

Final Technical Report for

OFFICE OF NAVAL RESEARCH

GRANT No. N00014-01-1-0857

RELAXOR FERROELECTRIC SINGLE CRYSTAL BASED  
HYBRID ACTUATOR FOR  
UNDERWATER ACOUSTIC NOISE GENERATION

Grant Period: June 1, 2001 to May 31, 2002

Principal Investigator

Dr. Nesbitt W. Hagood, IV  
nwh@ContinuumPhotonics.com  
(978) 670-4910

Department of Aeronautics and Astronautics  
Massachusetts Institute of Technology  
Cambridge, MA 02139





## **Acknowledgments**

The funding for this work, provided by ONR grant N00014-01-1-0857, is gratefully acknowledged.



# Contents

<b>1</b>	<b>Introduction</b>	<b>12</b>
1.1	Objective . . . . .	12
1.2	Motivation . . . . .	12
1.2.1	Piezoelectric materials . . . . .	12
1.2.2	The MHT concept . . . . .	14
1.3	Acoustic noise generation . . . . .	14
1.3.1	Example application . . . . .	14
1.3.2	Typical requirements . . . . .	15
1.4	The passive valve micropump . . . . .	16
1.4.1	Fabrication overview . . . . .	19
1.4.2	Test results . . . . .	21
1.4.3	Conclusions from the micropump development . . . . .	21
1.5	The MHT Chip-Level Active Valve Pump Device . . . . .	22
1.5.1	The Active Valves . . . . .	23
1.5.2	Features of the MHT Design . . . . .	25
1.6	Research Program Challenges . . . . .	27
1.6.1	Modeling and Design Challenges . . . . .	27
1.6.2	Device Fabrication, Assembly, and Testing Challenges . . . . .	28
1.7	Research Program Sub-Component Development Plan . . . . .	29
<b>2</b>	<b>System Design and Modeling</b>	<b>31</b>
2.1	Approach to the design of the MHT device . . . . .	31
2.2	Development of Simulation Tools . . . . .	33
2.2.1	Objective . . . . .	33
2.2.2	The Pump Chamber . . . . .	34
2.2.3	Active Valve . . . . .	35
2.2.4	Fluid Models . . . . .	36
2.2.5	Design Issues . . . . .	37
2.2.6	Design Parameters . . . . .	39
2.3	Contributions: Modeling . . . . .	39
<b>3</b>	<b>Supporting Experimental Investigations</b>	<b>45</b>
3.1	Investigation of Flow Losses Through Microscale Orifices . . . . .	45
3.1.1	Microsystems Fluidic Modeling Strategies . . . . .	45
3.1.2	Results . . . . .	45
3.1.3	Transition Reynolds number . . . . .	45
3.1.4	Valve Seat Width Dependence . . . . .	46
3.1.5	Contributions . . . . .	47
3.2	Determination of Fluid Filling and Sealing Procedures at the Microscale . . . . .	48
3.2.1	Objectives . . . . .	48
3.2.2	Filling techniques . . . . .	48
3.2.3	Sealing concepts . . . . .	52
3.2.4	Accomplishments . . . . .	54
3.3	Piezoelectric Material Properties . . . . .	55
3.3.1	Objective . . . . .	55
3.3.2	Characterization of Generalized Material Constants . . . . .	55

3.3.3	Characterization of Material Energy Density . . . . .	57
3.3.4	Accomplishments . . . . .	57
3.4	Identification of SOI Membrane Stress Limits . . . . .	59
3.4.1	Objectives . . . . .	59
3.4.2	Accomplishments . . . . .	59
3.5	Contributions: Supporting Experimental Investigations . . . . .	61
<b>4</b>	<b>Device Fabrication and Assembly</b>	<b>63</b>
4.1	Fabrication and Assembly Procedures for the MHT Device . . . . .	63
4.1.1	Overview . . . . .	63
4.1.2	Challenges and Procedures . . . . .	63
4.1.3	Conclusions . . . . .	71
4.2	Chip-Level MHT Device Fabrication Process Flow . . . . .	72
4.2.1	Overview . . . . .	72
4.2.2	Processes for the Silicon Layers . . . . .	72
4.2.3	Glass Layers . . . . .	73
4.2.4	Conclusions . . . . .	77
4.3	Contributions: Fabrication and Assembly . . . . .	77
<b>5</b>	<b>Key Technology Demonstrations Through Device Sub-Component Development</b>	<b>79</b>
5.1	Development of Testing Rigs and Procedures for Device Characterization . . . . .	79
5.1.1	Overview . . . . .	79
5.1.2	Test System Requirements . . . . .	79
5.1.3	The device test jigs . . . . .	79
5.1.4	The fluid test system . . . . .	80
5.1.5	Displacement measurement . . . . .	80
5.1.6	Data acquisition . . . . .	84
5.1.7	Basic testing protocols . . . . .	84
5.1.8	Summary . . . . .	84
5.2	Piezoelectric Drive Element Component Testing . . . . .	85
5.2.1	Overview . . . . .	85
5.2.2	Test-Plan . . . . .	85
5.2.3	Summary of Results . . . . .	87
5.2.4	Conclusions . . . . .	89
5.3	Hydraulic Amplification Component Testing . . . . .	92
5.3.1	Objectives . . . . .	92
5.3.2	Static hydraulic amplification tests . . . . .	92
5.3.3	Accomplishments . . . . .	96
5.4	Piezoelectric Active Valve Component Testing . . . . .	98
5.4.1	Overview . . . . .	98
5.4.2	Test-Plan . . . . .	98
5.4.3	Summary of Results . . . . .	99
5.4.4	Conclusions . . . . .	105
5.5	Contributions: Subcomponent Devices . . . . .	105

<b>6</b>	<b>MHT Pump Device Testing</b>	<b>107</b>
6.1	Overview and objectives . . . . .	107
6.2	Experimental test setup used for MHT pump testing . . . . .	107
6.3	Standard testing protocol . . . . .	108
6.3.1	Limitations of the pump testing . . . . .	109
6.4	MHT pump operation results . . . . .	109
6.5	Conclusions: MHT pump device testing . . . . .	113
<b>7</b>	<b>Conclusions and Recommendations</b>	<b>115</b>
7.1	Conclusions: An overview . . . . .	115
7.2	Systems modeling . . . . .	115
7.3	Valve flow loss modeling . . . . .	115
7.4	Piezoelectric material capabilities . . . . .	115
7.5	Silicon membranes . . . . .	116
7.6	Fluid filling and sealing capabilities . . . . .	116
7.7	Microscale hydraulic amplification . . . . .	116
7.8	Microvalve development . . . . .	116
7.9	The MHT device as a bi-directional micropump . . . . .	116
7.10	Recommendations for advancement of MHT Technology . . . . .	117
7.10.1	Recommendations for advancement of the technologies that were developed . . . . .	117
7.10.2	Recommendations for development of additional technologies . . . . .	118
7.11	Feasibility: Underwater acoustic noise generation and MHT technology . . . . .	118
<b>8</b>	<b>References</b>	<b>121</b>
<b>9</b>	<b>Summary of Publications Generated under this Project</b>	<b>125</b>
<b>10</b>	<b>Personnel</b>	<b>129</b>
10.1	Principal Investigator . . . . .	129
10.2	Faculty . . . . .	129
10.3	Scientific Staff . . . . .	129
10.4	Graduate Students . . . . .	129
10.5	Undergraduate Students . . . . .	129
<b>11</b>	<b>Patents</b>	<b>131</b>

# List of Figures

1	Upper bound on specific work vs. frequency for various actuation media . . . . .	13
2	Generic block diagrams of Micro-Hydraulic Transducer systems . . . . .	15
3	MHT Hydro-acoustic concept . . . . .	16
4	Radiated power of a sphere . . . . .	17
5	Pressure and flow requirements . . . . .	17
6	Radiated power of a sphere . . . . .	18
7	Pressure and flow requirements . . . . .	18
8	A passive valve MHT pump . . . . .	19
9	Fabrication flow - passive valve pump . . . . .	20
10	Passive valve MHT pump: Results . . . . .	21
11	Passive valve MHT pump: Results . . . . .	22
12	Photograph of a 9-layer MHT system. . . . .	23
13	Schematic of fabricated multi-layer MHT actuator device . . . . .	24
14	3-D schematic of the piezoelectrically driven hydraulic amplification microvalve . . . . .	25
15	Labeled cross-sectional schematic of the MHT device . . . . .	27
16	Labeled cross-sectional schematic of the MHT device - Detail . . . . .	28
17	MHT sub-component fabrication and testing plan . . . . .	30
18	MHT Design procedure. . . . .	31
19	Main aspects of the modeling performed on the MHT device. . . . .	34
20	MHT Active valve pump system simulation schematic. . . . .	35
21	Duty cycles of the harvesting chamber . . . . .	36
22	Pump Chamber Model. . . . .	41
23	Schematic of the active valve. . . . .	42
24	Simulation architecture of the active valve. . . . .	42
25	Simplified device schematic showing pressures at different locations. . . . .	43
26	Piston deflection for different tether thicknesses and widths . . . . .	43
27	Transition Reynolds number and Discharge coefficient . . . . .	46
28	Scaled data for valve #1 and valve #3, Curve fitting using 14 for valve #1 . . . . .	47
29	Bulk modulus vs. fluid pressure . . . . .	48
30	Vapor lines for a selection of linear siloxanes . . . . .	49
31	Filling system schematic . . . . .	50
32	Filling system photograph . . . . .	50
33	Filling test chip . . . . .	51
34	Static sealing concepts . . . . .	52
35	Schematic of the dynamic seal . . . . .	53
36	Model of the dynamic seal . . . . .	53
37	Dynamic seal results . . . . .	54
38	Generalized material constants . . . . .	56
39	Coupling coefficient ( $k_{33}$ ) . . . . .	57
40	Maximum energy density for various materials. . . . .	58
41	A SEM micrograph showing the fracture test specimen employed in this work. . . . .	59
42	Typical shape of etched fillet. . . . .	60
43	Schematic cross-section of a multi-layer MHT device structure . . . . .	63
44	DRIE etch characteristics of a tethered drive element piston structure . . . . .	65
45	Wafer-level silicon-silicon fusion and silicon-Pyrex anodic bond steps . . . . .	65
46	Piezoelectric element integration within the drive element structure . . . . .	68

47	Die-level bonding procedure for the active valve portion of an MHT device . . . . .	69
48	Die-level alignment and bonding jigs . . . . .	70
49	Electrical contact to an MHT device for anodic bonding . . . . .	71
50	Silicon membrane fabrication . . . . .	72
51	Cross Section: 10 Valve device . . . . .	74
52	3D Cross section . . . . .	74
53	Process flow for Layer 2 . . . . .	74
54	Process flow for Layer 4 . . . . .	75
55	Process flow for Layer 5 . . . . .	75
56	Process flow for Layer 7 . . . . .	76
57	Process flow for Layer 8 . . . . .	76
58	Test jig . . . . .	80
59	Top clamp . . . . .	81
60	Electrical clamp . . . . .	81
61	Fluid test rig . . . . .	82
62	Regulator bank . . . . .	83
63	The test rig - side view . . . . .	83
64	3-D schematic of a three piezoelectric element, double-layer piston drive element device .	85
65	Overview of the drive element sub-component test plan . . . . .	86
66	Photograph of an assembled drive element Device 4 . . . . .	87
67	Drive element Device 1 transfer function of piston velocity versus frequency . . . . .	88
68	Drive element Device 3 transfer function of piston velocity versus frequency . . . . .	89
69	Drive element Device 4 transfer function of piston velocity versus frequency . . . . .	90
70	Drive element Device 4 displacement time histories. . . . .	90
71	Drive element Device 4 piston center displacement versus applied voltage at 100Hz . . . .	91
72	Static hydraulic amplifier . . . . .	92
73	HAC Large piston model correlation . . . . .	93
74	HAC Small piston model correlation . . . . .	94
75	Amplification ratio . . . . .	94
76	Amplification sensitivity . . . . .	95
77	HAC Large piston model correlation . . . . .	95
78	HAC Small piston model correlation . . . . .	96
79	Amplification ratio . . . . .	97
80	Amplification sensitivity . . . . .	97
81	Active valve schematic . . . . .	99
82	Active valve frequency response . . . . .	100
83	Valve cap and piston deflection time histories . . . . .	102
84	Valve and piston deflection vs. voltage . . . . .	103
85	Device AV1 dynamic flow regulation at 1kHz vs. $\Delta P$ . . . . .	104
86	MHT pump test schematic . . . . .	107
87	Driving waveforms . . . . .	109
88	Pump performance . . . . .	111
89	Pump performance variation vs. valve motion . . . . .	111
90	Pump performance variation vs. $V_{p-p}$ . . . . .	112
91	Pump performance variation vs. frequency . . . . .	112
92	Comparison with the former passive valve pump . . . . .	113
93	Comparison with the former passive valve pump . . . . .	114
94	Roadmap for acoustic noise generation . . . . .	118

95	Layer 2 masks . . . . .	133
96	Layer 4 masks . . . . .	134
97	Layer 5 masks . . . . .	134
98	Layer 7 masks . . . . .	135
99	Layer 7 masks . . . . .	135
100	Layer 8 masks . . . . .	136
101	Layer 8 masks . . . . .	136
102	Layer 8 masks . . . . .	137
103	Glass layer masks . . . . .	138
104	MHT mask overlay . . . . .	139



List of Tables

1	Summary of preliminary design decisions. . . . .	39
2	Summary of design and performance parameters. . . . .	40
3	Fracture strength values. . . . .	60
4	Active Valve Actuation Capabilities . . . . .	104

# 1 Introduction

## 1.1 Objective

The objective of the work presented here was the development of a compact piezoelectric material based hybrid pump-actuator device for underwater acoustic noise generation applications. The eventual goal being to develop an underwater acoustic noise generator that could output approximately  $0.25W$  to  $0.5W$  of acoustic power under water at frequencies in the range of  $500Hz$  to  $1kHz$ . The size of the eventual device in question would be of the order  $2 - 3cm$  in radius. This application therefore requires a compact, high power density actuator.

Recent research at MIT has worked toward the development of high specific power micropumping technology (with specific powers  $\sim 100 - 1000W/kg$ ). In order to realize this technology, which can be used for compact actuation systems, as well as for compact power generation applications, a novel class of Micro-Hydraulic Transducer (MHT) devices has been introduced [1] [2] [3] [4] [5]. These devices combine bulk piezoelectric materials with stiff micromachined structural elements and are designed to enable pumping of fluid against pressure differentials on the order of  $\sim 1 - 2MPa$ , creating flow rates near or in excess of  $1ml/s$ . For lower pressure differentials, even higher flow rates are attainable. These devices rely on a high frequency ( $10 - 20kHz$ ) piezoelectric pumping piston that transports the hydraulic fluid from a low to a high pressure. This high pressure fluid can then be used for actuation purposes. The promise of high power density makes MHT technology an ideal candidate for underwater acoustic noise generation.

The literature abounds with research efforts around the world to develop compact liquid micropumping systems, the term “micro” referring to devices which are created with fabrication procedures capable of  $\mu m$ -size tolerances and which produce overall micropump dimensions on the order of a few millimeters to a few centimeters. However, the vast majority of these systems are designed for low pressure and low flow rate applications [6] [7] [8] [9] [12] such as drug dispensing and microdosing [13] [14] [15]. The higher performing of these systems are capable of pumping liquids with flow rates on the order of  $1000 - 3000\mu l/min$  ( $0.017 - 0.050ml/s$ ) against differential pressures of between  $10kPa$  and  $50kPa$ . With a typical device mass on the order of  $\sim 1$  gram, these performance values correlate to device-level specific powers below  $2.5W/kg$ .

MHT technology is therefore unique in its ability to harness the power density of high performance single crystal piezoelectric materials and combine it with the potential benefits of large scale microfabrication.

## 1.2 Motivation

### 1.2.1 Piezoelectric materials

Piezoelectric materials are well-suited for transducer applications because of their inherently high peak specific powers. Figure 1 provides a comparison of the single stroke specific energy ( $J/Kg$ ), bandwidth (kHz), and theoretical peak specific power ( $W/kg$ ) for a variety of transducer materials [16] [17] [18]. The product of a material’s single stroke specific energy and its bandwidth provides a value for the material’s specific power ( $W/kg$ ). Shape-memory alloy materials (denoted SMA), for example, possess a relatively large single stroke specific work ( $\sim 5000J/kg$ ) in comparison to that of standard polycrystalline piezoelectric materials such as PZT-5H ( $\sim 10J/kg$ ). The maximum operational frequency, or bandwidth ( $\sim 10Hz$ ), of SMA materials, however, is significantly less than that of standard piezoelectrics ( $\sim 100kHz$ ). SMA materials and standard piezoelectrics both possess specific powers near  $100W/kg$ , however, their optimal implementation as actuation mechanisms is far different. In an application where

low frequency, large stroke actuation is desired (such as an on-off microvalve), the use of an SMA material might be preferred over a standard piezoelectric material. Conversely, for an application where high frequency, low stroke actuation is required, a piezoelectric material may be preferred. In fact, for this reason, the vast majority of high frequency micropumping systems use piezoelectric materials as their actuation mechanism in conjunction with fast-acting valves. The recent development of single-crystal ferroelectric materials (e.g. PZN-PT), characterized by specific powers approaching  $10\text{ kW/kg}$  ( $\sim 100\times$  greater than those of standard polycrystalline PZT materials) [19], offers further advantages in strain capability over the standard piezoelectrics. These high performing materials, however, have until now not been integrated within high frequency micropumping systems. The work presented in this document represent the first efforts to exploit the benefits of these materials for micro-servohydraulic applications.

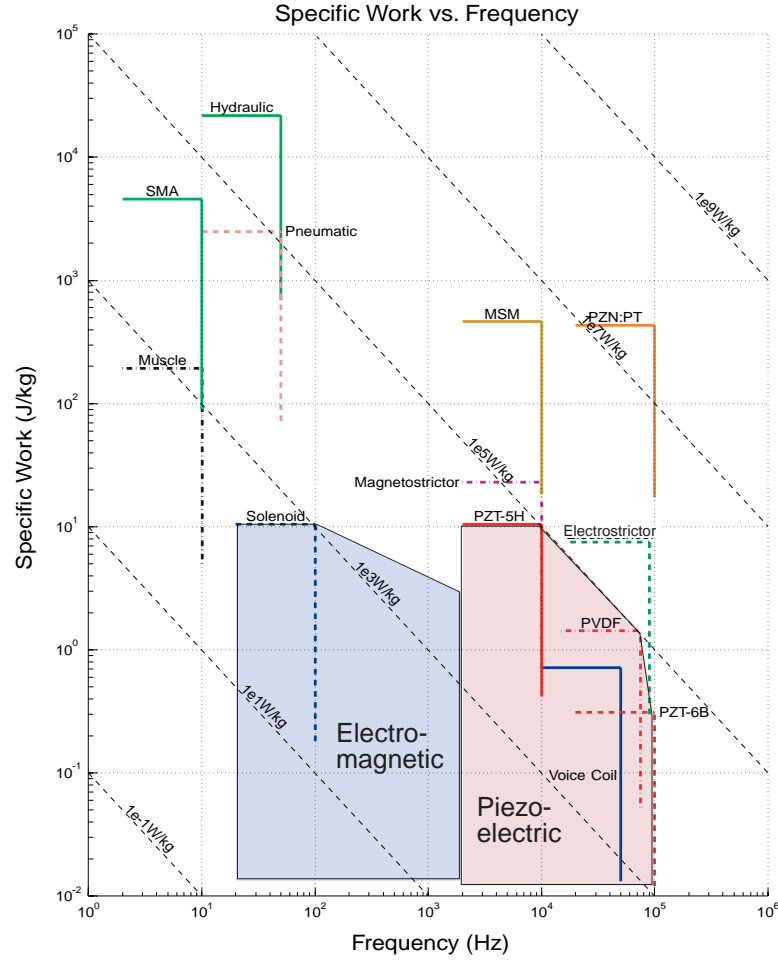


Figure 1: Upper bound on specific work vs. frequency for various actuation media. SMA is shape-memory alloy; PZN-PT is single-crystal piezoelectric; MSM is magnetic shape memory materials.

The piezoelectric micropumping devices and systems that have been presented in the literature up until this time typically utilize one of two actuation methods as a means to pump fluid: either (1) a deposited thin-film, thick disk, or bimorph of piezoelectric material [7] [8] [13] in contact with a compliant membrane, or (2) a direct-drive stack actuator in contact with a moveable silicon diaphragm. The thin-film, thick-film, and bimorph structural designs presented are not conducive to both high force and

high-frequency operation. The direct-drive stack actuation designs [20] [21] [22] are capable of achieving higher frequency operation than the thin-film, thick-film, and bimorph designs. However, these previously presented direct-drive stack designs require a significant length of piezoelectric actuation material to create the deflection and fluid pumping volume required for reasonable fluid flow rates. Due to this significant actuator size, an epoxy bonding agent and a relatively compliant silicon diaphragm are required to tolerance the piezoelectric material within the structures. The key design feature which differentiates Micro-Hydraulic Transducer devices from these previous piezoelectric micropumps is the incorporation of a stiff micromachined structural “piston-like” actuation element not only within the pumping chamber of the device, but also within accompanying flow regulation active valves. The annularly-tethered micromachined “piston” structure, driven by miniature bulk piezoelectric elements (almost an order of magnitude smaller than those used in [20] [21] [22]) attached using a thin-film eutectic alloy bond, can achieve structural frequencies well above 10kHz and can actuate against fluid pressurizations near 1MPa. The implementation of such a stiff structure within fluidic systems can enable significantly higher frequency, flowrate and/or pressurization capabilities than the previously presented piezoelectric micropumps.

### 1.2.2 The MHT concept

As shown in Figure 2, a Micro-Hydraulic Transducer system consists of a piezoelectric pump chamber, two actively controlled valves, and a low and high pressure fluid reservoir. In the MHT actuator, electrical energy supplied to the piezoelectric pump chamber results in a pumping of fluid through the valves from the low to high pressure reservoir. In the MHT power harvester, sequenced operation of the valves results in fluid flow from the high to low pressure reservoir, producing a “pinging” of the piezoelectric element within the pump chamber. This cyclic strain on the element induces electrical charge, which can be rectified and stored. For power harvesting operation, active valves are essential. For actuating (pumping operation), they are beneficial and also allows for bi-directional pumping. The specific power of these transducer devices scales linearly with the frequency of operation and the pressure drop across which the device can operate. Since structural frequencies scale inversely with the geometric size of the device, it is advantageous to build these systems as small as possible, hence the need for MEMS fabrication and process technologies.

## 1.3 MHT technology for hydro-acoustic actuation

### 1.3.1 Example application of MHT technology as an underwater acoustic noise source

One potential application of a small-scale servohydraulic actuator is that of underwater acoustic noise generation. The conceptual layout of such a device is shown in Figure 3. The size of the device shown would be approximately  $2.0cm \times 2.0cm \times 2.5cm$  in size. (See Figure 3 (A)) It is comprised of two or more bidirectional piezo-hydraulically driven pump modules stacked up in parallel configuration, and attached to a hydro-acoustic actuator head at the top. The bottom module of the device contains fluid supply reservoir and other accessories for the pumps. The fluid flow between the supply reservoir and the actuator-head at the top is transported via internal micro-flow channels. Additionally, other channels exist to connect the valves, pump, and the main fluid channels. The controls and drive electronics to power the valves and the pump drive element are integrated within the device.

The working principle of the device is schematically illustrated in Figure 3 (B). Each piezo pump comprises of a piezoelectrically driven fluid pumping chamber, two sets of actively controlled and piezo-electrically driven valves, and fluid channels. Each of the two sets of active valves, one set operating

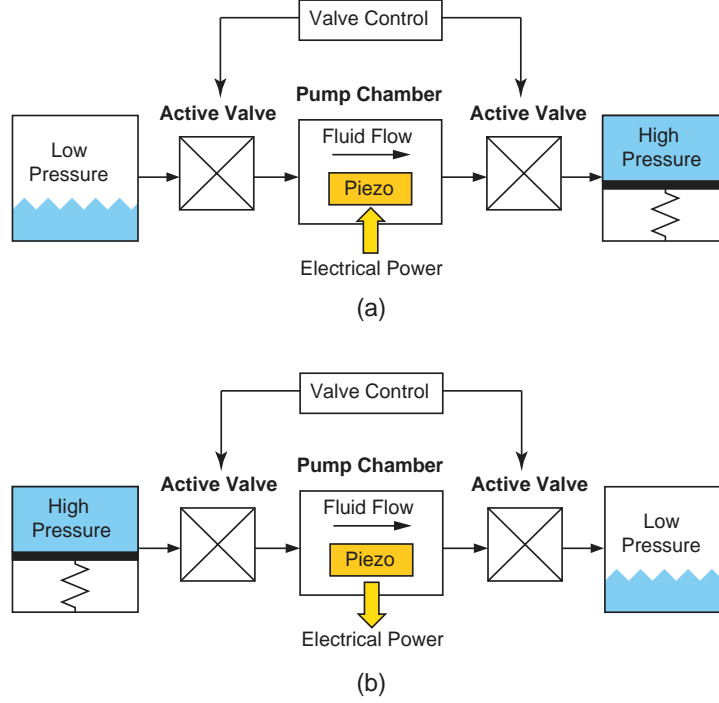


Figure 2: Schematics of Micro-Hydraulic Transducer systems: (a) MHT actuator system, (b) MHT power harvesting system. High specific power is achieved through the integration of piezoelectric material with structural stiff small-scale hydraulic systems.

between the fluid reservoir and the pump chamber and the other set operating between the pump chamber and the actuator head, regulate the fluid flow between the reservoir and the actuator head via the pumping chamber in a fully bi-directional manner. A tiny piezoelectric cylinder bonded to a thick disk of relatively larger area forms the drive piston element within the pump chamber. When an electric voltage is applied across the piezoelectric element, a finite strain is induced in the element, which causes the piston to move up and down, and thereby enables net volume oscillations in the pump chamber. A controller synchronized with the pump cycle signal controls the phase difference between the active valves, and simultaneously modulates the amplitudes of high frequency volume oscillations in the chamber in such a manner that results in a fully bi-directional fluid flow between the fluid reservoir and the hydro-acoustic actuator. The accumulated fluid in the hydro-acoustic actuator is directed to impinge on a flexible surface in contact with the water at low frequency, which in turn generates pressure pulse in the external water (not represented in the schematic). Thus, the high frequency small displacements of the piezo element are rectified into low frequency, high power acoustic energy by continuous sloshing of a stiff fluid back-and-forth from the reservoir to the actuator head.

### 1.3.2 Typical requirements for underwater acoustic noise generation

To illustrate the requirements of an underwater hydro-acoustic actuation scheme, consider the case of a sphere of radius  $a$ , radially oscillating in a fluid with surface velocity  $v = v_a \sin(\omega t)$ . The average radiated power is then given by [10] as:

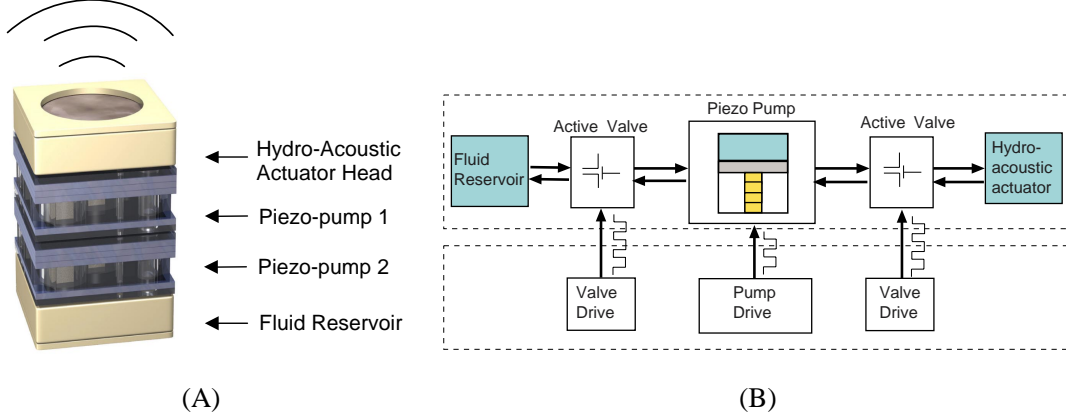


Figure 3: The MHT device as a hydro-acoustic actuator. (A) Conceptual 3D visualization, and (B) Schematic of the noise generator device.

$$P_{av} = \frac{(ka)^2}{1 + (ka)^2} \rho c \langle v^2 \rangle (4\pi a^2) \quad (1)$$

where  $k = \omega/c$  is the wave number. Figure 4 shows the radiated acoustic power of a sphere oscillating at  $500Hz$  in water. This figure shows that approximately  $0.25$  to  $0.5W$  of acoustic power can be delivered to the water at this frequency with a vibration stroke of  $\sim 60\mu m$ , using a sphere of radius  $\sim 20 - 30mm$ . Furthermore, the acoustic pressure is given by the relationship:

$$p = \sqrt{I_{ac} 2\rho c} \quad (2)$$

where  $I_{ac}$  is the sound intensity given by  $P_{av}/4\pi a^2$ . The associated r.m.s. flow rate<sup>1</sup>, assuming sinusoidal motion, for small vibrations, is:

$$Q \approx \pi \sqrt{8} a^2 v_a \quad (3)$$

It follows that for Figure 4, the associated acoustic pressure is  $\sim 10 - 15kPa$  and the required flow rate is  $\sim 300 - 500ml/s$ . (See Figure 5). Figures 6 and 7 show the same results for operation at  $1kHz$ . Operation at lower surface displacement amplitude would require similar power levels ( $0.25 - 0.5W$ ), pressures and flow rates. A typical pumping system would have to provide sufficient pressure to drive a radiating structural shell or piston to the desired amplitude of vibration. For typical materials, using a shell or piston robust enough to be submerged up to  $50m$  below the water surface, differential pressures of  $\sim 15 - 30kPa$  will be required to provide the necessary actuation force. The need therefore exists for a compact high power density actuation scheme. The work presented here explores MHT technology as a means of providing this actuation.

## 1.4 The passive valve micropump device as a technology demonstrator

To demonstrate the feasibility of the MHT concept, a passive valve micropump was built. (See Figure 8) [2] The micropump had a multi-layer structure. It included one fluid pump chamber and two identical

<sup>1</sup>The r.m.s. flow rate is used here, and not the peak flow rate. The net flow rate is zero, and the MHT device will allow bi-directional fluid flow.

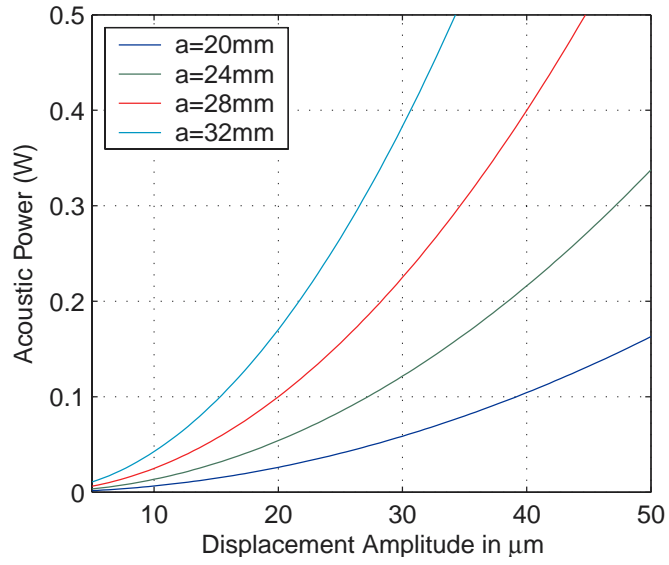


Figure 4: Radiated acoustic power of a sphere oscillating at 500 Hz.

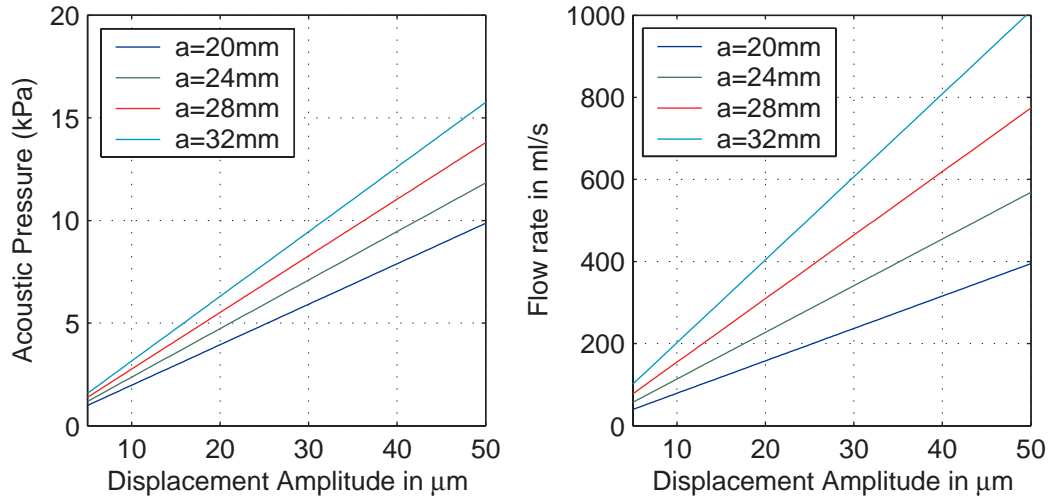


Figure 5: Pressure and flow requirements of a sphere oscillating at 500 Hz.

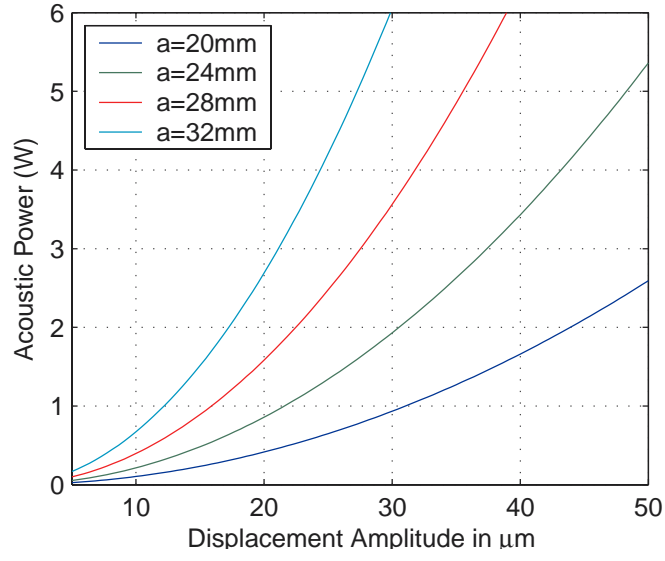


Figure 6: Radiated acoustic power of a sphere oscillating at 1000 Hz.

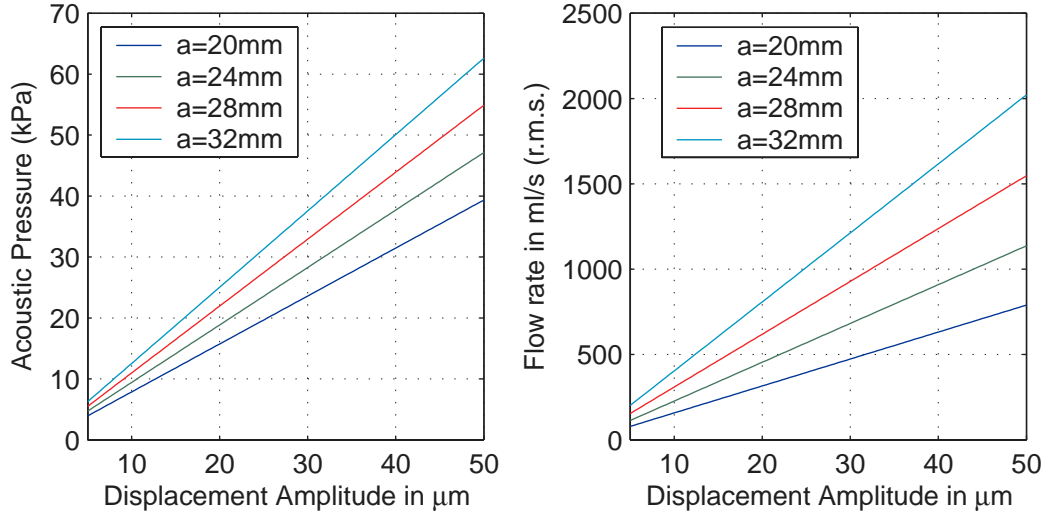


Figure 7: Pressure and flow requirements of a sphere oscillating at 1000 Hz.



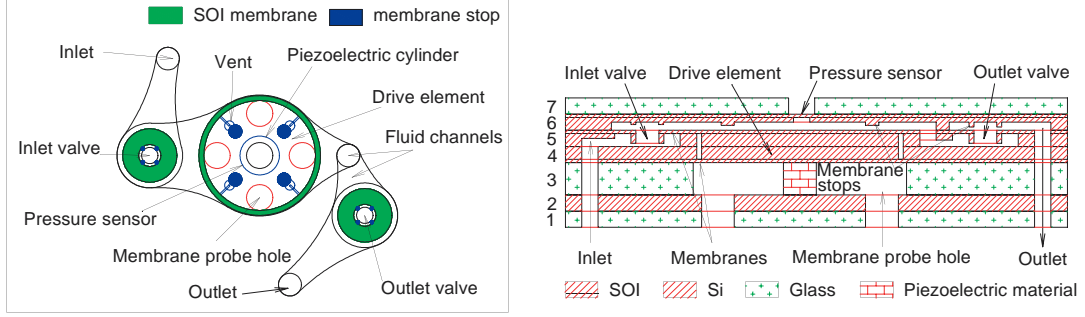


Figure 8: Passive valve MHT pump device previously demonstrated. [2]

passive check valves. The volume change in the fluid chamber is achieved by the vertical motion of the double layer cylindrical piston-like drive element (layers 4 and 5) attached to annular Si membranes and driven by a ceramic piezoelectric cylinder (Layer 3) 1mm in diameter and 1mm in height. In particular, this micropump demonstrated the following aspects:

- The feasibility of using a bulk piezoelectric element, precisely toleranced, in combination with a stiff pump piston structure, to enable high frequency, high flow rate and high pressure pumping.
- The feasibility of building a glass-silicon sandwich structure using a combination of silicon-glass anodic and silicon-silicon fusion bonds. This assembly scheme made it possible to build a device with a very stiff structure, giving the device its high pressure capabilities.
- The use of Deep Reactive Ion Etching (DRIE) to etch high-strength silicon membranes in SOI wafers. Although the use of SOI to form thin tethered membrane structures is not new, the micropump device combined four such structures into a single device - two for the main drive piston and one for each passive valve. This so-called "annular membrane with a rigid center boss" was also used for all moving parts in the final MHT device.

#### 1.4.1 Fabrication overview

The passive valve pump became a proving ground for many of the fabrication steps employed in the final MHT device. To minimize the size of the device, a compact design requiring a minimum number of layers, efficient use of the both surfaces in each layer, and therefore multiple lithography steps for the SOI wafers was implemented. As an example, Figure 9 shows the fabrication process flow for layer 5. The first step is the selection of the SOI wafer that has a 15 $\mu\text{m}$  thick SOI layer, a 0.4 $\mu\text{m}$  thick buried oxide, and a 380 $\mu\text{m}$  thick handle layer. Secondly, positive photoresist was coated on both sides of the wafer and the SOI side was patterned using standard lithography procedures. The photoresist on the handle side is to protect the handle surface from scratching in the lithography steps. This back surface protection method was used throughout the micro-fabrication processes. The wafer was then DRIE etched until the SOI layer was etched through. This step formed the fluid through holes in the SOI layer. Next, the wafer was cleaned and coated with positive photoresist on both sides again. The handle side was patterned with photoresist and etched down approximately 0.5 $\mu\text{m}$  in a RIE etcher to form the clearance between the valves and their seating surfaces. In the fourth step the wafer was oxidized at 1200°C for 5 hours to form 2 $\mu\text{m}$  of thermal oxide that is to be used as a nested mask and back surface protection from DRIE etching later on. The thermal oxide was etched in step 5 to form the nested mask

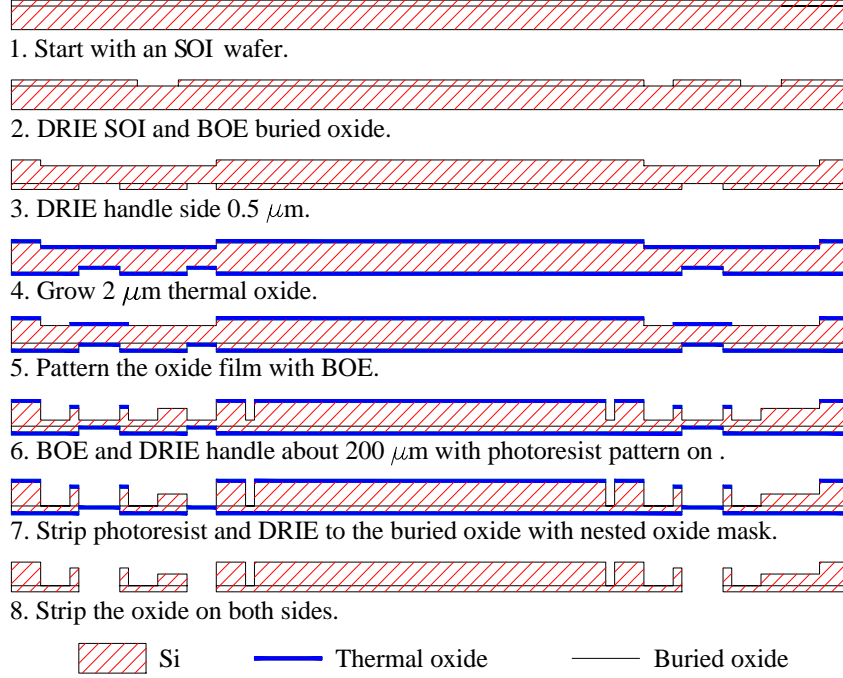


Figure 9: Fabrication flow of an SOI layer (Layer 5 in Figure 8) with the passive valves and half of the drive element piston.

and then another lithography process was performed on handle side to define the membranes in the drive element and in the passive valves in step 6. The wafer was etched first by DRIE about halfway though its thickness with photoresist as seen in step 6. Then the photoresist pattern was stripped and the nested thermal oxide mask was exposed for another DRIE step until it stopped at the buried oxide, as seen in step 7. The nested oxide mask was necessary to construct the  $200\mu\text{m}$  deep venting channels in the drive element and the fluid channels to the valves. Finally, the thermal oxide was stripped using BOE wet etching. Since all the membranes in this device have to operate under high stress and at high frequency, it is important to have a membrane structure with minimal stress concentration. A significant challenge in the micropump fabrication was controlling fillet radii in the range of  $20 - 40\mu\text{m}$  for stress reduction at the feet of the membranes. In the DRIE machine Si is etched at a rate of approximately  $2 - 4\mu\text{m}/\text{min}$ , depending on the feature size and exposed Si area. The etch front is usually a gradual curve in cross-section but varies depending on the etch conditions. An SOI membrane fillet radius is formed after the etch front reached the buried oxide and then the Si edges retreat horizontally to the side wall at a rate of approximately  $70 - 100\mu\text{m}/\text{min}$  as more oxide is exposed. There is a time window of approximately  $2 - 4\text{min}$ . to control the fillet radius in the desired range after approximately 2 hours of etching on the handle side. Therefore careful monitoring in the final stage of the DRIE is critical.

After the final DRIE etch and cleaning, the three SOI wafers were aligned using an Electronic Visions system and fusion bonded at  $1100^\circ\text{C}$  in nitrogen for 1 hour. The bonded wafer stack was cut into  $16.7\text{mm}$  by  $15.7\text{mm}$  chips with a die-saw, cleaned in water, acetone, methanol, and isopropanol successively, and finally dried in air. The glass wafers were processed with diamond drills and die-saw cut into small chips. All the interfaces between Si and glass were anodically bonded at  $300^\circ\text{C}$ . The Si and the piezoelectric

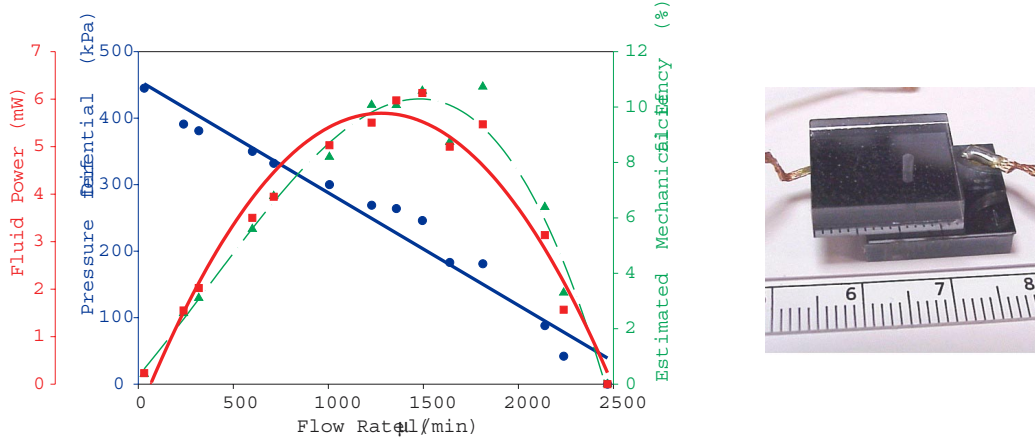


Figure 10: Passive valve MHT pump device - best results obtained.

material interfaces were eutectically bonded. To prepare for the eutectic bonding,  $500\text{\AA}$  of Ti film and  $5000\text{\AA}$  of Pt film were deposited on the Si surfaces through a shadow mask by e-beam and  $2\mu\text{m}$  of an Au-Sn (80–20%wt.) alloy films were deposited on the piezoelectric surfaces by sputtering. The composition of the metal films were chosen for surface wetting (Ti) and low eutectic bonding temperature (Au-Sn) so that the eutectic bonding and the last anodic bonding can be done simultaneously as required by the pump design.

#### 1.4.2 Test results

The working fluid for this pump, as well as for all of the other MHT devices, was a low viscosity silicone oil (Dow Corning DC200 0.65cst). Filling of the pump was performed under vacuum to minimize the risk of trapped air inside the device. Pumping operation was demonstrated at frequencies up to 12.5kHz. The MHT micropump device attained a maximum differential pressure of  $450\text{kPa}$  and a maximum flow rate of approximately  $2700\mu\text{l}/\text{min}$  at a  $12.5\text{kHz}$  operating frequency. (See Figure 10) These performance figures compared very favorably with the best micropump results reported in the literature at the time, and was only rivaled by electrokinetic (EK) pumps. EK pumps however, due to the nature of their operation, have a finite lifetime and are therefore not viable alternatives to piezoelectric MHT technology, despite their simplicity.

The micropump testing also highlighted the importance of fluidic resonances in microhydraulic systems. Figure 11 shows the large variations in flow rate for various frequencies of operation. The final MHT device was therefore designed to exploit these effects. These considerations are discussed in Section 2.2.4.

#### 1.4.3 Conclusions from the micropump development

In addition to demonstrating the feasibility of MHT technology, the passive valve pump also highlighted a number of issues related to the design, fabrication and testing of MHT devices. These include:

- Techniques for fluid filling and sealing of small devices.
- Control of the fillet feature at the bottom of a DRIE etched trench.

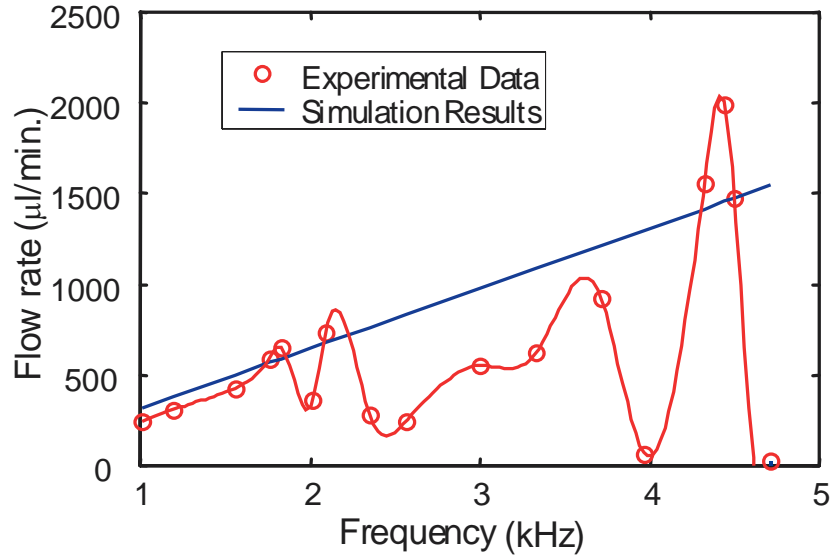


Figure 11: Passive valve MHT pump device - an example of the effect of fluidic resonances on the behavior of the device.

- Wafer handling and care throughout the fabrication process with eventual fusion bonding in mind - i.e. protecting the bond surfaces.
- Precise sorting and tolerancing of the piezoelectric elements.
- Fluidic resonances during operation that can either enhance or hurt device performance.

The passive valve micropump set an initial benchmark for the fluid power levels, pressures and flow rates attainable with MHT technology. It showed that high specific power MHT devices could become a reality, and provided the necessary motivation to proceed with the development of an active valve MHT device.

## 1.5 The MHT Chip-Level Active Valve Pump Device

In Section 1.2 a few basic functional requirements were implied for an MHT device:

- A piezoelectric pumping and generating chamber, with its piston attached to a piezoelectric element
- Two compact high frequency valves. For a high frequency pumping device, it is beneficial to have these valves actively controlled, to enable bi-directional pumping. By modulating the direction of flow at the required actuation frequency, a piezoelectric pump alone is sufficient for flow control and actuation, and additional hydraulic circuit elements could be done away with. In this manner, reduced complexity in the hydraulic circuit can be traded for a slight increase in pump complexity. Because the pump is microfabricated, however, the only added complexity may be a change in mask design.
- Connection to two external reservoirs - a high pressure reservoir or HPR, and a low pressure reservoir or LPR.

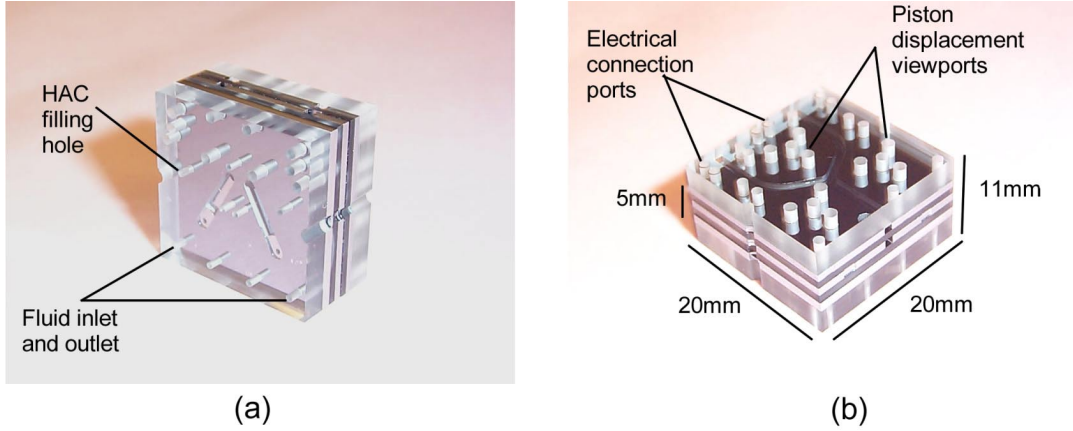


Figure 12: Photograph of a 9-layer silicon and glass chip-level MHT device. Dimensions of the device: 20mm x 20mm x 10mm.

A device to satisfy these requirements was built under this project. The completed device is shown in Figure 12. The result is a 9-layer device combining four microfabricated silicon layers with precision piezoelectric elements and five ultrasonically machined glass layers.

A 3-D schematic of the MHT pumping system, illustrating individual silicon and glass layers, is shown in Figure 13. The middle glass layer (Layer 3) forms the drive element support structure and the top (Layer 9 - not shown) and bottom (Layer 1 - not shown) glass layers provide structural support. The bottom silicon layer (Layer 2) and drive piston silicon layers (Layers 4,5) provide a path for electrical contact to the piezoelectric cylinders in each of the two active valves and within the harvesting chamber. The top four silicon layers (Layers 4,5,7,8) and glass layer (Layer 6) house the hydraulic amplification chamber (within the valves), valve cap and membrane structure, and fluid inlet and outlet channels. All silicon-silicon wafer interfaces are bonded with high-temperature ( $\sim 1100^\circ\text{C}$ ) fusion bonds, and all silicon-glass layer interfaces are bonded using low temperature ( $\sim 300^\circ\text{C}$ ) anodic bonds. Attachment of the top and bottom piezoelectric cylinder surfaces to the adjoining silicon is achieved with a low temperature ( $\sim 300^\circ\text{C}$ ) AuSn eutectic bond.

### 1.5.1 The Active Valves - Enabling Bi-Directional Pumping

The performance of these MHT systems is directly governed by the capabilities of the valves, which regulate flow into and out of the pump chamber. An ideal valve should have a minimal resistance when open, and should seal perfectly when closed. For bi-directional pumping, classical check valves will not suffice. As a result, to achieve high specific power Micro-Hydraulic Transducer devices, a compact high frequency, high pressure active valve is required. The microvalve subcomponent is shown schematically in Figure 14. This device is desired to achieve large valve cap stroke (up to  $\sim 40\mu\text{m}$ ) against high pressure loads ( $\sim 1\text{-}2\text{MPa}$ ) through a novel hydraulic amplification mechanism that converts the small displacement ( $\sim 1\mu\text{m}$ ) of a piezoelectric material element into a significantly larger valve cap stroke. The inherent stiffness of the piezoelectric material and the hydraulic fluid chamber enable both high-frequency and high-force actuation capabilities.

The active valve consists of three primary components: a piezoelectric drive element, an enclosed fluid amplification chamber, and a membrane with attached valve cap. The drive element incorporates a circular piston structure supported from beneath by one or more small bulk piezoelectric cylinders and

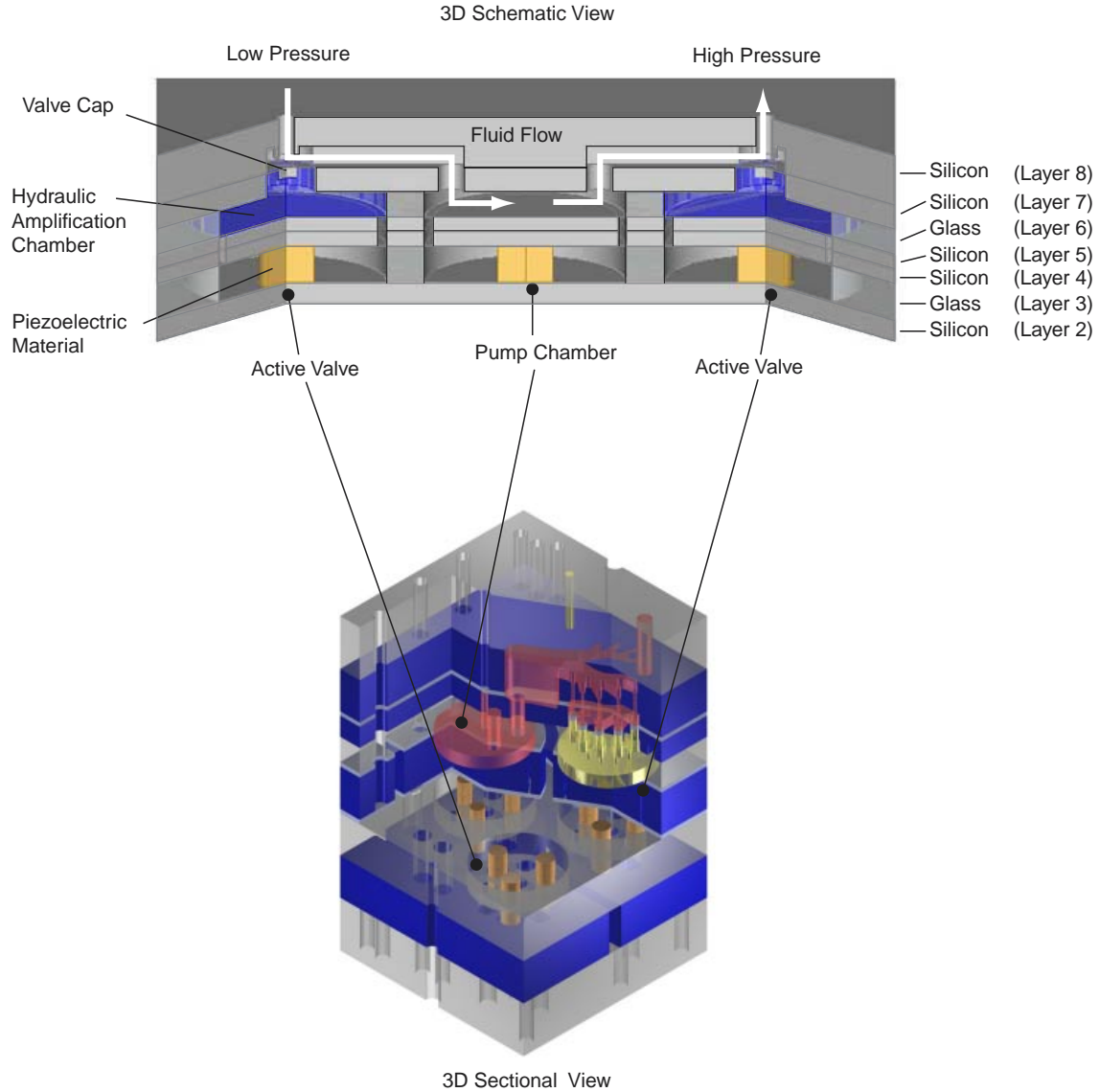


Figure 13: 3-D schematic of a Micro-Hydraulic Transducer multi-layer silicon and glass structure. Shown are both a linear 2D schematic and also a 3D section view of the device.

is suspended circumferentially from a surrounding support structure by thin annular micromachined tethers. This novel compact “piston-type” design enables high frequency actuation against a large external pressurization due to the high stiffness of the piston structure and integration of miniature bulk piezoelectric elements beneath the piston using a thin-film bond layer. The lateral dimensions of the tethers are designed to make the tethers compliant enough to allow for rigid piston motion up and down, yet stiff enough to resist bowing under pressurization caused by the hydraulic fluid above the tether during actuation. The tethers provide a seal between the hydraulic fluid above the piston and the piezoelectric chamber below the piston, and also provide a path for electrical contact to the top surface of the piezoelectric cylinders. The fluid chamber resides between the top surface of the drive element piston and the bottom surface of a thin, smaller diameter silicon micromachined valve cap membrane.

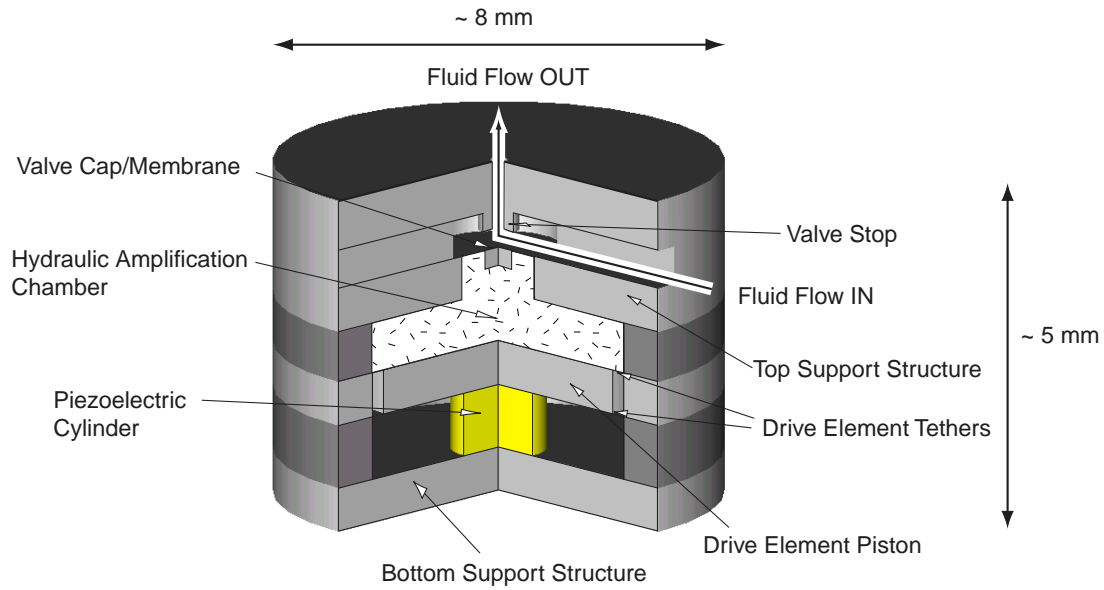


Figure 14: Schematic of a piezoelectrically-driven hydraulic amplification microvalve. The primary structural components are designated with arrows. External hydraulic system pressure loading is applied on the top surface of the valve cap and membrane.

In response to applied piezoelectric voltage, the piezoelectric material strains. The resulting deflection of the drive element piston generates a pressure within the hydraulic amplification chamber which in turn deflects the valve cap and membrane against a fluid orifice, thereby regulating fluid flow through the external hydraulic system. The pressure loadings on the valve cap and membrane during device operation depend on the external microfluidic system application. The piezoelectric material capabilities, the ratio of the piston diameter to the valve membrane diameter, the compliances of the fluid and structural elements in the chamber, the severity to which the valve cap membrane experiences nonlinear behavior, and the nature of the external loading all contribute to the performance of this microvalve device.

### 1.5.2 Features of the MHT Design

We now highlight more detailed design features of the MHT device. Some of these features will be discussed in further detail in later sections of this report. Using Figures 15 and 16 for reference, the following features were incorporated in the MHT device:

1. Pin contact for anodic bonding of Layer 3.
2. Viewport for displacement measurement of the piston.
3. Electrical contact (hole for spring pin contact) to piston layer.
4. Clearance in Layer 2 to prevent electrical short to contact to Layer 4. Also sufficient to prevent arcing.
5. Pin contact to Pyrex Layer 3 for anodic bonding.

6. Electrical pin contact to Layer 2.
7. Additional anodic bonding hole
8. Anodic bonding contact to SOI layer of layer 5 for bonding to Layer 6. (Eventually contacting Layer 4 was found to be sufficient for this design.
9. Piston membrane tethers. Proper design of these membranes for both strength and deflection was critical. Each device has six of these membranes attached to its three piezoelectrically driven pistons.
10. Piezoelectric piston. This particular one drives one of the active valves.
11. Piezo seat. These recesses, of order  $20\mu m$  deep, were individually etched to accommodate different size piezoelectric elements.
12. Electrical isolation trench in Layer 2. All three pistons were fully isolated and were thus capable of being supplied with "ungrounded" power.
13. Electrical isolation trench in Layers 4 and 5. This forms the other side of the electrical isolation of the piezoelectric piston assembly. Note also that Layer 6 is a glass layer, thus preventing capacitive coupling to Layers 7 and 8, that are grounded.
14. Piezo recess clearance in the Pyrex. Recesses were ultrasonically machined for every piezoelectric element, simplifying pick-and-place positioning.
15. Piezoelectric element. Only one piezoelectric element per piston is shown in this schematic. All MHT devices had three piezoelectric elements per piston, for a total of nine per device.
16. Shallow recess in glass Layer 3, to allow piston motion.
17. Vent channels between Layers 4 and 5. This is to prevent a sealed cavity from forming during the fusion bonding process.
18. Inlet pressure sensing membrane. This membrane was to be used to sense dynamic pressure of the device inlet, and was machined in Layer 7.
19. Flow inlet (or outlet - the device was symmetric and bi-directional).
20. Entrance to the valve. Flow experiments have shown that the nature of the entrance "step" into the poppet valve has a significant effect on the flow losses through it.
21. Valve seat. The seat width was also designed for minimum pressure drop.
22. Valve outlet channel.
23. Valve cap (central boss). This cross-sectional schematic depicts the harvesting device with 10 discrete valve caps per active valve unit, for a total of 20 per device. In addition, devices with one and two valve units were also microfabricated. Only the single valve devices were tested. Theoretically, a valve with 10 valve caps promised low pressure drops. Reliable fabrication of these membranes proved to be challenging.
24. Valve membrane tether.
25. Transfer port from Hydraulic Amplification Chamber (HAC) to valve cap.



26. Hydraulic Amplification Chamber. This was ultrasonically machined into Layer 6.
27. HAC filling port.
28. Main chamber.
29. Main chamber pressure sensor.
30. Outlet flow channel.
31. High frequency sealing channel for the hydraulic amplifier.
32. Central valve support. Care had to be taken to ensure the rigidity of this support. The compliance of the HAC had to be minimized to ensure proper amplification.
33. Flow outlet.
34. Outlet pressure sensor.
35. Electrical contact (pin contact) for anodic bonding of Layer 7 and 8 to Layer 9. (This hole was eventually deemed to be redundant.)
36. Electrical contact for anodic bonding of Layer 4 to Layer 3.

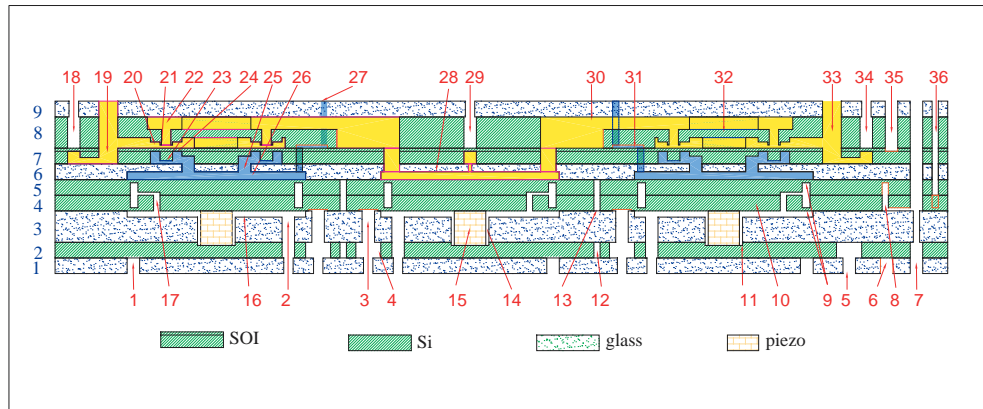


Figure 15: Cross-section schematic of the MHT device, highlighting major design features of the device.

## 1.6 Research Program Challenges

A significant number of challenges had to be overcome to realize a functional MHT system. These challenges, which can be organized into two major groupings: (1) modeling and design challenges and (2) fabrication, assembly, and testing challenges, are briefly introduced in this section and covered in detail in the remainder of this report.

### 1.6.1 Modeling and Design Challenges

The design philosophy for the MHT device was driven by requirements to produce a high power density, high performance, compact, energy generating device. As such, the design approach had to address the following issues and challenges. More attention will be given to these topics in Section 2.1:

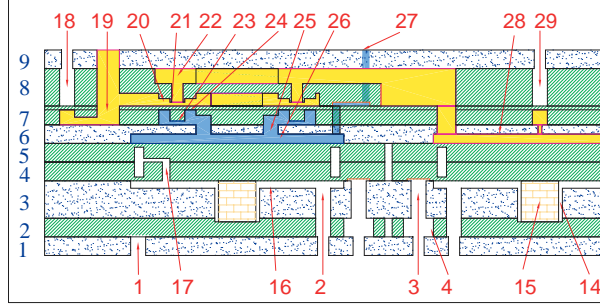


Figure 16: Cross-section schematic of the MHT device - a detail view.

**Design for Manufacturability** To design the MHT device, care had to be taken to ensure that the initial conceptual design was manufacturable using MEMS fabrication techniques. Where needed, enhancements could be made to existing fabrication technologies. Although new technologies and techniques were developed under this project that were particular to the MHT device, the majority of the silicon and glass layer fabrication relied on previously developed Deep Reactive Ion Etch (DRIE) and ultrasonic machining technologies. The same care had to be taken with the final design, to ensure that the device features were of dimensions that were manufacturable and not, for example, excessively fragile.

**Design for Performance** Performance of the device was of utmost importance. Therefore, many features of this device, structural, fluidic and electrical, were driven by a need to produce a well-performing MHT device. As in many MEMS devices there existed a strong coupling between the structural, fluidic and electrical energy domains, which required careful modeling to enable a design for maximal performance to be obtained.

**Design for Reliability and Strength** Hand in hand with performance came additional stresses on the materials used in the device, mainly silicon, glass, and the piezoelectric material of choice. Working with these brittle materials at high stress levels presented unique challenges when trying to ensure that a reliable device was designed.

**Design Refinement and Optimization** The MHT device, as a complex, coupled system demanded that attention be given to the modeling strategies, to ensure that the system-level simulations could be done quickly and effectively.

## 1.6.2 Device Fabrication, Assembly, and Testing Challenges

**Micromachining and Wafer-Bonding** Micromachining of the valve membrane and drive element tether structures within the MHT device is a critical step in the fabrication process. To achieve precise dimensional control of these thin-membrane structures, silicon-on-insulator (SOI) wafers containing a buried oxide etch-stop layer are used. In performing deep etches in these wafers, the surface roughness of the etch and the tailoring of the fillet radius profiles at the base of the etch must be well-controlled so as to maintain the strength and robustness of the structures. Additionally, upon completing the etching of the various silicon layers, wafer-level silicon-silicon fusion bonding and wafer-level silicon-glass anodic bonding procedures must be carried out to form multi-layer wafer stack structures, in preparation for device assembly.

**Piezoelectric Material Integration** Integration of bulk piezoelectric material within the thin-tethered drive element structures is the most critical step in the MHT assembly. Preparation of the material, including polishing, thin-film deposition, and core-drilling, is performed to provide an optimal surface finish of the material in preparation for eutectic bonding to the adjoining silicon layers within the device. Additionally, accurate measurement of the individual piezoelectric element dimensional thicknesses, prior to integration, is required to ensure optimal static and operational deflections of the piston structure which result in minimal stresses in the etched piston tethers. Incorporation of multiple smaller area piezoelectric materials spread out beneath the piston membrane is desired over placement of a single larger area piezoelectric material at the piston center, so as to reduce system compliances and increase actuation efficiency. However, tolerance issues become even more important when dealing with the requirements of multiple bonded elements.

**Fluid Filling and Sealing** Encapsulation of a working fluid in the device is a significant challenge at the microscale because surface-to-volume ratios are typically quite large, with surface energies playing a dominant role. Any gas bubbles present in the sealed active valves can create enormous system compliances, potentially rendering the system useless. The elimination of trapped gases during filling of the device and during encapsulation of the fluid port used for filling is critical for high-level performance. The development of a systematic fluid degassing and filling procedure is required for successful realization of a working active valve device.

**Device Testing** Experimental testing of a complex microfabricated device can be an extremely challenging activity, due primarily to the lack of physical access to the structures within the device. To thoroughly characterize the performance of the MHT system, drive element piston and valve cap deflections in response to applied voltages must be measured real-time. Additionally, dynamic pressures (between 0 and 2 MPa) upstream and downstream of the valve orifice and real-time fluid flow rates (as low as  $10 \mu L/min$  and as high as  $1 ml/s$ ) must be monitored. Development of a test-rig apparatus for carrying out these measurements is a critical task for proper evaluation of the device behavior.

## 1.7 Research Program Sub-Component Development Plan

A detailed sub-component testing plan for the MHT system is presented in Figure 17. This plan breaks the MHT systems into manageable sub-component structures according to the primary challenges already detailed. The piezoelectric drive element sub-component study proves the ability to micromachine the tethered piston structure and integrate bulk piezoelectric material beneath the piston structure of the active valves and harvesting chamber. The valve cap and membrane sub-component study validates the deflection behavior of the valve membrane structures contained within the active valves. The successful completion of these sub-component studies enables realization of the active valve system components. All of the fabrication and assembly challenges inherent in the realization of the active valve component structures are shared by the full MHT device, and as a result this sub-component testing plan enables step-by-step development of complete MHT systems.

Schematic Cross-Sections of Test Articles in the Test Plan

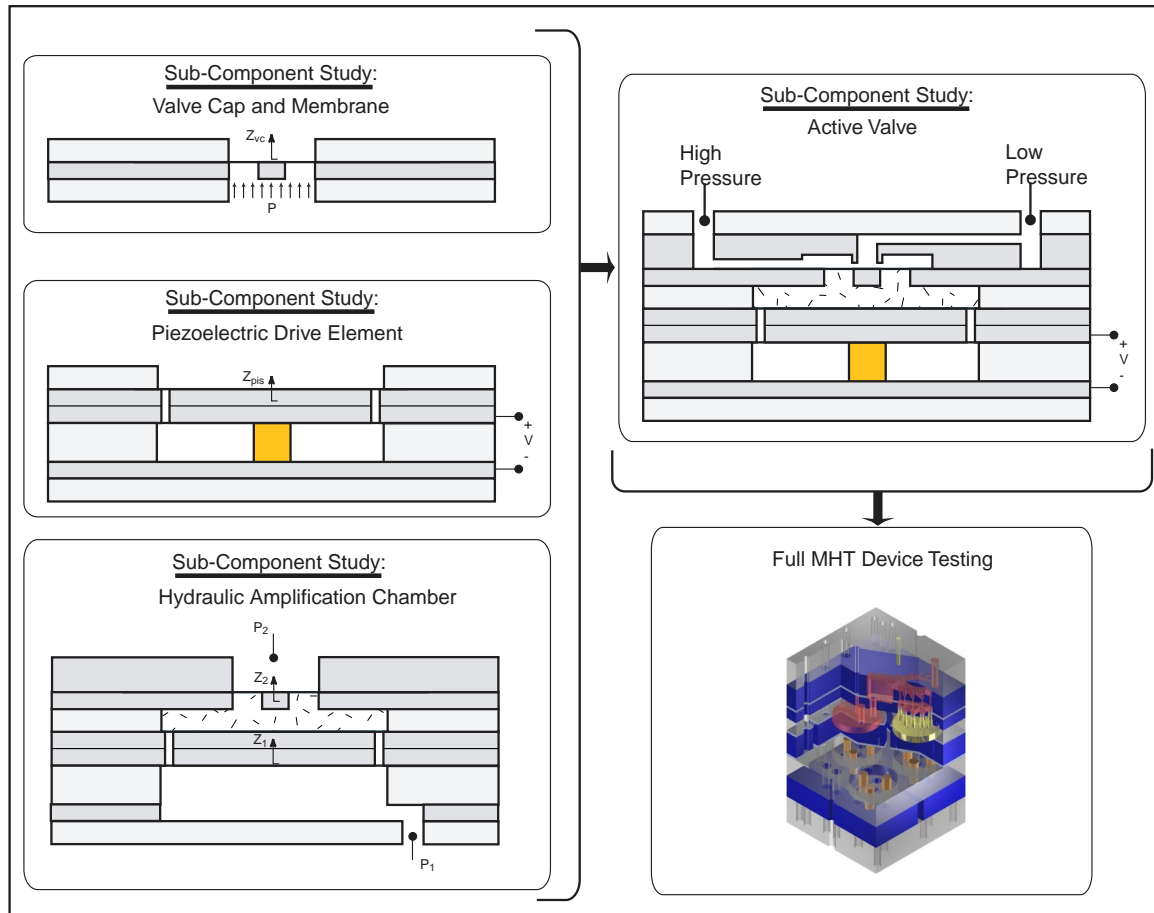


Figure 17: MHT sub-component testing plan. Realization of the full MHT system requires performance validation of piezoelectric drive element sub-component, valve cap and membrane sub-component, and active valve sub-component.

## 2 System Design and Modeling

Section 1 introduced the concept of the MHT system which, when operated in a pumping mode of operation, can be summarized into the following main components:

- The MHT device itself. At the heart of the MHT system is the MHT device, manufactured using a combination of microfabrication and conventional fabrication techniques.
- The drive electronics for the active valves and the pumping piston.
- A suitable packaging to enable the device and its electronics to be deployed as an underwater acoustic noise source.

The work described in this report focused primarily on the MHT device itself, with this component being by far the most challenging to design and manufacture. The design of this device was therefore approached in a systematic fashion, and this section deals with both the general approach and though process that resulted in the design of the MHT device, as well as a discussion of the simulation tools that were developed to produce the final design.

### 2.1 Approach to the design of the MHT device

We will now expand on the basic elements of the design process as described in Section 1.6.1. Presented here is a more detailed discussion of the design approach that led to the MHT device with the features as described in Section 1.5.2. This process is also represented schematically in Figure 18. Throughout this discussion, for references to items numbers and layers, the reader is referred back to Figures 15 and 16.

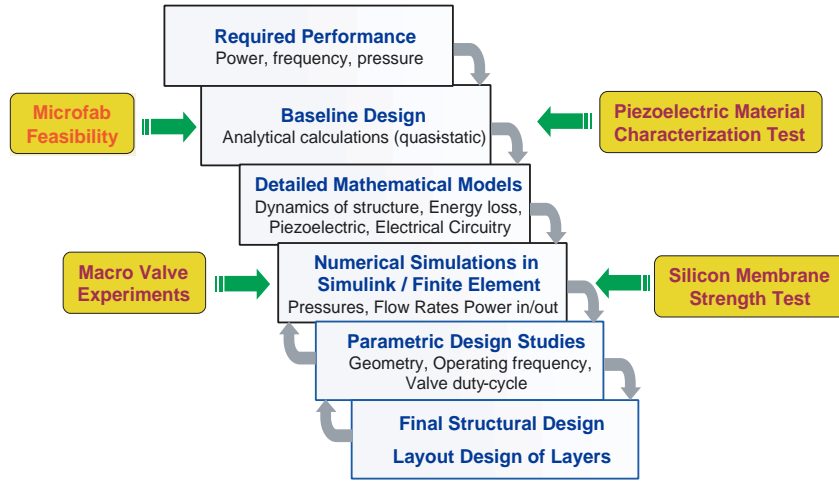


Figure 18: MHT Design procedure.

**Design for Manufacturability** Throughout the design procedure, manufacturability was a key consideration and determined, to a large extent, the layout and structure of the MHT device. What resulted was number of features that were mentioned in Section 1.5.2, and are discussed here in more detail.

1. Deep Reactive Ion Etching (DRIE) of silicon substrates. Using DRIE, which yields, in most instances, reliable "extruded" features, simplified mask layout and etching process development.
2. Ultrasonic machining for glass layers. Reliable, but limited in its capability to produce small features, ultrasonic machining was nonetheless chosen as the means for shaping the glass layers. All critical dimensions were therefore limited to the silicon layers.
3. Silicon-glass sandwich structure enabling die-level anodic bonding. By having been able to assemble devices on a one-by-one basis, it was possible to significantly increase the yield during the prototype development stage. Although this method is not desirable for large-scale production, it served well to yield devices that could be tested for performance.
4. Minimum thickness of SOI layers. The minimum thickness of the SOI layers was deemed to be  $7\mu m$ , due to both manufacturability and availability constraints, and this was then also the specified thickness for the valve membranes.
5. Recessed ultrasonic machining to make piezo alignment "pockets". By providing pockets in Layer 3 for aligning the piezoelectric elements, the "pick-and-place" assembly was greatly simplified.
6. Holes for anodic bonding. Spread throughout the device were holes for bonding almost any layer to any other layer, therefore giving various options for making electrical contact during assembly.
7. Individually etched piezo recesses. Due to unavoidable height variations in the piezoelectric elements, Layer 2 was designed to be etched on a die-by-die basis. Eventually, to obtain the desired depths, part-die masking was used to tailor individual piezo recesses. This procedure, once again, enabled the fabrication of prototype devices but is not desirable for mass production.

**Design for Performance** The following features in the design resulted primarily from an attempt to enhance the performance of the MHT device:

1. Double layer, double-tethered drive piston. This feature increases the first natural frequency of the drive piston. In addition, the stiffer piston provides for a less compliant chamber and hence a better performing device. See Section 5.2.
2. Stiff structure in general. The entire device was designed such that it would be sufficiently stiff to ensure that a minimal amount of energy is stored elastically, enabling maximum power transfer between the piezoelectric elements and the fluid.
3. Optimized stiffness of the membrane tether structures. As the most compliant members in the device, their flexibility contributed to a large extent to the compliance of the device, and as such had to be minimized, bearing in mind that a stiffer membrane would deflect less, giving less motion for a valve. It would also see higher stresses for a given deflection. This study is discussed in Section 2.2.5.
4. Pump chamber and hydraulic amplification chamber height of approximately  $200\mu m$ . This was found to be the lowest height that would not cause severe squeeze film damping effects.
5. Multiple valves instead of one large valve. This gives more flow area for a given valve opening, with less flow losses. This feature proved challenging to fabricate.
6. Three piezoelectric elements instead of a single one. Once again, to stiffen the system and raise the structural natural frequencies. Using this type of tripod configuration also ensured that the first vibrational mode of the piston, a tilt mode, was eliminated.

7. Deep electrical isolation trenches in Layer 2 and the Layer 4-5 pair. Electrical isolation was achieved during the dicing operation. This yielded a device with three fully isolated piezoelectric drive units.
8. Flow channel geometries chosen to exploit fluidic resonant behavior at the design frequency. Helmholtz resonator models were used.
9. Small sealing channels for dynamically sealing the hydraulic amplification units. These channels eliminated the need for a static seal for the prototype MHT devices. This allowed for the pressurization of the hydraulic amplification chambers to balance them with respect to the high and low pressure reservoirs.
10. The use of single crystal PZN-PT piezoelectric material for its superior electromechanical conversion capabilities.
11. The use of a low-viscosity (0.65cst) silicone oil with good silicon wetting properties reduced viscous losses in the device.

**Design for Reliability and Strength** The following steps, in terms of design and supporting investigations were taken to ensure that the final device would be reliable and functional:

1. Bonded SOI wafers ensure the use of single crystal device layers to form membranes of uniform thickness. (SOI wafers made using the SIMOX<sup>2</sup> process were found to be inadequate.)
2. Carefully controlled fillet radii at the bottom of the trenches that formed the membranes. This ensured reduced stress concentrations which allowed the membrane-piston structures to operate at larger deflections. The geometry of the fillet radii was specified after a set of membrane strength tests, described in Section 3.4, to ensure that the maximum stress in any tether structure does not exceed  $1GPa$  under the assembly and operating conditions of the device. For the valve membranes, this stress would be encountered during operation where the valves would deflect as much as  $15\mu m$  for the single valve devices and  $10\mu m$  for the ten-valve devices, experiencing fluid pressures as high as  $2MPa$ . For the pistons, this stress would be seen during assembly, and also during the poling step for the piezoelectric material. The combined oversizing of the piezoelectric elements and the additional deflection during poling could add up to as much as  $8\mu m$ , with the expected tolerances that were to be attained.
3. Determining the maximum stress limits of the piezoelectric materials to prevent compressive depolarization. (See Section 3.3)

**Design Refinement and Optimization** The remainder of Section 2 will address the design refinement procedure which took place whilst giving consideration to aspects of manufacturability, performance, reliability, strength and functionality.

## 2.2 Development of Simulation Tools

### 2.2.1 Objective

Given the complexity of MHT devices, comprehensive simulation tools were needed to produce a good design. Operation of each subcomponent of the device was coupled to the others and every design decision had to be made with remaining components in mind. In this case the approach was to create

---

<sup>2</sup>SIMOX: Separation by the IMplantation of OXYgen

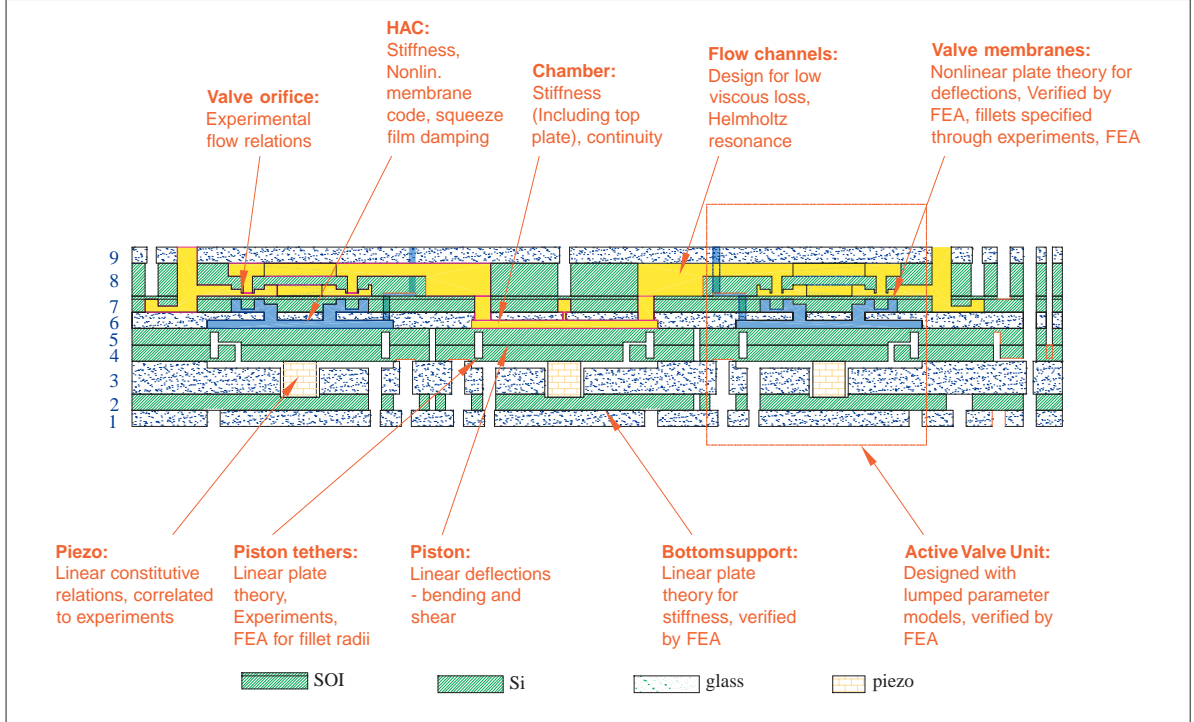


Figure 19: Main aspects of the modeling performed on the MHT device.

a system level simulation tool that enabled the monitoring of important parameters such as chamber pressure, flowrate, and various structural component deflections and stresses. This tool also combined the different energy domains, namely fluidic, structural and piezoelectric material. It was assumed that suitable drive electronics could be incorporated at a later stage with minimal additional effort. The system level simulation tool was supplemented by more detailed modeling and experimental methods in the following ways (See also Figure 19):

- Microscale fluid flow - by means of experimental investigations.
- Detailed finite element analysis of the structural components - the pistons, tethers and also the entire active valve unit.
- Including the nonlinear membrane behavior in the model using lookup tables to reduce the computational overhead.

Figure 20 depicts the entire system level simulation approach. For the purposes of designing the MHT device, most emphasis was placed on the "chip level simulation", and the Low Pressure Reservoir (LPR) and High Pressure Reservoir (HPR) were taken as constant pressure sources. In addition, the valve and pump piston drive electronics were not incorporated explicitly.

### 2.2.2 The Pump Chamber

The Pump Chamber consists of a fluid chamber, a piston and a piezoelectric cylinder. The piston converts the force exerted by the piezoelectric cylinder into a pressure in the chamber. The inlet and outlet valves operate  $180^\circ$  out of phase at high frequency and rectify the pressure fluctuations in the



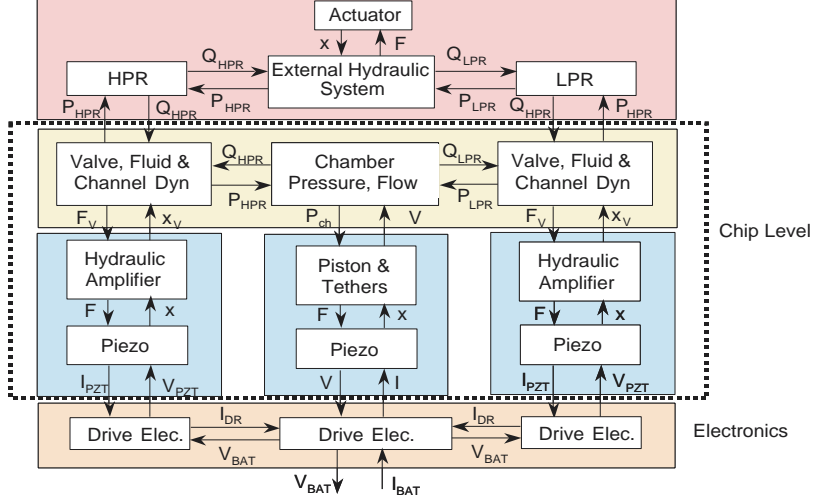


Figure 20: MHT Active valve pump system simulation schematic.

chamber into net flow rate from the low pressure reservoir to the high pressure reservoir. The generic operation and typical duty cycles are shown in Figure 21.

Figure 22 shows the structural components and the corresponding deformations which were used in the formulations of the governing equations. These deformations inside the pump chamber can be adequately represented by linear plate theory [38]. Each component is modeled as a plate with applied loading and boundary conditions to determine the deflections and swept volumes. In general, a symmetrically loaded circular plate will experience deflections due to bending as well as shearing. Since the radii of the structural components analyzed were significantly larger than the corresponding thicknesses, deformations only due to bending will be considered.

The equation governing the chamber continuity is:

$$P_{ch} = \frac{\beta_f}{V_o} \left( \int_0^t (Q_{in} - Q_{out}) dt + \Delta V_{pis} + \Delta V_{pb} + \Delta V_{te} - \Delta V_{tp} \right) \quad (4)$$

where  $\Delta V_{pis}$ ,  $\Delta V_{pb}$ ,  $\Delta V_{te}$ ,  $\Delta V_{tp}$  represent the swept volume due to the motion of the piston, deformation of the piston, deformation of the top tether and deformation of the top support structure respectively.

The elastic equations along with the chamber continuity equation and piezoelectric element constitutive relationships are solved in Maple and the coefficients required by the simulation architecture is calculated and fed to Simulink. The simulation architecture allows for integration of the elastic equations into the dynamic simulations as well as for monitoring important parameters like deflections and swept volumes of the individual structural components and stresses in the tethers.

### 2.2.3 Active Valve

The layout of the active valve is shown in Figure 23. The active valve structural components are modeled similarly using linear plate theory, with the exception of the valve membranes, whose deformation is nonlinear and a numerical code is used to calculate the deformation and stress of the membrane. The nonlinearity of the membrane structure is incorporated into the system level simulation using look-up

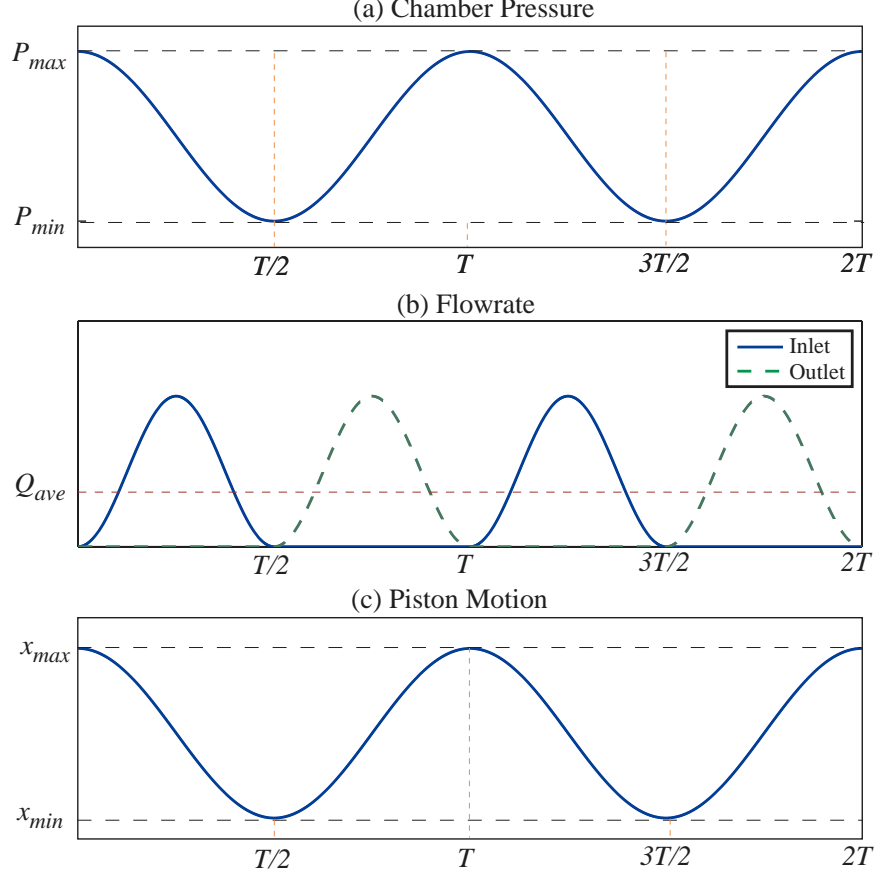


Figure 21: Duty cycles of generic operation of the pump chamber. The valve openings have the same duty cycle as the flowrates and are not shown here.

tables that are generated using the numerical code by running it for different pressure loading conditions on the active valve membrane. The Simulink architecture of the active valve is shown in Figure 24.

#### 2.2.4 Fluid Models

The schematic of the device with pressures at different locations within the system is shown in Figure 25 where  $P_{int-in}$  is the intermediate pressure at the exit of the inlet channel, and  $P_{int-out}$  is the intermediate pressure at the entrance to the outlet valve. Inlet and outlet channels have the same geometry.

**Valve Orifice Flow Relations** Work by previous researchers has shown that for small openings, poppet valves, such as the valve cap in the active valves within the MHT systems, behave as long orifices in which the effects of flow separation and subsequent re-attachment dominate the valve flow dynamics[5].

The valve orifice may be characterized as a flow contraction followed by a flow expansion. In the MHT power generator, Reynolds numbers are expected to fluctuate between approximately 10 and 20,000 as the valves open and close. For this reason, correction factors obtained from experimental results need to be employed to obtain estimates of the loss coefficients for these low turbulence and laminar flow regimes [37]. A loss coefficient for each of the contraction and expansion geometries,  $\zeta_{contraction}$  and

$\zeta_{expansion}$ , respectively, is used to approximate the total loss coefficient through the valve as detailed in the following relation:

$$\zeta_{orifice} = \zeta_{contraction}(f(Re), \frac{A_o}{A_2}) + \zeta_{expansion}(f(Re), \frac{A_o}{A_1}) \quad (5)$$

where the Reynolds number is defined as:

$$f(Re) = \frac{1}{\pi} \frac{Q}{R_{vc}\nu} \quad (6)$$

The pressure-flow relation for the full valve orifice geometry can be written as:

$$\Delta P = \frac{1}{2} \rho \zeta_{orifice} \left( \frac{Q^2}{A_o^2} \right) \quad (7)$$

These flow models are based on steady flow phenomena and do not capture frequency dependent losses. For a specific value of valve cap opening at a given time during the cycle, a relationship therefore exists for the instantaneous fluid flow through the valve as a function of the pressure drop across the valve.

**Flow in the Channels** Due to the high Reynolds numbers, the flow in the channels is expected to be inertia dominated. Furthermore, the compliance in the fluid channels is usually negligible due to the fact that the channels are surrounded by rigid walls and their volume is much smaller than that of the chamber. Under these assumptions the flow inside the channels is modeled as one dimensional inviscid and incompressible flow. The pressure-flowrate relationship in this case is given as:

$$\Delta P = I \frac{dQ}{dt} = \left( \frac{\rho L_c}{A_c} \right) \frac{dQ}{dt} \quad (8)$$

where  $I$  is defined as the fluid inductance inside the channel,  $\rho$  is the fluid density and  $L_c$  and  $A_c$  are the length and cross-sectional area of the fluid channel respectively. For a long channel with small cross-sectional area, one can expect fluid inertial effects to play a significant role as the pressure difference builds up to accelerate the fluid slug into the chamber. Conversely, for short channels with large cross-sectional areas, the inertial effects are negligible and the pressure  $P_{int-in}$  and  $P_{ch}$  or  $P_{ch}$  and  $P_{int-out}$  will not differ much. It is important to consider inertial effects when designing hydraulic systems containing small channels.

The governing equations for the fluid flow in the system, which are integrated into the system level simulation, can be obtained as:

$$P_{HPR} - P_{ch}(t) = R_{in}(Q_{in}, v_{oin})Q_{in}^2 + \left( \frac{\rho L_c}{A_c} \right) \frac{dQ_{in}}{dt} \quad (9)$$

$$P_{ch}(t) - P_{LPR} = R_{out}(Q_{out}, v_{oout})Q_{out}^2 + \left( \frac{\rho L_c}{A_c} \right) \frac{dQ_{out}}{dt} \quad (10)$$

where  $R_{in}$  and  $R_{out}$  are the fluid resistances of the inlet and outlet valves respectively.

## 2.2.5 Design Issues

**Fluidic Oscillations** Inertial effects should be considered when designing hydraulic systems containing small channels. In the MHT devices the fluid channels and the main chamber constitute a resonant system similar to a Helmholtz resonator which comprises a fluid channel and a chamber with an effective compliance. The fluidic channels have to be designed such that the device will operate at resonance

condition when operated at the design frequency. The motivation for operating at resonance is that the same pressure band can be achieved with smaller valve cap sizes or valve openings compared to the case of negligible or very large fluid inductance in the channels, resulting in reduced power consumption in the active valves.

**Chamber filling and evacuation** In order to attain the desired pressure bands inside the chamber, it is important to design the valve sizes, openings and the operating frequency accordingly. The combination of the valve size and the valve opening define the overall valve resistance. For a given operating frequency and pressure band, it is important to design the valve size and opening such that they will provide just enough filling and evacuation of the chamber in the required time interval, so that the chamber pressure fluctuates between the reservoir pressures in the most economical way.

**Tether Structure Optimization** Accurate design of the piston tether structure is very crucial for system operation. The tethers should be flexible enough to allow sufficient motion of the piston, yet stiff enough to avoid introduction of excessive compliance into the system. If the tether is either too thin or the tether width is very large, this results in low pressure in the chamber and small compression of the piezoelectric element since the compliance introduced by the tether is very large. In other words, pressure does not built up inside the chamber because of the excessive bending of the tether. If the tether is either too thick or the tether width is very small, the chamber compliance will be low, but the piston will be too stiff for the piezoelectric element to actuate it, and the stroke will be small, giving low flow rates. This suggests that for a design where the chamber diameter(or piston diameter) is determined, the tether structure has to be optimized in conjunction with fabrication limitations, such as thickness of the tether, which is determined by the SOI wafer being used.

Consider a chamber of the following geometric parameters:  $D_{ch} = 5mm$ ,  $D_p = 1mm$ ,  $L_p = 1mm$ , and  $H_{ch} = 200\mu m$ . An additional fluid volume,  $\Delta V_f = 10^{-11}m^3$ , is introduced into the chamber. Figure 26 shows piston deflection/piezoelectric element deflection for different tether thicknesses and widths. The tether width is varied by keeping the chamber diameter the same and changing the piston diameter. It can be seen that, for a given tether thickness, there exists a range of optimum tether widths. In this case the "perturbation" was an additional fluid volume. This produced a negative piston motion. A small voltage perturbation on the piezoelectric element will have a similar effect, with a positive piston motion. For the MHT device that was tested, the tether width was  $225\mu m$  and the thickness  $9\mu m$ .

The stresses calculated using linear theory give a reasonable estimate and provide a first order prediction about stresses seen in the piston membranes. However, for the final, refined design, consideration was also given to the membrane fillet feature. The work described in Section 3.4 highlighted the importance of having a sufficient, but not too large, fillet feature to reduce stress concentrations in these tethered membrane structures.

**Preliminary design decisions** The working fluid is chosen to be silicone oil due to its low viscosity and low density. It also has a comparable bulk modulus to that of water. PZN-PT is chosen as the piezoelectric element due to its high coupling coefficient, which results in efficient electromechanical energy conversion. The chamber height is chosen to be  $200\mu m$ . A preliminary study has shown that chamber heights smaller than this could cause squeeze film damping effect inside the chamber. On the other hand, larger chamber heights would increase the chamber compliance, which would decrease the efficiency of the system. The length of the piezoelectric element is chosen to be  $1mm$ . This parameter is determined by considering the actuation in the active valves, since all the piezoelectric cylinders within the system, namely the ones in the active valves and the one in the energy harvesting chamber, have the same length because of the layered structure of the device.

Design Decisions		
Piezoelectric material	PZN-PT	lowest flowrate requirement
Working fluid	silicone oil	low viscosity and density
Piezoelectric element length, $L_p$	1mm	active valve actuation
Chamber height, $H_{ch}$	200 $\mu m$	squeeze film damping
Parameters imposed by fabrication process		
Piston thickness, $t_{pis}$	800 $\mu m$	double layer piston
Top and bottom support structure thickness	2.5mm	packaging layers
Tether thickness	10 $\mu m$	fabrication feasibility
Material Limitations		
Depolarization stress of piezoelectric element, $\sigma_d$	10MPa	shouldn't be exceeded
Maximum allowable stress in tethers	1GPa	shouldn't be exceeded

Table 1: Summary of preliminary design decisions.

**Parameters imposed by active valve design** The basic limitation of the active valves is their bandwidth and the maximum pressure they can work against. Typical trade-offs in the active valve design are stroke, bandwidth and force. Also, the active valves impose a minimum pressure requirement, the bias pressure, due to cavitation considerations in the hydraulic amplification chamber(HAC) within the active valve structure.

**Parameters imposed by fabrication processes** The device consists of silicon and Pyrex micromachined layers. The thickness of the layers dictate the thicknesses of individual components. For example, a double layer piston structure, which consist of two silicon layers bonded to each other, will have a thickness of  $t_{pis} = 800\mu m$ . Since the tethers are created through deep reactive ion etching(DRIE) of a SOI wafer, the tether thickness is defined by the SOI layer. Also, the fillet radius control during the fabrication process imposes some limitations on the tether width. For example narrow tethers would be very stiff due to the relatively large fillet radius and the predictions of the linear theory used for the optimization would not valid beyond a certain tether width. The tether thickness was chosen to be 10 $\mu m$ . The thicknesses of the top and bottom support structures are determined by the number of layers used, including the packaging layers on top and bottom portions of the device. The compliance of the system is very important in terms of system performance and they should be kept as small as possible. Therefore it is desirable to have very thick top and bottom support structures. The effective thickness would also depend on the structure of the auxiliary system in which the device is packaged.

### 2.2.6 Design Parameters

This section presents the design parameters of the MHT Active Valve Pump device. The preliminary design decisions, parameters imposed by fabrication process and material limitations are summarized in Table 1. The final design parameters are listed in Table 2.

## 2.3 Contributions: Modeling

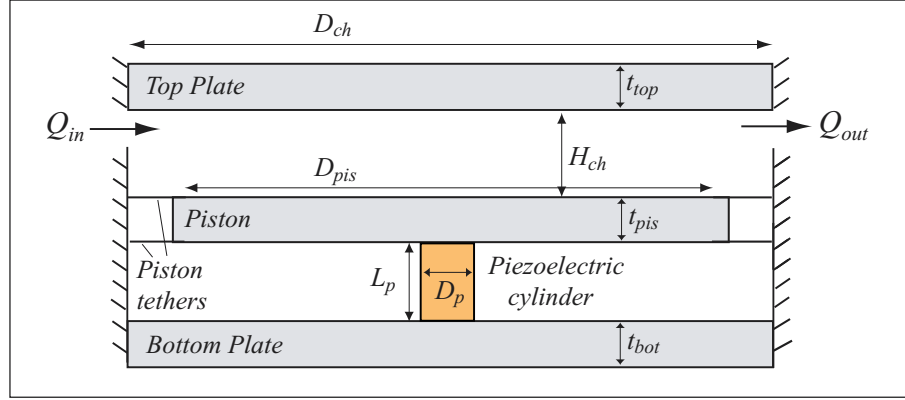
The contributions of the modeling of the MHT device can be summarized as follows:

1. A detailed systems level model of the MHT device that includes all the major parameters has been developed.

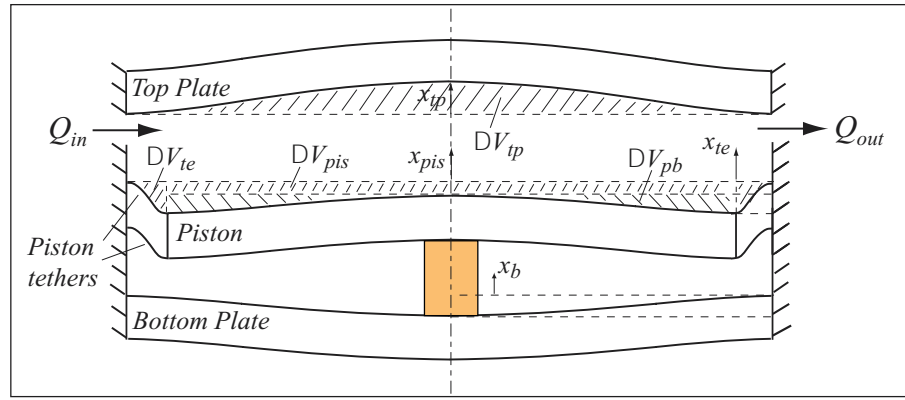
<b>Parameters imposed by active valve design</b>		
Operation frequency, $f$	$15kHz$	bandwidth of active valves
Bias Pressure, $P_b$	$0.4MPa$	cavitation in HAC chamber
High Pressure Reservoir Pressure, $P_{HPR}$	$2.4MPa$	membrane stress limitation
<b>Designed parameters</b>		
Piston Diameter, $D_{pis}$	$6.85mm$	-
Piezoelectric cylinder diameter, $D_p$	$2.05mm$	-
Battery voltage, $V_b$	$90V$	-
Tether width, $w_t$	$225\mu m$	optimization
Chamber diameter, $D_{ch}$	$7.3mm$	-
Fluid channel length to area ratio, $\frac{L_c}{A_c}$	$2000m^{-1}$	same for inlet and outlet
Valve cap radius, $R_{vc}$	$300\mu m$	same for inlet and outlet
Valve opening, $vo_{in}, vo_{out}$	$30\mu m$	same for inlet and outlet
<b>Performance parameters</b>		
Net flowrate, $Q_{net}$	$1ml/s$	-
Pressure Differential	$2MPa$	-

Table 2: Summary of design and performance parameters.

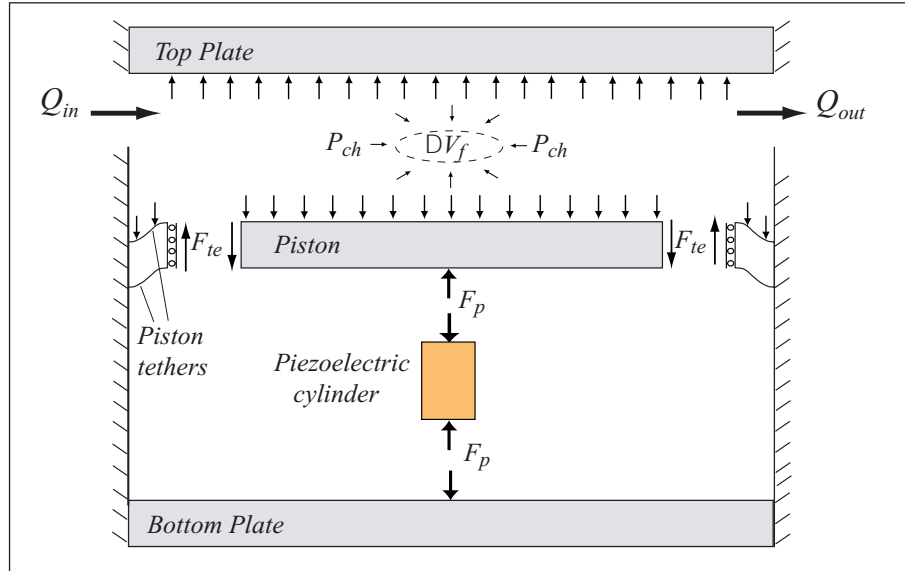
2. As a subset of this effort, a model has been developed for a annular plate with a rigid center boss undergoing large deflections. This enabled the taking into account of the large deflections of the valve membrane structures. This model was also used extensively in the active valve design effort.
3. A tether width optimization scheme was introduced to determine the optimal width for the piston and valve tethers.
4. A number of design features were introduced to improve either the manufacturability or the performance of the MHT device, or both.
5. As a final result, a detailed design for a bench top MHT device was produced.



(a)



(b)



(c)

Figure 22: Pump Chamber Model.

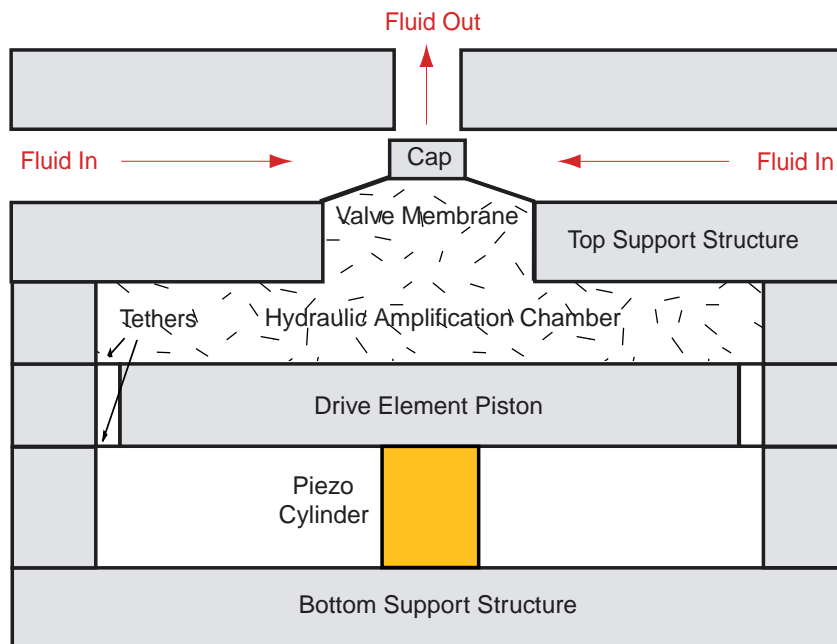


Figure 23: Schematic of the active valve.

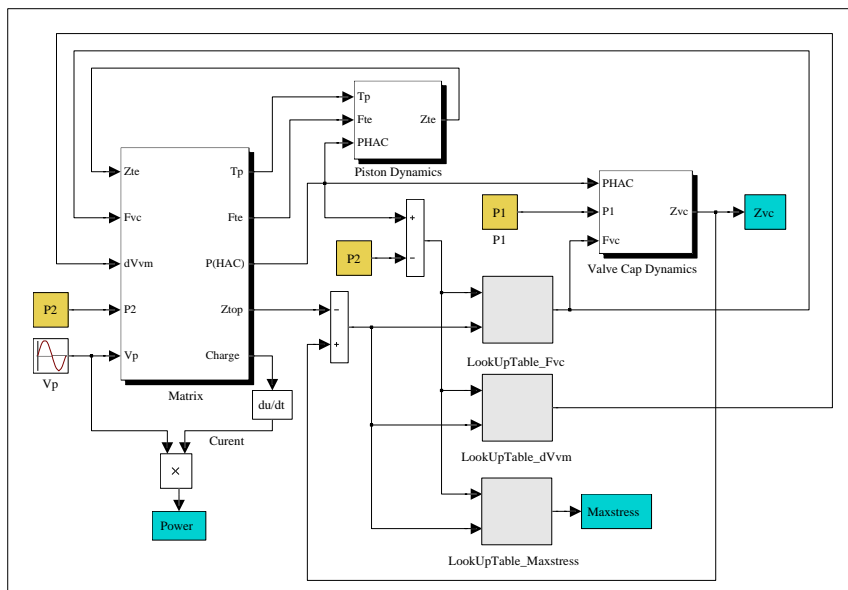


Figure 24: Simulation architecture of the active valve.



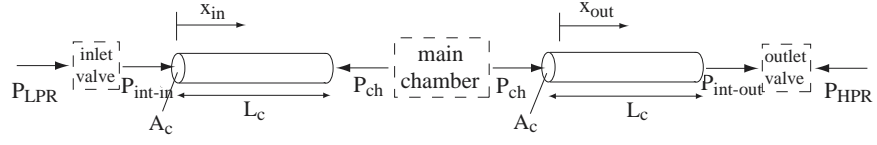


Figure 25: Simplified device schematic showing pressures at different locations.

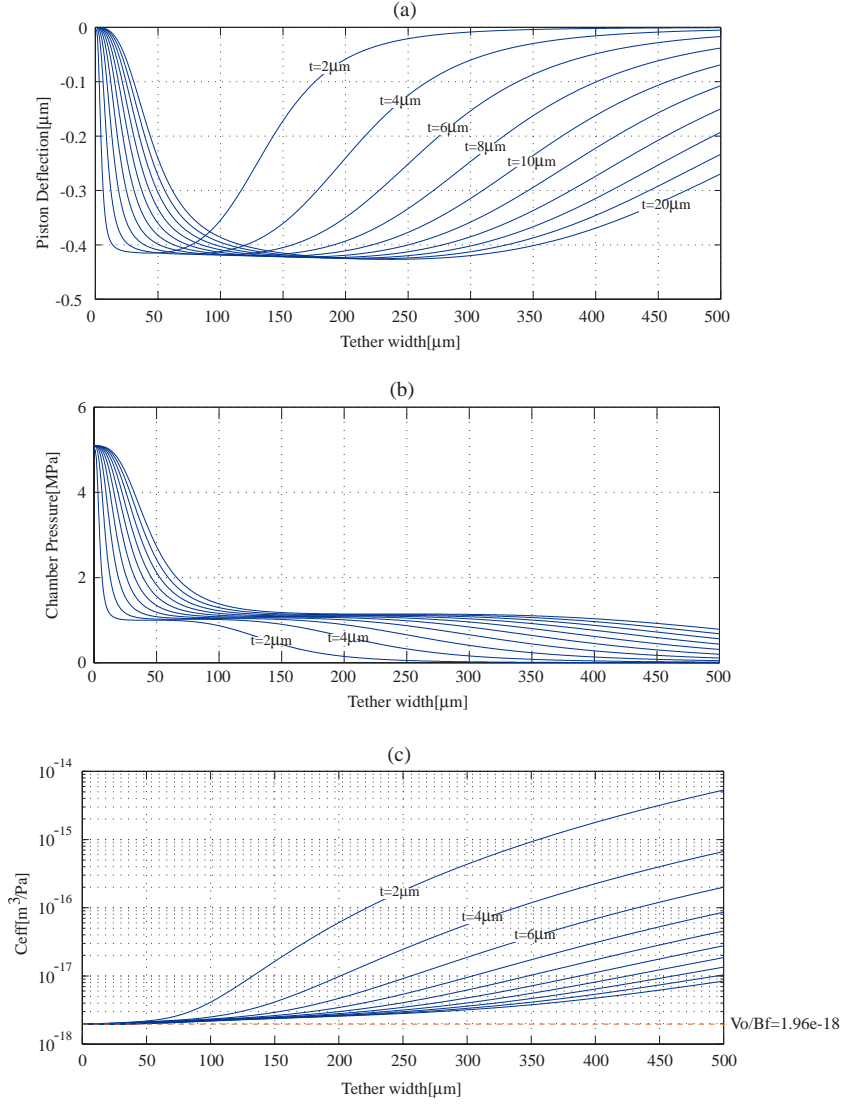


Figure 26: Piston deflection for different tether thicknesses and widths



## 3 Supporting Experimental Investigations

### 3.1 Investigation of Flow Losses Through Microscale Orifices

The rapid increase in the development of complex microfluidic devices has revealed a need for more accurate modeling of fluid behavior in small-scale microfabricated geometries. Microvalves tend to be one of the dominating elements in such systems, but at the same time their detailed behavior remains poorly understood and systematic studies of microvalve fluid mechanics are lacking.

In the case of the Micro Hydraulic Transducer program at MIT, the requirements on valve modeling take a different perspective. In this case the valve and head loss models are used as design tools. Typical orifice models will not capture geometry related sensitivities necessary for design and optimization. Furthermore, one of the goals of the MHT project is to harvest energy with this device, for this reason, and considering that the valve is the dominating head loss, it becomes critical to determine accurately the corresponding head losses and sensitivities. Only then will it be possible to design a more efficient valve.

The major fluid mechanics challenge is to model the steady and unsteady fluid behavior in these micron-scale geometries. The Reynolds number during one cycle varies between 1 and 20,000 with a Strouhal number of order 1. In this regime both inertial and viscous forces are important and unsteady effects cannot be ignored. The model needs to be accurate, yet implemented in a flexible manner suitable for design purposes and integration into full system simulations. Unfortunately, such models do not presently exist, and where partial models are available, they are typically neither calibrated nor validated for the small scales and unique geometries that are found in microfluidic systems. The purpose of this work is to provide such calibration and validation.

#### 3.1.1 Microsystems Fluidic Modeling Strategies

Previous experiences by Olsson, Bourouina and Gravesen have proven that the lumped element model is useful for the analysis of microfluidic systems. The lumped model has the added advantage that due to its similarity with circuit system-analysis existing software, such as SPICE and SIMULINK, can be used to obtain solutions. In this case the behavior of localized components needs to be characterized separately. In our case the microvalve dominates the flow regime and therefore is the focus of this work.

#### 3.1.2 Results

Numerical and analytical techniques are inadequate for characterizing valve flows in the low turbulence to transition regime therefore a experimental approach was favored. The experiments were carried out on a scaled up version of the valve for ease of instrumentation.

#### 3.1.3 Transition Reynolds number

Observing the experimental results for different valve sizes a unified formula for predicting the transition Reynolds number was formulated. The transition Reynolds number is described as a function of the valve opening ratio ( $h^*$ ) and the valve diameter ( $d^*$ ) ratio. Having an expression that predicts the transition Reynolds number for different valves and openings we can define a modified Reynolds number ( $Re_m$ ) such that all curves will experience transition at the same point. The curve is empirical in nature and no attempt is made to relate it to physical variables. The modified Reynolds number ( $Re_m$ ) is defined as

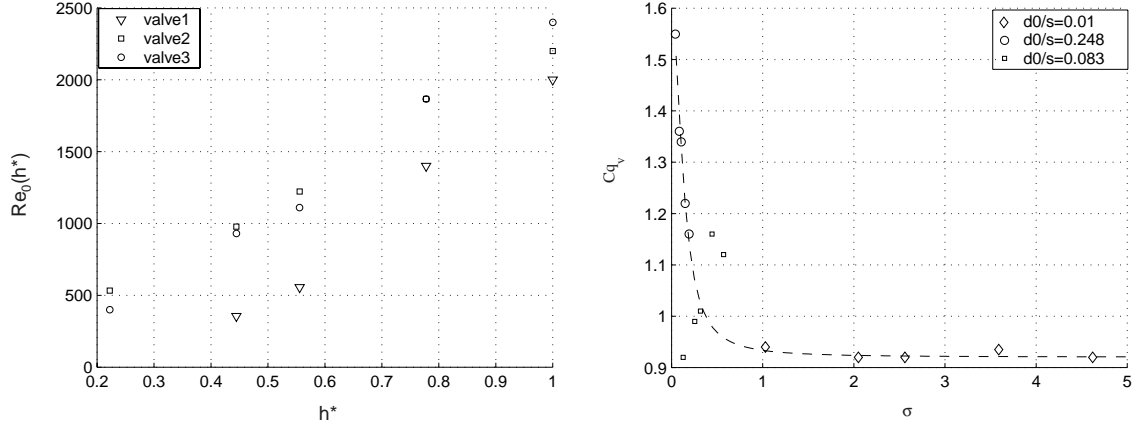


Figure 27: Transition Reynolds number vs valve opening ratio and ,Discharge coefficient ( $C_q$ ) vs. non-dimensional valve opening ( $h^*$ ) for the three valves; plate separation ( $h_p$ ) 450  $\mu\text{m}$ .  $h^*$

$$Re_m = Re_0 - h^* \left( \frac{1 - 0.692d^*}{2.483e^{-3} - 2.818e^{-3}d^*} \right) + \left( \frac{2942 - 2205d^*}{1 - 1.88d^*} \right) \quad (11)$$

where  $Re_0 = 4Q/(\pi d_0 \nu)$  is the Reynolds number based on the valve inlet diameter ( $d_0$ ),  $h^*$  is the valve opening ratio and  $d^*$  is the valve diameter ratio. The results of the scaling can be seen in Figure 27.

### 3.1.4 Valve Seat Width Dependence

The effect of the valve seat width was investigated with three valves of different seat widths ( $s$ ). The results are shown in Figure 27 where the  $x$ -axis shows the ratio of valve opening ( $h_v$ ) to seat width ( $s$ ), defined as ( $\sigma$ ). The  $y$ -axis uses the modified discharge coefficient  $C_m = C_q/(4h^*)$  where  $C_q = 4Q/(\pi d_0 h_p) \sqrt{\rho/(2\Delta P)}$ . One interesting result is that for values of  $\sigma > 1$  the modified discharge coefficient is not affected by the seat width,  $s$ . Once this threshold is passed, however, the discharge coefficient becomes very sensitive to the seat width and rises rapidly. Significant pressure recovery is observed, even surpassing  $C_m=1$ . This increase in discharge coefficient may be explained by drawing an analogy to thick orifices. For a thick orifice, the separation bubble tends to reattach within the throat area as shown by Sahin et al. The reattachment reduces the flow losses across the orifice. For the case where the non-dimensional seat width  $\sigma < 1$  the same phenomenon is observed and we theorize that the separated flow undergoes reattachment with the accompanying pressure recovery.

A curve fit for the discharge coefficient ( $C_m$ ) as a function of  $\sigma$ , the valve opening over seat width ratio, is given by

$$C_m = \left\{ 0.9203 + \frac{0.6755}{1 + \left( \frac{\sigma}{0.1327} \right)^{1.9361}} \right\} (h^*)^{-b}. \quad (12)$$

$$b = \frac{\frac{0.1}{1 + \exp\left(\frac{Re_m - 2050}{200}\right)}}{1 + 10^{\left(\frac{\ln(s/0.25)}{0.5}\right)}} \quad (13)$$

which is a function of the valve seat width ( $s$ ) and the modified Reynolds number.

The curve shown in Figure 28 can be approximated by using equation 14 as suggested by Lichtarowicz. The curve however requires different coefficients which were obtained using the curve fitting program DATAFIT. The equation is then given by :

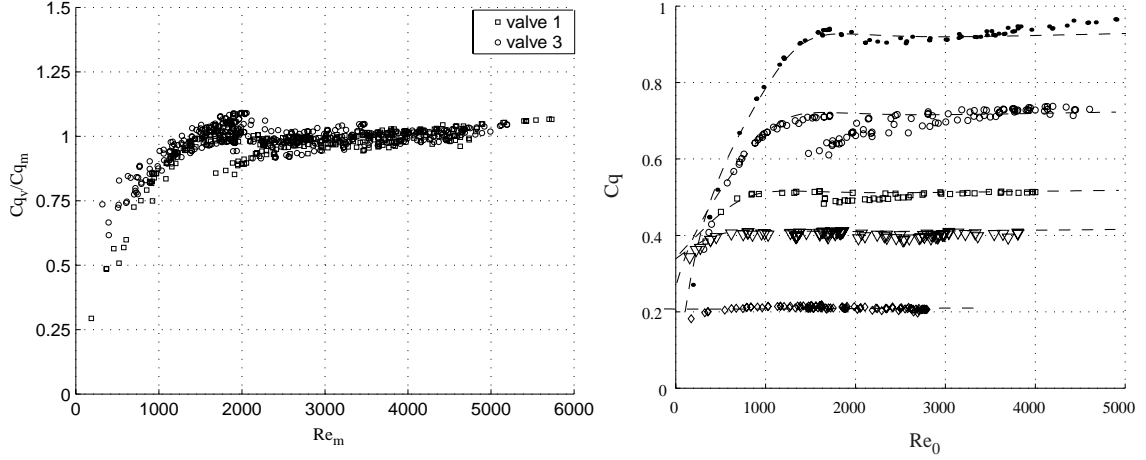


Figure 28: Scaled data for valve #1 and valve #3, Curve fitting using 14 for valve #1

$$\frac{1}{C_n} = \frac{C_m}{C_q} = 0.956 + \frac{364.89}{Re_m} - \frac{0.194}{1 + 2.608(\ln(0.000718Re_m))^2}. \quad (14)$$

where  $C_m$ (Equation 12) gives the magnitude of  $C_q$  at the turbulent regime limit and  $C_n$ (Equation 14) gives the necessary correction factors to account for the Reynolds number dependence in the transition and laminar flow regimes. The quality of the curve fit can be appreciated when compared to the original data. The results for valve #1 can be seen in Figure 28 showing that the curve fit describes accurately the valve behavior for different valve openings and Reynolds numbers.

### 3.1.5 Contributions

An hydraulic model for the Micro-Hydraulic Transducer was constructed based on a low-order lumped element model. The valve flow characteristics were investigated experimentally and parametric studies were carried out to obtain the flow dependencies and allow for a better estimation of the head losses. Data reduction and curve fitting resulted in a model comprised of three formulas which can be used to predict the discharge coefficient  $C_q$  of a poppet valve based on the Reynolds number and valve dimensions. The results presented can in turn be used as part a systems simulation for design and optimization purposes.

## 3.2 Determination of Fluid Filling and Sealing Procedures at the Microscale

### 3.2.1 Objectives

For effective hydraulic amplification, the compliance of the hydraulic amplification chambers had to be minimized. Hence, reliable filling and sealing techniques were required to ensure the stiffest hydraulic amplification chamber possible. This section describes filling techniques developed in conjunction with Boston MicroSystems. It also addresses the sealing techniques that were developed to properly seal the hydraulic amplification chambers for either static or dynamic sealing purposes.

### 3.2.2 Filling techniques

**Fluid requirements** For the full MHT device, the working fluid had to satisfy the following requirements:

- Low viscosity, for minimal viscous losses.
- High bulk modulus, for minimal compliance.
- Should wet silicon surfaces well, to ease filling of small cavities.
- Should be dielectric, due to the high voltage operation of the device.

Based on these requirements a volatile silicone oil, Hexamethyldisiloxane (Produced by Dow Corning under the trade name DC200 0.65cst), was chosen as the system fluid. This was also the fluid used in all devices tested in this document.

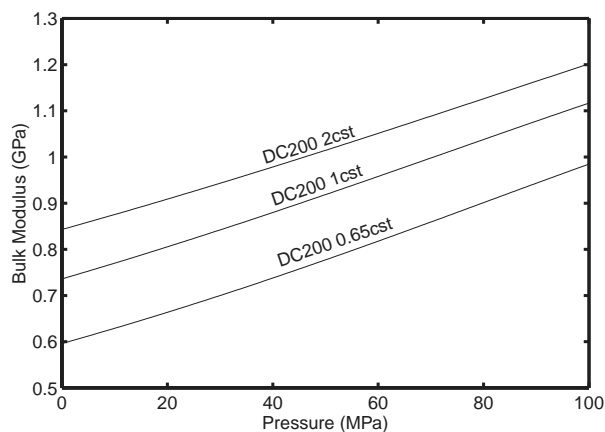


Figure 29: Bulk modulus vs. fluid pressure for a selection of volatile silicone oils, adapted from data as supplied by Dow Corning. Note that the amount of outgassing performed on these fluids is unknown.

The properties of various silicone oils indicate that there is a tradeoff between viscosity and bulk modulus. This is also shown in Figure 29. In the case where it is possible to use a different fluid in the HAC, it might pay off to investigate slightly more viscous fluids with higher bulk moduli. Note, however, that filling of the HAC, as described in the previous section, relies on the working fluid also possessing a high vapor pressure. This requirement eliminates most of the high viscosity oils. (See Figure 30)

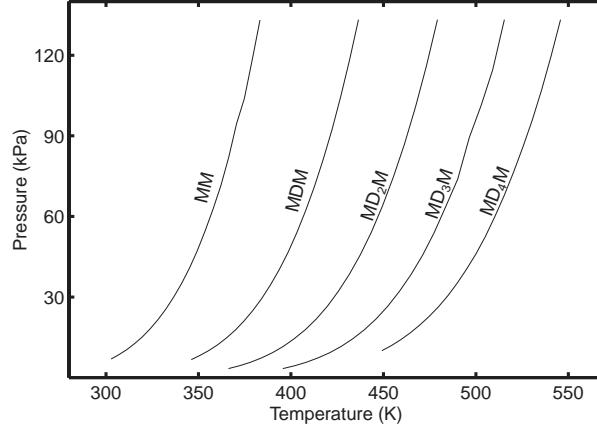


Figure 30: Vapor lines for a selection of linear siloxanes. The graphs show the vapor lines for Hexamethyldisiloxane ( $MM$ ), Octamethyltrisiloxane ( $MDM$ ), Decamethyltetrasiloxane ( $MD_2M$ ), Dodecamethylpentasiloxane ( $MD_3M$ ) and Tetradecamethylhexasiloxane ( $MD_4M$ ). Dow Corning DC200 0.65cst consists of  $MM$  and trace impurities. The other viscosities may contain blends of the compounds mentioned above.

**Filling process** To ensure bubble-free filling of the HAC, a filling system and associated filling process was developed. Figure 31 shows a schematic of the apparatus and Figure 32 is a photograph of the same apparatus.

To fill and seal an HAC, the following process was developed:

1. Set the initial condition of the system: All valves closed.
2. Open Tank B, and place the device test jig (Discussed in Section 5.1.3), as well as the device, inside. Do not mount the device in the jig yet. This will be done after filling. Also do not install any o-rings in the jig. They are installed after filling. Close Tank B.
3. Start vacuum pump VP1.
4. When sufficient vacuum has been attained in the cold traps, CT1 and CT2, fill CT1 and CT2 with liquid nitrogen. Open ball valves V5 and V1.
5. *Substep if Tank A is not already filled with silicone oil:* Connect silicone oil reservoir (not shown) to Tank A via V6. FT1 will filter the inlet stream. Open V6 and V2. This will draw the silicone oil into Tank A, and simultaneously outgas the oil. Dissolved gases tend to reduce the effective bulk modulus of the oil, an undesired effect. After Tank A is filled, Close V6 and V2. Disconnect silicone oil reservoir and vent Tank A to atmosphere through V6.
6. Open V3. Evacuate Tank B to  $5mmHg$  or less.
7. *Vapor purging step:* Slowly open V4 and allow a small amount of silicone oil to flow into Tank B. In this case, a fluid level of approximately  $10mm$  was used in Tank B. Close V4.
8. Continue pumping on Tank B for approximately 90 minutes. All of the oil in Tank B should have evaporated, and would have been caught in CT1. Ensure that Tank B is at a pressure of  $5mmHg$  or less.

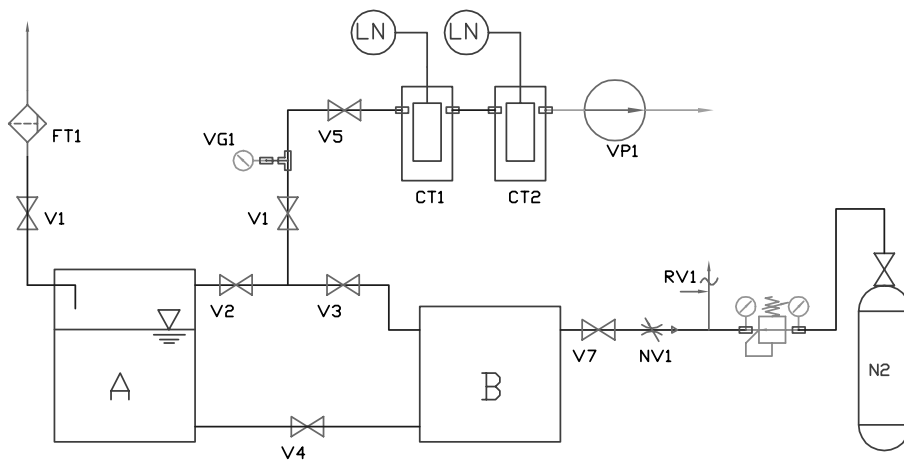


Figure 31: Schematic representation of the filling system

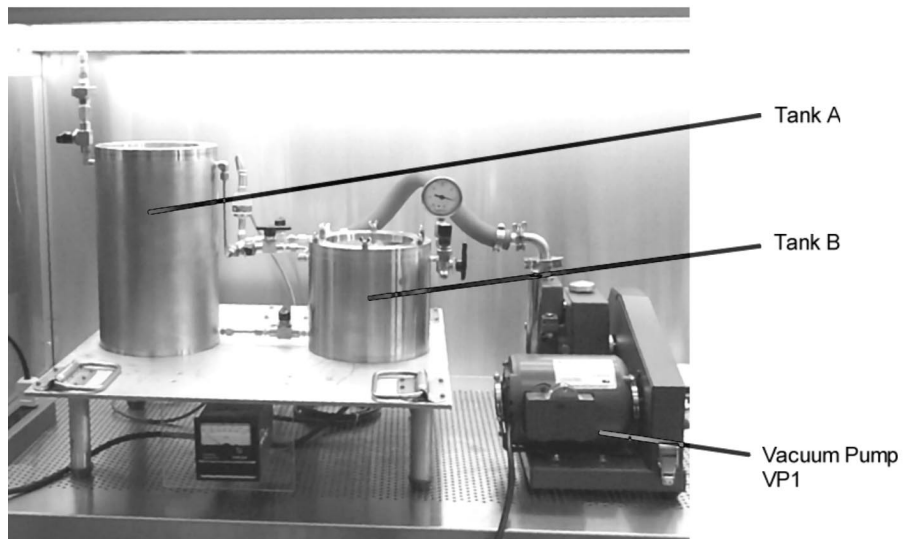


Figure 32: The fluid filling system. The cold traps are not shown in this photograph.



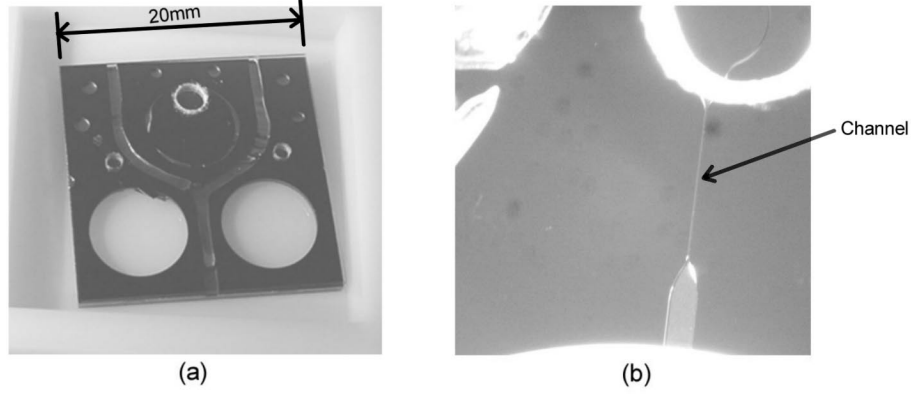


Figure 33: (a) Experimental filling test chip with two  $10\mu\text{m} \times 10\mu\text{m} \times 1\text{mm}$  channels and matching dead volumes. (b) Detail of the filling channel. The dead volume had to be evacuated through this channel prior to filling.

9. *Filling:* Close V3. Slowly open V4 and allow the fluid to submerge the jig and the device. Close V4 when the contents of Tank B are submerged.
10. *Pressurising:* Open V7 and needle valve NV1. Adjust the regulator, APR1, to provide an absolute pressure of  $1.5\text{atm}$ . This will ensure that the pressure in the HAC asymptotes to a slightly higher pressure than atmosphere.
11. Reduce the pressure in Tank B to  $1\text{atm}$  absolute pressure, and open Tank B.
12. With the device and the jig still submerged, insert the o-ring seals into the jig, mount the device and clamp to seal.

**Initial tests** In this work it was necessary to fill a dead volume of approximately  $8.3\mu\text{l}$  through a channel of dimensions  $10\mu\text{m} \times 10\mu\text{m} \times 1\text{mm}$ . The motivation for this channel will be discussed in Section 3.2.3. The nature of the design of the devices prevented any visual inspection of the HAC for bubbles after filling. It was therefore essential to verify the filling procedure described in Section 3.2.2, and to ensure that it was very robust. To this end, a set of experimental devices was fabricated in such a manner that the filling procedure could be seen through a suitable glass window. A device consisting of a glass-silicon-glass sandwich structure was fabricated using DRIE and a simple two step lithography process. A completed filling test chip is shown in Figure 33. Assembly was performed on the die level, using simultaneous anodic bonding of the top and bottom glass layers. In this case, conventional machining, using diamond tools, was used to drill holes in the top glass layer.

Using the procedure as described above, and visually monitoring the filling of each chamber using a microscope, it was verified that bubble-free filling could be obtained. The filling time after initiating the pressurization step was found to be approximately 7 minutes. After this time, no visible bubbles were detected. Two of these devices were assembled, giving a total of four chambers to be filled. Both chips were filled successfully on the first attempts to fill them. These results provided the needed confidence to fill and test the full hydraulic amplification devices.

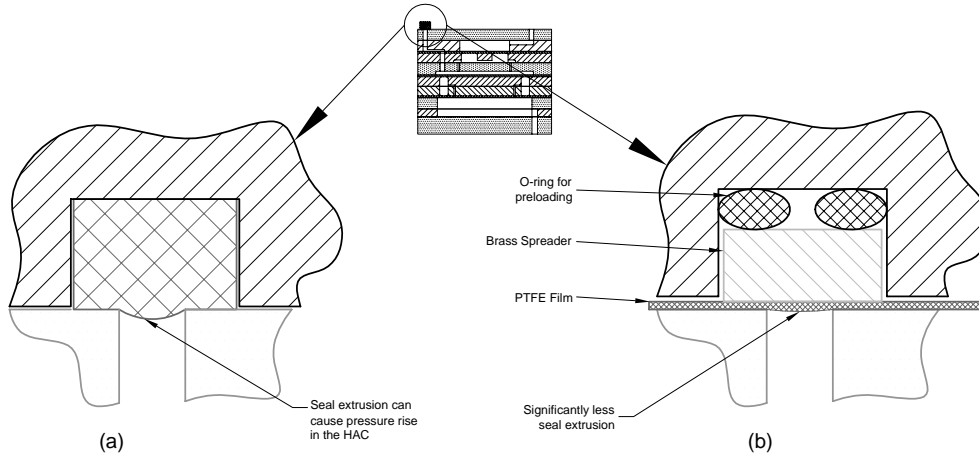


Figure 34: Static sealing of the hydraulic amplifier: a) The basic concept of a elastomeric or plastic seal. Seal compression could introduce large pressure changes in the HAC. b) Using a PTFE film for sealing, with a load spreader and a preloading element.

### 3.2.3 Sealing concepts

Sealing of an hydraulic amplifier can be challenging. One would like to maximize the stiffness of the hydraulic coupler. This also means that any imposed volume change, as might be introduced by a seal pressing against an opening and subsequently bulging could introduce a large pressure increase in the hydraulic amplification chamber. (See Figure 34a ). This led to the development of two sealing strategies for the two different types of tests performed on the hydraulic amplifiers evaluated in this work. The first type is a traditional static seal, as described above, and the second type, for high frequency hydraulic amplifiers, is a dynamic seal relying on a flow restriction.

**Static sealing** For static sealing of the hydraulic amplifiers a seal consisting of a Teflon sheet,  $125\mu\text{m}$  thick, backed by a brass plate and preloaded with an o-ring was used, as illustrated in Figure 34b. This method enabled reliable sealing of the hydraulic amplifiers while giving minimal seal compression and volume change in the HAC, even with a sealing hole diameter in the glass layer of  $800\mu\text{m}$ . Should seal compression be of greater concern, the sealing hole diameter can be further reduced by micromachining the inlet port to the HAC.

**Dynamic sealing** If the hydraulic amplifier is to be operated only at high frequencies, another sealing technique can be used. By providing a suitable flow restriction on the inlet port to the HAC, it can be shown that high frequency pressure fluctuations generated by the large piston inside the HAC will not be transmitted to the outside. This restriction will have the effect of a low pass filter, allowing low frequency pressure variations to enter and leave the HAC. Using this sealing technique, the concerns related to seal compression are eliminated and it becomes easier to control the static pressure in the HAC. These benefits come at the cost of an external pressurization system that must be added to the device. For experimental purposes, this was not a concern. Figure 35 illustrates the basic principle. In addition, the external pressurization system provides the benefit of setting a constant pressure bias in the HAC. This in turn allows for balancing of the steady-state pressure on the small piston, and can also be used to control the static position of the small piston, should an offset be desired as, for example, in the case of a valve [35]. Furthermore, placing a bias pressure on the HAC reduces the likelihood of

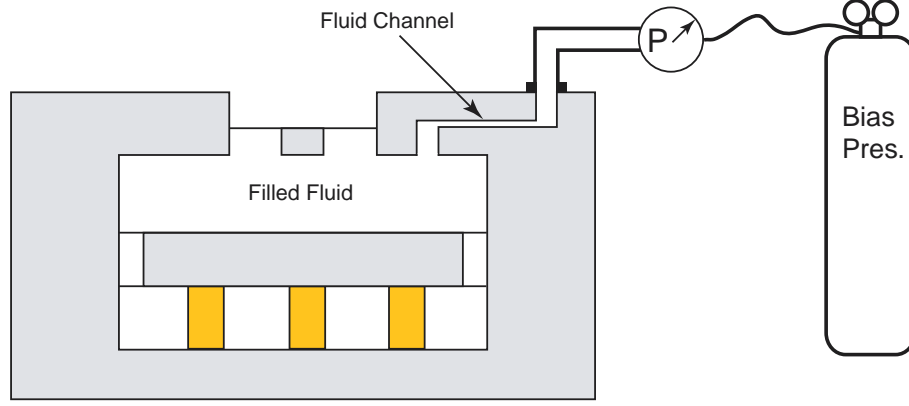


Figure 35: Schematic of the high resistance fluid channel between the HAC and an external bias pressure regulator. This channel was etched into the underside of Layer 7.

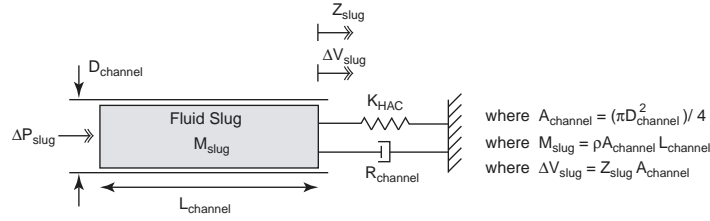


Figure 36: Model of the high resistance fluid channel between the HAC and an external bias pressure regulator. A fluid slug within the channel is modeled. This slug is acted upon by an external stiffness associated with the HAC chamber stiffness. Additionally, the flow resistance of this slug through the channel is modeled using laminar Hagen-Poiseuille flow relations.

cavitation that could be induced by high frequency operation of the large piston.

A simple way to design this type of seal is to assume it to be a channel of suitable dimensions, containing a fluid slug. (See Figure 36.) By selecting the appropriate boundary conditions for the fluid slug in the channel, and by estimating the losses in the channel using Hagen-Poiseuille flow, one can predict the cutoff frequency of such a channel. As discussed in [35], such a channel was designed using the following equation of motion, as given by Roberts, as a starting point:

$$\left( \frac{M_{slug}}{A_{channel}^2} \right) \Delta \ddot{V}_{slug} + R_{channel} \Delta \dot{V}_{slug} + K_{HAC} \Delta V_{slug} = \Delta P_{slug} \quad (15)$$

A channel of dimensions  $10\mu m \times 10\mu m \times 1mm$  was designed. Letting  $L_{channel} = 1mm$ ,  $D_{channel} = 11.3\mu m$ ,  $K_{HAC} = 1.0e^{17} Pa/m^3$ ,  $\rho_{fluid} = 760kg/m^3$ , and  $\mu_{fluid} = 6.5e^{-4} kg/(ms)$  gives a frequency of  $48Hz$  for which  $\Delta V_{slug}$  is 1% of the large piston volume change. For a further treatment of this subject, the reader is referred to [35].

Test results, as shown in Figure 37 clearly indicate the effectiveness of this channel. A lower cutoff frequency of approximately  $0.1Hz$  was observed. This frequency is even less than the design cutoff frequency. It is also significantly less than the design frequency for the hydraulic amplifier, of between 1 and  $15kHz$ . This ensures that the full pressure swing created by the piezoelectric actuators acting on the large piston is transferred to the smaller piston.

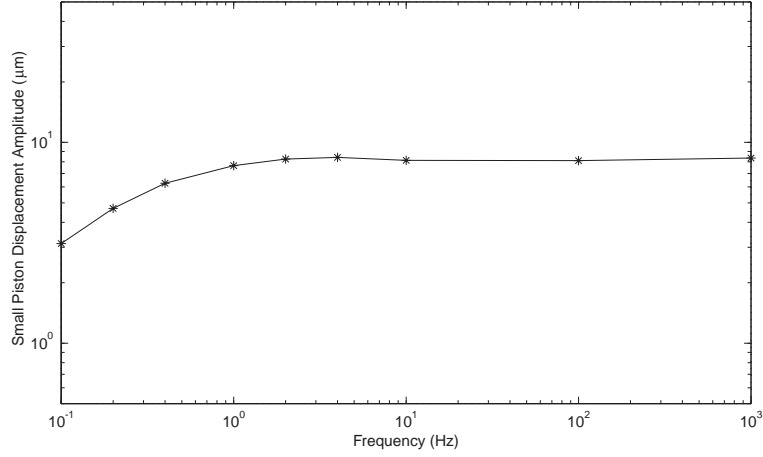


Figure 37: Experimental results of tests performed on a flow restriction-type dynamic seal. This test was performed by applying a sinusoidal excitation of  $200V_{p-p}$  to the piezoelectric element of the large piston, and measuring the displacement of the small piston for the frequencies shown. Note the good quasi-static performance down to 1Hz.

### 3.2.4 Accomplishments

The accomplishments in terms of filling and sealing of hydraulic amplifiers can be summarized as follows:

- Successful filling of micromachined dead volumes of approximately  $10\mu l$  in volume
- Successful static sealing of such volumes with minimal seal extrusion.
- Successful dynamic sealing of such volumes.

### 3.3 Piezoelectric Material Properties

#### 3.3.1 Objective

Although the system-level simulations contain the assumption that the material properties are independent of stress and frequency, this linearity may not be true in practice. Therefore, it is of interest to obtain experimental data of material constants as a function of stress and frequency. Especially with respect to stress, it is a major concern that the high compression parallel to the piezoelectric polarization direction may depolarize the materials [41].

This section will fully investigate the rate and stress effects. The common commercial piezoceramic PZT-5H <sup>3</sup> was selected for test because its moderate piezoelectric constant, stiffness, availability and low cost. Other modern engineered materials such as single crystal PZN-PT <sup>4</sup> and PMN-PT <sup>5</sup> were also evaluated because of their high piezoelectric constants and promise of high performance. PZN-PT was also the material of choice for the energy harvester.

#### 3.3.2 Characterization of Generalized Material Constants

To characterize the behavior of piezoelectric materials at different levels of compressive stress and frequency, a generalized material constant is first defined as the linear slope of material response with respect to the stress at different amplitudes and frequencies of the input stress. These generalized material constants include piezoelectric coupling constants  $d_{33}$  and  $g_{33}$ , and compliance  $s_{33}^E$  and  $s_{33}^D$ , which are required inputs of the simulation model. The  $d_{33}$  constant can determine how much current can be drawn from the specimen at short circuit condition. The  $g_{33}$  constant can determine how much potential can be generated on the specimen at open circuit condition. The stiffness can determine how much displacement the specimen deforms to and how much power is delivered into the specimen for a given input force.

Figure 38 shows the data of  $s_{33}^E$ ,  $s_{33}^D$ ,  $d_{33}$  and  $g_{33}$  as a function of stress at 10 Hz and 400 Hz for PZT-5H, PZN-PT and PMN-PT. As can be seen, the material properties is a strong function of the driving stress but, as expected, only a weak function of the driving frequency. Each data set can be fitted using a polynomial function of compressive stress  $T$  in MPa:

$$d_{33}^{PZT5H} = 679.186002848395 + 11.035909394745T - 0.284348262482T^2 \quad (16)$$

$$d_{33}^{PMNPT} = 958.755747212946 + 17.235290861948T - 0.720369973552T^2 \quad (17)$$

$$d_{33}^{PZNPT} = 1576.85195818796 + 47.839603507060T - 1.819780741040T^2 \quad (18)$$

$$g_{33}^{PZT5H} = 0.02019638833093 + 0.00012746071745T - 0.00004193544098T^2 + 0.00000232408964T^3 - 0.00000005774398T^4 + 0.00000000053195T^5 \quad (19)$$

$$g_{33}^{PMNPT} = 0.02701591972747 + 0.00051050517351T - 0.00010711068484T^2 + 0.00000316972139T^3 - 0.00000002843305T^4 \quad (20)$$

$$g_{33}^{PZNPT} = 0.036175902695820.00071800517313T - 0.00019501199244T^2 + 0.00000674820968T^3 - 0.00000007130516T^4 \quad (21)$$

$$s_{33}^{E PZT5H} = 23.75337763095130 + 0.11773640699360T - 0.00526783476887T^2 \quad (22)$$

---

<sup>3</sup>6.35mm cube supplied by Staveley Sensors in E. Hartford, CT.

<sup>4</sup>PZN-4.5%PT, 5.5mm cube, supplied by TRS Ceramics, Inc., State College, PA.

<sup>5</sup>6mm × 6mm × 4mm supplied by Crystal Associates Inc., East Hanover, NJ.

$$s_{33}^{E^{PMNPT}} = 39.28579064087646 + 0.70661572652481T - 0.00809493733445T^2 \quad (23)$$

$$s_{33}^{E^{PZNPT}} = 78.07645545991812 + 0.71686410336253T - 0.00661863533739T^2 \quad (24)$$

$$s_{33}^{D^{PZT5H}} = 10.27658431341368 - 0.03504827381062T + 0.00128025014264T^2 \quad (25)$$

$$s_{33}^{D^{PMNPT}} = 15.52573085816073 + 0.59993999592106T + 0.01433878548882T^2 \quad (26)$$

$$s_{33}^{D^{PZNPT}} = 15.79245215972361 + 0.10766785303148T - 0.15070056364832T^2 + 0.04032822016655T^3 - 0.00179313481186T^4 + 0.00002361991079T^5 \quad (27)$$

The variation in properties for the single crystal data at different frequencies might be due to the variation of different samples. A slight misalignment of the cutting of a single crystal specimen may result in a large variation in material properties, while the cutting has no major effect on a polycrystalline PZT-5H specimen. Amongst the four constants,  $g_{33}$  decreases most rapidly as the compression is increased. This also results in the sharp degeneration of the coupling coefficient  $k_{33}$  shown in Figure 39 and defined as:

$$k_{33}^2 = \frac{d_{33}g_{33}}{s_{33}^E} \quad (28)$$

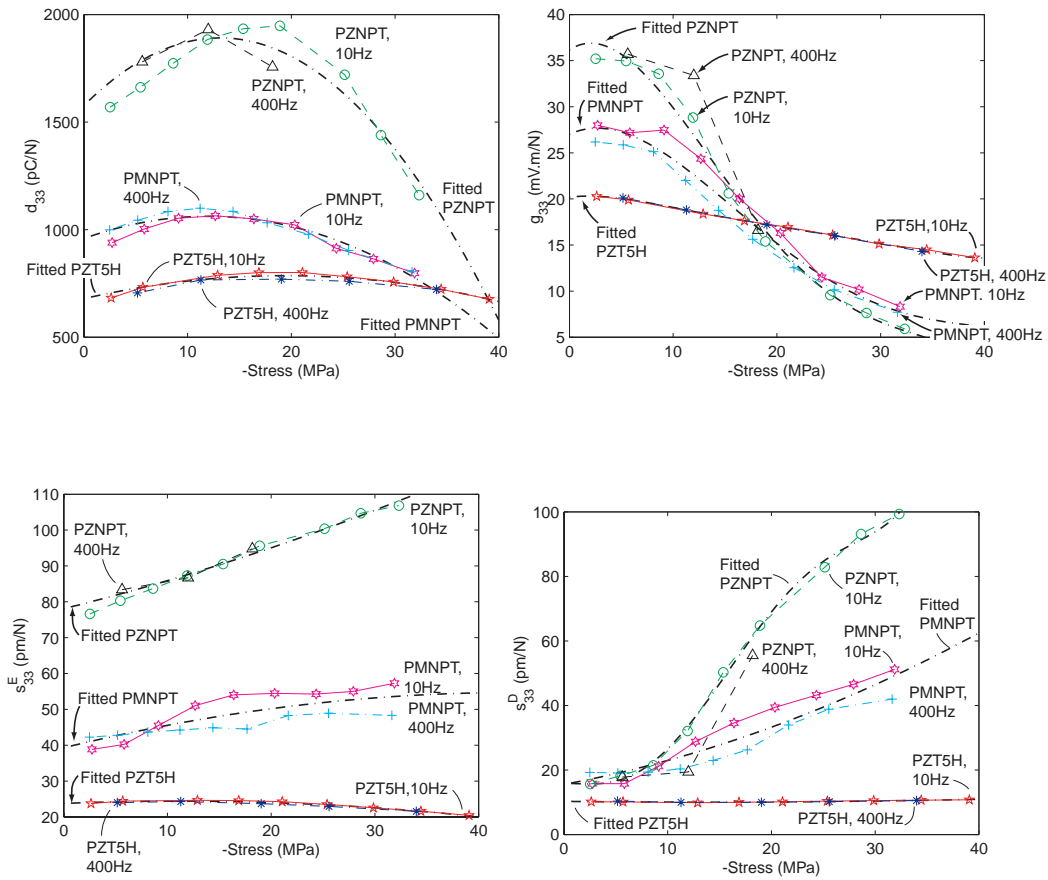


Figure 38: Generalized material constants  $d_{33}$ ,  $g_{33}$ ,  $s_{33}^E$  and  $s_{33}^D$  as a function of stress at 10Hz and 400 Hz for PZT-5H, PZN-PT and PMN-PT.

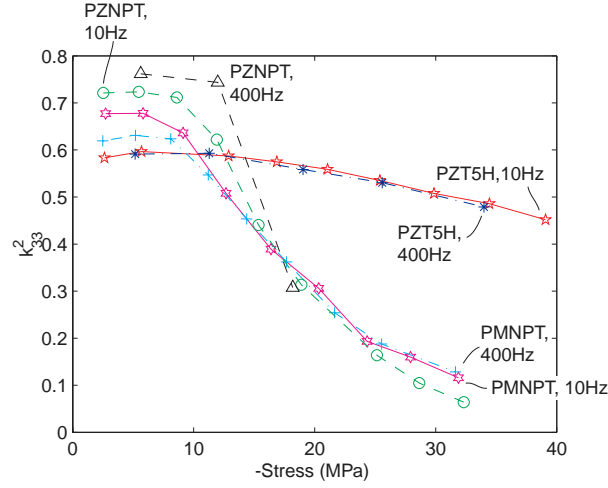


Figure 39:  $k_{33}$

### 3.3.3 Characterization of Material Energy Density

Tests were also performed to characterize the material energy density. In these particular tests, the piezoelectric material was subjected to a sinusoidally varying load and the response was rectified using a diode bridge. The power produced was delivered to a voltage source (representing a battery) at an optimum voltage for an impedance matched condition. Figure 40 shows the maximum energy density of different materials as a function of compressive stress using rectifying circuitry. The dashed lines are obtained assuming the materials are linear; however, the experiment shows that the materials degenerate at higher stress.

### 3.3.4 Accomplishments

In this work, the material properties for application to the MHT device were tested and show a significant dependence on applied stress but not a significant dependence on frequency. These material properties can be presented as generalized material constants as a function of stress, as shown in Figure 38. For PZT-5H, the material starts to depole when the compression is higher than 22MPa, while the material starts to degenerate at stress higher than 11Mpa for PZN-PT, and 15MPa for PMN-PT. Among others, PZN-PT at low stress has the largest energy density. However, at higher stress levels, the results indicate that ceramic piezoelectric materials such as PZT-5H may be a better alternative, as also shown in Figure 40. For a low-pressure, underwater acoustic noise generation application, PZN-PT is a good choice.

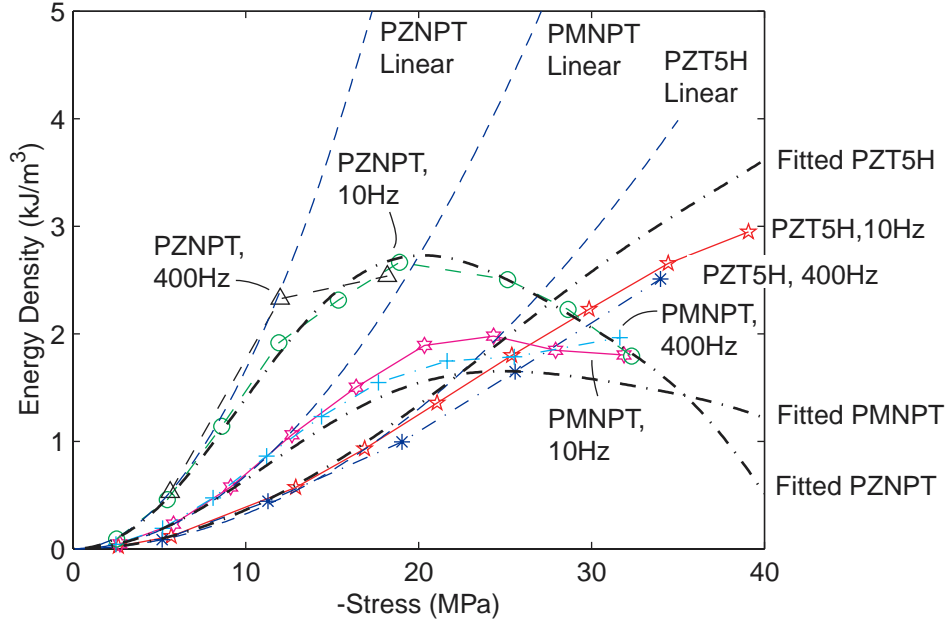


Figure 40: Maximum energy density using rectifying circuitry. The curves labeled as "Fitted" are obtained using generalized material constants described in Eq. 16, 17, 18, 19, 20 and 21. The curve labeled as "Linear" are obtained assuming constant material coefficients  $d_{33}$  and  $g_{33}$  at zero stress



## 3.4 Identification of SOI Membrane Stress Limits

### 3.4.1 Objectives

The drive elements and valves in the MHT device rely on thin single crystal silicon membranes. The membranes are fabricated by patterning the backside of a silicon-on-insulator (SOI) wafer and deep reactive ion etching (DRIE) to the buried oxide which acts as an etch stop. Maximizing the strength of the membranes is critical for device operation, thus a systematic study was performed to measure the strength of membranes fabricated using this technique. The primary objectives of this study was to understand the resulting etched geometry and to measure the fracture strength of such structures. Understanding the geometry and knowing the fracture strength are essential in designing MHT devices.

### 3.4.2 Accomplishments

The test structure employed mirrored the actual pistons in the MHT device. Figure 41 is a scanning electron microscope (SEM) micrograph of a test specimen that has been cross-sectioned. The specimen consists of an etched circular trench that forms a central boss supported by a thin tether membrane. A test system that applies a controlled displacement at the center of the central boss and measures load was constructed. Specimens were loaded until failure and the load measured. Through SEM examination of the etched features, the geometry of the fillet was determined so that it could be accurately modelled in finite element analyses of the test specimen and the device. Figure 42 is a SEM micrograph of the fillet at the base of the etched trench and demonstrates that the fillet has an elliptical shape.

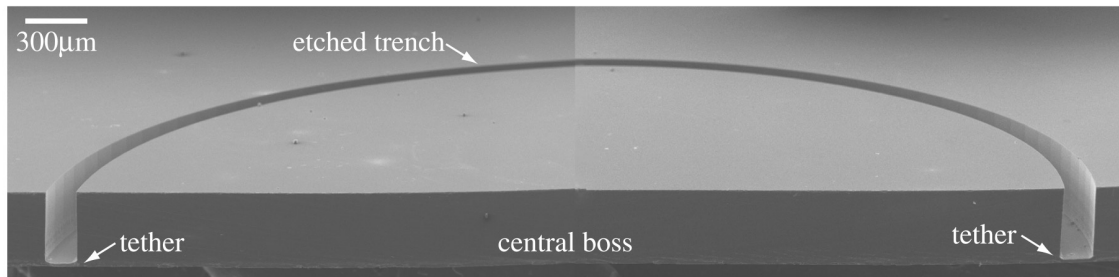


Figure 41: A SEM micrograph showing the fracture test specimen employed in this work.

A total of 129 specimens were fabricated and tested according to the above procedure. SOI wafers from two manufacturers, Motorola and BCO Technologies (now Analog Devices), were used in the tests. In addition, the study sought to address whether the oxide layer at the base the etched trench should be removed. Thus, there are four groups of specimens that were fabricated and tested. Details about the groups and the measured fracture strengths are listed in Table 3. The scatter in the strength results listed is result of variability in the fabrication process.

From the results listed in Table 3 two clear trends are observed. First, it is clear that removal of the oxide at the base of the trench reduces the fracture strength of the membranes by approximately 0.3 GPa. The other fact that is observed is that membranes fabricated from BCO SOI wafers are significantly stronger than the Motorola SOI wafers employed. This data and these trends provided critical information that guided the fabrication of actual MHT devices. Namely it lead to the use of all BCO SOI wafers for critical membrane elements and second it provided design stress guidelines. Further information about this work is provided in reference [29].

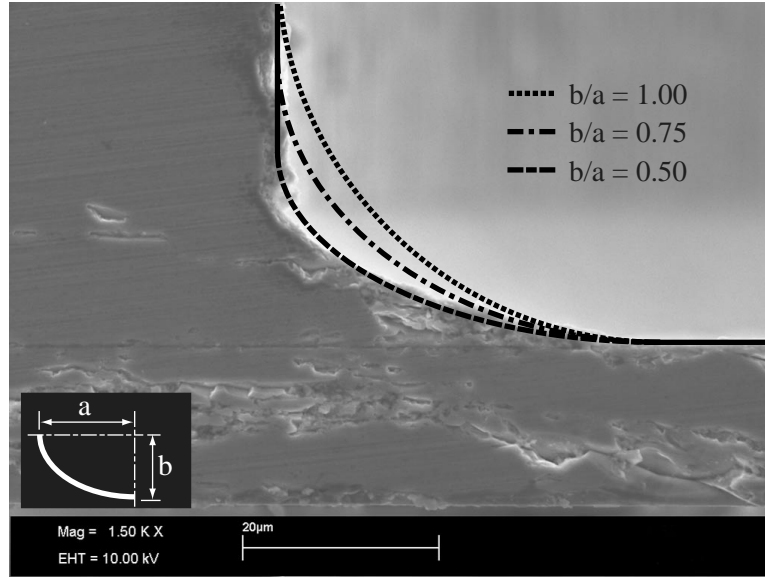


Figure 42: Typical shape of etched fillet.

Table 3: Fracture strength values.

Group	Manufacturer	Buried oxide present?	Mean (GPa)	C.V.	Number of Specimens
I	BCO	present	1.67	0.27	10
II	Motorola	present	0.77	0.22	12
III	BCO	removed	1.30	0.37	19
IV	Motorola	removed	0.48	0.26	88

### 3.5 Contributions: Supporting Experimental Investigations

A number of experimental studies were conducted to assist in the design of the MHT device. The contributions made with these studies are:

1. Empirical models for flow losses through microfabricated poppet-type valves were obtained. These results were found to correlate very well with eventual flow testing of the MHT valve units.
2. A technique was developed for the bubble-free filling of the Hydraulic Amplification Chambers (HAC's) of the MHT device. This technique proved to be robust and all devices tested were properly filled.
3. A static sealing option was introduced for the HAC, and used in the static hydraulic amplification tests.
4. A dynamic sealing technique was also introduced, which enabled pressure balancing of the active valve structures. This sealing technique proved to be very reliable for bench top testing.
5. A detailed characterization was performed on the energy harvesting capabilities of various piezo-electric materials, for use in the MHT device. For the final device, the chosen material was single crystal PZN-PT.
6. The strength of silicon membrane tethered structures was determined through extensive test specimen preparation and testing. A design value of  $1GPa$  was determined as a result of these tests. In addition, the tests also reconfirmed that a good fillet feature is essential to producing a strong membrane.



## 4 Device Fabrication and Assembly

### 4.1 Fabrication and Assembly Procedures for the MHT Device

#### 4.1.1 Overview

The full MHT system is fabricated using a combination of microscale (silicon patterning and etching) and macroscale (piezoelectric material integration) procedures. The chip-level MHT device consists of multiple layers of silicon and glass (Pyrex 7740) with integrated piezoelectric elements, all bonded together to form the important structural features of the device. These features are the tethered-piston piezoelectric drive element, the enclosed hydraulic amplification chamber, the valve membrane and orifice structure, and the fluid channels connecting the inlet and outlet valves to the central pump chamber.

A cross-section of a full MHT system, with an embedded pump chamber and two multi-layered active valves, is shown in Figure 43. Layers 1, 3, 6, and 9 of the device are each borosilicate glass (Pyrex 7740), the features of which are formed through wafer-level ultrasonic machining. Layers 2 and 8 are formed from standard silicon wafers and are etched using deep-reactive ion etching procedures. Layers 4, 5, and 7 are created from silicon-on-insulator (SOI) wafers. The drive element tethers supporting the piston structures in Layers 4 and 5 and the valve membrane and cap structures in Layer 7 are produced using deep-reactive etching, with the buried oxide acting as an etch stop for precise control of tether and membrane thicknesses. The three primary bonding mechanisms used to realize the device are silicon-silicon fusion bonding, silicon-glass anodic bonding, and silicon-piezoelectric material eutectic bonding.

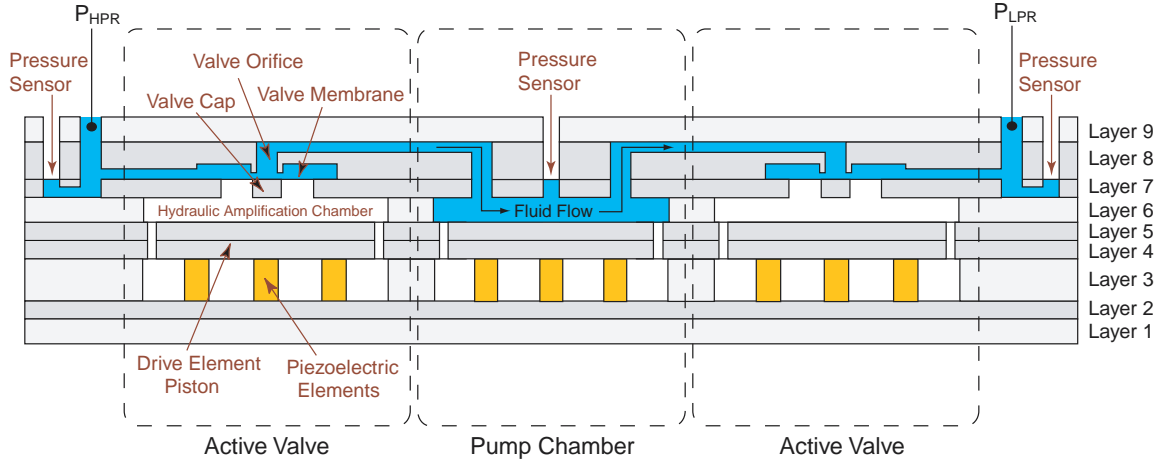


Figure 43: Cross-section schematic of a nine-layer multiple wafer MHT system with two embedded active valve structures. Realization of this system requires robust bonding of silicon-to-silicon and silicon-to-glass at the wafer-level and integration and bonding of piezoelectric material elements with silicon at the die-level.

#### 4.1.2 Challenges and Procedures

The critical challenges associated with the fabrication and assembly of this multi-layer MHT device were: (1) etching of the high-aspect ratio features in the silicon-on-insulator wafers to form the tethered drive element piston and valve membrane structures, (2) wafer-level silicon-silicon fusion bonding and wafer-

level silicon-glass anodic bonding, (3) preparation, integration, and bonding of the bulk piezoelectric material elements within the drive element structure and (4) die-level assembly and bonding of the silicon and glass layers. The procedures developed to overcome these challenges are detailed in the following sections.

**Etching of the Tethered Drive Elements and Valve Membranes** The drive element tethers and valve membranes within the pump chamber and active valves are designed to be quite thin (on the order of  $7 - 10\mu m$ ). To achieve precise dimensional control of these features, SOI wafers containing a buried oxide layer a preset distance from one side of the wafer were used. In performing deep etches into the silicon wafer down to the buried oxide layer, it was critical that the surface roughness of the etch and the tailoring of fillet radii profiles at the base of the etched profiles be well-controlled so as to maintain strength and robustness of the thin-membrane structures. Figure 44 illustrates etch profiles at the SOI interface of a typical drive element piston that can result, depending on the process chosen and care given to performing the etch. Ideally, one would like to create a fillet radius between the thin tether and the much thicker ( $\sim 400\mu m$ ) central piston structure to minimize stress concentrations, as shown in Figure 44(c). It is essential to avoid etch profiles such as the sharp corner shown in Figure 44(b) and the “footing” or “notching” profile shown in Figure 44(d). These serve to magnify stresses at these interface regions, thereby compromising the overall strength of the structure.

Considerable research work has been done in developing and optimizing deep etching processes for single-crystal silicon materials [23] [24]. The Deep-Reactive Ion Etching (DRIE) process used to create the MHT device is known as the Bosch Process [23]. This method involves repetitive cycles of plasma etching and passivation to create high aspect ratio deep trenches in silicon. Using photoresist as a masking agent, a timed plasma etch using  $SF_6$  is carried out. Following this timed etch, a passivating film using  $C_4F_8$  is deposited over all exposed surfaces of the wafer, including the etched trench bottom and sidewalls. During the next timed plasma etch, this passivating film is preferentially removed from the bottom of the trenches through ion bombardment, while the film on the sidewalls remains intact. This cyclic process is repeated until the buried-oxide etch stop layer is reached. At this juncture, carefully monitoring of the etch process is performed to ensure that fillet radii of a desired size (based on modeling specifications) are created. Figures 44(e)-(g) show SEM images of a successfully etched drive element piston structure with properly tailored fillet radii.

This final “fillet tailoring” step is a difficult one because once the silicon has been etched away such that portions of the oxide are visible, very little time is required for lateral etching of the remaining silicon above the oxide layer to be completely etched away, resulting in potential “footing” profiles at the interface. The rapid lateral etching has been studied and investigated by numerous individuals, and it is believed to result from plasma charging effects at the silicon/oxide interface [25] [26] [27]. Consistently controlling these fillet profiles is extremely hard to achieve, as etch parameters such as etch time, passivation time,  $SF_6$  flow rate, electrode power during etching, electrode power during passivation, and  $C_4F_8$  flow rate must be tuned and optimized. Procedures were developed within this program to adequately control fillet radius profiles within the membrane structures of the MHT device.

**Wafer-Level Bonding** For the multi-layer active valve structure presented in this thesis, various silicon-silicon and silicon-glass wafer-level bonds were performed. A silicon-silicon wafer-level fusion bonding process was used to bond Layers 4 and 5 together to form Stack 4-5 and Layers 7 and 8 together to form Stack 7-8. A silicon-glass wafer-level anodic bonding process was used to bond Layers 1 and 2 together to form Stack 1-2, Stack 4-5 and Layer 6 together to form Stack 4-5-6, and Stack 7-8 and Layer 9 together to form Stack 7-8-9. Following these wafer-level bonding steps, the stacks were die-sawed into individual dies and cleaned in preparation for die-level bonding and piezoelectric material integration. Figure 45 illustrates the various wafer-level silicon-silicon and silicon-glass bonding steps.

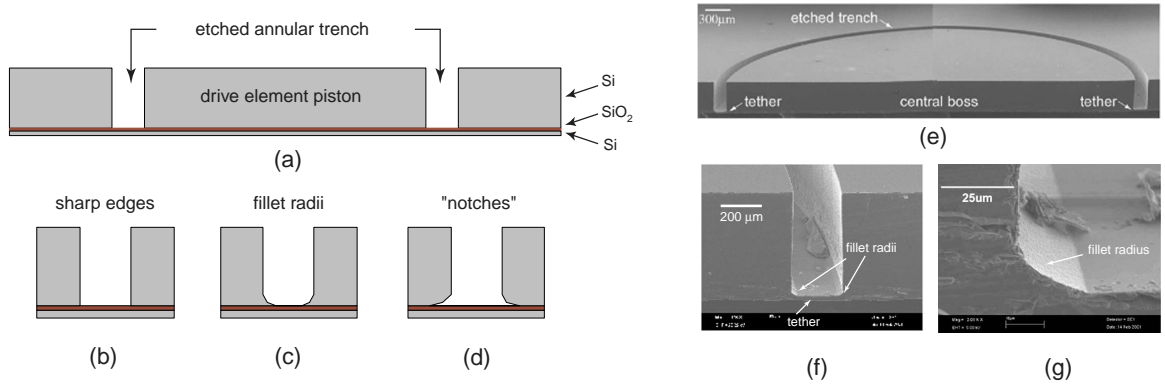


Figure 44: Etching of a typical drive element piston structure: (a) cross-section view of drive piston, (b) sharp corner etch features, (c) fillet radius features, and (d) “notching” or “footing” features, (e) SEM cross-section view of SOI piston structure, (f) SEM close-up of etched trench, and (g) further SEM close-up of fillet radius feature. In this structure, a 20 – 25 $\mu\text{m}$  fillet radius was achieved. Debris in background was generated during die-saw procedures.

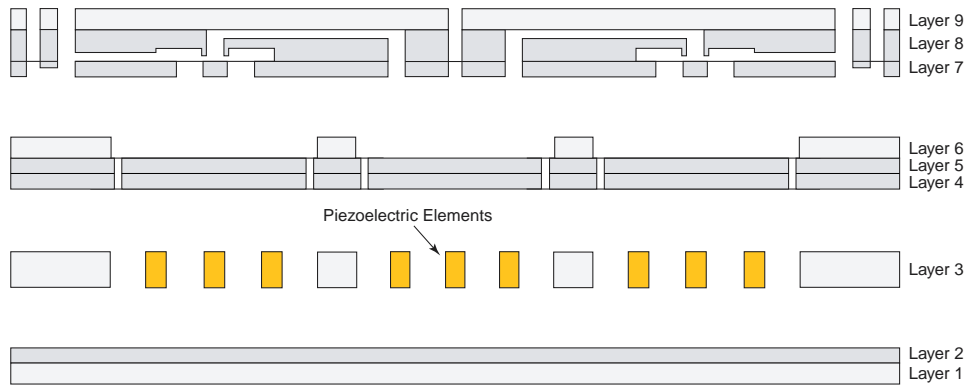


Figure 45: Wafer-level silicon-silicon fusion and silicon-glass anodic bonding steps are carried out prior to piezoelectric material integration.

The silicon-silicon fusion bonding process used to create wafer-level stacks for the active valve device is a well developed process and consists of three primary steps [28]: (1) preparation and treatment of the silicon wafer surface to produce a hydrophilic surface, (2) alignment and adhesion of two wafers together (weak van der Waals or hydrogen bonds maintain wafer-wafer adhesion) in a clean room-temperature environment, either in air, inert atmosphere, or vacuum, and (3) high temperature annealing of the wafer stack at 1000°C to promote strong covalent bonding. The strength of this fusion bond is dependent on the annealing temperature and time [29]. Paramount in the bonding process is the cleanliness of the silicon wafers prior to bonding and of the alignment and bonding apparatus itself. Particulate matter present between the silicon wafers during adhesion can result in significant defect regions characterized by little or no bonding.

The silicon-glass anodic bonding process used to create wafer-level stacks also is a well-developed process. This process involves three primary steps: (1) preparation and cleaning of the silicon and glass surfaces using a piranha soak and an oxygen ashing step, (2) alignment and clamping of the two wafers

together, and (3) application of a voltage (1000V) across the wafer interface at elevated temperature (300°). The negative electrode is applied to glass wafer surface not being bonded with the silicon wafer held at ground potential. As for the fusion bonding process, cleanliness of the wafers and the bonding apparatus is paramount for achieving high-quality and low-defect wafer-level bonds.

**Integration of the Bulk Piezoelectric Elements** Integration of the piezoelectric elements within the device constitutes a critical task in the assembly of the active valve device. The top and bottom surfaces of the piezoelectric elements are covered with a thin-film gold-tin (Au-Sn) eutectic alloy for bonding to the adjoining silicon layers at an elevated temperature. In order to achieve good bonding over the complete interface area, the piezoelectric material must possess smooth top and bottom surfaces. A rough surface of the piezoelectric material (and therefore of the metallized layer), would result in only pinpoint contacts between the piezoelectric material and the silicon and therefore a weak bond. Prior to bonding, sizing of the piezoelectric elements with respect to the surrounding Layer 3 glass and etching of seats in the Layer 2 silicon to compensate for thickness mismatch between the piezoelectric material and glass is critical for ensuring a deflection of the drive element piston below levels of fracture stress in the tethers. Each of these piezoelectric material integration issues is covered in detail in the following sections.

**Piezoelectric Material Preparation** Virgin piezoelectric materials are obtained from vendors in the form of thin plates, each with a thickness of  $\sim 1.1\text{mm}$  and diameter between 1 cm and 5 cm. As received, these plates possess a surface roughness as large as  $5\mu\text{m}$ . In order to achieve adequate eutectic bonding during device assembly, a surface roughness near  $0.5\mu\text{m}$  is required prior to metallization. To achieve this, the piezoelectric material plates are polished using coarse and fine grain diamond slurry polishing procedures. During polishing, each plate is sized to yield a thickness of  $1\text{mm} \pm 10\mu\text{m}$  with thickness variation across the plate of  $\sim 2\mu\text{m}$ . Prior to metallization, the material plates are solvent cleaned with a series of acetone, methanol, and isopropanol steps. Additionally, a further cleaning soak in a 20:1 water:nitric acid solution is carried out for 1 minute to remove particulate matter. At this point, the piezoelectric material plates are ready for metallization.

**AuSn Eutectic Bonding** To bond mechanically and to connect electrically the piezoelectric material cylinders to the adjoining silicon layers in the active valve device, a reliable bonding mechanism must be employed. This bonding mechanism must allow for tight dimensional control over the bond layer thickness and allow for a bonding temperature and environment that is compatible with the rest of the die-level assembly process. Numerous bonding methods that could potentially work in this device, ranging from polyimides and epoxies to brazing and soldering to gold-based eutectic alloys, have been presented in the literature. A detailed discussion of these research efforts, with application toward the development of MHT technology, is found in [29]. The resulting conclusion of initial work by Mlcak [30] and the subsequent work by Turner [29] was to employ a thin-film AuSn eutectic alloy (composition: 80 wt. % Au and 20 wt. % Sn) as the bonding mechanism within MHT devices.

A four layer film structure on the piezoelectric material and a three layer film structure on each of the adjoining silicon layers is deposited in preparation for bonding, as shown in Figure 46(a). The four layer structure on the piezoelectric material consists of 50 nm Ti, 250 nm Pt, 4000 nm AuSn, and 50 nm Au. The Ti serves as an adhesion layer, the Pt as a diffusion barrier, and the final Au as a capping layer to prevent oxidation of Sn in the AuSn alloy. The AuSn layer, chosen to be thick enough ( $4\mu\text{m}$ ) to compensate for the piezoelectric material surface roughness ( $\sim 0.5\mu\text{m}$ ), is sputtered from an alloy target with 80 wt. % Au and 20 wt. % Sn composition. Sputtering is chosen over evaporation because sputtering allows the stoichiometry of the target to be maintained in the deposited film [31]. The three



layer Ti-Pt-Au structure on each of the adjoining silicon pieces enables the eutectic alloy to wet the silicon and is deposited on the die-level using e-beam evaporation procedures.

**Dicing/Core-Drilling of Piezoelectric Elements** Following deposition of the eutectic alloy, the metallized piezoelectric material plates are core-drilled or diced to produce either cylindrical or square piezoelectric elements. As detailed in subsequent chapters of this thesis, devices integrating both cylindrical and square elements have been successfully fabricated and tested. The advantage of using square piezoelectric elements over cylindrical ones is that the process of dicing a piezoelectric material plate in a grid pattern results in the production of 2-3 times the number of elements than can be produced from core-drilling from a identical size plate. By sheer numbers and by the fact that closely located elements will possess almost identical thicknesses (relatively insensitive to variations in thickness across the material plates), the use of square elements increases the odds of being able to select multiple elements of identical thickness to insert into drive element structures. Once the material plate has been either core-drilled or diced, the resulting piezoelectric elements are individually measured for thickness using a hand-held precision micrometer. By calibrating the micrometer before each measurement with a precise thickness gauge block ( $1\text{mm} \pm 0.01 \mu\text{m}$ ) and averaging repeated series of measurements of the same elements, these thickness measurements are estimated to be accurate within  $\sim 0.5\mu\text{m}$ . The elements are then organized and sorted according to the thickness.

**Etching of the Piezoelectric Element Seats** One of the critical issues during integration of the piezoelectric material elements is guaranteeing an upward deflection of the drive element piston large enough to ensure a preload on the eutectic alloy interface during bonding, yet small enough to ensure stresses in the piston tethers below the critical value of 1 GPa. Typically, in the drive element structures designed, fabricated, and tested in this thesis, the piston tethers will reach a tensile stress of 1 GPa for displacements near  $\sim 9\mu\text{m}$ . Therefore, at any time during the bonding, poling, and operation of a device, it is desired to maintain piston displacements no greater than a safe value of  $\sim 6\mu\text{m}$ . In terms of preload on the eutectic interface, it is desired to ensure a “piston push-up” of  $\sim 2\mu\text{m}$ . These requirements therefore dictate that at the instant of eutectic bonding, the piezoelectric element(s) beneath the drive element piston must be forcing the piston upward by  $\sim 2\mu\text{m}$  and that for all time after that the piston must not be forced to displacements greater than  $\sim 6\mu\text{m}$ . Considering that this  $4\mu\text{m}$  range is 0.4% of the total piezoelectric element thickness, this task represents quite a challenge.

In preparation for piezoelectric element integration, the Layer 3 glass wafer was diced into individual dies, and each of these dies was measured using the micrometer. As received from the vendor, each of the ultrasonically-machined Layer 3 glass wafers possesses a thickness between  $967 \mu\text{m}$  and  $974 \mu\text{m}$ , with thickness variation across a given wafer less than  $1\mu\text{m}$ . At the time of integration, since the piezoelectric elements (with deposited eutectic alloy films) have thicknesses near  $1000 \mu\text{m}$  and the Layer 3 glass dies have thickness near  $970 \mu\text{m}$ , it is necessary to have the capability to remove this thickness difference of  $\sim 30\mu\text{m}$  between the piezoelectric material and the surrounding glass. Ideally, once integrated into the device, the piezoelectric elements’ top surfaces should be slightly above level with the Layer 3 glass top surface so as to produce predictable upward displacement of the drive element piston from its equilibrium position (“push-up”).

This thickness matching is achieved by plasma etching shallow seats for all of the piezoelectric elements in the Layer 2 bottom silicon wafer, as shown in Figure 46(b). An iterative process of carefully timed etches followed by depth measurements using a scanning profilometer can result in etch depth control to within  $\sim 0.5\mu\text{m}$ . With this capability to compensate for thickness mismatch between the piezoelectric elements and the surrounding Layer 3 glass, proper “push-up” of the drive element piston can be achieved during assembly and bonding. On the die-level, each Layer 2 silicon die is matched with a pre-measured ( $t_{\text{piezo}}$ ) grouping of one or three piezoelectric elements (depending on whether a single

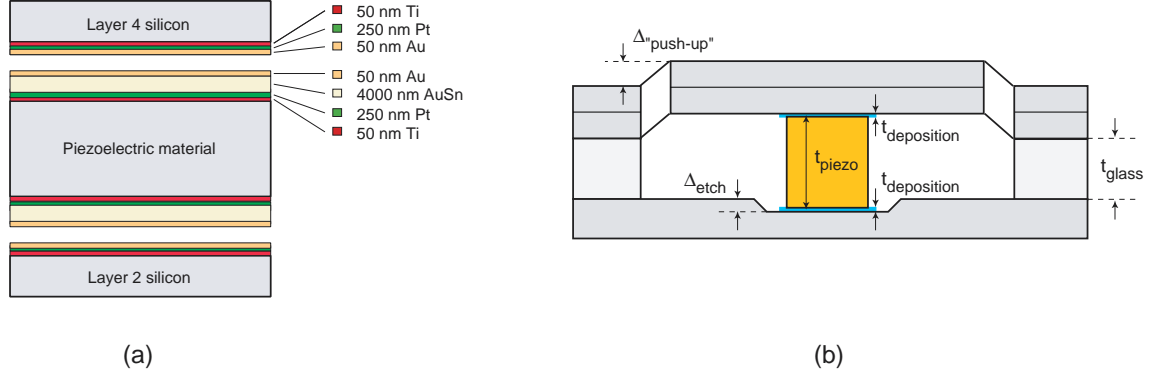


Figure 46: Piezoelectric integration within the drive element structure: (a) eutectic alloy deposition on the piezoelectric material and adjoining silicon layers. The piezoelectric material contains a 4 layer film structure and each of the silicon layers contains a 3 layer film structure, and (b) Tolerancing of the piezoelectric element within the structure by plasma etching shallow seats in the Layer 2 bottom silicon die. Precise control of the etch depth was necessary to achieve the desired “push-up” of the drive element piston.

or multiple piezoelectric valve is being fabricated) and with a pre-measured ( $t_{glass}$ ) Layer 3 glass die. With knowledge of the three-layer film thickness  $t_{deposition}$  that will subsequently be deposited on the underside of the drive element piston in Layer 4 and on the top surface of the “to be etched” seats in Layer 2, and with the value of  $\Delta_{push-up}$  desired after device assembly, the required etch depth ( $\Delta_{etch}$ ) in Layer 2 is determined, according to Equation 29.

$$\Delta_{etch} = t_{piezo} + 2t_{deposition} - t_{glass} - \Delta_{push-up} \quad (29)$$

Following etching of the seats, the Layer 1-2 silicon dies were cleaned and combined with Stack 4-5-6 silicon dies for deposition of the three-layer Ti-Pt-Au film structure required for eutectic bonding. This deposition was performed using e-beam evaporation through specially-machined shadow masks to allow for selective coating of the dies. For the Stack 4-5-6 dies, the underside of the drive element piston was coated, and for Layer 2 dies the inside of each of the etch seats was coated.

## Die-Level Assembly and Bonding

**Assembly and Bonding Procedure** The final assembly of the MHT device was performed at the die-level. As shown in Figure 47(a), which illustrates the procedures through the building of one of the active valves, wafer-level etching and bonding procedures, followed by dicing of the stacks into individual dies result in the creation of a Stack 7-8-9 die, a Stack 4-5-6 die, a Stack 1-2 die, and a Layer 3 die. Additionally, piezoelectric material preparations create individual piezoelectric elements ready for insertion. It was desirable to perform these bonding steps at the die-level, rather than the wafer-level, so as to allow for individual measurements of the Layer 3 glass die thickness and to enable individual control of the seat etching in Layer 2. Additionally, die-level bonding significantly reduced the risk of losing an entire multi-layer wafer structure during wafer-level processing. The die-level assembly process consists of four main steps, as shown in Figure 47(b), (c), (d).

1. Die-level anodic bonding of Stack 4-5-6 to Stack 7-8-9 at a temperature of 300°C and an applied voltage of 1000V across the Layer 6 - Layer 7 interface. This bond was performed at atmospheric

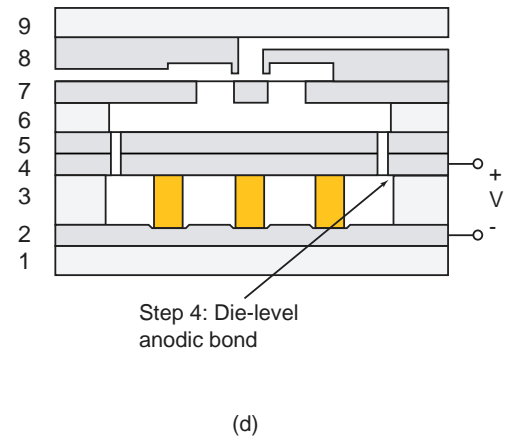
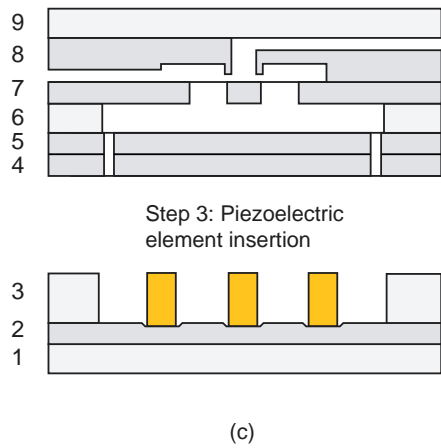
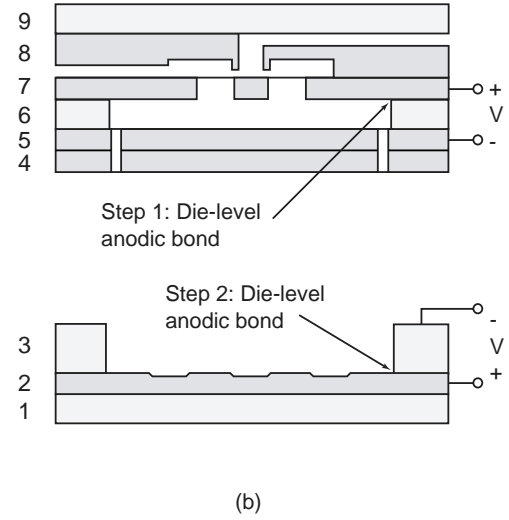
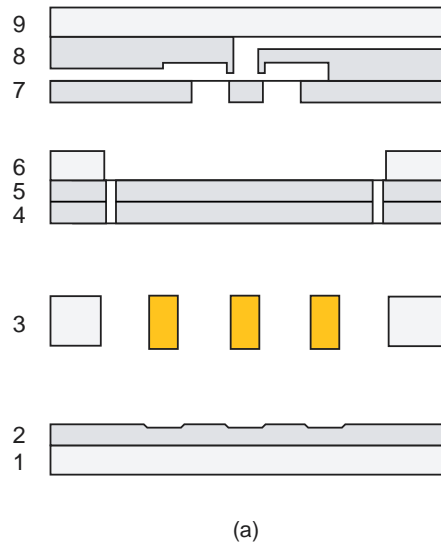


Figure 47: Die-level bonding procedure for the active valve portion of an MHT device: (a) beginning dies ready for assembly, (b) Step 1: anodic bonding of Stack 4-5-6 to Stack 7-8-9 ; Step 2: anodic bonding of Stack 1-2 to Layer 3, (c) Step 3: insertion of piezoelectric element(s), and (d) Step 4: anodic bonding of Stack 1-2-3 to Stack 4-5-6-7-8-9.

pressure. Time of bond = approximately 2 minutes.

2. Die-level anodic bonding of Stack 1-2 to Layer 3 at a temperature of 300°C and an applied voltage of 1000V across the Layer 2 - Layer 3 interface. This bond was performed at atmospheric pressure. Time of bond = approximately 2 minutes.
3. Alignment and placement of one or more piezoelectric material elements within the Stack 1-2-3 die.
4. Simultaneous die-level anodic bonding of Stack 1-2-3 to Stack 4-5-6-7-8-9 and eutectic bonding of piezoelectric element(s) to Layer 2 and Layer 4 silicon. This bond was performed in a reducing atmosphere of  $Ar-5\%H_2$  gas at pressure  $10^{-2}$  torr and temperature 300°C. Additionally, a voltage of 1000V was applied across the Layer 3 - Layer 4 interface. Time of bond = approximately 2 minutes.

A reducing atmosphere was chosen for the final simultaneous anodic/eutectic bond to ensure no oxidation of the Sn within the AuSn alloy and to achieve a void-free eutectic bond [29]. Additionally, following this bond, the device was cooled under vacuum to ensure removal of all trapped gases within the bond. Completion of these four die-level bonding steps produced an MHT structure that was ready for filling of the hydraulic amplification chamber.

**Assembly Jigs** The die-level anodic bonding discussed above was performed using the specially machined alignment and bonding jigs shown in Figure 48. The 1st-generation jig, shown in Figure 48(a), provided a large central contact surface onto which a die could be placed and the bottom surface held at either positive or negative voltage. An outer ring with attached spring clamps for clamping of one die onto another was held at ground potential. Once inserted into an oven, electrical contact was made through attached feet on the underside of the jig. Alignment, placement, and clamping of a dies and insertion of piezoelectric elements was facilitated by a vacuum chuck with 3-axis motion capability and a range in each of these directions of 1 cm. The 2nd-generation jig, shown in Figure 48(b), was more compact than the 1st-generation jig. It likewise provided electrical contact through thin wire clamps, but additionally allowed for edge alignment of the dies to a central area with ceramic insulating locator pins. Figure 49 illustrates an MHT device in the final bonding step using the 2nd-generation anodic bonding jig.

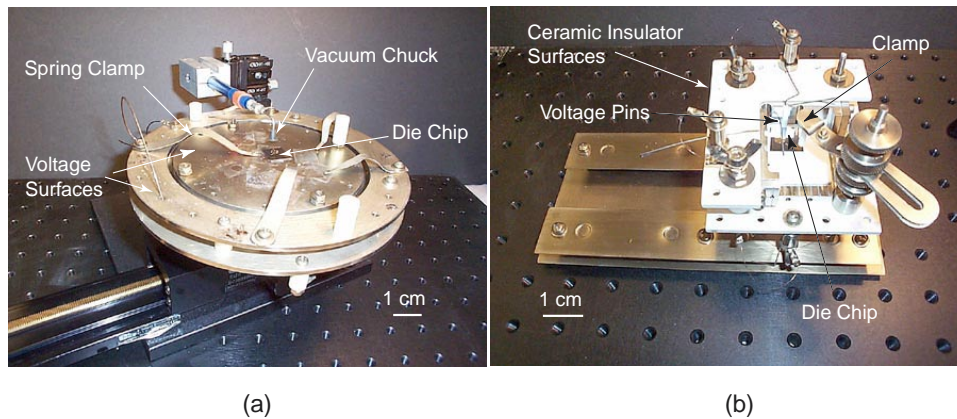


Figure 48: Die-level alignment and bonding jigs: (a) 1st-generation jig, (b) 2nd-generation jig.

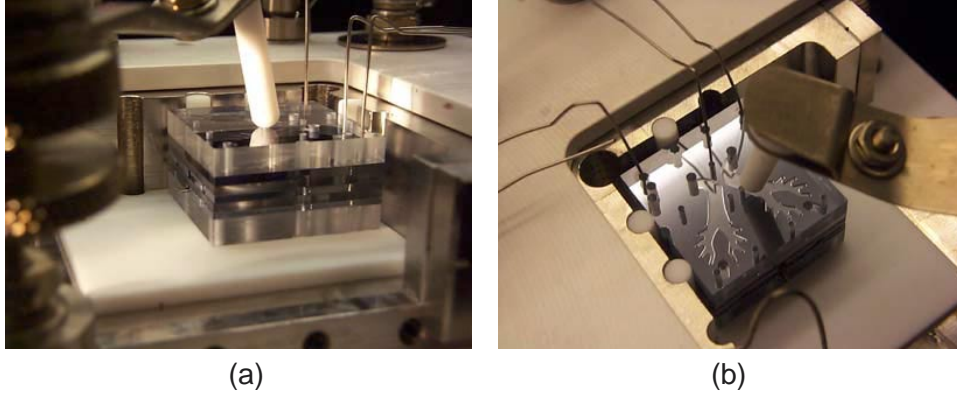


Figure 49: Electrical contact to an MHT device for anodic bonding: (a) side view of chip in jig and (b) top view of chip in jig. Electrical cantilever pins contact various layers of the device for bonding procedures.

**Fluid Filling/Sealing of HAC** Introducing fluid into the hydraulic amplification chamber of the active valve was a critical step in preparing the device for operation. Any bubbles or trapped residual gas within the amplification chamber would significantly increase its compliance, thereby eliminating efficient coupling between the drive element and valve membrane structure. The techniques and procedures used to fill and seal the device were presented in Section 3.2.

#### 4.1.3 Conclusions

The following critical challenges associated with the fabrication and assembly of this multi-layer MHT device were overcome: (1) etching of the high-aspect ratio features in the silicon-on-insulator wafers to form the tethered drive element piston and valve membrane structures, (2) wafer-level silicon-silicon fusion bonding and wafer-level silicon-glass anodic bonding, (3) preparation, integration, and bonding of the bulk piezoelectric material elements within the drive element structure, (4) die-level assembly and bonding of the silicon and glass layers, and (5) fluid filling and sealing of the hydraulic amplification chamber. With the developed procedures, multi-layer drive elements, active valves, and full MHT systems were successfully fabricated and assembled.

## 4.2 Chip-Level MHT Device Fabrication Process Flow

### 4.2.1 Overview

This section briefly outlines the fabrication approaches used to fabricate the silicon and glass layers of the MHT devices. The fabrication process required to produce a device can be divided into the following major subtasks:

- Silicon tethered membrane fabrication, using Silicon-On-Insulator (SOI) wafers.
- Structural silicon layer fabrication. Double-side polished wafers are used for this purpose.
- Glass layer fabrication by ultrasonic machining. The glass used was *Pyrex*<sup>TM</sup>7740 by Corning.
- Wafer scale fusion bonding of silicon-silicon wafer pairs and anodic bonding of silicon-glass wafer pairs.
- Die-level alignment, integration of the piezoelectric material and anodic bonding to complete the assembly. (See Section 4.1)

### 4.2.2 Processes for the Silicon Layers

All silicon layers were fabricated in the MIT Microsystems Technology Laboratory facilities (MTL). The fabrication relied heavily on two ST Systems ICP plasma etchers for DRIE (Deep Reactive Ion Etching). The most challenging part of the silicon layer fabrication process proved to be the etching of the silicon tethered membrane structures that formed the moving parts of all the devices.

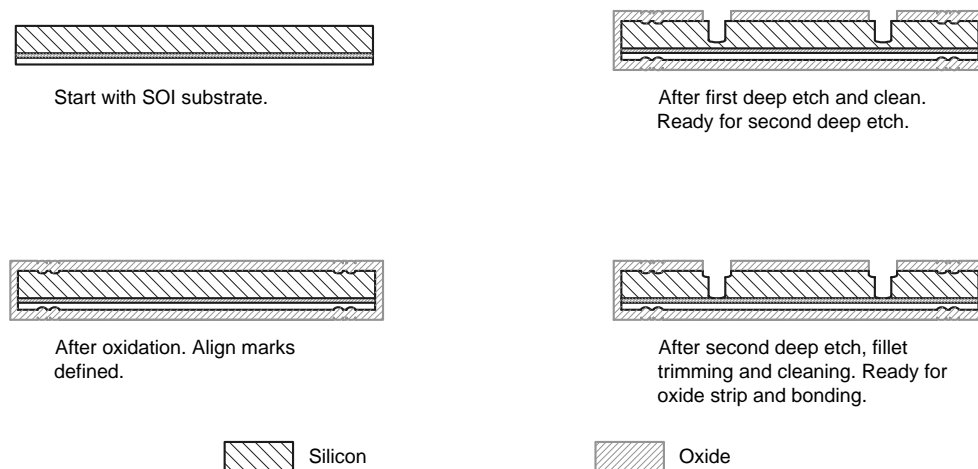


Figure 50: Selected steps of the process required to produce a tethered silicon membrane structure.

Figure 50 depicts the process used to produce the silicon membrane structures used in the devices characterized in this work. A scanning electron micrograph of such a structure is shown in Figure 41. The process flow for creating a structure like this from an SOI substrate can be summarized in the following steps:

1. Start with a Silicon on Insulator (SOI) wafer, double side polished. Device layer thicknesses of  $7\mu\text{m}$  to  $10\mu\text{m}$  were used. The wafer thicknesses ranged from  $300$  to  $400\mu\text{m}$ .

2. Grow first layer of protective thermal oxide at  $1100^{\circ}\text{C}$ ,  $0.6\mu\text{m}$  thick.
3. Pattern align marks on both sides, using OCG825 standard thin photoresist. Etch in 7:1 Buffered Oxide Etch (BOE).
4. Etch align marks in Silicon using reactive ion etching (RIE)..
5. Grow second layer of protective thermal oxide at  $1100^{\circ}\text{C}$ , to a total thickness of  $1.7\mu\text{m}$ .
6. Pattern oxide using BOE, to define the nested mask
7. Recoat with photoresist, using Clariant AZ4620 thick photoresist. A thickness of approximately  $10\mu\text{m}$  after baking is desired. Define the first Deep Reactive Ion Etching (DRIE) etch mask. Mount the wafer on a handle substrate using AZ4620 photoresist.
8. Perform the first deep etch using an STS ICP DRIE tool to approximately  $20\mu\text{m}$  away from the buried oxide. Dismount wafer in acetone and strip photoresist using a process consisting of burning the organic materials in an oxygen plasma ("ashing") and performing a chemical cleaning step, using a mixture of 3 parts  $\text{H}_2\text{SO}_4$  added to 1 part of  $\text{H}_2\text{O}_2$  ("Piranha cleaning").
9. Remount wafer on handle substrate and perform the final etch.
10. Dismount in acetone, and clean using again ashing and piranha. Just prior to fusion bonding, the oxide would be stripped with BOE and an RCA cleaning step would be performed.

The procedure described above will allow the fabrication of a basic tethered silicon membrane structure. It has been found that some amount of exposed silicon outside of the etched membrane features, as provided by the nested mask process, tends to simplify the fillet radius control procedure somewhat.

Additional features, e.g. flow channels, can be defined in the nested mask and the nested mask etch depth can be tailored (within the bounds of the wafer's structure) to suit the requirements of the features needed. In this work it has been found that features deeper than approximately  $20\mu\text{m}$  (and of in-plane dimensions greater than  $\sim 500\mu\text{m}$ ) will not be well suited to an additional lithography step involving the spin-casting of photoresist and subsequent exposure. Another observation is that the nested mask, a hard  $\text{SiO}_2$  mask, will generally provide a smoother sidewall than the initial photoresist mask. This can be attributed to a phenomenon sometimes referred to as "micromasking", where photoresist is removed from the top of the substrate by the DRIE process, and subsequently redeposited on the trench walls, leading to sidewall roughness.

Figure 51, shows, again, a cross-sectional view of all the layers of the MHT device. This figure is similar to Figures 13 and 43, and will be used to reference the process flows for the layers. An accompanying 3D sectional view is given in Figure 52, with the flow path for the working fluid shown in red, and the fluid of an hydraulic amplifier shown in yellow.

The process flows for the five silicon layers, Layers 2, 4, 5, 7 and 8, as shown in Figure 51 are now given in Figures 53, 54, 55, 56 and 57. For the mask layouts, the reader is referred to the appendices.

### 4.2.3 Glass Layers

The Pyrex glass layers were fabricated by ultrasonic machining. The masks for the glass layers (Layers 1, 3, 6 and 9) are also given in the appendices. This fabrication was performed by an outside vendor<sup>6</sup>.

For this device, the glass layers had the following thicknesses:

---

<sup>6</sup>Bullen Ultrasonics, 4613 Camden Road Eaton, OH 45320 Phone: (937) 456-7133 Fax: (937) 456-2779, <http://www.bullen-ultrasonics.com/>

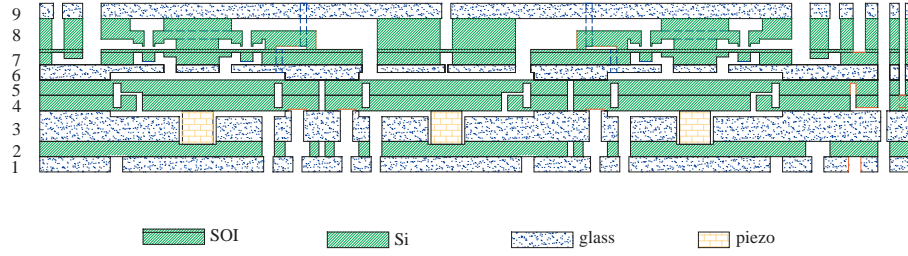


Figure 51: A schematic cross-sectional view of the 10-valve device. This figure is identical to Figures 13 and 43, except for the detail around the valves this figure will be used as a reference for discussion the process flows for fabricating the various layers.

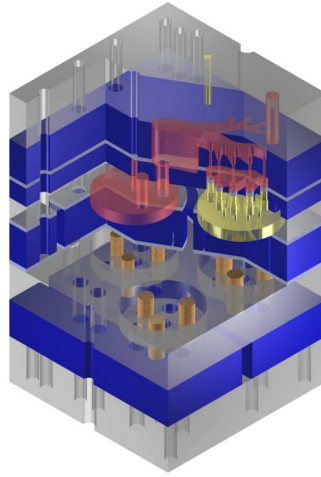


Figure 52: A 3D cross-sectional view of the MHT device with 10 small valves per valve unit. It is a more realistic 3-dimensional representation of the picture shown in Figure 51

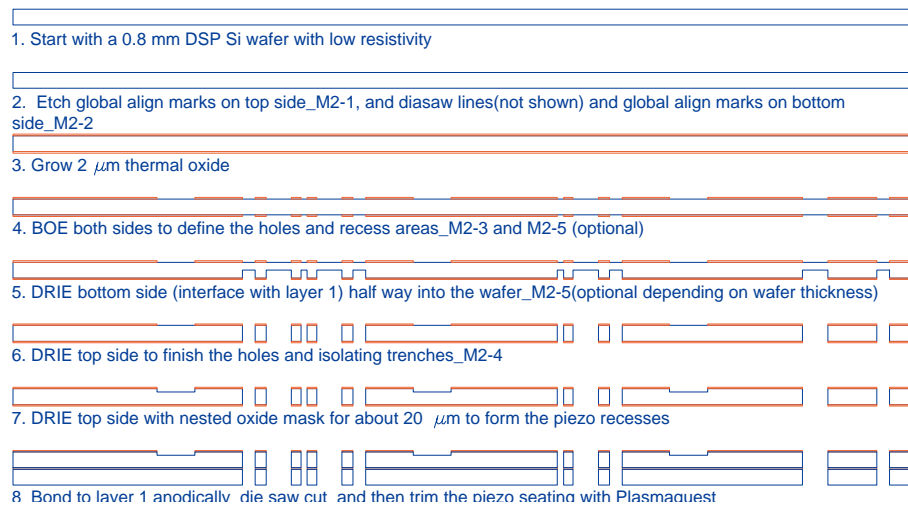


Figure 53: Process flow for Layer 2. This is the layer that provides the lower contact for the piezos.



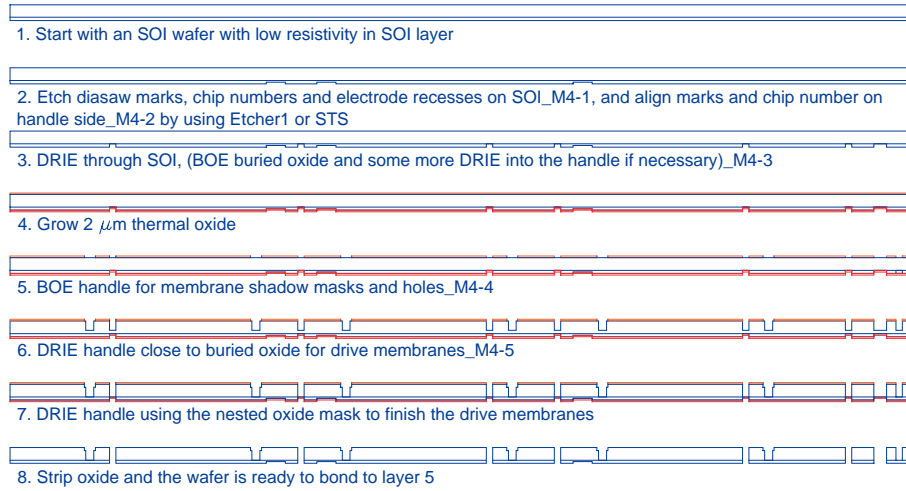


Figure 54: Process flow for Layer 4. This layer forms the lower part of the two-layer drive piston structure. Each device had three such pistons.

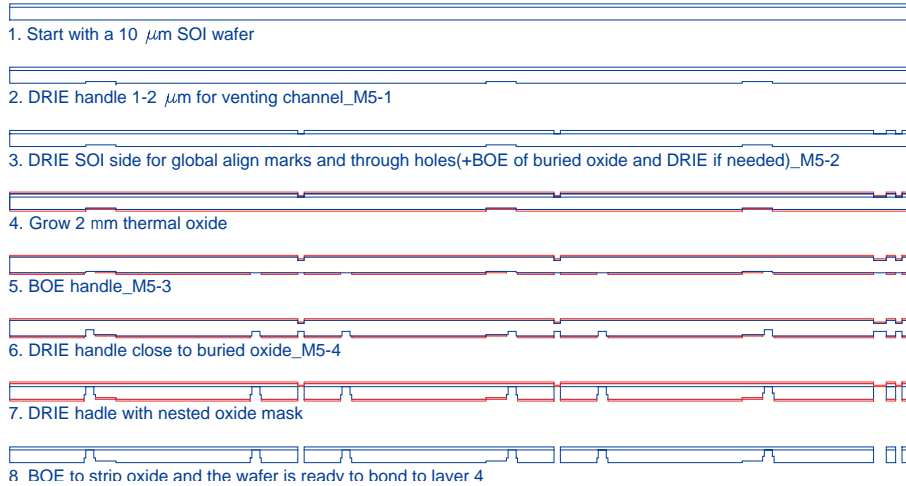


Figure 55: Process flow for Layer 5. This layer forms the upper part of the two-layer drive piston structure and mates to Layer 4.

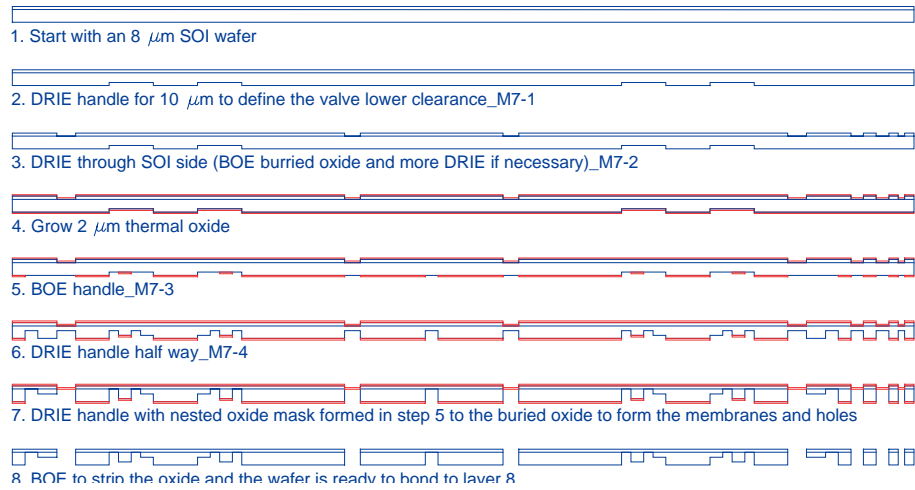


Figure 56: Process flow for Layer 7. This layer contains the valve caps and membranes.

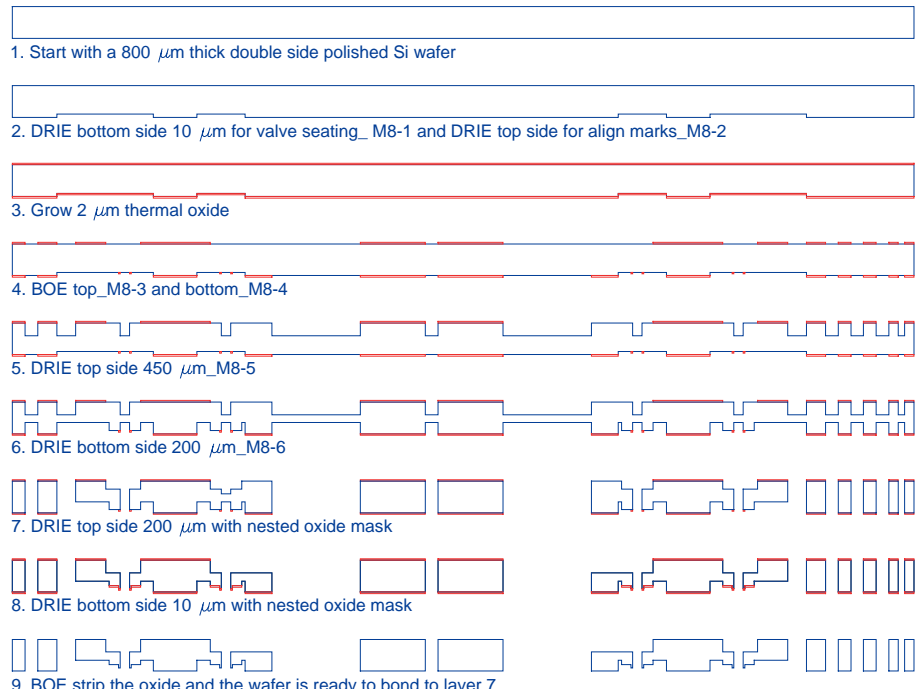


Figure 57: Process flow for Layer 8. This layer contains the flow paths for the various devices. For the valve test components, it provided two independent flow paths, and for the full MHT device, a flow path passing through the two valves and the pump chamber.

- Layer 1:  $3mm$
- Layer 3:  $970\mu m$ , nominal
- Layer 6:  $1mm$
- Layer 9:  $3mm$

In the case of layer 3, a recess was machined to provide clearance for the motion of the piston. In the case of Layer 6, a similar recess was machined, but in this case it was used to form the hydraulic amplification chamber. The fabrication of the Pyrex layers was a robust process, and few problems were encountered. For all Pyrex layers, prior to sending the wafers for the ultrasonic machining, align marks were patterned on the glass using BOE and a thin resist (OCG825 resist). The ultrasonic machining was then performed, aligned to these alignment features.

#### 4.2.4 Conclusions

This section presented the fabrication techniques used to produce the silicon and glass wafers for the MHT devices. The fabrication of multiple full wafersets of MHT devices was completed successfully to enable the fabrication of the devices discussed in later sections of this report. In terms of fabrication, this project had the following major achievements:

- Fabrication techniques for the fabrication of high-strength silicon-tethered membrane structures as moving parts.
- Multiple nested mask processes to form complex deep reactive ion etched structures. (See e.g. Figure 57)

By using a combination of silicon and glass layers, and by exploiting the benefits of both aligned wafer bonding and die-level bonding, it was possible, for these experimental devices, to avoid having to bond a full stack of wafers and thereby significantly reduce the risk in the fabrication process. For large-scale production, the assembly procedures could be refined to yield a full process flow on the wafer scale.

### 4.3 Contributions: Fabrication and Assembly

To summarize, the following was contributed in terms of fabrication and assembly of the MHT device:

1. Fabrication of fragile tethered membrane structures.
2. The fabrication of a nine-layer MEMS device.
3. Die level alignment and anodic bonding techniques.
4. Integration of bulk piezoelectric material in a microscale device.



## **5 Key Technology Demonstrations Through Device Sub-Component Development**

### **5.1 Development of Testing Rigs and Procedures for Device Characterization**

#### **5.1.1 Overview**

This section describes a testing system that was constructed to support the testing of the MHT device and its subcomponents. This test system allowed for the filling of devices with the working fluid, silicone oil, as described in Section 3.2. Furthermore, it allowed for the pressurization of the devices, and also for full measurement of all relevant pressures in the fluid circuit. Displacements were measured with a laser vibrometer.

#### **5.1.2 Test System Requirements**

The testing system had the following requirements:

- Enable the bubble free filling of the portion of the devices that would see fluid flow. This was accomplished by a vacuum system and a vapor purging process similar to the process described in Section 3.2.
- Enable the static pressurization of both the parts of the devices that would see fluid flow (valve subcomponents and pumps) as well as the hydraulic amplification chambers and also the upper part of the hydraulic amplification test units. Nitrogen was used to pressurize vessels containing the working fluid, and a regulator bank controlled the pressure.
- Accurate measurement of the relevant static pressures. Commercial pressure transducers were used.
- Measurement of the motion of both the valve caps and pistons of the devices. A scanning laser vibrometer was utilized for its high frequency capabilities and ease of use.
- Driving of the active valves and pump devices. A combination of a computer data acquisition and signal generation system combined with a bank of amplifiers were used for this purpose.

#### **5.1.3 The device test jigs**

The purpose of a test jig is to provide an interface between the microfabricated device, in this case the MHT device, and the macroscale environment with which it has to interact. Figures 58, 59 and 60 show the test jig that was designed. Figures 58 and 59 depict the test jig that was used to test the static hydraulic amplifiers, and Figure 60 shows the electrical clamp plate that was used instead of the one shown in Figure 59 (a) to test the active valve and full MHT devices. In the design of this test jig the following aspects were considered:

- Provide reliable sealing of all fluid connections to the device. Accomplished by o-rings.
- Provide sufficient, but not excessive, clamping force. Accomplished by using springs for preload.
- Expose as much of the device area as possible for ease of laser displacement measurement. This was done. In addition, the jig was manufactured from aluminum and anodized black, to minimize reflection.

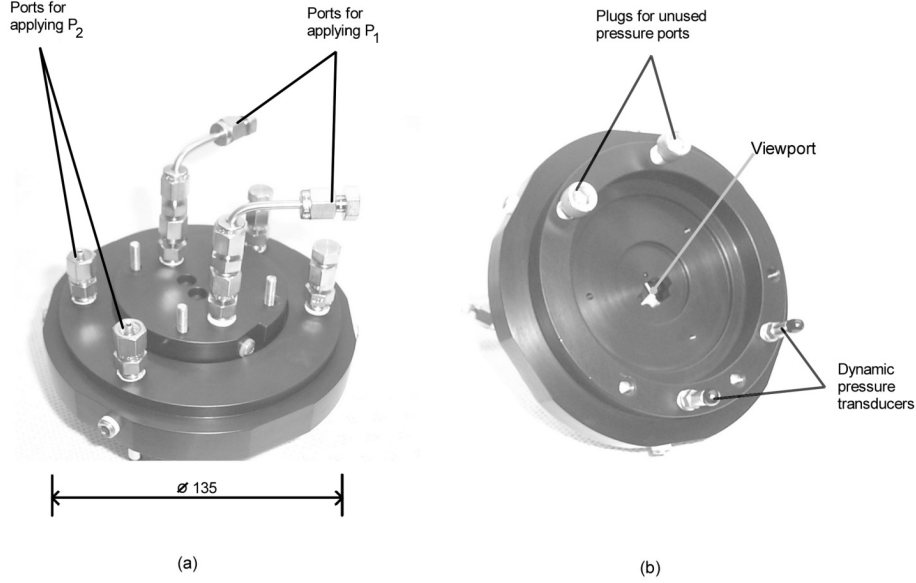


Figure 58: Two views of the test jig: Top view (a) and bottom view (b). Note the viewport for laser displacement measurement.

- Ensure proper electrical insulation. The device was insulated from the jig with an acetal-type plastic insert.
- Allow for measuring of dynamic pressure fluctuations near the device. Provision was made for the installation of PCB model 112A22 dynamic pressure transducers on the jig.
- Had to fit in the fluid filling system discussed in Section 3.2.
- Had to provide electrical connection capability for the active valve and full MHT devices.

#### 5.1.4 The fluid test system

Figures 61, 62 and 63 shows the entire fluid test rig that was built to test the MHT device and its subcomponents. All tubing was stainless steel. Nitrogen was used to pressurize the Dow Corning DC200 0.65cst silicone oil that was used for all tests where liquid was involved. More information about the fluid test systems can be found in [33].

#### 5.1.5 Displacement measurement

All displacement measurements were performed with a Polytec PI PSV-300 Scanning Laser Vibrometry system, as shown in Figures 61 and 63. Using doppler principles, this system measures the velocity of a moving target. By integration, displacement is obtained. The system was outfitted with a precision displacement measuring board with a rated resolution of  $2nm$ . Testing has shown that the actual resolution is dependent on the amount of ambient noise present, and also on the nature of the surface being measured. The best actual resolution obtained for near-zero frequency displacement measurements was found to be between  $10$  and  $50nm$ , depending on the noise present when the measurements were performed.

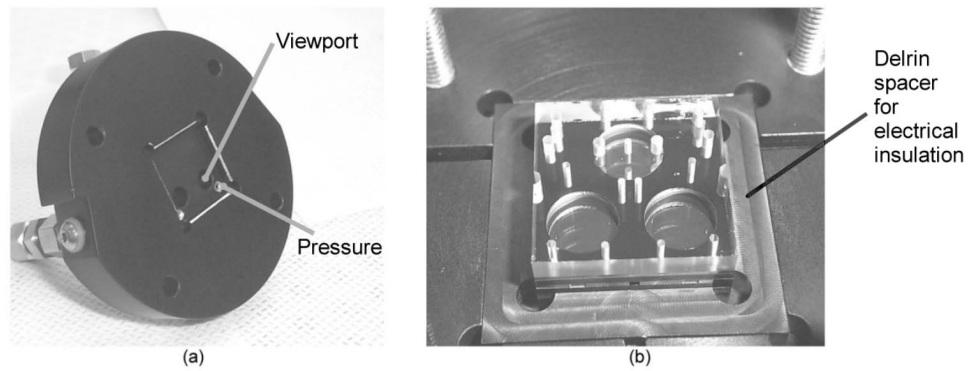


Figure 59: The top clamp (a) shows a recess for the device, two optical viewports and also two fluid pressurization ports. The device is inserted into the main jig (b) and then clamped with the top clamp.

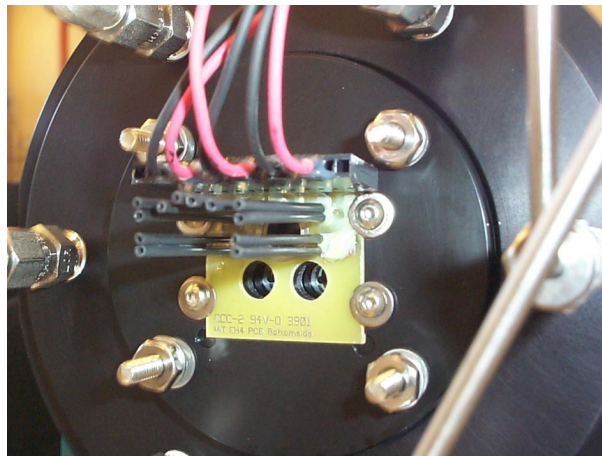


Figure 60: This picture shows the clamp that was used for the devices that required electrical connections. A printed circuit board was used, combined with spring-type contact pins, to make electrical contact. Each contact had two pins for redundancy. Viewports were made in the PC board to accommodate laser displacement measurement of the drive pistons.

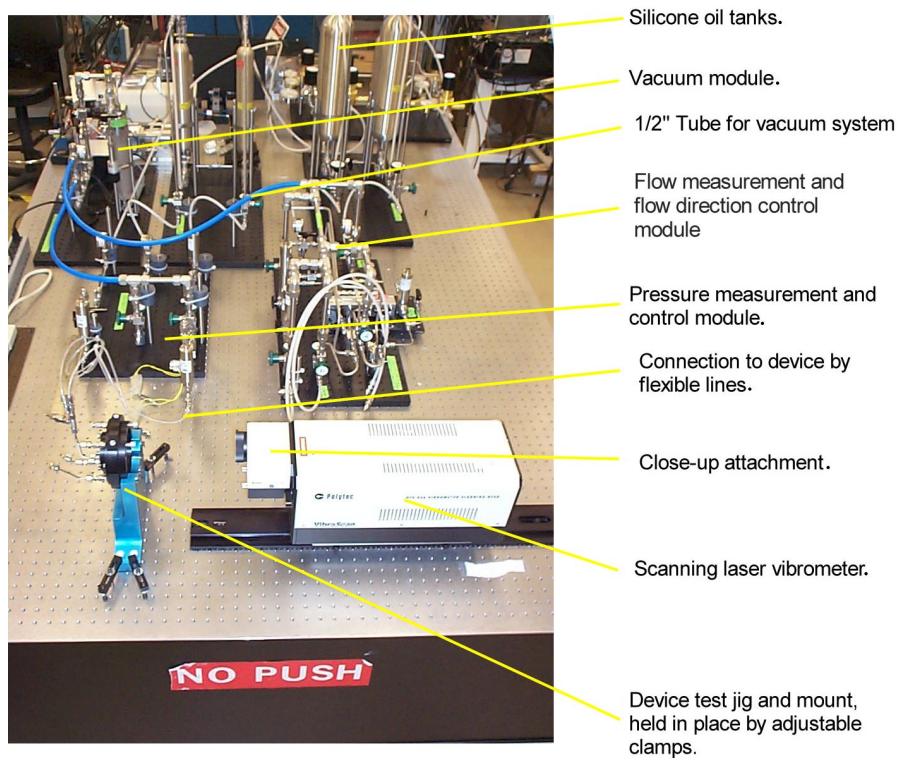


Figure 61: The fluid test system.



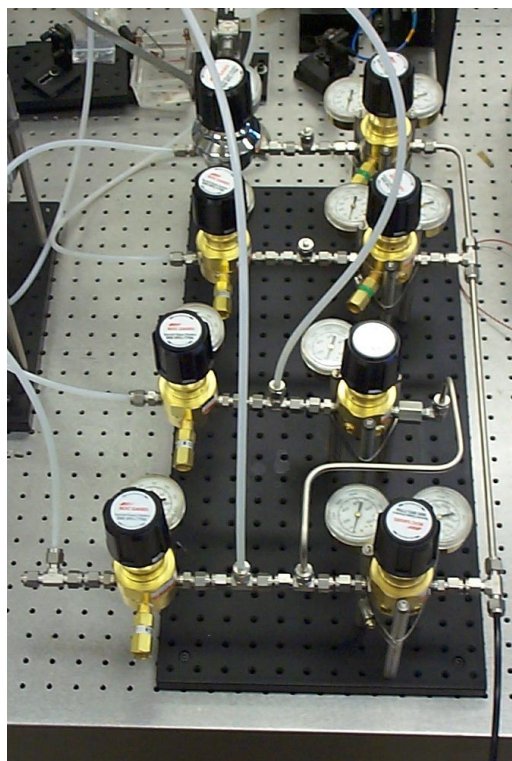


Figure 62: Regulator bank.

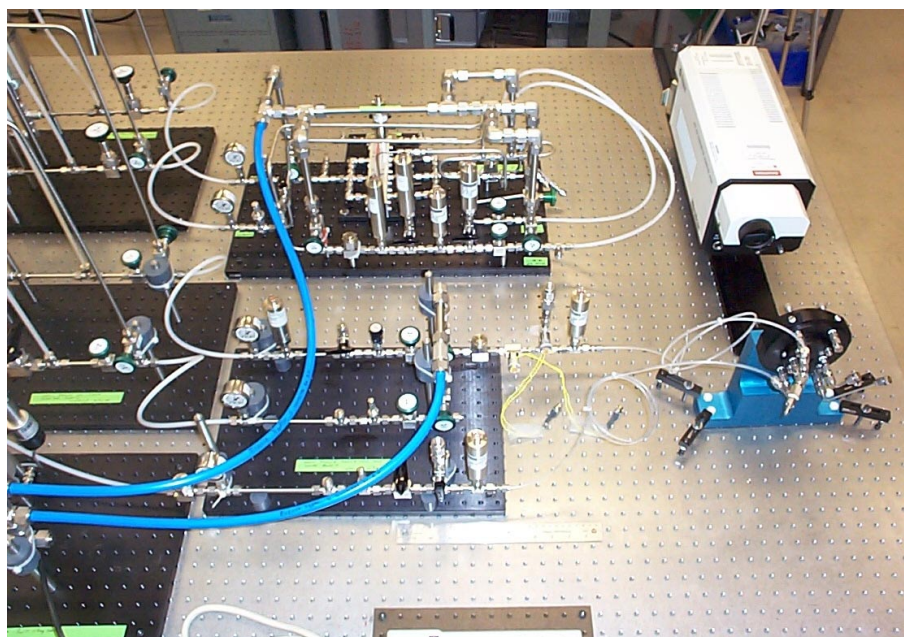


Figure 63: Side angle photograph of the test rig, with more detail on the pressure measurement and control module.

### 5.1.6 Data acquisition

All data acquisition was performed using two National Instruments PCI-6110 boards installed in a desktop computer with an Intel Pentium III 700MHz processor and 128MB RAM. The data acquisition system allowed the simultaneous, synchronized, measurement of up to eight input channels, at sampling rates of up to 4MHz. In addition, it also allowed for simultaneous synchronized generation of four arbitrary waveform outputs at frequencies up to 25kHz, using data acquisition software developed using the National Instruments LabView language.

### 5.1.7 Basic testing protocols

The various tests performed on the devices all had slightly different protocols, but the following general guidelines were followed in most cases to ensure that the devices are bubble-free and also that they would not be damaged during the startup of a particular test.

- *Filling of the flow circuit and the static pressurization systems:* The test rig was filled with silicone oil prior to inserting the device. This was done by evacuating the tubing system and then filling with silicone oil. The silicone oil itself was also outgassed by drawing a vacuum on the containing vessels.
- *Inserting the device:* During the mounting of the device in the test system care had to be taken not to introduce particles to the device. This was done by flowing silicone oil out of all connecting ports whilst connecting the device. This practice also ensured the minimum amount of entrapped bubbles in the system.
- *Preparing the device for operation:* Before any power could be supplied to the device, all the appropriate pressures had to be set to ensure that the valves were in the correct mean positions. This was done by setting the two  $P_{HAC}$ 's as well as  $P_{HPR}$  and  $\Delta P$  to the correct values. These values were then checked by measuring the valve displacement with the laser vibrometer, and also by using the nonlinear membrane code that was developed as part of this project.
- *Testing* After all the pressures were set, the voltages were applied to set the valves in motion. The valve excitation was controlled by the computer data acquisition system, which meant that the valves were sometimes started and stopped abruptly, when a new dataset was being taken. This abrupt starting and stopping did not damage the valves.

### 5.1.8 Summary

This section described the layout of the test system that was used to test the microfabricated MHT device and its subcomponents. A modular approach was used to design and construct this test system and the same system was used to test all devices. It enabled the bubble-free filling and sealing of the "flow" portion<sup>7</sup> of the devices, as well as a complete measurement of all the relevant pressures and flows.

---

<sup>7</sup>excluding the hydraulic amplifiers, which were filled using the techniques described in Section 3.2.

## 5.2 Piezoelectric Drive Element Component Testing

### 5.2.1 Overview

The purpose of this sub-component study was to evaluate the fabrication and assembly process flow of the piezoelectric drive element structure and to obtain quasi-static and high-frequency experimental data on completed devices. Successful integration of polycrystalline PZT-5H material elements, as well as single-crystal PZN-PT material elements, within DRIE etched and bonded tethered piston structures would demonstrate the potential for high-frequency, high-stiffness actuation within the active valve and pump chamber portions of the full MHT device.

In this study, drive element devices were constructed with both single-layer and double-layer pistons, with both PZT-5H and PZN-PT piezoelectric material elements, and with both single and multiple (three) piezoelectric elements beneath the drive element piston. The drive element final design within the active valve and pump chamber portions of the full MHT pump device incorporates three PZN-PT elements spread out beneath a double-layer piston structure. PZN-PT was chosen due to its enhanced strain capabilities over the polycrystalline PZT materials [34], such as PZT-5H. Three elements were chosen, rather than a single element located at the chamber center, to enhance the stiffness of the actuator by eliminating bending and tilting effects. And a double layer piston structure was decided upon, rather than a single-layer design, to reduce piston compliance and potentially enable piston lightweighting in future design iterations. Within this sub-component study, a device with each of these design variations was built as a means to gradually achieve the final design geometry.

### 5.2.2 Test-Plan

A double-layer, three piezoelectric element drive element device is illustrated in Figure 64. Within this study, over 10 devices were built and tested. A comprehensive overview of this study is found in [35]. For the purposes of this report, four distinct devices that highlight the important experimental results will be focused on. Schematic cross-sections of these devices are shown in Figure 65(a) and top-view schematics are illustrated in Figure 65(b). The three major design variations contained within this sub-component study were: (1) use of a single-layer silicon drive piston structure versus use of a double-layer piston structure, (2) integration of PZT-5H material versus integration of PZN-PT material, and (3) incorporation of a single piezoelectric element beneath the piston versus integration of three elements spread out beneath the piston.

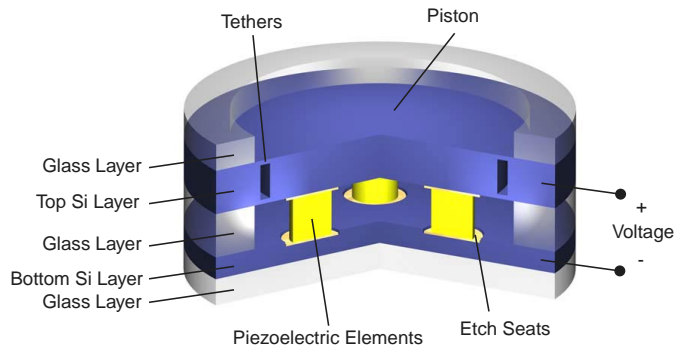


Figure 64: 3-D schematic of a piezoelectric element drive element device. Three piezoelectric cylinders are sandwiched between a lower support silicon layer and an upper double silicon layer tethered-piston structure. Voltage is carried along the upper and lower silicon layers.

Device 1 incorporated a single PZT-5H cylindrical piezoelectric element centrally located beneath the tethered piston. Device 2 incorporated a single PZN-PT cylindrical piezoelectric element also centrally located beneath the piston structure. Device 3 incorporated three PZT-5H cylindrical elements spread out uniformly beneath the piston. In these three devices, the piezoelectric cylinder thicknesses were  $\sim 1\text{mm}$ , while the drive piston had a thickness of  $390\mu\text{m}$  and the tether had a thickness of  $9\mu\text{m}$ . Device 4 incorporated three square PZN-PT elements beneath a double-layer piston structure. The piston and tether radial dimensions were slightly larger than those in Devices 1-3. In fact, the Device 4 dimensions were exactly those used within the active valve and pump chamber components of the full MHT device. As was the case for Devices 1-3, the piezoelectric element thicknesses were  $\sim 1\text{mm}$  in Device 4. Since the piston was comprised of two layers, its total thickness was  $780\mu\text{m}$  with each tether having a thickness of  $8\mu\text{m}$ . A photograph of Device 4 is shown in Figure 66.

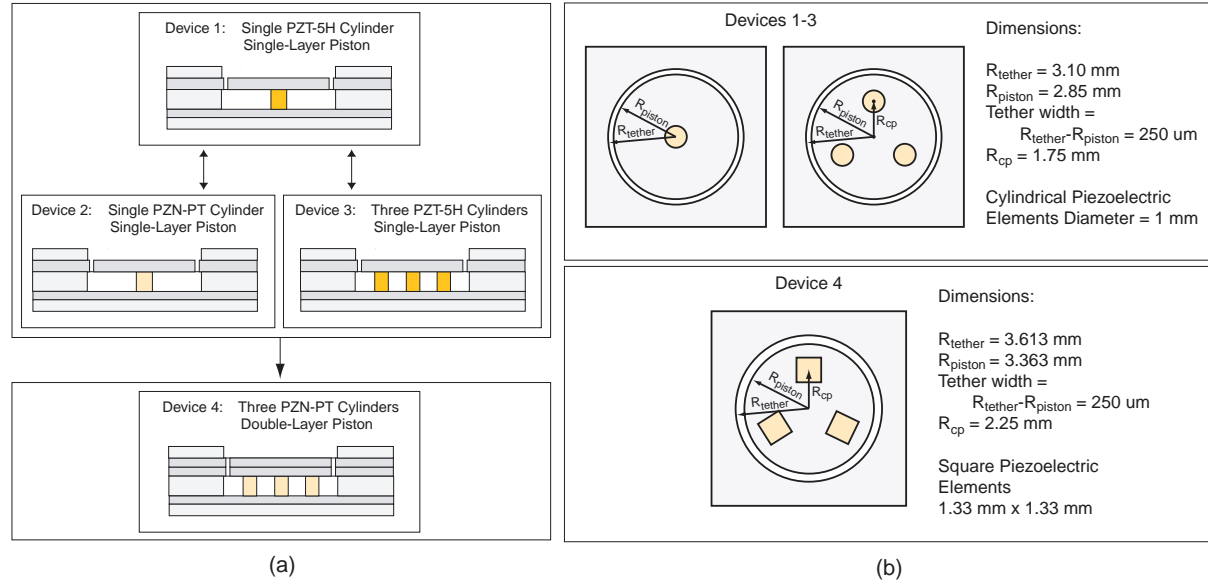


Figure 65: Overview of the drive element sub-component test plan. Devices incorporating single and three piezoelectric cylinders (both PZT-5H and PZN-PT) beneath single-layer and double-layer drive pistons were fabricated and tested.

The process of experimentally testing each drive element device consisted of three major steps. The first step involved careful microscopic inspection of the device to evaluate the fillet radius profile(s) along the etched drive element tether(s). These inspections were performed on the wafer-level prior to any bonding operations. Knowledge of the fillet radius sizes was important for later evaluation of device performance. The second step involved characterization of stand-alone piezoelectric material elements that originated from the same batch (plate) of material that yielded the elements that were integrated within the device. This was a critical procedure so that comparison of drive element device voltage-deflection behavior could be compared to that of representative piezoelectric material elements. The third step involved rigorous experimental testing of the device. Each device was rigidly clamped to a test-jig surface and experimentally evaluated using a scanning laser vibrometer system. Scan points were defined over the top surface of the tethered piston and along the circumferential boundary supporting the piston. Three measurement procedures were used to characterize device performance. In the first procedure, a low-voltage ( $0\text{V} \pm 25\text{V}$ ) sweep signal was applied to each device over a frequency range of  $10\text{kHz}$  to  $200\text{kHz}$  to determine the onset of dynamic modal characteristics. A transfer function of

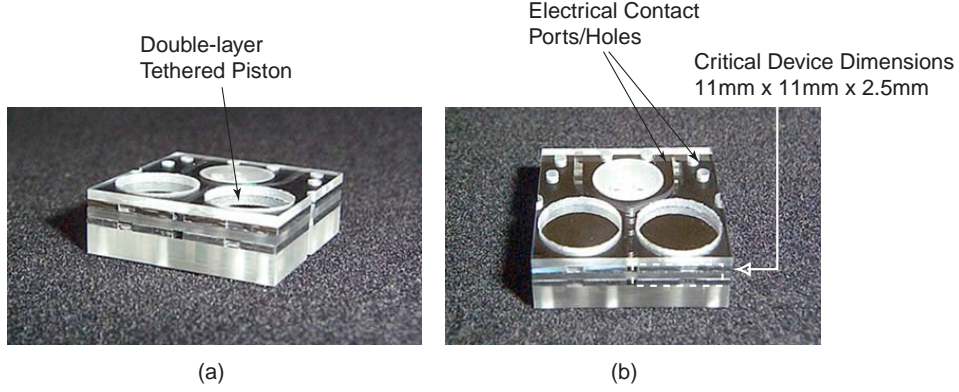


Figure 66: Photograph of an assembled three piezoelectric element, double-layer piston drive element device: thick glass packaging layers were used for clamping purposes during testing.

velocity (averaged over all scan points) versus frequency was recorded. Close-up frequency sweeps around dominant modal frequencies were then carried out to obtain high-resolution mode shape behavior. In the second procedure, a sinusoidal voltage of  $500V \pm 500V$  was applied to each device at selected frequencies of 15kHz and 7kHz to evaluate device behavior below the modal frequencies. At each of these low-frequencies, displacement time histories at the piston center and at an outer edge of the piston were recorded. In the third procedure, voltage-deflection curves (of the piston center) for varying levels of applied voltage were obtained at a frequency of 100Hz to determine the true quasi-static voltage dependent performance of the device.

### 5.2.3 Summary of Results

A detailed overview of the drive element sub-component study is found in [35]. The fillet radius inspection and the piezoelectric material voltage-deflection characterization steps discussed above, although detailed in [35], are not covered in this report. Rather, a concise overview of the experimental results and the impact of these results on the development of subsequent MHT active valve and pump devices is provided.

Figure 67(a) plots the transfer function of averaged velocity over the scanned piston surface versus frequency for Device 1. Figure 67(a) presents experimental mode shapes of the device at select modal frequencies. Device 1 experiences a “1 –  $\Theta$ ” tilt mode at  $f = 31kHz$ , followed by a “plunge” mode at  $f = 80kHz$ , and a “2 –  $\Theta$ ” mode at  $f = 131kHz$ . As shown in Figure 67(c), these modal frequencies correlate well with finite-element models of the device. The frequency difference in the “1 –  $\Theta$ ” mode between finite-element model and experiment is most likely attributed to imperfect placement of the piezoelectric cylinder beneath the piston or a non-uniform fillet radius around the tethered-piston. At a driving frequency of 15kHz and an applied voltage of 1000Vpp, the overall peak-peak deflection at the piston center was measured to be  $\delta_{p-p} = 0.69\mu m$ , slightly lower than the expected range of  $\delta_{p-p} = 0.75 - 0.82\mu m$ , based on the material characterization tests detailed in [35]. Most likely, this was a result of material property inconsistency within the batch of PZT-5H piezoelectric cylinders.

Dynamic tests on Device 2 resulted in very similar modal behavior to that of Device 1, however, the frequencies at which the modes occurred were shifted downward (see results in [35]). Device 2 experienced a “1 –  $\Theta$ ” tilt mode at  $f = 30kHz$ , followed by a “plunge” mode at  $f = 61kHz$ , and a “2 –  $\Theta$ ” mode at  $f = 112kHz$ . This frequency shift was expected since PZN-PT is a softer material than PZT-5H. At a driving frequency of 15kHz and an applied voltage of 1000Vpp, the overall peak-peak deflection at the piston center was measured to be  $\delta_{p-p} = 1.42\mu m$ , slightly lower than the expected



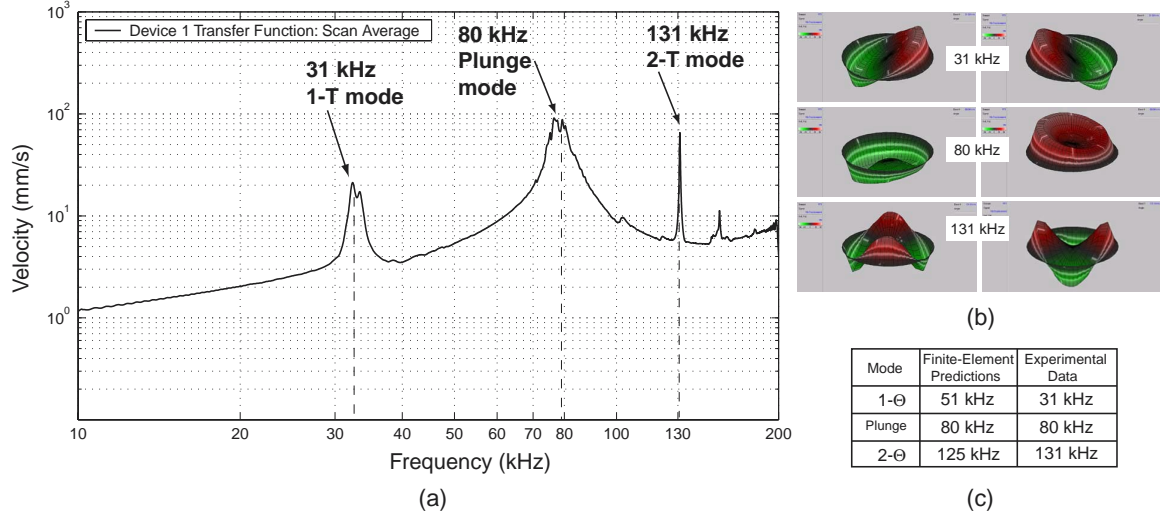


Figure 67: Device 2 dynamic behavior: (a) transfer function of piston velocity versus frequency for a sweep input from 10kHz to 200kHz and small signal drive voltage  $0V \pm 25V$ , (b) vibrometer scan images of mode shapes, and (c) model-experiment correlation for modal behavior. Phase information was not recorded for this device.

range of  $\delta_{p-p} = 1.35 - 1.55 \mu m$ , based on the material characterization tests detailed in [35]. This enhanced deflection capability is the reason for incorporation of PZN-PT material within the final MHT systems. Devices 1 and 2 both perform well as actuator mechanisms, however, the presence of a tilting mode at a frequency near 30kHz results in the potential for non-ideal rocking behavior when driving with frequencies near 15kHz. It was for this reason that subsequent devices were built and tested with multiple piezoelectric elements spaced out beneath the piston.

Figure 68(a) plots the transfer function of averaged velocity over the scanned piston surface versus frequency for Device 3. In comparing this dynamic response to that of Device 1, modal behavior is not observed until frequencies near  $f = 80 kHz$ . The placement of multiple cylinders beneath the piston eliminated tilting behavior at frequencies in the 30kHz to 80kHz range. As shown in Figure 68(b), initial modal behavior is characterized by non-symmetric motion of the piston surface, most likely due to unsymmetric placement of the piezoelectric elements beneath the piston, differences in material properties among the elements, or a non-uniform fillet radius profile along the tether circumference. A perfectly symmetric finite-element model of this device predicts 1st modal behavior at 225kHz. For low-frequency actuation, the multiple piezoelectric cylinder stiffening effect is justified in Figure 68(c) as the displacement profile at 15kHz experienced minimal tilting during actuation. As for Device 1, the magnitude of the piston center displacement in Device 3,  $\delta_{p-p} = 0.72 \mu m$ , was slightly lower than the expected range of  $\delta_{p-p} = 0.75 - 0.82 \mu m$ . Overall, integration of three PZT-5H elements within a single layer piston device was therefore proven. The next step was to validate incorporation of three PZN-PT elements beneath a double-layer piston structure, as required by the full MHT systems.

Figure 69(a) plots the transfer function of averaged velocity over the scanned piston surface versus frequency for Device 4. Modal behavior began near 50kHz and was characterized by non-symmetric tilting motion of the piston surface, most likely due to unsymmetric placement of the piezoelectric elements beneath the piston or differences in material properties among the elements. A perfectly symmetric finite-element model of this device predicted 1st modal behavior (piston plunge) at 155kHz and 2nd modal behavior (1- $\Theta$  piston tilting) at 288kHz. For low-frequency actuation at 15kHz and at a

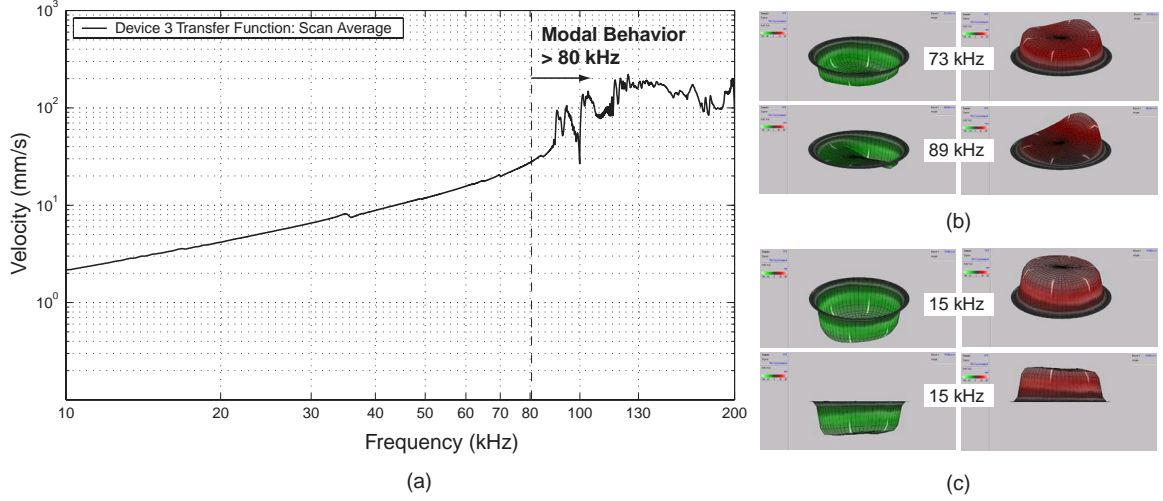


Figure 68: Device 3 dynamic behavior: (a) transfer function of piston velocity versus frequency for a sweep input from 10kHz to 200kHz and small signal drive voltage  $0V \pm 25V$ , (b) vibrometer scan images of mode shapes, and (c) vibrometer scan images of low-frequency motion. Phase information was not recorded for this device.

voltage of 1000V peak-peak, the drive element piston experienced minimal tilting (as shown in Figure 69(b)), indicating a well-built and tolerated drive element device.

The degree of piston tilting is illustrated more clearly in Figure 70. The displacement time history at the piston center (Figure 70(a)) is very smooth with no higher order oscillations. Likewise, the displacement time histories at the piston edge locations with maximum peak-peak motions (Figure 70(b)) are also completely free from higher order oscillations. In comparing the peak-peak deflections of these opposite piston edges, the magnitude of tilt is estimated to be  $\sim 4\%$  of the piston center deflection. The piston center displacement ( $\delta_{p-p} = 1.41\mu m$ ) correlates well with the expected range of  $\delta_{p-p} = 1.35 - 1.55\mu m$ . As was the case for the first generation drive element devices, the deflection behavior under quasi-static driving conditions is linear with the applied voltage. Figure 71 illustrates this voltage dependent behavior at 100Hz. The deflection response is linear with increasing voltage and the hysteresis contained within the motion is minimal.

## 5.2.4 Conclusions

The previously described drive element devices were fabricated in an effort to demonstrate that both standard polycrystalline PZT-5H piezoelectric material as well as higher-strain single-crystal PZN-PT piezoelectric material could be incorporated beneath micromachined piston structures. The integration of both single and three piezoelectric elements beneath the drive piston was proven to be reliable. The dynamic low-voltage and quasi-static high-voltage experimental results clearly indicate that the fabrication and assembly process flow for these component structures can enable high frequency actuation capabilities within the active valve and pump chamber portions of full MHT systems.

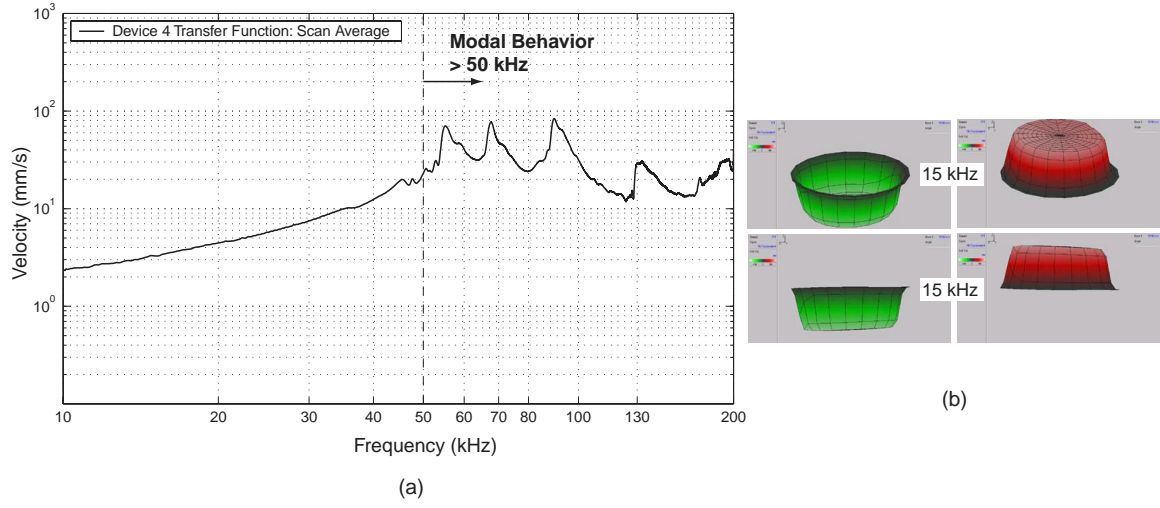


Figure 69: Device 4 dynamic behavior: (a) transfer function of piston velocity versus frequency for a sweep input from 10kHz to 200kHz and small signal drive voltage  $0V \pm 25V$  and (b) quasi-static behavior at 15kHz. Phase information was not recorded for this device.

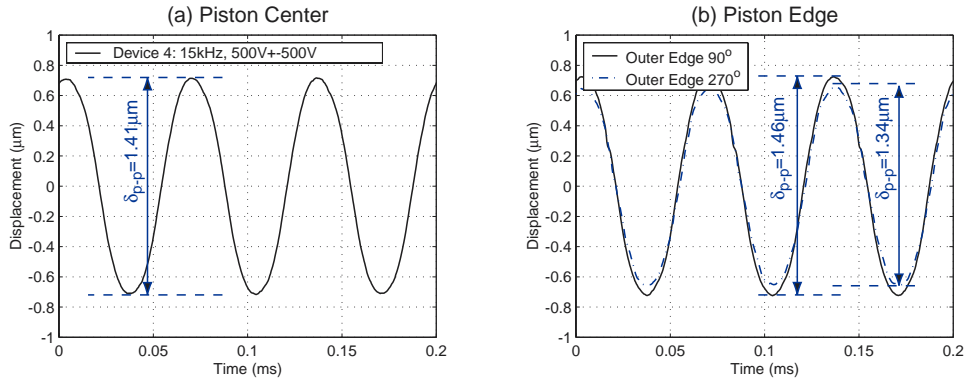


Figure 70: Device 4 displacement time histories for sinusoidal drive voltage of  $500V \pm 500V$  at  $f = 15\text{kHz}$ : (a) piston center displacement and (b) piston edge displacements. These results indicate a rigid well-toleranced device.



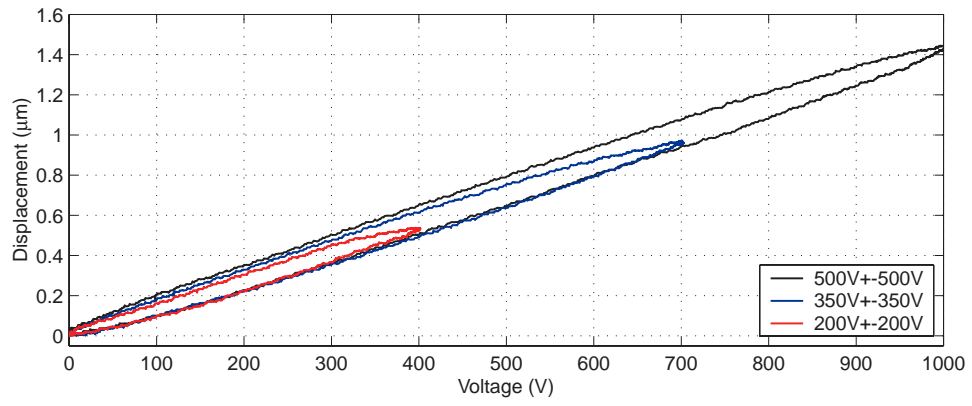


Figure 71: Device 4 piston center displacement versus applied voltage at 100Hz.

## 5.3 Hydraulic Amplification Component Testing

### 5.3.1 Objectives

Hydraulic amplification was chosen as the means for stroke amplification of the piezoelectric elements that actuate the valves of the MHT. This means of stroke amplification is both compact and stiff, provided that the hydraulic coupler that couples the small and large pistons can be made sufficiently stiff. This requires that the hydraulic amplifiers of the MHT be:

1. Properly evacuated prior to filling.
2. Filled without introducing any gas bubbles.
3. Sealed in an appropriate and reliable manner.

To this end, a study was performed on the hydraulic amplification units of the MHT device. This work is described in detail in [33], and is briefly summarized here. Using the test system described in Section 5.1, a series of static (pressure-actuated) tests were performed on the hydraulic amplifiers, in addition to dynamic tests that are described in Section 5.4. Tests were performed on two types of devices, namely:

- A device with one large piston of approximately  $7mm$  in diameter, and a smaller one of approximately  $0.5mm$  in diameter. (HAC Device 3)
- A device with one large piston, approximately  $7mm$  in diameter, and ten smaller pistons, each with diameter of approximately  $200\mu m$ . (HAC Device 4)

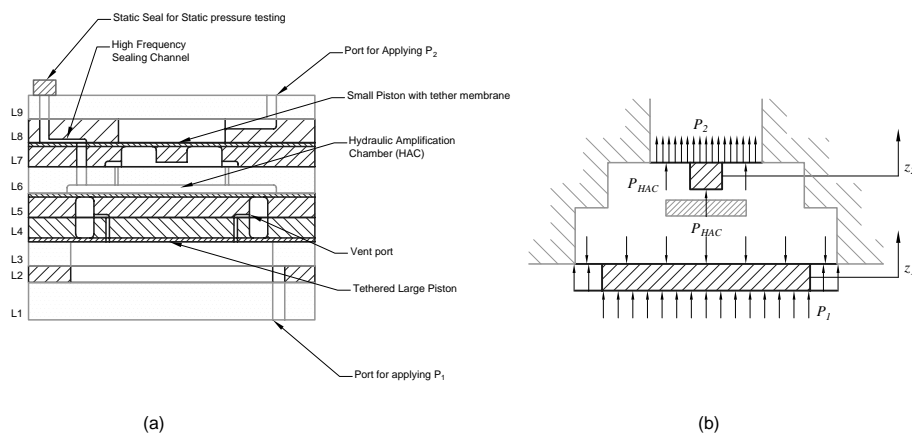


Figure 72: Two representations of the static hydraulic amplification device: (a) A detailed cross section schematic view, and (b) A simplified functional schematic, with nomenclature to be used.

### 5.3.2 Static hydraulic amplification tests

The static hydraulic amplification tests were performed on geometries schematically depicted in Figure 72. The nomenclature shown will be used for this section.

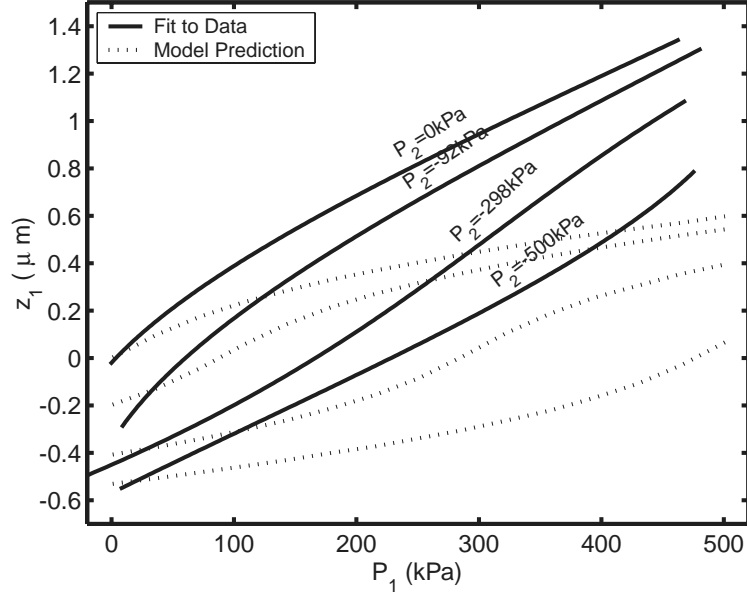


Figure 73: Motion of the large piston for varying pressure on the large piston ( $P_1$ ) and various values of pressure on the small piston. HAC Device 3.

**Tests performed, and correlation with nonlinear models: HAC Device 3** Figures 73 and 74 show the deflections of the large piston and one of the small pistons for  $P_1$  varying from 0 to  $500\text{ kPa}$  and for  $P_2$  having values 0, 92, 298 and  $500\text{ kPa}$ . The large piston acts as a pressure transfer element with very little pressure differential across this piston for the deflections seen in these tests. The small piston in turn responds to the pressure transferred by the large piston.

**Amplification ratio and amplification sensitivity: HAC Device 3** A suitable figure of merit in evaluating the performance of an hydraulic amplifier would be an amplification ratio or an amplification factor. This ratio can be computed using two different methods. The first method, which we will define as the amplification ratio, is defined as:

$$AR = \left( \frac{z_2(P_1) - z_2(0)}{z_1(P_1) - z_1(0)} \right)_{P_2=const} \quad (30)$$

Figure 75 shows this amplification ratio. Note that the amplification ratio is always a maximum near the "linear region" of the operating regime. The second method, shown in Figure 76 uses the incremental displacement amplification which allows us to write an expression for the amplification sensitivity:

$$AS = \left( \frac{\partial z_2}{\partial z_1} \right)_{P_1, P_2=const} \quad (31)$$

**Tests performed, and correlation with nonlinear models: HAC Device 4** Both hydraulic amplifiers in HAC Device 4 were tested. The results of the two devices match closely, and only one set is discussed here. Figures 77 and 78 show the deflections of the large piston and the small piston for  $P_1$  varying from 0 to  $200\text{ kPa}$  and for  $P_2$  having values 0, 53, 105, 153, 206 and  $253\text{ kPa}$ . As was the case for HAC Device 3, the large piston deflects significantly more than model predictions, indicating a reduced stiffness of the HAC.

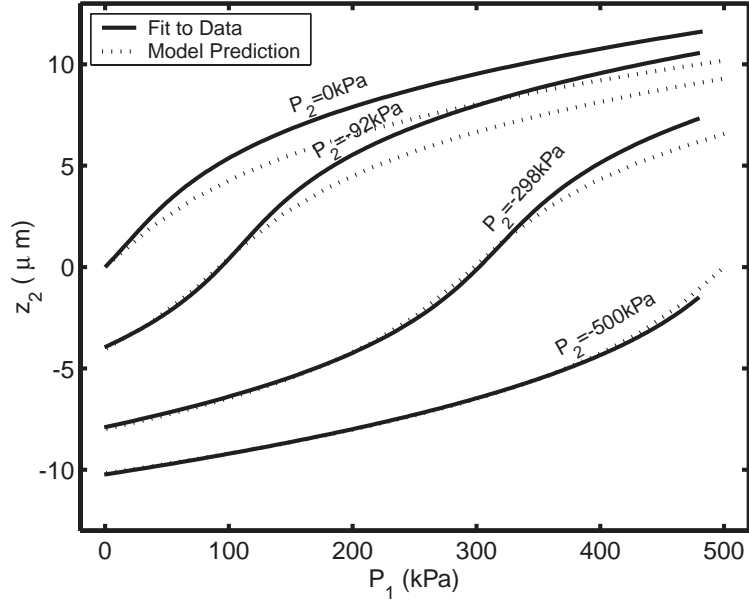


Figure 74: Motion of the small piston for varying pressure on the large piston ( $P_1$ ) and various values of pressure on the small piston. HAC Device 3.

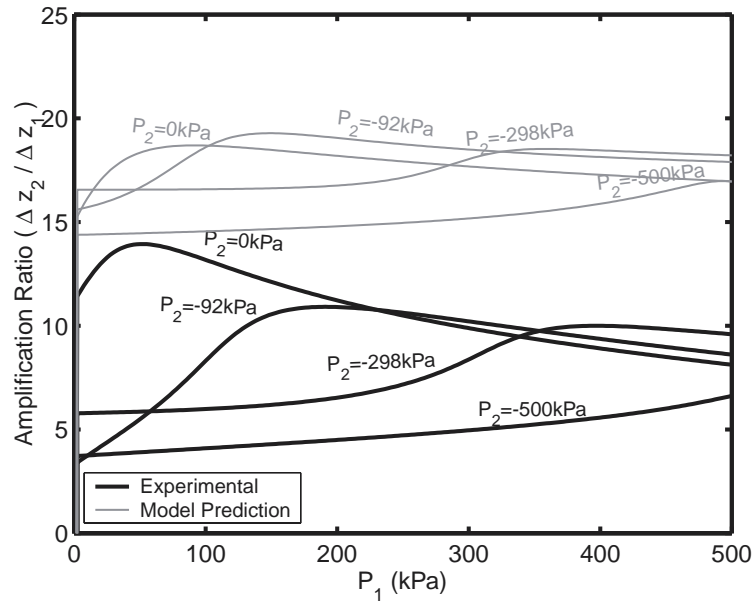


Figure 75: Amplification ratios for the tests performed. HAC Device 3.

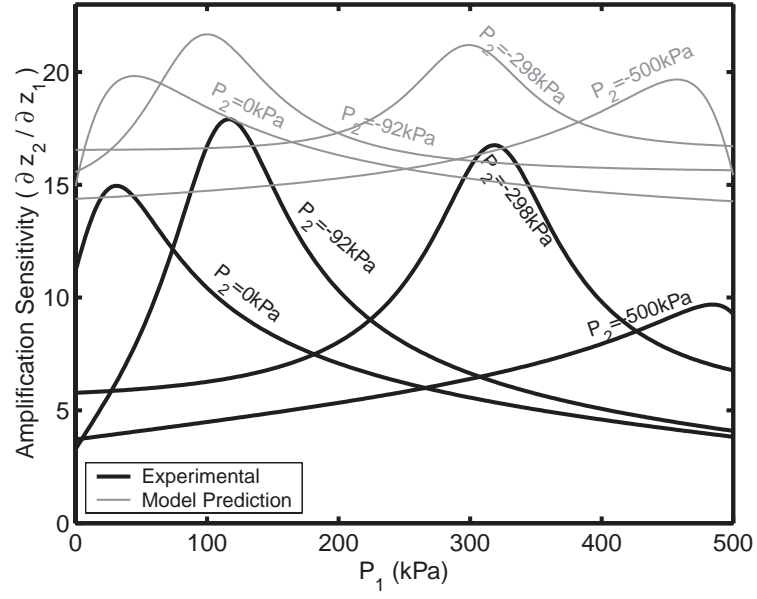


Figure 76: Amplification sensitivities for the tests performed. HAC Device 3.

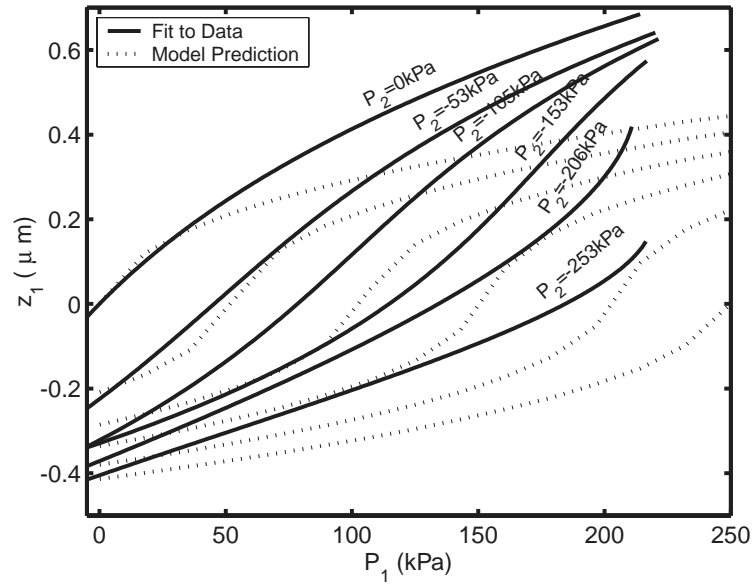


Figure 77: Motion of the large piston for varying pressure on the large piston ( $P_1$ ) and various values of pressure on the small piston. HAC Device 4.

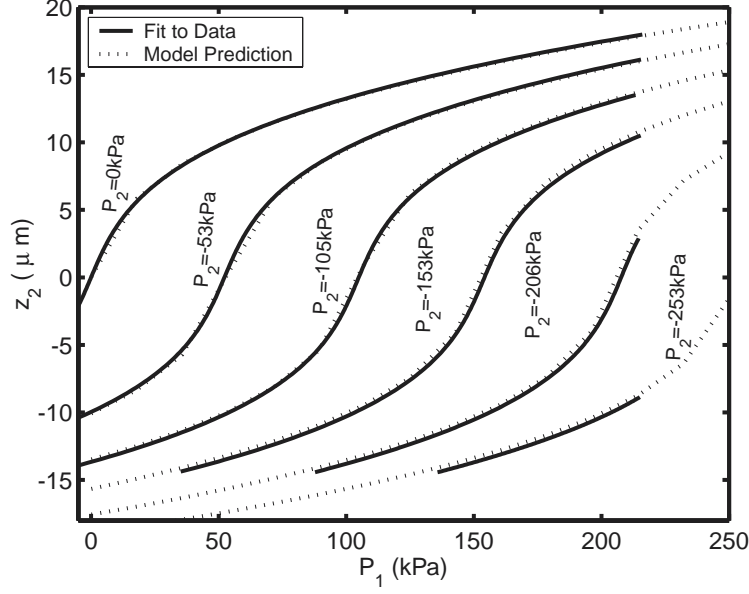


Figure 78: Motion of the small piston for varying pressure on the large piston ( $P_1$ ) and various values of pressure on the small piston. HAC Device 4. The good correlation is attributed to the fact that the large piston sees a very small  $\Delta P$ .

**Amplification ratio and amplification sensitivity: HAC Device 4** Using Equations 30 and 31, we proceed to compute the amplification ratio and amplification sensitivity for HAC Device 4. The results are shown in Figures 79 and 80. The amplification ratio is higher than predicted for  $P_2 = 0 \text{ kPa}$ . This could probably be attributed to a measurement irregularity. Also, in this case, the amplification sensitivity is higher for the experimental case. This is due to a smaller incremental change in  $z_1$  for the measured values.

In summary, two static hydraulic amplifiers with different theoretical amplification ratios have been tested. The same trends have been seen in the tests of both HAC Device 3 and HAC Device 4, with the latter device, HAC Device 4, appearing to be the one that was better filled and sealed. Amplification ratios of up to 40:1 were observed, when ignoring the  $P_2 = 0 \text{ kPa}$  result for HAC Device 4. In addition, amplification sensitivities of approximately 80:1 were obtained.

### 5.3.3 Accomplishments

The hydraulic amplification subcomponent testing yielded the following accomplishments:

- Hydraulic amplification with sufficient stiffness for piezoelectric active valve actuation were demonstrated.
- These devices also displayed acceptable amplification ratios which compared well with theoretical predictions.
- As technology subcomponents hydraulic amplifiers such as these show potential for use in microscale actuation, not limited to the actuation of valves in an MHT device

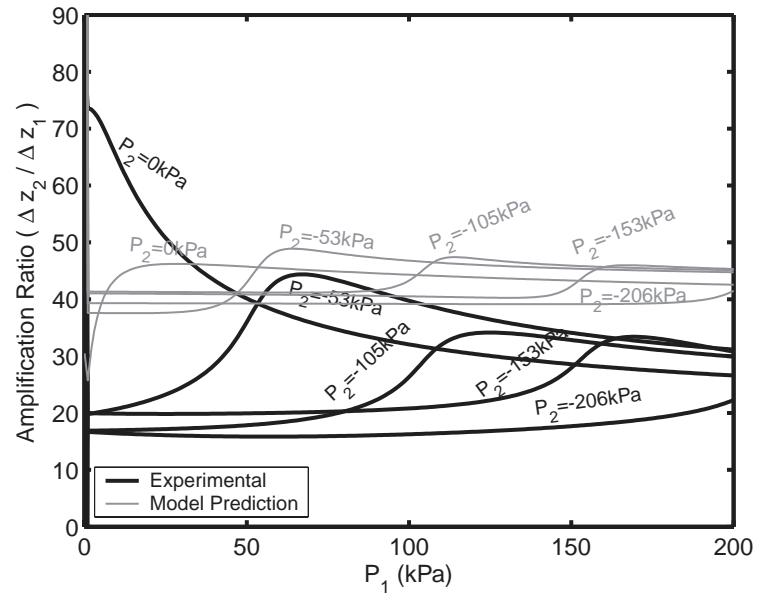


Figure 79: Amplification ratios for the tests performed. HAC Device 4.

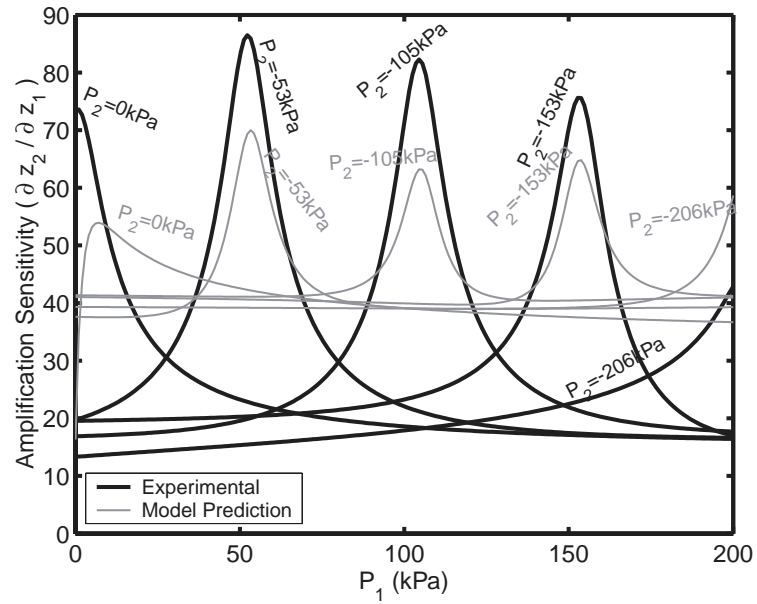


Figure 80: Amplification sensitivities for the tests performed. HAC Device 4.

## 5.4 Piezoelectric Active Valve Component Testing

### 5.4.1 Overview

The purpose of this component study was to evaluate the quasi-static and dynamic structural performance of the complete active valve device and to determine its limitations in regulating the flow of fluid against imposed differential pressures. Specifically, the four primary objectives of this study were:

1. To understand the dynamic behavior of the active valve device and to determine the range of driving frequency for which the valve behaves in a quasi-static manner.
2. To evaluate the amplification ratio of the active valve structure under a variety of voltage levels and internal and external bias pressures for a driving frequency below resonance to ensure quasi-static operation.
3. To characterize the differential pressure-flow rate curves for the valve cap and orifice geometry of the active valve device.
4. To characterize the dynamic capability of the active valve structure in regulating fluid flow against a preset differential pressure across the valve at a driving frequency below resonance to ensure quasi-static operation.

Successful operation of the valve structure in this manner proves its capabilities as a flow regulation device. A further goal is to identify the limiting differential pressures against which the active valve can function.

The dimensions of the fabricated final active valve device are illustrated in Figure 81. The device incorporated three PZN-PT piezoelectric square elements (each with cross-sectional area 1.06mm x 1.06mm) beneath a double-layer tethered piston structure. The top and bottom tethers of the piston were each  $250\mu\text{m}$  in width and each had a thickness of  $8\mu\text{m}$ . A valve cap and membrane structure was positioned above the hydraulic amplification chamber, with a structural stop (formed by the glass Layer 6 within the HAC chamber)  $\sim 16.5\mu\text{m}$  below the equilibrium position of the valve cap. Glass Layer 6 contained a series of “HAC through-holes” to carry the fluid from the lower to upper portion of the HAC chamber. The valve cap had a diameter of  $500\mu\text{m}$  and the valve membrane had an outer diameter of  $1400\mu\text{m}$  and thickness of  $6\mu\text{m}$ . A valve orifice was located  $\sim 16.5\mu\text{m}$  above the valve cap equilibrium position. The orifice had an inner diameter of  $450\mu\text{m}$ .

### 5.4.2 Test-Plan

Testing of the active valve device was divided into two primary efforts. The first effort focused on characterizing the actuation capabilities of the valve structure without the effects of differential pressure and flowing fluid above the structure. In this effort, the dynamic behavior of the active valve device was evaluated and the range of driving frequency for which the valve behaved in a quasi-static manner was determined. Additionally, at the determined maximum quasi-static operational frequency, the structural amplification ratio of the valve device was characterized as a function of applied voltage to the piezoelectric drive element. Once the device was proven to be a successful actuator, the second effort focused on evaluating its flow regulation capabilities and limitations. In this effort, the flow regulation capability of the valve device at the maximum quasi-static operational frequency of the structure was evaluated as a function of increasing differential pressure across the valve orifice. In this manner, the valve performance limitations could be determined as the differential pressure was increased.



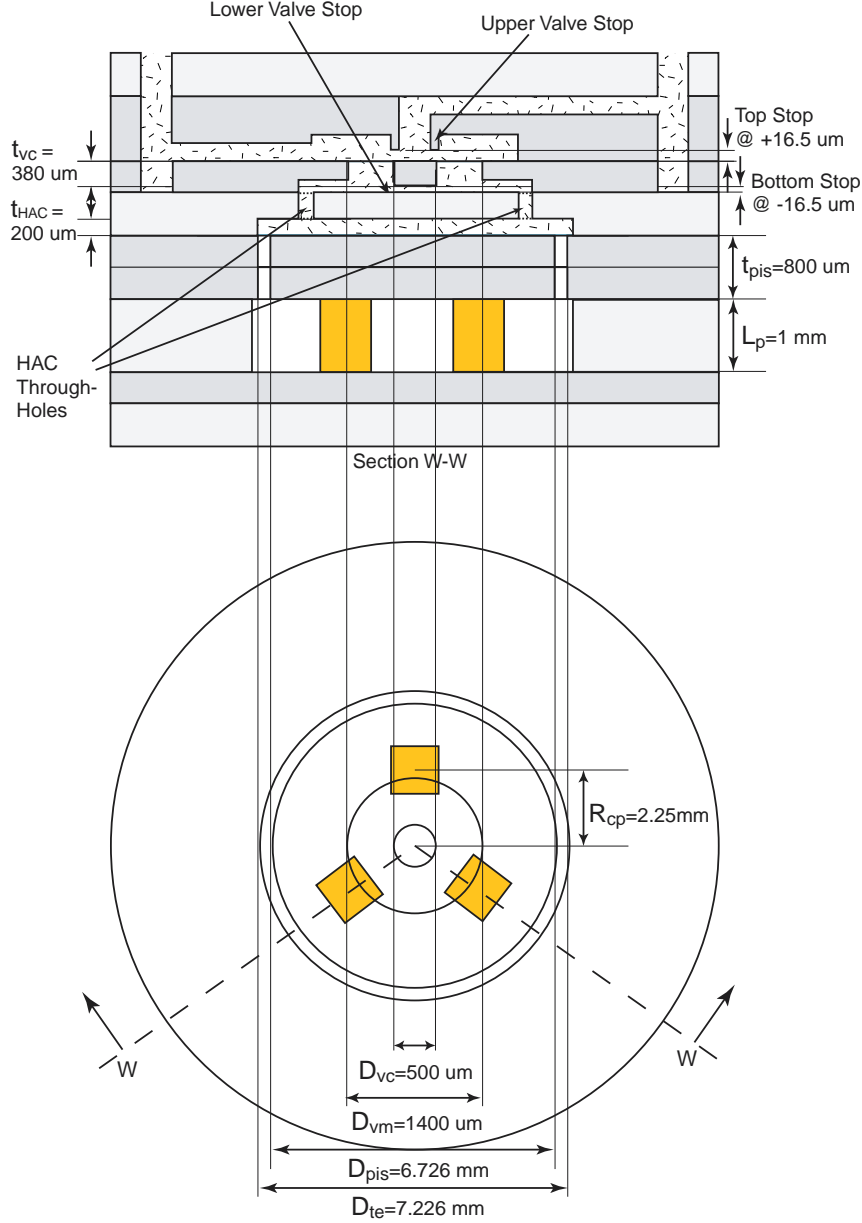


Figure 81: Dimensions of the fabricated active valve devices. Three square PZN-PT elements were incorporated beneath a double-layer tethered piston. A valve cap and membrane structure interacts with the fluid orifice structure at  $Z_{vc} = +16.5\mu m$  and with the glass Layer 6 structure within the HAC chamber at  $Z_{vc} = -16.5\mu m$ .

### 5.4.3 Summary of Results

**Device Actuation Capabilities** To characterize the frequency-dependent behavior of the active valve device, a low-voltage ( $0V \pm 5V$ ) sweep signal from 500Hz to 100kHz was applied to the piezoelectric drive element structure. The corresponding valve cap and piston displacements were measured using the laser vibrometer system. Figure 82 overlays the frequency response of the drive element piston with

that of the valve cap, for the case in which oil is present above the valve structure but for which no differential pressure or flowing fluid occurred across the valve orifice. These tests were performed with  $P_{bias} = 500kPa$  to eliminate the possibility of cavitation within the HAC chamber. Additionally, the pressures above the valve cap and membrane were maintained at  $P_{IN} = P_{OUT} = 500kPa$ .

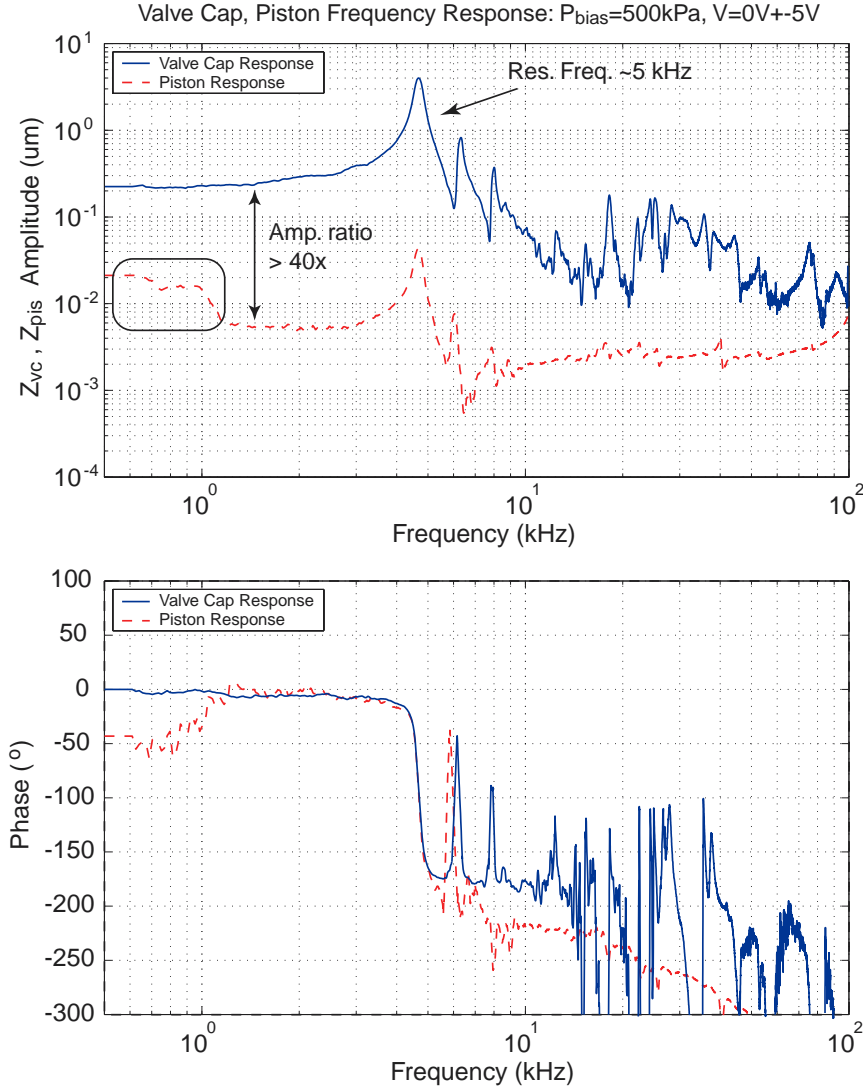


Figure 82: Low-voltage ( $0V \pm 5V$ ) piston and valve cap frequency responses from 500Hz to 100kHz, with oil present above the valve structure. The top figure plots the valve cap and piston amplitudes, while the bottom figure plots the corresponding phase. The bias pressure in these tests was maintained at  $P_{bias} = 500kPa$ . An amplification ratio between 40x-50x is observed for frequencies below 5kHz.

The piston and valve responses both followed the same patterns across the frequency range. The valve 1st modal frequency was observed to occur at  $\sim 5kHz$ . The additional peaks in the response were most likely a result of fluid-structure interactions between the oil and the experimental test-jig flow tubes external to the device or between the oil and the flow channels internal to the device. The increase in piston displacement amplitude at frequencies below 1kHz was due to measurement limitations in the

vibrometer system (essentially the magnitude of the measured velocities and displacements were of the same order as the noise floor of the system). The results indicate that the amplification ratio of the valve device was steady (between 40x-50x) over the range of frequencies below resonance.

The previous frequency sweep experimental tests found the 1st modal frequency of the device to be  $\sim 5\text{kHz}$ . In order to evaluate the quasi-static performance of the structure under the larger drive voltage levels at which the valve was designed to operate, a frequency of operation of  $1\text{kHz}$  was chosen. Figure 83 plots the valve cap and piston displacement time histories, respectively, at this drive frequency over a range of applied voltages from  $50\text{Vpp}$  to  $800\text{Vpp}$ . In Figure 83(a), the dotted lines at  $+16.5\mu\text{m}$  and  $-16.5\mu\text{m}$  indicate the position of the upper and lower valve stops, respectively. For an applied voltage of  $50\text{Vpp}$ , the response of the valve cap was purely sinusoidal. As the voltage was increased to  $800\text{Vpp}$ , the resulting valve cap displacement time history contained small amplitude higher frequency ( $\sim 5\text{kHz}$ ) oscillations due to the non-linear nature of the valve membrane structure. These oscillations became more pronounced as the voltage was increased. In Figure 83(b), the drive element deflection time histories were somewhat rough in nature due to the noise level of the measurement system. As the deflections increased in amplitude, the effect of this noise floor diminished. It is important to note that for a voltage of  $800\text{V}$ , the valve was not deflected sufficiently to close against the valve orifice. This was due to the fact that the actual piezoelectric material coefficient was only  $\sim 75\%$  of the expected value used for the original valve design (see further discussion in next paragraph).

Figure 84 takes these deflection time histories and plots the valve cap peak-peak displacement, piston peak-peak displacement, and corresponding device amplification ratio as a function of applied voltage to the piezoelectric drive element. The amplification ratio was observed to decrease from 50 to 40 as the voltage was increased. This decrease was a result of increased pressurization within the HAC chamber due to the non-linear increase in the valve membrane stiffness. As the voltage was increased, a smaller percentage of the drive element swept volume was transferred to the valve membrane since more volume was lost in the chamber compliances.

Figure 84 also includes model predictions for this behavior. Shown on this plot are three curves generated from the active valve simulation tools discussed previously. The first curve is the predicted response based on the assumed piezoelectric material coefficient value of  $d_{33} = 2000\text{pC/N}$  used in the original design of the active valve device. The second two model curves are based on limiting values of  $d_{33} = 1300 - 1500\text{pC/N}$  determined by measuring a large number of individual piezoelectric elements and observing the range of piezoelectric coefficients. Active valve performance was therefore compared to these limiting model cases rather than the ideal case since the piezoelectric elements were determined to be inferior to original design assumptions. The model correlation indicates that the experimental valve cap deflection curve falls slightly short (at  $800\text{Vpp}$  for example, the cap deflection was  $26\mu\text{mP-P}$  versus the predicted  $31\mu\text{mP-P}$ ) of the prediction limits for  $d_{33} = 1300 - 1500\text{pC/N}$ , while the experimental piston deflection curve falls within these limits for large enough applied voltage. Based on these results, it can be concluded that an additional compliance mechanism must exist within the HAC chamber, most likely due to a smaller than expected value of fluid bulk modulus. A fluid bulk modulus of  $K_f = 2\text{GPa}$  was assumed in the active valve models and simulations [35]. The corresponding device amplification ratio, as shown in Figure 84(c) decreased slightly from  $\sim 50\text{x}$  for a low voltage of  $100\text{Vpp}$  to  $\sim 40\text{x}$  for a high voltage of  $800\text{Vpp}$ , consistently within 5-10% of the limiting model predictions.

Table 4 summarizes the critical actuation capabilities of the active valve device in comparison to model predictions. As discussed previously, the valve 1st modal frequency occurred at  $\sim 5\text{kHz}$ . Finite-element models of this valve structure had predicted a 1st modal frequency of  $14\text{kHz}$ , however, these models did not include the presence of oil above the valve cap and membrane structure. It was this added mass of the oil that reduced the 1st modal frequency of the valve structure. Future modeling of the valve should more carefully include this added mass effect when predicting modal behavior. As for quasi-static operation at  $1\text{kHz}$ , as already discussed, the measured device valve cap deflection fell

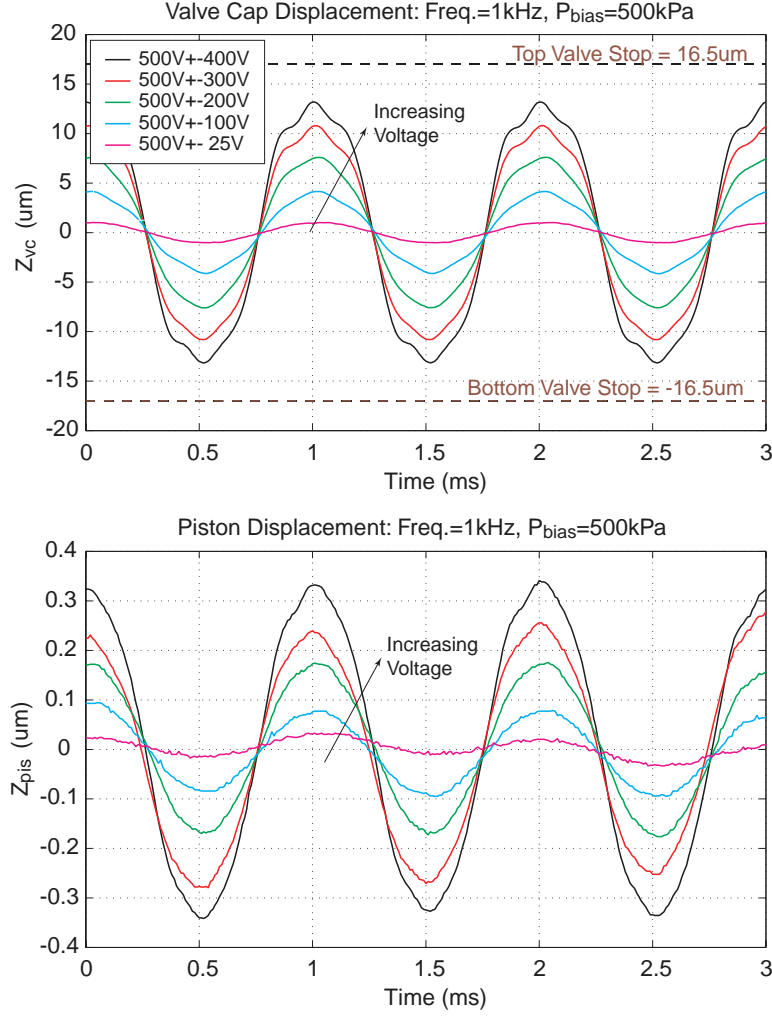


Figure 83: Valve cap and piston deflection time histories for a series of 1kHz sinusoidal drive voltage levels. As the voltage was increased, small amplitude 5kHz oscillations appeared in the deflection responses. Note that a voltage of 800Vpp was not sufficient to close valve cap against the valve orifice.

slightly short of predictions. However, the amplification ratio was in excellent agreement with model predictions. Overall, this encouraging device performance enabled further investigations into the valve's flow regulation capabilities.

**Device Flow Regulation Capabilities** To evaluate the capability of the active valve device to regulate flow at 1kHz, a series of tests was carried out for increasing imposed differential pressure across the valve orifice. Flow regulation tests were performed for differential pressures  $P_{IN} - P_{OUT} = 24\text{kPa}$ ,  $95\text{kPa}$ ,  $145\text{kPa}$ ,  $200\text{kPa}$ ,  $260\text{kPa}$ , and  $340\text{kPa}$ . By controlling  $P_{HAC}$  with respect to the magnitude of  $P_{IN}$  and  $P_{OUT}$  (using the high-frequency channel and corresponding bias pressure regulator set-up discussed previously), the valve cap was displaced statically upward to a deflection of  $Z_{vc} = 11\mu\text{m}$ . A sinusoidal voltage of 500Vpp was then applied to the piezoelectric drive element at 1kHz to actuate the valve cap

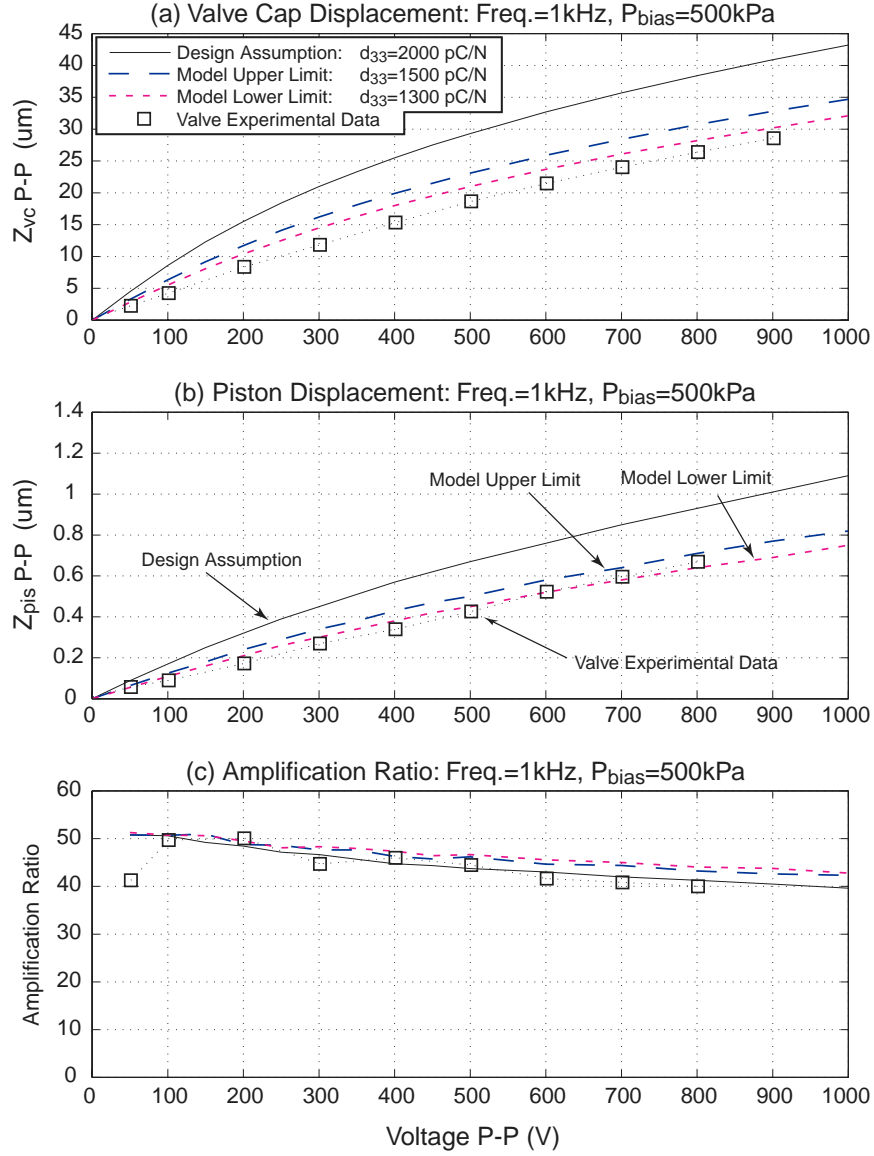


Figure 84: Active valve quasi-static 1kHz model correlation for increasing applied voltage: (a) the valve cap deflection curve was 5 – 10% below the limiting bounds for  $d_{33} = 1300 - 1500\text{pC/N}$ , (b) the piston deflection curve fell within the limiting bounds for large voltage, and (c) the device amplification ratio (between 40x and 50x) agreed very closely with the predicted limiting bounds.

upward against the valve orifice and downward toward the original equilibrium position of the valve cap. In all test runs, it was desired to just barely close the valve cap against the orifice at its maximum displacement, and to maintain  $Z_{vc} = 0$  at its minimum displacement. In others words, it was desired to always ensure a valve opening stroke of  $16.5\mu\text{m}$ .

Figure 85 plots the experimentally measured flow rates for each of the differential pressure test cases. An applied voltage of 500Vpp was held constant for all of the test cases, and the corresponding measured stroke of the valve cap during actuation is printed inside of each data bar. Figure 85 also

Performance Characteristics	Experimental Results	Model Predictions
1st Modal Frequency	5 kHz	14 kHz
Piston Deflection (@1kHz, 800Vpp)	$0.65\mu m$ pp	$0.72\mu m$ pp
Valve Cap Deflection (@1kHz, 800Vpp)	$26\mu m$ pp	$31\mu m$ pp
Amplification Ratio (@1kHz, 800Vpp)	40x	43x

Table 4: Active Valve Actuation Capabilities

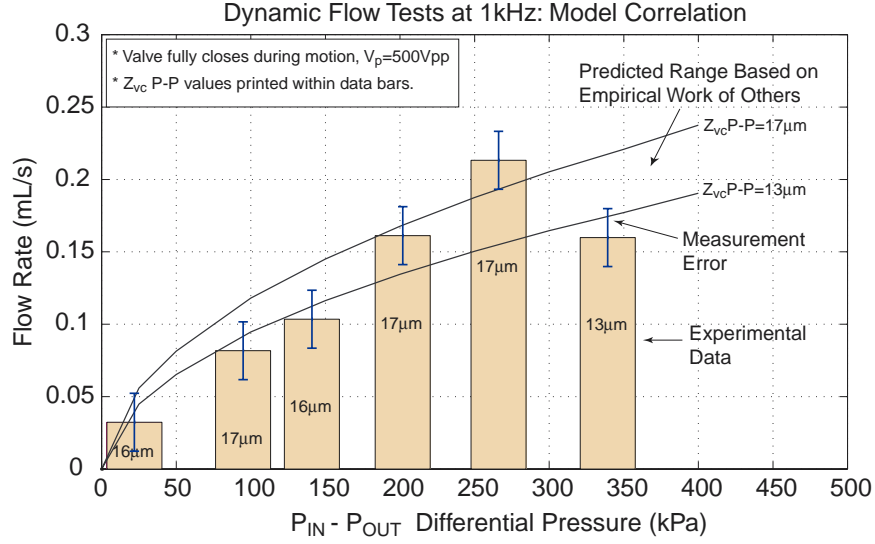


Figure 85: Dynamic flow regulation model correlation at 1kHz for varying differential pressures. Correlation is good over range of differential pressures. Error bars on the data indicate the measurement error, which was estimated based on the flow sensor calibration error and the accuracy of the applied differential pressure.

plots the experimental results versus the model expectations obtained using the active valve simulation tools detailed previously. Model predictions for chosen limiting valve strokes of  $Z_{vc,PP} = 13\mu m$  and  $Z_{vc,PP} = 17\mu m$  are shown. The model correlation indicates that the active valve regulates flow in excellent correlation with the model predictions. Since the flow loss coefficients are based on a compilation of empirical work from other researchers, the line of predicted behavior in Figure 85 is understood to be of only “limited accuracy”, in other words, it is not based on exact theory.

Subsequent test runs at differential pressures in excess of  $P_{IN} - P_{OUT} = 340kPa$  resulted in unstable oscillatory motion of the valve cap structure, and eventually fracture of the valve membrane. The nature of the flow behavior (based on Reynolds number) was investigated for a variety of valve opening situations in subsequent studies. The results indicated that these self-excited valve cap oscillations were most probably a result of transitional flow (between laminar and turbulence) through the valve orifice structure, a regime which limited the valve operation to relatively low differential pressures of no more than 340kPa. A comprehensive overview of these unstable oscillatory valve cap experiments is detailed

in [35]. Future research work should focus on a better understanding of the flow regimes through these microscale orifice structures and on a redesign effort to develop a valve geometry which is less sensitive to the flow behavior passing through the orifice. Additionally, this redesign should include an effort to increase the 1st modal frequency of the device, to potentially enable operation at or above a frequency of 10kHz. With these redesign efforts, a higher frequency, higher flow rate microvalve could be achieved.

#### 5.4.4 Conclusions

The piezoelectrically-driven hydraulic amplification microvalve, for use in full MHT systems, was successfully fabricated and tested. This concept of hydraulically amplifying the limited stroke of a miniature bulk piezoelectric material into a significantly larger motion of a valve cap structure enabled the valve to simultaneously meet a set of high frequency ( $\geq 1\text{kHz}$ ), high pressure ( $\geq 300\text{kPa}$ ), and large stroke ( $20\text{--}30\mu\text{m}$ ) requirements not previously satisfied by other microvalves. The active valve structural behavior and flow regulation capabilities were evaluated over a range of applied piezoelectric voltages, actuation frequencies, and differential pressures across the valve. For applied piezoelectric voltages up to  $500\text{V}_{\text{pp}}$  at  $1\text{kHz}$ , the valve devices demonstrated amplification ratios of drive element deflection to valve cap deflection of  $40\text{x--}50\text{x}$ . These amplification ratios correlated within  $5 - 10\%$  of the model expectations. Flow regulation experiments proved that a maximum average flow rate through the device of  $0.21\text{mL/s}$  for a  $1\text{kHz}$  sinusoidal drive voltage of  $500\text{V}_{\text{pp}}$ , with valve opening of  $17\mu\text{m}$ , against a differential pressure of  $260\text{kPa}$  could be obtained. Tests revealed that fluid-structural interactions between the valve cap and membrane components and flow instabilities (due to transition between the laminar and turbulent flow regimes through the valve orifice) limited the valve performance capabilities. These limitations have an effect on the capabilities of full MHT devices.

As a discrete valve, this device compares favorably with other microvalves reported in the literature in terms of flow rate, frequency of operation and maximum pressure. These tests have shown that it is possible to develop a high flow rate high pressure piezoelectric microvalve. A redesign to stiffen the valve and change its dynamics should allow it to operate at its initial design specifications.

### 5.5 Contributions: Subcomponent Devices

The evaluation of the MHT subcomponents proved to be quite valuable, and the following contributions can be summarized:

1. The drive piston subcomponent as the first MEMS device to use bulk piezoelectric material integrated by means of thin film bonding.
2. An understanding of the drive piston and its use as a fluidic actuator.
3. The first demonstration of hydraulic stroke amplification on the microscale, with amplification ratios as high as  $40:1$
4. The hydraulically amplified piezoelectric microvalve, capable of high flow rates and high frequencies of operation.





## 6 MHT Pump Device Testing

### 6.1 Overview and objectives

The previous sections described tests aimed at characterizing the subcomponents of the MHT device. With these results in hand, the MHT device itself could be tested. This section describes tests performed on two active valve MHT devices, using the testing system described in Section 5.1. Tests were performed under the following operating conditions:

- Frequency:  $625Hz$  and  $1kHz$
- Pump piston voltage: up to  $1200V_{p-p}$
- Active valve voltage: up to  $550V_{p-p}$
- $\Delta P$ : up to  $325kPa$

### 6.2 Experimental test setup used for MHT pump testing

The test setup used to test the MHT pump device, along with the key measurements, is shown schematically in Figure 86. For a detailed description of the actual test setup, the reader is referred to Section 5.1. During operation of the MHT pump device, the following measurements were performed:

1. Flow rate through and pressure drop across the device. ( $\Delta P$  and  $Q$ )
2. Steady (average) outlet pressure. ( $P_{HPR}$ )
3. The steady pressures in the hydraulic amplification chambers. ( $P_{HAC}$ )
4. The valve cap displacements (Only one at a time). ( $x_{valve}(t)$ )
5. The voltages and currents into each piezoelectric drive piston. ( $V(t), i(t)$ )

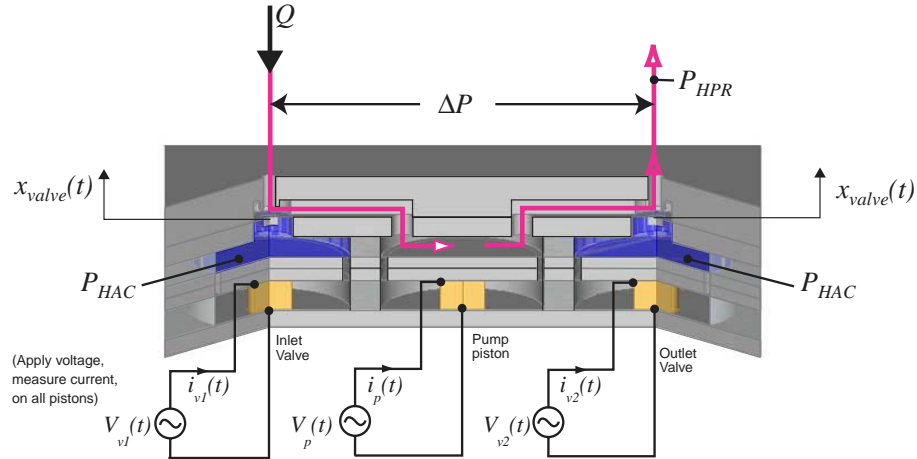


Figure 86: Schematic of the pump test setup. During testing of the device, all the pressures, flow rates, voltages and currents shown here were measured.

## 6.3 Standard testing protocol

All tests performed on the active valve MHT pump devices were aimed at determining the flow rate for a given  $\Delta P$ . Because the pressures in the HAC's were not coupled to  $P_{HPR}$  and  $P_{LPR}$ ,  $P_{HAC}$  for each valve had to be set individually for each new  $\Delta P$ . The following protocol was followed to ensure that, for a given  $\Delta P$ , the valves motions had the same mean position for a given valve drive voltage.

1. *Determine the correct valve and piston drive waveforms.* Although the valves were initially designed to be driven by half-sine type waveforms, it was later found to be beneficial, especially at lower pressures of operation, to have a stationary region in the valve motion as is depicted in Figure 87. This would give a "full" pressure swing in the chamber, between  $P_{HPR}$  and  $P_{LPR}$ . The piston drive voltage was always sinusoidal. In all experiments the drive waveforms were not allowed to go negative to prevent depoling of the  $PZN - PT$  material. This material was found to have a small negative coercive field and good field-strain linearity at high positive field and low preload. Therefore, the benefits of allowing the piezo voltage to go slightly negative seemed small compared to the risk of depoling.
2. *Decide on valve and piston drive voltages.* Higher valve and piston drive voltages were in general associated with better device performance, but also with an increased risk of breakage. Therefore, successive test runs were performed at ever increasing drive voltages for both the valves and the piston.
3. *Position valves at their equilibrium positions* Here the pressures are set such that  $P_{HAC} = P_{LPR} = P_{HPR} = P_{CH}$ . This ensures that the valves are in their zero deflection state.
4. *Start the electrical excitation at the desired voltage and frequency* start driving the piston and the valves electrically. At this point, a flow rate will be observed, but it may be low, due to the fact that the valves are not necessarily contacting the valve seats, resulting in reverse leakage.
5. *Adjust  $P_{HAC}$  for the correct valve steady positions.* The valve steady position is readjusted to allow the valves to *just* touch their seats at maximum travel. This allows sealing to occur during the suction and discharge cycles of the pump. The valve steady position is the rest position of the valve. It is given by the steady (or static) pressures acting on it, hence:  $P_{HAC}$ , the static pressure in the hydraulic amplification chamber, the pressure on the valve membrane, which is either  $P_{HPR}$  or  $P_{LPR}$ , and the pressure on the valve,  $P_{CH}$ , the pressure in the pump chamber. By assuming that  $P_{CH} \approx (P_{HPR} - P_{LPR})/2$ , all the pressures on the valve caps were known, and, using the nonlinear valve membrane deflection code described in [35], the steady position of the valve could be predicted and set using the various pressures. This estimation method was verified against direct displacement measurement of the valve using a Polytec PSV-300H scanning laser vibrometer (SLV), and was proven to be very accurate.
6. *Determine and set the desired pressure differential ( $\Delta P$ ).* The pressure differential was the varying parameter for each set of drive voltages and valve positions. During this step,  $\Delta P$  is raised to the desired level, and, along with it,  $P_{HAC}$  for the outlet valve is raised to retain contact of the valve with its seat. Valve contact was verified as a zero velocity signal using the Polytec PSV-300H SLV. The valve steady position was again backed out using the nonlinear analysis code. For reasons related to this particular experimental setup, it was easier to reduce  $P_{LPR}$  rather than increase  $P_{HPR}$  to increase  $\Delta P$ . This, however, required that  $P_{HPR}$  be set such that  $P_{LPR}$  remain high enough to prevent cavitation at the inlet. The minimum value for  $P_{LPR}$  varied between  $15kPa$  and  $200kPa$  for various test runs, with  $P_{LPR}$  being higher for higher performance tests. The minimum value for  $P_{LPR}$ , given a set of operating parameters, was not determined in this work. From the

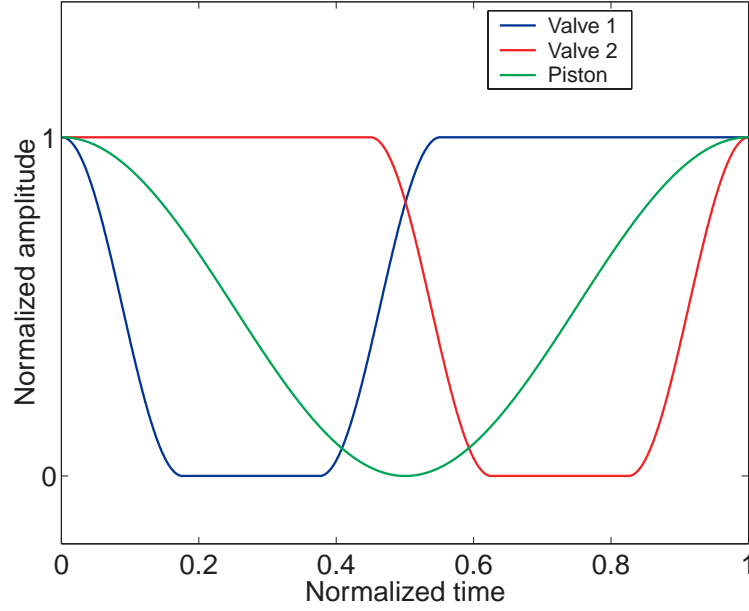


Figure 87: Active valve and piston drive waveforms for the pump device.

linearity observed in the  $\Delta P - Q$  plots, we can conclude that cavitation was not a significant issue in the experiments performed.

The above tests were performed using the testing system described in Section 5.1

### 6.3.1 Limitations of the pump testing: Difficulties at high flow rates

At very high (but not yet design level) flow rates, a limit for device operation was found. This was initially observed in the active valve tests, described in Section 5.4.3. When operated under very high flow rates, excessive valve oscillation was observed. In [35], this phenomenon is explained and is attributed to flow induced vibration in the transition flow regime between laminar and turbulent flow. Device operation under these conditions was not possible, and indeed, this was also the cause of failure of the best performing device. This phenomenon, also not captured by models, placed a fundamental limit on the capabilities of the devices tested here. A suitable redesign to eliminate this suspected mode of vibration should enable the devices to perform to their initial, quasi-steady design limits. It should be noted that under static loading conditions, the valve membranes saw deflections with associated stresses in the membranes close to the 1GPa design limits of the device. Therefore, if the flow-vibration problem could be eliminated, along with the associated high dynamic stresses, the devices should be able to perform as designed.

## 6.4 MHT pump operation results

This section presents results from the tests performed on two MHT pump devices. Both devices had a single inlet and a single outlet valve, identical to the valves that were described in Section 5.4. Therefore, these two MHT devices were tested within the limits set by the capabilities of those active valves.

Figure 88 shows the best data obtained from all the runs of active valve pump tests. This figure displays the pressure differential attained, the electrical power consumed, as well as the efficiency of the

device. For this result, the operating conditions of the device were as follows:

- Valve drive voltages:  $550V_{p-p}$ .
- Piston drive voltage:  $1200V_{p-p}$ .
- Resultant valve peak-to-peak displacement:  $\sim 11\mu m_{p-p}$ .
- Drive frequency:  $1kHz$ .

The  $\Delta P$  vs.  $Q$  curve shows a linear relationship between pressure differential and flow rate. This result was observed during all tests, and is consistent with model predictions. In fact, it is easy to show that the flow rate  $Q$  for a positive displacement piston-type pump with a compliant chamber, under quasi-static conditions, should depend approximately linearly on the pressure. (See e.g. [11]) All tests conducted were of the same type as the test shown in Figure 88. Hence, a set of drive voltages and a drive frequency would be picked, and then the flow rate would be measured at various differential pressures. In this case the pressure is shown on the vertical axis to be consistent with the typical head vs. flow rate curve that is often used to describe the performance of commercial pumps. Note that all curves shown, except where noted otherwise, are least squares fits to the data shown. The fluid power is defined as:

$$P_{fluid} = \Delta P \times Q \quad (32)$$

and the efficiency as:

$$\eta = \frac{P_{fluid}}{P_{electrical}} \quad (33)$$

Figure 89 shows the effect of changing the valve stroke as well as the mean position of the valve. This figure demonstrates the importance of the correct  $P_{HAC}$  and also valve drive voltage to ensure maximum performance is attained. The maximum (zero  $\Delta P$ ) flow rate does not change appreciably with increased valve motion, indicating that the pump is not being "choked" by the valves. In subsequent tests the goal was to ensure that the valves would always be fully sealed when at the top of their stroke by controlling  $P_{HAC}$ . Increasing the piston drive voltage, as shown in Figure 90, has the effect of increasing both the maximum flow rate as well as the maximum pressure delivered by the pump. The flow rate increases due to the increased stroke of the pumping piston, and the pressure increases due to higher pump chamber pressures associated with the larger piston stroke. Small variations in the valve mean position from test to test could explain why the curves are not parallel in Figure 90. Increasing the drive frequency has the effect of increasing the maximum flow rate but not the maximum pressure attained. Figure 91 shows the combined effect of increasing frequency and increasing voltage. Although the drive voltage differs in the two curves, the factor  $1.6\times$  increase in frequency does produce an increase in flow rate that is noticeably higher than the flow rate increases observed in Figure 90.

It is interesting to compare the results of the active valve MHT device to those of the passive valve micropump discussed in [2]. This device, built as an MHT technology demonstrator, had a  $3.6mm$  pumping piston and was driven at a maximum frequency of  $12.5kHz$ . The MHT device, driven at  $1kHz$ , with a piston diameter of  $6.8mm$ , compares favorably with this device. Figure 92 shows the comparison. The higher pressure attained by the passive valve device can most likely be attributed to an overall stiffer structure and less chamber compliance associated with the smaller piston. Figure 93 shows a rescaled version of Figure 92, where the flow rate for the MHT device was multiplied by 12.5, under the assumption that with a suitable redesign for higher frequency operation it should be possible to eliminate the current  $\sim 6kHz$  resonant frequency of the valve, or make it higher. Furthermore, the

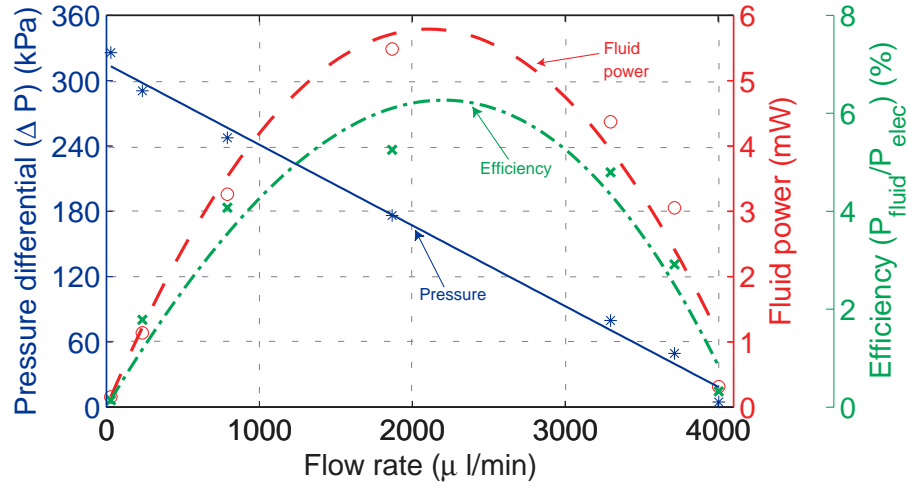


Figure 88: A graphical summary of the best results attained during the active valve pump testing experiments. The device failed during subsequent attempts to achieve better performance. The curves shown are least squares fits through the data.

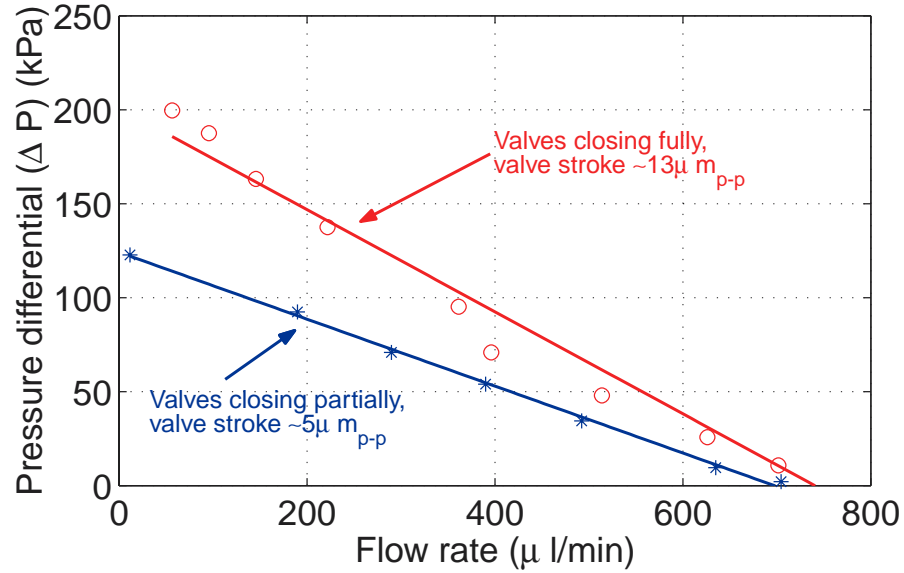


Figure 89: Effect of increasing valve motion from partially sealed to fully sealed operation. For these plots, the drive frequency was  $625\text{ Hz}$ , using a  $600V_{p-p}$  piston drive voltage and a  $350V_{p-p}$  valve drive voltage for the  $5\mu\text{m}_{p-p}$  results, whereas  $550V_{p-p}$  was used to obtain the  $13\mu\text{m}_{p-p}$  results. Fully sealed operation was verified by taking displacement-time laser vibrometer data. The lines are linear fits to the data.

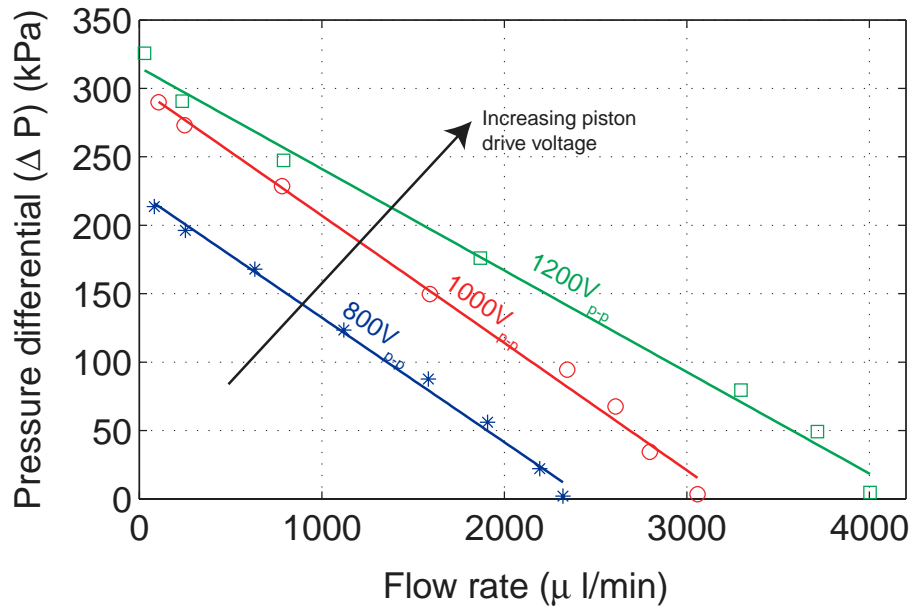


Figure 90: Effect of increasing drive voltage on pump performance. The drive frequency was  $1kHz$  and the valve drive voltage  $550V_{p-p}$  for all data shown.

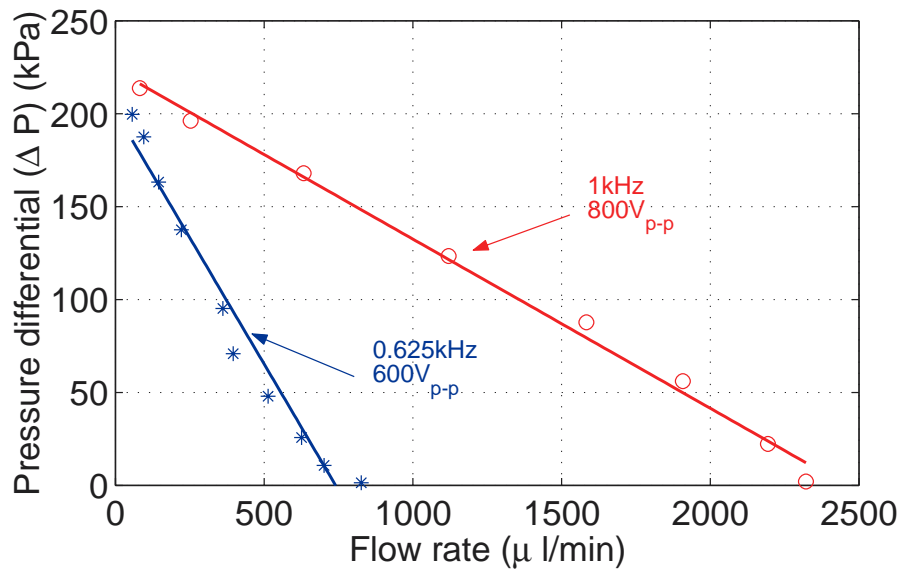


Figure 91: Combined effect of increasing frequency and drive voltage. Although the drive voltage differs in the two curves, the factor  $1.6\times$  increase in frequency does produce an increase in flow rate that is noticeably higher than the flow rate increases observed in Figure 90 for proportional voltage increases.

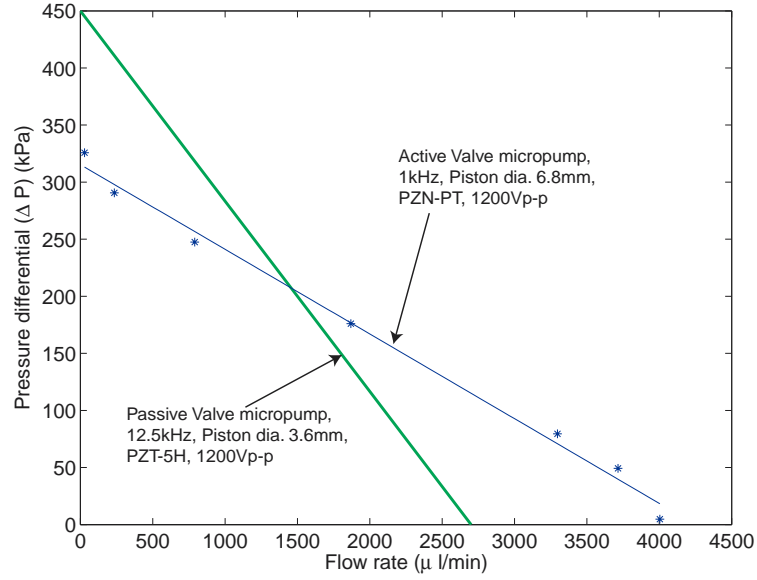


Figure 92: Performance of the active valve MHT pump compared to a previous passive valve technology demonstrator device. The former device (See [2]) had a  $3.6\text{mm}$  diameter piston, and was operated at a frequency of  $12.5\text{kHz}$ . The active valve MHT device has a pumping piston diameter of  $6.8\text{mm}$  and an operating frequency of  $1\text{kHz}$ .

flow rates were divided by the piston area to yield pressure-flow rate relations per unit piston area. This comparison suggests that the active valve MHT device could yield significant performance improvements over its predecessor. A peak power of approximately  $2\text{mW}/\text{mm}^2$  of piston area corresponds to a total fluid power of  $70\text{mW}$ . This comparison, however, did not alter the maximum pressure, which could also increase with a redesign of the valves. The target acoustic power for underwater noise generation of  $0.25$  to  $0.5\text{W}$  could be attained by utilizing an array of MHT devices in parallel, increasing the piston diameter or having pistons with a larger stroke. These strategies will be discussed further in the next chapter.

## 6.5 Conclusions: MHT pump device testing

The following accomplishments and other significant items were realized during testing of the MHT active valve pump device:

1. Two MHT pump devices were tested, with a maximum  $\Delta P$  of  $320\text{kPa}$ , and a maximum fluid power of  $5.5\text{mW}$ . The maximum efficiency was  $5.5\%$
2. By a rescaling of the results, it is projected that a maximum fluid power of  $70\text{mW}$  is attainable from this MHT device. By making suitable design changes and/or by combining a number of these devices in parallel, they could be a feasible means of hydraulic actuation for underwater acoustic noise generation.

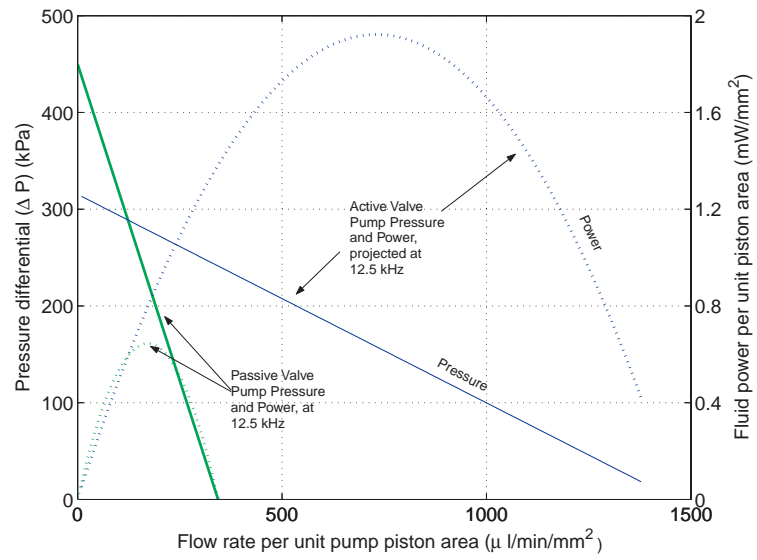


Figure 93: Performance comparison by rescaling Figure 92 to account for the mismatch in drive frequencies and piston diameters. The active valve MHT device shows a potential improvement in overall fluid power delivered, should it be redesigned to operate at higher frequencies.



## 7 Conclusions and Recommendations

### 7.1 Conclusions: An overview

In this project, several significant advancements were made in the following areas:

1. Systems modeling
2. Flow losses through annular poppet valves
3. Microfabrication techniques for silicon tethered membrane structures.
4. Integration of bulk piezoelectric material on the microscale.
5. Evaluation of the strength of silicon membranes for use as flexural seals, and the requirements placed on the fabrication of these structures.
6. Filling small micromachined dead volumes with liquids and sealing them.
7. Hydraulic amplification was proven on the microscale for the first time.
8. For the first time, an hydraulically amplified high-pressure high-frequency valve was demonstrated on the microscale.
9. The first active valve micropump was demonstrated.

These accomplishments will now be discussed in detail.

### 7.2 Systems modeling

- A full lumped parameter system modeling scheme was introduced, taking into account all the relevant material properties.
- To this lumped model was attached the results of a nonlinear membrane deflection code in the form of lookup tables to accurately model the valve motions of this device.

### 7.3 Valve flow loss modeling

- A macroscale test setup was constructed to measure the loss coefficients of annular poppet microvalves. These loss coefficients correlated well with measured values from experiments of the microfabricated valve devices.

### 7.4 Piezoelectric material capabilities

- Detailed nonlinear material models were derived for PZT-5H, PZN-PT and PMN-PT piezoelectric materials.
- Techniques were developed for incorporating small bulk piezoelectric actuation elements into a microfabricated structure with micron-size tolerances. This enabled the fabrication of power-MEMS devices with superior performance compared to similar devices attempting to use thin film piezoelectric materials.

## 7.5 Thin silicon membrane structures - strength and manufacturability

- Techniques were developed for the fabrication and testing of small silicon tethered membranes structures. The microfabrication techniques were centered around an increased emphasis on cleanliness during processing to minimize point defects, as well as careful inspection and covering of etched features during the final stages of deep etching.
- A testing apparatus was built, and strength numbers were obtained which were subsequently used in the design of the final energy harvester device.

## 7.6 Fluid filling and sealing capabilities

- Techniques were developed for reliably filling and sealing micromachined dead volumes, bubble free. By using a silicone oil that wetted the silicon surfaces well, and by using proper evacuation and purging prior to filling, a robust filling process was obtained.
- This project introduced a novel dynamic sealing technique using a flow restriction to isolate high frequency pressure fluctuations in the hydraulic amplification chambers from an external static pressure.

## 7.7 Microscale hydraulic amplification

- This project marked the first demonstration of hydraulic stroke amplification on the microscale.
- Good correlation with models were obtained, and it was shown that hydraulic amplification can be a stiff, compact means of stroke amplification, primarily as designed, for valve actuation, but with potential for other small-scale positioning and actuation applications.

## 7.8 Microvalve development

- This project presented the first hydraulically amplified piezoelectrically driven valve.
- In terms of combined pressure, flow and frequency capability, this valve addresses a niche area of applications for which until now there has not been such a device reported in the literature.
- Again, good correlation was seen with models.
- The device was limited by flow induced vibration. With a suitable geometric redesign, it should be possible to eliminate this problem.

## 7.9 The MHT device as a bi-directional micropump

- The MHT device was finally tested as a pump. A maximum flow rate of  $4000\mu l/min$  and a maximum pressure differential of  $320kPa$  was attained.
- This was the first microfabricated pump with active valves.

Indeed, the final MHT device is bi-directional in more than one sense: Thanks to its active valves and the symmetric design presented here, the pump itself is capable of delivering flow in both directions, by simply changing the phasing of the valve drive signals. In addition, it can be operated as either a pump or as an energy generator, hence having bi-directional energy flow.

## 7.10 Recommendations for advancement of MHT Technology

### 7.10.1 Recommendations for advancement of the technologies that were developed

For the technologies and achievements mentioned in the previous sections, the following steps are recommended should future work be undertaken:

- *Modeling:* The system modeling can benefit from additional work to better understand the chosen piezoelectric material and its capabilities. An efficiency of 70% was assumed for the piezo and its circuitry, and this assumption should be better accounted for. In addition, the dynamic design of the valve needs to be revisited to design a valve that (a) has a higher first natural frequency and (b) does not have any structural modes of vibration that can couple with fluid oscillations to create an unstable operating regime below the design frequencies and pressures. This need not necessarily be accounted for in the lumped parameter model, because this redesign will ensure that the initial assumptions in the lumped system model will still hold.
- *Bulk piezoelectric integration on the microscale:* This project has proven that there are tangible benefits to be had from using bulk piezoelectric material in a microfabricated device where superior actuation or energy conversion is needed. Therefore, it is recommended that an easier manufacturable approach for the integration of piezoelectric actuation elements be developed. A wafer-scale approach with active elements would be beneficial for a large number of small-scale actuation applications.
- *Silicon membrane fabrication:* This process needs to be improved to allow for the batch fabrication of these structures whilst maintaining good structural properties. Design changes have been proposed that involve an additional isotropic shallow etch from the SOI device side to form the fillet. A wider deep trench etch is then performed. By choosing the correct geometry, the maximum stress still occurs at the fillet, but in this case the fillet is much easier to etch.
- *Hydraulic amplification devices:* The hydraulic amplification devices can benefit from an exploration of different application prospects such as microactuation and positioning. In addition, further work is required to make the piezoelectrically driven hydraulic amplifiers self-contained in the sense that an external static pressurization is not required. Although this feature proved exceptionally useful during testing, it may not be practical for a real non-fluidic device such as a simple hydraulically amplified actuator. (In the case of a fluidic device, a design could be conceived where the dynamic seal connects directly to the low and high pressure reservoirs, hence making it self-contained).
- *Fluid filling:* The fluid filling techniques worked well for these experimental devices. However, for productions systems further refinement will be needed.
- *Microfabricated active valve:* It has been mentioned a number of times before, but the single biggest benefit from future work on the active valves would be a design effort that attempts to increase the natural frequency of this device. In addition, this device could also benefit from a good "static" sealing approach that would open a wide range of additional applications for this valve as a fast-acting, high pressure, high performance valve.
- *MHT Pump device:* This device would benefit most from a redesign of the active valves. There also remains some interesting work related to the cascading in series/parallel of these pumps. It may be possible to either attain very high pressures, flow rates or both from series-parallel combinations

of these devices. With the existing knowledge, it may also benefit to revisit the passive valve pump design as a simpler alternative for less demanding applications. As had been noted before, however, overall system complexity is not necessarily reduced by using a passive valve pump, since the external hydraulic system will now require active components such as valves and actuators. A more detailed study of the trade-offs may prove fruitful

### 7.10.2 Recommendations for development of additional technologies

The following aspect were not fully addressed in this project, but would need further study to enable MHT technology to become a practical technology for typical real-life applications:

- *Drive electronics:* The devices discussed in this report used conventional linear amplifiers and macro-scale drive electronics. This certainly has to change for MHT devices, and also valves and hydraulic amplifiers, to become feasible.
- *Hydraulic actuation system design and development:* Little attention was given to the design of a self-contained compact hydraulic actuation system. This needs to be developed, whether the application would be a compact underwater acoustic noise source or any other microscale servo-hydraulic actuation system. Integration of a fully enclosed, permanently sealed hydraulic system will make MHT technology a reality for real world applications.

## 7.11 Feasibility: Underwater acoustic noise generation and MHT technology

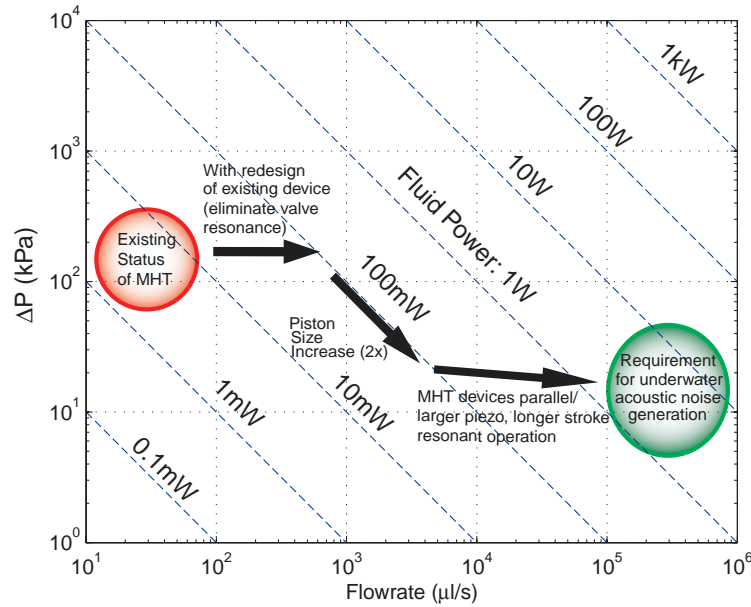


Figure 94: Roadmap for underwater acoustic noise generation using MHT technology. Although the existing devices fall short of the required flow rate and fluid power, they do provide higher pressure. By redesigning the MHT device to be better suited to the underwater acoustic noise application, the required flow rates and pressures should be attainable.

This project has gone to great lengths to develop the core technologies that are required to produce an MHT device that can function as a pump for an underwater acoustic noise generation system. As was discussed in Section 1.3, approximately  $0.5W$  of acoustic power can be attained with a acoustic radiation source of size  $\sim 30mm$ . This number corresponds to a required acoustic pressure of  $\sim 5kPa$  and a hydraulic actuation flow rate of  $\sim 300ml/s$ , or  $3 \times 10^5 \mu l/s$ . The existing MHT devices should be capable of delivering  $\sim 70mw$  per device with suitable design improvements, at flow rates of  $\sim 600 \mu l/s$ . Figure 94 shows a possible roadmap for developing an MHT device to satisfy the requirements. With a piston size increase of  $2.5\times$  to  $17mm$ , an increased piezo stroke of  $2\times$  and by using two devices in parallel, another factor 10 increase in fluid power can be attained. Resonance may also be used to enhance the performance of the MHT at a given pumping frequency. Resonant effects were shown to have a positive effect on the passive valve micropump performance. The active valve MHT was not able to operate at sufficiently high frequencies for this effect to come into play. A second generation redesign of the device, based on the foundations provided in the work presented in this document, should be able to yield a device that can satisfy this application.

In conclusion it can be said that, although the particular MHT *device* presented in this work falls short of its intended goal of being a pump for underwater acoustic noise generation purposes, MHT *technology* was demonstrated to be a very feasible means of achieving this goal. Furthermore, with a suitable set of drive electronics, as well as integration into a self-contained hydraulic system, MHT technology shows promise not only for underwater acoustic noise generation, but also for a variety of applications where compactness, large actuation force and bandwidth are required.



## 8 References

- [1] N.W. Hagood, D.C. Roberts, L. Saggere, K.S. Breuer, K.-S. Chen, J.A. Carretero, H.Q. Li, R. Mlcak, S. Pulitzer, M.A. Schmidt, S.M. Spearing, and Y.-H. Su, "Micro Hydraulic Transducer Technology for Actuation and Power Generation," Proceedings of SPIE: SPIE's 7th Annual International Symposium on Smart Structures and Materials, Vol. 3985, pp. 680-688, 2000.
- [2] H.Q. Li, D.C. Roberts, J.L. Steyn, K.T. Turner, J.A. Carretero, O. Yaglioglu, Y.-H. Su, L. Saggere, N.W. Hagood, S.M. Spearing, M.A. Schmidt, R. Mlcak, and K.S. Breuer, "A High Frequency High Flow Rate Piezoelectrically Driven MEMS Micropump," Proceedings of the IEEE Solid-State Sensor and Actuator Workshop, Hilton Head, SC. pp. 69-72, 2000.
- [3] D.C. Roberts, J.L. Steyn, H.Q. Li, K.T. Turner, R. Mlcak, L. Saggere, S.M. Spearing, M.A. Schmidt, and N.W. Hagood, "A High-Frequency, High-Stiffness Piezoelectric Micro-Actuator For Hydraulic Applications," Proceedings of the 2001 International Conference on Solid-State Sensors and Actuators (Transducers '01), 2001.
- [4] D.C. Roberts, N.W. Hagood, Y.-H. Su, H.Q. Li, and J.A. Carretero, "Design of a Piezoelectrically-Driven Hydraulic Amplification Microvalve for High Pressure, High Frequency Applications," Proceedings of SPIE's 7th International Symposium on Smart Structures and Materials, Vol. 3985, pp. 616-628, 2000.
- [5] D.C. Roberts, O. Yaglioglu, J. Carretero, Y.-H. Su, L. Saggere, and N.W. Hagood, "Modeling, Design, and Simulation of a Piezoelectric Microvalve for High Pressure, High Frequency Applications," Proceedings of SPIE's 8th International Symposium on Smart Structures and Materials, Vol. 4327, 2001.
- [6] H. Van Lintel, F. van de Pol, and A. Bouwstra, "Piezoelectric micropump based on micromachining of silicon", Sensors and Actuators, 15, pp. 153-167, 1988.
- [7] M. Stehr, S. Messner, H. Sandmaier, and R. Zengerle, "The VAMP - a new device for handling liquids or gases," Sensors and Actuators A, 57, pp. 153-157, 1996.
- [8] V. Gass, B. van der Schoot, S. Jeanneret, and N. de Rooij, "Integrated flow-regulated silicon micropump," Sensors and Actuators A, 43, pp. 335-338, 1994.
- [9] S. Shoji and M. Esashi, "Microflow devices and systems," Journal of Micromechanics and Microengineering, 4, pp. 157-171, 1994.
- [10] A. D. Pierce, "Acoustics: An introduction to its physical principles and applications." Woodbury, N.Y., Acoustical Society of America, 1989.
- [11] D. Accoto, M.C., Carrorozza and P Dario, "Modelling of micropumps using unimorph piezoelectric actuator and ball valves," Journal of Micromechanics and Microengineering, 10, pp. 277-281, 2000.
- [12] K. Ikuta, T. Hasewaga, and T. Adachi, "The Optimized SMA Micro Pump Chip Applicable to Liquids and Gases," Proceedings of the 2001 International Conference on Solid-State Sensors and Actuators (Transducers '01), 2001.
- [13] M. Koch, N. Harris, R. Maas, A. Evans, N. White, and A. Brunnschweiler, "Novel micropump design with thick-film piezoelectric actuation," Measurement Science and Technology, v.8 n.1, pp. 49-57, Jan 1997.

- [14] P. Watler and M. Sefton, "A Piezoelectric Driven Controlled Release Micropump for Insulin Delivery," *Trans Am Soc Artif Intern Organs*, Vol. XXXVI, pp. 70-77, 1990.
- [15] B. Wagner, H. Quenzer, S. Hoerschelmann, T. Lisec, and M. Juerss, "Micromachined bistable valves for implantable drug delivery systems," *Proceedings of the 18th Annual International Conference of the IEEE Engineering in Medicine and Biology Society*, pp. 254-255, 1997.
- [16] J.M. Hollerbach, I.W. Hunter, J. Ballantyne, "A comparative analysis of actuator technologies for robotics," *Robotics Review* 2, Eds. Khatib and Oussama, MIT Press, pp. 299-342.
- [17] J.E. Huber, N.A. Fleck, and M.F. Ashby, "The selection of mechanical actuators based on performance indices," *Proceedings of the Royal Society of London, Series A*, Vol. 453, No. 1965, p. 2185.
- [18] S.W. Pulitzer III, "Feasability Assessment and Design of Micro Hydraulic Solid-State Transducers," MIT Master's Thesis. June 1998.
- [19] S. Park and T. Shrout, "Characteristics of Relaxor-Based Piezoelectric Single Crystals for Ultrasonic Transducers," *IEEE Transactions on Ultrasonics, Ferroelectrics, and Frequency Control*, Vol. 44, No. 5, pp. 1140-1147, 1997.
- [20] M. Esashi, S. Shoji, and A. Nakano, "Normally Closed Microvalve and Micropump Fabricated on a Silicon Wafer," *Sensors and Actuators* 20, pp. 163-169, 1989.
- [21] M. Esashi, "Integrated Micro Flow Control Systems," *Sensors and Actuators*, A21-A23, pp. 161-167, 1990.
- [22] S. Shoji, B. Van der Schoot, N. de Rooij, and M. Esashi, "Smallest Dead Volume Microvalves for Integrated Chemical Analyzing Systems," *Proceedings of the 1991 International Conference on Solid-State Sensors and Actuators (Transducers '91)*, pp. 1052-1055, 1991.
- [23] A.A. Ayon, K-S. Chen, K.A. Lohner, S.M. Spearing, H.H. Sawin, and M.A. Schmidt, "Deep Reactive Ion Etching of Silicon," *Materials Research Society Symposium Proceedings*. v. 546, pp.51-61, 1999.
- [24] K-S. Chen, A. Ayon, and S.M. Spearing, "Controlling and Testing the Fracture Strength of Silicon on the Mesoscale," *Journal of the American Ceramic Society*, 83 [6], pp.1476-84, 2000.
- [25] J.C. Arnold and H.H. Sawin, "Charging of pattern features during plasma etching," *J. Appl. Phys.*, vol. 70, no. 10, pp.5314-5317, 1991.
- [26] T. Kinoshita, M. Hane, and J.P. McVittie, "Notching as an example of charging in uniform high-density plasmas," *J. Vac. Sci. Technol. B, Microelectron. Process. Phenom.*, vol. B14, no. 1, pp.560-565, 1996.
- [27] T. Nowaza, T. Kinoshita, T. Nishizawa, A. Narai, T. Inoue, and A. Nakaue, "The electron charging effects of plasma on notch profile defects," *Jpn. J. Appl. Phys.*, vol. 34, pt. 1, no. 4B, pp.2107-2113, 1995.
- [28] U. Gosele and Q.-Y. Tong. Semiconductor wafer bonding. *Annual Review of Materials Science*, 28, pp. 215-241, 1998.
- [29] K.T. Turner, "An Evaluation of Critical Issues for Microhydraulic Transducers: Silicon Wafer Bonding, Strength of Silicon on Insulator Membranes and Gold-Tin Solder Bonding," Master's Thesis, Massachusetts Institute of Technology, Cambridge, MA, June 2001.



- [30] R. Mlcak, Numerous presentations at MIT on the development of a bonding technology between piezoelectric material and silicon for use in MHT technology, 1997-2000.
- [31] M. Ohring. *The Materials Science of Thin Films*. Academic Press, New York, 1992.
- [32] R. Mlcak. *Wafer-scale Fluid Filling System: Standard Operating Procedure and Manual*. Document was provided to MIT from Boston Microsystems, Inc. in October 2000.
- [33] J.L. Steyn, "Hydraulic Amplification for Actuation in MicroElectroMechanical Systems," Master's Thesis, Massachusetts Institute of Technology, Cambridge, MA, February 2002.
- [34] S.E. Park and T.R. Shrout, "Characteristics of Relaxor-Based Piezoelectric Single Crystals for Ultrasonic Transducers," *IEEE Trans. Ultrasonics, Ferroelectrics, and Frequency Control*, Vol.44, No.5, Sept. 1997, pp. 1140-1147.
- [35] D.C. Roberts, "Design, Modeling, Fabrication, and Testing of a Piezoelectric Microvalve for High Pressure, High Frequency Hydraulic Applications," Ph.D. Thesis, Massachusetts Institute of Technology, Cambridge, MA, February 2002.
- [36] O. Yaglioglu, "Modeling and Design Considerations for a Micro-Hydraulic Piezoelectric Power Generator", S.M. Thesis, Massachusetts Institute of Technology, Cambridge, MA, June 2002.
- [37] J. A. Carretero. "Measurement and Modeling of the Flow Characteristics of Micro Disc Valves". *SM Thesis, Massachusetts Institute of Technology*, 2001.
- [38] S. Timoshenko. "Theory of Plates and Shells". McGraw-Hill, NewYork, NY, 1940.
- [39] I.E. Idelchik. "Handbook of Hydraulic Resistance", FL, 1994
- [40] Lin, Ching-Yu "Material Characterization and Modeling for Piezoelectric Actuation and Power Generation under High Electromechanical Loading", Doctoral Thesis, Massachusetts Institute of Technology, Cambridge, MA, June, 2002.
- [41] B. Jaffe, W. Cook, and H. Jaffe, *Piezoelectric Ceramics*, 1971, pp. 279
- [42] M. Goldfarb and L. D. Jones, "On the Efficiency of Electric Power Generation with Piezoelectric Ceramic." *Journal of Dynamic Systems, Measurement, and Control*. Transaction of ASME, vol. 121, September 1999, pp. 566 - 571.



## 9 Summary of Publications Generated under this Project

This section summarizes the publications that were produced as part of this project. They are attached in the appendices.

1. N.W. Hagood, D.C. Roberts, L. Saggere, M.A. Schmidt, S.M. Spearing, K.S. Breuer, R. Mlcak, J.A. Carretero, F. Ganji, H.Q. Li, K.S. Chen, Y.H. Su, S.W. Pulitzer, "Development of Micro Hydraulic Transducer Technology," *Proceedings of the 10th International Conference on Adaptive Structures and Technologies*, pp. 71-81, Paris, France, Oct. 11-13, 1999.
2. N.W. Hagood, D.C. Roberts, L. Saggere, K.S. Breuer, K.-S. Chen, J.A. Carretero, H.Q. Li, R. Mlcak, S. Pulitzer, M.A. Schmidt, S.M. Spearing, and Y.-H. Su, "Micro Hydraulic Transducer Technology for Actuation and Power Generation," *Proceedings of the SPIE 7th Annual International Symposium on Smart Structures and Materials*, Vol. 3985, pp. 680-688, Newport Beach, CA, March 5-9, 2000.
3. D.C. Roberts, N.W. Hagood, Y.-H. Su, H.Q. Li, and J.A. Carretero, "Design of a Piezoelectrically-Driven Hydraulic Amplification Microvalve for High Pressure, High Frequency Applications," *Proceedings of the SPIE 7th Annual International Symposium on Smart Structures and Materials*, Vol. 3985, pp. 616-628, Newport Beach, CA, March 5-9, 2000.
4. H.Q. Li, D.C. Roberts, J.L. Steyn, K.T. Turner, J.A. Carretero, O. Yaglioglu, Y.-H. Su, L. Saggere, N.W. Hagood, S.M. Spearing, M.A. Schmidt, R. Mlcak, and K.S. Breuer, "A High Frequency High Flow Rate Piezoelectrically Driven MEMS Micropump," *Proceedings of the IEEE Solid-State Sensor and Actuator Workshop*, Hilton Head, SC. pp. 69-72, June 4-8, 2000.
5. L. Saggere, N.W. Hagood, D.C. Roberts, H.Q. Li, J.L. Steyn, K.T. Turner, J.A. Carretero, O. Yaglioglu, Y.H. Su, R. Mlcak, S.M. Spearing, K.S. Breuer, and M.A. Schmidt, "Design, Fabrication, and Testing of a Piezoelectrically Driven High Flow Rate Micro-Pump," *Proceedings of the 12th IEEE International Symposium on the Applications of Ferroelectrics*, Honolulu, Hawaii, July 30-Aug. 2, 2000.
6. Y.H. Su and S.M. Spearing, "Large Deflection Analysis of an Annular Plate with a Rigid Boss Under Axisymmetric Loading," *Proceedings of the International Congress of Theoretical and Applied Mechanics 2000*, Chicago, IL, Aug. 29, 2000.
7. J.A. Carretero and K.S. Breuer, "Measurement and Modeling of the Flow Characteristics of Micro Disk Valves," *Proceedings of the 2000 International Mechanical Engineering Congress and Exposition: Microfluidics Symposium*. Orlando, FL, Nov. 2000.
8. D.C. Roberts, O. Yaglioglu, J. Carretero, Y.-H. Su, L. Saggere, and N.W. Hagood, "Modeling, Design, and Simulation of a Piezoelectric Microvalve for High Pressure, High Frequency Applications," *Proceedings of the SPIE 8th Annual International Symposium on Smart Structures and Materials*, Vol. 4327, pp. 366-380, Newport Beach, CA, March 4-8, 2001.
9. D.C. Roberts, J.L. Steyn, H.Q. Li, K.T. Turner, R. Mlcak, L. Saggere, S.M. Spearing, M.A. Schmidt, and N.W. Hagood, "A High-Frequency, High-Stiffness Piezoelectric Micro-Actuator For

- Hydraulic Applications,” *Proceedings of the 11th International Conference on Solid-State Sensors and Actuators (Transducers '01)*, Munich, Germany, pp. 686-689, June 10-14, 2001.
10. J.A. Carretero. “Measurement and Modeling of the Flow Characteristics of Micro Disc Valves”, S.M. Thesis, Massachusetts Institute of Technology, Cambridge MA. February 2001.
  11. K.T. Turner, “An Evaluation of Critical Issues for Microhydraulic Transducers: Silicon Wafer Bonding, Strength of Silicon on Insulator Membranes and Gold-Tin Solder Bonding.” S.M. Thesis, Massachusetts Institute of Technology, Cambridge, MA, June 2001.
  12. K.T. Turner, R. Mlcak, D.C. Roberts and S.M. Spearing, “Bonding of Bulk Piezoelectric Material to Silicon Using a Gold-Tin Eutectic Bond”, *2001 MRS Fall Meeting*, Boston, MA.
  13. Y.H. Su, K.S. Chen, D.C. Roberts, and S.M. Spearing, “Large Deflection Analysis of a Pre-Stressed Annular Plate With a Rigid Boss Under Axisymmetric Loading”, *Journal of Micromech. Microeng.* 11 (2001) pp. 645-653.
  14. D.C. Roberts, “Design, Modeling, Fabrication, and Testing of a Piezoelectric Microvalve for High Pressure, High Frequency Hydraulic Applications,” Ph.D. Thesis, Massachusetts Institute of Technology, Cambridge, MA, February 2002.
  15. D.C. Roberts, H.Q. Li, J.L. Steyn, K.T. Turner, R. Mlcak, L. Saggere, S.M. Spearing, M.A. Schmidt, and N.W. Hagood, “A High-Frequency, High-Stiffness Piezoelectric Actuator For Microhydraulic Applications,” *Sensors and Actuators: A. Physical*. Accepted for publication.
  16. O. Yaglioglu, Y.H. Su, D.C. Roberts, J. Carretero, N.W. Hagood, “Modeling, Simulation and Design of Piezoelectric Micro-Hydraulic Transducer Devices,” *To be presented at the Fifth International Conference on Modeling and Simulation of Microsystems*, April 21-25, San Juan, Puerto Rico, 2002.
  17. J.L. Steyn, H.Q. Li, D.C. Roberts, R. Mlcak, K.T. Turner, O. Yaglioglu, Y.-H. Su, M.A. Schmidt, S.M. Spearing, N.W. Hagood, “Hydraulic Amplification Devices for Microscale Actuation,” *TRF Solid-State Sensor and Actuator Workshop*, Hilton Head, SC, USA, 2002.
  18. J.L. Steyn, “Hydraulic Amplification for Actuation in MicroElectroMechanical Systems,” S.M. Thesis, Massachusetts Institute of Technology, Cambridge, MA, June 2002.
  19. O. Yaglioglu, “Modeling and Design Considerations for a Micro-Hydraulic Piezoelectric Power Generator,” S.M. Thesis, Massachusetts Institute of Technology, Cambridge, MA, June 2002.
  20. C.-Y. Lin, “Material Characterization and Modeling for Piezoelectric Actuation and Power Generation under High Electromechanical Loading,” Doctoral Thesis, Massachusetts Institute of Technology, Cambridge, MA, June, 2002.
  21. H.Q. Li, D.C. Roberts, J.L. Steyn, K.T. Turner, O. Yaglioglu, N.W. Hagood, S.M. Spearing, and M.A. Schmidt, “Fabrication of a microvalve with piezoelectric actuation,” *To be presented at the MEMS '03 conference*, Kyoto, Japan, 2003.

22. David C. Roberts, Hanqing Li, J. Lodewyk Steyn, Onnik Yaglioglu, S. Mark Spearing, Martin A. Schmidt, Nesbitt W. Hagood, "A Piezoelectric Microvalve for Compact High-Frequency, High Differential Pressure Hydraulic Micropumping Systems", Accepted for publication in the Journal of Microelectromechanical Systems.



## **10 Personnel**

### **10.1 Principal Investigator**

Hagood IV, Nesbitt W.

### **10.2 Faculty**

Breuer, Kenny S.

Schmidt, Martin A.

Spearing, S. Mark

### **10.3 Scientific Staff**

Atalla, Mauro J.

Li, Hanqing

Roberts, David C.

Robertson, David C.

Saggere, Laxminarayan

Su, Yu-Hsuan

### **10.4 Graduate Students**

Carretero, Jorge A. - S.M. in Aeronautics and Astronautics

Lin, Ching-Yu - Ph.D. in Aeronautics and Astronautics

Pulitzer III, Seward W. - S.M. in Mechanical Engineering

Roberts, David C. - Ph.D. in Mechanical Engineering

Steyn, J. Lodewyk - S.M. in Aeronautics and Astronautics

Turner, Kevin T. - S.M. in Mechanical Engineering

Yaglioglu, Onnik - S.M. in Mechanical Engineering

### **10.5 Undergraduate Students**

Bennett, David

Berte, Mark

Chang, Rick

Connelly, Blair

Daniels, Jeff

Gupta, Geeta

Gustafson, Peter A.

Hawrylchak, Michael Y.

Lu, James

Manka, Alexander K.

McKenny, Kurtis G.

Oliver, Todd

Sandoval, Daniel  
Stockham, Erik



## 11 Patents

“Microactuator Having Amplified Actuation Stroke,” by D.C. Roberts, N.W. Hagood, S.W. Pulitzer, M.A. Schmidt, H.Q. Li, J.L. Steyn, R. Mlcak, K.T. Turner, S.M. Spearing, K.S. Chen, Patent pending with United States Patent and Trademark Office. Filing Date: October 11, 2001



## Appendix - Masks

This appendix contains all the masks of the MHT 10 valve device and its subcomponents.

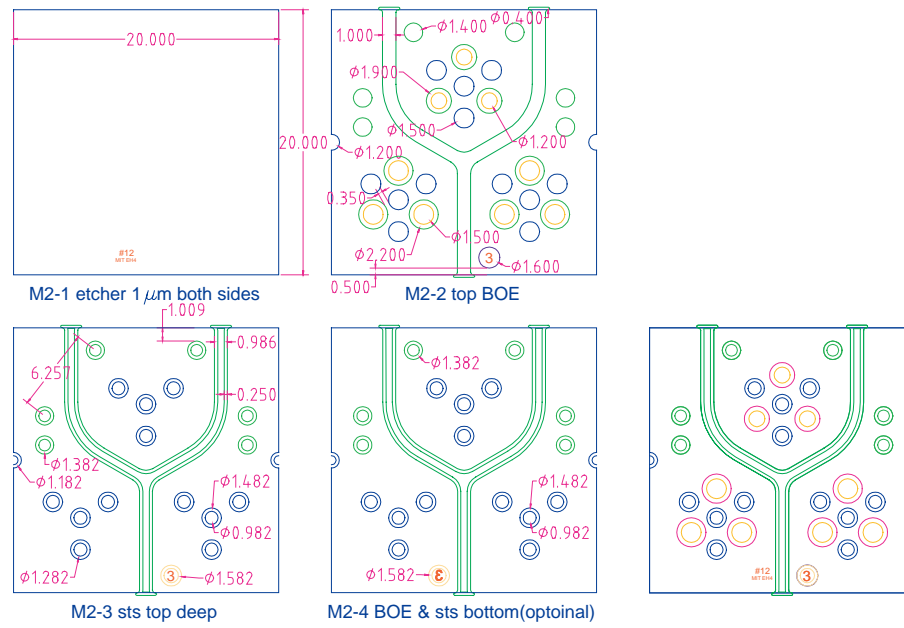


Figure 95: Layer 2 masks.

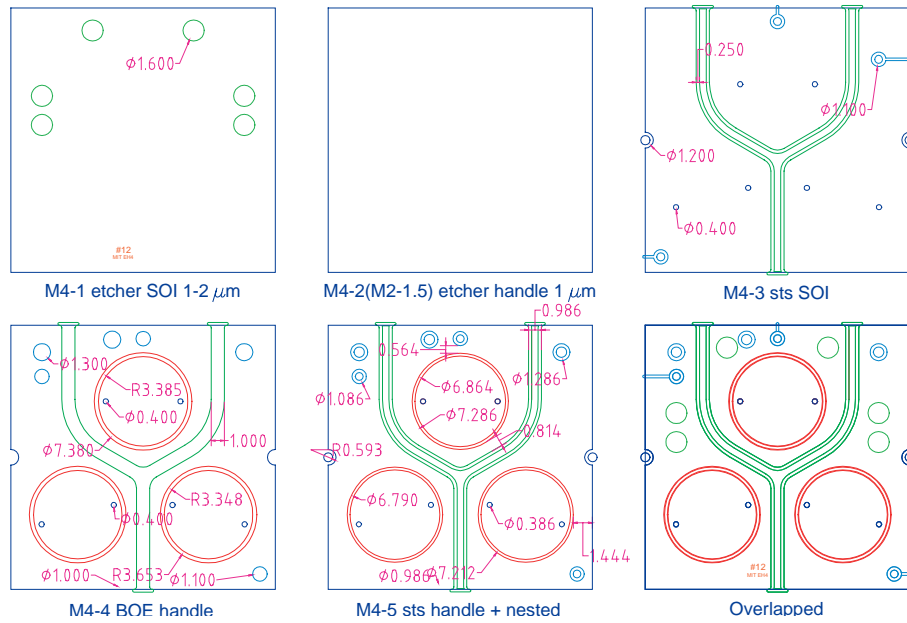


Figure 96: Layer 4 masks.

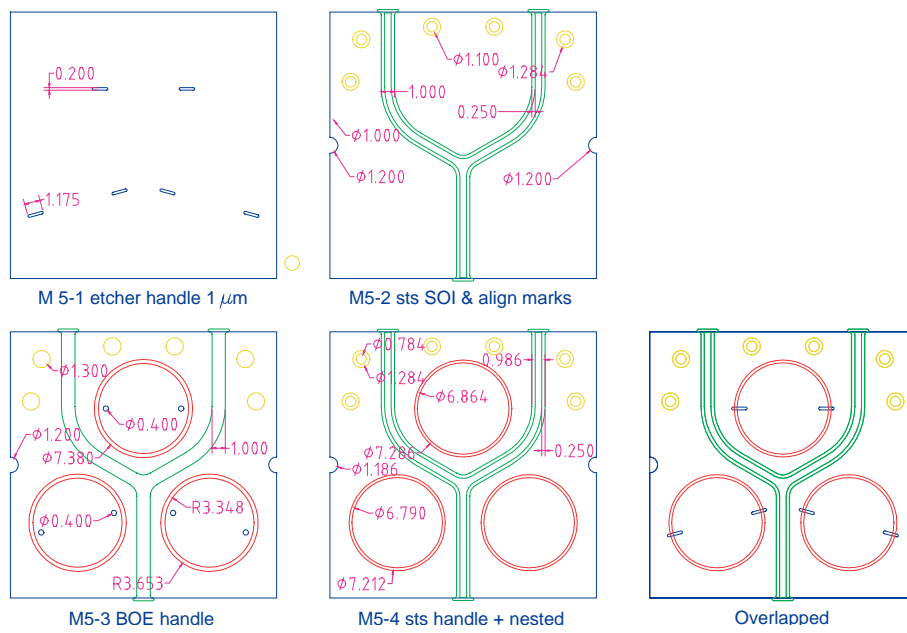


Figure 97: Layer 5 masks.

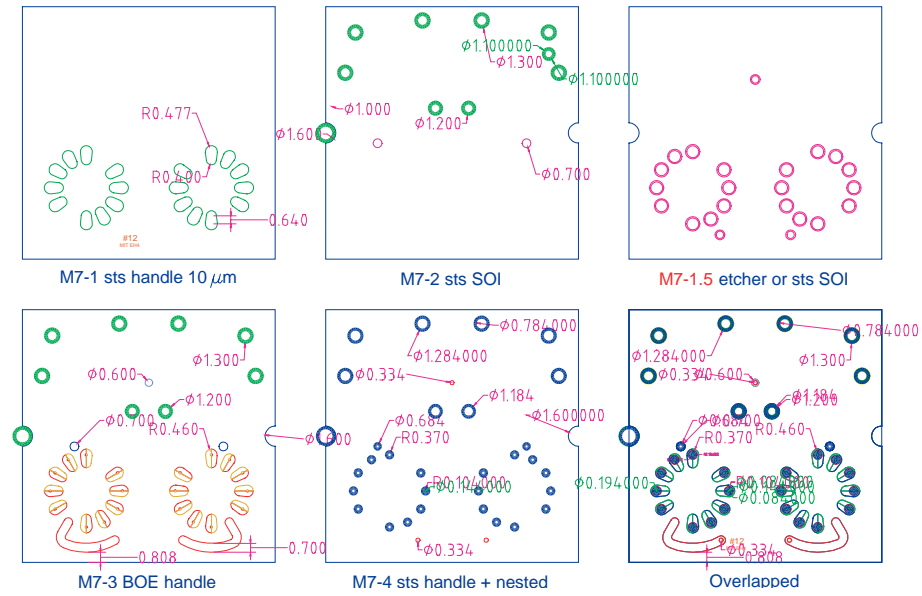


Figure 98: Layer 7 masks. MHT device with 10 small valves per valve unit

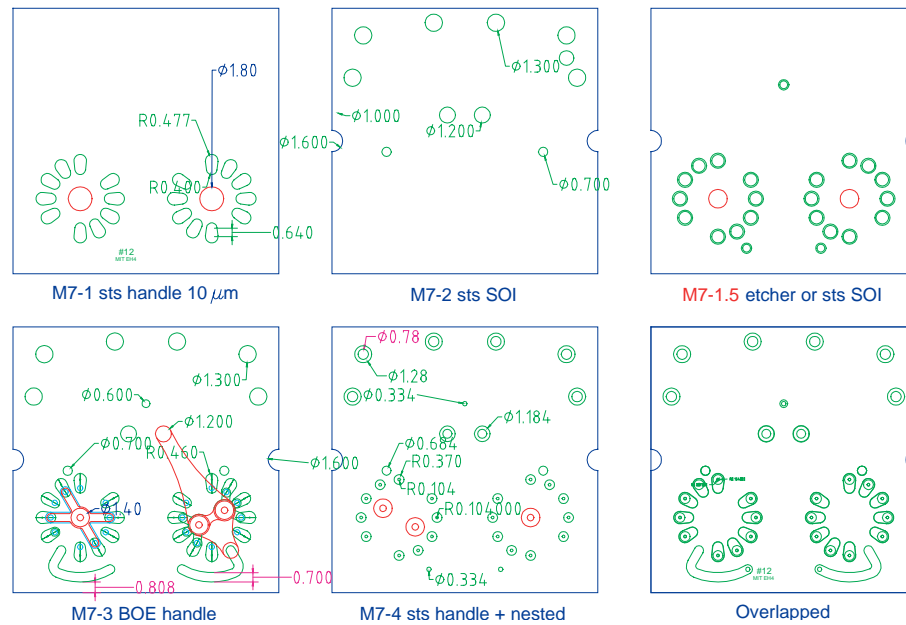


Figure 99: Layer 7 masks. MHT subcomponents with 1, 2 and 10 valve devices.

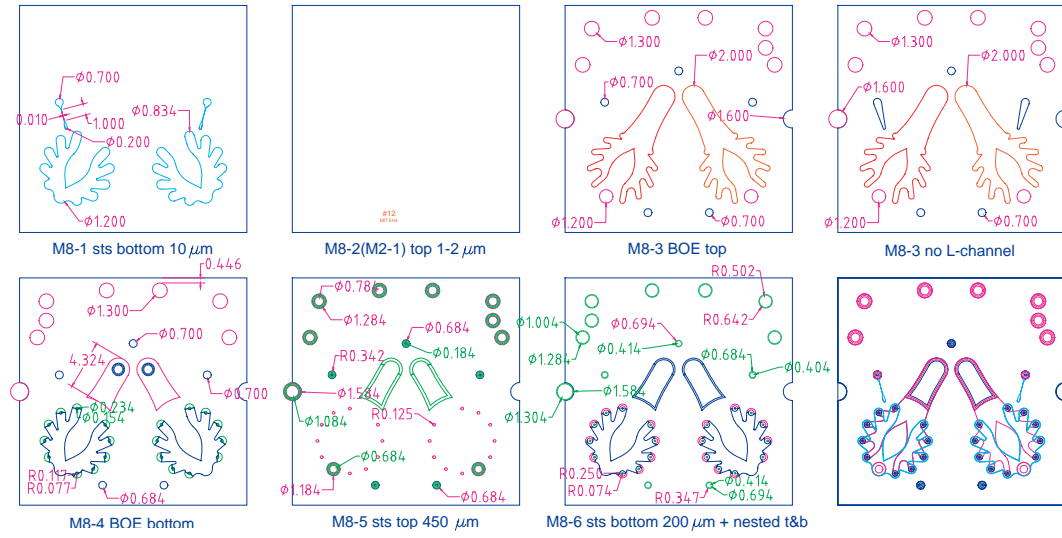


Figure 100: Layer 8 masks. MHT device with 10 small valves per valve unit

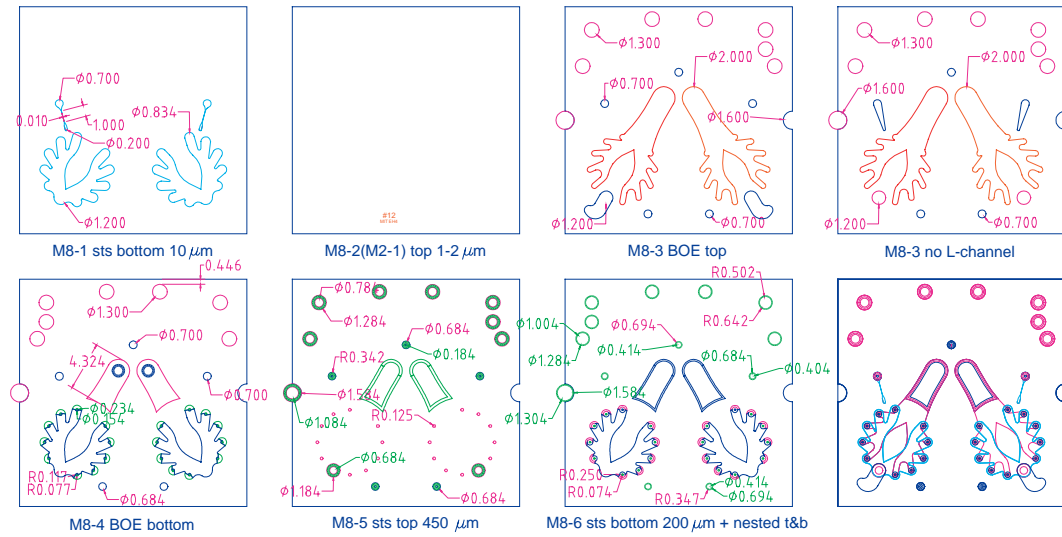


Figure 101: Layer 8 masks. MHT subcomponent device with 10 small valves per valve unit. The only difference is the inlet and outlet hole positions.

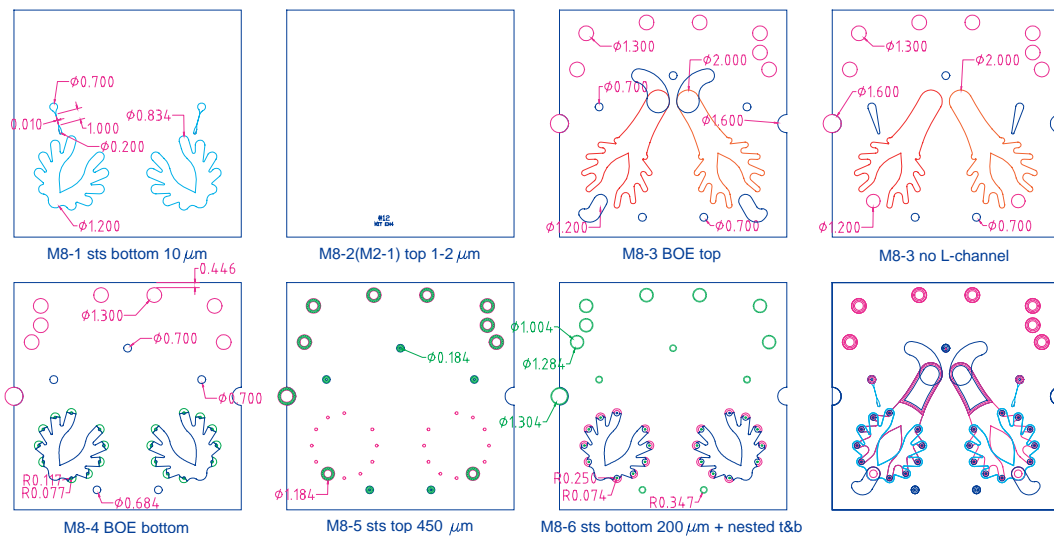


Figure 102: Layer 8 masks. MHT subcomponent device with 10 small valves per valve unit. This device has two discrete valve test units, and cannot function as a harvester.

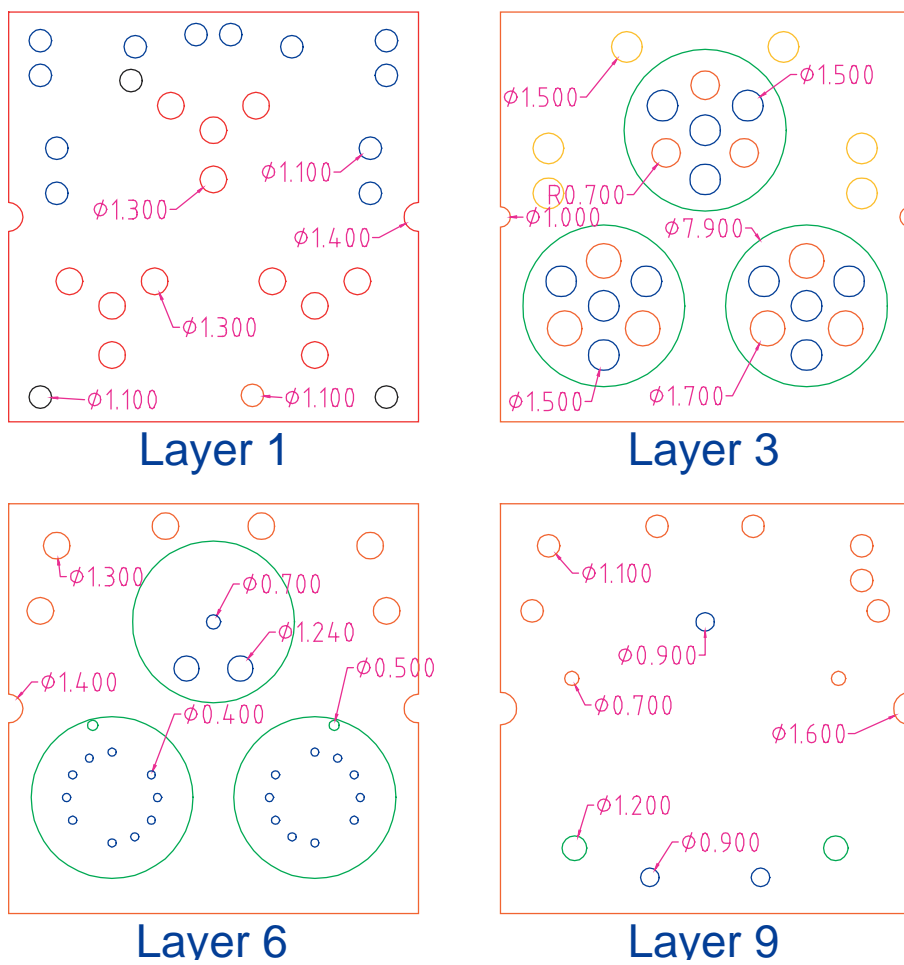
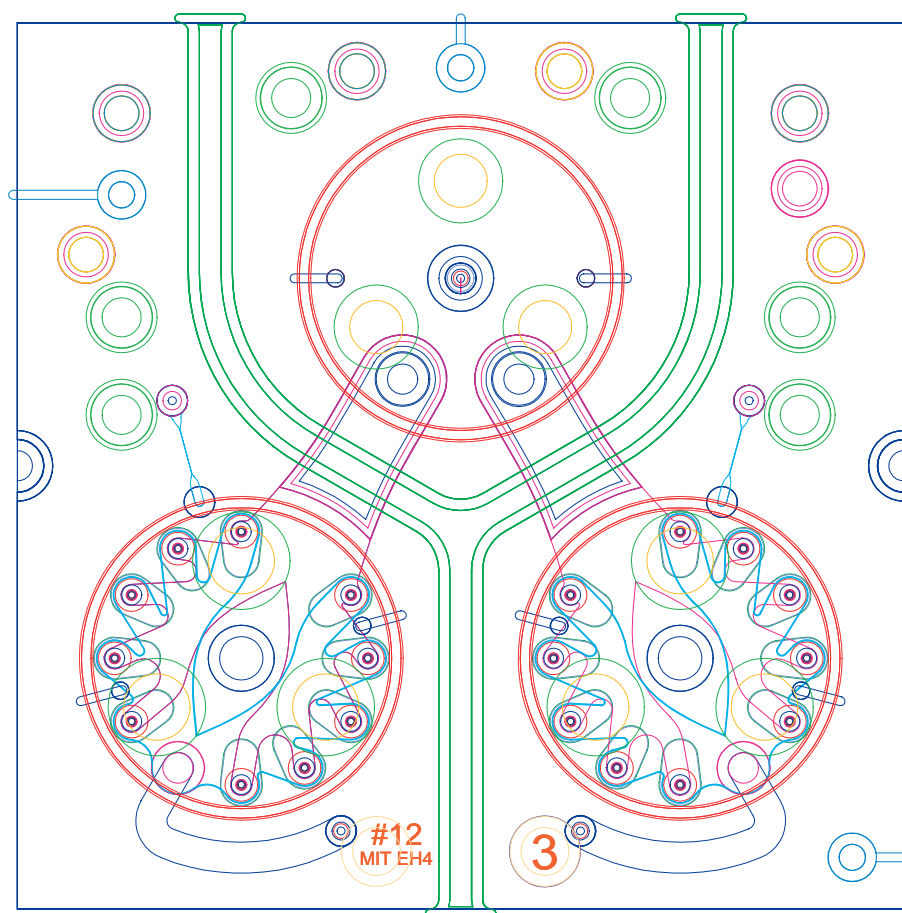


Figure 103: Glass layer masks.





## Overlapped

Figure 104: Overlay of all the masks of the MHT device



## Appendix - Copies of Publications and Theses

Attached are copies of publications and theses that were produced as part of this project. These are summarized in Section 9. The following publications have not yet been submitted for review:

- A journal copy of the paper presented at the Hilton Head 2002 Solid State Sensor and Actuator Workshop. ("Hydraulic Amplification Devices for Microscale Actuation", Steyn *et al*),
- "The Microhydraulic Transducer: A bi-directional pump and generator for small scale actuation and power generation", Steyn *et al*. A journal publication on the final results of the MHT project.

## Development of Micro-Hydraulic Transducer Technology

Nesbitt W. Hagood IV<sup>1</sup>, David C. Roberts<sup>1</sup>, Laxman Saggere<sup>1</sup>, Martin A. Schmidt<sup>2</sup>, Mark Spearing<sup>1</sup>, Kenneth S. Breuer<sup>3</sup>, Richard Mlcak<sup>4</sup>, Jorge A. Carretero<sup>1</sup>, Farid Ganji<sup>1</sup>, Hanqing Li<sup>1</sup>, Kuo-Shen Chen<sup>1</sup>, Yu-Hsuan Su<sup>1</sup>, Seward Pulitzer<sup>1</sup>

### ABSTRACT

A novel miniature transducer mechanism, called the solid-state micro-hydraulic transducer, is introduced. This transducer exploits the synergism of integrating the enabling micromachining technology, piezoelectrics, and microhydraulic concepts to achieve high performance. The transducer can function as both an actuator that supplies high mechanical force in response to electrical input and as an energy generator that transduces electrical energy from wasted mechanical energy in the environment. The transducer is capable of outputting energy at very high power density, and thus, has the potential to enable many novel applications. The concept, the design, and the potential applications of the transducers are presented. Present efforts towards the development of these transducers and the challenges involved therein are also discussed.

### INTRODUCTION

Transducers are a class of devices that interact with the environment in some way to transform physical energy from one form to another. Sensors, actuators and energy generators are some of the important types of transducers. Micromachined transducers possess feature sizes on the order of 10-100  $\mu\text{m}$  and are typically fabricated using the micromachining techniques developed for the integrated circuit industry. The focus of this paper is on the development of a novel type of micromachined transducer that can perform the dual function of both an actuator and energy generator.

The performance and usefulness of a transducer (actuator/energy generator) for most applications are highly dependent on two important characteristics: compactness and power density, that is, power output by the transducer per its unit mass. Conventional transducers, generally, not only tend to be heavy and bulky, but are also limited in their transducing power on account of their low bandwidths. For instance, conventional hydraulic systems possess high single-stroke work, but their power-densities are greatly reduced by their large mass. Recent advances in active materials technology has led to the development of many compact solid-state transducers. However, the power output from these solid-state transducers is fairly limited for most macro applications. Although the single-stroke work output of solid-state materials such as piezoelectrics is relatively small, such materials possess very high bandwidths, and as such, are capable of high power output. However, since most applications do not require high frequency actuation, the high bandwidth potential of piezoelectrics is

---

<sup>1</sup> Dept. of Aeronautics and Astronautics, MIT, 77 Massachusetts Ave., Cambridge, MA 02139 USA.

<sup>2</sup> Microsystems Technology Laboratories, MIT, 77 Massachusetts Ave., Cambridge, MA 02139 USA.

<sup>3</sup> Dept. of Engineering, Box D, Brown University, Providence, RI 02912-D USA.

<sup>4</sup> Boston MicroSystems Inc., 356 Wellesly, MA 02181 USA.

not fully utilized. Since a transducer's power output is the product of its single stroke energy and its bandwidth, it is feasible to create high performance transducers by combining high single-stroke force of a hydraulic system and high frequency displacements of a piezoelectric element in a synergistic manner. This concept can be further exploited to create high performance transducers with very high power densities by miniaturizing the transducer systems. The state-of-the-art micromachining (or MEMS) technology has the potential to allow for the implementation of this concept at the micro scale.

Research and development of microfluidic devices has received a significant amount of interest in the past few years [1]. The feasibility of micromachining many of the key building blocks (flow channels, pumps, active/passive valves) of a micro-fluidic system including the integration of solid-state materials such as piezoelectrics to actuate valves has already been demonstrated, and researchers are now striving to create complete microfluidic systems. However, the microfluidic devices developed thus far mostly feature small flow conductance, limited stroke, and low power density, and are mostly geared towards small flow/force applications such as microdosing of fluids.

This paper introduces the development a novel class of micromachined transducers called solid-state micro-hydraulic transducers that are capable of extremely high power density outputs on the order of 500-1000 W/Kg. A unique feature of these transducers is their ability to operate as both an actuator and a power generator, by merely reversing the direction of their operation. As actuators, these transducers transform electrical energy input into mechanical energy output, and as energy generators, the transducers transform mechanical energy input into electrical energy that can be stored in a battery or a capacitor.

These high performance transducers can significantly enhance the scope of micromachined transducers technology by enabling many novel applications. When utilized as actuators, they are capable of extending the usefulness of active material based structural actuation beyond small strain applications. A coordinated command of an array of tiny actuators integrated with a structure can generate a distributed strain in the structure which is far higher than that achievable through direct application of piezoelectrics. These actuators can also be useful in miniature robotics. As energy generators, the transducers can extract electrical energy from wasted mechanical energy sources such as vibrations of operating machinery and heel strike of human gait, and function as disposable batteries for numerous small electronic devices in both civilian and military arenas.

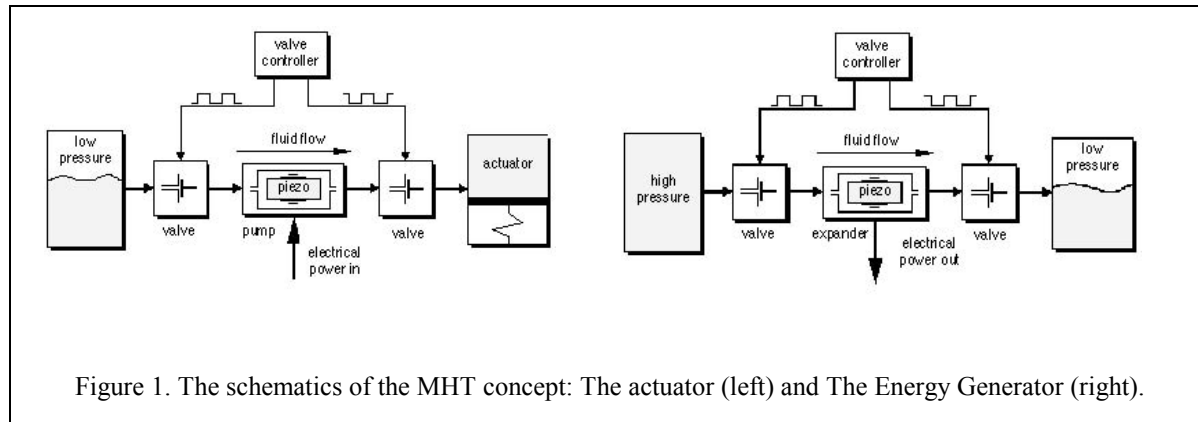
This paper introduces the concept, the design, and the technical challenges involved in the development of these transducers. The fabrication and testing of key components within these transducers are also presented.

## **MICRO-HYDRAULIC TRANSDUCERS (MHT)**

### **The Concept of MHT**

The concept of the micro-hydraulic transducer (MHT) is schematically illustrated in Figure 1. As shown in the figure, the transducer can be configured as both an actuator and an energy generator, and in either configuration, the transducer is comprised of the following generic components: a piezoelectric fluid pump chamber, two actively controlled valves, a low-pressure fluid reservoir (LPR), and a high-pressure fluid reservoir (HPR). The two active valves—one operating between the LPR and the pump chamber and the other one operating between the pump chamber and the HPR—regulate the fluid flow into and out of the pump chamber. The piezoelectric element within the pump chamber serves as the main energy transducing element.

In the actuator mode (see Figure 1(a)), an electric voltage applied to the piezoelectric induces a strain in the element resulting in a net volume change in the pump chamber. A controller synchronized



with the pump signal cycles the active valves out of phase with each other in a specified duty cycle, transforming the volume oscillations of the chamber into a net fluid flow from a low pressure reservoir to a high pressure reservoir. The accumulation of fluid in the high-pressure reservoir or the actuator increases the pressure and performs useful work on the load. After the actuator travels its full stroke, the flow direction is reversed and the actuator is evacuated as it returns to its initial position, completing the actuation cycle. In this way the high frequency, small displacements of the piezoelectric are rectified into low frequency, large stroke actuation.

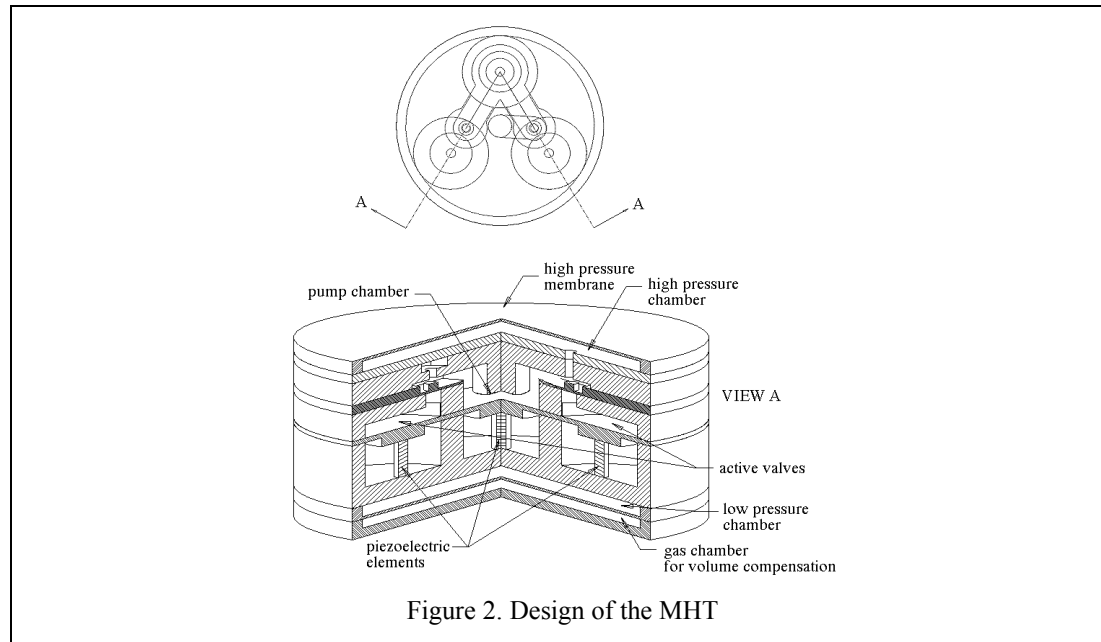
In the energy generator mode, the transducer operates in a manner that is reverse of the actuator. The controller toggles the valves with a phasing that allows fluid flow from the high pressure reservoir to the low pressure reservoir, thus transforming the static fluid pressure into high frequency pulses on the piezoelectric. Valve actuation at high frequency creates a near sinusoidal cyclic stress on the piezoelectric element, thereby generating electrical charge across the element. Coupled circuitry (not shown) rectifies this electrical energy and stores it capacitively.

## Design of MHT

A prototype design for the micro-hydraulic transducer mechanism with typical overall dimensions of 15mm×15mm×4mm is shown in Figure 2. The mechanism is comprised of three chambers, a main pump chamber and two active valve chambers, arranged in a triangular fashion (see top view in Figure 2) so as to minimize the channel lengths connecting the valves and the piezo/fluid chamber and to allow for an overall circular geometry of the mechanism to minimize device structural mass. In each chamber, a piezoelectric element is sandwiched between the rigid device structure and a moveable piston plate. The piston plate is sufficiently thick for rigidity and is tethered to the chamber wall through thin flexible diaphragms that extend radially from the outer edges of the cylinder. The structure effectively constitutes a piston that can move vertically up and down when a net force is applied to it.

Each active valve chamber incorporates a stiff fluid enclosed in the volume between the piston diaphragm and the valve diaphragm, and effectively serves as a hydraulic amplifier. As the piston in the active valve is displaced by the piezoelectric element, the pressure of the compressed fluid acts to deform the smaller area valve membrane located at the top of the chamber. Deflection of the rigid cap at the center of the valve membrane blocks fluid flow through the corresponding fluid orifice.

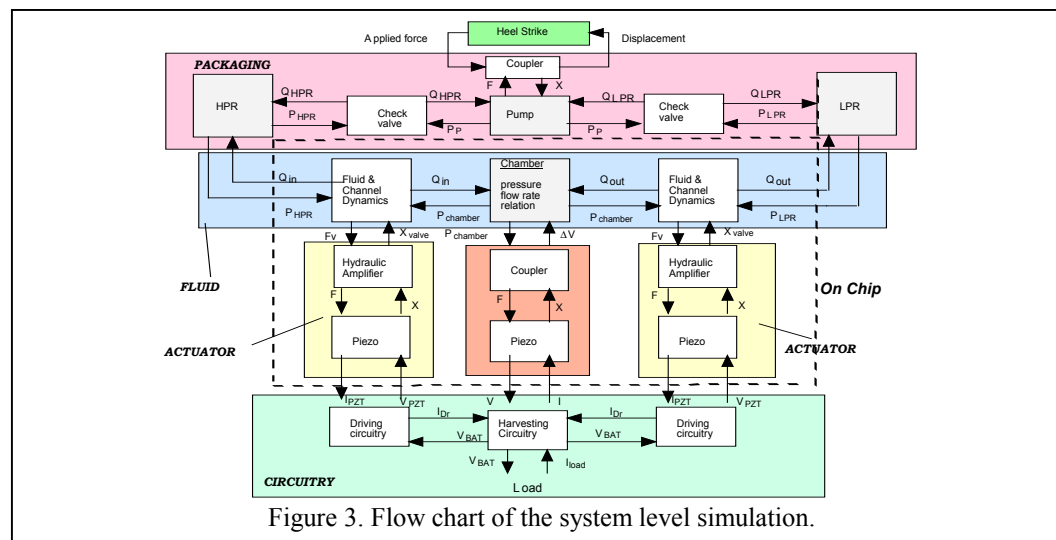
Two cylindrical volumes located on the upper and lower sides of the three chambers comprise the HPR and the LPR. Fluid travels between the LPR and the connected valve via a cylindrical vertical channel located in the center of the mechanism (not visible in the cutaway view), while three other



channels exist to connect the valves, pump, and HPR. A gas chamber, separated from the low-pressure chamber by a thin membrane, serves to compensate the volume change. In addition, the controls and drive electronics (not shown in the figure) to power the valves and to harvest electrical energy are integrated with the design.

### Simulation of MHT

To obtain a realistic prediction of MHT performance, detailed non-linear equations describing the analytical models of the canonical system components were built in the Matlab/Simulink<sup>®</sup> application and integrated to carry out system level simulations. These model/simulations include such effects as fluid viscous losses, fluid inertia, piezoelectric material behavior, pump chamber and valve structural



dynamics, and electrical circuit behavior. The entire system is highly coupled and a flow chart of the system as represented in system level simulations is shown in Figure 3. Computer simulations of the steady-state operation of the transducer design indicate power densities near 1 kW/kg and flow rates of 1.5 ml/s at efficiencies around 40%.

### **Highlights of the MHT Technology**

The proposed MHT devices derive their enhanced performance from several inherent design features. In order to maximize its power output, the device is operated at very high frequencies near the resonance of the piezoelectric element. The key to such high frequency operation is successful design and implementation of fast acting valves. Active valves with high frequency and high force are accomplished in the MHT design through a piezoelectrically driven hydraulically amplified mechanism. Within the valve, a hydraulic chamber serves to amplify the small displacements of the piezoelectric material into significantly larger displacements of the valve cap and effectively transmits the high force actuation capability of the piezoelectric material. The utilization of the hydraulic amplification chamber also leads to minimization of the actuator material, and thus helps in achieving high power densities. The ability to micromachine the device provides the scope to further miniaturize the system to micro scales, leading to higher valve frequencies and therefore enhanced device power densities.

The novel feature of the MHT design is the single configuration that allows for dual functionality of the transducer. This design of MHT devices enables the micro-hydraulics technology to create both actuators and energy generators with high flow rates and high power densities. This can potentially lead to many novel applications. One of the important intended applications of the MHT is to convert the mechanical energy generated by the low frequency human heel-strike into electrical energy by packaging the entire device into the heel of a standard boot, and store the energy in a battery within the device. Another important application of these transducers is in the active control of structures. Active materials are widely used for structural actuation. However, the full actuation authority of these materials cannot be exploited on account of the low bandwidth capability of most controlled structures. Since the MHT devices are capable of transducing the full actuation potential of piezoelectrics at high frequencies into low frequency and large hydraulic power, they can be applied to large deformation control of structures. These actuators can be operated as stand-alone devices, or may be comprised of any combination of several units in series or parallel to achieve desired output characteristics. Cascaded actuators can work against significantly larger overall pressure potentials than a single actuator and multiple parallel actuators can produce enhanced flow rates over a single actuator.

### **TECHNICAL CHALLENGES**

The development of the MHT design is currently ongoing. Realization of these devices involves overcoming significant technical challenges in design, modeling, fabrication, and system level integration.

**Design** Achieving high power densities in MHT devices is critically dependent on fast acting valves capable of operating at frequencies in the tens of kilohertz range and with sufficient actuation force to overcome pressures of ~1MPa. Therefore, the valves must be designed to be stiff, yet flexible enough to allow large stroke. In addition, the valve structural geometry and active driving means for the valves must be minimal in size and mass. Numerous microvalve designs have been reported in the literature up to this time, including those driven by electrostatic [2], electromagnetic [3], thermal bimetallic [4], thermo-pneumatic [5], and direct piezoelectric [6] means. However, none of these can



meet the aforementioned frequency, force, and size/mass requirements. The hydraulically amplified piezoelectric valve concept presented in this paper strives to meet the above design requirements.

**Modeling** Microscale fluid flows typically fall within the transition regime between inertia-dominated and viscous-dominated behavior, and are therefore quite difficult to accurately model. In comparison to macroscale flows, which are typically inertia dominated and far in excess of the transitional Reynolds number of 2300, microscale flows can experience significant viscous forces. As a result, the well-documented high Reynolds number steady flow correlations through such structures as elbows, expansions, contractions, and diffusers are not applicable. For these lower Reynolds number flows, few correlations exist and steady flow CFD models are often required to gain insight.

Modeling of unsteady flow phenomena at these scales is even more difficult. In micro-hydraulic transducer devices, active valve frequencies in the tens of kilohertz range result in rapidly moving boundary conditions (valve cap surface) with time. For complex geometries, CFD models are unable to accurately capture the flow behavior. Experimental correlation is the only possible method for developing models to represent these flows.

**Simulation** A realistic prediction of the MHT performance can only be gained by numerically integrating all the governing equations for the entire system. The system equations involving complex fluid-structure dynamic interactions are highly coupled and highly nonlinear. As such, system simulations are computationally intensive and difficult to solve.

**Electronics** Development of efficient drive electronics and efficient power harvesting circuitry for the power harvester device, and reliable controls as well as their packaging are also challenging issues.

**Micromachining** Micromachining of the MHT involves some critical issues that either require very accurate control of the process parameters or need innovation of new processes. The design requires 2-sided lithography in order to minimize the overall number of silicon wafers in the devices and thereby minimize the overall device mass and volume. Although single-sided lithography of silicon wafers is a mature and proven process, there is no existing standard for 2-sided lithography. Protection of fragile structures etched on a given side, while depositing and preparing photoresist on the opposite side is not a straightforward process. Furthermore, the buried oxide from the Deep-Reactive Ion Etching (DRIE) process required to etch the drive element and valve membranes in Silicon-On-Insulator (SOI) wafers can result in stresses in the membrane. Also, the multi-layer wafer bonding procedures required for the MHT devices are difficult to accomplish.

**System Level Integration** Integration of bulk piezoelectric material (ideally, single-crystal ferroelectric material) with silicon micromachined structures is a predominant challenge in the development of micro-hydraulic transducers. Due to the fact that piezoelectric materials degrade at temperatures far below those required for silicon-silicon fusion bonding, other structural materials and bonding procedures are required in the planar region directly surrounding the bulk piezoelectric material. Pyrex can be substituted for silicon, resulting in robust lower temperature anodic bonds between the pyrex and the upper and lower silicon wafers. Eutectic alloy compositions can be deposited on the top and bottom surfaces of the piezoelectric material and on the bordering silicon wafers to allow for strong, low-temperature eutectic bonds between the piezoelectric material and the silicon. In this way, the piezoelectric material integration and subsequent low-temperature bonding steps are the last to be performed.

In addition, successful piezoelectric integration depends on the accuracy to which the piezoelectric material thickness can be measured with respect to that of the surrounding material. Thickness variation between these two components can create unwanted static and operational deflections of the piston membrane and therefore potentially destructive stresses at the critical etched membrane silicon-oxide interfaces. Also, incorporation of multiple smaller area piezoelectric materials spread out under the piston membrane is desired over placement of a single larger area piezoelectric material at the piston center, so as to reduce system compliances and increase efficiency. However, tolerance issues become even more important when dealing with requirements on multiple bonded structures in the

same plane. Structural integrity of the etched membranes and high cycle fatigue of the bonds are additional critical issues for successful MHT development [7].

**Fluid filling and sealing** Encapsulation of a working fluid in the device is a significant challenge at the microscale because surface-to-volume ratios are typically quite large, with surface energies playing a dominant role. Any gas bubbles present in the sealed operational device can create enormous system compliances, potentially rendering the device useless. The elimination of trapped gasses during filling of the device and during encapsulation of the fluid ports used for filling is critical for high-level performance. The choice of fluid, degassing of the fluid, and post-filling encapsulation of the fluid are important to prevent the generation of any bubbles during the operation.

## **CURRENT EFFORTS TOWARDS THE DEVELOPMENT OF MHT**

### **Fabrication and Testing of the Drive Component**

Fabrication and testing of the main components of the transducer are currently underway. A first generation drive component that is common to both the pump and the active valve chambers has been successfully fabricated and tested. This drive component incorporates a single PZT-5H cylinder positioned at the center of the drive element chamber, eutectically bonded below to a silicon substrate and above to a silicon piston membrane. The pyrex layer in the middle is anodically bonded to silicon at the top and the bottom. Figure 4 shows a fabricated device whose dimensions are 10mm×10mm×2mm.

The drive elements have been statically and dynamically tested using an optical probe and laser scanning vibrometer system, and the measured results (shown in Figure 5) were found to be in excellent correlation with the theoretical results predicted by finite-element analysis. Finite-element models predicted dominant modal behavior at 70kHz (1- $\theta$  tilt mode), 110kHz (plunge mode), 175kHz (2- $\theta$  mode), and higher frequencies. Experimental results indicated modal behavior at 74 kHz (1- $\theta$  tilt mode), 110 kHz (plunge mode), and 130 kHz (2- $\theta$  mode).

### **Fabrication of the Complete Device**

The multi-layer device fabrication sequence plan and mask designs for the entire MHT device have been completed. Figure 6 shows the cross-section of the various layers in the fabrication of the device. Figure 7(A) shows the cross-section of the assembled device from the top. The drive piston diameter is 7.7 mm and the valve piston diameter is 6.0 mm. The valve head membrane is 1.6 mm in diameter. It may be noticed in Figure 6 that three identical piezos are symmetrically placed in a triangular configuration in each chamber instead of a single piezo at the center of each chamber as illustrated in Figure 2. Use of multiple piezos in the drive chambers enables higher power out and better efficiency of the device. The top view of each layer is shown in Figure 7(B). In layer 2, trenches are etched to separate the electrodes.

Figure 8 shows the assembly process involved in device fabrication. First, all of the layers above and all of the layers below the piezo level are bonded to form an upper die and a lower die. Then, accurately sized piezos are manually put in place between the two dies for the final anodic and eutectic bonding. Because of the involvement of manual assembly of the piezo, and the need for etching Si surface below each piezo, the last assembly step is done at chip level, that is, after the upper die and lower die are cut from wafer level.

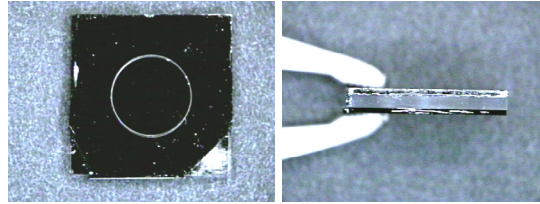


Figure 4. Fabricated drive-element component.

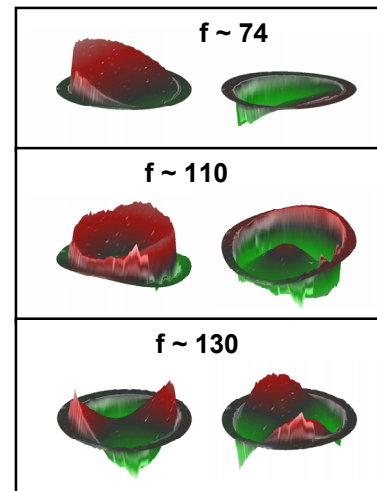


Figure 5. Experimental results showing frequencies and mode shapes of the drive component.

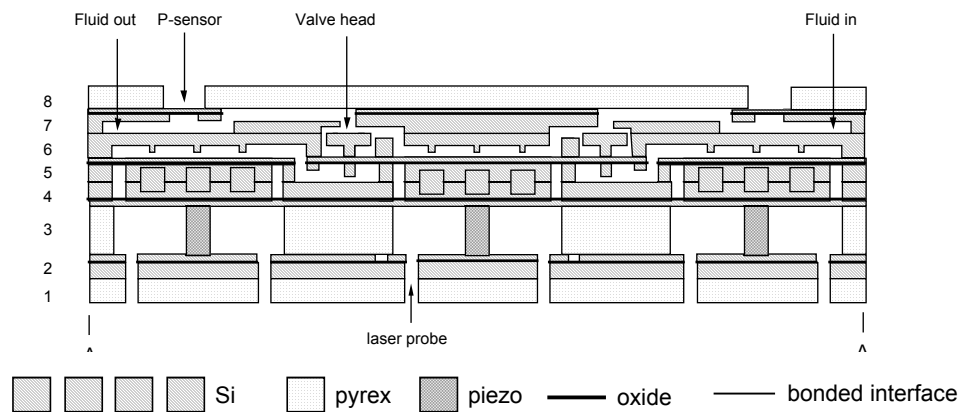
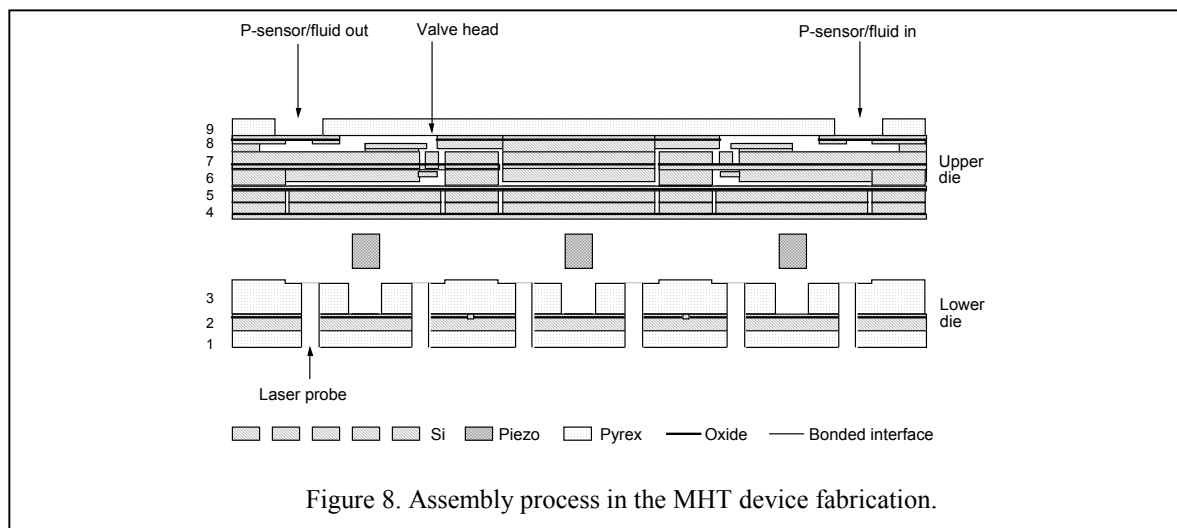
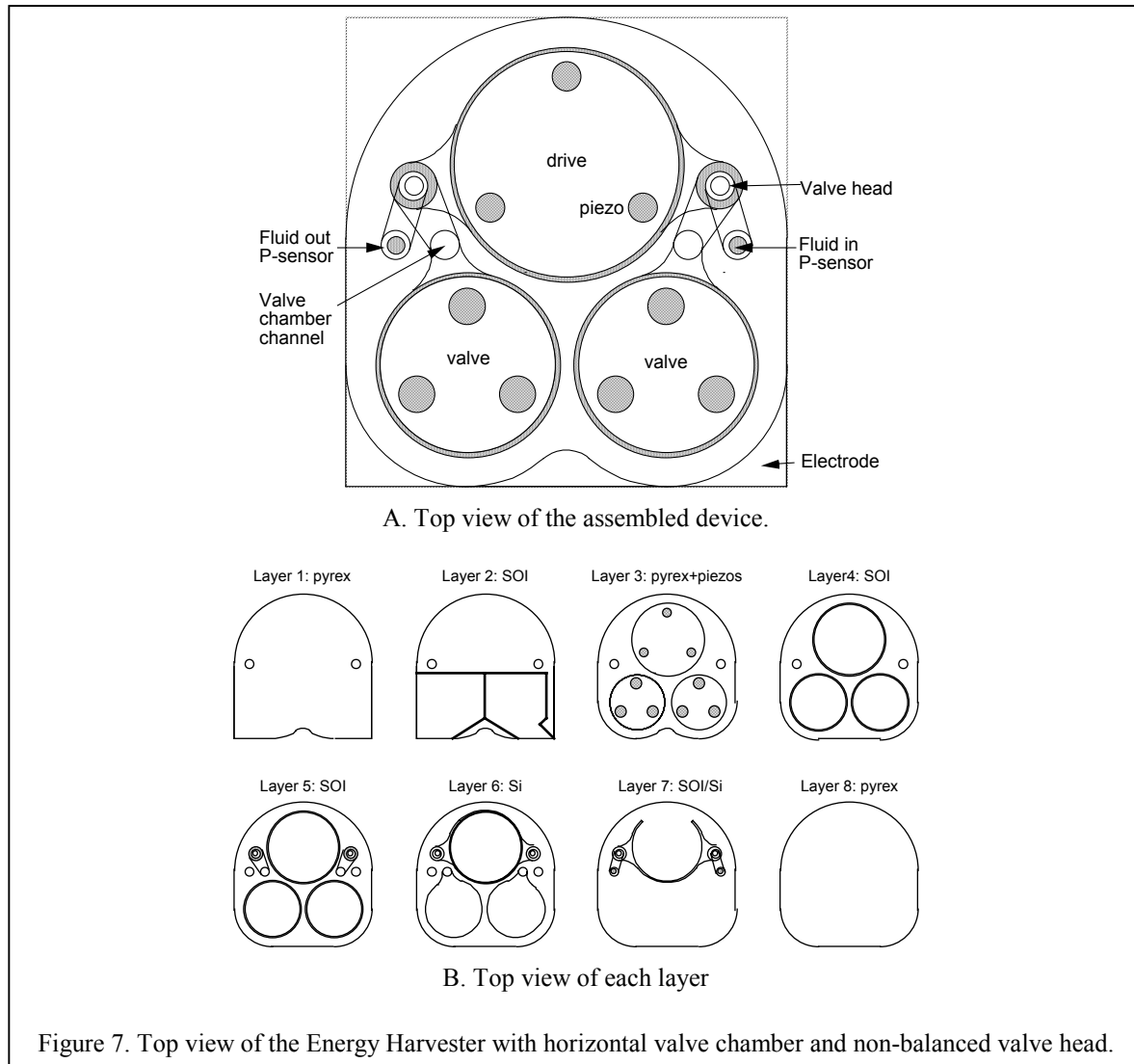


Figure 6. Cross-section of the Energy Harvester device with horizontal valve chamber.



## Fluid filling studies

To practically study the critical issues concerning fluid encapsulation in the device, several experiments on fluid-filling in specially fabricated micro channels have been conducted. A schematic of the experimental set-up is shown in Figure 9, and a photograph of the actual experimental set-up is shown in Figure 10. The chips with specially fabricated micro channels were connected to a fluid supply tank, a fluid drain, a vacuum pump and inert (and solvable) gas cylinders. The vacuum pump created a partial vacuum in the chips, which allowed for easy purging and filling of the channels. The fluid supply tank was wrapped with a heat tape, and connected to a vacuum pump, to enable fluid degassing. To create a partial vacuum, the fluid channels and cavities were first pumped down. This was followed by a few cycles of purging the channels with a solvable gas ( $\text{CO}_2$ ) and then evacuating. Finally, the channels were filled with the degassed fluid at a controlled rate, and the filled channels were inspected under a microscope for any entrapped bubbles. To investigate the effect of the fluid properties on filling, a few different fluids ( $\text{H}_2\text{O}$ , methanol, and silicone oil) were used. The results of these experimental studies indicated that filling of the small channels and the chambers is achievable with negligible gas entrapment especially with the silicone oil.

## CLOSURE

A novel micromachined transducer mechanism that can function as both an actuator and an energy generator is introduced. This transducer exploits the integration of micromachining technology with active materials and hydraulics for the first time to create a transducer capable of yielding high power densities near 1 kW/kg. This transducer technology offers exciting prospects for the unique interplay of technologies expanding the scope of applications for micromachined transducers.

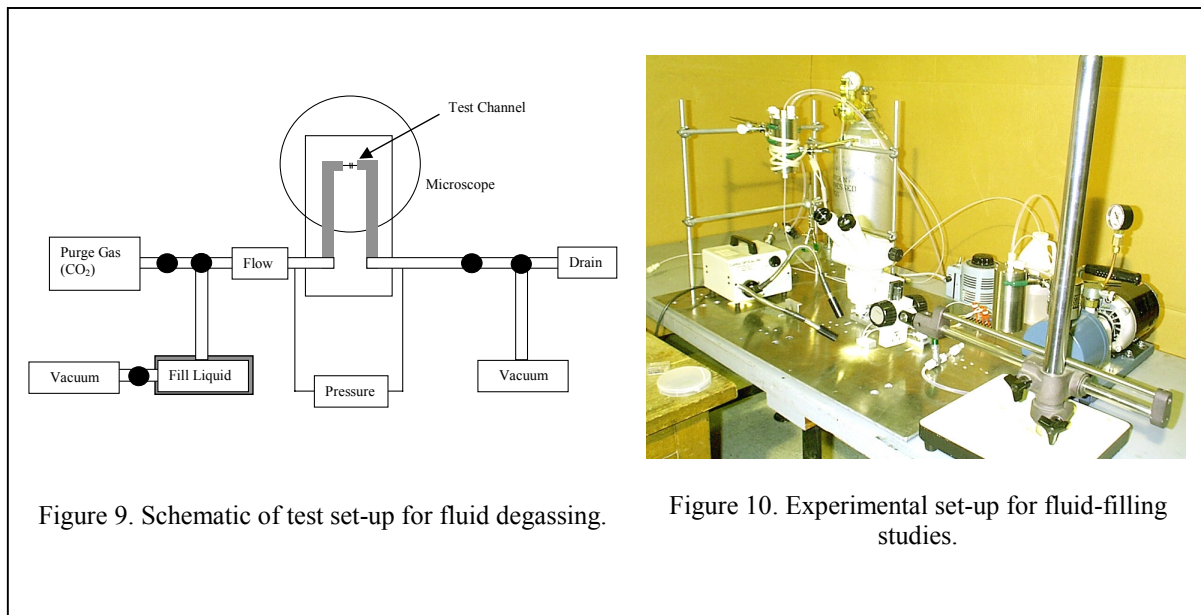


Figure 10. Experimental set-up for fluid-filling studies.

## REFERENCES

1. Gravesen, P., Branebjerg, J., Jensen, O. S., 1993, "Microfluidics-A Review," *J. Micromech. Microeng.*, 3 (1993), pp. 168-182.  
Burgess, S. C., Moore, D. F., Newland, D. E., and Klaubert, H. L., 1997, "A Study of Mechanical Configuration Optimisation in Micro-systems," *Research in Engineering Design*, Vol. 9, pp.46-60.
2. Huff, M. A., Mettner, M. S., Lober, T. A., Schmidt, M. A., "A Pressure-Balanced Electrostatically-Actuated Microvalve," *IEEE Solid-State Sensor and Actuator Workshop, 1990*, pp.123-7.
3. Meckes, A., Behrens, J., Benecke, W., "Electromagnetically Driven Microvalve Fabricated in Silicon," *Transducers '97, 1997 International Conference on Solid-State Sensors and Actuators*, pp.821-4.
4. Jerman, H., "Electrically-activated, normally-closed diaphragm valves," *Transducers '91, 1991 International Conference on Solid-State Sensors and Actuators.*, pp.1045-8.
5. Van de Pol, F. M., Wonnink, D. J., Elwenspoek, M., and Fluitman, J. J., "A Thermo-pneumatic Principle for a Microminiature Pump and other Micromechanical Devices," *Sensors and Actuators, 17* (1989), pp.139-143.
6. Esashi, M., Shoji, S., Nakano, A., "Normally-Closed Microvalve and Micropump Fabricated on a Silicon Wafer," *Sensors and Actuators, 20* (1989), pp.163-9.
7. Chen, K. S., Ayon, A. A., and Spearing, S. M., "Silicon Strength Testing for Mesoscale Structural Applications," *Microelectromechanical Structures for Materials Research. Symposium. Materials Research Society 1998*, pp. 123-30.

# Micro Hydraulic Transducer Technology for Actuation and Power Generation

Nesbitt W. Hagood<sup>a</sup>, David C. Roberts<sup>a</sup>, Laxminarayana Saggere<sup>a</sup>,  
Kenneth S. Breuer<sup>b</sup>, Kuo-Shen Chen<sup>a</sup>, Jorge A. Carretero<sup>a</sup>, Hanqing Li<sup>a</sup>,  
Richard Mlcak<sup>c</sup>, Seward Pulitzer<sup>a</sup>, Martin A. Schmidt<sup>a</sup>, S. Mark Spearing<sup>a</sup>, Yu-Hsuan Su<sup>a</sup>

<sup>a</sup>Massachusetts Institute of Technology, Cambridge, MA 02139

<sup>b</sup>Brown University, Providence, RI 02912

<sup>c</sup>Boston Microsystems, Inc., Woburn, MA 01801

## ABSTRACT

The paper introduces a novel transducer technology, called the solid-state micro-hydraulic transducer, currently under development at MIT. The new technology is enabled through integration of micromachining technology, piezoelectrics, and microhydraulic concepts. These micro-hydraulic transducers are capable of bi-directional electromechanical energy conversion, i.e., they can operate as both an actuator that supplies high mechanical force in response to electrical input and an energy generator that transduces electrical energy from mechanical energy in the environment. These transducers are capable of transducing energy at very high specific power output in the order of 1 kW/kg, and thus, they have the potential to enable many novel applications. The concept, the design, and the potential applications of the transducers are presented. Present efforts towards the development of these transducers, and the challenges involved therein, are also discussed.

**Keywords:** transducer, actuator, energy generator, micro-hydraulics.

## 1. INTRODUCTION

Transducers are a class of devices that interact with the environment in some way to transform physical energy from one form to another. The performance and usefulness of a transducer for most applications are highly dependent on two important characteristics: compactness and specific power output, that is, power output by the transducer per its unit mass. Conventional transducers, generally, not only tend to be heavy and bulky, but are also limited in their transducing power on account of their low bandwidths. Recent advances in active materials technology has led to the development of many compact solid-state transducers. However, the power output from these solid-state transducers is fairly limited for most macro applications. Although the single-stroke work output of solid-state materials such as piezoelectrics is relatively small, such materials possess very high bandwidths, and as such, are capable of high power output. However, since most applications do not require high frequency actuation, the high bandwidth potential of piezoelectrics is not fully utilized. Since a transducer's power output is the product of its single stroke energy and its bandwidth, it is feasible to create high performance transducers by combining high single-stroke force of a hydraulic system and high frequency displacements of a piezoelectric element in a synergistic manner. This concept can be further exploited to create high performance transducers with very high power densities by miniaturizing the transducer systems. The state-of-the-art micromachining (or MEMS) technology has the potential to allow for the implementation of this concept at the micro scale.

Research and development of microfluidic devices has received a significant amount of interest in the past few years [1]. The feasibility of micromachining many of the key building blocks (flow channels, pumps, active/passive valves) of a micro-fluidic system including the integration of solid-state materials such as piezoelectrics to actuate valves has already been demonstrated, and researchers are now striving to create complete microfluidic systems. However, the microfluidic devices developed thus far mostly feature small flow conductance, limited stroke, and low power density, and are mostly geared towards small flow/force applications such as microdosing of fluids.

This paper introduces the development a novel class of micromachined devices called solid-state micro-hydraulic transducers that are capable of extremely high power density outputs on the order of 500-1000 W/Kg, and potentially higher. A unique feature of these transducers is their ability to operate in a fully bi-directional manner, that is, both as actuators and as power generators, by reversing the direction of their operation. As actuators, these transducers transform electrical energy input into mechanical energy output, and as energy generators, the transducers transform mechanical energy input into electrical energy that can be stored in a battery or a capacitor.

These high performance transducers can significantly enhance the scope of micromachined transducers technology by enabling many novel applications. When utilized as actuators, they are capable of extending the usefulness of active material based structural actuation beyond small strain applications. A coordinated command of an array of tiny actuators integrated with a structure can generate a distributed strain in the structure which is far higher than that achievable through direct application of piezoelectrics. These actuators can also be useful in miniature robotics. As energy generators, the transducers can extract electrical energy from wasted mechanical energy sources such as vibrations of operating machinery and heel strike of human gait, and function as disposable batteries for numerous small electronic devices in both civilian and military arenas. This paper introduces the concept, the design, and the technical challenges involved in the development of these transducers. The fabrication and testing of key components within these transducers are also presented.

## 2. MICRO-HYDRAULIC TRANSDUCERS (MHT)

### 2.1 The Concept of MHT

The concept of the micro-hydraulic transducer (MHT) is schematically illustrated in Figure 1. As shown in the figure, the transducer can be configured as both an actuator and an energy generator, and in either configuration, the transducer is comprised of the following generic components: a piezoelectric fluid pump chamber, two actively controlled valves, a low-pressure fluid reservoir (LPR), and a high-pressure fluid reservoir (HPR). The two active valves—one operating between the LPR and the pump chamber and the other one operating between the pump chamber and the HPR— regulate the fluid flow into and out of the pump chamber. The piezoelectric element within the pump chamber serves as the main energy transducing element.

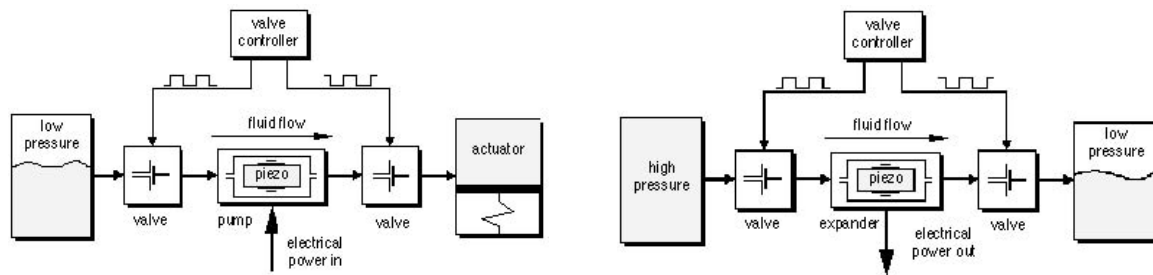


**Figure 1.** The schematics of the MHT concept: The actuator (left) and The Energy Generator (right).

In the actuator mode (see Figure 1(a)), an electric voltage applied to the piezoelectric induces a strain in the element resulting in a net volume change in the pump chamber. A controller synchronized with the pump signal cycles the active valves out of phase with each other in a specified duty cycle, transforming the volume oscillations of the chamber into a net fluid flow from a low-pressure reservoir to a high pressure reservoir. The accumulation of fluid in the high-pressure reservoir or the actuator increases the pressure and performs useful work on the load. After the actuator travels its full stroke, the flow direction is reversed and the actuator is evacuated as it returns to its initial position, completing the actuation cycle. In this way the high frequency, small displacements of the piezoelectric are rectified into low frequency, large stroke actuation.

In the energy generator mode, the transducer operates in a manner that is reverse of the actuator. The controller toggles the valves with a phasing that allows fluid flow from the high pressure reservoir to the low pressure reservoir, thus transforming the static fluid pressure into high frequency pulses on the piezoelectric. Valve actuation at high frequency creates a near sinusoidal cyclic stress on the piezoelectric element, thereby generating electrical charge across the element. Coupled circuitry (not shown) rectifies this electrical energy and stores it capacitively.

### 2.2 Design of MHT

A CAD model of the prototype design for the micro-hydraulic transducer mechanism with typical overall dimensions of 20mm×10mm×5mm is shown in Figure 2. The mechanism is comprised of three chambers, a main pump chamber and two active valve chambers. In each chamber, a piezoelectric element is sandwiched between the rigid bottom layer of the structure and a moveable piston plate. The piston plate is sufficiently thick for rigidity and is tethered to the chamber wall



through thin flexible diaphragms that extend radially from the outer edges of the cylinder. The structure effectively constitutes a piston that can move vertically up and down when a net force is applied to it. Each active valve chamber incorporates a stiff fluid enclosed in the volume between the piston diaphragm and the valve diaphragm, and effectively serves as a hydraulic amplifier. As the piston in the active valve is displaced by the piezoelectric element, the pressure of the compressed fluid acts to deform the smaller area valve membrane located at the top of the chamber. Deflection of the rigid cap at the center of the valve membrane blocks fluid flow through the corresponding fluid orifice.

Two cylindrical volumes located on the upper and lower sides of the three chambers comprise the HPR and the LPR. Fluid travels between the LPR and the connected valve via a cylindrical vertical channel located in the center of the mechanism (not seen in Figure 2), while three other channels exist to connect the valves, pump, and HPR. A gas chamber, separated from the low-pressure chamber by a thin membrane, serves to compensate the volume change. In addition, the controls and drive electronics (not shown in Figure 2) to power the valves and to harvest electrical energy are integrated with the design.

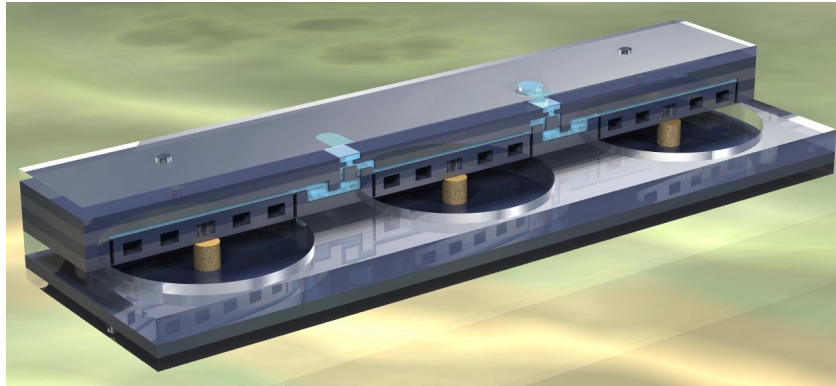


**Figure 2.** Design of MHT.

### 2.3 Simulation of MHT

To obtain a realistic prediction of MHT performance, detailed non-linear equations describing the analytical models of the canonical system components were built in the Matlab/Simulink<sup>®</sup> application and integrated to carry out system level simulations. These model/simulations include such effects as fluid viscous losses, fluid inertia, piezoelectric material behavior, structural compliances and dynamics of the pump chamber and valves, and electrical circuit behavior. The entire system is highly coupled and a flow chart of the system as represented in system level simulations (for the energy generator operation) is shown in Figure 3. Computer simulations of the steady-state operation of the transducer design indicate specific power output near 1 kW/kg and flow rates of 1.5 ml/s at efficiencies around 40%.

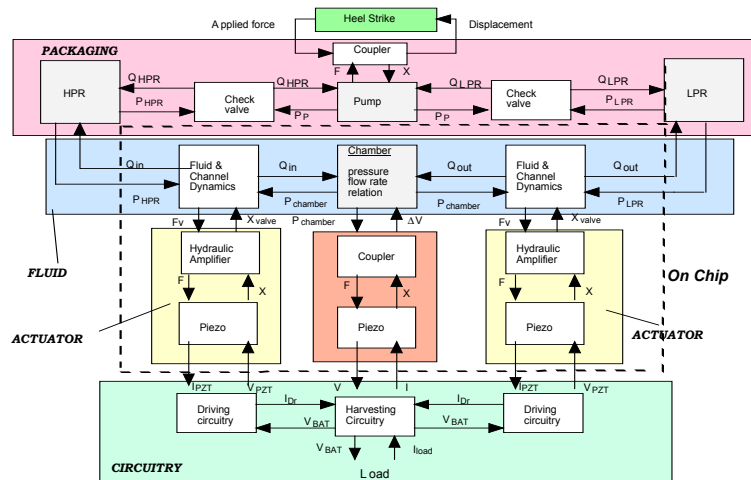


**Figure 3.** Flow chart of the system level simulation.

## 2.4 Highlights of the MHT Technology

The proposed MHT devices derive their enhanced performance from several inherent design features. One of the important objectives of developing the MHT technology is to accomplish high specific power from the devices. In order to achieve such high power output, the device is operated at very high frequencies at or near the resonance of the piezoelectric/fluid-structure system. The key to such high frequency operation is successful design and implementation of fast acting valves. Active valves with high frequency and high force are accomplished in the MHT design through a piezoelectrically driven hydraulically amplified mechanism. Within the valve, a hydraulic chamber serves to amplify the small displacements of the piezoelectric material into significantly larger displacements of the valve cap and effectively transmits the high force actuation capability of the piezoelectric material. The utilization of the hydraulic amplification chamber also leads to minimization of the actuator material, and thus helps in achieving high power densities. Another highlight of the MHT technology is the exploitation of micromachining capability to miniaturize the system to a compact micro scale device, leading to higher valve frequencies and enhanced specific power of the device.

The novel feature of the MHT design is the single configuration that allows for dual functionality of the transducer. This design of MHT devices enables the micro-hydraulics technology to create both actuators and energy generators with high flow rates and high power densities. This can potentially lead to many novel applications. One of the important intended applications of the MHT is to convert the mechanical energy generated by the low frequency human heel-strike into electrical energy by packaging the entire device into the heel of a standard boot, and store the energy in a battery within the device. Another important application of these transducers is in the active control of structures. Active materials are widely used for structural actuation. However, the full actuation authority of these materials cannot be exploited on account of the low bandwidth required for most controlled structures. Since the MHT devices are capable of transducing the full actuation potential of piezoelectrics at high frequencies into low frequency and large hydraulic power, they can be applied to large deformation control of structures.

The MHT devices can be operated as stand-alone devices, or may be comprised of any combination of several units in series or parallel to achieve desired output characteristics. Cascaded actuators can work against significantly larger overall pressure potentials than a single actuator and multiple parallel actuators can produce enhanced flow rates over a single actuator. Likewise, multiple energy generator units can be configured in parallel to yield higher cumulative electrical energy.

## 2.5 Technical challenges

The development of the MHT technology is currently ongoing. Realization of these devices involves overcoming significant technical challenges in design, modeling, fabrication, and system level integration. Some of the major challenges are highlighted below.

**Design** Achieving high specific power outputs in MHT devices is critically dependent on fast acting valves capable of operating at frequencies in the tens of kilohertz range and with sufficient actuation force to overcome pressures of about 1MPa. Therefore, the valves must be designed to be stiff, yet flexible enough to allow large stroke. In addition, since the valves are parasitic to the complete packaged device, the valve structural geometry and active driving means for the valves must be minimal in size and mass. Numerous microvalve designs have been reported in the literature up to this time, including those driven by electrostatic [2], electromagnetic [3], thermal bimetallic [4], thermo-pneumatic [5], and direct piezoelectric [6] means. However, none of these can meet the aforementioned frequency, force, and size/mass requirements. The hydraulically amplified piezoelectric valve concept presented briefly in this paper and in more detail in the companion paper [8], achieves the above design requirements.

**Modeling microfluidics** Microscale fluid flows for the MHT device scale typically fall within the transition regime between inertia-dominated and viscous-dominated behavior, and are therefore quite difficult to accurately model. In comparison to macroscale flows, which are typically inertia dominated and far in excess of the transitional Reynolds number of 2300, microscale flows can experience significant viscous forces. As a result, the well-documented high Reynolds number steady flow correlations through such structures as elbows, expansions, contractions, and diffusers are not applicable. For these lower Reynolds number flows, few correlations exist and steady flow CFD models are often required to gain insight.

Modeling of unsteady flow phenomena at these scales is even more difficult. In micro-hydraulic transducer devices, active valve frequencies in the tens of kilohertz range result in rapidly moving boundary conditions (valve cap surface) with time. For complex geometries, CFD models are unable to accurately capture the flow behavior. Experimental correlation is the only possible method for developing models to represent these flows.

**Simulation** A realistic prediction of the MHT performance can only be gained by numerically solving all the governing equations for the entire system. The system equations involving complex fluid-structure dynamic interactions are highly

coupled, highly nonlinear, and numerically stiff. As such, system level simulations are computationally intensive and difficult to solve. The complete system involves a large number of design variables that add complexity and difficulty to the system design and optimization.

**Electronics** Development of efficient high power drive electronics and efficient power harvesting circuitry for the power harvester device, and reliable controls are challenging. Packaging them into a compact size is a formidable task.

**Micromachining** Micromachining of the MHT involves some critical issues that either require very accurate control of the process parameters or need innovation of new processes. The design requires 2-sided lithography in order to minimize the overall number of silicon wafers in the devices and thereby minimize the overall device mass and volume. Although single-sided lithography of silicon wafers is a mature and proven process, there is no existing standard for 2-sided lithography. Protection of fragile structures etched on a given side, while depositing and preparing photoresist on the opposite side is not a straightforward process. Furthermore, the buried oxide removal from the Deep-Reactive Ion Etching (DRIE) process required to etch the drive element and valve membranes in Silicon-On-Insulator (SOI) wafers can result in stresses in the membrane. Also, the multi-layer wafer bonding procedures required for the MHT devices are difficult to accomplish.

**System Level Integration** Integration of bulk piezoelectric material (ideally, single-crystal ferroelectric material) with silicon micromachined structures is a predominant challenge in the development of micro-hydraulic transducers. Due to the fact that piezoelectric materials degrade at temperatures far below those required for silicon-silicon fusion bonding, other structural materials and bonding procedures are required in the planar region directly surrounding the bulk piezoelectric material. Pyrex can be substituted for silicon, resulting in robust lower temperature anodic bonds between the pyrex and the upper and lower silicon wafers. Eutectic alloy compositions can be deposited on the top and bottom surfaces of the piezoelectric material and on the bordering silicon wafers to allow for strong, low-temperature eutectic bonds between the piezoelectric material and the silicon. In this way, the piezoelectric material integration and subsequent low-temperature bonding steps are the last to be performed.

In addition, successful piezoelectric integration depends on the accuracy to which the piezoelectric material thickness can be measured with respect to that of the surrounding material. Thickness variation between these two components can create unwanted static and operational deflections of the piston membrane and therefore potentially destructive stresses at the critical etched membrane silicon-oxide interfaces. Also, incorporation of multiple smaller area piezoelectric materials spread out under the piston membrane is desired over placement of a single larger area piezoelectric material at the piston center, so as to reduce system compliances and increase efficiency. However, tolerance issues become even more important when dealing with requirements on multiple bonded structures in the same plane. Structural integrity of the etched membranes and high cycle fatigue of the bonds are additional critical issues for successful MHT development [7].

**Fluid filling and sealing** Encapsulation of a working fluid in the device is a significant challenge at the microscale because surface-to-volume ratios are typically quite large, with surface energies playing a dominant role. Any gas bubbles present in the sealed operational device can create enormous system compliances, potentially rendering the device useless. The elimination of trapped gasses during filling of the device and during encapsulation of the fluid ports used for filling is critical for high-level performance. The choice of fluid, degassing of the fluid, and post-filling encapsulation of the fluid are important to prevent the generation of any bubbles during the operation.

### 3. CURRENT EFFORTS TOWARDS THE DEVELOPMENT OF MHT

In order to practically evaluate the performance, and validate the design of the main components in the MHT, we are currently in the process of fabricating and testing the main components of the transducer. The main components being evaluated are the drive element (that is common to both the pump and the active valve chambers), and the full active valve component including hydraulic amplification mechanism. Efforts are also ongoing towards evaluating and minimizing the risks involved in accomplishing the necessary microfabrication processes including various bonding techniques, integration of piezoelectric materials with silicon micromachined structures, and fluid-filling and sealing operations in the micro device. As a precursor towards the development of the complete MHT device with actively controlled valves, a prototype of piezo-driven micro-pump with check (passive) valves was also fabricated and tested successfully. The details of each of these efforts are summarized in the following sub-sections.

### 3.1 Fabrication and Testing of the Drive Element

A first generation drive component has been successfully fabricated and tested. This drive component incorporates a single PZT-5H cylinder positioned at the center of the drive element chamber, eutectically bonded below to a silicon substrate and above to a silicon piston membrane. The pyrex layer in the middle is anodically bonded to silicon at the top and the bottom. Figure 4 shows a fabricated device whose dimensions are 10mm× 10mm×2mm.

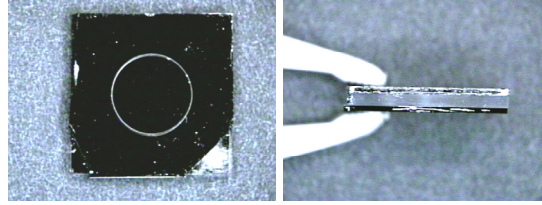


**Figure 4.** Fabricated drive-element component

The drive elements have been statically and dynamically tested using an optical probe and laser scanning vibrometer system, and the measured results (shown in Figure 5) were found to be in excellent correlation with the theoretical results predicted by finite-element analysis. Finite-element models predicted dominant modal behavior at 70kHz (1- $\theta$  tilt mode), 110kHz (plunge mode), 175kHz (2- $\theta$  mode), and higher frequencies. Experimental results indicated modal behavior at 74 kHz (1- $\theta$  tilt mode), 110 kHz (plunge mode), and 130 kHz (2- $\theta$  mode).

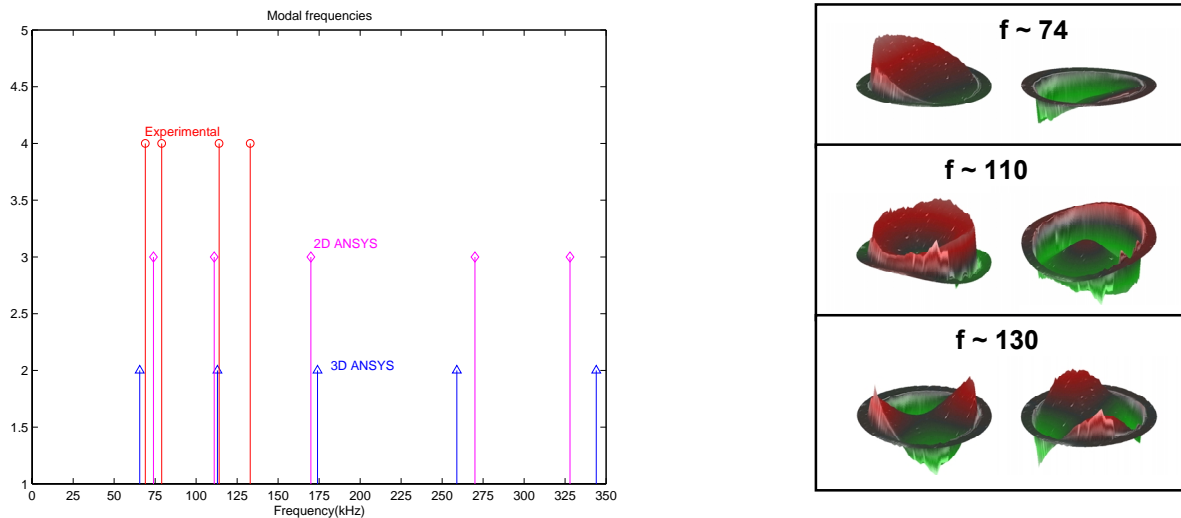


**Figure 5.** Experimental results showing frequencies and mode shapes of the drive component.

### 3.2 Development of the Active Valve Component

Efforts are currently underway to fabricate the hydraulic amplification component including microvalves and integrate it with the drive element discussed in the previous section in order to build the full active valve component as shown in Figure 6. The complete active valve component will comprise of drive element component with additional silicon and pyrex layers that form the fluid inlet and outlet ports, fluid channels, the valve cap/membrane, and the hydraulic amplification chamber. The performance and structural integrity of the complete active valve will be evaluated under varying system loads. Also, the feasibility of fluid filling and sealing, and membrane stress limitations will be practically evaluated. A numerical code has

been developed to accurately predict the highly non-linear valve membrane/cap deflections under large system pressures. Analytical models are being developed to estimate valve energy consumption so that new generation active valve designs can be made smaller in overall volume and mass and contain reduced amounts of active material. More details on the development of active valve component can be found in a companion paper presented at this conference [8].

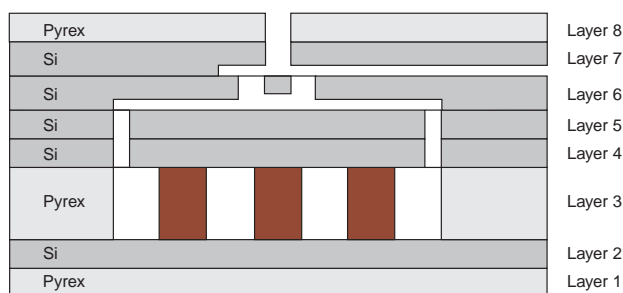


**Figure 6.** Configuration of active valve component

### 3.3 Fluid filling studies

To practically study the critical issues concerning fluid encapsulation in the device, several experiments on fluid-filling in specially fabricated micro channels have been conducted. A schematic of the experimental set-up is shown in Figure 14, and a photograph of the actual experimental set-up is shown in Figure 15. The chips with specially fabricated micro channels were connected to a fluid supply tank, a fluid drain, a vacuum pump and inert (and solvable) gas cylinders. The vacuum pump created a partial vacuum in the chips, which allowed for easy purging and filling of the channels. The fluid supply tank was wrapped with a heat tape, and connected to a vacuum pump, to enable fluid degassing. To create a partial vacuum, the fluid channels and cavities were first pumped down. This was followed by a few cycles of purging the channels with a solvable gas ( $\text{CO}_2$ ) and then evacuating. Finally, the channels were filled with the degassed fluid at a controlled rate, and the filled channels were inspected under a microscope for any entrapped bubbles. To investigate the effect of the fluid properties on filling, a few different fluids ( $\text{H}_2\text{O}$ , methanol, and silicone oil) were used. The results of these experimental studies indicated that filling of the small channels and the chambers is achievable with negligible gas entrapment especially with the silicone oil.

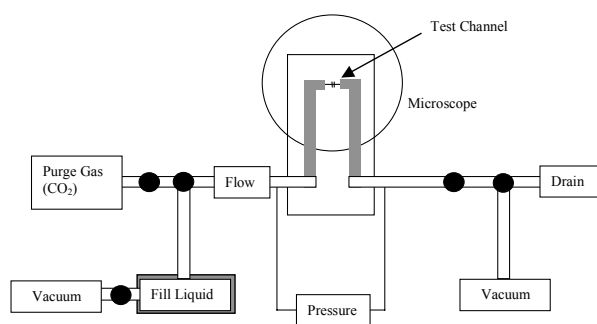


**Figure 14.** Schematic of test set-up for fluid degassing.



**Figure 15.** Experimental set-up for fluid-filling studies.

### 3.4 Fabrication and Testing of Passive Valve Micropump

To evaluate the technical feasibility towards the development of the MHT device with actively controlled valves, a prototype of piezo-driven micro-pump with passive check valves was fabricated and tested. The schematic and the photograph of the packaged prototype micro-pump is shown in Figure 7 and 8 respectively. The device utilizes a PZT-5H piezo element as the pumping element and two axisymmetric silicon micromachined membranes with hollow annular bosses for system check valves. The device was assembled from 7 independent layers (3 pyrex layers and 4 silicon layers) aligned and sandwiched together using diffusion bonding between SOI wafers, anodic bonding between Si and glass interfaces and eutectic bond between Si and the piezo material interfaces. Using Dow-Corning Silicon 200 oil as the working fluid and the experimental set-up shown in Figure 9, the performance of the micro-pump was tested by varying voltages from 0 to 1800V and at various frequencies between 1kHz to 10 kHz across the piezo element. The test results indicated successful pumping of fluid from the low pressure reservoir to high pressure reservoir at rates in the order of 2 ml/min at 4.5 kHz. Figure 10 illustrates the plot of flow Vs. rate pressure differential across the pump at 3.5kHz and 1600 V across the piezo element.

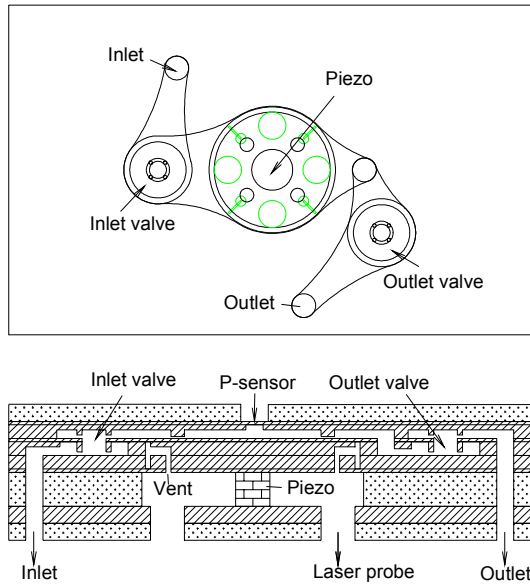


**Figure 7.** Schematic drawing of micro-pump with passive valves.

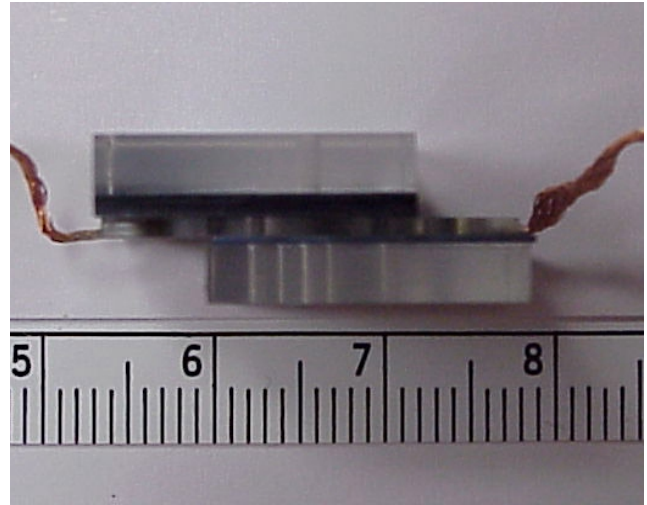


**Figure 8.** Side view of the fabricated prototype of micropump with passive valves.

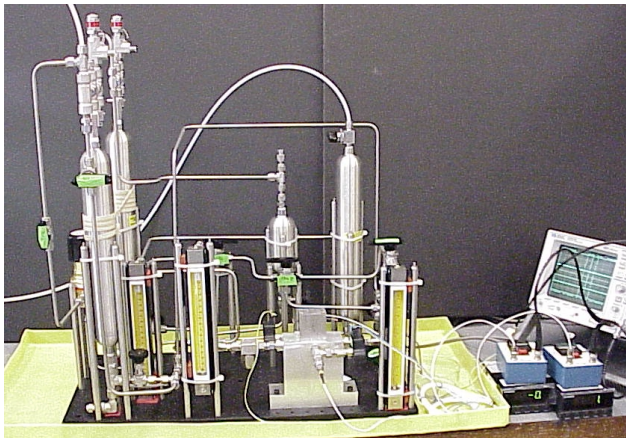


**Figure 9.** Experimental set-up for testing the passive valve micro-pump.

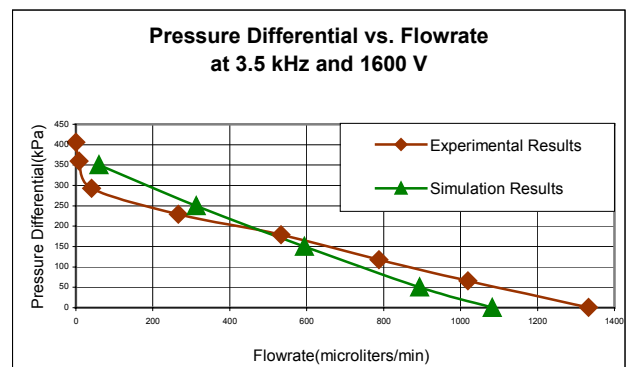


**Figure 10.** Plot of flow rate vs. pressure differential across the passive valve micro-pump.



## CLOSURE

A novel micromachined transducer mechanism that can function as both an actuator and an energy generator is introduced. This transducer exploits the integration of micromachining technology with active materials and hydraulics for the first time to create a transducer capable of yielding high power densities near 1 kW/kg. This transducer technology offers exciting prospects for the unique interplay of technologies expanding the scope of applications for micromachined transducers. However, there are number of technical challenges to overcome in realizing the transducer device. Efforts are currently underway to fabricate and test the main components of the transducer. Towards the development of the MHT device, a prototype of piezo-driven micro-pump with passive check valves was recently fabricated and tested. The success of the passive valve micro-pump has demonstrated the ability to overcome several critical risks involved in the development of MHT and has laid the groundwork for realization of the MHT energy generator.

## ACKNOWLEDGEMENTS

This research was sponsored by DARPA under Grant # DAAG55-98-0361 and by ONR under grant no Grant # N00014-97-1-0880.

## REFERENCES

1. Gravesen, P., Branebjerg, J., Jensen, O. S., 1993, "Microfluidics-A Review," *J. Micromech. Microeng.*, 3 (1993), pp. 168-182.
2. Burgess, S. C., Moore, D. F., Newland, D. E., and Klaubert, H. L., 1997, "A Study of Mechanical Configuration Optimisation in Micro-systems," *Research in Engineering Design*, Vol. 9, pp.46-60.
3. Huff, M. A., Mettner, M. S., Lober, T. A., Schmidt, M. A., "A Pressure-Balanced Electrostatically-Actuated Microvalve," *IEEE Solid-State Sensor and Actuator Workshop, 1990*, pp.123-7.
4. Meckes, A., Behrens, J., Benecke, W., "Electromagnetically Driven Microvalve Fabricated in Silicon," *Transducers '97, 1997 International Conference on Solid-State Sensors and Actuators*, pp.821-4.
5. Jerman, H., "Electrically-activated, normally-closed diaphragm valves," *Transducers '91, 1991 International Conference on Solid-State Sensors and Actuators.*, pp.1045-8.
6. Van de Pol, F. M., Wonnink, D. J., Elwenspoek, M., and Fluitman, J. J., "A Thermo-pneumatic Principle for a Microminiature Pump and other Micromechanical Devices," *Sensors and Actuators*, 17 (1989), pp.139-143.
7. Esashi, M., Shoji, S., Nakano, A., "Normally-Closed Microvalve and Micropump Fabricated on a Silicon Wafer," *Sensors and Actuators*, 20 (1989), pp.163-9.
8. Roberts, D., et al., "Design of a Piezoelectrically-Driven Hydraulic Amplification Microvalve for High Pressure, High Frequency Applications" *Smart Structures and Materials 2000: SPIE's 7<sup>th</sup> International Symposium on Smart Structures and Materials*, Newport Beach, CA, March 2000.

# Design of a Piezoelectrically-Driven Hydraulic Amplification Microvalve for High Pressure, High Frequency Applications

David C. Roberts<sup>\*</sup>, Nesbitt W. Hagood, Yu-Hsuan Su, Hanqing Li, Jorge A. Carretero

Active Materials and Structures Laboratory, Department of Aeronautics and Astronautics,  
Massachusetts Institute of Technology

## ABSTRACT

This paper reports the design of a piezoelectrically-driven microfabricated valve for high frequency control of large pressure fluid flows. The enabling concept of the valve is the ability to convert the small displacement of a piezoelectric element into a large valve cap stroke through the use of a hydraulic fluid, while maintaining high force capability. The current valve design, with operating frequency of 24 kHz and valve stroke of 40 $\mu$ m, has been tailored for use in microhydraulic actuation and energy-harvesting devices, which require high-frequency regulation of  $\sim$ 1ml/sec fluid flows across pressure differentials of 1-2 MPa.

**Keywords:** microvalve, hydraulic, amplification, piezoelectric, micromachined

## 1. INTRODUCTION

The development of a fluidic microvalve, capable of high frequency control of high pressure fluid flows, is important toward the realization of high power density micropumping technology. Examples of this potential technology are Micro-Hydraulic Transducer devices for actuation and power harvesting<sup>1</sup>. MHT actuators can be used in microrobotic applications and MHT power harvesters can be used in heel-strike power generation devices. These MHT devices combine active materials, such as piezoelectric or single-crystal ferroelectric material, with MEMS microfabrication techniques and hydraulic fluid to create high frequency pumping excitation in small mass systems. Both types of transducers consist of a piezoelectric pump chamber, two actively controlled valves, and a low and high pressure fluid reservoir. In the MHT actuator, electrical energy supplied to the piezoelectric pump chamber results in pumping of fluid through the valves from the low to high pressure reservoir. In the MHT power harvester, sequenced operation of the valves results in fluid flow from the high to low pressure reservoir, producing a “pinging” of the piezoelectric element within the pump chamber. This cyclic strain on the element induces electrical charge, which can be rectified and stored. The power density of these transducer devices scales linearly with the frequency of operation and the pressure drop across which the device can operate and inversely with scale of the device. Therefore, a MEMS-scale high frequency, high pressure active valve is required.

Although a significant amount of literature is available describing the development of active valve devices and technology, few if any have been designed for high frequency control of high pressure fluid flows. Novel microvalve designs using thermopneumatic actuation<sup>2</sup>, thermal bimetallic actuation<sup>3</sup>, electrostatic actuation<sup>4</sup>, electromagnetic actuation<sup>5</sup>, and piezoelectric bender-type actuation<sup>6</sup> have been presented. Thermal actuation designs are severely limited in their response times. Electrostatic, electromagnetic, and piezoelectric bender-type designs are limited in their ability to generate both high force and large deflection output. One method to obtain both high frequency and high force output is to use a bulk or stack-type piezoelectric actuator material to drive the valve membrane. A piezoelectric-stack driven device in which the stack is attached directly to the moveable valve membrane is presented in the literature<sup>7</sup>. However, in order to attain reasonable valve deflection, the piezoelectric stack material is required to be excessively long, and therefore the overall device mass and size are too large. A unique solution to this problem is to design a microvalve with a means to hydraulically amplify the stroke of a piezoelectric bulk-type material into a significantly larger (10x-20x) valve membrane stroke, yet still maintain high frequency, high force capability.

Numerous macroscale piezoelectric hydraulic amplification mechanisms have been presented in the literature. In an application for active vibration control, a piezoelectric actuator uses the volume change of a piezoelectric ring to create a

---

<sup>\*</sup> Correspondence: Email: dcrobert@mit.edu; Telephone: (617) 253-6462; Fax: (617) 258-5940



large deflection of a smaller area contact surface<sup>8</sup>. In an application for vibration control of a rotary dynamic system, the deflection of a stack-type piezoelectric actuator is coupled through a hydraulic line to a smaller size piston, which helps to control the motion of a rotating shaft<sup>9</sup>. These and other<sup>10</sup> piezoelectric hydraulic amplification mechanisms are novel in design, yet do not face the difficult fabrication challenges inherent in the development of high frequency MEMS-scale devices.

This paper develops the concept of and a detailed analytic and numerical model for a bulk piezoelectric hydraulic-amplification microvalve for high frequency control of high pressure fluid flows. Section 2 presents the conceptual design of the microvalve. Section 3 outlines the assumptions underlying the microvalve model. Section 4 presents the detailed theory of the microvalve behavior and interactions of its sub-components. Section 5 compares the results of the analytic and numerical valve model to a finite-element model and presents a first generation design of the microvalve. Section 6 details the fabrication process and challenges associated with the valve development. Section 7 presents experimental testing results of microfabricated subcomponent drive element structures. Section 8 presents the conclusions and future work.

## 2. GEOMETRY

Figure 1 presents a schematic of the proposed piezoelectrically driven hydraulic amplification microvalve. The axisymmetric valve is comprised of three primary sub-structures: a piezoelectric drive element, a closed fluid amplification chamber, and a membrane with attached valve cap. The drive element sub-structure consists of multiple bulk piezoelectric material cylinders in parallel, each bonded on its top surface to a silicon micromachined piston and on its bottom surface to a silicon support structure. The drive element piston is attached along its outer circumference to a silicon support structure with two thin silicon tethers. The fluid chamber resides between the top surface of the drive element piston and the bottom surface of a smaller diameter silicon micromachined valve cap membrane.

In response to applied piezoelectric voltage, a small deflection of the drive element piston translates into much larger deflection of the valve cap membrane. The ratio of the piston diameter to the valve membrane diameter, the compliances of the fluid and structural chamber, the severity to which the valve cap membrane experiences nonlinear behavior, and the piezoelectric material performance determine the potential valve stroke for a given piezoelectric voltage. Typical dimensions that allow the microvalve to achieve 1ml/s fluid flows across pressure differentials of 1-2 MPa are:  $N_{\text{PIEZO}} = 3$ ,  $L_{\text{PIEZO}} = 1\text{mm}$ ,  $D_{\text{PIEZO}} = 1.385\text{mm}$ ,  $D_{\text{PISTON}} = 6\text{mm}$ ,  $t_{\text{PISTON}} = 1000\mu\text{m}$ ,  $t_{\text{TETHER}} = 10\mu\text{m}$ ,  $D_{\text{HAC}} = 6.3\text{mm}$ ,  $H_{\text{HAC}} = 100\mu\text{m}$ ,  $t_{\text{CHAMBER}} = 1000\mu\text{m}$ ,  $D_{\text{VM}} = 1.6\text{mm}$ ,  $t_{\text{VM}} = 5\mu\text{m}$ ,  $D_{\text{CAP}} = 620\mu\text{m}$ , and  $t_{\text{CAP}} = 300\mu\text{m}$ . These are described in detail in Section 5.

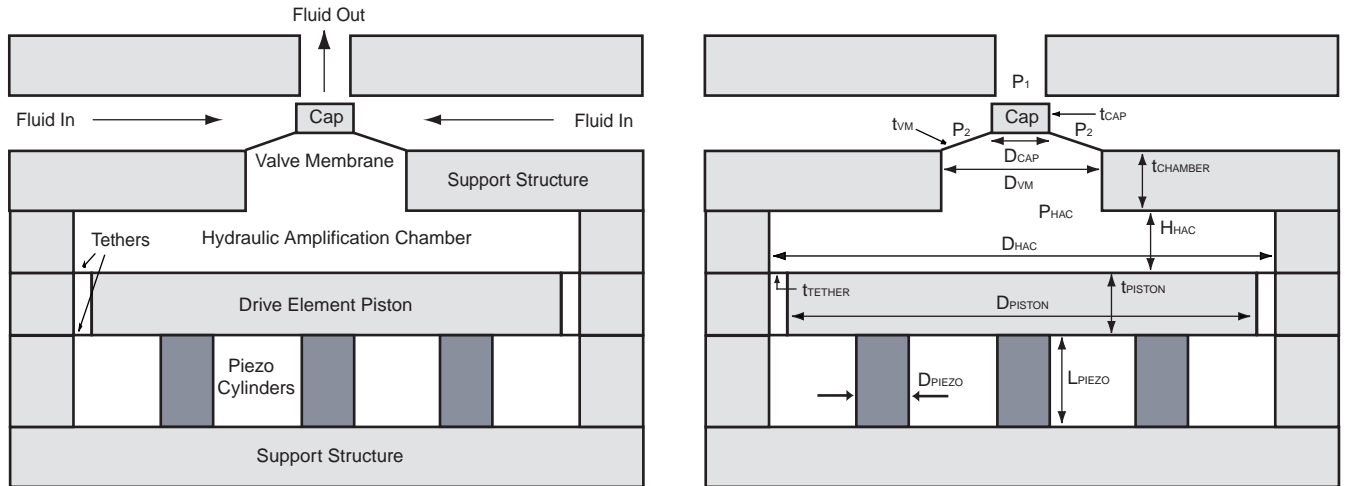


**Figure 1: Schematic of active valve illustrating valve membrane and cap closing against fluid outlet port.**

The geometric and loading variables of the valve are listed below.

$L_{\text{PIEZO}}$	Piezoelectric cylinder length
$D_{\text{PIEZO}}$	Piezoelectric cylinder diameter

$N_{\text{PIEZO}}$	# of piezoelectric cylinders in drive element
$D_{\text{PISTON}}$	Drive element piston diameter
$t_{\text{PISTON}}$	Drive element piston thickness
$t_{\text{TETHER}}$	Drive element tether thickness
$D_{\text{HAC}}$	Hydraulic amplification chamber diameter
$H_{\text{HAC}}$	Main hydraulic amplification chamber height
$t_{\text{CHAMBER}}$	Top chamber structure thickness
$D_{\text{VM}}$	Valve membrane outer diameter
$t_{\text{VM}}$	Valve membrane thickness
$D_{\text{CAP}}$	Valve cap diameter
$t_{\text{CAP}}$	Valve cap thickness
$P_{\text{HAC}}$	Hydraulic amplification chamber pressure
$P_1$	External pressure over valve cap
$P_2$	External pressure over valve membrane
$V_{\text{PIEZO}}$	Applied piezoelectric voltage

In developing a comprehensive analytical model for the active valve, the following aspects need to be accurately represented: (1) piezoelectric material behavior, (2) drive element piston and tether deflection behavior, (3) fluid compressibility, (4) hydraulic amplification chamber structural compliance, and (5) valve membrane/cap deflection behavior. The efficiency of the valve drive is a function of how much volume is created in the various system compliances. The ideal design would call for a hydraulic fluid with infinite bulk modulus and a completely rigid drive element piston and chamber structure. In this case, all of the volume change created by the drive element deflection would exhibit itself in the volume change associated with the valve membrane deflection. In reality, these compliances cannot be ignored.

### 3. ASSUMPTIONS

#### Drive Element

- Bending of silicon structural support underneath piezoelectric cylinders within drive element is neglected.
  - In a packaged device, it is likely that the bottom support structure would be sufficiently thick to allow almost zero negative deflection of the entire drive element structure. In fact, to minimize overall device volume and mass, this bottom support structure would be a hollowed out structure with support pieces solely under the location of the piezoelectric cylinders. Nevertheless, in future generations of the valve model, this compliant effect will be included.
- Bending of drive element piston is neglected.
  - The drive element piston structure is a sandwich of two 400 $\mu\text{m}$  thick silicon wafers. This thickness, coupled with the fact that multiple piezoelectric cylinders are spread out spatially under the piston, severely limit the amount of bending that the drive element piston can experience. Studies of piston compliance have been performed and results indicate that this assumption is a reasonable one.
- Tether behavior is within linear bending regime.
  - The drive element deflection is within the range of 0-5  $\mu\text{m}$  during device operation. Since the drive element tethers have thickness of 10  $\mu\text{m}$ , this tether bending behavior can be assumed linear.

#### Valve Cap/Membrane

- Bending of valve cap is neglected.
  - The valve membrane/cap structure is created from etching a 300 $\mu\text{m}$  or 400 $\mu\text{m}$  silicon wafer. The thickness of the cap is very large compared to the membrane thickness ( $\sim 5\mu\text{m}$ ). Therefore, minimal cap bending results. Studies of this cap bending have been performed and results indicate that this assumption is a valid one.

As a result of these assumptions, the primary sources of system compliance that remain to be included in the valve model are the fluid compressibility, the hydraulic amplification chamber structural compliance, and the valve membrane compliance.

## 4. THEORY

The five primary modeling tasks were discussed at the conclusion of Section 2. Each of these tasks is now presented in detail. This section will conclude with an overview of the full analytical/numerical model and its solution process.

### 1. Piezoelectric Material Behavior

The piezoelectric material cylinders within the valve drive element experience a compressive loading due to the hydraulic amplification chamber pressure acting over the piston top surface, the tensile drive element tether force, and the applied piezoelectric voltage. For a bulk cylindrical piezoelectric material, as shown in Figure 2, subject to a compressive axial stress  $T_{PIEZO}$  and an applied voltage  $V_{PIEZO}$ , the material axial strain is:

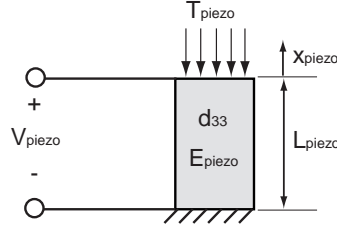


Figure 2: Cylindrical piezoelectric element with applied voltage and stress loading.

$$\epsilon_{piezo} = \frac{x_{piezo}}{L_{piezo}} = \frac{d_{33} V_{piezo}}{L_{piezo}} - \frac{T_{piezo}}{E_{piezo}}. \quad (1)$$

$d_{33}$  is the piezoelectric material coefficient and  $E_{PIEZO}$  is the modulus of elasticity. Under the case of zero external loading,  $T_{PIEZO}=0$ , the material experiences a maximum strain, termed the *free strain*. Under the case of an external load of  $T_{PIEZO}=d_{33}V_{PIEZO}E_{PIEZO}/L_{PIEZO}$ , the material experiences no net strain. This is termed the *blocked force condition*. These are the limiting cases for piezoelectric actuation. Equation 1 assumes perfect 33-actuation. In reality, this is not exactly true due to transverse clamping of the piezoelectric element at its top and bottom. However, the incorporation of multiple, smaller diameter piezoelectric elements rather than a single large diameter element helps to reduce this clamping effect and supports the assumption.

### 2. Drive Element Piston/Tether Behavior

The drive element provides a volume change, which is transferred to the valve cap/membrane through the use of hydraulic fluid. The drive element piston/tether experiences loading in the form of a pressure  $P_{HAC}$  acting on the top surface of the piston and tether and a stress  $T_{PIEZO}$  acting on the bottom surface of the piston at the locations of piezoelectric cylinder attachment. Figure 3a illustrates this loading. Under the assumption of a rigid drive element piston, this loading scenario can

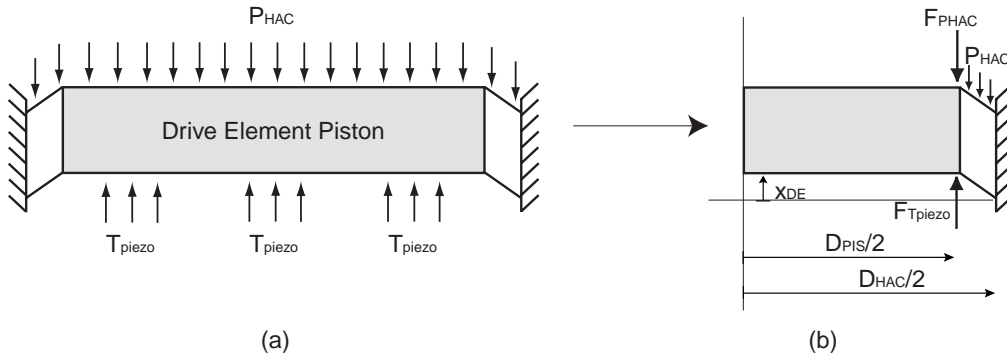


Figure 3: Simplification of pressure /stress loading on drive element piston for use in linear deflection analysis of drive element tethers.

be simplified into a pressure  $P_{HAC}$  acting on the top surface of the upper drive element tether and two concentrated forces,  $F_{PHAC}$  and  $F_{TPIEZO}$ , acting along the inner circumference of the upper and lower tether. Figure 3b illustrates this simplified loading.  $F_{PHAC}$  is the total force due to the pressure acting over the top surface of drive element piston and  $F_{TPIEZO}$  is the total force due to the piezoelectric material stress acting over the corresponding bottom surface of the piston.

Focusing on each tether as an annular plate with the loadings stated above, the deflection and volume change of the drive element piston are determined using linear plate theory. The relations take the following general forms:

$$x_{DE} = C_1 T_{PIEZO} - C_2 P_{HAC} \quad (2)$$

$$\Delta V_{DE} = C_3 T_{PIEZO} - C_4 P_{HAC} + A_{PISTON} x_{DE} \quad (3)$$

where the coefficients  $C_1$  and  $C_3$  are associated with the  $T_{PIEZO}$  loading and the coefficients  $C_2$  and  $C_4$  are associated with the  $P_{HAC}$  loading. These relations are derived from first principles, solving the bending equation for an axisymmetrically loaded circular plate with appropriate boundary conditions<sup>11</sup>. See Appendix for equations and boundary conditions.

### 3. Fluid Compressibility

In response to increased pressures generated within the hydraulic amplification chamber, the contained fluid will be compressed. A portion of the drive element volume change will be lost in this undesired volume change of the fluid. The relationship between the fluid volume change  $\Delta V_{HAC}$  and the fluid pressure change  $\Delta P_{HAC}$  is

$$\Delta V_{HAC} = \left( \frac{-V_{i,HAC}}{\kappa_f} \right) \Delta P_{HAC} \quad (4)$$

where  $\kappa_f$  is the fluid bulk modulus and  $V_{i,HAC}$  is the initial volume of the hydraulic amplification chamber. Assuming the initial pressure of the hydraulic amplification chamber to be zero, the term  $\Delta P_{HAC}$  can be replaced by  $P_{HAC}$ .

### 4. Hydraulic Amplification Chamber Structural Compliance

It is important to ensure that the hydraulic amplification chamber compliance is minimal so that only a small portion of the drive element volume change is lost in the chamber deformation. The top chamber structure can be modeled as an annular plate with a pressure loading on its underside and an effective circumferential force at the inner radius due to the tensile reaction of the valve membrane. Figure 4 illustrates this model. Linear theory can be safely assumed since the structural deflections are significantly less than the structural thicknesses.

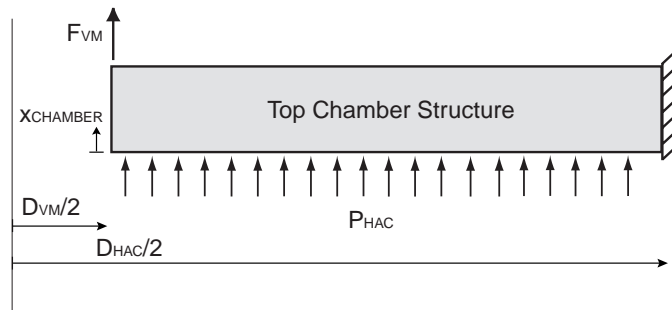


**Figure 4: Hydraulic amplification chamber structural deformation under  $P_{HAC}$  loading and the valve membrane tensile force.**

The inner circumference deflection and total volume change of the chamber structure are determined using linear plate deflection theory and take the following general forms:

$$x_{CHAMBER} = C_5 P_{HAC} - C_6 F_{VM} \quad (5)$$

$$\Delta V_{\text{CHAMBER}} = C_7 P_{\text{HAC}} - C_8 F_{\text{VM}} + A_{\text{VM}} x_{\text{CHAMBER}} \quad (6)$$

where the coefficients  $C_5$ ,  $C_6$ ,  $C_7$ , and  $C_8$  are associated with the loading conditions shown in Figure 4. As for the drive element relations, the chamber compliance relations are derived from first principles, taking into account deflection and shearing effects. See Appendix for equations and boundary conditions. The vertical component of the tensile reaction force of the valve membrane is simply the net force due to all the pressures acting over the valve membrane and cap. In reality, the region above the annular chamber structure will not be completely unsupported. As a result, this model provides a worst-case value for the structural chamber volume change.

## 5. Valve Membrane Behavior

During device operation, the valve cap may experience deflections significantly larger than the valve membrane thickness. As a result, modeling the non-linear behavior of the valve membrane is a critical task in capturing accurate behavior of the valve. For the fluid flow directionality shown in Figure 1, a pressure drop occurs as the fluid flows radially inward over the valve membrane, through the contraction over the valve cap, and finally through the expansion into the exit channel. Assuming the valve cap opening is small compared to the valve cap thickness, the majority of this pressure drop occurs through the contraction and expansion ( $r = D_{\text{CAP}}/2$ ). As a result, the pressure  $P_2$  is constant over the valve membrane area and the pressure  $P_1$  is constant over the valve cap area.

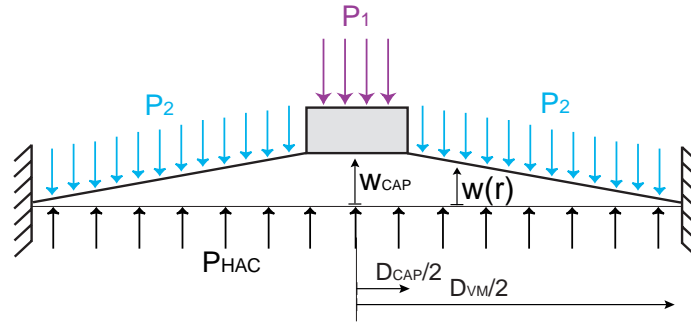


**Figure 5: Valve membrane and cap, deflected upward from equilibrium position, under pressure loadings  $P_{\text{HAC}}$ ,  $P_1$ , and  $P_2$ .**

As shown in Figure 5, the valve membrane experiences a pressure loading  $P_{\text{HAC}}$  over the entirety of its bottom surface, a pressure loading  $P_1$  over the valve cap top surface, and a pressure loading  $P_2$  over the top surface of the valve membrane. For linear theory, the deflection and volume relations for the valve cap/membrane are simply:

$$w_{\text{CAP}} = C_9 P_{\text{HAC}} - C_{10} F_{\text{VM}} \quad (7a)$$

$$\Delta V_{\text{VM}} = C_{11} P_{\text{HAC}} - C_{12} F_{\text{VM}} + A_{\text{CAP}} w_{\text{CAP}} \quad (7b)$$

where the coefficients  $C_9$ ,  $C_{10}$ ,  $C_{11}$ , and  $C_{12}$  are associated with the loading conditions shown in Figure 5. As for the drive element and chamber compliance relations, these linear valve membrane relations are derived from first principles, taking into account deflection and shearing effects.

Linear theory, however, is inadequate for capturing the large deflection behavior of the valve membrane. During operation, the valve membrane experiences deflections significantly larger than its thickness. As a result, a numerical code has been developed by the author to accurately capture the large deflection behavior of an annular membrane with a rigid boss under axisymmetric loading<sup>12</sup>. For given membrane dimensions and material constants, the code calculates the valve membrane deflection  $w(r)$ , the total swept volume under the membrane  $\Delta V_{\text{VM}}$ , and the radial stress in the membrane  $\sigma(r)$  for the three pressure loading inputs  $P_{\text{HAC}}$ ,  $P_1$ , and  $P_2$ ,

$$[w(r), \Delta V_{\text{VM}}, \sigma(r)] = F_{\text{NON-LINEAR}}(P_{\text{HAC}}, P_1, P_2). \quad (7)$$

Figure 6 compares the valve cap deflection predicted by this non-linear code with that predicted by basic linear theory, for an assumed valve cap and membrane geometry  $D_{CAP} = 0.62\text{mm}$ ,  $D_{VM} = 1.60\text{mm}$ , and  $t_{VM} = 5\mu\text{m}$  and assumed silicon material properties  $E_{Si} = 165\text{GPa}$  and  $\nu_{Si} = 0.22$ . The applied loading in this case is zero pressure acting on the top surface of the valve cap and membrane ( $P_1 = P_2 = 0$ ) and pressure  $P_{HAC}$  acting underneath the cap and membrane.

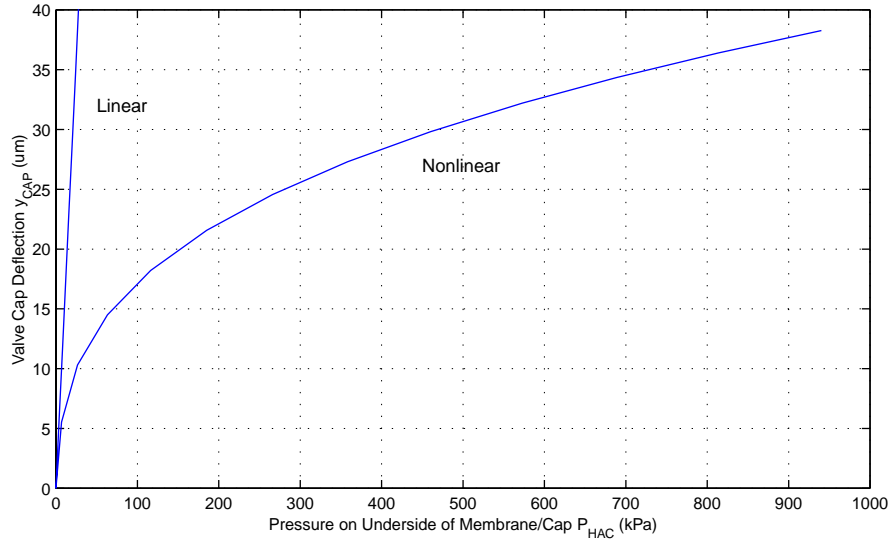


**Figure 6: Comparison of valve cap deflection predicted by non-linear theory and linear theory.**

As seen in Figure 6, significantly larger pressures are required to produce identical cap deflections in the non-linear case than in the linear case for large deflection behavior. For example, whereas in linear theory a pressure of 20kPa is necessary to deflect the cap 20um, in non-linear theory the required pressure to create the same deflection is 160kPa. This is due to increased membrane stiffening as the membrane experiences deflections significantly larger than its thickness. In large deflection regimes, membrane stresses due to in-plane stretching dominate those stresses due to simple bending. This non-linear code successfully predicts the highly non-linear deflection behavior of the valve membrane and cap under large pressure loadings. Only by incorporating this non-linear deflection behavior of the valve membrane can a realistic model of the full active valve be realized.

## 6. Full Valve Model

The complete active valve quasi-static model takes as input the geometry, material properties, and applied loading ( $V_{PIEZO}$ ,  $P_1$ , and  $P_2$ ). Because the valve behavior is non-linear, the process for obtaining an equilibrium solution requires a series of iterations in  $P_{HAC}$ . This process is illustrated in Figure 7. A linear model of the valve is first solved in order to gain an initial guess for  $P_{HAC}$ . This linear model consists of Eqs (1), (2), (3), (4), (5), (6), (7a), (7b), and the following geometric relation:

$$\Delta V_{DE} + \Delta V_{HAC} - \Delta V_{CHAMBER} - \Delta V_{VM} = 0 \quad (8)$$

With this initial guess for  $P_{HAC}$ , the model then proceeds to the non-linear solver block. This block takes  $P_{HAC}$  as an input and proceeds to evaluate Eqs (1), (2), (3), (4), (5), (6), (7), and the following geometric relation:

$$\Delta V_{CHECK} = \Delta V_{DE} + \Delta V_{HAC} - \Delta V_{CHAMBER} - \Delta V_{VM} \quad (9)$$

$\Delta V_{CHECK}$  will be non-zero as long as the assumed  $P_{HAC}$  is incorrect. If  $\Delta V_{CHECK} > 0$ ,  $P_{HAC}$  is increased for the subsequent iteration. If  $\Delta V_{CHECK} < 0$ ,  $P_{HAC}$  is reduced for the subsequent iteration. This process continues until the magnitude of  $\Delta V_{CHECK}$  is within a specified tolerance. The result of this procedure is an accurate solution for the quasi-static behavior of the full active valve.

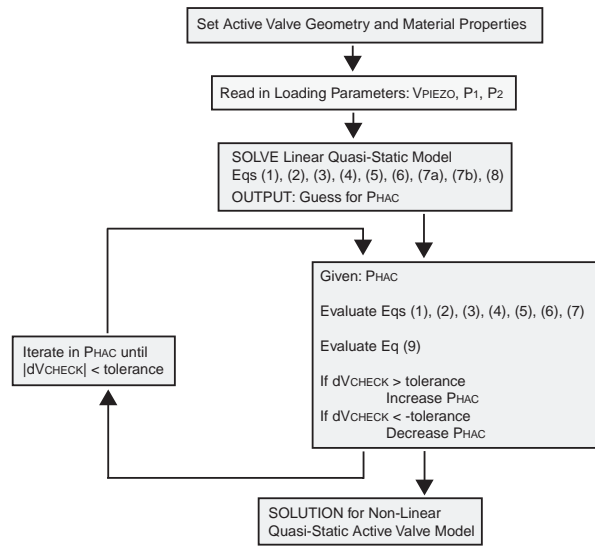


**Figure 7: Flowchart for analytical/numerical non-linear active valve model.**

## 5. RESULTS/CURRENT DESIGN

A proposed geometric design for the valve is detailed in this section. Based on input from full-scale MHT transducer simulations, the pressures over the valve membrane at the instant when it is fully open are  $P_1 = 0.8$  MPa and  $P_2 = 1.6$  MPa and the pressures over the valve membrane when it is fully closed are  $P_1 = P_2 = 1.6$  MPa. The valve must therefore overcome an increasing pressure as it closes. In order to control a system flow rate of 1 mL/s, the valve geometry detailed in Table 1 has been determined, with the specific materials properties documented. Table 2 details the loading conditions and valve performance for the fully open and fully closed valve situations, and compares the analytic/numerical results with those of an ANSYS finite-element model.

**Table 1: Active Valve Geometry and Material Properties**

Active Valve Geometry				
$L_{PIEZO} = 1\text{mm}$	$D_{PISTON} = 6\text{mm}$	$D_{HAC} = 6.3\text{mm}$	$D_{VM} = 1.6\text{mm}$	$D_{CAP} = 0.62\text{mm}$
$D_{PIEZO} = 1.385\text{mm}$	$t_{PISTON} = 1000\mu\text{m}$	$H_{HAC} = 100\mu\text{m}$	$t_{VM} = 5\mu\text{m}$	$t_{CAP} = 300\mu\text{m}$
$N_{PIEZO} = 3$	$t_{TETHER} = 10\mu\text{m}$	$t_{CHAMBER} = 1000\mu\text{m}$		

Material Properties		
PZN-PT Single Crystal Material	Single Crystal Silicon	Dow-Corning Silicon Oil
$d_{33} = 2100 \text{ e-12 pC/N}$	$E_{SILICON} = 165 \text{ GPa}$	$\rho_{FLUID} = 816 \text{ kg/m}^3$
$E_{PIEZO} = 7.69 \text{ GPa}$	$\nu_{SILICON} = 0.22$	$\kappa_{FLUID} = 2.105 \text{ GPa}$

**Table 2: Active Valve Analytic/Numerical Results vs. Finite-Element Results**

Valve Condition	Loading	Analytical/Num. Results	FEM Results
FULLY OPEN	$P_1 = 0.8 \text{ MPa}$ $P_2 = 1.6 \text{ MPa}$ $V_{PIEZO} = 75 \text{ V}$	$w_{CAP} = -20.001 \mu\text{m}$ $x_{DE} = -0.773 \mu\text{m}$ $P_{HAC} = 1.136 \text{ MPa}$ $T_{PIEZO} = 7.155 \text{ MPa}$ $\sigma_{VM} = 1.017 \text{ GPa}$	$w_{CAP} = -19.698 \mu\text{m}$ $x_{DE} = -0.800 \mu\text{m}$ $P_{HAC} = 1.158 \text{ MPa}$ $T_{PIEZO} = 7.367 \text{ MPa}$ $\sigma_{VM} = 1.030 \text{ GPa}$
FULLY CLOSED	$P_1 = 1.6 \text{ MPa}$ $P_2 = 1.6 \text{ MPa}$ $V_{PIEZO} = 1200 \text{ V}$	$w_{CAP} = 20.058 \mu\text{m}$ $x_{DE} = 0.972 \mu\text{m}$ $P_{HAC} = 1.751 \text{ MPa}$ $T_{PIEZO} = 11.902 \text{ MPa}$ $\sigma_{VM} = 0.797 \text{ GPa}$	$w_{CAP} = 20.701 \mu\text{m}$ $x_{DE} = 0.995 \mu\text{m}$ $P_{HAC} = 1.733 \text{ MPa}$ $T_{PIEZO} = 11.725 \text{ MPa}$ $\sigma_{VM} = 0.778 \text{ GPa}$

This active valve geometry results in a deflection of the valve cap from  $-20.001 \mu\text{m}$  in its fully open state to  $+20.058 \mu\text{m}$  in its closed state (total stroke =  $40.059 \mu\text{m}$ ) for an applied voltage on three piezoelectric material cylinders from  $75 \text{ V}$  to  $1200 \text{ V}$ , under the pressure loading stated above. The analytic/numerical model used for this design procedure correlates extremely well to an ANSYS finite-element model. The natural frequency of this valve is determined with an ANSYS modal analysis to be  $24.6 \text{ kHz}$ . Two important constraints exist in the development of the device: (1) maintaining the maximum membrane stress below its failure limit and (2) maintaining the piezoelectric material compressive stress below its depolarization stress. For single crystal silicon, this failure stress has been estimated to be  $1 \text{ GPa}$ <sup>13</sup>. Although not documented in the literature, the compressive depolarization stress is estimated to be  $30 \text{ MPa}$ , the same as that for PZT-5H. In the active valve design described by Tables 1 and 2, the piezoelectric voltage was optimized to ensure that the valve membrane experiences equal amplitude negative and positive deflections during the cycle. This allows the valve stroke to be maximized under the limitations of the  $1 \text{ GPa}$  membrane stress.

To demonstrate the highly non-linear nature of this active valve geometry, Figure 8 plots the linear and non-linear valve behavior versus applied piezoelectric voltage under zero loading conditions,  $P_1 = P_2 = 0$ . Although these loading conditions differ significantly from those predicted during operation in MHT devices, they allow for clear comparison between linear and non-linear valve performance, and support the effort to include non-linear valve deflection behavior in this active valve model. Plots (a)-(c) illustrate the valve cap deflection, maximum valve membrane stress, and hydraulic amplification chamber pressure versus the applied piezoelectric voltage, respectively.

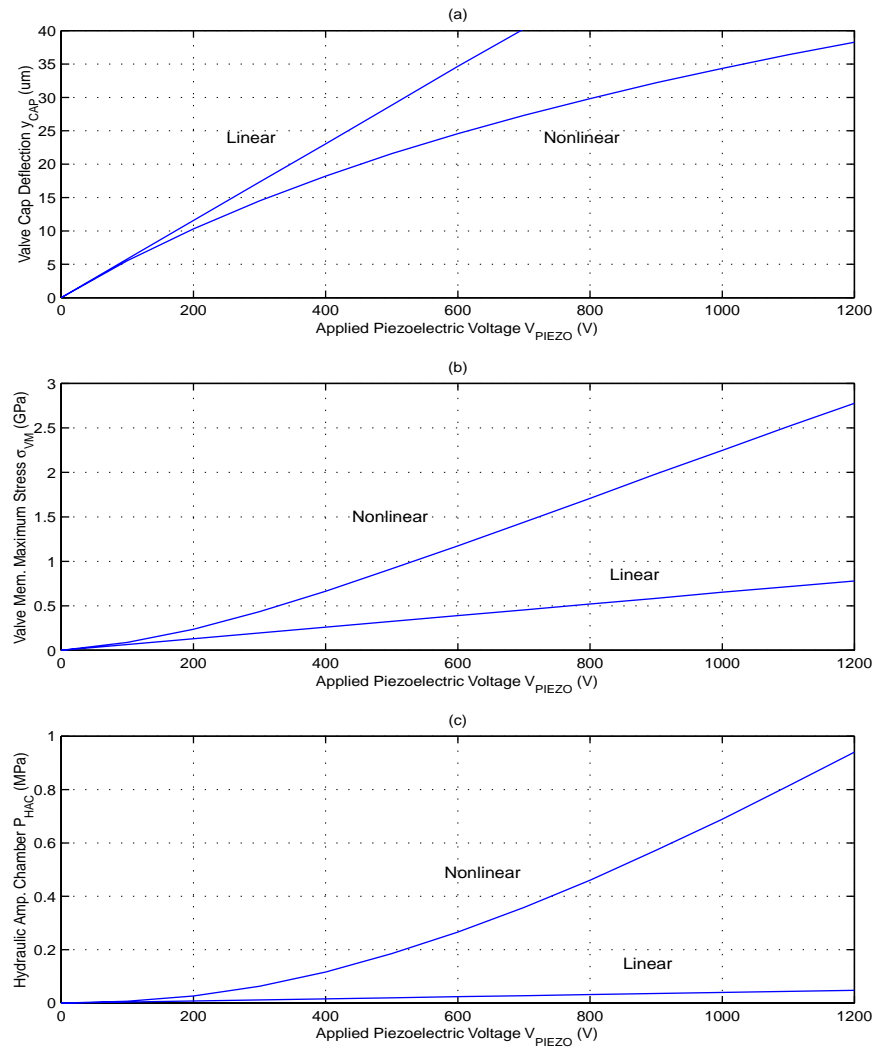


**Figure 8: Non-linear behavior of active valve: (a) valve cap deflection versus applied piezoelectric voltage, (b) maximum valve membrane stress versus applied piezoelectric voltage, and (c) hydraulic amplification chamber pressure versus applied piezoelectric voltage.**



Clearly, from plots (a) and (c), the valve exhibits both a non-linear deflection versus voltage relationship and chamber pressure versus voltage relationship. Plot (c) illustrates the non-linear nature of the maximum membrane stress. The analytical/numerical model developed in this work captures the highly non-linear nature of this active valve and provides a tool for future valve geometry optimization.

## 6. FABRICATION

The proposed fabrication process for this microvalve involves the integration of 5 silicon wafers and 3 layers of pyrex glass. A schematic of the device, illustrating individual silicon and pyrex layers, is shown in Figure 9. The middle pyrex layer (3) forms the drive element support structure and the top (8) and bottom (1) pyrex layers provide structural support for the bench-top device. The bottom silicon layer (2) provides support for and electrical contact to the piezoelectric cylinders. The top four silicon layers (4, 5, 6, and 7) house the hydraulic amplification chamber, valve cap/membrane structure, and fluid inlet and outlet channels. All silicon-silicon wafer interfaces are bonded with high-temperature (~1300C) fusion bonding, and all silicon-pyrex layer interfaces are bonded using low temperature (~300C) anodic bonding. Attachment of the top and bottom piezoelectric cylinder surfaces to the adjoining silicon is achieved with low temperature (300-500C) eutectic bonding. Piezo integration is performed after layers 1 and 2 have been bonded together and after layers 4, 5, 6, 7, and 8 have been bonded together. The final step is therefore the anodic and eutectic bonding of these top and bottom pre-bonded sections with pyrex layer 3 and the piezoelectric cylinders, respectively.

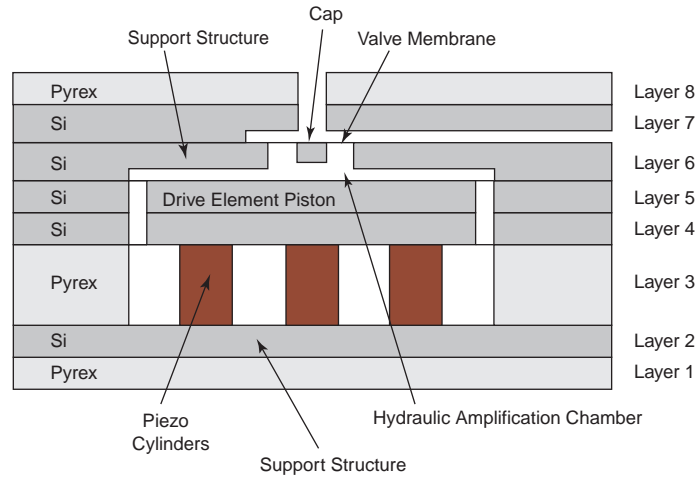


**Figure 9: Wafer-level schematic of fabricated microvalve, including placement of multiple piezoelectric cylindrical elements within drive element.**

Three significant challenges exist in the development of this novel valve. These are micromachining challenges, piezoelectric material integration challenges, and fluid filling and sealing challenges.

### Micromachining

Micromachining of the valve involves some critical issues that either require very accurate control of the process parameters or need innovation of new processes. The design requires 2-sided lithography in order to minimize the overall number of silicon wafers in the devices and thereby minimize the overall device mass and volume. Although single-sided lithography of silicon wafers is a mature and proven process, there is no existing standard for 2-sided lithography. Protection of the fragile valve membrane structures etched on a given side, while depositing and preparing photoresist on the opposite side is not a straightforward process. Furthermore, the buried oxide from the Deep-Reactive Ion Etching (DRIE) process required to etch the drive element and valve membranes in Silicon-On-Insulator (SOI) wafers can result in stresses in the membrane.

### Piezoelectric Material Integration

Integration of bulk piezoelectric material (ideally, single-crystal ferroelectric material) with silicon micromachined structures is a challenge. Due to the fact that piezoelectric materials degrade at temperatures far below those required for silicon-silicon

fusion bonding, other structural materials and bonding procedures are required in the planar region directly surrounding the bulk piezoelectric material. Pyrex can be substituted for silicon, resulting in robust lower temperature anodic bonds between the pyrex and the upper and lower silicon wafers. Eutectic alloy compositions can be deposited on the top and bottom surfaces of the piezoelectric material and on the bordering silicon wafers to allow for strong, low-temperature eutectic bonds between the piezoelectric material and the silicon. In this way, the piezoelectric material integration and subsequent low-temperature bonding steps are the last to be performed.

In addition, successful piezoelectric integration depends on the accuracy to which the piezoelectric material thickness can be measured with respect to that of the surrounding pyrex material. Thickness variation between these two components can create unwanted static and operational deflections of the piston membrane and therefore potentially destructive stresses at the critical etched membrane silicon-oxide interfaces. Also, incorporation of multiple smaller area piezoelectric materials spread out under the piston membrane is desired over placement of a single larger area piezoelectric material at the piston center, so as to reduce system compliances and increase efficiency. However, tolerance issues become even more important when dealing with requirements on multiple bonded structures in the same plane. Structural integrity of the etched membranes and high cycle fatigue of the bonds are additional critical issues for successful valve development.

### Fluid Filling and Sealing

Encapsulation of a working fluid in the device is a significant challenge at the microscale because surface-to-volume ratios are typically quite large, with surface energies playing a dominant role. Any gas bubbles present in the sealed operational device can create enormous system compliances, potentially rendering the device useless. The elimination of trapped gasses during filling of the device and during encapsulation of the fluid port used for filling is critical for high-level performance. The choice of fluid, degassing of the fluid, and post-filling encapsulation of the fluid are important to prevent the generation of any bubbles during the operation.

## 7. EXPERIMENTAL TESTING OF DRIVE ELEMENT

A series of first-generation drive element devices has successfully been fabricated and tested. Each device incorporates a single PZT-5H material cylinder, with diameter 1mm and length 1mm, within a drilled 6mm diameter, 1mm thick pyrex chamber. Prior to integration, a thin 1um layer of Au-Si eutectic alloy was deposited on the top and bottom surfaces of the piezoelectric element. A 500um thick SOI wafer, with a Deep-Reactive Ion Etched (DRIE) annular trench to form the drive piston, was bonded to the top surface of the pyrex layer using anodic bonding. A silicon wafer with a DRIE etched piezo seat was bonded to the bottom surface of the pyrex layer with anodic bonding as well. As a last step, a eutectic bond was formed between the piezoelectric element and the top and bottom silicon layers by heating the device to a temperature of ~500C, allowing the alloy layer to flow. The device was poled as it cooled. Figures 10 and 11 illustrate the fabrication sequence and device geometry.

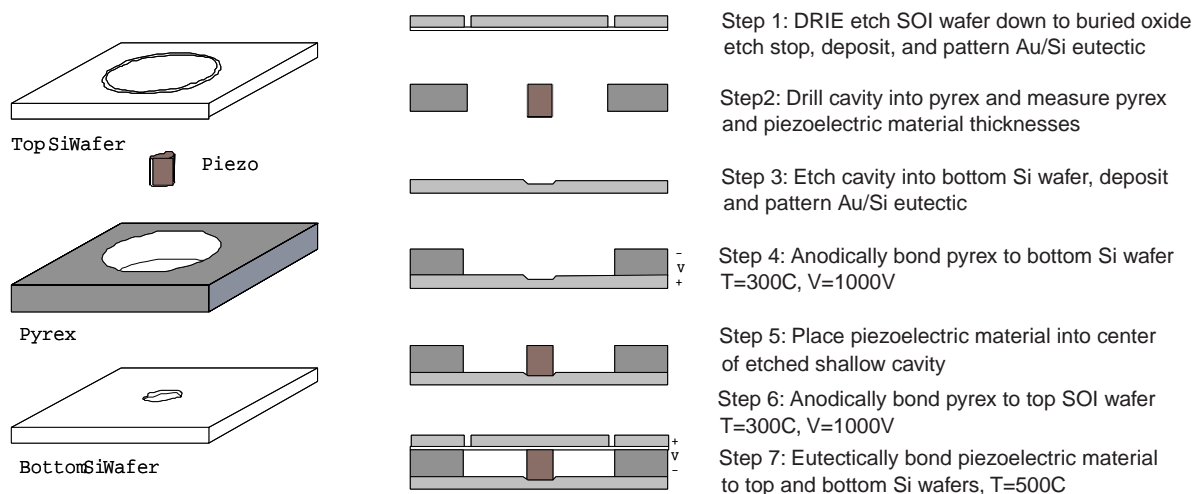


**Figure 10: Geometry and fabrication sequence of a first-generation drive element device.**

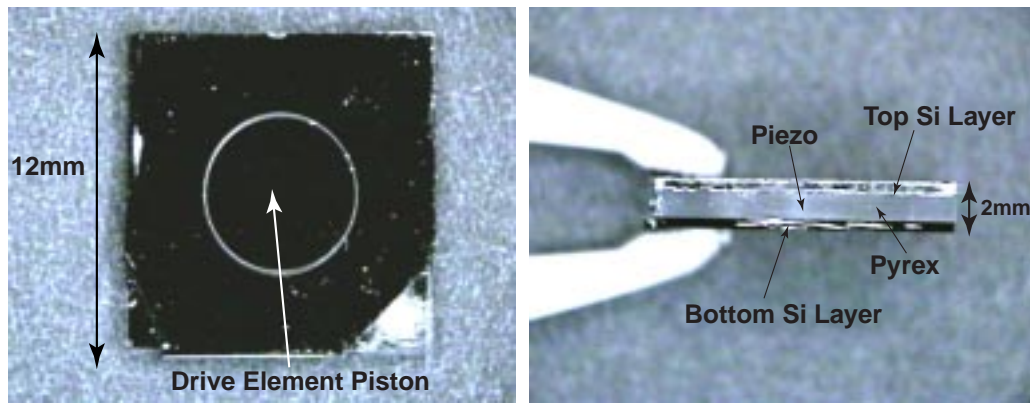


**Figure 11: Top and side view of 1st generation drive element device.**

The drive element devices were statically and dynamically tested using an optical probe and laser scanning vibrometer system, and the measured results (shown in Figure 12) were found to be in excellent correlation with the theoretical results predicted by finite-element analysis. Finite-element models predicted dominant modal behavior at 70kHz (1- $\theta$  tilt mode), 110kHz (plunge mode), 175kHz (2- $\theta$  mode), and higher frequencies. Experimental results indicated modal behavior at 74 kHz (1- $\theta$  tilt mode), 110 kHz (plunge mode), and 130 kHz (2- $\theta$  mode). These fabrication and experimental efforts have demonstrated the feasibility of integrating bulk piezoelectric material elements with microfabricated structures and systems.

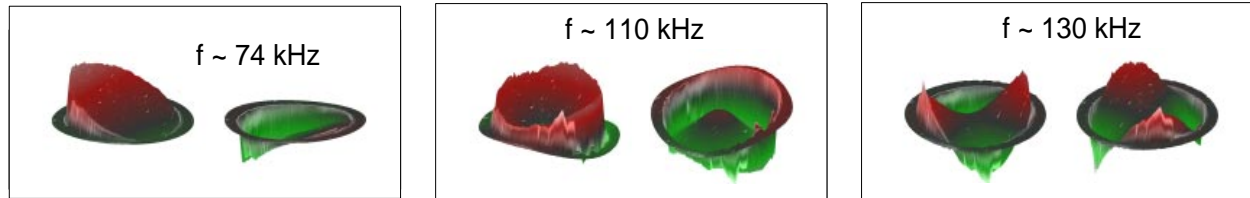


**Figure 12: Experimental mode shapes of a 1st-generation drive element device. Shown is the behavior of the drive element piston at various frequencies. These results were obtained with a laser scanning vibrometer system.**

## 8. CONCLUSIONS/FUTURE WORK

This paper has proposed a novel design for a piezoelectrically-driven hydraulic amplification microvalve for high pressure, high flow applications. An analytical and numerical model of this valve that captures the piezoelectric material behavior, fluid and structural compliance effects, and the highly non-linear behavior of the thin silicon valve cap membrane has been presented. Analytical modeling results indicate excellent correlation with finite-element models. In addition, 1<sup>st</sup> generation drive element devices have successfully been fabricated and tested, proving the capability to integrate bulk piezoelectric material elements with microfabricated structures and systems. An important issue for further study is the development of particular valve geometries that minimize energy consumption in the valve. As mentioned in Section 5, the valves in MHT devices are predicted to experience larger overall external pressures during closing as compared to during opening, and as a result lose energy to the pumping fluid environment. Future work will focus on the optimization of this valve geometry in an effort to minimize valve energy consumption and required active material volume and to maximize valve natural frequencies. In addition, 2<sup>nd</sup> generation drive element devices (incorporating three piezoelectric cylinders in parallel under the drive element piston) and full active valve structures will be fabricated and tested to validate performance.

## 9. REFERENCES

1. N.W. Hagood, D.C. Roberts, L. Saggere, M.A. Schmidt, S.M. Spearing, K.S. Breuer, R. Mlcak, J.A. Carretero, F. Ganji, H.Q. Li, K.-S. Chen, Y.-H. Su, and S. Pulitzer, "Development of Micro-Hydraulic Transducer Technology", 10<sup>th</sup> International Conference on Adaptive Structures and Technologies, Paris. 1999.

2. K. Henning, "Liquid and gas-liquid phase behavior in thermopneumatically actuated microvalves", *Proceedings of SPIE– The International Society for Optical Engineering* v3515, pp. 53-63, 1998.
3. H. Jerman, "Electrically-Activated, Micromachined Diaphragm Valves", *Transducers '91: 1991 International Conference on Solid-State Sensors and Actuators*, pp. 1045-1048, 1991.
4. M.A. Huff and M.A. Schmidt, "Fabrication, Packaging, and Testing of a Wafer-Bonded Microvalve", *Proceedings of the IEEE Solid-State Sensor and Actuator Workshop, Hilton Head, SC*, pp. 194-197, 1992.
5. A. Meckes, J. Behrens, and W. Benecke, "Electromagnetically Driven Microvalve Fabricated in Silicon", *Transducers '97: 1997 International Conference on Solid-State Sensors and Actuators*, pp. 821-824, 1997.
6. J.G. Smits, "Piezoelectric Micropump with Microvalves", *Proc Eighth Bienn Univ Gov Ind Microelectron Symp. (IEEE n 89CH2769-8), Piscataway, NJ, USA*. p 92-94
7. M. Esashi, S. Shoji, and A. Nakano, "Normally Closed Microvalve and Micropump Fabricated on a Silicon Wafer", *Sensors and Actuators* 20, pp. 163-169, 1989.
8. J. Garcia-Bonito, M.J. Brennan, S.J. Elliot, A. David, and R.J. Pinnington, "A novel high-displacement piezoelectric actuator for active vibration control", *Smart Mater. Struct.* 7, pp. 31-42, 1998.
9. P. Tang, A. Palazzolo, A. Kascak, G. Montague, and W. Li, "Combined Piezoelectric-Hydraulic Actuator Based Active Vibration Control for Rotordynamic System", *Journal of Vibration and Acoustics* 117, pp. 285-293, 1995.
10. Tsukamoto, "Piezo-Actuator's Displacement Magnifying Mechanism", US Patent 5,233,834. 1993.
11. S. Timoshenko, *Theory of Plates and Shells*, Ch.3, McGraw-Hill, New York, 1940.
12. Y.H. Su, D.C. Roberts, and S.M. Spearing, "Large deflection analysis of a prestressed annular plate with a rigid boss under axisymmetric loading", *ASME Journal of Applied Mechanics*, Currently Under Review.
13. S.M. Spearing and K.S. Chen, "Micro-gas turbine engine materials and structures", *Ceramic Engineering & Science Proceedings*. v 18 n 4 B, p 11-18, 1997.

## APPENDIX

### Drive Element Tether Behavior

The drive element relations are derived from first principles, solving the bending equation for an axisymmetrically loaded circular plate with appropriate boundary conditions<sup>11</sup>.

$$\frac{\partial}{\partial r} \left( \frac{1}{r} \frac{\partial}{\partial r} \left( r \frac{\partial x(r)}{\partial r} \right) \right) = \frac{Q(r)}{D} \quad (\text{A.1})$$

$$\text{BCs: } x \left( r = \frac{D_{\text{HAC}}}{2} \right) = 0; \quad \frac{\partial x}{\partial r} \left( r = \frac{D_{\text{HAC}}}{2} \right) = 0; \quad \frac{\partial x}{\partial r} \left( r = \frac{D_{\text{PISTON}}}{2} \right) = 0 \quad (\text{A.2})$$

where  $Q(r)$  is the shearing force and  $D$  is the plate flexural rigidity, and solving the following shear deformation relation with appropriate boundary conditions:

$$\frac{\partial}{\partial r} x(r) = - \frac{\alpha Q(r)}{G t_{\text{TETHER}}} \quad (\text{A.3})$$

$$\text{BC: } x \left( r = \frac{D_{\text{HAC}}}{2} \right) = 0 \quad (\text{A.4})$$

where  $\alpha$  is the shear coefficient of the cross-section and  $G$  is the shear modulus of elasticity. The majority of the drive element tether deflection is a result of bending, not shear. However, the shear contribution is included for completeness.

### Hydraulic Amplification Chamber Compliance

As for the drive element relations, the chamber compliance relations are derived from first principles, taking into account deflection and shearing effects, with the following boundary conditions:

$$\text{BCs: } x \left( r = \frac{D_{\text{HAC}}}{2} \right) = 0; \quad \frac{\partial x}{\partial r} \left( r = \frac{D_{\text{HAC}}}{2} \right) = 0; \quad \frac{\partial}{\partial r} \left( \frac{\partial x}{\partial r} \right) + \frac{\nu}{r} \left( \frac{\partial x}{\partial r} \right) = 0 \text{ at } \left( r = \frac{D_{\text{VM}}}{2} \right) \quad (\text{A.5})$$

where  $\nu$  is the Poisson ratio. The majority of the top chamber structure deflection is a result of shear, not bending. However, both effects are included for completeness.

**H.Q. Li, D.C. Roberts, J.L. Steyn, K.T. Turner, J. A. Carretero, O. Yaglioglu,  
Y.-H. Su, L. Saggere, N.W. Hagood, S.M. Spearing, and M.A. Schmidt**  
Massachusetts Institute of Technology  
Cambridge, MA 02139

**R. Mlcak**  
Boston Microsystems, Inc.  
Woburn, MA 01801

**K.S. Breuer**  
Brown University  
Providence, RI 02912

## ABSTRACT

A piezoelectrically driven fluidic micropump was fabricated and tested. Microelectromechanical systems (MEMS) fabrication technology was used. Small cylindrical piezoelectric material elements were integrated with microfabricated silicon, silicon on insulator (SOI), and glass chips using eutectic bonding and anodic bonding processes. SOI wafers were used to form the thin membranes within the moving parts (a drive element and two passive valves). The design, microfabrication process, and assembly of the device are described in this paper. Fabrication issues such as control of fillet radii at the feet of the Si membranes for stress reduction and simultaneous eutectic and anodic bonding were discussed. A flow rate as high as 3000  $\mu\text{l}/\text{min}$  was recorded. Experimental and simulation results of the dependences of the pump flow rate on the voltage and frequency applied on the piezoelectric material are shown and discussed.

## INTRODUCTION

This paper presents the fabrication and testing of a high pressure, high flow rate piezoelectrically driven fluidic micropump with passive valves. In comparison to other piezoelectrically driven micropumps in the literature [1-4], this device incorporates the integration of bulk piezoelectric material with MEMS microfabrication techniques to allow for high structural driving frequencies in the tens of kHz range and implements novel methods of anodic and eutectic bonding to join silicon, glass, and piezoelectric components, enabling minimal device mass and therefore high power density. It requires a compact design that brings about challenging fabrication issues such as multi-layer wafer bonding, multiple lithography and deep reactive ion etch (DRIE) steps for the SOI wafers, use of nested oxide masks, and integration of small piezoelectric material elements. The need for high frequency and high flow rate calls for precisely micro-machined Si membranes capable of large deflection as the moving components in the pump chamber and the passive valves of the micropump. SOI wafers are good choices for this purpose because they have a uniform thin Si layer, their buried oxide can be used as the etch stop during DRIE processes, and the fillet radii of the membranes that are critical to the strength of the membranes are easier to control in the presence of the buried oxide. Another advantage of SOI wafers is that separate electrodes can be formed in the SOI layer during microfabrication, with the buried oxide as the insulator. Eutectic bonding has been used to integrate the piezoelectric elements into the MEMS devices. For this micropump it is necessary to choose low melting point eutectic bonding alloys so that the eutectic bonding can be performed simultaneously with the anodic bonding of the Si and SOI layers to the glass layer that encloses the piezoelectric material for

insulation. The successful fabrication of the micropump is a major step toward the realization of high power density transducer devices for micro-robotic actuation and heel-strike power generation applications [5, 6].

## MICROPUMP STRUCTURE

The micropump has a multi-layer structure, schematically shown in Figure 1. It includes one fluid pump chamber and two identical passive check valves [7]. The volume change in the fluid chamber is achieved by the vertical motion of the double layer cylindrical piston-like drive element (layers 4 and 5) attached to annular Si membranes and driven by a ceramic piezoelectric cylinder (layer 3) 1 mm in diameter and 1 mm in height. When a voltage is applied to the piezoelectric cylinder, it pushes the drive element piston up, producing a high pressure in the fluid chamber that closes the inlet valve and opens the outlet valve so that fluid can flow out of the fluid pump chamber. Next, when the voltage is

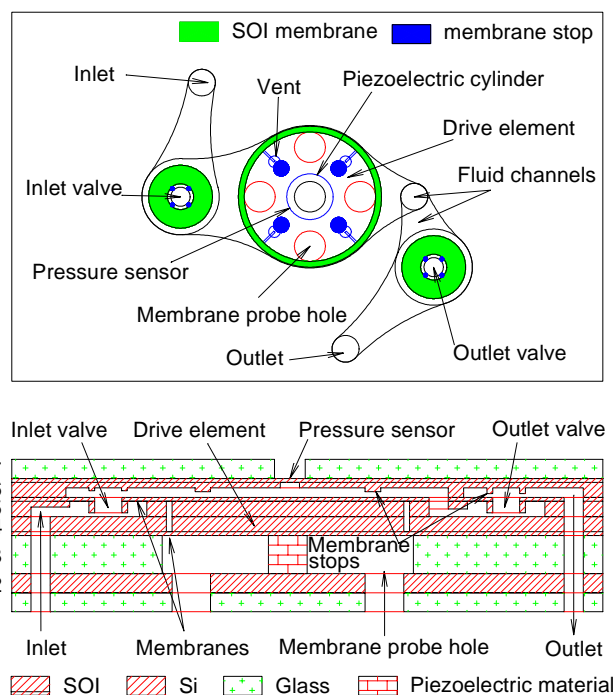


*Figure 1. Top view and cross-section view of the micropump. The cross-section view is from a zig-zag cut to show all the features. reduced the piezoelectric cylinder contracts and the drive element piston moves down, resulting in a low pressure in the fluid chamber that closes the outlet valve and opens the inlet valve so*



repeating these steps at high frequency.

The drive element piston is 3.6 mm in diameter and each of the two SOI layers 4 and 5 forming the piston is about 400  $\mu\text{m}$  thick. The annular drive element SOI membranes are 150  $\mu\text{m}$  wide and 10  $\mu\text{m}$  thick in the lower layer and 15  $\mu\text{m}$  thick in the upper layer which also includes the valves. SOI wafers (layers 4, 5, and 6) were chosen to construct the membranes in the device for two reasons: 1) to control precisely the membrane thickness by using the buried oxide in the SOI as an etch stop in the DRIE process, and 2) to use the lower SOI (layer 4) as an electrode to the piezoelectric cylinder and the buried oxide as an insulator between the piezoelectric cylinder and the remaining part of the micropump. The thickness of the SOI membranes in layer 5 was determined mainly by the design specifications of the passive valves that were subject to much larger deflections than the drive element piston membrane. Venting channels in layer 5 and holes in layer 4 (not shown in Fig. 1) were formed to release pressure in the cavity between the drive element membranes during the wafer diffusion bonding. The passive valves consist of a 0.5 mm center hole and a 15  $\mu\text{m}$  thick annular SOI membrane with an inner diameter of 0.70 mm and an outer diameter of 1.65 mm. When not deflected the valves are only 0.5  $\mu\text{m}$  from layer 4 to minimize back leaking.

The fluid chamber above the drive element piston and fluid channels to and from the valves are located in layer 6. Small cylindrical motion stops about 8  $\mu\text{m}$  from the drive element and about 18  $\mu\text{m}$  from the valves respectively were also formed in layer 6 to prevent the membranes from excessive deflections. A pressure sensor in the shape of a circular membrane 0.8 mm in diameter and 20  $\mu\text{m}$  thick was formed in the fluid chamber for on-site pressure measurement. A ceramic PZT-5H piezoelectric cylinder 1 mm in diameter and 1 mm in height was incorporated in the middle glass layer 3 as the active drive component of the micropump. The Si layer below the piezoelectric cylinder was used as the other electric contacts to the piezoelectric cylinder. 3 mm thick borosilicate glass was used in the top and bottom layers 1 and 7 for structural strengthening of this bench top device.

## MICROFABRICATION PROCESSES

To minimize the size of the device, a compact design requiring a minimum number of layers, efficient use of the both surfaces in each layer, and therefore multiple lithography steps for the SOI wafers was implemented. As an example, Figure 2 shows the fabrication process flow for layer 5. The first step is the selection of the SOI wafer that has a 15  $\mu\text{m}$  thick SOI layer, a 0.4  $\mu\text{m}$  thick buried oxide, and a 380  $\mu\text{m}$  thick handle layer. Secondly, positive photoresist was coated on both sides of the wafer and the SOI side was patterned using standard lithography procedures. The photoresist on the handle side is to protect the handle surface from scratching in the lithography steps. This back surface protection method was used throughout the micro-fabrication processes. The wafer was then put in a DRIE machine until the SOI layer was etched through. This step formed the fluid through holes in the SOI layer. Next, the wafer was cleaned and coated with positive photoresist on both sides again. The handle side was patterned with photoresist and etched down about 0.5  $\mu\text{m}$  in a RIE etcher to form the clearance between the valves and their seating surfaces. In the fourth step the wafer was oxidized at 1100°C for 5 hours to form 2  $\mu\text{m}$  of thermal oxide that is to be used as a nested mask and back surface protection from DRIE etching later on. The thermal oxide was etched in step 5 to form the nested mask and then another lithography process was

first by DRIE about halfway through its thickness with photoresist as seen in step 6. Then the photoresist pattern was stripped and the nested thermal oxide mask was exposed for another DRIE step until it stopped at the buried oxide, as seen in step 7. The nested oxide mask was necessary to construct the 200  $\mu\text{m}$  deep venting channels in the drive element and the fluid channels to the valves. Finally, the thermal oxide was stripped using BOE wet etching.

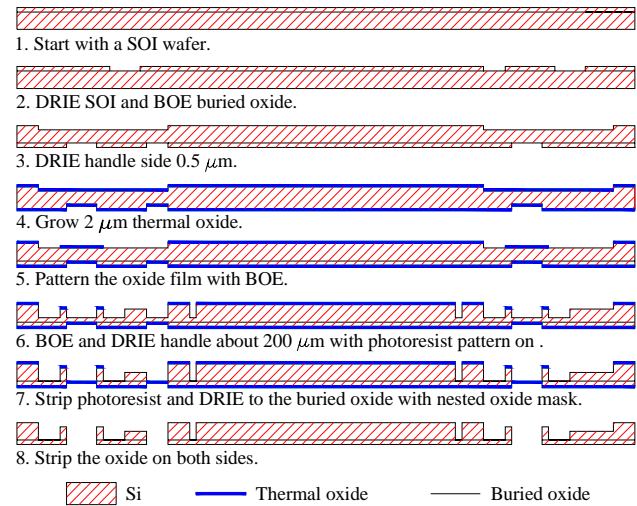


Figure 2. Fabrication flow of an SOI layer (layer 5 in Fig. 1) with the passive valves and half of the drive element piston.

Since all the membranes in this device have to operate under high stress and at high frequency, it is important to have a membrane structure with minimal stress concentration. A significant challenge in the micropump fabrication was controlling fillet radii in the range of 20-40  $\mu\text{m}$  for stress reduction at the feet of the membranes. In the DRIE machine Si is etched at a rate of about 2-4  $\mu\text{m}/\text{min}$ . depending on the feature size and exposed Si area. The etch front is usually a gradual curve in cross-section but varies depending on the etch conditions. An SOI membrane fillet radius is formed after the etch front reached the buried oxide and then the Si edges retreat horizontally to the side wall at a rate of about 70-100  $\mu\text{m}/\text{minute}$  as more oxide is exposed. There is a time window of only about 2-4 minutes to control the fillet radius in the desired range after about 2 hours etch of the handle side. Therefore careful monitoring in the final stage of the DRIE is critical. Figure 3 shows a 150  $\mu\text{m}$  wide drive element membrane with a gradual fillet about 25  $\mu\text{m}$  long horizontally.

## ASSEMBLY OF THE DEVICE

After the final DRIE etch and cleaning, the three SOI wafers were aligned using an Electronic Visions system and fusion bonded at 1100°C in nitrogen for 1 hour. The bonded wafer stack was cut into 16.7 mm by 15.7 mm chips with a die-saw, cleaned in water, acetone, methanol, and isopropanol successively, and finally dried in air. The glass wafers were processed with diamond drills and die-saw cut into small chips. All the interfaces between Si and glass were anodically bonded at about 300°C. The Si and the piezoelectric material interfaces were eutectically bonded.

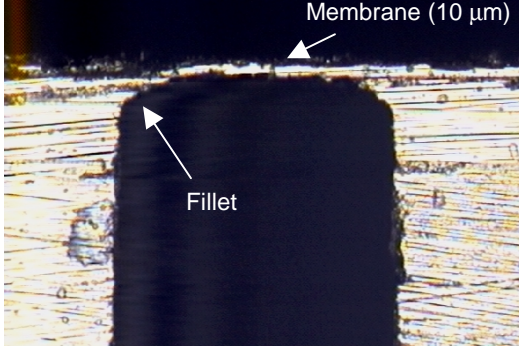


Figure 3. Optical cross-section picture of a drive element membrane, the membrane thickness is about 10  $\mu\text{m}$ .

To prepare for the eutectic bonding, 500 Å of Ti film and 5000 Å of Pt film were deposited on the Si surfaces through a shadow mask by e-beam and 2  $\mu\text{m}$  of an Au-Sn (80-20% wt.) alloy films were deposited on the piezoelectric surfaces by sputtering. The composition of the metal films were chosen for surface wetting (Ti) and low eutectic bonding temperature (Au-Sn) so that the eutectic bonding and the last anodic bonding can be done simultaneously as required by the pump design. The height of the piezoelectric cylinders were designed to be 2-3  $\mu\text{m}$  larger than the height of the middle glass piece (layer 3 in Fig. 1) so that the drive element piston is preloaded and when the chamber is expanded there is no pulling of the drive element piston by the piezoelectric cylinder that might delaminate the eutectic bonding. For this reason, an oxide mask that defines the piezoelectric seating was left on each Si chip below the piezoelectric (layer 2 in Fig. 1) for height compensation by individually trimming etch of the Si chips. Finally wires were soldered on the Ti/Pt electrode pads that were deposited at the same time as the eutectic bonding films were deposited. Figure 4 shows a picture of an assembled micropump.

The key components of this bench top device were built in an area of about 8.6 mm by 7.7 mm, while the electric contacts and

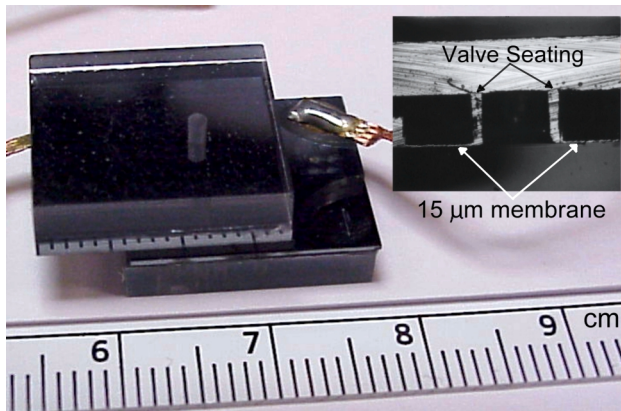


Figure 4. An assembled micropump with electric leads. Small graduations are in mm. The inset is a cross-section picture of a passive valve with 15  $\mu\text{m}$  thick membrane.

the supporting glass pieces take most space of this bench-top device. The inset of Fig. 4 is a cross-section photograph of a passive check valve with 15  $\mu\text{m}$  thick membrane.

## TEST RESULTS

that includes fluid reservoirs, valves, pressure sensors, and flow meters, as shown in Figure 5. The inset in Fig. 5 is an picture of the test jig with a micropump sealed in it by rubber O-rings. The system was first evacuated and then filled with 1 centistoke silicone oil. The piezoelectric cylinders were driven by AC signals with peak to peak voltages in the range of 0-1600 V, bias voltages in the range of 300-600 V, and frequencies in the range of 1-12.5 kHz. The inlet pressure was maintained at 850 kPa in all the tests. The highest flow rate recorded is 3000  $\mu\text{L}/\text{min}$  at 1200 V peak to peak voltage, 600 V bias voltage, and 4.5 kHz, and zero differential pressure.

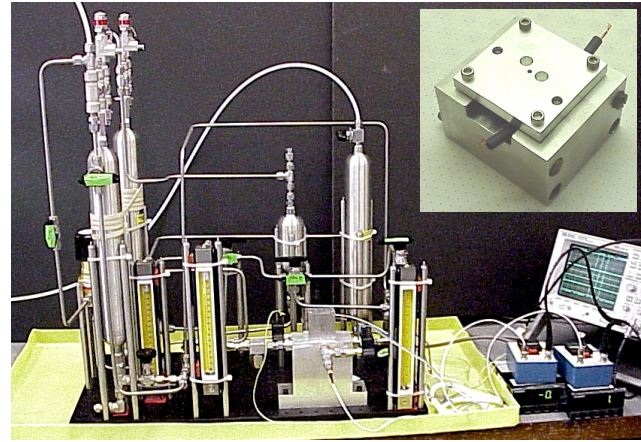


Figure 5. The experimental setup for micropump test. The inset is the package jig holding the micropump.

Figure 6 shows the experimental and quasi-static simulation results of the dependence of flow rate on peak to peak voltage. This test was done at a drive frequency of 3.5 kHz, a bias voltage of 600 V, and zero differential pressure. The flow rate increases with the voltage monotonically but not linearly. In Simulation 1 a rigid chamber structure was assumed. It is believed that the flow rate of Simulation 1 is higher than the experimental results because the micropump has, as part of the fluid chamber, flexible SOI

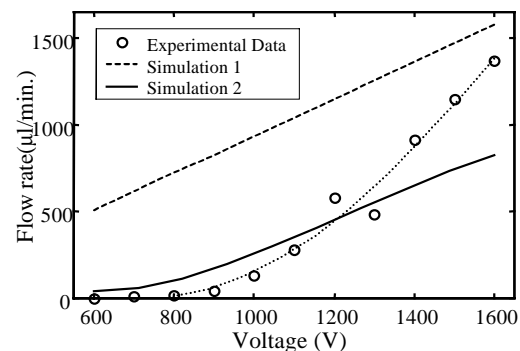


Figure 6. Flow rate vs. piezo peak to peak voltage at 3.5 kHz drive frequency. The results of two quasi-static simulations with different chamber compliance are also shown.

membranes attached to the drive element piston and the two passive check valves (see Fig. 1). An increased fluid chamber compliance was included in Simulation 2 and its results are closer to the experimental data as can be seen from Fig. 6. However, at high drive voltage the experimental flow rate increased with the drive voltage much faster than the results of Simulation 2. This is probably because the membranes deflect more and become stiffer

rate, while in Simulation 2 this increase of membrane stiffness was not accounted for.

Figure 7 shows the relation between the inlet-outlet differential pressure and the flow rate. In this experiment the piezoelectric cylinder was driven at 1200 V peak to peak voltage, 600 V bias voltage, and 3.5 kHz.

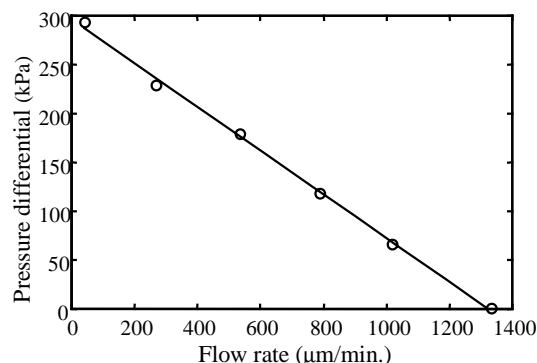


Figure 7. Inlet to outlet differential pressure vs. flow rate.

The flow rate vs. piezoelectric cylinder drive frequency curve of the same device and a quasi-static simulation result are shown in Figure 8. Other experimental conditions of this test were: peak to peak voltage at 1200 V, bias voltage at 300 V, and zero differential pressure. Figure 8 clearly shows some form of resonance effect that is not present in the simulation. We found that changing the bias voltage to the piezoelectric material and changing the pressure difference between the inlet and outlet have an influence on the value of the flow rate but not on the resonance peak positions. The flow resonance could be due to the pressure wave effects at abrupt corners of the package of the micropump or due to the internal structure of the device. A systematic study of the micropumps is under way to better understand their behavior and to improve their performance.

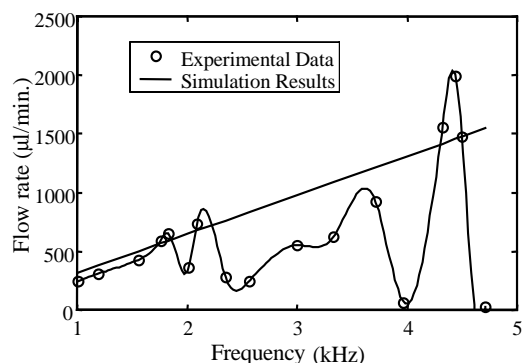


Figure 8. Flow rate vs. drive frequency of the micropump.

## CONCLUSIONS

The work in this paper is part of a larger effort to develop high power density transducer devices [5] for micro-robotic actuation and human heel-strike power generation applications. The successful fabrication of the micropump has validated the MEMS process design and bonding techniques to be used for these devices. Since device power is generally proportional to flow rate,

multiple piezoelectric cylinders are currently being developed. A further increase in flow rate can be realized by using newly developed single crystal piezoelectric materials [8]. A performance improvement of 10 times is expected in micropumps that combine larger drive elements and single crystal piezoelectric materials. In order to examine the effect of resonance on the performance of the micropump, the internal device structure and external test set-up are under investigation. In addition, it may be possible to use this resonance behavior to maximize the flow rate by tuning the device to a desired resonance frequency.

## ACKNOWLEDGEMENT

We would like to thank the staff members of the Microsystems Technology Laboratories at MIT, especially Kurt Broderick, for their help in the microfabrication of the micropumps. We also thank Dr. Arturo Ayon of MIT for his help with the diffusion bonding of the SOI wafers. This work is funded by DARPA.

## REFERENCES

1. S. Shoji and M. Esashi, "Microflow Devices and Systems", *Journal of Micromechanics and Microengineering*, 4, 157, (1994).
2. M. Koch, A.G.R. Evans, and A. Brunnschweiler, "The Dynamic Micropump Driven with a Screen Printed PZT Actuator", *Journal of Micromechanics and Microengineering*, 8, 119, (1998).
3. M. Esashi, S. Shoji, and A. Nakano, "Normally Closed Microvalve and Micropump Fabricated on a Silicon Wafer", *Sensors and Actuators*, vol. 20, pp 163-169, 1989.
4. D. Maillefer, H. Van Lintel, G. Rey-Mermet, R. Hirschi, "A High Performance Si Micropump for an Implantable Drug Delivery System", *Technical Digest, IEEE International MEMS'99 Conference*, pp. 541-6, (1999).
5. Nesbitt W. Hagood IV, *et al.* "Micro-hydraulic Transducer Technology for Actuation and Power Generation", submitted to SPIE 7<sup>th</sup> International Symposium on Smart Structures and Materials, Newport Beach, CA, March 5-9, 2000.
6. D.C. Roberts *et al.* "Design of Piezoelectrically-driven Hydraulic Amplification for High Pressure, High Frequency Applications", submitted to SPIE 7<sup>th</sup> International Symposium on Smart structures and Materials, Newport Beach, CA, March 5-9, 2000.
7. H.T.V. Van Lintel, F.C.M. Van De Poll, and S. Bouwstra, "A Piezoelectric Micropump Based on Micromachining of Silicon", *Sensors and Actuators* 20, 163, (1989).
8. Seung-Erg Park and Thomas R. Shrout, "Characteristics of Relaxor-Based Piezoelectric Single Crystals for Ultrasonic Transducers", *IEEE Trans. Ultrasonics, Ferroelectrics, and Frequency Control*, 44, 1140 (1997).



# Design, Fabrication, and Testing of a Piezoelectrically Driven High Flow Rate Micro-Pump

L. Saggere<sup>1</sup>, N. W. Hagood<sup>1</sup>, D. C. Roberts<sup>1</sup>, H.-Q. Li<sup>1</sup>, J. L. Steyn<sup>1</sup>, K. Turner<sup>1</sup>, J. A. Carretero<sup>1</sup>, O. Yaglioglu<sup>1</sup>, Y.-H. Su<sup>1</sup>, R. Mlcak<sup>2</sup>, S. M. Spearing<sup>1</sup>, K. S. Breuer<sup>3</sup>, M. A. Schmidt<sup>1</sup>

<sup>1</sup>Massachusetts Institute of Technology, Cambridge, MA 02139 USA

<sup>2</sup>Boston Microsystems, Inc., Woburn, MA 01801 USA

<sup>3</sup>Brown University, Providence, RI 02912 USA

**Abstract** — Towards the development of novel class of miniature transducers with very high specific power, a high frequency and high flow rate hydraulic micro-pump with passive check valves was fabricated and tested. The micro-pump features a small piezoelectric (PZT-5H/PZN-PT) cylinder integrated into micromachined silicon and pyrex chips. The piezoelectric cylinder bonded to a thick circular disk serves as the drive element in the pump chamber, and two axisymmetric silicon membranes with hollow annular bosses serve as system check valves. Using silicone oil as the working fluid, the performance of the micro-pump was tested by varying voltages from 0 to 1600V and frequencies from 1 kHz to 12 kHz. The micro-pump with PZT-5H element achieved a high flow rate of 2.5 ml/min at 1200 V and 4.5 kHz.

## INTRODUCTION AND MOTIVATION

Recent advances in active materials technology has led to the development of many new solid-state actuators. However, the specific power (power per unit mass) output of these solid-state actuators is fairly limited. A major program with the broad goal of developing miniaturized transducers, called Micro-Hydraulic Transducers (MHT), with very high specific power in the order of 1 kW/kg is currently underway at MIT [1]. This program derives its impetus from an evolving realization that attractive output power densities are achievable by active materials with decreasing size and high frequency operation, and exploits from the integration of the piezoelectric technology with the micro-machining (MEMS) technology and micro-hydraulic concepts. The essential building unit of the MHT is a micro-pump with actively controlled valves that rectify fluid-flow from one pressure potential to another at very high frequencies and high flow-rates against high pressures, yielding a high power output. These operating requirements of the micro-pump are more demanding than any micro-fluidic device developed so far. Several micro-pumps based on different principles have been reported, however, mostly they feature either small flows or low output pressures [2,3].

Development of an active valve micro-pump for MHT involves several critical challenges in design, fabrication and system level integration. The motivation for the work

presented in this paper stemmed mainly from the need to demonstrate the technical feasibility and to minimize the risks involved in the development of an active valve micro-pump for MHT. This purpose was accomplished through a successful development of a slightly simpler version of the device, that is, a micro-pump with passive (check) valves, with similar performance goals of high flow and high pressure. This paper reports the design, modeling, fabrication and testing of the passive valve micro-pump.

## WORKING PRINCIPLE AND DESIGN

The micro-pump is comprised of the following generic components: pump chamber, a piezoelectric element, a low-pressure fluid reservoir (LPR), a high-pressure fluid reservoir (HPR), and two check valves—one operating between the LPR and the pump chamber and the other one operating between the pump chamber and the HPR—as schematically shown in Figure 1. An electric voltage applied to the piezo induces a strain in the element resulting in a net volume change in the pump chamber. The two valves transform the volume oscillations of the chamber into a net fluid flow from LPR to HPR. The accumulation of fluid in the HPR increases the pressure and performs useful work on the load. After the actuator travels its full stroke, the flow direction is reversed (not illustrated in Figure 1) and the actuator is evacuated as it returns to its initial position, completing the actuation cycle. In this way the high frequency, small displacements of the piezoelectric are rectified into low frequency, large stroke actuation.

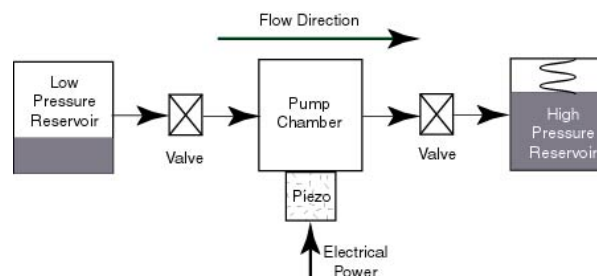


Figure 1. Working principle of the micro-pump.

The micro-pump configuration is shown in Figure 2. The pump chamber at the center encloses a piezo element sandwiched between a moveable thick circular disk and the rigid bottom. The moveable disk is tethered to the chamber wall through thin flexible membranes around the circumference. The moveable plate and the piezo together effectively constitute a piston-like structure that can move vertically up and down when the piezo is strained by applying electric voltage across its ends. The volume between the chamber ceiling and the piston surface encloses the working fluid that is pumped. Two axisymmetric silicon micromachined membranes with hollow annular bosses serve as system check valves between the inlet/outlet port and the pump chamber.

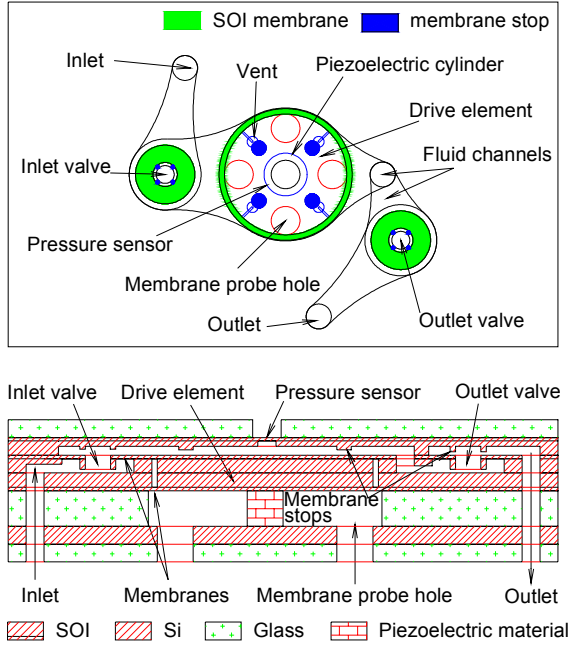


Fig. 2: Top view and cross-sectional view (along a zig-zag cut in the top view) of the micropump.

The approximate dimensions of the piezo cylinder and the chamber were first determined analytically to satisfy the requirement of an average flow rate of 1 ml/s at 20 kHz operating frequency. The dimensions of passive valves were chosen such that their first natural frequency is well above the valve operating frequency, and the membranes stresses are within allowable limits at a maximum stroke of about 20  $\mu\text{m}$ , and other dimensions were chosen suitably. The design was then verified and dimensions adjusted for best performance through computer simulations. The primary transduction element in the device, PZT-5H piezo cylinder is about 1 mm in diameter and 1 mm in height. The diameter of the pumping chamber is 3.6 mm, and its height from the piston surface is 200  $\mu\text{m}$ . The width of the tethers membrane around the piston is 150  $\mu\text{m}$  and their thickness is about 15  $\mu\text{m}$ . The membranes comprising the passive valves are 15  $\mu\text{m}$  thick, and have an inner diameter of 0.70 mm and an outer diameter of 1.65 mm. The hole at

the center of the rigid boss through which the fluid can pass through when the valve is open is 0.5 mm in diameter. When not in motion, the valves are normally closed with a minimal 0.5  $\mu\text{m}$  gap between the valve and the seating to minimize any back flows.

## MODELING AND SIMULATION

Dynamic simulations of the micro-pump system were carried out to gain insight into the performance of the micro-pump. Detailed analytical models of the canonical components of the system and the fluid-flow models including fluid inductance and fluidic and structural compliances were built in the Matlab/Simulink® application and system level simulations were carried out by numerically integrating the coupled governing equations. The entire system is highly coupled as can be seen in the block diagram of the system in Figure 2.

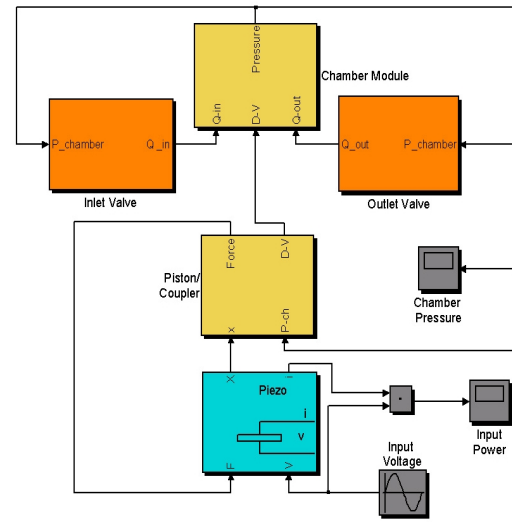


Figure 2: Flow chart of the simulations.

The key components in the micro-pump are: *drive element*, *pump chamber*, *passive valves*, and *flow channels*. All the structural components were modeled as lumped single DOF, and this is adequate since the operational frequency of the device is well below the first natural frequency of any structural component. The liquid in the pump chamber is assumed to be quasi-statically compressible. Further, the interior pressure distributions in the system cavities are assumed to be uniform and the flow is assumed to be steady.

**Drive Element:** The equations describing the dynamic motion of the drive element which includes piezo and piston is as follows:

$$M\ddot{x} + b\dot{x} + kx - p_c A_{pis} = F$$

$$x = d_{33}V_e - \frac{F}{k}$$

$$\Delta V = x A_{pis}$$

where  $x$  = piston displacement,  $M$  = effective mass of the piston element,  $b$  = damping coefficient,  $k$  = stiffness of the tethers attached to the piston,  $F$  = internal force at the

interface of piston and the piezo,  $d_{33}$  = dielectric constant of the piezo,  $A_{pis}$  = area of the piston,  $p_c$  = pressure in the chamber,  $V_e$  = applied voltage across the piezo, and  $\Delta V$  = change in volume of the pump chamber.

*Pump Chamber:* The following equation, obtained by the application of continuity to the control volume, governs the pressure variation in the pump chamber.

$$\dot{p}_c = \left( \frac{V_0 - \Delta V}{C_s} + \frac{1}{K_f} \right)^{-1} (Q_{in} - Q_{out} + \Delta V)$$

where  $V_0$  is the volume of fluid initially contained within the chamber when the volume source is undeformed,  $K_f$  is the bulk modulus of the fluid, and  $C_s$  is the hydraulic capacitance of the chamber structure.

*Check Valve and Channel Dynamics:* The check valves rectify the fluid flow by opening or closing the fluid flow path from the reservoir to the chamber in response to the pressure differential between the two sides. The valve opening is modeled as a quasi-static linear function of the pressure differential across the valve. The flow rate  $Q$ , and the pressure drop across the valve,  $\Delta P$ , are related as:

$$\Delta P = \frac{1}{2} \rho \zeta \left( \frac{Q}{A} \right)^2 + I \dot{Q}$$

where  $\rho$  = density of the fluid,  $I$  = channel inductance,  $A$  = surface area of the valve opening for flow across the valve,  $\zeta$  = the loss coefficient, a function of Reynold's number corresponding to the instantaneous flow rate, determined from a standard look-up table.

## FABRICATION

The micro-pump is fabricated as a multi-layer structure as schematically illustrated in Figure 1. The device is assembled from seven layers—3 SOI wafers, 1 Si layer and 3 pyrex layers—as shown numbered in the cross-section figure in Fig. 1. To achieve a compact design using minimum number of layers, both surfaces of each layer were efficiently utilized by implementing multiple lithography steps for the SOI wafers. For complete details on the microfabrication of the layers, interested readers may refer [4]. After the microfabrication process, the top three SOI wafers (layers 4, 5, and 6) were aligned using an Electronic Visions system and fusion bonded at 1100°C in nitrogen for 1 hour. The bonded wafer stack was cut into chips of size 16.7 mm by 15.7 mm chips using a die-saw, cleaned in water, acetone, methanol, and isopropanol successively, and finally dried in air. The glass wafers were processed with diamond drills and die-saw cut into small chips. Then, the Si and glass interface in the bottom stack (layers 1, 2, and 3) and in top stack (layer 7 and the bonded stack 4, 5, 6) were separately anodically bonded at about 300°C. A ceramic PZT-5H piezoelectric cylinder 1 mm in diameter and 1 mm in height was manually placed in the middle of the glass layer 3 in the bottom stack, and the piezo-Si interfaces were eutectically bonded using a Ti-Pt and Au-Sn alloys. Figure 4 shows a picture of a fully assembled

micropump with electrical leads. The packaged device has dimensions 22.7mm × 15.7mm × 8.6mm. However, the packaging volume is not optimized and as such, the total volume of the device could be much smaller.

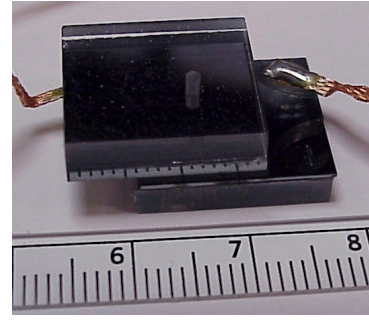


Figure 4. Assembled micro-pump with electrical leads.

## TESTING AND MODEL CORRELATION

An experimental rig (Figure 5) that includes low and high-pressure reservoirs, control valves, pressure, voltage, and current sensors and flow meters was constructed to test the micro-pump. The micro pump device is placed in a specially designed aluminum jig (shown in the inset in Figure 5) with O-rings for connection to the inlet and outlet fluid channels. Static and dynamic pressure sensors are placed directly before and after the device to monitor the LPR and HPR pressures. A micromachined membrane within the top structure of the device pump chamber allows for measurement of the internal pressure as a function of the membrane deflection using an MTI laser probe deflection sensor. In order to avoid any air bubbles in the device, the fluid channels and cavities in the micro pump were first evacuated with the aid of a vacuum pump followed by a few cycles of purging the channels with a solvable gas ( $N_2$ ) and evacuating. Finally, the device was filled with the degassed fluid at a controlled rate.

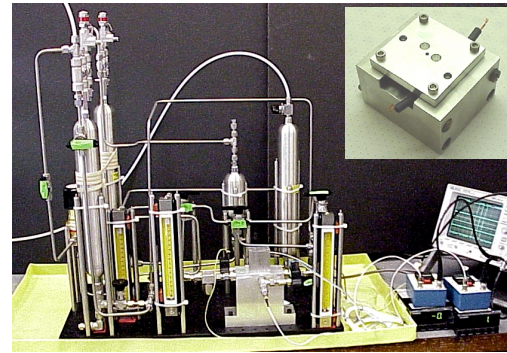


Figure 5. The experimental rig for testing micro-pump. The inset shows packaging jig holding the micro-pump.

The performance of the micro-pump was evaluated by varying voltages across the piezo from 0 to 1600V with bias voltages in the range of 300-600 V, and frequencies from 1 kHz to 12 kHz. The inlet pressure was maintained at 850 kPa, and the differential pressure across the pump

was varied from 0 to 500 kPa. Flow rates were measured using fluid rotameters directly before and after the device, and pressure signals were acquired using the Lab View data acquisition system. Highest flow rate recorded was 2500  $\mu\text{l}/\text{min}$  at 1200 V peak-to-peak voltage, 600 V bias voltage, and 4.5 kHz, and zero differential pressure.

Figures 6, 7, and 8 show the model correlation curves illustrating the performance characteristics of the micro-pump. In Figure 6, the plot of flow rate as a function of drive frequency at zero pressure differential is shown. It can be seen that a good correspondence between the model and experiment was achieved in low frequency regime, however, in the high frequency regime, fluidic resonance effects that were not predicted in the simulation were observed. The resonance effects are attributed to the geometry of the experimental rig.

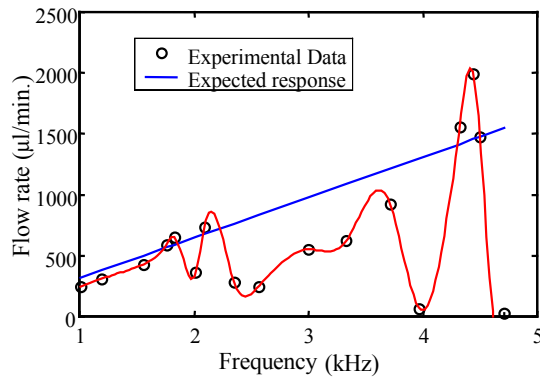


Figure 7. Flow rate versus drive frequency at 1200 V peak-to-peak voltage, and zero differential pressure.

Figure 7 shows the plot of the flow rate versus the pressure differential across the inlet-outlet at 3.5 kHz and 1200 V P-P drive voltage and 600 V bias voltage.

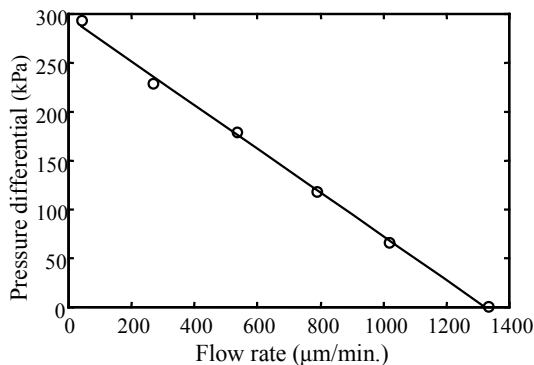


Figure 7. Pressure differential versus flow rate.

Figure 8 shows the relation between the flow rate and the peak-to-peak voltage across the piezo element at a drive frequency of 3.5 kHz, a bias voltage of 600 V, and zero differential pressure. The flow rate increases with the voltage monotonically but not linearly. The slight difference in the slopes of the model and experimental curves is attributed to the non-linear behavior of the tethers that was not modeled in the simulation.

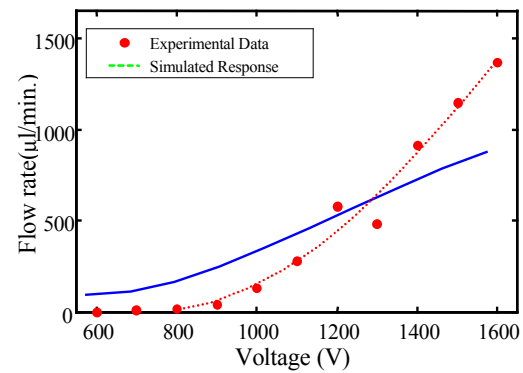


Figure 8. Flow rate vs. piezo peak to peak voltage at 3.5 kHz drive frequency

## CONCLUDING REMARKS

A piezoelectrically driven passive valve hydraulic micro-pump operating at very high frequencies and yielding a high flow rate of 2.5 ml/min has been successfully fabricated and tested. This work has demonstrated the technical feasibility of critical micro-fabrication processes, bulk piezo-silicon integration, and fluid-filling techniques, and thus offers exciting prospects for accomplishing high specific power micro-hydraulic transducers, a new technology under development at MIT. A more rigorous and systematic study is under way to better understand the behavior and to improve the micro-pump performance by either eliminating or exploiting the fluidic resonance effects. The next generation micro-pumps, currently under development, will feature active valves and the single crystal piezo (PZT-PT) element for drive both in the pump chamber and the valves. As a result, a ten-fold increase in the performance is expected.

## ACKNOWLEDGEMENTS

This research was sponsored by DARPA under Grant # DAAG55-98-0361 and by ONR under Grant # N00014-97-1-0880.

## REFERENCES

- [1] Hagood, N., *et al.* "Micro-hydraulic Transducer Technology for Actuation and Power Generation", *Proceedings of SPIE*, Vol. 3985(2000), Newport Beach, CA, March 5-9, 2000, pp. 680-688.
- [2] Gravesen, P., Branebjerg, J., Jensen, O. S., 1993, "Microfluidics-A Review," *J. Micromech. Microeng.*, **3** (1993), pp. 168-182.
- [3] Shoji, S., and Esashi, M., "Microflow Devices and Systems," *J. Micromech. Microeng.* **4** (1994), pp. 157-171.
- [4] Li, H.-Q. *et al.*, "A High Frequency High Flow Rate Piezoelectrically Driven MEMS Micropump," *Proceedings (CD ROM), Solid State Sensor and Actuator Workshop*, Hilton Head Island, SC, June 4-8, 2000, pp. 69-72.



# MEASUREMENT AND MODELING OF THE FLOW CHARACTERISTICS OF MICRO DISC VALVES

J. A. Carretero  
Mass. Institute of Technology  
Dept. of Aeronautics & Astronautics  
Cambridge MA 02139  
Email: jorgcb@mit.edu

K.S. Breuer  
Brown University  
Division of Engineering, Box D  
Providence RI 02912  
Email: kbreuer@brown.edu

## ABSTRACT

The head losses in microfluidic systems such as micropumps are dominated by losses in microvalves, where microfabrication constraints limit significantly possible microvalve designs. This makes them quite different from conventional valves. In particular, flow characteristics in the laminar and low-Reynolds turbulent regimes are not understood clearly, and detailed information about the flow losses is lacking. This paper addresses this issue by using a scaled-up (10:1) valve experiment to measure pressure losses in typical microfabricated valve geometries. The macroscale model is fully instrumented and discharge coefficients and sensitivities to stroke, seat width and Reynolds number are presented.

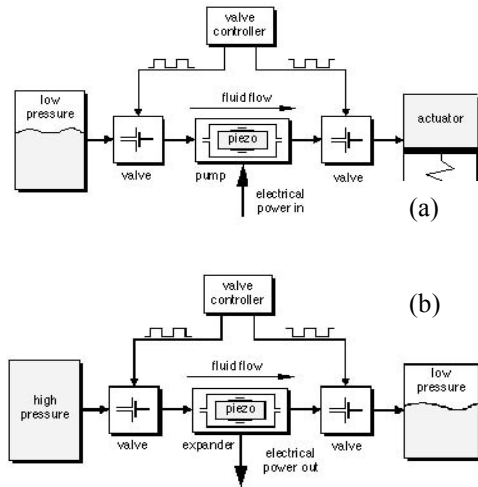


**Figure 1. Schematic representation of a bidirectional MicroHydraulic Transducer system in (a) pump and (b) energy harvester modes.**

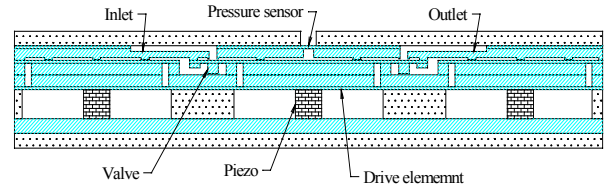


**Figure 2. Cross-sectional view of a multiple wafer micropump with active valves**

## INTRODUCTION

The rapid increase in the development of complex microfluidic devices has revealed a need for more accurate modeling of fluid behavior in small-scale microfabricated geometries. This paper discusses the fluid mechanics modeling strategy undertaken as part of the development effort for the MIT Micro Hydraulic Transducer project. The concept of the Micro Hydraulic Transducer (MHT) integrates the large single-stroke force of a hydraulic system with the high-frequency small stroke available from a piezoelectric element. The combination is used to create high-performance transducers (Hagood *et al.* [1]). The device can operate as an actuator (transforming electrical to mechanical energy) or as an energy harvester (converting mechanical to electrical energy) as shown schematically in Figure 1. The MHT architecture resembles that of a reciprocating internal combustion engine cylinder as seen in Figure 2. The fluid at high pressure comes into the cylinder chamber through an inlet valve, compresses the piston (which in turn compresses the piezoelectric crystal). The piezo then expands, driving the piston up and forcing the fluid out through the outlet valve. In the current design, the piston is approximately 8 mm in diameter, and the valves are poppet type disc valves ( $\varnothing$  500  $\mu$ m) with strokes of less than 40  $\mu$ m operating at approximately 20 kHz. In order to obtain this stroke at such high frequencies the valve is actuated by a piezoelectric aided by an amplification chamber as detailed by Roberts *et al.* [2].

A critical need in the design of the MHT is an accurate fluid mechanics model. The major fluid mechanics challenge is to

model the steady and unsteady fluid behavior in these micron-scale geometries. The Reynolds number during one cycle varies between 1 and 20,000 with a Strouhal number of order 1. In this regime both inertial and viscous forces are important and unsteady effects cannot be ignored. The model needs to be accurate, yet implemented in a flexible manner suitable for design purposes and integration into full system simulations. Unfortunately, such models do not presently exist, and where partial models are available, they are typically neither calibrated nor validated for the small scales and unique geometries that are found in microfluidic systems. The purpose of this paper is to provide such calibration and validation.

## NOMENCLATURE

$C_m$	Modified discharge coefficient	-
$C_q$	Discharge coefficient	-
$d_0$	Inlet diameter	m
$d_{sys}$	Characteristic length	m
$d_v$	Valve cap diameter	m
$f$	Driving frequency	Hz
$h^*$	$h_v/h_p$	-
$h_p$	Plate separation	m
$h_v$	Valve opening	m
$k$	Isothermal bulk modulus	Pa
$l$	Channel length	m
$m$	Scaling power	-
$Q$	Volumetric flow rate	m <sup>3</sup> /s
$Re$	Reynolds number	-
$s$	Seat width	m
$U$	Local flow velocity	m/s
$A_0$	Throat flow area	m <sup>2</sup>
$A_1$	Upstream flow area	m <sup>2</sup>
$A_2$	Downstream flow area	m <sup>2</sup>
$\Delta P$	Pressure drop	Pa
$\alpha$	Non-dimensional frequency	-
$\varepsilon$	Loss coefficient correction factor	-
$\lambda$	wavelength	m
$\mu$	Dynamic viscosity	Pa s
$\nu$	Kinematic viscosity	m <sup>2</sup> /s
$\rho$	Fluid density	Kg/m <sup>3</sup>
$\sigma$	$h_v/s$	-
$\zeta_{quad}$	Turbulent loss coefficient	-
$\zeta_\phi$	Loss coefficient correction factor	-

## LUMPED ELEMENT HYDRAULIC MODEL

For initial designs, the hydraulic system has been modeled using lumped elements. The lumped model has proven to be useful for the analysis of microfluidic systems by Olsson, Bourouina, and Gravesen [3,4,5]. The model is easy to integrate to overall system simulations that may include electrical and structural components. This model, however, is limited to short channels. Wylie and Streeter [6] have proposed a rule-of-thumb criterion in which they suggest that the maximum channel

length ( $l$ ) should be less than 4% of the acoustic wavelength ( $\lambda$ ) as shown by :

$$l \leq 0.04\lambda = \left(\frac{0.04}{f}\right) \sqrt{\frac{k}{\rho}} \quad (1)$$

Equation (1) assumes that the flow channel has rigid walls, and therefore the acoustic wavelength ( $\lambda$ ) is only a function of the frequency of the pressure oscillations ( $f$ ), the fluid bulk modulus ( $k$ ) and the fluid density ( $\rho$ ).

With the lumped element model, the fluidic components are characterized by equivalent capacitances, resistances and inductances. The flow resistances in each element were modeled using published experimental loss coefficients (Idelchik [7]), which were corrected according to the local Reynolds number ( $Re$ ). However, flow correlations at these low Reynolds numbers are not always reliable and need to be validated through experiment and computations. The dominant inductance element is the fluid mass contained in the channels of the system while the dominant capacitance is the compliance of the piston chamber (the fluid itself is close to incompressible). In order to establish a uniform system model, the different resistive components were referenced to a characteristic system length with which we can define a system-wide Reynolds number. The characteristic length chosen was the valve inlet diameter ( $d_{sys}$ ).

Initial results indicate (not surprisingly) that the valves are the dominant loss element in the system. Thus is not unusual, and Gravesen [5] notes that the valves are usually the dominant loss element due to the fact that the entire flow has to pass through the small valve openings. For this reason the design of the valves require special attention and are therefore the focus of this paper.

## Micro-Scale Valves

Microvalves may be classified as active (with an actuator) or passive (without actuator). Many different examples of both types of microvalves exist in the literature. A review by Shoji, Esashi [8], and Gravesen [5] indicates that most microvalves have been designed for gas control, while not many have been demonstrated for liquid applications due to their low conductance.

The low conductance of microvalves is directly related to microfabrication constraints, which limits available geometries to low aspect ratio, prismatic elements due to the line-of-sight nature of microfabrication techniques. This greatly limits the available geometries of fluidic devices. For instance valves cannot have three-dimensional structures such as 45° poppets, rounded edges and fillets (although some limited fillet capabilities have been demonstrated in highly stressed MEMS structures; Ayon, *et al.* [9]). The high temperatures required for bonding the devices preclude the use of polymers and soft materials for the valve seats. Available actuation options are

limited in stroke and control authority further constraining valve response time and performance. The above-mentioned constraints have made typical microvalve designs quite different from macro scale valves.

In most cases valves are fabricated and then characterized experimentally, primarily because detailed analysis of the flow characteristics and sensitivities to different relevant parameters is lacking. One of the main reasons for this is that instrumenting a microvalve to measure both flow rate and pressure as functions of the valve position is very difficult.

### **Macro scale valves**

In contrast, much research has been conducted on “normal”-sized valves. However, the complex geometries make the flow in valves very complicated and valve-dependant. Thus comparison between different experimental measurements and numerical simulations is difficult, even impractical. In the past, researchers have investigated such flows using a variety of analytical techniques (Von Mises, [10]) and numerical techniques (Vaughan, [11]). These techniques suffer from the fact that flow separation, cavitation, transition, reattachment and relaminarization are difficult to model mathematically and expensive numerically. Other researchers have employed an experimental approach (Stone, [12]; Johnston, [13]) but have focused primarily on the turbulent flow regime. These efforts have shown that, for small openings, poppet valves behave like long orifices, a suggestion that supports the thought that the effects of flow separation and subsequent reattachment dominate the valve dynamics.

### **RESEARCH STRATEGY**

Our approach to the detailed study of poppet-type microvalves consists of parallel experiments, computations and low-order modeling. The measurements are conducted using two parallel experimental facilities, one at the macro-scale (approximately 1 cm valve head diameter, with full instrumentation) and one at full-scale (500  $\mu\text{m}$  valve head, with limited instrumentation). Both Reynolds and Strouhal numbers are matched in the two experiments. The results from the macro-scale experiment are presented in this paper.

### **Order of magnitude valve model**

The order-of-magnitude model allowed us to make initial estimates of the head losses through the valves. This model also gave a starting point for designing the valve experiments. As mentioned above, previous work (Schrenk [14]; Stone [12]; Johnston [13]) has suggested that the valve can be modeled as an orifice. The initial order-of-magnitude model was constructed based on an orifice analogy.

Most of the information gathered on orifices is based on experiments carried out in pipes of 2 in diameter and higher. It has been noted that orifices in pipes of smaller diameter have

higher discharge coefficients due to second-order effects, such as surface tension (Ramamurthi [15]). For Reynolds less than  $10^4$ , the discharge coefficient has to be corrected for Reynolds dependency and surface conditions, and these correlations are less common and less reliable than those for fully rough turbulent regime. Thus, the orifice model should be able to capture the flow physics, but should be considered only as an approximation to the correct values.

To a certain extent the orifice itself may be thought of as a contraction of the flow and a subsequent expansion. An integral analysis gives a relationship for the combined effect of the flow expansion and contraction. The quadratic local loss coefficient ( $\zeta_{quad}$ ) is defined as the total pressure drop ( $\Delta P$ ) over the dynamic pressure based on the orifice local mean velocity ( $U$ ):

$$\zeta_{quad} = \frac{\Delta P}{\frac{1}{2} \rho U^2} = \left[ \frac{1}{2} \left( 1 - \frac{A_0}{A_1} \right)^{\frac{3}{4}} + \left( 1 - \frac{A_0}{A_2} \right)^2 \right]. \quad (2)$$

The loss coefficient,  $\zeta_{quad}$ , is a function of both the ratio of the orifice throat area to the upstream area ( $A_0/A_1$ ) and the ratio of the orifice throat area to downstream area ( $A_0/A_2$ ). The loss coefficient in equation 2 disregards any Reynolds number dependency and therefore needs to be corrected. Idelchik [7] uses two empirical correction factors ( $\zeta_\phi$  and  $\varepsilon$ ) based on the local Reynolds number, and with this, a modified loss coefficient ( $\zeta$ ) can be defined:

$$\zeta = \zeta_\phi(\text{Re}) + \varepsilon(\text{Re}) \zeta_{quad}. \quad (3)$$

For the initial model, experimental correlations published by Idelchik [7] were used to compute the loss coefficient for a variety of geometries.

### **Scaling considerations**

The macro scale experiment uses a scaled-up version of the micro disc valve that is fabricated in the full-size MHT. Geometrical and dynamic similarity concepts were employed to relate the macro to the micro scale results. Both Reynolds and Strouhal numbers were fixed and a suitable scaling factor was chosen. The main considerations in picking the right scale were to make it easy to instrument, to take advantage of the fact that the driving frequency scales like the square of the length scale and to make it amenable to traditional fabrication processes. A scaling factor of ten was chosen for the macro-scale experiment, resulting in a valve of approximately 1cm in diameter. The stroke of the valve also scales linearly, and thus the 40  $\mu\text{m}$  stroke in the microscale becomes 400  $\mu\text{m}$  in the macro-scale experiment.

The scaling of the driving frequency ( $f$ ) was explored by defining the non-dimensional frequency, or Stokes number,  $St$ , which is the product of the Reynolds number and the Strouhal number:

$$St = \left( \frac{U d_{sys}}{\nu} \right) \left( \frac{d_{sys} f}{U} \right) = \frac{d_{sys}^2 f}{\nu} \quad (4)$$

This is a function of only the characteristic length scale ( $d_{sys}$ ), system frequency ( $f$ ) and kinematic viscosity ( $\nu$ ). This indicates that a geometric scale increase of ten corresponds to a reduction by a factor of a 100 of the driving frequency ( $f$ ). The microscale driving frequency of 12kHz was thus reduced to 120 Hz in the macro-rig, significantly simplifying the instrumentation and actuation requirements. Flow rates scale linearly with length and for the range of Reynolds numbers examined, the maximum flow rate needed was 3 liters-per-minute.

One disadvantage of scaling up a system is that some parameters are difficult, or impossible to properly scale. In the present case, the most obvious parameter that was not matched was that of the surface finish, but this is thought to be less important. However, one attribute of microfabrication that is important to match is the sharp corners that define MEMS-fabricated edges. Care was taken to ensure that this feature was preserved in the macro-rig.

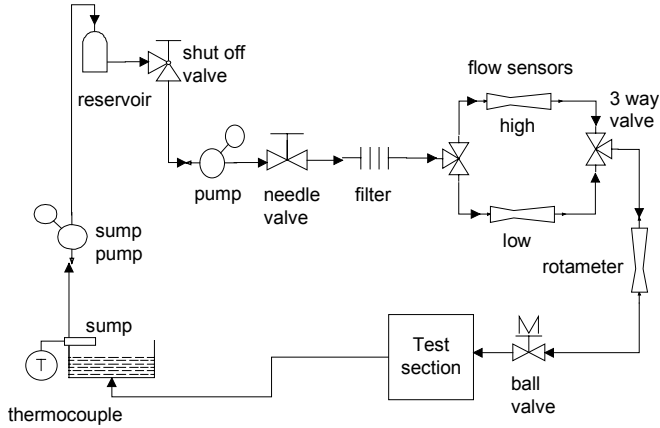


**Figure 3. Schematic of the macro-scale test facility layout.**

## MACRO SCALE EXPERIMENTAL SETUP

A schematic of the experimental setup is shown in Figure 3. The range of flowrates explored in the experiments required the use of multiple pressure sensors and flowmeters in order to accurately monitor the spectrum of test conditions.

The setup includes two Cole-Palmer differential pressure liquid flowmeters each with an uncertainty of 3 % (full scale). The low discharge flowmeter has a maximum flow rate of 1 liter/min and the high discharge flowmeter has a maximum discharge of 5 liters/min. Both flowmeters have a 0-5 volt output to the data acquisition system. A rotameter was placed in series with the flowmeters to ensure consistency in the measured flowrates. The calibration of each flowmeter was measured gravimetrically prior to the experiments. The temperature of the water was measured using an Omega K-type

submersible thermocouple and corroborated with a regular thermometer. The Temperature ( $T$ ) data was used to correct the dynamic viscosity ( $\mu$ ) of the deionized water according to:

$$\mu = \left( \frac{0.1}{-120 + 2.1428(T [C] - 8.435) + \sqrt{8078.4 + (T [C] - 8.435)^2}} \right) \quad (5)$$

obtained from Richter [16]. Pressure sensing both upstream and downstream of the valve was performed using two wet-wet differential pressure transducers. The low-side transducer was a Setra model 230 with a pressure range of 0-2 psid and accuracy of  $\pm 0.25$  % (FS). The high-side sensor was a sensotec model FDW1VJ with a range from 0-150 psid. The accuracy of this sensor is quoted as 0.1 % (FS).

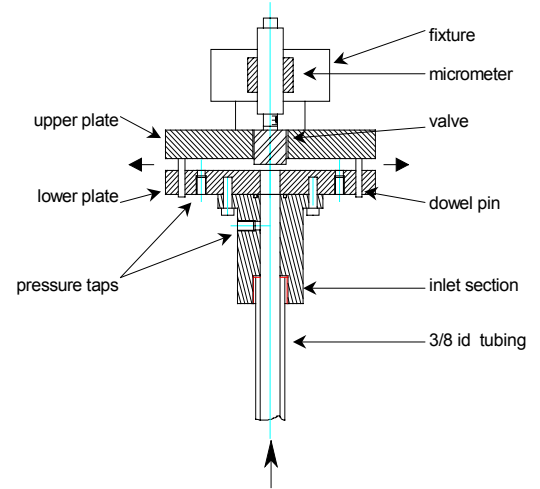


**Figure 4. Test section detail of the macro scale test facility.**

The test section, illustrated in Figure 4, is axisymmetric with the test fluid flowing in from the center tube and exhausting radially outward. The test section may be subdivided into three subsections: inlet, valve and positioning section. The inlet section consists of a 3/8" aluminum tube, 36" (96 diameters) long. The tube is connected to the valve section and special care was taken to ensure that the inside surface was free of gaps and steps.

The valve section has two cylindrical plates, which were ground flat to a specified planarity of less than 1 mil (Checked with dial gauge). Accurate control of the separation of the two plates is critical to the experiment, and so, to ensure that the plates were parallel, they were separated by three thickness gauges placed 120° apart, and tightened with screws. The separation was then re-checked with thickness gauges and a depth micrometer. Dowel pins ensured the concentricity of the upper and lower plates. The upper plate also serves as guide for the valve, which slides up and down inside a sleeve.



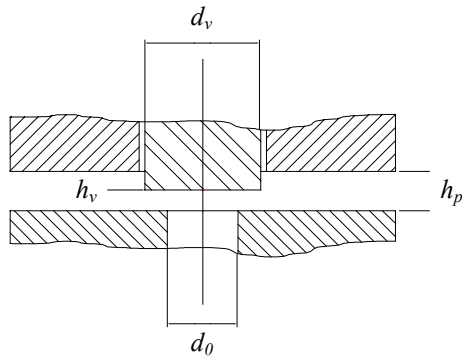


**Figure 5. Valve geometry detail.**

The valves, as well as the seats, were fabricated such that all the edges remained sharp with no appreciable fillets (checked under a microscope). This is important because, as mentioned above, the flow is quite sensitive to rounded edges which would not be present in a MEMS-fabricated fluidic system. Pressure was sensed both upstream and downstream of the valve. Two pressure-sensing ports, 180° apart, were used downstream, to ensure that the flow was symmetric. The valve head was positioned using a micrometer (accuracy  $\pm 5 \mu\text{m}$ ) with a special non-rotating head, bonded to the valve. The valve position was measured before and after each measurement with a thickness gauge.

The valve geometry employed for the experiments is detailed in Figure 5. The inlet diameter ( $d_0$ ) was 3/8 in (9.525 mm), plate separation ( $h_p$ ) was set at 450  $\mu\text{m}$ . The valve opening ( $h_v$ ) was varied from fully-closed to fully-open. Three valve diameters were employed, as shown in Table 1. For each of these configurations, the loss coefficient was measured as functions of the Reynolds number, valve stroke ( $h^* = h_v/h_p$ ) and seat width.

**Table 1 Valve diameters ( $d_v$ ) with corresponding seat widths ( $s$ ) and non-dimensional seat widths ( $\sigma$ )**

	Valve diameter ( $d_v$ )	Valve seat width ( $s$ )	$\sigma$
1	0.383 in (9.72 mm)	0.004 in (0.10 mm)	0.01
2	0.437 in (11.10 mm)	0.031 in (0.78 mm)	0.08
3	0.562 in (14.24 mm)	0.093 in (2.36 mm)	0.25

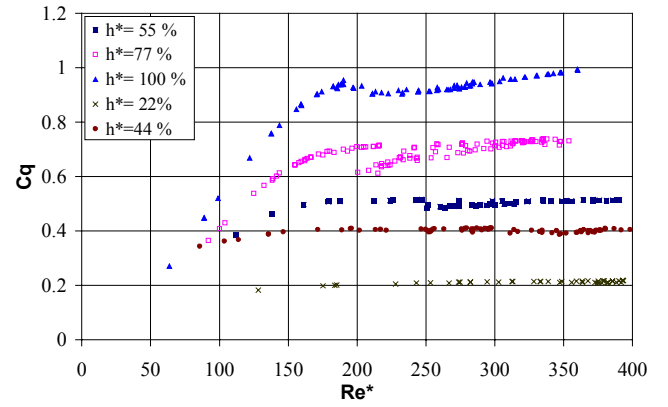


**Figure 6. Discharge Coefficient vs. Reynolds number for different percentages of valve opening ( $h^*$ ) for valve 1. The plate separation ( $h_p$ ) was 450  $\mu\text{m}$ .**

## RESULTS AND DISCUSSION

The flow is characterized by a discharge coefficient ( $C_d$ ) which is a function of the volumetric flow rate ( $Q$ ), the inlet diameter ( $d_0$ ), the fluid density ( $\rho$ ), and the static pressure difference ( $\Delta p$ ) as shown by:

$$C_d = \frac{4Q}{\pi d_0^2} \sqrt{\frac{\rho}{2\Delta p}} \quad (6)$$

This represents the measured flow rate, normalized by the ideal flow rate based on the applied pressure drop and inlet area. The Reynolds number is a function of the volumetric flow rate ( $Q$ ), the kinematic viscosity ( $\nu$ ) and the valve opening ( $h_v$ ) and is defined as:

$$Re^* = \sqrt{\frac{Q}{\nu h_v}} \quad (7)$$

This scaling is chosen so that, in the laminar flow regime where the flow rate is proportional to the pressure drop, the discharge coefficient is proportional to the Reynolds number.

In Figure 6 the discharge coefficient  $C_d$  is plotted versus the Reynolds number  $Re^*$  for different percentages of valve opening ( $h^*$ ). It is observed that in the turbulent regime, as expected, the discharge coefficient ( $C_d$ ) becomes a weak function of the Reynolds number and therefore remains almost constant.

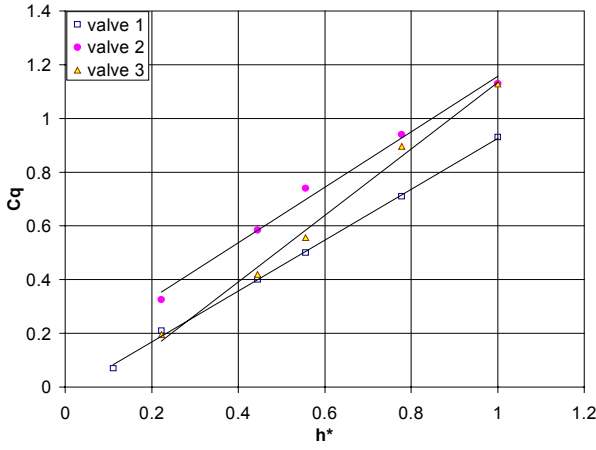


**Figure 7. Discharge coefficient ( $C_q$ ) vs. non-dimensional valve opening ( $h^*$ ) for the three valves; plate separation ( $h_p$ ) 450  $\mu\text{m}$ .**

In the laminar regime the pressure drop ( $\Delta p$ ) becomes proportional to the flow rate ( $\Delta p \propto Q$ ). The discharge coefficient is then directly proportional to the square root of the flow rate and linearly proportional to the Reynolds number, as defined above. It should be pointed out that closer analysis of the data presented in Figure 6 indicates that only the curves for 77% and 100% aperture achieved laminar flow. The remaining curves show a transition regime behavior with  $\Delta p \propto Q^{1.6-1.8}$  depending on the case. Drawing an analogy to pipe flow this is reminiscent of classical low-Reynolds number turbulent behavior as described by Blasius [17].

The qualitative change in the transition point from laminar to turbulent as the percentage of valve opening ( $h^*$ ) changes can be explained if we consider that we have two competing flows. The first one is the parallel plate axisymmetric radially divergent flow that is continually decelerating. This flow shows a transition at Reynolds numbers  $Re_d \cong 2000$ , as shown by Moller [18]. The second flow is an orifice-type flow, which remains turbulent at much lower Reynolds numbers. This explains the fact that as the valve closes the orifice-type effect becomes dominant and turbulent flow continues, even for  $Re_d < 2000$ .

It should also be pointed out that, in some cases, hysteresis was observed as measurements were taken cycling from lower to higher flow rates ( $Q$ ) and viceversa. Hysteresis is clearly visible for the 77% ( $h^*$ ) curve, and is consistent with observations of Schrenk [14].

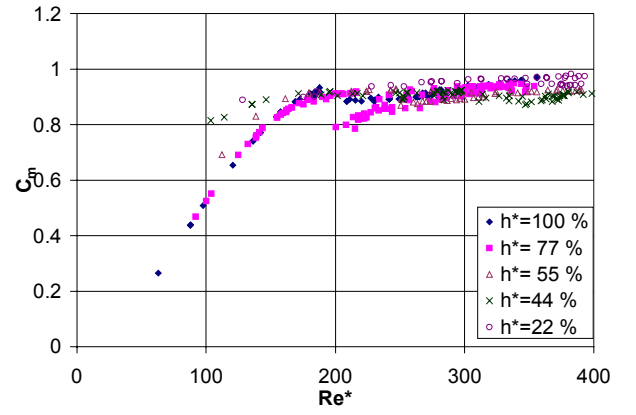


**Figure 8. Modified discharge coefficient  $C_m$  vs. Reynolds number for valve #1 and plate separation  $h_p=450 \mu\text{m}$**

### Valve opening dependence

The pressure drop vs. valve opening relationship for turbulent flow was explored further and the results are shown in Figure 7, where the discharge coefficient,  $C_q$ , is plotted versus the percentage of valve opening ( $h^*$ ) for the three different valves. The discharge coefficient,  $C_q$ , is observed to vary linearly with the valve opening, and to be more-or-less independent of the valve geometry, and shows that, based on definition of  $C_q$  in equation (6), the static pressure difference is proportional to the square of the non-dimensional valve opening ( $h^*$ ). This result emphasizes the importance of maximizing the stroke for these valves in system designs.

Knowing the dependence of the discharge coefficient ( $C_q$ ) to the non-dimensional valve opening ( $h^*$ ) allows us to define a modified discharge coefficient ( $C_m$ ) such that all the curves can be collapsed onto one band for the turbulent flow regime. This modified discharge coefficient is based on the valve opening ( $h_v$ ) raised to some power  $m$ , and on the inlet diameter ( $d_0$ ) having the form:

$$C_m = \frac{Q}{\pi d_0 h_v^m} \sqrt{\frac{\rho}{2\Delta P}} \quad (8)$$

The advantage of doing this is that a valve may be modeled rather accurately using a single corrected discharge coefficient formula. Such a scaling can be seen in Figure 8. where, for valve #1, the scaling power ( $m$ ) had a value of one. Here, we see that, for all valve openings, the modified discharge coefficient ( $C_m$ ) lies between 0.88 - 0.93. It should be noticed that as transition effects start to become important this approximation fails and should therefore be employed with caution. This behavior also supports the analogy between poppet disc valves and orifices. The same behavior was also observed in the other valves, although the proper scaling coefficient varied slightly. A numerical curve fit indicated that, for valves #2 and #3, a value of  $m=0.8$  provided a better collapse of the data in the high-flow regime.

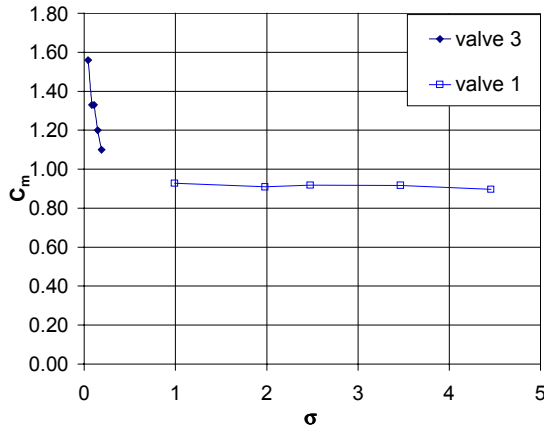


**Figure 9. Discharge coefficient vs. non-dimensional seat width ( $\sigma$ ). The plate separation was  $h_p=450 \mu\text{m}$ .**

### Valve seat width dependence

The effect of the valve seat width was investigated with two valves of different seat widths ( $s$ ). The results are shown in Figure 9 where the x-axis shows the ratio of valve opening ( $h_v$ ) to seat width ( $s$ ), defined as ( $\sigma$ ). The y-axis uses the modified discharge coefficient ( $C_m$ ) with a scaling power  $m=1$ . One interesting result is that up to a value of  $\sigma > 1$  the modified discharge coefficient is not affected by the seat width,  $\sigma$ . Once this threshold is passed, however, the discharge coefficient becomes very sensitive to the seat width and rises rapidly. Significant pressure recovery is observed, even surpassing  $C_m=1$ . This increase in discharge coefficient may be explained by drawing an analogy to thick orifices. For a thick orifice, the separation bubble tends to reattach within the throat area as shown by Sahin *et al.*[19]. The reattachment reduces the flow losses across the orifice. For the case where the non-dimensional seat width  $\sigma < 1$  the same phenomenon is observed and we theorize that the separated flow undergoes reattachment with the accompanying pressure recovery.

The results shown in Figure 9 are consistent with those obtained by Johnston and co-workers [2]. The main difference observed, though, is that Johnston observed a minimum  $C_m$  of 0.75 where we observed a higher value of approximately 0.9. The reason for this difference is attributed to geometrical differences in the valve test setup. However it is recognized that although the trends are similar to those of other researchers more experiments are required to fully characterize this behavior.

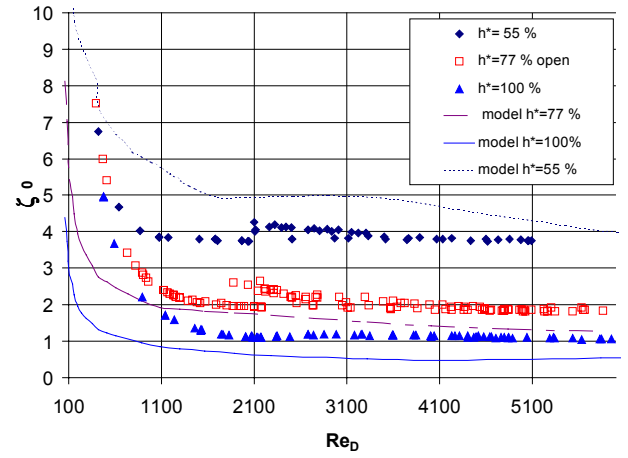


**Figure 10. Loss coefficient vs. Reynolds number comparison between experimental results and the lumped model for various valve opening percentages ( $h^*$ ).**

### Comparison of lumped model to data

A comparison of the original lumped model and the data for valve #1 is presented in Figure 10, where the x-axis is the Reynolds number based on the inlet flow area ( $A_I$ ), as defined by:

$$\text{Re}_d = \left( \frac{4Q}{\pi d_0 v} \right) \quad (9)$$

and the y-axis is a loss coefficient  $\zeta_0$  defined by:

$$\zeta_0 = \frac{\Delta P_0}{\frac{1}{2} \rho \left( \frac{Q}{\pi d_0 h_v} \right)^2} \quad (10)$$

where  $\Delta P_0$  is the total pressure drop,  $\rho$  is the fluid density,  $Q$  is the volumetric flow rate,  $d_0$  is the inlet diameter and  $h_v$  is the valve opening. It is observed that the original order-of-magnitude flow model captures correctly the flow physics of the valve although the numerical values are off by a factor of 2 with respect to experimental values. In addition, the original model does not accurately capture the transition point. A new corrected model is currently being developed to closer match the experimental data, while still maintaining generality.

## CONCLUSIONS

The flow characteristics of a poppet type disc valves with geometries defined by standard microfabrication techniques have been studied employing a 10:1 scale experimental facility. The experiments have shown that the commonly used orifice analogy is a good approximation in the turbulent regime. Transition effects, however are not properly captured by such model. This is attributed to the competing nature of the axisymmetric divergent flow between two parallel plates and the small orifice flow for different valve openings.

The sensitivity to valve stroke has been characterized for the turbulent regime and it was shown that  $\Delta P$  becomes proportional to the square of the valve opening to plate separation ratio ( $h^*$ ).

The valve seat width effect has been investigated showing that for the turbulent regime the modified discharge coefficient,  $C_m$ , (Equation 8) is independent of the valve opening to seat width ratio,  $\sigma$ . It has also been seen that for  $\sigma$  less than one, the modified discharge coefficient rises significantly, presumably due to reattachment.

What is particularly encouraging, however, is that the simple model does capture both the character and (with a factor of about two), the numerical values of the loss-coefficients. This is extremely valuable for the complex design in which many tradeoffs need to be balanced to ensure a functional, robust and efficient micro-hydraulic transducer. More experiments will be pursued in the near future, including unsteady measurements and measurements in the full-scale (micro) device.

## ACKNOWLEDGMENTS

This research was sponsored by DARPA under Grant # DAAG55-98-1-0361 and ONR under Grant # N00014-97-1-0880. We would like to thank everyone in the MHT project for their support, advice, help and friendship during the good times and the bad times. These lines are not enough to mention all the people that have in one way or another helped us along the way. After all two roads diverged in a yellow wood... Frost, 1915.

## REFERENCES

- Hagood, N. W., Roberts, D. C., Saggere, L., Breuer, K. S., Chen, K.-S., Carretero, J. A., Li, H. Q., Mlcak, R., Pulitzer, S., Schmidt, M. A., Spearing, S. M., Su, Y.-H., 2000 "Micro Hydraulic Transducer Technology for Actuation and Power Generation," Smart Structures and Materials 2000: Smart Structures and Integrated Systems, **3985** Newport Beach, CA, March 2000.
- Roberts, D. C., Hagood, N. W., Su, Y. H., Li, H. Q., Carretero, J. A., 2000 "Design of a Piezoelectrically-Driven Hydraulic Amplification Microvalve for High Pressure, High Frequency Applications" Smart Structures and Materials 2000: Smart Structures and Integrated Systems, **3985** Newport Beach, CA, March 2000.
- Olsson, A. Stemme, G., Stemme, E., 1999, "A numerical design study of the valveless diffuser pump using a lumped- mass model," Journal of Micromechanics & Microengineering. **9** pp 34-44
- Bourouina, T., Grandchamp, J-P., 1996, "Modeling micropumps with electrical equivalent networks," Journal of Micromechanics & Microengineering. **6** pp 398-404
- Gravesen, P. Branebjerg, J. Sondegard, O., 1993, "Microfluidics- a review," Journal of Micromechanics & Microengineering. **3** pp 168-182
- Wylie, B. E., Streeter, V. L., 1993, *Fluid Transients in Systems*, Prentice Hall, Englewood Cliffs, NJ
- Idel'chik, I. E., 1994, *Handbook of hydraulic resistance*, CRC Press, Boca Raton, FL
- Shoji, S., Esashi, M., 1994, "Microflow devices and systems," Journal of Micromechanics & Microengineering. **4** n 4 Dec 1994. pp 157-171
- Ayon, A., Chen, K.-S., Lohner, K. A., Spearing, S. M., Sawin, H.H, Schmidt, M. A., 1999, "Deep reactive ion etching of silicon," Proceedings of the 1998 MRS Fall Meeting - Symposium AA, Materials Science of Microelectromechanical Systems (MEMS). Boston, MA, USA. 19981201-19981202.
- Von Mises, R., 1917, "The calculation of flow coefficient for nozzle and orifice", VDA, **61** (21-23)
- Vaughan, N. D., Johnston, D. N., Edge, K.A., 1992, "Numerical simulation of fluid flow in poppet valves", Proceedings of the Institution of Mechanical Engineers, Part C: Mechanical Engineering Science. **206** n 2 1992 pp 119-127.
- Stone, J. A., 1960, "Discharge coefficients and Steady-State Flow Forces for Hydraulic Poppet Valves," Transactions ASME , Journal of Basic Engineering," March 1960, pp 144-154
- Johnston, D. N., Edge, K. A., Vaughan N. D., 1991, "Experimental investigation of flow and force characteristics of hydraulic poppet and disc valves," Proceedings of the Institution of Mechanical Engineers, Part A: Power & Process Engineering. **205** n 3 1991 p 161-171.
- Schrenk, E., 1957, "Disc valves, flow patterns, resistance and loading," Translation from German , BHRA T547
- Ramamurthi, K. Nandakumar, K. 1999, "Characteristics of flow through small sharp-edged cylindrical orifices," Flow measurement and Instrumentation, **10** 133-143
- Richter, M., Woias, P. Weib, D., 1997, "Microchannels for applications in liquid dosing and flow rate measurement," Sensors and Actuators A **62** pp 480-483
- White. F., 1994, *Fluid Mechanics*, McGraw-Hill, Inc. New York
- Moller , P. S., 1962, "Radial Flow without swirl between parallel discs," Aeronautical Quarterly, **14** pp 163-185
- Sahin, B., Ceyhan, H., 1996, "Numerical and experimental analysis of laminar flow through square-edged orifice with variable thickness, " Transactions of the Institute of Mechanical Engineers, **18** n. 4 pp. 166-174

# Modeling, Design, and Simulation of a Piezoelectrically Driven Microvalve for High Pressure, High Frequency Applications

David C. Roberts<sup>a</sup>, Onnik Yaglioglu, Jorge Carretero, Yu-Hsuan Su,  
Laxman Saggere, Nesbitt W. Hagood

Active Materials and Structures Laboratory, Department of Aeronautics and Astronautics,  
Massachusetts Institute of Technology

## ABSTRACT

This paper reports the modeling, design, and dynamic simulation of a piezoelectrically-driven microfabricated valve for high frequency regulation of high pressure fluid flows. The enabling concept of the valve is the ability to convert the small displacement of a piezoelectric element into a large valve cap stroke through the use of a hydraulic fluid, while maintaining high force capability. The paper focuses on the development of a systematic procedure to arrive at a geometric valve design for given performance requirements. Modeling of the non-linear large deflection behavior of the valve membrane and design of this structure to maintain stresses below critical levels are discussed. Design of the piezoelectric material drive portion of the valve to create a stiffness match with the valve membrane and external hydraulic system is detailed. In addition, this paper presents a dynamic simulation of the active valve, including effects such as valve cap dynamics and fluid damping, that allow for understanding and prediction of valve performance under various loading conditions.

**Keywords:** microvalve, hydraulic, amplification, piezoelectric, micromachined

## 1. INTRODUCTION

The development of an active microvalve, capable of high frequency ( $\sim 10\text{kHz}$ ) control of large pressure differential ( $\sim 1\text{MPa}$ ) fluid flows, is critical toward the realization of high energy density microfluidic devices. Such a valve is being developed at MIT to regulate fluid flow in Micro-Hydraulic Transducer devices for actuation and power harvesting.<sup>1</sup> These MHT devices combine active materials, such as piezoelectric or single-crystal ferroelectric material, with MEMS microfabrication techniques and hydraulic fluid to create high frequency pumping excitation in small mass systems. Both types of transducers consist of a piezoelectric pump chamber, two actively controlled valves, and a low and high pressure fluid reservoir. In the MHT actuator, electrical energy supplied to the piezoelectric pump chamber results in pumping of fluid through the valves from the low to high pressure reservoir. In the MHT power harvester, sequenced operation of the valves results in fluid flow from the high to low pressure reservoir, producing a "pinging" of the piezoelectric element within the pump chamber. This cyclic strain on the element induces electrical charge, which can be rectified and stored. The specific power of these transducer devices scales linearly with the frequency of operation and the pressure drop across which the device can operate and inversely with scale of the device. As a result, MHT device performance relies on the high frequency, high force, and high stroke capabilities of the active valves employed.

A novel piezoelectrically-driven microvalve design for use in such microfluidic systems was first introduced in [2]. This paper extends that work by introducing a systematic design procedure for the valve and dynamic simulation tools to understand device performance. The organization of the paper is as follows: Section 2 reviews the active valve geometry, its principle of operation, and the requirements placed on the valve by a typical MHT microfluidic system. Section 3 details the linear and non-linear modeling tools that have been developed to accurately predict active valve behavior. Section 4 presents a systematic procedure for designing the valve geometry for a given set of performance requirements. Section 5 presents a complete valve system model and associated simulation results that confirm the design procedure. Section 6 presents conclusions and future work.

---

<sup>a</sup> Address: 77 Massachusetts Ave, Rm 37-358A, Cambridge, MA 02139 E-mail: dcrobert@mit.edu

## 2. SYSTEM

### 2.1. Valve Geometry/Working Principle

The proposed piezoelectrically-driven hydraulically-amplified microvalve is shown in Figure 1. This device is able to achieve large valve cap stroke ( $\sim 20 - 30\mu\text{m}$ ) against high pressure loads ( $\sim 1\text{MPa}$ ) through a novel hydraulic amplification mechanism that converts the small strain ( $\sim 1\mu\text{m}$ ) of a piezoelectric material element into a significantly larger valve cap stroke. The inherent stiffness of the piezoelectric material and the hydraulic fluid chamber enable both high-frequency and high-force actuation capabilities.

The active valve consists of three primary components: a piezoelectric drive element, a closed fluid amplification chamber, and membrane with attached valve cap. The drive element sub-structure consists of one or more tiny piezoelectric material cylinders, each bonded on its top surface to a silicon micromachined piston and on its bottom surface to a silicon support structure. To achieve a fluid seal between the hydraulic amplification chamber and the piezoelectric material yet allow for minimally-restrained motion of the drive element piston, thin micromachined silicon tethers along the piston outer circumference serve as flexural attachments to an outer silicon support structure. The fluid chamber resides between the top surface of the drive element piston and the bottom surface of a thin, smaller diameter silicon micromachined valve cap membrane.

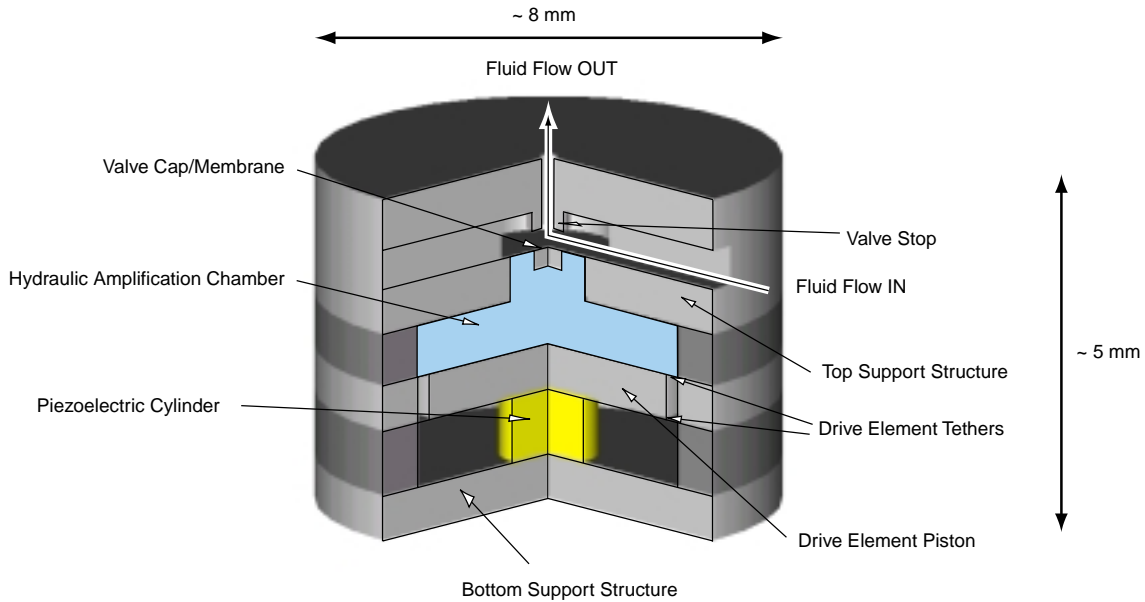


**Figure 1.** Schematic of a piezoelectrically-driven hydraulic amplification microvalve. Primary structural components are designated with arrows. External loading exists on top surface of valve cap and membrane.

In response to applied piezoelectric voltage, the piezoelectric material strains. The resulting deflection of the drive element piston generates a pressure within the hydraulic amplification chamber which in turn deflects the valve cap and membrane against a fluid orifice thereby regulating fluid flow through the external hydraulic system. The pressure loadings on the valve cap and membrane during device operation depend on the external microfluidic system application. The piezoelectric material capabilities, the ratio of the piston diameter to the valve membrane diameter, the compliances of the fluid and structural elements in the chamber, the severity to which the valve cap membrane experiences nonlinear behavior, and the nature of the external loading all contribute to the performance of this microvalve device.

## 2.2. System Requirements on Valve

This active valve geometry has been baselined for use in the MHT technology currently under development at MIT. A schematic of a positive displacement pump in used in MHT power harvesting is shown in Figure 2. Out of phase operation of two active valves results in a pulsing flow of fluid from a high pressure reservoir ( $P_{HPR}$ ) to a low pressure reservoir ( $P_{LPR}$ ) through a central piezoelectric harvesting chamber.<sup>1</sup> With each cycle of device operation, the increasing and decreasing fluid pressure  $P_{EHC}$  in the harvesting chamber (as the chamber fills and evacuates) results in a stressing of the piezoelectric material element(s) and a subsequent generation of charge. For a given harvesting chamber geometry, the system operational frequency and the peak-peak pressure  $P_{EHC}$  fluctuation in the chamber directly determine the achievable power generation levels. The required cyclic flow rates into and out of the chamber,  $Q_{in}$  and  $Q_{out}$ , are functions of this pressure fluctuation and the structural chamber volumetric stiffness. For known values of  $P_{HPR}$  and  $P_{LPR}$ , active valves must therefore be implemented with these frequency, pressure, and flow rate capabilities. For the example system shown in Figure 2, the inlet valve membrane experiences a constant high pressure  $P_{HPR}$  over its top surface while the valve cap sees a changing pressure  $P_{EHC}^*$  as the chamber fills and evacuates. Likewise, the outlet valve membrane experiences a constant low pressure  $P_{LPR}$  over its top surface while the valve cap sees a changing pressure  $P_{EHC}^{**}$  as the chamber fills and evacuates. The amounts by which  $P_{EHC}^*$  and  $P_{EHC}^{**}$  differ from  $P_{EHC}$  are functions of the fluid inertial effects in the inlet and outlet flow channels (see Section 3.2.2). With an understanding of external system pressure and flow rate requirements such as in this MHT microfluidic system, piezoelectric active valves can be properly designed.

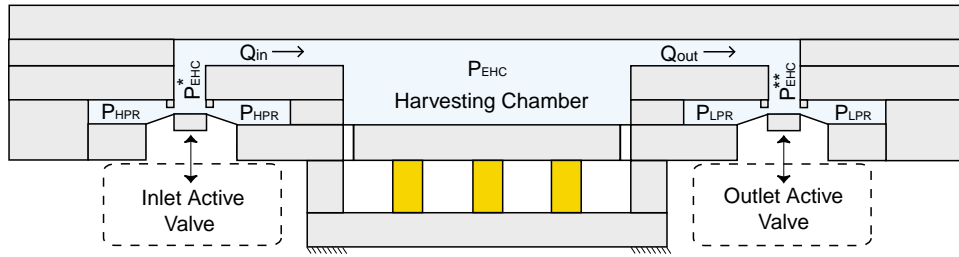


**Figure 2.** Schematic of an MHT power harvesting device. Two active valves regulate flow at high frequency from a high pressure  $P_{HPR}$  to a low pressure  $P_{LPR}$ . Cyclic pressure change in harvesting chamber  $P_{EHC}$  creates a stressing of the piezoelectric material and a subsequent generation of charge.

## 2.3. Design Goals and Issues

This paper focuses on the development of modeling tools and design strategies for implementation of piezoelectric active valve technology in microfluidic systems. Although the design procedure is generic to both actuator and harvesting applications, for purposes of clarity, the discussions in this paper will center on the design of active valves to be used in the previously described MHT power harvesting system. Furthermore, without any loss of generality, the focus will be solely on the design and simulation of the inlet active valve.

To regulate flow into the MHT harvesting chamber so as to meet overall system requirements, the inlet valve membrane and cap must be sized properly to ensure adequate *stroke* of the cap and allow sufficient *flow rate* to successfully fill the chamber in the allotted time, while withstanding the pressure loads without exceeding the *membrane stress* fracture levels. In addition, the piezoelectric drive portion of the valve must be designed so as to *minimize the overall footprint* of the device, yet still provide adequate *actuation capabilities* in pressurizing and producing volume change to the hydraulic amplification chamber. These design and modeling issues are detailed in the following sections.

## 3. MODELING

The modeling effort is sub-divided into two parts in order to capture the physics of the active valve and predict its performance as it regulates flow in the external hydraulic microfluidic system. The first part focuses on the development of an active valve model to capture the behavior of the full valve under generic external loading conditions. The second part focuses on the external hydraulic system to develop pressure-flow relations that govern

the filling of the MHT harvesting chamber. These parts, when coupled together, allow for an understanding of the full valve and external system behavior.

### 3.1. Active Valve Model

The modeling techniques for capturing the active valve behavior under the external loading discussed in Section 2.2 are detailed in this section. A more comprehensive overview of these modeling tools is found in [2]. One major assumption in this valve active model is that linear theory is appropriate for the majority of structural components. This is valid since these structural components are expected to deform in small deflection regimes.<sup>3</sup> The sole exception is that of the valve membrane, which experiences peak deflections that exceed the membrane thickness. This large deflection behavior will be an important focus of this section. A second major issue involves the benefits of incorporating multiple small-area piezoelectric elements in the drive structure rather than a single large element. Although not detailed in this paper, finite-element studies have shown that the use of these elements spread out above the bottom support structure and below the drive piston significantly reduces the structural compliance of these components to levels where their effect on overall device performance is small. As a result, the bottom support structure and the drive piston are assumed rigid in the model. A discussion of the modeling techniques for each of the remaining valve components follows. Figure 3 provides a reference for valve dimensions, performance variables, and the complete set of active valve relations. The coefficients  $\beta_1$ - $\beta_8$  found in Figure 3(c) are derived from linear plate theory but are not discussed explicitly in this paper (see [2] for further details).

#### 3.1.1. Piezoelectric Material

The piezoelectric material elements within the valve drive structure experience a compressive stress loading  $T_p$  during voltage actuation  $V_p$ . The displacement  $Z_p$  of these piezoelectric elements is governed by Eq (1). This relation assumes perfect  $d_{33}$  actuation. Although not exactly true due to transverse clamping of the piezoelectric elements at their top and bottom surfaces, the incorporation of multiple small diameter piezoelectric material elements rather than a single large element helps to reduce this clamping effect and supports this assumption.

#### 3.1.2. Drive Piston and Tethers

The drive element piston experiences a pressure loading  $P_{HAC}$  over its top surface area  $A_{pis} = \pi R_{pis}^2$  and a stress loading  $T_p$  on its bottom surface over the summed piezoelectric element area  $A_p$ . In addition, the tethers provide a total force  $F_{te}$  on the piston outer circumference. The dynamic motion of the piston is expressed in Eq 4, where  $M_{pis}$  is the piston mass and  $C_{pis}$  is a damping parameter. The tether deflection and swept volume are determined using linear plate theory (see [2]) and are therefore functions of  $F_{te}$  acting on the tether inner circumference and  $P_{HAC}$  acting over the top tether surface, as expressed in Eqs 3 and 2, respectively. As defined in this paper, the tether swept volume  $dV_{te}$  includes the swept volume of the piston and therefore is additionally a function of  $Z_{te}$ . Since the piston is assumed rigid,  $Z_p = Z_{te}$ .

#### 3.1.3. HAC Fluid

Fluid compressibility effects are included to describe the pressure  $P_{HAC}$  - volume  $dV_{fluid}$  relationship within the hydraulic amplification chamber, according to Eq 6.  $V_o = \pi R_{te}^2 t_{HAC}$  is the initial volume of the HAC chamber and  $K_{fluid}$  is the fluid bulk modulus.

#### 3.1.4. Top Support Structure

The top support structure is modeled as an annular plate clamped at its outer circumference  $R_{te}$  and free at its inner circumference  $R_{vm}$ . Pressure loading  $P_{HAC}$  acts on the underside of this plate and a force  $F_{vm}$ , due to the forces on the valve membrane, acts at  $R_{vm}$ . The deflection  $Z_{top}$  and the plate swept volume  $dV_{top}$  are governed by Eqs 8 and 7 respectively.  $dV_{top}$  includes the swept volume beneath the valve cap and membrane corresponding to  $Z_{top}$ , as shown in Figure 3(b).



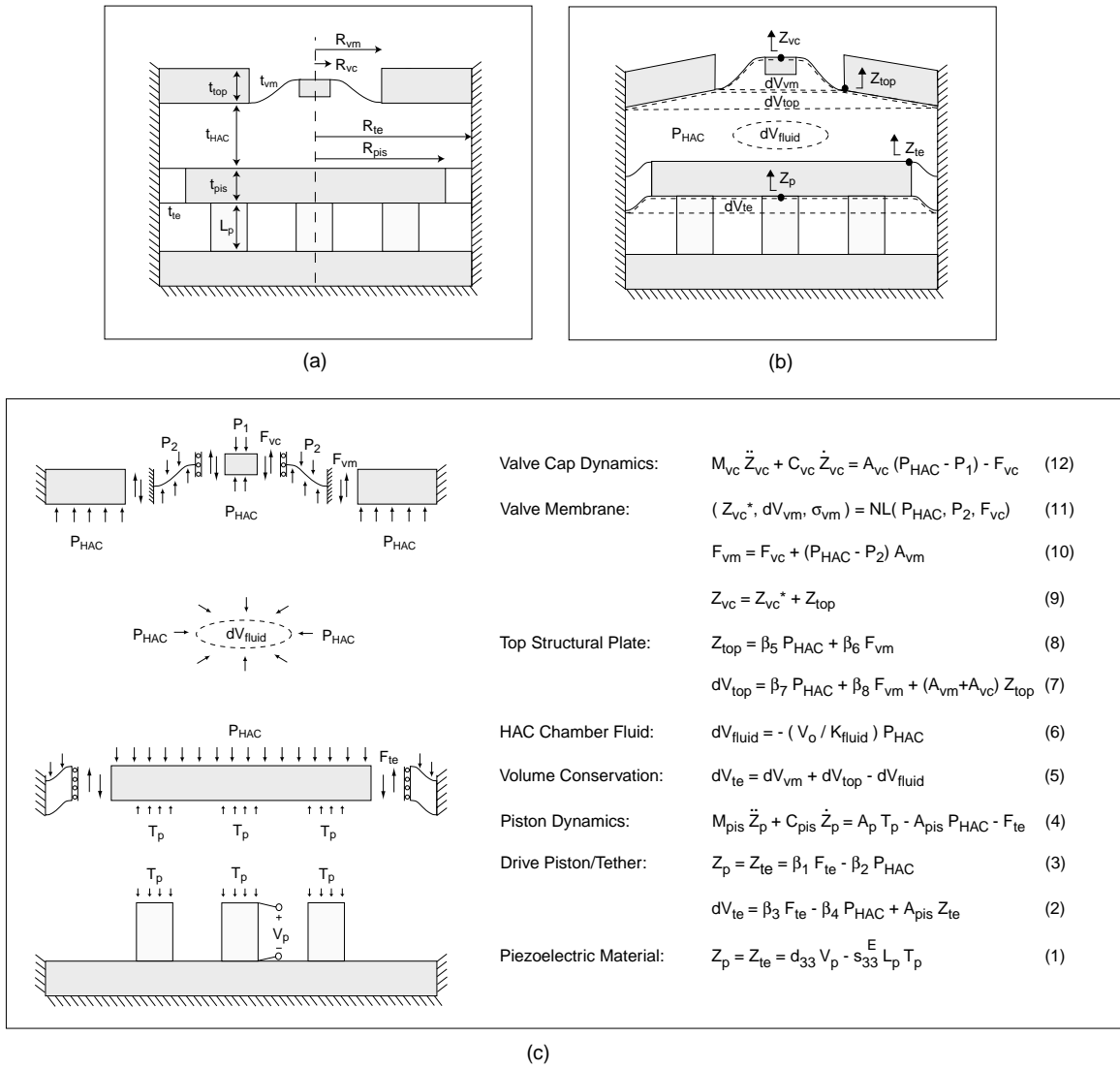


**Figure 3.** Modeling schematic of active valve with related equations: (a) schematic illustrating the dimensional parameters of each of the valve sub-component structures, (b) schematic highlighting important deflection and swept volume parameters, and (c) free-body diagrams of valve sub-components and corresponding modeling equations.

### 3.1.5. Valve Cap and Membrane

The valve cap is significantly thicker than the membrane and is therefore assumed rigid. As will be discussed in Section 3.2.3, the cap is assumed to experience a net upward pressure of  $P_{vc} = P_{HAC} - P_{EHC}^*$  over its area  $A_{vc}$  and a force  $F_{vc}$  due to valve membrane behavior along its outer circumference  $R_{vc}$ . The dynamic motion of the valve cap is expressed in Eq 12, where  $M_{vc}$  is the valve cap mass and  $C_{vc}$  is a damping parameter. Since the valve cap and membrane experience significant deflections during actuation, non-linear large deflection modeling capabilities must be implemented in the model. In general, the deflection of a structural plate can be represented using linear deformation theory only if the deflection of the plate is less than about half the plate's thickness.<sup>3</sup> For plates that experience large deflection behavior, in-plane tensile stresses are generated and significant plate stiffening effects occur. Since in this active valve device, cap deflections on the order of  $15 - 30\mu m$  are expected for membranes with thicknesses between  $5 - 10\mu m$ , modeling of these stiffening effects and stresses is crucial for the design of robust valve membrane components.

A general numerical technique has been developed for calculating the quasi-static non-linear large-deflection behavior of annular plates with rigid central caps under axisymmetric loading.<sup>4</sup> This technique serves as the backbone for a series of modeling tools developed to predict the non-linear valve membrane deformation during active valve operation. As shown in Figure 3(c) and discussed in 3.2.3, the valve membrane is assumed to experience a net pressure upward of  $P_{vm} = P_{HAC} - P_{HPR}$  over its area  $A_{vm} = \pi(R_{vm}^2 - R_{vc}^2)$  and a force  $F_{vc}$  at its inner circumference. These non-linear modeling tools, as expressed in Eq 11, are capable of determining the valve cap deflection  $Z_{vc}^*$  with respect to the top support structure, the swept volume under the membrane and cap  $dV_{vm}$  and the complete stress field in the membrane  $\sigma_{vm}$  for applied loading  $P_{HAC}$ ,  $P_{HPR}$ , and  $F_{vc}$ . The absolute valve cap deflection  $Z_{vc}$  is the sum of  $Z_{vc}^*$  and  $Z_{top}$ , as expressed in Eq 9.

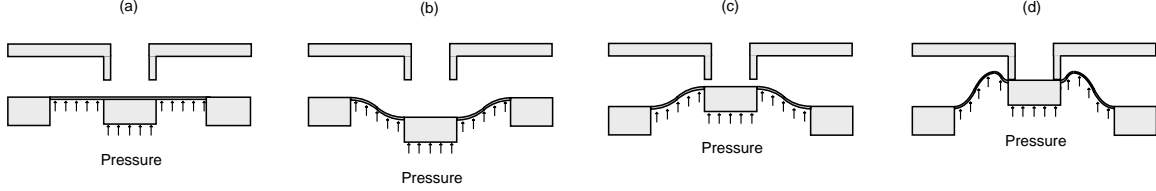


**Figure 4.** Pressure-deflection scenarios of valve cap and membrane: (a)  $P_{vm} = 0$  and  $F_{vc} = 0$ , (b)  $P_{vm} < 0$  and  $F_{vc} < 0$ , cap deflection negative, (c)  $P_{vm} > 0$  and  $F_{vc} > 0$ , cap deflection positive but less than valve stop, and (d)  $P_{vm} > 0$  and  $F_{vc} < 0$ , cap deflection positive and restrained against valve stop.

During valve actuation, the cap and membrane structure experience deformation modes as shown in Figure 4. Negative valve cap deflections 4(b) allow for large external system flow rates while positive valve cap deflections 4(c) correspond to small valve openings and therefore small external flow rates. As the cap is forced shut against the fluid orifice 4(d), bowing of the valve membrane can result. It is desired to operate these valve membranes in this positive/negative deflection regime so as to minimize valve membrane stresses yet maximize total valve cap stroke.

## 3.2. External Hydraulic System Model

The inlet active valve within the example MHT power harvesting device regulates flow from a high pressure reservoir to the harvesting chamber. As fluid passes over the valve membrane and cap, it exerts pressures on these structures. These pressures and flow rates are a function of the opening and closing action of the valve cap against its stop, the geometry of the fluid channel that carries fluid from the valve to the chamber, and the effective hydraulic stiffness of the harvesting chamber being filled. This section details the techniques used to model the pressure-flow relations for each of these system features.

### 3.2.1. MHT Chamber Stiffness

During the first half of a complete device cycle, the inlet valve is open and the outlet valve is closed. As fluid passes through the valve into the harvesting chamber, the chamber pressure increases. The relationship between the amount of fluid entering the chamber and the pressure rise within the chamber is determined by the effective hydraulic chamber stiffness,  $K_{EHC}$ . Figure 5(a) shows a simplified schematic of this filling process.

$K_{EHC}$  is a function of the chamber geometry, material properties, and fluid initial volume. A large  $K_{EHC}$  means that a small amount of fluid  $dV_{EHC} = \int Q_{in}(t)dt$  flowing into the chamber will result in a large increase in chamber pressure  $P_{EHC}$ , whereas a small  $K_{EHC}$  means that a small amount of fluid flow into the chamber will result in a small chamber pressure increase. The chamber pressure increase as a function of time can be written as

$$\frac{dP_{EHC}}{dt} = K_{EHC}Q_{in}(t). \quad (14)$$

A similar model can be used to evaluate the evacuation of fluid through the outlet valve, resulting in a chamber pressure decrease as fluid flows to a low pressure  $P_{LPR}$  (see Figure 5(b)). For illustration purposes in this paper, however, only the inlet valve and corresponding filling of the harvesting chamber are considered.

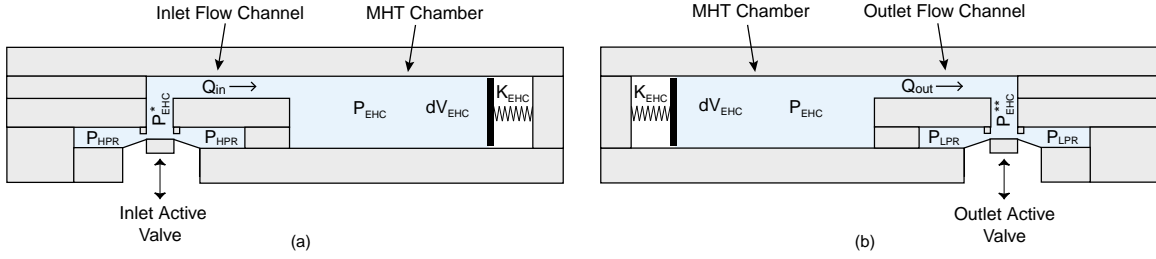


**Figure 5.** Filling and evacuation models for MHT: (a) During inlet valve opening and closing, fluid fills the harvesting chamber. (b) During outlet valve opening and closing, fluid evacuates the harvesting chamber. The associated chamber pressure time history  $P_{EHC}(t)$  during filling and evacuation is a function of the amount of fluid entering/evacuating the chamber and the chamber volumetric stiffness  $K_{EHC}$ .

### 3.2.2. Valve Channel Inertial Effects

Fluid inertial effects within the flow channel connecting the valve to the harvesting chamber can play a significant role in determining the difference between  $P_{EHC}^*(t)$  and  $P_{EHC}(t)$  during device operation. This pressure-flow relation can be written as

$$P_{EHC}^*(t) - P_{EHC}(t) = \left( \frac{\rho L_c}{A_c} \right) \dot{Q}_{in} \quad (15)$$

where  $\rho$  is the fluid density,  $L_c$  is the channel length, and  $A_c$  is the channel area. For a long channel with small cross-section area, one can expect fluid inertial effects to play a significant role as the pressure  $P_{EHC}^*$  builds up to accelerate the fluid slug into the chamber. Conversely, for short channels with large areas, the inertial effects are negligible and the pressure  $P_{EHC}^*(t)$  and  $P_{EHC}(t)$  do not differ at all. It is important to be aware of these inertial effects when designing and modeling any sort of hydraulic system that contains small channels. For simplicity in this paper, however, it will be assumed that the channel geometry within the external hydraulic system has been designed in such a way that fluid inertial effects are negligible.

### 3.2.3. Valve Orifice Flow Relations

Work by previous researchers<sup>67,8</sup> has shown that for small openings, poppet valves (such as the valve cap in this proposed device) behave as long orifices in which the effects of flow separation and subsequent reattachment dominate the valve flow dynamics.

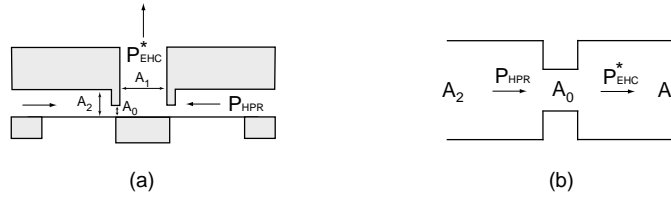


**Figure 6.** Valve orifice representation: (a) valve cap geometry and fluid flow areas, (b) representation of flow through valve as a flow contraction followed by a flow expansion.

Qualitatively, the valve flow can be approximated by a simplified order-of-magnitude valve model. The valve orifice may be characterized as a flow contraction followed by a flow expansion as shown in Figure 6(a) and (b). An integral analysis gives a relationship for the combined effect of the flow expansion and contraction. The loss coefficient  $\zeta_{orifice}$  is defined as the total pressure drop  $\Delta P = P_{HPR} - P_{EHC}^*$  over the dynamic pressure based on the orifice local mean velocity ( $\bar{u} = \frac{Q}{A_o}$ )

$$\zeta_{orifice} = \frac{\Delta P}{\frac{1}{2}\rho\bar{u}^2} = \left[ \frac{1}{2} \left( 1 - \frac{A_0}{A_1} \right)^{\frac{3}{4}} + \left( 1 - \frac{A_0}{A_2} \right)^2 \right] \quad (16)$$

where the upstream flow area can be approximated as  $A_2 = 2\pi R_{vc} H_{upstream}$ , the throat area can be approximated by  $A_0 = 2\pi R_{vc} Z_{stroke}$ , and the downstream flow area can be approximated as  $A_1 = \pi R_{vc}^2$ .  $H_{upstream}$  is the height of the radial flow channel above the valve membrane to the cap and  $Z_{stroke}$  is the valve cap opening distance from the valve stop structure.

This approximation, however, holds only for Reynolds numbers of order  $Re > 10,000$ . In microfluidic systems, such as the MHT power harvester, much lower Reynolds numbers are expected.<sup>5</sup> For this reason, correction factors (obtained from experimental results) are employed to obtain better estimates of the loss coefficients for these low turbulence and laminar flows.<sup>5</sup> Although not detailed explicitly in this paper, these higher order loss effects can be represented with a Reynold's number dependant coefficient  $C(Re)$  as a multiplier of  $\zeta_{orifice}$ . As a result, the pressure-flow relation for this orifice can be written as

$$\Delta P = P_{HPR} - P_{EHC}^* = \frac{1}{2}\rho C(Re)\zeta_{orifice} \left( \frac{Q^2}{A_0^2} \right). \quad (17)$$

All subsequent fluid models discussed in this paper incorporate these higher-order correction factors to obtain an accurate estimation of the flow behavior. The following assumptions are made to define the valve cap and membrane areas over which the upstream pressure  $P_{HPR}$  and the downstream pressure  $P_{EHC}^*$  act. Since the valve cap stroke during operation is significantly less than  $H_{upstream}$ ,  $R_{vm}$ , and  $R_{vc}$ , the majority of pressure drop through the valve structures occurs across the contraction and expansion at the valve cap circumference. As a result, at any given instant of time, the pressure acting over the valve membrane area can be approximated as the reservoir pressure  $P_{HPR}$  and the pressure acting over the valve cap area can be approximated as  $P_{EHC}^*$ . For a specific value of valve cap opening at a given time during the cycle, a relationship therefore exists for the instantaneous fluid flow through the valve as a function of the pressure drop across the valve.

## 4. DESIGN PROCEDURE

### 4.1. Overview

This section introduces a systematic design procedure that can be implemented to calculate dimensions of the valve cap, valve membrane, hydraulic amplification chamber, and drive element portion of the inlet active valve to satisfy requirements set forth by the external hydraulic system. This design procedure is based upon quasi-static valve piston and valve cap behavior (ie:  $\ddot{Z}_{vc} = \dot{Z}_{vc} = \ddot{Z}_{pis} = \dot{Z}_{pis} = 0$ ). Depending upon the frequency of operation, this assumption may or may not be a valid one, since system dynamic effects could be excited. It is therefore the purpose of this quasi-static design procedure to generate a 1st-order design, from which a full dynamic simulation can be run to evaluate the goodness of the design and used as a tool for fine-tuning of the valve geometries. Section 5 will present full dynamic simulations as a check to this design procedure.

Figure 7 presents a generalized flowchart for this quasi-static design process. Given external system requirements, such as the chamber stiffness  $K_{EHC}$ , the  $P_{EHC}$  pressure fluctuation from a  $P_{min}$  to a  $P_{max}$  during filling, the reservoir pressure  $P_{HPR}$ , and the overall desired system frequency  $f_{sys}$ , the following steps are carried out: (1) the valve cap radius  $R_{vc}$  (for a chosen valve stroke  $Z_{stroke}$ ) is calculated to allow for adequate filling of the harvesting chamber, (2) the valve membrane thickness  $t_{vm}$ , outer radius  $R_{vm}$ , and required  $P_{HAC}(t)$  time history are calculated to allow for motion of the cap along its desired trajectory against the known external loads while at the same time ensuring membrane stresses below critical levels, and (3) the drive element piston area  $A_{pis}$  and piezo area  $A_p$  are calculated to provide a stiffness match between the drive piston structure and the load that it encounters and to ensure adequate actuation capabilities.

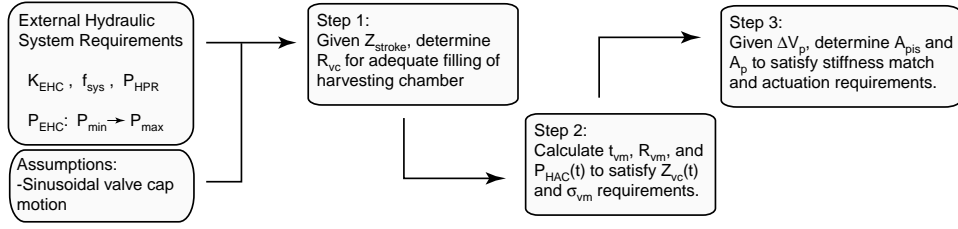


**Figure 7.** Flowchart organizing design procedure for inlet active valve.

## 4.2. System Requirements

To facilitate the understanding of the design procedure detailed in the following subsections, numerical system requirements characteristic of a typical MHT are presented here. For  $P_{HPR} = 1.2 \text{ MPa}$ , the inlet valve opens in a sinusoidal manner to fill a harvesting chamber with  $K_{EHC} = 1.5e^{16} \frac{\text{Pa}}{\text{m}^3}$ . The system frequency is chosen to be  $f_{sys} = 10 \text{ kHz}$  and it is desired that during this filling process,  $P_{EHC}$  should rise from a minimum pressure  $P_{min} = 0.2 \text{ MPa}$  to a maximum pressure  $P_{max} = 1.0 \text{ MPa}$ . It is assumed that the outlet valve is designed properly to allow evacuation from  $P_{max} = 1.0 \text{ MPa}$  to  $P_{min} = 0.2 \text{ MPa}$  during the time that the inlet valve is closed. In addition, it can be assumed that channel dimensions  $L_c$  and  $A_c$  are chosen to ensure that fluid inertial effects in the channel are negligible (ie:  $P_{EHC} = P_{EHC}^*$  at all times).

## 4.3. Step 1: Design of Valve Cap

In the first step of the design procedure, the valve cap radius  $R_{vc}$  is calculated so as to allow for exact filling of the harvesting chamber. With the imposed valve cap motion  $Z_{vc}(t)$  and the external hydraulic system modeling tools described in Section 3.2,  $R_{vc}$  is determined such that the pressure rise in the harvesting chamber increases from its initial minimum of  $P_{min}$  to the desired maximum pressure  $P_{max}$  at the time the valve completely closes again. Equations 14, 15, 16, 17 are solved in a simulation format for this purpose. Insufficient filling will result if  $R_{vc}$  is not large enough. Conversely, if  $R_{vc}$  is too large, the chamber will be filled in excess. For the example MHT system, a value of  $R_{vc} = 241 \mu\text{m}$  is determined that results in a harvesting chamber pressure rise from  $P_{EHC} = 0.2 \text{ MPa}$  to  $P_{EHC} = 1.0 \text{ MPa}$  during the time that the inlet valve is open. Figure 8(a) illustrates the imposed valve cap deflection for this case. The valve is completely closed when  $Z_{vc} = +20 \mu\text{m}$  and is fully open when  $Z_{vc} = -20 \mu\text{m}$ . Figure 8(b) shows the corresponding flow rate  $Q_{in}$  through the valve and Figure 8(c) details the resulting  $P_{EHC}(t)$  time history. Note that the chamber fills properly since the pressure at the instant of valve closing is  $1.0 \text{ MPa}$ . Since a complete  $P_{EHC}(t)$  time history is needed for further steps in the design procedure, it is assumed that an outlet valve for the system has been sufficiently designed to evacuate the fluid during the second half of the device cycle, creating the evacuation pressure behavior shown in Figure 8(c).

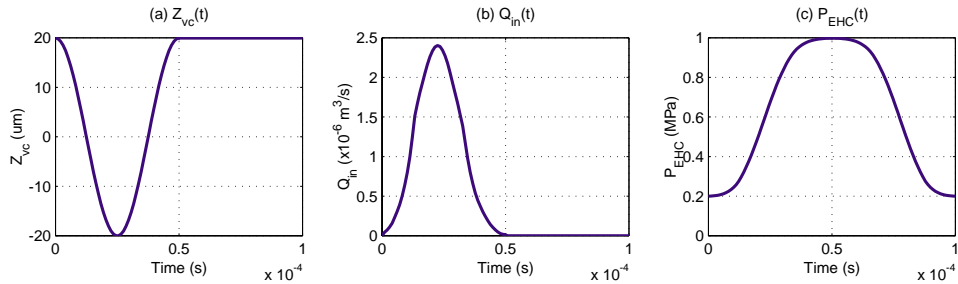


**Figure 8.** Chamber filling plots corresponding to  $Z_{stroke} = 40 \mu\text{m}$  and  $R_{vc} = 241 \mu\text{m}$ : (a) imposed valve cap deflection  $Z_{vc}(t)$ , (b) flow rate through valve  $Q_{in}(t)$ , and (c) resulting  $P_{EHC}(t)$  during filling (and evacuation).

#### 4.4. Step 2: Design of Valve Membrane

In the second step of the design procedure, the valve membrane thickness  $t_{vm}$  and outer radius  $R_{vm}$ , and the required  $P_{HAC}(t)$  time history are calculated such that the valve cap properly follows its imposed trajectory  $Z_{vc}(t)$  and experiences a maximum tensile membrane stress during this motion of  $\sigma_{vm} = \sigma_{limit}$ . The code calculates the entire stress field along the membrane, however it records only the maximum tensile value for each time instant during the cycle and calls it  $\sigma_{vm}$ . A limiting value for  $\sigma_{limit} = 1.0GPa$  is taken from.<sup>9</sup> Since a small value of  $t_{vm}$  is desired to minimize actuation requirements, an initial guess of  $t_{vm} = 7\mu m$  is employed. For this value, a guess for  $R_{vm}$  is taken. Under the constant  $P_{HPR}$  loading on the valve membrane and the time-varying loading  $P_{EHC}^*(t)$  on the valve cap calculated in Step 1, the required  $P_{HAC}(t)$  time history is calculated to force the valve membrane and cap to follow its imposed trajectory  $Z_{vc}(t)$ . During this time cycle,  $\sigma_{vm}$  is monitored. This procedure becomes an iterative process in  $R_{vm}$  until a value of  $R_{vm}$  is determined such that at some time during the complete cycle, a peak tensile stress of  $\sigma_{limit}$  is reached. For the example MHT system, a value of  $R_{vm} = 757\mu m$  is determined for  $t_{vm} = 7\mu m$ . The required  $P_{HAC}(t)$  time history, swept volume time history under the membrane and cap  $dV_{vm}(t)$ , and the associated membrane stress time history  $\sigma_{vm}(t)$  are shown in Figures 9(a), (b), and (c) respectively. In Figure 9(c), notice that the maximum stress in the membrane during the cycle occurs when the cap is deflected to its minimum value of  $Z_{vc} = -20\mu m$ . The membrane again experiences a stress of  $1.0GPa$  when the cap is at its maximum deflection of  $Z_{vc} = +20\mu m$ . This reconfirms the design choice to force the membrane into symmetric upward and downward motion so as to maximum total valve cap stroke when restricted to limited membrane stress levels.

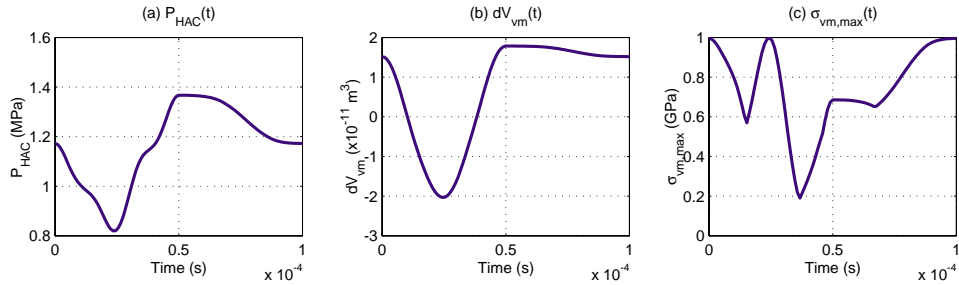


**Figure 9.** Valve membrane behavior corresponding to  $Z_{stroke} = 40\mu m$ ,  $R_{vc} = 241\mu m$ ,  $t_{vm} = 7\mu m$ , and  $R_{vm} = 757\mu m$ : (a) required hydraulic amplification chamber  $P_{HAC}(t)$ , (b) corresponding valve cap and membrane swept volume  $dV_{vm}(t)$ , and (c) peak stress in valve membrane  $\sigma_{vm}(t)$ .

#### 4.5. Step 3: Design of Piezoelectric Drive Element

In the third step of the design procedure, the piezoelectric material area and drive element piston area are determined so as to create a quasi-static stiffness match with the loading seen by this structure. The goal in doing this is to maximize the energy transfer from the piezoelectric material to the load. As shown in Figure 10, the valve cap/membrane and external hydraulic system appear to the drive structure as a stiffness  $K_{vm}$  in series with a fluid stiffness  $K_{HAC}$  of the hydraulic amplification chamber. A linearization of the actuation curve associated with the motion of the valve cap (described by the time histories  $P_{HAC}(t)$  and  $dV_{vm}(t)$  calculated in Step 2 of the design procedure and plotted against one another in Figure 10(a)) provides an approximation for this  $K_{vm}$  stiffness. Combining  $K_{vm}$  and  $K_{HAC}$  together produces an overall load  $K_{load}$  seen by the piezoelectric element. The requirement of a stiffness match between  $K_{piezo}$  and  $K_{load}$  therefore results in the following equality,

$$K_{piezo} = K_{load} \quad \rightarrow \quad \frac{E_p A_p}{L_p} = \frac{A_{pis}^2}{\left( \frac{\Delta V_{vm}}{\Delta P_{HAC}} \right) + \left( \frac{A_{pis} H_{HAC}}{K_{fluid}} \right)}. \quad (18)$$

The piezoelectric material actuation requirement to drive the valve cap and membrane against the external hydraulic system in a stiffness match configuration produces the following relation:

$$\frac{1}{2}d_{33}V_p = \left( \frac{1}{A_{pis}} \right) \left[ \Delta V_{vm} + \left( \frac{A_{pis}H_{HAC}}{K_{fluid}} \right) \Delta P_{HAC} \right]. \quad (19)$$

Therefore, equations 18 and 19 form a set of two equations with three unknowns  $A_{pis}$ ,  $A_p$ , and  $V_p$ . Equation 18 sets the relationship between  $A_{pis}$  and  $A_p$  for a stiffness match between piezo and load to be achieved while equation 19 defines the condition under which valve performance is met, relating the input piezo voltage  $V_p$  to the  $A_{pis}$ . In observing these equations, it is clear that the smaller the voltage  $V_p$ , the larger the values of  $A_{pis}$  and  $A_p$  need to be. Since one of the goals in the design of this active valve is make its footprint as small as possible, this implies that the valve should work at as large a voltage as possible. In real devices, a limitation of electrical breakdown across the air gap between drive element piston and the bottom structural plate exists, and therefore a maximum allowable  $V_p$  for the given piezo length  $L_p$  is set. As a result, in the design of this valve, voltage now becomes an imposed quantity. The set of two equations can be solved for the two remaining geometric free design variables  $A_{pis}$  and  $A_p$  to create a quasi-static stiffness match condition between the piezo and load and to ensure adequate valve performance to satisfy the actuation requirements passed down from the membrane and cap design steps.

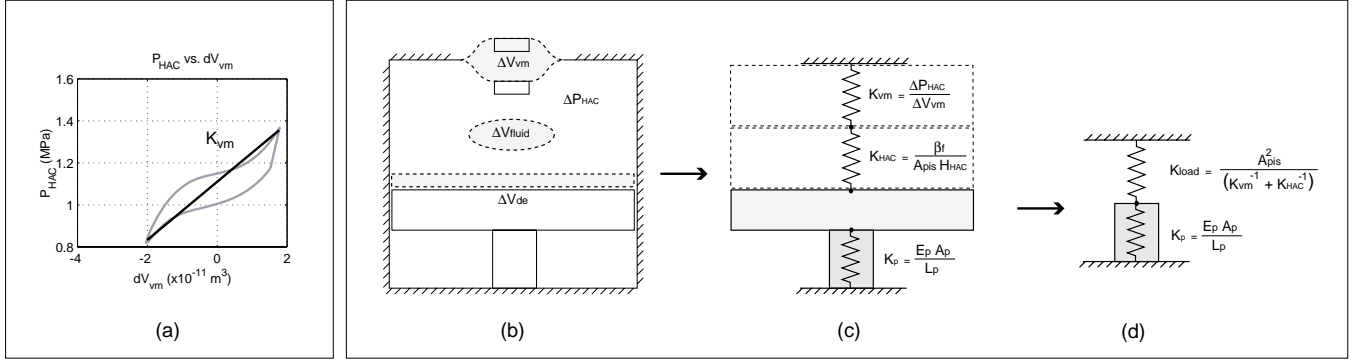


**Figure 10.** Simplification of active valve device to quasi-static stiffness match analogy: (a) determination of linearized  $K_{vm}$  stiffness load, (b) important actuation volume change and pressure variables, (c) valve membrane volumetric stiffness in series with fluid hydraulic stiffness acting through piston area against piezo displacement stiffness, and (d) lumped linear load spring acting against piezo material.

For the example MHT system, the piezoelectric material thickness is assumed to be  $L_p = 1mm$  and the applied peak-peak voltage is assumed to be  $V_p = 1000V$ . Under these assumptions, a drive piston area and piezo area are calculated to correspond to  $R_{pis} = 3.59mm$  and  $R_p = 0.88mm$ . Figures 11(a), (b), and (c) show the required piezoelectric voltage time history  $V_p$  to force the valve cap to follow the desired trajectory  $Z_{vc}(t)$ , the drive element  $P_{HAC}$  vs.  $dV_{de}$  actuation curve, and the resulting piezoelectric material stress time history  $T_p$ , respectively. In comparing Figure 11(b) to Figure 10(a), notice the increased volume change between  $dV_{de}$  and  $dV_{vm}$ . This difference is exactly equal to the fluid compressibility volume change  $dV_{HAC}$  under the pressure loading  $P_{HAC}(t)$ . At this point, a design for the active valve has been achieved. Simulations are now run with all structural and dynamic effects included to evaluate this valve design.

## 5. SIMULATION

The systematic design procedure presented in the previous section was based on quasi-static valve behavior. In reality dynamic effects, such as drive piston inertia and damping and valve cap inertia and damping, could have an effect on valve performance if the frequency of operation is close to valve structural resonances. This section presents a Simulink simulation architecture that includes these dynamic effects.

### 5.1. Simulink Implementation/Architecture

A complete simulation architecture is implemented that includes the active valve model (with dynamics) and the external hydraulic system model. Figure 12 illustrates the active valve portion of this complete system. Although not

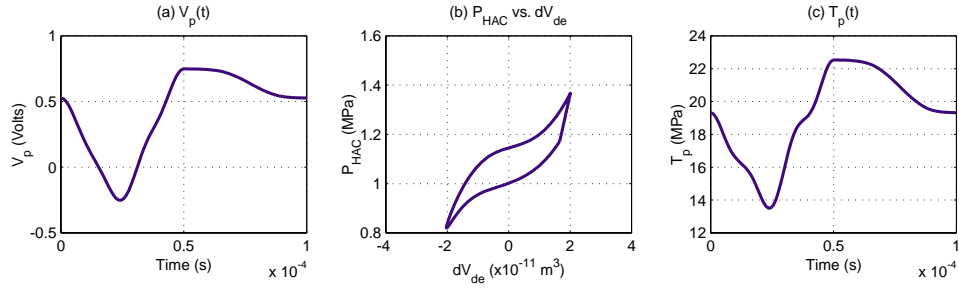


**Figure 11.** Drive element behavior corresponding to  $R_{pis} = 3.59mm$  and  $R_p = 0.88mm$ : (a) required piezoelectric voltage  $V_p(t)$ , (b) corresponding drive element actuation curve, and (c) stress on piezoelectric material  $T_p(t)$ .

shown in this figure, the additional external hydraulic system architecture (including the effects of the fluid orifice pressure-flow relations, the valve channel inertia, and the chamber stiffness) is coupled to this active valve system to simulate full filling and evacuation.

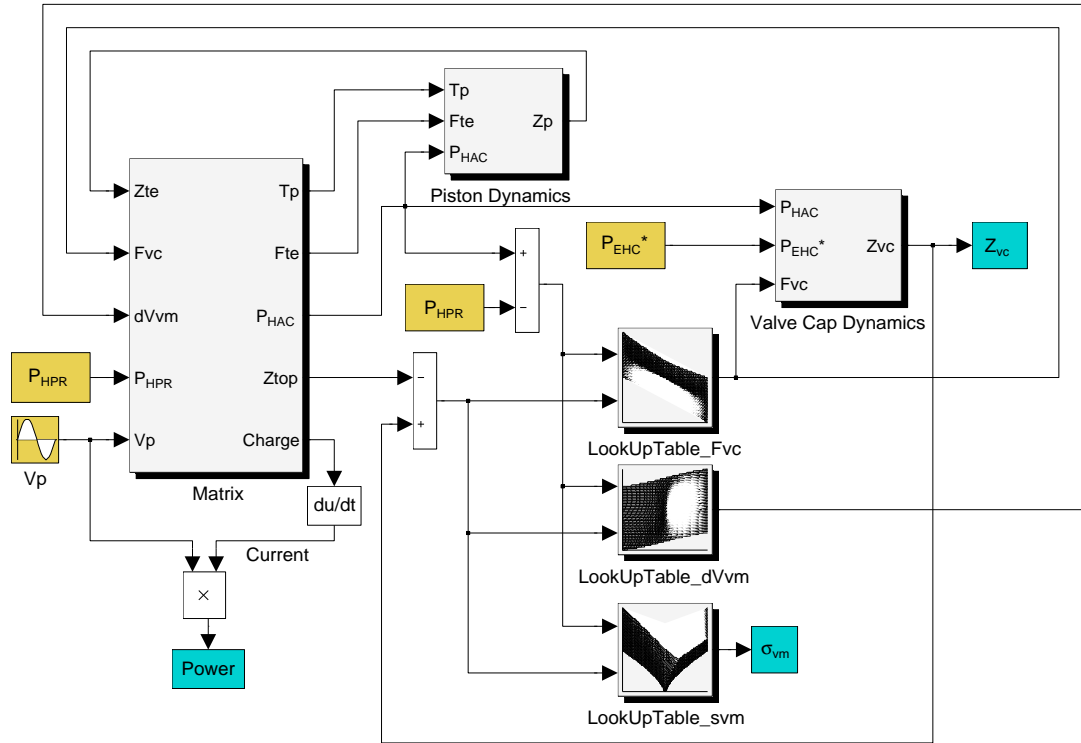


**Figure 12.** Complete Simulink system architecture, showing linear equation matrix, non-linear look-up tables, valve cap dynamics block, and drive element piston dynamics block. Simulation parameters included in the figure correspond to those in Figure 3(c). Note that  $P_1 = P_{EHC}^*$  and  $P_2 = P_{HPR}$ .

The active valve simulation architecture in Figure 12 can be broken down into four major subsystems: a matrix of linear coefficients describing active valve behavior, non-linear look-up tables that capture the large-deflection valve membrane deformation, a valve cap dynamics block, and a drive piston dynamics block.



### 5.1.1. Linear Matrix Relations

As discussed in Section 3.1, all of the structural elements except the valve membrane operate in linear deformation regimes. Within the simulation, therefore, a matrix of compliance and parameter coefficients are included for these linear relations:

$$\begin{bmatrix} T_p \\ F_{te} \\ P_{HAC} \\ Z_{top} \\ Charge \end{bmatrix} = \begin{bmatrix} A_{1,1} & A_{1,2} & A_{1,3} & A_{1,4} & A_{1,5} \\ A_{2,1} & A_{2,2} & A_{2,3} & A_{2,4} & A_{2,5} \\ A_{3,1} & A_{3,2} & A_{3,3} & A_{3,4} & A_{3,5} \\ A_{4,1} & A_{4,2} & A_{4,3} & A_{4,4} & A_{4,5} \\ A_{5,1} & A_{5,2} & A_{5,3} & A_{5,4} & A_{5,5} \end{bmatrix} \begin{bmatrix} Z_{te} \\ F_{vc} \\ dV_{vm} \\ P_{HPR} \\ V_p \end{bmatrix} \quad (20)$$

Inputs to this matrix are the  $Z_p$  and  $Z_{vc}$  variables fed back from the piston and valve cap dynamic blocks respectively,  $dV_{vm}$  fed back from the non-linear valve membrane look-up table, and the active valve loadings  $V_p$  and  $P_{HPR}$ . Outputs of this matrix are  $T_p$ ,  $F_{te}$ ,  $P_{HAC}$ , and  $Z_{top}$ . These outputs are fed to the other subsystems within the active valve model. These matrix coefficients are generated in an external Maple code and read into the Simulink model.

### 5.1.2. Non-Linear Look-Up Tables

As discussed in Section 3.1.5, numerical tools have been developed to calculate the non-linear large deflection behavior of the valve membrane. One possibility for capturing the non-linear behavior in the Simulink simulation would be to call the numerical code at each and every time step during a simulation run. However, the required computation for the simulation using this procedure is quite intensive. As a result, a method is implemented by which the numerical code is used to generate look-up tables for important non-linear behavioral variables, as shown in Figure 13. Taking as inputs the valve cap displacement  $Z_{vc}$  and the net pressure across the valve membrane  $P_{vm} = P_{HAC} - P_{HPR}$ , a lookup table is employed for each of the output variables  $F_{vc}$ ,  $dV_{vm}$ , and  $\sigma_{vm}$ . The size of the look-up tables is governed by the number of calculation points between the upper and lower limits of the inputs  $Z_{vc}$  and  $P_{vm}$ . For example, the look-up tables used in the simulations in this paper take as inputs a  $Z_{vc}$  vector 100 elements in length, covering a range from  $Z_{vc} = -50\mu m$  to  $Z_{vc} = +50\mu m$ , and a  $P_{vm}$  vector 100 elements in length, covering a range from  $P_{vm} = -1.5MPa$  to  $P_{vm} = +1.5MPa$ . Convergence studies were performed to validate that these vector resolutions were fine enough for accurate results.

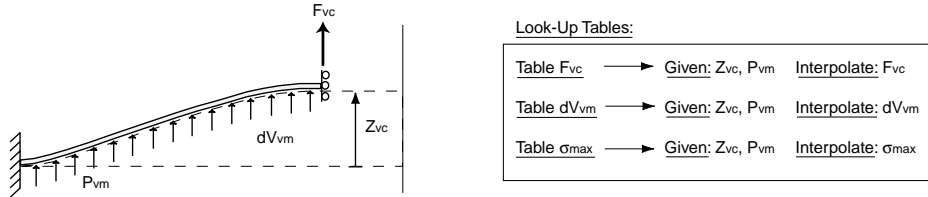


**Figure 13.** Numerical modeling tools are used to generate look-up tables for the non-linear large deflection behavior of the valve cap and membrane. Given a prescribed valve cap displacement  $Z_{vc}$  and pressure loading across the membrane  $P_{vm}$ , a look-up table for each of  $F_{vc}$ ,  $dV_{vm}$ , and  $\sigma_{vm}$  is created.

### 5.1.3. Piston and Valve Cap Dynamics

The dynamic behavior of the drive piston structure is governed by Eq 4. The damping coefficient  $C_{pis}$  is a lumped parameter that is meant to include the effects of structural damping in the tethers and damping due to fluid interaction. In a similar fashion, the dynamic behavior of the valve cap is represented by Eq 12. The damping coefficient  $C_{vc}$  is a lumped parameter that includes effects of structural damping in the membrane, squeeze film damping due to valve cap motion when closing the valve, and damping due to fluid interaction. Exact values of  $C_{pis}$  and  $C_{vc}$  are not known. Values are therefore chosen that result in dynamic responses that are relatively free of high-order oscillations (see results in Figure 14), yet still exhibit inertia and phase lag effects. Estimations for the damping ratios of the piston and valve cap ( $\zeta_{pis}$  and  $\zeta_{vc}$ ) are calculated from these  $C_{pis}$  and  $C_{vc}$  values by observing the resonant frequency  $\omega_n$  of each component in small deflection linear regimes, according to the relations  $\zeta_{pis} = \frac{C_{pis}}{2\omega_{pis}}$  and  $\zeta_{vc} = \frac{C_{vc}}{2\omega_{vc}}$  respectively.

The Simulink block which captures this valve cap dynamic behavior also includes the effect of the valve cap as it comes into contact with the valve stop. This hitting behavior is modeled as an inelastic collision between the cap and the stop. The assumption here is that if the cap impacts the stop with a velocity  $V_1$ , it will bounce back with a lesser velocity  $V_2$ , according to the relation  $V_2 = \sqrt{r}V_1$ , where  $r < 1$  is called the coefficient of restitution. The above formulation for the hitting can be implemented in Simulink by setting  $V_2$  as the initial condition for the valve velocity at the subsequent time step immediately following impact.

## 5.2. Simulation Results

As mentioned in the previous section, the additional external hydraulic system flow behavior (including the effects of the fluid orifice pressure-flow relations, the valve channel inertia, and the chamber stiffness) is coupled to the active valve system shown in Figure 12 to simulate full filling and evacuation. In fact, to evaluate the goodness of the active valve geometry created in the systematic design procedure from Section 4, a complete MHT system with both inlet and outlet active valves and harvesting chamber and fluid channel structures is implemented. In order to provide a reasonable framework for comparison for the inlet valve behavior, the outlet valve is sized and operated to properly evacuate the harvesting chamber to the desired  $P_{min} = 0.2 \text{ MPa}$  prior to inlet valve opening. Using this procedure, a comparison between the system performance requirements set forth in Section 4.2 and the actual dynamic system behavior with the determined valve geometry can be performed.

The active valve geometry created during the systematic design procedure of Section 4 is implemented in this full dynamic system simulation to evaluate whether it can in fact achieve the system performance requirements set forth in Section 4.2, namely an adequate  $P_{EHC}(t)$  pressure rise from  $0.2 \text{ MPa}$  to  $1.0 \text{ MPa}$  during operation. In addition, critical valve variables, such as  $\sigma_{vm}(t)$ ,  $Z_{vc}(t)$ , and  $P_{HAC}(t)$  are monitored. In this simulation, a positive valve stop at a location of  $Z_{vc} = 20 \mu\text{m}$  is implemented. The results of this simulation for two different values of valve cap damping are shown in Figure 14.

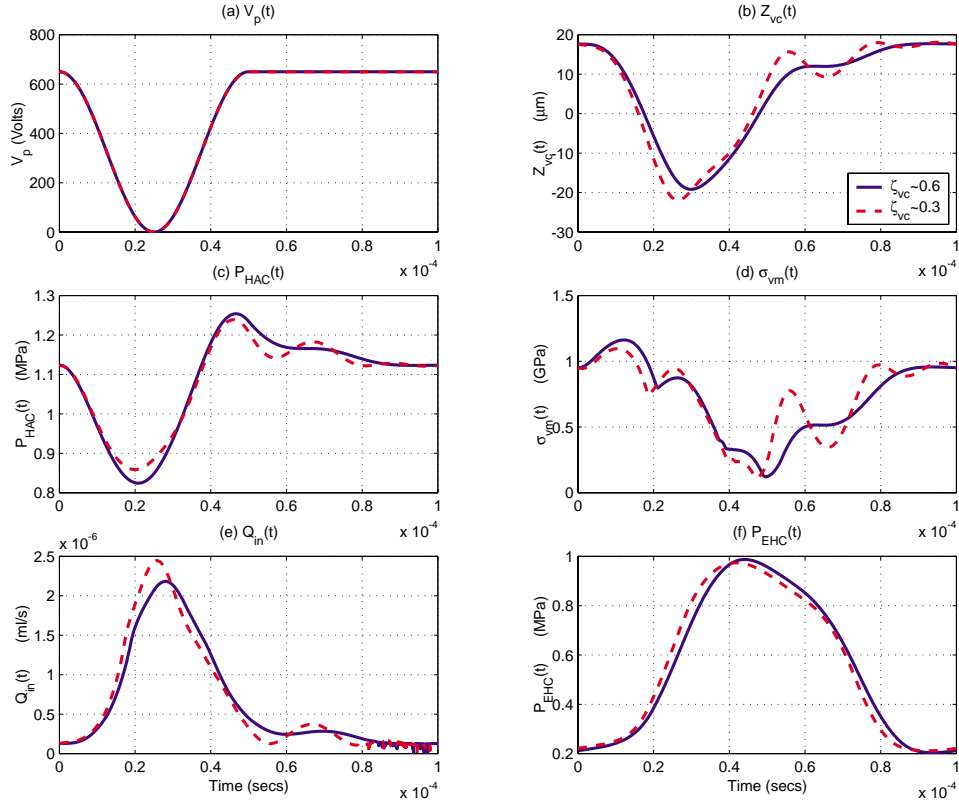


**Figure 14.** Full system simulations: (a) solid line represents case in which  $\zeta_{pis} = 0.7$ ,  $\zeta_{vc} = 0.6$ , (b) dashed line represents case in which  $\zeta_{pis} = 0.7$ ,  $\zeta_{vc} = 0.3$ . Note that in these cases, the valve cap does not hit the stop.

Due to dynamic effects in the active valve system, an applied peak-peak voltage of only 650V (compared to the quasi-static prediction of 1000V) is required to actuate the valve and produce the proper filling behavior of the harvesting chamber. Notice that the valve cap  $Z_{vc}(t)$ , HAC pressure  $P_{HAC}(t)$ , inlet flow rate  $Q_{in}(t)$ , and resulting harvesting chamber pressure  $P_{EHC}(t)$  time histories all correlate very closely to those predicted by the systematic quasi-static design procedure. One interesting note is that the valve membrane stress  $\sigma_{vm}$  time history differs slightly from the quasi-static prediction in the region when the valve cap is just beginning to open. Rather than immediately decreasing, as is predicted in the quasi-static procedure,  $\sigma_{vm}$  actually begins to increase to a peak value of  $1.15GPa$  (for  $\zeta_{vc} = 0.6$ ) and to a peak value of  $1.05GPa$  (for  $\zeta_{vc} = 0.3$ ) just after opening. This phenomenon is due to the dynamic effects on the valve membrane. Essentially, the  $P_{HAC}$  pressure below the membrane decreases substantially before the valve cap is able to move downward (due to the cap's inertia and the effect of damping), resulting in an enhanced membrane curvature at  $R_{vc}$  and therefore an increase in  $\sigma_{vm}$ . These important observations on the membrane stress can be fed back to the quasi-static design procedure. Using a smaller value of limiting stress  $\sigma_{limit}$ , a slightly modified valve geometry can be generated so that dynamic membrane stresses do not exceed the desired bound.

## 6. CLOSURE

This paper has introduced design, modeling, and simulation tools that can be implemented to develop a piezoelectrically-driven hydraulically-amplified valve geometry for use in high pressure, high frequency hydraulic system applications. A systematic design procedure, based on quasi-static valve behavior (ie: no valve cap or piston dynamics), has been presented that allows the designer to generate a geometric valve design and understand the basic governing behavior. With these valve geometric dimensions, a full dynamic valve and system simulation is carried out that includes valve cap and piston dynamics. The effects of valve cap and piston inertia and damping on important system parameters, such as valve membrane stress, are evaluated. The quasi-static design procedure has been verified with dynamic simulations for the range of operating frequencies 10 – 20kHz. Future experimental work will be carried out on micro-fabricated active valves to obtain a more accurate understanding of damping effects in this system.

## ACKNOWLEDGMENTS

This research was sponsored by DARPA Grant #DAAG55-98-0361 and by ONR Grant #N00014-97-1-0880.

## REFERENCES

1. N.W. Hagood, D.C. Roberts, L. Saggere, K.S. Breuer, K-S. Chen, J.A. Carretero, H.Q. Li, R. Mlcak, S. Pulitzer, M.A. Schmidt, S.M. Spearing, and Y-H. Su, "Micro Hydraulic Transducer Technology for Actuation and Power Generation", Proceedings of SPIE, Vol. 3985 (2000), Newport Beach, CA, March 5-9, 2000, pp.680-688.
2. D.C. Roberts, N.W. Hagood, Y-H. Su, H.Q. Li, and J.A. Carretero, "Design of a Piezoelectrically-Driven Hydraulic Amplification Microvalve for High Pressure, High Frequency Applications," Proceedings of SPIE, Vol. 3985 (2000), Newport Beach, CA, March 5-9, 2000, pp.616-628.
3. S. Timoshenko, *Theory of Plates and Shells*, p. 329, McGraw-Hill, New York, 1940.
4. Y-H. Su, K-S. Chen, D.C. Roberts, and S.M. Spearing, "Large Deflection Analysis of a Prestressed Annular Plate with a Rigid Boss under Axisymmetric Loading," Submitted to *Journal of Micromechanics and Micro-engineering*.
5. J. Carretero and K.S. Breuer, "Measurement and Modeling of the Flow Characteristics of Micro Disk Valves," Proceedings of the 1994 International Mechanical Engineering Conference and Exposition: Microfluidics Symposium, Orlando, FL, Nov. 2000.
6. E. Schrenk, "Disc valves, flow patterns, resistance and loading," BHRA T, 1957 (547). Translation from German.
7. A. Lichtarowicz, "Flow and Force Characteristics of Flapper Valves," Third International Symposium on Fluid Power, Turin, 1973, pp. B1-1.
8. D.N. Johnston, K.A. Edge, and N.D. Vaughan, "Experimental investigation of flow and force characteristics of hydraulic poppet and disc valves," Proceedings of the Institution of Mechanical Engineers, Part A: Power & Process Engineering, 1991 Vol 205, No 3, pp. 161-171.
9. S.M. Spearing and K.S. Chen, "Micro-gas turbine engine materials and structures," *Ceramic Engineering & Science Proceedings v.18n 4B*, p. 11-18, 1997.

# A High-Frequency, High-Stiffness Piezoelectric Micro-Actuator For Hydraulic Applications

David C. Roberts\*, J. Lodewyk Steyn\*, Hanqing Li\*, Kevin T. Turner\*, Richard Mlcak\*\*, Laxman Saggere\*, S. Mark Spearing\*, Martin A. Schmidt\*, and Nesbitt W. Hagood\*

\*Massachusetts Institute of Technology, Cambridge, MA 02139 USA

\*\*Boston MicroSystems, Inc., Woburn, MA 01801 USA

## SUMMARY

A piezoelectric micro-actuator capable of high stiffness actuation in micro-hydraulic systems was fabricated and experimentally tested to frequencies in excess of 100 kHz. The actuator was fabricated from a bonded stack of micromachined silicon-on-insulator (SOI) and borosilicate glass layers. Actuation was provided by 1mm sized piezoelectric cylinders, which were integrated within a tethered piston structure and electrically and mechanically attached using a thin-film AuSn eutectic bond. Die-level anodic bonding techniques were developed to assemble the supporting structural silicon and glass layers. The microfabrication, device assembly, experimental testing procedures, and actuator performance are discussed in this paper. Issues such as piezoelectric material preparation, requisite dimensional tolerancing, micromachining of the silicon tethered structures, and integration of multiple piezoelectric elements within the micro-actuator structure are detailed.

**Keywords:** actuator, piezoelectric, micromachined

## INTRODUCTION

In order to realize high specific power transducers, a novel approach integrating micro-hydraulics, piezoelectric materials and micromachining technology is being developed [1,2,3]. These micro-hydraulic transducers (MHT) rely on a high frequency fluid pumping mechanism and equally fast actively controlled valves to achieve high system flow rates (~1ml/s) against large differential pressures (~1-2MPa). The pumping and valving functions in MHT systems require a positive-displacement micro-actuator structure that can produce fluid volume oscillations at high frequency (10-20 kHz) and exhibit high structural stiffness so as to minimize compliance against the large differential system pressures. The actuator is required to be compact, low mass, and amenable to integration with other micromachined components of the hydraulic system. Motivated by the need for such an actuator for use in MHT technology, and potentially, other similar

microhydraulics applications, a novel piezoelectrically driven micro-actuator has been developed and tested. The paper highlights the development of this actuator.

Conceptually, the proposed micro-actuator incorporates a circular piston structure supported from beneath by one or more small bulk piezoelectric cylinders and suspended circumferentially from a surrounding support structure by thin annular micromachined tethers. This unique design provides the actuator not only the desired performance characteristics, but also enables higher specific actuation authority (force per unit mass) than a similar class of piezoelectrically-driven micro-actuators using tall stacks of piezoelectric layers or thick piezoelectric films previously reported [4,5]. In addition, the integration of high performance single-crystal PZN-PT piezoelectric material over standard polycrystalline PZT-5H piezoelectric material allows for enhanced actuation capabilities [6].

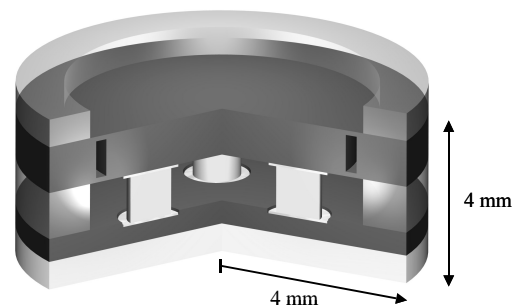


**Figure 1: Schematic of a micro-actuator device, with three piezoelectric material cylinders beneath a double layer micromachined piston and tether structure.**

Development of the actuator reported in this paper involved overcoming several technical challenges including (1) reliable bonding of bulk piezoelectric material to silicon using a thin-film AuSn eutectic bond, (2) tight control tolerances of piezoelectric cylinder lengths and surface roughness, and (3) controlled Si etching of the thin tether structures. The following sections present the details of design, microfabrication, and assembly of the actuator, and experimental validation of the actuator performance.

## DEVICE DESIGN

The micro-actuator device is illustrated in Figures 1 and 3. It consists of one or more piezoelectric cylinders sandwiched between a rigid bottom silicon layer and a top micromachined silicon piston/tether structure. Each of the piezoelectric cylinders has a thickness of 1mm and a diameter of 1mm. The top and bottom surfaces of each piezoelectric element are coated with a eutectic bond layer consisting of 50nm Ti, 250nm Pt, 4000nm AuSn alloy, and 20nm Au. The Ti serves as an adhesion layer to the piezoelectric material, the Pt serves as a diffusion barrier, and the Au serves as a capping layer to ensure no oxidation of the Sn. The bottom silicon layer incorporates an etch seat for each of the piezoelectric elements, to allow for tolerancing of the elements with respect to the surrounding glass layer. The tethered piston (diameter=6.2mm) is created by wafer fusion bonding two micromachined SOI layers together. In response to a sinusoidal voltage, the piezoelectric material expands and contracts, thereby actuating the piston against an external load. In a typical MHT system that incorporates this actuator element, hydraulic fluid above the piston and tether would be pressurized and depressurized, for the purpose of either pumping fluid [1,3] or actuating a valve head [2].

## DEVICE FABRICATION

**Piezoelectric Material** Virgin piezoelectric materials, both PZT-5H and PZN-PT, are obtained in plate form and subsequently double-side polished to a thickness of  $1\text{mm} \pm 10\mu\text{m}$ . The surface roughness after polishing is  $0.5\mu\text{m}$ . This ensures adequate roughness for adhesion of the eutectic film, yet sufficient smoothness for surface contact between the piezoelectric and Si surfaces during bonding. The Ti-Pt-AuSn-Au multi-layer film (as described in the previous section) is sputter-deposited onto both sides of the substrate plate. From this plate, 1mm diameter cylinders are core-drilled, cleaned, and measured.

**Piston and Tether Structure** The piston/tether structure is created by Deep Reactive Ion Etching (DRIE) of a SOI wafer. The tether thickness ( $\sim 10\mu\text{m}$ ) is defined by the SOI device layer, and the buried oxide acts as the etch stop. Control of the fillet radii at the base of the etch trench is critical for the minimization of stress concentrations and is accomplished with a carefully timed deep etch. Double layer drive pistons are desired to minimize piston bending during actuation. This is accomplished by individually etching two SOI wafers, each  $400\mu\text{m}$  thick, and then fusion bonding them together. Vent channels are included within the piston

structure to prevent pressurization between the tethers during wafer annealing (see Figure 2).

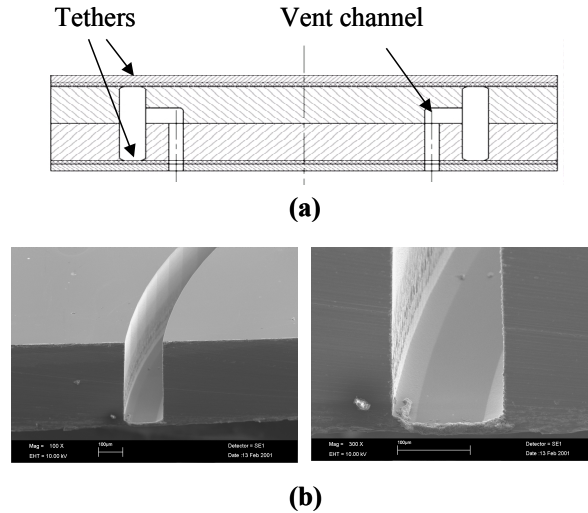


**Figure 2: Micromachined tethered piston structure: (a) cross section schematic view of a double-layer piston and (b) Scanning Electron Micrograph of cross-sectioned single layer piston wafer. Note fillet radius features at base of tether.**

**Glass Layers** All glass layers are Pyrex 7740 and are patterned by conventional diamond core drilling. The middle glass layer is measured for tolerancing purposes when integrating the piezoelectric elements.

**Piezoelectric Cylinder Etch Seats** The bottom silicon layer is  $400\mu\text{m}$  thick and contains etched cavity seats for placement of the piezoelectric cylinders. The depth of these seats is determined by the thickness mismatch between the middle glass layer and the piezoelectric cylinders. It is desired to size the cylinders slightly larger ( $\sim 1\text{--}2\mu\text{m}$ ) than the glass and seat depth so as to create a preload during assembly, thereby ensuring that the eutectic bond remains in compression. Reactive Ion Etching (RIE) was used to etch the cavities down to the required depth. The top surface of the etch seats and the bottom surface of the piston are coated with 50nm Ti, 250nm Pt, and 50nm Au to facilitate adhesion of the eutectic bond layer. This film is deposited by electron beam evaporation, on the die level, through a shadow mask. After this deposition step, the subcomponents are ready for assembly.

## DEVICE ASSEMBLY

As illustrated in Figure 3, the final assembly of the device requires multiple layers to be bonded. First, die level anodic bonds between the top and bottom silicon layers and the glass packaging layers (not shown in

Figure 3) are completed at a temperature of 300°C and an applied potential of 1000V. The middle glass layer, bottom silicon layer and piezoelectric cylinders are selected to provide the proper preload on the piston and piezoelectric element. A die level anodic bond between the bottom silicon layer and middle glass layer is then carried out under the conditions identified previously. The piezoelectric cylinders are inserted in the center cavity and aligned within the etched seats in the bottom silicon layer. The top silicon layer, which contains the tethered piston structure, is aligned and clamped to the lower structure. The clamped structure is heated to 300°C and a voltage of 1000 V is applied to form an anodic bond between the top silicon layer and the middle glass layer.

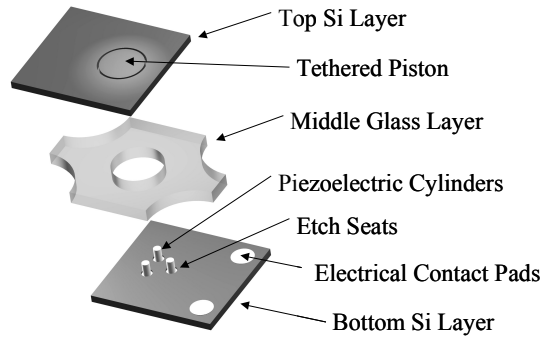
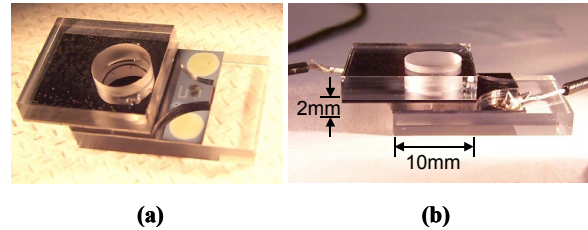


**Figure 3: Exploded view of primary layers in single-layer piston micro-actuator structure (top and bottom support glass layers not shown).**

The 300°C temperature allows the AuSn eutectic alloy to melt. The alloy flows and wets the Ti-Pt-Au film on the top and bottom silicon layers. The 4μm thick eutectic film is sized to be sufficiently thick to compensate for the dimensional tolerance ( $\pm 1\mu\text{m}$ ) of the piezoelectric elements. Upon cooling, the AuSn alloy solidifies and bonds the piezoelectric cylinders to the silicon layers in the device. Following the final bonding step, lead wires, which provide electrical connection to the piezoelectric element, are soldered to gold contact pads on the upper and lower silicon layers. Poling of the piezoelectric material within the device is performed following the assembly procedure. This is accomplished by heating the device to approximately half the Curie temperature and applying an electric field equal to twice that of the coercive field of the piezoelectric material, which in the case of PZT-5H are 90°C and 1100V, respectively.

## TESTING AND RESULTS

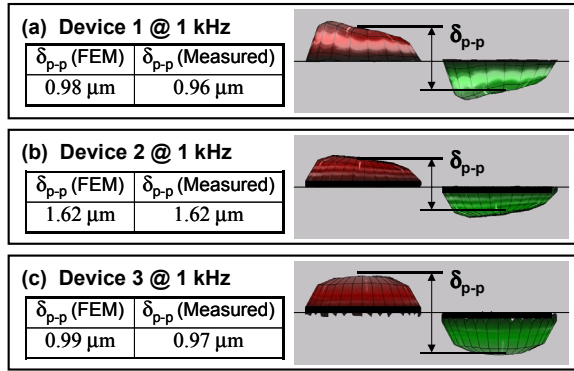
Three distinct micro-actuator devices have been fabricated and tested. The first and second devices incorporate a centrally-located PZT-5H cylinder and PZN-PT cylinder, respectively, beneath a single layer piston. The third device incorporates three PZT-5H cylinders evenly spaced beneath a single layer piston. Work on integrating three PZN-PT cylinders in conjunction with double layer pistons is currently in progress. Device 1 is shown in Figure 4.



**Figure 4: Close-up photographs of Device 1: (a) w/o electrical leads, (b) with electrical leads.**

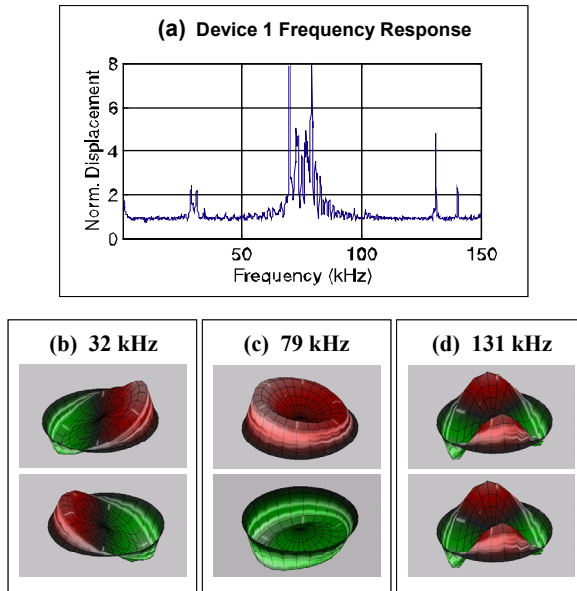
Each of the fabricated devices was tested using a scanning laser vibrometer system. To determine quasi-static performance, a sinusoidal voltage of  $500\text{V} \pm 500\text{V}$  was applied at a frequency of 1 kHz. The piston center point peak-peak displacement  $\delta_{p-p}$  was recorded to evaluate the voltage-displacement response of the device. To observe higher-order dynamic modal behavior, a reduced sinusoidal voltage was applied over a range from 1 kHz to 500 kHz and mode shape frequencies were recorded. For both the quasi-static and modal experiments, recorded data was compared to results from finite-elements models.

Figure 5 displays the quasi-static deformation of each of the three devices at 1 kHz and a comparison of expected  $\delta_{p-p}$  to experimentally measured  $\delta_{p-p}$ . Ideally, a perfect micro-actuator device would exhibit flat piston motion as it transverses a complete cycle of deflection. As can be seen in Figure 5a and Figure 5b, the piston for each of the single piezoelectric cylinder devices tilts as it cycles, due to imperfect placement of the cylinder beneath the piston. Non-uniform fillet radii or membrane tether thickness around the piston could also contribute to this behavior, however, for these two devices, careful measurement and evaluation of the membrane structures prior to device assembly revealed very uniform etch profiles. Figure 5c illustrates the piston deformation for Device 3. As compared to the single cylinder devices, incorporation of three PZT-5H cylinders beneath the piston enables closer to ideal flat piston actuation throughout a cycle. The measured deflections of all three devices correlate well with those predicted by finite-element analyses.



**Figure 5: Quasi-static side-view deformations at 1 kHz: (a) Device 1, (b) Device 2, and (c) Device 3. Devices 1 and 2 exhibit tilted piston behavior whereas Device 3 operates with a more uniform flat profile.**

Dynamic modal behavior of these devices can provide important insight into how well a given device has been fabricated. The frequency response and selected mode shapes for Device 1 are shown in Figure 6 as an example. The first mode shape at 32 kHz (see Figure 6b) is characterized by uneven tilting of the piston. Finite-element models predict this first mode to occur at 50 kHz. The discrepancy is most likely due to an un-centered piezoelectric cylinder. Figures 6c and 6d illustrate a plunge mode at 79 kHz and a higher order 2 $\Theta$  mode at 131 kHz. Predictions for these modes from finite-element models are 80 kHz and 125 kHz, respectively. For Device 3, modal behavior is not



**Figure 6: Device 1 modal behavior: (a) selected frequency response between 1kHz and 150kHz, (b) mode shape at 32kHz, (c) mode shape at 79kHz, and (d) mode shape at 131kHz.**

observed until frequencies in excess of 70 kHz, due to the additional stiffening effects provided by multiple piezoelectric cylinders beneath the actuator piston.

## CLOSURE

A novel piezoelectric micro-actuator device for use in high frequency fluidic pumping applications has been developed. Small bulk piezoelectric material cylinders were integrated within a microfabricated tethered piston structure using a AuSn eutectic bond to provide high stiffness actuation. A series of micro-actuator devices has been fabricated and experimentally tested. Benefits of incorporating high performance PZN-PT material rather than standard PZT-5H piezoelectric material and the incorporation of multiple piezoelectric cylinders beneath the actuator piston rather than a single centrally-located cylinder have been demonstrated. Development of actuators incorporating multiple piezoelectric cylinders beneath double layer piston structures to further improve actuator performance is underway.

## ACKNOWLEDGEMENTS

This research was sponsored by DARPA under Grant #DAAG55-98-0361 and by ONR under Grant #N00014-97-1-0880.

## REFERENCES

- [1] N.W. Hagood, et. al., "Development of Micro-Hydraulic Transducer Technology," *Proc. of 10<sup>th</sup> Int. Conf. On Adaptive Structures and Technologies*, Oct. 11-13, 1999, Paris, France, pp. 71-81.
- [2] D.C. Roberts, et. al., "Modeling, Design, and Simulation of a Piezoelectrically-Driven Microvalve for High Pressure, High Frequency Applications," *Proc. of SPIE*, Vol. 4327, Newport Beach, CA, March 4-8, 2001.
- [3] H.Q. Li, et. al., "A High Frequency High Flow Rate Piezoelectrically Driven MEMS Micropump," *Proc. Of Solid State Sensor and Actuator Workshop*, June 4-8, 2000, Hilton Head, SC, pp.69-72.
- [4] M. Esashi, S. Shoji, and A. Nakano, "Normally Closed Microvalve and Micropump Fabricated on a Silicon Wafer," *Sensors and Actuators*, 20, 1989, pp.163-169.
- [5] M. Koch, et al. "Novel Micropump Design with Thick-Film Piezoelectric Actuation," *Measurement Science and Technology*, v8 n1 Jan 1997, p.49-57.
- [6] S-E. Park and T.R. Shrout, "Characteristics of Relaxor-Based Piezoelectric Single Crystals for Ultrasonic Transducers," *IEEE Trans. Ultrasonics, Ferroelectrics, and Frequency Control*, 44, 1997, pp.1140-1147.



# Measurement and Modeling of the Flow Characteristics of Micro Disc Valves

by

Jorge Alejandro Carretero Benignos

B.S. Mechanical Engineering

Universidad de las Americas- Puebla, 1996

Submitted to the Department of Aeronautics and Astronautics  
in partial fulfillment of the requirements for the degree of

Master of Science in Aeronautics and Astronautics

at the

MASSACHUSETTS INSTITUTE OF TECHNOLOGY

February 2001

©Jorge Alejandro Carretero Benignos, ASME International, MMI.

All rights reserved.

The author hereby grants to MIT permission to reproduce and to  
distribute publicly paper and electronic copies of this thesis document  
in whole or in part.

Author .....  
Department of Aeronautics and Astronautics  
Jan 19, 2001

Certified by .....  
Kenneth S. Breuer  
Visiting Associate Professor of Aeronautics and Astronautics, MIT  
Associate Professor Division of Engineering Brown University  
Providence, RI  
Thesis Supervisor

Accepted by .....  
Wallace E. Vander Velde  
Chairman, Department Committee on Graduate Students



# Measurement and Modeling of the Flow Characteristics of Micro Disc Valves

by

Jorge Alejandro Carretero Benignos

Submitted to the Department of Aeronautics and Astronautics  
on Jan 19, 2001, in partial fulfillment of the  
requirements for the degree of  
Master of Science in Aeronautics and Astronautics

## Abstract

The head losses in microfluidic systems such as micropumps are dominated by losses in microvalves, where microfabrication constraints limit significantly possible microvalve designs. This makes them quite different from conventional valves. In particular, flow characteristics in the laminar and low-Reynolds turbulent regimes are not understood clearly, and detailed information about the flow losses is lacking. This work addresses this issue by using a scaled-up (10:1) valve experiment to measure pressure losses in typical microfabricated valve geometries. The macroscale model is fully instrumented and discharge coefficients and sensitivities to stroke, seat width and Reynolds number are presented.

Thesis Supervisor: Kenneth S. Breuer

Title: Visiting Associate Professor of Aeronautics and Astronautics, MIT

Associate Professor Division of Engineering Brown University Providence, RI

# Acknowledgments

Two roads diverged in a yellow wood... and I, I took the one less traveled by, and that has made all the difference. I have come to understand that in many cases life presents many possible paths for us and that none of them is better than the others, they are only different. The paths I've taken I took because I wanted, it has been my choice and I have no regrets.

My time at MIT has been both the best and the worst. I have met wonderful people and learned a lot from them. I have also gone through very hard times and it has been during those times that I feel that I have matured the most. The path hasn't been easy, but the help of my friends has made it a lot easier. I dedicate this thesis to my family, friends and all the people who have been there when I needed them the most.

First of all I would like to thank my advisor Prof. Kenny Breuer. I thank him for trusting me with this project, for his unending support and infinite patience. Kenny believed and supported me in those times when everything was falling apart. I greatly appreciate his technical expertise, his attention to detail and quality in research and above all his support. Kenny has been not only my advisor but a good friend. Thanks Kenny I am very grateful for all you've done for me. I would also like to thank Professors Mark Spearing, Nesbitt Hagood and Marty Schmidt for their continued support and guidance throughout this time.

The MHT guys, what a group! It has been amazing to work with such a wonderful and diverse group of people. Dave, Rick, Farid, Hanqing, Kuo-Shen, Su, Laxman, Lodewyk, Onnik and Kevin. Guys it has been a pleasure to work with you and one of the best experiences I've had.

Special thanks are due to Dave Robertson and Fred Cote for all their help setting up the experiments. I should also thank James Lu, Todd Oliver and Daniel Sandoval for their hard work and patience.

I would also like to thank my friends at the different aero/astro labs: FDRL (the only lab staffed 24 hours a day), AMSL, Man-vehicle, SSL and the whole aero gang.

The mexican guys, all my friends who have had the patience to hang out with me. We have shared beers, late night movies and coffees they have made my time at MIT both enjoyable and unforgettable. Special thanks to the core group : Ante, Rodrigoq, Raymundo, Mescobar, AB, Juliocc, Joseicv, Kate, Jordi, Dara, Magdalena, Mhurtado, Belen, Anap and Mhadis. You guys have made me feel at home away from home. Thanks guys and I wish everyone the best of the best.

Finally, thinking about home... my friends at home. First of all Edgar, thanks for your support throughout this time. Those late night email sessions we had really made a difference. Thanks for all your help. Special thanks are in order for Diana, Yuria, Gabriel, Samuel, Ramon (aka Livingston), Caro, Karla, Pliego and my aunt Beatriz. Les doy las gracias, sepan que los aprecio y que siempre los he extranado. Estaremos lejos fisicamente, pero siempre han estado cerca de mi pensamiento.

Casi para terminar, queda el espacio para aquellas ninas que he querido. Como se dijo por ahi... hay anecdotas que contare, y otras que no... estas mejor las dejaremos asi. A ellas tengo mucho que agradecerles aun cuando las cosas no hayan funcionado. A mi asesorada estrella, siento que no hayamos coincidido, pero te agradezco el que me hayas hecho pensar sobre muchas cosas y ello ha tenido un profundo impacto en mi vida. A su tocaya, solo me queda decirle que aunque las cosas no salieron siempre tendra un lugar muy especial en mi corazon y le deseo la mejor de las suertes en su vida.

Finally, my family. My mom, dad, and brother. I have missed you these years so much and I cherish every moment I have been able to share with you. Ustedes han sido mi inspiracion para seguir adelante y una fuente inagotable de amor. Si he llegado hasta aca ha sido por ustedes. Gracias de todo corazon. Muy especialmente dedico esta tesis a mis abuelos Herman, Olga Alicia, Alfonso y Evita.

This research would not have been possible without the generous of DARPA under grant # *DAAG55-98-1-0361* and ONR under Grant # *N00014-97-1-0880*. I would like to acknowledge CONACYT for supporting me throughout my first year at MIT.

$C_m$	Modified discharge coefficient
$C_q$	Discharge coefficient
$d_0$	Inlet diameter
$d_{sys}$	Characteristic length
$d_v$	Valve cap diameter
$f$	Driving frequency
$h^*$	$h_v/h_p$
$h_p$	Plate separation
$h_v$	Valve opening
$k$	Isothermal bulk modulus
$K$	Stiffness
$l_o$	Channel length
$M$	mass
$Q$	Volumetric flow rate
$Re$	Reynolds number
$s$	Seat width
$\bar{u}$	Local flow velocity
$A_o$	Throat flow area
$A_1$	Upstream flow area
$A_2$	Downstream flow area
$\Delta P$	Pressure drop
$\epsilon$	Loss coefficient correction factor
$\lambda$	Acoustic wavelength
$\mu$	Dynamic viscosity
$\nu$	Kinematic viscosity
$\rho$	Fluid density
$\sigma$	$h_v/s$
$\zeta_{quad}$	Turbulent loss coefficient
$\zeta_\phi$	Loss coefficient correction factor

$E$	Young's modulus
$I_A$	Moment of Inertia
$A_c$	Cross-sectional area
$l$	Generic length scale
$\omega_n$	circular natural frequency
$P$	Pressure
$C$	Capacitance
$\Delta V_f$	Fluid volume change
$\Delta V_s$	Structural volume change
$R$	Fluid Resistance
$\dot{\Phi}$	Heat transfer rate
$e$	Internal energy
$h$	Enthalpy
$D$	Channel Diameter
$n$	Scaling power
$\hat{n}$	Unit normal vector
$\dot{W}$	Work rate
$m$	Scaling power
$C_d$	Orifice discharge coefficient
$\beta$	Diameter ratio d/D
$d$	Orifice diameter
$A_r$	Orifice correction factor
$M_2$	Orifice correction factor
$C_\infty$	Ultimate Orifice discharge coefficient
$\Delta P_+$	Forward pressure drop
$\Delta P_-$	Backflow pressure drop
$Di$	Diodicity
$S$	Strouhal number

$Fr$	Froude number
$g$	gravity
$t$	orifice thickness
$I$	Lumped element Inductance $l/A$
$F$	Force
$\vec{v}$	Fluid velocity vector
$u$	x-direction absolute velocity
$u_r$	Normal exterior relative velocity to the control surface
$u_c$	Normal exterior fluid velocity in the $x$ -direction
$x_1$	Wafer thickness
$x_s$	Valve displacement
$a$	area
$\dot{V}_p$	Volume rate of change due to piston movement
$V_0$	Initial piston chamber volume
$d_h$	Hydraulic diameter

# Contents

<b>1</b>	<b>Introduction</b>	<b>15</b>
1.1	Overview of the Micro-Hydraulic Transducer . . . . .	15
1.2	Motivation . . . . .	16
1.3	Challenges . . . . .	17
1.4	Contributions . . . . .	17
<b>2</b>	<b>Literature Background</b>	<b>18</b>
2.1	MEMS Scaling Issues . . . . .	18
2.2	Microsystems Fluidic Modeling Strategies . . . . .	19
2.3	Micro Scale Valves . . . . .	21
2.3.1	Passive Microvalves . . . . .	21
2.3.2	Active microvalves . . . . .	24
2.4	Macro-scale Valves . . . . .	28
2.5	Summary . . . . .	30
<b>3</b>	<b>Modeling of Hydraulic Microsystems</b>	<b>31</b>
3.1	The MHT Hydraulic Model . . . . .	32
3.1.1	Valve Cap Force Calculation . . . . .	34
3.1.2	Capacitance modeling . . . . .	36
3.1.3	Inductance in fluid channels . . . . .	38
3.1.4	Resistive Elements . . . . .	39
3.2	SIMULINK Model Implementation . . . . .	43
3.3	Summary . . . . .	46



<b>4</b>	<b>Experimental Setup</b>	<b>47</b>
4.1	Experiment Design . . . . .	47
4.1.1	Scale Effects . . . . .	49
4.2	Macro-scale setup . . . . .	51
4.2.1	Fluid Delivery Section . . . . .	51
4.2.2	Test Section . . . . .	52
4.2.3	Valve Geometry . . . . .	54
4.2.4	Experimental Procedure . . . . .	55
4.2.5	Calibration Experiments . . . . .	55
4.3	Summary . . . . .	57
<b>5</b>	<b>Experimental Results and Correlations</b>	<b>58</b>
5.1	Experimental Results . . . . .	58
5.1.1	Valve Opening Dependence . . . . .	62
5.1.2	Valve Seat Width Dependence . . . . .	64
5.1.3	Comparison of Lumped Model to Data . . . . .	67
5.2	Modified model . . . . .	67
5.2.1	Detailed orifice model background . . . . .	67
5.2.2	Modified valve model . . . . .	70
5.3	Summary . . . . .	73
<b>6</b>	<b>Conclusions and Recommendations</b>	<b>74</b>
<b>A</b>	<b>Valve Plots and Summary of Model Equations</b>	<b>76</b>

# List of Figures

1-1	Conceptual Diagram of Bidirectional Microdevice . . . . .	16
2-1	Typical Architectures of Passive Microvalves [37] . . . . .	22
2-2	NMP Passive Microvalves, Olsson [22] and Forster[4] . . . . .	23
2-3	Thermopneumatic Active Microvalve [7] . . . . .	25
2-4	Electrostatically Actuated Microvalve [30] . . . . .	26
2-5	Electromagnetic Actuated microvalve [9] . . . . .	27
2-6	MHT Amplification Chamber,[27] . . . . .	28
3-1	Cross-sectional view of a multiple wafer energy harvester with active valves . . . . .	32
3-2	Schematic of the MHT hydraulic system . . . . .	32
3-3	Hydraulic Systems Control Volume Representation . . . . .	33
3-4	Schematic of the inlet valve section . . . . .	33
3-5	Valve Sections: Lumped Model Equivalents . . . . .	34
3-6	control volume for valve cap force calculation . . . . .	35
3-7	Energy Harvesting Chamber Representation . . . . .	37
3-8	Valve schematic for the order-of-magnitude model . . . . .	41
3-9	Order of magnitude valve model. Results are shown for different valve openings $h_v$ . . . . .	42
3-10	Comparison of component loss coefficients vs $Re_s$ . . . . .	43
3-11	Generic Architecture of Fluidic resistances in Simulink . . . . .	44
3-12	Simulink Representation of the Flow Rate Equation 3.20 . . . . .	45

3-13	Time histories of chamber pressure, inlet valve flow rate, outlet valve flow rate and valve openings for the resonance condition of an Energy Harvester,[36]. Continuous lines are for inlet parameters . . . . .	45
4-1	Schematic of the macro-scale test facility layout. . . . .	51
4-2	Test section detail of the macro scale test facility. . . . .	53
4-3	Valve geometry detail. . . . .	53
4-4	Test orifice for calibration . . . . .	56
4-5	Test orifice discharge coefficient vs Reynolds number. . . . .	57
5-1	Discharge Coefficient vs. Reynolds number for different percentages of valve opening ( $h^*$ ) for valve 1. The plate separation ( $h_p$ ) was $450\text{ }\mu\text{m}$	59
5-2	Transition Reynolds number vs valve opening ratio, $h^*$ . . . . .	61
5-3	Discharge coefficient ( $C_q$ ) for valve #1 vs modified Reynolds number ( $Re_m$ ) . . . . .	61
5-4	Discharge coefficient ( $C_q$ ) vs. non-dimensional valve opening ( $h^*$ ) for the three valves; plate separation ( $h_p$ ) $450\text{ }\mu\text{m}$ . . . . .	62
5-5	Modified discharge coefficient ( $C_m$ ) vs. Reynolds number for valve #1 and plate separation $h_p = 450\mu\text{m}$ . . . . .	63
5-6	Discharge coefficient vs. non-dimensional seat width ( $\sigma$ ). The plate separation was $h_p=450\text{ }\mu\text{m}$ . . . . .	64
5-7	Seat width effect on discharge coefficient from Johnston <i>et al</i> [14] . .	65
5-8	Loss coefficient vs. Reynolds number comparison between experimental results and the lumped model for various valve opening percentages ( $h^*$ ). . . . .	66
5-9	Sharp edged orifice discharge coefficient vs Reynolds number . . . . .	69
5-10	Long orifice $t/d=0.5$ from Lichtarowicz [16] . . . . .	71
5-11	Long orifice $t/d=0.5$ from Lichtarowicz [16] . . . . .	71
5-12	Scaled data for valve #1 and valve #3 . . . . .	72
5-13	Curve fitting using 5.14 for valve #1 . . . . .	73

A-1	Reynolds number vs Discharge coefficient for valve 2 (dv=11.10 mm)	77
A-2	Reynolds number vs Discharge coefficient for valve 3 (dv=14.24 mm)	77

# List of Tables

4.1 Valve diameters ( $d_v$ ) with corresponding seat widths ( $s$ ) and non-  
dimensional seat widths ( $\sigma$ ) . . . . . 54

# Chapter 1

## Introduction

Many definitions exist to describe what are commonly known as Micro-Electro Mechanical Systems (MEMS). In general MEMS devices are those that fall within the range of  $1\ \mu\text{m} - 1\ \text{mm}$  in size. These devices are typically made out of Silicon wafers and machined using Integrated Circuit (IC) manufacturing techniques. A distinctive feature of MEMS is that they operate outside the realm of IC circuits, finding applications in solid mechanics, fluids, optics, magnetics and others. The focus of this work is on integrated microfluidic systems, particularly on the fluid mechanics aspect of these systems. This thesis discusses the fluid mechanics modeling strategy undertaken as part of the development effort for the MIT Micro Hydraulic Transducer project. The approach and results, however, are by no means limited to this particular system, they are relevant to fluidic microsystems in general.

### 1.1 Overview of the Micro-Hydraulic Transducer

The immediate application of this work is to the Micro-hydraulic Transducer (MHT) program, although the phenomena described applies to micropumps in general. The concept of the MHT, as shown schematically in Figure 1-1, integrates the large single-stroke force of an hydraulic system with the high-frequency small stroke available from a piezoelectric element. The combination is used to create high-performance transducers (Hagood *et al*, [6]). The device can operate as an actuator (transforming

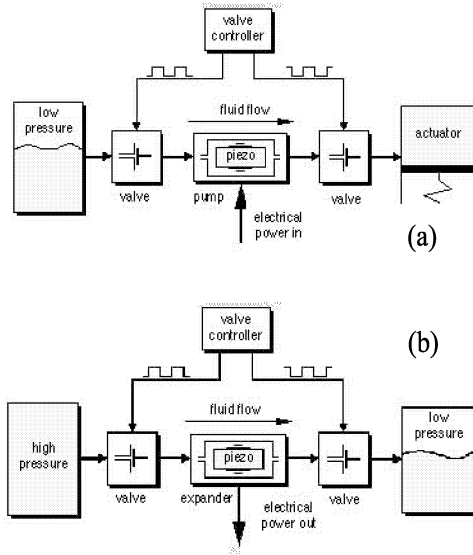


Figure 1-1: Conceptual Diagram of Bidirectional Microdevice

electrical to mechanical energy, (Figure 1-1,a) or as an energy harvester (converting mechanical to electrical energy), Figure 1-1,b. The MHT architecture resembles that of a reciprocating internal combustion engine cylinder. The fluid at high pressure comes into the cylinder chamber through an inlet valve, compresses the piston and in turn the piezoelectric crystal. The cycle is completed when the piezo expands driving the piston up and forcing the fluid out through the outlet valve. In the current design, the piston is approximately 8 mm in diameter, and the valves are poppet type disc valves ( $\varnothing$  500 $\mu$ m) with strokes of less than 40  $\mu$ m operating at approximately 20 kHz. In order to obtain this stroke at such high frequencies the valve is actuated by a piezoelectric element aided by an amplification chamber as detailed by Roberts *et al* [27].

## 1.2 Motivation

The rapid increase in the development of complex microfluidic devices has revealed a need for more accurate modeling of fluid behavior in small-scale microfabricated geometries. Microvalves tend to be one of the dominating elements in such systems, but

at the same time their detailed behavior remains poorly understood and systematic studies of microvalve fluid mechanics are lacking.

In the case of the Micro Hydraulic Transducer program at MIT, the requirements on valve modeling take a different perspective. In this case the valve and head loss models are used as design tools. Typical orifice models will not capture geometry related sensitivities necessary for design and optimization. Furthermore, one of the goals of the MHT project is to harvest energy with this device, for this reason, and considering that the valve is the dominating head loss, it becomes critical to determine accurately the corresponding head losses and sensitivities. Only then will it be possible to design a more efficient valve.

## **1.3 Challenges**

The major fluid mechanics challenge is to model the steady and unsteady fluid behavior in these micron-scale geometries. The Reynolds number during one cycle varies between 1 and 20,000 with a Strouhal number of order 1. In this regime both inertial and viscous forces are important and unsteady effects cannot be ignored. The model needs to be accurate, yet implemented in a flexible manner suitable for design purposes and integration into full system simulations. Unfortunately, such models do not presently exist, and where partial models are available, they are typically neither calibrated nor validated for the small scales and unique geometries that are found in microfluidic systems. The purpose of this thesis is to provide such calibration and validation.

## **1.4 Contributions**

An hydraulic model for the Micro-Hydraulic Transducer was constructed based on a low-order lumped element model. The valve flow characteristics were investigated experimentally and parametric studies were carried out to obtain the flow dependencies and allow for a better estimation of the head losses.



# Chapter 2

## Literature Background

### 2.1 MEMS Scaling Issues

The miniaturization of systems presents several interesting performance advantages. One of the major advantages that comes with miniaturization is that as a system is scaled down its mass ( $M$ ) reduces like the third power of the length scale ( $l$ ), (ie  $m \propto l^3$ ). This dramatic mass reduction increases the natural frequency ( $\omega_n$ ) of a system as shown for a simple cantilever beam:

$$\omega_n = \sqrt{\frac{K}{M}} = \sqrt{\frac{3EI_A}{l^4\rho A_c}} = c\frac{1}{l} \quad (2.1)$$

where  $k$  is the stiffness and  $m$  the mass of the beam. The stiffness ( $K$ ) is given by Young's modulus ( $E$ ), the area moment ( $I_A$ ) and the beam length ( $l$ ). The mass ( $M$ ) is given by the length ( $l$ ), the cross-sectional area ( $A_c$ ) and the material density ( $\rho$ ). As it can be appreciated in equation 2.1 the natural frequency ( $\omega_n$ ) scales like  $1/l$ . This allows for a significant increase in operating frequencies for micromachined devices as described in detail by Burgess [3]. The previous argument has been one of the major driving forces towards the development of MEMS. However, not all phenomena scale as favorably as inertia, for instance viscous effects and other surface-driven phenomena become relatively more important as scale decreases. In our case we are particularly interested on Microfluidic MEMS and for this reason, we

will study in detail the fluidic behavior at these scales.

Microfluidic systems encompass many different applications from on-chip chemical systems to micro-mixers, micropumps and microtransducers to name a few. As scale decreases the surface-to-volume ratio increases making such effects as viscosity, Van der Waals forces, electrostatic forces, etc. important and in some cases detrimental to system performance. An introductory discussion of such scaling effects can be seen in Ho and Tai's microfluidics review paper,[10].

In particular the focus of this work is on modeling the fluidic behavior in microfluidic transducers. One of the major questions is to understand how hydraulic systems and their components behave at the microscales and how macro-scale results scale down.

In the first part of this chapter a brief literature review of existing modeling approaches for micro-hydraulic systems is presented. The second part of the chapter focuses on microvalves due to their importance in micro-hydraulic MEMS. The main purpose of this chapter is to set the stage for this thesis work by presenting what has been done by other researchers in the field.

## **2.2 Microsystems Fluidic Modeling Strategies**

Several modeling approaches have been proposed for integrated microsystems. From the fluids point of view there are several options: Navier-Stokes simulations, Characteristic equations, impedance models (distributed models), and electrical analogy or lumped models.

The direct simulation of the flow in these systems by solving the Navier-Stokes equations is not feasible due to the complicated geometries, moving boundaries, fluid/structure interactions, and the unsteady nature of the phenomena described making them at best impractical.

A second approach is to use the characteristic equations method. This approach transforms the flow's partial differential equations, into ordinary differential equations significantly simplifying the problem. These equations can then be integrated forward

in time to obtain a solution. This method will give a solution that usually would only be surpassed in accuracy by a direct simulation of the Navier-Stokes equations[35]. However, localized head losses like elbows, valves, etc. still need to be characterized separately and fed to the model. The quality of the model will thus depend on how well these localized losses are modeled. Two important disadvantages of this approach is that integration to structural and electrical models is not straightforward and that a full-system simulation becomes computationally expensive.

A third option is comprised by distributed parameter models or impedance-based models. This approach is part of the so-called electrical analogy methods used traditionally in acoustics. This approach assumes that the pressure is analogous to electrical voltage and that the flow rate is analogous to electrical current. The impedance is defined as the ratio of the dependent variables pressure ( $P$ ) and flow rate ( $Q$ ) respectively for each section. In such manner the system may be solved as an eigenvalue problem.

In those cases in which pipe lengths are short the distributed parameter model can be simplified even further to a "lumped" element model. Previous experiences by Olsson[23], Bourouina[2], and Gravesen[5] have proven that the lumped element model is useful for the analysis of microfluidic systems. The advantage of lumped models is that they are easily integrated to full system simulations which may also include structural and electrical components. The intrinsic modularity of this type of model makes it easy to modify and build up on. The lumped model has the added advantage that due to its similarity with circuit system-analysis existing software, such as SPICE and SIMULINK, can be used to obtain solutions.

In this case as in previous approaches the behavior of localized components needs to be characterized separately. Thus the results of a given simulation will be a function of how accurately the system is modeled and how well the subcomponent's behavior is known.

Microvalves are in most cases the most difficult subcomponents to characterize in microhydraulic systems. Incidentally microvalves are also the main dissipative elements of these hydraulic systems. A literature review of existing microvalves is

presented next to set the context for this thesis experimental work.

## 2.3 Micro Scale Valves

Microvalves may be classified as active (with an actuator) or passive (without actuator). Many different examples of both types of microvalves exist in the literature. A review by Shoji and Esashi [31], and Gravesen [5] indicates that most microvalves have been designed for gas control, while not many have been demonstrated for liquid applications due to their low conductance.

The low conductance of microvalves is directly related to microfabrication constraints, which limits available geometries to low aspect ratio, prismatic elements due to the line-of-sight nature of microfabrication techniques. This greatly limits the available geometries of fluidic devices. For instance valves cannot have three-dimensional structures such as  $45^\circ$  poppets, rounded edges and fillets (although some limited fillet capabilities have been demonstrated in highly stressed MEMS structures; Ayon, et al.[1]). The high temperatures required for wafer bonding preclude the use of polymers and soft materials for the valve seats. Available actuation options are limited in stroke and control authority further constraining valve response time and performance. The above-mentioned constraints have made typical microvalve designs quite different from macro scale valves and yielded highly suboptimal microvalves.

In most cases valves are fabricated and then characterized experimentally, primarily because detailed analysis of the flow characteristics and sensitivities to different relevant parameters is lacking. One of the main reasons for this is that instrumenting a microvalve to measure both flow rate and pressure as functions of the valve position is very difficult.

### 2.3.1 Passive Microvalves

Passive valves may be subdivided into moving parts valves and No Moving Parts (NMP) valves. The first group mainly has valves which open and close in response to a net force acting on them. These microvalves usually have a micromachined

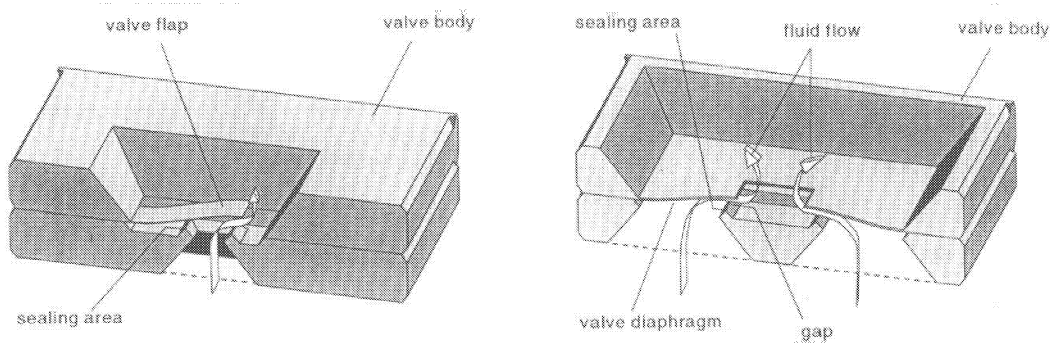


Figure 2-1: Typical Architectures of Passive Microvalves [37]

Silicon membrane that is free to deflect in one direction. The resulting behavior is equivalent to that of a macro-scale check valve. The moving membranes have been fabricated in many different sizes and thicknesses, with annular shapes, cantilever type flaps and tethered structures. This class of micro-valves, however, have some generic characteristics: one way flow, limited stroke, and in many cases they are susceptible to clogging.

A survey of existing micro-check-valves by Shoji [31] shows that typical passive check valves range in size from  $800\text{ }\mu\text{m}$  to about  $7\text{ mm}$ , and only one valve in the  $100\text{ }\mu\text{m}$  range has been reported. All of these valves were Silicon micromachined valves and were either cantilever or circular membrane type check valves as shown in Figure 2-1. The Reverse flow rates (leak flow) of these valves were in the order of  $1\text{ }\mu\text{l/min}$  for water. The forward flow rate was generally two to three orders of magnitude higher than the reverse (leak) flow rate. It should be observed, though, that these comparisons suffer from the fact that the reported results for each valve were based on different applied pressures but they do convey the general capabilities of such systems.

One of the contributing factors to the low conductance of microvalves is the limited stroke. In the case of passive valves, the stroke depends on the surrounding fluid pressure, membrane thickness and valve size. In some cases the valve deflection is larger than the membrane thickness resulting in nonlinear behavior and therefore

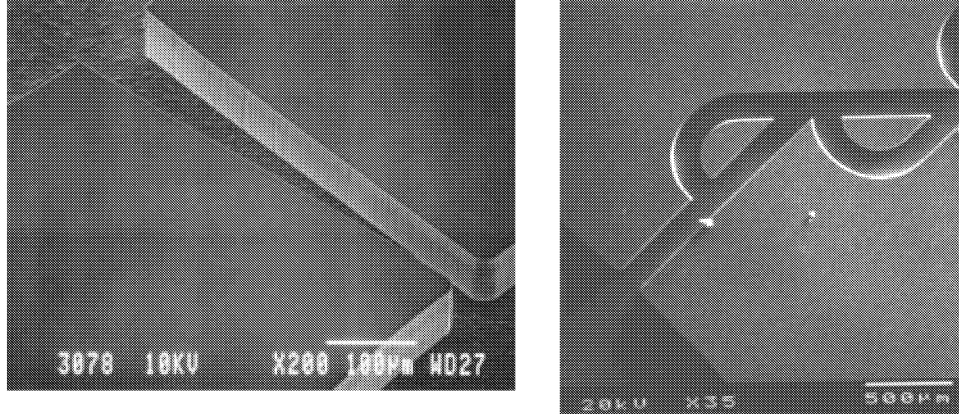


Figure 2-2: NMP Passive Microvalves, Olsson [22] and Forster[4]

smaller displacements per applied pressure.

From the fluid mechanics point of view the flow characterization of this valves is difficult since the valve position and capacitance are pressure dependent.

The second major type of passive valves are No-Moving-Parts (NMP) valves. These valves are carefully contoured so that flow is preferential in one direction. The aim, as in the case of the micro-check-valves is to obtain a high conductance in one direction and a comparatively low conductance in the reverse flow condition. Several examples of these valves exist, the geometries are different but the operating principle is the same as seen in Figure 2-2. In-depth studies have been carried out by Stemme and Olsson [22] with a diffuser/nozzle design and Forster *et al*[4] with Tesla type valves. These valves are characterized by high reverse flow rates (compared to moving part check valves), however these designs are compensated by their ease to manufacture, robustness, and their ability to transport particle laden fluids.

A figure of merit used to estimate the quality of a given design is the diodicity. The diodicity ( $Di$ ) is defined as

$$Di = \frac{\Delta P_-}{\Delta P_+} \quad (2.2)$$

where the  $\Delta P_+$  is the pressure drop in the forward (or positive direction) and  $\Delta P_-$  is the pressure drop in the reverse (leak) direction. NMP valves or fluidic diodes

usually have a diodicity of about 1.1- 1.3. Considering that for laminar flow the flow rate ( $Q$ ) is a linear function of the pressure drop, we can estimate that micro check valves with moving parts would have a diodicity roughly two orders of magnitude higher than NMP valves. It has been suggested, though, that probably a better figure of merit would be reverse pressure differential per flow rate which for very low flow rates should be a constant.

### 2.3.2 Active microvalves

The microvalve actuator plays a fundamental role in determining the efficiency and overall design of a valve. Many designs and actuation principles have been proposed the most common options are electrical, thermal, magnetic, and piezoelectric.

Ideally an actuator system should be easy to miniaturize, efficient, have a large stroke and fast response time. Currently, no actuation system fulfills the previously mentioned characteristics of the "ideal actuator". Considering this certain types of actuators are better suited to some applications than others. The strengths and weaknesses of the most common actuation systems are outlined next.

Thermal based systems can be categorized into thermopneumatic, bimetallic, and Shape-Memory-Alloys (SMA) actuators. Thermopneumatic based actuators for microvalves have been investigated by Zdeblick, Henning and coworkers [8],[7] resulting in a commercially available microvalve (Redwood microsystems) . The thermopneumatic normally-open valve as shown in Figure 2-3 has a cavity which is filled with Fluorinert. The orifice size as reported varies from 25 to 500  $\mu\text{m}$ , with membrane diameter of roughly 6 mm. The Fluorinert is heated with a Platinum resistor deflecting the cavity membrane and closing the valve. The response time is in the order of 0.1–1 sec, with maximum reported strokes of 50  $\mu\text{m}$ . It is suggested that a change of heat transfer mode from conduction to phase change may reduce the response time down to tenths of milliseconds. Cycling the valve, however, poses a greater challenge, for the system would have to be heated and cooled rapidly. The advantage of this type of actuation is that it has the widest temperature range from  $-20^{\circ}\text{C}$  to  $70^{\circ}\text{C}$ . Applications for the control of refrigerant liquids have been suggested.

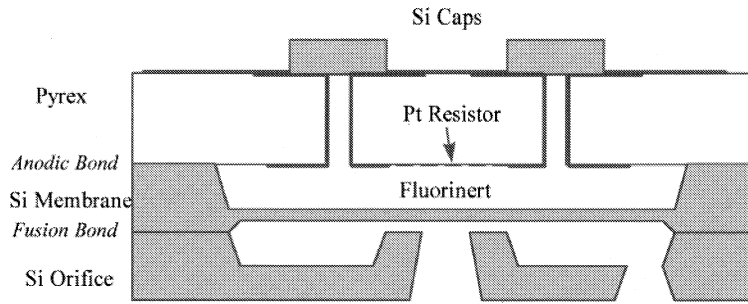


Figure 2-3: Thermopneumatic Active Microvalve [7]

The second thermal actuation system found in the literature are bimetallic systems. The bimetallic actuator usually consists of a circular Silicon membrane connected to a thin annular metallic ring. The system is heated and the effect is such that due to the dissimilar thermal expansion coefficients the membrane deflects. Theoretical estimates by Jerman[13] suggest that for a 2.5 mm diameter, 8  $\mu\text{m}$  thick Si membrane with 5  $\mu\text{m}$  of deposited Aluminum and b/a ratio of 0.5 displacements in the order of 25-30  $\mu\text{m}$  with symmetrical vertical travel are achievable. This actuation mechanism, however, is limited in its response time due to the heating and cooling of the bimetallic materials. The response time oscillates between 1 msec and 1 sec depending on the details of the configuration. For the previously described configuration Jerman has shown experimentally response times of 100 to 300 msec. Bimetallic actuated valves have been proposed for systems in which proportional valve control is required. They have approximately the same operating range of thermopneumatic valves but without the further complication of sealing liquid in a cavity.

Shape-memory-alloy based systems have the ability to produce large strokes, however due to their non-linear response to temperature are difficult to control and response times are in the order of 10 seconds. This valves may have large stroke but are difficult to control and therefore have only been used as on-off valves.

Electrostatically actuated valves typically rely on two Silicon wafers to act as electrodes. The Silicon plates are insulated by grown oxide and separated by another layer usually of pyrex in a "sandwich" fashion as seen on Figure 2-4. The



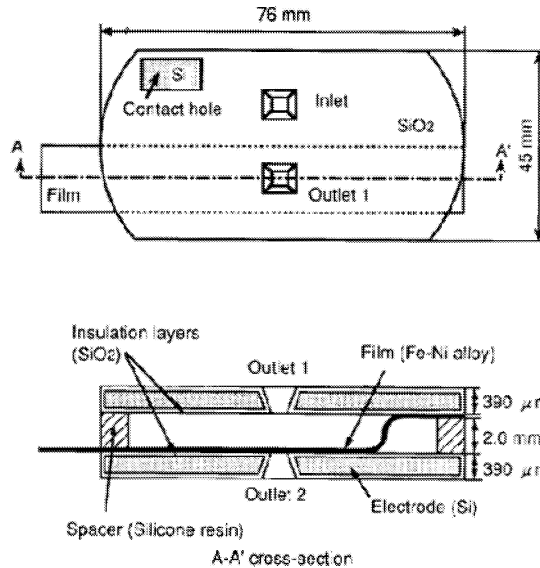


Figure 2-4: Electrostatically Actuated Microvalve [30]

moving part of the valve is a metallic flapper which is attracted either to the lower or upper electrode depending on the field direction. The fundamental limitation of these systems is that the actuation force is inversely proportional to the square of the distance between the flapper and the electrode. This limits the field of usage of these valves to low pressures and relatively short strokes. Experimental results by Shikida[30] showed a maximum block force of  $\sim 20$  mN. The major advantage of this architecture is that fast response times of the order of 0.1 msec can be attained. This actuation system can provide actuation for large strokes but low forces. It has been successfully employed for the control of rarefied gas systems such as Molecular Beam Epitaxy (MBE).

Electromagnetic actuation has been explored by Hirano, Yanagisawa and coworkers[9]. The major problem of this actuation system is the requirement for a miniaturized coil as seen in Figure 2-5.

Piezoelectrically based actuators represent one of the fastest options for opening and closing a microvalve. Piezoelectric actuators however, have very small strokes and this has significantly limited their use for microvalves. Active microvalves with piezoelectric actuators have been proposed by Shoji and Esashi [31] and Roberts *et*

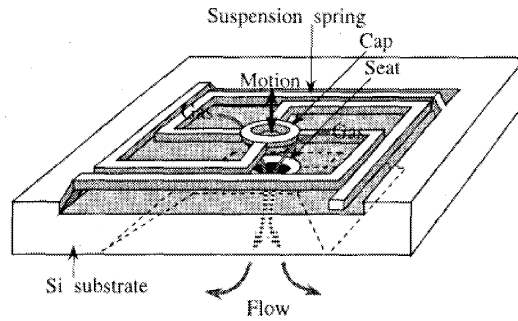


Figure 2-5: Electromagnetic Actuated microvalve [9]

*al.*[27]. Shoji and Esashi have shown experimentally response times of the order of 1 msec with gas flows of 40 ml/min. The design proposed by Roberts, Figure 2-6, uses an amplification chamber to obtain more stroke out of a piezoelectric while retaining the force and rapid reaction available with a piezoelectric.

### Lessons Learned from Existing Microvalves

One can observe from reviewing the existing literature on microvalves and integrated microsystems that virtually all the proposed valve flow models make the following assumptions:

The valve is the dominating flow loss in the system. This means that in most cases the only flow resistance or head loss needed to describe a system is the valve.

The unsteady state head losses are modeled with steady state head loss models. This approximation is made because in many cases the frequency dependent resistance term is difficult to model and experimental results are lacking.

Microvalves are approximated as variable area orifices. This approximation is based on the assumption that inertial losses ( $\Delta P \propto Q^2$ ) are the dominating loss mechanisms in the valves. It should be pointed out that although such approximations do capture the physical flow behavior they will be only order of magnitude models.

Valve stroke, as seen in the literature is one of the key elements required of an actuation system in order to obtain high conductance.

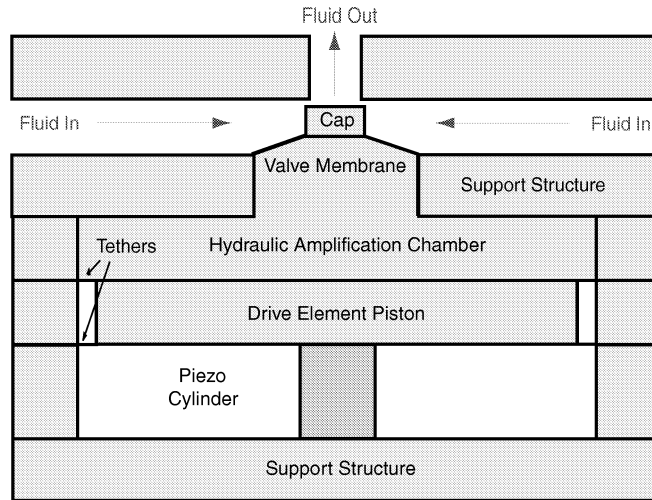


Figure 2-6: MHT Amplification Chamber,[27]

The closing force, leakage, and response times are important but their requirements are heavily dependent on the application at hand.

Microvalves for gas flow applications are characterized by low Reynolds numbers of order 100-1000, but the flows may approach Mach 1. For this reason choked flow in the valve orifice is observed in many cases. The most common flow model is a quasi 1-d gas flow model for subsonic flow and in certain cases for choked flow.

In the case of liquids such as water and Silicon oils, the situation is not much different. Flow models reduce the valve behavior again to a variable area orifice. In most cases these models are used to analyze obtained experimental results. Corrected discharge coefficients are computed and curves fitted to the data.

The systematic study of the valve behavior and sensitivities of the different flow parameters is usually not performed.

## 2.4 Macro-scale Valves

Macro-scale poppet and disc valves have many applications most notably in internal combustion engines, pressure control and relief valves, compressor valves and even for homogenizing milk.

In contrast to microvalves, much research has been conducted on "normal"-sized valves. However, the complex geometries make the flow in valves very complicated and valve-dependent. Thus comparison between different experimental measurements and numerical simulations is difficult, even impractical. In the past, researchers have investigated such flows using a variety of analytical techniques such as potential flow analysis (Von Mises, [17]), his work predicted the flow contraction but ignored the reattachment and pressure recovery phenomena. Other experimental results have shown that the flow behavior is highly dependent on the details of the valve geometry and the separated jet. The effects of these two parameters are very difficult to model mathematically.

Numerical techniques have been employed to analyze the flow behavior of poppet and disc valves, but as Vaughan [33], points out typical turbulence models (such as the  $\kappa - \epsilon$  model) have been shown to give inaccurate results. Vaughn and coworkers concluded that numerical simulations can show qualitative trends but the results may be quantitatively inaccurate. They further point out that the popular  $\kappa - \epsilon$  model is inadequate for solving this flows and suggest that a Reynolds-stress based model should give a better approximation to the real flow. It follows from their conclusions that numerical simulations need to be validated against experiments whenever possible.

In summary all these techniques suffer from the fact that flow separation, cavitation, transition, reattachment and relaminarization are difficult to model mathematically and expensive numerically.

The preferred approach to this type of problem is experimental. Previous work on macro-scale valves traces back to the work of Schrenk (1925), Stone,[32] and Johnston[14]. Schrenk reported discharge coefficients on poppet and disc valves. Stone concentrated on sharp edged poppet valves and low turbulence flows. His results however show considerable scatter and as he suggests more research is needed. Johnston and coworkers concentrated on measuring the discharge coefficients and force acting on poppet and disc type valves. Their work concentrated on the fully turbulent regime (i.e.  $Re \gg 2500$ ). Johnston makes no reference to transition effects

or low turbulence behavior.

One important conclusion that can be obtained from these efforts is that, for small openings, poppet valves behave like long orifices, a suggestion that supports the thought that the effects of flow separation and subsequent reattachment dominate the valve dynamics.

A second important conclusion is that although qualitatively the flow behavior may be analogous to that of a long orifice the actual value of the discharge coefficients is a strong function of the valve geometry and the upstream and downstream conditions. For this reason, it is important to investigate experimentally the fluidic behavior for the particular geometry under study.

## 2.5 Summary

In this chapter a literature review of the most common micro-hydraulic system modeling strategies was undertaken. The main advantages and disadvantages of the different approaches were shown. It was concluded that most of these strategies required separate submodels for their subcomponents (i.e. valves, elbows, etc.). Considering that microvalves are in most cases the dominant dissipative element a separate literature review was undertaken.

The microvalve review showed, as pointed before, that there is very little information regarding the flow characteristics of reported microvalves. Most flow models identified the valve as an orifice correlating adequately with the results. These models gave, however, little insight to the flow sensitivity to valve geometry and Reynolds number. The third part of the chapter concentrated on macro-scale valves that may be similar to those found in microsystems. The complication, as it was pointed out, is that there is a lack of information for disc valves operating at low turbulence and transition regimes. As a conclusion, two decisions were made: to construct an order of magnitude model for the valve based on available orifice information and to explore experimentally, via a macro-scale valve, the valve flow characteristics at low turbulent Reynolds numbers.

## Chapter 3

# Modeling of Hydraulic Microsystems

Based on the literature review, for initial designs and system analysis, the hydraulic system of the MHT has been modeled using lumped elements. As mentioned in the literature review the lumped model is limited to short channels. Wylie and Streeter[35] have proposed a conservative rule-of-thumb criterion in which they suggest that the maximum channel length ( $l$ ) should be less than 4% of the acoustic wavelength ( $\lambda$ ) as shown by :

$$l \leq 0.04\lambda = \left(\frac{0.04}{f}\right) \sqrt{\frac{k}{\rho}}. \quad (3.1)$$

Equation 3.1 assumes that the flow channel has rigid walls, and therefore the acoustic wavelength ( $\lambda$ ) is only a function of the frequency of the pressure oscillations ( $f$ ), the fluid bulk modulus ( $k$ ) and the fluid density ( $\rho$ ).

The lumped model breaks up the hydraulic system into subcomponents or elements. The subcomponent's behavior is described by three 'properties': inductivity, resistivity and capacity. The inductivity represents the fluid mass or inertia. The resistivity is related to the dissipative characteristics of the element. Finally the capacity describes the fluid storage capability of a given component. Different elements will have different combinations of these properties and in some cases the effect of

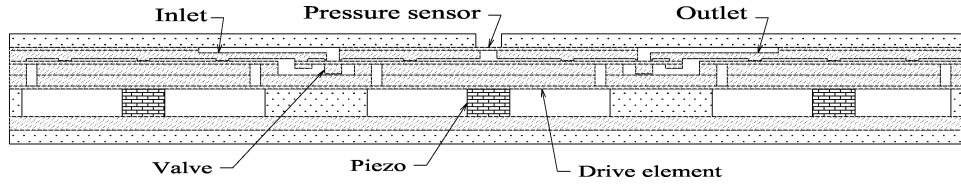


Figure 3-1: Cross-sectional view of a multiple wafer energy harvester with active valves

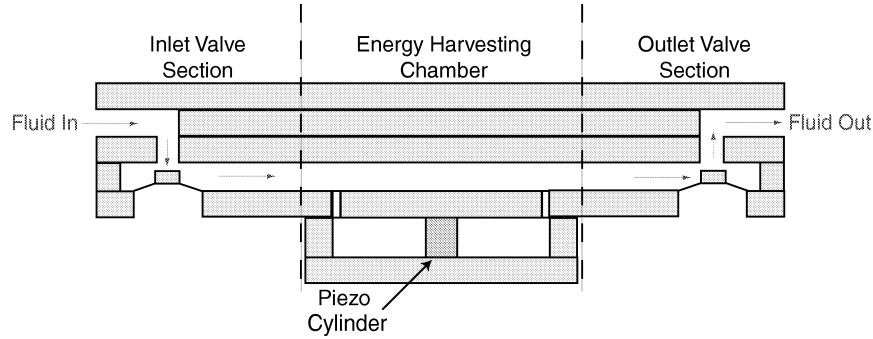


Figure 3-2: Schematic of the MHT hydraulic system

some will be negligible compared to others. The end effect is a system of equations that resembles those used for electrical circuit analysis.

### 3.1 The MHT Hydraulic Model

The MHT's hydraulic system to be modeled is shown in figure 3-1. A schematic representation of the flow path can be seen in Figure 3-2. The flow paths are rather tortuous being characterized by sudden expansions, contractions,  $90^\circ$  turns, short tubes and valves. The hydraulic system is divided into three main sections: the inlet valve section, Energy Harvesting Chamber (EHC) section, and Outlet valve section as shown schematically in Figure 3-2 and 3-3.

As mentioned before the lumped element model classifies the fluidic components into equivalent capacitances, resistances and inductances. The lumped element representation of the inlet and outlet valve sections is presented in Figure 3-5. The inlet

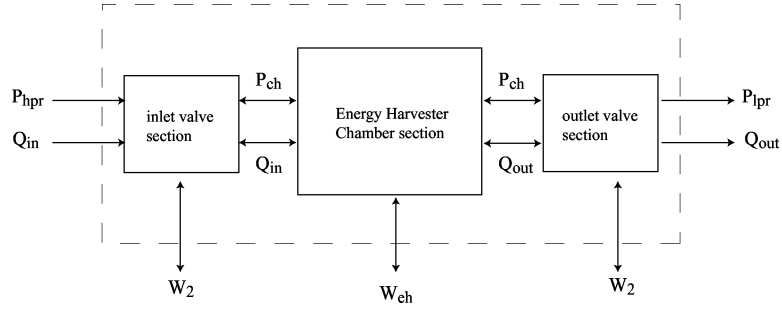


Figure 3-3: Hydraulic Systems Control Volume Representation

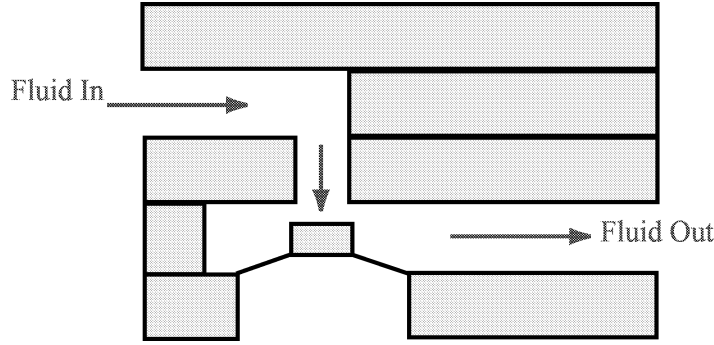


Figure 3-4: Schematic of the inlet valve section

and outlet valve sections are presented schematically in Figure 3-4 and in lumped element representation in Figure 3-5 showing that the dominating effects are of inductive ( $I_i$ ) and resistive nature ( $R_i(Q)$ ). The channel capacitance is neglected on the grounds that the channels have rigid walls and the fact that the fluid is nearly incompressible.

The lumped model equation for the inlet valve is given by :

$$P_{hpr} - P_{ch} = (I_1 + I_2)\dot{Q} + (R_1(Q) + R_{v1}(Q) + R_2(Q))Q + \Delta P_{vp} \quad (3.2)$$

where as seen in Figure 3-5 there are two inductance elements  $I_1$  and  $I_2$ , and three major groups of resistive elements shown as  $R_i$ . It should be pointed out that these resistive terms are in general non-linear which may make the numerical solution more difficult. In the case of the outlet valve the flow equation is similar :



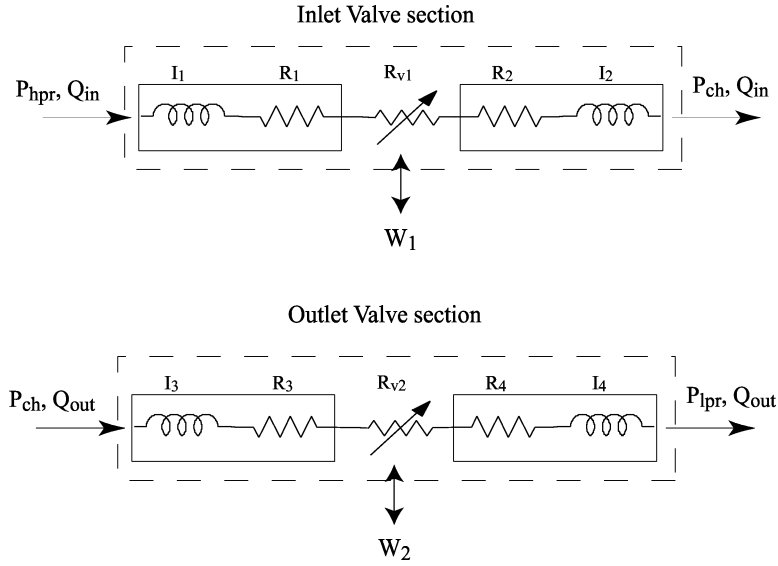


Figure 3-5: Valve Sections: Lumped Model Equivalents

$$P_{ch} - P_{lpr} = (I_1 + I_2)\dot{Q} + (R_1(Q) + R_{v1}(Q) + R_2(Q))Q + \Delta P_{vp}. \quad (3.3)$$

The major difference found in this model relative to other models available in the literature comes from the term  $\Delta P_{vp}$  which describes the work done by the valve cap on the fluid and viceversa. This term is of the form:

$$\Delta P_{vp} = \frac{\dot{W}}{Q} = \frac{1}{Q} \frac{d \left( \int \vec{F} \cdot d\vec{x} \right)}{dt} \quad (3.4)$$

where the change in pressure  $\Delta P_{vp}$  is equal to the rate of work ( $\dot{W}$ ), done on the system by the valve cap, over the instantaneous flow rate ( $Q$ ).

### 3.1.1 Valve Cap Force Calculation

The fluid force acting on the valve cap is calculated using the unsteady integral momentum equation given by

$$\vec{F} = \frac{\partial}{\partial t} \int (\rho \vec{v}) dV + \oint (\rho \vec{v} \cdot d\vec{S}) \vec{v} \quad (3.5)$$

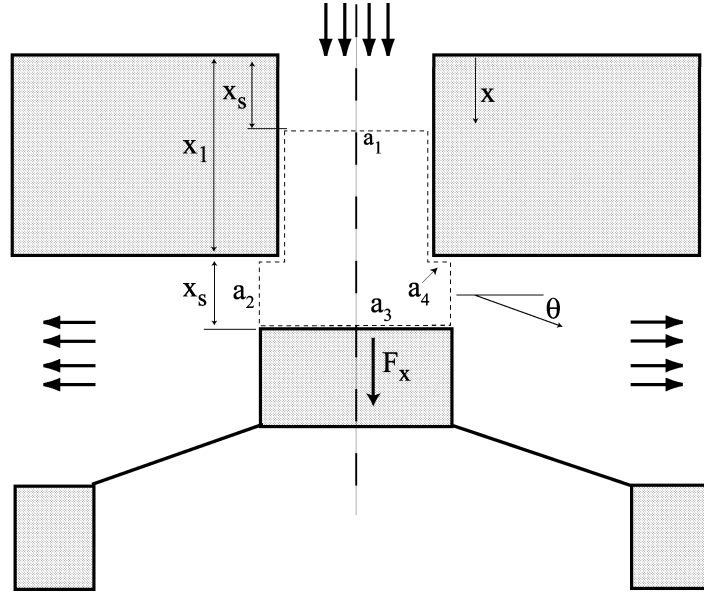


Figure 3-6: control volume for valve cap force calculation

where  $\vec{F}$  is the resultant force acting on the control volume,  $\rho$  is the fluid density, and  $\vec{v}$  is the fluid velocity vector. A schematic of the valve and the control volume used to calculate the force is shown in Figure 3-6. The valve force calculation, as seen in Figure 3-6, only requires the use of the  $x$ -direction momentum equation. The calculation assumes that the control volume moves with the valve cap, that friction forces are negligible, and that the fluid is incompressible. Following Ikebe's[12] method we obtain the  $x$ -direction momentum equation :

$$F_x = \rho \left\{ \frac{d}{dt} \oint x u_c dS + \oint u u_r dS \right\} \quad (3.6)$$

where  $F_x$  is the  $x$ -direction force acting on the fluid,  $\rho$  is the fluid density,  $u_c$  is the normal exterior fluid velocity in the  $x$ -direction, and  $u_r$  is the normal exterior relative velocity to the control surface. Applying equation 3.6 to all the control surfaces in Figure 3-6 we obtain:

$$\frac{F_x}{\rho} = (x_1 + x_s)\ddot{x}_s + (\dot{x}_s)^2 a_3 + (x_1 - \frac{x_s}{2})\dot{Q} + \frac{\dot{x}_s}{2}Q + \left( \frac{\tan \theta}{a_2} - \frac{1}{a_1} \right) Q^2 \quad (3.7)$$

where  $F_x$  is the  $x$ -direction force,  $\rho$  is the fluid density,  $x_s$  is the valve displacement,  $x_1$  is the height of the control volume,  $Q$  is the instantaneous flow rate,  $\theta$  is the fluid jet angle, and  $a_i$  are the control surfaces. The surface areas are given by

$$\begin{aligned} a_1 &= \frac{\pi}{4}d_0^2 \\ a_2 &= \pi x_s d_v \\ a_3 &= \frac{\pi}{4}d_v^2 \end{aligned}$$

where  $d_0$  is the inlet diameter,  $d_v$  is the valve diameter, and  $x_s$  is the valve displacement.

A simplification of the equation can be obtained if we assume that  $x_1 \gg x_s$  in that case we obtain:

$$\frac{F_x}{\rho} = (x_1)\ddot{x}_s + (\dot{x}_s)^2 a_3 + (x_1)\dot{Q} + \frac{\dot{x}_s}{2}Q + \left(\frac{\tan \theta}{a_2} - \frac{1}{a_1}\right)Q^2. \quad (3.8)$$

This result allows us to calculate the unsteady force on the valve cap ( $F_x$ ) as a function of the flow rate ( $Q$ ) and valve displacement ( $x_s$ ). Experimental results by Nakada and Ikebe[21] have shown that for spool valves this modeling approach gives reasonably accurate results.

### 3.1.2 Capacitance modeling

The Piston chamber or EHC is the dominant capacitance of the system. The compliance of the piston chamber results from the compression of the fluid ( $\Delta V_f$ ), the structural compliances ( $\Delta V_s$ ) and the oscillatory movement of the piston. The change in pressure ( $\dot{P}$ ) due to capacitive effects is defined as :

$$\dot{P} = \frac{1}{C} (Q_{in} - Q_{out} - \dot{V}_p) \quad (3.9)$$

where  $C$  is equivalent capacitance,  $Q_{in}$  is the flow rate into the control volume,

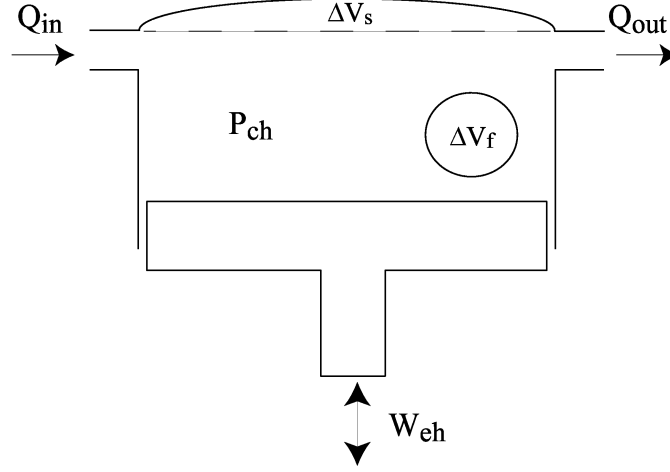


Figure 3-7: Energy Harvesting Chamber Representation

$Q_{out}$  is the flow rate leaving the control volume and  $\dot{V}_p$  is the change of volume due to the piston movement. In general the equivalent capacitance for the piston chamber is of the form :

$$C = \frac{\partial V_s}{\partial P} + \frac{\partial V_f}{\partial P} \quad (3.10)$$

where the first term refers to the change in volume by the structure for a given pressure. This relation is obtained from structural calculations and FEA analyses (outside the scope of this thesis). The second term describes fluid compressibility which can be estimated using the isothermal bulk modulus. The underlying assumption here is that the temperature is nearly constant, making the thermal expansion coefficient effect negligible.

The fluidic capacitance ( $C_f$ ) is related to the isothermal bulk modulus ( $k$ ) by the following equation:

$$C_f = \frac{V_0}{k} \quad (3.11)$$

where  $V_0$  is the initial volume.

### 3.1.3 Inductance in fluid channels

The compliance in the fluid channels is usually much smaller than that of the piston chamber due to the fact that the channels are surrounded by rigid walls and that their fluid volume is smaller than that of the chamber.

The inductance element is the fluid mass contained in the channels of the system and it has been modeled by assuming inviscid flow (i.e.  $R_1 = R_2 = 0$ ). For an unsteady constant area channel flow the energy equation can be written as

$$\dot{\Phi} - \dot{W} = \int \int \int_{cv} \left( e + \frac{1}{2}u^2 \right) \rho dV + \int \int_s \left( h + \frac{1}{2}u^2 \right) \rho (\vec{u} \cdot \hat{n}) dS \quad (3.12)$$

where  $\dot{\Phi}$  is the heat transfer into the system,  $\dot{W}$  is the work done by the system,  $e$  is the internal energy,  $u$  is the flow velocity,  $\rho$  is the fluid density and  $h$  is the fluid enthalpy. For an adiabatic, inviscid flow in a constant area channel the expression reduces to :

$$\Delta P = \frac{1}{Q} \int \int \int_{cv} \left( e + \frac{1}{2}u^2 \right) \rho dV \quad (3.13)$$

further assuming a uniform velocity profile we obtain the following result:

$$\Delta P = I \dot{Q} = \left( \frac{\rho l}{A} \right) \dot{Q} \quad (3.14)$$

where  $I$  is defined as the inductance which is a function of the fluid density ( $\rho$ ), the channel length ( $l$ ) and the channel cross-sectional area ( $A$ ).

The approximation is now compared to cases where we have fully developed viscous velocity profiles. In those cases where the flow is laminar it has been shown by Morris *et al*[19] that the formula underestimates the correct value by about 30%. This can be easily explained if we consider that in deriving the inviscid Inductance ( $I$ ), the underlying assumption is that of a uniform velocity profile. For laminar flow this approximation is inaccurate since the velocity profile is parabolic. Using the parabolic velocity profile to compute the change of the kinetic energy in the system we obtain the correct inductance value which is  $\frac{4}{3}$  times higher than the inviscid case

as shown by Olsson [23]. For turbulent flows, assuming a velocity profile ( $u$ ):

$$u \simeq u_0 \left(1 - \frac{2r}{D}\right)^n \quad (3.15)$$

where  $u_0$  is the maximum axial velocity,  $r$  is the radial location,  $D$  is the pipe diameter and  $n$  is the scaling power. The scaling power  $n$  is set to  $\frac{1}{7}$ . Compared to the constant velocity profile the correction factor is only 1.02.

### 3.1.4 Resistive Elements

For the resistive elements the microvalves have been identified as the major fluidic resistance of most existing micropumps. Gravesen [5] notes that the valves are usually the dominant loss element due to the fact that the entire flow has to pass through the small valve openings. For a first approximation to the valve head loss they were modeled as a simple orifices.

The flow resistance of each element ( $R_i$ = elbows, contractions, channels,etc.) is modeled using published experimental loss coefficients (Idelchik [11]), which were corrected according to the local Reynolds number (Re).

The quadratic loss coefficient ( $\zeta$ ) is defined by :

$$\zeta_{quad} = \frac{\Delta P}{\frac{1}{2}\rho\bar{u}^2} \quad (3.16)$$

where  $\Delta P$  is the total pressure drop,  $\rho$  is the fluid density and  $\bar{u}$  is the local bulk flow velocity. Published values of the loss coefficient ( $\zeta$ ) for different components such as elbows, expansions and contractions are reported usually for fully turbulent regimes. In this regime pressure losses are inertially dominated and qualitatively behave like ( $\Delta P \propto \bar{u}^2$ ). This clearly shows that the reported loss coefficients will tend to be weak functions (or independent) of the Reynolds number. This approximation, however, only holds for Reynolds numbers of order  $Re > 10,000$ . Microfluidic systems, like the MHT, usually operate at lower Reynolds numbers. For this reason correction factors or experimental results are employed to obtain better estimates of the loss coefficients for low turbulence flows.

Idelchik modifies the quadratic loss coefficient ( $\zeta_{quad}$ ) with two empirical correction factors ( $\zeta_\phi$  and  $\epsilon$ ) based on the local Reynolds number ( $Re$ ), and with this, a modified loss coefficient ( $\zeta$ ) can be defined:

$$\zeta = \zeta_\phi(Re) + \epsilon(Re)\zeta_{quad}. \quad (3.17)$$

In this manner the flow resistances of the different components were estimated. In order to establish a uniform system model, the different resistive components were referenced to a characteristic system length with which a system-wide Reynolds number ( $Re_{sys}$ ) is defined. The characteristic length chosen was the valve inlet diameter ( $d_{sys}$ ).

### Order of Magnitude Valve Model for the MHT

For initial estimates an order-of-magnitude valve model was constructed. This model also gave a starting point for designing the valve experiments. As mentioned above, previous work (Schrenk [29]; Stone [32]; Johnston [14]) has suggested that the valve can be modeled as an orifice. The initial order-of-magnitude model was constructed based on an orifice analogy. The disk valve to be modeled can be seen in Figure 3-8. The valve is characterized by three areas :  $A_1$  the upstream flow area,  $A_0$  the throat flow area and  $A_2$  the downstream area.

Most of the information gathered on orifices is based on experiments carried out in pipes of 2in diameter and higher[25]. It has been noted that orifices in pipes of smaller diameter have higher discharge coefficients due to second-order effects, such as surface tension (Ramamurthi [24]).

Thus, the orifice model should be able to capture the flow physics, but should be considered only as an approximation to the correct values.

To certain extent the orifice itself may be thought of as a contraction of the flow and a subsequent expansion. An integral analysis gives a relationship for the combined effect of the flow expansion and contraction. The quadratic local loss coefficient ( $\zeta_{quad}$ ) is defined as the total pressure drop ( $\Delta P$ ) over the dynamic pressure based on the

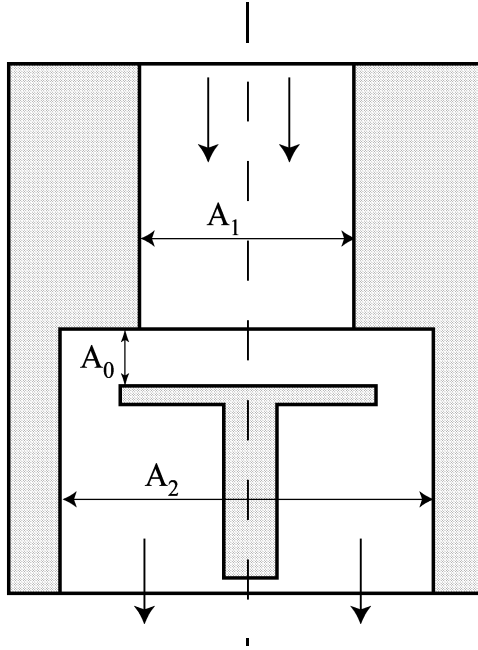


Figure 3-8: Valve schematic for the order-of-magnitude model

orifice local mean velocity ( $\bar{u}$ ):

$$\zeta_{quad} = \frac{\Delta P}{\frac{1}{2}\rho\bar{u}^2} = \left[ \frac{1}{2} \left( 1 - \frac{A_0}{A_1} \right)^{\frac{3}{4}} + \left( 1 - \frac{A_0}{A_2} \right)^2 \right] \quad (3.18)$$

The loss coefficient,  $\zeta_{quad}$ , is a function of both the ratio of the orifice throat area to the upstream area ( $A_0/A_1$ ) and the ratio of the orifice throat area to downstream area ( $A_0/A_2$ ).

For the initial model, experimental correlations published by Idelchik [11] were used to compute the loss coefficient for a variety of geometries. The order of magnitude valve model is shown in Figure 3-9 where the  $x$ -axis represents the Reynolds number and the  $y$ -axis represents the loss coefficient ( $\zeta$ ) values for different valve openings ( $h_v$ ). The model shows that in the turbulent regime the loss coefficient is a weak function of the Reynolds number (as expected). As the Reynolds number decreases, transition to the laminar regime starts and eventually for sufficiently low Reynolds numbers the flow becomes laminar. Figure 3-9 also shows the significant dependence of the loss coefficient ( $\zeta$ ) to the valve opening ( $h_v$ )



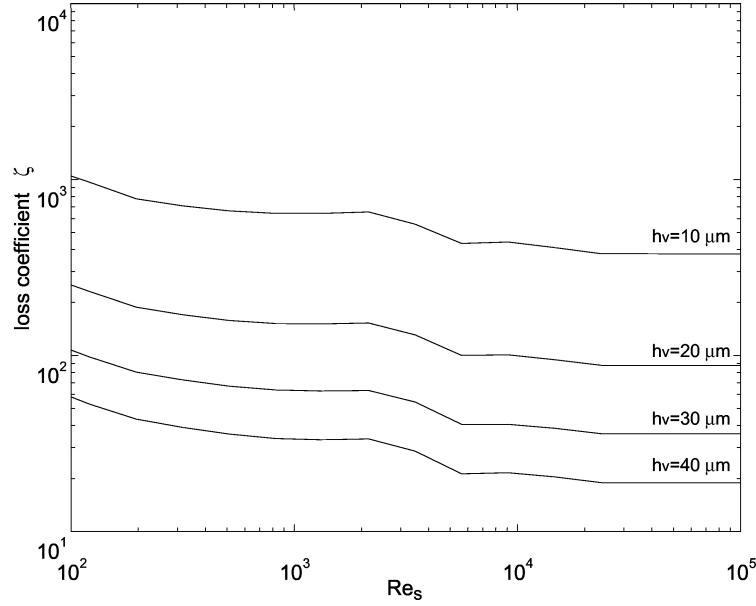


Figure 3-9: Order of magnitude valve model. Results are shown for different valve openings  $h_v$

This order of magnitude model aims to capture the flow physics of the valve and establish within an order of magnitude the head losses. The model takes into account such effects as valve opening ( $h_v$ , valve cap diameter ( $d_v$ ) and downstream chamber height ( $h_p$ ). This model, however will not be able to capture the effect of the seat width ( $s$ ).

### Comparison of Resistive Elements

The comparison of loss coefficients ( $\zeta$ ) versus a system wide Reynolds number. The system-wide-Reynolds-number ( $Re_s$ ) is based on one representative reference length for the whole system. In the MHT case the selected reference length is the valve inlet diameter ( $d_0$ ). The local Reynolds numbers are converted to the system-wide-Reynolds-number by using:

$$Re_s = \frac{d_h}{d_0} Re \quad (3.19)$$

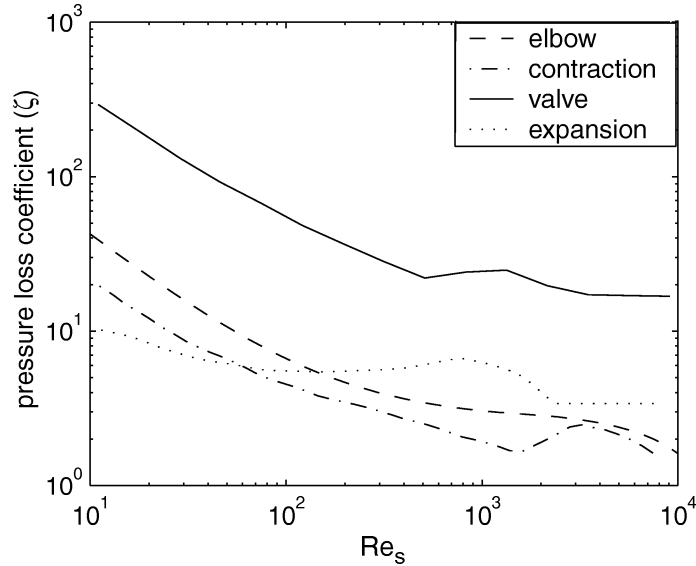


Figure 3-10: Comparison of component loss coefficients vs  $Re_s$

where  $d_h$  is the local hydraulic diameter,  $d_0$  is the reference length for the system, and  $Re$  is the local Reynolds number.

is shown in Figure 3-10. It should be pointed out that because flow correlations at these low Reynolds numbers are not always reliable they need to be validated through experiment and computations.

Initial results shown in figure 3-10 indicate (confirming previous assumptions) that the valves are the dominant loss element in the hydraulic system. For this reason the valve design and analysis required special attention.

## 3.2 SIMULINK Model Implementation

SIMULINK is a graphical interface (based on the MATLAB architecture) for modeling, simulating and analysing dynamical systems. SIMULINK allows the user to break-up a system into smaller interchangeable modules giving flexibility without sacrificing performance.

The implementation of the hydraulic lumped model into SIMULINK is divided into two major areas: the implementation of the previously described fluidic resis-

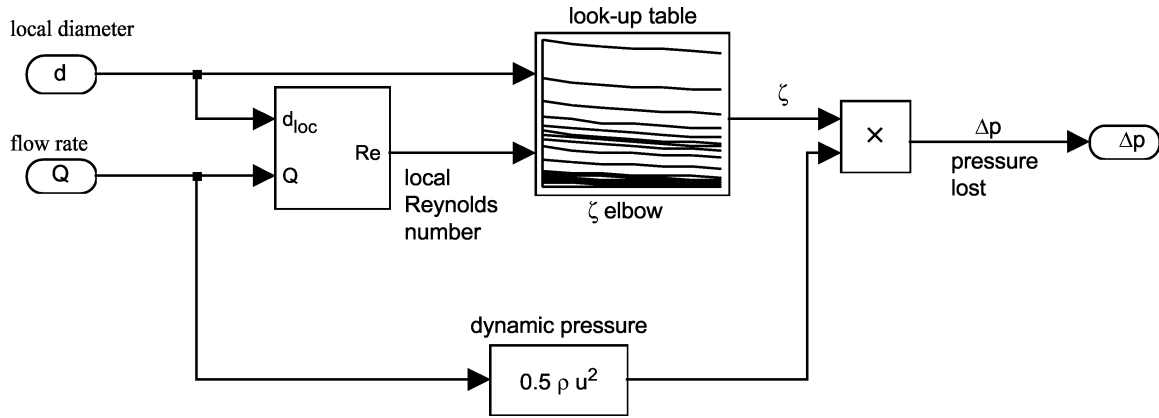


Figure 3-11: Generic Architecture of Fluidic resistances in Simulink

tances and the coding of the flow rate equations.

Each fluidic resistance was coded into a generic fluidic resistance module. Considering that the pressure losses due to fluidic resistances undergo significant qualitative changes for different flow rates the values for each element were coded as two-dimensional look-up tables. The advantage of doing this is that SIMULINK only has to interpolate the correct head loss value from given local flow conditions from the look-up table. This operation is computationally inexpensive and more accurate than using correlation formulas. The look-up tables have as input the local Reynolds number which is computed from the instantaneous flow rate and the dimensions of the element (i.e. diameter, length, etc.) The result is given as a loss coefficient ( $\zeta$ ) which is then converted to a pressure loss by substituting the loss coefficient into equation 3.16. A typical fluidic resistance block is shown in Figure 3-11.

The flow rate equations 3.2 and 3.3 were coded in the following manner to accomodate for SIMULINK's architecture:

$$Q = \int \left( \frac{P_{hpr} - P_{ch} - \Delta P_v(Q) - \Delta P_1(Q) - \Delta P_2(Q)}{I} \right). \quad (3.20)$$

In equation 3.20  $Q$  is the flow rate,  $P_{hpr}$  is the upstream pressure (Pressure in the high pressure reservoir),  $P_{ch}$  is the downstream pressure (pressure in the chamber),

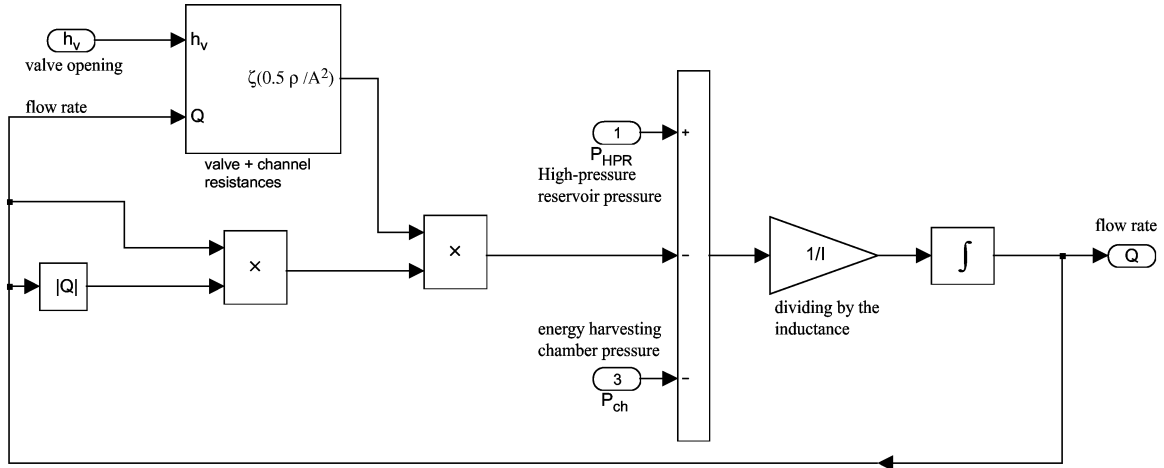


Figure 3-12: Simulink Representation of the Flow Rate Equation 3.20

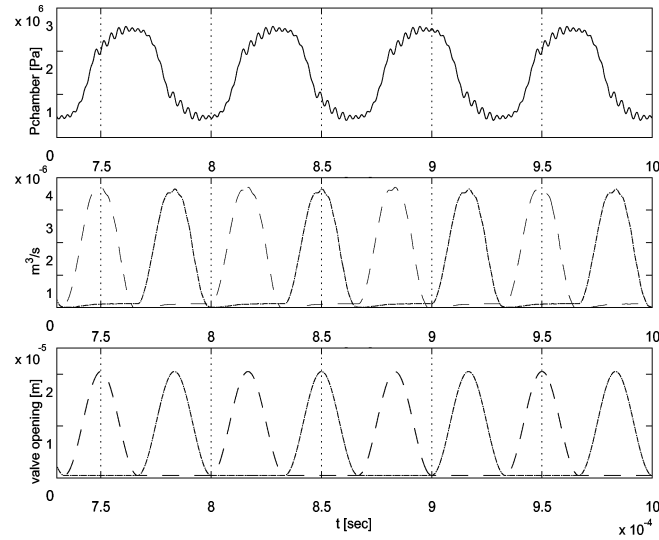


Figure 3-13: Time histories of chamber pressure, inlet valve flow rate, outlet valve flow rate and valve openings for the resonance condition of an Energy Harvester,[36]. Continuous lines are for inlet parameters

$\Delta P_v(Q)$  is the head lost at the valve and  $I$  is the fluid inductance defined by equation 3.14. It should be noted that the head loss across the valve is also a function of the flow rate ( $Q$ ) and that the equation is solved iteratively by SIMULINK. Equation 3.20 is shown in its SIMULINK representation in figure 3-12.

Plots of sample simulations are shown in Figure 3-13. The high frequency ripples of the chamber pressure signal are due to piston dynamics included in the model.

### 3.3 Summary

This chapter described the lumped parameter model chosen for initial designs and calculations. A detailed explanation of the lumped model structure for the Micro-Hydraulic Transducer was formulated. The dominating components were identified and order of magnitude comparisons between components were made. The microvalve was identified as the dominating resistance suggesting the need of a more accurate model to optimize the valve. The SIMULINK version of the model was presented and sample time histories have been included.

# Chapter 4

## Experimental Setup

The research strategy previously discussed called primarily for an experimental approach to study the microvalve behavior. As mentioned before, even partial instrumentation of a microvalve is not trivial, for this reason a scaled up version, a macro-scale valve experiment was considered.

In this chapter, the geometrical and dynamic similarity concepts employed to relate the macro to micro-scale scale results are discussed. The relevant non-dimensional numbers are defined and the scaling effects are explored. The second section of the chapter will cover the experimental macro-scale facility. Fabrication, instrumentation, and setup capability issues are addressed. Finally, the experimental methodology and data validation tests are presented.

### 4.1 Experiment Design

The flow conditions between a model and a prototype are similar if geometric, kinematic and dynamic similarity is achieved. Once similarity is achieved the results obtained with the model can be related to the prototype via previously defined scaling laws.

Geometrical similarity is attained by replicating the geometry of the full scale (microvalve) at the macro-scale. Kinematic similarity is obtained if the model and prototype have homologous length-scale ratio and time-scale ratio. A result of the

temporal and spatial ratio equivalence will be a similar velocity ratio and therefore a kinematic similarity. Dynamic similarity refers to a model/prototype system with equivalent force-scale ratio throughout. Dynamic and kinematic similarity are attained by matching the Reynolds and Strouhal numbers [34].

The Reynolds number

$$Re = \frac{l\bar{u}}{\nu} \quad (4.1)$$

represents the ratio of inertial to viscous forces and is a function of the length scale ( $l$ ), the local mean flow velocity ( $\bar{u}$ ), and kinematic viscosity ( $\nu$ ). Expressing the Reynolds number as a function of a flow rate ( $Q$ ), we obtain

$$Re = \frac{Q}{\nu l}. \quad (4.2)$$

For a fixed flow rate ( $Q$ ), the Reynolds number scales linearly with the length scale ( $l$ ).

The Strouhal number is used to describe the unsteadiness of a flow, and it is defined as:

$$S = \frac{fl}{\bar{u}} \quad (4.3)$$

where  $f$  is the oscillatory frequency of the flow,  $l$  is the characteristic length scale, and  $\bar{u}$  is the local flow velocity. For a fixed Reynolds and Strouhal number, the driving frequency ( $f$ ) scales as the reciprocal of the length scale squared ( $f \propto l^{-2}$ ).

The pressure drop in a scaled-up model of the micro-valve is also a function of the length scale. In this case, assuming that the head loss across a microvalve is characterized by a loss coefficient as defined by equation 3.16. Replacing the flow velocity ( $\bar{u}$ ), by the Reynolds number, and solving for the pressure drop we obtain:

$$\Delta P = \frac{\zeta}{2}\rho \left( \frac{Re \cdot \nu}{l} \right)^2 \quad (4.4)$$

which shows that the pressure drop ( $\Delta P$ ) is inversely proportional to the square

of the length scale ( $l$ ).

### 4.1.1 Scale Effects

One disadvantage of scaling up a system is that some parameters are difficult, or impossible to scale properly. In the present case, the most obvious parameter that was not matched was that of the surface finish, but this is thought to be less important. However, one attribute of microfabrication that is important to match is the sharp corners that define MEMS-fabricated edges. Care was taken to ensure that this feature was preserved in the macro-rig.

Another disadvantage of scaling up a system is that some effects that may be considered negligible in the full scale (micro-scale) system do have an important effect as the system is scaled up. An important scale effect observed in the macro-scale facility was that of gravity. The Froude number is defined as

$$Fr = \frac{(Re \cdot \nu)^2}{l^3 g} \quad (4.5)$$

where the  $Re$  is the Reynolds number,  $\nu$  is the kinematic viscosity,  $l$  is the length scale and  $g$  is the gravitational constant. For a fixed Reynolds number Froude is inversely proportional to the third power of the length scale. In the micro-scale  $Fr \approx 30000$  which tells that gravity effects are negligible. For the macro-scale experiment the Froude number becomes about 30 which shows that gravity effects are important.

Once the scaling relations were known, it was important to relate these parameters to practical experimental considerations. In choosing a convenient scale factor several issues needed to be addressed :

- Machining limitations
- Instrumentation
- Actuation frequency
- Flow rates
- Expected pressures



A scaled up version of the microvalve should be machined using traditional methods such as milling and turning. The use of standard machine shop technology significantly reduced lead times and allowed for quick modifications of parts.

A properly scaled macrovalve would permit the use of off-the-shelf instrumentation such as pressure sensors, flowmeters and temperature sensors. A fundamental advantage of the scaled-up system is that there is enough space for instrumenting the valve test section and monitoring the flow rates, pressures, valve position and temperature of the fluid at the same time. The ability to measure all these parameters gives a clearer picture of the flow behavior.

The actuation frequency ( $f$ ) of the valve is an important factor for the sizing of the macro-scale experiment. It should be pointed out that although this parameter has no effect on steady-state measurements, the same setup will be employed for future unsteady macro-scale experiments and therefore should be considered as a design requirement. The intent is to lower the operational frequency so that a conventional actuator may be employed to drive the valve.

Considering all the above listed requirements and issues, a scaling factor of ten was chosen for the macro-scale experiment, resulting in a valve of approximately 1 cm in diameter. The stroke of the valve is 400  $\mu\text{m}$ . The size of the setup allowed for complete instrumentation. The driving frequency for an actuated valve would be in the range of 100 Hz. The maximum flow rate needed was in the order of 3 liters-per-minute. The expected pressures were in the range of 1000 to 20,000 Pa. These were the functional requirements that drove the experimental setup design.

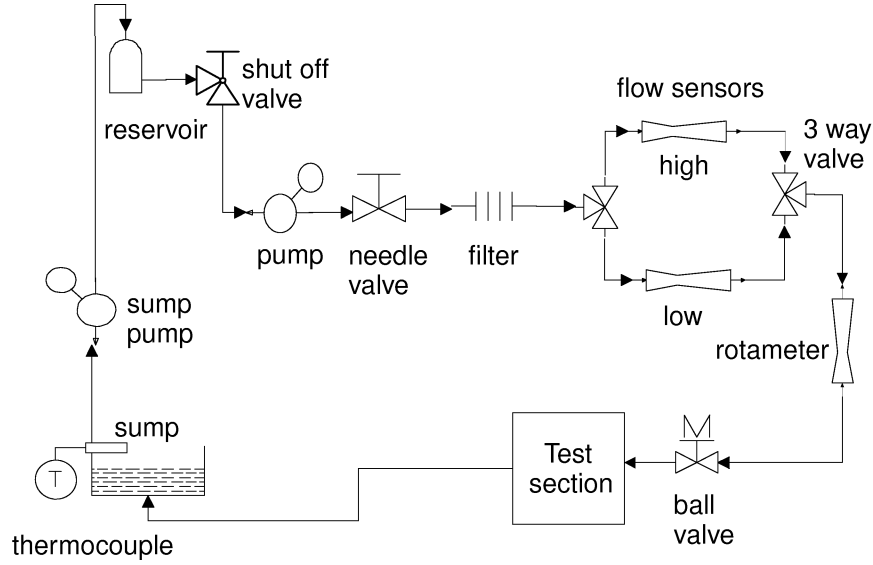


Figure 4-1: Schematic of the macro-scale test facility layout.

## 4.2 Macro-scale setup

### 4.2.1 Fluid Delivery Section

A schematic of the experimental setup is shown in Figure 4-1. The fluid used for the experiments is deionized water which flows from the reservoir to a 1/15 HP centrifugal pump passing through a control needle valve and into a 50  $\mu\text{m}$  particulate filter. The purpose of the filter is to remove any particulates that could clog the flowmeters and doubles as a settling chamber for the incoming fluid.

The range of flowrates explored in the experiments required the use of multiple pressure sensors and flowmeters in order to accurately monitor the spectrum of test conditions. The setup includes two Cole-Palmer differential pressure liquid flowmeters (Cole-Parmer model 32916-16 and 14) each with an uncertainty of 3% (full scale). The low discharge flowmeter has a maximum flow rate of 1 liter/min and the high discharge flowmeter has a maximum discharge of 5 liters/min. Both flowmeters have a 0-5 volt output to the data acquisition system. A rotameter was placed in series with the flowmeters to ensure consistency in the measured flowrates. The calibration of each flowmeter was checked gravimetrically prior to the experiments.

The water then flowed into the test section and to the sump where the temperature of the water was measured. The temperature was measured using an Omega K-type submersible thermocouple and corroborated with a regular thermometer. The Temperature ( $T$ ) data was used to correct the dynamic viscosity ( $\mu$ ) of the deionized water according to:

$$\mu = \left\{ \frac{0.1}{-120 + 2.1428 (T[^\circ C] - 8.435 + \sqrt{8078.4 + (T[^\circ C] - 8.435)^2})} \right\} \quad (4.6)$$

obtained from Richter [26]. Once in the sump, the water was pumped back to the reservoir using an automatic sump pump completing the circuit.

### 4.2.2 Test Section

The test section, illustrated in Figure 4-2, is axisymmetric with the test fluid flowing in from the center tube and exhausting radially outward. The test section may be subdivided into three subsections: inlet, valve and positioning section. The inlet section consists of a 3/8in Aluminum tube, 36in (96 diameters) long. The tube is connected to the valve section and special care was taken to ensure that the inside surface was free of gaps and steps.

The valve section has two cylindrical plates, which were ground flat to a specified planarity of less than 1 mil (checked with dial gauge). Accurate control of the separation of the two plates is critical to the experiment, and so, to ensure that the plates were parallel, they were separated by three thickness gauges placed 120° apart, and tightened with screws. The separation was then re-checked with thickness gauges and a depth micrometer. Dowel pins ensured the concentricity of the upper and lower plates. The upper plate also serves as guide for the valve, which slides up and down inside a sleeve.

The valves, as well as the seats, were fabricated such that all the edges remained sharp with no appreciable fillets (checked under a microscope). This is important

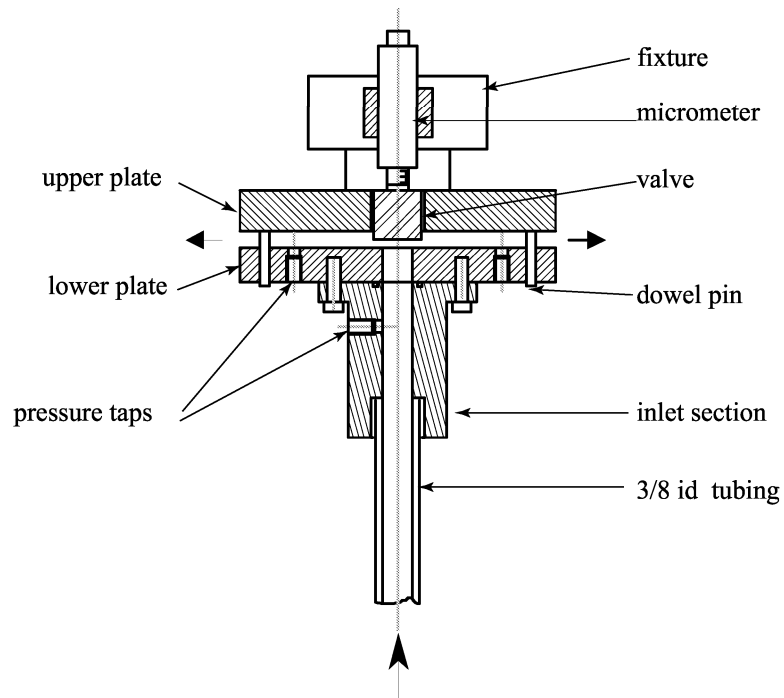


Figure 4-2: Test section detail of the macro scale test facility.

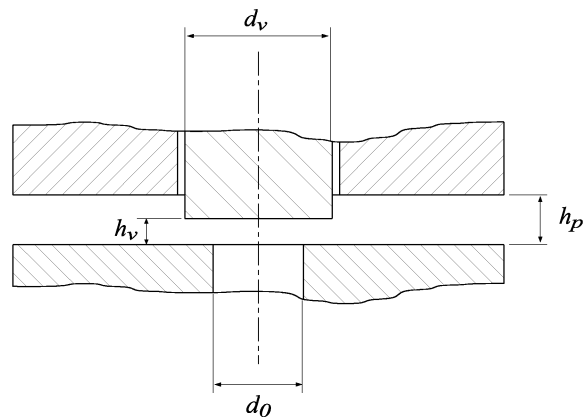


Figure 4-3: Valve geometry detail.

Table 4.1: Valve diameters ( $d_v$ ) with corresponding seat widths ( $s$ ) and non-dimensional seat widths ( $\sigma$ )

	Valve diameter ( $d_{sys}$ )	Valve seat width ( $s$ )	$\sigma$
1	0.383 in (9.72 mm)	0.004 in (0.10 mm)	0.01
2	0.437 in (11.10 mm)	0.031 in (0.78 mm)	0.08
3	0.562 in (14.24 mm)	0.093 in (2.36 mm)	0.25

because, as mentioned above, the flow is quite sensitive to rounded edges which would not be present in a MEMS-fabricated fluidic system. Pressure was sensed both upstream and downstream of the valve. Two pressure-sensing ports, 180° apart, were used downstream, to ensure that the flow was symmetric. Pressure sensing both upstream and downstream of the valve was performed using two wet-wet differential pressure transducers. The low-side transducer was a Setra model 230 with a pressure range of 0-2 psid and accuracy of  $\pm 0.25\%$ (FS). The high-side sensor was a sensotec model FP2000FDW1VJ with a range from 0-150 psid. The accuracy of this sensor is quoted as 0.1%(FS).

The valve head was positioned using a micrometer (accuracy  $\pm 5 \mu\text{m}$ ) with a special non-rotating head, bonded to the valve. The valve position was measured before and after each measurement with a thickness gauge.

### 4.2.3 Valve Geometry

The valve geometry employed for the experiments is detailed in Figure 4-3. The inlet diameter ( $d_0$ ) was 3/8 in (9.525 mm), plate separation ( $h_p$ ) was set at 450  $\mu\text{m}$ . The valve opening ( $h_v$ ) was varied from fully-closed to fully-open. Three valve diameters were employed, as shown in Table 4.1. For each of these configurations, the loss coefficient was measured as function of the Reynolds number, valve stroke ( $h^* = h_v/h_p$ ) and seat width ( $s$ ).

#### 4.2.4 Experimental Procedure

The experimental procedure followed for each experimental run is detailed next. The idea behind such a methodology is to minimize the probability of externally induced variations in the test conditions and to minimize the effect of known disturbances such as bubbles, instrument tare offset and temperature transients.

The setup is energized, and the tare of the flowmeters is reset. The position of the valve is set with the micrometer and checked with the corresponding feeler gauge. The valves are then opened and the pump started. In order to dislodge any existing bubbles the flow rate is stepped up to its maximum value. The readout of the flowmeter is checked with the rotameter to assure the consistency of the flow measurements.

The wet-wet differential pressure sensor is purged via the drain screws and the signal is observed in the oscilloscope. The system runs for 5 minutes before any measurement is taken in order to ensure steady state conditions.

The data acquisition system was a National Instruments board and the software employed was LABVIEW release 5.1. The data was sampled at 2 kHz with an over-sampling of 10 points, averaged over 4 periods of 5 seconds each resulting in a total of 10,000 points per reported point. Multiple runs were made cycling from lower to higher flows and viceversa in order to establish if any hysteretic behavior was present.

The data points were converted using the conversions functions provided with each sensor. For each data point the time average and standard deviation were calculated. This information was then saved for further analysis.

#### 4.2.5 Calibration Experiments

In order to ascertain if the test setup and data acquisition systems were properly installed a test experiment was performed. The test experiment was a simple orifice experiment. The test section in this case was substituted by that shown in figure 4-4. This orifice test setup is made of Aluminum and is comprised of 3 parts the upstream section, the orifice plate and the downstream section. The pipe diameter ( $D$ ) is

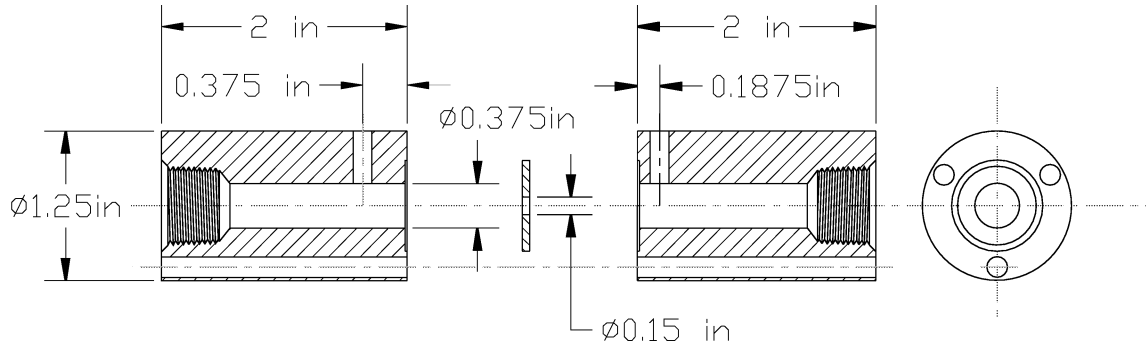


Figure 4-4: Test orifice for calibration

$D = 3/8$  in. The orifice diameter ( $d$ ) is  $d = 0.15$  in and the plate is  $t = 1/16$  in thick. The upstream pressure tap is located  $1D$  diameters from the orifice plate and the downstream pressure tap is located  $1/2 D$  diameters from the orifice plate.

The results of the experiment are shown in Figure 4-5 where the x-axis shows the Reynolds number based on pipe diameter ( $D$ ) and the y-axis is the orifice discharge coefficient. The orifice discharge coefficient  $C_d$  is defined by :

$$C_d = \frac{Q}{A_o} \sqrt{\left( \frac{\rho(1 - \beta^4)}{2\Delta P} \right)} \quad (4.7)$$

where  $Q$  is the flow rate,  $A_o$  is the orifice area,  $\beta$  is the orifice to pipe diameter ratio,  $\rho$  is the fluid density and  $\Delta P$  is the static pressure drop across the orifice. The orifice tested is classified as a thick orifice ( $t^* = 0.425$ ) as opposed to thin orifices which have a  $t^* \leq 0.02$ . For thick orifices the separation bubble created at the orifice leading edge tends to reattach to the orifice walls thus reducing the head loss.

Figure 4-5 shows that the experimental values obtained are approximately 3% higher than those expected for small orifices with reattached flow from published data by Lichtarowicz[16].

As it can be appreciated the data shown is nearly independent of the Reynolds number consistent with the known behavior of orifices for turbulent flow. Another important factor to be noted for this test experiment is that the data shows good

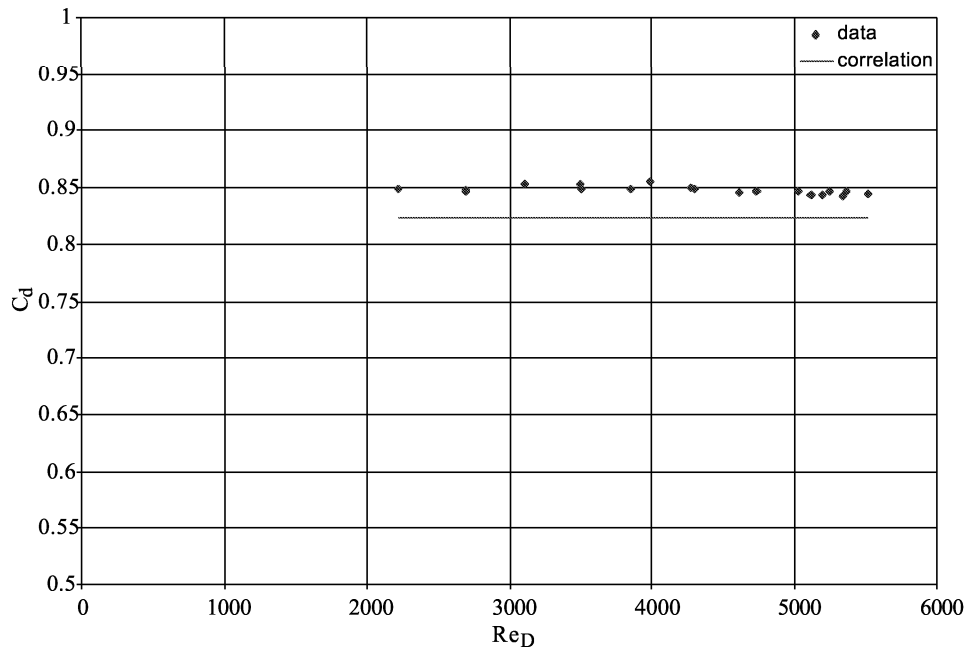


Figure 4-5: Test orifice discharge coefficient vs Reynolds number.

repeatability.

### 4.3 Summary

In this chapter the scaling issues associated with a macro-scale experiment have been discussed. The relevant non-dimensional numbers were defined and scaling powers derived. Practical considerations of scaling up a system were addressed and finally a scaling factor of ten was chosen for the macro-scale facility.

The second part of the chapter focused on the experimental setup of the macro-scale facility. The general architecture of the system was described, and the sensing capabilities of the system were discussed. Finally calibration data is presented and compared to published results.



# Chapter 5

## Experimental Results and Correlations

In this chapter the experimental results for the three valves described previously are reported. The characteristics and sensitivities to various parameters are reported and finally the modified valve model is presented.

### 5.1 Experimental Results

The flow is characterized by a discharge coefficient ( $C_q$ ) which is a function of the volumetric flow rate ( $Q$ ), the inlet diameter ( $d_0$ ), the fluid density ( $\rho$ ), and the static pressure difference ( $\Delta P$ ) as shown by:

$$C_q = \frac{4Q}{\pi d_0 h_p} \sqrt{\frac{\rho}{2\Delta P}} \quad (5.1)$$

This represents the measured flow rate, normalized by the ideal flow rate based on the applied pressure drop and an equivalent area. The Reynolds number is a function of the volumetric flow rate ( $Q$ ), the kinematic viscosity ( $\nu$ ) and the valve opening ( $h_v$ ) and is defined as:

$$Re^* = \sqrt{\frac{Q}{\nu h_v}} \quad (5.2)$$

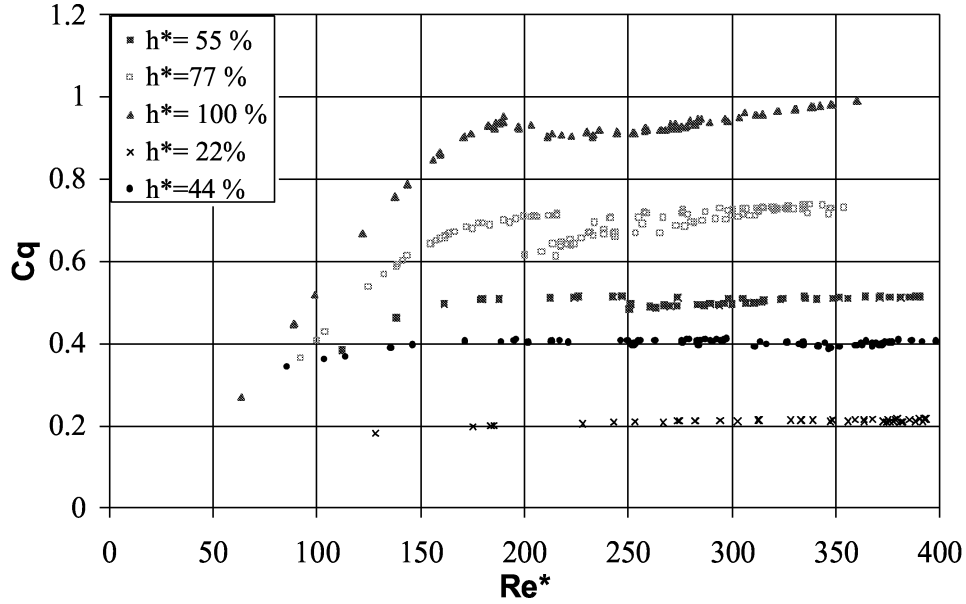


Figure 5-1: Discharge Coefficient vs. Reynolds number for different percentages of valve opening ( $h^*$ ) for valve 1. The plate separation ( $h_p$ ) was  $450 \mu\text{m}$

This scaling is chosen so that, in the laminar flow regime where the flow rate is proportional to the pressure drop, the discharge coefficient is proportional to the Reynolds number. In Figure 5-1 the discharge coefficient  $C_q$  is plotted versus the Reynolds number  $Re^*$  for different percentages of valve opening ( $h^*$ ). It is observed that in the turbulent regime, as expected, the discharge coefficient ( $C_q$ ) becomes a weak function of the Reynolds number and therefore remains almost constant.

In the laminar regime the pressure drop ( $\Delta P$ ) becomes proportional to the flow rate ( $\Delta P \propto Q$ ). The discharge coefficient is then directly proportional to the square root of the flow rate and linearly proportional to the Reynolds number, as defined above. It should be pointed out that closer analysis of the data presented in Figure 5-1 indicates that only the curves for 77% and 100% aperture achieved laminar flow. The remaining curves show a transition regime behavior with  $\Delta P \propto Q^{1.6-1.8}$  depending on the case. Drawing an analogy to pipe flow this is reminiscent of classical low-Reynolds number turbulent behavior as described by Blasius[34]. The qualitative change in the transition point from laminar to turbulent as the percentage of valve opening ( $h^*$ )

changes can be explained if we consider that we have two competing flows. The first one is the parallel plate axisymmetric radially divergent flow that undergoes a continuous deceleration. This flow shows a transition at Reynolds numbers  $Re_0 \approx 2000$ , as shown by Moller[18]. The second flow is an orifice-type flow, which remains turbulent at much lower Reynolds numbers. This explains the fact that as the valve closes the orifice-type effect becomes dominant and turbulent flow continues, even for  $Re_0 < 2000$ .

It should also be pointed out that, in some cases, hysteresis was observed as measurements were taken cycling from lower to higher flow rates ( $Q$ ) and viceversa. Hysteresis is clearly visible for the 77% ( $h^*$ ) curve, and is consistent with observations of Schrenk[29].

Inspection of figures A-2, A-1 and 5-1 shows that the transition Reynolds number varies with valve opening ( $h_v$ ) and seat width ( $s$ ). Observation of the Reynolds number behavior for the different valves suggests that for a given valve the transition Reynolds number is nearly a linear function of the valve opening ratio ( $h^*$ ) as seen in Figure 5-2. Observing that the slopes are similar, a unified formula for the transition Reynolds number is proposed. The transition Reynolds number is described as a function of the valve opening ratio ( $h^*$ ) and the valve diameter ( $d^*$ ) ratio. Having an expression that predicts the transition Reynolds number for different valves and openings we can define a modified Reynolds number ( $Re_m$ ) such that all curves will experience transition at the same point. The curve is empirical in nature and no attempt is made to relate it to physical variables. The modified Reynolds number ( $Re_m$ ) is defined as

$$Re_m = Re_0 - h^* \left( \frac{1 - 0.692d^*}{2.483e^{-3} - 2.818e^{-3}d^*} \right) + \left( \frac{2942 - 2205d^*}{1 - 1.88d^*} \right) \quad (5.3)$$

where  $Re_0$  is the Reynolds number based on the valve inlet diameter ( $d_0$ ),  $h^*$  is the valve opening ratio and  $d^*$  is the valve diameter ratio. The results of the scaling can be seen in Figure 5-3.

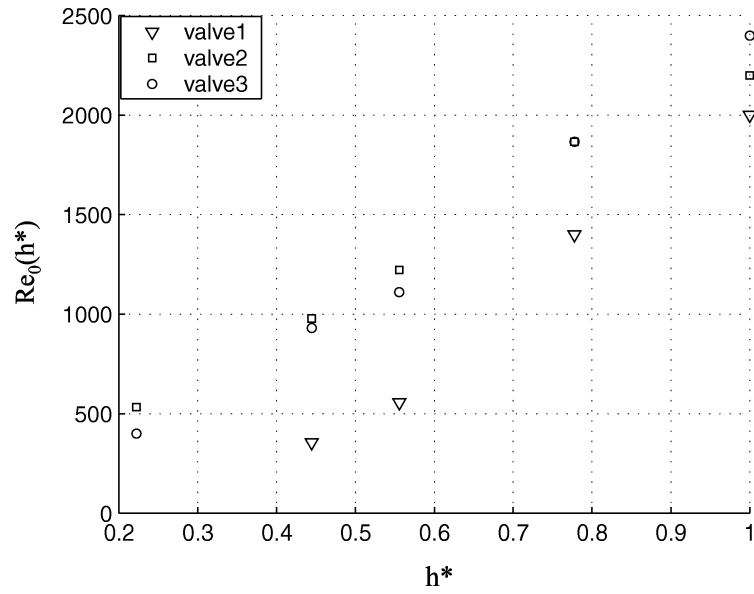


Figure 5-2: Transition Reynolds number vs valve opening ratio,  $h^*$

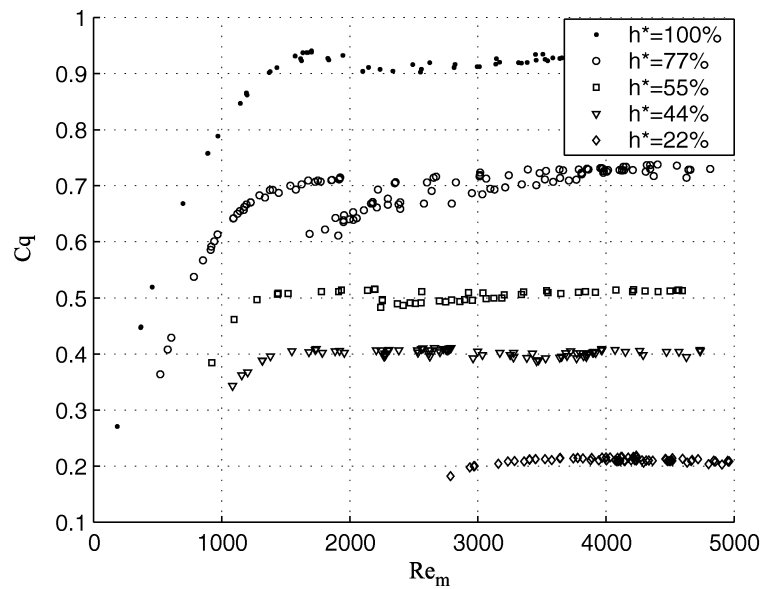


Figure 5-3: Discharge coefficient ( $C_d$ ) for valve #1 vs modified Reynolds number ( $Re_m$ )

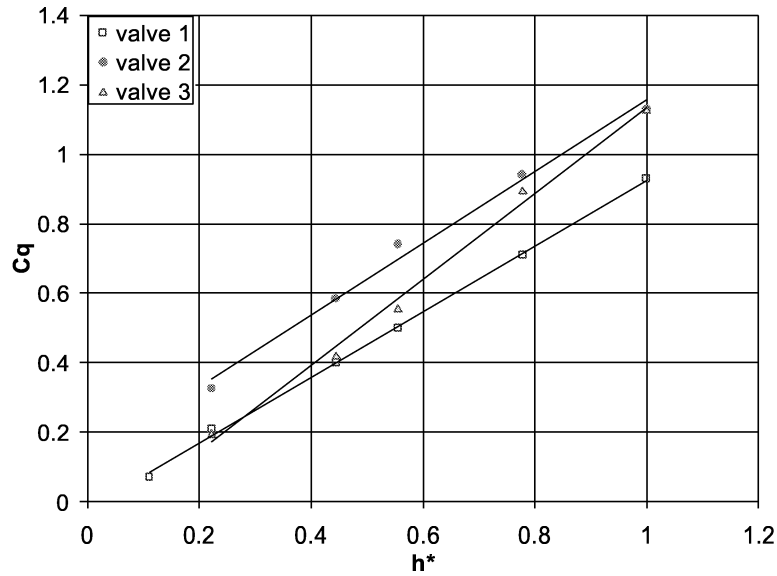


Figure 5-4: Discharge coefficient ( $C_q$ ) vs. non-dimensional valve opening ( $h^*$ ) for the three valves; plate separation ( $h_p$ )  $450\ \mu\text{m}$ .

### 5.1.1 Valve Opening Dependence

The pressure drop vs. valve opening relationship for turbulent flow was explored further and the results are shown in Figure 5-4, where the discharge coefficient,  $C_q$ , is plotted versus the percentage of valve opening ( $h^*$ ) for the three different valves. The discharge coefficient,  $C_q$ , is observed to vary linearly with the valve opening, and to be more-or-less independent of the valve geometry, and shows that, based on the definition of  $C_q$  in equation 5.1, the static pressure difference is proportional to the square of the non-dimensional valve opening ( $h^*$ ). This result emphasizes the importance of maximizing the stroke for these valves in system designs.

Knowing the dependence of the discharge coefficient ( $C_q$ ) to the non-dimensional valve opening ( $h^*$ ) allows us to define a modified discharge coefficient ( $C_m$ ) such that all the curves can be collapsed onto one band for the turbulent flow regime. This modified discharge coefficient is based on the valve opening ( $h_v$ ) raised to some power  $m$ , and on the inlet diameter ( $d_0$ ) having the form:

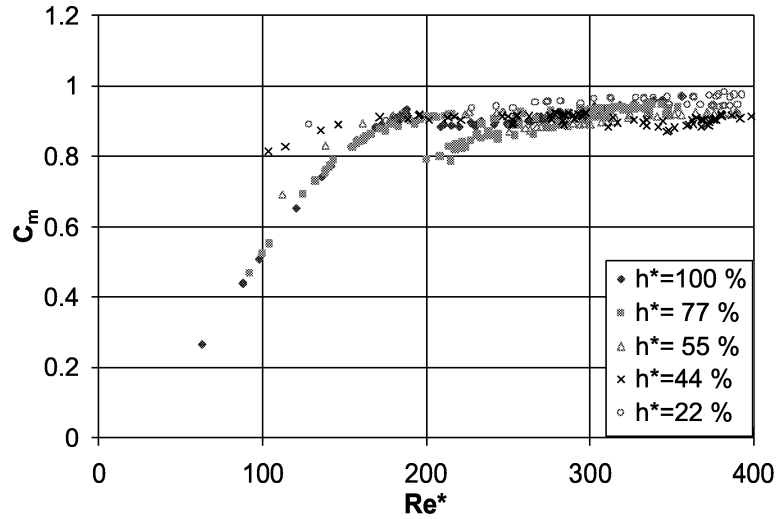


Figure 5-5: Modified discharge coefficient ( $C_m$ ) vs. Reynolds number for valve #1 and plate separation  $h_p = 450\mu\text{m}$

$$C_m = \frac{Q}{\pi d_0 h_v^m} \sqrt{\frac{\rho}{2\Delta P}}. \quad (5.4)$$

The advantage of doing this is that a valve may be modeled rather accurately using a single corrected discharge coefficient formula. Such a scaling can be seen in Figure 5-5 where, for valve #1, the scaling power ( $m$ ) had a value of one. Here, we see that, for all valve openings, the modified discharge coefficient ( $C_m$ ) lies between 0.88 – 0.93. It should be noticed that as transition effects start to become important this approximation fails and should therefore be employed with caution. This behavior also supports the analogy between poppet disc valves and orifices. The same behavior was also observed in the other valves, although the proper scaling coefficient varied slightly. A numerical curve fit indicated that, for valves #2 and #3, a value of  $m = 0.8$  provided a better collapse of the data in the high-flow regime. The change in the value of  $m$  is a consequence of flow reattachment to the valve seat as the valve opening to seat width ratio becomes smaller. This effect is addressed in detail in the following subsection.

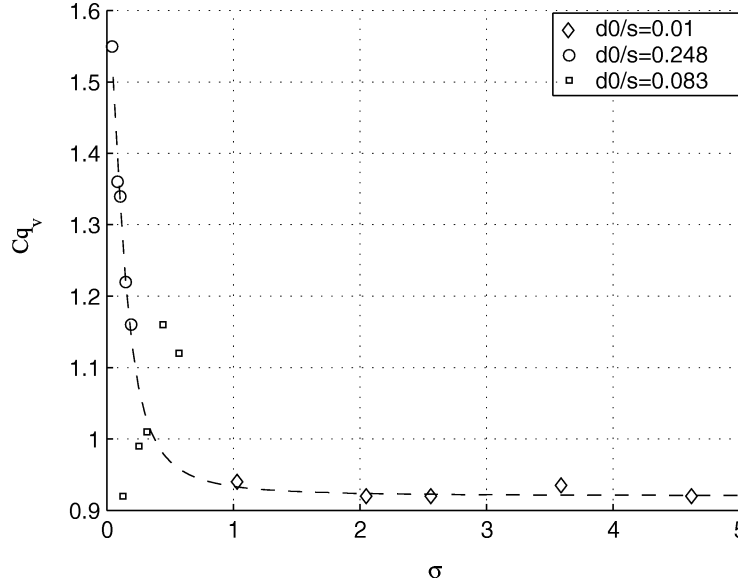


Figure 5-6: Discharge coefficient vs. non-dimensional seat width ( $\sigma$ ). The plate separation was  $h_p=450 \mu\text{m}$ .

### 5.1.2 Valve Seat Width Dependence

The effect of the valve seat width was investigated with three valves of different seat widths ( $s$ ). The results are shown in Figure 5-6 where the  $x$ -axis shows the ratio of valve opening ( $h_v$ ) to seat width ( $s$ ), defined as ( $\sigma$ ). The  $y$ -axis uses the modified discharge coefficient ( $C_m$ ) with a scaling power  $m=1$ . One interesting result is that for values of  $\sigma > 1$  the modified discharge coefficient is not affected by the seat width,  $s$ . Once this threshold is passed, however, the discharge coefficient becomes very sensitive to the seat width and rises rapidly. Significant pressure recovery is observed, even surpassing  $C_m=1$ . This increase in discharge coefficient may be explained by drawing an analogy to thick orifices. For a thick orifice, the separation bubble tends to reattach within the throat area as shown by Sahin et al.[28]. The reattachment reduces the flow losses across the orifice. For the case where the non-dimensional seat width  $\sigma < 1$  the same phenomenon is observed and we theorize that the separated flow undergoes reattachment with the accompanying pressure recovery.

The results shown in Figure 5-6 are consistent with those obtained by Johnston *et*

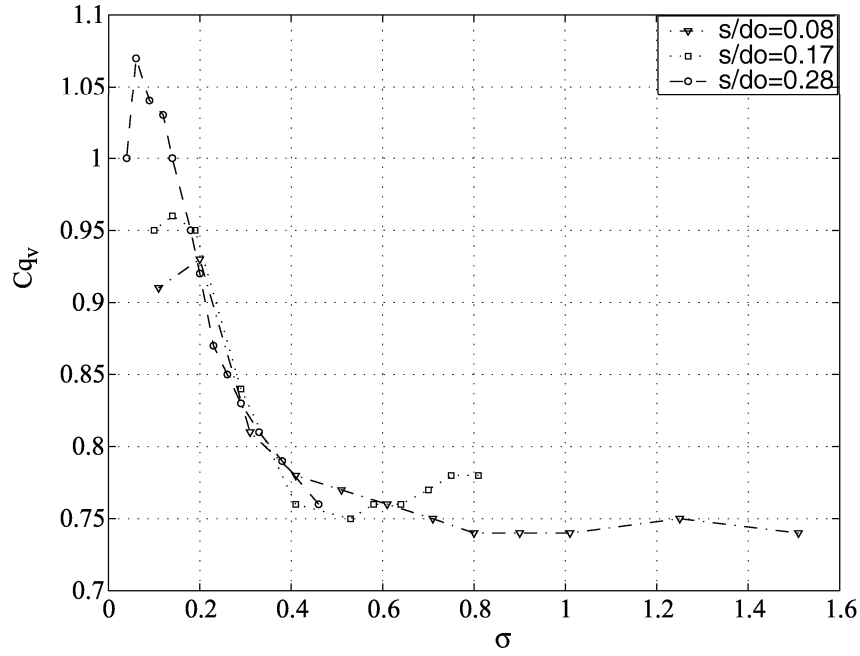


Figure 5-7: Seat width effect on discharge coefficient from Johnston *et al* [14]

*al*[14], shown in Figure 5-7, and Lichtarowicz[15] . The main difference seen, though, is that Johnston observed a minimum  $C_m$  of 0.75 where we observed a higher value of approximately 0.9. The reason for this difference is attributed to geometrical differences in the valve test setup. However it is recognized that although the trends are similar to those of other researchers more experiments are required to fully characterize this behavior. A curve fit for the discharge coefficient ( $C_m$ ) as a function of  $\sigma$ , the valve opening over seat width ratio, is given by

$$C_m = \left\{ 0.9203 + \frac{0.6755}{1 + \left( \frac{\sigma}{0.1327} \right)^{1.9361}} \right\} (h^*)^{-b}. \quad (5.5)$$

where  $b$  is given by

$$b = \frac{\frac{0.1}{1 + \exp\left(\frac{Rem - 2050}{200}\right)}}{1 + 10^{\left(\frac{\ln(s/0.25)}{0.5}\right)}} \quad (5.6)$$

which is a function of the valve seat width ( $s$ ) and the modified Reynolds number. The value of  $b$  oscillates from 0 to 0.1 depending on flow conditions. The valve opening



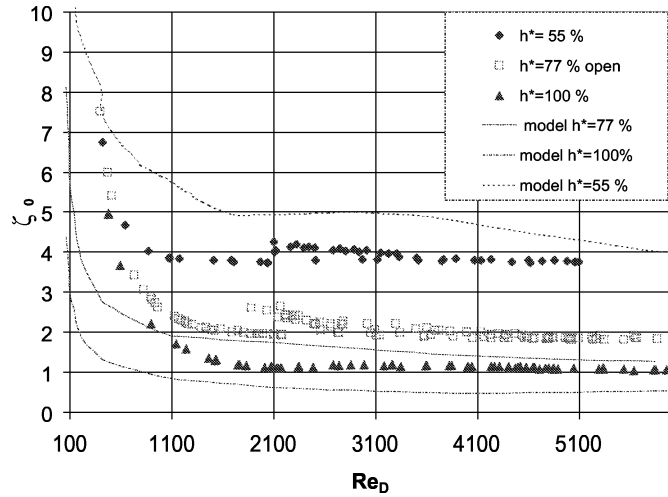


Figure 5-8: Loss coefficient vs. Reynolds number comparison between experimental results and the lumped model for various valve opening percentages ( $h^*$ ).

dependence changes slightly as the Reynolds number decreases reaching the transition zone changing the exponent  $b$  from 0 to 0.1. The effect is related to the Reynolds number dependence of the reattachment point as pointed out by Nakabayashi and Ichikawa[20].

One important factor to mention is the behavior observed with valve #2, this valve shows a flow reattachment similar as that shown by valve #3. The behavior of valve # 2, however reaches a maximum and then a sharp decrease of the discharge coefficient is observed. In this case it is hypothesized that surface friction forces become important diminishing the effect of the pressure recovery product of the flow reattachment as pointed out by Lichtarowicz[15]. More experiments are required in the future to map and understand this behavior and available data from other researchers shows considerable scatter making more difficult the task of identifying the point where the maximum is reached.

### 5.1.3 Comparison of Lumped Model to Data

A comparison of the original lumped model and the data for valve #1 is presented in Figure 5-8, where the  $x$ -axis is the Reynolds number based on the inlet flow area ( $A1$ ), as defined by:

$$Re_0 = \left( \frac{4Q}{\pi d_0 \nu} \right) \quad (5.7)$$

and the  $y$ -axis is a loss coefficient  $\zeta_0$  defined by:

$$\zeta_0 = \frac{\Delta P_0}{\frac{1}{2} \rho \left( \frac{Q}{\pi d_0 h_v} \right)^2} \quad (5.8)$$

where  $\Delta P_0$  is the total pressure drop,  $\rho$  is the fluid density,  $Q$  is the volumetric flow rate,  $d_0$  is the inlet diameter and  $h_v$  is the valve opening. It is observed that the original order-of-magnitude flow model captures correctly the flow physics of the valve although the numerical values are off by a factor of 2 with respect to experimental values. In addition, the original model does not accurately capture the transition point.

## 5.2 Modified model

It may be argued that the valve flow cycles from a dominant axisymmetric radially divergent parallel plate flow to an orifice flow depending as a function of the valve opening. In order to establish a more accurate prediction for the start of transition regime a closer look at the flows is important.

### 5.2.1 Detailed orifice model background

The thin sharp edged orifice flows have been studied in detail by many researchers. The turbulent behavior of orifices is heavily documented and because of its use as flowmeter, standard empirical correlations exist. Transition in this flows is observed for Reynolds numbers (based in the orifice diameter) in the range of 3000 – 4500 as

reported by Reader-Harris[25]. Reader-Harris and coworkers presented a new correlation for the enlarged EEC/API database. The database includes data for orifices from 50 and 600 mm pipes. The improved orifice discharge ( $C_d$ ) equation[25] is given by:

$$\begin{aligned}
C_d = & 0.5934 + .0232\beta^{1.3} - 0.2010\beta^8 + .000515 \left( \frac{1e^6\beta}{Re_D} \right)^{0.7} \\
& + (0.0187 + 0.04A_r)\beta^{3.5} \max \left\{ \left( \frac{1e^6}{Re_D} \right)^{0.3}, 23.1 - 4800 \frac{Re_D}{1e^6} \right\} \\
& + (0.043 + (0.090 - A_r) \exp^{-10l_1} - (0.133 - A_r) \exp^{(-7l_1)})(1 - A_r) \left( \frac{\beta^4}{1 - \beta^4} \right) \\
& - 0.031(M_2 - 0.8M_2^{1.1}) \left[ 1 + 8 \max \left\{ \log \left( \frac{3700}{Re_D} \right), 0.0 \right\} \right] \beta^{1.3} \\
& + 0.0015 \max \left( \frac{0.05}{\beta D} - 1, 0 \right)
\end{aligned} \tag{5.9}$$

where

$$M_2 = \frac{2l_2}{1 - \beta} \tag{5.10}$$

and

$$A_r = \left( \frac{2100\beta}{Re_D} \right)^{0.9}. \tag{5.11}$$

The orifice discharge coefficient ( $C_d$ ) is seen to be a function of the orifice to pipe diameter ratio ( $\beta$ ), the Reynolds number ( $Re_D$ ) based on the pipe diameter ( $D$ ), the distance between the upstream pressure tap to pipe diameter ratio ( $l_1$ ) and the distance between the downstream pressure tap to pipe diameter ratio ( $l_2$ ).

The discharge coefficient for orifices at lower Reynolds numbers ( $Re_d < 1000$ ) is not as well known. Results by Mills[34] and Sahin[28] suggest that for Reynolds numbers up to  $Re_d \approx 25$  the orifice discharge coefficient for laminar flow[34] is given by:

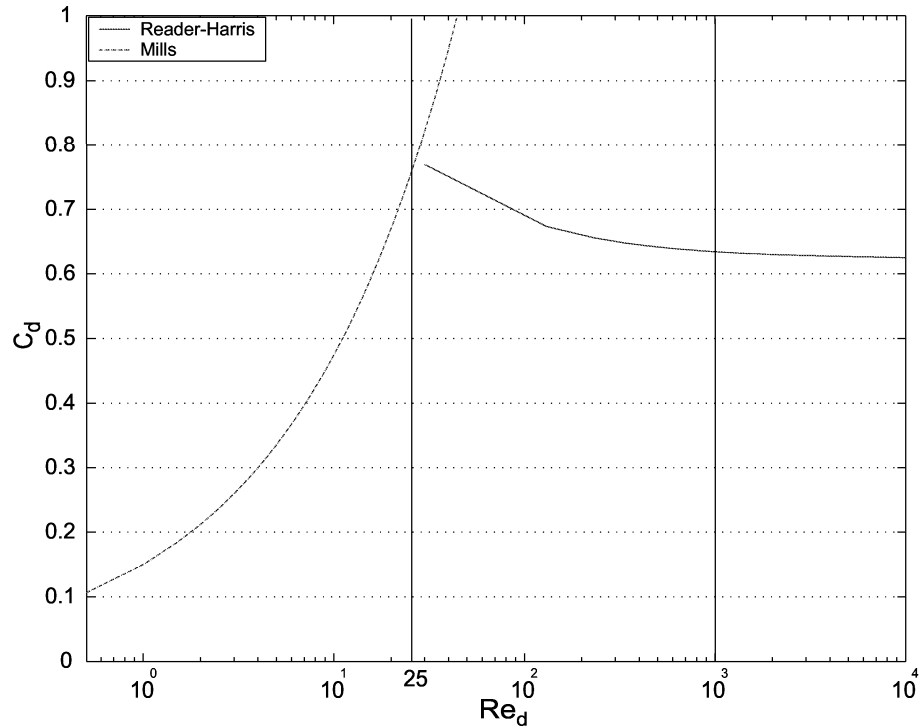


Figure 5-9: Sharp edged orifice discharge coefficient vs Reynolds number

$$C_d = 0.15\sqrt{Re}. \quad (5.12)$$

Combining the known turbulent behavior described by equation 5.9 and the laminar flow behavior of equation 5.12 a map for the behavior of a simple thin sharp edged orifice is shown in figure 5-9. The transition region ranges from  $Re \approx 25$  to  $Re \approx 4500$ .

For Reynolds less than  $10^4$ , the discharge coefficient has to be corrected for Reynolds dependency and surface conditions, and these correlations are less common and less reliable than those for fully rough turbulent regime.

In the case of long orifices results by Lichtarowicz[16] showed that the discharge coefficients are significantly higher than those predicted for thin sharp edged orifices. In particular for non-cavitating long orifices for  $1 \leq Re \leq 10000$  he proposes a curve fit

based on a modified Reynolds numbers ( $Re_h$ ):

$$Re_h = \left( \frac{2\Delta P}{\rho} \right)^{0.5} \frac{d}{\nu} \quad (5.13)$$

which is based on the pressure drop across the orifice ( $\Delta P$ ), the fluid density ( $\rho$ ), the orifice diameter ( $d$ ) and the kinematic viscosity ( $\nu$ ). Lichtarowicz[16] curve fit for the orifice discharge coefficient is given by:

$$\frac{1}{C_d} = \frac{1}{C_\infty} + \frac{20}{Re_h} \left( 1 + 2.25 \frac{l}{d} \right) - \frac{0.005 \frac{l}{d}}{1 + 7.5(\ln(0.00015 Re_h))^2} \quad (5.14)$$

where  $C_\infty$  is the discharge coefficient for  $Re_h > 10000$ ,  $l$  is the thickness of the orifice, and ( $d$ ) is the orifice diameter. The curve fit is very good and describes accurately the results obtained by various researchers for Reynolds numbers between 1 and 10000. Beyond this value the discharge coefficient becomes independent of the Reynolds number (or nearly so) and is described by the equation[16]:

$$C_\infty = 0.827 - 0.0085 \frac{l}{d} \quad (5.15)$$

becoming only a function of length ( $l$ ) to orifice diameter ( $d$ ) ratio. The higher discharge coefficients are attributed to flow reattachment and the subsequent pressure recovery that this brings. For  $l/d = 0.5$  Lichtarowicz found that the orifice discharge coefficient rose rapidly, reaching a peak at about  $Re_h \approx 700$  and then falling rapidly to the ultimate discharge coefficient ( $C_\infty$ ). For longer orifices, the sharp change smoothes out and the irregularity almost disappears.

### 5.2.2 Modified valve model

The similarity between the orifice results of Lichtarowicz (see Figure 5-10 and 5-11) and the present investigation valve results (Figure 5-1) is striking. It is interesting to note how the shape of the curve varies as the length to diameter ratio of the orifice varies. Analogously the valve curve profile varies in the same manner as the opening changes. Qualitatively, as was originally hypothesized, the valve can be seen to behave

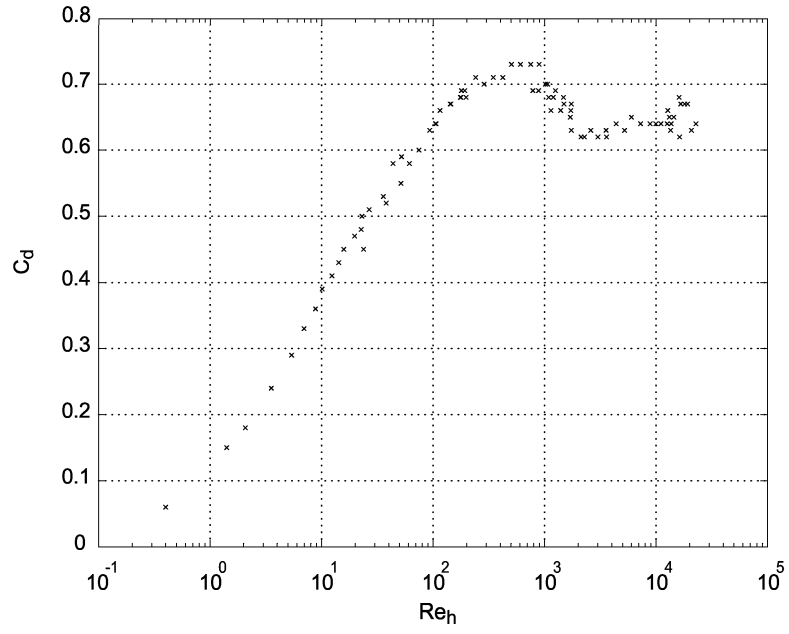


Figure 5-10: Long orifice  $t/d=0.5$  from Lichtarowicz [16]

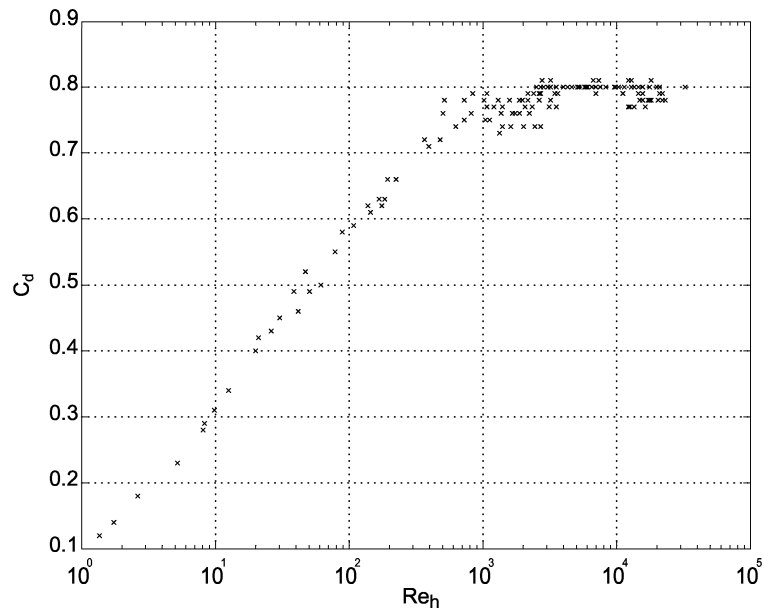


Figure 5-11: Long orifice  $t/d=0.5$  from Lichtarowicz [16]

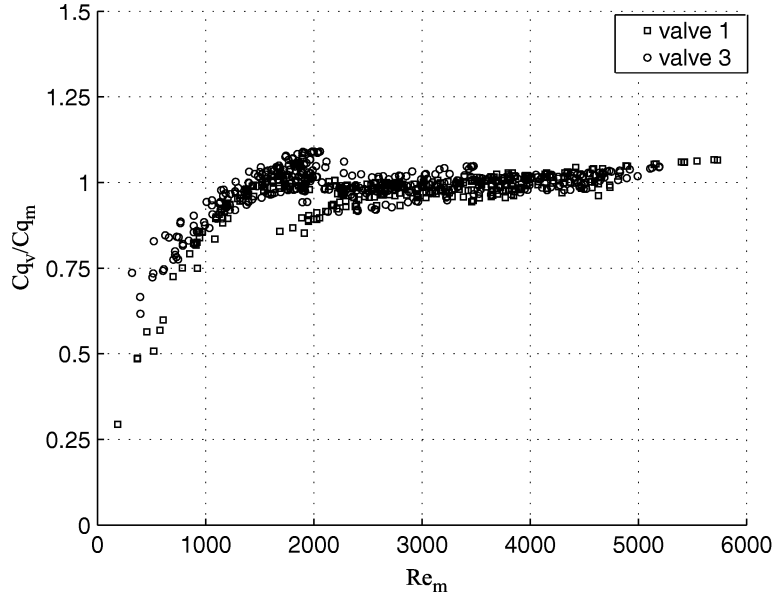


Figure 5-12: Scaled data for valve #1 and valve #3

just as a long orifice but the analogy may be extended to the laminar regime.

Considering the resemblance between the orifice and valve model it is tempting to attempt to correlate the current valve data with an equation similar to Lichtarowics equation 5.14. Using a curve fitting program (DATAFIT by Oakdale Engineering) it is seen that the curves of individual experiments correlate well. In the interest to obtain only one curve for all experiments the current data is scaled using equations 5.3, 5.5 and 5.6. Using this scaling functions the transformed data collapses into one curve as seen in Figure 5-12

The curve shown in Figure 5-12 can be approximated by using equation 5.14 as suggested by Lichtarowicz. The curve however requires different coefficients which were obtained using the curve fitting program DATAFIT. The equation is then given by :

$$\frac{1}{Cq} = 0.956 + \frac{364.89}{Re_m} - \frac{0.194}{1 + 2.608(\ln(0.000718Re_m))^2}. \quad (5.16)$$

The results for valve #1 can be seen in Figure 5-13. The corresponding plots for valves #2 and #3 and a summary of the equations can be found in Appendix A.

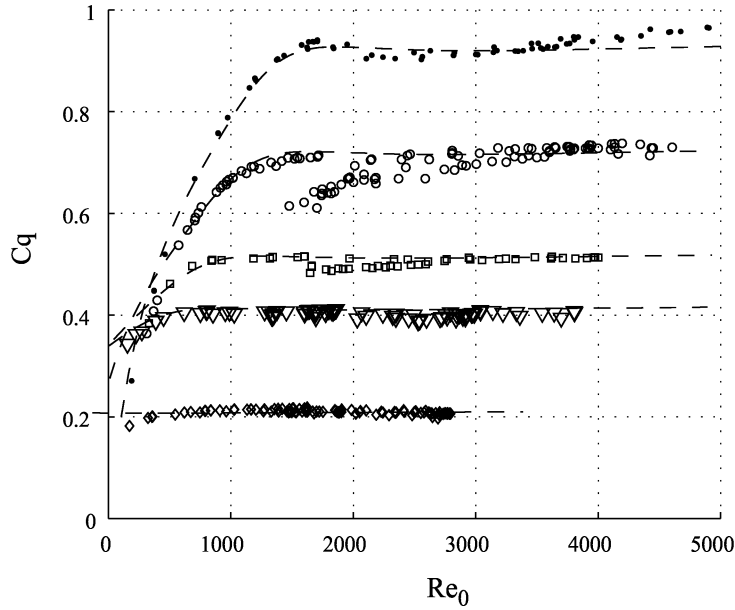


Figure 5-13: Curve fitting using 5.14 for valve #1

### 5.3 Summary

In this chapter the steady state experimental results for three valves of different diameters have been presented. Parametric studies were done for the Reynolds number dependency, valve aperture dependence, and seat width dependence. The results were compared to those the original order of magnitude valve model and found a factor of 2 difference. More detailed analysis revealed that the valve behavior approximated that of a long orifice even in the transition and laminar regimes. For comparison curve fits using an empirical formula for orifices was employed with good results further confirming the analogy in this low turbulence regimes. Finally a generalized coefficient formula as function of valve opening and valve diameter was obtained.



# Chapter 6

## Conclusions and Recommendations

From the outset of this research, the goal has been to generate a model that describes accurately the hydraulic behavior of microsystems. A low-order lumped model was constructed and integrated to a full system simulation. The need to obtain a better representation of microvalve behavior led to experiments to characterize their behavior.

The flow characteristics of a poppet type disc valves with geometries defined by standard microfabrication techniques have been studied employing a 10:1 scale experimental facility. The experiments have shown that the commonly used orifice analogy is a good approximation in the turbulent regime. Transition effects, however are not properly captured by such model. This is attributed to the competing nature of the axisymmetric divergent flow between two parallel plates and the small orifice flow for different valve openings.

The sensitivity to valve stroke has been characterized for the turbulent regime and it was shown that  $\Delta P$  becomes proportional to the square of the valve opening to plate separation ratio ( $h^*$ ).

The valve seat width effect has been investigated showing that for the turbulent regime the modified discharge coefficient,  $C_m$ , is independent of the valve opening to seat width ratio,  $\sigma$ . It has also been seen that for  $s$  less than one, the modified discharge coefficient rises significantly, presumably due to reattachment.

What is particularly encouraging, however, is that the simple model does capture

both the character and (with a factor of about two), the numerical values of the loss-coefficients. This is extremely valuable for the complex design in which many trade-offs need to be balanced to ensure a functional, robust and efficient micro-hydraulic transducer.

A more detailed analysis of the data showed that qualitatively the flow behavior is strikingly similar to that of long orifice for the transition and laminar regimes. The present results were fitted to empirical orifice correlations for Reynolds numbers  $Re_h \leq 10000$ . The resulting model is comprised of two scaling formulas : a modified Reynolds number formula and a discharge coefficient formula (as function of the valve opening to seatwidth ratio). These two formulas allow the re-scaling of the curves into one similarity curve. This curve may in turn be fitted to an orifice empirical orifice formula as in Lichtarowicz[16].

More experiments will be pursued in the near future, including unsteady measurements and measurements in the full-scale (micro) device. A second step in the systematic study of the valve will be unsteady measurements to obtain a better understanding of the unsteady behavior at high frequencies valves. Finally the experiments will be taken to the full-scale prototype microvalves. In this experiments comparisons between the results obtained with the macro-scale valve will be evaluated for the steady and unsteady state.

# Appendix A

## Valve Plots and Summary of Model Equations

The model used for predicting the flow losses is comprised of three main formulas: a Reynolds number scaling, a discharge coefficient scaling and the equation that relates the scaled Reynolds number to the scaled discharge coefficient.

$$Re_m = Re_0 - \frac{1}{h^*} \left( \frac{1 - 0.692d^*}{2.483e - 3 - 2.818e - 3d^*} \right) + \frac{2942 - 2205d^*}{1 - 1.88d^*} \quad (\text{A.1})$$

$$b = \frac{0.1}{1 + \exp\left(\frac{Re_m - 2050}{200}\right)} \left\{ \frac{1}{1 + 10^{\left(\frac{\ln(\sigma) - \ln(0.25)}{0.5}\right)}} \right\} \quad (\text{A.2})$$

$$C_f = \left[ 0.9203 + \frac{0.6755}{1 + \left(\frac{\sigma}{0.1327}\right)^{1.9361}} \right] (h^*)^{-b} \quad (\text{A.3})$$

$$\frac{1}{C} = \frac{C_f}{C_m} = 0.956 + \frac{364.89}{Re_m} - \frac{0.194}{1 + 2.608(\ln(0.000718Re_m))^2}. \quad (\text{A.4})$$

$$C_m = \frac{Q}{\pi h_v d_0} \sqrt{\frac{\rho}{2\Delta P}} \quad (\text{A.5})$$

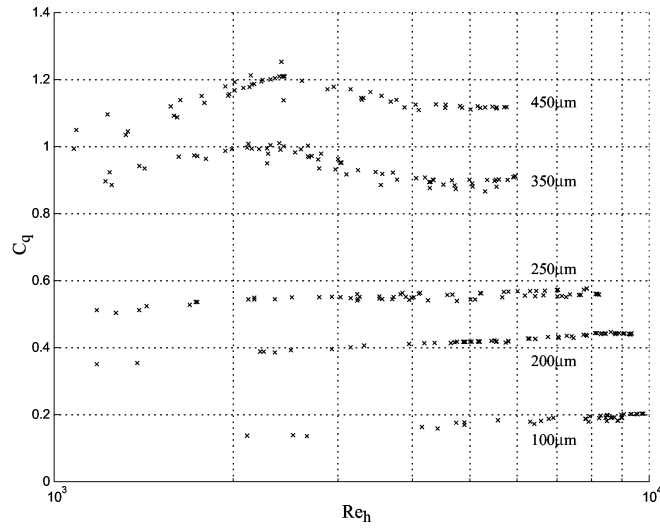


Figure A-1: Reynolds number vs Discharge coefficient for valve 2 ( $d_v=11.10$  mm)

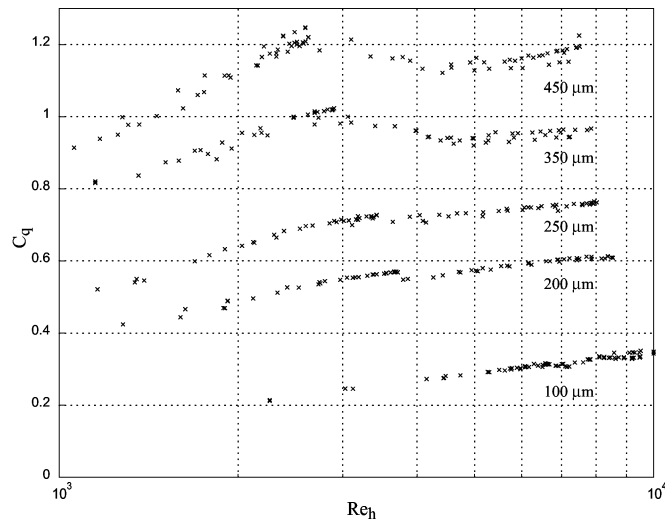


Figure A-2: Reynolds number vs Discharge coefficient for valve 3 ( $d_v=14.24$  mm)

# Bibliography

- [1] A. Ayon, K.-S. Chen, K. A. Lohner, S. M. Spearing, H.H Sawin, and M. A. Schmidt. Deep reactive ion etching of silicon. *Proceedings of the 1998 MRS Fall Meeting - Symposium AA, Materials Science of Microelectromechanical Systems (MEMS). Boston, MA, USA*, 1998.
- [2] T. Bourouina and J. P. Grandchamp. Modeling micropumps with electrical equivalent networks. *Journal of Micromechanics and Microengineering*, pages 398–404, 1996.
- [3] S. C. Burgess, D. F. Moore, D. E. Newland, and H. L. Klaubert. A study of mechanical configuration optimization in micro-systems. *Research in Engineering Design*, 9:46–60, 1997.
- [4] F. K. Forster, R. L. Bardell, M. A. Afromowitz, N. R. Sharma, and A. Blanchard. Design, fabrication and testing of fixed-valve micro-pumps. *Proceedings of the ASME Fluids Engineering Division, ASME*, 234:39–44, 1995.
- [5] P. Gravesen, J. Branebjerg, and O. Sondegard. Microfluidics – a review. *Journal of Micromechanics & Microengineering*, 3:168–182, 1993.
- [6] N. W. Hagood, D. C. Roberts, L. Saggere, K. S. Breuer, K.-S Chen, J. A. Carretero, H. Q. Li, R. Mlcak, S. Pulitzer, M. A. Schmidt, S. M. Spearing, and Y.-H. Su. Micro hydraulic transducer technology for actuation and power generation. *Smart Structures and Materials 2000: Smart Structures and Integrated Systems, Newport Beach, CA*, 3985, March 2000.
- [7] A. K. Henning. Microfluidic mems. *IEEE Aerospace Applications Conference Proceedings, Los Alamitos, CA*, 1:471–486, 1998. This is a full ARTICLE entry.
- [8] A. K. Henning, J. S. Fitch, J. M. Harris, E. B. Dehan, B. A. Cozad, L. Christel, Y. Fathi, Jr. D. A Hopkins, L. J. Lilly, w. McCulley, W. A. Weber, and M. Zdeblick. Microfluidic mems for semiconductor processing. *IEEE Transactions on Components Packaging & Manufacturing Technology Part B-Advanced Packaging.*, 21(4):329–337, November 1998.
- [9] M. Hirano, K. Yanagisawa, H. Kuwano, and S. Nakano. Microvalve with ultra-low leakage. *Proceedings of the IEEE Micro Electro Mechanical Systems (MEMS) 1997. IEEE, Piscataway, NJ*, pages 323–326, 1997.

- [10] C.-M. Ho and Y.-C. Tai. Micro-electro-mechanical-systems (mems) and fluid flows. *Annual Review of Fluid Mechanics*, 30:579–612, 1998.
- [11] I. E. Idelchik. *Handbook of Hydraulic Resistance*. CRC Press, Boca Raton, FL, 1994.
- [12] Y. Ikebe and H. Ohuchi. Generalized formulation of momentum theory. *Fluidics Quarterly*, 10(4):27–46, 1978.
- [13] H. Jerman. Electrically-activated, normally-closed diaphragm valves. *Journal of Micromechanics & Microengineering*, 4(4):210–216, December 1994.
- [14] D. N. Johnston, K. A. Edge, and N. D. Vaughan. Experimental investigation of flow and force characteristics of hydraulic poppet and disc valves. *Proceedings of the Institution of Mechanical Engineers, Part A: Power & Process Engineering*, 205(3):161–171, 1991.
- [15] A. Lichtarowicz. Flow and force characteristics of flapper valves. *Third International Symposium on Fluid Power Turin*, pages B1–1, 1973.
- [16] A. Lichtarowicz, R. K. Duggins, and E. Markland. Discharge coefficients for incompressible non-cavitating flow through long orifices. *Journal of Mechanical Engineering Science*, 7(2):210–219, 1965.
- [17] R. Von Mises. The calculation of flow coefficient for nozzle and orifice. *VDA*, 61:21–23, 1917.
- [18] P. S. Moller. Radial flow without swirl between parallel discs. *Aeronautical Quarterly*, 14:163–185, 1962.
- [19] C. J. Morris and Fred K. Forster. The design-fix for fixed-valve micropumps. *Late News Poster Session, Solid-State Sensor and Actuator Workshop. Hilton Head Is. SC*, pages 11–12, June 2000.
- [20] K. Nakabayahsi and T. Ichikawa. Annular separation bubble near the inlet corner and viscous radial flow between two parallel disks. *Nippon Kikai Gakkai Ronbunshu, B Hen.*, 56(525):1267–1273, May 1990.
- [21] T. Nakada and Y. Ikebe. Measurement of the unsteady axial flow force on a spool valve. *Pneumatic and Hydraulic Components and Instruments in Automatic Control, Proceedings of the IFAC Symposium, Warsaw, Pol.*, pages 193–198, 1980.
- [22] A. Olsson, G. Stemme, and E. Stemme. Simulation studies of diffuser and nozzle elements for valve-less micropumps. *Transducers '97 and International Conference on Solid-State Sensors and Actuators and Chicago*, pages 1039–1042, June 1997.

- [23] A. Olsson, G. Stemme, and E. Stemme. A numerical design study of the valve-less diffuser pump using a lumped-mass model. *Journal of Micromechanics and Microengineering*, 9:34–44, 1999.
- [24] K. Ramamurthi and K. Nandakumar. Characteristics of flow through small sharp-edged cylindrical orifices. *Flow measurement and Instrumentation*, 10:133–143, 1999.
- [25] M. J. Reader-Harris, J. A. Sattary, and E. P. Spearman. The orifice plate discharge coefficient equation- further work. *Flow Measurement and Instrumentation*, 6(2):101–114, 1995.
- [26] M. Richter, P. Woias, and D. Weib. Microchannels for applications in liquid dosing and flow rate measurement. *Sensors and Actuators A*, 62:480–483, 1997.
- [27] D. C. Roberts, N. W. Hagood, Y. H. Su, H. Q. Li, and J. A. J. A. Carretero. Design of a piezoelectrically-driven hydraulic amplification microvalve for high pressure, high frequency applications. *Smart Structures and Materials 2000: Smart Structures and Integrated Systems*, Newport Beach, CA, 3985, March 2000.
- [28] B. Sahin and H. Ceyhan. Numerical and experimental analysis of laminar flow through square-edged orifice with variable thickness. *Transactions of the Institute of Mechanical Engineers*, 18(4):166–174, 1996.
- [29] E. Schrenk. Disc valves, flow patterns, resistance and loading. *BHRA T*, (547), 1957. Translation from German.
- [30] M. Shikida, K. Sato, S. Tanaka, Y. Kawamura, and Y. Fujisaki. Electrostatically driven gas valve with high conductance. *Journal of Microelectromechanical Systems*, 3(2):76–80, June 1994.
- [31] S. Shoji and M. Esashi. Microflow devices and systems. *Journal of Micromechanics & Microengineering*, 4(4):157–171, December 1994.
- [32] J. A. Stone. Discharge coefficients and steady-state flow forces for hydraulic poppet valves. *Transactions ASME , Journal of Basic Engineering*, pages 144–154, 1960.
- [33] N. D. Vaughan, C. Johnston, and K.A. Edge. Numerical simulation of fluid flow in poppet valves. *Proceedings of the Institution of Mechanical Engineers, Part C: Mechanical Engineering Science.*, 206(2):119–127, 1992.
- [34] F. White. *Fluid Mechanics*. McGraw-Hill, Inc., New York, 1994.
- [35] E. B. Wylie, V. L. Streeter, and L. Suo. *Fluid Transients in Systems*. Prentice-Hall Inc., Englewood Cliffs, New Jersey, 1993.
- [36] O. Yaglioglu, Y.-H. Su, J. A. Carretero, D. C. Roberts, and L. Saggere. Mht:energy harvester simulink simulation. in-project design tool, August 2000.

- [37] R. Zengerle and M. Richter. Simulation of microfluid systems. *Journal of Micromechanics and Microengineering*, 4:192–204, 1994.



**An Evaluation of Critical Issues for  
Microhydraulic Transducers: Silicon Wafer  
Bonding, Strength of Silicon on Insulator  
Membranes and Gold-Tin Solder Bonding**

by

Kevin Thomas Turner

B.S. Mechanical Engineering, The Johns Hopkins University, 1999

Submitted to the Department of Mechanical Engineering  
in partial fulfillment of the requirements for the degree of

Master of Science in Mechanical Engineering

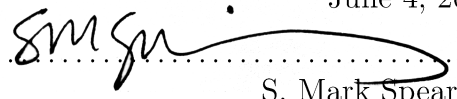
at the

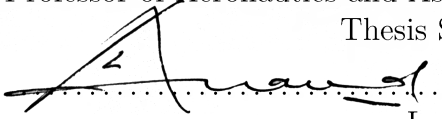
MASSACHUSETTS INSTITUTE OF TECHNOLOGY

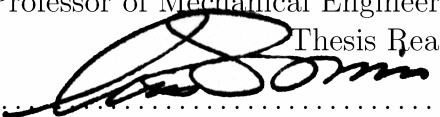
June 2001

© Massachusetts Institute of Technology 2001. All rights reserved.

Author .....   
Department of Mechanical Engineering  
June 4, 2001

Certified by .....   
S. Mark Spearing  
Esther and Harold Edgerton Associate Professor of Aeronautics and Astronautics  
Thesis Supervisor

Certified by .....   
Lallit Anand  
Professor of Mechanical Engineering  
Thesis Reader

Accepted by .....   
Ain Sonin  
Chairman, Department Committee on Graduate Students



# **An Evaluation of Critical Issues for Microhydraulic Transducers: Silicon Wafer Bonding, Strength of Silicon on Insulator Membranes and Gold-Tin Solder Bonding**

by

Kevin Thomas Turner

Submitted to the Department of Mechanical Engineering  
on June 4, 2001, in partial fulfillment of the  
requirements for the degree of  
Master of Science in Mechanical Engineering

## **Abstract**

Microhydraulics transducers (MHT) are a class of microelectromechanical systems (MEMS) currently being developed to produce bi-directional transducers with high power densities (500–1000 W/kg). The development of these devices, which combine microfabrication technology and piezoelectric materials, requires the use of variety of materials and fabrication technologies that are not fully developed. Three materials and structures issues, which are essential to the development of MHT devices, are silicon wafer bonding, strength of silicon-on-insulator (SOI) membranes, and gold-tin bonding. Each of these topics was addressed independently. The mechanical integrity of silicon fusion bonds as a function of processing parameters was examined using a four-point bend delamination specimen. The study showed that the specimen was effective for characterizing low toughness bonds and that certain processing conditions can have a profound impact on bond toughness. Bond toughness increased with anneal time and temperature, but, initial contacting conditions, such as time and clamping pressure, proved to have little effect on final bond toughness. The fracture strength of membranes fabricated from SOI wafers using deep reactive ion etching was experimentally measured. Results showed that the strengths of these membranes was less than that of structures etched from bulk silicon and that the strength was dependent on SOI manufacturer. Finally, a thin film gold-tin solder bond was developed to bond bulk piezoelectric material to silicon structures. The process, which uses a sputtered gold-tin eutectic alloy (80wt%Au–20wt%Sn), was refined to produce void-free bonds. Preliminary tensile tests indicated failure was likely to occur in the piezoelectric material itself or along the solder-piezoelectric material interface. The results of these three studies provide information that is essential to the development of MHT devices as well as a wide range of MEMS devices.

Thesis Supervisor: S. Mark Spearing

Title: Esther and Harold E. Edgerton Associate Professor of Aeronautics and Astronautics



# Acknowledgments

The work reported in this thesis would not have been possible without the help of many people along the way. First and foremost, I would like to thank my advisor, Mark, for his guidance and advice throughout this work. The help of all the students, staff and faculty on the MHT project is greatly appreciated. In particular, I would like to thank Lodweyk Steyn and Hanqing Li for their help in the tedious task of specimen fabrication and providing general advice regarding microfabrication. Also, numerous discussions with Dave Roberts and Yu-Hsuan Su were indispensable in completing this work. The assistance and guidance provided by Arturo Ayon allowed the study of silicon fusion bond strength to be completed. The help of several undergraduates, Nate Fitzgerald, Rogelio Garcia, Federico Gutierrez, and John Seminatore, was essential in carrying out the silicon fracture and fusion bond tests. Last, but certainly not least, I would like to express my gratitude to the staff of the Microsystems Technology Laboratory (MTL), the Active Materials and Structures Laboratory (AMSL), and the Technology Laboratory for Advanced Composites (TELAC), particularly Dave Robertson and John Kane, for their assistance throughout.

This work was sponsored by DARPA under contract DAAG55-98-1-0361.



# Contents

<b>1</b>	<b>Introduction</b>	<b>17</b>
1.1	Motivation . . . . .	17
1.2	Objectives . . . . .	19
1.3	Scope of Thesis . . . . .	20
<b>2</b>	<b>Silicon Wafer Bonding</b>	<b>23</b>
2.1	Introduction . . . . .	23
2.2	Background . . . . .	25
2.2.1	Silicon Fusion Bonding . . . . .	25
2.2.2	Mechanical Characterization of Bond Strength . . . . .	27
2.3	Test Specimen . . . . .	30
2.4	Crack Initiation and Propagation . . . . .	33
2.4.1	Crack Initiation . . . . .	33
2.4.2	Bond Area Reduction . . . . .	34
2.4.3	Chevron Notch . . . . .	35
2.5	Specimen Fabrication . . . . .	37
2.6	Experimental Procedure . . . . .	40
2.6.1	Test Apparatus . . . . .	40
2.6.2	Alignment . . . . .	40
2.6.3	Test Procedure . . . . .	44
2.7	Test Results . . . . .	44
2.7.1	Effectiveness of Specimen . . . . .	45
2.7.2	Effect of Process Parameters on Bond Quality . . . . .	47

2.8	Conclusion and Recommendations . . . . .	49
<b>3</b>	<b>Silicon-on-Insulator Membranes</b>	<b>51</b>
3.1	Introduction . . . . .	51
3.2	Background . . . . .	53
3.3	Experimental Method . . . . .	54
3.3.1	Specimen Geometry and Loading . . . . .	55
3.3.2	Specimen Fabrication . . . . .	57
3.3.3	Test Apparatus . . . . .	59
3.3.4	Test Procedure . . . . .	62
3.4	Finite Element Modeling and Data Reduction . . . . .	64
3.5	Results . . . . .	67
3.6	Conclusions . . . . .	72
<b>4</b>	<b>Gold-Tin Bonding</b>	<b>75</b>
4.1	Introduction . . . . .	75
4.2	Bond Selection . . . . .	76
4.2.1	Bond Requirements . . . . .	76
4.2.2	Bonding Techniques . . . . .	77
4.3	Gold-Tin Bonding Background . . . . .	79
4.3.1	Applications . . . . .	79
4.3.2	Material Properties . . . . .	80
4.3.3	Process Overview . . . . .	81
4.3.4	Mechanical Integrity . . . . .	83
4.4	Device Assembly . . . . .	84
4.5	Bonding Process . . . . .	87
4.6	Qualitative Evaluation of Bond Quality . . . . .	90
4.7	Tensile Tests . . . . .	94
4.7.1	Experimental Procedure . . . . .	94
4.7.2	Results . . . . .	95
4.8	Conclusions and Recommendations . . . . .	99



<b>5</b>	<b>Conclusions and Recommendations</b>	<b>101</b>
<b>A</b>	<b>Photolithography Masks</b>	<b>103</b>
<b>B</b>	<b>Finite Element Code</b>	<b>109</b>



# List of Figures

1-1	A typical MHT device: a piezoelectric micropump. . . . .	18
2-1	Techniques to evaluate bond strength. . . . .	27
2-2	Schematic of four-point bend delamination specimen. . . . .	30
2-3	Ideal load-displacement curve. . . . .	32
2-4	Procedure for creating precrack. . . . .	34
2-5	Effect of bonded area ratio on toughness. . . . .	36
2-6	Standard and chevron notch specimen geometries. . . . .	37
2-7	IR image of a bonded wafer pair. . . . .	39
2-8	Micrograph of specimen showing interfacial notch. . . . .	39
2-9	Strain-displacement for a misaligned specimen. . . . .	41
2-10	Schematic of misalignment. . . . .	42
2-11	Schematic of alignment fixture. . . . .	42
2-12	Strain-displacement for an aligned specimen. . . . .	43
2-13	Load-displacement plot for a typical test. . . . .	45
2-14	Chevron-notch specimen failure. . . . .	46
2-15	Bond toughness as a function of anneal temperature. . . . .	47
2-16	Bond toughness as a function of anneal time. . . . .	48
2-17	Bond toughness as a function of contacting pressure. . . . .	49
2-18	Bond toughness as a function of contacting time. . . . .	50
3-1	A SEM micrograph showing a typical MHT drive membrane. . . . .	52
3-2	Fracture strength measurement approach. . . . .	55
3-3	Schematic of test specimen for measurement of fracture strength. . .	56

3-4	Potential silicon membrane loading configurations. . . . .	57
3-5	Different approaches for etching fillets, (a) ‘standard’, (b) ‘alternate’. . . . .	58
3-6	Silicon fracture test machine. . . . .	60
3-7	Effect of misalignment on maximum stress in a specimen. . . . .	62
3-8	Typical fillet radius, (a) viewed from the top, (b) cross-section view. . . . .	63
3-9	Typical defect in fillet radius. . . . .	64
3-10	Finite element model of specimen. . . . .	65
3-11	Typical shape of etched fillet radius. . . . .	66
3-12	Effect of $b/a$ ratio on maximum stress. . . . .	67
3-13	Strength results for specimens with oxide. . . . .	70
3-14	Strength results for specimens without oxide. . . . .	70
4-1	Gold-tin equilibrium phase diagram. . . . .	80
4-2	Final MHT bonding process. . . . .	85
4-3	Bond pressure as a function of tether width and piezoelectric element oversize. . . . .	86
4-4	Deposited metal layers used to fabricate the gold-tin solder bonds. . . . .	88
4-5	Solder bonding jig. . . . .	89
4-6	Temperature and pressure cycle to complete bond. . . . .	91
4-7	Two examples of poor bonding, (a) due to the presence of trapped gas, (b) due to poor cleaning. . . . .	92
4-8	Void-free AuSn bond of silicon to silicon. . . . .	93
4-9	Void-free AuSn bond of PZT-5H to silicon. . . . .	93
4-10	Void-free AuSn bond PZN-PT to silicon. . . . .	94
4-11	Tensile specimen geometry. . . . .	95
4-12	Tensile specimen, (a) mounted to studs, (b) mounted in test machine. . . . .	96
4-13	Micrograph of fracture surface of specimen C. . . . .	97
4-14	Micrograph of fracture surface of specimen B. . . . .	98
A-1	Mask layout to define shallow grooves in standard 4-point specimen. . . . .	104
A-2	Mask layout to define shallow grooves in 4-point chevron specimen. . . . .	105

A-3 Mask layout to define deep trench in 4-point specimens. . . . . 106

A-4 Mask layout to define alignment marks and specimen edges in device  
layer of fracture strength specimen. . . . . 107

A-5 Mask layout to define deep trenches in handle wafer of fracture strength  
specimen. . . . . 108



# List of Tables

3.1	Process conditions of fabricated wafers. . . . .	68
3.2	Fracture strength values of tested wafers. . . . .	69
3.3	Consolidated fracture strength values. . . . .	69
4.1	Room temperature mechanical Properties of 80 wt.% Au and 20 wt% Sn alloy. . . . .	81
4.2	Typical processing conditions for AuSn preform solder bonds. . . . .	82
4.3	Typical processing conditions for AuSn thin-film solder bonds. . . . .	83
4.4	Tensile test results. . . . .	96





# Chapter 1

## Introduction

### 1.1 Motivation

A class of Microelectromechanical Systems (MEMS) known as Micro-Hydraulic Transducers (MHT) is currently being developed to produce bi-directional transducers with high power densities (500–1000 W/kg) [1], [2], [3], [4]. The transducers can act as actuators by transforming electrical energy into mechanical energy or as energy harvesting devices by transforming mechanical energy into electrical energy. Potential applications include actuators for distributed arrays and miniature robotics, as well as energy harvesting devices for recovery of electrical energy from human motion. Current efforts are focused on developing and validating the technology required to produce such devices.

MHT devices utilize piezoelectric material as the conversion medium between electrical and mechanical energy. Piezoelectric materials have high bandwidth and are capable of high power output, if this bandwidth is utilized. For this reason, MHT devices are designed to operate at high frequencies (tens of kilohertz) and thus require small length scales to achieve high structural natural frequencies. Microfabrication technology allows mechanical structures to be fabricated with the required dimensions. The combination of high frequencies and piezoelectric material leads to a device with high power output, however, most applications require a relatively low frequency mechanical input/output. In MHT devices, the high frequency operation

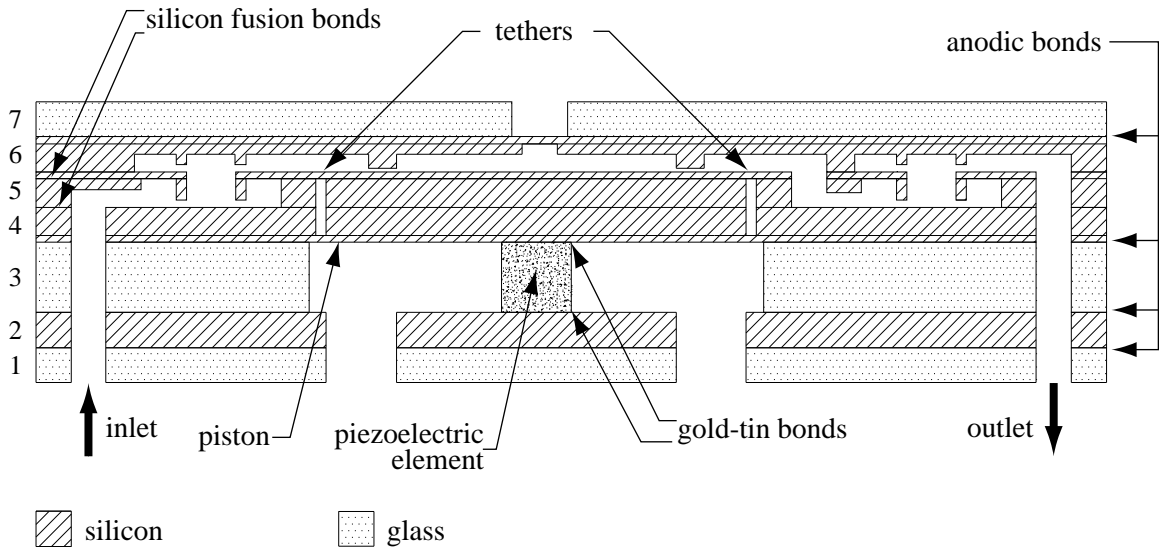


Figure 1-1: A typical MHT device: a piezoelectric micropump.

of the piezoelectric element is rectified to a more useful low frequency mechanical motion through the use of a fluid transfer medium and a series of valves. By incorporating piezoelectric materials, hydraulics, and microfabrication technology, high power density transducers can be produced.

A cross-section of a piezoelectrically driven micropump is shown in Figure 1-1. While this a specific MHT device, it illustrates the basic design and fabrication approach for a wide range of MHT devices [5]. MHT devices are fabricated by bonding multiple bulk micromachined wafers. Moving mechanical components, such as pistons, membranes, and valves, which require precise dimensional control, are micromachined from silicon and silicon-on-insulator (SOI) wafers using a deep reactive ion etching (DRIE) process. The outer packaging layers (layers 1 and 7) and the center isolation layer (layer 3) are fabricated from borosilicate glass wafers, specifically Pyrex 7740, using either conventional diamond drilling or ultrasonic machining techniques. A unique feature of MHT devices is the use of bulk piezoelectric material, rather than thin films. The piezoelectric elements are fabricated from bulk piezoelectric disks, which are ground and polished to the desired thickness and then subsequently core drilled or diced into smaller elements. Assembly of the device is completed through a series of bonding steps that begins with bonding of the silicon

layers to one another. Bonding between the silicon layers is accomplished using silicon fusion bonding. The silicon structures are then bonded to the glass packaging and isolation layers using field-assisted glass bonding (anodic bonding) [6]. Coincident with the bonding of the glass isolation layer to the silicon layers, the piezoelectric element must be inserted and bonded to the lower silicon layer and the silicon piston. A gold-tin solder bond provides the mechanical and electrical connection between the silicon layers and the piezoelectric elements.

The fabrication of the device involves a multitude of different processes, each with its own unique challenges and limitations. In order to ensure a robust and reliable device, the fabrication technologies outlined above must be well understood and controlled. A direct coupling exists between fabrication route and the performance and reliability of the device. While technologies such as anodic bonding have seen widespread use in MEMS devices and are well developed and robust, other technologies employed in the device are not. In order for the development of MHT devices, as well as other MEMS devices, to progress successfully, issues pertaining to silicon fusion bonding, deep reactive ion etched silicon-on-insulator membranes, and bonding of bulk piezoelectric material to silicon must be addressed.

## 1.2 Objectives

The primary goal of this work is to address the materials and structures issues that are most critical to the development of MHT devices. This overall goal, the nature of the design and fabrication of the device, and the existing technology has resulted in three main objectives for this work. These objectives are diverse and distinct from one another, but contribute to the common goal of developing MHT devices. The three main objectives of this work are:

- To develop a reliable technique for measuring wafer bond quality and to examine the effect of various processing conditions on silicon fusion bond toughness.
- To measure the mechanical strength of membranes fabricated from SOI wafers

using deep reactive ion etching and to make recommendations regarding the fabrication and design of such structures.

- To develop a thin film gold-tin solder bond to secure piezoelectric elements to the silicon structure of the device and to evaluate the mechanical integrity of the bond.

While the overall goal of this work is clearly to validate the technology necessary for the development of MHT devices, a subsequent goal has resulted from the need to characterize accurately various materials properties. The lack of standard test techniques for measuring mechanical properties of MEMS materials and structures requires that test structures and specimens be developed to measure accurately the quantity of interest. Thus, a secondary goal of this work is to develop and validate test methods and tools, which not only provide the information critical to the design of MHT devices, but also have the ability to be applied to a variety of MEMS materials.

## 1.3 Scope of Thesis

The outline of this thesis is straightforward and follows the objectives outlined in Section 1.2. Chapter 2 addresses the use of a four-point bend delamination specimen to quantify silicon fusion bond quality. It gives a brief review of silicon fusion bonding as well as test techniques commonly employed to measure bond quality. The chapter details the four-point bend specimen employed, the specimen fabrication and bonding process, and the test method. Results for silicon fusion bond toughness as a function of processing conditions are presented and recommendations are made regarding the use of the four-point specimen for evaluation of bond quality. Chapter 3 discusses issues pertaining to the strength of thin silicon membranes fabricated from SOI wafers by deep reactive ion etching. A review of previous work pertaining to the mechanical strength of single crystal silicon is given, followed by an outline of the process employed in the fabrication of membranes for MHT devices. Details are given with regard to specimen fabrication, test method and test apparatus. Experimental

results that were obtained are given as well as design recommendations. Chapter 4 covers the development and testing of a thin film gold-tin eutectic solder bond. Previous work with regard to gold-tin bonding and bonding for microsystems is discussed. Specifics with regard to the bond material selection, process development and refinement are given. Qualitative results demonstrating void-free bonding and quantitative results obtained from simple tensile tests are presented. The final chapter, chapter 5, gives overall recommendations and conclusions regarding the materials and structures issues for MHT devices discussed.



# Chapter 2

## Silicon Wafer Bonding

### 2.1 Introduction

In recent years, the number of MEMS devices that are fabricated by bonding multiple bulk micromachined wafers has been steadily increasing. The success of these multi-wafer devices relies on advances in etching technology and reliable bonding between wafers [7], [8], [9]. MHT devices are a typical example and rely on achieving wafer scale silicon-silicon and silicon-glass bonds. Many devices that are currently under development, [10], as well as some devices that are currently produced commercially, [11], [12], employ wafer scale-bonding to produce complex microstructures or to meet packaging requirements. Since silicon remains the material of choice for bulk micromachining operations, a significant amount of work has been devoted to developing robust bonds between etched silicon wafers.

A variety of techniques exist to bond two or more silicon wafers to one another. The more popular techniques include gold-silicon eutectic bonding, anodic bonding and silicon fusion bonding (silicon direct bonding). Gold-silicon eutectic bonding involves depositing a thin layer of gold on one of the wafers to be bonded, placing the wafers in contact, and subsequently heating to above the Au-Si eutectic temperature, 363°C. Upon cooling, the Au-Si eutectic alloy solidifies and secures the wafers together. This bonding method is attractive because it offers a low processing temperature and is electrically and thermally conductive. However, it can be difficult to

achieve large area void-free bonds and the large thermal expansion mismatch between gold and silicon can lead to stresses in the bonded wafers. Anodic bonding, while traditionally used to bond silicon to borosilicate glass wafers, has recently been employed to bond silicon wafers to one another with a thin glass intermediate layer [13], [14]. This is accomplished by either sputtering or evaporating a thin layer of borosilicate glass that has a thermal expansion coefficient close to that of silicon (typically Pyrex 7740 or Schott 8329) on one of the surfaces to be bonded. The wafers are then contacted, heated to 300-500°C, and a potential of 800-1200 V is applied across the interface. A strong hermetic bond is formed at the interface with relatively little residual stress. However, the bond is not electrically conductive and the strength is often limited by that of the glass. Silicon fusion bonding (silicon direct bonding) requires no intermediate bonding layers and can be accomplished between two mirror-polished silicon wafers. Two wafers, which have been cleaned thoroughly, are brought into contact and then annealed at a temperature in the range of 1000°C. The absence of an intermediate layer eliminates thermally induced residual stresses, and bonds with strengths that approach that of silicon can be achieved. Unfortunately, the high anneal temperature prohibits processing steps, such as the deposition of metals, or the integration of sensitive electronics prior to the bonding step.

Despite the high anneal temperatures that are required for silicon fusion bonding, it has gained widespread acceptance in the fabrication of MEMS devices. The fact that it has the potential to yield bonds with mechanical properties virtually identical to silicon itself without inducing residual stresses has made it a very appealing option in device design. Significant effort has been devoted towards characterizing bond integrity as a function of process conditions. A review of this work is given in Section 2.2. This work has demonstrated the profound effect processing route can have on bond integrity and has highlighted the fact that it may be possible to achieve high strength bonds at lower temperatures. The previous work has examined a variety of process conditions and has used various mechanical testing techniques to measure bond integrity. The current study builds on previous work, [15], [16], and focuses on employing a four-point flexure delamination specimen to measure reliably silicon



fusion bond toughness as a function of processing conditions. The study specifically examines the effect of contacting conditions, anneal time, and anneal temperature on bond toughness.

## 2.2 Background

### 2.2.1 Silicon Fusion Bonding

There has been an intense effort over the past 15 years to develop wafer scale silicon-silicon bonds where the wafers have a thermally grown oxide or a thin native oxide on the surfaces to be bonded. The concept of bonding silicon wafers with a thermally grown oxide layer at the interface using a room temperature contacting step followed by a high temperature anneal was first demonstrated by Lasky et al. [17], [18] at IBM in 1985 as a means of fabricating silicon-on-insulator wafers for electronic applications. At approximately the same time, Shimbo and colleagues at Toshiba reported bonding silicon wafers with a native oxide and hydrophilic surfaces at room temperature [19]. Shimbo et al. reported that following an anneal step at 1000°C, the bond strength reaches that of bulk silicon and the electrical resistivity across the interface is low. This early work sparked interest in the field that has continued to the present day. A significant number of papers have been published that examine a variety of different topics relating to silicon-silicon direct bonding. Several review articles [20], [21] as well as a book [22] on the subject offer a comprehensive review of direct wafer bonding. A brief review of the work relevant to the current study, concerning bonding of hydrophilic wafers without a thermally grown oxide on a surface, is provided below.

The silicon fusion bonding process is relatively well developed and in general consists of three basic steps [20]:

- I. The surfaces of two flat, mirror polished wafers are prepared to achieve the desired surface conditions. On wafers with a thin native oxide, various treatments are used to produce a hydrophilic surface on the wafer.
- II. The two wafers are brought into contact at room temperature in a suffi-

ciently clean environment. This step can be carried out in air, an inert atmosphere, or a vacuum. The most critical factor is the cleanliness of the environment, which is essential in avoiding particles between the wafers.

III. Following the room temperature bonding step, the wafers are bonded with weak van der Waals or hydrogen bonds. These bonds are sufficient to adhere the wafers to one another, but have inadequate strength for most applications. To achieve the full strength, the wafer pair is annealed at high temperatures near  $1000^{\circ}\text{C}$ . The result is covalent bonds at the interface which are approximately two orders of magnitude stronger than the initial secondary bonds.

While the general steps are well known, the literature reports a wide array of processing parameters that may be employed at each step. The discussion here is limited to the work that has examined the effect of varying the anneal time and temperature.

The high temperature anneal step is a critical step and essential to achieving robust bonds. The length and temperature of the anneal step has been varied in previous work to examine the effect on bond quality. The initial work by Shimbo, [19] et al. demonstrated the profound effect of anneal temperature. Bonds were fabricated using a 2 hour anneal, at temperatures from 200 to  $1200^{\circ}\text{C}$ . Bond strength measurements indicated that above  $300^{\circ}\text{C}$ , the strength increased with increasing temperature. While the increase was monotonic, the strength reached a plateau between 600 and  $800^{\circ}\text{C}$  and then increased and reached another plateau above  $1000^{\circ}\text{C}$ . Work by Tong et al., [23] yielded similar results for the bond energy as a function of temperature. Bond energy was measured for specimens annealed for 100 hours at temperatures from 25 to  $900^{\circ}\text{C}$ . Between 150 and  $800^{\circ}\text{C}$  the bond energy was approximately half of the value when annealed at high temperatures. Above  $800^{\circ}\text{C}$  the strength increased rapidly and reached its maximum value at  $900^{\circ}\text{C}$ .

The effect of annealing time has been investigated less than that of annealing temperature. Work has been done to characterize bond energy as a function of time for temperatures of  $43^{\circ}\text{C}$  and  $150^{\circ}\text{C}$ , [23]. Results indicated that the bond

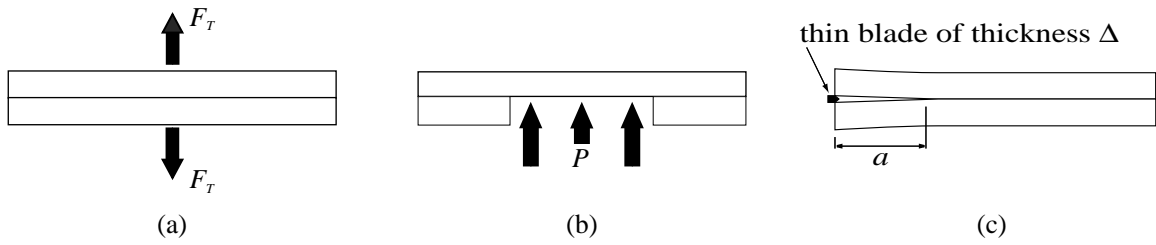


Figure 2-1: Techniques to evaluate bond strength.

energy approached a saturated value, which was more than an order of magnitude less than the bond energy obtained from a high temperature anneal, after approximately 100 hours. A more complete study was conducted in which temperatures from 195 to 700°C and times up to 1106 hours were investigated [24]. Tensile tests demonstrated that at 700°C, the strength was increased by 2.5 times when the anneal time was increased from 1 to 66 hours. However, the strength of specimens annealed at 195°C for 1106 hours only had strengths that were approximately two thirds of the strength that could be achieved by annealing for 66 hours at 700°C. This data, while not comprehensive, does indicate the possibility of achieving robust silicon-silicon fusion bonds at lower temperatures.

### 2.2.2 Mechanical Characterization of Bond Strength

The quality of silicon fusion bonds has been examined qualitatively and quantitatively using a variety of non-destructive as well as destructive techniques. The discussion here is limited to quantitative techniques that provide either a bond failure stress or a bond toughness value. While there are a range of techniques available to measure bond strength or toughness, three tests in particular have been used in the characterization of silicon fusion bond quality. These tests, which are illustrated in Figure 2-1, are tensile tests, pressure-burst tests and the crack opening method.

The tensile test, which is illustrated in Figure 2-1(a), is attractive due to the ease of specimen fabrication and testing. However, tensile tests may present problems in quantifying the process because the failure load,  $F_T$ , is not only a function of the material properties at the interface, but also a function of geometry. Thus, defects

in the bond or damage at the edges due to specimen preparation and handling can lead to low failure stresses with a significant degree of scatter in the data set. In addition, the stress-state at the interface may be dependent on the exact specimen geometry employed, which makes comparing data between different tests difficult. To eliminate the possibility of edge damage, researchers have used patterned wafers to bond selective areas of a wafer [25]. These wafers were then diced, such that the bonded region was far from the dicing path. This eliminated the chance of introducing flaws at the bonded interface that can lead to erroneous failure loads. Despite these efforts though, significant scatter still existed in the reported strength values. Abe et al. utilized a tensile loading as well, but adopted a different geometry in an attempt to eliminate problems such as residual damage. The tests were conducted on a bonded pair, where one layer had been thinned to 2-3  $\mu\text{m}$ . A stud with a 5.7 mm<sup>2</sup> bonding area was affixed using epoxy to the surface of the thinned wafer and subsequently pulled in tension. Since the layer was thin, the measured fracture load was primarily controlled by the bond between the silicon layers. The data obtained showed relatively little scatter, but in strong bonds, failure would occur in the adhesive layer which secures the stud to the silicon.

The pressure-burst test, which is shown in Figure 2-1(b) has been employed to measure failure stress of silicon fusion bonds [19]. Fabrication of the test structures was straightforward and was accomplished by etching through holes in one of the wafers to be bonded. Following bonding, the wafer pair was diced into specimens and the dies were mounted in a fixture which allowed a hydrostatic oil pressure to be applied from beneath. The failure stress was calculated from the applied pressure,  $P$ , at failure. While specimen fabrication is simple, the stress state at the interface is complicated and difficulties similar to those of the tensile test may be encountered.

The limitations and complications of these stress-based approaches are clear and well documented. Mazara et al. [26] recognized the difficulties of these tests and employed the double cantilever beam geometry shown in Figure 2-1(c) to quantify the strength of wafer bonds for silicon-on-insulator fabrication. The test, also known as the crack opening method, is accomplished by inserting a thin blade between the

wafers and measuring the extent of the crack propagation. Crack length is typically measured using IR imaging from above or with an optical microscope from the side. The distance the crack propagates can be directly related to bond quality through an energy balance. Based on the thickness of the blade,  $\Delta$ , the thickness of the bonded layers,  $h$ , the elastic properties of the layers,  $E$  and  $\nu$ , and the crack length,  $a$ , the critical strain energy release rate,  $G_c$ , or the bond toughness can be calculated as:

$$G_c = \frac{3}{16} \frac{\Delta^2 h^3}{a^4} \frac{E}{1 - \nu^2}. \quad (2.1)$$

Equation 2.1 is for the specific case where the bonded layers have the same thickness and elastic properties. Similar expressions exist for the general case where the layers are different materials and have different dimensions [27]. Many researchers, who have employed this technique, report specific surface energy values,  $\gamma_s$  rather than the critical strain energy release rate. The two quantities are closely related and simply differ by a factor of two, where  $G_c = 2\gamma_s$ .

The crack opening method is advantageous because it offers a well defined loading at the interface. The extent of crack propagation is largely unaffected by small flaws at the edges and in general the measured toughness is less sensitive to geometry than the failure stress values in the tensile and pressure tests. However, the technique is not without its limitations and difficulties. The most important concern is the fourth order dependence of  $G_c$  on crack length [8], which is seen in equation 2.1. Crack length is a difficult quantity to measure accurately and slight errors in measurement can lead to large errors in the  $G_c$  value. In addition, it has been observed that the crack length is dependent on time and humidity, which can make repeatability difficult [28]. Finally, in well-bonded wafers, insertion of the blade is difficult and often leads to wafer fracture. Despite the limitations, it has been the most widely used test in the characterization of silicon-silicon wafer bonds up to this point.

An alternative technique to measure critical strain energy release rate is a four-point bend delamination specimen. The specimen, which was developed for evaluating bimaterial interfaces, does not require the measurement of crack length, [27],[29],[30].

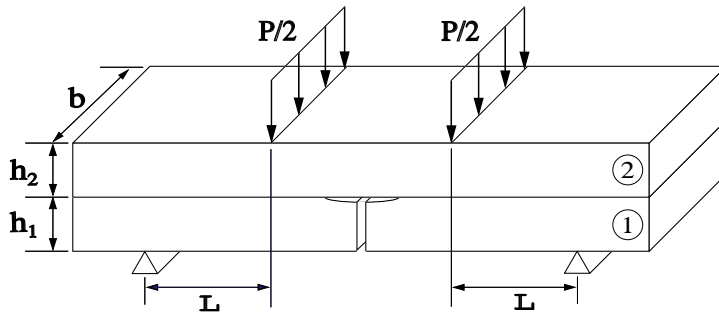


Figure 2-2: Schematic of four-point bend delamination specimen.

The critical strain energy release rate can be determined from a critical load and the dimensions and elastic properties of the specimen. The specimen offers a well-defined loading similar to that of the double cantilever beam and is relatively simple to fabricate. The specimen has not been employed previously to characterize silicon fusion bonds, but has been used to quantify the integrity of wafer-scale gold-gold thermocompression bonds, [31]. Based on the literature, the specimen appears to be an attractive alternative to the crack opening method.

## 2.3 Test Specimen

The four point bend specimen, which is shown schematically in Figure 2-2, consists of two bonded layers with a central notch and symmetric interfacial pre-cracks. The loading configuration creates a constant moment between the inner loading points. Thus, while the crack is within the inner loading points, the strain energy release rate,  $G$ , is independent of crack length. The energy release rate for the case where the crack is within the inner loading points can be determined analytically by calculating the difference in the strain energy in the uncracked and cracked beam [29]. Using Euler-Bernoulli beam theory, the strain energy release rate is expressed as

$$G = \frac{M^2}{2E_2'b} \left( \frac{1}{I_2} - \lambda \frac{1}{I_c} \right) \quad (2.2)$$

where  $M$  is the moment between the inner loading points and can be written in terms of the applied load,  $P$ , and the distance between the inner and outer loading points,

$L$ .

$$M = PL/2 \quad (2.3)$$

The additional terms of equation 2.2 are simply functions of the geometry and the elastic properties of the specimen layers, and are defined as

$$\lambda = \frac{E'_2}{E'_1} \quad (2.4)$$

$$I_c = b \left( \frac{1}{12}h_1^3 + \frac{1}{12}h_2^3\lambda + \frac{\lambda h_1 h_2 (h_1 + h_2)^2}{4(h_1 + \lambda h_2)} \right) \quad (2.5)$$

$$I_2 = \frac{1}{12}bh_2^3. \quad (2.6)$$

The subscripts 1, 2, and  $c$  refer to the properties of the lower, upper, and composite beams, respectively. The geometry is defined by the thickness of the layers,  $h_1, h_2$ , and the width,  $b$ , as shown in Figure 2-2. The appropriate choice of  $E'$  depends on the geometry of the specimen. In the case of plane stress

$$E'_n = E_n \quad (2.7)$$

and for plane strain

$$E'_n = \frac{E_n}{1 - \nu_n^2}. \quad (2.8)$$

When employing the four-point-bend delamination specimen to measure critical strain energy release rate, it is assumed that at a critical load,  $P_c$ , the strain energy release rate at the interface,  $G$ , will exceed the critical strain energy release rate (toughness) of the bond,  $G_c$ , and delamination will begin. When the interface toughness is constant, the crack will propagate at a constant load while advancing between the inner loading points. A ideal load-displacement curve for a specimen that delaminates at a critical load,  $P_c$ , is shown in Figure 2-3. As seen in Figure 2-3, the critical load can clearly be identified from the plateau in the load-crosshead displacement curve. Using the measured critical load and the dimensions and elastic properties of the specimen, critical strain energy rate can be determined using equations 2.2-2.8.

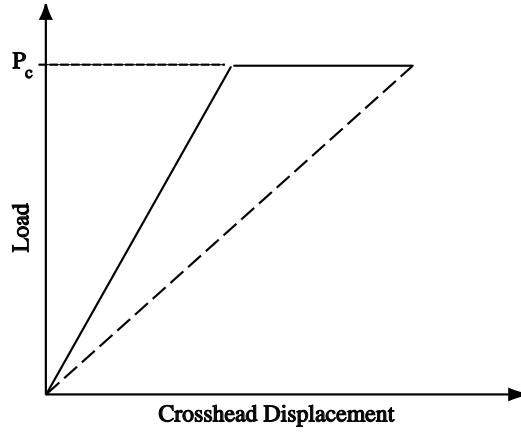


Figure 2-3: Ideal load-displacement curve.

For the current study, layers 1 and 2 are of equal thickness,  $h$ , and have the same elastic properties,  $E, \nu$ . In addition, plane strain is assumed. With these conditions, the critical strain energy release rate,  $G_c$ , can be determined using

$$G_c = \frac{21}{16} \frac{P_c^2 L^2}{b^2 h^3} \frac{1 - \nu^2}{E}. \quad (2.9)$$

The loading at the interface of the four-point-bend specimen is mixed-mode. The exact phase angle of loading,  $\Psi$ , which describes the ratio of mode I to mode II loading, is a function of the ratio of moduli and thickness of the bonded layers [29]. While the crack is within the inner loading points, the phase angle is independent of crack length. For the geometry employed in present study, where  $E_1 = E_2, h_1 = h_2$ ,  $\Psi \approx 40^\circ$ , which indicates slightly more tensile opening than sliding at the interface ( $\frac{G_{II}}{G_I} \approx 0.85$ ). While the mixed-mode conditions may in fact be closer to the types of loading incurred in real devices, the mixed-mode properties of the specimen pose some challenges in testing. The principal difficulty arises from the fact that in a monolithic material, cracks tend to follow the most energetically favorable path, which is a mode I path. For the majority of applications of the four-point delamination specimen, the interface has a lower toughness than the adjoining layers, such that the crack follows the interface. However, as was stated earlier, silicon fusion bonds have the potential to achieve mechanical properties similar to those of silicon itself. Thus, in



a well-bonded specimen, the crack will not propagate along the interface, but will follow the mode I path and lead to fracture through the middle of the specimen.

## 2.4 Crack Initiation and Propagation

The two most difficult challenges in employing the four point bend specimen are initiating the crack at the interface and forcing the crack to follow the interface. The latter is due to the mixed-mode conditions and the fact that silicon fusion bonds can be quite strong. Crack initiation is also made difficult by the strength of the bond, but is further complicated by the scale and fabrication method of the specimens. Several different specimen design and fabrication processes were attempted to try to overcome these challenges.

### 2.4.1 Crack Initiation

Typically, cracks are initiated at the interface of the four-point-bend specimen using a two-step process [27],[31]. First, a cut is made in the lower layer of specimen to define the position of the central notch. The cut is made using a thin saw blade and the depth is set so that the resulting cut falls short of the interface. Following the cut, the specimen is loaded in three-point bending, with the center loading point acting on the upper layer and positioned above the notch that was previously cut. Upon loading in three point bending, a crack initiates at the tip of the saw cut and propagates and branches into the interface. The crack arrests a short distance from the notch since the driving force at the interface diminishes with distance from the center loading point. This technique works well for bimaterial specimens or specimens with intermediate bonding layers. However, in a silicon fusion bond specimen it is unlikely that the crack would deflect at the interface, but would rather continue past the interface into the upper layer.

Recognizing this limitation, an alternate technique for precracking the specimen was developed. Figure 2-4 illustrates the basic approach that was employed. Prior to bonding, a trench was etched in the lower layer of the specimen. The layers were

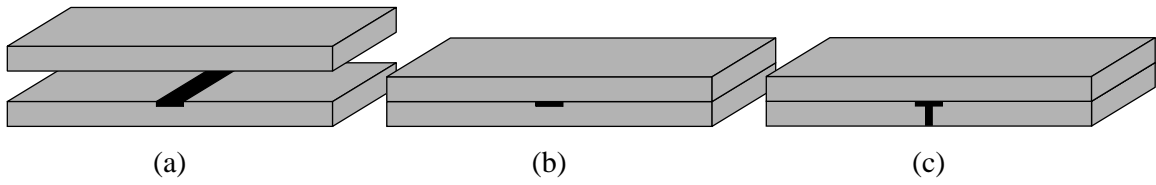


Figure 2-4: Procedure for creating precrack.

subsequently bonded and then a saw cut was made that intersected the previously etched trench. The presence of the trench allows the cut to be made without damaging the upper layer of the specimen. The combination of an etched trench and saw cut form the central notch and precrack.

### 2.4.2 Bond Area Reduction

The mixed-mode conditions at the interface coupled with the potential strength of silicon fusion bonds created a situation in which it was difficult to force the crack to follow the interface. Analysis indicates for geometries similar to the one used in this study that the ratio of interface to layer toughness determines whether the crack will follow the interface or proceed into the layer above [32]. A novel approach, which entailed reducing the effective interface toughness via a bond area reduction, was employed to alter the ratio of interface toughness to layer toughness. The hope was that by reducing the interface toughness sufficiently, it would become energetically favorable for the crack to propagate along the interface rather than along the mode I path. The bond area reduction at the interface was accomplished by etching shallow grooves, 1-3  $\mu\text{m}$  in depth, on one of the bonding surfaces. The grooves, which run parallel to the length of the specimen, prevent bonding in certain areas, but do not significantly alter the stiffness of the 525  $\mu\text{m}$  thick layer.

By reducing the bond area at the interface, the effective ‘global’ bond toughness is reduced. While the areas that are bonded have the true interface toughness, the toughness that is measured using the four-point bend specimen is lower because of the reduced area. Toughness, or critical strain energy release rate, for a specimen of

constant width is defined as

$$G = \frac{1}{b} \frac{\partial U}{\partial a} \quad (2.10)$$

where  $U$  is the stored energy,  $b$  is the width of the specimen, and  $a$  is the crack length. Since the grooves are parallel to the length of the specimen, the grooves effectively reduce the width of the specimen in equation 2.10 but do not affect the stored energy. Noting this fact and examining equation 2.10, it is seen that the ‘true’ toughness of the interface can be calculated from the measured toughness of a specimen with reduced bond area,

$$G_{true} = \frac{1}{AR} G_{measured} \quad (2.11)$$

where  $AR$  is the area ratio of the specimen and is defined as the bonded area divided by total specimen area. The validity of equation 2.11 was verified experimentally by testing specimens with various area ratios that were processed under identical conditions. Figure 2-5 shows the results of two such sets of specimens that have been corrected using equation 2.11. In Figure 2-5, specimen set A, which contains 7 specimens, has a mean of 1.51 J/m<sup>2</sup> and a coefficient of variation of 0.05, while set B, which contains 5 specimens, has a mean of 1.57 J/m<sup>2</sup> and a coefficient of variation of 0.04. These results clearly validate equation 2.11. In the current study, bonded area ratios,  $AR$ , ranging from 0.1 to 0.9 were utilized so that specimens with a range of interface toughness could be tested.

### 2.4.3 Chevron Notch

As will be discussed in detail in Section 2.7.1, the use of the etched trench and central notch as the crack initiation site proved successful for specimens with low to intermediate interface toughness values. However, in well bonded specimens, the crack would fail to initiate in the interface and would fracture via a crack propagating through the upper layer. A chevron notch geometry was employed at the end of the bonded areas in an attempt to alleviate this problem. Figure 2-6 illustrates the geometry of the chevron notch specimen as compared to the initial specimen geometry. In the standard specimen, the intersection between the bonded areas and the central

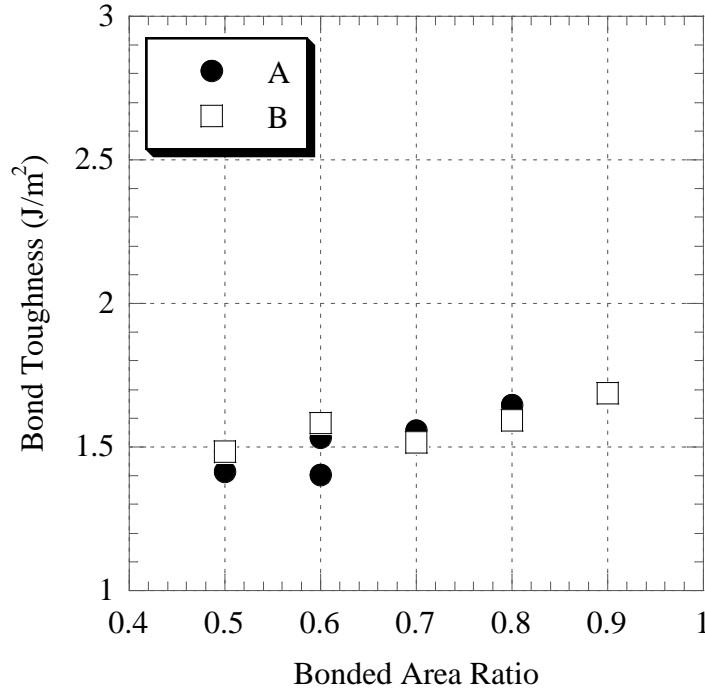


Figure 2-5: Effect of bonded area ratio on toughness.

notch was a line, with a length equal to the width of the bonded areas. The bonded areas in the chevron notch specimens met the central notch at a point. The point was created by incorporating a triangular region at the end of the bonded areas with an included angle of  $60^\circ$ .

The premise of the chevron notch design was that the reduced bonded area at the notch should make it easier for a crack to initiate at the interface. Once the crack has initiated at the interface, it should continue to propagate along the interface if the bonded area is sufficiently low. The fact that the width of the bonded regions vary near the central notch means that delamination in this region will not occur at a constant load. However, once the crack has propagated past the triangular ends of the bonded regions, the specimen will delaminate at a constant load and a plateau will be observed in the load displacement curve. Based on this load, the critical strain energy release rate can be calculated. In the specimens used in this study, the distance from the central notch to the inner loading points was 10 mm and the maximum length

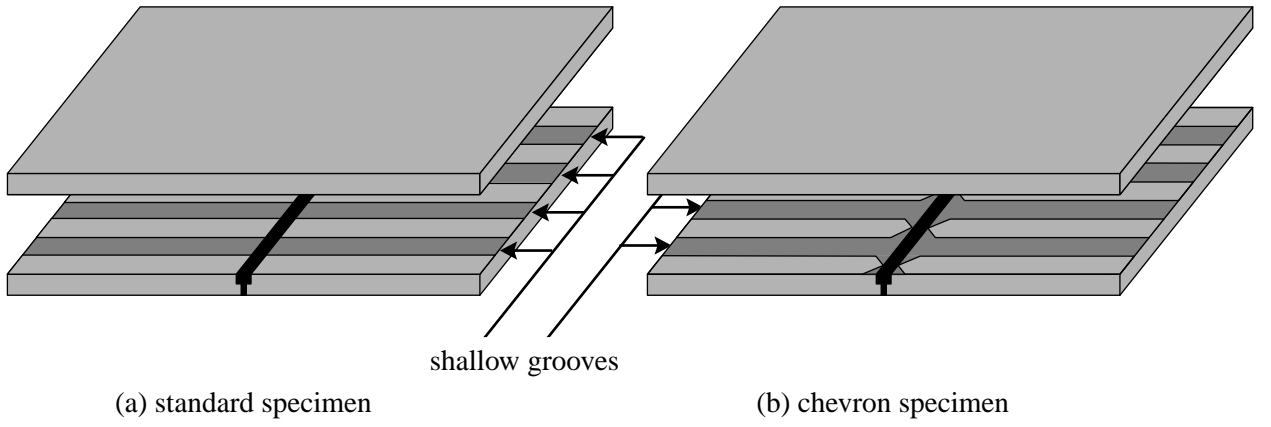


Figure 2-6: Standard and chevron notch specimen geometries.

of the triangular regions was 0.8 mm. Based on these dimensions, it is clear that a large plateau should be observed from which the critical load can be determined.

## 2.5 Specimen Fabrication

The fabrication process was a two mask process and required two lithography steps, two etches, two ‘piranha’ cleans, an RCA clean, and the final bonding step. The first mask was used to define the pattern for the shallow grooves, which reduced the bonded area at the interface. The mask layouts for the standard and chevron specimens are included in Appendix A. The pattern was designed so that nine specimens, each 8 mm wide, with varying area ratios from 0.1 to 0.9, were fabricated on a single 4” wafer. The etched shallow grooves resulted in bonded regions varying from 0.1 to 0.9 mm in width. The second mask, which is also included in Appendix A, was used to define a deep trench, which formed the central notch in either the standard or chevron specimens. The central notch was 0.6mm wide and ends short of the edges of the wafer in order to protect against possible wafer fracture. Alignment marks were included in both masks to permit precise positioning between the two etches.

All specimens were fabricated from single-side polished 4”, n-type, (100) Czochralski grown, silicon wafers with an average thickness of 525  $\mu\text{m}$ . The pattern for the shallow grooves was defined in a layer of OCG825 photoresist. The wafers were deep reactive ion etched for a brief period to form grooves 1-3  $\mu\text{m}$  deep. The wafers were

subsequently cleaned using a standard ‘piranha’ clean (3:1  $\text{H}_2\text{SO}_4\text{:H}_2\text{O}_2$ ) to remove the remaining resist. The wafers were then coated with thick resist, AZ4620, and patterned to define the deep trench. The trench was deep reactive ion etched to a depth of 100  $\mu\text{m}$  at an average etch rate of 2.5  $\mu\text{m}/\text{min}$ . Following etching, a ‘piranha’ clean was used to remove the resist from the wafers.

To prepare for bonding, an etched silicon wafer and bare silicon wafer were cleaned using a standard RCA<sup>™</sup> clean. In the RCA<sup>™</sup> clean, organics are removed using a 5:1:1  $\text{H}_2\text{O}:\text{H}_2\text{O}_2:\text{NH}_4\text{OH}$  solution. A thin silicon dioxide layer is then removed using a 50:1  $\text{H}_2\text{O}:\text{HF}$  solution. An ionic clean in 6:1:1  $\text{H}_2\text{O}:\text{H}_2\text{O}_2:\text{HCl}$  solution followed by distilled water rinse and spin dry are the final steps of the clean procedure. The RCA<sup>™</sup> clean results in a surface that is hydrophilic and ready to be contacted. Immediately following the RCA clean, an etched wafer was aligned to a bare wafer and transferred to an Electronic Visions AB1-PV bonder. The chamber was purged with nitrogen and then evacuated to  $5 \times 10^{-2}$  mbar. After the desired chamber pressure had been achieved, the wafers were contacted and clamped with a specified pressure. A pressure of 4000 mbar applied over a period of 30 s is the baseline process. In this study, the magnitude and duration of the applied pressure were varied systematically between 150-2000 mbar and 60-1200 s respectively. Following contacting, the chamber was vented to atmosphere and the wafer pair was removed. The wafer pair, which is held together by weak surface forces following contacting, was inspected for large voids using IR imaging. A typical IR image of a bonded wafer pair is shown in Figure 2-7. To achieve full bond strength, the bonded pair was annealed in a nitrogen atmosphere. The effect of annealing time and temperature were the primary interest in this work, thus a considerable range was examined. A series of six bonded pairs were annealed for 24 hours at temperatures from 500-1000°C in increments of 100°C to examine the effect of annealing temperature. The effect of annealing time was investigated by fabricating seven bonded pairs at an anneal temperature of 600°C for anneal times from 48 to 336 hours in 48 hour increments.

Following bonding, the location of specimens were marked on the exterior of the bonded wafer pair using IR imaging. Following marking, one cut using a wet diamond

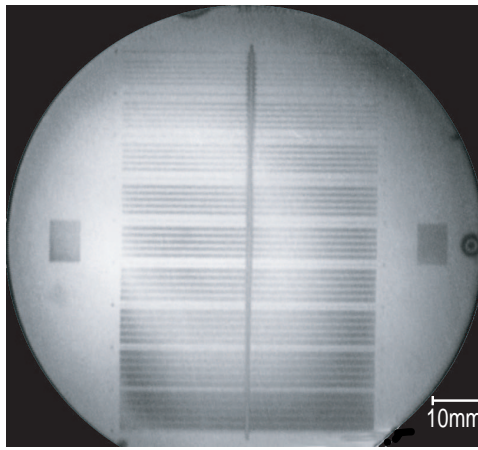


Figure 2-7: IR image of a bonded wafer pair.

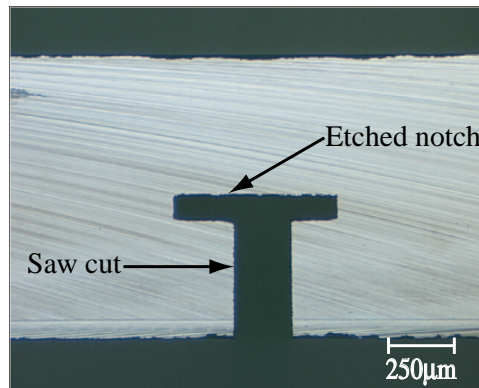


Figure 2-8: Micrograph of specimen showing interfacial notch.

wafer saw was made at each end of the wafer parallel to the specimens. These cuts allowed the location of the deep trench to be viewed directly and marked accurately. Marking the location of the deep trench using this procedure proved to be significantly more accurate than marking it using IR imaging. Mechanical testing specimens were then fabricated from the bonded wafer pairs with two sequences of cuts using a wet diamond wafer saw. First, the saw was used to cut through the lower wafer and intersect with the deep trench. This saw cut and the deep etched trench form the central notch as shown in Figure 2-8. Following the fabrication of the central notch, nine specimens were cut from each wafer by dicing into 8 mm wide strips. Finally, the diced specimens were removed from the mounting tape, which is required for the dicing saw, and cleaned thoroughly with an acetone rinse.

## 2.6 Experimental Procedure

### 2.6.1 Test Apparatus

Testing was carried out in a commercial servo-hydraulic test machine fitted with a four-point loading fixture. The four-point loading fixture is a commercial fixture and accepts specimens up to 8 mm wide of any thickness. The inner loading points are 20 mm apart and are centered between the outer rollers which are spaced 40 mm apart. The rollers are 4.8 mm diameter carbon steel pins and rest on half-moon shaped alumina supports. The half-moon supports allow the rollers to articulate around the longitudinal axis of the specimen. The test machine offers direct measurement of crosshead displacement and a 100 N load cell was used to ensure accurate load measurement in the range of interest. The load and crosshead displacement were monitored and recorded using a microcomputer with a data acquisition board and LabVIEW™ software. While not required, crack propagation was monitored using a Questar™ telemicroscope.

### 2.6.2 Alignment

Early tests revealed that the alignment of the standard four-point test fixture was quite poor. The presence of the misalignment was identified from force-displacement plots of tests and observations through a telemicroscope. The plots showed that delamination was not occurring at a constant load and crack opening observations revealed that the crack would consistently propagate first on one side of the fixture. This behavior is indicative of a jig that is misaligned such that one of the inner rollers contacts the specimen before the other inner roller. This results in three-point bending initially and a larger loading on one side of the specimen. This behavior was verified by instrumenting an 8 mm wide by 1 mm thick silicon beam with two piezoresistive strain gages. The strain gages were mounted on the bottom of the beam and positioned 20 mm apart on center. The beam was placed in the four-point fixture such that the gages were aligned with the inner loading points. While loading



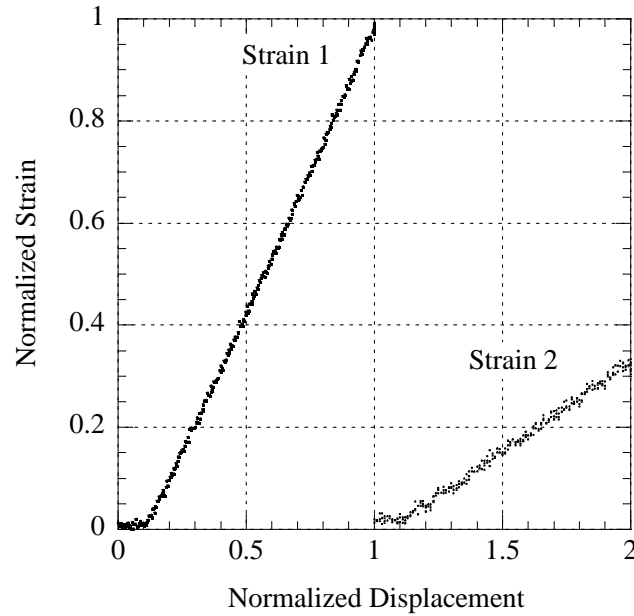


Figure 2-9: Strain-displacement for a misaligned specimen.

the specimen under displacement control, the strain was monitored on the two gages to observe the relative loading of the two sides of the specimen. By comparing the strain-crosshead displacement curves for the two strain gages, it can be determined whether or not the jig is properly aligned to provide four-point bending. Figure 2-9 shows the strain-displacement curves obtained from a specimen that was tested using the standard four-point test jig. Since this test is simply a comparison between the two strain gages, the strain and displacement values have been normalized. The strain 2 curve was shifted by 1.0 on the displacement axis to permit a clearer representation of the data. The important point to recognize from Figure 2-9 is that the slopes of the two curves are significantly different, and at equal displacements strain 2 is significantly lower than strain 1. This indicates that the roller located above strain gage 1 comes into contact with the specimen prior to the roller above strain gage 2. This type of misalignment is illustrated in Figure 2-10.

To correct for the misalignment, a custom fixture was designed and constructed. The fixture, which is illustrated schematically in Figure 2-11, consists of two aluminum plates pivoted on a center roller. Two springs on the ends of the plates provide a

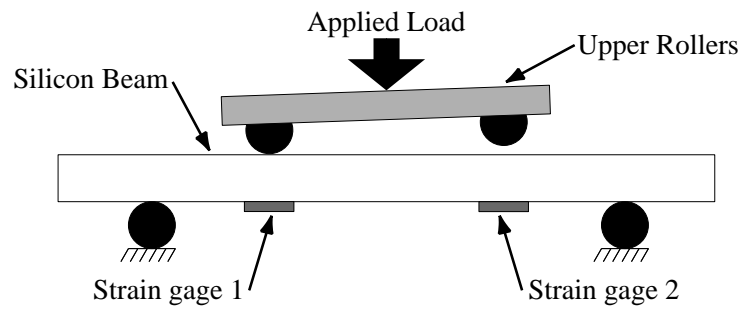


Figure 2-10: Schematic of misalignment.

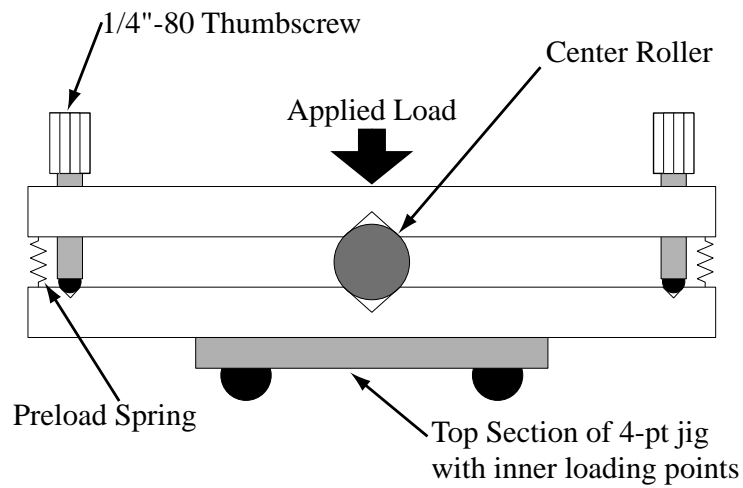


Figure 2-11: Schematic of alignment fixture.

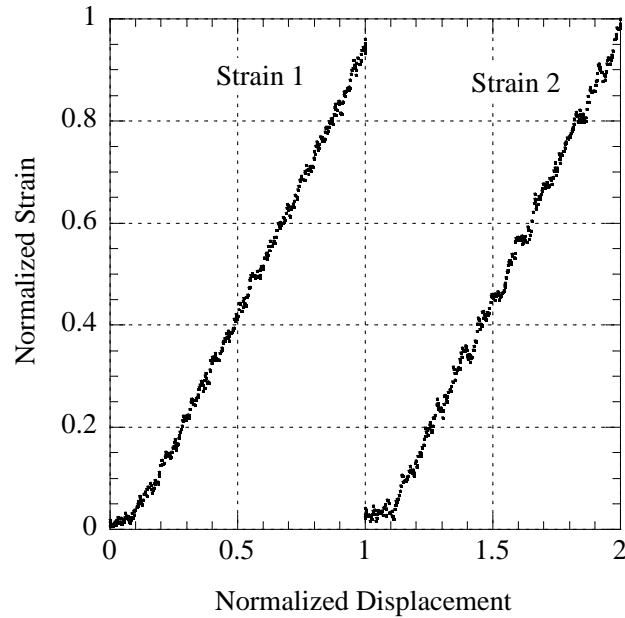


Figure 2-12: Strain-displacement for an aligned specimen.

preload, which keeps the plates firmly against the center roller. Two 1/4"-80 thumbscrews are mounted in the top plate and allow the relative angle between the two plates to be varied by approximately  $\pm 10^\circ$  from the parallel position. Care must be taken when using the alignment fixture to avoid displacing the thumbscrews too far and lifting the plates off of the center roller. If the plates are separated from the center roller, the jig will be unstable. To be effective, the center line of the alignment jig must be aligned with the center line of the four-point-loading fixture.

Employing this alignment fixture and adjusting it appropriately resulted in a uniform loading of the specimen. Strain-displacement curves obtained using a strain-gaged beam are plotted in Figure 2-12. It is evident from the similar slopes of the two curves shown in Figure 2-12 that the misalignment was significantly reduced. While the alignment jig provides the potential to achieve good alignment, as seen in Figure 2-12, it does not guarantee it. The jig must be adjusted carefully to ensure that the specimen is uniformly loaded. Proper adjustment of the alignment jig was an iterative process, and involved loading a strain gaged beam specimen up to a specified displacement that corresponds to a range similar to that expected in actual

tests. While the beam had a static load applied, the thumbscrews were adjusted to balance the strains on the two sides. The specimen was then unloaded and reloaded to ensure the strain-displacement curves had similar slopes. Experience demonstrated that several loading and adjustment steps are required to achieve balanced loading on the two strain gages. Following alignment, load-displacement curves obtained on delamination specimens exhibited the load plateau that was expected.

### 2.6.3 Test Procedure

Specimens were placed in the four-point bending fixture such that the central notch of the specimen fell within the inner loading points. While exact alignment is not critical, since the moment between the inner rollers is constant, an attempt was made to align the central notch of the specimen with the center line of the fixture. Centering the specimen allows the maximum amount of crack growth at a constant load and hence a larger plateau in the force-displacement curve. Friction between the rollers and specimen, which can have a significant effect on the measured  $G_c$  value [30], was minimized through the use of a dry graphite lubricant. Specimens were loaded under displacement control at a constant rate of 0.15 mm/min. Crack propagation was permitted to continue until the crack reached the inner loading points, at which point the specimen was unloaded. The actual dimensions of the specimen, including the overall width, the interface grooves, and the thickness of the layers, were measured. The width and thickness were measured using a digital micrometer and the groove dimensions were measured using an optical microscope with a measurement feature. These dimensions and the critical load from the test were used to calculate  $G_c$  values using equations 2.9 and 2.11.

## 2.7 Test Results

A force-displacement plot from a typical test is shown in Figure 2-13. The specimen loads elastically until a critical load is reached. This elastic loading region is observed in Figure 2-13. The fact that the loading is not entirely smooth was a result of

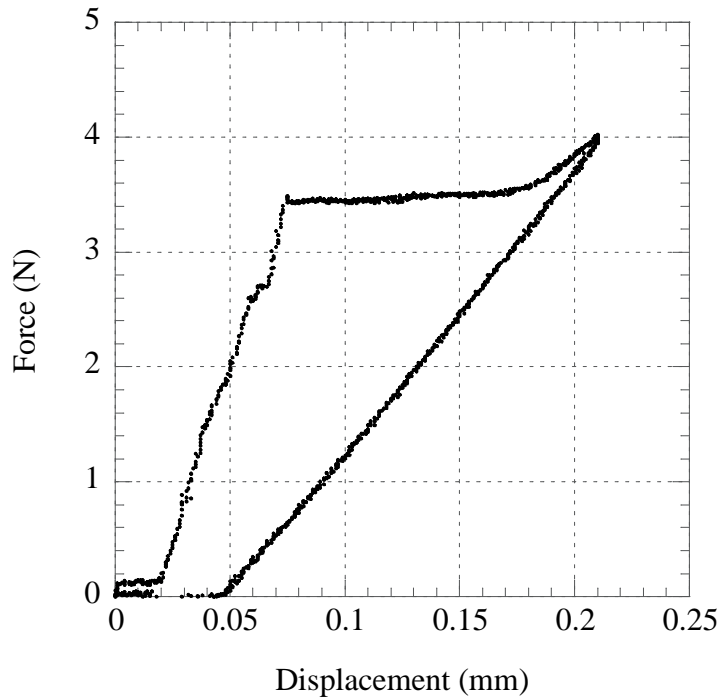


Figure 2-13: Load-displacement plot for a typical test.

the specimen and rollers seating themselves. At a critical load of approximately 3.5 N, delamination began and proceeded at a constant load. After propagating at a constant load, the load began to increase, which indicates the crack had reached the outer loading points. Following this, the specimen was unloaded. The specimen unloaded in an elastic manner and was more compliant because of the crack growth at the interface. The unloading path does not pass through the origin of the plot because the crack fails to close completely due to particulates that accumulate at the interface after delamination.

### 2.7.1 Effectiveness of Specimen

Delamination and steady-state crack growth, as observed in Figure 2-13, was routinely obtained for low toughness bonds ( $G_c < 2.5 \text{ J/m}^2$ ). While the test specimen allowed low toughness bonds to be characterized, it proved ineffective in quantifying the toughness of well bonded wafers. Rather than delaminating along the interface, the

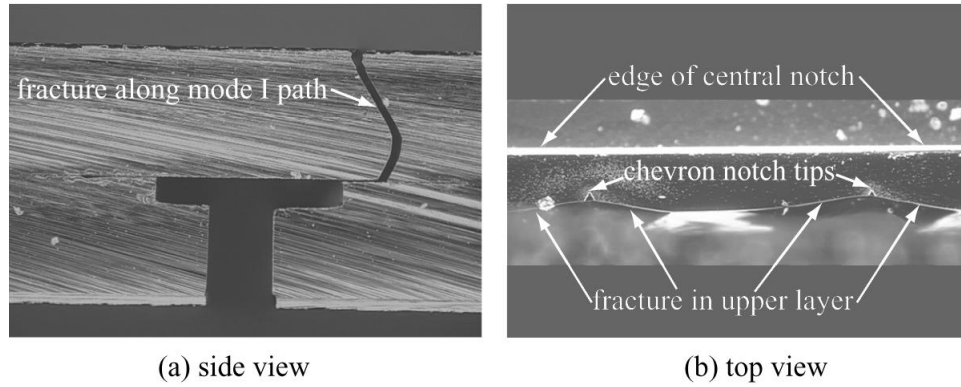


Figure 2-14: Chevron-notch specimen failure.

crack would either fail to initiate or would propagate a short distance along the interface and quickly deflect into the unnotched silicon layer. When either of these situations occurred, exact bond toughness values, could not be obtained, but a lower limit could be established. The reduction of the bonded area at the interface and the chevron notch had a limited effect in mitigating these difficulties.

The use of shallow grooves to reduce the effective toughness proved unsuccessful in preventing crack deflection. Tests of specimens with low toughness bonds verified equation 2.11 and demonstrated that the shallow grooves reduce the effective ‘global’ toughness of the interface. However, this proved to be inadequate in preventing crack deflection in well bonded specimens. It is believed that this occurred because of the scale of the groove pattern and that while the ‘global’ interface toughness is reduced, the ‘local’ toughness in the bonded regions is the quantity that actually controls crack deflection. A crack that is propagating along one of the bonded regions, which is hundreds of microns wide, deflects from the interface to follow a mode I path and subsequently leads to fracture of the upper silicon beam

The chevron notch geometry, which was implemented to encourage crack initiation at interface, did not notably change the delamination success rate in well-bonded specimens. In specimens annealed at temperatures greater than 800°C, failure through the upper silicon layer was common. A specimen that fractured through the upper silicon layer is shown in Figure 2-14. The path of the crack shown in Figure 2-14(a) is typical of the majority of failures observed. Figure 2-14(b) demonstrates that in

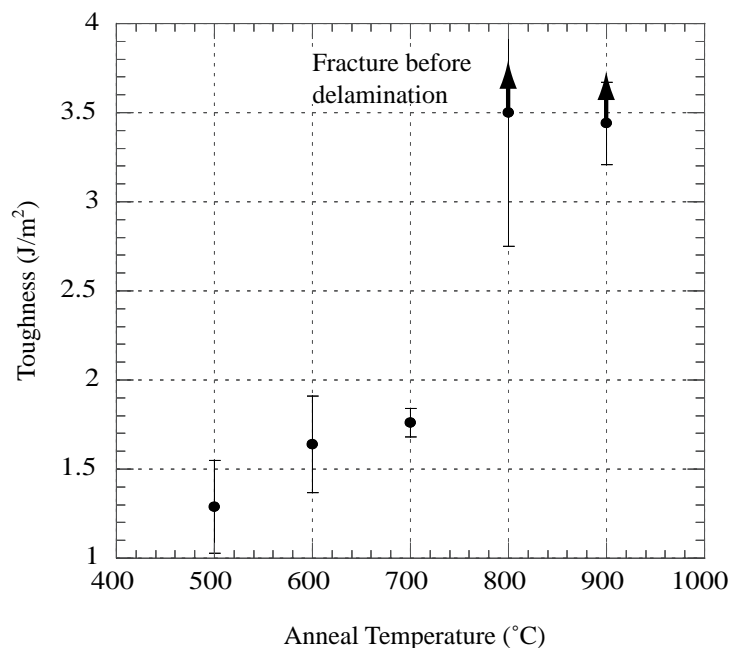


Figure 2-15: Bond toughness as a function of anneal temperature. Anneal time, contacting pressure, and contacting time held constant at 24 hours, 4000 mbar and 30 s, respectively.

well-bonded specimens, the crack often fails to propagate a significant distance along the interface. As illustrated from these micrographs, the chevron notch geometry, did not offer a notable improvement over the original specimen design.

### 2.7.2 Effect of Process Parameters on Bond Quality

Despite the limitations of the specimen, mixed-mode toughness values were obtained for silicon fusion bonds under various processing conditions. The reported data is limited to low toughness bonds and includes data from specimens fabricated under various annealing temperatures and times, and contacting conditions. For each set of processing conditions, multiple specimens from a single wafer pair were tested. Thus, in the plots that follow each data point represents an average of the specimens tested, typically four to five specimens. The error bars indicate the standard deviation of the data set.

Figures 2-15 and 2-16 demonstrate the effect of annealing temperature and time, respectively. All the specimens in Figure 2-15 were annealed for 24 hours at the spec-

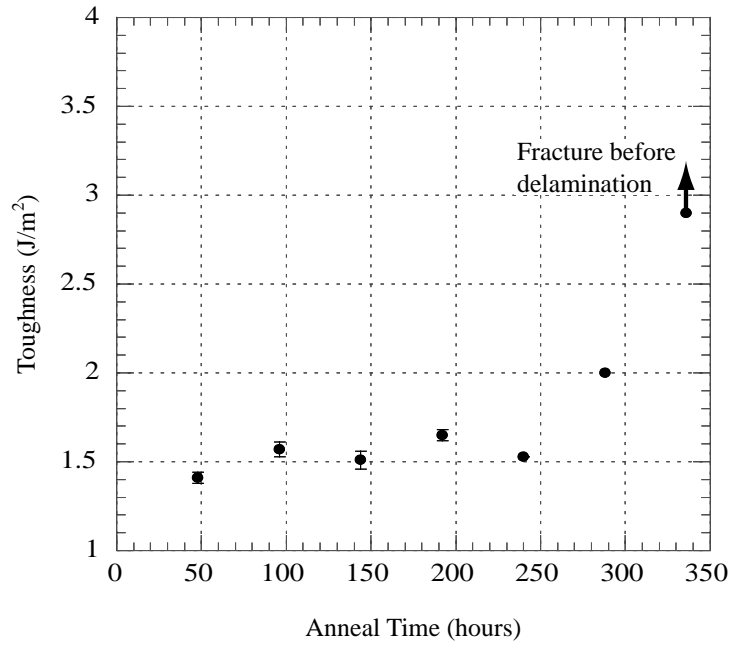


Figure 2-16: Bond toughness as a function of anneal time. Anneal temperature, contacting pressure, and contacting time held constant at 600 C, 4000 mbar and 30 s, respectively.

ified temperature. Figure 2-15 shows that bond toughness increases monotonically, but not linearly, with temperature. The specimens that were annealed at 800°C and 900°C failed to delaminate. As indicated on the plot, the measured toughness values for bonds at 800°C and 900°C only provide a lower limit on toughness. The lack of delamination indicates strong bonds, but specific values could not be obtained for  $G_c$ . The specimens used to obtain the data plotted in Figure 2-16 were annealed at 600°C for varying lengths of time. Delamination did not occur in the set of specimens annealed for 336 hours, thus, the data represents a lower limit on bond toughness at that point. Figure 2-16 suggests that annealing time has little effect on bond strength until some critical time is reached, at which point bond strength increases dramatically. The data in Figure 2-16 and the fact that specimens annealed at 336 hours did not delaminate suggests that bond strength can be increased after long anneal times. The trends observed with respect to annealing time and temperature are consistent with data for silicon fusion bonds reported elsewhere [20].

The effect of the parameters used during the initial contact of the wafers was



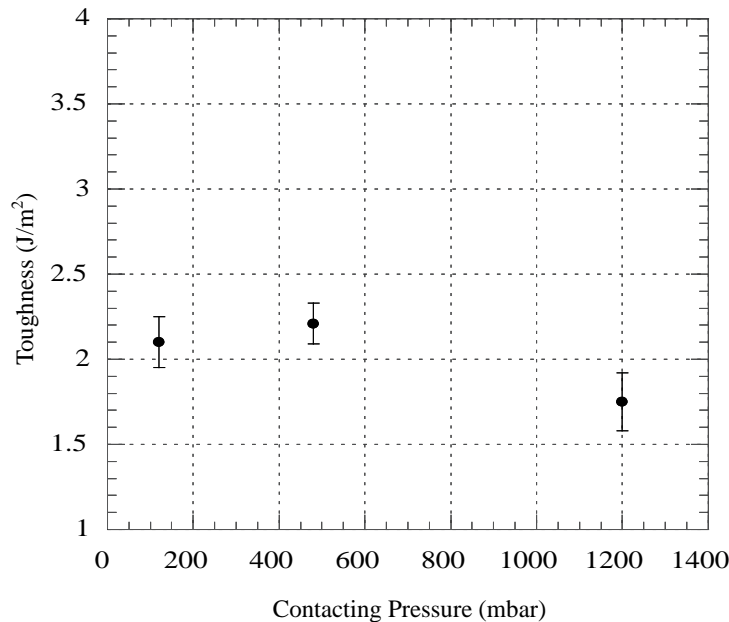


Figure 2-17: Bond toughness as a function of contacting pressure. Anneal temperature, anneal time, and contacting time held constant at 700 C, 24 hours and 30 s, respectively.

also examined in this study. To examine the effect of these, the anneal temperature and time were held constant at 700°C for 24 hours. The magnitude and time of the pressure applied during contacting were varied systematically. Figures 2-17 and 2-18 show the effect of the magnitude and time, respectively. Both parameters seem to have little effect on bond toughness. This is reasonable considering contacting is performed at room temperature and the lengths of time are relatively short.

## 2.8 Conclusion and Recommendations

A four-point bend delamination specimen has been employed to characterize the quality of silicon fusion bonds. A wafer-scale specimen fabrication process was demonstrated and test techniques developed. The study illustrated the need for proper alignment and provided a means to achieve it. The specimen was effective in characterizing low toughness bonds, however delamination and crack propagation along the interface could not be achieved in well-bonded specimens. The reduction of bonded area at the interface and the use of a chevron notch geometry proved ineffective in

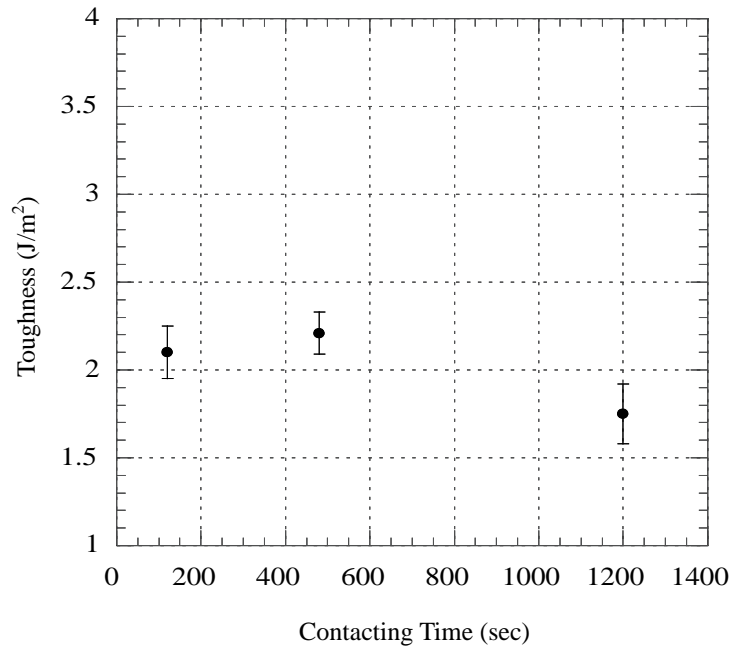


Figure 2-18: Bond toughness as a function of contacting time. Anneal temperature, anneal time, and contacting pressure held constant at 700 C, 24 hours and 4000 mbar, respectively.

encouraging crack initiation in high toughness interfaces. Tests of specimens with interface toughness values less than 2.5 J/m<sup>2</sup> were quite successful and demonstrated the expected behavior of stable crack propagation at a constant load. The increase in bond strength with annealing time and temperature that was observed is consistent with results reported elsewhere. The effect of contacting pressure and time were examined and found to have little effect on bond quality. The study clearly showed the applicability as well as the limitations of the four-point bend delamination specimen in characterizing silicon fusion bonds.

While the test technique has been developed and bonds have been characterized, further tests are required to completely map the process parameters of interest. The limitations of the specimen prevented bond toughness measurements on specimens fabricated under the full-range of process conditions. To examine the full range of process conditions, a different specimen geometry that permits delamination rather than fracture of specimens with well-bonded interfaces is required.

# Chapter 3

## Silicon-on-Insulator Membranes

### 3.1 Introduction

A common technique for producing thin single crystal silicon membranes of uniform thickness is to etch a cavity in the backside of a silicon-on-insulator (SOI) wafer. The thin oxide layer, which bonds the substrate to the device layer, acts as an etch stop. Thus, the membrane thickness is defined by the thickness of the device layer, which can range from less than 1  $\mu\text{m}$  up to several hundred microns. The tethered pistons in MHT devices, which can be seen in Figure 1-1, are fabricated from SOI wafers using this basic approach. To produce the piston structure, a circular trench is deep reactive ion etched (DRIE) in the backside of the wafer, resulting in a central boss connected to the substrate via a thin tether. A typical tethered piston structure that has been cross-sectioned is shown in Figure 3-1. The central boss is the total thickness of the wafer and the tether thickness is defined by the device layer thickness. In typical MHT devices, the membrane is 5-15  $\mu\text{m}$  thick, the boss is 405-415  $\mu\text{m}$  thick, the boss has a diameter of 5-8 mm, and the trench is 150-225  $\mu\text{m}$  wide.

The pistons are the primary moving mechanical components in MHT devices and allow the motion of the piezoelectric element to be transferred to the fluid medium. The tether serves as a seal, while permitting motion of the piston. The tethered pistons are loaded severely and two competing requirements are placed on the piston structure. The piston must allow for large displacements of the piezoelectric element,

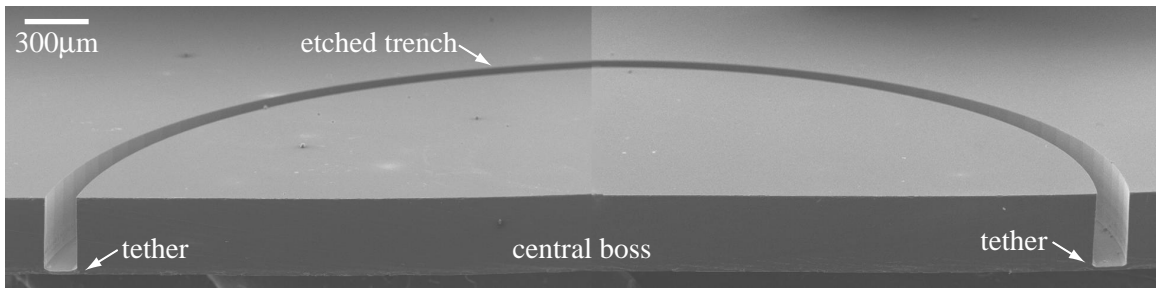


Figure 3-1: A SEM micrograph showing a typical MHT drive membrane.

but must also be stiff enough to withstand the high pressure loads from the fluid. This means that relatively stiff pistons must have the ability to withstand large deflections. Based on this, it is clear that high stresses cannot be avoided in the structure. Device modeling has indicated a clear link between device performance and the maximum allowable stress on the silicon structures [33]. Clearly, utilizing the full strength of the silicon membranes is required to achieve maximum device performance.

Single crystal silicon, while primarily used for microelectronics applications, has seen use as a mechanical material for close to three decades [34]. It is a high strength material and reported fracture strengths often exceed 1 GPa. The difficulty with employing this material for high stress applications is that it has a low fracture toughness, and thus the tensile fracture strength is highly dependent on the presence of defects and the surface roughness of the structure. Furthermore, the surface roughness is highly dependent on fabrication process. Thus, while strength values are reported in the literature, the actual strength of silicon components must often be measured experimentally to ensure optimal and safe device design. The purpose of this work is to measure the strength of silicon membranes fabricated from SOI wafers in order to provide a realistic design strength for the development of MHT devices. This was accomplished by carrying out tests on specimens with a fabrication process and geometry similar to the piston structures found in MHT devices. Background material regarding the strength of silicon is followed by a summary of the specimens and the test method employed. The results of the mechanical tests are presented and recommendations regarding further process development and testing are made.

## 3.2 Background

While no published data exists on the strength of membranes fabricated from SOI wafers, several researchers have investigated the strength of single crystal silicon as a function of processing conditions. One of earliest investigations was completed by Hu in 1982 [35]. Hu loaded simply supported specimens at the center and measured fracture strengths for wafers with various surface treatments. For well polished (100) wafers, a mean fracture strength of 2.8 GPa with a standard deviation of 1.2 GPa was reported. The range of strengths observed in the study was large, with a low value of 0.3 GPa and a high value of 6.9 GPa. Wilson et al. loaded microcantilever silicon beams, which had been etched from (100) wafers using a KOH solution, to fracture [36]. A strong dependence of strength on surface roughness was observed. Mean fracture strengths between 1.0 and 3.6 GPa were reported. Chen et al. examined the strength of silicon using two different specimens, a biaxial flexure specimen and a geometry termed the radiused hub flexure specimen, in which a circular trench is etched and a load is applied on the resulting central hub [37], [38], [39]. The data was presented in Weibull form, which is typically used to present strength data of brittle materials. For specimens with various surface conditions, reference strengths from 1.2 to greater than 4 GPa were reported, with Weibull moduli ranging from 2.7 to 7.5. While the reference strengths indicate that high fracture strengths can be achieved, the low Weibull moduli indicate a large degree of scatter in the data. Of particular interest to the current study, are the results of radiused hub flexure specimens, which were fabricated by DRIE and had a geometry similar to the pistons in MHT devices. Using these specimens, Chen et al. demonstrated that the strength of DRIE structures could be improved significantly using either an isotropic wet etch or a  $\text{SF}_6$  dry etch following the DRIE step.

The brittle nature of silicon, makes the fracture toughness an important quantity when considering the mechanical integrity of silicon structures. The fracture toughness determines the sensitivity of the fracture strength to flaws. Several studies report fracture toughness values for single crystal silicon. Early work, in which a

specimen with a flaw was loaded in four-point bending, measured fracture toughness as a function of crystal orientation. The highest fracture toughness, which was observed in the  $\{100\}$  orientation, was  $0.95 \text{ MN/m}^{3/2}$ . A lower fracture toughness of  $0.82 \text{ MN/m}^{3/2}$  was observed for specimens with  $\{111\}$  orientation [40]. More recent work supports these findings and reports fracture toughness values of  $0.83 \text{ MN/m}^{3/2}$  for specimens with a  $\{111\}$  orientation and  $0.91 \text{ MN/m}^{3/2}$  for specimens with a  $\{100\}$  orientation [41].

Based on the reported strength values, it is clear that the strength of silicon is highly dependent on the fabrication route and geometry of the structure. The previous work provides a range of strength values, but is insufficient to use for design purposes. The reported fracture toughness values provide insight into the factors that control strength in silicon structures. The low fracture toughness suggests that the fracture strength is highly sensitive to flaws. The wide range of stress values and the low fracture toughness support the assertion that to obtain accurate design data, measurement of strength on specimens with a fabrication process and geometry similar to actual structures is required.

### 3.3 Experimental Method

The approach employed in the current study to measure the fracture strength of silicon membranes is illustrated in Figure 3-2. Specimens, which had a geometry similar to the drive pistons in MHT devices, were simply supported at the edges while a point load was applied at the center of the boss. The center loading point was actuated at a constant displacement rate until fracture of the membrane occurred. Based on the failure load and the measured geometry of the specimen, the fracture stress was determined using a finite element model. The details regarding the test specimen, apparatus, and procedure are presented below.

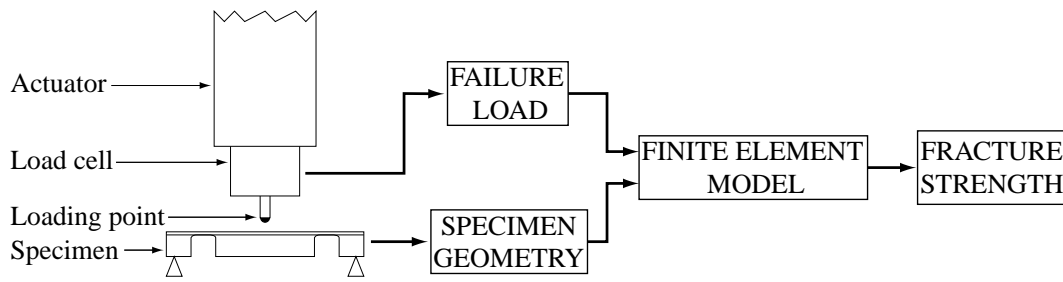


Figure 3-2: Fracture strength measurement approach.

### 3.3.1 Specimen Geometry and Loading

The test specimen was designed such that the geometry replicated the tethered drive pistons in the MHT device. This was done to ensure that the measured strength was an accurate representation of the strength expected in the device. The geometry must be similar because issues relating to etching, such as surface roughness, fillet radius control and etch rate, all depend on the geometry. The goal was to replicate faithfully the process used in device fabrication in order to not only quantify the strength, but to also gain a better understanding of the actual etched geometry and the difficulties in fabricating these structures. While these specimens allow the measurement of strength for these structures, the results may not be generally applicable due to the specific geometry.

The test specimen that was employed is shown in Figure 3-3. The specimen consisted of a central boss, 5.7 mm in diameter, connected via a 150  $\mu\text{m}$  wide tether to a 10  $\times$  10 mm die. The membrane thickness, which was defined by the thickness of the SOI device layer, varied in the current study from 5 to 18  $\mu\text{m}$ . The tether was defined by etching a trench through the 400  $\mu\text{m}$  thick substrate and controlling the etch appropriately to achieve a fillet radius at the bottom of the trench. The geometry is representative of that found in MHT devices, however, due to varying design requirements, the exact dimensions of the structures may vary. Pistons in current MHT devices have central bosses with diameters from 5 to 8 mm and tether widths from 150 to 225  $\mu\text{m}$ .

In addition to matching the geometry, an effort was also made to achieve a stress distribution in the specimen similar to that in the device. The loading on the piston

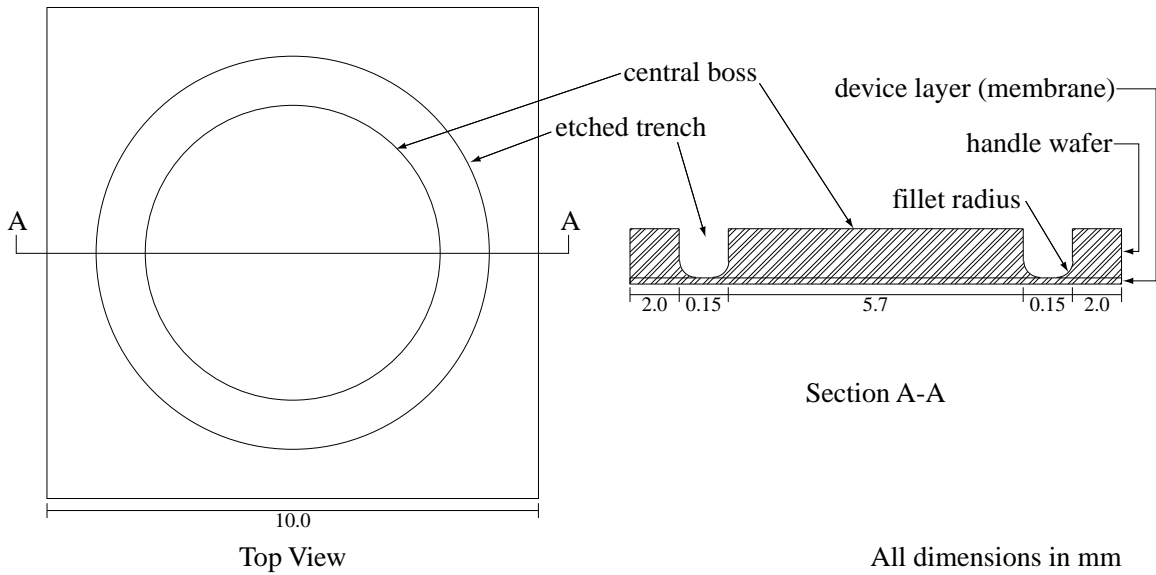


Figure 3-3: Schematic of test specimen for measurement of fracture strength.

structure during assembly and operation in MHT devices is quite complicated. Various combinations of pressure loads and displacements are applied to the tether during the device's lifetime. The highest tensile stresses are typically observed at the fillet radius at the base of the trench. Thus, a loading configuration that resulted in high tensile stresses at the fillet was chosen for this study. Two loading configurations, which are shown in Figure 3-4, that satisfy this requirement are a pressure load and a central point-load. The stress distribution does vary between the two cases, but, for the current geometry, the maximum tensile stress is found in the fillet for either loading scenario. The difficulty with the pressure load is that the specimen must be mounted securely in order to apply pressure from beneath. This mounting can induce residual stresses in the membrane and can be difficult to model accurately since the boundary conditions are not ideal. The point-load configuration, however, can be simply supported at the edges, which makes specimen mounting simpler and quicker. In addition, it is felt that the boundary conditions are easier to model accurately. Hence, in the current work, the specimen is simply supported at the edges and a load is applied at the center of the boss, as shown in Figure 3-4(b).



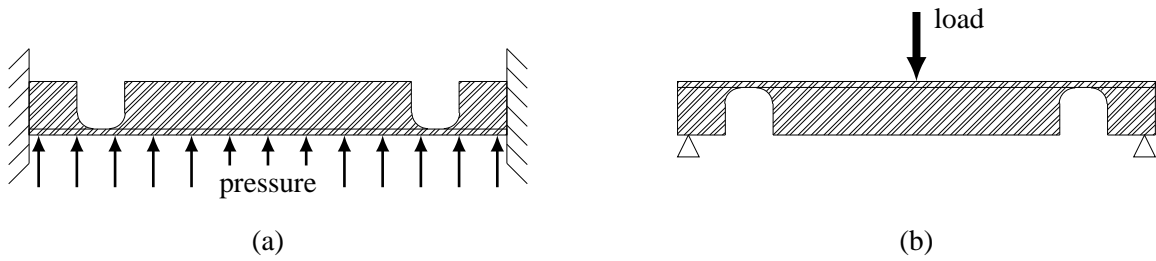


Figure 3-4: Potential silicon membrane loading configurations.

### 3.3.2 Specimen Fabrication

Specimens were fabricated from 4", (100), n-type double-side polished SOI wafers. The SOI wafers, which were purchased commercially, had been fabricated by bonding two (100) Czochralski grown silicon wafers together with a thermal oxide at the interface. Following bonding, the device layer was thinned using chemical-mechanical polishing. The specimens had features that required lithography and etching on both sides of the wafer. On the device layer, a shallow etch was used to create features that indicated the center of specimen, the specimen location on the wafer, and the edges of the specimen for dicing. A deep-etch from the backside was used to create the trenches that define the piston-like structure.

In order to achieve a fillet radius at the base of the trench, the deep etch must be controlled precisely. Control is difficult, and two different approaches to form and control the fillet radius were employed in the fabrication of specimens. The ‘standard’ approach, shown in Figure 3-5(a), is to etch a trench with straight sidewalls and carefully time the etch so that a fillet radius remains at the base of the trench. This approach is difficult because the etch must be controlled to within a few microns. Variations in etch uniformity across the wafer require that the wafer be inspected and that complete membranes be manually covered with photoresist, while etching is completed on others. An alternative approach employed is shown in Figure 3-5(b). A narrow trench is etched partially through the wafer, then a mask with a wider opening is used to complete the trench. This approach allows better control because the fillet does not recede as quickly during etching. While control is better, individual inspection and covering is still required.

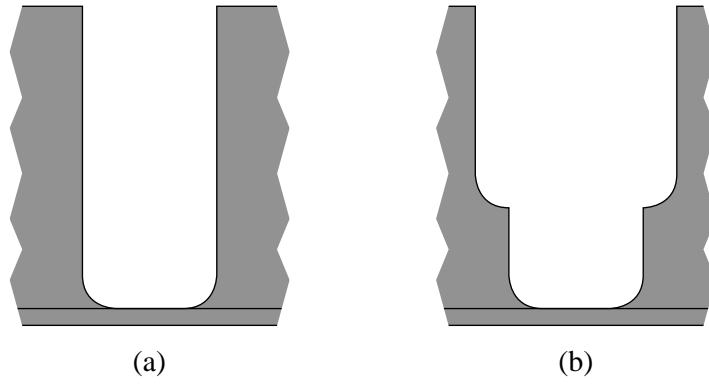


Figure 3-5: Different approaches for etching fillets, (a) ‘standard’, (b) ‘alternate’.

To fabricate the standard test specimens, the device layer was coated with OCG825 thin photoresist. The resist was patterned to define alignment marks at the center of each specimen as well as marks to facilitate die-sawing. The wafer was etched briefly using DRIE to create features  $\approx 4\text{-}6\text{ }\mu\text{m}$  deep. Following etching, the resist was stripped and the backside was coated with AZ4620 resist. The pattern to form the deep trench was defined in the resist. Alignment between the patterns on the two sides of the wafer was accomplished through the use of alignment features on the masks and a mask aligner with backside alignment capability. The trenches were etched at a rate of approximately  $3\text{ }\mu\text{m}/\text{min}$  using DRIE. When the trench approached the oxide layer, the wafer was removed and the membranes were inspected. Membranes that had a suitable fillet radius were covered with resist using a swab and then baked to cure the resist. Following protection of complete membranes, the wafer was etched further to complete the remaining membranes. This process of inspection, protection and additional etching was repeated until all specimens had suitable fillet radii. Given the nature of this process, it is easy to see that it is time consuming and has the potential for large variations in quality. On a portion of the specimens fabricated, the oxide at the base of the trench was removed using a buffered oxide etch (BOE). Finally, specimens were mounted on a handle wafer using photoresist and separated into  $10 \times 10\text{ mm}$  dies using a diamond wafer saw. The mask layout used permitted 48 specimens to be fabricated per 4” wafer.

The ‘alternate’ specimen geometry was fabricated using the same process as the

standard specimens, with the exception of the backside etch. The trenches were fabricated using a nested mask to allow the stepped geometry to be formed. The nested mask consisted of an oxide mask, which defined the wider trench, and a photoresist mask to define the narrow section. Using the resist mask, a narrow trench was etched 100–200  $\mu\text{m}$  deep. The resist was then stripped, and the oxide mask was used to etch the wider trench. The second etch, using the oxide mask, forms the step in the wall and completes the narrow trench in the center. The second etch is continued until the oxide is exposed. The fillet radii are then trimmed using the same procedure as employed on the standard specimens.

The basic DRIE process consists of sequential  $\text{SF}_6$  dry etch and polymer passivation steps. The etch removes material and the passivation layer protects the sidewalls of the feature being etched. As discussed previously, Chen indicated the possibility to increase fracture strength of silicon by conducting a dry  $\text{SF}_6$  etch without passivation at the end of a deep etch [38]. A portion of the specimens fabricated utilized this approach in an attempt to increase strength. This was accomplished by etching the majority of the depth using the standard DRIE process and then completing the final fillet radius trimming using a dry  $\text{SF}_6$  etch. This process results in more mask undercutting and slightly wider trenches, since the  $\text{SF}_6$  etches isotropically, however, surface finish is improved.

### 3.3.3 Test Apparatus

Typical failure loads for specimens employed in this study were between 1 and 15 N depending on the exact membrane thickness and fillet dimensions. In addition to the relatively low loads, the maximum deflection at failure for these specimens was typically less than 6  $\mu\text{m}$ . Thus, to test mechanically such specimens, a test machine that permitted submicron actuation and had the ability to measure loads well under 1 N was required. Furthermore, the test machine had to allow the specimens to be mounted and provide a means to align the loading point to the center of the specimen. The test machine that was developed and constructed for the current study based on these requirements is illustrated schematically and pictured in Figure 3-6.

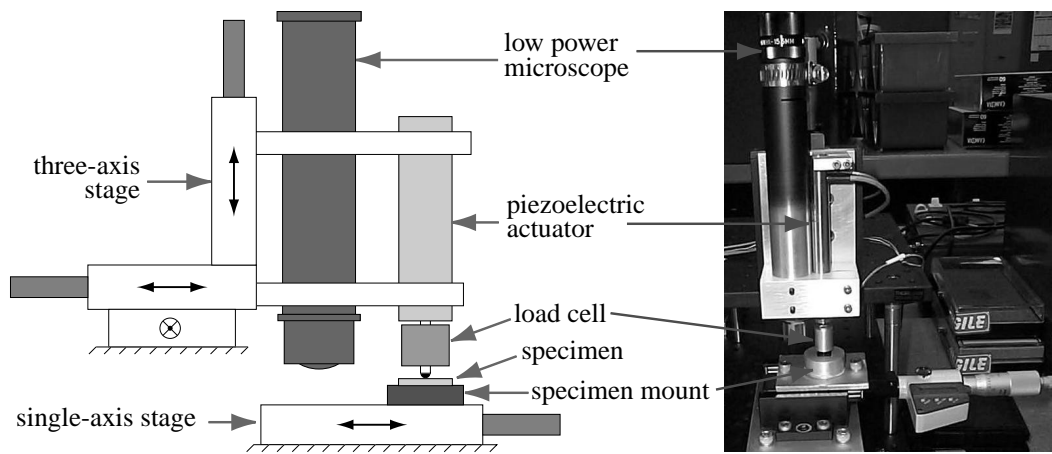


Figure 3-6: Silicon fracture test machine.

The layout of the test machine shown in Figure 3-6 is straightforward and consists of five basic components: an actuator, a load cell, a low-power microscope, a three-axis translation stage, and a precision single-axis translation stage. The basic theory of operation was that using the three-axis stage, the microscope, which contains a reticle with cross-hairs, was aligned to the etched feature at the center of the specimen. Following alignment, the single-axis stage was translated a fixed amount such that the loading point was aligned to the center of the specimen. The actuator was then used to displace the loading point and load the specimen. The load cell, which sits between the actuator and loading point, measured the force applied to the specimen.

The small displacements that were required, were achieved through the use of a commercially available piezoelectric stack actuator with a range of  $60\text{ }\mu\text{m}$ . Loads were measured with a commercially available strain-gage based load cell with a full-scale range of  $20\text{ N}$ . The load cell was calibrated in compression by applying a static load using weights. The results of multiple calibrations throughout the testing program demonstrated that the load cell sensitivity was repeatable to within  $\pm 5\%$  of the original calibration. The single-axis stage used was a commercial optical stage fitted with a digital micrometer with a quoted accuracy of  $\pm 1\text{ }\mu\text{m}$ . The other essential components in the test setup included the specimen mount, loading point, and the data acquisition system. The specimen mount, which sits on the single axis translation stage, was an aluminium block with a machined groove to locate the specimen

and a through hole 6.4 mm in diameter to permit the membrane to deflect. The loading-point was a 1.5 mm steel ball that was mounted to the end of the load cell. The actuator was controlled and the load was recorded using a microcomputer and LabVIEW™ data acquisition software.

Extensive efforts were taken to ensure proper alignment and calibration of the test machine. As stated previously, the calibration of the load cell was checked periodically throughout the testing program. An additional source of error that was of concern was misalignment of the loading point with respect to the center of the specimen. While alignment marks are etched on the center of each specimen, the process of aligning to the marks using the reticle and then translating the stage to align the loading point is a potential source of error. To ensure that the loading-point position matched that of the reticle once translated, a series of tests were completed in which a soft wax was indented to check the alignment and positioning accuracy. The results of the tests demonstrated that the loading-point could be repeatedly aligned to within  $\pm 50 \mu\text{m}$  of the initial position of the reticle. The effect of this error on the stress state in the specimen was examined using a linear 3-D finite element model of a typical specimen. The model, which consisted of half of a specimen with a 3 mm outer diameter,  $150 \mu\text{m}$  tether width,  $400 \mu\text{m}$  thick boss and  $10 \mu\text{m}$  thick membrane, was solved using the commercial finite element package ANSYS™. A copy of the batch file defining the model is included in Appendix B. A  $5 \mu\text{m}$  fillet radius was assumed at the base of the trench and a 2 N point load was applied near the center of the boss. The position of the point load was shifted different distances from the center of the specimen to observe the effect of misalignment on the maximum stress in the structure at the fillet radius. Figure 3-7 shows the percent change in maximum stress as the 2 N point load is shifted from the center. It is seen that if the position error is less than  $50 \mu\text{m}$ , the maximum stress increases by less than 4%. This result is quite reasonable considering the stiffness of the boss relative to the membrane and the relatively large diameter of the boss compared to the magnitude of the position error.

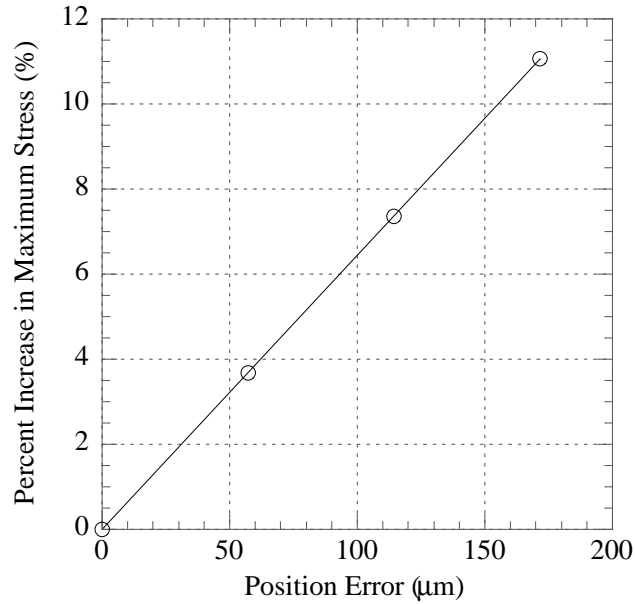


Figure 3-7: Effect of misalignment on maximum stress in a specimen.

### 3.3.4 Test Procedure

Following specimen fabrication and dicing, the specimens were separated from the handle wafer and cleaned in acetone. The trench width and fillet radius of the specimens were measured using an optical microscope with a calibrated digital measuring feature. The top width and fillet radii were measured in three locations around the circumference of the trench. The fillet radius was measured by viewing the bottom of the etched trench and measuring the width of the membrane between the fillets as seen in Figure 3-8(a). The fillet radius was then calculated by subtracting this length from the measured top width and dividing by two. This method is only valid when the sidewalls of the trench are straight, the fillets on both sides of the trench are equal size and the fillet geometry can be inferred from the length alone. Numerous specimens were cross-sectioned to verify that these conditions were true for the specimens in this work. The straight sidewalls and equal size fillets can be seen in Figure 3-8(b). The fillet shape appears to scale relatively well with length and the effect of slight variations in exact fillet geometry do not effect the calculated stress values significantly as discussed in Section 3.4. The features observed in Figure 3-8(b)

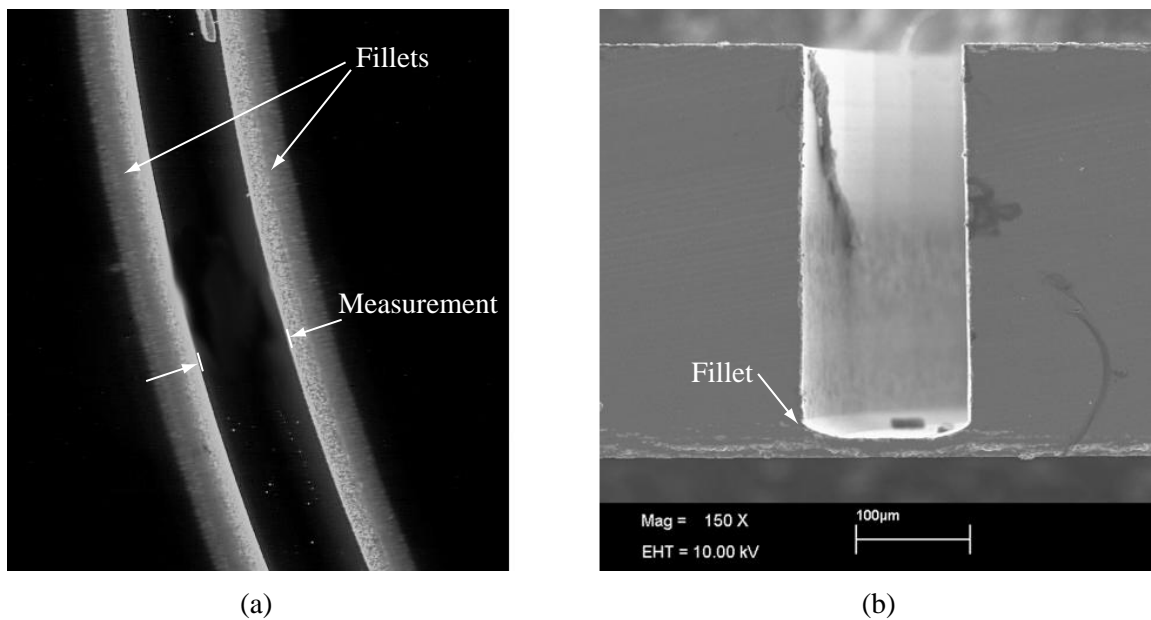


Figure 3-8: Typical fillet radius, (a) viewed from the top, (b) cross-section view.

were consistent among the specimens cross-sectioned, thus it was concluded that it was reasonable to measure the fillet geometry using the method described. For the ‘alternate’ specimen geometry, a similar procedure was used, but, the width of the trench at the step was also measured to allow the fillet radius to be calculated.

In addition to the measurements with the optical microscope, several specimens from each wafer were cross-sectioned and the membrane thickness was measured using a scanning electron microscope (SEM). The calibration of the SEM was checked using a measurement standard with 1.9 and 10  $\mu\text{m}$  features, immediately prior to measuring any specimens. It is assumed that the thickness of the membrane is uniform across the wafer, thus, measurements from 1 or 2 specimens were used to determine the thickness of all the specimens on a wafer.

Along with the measurements, the specimens were also inspected for defects in the membrane or fillet using an optical microscope. Defects in the fillet are common and specimens with large defects were not tested. Defects, such as the example shown in Figure 3-9, are caused by poor photoresist coverage during the inspection and protection stage of the fabrication process. This problem has recently been solved by using a thin photoresist and increasing the bake times during the individual fillet

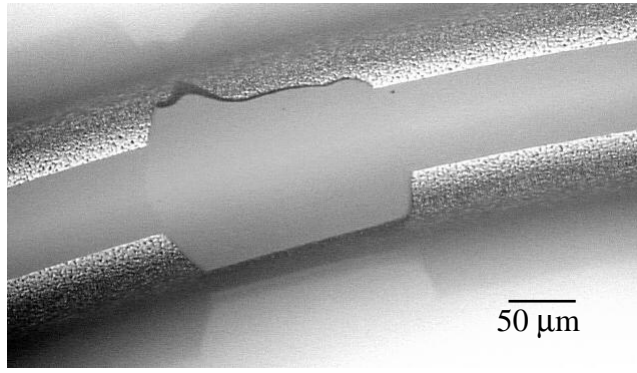


Figure 3-9: Typical defect in fillet radius.

protection process. Between defects such as these, membranes that were over or under-etched, and membranes that fractured during fabrication and handling, the typical specimen yield on a wafer was 30 to 50%.

Following measurement and inspection, the specimens were mounted in the test machine. The specimens were aligned and loaded at a constant displacement rate to fracture, as discussed in Section 3.3.3. The load was recorded as a function of time using LabVIEW™. The failure load was obtained from the recorded data and a failure stress was obtained from a simple finite element model using this load value and the measured geometry of the specimen. The finite element model is detailed in the following section.

### 3.4 Finite Element Modeling and Data Reduction

To extract the failure stress from the measured failure load and geometry, a finite element analysis of the specimen was used. A full three dimensional model was too computationally expensive to use for this stress analysis, thus a 2-D axisymmetric model was employed. The basic form of the model, including boundary conditions and loading is shown in Figure 3-10. The model was meshed with 8-node plane strain axisymmetric elements as seen in Figure 3-10. Single crystal silicon, which is an anisotropic material with diamond cubic symmetry, has stiffness coefficients  $C_{11}=1.657$ ,  $C_{12}=0.639$ , and  $C_{44}=0.796 \cdot 10^{11}$  Pa [42]. For the purposes of the axisym-



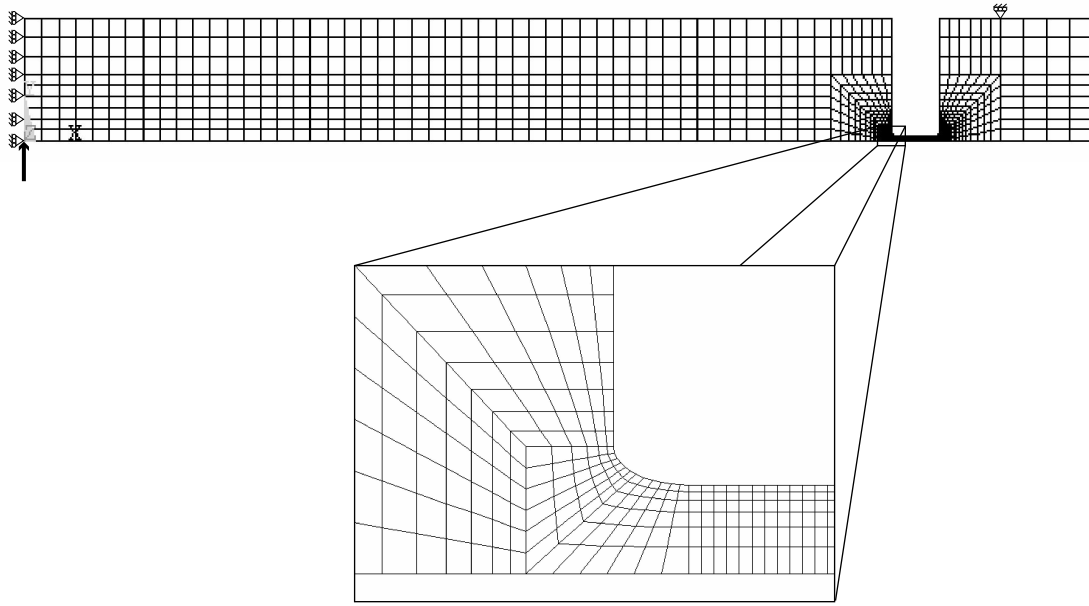


Figure 3-10: Finite element model of specimen.

metric finite element model, an isotropic equivalent Young's modulus of 165 GPa and a Poisson's ratio of 0.22 were assumed. The material is linear elastic up to the fracture point, thus material nonlinearities were not included. However, the deflections of the structure have the potential to be large relative to the membrane thickness, thus, nonlinearities due to large deflections and stress stiffening were included.

To extract the stress from a measured failure load, the geometry of the model was defined using the experimentally measured values. The measured trench width, membrane thickness, and fillet radius were used when determining the fracture stress for each specimen. The shape of the fillet radius was assumed to be a quarter-ellipse as seen in Figure 3-11. The  $b/a$  ratio, which defines the aspect ratio of the ellipse, was assumed to be 0.5 for all specimens. From the specimen cross-sections examined, it was seen that the  $b/a$  ratio was typically near 0.5, but occasionally was greater. A  $b/a$  ratio greater than 1.0 was never observed. The sensitivity of the maximum stress to the  $b/a$  ratio of the fillet was examined for a typical specimen with a 6 mm outer diameter, 5.7 mm inner diameter, 12  $\mu\text{m}$  thick membrane, and a 6 N load applied at the center. The maximum stress as a function of fillet radius length,  $a$ , for  $b/a$  ratios from 0.5 to 1.0 is plotted in Figure 3-12. It is seen that the effect of the exact fillet

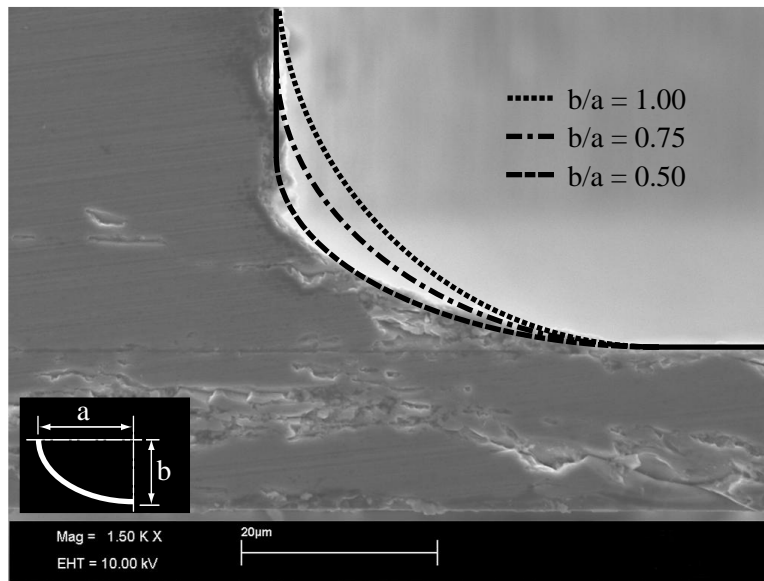


Figure 3-11: Typical shape of etched fillet radius.

radius shape on the maximum stress in the structure is small. This suggests that it is reasonable to assume  $b/a = 0.5$  for all specimens and to infer the fillet geometry from the measured fillet length alone.

This finite element model, for which the batch file is included in Appendix B, was used to determine the fractures strength of all specimens tested. The fracture strength was taken as the maximum tensile stress (the first principal stress), which was located near the base of the fillet. Since silicon is a brittle material, failure does not simply depend on the maximum stress, but rather depends on the probability of a critically sized flaw being located and oriented relative to a tensile stress. Thus, strength data for brittle materials is usually represented using Weibull statistics, where the probability of failure depends on the stress distribution over a volume or surface area. Chen et al. used Weibull statistics to represent strength data of DRIE silicon and found the data only fit the Weibull distribution moderately well [38]. In the current study, significant scatter was present in the data and it did not appear to fit a Weibull distribution well. Thus, the data is presented in terms of maximum stress in the structure at failure. This approach is reasonable since the area and stress distribution of the specimen and the structures in MHT devices are quite similar. While this data may not necessarily be used to design a broad range of structures, it

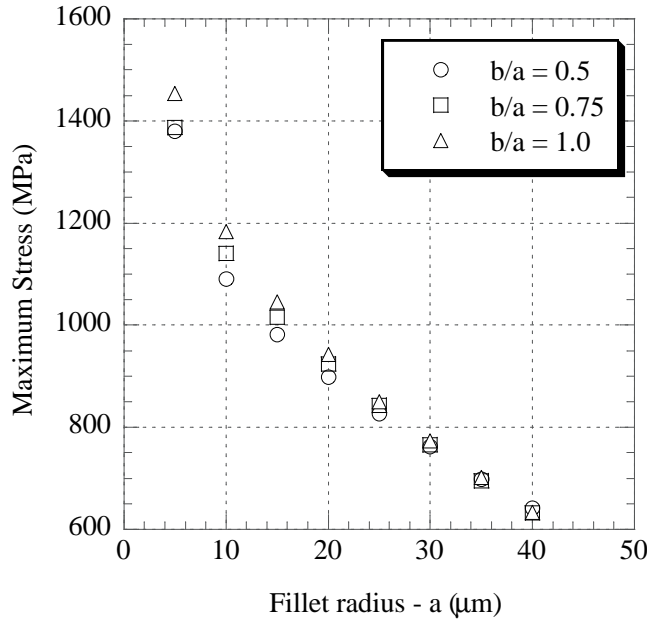


Figure 3-12: Effect of  $b/a$  ratio on maximum stress.

should provide moderately good estimates for the design of MHT devices.

### 3.5 Results

Through the course of this study, 7 wafers were fabricated and tested, yielding 129 specimens. The nominal thickness of the device layer, manufacturer of the wafer, and details with regard to the process, such as the use of a dry  $\text{SF}_6$  etch or the removal of oxide are listed in Table 3.1. The wafers with 5  $\mu\text{m}$  thick device layers were purchased from BCO Technologies<sup>1</sup>, while the wafers with thicker device layers, 12.5 and 18  $\mu\text{m}$ , were donated to the MIT Microsystems Technology Laboratory several years ago by Motorola. The specimens listed in Table 3.1 were fabricated in two batches. The first batch, which included wafers A and B, were fabricated using the standard process outlined in Section 3.3.2. The dry  $\text{SF}_6$  etch was not used and the oxide at the base of the trenches was not removed. The second batch, which included wafers C through G, were fabricated with either the standard or alternate fabrication process discussed

<sup>1</sup>BCO Technologies, 5 Hannahstown Hill, Belfast, BT17 OLT United Kingdom

Table 3.1: Process conditions of fabricated wafers.

Wafer	Thickness	Manufacturer	Process	SF <sub>6</sub> dry etch?	Oxide removed?
A	5 $\mu\text{m}$	BCO	standard	no	no
B	18 $\mu\text{m}$	Motorola	standard	no	no
C	18 $\mu\text{m}$	Motorola	standard	yes	yes
D	18 $\mu\text{m}$	Motorola	standard	yes	yes
E	5 $\mu\text{m}$	BCO	standard	yes	yes
F	12.5 $\mu\text{m}$	Motorola	alternate	yes	yes
G	18 $\mu\text{m}$	Motorola	alternate	yes	yes

in Section 3.3.2. The fillet radius trimming was completed using the dry SF<sub>6</sub> etch and the oxide at the base of the etched trenches was removed. The oxide was removed at the base of the trenches because process development for the MHT device revealed that this oxide would have to be removed when fabricating the actual device.

All wafers were measured and tested according to the procedures outlined above. The fracture strength mean and coefficient of variation ( $C.V. = \frac{Std.Dev}{Mean}$ ) for each wafer is listed in Table 3.2. In addition, the number of specimens tested from each wafer is provided. From the values listed, it is seen that the mean fracture strengths vary considerably between the BCO and Motorola wafers. One also notices that the coefficient of variation among specimens from a single wafer is quite large, typically near 0.25. This large coefficient of variation, which indicates considerable scatter in the data, is not entirely surprising given the fact that silicon is a brittle material. An additional factor, which may contribute to the scatter in the data, is the fact that the size of the fillet radius often varied by as much 50% around the circumference of the membrane. For the purpose of calculating fracture stress, an average fillet width was used, which yields a more conservative estimate of strength than if the minimum fillet dimension is used.

While the data in Table 3.2 summarizes the data from all the wafers, it is useful to group specimens with the same manufacturer and similar fabrication processes. The strength data presented in Table 3.2 was consolidated into four groups:

- I. This group includes all the specimens from wafer A. The starting SOI wafer was from BCO, the SF<sub>6</sub> dry etch was not used, and the oxide was

Table 3.2: Fracture strength values of tested wafers.

Wafer	Measured Thickness	Mean (GPa)	C.V.	Number of Specimens
A	5.3 $\mu\text{m}$	1.67	0.27	10
B	17.5 $\mu\text{m}$	0.77	0.22	12
C	17.1 $\mu\text{m}$	0.54	0.26	26
D	17.4 $\mu\text{m}$	0.47	0.24	25
E	4.6 $\mu\text{m}$	1.30	0.37	19
F	13.1 $\mu\text{m}$	0.46	0.19	24
G	17.8 $\mu\text{m}$	0.40	0.29	13

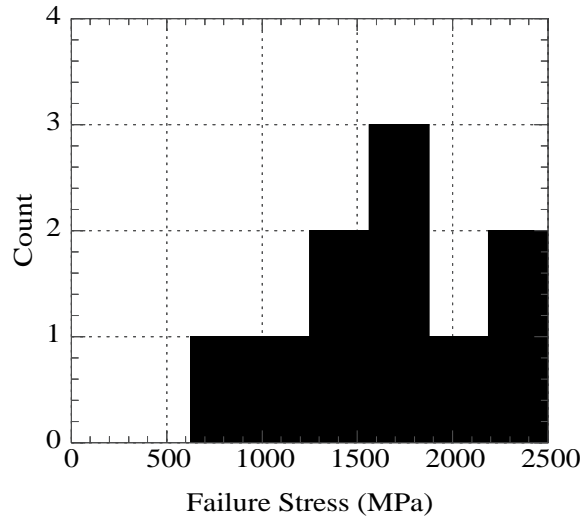
Table 3.3: Consolidated fracture strength values.

Group	Mean (GPa)	C.V.	Number of Specimens
I	1.67	0.27	10
II	0.77	0.22	12
III	1.30	0.37	19
IV	0.48	0.26	88

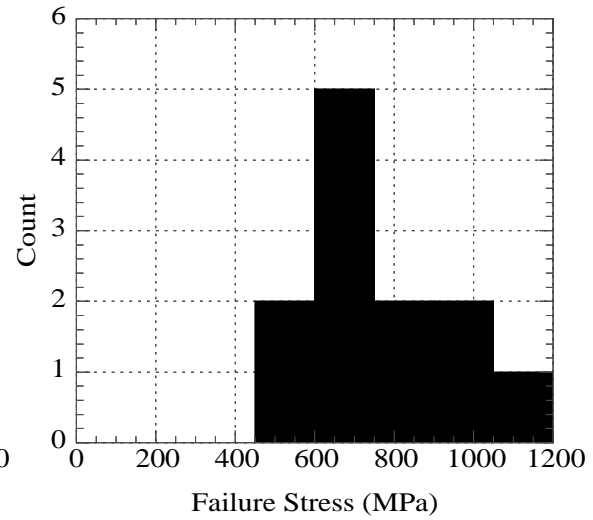
not removed. The distribution of strength for this set is shown in Figure 3-13(a).

- II. This group includes all the specimens from wafer B. The starting SOI wafer was from Motorola, the  $\text{SF}_6$  dry etch was not used, and the oxide was not removed. The distribution of strength values for this set is shown in Figure 3-13(b).
- III. This group includes all the specimens from wafer E. The starting SOI wafer was from BCO, the  $\text{SF}_6$  dry etch was used, and the oxide was removed. The distribution of strength values for this set is shown in Figure 3-14(a).
- IV. This group includes all the specimens from wafers C,D,F, and G. This set includes wafers fabricated using the 'standard' and 'alternate' trench geometries. The starting SOI wafers were from Motorola, the  $\text{SF}_6$  dry etch was used, and the oxide was removed. The distribution of strength values for this set is shown in Figure 3-14(b).

The fracture strength mean and coefficient of variation for each group listed above are summarized in Table 3.3.

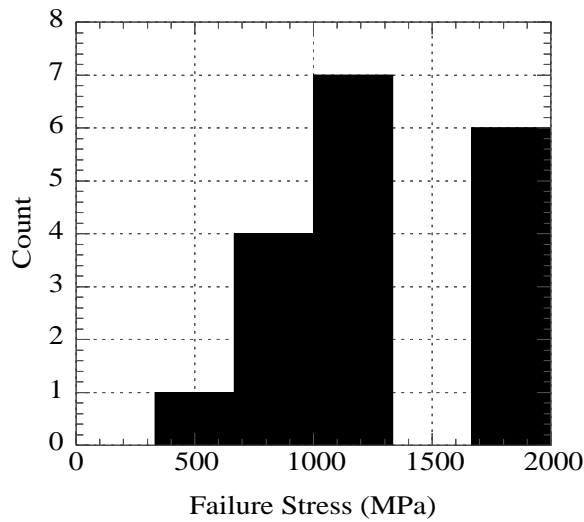


(a) BCO wafer.

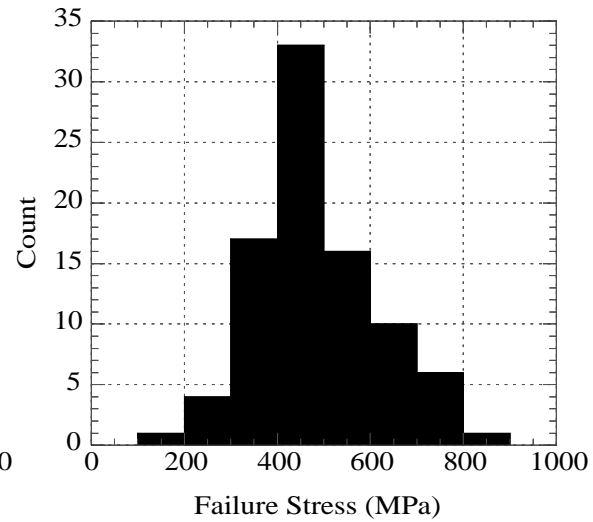


(b) Motorola wafer.

Figure 3-13: Strength results for specimens with oxide.



(a) BCO wafer.



(b) Motorola wafers.

Figure 3-14: Strength results for specimens without oxide.

Based on the mean fracture strengths of the four groups discussed above, two clear trends can be identified. The first is that removal of the oxide at the base of the trench reduces fracture strength. The data shows a clear decrease of approximately 0.3-0.4 GPa in the strength of specimens when the oxide is removed. While this is a concern, it is a reasonable result. The oxide, which most likely contains a compressive residual stress, maintains a compressive stress on the surface of the structure. The compressive stress on the surface reduces the effective tensile stress on flaws and thus allows the structure to carry a higher load. The other trend, which is clear from the data, is that the BCO wafers are significantly stronger than the Motorola wafers. While one could argue that this may be due to the size effect, since the BCO specimens had thinner membranes than the Motorola specimens, it is unlikely this is the cause, since strength controlling defects in single crystal silicon are usually on the surface. While the volume of these specimens is different, the surface area and stress distribution is nearly the same. Thus, one would expect the two thicknesses to have similar failure probabilities. A more likely explanation is that there is a difference in the quality of the SOI wafers themselves. While both the Motorola and BCO wafers were manufactured with the same basic process, slight differences in the individual vendor's process may effect the strength. In addition, SOI fabrication is still a developing field and the Motorola wafers were fabricated several years before the BCO wafers, thus it is likely process improvements have been made since the Motorola wafers were fabricated.

An unfortunate artifact of how the specimens were fabricated is that all the specimens which had the oxide removed, also had the  $\text{SF}_6$  dry etch. Since the oxide effects the strength, the effect of the  $\text{SF}_6$  etch could not be observed in the data. While it is possible that the  $\text{SF}_6$  etch could actually reduce the strength and be responsible for the decrease in strength attributed to the removal of the oxide, it is unlikely. SEM observations of the etched trench clearly show that specimens trimmed with the  $\text{SF}_6$  have smoother etched surfaces. The smoother surfaces should result in higher strength, not lower strength as was observed. Thus, it is believed that the conclusion, that the removal of oxide reduces the strength, is a valid one.

While there are clear trends observed, the degree of scatter present is a concern. The scatter is present despite attempts to inspect specimens for defects prior to testing. The reason that this inspection process does not result in a tight strength distribution is because of the scale of the defects detected in the inspection process. During the inspection, defects with sizes on the order of 10-100 microns were observed. The difficulty arises from the fact that the defects that control strength are several orders of magnitude smaller than this. Using an average fracture toughness of silicon of  $K_{IC}=0.89 \text{ MN/m}^{3/2}$  and assuming failure occurs at a stress,  $\sigma_f$ , the critical flaw size that results in failure is,

$$a_{crit} \geq \frac{1}{\pi} \left( \frac{K_{IC}}{\sigma_f} \right)^2. \quad (3.1)$$

Based on this, it easily seen that to achieve a fracture stress of 0.5 GPa, flaws must be less than  $1.0 \text{ } \mu\text{m}$  in size. Furthermore, to achieve a strength of 1 GPa, the maximum flaw size must be less than  $0.25 \text{ } \mu\text{m}$ . These flaws are well below the resolution of the inspection process used, and it would be difficult to inspect the entire structure, which is on the order of millimeters, for flaws less than  $1 \text{ } \mu\text{m}$  in dimension. Thus, the scatter in the data is not unreasonable. A degree of scatter is to be expected in strength data of brittle materials and that is why failure probabilities rather than strengths are often defined. Unfortunately, the data in the current study did not fit the typical Weibull distribution well and thus, strengths are reported rather than failure probabilities. The most likely cause of the poor fit is that there are several types of defects that control the strength.

### 3.6 Conclusions

In this study, the fracture strength of tethered piston structures fabricated from SOI wafers has been measured. The results indicate a strong dependence of strength on the SOI manufacturer as well as the processing route. It was observed that of the SOI wafers currently used in the fabrication of MHT devices, the strength of the BCO



wafers was significantly higher than that of the Motorola wafers. While no qualitative difference between the wafers could be observed, the strength tests clearly indicate a difference in quality. In addition, it was also observed that removal of the oxide at the base of the etched trench appears to reduce the fracture strength of the membrane structures. There was a large degree of scatter in the data and coefficient of variations of 0.25 were common. The strength values measured for these DRIE SOI structures was well below strengths reported elsewhere for similar DRIE structures fabricated from bulk silicon wafers [38]. The cause of this difference in strength between SOI wafers and bulk silicon wafers is not clear.

The study clearly indicated the need to develop a better fabrication process for membranes. Controlling the size of the fillet is difficult and variations in geometry are believed to be partly responsible for the scatter in the data. A better process is essential for improving yield and reducing manufacturing time. Based on the strength data, it clear that SOI wafers from different sources should be tested to verify the strength prior to integration in a device. Finally, it would be highly desirable to obtain additional strength data and to fit the data to a suitable statistical distribution. This would allow probabilistic design techniques to be used to ensure the reliability of MHT devices.



# Chapter 4

## Gold-Tin Bonding

### 4.1 Introduction

The integration of bulk piezoelectric material is a key factor in the design of microhydraulic transducers that allows high power density devices to be achieved. The bulk piezoelectric material, which may be a polycrystalline material such as PZT-5H (lead zirconate titanate) or a single crystal material such as PMN-PT (lead magnesium niobate-lead titanate) or PZN-PT (lead zinc niobate-lead titanate), allows significantly more actuation capability than thin-film piezoelectric materials that are typically found in microscale devices. In order to use the full potential of bulk piezoelectric materials, a reliable means of bonding the material to micromachined silicon structures is required. The bond must provide a mechanical and electrical connection, allow adequate dimensional control, and be compatible with the device fabrication process.

The focus of the current work is the development of the bonding process and preliminary mechanical characterization of bond strength. In this chapter, the requirements of the bond and the selection of the gold-tin solder bond are detailed. Previous work pertaining to gold-tin solder is briefly reviewed to establish a basic process and typical bond strength values. The process that has been developed to produce void-free bonds is described and the critical factors necessary to achieve robust bonds are identified. Results of tensile tests that were conducted to verify the

mechanical integrity of the bond and demonstrate potential weaknesses are presented. Recommendations regarding further process development and characterization are given.

## 4.2 Bond Selection

### 4.2.1 Bond Requirements

The primary function of the bond is to provide a mechanical connection between the piezoelectric element and the silicon structure. While efforts are made to keep the bond in compression during device operation, scenarios exist where a tensile load may be applied to the bond. In addition, the bond is subjected to cyclic shear strains from the lateral expansion of the piezoelectric element. Large numbers of cycles are expected to accumulate quickly, given that typical drive frequencies are between 10 and 30 kHz. These factors all contribute to a general requirement that the bond be mechanically robust. Equally important, the bond must provide an electrical connection between the silicon electrode and the piezoelectric element. While actuation could be achieved with a dielectric layer between the piezoelectric element and the silicon, the layer would act as a capacitor and would result in a voltage drop across the bond, thus requiring higher drive voltages. For a typical piezoelectric element (dielectric constant,  $\kappa \approx 5000$ ) of height 1 mm bonded with a 1  $\mu\text{m}$  thick bond of epoxy or glass ( $\kappa \approx 5$ ) on both ends, the drive voltage required would be approximately three times higher than if the bond was conductive. An increase of drive voltage by a factor of three is a serious issue, since typical design voltages are near 1000 V. Finally, the bonding technique must also be compatible with the materials and fabrication processes of the device. Bonding mediums that have low maximum temperatures are not feasible because the final anodic bond, which requires a processing temperature of 300°C, must be completed coincident with or following the piezoelectric bonding step. Similarly, bonds which require high temperatures are limited by the softening point of the Pyrex glass, which is near 800°C, and the upper processing limit of

the piezoelectric material. It should be noted that at temperatures above 100°C the piezoelectric material de-poles, but it can easily be re-poled following bonding. These requirements dictate the selection of a suitable bonding technique.

### 4.2.2 Bonding Techniques

Bonding of dissimilar materials to construct mechanical structures on the microscale is an area of limited research. However, the area of packaging microdevices and die-attach techniques is a rich subject and is closely related to the task at hand. Packaging individual devices usually involves bonding dissimilar materials (one of them often silicon and the other often a ceramic) with relatively small areas, typically 4-100 mm<sup>2</sup>. The piezoelectric elements in MHT devices must be bonded to silicon and have bonding areas approximately 1-3 mm<sup>2</sup>. Thus, many of the techniques that were considered for the current application were based on die-attach and packaging techniques. Among the methods that were considered are solder bonding or brazing, organic adhesives, and glass bonding mediums.

Organic adhesives, such as polyimides and epoxies can be filled with a metal powder to provide electrical conductivity [43], however their temperature range is limited. The maximum service temperature, which is near 200°C for high performance adhesives, is inadequate to withstand the 300°C temperature required for the anodic bond. Glass frit bonds and anodic bonds, which permit bonding of dissimilar materials through the use of a thin intermediate glass layer, can withstand the required temperatures of the final bond step of the device. A glass frit bond, where the glass acts as an adhesive, is accomplished by applying a glass layer at the interface, then heating sufficiently to drive out the organic binders that are present in the glass. The glasses can be metal filled to produce an electrically conductive bond and low temperature glasses with processing temperatures near 400°C are available. The primary drawback of this method, though, is that it is difficult to remove the solvents and binders in the glass completely [44]. This problem is further complicated by the fact that, in MHT devices, the bond is contained in a small cavity. The other method in which a glass layer can be used to bond piezoelectric material to silicon

is to sputter or evaporate a thin layer of borosilicate glass on the piezoelectric element. An anodic bond can then be formed between the silicon and the glass layer by heating to a temperature of 300-500°C and applying an electric potential across the interface. This approach has successfully been used to bond bulk piezoceramics to silicon wafers [45], [46]. The use of an anodic bond is attractive because the thermal expansion of the glass can closely match that of silicon and the temperatures required are compatible with the existing processes in the device. The difficulty with the anodic bonding technique is that the glass can not be electrically conductive because of the voltage that must be applied across the interface to achieve a bond.

Brazing and soldering involve a wide range of materials and processing conditions. A typical process consists of heating the bond material, which is typically a metal alloy, above its liquidus temperature, allowing it to wet the surfaces to be bonded, and then cooling to solidify. The only difference between soldering and brazing is the temperature at which the bond is completed. If the alloy being used melts above 450°C, it is considered a braze, and if it falls below this temperature it is a solder. Solders are more prevalent in the realm of microelectronics packaging, because the lower processing temperatures prevent damage of sensitive electronics. In general, solders are divided into two basic categories, soft and hard. Soft solders typically have melting temperatures below 200°C, have low yield strengths, and are more susceptible to thermal fatigue and creep. Hard solders, which include eutectic compositions of AuSi (97wt.%Au-3wt.%Si), AuSn (80wt.%Au-20wt.%Sn) and AuGe (87.5wt.%Au-27.5wt.%Ge), have higher melting temperatures and yield strengths and are used more frequently in packaging applications, [43], [44]. Besides packaging applications, AuSi has also been used to bond three dimensional silicon microstructures [47], and AuGe to bond quartz layers in an accelerometer, [48].

The gold-based eutectic solders have excellent mechanical properties and are electrically conductive, which make them an attractive option for the bonding of piezoceramics to silicon. In addition, the bonds can be completed in a reducing atmosphere without the use of flux. The AuSi, AuSn, and AuGe eutectic solders melt at 363, 278 and 361°C, respectively. To ensure complete melting, bonds are often completed at

20-40°C above these temperatures. Thus, the fabrication temperatures are compatible with those required for the anodic bond. Further, the gold-tin processing temperature, which is close to 300°C, allows the anodic bond and silicon-piezoelectric bond to be accomplished simultaneously. Gold-tin has the lowest melting temperature, highest yield strength, and lowest modulus of the gold-based eutectic solders discussed [49]. The principal disadvantages of the gold-tin solder are the large thermal expansion coefficient of the solder, which can lead to large residual stresses, and the high gold content, which makes the bonding method expensive. Despite these drawbacks, the advantages of the gold-tin solder lead it to its selection to bond piezoelectric elements to silicon in MHT devices. The gold-tin is a clear choice, however there have been various gold-tin bonding processes reported and the exact implementation of the bond was based on previous work and factors specific to the MHT device.

## 4.3 Gold-Tin Bonding Background

### 4.3.1 Applications

Gold-tin alloys have been used in a variety of packaging and microelectronic applications for more than 20 years. The principle use of the solder has been for die-attach applications, in which the gold-tin bond secures a silicon or gallium arsenide (GaAs) die to a ceramic substrate, such as alumina. The excellent thermal conductivity and high yield strength of the bond are often cited as the important factors in selecting gold-tin. More recently, gold-tin bonds have been used for optoelectronic packaging applications that require bonding of laser dies to diamond or silicon substrates. The relatively high melting temperature of the gold-tin, compared to typical lead-based solders, make the gold-tin system well-suited for these devices, which operate at elevated temperatures. Gold-tin bonds have also recently been used in electronic flip-chip applications [50], and the packaging of MEMS devices. In particular, it has been used to form interconnects in chemical sensors, [51], and is used to hermetically seal a glass cover on a commercial electrostatic projection display [52].

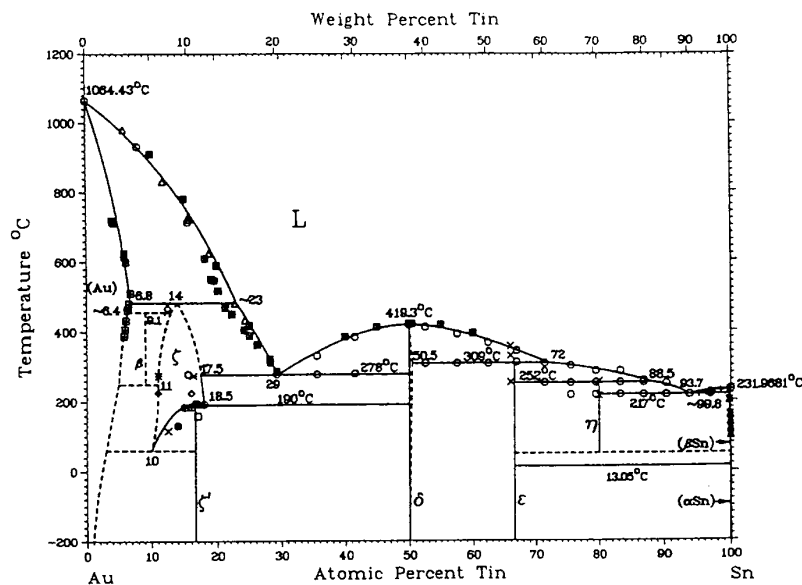


Figure 4-1: Gold-tin equilibrium phase diagram. [53].

### 4.3.2 Material Properties

The equilibrium phase diagram of the gold-tin binary system is shown in Figure 4-1 [53]. It is one of the more complicated binary systems and has two eutectic points. The common eutectic composition of 80 wt.% Au and 20 wt.% Sn melts at 278°C. Alloys of the second eutectic composition, 10 wt.% Au and 90 wt.% Sn melt at 217°C. A detailed review of the metallurgy is provided in reference [54]. Virtually all applications of the gold-tin system as a solder utilize the 80/20 eutectic composition.

Limited data exists on the mechanical properties of the gold-tin alloy. Olsen et al. report values for the thermal expansion, elastic modulus, and strength as a function of temperature for the 80 wt.% Au and 20 wt.% Sn alloy [49]. The room temperature values are listed in Table 4.1. These values were obtained from tensile tests conducted on cast specimens with a 2.8 cm gage length and cross-sections ranging from 0.12 to 0.2 cm<sup>2</sup>. The size and fabrication of the specimen are significantly different than those of typical bonds. However, the values for thermal expansion and modulus should be reasonably good approximations. The strength values, though, will likely be different given the significant difference in geometry and loading between the specimens used and an actual bond.



Table 4.1: Room temperature mechanical properties of 80 wt.% Au and 20 wt% Sn alloy [49].

Young's Modulus	59.2 GPa
CTE	15.93 $\mu\text{m}/\text{m}^\circ\text{C}$
Yield Strength	275 MPa
Ultimate Strength	275 MPa

### 4.3.3 Process Overview

Two primary methods have been employed for fabricating gold-tin bonds. The difference between the two methods is in how the gold-tin material is applied. The traditional approach is to use a gold-tin preform, which is a thin strip of the alloy that is typically 25-50  $\mu\text{m}$  thick. The bond is accomplished by placing the preform between the die and substrate and heating to above the melting temperature of the alloy. The surfaces to be bonded must typically be metallized so that the solder wets the components. In addition, a clamping pressure or a scrubbing motion is used to promote wetting and break the tin oxide, which is found on the as-fabricated preforms. The alternative approach is to deposit a series of gold and tin layers on one of the components to be bonded. Upon heating, the gold and tin melt and interdiffuse to form a gold-tin alloy. This approach was developed so that thinner bonding layers could be achieved and oxide on the surface reduced. The tin-oxide on the surface is prevented by depositing the gold and tin layers such that gold is the final layer deposited, thus protecting the tin layer from atmosphere and oxidation. Details of these methods, which have been used in previous work to bond silicon and GaAs dies to alumina substrates, are described below.

Preforms are commercially available in a variety of dimensions and can be purchased in ribbon form or stamped geometries. The solder will not readily wet silicon dies, GaAs dies, or ceramic substrates, thus the bonding surfaces need to be metallized prior to bonding. The metallizations typically employed consist of multiple layers and must adhere well to the components, protect against diffusion, and provide a layer that is easily wetted. Successful bonding of silicon and GaAs dies to alumina substrates has been reported using gold-tin preforms, where a chromium and a gold

Table 4.2: Typical processing conditions for AuSn preform solder bonds.

	DIE			SUBSTRATE	
	Material	Deposition ( $\mu\text{m}$ )	Size	Material	Deposition ( $\mu\text{m}$ )
A	GaAs	0.04 Cr, 0.5 Au	4x4 mm	alumina	0.025 Cr, 5.0 Au
B	Si	0.04 Cr, 0.5 Au	4x4 mm	alumina	0.025 Cr, 5.0 Au
C	GaAs	0.1 Ti, 0.5 Au	5.14x5.18 mm	alumina	0.5 Cr, 7.0 Au
D	GaAs	0.1 Ti, 0.5 Au	1.16x0.81 mm	alumina	0.5 Cr, 7.0 Au

	PROCESS			STRENGTH		Ref.
	Temperature	Atmosphere	Pressure (MPa)	Loading	Value (MPa)	
A	310°C	H <sub>2</sub> ,N <sub>2</sub>	0.28-0.42	shear	2.45-6.8 MPa	[56]
B	305°C	H <sub>2</sub>	0.14	tensile	>1.4 MPa	[57]
C	310°C	N <sub>2</sub>	0.05 w/ scrubbing	shear	>4.5 MPa	[58]
D	310°C	N <sub>2</sub>	0.05 w/ scrubbing	shear	19.6-23.6 MPa	[58]

capping layer were deposited on the dies and substrates. The chromium layer, which was deposited first, served as an adhesion layer and a diffusion barrier, and the gold layer was employed to promote wetting [55], [56], [57]. Other studies have reported the use of a two-layer metallization of titanium and gold to achieve similar results [58]. To complete the bond, the gold-tin preform is placed between the metallized components and heated to approximately 310°C. A nitrogen or hydrogen ambient is typically used to prevent oxidation during heating [56], [58]. A scrubbing technique or an applied static pressure has been used to break the surface oxide and produce bonds with good homogeneity and relatively few voids. The magnitude of the clamping pressures used range from 0.05 to 0.42 MPa. The details of the work discussed above are summarized in Table 4.2.

The alternative approach that has been employed to form gold-tin bonds is to deposit layers of gold and tin on one of the components to be bonded. In previous work, the gold and tin films were deposited using evaporation over an adhesion layer of chromium or titanium, which was deposited on to the silicon or GaAs dies [59], [60], [61]. All the films are deposited in one vacuum cycle to avoid oxidation of the tin. The component that mates with the layer containing the gold-tin composite must be metallized. Typical metallization schemes have included a chromium or titanium adhesion layer followed by a gold capping layer. To complete the bond,

Table 4.3: Typical processing conditions for AuSn thin-film solder bonds.

DIE				SUBSTRATE	
	Material	Deposition ( $\mu\text{m}$ )	Size	Material	Deposition ( $\mu\text{m}$ )
A	Si	0.1 Cr, 0.1 Au, 1.0 Sn, 0.1 Au	10x10 mm	Si	0.1 Cr, 1.0 Au
B	GaAs	0.07 Cr, 0.815 Sn, 0.065 Au	5x5 mm	Si	0.07 Cr, 1.6 Au
C	GaAs	0.03 Cr, 0.5 Au, 2.25 Sn, 0.75 Au	4x4 mm	alumina	0.03 Cr, 6.4 Au

PROCESS				STRENGTH		
	Temperature	Atmosphere	Pressure (MPa)	Loading	Value (MPa)	Ref.
A	350°C	air	0.07	tensile	2.0 MPa	[60]
B	272 or 286°C	H <sub>2</sub> w/ N <sub>2</sub>	used, not specified	-stronger than GaAs-		[61]
C	320°C	H <sub>2</sub>	0.28	-not tested-		[59]

the pieces were assembled and heated in an inert or reducing atmosphere to a temperature between 310° and 350°C. It should be noted that this multilayer concept is only effective because of the fact that the tin melts at 232°C, which is lower than the melting temperature of the 80/20 eutectic alloy. This approach would not work for the AuSi or AuGe solders in which the individual constituents melt at a higher temperature than the eutectic compositions [59]. With the gold-tin multilayer bonds, a static pressure of the same magnitude as that used for preform bonding was used. It is interesting that a pressure appears to be required despite the absence of the tin-oxide layer. Specific processes that have been employed to achieve bonds with few voids are detailed in Table 4.3.

#### 4.3.4 Mechanical Integrity

Reported failure stress values are listed in Tables 4.2 and 4.3 for gold-tin bonds formed using preforms and thin-films. The degree of mechanical characterization is quite limited in the work outlined above. The relative paucity of the data is primarily due to the fact that the majority of work has been devoted towards packaging applications. Detailed understanding of the mechanical integrity of the bond is often not the objective of the work, but rather the focus is to determine whether or not the bond is comparable to other packaging technologies. This is often assessed by conducting simple tensile or shear tests and comparing the results to guidelines

outlined in a specific standard. A common standard, which was used to assess bond strength in references [56], [57], and [58], is MIL-STD-883 [62]. The standard gives simple criteria, which consist of certain failure loads that dies of different sizes must be able to withstand for various loading configurations. Thus, data on the mechanical properties of the bond are limited.

Despite the limited data, it is possible to establish a general range of expected bond strengths from the values listed in Tables 4.2 and 4.3. Typical strengths are below 10 MPa and the highest value that was reported is 23.6 MPa. The type of tests used to obtain these values are quite sensitive to the exact geometry tested and any flaws that may be present. In addition, the failure stress values are likely a function of the substrate and die material being bonded. Researchers have reported die fracture rather than failure in the bonding layer in several studies [57], [55]. Thus, while values given Tables 4.2 and 4.3 establish a general range of bond strength values, the factors discussed above should be considered when examining this data.

## 4.4 Device Assembly

In order to design the bonding process, an understanding of the MHT device assembly process is required. The bonding of the piezoelectric element to the silicon is one of the final fabrication steps of the device. This bond is completed on the die-level with the upper and lower layers fully assembled. Figure 4-2 illustrates the basic process of the final bonding step. The lower layer, composed of two glass layers and one silicon layer, forms a chamber which holds the piezoelectric element. The top layer includes a stack of multiple silicon wafers bonded to a glass packaging layer. The drive piston, which the piezoelectric element actuates during device operation, is located in the silicon structure of the upper layer. Assembly is accomplished by manually placing a small piezoelectric cylinder in the lower chamber and aligning and bonding the upper stack to the lower stack using an anodic bond. A gold-tin solder layer on the ends of the piezoelectric element is melted by heating to approximately 300°C, the temperature used for the anodic bond. Upon cooling, the solder layer bonds

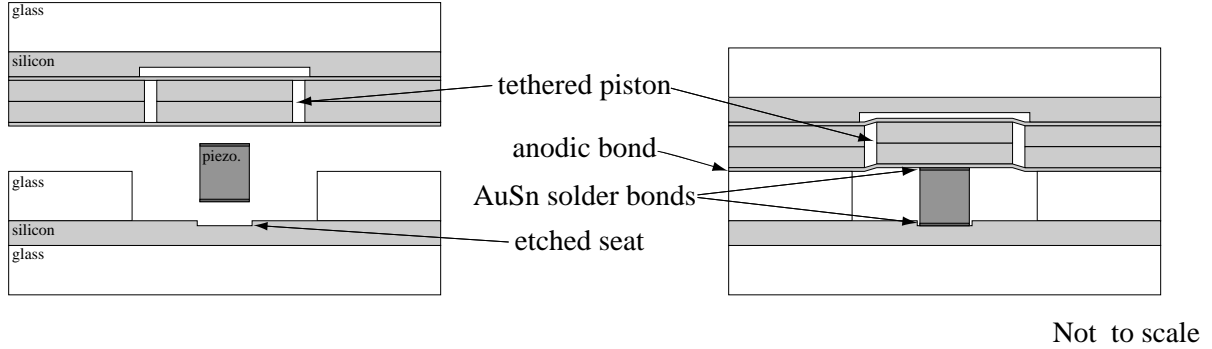


Figure 4-2: Final MHT bonding process.

the piezoelectric element to the silicon piston. A shallow etch in the lower silicon layer defines a seat, which allows precise positioning of the piezoelectric element. The height of the piezoelectric element, the height of the middle glass layer, and the depth of the etched seat are carefully controlled and measured such that the piezoelectric element is oversized and causes the membrane to be displaced 1-2  $\mu\text{m}$  prior to any actuation. The displacement of the piston leads to a preload on the piezoelectric element, which supplies a clamping pressure to the bond and assists in keeping the bond in compression during device operation.

The magnitude of this pressure is important in designing the bonding process since it is the only clamping force that can be applied to the joint during bonding. The oversized piezoelectric element displaces the tethered piston, compresses the piezoelectric element slightly, and causes limited deflection in the lower plate. The tethered piston, which typically has tethers 10-20  $\mu\text{m}$  thick, and the piezoelectric element, which has a relatively low elastic modulus ( $E_{PZT-5H} = 63 \text{ GPa}$ ,  $E_{PZN-PT} = 9 \text{ GPa}$ ), are the most compliant components in the system. The bottom plate, which is a 500  $\mu\text{m}$  thick silicon layer laminated to a 3 mm layer of glass, is assumed to be rigid compared to the membrane and piezoelectric element. Based on these assumptions, the force

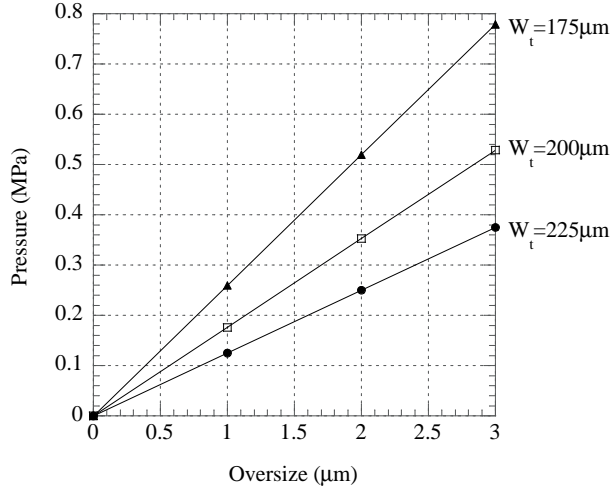


Figure 4-3: Bond pressure as a function of tether width and piezoelectric element oversize.

acting on the piezoelectric element,  $F_P$ , due to an oversize,  $\delta$ , can be written as

$$F_P = \delta \frac{k_m k_p}{k_p + k_m}, \quad (4.1)$$

where  $k_m$  and  $k_p$  are the stiffness of the membrane and the piezoelectric element, respectively. The force on the piston and the corresponding pressures on the bond were calculated for a range of typical oversize values,  $\delta$ . The results, which are plotted in Figure 4-3, are for a typical double layer piston geometry with a 6.8 mm inner diameter, a tether thickness of  $10 \mu m$ , and the tether widths shown. It was assumed there were three PZN-PT piezoelectric elements in the chamber each with a diameter of 1.5 mm and a length of 1 mm. These results are for a specific case, however, it is believed that the values chosen above result in the most conservative pressure estimate (the lowest applied pressure possible is seen as the conservative case, since higher applied pressures appear to lead to better bonding) based on the current design of MHT devices. Since a minimum oversize of  $1 \mu m$  is expected and  $225 \mu m$  is currently the widest tether in the design, the bond should have a minimum of 0.13 MPa applied during device assembly.

## 4.5 Bonding Process

The previous work using gold-tin bonding summarized in Section 4.3.3 illustrates the basic bonding process and the approaches that have been employed. The dimensional tolerances required in MHT devices led to the selection of a thin film gold-tin bond rather than the use of a preform. The piezoelectric element with the bonding layer must be sized to within  $1\text{ }\mu\text{m}$  of the specified length. Commercially available preforms have thicknesses between 25 and  $50\text{ }\mu\text{m}$  and thickness tolerances of  $\pm 5\text{ }\mu\text{m}$ . This tolerance, along with the difficulty of handling a preform that is  $25\text{ }\mu\text{m}$  thick and 1-2 mm in diameter, were the principal factors in choosing to use a thin-film bond. The approach adopted differs from the thin-film bonding techniques discussed in Section 4.3.3 in that the gold-tin is deposited as an alloy rather than alternating layers of gold and tin. The device geometry and assembly prohibits the use of a scrubbing technique and requires that a static pressure be applied to the bond. The process was developed with these constraints in mind. The details of the bonding process that has been developed are given below.

The multiple layers of metal that are deposited on the silicon and the piezoelectric components to be bonded are shown in Figure 4-4. The starting piezoelectric material were PZT-5H or PZN-PT plates, 12 to 25 mm in diameter, that were ground and polished to a thickness of 1 mm and a surface roughness of  $0.5\text{ }\mu\text{m}$ . Prior to deposition, the plates were cleaned using a weak nitric acid solution (20:1  $\text{H}_2\text{O}:\text{HNO}_3$ ) followed by a deionized water rinse. The four layer film structure on the piezoelectric plates was deposited in one vacuum cycle using RF sputtering. The 50 nm thick titanium layer and the 250 nm thick platinum layer serve as the adhesion layer and diffusion barrier, respectively. The gold-tin layer, which is  $4\text{ }\mu\text{m}$  thick, is sputtered from an alloy target that has an 80 wt.% Au - 20 wt.% Sn composition. Sputtering was chosen over evaporation because sputtering allows the stoichiometry of the target to be maintained in the deposited film [63]. The final layer is a gold capping layer, 50 nm thick, that serves to prevent the gold-tin film from oxidizing. The multi-layer film structure on the silicon pieces allows the solder to wet the silicon. The films were

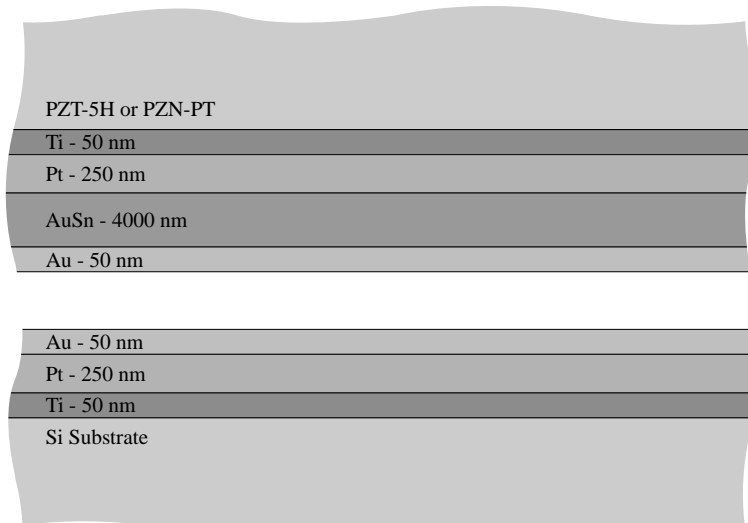


Figure 4-4: Deposited metal layers used to fabricate the gold-tin solder bonds.

deposited on the silicon pieces, which had been cleaned with a standard ‘piranha’ clean (3:1  $\text{H}_2\text{SO}_4\text{:H}_2\text{O}_2$ ), using electron-beam evaporation in one vacuum cycle. For the test bonds in this study, the metallization layer was deposited uniformly on a 4” silicon wafer. In the actual device, where selective deposition of the metallization layer is required, deposition is done on the die-scale using a shadow mask. The titanium adheres well to the silicon and the platinum helps to prevent diffusion. The gold layer ensures that the gold-tin solder can easily wet the surface. The gold capping layer on the silicon pieces as well as the piezoelectric elements causes the gold-tin alloy to become slightly gold-rich. However, since the gold layers are thin (50 nm), as compared to the 4  $\mu\text{m}$  thick gold-tin layer, the change is small and the gold fraction in the final bond remains less than 80.5 wt.%.

The test specimens used in developing the process were nominally 2.5×2.5 mm and 3.5×3.5 mm piezoelectric pieces bonded to 10×10 mm silicon dies. The individual piezoelectric pieces and silicon dies were cut from the larger piezoelectric plates and silicon wafers using a diamond wafer saw. Prior to dicing, the surfaces were coated with a thin layer of Crystallbond™ thermal wax, which was applied by heating the pieces to 100°C and spreading the wax. The wax, which is hard at room temperature, was used to suppress chipping of the film at the die edges and to protect the surface



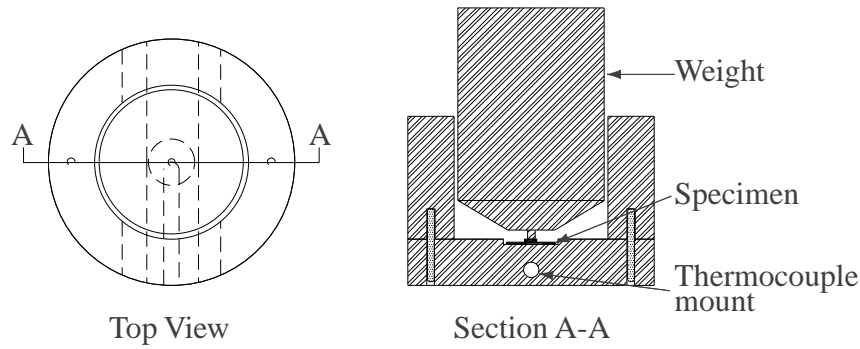


Figure 4-5: Solder bonding jig.

from particulates during dicing. While this method has proved successful in protecting the specimens during dicing, heating to 100°C has the possibility to lead to oxidation of the tin. The wax was removed by soaking the diced pieces in acetone. Complete removal of the wax was ensured by a second acetone clean in an ultrasonic bath. Immediately prior to bonding, the silicon and piezoelectric components were cleaned with sequential acetone, methanol, and isopropanol rinses. The specimens were dried with filtered N<sub>2</sub> following the isopropanol rinse.

The bonds were assembled and a clamping pressure was applied using a special jig. The jig, which is illustrated in Figure 4-5, applies a static pressure using a weight. A weight was used to provide the loading in order to avoid changes in clamping pressure due to thermal expansion of the jig. The jig dimensions were chosen such that the pressure applied on the specimen was near the minimum clamping pressure expected in the device, 0.13 MPa. A type K thermocouple, located in the jig directly beneath where the specimen sits, permitted an accurate measurement of the temperature of the specimen. Following assembly and mounting, the specimen and jig were transferred to a vacuum oven. The vacuum oven used has the capability to heat to 600°C and maintain pressures as low as  $5 \times 10^{-3}$  torr.

To prevent oxidation of the tin in the solder, bonding was carried out in an Ar-5%H<sub>2</sub> atmosphere. The presence of H<sub>2</sub> in the atmosphere produces a reducing atmosphere that can help to remove any stable oxides that may be present on the solder. To achieve the desired atmosphere in the oven, the chamber was evacuated to

$10^{-2}$  torr and then purged with the Ar-5% $H_2$  gas. The chamber was backfilled with the gas until a pressure of 20 inHg was reached. The chamber was then evacuated a second time to  $10^{-2}$  torr. The chamber was backfilled again with the reducing atmosphere until a pressure of 20 inHg was reached. A slight vacuum of 20 inHg was maintained when backfilling because the seals on the oven do not support positive pressures. Following the two evacuation and purge sequences, the chamber was heated to a maximum temperature between 300 and 325°C. A range of temperatures is given because it was discovered that solder from different deposition runs often melt at slightly different temperatures. This variation is believed to be due to slight compositional variations in the solder. Once the maximum temperature was reached, the chamber was evacuated to  $10^{-2}$  torr. The bond was allowed to soak at the desired temperature for approximately  $\frac{1}{2}$  to 1 hour. Following the soak time, the bond was cooled under vacuum. The soak and cool stages are completed under vacuum to ensure that any trapped gases are removed from the bond. The temperature and pressure cycle used to complete a bond is summarized in Figure 4-6. As seen in Figure 4-6, the heat and cool times are quite long. The length of these times is due to the nature of the oven and the mass of the jig that was used. It is believed that shorter times could be realized if different equipment was employed.

Following cooling, the bond was removed from the oven. Bonds produced via this process were examined for voids and mechanically tested using a tensile loading. The process outlined above was developed iteratively based on the results of these experiments. The details and results of the qualitative evaluation of bond quality and the mechanical characterization are detailed in the following sections.

## 4.6 Qualitative Evaluation of Bond Quality

The primary focus of the process development work was to produce void-free bonds. Elimination of voids in the bond is critical. Voids inherently reduce the strength of the bond and are stress raisers, which can serve as fatigue crack initiation sites. To inspect for voids, bonded specimens were cross-sectioned and polished, then examined using

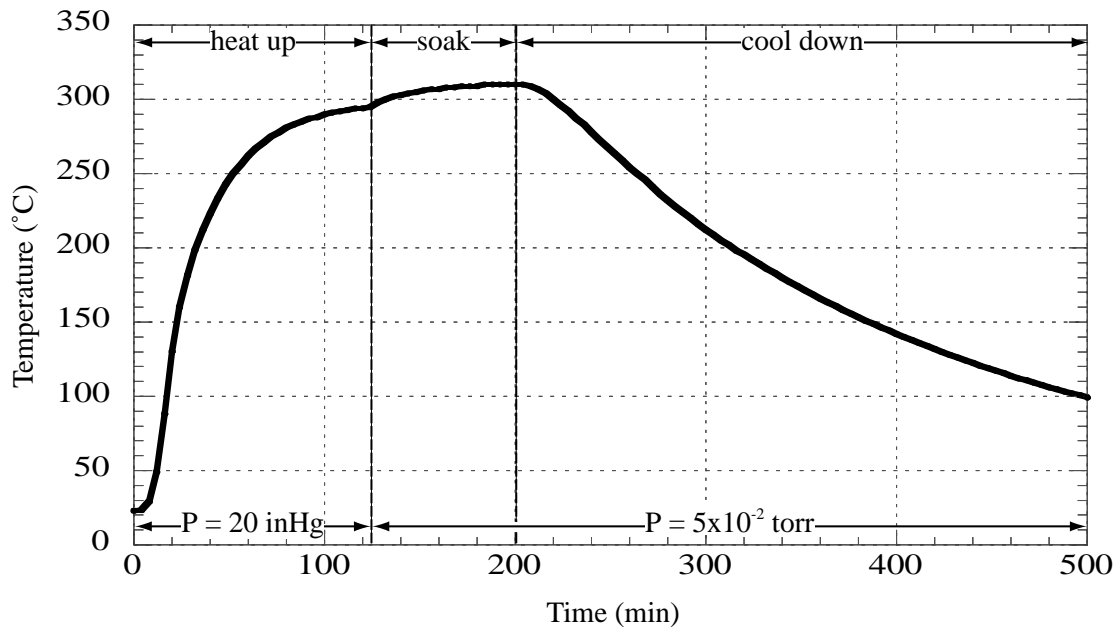


Figure 4-6: Temperature and pressure cycle to complete bond.

a scanning electron microscope (SEM). The inspection process, while destructive, is straightforward and allows small voids to be identified. The results of several examinations of gold-tin bonds between two silicon pieces or silicon and PZT-5H or PZN-PT are discussed below. All the bonds discussed were fabricated according to the process outlined in Section 4.5 except where differences are noted. The bonds between two silicon pieces were carried out identically to the silicon-piezoelectric bonds, except for the fact that the substrate with the gold-tin layer was silicon rather than a piezoelectric material.

Figure 4-7 shows two examples of early bond attempts. While the bonds appeared mechanically sound, the cross-sections revealed that the bond contained numerous voids and un-bonded regions. The bond in Figure 4-7(a) was bonded with no applied pressure and cooled in an Ar-5% $H_2$  environment with a pressure of 5 inHg. It was found that voids such as those shown in Figure 4-7(a) could be eliminated by applying a static pressure during bonding and cooling under vacuum. Experiments indicated that either cooling under vacuum or applying a static pressure alone, was not sufficient to eliminate voids of this nature. The use of both appears to be required to consistently prevent voids such as these. Figure 4-7(b) shows a poorly bonded inter-

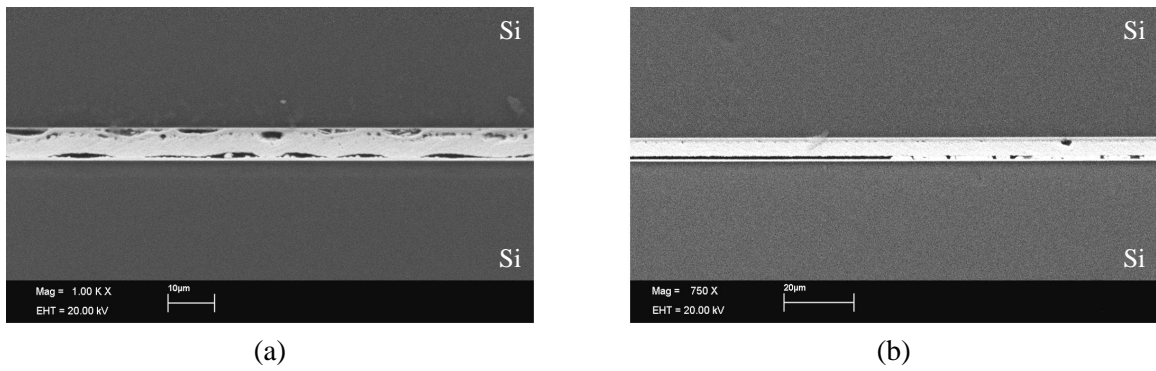


Figure 4-7: Two examples of poor bonding, (a) due to the presence of trapped gas, (b) due to poor cleaning.

face of a different nature. Large un-bonded regions are visible at the interface, where the layer with the deposited gold-tin solder mates with the substrate with the gold metallization layer. It is believed that poor bonds such as these are a result of poor cleaning of the interfaces prior to bonding.

Void-free bonds, such as the one shown in Figure 4-8, were routinely obtained if the cleaning procedure and process outlined in Section 4.5 were followed. Figure 4-8 shows a void-free bond between two silicon pieces. The final bonding layer is  $5.4\ \mu\text{m}$  thick, which is thicker than the total specified thickness of the deposited films. Bonds with thicknesses varying from  $3.5\ \mu\text{m}$  to  $5.5\ \mu\text{m}$  have been observed. It is believed this is due to variations in the thickness of the deposited films, since specimens cut from the same silicon wafer or piezoelectric disk tend to have similar bond thickness. A variation of  $1\text{-}2\ \mu\text{m}$  from the design value is not a major concern in device fabrication, since the piezoelectric element dimensions are measured following deposition and the fact that the device fabrication process permits compensation of small deviations. However, it should be possible to obtain films of consistent thickness, if the deposition system is well calibrated and the same system is used for all depositions. Deposition in the current study was outsourced and two different vendors<sup>12</sup>, were used over the course of this work.

Once a reasonable process was established for producing void-free gold-tin bonds

<sup>1</sup>Vacuum Process Engineering, 4261 Power Inn Road, Sacramento, CA 95826

<sup>2</sup>Professor Sy-Hwang Liou, University of Nebraska, 364 Behlen, Lincoln, NE 68588

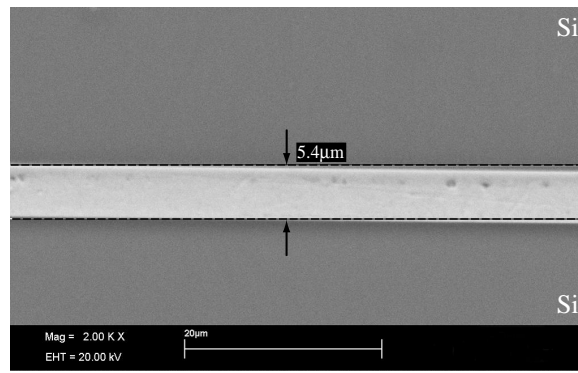


Figure 4-8: Void-free AuSn bond of silicon to silicon.

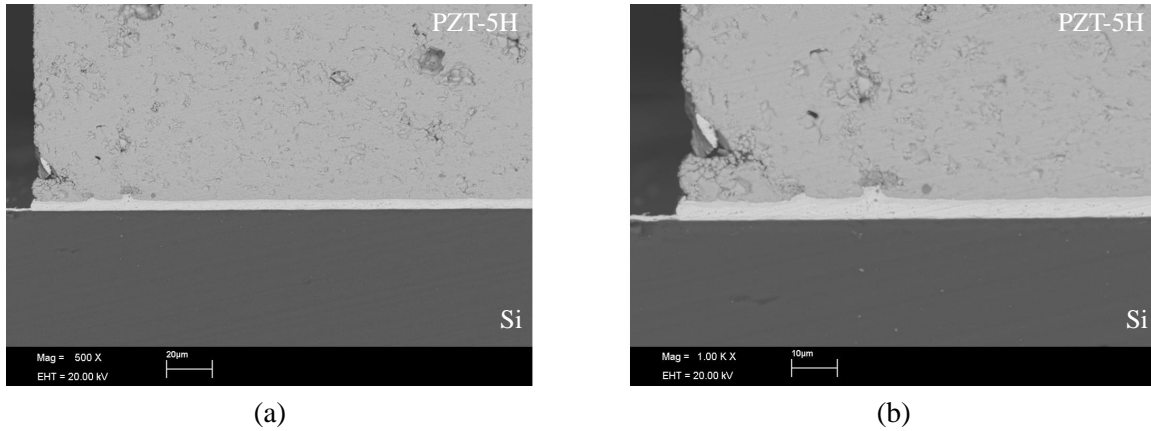


Figure 4-9: Void-free AuSn bond of PZT-5H to silicon.

between two silicon components, PZT-5H/Si and PZN-PT/Si bonds were fabricated. A cross-section of a gold-tin bond between PZT-5H and Si is shown in Figure 4-9. The specimen appears well bonded and to be void free. While the PZT-5H is polished prior to bonding, small surface defects are sometimes present. Small defects in the PZT-5H that were filled by the solder are clearly observed in the cross-sections shown in Figure 4-9. This is encouraging because it indicates that the solder allows for compensation of rough or imperfect surfaces. The final important feature to recognize in Figure 4-9 is the geometry of the bond layer at the edge. A fillet is not formed and there appears to have been little flow of the solder beyond the edge of the PZT-5H material. This behavior was routinely observed and has the potential to limit the load carrying capability of the bond.

The gold-tin bonds between PZN-PT and silicon had appearances similar to the

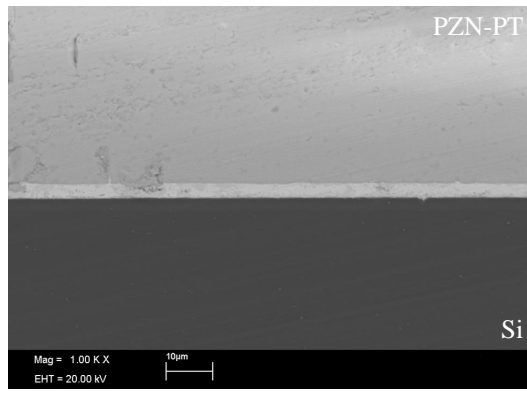


Figure 4-10: Void-free AuSn bond PZN-PT to silicon.

bonds fabricated between PZT-5H and silicon components. A PZN-PT element bonded to a Si substrate is shown in Figure 4-10. The bond layer is continuous and void-free. Again, the capability of the gold-tin to fill imperfections in the surface can be observed.

The SEM evaluations of the bonds allowed a bonding process to be developed to produce void free bonds. The results presented demonstrate that bonds can be achieved between two silicon pieces, or a silicon and a PZT-5H or PZN-PT piece. While these results were encouraging and were useful for process development, they did not provide any information pertaining to the mechanical strength of the bond. Thus, following development of a process to produce void-free bonds, simple mechanical tests were conducted to gain additional information regarding the bond integrity.

## 4.7 Tensile Tests

### 4.7.1 Experimental Procedure

Simple tensile tests were performed on piezoelectric elements bonded to silicon substrates using the thin film gold-tin solder bond developed in this work. The purpose of these tests was not to investigate systematically the effect of processing parameters, but, rather was to establish typical strength values for the bonds and to identify potential weaknesses of the bonding technique. The specimens were designed to replicate closely the actual geometry found in the device. The specimen, which is shown

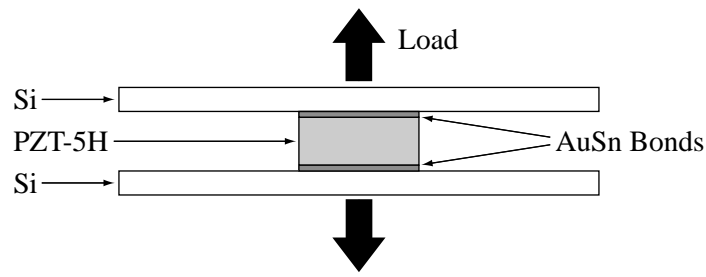


Figure 4-11: Tensile specimen geometry.

schematically in Figure 4-11, consists of a nominally  $2.5 \times 2.5$  mm or  $3.5 \times 3.5$  mm PZT-5H element bonded between two  $10 \times 10$  mm silicon dies. The specific specimen geometry was chosen to facilitate specimen gripping and mounting. The area-ratio between the silicon plates and the solder-bonds allow bonds with strengths greater than that of the epoxy used to mount the specimen to be tested. It should be noted though, that while the specimen geometry makes mounting possible, the presence of two interfaces increases the probability that a specimen will fail at a lower load. Specimens were fabricated using the process outlined in Section 4.5.

The specimens were mounted to aluminum studs using Devcon 5-Minute Epoxy<sup>TM</sup>. A mounted specimen is pictured in Figure 4-12(a). As shown in Figure 4-12(b), the aluminum studs were secured into two collars mounted in a standard servo-hydraulic testing machine. The lower collar was mounted to the movable crosshead of the test machine. The upper collar was attached to a 100 N load cell mounted on the fixed crosshead. The upper collar was connected to the load cell via a 0.3 m long 0.5 mm diameter steel cable. The cable provided a compliant coupling between the test machine and the load cell and was included to mitigate the effects of any misalignment that may have been present. Specimens were loaded at a constant displacement rate of 0.3 mm/min until failure occurred. The failure stress was calculated from the load at failure and the cross-sectional area of the specimen as measured using a micrometer.

## 4.7.2 Results

The results of five tensile tests that were conducted on PZT-5H bonded to silicon are listed in Table 4.7.2. The failure stress values listed span an order of magnitude,

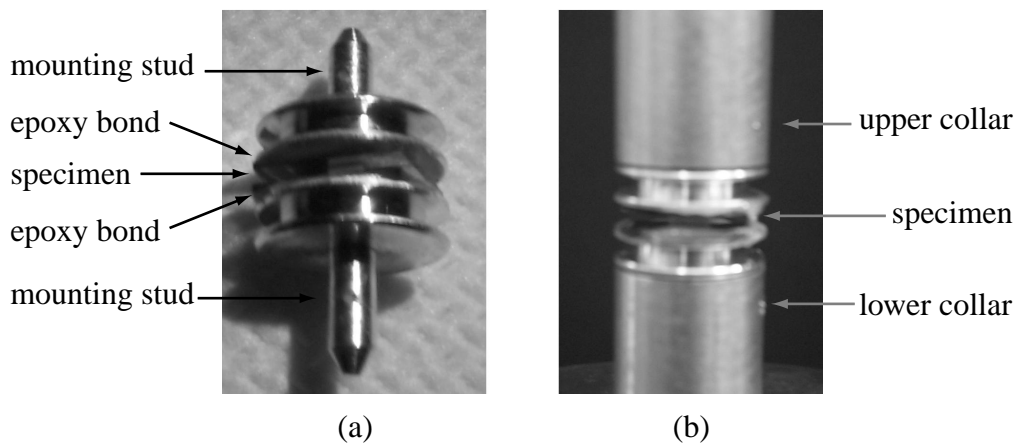


Figure 4-12: Tensile specimen, (a) mounted to studs, (b) mounted in test machine.

Table 4.4: Tensile test results.

Specimen	Processing Temperature (°C)	Applied Pressure (MPa)	Failure Stress (MPa)
A	305	0.15	2.8
B	305	0.15	3.2
C	305	0.15	9.0
D	325	0.15	0.8
E	305	0.31	5.0

0.8 MPa to 9.0 MPa. The scatter in the data is not entirely surprising given the geometry of the specimen. The measured failure load is very sensitive to defects in the bond or piezoelectric material. While there is scatter in the data, a degree of correlation exists between the failure stresses measured and the appearance of the fracture surfaces.

Significant differences in the appearance of the fracture surfaces were observed between the specimens that failed at higher loads, specimens C and E, and the specimens that had lower failure stresses, specimens A, B, and D. Figure 4-13 and Figure 4-14 show the fracture surfaces of specimens C and B, respectively. In specimen C, the failure occurred primarily along the interface between the PZT-5H and the titanium adhesion layer. The speckled pattern observed on the surfaces in Figure 4-13 are small PZT-5H pieces that have pulled out from the surface of the piezoelectric element. Over a small area near the center of the specimen, failure did not occur at the PZT-5H/film interface, but, rather occurred within the bonding layer. The fracture



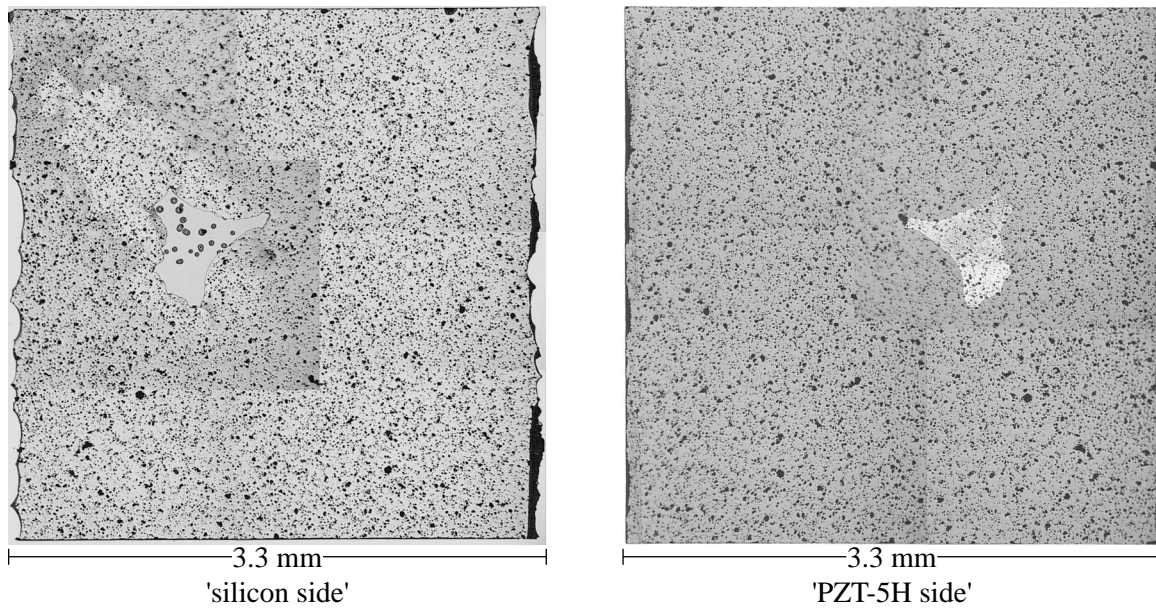


Figure 4-13: Micrograph of fracture surface of specimen C.

surface of this specimen indicates that at high failure loads the interface between the film and the piezoelectric element is the factor that limits bond strength.

The fracture surface of specimen B, pictured in Figure 4-14, is similar in appearance to the surfaces of specimens A and D. The following features, which can be observed in Figure 4-14, were present on all of these specimens that failed at relatively low stresses.

- Areas with pull-out of large pieces of piezoelectric material. These areas, which appear as black regions, are where significant fracture has occurred in the piezoelectric material.
- Small areas where failure has occurred between the film and the PZT-5H. These areas are identical to those observed in specimen C and consist of delamination between the titanium film and the PZT-5H as well as the pull-out of small pieces of PZT-5H.
- Large areas of failure within the bonding layer. This failure is believed to occur at the interface between the gold-tin alloy and the gold metallization layer on the silicon substrates.

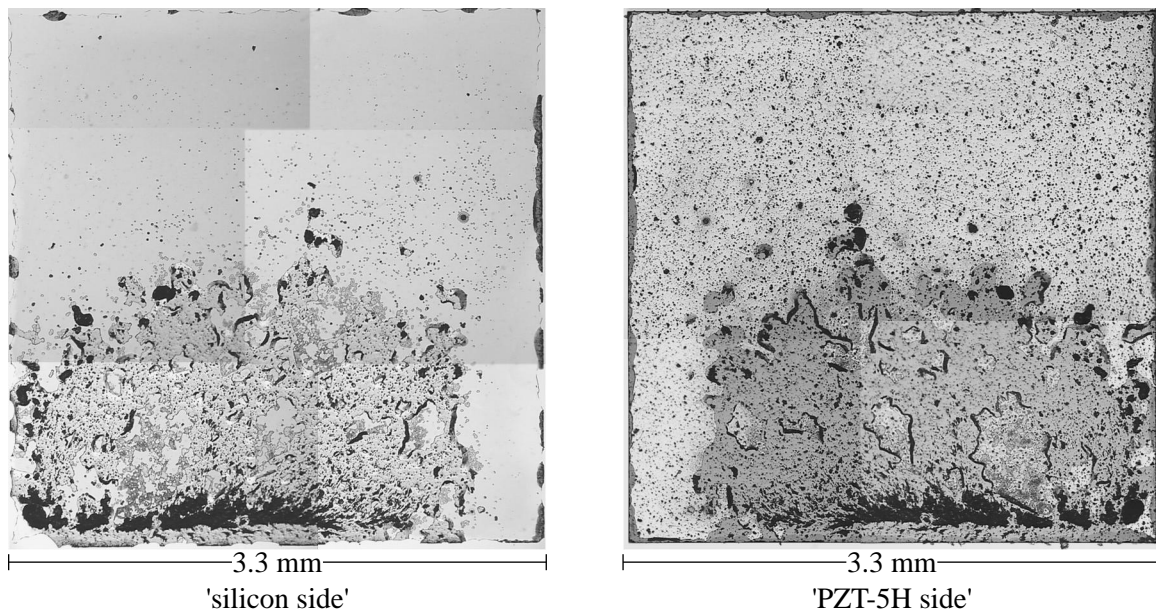


Figure 4-14: Micrograph of fracture surface of specimen B.

These features indicate two possible failure modes for these specimens. The first, which is suggested by the large fractured regions in the piezoelectric material, is that the PZT-5H element contained a flaw that led to fracture of the PZT-5H at a low load. The other possible failure mode is that a section of the interface was poorly bonded and fracture was able to begin in the bond itself. Once a portion of the solder layer failed, the local stress on the well-bonded regions increased and lead to fracture in the PZT-5H. If the latter case is the true mode of failure, it is possible that poor bonding may have been caused by contamination on the surface and inadequate cleaning.

Despite the uncertainty with respect to the exact failure mode of the specimen, the potential limiting factors of the bond strength can be identified. The primary mode of failure that was observed in the specimens with high failure stresses was clearly adhesive failure between the PZT-5H and the titanium adhesion layer. This failure is believed to be a combination of the low strength of the PZT-5H, as indicated by the pull-out, and the quality of adhesion of the titanium film. The lower failure stresses that were incurred in specimens A, B, and D are believed to be due to flaws in the PZT-5H material or a poorly bonded interface. However, the qualitative evaluation of

bond quality discussed in Section 4.6 indicates that homogenous bonds with few voids can be formed, and suggests that poorly bonded interfaces can be avoided. Thus, it appears that the limiting factor of the bond strength is the PZT-5H material and its interface with the titanium adhesion layer.

## 4.8 Conclusions and Recommendations

A process to produce thin-film gold-tin bonds between piezoelectric elements and silicon substrates has been developed. The bonding method was selected based on the requirements of the MHT device. The process has been developed such that void-free bonds can routinely be fabricated. Bonds were cross-sectioned and examined to verify the uniformity of the bonds and the absence of voids. Simple tensile tests were conducted on PZT-5H elements bonded to silicon. The results, although limited, indicate the strength of the bond is limited by the strength of the titanium - PZT-5H interface. It is unclear whether a different adhesion layer would result in higher bond strengths, since fracture of the PZT-5H itself is often observed when the interface fails.

While a bond process has been developed, the degree of mechanical characterization of bond quality has been limited. In order to ensure reliable device design and an optimal fabrication process, further tests must be conducted. In particular, the fatigue behavior and long term reliability of the bond need to be studied. In addition, a detailed study with systematic variations in the process conditions is required in order to ensure an optimal process. The fatigue behavior of the bond is probably best observed through the operation of prototype devices. Actual devices permit accurate representation of the stress-state at the interface and allow a large number of cycles to be applied. The study of the effect of the process parameters on bond quality could be conducted using a specimen similar in geometry to the DCB or 4-point bend specimens discussed in Chapter 2. These specimens would decrease the sensitivity of the measured values to the exact geometry of the specimen. While these tasks are required to fully validate the bonding technology, the current work has clearly

demonstrated the potential to employ gold-tin bonds to bond piezoelectric elements to silicon in MHT devices.

# Chapter 5

## Conclusions and Recommendations

This work has addressed several issues that are critical to the development of MHT devices. These issues, while particularly relevant to MHT devices, may also have relevance in the development of other microscale devices. Three distinct topics have been investigated in the current work: silicon fusion bonding, strength of SOI membranes, and gold-tin bonding. In each area, key accomplishments have been made. The key achievements of this work are highlighted below.

- A four-point bend delamination specimen was employed to measure the toughness of silicon fusion bonds. It was demonstrated that the specimen was effective for characterizing low toughness bonds, but was not suited for testing bonds where the toughness approaches that of the bulk material.
- Silicon fusion bond toughness was measured as a function of processing conditions for bonds with toughnesses lower than  $2.5 \text{ J/m}^2$ . It was shown that while the initial contacting conditions, such as time and pressure do not have a significant effect on bond quality, the anneal temperature and time have a profound impact on bond toughness.
- The fracture strength of membranes fabricated from SOI wafers using deep reactive ion etching was measured. The results indicated that the fracture strength, which was considerably lower than that reported for deep reactive ion etched bulk silicon, was highly dependent on the SOI manufacturer.

- A process has been developed for producing void-free thin-film gold-tin eutectic bonds between silicon substrates and piezoelectric elements. Tensile tests demonstrated that the strength of the bonds is limited by the PZT-5H/solder interface.

While significant progress has been made in this work, the results of the work also lead to additional questions and demonstrate the need for further investigation of certain issues. Based on this, several recommendations for future work are itemized below.

- To fully map the effect of process parameters on silicon fusion bond toughness, additional tests must be completed. It is likely that an alternative specimen geometry will be required, so that bonds with higher toughnesses can be tested.
- To provide a more reliable strength value for the design of SOI membrane structures, variation in the fabrication and processing of such structures must be reduced. While variation will always be present in strength data of silicon, which is brittle, reduction of the variation would allow the data to be fit to a statistical distribution and permit the use of probabilistic design techniques.
- In order to refine the gold-tin bonding process that has been developed, a systematic investigation of processing conditions on the bond strength is required. To complete this study, however, it is highly recommended that a mechanical testing specimen, which is less sensitive to geometry than a tensile specimen, be employed.
- To ensure the reliability of MHT devices, a detailed study of the effects of cyclic loading on the gold-tin bond must be completed.

Despite these issues, which should be investigated further, it is clear that this work has made progress and provided insight into the principal materials and structures concerns that must be addressed to permit the development of MHT devices.

# Appendix A

## Photolithography Masks

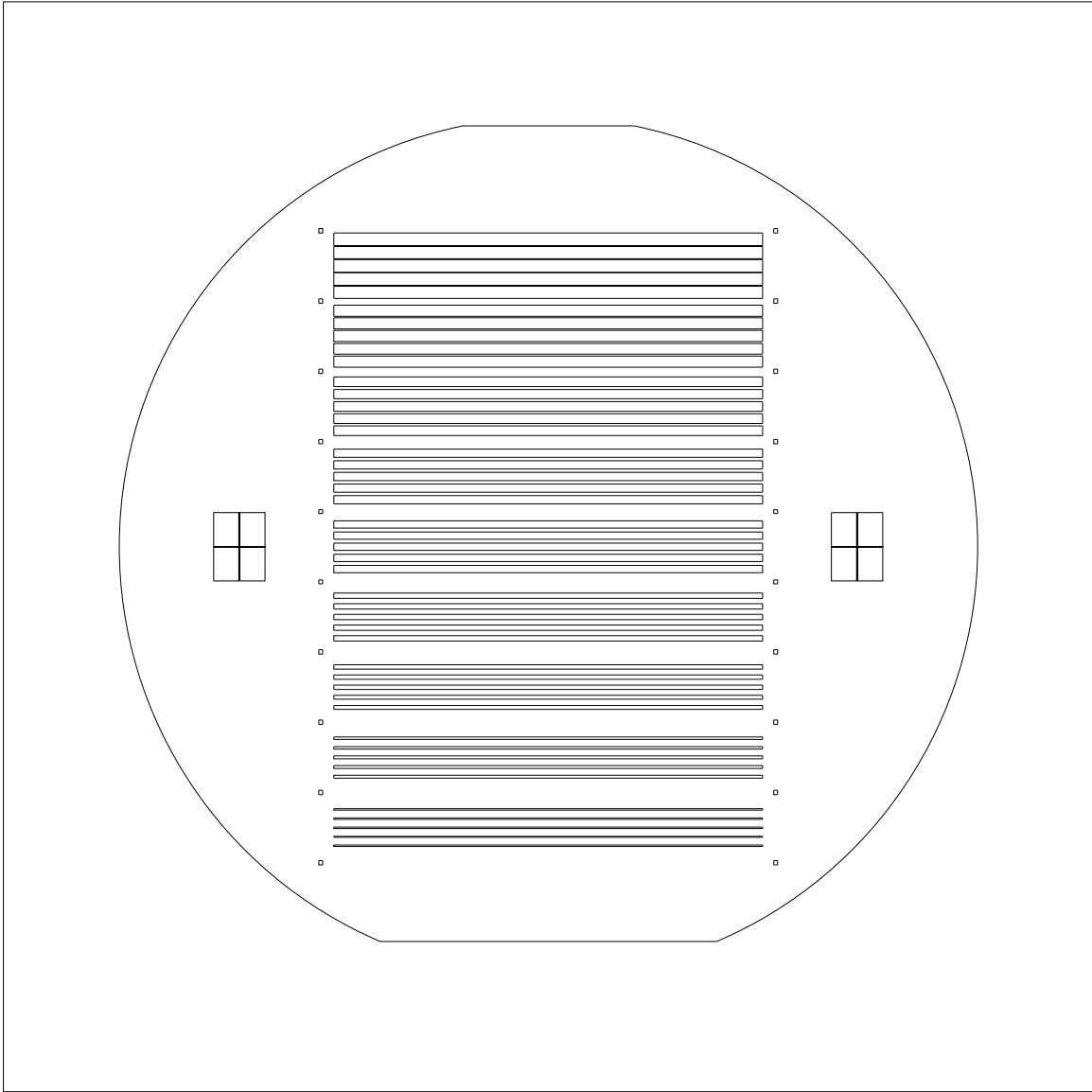


Figure A-1: Mask layout to define shallow grooves in standard 4-point specimen.



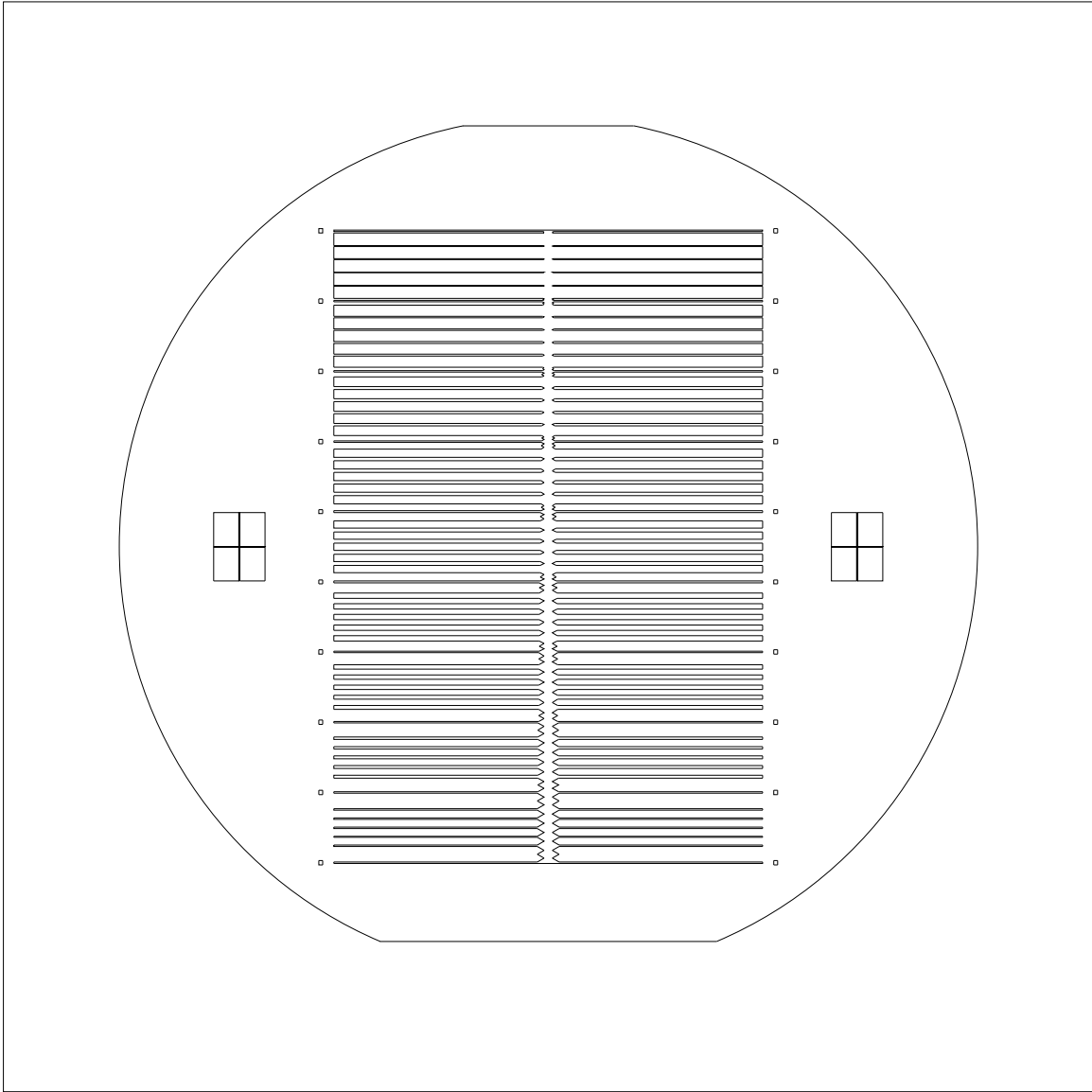


Figure A-2: Mask layout to define shallow grooves in 4-point chevron specimen.

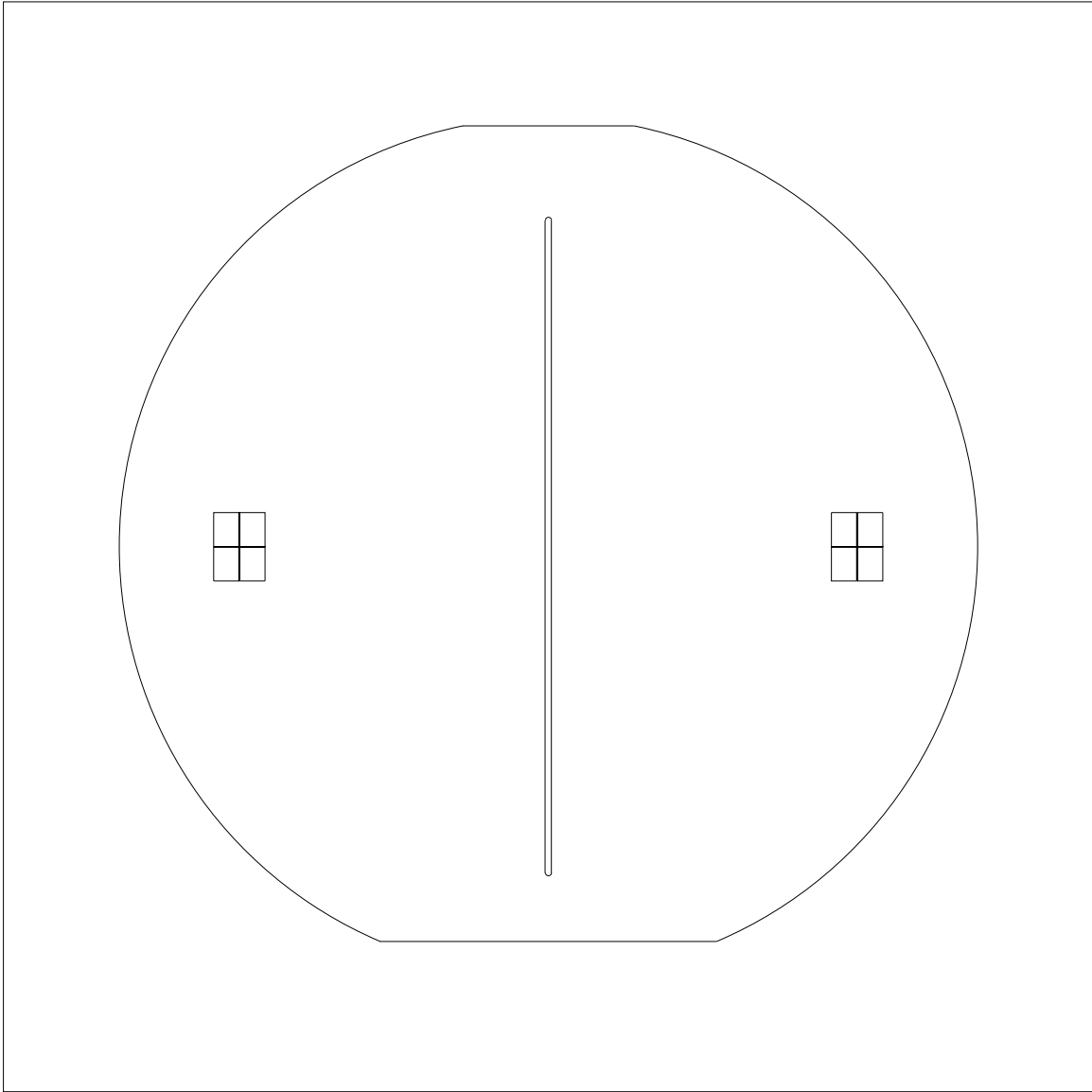


Figure A-3: Mask layout to define deep trench in 4-point specimens.

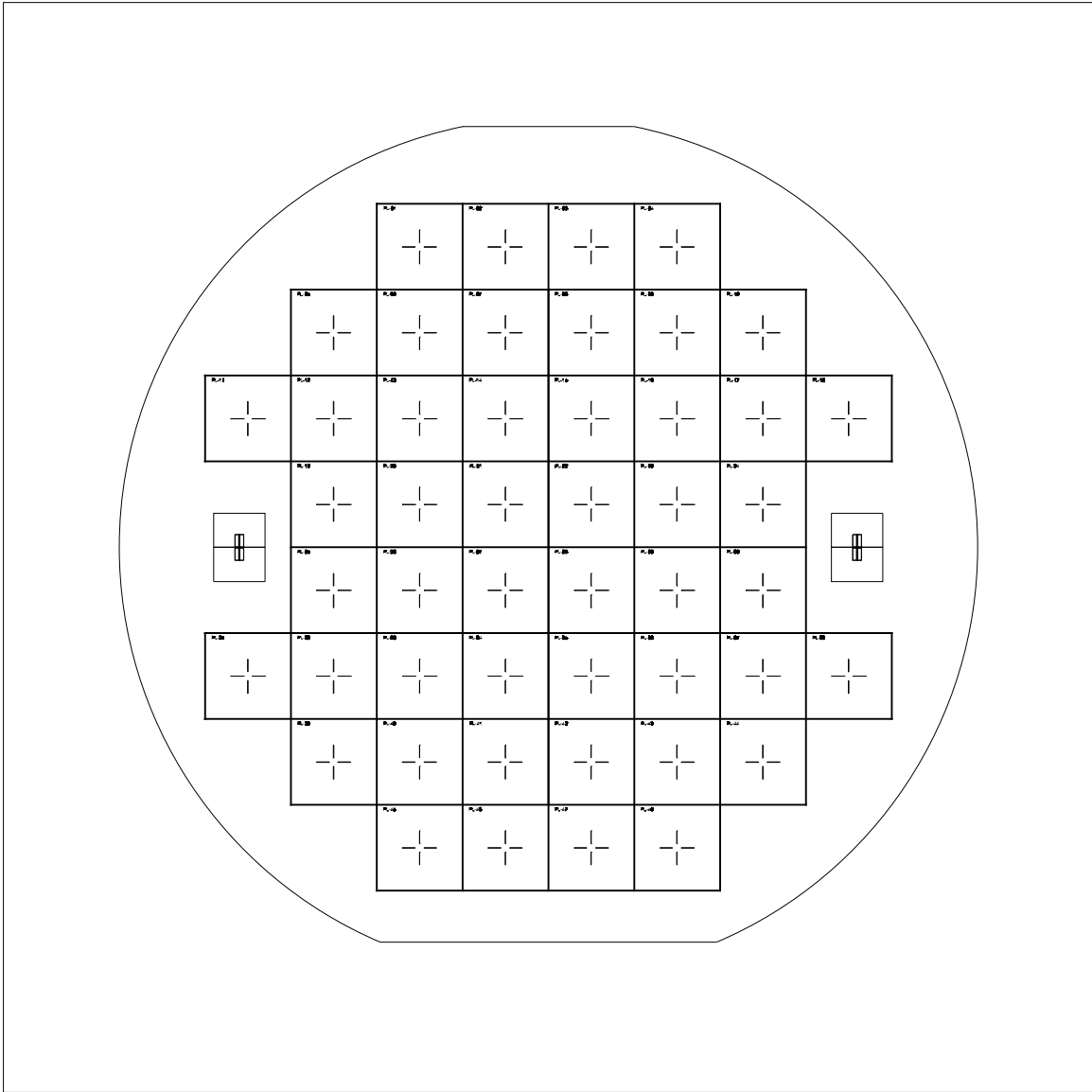


Figure A-4: Mask layout to define alignment marks and specimen edges in device layer of fracture strength specimen.

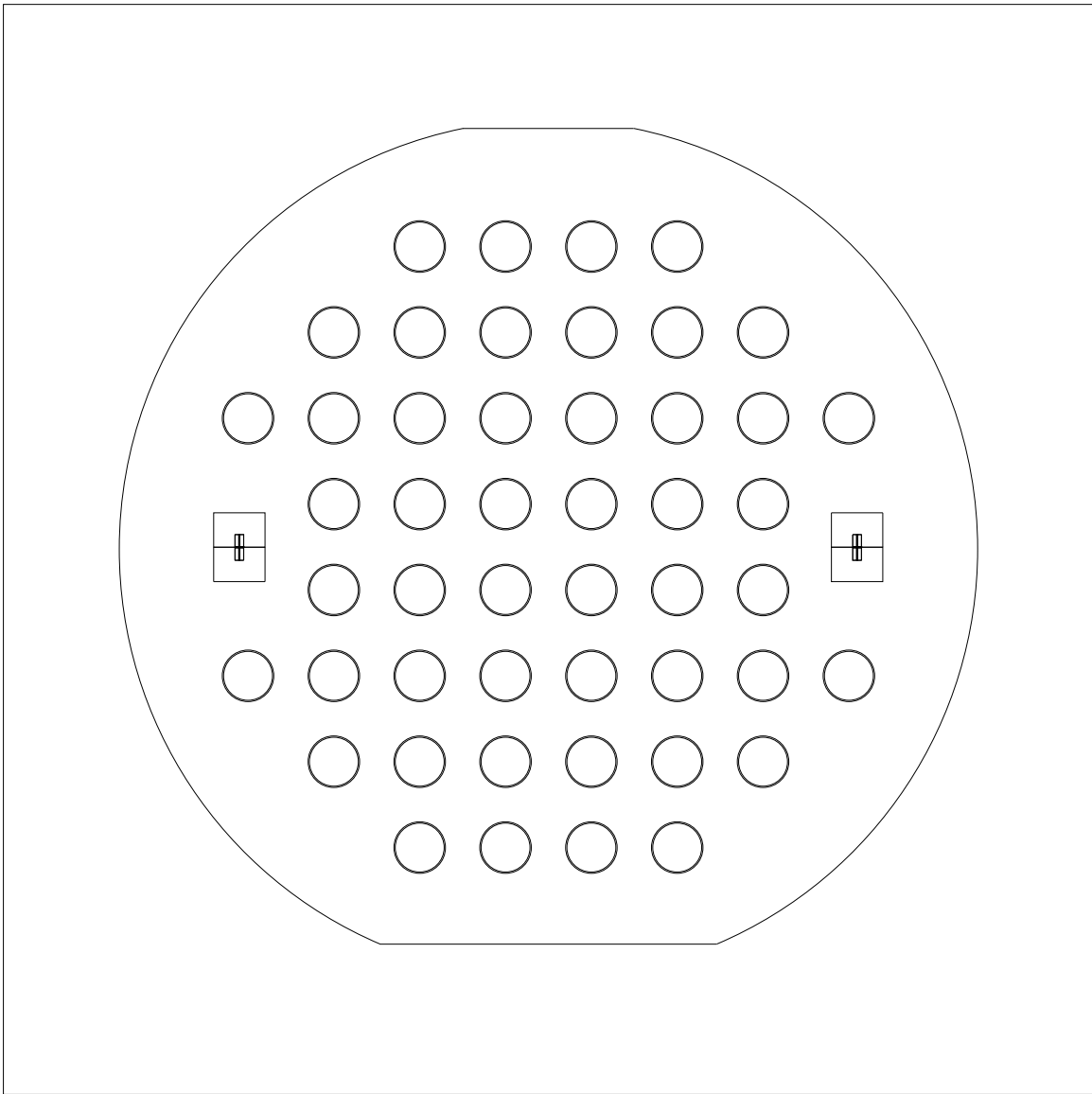


Figure A-5: Mask layout to define deep trenches in handle wafer of fracture strength specimen.

# Appendix B

## Finite Element Code

# Silicon membrane specimen finite element model: 3-D main model.

```

! si_mainmodel.txt
! This is a 3-D model of the silicon membrane specimen (half
! model). It is used to determine the effect of off-center
! loading on the stress in the fillet.

! This model includes the basic structure of the specimen,
! but does not include the fillet at the base of the
! trench. To determine the stresses in the actual fillet,
! this model must be run in conjunction with
! si_submodel.txt, which includes the fillet geometry.
! The results of this model are transferred and used in
! si_submodel.txt, using the ANSYS submodeling technique.

! This is a linear model.

! The units used in the model are N, mm, s
finish
/clear

/filename,si_mainmodel.txt
/title,Coarse Model

/prep7
csys,1

!---Geometry---
r1 = 3000.0e-3      ! outer radius
r2 = 2850.0e-3      ! inner radius
r3 = 2750.0e-3

z1 = 410.0e-3      ! thickness
z2 = 300.0e-3
z3 = 400.0e-3

eps = 1e-5

!---Mesh Density---
N1=2
N2=2
N3=2
N4=4
N5=3
N6=2
N8=6
N9=48

!---Loading---
Force = -2.0      ! force

NO = 4      ! offset in elements
os = ((2750/n9)*NO)*.001 ! offset in mm

!---Material Properties---
mp,ex,1,165.0e3
mp,prxy,1,0.22

!---Element Types---
et,1,solid95
et,2,solid45

!---Keypoint Definition---
k,1,0,0,z1
k,2,r3,0,z1
k,3,r2,0,z1
k,4,r1,0,z1
k,5,0,0,z3
k,6,r3,0,z3
k,7,r2,0,z3
k,8,r1,0,z3
k,9,r3,0,z2
k,10,r2,0,z2
k,11,0,0,0
k,12,r2,0,0
k,13,0,0,z2

k,101,0,90,z1
k,201,r3,90,z1
k,301,r2,90,z1
k,401,r1,90,z1
k,501,0,90,z3
k,601,r3,90,z3
k,701,r2,90,z3
k,801,r1,90,z3
k,901,r3,90,z2
k,1001,r2,90,z2
k,1101,0,90,0
k,1201,r2,90,0

k,111,0,180,z1
k,211,r3,180,z1
k,311,r2,180,z1
k,411,r1,180,z1
k,511,0,180,z3
k,611,r3,180,z3
k,711,r2,180,z3
k,811,r1,180,z3
k,911,r3,180,z2
k,1011,r2,180,z2
k,1111,0,180,0
k,1211,r2,180,0

!---Lines---
l,1,2      ! Line 1
l,2,3      ! Line 2
l,3,4      ! Line 3
l,1,5      ! Line 4
l,2,6      ! Line 5
l,3,7      ! Line 6
l,4,8      ! Line 7
l,5,6      ! Line 8
l,6,7      ! Line 9
l,7,8      ! Line 10
l,5,11     ! Line 11
l,6,9      ! Line 12
l,7,10     ! Line 13
l,9,10     ! Line 14

```

```

1.10.12 ! Line 15
1.11.12 ! Line 16

1.1.201 ! Line 17
1.201.301 ! Line 18
1.301.401 ! Line 19
1.201.601 ! Line 20
1.301.701 ! Line 21
1.401.801 ! Line 22
1.5.601 ! Line 23
1.601.701 ! Line 24
1.701.801 ! Line 25
1.601.901 ! Line 26
1.701.1001 ! Line 27
1.901.1001 ! Line 28
1.1001.1201 ! Line 29
1.11.1201 ! Line 30

1.1.211 ! Line 31
1.211.311 ! Line 32
1.311.411 ! Line 33
1.211.611 ! Line 34
1.311.711 ! Line 35
1.411.811 ! Line 36
1.5.611 ! Line 37
1.611.711 ! Line 38
1.711.811 ! Line 39
1.611.911 ! Line 40
1.711.1011 ! Line 41
1.911.1011 ! Line 42
1.1011.1211 ! Line 43
1.11.1211 ! Line 44

larc.4.401.1,r1 ! Arc 1 Line 45
larc.3.301.1,r2 ! Arc 2 Line 46
larc.2.201.1,r3 ! Arc 3 Line 47
larc.8.801.5,r1 ! Arc 4 Line 48
larc.7.701.5,r2 ! Arc 5 Line 49
larc.6.601.5,r3 ! Arc 6 Line 50
larc.10.1001.13,r2 ! Arc 7 Line 51
larc.9.901.13,r3 ! Arc 8 Line 52
larc.12.1201.11,r2 ! Arc 9 Line 53

larc.411.401.1,r1 ! Arc 10 Line 54
larc.311.301.1,r2 ! Arc 11 Line 55
larc.211.201.1,r3 ! Arc 12 Line 56
larc.811.801.5,r1 ! Arc 13 Line 57
larc.711.701.5,r2 ! Arc 14 Line 58
larc.611.601.5,r3 ! Arc 15 Line 59
larc.1011.1001.13,r2 ! Arc 16 Line 60
larc.911.901.13,r3 ! Arc 17 Line 61
larc.1211.1201.11,r2 ! Arc 18 Line 62

!---Areas--
al.1.4.5.8 ! Area 1
al.2.5.6.9 ! Area 2
al.3.6.7.10 ! Area 3
al.8.11.12.14.15.16 ! Area 4
al.9.12.13.14 ! Area 5
al.17.4.20.23 ! Area 6
al.18.20.21.24 ! Area 7
al.19.21.22.25 ! Area 8

al.23.11.26.28.29.30 ! Area 9
al.24.26.27.28 ! Area 10
al.31.4.34.37 ! Area 11
al.32.34.35.38 ! Area 12
al.33.35.36.39 ! Area 13
al.37.43.40.42.11.44 ! Area 14
al.38.40.41.42 ! Area 15

al.7.22.45.48 ! Area 16
al.48.49.10.25 ! Area 17
al.13.27.49.51 ! Area 18
al.15.29.51.53 ! Area 19
al.16.30.53 ! Area 20
al.30.44.62 ! Area 21
al.29.43.62.60 ! Area 22
al.27.41.60.58 ! Area 23
al.25.39.58.57 ! Area 24
al.22.36.54.57 ! Area 25
al.19.33.54.55 ! Area 26
al.18.32.55.56 ! Area 27
al.17.31.56 ! Area 28
al.1.17.47 ! Area 29
al.2.18.47.46 ! Area 30
al.3.19.46.45 ! Area 31

al.9.24.49.50 ! Area 32
al.8.23.50 ! Area 33
al.23.37.59 ! Area 34
al.24.38.58.59 ! Area 35
al.21.35.58.55 ! Area 36
al.20.34.59.56 ! Area 37
al.5.20.47.50 ! Area 38
al.6.21.46.49 ! Area 39
al.12.26.50.52 ! Area 40
al.14.28.51.52 ! Area 41
al.26.40.59.61 ! Area 42
al.28.42.60.61 ! Area 43

!---Volumes--
va.13.8.24.25.26.36 ! Volume 1
va.12.7.27.35.36.37 ! Volume 2
va.11.6.34.37.28 ! Volume 3
va.1.6.29.33.38 ! Volume 4
va.2.7.30.32.38.39 ! Volume 5
va.3.8.31.16.17.39 ! Volume 6
va.15.10.23.35.42.43 ! Volume 7
va.14.9.34.21.22.43.42 ! Volume 8
va.4.9.33.40.41.19.20 ! Volume 9
va.5.10.32.18.40.41 ! Volume 10

!---Mesh Definition--
lset,s,1,4,7
lset,a,1,20,22
lset,a,1,34,36
lesize,all,,N1

lset,s,1,12,13
lset,a,1,26,27
lset,a,1,40,41
lesize,all,,N2

```

```

lsel,s,line,,15,15
lsel,a,line,,29,29
lsel,a,line,,43,43
lesize,all,,N3

lsel,s,line,,11,11
lesize,all,,N4

lsel,s,line,,3,3
lsel,a,line,,19,19
lsel,a,line,,33,33
lsel,s,line,,10,10
lsel,a,line,,25,25
lsel,a,line,,39,39
lesize,all,,N5

lsel,s,line,,2,2
lsel,a,line,,9,9
lsel,a,line,,14,14
lsel,s,line,,18,18
lsel,a,line,,24,24
lsel,a,line,,28,28
lsel,s,line,,32,32
lsel,a,line,,38,38
lsel,a,line,,42,42
lesize,all,,N6

lsel,s,line,,16,16
lsel,a,line,,30,30
lsel,a,line,,44,44
lsel,a,line,,53,53
lsel,a,line,,62,62
lesize,all,,N8

lsel,s,line,,45,52
lsel,a,line,,54,61
lesize,all,,N9

!---Mesh Volumes---
vsel,s,volu,,3,4
type,2
meshape,0,3D
vmesh,all

vsel,s,volu,,1,2
vsel,a,volu,,5,7
vsel,a,volu,,10,10
type,1
meshape,0,3D
vmesh,all

vsel,s,volu,,8,9
type,1
meshape,1,3D
vmesh,all

!---Boundary Conditions---
nsel,s,loc,x,r1-eps,r1+eps
d,all,all,0
csys,0

! symmetry BC
nsel,s,loc,y,0-eps,0+eps
d,all,uy,0
csys,1
alls
!---Solve---
/solu
antype,static
nsel,s,loc,z,z1-eps,z1+eps
nsel,r,loc,y,0-eps,0+eps
nsel,r,loc,x,(0+os)-eps,(0+os)+eps
f,all,fz,force
alls
save
solve
save
finish
/post1
nsel,s,loc,z,z1-eps,z1+eps
nsel,r,loc,x,r2-eps,r2+eps
nsel,u,loc,y,0+eps,45-eps
nsel,u,loc,y,45+eps,90-eps
nsel,u,loc,y,90+eps,135-eps
nsel,u,loc,y,135+eps,180-eps
prnsol,u,z
alls

```



```

! si_submodel.txt
! This is a 3-D model of the fillet of the silicon membrane
! specimen (half model). It is used to determine the
! effect of off-center loading on the stress in the fillet.
! This model is only the fillet and serves as a submodel,
! this file uses information from si_mainmodel.txt and thus
! it must be run before using this model.

! The fillet is assumed to be a quarter circle.

! This is a linear model.

! The units used in the model are N, mm, s

finish
/clear
/filename,si_submodel
/title,Sub Model
/prep7
csys,1

!---Geometry---
cr = 2750.0e-3
x1 = cr+90.0e-3
x2 = cr+100.0e-3
x3 = cr+200.0e-3

rad = 5.0e-3
filldist = (rad-(rad/(2.0*0.5))) ! fillet radius
cz=(300e-3)-rad
z1=cz+100e-3
z2=cz+rad+100e-3
z3=cz+rad+110e-3

sp1=45
sp2=90
sp3=135
sp4=180
eps=1e-5

!---Mesh Density---
N1=2
N2=3
N3=2
N4=N2
N5=2
N6=87
N7=22

!---Material Properties---
mp,ex,1,165.0e3
mp,prxy,1,0.22

!---Element Type---
et,1,solid95
!---Keypoints---
k,1,cr,0,z3
k,2,x1,0,z3
k,3,x2+rad,0,z3
k,4,x3,0,z3
k,5,cr,0,z1
k,6,x1,0,z1
k,7,x2,0,z1
k,8,x2+filldist,0,z2-filldist
k,9,x2+rad,0,z2
k,10,x3,0,z2
k,11,cr,0,cz
k,12,x1,0,cz
k,13,x2,0,cz

k,14,cr,sp1,z3
k,15,x1,sp1,z3
k,16,x2+rad,sp1,z3
k,17,x3,sp1,z3
k,18,cr,sp1,z1
k,19,x1,sp1,z1
k,20,x2,sp1,z1
k,21,x2+filldist,sp1,z2-filldist
k,22,x2+rad,sp1,z2
k,23,x3,sp1,z2
k,24,cr,sp1,cz
k,25,x1,sp1,cz
k,26,x2,sp1,cz

k,27,cr,sp2,z3
k,28,x1,sp2,z3
k,29,x2+rad,sp2,z3
k,30,x3,sp2,z3
k,31,cr,sp2,z1
k,32,x1,sp2,z1
k,33,x2,sp2,z1
k,34,x2+filldist,sp2,z2-filldist
k,35,x2+rad,sp2,z2
k,36,x3,sp2,z2
k,37,cr,sp2,cz
k,38,x1,sp2,cz
k,39,x2,sp2,cz

k,101,cr,sp3,z3
k,201,x1,sp3,z3
k,301,x2+rad,sp3,z3
k,401,x3,sp3,z3
k,501,cr,sp3,z1
k,601,x1,sp3,z1
k,701,x2,sp3,z1
k,801,x2+filldist,sp3,z2-filldist
k,901,x2+rad,sp3,z2
k,1001,x3,sp3,z2
k,1101,cr,sp3,cz
k,1201,x1,sp3,cz
k,1301,x2,sp3,cz

k,1401,cr,sp4,z3
k,1501,x1,sp4,z3

```

```

k.1601,x2+rad,sp4,z3
k.1701,x3,sp4,z3
k.1801,cr,sp4,z1
k.1901,x1,sp4,z1
k.2001,x2,sp4,z1
k.2101,x2+fldist,sp4,z2-fldist
k.2201,x2+rad,sp4,z2
k.2301,x3,sp4,z2
k.2401,cr,sp4,cz
k.2501,x1,sp4,cz
k.2601,x2,sp4,cz

!---Lines---
1.1,2      ! Line 1
1.2,3      ! Line 2
1.3,4      ! Line 3
1.1,5      ! Line 4
1.2,6      ! Line 5
1.2,8      ! Line 6
1.3,9      ! Line 7
1.4,10     ! Line 8
1.5,6      ! Line 9
1.6,7      ! Line 10
1.9,10     ! Line 11
1.5,11     ! Line 12
1.6,12     ! Line 13
1.7,13     ! Line 14
1.11,12    ! Line 15
1.12,13    ! Line 16

1.14,15    ! Line 17
1.15,16    ! Line 18
1.16,17    ! Line 19
1.14,18    ! Line 20
1.15,19    ! Line 21
1.15,21    ! Line 22
1.16,22    ! Line 23
1.17,23    ! Line 24
1.18,19    ! Line 25
1.19,20    ! Line 26
1.22,23    ! Line 27
1.18,24    ! Line 28
1.19,25    ! Line 29
1.20,26    ! Line 30
1.24,25    ! Line 31
1.25,26    ! Line 32

1.27,28    ! Line 33
1.28,29    ! Line 34
1.29,30    ! Line 35
1.27,31    ! Line 36
1.28,32    ! Line 37
1.28,34    ! Line 38
1.29,35    ! Line 39
1.30,36    ! Line 40
1.31,32    ! Line 41
1.32,33    ! Line 42
1.35,36    ! Line 43
1.31,37    ! Line 44
1.32,38    ! Line 45
1.33,39    ! Line 46
1.37,38    ! Line 47

1.38,39    ! Line 48
1.4,17     ! Line 49
1.3,16     ! Line 50
1.2,15     ! Line 51
1.1,14     ! Line 52
1.10,23    ! Line 53
1.9,22     ! Line 54
1.8,21     ! Line 55
1.7,20     ! Line 56
1.6,19     ! Line 57
1.5,18     ! Line 58
1.13,26    ! Line 59
1.12,25    ! Line 60
1.11,24    ! Line 61

1.17,30    ! Line 62
1.16,29    ! Line 63
1.15,28    ! Line 64
1.14,27    ! Line 65
1.23,36    ! Line 66
1.22,35    ! Line 67
1.21,34    ! Line 68
1.20,33    ! Line 69
1.19,32    ! Line 70
1.18,31    ! Line 71
1.26,39    ! Line 72
1.25,38    ! Line 73
1.24,37    ! Line 74

larc.7,8,9,rad ! Line 75
larc.8,9,7,rad ! Line 76
larc.20,21,22,rad ! Line 77
larc.21,22,20,rad ! Line 78
larc.33,34,35,rad ! Line 79
larc.34,35,33,rad ! Line 80

1.101,201  ! Line 81
1.201,301  ! Line 82
1.301,401  ! Line 83
1.101,501  ! Line 84
1.201,601  ! Line 85
1.201,801  ! Line 86
1.301,901  ! Line 87
1.401,1001 ! Line 88
1.501,601  ! Line 89
1.601,701  ! Line 90
1.901,1001 ! Line 91
1.501,1101 ! Line 92
1.601,1201 ! Line 93
1.701,1301 ! Line 94
1.1101,1201 ! Line 95
1.1201,1301 ! Line 96

1.1401,1501 ! Line 97
1.1501,1601 ! Line 98
1.1601,1701 ! Line 99
1.1401,1801 ! Line 100
1.1501,1901 ! Line 101
1.1501,2101 ! Line 102
1.1601,2201 ! Line 103
1.1701,2301 ! Line 104
1.1801,1901 ! Line 105

```

```

1.1901.2001      ! Line 106
1.2201.2301      ! Line 107
1.1801.2401      ! Line 108
1.1901.2501      ! Line 109
1.2001.2601      ! Line 110
1.2401.2501      ! Line 111
1.2501.2601      ! Line 112

1.401.1701       ! Line 113
1.301.1601       ! Line 114
1.201.1501       ! Line 115
1.101.1401       ! Line 116
1.1001.2301      ! Line 117
1.901.2201       ! Line 118
1.801.2101       ! Line 119
1.701.2001       ! Line 120
1.601.1901       ! Line 121
1.501.1801       ! Line 122
1.1301.2601      ! Line 123
1.1201.2501      ! Line 124
1.1101.2401      ! Line 125

1.401.30         ! Line 126
1.301.29         ! Line 127
1.201.28         ! Line 128
1.101.27         ! Line 129
1.1001.36        ! Line 130
1.901.35         ! Line 131
1.801.34         ! Line 132
1.701.33         ! Line 133
1.601.32         ! Line 134
1.501.31         ! Line 135
1.1301.39        ! Line 136
1.1201.38        ! Line 137
1.1101.37        ! Line 138

larc.701.801.901.rad
larc.801.901.701.rad
larc.2001.2101.2201.rad
larc.2101.2201.2001.rad

!---Areas---
al.1.4.5.9       ! Area 1
al.5.6.10.75     ! Area 2
al.2.6.7.76       ! Area 3
al.3.7.8.11       ! Area 4
al.9.12.13.15     ! Area 5
al.10.13.14.16    ! Area 6

al.17.20.21.25    ! Area 7
al.21.22.26.77    ! Area 8
al.18.22.23.78    ! Area 9
al.19.23.24.27    ! Area 10
al.25.28.29.31    ! Area 11
al.26.29.30.32    ! Area 12

al.33.36.37.41    ! Area 13
al.37.38.42.79    ! Area 14
al.34.38.39.80    ! Area 15
al.35.39.40.43    ! Area 16
al.41.44.45.47    ! Area 17
al.42.45.46.48    ! Area 18

al.3.19.49.50     ! Area 19
al.8.24.49.53     ! Area 20
al.11.27.53.54     ! Area 21
al.7.23.50.54     ! Area 22
al.2.18.50.51     ! Area 23
al.76.78.54.55    ! Area 24
al.6.22.51.55     ! Area 25
al.75.77.55.56    ! Area 26
al.10.26.56.57    ! Area 27
al.5.21.51.57     ! Area 28
al.1.17.51.52     ! Area 29
al.4.20.52.58     ! Area 30
al.9.25.58.57     ! Area 31
al.12.28.58.61    ! Area 32
al.15.31.60.61    ! Area 33
al.13.29.57.60    ! Area 34
al.14.30.56.59    ! Area 35
al.16.32.59.60    ! Area 36

al.19.35.62.63    ! Area 37
al.24.40.62.66    ! Area 38
al.27.43.66.67    ! Area 39
al.23.39.63.67    ! Area 40
al.18.34.63.64    ! Area 41
al.78.80.67.68    ! Area 42
al.22.38.64.68    ! Area 43
al.77.79.68.69    ! Area 44
al.21.37.64.70    ! Area 45
al.26.42.69.70    ! Area 46
al.30.46.69.72    ! Area 47
al.32.48.72.73    ! Area 48
al.29.45.70.73    ! Area 49
al.31.47.74.73    ! Area 50
al.28.44.74.71    ! Area 51
al.25.41.71.70    ! Area 52
al.17.33.64.65    ! Area 53
al.20.36.65.71    ! Area 54

al.81.84.85.89    ! Area 55
al.85.86.90.139   ! Area 56
al.82.86.87.140   ! Area 57
al.83.87.88.91    ! Area 58
al.92.89.93.95    ! Area 59
al.90.93.94.96    ! Area 60

al.97.100.101.105 ! Area 61
al.101.102.106.141 ! Area 62
al.98.102.103.142 ! Area 63
al.103.99.104.107 ! Area 64
al.108.105.109.111 ! Area 65
al.106.109.110.112 ! Area 66

al.97.81.116.115  ! Area 67
al.98.82.115.114  ! Area 68
al.99.83.114.113  ! Area 69
al.104.88.113.117 ! Area 70
al.103.87.118.114 ! Area 71
al.102.86.115.119 ! Area 72
al.101.85.115.121 ! Area 73
al.100.84.116.122 ! Area 74
al.105.89.122.121 ! Area 75
al.90.106.121.120 ! Area 76

```

```

al,141,139,120,119 ! Area 77
al,142,140,119,118 ! Area 78
al,107,91,118,117 ! Area 79
al,110,94,120,123 ! Area 80
al,109,93,121,124 ! Area 81
al,108,92,122,125 ! Area 82
al,111,95,125,124 ! Area 83
al,112,96,124,123 ! Area 84

al,33,81,129,128 ! Area 85
al,34,82,128,127 ! Area 86
al,35,83,127,126 ! Area 87
al,40,88,126,130 ! Area 88
al,39,87,127,131 ! Area 89
al,38,86,128,132 ! Area 90
al,37,85,128,134 ! Area 91
al,36,84,129,135 ! Area 92
al,41,89,135,134 ! Area 93
al,42,90,134,133 ! Area 94
al,79,139,133,132 ! Area 95
al,80,140,132,131 ! Area 96
al,43,91,131,130 ! Area 97
al,44,92,135,138 ! Area 98
al,45,93,134,137 ! Area 99
al,46,94,133,136 ! Area 100
al,47,95,138,137 ! Area 101
al,48,96,137,136 ! Area 102

!---Volumes---
va,1,7,28,29,30,31 ! Volume 1
va,2,8,25,26,27,28 ! Volume 2
va,3,9,22,23,24,25 ! Volume 3
va,4,10,19,20,21,22 ! Volume 4
va,5,11,31,32,33,34 ! Volume 5
va,6,12,27,34,35,36 ! Volume 6
va,7,13,45,52,53,54 ! Volume 7
va,8,14,43,44,45,46 ! Volume 8
va,9,15,40,41,42,43 ! Volume 9
va,10,16,37,38,39,40 ! Volume 10
va,11,17,49,50,51,52 ! Volume 11
va,12,18,46,47,48,49 ! Volume 12
va,61,55,67,73,74,75 ! Volume 13
va,62,56,72,73,76,77 ! Volume 14
va,63,57,68,71,72,78 ! Volume 15
va,64,58,69,70,71,79 ! Volume 16
va,65,59,75,81,82,83 ! Volume 17
va,66,60,80,81,76,84 ! Volume 18
va,55,13,85,91,92,93 ! Volume 19
va,56,14,90,91,94,95 ! Volume 20
va,57,15,86,89,90,96 ! Volume 21
va,58,16,87,88,89,97 ! Volume 22
va,59,17,93,98,99,101 ! Volume 23
va,60,18,94,99,100,102 ! Volume 24

!---Mesh Definition---
lsel,s,LINE,,3,3
lsel,a,LINE,,19,19
lsel,a,LINE,,35,35
lsel,a,LINE,,83
lsel,a,LINE,,99
lesize,all,,N1

lsel,s,LINE,,3
lsel,a,LINE,,6
lsel,a,LINE,,10
lsel,a,LINE,,18
lsel,a,LINE,,22
lsel,a,LINE,,26
lsel,a,LINE,,32
lsel,a,LINE,,34
lsel,a,LINE,,38
lsel,a,LINE,,42
lsel,a,LINE,,48
lsel,a,LINE,,82
lsel,a,LINE,,86
lsel,a,LINE,,106
lsel,a,LINE,,96
lsel,a,LINE,,98
lsel,a,LINE,,102
lsel,a,LINE,,106
lsel,a,LINE,,112
lesize,all,,N2

lsel,s,LINE,,1
lsel,a,LINE,,9
lsel,a,LINE,,15
lsel,a,LINE,,17
lsel,a,LINE,,25
lsel,a,LINE,,31
lsel,a,LINE,,33
lsel,a,LINE,,41
lsel,a,LINE,,47
lsel,a,LINE,,81
lsel,a,LINE,,89
lsel,a,LINE,,95
lsel,a,LINE,,97
lsel,a,LINE,,105
lsel,a,LINE,,111
lesize,all,,N3

lsel,s,LINE,,4,8
lsel,a,LINE,,20,24
lsel,a,LINE,,36,40
lsel,a,LINE,,84,88
lsel,a,LINE,,100,104
lesize,all,,N4

lsel,s,LINE,,12,14
lsel,a,LINE,,28,30
lsel,a,LINE,,44,46
lsel,a,LINE,,92,94
lsel,a,LINE,,108,110
lesize,all,,N5

lsel,s,LINE,,49,51
lsel,a,LINE,,53,57
lsel,a,LINE,,59,60
lsel,a,LINE,,62,64

```

```

lsel,a,line,,66,70
lsel,a,line,,72,73
lsel,a,line,,113,115
lsel,a,line,,117,121
lsel,a,line,,123,124
lsel,a,line,,126,128
lsel,a,line,,130,134
lsel,a,line,,136,137

lesize,all,,N6

lsel,s,line,,52
lsel,a,line,,65
lsel,a,line,,116
lsel,a,line,,129
lsel,a,line,,58
lsel,a,line,,71
lsel,a,line,,122
lsel,a,line,,135
lsel,a,line,,61
lsel,a,line,,74
lsel,a,line,,125
lsel,a,line,,138

lesize,all,,N7

!---Mesh Volumes---
vsel,s,volu,,2,4
vsel,a,volu,,6
vsel,a,volu,,8,10
vsel,a,volu,,12
vsel,a,volu,,14,16
vsel,a,volu,,18
vsel,a,volu,,20,22
vsel,a,volu,,24
meshape,0,3D
vmesh,all

vsel,s,volu,,1
vsel,a,volu,,5
vsel,a,volu,,7
vsel,a,volu,,11
vsel,a,volu,,13
vsel,a,volu,,17
vsel,a,volu,,19
vsel,a,volu,,23
meshape,1,3D
vmesh,all

!---Boundary Conditions---
csys,0
nsel,s,loc,y,0-eps,0+eps
d,all,uy,0
csys,1

!---Cut Boundaries---
nsel,s,loc,x,cr-eps,cr+eps
nsel,a,loc,z,cz-eps,cz+eps
nsel,a,loc,x,x3-eps,x3+eps
nwrite

!---Write to database---
alls
save

!---Resume database from coarse model and obtain data--
resume,si_mainmodel.db

/post1
file,si_mainmodel,rst
set
cbdo
finish

!---Resume the submodel database---
resume,

!---Solve---
/solu
antype,static
/input,,cbdo

alls
solve
save
finish

!---Post Processing---
/post1
rsys,1

nsel,s,loc,z,z3-eps,z3+eps
nsel,r,loc,x,cr-eps,cr+eps
nsel,u,loc,y,0+eps,45-eps
nsel,u,loc,y,45+eps,90-eps
nsel,u,loc,y,90+eps,135-eps
nsel,u,loc,y,135+eps,180-eps
prnsol,u,z

nsel,s,loc,z,z3-eps,z3+eps
nsel,r,loc,x,x3-eps,x3+eps
nsel,u,loc,y,0+eps,45-eps
nsel,u,loc,y,45+eps,90-eps
nsel,u,loc,y,90+eps,135-eps
nsel,u,loc,y,135+eps,180-eps
prnsol,u,z

dsys,1
rsys,1
nsel,s,loc,x,x2+rad-eps,x2-rad+eps
nsel,r,loc,z,z2-eps,z2+eps
nsort,loc,y,1,0
/page,1000,80,1000,132
/output,check.txt,~/,append
prnsol,u,z
prnsol,s
dsys,0

```

# Silicon membrane specimen finite element model: 2-D axisymmetric model.

```

! si_fracture.txt
! This is a 2-D axisymmetric model of the silicon membrane
! specimen. It is used to determine the maximum stress in
! the specimen for a given geometry and load.

! The fillet is assumed to be an ellipse and the aspect ratio
! can be varied from 0.1 to 1.0 (quarter circle). An aspect
! ratio of 0.5 is believed to be the most realistic for the
! current specimens.

! This is a non-linear model.

! Note that all units are given in mm and N, for some
! reason the program will not mesh arcs less than 10e-6. Thus
! we use mm as our base unit of length and everything works
! fine.

finish
/clear,nostart

/filename,si_fracture.txt
/title,Membrane Study

/prep7

!---Geometry---
tether = 0.155
Rmid = (2.845+3.00)/2.0
Ri = Rmid-tether/2.0
Ro = Rmid+tether/2.0
Rd = 3.500
Rm = 200.0e-3
tm = 17.53e-3
tw = 400.0e-3
L = 15.0e-3
H = 0.50*L
RHL = H/L
RF = L

!---Load---
force = 10.0 ! force applied in newtons

!---Variables---
r1 = Ri-Rm
r2 = Ri-tm
r3 = Ri
r5 = Ri+L
r6 = Ro-L
r8 = Ro
r9 = Ro+tm
r10 = Ro+Rm
r11 = Rd

h1 = tm
h3 = tm+H
h4 = tm+Rm
h5 = tw

!---Mesh Parameters---
N1 = 50
N2 = 6
N3 = 6
N4 = 15
N5 = 3
N6 = 48
N7 = 4
eps = 1e-10

!---Coordinate Systems---
local,11,1,f5,h3,0,0,0,0,RHL
local,12,1,f6,h3,0,0,0,0,RHL
csys,0

!---Element Type---
et,1,Plane82
keyopt,1,3,1

!---Material Properties---
mp,ex,1,165e3
mp,prxy,1,0.22

!---Keypoints---
csys,0
k,1,0,0
k,2,r1,0
k,3,r2,0
k,4,r5,0
k,5,r6,0
k,6,r9,0
k,7,r10,0
k,8,r11,0
k,9,r5,h1
k,10,r6,h1
k,13,r2,h3
k,14,r3,h3
k,15,r8,h3
k,16,r9,h3
k,17,0,h4
k,18,r1,h4
k,19,r3,h4
k,20,r8,h4
k,21,r10,h4
k,22,r11,h4
k,23,0,h5
k,24,r1,h5
k,25,r3,h5
k,26,r8,h5
k,27,r10,h5
k,28,r11,h5
csys,11
k,11,L,-135,0

csys,12
k,12,L,-45,0

```

```

!--Lines--
csys, 0
! #1
! #2
! #3
! #4
! #5
! #6
! #7
! #8
! #9
! #10
! #11
! #12
! #13
! #14
! #15
! #16
! #17
! #18
! #19
! #20

csys, 11
! #21
! #22
! #23

csys, 12
! #24
! #25

csys, 0
! #26
! #27
! #28
! #29
! #30
! #31
! #32
! #33
! #34
! #35
! #36
! #37
! #38
! #39
! #40
! #41
! #42

!--Mesh Density--
lesize, 23,,,N1
lesize, 4,,,N1

lsel,s_line,,11,14,3
lesize,all,,,N2,0.25

lsel,s_line,,12,13
lsel,a_line,,20,26,6
lesize,all,,,N2,0.25

lsel,s_line,,29,30
lsel,a_line,,40,41
lesize,all,,,N2

lsel,s_line,,3,5,2
lsel,a_line,,21,22
lsel,a_line,,24,25
lesize,all,,,N3

lsel,s_line,,10,15,5
lsel,a_line,,9,16,7
lsel,a_line,,8
lsel,a_line,,17
lesize,all,,,N3

lsel,s_line,,2,6,4
lsel,a_line,,19,27,8
lsel,a_line,,31,32
lesize,all,,,N4,10

lsel,s_line,,33,38
lesize,all,,,N5

lsel,s_line,,1,18,17
lsel,a_line,,39
lesize,all,,,N6

lsel,s_line,,7,28,21
lsel,a_line,,42
lesize,all,,,N7

lsel,all

!--Areas--
al,1,9,18,8 ! #1
al,2,10,19,9 ! #2
al,10,11,21,20 ! #3
al,11,3,12,22 ! #4
al,12,4,13,23 ! #5
al,13,5,14,24 ! #6
al,14,15,26,25 ! #7
al,15,6,16,27 ! #8
al,16,7,17,28 ! #9
al,18,34,39,33 ! #10
al,34,29,35,40 ! #11
al,36,30,37,41 ! #12
al,37,28,38,42 ! #13
al,19,20,31,29 ! #14
al,32,26,27,30 ! #15

!--Mesh Areas--
asel,s_area,,3,4 ! areas 3,4,6,7
asel,a_area,,6,7
mshape,,2D
amesh,all

asel,s_area,,5,5 ! area 5

```

```

meshape,0,2D
amesh,all

asel,s,area,,14,15 ! areas 14,15
asel,a,area,,2,8,6 ! areas 2,8
meshape,0,2D
amesh,all

asel,s,area,,11,12 ! area 11,12
meshape,0,2D
amesh,all

asel,s,area,,1,1 ! area 1
meshape,0,2D
amesh,all

asel,s,area,,10,10 ! area 10
meshape,0,2D
amesh,all

asel,s,area,,9,9 ! area 9
meshape,0,2D
amesh,all

asel,s,area,,13,13 ! area 13
meshape,0,2D
amesh,all

alls

!---Displacement B.C.---
nrel,s,loc,x,0-eps,0+eps
d,all,ux,0

nrel,s,loc,y,h5-eps,h5+eps
nrel,r,loc,x,r9-eps,r1+eps
nrel,r,loc,x,3.2-eps,3.2+eps
d,all,uy,0

alls

!---Solve---
/solu
antype,static

nrel,s,loc,x,0-eps,0+eps
nrel,r,loc,y,0-eps,0+eps
f,all,fy,force

nlgeom,on
nropt,full,off
satisf,on
autots,on
lnsrch,on
neqit,30
cnvtol,f,0.005,2,1e-8
nsubst

alls
save

```

```

solve
finish

!---Post Processing---
/post1
nrel,s,loc,x,r2-eps,r2+eps
nrel,r,loc,y,h3-eps,h3+eps
prnsol,u,y

nrel,all
esel,all
plnsol,s,1

nrel,s,loc,x,(Ri+L-eps),(Ri+L+eps)
nrel,r,loc,y,(tm*(1-0.29874166*1/4)-1e-7),(tm*(1-0.29874166*1/4)+1e-7)
prnsol,s,prin

nrel,s,loc,x,Ri-eps,Rd+eps

```



# References

- [1] Seward Webb Pulitzer III. Feasibility assessment and design of micro hydraulic solid-state transducers. Master's thesis, Massachusetts Institute of Technology, 1998.
- [2] N.W. Hagood IV, D.C. Roberts, L. Saggere, M.A. Schmidt, M. Spearing, K.S. Breuer, R. Mlcak, J.A. Carretero, F. Ganji, H. Li, K.-S. Chen, Y.-H. Su, and S. Pulitzer. Development of micro-hydraulic transducer technology. In *The 10th International Conference on Adaptive Structures and Technologies (ICAST '99)*, October 1999.
- [3] N.W. Hagood, D.C. Roberts, L. Saggere, K.S. Breuer, K.-S. Chen, J.A. Carretero, H. Li, R. Mlcak, S. Pulitzer, M.A. Schmidt, S.M. Spearing, and Y.-H. Su. Micro hydraulic transducer technology for actuation and power generation. In *Proceedings of the SPIE: Smart Structures and Materials 2000-Smart Structures and Integrated Systems*, volume 3985, pages 680–688, 2000.
- [4] D.C. Roberts, J.L. Steyn, H. Li, K.T. Turner, R. Mlcak, L. Saggere, S.M. Spearing, M.A. Schmidt, and N.W. Hagood. A high-frequency, high-stiffness piezoelectric micro-actuator for hydraulic applications. In *Transducers '01*, 2001.
- [5] H. Q. Li, D. C. Roberts, J. L. Steyn, K. T. Turner, J. A. Carretero, O. Yaglioglu, Y.-H. Su, L. Saggere, N. W. Hagood, S. M. Spearing, M.A. Schmidt, R. Mlcak, and K. S. Breuer. A high frequency high flow rate piezoelectrically driven MEMS micropump. In *Solid-State Sensor and Actuator Workshop 2000*, pages 69–72, June 2000.

- [6] G. Wallis and D.I. Pomerantz. Field assisted glass-metal sealing. *Journal of Applied Physics*, 40(10):3946–3949, 1969.
- [7] E. H. Klaassen, K. Petersen, M. J. Noworolski, J. Logan, N. I. Maluf, J. Brown, C. Storment, W. McCulley, and G. A. Kovacs. Silicon fusion bonding and deep reactive ion etching: a new technology for microstructures. *Sensors and Actuators*, A52:132–139, 1996.
- [8] M. A. Schmidt. Wafer-to-wafer bonding for microstructure formation. *Proceedings of the IEEE*, 86(8):1575–1585, August 1998.
- [9] A.R. Mizra and A.A. Ayon. Silicon wafer bonding: key to high-volume manufacturing. *Sensors*, December 1998.
- [10] A. Mehra, A. Ayon, I.A. Waitz, and M.A. Schmidt. Microfabrication of high-temperature silicon devices using wafer bonding and deep reactive ion etching. *Journal of Microelectromechanical Systems*, 8(2):152–156, 1999.
- [11] H.-J. Kress, F. Bantien, J. Marek, and M. Willmann. Silicon pressure sensor with integrated CMOS signal-conditioning circuit and compensation of temperature coefficient. *Sensors and Actuators*, 25(1):21–26, 1990.
- [12] L. Spangler and C.J. Kemp. ISAAC-integrated silicon automotive accelerometer. In *Transducers '95*, pages 25–29, 1995.
- [13] P. Krause, M. Sporys, E. Obermeier, K. Lange, and S. Grigull. Silicon to silicon anodic bonding using evaporated glass. In *Transducers '95*, pages 228–231, 1995.
- [14] S. Weichel, Roger de Reus, and Michael Lindahl. Silicon-to-silicon wafer bonding using evaporated glass. *Sensors and Actuators*, A70:179–184, 1998.
- [15] Bruno Miller. Hybrid silicon/silicon carbide microstructures and silicon bond strength tests for the MIT microengine. Master’s thesis, Massachusetts Institute of Technology, 1998.

- [16] K.T. Turner, A.A. Ayon, D. Choi, B. Miller, and S.M. Spearing. Characterization of silicon fusion bonds using a four-point bend specimen. In *Materials Science of Microelectromechanical Systems (MEMS) Devices III*, volume 657. MRS, September 2000.
- [17] J.B. Lasky, S.R. Stiffler, F.R. White, and J.R. Abernathy. Silicon-on-insulator (SOI) by bonding and etch-back. In *International Electron Devices Meeting. Technical Digest*, pages 684–687. IEEE, 1985.
- [18] J.B. Lasky. Wafer bonding for silicon on insulator technologies. *Applied Physics Letters*, 48(1):78–80, 1986.
- [19] M. Shimbo, K. Furukawa, K. Fukuda, and K. Tanzawa. Silicon-to-silicon direct bonding method. *Journal of Applied Physics*, 60(8):2987–2989, 1986.
- [20] U. Gosele and Q.-Y. Tong. Semiconductor wafer bonding. *Annual Review of Materials Science*, 28:215–241, 1998.
- [21] U. Gosele, Y. Bluhm, G. Kastner, P. Kopperschmidt, G. Krauter, R. Scholz, A. Schumacher, St. Senz, Q.-Y. Tong, L.-J. Huang, Y.-L. Chao, and T.H. Lee. Fundamental issues in wafer bonding. *Journal of Vacuum Science and Technology A*, 17(4):1145–1152, 1999.
- [22] Q.-Y. Tong and U. Gosele. *Semiconductor wafer bonding : science and technology*. Wiley, New York, 1999.
- [23] Q.-Y. Tong, G. Cha, R. Gafiteanu, and U. Gosele. Low temperature wafer direct bonding. *Journal of Microelectromechanical Systems*, 3(1):29–35, 1994.
- [24] B.E. Roberds and S.N. Farrens. Low temperature silicon direct bonding. In *Proceeding of the First International Symposium on Semiconductor Wafer Bonding: Science, Technology, and Applications*, pages 240–248, 1992.
- [25] S.N. Farrens, B.E. Roberds, J.K. Smith, and C.E. Hunt. Analysis of bond characteristics in Si direct-bonded materials. In *Proceeding of the Second International*

- [26] W.P. Mazara, G. Goetz, A. Caviglia, and B. McKitterick. Bonding of silicon wafers for silicon on insulator. *Journal of Applied Physics*, 64(10):4943–4950, 1988.
- [27] H.C. Cao and A.G. Evans. An experimental study of the fracture resistance of bimaterial interfaces. *Mechanics of Materials*, 7:295–304, 1989.
- [28] T. Martini, J. Steinkirchner, and U. Gosele. The crack opening method in silicon wafer bonding: how useful is it? *Journal of the Electrochemical Society*, 144(1):354–357, 1997.
- [29] P.G. Charalambides, J. Lund, A.G. Evans, and R.M. McMeeking. A test specimen for determining the fracture resistance of bimaterial interfaces. *Journal of Applied Mechanics*, 56:77–82, 1989.
- [30] P.G. Charalambides, H.C. Cao, J. Lund, and A.G. Evans. Development of a test method for measuring the mixed mode fracture resistance of bimaterial interfaces. *Mechanics of Materials*, 8:269–283, 1990.
- [31] C.H. Tsau, M.A. Schmidt, and S.M. Spearing. Characterization of low temperature, wafer-level gold-gold thermocompression bonds. In *Materials Science of Microelectromechanical Systems (MEMS) Devices II*, volume 605, pages 171–176. MRS, September 1999.
- [32] M.-Y. He and J.W. Hutchinson. Crack deflection at an interface between dissimilar elastic materials. *International Journal of Solids and Structures*, 25(9):1053–1067, 1989.
- [33] Personal communication with David C. Roberts.
- [34] K.E. Petersen. Silicon as a mechanical material. *Proceedings of the IEEE*, 70(5):420–457, 1982.

- [35] S.M. Hu. Critical stress in silicon brittle fracture, and effect of ion implantation and other surface treatments. *Journal of Applied Physics*, 53(5):3576–3580, 1982.
- [36] C.J. Wilson, A. Omeggi, and M. Narbutovskih. Fracture testing of silicon microcantilever beams. *Journal of Applied Physics*, 79(5):2386–2393, 1996.
- [37] K.-S. Chen, A.A. Ayon, K.A. Lohner, M.A. Kepets, T.K. Melconian, and S.M. Spearing. Dependence of silicon fracture strength and surface morphology on deep reactive ion etching parameters. In *Materials Science of Microelectromechanical Systems (MEMS) Devices*, volume 546, pages 21–26. MRS, September 1998.
- [38] K.-S. Chen. *Materials characterization and structural design of ceramic micro turbomachinery*. PhD thesis, Massachusetts Institute of Technology, 1999.
- [39] K.-S. Chen, A. Ayon, and S.M. Spearing. Controlling and testing the fracture strength of silicon on the mesoscale. *Journal of the American Ceramic Society*, 83(6):1476–1484, 2000.
- [40] C.P. Chen and M.H. Leipold. Fracture toughness of silicon. *Ceramic Bulletin*, 59(4):469–472, 1980.
- [41] F. Ericson, S. Johansson, and J.-A. Schweitz. Hardness and fracture toughness of semiconducting materials studied by indentation and erosion techniques. *Materials Science and Engineering*, A105/106:131–141, 1988.
- [42] J.J. Wortman and R.A. Evans. Young’s modulus, shear modulus, and poisson’s ratio in silicon and germanium. *Journal of Applied Physics*, 36(1):153–156, 1965.
- [43] G.S. Selvaduray. Die bond materials and bonding mechanisms in microelectronic packaging. *Thin Solid Films*, 153:431–445, 1987.
- [44] R.K. Shukla and N.P. Mencinger. A critical review of VLSI die-attachment in high reliability applications. *Solid State Technology*, pages 67–74, July 1985.

- [45] G. Sasaki, H. Fukunaga, T. Suga, and K. Tanaka. Mechanism of the anodic bonding between PZT ceramics and silicon wafer. *Materials Chemistry and Physics*, 51:174–177, 1997.
- [46] K. Tanaka, E. Takata, and K. Ohwada. Anodic bonding of lead zirconate titanate ceramics to silicon with intermediate glass layer. *Sensors and Actuators*, A69:199–203, 1998.
- [47] A.-L. Tiensuu, M. Bexell, J.A. Schweitz, L. Smith, and S. Johansson. Assembling three-dimensional microstructurea using gold-silicon eutectic bonding. *Sensors and Actuators*, A45:227–236, 1994.
- [48] P.T. Vianco and J.A. Rejent. Solder bond applications in a piezoelectric sensor assembly. In *Forty-Fifth Annual Symposium on Frequency Control*, pages 266–280. IEEE, 1991.
- [49] D.R. Olsen and H.M. Berg. Properties of die bond alloys relating to thermal fatigue. *IEEE Transactions on Components, Hybrids, and Manufacturing Technology*, CHMT-2(2):257–263, 1979.
- [50] C. Kallmayer, D. Lin, J. Kloeser, H. Opperman, E. Zakel, and H. Reichl. Fluxless flip-chip attcahment techniques using the Au/Sn metallurgy. In *Proceedings of the Seventeenth Electronic Manufacturing Technology Symposium*, pages 20–28. IEEE, 1995.
- [51] Eniko T. Enikov and J.G. Boyd. Electroplated-fluidic interconnects for chemical sensors. *Sensors and Actuators*, A84:161–164, 2000.
- [52] S.D. Senturia. *Microsystem Design*. Kluwer, Boston, MA, 2001.
- [53] H. Okamoto and T.B. Massalski. *Phase Diagrams of Binary Gold Alloys*. ASM International, Metals Park, OH, 1987.
- [54] G.S. Matijasevic, C.C. Lee, and C.Y. Wang. Au-Sn alloy phase diagram and properties related to its use as a bonding medium. *Thin Sold Films*, 223:276–1287, 1993.

- [55] C.C. Lee and G.S. Matijasevic. Highly reliable die attachment on polished GaAs surfaces using gold-tin eutectic alloy. *IEEE Transactions on Components, Hybrids, and Manufacturing Technology*, 12(3):406–409, 1989.
- [56] G.S. Matijasevic and C.C. Lee. A reliability study of Au-Sn eutectic bonding with GaAs dice. In *Proceeding of the 27th Annual Reliability Physics Symposium*, pages 137–140. IEEE, 1989.
- [57] G.S. Matijasevic, C.Y. Wang, and C.C. Lee. Void free bonding of large silicon dice using gold-tin alloys. *IEEE Transactions on Components, Hybrids, and Manufacturing Technology*, 13(4):1128–1134, 1990.
- [58] M. Nishiguchi, N. Goto, and H. Nishizawa. Highly reliable Au-Sn eutectic bonding with back-ground GaAs LSI chips. In *Electronic Manufacturing Technology Symposium, 1990 Proceedings, Competitive Manufacturing for the Next Decade*, pages 216–222. IEEE, 1990.
- [59] C.C. Lee, C.Y. Wang, and G.S. Matijasevic. A new bonding technology using gold and tin multilayer composite structures. *IEEE Transactions on Components, Hybrids, and Manufacturing Technology*, 14(2):407–412, 1991.
- [60] C. Christensen and S. Bouwstra. Eutectic bonds on wafer scale by thin film multilayers. In *Proceedings of the SPIE: Micromachining and Microfabrication Process Technology II*, volume 2879, pages 288–290, 1996.
- [61] G.R. Dohle, J.J. Callahan, K.P. Martin, and T.J. Drabik. Bonding of epitaxial lift off (ELO) devices with AuSn. In *Proceedings of the 45th Electronic Components and Technology Conference*, pages 423–427. IEEE, 1995.
- [62] U.S. Department of Defense, Washington D.C. *MIL-STD-883E: Test Methods and Procedures for Microelectronics*, 1996.
- [63] M. Ohring. *The Materials Science of Thin Films*. Academic Press, New York, 1992.

# BONDING OF BULK PIEZOELECTRIC MATERIAL TO SILICON USING A GOLD-TIN EUTECTIC BOND

**Kevin T. Turner<sup>1</sup>, Richard Mlcak<sup>2</sup>, David C. Roberts<sup>1</sup> and S. Mark Spearing<sup>1</sup>**

<sup>1</sup>Massachusetts Institute of Technology, Cambridge, MA 02139 USA

<sup>2</sup>Boston MicroSystems, Inc., Woburn, MA 01801 USA

## ABSTRACT

A class of MEMS devices, which utilizes microfabrication technology and bulk piezoelectric material, is currently being developed to produce high power density transducers. A thin-film gold-tin eutectic solder bond has been developed to bond electrically and mechanically bulk piezoelectric elements to microfabricated silicon structures in these devices. A 4.3  $\mu\text{m}$  thick multilayer film structure, consisting of a titanium adhesion layer, a platinum diffusion barrier, a gold-tin (80 wt.% Au - 20 wt.% Sn) alloy layer, and a pure gold capping layer, was sputter deposited on the piezoelectric components to be bonded. Bonding was accomplished by mating the piezoelectric components with silicon components metallized with a titanium-platinum-gold multilayer film and heating to approximately 300°C in a reducing atmosphere. The bonding technology allows thin, electrically conductive bonds to be formed between dissimilar materials with minimal amounts of applied pressure during bonding. Successful bonding has been achieved between single crystal silicon and polycrystalline lead-zirconate-titanate (PZT-5H) as well as between silicon and single crystal lead zinc niobate-lead titanate (PZN-PT). The process was optimized to produce mechanically robust, void-free bonds. The absence of voids was verified through scanning electron microscope examinations of bond cross-sections. Tensile tests conducted on representative structures indicated that the strength of the bond was limited by the strength of the titanium – PZT-5H interface.

## INTRODUCTION

A class of MEMS devices known as micro-hydraulic transducers (MHT), are currently being developed for actuation and power generation applications [1,2]. To achieve the desired power densities and actuation capabilities, there is a need to integrate bulk piezoelectric (rather than thin-film) material into these devices. These devices are constructed by bonding multiple micromachined glass and silicon wafers. Figure 1 illustrates the basic construction of an MHT device and demonstrates the final bond step, a novel anodic bond between glass and silicon in which the piezoelectric elements (typically cylinders 0.5-2 mm in diameter and 1 mm thick) are simultaneously bonded using a gold-tin eutectic bond within the structure. The bond between the piezoelectric elements and silicon layers must provide both a mechanical and electrical connection, and must be compatible with the preferred anodic bond temperature of 300°C. Gold-tin eutectic (80 wt.% Au - 20 wt.% Sn) solder bonding is an attractive option for this application because it has a eutectic temperature slightly less than 300°C, it is a hard solder with a relatively high yield strength, and is electrically conductive. The current work details the gold-tin bonding process developed for bonding bulk piezoelectric material to silicon during the final anodic bond in MHT device assembly.

Gold-based eutectic solders, including gold-silicon, gold-tin, and gold-germanium, are part of a class of hard solders, which have melting temperatures, yield-strengths, and moduli that are higher than those of more common soft solders. Gold-tin has the lowest melting temperature,



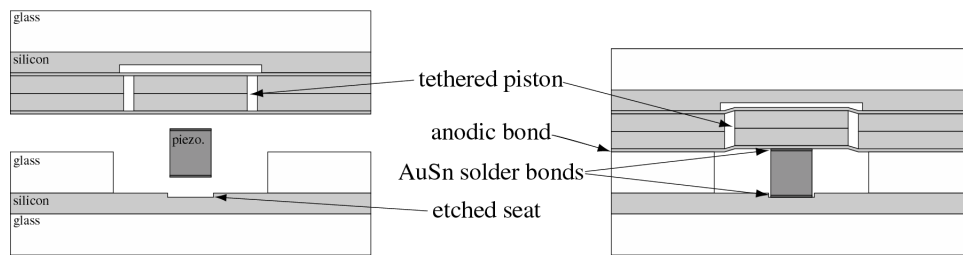


**Figure 1:** Basic MHT device structure. Bulk piezoelectric elements are bonded to the silicon support structure and the silicon piston using gold-tin solder bonds.

278°C (for the 80 wt.% Au - 20 wt.% Sn eutectic composition), of the gold based-solders. Gold-tin has been used in a variety of applications, including: die-attach [3],[4], flip-chip packaging [5], and chemical sensors [6]. Two primary techniques have been reported for fabricating gold-tin bonds. The traditional technique that has been used is to place a preform of the solder material, typically 25  $\mu\text{m}$  thick, between the adherends, which have been metallized if necessary, and then to heat the assembly above the melting temperature of the alloy. To achieve bonding using gold-tin preforms, the joint is heated to approximately 305°C (25°C above the melting temperature) and a scrubbing motion is applied to break the oxide, which exists on the surface of the perform [3]. The alternative approach to preforms that has been employed is to deposit directly the gold-tin material on the components to be bonded. Several researchers have reported achieving robust bonds between GaAs and silicon by evaporating alternating layers of gold and tin, where the thickness ratios of the layers are set to achieve the desired 80/20 weight ratio, on the surfaces to be bonded [4]. Bonding is achieved by mating the components and heating to a temperature near 300°C while applying a static pressure ( $< 0.3 \text{ MPa}$ ) to the joint. This technique is attractive because thinner joints with better dimensional control can be achieved. In addition, the films are deposited such that gold is the outer layer, thus preventing surface oxidation of tin and eliminating the need for the scrubbing motion during bonding.

## BONDING PROCESS

Dimensional tolerance requirements coupled with the inability to apply a scrubbing motion during device fabrication dictated that a thin-film gold-tin bond be employed in the fabrication of MHT devices. The approach that was adopted differs from the thin-film bonding technique discussed above in that the gold-tin is sputter-deposited as an alloy, rather than as alternating layers of gold and tin. The bonding process was developed to produce mechanically sound, void-free bonds. Details of the refined process are presented below.

The metal layers deposited onto the silicon and piezoelectric surfaces to be bonded are shown in Figure 2. PZT-5H or PZN-PT piezoelectric plates, 12 to 25 mm in diameter, were first ground and polished to a thickness of 1 mm and a surface roughness of better than 0.5  $\mu\text{m}$ . Prior to deposition, the plates were cleaned using a weak nitric acid solution (20:1  $\text{H}_2\text{O}:\text{HNO}_3$ ). The four-layer film structure on the piezoelectric plates was deposited in one vacuum cycle using sputtering. The 50 nm thick titanium layer and the 250 nm thick platinum layer serve as an adhesion layer and diffusion barrier, respectively. A 4  $\mu\text{m}$  thick gold-tin eutectic layer was sputtered from an alloy target of 80 wt.% Au - 20 wt.% Sn composition. Sputtering was chosen over evaporation because sputtering allows the stoichiometry of the target to be maintained in the deposited film. The final layer is a gold capping layer, 50 nm thick, that serves to prevent tin oxidation in the gold-tin alloy. The Ti-Pt-Au multi-layer film on the silicon pieces provides both

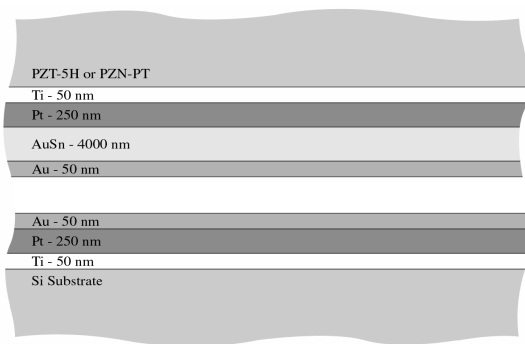


**Figure 2:** Arrangement and thickness of metal layers deposited on components for gold-tin bonding.

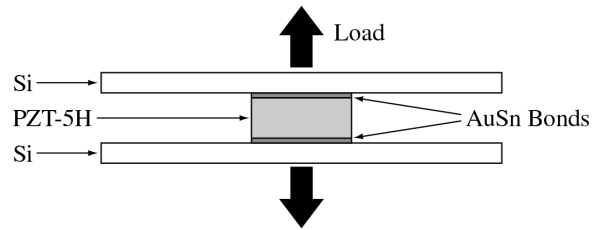


**Figure 3:** Schematic of bond test geometry. A tensile load is applied to the bond during testing.

a surface that can be wet by the gold-tin alloy and a diffusion barrier to prevent gold-silicon alloying during the bond process. The silicon surfaces were first prepared by a standard piranha clean, and the Ti-Pt-Au film was deposited in one vacuum cycle using electron-beam evaporation. For the bond experiments in this study, the silicon metallization layers were deposited uniformly onto 100 mm silicon wafers. However, in device fabrication, a shadow mask was employed to achieve spatially selective deposition, thereby eliminating the need for photolithographic patterning of the fragile silicon components. The gold capping layer on the silicon pieces, as well as the piezoelectric elements, causes the gold-tin eutectic alloy to become slightly gold-rich. However, the 50 nm gold layers are thin as compared to the 4  $\mu\text{m}$  thick gold-tin layer and the gold fraction in the final bond remains less than 80.5 wt.%.

The test specimens employed in developing this process were nominally 2.5×2.5 mm or 3.5×3.5 mm piezoelectric pieces bonded to 10×10 mm silicon dies, as shown in Figure 3. The piezoelectric pieces and silicon dies were cut from the larger wafers and plates using a diamond dicing saw. The surfaces were protected during dicing using a low temperature wax, which was removed after dicing. Immediately prior to bonding, the piezoelectric and silicon pieces were cleaned using sequential acetone, methanol, and isopropanol rinses, and were dried with filtered  $\text{N}_2$ . The pieces were assembled and clamped using a jig that provides approximately 0.15 MPa of pressure to the joint during bonding. This pressure was selected to correlate with the clamping pressure applied to the bond during the anodic bond process in MHT device assembly. The clamped joint was heated to 305°C in a vacuum oven that was first evacuated to  $5 \times 10^{-3}$  torr and backfilled with argon containing 5% hydrogen. The presence of hydrogen in the purging gas provided a reducing atmosphere to prevent tin oxidation during the bond process, and possibly to remove oxidizing adsorbates on the original gold surfaces. Once the maximum temperature of 305°C was reached, the chamber was evacuated to  $5 \times 10^{-3}$  torr. After a soak time of approximately 30 min, the joint was cooled to room temperature. The soak and cool periods are completed under vacuum to remove trapped gases in the bond layer and to ensure void-free bonds.

## EXPERIMENTAL EVALUATION

The bonding process detailed above was developed and refined based on data from experimental evaluations of the bond. The primary focus of the process development work was to produce void-free bonds, as voids inherently reduce the strength of the bond and can serve as fatigue crack initiation sites. This is particularly important in MHT devices where the bonds are subjected to a large number of cyclic shear strains during operation. To inspect for voids,

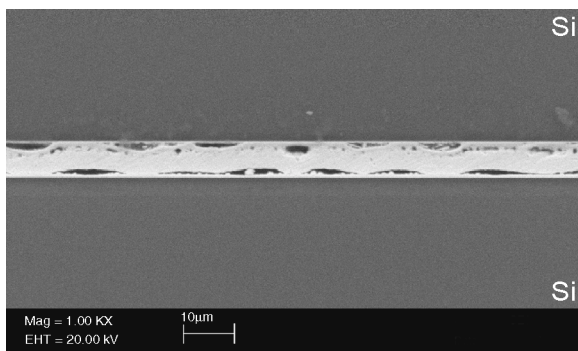


**Figure 4:** An example of poor bonding believed to be a result of trapped gases at the interface.

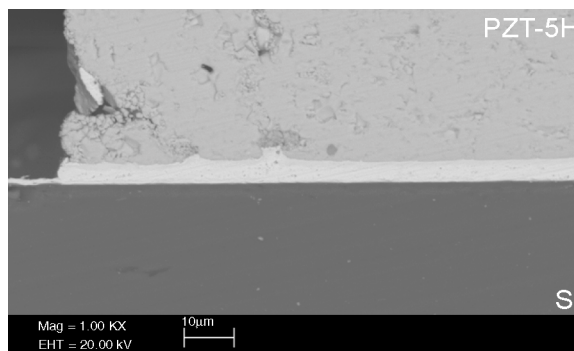


**Figure 5** SEM micrograph showing a void-free gold-tin bond joining bulk PZT-5H to silicon.

bonded specimens were cross-sectioned and polished, then examined using a scanning electron microscope (SEM). The inspection process, while destructive, is straightforward and allows small voids to be identified. In addition to the inspection of bond cross-sections, mechanical testing specimens with the geometry shown in Figure 3 were fabricated and tested. The specimen was designed to replicate a typical MHT component and was selected to elucidate potential failure modes, rather than provide data for process optimization. The specimens were mounted to aluminum studs using an epoxy and loaded to failure in tension using a standard servo-hydraulic test machine. Failure stress values were calculated based on the failure load and nominal bonded area. The fracture surfaces were examined using an optical microscope to identify the types of failure incurred.

## RESULTS AND DISCUSSION

Initial process development work was completed on silicon-silicon specimens rather than the silicon-piezoelectric specimens described above. The specimens are identical to those described above, with the exception that the gold-tin layer is deposited on silicon rather than a piezoelectric substrate. Figure 4 shows an early bond attempt between two silicon components. While the bond appeared mechanically sound, the cross-section revealed that the bond contained numerous voids. The bond shown in Figure 4 was fabricated using a process similar to that described above, however no clamping pressure was applied during bonding and cooling was not performed under vacuum. Subsequent experiments demonstrated that these voids could be eliminated by applying a moderate clamping pressure (0.15 MPa) and cooling under vacuum. Both of these precautions were found to be required in order to eliminate consistently voids of this type. Cross-sectional analysis also showed that large unbonded regions occasionally formed when the components were not thoroughly cleaned with the sequential acetone, methanol, and isopropanol rinses and N<sub>2</sub> dry immediately prior to bonding.

Figures 5 and 6 are SEM micrographs showing void-free gold-tin bonds between bulk piezoelectric material and silicon. Figure 5 shows a bond between PZT-5H and silicon. The bond is void-free and it can be observed that the gold-tin solder has the ability to fill defects that exist on the surface of the PZT-5H. The other important feature evident in Figure 5 is the absence of a fillet at the bond edge, as there appears to be negligible flow of the solder from the bond space to the edge of the PZT-5H. This behavior was routinely observed and has the potential to limit the load carrying capability of the bond. Figure 6 is a micrograph of a gold-tin bond between PZN-PT and silicon, again showing a continuous and void-free bond layer and the capability for gold-tin to fill imperfections in the piezoelectric material.

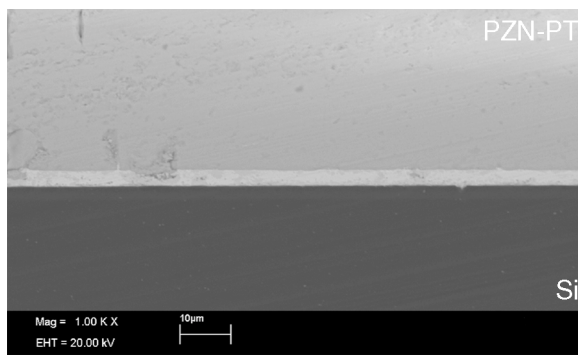


**Figure 6:** SEM micrograph showing a void-free gold-tin bond joining bulk PZN-PT to silicon.

**Table 1:** Failure stresses obtained from tensile tests on gold-tin bonds between silicon and PZT-5H.

<i>Specimen</i>	<i>Failure Stress (MPa)</i>
<i>A</i>	2.8
<i>B</i>	3.2
<i>C</i>	9.0
<i>D</i>	0.8
<i>E</i>	5.0

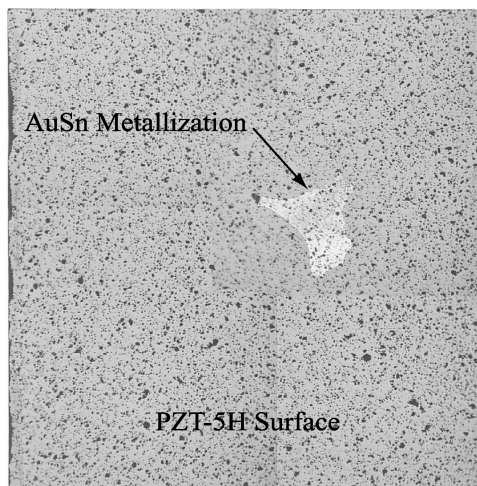
The SEM evaluation of the bond cross-sections allowed a bond process that yields void-free bonds to be developed. Following the development of the refined process, tensile specimens with the geometry shown in Figure 3 were fabricated and tested. Results from five tests are given in Table 1. The failure stress values span an order of magnitude, from 0.8 to 9.0 MPa. The scatter in the data is not entirely surprising, since the measured failure load is very sensitive to defects in the piezoelectric material or the bond layer. Despite the scatter, there is a degree of correlation between the measured failure stresses and the appearance of the fracture surfaces. Figure 7 is an optical micrograph showing the PZT-5H surface of specimen C after testing. Failure occurred primarily along the interface between the titanium adhesion layer and the PZT-5H. A small patch of the gold-tin bond layer remains attached, but the majority of the surface in Figure 7 is bare PZT-5H. The speckled pattern observed on the surface consists of small divots where PZT-5H pieces have pulled out. This overall failure pattern was observed in specimens C and E, the specimens with the highest failure stresses. This suggests that the strength of the bond is limited by interface between the PZT-5H and the bond layer.

Figure 8 shows the fracture surface of specimen B, and is similar in appearance to the fracture surfaces of specimens A and D. The surface consists of areas where fracture has occurred in the bond layer as well as areas where significant fracture of the PZT-5H has occurred. The fracture surface shown in Figure 8 suggests two possible modes of failure for specimens A, B, and D, which had the lowest failure stresses of the specimens tested. The first possible mode of failure, which is suggested by the large fractured regions in the PZT-5H, is that a flaw existed in the PZT-5H and led to fracture at a low load. The other possible failure mode is that the interface was poorly bonded due to contamination and fracture began within the bond layer itself. Once a portion of the solder layer failed, the local stress on the well bonded regions increased and led to the fracture of the PZT-5H. The SEM evaluations established that void-free bonds can routinely be produced, which suggests the second possible mode of failure can be avoided. Thus, based on the results of the tensile tests, it is clear the limiting factor in bond strength is the interface between the PZT-5H and the bond layer. Based on the examinations of the fracture surfaces it is unclear whether it due to poor adhesion between the PZT-5H and the titanium or whether failure occurs due to fracture and pull-out of the PZT-5H itself.

## CONCLUSIONS

A thin-film gold-tin eutectic bond was developed to provide reproducible, void-free electrical and mechanical bonds between piezoelectric elements and silicon substrates. The bonding process is compatible with and can be performed during anodic bond assembly of





**Figure 7:** PZT-5H surface of a tensile specimen that failed at 9.0 MPa.

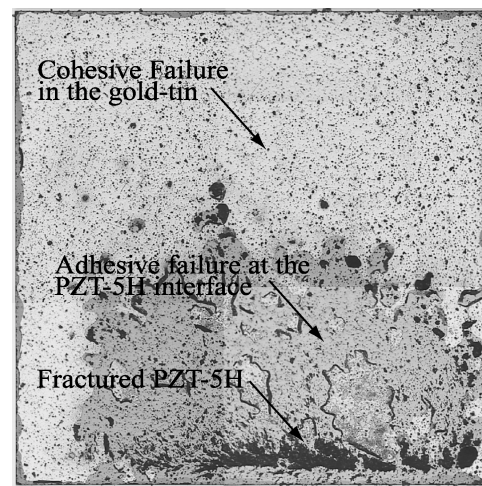


**Figure 8:** PZT-5H surface of a tensile specimen that failed at 3.2 MPa.

micro-hydraulic transducers. Bonds were cross-sectioned and examined to verify bond uniformity and the absence of voids. Tensile tests were conducted on PZT-5H elements bonded to silicon. The results indicate the strength of the bond is limited by the strength of the titanium - PZT-5H interface. It is unclear whether a different adhesion layer would result in higher bond strengths, since fracture of the PZT-5H itself is often observed when the interface fails. To validate fully and further develop the process, a systematic process optimization should be completed and the fatigue behavior of the bond studied. Despite the need for further work, the current study has clearly demonstrated the potential to integrate bulk piezoelectric material into microdevices using a gold-tin eutectic bond.

## ACKNOWLEDGEMENT

This work was sponsored by DARPA under contract DAAG55-98-0361.

## REFERENCES

1. N.W. Hagood, D.C. Roberts, L. Saggere, K.S. Breuer, K.-S. Chen, J.A. Carretero, H. Li, R. Mlcak, S. Pulitzer, M.A. Schmidt, S.M. Spearing, and Y.-H. Su, *Proceedings of the SPIE* **3985**, 680-688 (2000).
2. D.C. Roberts, J.L. Steyn, H. Li, K.T. Turner, R. Mlcak, L. Saggere, S.M. Spearing, M.A. Schmidt, and N.W. Hagood. *Transducers' 01* (2001).
3. M. Nisguchi, N. Goto, and H. Nishizawa. *IEEE Electronic Manufacturing Technology Symposium*, 216-222 (1990).
4. C.C. Lee, C.Y. Wang, and G.S. Matijasevic, *IEEE Transactions on Components, Hybrids and Manufacturing Technology*, **14**, 407-412 (1991).
5. C. Kallmayer, D. Lin, J. Kloesser, H. Opperman, E. Zakel, and H. Reichl. *IEEE Seventeenth Electronic Manufacturing Technology Symposium*, 20-28 (1995).
6. E. T. Enikov and J.G. Boyd. *Sensors and Actuators*, **A84**, 161-164 (2000).

# Large deflection analysis of a pre-stressed annular plate with a rigid boss under axisymmetric loading

Y H Su<sup>1</sup>, K S Chen<sup>2</sup>, D C Roberts<sup>3</sup> and S M Spearing<sup>4</sup>

<sup>1</sup> Department of Mechanical Engineering, State University of New York at Stony Brook, USA

<sup>2</sup> Department of Mechanical Engineering, National Cheng-Kung University, Tainan, Taiwan, Republic of China, 701

<sup>3</sup> Department of Mechanical Engineering, Massachusetts Institute of Technology, Cambridge, MA, USA

<sup>4</sup> Department of Aeronautics and Astronautics, Massachusetts Institute of Technology, Cambridge, MA, USA

Received 9 November 2000, in final form 1 October 2001

Published 12 October 2001

Online at [stacks.iop.org/JMM/11/645](http://stacks.iop.org/JMM/11/645)

## Abstract

The large deflection analysis of a pre-stressed annular plate with a central rigid boss subjected to axisymmetric loading is presented. The factors affecting the transition from plate behaviour to membrane behaviour (e.g. thickness, in-plane tension and material properties) are studied. The effect of boss size and pre-tension on the effective stiffness of the plate are investigated. The extent of the bending boundary layers at the edges of the plate are quantified. All results are presented in non-dimensional form. The design implications for microelectromechanical system components are assessed.

## 1. Introduction

Over the past decade, the development of precision micromachining technology has led to the realization of complex miniature mechanical devices which are integrated with microelectronics at the ‘chip’ level. Such microelectromechanical systems (MEMS) offer great potential for compact, low-cost sensors, actuators and power sources. One structure common to numerous MEMS devices is that of a thin circular plate or membrane with a central circular boss or proof mass. Structures of this type can be found in pressure sensors, accelerometers, micro valves [1], and micro hydraulic transducers [2]. Often during operation, such structures are loaded into the large deflection regime where linear deformation theory no longer applies. In addition, these structures are often created by wafer-bonding operations [3], which may introduce in-plane residual stress due to thermal expansion, mismatch between adjacent wafers, or due to other process related effects. In extreme cases thermal-induced buckling may occur.

This paper presents a mechanical analysis of these issues, and builds upon previous work by others, notably [4–8]. In particular, this paper extends the work of [8] to study

the large deflection of a pre-tensioned annular plate bonded with a rigid boss under axisymmetric pressure and in-plane loading. A comprehensive review of the literature can be found in [8]. The structure of this paper is as follows. In section 2, the derivation of the nonlinear governing equations is detailed. The numerical algorithm used to solve the problem is introduced in section 3. The membrane response and the plate response are compared in section 4. In section 5, nonlinear effects due to large deformations are compared with the results obtained from linear theory. The effects of boss size, pre-tension, and compliance of the boss are also addressed in this section. In section 6, several assumptions made in section 2 are justified *a posteriori*. The important conclusions of this work are summarized in section 7.

## 2. Formulation

We consider an annular plate with inner radius  $r_b$ , outer radius  $r_a$  and thickness  $h$  bonded with a rigid boss and pre-stressed by an uniform in-plane loading  $N_r = N_0$  along its outer circumference. Then a uniform pressure  $p_0$  is applied under the plate as shown in figure 1.

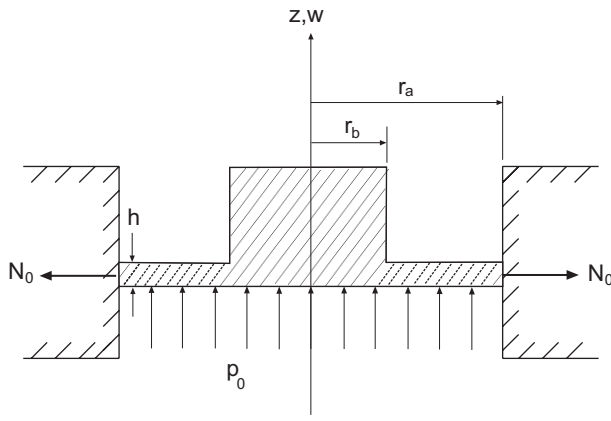


Figure 1. Geometric configuration.

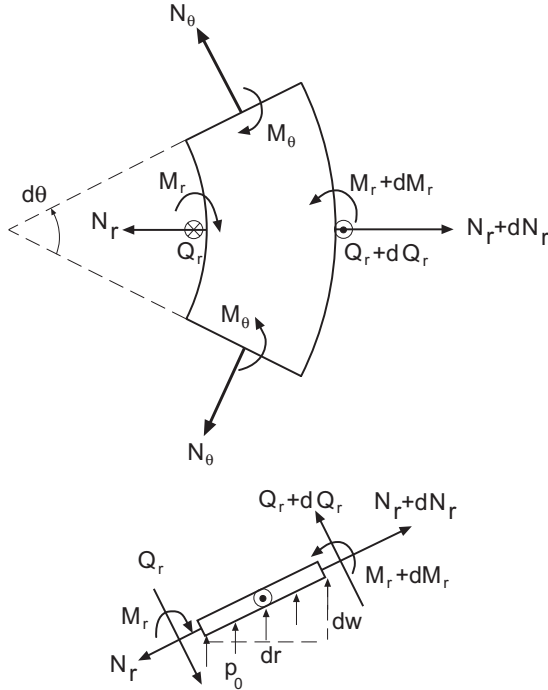


Figure 2. Force definitions and sign conventions.

Following the von Karman plate theory [9], the vertical displacement  $w$  is assumed to be much larger than the lateral displacements  $u$  and  $v$ , and the normals to the undeformed middle surface remain the normals to the deformed middle surface. Thus the deformed shape of the thin plate can be fully described by the geometry of the neutral surface. In the present analysis, only quadratic nonlinear terms will be retained.

Referring to figure 2, the equilibrium equations for the bending of the plate give

$$\frac{dN_r}{dr} + \frac{N_r - N_\theta}{r} = 0 \quad (1)$$

$$\frac{d}{dr}(rQ_r) + \frac{d}{dr}\left(rN_r \frac{dw}{dr}\right) + rp_0 = 0 \quad (2)$$

and

$$Q_r = \frac{dM_r}{dr} + \frac{M_r - M_\theta}{r} \quad (3)$$

where  $N_r$  is the radial force per unit length along the circumference (its direction is always tangential to the deformed neutral surface),  $N_\theta$  is the circumferential force per unit length, and  $Q_r$  is the shearing force per unit length and is normal to the deformed middle surface.

Moment equilibrium gives<sup>1</sup>

$$M_r = D(\kappa_r + \nu\kappa_\theta), \quad M_\theta = D(\kappa_\theta + \nu\kappa_r) \quad (4)$$

where

$$D \equiv \frac{Eh^3}{12(1-\nu^2)}.$$

Kinematic considerations give<sup>2</sup>

$$\kappa_r = -\frac{d^2w}{dr^2}, \quad \kappa_\theta = -\frac{1}{r} \frac{dw}{dr}. \quad (5)$$

With simple algebra, we obtain

$$\frac{d^3w}{dr^3} + \frac{1}{r} \frac{d^2w}{dr^2} - \frac{1}{r^2} \frac{dw}{dr} - \frac{N_r}{D} \frac{dw}{dr} = \frac{p_0 r}{2D}. \quad (6)$$

The strain-displacement relationship can be written as follows<sup>3</sup>

$$\epsilon_r = \frac{du}{dr} + \frac{1}{2} \left( \frac{dw}{dr} \right)^2, \quad \epsilon_\theta = \frac{u}{r}. \quad (7)$$

In order to eliminate  $u$ , we rewrite the strain-displacement relationship as follows

$$r \frac{d\epsilon_\theta}{dr} + \epsilon_\theta - \epsilon_r + \frac{1}{2} \left( \frac{dw}{dr} \right)^2 = 0. \quad (8)$$

The material is assumed to follow Hooke's law, i.e. for a material with Young's modulus  $E$  and Poisson's ratio  $\nu$ ,<sup>4</sup>

$$\epsilon_r = \frac{1}{E} \left( \frac{N_r}{h} - \nu \frac{N_\theta}{h} \right), \quad \epsilon_\theta = \frac{1}{E} \left( \frac{N_\theta}{h} - \nu \frac{N_r}{h} \right). \quad (9)$$

Substituting equation (9) into (8) gives

$$\frac{dN_\theta}{dr} - \frac{N_r - N_\theta}{r} + \frac{Eh}{2r} \left( \frac{dw}{dr} \right)^2 = 0. \quad (10)$$

Equations (1), (6) and (10) form three nonlinear differential equations with three unknowns  $N_r$ ,  $N_\theta$  and  $w$ .

The boundary conditions that must be satisfied are

$$\frac{dw}{dr} = 0, \quad u = r\epsilon_\theta = 0 \quad \text{at} \quad r = r_b \quad (11)$$

<sup>1</sup> Note that the assumption of plane sections remaining plane is applied here; shearing deformation is not taken into account.

<sup>2</sup>

$$\kappa_r = -\frac{(d^2w/dr^2)}{\sqrt{[1 + (dw/dr)^2]^3}} \sim -\frac{d^2w}{dr^2} \left[ 1 - \frac{3}{2} \left( \frac{dw}{dr} \right)^2 + \dots \right].$$

Since the second term is of cubic order, it will be dropped.

<sup>3</sup> More fully,

$$\epsilon_r = \frac{du}{dr} + \frac{1}{2} \left[ \left( \frac{du}{dr} \right)^2 + \left( \frac{dw}{dr} \right)^2 \right].$$

Since  $u \ll w$ , the term  $(du/dr)^2$  is negligible.

<sup>4</sup> Note that plane stress is assumed here.

and

$$\frac{dw}{dr} = 0, \quad u = r\epsilon_\theta = 0 \quad \text{at} \quad r = r_a. \quad (12)$$

The linear solution of the initial in-plane pre-stress resulting from a uniform tension load  $N_r = N_0$  applied at  $r = r_a$  and zero displacement  $u = 0$  at  $r = r_b$  can be shown to be

$$N_{r0} = C \left[ 1 + \beta^2 \left( \frac{r_a}{r} \right)^2 \right] \quad (13)$$

$$N_{\theta 0} = C \left[ 1 - \beta^2 \left( \frac{r_a}{r} \right)^2 \right] \quad (14)$$

where

$$\beta = \sqrt{\frac{1-\nu}{1+\nu}} \xi_b \quad (15)$$

$$C = \frac{N_0}{1+\beta^2} \quad (16)$$

and

$$\xi_b = \frac{r_b}{r_a}. \quad (17)$$

This was obtained from equations (1)–(7) by setting  $w = 0$  and  $p_0 = 0$ . Note that the stresses vary with  $r$ , instead of being constant as in the case of a uniform circular plate without a central boss.

After the pre-stress is applied, the plate is subjected to a transverse pressure  $p_0$ . The lateral loads are then decomposed as follows

$$N_r = N_{r0} + \tilde{N}_r \quad \text{and} \quad N_\theta = N_{\theta 0} + \tilde{N}_\theta. \quad (18)$$

The three nonlinear governing equations can then be rewritten as

$$\frac{d\tilde{N}_r}{dr} + \frac{\tilde{N}_r - \tilde{N}_\theta}{r} = 0 \quad (19)$$

$$\frac{d^3 w}{dr^3} + \frac{1}{r} \frac{d^2 w}{dr^2} - \frac{(\beta^2 r_a^2 C)/D + 1}{r^2} \frac{dw}{dr} - \frac{\tilde{N}_r + C}{D} \frac{dw}{dr} = \frac{p_0 r}{2D}. \quad (20)$$

$$\frac{d\tilde{N}_\theta}{dr} - \frac{\tilde{N}_r - \tilde{N}_\theta}{r} + \frac{Eh}{2r} \left( \frac{dw}{dr} \right)^2 = 0. \quad (21)$$

### 2.1. Non-dimensionalization

After Sheplak [8], the following characteristic quantities are introduced to non-dimensionalize equations (19)–(21)

$$\begin{aligned} \xi &= \frac{r}{r_a}, & ()' &= \frac{d}{d\xi}, & W &= \frac{w}{h}, & U &= \frac{u}{h} \\ \theta &= \frac{dW}{d\xi} = \frac{r_a}{h} \frac{dw}{dr}, & \Psi &= \frac{d\theta}{d\xi} = \frac{r_a^2}{h} \frac{d^2 w}{dr^2} \\ S_r &= \frac{\tilde{N}_r r_a^2}{Eh^3}, & S_\theta &= \frac{\tilde{N}_\theta r_a^2}{Eh^3}. \end{aligned} \quad (22)$$

The dimensionless forms of equations (19)–(21) are thus

$$\theta'' + \frac{\theta'}{\xi} - \left( k^2 + \frac{s^2 + 1}{\xi^2} \right) \theta - 12(1-\nu^2) S_r \theta = 6(1-\nu^2) P \xi \quad (23)$$

$$S_r' + \frac{S_r - S_\theta}{\xi} = 0 \quad (24)$$

and

$$S_\theta' - \frac{S_r - S_\theta}{\xi} = -\frac{1}{2\xi} \theta^2 \quad (25)$$

where  $k$  and  $s$  are dimensionless pre-tension parameters, and  $P$  is a loading parameter, which are defined as follows

$$k = \frac{r_a}{h} \sqrt{\frac{12(1-\nu^2)}{1+\beta^2} \frac{N_0}{Eh}}, \quad s = \beta k \quad (26)$$

$$\text{and} \quad P = \frac{p_0 r_a^4}{Eh^4}.$$

The corresponding dimensionless boundary conditions can be expressed as

$$\theta = 0, \quad S_\theta - \nu S_r = 0 \quad \text{at} \quad \xi = \xi_b = \frac{r_b}{r_a} \quad (27)$$

and

$$\theta = 0, \quad S_\theta - \nu S_r = 0 \quad \text{at} \quad \xi = \xi_a = 1. \quad (28)$$

Here, equations (1) and (9) are used to simplify equations (11) and (12).

In order to solve equations (23)–(25), we first substitute equation (24) into (25) to eliminate  $S_\theta$

$$\xi^2 S_r'' + 3\xi S_r' = -\frac{\theta^2}{2}. \quad (29)$$

Equation (23) can be rewritten as follows

$$\xi^2 \theta'' + \xi \theta' - \left[ (s^2 + 1) + \xi^2 (k^2 + 12(1-\nu^2) S_r) \right] \theta = 6(1-\nu^2) P \xi^3. \quad (30)$$

The boundary conditions which must be satisfied are

$$\theta = 0, \quad \xi S_r' + (1-\nu) S_r = 0 \quad \text{at} \quad \xi = \xi_b \quad (31)$$

and

$$\theta = 0, \quad \xi S_r' + (1-\nu) S_r = 0 \quad \text{at} \quad \xi = \xi_a. \quad (32)$$

A careful examination of the dimensionless equations (29)–(32) reveals that for a given material (more specifically,  $\nu$ ) the problem is characterized by three dimensionless parameters: the modified boss size  $\beta$ , the pre-tension  $k$ , and the loading  $P$ . Note that the modified boss size  $\beta$  plays roles only in defining the boundary conditions and in determining  $k$ . However, the effect of  $\beta$  on  $k$  is very limited. More interestingly, the thickness  $h$  plays no explicit role in the problem.

### 2.2. Stress calculation

After solving equations (29)–(32), we obtain the distributions of  $S_r$  and  $\theta$ . To calculate the stress fields, we define the dimensionless parameters of the in-plane pre-stress,  $S_{r0}$  and  $S_{\theta 0}$ , as follows

$$S_{r0} = \frac{N_{r0} r_a^2}{Eh^3} = \frac{k^2}{12(1-\nu^2)} \left[ 1 + \beta^2 \left( \frac{r_a}{r} \right)^2 \right] \quad (33)$$

$$S_{\theta 0} = \frac{N_{\theta 0} r_a^2}{Eh^3} = \frac{k^2}{12(1-\nu^2)} \left[ 1 - \beta^2 \left( \frac{r_a}{r} \right)^2 \right]. \quad (34)$$



Then the corresponding dimensionless radial stress can be expressed as

$$\sigma_r = S_{r0} + S_r - \frac{z}{(1-\nu^2)h} \left( \Psi + \frac{\nu\theta}{\xi} \right) \quad (35)$$

and the corresponding dimensionless circumferential stress can be written as

$$\sigma_\theta = S_{\theta0} + S_\theta - \frac{z}{(1-\nu^2)h} \left( \nu\Psi + \frac{\theta}{\xi} \right). \quad (36)$$

$S_\theta$  can be evaluated through equation (24) as follows

$$S_\theta = \xi S'_r + S_r. \quad (37)$$

### 3. Numerical integration

Finite difference methods provide an efficient means of solving the governing equations derived above. Previous work [8] on a similar configuration has identified the importance of thin boundary layers near clamped edges<sup>5</sup>. In order to resolve the boundary layers for the present case using numerical integration, two coordinate transformations, similar to those used in [8] were introduced to achieve better resolution near the boundary layer regions as follows.

For  $\xi_b \leq \xi \leq 0.5(\xi_a + \xi_b)$ ,

$$\xi = \xi_b + (\alpha - 1)(\xi_c - \xi_b) \frac{r - r^{\bar{\xi}}}{1 + r^{\bar{\xi}}}, \quad 0 \leq \bar{\xi} \leq 1 \quad (38)$$

where  $\alpha$  can be thought of as the coordinate stretching parameter and

$$r \equiv \left[ \frac{\alpha + 1}{\alpha - 1} \right].$$

For  $0.5(\xi_a + \xi_b) \leq \xi \leq \xi_a$ ,

$$\xi = \xi_a + (\alpha - 1)(\xi_c - \xi_a) \frac{r - r^{\bar{\xi}}}{1 + r^{\bar{\xi}}}, \quad 0 \leq \bar{\xi} \leq 1. \quad (39)$$

For  $0 \leq \eta \leq 0.5$ ,

$$\eta = 0.5 - 0.5\bar{\xi}$$

and for  $0.5 \leq \eta \leq 1$ ,

$$\eta = 0.5 + 0.5\bar{\xi}.$$

Conversely, for  $0.5(\xi_a + \xi_b) \leq \xi \leq \xi_a$  we have

$$\bar{\xi} = \frac{1}{\ln(r)} \frac{r(\alpha - 1)(\xi_c - \xi_a) - (\xi - \xi_a)}{(\alpha - 1)(\xi_c - \xi_a) + (\xi - \xi_a)}.$$

Setting  $m \equiv (\alpha - 1)(\xi_c - \xi_a)$  for convenience gives

$$\bar{\xi} = \frac{1}{\ln(r)} \ln \left[ \frac{mr - (\xi - \xi_a)}{m + (\xi - \xi_a)} \right].$$

For the derivatives, we have

$$\frac{d\bar{\xi}}{d\xi} = -\frac{1}{\ln(r)} \frac{m(1+r)}{[mr - (\xi - \xi_a)][m + (\xi - \xi_a)]} \quad (40)$$

<sup>5</sup> This will be explained later in section 4.

**Table 1.** Comparison of finite element and finite difference solutions.

	$r_b$ (mm)				
	0.0	0.2	0.4	0.6	0.75
Finite element ( $\mu\text{m}$ )	38.7	32.8	22.3	9.00	1.89
Finite difference ( $\mu\text{m}$ )	38.67	32.76	22.27	8.95	1.83

$$\frac{d^2\bar{\xi}}{d\xi^2} = \frac{1}{\ln(r)} \frac{m(1+r)(m_2 - 2\xi)}{([mr - (\xi - \xi_a)][m + (\xi - \xi_a)])^2} \quad (41)$$

where

$$m_1 = (mr + \xi_a)(m - \xi_a), \quad m_2 \equiv (mr - m + 2\xi_a).$$

For  $\xi_b \leq \xi \leq 0.5(\xi_a + \xi_b)$ ,  $r_a$  is replaced with  $r_b$  in the previous equations (40) and (41). In the present case, the stretching parameter  $\alpha = 1.05$  is used.

The governing equation in the transformed coordinate system can be written as follows

$$\begin{aligned} \xi^2(\bar{\xi}) \left( \frac{d\bar{\xi}}{d\xi} \right)^2 \frac{d^2\theta}{d\bar{\xi}^2} + \left[ \xi(\bar{\xi}) \frac{d\bar{\xi}}{d\xi} + \xi^2(\bar{\xi}) \left( \frac{d^2\bar{\xi}}{d\xi^2} \right) \right] \frac{d\theta}{d\bar{\xi}} \\ - [(s^2 + 1) + \xi^2(\bar{\xi})(k^2 + 12(1-\nu)S_r(\bar{\xi}))] \theta(\bar{\xi}) \\ = 6(1-\nu^2)P\xi^3(\bar{\xi}) \end{aligned} \quad (42)$$

and

$$\begin{aligned} \xi^2(\bar{\xi}) \left( \frac{d\bar{\xi}}{d\xi} \right)^2 \frac{d^2S_r}{d\bar{\xi}^2} + \left[ 3\xi(\bar{\xi}) \frac{d\bar{\xi}}{d\xi} + \xi^2(\bar{\xi}) \left( \frac{d^2\bar{\xi}}{d\xi^2} \right) \right] \frac{dS_r}{d\bar{\xi}} \\ = -\frac{\theta^2(\bar{\xi})}{2}. \end{aligned} \quad (43)$$

The boundary conditions to be satisfied are

$$\theta = 0, \quad \xi_b \frac{d\eta}{d\bar{\xi}} \frac{dS_r}{d\eta} + (1-\nu)S_r = 0 \quad \text{at } \eta = 0 \quad (44)$$

$$\theta = 0, \quad \xi_a \frac{d\eta}{d\bar{\xi}} \frac{dS_r}{d\eta} + (1-\nu)S_r = 0 \quad \text{at } \eta = 1. \quad (45)$$

The governing equations were implemented using a second-order central-difference scheme, while the boundary conditions were implemented by using second-order forward and backward differencing schemes, respectively. The under-relaxation technique was used to accelerate convergence. In the present case, the under-relaxation parameter  $\omega = 0.25$  is used.

In order to assess the accuracy of the finite difference schemes, a finite element model (FEM) was created (using the commercial FEM program ANSYS<sup>TM</sup> version 5.6, 400 three-dimensional (3D) axisymmetric solid elements with nonlinear analysis are used). The following material and geometrical parameters were used:  $E = 165$  GPa;  $\nu = 0.22$ ;  $r_a = 0.8$  mm;  $h = 10$   $\mu\text{m}$ ;  $p_0 = 1$  MPa;  $N_0 = 0$  and  $r_b = 0.0, 0.2, 0.4, 0.6$  and  $0.75$  mm, respectively<sup>6</sup>. These parameters are representative of the micro-hydraulic transducer element made of silicon described in [2]. Table 1 shows the comparison between the centre deflections obtained from FEM and those

<sup>6</sup> Here silicon, an anisotropic material, is modelled as an isotropic material for simplicity. For the particular case of a  $\langle 100 \rangle$  silicon wafer loaded axisymmetrically this is a valid assumption due to the invariance of the effective modulus  $E/(1-\nu)$ . For other orientations and non-axisymmetric loading this assumption only allows for an approximate solution [10, 11].

obtained from the present method. The two results agree with each other very well. Note that the largest discrepancy between the two analyses occurs when  $r_b$  approaches  $r_a$ . This is due to the neglect of the shear deformation in the derivation of the governing equations.

#### 4. Differences between membrane and thin plate behaviours

By definition, membranes can sustain only tensile stress, but no bending moment. In MEMS applications, unsupported thin films are typical examples. In contrast, plates can sustain both tensile stress and bending moments. In the limiting case of a very thin plate, the bending stress becomes insignificant compared to the tensile stress, and the membrane behaviour is recovered. In the context of designing MEMS, it is important to identify the transition from plate to membrane-dominated behaviour. When the thickness of the plate becomes very thin, the bending stress becomes insignificant compared to the tensile stress and the difference between a membrane and a thin plate diminishes. It is therefore interesting to compare the two results under this limit.

##### 4.1. Membrane response

The governing equations describing the response of the structure shown in figure 1, if it acts as a pure membrane, can be obtained by neglecting the shear  $Q_r$  and bending moments  $M_r$  and  $M_\theta$  in the derivation given in section 2. The resulting dimensionless equations can be written as follows

$$\left[ S_r + \frac{k^2 + (s/\xi)^2}{12(1-\nu^2)} \right] \theta = -\frac{1}{2} P \xi, \quad \xi_b \leq \xi \leq \xi_a \quad (46)$$

and

$$\xi^2 S_r'' + 3\xi S_r' = -\frac{\theta^2}{2} \quad (47)$$

where  $k$  and  $s$  are defined in equation (26).

The boundary conditions to be satisfied are

$$\xi S_r' + (1-\nu)S_r = 0 \quad \text{at} \quad \xi = \xi_b \quad (48)$$

and

$$\xi S_r' + (1-\nu)S_r = 0 \quad \text{at} \quad \xi = \xi_a. \quad (49)$$

Note that the boundary conditions  $\theta = 0$  at  $\xi = \xi_b$  and  $\xi_a$ , assumed in the plate case, no longer apply, since the membrane cannot sustain bending moments. The same solution algorithm used for the plate case can be applied to the membrane case.

Linearization of equation (46) indicates that a membrane without pre-tension ( $k, s = 0$ ) cannot sustain any lateral loading  $P$  under linearized theory.

For the purpose of illustration, a thin silicon plate ( $E = 165$  GPa,  $r_a = 0.8$  mm,  $t = 5$   $\mu$ m) without a rigid boss is chosen, i.e.  $r_b = 0$ , and a uniform transverse pressure  $p_0 = 2$  MPa is applied. (The corresponding dimensionless parameters are  $P = 7934$ ,  $\beta = 0$  and  $k = 0$ .) The problems shown in figure 3 are analysed. The balloon case is shown only for the demonstration of the constant curvature phenomenon. The deflection curves for both cases are plotted in figure 4. Away from the boundaries, the membrane under

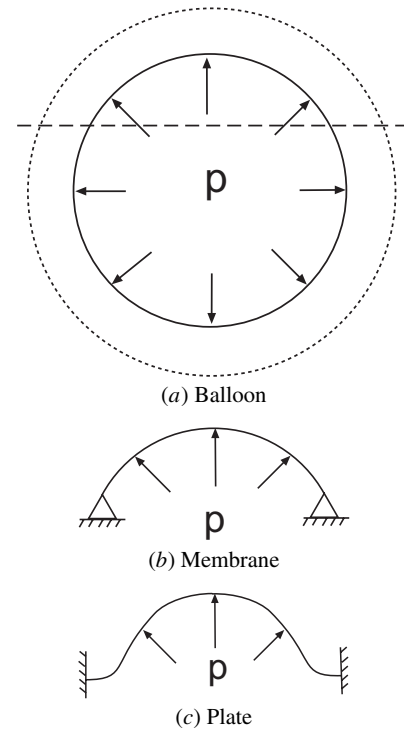


Figure 3. Comparison between balloon, membrane and plate cases.

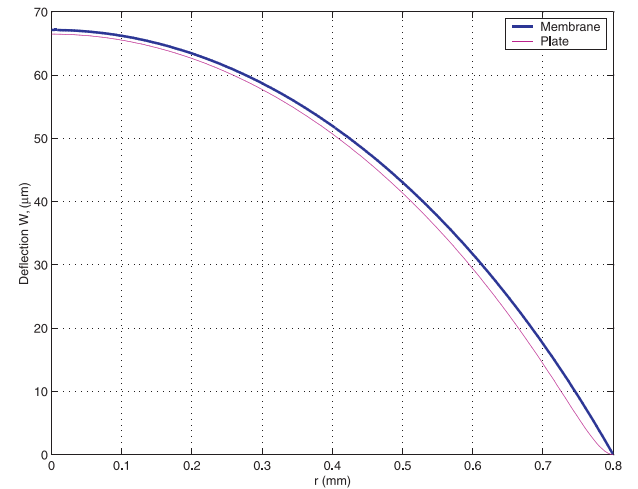
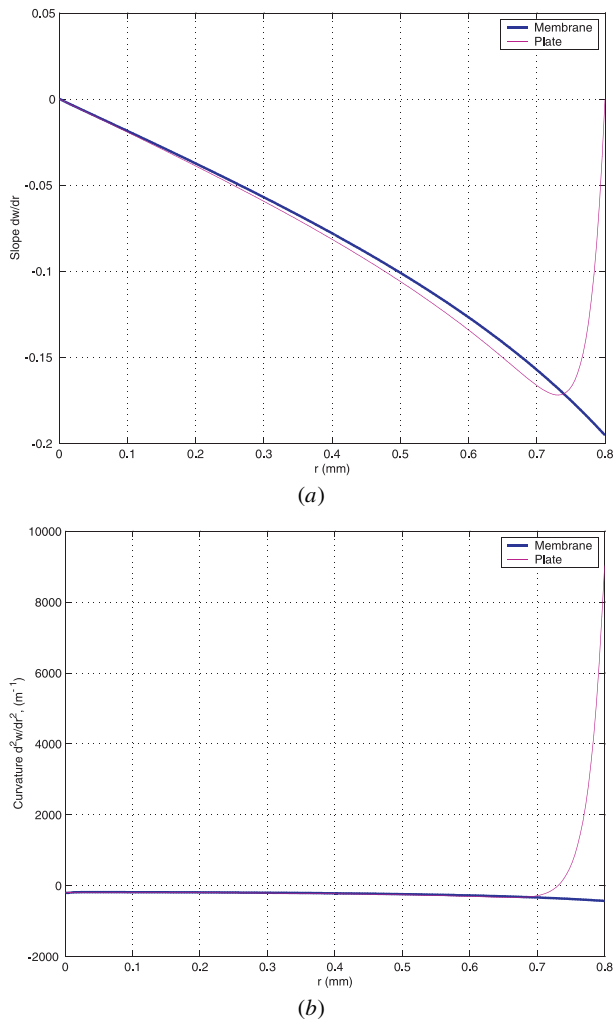


Figure 4. Comparison of the deflection curves between the membrane and plate cases.

constant pressure acts very similarly to the equivalent segment of a balloon with constant internal pressure. Furthermore, the extremely thin plate also behaves essentially as a membrane.

The effect of the boundary condition is seen more clearly in the slope and curvature of the structures shown in figure 3. A boundary layer exists near  $\xi = \xi_a$  as indicated in figure 5(a). This implies that the bending stress of the plate is significant only within the thin boundary layer where the two results differ. This effect is shown explicitly in figure 5(b). Note that in both cases the curvature is nearly constant everywhere away from the wall.

The in-plane stresses for the membrane and plate cases are shown in figure 6. Note that in both cases there is no in-plane pre-stress applied. Clearly the in-plane stresses



**Figure 5.** (a) Comparison of the slope curves between the membrane and plate cases. (b) Comparison of the curvature curves between the membrane and plate cases.

behave similarly to each other. This indicates that the in-plane stress dominates in the plate case. Interestingly, the in-plane stresses decrease with the increasing radial coordinate. The stresses become singular near the centre in both cases since the tangential slopes are horizontal at the centre.

## 5. Linear versus nonlinear analysis

As discussed in the introduction thin plate structures are often used in the large deflection regime. It is therefore important to understand the limitations of using linear solutions to predict their behaviour. It is very tempting to approximate this nonlinear deflection by superposing the linear bending deflection with the deflection caused by the in-plane pre-stress. Unfortunately, the deflection due to bending is very often overestimated by several orders of magnitude and the deflection due to in-plane pre-stress is always zero because of the lack of coupling between in-plane pre-stress and bending stress. Another possible way to approximate the nonlinear deflection is to make use of the linearized systems of equations (19)–(21). Unfortunately, this leads to the same difficulty mentioned above. The significant difference between

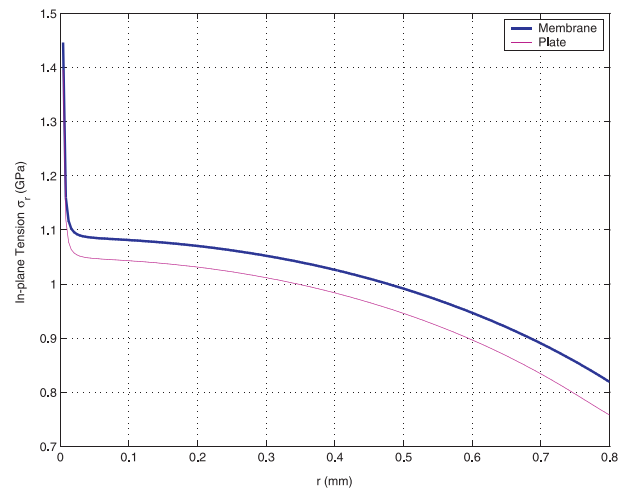


**Figure 6.** Comparison of the in-plane stresses between the membrane and plate cases.

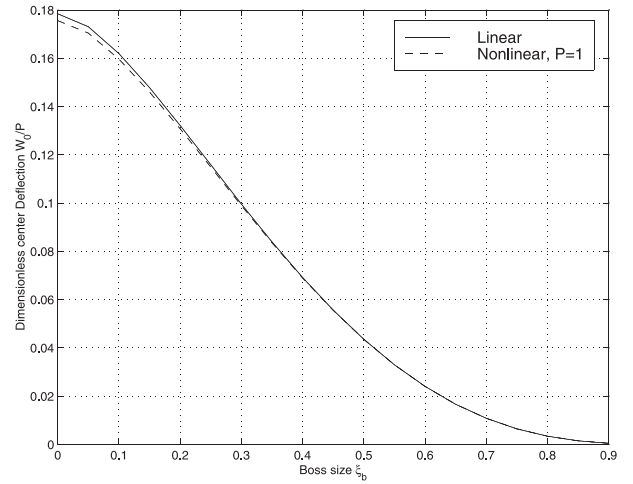


**Figure 7.** Centre deflection normalized by loading as a function of boss size.

the linear and nonlinear cases will be illustrated in the following discussion.

### 5.1. Effect of boss size

Results of the linear calculations of the centre deflection  $W_0$  for various boss sizes  $\xi_b$  are given in figure 7. The results based on nonlinear theory for  $P = 1$  are also plotted on the same diagram. The two curves are essentially the same, since the deflection under this pressure level is still much smaller than the plate thickness.

The centre deflections calculated using nonlinear theory versus boss size under various pressure levels are presented in figure 8. The corresponding results based on linear theory can be obtained by multiplying the deflection curve in figure 7 by  $P$ . As can be seen from figure 8, there are large differences corresponding to several orders of magnitude between the linear and nonlinear results. Obviously, the linear theory is not appropriate for predicting the behaviour of MEMS structures with large deflections.

Figure 9 shows the distribution of the normalized slope in a plate with  $\xi_b = 0.4$  under various pressure levels ( $P = 1-10^5$ ).

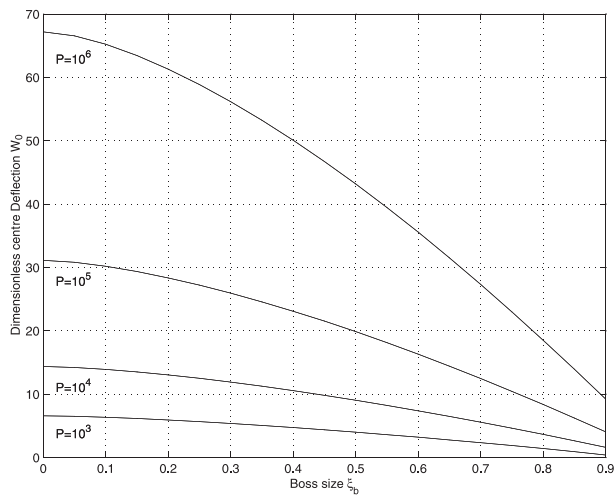


**Figure 8.** Dimensionless centre deflection as a function of boss size.

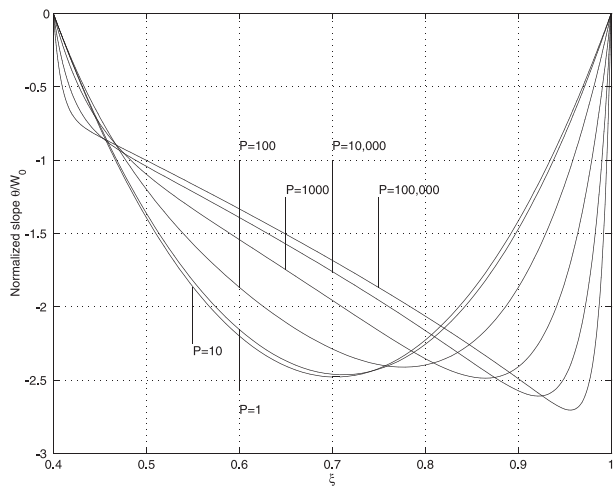


**Figure 9.** Normalized slope of the deflected shapes.

As shown in the diagram, the importance of the bending stress compared with the membrane stress decreases with the increasing pressure level. Bending effects are thus confined within a very thin boundary region when  $P \gg 1$ . Away from the boundary layers, the curve is almost straight which signifies a constant curvature behaviour. This indicates that the membrane stress dominates over this region.

The distributions of the deflection, slope, and curvature in the plates with various boss sizes under pressure  $P = 10^4$  are shown in figures 10–12. As indicated in figure 11, boundary layers form at each of the two edges as expected. The nearly constant curvature behaviour away from the boundary layers is illustrated in figure 12.

### 5.2. Effect of pre-tension

Pre-tension tends to stiffen the plate both in linear and nonlinear theory. This plays an important role in determining the plate behaviour. This is best illustrated in figure 13. When the pre-tension  $k$  is small, the pre-tension has little effect on the plate stiffness. This is shown by the flat regions in figure 13. When the pre-tension  $k$  is very large, the stiffness of the plate is increased significantly which in turn determines the

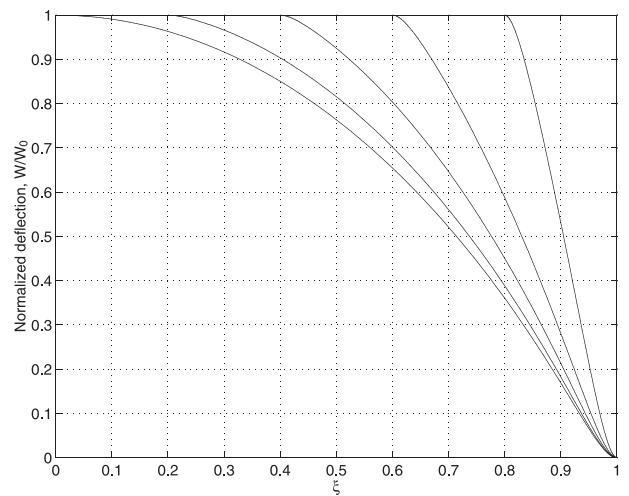


**Figure 10.** Normalized deflected shapes of the thin plate.

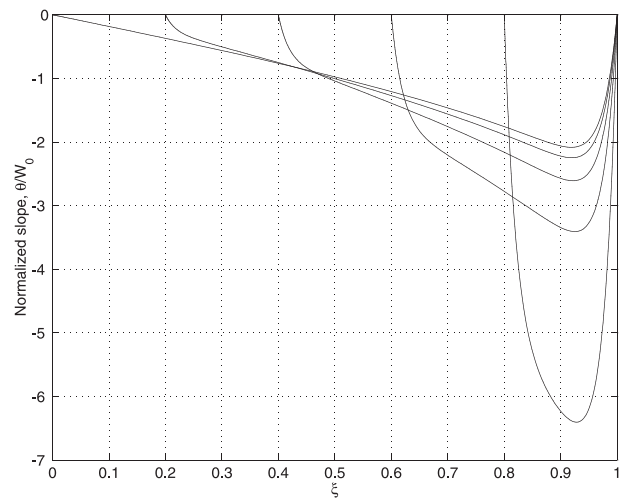


**Figure 11.** Normalized slope of the deflected plates.

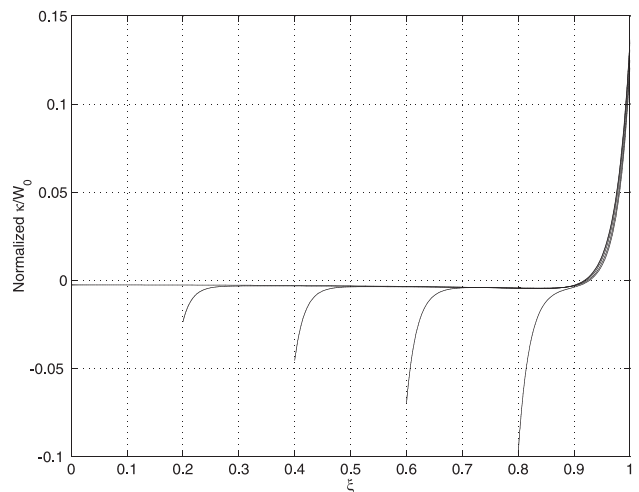


**Figure 12.** Normalized curvatures of the deflected plates.

deflection. This is confirmed by the significant reduction in the deflection in figure 13. Interestingly, the linear and nonlinear solutions coincide with each other in this limit. This indicates

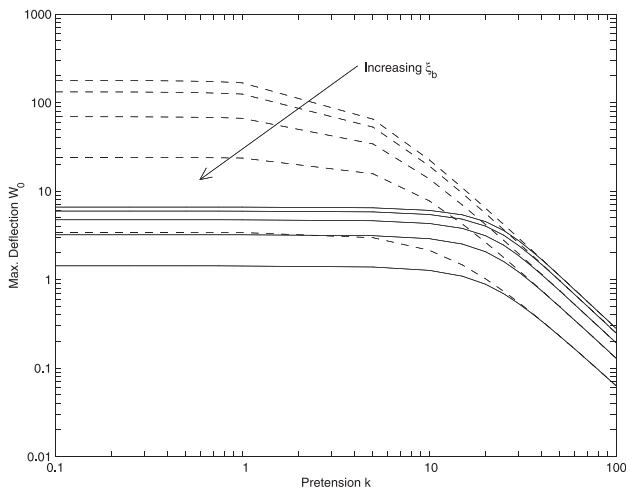


**Figure 13.** Centre deflection as a function of in-plane pre-tension  $k$  for different boss sizes  $\xi_b = 0, 0.2, 0.4, 0.6$  and  $0.8$ . Both the linear (dashed) and nonlinear (solid) cases are shown.

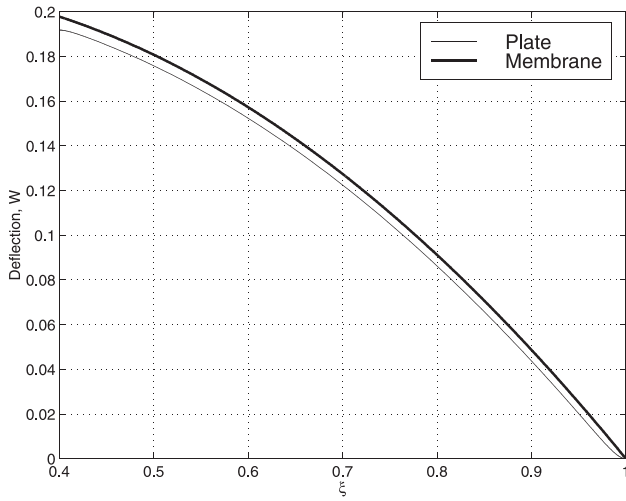


**Figure 14.** Comparison between the deflected shapes of the plate case and the membrane case.

that the pre-tension dominates over the plate behaviour and effectively causes the structure to behave more as a membrane, except in the boundary regime. This is demonstrated further in figures 14–16. Figure 14 shows the distribution of deflection of a thin plate with a rigid boss of size  $\xi_b = 0.4$  subjected to pressure  $P = 1000$  and pre-tension  $k = 100$ . Also shown in the same diagram is the deflection curve obtained by treating the plate as a hinged membrane (thick curve). Figures 15 and 16 show excellent agreement between the two models in the regions away from the boundary layers.

Another interesting observation, originally made by Sheplak and Dugundji [8], is that the centre deflection  $W_0$  of a thin plate without a rigid boss varies linearly with loading  $P$  when  $P$  is small and  $W_0 \sim P^{1/3}$  when  $P$  is large. For a large pre-tension  $k$ , the linear region grows reflecting the increased dominance of the membrane response. The same phenomenon is also observed in the cases of a plate with a rigid boss, as shown in figure 17.

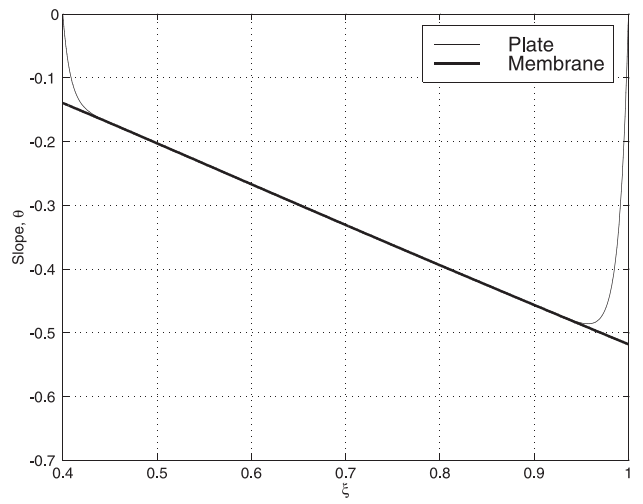


**Figure 15.** Comparison between the slopes of the plate case and the membrane case.

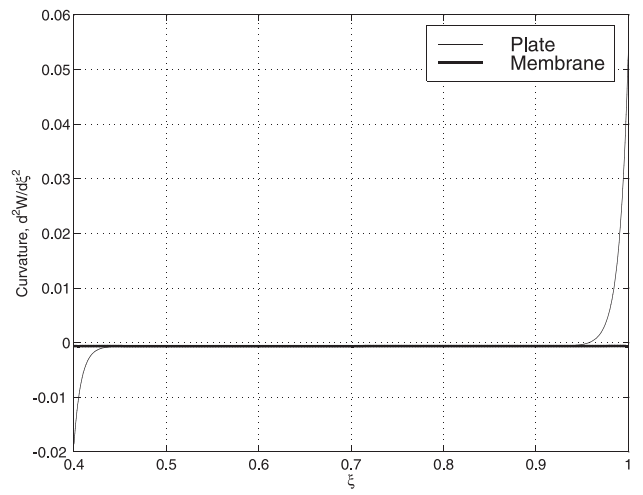


**Figure 16.** Comparison between the curvatures of the plate case and the membrane case.

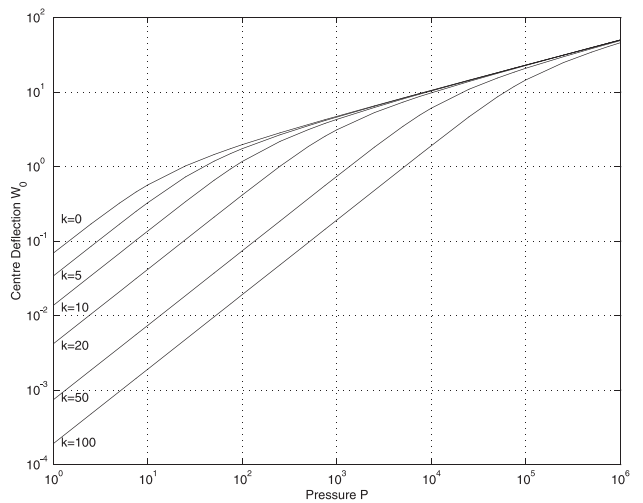


**Figure 17.** Centre deflection as a function of loading for in-plane pre-tension  $k = 0, 5, 10, 20, 50$  and  $100$  ( $\xi_b = 0.4$ ).

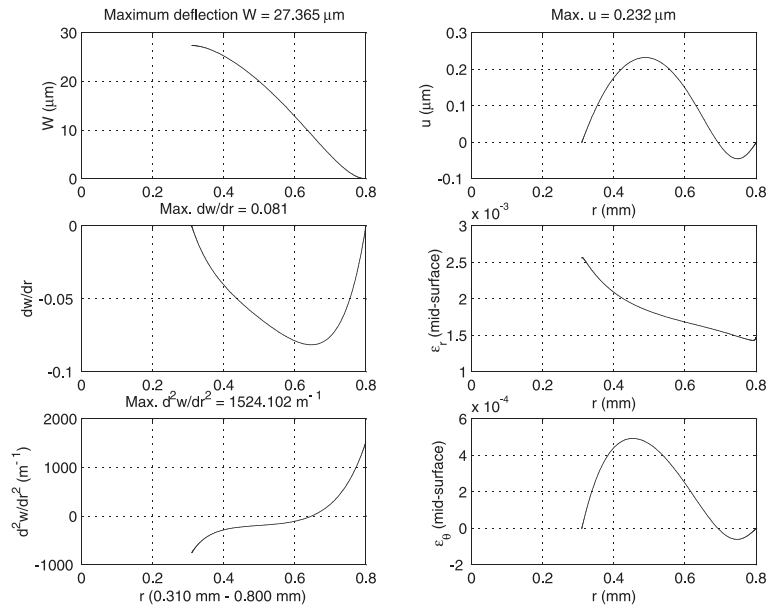


**Figure 18.** Displacement and strain fields for an annular plate with  $r_b = 0.31$  mm,  $r_a = 0.8$  mm,  $h = 10$   $\mu$ m, under pressure  $P = 1$  MPa.

## 6. Justification *a posteriori*

Several assumptions have been made in the previous analysis. Before concluding it is appropriate to evaluate these assumptions. In particular, the assumptions of  $u \ll w$  and the applicability of Hooke's law lie at the heart of this analysis. In order to investigate further, let us take the following examples:  $E = 165$  GPa,  $\nu = 0.22$ , and a failure stress  $\sigma_u = 1.0$  GPa (typical for a Si wafer),  $r_b = 0.31$  mm,  $r_a = 0.8$  mm,  $h = 10$   $\mu$ m,  $P = 1.0$  MPa. Figure 18 shows the displacement and strain fields of the corresponding structure. The maximum radial displacement  $u$  is  $0.232$   $\mu$ m and the maximum vertical deflection  $w$  is  $27.4$   $\mu$ m. Clearly,  $u \ll w$  is a valid assumption. It is also seen from the diagram that the maximum radial strain  $\epsilon_r = 2.5 \times 10^{-3}$  which is smaller than the ultimate strain  $\sigma_u/E = 6 \times 10^{-3}$ . Since silicon is a brittle material, this implies that Hooke's law is still valid. More specifically, this is a typical example of the large deformation but small strain problem.

## 7. Conclusion

The deflection of pre-tensioned annular plates containing rigid bosses has been examined. The conditions for the transition from plate behaviour under low loads to membrane behaviour under higher pressure and pre-tension have been identified. The presentation of the results in dimensionless form allows them to be readily applied to the design and analysis of structures of this configuration. The effect of large deflection and the influence of radial pre-stress are important factors that must be accounted for in the design of MEMS elements. The semi-analytical solutions presented herein have been shown to be accurate to within 3% for typical MEMS structures and materials given the assumptions on boundary conditions and material properties. Future work (currently undergoing) will provide experimental evidence to test these assumptions. The use of semi-analytical methods to derive these solutions allows

parametric studies to be conducted more efficiently than if finite element methods were used. Furthermore, the solutions can be incorporated directly into the dynamic simulations required to validate the operation of MEMS devices.

## Acknowledgments

This work has been sponsored by DARPA under grant No. DAAG55-98-1-0361 and ONR under grant No. N00014-97-1-0880. The authors would like to thank Professor John Dugundji for his generous help and insightful remarks.

## References

- [1] Huff M *et al* 1990 A pressure-balanced electrostatically-actuated microvalve *IEEE Solid-State Sensor and Actuator Workshop (Hilton Head, SC, USA)* pp 123–7
- [2] Hagood N *et al* 1999 Development of micro hydraulic transducer technology *Proc. 10th Int. Conf. on Adaptive Structures and Technologies (Paris)*
- [3] Schmidt M A 1998 Wafer-to-wafer bonding for microstructure *Proc. IEEE* **86** 1575–85
- [4] Timoshenko S and Woinowsky-Krieger S 1959 *Theory of Plates and Shells* 2nd edn (New York: McGraw-Hill)
- [5] Nadai A 1925 *Elastische Platten* (Berlin: Springer) p 288
- [6] Way S 1934 Bending of circular plates with large deflection *Trans. ASME* **56** 627–36
- [7] Voorthuyzen J A and Bergveld P 1984 The influence of tensile forces on the deflection of circular diaphragms in pressure sensors *Sensors Actuators A* **6** 201–13
- [8] Sheplak M and Dugundji J 1998 Large deflections of clamped circular plates under initial tension and transitions to membrane behavior *J. Appl. Mech.* **65** 107–15
- [9] Stoker J J 1968 *Nonlinear Elasticity* (London: Gordon and Breach)
- [10] Brantley W A 1973 Calculated elastic constants for stress problems associated with semiconductor devices *J. Appl. Phys.* **44** 534–5
- [11] Chen Kuo-Shen 1999 Materials characterization and structural design of ceramic micro turbomachinery *PhD Thesis MIT*

# Design, Modeling, Fabrication, and Testing of a Piezoelectric Microvalve for High Pressure, High Frequency Hydraulic Applications

by

David C. Roberts

S.B., Mechanical Engineering  
Massachusetts Institute of Technology, 1995

S.M., Mechanical Engineering  
Massachusetts Institute of Technology, 1998

SUBMITTED TO THE DEPARTMENT OF MECHANICAL ENGINEERING  
IN PARTIAL FULFILLMENT OF THE DEGREE OF

DOCTORATE OF PHILOSOPHY

at the

MASSACHUSETTS INSTITUTE OF TECHNOLOGY

February 2002

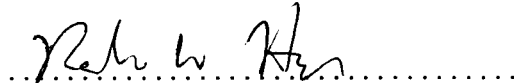
© 2002 Massachusetts Institute of Technology  
All rights reserved

Signature of Author .....



Department of Mechanical Engineering  
January 10, 2002

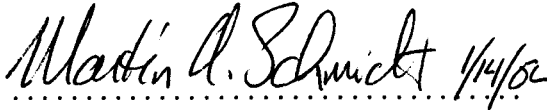
Certified by Doctoral Committee



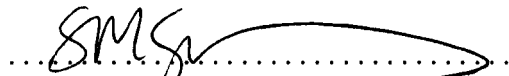
Nesbitt W. Hagood (Co-Chair), Associate  
Professor of Aeronautics and Astronautics



David L. Trumper (Co-Chair), Associate  
Professor of Mechanical Engineering



Martin A. Schmidt  
Professor of Electrical Engineering



S. Mark Spearing, Associate  
Professor of Aeronautics and Astronautics

Accepted by .....



Professor Ain Sonin  
Chairman, Department Graduate Committee





# Design, Modeling, Fabrication, and Testing of a Piezoelectric Microvalve for High Pressure, High Frequency Hydraulic Applications

by

David C. Roberts

Submitted to the Department of Mechanical Engineering on January 10, 2002, in partial fulfillment of the requirements for the Degree of Doctor of Philosophy in Mechanical Engineering.

## Abstract

A piezoelectrically-driven hydraulic amplification microvalve for use in high specific power hydraulic pumping applications was designed, fabricated, and experimentally characterized. High frequency, high force actuation capabilities were enabled through the incorporation of one or more bulk piezoelectric material elements beneath a micromachined annular tethered-piston structure. An hydraulic amplification mechanism was employed to amplify the limited stroke of this piezoelectrically-driven piston structure to a significantly larger motion (40-50x) of a micromachined valve membrane with attached valve cap. This valve cap was actuated through its stroke to open and close against a fluid orifice. These design features enabled the valve device to simultaneously meet a set of high frequency (1-10kHz), high pressure(0.1-1MPa), and large stroke (15-40 $\mu$ m) requirements that had not previously been satisfied by other microvalves presented in the literature.

This research was carried out through a series of modeling, design, fabrication, assembly, and experimental testing tasks. Linear and non-linear modeling tools characterizing the structural deformations of the active valve sub-systems were developed. These tools enabled accurate prediction of real-time stresses along the micromachined valve membrane structure during deflection into its non-linear large-deflection regime. A systematic design procedure was developed to generate an active valve geometry to satisfy membrane stress limitations and valve power consumption requirements set forth by external hydraulic system performance goals. Fabrication challenges, such as deep-reactive ion etching (DRIE) of the drive element and valve membrane structures, wafer-level silicon-to-silicon fusion bonding and silicon-to-glass anodic bonding operations, preparation and integration of piezoelectric material elements within the micromachined tethered piston structure, die-level assembly and bonding of silicon and glass dies, and filling of degassed fluid within the hydraulic amplification chamber were overcome.

The active valve structural behavior and flow regulation capabilities were evaluated over a range of applied piezoelectric voltages, actuation frequencies, and differential pressures across the valve. For applied piezoelectric voltages up to 500Vpp at 1kHz, the valve devices demonstrated amplification ratios of drive element deflection to valve cap deflection of 40-50x. These amplification ratios correlated within 5 – 10% of the model expectations. Flow regulation experiments proved that a peak average flow rate through the device of 0.21mL/s under a 1kHz sinusoidal drive voltage of 500Vpp, with valve opening of 17 $\mu$ m, against a differential pressure of 260kPa could be obtained. Tests revealed that fluid-structural interactions between the valve cap and membrane components and flow instabilities (due to transition between the laminar and turbulent flow regimes through the valve orifice) limited the valve performance capabilities.

Thesis Supervisor: Dr. Nesbitt W. Hagood

Title: Associate Professor of Aeronautics and Astronautics



# Acknowledgements

This research work was sponsored by DARPA under Grant #DAAG55-98-1-0361  
and by ONR under Grant #N00014-97-1-0880.

The research presented in this thesis could not have been accomplished without the generous support and hard work of a large group of individuals. First and foremost, I would like to thank my advisor, Dr. Nesbitt Hagood, for providing the programmatic resources and support for this research, as well as the numerous opportunities to present this work within the MIT community and at academic conferences. Additionally, his ability to always be one step ahead of the game kept me sharp and forced me to defend and clearly justify all of the decisions made along the path of my PhD work. I would also like to acknowledge my doctoral committee members, Dr. Martin Schmidt, Dr. Mark Spearing, and Dr. David Trumper, for their advice and direction during this work. These interactions have helped me to mature, both intellectually and personally. Additionally, I would like to acknowledge Dr. Kenneth Breuer, at Brown University, for his very helpful guidance on microscale fluid related issues.

I owe a great deal of thanks to Dr. Richard Mlcak, at Boston Microsystems, Inc, for his introduction to the world of MEMS, through initial piezoelectric material integration studies at the onset of the MHT research program four years ago and his continued support in the area of microscale fluid filling and sealing. Additionally, instrumental to the accomplishments embodied within this work were Dr. Laxman Saggere, for his advice on modeling assumptions within my active valve optimization code; Kevin Turner, for his contributions in the area of eutectic bonding; Blair Connelly, for her hard work in the development of testing apparatus for use with the laser vibrometer system used in this work; David Robertson, for his lab organization and debugging activities; Tim Glenn, for his generous support in providing exceptional renderings of MEMS devices for the MHT program; and Seward (Chip) Pulitzer, for his initial system modeling work at the beginning of the program.

Jorge Carretero and Onnik Yaglioglu have been sources of continual support in the development of fluid flow models and full system-level simulations for this active valve device and for MHT systems, in general. Dr. Yu-Hsuan Su was essential to the development of the finite-difference numerical modeling scheme, which serves as the backbone of the non-linear large deflection valve membrane code presented in Chapter 2 of this thesis. Dr. Hanqing Li deserves an unbelievable amount of recognition for his dedication in and out of the cleanroom, providing the MHT program with repeatable and robust fabrication processes for the creation of etched silicon wafers and silicon-glass bonded stacks. Lastly, from the programmatic side of things, I have to give a great deal of thanks to Lodewyk Steyn, who throughout his time on the MHT program, has performed duties above and beyond what were required of him in an effort to unselfishly move the program forward. Without his dedication, especially on the experimental testing side of the program, the validation of fluid-filled active valve devices would not have been accomplished in such an aggressive time frame.

Finally, I would like to thank my family. None of this work could have been accomplished without the positive support from my Mom, Dad, and brother Will. Most importantly, I have to thank my wife, Heather, for her unbelievable support and patience through four and half years of sometimes frustrating, sometimes exhilarating, and all the time stressful research work.



# Contents

<b>1</b>	<b>Introduction</b>	<b>25</b>
1.1	Motivation . . . . .	25
1.2	Overview of Previous Microvalve Technology . . . . .	28
1.3	Concept . . . . .	33
1.4	Challenges . . . . .	35
1.4.1	Modeling and Design Challenges . . . . .	36
1.4.2	Device Fabrication, Assembly, and Testing Challenges . . . . .	37
1.5	Objectives . . . . .	39
1.6	Approach . . . . .	39
1.7	Thesis Executive Summary . . . . .	41
<b>2</b>	<b>Active Valve Linear Model</b>	<b>47</b>
2.1	Valve Geometry and Modeling Procedure . . . . .	47
2.2	Overview of Linear Plate Theory . . . . .	48
2.2.1	Deflections Due to Bending . . . . .	49
2.2.2	Deflections Due to Shearing . . . . .	50
2.2.3	Combined Deflection Due to Bending and Shearing . . . . .	51
2.2.4	Comparison of Bending/Shearing Deflections . . . . .	51
2.3	Detailed Structural Modeling . . . . .	52
2.3.1	Piezoelectric Material Behavior . . . . .	52
2.3.2	Drive Element Piston and Tether Behavior . . . . .	53
2.3.3	Bottom Structural Compliance . . . . .	57
2.3.4	Fluid Compressibility . . . . .	58
2.3.5	Top Structural Compliance . . . . .	58
2.3.6	Valve Cap and Membrane Behavior . . . . .	59
2.4	Full Active Valve Linear Model . . . . .	61
2.5	Impact of Multiple Piezoelectric Cylinders . . . . .	62
2.5.1	Finite-Element Analysis of Piston . . . . .	62

2.5.2	Finite-Element Analysis of Bottom Plate . . . . .	65
2.6	Further Modeling Issues . . . . .	66
2.7	Conclusions . . . . .	67
<b>3</b>	<b>Non-Linear Deformation of the Valve Cap and Membrane</b>	<b>69</b>
3.1	Introduction . . . . .	69
3.2	Plate Geometry . . . . .	70
3.3	Theory . . . . .	70
3.3.1	Assumptions . . . . .	70
3.3.2	Equilibrium Equations . . . . .	71
3.3.3	Geometric Compatibilities . . . . .	72
3.3.4	Constitutive Laws . . . . .	73
3.3.5	Governing Equations . . . . .	73
3.3.6	In-Plane Prestress . . . . .	74
3.3.7	Non-Dimensionalized Governing Equations . . . . .	76
3.3.8	Finite-Difference Implementation . . . . .	78
3.3.9	Post-Processing Calculations . . . . .	81
3.4	Results of Numerical Code . . . . .	83
3.4.1	Loading: $P_1 = P_2 = 0$ , $P_3 = 100kPa$ , $N_o = 0$ . . . . .	84
3.4.2	Loading: $P_1 = 2.90MPa$ , $P_2 = 0$ , $P_3 = 1.30MPa$ , $N_o = 0$ . . . . .	84
3.4.3	Loading: $P_1 = P_2 = 0$ , Varying $P_3$ , $N_o = 0$ . . . . .	85
3.4.4	Loading: $P_1 = P_2 = 0$ , $P_{HAC} = 100kPa$ , Varying $N_o$ . . . . .	86
3.5	Matlab Non-Linear Tools . . . . .	87
3.6	Conclusions . . . . .	89
<b>4</b>	<b>Active Valve Non-Linear Model and Simulation</b>	<b>91</b>
4.1	Quasi-Static Active Valve Model . . . . .	91
4.2	Accuracy of Quasi-Static Model . . . . .	93
4.2.1	Assumptions in Model . . . . .	93
4.2.2	FEM Model Geometries and Correlation Procedure . . . . .	94
4.2.3	Model Correlation Procedure . . . . .	95
4.2.4	Valve Geometry . . . . .	96
4.2.5	Model Correlation . . . . .	97
4.3	Finite-Element Resonant Behavior . . . . .	101
4.4	Dynamic Active Valve Simulation . . . . .	102
4.4.1	Linear Matrix Relations . . . . .	102
4.4.2	Non-Linear Look-Up Tables . . . . .	103
4.4.3	Piston and Valve Cap Dynamics . . . . .	104

4.5	Conclusions . . . . .	106
<b>5</b>	<b>Active Valve Design Procedure</b>	<b>109</b>
5.1	Valve Requirements in Generic MHT System . . . . .	110
5.2	Modeling of External Hydraulic System . . . . .	111
5.2.1	MHT Chamber Stiffness . . . . .	112
5.2.2	Valve Channel Inertial Effects . . . . .	113
5.2.3	Valve Orifice Flow Relations . . . . .	113
5.2.4	Chamber Filling Simulation Tool . . . . .	116
5.3	Systematic Design Procedure . . . . .	118
5.3.1	Overview . . . . .	118
5.3.2	System Requirements . . . . .	119
5.3.3	Step 1: Design of Valve Cap . . . . .	119
5.3.4	Step 2: Design of Valve Membrane . . . . .	121
5.3.5	Step 3: Design of Piezoelectric Drive Element . . . . .	122
5.4	Design Freedoms Within Procedure . . . . .	125
5.4.1	Design Freedom: $Z_{vc,stroke}$ . . . . .	125
5.4.2	Design Freedom: $t_{vm}$ . . . . .	126
5.5	Power Consumption in Active Valve . . . . .	134
5.5.1	Overview of Energy/Power Consumption . . . . .	134
5.5.2	Benefit of Multiple Valve Heads . . . . .	135
5.6	Results of Systematic Design Procedure . . . . .	138
5.7	Correlation With Dynamic Simulation . . . . .	142
5.8	Conclusions . . . . .	145
<b>6</b>	<b>Device Fabrication and Preparation for Testing</b>	<b>147</b>
6.1	Introduction . . . . .	147
6.2	Fabrication Challenges and Procedures . . . . .	148
6.2.1	Etching of Tethered Drive Element and Valve Membranes . . . . .	149
6.2.2	Wafer-Level Bonding . . . . .	151
6.2.3	Integration of Bulk Piezoelectric Elements . . . . .	152
6.2.4	Die-Level Assembly and Bonding . . . . .	157
6.2.5	Fluid Filling/Sealing of HAC . . . . .	161
6.3	Sub-Component Testing Plan . . . . .	165
6.3.1	Piezoelectric Drive Element . . . . .	165
6.3.2	Valve Cap and Membrane . . . . .	166
6.3.3	Full Active Valve . . . . .	167
6.4	Testing Apparatus . . . . .	167

6.4.1	Laser Vibrometer System . . . . .	167
6.4.2	Fluids Test-Rig . . . . .	168
6.5	Conclusions . . . . .	168
<b>7</b>	<b>Sub-Component Study: Piezoelectric Drive Element</b>	<b>173</b>
7.1	Objectives . . . . .	173
7.2	Device Test-Plan . . . . .	174
7.2.1	1st Generation Devices . . . . .	174
7.2.2	2nd Generation Device . . . . .	176
7.3	Device Assembly . . . . .	177
7.4	Testing Procedure . . . . .	180
7.5	Experimental Results . . . . .	180
7.5.1	1st Generation Devices . . . . .	180
7.5.2	2nd Generation Device . . . . .	196
7.6	Conclusions . . . . .	200
<b>8</b>	<b>Sub-Component Study: Valve Cap and Membrane</b>	<b>203</b>
8.1	Objectives . . . . .	203
8.2	Device Test-Plan . . . . .	204
8.2.1	Geometry . . . . .	204
8.2.2	Device Assembly . . . . .	205
8.2.3	Testing Procedure . . . . .	205
8.3	Theoretical Predictions . . . . .	206
8.3.1	1st Modeling Procedure: Numerical Non-linear Deflection Code . . . . .	206
8.3.2	2nd Modeling Procedure: Finite-element Code . . . . .	207
8.4	Experimental Results . . . . .	213
8.4.1	Fillet Radius Inspection . . . . .	213
8.4.2	Pressure-Deflection Results . . . . .	213
8.5	Conclusions . . . . .	214
<b>9</b>	<b>Active Valve Testing</b>	<b>217</b>
9.1	Objectives . . . . .	217
9.2	Device Test-Plan . . . . .	218
9.2.1	Geometry . . . . .	218
9.2.2	Plan of Study . . . . .	218
9.3	Experimental Testing Section 1: Active Valve Structural Performance . . . . .	220
9.3.1	Testing Section 1: Active Valve Structural Performance . . . . .	220
9.3.2	Testing Section 2: Active Valve Fluid Flow Regulation . . . . .	252



9.4	Conclusions . . . . .	276
<b>10</b>	<b>Conclusions and Recommendations</b>	<b>279</b>
10.1	Summary and Conclusions . . . . .	279
10.1.1	Thesis Summary . . . . .	279
10.1.2	Thesis Contributions . . . . .	284
10.2	Recommended Further Work and the Future of MHTs . . . . .	285
10.2.1	Redesign for Enhanced Operational Frequency . . . . .	286
10.2.2	Understanding of Flow Induced Structural Instabilities . . . . .	287
10.2.3	Materials Characterization . . . . .	290
10.2.4	Microfabrication Issues . . . . .	291
10.2.5	Future of MHTs . . . . .	292
<b>A</b>	<b>Support Documentation for Active Valve Linear Model</b>	<b>295</b>
A.1	ChapterExample.mws . . . . .	296
A.2	FullActiveValve(LINEAR).mws [see Section 2.4] . . . . .	299
<b>B</b>	<b>Support Documentation for Non-Linear Valve Cap/Membrane</b>	<b>313</b>
B.1	NLValveCapMembrane-CaseA.m [see Section 3.5] . . . . .	314
B.2	NLValveCapMembrane-CaseB.m [see Section 3.5] . . . . .	318
B.3	NLValveCapMembrane-CaseC.m [see Section 3.5] . . . . .	322
<b>C</b>	<b>Support Documentation for Full Non-Linear Active Valve Model</b>	<b>327</b>
C.1	FullActiveValve(Non-Linear).mws [Section 4.1] . . . . .	328
C.2	NLActiveValveMatlab.m [Section 4.1] . . . . .	334



# List of Figures

1.1	Upper bound on specific work vs. frequency for various actuation media . . . . .	27
1.2	Generic block diagrams of Micro-Hydraulic Transducer systems . . . . .	28
1.3	Selected thermal, electrostatic, and electromagnetic microvalves previously re- ported in the literature . . . . .	29
1.4	Selected piezoelectrically-driven microvalves previously reported in the literature	31
1.5	3-D schematic of the piezoelectrically driven hydraulic amplification microvalve .	34
1.6	Schematic of the fabricated multi-layer active valve structure . . . . .	36
1.7	Schematic of fabricated multi-layer MHT actuator device . . . . .	37
1.8	Active valve sub-component fabrication and testing plan . . . . .	41
1.9	Photograph of a 9-layer piezoelectrically-driven hydraulic amplification microvalve.	42
2.1	2-D schematic of the piezoelectrically-driven hydraulic amplification microvalve. .	48
2.2	Linear plate theory for a generic circular plate. . . . .	49
2.3	Bending and shearing contributions to plate deformation . . . . .	52
2.4	Modeling of the piezoelectric material element . . . . .	53
2.5	Modeling of the drive element tethered piston structure . . . . .	54
2.6	Modeling of the bottom structural plate . . . . .	58
2.7	Modeling of the top structural plate . . . . .	59
2.8	Linear modeling of the valve cap and membrane structure . . . . .	59
2.9	Simplified schematic of the valve membrane structure . . . . .	60
2.10	Blow-up view of the modeled components in the microvalve . . . . .	61
2.11	Finite-element schematics of the drive element piston . . . . .	63
2.12	Compliance coefficients for the drive element piston with multiple piezoelectric cylinders . . . . .	64
2.13	Finite-element schematics of the bottom plate structure . . . . .	65
2.14	Compliance coefficients of the bottom plate structure with multiple piezoelectric cylinders . . . . .	66
3.1	Simplified schematic of the valve membrane structure . . . . .	70

3.2	Force and moment diagrams for a plate section . . . . .	71
3.3	Schematic of a pretensioned annular plate . . . . .	75
3.4	Coordinate transformation used within numerical code . . . . .	79
3.5	Pressure loading terminology on an annular plate . . . . .	83
3.6	Deflection of a thin annular plate under loading scenario 1 . . . . .	84
3.7	Deflection of a thin annular plate under loading scenario 2 . . . . .	86
3.8	Deflection of a thin annular plate under loading scenario 3 . . . . .	87
3.9	Deflection of a thin annular plate under loading scenario 4 . . . . .	88
3.10	Numerical code tools to be used throughout thesis . . . . .	89
4.1	Quasi-static non-linear active valve model overview . . . . .	92
4.2	Finite-element model of the active valve without fillet radii . . . . .	94
4.3	Finite-element model of the active valve with fillet radii . . . . .	95
4.4	Boundary conditions imposed in the active valve finite-element models . . . . .	96
4.5	Monitored variables in the active valve models . . . . .	97
4.6	Finite-element stresses predicted in the active valve device . . . . .	100
4.7	Finite-element modal behavior of the active valve . . . . .	102
4.8	Dynamic simulation architecture of the active valve . . . . .	103
4.9	Look-up tables describing valve membrane large deflection behavior . . . . .	104
4.10	Piston dynamics included in the simulation . . . . .	105
4.11	Valve cap dynamics included in the simulation . . . . .	105
5.1	Schematic of a generic MHT power harvesting device . . . . .	110
5.2	Filling/evacuation of the harvesting chamber through the valves . . . . .	112
5.3	Modeling of the valve orifice . . . . .	113
5.4	Look-up tables for valve orifice coefficients . . . . .	115
5.5	Simulation architecture for chamber filling through active valve . . . . .	117
5.6	Simulation architecture for active valve orifice and channel . . . . .	117
5.7	Flowchart for the quasi-static systematic active valve design procedure . . . . .	118
5.8	Chamber filling as a function of valve cap radius . . . . .	120
5.9	Design plots for the valve membrane . . . . .	121
5.10	Modeling of the active valve structure in an impedance match condition . . . . .	123
5.11	Drive element behavior design plots . . . . .	124
5.12	Valve cap size vs. imposed valve cap stroke . . . . .	126
5.13	Valve membrane size and thickness vs. imposed valve cap stroke: Case 1 . . . . .	127
5.14	Maximum valve membrane stress vs. membrane radius: Case 1 . . . . .	128
5.15	Example valve membrane deflection plots: Case 1 . . . . .	129
5.16	Valve membrane size and thickness vs. imposed valve cap stroke: Case 2 . . . . .	130

5.17	Maximum valve membrane stress vs. membrane radius: Case 2 . . . . .	131
5.18	Example valve membrane deflection plots: Case 2 . . . . .	133
5.19	Hysteretic energy loss in active valve . . . . .	134
5.20	Full quasi-static design procedure results: Part 1 . . . . .	139
5.21	Full quasi-static design procedure results: Part 2 . . . . .	140
5.22	Full quasi-static design procedure results: Part 3 . . . . .	141
5.23	Simulation architecture for the filling/evacuation of the MHT system . . . . .	143
5.24	System simulation plots using the designed active valve geometry . . . . .	144
6.1	Schematic cross-section of a multi-layer MHT/active valve structure . . . . .	148
6.2	DRIE etch characteristics of a drive element piston and tether . . . . .	149
6.3	SEM etch images of a drive element piston and tether . . . . .	150
6.4	Wafer-level silicon-silicon fusion and silicon-pyrex anodic bond steps . . . . .	151
6.5	Piezoelectric material surface roughness scans . . . . .	153
6.6	Piezoelectric thin-film eutectic alloy composition . . . . .	154
6.7	Precision micrometer measurement of a piezoelectric element thickness . . . . .	155
6.8	Piezoelectric element tolerancing within drive element structure . . . . .	156
6.9	Die-level bonding procedure for active valve device . . . . .	158
6.10	Die-level alignment and bonding jigs . . . . .	160
6.11	Electrical contact to an active valve chip for anodic bonding . . . . .	160
6.12	Fluid filling apparatus to fill active valve devices . . . . .	161
6.13	Fluid filling schematic of component connections . . . . .	162
6.14	Schematic of the high resistance fluid channel between the HAC and an external bias pressure . . . . .	163
6.15	Model of the high resistance fluid channel between the HAC and an external bias pressure . . . . .	164
6.16	Active valve sub-component fabrication and testing plan . . . . .	165
6.17	Drive element sub-component test structures . . . . .	166
6.18	Valve membrane sub-component study and full active valve study . . . . .	167
6.19	Fluids test-rig for testing of the active valve and its sub-components . . . . .	169
7.1	3-D schematic of a piezoelectric drive element device . . . . .	174
7.2	Overview of the drive element sub-component test plan . . . . .	175
7.3	Drive element geometries and piezoelectric element layout . . . . .	176
7.4	Exploded view of drive element structure . . . . .	177
7.5	Assembly of a piezoelectric drive element device . . . . .	178
7.6	Photographs of fabricated 1st-generation drive element device . . . . .	179
7.7	Photograph of an assembled 2nd-generation drive element device . . . . .	179

7.8	Measurement points on drive element piston surface using scanning laser vibrometer	181
7.9	Inspection of fillet radii on 1st-generation devices . . . . .	182
7.10	Piezoelectric material characterization of representative elements . . . . .	183
7.11	Device 1 transfer functions of piston velocity versus frequency . . . . .	185
7.12	Device 1 modal behavior . . . . .	186
7.13	Vibrometer scan images of Device 1 low-frequency 15kHz displacement profile . .	186
7.14	Device 1 displacement time histories for a sinusoidal drive voltage of $500V \pm 500V$ at $f = 15kHz$ . . . . .	187
7.15	Device 1 displacement time histories for a sinusoidal drive voltage of $500V \pm 500V$ at $f = 7kHz$ . . . . .	187
7.16	Device 1 piston center displacement versus applied voltage at 100Hz . . . . .	187
7.17	Device 2 transfer functions of piston velocity versus frequency . . . . .	189
7.18	Device 2 modal behavior . . . . .	190
7.19	Vibrometer scan images of Device 2 low-frequency 15kHz displacement profile . .	190
7.20	Device 2 displacement time histories for a sinusoidal drive voltage of $500V \pm 500V$ at $f = 15kHz$ . . . . .	191
7.21	Device 2 displacement time histories for a sinusoidal drive voltage of $500V \pm 500V$ at $f = 7kHz$ . . . . .	191
7.22	Device 2 piston center displacement versus applied voltage at 100Hz . . . . .	191
7.23	Device 3 transfer functions of piston velocity versus frequency . . . . .	193
7.24	Vibrometer scan images of selected Device 4 modal behavior . . . . .	194
7.25	Device 3 ANSYS finite-element model prediction for 1st mode . . . . .	194
7.26	Vibrometer scan images of Device 3 low-frequency 15kHz displacement profile . .	194
7.27	Device 3 displacement time histories for a sinusoidal drive voltage of $500V \pm 500V$ at $f = 15kHz$ . . . . .	195
7.28	Device 3 displacement time histories for a sinusoidal drive voltage of $500V \pm 500V$ at $f = 7kHz$ . . . . .	195
7.29	Device 3 piston center displacement versus applied voltage at 100Hz . . . . .	195
7.30	Device 4 transfer functions of piston velocity versus frequency . . . . .	197
7.31	Vibrometer scan images of selected Device 4 modal behavior . . . . .	198
7.32	Vibrometer scan images of Device 4 low-frequency 15kHz displacement profile . .	198
7.33	Device 4 displacement time histories for a sinusoidal drive voltage $500V \pm 500V$ at $f = 15kHz$ . . . . .	199
7.34	Device 4 piston center displacement versus applied voltage at 100Hz . . . . .	199
8.1	2-D schematic of a valve cap and membrane structure . . . . .	204
8.2	Dimensions of the fabricated valve cap and membrane structures . . . . .	204

8.3	Valve cap and membrane sub-component structure . . . . .	205
8.4	Baseline valve cap and membrane design dimensions . . . . .	209
8.5	Sensitivity of baseline valve cap and membrane design to variations in valve membrane thickness . . . . .	210
8.6	Finite-element mesh of valve cap and membrane structure . . . . .	211
8.7	Finite-element stress contours resulting from applied differential pressure loading	211
8.8	Sensitivity of baseline valve cap and membrane design to variations in fillet radius size . . . . .	212
8.9	Valve cap and membrane experimental pressure-deflection results . . . . .	214
9.1	Dimensions of active valve devices AV1 and AV2 . . . . .	219
9.2	Device AV1 low-voltage valve cap frequency response from 500Hz to 100kHz, with and without oil present above the valve structure. . . . .	223
9.3	Device AV1 low-voltage piston and valve cap frequency responses from 500Hz to 100kHz, with oil present above the valve structure. . . . .	224
9.4	Device AV1 low-voltage valve cap frequency responses from 500Hz to 100kHz, for varying $P_{bias}$ . . . . .	225
9.5	Device AV1 low-voltage valve cap frequency responses from 500Hz to 100kHz, for varying differential pressure applied to valve cap and membrane structure. . .	226
9.6	Device AV1 valve cap frequency responses from 500Hz to 3kHz, for $P_{bias} =$ $500kPa$ and increasing high voltage drive levels. . . . .	227
9.7	Device AV1 high-voltage piston and valve cap frequency responses from 500Hz to 3kHz, for $P_{bias} = 500kPa$ . . . . .	228
9.8	Device AV1 valve cap and piston deflection time histories for 1kHz sinusoidal drive voltage levels. . . . .	230
9.9	Device AV1 valve cap peak-peak motion, piston peak-peak motion, and device amplification ratio as a function of 1kHz sinusoidal drive voltage levels. . . . .	231
9.10	Device AV1 valve cap peak-peak motion, piston peak-peak motion, and device amplification ratio as a function of 1kHz sinusoidal drive voltage levels, with $P_{vc,vm} = 50kPa$ . . . . .	232
9.11	Experimental verification of the high-frequency channel in device AV1. . . . .	233
9.12	Device AV2 low-voltage valve cap frequency response from 500Hz to 100kHz, with and without oil present above the valve structure. . . . .	236
9.13	Device AV2 low-voltage valve cap frequency responses from 500Hz to 100kHz, for varying $P_{bias}$ . . . . .	237
9.14	Device AV2 valve cap frequency responses from 500Hz to 3kHz, for $P_{bias} =$ $500kPa$ and increasing high voltage drive levels. . . . .	238

9.15	Device AV2 high-voltage piston and valve cap frequency responses from 500Hz to 3kHz, for $P_{bias} = 500kPa$ . . . . .	239
9.16	Device AV2 valve cap and piston deflection time histories for 1kHz sinusoidal drive voltage levels. . . . .	240
9.17	Device AV2 valve cap peak-peak motion, piston peak-peak motion, and device amplification ratio as a function of 1kHz sinusoidal drive voltage levels. . . . .	241
9.18	Device AV1 and device AV2 quasi-static 1kHz model correlation for fluid bulk modulus $K_f = 2.0GPa$ . . . . .	244
9.19	Device AV1 and device AV2 quasi-static 1kHz model correlation for varying fluid bulk modulus $K_f$ . . . . .	245
9.20	Finite-element active valve modal frequency sensitivity studies . . . . .	248
9.21	Finite-element modal frequency sensitivity to valve cap added mass . . . . .	251
9.22	Model correlation to device AV1 quasi-static fluid flow rate versus valve opening behavior for differing imposed differential pressures . . . . .	253
9.23	Schematic of valve cap and membrane orifice structure. . . . .	257
9.24	Representative displacement signals corresponding to stable and unstable valve cap behavior during quasi-static opening. . . . .	258
9.25	Representative plots for valve cap behavior, differential pressure, and flow rate during quasi-static opening for $P_1 - P_2 = 80kPa$ . . . . .	259
9.26	Valve cap Instability Values during quasi-static opening for $P_1 - P_2 = 80kPa$ , $P_1 - P_2 = 130kPa$ , and $P_1 - P_2 = 160kPa$ . . . . .	260
9.27	Valve cap Instability Values during quasi-static opening for $P_1 - P_2 = 200kPa$ , $P_1 - P_2 = 230kPa$ , and $P_1 - P_2 = 240kPa$ . . . . .	261
9.28	Valve cap Instability Values during quasi-static opening for $P_1 - P_2 = 305kPa$ and $P_1 - P_2 = 360kPa$ . . . . .	262
9.29	Complete grouping of all valve cap Instability Values plotted as $P_1 - P_2$ vs. $Z_{vc,opening}$ . . . . .	263
9.30	Estimated boundaries for smooth, rough, and oscillatory regions plotted as $P_1 - P_2$ vs. $Z_{vc,opening}$ . . . . .	264
9.31	Estimated boundaries for unstable and stable regions plotted as $P_1 - P_2$ vs. $Z_{vc,opening}$ . . . . .	265
9.32	Estimated constant Reynolds number curves plotted as $P_1 - P_2$ vs. $Z_{vc,opening}$ . . . . .	266
9.33	Constant Reynolds number curves (experimental vs. model predictions) plotted as $P_1 - P_2$ vs. $Z_{vc,opening}$ . . . . .	267
9.34	Plot of flow resistance coefficient versus Reynolds number for a generic flow orifice contraction structure. . . . .	268



9.35	Device AV1 estimated laminar, transition, and turbulent flow regimes based on experimental data. . . . .	269
9.36	Schematic of vorticity formation in contraction and expansion fluid flow sections.	270
9.37	Laminar, transition, and turbulent representative flow behavior . . . . .	271
9.38	Device AV1 valve cap time histories under varying duty cycle voltage waveforms to piezoelectric drive element. . . . .	273
9.39	Device AV1 model correlation to experimental flow rate results for varying duty cycles. . . . .	274
9.40	Device AV1 dynamic flow regulation model correlation at 1kHz for varying differential pressures. . . . .	275



# Nomenclature

$A_c$	high frequency channel cross-sectional area
$A_p$	piezoelectric material area
$A_{pis}$	drive element piston area
$A_{vc}$	valve cap area
$A_{vm}$	valve membrane area
$dP_{HAC}$	hydraulic amplification chamber pressurization
$dV_{EHC}$	fluid volume change within external energy harvesting chamber
$dV_{fluid}$	hydraulic amplification chamber fluid volume change
$dV_{pis}$	drive element piston swept volume
$dV_{te}$	drive element tether swept volume
$dV_{de}$	drive element total swept volume
$dV_{top}$	top structural plate volume change
$dV_{vm}$	valve cap and membrane swept volume
$d_{33}$	piezoelectric material coefficient
$E_p$	piezoelectric material Young's modulus
$E_{si}$	silicon Young's modulus
$E_{pyrex}$	Pyrex Young's modulus
$fR$	fillet radius
$F_{vc}$	force on valve cap structure
$F_{vm}$	valve membrane force on top structural plate
$G_{si}$	silicon shear modulus
$H_{HAC}$	hydraulic amplification chamber height
$K_{EHC}$	generalized external energy harvesting chamber stiffness
$K_f$	fluid bulk modulus
$L_c$	high frequency channel length
$L_p$	piezoelectric material length
$N_{vh}$	number of valve heads used in parallel within active valve
$P_{bias}$	hydraulic amplification chamber bias pressure
$P_{EHC}$	external energy harvesting chamber pressure
$P_{EHC}^*$	pressure within inlet valve orifice channel
$P_{EHC}^{**}$	pressure within outlet valve orifice channel

$P_{HAC}$	hydraulic amplification chamber pressure
$P_{HPR}$	high pressure reservoir pressure
$P_{LPR}$	low pressure reservoir pressure
$P_{pis}$	applied pressure beneath drive element piston
$P_1$	generalized pressure above valve cap
$P_2$	generalized pressure above valve membrane
$Q_{in}$	flow rate through inlet valve
$Q_{out}$	flow rate through outlet valve
$R_{bot}, D_{bot}$	bottom structural plate radius, diameter
$R_{cp}$	piezoelectric material spacing radius from drive element center
$R_{orifice}, D_{orifice}$	valve fluid orifice radius, diameter
$R_p, D_p$	piezoelectric material radius, diameter
$R_{pis}, D_{pis}$	drive element piston radius, diameter
$R_{te}, D_{te}$	drive element tethers outer radius, diameter
$R_{top}, D_{top}$	top structural plate radius, diameter
$R_{vc}, D_{vc}$	valve cap radius, diameter
$R_{vm}, D_{vm}$	valve membrane radius, diameter
$RE$	generalized Reynolds number
$RE_{Dorifice}$	Reynolds number through valve orifice
$t_{bot}$	bottom structural plate thickness
$t_{pis}$	drive element piston thickness
$t_{tetop}$	top drive element tether thickness
$t_{tebot}$	bottom drive element tether thickness
$t_{top}$	top structural plate thickness
$t_{vc}$	valve cap thickness
$t_{vm}$	valve membrane thickness
$T_p$	piezoelectric material stress
$V_p$	piezoelectric material voltage
$V_{HAC}$	hydraulic amplification chamber volume
$W_{hys}$	hysteretic energy consumption of active valve
$Z_{bot}$	bottom structural plate deflection
$Z_{de}$	drive element total deflection
$Z_p$	piezoelectric material deflection
$Z_{pis}$	drive element piston deflection

$Z_{te}$	top drive element tether deflection
$Z_{top}$	top structural plate deflection
$Z_{vc}$	valve cap deflection (absolute)
$Z_{vc,opening}$	valve cap opening distance from orifice
$Z_{vc,stroke}$	valve cap peak-peak stroke
$\alpha_{si}$	silicon shear correction factor
$\epsilon_p$	piezoelectric material strain
$\nu_p$	piezoelectric material Poisson ratio
$\nu_{Pyrex}$	Pyrex Poisson ratio
$\nu_{si}$	silicon Poisson ratio
$\rho_{fluid}$	fluid density
$\sigma_{vm}$	valve membrane radial stress
$\sigma_{vm,max}$	maximum valve membrane radial stress
$\zeta_{orifice}$	valve orifice loss coefficient
$\Xi_{Zpis}^P, \Xi_{Zpis}^T, \Xi_{dVpis}^P, \Xi_{dVpis}^T$	drive element piston compliance coefficients
$\Xi_{Ztetop}^F, \Xi_{Ztetop}^P, \Xi_{dVtetop}^F, \Xi_{dVtetop}^P$	top drive element tether compliance coefficients
$\Xi_{Ztebot}^F, \Xi_{Ztebot}^P$	bottom drive element tether compliance coefficients
$\Xi_{Zbot}^T$	bottom structural plate compliance coefficient
$\Xi_{Ztop}^F, \Xi_{Ztop}^P, \Xi_{dVtop}^F, \Xi_{dVtop}^P$	top structural plate compliance coefficients
$\Xi_{Zvc}^F, \Xi_{Zvc}^P, \Xi_{dVvm}^F, \Xi_{dVvm}^P$	valve cap and membrane compliance coefficients
	(linear deformation theory)



# Chapter 1

## Introduction

### 1.1 Motivation

The development of a fluidic microvalve, capable of high frequency control of high pressure liquid fluid flows, is a key task in the realization of high specific power ( $\frac{W}{kg}$ ) micropumping technology. Currently, many research efforts around the world are underway to develop compact liquid micropumping systems, the term “micro” referring to devices which are created with fabrication procedures capable of  $\mu m$ -size tolerances and which produce overall micropump dimensions on the order of a few millimeters to a few centimeters. However, the vast majority of these systems are designed for low pressure and low flow rate applications [1] [2] [3] [4] [5] such as drug dispensing and microdosing [6] [7] [8]. The higher performing of these systems are capable of pumping liquids with flow rates on the order of  $1000-3000 \frac{\mu L}{min}$  ( $0.017-0.050 \frac{mL}{s}$ ) against differential pressures of between 10kPa and 50kPa. With a typical device mass on the order of  $\sim 1$  gram, these performance values correlate to device-level specific powers below  $2.5 \frac{W}{kg}$ .

In an effort to develop high specific power micropumping technology (with specific powers  $\sim 100-1000 \frac{W}{kg}$ ) for both actuation and power generation applications, a novel class of Micro-Hydraulic Transducer (MHT) devices has been introduced [1] [10] [11] [12] [13]. These devices combine bulk piezoelectric materials with stiff micromachined structural elements and are designed to enable high frequency pumping of fluid (10-20kHz) against pressure differentials on the order of  $\sim 1-2$ MPa, creating flow rates near or in excess of  $1 \frac{mL}{s}$ .

Piezoelectric materials are well-suited for transducer applications because of their inherently high peak specific powers. Figure 1.1 provides a comparison of the single stroke specific energy ( $\frac{J}{kg}$ ), bandwidth (kHz), and theoretical peak specific power ( $\frac{W}{kg}$ ) for a variety of transducer materials [14] [15] [16]. The product of a material’s single stroke specific energy and its bandwidth provides a value for the material’s specific power ( $\frac{W}{kg}$ ). Shape-memory alloy materials (denoted SMA), for example, possess a relatively large single stroke specific work ( $\sim 5000 \frac{J}{kg}$ ) in com-

parison to that of standard polycrystalline piezoelectric materials such as PZT-5H ( $\sim 10 \frac{J}{kg}$ ). The maximum operational frequency, or bandwidth ( $\sim 10\text{Hz}$ ), of SMA materials, however, is significantly less than that of standard piezoelectrics ( $\sim 100\text{kHz}$ ). SMA materials and standard piezoelectrics both possess specific powers near  $100 \frac{W}{kg}$ , however, their optimal implementation as actuation mechanisms is far different. In an application where low frequency, large stroke actuation is desired (such as an on-off microvalve), the use of an SMA material might be preferred over a standard piezoelectric material. Conversely, for an application whereby high frequency, low stroke actuation is required, a piezoelectric material may be preferred. In fact, for this reason, the vast majority of high frequency micropumping systems use piezoelectric materials as their actuation mechanism in conjunction with fast-acting valves. The recent development of single-crystal ferroelectric materials (e.g. PZN-PT), characterized by specific powers approaching  $10 \frac{kW}{kg}$  ( $\sim 100\times$  greater than those of standard polycrystalline PZT materials) [17], offers further advantages in strain capability over the standard piezoelectrics. These high performing materials, however, have yet to be integrated within high frequency micropumping systems.

The piezoelectric micropumping devices and systems that have been presented in the literature up until this time typically utilize one of two actuation methods as a means to pump fluid: either (1) a deposited thin-film, thick disk, or bimorph of piezoelectric material [2] [3] [6] in contact with a compliant membrane, or (2) a direct-drive stack actuator in contact with a moveable silicon diaphragm. The thin-film, thick-film, and bimorph structural designs presented are not conducive to both high force and high-frequency operation. The direct-drive stack actuation designs [18] [19] [20] are capable of achieving higher frequency operation than the thin-film, thick-film, and bimorph designs, however the presented micropump devices using these designs are limited in their flow rate, pressurization, and frequency capabilities due to inadequacies of the accompanying one-way passive valves used to regulate the fluid flow. Additionally, these previously presented direct-drive stack designs require a significant length of piezoelectric actuation material to create the deflection and fluid pumping volume required for reasonable fluid flow rates. Due to this significant actuator size, an epoxy bonding agent and a relatively compliant silicon diaphragm are required to tolerance the piezoelectric material within the structures. The key design feature which differentiates Micro-Hydraulic Transducer devices from these previous piezoelectric micropumps is the incorporation of a stiff micromachined structural “piston-like” actuation element not only within the pumping chamber of the device, but also within accompanying flow regulation active valves. The annularly-tethered micromachined “piston” structure, driven by miniature bulk piezoelectric elements (almost an order of magnitude smaller than those used in [18] [19] [20]) attached using a thin-film eutectic alloy bond, can achieve structural frequencies well above  $10\text{kHz}$  and can actuate against fluid pressurizations near  $1\text{MPa}$ . The implementation of such a stiff structure within fluidic systems can enable significantly higher frequency and pressurization capabilities than the previously



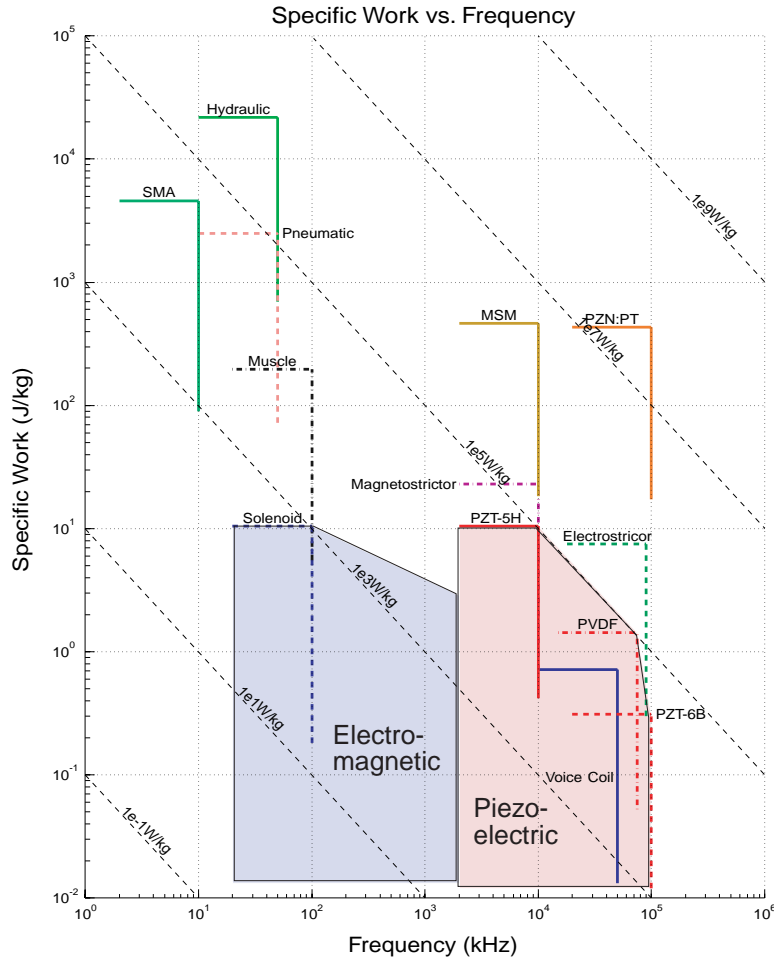


Figure 1.1: Upper bound on specific work vs. frequency for various actuation media. SMA is shape-memory alloy; PZN-PT is single-crystal piezoelectric; MSM is magnetic shape memory materials.

presented piezoelectric micropumps.

As shown in Figure 1.2, a Micro-Hydraulic Transducer system consists of a piezoelectric pump chamber, two actively controlled valves, and a low and high pressure fluid reservoir. In the MHT actuator, electrical energy supplied to the piezoelectric pump chamber results in a pumping of fluid through the valves from the low to high pressure reservoir. In the MHT power harvester, sequenced operation of the valves results in fluid flow from the high to low pressure reservoir, producing a “pinging” of the piezoelectric element within the pump chamber. This cyclic strain on the element induces electrical charge, which can be rectified and stored. The specific power of these transducer devices scales linearly with the frequency of operation and the pressure drop across which the device can operate. Since structural frequencies scale inversely with the geometric size of the device, it is advantageous to build these systems as small as

possible, hence the need for MEMS fabrication and process technologies. The performance of these MHT systems is directly governed by the capabilities of the active valves, which regulate flow into and out of the pump chamber. As a result, to achieve high specific power Micro-Hydraulic Transducer devices, a compact high frequency, high pressure active valve is required. The development of such an active valve is the subject of this thesis.

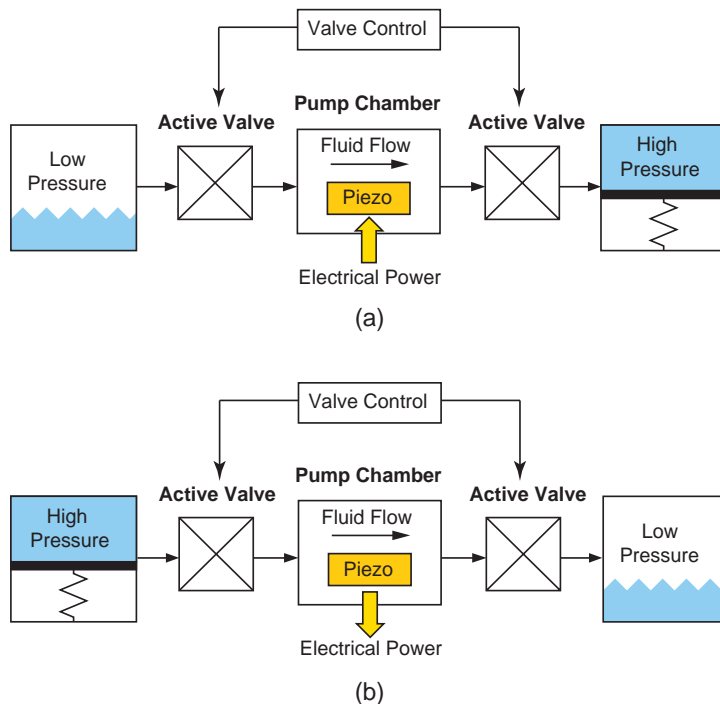


Figure 1.2: Schematics of Micro-Hydraulic Transducer systems: (a) MHT actuator system, (b) MHT power harvesting system. High specific power is achieved through the integration of piezoelectric material with structural stiff small-scale hydraulic systems.

## 1.2 Overview of Previous Microvalve Technology

Although a significant amount of literature is available describing the development of active valve devices and technology, few if any have been designed for high frequency control of high pressure liquid fluid flows. Novel microvalve designs using thermopneumatic actuation [21] [22], thermal bimetallic actuation [24], SMA actuation [23], electrostatic actuation [25] [26], electromagnetic actuation [27] [28], piezoelectric bender-type actuation (both thin-film and thick film) [29] [30] [31], and piezoelectric stack-type actuation [18] [19] [20] have been presented. A sampling of previously reported microvalves is shown in Figure 1.3 and Figure 1.4.

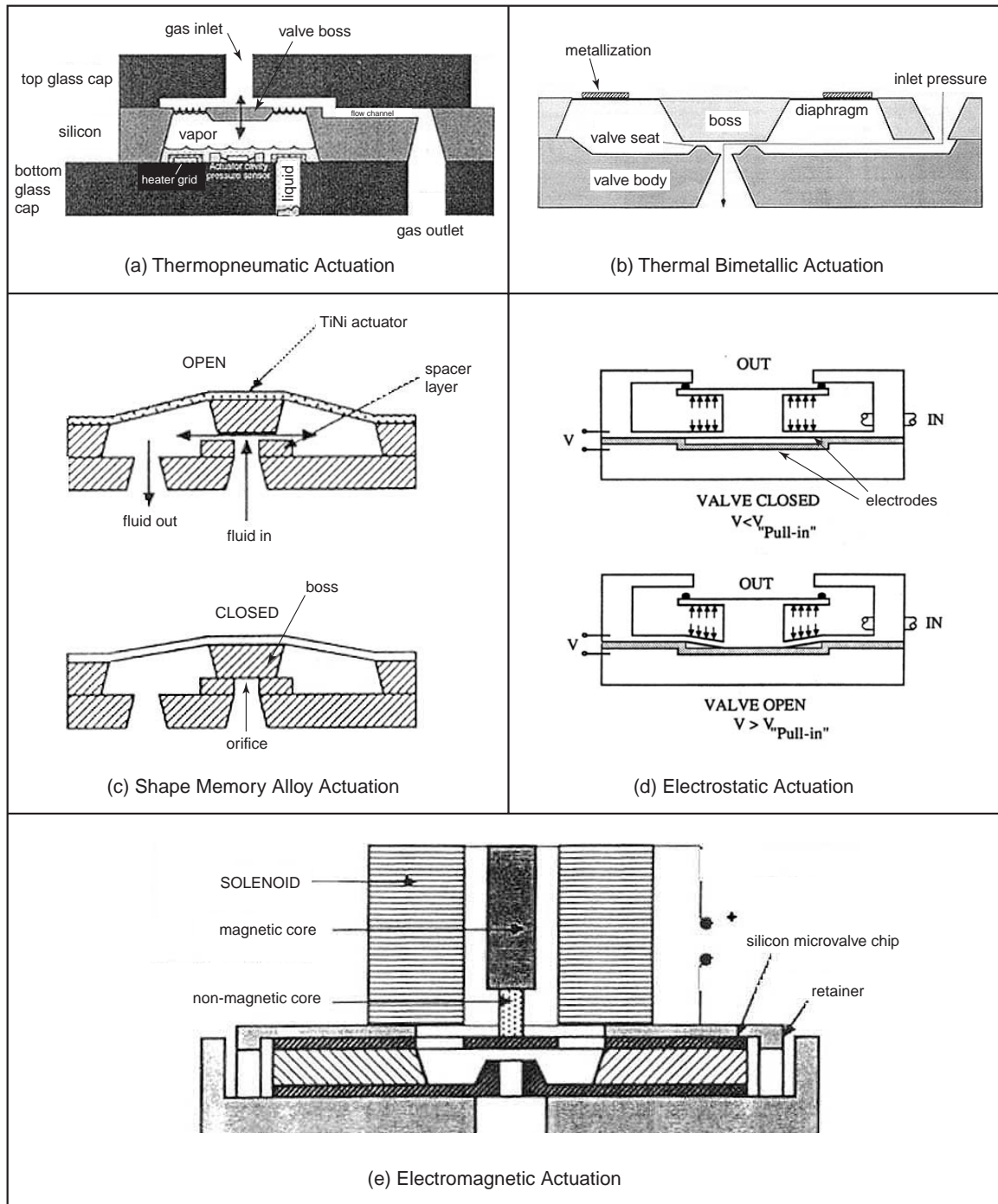


Figure 1.3: Previously reported microvalves: (a) thermopneumatic actuation, Rich [22], (b) thermal bimetallic actuation, Jerman [24], (c) shape memory alloy actuation, Huff [23], (d) electrostatic actuation, Huff [25], and (e) electromagnetic actuation, Pourahmadi [27].

Figure 1.3(a) shows a thermopneumatic microvalve [22] for control of gas flows. A valve central boss is supported by a corrugated silicon membrane. The deflection of the boss is controlled by the vapor pressure of the heated working fluid (parylene) within the contained chamber. A micromachined heater grid exists within the chamber to increase the fluid temperature. For typical operation, a temperature of  $80^{\circ}\text{C}$  (and a corresponding power dissipation of 300mW) is required to move the valve boss through a stroke of  $9\mu\text{m}$  in a time of approximately 15 seconds. Maximum pressure rise within the fluid chamber was reported to be 100kPa.

Figure 1.3(b) illustrates a thermal bimetallic valve [24] for use in pneumatic closed-loop pressure or flow control applications. The valve consists of a diaphragm actuator with a central boss which mates to an etched silicon valve body. The actuator includes a circular silicon diaphragm with integrated diffused resistors and an annular region of deposited aluminum. As current is passed through the resistors, the diaphragm increases in temperature. The thermal expansion mismatch between the silicon and aluminum results in a controlled displacement of the central boss. An operational boss deflection of  $15\mu\text{m}$  was obtained in response to a temperature increase of  $100^{\circ}\text{C}$  (and a reported corresponding power dissipation of 1W). Regulation of 200kPa differential pressure gas flows in an on-off fashion was demonstrated, resulting in gas flow rates of up to 2mL/s. No actuation response time was reported.

Figure 1.3(c) displays a shape-memory alloy (titanium nickel) actuated microvalve [23] for precise regulation of liquid fluid flow in micro-chemical analysis and drug delivery applications. The shape-memory effect is an athermal phase transformation between the austenitic (high temperature rigid) and martensitic (low temperature ductile) phases. In this valve, a TiNi diaphragm with attached silicon boss is actuated to open and close against a micromachined orifice. The valve was tested in an on-off fashion and it was reported to enable a liquid (DI water) flow rate of 0.1mL/s for an applied differential pressure of 5kPa. Maximum stroke of the valve boss was not reported.

Figure 1.3(d) displays an electrostatic microvalve [25] with a pressure-balancing structural feature that allows it to control fluids at pressures significantly larger than the necessary actuation pressure. The fluid provides a balancing force on the moving part of the structure thereby reducing the force required to open the valve. The moving part of the valve is a plunger which is actuated vertically, and consists of a center-bossed circular base and cap. Electrostatic actuation is enabled through a small gap between the underside of the membrane and the top surface of a bottom support structure. This on-off valve was able to control 220kPa differential gas flows with an actuation voltage of 210V, resulting in a peak flow rate of 2.5mL/s. Due to significant ohmic heating in the device (because of a poor oxide layer), power dissipation was reported to be greater than 10W.

Figure 1.3(e) illustrates an electromagnetic microvalve [27] designed for applications requiring large stroke and large on-off gas flow rates. The microvalve consists of a solenoid housing

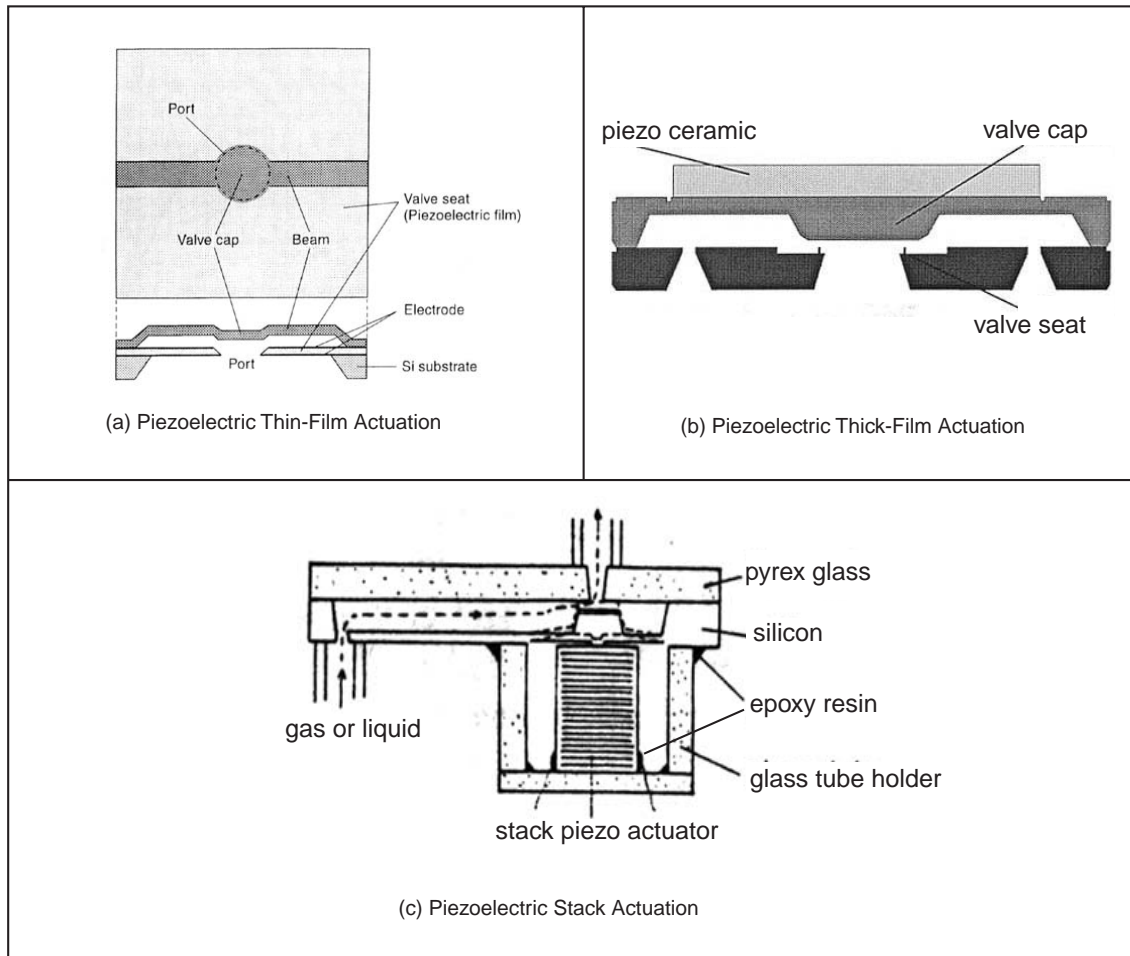


Figure 1.4: Previously reported piezoelectric microvalves: (a) piezoelectric thin-film actuation, Watanabe [30], (b) piezoelectric thick-film actuation, Kluge [31], and (c) piezoelectric stack actuation, Esashi [19].

and a plunger which is rigidly attached to a diaphragm structure. Current applied to the solenoid results in a motion of the plunger against a micromachined orifice. Dimensions of the solenoid attachment are unknown, however the author states that the application for this valve does not require the device to fit within a compact volume. For on-off operation, this direct drive is reported to achieve a maximum valve cap displacement of  $100\mu\text{m}$  against a differential pressure of  $90\text{kPa}$ , resulting in peak flow rates near  $5\text{mL/s}$ . Power dissipation was reported to be greater than  $1\text{W}$ .

Figure 1.4(a) displays a portion of a piezoelectrically-driven microvalve matrix [30] for controlling precise levels of gas flow. The valve is constructed of a thin beam with a round valve cap at the center and a valve seat of piezoelectric thin-film bifurcated in the normal direction.

The valve is normally closed due to a residual stress in the beam. For voltage applied to the valve seat, the piezoelectric film shrinks and the inner edge moves radially outward thereby increasing the flow area between the valve cap and this inner edge. The outer diameter of the piezoelectric thin-film is  $600\mu\text{m}$  and its thickness is  $1\mu\text{m}$ . In response to a voltage of 1V, the valve was reported to actuate against a differential pressure of 0.1kPa, resulting in a gas flow rate of 2mL/s.

Figure 1.4(b) illustrates a thick-film piezoelectrically-actuated microvalve [31] for use in high gas flow applications. The valve consists of a micromachined valve cap and membrane structure with an attached (via epoxy) piezoceramic disk to actuate the valve cap against a micromachined valve seat orifice. The valve seat diameter is 2.25mm and the achievable stroke of the valve cap is  $30\mu\text{m}$  for an applied voltage of up to 3000V. For on-off operation, the valve was reported to regulate gas flow at 11.6Hz against a differential pressure of 400kPa. The thickness of the piezoceramic disk structure was not detailed.

Figure 1.4(c) displays a piezoelectrically-driven microvalve [19] using a direct drive piezoelectric stack as the actuation mechanism. This valve was designed for use in a liquid micropumping system. The microvalve consists of one silicon and two glass layers anodically bonded together. The silicon contains a inlet through hole, a flow channel, and a moveable diaphragm with a central boss structure. A piezoelectric stack 9mm in length is attached to the underside of the boss using epoxy. In response to a voltage of 90V at a frequency of 30Hz, an estimated liquid pressurization of 8kPa in the pumping chamber of the micropump and a corresponding flow rate of 0.00025mL/s was reported.

The previously described microvalves were selected to illustrate the wide variety of actuation concepts previously reported in the literature. All of these microvalves share a common operational geometry (except for Watanabe [30]) in that a valve boss is affixed to a diaphragm or membrane structure which carries the boss through a predetermined stroke, in response to some form of actuation principle. The majority of these valves were designed for gas flows, and as such estimating their capabilities in handling liquids is difficult to do, although typically flow rates of liquids for a given differential pressure can be expected to be 100-1000x smaller than gas flow rates under the same differential pressures. In general, based on their reported capabilities, it can be concluded that none of these valves is capable of simultaneously satisfying the set of high frequency (1-10kHz), high pressure (0.1-1MPa), and large stroke ( $15\text{-}40\mu\text{m}$ ) requirements needed within full MHT liquid micropumping systems.

The thermal actuation designs (based on thermopneumatic, thermal bimetallic, and shape memory alloy principles) potentially can achieve large stroke and reasonable actuation force. However, these thermally-based devices exhibit excessive power consumption and poor response times on the order of seconds. High-frequency actuation in the kHz range is therefore unachievable. The electrostatic devices are limited in their deflection and pressure generation capabili-

ties, since the electrostatic force generated between two parallel plates scales inversely with their spacing and since electrical breakdown across the gap must be avoided. The electromagnetic concept is impeded by the overall size of external solenoid and housing structures needed to actuate the valve structure. Piezoelectric thin-film and thick-film bender-type designs are limited in their ability to generate both high force and large deflection output. Shoji and Esashi's work aimed at solving this problem through the use of a stack-type piezoelectric actuator material to directly drive the valve membrane. In doing so, however, the piezoelectric stack material was required to be long ( $\sim 9\text{mm}$ ), resulting in a large actuator mass and size. The operational frequency of this device was reported only up to 30Hz.

A promising method for achieving high frequency operation in conjunction with large force and high stroke capability would be to design a microvalve with a means to amplify the stroke of a piezoelectric bulk-type material (for example 1mm in thickness - almost an order of magnitude smaller in length than Shoji and Esashi's stack) into a larger valve membrane stroke. This could be done using a stiff hydraulic fluid within an enclosed chamber to couple the piezoelectric material motion to the valve cap motion using an area ratio amplification concept. This type of structure would thereby achieve high frequency, high pressure, and large valve cap stroke actuation with minimal device power consumption (a further advantage of piezoelectric materials). Numerous macroscale piezoelectric hydraulic amplification mechanisms have been presented in the literature. In an application for active vibration control, a piezoelectric actuator uses the volume change of a piezoelectric ring to create a large deflection of a smaller area contact surface [32]. In an application for vibration control of a rotary dynamic system, the deflection of a stack-type piezoelectric actuator is coupled through a hydraulic line to a smaller size piston, which helps to control the motion of a rotating shaft [33]. These and other [34] piezoelectric hydraulic amplification mechanisms are novel in design, yet do not face the difficult fabrication, assembly, and tolerancing challenges inherent in the development of high frequency MEMS-scale devices.

### 1.3 Concept

This thesis focuses on the design, modeling, fabrication, and experimental testing of a piezoelectrically driven hydraulic amplification microvalve for high pressure, high frequency applications. The proposed microvalve is shown in Figure 1.5. This device is desired to achieve large valve cap stroke (up to  $\sim 40\mu\text{m}$ ) against high pressure loads ( $\sim 0.1\text{-}1\text{MPa}$ ) through a novel hydraulic amplification mechanism that converts the small displacement ( $\sim 1\mu\text{m}$ ) of a piezoelectric material element into a significantly larger valve cap stroke. The inherent stiffness of the piezoelectric material and the hydraulic fluid chamber enable both high-frequency and high-force actuation capabilities.

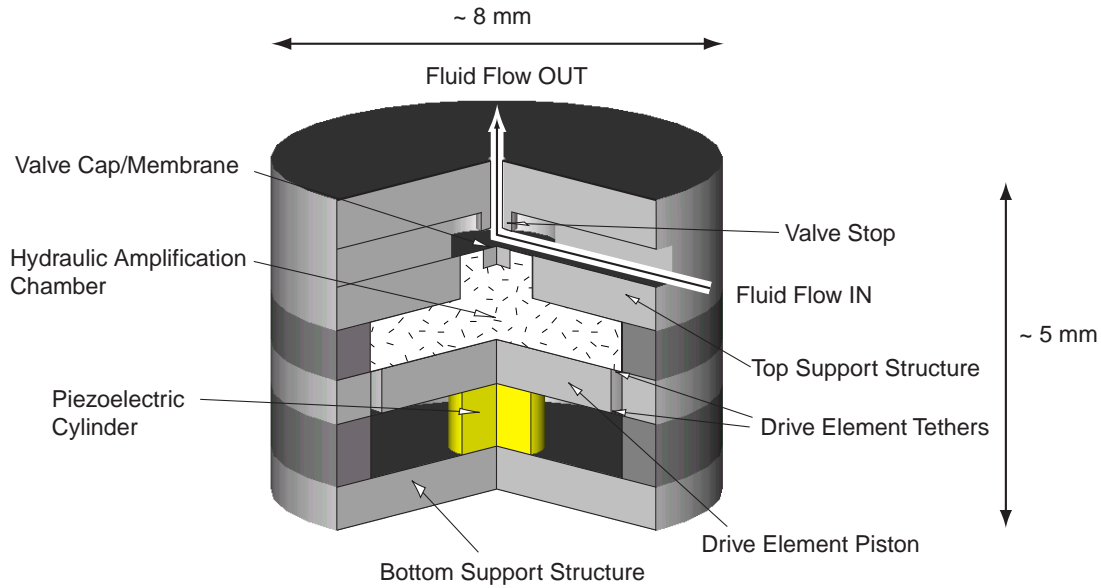


Figure 1.5: Schematic of a piezoelectrically-driven hydraulic amplification microvalve. The primary structural components are designated with arrows. External hydraulic system pressure loading is applied on the top surface of the valve cap and membrane.

The active valve consists of three primary components: a piezoelectric drive element, an enclosed fluid amplification chamber, and a membrane with attached valve cap. The drive element incorporates a circular piston structure supported from beneath by one or more small bulk piezoelectric cylinders and is suspended circumferentially from a surrounding support structure by thin annular micromachined tethers. This novel compact “piston-type” design enables high frequency actuation against a large external pressurization due to the high stiffness of the piston structure and integration of miniature bulk piezoelectric elements beneath the piston using a thin-film bond layer. The lateral dimensions of the tethers are designed to make the tethers compliant enough to allow for rigid piston motion up and down, yet stiff enough to resist bowing under pressurization caused by the hydraulic fluid above the tether during actuation. The tethers provide a seal between the hydraulic fluid above the piston and the piezoelectric chamber below the piston, and also provide a path for electrical contact to the top surface of the piezoelectric cylinders. The fluid chamber resides between the top surface of the drive element piston and the bottom surface of a thin, smaller diameter silicon micromachined valve cap membrane. These design features enable the valve device to simultaneously meet a set of high frequency, high pressure, and large stroke requirements that have not previously been satisfied by other microvalves presented in the literature.



In response to applied piezoelectric voltage, the piezoelectric material strains. The resulting deflection of the drive element piston generates a pressure within the hydraulic amplification chamber which in turn deflects the valve cap and membrane against a fluid orifice, thereby regulating fluid flow through the external hydraulic system. The pressure loadings on the valve cap and membrane during device operation depend on the external microfluidic system application. The piezoelectric material capabilities, the ratio of the piston diameter to the valve membrane diameter, the compliances of the fluid and structural elements in the chamber, the severity to which the valve cap membrane experiences nonlinear behavior, and the nature of the external loading all contribute to the performance of this microvalve device.

The proposed fabrication process for this microvalve involves the assembly of five silicon layers and four glass layers. A 2-D schematic of the microvalve device, illustrating individual silicon and glass layers, is shown in Figure 1.6. The middle glass layer (Layer 3) forms the drive element support structure and the top (Layer 9) and bottom (Layer 1) glass layers provide structural support. The bottom silicon layer (Layer 2) and drive piston silicon layers (Layers 4,5) provide a path for electrical contact to the piezoelectric cylinders. The top four silicon layers (Layers 4,5,7,8) and glass layer (Layer 6) house the hydraulic amplification chamber, valve cap and membrane structure, and fluid inlet and outlet channels. All silicon-silicon wafer interfaces are bonded with high-temperature ( $\sim 1300^{\circ}\text{C}$ ) fusion bonds, and all silicon-glass layer interfaces are bonded using low temperature ( $\sim 300^{\circ}\text{C}$ ) anodic bonds. Attachment of the top and bottom piezoelectric cylinder surfaces to the adjoining silicon is achieved with a low temperature ( $\sim 300^{\circ}\text{C}$ ) AuSn eutectic bond.

Shown in Figure 1.7 is a 3-D schematic of a fabricated silicon and glass multi-layer Micro-Hydraulic Transducer actuator system. This system consists of an inlet and outlet piezoelectrically driven active valve and a centrally-located piezoelectric pump chamber. The pump chamber is comprised essentially of the same drive element structure contained within each active valve component. All of the fabrication and assembly challenges (see Section 1.4.2) inherent in the realization of the active valve component structures are shared by the full MHT device, and as a result the efforts documented within this thesis to successfully fabricate a workable valve device at the same time demonstrate the ability to realize complete MHT systems.

## 1.4 Challenges

A significant number of challenges had to be overcome to realize a functional piezoelectrically driven hydraulic amplification microvalve. These challenges can be organized into two major groupings: (1) modeling and design challenges and (2) fabrication, assembly, and testing challenges. These challenges are highlighted in the following sections.

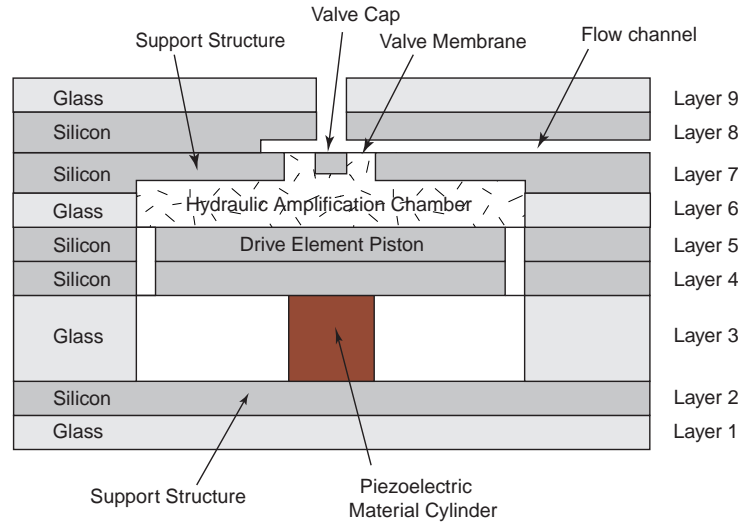


Figure 1.6: 2-D schematic of a microvalve multi-layer silicon and glass structure. Five silicon layers, four glass layers, and one or more piezoelectric material cylinders are joined together to form the microvalve. Enclosed fluid within the hydraulic amplification chamber couples the drive element piston deflection to the valve cap motion.

### 1.4.1 Modeling and Design Challenges

#### Structural Modeling of Active Valve

The development of a comprehensive structural model for the active valve requires detailed modeling of the piezoelectric material behavior, the bottom support plate structural compliance, the drive element piston and tether compliances, the hydraulic chamber fluid stiffness, the top support plate structural compliance, and the valve membrane deflection behavior. Stresses within the piezoelectric material, the drive piston tethers, and the valve membrane must be calculated to ensure structural integrity of the device under worst-case system loading conditions. Linear plate deformation theory is adequate for calculating the deflections and stresses associated with the drive piston tether and chamber compliances since these structural deflections are small in comparison to the respective structural thicknesses. However, modeling of the valve membrane requires more advanced non-linear deformation theory.

#### Non-linear Modeling of Valve Membrane

To achieve a high stroke actuation capability within the active valve device, the valve membrane/plate structure is designed to experience peak deflection magnitudes which exceed the plate structural thickness. This type of large-deflection deformation behavior is characterized by an elongation or stretching of the plate structure and a subsequent generation of a non-zero in-plane tensile stress along the neutral axis. As the plate is deformed significantly into the

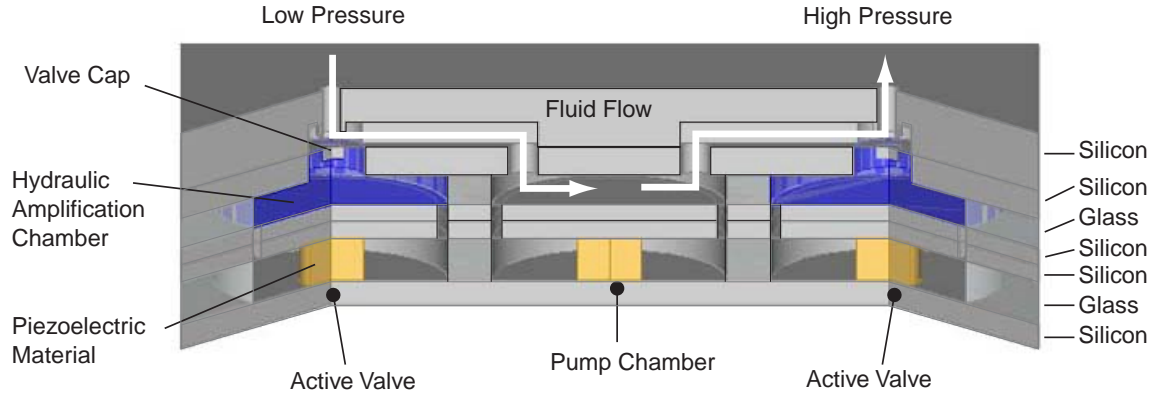


Figure 1.7: 3-D schematic of a Micro-Hydraulic Transducer multi-layer silicon and glass structure. Since a complete MHT system relies on identical fabrication and assembly procedures to those of the component valve, successful testing of the piezoelectrically driven active valve device validates the capability to realize the full MHT system.

large deflection regime, the in-plane tensile stress begins to exceed the bending stresses and the plate stiffness increases. Linear plate theory is inadequate to capture these stiffening effects, and as a result, tools have been developed to accurately model the non-linear large deflection behavior of the valve membrane/plate structure.

### Development of Systematic Active Valve Design Procedure

The design and formulation of an active valve geometry which can satisfy performance requirements imposed by an external hydraulic system is an important step in the development of MHT systems. Accurate modeling of the fluid flow behavior through the hydraulic system and interaction of the valve structure with this external system must be developed. Additionally, design parameter variations, such as valve membrane thickness, valve cap stroke, and the number of valve membranes working together in parallel within the active valve device must be properly investigated so as to create an active valve whose membrane structures experience stresses below fracture limits and, as a whole, that consumes as little power as possible during operation.

#### 1.4.2 Device Fabrication, Assembly, and Testing Challenges

##### Micromachining and Wafer-Bonding

Micromachining of the valve membrane and drive element tether structures within the active valve device is a critical step in the fabrication process. To achieve precise dimensional control of these thin-membrane structures, silicon-on-insulator (SOI) wafers containing a buried oxide

etch-stop layer are used. In performing deep etches in these wafers, the surface roughness of the etch and the tailoring of the fillet radius profiles at the base of the etch must be well-controlled so as to maintain the strength and robustness of the structures. Additionally, upon completing the etching of the various silicon layers, wafer-level silicon-silicon fusion bonding and wafer-level silicon-glass anodic bonding procedures must be carried out to form multi-layer wafer stack structures, in preparation for device assembly.

## **Piezoelectric Material Integration**

Integration of bulk piezoelectric material within the thin-tethered drive element structures is the most critical step in the active valve assembly. Preparation of the material, including polishing, thin-film deposition, and core-drilling, is performed to provide an optimal surface finish of the material in preparation for eutectic bonding to the adjoining silicon layers within the device. Additionally, accurate measurement of the individual piezoelectric element dimensional thicknesses, prior to integration, is required to ensure optimal static and operational deflections of the piston structure which result in minimal stresses in the etched piston tethers. Incorporation of multiple smaller area piezoelectric materials spread out beneath the piston membrane is desired over placement of a single larger area piezoelectric material at the piston center, so as to reduce system compliances and increase actuation efficiency. However, tolerance issues become even more important when dealing with the requirements of multiple bonded elements.

## **Fluid Filling and Sealing**

Encapsulation of a working fluid in the device is a significant challenge at the microscale because surface-to-volume ratios are typically quite large, with surface energies playing a dominant role. Any gas bubbles present in the sealed operational device can create enormous system compliances, potentially rendering the device useless. The elimination of trapped gases during filling of the device and during encapsulation of the fluid port used for filling is critical for high-level performance. The development of a systematic fluid degassing and filling procedure is required for successful realization of a working active valve device.

## **Device Testing**

Experimental testing of a complex microfabricated device can be an extremely challenging activity, due primarily to the lack of physical access to the structures within the device. To thoroughly characterize the performance of the active valve device presented in this thesis, drive element piston and valve cap deflections in response to applied voltages must be measured real-time. Additionally, dynamic pressures (between 0 and 2 MPa) upstream and downstream of the valve orifice and real-time fluid flow rates (as low as  $10 \frac{\mu L}{min}$  and as high as  $1 \frac{mL}{s}$ ) must

be monitored. Development of a test-rig apparatus for carrying out these measurements is a critical task for proper evaluation of the device behavior.

## 1.5 Objectives

The primary objective of this thesis is to develop a piezoelectrically driven hydraulic amplification microactuator structure, which can be operate as a microvalve for high frequency control of high pressure fluid flows. This research is carried out through a series of modeling, design, fabrication, assembly, and experimental testing tasks. This work will demonstrate the microactuator and valve concepts and evaluate their experimental performance in comparison to behavior predicted by the models developed in the thesis.

A secondary goal of this thesis is to provide a framework of linear and non-linear structural modeling tools and design procedures that can be implemented in the development of high frequency piezoelectric micropumping and microvalving systems. Additionally, a further goal of this thesis is to present a method for small-scale bulk piezoelectric material integration within silicon micromachined thin-tethered structures, a procedure which can enable the realization of compact high-frequency high-stiffness hydraulic actuator structures.

## 1.6 Approach

The overall scope of this thesis includes each of the challenges presented in Section 1.4, and consequently the thesis is divided into two major parts. The first part (Chapters 2 through 5) focuses on active valve modeling and design. The second part (Chapters 6 through 9) concentrates on active valve fabrication, assembly, and testing. Use of the modeling tools developed in the first part of the thesis enables model-experiment correlation in the later sections.

**Chapter 2** introduces the concept of the active valve device and details the procedures used to model the structural valve component compliances. Linear plate theory, with bending and shearing deformation effects included, is implemented. Additionally, the benefits of multiple piezoelectric elements spread out beneath the drive element piston rather than a single centrally-located element are presented through a series of finite-element studies.

**Chapter 3** presents the development of a numerical code to model the large deflection behavior of a thin annular plate structure with rigid central cap under pressure loading. This theory has been specifically developed to capture the non-linear stiffening effects present in the valve membrane structure of the active valve, effects which are unaccounted for in the basic linear plate theory presented in Chapter 2. The finite-differencing scheme presented in this chapter is based upon the work of Su [1].

**Chapter 4** combines the linear and non-linear modeling tools presented in Chapters 2 and 3 to create a quasi-static structural model of the active valve. In addition, the chapter introduces a dynamic simulation architecture for the valve, which includes inertia and damping associated with the drive element piston and valve cap structural elements. Calculation of the coupled fluid-structure resonant valve frequency, based on finite-element analyses, is also presented.

**Chapter 5** uses the modeling tools and simulations developed in the first three chapters to formulate a systematic quasi-static design procedure that can be used to design an active valve geometry based on external hydraulic system performance requirements. This design procedure incorporates the governing fluid flow relations linking the valve cap motion to the external hydraulic system pressures and enables variation of key parameters within the active valve geometry to minimize power consumption. As a check, full system dynamic simulations are run to validate the quality of the valve geometry created using the quasi-static procedure.

**Chapter 6** presents an overview of the fabrication challenges encountered and the solutions implemented in the development of the active valve device. A detailed sub-component testing plan for the active valve is presented as well. This systematic plan, as shown in Figure 1.8, breaks the complete active valve structure into manageable sub-component structures according to the primary challenges already detailed. The piezoelectric drive element sub-component study proves the ability to micromachine the tethered piston structure and integrate bulk piezoelectric material beneath the piston. The valve cap and membrane sub-component study validates the non-linear large deflection behavior of the valve membrane structure. Following successful completion of these sub-component studies, a complete active valve device can be fabricated and tested.

**Chapter 7** details the piezoelectric drive element sub-component study. Devices are fabricated that incorporate both standard polycrystalline PZT-5H piezoelectric material elements as well as higher-strain single-crystal PZN-PT piezoelectric material. Additionally, devices with three piezoelectric elements spread out beneath the drive piston are compared to single element devices to demonstrate the stiffening benefit of incorporating multiple piezoelectric elements within the drive element structure. These devices are quasi-statically and dynamically characterized to frequencies in excess of 100 kHz.

**Chapter 8** details the valve cap and membrane sub-component study. Valve membrane structures are fabricated and inspected to ensure adequate fillet radius control at the base of the etched features. Pressure-deflection experiments are carried out to characterize the degree of non-linearity present in these structures. Experimental results are compared to analytical and finite-element model results in which key parameters have been varied (membrane thickness and fillet radius size) in an effort to determine the sensitivity of the membrane behavior to these parameters.

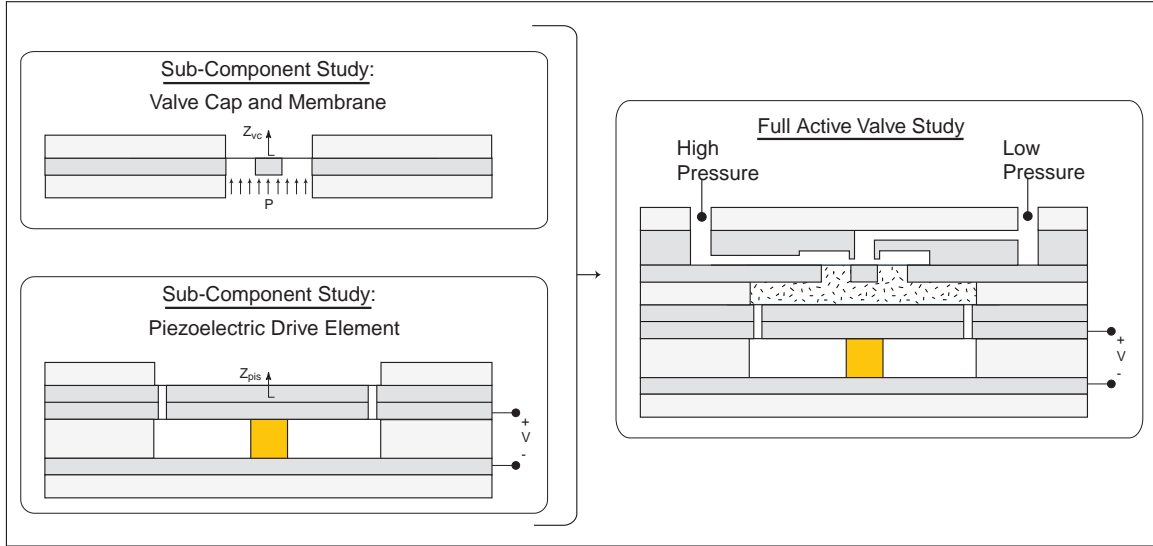


Figure 1.8: Active valve sub-component testing plan. Realization of the full active valve requires performance validation of piezoelectric drive element sub-component, valve cap and membrane sub-component, and hydraulic amplification chamber sub-component.

**Chapter 9** presents the experimental testing of the full active valve device, with a focus on voltage-valve cap deformation frequency-dependent behavior, as well as differential pressure-flow characterization of the valve. Correlation to quasi-static and dynamic models is presented.

Lastly, **Chapter 10** concludes the thesis with a summary of accomplishments. Conclusions are drawn and recommendations are made for future work. Appendices are also included, which detail many of the structural models and dynamic simulations presented throughout the thesis.

## 1.7 Thesis Executive Summary

This thesis demonstrates, through a series of modeling, design, fabrication, assembly, and experimental testing tasks, successful operation of a piezoelectrically-driven hydraulic amplification microvalve for use in Micro-Hydraulic Transducer systems. Linear and non-linear modeling tools characterizing the structural deformations of the active valve sub-systems were developed. These tools enabled accurate prediction of real-time stresses along the micromachined valve membrane structure as it was deflected into its non-linear large-deflection regime. A systematic design procedure was developed to generate an active valve geometry to satisfy membrane stress limitations and valve power consumption requirements set forth by external hydraulic system performance goals. Fabrication challenges, such as deep-reactive ion etching (DRIE) of the drive element and valve membrane structures, wafer-level silicon-to-silicon

fusion bonding and silicon-to-glass anodic bonding operations, preparation and integration of piezoelectric material elements within the micromachined tethered piston structure, die-level assembly and bonding of silicon and glass dies, and filling of degassed fluid within the hydraulic amplification chamber were overcome. A photograph of the completed 9-layer microfabricated valve is shown in Figure 1.9.

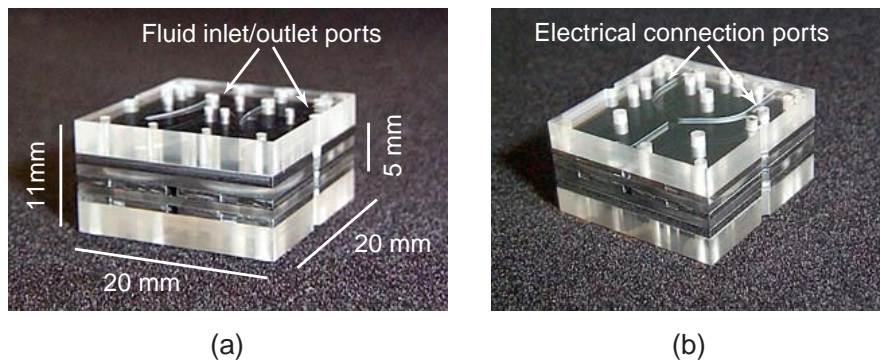


Figure 1.9: Photograph of a 9-layer silicon and glass piezoelectrically-driven hydraulic amplification microvalve, as part of a full MHT system. Dimensions of the valve structure within the full MHT chip are 8mm x 8mm x 5mm.

The active valve structural behavior and flow regulation capabilities were evaluated over a range of applied piezoelectric voltages, actuation frequencies, and differential pressures across the valve. For applied piezoelectric voltages up to 500Vpp at 1kHz, the valve devices demonstrated amplification ratios of drive element deflection to valve cap deflection of 40-50x. These amplification ratios correlate within 5 – 10% of the model expectations. Flow regulation experiments proved that a peak average flow rate through the device of 0.21mL/s under a sinusoidal drive voltage of 500Vpp, with valve opening of  $17\mu\text{m}$ , against a differential pressure of 260kPa could be obtained. Tests revealed that fluid-structural interactions between the valve cap and membrane components and flow instabilities (due to transition between the laminar and turbulent flow regimes through the valve orifice) limited the valve performance capabilities.



# Bibliography

- [1] H. Van Lintel, F. van de Pol, and A. Bouwstra, "Piezoelectric micropump based on micro-machining of silicon", *Sensors and Actuators*, 15, pp. 153-167, 1988.
- [2] M. Stehr, S. Messner, H. Sandmaier, and R. Zengerle, "The VAMP - a new device for handling liquids or gases," *Sensors and Actuators A*, 57, pp. 153-157, 1996.
- [3] V. Gass, B. van der Schoot, S. Jeanneret, and N. de Rooij, "Integrated flow-regulated silicon micropump," *Sensors and Actuators A*, 43, pp. 335-338, 1994.
- [4] S. Shoji and M. Esashi, "Microflow devices and systems," *Journal of Micromechanics and Microengineering*, 4, pp. 157-171, 1994.
- [5] K. Ikuta, T. Hasewaga, and T. Adachi, "The Optimized SMA Micro Pump Chip Applicable to Liquids and Gases," *Proceedings of the 2001 International Conference on Solid-State Sensors and Actuators (Transducers '01)*, 2001.
- [6] M. Koch, N. Harris, R. Maas, A. Evans, N. White, and A. Brunnschweiler, "Novel micropump design with thick-film piezoelectric actuation," *Measurement Science and Technology*, v.8 n.1, pp. 49-57, Jan 1997.
- [7] P. Watler and M. Sefton, "A Piezoelectric Driven Controlled Release Micropump for Insulin Delivery," *Trans Am Soc Artif Intern Organs*, Vol. XXXVI, pp. 70-77, 1990.
- [8] B. Wagner, H. Quenzer, S. Hoerschelmann, T. Lisec, and M. Jueress, "Micromachined bistable valves for implantable drug delivery systems," *Proceedings of the 18th Annual International Conference of the IEEE Engineering in Medicine and Biology Society*, pp. 254-255, 1997.
- [9] N.W. Hagood, D.C. Roberts, L. Saggere, K.S. Breuer, K.-S. Chen, J.A. Carretero, H.Q. Li, R. Mlcak, S. Pulitzer, M.A. Schmidt, S.M. Spearing, and Y.-H. Su, "Micro Hydraulic Transducer Technology for Actuation and Power Generation," *Proceedings of SPIE: SPIE's 7th Annual International Symposium on Smart Structures and Materials*, Vol. 3985, pp. 680-688, 2000.

- [10] H.Q. Li, D.C. Roberts, J.L. Steyn, K.T. Turner, J.A. Carretero, O. Yaglioglu, Y.-H. Su, L. Saggere, N.W. Hagood, S.M. Spearing, M.A. Schmidt, R. Mlcak, and K.S. Breuer, "A High Frequency High Flow Rate Piezoelectrically Driven MEMS Micropump," Proceedings of the IEEE Solid-State Sensor and Actuator Workshop, Hilton Head, SC. pp. 69-72, 2000.
- [11] D.C. Roberts, J.L. Steyn, H.Q. Li, K.T. Turner, R. Mlcak, L. Saggere, S.M. Spearing, M.A. Schmidt, and N.W. Hagood, "A High-Frequency, High-Stiffness Piezoelectric Micro-Actuator For Hydraulic Applications," Proceedings of the 2001 International Conference on Solid-State Sensors and Actuators (Transducers '01), 2001.
- [12] D.C. Roberts, N.W. Hagood, Y.-H. Su, H.Q. Li, and J.A. Carretero, "Design of a Piezoelectrically-Driven Hydraulic Amplification Microvalve for High Pressure, High Frequency Applications," Proceedings of SPIE's 7th International Symposium on Smart Structures and Materials, Vol. 3985, pp. 616-628, 2000.
- [13] D.C. Roberts, O. Yaglioglu, J. Carretero, Y.-H. Su, L. Saggere, and N.W. Hagood, "Modeling, Design, and Simulation of a Piezoelectric Microvalve for High Pressure, High Frequency Applications," Proceedings of SPIE's 8th International Symposium on Smart Structures and Materials, Vol. 4327, 2001.
- [14] J.M. Hollerbach, I.W. Hunter, J. Ballantyne, "A comparative analysis of actuator technologies for robotics," *Robotics Review* 2, Eds. Khatib and Oussama, MIT Press, pp. 299-342.
- [15] J.E. Huber, N.A. Fleck, and M.F. Ashby, "The selection of mechanical actuators based on performance indices," Proceedings of the Royal Society of London, Series A, Vol. 453, No. 1965, p. 2185.
- [16] S.W. Pulitzer III, "Feasability Assessment and Design of Micro Hydraulic Solid-State Transducers," MIT Master's Thesis. June 1998.
- [17] S. Park and T. Shrout, "Characteristics of Relaxor-Based Piezoelectric Single Crystals for Ultrasonic Transducers," IEEE Transactions on Ultrasonics, Ferroelectrics, and Frequency Control, Vol. 44, No. 5, pp. 1140-1147, 1997.
- [18] M. Esashi, S. Shoji, and A. Nakano, "Normally Closed Microvalve and Micropump Fabricated on a Silicon Wafer," *Sensors and Actuators* 20, pp. 163-169, 1989.
- [19] M. Esashi, "Integrated Micro Flow Control Systems," *Sensors and Actuators*, A21-A23, pp. 161-167, 1990.
- [20] S. Shoji, B. Van der Schoot, N. de Rooij, and M. Esashi, "Smallest Dead Volume Microvalves for Integrated Chemical Analyzing Systems," Proceedings of the 1991 Interna-

- tional Conference on Solid-State Sensors and Actuators (Transducers '91), pp. 1052-1055, 1991.
- [21] K. Henning, "Liquid and gas-liquid phase behavior in thermopneumatically actuated microvalves," Proceedings of SPIE- The International Society for Optical Engineering v3515, pp. 53-63, 1998.
  - [22] C. Rich and K. Wise, "A Thermopneumatically-Actuated Microvalve With Improved Thermal Efficiency and Integrated State Sensing," Proceedings of the IEEE Solid-State Sensor and Actuator Workshop, Hilton Head, SC, pp. 234-237, 2000.
  - [23] M.A. Huff and W.L. Benard, "Thin film titanium-nickel shape memory alloy microfluidic devices," Proceedings of the Third International Symposium on Microstructures and Microfabricated Systems, pp. 26-38, 1997.
  - [24] H. Jerman, "Electrically-Activated, Micromachined Diaphragm Valves," Proceedings of the 1991 International Conference on Solid-State Sensors and Actuators (Transducers '91), pp. 1045-1048, 1991.
  - [25] M.A. Huff, "Silicon Micromachined Wafer-Bonded Valves," Ph.D. Thesis, Massachusetts Institute of Technology, 1993.
  - [26] M. Shikida, K. Sato, S. Tanaka, Y. Kawamura, and Y. Fujisaki, "Electrostatically driven gas valve with high conductance," Journal of Microelectromechanical Systems, 3(2), pp.76-80, June 1994.
  - [27] F. Pourahmadi, L. Christel, K. Petersen, J. Mallon, and J. Bryzek, "Variable-Flow Micro-Valve Structure Fabricated with Silicon Fusion Bonding," Proceedings of the IEEE Solid-State Sensor and Actuator Workshop, Hilton Head, SC, pp. 78-81, 1990.
  - [28] A. Meckes, J. Behrens, and W. Benecke, "Electromagnetically Driven Microvalve Fabricated in Silicon," Proceedings of the 1997 International Conference on Solid-State Sensors and Actuators (Transducers '97), pp. 821-824, 1997.
  - [29] J.G. Smits, "Piezoelectric Micropump with Microvalves", Proc Eighth Bienn Univ Gov Ind Microelectron Symp. (IEEE n 89CH2769-8), Piscataway, NJ, USA. p 92-94
  - [30] T. Watanabe and H. Kuwano, "A microvalve matrix using piezoelectric actuators," Microsystem Technologies, pp. 107-111, 1997.
  - [31] S. Kluge, G. Neumayer, U. Schaber, and M. Wackerle, "Pneumatic Silicon Microvalves with Piezoelectric Actuation," Proceedings of the 2001 International Conference on Solid-State Sensors and Actuators (Transducers '01), 2001.

- [32] J. Garcia-Bonito, M.J. Brennan, S.J. Elliot, A. David, and R.J. Pinnington, "A novel high-displacement piezoelectric actuator for active vibration control," *Smart Mater. Struct.* 7, pp. 31-42, 1998.
- [33] P. Tang, A. Palazzolo, A. Kascak, G. Montague, and W. Li, "Combined Piezoelectric-Hydraulic Actuator Based Active Vibration Control for Rotordynamic System," *Journal of Vibration and Acoustics* 117, pp. 285-293, 1995.
- [34] Tsukamoto, "Piezo-Actuator's Displacement Magnifying Mechanism," US Patent 5,233,834. 1993.
- [35] Y.H. Su, K.S. Chen, D.C. Roberts, and S.M. Spearing, "Large Deflection Analysis of a Pre-Stressed Annular Plate With a Rigid Boss Under Axisymmetric Loading", *Journal of Micromech. Microeng.* 11 (2001) pp. 645-653.

## Chapter 2

# Active Valve Linear Model

This chapter presents the analytical modeling structure of the active valve, focusing on the linear deformation behavior of the various structural components. This chapter begins with an overview of each of the components of the active valve, detailing the corresponding structural geometries and associated assumptions used to model them. This first-level active valve model assumes a single cylindrical piezo material under the drive element piston for ease of modeling. Toward the conclusion of the chapter, the effects of incorporating multiple piezoelectric cylinders are discussed and the corresponding benefits to structural stiffnesses of the piston and the bottom structural plate are presented. The chapter concludes with an identification of the valve components that require further development of non-linear theory.

### 2.1 Valve Geometry and Modeling Procedure

The proposed piezoelectrically driven hydraulic amplification microvalve is schematically shown in Figure 2.1. The axisymmetric valve is comprised of three primary sub-structures: a piezoelectric drive element, a closed hydraulic amplification chamber, and a membrane with attached valve cap. The drive element sub-structure consists of one or more bulk piezoelectric material cylinders located at the center of the device, each bonded on its top surface to a silicon micromachined piston and on its bottom surface to a silicon support structure. The drive element piston is attached along its outer circumference to a silicon support structure with two thin silicon tethers. The fluid chamber resides between the top surface of the drive element piston and the bottom surface of a smaller diameter silicon micromachined valve cap membrane. In response to an applied piezoelectric voltage, a small deflection of the drive element piston translates into a much larger deflection of the valve cap membrane. The ratio of the piston diameter to the valve membrane diameter, the compliances of the fluid and structural chamber, the severity to which the valve cap membrane experiences nonlinear behavior, and the piezoelectric material performance determine the potential valve stroke for a given applied piezoelectric voltage.

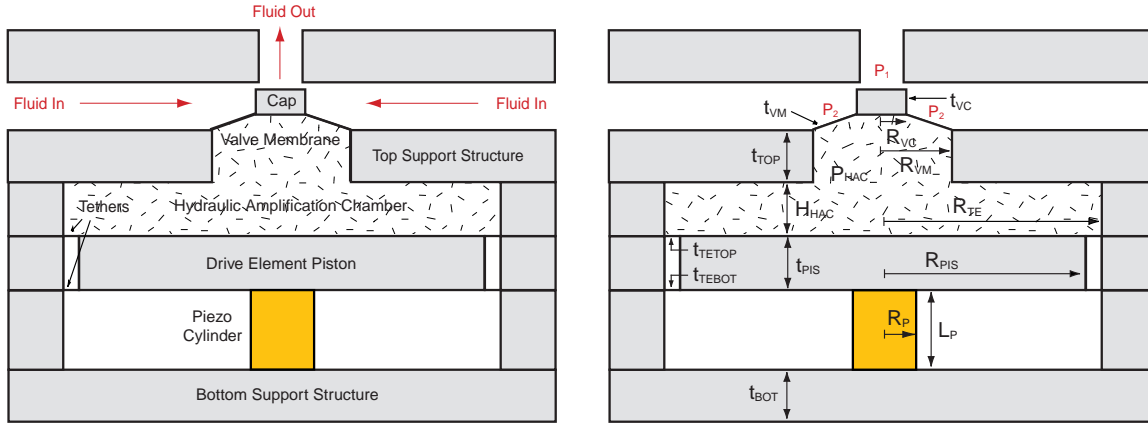


Figure 2.1: 2-D schematic of the piezoelectrically-driven hydraulic amplification microvalve. The nomenclature and key dimensions are detailed.

In developing a comprehensive analytical model for the active valve, the following aspects need to be accurately represented: (1) piezoelectric material behavior, (2) drive element piston and tether deflection behavior, (3) fluid compressibility, (4) hydraulic amplification chamber structural compliance, (5) valve cap and membrane deflection behavior, and (6) bottom structural plate behavior beneath piezoelectric material. The efficiency of the valve drive is a function of how much volume is created due to the various system compliances. The ideal design would call for a very stiff hydraulic fluid and a completely rigid drive element piston and chamber structure. In this case, all of the volume change created by the drive element deflection would exhibit itself in the volume change associated with the valve membrane deflection. Modeling of aspects (2), (4), (5), and (6) require a detailed understanding of linear plate theory. Each of these aspects will be modeled as a plate with applied loading and boundary conditions to determine the deflections and swept volumes due to bending and shearing effects. Non-linear issues such as in-plane stretching will be discussed at the close of the chapter.

## 2.2 Overview of Linear Plate Theory

In general, a symmetrically loaded circular plate will experience deflections due to bending and shearing. If the plate thickness is small compared to the plate outer radius, the deflection due to bending will be significantly larger than that due to shearing. If the plate thickness is of the same order of magnitude as the plate outer radius, however, the deflection contribution due to shearing effects will no longer be negligible. In these cases, it is advisable to obtain the total deflection as a sum of these two contributing effects. As detailed above, the top chamber structure, the drive element piston, the drive element tethers, the bottom chamber structure, and the valve cap/membrane can be modeled using linear plate theory. The degree to which

each of these structural components may experience non-linear deflection behavior is discussed at the conclusion of this chapter. This section presents the methodology used to model these plate behaviors (in a linear fashion) by way of a simple example. The following sections then detail each of the modeled valve compliances.

An example of a symmetrically loaded circular plate is shown in Figure 2.2. This plate is clamped at its outer radius ( $r=a$ ), guided at its inner radius ( $r=b$ ), and subjected to a pressure loading  $P$  over its bottom surface. The plate will experience deflections due to bending and shearing effects.

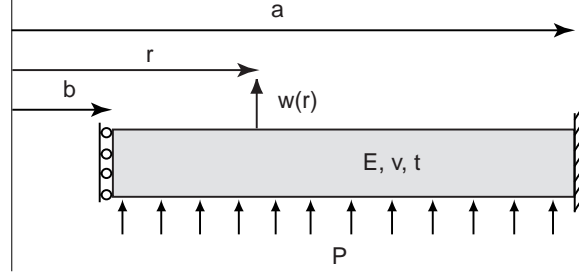


Figure 2.2: Circular plate under axisymmetric pressure loading, with a guided boundary condition at inner radius  $b$  and a clamped boundary condition at outer radius  $a$ .

### 2.2.1 Deflections Due to Bending

The governing differential equation for the symmetrical bending of a circular plate can be written as:

$$\frac{d}{dr} \frac{d}{dr} r \left( \frac{d}{dr} w(r) \right) = \frac{Q(r)}{D} \quad (2.1)$$

where  $D = \frac{Et^3}{12(1-\nu^2)}$  is the flexural rigidity of the plate and  $Q(r)$  is the shear force per unit length as a function of  $r$ .  $Q(r)$  depends on the nature of the plate loading. In this example case, the shear force is:

$$Q(r) = \frac{P(r^2 - b^2)}{2r} \quad (2.2)$$

The boundary conditions in this example case are:

$$BC1 : w(r = a) = 0 \quad (2.3)$$

$$BC2 : \frac{dw}{dr}(r = a) = 0 \quad (2.4)$$

$$BC3 : \frac{dw}{dr}(r = b) = 0 \quad (2.5)$$

By integrating the governing differential equation and applying the imposed boundary conditions, the deflection of the plate  $w(r)$  can be determined. In addition, the swept volume associated with the deflection can then be calculated as follows:

$$dV = \int 2\pi r w(r) \partial r. \quad (2.6)$$

For this example plate bending case, the plate deflection at the inner radius ( $r=b$ ) and the swept volume are found to be:

$$w_{bending}(b) = \left[ \Xi_{w_{bending}(b)}^P \right] P \quad (2.7)$$

$$dV_{bending} = \left[ \Xi_{dV_{bending}}^P \right] P \quad (2.8)$$

where  $\Xi_{w_{bending}(b)}^P$  and  $\Xi_{dV_{bending}}^P$  are the plate bending compliances,

$$\Xi_{w_{bending}(b)}^P = \left( \frac{1}{64D(b^2 - a^2)} \right) \left( 3b^6 + a^2b^4 \left( -7 + 4 \ln \left[ \frac{b}{a} \right] - 16 \ln \left[ \frac{b}{a} \right]^2 \right) + a^4b^2 \left( 5 - 4 \ln \left[ \frac{b}{a} \right] \right) - a^6 \right) \quad (2.9)$$

$$\Xi_{dV_{bending}}^P = \left( \frac{-\pi}{192D(b^2 - a^2)} \right) \left( a^8 - 10a^6b^2 + 24a^4b^4 \left( 1 - \ln \left[ \frac{b}{a} \right] \right) + a^2b^6 \left( -22 + 24 \ln \left[ \frac{b}{a} \right] \right) + 7b^8 \right) \quad (2.10)$$

These compliance coefficients are derived in detail in Appendix A.1.

### 2.2.2 Deflections Due to Shearing

In cases where the plate thickness is not small compared to the plate outer radius, shearing effects may contribute significantly to the overall deflection. The following analysis structure will allow for estimations of this deflection due to shear.

In general, shearing stresses vary across the thickness of a plate according to the same principle as for beams of narrow rectangular cross-sectional area [3]. The corresponding shearing strain can be written as:

$$\frac{dw}{dr} = \frac{-\alpha Q(r)}{Gt} \quad (2.11)$$

where  $G = \frac{E}{2(1-\nu)}$  is the modulus of elasticity in shear of a plate,  $t$  is the plate thickness, and  $Q(r)$  is, again, the shear force per unit length as a function of  $r$ . The coefficient  $\alpha$  is the shear correction factor. The boundary condition in this example case is:



$$BC4 : w(r = a) = 0 \quad (2.12)$$

By integrating the differential equation and applying the imposed boundary condition, the deflection of the plate  $w(r)$  can be determined. The swept volume associated with this deflection can be calculated according to Equation (2.6). For this example plate shearing case, the plate deflection at the inner radius ( $r=b$ ) and the swept volume under the plate are found to be:

$$w_{shear}(b) = \left[ \Xi_{w_{shear}(b)}^P \right] P \quad (2.13)$$

$$dV_{shear} = \left[ \Xi_{dV_{shear}}^P \right] P \quad (2.14)$$

where  $\Xi_{w_{shear}(b)}^P$  and  $\Xi_{dV_{shear}}^P$  are the plate shear compliances,

$$\Xi_{w_{shear}(b)}^P = \left( \frac{\alpha}{4Gh} \right) \left( a^2 + b^2 \left( -1 + 2 \ln \left[ \frac{b}{a} \right] \right) \right) \quad (2.15)$$

$$\Xi_{dV_{shear}}^P = \left( \frac{\pi \alpha}{8Gh} \right) \left( a^4 - 4a^2b^2 + b^4 \left( 3 - 4 \ln \left[ \frac{b}{a} \right] \right) \right) \quad (2.16)$$

These compliance coefficients are derived in detail in Appendix A.1.

### 2.2.3 Combined Deflection Due to Bending and Shearing

The total deflection at ( $r=b$ ) and swept volume of the plate are sums of those contributions due to pure bending effects and shearing effects. In this example case, the plate deflection and swept volume can therefore be written, respectively, as:

$$w(b) = \left[ \Xi_{w_{bending}(b)}^P + \Xi_{w_{shear}(b)}^P \right] P = \left[ \Xi_{w(b)}^P \right] P \quad (2.17)$$

$$dV = \left[ \Xi_{dV_{bending}}^P + \Xi_{dV_{shear}}^P \right] P = \left[ \Xi_{dV}^P \right] P \quad (2.18)$$

It is clear from this example that the plate deflection at a desired location and the swept volume can be expressed as linear functions of the loading parameters.

### 2.2.4 Comparison of Bending/Shearing Deflections

To illustrate the importance of the bending and shearing contributions to the example symmetric annular plate discussed thus far, the overall radial dimensions of the plate and the applied pressure loading are held constant and the plate thickness is varied from a value that is small compared to the plate radial dimensions to a value that is of the same order of magnitude as the radial dimensions. In doing this, one would expect to observe an increasing importance of

the shearing contribution as the plate thickness increases. The following dimensions, material constants, and loading parameters are assigned to the example case, and are typical of those found in the proposed active valve:

$$a = 3\text{mm}, b = 0.5\text{mm}, E = 165\text{GPa}, \nu = 0.22, \alpha = 1.5, P = 1\text{MPa}. \quad (2.19)$$

Deflections (at  $r=b$ ) due to bending and shearing are calculated as the plate thickness is varied from  $t = 20\mu\text{m}$  to  $t = 2\text{mm}$ . The results are shown in Figure 2.3.

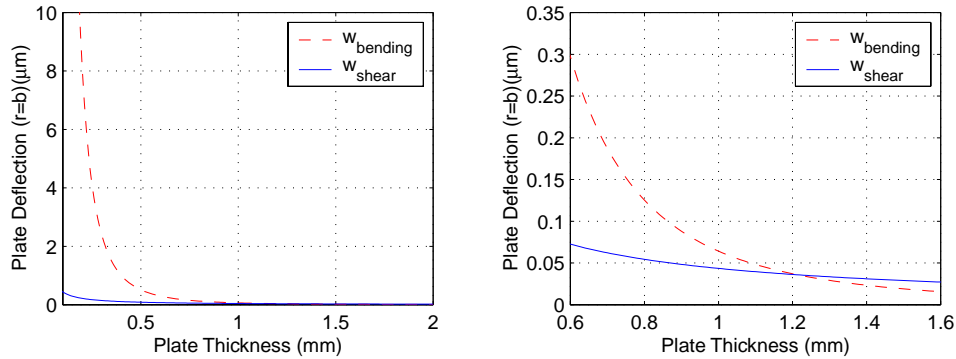


Figure 2.3: Bending and shearing contributions to plate deflection at inner radius ( $r=b$ ). The plot on the right is a close-up view. As the ratio of plate thickness to plate outer radius approaches 1, the deflection due to shearing becomes important. For ratios  $\ll 1$ , shearing effects are inconsequential compared to bending effects.

These results illustrate the importance of shearing effects as the ratio of plate thickness to plate outer radius approaches 1. For ratios significantly less than 1, deflections due to bending far exceed those due to shearing. In this case, neglecting the shear contributions would have little effect on the calculated deformation. On the other hand, for ratios near and greater than 1, shear contributions are important and therefore, neglecting them would result in overall deformations smaller than those expected in reality. For each of the compliant plate structures within the active valve, except for the valve membrane (where its thickness  $\ll$  radial dimensions), both bending and shear effects are included in the deformation analyses.

## 2.3 Detailed Structural Modeling

### 2.3.1 Piezoelectric Material Behavior

The piezoelectric material cylinder within the valve drive element strains when a voltage is applied to it. Often, the loading on the material may increase during this actuation step. In the drive element structure, this actuation compressive loading is a combination of the hydraulic

amplification chamber pressure acting over the piston top surface and the tensile drive element tether force acting along the piston outer circumference. In general, for a bulk cylindrical piezoelectric element, as shown in Figure 2.4, subject to an applied voltage  $V_p$  and an actuation compressive axial stress  $\Delta T_p$ , the material axial strain is:

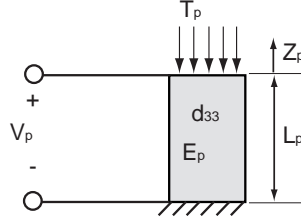


Figure 2.4: Cylindrical piezoelectric element with applied voltage and stress loading.

$$\varepsilon_p = \frac{\Delta Z_p}{L_p} = \frac{d_{33} V_p}{L_p} - \frac{\Delta T_p}{E_p} \quad (2.20)$$

The parameter  $d_{33}$  is the piezoelectric material coefficient and  $E_p$  is the modulus of elasticity. Under the case of zero actuation loading,  $\Delta T_p = 0$ , the material experiences a maximum strain in response to a voltage  $V_p$ . This is termed the free strain condition,  $\varepsilon_{p,free} = \frac{d_{33} V_p}{L_p}$ . At a sufficiently large external load, the material experiences no net strain in response to a voltage. This is termed the blocked force condition,  $\Delta T_{p,blocked} = \frac{d_{33} V_p E_p}{L_p}$ .

Equation 2.20 assumes perfect 33-direction actuation. In reality, this is not achieved due to transverse clamping of the piezoelectric element at its top and bottom. However, the incorporation of multiple, smaller diameter piezoelectric elements rather than a single large diameter element helps to reduce this clamping effect and supports the assumption. The implementation of multiple, smaller diameter piezoelectric elements is discussed in Section 2.5. For the purposes of the active valve model development in this section, however, a single piezoelectric material cylinder placed at the center of the drive element chamber is assumed.

### 2.3.2 Drive Element Piston and Tether Behavior

The drive element substructure provides a volume change, which is transferred to the valve cap/membrane through the use of hydraulic fluid. In an ideal case, the drive piston would be a rigid structure and the drive element tethers would be stiff enough to resist significant volume deformation due to the hydraulic amplification chamber pressure, yet compliant enough to allow for adequate piston deflection and to ensure tether stresses below critical levels. The drive element piston and tether structure can be broken into two linked sub-models, as shown in Figure 2.5. The first sub-model captures the behavior of the drive piston and the second sub-model captures the behavior of the drive element tethers.

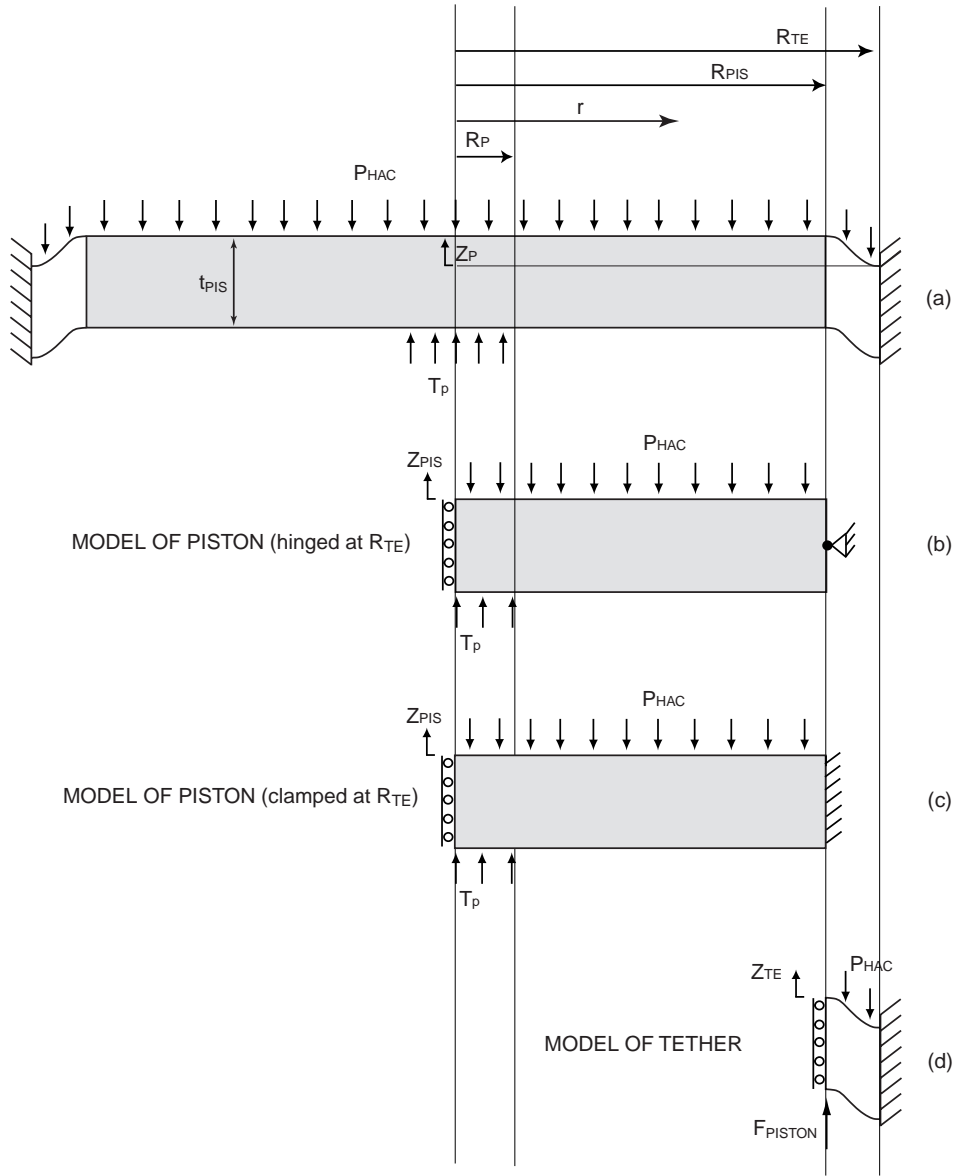


Figure 2.5: Simplification of pressure and stress loading on the drive element piston for use in the linear deflection analysis of the drive element tethers.

## Drive Element Piston

Figures 2.5(b) and 2.5(c) present two potential ways to model the deformation of the drive element piston. Both scenarios model the piston as a circular plate with outer radius  $R_{pis}$  and thickness  $t_{pis}$  and assume the plate to experience a guided boundary condition at its center. Finite-element models have shown this to be a more appropriate (and conservative) boundary condition than enforcing a guided boundary condition at the edge of piezo material,  $R_p$ . The piezoelectric material is not infinitely rigid, and therefore does allow for plate bending over the region where the material contacts the piston. The primary difference in the two scenarios is the boundary condition assumptions at the outer piston radius  $R_{pis}$ . If the drive element tethers possessed negligible stiffness, one could assume that they exert an insignificant bending moment on the drive piston, resulting in an appropriate hinged boundary condition at  $R_{pis}$ , as shown in Figure 2.5(b). On the other hand, if the tethers possessed an infinite stiffness, one could assume them to create a rigid boundary on the piston at this location, as shown in Figure 2.5(c). Finite-element studies have shown that for the typical range of design space for the tethers and piston in this active valve device, the actual structural behavior is approximately halfway between these two limiting scenarios. Therefore, the drive element piston compliances are taken as the average of these limiting scenarios. The hydraulic amplification chamber pressure  $P_{HAC}$  acts over the entire top surface of the plate from  $r = 0$  to  $r = R_{pis}$  and the piezoelectric material stress  $T_p$  acts over the bottom surface of the plate from  $r = 0$  to  $r = R_p$ . The piston center deflection  $Z_{pis}$  and piston swept volume  $dV_{pis}$  (referenced to the hinged outer radius) can therefore be represented by the following relations,

$$Z_{pis} = \left[ \Xi_{Z_{pis}}^T \right] T_P - \left[ \Xi_{Z_{pis}}^P \right] P_{HAC} \quad (2.21)$$

$$dV_{pis} = \left[ \Xi_{dV_{pis}}^T \right] T_P - \left[ \Xi_{dV_{pis}}^P \right] P_{HAC} \quad (2.22)$$

where  $\Xi_{Z_{pis}}^T$ ,  $\Xi_{Z_{pis}}^P$ ,  $\Xi_{dV_{pis}}^T$ , and  $\Xi_{dV_{pis}}^P$  are the compliance coefficients defined explicitly in Appendix A.2.

## Drive Element Tethers

In Figure 2.5(c), each drive element tether is modeled as a circular plate with inner radius  $R_{pis}$  and outer radius  $R_{ch}$ . In order to allow for flexibility in design, the top and bottom tethers are defined to have different thicknesses ( $t_{tetop}$  or  $t_{tebot}$ ). Again, assuming that the piston slope at  $R_{pis}$  is zero, the boundary condition on each tether at this location is that of a guided interface. At  $R_{ch}$ , each plate is rigidly clamped to the valve support structure. The top tether experiences a concentrated force  $F_{tetop}$  at  $r = R_{pis}$  and a pressure loading  $P_{HAC}$  from  $r = R_{pis}$  to  $r = R_{ch}$

while the bottom tether experiences only a concentrated force  $F_{tebot}$  at  $r = R_{pis}$ . The deflection (at  $r = R_{pis}$ ) and swept volume of the top tether alone can be written as,

$$Z_{tetop} = \left[ \Xi_{Z_{tetop}}^F \right] F_{tetop} - \left[ \Xi_{Z_{tetop}}^P \right] P_{HAC} \quad (2.23)$$

$$dV_{tetop} = \left[ \Xi_{dV_{tetop}}^F \right] F_{tetop} - \left[ \Xi_{dV_{tetop}}^P \right] P_{HAC} + A_{pis} Z_{tetop} \quad (2.24)$$

where  $\Xi_{Z_{tetop}}^F$ ,  $\Xi_{Z_{tetop}}^P$ ,  $\Xi_{dV_{tetop}}^F$ , and  $\Xi_{dV_{tetop}}^P$  are coefficients defined explicitly in Appendix A.2.

The deflection (at  $r = R_{pis}$ ) and swept volume of the bottom tether alone can be written as,

$$Z_{tebot} = \left[ \Xi_{Z_{tebot}}^F \right] F_{tebot} \quad (2.25)$$

$$dV_{tebot} = \left[ \Xi_{dV_{tebot}}^F \right] F_{tebot} + A_{pis} Z_{tebot} \quad (2.26)$$

where  $\Xi_{Z_{tebot}}^F$  and  $\Xi_{dV_{tebot}}^F$  are coefficients defined explicitly in Appendix A.2.

Although the equations for the behavior of each tether alone are straightforward, the behavior resulting from both tethers together is more complex. In a two-tether system, both tethers share the same deflection at  $r = R_{pis}$ ; that is,  $Z_{te} = Z_{tetop} = Z_{tebot}$ . Additionally, the sum of the piston forces on the tethers must be equal to the total force on the piston itself,

$$F_{tetop} + F_{tebot} = F_{piston} = A_p T_p - A_{pis} P_{HAC}. \quad (2.27)$$

The distribution of this force on the tethers is determined by the relative stiffnesses of the tethers, and therefore, the force taken by the top tether can be written as,

$$F_{tetop} = \left[ \frac{\Xi_{Z_{tebot}}^F}{\Xi_{Z_{tebot}}^F + \Xi_{Z_{tetop}}^F} \right] F_{piston} \quad (2.28)$$

One can observe from this relation that if the bottom tether has a thickness much less than that of the top tether (ie:  $\Xi_{Z_{tebot}}^F \gg \Xi_{Z_{tetop}}^F$ ), then all of the piston load is taken by the top tether,  $F_{tetop} \approx F_{piston}$ . Likewise, if the tethers have the same thickness, then each tether carries half of the piston force. Following these arguments, the tether deflection (at  $r = R_{pis}$ ) and the tether swept volume can be expressed as,

$$Z_{te} = Z_{tetop} = \left[ \frac{\Xi_{Z_{tetop}}^F \Xi_{Z_{tebot}}^F}{\Xi_{Z_{tebot}}^F + \Xi_{Z_{tetop}}^F} \right] (A_p T_p - A_{pis} P_{HAC}) - \left[ \frac{\Xi_{Z_{tetop}}^P \Xi_{Z_{tebot}}^P}{\Xi_{Z_{tebot}}^P + \Xi_{Z_{tetop}}^P} \right] P_{HAC} \quad (2.29)$$

$$dV_{te} = dV_{tetop} = \left[ \frac{\Xi_{dV_{tetop}}^F \Xi_{Z_{tebot}}^F}{\Xi_{Z_{tebot}}^F + \Xi_{Z_{tetop}}^F} \right] (A_p T_p - A_{pis} P_{HAC}) - \left[ \frac{\Xi_{dV_{tetop}}^P \Xi_{Z_{tebot}}^P}{\Xi_{Z_{tebot}}^P + \Xi_{Z_{tetop}}^P} \right] P_{HAC} + A_{pis} Z_{te} \quad (2.30)$$

In this manner, the deflection of the drive element piston outer radius and the swept volume of the piston and top tether is determined.

### Combined Piston and Tether Behavior

Having modeled the piston and tethers individually, it is now possible to express the complete piston/tether deflection and swept volume. The drive element piston center deflection with respect to the active valve structural support is the sum of the piston deflection in the first sub-model and the tether deflection in the second sub-model,

$$Z_{de} = Z_{pis} + Z_{te}. \quad (2.31)$$

Likewise, the total drive element volume change is the sum of the piston swept volume in the first sub-model and the top tether swept volume in the second sub-model,

$$dV_{de} = dV_{pis} + dV_{te}. \quad (2.32)$$

These relations, therefore, fully describe the drive element center deflection and swept volume as a function of the piston and tether stiffness coefficients and the loading,  $T_p$  and  $P_{HAC}$ .

### 2.3.3 Bottom Structural Compliance

A rigid valve structure beneath the piezoelectric material cylinder would ensure that all of the piezoelectric strain during actuation goes into the drive element volume change needed for valve cap motion. In reality, this structure is not rigid and as a result this bottom structure deformation serves only to reduce the effective volume change that can be produced by the drive element.

As shown in Figure 2.6, this structure can be modeled as a circular plate with thickness  $t_{bot}$ , guided at its center, and clamped at outer radius  $R_{ch}$ . Again, as for the drive element piston, the assumption that the piezo in no way helps to stiffen the plate is taken as a conservative estimate. The only loading applied to the plate is the piezoelectric material stress  $T_p$  from  $r = 0$  to  $r = R_p$ . The bottom plate center deflection  $Z_{bot}$  can therefore be represented by the following relation,

$$Z_{bot} = - \left[ \Xi_{Z_{bot}}^T \right] T_p \quad (2.33)$$

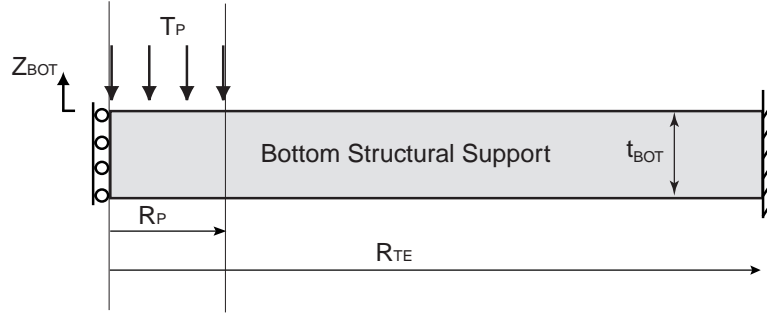


Figure 2.6: Compliance of bottom structure beneath piezoelectric material.

where  $\Xi_{Z_{bot}}^T$  is defined explicitly in Appendix A.2.

### 2.3.4 Fluid Compressibility

During valve actuation, increased pressure within the hydraulic amplification chamber results in compression of the contained fluid. A portion of the drive element volume change will be lost in this undesired volume change of the fluid. The relationship between the fluid volume change  $dV_{HAC}$  and the fluid pressure change  $dP_{HAC}$  is:

$$dV_{HAC} = - \left( \frac{V_{HAC}}{K_f} \right) dP_{HAC} \quad (2.34)$$

where  $K_f$  is the fluid bulk modulus and  $V_{HAC}$  is the total fluid volume of the hydraulic amplification chamber.

### 2.3.5 Top Structural Compliance

For efficient hydraulic amplification within the active valve, the top structural compliance should be small so that minimal drive element actuation volume is lost in this chamber deformation. As shown in Figure 2.7, the top chamber structure can be modeled as an annular plate with inner radius  $R_{vm}$ , outer radius  $R_{ch}$ , and thickness  $t_{top}$ . At  $R_{vm}$ , the plate is free and experiences a concentrated force  $F_{vm}$ , corresponding to the sum of all the forces acting on the valve cap and membrane,

$$F_{vm} = P_{HAC} A_{vm} - P_1 A_{vc} - P_2 (A_{vm} - A_{vc}). \quad (2.35)$$

The plate is rigidly clamped at  $R_{te}$ . The plate experiences a pressure loading  $P_{HAC}$  on its underside.

The top plate inner radius deflection  $Z_{top}$  and swept volume  $dV_{top}$  can therefore be represented by the following relation,



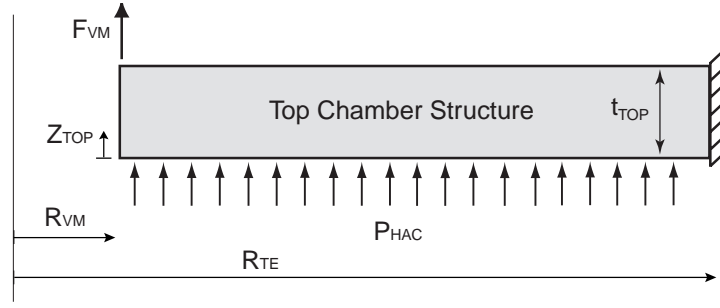


Figure 2.7: Hydraulic amplification chamber structural deformation under  $P_{HAC}$  and  $F_{vm}$  loading.

$$Z_{top} = \left[ \Xi_{Z_{top}}^P \right] P_{HAC} + \left[ \Xi_{Z_{top}}^F \right] F_{vm} \quad (2.36)$$

$$dV_{top} = \left[ \Xi_{dV_{top}}^P \right] P_{HAC} + \left[ \Xi_{dV_{top}}^F \right] F_{vm} + A_{vm} Z_{top} \quad (2.37)$$

where  $\Xi_{Z_{top}}^P$ ,  $\Xi_{Z_{top}}^F$ ,  $\Xi_{dV_{top}}^P$ , and  $\Xi_{dV_{top}}^F$  are defined explicitly in Appendix A.2. In reality, the region above the annular chamber structure will not be completely unsupported. As a result, this model provides a worst-case value for the structural chamber volume change.

### 2.3.6 Valve Cap and Membrane Behavior

For the fluid flow directionality shown in Figure 2.1, a pressure drop occurs as the fluid flows radially inward over the valve membrane, through the contraction over the valve cap, and finally through the expansion into the exit channel. In the structural modeling of the valve cap and membrane, the pressure  $P_2$  is assumed constant over the valve membrane area and the pressure  $P_1$  is assumed constant over the valve cap area (see Chapter 5 for further discussion of these fluid modeling assumptions).

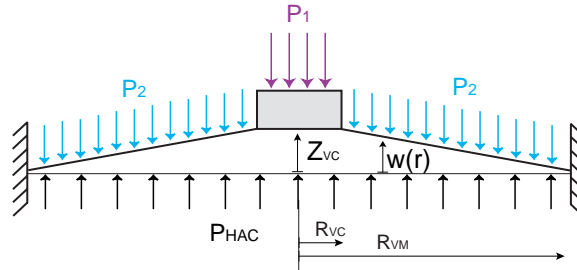


Figure 2.8: Valve membrane and cap, deflected upward from their equilibrium position, under pressure loadings  $P_{HAC}$ ,  $P_1$ , and  $P_2$ .

As shown in Figure 2.8, the valve membrane experiences a pressure loading  $P_{HAC}$  over its entire bottom surface, a pressure loading  $P_1$  over the valve cap top surface, and a pressure loading  $P_2$  over the top surface of the valve membrane. The valve membrane can be modeled as a circular plate with thickness  $t_{vm}$ , a guided boundary condition at  $r = R_{vc}$ , and a clamped boundary condition at  $r = R_{vm}$ , with a pressure loading  $P_{vm} = (P_{HAC} - P_2)$  on the underside of the membrane and a concentrated force  $F_{vc} = A_{vc}(P_{HAC} - P_1)$  acting in the upward direction at  $r = R_{vc}$  (see Figure 2.9). Bending of the valve cap is neglected in this model. For typical valve cap and membrane dimensions within the active valve structure, finite-element studies have shown that this rigid cap assumption is valid.

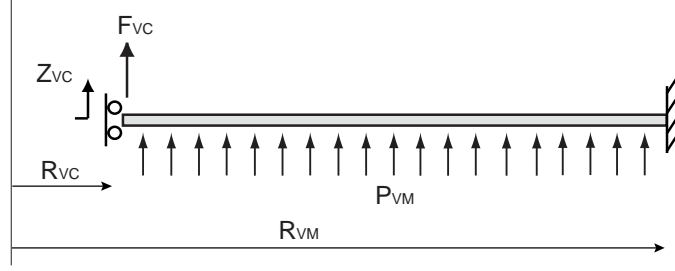


Figure 2.9: Simplified model of the valve cap and membrane with imposed boundary conditions and applied loading.

For linear theory, the inner radius deflection  $Z_{vc}$  and the swept volume  $dV_{vm}$  can be represented by the following relations,

$$Z_{vc} = \left[ \Xi_{Z_{vc}}^P \right] P_{vm} + \left[ \Xi_{Z_{vc}}^F \right] F_{vc} \quad (2.38)$$

$$dV_{VM} = \left[ \Xi_{dV_{vm}}^P \right] P_{vm} + \left[ \Xi_{dV_{vm}}^F \right] F_{vc} + A_{vc} Z_{vc} \quad (2.39)$$

where  $\Xi_{Z_{vc}}^P$ ,  $\Xi_{Z_{vc}}^F$ ,  $\Xi_{dV_{vm}}^P$ , and  $\Xi_{dV_{vm}}^F$  are defined explicitly in Appendix A.2.

## 2.4 Full Active Valve Linear Model

The complete quasi-static active valve model consists of Equations 6.2, 6.3, 6.4, 2.29, 2.30, 2.33, 2.34, 2.35, 2.36, 2.37, 2.38, and 2.39, combined with the following two equations for displacement matching and volume conservation,

$$Z_p + Z_{bot} = Z_{te} + Z_{pis} \quad (2.40)$$

$$dV_{te} + dV_{pis} + dV_{fluid} - dV_{top} - dV_{vm} = 0. \quad (2.41)$$

Figure 2.10 summarizes the modeling components of the active valve. All equations are represented in a Maple code that solves for  $T_p$  and all of the structural component displacements and swept volumes, given the voltage input  $V_p$  and the external valve cap and membrane pressure loadings  $P_1$  and  $P_2$ . This model is included in Appendix A.2 for reference.

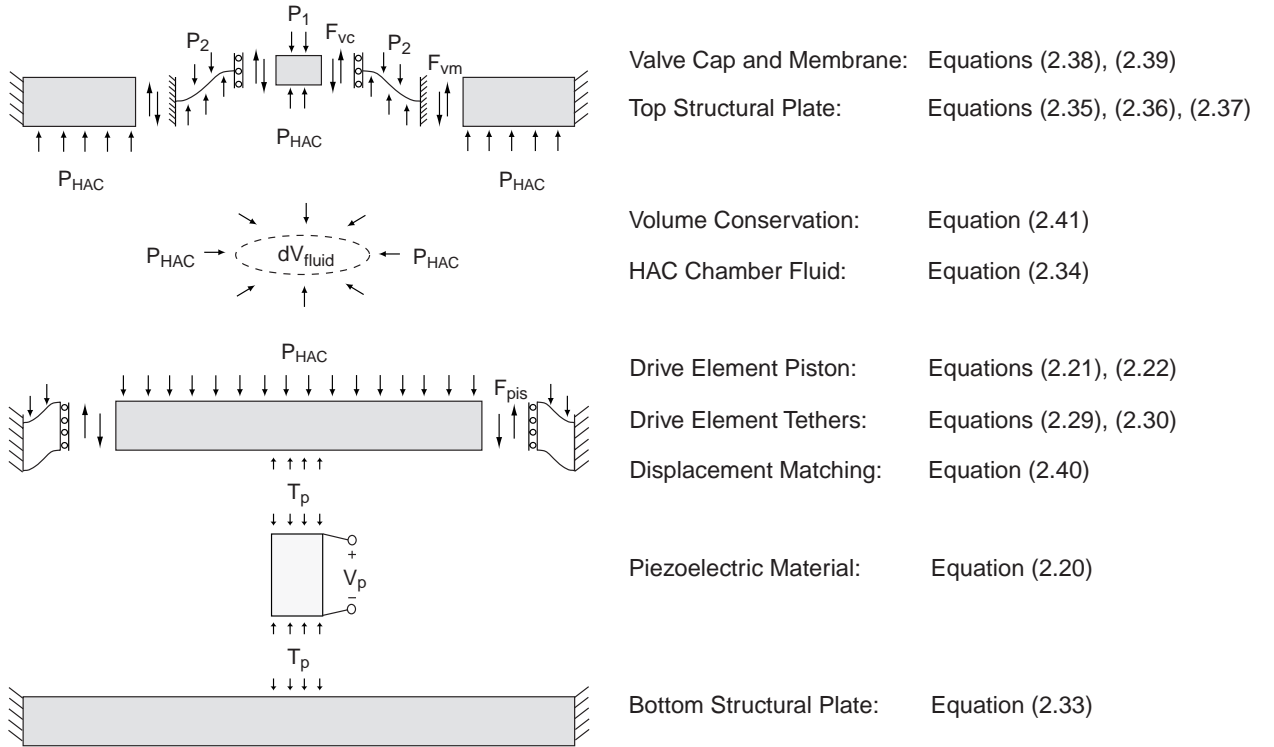


Figure 2.10: Complete linear quasi-static active valve structural model.

## 2.5 Impact of Multiple Piezoelectric Cylinders

The previous development of analytical theory for the active valve has assumed the piezoelectric actuation material to be a single cylinder located at the center of the drive element piston. To stiffen the drive element actuator structure, it would be desirable to incorporate a matrix of small diameter piezoelectric rods under the piston rather than a single centrally-located large-size cylinder (as long as the rods are sized properly to avoid buckling). Although incorporation of a matrix of rod structures is beyond the scope of this thesis, the use of three smaller diameter piezoelectric cylinders spread out beneath the piston is realizable (Chapter 8 experimentally evaluates this concept). This modeling section investigates the benefits of using three smaller diameter piezoelectric cylinders rather than a single centrally-located one in order to effectively “stiffen” the drive element piston and bottom plate structures.

Since the analytical relations developed thus far have assumed plate theory with boundary conditions corresponding to a single centrally-located piezoelectric cylinder, and since derivation of 3-dimensional plate behavior for multiple cylinder geometries is complex, finite-element models of the structural components are required. This section demonstrates, through example cases, how finite-element models of the drive element piston structure and bottom plate structure can be used to determine the  $\Xi_{Z_p}^T$ ,  $\Xi_{Z_p}^P$ ,  $\Xi_{dV_{pis}}^T$ ,  $\Xi_{dV_{pis}}^P$ , and  $\Xi_{Z_{bot}}^T$  compliance coefficients for three-piezoelectric cylinder geometries. Once determined, these coefficients can simply be substituted into the corresponding structural equations developed for the single-cylinder geometry presented in Sections 2.3.2 and 2.3.3.

### 2.5.1 Finite-Element Analysis of Piston

As presented in Section 2.3.2, the  $\Xi$  compliance coefficients for the piston structure are taken as the average of the hinged and clamped boundary condition scenarios at  $R_p$ . For clarity, this section will analyze the effects of three piezoelectric cylinders on a drive piston in the hinged boundary condition scenario. A similar procedure can be carried out for the clamped scenario, but is not documented in the section.

To illustrate the benefits of using three piezoelectric cylinders, a finite-element study comparing a single piezoelectric cylinder piston geometry to geometries with three piezoelectric cylinders is presented. In this study, representative piston geometry and material properties are taken to be:  $R_{pis} = 3mm$ ,  $t_{pis} = 800\mu m$ ,  $E_{Si} = 165GPa$ , and  $\nu_{Si} = 0.22$ . For the single piezoelectric cylinder geometry, the cylinder radius is  $R_p = 1mm$ . For the three piezoelectric cylinder geometry, the radius of each cylinder is sized ( $R_p = 0.577mm$ ) such that the total area of all three is identical to the area of the cylinder in the single piezoelectric cylinder case. The distance  $R_{cp}$  of each cylinder from the piston center is varied in this study to illustrate the effect of cylinder placement on the piston compliance. Schematics of the single cylinder and

three cylinder finite-element model geometries are shown in Figure 2.11. The piston structure is guided at its center ( $r = 0$ ) and hinged at its outer radius ( $r = R_{pis}$ ).

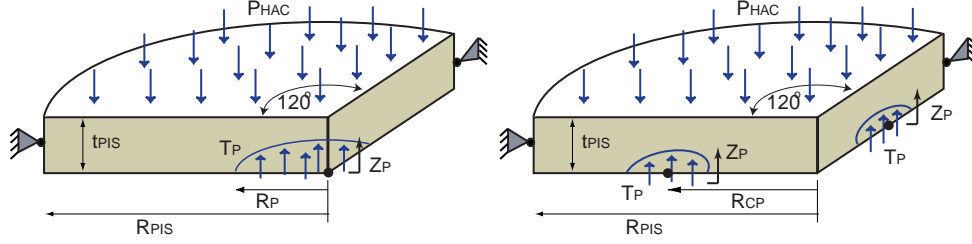


Figure 2.11: Finite-element (ANSYS) models of (a) a single centrally located piezoelectric cylinder beneath the drive element piston, and (b) a three piezoelectric cylinder design with the cylinders spread out beneath the drive element piston.

To determine the compliance coefficients  $\Xi_{Z_p}^T$  and  $\Xi_{dV_{pis}}^T$  for the drive piston structure, a stress  $T$  is applied on the underside of the piston where the cylinder(s) make contact. The resulting displacement at the center of the cylinder(s),  $Z_p$ , and the resulting swept volume of the piston structure,  $dV_{pis}$  are recorded. Similarly, to determine the compliance coefficients  $\Xi_{Z_p}^P$  and  $\Xi_{dV_{pis}}^P$ , a pressure  $P$  is applied on the entire top surface of the piston. The resulting displacement at the center of the cylinder(s),  $Z_p$ , and the resulting swept volume of the piston structure,  $dV_{pis}$  are recorded. From these responses, the compliance coefficients are calculated.

### Single Piezoelectric Cylinder Geometry

In performing finite-element analyses for this single cylinder geometry, the resulting piston compliance coefficients were found to be:

Loading	$Z_p$ Compliance	$dV_{de}$ Compliance
Stress	$\Xi_{Z_p}^T = 2.09e^{-13} \frac{m}{Pa}$	$\Xi_{dV_{pis}}^T = 2.42e^{-18} \frac{m^3}{Pa}$
Pressure	$\Xi_{Z_p}^P = 8.20e^{-13} \frac{m}{Pa}$	$\Xi_{dV_{pis}}^P = 1.08e^{-17} \frac{m^3}{Pa}$

### Three Piezoelectric Cylinder Geometries

Finite-element analyses for the three cylinder geometry were performed, with  $R_{cp}$  varying from 1 mm to 2.25 mm. Figure 2.12 plots the compliance coefficients of the three-cylinder geometries as a function of  $R_{cp}$ . Taking as an example case,  $R_{cp} = 2.25mm$ , the compliance coefficients were found to be:

Loading	$Z_p$ Compliance	$dV_{de}$ Compliance
Stress	$\Xi_{Z_p}^T = 0.36e^{-13} \frac{m}{Pa}$	$\Xi_{dV_{pis}}^T = 0.94e^{-18} \frac{m^3}{Pa}$
Pressure	$\Xi_{Z_p}^P = 3.12e^{-13} \frac{m}{Pa}$	$\Xi_{dV_{pis}}^P = 1.08e^{-17} \frac{m^3}{Pa}$

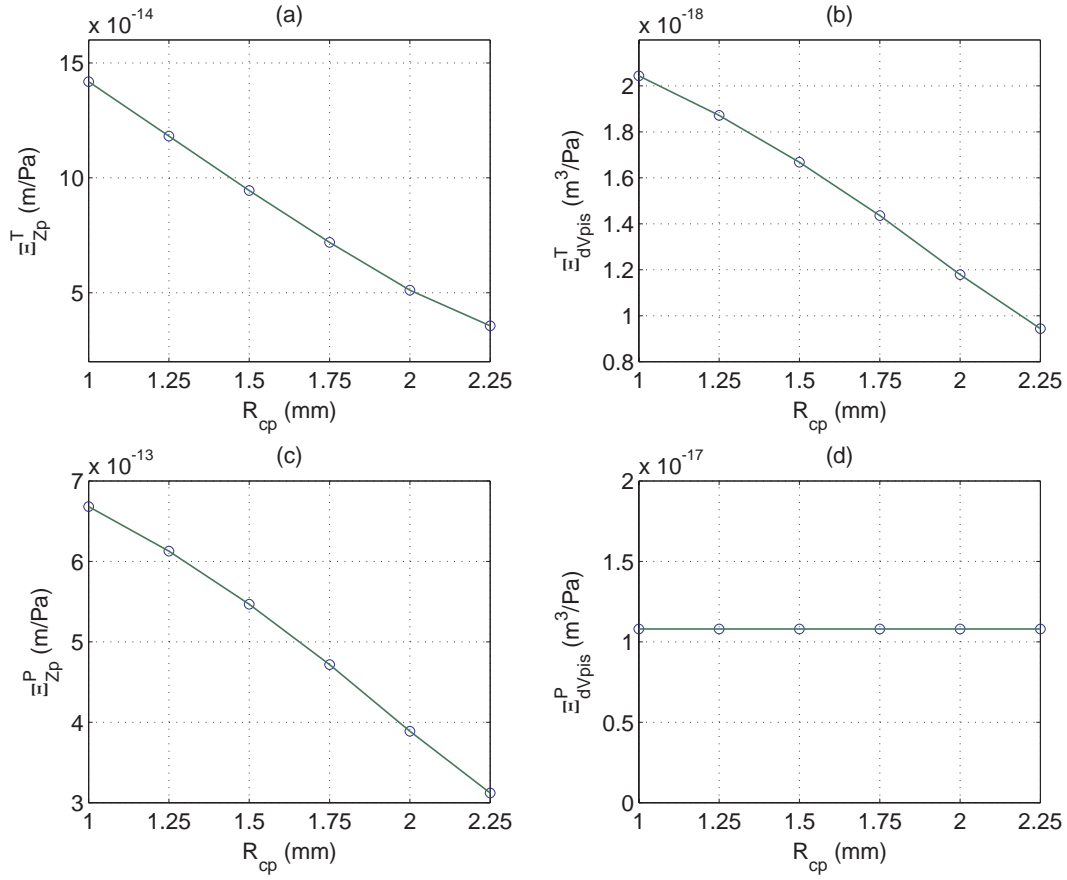


Figure 2.12: Compliance coefficients of the three cylinder piston geometry for varying  $R_{cp}$ : (a)  $\Xi_{Zp}^T$ , (b)  $\Xi_{dVpis}^T$ , (c)  $\Xi_{Zp}^P$ , and (d)  $\Xi_{dVpis}^P$ .

In comparing these results (for  $R_{cp}=2.25$  mm) to those of the single cylinder geometry, it is observed that  $\Xi_{Zp}^T$  is reduced by 5.8x,  $\Xi_{dVpis}^T$  is reduced by 2.6x, and  $\Xi_{Zp}^P$  is reduced by 2.6x. Clearly, the use of three cylinders spread out beneath the piston is beneficial in reducing these coefficients, and therefore stiffening the structure.  $\Xi_{dVpis}^P$ , however, remains the same. This is expected since the swept volume of the piston structure (with no cylinders present below) in response to an applied pressure on the piston top surface should be identical for the single and three cylinder geometries. These results demonstrate the stiffening benefits of incorporating three piezoelectric cylinders beneath the drive element piston rather than a single centrally-located one. With these types of finite-element models, one can obtain compliance coefficients for a particular three cylinder drive piston geometry and use these coefficients in the analytical equations developed in Section 2.3.2 to accurately model the valve structural behavior.

### 2.5.2 Finite-Element Analysis of Bottom Plate

To illustrate the stiffening benefit of using three piezoelectric cylinders above the bottom plate, a finite-element study comparing a single piezoelectric cylinder bottom plate geometry to geometries with three piezoelectric cylinders is presented. In this study, the chamber bottom plate geometry and material properties are assumed to be:  $R_{te} = 3.2\text{mm}$ ,  $t_{pis} = 1000\mu\text{m}$ ,  $E_{Si} = 165\text{GPa}$ , and  $\nu_{Si} = 0.22$ . For the single piezoelectric cylinder geometry, the cylinder radius is  $R_p = 1\text{mm}$ . For the three piezoelectric cylinder geometry, the radius of each cylinder is sized ( $R_p = 0.577\text{mm}$ ) such that the total area of all three is identical to the area of the cylinder in the single piezoelectric cylinder case. Schematics of the single cylinder and three cylinder finite-element model geometries are shown in Figure 2.13. The piston structure is guided at its center ( $r = 0$ ) and clamped at its outer radius ( $r = R_{te}$ ).

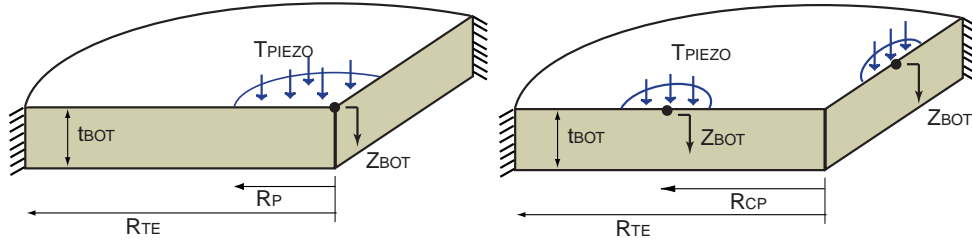


Figure 2.13: Finite-element (ANSYS) models of bottom plate structure with (a) a single centrally located cylinder above the bottom plate, and (b) a three cylinder design, with the cylinders spread out above the bottom plate.

To determine the compliance coefficient for the bottom plate structure  $\Xi_{Z_{bot}}^T$ , a pressure (stress)  $T$  is applied to the top surface of the plate where the cylinder(s) make contact. The resulting displacement at the center of the cylinder(s),  $Z_{bot}$  is recorded. From this response, the compliance coefficient is calculated.

#### Single Piezoelectric Cylinder Geometry

In performing the finite-element analysis for this single cylinder geometry, the resulting piston compliance coefficient was found to be:

Loading	$Z_{bot}$ Compliance
Stress	$\Xi_{Z_{bot}}^T = 4.79e^{-14} \frac{m}{Pa}$

#### Three Piezoelectric Cylinder Geometries

Finite-element analyses for the three cylinder geometry were performed, with  $R_{cp}$  varying from 1 mm to 2.25 mm. Figure 2.14 plots the compliance coefficient  $\Xi_{Z_{bot}}^T$  of the three-cylinder

geometry as a function of this varying  $R_{cp}$ . Taking as an example case,  $R_{cp} = 2.25\text{mm}$ , the compliance coefficient was found to be:

Loading	$Z_{bot}$ Compliance
Stress	$\Xi_{Z_{bot}}^T = 0.98e^{-14} \frac{m}{Pa}$

In comparing this result (for  $R_{cp}=2.25\text{ mm}$ ) to that of the single cylinder geometry, it is observed that  $\Xi_{Z_p}^T$  is reduced by 4.9x. Clearly, the use of three cylinders spread out above the bottom plate is beneficial in reducing the amount by which the centers of the cylinders move downward into the plate. These results demonstrate the stiffening benefits of incorporating three piezoelectric cylinders above the bottom plate structure rather than a single centrally-located one. With this type of finite-element model, one can obtain the compliance coefficient for a particular three cylinder bottom plate geometry and use this coefficient in the analytical equations developed in Section 2.3.3 to accurately model the valve structural behavior.

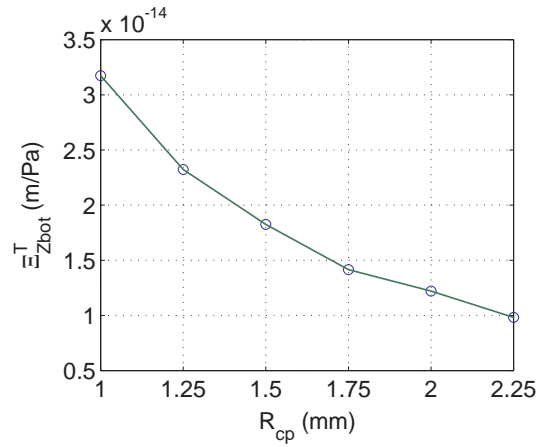


Figure 2.14: Compliance coefficient  $\Xi_{Z_{bot}}^T$  of the three cylinder bottom plate geometry for varying  $R_{cp}$ .

## 2.6 Further Modeling Issues

The structural component that requires additional modeling focus is that of the valve cap and membrane. For the typical design space in the proposed active valve, this plate/membrane structure is designed to have a thickness of approximately  $10\text{ }\mu\text{m}$ , yet experience deflections on this order or larger. In this deflection regime, the plate will begin to stretch, resulting in the generation of in-plane tensile stresses that are unaccounted for in the linear plate theory presented in this chapter. The drive element tethers also possess thicknesses near  $10\text{ }\mu\text{m}$ , however, because the piston deflection during device operation is expected to be only  $1\text{-}2\text{ }\mu\text{m}$ , these tethers can be accurately modeled by the linear relations detailed thus far.



## 2.7 Conclusions

This chapter has developed a linear, quasi-static structural model of the proposed active valve device, including piezoelectric material behavior, deformation of the drive element tethers and the valve cap/membrane structure, and the compliances associated with the drive element piston, bottom structural plate, top structural plate, and hydraulic fluid. In addition, the chapter has demonstrated, through the use of representative finite-element models, the benefits of incorporating multiple piezoelectric cylinders spread out beneath the drive element piston rather than a single centrally-located one. The following chapter will detail the development of numerical non-linear modeling tools for understanding the large deflection deformation behavior of the valve cap and membrane structure.

# Bibliography

- [1] S. Timoshenko. *Theory of Plates and Shells*. McGraw-Hill Book Company, Inc., New York and London, 1940.

## Chapter 3

# Non-Linear Deformation of the Valve Cap and Membrane

This chapter presents the development of a numerical code for the non-linear large-deflection modeling of a thin annular plate structure with rigid central cap under pressure loading. This theory has been specifically developed to model the valve cap and membrane behavior in the proposed active valve device. The chapter begins within an introduction to the valve cap geometry under investigation and the associated nature of the geometric non-linearity. The theory behind this non-linear deformation is then presented, with detailed derivation of the governing equations used in the numerical integration. Representative loading plots for a given valve geometry are then presented to illustrate the numerical code's capability to capture in-plane tensile stresses and boundary layer phenomena. Lastly, three Matlab<sup>TM</sup> codes are presented that serve as non-linear modeling tools for use in Chapters 4, 5, and 8 of this thesis. The finite-differencing scheme presented in this chapter is based upon the work of Su [1].

### 3.1 Introduction

In general, the deflection of a structural plate can be represented using linear deformation theory only if the deflection of the plate is less than about half the thickness of the plate. In this small deflection regime, it can be assumed that the plate's neutral axis is unchanged in length as it deforms, ie: it experiences no tensile stress. The only stresses that exist in this plate are the compressive and tensile bending stresses above and below this neutral axis. In a plate experiencing large deflections (that is, deflections greater than half the thickness of the plate), however, the plate begins to stretch and the assumption of zero in-plane tensile stress at the neutral axis is no longer valid. As the plate is deformed more and more into the large deflection regime, the in-plane tensile stress begins to dominate the bending stresses, thereby

increasing the plate stiffness. This marks the onset of membrane behavior, characterized by the inability to withstand bending moments. For plates that experience loads that create this large deflection behavior, it is critical that this in-plane stress be modeled and that the plate stiffening effects be captured.

## 3.2 Plate Geometry

The plate geometry under consideration in this chapter is shown in Figure 3.1. The plate has outer radius,  $r_a$ , inner radius  $r_b$ , thickness  $t$ , a Young's Modulus  $E$ , and a poisson ratio  $\nu$ . The plate is clamped at its outer radius and guided at its inner radius. The assumption of a guided boundary condition at  $r_b$  is a reasonable one since bending of the valve cap is negligible. The plate experiences a pressure loading  $p$  underneath the plate from  $r_b$  to  $r_a$  and a concentrated circumferential force  $f$  at  $r_b$ .

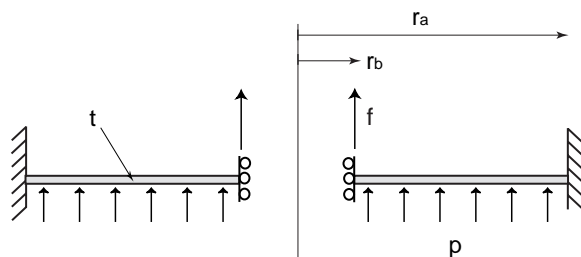


Figure 3.1: Schematic of an annular plate with a rigid central boss under pressure loading.

## 3.3 Theory

The work presented in this chapter is an extension of Sheplak and Dugundji's work on the large deflection behavior of clamped circular plates (without rigid central caps) [2]. Additionally, the finite-difference implementation contained within this chapter is the result of work done by Su [1].

### 3.3.1 Assumptions

This chapter follows von Karman plate theory, in which the vertical displacement of the plate  $w$  is assumed to be much larger than the lateral displacement  $u$  and  $v$  and the normals to the undeformed middle surface remain the normals to the deformed middle surface. As a result, the deformed shape of the thin plate can be fully described by the geometry of the neutral surface. In this analysis, only quadratic non-linear terms are retained.

### 3.3.2 Equilibrium Equations

The forces and moments experienced by a small section of the plate are shown in Figure 3.2, where  $M_r$  and  $M_\theta$  are the radial and tangential moments respectively,  $N_r$  is the in-plane tension load per unit circumference, and  $Q_r$  is the shear force per unit circumference.

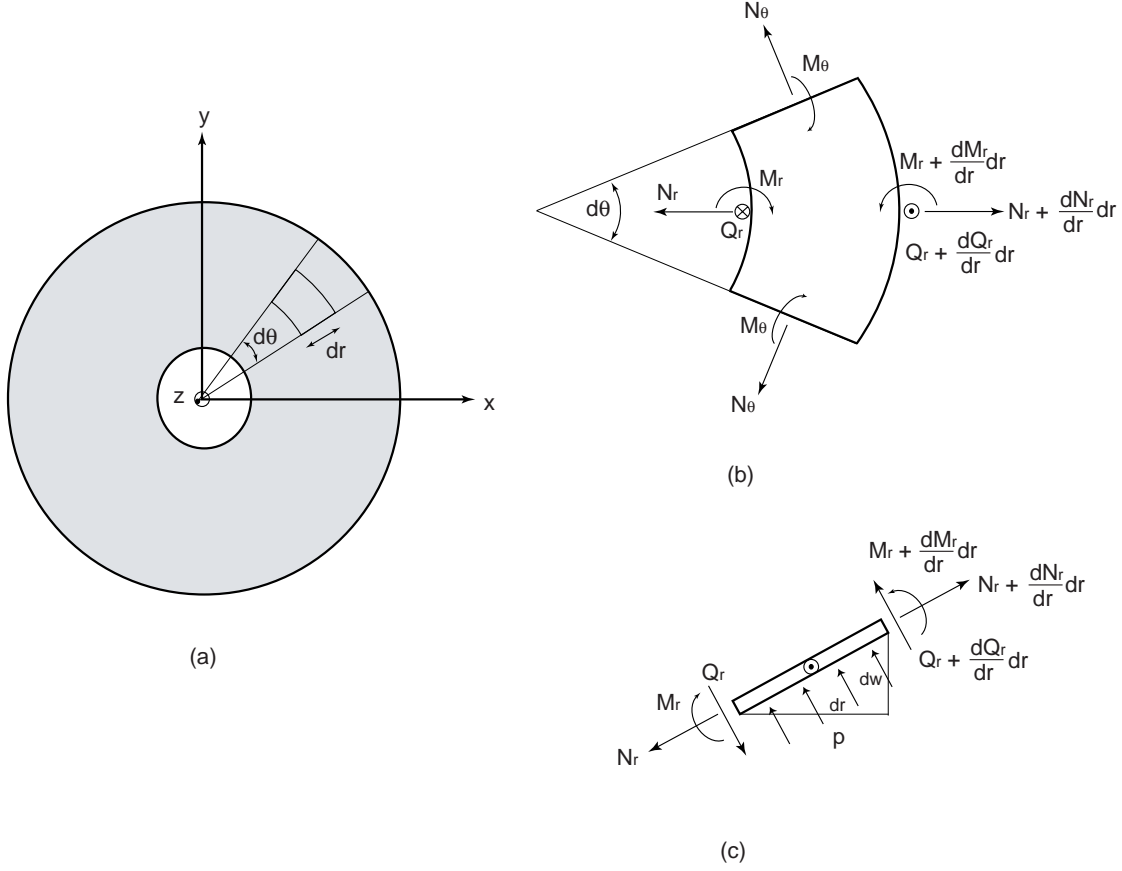


Figure 3.2: Force and moment free-body diagrams for an infinitesimal annular plate section: (a) top view of plate, (b) top view of plate section, (c) side-view of plate section.

To obtain the equilibrium equations for this plate, a radial force balance, a z-direction force balance, and a circumferential moment balance are performed.

The radial force balance produces the following initial relation,

$$\begin{aligned} \sum F_r \rightarrow & (N_r + \frac{dN_r}{dr}dr)(\cos \frac{dw}{dr})(r + dr)d\theta - N_r(\cos \frac{dw}{dr})rd\theta - 2N_\theta(\sin \frac{d\theta}{2})dr - \\ & (Q_r + \frac{dQ_r}{dr}dr)(\sin \frac{dw}{dr})(r + dr)d\theta + Q_r(\sin \frac{dw}{dr})rd\theta - p(\sin \frac{dw}{dr})rdrd\theta = 0. \end{aligned} \quad (3.1)$$

The z-direction force balance produces the following initial relation,

$$\begin{aligned} \sum F_z \rightarrow & (N_r + \frac{dN_r}{dr}dr)(\sin\frac{dw}{dr})(r + dr)d\theta - N_r(\sin\frac{dw}{dr})rd\theta + \\ & (Q_r + \frac{dQ_r}{dr}dr)(\cos\frac{dw}{dr})(r + dr)d\theta - Q_r(\cos\frac{dw}{dr})rd\theta + p(\cos\frac{dw}{dr})rdrd\theta = 0. \end{aligned} \quad (3.2)$$

The circumferential moment balance produces the following initial relation,

$$\sum M_r \rightarrow (M_r + \frac{dM_r}{dr}dr)(r + dr)d\theta - M_r rd\theta + (Q_r + \frac{dQ_r}{dr}dr)(r + dr)(r + dr)d\theta - Q_r r^2 d\theta = 0. \quad (3.3)$$

Using the following simplifying relations which hold true for the plate section,

$$\cos\frac{dw}{dr} \sim 1 \quad , \quad \sin\frac{dw}{dr} \sim \frac{dw}{dr} \quad , \quad \sin\frac{d\theta}{2} \sim \frac{d\theta}{2} \quad , \quad (dr)^2 \ll dr$$

the force and moment equilibrium balances can be simplified to the following equations respectively,

$$N_r - N_\theta + r \left( \frac{dN_r}{dr} \right) = 0, \quad (3.4)$$

$$\frac{d}{dr} \left( N_r r \frac{dw}{dr} \right) + \frac{d}{dr} (Q_r r) + pr = 0, \quad (3.5)$$

and

$$Q_r + \frac{dM_r}{dr} + \left( \frac{M_r - M_\theta}{r} \right) = 0. \quad (3.6)$$

### 3.3.3 Geometric Compatibilities

The radial elongation of the neutral axis during deformation can be represented by the following strain displacement relation [3],

$$\epsilon_r = \frac{du}{dr} + \frac{1}{2} \left[ \left( \frac{du}{dr} \right)^2 + \left( \frac{dw}{dr} \right)^2 \right]. \quad (3.7)$$

Based on the assumption that  $u \ll w$ , it follows that the term  $(\frac{du}{dr})^2$  is negligible compared to the term  $(\frac{dw}{dr})^2$ . Therefore, the radial strain displacement relation can be simplified to

$$\epsilon_r = \frac{du}{dr} + \frac{1}{2} \left( \frac{dw}{dr} \right)^2. \quad (3.8)$$

The circumferential strain-displacement relationship is

$$\epsilon_\theta = \frac{u}{r}. \quad (3.9)$$

The first and second principle curvatures for the plate are [3]

$$\kappa_r = -\frac{d^2 w}{dr^2} \quad , \quad \kappa_\theta = -\frac{1}{r} \frac{dw}{dr}. \quad (3.10)$$

### 3.3.4 Constitutive Laws

Assuming that the plate experiences plane stress, ie: no variations in stress occur through the thickness of the plate, the material Hooke's Law can be written as

$$\epsilon_r = \frac{1}{E} \left( \frac{N_r}{t} - \nu \frac{N_\theta}{t} \right) \quad , \quad \epsilon_\theta = \frac{1}{E} \left( \frac{N_\theta}{t} - \nu \frac{N_r}{t} \right) \quad (3.11)$$

where  $E$  and  $\nu$  are the material Young's Modulus and Poisson Ratio respectively. Moment equilibrium in the plate yields

$$M_r = -D(\kappa_r + \nu \kappa_\theta) \quad , \quad M_\theta = -D(\kappa_\theta + \nu \kappa_r) \quad (3.12)$$

where  $D$  is the plate flexural rigidity, defined by

$$D = \frac{Eh^3}{12(1 - \nu^2)}. \quad (3.13)$$

### 3.3.5 Governing Equations

Beginning with the three equilibrium equations (5.9), (5.10), and (3.6), the governing differential equations for the plate can be derived. Integrating (5.10) with respect to  $r$  from  $r_b$  to  $r$  yields

$$(Q_r r - Q_{r_b} r_b) + \left( N_r \frac{dw}{dr} - N_{r_b} \left( \frac{dw}{dr} \right)_{r_b} \right) + \frac{1}{2} p(r^2 - r_b^2) = 0 \quad (3.14)$$

Since the shear force at  $r_b$  is  $Q_{r_b} = \frac{-f}{2\pi r_b}$  and since  $(\frac{dw}{dr})_{r_b} = 0$ , it follows that

$$Q_r + N_r \frac{dw}{dr} + \frac{f}{2\pi r} + \frac{p(r^2 - r_b^2)}{2r} = 0. \quad (3.15)$$

Substituting the moment-curvature relations (3.12) into (3.6) gives

$$Q_r + D \left( \frac{d^3 w}{dr^3} + \frac{1}{r} \frac{d^2 w}{dr^2} - \frac{1}{r^2} \frac{dw}{dr} \right) = 0. \quad (3.16)$$

Combining (3.16) with (3.15) produces

$$\frac{d^3 w}{dr^3} + \frac{1}{r} \frac{d^2 w}{dr^2} - \frac{1}{r^2} \frac{dw}{dr} - \frac{N_r}{D} \frac{dw}{dr} = \frac{f}{2\pi r D} + \frac{p(r^2 - r_b^2)}{2rD}. \quad (3.17)$$

Rewriting the strain-displacement relations (3.8) and (3.9) in the following manner,

$$r \frac{d\epsilon_r}{dr} + \epsilon_\theta - \epsilon_r + \frac{1}{2} \left( \frac{dw}{dr} \right)^2 = 0, \quad (3.18)$$

and substituting the material Hooke's Law relations (3.11) into (3.18) produces

$$\frac{dN_\theta}{dr} - \left( \frac{N_r - N_\theta}{r} \right) + \frac{Eh}{2r} \left( \frac{dw}{dr} \right)^2 = 0. \quad (3.19)$$

Equations (5.9), (3.17), and (3.19), therefore form a set of three non-linear differential equations in the three unknowns  $N_r$ ,  $N_\theta$ , and  $w$ . The boundary conditions corresponding to these equations can be written as follows:

$$\text{at } r = r_b : \quad u = r\epsilon_\theta = 0 \rightarrow N_\theta - \nu N_r = 0, \quad \frac{dw}{dr} = 0 \quad (3.20)$$

$$\text{at } r = r_a : \quad u = r\epsilon_\theta = 0 \rightarrow N_\theta - \nu N_r = 0, \quad \frac{dw}{dr} = 0 \quad (3.21)$$

It is interesting to note at this point that these equations are non-linear because of the term  $\frac{N_r}{D} \frac{dw}{dr}$  in (3.17). If the plate were deforming only in the linear regime, the term  $N_r = 0$ , and therefore the three governing differential equations would condense into the following single linear equation,

$$\frac{d^3 w}{dr^3} + \frac{1}{r} \frac{d^2 w}{dr^2} - \frac{1}{r^2} \frac{dw}{dr} = \frac{f}{2\pi r D} + \frac{p(r^2 - r_b^2)}{2rD} \quad (3.22)$$

which could be integrated three times to obtain a solution for  $w(r)$ , as was detailed in Chapter 2 of this thesis.

### 3.3.6 In-Plane Prestress

As often is the case with micromachined thin plate structures, residual tensile stresses in the plate can exist prior to transverse loading. These initial in-plane loads serve to pretension the plate and can significantly affect the resulting deformation behavior. The complete loading parameters,  $N_r$  and  $N_\theta$ , can therefore be decomposed into initial in-plane prestressing components  $N_{r0}$  and  $N_{\theta0}$ , and into components due to the transverse pressure loading  $\tilde{N}_r$  and  $\tilde{N}_\theta$ , as



follows:

$$N_r = N_{ro} + \tilde{N}_r \quad (3.23)$$

$$N_\theta = N_{\theta o} + \tilde{N}_\theta. \quad (3.24)$$

These parameters,  $\tilde{N}_r$  and  $\tilde{N}_\theta$ , can be thought of as incremental changes in  $N_r$  and  $N_\theta$  due to the application of the transverse loading on top of the already prestressed plate.

### Derivation of $N_{ro}$ and $N_{\theta o}$

It is desired to obtain expressions for the in-plane prestress that results from a uniform tension load  $N_r = N_o$  applied at  $r = r_a$  with zero displacement  $u = 0$  at  $r = r_b$ . Since  $p = 0$  and  $w(r)$  and its derivatives with respect to  $r$  are zero, only (5.9) of the three governing equations remains. The strain-displacement relations (3.8) and (3.9) can be simplified to:

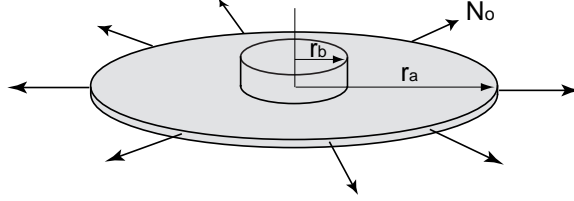


Figure 3.3: Schematic of an annular plate with a rigid central boss under pretension. Loading  $N_o$  is applied radially outward at  $r = r_a$

$$\epsilon_r = \frac{du}{dr} \quad , \quad \epsilon_\theta = \frac{u}{r}. \quad (3.25)$$

Substituting (3.25) into (3.11) and rearranging for  $N_r$  and  $N_\theta$  produces

$$N_r = \left( \frac{Et}{1 - \nu^2} \right) \left( \frac{du}{dr} + \frac{\nu u}{r} \right) \quad , \quad N_\theta = \left( \frac{Et}{1 - \nu^2} \right) \left( \nu \frac{du}{dr} + \frac{u}{r} \right). \quad (3.26)$$

Inserting (3.26) into (5.9) results in a solution for  $u(r)$ :

$$u(r) = \frac{N_o}{\left( \frac{Et}{1 - \nu^2} \right) [(1 + \nu) + \left( \frac{r_b}{r_a} \right)^2 (1 - \nu)]} \left[ r - \frac{r_b^2}{r} \right]. \quad (3.27)$$

Inserting this relation for  $u(r)$  back into (3.26) yields the following expressions for the initial in-plane tensile loads:

$$N_{ro} = \left( \frac{N_o}{1 + \beta^2} \right) \left[ 1 + \beta^2 \left( \frac{r_a}{r} \right)^2 \right] \quad (3.28)$$

and

$$N_{\theta o} = \left( \frac{N_o}{1 + \beta^2} \right) \left[ 1 - \beta^2 \left( \frac{r_a}{r} \right)^2 \right] \quad (3.29)$$

where

$$\beta = \left( \frac{r_b}{r_a} \right) \sqrt{\frac{1 - \nu}{1 + \nu}}. \quad (3.30)$$

It is interesting to observe here that these in-plane tensile loads vary with  $r$ , unlike the in-plane tensile loads for a circular plate with no rigid central boss, which do not vary with  $r$ ,

$$N_{ro} = N_{\theta o} = \frac{N_o(1 - \nu)^2}{Et}. \quad (3.31)$$

### Governing Equations for Complete Loading

Having found expressions for the initial prestressing in-plane loads, (5.2) and (3.29) can be substituted into the three previous governing differential equations (5.9), (3.17), and 3.19) to produce the following three refined governing equations, in terms of  $\tilde{N}_r$ ,  $\tilde{N}_\theta$ , and  $N_o$ ,

$$\frac{d\tilde{N}_r}{dr} + \frac{\tilde{N}_r - \tilde{N}_\theta}{r} = 0, \quad (3.32)$$

$$\frac{d^3 w}{dr^3} + \frac{1}{r} \frac{d^2 w}{dr^2} - \left( \frac{\frac{\beta^2 r_a^2 N_o}{D(1 + \beta^2)} + 1}{r^2} \right) \frac{dw}{dr} - \left( \frac{\tilde{N}_r}{D} + \frac{N_o}{D(1 + \beta^2)} \right) \frac{dw}{dr} = \frac{f}{2\pi r D} + \frac{p(r^2 - r_b^2)}{2r D}, \quad (3.33)$$

and

$$\frac{d\tilde{N}_r}{dr} - \left( \frac{\tilde{N}_r - \tilde{N}_\theta}{r} \right) + \frac{Et}{2r} \left( \frac{dw}{dr} \right)^2 = 0. \quad (3.34)$$

### 3.3.7 Non-Dimensionalized Governing Equations

In order to generalize these equations for ease of use, the non-dimensionalization procedure of Sheplak and Dugundji is followed, with the subsequent non-dimensional parameters being defined,

$$\begin{aligned} \xi &= \frac{r}{r_a} & ()' &= \frac{d}{d\xi} & W &= \frac{w}{t} & U &= \frac{u}{h} \\ \theta &= \frac{dW}{d\xi} = \frac{r_a}{t} \frac{dw}{dr} & \Psi &= \frac{d\theta}{d\xi} = \frac{r_a^2}{t} \frac{d^2 w}{dr^2} \end{aligned}$$

$$S_r = \frac{\tilde{N}_r r_a^2}{Et^3} \quad S_\theta = \frac{\tilde{N}_\theta r_a^2}{Et^3}. \quad (3.35)$$

The governing equations (3.32), (3.33), and (3.34) can therefore be reexpressed in non-dimensional form as

$$S'_r + \frac{S_r - S_\theta}{\xi} = 0, \quad (3.36)$$

$$\theta'' + \frac{\theta'}{\xi} - \left( k^2 + \frac{s^2 + 1}{\xi^2} \right) \theta - 12(1 - \nu^2) S_r \theta = 6(1 - \nu^2) \left( P\xi - \frac{P}{\xi} \left( \frac{r_b}{r_a} \right)^2 + \frac{F}{\xi} \right), \quad (3.37)$$

and

$$S'_\theta - \left( \frac{S_r - S_\theta}{\xi} \right) = -\frac{1}{2\xi} \theta^2 \quad (3.38)$$

where

$$k = \left( \frac{r_a}{t} \right) \sqrt{\frac{12(1 - \nu^2)N_o}{Et(1 + \beta^2)}} \quad , \quad s = \beta k \quad , \quad P = \frac{pr_a^4}{Et^4}, \quad F = \frac{fr_a^2}{\pi Et^4}. \quad (3.39)$$

The parameters  $k$  and  $s$  are dimensionless pretension parameters and  $P$  is a dimensionless transverse loading parameter. The boundary conditions can be written as

$$\text{at } \xi = \xi_b = \frac{r_b}{r_a} : \quad S_\theta - \nu S_r = 0 \quad , \quad \theta = 0 \quad (3.40)$$

$$\text{at } \xi = \xi_a = 1 : \quad S_\theta - \nu S_r = 0 \quad , \quad \theta = 0. \quad (3.41)$$

For use in the numerical finite-difference code to be discussed in the next section, (3.36), (3.37), and (3.38) can be simplified to two non-dimensional governing equations in the variables  $S_r$  and  $\theta$  by substituting (3.36) into (3.38) to eliminate  $S_\theta$ . Therefore, the following set of equations is ready for finite-difference implementation:

$$\xi^2 S''_r + 3\xi S'_r = -\frac{\theta^2}{2} \quad (3.42)$$

$$\xi^2 \theta'' + \xi \theta' - [(s^2 + 1) + \xi^2(k^2 + 12(1 - \nu^2)S_r)]\theta = 6(1 - \nu^2) \left( P\xi^3 - P\xi \left( \frac{r_b}{r_a} \right)^2 + F\xi \right) \quad (3.43)$$

where

$$k = \left(\frac{r_a}{t}\right) \sqrt{\frac{12(1-\nu^2)N_o}{Et(1+\beta^2)}} \quad s = \beta k \quad P = \frac{pr_a^4}{Et^4} \quad F = \frac{fr_a^2}{\pi Et^4} \quad (3.44)$$

Boundary Conditions:

$$at \quad \xi = \xi_b : \quad \xi S_r' + (1-\nu)S_r = 0 \quad , \quad \theta = 0 \quad (3.45)$$

$$at \quad \xi = \xi_a : \quad \xi S_r' + (1-\nu)S_r = 0 \quad , \quad \theta = 0 \quad (3.46)$$

Post-Equation:

$$S_\theta = \xi S_r' + S_r. \quad (3.47)$$

### 3.3.8 Finite-Difference Implementation

The non-linear dimensionless governing differential equations (3.42) and (3.43) can not be solved directly due to the presence of the non-linear term  $S_r\theta$  in (3.43). As a result, they must be numerically solved. This section details the implementation of a finite-difference scheme to accomplish this goal. Sheplak and Dugundji's work on the non-linear deflection of clamped circular plates highlights the importance of a boundary layer region near the plate's clamped outer radius. For large deflections, it is within this region that a transition from membrane behavior to plate bending behavior occurs. To accurately model this region, Sheplak and Dugundji introduced a coordinate transformation that clusters a higher density of finite-difference grid points in this region than in the central regions of the plate.

In the case of an annular plate with clamped outer radius and guided inner radius (corresponding to a rigid central cap), a similar procedure can be carried out. However, in this situation, it is necessary to introduce a more detailed coordinate transformation that clusters grid points at both  $r = r_a$  and  $r = r_b$  so that the two corresponding boundary layer regions can be accurately resolved. Letting  $\xi_c = \frac{1}{2}(\xi_b + \xi_a)$  and defining  $\eta$  to be a set of equally spaced grid points between 0 and 1, a proposed coordinate transformation is:

$$for \quad 0 \leq \eta \leq 0.5 : \quad \xi = \xi_b + (\alpha - 1)(\xi_c - \xi_b) \left( \frac{\phi - \phi^{1-2\eta}}{1 + \phi^{1-2\eta}} \right) \quad (3.48)$$

$$for \quad 0.5 < \eta \leq 1 : \quad \xi = \xi_a + (\alpha - 1)(\xi_c - \xi_a) \left( \frac{\phi - \phi^{2\eta-1}}{1 + \phi^{1-2\eta}} \right) \quad (3.49)$$

where  $\alpha$  is a coordinate stretching parameter varying between 1 and  $\infty$  and  $\phi = [\frac{\alpha+1}{\alpha-1}]$ .

The closer  $\alpha$  is to 1, the higher the mesh density near  $r = r_b$  and  $r = r_a$  in the coordinate transformation.

An example of this coordinate transformation is illustrated in Figure 3.4, for the case of  $\xi_b = 0.1$  and for 20 grid points existing between  $\xi_b$  and  $\xi_a$ . In Plot 3.4(a), a value of  $\alpha = 10$  results in an evenly spaced finite-difference grid mesh between the inner and outer dimensionless boundary of the plate. As  $\alpha$  approaches 1 in Plots 3.4(c) and 3.4(d), an increase in the mesh density begins to appear near the boundaries. For the numerical code implemented in this thesis, values of  $\alpha$  between 1.01 and 1.05 and number of grid points between 100 and 200 were commonly employed.

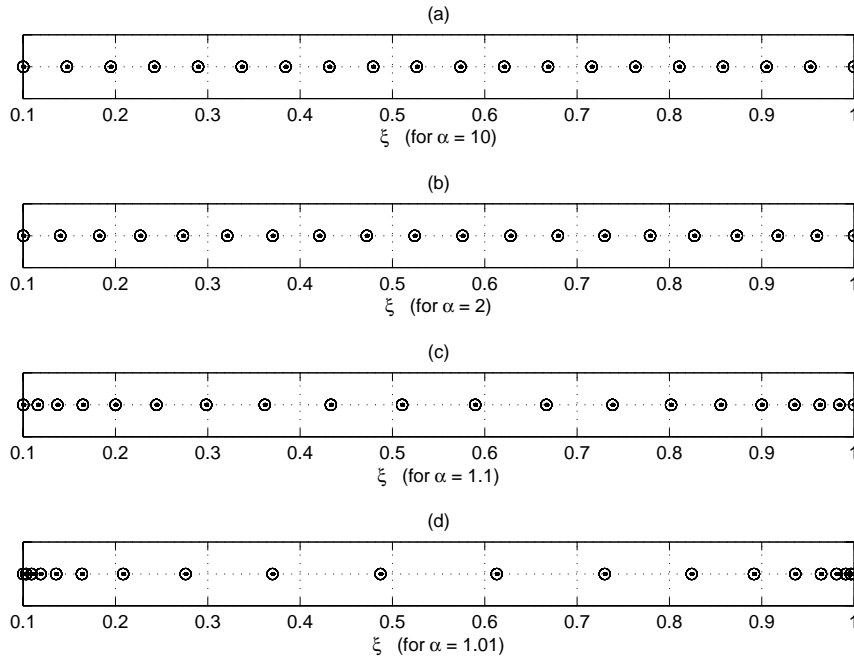


Figure 3.4: Coordinate transformation grid point locations for differing values of  $\alpha$ .

Having defined these coordinate transformations, it is required to derive equations for  $\eta$ ,  $\frac{d\eta}{d\xi}$ , and  $\frac{d^2\eta}{d\xi^2}$  as functions of  $\xi$  for use in the final coordinate transformation governing differential equations to be presented on the following pages. Rearranging (3.48) and (3.49) and taking derivatives with respect to  $\xi$  produces the following relations:

For  $\xi_b \leq \xi \leq \xi_c$ :

$$\eta = \frac{1}{2} \left( 1 - \left( \frac{1}{\ln \phi} \right) \ln \left( \frac{m\phi - (\xi - \xi_b)}{m + (\xi - \xi_b)} \right) \right) \quad (3.50)$$

$$\frac{d\eta}{d\xi} = \frac{1}{2 \ln \phi} \left( \frac{m(1 + \phi)}{(m\phi - (\xi - \xi_b))(m + (\xi - \xi_b))} \right) \quad (3.51)$$

$$\frac{d^2\eta}{d\xi^2} = \frac{-1}{2\ln\phi} \left( \frac{m(1+\phi)(n-2\xi)}{[(m\phi - (\xi - \xi_b))(m + (\xi - \xi_b))]^2} \right) \quad (3.52)$$

$$\text{where} \quad m = (\alpha - 1)(\xi_c - \xi_b) \quad (3.53)$$

$$\text{where} \quad n = m\phi - m + 2\xi_b.$$

For  $\xi_c \leq \xi \leq \xi_a$ :

$$\eta = \frac{1}{2} \left( 1 + \left( \frac{1}{\ln\phi} \right) \ln \left( \frac{m\phi - (\xi - \xi_a)}{m + (\xi - \xi_a)} \right) \right) \quad (3.54)$$

$$\frac{d\eta}{d\xi} = \frac{-1}{2\ln\phi} \left( \frac{m(1+\phi)}{(m\phi - (\xi - \xi_a))(m + (\xi - \xi_a))} \right) \quad (3.55)$$

$$\frac{d^2\eta}{d\xi^2} = \frac{1}{2\ln\phi} \left( \frac{m(1+\phi)(n-2\xi)}{[(m\phi - (\xi - \xi_a))(m + (\xi - \xi_a))]^2} \right) \quad (3.56)$$

$$\text{where} \quad m = (\alpha - 1)(\xi_c - \xi_a) \quad (3.57)$$

$$\text{where} \quad n = m\phi - m + 2\xi_a.$$

Incorporating these coordinate transformations into the set of Equations (3.42) - (3.47), the transformed set of equations can be written as

$$\xi^2(\eta) \left( \frac{d\eta}{d\xi} \right)^2 \frac{d^2 S_r(\eta)}{d\eta^2} + \left( \xi^2(\eta) \frac{d^2 \eta}{d\xi^2} + 3\xi(\eta) \frac{d\eta}{d\xi} \right) \frac{dS_r(\eta)}{d\eta} = -\frac{\theta^2(\eta)}{2} \quad (3.58)$$

$$\begin{aligned} \xi^2(\eta) \left( \frac{d\eta}{d\xi} \right)^2 \frac{d^2 \theta(\eta)}{d\eta^2} + \left( \xi^2(\eta) \frac{d^2 \eta}{d\xi^2} + \xi(\eta) \frac{d\eta}{d\xi} \right) \frac{d\theta(\eta)}{d\eta} - [(s^2 + 1) + \xi^2(\eta)(k^2 + 12(1 - \nu^2)S_r(\eta))] \theta(\eta) \\ = 6(1 - \nu^2) \left( P\xi^3(\eta) - P\xi(\eta) \left( \frac{r_b}{r_a} \right)^2 + F\xi(\eta) \right) \end{aligned} \quad (3.59)$$

Boundary Conditions:

$$\text{at } \eta = 0 : \quad \xi \left( \frac{d\eta}{d\xi} \right) \left( \frac{dS_r}{d\eta} \right) + (1 - \nu)S_r(\eta) = 0 \quad , \quad \theta(\eta) = 0 \quad (3.60)$$

$$\text{at } \eta = 1 : \quad \xi \left( \frac{d\eta}{d\xi} \right) \left( \frac{dS_r}{d\eta} \right) + (1 - \nu)S_r(\eta) = 0 \quad , \quad \theta(\eta) = 0 \quad (3.61)$$

Post-Equation:

$$S_\theta(\eta) = \xi(\eta) \left( \frac{d\eta}{d\xi} \right) \frac{dS_r(\eta)}{d\eta} + S_r(\eta). \quad (3.62)$$

These equations are solved using a 2nd-order central finite difference scheme for the interior grid points, a 2nd-order forward difference scheme for the grid point corresponding to the boundary condition at the inner radius, and a 2nd-order backward difference scheme for the grid point corresponding to the boundary condition at the outer radius. These equations are cast into two matrix relations as follows:

$$[A]\theta = C \quad (3.63)$$

$$[B]S_r = -\frac{1}{2}\theta^2. \quad (3.64)$$

An initial guess for  $\theta$  is taken based on the solution to the linear problem. Based on this  $\theta$ ,  $S_r$  is determined and the nonlinear term  $12(1 - \nu^2)\xi^2(\eta)S_r$  is calculated. Having incorporated this nonlinear term into  $[A]$ , the new solution for  $\theta$  is determined. The error between the previous  $\theta$  and the newly obtained  $\theta$  is calculated. If this error is sufficiently small, then the procedure is complete and the solution vector  $\theta$  has been found. If the error is too large, an under relaxation technique is used to produce a new  $\theta$  guess and the procedure is repeated. This iteration scheme continues until  $\theta$  converges to a sufficiently accurate result.

### 3.3.9 Post-Processing Calculations

Once the non-linear solution procedure has been completed and  $S_r$ ,  $S_\theta$ , and  $\theta$  have been found, it is desired to obtain the deflection  $w$  of the plate, the curvature  $\frac{d^2w}{dr^2}$  of the plate, and the stresses  $\sigma_r$  and  $\sigma_\theta$  within the plate. These calculations are described in the following sections.

#### Calculation of $w$

As detailed in (3.35),  $\theta = \frac{dW}{d\xi} = \frac{r_a}{t} \frac{dw}{dr}$ . To calculate  $w$ , finite differences are implemented to express  $\theta$  in terms of  $W$ ,

$$\theta = [W_{matrix}]W. \quad (3.65)$$

Then, since the vector  $\theta$  is known, this relation is rearranged to solve for  $W$ ,

$$W = [W_{matrix}]^{-1}\theta. \quad (3.66)$$

Finally, the dimensional vector  $w$  is calculated,

$$w = Wt. \quad (3.67)$$

### Calculation of $\frac{d^2 w}{dr^2}$

The non-dimensional plate curvature  $\Psi$  is calculated, according to (3.35), using 2nd-order finite difference schemes,

$$\Psi = \frac{d\theta}{d\xi}. \quad (3.68)$$

The dimensional plate curvature is then calculated,

$$\frac{d^2 w}{dr^2} = \Psi \frac{t}{r_a^2}. \quad (3.69)$$

### Calculation of $\sigma_r$ and $\sigma_\theta$

In general, the dimensional plate stresses can be expressed as

$$\sigma_r = \frac{Et^2}{r_a^2} (S_{ro} + S_r + S_{r,bending}) \quad (3.70)$$

$$\sigma_\theta = \frac{Et^2}{r_a^2} (S_{\theta o} + S_\theta + S_{\theta,bending}) \quad (3.71)$$

where  $S_{ro}$  and  $S_{\theta o}$  are the dimensionless initial in-plane stresses prior to plate transverse loading,  $S_r$  and  $S_\theta$  are the dimensionless in-plane stresses created during plate deflection, and  $S_{r,bending}$  and  $S_{\theta,bending}$  are the dimensionless bending stresses created during plate deflection. Each of these contributions is considered as follows.

$S_{ro}$  and  $S_{\theta o}$  Combining (5.2), (3.29), and (3.35), the dimensional initial in-plane stresses are found to be

$$S_{ro} = S_{\theta o} = \left( \frac{k^2}{12(1-\nu^2)} \right) \left[ 1 + \beta^2 \left( \frac{r_a}{r} \right)^2 \right]. \quad (3.72)$$

$S_r$  and  $S_\theta$  These are the results directly from the numerical code.

$S_{r,bending}$  and  $S_{\theta,bending}$  For plate bending, the radial and tangential strains are functions of the distance from the neutral axis [3],

$$\epsilon_{r,bending} = -z \frac{d^2 w}{dr^2}, \quad \epsilon_{\theta,bending} = -\frac{z}{r} \frac{dw}{dr}. \quad (3.73)$$

According to (3.11),



$$\epsilon_r = \frac{1}{E}(\sigma_r - \nu\sigma_\theta) \quad , \quad \epsilon_\theta = \frac{1}{E}(\sigma_\theta - \nu\sigma_r). \quad (3.74)$$

Substituting (3.73) into (3.74) and rearranging in terms of  $\sigma_r$  and  $\sigma_\theta$ , then incorporating (3.35) yields,

$$S_{r,bending} = S_{r,bending}(z) = \frac{-z}{(1-\nu^2)t} \left( \Psi + \frac{\nu\theta}{\xi} \right) \quad (3.75)$$

$$S_{\theta,bending} = S_{\theta,bending}(z) = \frac{-z}{(1-\nu^2)t} \left( \frac{\theta}{\xi} + \nu\Psi \right). \quad (3.76)$$

Therefore, the dimensional plate stresses  $\sigma_r$  and  $\sigma_\theta$  can be assembled from these three stress contributions.

### 3.4 Results of Numerical Code

This section presents results to illustrate the capability of the numerical code to capture the non-linear large deflection behavior of a thin annular plate with a rigid central cap. As an example, consider a silicon plate with  $r_b = 400\mu m$ ,  $r_a = 800\mu m$ ,  $t_{vm} = 7\mu m$ ,  $E_{si} = 165GPa$ , and  $\nu = 0.22$ . This structure is shown in Figure 3.5. The following subsections use this plate geometry under varying loads to show important non-linear phenomena. Sections 3.4.1 and 3.4.2 highlight the differences between linear and non-linear deflection theory for two distinct loading scenarios. Section 3.4.3 focuses on the presence of thin boundary layer regions near the clamped boundaries and the change in these regions as the plate is deflected more and more into the large deflection regime. And Section 3.4.4 discusses the effect that initial in-plane tension can have on the plate deflection behavior.

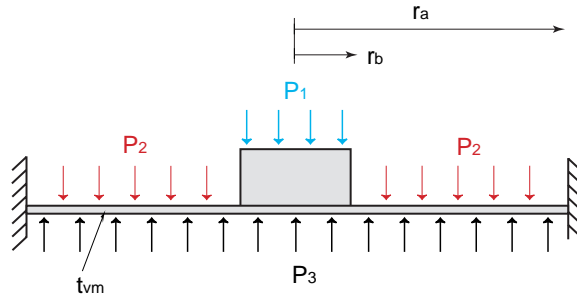


Figure 3.5: Schematic of an annular plate with a rigid central boss under pressure loading  $P_1$ ,  $P_2$ , and  $P_3$ .

### 3.4.1 Loading: $P_1 = P_2 = 0$ , $P_3 = 100kPa$ , $N_o = 0$

Figure 3.6 displays the linear and non-linear plate behavior for loading of  $P_1 = P_2 = 0kPa$  and  $P_3 = 100kPa$  and zero initial in-plane tension. From plot(a), it is clear that the deflection ( $= 11.5\mu m$ ) calculated using the numerical code is significantly less than that ( $= 31.5\mu m$ ) predicted by linear theory. Thin plate structures, such as the one under consideration, experience significant in-plane stresses as the deflections grow larger than the plate thickness. It is evident that this non-linear code captures this behavior. Shown in plots (b) and (c) are the dimensional linear and non-linear plate slopes ( $\frac{dw}{dr}$ ) and curvatures ( $\frac{d^2w}{dr^2}$ ). Note the boundary condition enforcement of zero slope at  $r_b$  and  $r_a$ . Plot (d) illustrates the stress  $\sigma_r$  at the top and bottom plate surfaces predicted by the non-linear code. In this case, the peak tensile stress in the plate is  $0.45GPa$  and occurs on the underside of the plate at  $r_a$ .

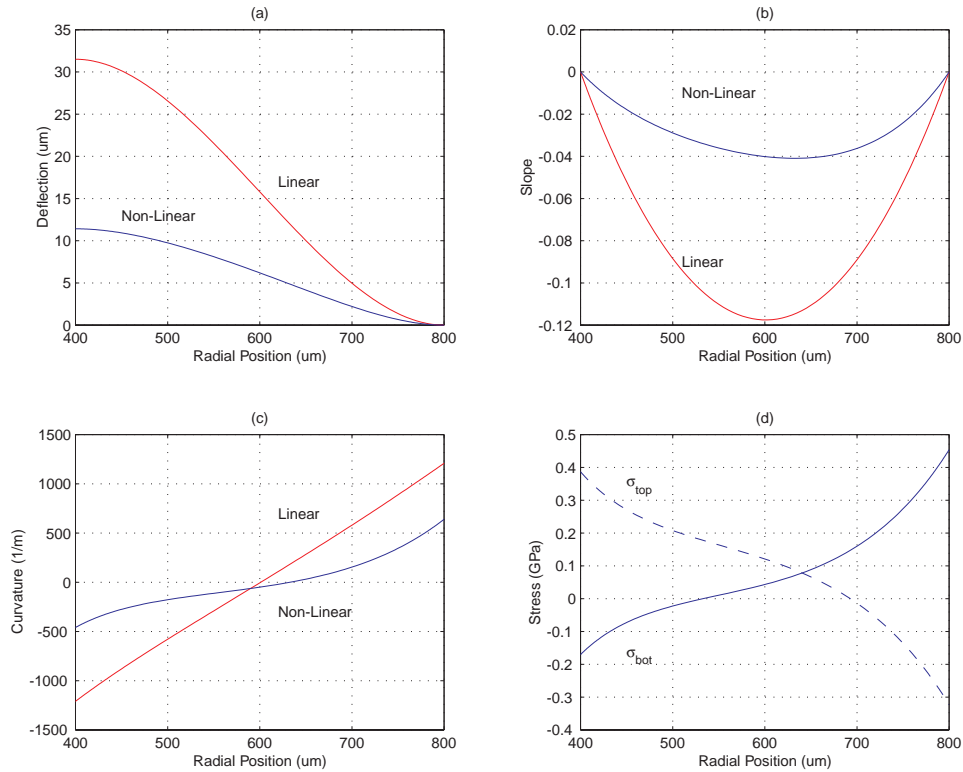


Figure 3.6: Deflection of thin annular plate under loading  $P_1 = P_2 = 0$ ,  $P_3 = 100kPa$ . Plate dimensions and properties:  $r_b = 400\mu m$ ,  $r_a = 800\mu m$ ,  $t = 7\mu m$ ,  $E_{si} = 165GPa$ , and  $\nu = 0.22$ .

### 3.4.2 Loading: $P_1 = 2.90MPa$ , $P_2 = 0$ , $P_3 = 1.30MPa$ , $N_o = 0$

Figure 3.7 displays the linear and non-linear plate behavior for loading of  $P_1 = 2.90MPa$ ,  $P_2 = 0MPa$  and  $P_3 = 1.30MPa$ , and zero initial in-plane tension loading. These pressure

loadings were chosen to illustrate the difference between linear and non-linear theory even when the valve cap deflection predicted in both cases is identical. From plot(a), it is clear that the inner radius deflection predicted by both the linear and non-linear code is identical ( $= 0.7\mu m$ ). However, the deflection behavior of the interior sections of the plate are quite different, due to the stiffening effect of the plate, which is accurately captured by the non-linear code. Linear theory predicts a peak plate deflection near  $18\mu m$  whereas non-linear theory predicts a plate deflection near  $9\mu m$ . Shown in plots (b) and (c) are the dimensional linear and non-linear plate slopes ( $\frac{dw}{dr}$ ) and curvatures ( $\frac{d^2w}{dr^2}$ ). Again, note the boundary condition enforcement of zero slope at  $r_b$  and  $r_a$ . Also, note the presence of near constant curvature toward the central portions of the plate for the non-linear theory. This is due to the fact that the structure is behaving more like a membrane than a plate in these sections. At values of  $r$  closer to the boundaries at  $r_b$  and  $r_a$ , the curvature changes significantly. It is in these boundary layer regions that the bending stresses become greater than the in-plane tensile stresses, and the structure transitions back to plate behavior. Plot (d) further illustrates this point. The total stress  $\sigma_r$  at the top and bottom plate surfaces remain almost constant in these central membrane sections, however they increase sharply toward the boundaries. It is here that the bending stresses dominate. In this case, the peak tensile stress in the plate is approximately  $1.80GPa$  and occurs on the bottom of the plate at  $r_b$ . In this loading situation, although, the inner radius deflection is predicted to be the same by the linear and non-linear code, the deflection of the interior portions of the plate are quite different. When analyzing the active valve behavior, the volume swept under the membrane would be overestimated if linear theory were to be used.

### 3.4.3 Loading: $P_1 = P_2 = 0$ , Varying $P_3$ , $N_o = 0$

To understand the concept of increasing plate stiffness and the presence of thin boundary layers regions near  $r_b$  and  $r_a$  as the plate is pushed further into the large deflection regime, the plate is subjected to varying pressure  $P_3$  beneath the membrane and cap and no other loading. Figure 3.8(a) illustrates the cap deflection at  $r = r_b$  for increasing applied pressure  $P_3$  from 0 to 10 MPa. A non-linear pressure-deflection curve is evident. As the plate experiences larger deflections, higher pressure increase increments are required to produce the same deflection increments. The plate is becoming stiffer as its deflection increases. Figure 3.8(b) shows a magnification of part of this curve, from 0 to 0.06 MPa applied pressure. Notice that the pressure-deflection curve is linear up to deflections of approximately half the plate thickness,  $t_{vm} = 3.5\mu m$ . Linear deflection theory is accurate for this small deflection regime.

Figure 3.8(c) displays the normalized plate deflection shapes for  $P_3$  loading of 0.01MPa, 0.1MPa, 1MPa, 10MPa, and 100MPa. When  $P_3 = 0.01MPa$ , the plate deflection is very small ( $2.8\mu m$ ), and therefore the plate experiences only bending stresses. When  $P_3 = 0.1MPa$ , the plate deflection is  $11\mu m$  and therefore the plate has entered the large deflection regime. From

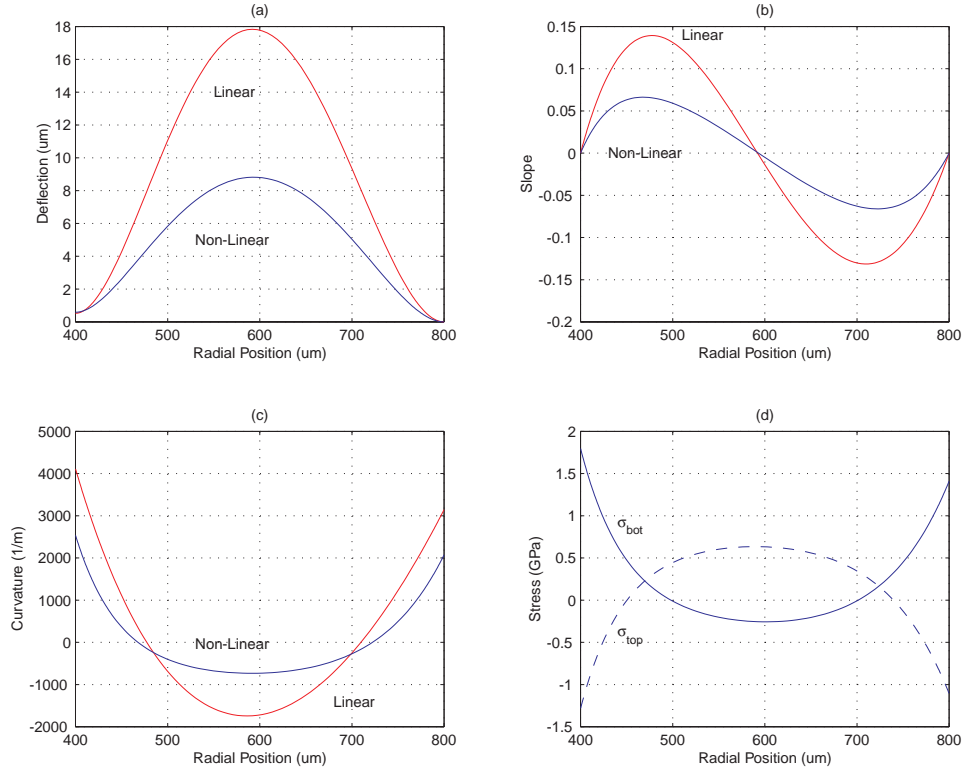


Figure 3.7: Deflection of thin annular plate under loading  $P_1 = 2.9MPa$ ,  $P_2 = 0$ ,  $P_3 = 1.3MPa$ . Plate dimensions and properties:  $r_b = 400\mu m$ ,  $r_a = 800\mu m$ ,  $t = 7\mu m$ ,  $E_{si} = 165GPa$ , and  $\nu = 0.22$ .

Figure 3.8(d), one can observe a slight reduction in the size of boundary layer regions near  $r_b$  and  $r_a$ . When  $P_3 = 10MPa$ , the deflection is relatively large (  $64\mu m$ ). The boundary layers have been decreased to very thin regions. In the central portions of the plate, the in-plane tensile stresses dominate the bending stresses and therefore the plate curvature is constant. However, near the boundaries, the bending stresses are not negligible and therefore the plate curvature changes significantly. This is the region of transition from membrane to plate behavior.

#### 3.4.4 Loading: $P_1 = P_2 = 0$ , $P_{HAC} = 100kPa$ , Varying $N_o$

It is also interesting to note the effect of pretensioning on the plate deflection. Pretensioning the plate in the radial direction has the same effect as forcing the plate to experience large deflections, in that it increases the in-plane tensile stress within the plate. Figure 3.9 illustrates this phenomenon for the plate described above under pressure loading  $P_1 = P_2 = 0$  and  $P_3 = 100kPa$ . As the plate pretension (in units of stress) is increased from zero to  $750MPa$ , the plate deflection at  $r_b$  decreases from  $11.5\mu m$  to  $1.3\mu m$ . It is therefore critical when micromachining thin plate structure to estimate the magnitude of residual in-plane stresses that could result from

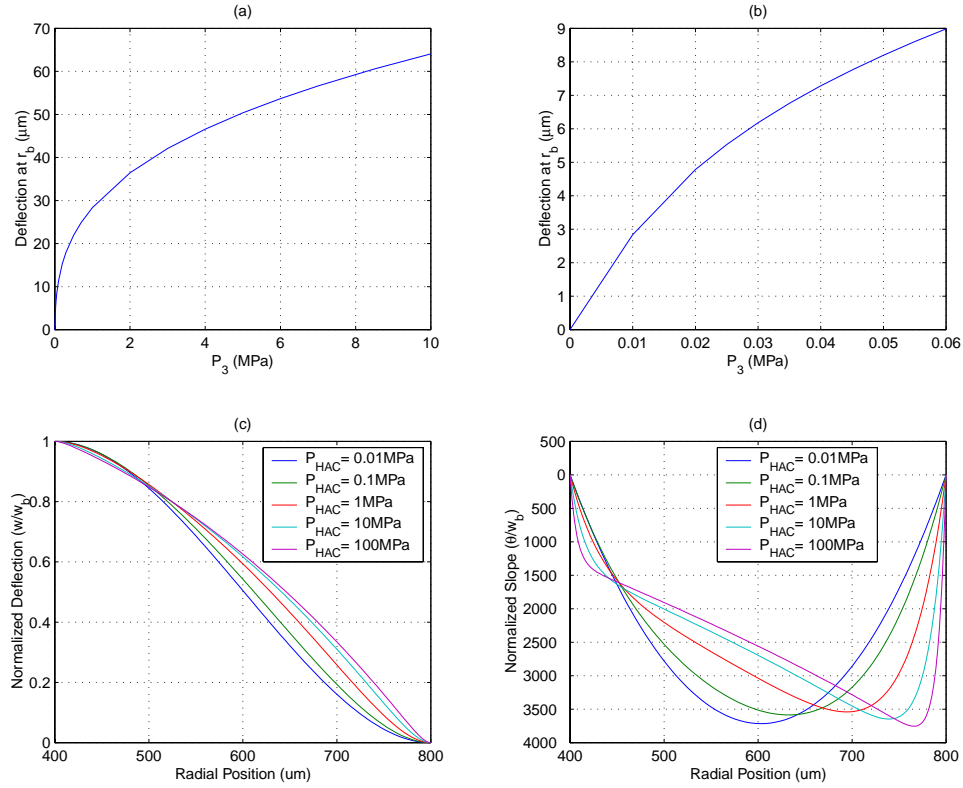


Figure 3.8: Deflection of thin annular plate under varying  $P_3$  loading with  $P_1 = P_2 = 0$  and  $N_o = 0$ . Plate dimensions and properties:  $r_b = 400\mu m$ ,  $r_a = 800\mu m$ ,  $t = 7\mu m$ ,  $E_{si} = 165GPa$ , and  $\nu = 0.22$ .

wafer processing. The presence of any such stresses could substantially alter the performance from that predicted by theory.

### 3.5 Matlab Non-Linear Tools

The previous results have proven the capability of this numerical code to predict the non-linear deformation behavior of a thin plate structure with a rigid central cap. In the subsequent active valve design, modeling, and optimization chapters of the thesis, this large deflection numerical code is implemented in three distinct ways to allow for a variety of approaches to understanding the non-linear behavior of the valve cap and membrane. Each of these approaches is contained in a separate Matlab<sup>TM</sup> numerical code, and therefore act as a modeling tool for future use. These approaches are illustrated in Figure 3.10.

The first approach, detailed in Figure 3.10(a), calculates the valve cap deflection and associated plate behavior, given the pressure across the valve membrane  $P_{vm}$  and the effective force acting on the valve cap  $F_{vc}$ . For the loading terminology in this chapter, the effective

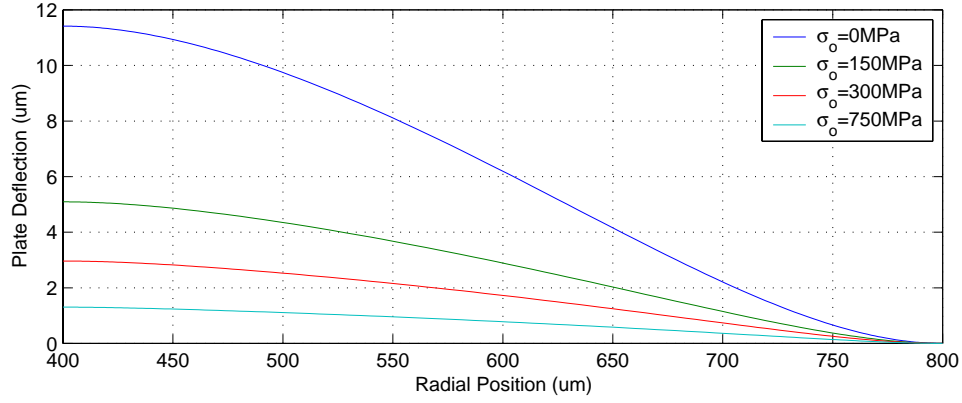


Figure 3.9: Deflection of a thin annular plate under loading  $P_1 = P_2 = 0$ ,  $P_{HAC} = 100kPa$ , with varying  $N_o$ . Plate dimensions and properties:  $r_b = 400\mu m$ ,  $r_a = 800\mu m$ ,  $t = 7\mu m$ ,  $E_{si} = 165GPa$ , and  $\nu = 0.22$ .

force on the valve cap would be  $F_{vc} = A_{vc}(P_3 - P_1)$ . The effective force could be the resultant of only pressures  $P_3$  and  $P_1$  (acting over the valve cap area) if the valve cap is unrestrained, or it could be the resultant of pressures  $P_3$ ,  $P_1$ , and a reaction force imposed on the valve cap by an external structure if the cap is closed against a valve stop. This Matlab<sup>TM</sup> code, labeled NLValveCapMembrane-CaseA.m and included for reference in Appendix B.1, will be used in Chapter 3 as a part of the complete non-linear active valve quasi-static model.

The second approach, detailed in Figure 3.10(b), calculates the pressure across the valve membrane  $P_{vm}$  such that the valve deflection attains a certain value  $Z_{vc}$ , given a known value of  $F_{vc}$ . This Matlab<sup>TM</sup> code, labeled NLValveCapMembrane-CaseB.m and included for reference in Appendix B.2, will be important in Chapter 5 for determining the necessary  $P_{HAC}(t)$  time history within the active valve in order to produce a desired  $Z_{vc}(t)$  trajectory when the external loading time histories  $P_1(t)$  and  $P_2(t)$  are given.

The third approach, detailed in Figure 3.10(c), calculates the force on the valve cap  $F_{vc}$  required to produce a particular valve cap deflection  $Z_{vc}$  under a known loading  $P_{vm}$ . This Matlab<sup>TM</sup> code, labeled NLValveCapMembrane-CaseC.m and included for reference in Appendix B.3, will be used in Chapter 3 to determine the reaction force exerted by a valve stop structure on the valve cap when given all three pressure loadings  $P_1$ ,  $P_2$ ,  $P_3$ , and an imposed valve cap deflection (ie: hitting a stop).

All three of these Matlab<sup>TM</sup> tools share the same non-linear theory and finite-difference implementation as presented in this chapter. They differ only in the organization of the system matrices and the procedure in which the various known and unknown quantities are handled. All are capable of outputting the entire plate spatial deflection vector, as well as the spatial slope and curvature vectors, and the plate top and bottom surface spatial stress vectors. The

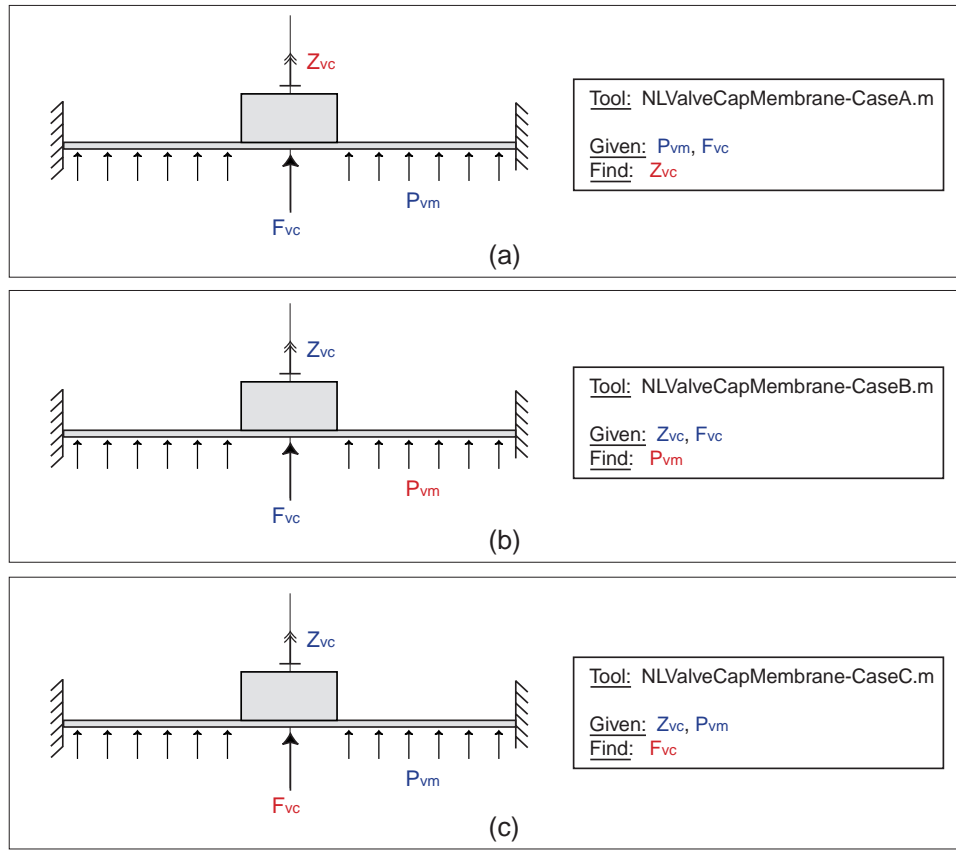


Figure 3.10: Matlab Tools for Use in Subsequent Chapters: (a) NLValveCapMembrane-CaseA.m, (b) NLValveCapMembrane-CaseB.m, and (c) NLValveCapMembrane-CaseC.m.

codes included in Appendix B are written as Matlab<sup>TM</sup> functions.

### 3.6 Conclusions

This chapter has presented the theory governing the non-linear deflection of a thin annular plate with a rigid central cap and has detailed the development of a numerical code to capture this behavior. The results of the code have been compared to linear theory and important phenomena such as in-plane pretension effects and plate/membrane boundary layer regions have been discussed. Since this theory is critical for the development of the active valve device proposed in this thesis, three distinct Matlab<sup>TM</sup> codes/tools have been written for use in the design, modeling, and valve optimization chapters that follow.

# Bibliography

- [1] Y.H. Su, K.S. Chen, D.C. Roberts, and S.M. Spearing, “Large Deflection Analysis of a Pre-Stressed Annular Plate With a Rigid Boss Under Axisymmetric Loading”, *Journal of Micromech. Microeng.* 11 (2001) pp. 645-653.
- [2] M. Sheplak and J. Dugundji, “Large Deflections of Clamped Circular Plates Under Initial Tension and Transitions to Membrane Behavior”, *Journal of Applied Mechanics*, Vol. 65, pp.107-115, March 1998.
- [3] S. Timoshenko. *Theory of Plates and Shells*. McGraw-Hill Book Company, Inc., New York and London, 1940.



## Chapter 4

# Active Valve Non-Linear Model and Simulation

This chapter combines the linear and non-linear modeling tools presented in Chapters 2 and 3 to create a quasi-static structural model of the full piezoelectrically-driven active valve. In addition, the chapter introduces a dynamic simulation architecture for the valve, which includes the inertia and damping associated with the drive element piston and valve cap structural elements. Calculation of the coupled fluid-structure resonant valve frequency, based on finite-element models, is also presented.

### 4.1 Quasi-Static Active Valve Model

A quasi-static active valve model, incorporating only linear structural behavior, was presented in Chapter 2. By combining this model with the numerical code developed in Chapter 3 to model the large-deflection behavior of the valve membrane, a complete quasi-static non-linear active valve model can be formulated. This model consists of two primary solving steps, as shown in Figure 4.1. In the first step, a matrix  $A$  is generated which captures all linear relationships within the valve structure. In the second step, this matrix is used in combination with one of the previously described non-linear tools, `NLValveCapMembrane-CaseA.m`, to solve iteratively for the complete active valve behavior.

Since the valve membrane is the only structural component of the active valve for which non-linear modeling is required, the linear compliance matrix  $A$  can be defined by:

$$Y = [A]U. \quad (4.1)$$

where  $Y$  is a vector of active valve variables to be calculated using linear theory, and  $U$  is a vector of input variables required to calculate  $Y$ . This matrix relation can be rewritten in

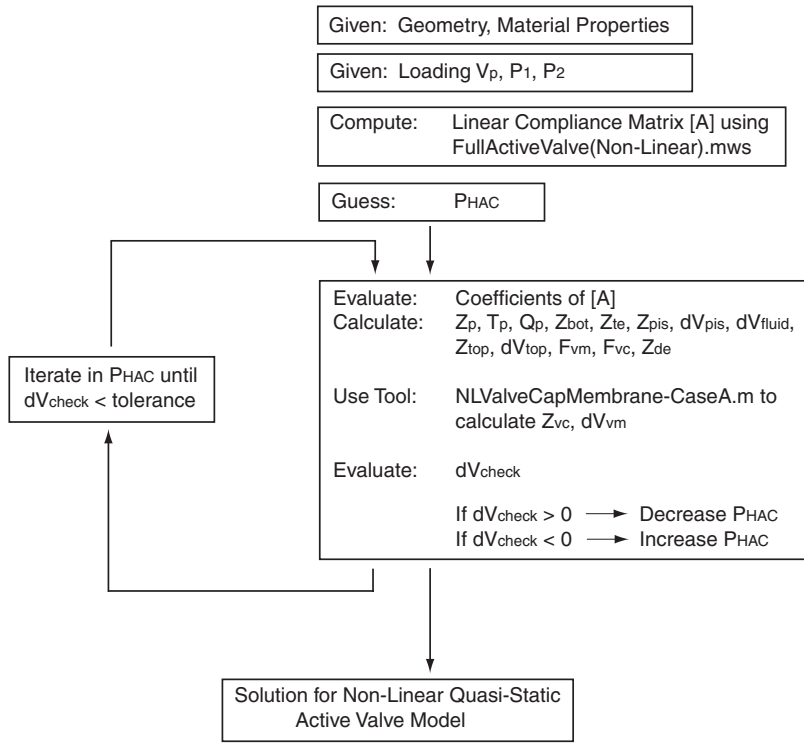


Figure 4.1: Calculation procedure for non-linear quasi-static active valve model.

more detail as:

$$\begin{bmatrix} Z_p \\ T_p \\ Q_p \\ Z_{bot} \\ Z_{te} \\ dV_{te} \\ Z_{pis} \\ dV_{pis} \\ dV_{fluid} \\ Z_{top} \\ dV_{top} \\ F_{vm} \\ F_{vc} \\ Z_{de} \end{bmatrix} = \begin{bmatrix} A_{1,1} & A_{1,2} & A_{1,3} & A_{1,4} \\ A_{2,1} & A_{2,2} & A_{2,3} & A_{2,4} \\ A_{3,1} & A_{3,2} & A_{3,3} & A_{3,4} \\ A_{4,1} & A_{4,2} & A_{4,3} & A_{4,4} \\ A_{5,1} & A_{5,2} & A_{5,3} & A_{5,4} \\ A_{6,1} & A_{6,2} & A_{6,3} & A_{6,4} \\ A_{7,1} & A_{7,2} & A_{7,3} & A_{7,4} \\ A_{8,1} & A_{8,2} & A_{8,3} & A_{8,4} \\ A_{9,1} & A_{9,2} & A_{9,3} & A_{9,4} \\ A_{10,1} & A_{10,2} & A_{10,3} & A_{10,4} \\ A_{11,1} & A_{11,2} & A_{11,3} & A_{11,4} \\ A_{12,1} & A_{12,2} & A_{12,3} & A_{12,4} \\ A_{13,1} & A_{13,2} & A_{13,3} & A_{13,4} \\ A_{14,1} & A_{14,2} & A_{14,3} & A_{14,4} \end{bmatrix} \begin{bmatrix} V_p \\ P_1 \\ P_2 \\ P_{HAC} \end{bmatrix}. \quad (4.2)$$

For a given active valve geometry, the coefficients of the linear compliance matrix  $A$  are calculated (see Maple<sup>TM</sup> code FullActiveValve(Non-Linear).mws in Appendix C.1). For a known set of loadings  $V_p$ ,  $P_1$ , and  $P_2$ , an initial guess for the equilibrium pressure  $P_{HAC}$  is assumed,

and the variables contained in  $Y$  are calculated. With this value of  $P_{HAC}$ , the non-linear tool NLValveCapMembrane-CaseA.m is called to calculate  $Z_{vc}$  and  $dV_{vm}$ . A check is then made of the summation of swept volumes,

$$dV_{check} = dV_{vm} + dV_{top} - dV_{te} - dV_{pis} - dV_{fluid}. \quad (4.3)$$

If  $dV_{check} > 0$ , the initial guess for  $P_{HAC}$  was too large. Conversely, if  $dV_{check} < 0$ , the initial guess for  $P_{HAC}$  was too small. Depending on the result, a modified value of  $P_{HAC}$  is attempted. This iteration procedure is carried out until subsequent iteration values of  $dV_{check}$  are confined to within a specified tolerance. At this point, an equilibrium solution for the active valve under the specified loading conditions has been achieved.

## 4.2 Accuracy of Quasi-Static Model

The accuracy of this quasi-static active valve model can be verified by comparing its results under various loading conditions to those of a finite-element model. In making this comparison, the goodness of the assumptions used in this analytical model can be evaluated.

### 4.2.1 Assumptions in Model

The analytical active valve model uses linear and non-linear plate theory to model the compliances of the structural components. Boundary conditions for each of the components were chosen in an effort to accurately represent the geometries of a real device. However, it would be impossible to achieve 100% perfect correlation between the analytical model and a finite-element model, or a real device. Therefore, prior to comparing the analytical and finite-element models, the following thoughts concerning model correlation are put forth:

1. Both the valve membrane structure and the drive element piston tethers have been modeled with rigid boundary conditions along their respective inner and outer circumferences. In reality, because these interfaces are not in fact rigid, one might expect a “local” softening effect at these locations that would make these plate structures softer than predicted by theory.
2. Bending and shearing effects have been accounted for in the linear analytical equations governing the drive element piston, the top plate structure, and the bottom plate structure. Due to the fact that shearing coefficients are not well understood for these types of plate geometries, some non-correlation between analytical and finite-element results is expected. Additionally, because these plate geometries and associated boundary conditions are somewhat complex (ie: the presence of the piezoelectric cylinder beneath the piston and above the bottom plate), some degree of non-correlation is expected.

It is hoped, however, that even with all of these uncertain issues associated with material properties and geometric boundary conditions, the correlation between the analytical and finite-element model will be within  $\sim 10\%$  for a range of loading parameters that covers the design space for the proposed active valve.

#### 4.2.2 FEM Model Geometries and Correlation Procedure

Two finite-element models of the active valve have been developed to estimate the accuracy of the analytical quasi-static active valve model. The first model, illustrated in Figure 4.2, uses 8-node axisymmetric plane elements for all of the component structures, including the fluid. Material properties for silicon and pyrex are assigned appropriately, as are the bulk modulus properties for the contained hydraulic fluid. As shown in Figures 4.2(b) and 4.2(c), the valve membrane and drive element tethers structures do not include fillet radius features. Since the analytical model does not include the effect of fillet radii either, this allows for a level comparison. Estimates of maximum stress in these structures, however, will not be accurate.

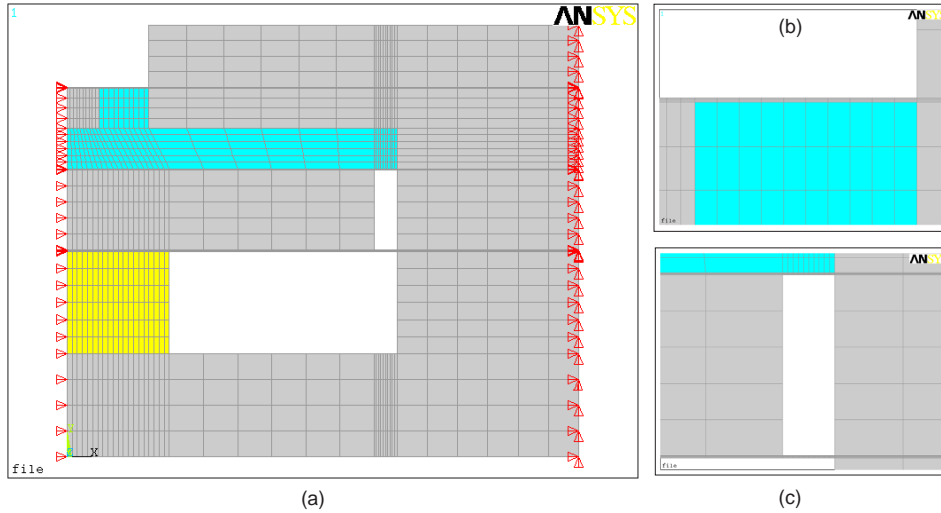


Figure 4.2: An ANSYS<sup>TM</sup> finite-element model of the full active valve without fillet radius features on the valve membrane and drive element tether structures : (a) entire device, (b) close-up view of valve cap and membrane, and (c) close-up view of drive element tethers.

The second model, illustrated in Figure 4.3, also used 8-node axisymmetric plane elements and the same material definitions. However, this model does include adjustable size fillet radius features on the valve membrane and the drive element tether structures. Figures 4.3(b) and 4.3(c) show close-ups of these regions. This enables a determination of the degree of stiffening that the fillets add to the structures and also allows for accurate estimation of stress concentrations in the structures. Both finite-element models have gone through a convergence

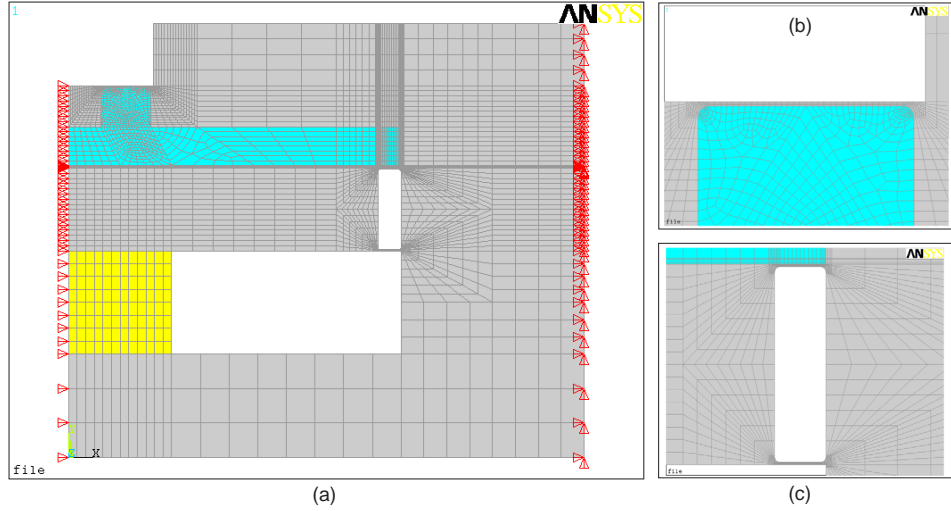


Figure 4.3: ANSYS finite-element model of full active valve with fillet radius features included: (a) entire device, (b) close-up view of valve cap and membrane, and (c) close-up view of drive element tethers.

study to ensure that the element mesh densities are fine enough to produce reliable results.

#### 4.2.3 Model Correlation Procedure

The procedure for comparing the analytical quasi-static active valve model to the finite-element models is documented below. The procedure involves a systematic study of the correlation between these models for varying boundary condition and fillet radius assumptions.

1. To determine the modeling accuracy of the piezoelectric material, valve membrane, drive element tethers, and hydraulic fluid in the analytical model, all other structural components (valve cap, drive piston, top plate, and bottom plate) in the model are made rigid (ie:  $\Xi_{Z_{bot}}^T = \Xi_{Z_{pis}}^T = \Xi_{dV_{pis}}^T = \Xi_{Z_{pis}}^P = \Xi_{dV_{pis}}^P = \Xi_{Z_{top}}^P = \Xi_{Z_{top}}^F = 0$ ). Behavior of the analytical valve is compared to the finite-element model (without fillets) with identical conditions on the component stiffnesses. Figure 4.4(a) illustrates the FEM model. Infinitely stiff regions are shaded dark.
2. To determine the modeling accuracy of the drive piston, top structural plate, and bottom structural plate, the analytical model is run with all compliances in their normal state. Behavior of the analytical model is compared to the finite-element model (without fillets) with infinitely stiff regions as shown in Figure 4.4(b). This comparison will validate the accuracy of the full analytical model with all compliances included.
3. To evaluate the effect of the fillet radius features and additional sidewall material on the

valve behavior, the finite-element model (with fillet radius =  $25 \mu m$ ) with no regions of infinite stiffness is run, as illustrated in Figure 4.4(c). The boundary condition in this model is at the outer radius of the entire structure rather than at the outer radius of the hydraulic amplification chamber. This is a more realistic model of a fabricated valve device. Comparison is made to the full analytical model with all compliances in their normal state.

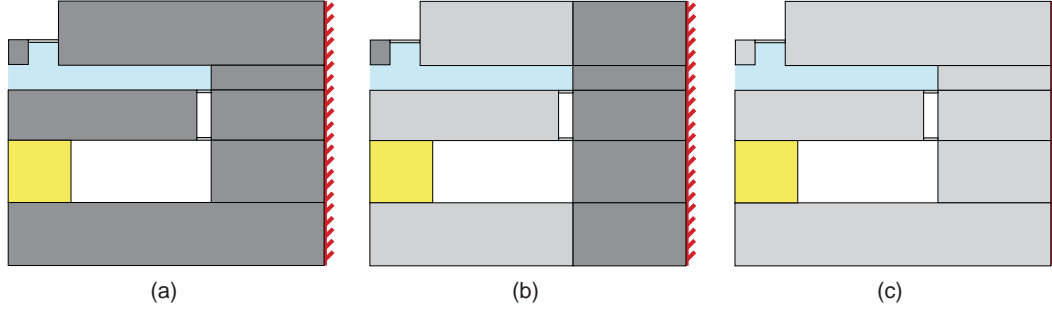


Figure 4.4: ANSYS<sup>TM</sup> finite-element comparison stages: (a) Top plate, bottom plate, piston, valve cap, and side structures are rigid, (b) Only valve cap and side structures are rigid, and (c) No structures rigid.

To cover the design space for the active valve geometry under consideration, the following three loading scenarios are applied:

1.  $V_p=1000 \text{ V}$ ,  $P_1=0$ ,  $P_2 = 0$
2.  $V_p=0$ ,  $P_1=1 \text{ MPa}$ ,  $P_2 = 1 \text{ MPa}$
3.  $V_p=500 \text{ V}$ ,  $P_1=0.5 \text{ MPa}$ ,  $P_2 = 0$ .

These loading scenarios are chosen to capture the valve behavior throughout a complete cycle of deflection. The first loading scenario produces a large positive valve cap deflection, the second loading scenario produces a large negative valve cap deflection, and the third scenario produces a small positive valve cap deflection. The comparison procedure detailed above is carried out for each of the loading scenarios to evaluate the accuracy of the analytical quasi-static active valve model.

#### 4.2.4 Valve Geometry

The active valve geometry used in this comparison study is detailed in the following table. These dimensions are chosen to represent a typical active valve device.

Geometric Dimensions:

Component	Parameters			
Valve Cap	$R_{vc} = 310\mu m$	$R_{vm} = 800\mu m$	$t_{vm} = 10\mu m$	$t_{vc} = 400\mu m$
Top/Bottom Plate	$t_{top} = 1000\mu m$	$t_{bot} = 1000\mu m$		
HAC Chamber	$R_{te} = 3.225mm$	$H_{HAC} = 400\mu m$		
Piston/Tethers	$R_{pis} = 3mm$	$t_{pis} = 800\mu m$	$t_{tetop} = 10\mu m$	$t_{tebot} = 10\mu m$
Piezo	$L_p = 1mm$	$R_p = 1mm$		

Material Properties:

Material	Properties		
Silicon	$E_{Si} = 165GPa$	$\nu_{Si} = 0.22$	$\alpha_{Si} = 1.25$
Pyrex	$E_{pyrex} = 48GPa$	$\nu_{pyrex} = 0.20$	
Piezo	$d_{33} = 2000\frac{pC}{N}$	$E_{piezo} = 9.01GPa$	
Fluid	$K_{fluid} = 2.0GPa$		

The critical valve parameters chosen to serve as comparisons between the two models are the valve cap deflection  $Z_{vc}$ , the top plate structure deflection  $Z_{top}$ , the hydraulic amplification chamber pressure  $P_{HAC}$ , the drive piston center deflection  $Z_{pis}$ , the top tether deflection  $Z_{te}$ , and the bottom plate structure center deflection  $Z_{bot}$ . These parameters are reviewed in Figure 4.5. In addition, for the finite-element model with fillet radius features, the maximum membrane stress in the model is also monitored.

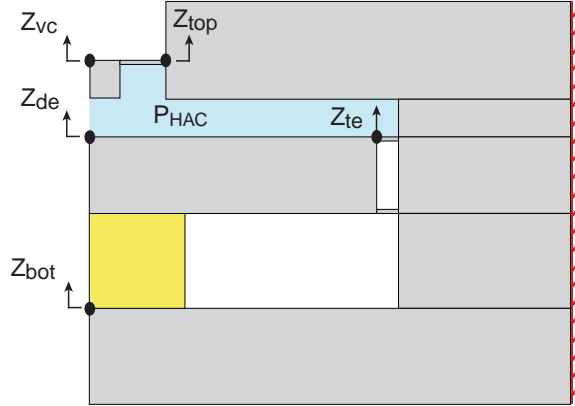


Figure 4.5: Variables monitored in analytic and FEM models.

#### 4.2.5 Model Correlation

##### Finite-Element Model (without fR), Rigid Compliances

In comparing the analytical model to the finite-element model without fillet radius features for the case where the drive piston, the top structural compliance, the bottom structural compliance, and the valve cap are all designated to be rigid, the results correlate extremely well. Table

4.1 shown below compares these results for the three loading scenarios. For each of the three loading scenarios, the valve cap deflection correlates within 0.4%. All of the other parameters also correlate very well, within 1%. This correlation proves that the valve membrane non-linear relations, the drive element tether relations, the fluid compliance, and the piezoelectric material behavior are all modeled very accurately in the non-linear quasi-static analytical active valve model.

TABLE 4.1: Model Correlation (without fR), Rigid Compliances

Loading	Model	Variables to Monitor						
		$Z_{vc}$ ( $\mu m$ )	$Z_{de}$ ( $\mu m$ )	$Z_{te}$ ( $\mu m$ )	$Z_{top}$ ( $\mu m$ )	$Z_{bot}$ ( $\mu m$ )	$P_{HAC}$ ( $kPa$ )	$\sigma_{max}$ ( $GPa$ )
Scenario 1 $V_p = 1000V$ $P_1 = 0, P_2 = 0$	Analytic	26.269	1.136	1.136	0	0	781	1.45
	FEM	26.218	1.143	1.143	0	0	775	n/a
	% Dif	0.2 %	0.6 %	0.6 %	0 %	0 %	0.8 %	n/a
Scenario 2 $V_p = 0V$ $P_1 = 1MPa, P_2 = 1MPa$	Analytic	-20.770	-0.597	-0.597	0	0	567	0.96
	FEM	-20.858	-0.591	-0.591	0	0	562	n/a
	% Dif	0.4 %	1.0 %	1.0 %	0 %	0 %	0.9 %	n/a
Scenario 3 $V_p = 500V$ $P_1 = 0.5MPa, P_2 = 0$	Analytic	14.207	0.612	0.612	0	0	349	0.66
	FEM	14.175	0.614	0.614	0	0	347	n/a
	% Dif	0.2 %	0.3 %	0.3 %	0 %	0 %	0.6 %	n/a

### Finite-Element Model (without fR), Normal Compliances

In comparing the analytical model to the finite-element model without fillet radius features for the case where the drive piston, the top structural compliance, and the bottom structural compliance are returned to their normal values, the results correlate fairly well. The valve cap deflection for the first loading scenario correlates within 3.7%, for the second loading scenario within 0.4%, and for the third loading scenario within 7.5%. This larger value of 7.5% is not that bad since the valve cap deflection is relatively small. As loading is applied that forces the valve cap near zero deflection, one would expect the % error to increase even though the absolute difference between the model deflections is much smaller than  $1\mu m$ .

TABLE 4.2: Model Correlation (without fR), Normal Compliances



Loading	Model	Variables to Monitor						
		$Z_{vc}$ ( $\mu m$ )	$Z_{de}$ ( $\mu m$ )	$Z_{te}$ ( $\mu m$ )	$Z_{top}$ ( $\mu m$ )	$Z_{bot}$ ( $\mu m$ )	$P_{HAC}$ ( $kPa$ )	$\sigma_{max}$ ( $GPa$ )
Scenario 1 $V_p = 1000V$ $P_1 = 0, P_2 = 0$	Analytic	21.787	1.213	0.792	0.087	-0.251	482	1.03
	FEM	22.629	1.267	0.837	0.094	-0.249	510	n/a
	% Dif	3.7 %	4.3 %	5.4 %	7.5 %	0.8 %	5.5 %	n/a
Scenario 2 $V_p = 0V$ $P_1 = 1MPa, P_2 = 1MPa$	Analytic	-24.107	-0.560	-0.846	0.031	-0.179	371	1.25
	FEM	-24.009	-0.532	0.834	0.039	-0.180	396	n/a
	% Dif	0.4 %	5.0 %	1.4 %	20.5 %	0.6 %	6.3 %	n/a
Scenario 3 $V_p = 500V$ $P_1 = 0.5MPa, P_2 = 0$	Analytic	9.654	0.595	0.378	0.042	-0.129	249	0.45
	FEM	10.436	0.628	0.409	0.044	-0.126	259	n/a
	% Dif	7.5 %	5.3 %	7.6 %	4.5 %	2.3 %	3.9 %	n/a

In looking at the other monitored variables, one notices that they all correlate within 7.5%, except for  $Z_{top}$  in Loading Scenario 1. Again, though, this deflection is extremely small, and therefore such a significant error has negligible effect on the rest of the system performance. In fact, from Loading Scenario 1, the following swept volumes are obtained from the analytical model:  $dV_{pis} = 4.03e^{-12}m^3$ ,  $dV_{te} = 2.38e^{-11}m^3$ ,  $dV_{top} = 1.11e^{-12}m^3$ ,  $dV_{fluid} = -3.32e^{-12}m^3$ , and  $dV_{vm} = 2.34e^{-11}m^3$ . From these, it is calculated that the volume of fluid lost in the top structural plate compliance is approximately 4% of the swept volume of piston and tether together (the actuation swept volume). Overall, this 4% loss is important, but 20.5% of this 4% is not. In conclusion, the analytical valve model predicts the valve cap deflection very well.

### Finite-Element Model (with fR), Normal Compliances

In order to evaluate the accuracy of the analytical valve model with respect to a finite-element model that is more characteristic of the real device, no rigidities are assumed in the finite-element model and fillet radius features are taken into consideration. The finite-element results for Loading Scenario 1 are illustrated graphically in Figure 4.6.

A major realistic effect that is considered in this model is the presence of the rigid boundary condition at the outer radius of the device rather than at  $R_{te}$ . This condition serves to soften the top and bottom plate compliances. From Table 4.3 below, it is clear that in all three loading scenarios,  $Z_{top}$  and  $Z_{bot}$  show very large correlation errors near 50%. This is a result of this softening. It is interesting, however, that even with these large deviations in  $Z_{top}$  and  $Z_{bot}$ , the overall valve cap deflection correlation is excellent (less than 4% for all loading scenarios). The principal reason for this, again, that the absolute swept volumes associated with these deflections are not very large.

TABLE 4.3: Model Correlation (with fR), Rigid Compliances

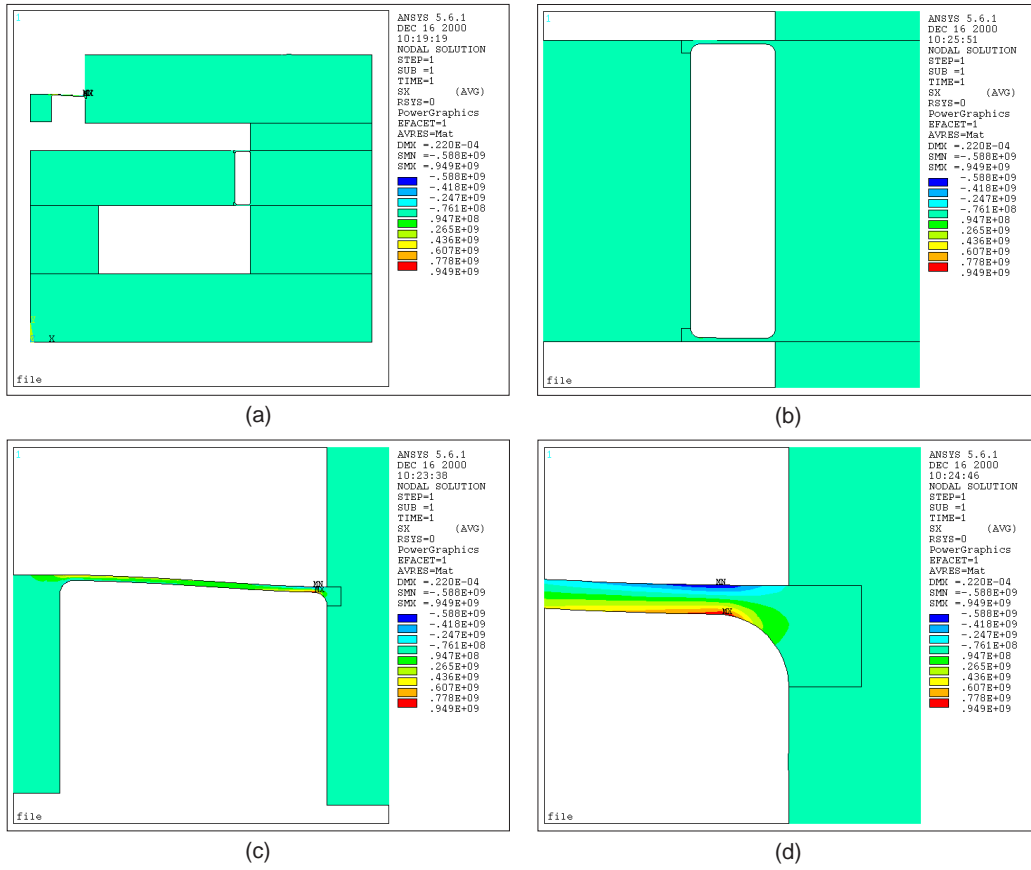


Figure 4.6: ANSYS<sup>TM</sup> FEM stress contour plots for Loading Scenario 1 on fillet radius model.

Loading	Model	Variables to Monitor							
		$Z_{vc}$ ( $\mu m$ )	$Z_{de}$ ( $\mu m$ )	$Z_{te}$ ( $\mu m$ )	$Z_{top}$ ( $\mu m$ )	$Z_{bot}$ ( $\mu m$ )	$P_{HAC}$ ( $kPa$ )	$\sigma_{max}$ ( $GPa$ )	
Scenario 1 $V_p = 1000V$ $P_1 = 0, P_2 = 0$	Analytic	21.787	1.213	0.792	0.087	-0.251	482	1.03	
	FEM	22.002	1.225	0.809	0.157	-0.333	464	0.95	
	% Dif	1.0 %	1.0 %	2.1 %	44.6 %	24.6 %	3.7 %	7.8 %	
Scenario 2 $V_p = 0V$ $P_1 = 1MPa, P_2 = 1MPa$	Analytic	-24.107	-0.560	-0.846	0.031	-0.179	371	1.25	
	FEM	-24.269	-0.552	-0.826	0.071	-0.237	365	1.05	
	% Dif	0.7 %	1.4 %	2.4 %	56.3 %	24.5 %	1.6 %	16.0 %	
Scenario 3 $V_p = 500V$ $P_1 = 0.5MPa, P_2 = 0$	Analytic	9.654	0.595	0.378	0.042	-0.129	249	0.45	
	FEM	9.283	0.590	0.371	0.078	-0.176	246	0.41	
	% Dif	3.8 %	0.8 %	1.9 %	46.2 %	26.7 %	1.2 %	8.9 %	

Another reason, though, has to do with the behavior of the valve cap membrane. Thinking about the valve cap and membrane structure, because the valve cap is no longer rigid, the local behavior at the interface between the membrane and the cap may result in a softer structure. This appears to be the case since a 3.7% less  $P_{HAC}$  pressure deflects the valve cap 1.0% more

in the realistic finite-element model than in the analytical model. A counter-effect which most likely helps to minimize this softening of the valve cap and membrane is the presence of the fillet radii. Each fillet radius provides significantly more material at this interface and hence stiffens the structure.

To conclude this section on the analytical quasi-static active valve model, the comparisons between the analytical model and finite-element models have proven that the analytical model very accurately predicts the quasi-static active valve behavior of finite-element models with boundary conditions similar to those expected in fabricated devices. These quasi-static modeling techniques will now serve as the basis for dynamic models which will be able to capture higher-order dynamic effects within the active valve structure.

### 4.3 Finite-Element Resonant Behavior

To gain a rough idea of the frequency capabilities of this valve structure, a 2-D finite-element model without fillet radius features was evaluated using modal analyses in ANSYS<sup>TM</sup>. By definition, modal analyses are only valid for purely linear systems. Consequently, the resulting resonant frequencies are good predictions of active valve behavior only if the valve is operated such that valve cap and membrane deflections are within the small-deflection regime (ie: small applied voltage to the piezoelectric material). This model incorporates four-node plane elements for the silicon and glass structural parts of the valve and 4-node acoustic fluid elements for the liquid contained within the hydraulic amplification chamber. These acoustic elements enable fluid-structure interaction between the fluid and the surrounding structure of the HAC chamber. For the active valve geometry used in this chapter, the modal analysis results indicate a first modal frequency at  $f_1 = 25.6kHz$  and a second modal frequency at  $f_2 = 102.7kHz$ , as shown in Figure 4.7.

Since, during real valve operation, the valve cap and membrane structure are required to experience deflections well into the non-linear regime, this first modal frequency can be taken as a lower limit to the actual resonant excitation. As a note to the reader, the active valve geometry considered in this chapter is slightly different from the valve devices built and tested in later parts of this thesis. The valve membrane is slightly thicker ( $t_{vm} = 10\mu m$ ) than in the experimental devices ( $t_{vm} = 6\mu m$ ) and the HAC chamber is slightly reduced in size ( $R_{te} = 3.225mm$ ) than in the experimental devices ( $R_{te} = 3.613mm$ ), differences which serve to make the experimental devices softer than the geometry evaluated in this chapter. As a result, a slightly reduced modal frequency can be expected in the experimental valve device, as detailed in Chapter 9. The modal finite-element models used through this thesis, however, are identical to the one presented in this chapter.

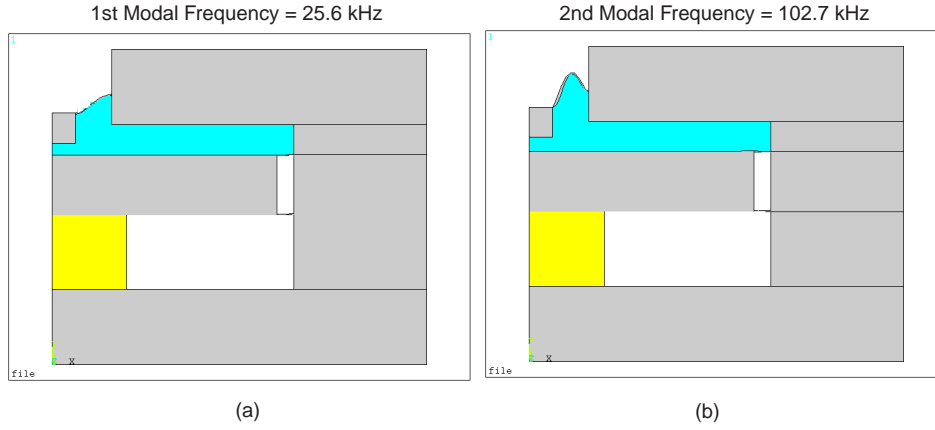


Figure 4.7: ANSYS<sup>TM</sup> FEM mode shapes: (a) 1st modal frequency = 25.601 kHz, (b) 2nd modal frequency = 102.67 kHz.

## 4.4 Dynamic Active Valve Simulation

To properly capture the non-linear effects of the valve membrane deformation at high frequency, and to include important dynamic effects, such as the drive element piston inertia and the valve cap inertia and damping, a Simulink<sup>TM</sup> simulation architecture is presented in this section. The structural compliances within the active valve simulation are based exactly upon the linear and non-linear modeling tools presented in Chapters 2 and 3 of this thesis. The simulation architecture can be broken down into four major subsystems, as illustrated in Figure 4.8: a matrix of linear coefficients describing the bulk of the active valve behavior, a series of non-linear look-up tables that captures the large-deflection valve membrane deformation and stress, a valve cap dynamics block, and a drive piston dynamics block.

### 4.4.1 Linear Matrix Relations

As discussed in Chapter 2, all of the structural elements except the valve membrane operate in linear deformation regimes. Within the simulation, therefore, a matrix of compliance and parameter coefficients are included for these linear relations:

$$\begin{bmatrix} T_p \\ F_{te} \\ P_{HAC} \\ Z_{top} \\ Charge \end{bmatrix} = \begin{bmatrix} A_{1,1} & A_{1,2} & A_{1,3} & A_{1,4} & A_{1,5} \\ A_{2,1} & A_{2,2} & A_{2,3} & A_{2,4} & A_{2,5} \\ A_{3,1} & A_{3,2} & A_{3,3} & A_{3,4} & A_{3,5} \\ A_{4,1} & A_{4,2} & A_{4,3} & A_{4,4} & A_{4,5} \\ A_{5,1} & A_{5,2} & A_{5,3} & A_{5,4} & A_{5,5} \end{bmatrix} \begin{bmatrix} Z_{te} \\ F_{vc} \\ dV_{vm} \\ P_{HPR} \\ V_p \end{bmatrix} \quad (4.4)$$

Inputs to this matrix are the  $Z_p$  and  $Z_{vc}$  variables fed back from the piston and valve cap dynamic blocks respectively,  $dV_{vm}$  fed back from the non-linear valve membrane look-up table,



variables  $F_{vc}$ ,  $dV_{vm}$ , and  $\sigma_{vm}$ . The size of the look-up tables is governed by the number of calculation points between the upper and lower limits of the inputs  $Z_{vc}$  and  $P_{vm}$ . For example, the look-up tables used in the simulations in this section take as inputs a  $Z_{vc}$  vector 100 elements in length, covering a range from  $Z_{vc} = -50\mu m$  to  $Z_{vc} = +50\mu m$ , and a  $P_{vm}$  vector 100 elements in length, covering a range from  $P_{vm} = -1.5MPa$  to  $P_{vm} = +1.5MPa$ . Convergence studies were performed to validate that these vector resolutions were fine enough for accurate results. The Matlab<sup>TM</sup> file, NLValveCapMembrane-CaseC.m, detailed at the conclusion of Chapter 3 and included in Appendix B.3, is used to create these look-up tables.

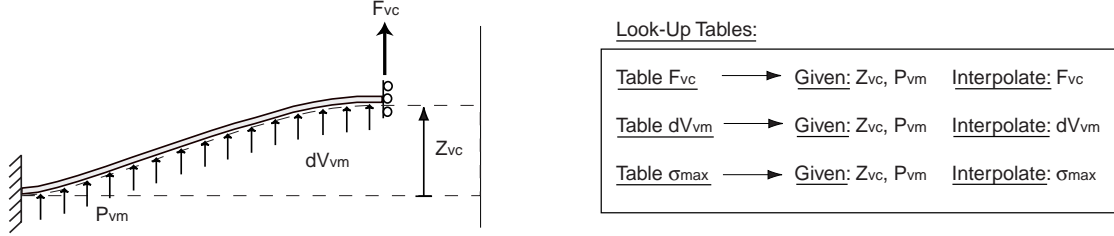


Figure 4.9: Numerical modeling tools are used to generate look-up tables for the non-linear large deflection behavior of the valve cap and membrane. Given a prescribed valve cap displacement  $Z_{vc}$  and pressure loading across the membrane  $P_{vm}$ , a look-up table for each of  $F_{vc}$ ,  $dV_{vm}$ , and  $\sigma_{vm}$  is created.

#### 4.4.3 Piston and Valve Cap Dynamics

The dynamic behavior of the drive piston structure is governed by the following relation:

$$M_{pis}\ddot{Z}_{pis} + C_{pis}\dot{Z}_{pis} = A_p T_p - A_{pis} P_{HAC} - F_{te} \quad (4.5)$$

The damping coefficient  $C_{pis}$  is a lumped parameter that is meant to include the effects of structural damping in the tethers and damping due to fluid interaction. Figure 4.10 displays a schematic of the valve cap mass and the corresponding Simulink block architecture included within the full active valve simulation.

In a similar fashion, the dynamic behavior of the valve cap is represented by the following relation:

$$M_{vc}\ddot{Z}_{vc} + C_{vc}\dot{Z}_{vc} = A_{vc}(P_{HAC} - P_1) - F_{vc} \quad (4.6)$$

The damping coefficient  $C_{vc}$  is a lumped parameter that includes the effects of structural damping in the membrane, squeeze film damping due to the valve cap motion when closing the valve, and damping due to fluid-structure interaction. Figure 4.11 displays a schematic of

the valve cap mass and the corresponding Simulink block architecture included within the full active valve simulation.

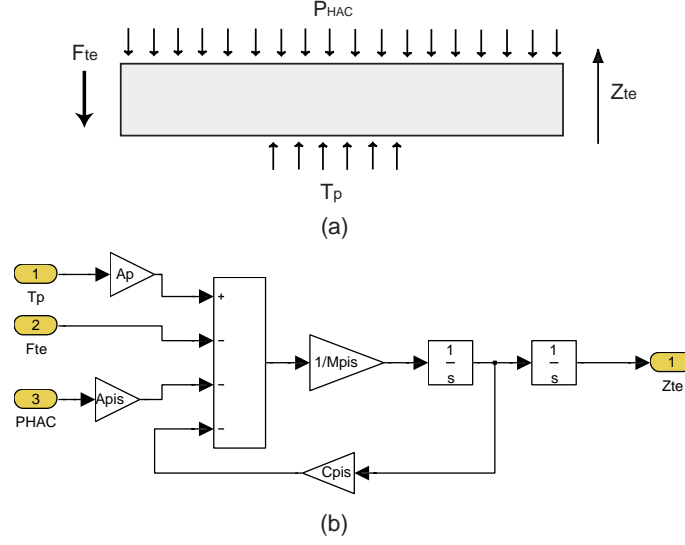


Figure 4.10: Piston Dynamics: (a) free-body diagram of piston structure, and (b) Simulink block architecture.

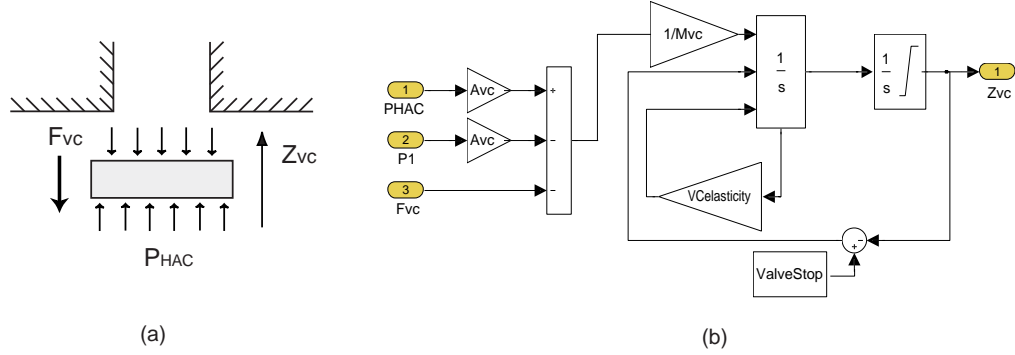


Figure 4.11: Valve cap dynamics: (a) free-body diagram of valve cap structure, and (b) Simulink block architecture.

Exact values of  $C_{pis}$  and  $C_{vc}$  are difficult to estimate accurately. Values are therefore chosen that result in dynamic responses that are relatively free of high-order oscillations (see results in Figure 5.24), yet still exhibit inertia and phase lag effects. Estimates for the damping ratios of the piston and valve cap ( $\zeta_{pis}$  and  $\zeta_{vc}$ ) are calculated from these  $C_{pis}$  and  $C_{vc}$  values by observing the resonant frequency  $\omega_n$  of each component in small deflection linear regimes, according to the relations  $\zeta_{pis} = \frac{C_{pis}}{2\omega_{pis}}$  and  $\zeta_{vc} = \frac{C_{vc}}{2\omega_{vc}}$  respectively.

The Simulink block which captures this valve cap dynamic behavior also includes the effect

of the valve cap as it comes into contact with valve stops, either above and/or below the valve cap. This hitting behavior is modeled as an inelastic collision between the cap and the stop. The assumption here is that if the cap impacts the stop with a velocity  $V_1$ , it will bounce back with a lesser velocity  $V_2$ , according to the relation  $V_2 = \sqrt{r}V_1$ , where  $r < 1$  is called the coefficient of restitution. The above formulation for the hitting can be implemented in Simulink by setting  $V_2$  as the initial condition for the valve velocity at the subsequent time step immediately following impact. For further details on active valve and full MHT system simulation results, see Yaglioglu's MIT Master's thesis [8].

## 4.5 Conclusions

This chapter has presented a complete quasi-static analytical active valve model and a full dynamic active valve simulation architecture for use in predicting structural behavior of a given active valve geometry to a variety of loading conditions. Both models integrate the linear and non-linear tools presented in Chapters 2 and 3, respectively. Overall, the quasi-static analytical active valve model correlates very well with representative finite-element models, thereby justifying many of the boundary condition assumptions in the analytical model. The dynamic simulation architecture enables further investigation of higher-order dynamic effects in the drive element piston and valve cap structures.



# Bibliography

- [1] O. Yaglioglu. Master's Thesis, Massachusetts Institute of Technology, 2002.



## Chapter 5

# Active Valve Design Procedure

So far, this thesis has presented detailed linear and non-linear structural modeling tools that can be used to predict the performance of a given active valve geometry, in response to an applied voltage on the piezoelectric material elements and against known external pressure loadings on the valve cap and membrane structure. Although it is quite important to be able to predict the performance of a predetermined active valve geometry, it is also critical to be able to design a structural geometry that can meet the specifications of and therefore be used within a complete MHT system. In order to accomplish this, relations governing the fluid flow behavior through the MHT system and the interaction of the valve structure with this external hydraulic system must be developed. The goals of this chapter, therefore, are (1) to present modeling tools that capture the interaction between the valve structure and the external hydraulic system, (2) to develop a systematic design procedure that can be used to formulate of an active valve geometry which will satisfy the pressure-flow requirements set by an overall MHT system, and (3) to present higher-order design benefits of incorporating multiple valve cap and membrane structures within the active valve so as to minimize power consumption of the valve.

Section 5.1 revisits a generic MHT system and discusses the performance requirements that this system demands from its active valves. Section 5.2 presents the tools for modeling the pressure-flow relationships in the hydraulic system external to the active valve and develops a related simulation tool for use in the subsequent design procedure. Section 5.3 details the systematic procedure used to design a single valve cap and membrane active valve geometry. This procedure demonstrates the fundamental steps involved in the design of the active valve, but does not include design options for multiple valve heads. Section 5.4 highlights some important issues associated with free design variables within the procedure. Section 5.5 presents the theory behind valve power consumption and the benefit of incorporating multiple valve caps and membranes within the active valve structure. Section 5.6 presents results of the updated systematic design procedure, which allows for inclusion of multiple valve caps and membranes in the design process. Finally, Section 5.7 validates the capability of the quasi-static design

procedure by comparing the performance of a generated active valve geometry to that of a full dynamic simulation.

## 5.1 Valve Requirements in Generic MHT System

A schematic of an MHT power harvesting device is shown in Figure 5.1. Out of phase operation of two active valves results in a pulsing flow of fluid from a high pressure reservoir ( $P_{HPR}$ ) to a low pressure reservoir ( $P_{LPR}$ ) through a central piezoelectric harvesting chamber [1]. With each cycle of device operation, the increasing and decreasing fluid pressure  $P_{EHC}$  in the harvesting chamber (as the chamber fills and evacuates) results in a stressing of the piezoelectric material element(s) and a subsequent generation of charge. For a given harvesting chamber geometry, the system operational frequency  $f_{sys}$  and peak-peak pressure  $P_{EHC}$  fluctuation in the chamber directly determine the achievable power generation levels. The required cyclic flow rates into and out of the chamber,  $Q_{in}$  and  $Q_{out}$ , are functions of this pressure fluctuation and the structural chamber volumetric stiffness. Therefore, assuming that a harvesting chamber structural geometry is known, and that  $f_{sys}$ ,  $P_{HPR}$ ,  $P_{LPR}$ , and a desired  $P_{EHC}$  pressure fluctuation are also required, then an inlet and outlet active valve can be designed to permit this overall MHT system performance.

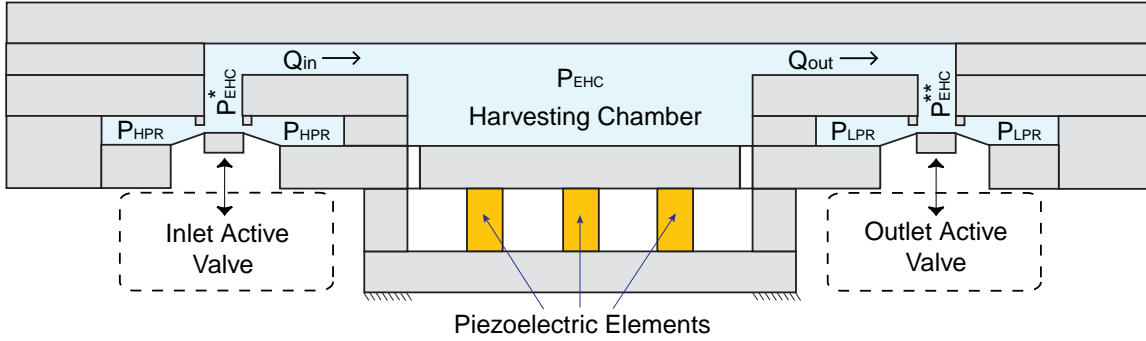


Figure 5.1: Schematic of an MHT power harvesting device. Two active valves regulate flow at high frequency from a high pressure  $P_{HPR}$  to a low pressure  $P_{LPR}$ . Cyclic pressure change in the harvesting chamber  $P_{EHC}$  creates a stressing of the piezoelectric material and a subsequent generation of charge.

In the example MHT power harvesting system shown in Figure 5.1, the top surface of the inlet valve membrane is in contact with the high pressure reservoir and therefore experiences a constant  $P_{HPR}$ . The valve cap, on the other hand, sees a changing pressure  $P_{EHC}^*$  as the chamber fills and evacuates. Likewise, the top surface of the outlet valve membrane is in contact with the low pressure reservoir and therefore experiences a constant  $P_{LPR}$  while the valve cap

sees a changing pressure  $P_{EHC}^{**}$  as the chamber fills and evacuates. The assumptions for the areas over which these system pressures act is further detailed in Section 5.2.3. The amounts by which  $P_{EHC}^*$  and  $P_{EHC}^{**}$  differ from  $P_{EHC}$  are functions of the fluid inertial effects in the inlet and outlet flow channels (see Section 5.2.2). With the ability to model these pressure-flow relations through the MHT system, a design procedure can be developed and implemented to design the active valve geometries for the system.

The systematic active valve design procedure that is developed in this chapter is based on quasi-static valve structural behavior. In other words, dynamic effects within the active valve such as those associated with the valve cap mass, the drive element piston mass, and any damping effects are not included. In this way, the basic process of the design procedure can be well understood and estimates for valve geometries to satisfy the MHT system requirements can be generated. Once an active valve geometry is designed in this way, full dynamic simulations of the structure can be run in order to evaluate the goodness of the quasi-static valve design and to enable tweaking of the valve geometries to achieve higher performance. Although this quasi-static design procedure is generic to both the MHT actuator and power harvesting applications, for purposes of clarity, the discussions in this thesis will center on the design of active valves to be used in the previously described MHT power harvesting system. Furthermore, without any loss of generality, the focus of this chapter will be solely on the design of the inlet active valve for the harvesting system.

To regulate flow into the MHT harvesting chamber so as to meet the overall system requirements, the inlet valve membrane and cap structure must be sized properly to ensure adequate stroke of the valve cap and to allow sufficient fluid flow through the orifice to fill the chamber in the allotted time. In addition, under these external pressure loadings, stresses within the valve cap and membrane structure must be kept below the fracture strength of the membrane material. The piezoelectric drive portion of the valve must be designed so as to minimize the overall volume of the device, yet still provide adequate actuation for pressurizing and producing volume change to the hydraulic amplification chamber. Further design issues, such as valve power consumption and the incorporation of multiple valve heads within a single active valve structure, will be covered in detail in this chapter.

## 5.2 Modeling of External Hydraulic System

Before presenting the quasi-static active valve design procedure, the modeling of the fluid-flow relations in the MHT system external to the active valve structure must be discussed. The inlet active valve within the example MHT power harvesting device regulates flow from the high pressure reservoir to the harvesting chamber. As fluid passes over the valve membrane and cap, it exerts pressures on these structures. These pressures and flow rates are a function

of the opening and closing action of the valve cap against its stop, the geometry of the fluid channel that carries fluid from the valve to the chamber, and the effective hydraulic stiffness of the harvesting chamber being filled. This section details the techniques used to model the pressure-flow relations for each of these system features. In the following discussions, it is assumed that that inlet and outlet valves operate each with a 50% duty cycle, ie: the inlet valve is open exactly for the first half of the MHT system period  $T_{sys} = \frac{2\pi}{f_{sys}}$  while the outlet valve is open for exactly the second half of the system period.

### 5.2.1 MHT Chamber Stiffness

During the first half of a complete device cycle, the inlet valve is open and the outlet valve is closed. As fluid passes through the valve into the harvesting chamber, the chamber pressure increases. The relationship between the amount of fluid entering the chamber and the pressure rise within the chamber is determined by the effective hydraulic chamber stiffness,  $K_{EHC}$ . Figure 5.2(a) shows a simplified schematic of this filling process.

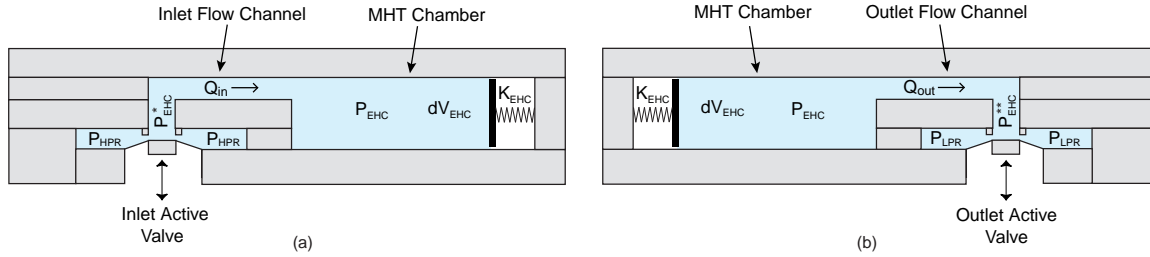


Figure 5.2: Filling and evacuation models for an MHT system: (a) During inlet valve opening and closing, fluid fills the harvesting chamber. (b) During outlet valve opening and closing, fluid evacuates the harvesting chamber. The associated chamber pressure time history  $P_{EHC}(t)$  during filling and evacuation is a function of the amount of fluid entering/evacuating the chamber and the chamber volumetric stiffness  $K_{EHC}$ .

$K_{EHC}$  is a function of the chamber geometry, material properties, and fluid initial volume. A large  $K_{EHC}$  means that a small amount of fluid  $dV_{EHC} = \int Q_{in}(t)dt$  flowing into the chamber will result in a large increase in chamber pressure  $P_{EHC}$ , whereas a small  $K_{EHC}$  means that even a large amount of fluid flow into the chamber will result in only a small chamber pressure increase. The chamber pressure increase as a function of time can be written as

$$\frac{dP_{EHC}}{dt} = K_{EHC}Q_{in}(t). \quad (5.1)$$

A similar model can be used to evaluate the evacuation of fluid through the outlet valve, resulting in a chamber pressure decrease as fluid flows to a low pressure  $P_{LPR}$  (see Figure

5.2(b)). For the purposes of this thesis, however, only the inlet valve and corresponding filling of the harvesting chamber are considered.

### 5.2.2 Valve Channel Inertial Effects

Fluid inertial effects within the flow channel connecting the valve to the harvesting chamber can play a significant role in determining the difference between  $P_{EHC}^*(t)$  and  $P_{EHC}(t)$  during device operation. This pressure-flow relation can be written as

$$P_{EHC}^*(t) - P_{EHC}(t) = \left( \frac{\rho L_c}{A_c} \right) \dot{Q}_{in} \quad (5.2)$$

where  $\rho$  is the fluid density,  $L_c$  is the channel length, and  $A_c$  is the channel area. For a long channel with small cross-section area, one can expect fluid inertial effects to play a significant role as the pressure  $P_{EHC}^*$  builds up to accelerate the fluid slug into the chamber. Conversely, for short channels with large areas, the inertial effects are negligible and the pressure  $P_{EHC}^*(t)$  and  $P_{EHC}(t)$  will not differ at all. It is important to be aware of these inertial effects when designing and modeling any sort of hydraulic system that contains small channels.

### 5.2.3 Valve Orifice Flow Relations

Work by previous researchers [3] [4] [5] has shown that for small openings, poppet valves (such as the valve cap in this proposed active valve device) behave as long orifices in which the effects of flow separation and subsequent reattachment dominate the valve flow dynamics.

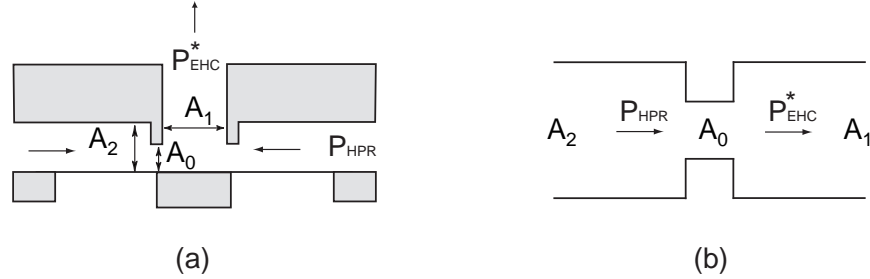


Figure 5.3: Valve orifice representation: (a) valve cap geometry and fluid flow areas, (b) representation of flow through valve as a flow contraction followed by a flow expansion.

Qualitatively, the valve flow can be approximated by a simplified order-of-magnitude valve model. The valve orifice may be characterized as a flow contraction followed by a flow expansion as shown in Figure 5.3(a) and (b). An integral analysis gives a relationship for the combined effect of the flow expansion and contraction. The loss coefficient  $\zeta_{orifice}$  is defined as the total

pressure drop  $\Delta P = P_{HPR} - P_{EHC}^*$  over the dynamic pressure based on the orifice local mean velocity ( $\bar{u} = \frac{Q}{A_o}$ )

$$\zeta_{orifice} = \frac{\Delta P}{\frac{1}{2}\rho\bar{u}^2} = \left[ \frac{1}{2} \left( 1 - \frac{A_0}{A_1} \right)^{\frac{3}{4}} + \left( 1 - \frac{A_0}{A_2} \right)^2 \right] \quad (5.3)$$

where the upstream flow area can be approximated as  $A_2 = 2\pi R_{vc} H_{upstream}$ , the throat area can be approximated by  $A_0 = 2\pi R_{vc} Z_{stroke}$ , and the downstream flow area can be approximated as  $A_1 = \pi R_{vc}^2$ .  $H_{upstream}$  is the height of the radial flow channel above the valve membrane to the cap and  $Z_{stroke}$  is the valve cap opening distance from the valve stop structure.

This approximation, however, is independent of the Reynolds number and therefore holds only for  $Re > 10,000$ , where fully turbulent flow regimes exist. In microfluidic systems, such as the MHT power harvesting device, Reynolds numbers are expected to fluctuate between approximately 10 and 20,000 as the valve opens and closes [2]. For this reason, correction factors (obtained from experimental results) need to be employed to obtain better estimates of the loss coefficients for these low turbulence and laminar flow regimes [2]. A loss coefficient for each of the contraction and expansion geometries ( $\zeta_{contraction}$  and  $\zeta_{expansion}$ , respectively) is used to approximate the total loss coefficient through the valve, as detailed in the following relation

$$\zeta_{orifice}^* = \zeta_{contraction}(Re, \frac{A_0}{A_2}) + \zeta_{expansion}(Re, \frac{A_0}{A_1}) \quad (5.4)$$

where the Reynolds number is defined as

$$Re = \frac{1}{\pi} \frac{Q}{R_{vc}\nu}. \quad (5.5)$$

Figure 5.4(a) plots  $\zeta_{contraction}$  as a function of  $Re$  and the contraction area ratio  $\frac{A_0}{A_2}$  and Figure 5.4(b) plots  $\zeta_{expansion}$  as a function of  $Re$  and the expansion area ratio  $\frac{A_0}{A_1}$ . As a result, the pressure-flow relation for the full valve orifice geometry can be written as

$$\Delta P = P_{HPR} - P_{EHC}^* = \frac{1}{2} \rho \zeta_{orifice}^* \left( \frac{Q^2}{A_0^2} \right). \quad (5.6)$$

All subsequent fluid models discussed in this thesis incorporate these higher-order correction factors to obtain an accurate estimation of the flow behavior. These flow models are based on steady flow phenomenon and do not capture frequency dependent losses. The following assumptions are made to define the valve cap and membrane areas over which the upstream pressure  $P_{HPR}$  and the downstream pressure  $P_{EHC}^*$  act. Since the valve cap stroke during



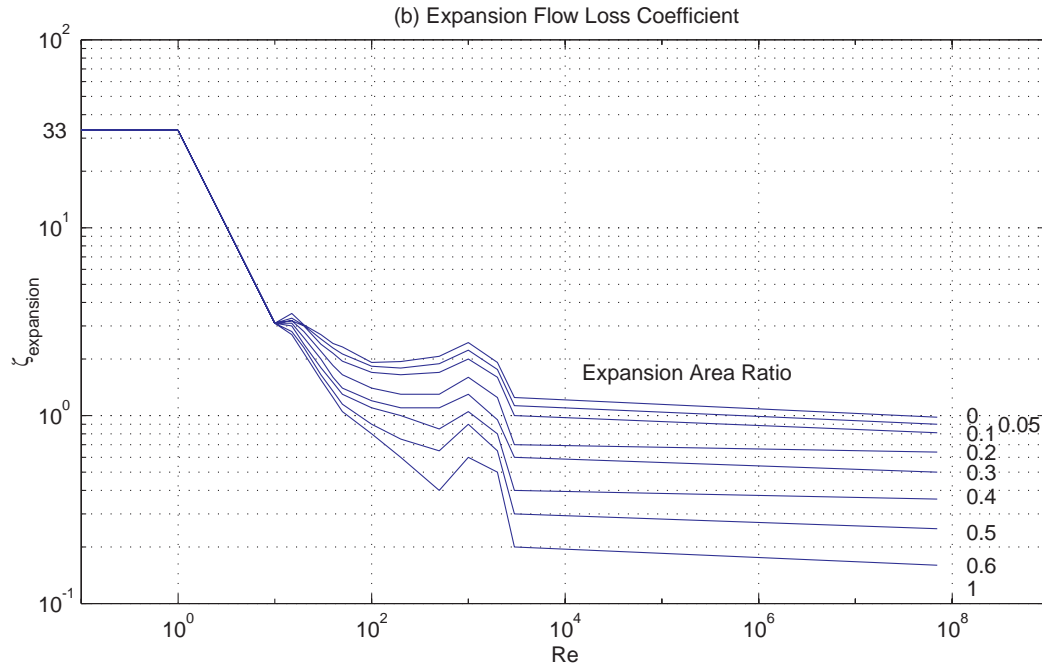
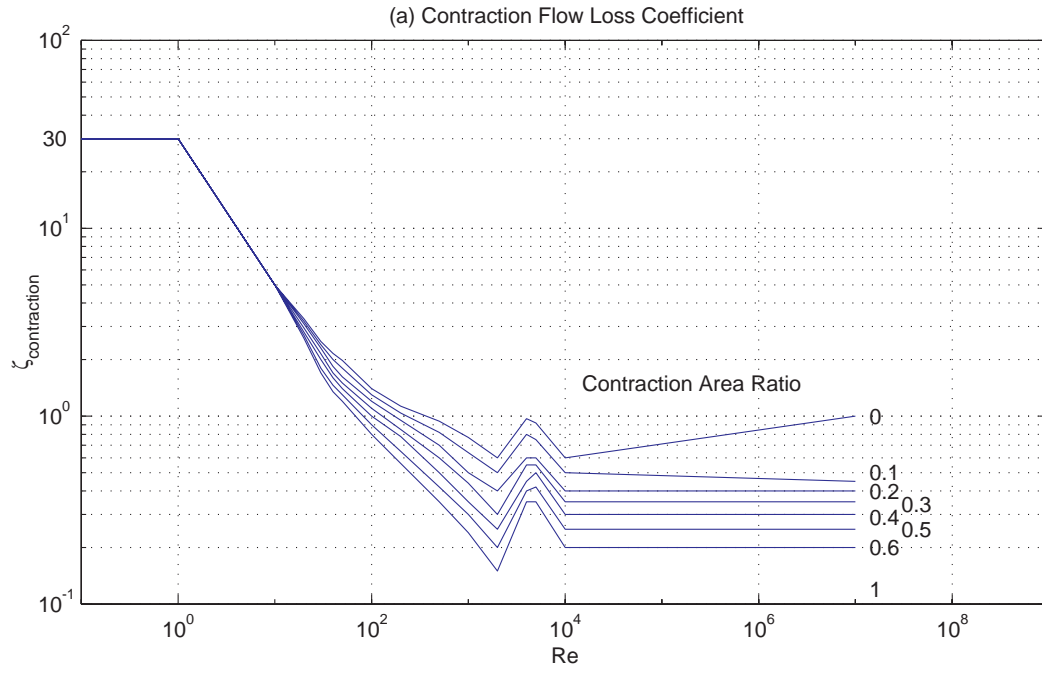


Figure 5.4: Look-Up Tables for flow loss contraction and expansion coefficients. For further details, see [2].

operation is significantly less than  $H_{upstream}$ ,  $R_{vm}$ , and  $R_{vc}$ , the majority of pressure drop through the valve structures occurs across the contraction and expansion at the valve cap circumference. As a result, at any given instant of time, the pressure acting over the valve membrane area can be approximated as the reservoir pressure  $P_{HPR}$  and the pressure acting over the valve cap area can be approximated as  $P_{EHC}^*$ . For a specific value of valve cap opening at a given time during the cycle, a relationship therefore exists for the instantaneous fluid flow through the valve as a function of the pressure drop across the valve.

#### 5.2.4 Chamber Filling Simulation Tool

The previously described pressure-flow relations for the harvesting chamber stiffness, valve orifice, and flow channel connecting the valve and chamber can be recast in Simulink<sup>TM</sup> to create a simulation tool for fluid filling of the harvesting chamber. For known dimensions of the valve cap, the surrounding structure forming the upstream and downstream flow areas, the valve channel dimensions, the harvesting chamber dimensions and material properties,  $P_{HPR}$ , and the desired minimum pressure in the harvesting chamber  $P_{EHC,min}$  (the pressure immediately when the outlet valve has closed), and for an assumed valve cap opening profile  $Z_{vc,opening}$ , the filling behavior of the system through the inlet valve orifice can be simulated. Figure 5.5 illustrates the high-level Simulink<sup>TM</sup> model, and Figure 5.6 shows the fluid orifice and valve channel block diagram structure.

A major assumption underlying this simulation is that the accompanying outlet valve of the MHT system has been designed properly to ensure that the harvesting chamber pressure  $P_{EHC}$  has decreased to a value of  $P_{EHC,min}$  at the instant the outlet valve fully closes. Furthermore, the variable  $Z_{vc,opening}$  is the distance between the valve stop and the surface of the valve cap. For example, if the valve being modeled is forced to experience a sinusoidal absolute deflection history from  $Z_{vc} = -20\mu m$  (fully open) to  $Z_{vc} = +20\mu m$  (fully closed), the corresponding  $Z_{vc,opening}$  values are  $Z_{vc,opening} = +40\mu m$  (fully open) to  $Z_{vc,opening} = 0\mu m$  (fully closed).

This filling simulation will be an important part of the systematic active valve design procedure detailed in the following sections. It will allow for the determination of a valve cap size and imposed valve opening so as to achieve the required  $P_{EHC}$  pressure excursion during MHT system filling.

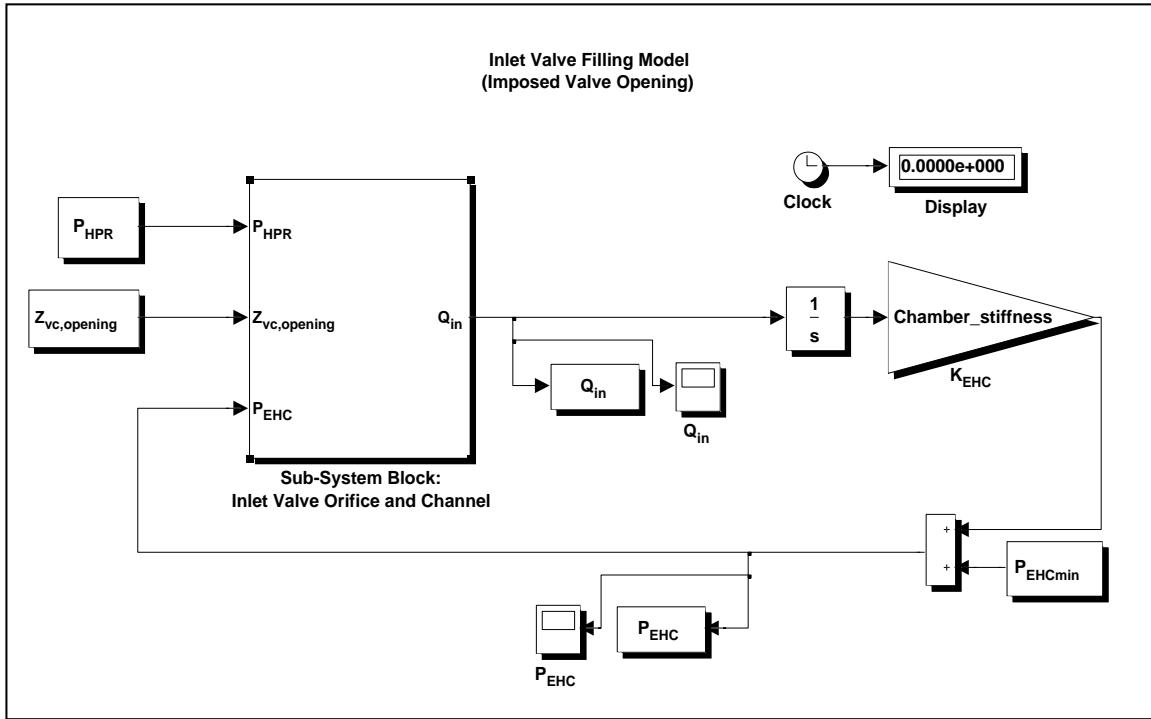


Figure 5.5: Simulink<sup>TM</sup> high-level simulation overview for filling of the MHT system through the inlet active valve.

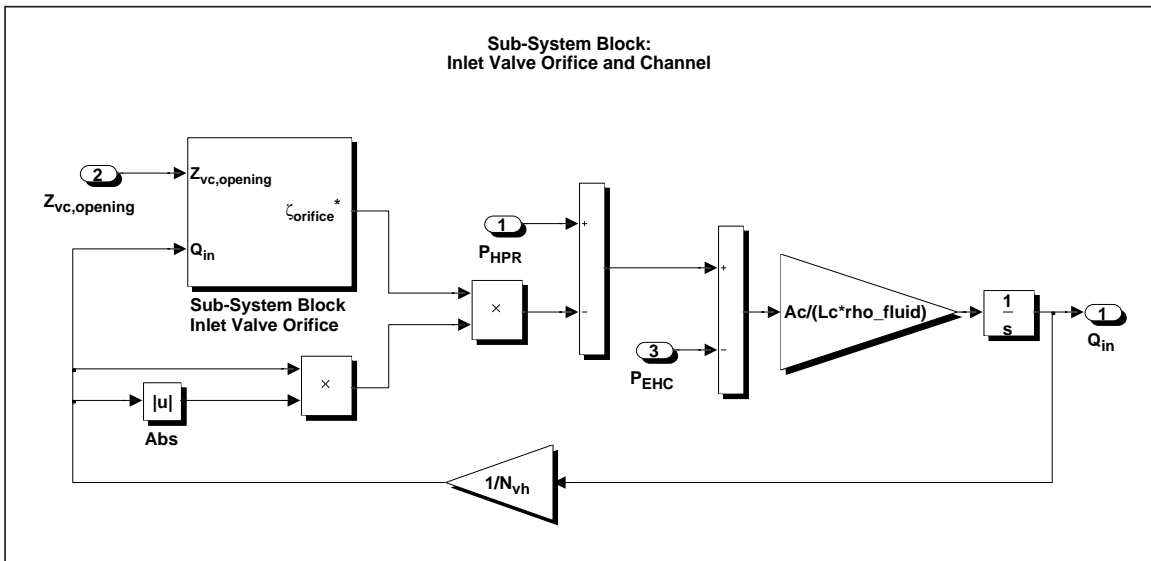


Figure 5.6: Simulink<sup>TM</sup> valve orifice and channel sub-system block for filling of the MHT system through the inlet active valve.

## 5.3 Systematic Design Procedure

This section introduces a systematic design procedure that can be implemented to calculate dimensions of the valve cap, valve membrane, hydraulic amplification chamber, and drive element portion of the inlet active valve to satisfy requirements set forth by the external hydraulic system. This design procedure is based upon quasi-static valve piston and valve cap behavior (ie:  $\ddot{Z}_{vc} = \dot{Z}_{vc} = \ddot{Z}_{pis} = \dot{Z}_{pis} = 0$ ). Depending upon the frequency of operation, this assumption may or may not be a valid one, since system dynamic effects could come into play. It is therefore the purpose of this quasi-static design procedure to generate a valve design, from which a full dynamic simulation can be run to evaluate the goodness of the design and be used as a tool for fine-tuning the valve geometry.

### 5.3.1 Overview

Figure 5.7 presents a generalized flowchart for this quasi-static design process. Given external system requirements, such as the chamber stiffness  $K_{EHC}$ , the  $P_{EHC}$  pressure fluctuation from a  $P_{EHC,min}$  to a  $P_{EHC,max}$  during filling, the reservoir pressure  $P_{HPR}$ , and the overall desired system frequency  $f_{sys}$ , the following steps are carried out:

1. The valve cap radius  $R_{vc}$  (for a chosen valve stroke  $Z_{stroke}$ ) is calculated to allow for adequate filling of the harvesting chamber.
2. The valve membrane outer radius  $R_{vm}$  and required  $P_{HAC}(t)$  time history (for a given membrane thickness  $t_{vm}$ ) are calculated to allow for motion of the cap along its desired trajectory against the known external loads while at the same time ensuring membrane stresses below critical levels.
3. The drive element piston area  $A_{pis}$  and piezo area  $A_p$  are calculated to provide a stiffness match between the drive piston structure and the load that it encounters and to ensure adequate actuation capabilities.

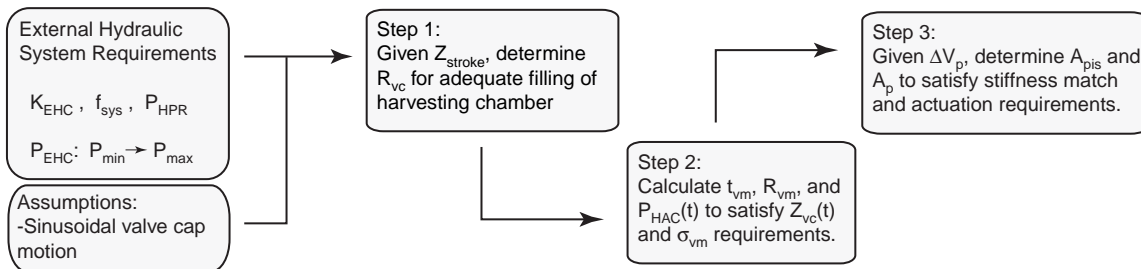


Figure 5.7: Flowchart illustrating the design procedure for the inlet active valve.

The full active valve design procedure, which will be discussed in Section 5.6, includes the ability to consider single valve cap and membrane designs as well as multiple valve cap and membrane designs (from now on  $N_{vh}$  is designated as the number of valve heads in the design), varying valve cap strokes  $Z_{vc,stroke}$ , and varying valve membrane thicknesses  $t_{vm}$ . There are important and interesting design issues associated with each of these design freedoms. Sections 5.4.1, 5.4.2, and 5.5 detail these issues. However, in this section, in order to present clearly the physical intuition behind the main steps in the design procedure, the following assumptions are made. First, this section focuses on generation of a single valve cap and membrane valve design. Second, in Step 1 when calculating the valve cap radius for adequate filling of the harvesting chamber, a value for  $Z_{vc,stroke}$  is assumed. Third, in Step 2, the valve membrane radius  $R_{vm}$  and required  $P_{HAC}(t)$  are calculated for an assumed valve membrane thickness  $t_{vm}$ .

### 5.3.2 System Requirements

To facilitate the understanding of the basic steps in the design procedure detailed in the following subsections, numerical system requirements characteristic of a typical MHT are presented here. For  $P_{HPR} = 1.2MPa$ , the inlet valve opens in a sinusoidal manner to fill a harvesting chamber with  $K_{EHC} = 1.5e^{16} \frac{Pa}{m^3}$ . The system frequency is chosen to be  $f_{sys} = 10kHz$  and it is desired that during this filling process,  $P_{EHC}$  should rise from a minimum pressure  $P_{min} = 0.2MPa$  to a maximum pressure  $P_{max} = 1.0MPa$ . It is assumed that the outlet valve is designed properly to allow evacuation from  $P_{max} = 1.0MPa$  to  $P_{min} = 0.2MPa$  during the time that the inlet valve is closed. In addition, for this example system, the channel dimensions  $L_c$  and  $A_c$  are chosen to ensure that fluid inertial effects in the channel are negligible (ie:  $P_{EHC} = P_{EHC}^*$  at all times).

### 5.3.3 Step 1: Design of Valve Cap

In the first step of the design procedure, the valve cap radius  $R_{vc}$  is calculated so as to allow for exact filling of the harvesting chamber. With the imposed valve cap motion  $Z_{vc}(t)$  and the external hydraulic system modeling tools described in Section 5.2,  $R_{vc}$  is determined such that the pressure rise in the harvesting chamber increases from its initial minimum of  $P_{min}$  to the desired maximum pressure  $P_{max}$  at the time the valve completely closes again. In this example procedure, the valve cap stroke is taken to be  $Z_{stroke} = 40\mu m$ . Equations 5.1, 5.2, 5.3, 5.6 are solved in the previously described Simulink simulation for this purpose. Insufficient filling will result if  $R_{vc}$  is not large enough. Conversely, if  $R_{vc}$  is too large, the chamber will be filled in excess. Figure 5.8 illustrates adequate and inadequate filling scenarios.

For the example MHT system, a value of  $R_{vc} = 241\mu m$  is determined, through iteration, that results in a harvesting chamber pressure rise from  $P_{EHC} = 0.2MPa$  to  $P_{EHC} = 1.0MPa$

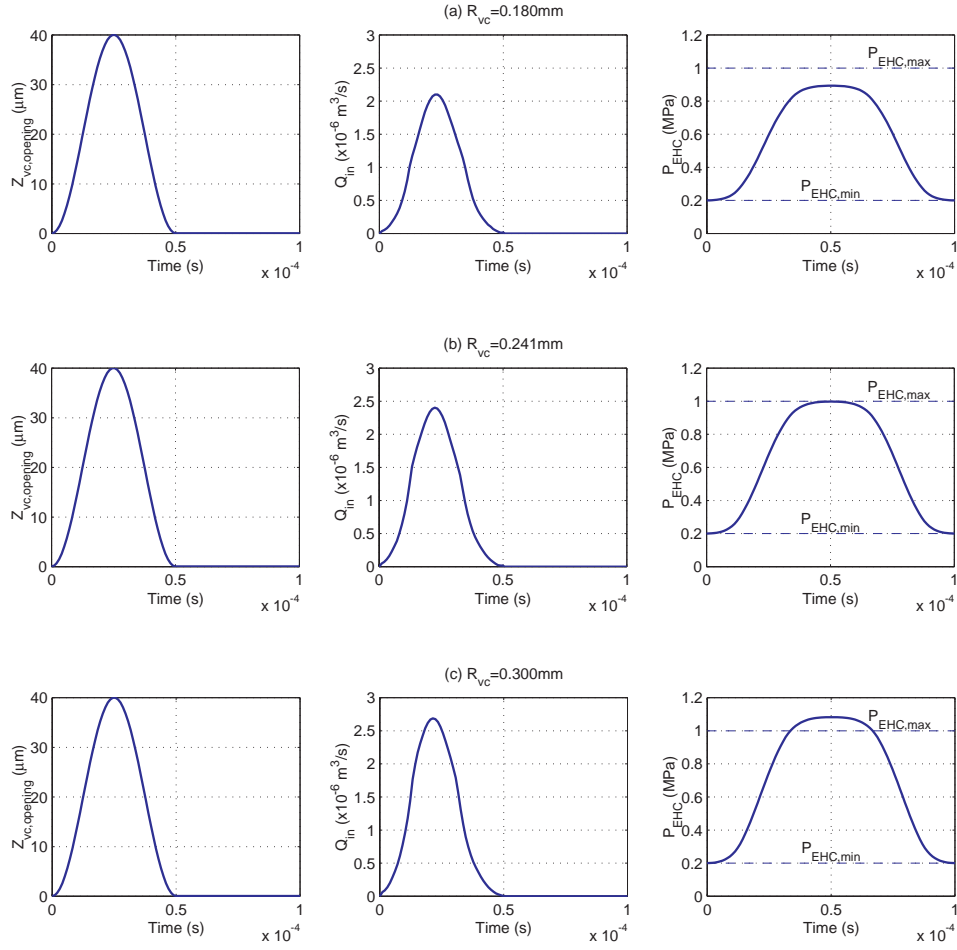


Figure 5.8: Chamber filling plots corresponding to  $Z_{stroke} = 40\text{ }\mu\text{m}$  and differing values of  $R_{vc}$ : (a) if  $R_{vc} = 180\text{ }\mu\text{m}$ , the chamber can not fill adequately, (b) if  $R_{vc} = 241\text{ }\mu\text{m}$ , the chamber fills the desired amount, and (c) if  $R_{vc} = 300\text{ }\mu\text{m}$ , the chamber fills in excess of the desired amount.

during the time that the inlet valve is open. Figure 5.8(b) displays the imposed valve cap deflection, the corresponding flow rate  $Q_{in}$  through the valve, and the resulting  $P_{EHC}(t)$  time history for this case. The valve is completely closed when  $Z_{vc,opening} = 0\text{ }\mu\text{m}$  and is fully open when  $Z_{vc,opening} = +40\text{ }\mu\text{m}$ . Note that the chamber fills properly since the pressure at the instant of valve closing is  $1.0\text{ MPa}$ . Since a complete  $P_{EHC}(t)$  time history is needed for further steps in the design procedure, it is assumed that an outlet valve for the system has been sufficiently designed to evacuate the fluid during the second half of the device cycle. Figure 5.8(a) shows the corresponding results for the case where the valve cap radius is too small,  $R_{vc} = 180\text{ }\mu\text{m}$ . Here, the chamber pressure is only able to rise to  $P_{EHC} = 0.9\text{ MPa}$  at the instant the inlet valve closes. Figure 5.8(c) shows the corresponding results for the case where the valve cap radius is too large,  $R_{vc} = 300\text{ }\mu\text{m}$ . Here, the chamber pressure rises in excess of

the desired value to  $P_{EHC} = 1.08 MPa$  at the instant the inlet valve closes.

### 5.3.4 Step 2: Design of Valve Membrane

In the second step of the design procedure, for a given valve membrane thickness  $t_{vm}$ , the outer membrane radius  $R_{vm}$  and required  $P_{HAC}(t)$  time history are calculated such that the valve cap properly follows its imposed trajectory  $Z_{vc}(t)$  and experiences a maximum tensile membrane stress during this motion of  $\sigma_{vm} = \sigma_{limit}$ . The code calculates the entire stress field along the membrane, however it records only the maximum tensile value for each time instant during the cycle and calls it  $\sigma_{vm}$ . A limiting value for  $\sigma_{limit} = 1.0 GPa$  is taken from [6] [5]. Since a small value of  $t_{vm}$  is desired to minimize actuation requirements, an initial value of  $t_{vm} = 7 \mu m$  is employed. For the given value of  $t_{vm}$ , a guess for  $R_{vm}$  is taken. Under the constant  $P_{HPR}$  loading on the valve membrane and the time-varying loading  $P_{EHC}^*(t)$  on the valve cap calculated in Step 1, the required  $P_{HAC}(t)$  time history is calculated to force the valve membrane and cap to follow its imposed trajectory  $Z_{vc}(t)$ . During this time cycle,  $\sigma_{vm}$  is monitored. This procedure becomes an iterative process in  $R_{vm}$  until a value of  $R_{vm}$  is determined such that at some time during the complete cycle, a peak tensile stress of  $\sigma_{limit}$  is reached. As will be discussed in Section 5.4.2, it might be the case that it is impossible to arrive at a membrane design for this particular value of  $t_{vm}$  due to high stresses in the membrane, at which point it will be necessary to increase the membrane thickness. However, this issue is held off until Section 5.4.2.

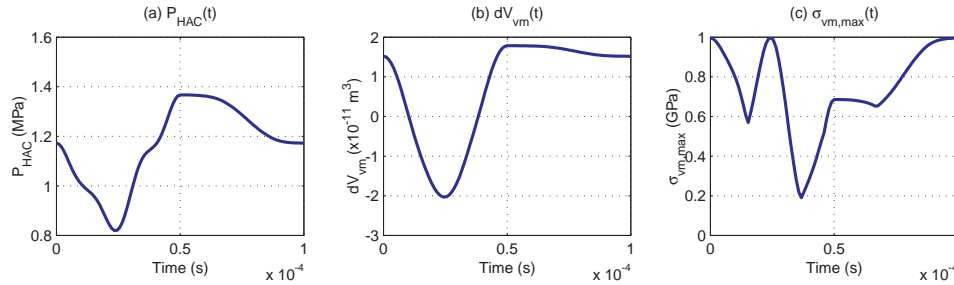


Figure 5.9: Valve membrane behavior corresponding to  $Z_{stroke} = 40 \mu m$ ,  $R_{vc} = 241 \mu m$ ,  $t_{vm} = 7 \mu m$ , and  $R_{vm} = 757 \mu m$ : (a) required hydraulic amplification chamber  $P_{HAC}(t)$ , (b) corresponding valve cap and membrane swept volume  $dV_{vm}(t)$ , and (c) peak stress in valve membrane  $\sigma_{vm}(t)$ .

For the example MHT system, a value of  $R_{vm} = 757 \mu m$  is determined for  $t_{vm} = 7 \mu m$ . The required  $P_{HAC}(t)$  time history, swept volume time history under the membrane and cap  $dV_{vm}(t)$ , and the associated membrane stress time history  $\sigma_{vm}(t)$  are shown in Figures 5.9(a), (b), and (c) respectively. In Figure 5.9(c), notice that the maximum stress in the membrane during the cycle occurs when the cap is deflected to its minimum value of  $Z_{vc} = -20 \mu m$ . The

membrane again experiences a stress of  $1.0GPa$  when the cap is at its maximum deflection of  $Z_{vc} = +20\mu m$ . This reconfirms the design choice to force the membrane into symmetric upward and downward motion so as to maximize total valve cap stroke when restricted to limited membrane stress levels.

### 5.3.5 Step 3: Design of Piezoelectric Drive Element

In the third step of the design procedure, the piezoelectric material area and drive element piston area are determined so as to create a quasi-static stiffness match with the loading seen by this structure. The goal in doing this is to maximize the energy transfer from the piezoelectric material to the load. As shown in Figure 5.10, the valve cap/membrane and external hydraulic system appear to the drive structure as a stiffness  $K_{vm}$  in series with a fluid stiffness  $K_{HAC}$  of the hydraulic amplification chamber. A linearization of the actuation curve associated with the motion of the valve cap (described by the time histories  $P_{HAC}(t)$  and  $dV_{vm}(t)$  calculated in Step 2 of the design procedure and plotted against one another in Figure 5.10(a)) provides an approximation for this  $K_{vm}$  stiffness. Combining  $K_{vm}$  and  $K_{HAC}$  together produces an overall load  $K_{load}$  seen by the piezoelectric element. This model neglects the stiffness of the drive piston tethers. Studies have shown that the stiffnesses of these tethers in relation to the  $K_{vm}$  and  $K_{HAC}$  are small for typical active valve designs. The requirement of a stiffness match between  $K_{piezo}$  and  $K_{load}$  therefore results in the following equality,

$$K_{piezo} = K_{load} \quad \rightarrow \quad \frac{E_p A_p}{L_p} = \frac{A_{pis}^2}{\left(\frac{\Delta V_{vm}}{\Delta P_{HAC}}\right) + \left(\frac{A_{pis} H_{HAC}}{K_{fluid}}\right)}. \quad (5.7)$$

Substituting this requirement into the following piezoelectric material actuator equation, one obtains a relationship between  $Z_p$  and  $V_p$ ,

$$Z_p = d_{33}V_p - \frac{F_p}{K_p} = d_{33}V_p - \left(\frac{K_{load}}{K_{piezo}}\right) Z_p \quad \rightarrow \quad Z_p = \frac{1}{2}d_{33}V_p. \quad (5.8)$$

In addition to this impedance match requirement on  $Z_p$ ,  $Z_p$  must also satisfy the volume conservation relation within the active valve structure,

$$Z_p = \frac{\Delta V_{de}}{A_{pis}} = \frac{\Delta V_{vm} + \Delta V_{fluid}}{A_{pis}} = \left(\frac{1}{A_{pis}}\right) \left[\Delta V_{vm} + \left(\frac{A_{pis} H_{HAC}}{K_{fluid}}\right) \Delta P_{HAC}\right]. \quad (5.9)$$

Eliminating  $Z_p$  in Equations 5.8 and 5.9 results in the following equality,

$$\frac{1}{2}d_{33}V_p = \left(\frac{1}{A_{pis}}\right) \left[\Delta V_{vm} + \left(\frac{A_{pis} H_{HAC}}{K_{fluid}}\right) \Delta P_{HAC}\right]. \quad (5.10)$$



Therefore, equations 5.7 and 5.10 form a set of two equations with three unknowns  $A_{pis}$ ,  $A_p$ , and  $V_p$ . Equation 5.7 sets the relationship between  $A_{pis}$  and  $A_p$  for a stiffness match between piezo and load to be achieved while equation 5.10 defines the condition under which valve performance is met, relating the input piezo voltage  $V_p$  to the  $A_{pis}$ . In observing these equations, it is clear that the smaller the voltage  $V_p$ , the larger the values of  $A_{pis}$  and  $A_p$  need to be. Since one of the goals in the design of this active valve is make its total volume as small as possible, this implies that the valve should work at as large a voltage as possible. In real devices, a limitation of electrical breakdown across the air gap between drive element piston and the bottom structural plate exists, and therefore a maximum allowable  $V_p$  for the given piezo length  $L_p$  is set. As a result, in the design of this valve, voltage now becomes an imposed quantity. The set of two equations can be solved for the two remaining geometric free design variables  $A_{pis}$  and  $A_p$  to create a quasi-static stiffness match condition between the piezo and load and to ensure adequate valve performance to satisfy the actuation requirements passed down from the membrane and cap design steps.

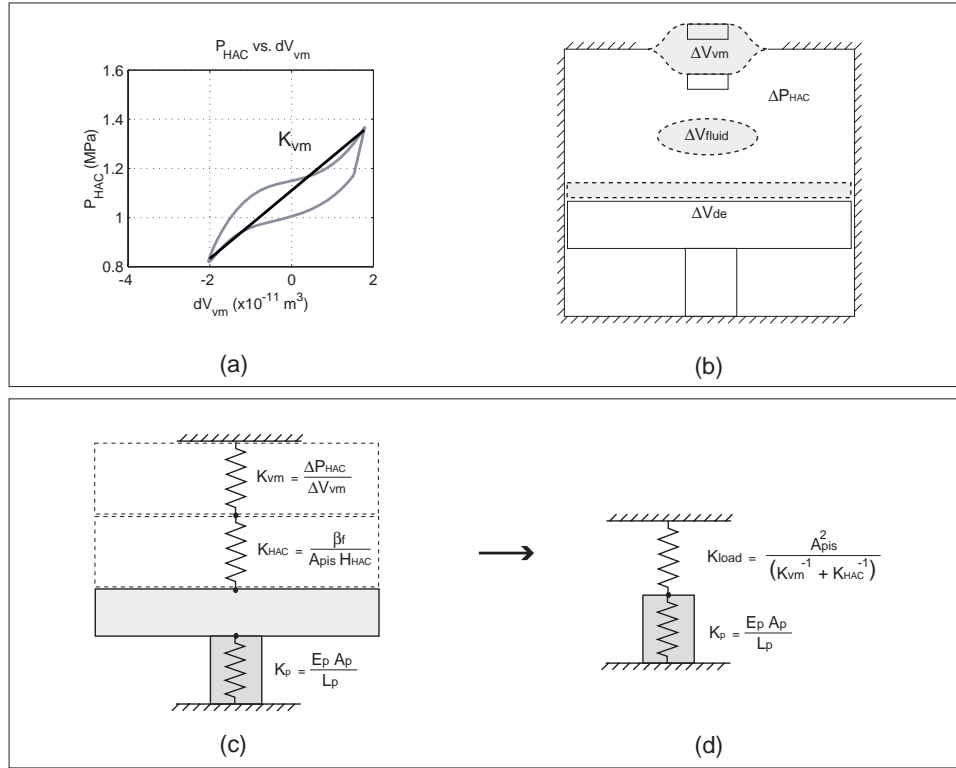


Figure 5.10: Simplification of the active valve device in a quasi-static stiffness match analogy: (a) determination of linearized  $K_{vm}$  stiffness load, (b) important actuation volume change and pressure variables, (c) valve membrane volumetric stiffness in series with fluid hydraulic stiffness acting through piston area against piezo displacement stiffness, and (d) lumped linear load spring acting against piezo material.

For the example MHT system, the piezoelectric material thickness is assumed to be  $L_p = 1mm$  and the applied peak-peak voltage is assumed to be  $V_p = 1000V$ . Under these assumptions, a drive piston area and piezo area are calculated to correspond to  $R_{pis} = 3.59mm$  and  $R_p = 0.88mm$ . Figures 5.11(a), (b), and (c) show the required piezoelectric voltage time history  $V_p$  to force the valve cap to follow the desired trajectory  $Z_{vc}(t)$ , the drive element  $P_{HAC}$  vs.  $dV_{de}$  actuation curve, and the resulting piezoelectric material stress time history  $T_p$ , respectively. In comparing Figure 5.11(b) to Figure 5.10(a), notice the increased volume change between  $dV_{de}$  and  $dV_{vm}$ . This difference is exactly equal to the fluid compressibility volume change  $dV_{HAC}$  under the pressure loading  $P_{HAC}(t)$ . At this point, a design for the active valve has been achieved.

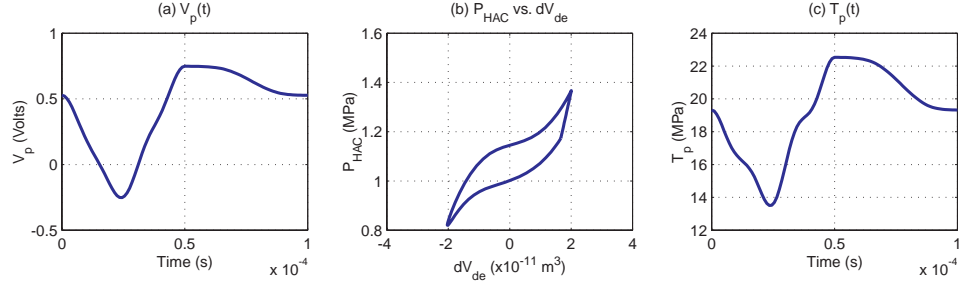


Figure 5.11: Drive element behavior corresponding to  $R_{pis} = 3.59mm$  and  $R_p = 0.88mm$ : (a) required piezoelectric voltage  $V_p(t)$ , (b) corresponding drive element actuation curve, and (c) stress on piezoelectric material  $T_p(t)$ .

## 5.4 Design Freedoms Within Procedure

The basic design procedure for the active valve discussed in Section 5.3 was simplified in three ways in order to ease the explanation of the main steps. First, the valve design was carried out for a valve geometry with only a single valve cap and membrane above the hydraulic amplification chamber ( $N_{vh} = 1$ ). Second, the design assumed a predetermined stroke  $Z_{vc,stroke}$  of the valve cap. Third, the design assumed that a value of  $t_{vm}$  could be chosen that would result in the successful calculation of the valve membrane outer radius  $R_{vm}$  to guarantee stresses below a limiting value. In reality, when designing the active valve structure, one would like to relax all three of these design restrictions so that the design process creates an optimal valve geometry. It might therefore be the case that the optimal active valve design uses five valve caps and membranes in parallel above the hydraulic amplification chamber rather than a single valve cap and membrane, or that the stroke(s) of the valve cap(s) should be  $20\mu m$  rather than  $40\mu m$ , or that  $8\mu m$  is the minimal valve membrane thickness that can be used to create a strong enough valve membrane structure. This section will discuss two of these three design freedoms,  $Z_{vc,stroke}$  and  $t_{vm}$ . The third design freedom,  $N_{vh}$ , will be discussed in Section 5.5. All three design freedoms will then be included in the final systematic design procedure presented in Section 5.6.

### 5.4.1 Design Freedom: $Z_{vc,stroke}$

In the example active valve design procedure presented in Section 5.3, the required valve cap size  $R_{vc}$  was calculated that would allow for adequate filling of the harvesting chamber, given that the valve cap was allowed to move through a stroke of  $Z_{vc,stroke} = 40\mu m$ . It would have also been possible to determine a value for  $R_{vc}$  if  $Z_{vc,stroke} = 20\mu m$ . To maintain fluid flow resistance through the valve structure, it makes sense that as the valve cap stroke is decreased, the radius of the valve cap itself must be increased. Figure 5.12 displays the calculated valve cap radius  $R_{vc}$  for a series of different valve cap strokes  $Z_{vc,stroke}$  for the example MHT system described in the previous section. For an imposed  $Z_{vc,stroke} = 40\mu m$ , the design code simulation requires a value of  $R_{vc} = 241\mu m$  to ensure proper filling of the harvesting chamber. Alternatively, for an imposed  $Z_{vc,stroke} = 20\mu m$ , the design code simulation requires a value of  $R_{vc} = 688\mu m$  to ensure proper filling of the harvesting chamber. Therefore, different combinations of  $Z_{vc,stroke}$  and  $R_{vc}$  can effectively fill the chamber, but as the full design procedure in Section 5.6 will illustrate, one combination may be better than others in designing the remaining structures of the valve.

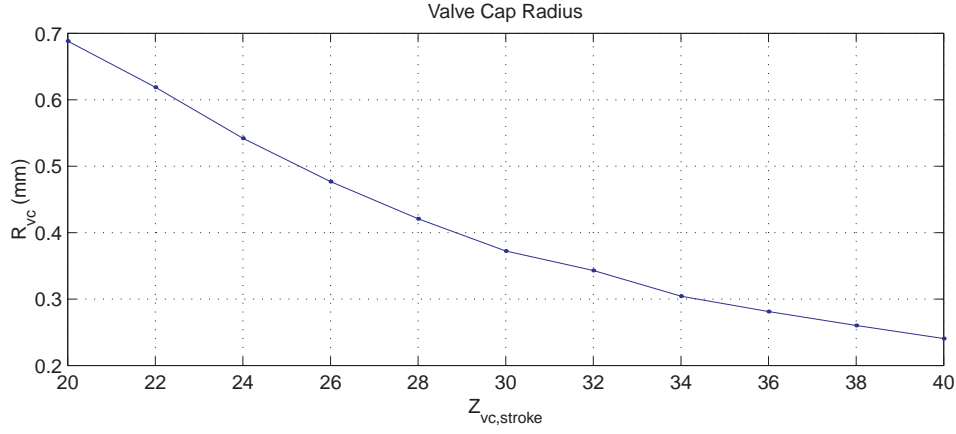


Figure 5.12: Design of valve cap, for  $P_{HPR} = 1.2MPa$ ,  $f_{sys} = 10kHz$ ,  $P_{EHC,min} = 0.2MPa$ ,  $P_{EHC,max} = 1.0MPa$ , and varying  $Z_{vc,stroke}$ .

#### 5.4.2 Design Freedom: $t_{vm}$

For a given size valve cap (value of  $R_{vc}$ ), the next step in the design procedure is to design a membrane structure which can carry this valve cap through the imposed opening time history against the external pressure loadings,  $P_{HPR}$  and  $P_{EHC}(t)$ . During filling of the chamber, as was discussed in previous sections,  $P_{HPR}$  is constant with time over the valve membrane, however,  $P_{EHC}$  varies from a minimum to a maximum. The valve membrane radius  $R_{vm}$  and thickness  $t_{vm}$  must be determined to achieve the desired behavior.

Two example studies will be included in this section to illustrate some important issues concerning the design of the valve membrane structure. The first study will look at the design of the valve membranes for each of the valve cap sizes arrived at in Section 5.4.1, assuming that  $P_{HPR} = P_{EHC} = 1.2MPa$  for all time during the opening and closing of the valve cap and membrane. This situation, where the pressures above the cap and membrane structure are constant with time, would never occur in reality. However, the purpose of this study is to illustrate an important point associated with the structural design of the membrane. The second study will then focus on the real case, where  $P_{HPR} = 1.2MPa$  during opening and closing, but  $P_{EHC}$  does vary as calculated in the design code simulation. The overall conclusion from these comparative studies will be that this changing  $P_{EHC}$  pressure with time in certain circumstances does not allow for a valve design of a particular membrane thickness to be calculated that can satisfy the membrane stress limitations. In such cases, it will be necessary to iterate to larger membrane thicknesses to achieve a reasonable design.

**Example Study:**  $P_{HPR} = 1.2MPa$  and  $P_{EHC}(t) = 1.2MPa$

In this example study, for each of the valve cap designs presented in Figure 5.12, the design code calculates the valve membrane radius so that for the imposed valve cap displacements and under the constant external loading  $P_{HPR} = P_{EHC} = 1.2MPa$ , the membrane experiences a peak stress of  $\sigma_{vm} = 1GPa$  during its opening/closing cycle. The valve membrane thickness is assumed to be  $t_{vm} = 7\mu m$  for these calculations. This is really a lower limit for membrane thickness based on fabrication restrictions.

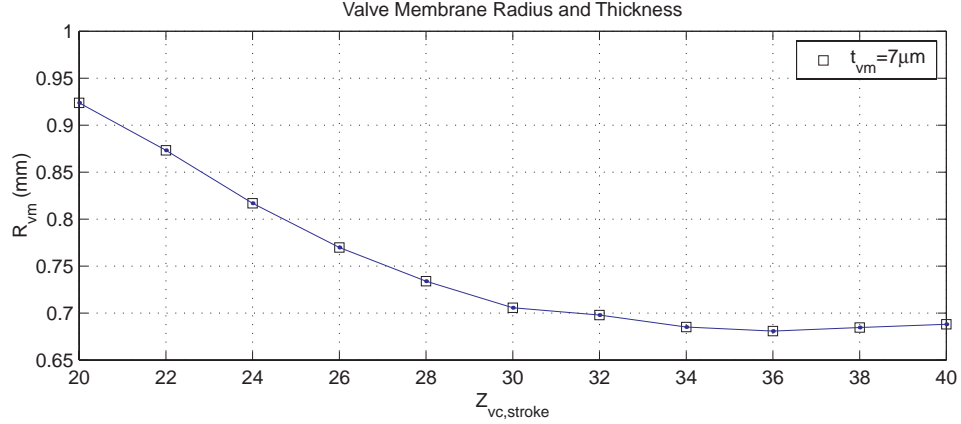


Figure 5.13: Design of valve membrane for the case where the external pressure loading on the valve cap and membrane are held constant during the time that the cap opens and closes,  $P_{HPR} = P_{EHC} = 1.2MPa$  constant with time.

Figure 5.13 displays the calculated  $R_{vm}$  values for each of the imposed  $Z_{vc,stroke}$  and previously calculated  $R_{vc}$  values. For an imposed  $Z_{vc} = 40\mu m$  and therefore for the previously calculated  $R_{vc} = 241\mu m$ , the design code procedure calculates a membrane radius of  $R_{vm} = 688\mu m$  to ensure stresses below the limit. For an imposed  $Z_{vc} = 20\mu m$  and therefore for the previously calculated  $R_{vc} = 688\mu m$ , the design code procedure calculates a membrane radius of  $R_{vm} = 924\mu m$  to ensure stresses below the limit. In all cases for the imposed valve cap stroke between  $20\mu m$  and  $40\mu m$ , the membrane is able to designed with  $t_{vm} = 7\mu m$ .

To illustrate how the code determines  $R_{vm}$ , take the point design for an imposed  $Z_{vc,stroke} = 20\mu m$ . The valve cap radius has been previously calculated to be  $R_{vc} = 688\mu m$ . The code begins by guessing a value of  $R_{vm}$ , and then determines the required  $P_{HAC}$  pressure underneath the cap and membrane at each instant of time to satisfy the required cap displacement against the external pressure loadings. The membrane stress is recorded for all time instants during the complete opening/closing cycle of the valve cap. The code then iterates in  $R_{vm}$  until a value is determined that results in the desired peak stress occurring during the valve cap opening/closing cycle.

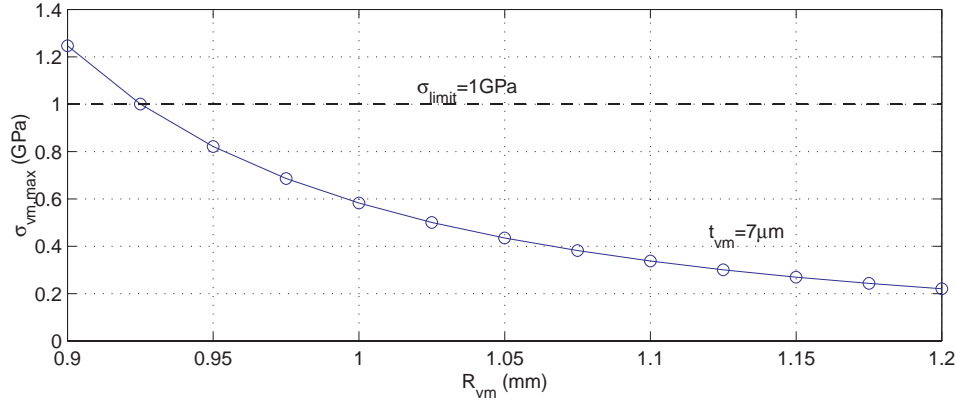


Figure 5.14: For  $Z_{vc,stroke} = 20\mu m$ ,  $R_{vc} = 688\mu m$ ,  $P_{HPR} = P_{EHC} = 1.2MPa$  constant with time, and  $t_{vm} = 7\mu m$ , the membrane peak stress  $\sigma_{vm,peak}$  during valve cap motion decreases as  $R_{vm}$  is decreased. An  $R_{vm}$  to meet the desired  $\sigma_{vm,peak} = 1GPa$  can be determined.

Figure 5.14 plots the peak membrane stress during a complete valve membrane cycle for guesses of  $R_{vm}$ . Notice that the value of  $R_{vm}$  for which  $\sigma_{vm,max} = 1.0$  is  $924\mu m$ . For a small value of  $R_{vm} = 900\mu m$ , the membrane stress reaches a peak stress of  $\sigma_{vm} = 1.24GPa$  during the cycle, whereas for a large value of  $R_{vm} = 1200\mu m$ , the membrane stress reaches a peak stress of only  $\sigma_{vm} = 0.22GPa$  during the cycle. For a value of  $R_{vm} = 1010\mu m$  (chosen for demonstration purposes), a peak stress of  $\sigma_{vm} = 0.52GPa$  during the cycle is determined. For all of these membrane designs, the peak stress occurs at the time during the cycle when the valve membrane is at peak positive displacement. Figure 5.15 illustrates the spatial displacement and stress distributions of the membrane for these three membrane designs. Notice in Figure 5.15(a), for  $R_{vm} = 1200\mu m$ , that the stress is low because of the minimal curvature in the membrane at the inner and outer boundaries. Also, there is only a slight shift in the mean stress on the top and bottom membrane surfaces (ie: the membrane is experiencing non-linear stretching of the neutral axis, but only slightly). In Figure 5.15(c), for  $R_{vm} = 900\mu m$ , the stress is high because of the significant curvature in the membrane at the inner and outer boundaries. In this case, there is a significant shift in the mean stress ( $\sim 0.25GPa$ ) on the top and bottom membrane surfaces as the membrane experiences quite a bit of non-linear stretching. And in Figure 5.15(b), for  $R_{vm} = 1010\mu m$ , the membrane behavior is between the previous two cases.

The important conclusion from this example study with a constant  $P_{EHC}$  above the valve cap during the design of the valve membrane structure is that for the variety of valve cap strokes imposed, a valve membrane with thickness  $t_{vm}$  is able to be determined to satisfy the stress limitations. As will be shown in the following example study, as  $P_{EHC}$  is allowed to vary, as it would in a real system, different membrane thicknesses will have to be considered.

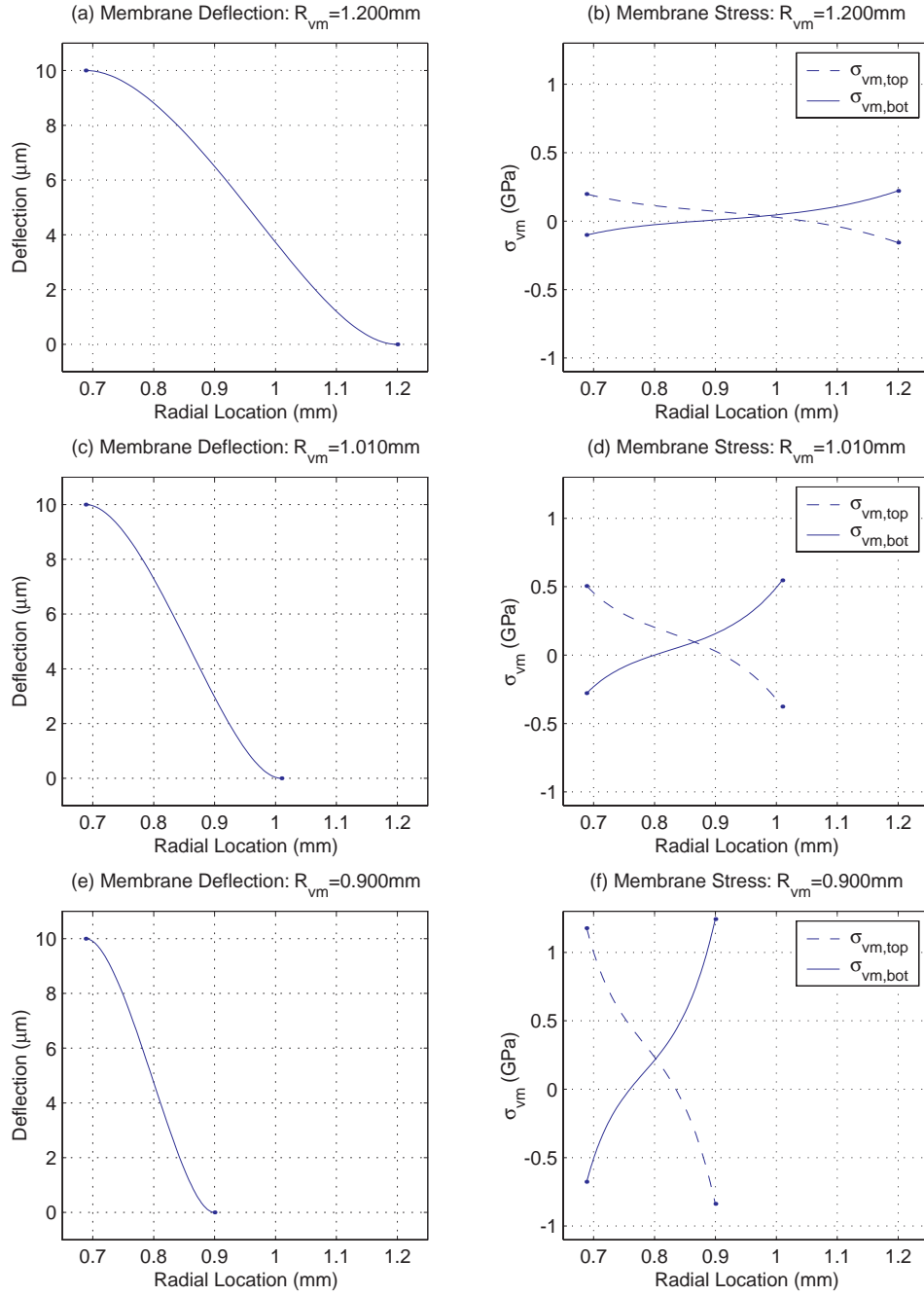


Figure 5.15: Example valve membrane deflection and stress plots for  $Z_{vc,stroke} = 20\mu m$ ,  $R_{vc} = 688\mu m$ ,  $P_{HPR} = P_{EHC} = 1.2\text{MPa}$  constant with time, and  $t_{vm} = 7\mu m$ : (a)  $R_{vm} = 1200\mu m$ , (b)  $R_{vm} = 1010\mu m$ , and  $R_{vm} = 900\mu m$ .

**Example Study:**  $P_{HPR} = 1.2MPa$  and  $P_{EHC}(t) = \text{varying}$

In this example study, for each of the valve cap designs presented in Figure 5.12, the design code calculates the valve membrane radius so that for the imposed valve cap displacements and under the external loading  $P_{HPR} = 1.2MPa$  and  $P_{EHC} = 0.2MPa \rightarrow 1.0MPa$ , the membrane experiences a peak stress of  $\sigma_{vm} = 1GPa$  during its opening/closing cycle. The valve membrane thickness is desired to be  $t_{vm} = 7\mu m$  for these calculations, however, if a membrane design at a certain thickness can not be found, then the thickness is increased. Figure 5.16 displays the calculated  $R_{vm}$  values for each of the imposed  $Z_{vc,stroke}$  and previously calculated  $R_{vc}$  values.

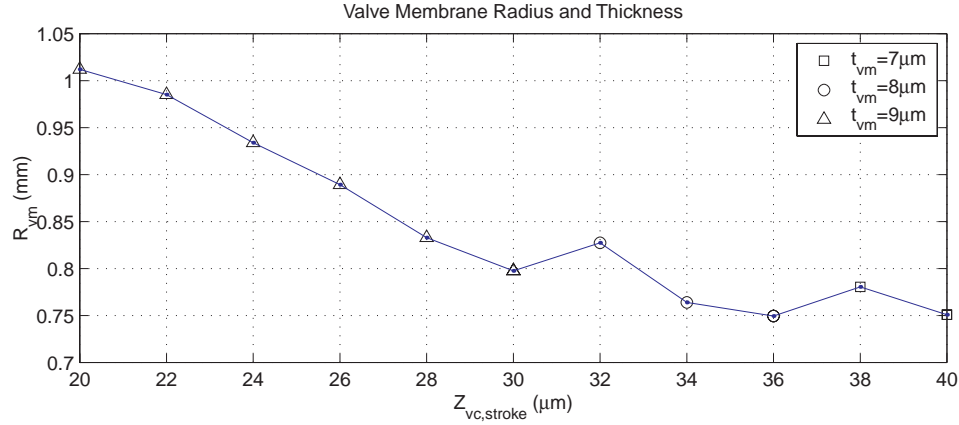


Figure 5.16: Design of the valve membrane for the case where  $P_{HPR} = 1.2MPa$  and the external pressure loading on the valve cap  $P_{EHC}$  is allowed to vary with time, as it would in a real hydraulic system.

In comparison to the previous example study where a valve membrane with  $t_{vm} = 7\mu m$  could be designed for each of the valve cap strokes, in this example study, as  $Z_{vc,stroke}$  is reduced from  $40\mu m$  to  $20\mu m$ ,  $t_{vm}$  must be increased from  $7\mu m$  so as to determine  $R_{vm}$  values that satisfy the stress requirements. This is a result of the changing  $P_{EHC}$  pressure over the valve cap as the cap moves through its cycle. For an imposed  $Z_{vc,stroke} = 40\mu m$  and therefore for the previously calculated  $R_{vc} = 241\mu m$ , the design code procedure is able to determine a membrane radius of  $R_{vm} = 751\mu m$  for  $t_{vm} = 7\mu m$  to ensure stresses below the limit. For an imposed  $Z_{vc,stroke} = 20\mu m$  and therefore for the previously calculated  $R_{vc} = 688\mu m$ , however, the design code procedure is not able to determine a satisfactory  $R_{vm}$  for either  $t_{vm} = 7\mu m$  or  $t_{vm} = 8\mu m$ . Rather, it must increase the membrane thickness to  $t_{vm} = 9\mu m$  in order to find a satisfactory membrane radius of  $R_{vm} = 1010\mu m$  that ensures stresses below the limit.

Figure 5.17 plots the peak membrane stress during a complete valve membrane cycle for the case of imposed  $Z_{vc,stroke} = 20\mu m$  for guesses of  $R_{vm}$  at the three thicknesses  $t_{vm} = 7\mu m$ ,  $t_{vm} = 8\mu m$ , and  $t_{vm} = 9\mu m$ . For  $t_{vm} = 7\mu m$ , no value of  $R_{vm}$  can be chosen to bring



the stress below the critical limit of  $\sigma_{limit} = 1GPa$ . At this thickness, small values of  $R_{vm}$  and large values of  $R_{vm}$  both result in large stresses due to high membrane curvature at the membrane boundaries. In the case of small  $R_{vm}$ , the high curvature is a result of the membrane being so short in width, whereas for the case of large  $R_{vm}$ , the high curvature is a result of bowing of the membrane under the large negative pressure differential across the membrane (see later discussion). For  $t_{vm} = 8\mu m$ , again no value of  $R_{vm}$  can be determined, although the minimum of the curve is approaching  $\sigma_{limit}$ . Finally, for  $t_{vm} = 9\mu m$ , a valve membrane radius is achievable. In fact, there are two potential solutions, one at  $R_{vm} = 1130\mu m$  and the other at  $R_{vm} = 1015\mu m$ . During the design procedure, the code picks the smaller of the two values, so as to minimize the valve size.

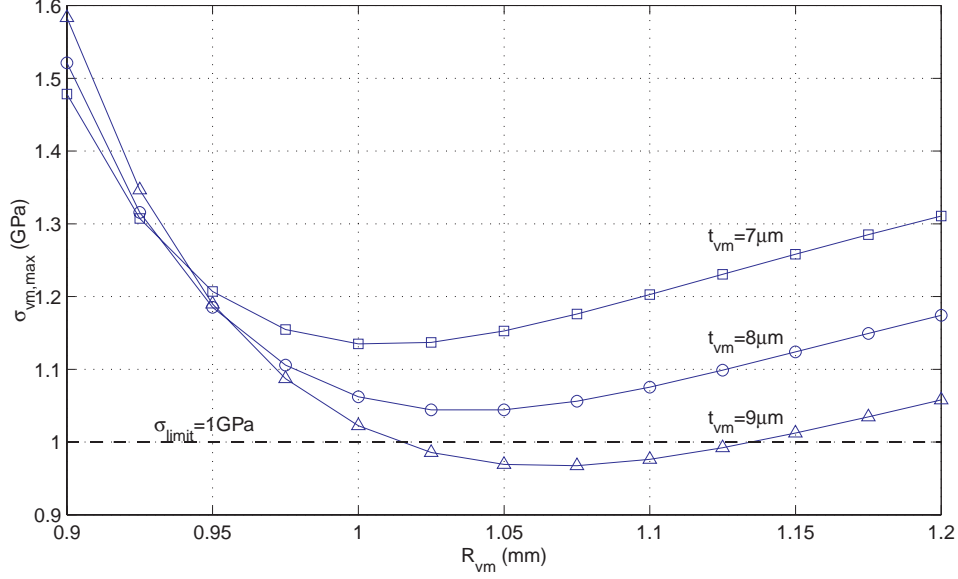


Figure 5.17: For  $Z_{vc,stroke} = 20\mu m$ ,  $R_{vc} = 688\mu m$ ,  $P_{HPR} = 1.2MPa$ ,  $P_{EHC}$  varying with time, and for different  $t_{vm}$ , the membrane peak stress  $\sigma_{vm,peak}$  during valve cap motion reaches a minimum at a particular  $R_{vm}$ . A satisfactory  $R_{vm}$  for  $t_{vm} = 7\mu m$  and for  $t_{vm} = 8\mu m$  can not be found, however an  $R_{vm}$  for  $t_{vm} = 9\mu m$  can be determined to meet the desired  $\sigma_{vm,peak} = 1GPa$ .

Figure 5.15 illustrates the spatial displacement and stress distributions of the membrane for three values of membrane radius  $R_{vm} = 1200\mu m$ ,  $R_{vm} = 1010\mu m$ , and  $R_{vm} = 900\mu m$ , all for  $t_{vm} = 9\mu m$ . Notice in Figure 5.18(a), for  $R_{vm} = 1200\mu m$ , that the stress is large because of the significant curvature in the membrane at the inner boundary due to the negative bowing of the membrane. This bowing develops because at the instant when the valve cap is at its maximum deflection upward, the pressure acting on the top surface of the valve cap is at its minimum  $P_{EHC} = 0.2MPa$ . Therefore, the required  $P_{HAC}$  within the valve hydraulic

amplification chamber at this time instant is low, resulting in a significant negative pressure across the valve membrane. In Figure 5.18(c), for  $R_{vm} = 900\mu m$ , the stress is high because of the significant curvature in the membrane at the inner and outer boundaries, due to the minimal width of the membrane. And in Figure 5.18(b), for  $R_{vm} = 1010\mu m$ , the peak membrane stress is  $\sigma_{vm,peak} = 1.0GPa$  and occurs at the inner membrane boundary.

This study has shown that in designing to valve membranes to work under varying pressure time histories, depending on the magnitude of the external pressures and their behavior with time, it is sometimes impossible to determine a valve membrane radius for a given membrane thickness to achieve stresses below the critical limits. As a result of this, the final systematic active valve design procedure presented in Section 5.6 is capable of recognizing these restrictions and iterating on the membrane thickness until a satisfactory membrane design is achieved.

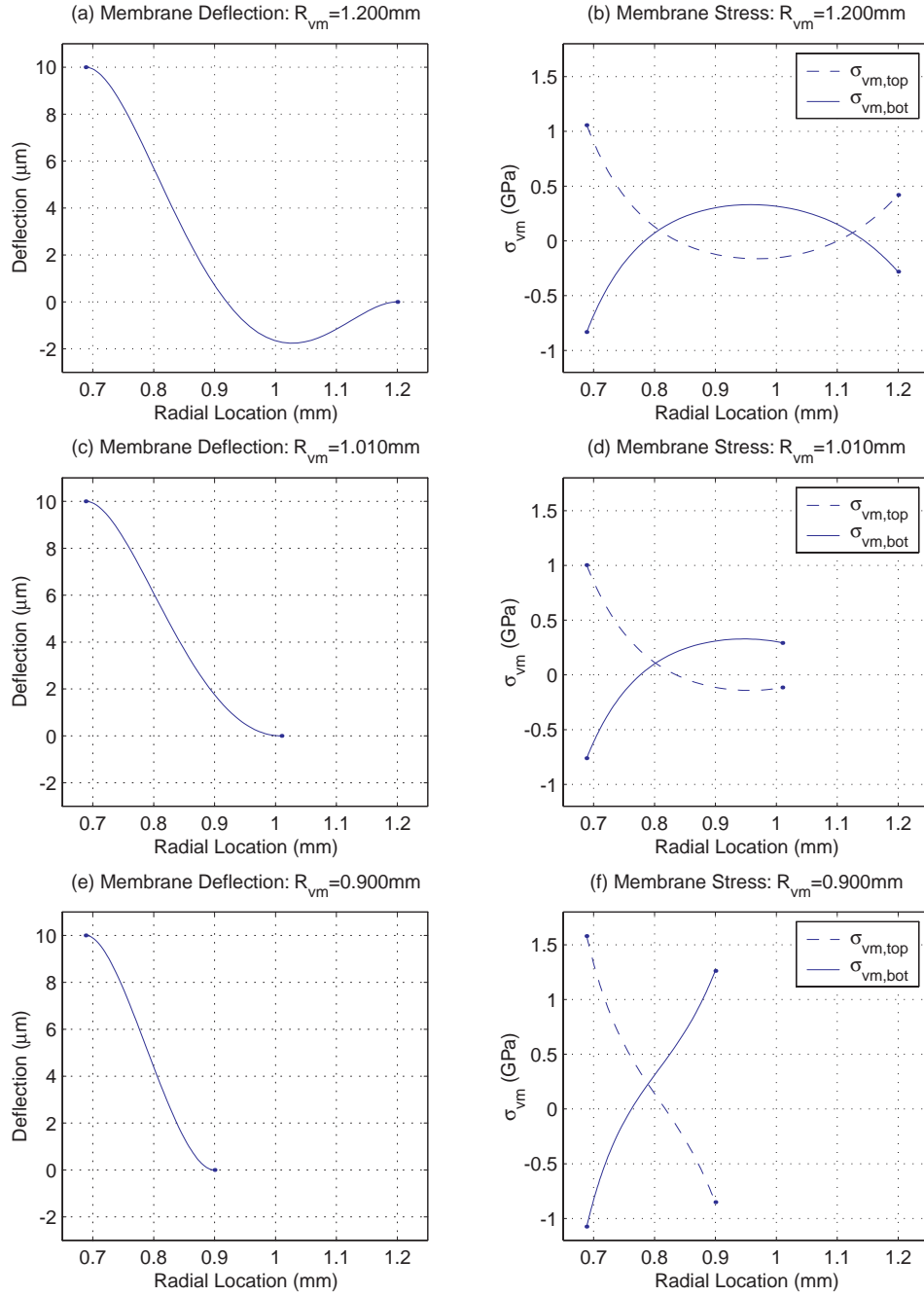


Figure 5.18: Example valve membrane deflection and stress plots for  $Z_{vc,stroke} = 20\mu\text{m}$ ,  $R_{vc} = 688\mu\text{m}$ ,  $P_{HPR} = 1.2\text{MPa}$ ,  $P_{EHC}$  varying with time, and  $t_{vm} = 9\mu\text{m}$ : (a)  $R_{vm} = 1200\mu\text{m}$ , (b)  $R_{vm} = 1010\mu\text{m}$ , and (c)  $R_{vm} = 900\mu\text{m}$ .

## 5.5 Power Consumption in Active Valve

During each cycle of operation of the active valve, electrical energy flows into and out of the piezoelectric material. The amount of energy required is dependent on the strain of the material and the load that it actuates against. To create a simple method for evaluating these energies in a given active valve geometry, the drive element portion of the valve will be focused on. In the final step of the design procedure, the piezoelectric material diameter and drive element piston diameter were calculated to create a stiffness match condition with the loading that the drive element experienced (see details in Section 5.3.5). Figure 5.11(b) illustrated the drive element actuation curve for the example design in Section 5.3.2. This type of curve will be the basis for evaluating cyclic energy flow in the valve.

### 5.5.1 Overview of Energy/Power Consumption

Figure 5.19 displays representative drive element actuation plots for a typical active valve design. In Figure 5.19(a), as the piezoelectric material expands and creates a positive drive element volume change  $dV_{de}$ , the pressure within the hydraulic amplification chamber  $P_{HAC}$  increases, due to the stiffness of the valve membrane and the external pressure loading time histories  $P_{HPR}$  and  $P_{EHC}(t)$ . The piezoelectric material therefore does work  $W_1$  on its environment. In Figure 5.19(b), the piezoelectric material deflection is decreasing, and the corresponding work done by the environment on the piezoelectric material (the drive element) is  $W_2$ . Throughout a full cycle of the valve, a total hysteretic valve energy loss of  $W_{hys} = W_1 - W_2$  results. This is due to the fact that during drive element motion upward, the average  $P_{HAC}$  pressure that the piston moves against is larger than that which exists to help move the piston downward in the second portion of the valve cycle. This hysteretic energy loss per valve cycle is being put into the external hydraulic system.

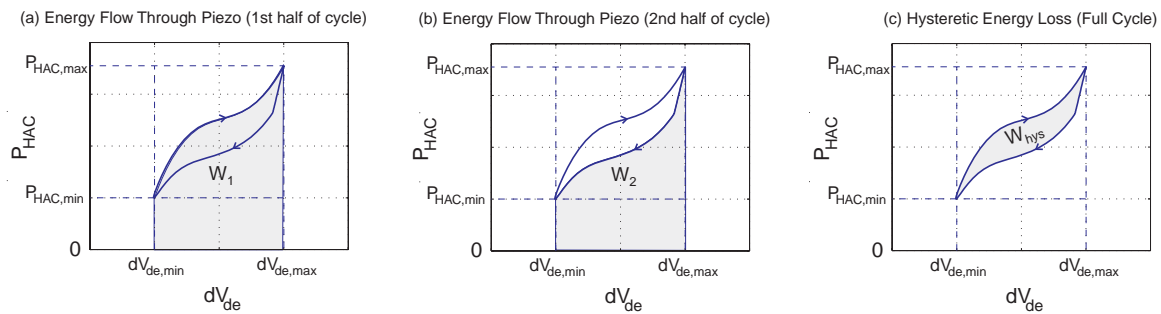


Figure 5.19: Schematic representation of energy flows and losses in active valve, based on drive element actuation behavior: (a) work done by piezo material on load during first half of valve cycle, (b) work done by load on piezo material during second half of valve cycle, and (c) hysteretic energy loss during a full valve cycle.

This hysteretic energy loss can be written in integral form as

$$W_{hys} = W_1 + W_2 = \int_1 P_{HAC} d(dV_{de}) + \int_2 P_{HAC} d(dV_{de}). \quad (5.11)$$

Note here that  $W_2$  is a negative quantity since work is done by the environment on the drive element. If the piezoelectric material and attached circuitry were 100% efficient, then no other energy loss mechanisms would exist within the valve system. In reality, though, the piezoelectric material and the attached circuitry are not perfectly efficient. Assuming a lumped parameter  $\gamma_{loss}$  as the fraction of energy flowing through the piezoelectric material during a full valve cycle that is lost due to material and circuitry inefficiencies, the total amount of cyclic energy lost in these mechanisms is therefore

$$W_{loss} = \gamma_{loss} (W_1 + |W_2|). \quad (5.12)$$

In order to calculate the power consumption of the valve design, the frequency of operation of the valve  $f_{sys}$  is incorporated into the previous relations. The total valve power consumption is thus the product of the valve frequency of operation and the total energy lost by the valve during a single cycle of operation,

$$P_{consumption} = f_{sys} [W_{hys} + W_{loss}]. \quad (5.13)$$

These power consumption quantities  $P_{hys}$ ,  $P_{loss}$ , and  $P_{consumption}$  will be monitored in carrying out the full valve systematic design code in order to evaluate the benefits of a particular valve design over another one.

### 5.5.2 Benefit of Multiple Valve Heads

The incorporation of multiple smaller-sized valve heads (which are designed to achieve the same external system flow performance as a single larger valve head) has the potential to reduce hysteretic energy loss of the active valve device. This phenomenon will be presented from the point of view of the valve cap and membrane acting against the external pressure loadings, since this is the actual structural interface between the active valve and the rest of the MHT system. The hysteretic energy loss of the active valve per cycle is the same whether it is looked at from the point of view of the drive element or the point of view of the valve cap and membrane. This is true because no energy loss mechanisms exist within the valve between the drive piston and the valve cap and membrane. Certainly, structural compliances do exist, but these are energy storage elements, not loss mechanisms. Therefore, it is possible to calculate

the hysteretic energy loss by focusing on just the motion of the valve cap and membrane against the external pressure loadings encountered. Furthermore, since the valve membrane experiences a constant pressure  $P_{HPR}$  during the complete actuation cycle, no cyclic work is being done through the valve membrane interface. Therefore, the estimation of valve hysteretic energy loss can be made simply by looking at the valve cap itself, its motion against the time-varying external pressure loading  $P_{EHC}(t)$  during a full actuation cycle.

This method of estimating valve hysteretic energy consumption will be used to explain the fundamental benefit of incorporating multiple valve heads within the active valve device rather than just a single valve head. For a given valve cap radius  $R_{vc}$ , imposed motion  $Z_{vc}(t)$ , and known external loading  $P_{EHC}(t)$  on the valve cap, the hysteretic energy consumption of the valve during a full actuation cycle can be written as

$$W_{hys} = \int P_{EHC}(t) d(V_{vc}) = \int P_{EHC}(t) \pi(R_{vc})^2 dZ_{vc}. \quad (5.14)$$

where  $dV_{vc}(t)$  is the swept volume of the valve cap. For simplicity in the following arguments, this relation can be simplified to the following proportionality,

$$W_{hys} \propto \Delta P_{EHC}^* \pi(R_{vc})^2 Z_{vc,stroke} \quad (5.15)$$

where  $\Delta P_{EHC}^*$  is the difference between the average encountered pressure as the valve moves upward and the average encountered external pressure as the valve moves downward. Also for the given values of  $R_{vc}$  and  $Z_{vc,stroke}$ , the peak area through which fluid can flow during an actuation cycle is

$$A_{flow} = 2\pi R_{vc} Z_{vc,stroke}. \quad (5.16)$$

Therefore, for a given valve cap size, imposed stroke, and known external pressure loading time history on the valve cap, the hysteretic energy loss per cycle and the peak fluid flow area can be related by

$$\frac{W_{hys}}{A_{flow}} \propto R_{vc}. \quad (5.17)$$

This relation basically states that the ratio of the valve cap structural area (which is proportional to  $W_{hys}$ ) to the valve cap circumference (which is proportional to fluid flow area) can be decreased by reducing the size of the valve cap radius  $R_{vc}$ . To reduce hysteretic energy consumption in the active valve, therefore, the goal should be to reduce this  $\frac{W_{hys}}{A_{flow}}$  as much as

possible, while keeping  $A_{flow}$  constant. This can be achieved by making individual valve caps smaller and placing many in parallel with multiple valve orifices connecting the high pressure reservoir to the harvesting chamber. Updating Equations 5.15 and 5.16 above to include the freedom to choose a particular number of valve heads  $N_{vh}$  within the design leads to

$$W_{hys, N_{vh}} \propto N_{vh} \Delta P_{EHC}^* \pi R_{vc, N_{vh}}^2 Z_{vc, stroke, N_{vh}} \quad (5.18)$$

and

$$A_{flow, N_{vh}} = N_{vh} 2\pi R_{vc, N_{vh}} Z_{vc, stroke, N_{vh}}. \quad (5.19)$$

If the goal is to design a valve with  $N_{vh} > 1$  that has the same total flow area as a valve with a single valve head, the following proportionality must be maintained (calculated by equating Equations 5.16 and 5.19),

$$\frac{R_{vc, N_{vh}}}{R_{vc}} \propto \frac{1}{N_{vh}} \frac{Z_{vc, stroke}}{Z_{vc, stroke, N_{vh}}}. \quad (5.20)$$

Inserting this proportionality into Equation 5.18 results in a relation for the hysteretic energy consumption as a function of the number of valve heads employed and the imposed valve cap stroke for the case of multiple valve heads versus the case of just a single valve head,

$$\frac{W_{hys, N_{vh}}}{W_{hys}} \propto \frac{1}{N_{vh}} \frac{Z_{vc, stroke}}{Z_{vc, stroke, N_{vh}}}. \quad (5.21)$$

Therefore, the potential exists to reduce significantly the hysteretic energy consumption in the active valve by incorporating multiple valve heads above the hydraulic amplification chamber rather than a single valve head. For example, by letting  $N_{vh} = 10$  and requiring that each of the ten valve heads move through one-half the stroke of a single valve head design, the hysteretic energy consumption of the 10-valve design will be 20% of that of the single valve design. The updated systematic design code detailed in the following section, includes this ability to compare and contrast valve designs with varying  $N_{vh}$  and different imposed valve cap strokes  $Z_{vc, stroke}$ . An additional benefit of incorporating multiple valve heads (that each move a smaller stroke than a single large valve head) is that it becomes easier to structurally design the valve membranes (in that small valve membrane thicknesses are achievable) to support these valve caps within the required stress limitations. This will be illustrated in Section 5.6.

## 5.6 Results of Systematic Design Procedure

This section presents results of the full systematic active valve design procedure for the example valve requirements defined in Section 5.3.2. As detailed in previous sections, this quasi-static procedure will now incorporate the three design freedoms that were not included in the basic design procedure detailed in Section 5.3, namely the ability to design a valve structure for multiple valve heads ( $N_{vh} > 1$ ), with varying valve cap strokes, and for differing valve membrane thicknesses. Specifically, the results presented in this section focus on a variety of chosen number of valve heads ( $N_{vh} = 1, 2, 3, 5$ ), imposed valve cap strokes between  $Z_{vc,stroke} = 8\mu m$  and  $Z_{vc,stroke} = 40\mu m$ , and available valve membrane thicknesses from  $t_{vm} = 7\mu m$  and upward in increments of  $1\mu m$ . The results clearly demonstrate the potential benefits of multiple valve head geometries for reducing total valve power consumption.

Figure 5.20 plots the calculated valve cap radius, valve membrane thickness and radius, and drive element piston diameter for the variety of  $N_{vh}$  and  $Z_{vc,stroke}$  values under question. Note that in Figure 5.20(b), for  $N_{vh} \geq 2$ , valve membranes with  $t_{vm} = 7\mu m$  are achievable for all the imposed  $Z_{vc,stroke}$  values. As more valve heads are allowed in parallel, each valve membrane gets smaller in size, resulting in reduced “bowing” of the membrane under the pressure loadings. This is the identical phenomenon to that discussed in Section 5.4.2. Also, notice in Figure 5.20(c) that as more valve heads are employed in the design, smaller drive piston dimensions are achieved, due to the fact that less swept volume is required by the valve membranes during actuation.

Figure 5.21 plots the calculated effective piezoelectric material diameter and the maximum compressive stress on the piezoelectric material during a full valve actuation cycle. Notice in Figure 5.21(a) that the required piezoelectric material diameter is generally increasing with increasing  $N_{vh}$ . This is due to the fact that the  $P_{HAC}(t)$  actuation requirements are increased because of the increased stiffness of the valve membranes. It is important also to monitor the compressive stress seen by the piezoelectric material to ensure that it is below the compressive depolarization limits.

Figure 5.22 plots the estimated hysteretic power consumption, material and circuitry power loss, and total valve power consumption. As seen in Figure 5.22(a), the hysteretic power consumption can be significantly reduced by incorporating multiple valve heads working with moderate valve strokes. In addition, as shown in Figure 5.22(b) material and circuitry losses can also be reduced, since total energy flowing through the piezoelectric material is lessened. Finally, Figure 5.22(c) plots the combined power consumption for the various active valve designs. As indicated in this plot, the valve design that results in the minimum power consumption uses ten valve heads  $N_{vh} = 5$ , each traveling through a stroke of  $Z_{vc,stroke} = 22\mu m$ . These results demonstrate the capabilities of this systematic active valve design procedure in evaluating single



and multiple valve head designs under loading conditions put forth by a typical MHT system.

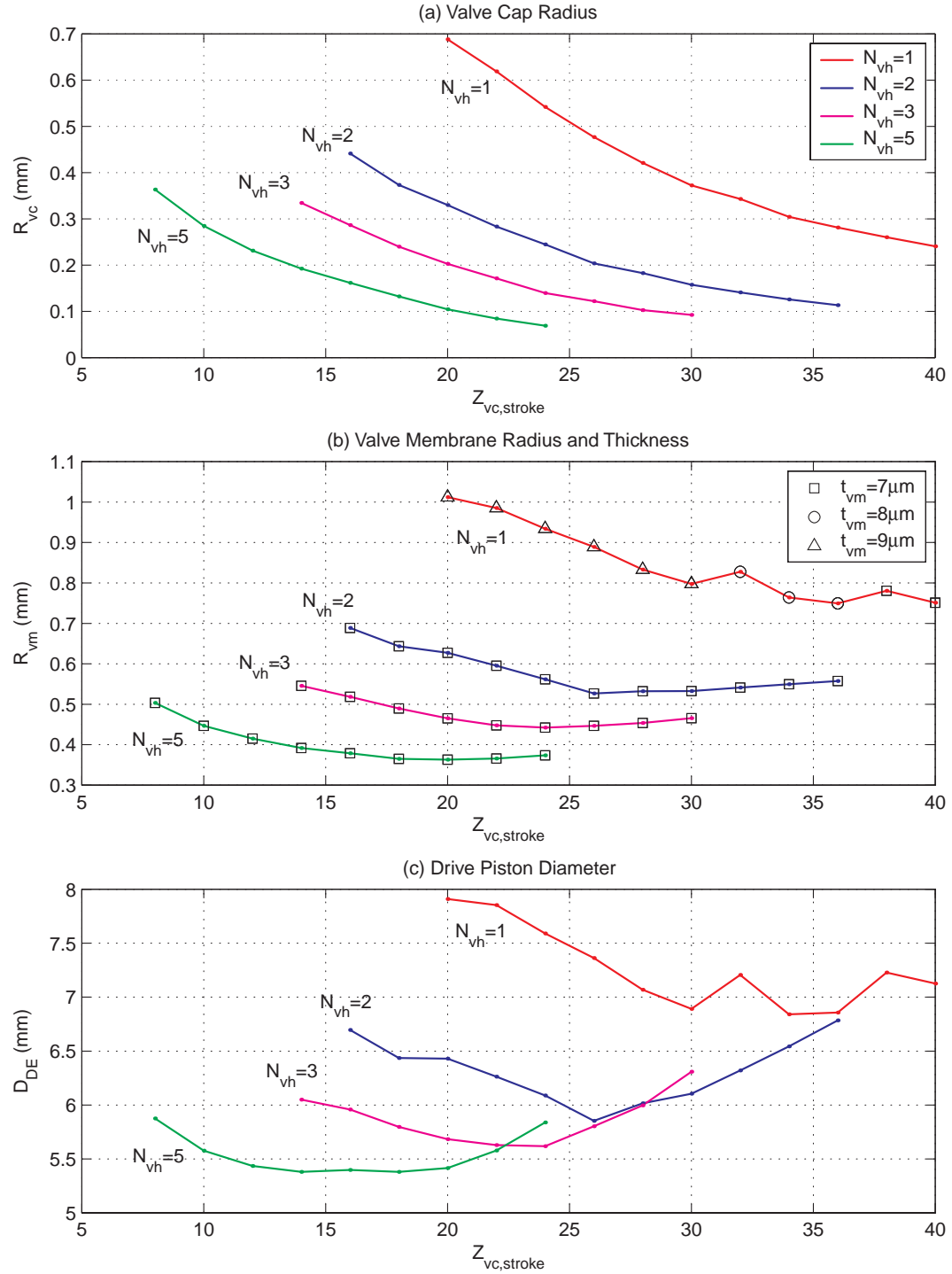


Figure 5.20: Multiple valve head comparison Plot 1

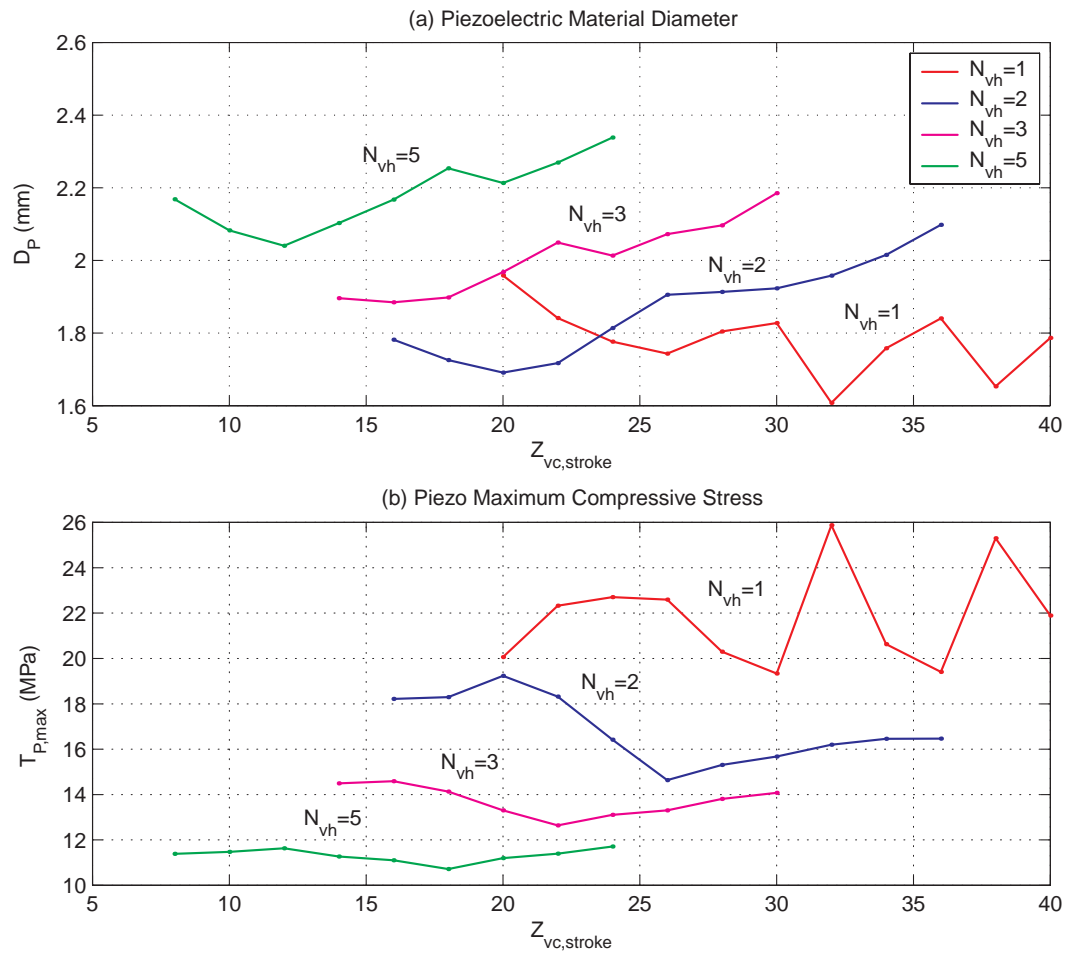


Figure 5.21: Multiple valve head comparison Plot 2

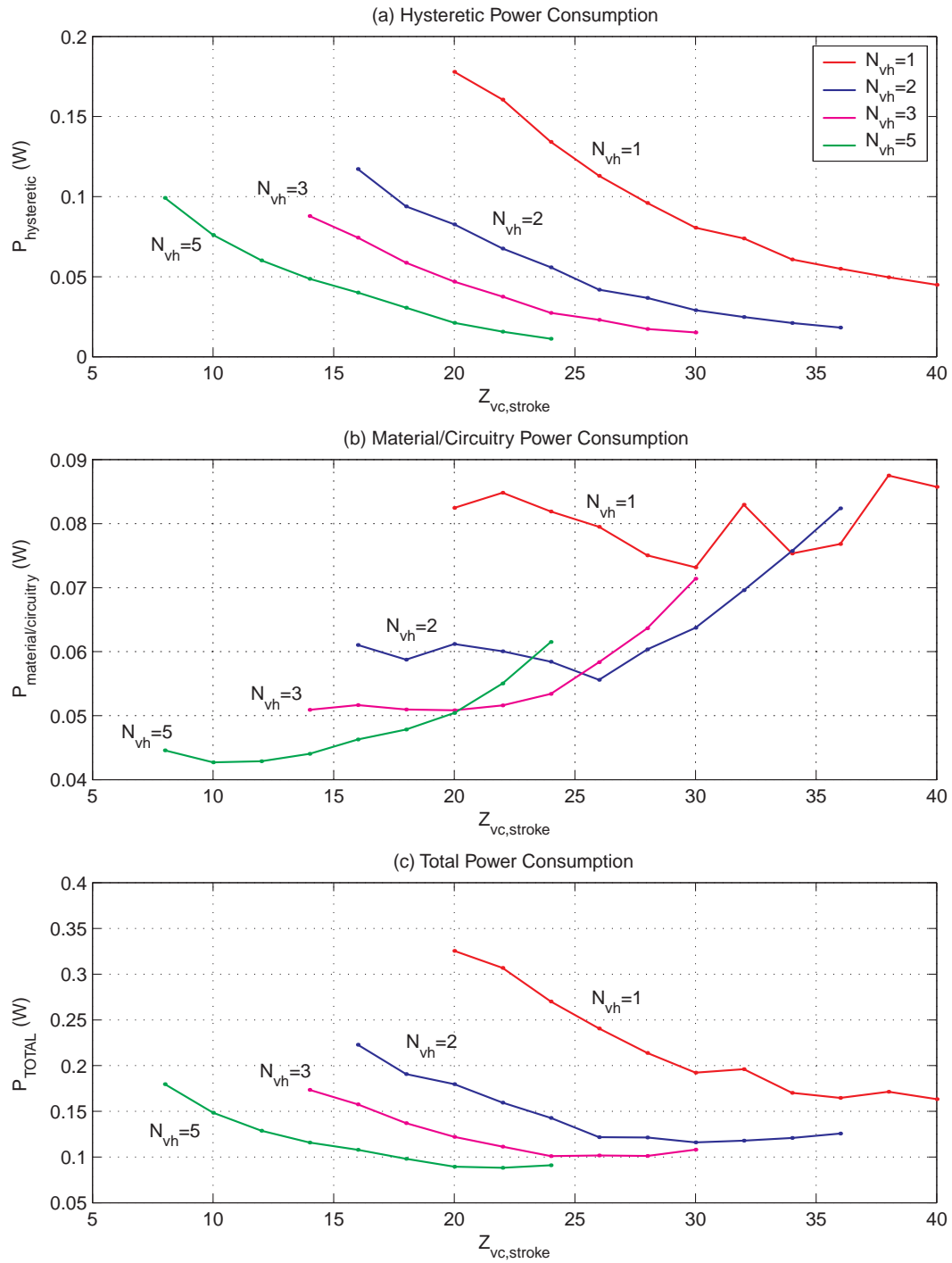


Figure 5.22: Multiple valve head comparison Plot 3

## 5.7 Correlation With Dynamic Simulation

The systematic design procedure presented in this chapter has been based on quasi-static structural behavior. In reality, dynamic effects within the active valve may result in performance of the valve that differs from quasi-static behavior. This section will take one of the active valve geometries formulated using the systematic design procedure in Section 5.6 and perform a full-scale dynamic simulation of this structure. The results will indicate that, indeed, the design formulated through the quasi-static procedure performs very close to expectations, thereby validating the use of the quasi-static procedure as a powerful tool for designing an active valve structure within a full hydraulic system.

The valve structure that was chosen for simulation is that corresponding to  $N_{vh} = 1$  and  $Z_{stroke} = 40\mu m$ . Revisiting Figures 5.20, 5.21, and 5.22 in Section 5.6, the valve geometry is as follows:  $R_{vc} = 241\mu m$ ,  $t_{vm} = 7\mu m$ ,  $R_{vm} = 757\mu m$ ,  $R_{pis} = 3.59mm$ , and  $R_p = 0.88mm$ . The peak-peak voltage applied to the piezoelectric material is 1000V at a frequency of  $f = 10kHz$ . Referring to Figures 5.8(b), 5.9, and 5.11, this active valve geometry is able to quasi-statically achieve the performance requirements set by the external hydraulic system, namely a pressure fluctuation in the harvesting chamber (with  $K_{EHC} = 1.5e^{16} \frac{Pa}{m^3}$ ) from 0.2MPa to 1.0MPa, given reservoir pressures of  $P_{HPR} = 1.2MPa$  and  $P_{LPR} = 0$ .

In order to evaluate this active valve geometry in a full dynamic simulation, a complete simulation architecture is implemented that includes the active valve simulation (presented in Chapter 4) and the external hydraulic system relations detailed in Section 5.2. Figure 5.23 shows this full simulation architecture. The additional external hydraulic system architecture (including the effects of the fluid orifice pressure-flow relations, the valve channel inertia, and the chamber stiffness) is coupled to this active valve system to simulate full filling and evacuation. In order to create full system pumping behavior, a chamber with both an inlet and outlet active valve is included in the simulation. In addition, critical valve variables, such as  $\sigma_{vm}(t)$ ,  $Z_{vc}(t)$ , and  $P_{HAC}(t)$  are monitored. In this simulation, a positive valve stop at a location of  $Z_{vc} = 20\mu m$  is implemented. The results of this simulation for two different values of valve cap damping are shown in Figure 5.24. For further details on full MHT system simulations, refer to [8].



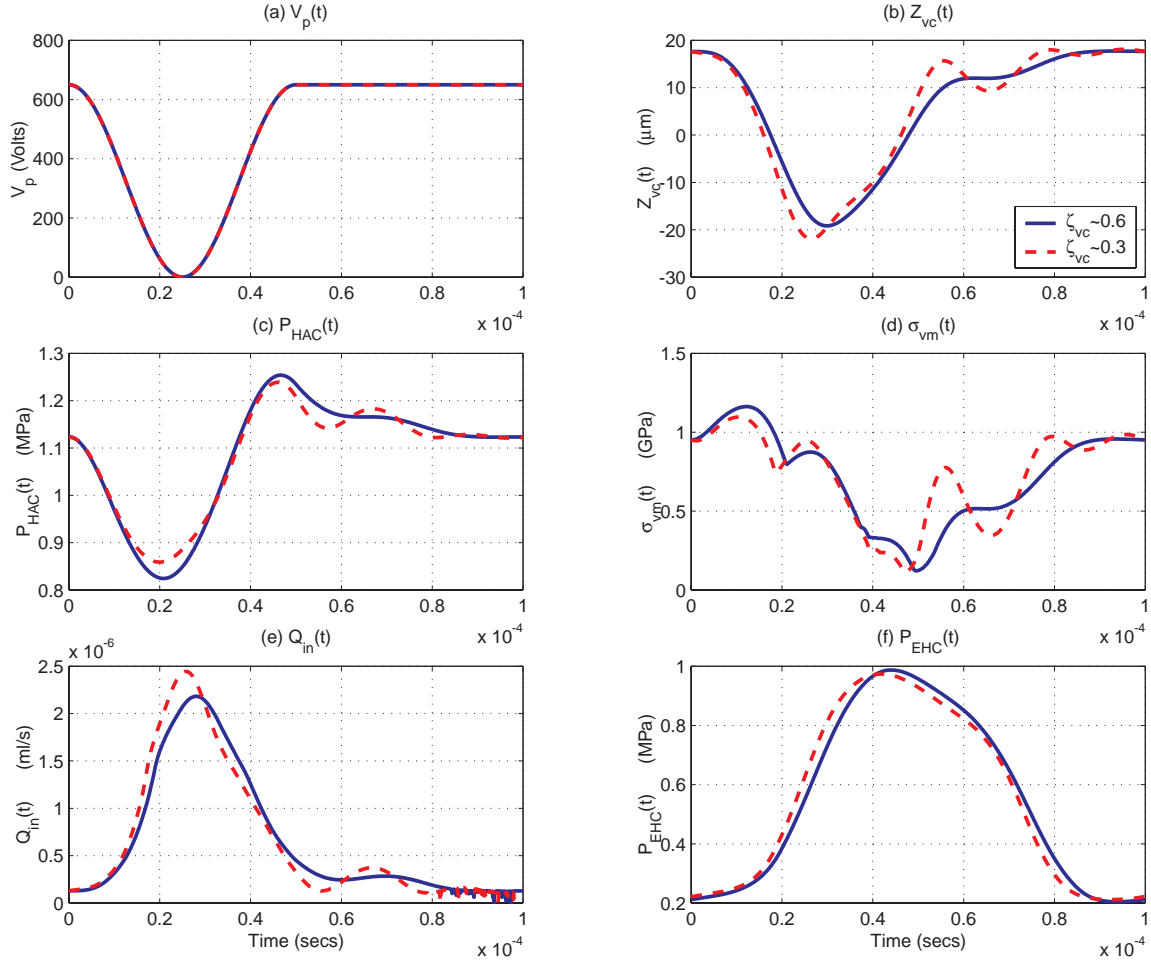


Figure 5.24: Full system simulations: (a) solid line represents case in which  $\zeta_{pis} = 0.7$ ,  $\zeta_{vc} = 0.6$ , (b) dashed line represents case in which  $\zeta_{pis} = 0.7$ ,  $\zeta_{vc} = 0.3$ . Note that in these cases, the valve cap does not hit the stop. In these plots,  $V_p$  is the applied piezoelectric voltage,  $Z_{vc}(t)$  is the position of the valve cap,  $P_{HAC}(t)$  is the hydraulic amplification chamber pressure,  $\sigma_{vm}(t)$  is the maximum valve membrane stress,  $Q_{in}(t)$  is the flow rate through the valve, and  $P_{EHC}(t)$  is the external chamber pressure.

Due to dynamic effects in the active valve system, an applied peak-peak voltage of only 650V (compared to the quasi-static value of 1000V) is required to actuate the valve and to produce the proper filling behavior of the harvesting chamber. Notice that the valve cap  $Z_{vc}(t)$ , HAC pressure  $P_{HAC}(t)$ , inlet flow rate  $Q_{in}(t)$ , and resulting harvesting chamber pressure  $P_{EHC}(t)$  time histories all correlate very closely to those predicted by the systematic quasi-static design procedure. One interesting note is that the valve membrane stress  $\sigma_{vm}$  time history differs slightly from the quasi-static prediction in the region when the valve cap is just beginning to open. Rather than immediately decreasing, as is predicted in the quasi-static procedure,  $\sigma_{vm}$  actually begins to increase to a peak value of  $1.15GPa$  (for  $\zeta_{vc} = 0.6$ ) and to a peak value of  $1.05GPa$  (for  $\zeta_{vc} = 0.3$ ) just after opening. This phenomenon is due to the dynamic effects on the valve membrane. Essentially, the  $P_{HAC}$  pressure below the membrane decreases substantially before the valve cap is able to move downward (due to the cap's inertia and the effect of damping), resulting in an enhanced membrane curvature at  $R_{vc}$  and therefore an increase in  $\sigma_{vm}$ .

These important observations on the membrane stress can be fed back to the quasi-static design procedure. Using a smaller value of limiting stress  $\sigma_{limit}$ , a slightly modified valve geometry can be generated so that dynamic membrane stresses do not exceed the desired bound. Overall, the dynamic performance of the active valve geometry formulated using the systematic quasi-static design procedure detailed in this chapter matches fairly well to desired requirements. This design procedure, therefore, can be very useful in developing valve geometries for use in full hydraulic systems.

## 5.8 Conclusions

This chapter has introduced the physical equations governing the fluid flow behavior within a generic MHT system, external to the valve cap and membrane structure of the active valve. With these relations, a comprehensive and systematic quasi-static design procedure has been presented that enables a designer to formulate an active valve geometry for use within an MHT system to satisfy certain pressure-flow requirements. This procedure formulates designs and evaluates valve power consumption for geometries with one or more valve heads acting in parallel above the hydraulic amplification chamber and for differing valve cap strokes. Additionally, valve membrane structures are designed to guarantee peak stress levels below a critical value during complete valve time histories. Active valve geometries produced by this design procedure have been analyzed using full dynamic system simulations, and results indicate that dynamic effects do not significantly affect the ability to meet the performance requirements. Overall, this design procedure enables the generation of active valve geometries for a potentially wide variety of hydraulic systems.

# Bibliography

- [1] N.W. Hagood, D.C. Roberts, L. Saggere, K.S. Breuer, K-S. Chen, J.A. Carretero, H.Q. Li, R. Mlcak, S. Pulitzer, M.A. Schmidt, S.M. Spearing, and Y-H. Su, "Micro Hydraulic Transducer Technology for Actuation and Power Generation", Proceedings of SPIE, Vol. 3985 (2000), Newport Beach, CA, March 5-9, 2000, pp.680-688.
- [2] J. Carretero and K.S. Breuer, "Measurement and Modeling of the Flow Characteristics of Micro Disk Valves," Proceedings of the 1994 International Mechanical Engineering Conference and Exposition: Microfluidics Symposium, Orlando, FL, Nov. 2000.
- [3] E. Schrenk, "Disc valves, flow patterns, resistance and loading," BHRA T, 1957 (547). Translation from German.
- [4] A. Lichtarowicz, "Flow and Force Characteristics of Flapper Valves," Third International Symposium on Fluid Power, Turin, 1973, pp. B1-1.
- [5] D.N. Johnston, K.A. Edge, and N.D. Vaughan, "Experimental investigation of flow and force characteristics of hydraulic poppet and disc valves," Proceedings of the Institution of Mechanical Engineers, Part A: Power & Process Engineering, 1991 Vol 205, No 3, pp. 161-171.
- [6] S.M. Spearing and K.S. Chen, "Micro-gas turbine engine materials and structures," *Ceramic Engineering & Science Proceedings v.18n 4B*, p. 11-18, 1997.
- [7] K.T. Turner, An Evaluation of Critical Issues for Microhydraulic Transducers: Silicon Wafer Bonding, Strength of Silicon on Insulator Membranes and Gold-Tin Solder Bonding, Massachusetts Institute of Technology, Master's Thesis, 2001.
- [8] O. Yaglioglu. Master's Thesis, Massachusetts Institute of Technology, 2002.



## Chapter 6

# Device Fabrication and Preparation for Testing

### 6.1 Introduction

The proposed piezoelectrically-driven hydraulic-amplification microvalve is fabricated using a combination of microscale (silicon patterning and etching) and macroscale (piezoelectric material integration) procedures. As detailed in previous chapters of this thesis, the valve consists of multiple layers of silicon and glass (Pyrex 7740) with integrated piezoelectric elements, all bonded together to form the important structural features of the device. These features are the tethered-piston piezoelectric drive element, the enclosed hydraulic amplification chamber, the valve membrane and orifice structure, and the fluid channels to and from the valve. A cross-section of a full MHT system, with embedded multi-layered active valve structure, is shown in Figure 6.1. Successful fabrication and assembly of a complete MHT system involves overcoming the identical challenges associated with realizing a working active valve device, since the valve structure and full MHT system span the same layers. As a result, the fabrication and assembly processes presented in this chapter are not unique to the active valve, but rather provide a platform of procedures that can be implemented to create a wide variety of micro-hydraulic systems. For the purposes of this thesis, however, only the geometry of the active valve is referred to in the fabrication and assembly discussions.

Layers 1, 3, 6, and 9 of the active valve structure (shown in Figure 6.1) are each borosilicate glass (Pyrex 7740), the features of which are formed through wafer-level ultrasonic machining. Layers 2 and 8 are formed from standard silicon wafers and are etched using deep-reactive ion etching procedures. Layers 4, 5, and 7 are created from silicon-on-insulator (SOI) wafers. The drive element tethers supporting the piston structure in Layers 4 and 5 and the valve membrane and cap structure in Layer 7 are produced using deep-reactive etching, with the buried oxide

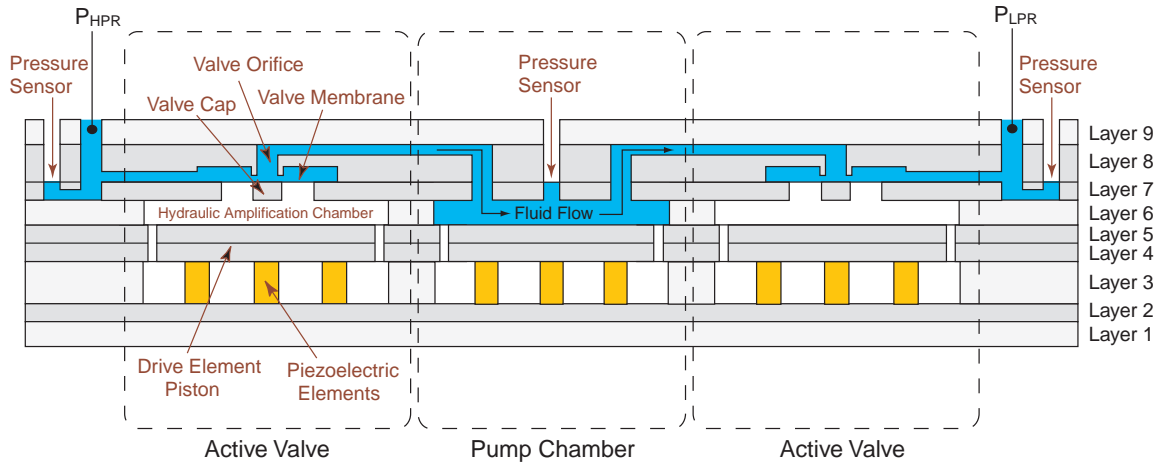


Figure 6.1: Cross-section schematic of a nine-layer multiple wafer MHT system with two embedded active valve structures. Realization of this active valve requires robust bonding of silicon-to-silicon and silicon-to-glass at the wafer-level and integration and bonding of piezoelectric material elements with silicon at the die-level, as will be discussed later in this chapter.

acting as an etch stop for precise control of tether and membrane thicknesses. Three primary bonding mechanisms are used to realize a complete valve device: silicon-silicon fusion bonding, silicon-glass anodic bonding, and silicon-piezoelectric material eutectic bonding.

This chapter first details the critical challenges associated with the fabrication and assembly of this multi-layer active valve device, namely (1) etching of the high-aspect ratio features in silicon-on-insulator wafers to form the tethered drive element piston and valve membrane structures, (2) wafer-level silicon-silicon fusion bonding and wafer-level silicon-glass anodic bonding, (3) preparation, integration, and bonding of the bulk piezoelectric material elements within the drive element structure, (4) die-level assembly of multiple silicon and glass layers, and (5) fluid filling and sealing of the hydraulic amplification chamber. Having laid out the details of these fabrication issues and the procedures used to overcome these obstacles, the chapter then presents a systematic fabrication and testing plan of important active valve sub-components, as a means to prove out the fabrication challenges. Details of each of the sub-component studies leading up to the full active valve are then documented in subsequent chapters of this thesis.

## 6.2 Fabrication Challenges and Procedures

This section attempts to follow the fabrication and assembly process in order of the steps and challenges involved. The first two challenges focus on the activities relating to wafer-level processing: etching of the drive element tether and valve membrane structures and silicon-silicon and silicon-glass wafer bonding procedures. The second two challenges are concerned

with die-level processing: preparation and integration of the piezoelectric elements within the device and the process flow associated with the die-level silicon-glass anodic bonding. The final challenge focuses on filling and sealing of fluid in the device once the active valve device has been successfully fabricated and assembled at the die-level.

### 6.2.1 Etching of Tethered Drive Element and Valve Membranes

The drive element tethers and valve membranes within the active valve device are designed to be quite thin (on the order of  $7 - 10\mu m$ ). To achieve precise dimensional control of these features, SOI wafers containing a buried oxide layer a preset distance from one side of the wafer are used. In performing deep etches into the silicon wafer down to the buried oxide layer, it is critical that the surface roughness of the etch and the tailoring of fillet radii profiles at the base of the etched profiles be well-controlled so as to maintain strength and robustness of the thin-membrane structures. Figure 6.2 illustrates etch profiles at the SOI interface of a typical drive element piston that can result, depending on the process chosen and care given to performing the etch. Ideally, one would like to create a fillet radius between the thin tether and the much thicker ( $\sim 400\mu m$ ) central piston structure to minimize stress concentrations, as shown in Figure 6.2(c). It is essential to avoid etch profiles such as the sharp corner shown in Figure 6.2(b) and the “footing” or “notching” profile shown in Figure 6.2(d). These serve to magnify stresses at these interface regions, thereby compromising the overall strength of the structure.

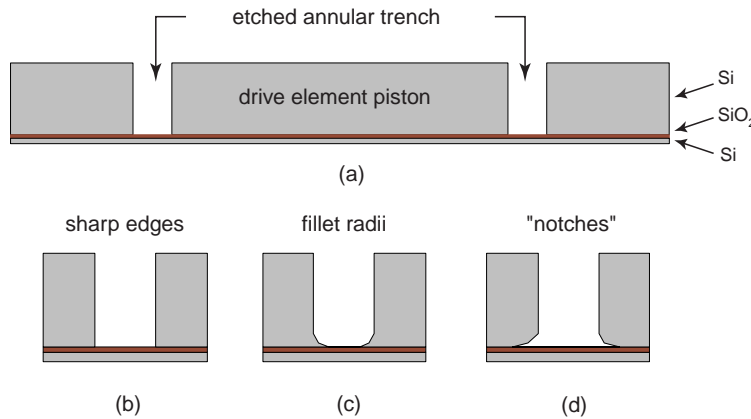


Figure 6.2: Etching of a typical drive element piston structure: (a) cross-section view of drive piston, (b) sharp corner etch features, (c) fillet radius features, and (d) “notching” or “footing” features.

Considerable research work has been done in developing and optimizing deep etching processes for single-crystal silicon materials [1] [2]. The Deep-Reactive Ion Etching (DRIE) process



and optimized. The details of these DRIE process parameters are beyond the scope of this thesis. The purpose of this section, rather, has been to present the significant challenges and obstacles faced in the etching of thin-membrane structures with desired fillet radii profiles. A designer may specify a particular fillet size, but the cleanroom process of achieving that profile is often a time-consuming one.

### 6.2.2 Wafer-Level Bonding

For the multi-layer active valve structure presented in this thesis, various silicon-silicon and silicon-glass wafer-level bonds are performed. A silicon-silicon wafer-level fusion bonding process is used to bond Layers 4 and 5 together to form Stack 4-5 and Layers 7 and 8 together to form Stack 7-8. A silicon-glass wafer-level anodic bonding process is used to bond Layers 1 and 2 together to form Stack 1-2, Stack 4-5 and Layer 6 together to form Stack 4-5-6, and Stack 7-8 and Layer 9 together to form Stack 7-8-9. Following these wafer-level bonding steps, the stacks are die-sawed into individual dies and cleaned in preparation for die-level bonding and piezoelectric material integration. Further discussion of why certain bond steps are performed at the wafer-level and others at the die-level is covered in Section 6.2.4. Figure 6.4 illustrates the various wafer-level silicon-silicon and silicon-glass bonding steps.

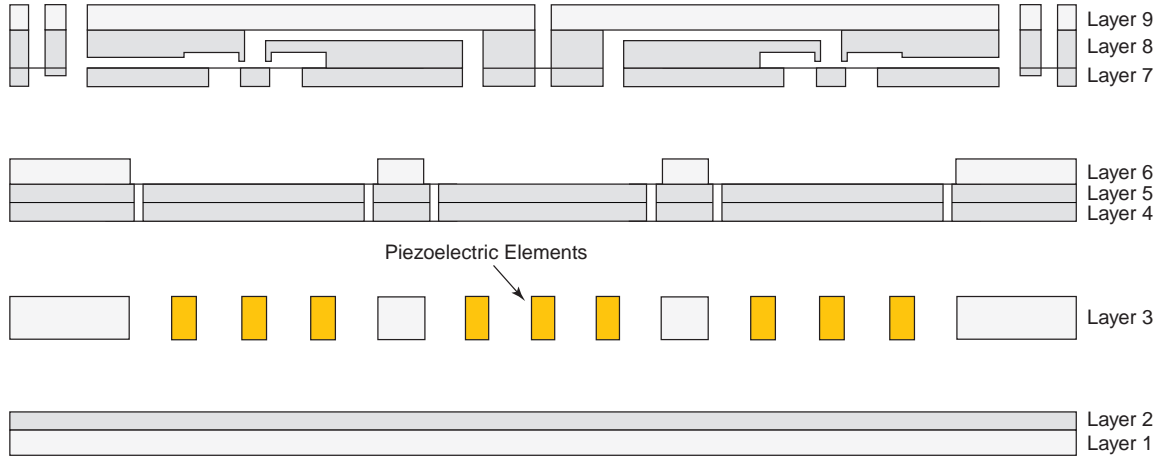


Figure 6.4: Wafer-level silicon-silicon fusion and silicon-glass anodic bonding steps are carried out prior to piezoelectric material integration.

The silicon-silicon fusion bonding process used to create wafer-level stacks for the active valve device is a well developed process and consists of three primary steps [6]: (1) preparation and treatment of the silicon wafer surface to produce a hydrophilic surface, (2) alignment and adhesion of two wafers together (weak van der Waals or hydrogen bonds maintain wafer-wafer adhesion) in a clean room-temperature environment, either in air, inert atmosphere, or vacuum, and (3) high temperature annealing of the wafer stack at 1000°C to promote strong covalent

bonding. The strength of this fusion bond is dependent on the annealing temperature and time [2]. Paramount in the bonding process is the cleanliness of the silicon wafers prior to bonding and of the alignment and bonding apparatus itself. Particulate matter present between the silicon wafers during adhesion can result in significant defect regions characterized by little or no bonding.

The silicon-glass anodic bonding process used to create wafer-level stacks also is a well-developed process. This process involves three primary steps: (1) preparation and cleaning of the silicon and glass surfaces using a piranha soak and an oxygen ashing step, (2) alignment and clamping of the two wafers together, and (3) application of a voltage (1000V) across the wafer interface at elevated temperature (300°). The negative electrode is applied to glass wafer surface not being bonded with the silicon wafer held at ground potential. As for the fusion bonding process, cleanliness of the wafers and the bonding apparatus is paramount for achieving high-quality and low-defect wafer-level bonds.

### 6.2.3 Integration of Bulk Piezoelectric Elements

Integration of the piezoelectric elements within the device constitutes a critical task in the assembly of the active valve device. This section discusses the important issues related to preparing and tolerancing of the piezoelectric material elements with respect to other features in the device. Details of the actual die-level assembly procedure will be provided in Section 6.2.4.

The top and bottom surfaces of the piezoelectric elements are covered with a thin-film gold-tin (Au-Sn) eutectic alloy for bonding to the adjoining silicon layers at an elevated temperature. In order to achieve good bonding over the complete interface area, the piezoelectric material must possess smooth top and bottom surfaces. A rough surface of the piezoelectric material (and therefore of the metallized layer), would result in only pinpoint contacts between the piezoelectric material and the silicon and therefore a weak bond. Prior to bonding, sizing of the piezoelectric elements with respect to the surrounding Layer 3 glass and etching of seats in the Layer 2 silicon to compensate for thickness mismatch between the piezoelectric material and glass is critical for ensuring a deflection of the drive element piston below levels of fracture stress in the tethers. Each of these piezoelectric material integration issues is covered in detail in the following sub-sections.

### Piezoelectric Material Preparation

Virgin piezoelectric materials are obtained from vendors in the form of thin plates, each with a thickness of  $\sim 1.1mm$  and diameter between 1 cm and 5 cm. As received, these plates possess a surface roughness as large as  $5\mu m$ . In order to achieve adequate eutectic bonding during

device assembly, a surface roughness near  $0.5\mu\text{m}$  is required prior to metallization. To achieve this, the piezoelectric material plates are polished using coarse and fine grain diamond slurry polishing procedures. Figure 6.5 displays typical profilometer scans before and after material polishing for the two primary types of piezoelectric materials used in the valve, PZT-5H and PZN-PT.

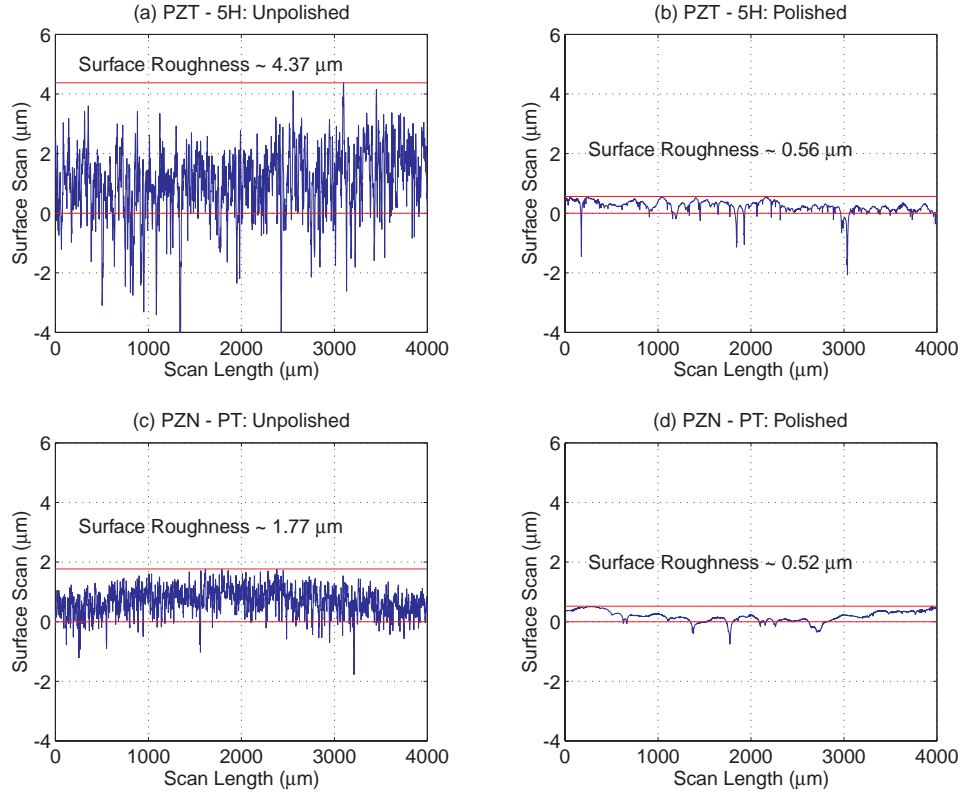


Figure 6.5: Profilometer surface roughness scans of PZT-5H and PZN-PT piezoelectric material plates before and after polishing steps: (a) unpolished PZT-5H material, (b) polished PZT-5H material, (c) unpolished PZN-PT material, (d) polished PZN-PT material. Note that thin deep trenches are not counted within the roughness estimate. However, thin tall “mountains” must be accounted for since these would serve to separate an adjoining layer of material.

During polishing, each plate is sized to yield a thickness of  $1\text{mm} \pm 10\mu\text{m}$  with thickness variation across the plate of  $\sim 2\mu\text{m}$ . Prior to metallization, the material plates are solvent cleaned with a series of acetone, methanol, and isopropanol steps. Additionally, a further cleaning soak in a 20:1 water:nitric acid solution is carried out for 1 minute to remove particulate matter. At this point, the piezoelectric material plates are ready for metallization.

## AuSn Eutectic Bonding

To bond mechanically and to connect electrically the piezoelectric material cylinders to the adjoining silicon layers in the active valve device, a reliable bonding mechanism must be employed. This bonding mechanism must allow for tight dimensional control over the bond layer thickness and allow for a bonding temperature and environment that is compatible with the rest of the die-level assembly process. Numerous bonding methods that could potentially work in this device, ranging from polyimides and epoxies to brazing and soldering to gold-based eutectic alloys, have been presented in the literature. A detailed discussion of these research efforts, with application toward the development of MHT technology, is found in [2]. The resulting conclusion of initial work by Mlcak [8] and the subsequent work by Turner [2] was to employ a thin-film AuSn eutectic alloy (composition: 80 wt. % Au and 20 wt. % Sn) as the bonding mechanism within MHT devices in general, and specifically within the active valve device presented in this thesis.

A four layer film structure on the piezoelectric material and a three layer film structure on each of the adjoining silicon layers is deposited in preparation for bonding, as shown in Figure 6.6. The four layer structure on the piezoelectric material consists of 50 nm Ti, 250 nm Pt, 4000 nm AuSn, and 50 nm Au. The Ti serves as an adhesion layer, the Pt as a diffusion barrier, the AuSn as the eutectic alloy, and the final Au as a capping layer to prevent oxidation of Sn in the AuSn alloy. The AuSn layer, chosen to be thick enough ( $4\ \mu\text{m}$ ) to compensate for the piezoelectric material surface roughness ( $\sim 0.5\ \mu\text{m}$ ), is sputtered from an alloy target with 80 wt. % Au and 20 wt. % Sn composition. Sputtering is chosen over evaporation because sputtering allows the stoichiometry of the target to be maintained in the deposited film [9]. The three layer Ti-Pt-Au structure on each of the adjoining silicon pieces enables the eutectic alloy to wet the silicon and is deposited on the die-level using e-beam evaporation procedures.

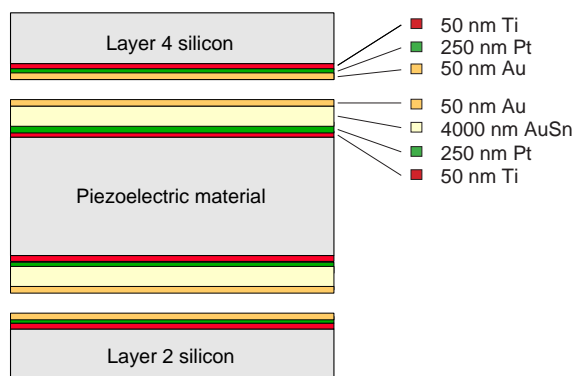


Figure 6.6: Eutectic alloy deposition on the piezoelectric material and adjoining silicon layers. The piezoelectric material contains a 4 layer film structure and each of the silicon layers contains a 3 layer film structure.



## Dicing/Core-Drilling of Piezoelectric Elements

Following deposition of the eutectic alloy, the metallized piezoelectric material plates are core-drilled or diced to produce either cylindrical or square piezoelectric elements. As detailed in subsequent chapters of this thesis, devices integrating both cylindrical and square elements have been successfully fabricated and tested. The advantage of using square piezoelectric elements over cylindrical ones is that the process of dicing a piezoelectric material plate in a grid pattern results in the production of 2-3 times the number of elements than can be produced from core-drilling from a identical size plate. By sheer numbers and by the fact that closely located elements will possess almost identical thicknesses (relatively insensitive to variations in thickness across the material plates), the use of square elements increases the odds of being able to select multiple elements of identical thickness to insert into drive element structures. Once the material plate has been either core-drilled or diced, the resulting piezoelectric elements are individually measured for thickness using a hand-held precision micrometer, as shown in Figure 6.7. By calibrating the micrometer before each measurement with a precise thickness gauge block ( $1\text{mm} \pm 0.01 \mu\text{m}$ ) and averaging repeated series of measurements of the same elements, these thickness measurements are estimated to be accurate within  $\sim 0.5\mu\text{m}$ . The elements are then organized and sorted according to the thickness.

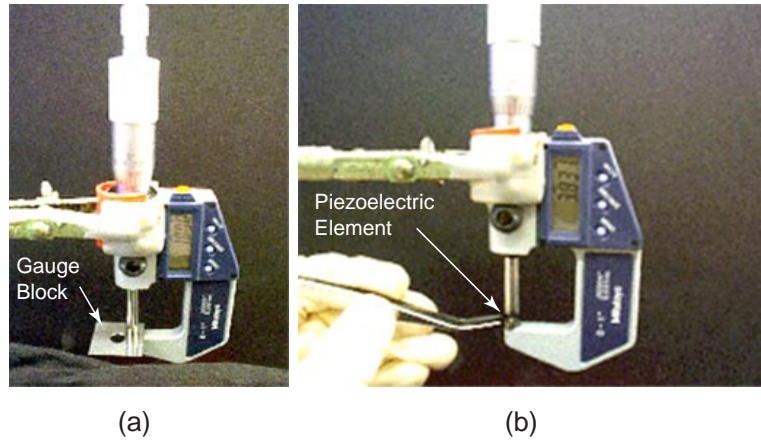


Figure 6.7: Precision micrometer used for thickness measurement of the piezoelectric elements and Layer 3 glass dies prior to device assembly: (a) calibration of micrometer with respect to a 1 mm gauge block, and (b) measurement of an individual piezoelectric element.

## Etching of Piezoelectric Element Seats

One of the critical issues during integration of the piezoelectric material elements is guaranteeing an upward deflection of the drive element piston large enough to ensure a preload on the eutectic

alloy interface during bonding, yet small enough to ensure stresses in the piston tethers below the critical value of 1 GPa. Typically, in the drive element structures designed, fabricated, and tested in this thesis, the piston tethers will reach a tensile stress of 1 GPa for displacements near  $\sim 9\mu m$ . Therefore, at any time during the bonding, poling, and operation of a device, it is desired to maintain piston displacements no greater than a safe value of  $\sim 6\mu m$ . In terms of preload on the eutectic interface, it is desired to ensure a “piston push-up” of  $\sim 2\mu m$ . These requirements therefore dictate that at the instant of eutectic bonding, the piezoelectric element(s) beneath the drive element piston must be forcing the piston upward by  $\sim 2\mu m$  and that for all time after that the piston must not be forced to displacements greater than  $\sim 6\mu m$ . Considering that this  $4\mu m$  range is 0.4% of the total piezoelectric element thickness, this task represents quite a challenge.

In preparation for piezoelectric element integration, the Layer 3 glass wafer is diced into individual dies, and each of these dies is measured using the hand-held micrometer. As received from the vendor, each of the ultrasonically-machined Layer 3 glass wafers possesses a thickness between  $967\mu m$  and  $974\mu m$ , with thickness variation across a given wafer less than  $1\mu m$ . At the time of integration, since the piezoelectric elements (with deposited eutectic alloy films) have thicknesses near  $1000\mu m$  and the Layer 3 glass dies have thickness near  $970\mu m$ , it is necessary to have the capability to remove this thickness difference of  $\sim 30\mu m$  between the piezoelectric material and the surrounding glass. Ideally, once integrated into the device, the piezoelectric elements’ top surfaces should be slightly above level with the Layer 3 glass top surface so as to produce predictable upward displacement of the drive element piston from its equilibrium position (“push-up”).

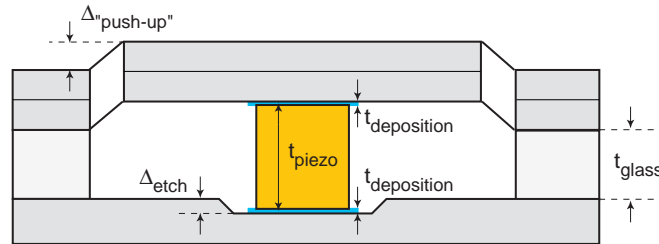


Figure 6.8: Compensation of the piezoelectric element - Layer 3 glass thickness mismatch by plasma etching shallow seats in the Layer 2 bottom silicon die. Precise control of the etch depth is necessary to achieve the desired “push-up” of the drive element piston.

This thickness matching is achieved by plasma etching shallow seats for all of the piezoelectric elements in the Layer 2 bottom silicon wafer, as shown in Figure 6.8. An iterative process of carefully timed etches followed by depth measurements using a scanning profilometer can result in etch depth control to within  $\sim 0.5\mu m$ . With this capability to compensate for thickness mismatch between the piezoelectric elements and the surrounding Layer 3 glass, proper

“push-up” of the drive element piston can be achieved during assembly and bonding. On the die-level, each Layer 2 silicon die is matched with a pre-measured ( $t_{piezo}$ ) grouping of one or three piezoelectric elements (depending on whether a single or multiple piezoelectric valve is being fabricated) and with a pre-measured ( $t_{glass}$ ) Layer 3 glass die. With knowledge of the three-layer film thickness  $t_{deposition}$  (see Section 6.2.3) that will subsequently be deposited on the underside of the drive element piston in Layer 4 and on the top surface of the “to be etched” seats in Layer 2, and with the value of  $\Delta_{“push-up”}$  desired after device assembly, the required etch depth ( $\Delta_{etch}$ ) in Layer 2 is determined, according to 6.1.

$$\Delta_{etch} = t_{piezo} + 2t_{deposition} - t_{glass} - \Delta_{“push-up”} \quad (6.1)$$

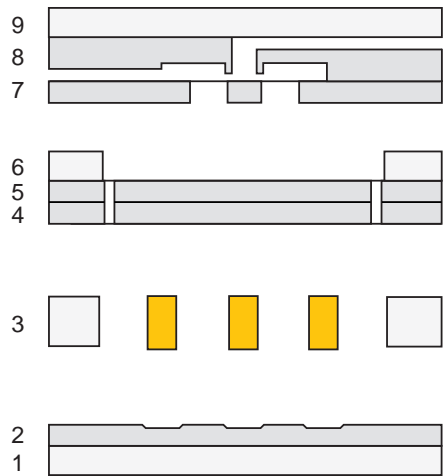
Following etching of the seats, the Layer 1-2 silicon dies are cleaned and combined with Stack 4-5-6 silicon dies for deposition of the three-layer Ti-Pt-Au film structure required for eutectic bonding. This deposition is performed using e-beam evaporation through specially-machined shadow masks to allow for selective coating of the dies. For the Stack 4-5-6 dies, the underside of the drive element piston is coated, and for Layer 2 dies the inside of each of the etch seats is coated.

## 6.2.4 Die-Level Assembly and Bonding

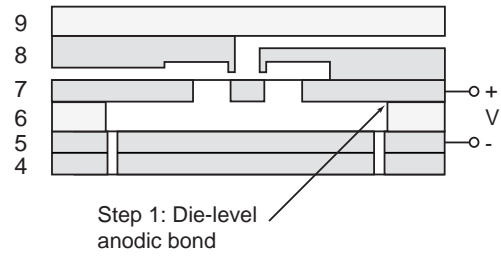
### Assembly and Bonding Procedure

Final assembly of the active valve device is performed at the die-level. As shown in Figure 6.9(a), wafer-level etching and bonding procedures, followed by dicing of the stacks into individual dies have resulted in the creation of a Stack 7-8-9 die, a Stack 4-5-6 die, a Stack 1-2 die, and a Layer 3 die. Additionally, piezoelectric material preparations have created individual piezoelectric elements ready for insertion. It is desirable to perform these bonding steps at the die-level, rather than the wafer-level, so as to allow for individual measurements of the Layer 3 glass die thickness and to enable individual control of the seat etching in Layer 2. Additionally, die-level bonding significantly reduces the risk of losing an entire multi-layer wafer structure during wafer-level processing. The die-level assembly process consists of four main steps, as shown in Figure 6.9(b), (c), (d).

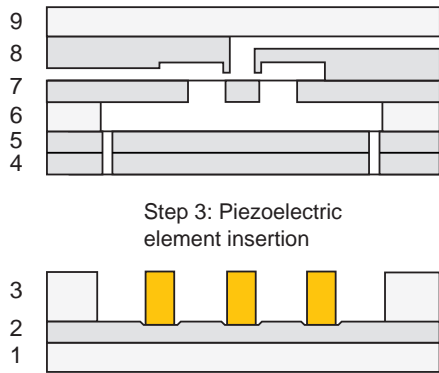
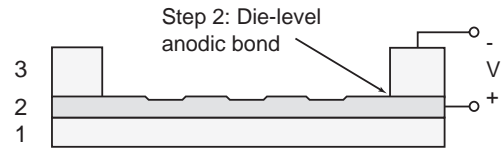
1. Die-level anodic bonding of Stack 4-5-6 to Stack 7-8-9 at a temperature of 300°C and an applied voltage of 1000V across the Layer 6 - Layer 7 interface. This bond is performed at atmospheric pressure. Time of bond = 20 minutes.
2. Die-level anodic bonding of Stack 1-2 to Layer 3 at a temperature of 300°C and an applied voltage of 1000V across the Layer 2 - Layer 3 interface. This bond is performed at atmospheric pressure. Time of bond = 45 minutes.



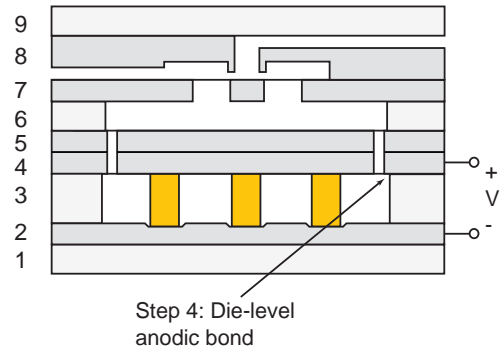
(a)



(b)



(c)



(d)

Figure 6.9: Die-level bonding procedure for active valve device: (a) beginning dies ready for assembly, (b) Step 1: anodic bonding of Stack 4-5-6 to Stack 7-8-9 ; Step 2: anodic bonding of Stack 1-2 to Layer 3, (c) Step 3: insertion of piezoelectric element(s), and (d) Step 4: anodic bonding of Stack 1-2-3 to Stack 4-5-6-7-8-9.

3. Alignment and placement of one or more piezoelectric material elements within the Stack 1-2-3 die.
4. Simultaneous die-level anodic bonding of Stack 1-2-3 to Stack 4-5-6-7-8-9 and eutectic bonding of piezoelectric element(s) to Layer 2 and Layer 4 silicon. This bond is performed in a reducing atmosphere of  $Ar - 5\%H_2$  gas at pressure  $10^{-2}$  torr and temperature  $300^\circ C$ . Additionally, a voltage of 1000V is applied across the Layer 3 - Layer 4 interface. Time of bond = 60 minutes.

A reducing atmosphere is chosen for the final simultaneous anodic/eutectic bond to ensure no oxidation of the Sn within the AuSn alloy and to achieve a void-free eutectic bond [2]. Additionally, following this bond, the device is cooled under vacuum to ensure removal of all trapped gases within the bond. Completion of these four die-level bonding steps produces an active valve structure that is ready for filling of the hydraulic amplification chamber.

### Assembly Jigs

The die-level anodic bonding discussed above is performed using the specially machined alignment and bonding jigs shown in Figure 6.10. The 1st-generation jig, shown in Figure 6.10(a), provides a large central contact surface onto which a die can be placed and the bottom surface held at either positive or negative voltage. An outer ring with attached spring clamps for clamping of one die onto another is held at ground potential. Once inserted into an oven, electrical contact is made through attached feet on the underside of the jig. Alignment, placement, and clamping of a dies and insertion of piezoelectric elements is facilitated by a vacuum chuck with 3-axis motion capability and a range in each of these directions of 1 cm. The 2nd-generation jig, shown in Figure 6.10(b), is more compact than the 1st-generation jig. It likewise provides electrical contact through thin wire clamps, but additionally allows for edge alignment of dies to a central area with ceramic insulating locator pins. Figure 6.11 illustrates an active valve device in the final bonding step using the 2nd-generation anodic bonding jig.

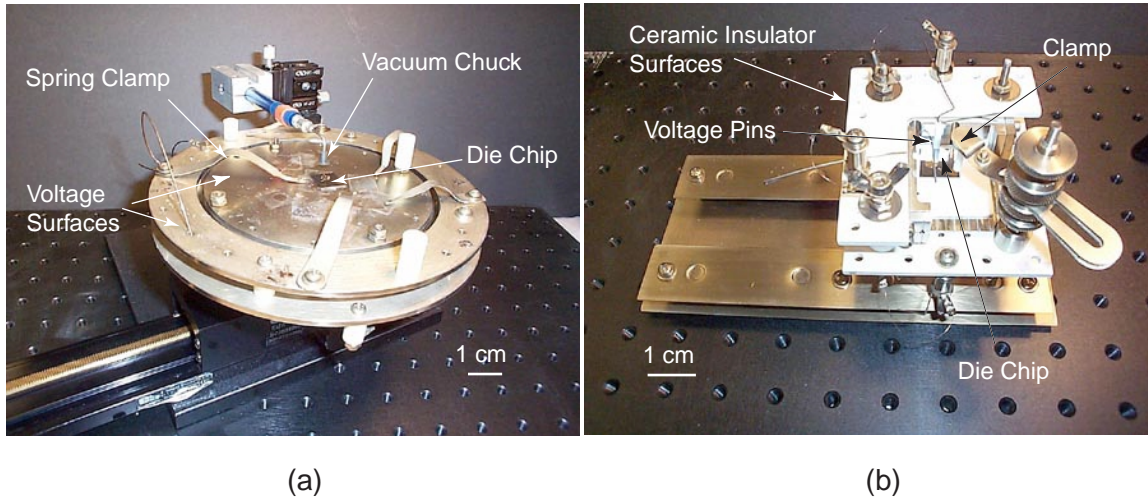


Figure 6.10: Die-level alignment and bonding jigs: (a) 1st-generation jig, (b) 2nd-generation jig.

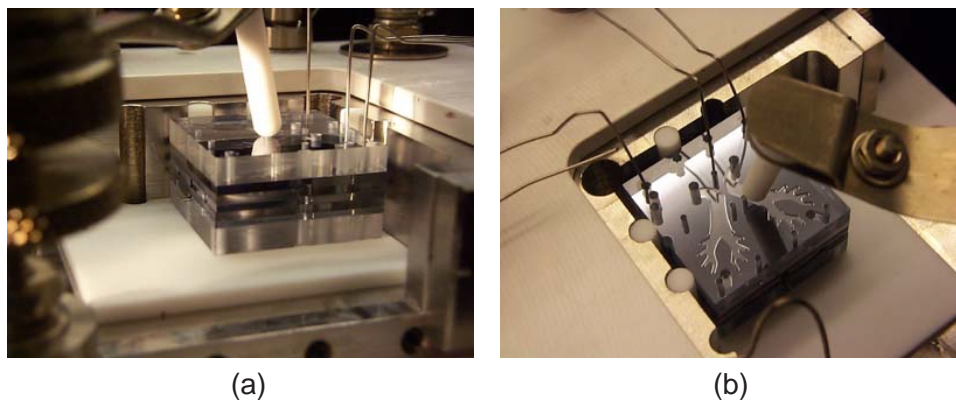


Figure 6.11: Electrical contact to an active valve chip for anodic bonding: (a) side view of chip in jig and (b) top view of chip in jig. Electrical cantilever pins contact various layers of the device for bonding procedures.

### 6.2.5 Fluid Filling/Sealing of HAC

Introducing fluid into the hydraulic amplification chamber of the active valve is a critical step in preparing the device for operation. Any bubbles or trapped residual gas within the amplification chamber will significantly increase its compliance, thereby eliminating efficient coupling between the drive element and valve membrane structure. This section briefly details the fluid filling procedure and issues associated with sealing.

#### Procedure for Filling

A fluid-filling apparatus and procedure developed by Richard Mlcak (Boston Microsystems, Inc) and updated by Lodewyk Steyn (MIT) was used to fill the active valve devices developed in this thesis. The apparatus, shown in Figure 6.12, consists of a filling chamber, a fluid reservoir chamber, a vacuum pump, and a series of valves connecting these components together. A schematic of the component connections is shown in Figure 6.13. A detailed explanation of the filling procedure and issues associated with the development of this procedure can be found in [10] and [11]. The major steps in the filling process are as follows:

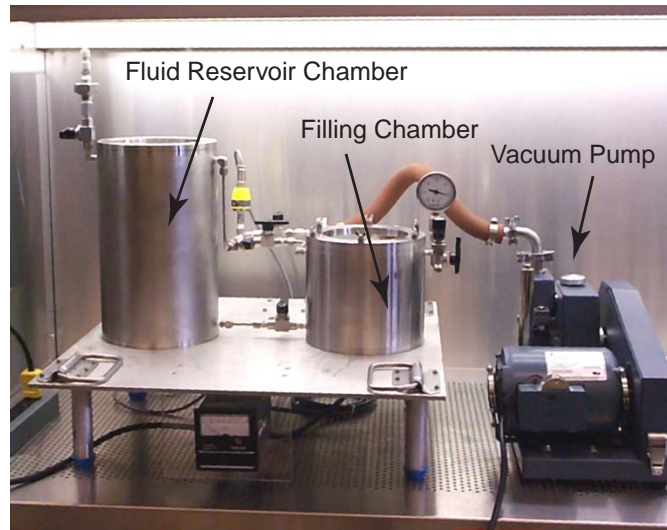


Figure 6.12: Fluid filling apparatus to fill active valve devices. System consists of a fluid reservoir chamber, a filling chamber, a vacuum pump, and series a valves connecting all components together.

1. The assembled, bonded, and poled active valve device is inserted into the filling chamber. The chamber is then closed, with no fluid present in this chamber. Valve 1, Valve 3, and Valve 5 are closed.

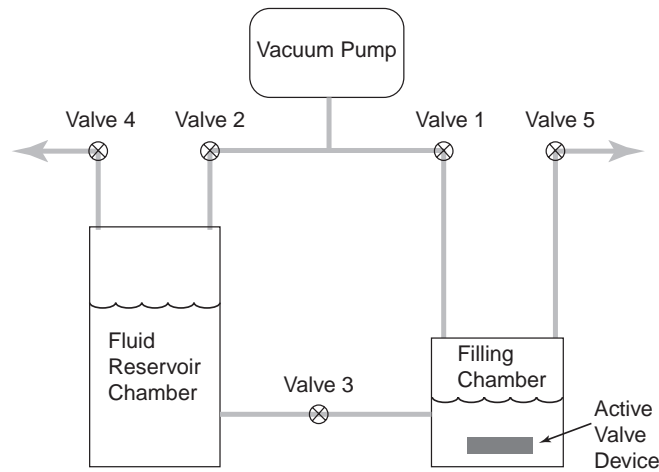


Figure 6.13: Fluid filling schematic of component connections.

2. With the fluid reservoir chamber full of fluid, Valve 4 is closed and Valve 2 is opened. The vacuum pump is initiated to outgas the fluid in the reservoir chamber. After a period of 1 hour, Valve 2 is closed. Valve 4 is then opened to bring the reservoir pressure back to atmospheric pressure.
3. Valve 3 is opened to introduce a small amount of fluid into the filling chamber from the reservoir chamber. Valve 3 is then closed. Valve 1 is then opened and the filling chamber is evacuated to approximately 1 torr. This evacuation acts to boil off the fluid introduced into the filling chamber. The hydraulic amplification chamber and other fluidic channels in the device are thereby filled with silicon oil vapor, which easily wets the walls of these structures. After 10 minutes, Valve 1 is closed.
4. Valve 3 is opened for a sufficient time to deliver to the filling chamber a volume of fluid that submerges the valve device and the jig within which it rests. Valve 3 is then closed.
5. Valve 5 is opened to pressurize the filling chamber to atmospheric pressure. This step, which lasts for approximately 1 hour, serves to “push” the fluid into the hydraulic amplification chamber. The device is then removed from the filling chamber and is ready for testing.

During this filling procedure, the active valve device is securely clamped within a test-jig apparatus. Prior to removal from the filling chamber, a valve located on the test jig that leads to the HAC chamber is closed. Once hooked up to the experimental testing apparatus, this valve is opened to an external pressure regulator (see next section).



## Sealing Issues

In order to maintain a compressive stress on the piezoelectric elements at all times and to eliminate the potential for cavitation within the hydraulic amplification chamber during actuation, the fluid within the chamber is required to be held at a positive bias pressure (typically 0.5-2MPa). The value of this bias pressure  $P_{bias}$  is determined based on the  $P_{HAC}$  pressure fluctuations expected during active valve operation (determined using numerical simulation).  $P_{bias}$  should be chosen to ensure that  $P_{HAC}$  never passes below zero during actuation. Sealing of the HAC chamber at a desired bias pressure was not an option in this thesis because such a procedure had not been developed. Further discussion of sealing and encapsulation studies for these types of devices can be found in [11]. For the purposes of the active valve described in this thesis, therefore, it was required to develop a means to bias the  $P_{HAC}$  after the fluid filling operation was complete and without completely sealing the chamber.

To accomplish this objective, a small cross-sectional area fluid channel was etched into the underside of Layer 7 so to provide a connecting path between the hydraulic amplification chamber and an external pressure regulator. Figure 6.14 illustrates this concept. By incorporating a high resistance fluid channel in this location, static bias pressures dictated by the external regulator can be imposed on the chamber, however, high frequency pressure fluctuations created during actuation remain confined to the chamber. In essence, this channel acts as a low pass filter for transmission of pressure fluctuations into and out of the chamber. The channel length, width, and height were designed to be 1mm,  $10\mu m$ , and  $10\mu m$  respectively. The channel was desired to be long and thin so as to create a large flow resistance during actuation. However, the channel width and height were designed large enough so as to be able to initially fill the device with fluid using the procedure detailed above in a reasonable amount of time (on the order of 20 minutes).

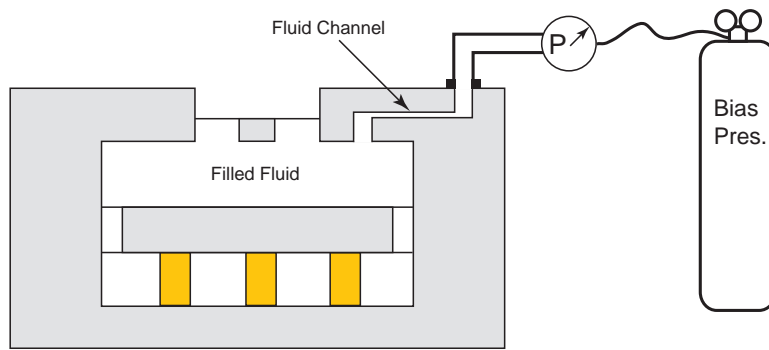


Figure 6.14: Schematic of the high resistance fluid channel between the HAC and an external bias pressure regulator. This channel was etched into the underside of Layer 7.

To design properly this high resistance flow channel for use in the active valve geometry

detailed in this thesis, a model was developed to capture the inertia and flow resistance associated with a fluid slug within the channel (see Figure 6.15). The assumptions in this model are: (1) the fluid slug occupies the entire length of the channel, (2) the fluid slug interacts with the volumetric stiffness of the hydraulic amplification chamber (designated as  $K_{HAC}$ ), and (3) the fluid slug flow behavior is governed by Hagen-Poiseuille flow relations. The variable  $\Delta V_{slug}$  is defined as the volume of fluid pushed into/pulled out of the HAC chamber during an actuation cycle of the active valve. The variable  $\Delta P_{slug}$  is defined as the differential pressure seen across the fluid slug during this actuation cycle due to pressure fluctuations within the HAC chamber.

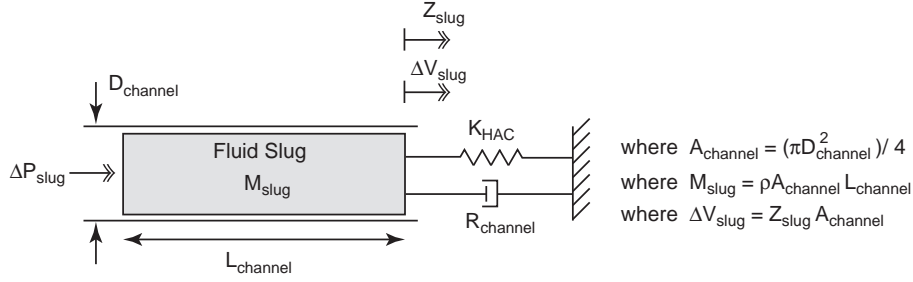


Figure 6.15: Model of the high resistance fluid channel between the HAC and an external bias pressure regulator. A fluid slug within the channel is modeled. This slug is acted upon by an external stiffness associated with the HAC chamber stiffness. Additionally, the flow resistance of this slug through the channel is modeled using laminar Hagen-Poiseuille flow relations.

Based on the model schematic in Figure 6.15, a differential equation for the slug behavior can be written,

$$\left( \frac{M_{slug}}{A_{channel}^2} \right) \Delta \ddot{V}_{slug} + R_{channel} \Delta \dot{V}_{slug} + K_{HAC} \Delta V_{slug} = \Delta P_{slug} \quad (6.2)$$

where  $R_{channel} = \left( \frac{128\mu L_{channel}}{\pi D_{channel}^4} \right)$  is based on Hagen-Poiseuille flow in a circular channel [8]. In this relation,  $\mu$  is the viscosity of the fluid. Inserting this flow relation into Equation 6.2 and rearranging in the frequency domain, a transfer function relating  $\Delta V_{slug}$  to  $\Delta P_{slug}$  is obtained

$$\frac{\Delta V_{slug}}{\Delta P_{slug}} = \frac{\left( \frac{\pi D_{channel}^2}{4\rho L_{channel}} \right)}{s^2 + \left( \frac{32\mu}{\rho D_{channel}^2} \right) s + \left( \frac{K_{HAC} \pi D_{channel}^2}{4\rho L_{channel}} \right)} \quad (6.3)$$

where  $\rho$  is the density of the fluid in the channel. The natural frequency (known as the Helmholtz frequency) of this fluid-structure interaction event can be written as

$$f_{Helmholtz} = \frac{1}{2\pi} \sqrt{\frac{K_{HAC} \pi D_{channel}^2}{4\rho L_{channel}}}. \quad (6.4)$$

In designing the channel dimensions, the following parameter values (which correlate with the active valve geometry fabricated in this thesis) were assumed:  $L_{channel} = 1mm$ ,  $D_{channel} = 11.3\mu m$ ,  $K_{HAC} = 1.0e^{17} \frac{Pa}{m^3}$ ,  $\rho = 760 \frac{kg}{m^3}$ , and  $\mu = 6.5e^{-4} \frac{kg}{ms}$ . These values result in a frequency of 48Hz for which  $\Delta V_{slug}$  is 1% of the drive element volume change. Additionally, a Helmholtz frequency of  $f_{Helmholtz} = 578Hz$  results. However, Helmholtz resonant behavior of this slug is non-existent due to the dominant fluid viscous losses in the channel. Additionally, with these channel dimensions, it is estimated that during initial fluid filling, the HAC chamber should fill in approximately 5-10 minutes under atmospheric pressurization in Step 5 of the above fluid filling procedure. Chapter 9 includes experimental verification of the performance of this high fluid resistance channel within working high frequency active valve devices.

### 6.3 Sub-Component Testing Plan

To solve and to overcome the previously described fabrication challenges, a fabrication and experimental test plan was developed. This plan divides the full piezoelectrically-driven active valve device into simpler decoupled sub-components structures, which can be independently fabricated, assembled, and tested. The sub-component structures are the piezoelectric drive element and the valve cap and membrane structure. Figure 6.16 outlines this plan. This section provides a general overview of the sub-component geometries and the important questions that need to be answered in each of the sub-component studies. Subsequent chapters of this thesis go on to provide complete and detailed experimental validation of each of the sub-components.

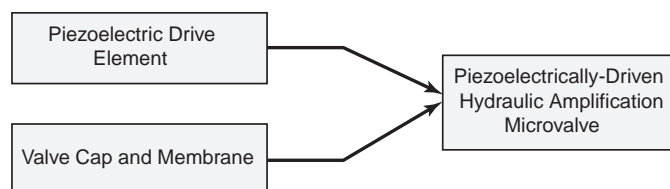


Figure 6.16: Sub-component fabrication and testing plan. Realization of a full piezoelectrically-driven hydraulic amplification microvalve depends on successful validation of the piezoelectric drive element and the valve cap and membrane deformation behavior. Fluid filling success is evaluated with the full active valve device.

#### 6.3.1 Piezoelectric Drive Element

The piezoelectric drive element provides actuation volume change and pressurization to the hydraulic amplification chamber and therefore the valve cap and membrane as it opens and closes against a fluid orifice. This sub-component study proves that etching of the high-aspect ratio tethered piston structures and control of fillet radii at the base of these etches can be

performed in a repeatable fashion. Additionally, wafer-level silicon-silicon fusion bonding were validated to form Stack 4-5. As shown in Figure 6.17, devices were constructed with single-layer pistons as well as double-layer pistons for stiffness comparison. Piezoelectric material, both PZT-5H and PZN-PT, were processed to create individual piezoelectric elements for insertion into drive element structures. Sub-component devices with a single element placed centrally beneath the drive piston as well as devices with three piezoelectric elements spaced out uniformly beneath the drive piston were fabricated to validate enhanced stiffening benefits of drive element actuators with multiple piezoelectric elements (again see Figure 6.17. The drive element sub-component devices were experimentally tested to evaluate both quasi-static deformation behavior (frequencies  $\leq 15$  kHz) and dynamic modal behavior (up to 200 kHz) under a wide range of applied voltages. Completion of this sub-component study enables incorporation of the drive element actuator structure within complete active valve structures.

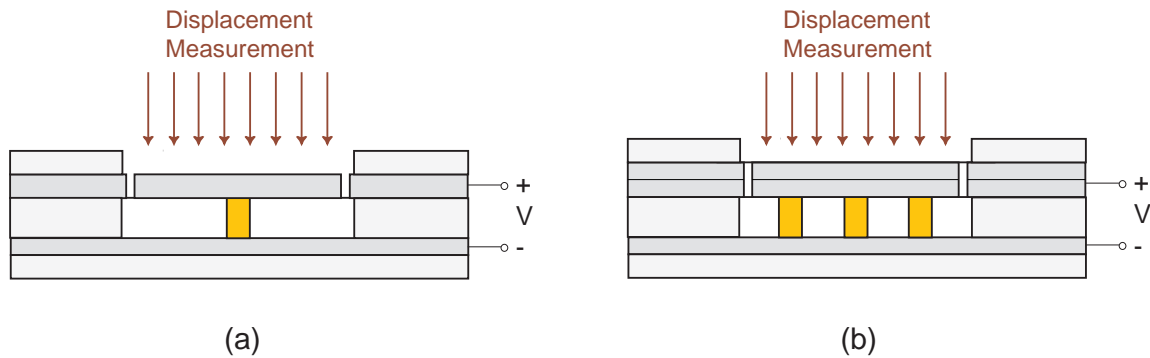


Figure 6.17: Drive element sub-component study: (a) devices with a single piezoelectric element centrally-located beneath the piston as well as devices with single-layer pistons will be fabricated, (b) devices with three piezoelectric elements positioned beneath the piston and devices with double-layer pistons will also be fabricated.

### 6.3.2 Valve Cap and Membrane

The valve cap and membrane structure reacts to differential pressures to open and close against a fluid orifice. This sub-component study validates the etching of the membrane and control of fillet radii at the oxide etch stop. Valve membrane structures were tested to verify non-linear pressure-deflection behavior, and results were compared to the non-linear numerical models presented in Chapter 3 of this thesis. The sub-component structure used for these tests is shown in Figure ??(a). Gas pressure was introduced into the amplification chamber to directly force the valve cap and membrane structure upward. Additionally, gas pressure was introduced above the membrane as well to deform the structure in the downward direction. Deflection of the valve cap was measured using a laser vibrometry system. Completion of this sub-component

study provides an understanding of the valve membrane stiffness in response to applied pressures and therefore enables subsequent fluid filling and testing of full active valve devices.

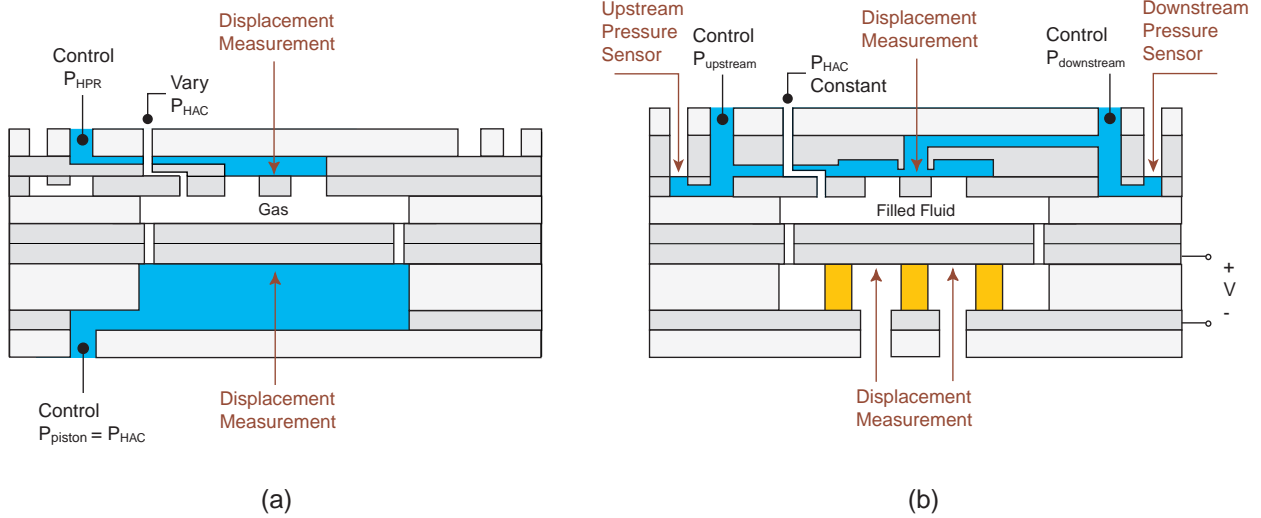


Figure 6.18: Valve membrane sub-component study and full active valve study: (a) valve cap and membrane within assembled chamber were deformed with gas pressure to determine structural stiffness, (b) the active valve device was fully characterized for pressure-flow behavior and limitations in dynamic performance. Note that the high resistance flow channel and the external fluid flow path above valve cap overlap in this schematic. In reality, these channels are offset spatially from one another.

### 6.3.3 Full Active Valve

Having successfully completed the two sub-component studies, a full active valve device was tested. The structure of this device is shown in Figure 6.18. Displacements of the valve cap in response to applied piezoelectric voltage were determined. In addition to evaluating the opening and closing capability of the valve in response to voltage, differential pressure - flow relations were established across the flow channel. Dynamic transfer functions of the full valve device were obtained and limitations in device performance were established.

## 6.4 Testing Apparatus

### 6.4.1 Laser Vibrometer System

A laser vibrometer system was used to measure the structural vibrations of the drive element piston and valve cap during the experimental testing of the full active valve and its sub-component structures. This system uses a technique known as laser doppler vibrometry to detect the ve-

locity of a moving surface. The wave used for this purpose is a laser, typically HeNe or of similar wavelength. When this wave strikes a moving surface and reflects back, a frequency shift is introduced. If the reflected wave is compared with the incident wave, the frequency shift results in a beating phenomenon, where the beat frequency is proportional to the velocity of the moving surface. Measuring this beat frequency therefore gives the velocity of the surface being measured.

During testing of the active valve and its sub-components, some of the measurements were taken through a medium of air in contact with the moving surface and some were taken through a medium of silicon oil in contact with the moving surface. As described in [13], the Doppler frequency shift, and hence the beat frequency, is proportional to the target velocity and also proportional to the refractive index of the medium in contact with the target. The silicon oil used in the valve (Dow Corning DC200 0.65 centistoke oil) has a refractive index of 1.375. Therefore, in taking measurements using this laser vibrometer system, any measurement values taken with this oil in contact with the moving surface were divided by 1.375 to obtain the proper values. All results incorporating oil in contact with the valve cap in subsequent chapters have been properly scaled by this value.

### 6.4.2 Fluids Test-Rig

The fluids testing rig used in the active valve and sub-component studies documented in this thesis was designed, built, and constructed by Lodewyk Steyn. Figure 6.19 illustrates a portion of this set-up. The explicit details of this test-rig are contained in [11]. In summary, this set-up enables the control of a wide range of pressure loadings on the drive element piston, within the HAC chamber, and on the valve cap and membrane upstream and downstream of the valve orifice flow channel for the active and sub-component studies. Fluid reservoirs contain degassed silicon oil for the purposes of creating fluid flow in testing the active valve device. A series of absolute and differential pressure sensors are located throughout the set-up to enable real-time measurements of the static and dynamic pressures at critical locations within the valve device. Further discussions of which pressures were measured for which experiments are included in the subsequent experimental chapters of this thesis.

## 6.5 Conclusions

This chapter has presented the fabrication and assembly challenges faced in realizing a working piezoelectrically driven hydraulic amplification microvalve. The wafer-level fabrication process, piezoelectric material preparation and integration issues, and die-level assembly and bonding procedures were discussed. Additionally, an overview of the active valve sub-component test plan was presented. The details of these sub-component studies are covered in subsequent

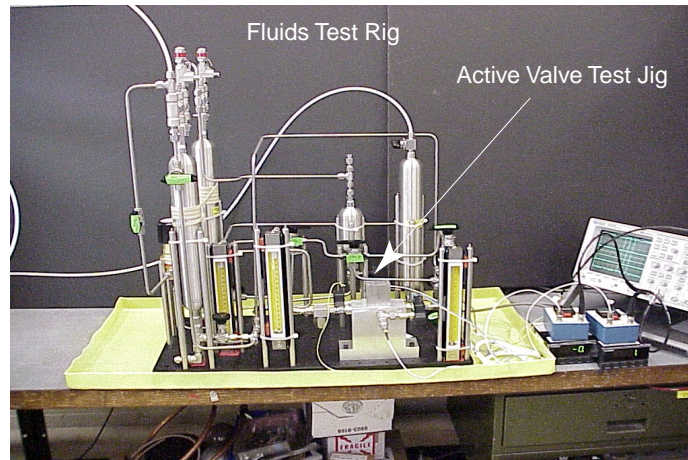


Figure 6.19: Fluids test-rig for testing of the active valve and its sub-components. This set-up contains fluid reservoirs, static and dynamic pressure sensors, flow sensors, and absolute and differential pressure sensors for evaluating device performance during testing.

chapters.

# Bibliography

- [1] A.A. Ayon, K-S. Chen, K.A. Lohner, S.M. Spearing, H.H. Sawin, and M.A. Schmidt, "Deep Reactive Ion Etching of Silicon," *Materials Research Society Symposium Proceedings*. v. 546, pp.51-61, 1999.
- [2] K-S. Chen, A. Ayon, and S.M. Spearing, "Controlling and Testing the Fracture Strength of Silicon on the Mesoscale," *Journal of the American Ceramic Society*, 83 [6], pp.1476-84, 2000.
- [3] J.C. Arnold and H.H. Sawin, "Charging of pattern features during plasma etching," *J. Appl. Phys.*, vol. 70, no. 10, pp.5314-5317, 1991.
- [4] T. Kinoshita, M. Hane, and J.P. McVittie, "Notching as an example of charging in uniform high-density plasmas," *J. Vac. Sci. Technol. B, Microelectron. Process. Phenom.*, vol. B14, no. 1, pp.560-565, 1996.
- [5] T. Nowaza, T. Kinoshita, T. Nishizawa, A. Narai, T. Inoue, and A. Nakae, "The electron charging effects of plasma on notch profile defects," *Jpn. J. Appl. Phys.*, vol. 34, pt. 1, no. 4B, pp.2107-2113, 1995.
- [6] U. Gosele and Q.-Y. Tong. Semiconductor wafer bonding. *Annual Review of Materials Science*, 28, pp. 215-241, 1998.
- [7] K.T. Turner, An Evaluation of Critical Issues for Microhydraulic Transducers: Silicon Wafer Bonding, Strength of Silicon on Insulator Membranes and Gold-Tin Solder Bonding. MIT Master's Thesis. June 2001.
- [8] R. Mlcak, Numerous presentations at MIT on the development of a bonding technology between piezoelectric material and silicon for use in MHT technology, 1997-2000.
- [9] M. Ohring. *The Materials Science of Thin Films*. Academic Press, New York, 1992.
- [10] R. Mlcak. *Wafer-scale Fluid Filling System: Standard Operating Procedure and Manual*. Document was provided to MIT from Boston Microsystems, Inc. in October 2000.



- [11] J.L. Steyn, Master's Thesis, Massachusetts Institute of Technology, 2002.
- [12] F.M. White, *Fluid Mechanics*, 2nd ed. McGraw-Hill Inc, 1986.
- [13] H.D. Young, *University Physics*, 8th ed. Addison Wesley, 1992.



## Chapter 7

# Sub-Component Study: Piezoelectric Drive Element

### 7.1 Objectives

The purpose of this sub-component study was to evaluate the fabrication and assembly process flow of the piezoelectric drive element structure, shown in Figure 7.1, and to obtain quasi-static and high-frequency experimental data on completed devices. Specifically, the three primary objectives of this study were:

1. To determine whether both single-layer and double-layer piston structures could be fabricated and assembled in drive element devices. As compared to single-layer pistons, the double-layer design enhances the structural stiffness of the micro-actuator device.
2. To determine whether standard polycrystalline PZT-5H and higher-performing single-crystal PZN-PT materials [4] could be processed and integrated within tethered-piston drive element structures. Although the final active valve devices (detailed in Chapter 9) incorporated solely PZN-PT material, the high cost of this material forced initial studies to work with less costly PZT-5H material.
3. To determine whether both single and multiple piezoelectric elements could be successfully integrated beneath the drive element piston. Multiple elements spread out beneath the piston serve to stiffen the micro-actuator structure. However, tolerancing and bonding of multiple elements within the device is more challenging.

Successful integration of these types of piezoelectric materials with properly etched and bonded tethered piston structures demonstrates the potential for high-frequency, high-stiffness actuation within full active valve devices.

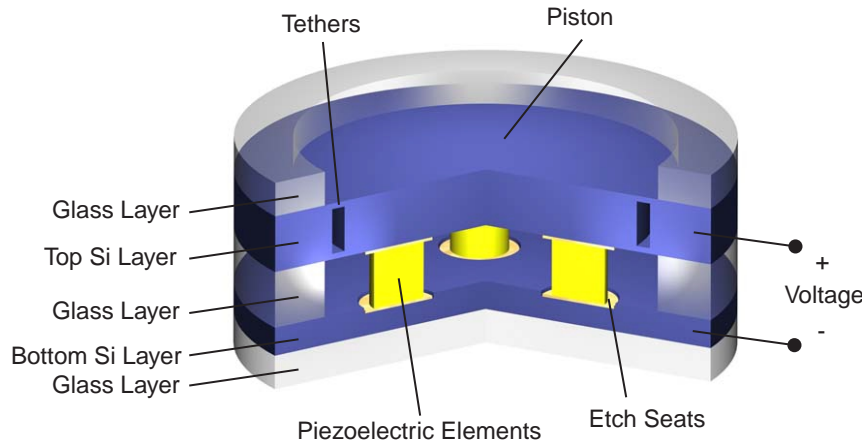


Figure 7.1: 3-D schematic of a piezoelectric drive element device. Three piezoelectric cylinders are sandwiched between a lower support silicon layer and an upper double silicon layer tethered-piston structure. Voltage is carried along the upper and lower silicon layers.

## 7.2 Device Test-Plan

The overall piezoelectric drive element sub-component study was divided into two parts. In the first part, “1st-generation” drive element devices were fabricated and tested. In the second part, “2nd-generation” drive element devices, slightly different in geometry than the “1st-generation” devices, were fabricated and tested. Ideally, a consistent geometry would have been preferred throughout the full study. Unfortunately, due to research program scheduling and resource limitations, the use of different geometries was unavoidable. The experimental results of the two sub-studies combined together, however, do provide overwhelming evidence that integration of piezoelectric elements within micromachined silicon thin-tethered piston structures is achievable. The overall device test plan is illustrated in Figure 7.2. The three major design variations contained within this sub-component study were: (1) use of a single-layer silicon drive piston structure versus use of a double-layer piston structure, (2) integration of PZT-5H material versus integration of PZN-PT material, and (3) incorporation of a single piezoelectric element beneath the piston versus integration of three elements spread out beneath the piston.

### 7.2.1 1st Generation Devices

As shown in Figure 7.2, the 1st-generation study included the fabrication and testing of three unique drive element devices, all incorporating a single-layer silicon drive piston. Device 1 incorporates a single PZT-5H cylindrical piezoelectric element centrally located beneath the tethered piston. Device 2 incorporates a single PZN-PT cylindrical piezoelectric element also

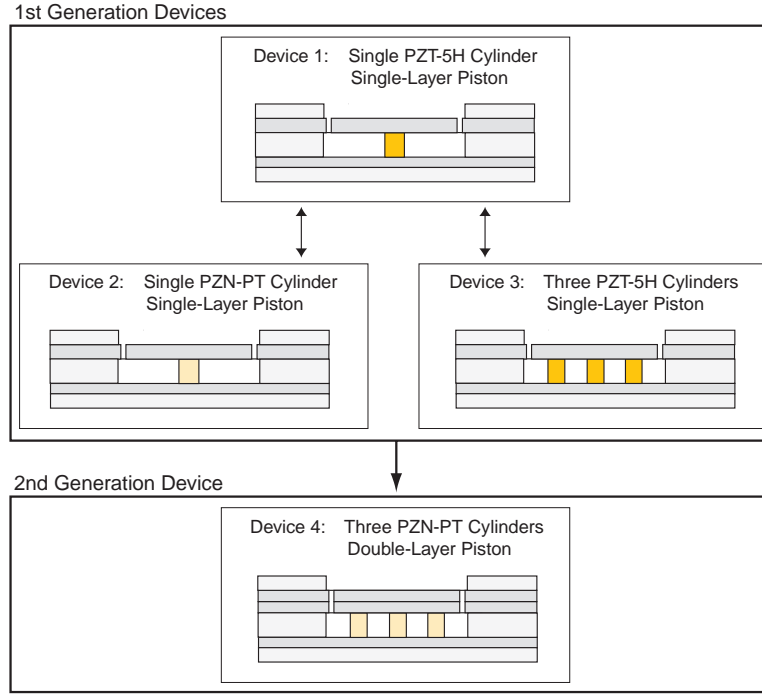


Figure 7.2: Overview of the drive element sub-component test plan. Within the 1st generation study, devices incorporating single and three piezoelectric cylinders (both PZT-5H and PZN-PT) beneath single-layer drive pistons were fabricated and tested. Within the 2nd generation study, devices with three PZN-PT square piezoelectric elements beneath double-layer drive pistons were fabricated and tested.

centrally located beneath the piston structure. Device 3 incorporates three PZT-5H cylindrical elements spread out uniformly beneath the piston. In all three devices, the piezoelectric cylinder thicknesses are  $\sim 1\text{mm}$ , while the drive piston has a thickness of  $390\mu\text{m}$  and the tether has a thickness of  $9\mu\text{m}$ . Figures 7.3(a) and (b) illustrate the top-view layout and dimensions of these single-cylinder and three-cylinder 1st-generation drive element devices, respectively. Experimental comparison of Device 2 with Device 1 demonstrates the benefits and drawbacks of incorporating the higher-strain capability, yet lower stiffness PZN-PT material versus PZT-5H material. Experimental comparison of Device 3 with Device 1 demonstrates the enhanced stiffening effects of incorporating multiple piezoelectric elements rather than a single centrally-located one within the drive element structure. Additionally, this comparison uncovers any potential difficulties involved in obtaining adequate eutectic bonding between all three cylinders and the adjacent silicon surfaces.

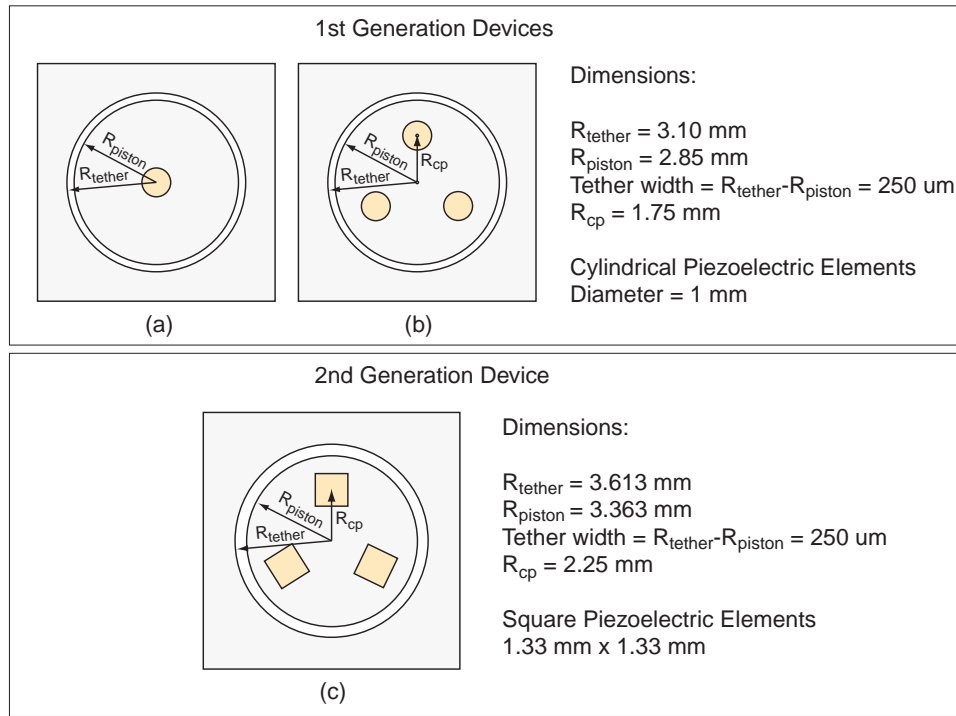


Figure 7.3: Drive element geometries and piezoelectric material layout for 1st and 2nd-generation devices: (a) 1st-generation device with a single piezoelectric cylinder, (b) 1st-generation device with three piezoelectric cylinders, and (c) 2nd-generation device with three piezoelectric square elements.

### 7.2.2 2nd Generation Device

As shown in Figure 7.2, the 2nd-generation study focused on the integration of three PZN-PT material elements beneath a double-layer drive element piston structure. This double-layer structure, as contained in the final design of the microvalve presented in Chapter 9, is critical for reducing compliance effects within the active valve during piezoelectric actuation. As for the 1st-generation devices, the piezoelectric element thicknesses are  $\sim 1\text{mm}$ . Since the piston is comprised of two layers, its total thickness is  $780\text{ }\mu\text{m}$  with each tether having a thickness of  $8\text{ }\mu\text{m}$ . Figure 7.3(c) illustrates the top-view layout and dimensions of this 2nd-generation drive element device, Device 4. In order to maximize use of PZN-PT material, square elements rather than cylindrical elements were incorporated in this structure (significantly more piezoelectric elements can be created by dicing a given size plate into squares rather than core-drilling cylinders from this plate). Successful fabrication and experimental evaluation of this final drive element device proves that such a micro-actuator structure can be implemented in the full active valve.

### 7.3 Device Assembly

As shown in Figure 7.4, the drive element structures consist of five primary layers, two of which are silicon and three of which are glass. The bottom silicon layer contains etched seats for thickness compensation of the piezoelectric elements with respect to the surrounding glass and also contains gold pads for electrical contact. The top silicon layer contains the etched tethered-piston structure. For 1st-generation devices, this layer is formed from a single silicon wafer, whereas for 2nd-generation devices, this layer is formed through wafer-level bonding of two etched silicon wafers. The top and bottom glass layers provide support for clamping during device testing.

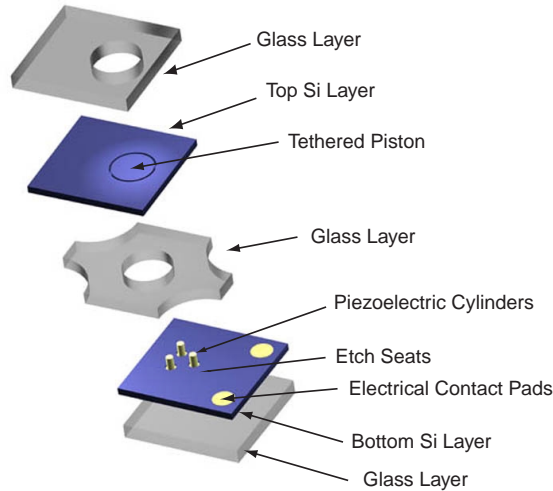


Figure 7.4: Exploded view of a 1st-generation piezoelectric drive element structure. One or more piezoelectric cylinders are arranged within a circular glass chamber, supported beneath a silicon layer with etched seats and bonded above to a micromachined piston.

As shown in Figure 7.5 and detailed in Chapter 6, a series of wafer-level/die-level anodic bonding steps and a final simultaneous anodic-eutectic bonding step were carried out to complete each of the drive element devices. Following this assembly, wires were soldered to the contact pads on the top and bottom silicon layers to provide electrical contact to the piezoelectric material. Poling of the device was performed by heating the device to approximately half the piezoelectric material Curie temperature ( $T_{curie} = 190^{\circ}C$  for PZT-5H and  $T_{curie} = 150^{\circ}C$  for PZN-PT) and applying a voltage of 1000V. Photographs of a 1st-generation drive element device prior to and following electrical lead attachment are shown in Figure 7.6(a) and (b) respectively. Photographs of a 2nd-generation drive element are shown in Figure 7.7.

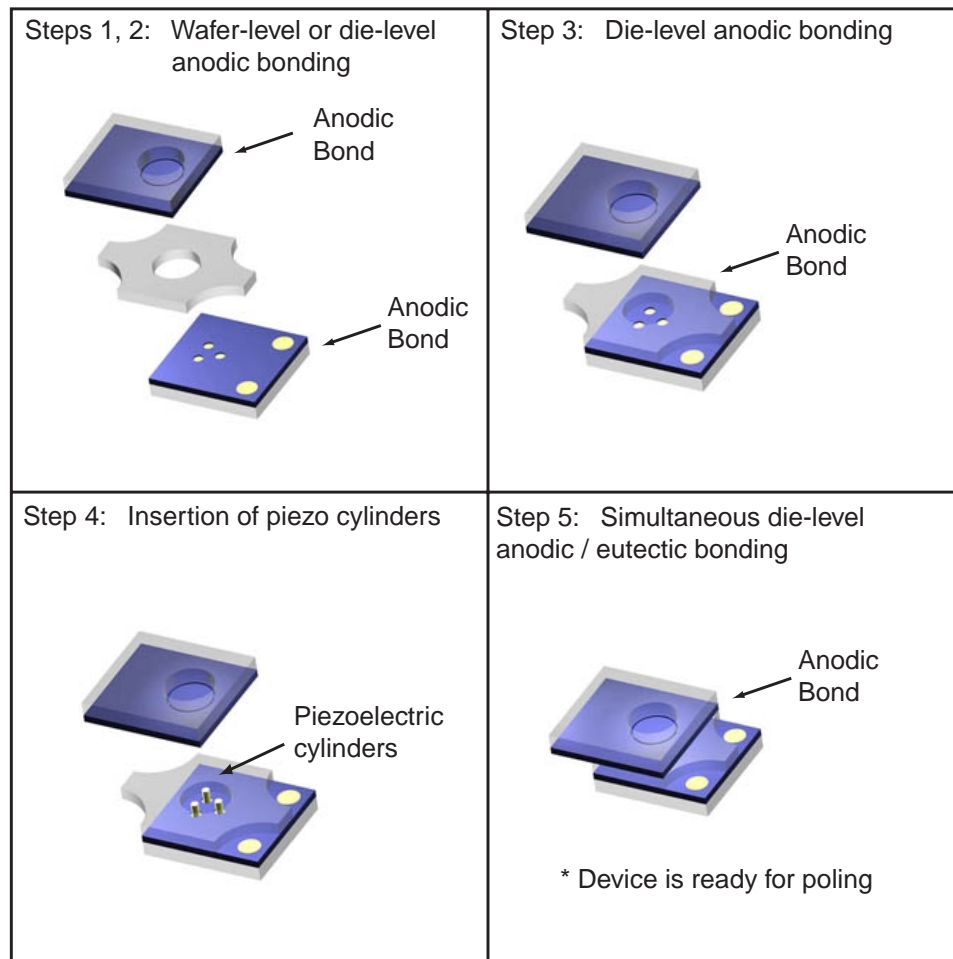


Figure 7.5: Assembly of a piezoelectric drive element device. Die-level anodic bonding procedures at  $T=300^{\circ}$  and 1000V were carried out to bond five layers together. The final anodic bonding step also serves to melt the eutectic alloy, forming the bond between the piezoelectric cylinders and the top and bottom silicon layers.



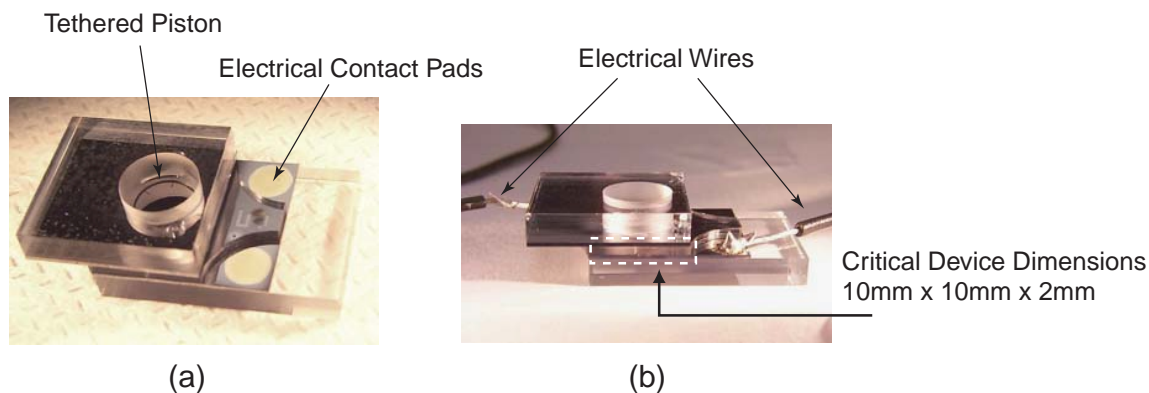


Figure 7.6: Photographs of an assembled 1st-generation piezoelectric drive element device: (a) a packaged device ready for attachment of electrical wires, prior to device poling, (b) a device ready for experimental testing. The critical device dimensions are 10mm x 10mm x 2mm. Thick glass packaging layers were used for clamping purposes during testing.

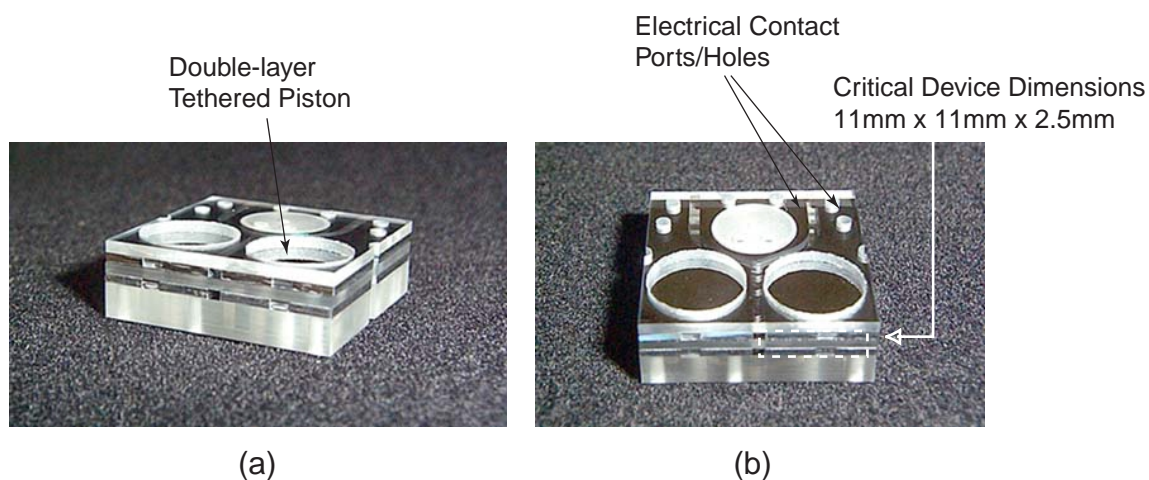


Figure 7.7: Photograph of an assembled 2nd-generation piezoelectric drive element device: thick glass packaging layers were used for clamping purposes during testing.

## 7.4 Testing Procedure

The process of experimentally testing a given drive element device consisted of three major steps. The first step involved careful microscopic inspection of the device to evaluate the fillet radius profile along the etched drive element tether. For 1st-generation devices, where single-layer pistons were used, measurements were taken following device assembly. However, for 2nd-generation devices, where a bonded double-layer piston prevented viewing of the piston etch, measurements were taken on each of the drive element tethers prior to wafer-level bonding. Knowledge of the fillet radius sizes was important for later evaluation of device performance.

The second step involved characterization of stand-alone piezoelectric material elements that came from the same batch (plate) of material that yielded the elements that were integrated within the device. This was a critical procedure so that comparison of drive element device voltage-deflection behavior could be compared to that of representative piezoelectric material elements.

The third step involved rigorous experimental testing of the device. Each device was rigidly clamped to a test-jig surface and experimentally evaluated using a scanning laser vibrometer system. As shown in Figure 7.8, scan points were defined over the top surface of the tethered piston and along the circumferential boundary supporting the piston. Three measurement procedures were used to characterize device performance. In the first procedure, a low-voltage ( $0V \pm 25V$ ) sweep signal was applied to each device over a frequency range of 10kHz to 200kHz to determine the onset of dynamic modal characteristics. A transfer function of velocity (averaged over all scan points) versus frequency was recorded. Close-up frequency sweeps around dominant modal frequencies were then carried out to obtain high-resolution mode shape behavior. In the second procedure, a sinusoidal voltage of  $500V \pm 500V$  was applied to each device at selected frequencies of 15kHz and 7kHz to evaluate device behavior below the modal frequencies. At each of these low-frequencies, displacement time histories at the piston center and at an outer edge of the piston were recorded. In the third procedure, voltage-deflection curves (of the piston center) for varying levels of applied voltage were obtained at a frequency of 100Hz to determine the true quasi-static voltage dependent performance of the device.

## 7.5 Experimental Results

### 7.5.1 1st Generation Devices

#### Measurement of Fillet Radius Profiles

Following assembly of each 1st-generation drive element device, careful inspection of the drive element piston tether was performed to characterize the uniformity of the fillet radii along the tether circumference. As shown in Figure 7.9(a), measurements were taken at eight equally

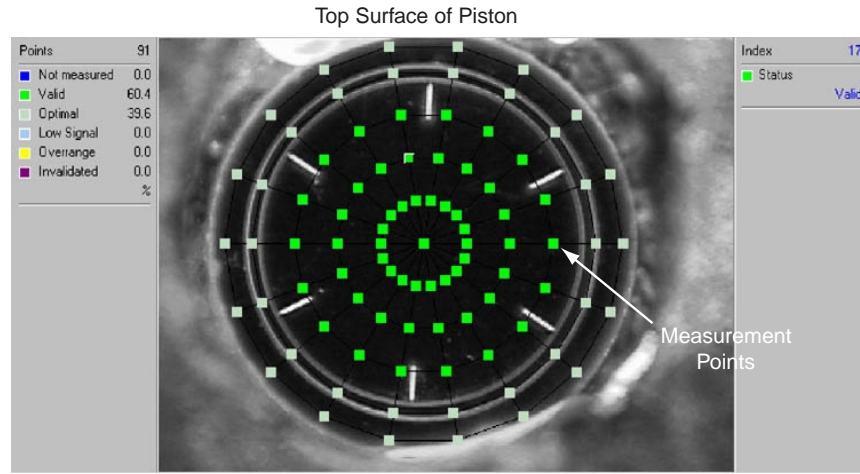


Figure 7.8: A scanning laser vibrometer system was used to characterize modal and quasi-static performance of each device. Measurement points are defined on the top surface of the piston.

spaced locations along the circumference. The first measurement point is located at 12 o'clock and numbering proceeds in the clockwise direction. The measurement terminology is illustrated in Figure 7.9(b). Using a microscope eyepiece with calibrated graduations, the tether width from the base of one fillet radius to the base of the opposite fillet radius was recorded. Additionally, the total trench width was measured. From these measurements, an average value for the fillet radius on each side of the trench was determined. Figure 7.9(c), (d), and (e) present the tether width and fillet radius measurements as a function of location along the tether circumference for Devices 1, 2, and 3, respectively. For Device 1, the tether width varies between  $138\mu m$  and  $163\mu m$  in a single sinusoidal cycle along the circumference (ie: the fillet radii vary from  $43\mu m$  to  $56\mu m$ ). Likewise, the tether width of Device 2 also varies sinusoidally, but with slightly larger variation, between  $165\mu m$  and  $200\mu m$ . For these two devices, due to this tether variation, the overall piston/tether stiffness is non-uniform around the circumference. For Device 3, tether width variation is also observed, however, in a more random fashion between  $178\mu m$  and  $195\mu m$ .

### Characterization of Piezoelectric Material

In order provide a basis for voltage-deflection comparison when testing completed drive element devices, representative PZT-5H and PZN-PT material cylinders were individually characterized (sufficiently long after poling, four days, to ensure adequate relaxation of the material). Figure 7.10 plots the results for three cylinders of each material at 10Hz for a driving voltage of  $500V \pm 500V$ . A very low frequency was chosen to guarantee true quasi-static behavior. The three PZT-5H cylinders exhibited peak deflections at 1000V between  $0.75\mu m$  and  $0.82\mu m$ . The three PZN-PT cylinders exhibited peak deflections at 1000V between  $1.35\mu m$  and  $1.55\mu m$ .

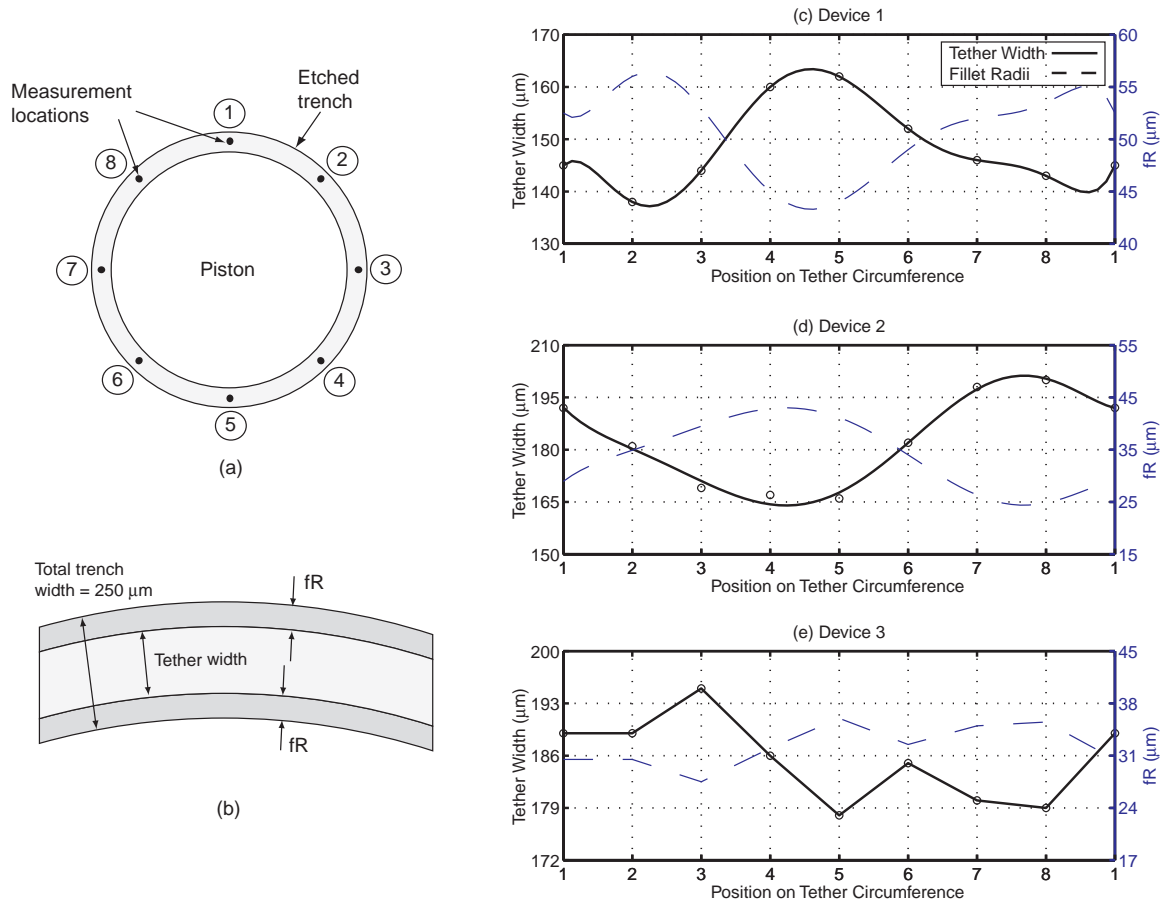


Figure 7.9: Inspection of tether width and fillet radii on Device 1, 2, and 3 tethered pistons: (a) definition of measurement locations around trench circumference, (b) average  $fR = \frac{1}{2}(\text{total trench width} - \text{measured tether width})$ , (c) Device 1 measurements, (d) Device 2 measurements, and (e) Device 3 measurements.

Finite-element models of drive element devices have indicated that the stiffness of the tether is insignificant compared to that of the piezoelectric materials, and therefore it does little to restrict the free-strain deflection of the piezoelectric material. As a result, these stand-alone piezoelectric element results provide an accurate expectation for quasi-static drive element device voltage-deflection performance.

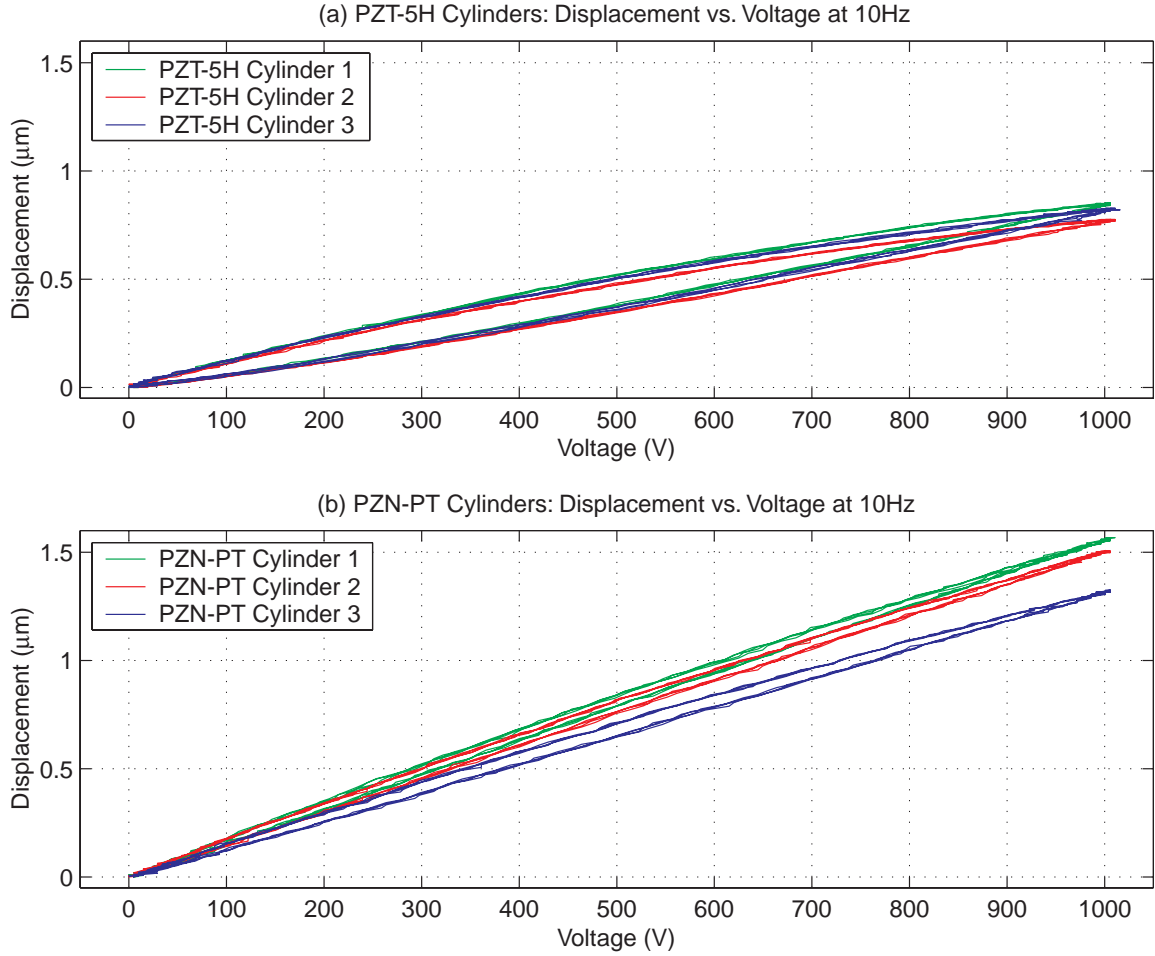


Figure 7.10: Piezoelectric material characterization on representative stand-alone PZT-5H and PZN-PT cylinders: (a) voltage-deflection responses at 10Hz for three different PZT-5H cylinders for  $V = 500V \pm 500V$  (these cylinders were taken from the identical PZT-5H material plate that yielded the cylinders used in Devices 1 and 3), (b) voltage-deflection responses at 10Hz for three different PZN-PT cylinders for  $V = 500V \pm 500V$  (these cylinders were taken from the identical PZN-PT material plate that yielded the cylinder used in Device 2).

## Experimental Testing of Device 1

Figure 7.11(a) plots the transfer function of averaged velocity over the scanned piston surface versus frequency for Device 1. Figure 7.11(b) plots these transfer functions for specific locations on the piston surface, at the center and at an outer edge. Figure 7.12(a) presents experimental mode shapes of the device at selected modal frequencies. The device experiences a “1 –  $\Theta$ ” tilt mode at  $f = 31kHz$ , followed by a “plunge” mode at  $f = 80kHz$ , and a “2 –  $\Theta$ ” mode at  $f = 131kHz$ . As shown in Figure 7.12, these modal frequencies correlate well with finite-element models of the device. The frequency difference in the “1 –  $\Theta$ ” mode between finite-element model and experiment could be attributed to imperfect placement of the cylinder beneath the piston or non-uniform fillet radii around the piston tether. In looking at Figure 7.11(b), notice that the velocity amplitudes are significantly more pronounced at the piston edge compared to the piston center. This is especially true for the “1 –  $\Theta$ ” tilt mode and the “plunge” mode.

Figure 7.13 illustrates the displacement profile of the device at 15kHz with an applied sinusoidal voltage of  $500V \pm 500V$ . Slight tilting of the piston surface is observed, and is again likely influenced by imperfect piezoelectric cylinder placement or non-uniformity in fillet radius etching. Figure 7.14 displays the corresponding displacement profiles at the piston center and piston edge. Higher-order dynamic oscillations of  $f = 80kHz$  are observed within the lower 15kHz drive frequency. These higher-order oscillations are more pronounced at the piston edge than at the piston center, which could be attributed to non-linearities inherent in the piezoelectric material or in the tether structure. The overall measured peak-peak deflection at the piston center,  $\delta_{p-p} = 0.69\mu m$ , is slightly lower than the expected range of  $\delta_{p-p} = 0.75 - 0.82\mu m$ . Most likely, this is a result of material inconsistency among the piezoelectric cylinders.

Figure 7.15 displays the displacement profiles at the piston center and piston edge at a driving frequency of 7kHz. Higher-order dynamic oscillations of  $f = 80kHz$  are again observed in the piston edge displacement signal, but with a lower magnitude. As for the piston center response at 15kHz, the overall measured peak-peak deflection at the piston center at 7kHz,  $\delta_{p-p} = 0.70\mu m$ , is slightly lower than the expected range of  $\delta_{p-p} = 0.75 - 0.82\mu m$ . Figure 7.16 plots the voltage-deflection curves for the piston center at 100Hz as a function of varying applied voltage levels, from  $100V \pm 100V$  to  $500V \pm 500V$ . Hysteresis in the PZT-5H material is clearly evident from the wide sweeping shapes of the curves. Overall, however, the peak displacement is close to linear with applied voltage.

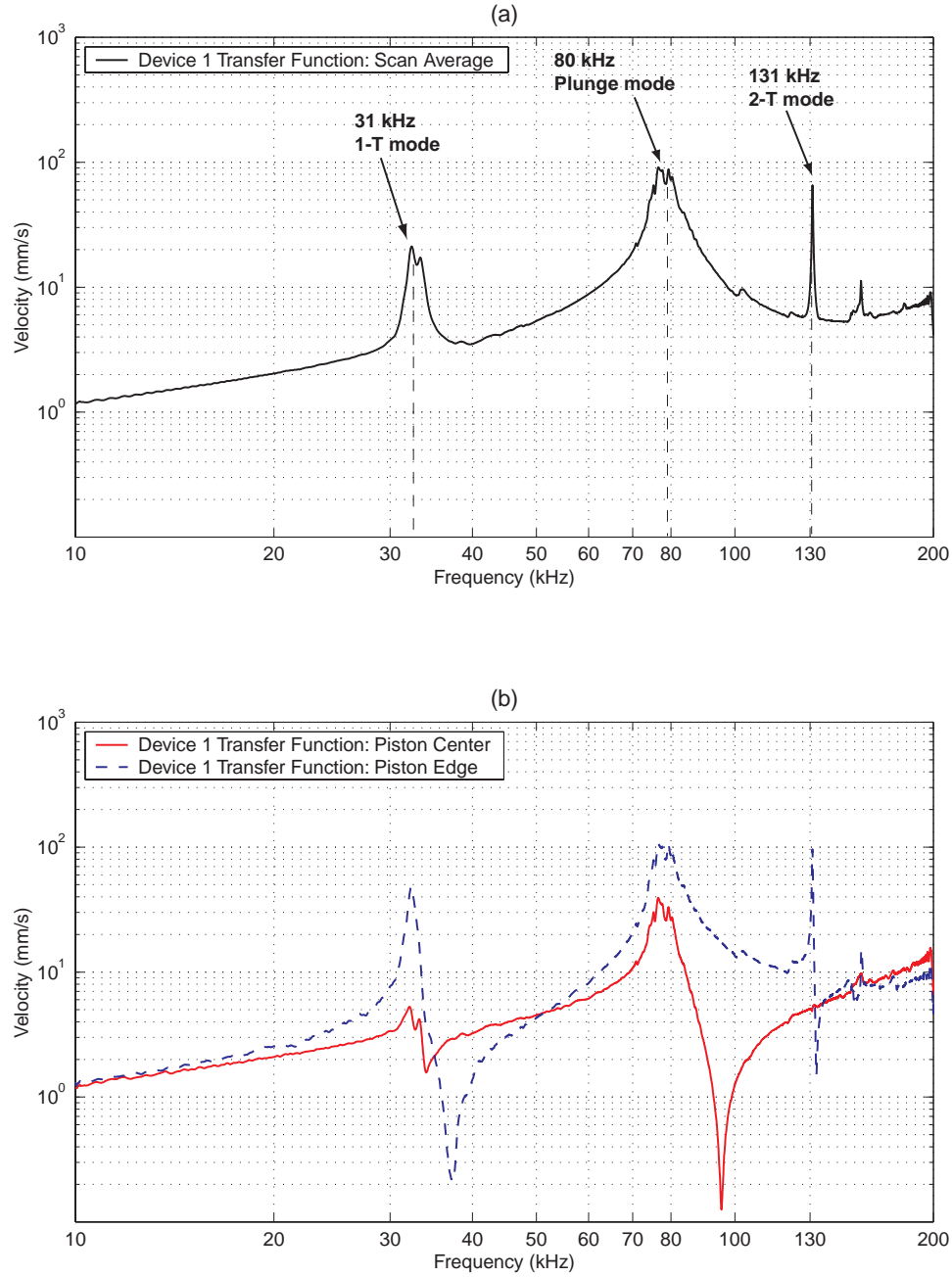


Figure 7.11: Device 1 transfer functions of piston velocity versus frequency for a sweep input from 10kHz to 200kHz and small signal drive voltage  $0V \pm 25V$ : (a) averaged velocity over piston surface, and (b) velocity at center and edge locations on piston surface. Modal behavior is present at 31kHz, 80kHz, and 131kHz. Phase information was not recorded for this device.

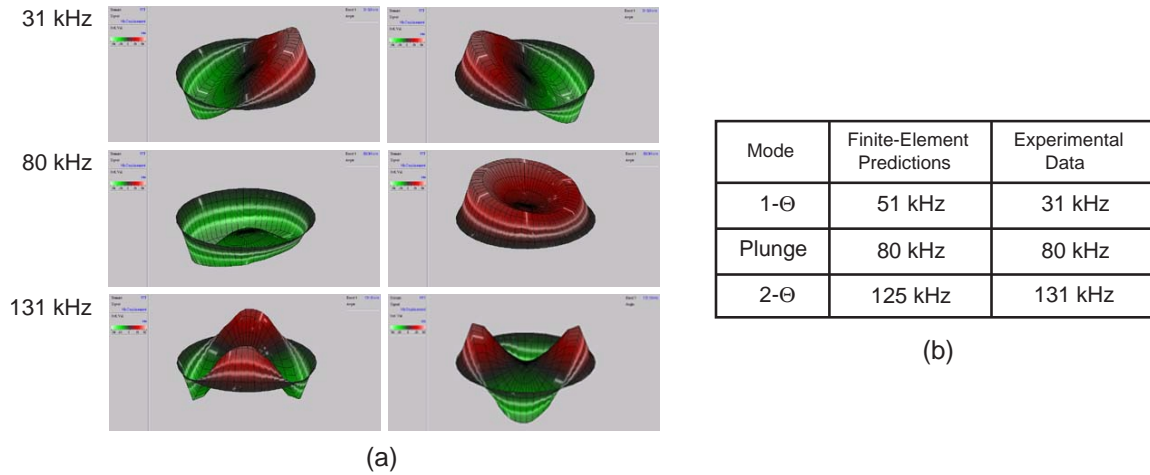


Figure 7.12: Device 1 modal behavior: (a) vibrometer scans of device: “1 –  $\Theta$ ” tilt mode at  $f = 31kHz$ , “plunge” mode at  $f = 80kHz$ , and “2 –  $\Theta$ ” mode at  $f = 131kHz$ , (b) comparison to results from the ANSYS finite-element model.

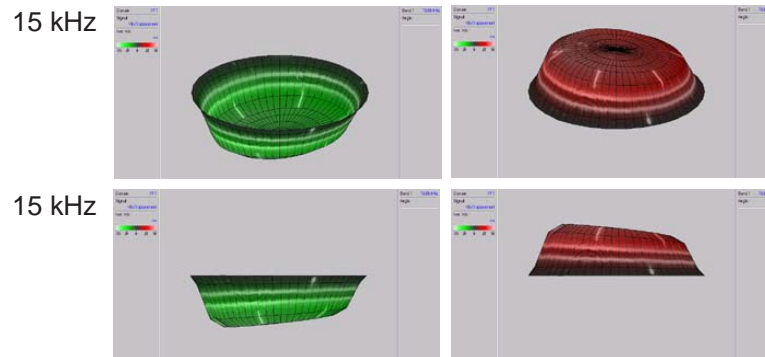


Figure 7.13: Vibrometer scan images of Device 1 low-frequency 15kHz displacement profile. The tilting of the piston surface is likely due to an uncentered piezoelectric cylinder or a non-uniform fillet radius in etched piston trench.



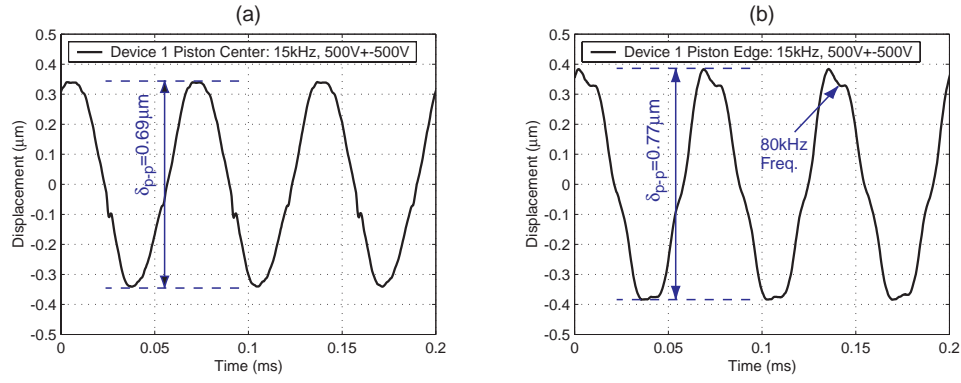


Figure 7.14: Device 1 displacement time histories for a sinusoidal drive voltage of  $500V \pm 500V$  at  $f = 15kHz$ : (a) piston center displacement and (b) piston edge displacement. Note the presence of 80kHz oscillations in the edge displacement time history.

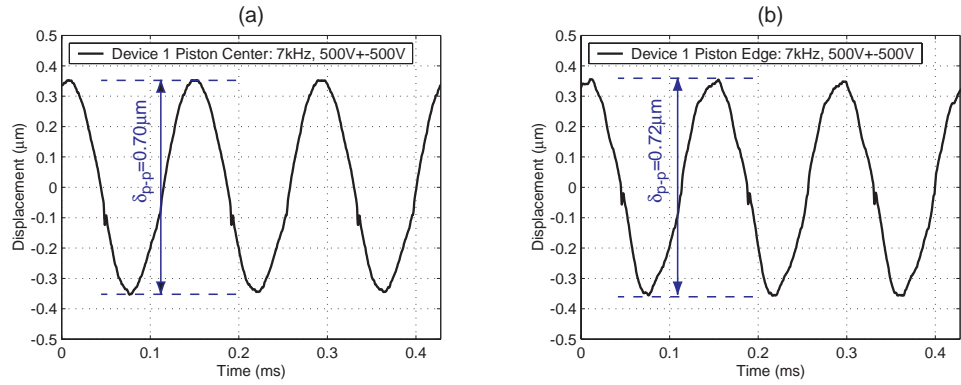


Figure 7.15: Device 1 displacement time histories for a sinusoidal drive voltage of  $500V \pm 500V$  at  $f = 7kHz$ : (a) piston center displacement and (b) piston edge displacement.

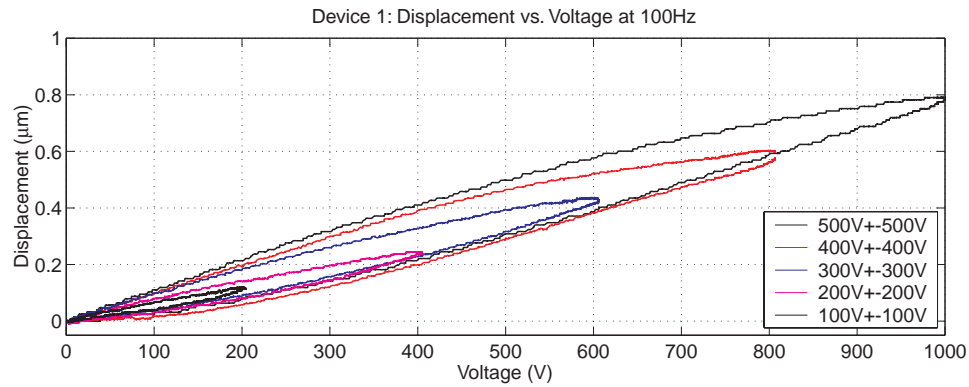


Figure 7.16: Device 1 piston center displacement behavior versus applied voltage at 100Hz.

## Experimental Testing of Device 2

Figure 7.17(a) plots the transfer function of averaged velocity over the scanned piston surface versus frequency for Device 2. Figure 7.17(b) plots these transfer functions for specific locations on the piston surface, at the center and at an outer edge. Figure 7.18(a) presents experimental mode shapes of the device at selected modal frequencies. In comparing this dynamic response to that of Device 1, the overall modal shapes are similar, however, the frequencies at which they occur are shifted downward. The “1 –  $\Theta$ ” tilt mode occurs at  $f = 30kHz$ , the “plunge” mode at  $f = 61kHz$ , and the “2 –  $\Theta$ ” mode at  $f = 112kHz$ . This frequency shift is expected since PZN-PT is a softer material than PZT-5H. As shown in Figure 7.18(b), these modal frequencies correlate well with finite-element models of the device. In looking at Figure 7.17(b), notice that the velocity amplitudes are significantly more pronounced at the piston edge compared to the piston center. This is especially true for the “1 –  $\Theta$ ” tilt mode and the “plunge” mode.

The displacement profile of Device 2 at 15kHz with an applied sinusoidal voltage of  $500V \pm 500V$  exhibits a non-uniform tilt (see Figure 7.19) in much the same manner as Device 1. The displacement time history at the piston edge exhibits components of the device “plunge” mode (see Figure 7.20). However, in comparison with Device 1 the magnitude of the piston center displacement in Device 2 is significantly increased to  $\delta_{p-p} = 1.42\mu m$ . This value correlates well with the expected peak-peak displacement range of  $\delta_{p-p} = 1.35 - 1.55\mu m$ .

Figure 7.21 displays the displacement profiles at the piston center and piston edge at a driving frequency of 7kHz. Dynamic oscillations of  $f = 61kHz$  are again observed in the piston edge displacement signal, and this signal has a decreased overall amplitude from the 15kHz response. As for the piston center response at 15kHz, the overall measured peak-peak deflection of the piston center at 7kHz,  $\delta_{p-p} = 1.39\mu m$ , correlates well to the expected range of  $\delta_{p-p} = 1.35 - 1.55\mu m$ . Figure 7.22 plots the voltage-deflection curves for the piston center at 100Hz as a function of varying applied voltage levels, from  $100V \pm 100V$  to  $500V \pm 500V$ . Comparing these curves to those of Device 1, it is clear that the PZN-PT material exhibits significantly reduced hysteretic behavior than the PZT-5H material. Additionally, the peak displacement is seen to be linear with applied voltage.

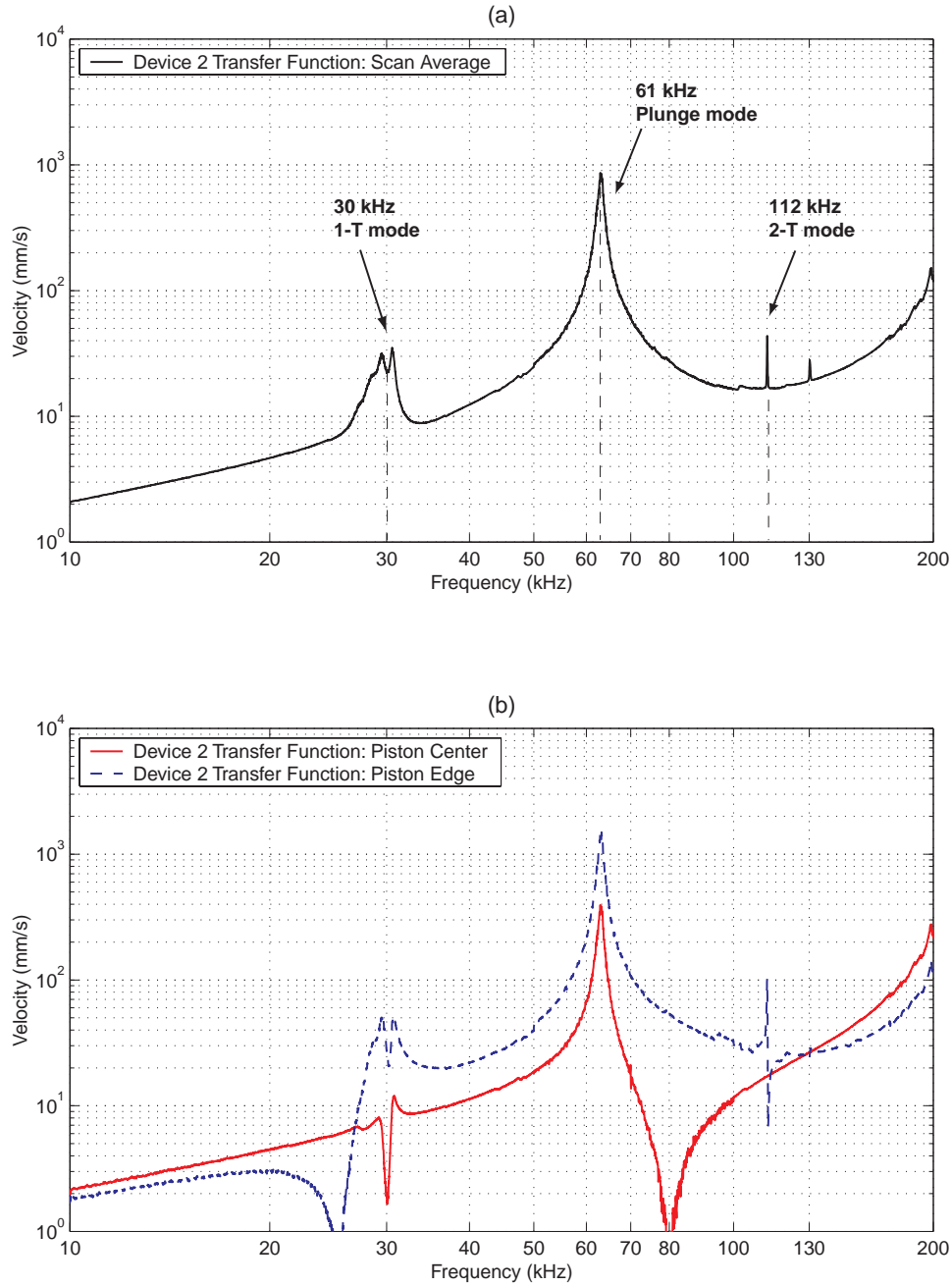


Figure 7.17: Device 2 transfer functions of piston velocity versus frequency for a sweep input from 10kHz to 200kHz and small signal drive voltage  $0V \pm 25V$ : (a) averaged velocity over piston surface, and (b) velocity at center and edge locations on piston surface. Modal behavior is present at 30kHz, 61kHz, and 112kHz. Phase information was not recorded for this device.

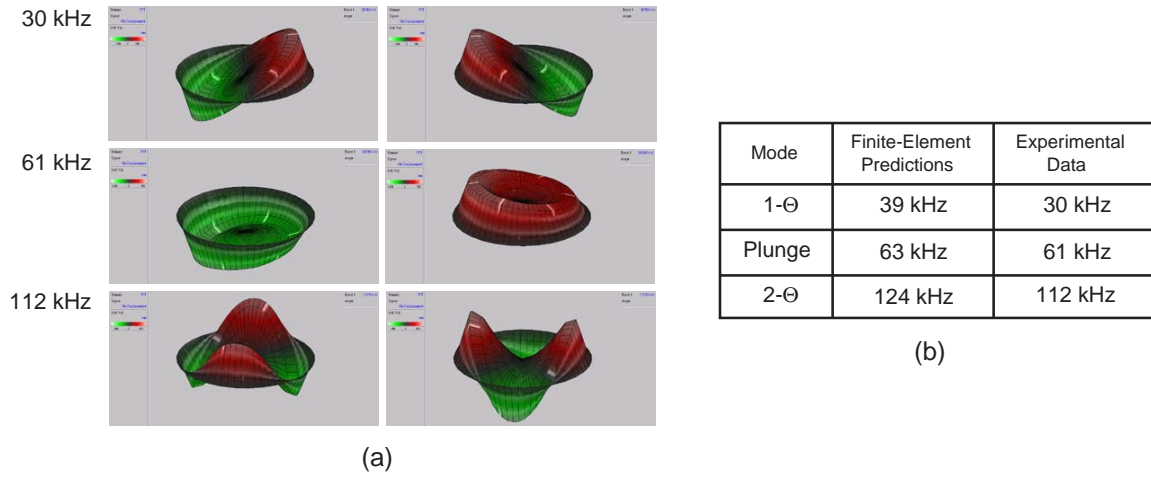


Figure 7.18: Device 2 modal behavior: (a) vibrometer scan images of device behavior: “1 –  $\Theta$ ” tilt mode at  $f = 30kHz$ , “plunge” mode at  $f = 61kHz$ , and “2 –  $\Theta$ ” mode at  $f = 112kHz$ , (b) comparison to results from the ANSYS finite-element model.

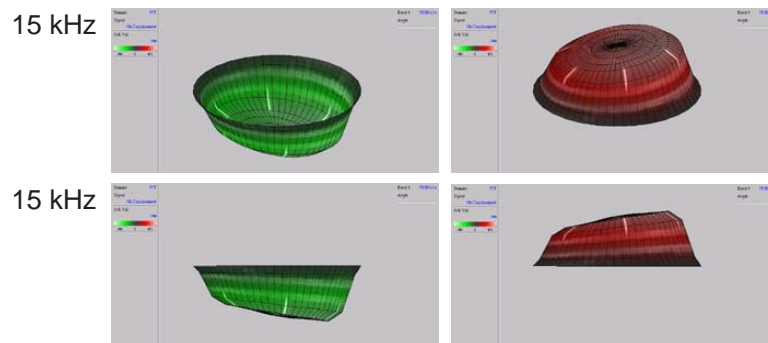


Figure 7.19: Vibrometer scan images of Device 2 low-frequency 15kHz displacement profile. The tilting of the piston surface is likely due to an uncentered piezoelectric cylinder or non-uniform fillet radius in etch piston trench.

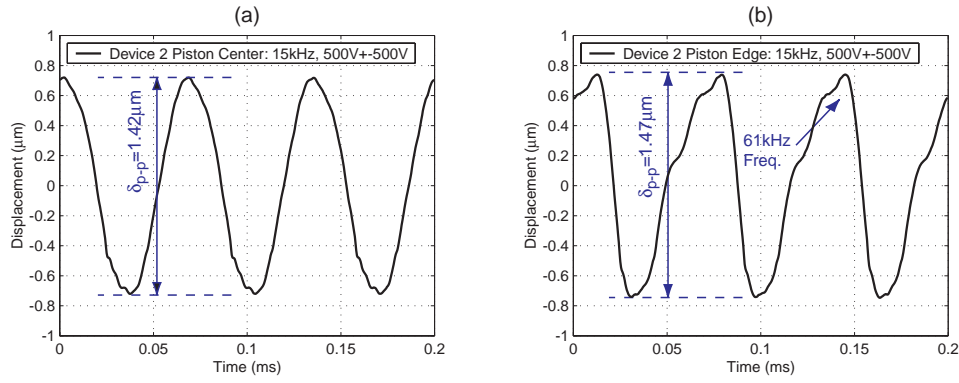


Figure 7.20: Device 2 displacement time histories for a sinusoidal drive voltage of  $500V \pm 500V$  at  $f = 15kHz$ : (a) piston center displacement and (b) piston edge displacement. Note the presence of 61kHz oscillations in the edge displacement time history.

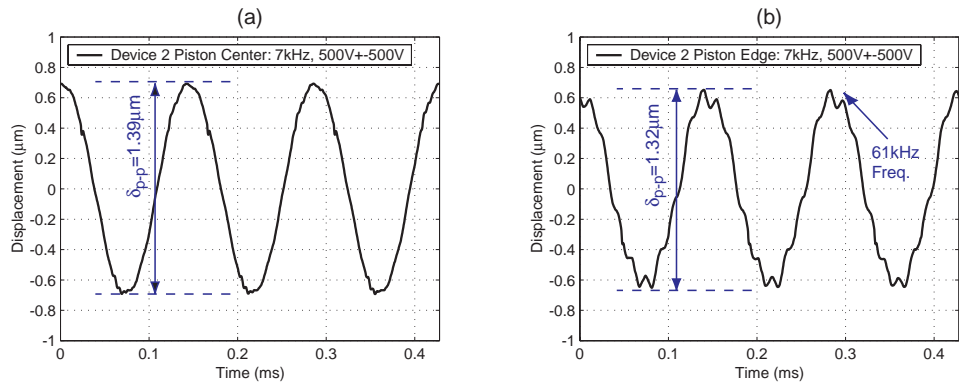


Figure 7.21: Device 2 displacement time histories for a sinusoidal drive voltage of  $500V \pm 500V$  at  $f = 7kHz$ : (a) piston center displacement and (b) piston edge displacement.

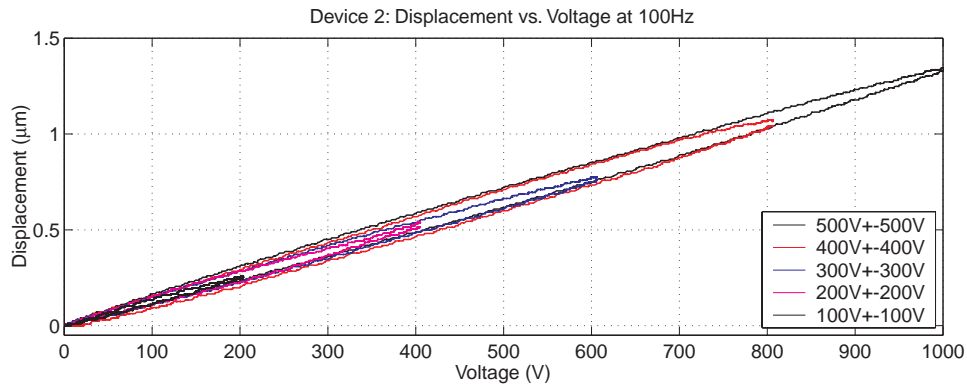


Figure 7.22: Device 2 piston center displacement versus applied voltage at 100Hz.

### Experimental Testing of Device 3

Figure 7.23(a) plots the transfer function of averaged velocity over the scanned piston surface versus frequency for Device 3. Figure 7.23(b) plots these transfer functions for specific locations on the piston surface, at the center and at an outer edge. In comparing this dynamic response to that of Device 1, modal behavior is not observed until frequencies near  $f = 80kHz$ . The placement of multiple cylinders beneath the piston eliminates tilting behavior at frequencies in the 30kHz to 80kHz range. As shown in Figure 7.24, initial modal behavior is characterized by non-symmetric motion of the piston surface, most likely due to unsymmetric placement of the piezoelectric elements beneath the piston, differences in material properties among the elements, or a non-uniform fillet radius profile along the tether circumference. A perfectly symmetric finite-element model of this device predicts 1st modal behavior at 225kHz (see Figure 7.25).

For low-frequency actuation, the multiple piezoelectric cylinder stiffening effect is observed in Figure 7.26 as the displacement profile at 15kHz experiences minimal tilting during actuation. In addition, as shown in Figure 7.27, the displacement time histories at the piston center and piston edge are relatively free from higher order oscillations. A small contribution with frequency  $f \sim 90kHz$  is evident in the piston edge displacement time history. As for Device 1, the magnitude of the piston center displacement in Device 3,  $\delta_{p-p} = 0.72\mu m$ , is slightly lower than the expected range of  $\delta_{p-p} = 0.75 - 0.82\mu m$ .

Figure 7.28 displays the displacement profiles at the piston center and piston edge at a driving frequency of 7kHz. Again, almost perfect displacement behavior free from higher-order oscillations is observed. The overall measured peak-peak deflection at the piston center at 7kHz,  $\delta_{p-p} = 0.76\mu m$ , is within the expected range of  $\delta_{p-p} = 0.75 - 0.82\mu m$ . As was the case for Device 1, the deflection behavior under quasi-static driving conditions (see Figure 7.29) is linear with the applied voltage. Overall, these results indicate that the incorporation of multiple piezoelectric cylinders spread out beneath the tethered piston is achievable.

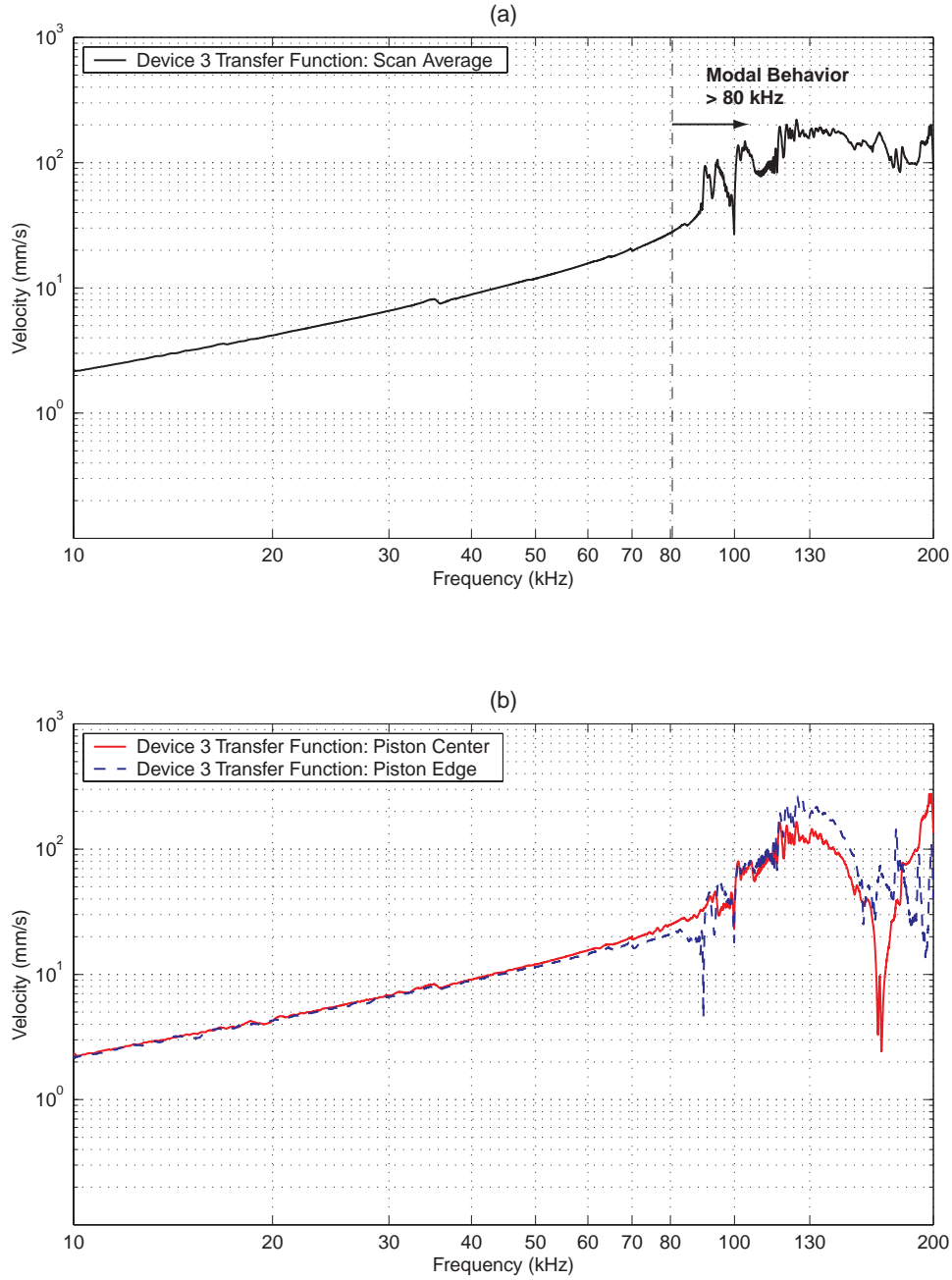


Figure 7.23: Device 3 transfer functions of piston velocity versus frequency for a sweep input from 10kHz to 200kHz and small signal drive voltage  $0V \pm 25V$ : (a) averaged velocity over piston surface, and (b) velocity at center and edge locations on piston surface. Modal behavior is not present below 80kHz. Phase information was not recorded for this device.

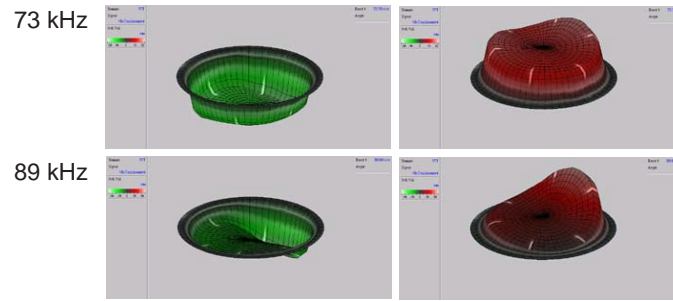


Figure 7.24: Vibrometer scan images of selected Device 3 modal behavior above 70kHz: behavior at 73kHz and 89kHz.

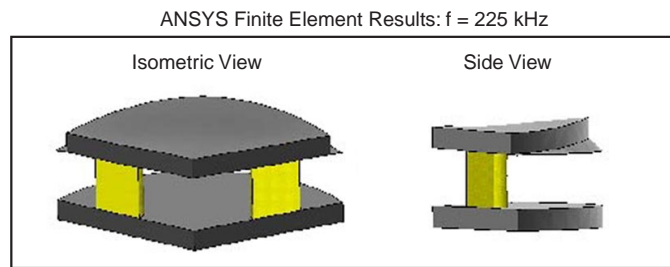


Figure 7.25: Device 3 ANSYS finite-element model prediction for 1st mode shape at 225 kHz.

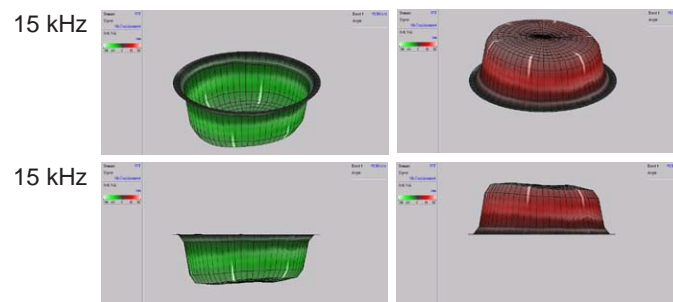


Figure 7.26: Vibrometer scan images of Device 3 low-frequency 15kHz displacement profile. Presence of multiple piezoelectric cylinders beneath piston serves to stiffen actuator structure and reduce tilting behavior.



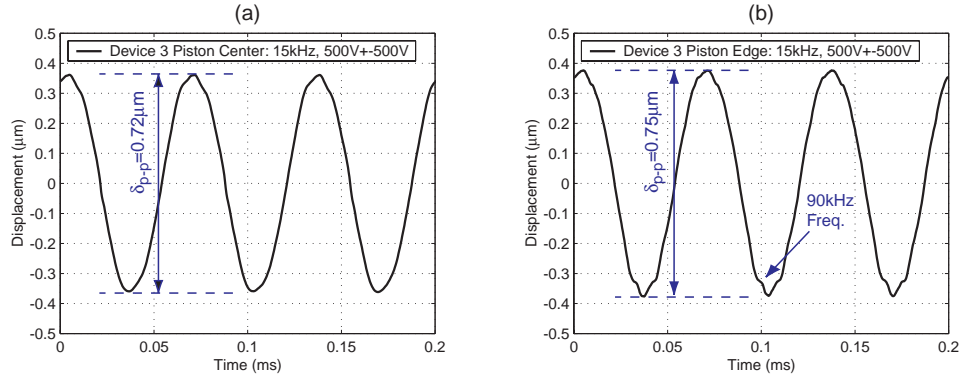


Figure 7.27: Device 3 displacement time histories for a sinusoidal drive voltage of  $500\text{V} \pm 500\text{V}$  at  $f = 15\text{kHz}$ : (a) piston center displacement and (b) piston edge displacement. Note the slight presence of a 90kHz oscillation in the edge displacement time history.

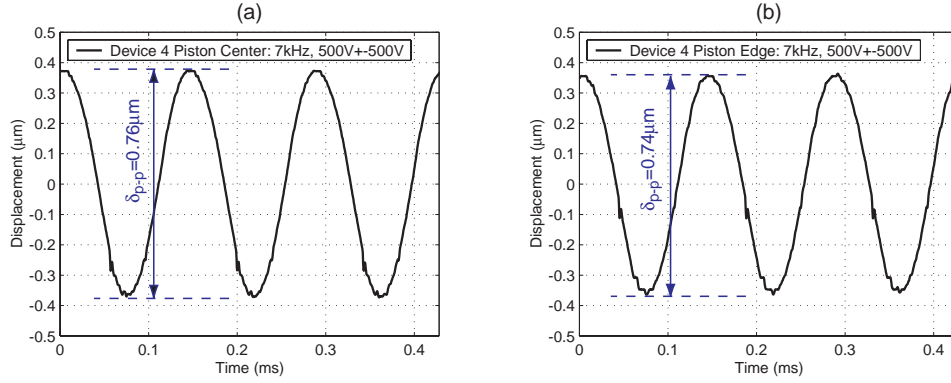


Figure 7.28: Device 3 displacement time histories for a sinusoidal drive voltage of  $500\text{V} \pm 500\text{V}$  at  $f = 7\text{kHz}$ : (a) piston center displacement and (b) piston edge displacement.

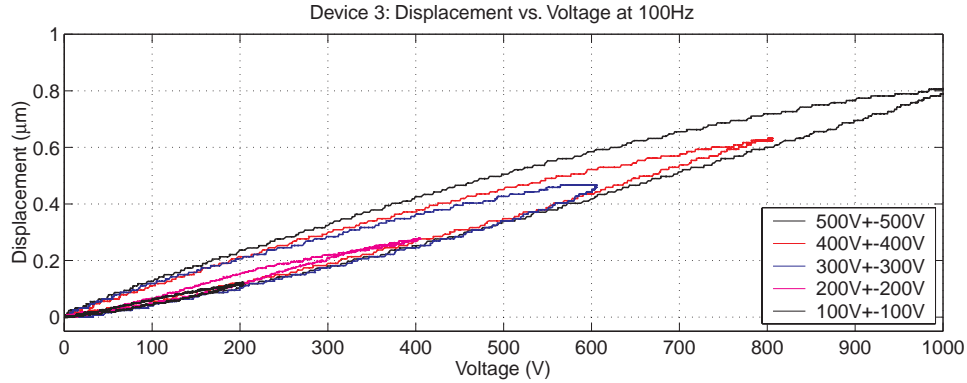


Figure 7.29: Device 3 piston center displacement versus applied voltage at 100Hz.

## 7.5.2 2nd Generation Device

### Measurement of Fillet Radius Profiles

As was performed for the 1st-generation drive element devices, careful inspection of the drive element tethers in Device 4 was also carried out. Since this device incorporates a double-layer piston structure, these inspections were performed prior to wafer-level Si-Si fusion bonding of the piston structure. For the lower piston tethers and upper piston tethers, fillet radii between 25-35  $\mu m$  (ie: tether widths between 180-200  $\mu m$ ) were measured with no observable defects along the tethers, indicating excellent uniformity during the previous DRIE etching procedures.

### Characterization of Piezoelectric Material

PZN-PT material similar to that in the 1st-generation drive element devices was used in Device 4. As a result, the PZN-PT material squares were expected to produce voltage-deflection behavior in the same range as shown in Figure 7.10 (ie: peak deflections at 1000V between 1.35 $\mu m$  and 1.55 $\mu m$ ).

### Experimental Testing of Device 4

Figure 7.30(a) plots the transfer function of averaged velocity over the scanned piston surface versus frequency for Device 4. Figure 7.30(b) plots these transfer functions for specific locations on the piston surface, at the center and at an outer edge. As shown in Figure 7.31, modal behavior begins near 50kHz and is characterized by non-symmetric tilting motion of the piston surface, most likely due to unsymmetric placement of the piezoelectric elements beneath the piston or differences in material properties among the elements. A perfectly symmetric finite-element model of this device predicts 1st modal behavior (piston plunge) at 155kHz and 2nd modal behavior (1- $\Theta$  piston tilting) at 288kHz.

For low-frequency actuation at 15kHz and at a voltage of 1000V peak-peak, the drive element piston experiences minimal tilting (as shown in Figure 7.32), indicating a well-built and toleranced drive element device. The degree of piston tilting is illustrated more clearly in Figure 7.33. The displacement time history at the piston center (Figure 7.33(a)) is very smooth with no higher order oscillations. Likewise, the displacement time histories at the piston edge locations with maximum peak-peak motions (Figure 7.33(b)) are also completely free from higher order oscillations. In comparing the peak-peak deflections of these opposite piston edges, the magnitude of tilt is estimated to be  $\sim 4\%$  of the piston center deflection. The piston center displacement ( $\delta_{p-p} = 1.41\mu m$ ) correlates well with the expected range of  $\delta_{p-p} = 1.35 - 1.55\mu m$ . As was the case for the first generation drive element devices, the deflection behavior under quasi-static driving conditions is linear with the applied voltage. Figure 7.34 illustrates this voltage dependent behavior at 100Hz.

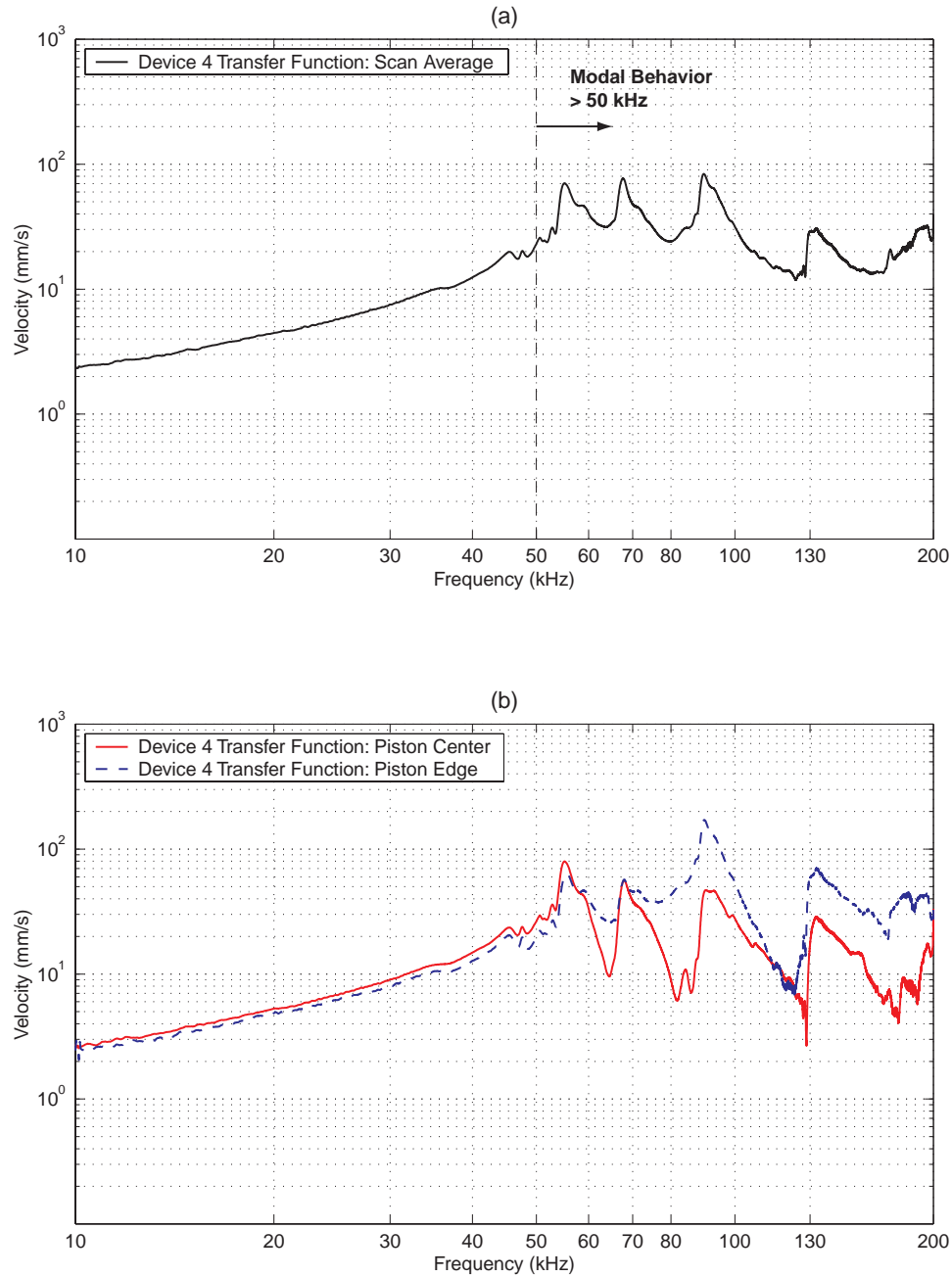


Figure 7.30: Device 4 transfer functions of piston velocity versus frequency for a sweep input from 10kHz to 200kHz and small signal drive voltage  $0V \pm 25V$ : (a) averaged velocity over piston surface, and (b) velocity at center and edge locations on piston surface. Modal behavior is present near 50kHz. Phase information was not recorded for this device.

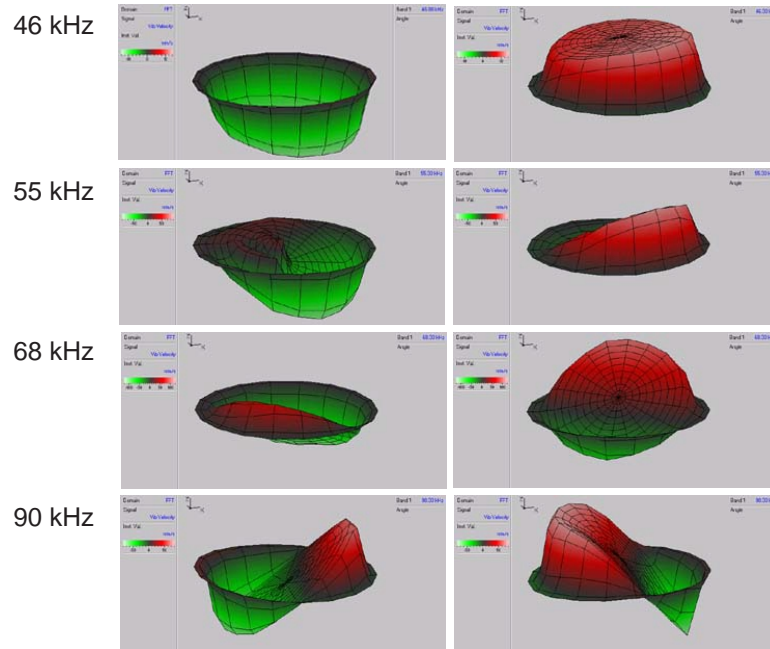


Figure 7.31: Vibrometer scan images of selected Device 4 modal behavior between 45kHz and 90kHz.

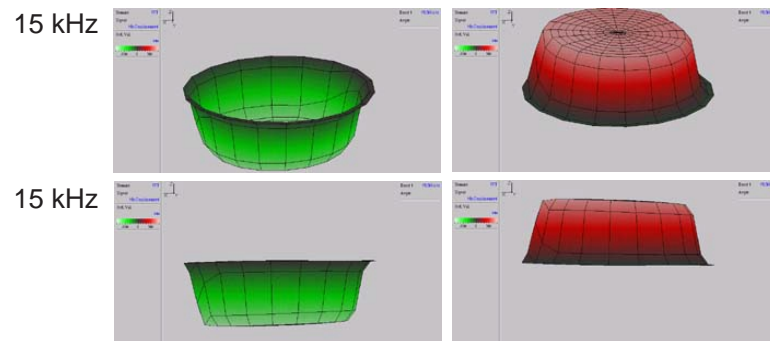


Figure 7.32: Vibrometer scan images of Device 4 low-frequency 15kHz displacement profile. This multiple piezoelectric cylinder device exhibits minimal tilting behavior at 15kHz.

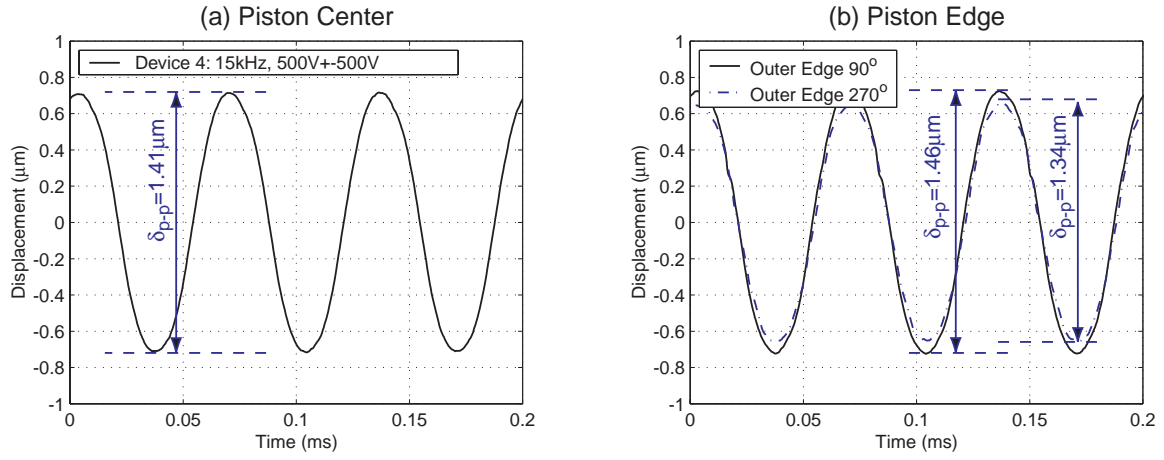


Figure 7.33: Device 4 displacement time histories for sinusoidal drive voltage of  $500V \pm 500V$  at  $f = 15kHz$ : (a) piston center displacement and (b) piston edge displacements. These results indicate a rigid well-toleranced device.

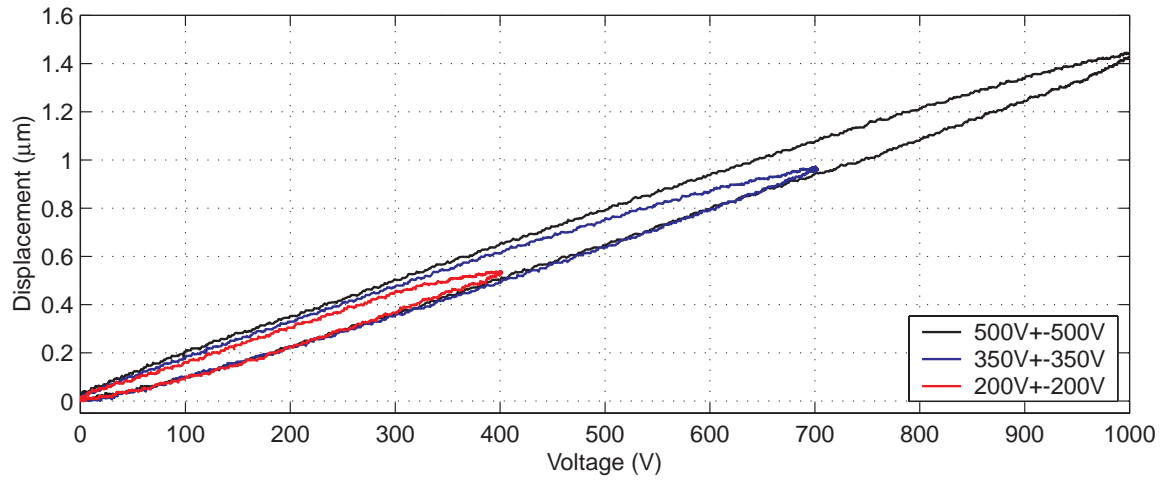


Figure 7.34: Device 4 piston center displacement versus applied voltage at  $100Hz$ .

## 7.6 Conclusions

This chapter has presented the development and testing of a variety of piezoelectric drive element devices. The results indicate that the incorporation of a single centrally-located piezoelectric element and the incorporation of multiple elements spread out symmetrically beneath single-layer and double-layer tethered piston structures can be performed in a repeatable and predictable fashion. Additionally, processing, tolerancing, and drilling/dicing procedures of high performing PZN-PT elements, in addition to standard polycrystalline PZT-5H elements, have been proven. This drive element manufacturing capability serves now as a foundation for the development and assembly of the full active valve devices presented in the following chapters.

# Bibliography

- [1] S.E. Park and T.R. Shrout, "Characteristics of Relaxor-Based Piezoelectric Single Crystals for Ultrasonic Transducers," *IEEE Trans. Ultrasonics, Ferroelectrics, and Frequency Control*, Vol.44, No.5, Sept. 1997, pp. 1140-1147.
- [2] D.C. Roberts, J.L. Steyn, H.Q. Li, K.T. Turner, R. Mlcak, L. Saggere, S.M. Spearing, M.A. Schmidt, and N.W. Hagood, "A High-Frequency, High-Stiffness Piezoelectric Micro-Actuator For Hydraulic Applications," *Proceedings of the 11th International Conference on Solid-State Sensors and Actuators, Munich, Germany, June 10-14, 2001*.





## Chapter 8

# Sub-Component Study: Valve Cap and Membrane

### 8.1 Objectives

The purpose of this study was to evaluate the fabrication process flow of the valve cap and membrane sub-component structure, shown in Figure 8.1, and to experimentally characterize the deflection behavior of a series of these membrane structures to differential pressure loadings. Specifically, the three primary objectives of this study were:

1. To demonstrate the capability to etch valve cap and membrane structures from silicon-on-insulator wafers, with accurate control over the fillet radii at the base of the etch.
2. To experimentally characterize the pressure-deflection behavior of the valve cap and membrane structures, and correlate these results to predictions from the structural models presented in Chapter 3 of this thesis. These structures are pressurized to significant levels at which non-linear large deformation behavior is expected.
3. To provide sensitivity analyses on key geometric parameters such as membrane thickness and fillet radius size to provide an understanding of fabrication process variability on structural pressure-deflection behavior.

Successful fabrication and experimental evaluation of these valve cap and membrane structures enables the further assembly and testing of full active valve devices.

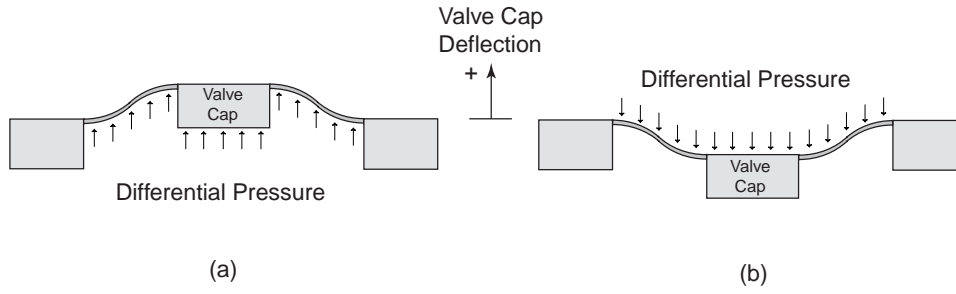


Figure 8.1: 2-D schematic of a valve cap and membrane structure: (a) deformation in response to a positive differential pressure, and (b) deformation in response to negative differential pressure.

## 8.2 Device Test-Plan

### 8.2.1 Geometry

The valve cap and membrane structures fabricated for this study had the dimensions illustrated in Figure 8.2. No valve stop exists above the valve cap in the positive direction (unlike in the full active valve device where the fluid orifice is present) in order to facilitate measurement of the valve cap and membrane deflections from above. However, a valve stop in the negative direction, situated  $15\mu m$  below the underside of the valve cap, does exist. In response to positive differential pressures across the structure (creating positive valve cap deflections), the membrane is therefore unrestrained. In response to negative differential pressures, however, the valve cap deflection is limited to  $-15\mu m$ .

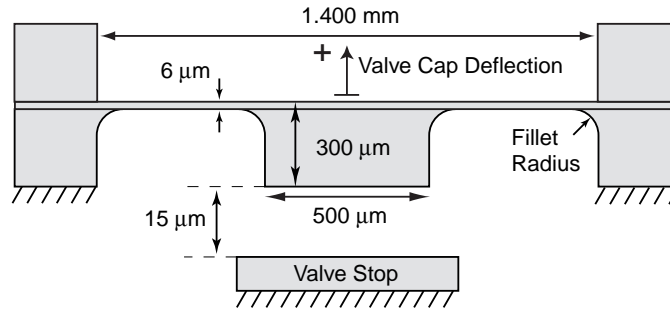


Figure 8.2: Dimensions of the fabricated valve cap and membrane structures: valve cap thickness =  $300\mu m$ , membrane thickness =  $6\mu m$ , valve cap diameter =  $500\mu m$ , and valve membrane outer diameter =  $1.4\text{ mm}$ . Fillet radii are shown in schematic.

### 8.2.2 Device Assembly

As presented in Chapter 7, testing of the valve cap and membrane structure is enabled through fabrication and assembly of the test device illustrated in Figure 8.3. This device consists of Layers N1, N2, N3, 4, 5, 6, N7, N8, and N9. Layers 4, 5, and 6 are identical to those layers used in a full active valve device, however the remaining layers are substituted for the final active valve layers to provide measurement access to the various components. Valve membrane deflection measurements are performed for applied gas pressure to the inside of the HAC chamber and to the top surface of the valve cap and membrane.

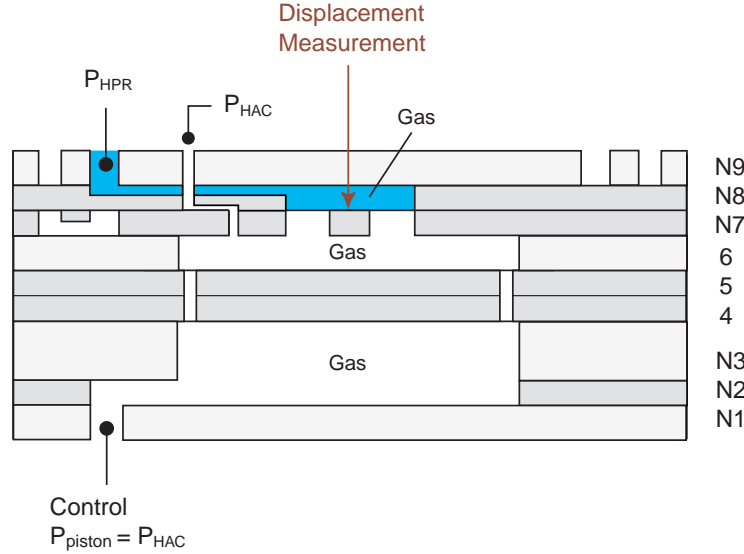


Figure 8.3: Valve cap and membrane sub-component structure. Gas pressure is used above and below the valve structure to obtain pressure-deflection measurements.

### 8.2.3 Testing Procedure

The valve membrane sub-component device was inserted into the fluids test-rig discussed in Chapter 7 for experimental testing. Gas pressure was independently regulated inside of the hydraulic amplification chamber ( $P_{HAC}$ ) and above the valve cap and membrane surface ( $P_{HPR}$ ) so as to provide either a positive or negative differential pressure across the valve cap and membrane structure. The pressure below the unrestrained drive element piston ( $P_{piston}$ ) was maintained at the same value as  $P_{HAC}$  to ensure zero deflection of this structure, thereby minimizing its potential for breaking. Through glass Layer 9, the deflection of the valve cap was monitored using a laser vibrometer system. Differential pressures from -0.40 MPa to 0.40 MPa were imposed on the valve cap and membrane structures and resulting deflection measurements were obtained.

## 8.3 Theoretical Predictions

In order to accurately predict the response of these valve membrane test structures to various pressure loadings, detailed modeling of the non-linear deflection behavior is required. In addition, sensitivity analyses on the membrane thickness and the fillet radius size are necessary to understand potential differences between predicted and experimental behavior. To accomplish these objectives, two parallel modeling procedures were implemented. The first procedure uses the numerical non-linear deflection code presented in Chapter 3 of this thesis to understand the effects of varying membrane thickness on the deflection behavior of the structure. Because this code is based on simplified plate theory, it does not include fillet radii geometries. As a result, a second procedure is implemented to develop finite-element models of the valve cap and membrane structures, which incorporate fillet radius features. Through the use of both modeling procedures, thorough understanding of the experimental results can be obtained.

### 8.3.1 1st Modeling Procedure: Numerical Non-linear Deflection Code

The Matlab<sup>TM</sup> codes, DAVE80200NLValveCaseA.m and DAVE80200NLValveCaseC.m (previously discussed in Chapter 3 and included for reference in Appendix B), are combined to capture the behavior of the valve cap and membrane structure for positive and negative differential pressure loadings. The results are discussed in the following sub-sections.

#### Baseline Design Pressure-Deflection Behavior

Figure 8.4 plots the valve cap deflection and maximum membrane tensile stress as a function of applied differential pressure from -0.40 MPa to 0.40 MPa. Results for linear and non-linear theory are shown. In comparing these curves, it is clear that non-linear deformation theory is required for accurate prediction of the valve membrane structural behavior. For the peak positive differential pressure of 0.40 MPa, a valve cap deflection of 22.6  $\mu m$  and corresponding maximum membrane stress of 1.06 GPa are predicted. Due to the presence of a valve stop in the negative direction, a valve cap deflection of -15  $\mu m$  and a corresponding maximum membrane stress of 1.00 GPa are predicted for an applied differential pressure of -0.40 MPa.

#### Sensitivity to Valve Membrane Thickness

Although the valve cap and membrane structures tested in this study have measured membrane thicknesses between 6  $\mu m$  and 7  $\mu m$ , these measurements are only accurate to within  $\pm 1 \mu m$ . As a result, it is important to predict the structural behavior over a range of membrane thickness. Figure 8.5 plots the valve cap deflection and maximum membrane tensile stress as a function of applied differential pressure from -0.40 MPa to 0.40 MPa for membrane thicknesses of 6  $\mu m$ , 7  $\mu m$ , and 8  $\mu m$ . In comparison to predictions for the 6  $\mu m$  membrane (valve cap deflection=22.6

$\mu m$ ), the 7  $\mu m$  membrane is predicted to deflect 20.8  $\mu m$  (8 % difference), and the 8  $\mu m$  membrane is predicted to deflect 19.6  $\mu m$  (13 % difference) for an applied differential pressure of 0.40 MPa. The corresponding stresses also differ by similar percentages. Based on these predictions, variations in membrane thickness should not drastically effect structural behavior, although it is an important fabrication uncertainty to keep in mind.

### **Sensitivity to Membrane In-Plane Prestress**

During fabrication procedures of the valve cap and membrane structures, the oxide above the membrane is stripped. Ideally, this procedure should eliminate any residual stress contained within the membrane structure. However, other procedures, such as anodic bonding of device layers, could potentially create residual stresses along the valve membrane due to thermal expansion mismatch between the silicon and pyrex layers. Calculations have indicated that these valve membrane structures will experience at most a residual tensile stress of 5 MPa for an anodic bonding temperature of up to 330C (50C above the ideal matched anodic bonding temperature of 280C) [1], a stress which has negligible effect on the stiffness of the valve membranes structures in response to pressure loading. As a result, since the anodic bonding procedures in this thesis are always carried out at 300C, these valve membranes should be free of residual tensile stress.

### **8.3.2 2nd Modeling Procedure: Finite-element Code**

Finite-element models have been developed that incorporate fillet radius features along the inner and outer circumference of the valve membrane. Figure 8.6 displays a mesh of the valve cap and membrane geometry, with detailed focus on the meshing grid around the fillet radius features. In this figure, the fillet radius has size 30 $\mu m$ . Figure 8.7 shows a representative stress contour plot of the structure when subjected to a positive differential pressure of 0.30MPa.

### **Sensitivity to Fillet Radius Size**

Using these finite-element models, valve cap deflection and maximum membrane stress plots as a function of varying fillet radius are acquired, as shown in Figure 8.8. The fillet radius at the inner and outer valve membrane circumference is varied to be 15  $\mu m$ , 30  $\mu m$ , 45  $\mu m$ , and 60  $\mu m$ . As evidenced in the plots, an increase in the fillet size serves to stiffen the overall membrane structure, resulting in reduced valve cap deflections. For example, for an applied differential pressure of 0.40 MPa, the valve cap with fR=15 $\mu m$  experiences a deflection of almost 23  $\mu m$  whereas the valve cap with fR=60 $\mu m$  experiences a deflection of approximately 20  $\mu m$ . The maximum membrane stress curves follow a similar pattern. In the valve cap and membrane

experiments discussed later in this chapter, careful inspection of the membrane fillet radii is performed prior to testing to enable understanding of the structural behavior.

### **Note on Theoretical Predictions**

The presence of a fillet radius along the valve membrane inner and outer membrane surfaces clearly has an effect on the structural stiffness, as evidenced in comparing Figures 8.5 and 8.8. For very small fillet radius sizes, these features act as stress concentrations. As such, the finite-element models with small fillet radii predict stresses significantly larger than those predicted by the numerical code (which includes no effect of fillet radii). Conversely, the finite-element models with large fillet radii predict smaller stresses than those predicted by the numerical code, mainly because the fillet structure actually results in a stiffening of the membrane and a subsequent reduction in the deflection magnitude of the valve cap. The fillet radii features present on the fabricated valve membrane structures discussed in the following experimental section were able to be controlled to within  $35 - 50\mu m$ , a range which is characterized by reasonably good correlation between finite-element and numerical pressure-deflection predictions. As such, when comparing experimental pressure-deflection behavior with theory in the following section of this chapter, the numerical predictions will be used.

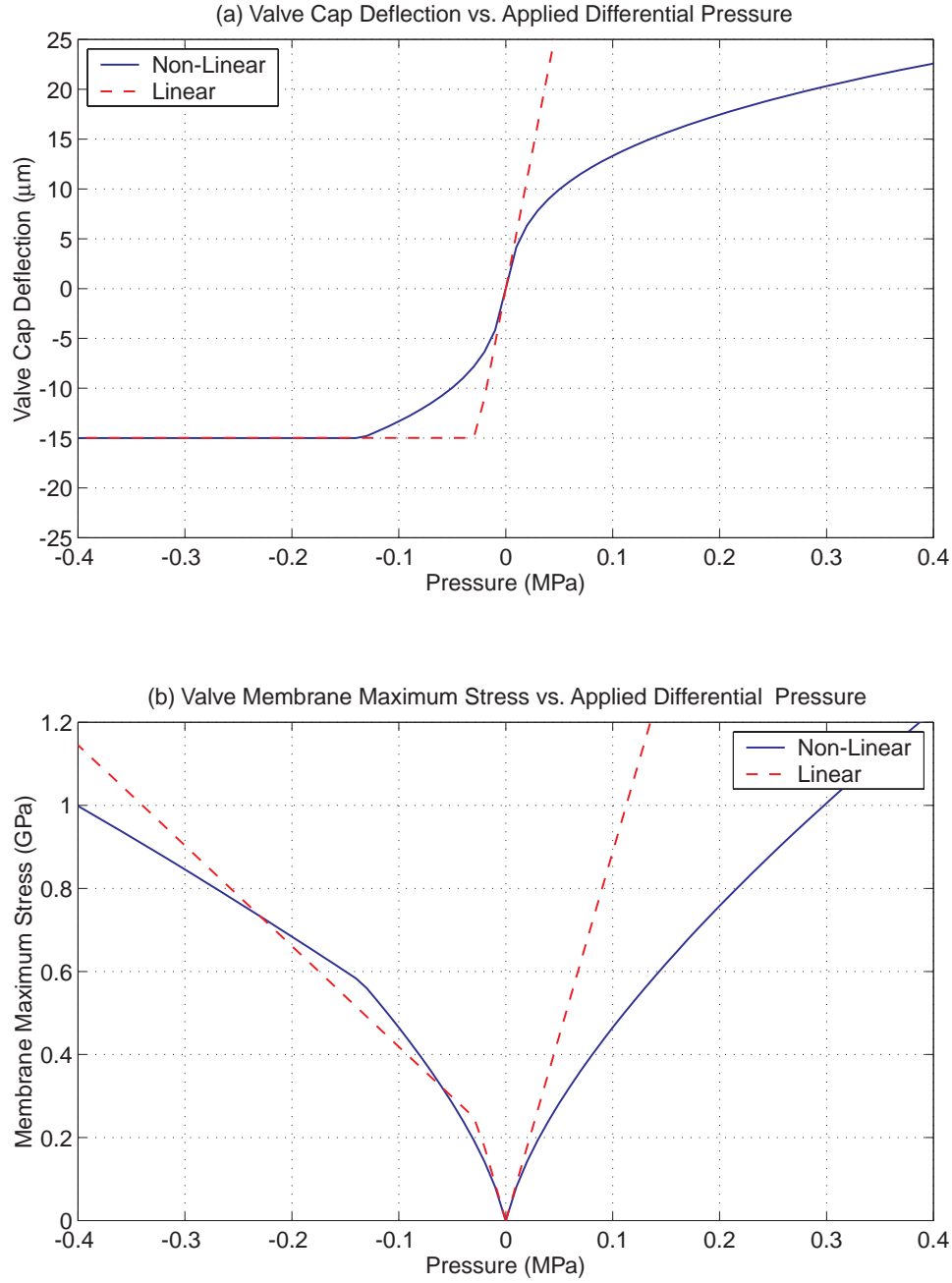


Figure 8.4: Baseline valve cap and membrane design  $\rightarrow r_{vc} = 250\mu\text{m}$ ,  $r_{vm} = 700\mu\text{m}$ ,  $t_{vm} = 6\mu\text{m}$ : (a) valve cap deflection vs. applied differential pressure, and (b) maximum stress in valve membrane vs. applied differential pressure. Note: valve stop present at  $-15\mu\text{m}$ .

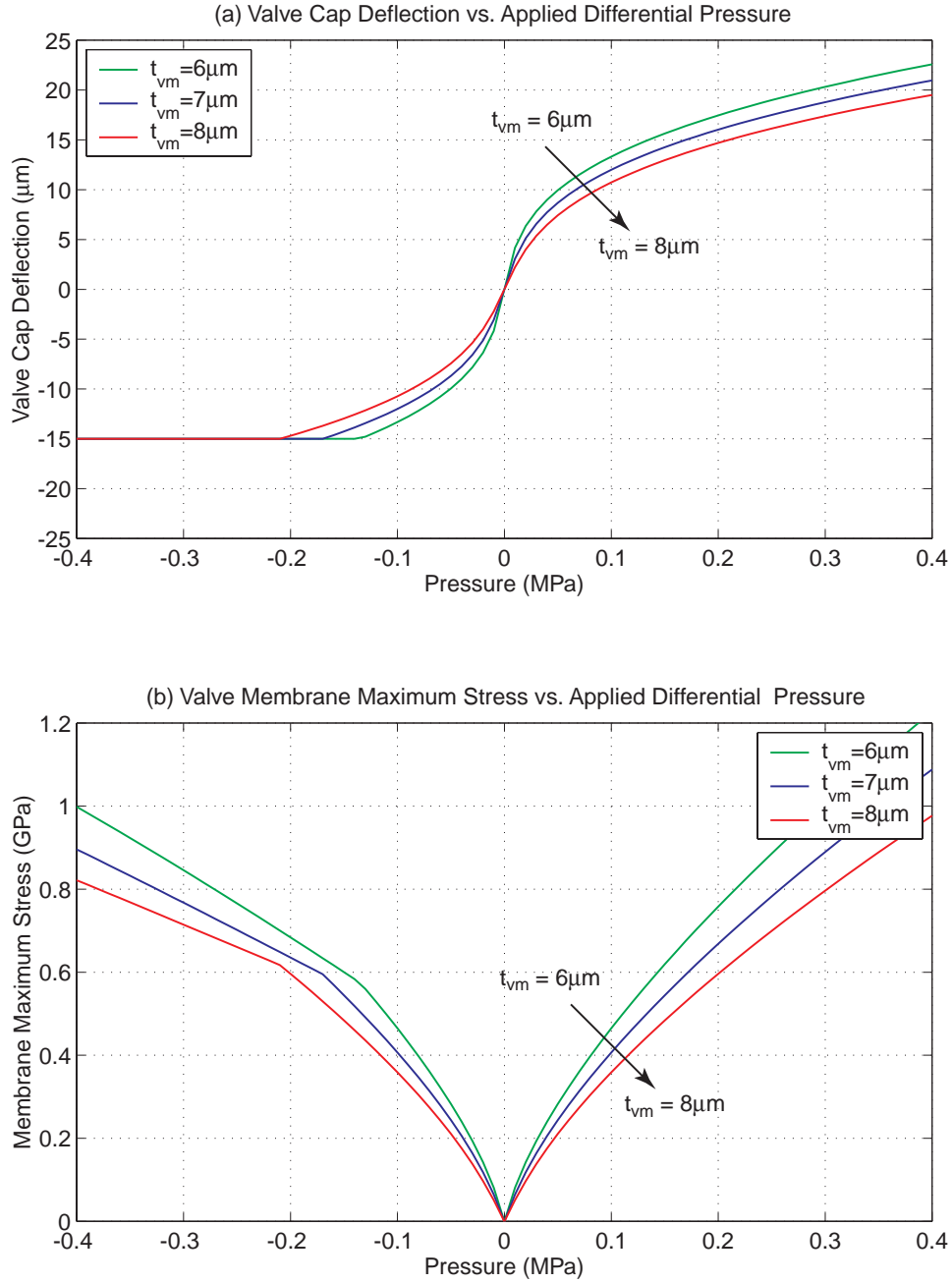


Figure 8.5: Sensitivity of baseline valve cap and membrane design to variations in valve membrane thickness  $\rightarrow r_{vc} = 250\mu\text{m}$ ,  $r_{vm} = 700\mu\text{m}$ ,  $t_{vm} = [6\mu\text{m}, 7\mu\text{m}, 8\mu\text{m}]$ : (a) valve cap deflection vs. applied differential pressure, and (b) maximum stress in valve membrane vs. applied differential pressure. Note: valve stop present at  $-15\mu\text{m}$ .



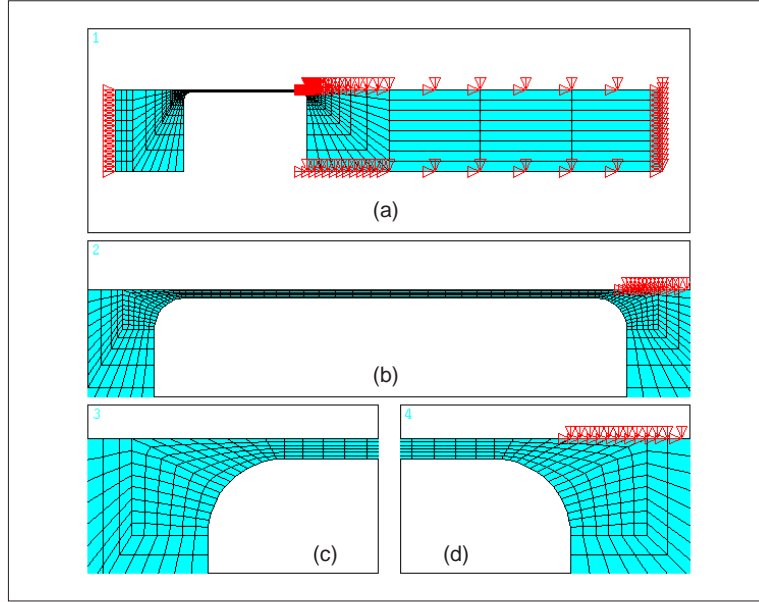


Figure 8.6: Finite-element mesh (ANSYS<sup>TM</sup>) of valve cap and membrane structure: (a) full view of 2-D axisymmetric model, (b) close-up view of membrane, (c) close-up view of inner fillet radius, and (d) close-up view of outer fillet radius.

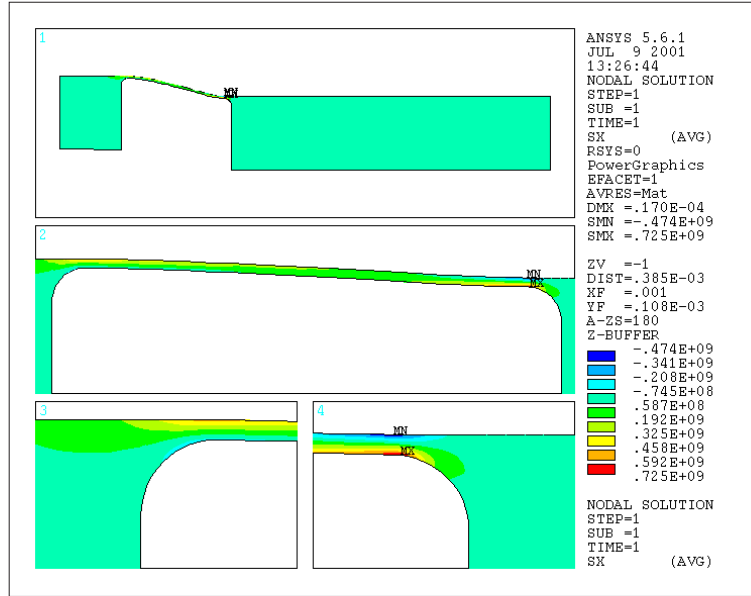


Figure 8.7: Finite-element stress contours resulting from applied differential pressure loading of 0.30 MPa. Fillet radii in model are  $fR = 30\mu m$ . Peak tensile stress (0.868 MPa) occurs at base of fillet radius along outer membrane circumference.

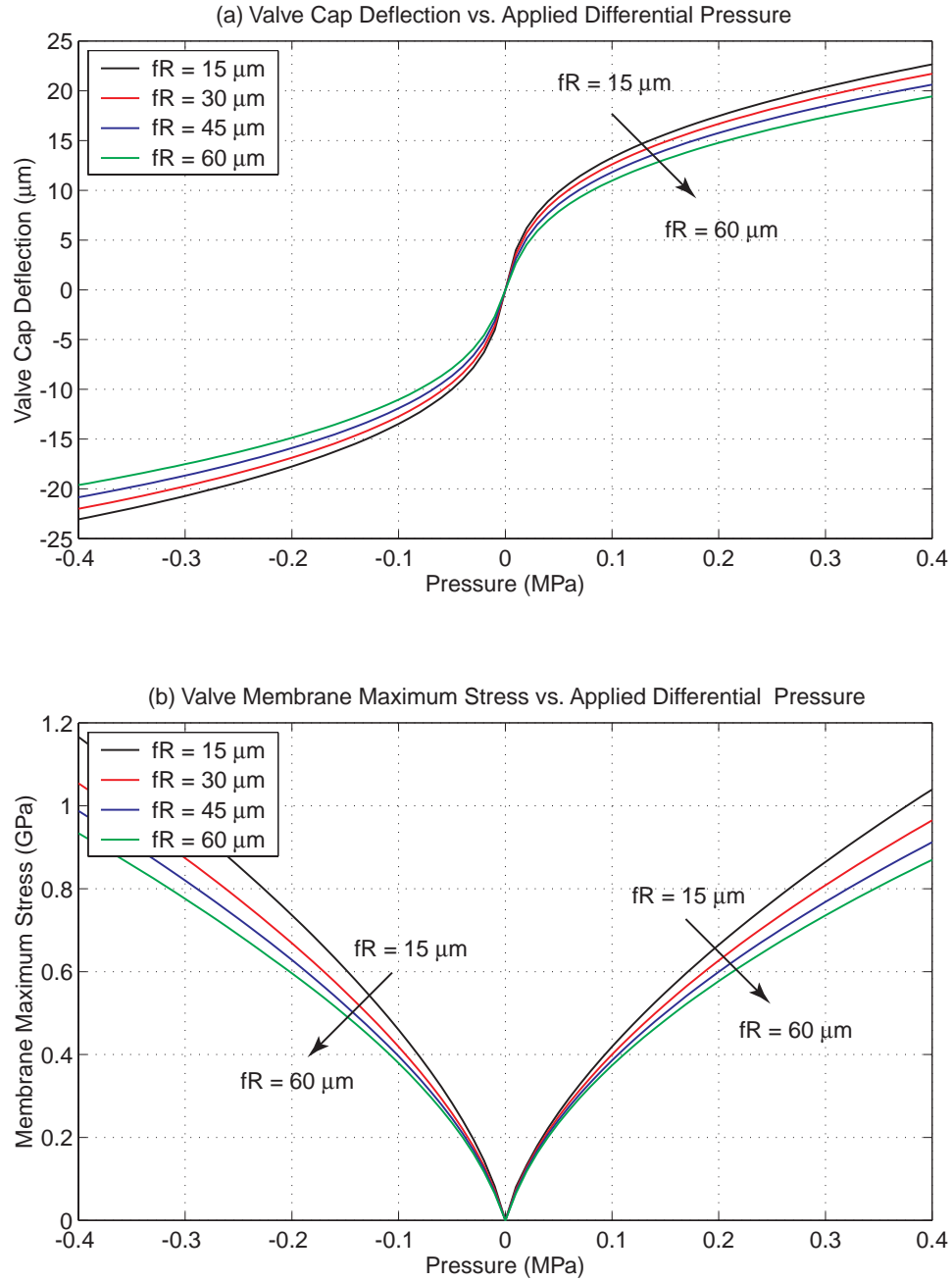


Figure 8.8: Sensitivity of baseline valve cap and membrane design to variations in fillet radius size  $\rightarrow r_{vc} = 250\mu m$ ,  $r_{vm} = 700\mu m$ ,  $t_{vm} = 6\mu m$ ,  $fR=[15\mu m, 30\mu m, 45\mu m, 60\mu m]$ : (a) valve cap deflection vs. applied differential pressure, and (b) maximum stress in valve membrane vs. applied differential pressure. Note: valve stop at  $-15\mu m$  not implemented in this finite-element model.

## 8.4 Experimental Results

Three representative valve cap and membrane sub-component structures (referred to as Valve Membrane 1, Valve Membrane 2, and Valve Membrane 3 in subsequent discussions) were experimentally tested to validate structural behavior. Prior to testing and before die-level bonding of Stack 4-5-6 to Stack N7-N8-N9, inspection of the valve membrane fillet radii in Layer N7 was performed. This section details these inspections, as well as the experimental pressure-deflection results for each of these membrane structures.

### 8.4.1 Fillet Radius Inspection

Each of the three representative valve membrane structures was inspected for the presence of defects along the etched membrane and for consistency in fillet radius size. Valve Membrane 1 possessed a consistent fillet radius size of 45-50  $\mu m$  and no defects along the membrane. Valve Membrane 2 possessed a consistent fillet radius size of 40-50  $\mu m$  and no defects along the membrane. And similarly, Valve Membrane 3 possessed a fillet radius size of 35-40  $\mu m$  and no defects along the membrane. Overall, these three valve membrane structures well represent the majority of etched valve membrane structures in their fillet radius consistency and lack of defects.

### 8.4.2 Pressure-Deflection Results

In order to determine the pressure-deflection behavior of these valve membrane structures, a pressure time history was imposed on the structure using a valve and pressure sensor set-up and the valve cap deflection was measured using a laser vibrometer system. Figure ?? overlays the pressure-deflection results for Valve Membranes 1, 2, and 3 with the structural predictions for  $t_{vm} = 6\mu m$  and  $t_{vm} = 7\mu m$  presented previously. Overall, all three membrane structures correlate well with each other and with predictions. Note that the valve membrane stops vary between -15 and -16  $\mu m$  due to non-uniform etch depths during fabrication.

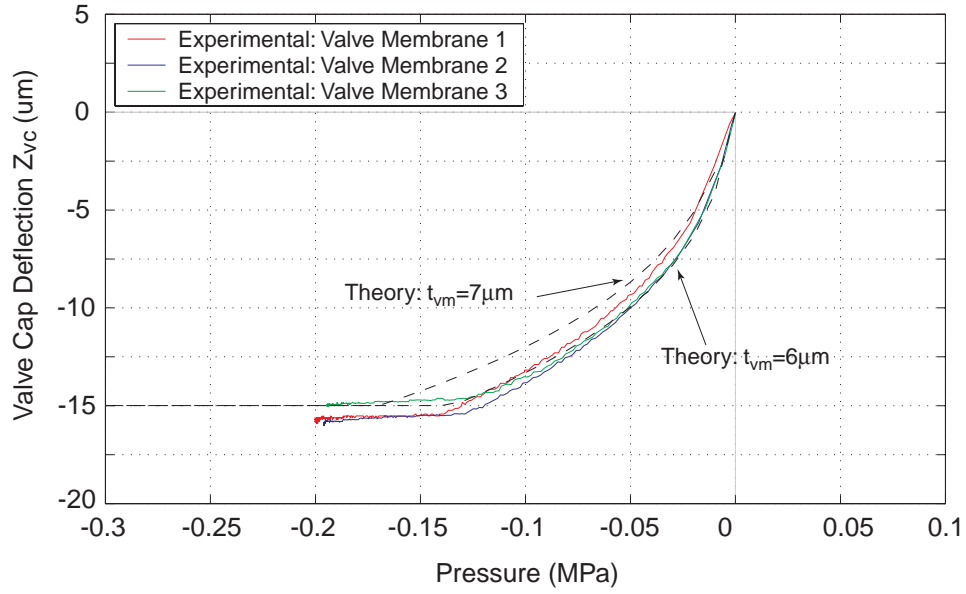


Figure 8.9: Valve cap and membrane experimental pressure-deflection results compared to theoretical expectations. The three representative valve cap and membrane structures correlate well with each other and with predicted behavior. Note that valve stops vary between  $-15$  and  $-16 \mu m$  due to non-uniformity in etching these features.

## 8.5 Conclusions

This chapter has presented successful correlation between valve membrane structural behavior and modeling predictions. Representative valve membranes that possessed consistent fillet radius profiles around the membrane and the absence of any significant etch defects were experimentally characterized. Pressure-deflection results correlate extremely well with predicted behavior obtained using finite-element models and the non-linear deformation code presented in Chapter 3. Overall, this chapter has verified that these valve membrane structures can be consistently fabricated for use in full active valve devices, and that these structures exhibit expected pressure-deflection behavior.

# Bibliography

- [1] Corning web information on the thermal expansion behavior of Pyrex 7740 and its use with Silicon for anodic bonding. (<http://www.corning.com/lightingmaterials/waferglass.html>)



## Chapter 9

# Active Valve Testing

### 9.1 Objectives

The purpose of this testing study was to evaluate the quasi-static and dynamic structural performance of the complete active valve device and to determine its limitations in regulating the flow of fluid against imposed differential pressures. Specifically, the four primary objectives of this study are:

1. To understand the dynamic behavior of the active valve device and to determine the range of driving frequency for which the valve behaves in a quasi-static manner. In essence, this goal focuses on locating the resonant frequencies of the structure. The effect of having or not having fluid present in the flow channel above the valve cap and membrane on the onset of valve resonant behavior is determined.
2. To evaluate the amplification ratio of the active valve structure under a variety of voltage levels and internal and external bias pressures for a driving frequency below resonance to ensure quasi-static operation. This is accomplished by measuring the drive piston and valve cap deflections under conditions that force the valve cap through its full stroke of operation, including interaction with the valve stops above and below the valve cap.
3. To characterize the differential pressure-flow rate curves for the valve cap and orifice geometry of the active valve device. This is accomplished by measuring an average fluid flow rate through the valve orifice as a function of valve cap opening downward from the upper valve stop. Motion of the valve cap through its stroke is controlled at a very slow rate to achieve quasi-static measurements of flow rate at given valve openings.
4. To characterize the dynamic capability of the active valve structure in regulating fluid flow against a preset differential pressure across the valve at a driving frequency below resonance to ensure quasi-static operation. Successful operation of the valve structure in

this manner proves its capabilities as a flow regulation device. A further goal is to identify the limiting differential pressures against which the active valve can function.

## 9.2 Device Test-Plan

### 9.2.1 Geometry

A schematic of the fabricated active valve device is illustrated in Figure 9.1. The device incorporates three PZN-PT piezoelectric square elements (each with cross-sectional area 1.06mm x 1.06mm) beneath a double-layer tethered piston structure. The top and bottom tethers of the piston are each 250 $\mu$ m in width and each have a thickness of 8 $\mu$ m. A valve cap and membrane structure is positioned above the hydraulic amplification chamber, with a structural stop (formed by the glass Layer 6 within the HAC chamber)  $\sim$  16.5 $\mu$ m below the equilibrium position of the valve cap. Glass Layer 6 contains a series of “HAC through-holes” and “HAC radial channels” to carry the fluid from the lower to upper portion of the HAC chamber. The valve cap has a diameter of 500  $\mu$ m and the valve membrane has an outer diameter of 1400  $\mu$ m. A valve orifice is located  $\sim$  16.5 $\mu$ m above the valve cap equilibrium position. The orifice has an inner diameter of 450 $\mu$ m. The drive element piston structure is consistent with the 2nd-generation drive element devices (except for the use of slightly reduced-area square piezoelectric elements) fabricated and tested as part of the drive element sub-component study detailed in Chapter 7. In addition, the valve cap and membrane structure is consistent with the valve structures fabricated and tested as part of the valve cap and membrane sub-component study detailed in Chapter 8.

### 9.2.2 Plan of Study

As detailed in the introduction to this chapter, the characterization of each active valve device was carried out through a series of four experimental testing studies. The first two studies focus on the dynamic and quasi-static behavior of the active valve structure, while the second two studies focus on the fluid flow regulation capability of the structure. In evaluating these objectives, numerous active valve devices were built. Two of these devices are covered in detail in this chapter (and thesis). The first active valve device (subsequently referred to as device AV1) successfully made it through the majority of all four testing studies. It failed during an experiment to determine its limitations in regulating high pressure flows. The second device (subsequently referred to as device AV2) broke during completion of the first two studies, and as a result, no flow regulation data was taken for this device. A discussion of this failure is described in the chapter. This chapter is organized into two primary sections, in accordance with these experimental testing studies. The first section details the results of the dynamic and



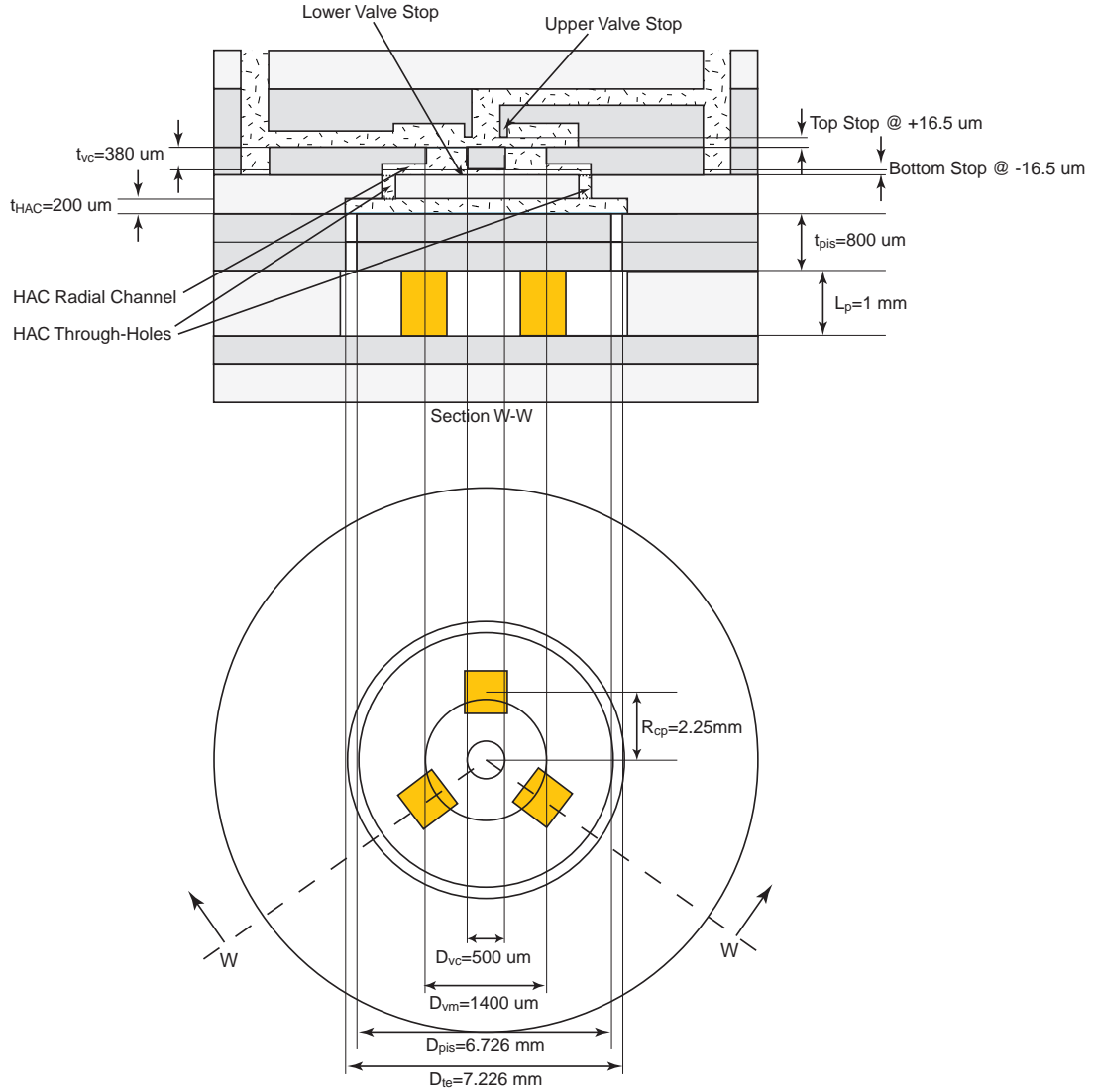


Figure 9.1: Dimensions of active valve devices AV1 and AV2. Three square PZN-PT elements are incorporated beneath a double-layer tethered piston. A valve cap and membrane structure interacts with the fluid orifice structure at  $Z_{vc} = +16.5\mu m$  and with the glass Layer 6 structure within the HAC chamber at  $Z_{vc} = -16.5\mu m$ . In the lower figure, only geometries beneath the valve cap structure (ie: beneath Layer 7) are detailed.

quasi-static active valve testing studies (for both device AV1 and device AV2), and the second section covers the valve flow regulation studies (for device AV1).

## 9.3 Experimental Testing Section 1: Active Valve Structural Performance

### 9.3.1 Testing Section 1: Active Valve Structural Performance

To characterize the frequency dependant behavior of each active valve device, the following tests were performed. A low-voltage ( $0V \pm 5V$ ) sweep signal from 500Hz to 100kHz was applied to the piezoelectric drive element structure. The corresponding valve cap and piston displacements were measured using a laser scanning vibrometer system. The effect of bias pressure (ie:  $P_{bias} = P_{HAC} = P_1 = P_2$ , where  $P_{bias} \geq 0$ ), up to 500 kPa, on the frequency response of the active valve device was evaluated. Additionally, higher-voltage (up to  $600V_{pp}$ ) sweep signals were applied over a lower range of frequency from 500Hz to 3kHz to evaluate the valve cap and piston behavior in a range of quasi-static frequencies below resonance.

To characterize the quasi-static behavior of each active valve device, a series of tests was run at a chosen frequency of operation (ie: 1kHz for these tests) sufficiently below the resonant frequency to ensure quasi-static structural behavior. The effects of increasing voltage and increasing bias pressure on the device amplification ratio were determined. Additionally, the capability of the device to open and close the valve cap against the fluid orifice was evaluated.

#### Active Valve Device AV1

Figures 9.2 through 9.7 display the structural testing results for active valve device AV1. Figure 9.2 plots the valve cap frequency response from 500Hz to 100kHz for an applied low-voltage sweep signal of  $0V \pm 5V$  under the condition that silicon oil is not present above the valve cap and membrane structure and under the condition that silicon oil is present above the valve cap and membrane structure. These tests were performed with  $P_{bias} = 500kPa$  to ensure that cavitation of the fluid within the HAC did not occur. Without oil, the resonant frequency of the structure is 10kHz. With oil, this frequency drops to slightly less than 5kHz. This reduction is due to the added mass of the fluid on the top surface of the valve cap and membrane. It is interesting to notice the presence of numerous resonant peaks (at 6.5kHz and 8kHz), in addition to the primary resonant peak at 5kHz, for the response with oil. Without oil, no additional resonant behavior is observed beyond the primary 10kHz resonance until approximately 40kHz. The additional peaks in the response with oil present are most likely a result of fluid-structure interactions between the oil and the experimental test-jig flow tubes external to the device or between the oil and the flow channels internal to the device. Pressure waves could be interacting within these channels and affecting the valve behavior. Additionally, the primary resonant peak of the response (at 5kHz) with oil above the structure is not as sharp as that without oil, due to the increased damping introduced by the fluid within the system. Based on the experimental

resonant peak amplitude, in comparison to expected behavior determined from the active valve model described in Chapter 5, the damping ratio of this structure is estimated to be 0.16.

Figure 9.3 overlays the frequency response of the drive element piston with that of the valve cap, for the case in which oil is present above the valve structure at the same operating conditions as previously described. The piston response exhibits the same resonant peak behavior as the valve cap response. The increase in piston displacement amplitude at frequencies below 1kHz is due to measurement limitations in the vibrometer system (essentially the magnitude of the measured velocities and displacements are of the same order as the noise floor of the system). The results indicate that the amplification ratio of the valve device is steady (between 40x-50x) over the range of frequencies below resonance.

Figure 9.4 plots the low-voltage valve cap frequency response from 500Hz to 100kHz for a varying bias pressure from  $P_{bias} = 100kPa$  to  $P_{bias} = 500kPa$ . For the PZN-PT material integrated within these valve devices, material testing results by Lin [1] indicate that the piezoelectric material strain capability degrades near a compressive stress of 10MPa. For the geometry of these active valve devices tested, a bias pressure of  $P_{bias} = 500kPa$  correlates to a compressive stress on the piezoelectric square elements beneath the piston of approximately 6.1MPa. These bias pressure tests therefore evaluate whether degradation occurs up to 6.1MPa. Higher bias pressure tests were to be performed following the completion of all four major testing sections. Clearly from the results, a variation in  $P_{bias}$  from 100kPa to 500kPa has no noticeable effect on the frequency response of the structure. Again, the upper limit to  $P_{bias}$  was not evaluated until all other experimental tests on the active valve device were completed, for safety reasons, to minimize potential breakage of the device.

Each of the previous frequency sweeps was carried out with the valve cap and membrane structure at its equilibrium position (zero deflection upward or downward) by ensuring that the pressures above the valve cap and membrane structure ( $P_1$  and  $P_2$ ) were identical to the pressure within the hydraulic amplification chamber ( $P_{HAC}$ ). Under these conditions, in order to close the valve cap against the valve orifice (+16.5 $\mu m$  above this equilibrium position) during quasi-static sinusoidal operation, a large voltage on the piezoelectric drive element could be required. Another potential way of operating the active valve device to ensure that the valve cap can close against the valve orifice for lower operating voltages is to impose a differential pressure (referred to as  $\Delta P_{vc,vm} = P_{HAC} - P_1$ , where  $P_1 = P_2$  for example) across the valve cap and membrane structure to create a positive offset deflection of the valve cap about which oscillation can then occur. This method reduces the overall stroke of the valve cap (due to the non-linearity of the valve membrane - see next paragraph), but ensures valve closure against the orifice. To evaluate this alternative operation concept on the resonant behavior of active valve device, additional low-voltage frequency sweeps were carried out with  $\Delta P_{vc,vm} = 20kPa$  and  $\Delta P_{vc,vm} = 50kPa$ , which produce offset valve cap displacements of  $Z_{vc} \sim +6\mu m$  and  $Z_{vc} \sim +10\mu m$  respectively.

Figure 9.5 compares the results.

With increasing offset displacement of the valve cap above its equilibrium position, the effective stiffness of the valve membrane structure for low-voltage (and therefore low amplitude) oscillations should increase since the membrane moves into its large-deflection regime. As a result, one would expect the resonant peak to shift to a increased frequency (due to the higher stiffness) and the magnitude of this peak to be reduced (also due to the higher stiffness). As shown in Figure 9.5(a), both of these results are clearly observed. As  $\Delta P_{vc,vm}$  is increased from 0kPa to 20kPa to 50kPa, the resonant peak increases from  $\sim 5kHz$  to  $\sim 6kHz$  to  $\sim 6.5kHz$ , respectively. Additionally, the valve cap oscillation amplitude decreases from  $\sim 4\mu m$  to  $\sim 1.6\mu m$  to  $\sim 0.8\mu m$  for this increase in  $\Delta P_{vc,vm}$ . This amplitude reduction is most clearly seen in Figure 9.5(b), which plots the amplitude on a linear scale. High-voltage quasi-static active valve operation under these differential pressure conditions is discussed further in the later half of Testing Section 1.

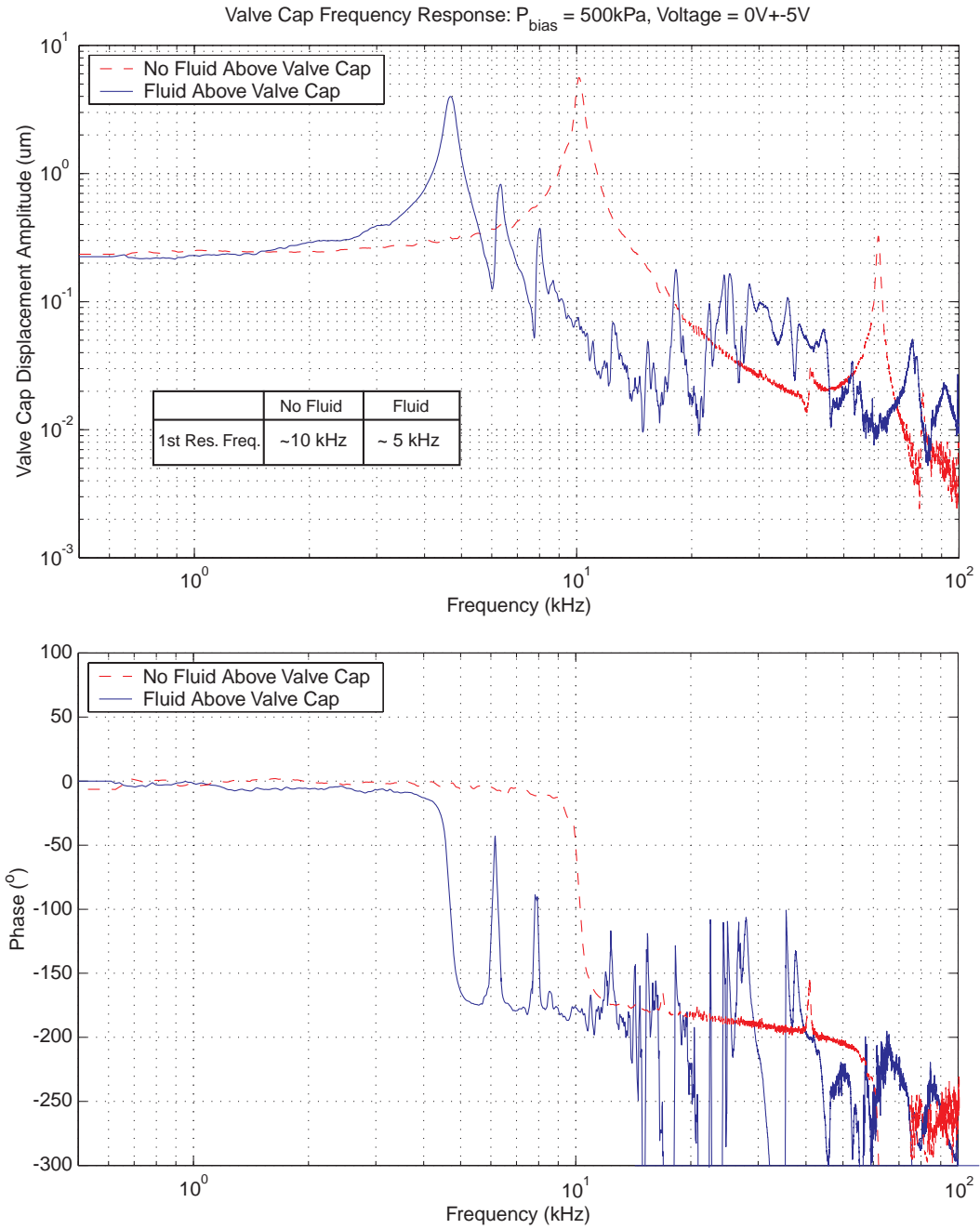


Figure 9.2: Device AV1 low-voltage ( $0V \pm 5V$ ) valve cap frequency response from 500Hz to 100kHz, with and without oil present above the valve structure. The bias pressure in these tests was maintained at  $P_{bias} = 500\text{kPa}$ . The presence of oil in the flow channel above the valve cap creates an added mass that reduces the resonant frequency from 10kHz to 5kHz.

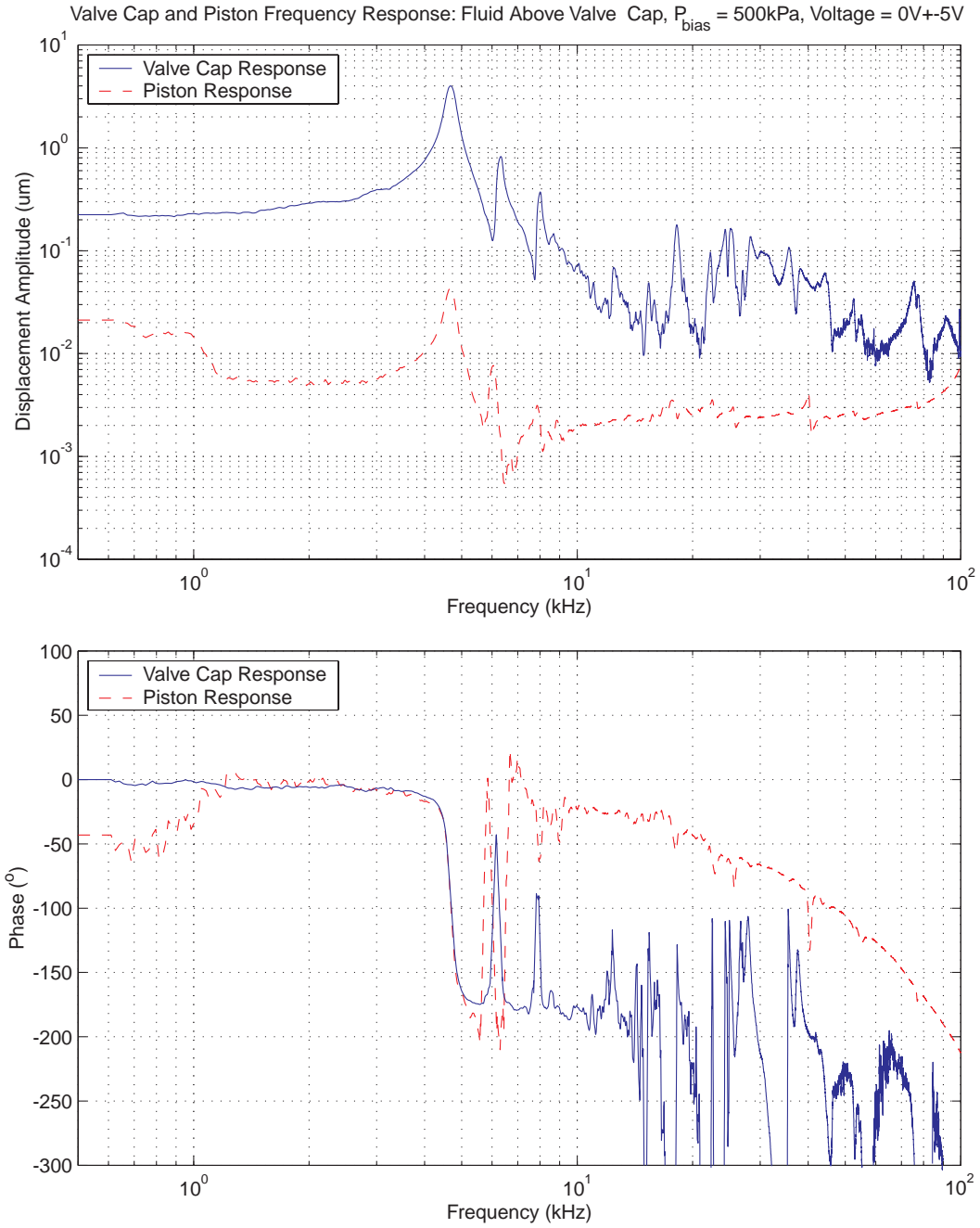


Figure 9.3: Device AV1 low-voltage ( $0V \pm 5V$ ) piston and valve cap frequency responses from 500Hz to 100kHz, with oil present above the valve structure. The bias pressure in these tests was maintained at  $P_{bias} = 500\text{kPa}$ . An amplification ratio between 40x-50x is observed for frequencies below resonance.

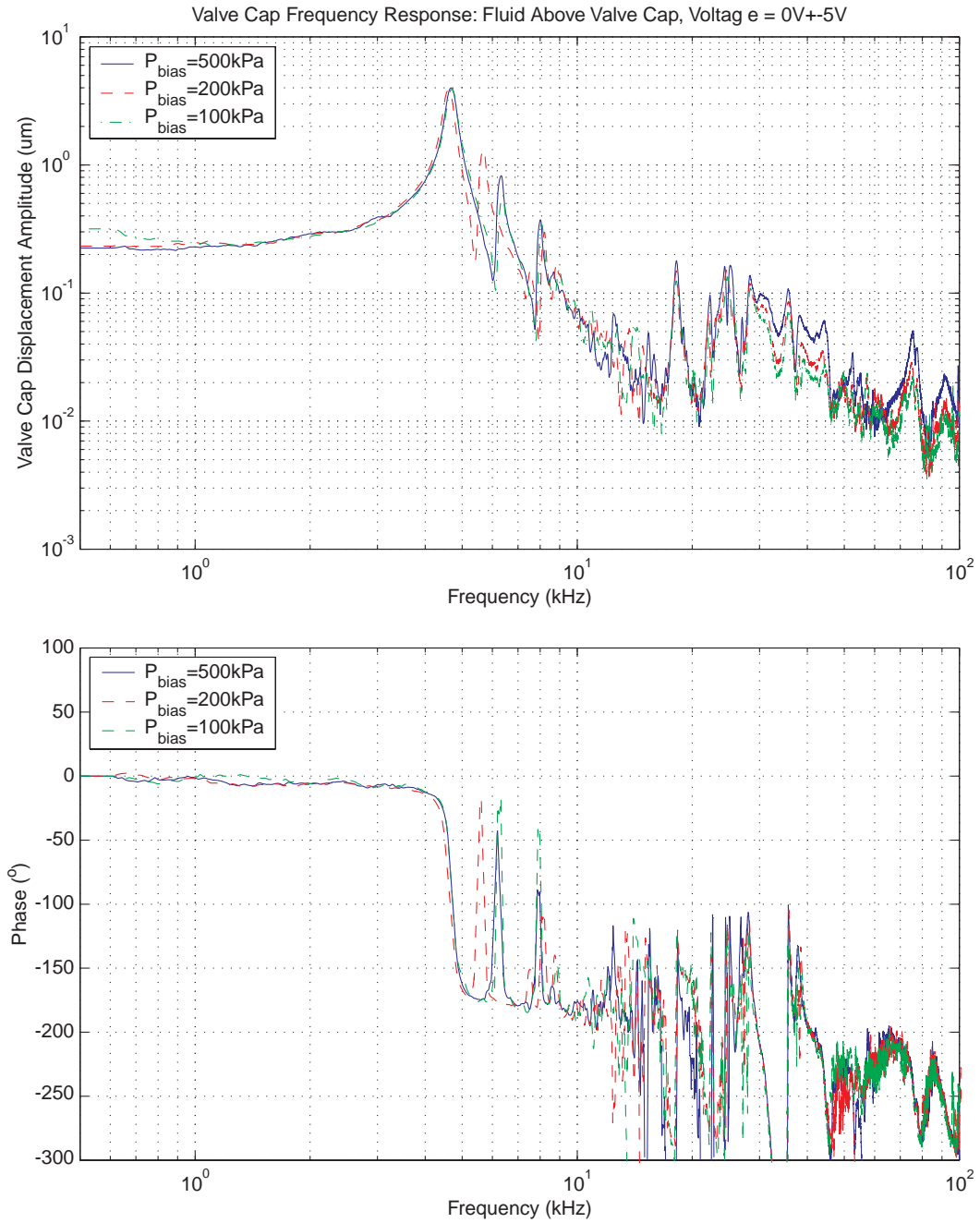


Figure 9.4: Device AV1 low-voltage valve cap frequency responses from 500Hz to 100kHz, for varying  $P_{bias}$ . Results indicate that frequency behavior is not affected by an increase in bias pressure from  $P_{bias} = 100\text{kPa}$  to  $P_{bias} = 500\text{kPa}$ .

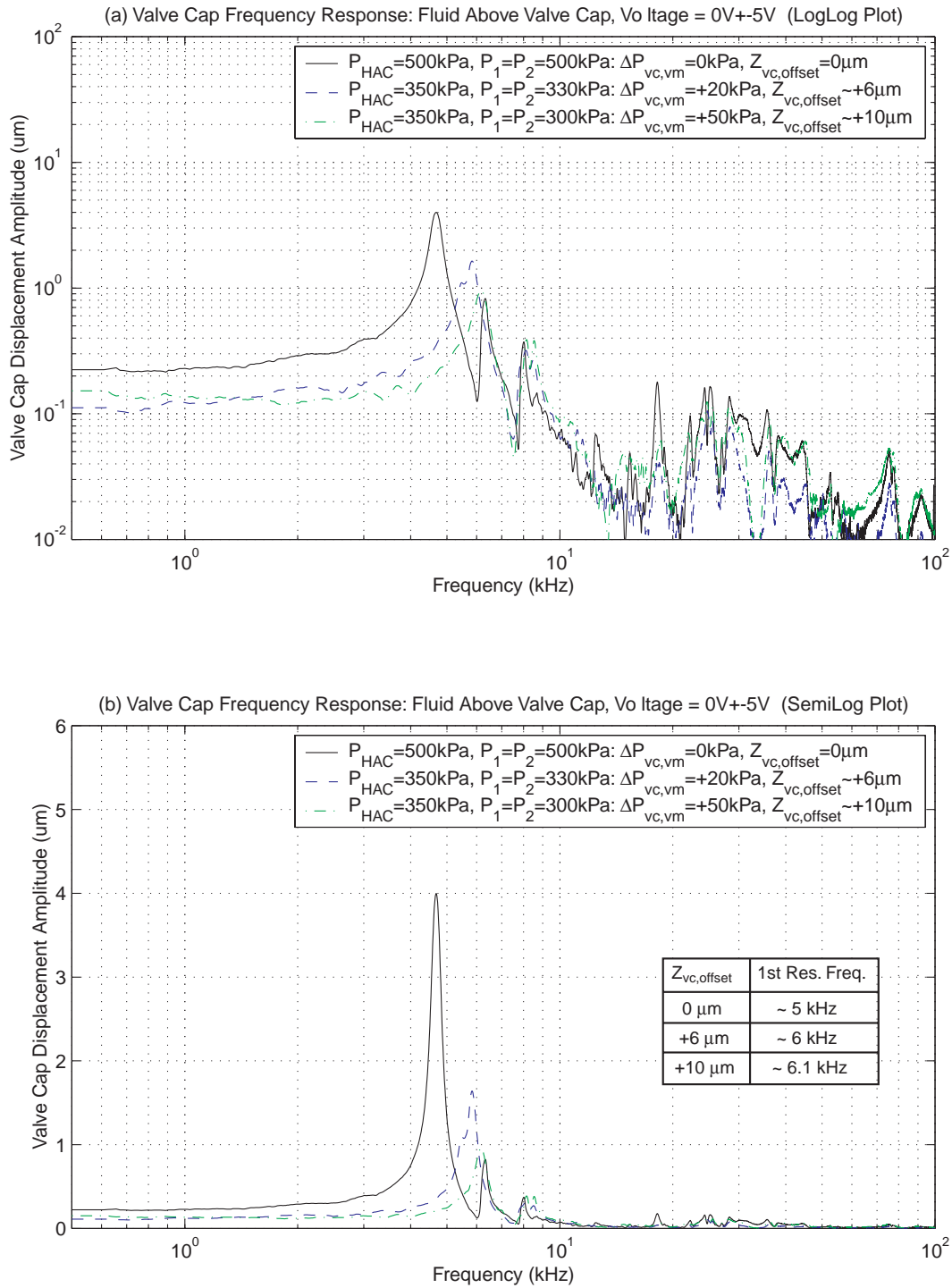


Figure 9.5: Device AV1 low-voltage valve cap frequency responses from 500Hz to 100kHz, for varying differential pressure applied to valve cap and membrane structure. For increasing differential pressure  $\Delta P_{vc,vm}$  across valve cap and membrane, the resonant peak shifts upward and the valve cap vibration amplitude decrease. These phenomena are due to the membrane stiffening as it is forced higher into its large-deflection regime.



A series of tests was also run on active valve device AV1 to characterize the high-voltage frequency response of the structure for a range of frequencies below resonance. Since the resonant peak of this device is present at 5kHz, a range was chosen to include 500Hz to 3kHz. Figure 9.6 plots the valve cap frequency response from 500Hz to 3kHz for a series of increasing drive voltage levels from 50Vpp to 600Vpp, all with  $P_{bias} = 500kPa$ . At the lower voltage drive levels, the valve cap deflection amplitude is essentially constant over these frequencies. As the voltage is increased, regions of increased valve cap deflection appear near 1.7-1.9kHz. This frequency value is approximately  $\frac{1}{3}$  of the low-voltage resonant frequency of the active valve device. This region, therefore, is a result of sub-harmonic excitation of the device. Figure 9.7 plots the valve cap versus piston deflection amplitude over this frequency range for an applied voltage of 600Vpp. In comparing these frequency responses, the amplification capabilities of the active valve device is evident. Figure 9.7(a) plots these curves on a logarithmic amplitude scale, and Figure 9.7(b) plots the curves on a linear amplitude scale. Over this range of frequencies, the amplification ratio is between 40x-50x.

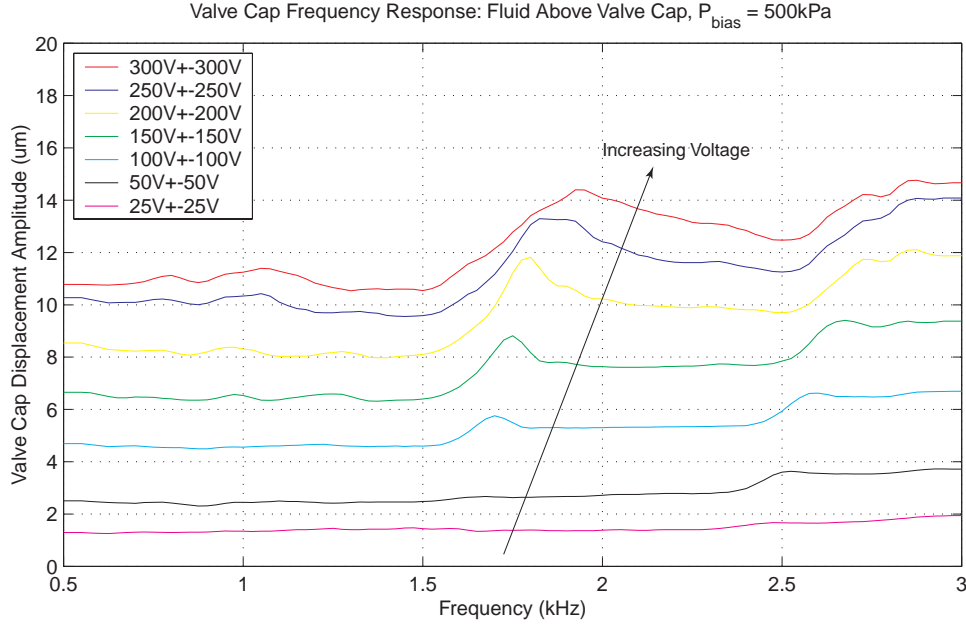


Figure 9.6: Device AV1 valve cap frequency responses from 500Hz to 3kHz, for  $P_{bias} = 500kPa$  and increasing high voltage drive levels. Harmonic excitation behavior near  $\sim 1.7 - 1.9kHz$  becomes evident as voltage levels are increased (ie: as valve membrane structure moves further into its non-linear large-deflection regime).

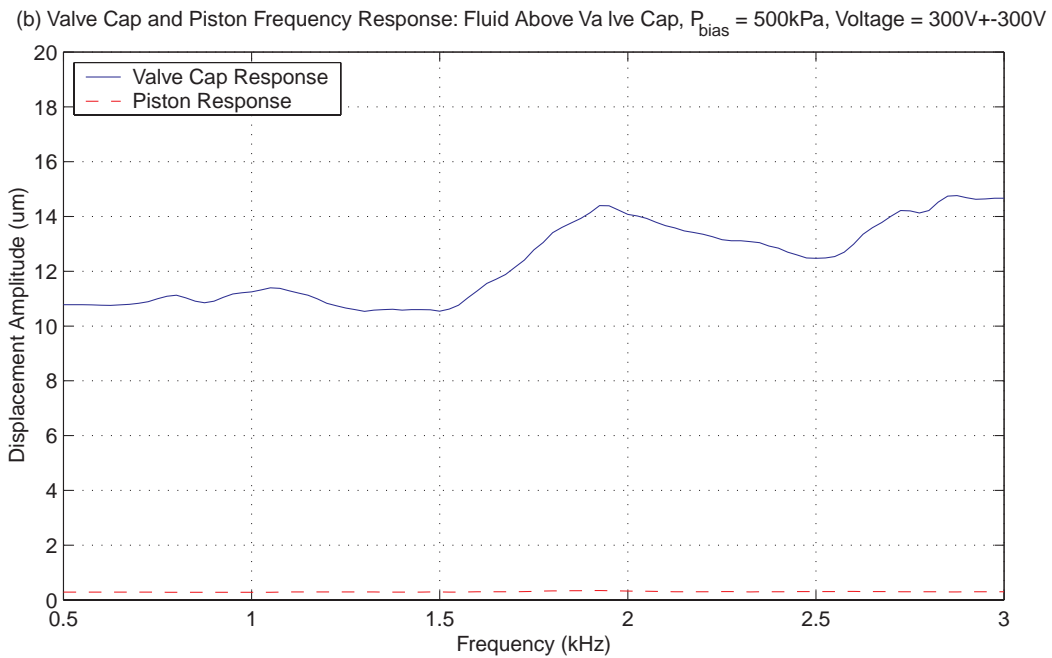
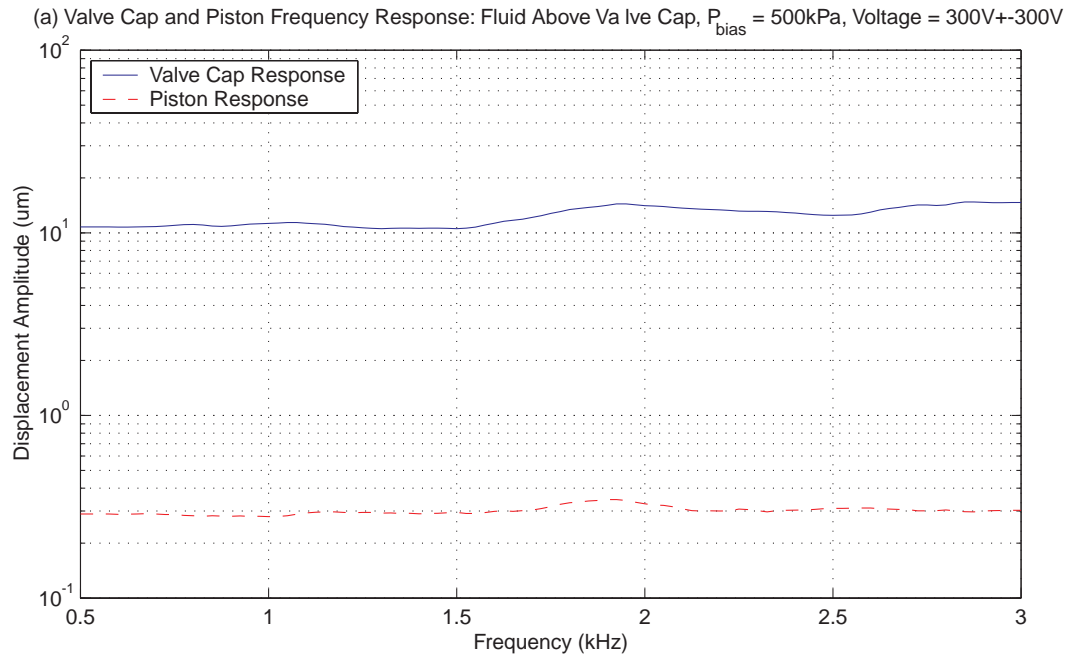


Figure 9.7: Device AV1 high-voltage piston and valve cap frequency responses from 500Hz to 3kHz, for  $P_{bias} = 500\text{kPa}$ . Amplification of active valve device is consistent between 40x-50x over this range of frequency.

The previous frequency sweep experimental tests found the resonant frequency of device AV1 to be  $\sim 5kHz$ . In order to evaluate the quasi-static performance of the structure under the larger drive voltage levels at which the valve was designed to operate, a frequency of operation of 1kHz was chosen. All subsequent structural testing was performed at this frequency. Figure 9.8 plots the valve cap and piston displacement time histories, respectively, over a range of applied voltages from 50Vpp to 600Vpp. In Figure 9.8(a), the dotted lines at  $+16.5\mu m$  and  $-16.5\mu m$  indicate the position of the upper and lower valve stops, respectively. For an applied voltage of 50Vpp, the response of the valve cap is purely sinusoidal. As the voltage is increased to 600Vpp, the resulting valve cap displacement time history contains small amplitude higher frequency ( $\sim 5kHz$ ) oscillations due to the non-linear nature of the valve membrane structure. These oscillations become more pronounced as the voltage is increased. In Figure 9.8(b), the drive element deflection time histories are somewhat rough in nature due to the noise level of the measurement system. As the deflections increase in amplitude, the effect of this noise floor diminishes.

Figure 9.9 takes these deflection time histories (at  $P_{bias} = 500kPa$ ), and plots the valve cap peak-peak displacement, piston peak-peak displacement, and corresponding device amplification ratio as a function of applied voltage to the piezoelectric drive element. The amplification ratio is observed to decrease from 49 to 41 with increasing voltage. This decrease is a result of increased pressurization within the HAC chamber due to the increase in the valve membrane stiffness, and therefore increased deformation of the structure and fluid within the chamber, for increased voltage. In essence, as the voltage is increased, a smaller percentage of the drive element swept volume is transferred to the valve membrane since more volume is lost in chamber compliances. Overall, as will be detailed in the model correlation part of Testing Section 1, this range of amplification ratio correlates extremely well with the expected range based on the models developed in the first half of this thesis. These tests were also performed under decreased bias pressures, and these results are additionally presented in Figure 9.9. For decreased  $P_{bias}$ , the valve cap and piston deflections slightly increase, most likely due to better performance of the piezoelectric material under lower loading. As expected, however, the amplification ratio is not affected by the reduced bias pressure.

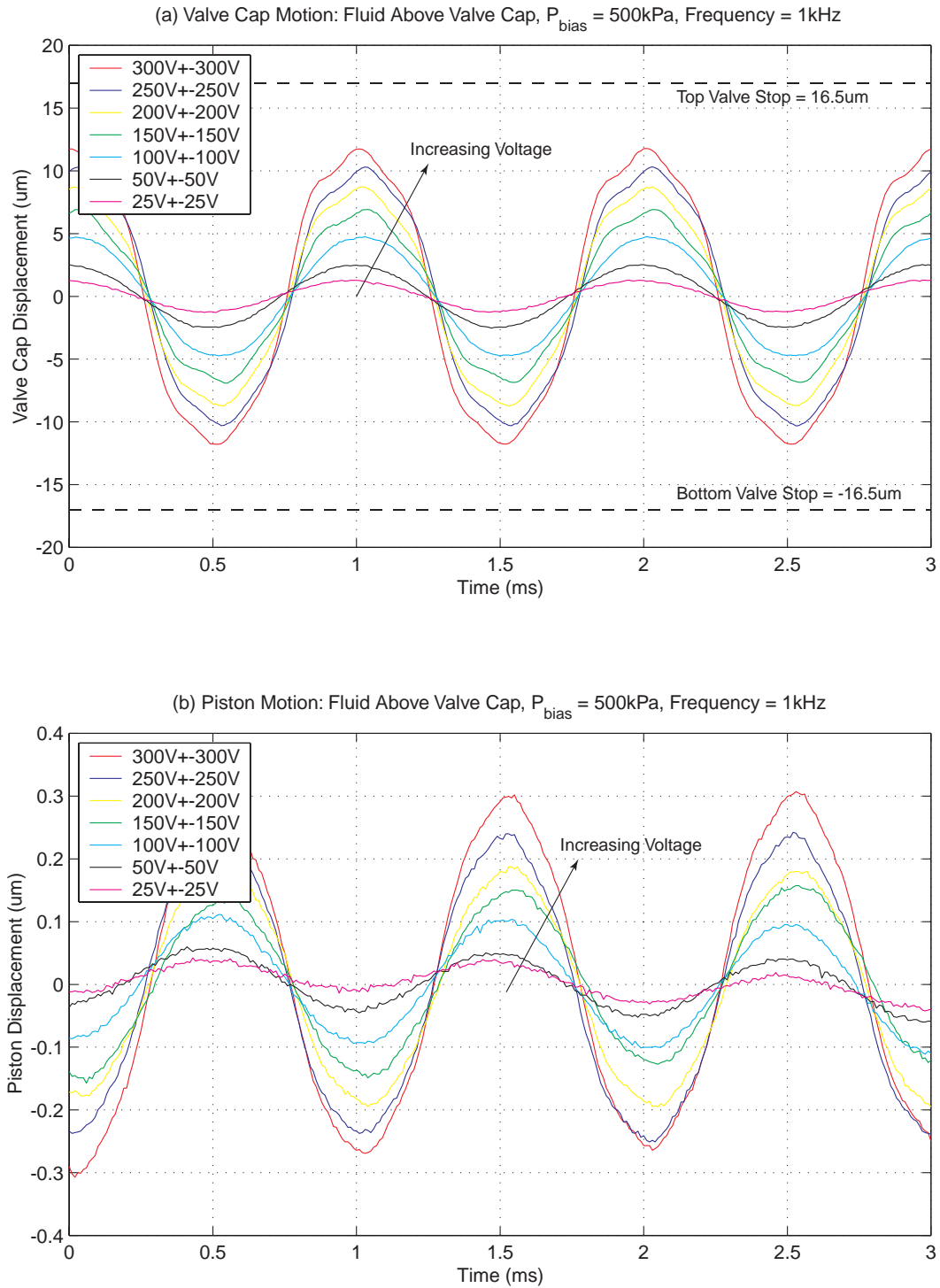


Figure 9.8: Device AV1 valve cap and piston deflection time histories for 1kHz sinusoidal drive voltage levels. As voltage is increased, small amplitude 5kHz oscillations appear in deflection responses. A voltage of 600Vpp is not sufficient to close valve cap against the valve orifice.

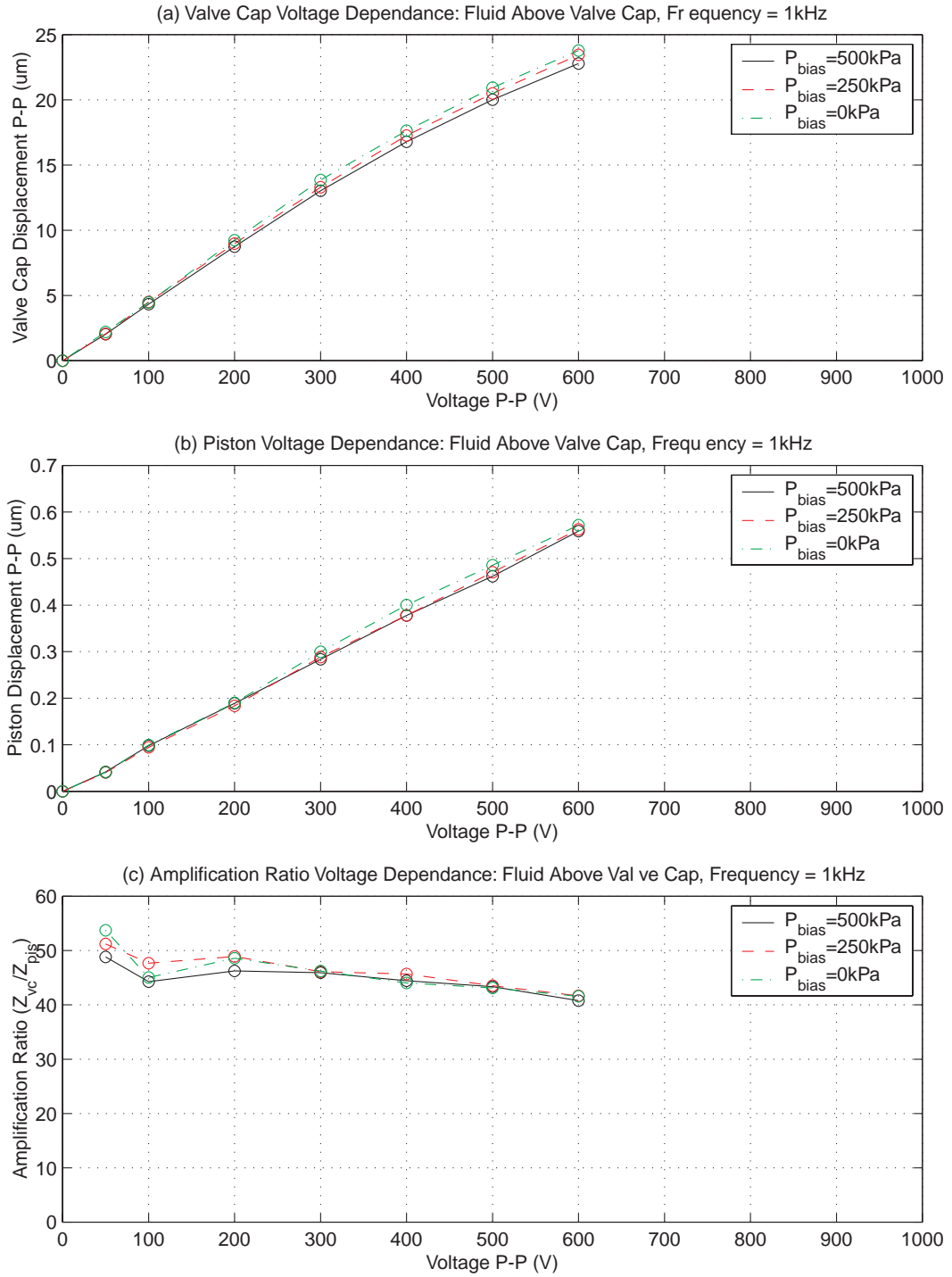


Figure 9.9: Device AV1 valve cap peak-peak motion, piston peak-peak motion, and device amplification ratio as a function of 1kHz sinusoidal drive voltage levels. Due to non-linear stiffness of the valve membrane structure, the amplification ratio decreases from  $\sim 50x$  to  $\sim 40x$  as the drive voltage is increased to 600Vpp.

In the previous tests at 1kHz, applied voltages were limited to 600Vpp to minimize the potential for device failure (due to stresses in drive element tethers - see the AV2 testing part of Testing Section 1 for an explanation). As a result, the valve cap never was able to close against the valve orifice. In order to observe valve closing and verify that the valve membrane is able to withstand these deflection magnitudes during dynamic operation, a series of tests was performed whereby a differential pressure of  $P_{vc,vm} = 50kPa$  was applied across the valve cap and membrane to deflect it to an offset position of  $\sim +10\mu m$ . Voltages from 50Vpp to 600Vpp were then applied to evaluate closing behavior. Figure 9.10 plots the resulting valve cap deflection time histories. Notice that applied voltages of 500Vpp and 600Vpp successfully force the valve cap closed. Since the valve membrane is offset into its large deflection regime, the higher voltage deflection time histories become non-symmetric about this offset deflection. Additionally, the rounded nature of these curves as the cap hits the upper valve stop (valve orifice) indicates that squeeze-film damping may be playing a positive role in damping out potential vibrations due to high velocity impact of the valve cap on the valve stop.

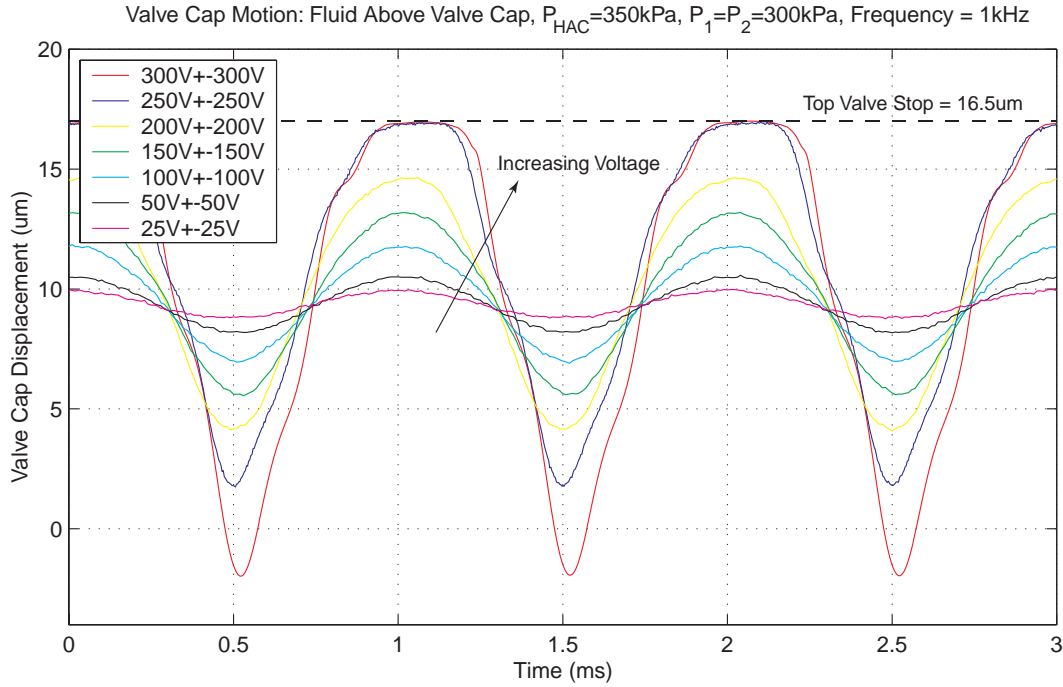


Figure 9.10: Device AV1 valve cap peak-peak motion, piston peak-peak motion, and device amplification ratio as a function of 1kHz sinusoidal drive voltage levels, with  $P_{vc,vm} = 50kPa$ . As the valve cap impacts the orifice stop, squeeze film damping may be aiding to damp undesired structural vibrations.

Overall, these series of low-voltage frequency sweep tests and higher-voltage quasi-static 1kHz tests have proven that active valve device AV1 successfully operates as a piezoelectrically-

driven hydraulic amplification microactuator structure. The series of tests detailed in Testing Section 2 will evaluate its capability to regulate fluid flow at high-frequency.

**Evaluation of Device AV1 High-Frequency Channel** The experimental data for device AV1 described in the previous sections was taken using the micromachined high-frequency channel (detailed in Chapter 6) as a means to control the static pressure  $P_{HAC}$  within the hydraulic amplification chamber, yet also to allow dynamic pressure fluctuations within the chamber created by piezoelectric actuation of the drive element. This channel, located between the HAC chamber and the external pressure port in the device, was designed to have a length of 1mm, a width of  $10\mu m$ , and a height of  $10\mu m$ . Although the previous set of data clearly indicates that this high-frequency channel must be satisfying its objective, the specific limitations of the channel are not clear. In an effort to evaluate the lower-limit frequency at which fluid begins to leak out of this channel during the positive stroke of the drive element actuation cycle, a series of tests for varying applied voltage to the piezoelectric elements were carried out.

In each test, the valve cap displacement amplitude was measured for an applied piezoelectric sinusoidal voltage (100Vpp, 200Vpp, and 400Vpp) over a frequency range from 1kHz to 0.1Hz. Figure 9.11 plots the valve cap displacement amplitude as function of frequency for these different applied voltage levels. Overall, the results indicate that this high-frequency channel behaves as a low pass filter with  $\sim 1\%$  reduction in performance at a frequency of  $\sim 1 - 2Hz$ . These experimental results correlate quite well to the conservative channel design procedure (detailed in Chapter 6) in which a 1% reduction in performance was estimated to occur at a frequency of 48Hz. As a result, during actuation of the active valve at the desired frequencies in excess of 500Hz, the channel allows negligible fluid volume to move into and out of the hydraulic amplification chamber.

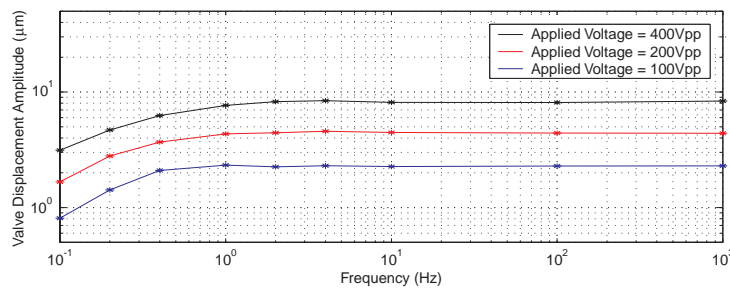


Figure 9.11: Experimental verification of the high-frequency channel in device AV1. The channel, with a length of 1mm, a width of  $10\mu m$ , and a height of  $10\mu m$ , successfully restricts fluid flow from the chamber during cyclic actuation down to a cutoff frequency near 1Hz.

## Active Valve Device AV2

This section documents the frequency response characteristics and quasi-static operational capabilities of active valve device AV2. The tests performed were identical to those carried out for device AV1. As such, only selected plots are included in this section. The overall objective of this section is to demonstrate that both devices behave in the same manner. As a result, a conclusion can be made that repeatability in fabricating and assembling these devices is excellent.

Figure 9.12 plots the valve cap frequency response from 500Hz to 100kHz for an applied low-voltage sweep signal of  $0V \pm 5V$  under the condition that silicon oil is not present above the valve cap and membrane structure and under the condition that silicon oil is present above the valve cap and membrane structure. As for device AV1, these tests were performed with  $P_{bias} = 500kPa$  to ensure that cavitation of the fluid within the HAC did not occur. Without oil, the resonant frequency of the structure is evident at 10.5kHz. With oil, this frequency drops to slightly less than 5kHz. These results are essentially the same as those found for device AV1.

Figure 9.13 plots the valve cap frequency responses under these voltage sweep signal inputs for a varying bias pressure. Clearly from the results, a variation in  $P_{bias}$  from 100kPa to 500kPa has no noticeable effect on the frequency response of the structure.

Figure 9.14 plots a series of valve cap frequency responses from 500Hz to 3kHz for increasing drive voltage levels from 50Vpp to 500Vpp, all with  $P_{bias} = 500kPa$ . As was observed for device AV1, as the voltage is increased, regions of increased valve cap deflection appear near 1.7-1.9kHz. This frequency value is approximately  $\frac{1}{3}$  of the low-voltage resonant frequency of the active valve device. This region, therefore, is a result of sub-harmonic oscillations of the device. Figure 9.15 plots the valve cap versus piston deflection amplitude over this frequency range for an applied voltage of 500Vpp. In comparing these frequency responses, the amplification capability of the active valve device is evident. Figure 9.15(a) plots these curves on a logarithmic amplitude scale, and Figure 9.15(b) plots them on a linear amplitude scale. Over this range of frequencies, the amplification ratio is in the range of 40x-50x, an identical result as for the amplification ratio found for device AV1.

In order to evaluate the quasi-static performance of device AV2, a frequency of operation of 1kHz was chosen. Figure 9.16(a) and (b) plot the valve cap and piston displacement time histories, respectively, over a range of applied voltages from 50Vpp to 900Vpp. In Figure 9.16(a), the dotted lines at  $+16.5\mu m$  and  $-16.5\mu m$  indicate the position of the upper and lower valve stops, respectively. For an applied voltage of 50Vpp, the response of the valve cap is purely sinusoidal. As the voltage is increased to 900Vpp, the resulting valve cap displacement time history contains significant higher frequency ( $\sim 5kHz$ ) oscillations due to the non-linear nature of the valve membrane structure. These oscillations become more pronounced as the voltage is increased. In the chronology of the testing procedure for devices AV1 and AV2,



device AV2 was tested before device AV1 was tested. During testing of device AV2, voltage was increased to 1000Vpp. At this voltage level, the drive element piston tethers broke and silicon oil leaked out of the HAC chamber. Data was therefore only able to be taken on the valve cap behavior up to 900Vpp and on the piston behavior up to 800Vpp. This is the reason that device AV1 was tested only up to 600Vpp (see previous section).

Figure 9.17 takes these deflection time histories (at  $P_{bias} = 500kPa$ ), and plots the valve cap peak-peak displacement, piston peak-peak displacement, and corresponding device amplification ratio as a function of applied voltage to the piezoelectric drive element. The amplification ratio is observed to vary from 40x to 50x, mainly decreasing with increasing voltage. As for device AV1, this decrease is a result of increased pressurization within the HAC chamber, and therefore increased deformation of the structure and fluid within the chamber, for increased voltage. In essence, as the voltage is increased, a smaller percentage of the drive element swept volume is transferred to the valve membrane since more volume is lost in chamber compliances. Overall, however, this range of amplification ratio correlates well with the expected range based on the models developed in the first half of this thesis (see Model Correlation part of Testing Section 1).

Piston failure in device AV2 is attributed to the fact that, although the drive element tethers were designed to have a thickness of  $8\mu m$ , their measured thickness was closer to  $6\mu m$ . As a result, under the calculated pressure loading of  $\sim 700kPa$  (corresponding to drive voltage of 1000V and  $P_{bias} = 500kPa$ ), the drive element tethers were expected to experience a stress approaching 1GPa, a value which is taken as a limit for the structural integrity of the silicon membrane structures [2]. Future drive element piston structures incorporate tethers which have a thickness of  $8\mu m$ . Although the complete series of tests that were performed on device AV1 were not able to be carried out on device AV2, the test results documented in this section indicate that this valve device also successfully operated as a piezoelectrically-driven hydraulic amplification microactuator structure.

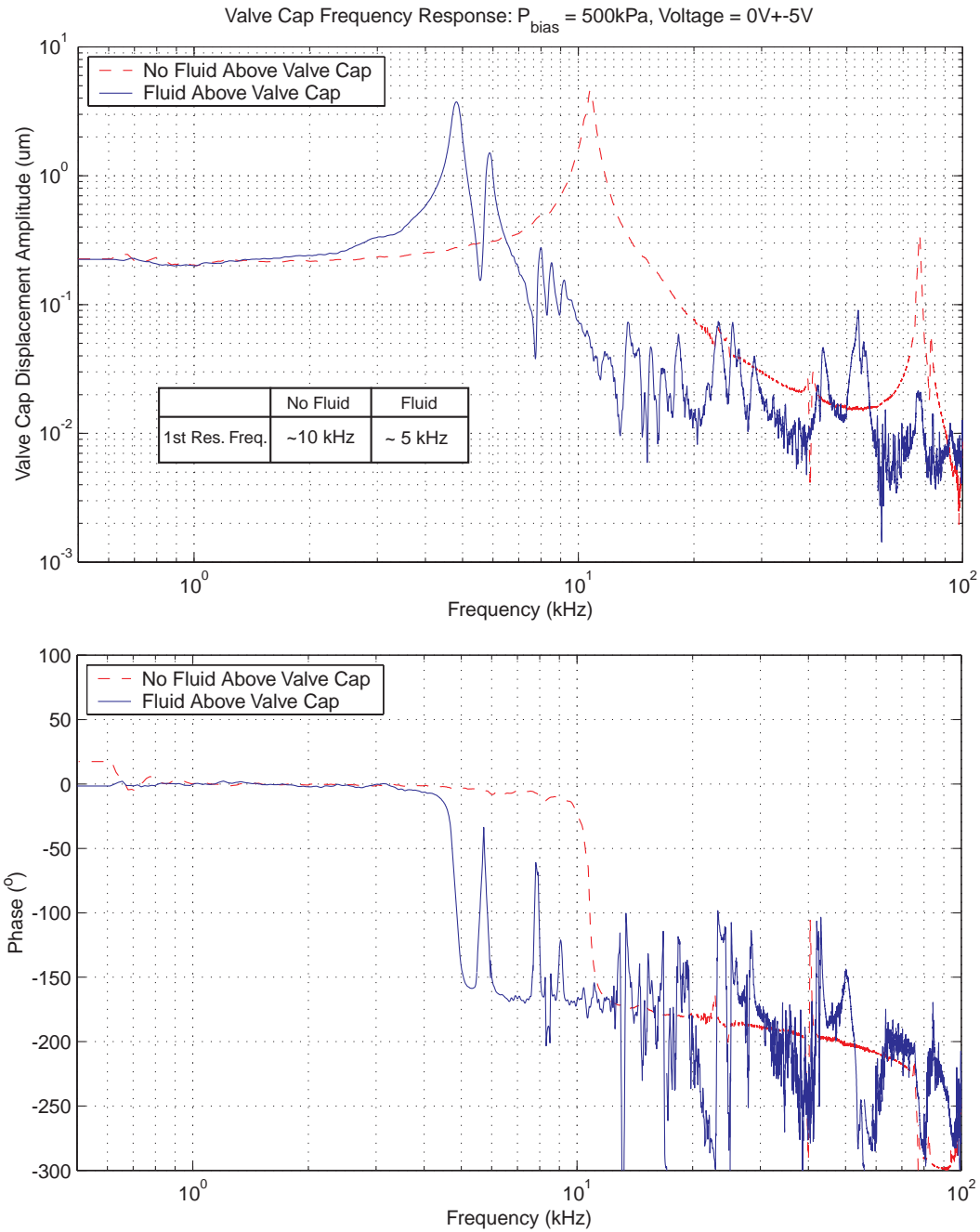


Figure 9.12: Device AV2 low-voltage ( $0V \pm 5V$ ) valve cap frequency response from 500Hz to 100kHz, with and without oil present above the valve structure. The bias pressure in these tests was maintained at  $P_{bias} = 500\text{kPa}$ . The presence of oil in the flow channel above the valve cap creates an added mass that reduces the resonant frequency from 10.5kHz to 5kHz.

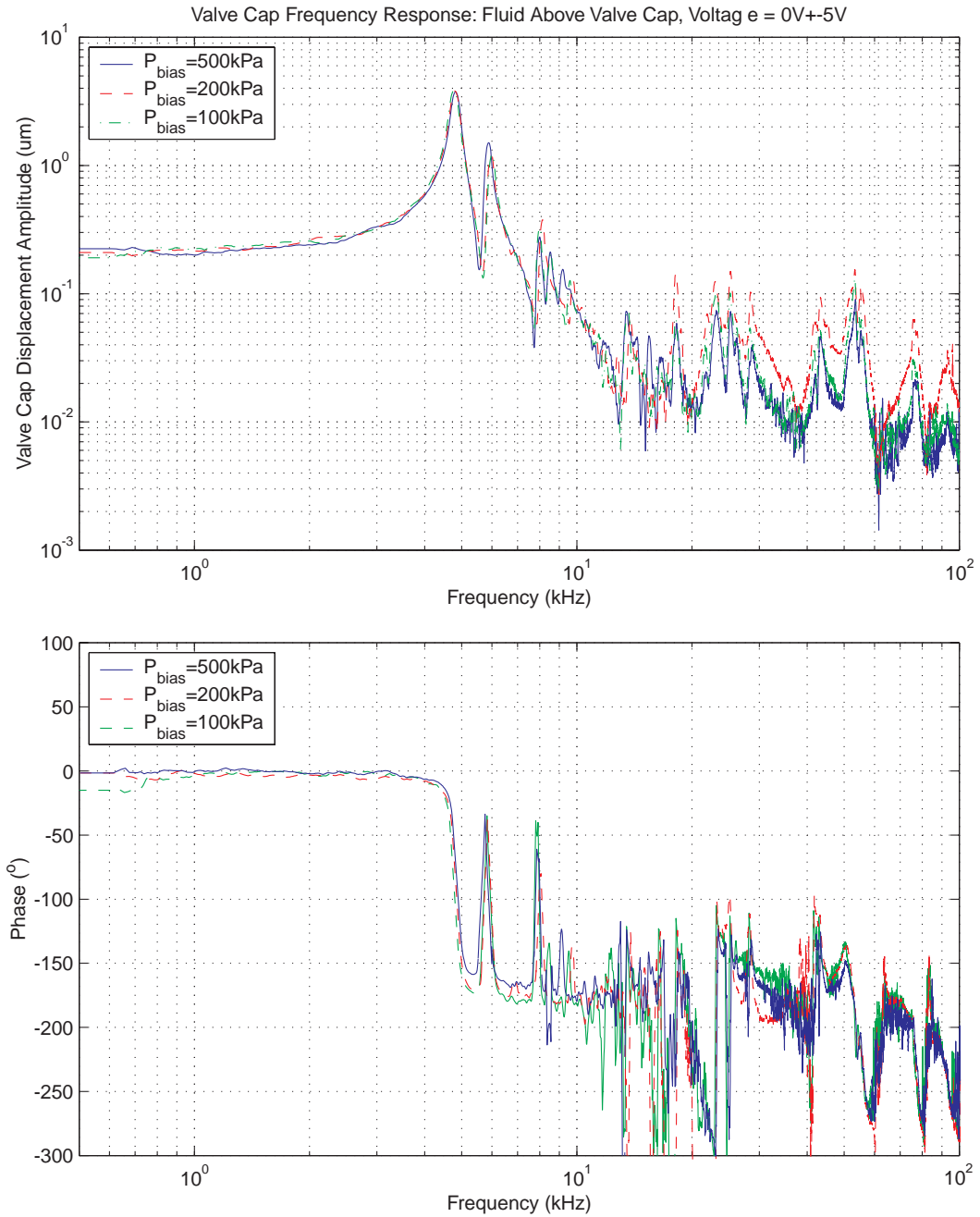


Figure 9.13: Device AV2 low-voltage valve cap frequency responses from 500Hz to 100kHz, for varying  $P_{\text{bias}}$ . Results indicate that frequency behavior is not affected by an increase in bias pressure from  $P_{\text{bias}} = 100\text{kPa}$  to  $P_{\text{bias}} = 500\text{kPa}$ .

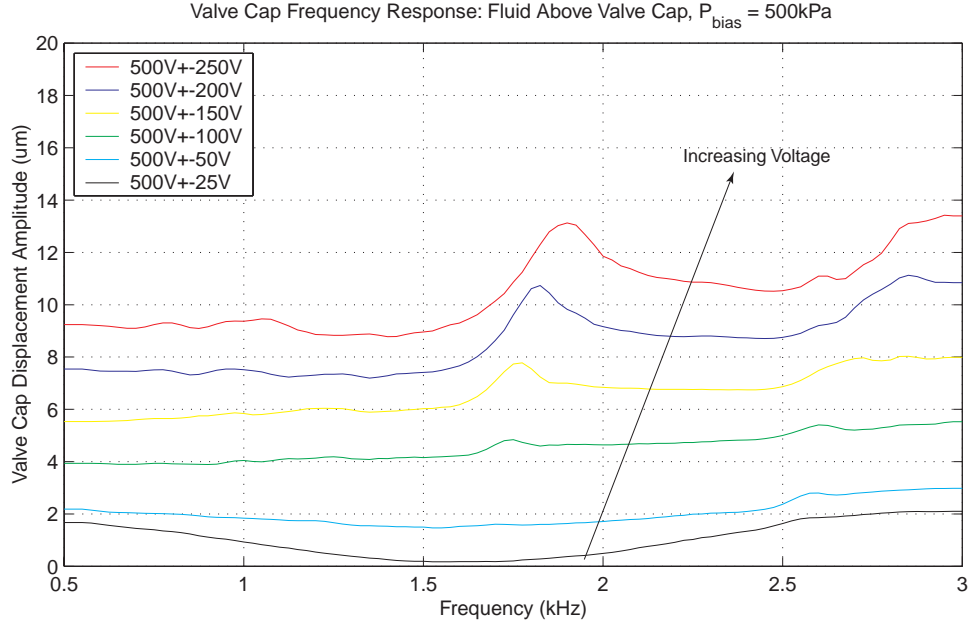


Figure 9.14: Device AV2 valve cap frequency responses from 500Hz to 3kHz, for  $P_{bias} = 500kPa$  and increasing high voltage drive levels. Harmonic excitation behavior near  $\sim 1.7 - 1.9kHz$  becomes evident as voltage levels are increased (ie: as valve membrane structure moves further into its non-linear large-deflection regime). It is unknown why the valve cap displacement dips downward between 500Hz and 2.5kHz for the voltage drive levels of 50Vpp and 100Vpp.

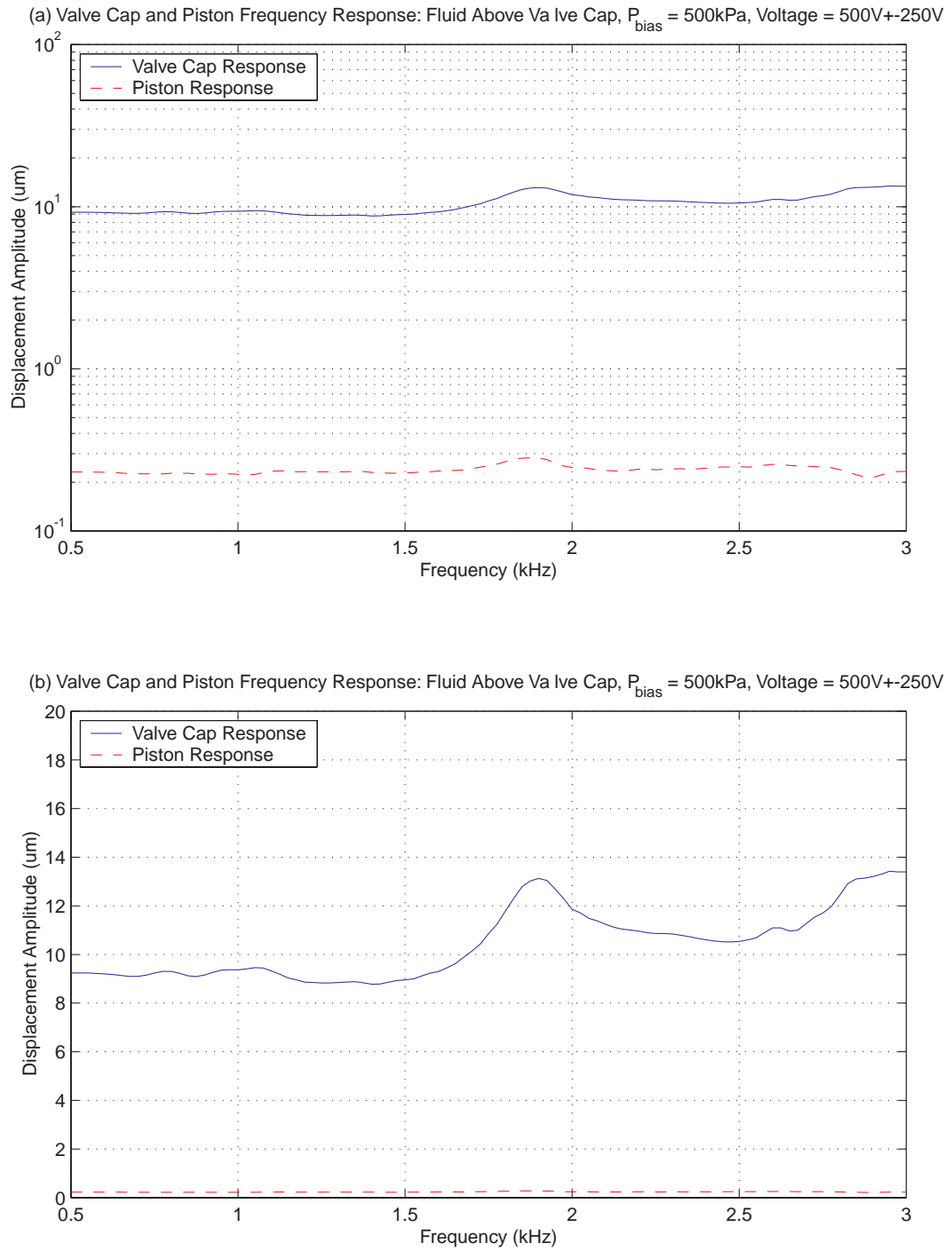


Figure 9.15: Device AV2 high-voltage piston and valve cap frequency responses from 500Hz to 3kHz, for  $P_{bias} = 500kPa$ . Amplification of active valve device is consistent between 40x-50x over this range of frequency.

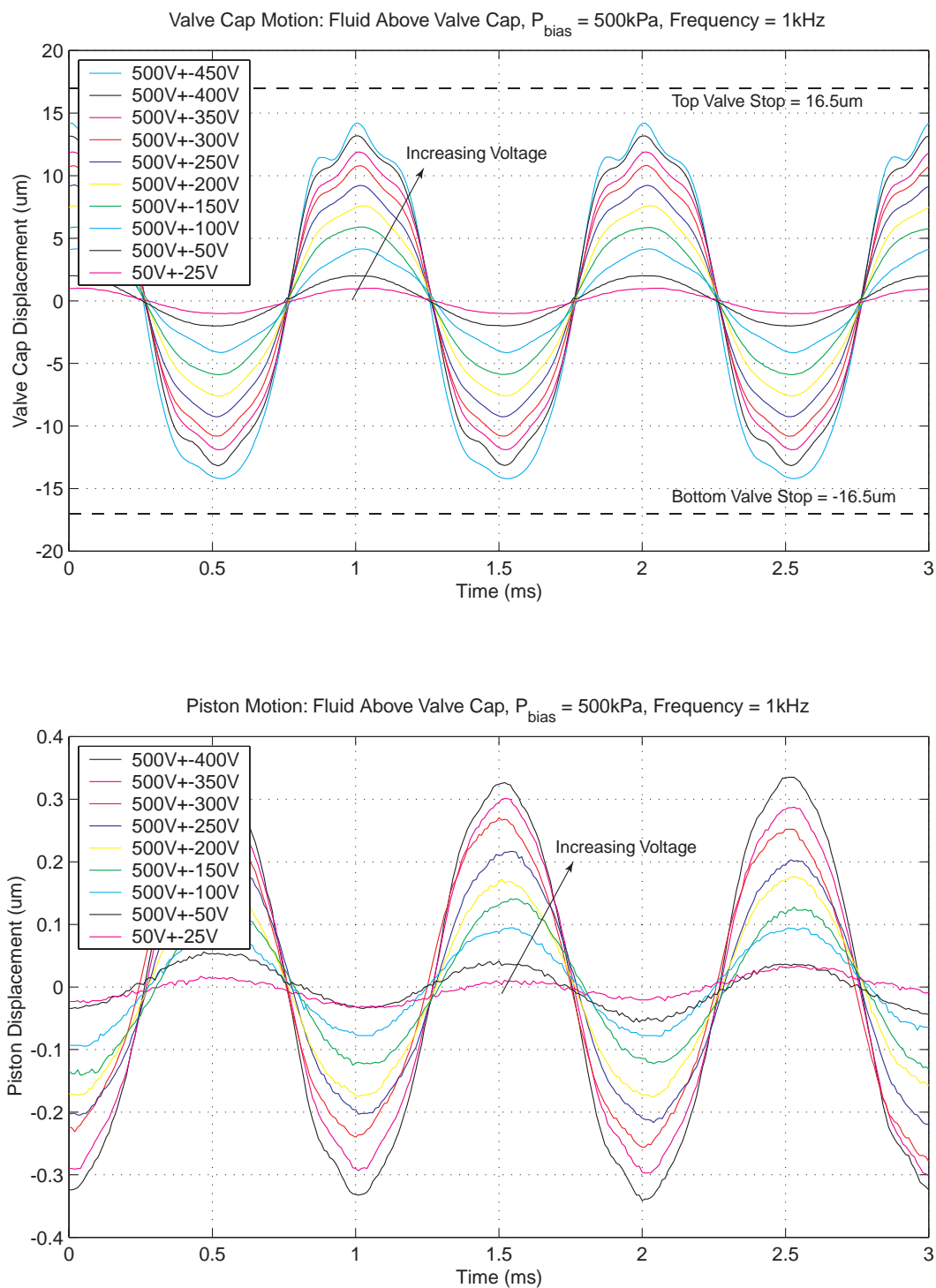


Figure 9.16: Device AV2 valve cap and piston deflection time histories for 1kHz sinusoidal drive voltage levels. As voltage is increased, small amplitude 5kHz oscillations appear in deflection responses. A voltage of 900Vpp is not sufficient to close the valve cap against the valve orifice.

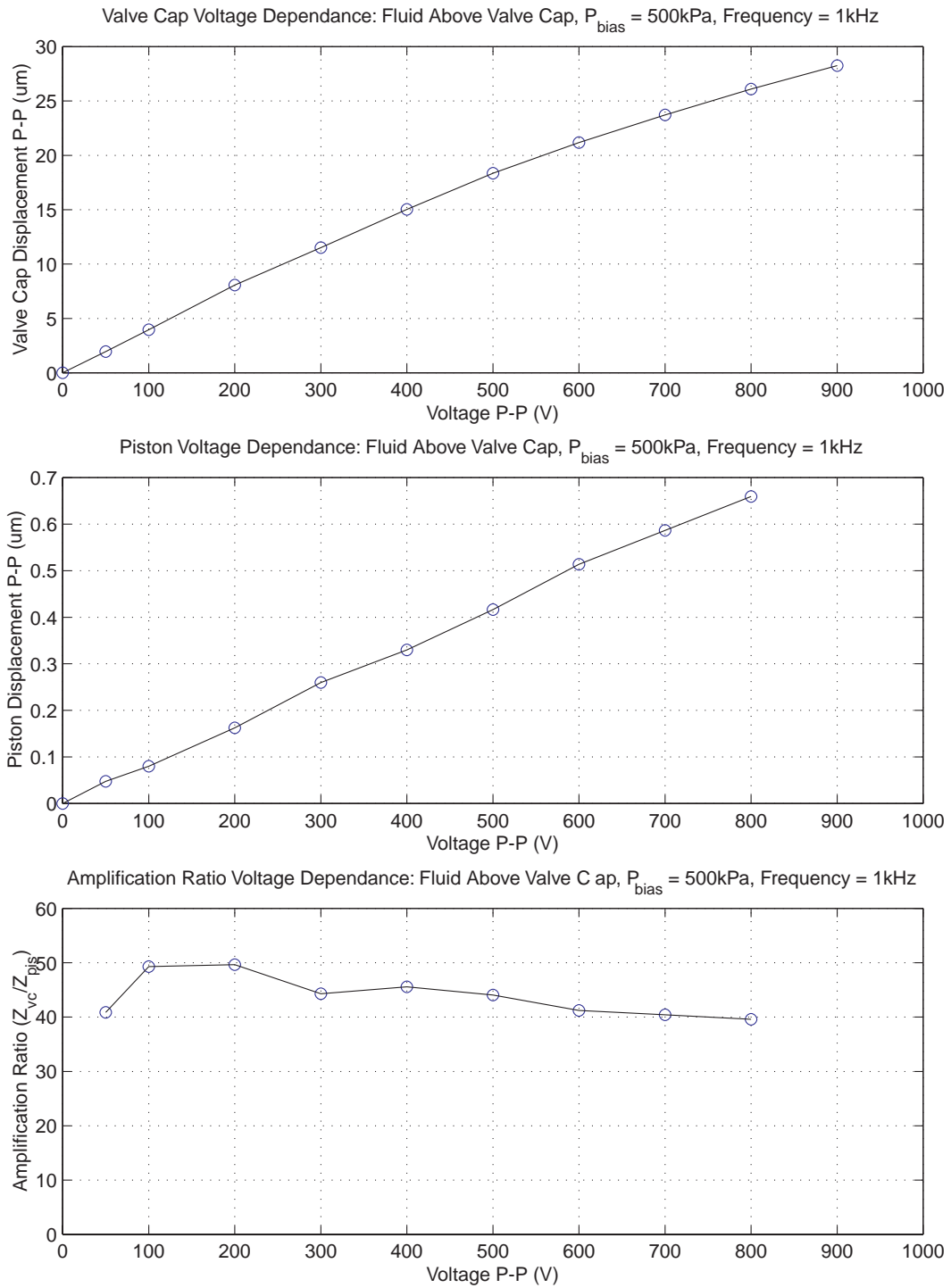


Figure 9.17: Device AV2 valve cap peak-peak motion, piston peak-peak motion, and device amplification ratio as a function of 1kHz sinusoidal drive voltage levels. Due to the non-linear stiffness of the valve membrane structure, the amplification ratio decreases from  $\sim 50x$  to  $\sim 40x$  as the drive voltage is increased to 900Vpp.

## Model Correlation

With the data presented in the previous section, model correlation efforts were pursued to compare these results to the expected results from the analytical and finite-element models documented in the first series of chapters in this thesis. In this section, the high-voltage quasi-static performance at 1kHz is correlated to model expectation using the full non-linear analytical active valve model presented in Chapter 4. Following this, the low-voltage frequency response performance is correlated to the predictions from the active valve finite-element model presented in Chapter 4, as well.

**1kHz Quasi-Static Correlation** Prior to comparing results for the 1kHz operating conditions, a static pressurization test was performed on the drive element structure within device AV1 to determine the mechanical stiffness of the piezoelectric material elements. In this test, the pressure within the hydraulic amplification chamber was increased from  $P_{HAC} = 0kPa$  to  $P_{HAC} = 500kPa$  over a time span of 90 seconds, and the displacement of the drive element piston was measured in real-time using the laser vibrometer system. In response to this 500kPa pressurization, the piston moved through a displacement of  $0.90\mu m$ . With this result and with the geometry of the structure presented in Figure 9.1, the Young's Modulus of the PZN-PT material was determined to be  $E_p = 6.76GPa$ . This value is 74% of the nominal modulus ( $E_p = 9.01GPa$ ) given by the manufacturer [3] and assumed for active valve design optimization throughout the earlier chapters of this thesis. It should be stated that the manufacturer's material data sheet [3] quoted the modulus within only  $\pm 20\%$ , and as a result, this experimentally determined reduced modulus from nominal was not completely unexpected. In the model correlation studies that follow, the effect of piezoelectric material Young's Modulus variation is evaluated. Additionally, as presented in Chapter 1, the piezoelectric coefficient assumed in the active valve design procedures was  $d_{33} = 2000pC/N$ . As shown in Chapter 7, in evaluating performance of the drive element devices, the actual coefficient for high-voltage behavior of this material was found to be in the range of  $d_{33} = 1300 - 1500pC/N$ . In the model correlation studies that follow, the effect of piezoelectric  $d_{33}$  variation is also evaluated.

Figure 9.18 plots the experimental 1kHz sinusoidal voltage drive data for devices AV1 and AV2 against theoretical plots obtained from the full valve analytical model. The operational conditions for these tests and simulations are: a bias pressure  $P_{bias} = 500kPa$ , a frequency 1kHz, and a varying applied voltage to the piezoelectric material. Shown on this plot are a series of model curves that span the range of  $d_{33}$  and  $E_p$  coefficients. For example, Model Case 1 assumes an ideal  $d_{33} = 2000pC/N$  and an  $E_p = 9.01GPa$ . At a peak-peak voltage of  $V_{p,PP} = 600V$ , for example, the model deflection is  $Z_{vc,PP} = 32.7\mu m$ , as compared to the experimental deflection for device AV1 of  $Z_{vc,PP} = 23.1$  and for device AV2 of  $Z_{vc,PP} = 21.6$ . Reducing the piezoelectric coefficient to  $d_{33} = 1500pC/N$  and maintaining  $E_p = 9.01GPa$



produces the curve for Model Case 2. A sharp reduction in valve cap deflection is observed. At  $V_{p,PP} = 600V$ , the model deflection is  $Z_{vc,PP} = 27.5\mu m$ . Now, reducing the modulus to  $E_p = 6.76GPa$  for the expected range of piezoelectric coefficient  $d_{33} = 1300 - 1500pC/N$  produces Model Case 3 and Model Case 4, respectively. These are the curves within which the experimental data should lie, since the  $d_{33}$  and  $E_p$  coefficients are taken from previous experimental studies. For Model Case 3, the model deflection is  $Z_{vc,PP} = 25.9\mu m$ , and for Model Case 4 the model deflection is  $Z_{vc,PP} = 23.7\mu m$ .

In observing 9.18(b), the piston deflection experimental data points do fall within these bounds. The experimental valve cap deflection data points, however, lie slightly below the lower bound. These two observations indicate that the drive element structure is well characterized by the values of  $d_{33} = 1300 - 1500pC/N$  and  $E_p = 6.76GPa$ . The lower than expected valve cap deflection experimental data, in comparison to the models, must therefore be a result of additional compliance within the hydraulic coupler mechanism itself. Since Chapter 7 validated that the valve membrane structures correlate extremely well with the non-linear model code, this compliance must be associated with either the fluid itself or a structural compliance of the hydraulic amplification chamber walls. This theory is supported by the amplification ratio data shown in Figure 9.18(c), where the amplification ratio as a function of applied voltage is slightly less than model predictions. However, all amplification ratio data indicate very good correlation within 5 – 10% of model predictions.

In order to further evaluate the issue of a lower than modeled fluid bulk modulus, two further model correlation cases were carried out. In all design chapters of this thesis, the fluid bulk modulus of the silicon oil was assumed to be  $K_f = 2.0GPa$  [4]. The previous plots just discussed assumed this value. Depending on how well the fluid is degassed and free of bubbles, this value could be substantially lower. To evaluate the effect of a reduced fluid bulk modulus, Model Case 4 was repeated (with  $d_{33} = 1300pC/N$  and  $E_p = 6.76GPa$ ) for  $K_f = 1.0GPa$  and  $K_f = 0.5GPa$ . These cases are label Model Case 5 and Model Case 6, respectively. As shown in Figure 9.19, a change in fluid bulk modulus does indeed result in expectations closer to the experimental data. Even for a reduction in fluid stiffness of 4 times, however, the amplification mechanism still performs well. This is a result of the fact that, in general, the fluid is stiff enough that its volume reduction during pressurization is significantly smaller than the actuation volume change produced by the drive element during operation.

These model correlation studies indicate that for the experimentally determined piezoelectric material properties  $d_{33} = 1300 - 1500pC/N$  and  $E_p = 6.76GPa$ , active devices AV1 and AV2 perform very close to model predictions for quasi-static operation at 1kHz. Slight discrepancies in performance can most likely be attributed to a smaller than expected fluid bulk modulus or equivalent structural compliance within the hydraulic amplification chamber.

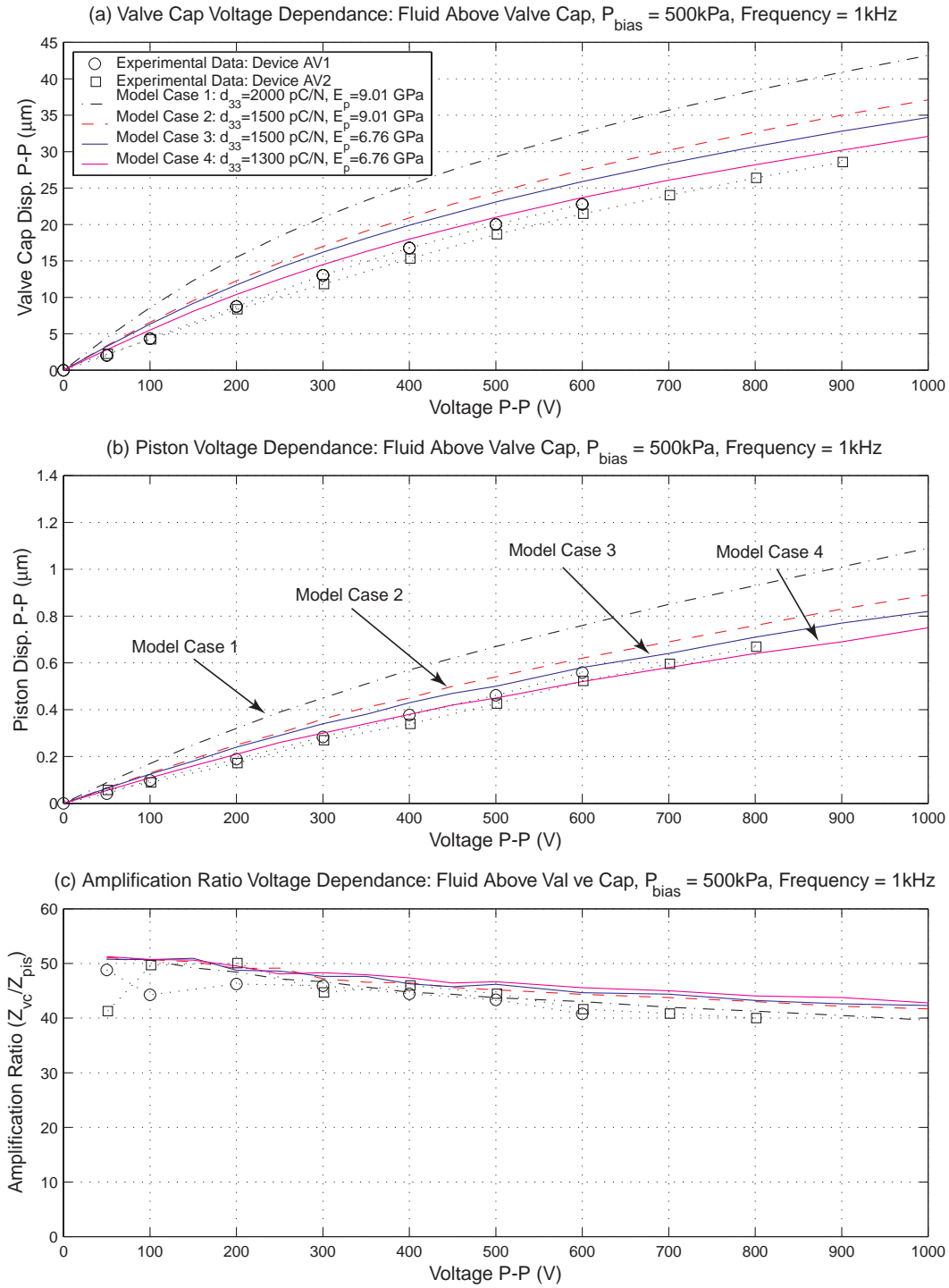


Figure 9.18: Device AV1 and device AV2 quasi-static 1kHz model correlation for fluid bulk modulus  $K_f = 2.0\text{GPa}$ . Results indicate the piston deflection is very close to the expected theoretical bounds for  $d_{33} = 1300 - 1500\text{pC/N}$  and  $E_p = 6.76\text{GPa}$ . Due to the fact that the valve cap deflection is further from the theoretical bounds, it is believed that fluid compliance or HAC structural compliance is creating a loss mechanism.

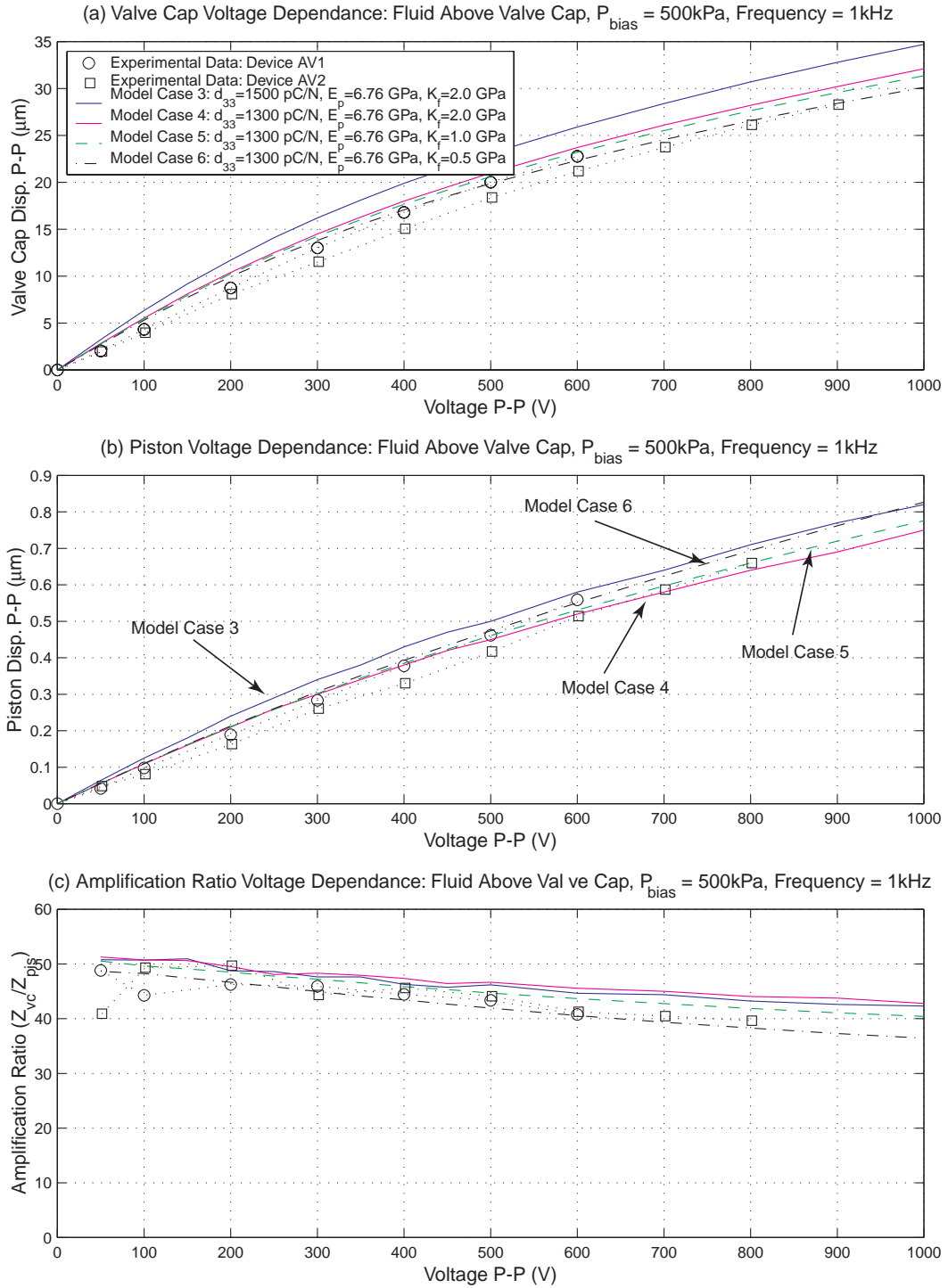


Figure 9.19: Device AV1 and device AV2 quasi-static 1kHz model correlation for varying fluid bulk modulus  $K_f$ . Results indicate a 75% reduction in the fluid bulk modulus would enable good correlation between experimental and theoretical results.

**Low-Voltage Frequency Response** Having correlated the quasi-static 1kHz high-voltage structural behavior of the microvalve to expected results based on the analytic models presented in this thesis, an effort is now made to understand the resonant frequency behavior at low-voltage. The 1st set of tests on device AV1 and device AV2 determined the onset of resonance for a low-voltage ( $0V \pm 5V$ ) sweep signal over a frequency range from 500Hz to 100kHz. These voltage levels were used to ensure that non-linear stretching of the valve membrane structure did not occur. Non-linearities in the structure would create a stiffer operational regime and, therefore, a corresponding increase in the frequency at which “resonance” occurs. As a result, low-voltage excitation produces a conservative estimate for resonant behavior, which can then be used to determine a desirable quasi-static frequency of operation for the valve. Without fluid above the valve cap and membrane structure, devices AV1 and AV2 were found to exhibit resonance at  $\sim 10kHz$ . With fluid present above the valve cap and membrane structure, resonance was observed at  $\sim 5kHz$ . In this model correlation section, an effort is made to correlate the active valve resonant behavior without the presence of external fluid to theoretical expectations based on the finite-element model described in Chapter 4. Furthermore, an effort is made to estimate the effect of the external fluid added mass on the active valve resonant frequency and to correlate this effect to the experimental downward shift in resonant frequency from  $\sim 10kHz$  to  $\sim 5kHz$ .

**Without Fluid Above Valve Cap and Membrane** An axisymmetric 2-D finite-element model was built for this correlation study with no fluid present above the valve cap and membrane. This model incorporates four-node plane elements for the silicon and glass structural parts of the valve and 4-node acoustic fluid elements for the liquid contained within the hydraulic amplification chamber. These acoustic elements enable fluid-structure interaction between the fluid and the surrounding structure of the HAC chamber. Sensitivity analyses were carried out to evaluate the first resonant frequencies of the coupled system, as a function of variations in important structural parameters and material properties. The parameters investigated were (1) the HAC fluid bulk modulus  $K_f$ , (2) the valve membrane thickness  $t_{vm}$ , (3) the piezoelectric material stiffness  $E_p$ , (4) the HAC fluid chamber height  $t_{HAC}$ , (5) the bottom support plate thickness  $t_{bot}$ , and (6) the top structural plate thickness  $t_{top}$ . The results of these sensitivity analyses are shown in Figure 9.20. In each analysis, the experimental baseline design for the active valve is specified. This baseline design includes the following values for the parameters under investigation:  $K_f = 2GPa$ ,  $t_{vm} = 6\mu m$ ,  $E_p = 6.76GPa$ ,  $t_{bot} = 1000\mu m$ ,  $t_{top} = 1000\mu m$ , and  $t_{HAC} = 200\mu m$ . With these baseline parameter values, a first modal frequency of 14.1kHz was determined. This theoretical value is significantly larger than the experimentally determined 1st modal frequency of 10kHz, and as a result, the sensitivity analyses that follow are meant to determine why this is.

Figure 9.20(a) shows the effect of reduced bulk modulus on the valve first modal frequency. The active valve was designed assuming a fluid bulk modulus value of  $K_f = 2GPa$ . The previous quasi-static model correlation section concluded that a reduction in bulk modulus down to  $K_f = 0.5GPa$  could explain the voltage-valve cap deflection performance reduction seen experimentally at 1kHz. From this modal analysis, however, it is clear that this reduction in modulus to  $K_f = 0.5GPa$  has minimal effect on the 1st modal frequency, dropping it only to 13.7kHz. In fact, a reduction to  $K_f = 0.02GPa$  is required to bring the 1st modal frequency down to 10kHz. It is therefore concluded that the expected fluid bulk modulus value of  $K_f = 0.5GPa$  is not the prime reason for the lower-than expected 1st modal frequency.

Figure 9.20(b) shows the effect of valve membrane thickness on the valve first modal frequency. Based on the valve membrane pressure-deflection results detailed in Chapter 8 (for which there was excellent correlation between theoretical and experimental results for  $t_{vm} = 6\mu m$ ), it is quite certain that the valve membrane thickness is very near to  $t_{vm} = 6\mu m$ . Figure 9.20(b) (solid line) shows that even if the thickness were to deviate anywhere within  $t_{vm} = 5 - 7\mu m$ , the effect on the first modal frequency would be quite small. It is therefore concluded that a slight deviation in valve membrane thickness from the experimentally verified value of  $t_{vm} = 6\mu m$  would not be sufficient to reduce the first modal frequency from 14.1kHz to 10kHz. Additionally, the dotted line in this plot illustrates the first modal frequency of the stand-alone valve cap and membrane structure (with no fluid in contact with its bottom surface) as a function of valve membrane thickness. One observes, in this case, that the modal frequency is very sensitive to valve membrane thickness. The important observation here is that the presence of the fluid in the HAC chamber serves to reduce the modal frequency (from 32.9kHz for the stand-alone valve membrane to 19.6kHz for the active valve coupled system) for a large thickness valve membrane (added mass effect to be discussed shortly) whereas for a small thickness valve membrane the presence of fluid in the HAC serves to increase the modal frequency (from 8.7kHz for the stand-alone valve membrane to 12.6kHz for the active valve coupled system). This illustrates the importance of performing full fluid-structural interaction analyses to predict the full valve modal frequency rather than estimating this modal frequency based on just one of the stand-alone structural components of the full valve.

Figure 9.20(c) shows the effect of piezoelectric material modulus  $E_p$  on the valve first modal frequency. In Chapter 9, this  $E_p$  value was experimentally determined to be 6.76GPa. It is clear from this plot that the valve modal frequency is insensitive to slight variations (between  $E_p = 6 - 8GPa$ ) in this value. It is therefore concluded that the reduction in the first modal frequency from 14.1kHz to 10kHz can not be attributed to an unexpected value of  $E_p$ .

Figures 9.20(d) and 9.20(e) illustrate the effect of the top and bottom structural plate thicknesses on the valve first modal frequency. It makes sense that if the bottom structural plate were to be significantly reduced in thickness, then the drive element portion of the valve

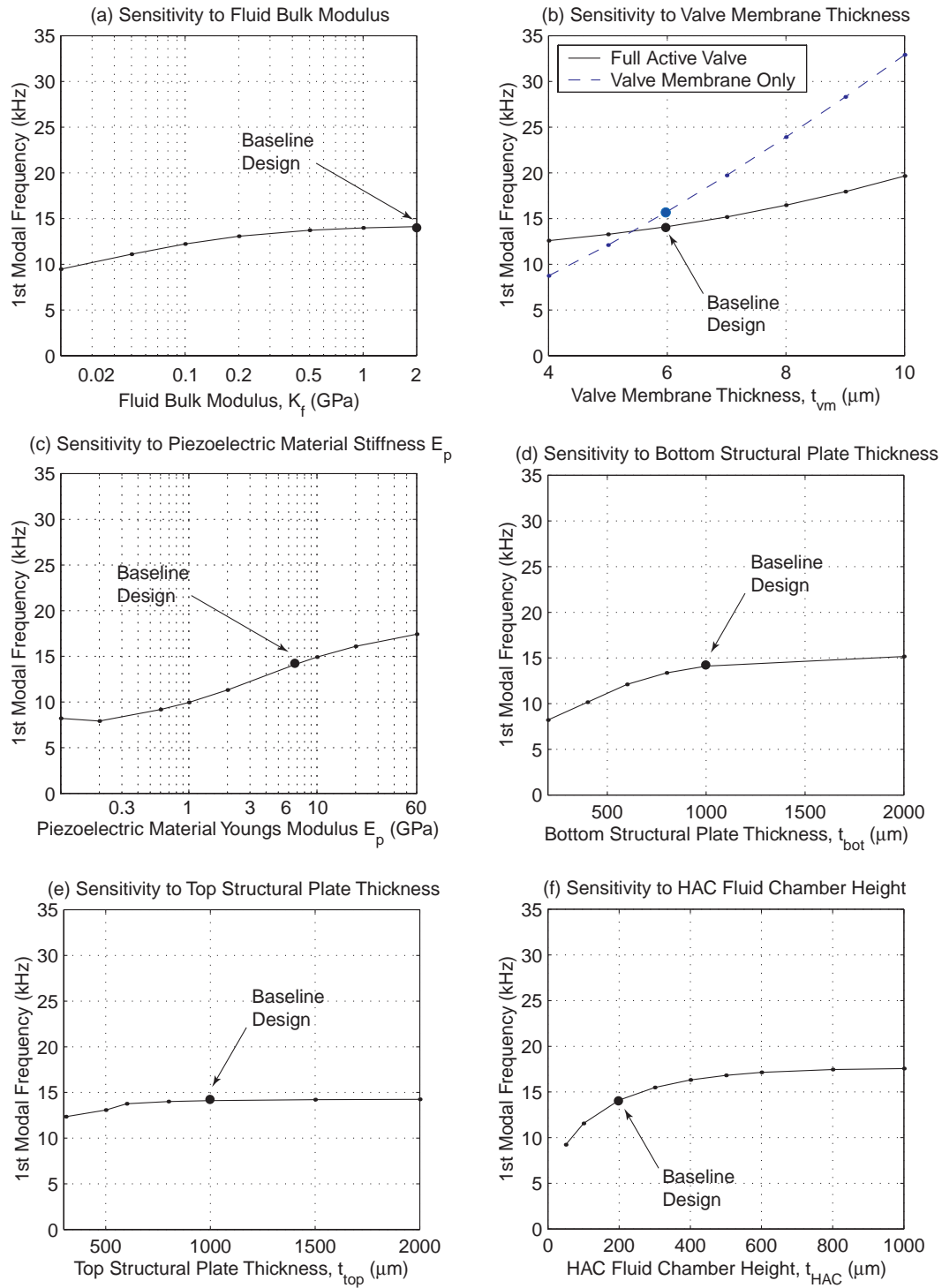


Figure 9.20: Finite-element active valve modal frequency sensitivity studies for (a) the HAC fluid bulk modulus  $K_f$ , (b) the valve membrane thickness  $t_{vm}$ , (c) the piezoelectric material stiffness  $E_p$ , (d) the HAC fluid chamber height  $t_{HAC}$ , (e) the bottom support plate thickness  $t_{bot}$ , and (f) the top structural plate thickness  $t_{top}$ .

would become much softer than in the baseline design, and the full valve modal frequency could be expected to drop. This phenomenon is observed in Figure 9.20(d). Likewise, if the top structural plate were to be significantly reduced in thickness, the HAC structural chamber would become much softer than in the baseline design, and the full valve modal frequency could be expected to drop. This phenomenon is observed in Figure 9.20(e). In the active valve devices experimentally tested in this thesis, however, the thicknesses of these two plates are well-characterized to each have a thickness of at least  $1000\mu m$ . Therefore, it is concluded that the top and bottom plate thicknesses do not contribute to the reduction in the active valve first modal frequency from 14.1kHz to 10kHz.

Figure 9.20(f) shows the effect of the HAC fluid chamber height  $t_{HAC}$  on the the valve first modal frequency. The plot illustrates that the modal frequency is extremely sensitive to a reduction in this chamber height from the baseline design value of  $t_{HAC} = 200\mu m$  (where the first modal frequency is 14.1kHz) to a smaller value of  $t_{HAC} = 50\mu m$  (where the 1st modal frequency is 9.2kHz). The reason for this significant frequency reduction as the chamber height is reduced is the presence of inertial coupling between the moving drive element piston and the adjacent glass surfaces that form the top of the HAC chamber. A comprehensive discussion of inertia coupling is found in Blevins [5]. The following excerpt is taken from [5]:

As a cross section accelerates in a fluid, pressure gradients will be generated in the surrounding fluid. These pressure gradients can exert fluid forces on adjacent structures. If the adjacent structures are not rigid, they will in turn deflect and generate forces on the accelerating cross section. This interaction between adjacent elastic structures is called inertial coupling. Inertial coupling increases as the distance between structures decreases. Inertial coupling can significantly affect the natural frequencies and mode shapes of [closely-packed structures] if the density of the surrounding fluid is comparable to or larger than the average density of the [structures]. *Blevins, p.403*

Prior to assembly of devices AV1 and AV2, the chamber height  $t_{HAC}$  of these devices was measured to be  $\sim 200\mu m$ . However, the geometry of the glass layer that forms this chamber is significantly more complex (see valve structure shown in Figure 9.1) than just having a volume of fluid  $200\mu m$  in height above the drive element piston and beneath the valve cap and membrane. In reality, a series of fluid channels exists (termed “HAC Through Holes” and “HAC Radial Channels” in Figure 9.1) through this glass layer to allow fluid to couple the piston motion to the valve membrane motion. During the design stages of the active valve device, a bottom structural stop beneath the valve cap (at  $Z_{vc} = -16.5\mu m$ ) was set as a requirement. These channels were therefore implemented to satisfy this requirement. The heights of the “HAC Radial Channel” features in Layer 7 are no more than  $100\mu m$ , and as a

result, acceleration of fluid in these channels could be a significant inertial coupling effect. Based on these arguments, it is concluded that the small-size fluid pathways through the complex glass Layer 6 HAC chamber are the most probable reason for the reduction in active valve modal frequency from the baseline design FEM expectation of  $14.1kHz$  to the experimentally-determined frequency of  $10kHz$ . Future valve design iterations should include larger  $t_{HAC}$  chamber heights (ie:  $t_{HAC} = 500\mu m$ ) with no complex fluid routing pathways. Eliminating the presence of the valve cap bottom structural stop might be a necessary consequence.

**With Fluid Above Valve Cap and Membrane** The previous model correlation section determined that inertial coupling effects between the accelerating fluid and the piston structure within the HAC chamber were the most likely reason for the lower-than expected active valve first modal frequency, when no fluid was present above the valve cap and membrane structure of the valve. Experimentally, without this fluid above the valve cap and membrane, the first modal frequency was found to be  $\sim 10kHz$ . With this fluid above the valve cap and membrane, the modal frequency was found to be  $\sim 5kHz$ . The following section attempts to explain this downward shift in valve modal frequency.

The conclusion of this section will be that the presence of fluid above the valve cap and membrane structure serves to increase the effective mass of the valve cap and membrane, thereby reducing the overall modal frequency. This statement is consistent with a discussion found in Blevins [5] concerning the effect of surrounding fluid on a circular plate in vibration. The following excerpt is taken from [5]:

As an elastic plate vibrates in a fluid, the fluid immediately surrounding the plate is set into motion and the plate will radiate sound waves into the far field... In general, the fluid will impose both added mass and damping forces on the plate. The added mass will lower the natural frequency of the plate from that which would be measured in a vacuum, and the damping of the plate will be increased. *Blevins, p.413*

Taking as an example a circular disk with radius  $r_a$  exposed on one side to an inviscid compressible fluid of density  $\rho_{fluid}$  (Blevins, p.414), the added mass of the disk for acceleration perpendicular to the plane of the disk can be estimated as  $M_{added} = \frac{8}{3}\rho_{fluid}r_a^3$ . For a back-of-the-envelope calculation on the valve cap and membrane in the active valve, let  $r_a = R_{vm}$ . The corresponding added mass is therefore  $M_{added} = \frac{8}{3}(777\frac{kg}{m^3})(700\mu m)^3 = 7.11e^{-7}kg$ . The baseline mass of the valve cap structure is  $M_{vc} = \rho_{Si}\pi R_{vc}^2 t_{vc} = (2200\frac{kg}{m^3})\pi(250\mu m)^2(300\mu m) = 1.30e^{-7}kg$ .

To therefore estimate the reduction in active valve first modal frequency due to the presence of fluid above the valve cap and membrane, the finite-element model from the previous section



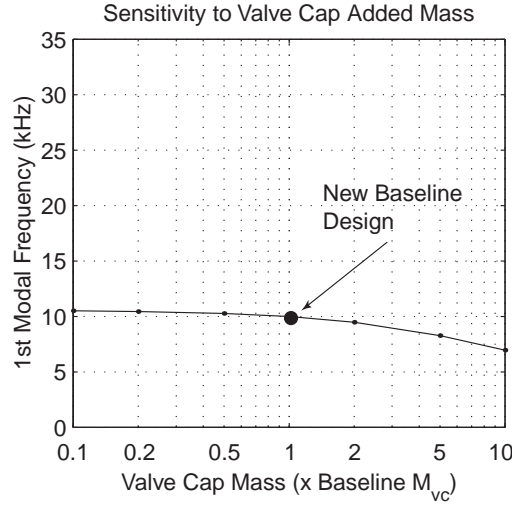


Figure 9.21: Finite-element modal frequency sensitivity to valve cap added mass. The presence of fluid above the valve cap and membrane structure creates an effective added mass to the coupled structure which serves to reduce the first modal frequency of the active valve device.

was run with a modified density of the valve cap material such that its mass was equal to  $M_{vc,modified} = M_{vc} + M_{added} = 8.42e^{-7}kg$  (an increase from the original valve cap mass of 6.5 times). In this comparison study, a new baseline valve design was chosen to include a fluid bulk modulus value of  $K_f = 0.5GPa$  and an HAC chamber height of  $t_{HAC} = 66\mu m$  so that the first modal frequency of the valve without the added mass was exactly 10.0kHz. This baseline FEM model therefore matched the experimental result without fluid above the valve cap and membrane. Now, with the addition of the added mass (x6.5), the first modal frequency of the valve was determined to be 7.8kHz (a 22% decrease from the new baseline design modal frequency of 10.0kHz). Figure 9.21 illustrates the theoretical effect of added mass (from x0.1 to x10) on the first modal frequency of the active valve structure. Over this range of added mass, the first modal frequency is affected, but not substantially.

For the active valve devices tested experimentally, there is a 50% reduction in the first modal frequency (from  $\sim 10kHz$  to  $\sim 5kHz$ ) due to the presence of fluid above the valve cap and membrane. The above study on the new baseline design (in which a 22% reduction was calculated) provides for an added mass argument that also applies to the experimental results, however, this value of added mass only partially reduces the first modal frequency to correlate with the experimental results. Since this added mass calculation was for a circular plate in an infinite fluid medium, and since in the real active valve structure, there exist structural surfaces within  $50-100\mu m$  of the top surface of the valve cap and membrane, it is likely that the same sort of inertial coupling effects as discussed in the previous section are coming into play. These unmodeled effects could potentially cause a further reduction in first modal frequency.

It is therefore concluded that the fluid mass (acceleration and inertia effects) above the valve cap and membrane and the presence of the flow channel structure near to this valve cap and membrane provide an additional mass seen by the active valve structure as it vibrates, thereby reducing the valve first modal frequency from the case when no fluid exists above the valve cap and membrane. Future active valve design iterations should more thoroughly evaluate this added mass effect on valve dynamic performance. The recommendation section of Chapter 10 further discusses these recommended future analyses.

### 9.3.2 Testing Section 2: Active Valve Fluid Flow Regulation

To characterize the flow regulation capability of the active valve devices documented in this thesis, a series of tests was performed. The first test focused on experimentally determining the quasi-static flow rate versus valve cap opening curves for varying applied differential pressures  $P_1 - P_2$  across the valve orifice. These results were then compared to predictions based on the flow models developed in Chapter 5 of this thesis and based on [2]. The second test evaluated the flow regulation capability of the active valve by varying the duty cycle of valve opening at a prescribed differential pressure  $P_1 - P_2$  and measuring the average flow rate through the valve orifice. The third test evaluated the flow regulation capability of the active valve at a prescribed operating frequency of 1kHz for increasing differential pressures across the valve orifice. Limitations in valve performance could therefore be determined as this differential pressure was increased. For each of these tests, an estimate of the measurement error is included in the experimental results plots detailed in this section.

#### Static Flow Tests

To determine the quasi-static flow rate versus valve opening curves for a series of imposed differential pressures across the valve orifice, the fluids test-rig (described in Chapter 6) was used. In these tests, no voltage was applied to the piezoelectric material. Rather, the valve cap position was controlled by regulating the pressure  $P_{HAC}$  to the hydraulic amplification chamber. For a given test run at a desired differential pressure  $P_1 - P_2$ ,  $P_{HAC}$  was first increased to move the valve cap upward against the fluid orifice (with  $P_1 = P_2 = 0$ ).  $P_1$  and  $P_2$  were then independently increased to set the desired differential pressure across the orifice. In order to maintain the valve cap against the orifice,  $P_{HAC}$  was varied real-time in conjunction with the increases in  $P_1$  and  $P_2$ . With the proper differential pressure set, a data acquisition system was started, into which the valve cap displacement, pressure measurement of  $P_{HAC}$ , pressure measurement of  $P_1$ , pressure measurement of  $P_2$ , and flow sensor measurement  $Q_{avg}$  were input. As detailed in Chapter 6, the flow rate measurements were taken using a calibrated flow orifice system.

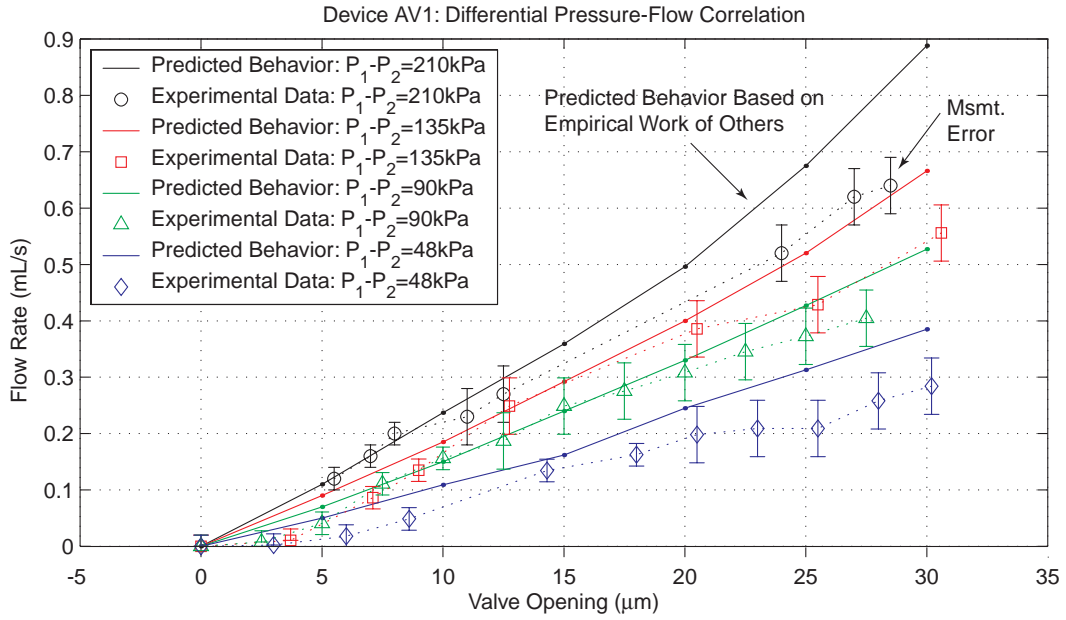


Figure 9.22: Model correlation to device AV1 quasi-static fluid flow rate versus valve opening behavior for differing imposed differential pressures. The experimental flow rates fall approximately 10 – 30% short of predictions based on the empirical work of others. Error bars on the data indicate estimates of measurement error. Two flow sensors of different ranges were used in these experiments, resulting in different levels of measurement error for lower and higher flow rates. These measurement errors were estimated based on the flow sensor calibration errors, the accuracy of the applied differential pressure, and human error associated with controlling the quasi-static nature of the experiments.

In order to obtain quasi-static flow measurements for a given valve cap opening,  $P_{HAC}$  was decreased slowly over a period of approximately 10 minutes. The valve cap was allowed to move through its full stroke of 30–33 $\mu\text{m}$ . The time constant of the flow orifice sensor was on the order of a few seconds, and therefore this measurement procedure enabled quasi-static measurements. Tests were performed for differential pressures of  $P_1 - P_2 = 48\text{kPa}$ , 90kPa, 135kPa, and 210kPa. For each test run, selected points were chosen to plot. Figure 9.22 overlays these experimental results with the predicted behavior based on the flow models used in Chapter 5 of this thesis. Since the Chapter 5 flow models are based on a compilation of empirical work from other researchers, the line of predicted behavior in Figure 9.22 is understood to be of only “limited accuracy”, in other words, it is not based on exact theory. In general, this comparison shows that the predicted behavior based on the empirical work of others overpredicts the flow rate behavior by approximately 10 – 30%. This is most likely due to differing geometric features between the orifice structures contained within the empirical results and the valve orifice structure in this thesis. Specifically, since the empirical results are based on macroscale orifice structures

with rounded and filleted features, one would expect better flow rate capabilities for given applied differential pressure and valve opening than in the microscale valve orifice structure detailed in this thesis, which possesses comparatively sharp corners. Furthermore, at small valve openings, the flow rate appears to be choked. Only when the valve cap reaches an opening of  $\sim 4\mu m$  does the fluid really begin to flow. Based on this data, active valve device AV1 can be characterized as a flow control device. These differential-pressure flow experiments were performed for differential pressures up to  $P_1 - P_2 = 210kPa$ . When tested to differential pressures greater than this value, interesting oscillatory behavior of the valve cap structure occurred. These observations and the corresponding efforts to determine the cause of these phenomena are detailed in the following section.

### Self-Oscillatory Behavior of Valve Cap During Static Flow Tests

The original objective of the static flow tests described above was to evaluate the differential pressure-flow behavior through the valve orifice for  $P_1 - P_2$  up to 800kPa, since this was the designed-for maximum differential pressure to be experienced in a complete MHT micropumping system. However, in testing the valve beyond  $P_1 - P_2 = 210kPa$ , self-oscillatory behavior of the valve cap at its resonant frequency of  $5kHz$  was observed and measured (remember, in these tests, there is no actuation of the piezoelectric drive elements – all pressures are controlled via external regulators). It is believed that this oscillatory behavior may be induced by vortices and unsteady flow phenomena as the flow transitions from the laminar to the turbulent flow regime. In an effort to evaluate this hypothesis, the following experiments were carried out.

For each of a series of differential pressures ( $P_1 - P_2 = 80kPa, 130kPa, 160kPa, 200kPa, 230kPa, 240kPa, 305kPa, \text{ and } 360kPa$ ), the valve cap was controlled to slowly open from its closed position using the same procedure as for the static flow tests. During this process, the valve opening  $Z_{vc,opening}$ , the quasi-static flow rate  $Q_{avg}$ , and the imposed differential pressure  $P_1 - P_2$  were measured real-time. The valve orifice geometry is shown in Figure 9.23. Numerous data points were selected and post-processing operations were performed to calculate the Reynolds number of the flow through the valve orifice, according to the relation  $RE_{Dorifice} = \frac{Q_{avg}}{D_{orifice}\nu}$ . Additionally, an “Instability Value” was determined for each data point corresponding to the behavior of the valve cap as it opened. The three types of valve cap behaviors observed (using the laser vibrometer system) during these tests were (1) smooth steady motion of the valve cap, (2) slightly rough motion of the valve cap (but always with negligible amplitude), and (3) oscillatory motion of the valve cap at a frequency of  $5kHz$  and with peak-peak displacement of  $3 - 4\mu m$ . Figure 9.24 displays typical displacement signals over a time period of 10 ms for each of these types of behaviors. At each data point, an Instability Value of 1, 2, or 3 was assigned for each of the respective measured behaviors. Since the valve cap structure essentially reacts as a sensor to any pressure fluctuations in the flow channel above

it, these assigned Instability Values can provide some insight into the behavior of the fluid as it flows through the orifice.

Figure 9.25 displays an example test run for the case of  $P_1 - P_2 = 80kPa$ . Plots of the Instability Value versus  $Z_{vc,opening}$ ,  $P_1 - P_2$  versus  $Z_{vc,opening}$ ,  $Q_{avg}$  versus  $Z_{vc,opening}$ , and  $RE_{Dorifice}$  versus  $Z_{vc,opening}$  are included. Notice that since the Reynolds number is proportional to the average flow rate, the  $Q_{avg}$  and  $RE_{Dorifice}$  curves in Figure 9.25(c) are identical, only the axes are scaled differently. Additionally, notice that  $P_1 - P_2$  is not constant over the length of the run. During the testing, it was very difficult to maintain the differential pressure at a constant value. For this test case of  $P_1 - P_2 = 80kPa$ , the valve cap smoothly moves through an opening trajectory, up to approximately  $Z_{vc,opening} = 19\mu m$ . At these conditions, the valve cap displacement begins to exhibit a slight roughness in its measured displacement (with roughness amplitude less than  $0.4\mu m$ ), but continues to open with no effect on valve cap position. At  $Z_{vc,opening} = 28\mu m$ , the valve cap displacement returns to smooth behavior. The corresponding Reynolds numbers for these transition points are  $RE_{Dorifice} = 788$  and  $RE_{Dorifice} = 928$ , respectively. In Figure 9.25(a), an Instability Value of 1 represents the smooth motion of the valve cap. An Instability Value of 2 represents slightly rough motion.

In order to obtain some understanding of the relationship between the valve cap behavior and the corresponding  $RE_{Dorifice}$ , test runs were carried out for the 8 differential pressure settings detailed above. Figure 9.26 plots the Instability Value versus  $Z_{vc,opening}$  curve for  $P_1 - P_2 = 80kPa$ ,  $P_1 - P_2 = 130kPa$ , and  $P_1 - P_2 = 160kPa$  respectively. Figure 9.27 plots the Instability Value versus  $Z_{vc,opening}$  curve for  $P_1 - P_2 = 200kPa$ ,  $P_1 - P_2 = 2300kPa$ , and  $P_1 - P_2 = 240kPa$  respectively. Figure 9.28 plots the Instability Value versus  $Z_{vc,opening}$  curve for  $P_1 - P_2 = 305kPa$  and  $P_1 - P_2 = 360kPa$  respectively. In observing these plots, it is clear that oscillatory behavior does not occur until the case of  $P_1 - P_2 = 200kPa$ . Under this differential pressure, at a value of  $Z_{vc,opening} = 8\mu m$ , the valve cap experiences a transition from smooth motion to oscillatory behavior with a frequency of 5kHz and a peak-peak displacement of  $6 - 8\mu m$ . The corresponding Reynolds number for this transition is  $RE_{Dorifice} = 615$ . At a deflection of  $Z_{vc,opening} = 19\mu m$ , the valve cap stops oscillating and exhibits only slightly rough behavior. The corresponding Reynolds number for this transition is  $RE_{Dorifice} = 969$ . And finally, when the valve cap approaches the lower valve stop, its motion once again becomes smooth, most likely caused by interaction with the solid surface below it. The corresponding Reynolds number for this transition is  $RE_{Dorifice} = 2000$ . Similar behavior is observed for larger imposed differential pressures as well. For the case of  $P_1 - P_2 = 360kPa$ , multiple transitions between smooth, oscillatory, and rough are observed. It appears as though upon separation from the upper valve orifice stop, the valve cap immediately begins to oscillate. It then transitions back to smooth behavior at  $Z_{vc,opening} = 4.5\mu m$ , back to oscillatory motion at  $Z_{vc,opening} = 7.5\mu m$ , back to smooth motion at  $Z_{vc,opening} = 13\mu m$ , and then to rough behavior

at  $Z_{vc,opening} = 20\mu m$ .

To better understand the relationship between these transition behaviors and the Reynolds number at which they occur, all 8 plots are combined in Figure 9.29. Regions of smooth, rough, and oscillatory behavior are clearly evident. Figure 9.30 is produced by estimating the boundaries between these regions and labeling the corresponding  $RE_{Dorifice}$  values at these boundary data points. In this plot, the distinct regions are detailed. Notice that a transition to rough valve cap motion occurs for Reynolds numbers between  $RE_{Dorifice} = 800 - 1100$ . Additionally, for large differential pressures, oscillatory valve cap behavior begins typically at  $RE_{Dorifice} = 500 - 600$ . Since rough valve cap behavior is characterized by only a tiny roughness in the displacement response (typically peak-peak displacement of less than  $0.4\mu m$ ), the valve cap itself remains in a stable operating condition. It is only when large amplitude oscillatory response occurs that the valve cap becomes unstable. Figure 9.31 plots this stable versus unstable representation. In essence, smooth and rough valve cap behavior have been grouped together to form the stable regions. Figure 9.32 plots experimental lines of constant Reynolds number over the data points for all 8 test cases and Figure 9.33 compares these lines of constant Reynolds number to the expected lines obtained from model simulations presented in Chapter 4. Notice that all of the experimentally determined lines of constant  $RE_{Dorifice}$  are very close to the theoretical predictions for low to moderate values of imposed differential pressure (ie: up to  $P_1 - P_2 = 150kPa$ ). Once the differential pressure is increased further, experimental correlation to theory is still good for low valve openings (lines of constant  $RE_{Dorifice}=400, 500, 800$ ), however the experimental lines of larger constant  $RE_{Dorifice} = 1000, 1500, 2200$  begin to bend more sharply upward from the theoretical predictions. This bending is directly in relation to the region of oscillatory behavior, which is bounded by a value of  $RE_{Dorifice} \sim 1000 - 1100$  for the larger differential pressures. If one were to conclude that the measurements of smooth valve cap motion correspond to a laminar flow regime and that the slightly rough valve cap motion corresponds to a turbulent flow regime, it could therefore be argued that the oscillatory behavior of the valve cap structure occurs in a transition regime (characterized by  $RE_{Dorifice}$  between  $\sim 500$  and  $\sim 1100$ ).

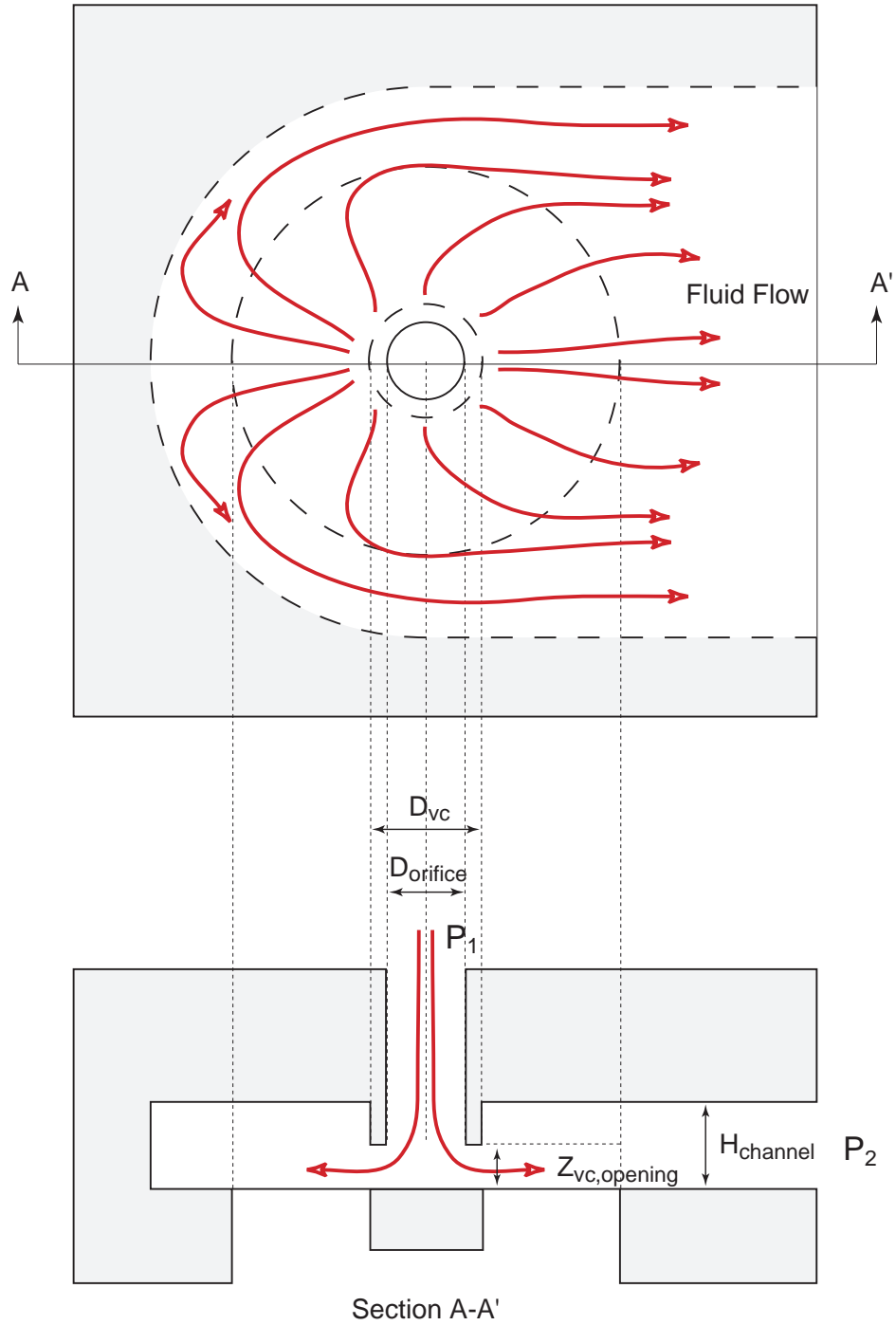


Figure 9.23: Schematic of valve cap and membrane orifice structure. For the active valve geometry tested in this thesis,  $D_{orifice} = 500\mu m$ ,  $Z_{vc,opening} = 0-30\mu m$ , and  $H_{channel} \sim 100\mu m$ . Notice that the fluid flows radially outward over valve membrane, primarily to one side of the structure. The other side is blocked.

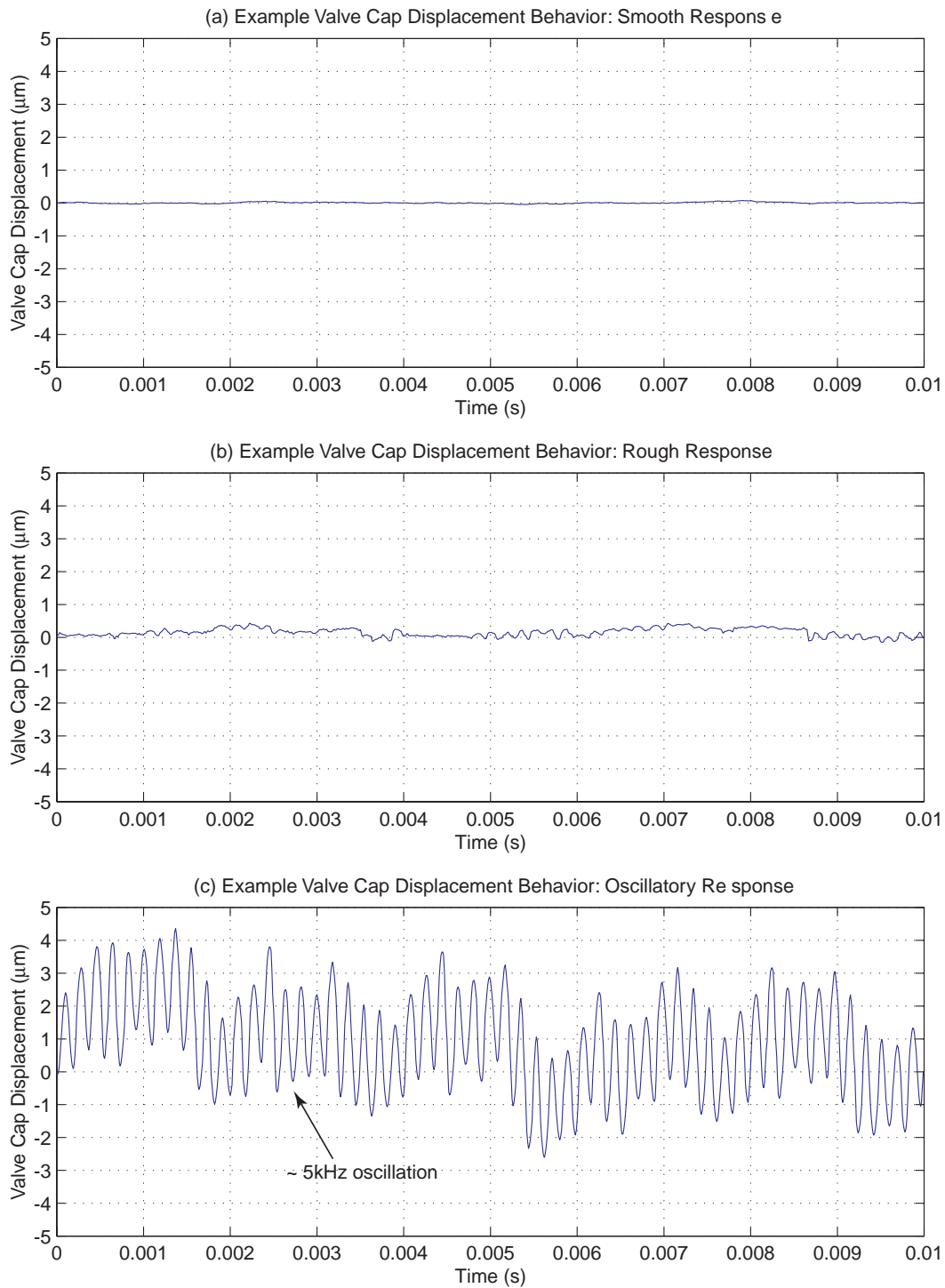


Figure 9.24: Representative displacement signals corresponding to stable and unstable valve cap behavior during quasi-static opening: (a) smooth displacement response (Instability Value=1), (b) slightly rough displacement response (Instability Value=2), characterized by random peak-peak motion less than  $0.4\mu\text{m}$ , and (c) oscillatory response characterized by  $3 - 4\mu\text{m}$  peak-peak oscillations at 5kHz (Instability Value=3).



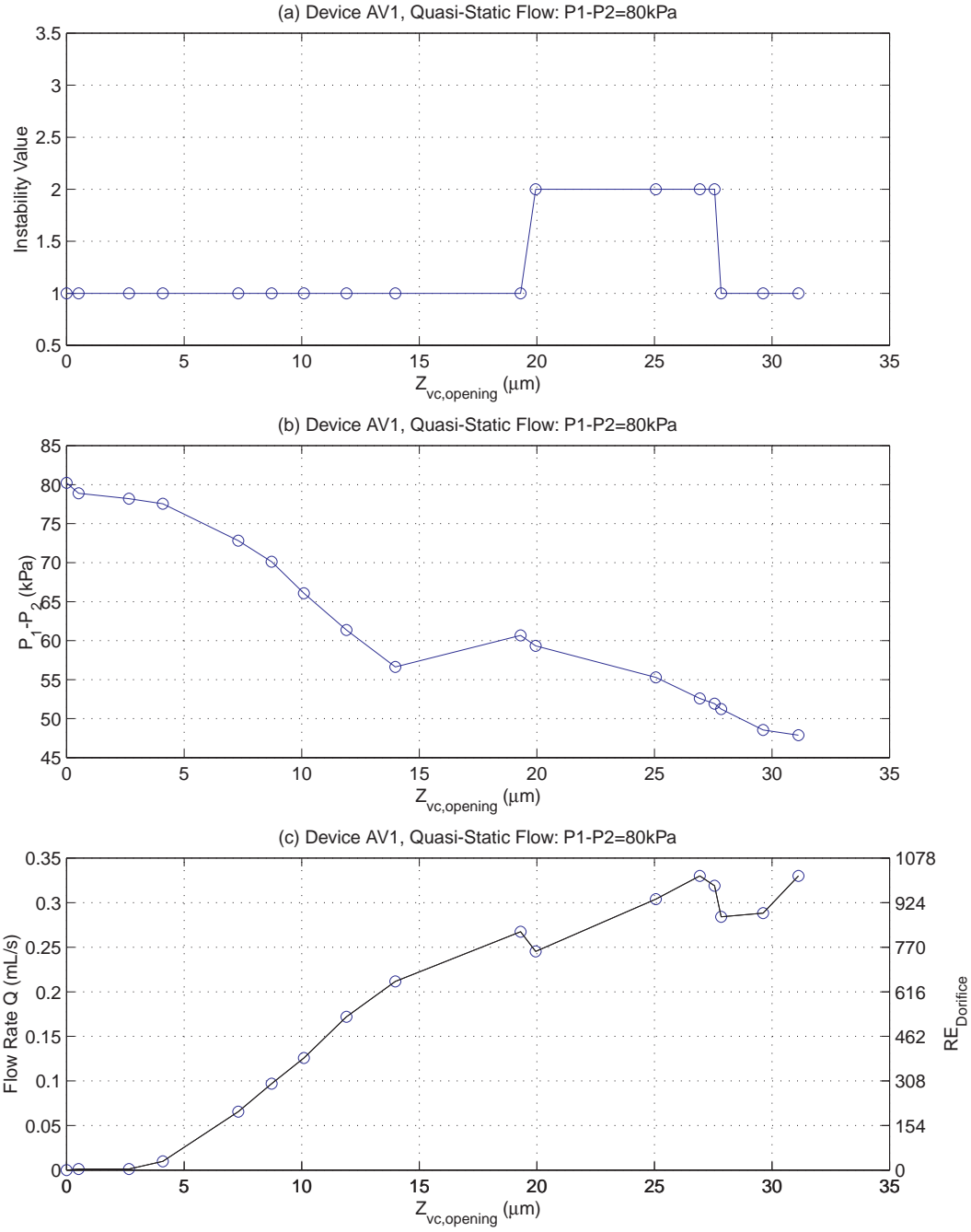


Figure 9.25: Representative plots for valve cap behavior, differential pressure, and flow rate during quasi-static opening for  $P_1 - P_2 = 80 \text{ kPa}$ . The valve cap opening motion transitions from smooth behavior to rough behavior at a deflection of  $Z_{vc, opening} = 19 \mu\text{m}$  and transitions back to smooth behavior at a deflection of  $Z_{vc, opening} = 28 \mu\text{m}$ .

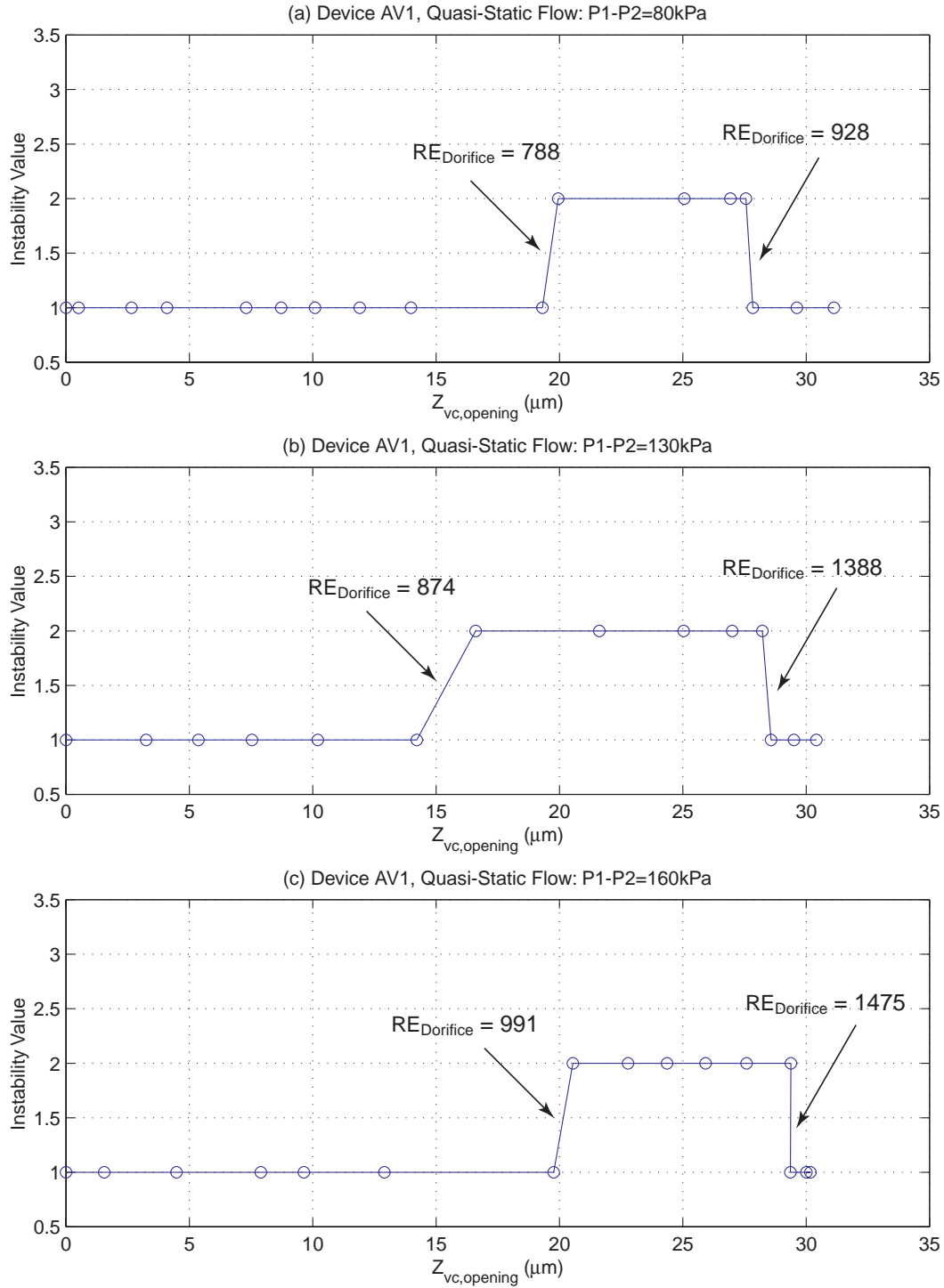


Figure 9.26: Valve cap Instability Values during quasi-static opening for  $P_1 - P_2 = 80 \text{ kPa}$ ,  $P_1 - P_2 = 130 \text{ kPa}$ , and  $P_1 - P_2 = 160 \text{ kPa}$ . Corresponding Reynolds numbers are labeled at the transition locations.

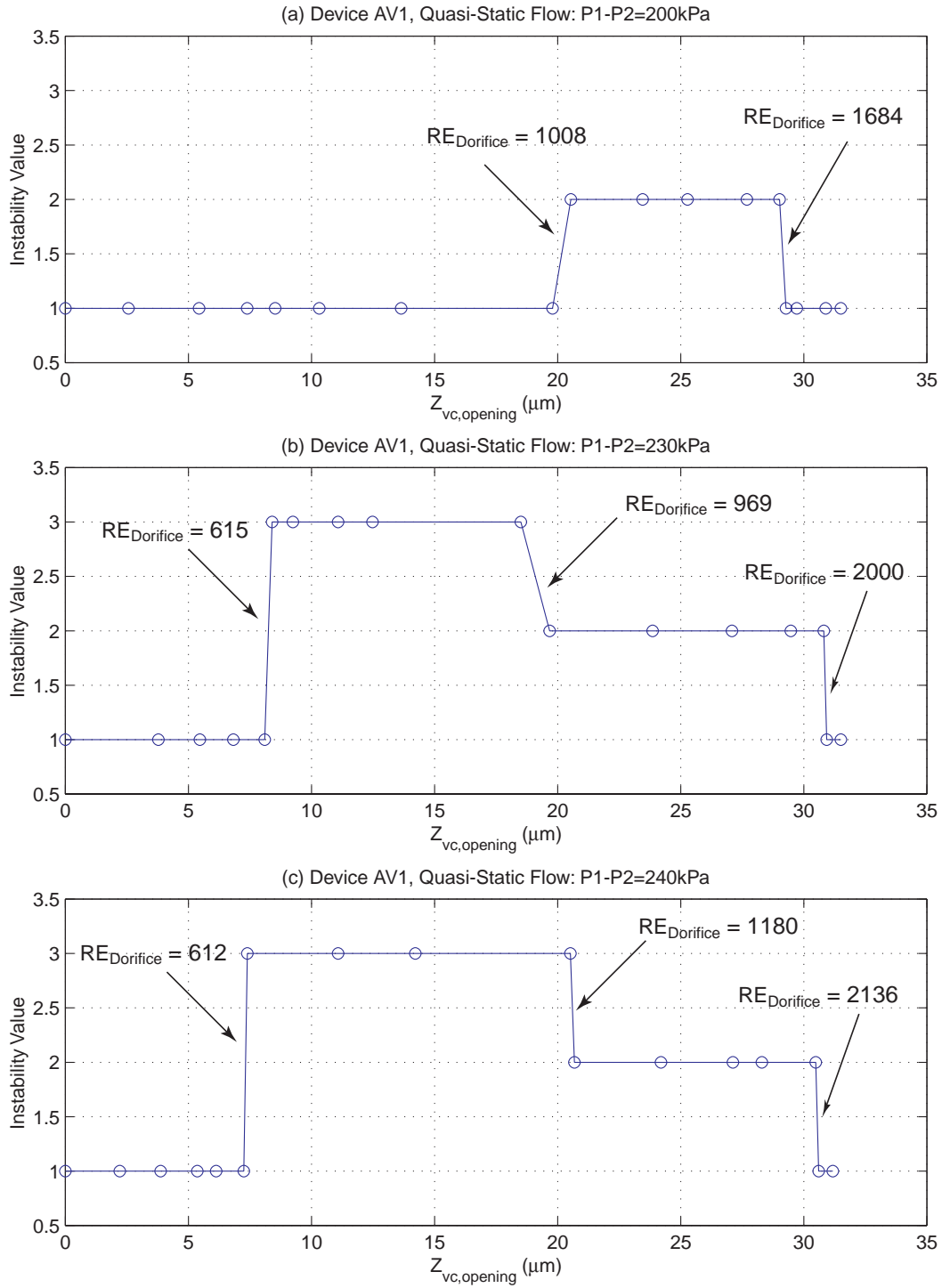


Figure 9.27: Valve cap Instability Values during quasi-static opening for  $P_1 - P_2 = 200 \text{ kPa}$ ,  $P_1 - P_2 = 230 \text{ kPa}$ , and  $P_1 - P_2 = 240 \text{ kPa}$ . Corresponding Reynolds numbers are labeled at the transition locations.

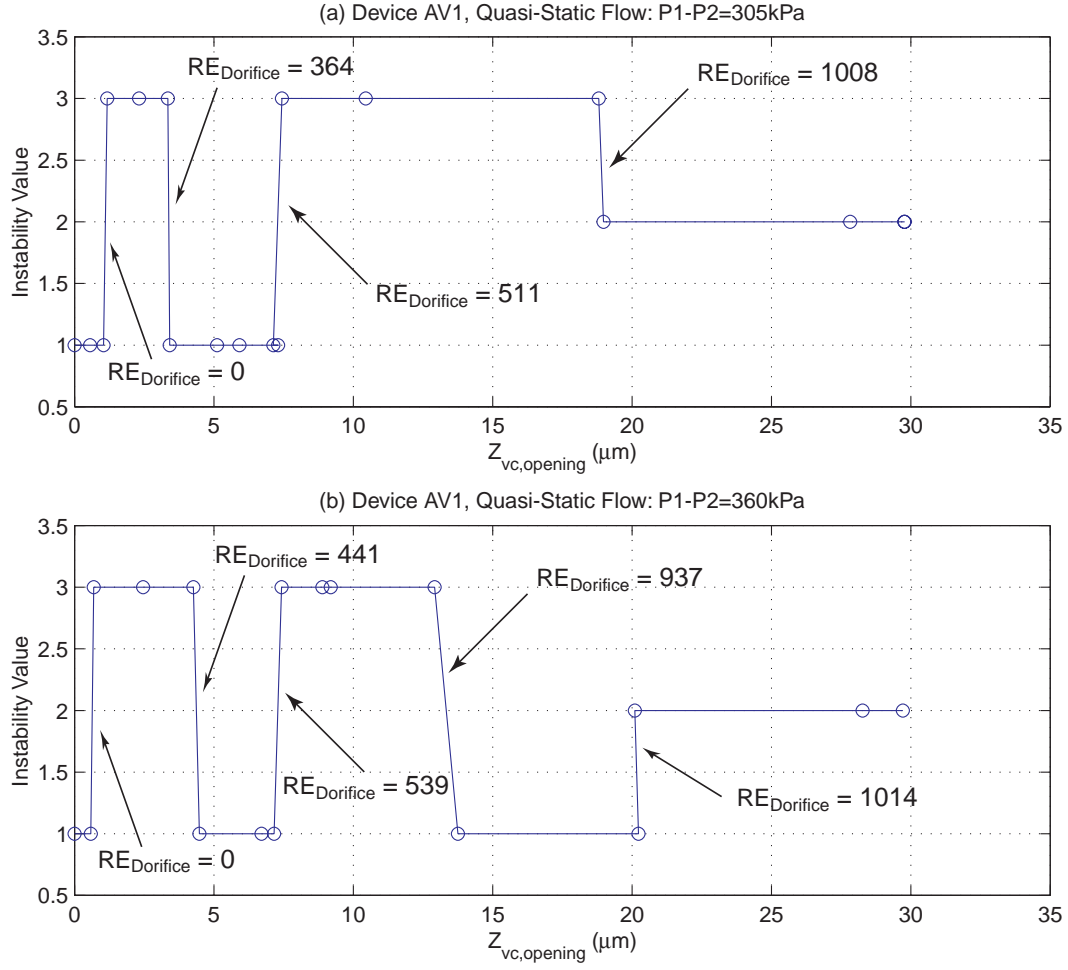


Figure 9.28: Valve cap Instability Values during quasi-static opening for  $P_1 - P_2 = 305 \text{ kPa}$  and  $P_1 - P_2 = 360 \text{ kPa}$ . Corresponding Reynolds numbers are labeled at the transition locations.

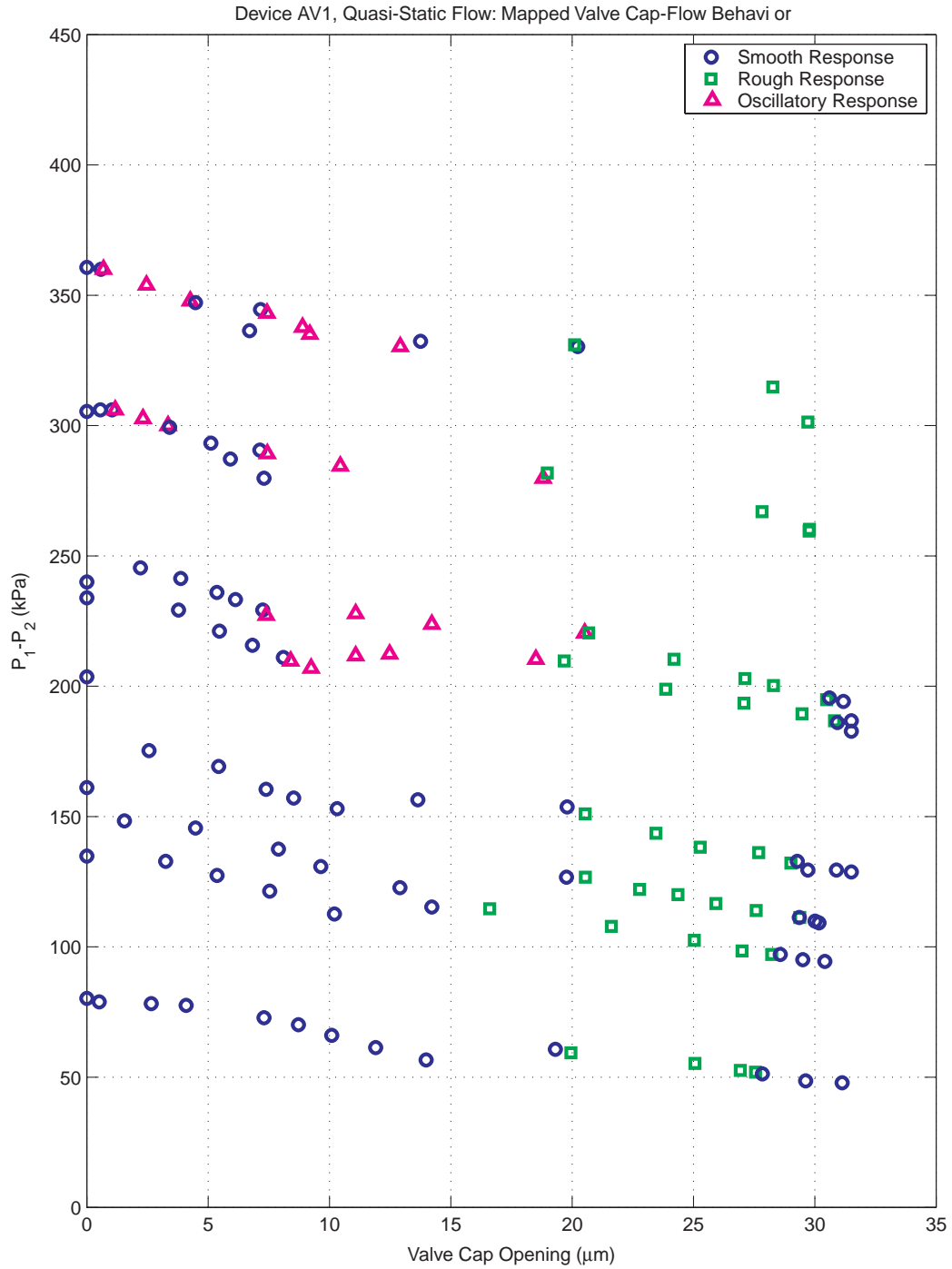


Figure 9.29: Complete grouping of all valve cap Instability Values plotted as  $P_1 - P_2$  vs.  $Z_{vc,opening}$ . Region of valve cap oscillation defined by triangular data points.

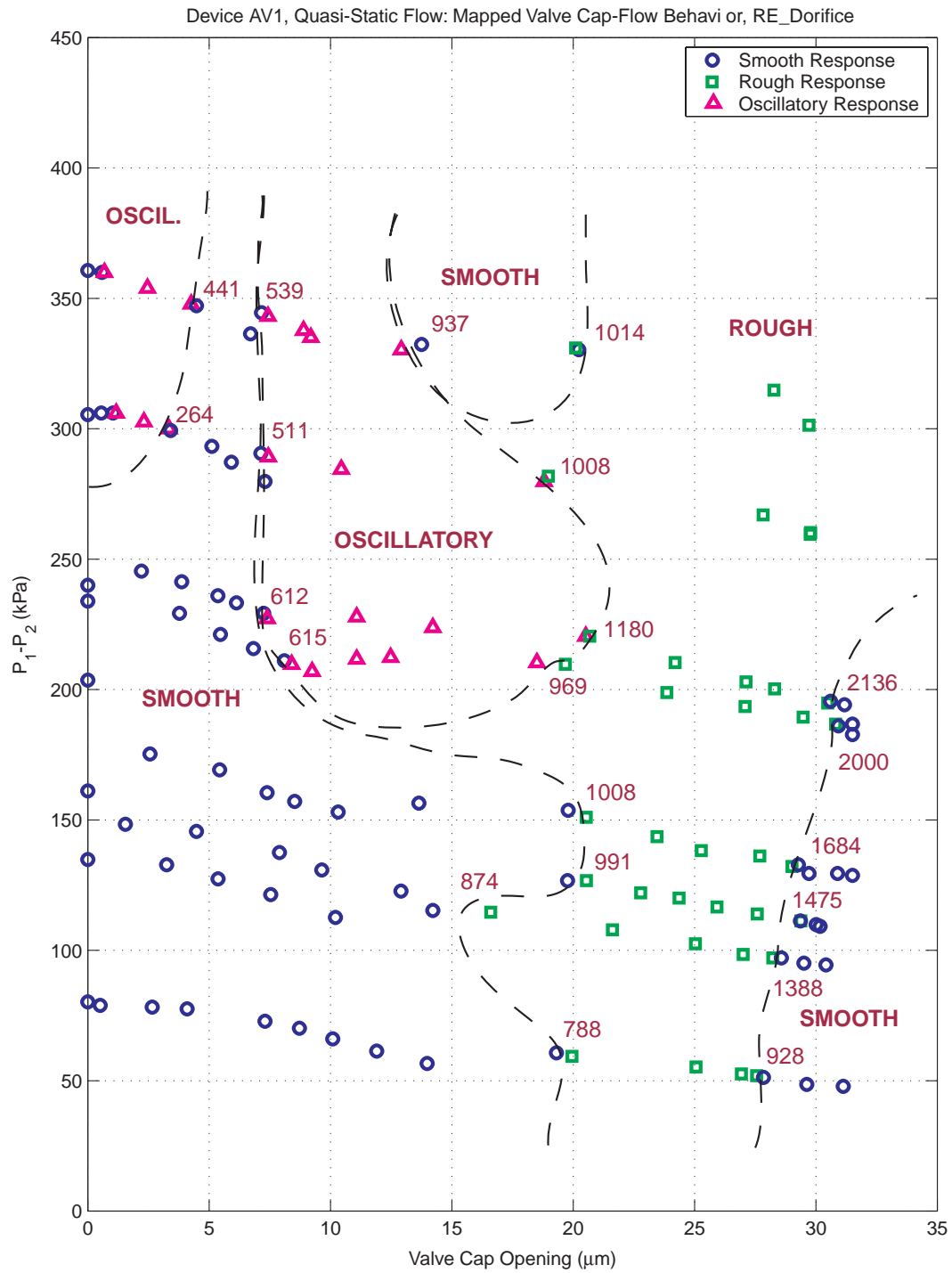


Figure 9.30: Estimated boundaries for smooth, rough, and oscillatory regions plotted as  $P_1 - P_2$  vs.  $Z_{vc, opening}$ . Corresponding transition Reynolds numbers are displayed along these boundary lines.

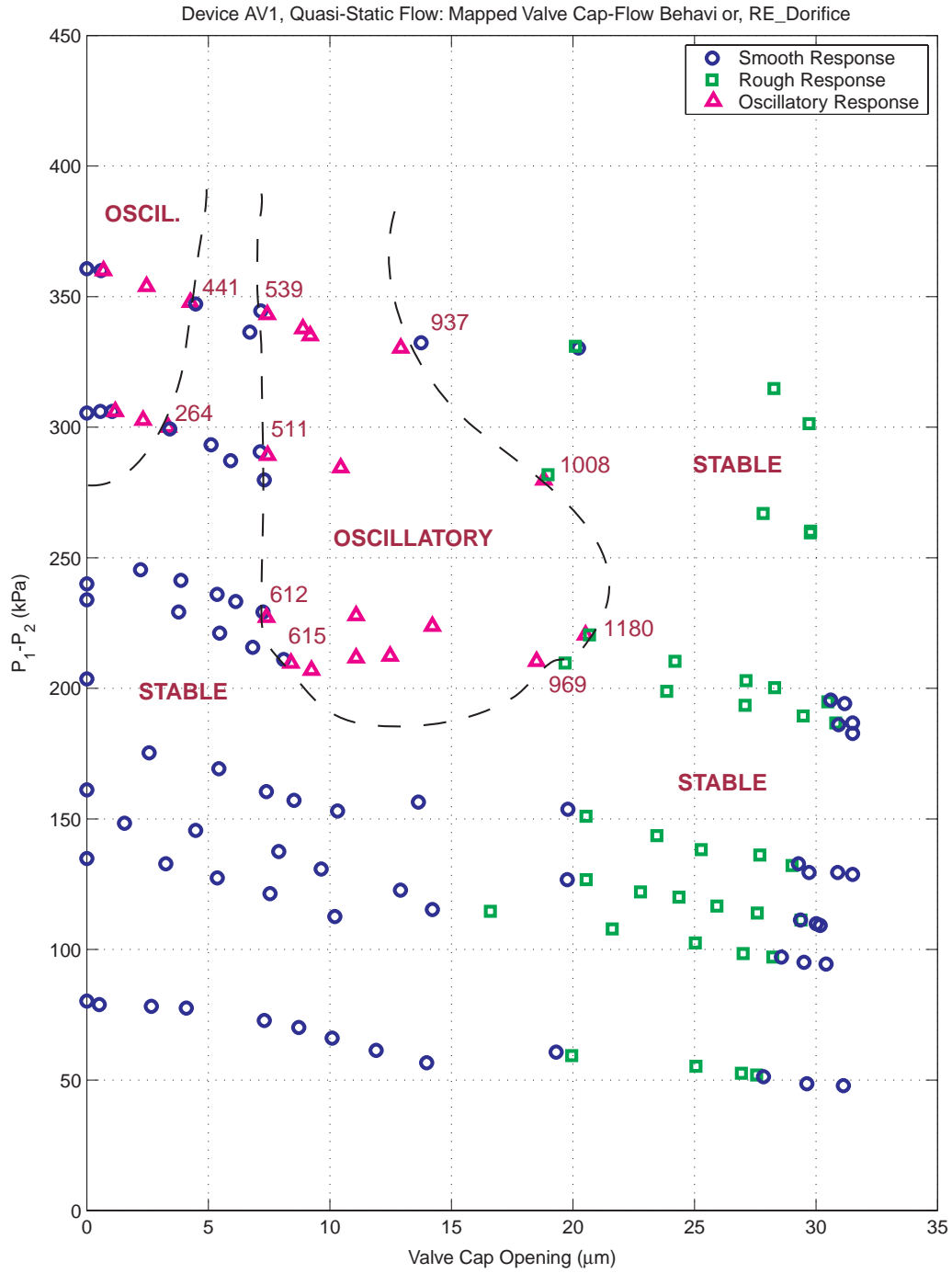


Figure 9.31: Estimated boundaries for unstable and stable regions plotted as  $P_1 - P_2$  vs.  $Z_{vc,opening}$ . Corresponding transition Reynolds numbers are displayed along these boundary lines.

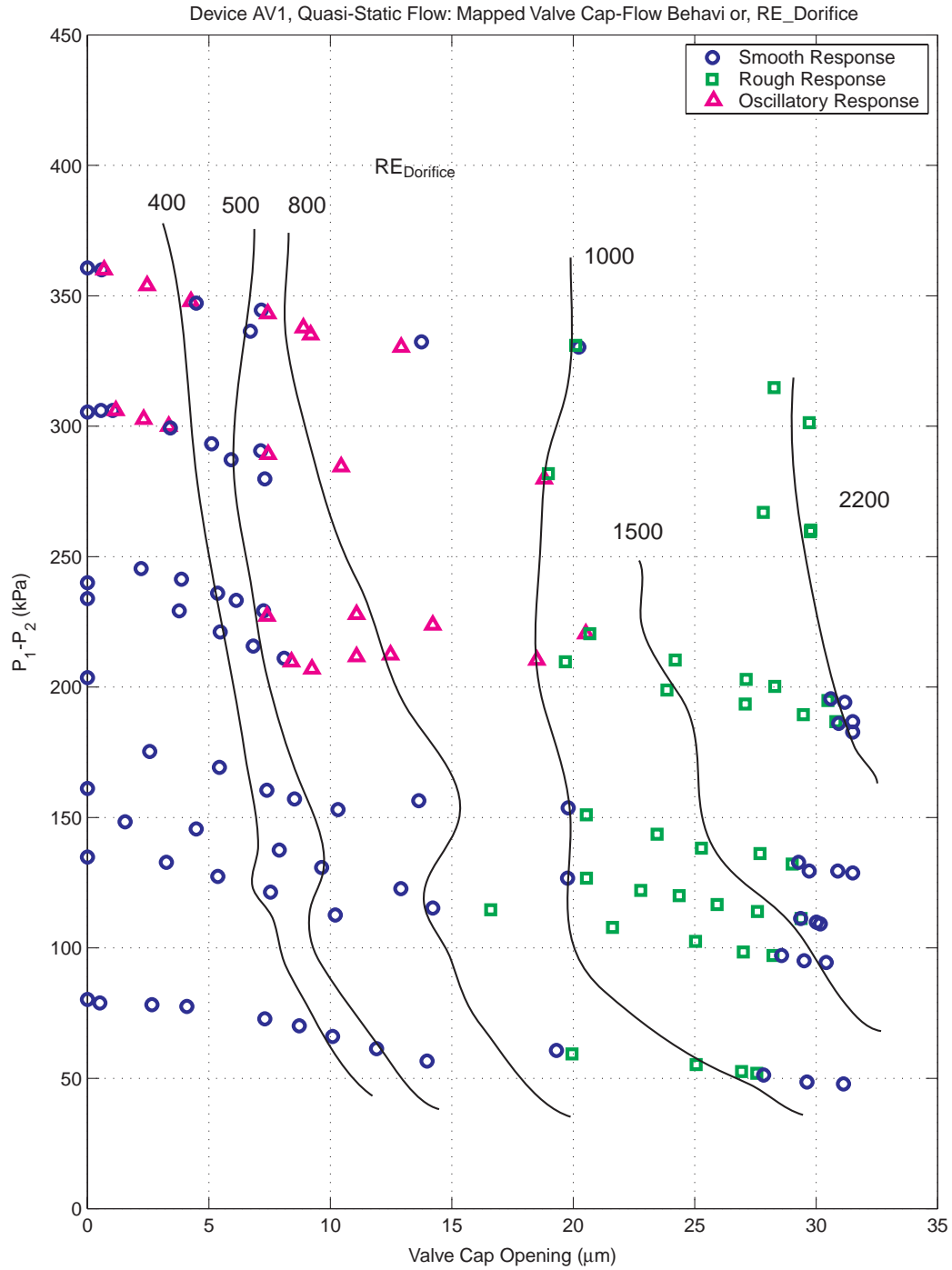


Figure 9.32: Estimated constant Reynolds number curves plotted as  $P_1 - P_2$  vs.  $Z_{vc,opening}$ . Lines are estimated by interpolating between adjacent data points.



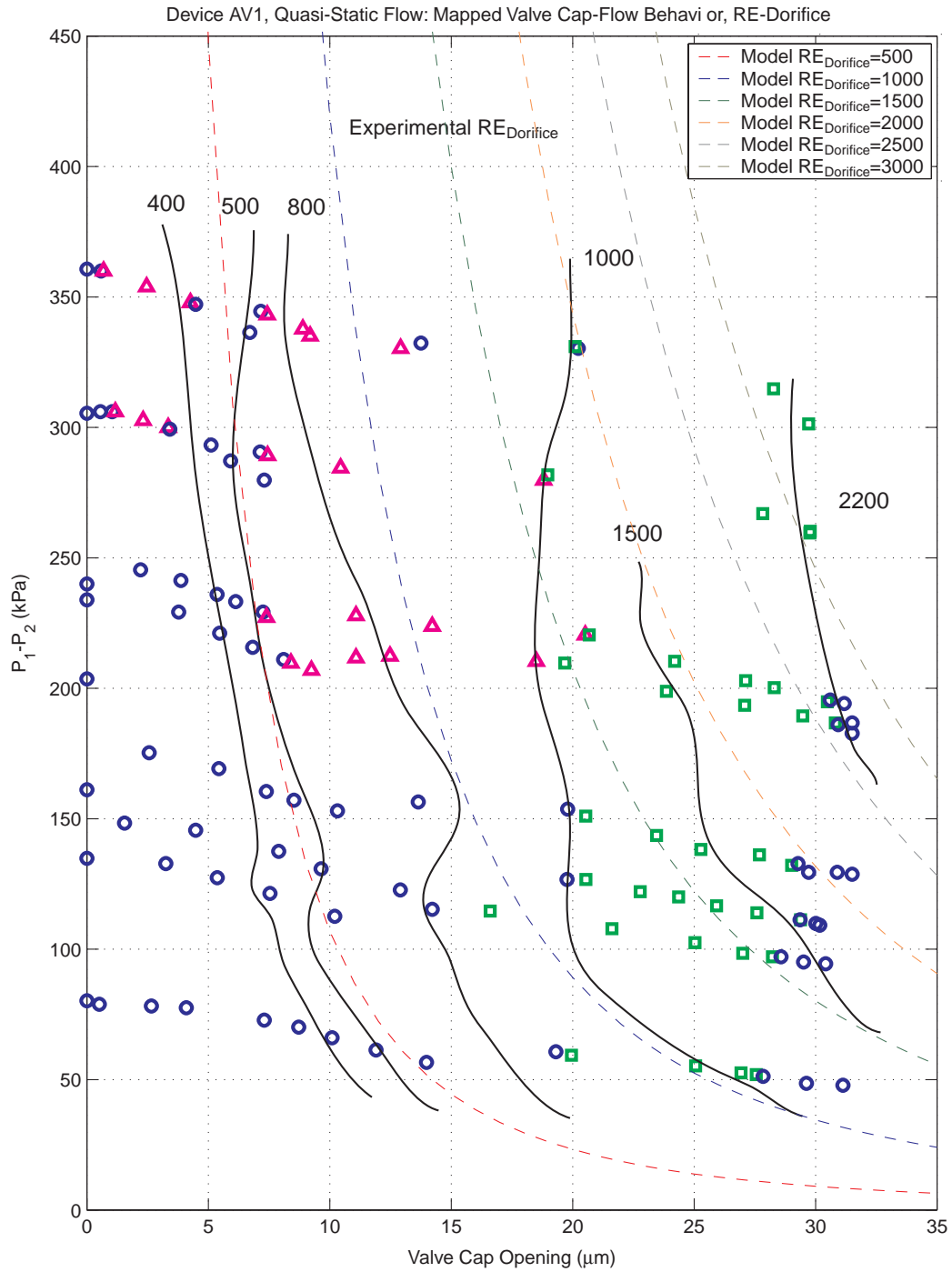


Figure 9.33: Constant Reynolds number curves (experimental vs. model predictions) plotted as  $P_1 - P_2$  vs.  $Z_{vc, opening}$ . Experimental lines are estimated by interpolating between adjacent data points.

The presence of a transition regime between laminar and turbulent flow for the experimental data can be further illustrated by plotting the data in a different way. Typically, in characterizing the physical sections of a fluid system (ie: a constant area pipe, a bend, an orifice, etc), a fluid resistance coefficient for each of the sections can be defined. This resistant coefficient  $\zeta$  is defined as the total pressure lost through the flow section divided by the dynamic pressure within the flow section [7], written in equation form as

$$\zeta = \frac{\Delta P}{\frac{1}{2}\rho_{fluid}u_{local}^2}, \quad (9.1)$$

where  $\Delta P$  is the pressure drop through the flow section (in the case of the valve orifice  $\Delta P = P_1 - P_2$ ) and  $u_{local}$  is the fluid velocity through the section (in the case of the valve orifice  $u_{local} = \frac{Q_{avg}}{A_{orifice}} = \frac{4Q_{avg}}{\pi D_{orifice}^2}$ ). A universal method for observing the transition between laminar and turbulent flow in a physical section of a flow system is to plot this flow resistance coefficient  $\zeta$  versus the Reynolds number in that section (in the case of the valve orifice  $RE_{D_{orifice}}$ ). Figure 9.34, taken from [7], shows an example of this type of plot for a generic fluid orifice contraction section of a fluid system, where the quantity  $\frac{F_0}{F_1}$  defines the geometric contraction ratio. Notice that for low Reynolds number,  $\zeta$  is inversely proportional to RE (laminar flow regime) whereas for large RE,  $\zeta$  is independent of RE (turbulent flow regime). In between these two regions is defined the transition regime where the flow transitions from laminar to turbulent.

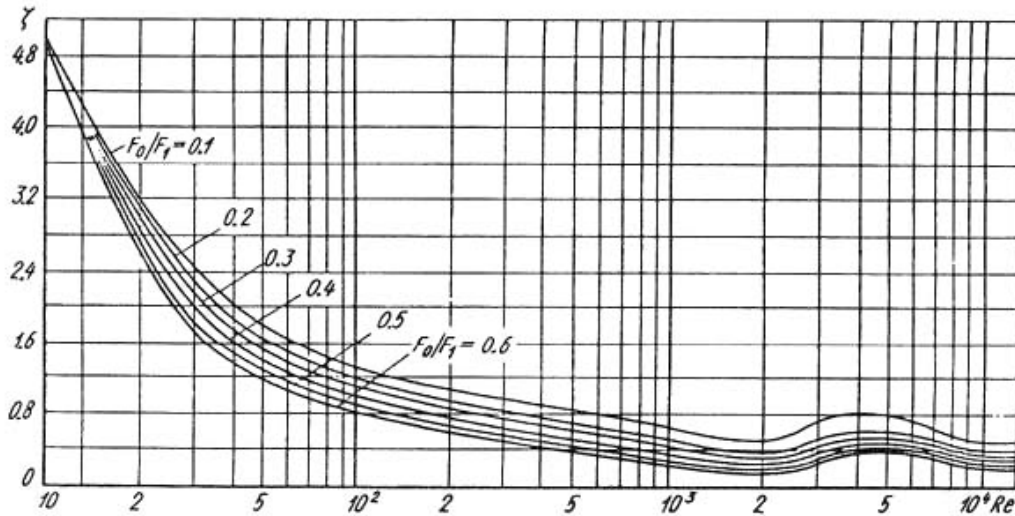


Figure 9.34: Plot of flow resistance coefficient  $\zeta$  versus Reynolds number for a generic flow orifice contraction structure [7]. The laminar flow regime is characterized by an inversely proportional relationship between  $\zeta$  and Reynolds number whereas the turbulent flow regime is characterized by no relation between  $\zeta$  and RE. Transition occurs between these two regimes.

For laminar fluid flow through an orifice, the flow rate is proportional to the applied differential pressure ( $Q_{avg} \propto \Delta P$ ) [2] [7], whereas for turbulent flow the flow rate is quadratically related to the differential pressure ( $Q_{avg} \propto \sqrt{\Delta P}$ ) [2] [7]. Substituting these pressure-flow relations into 9.1, it can be determined that in the laminar flow regime  $\zeta$  is inversely proportional to the Reynolds number, and that in the turbulent flow regime  $\zeta$  is independent of the Reynolds number. This is consistent with Figure 9.34. Therefore, for the experimental data in this thesis, a plot similar to Figure 9.34 should be able to be created, where the slope of the  $\zeta$  curve transitions from a negative value to a value of zero as  $RE_{Dorifice}$  increases. In doing this, a determination as to whether the oscillatory valve cap behavior correlates to the transition between the laminar and turbulent flow regimes can be obtained. To evaluate this hypothesis, the experimental data is replotted as  $\zeta_{orifice}$  versus  $RE_{Dorifice}$  in Figure 9.35.

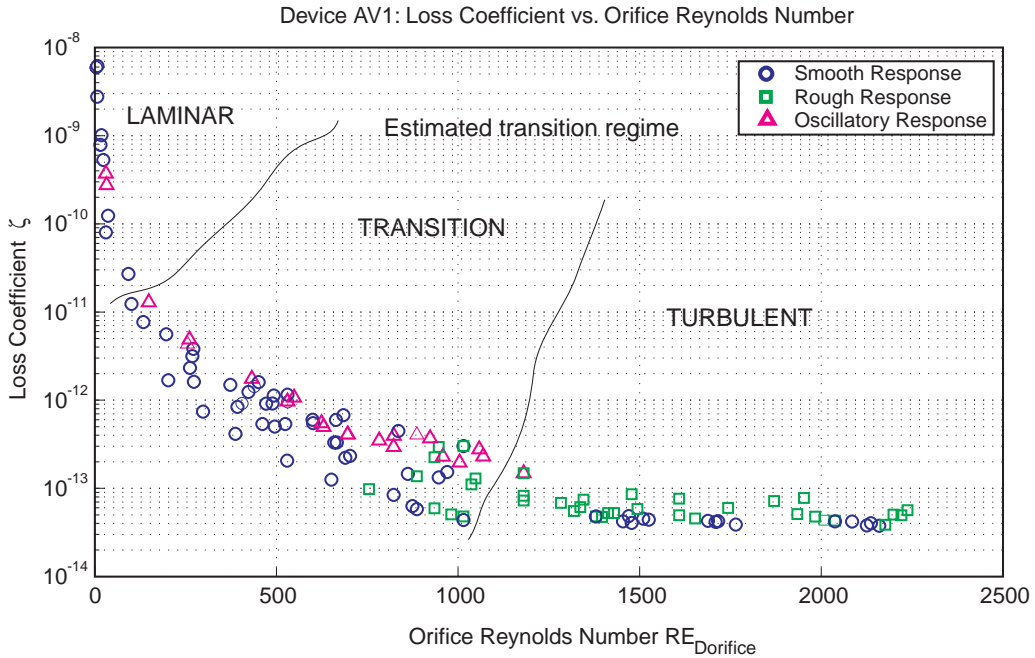


Figure 9.35: Device AV1 estimated laminar, transition, and turbulent flow regimes as a function of  $RE_{Dorifice}$  based on experimental data. Laminar regime is characterized by  $\zeta \propto \frac{1}{RE_{Dorifice}}$  and turbulent regime is characterized by  $\zeta$  being independent of  $RE_{Dorifice}$ . The majority of oscillatory data points occur within estimated boundaries of this transition regime.

Notice that, indeed, for increasing  $RE_{Dorifice}$  from 0 to 500,  $\zeta$  monotonically decreases, and for increasing  $RE_{Dorifice}$  from 1100 to 2500,  $\zeta$  remains constant. One may notice that the points above  $RE_{Dorifice} = 1100$  contain both smooth and rough valve cap behavior. Due to the fact that the differentiation between smooth and rough was a difficult task, it could be that in reality the smooth data points were mistaken for rough behavior. However, the important data

points of oscillatory behavior were clearly differentiable from both smooth and rough behavior and therefore there is no question as to their validity. These observations indicate the presence of reasonably well-defined laminar and turbulent flow regimes within the experimental results. Furthermore, the vast majority of the oscillatory data points lie within the region between  $RE_{Dorifice} = 500$  and  $RE_{Dorifice} = 1100$ . Based on these results, it can be argued that the oscillatory behavior of the valve cap is directly related to the presence of transition between laminar and turbulent flow in the valve orifice.

The following question must now be addressed: Does this conclusion that valve cap oscillatory behavior is related to the transition between laminar and turbulent fluid flow make sense? This question is answered through a discussion of laminar, turbulent, and transitional flow regimes based on literature contained within the fluids mechanics community.

As detailed in the fluid modeling portion of Chapter 5, the valve cap and orifice structure consists of two physical flow sections in series: a contraction section followed by an expansion section. Both of these types of flow sections result in the formation of vortices, the severity of which increases as the Reynolds number grows larger. Figure 9.36 (a) and (b) illustrate schematics of a typical fluid expansion section and a fluid contraction section, respectively, and the corresponding regions where vortices are present [7]. In general as fluid passes through these sections, the fluid boundary layers present upstream of the section are not able to remain intact in passing through the section. Shear layers form where the boundary layers separate from the original structural surfaces, and these shear layers tend to roll up in swirling vortices, which create unsteady forces on any surrounding structure [5] (such as the valve cap and membrane in the active valve).

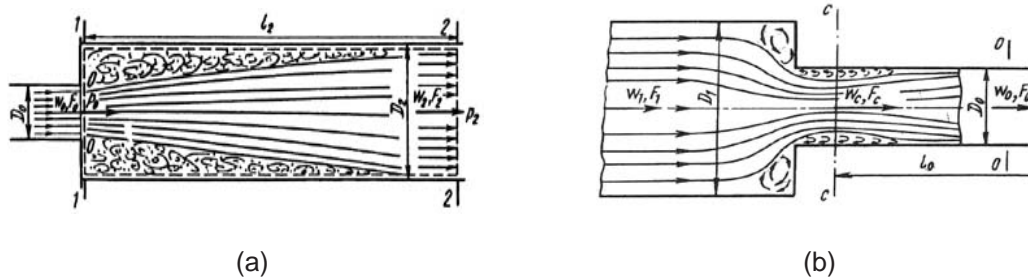


Figure 9.36: Schematic of vorticity formation in contraction and expansion fluid flow sections [7]: (a) expansion section, (b) contraction section.

This unsteady forcing is further enhanced if the flow is experiencing transition between laminar and turbulent behavior. In general, laminar viscous flow is characterized by smooth and steady fluid motion, whereas turbulent flow is characterized by continuous and almost random fluctuation in the velocities of the fluid particles. Both regimes have been studied for

a wide variety of flow geometries. Laminar flow theory is mathematically understood for many of these geometries. Turbulent flow behavior, however, is primarily an experimentally observed fact, which can be analyzed only through statistical understanding [8]. The transition between these two regimes is understood hardly at all. The transition regime is defined as the change (over space, time, and a certain Reynolds number range) of a laminar flow into a turbulent flow. Figure 9.37 illustrates a time history comparison of these three flow regime behaviors.

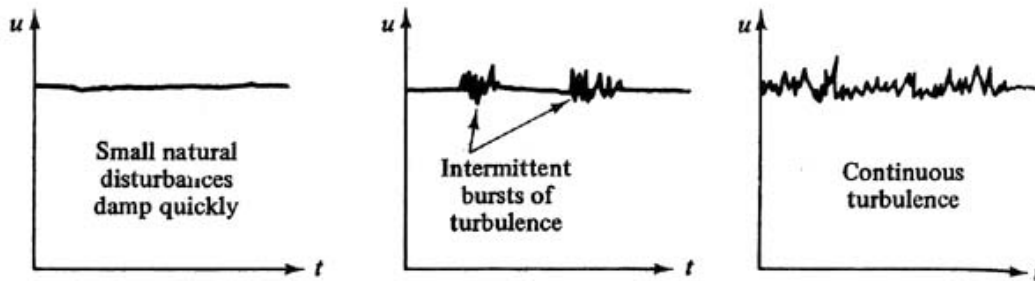


Figure 9.37: Laminar, transition, and turbulent representative flow behavior [8]: (a) laminar flow, (b) transition flow characterized by intermittent bursts of turbulent flow, and (c) turbulent flow.

In laminar flow, there may be occasional natural disturbances in the flow, however, they damp out very quickly. In fully turbulent flow, continuous rapid and random fluctuations are present. In transition, there exist sharp bursts of turbulent fluctuation as the increasing Reynolds number causes a breakdown or instability of laminar motion. Transition through the valve orifice in this thesis, therefore, could very well be characterized by intermittent increases and decreases in the intensity level of the vorticity formation through the orifice, thereby resulting in a significant oscillation of the forcing on the valve cap and the compliant valve membrane structure. It is this vortex-induced structural interaction between the fluid flow and the elastic valve structure that could be setting the valve cap oscillations into motion.

The experimental results presented in this section have provided insight into the approximate value of Reynolds number for which the valve cap structure begins to experience unstable oscillatory behavior. In the valve flow regulation experiments that follow, results will first be obtained for relatively low differential pressure situations to avoid the potential for valve failure due to these oscillations. Once flow regulation has been proved at low differential pressures, tests will then be performed at higher differential pressures to test the limits of the active valve device under these unknown flow regime conditions.

## Duty Cycle Flow Regulation Tests

To evaluate the capability of the active valve to regulate flow for applied voltage to the piezo-electric elements, a series of varying duty cycle test runs were carried out for an imposed differential pressure across the valve orifice of  $P_1 - P_2 = 35kPa$ . This low differential pressure was chosen to ensure flow regimes that do not excite valve cap oscillatory behavior. For each duty cycle run, the valve cap motion was controlled between a minimum valve cap absolute displacement (from its equilibrium position) of  $Z_{vc} = 4.0\mu m$  to a maximum valve cap absolute displacement of  $Z_{vc} = 11.5\mu m$ . Since the valve orifice is located a distance of  $16.5\mu m$  above the equilibrium position of the valve cap, it can be stated equivalently that the valve cap opening was controlled between a minimum opening of  $Z_{vc,opening} = 5\mu m$  to a maximum opening of  $Z_{vc,opening} = 12.5\mu m$ . Duty cycle voltage waveforms from zero to 100 were applied to the active valve such that the resulting valve cap motions shown in Figure 9.38 were obtained. A duty cycle of zero means that the valve cap was maintained constantly at its minimum opening of  $Z_{vc,opening} = 5\mu m$  and a duty cycle of 100 means that the valve cap was maintained constantly at its maximum opening of  $Z_{vc,opening} = 12.5\mu m$ . A duty cycle of 30, for example, means that the valve cap was effectively held at its minimum opening for 70% of the cycle and at its maximum opening for 30% of the cycle.

The results of these tests are shown in Figure 9.39. As the duty cycle is increased from zero to 100, the average flow rate through the valve orifice increases monotonically, thereby proving that the valve device is capable of regulating flow. Using the simulation tools detailed in Chapter 5 of this thesis, predicted results for the flow rates were calculated. These are overlayed with the experimental results in Figure 9.39. The comparison indicates that for reasonable valve openings, the measured flow rate correlates quite well with the model predictions. However, for small valve openings near  $Z_{vc,opening} = 5\mu m$ , the measured flow rate is significantly less than predicted. In essence, the flow appears to be choked more than expected at small valve openings. This observation agrees with the results at small valve openings of the quasi-static flow rate versus valve opening curves discussed previously. As discussed in the previous static flow test section, since the Chapter 5 flow models are based on a compilation of empirical work from other researchers, the lines of predicted behavior in Figure 9.39 are understood to be of only “limited accuracy”, in other words, they are not based on exact theory. In addition to modeling the case of a controlled valve opening of  $Z_{vc,opening} = 5 - 12.5\mu m$ , model predictions for a controlled valve opening of  $Z_{vc,opening} = 7 - 14.5\mu m$  and a controlled valve opening of  $Z_{vc,opening} = 8.5 - 16.5\mu m$  were also determined. These results are also shown in Figure 9.39 to convey the sensitivity of the offset valve opening on flow rate through the orifice. Shifts of a just a few  $\mu m$ s in the opening direction within the flow models result in significantly increased flow rate values.

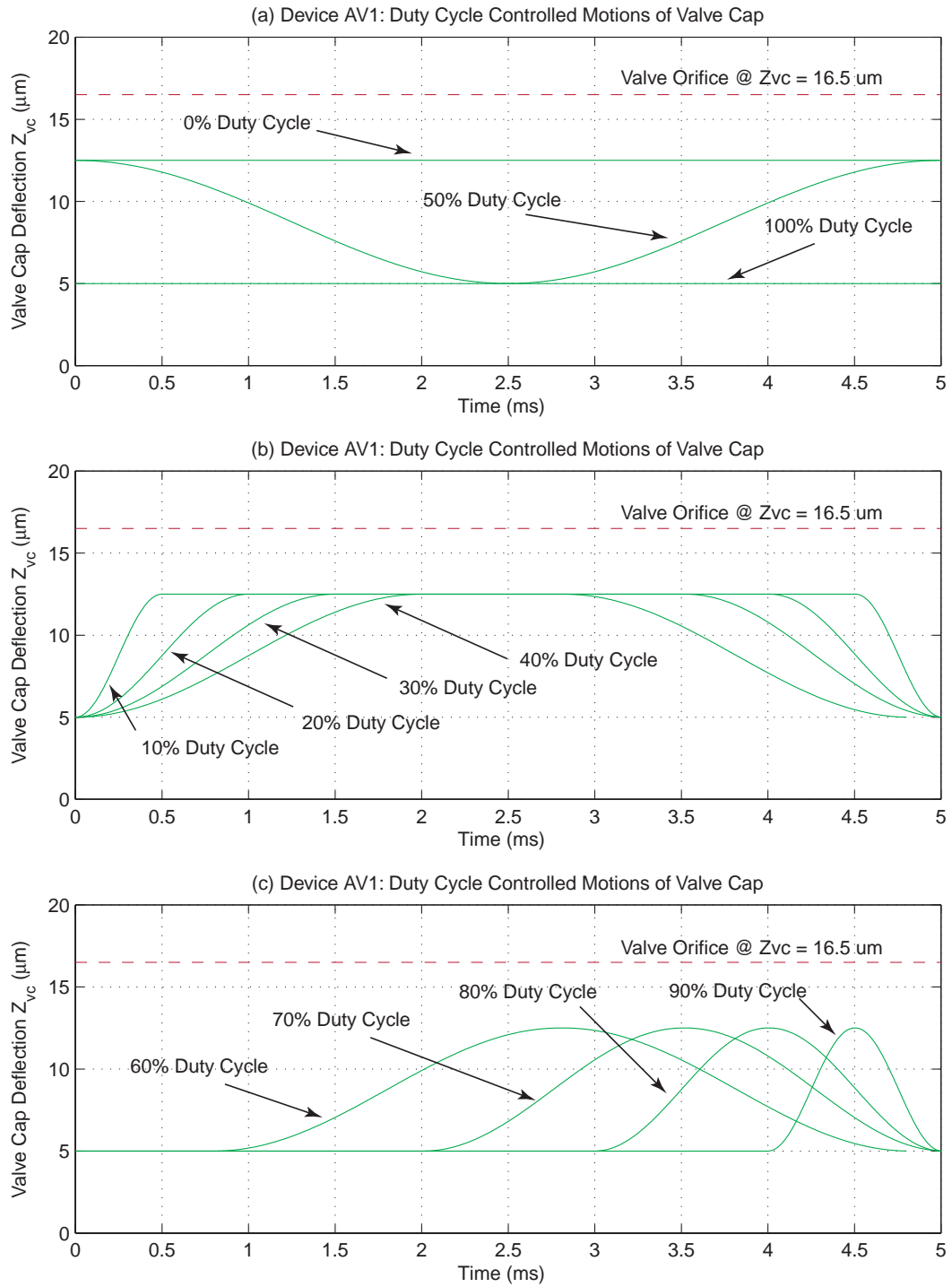


Figure 9.38: Device AV1 valve cap time histories under different duty cycle voltage waveforms to piezoelectric drive element. The valve cap is controlled to reach a maximum valve cap displacement of  $Z_{vc} = 12.5 \mu m$  and to reach a minimum valve cap displacement of  $Z_{vc} = 4 \mu m$ .

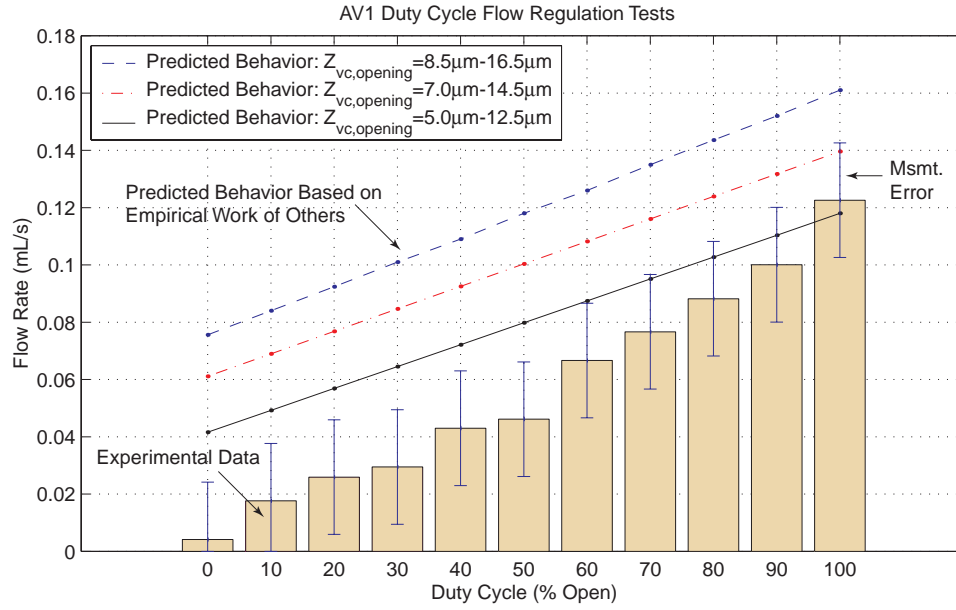


Figure 9.39: Device AV1 model correlation to experimental flow rate results for varying duty cycle inputs. Comparison illustrates good correlation for larger valve openings. For small opening, the flow appears choked. Error bars on the data indicate the measurement error, which was estimated based on the flow sensor calibration error and the accuracy of the applied differential pressure.

### 1kHz Flow Regulation Tests at Increasing Differential Pressure

To evaluate the capability of the active valve device to regulate flow at 1kHz, a series of tests was carried out for increasing differential pressures across the valve orifice. In addition to proving flow regulation at 1kHz, a further purpose of this study was to determine the maximum differential pressure across which the valve could operate. Since the magnitude of the unstable oscillatory behavior observed for the static flow tests at differential pressures greater than  $P_1 - P_2 = 210kPa$  was no more than  $3 - 4\mu m$  peak-peak, it was hoped that by operating the active valve device dynamically at 1kHz with total valve cap stroke of  $15 - 20\mu m$ , the effect of the 5kHz oscillations might not affect the overall flow regulation capability of the valve. As such, tests were performed for differential pressures in excess of  $P_1 - P_2 = 210kPa$ .

Flow regulation tests at 1kHz were performed for differential pressures  $P_1 - P_2 = 24kPa$ ,  $95kPa$ ,  $145kPa$ ,  $200kPa$ ,  $260kPa$ , and  $340kPa$ . By controlling  $P_{HAC}$  with respect to the magnitude of  $P_1$  and  $P_2$ , the valve cap was displaced statically upward to a deflection of  $Z_{vc} = 11\mu m$ . A sinusoidal voltage of  $500V_{pp}$  was then applied to the piezoelectric drive element at 1kHz to actuate the valve cap upward against the valve orifice and downward toward the original equilibrium position of the valve cap. In all test runs, it was desired to just barely close the valve cap against the orifice at its maximum displacement, and to maintain  $Z_{vc} = 0$  at its



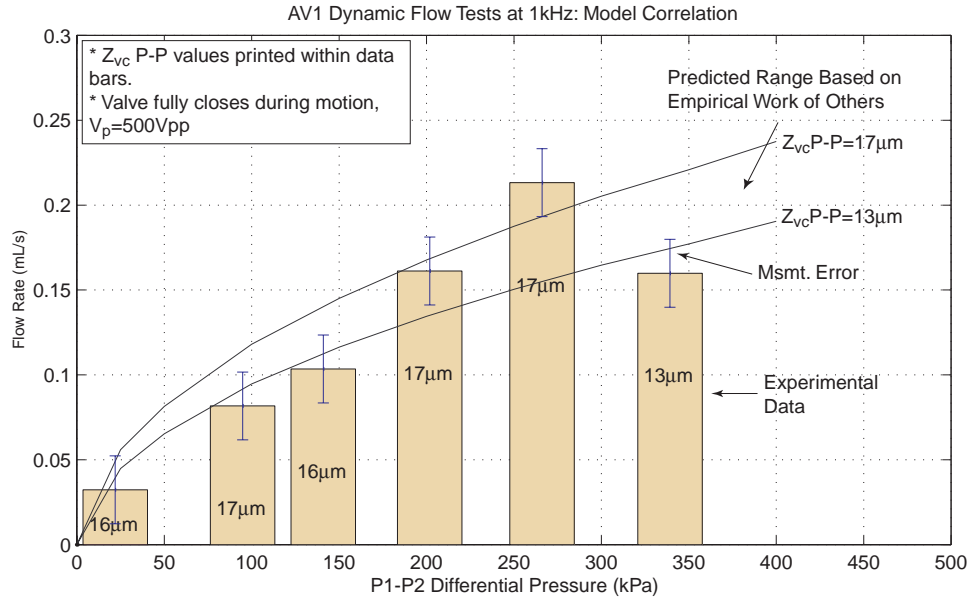


Figure 9.40: Device AV1 dynamic flow regulation model correlation at 1kHz for varying differential pressures. Correlation is good over range of differential pressures. Error bars on the data indicate the measurement error, which was estimated based on the flow sensor calibration error and the accuracy of the applied differential pressure.

minimum displacement. In others words, it was desired to always ensure a valve opening stroke of  $16.5\mu m$ . Figure 9.40 plots the experimentally measured flow rates for each of the differential pressure test cases. Because of the difficulty in achieving a valve cap stroke during actuation of  $Z_{vc,opening} = 16.5\mu m$ , the actual measured stroke of the valve cap during actuation is printed inside of each data bar. An applied voltage of 500Vpp was held constant for all of these test runs. It was noticed that for the differential pressure case of  $P_1 - P_2 = 340kPa$ , a valve cap stroke of  $13\mu m$  resulted, rather than the typical  $16 - 17\mu m$  of the previous test cases. It was believed in this case that the piezoelectric material capability may have been affected by the high pressure excursions (estimated maximum to be  $P_{HAC} \sim 600kPa$ ) within the HAC chamber.

Figure 9.40 also plots the experimental results versus the model expectations obtained using the active valve simulation tools developed in Chapter 5. Model predictions for the limiting cases of  $Z_{vc,opening} = 13\mu m$  and  $Z_{vc,opening} = 17\mu m$  are shown. The model correlation indicates that the active valve regulates flow in excellent correlation with the model predictions. As discussed in the previous flow testing sections, since the Chapter 5 flow models are based on a compilation of empirical work from other researchers, the line of predicted behavior in Figure 9.40 is understood to be of only “limited accuracy”, in other words, it is not based on exact theory. Upon carrying out a subsequent test run at  $P_1 - P_2 = 450kPa$ , as the differential pressure was being set across the valve orifice, the valve cap was observed to begin oscillating (with no

applied piezoelectric drive element voltage at this point). Very quickly afterward (fractions of a second, the valve cap lodged itself permanently against the bottom orifice. Subsequent efforts to move the valve cap upward by pressurizing and depressurizing the HAC chamber resulted in a  $1\mu\text{m}$  amplitude tilting of the valve cap. Based on this response, it is believed that the valve membrane fractured in response to the oscillatory valve cap motion caused by unstable transitional flow through the valve orifice. Because this device failed in this manner, experimental testing of active valve device AV1 was concluded.

## 9.4 Conclusions

This chapter has summarized the experimental tests performed on active valve devices AV1 and AV2. Both devices were proven to successfully operate as piezoelectrically-driven hydraulic amplification micro-actuator structures. For applied piezoelectric voltages up to 600Vpp at 1kHz, these devices demonstrated amplification ratios of drive element deflection to valve cap deflection of 40x-50x. These amplification ratios correlate within 5 – 10% of the model expectations. Although valve cap peak-peak deflections for the applied voltage levels were measured to be 20 – 30% lower than model expectations for the idealized  $E_p$  and  $d_{33}$  piezoelectric material coefficients used in the design optimization chapters of this thesis, correlation to model results that incorporate modified piezoelectric material properties based on proper experimental characterization of the material is within 5 – 10%.

Flow regulation experiments on active valve device AV1 proved that this valve structure can successfully regulate fluid flow at a frequency of 1kHz for valve cap peak-peak displacements of  $17\mu\text{m}$  up to differential pressures of 260kPa. For this condition, a peak average flow rate through the device of 0.21mL/s was obtained under a sinusoidal drive voltage of 500Vpp. Additionally, quasi-static differential pressure-flow rate curves were measured up to a differential pressure of 210kPa for the full range of valve cap stroke up to  $33\mu\text{m}$ . The measured flow rates were 10 – 30% lower than the expected flow rates based on the models presented in Chapter 4. Self-oscillatory motion of the valve membrane was observed for various combinations of valve cap opening and differential pressures in excess of 210kPa. The nature of the flow behavior (based on Reynolds number) was studied for a variety of valve opening situations. The results indicate that these self-excited valve cap oscillations were most probably a result of transitional flow (between laminar and turbulence) through the valve orifice structure, a regime which limited the valve operation to relatively low differential pressures below 350kPa. Overall, this piezoelectrically-driven hydraulic amplification microvalve was successfully proven to regulate fluid flow through microscale channels at high frequency.

# Bibliography

- [1] C.Y. Lin, Ph.D. Thesis. MIT. 2002.
- [2] K.T. Turner, An Evaluation of Critical Issues for Microhydraulic Transducers: Silicon Wafer Bonding, Strength of Silicon on Insulator Membranes and Gold-Tin Solder Bonding. MIT Master's Thesis. June 2001.
- [3] TRS Ceramics Data Sheet for PZN-PT.
- [4] Dow-Corning data sheet on silicon oil.
- [5] R.D. Blevins, Formulas for Natural Frequency and Mode Shape, R.E. Krieger, Malabar, FL, 1984.
- [6] J. Carretero and K.S. Breuer, "Measurement and Modeling of the Flow Characteristics of Micro Disk Valves," Proceedings of the 1994 International Mechanical Engineering Conference and Exposition: Microfluidics Symposium, Orlando, FL, Nov. 2000.
- [7] I.E. Idelchik, "Handbook of Fluid Resistance," CRC Press, Boca Raton, FL, 1994.
- [8] F.M. White, "Viscous Fluid Flow," McGraw-Hill, New York, NY, 1991.



## Chapter 10

# Conclusions and Recommendations

This chapter summarizes the modeling, design, fabrication, and testing research presented in this thesis. The thesis objectives and the thesis contributions are reviewed. Conclusions are drawn based on the results presented and recommendations for future work are detailed. Additionally, it is the purpose of this chapter to evaluate the impact of these thesis results on the performance capabilities and overall future of Micro-Hydraulic Transducer systems.

### 10.1 Summary and Conclusions

#### 10.1.1 Thesis Summary

The primary objective of this thesis was to develop, from the initial concept stage to the experimental testing of a fabricated device, a piezoelectrically driven hydraulic amplification microvalve for high frequency control of high pressure fluid flow. This research was carried out through a series of modeling, design, fabrication, assembly, and experimental testing tasks. This work demonstrated the valve concept and evaluated the valve performance in comparison to behavior predicted by the models developed in the thesis.

A secondary goal of this thesis was to provide a framework of linear and non-linear structural modeling tools and design procedures that can be implemented in the development of high frequency piezoelectric micropumping and microvalving systems. Additionally, a further goal of this thesis was to present a method for small-scale bulk piezoelectric material integration within silicon micromachined thin-tethered structures, a procedure which can enable the realization of compact high-frequency high-stiffness hydraulic actuator structures.

These objectives were divided into two major sections of the thesis. The first section, consisting of Chapters 1 through 5, focused on the conceptual design of the active valve structure, the development of structural modeling tools to predict the important linear and non-linear structural behaviors of the device component structures, the implementation of these modeling

tools within an active valve simulation architecture, and the development of a systematic design procedure that can be used to generate an active valve geometry based on external hydraulic system performance requirements. The second section, consisting of Chapters 6 through 9, highlighted the fabrication challenges inherent in building this active valve device and defined the fabrication process flow for the assembly of the device, including piezoelectric material integration. Additionally, comprehensive experiments were carried out to experimentally evaluate the piezoelectric drive element sub-component structure, the valve cap and membrane sub-component structure, and the full piezoelectrically-driven hydraulic amplification microvalve device. Each of the chapters is summarized below.

**Chapter 1** introduced the concept of the piezoelectrically-driven hydraulic amplification microvalve for use in high specific power hydraulic pumping applications. High frequency, high force actuation capability in the valve is enabled through the incorporation of solid-state bulk piezoelectric material elements beneath a compact and stiff structural piston mechanism. High stroke valve motion is achieved through the incorporation of a hydraulic amplification chamber between the moveable piston structure and a micromachined valve membrane. This enclosed fluid chamber, connecting the large cross-sectional area piston structure to a smaller cross-sectional area valve membrane structure, enables an amplification ( $40 - 50x$ ) of the limited piezoelectric material stroke into a significantly increased valve membrane and valve cap deflection. These design features enable the valve device to simultaneously meet a set of high frequency, high pressure, and large stroke requirements that have not previously been satisfied by other microvalves presented in the literature.

**Chapter 2** introduced the geometry of the active valve device and detailed the important structural elements within the device that needed to be accurately modeled. The structural deformations of the piezoelectric material elements, the drive element piston, the bottom support structure, the hydraulic amplification chamber, the top support structure, and the valve cap and membrane structure were modeled using linear plate theory, with bending and shearing deformation effects included. Additionally, theoretical studies were performed to demonstrate the benefits, by stiffening the drive element piston actuation structure, of integrating multiple piezoelectric material elements spread out beneath the drive element piston rather than integrating just a single centrally-located material element beneath the piston. These studies provided the optimal dimensional spacing of the three piezoelectric elements beneath the drive element piston in the fabricated and experimentally characterized active valve devices presented in Chapter 9.

**Chapter 3** presented the development of a numerical code to model the large deflection behavior of a thin annular plate structure with rigid central cap under pressure loading. The work presented in this chapter was based on a finite-difference scheme developed by Su [1]. This numerical code served as a modeling tool for use in the full active valve non-linear model and

system simulation presented in Chapter 4. The theory was specifically developed to capture the non-linear stiffening effects present in the valve membrane structure of the active valve. The linear plate theory representation that was presented in Chapter 2 is not able to capture these stiffening effects. A series of valve cap and membrane geometries and pressure loading scenarios, characteristic of those found and experienced in the final active valve device, was presented to demonstrate the capabilities of this modeling tool to capture the large deflection behavior of the structure.

**Chapter 4** presented a complete quasi-static structural model of the active valve. This model was comprised of the linear and non-linear modeling tools presented in Chapters 2 and 3, respectively. An evaluation of the assumptions within the structural model was performed through a series of comparison studies to a finite-element model of the active valve structure for a variety of loading scenarios. In addition, the chapter introduced a dynamic simulation architecture for the valve, which included inertia and damping associated with the drive element piston and valve cap structural elements. Calculation of the coupled fluid-structure resonant valve frequency, based on finite-element analyses, was also presented. The predicted resonance was based on a finite-element model that did not include the added mass of the fluid above the valve cap and membrane structure. As a result, this model overpredicted the valve resonant frequency in comparison to experimental results on the fabricated valve devices detailed in Chapter 9.

**Chapter 5** formulated a systematic quasi-static design procedure that can be used to generate an active valve geometry based on external hydraulic system performance requirements. This design procedure was based on the modeling tools and simulations developed in Chapters 2, 3, and 4 of the thesis. Additionally, the procedure incorporated the governing fluid flow relations linking the valve cap motion to the external hydraulic system pressures and enabled variation of key parameters within the active valve geometry (such as valve membrane thickness and the number of valve membranes used in parallel) to satisfy predetermined valve membrane stress limitations. A powerful characteristic of the systematic design procedure is the ability to monitor the stress at all positions along the valve membrane for any and all potential pressure loading scenarios experienced by the structure. This enables the designer to very accurately predict the maximum stress that the valve membrane will experience during its full actuation cycle as it opens and closes against the fluid orifice. As a check, full system dynamic simulations were run to validate the goodness of the valve geometry created using the quasi-static design procedure.

**Chapter 6** presented an overview of the fabrication challenges encountered and the solutions implemented in the development of the active valve device. These challenges included the wafer-level etching of the drive element and valve membrane structures, the wafer-level silicon-to-silicon and silicon-to-glass bonding operations, preparation and integration of the piezoelec-

tric material elements with the device, die-level assembly and bonding procedures, and the filling of degassed fluid within the hydraulic amplification chamber following device assembly. Additionally, the modeling and design of a micromachined high-resistance fluid channel was documented that enabled a static bias pressure to be imposed on the hydraulic amplification chamber without affecting the high-frequency actuation behavior of the active valve device.

Chapter 6 also presented a detailed sub-component testing plan for the active valve structure. This systematic plan separated the complete active valve structure into manageable sub-component devices according to the primary challenges previously detailed. The piezoelectric drive element sub-component study, whose purpose it was to prove the ability to micromachine the tethered piston structure and integrate bulk piezoelectric material beneath the piston, and the valve cap and membrane sub-component study, whose objective it was to validate the non-linear large deflection behavior of the valve membrane structures, were outlined. Additionally, the full active valve testing plan was outlined.

**Chapter 7** presented the experimental results for the piezoelectric drive element sub-component study. A series of drive element devices was fabricated in an effort to demonstrate that both standard polycrystalline PZT-5H piezoelectric material as well as higher-strain single-crystal PZN-PT piezoelectric material could be incorporated beneath micromachined piston structures. An additional goal was to demonstrate that devices with three piezoelectric elements spread out beneath the drive piston could be manufactured in a reliable manner. Quasi-static high-voltage experimental tests were performed on these devices at a frequency of 15kHz and dynamic low-voltage frequency tests were carried out between frequencies of 10kHz and 200kHz to identify modal characteristics.

The results indicated that the procedure formulated in Chapter 6 for integrating piezoelectric material elements, both PZT-5H and PZN-PT, within these micromachined structures is repeatable. All devices fabricated experienced a tolerance match between the piezoelectric elements and the surrounding supporting structures within  $\sim 1\mu m$ , thereby ensuring predictable “push-up” of the piston structure during assembly. Drive element devices incorporating a single piezoelectric material beneath the piston experienced modal “1- $\Theta$ ” tilting behavior at frequencies as low as 30kHz. Additionally, quasi-static actuation of the devices at 15kHz and 1000Vpp resulted in a slight tilting of the piston structures as they moved up and down through their actuation cycles. These tilting effects were attributed to imperfect placement of the piezoelectric element beneath the center of the piston and to non-uniform fillet radius etch profiles, characterized through microscope measurements, around the etched tether of the piston. Drive element devices incorporating three piezoelectric material elements experienced negligible tilting behavior during actuation at 15kHz and 1000Vpp due to the enhanced support of the piston from below. For these devices, modal behavior was not observed until frequencies in excess of 50kHz. This sub-component study successfully demonstrated the capability to fabricate and



assemble these component structures for use in full active valve devices.

**Chapter 8** presented the experimental results for the valve cap and membrane sub-component study. A series of valve membrane structures was fabricated and inspected to ensure adequate fillet radius control at the base of the etched features. Pressure-deflection experiments were carried out for differential pressures across the structure of up to 200kPa in an effort to characterize its non-linear large deflection behavior. Theoretical studies, using the non-linear numerical tools presented in Chapter 3, were carried out to determine deformation and membrane stress sensitivities to valve membrane thickness and fillet radius size. The experimental valve cap deflections, in response to pressure loading, were found to correlate within  $\sim 5\%$  of theoretical expectations. The valve membranes were deflected sufficiently to impact the valve stop in glass Layer 6, a condition which results in a predicted membrane stress of 0.65GPa. In these tests, no membranes fractured. This sub-component study successfully demonstrated the capability to fabricate the valve cap and membrane structure required in the full active valve device and verified that this structure behaves as predicted in its non-linear large deflection regime.

**Chapter 9** presented the experimental results of the full active valve testing study. The goals of these experiments were to evaluate the quasi-static and dynamic structural performance of the active valve device and determine some initial limitations in its ability to regulate fluid flow against imposed differential pressures. For the purposes of this study, two active valve devices were built and experimentally characterized. Both devices were proven to successfully operate as piezoelectrically-driven hydraulic amplification microactuator structures. For applied piezoelectric voltages up to 600Vpp at 1kHz, these devices demonstrated amplification ratios of drive element deflection to valve cap deflection of 40x-50x. These amplification ratios correlate within 5 – 10% of the model expectations. Although valve cap peak-peak deflections for the applied voltage levels were measured to be 20 – 30% lower than model expectations for the idealized  $E_p$  and  $d_{33}$  piezoelectric material coefficients used in the design optimization chapters of this thesis, correlation to model results that incorporate modified piezoelectric material properties based on proper experimental characterization of the material is within 5 – 10%.

Flow regulation experiments proved that this valve structure can successfully regulate fluid flow at a frequency of 1kHz for valve cap peak-peak displacements of  $17\mu m$  up to differential pressures of 260kPa. For this condition, a peak average flow rate through the device of 0.21mL/s was obtained under a sinusoidal drive voltage of 500Vpp. Additionally, quasi-static differential pressure-flow rate curves were measured up to a differential pressure of 210kPa for the full range of valve cap stroke up to  $33\mu m$ . The measured flow rates are 10 – 30% lower than those expected based on the models presented in Chapter 4. The onset of transition and turbulent flow regimes, which depending on the valve cap opening and the differential pressure could set the valve cap into self-excited oscillatory motion, was identified for differential pressures in excess of 210kPa. The nature of the flow behavior (based on Reynolds number) was studied

for a variety of valve opening situations. The results indicate that these self-excited valve cap oscillations were most likely a result of a transition flow regime between laminar and turbulence through the valve orifice structure, a regime which limits the valve operation to relatively low differential pressures below 350kPa. Overall, though, this piezoelectrically-driven hydraulic amplification microvalve has been successfully proven to regulate fluid flow through microscale channels at high frequency.

### 10.1.2 Thesis Contributions

The results presented in this thesis support the following conclusions, which address the primary objectives of this research:

1. A piezoelectrically-driven hydraulic amplification microvalve is a viable concept for the regulation of high differential pressure ( $> 300kPa$ ) fluid flows at high frequency ( $\geq 1kHz$ ), resulting in significant fluid flow capability.
2. Integration of miniaturized bulk piezoelectric materials (with dimensions less than 1mm x 1mm x 1mm) within micromachined thin-tethered piston structures is a viable method for achieving compact high frequency, high force actuation capability in microhydraulic systems.
3. Linear and non-linear modeling tools for the design of active valve devices, such as this one which incorporate thin-membrane valve structures, have been developed. These modeling tools enable accurate monitoring of real-time membrane stress levels at all locations along the membrane for all potential pressure loading scenarios experienced by the structure.

Although performing short of the original frequency and differential pressure design specifications set forth at the beginning of this thesis, the demonstrated valve capabilities place this device superior to any other microvalve presented in the literature (see Chapter 1) for simultaneously meeting a set of high frequency (1-10kHz), high pressure(0.1-1MPa), and large stroke ( $15\text{-}40\mu m$ ) requirements for regulating liquid fluid flows in micro hydraulic systems. It is the belief of this author that future design iterations could be successful in creating a microvalve structure that could operate at a frequency of 10-15kHz against differential pressures approaching 1MPa. The following section details further work that could enable this design goal and addresses the question “What do the results of this thesis mean to the overall future of high-specific power Micro-Hydraulic Transducer systems?”.

## 10.2 Recommended Further Work and the Future of MHTs

The results presented in this thesis have identified a number of issues and areas which require further development and investigation. In this section, these issues will first be organized into those that are deemed fundamentally critical for the development of the next generation piezoelectrically-driven hydraulic amplification active valve to meet the high frequency ( $>10\text{kHz}$ ) and large differential pressure ( $\sim 1\text{MPa}$ ) requirements set forth at the beginning of this thesis, and those that are worth investigating as a means to make modest improvements in device performance and to ease manufacturability concerns. Once this overall list has been defined, each of the issues will then be discussed in detail.

Based on the results of this thesis, it is clear that a piezoelectrically-driven hydraulic amplification microvalve can be designed, built, and successfully operated to regulate liquid fluid flows. The valve design experimentally characterized in this thesis, however, fell short of its operational goals in two primary ways. The first of these shortcomings was the valve's low 1st modal structural frequency ( $5\text{kHz}$ ), which limited valve quasi-static operation frequency to  $1\text{-}2\text{kHz}$ . Since the original design goal was to operate this valve within an MHT system at a frequency of at least  $10\text{kHz}$ , it can be stated that the valve severely underperformed. This is a shortcoming that this author believes can be overcome in future design iterations with more attention given to the important fluid-structural coupling and added mass phenomena that directly affect the valve's dynamic behavior. The second of these shortcomings was the unexpected interaction between the valve structure and the fluid flow at differential pressures in excess of  $210\text{kPa}$ . Chapter 9 included a thorough analysis of the related experimental data, resulting in the conclusion that the unstable self-oscillatory valve cap behavior was most probably caused by instabilities within the flow regime (such as vortices) as a transition from laminar to turbulence occurs. Whereas the first shortcoming can be overcome fairly easily within a redesign effort, this flow-induced instability issue is likely to require significantly more effort in the future (both in modeling and in detailed experimentation) to better characterize the fluid flow regimes that occur through these sorts of microvalve orifices and to more accurately capture interactions between these flow phenomena and adjacent compliant structures (such as the valve cap and membrane in this active valve design).

The two issues previously discussed are the critical ones which have most severely limited this active valve to lower than desired performance levels. On the positive side, however, it can be confidently stated that all of the structural models developed in this thesis for predicting quasi-static valve performance (Chapters 1-5) were in extremely good correlation with the  $1\text{kHz}$  experimental data presented in Chapter 9. The experimentally characterized valve cap deflections and valve amplification ratios for the full range of operating voltages were within  $5\text{-}10\%$  of model expectations, a result which confirms these documented models as important

tools within future valve design iterations. The additional areas of recommended future work (in addition to the two major issues discussed above), therefore, fall not within the realm of active valve structural modeling, but rather within the area of material characterization and microfabrication. Under the heading of material characterization is, first, the need for better understanding of single-crystal PZN-PT piezoelectric materials and, second, the need for better understanding of the stress limitations within etched single-crystal silicon material (especially SOI wafers). Under the heading of microfabrication are a variety of issues relating to the manufacturability of this highly-complex, multilayer valve structure.

In summary, the recommended future work is divided into the following sections: (1) a valve structural redesign phase to enable quasi-static operational frequencies at or above 10kHz, (2) a major program to characterize the flow regimes through microvalve orifices and to understand the potential impact that this flow behavior has in interacting with adjacent compliant structures (flow induced structural instabilities), (3) further characterization of the actuation capabilities of single-crystal piezoelectric materials and the stress limitations of SOI etched structures, and (4) the re-evaluation of user-intensive microfabrication steps and the development of a less complex active valve structure. These sections of recommended future work are discussed in detail in the following sections.

### 10.2.1 Redesign for Enhanced Operational Frequency

The modal frequency model correlation studies performed in Chapter 9 identified the hydraulic amplification chamber geometry as a key contributor to the reduction in frequency of the valve 1st modal frequency. Additionally, it was determined that the added mass of the external fluid above the valve cap and membrane structure had an important effect in limiting this frequency as well. A redesign effort should be performed on this active valve to increase its first modal frequency to within the range of 10-15kHz. The active valve geometry tested in this thesis incorporated a Layer 6 HAC chamber geometry characterized by a chamber height of  $t_{HAC} = 200\mu m$  and a series of small dimensioned through-holes and flow channels (with dimensions as small as  $100\mu m$ ) connecting the lower half of the HAC chamber to the upper half of the chamber. This intricate geometry was required in order to guarantee the presence of a rigid motion stop  $\sim 16.5\mu m$  below the underside of the valve cap. In such closely-packed structures, inertial coupling between the structural elements and the accelerating fluid can significantly reduce modal frequencies of the system, as discussed in Chapter 9. The next generation active valve should incorporate an HAC chamber with reasonable height (ie:  $t_{HAC} = 500\mu m$ ) and without any complex arrangement of holes and channels. The chamber should be a single simple cylindrical volume defined on its bottom surface by the tethered piston and on its top surface by the valve cap membrane and top support structure. In this re-design, no bottom stop would be present, a necessary consequence. Based on experimental

testing in this thesis, the valve should still operate successfully without this stop present. The simplification of this chamber geometry will, therefore, minimize the effect of inertia coupling and allow for a higher 1st modal frequency. One may argue that a larger volume fluid chamber will increase the compliance of this coupling mechanism between the piston and the valve membrane, an argument which is true. However, the degree to which performance would be reduced is negligible compared to the benefit of a higher operating frequency. Additionally, by incorporating the external fluid above the valve cap and membrane within future finite-element models, the influence if this added mass can be taken into account in designing a valve to meet a quasi-static frequency greater than 10kHz.

The modal frequency model correlation study performed in Chapter 9 also presented the effect of valve membrane thickness on the overall 1st valve modal frequency. It was shown that an increase in valve membrane thickness from  $t_{vm} = 6\mu m$  to  $t_{vm} = 10\mu m$  would increase the 1st modal frequency of the active valve from 14kHz to 20kHz (without fluid above valve cap and membrane). This is based on the fact that, in general, the stiffness of a plate scales with the cube of its thickness. This stiffening would help to increase the modal frequency, however, it would require more actuation authority from the drive element portion of the valve. Based on the tradeoffs documented in Chapter 5 of this thesis, such a tradeoff in frequency for a slightly larger piezoelectric material volume beneath the piston is worthy of investigation in the next generation design. Careful attention to the potential deflections and predicted stress levels seen in this larger thickness membrane during actuation would be required to maintain structural integrity. In essence, this redesign effort should use the exact modeling tools documented in Chapter 5 of this thesis, but include a more rigorous modal frequency evaluation during the process. An additional benefit of a thicker valve membrane would be the potential for reducing the magnitude of the flow-induced instability (to be discussed in the following section) caused by the interaction of the fluid flow through the orifice with the adjacent compliant valve membrane. A significantly stiffer membrane structure might eliminate the severity of this interaction all together.

## 10.2.2 Understanding of Flow Induced Structural Instabilities

For the active valve devices experimentally characterized in this thesis, flow-induced structural vibrations of the valve cap and membrane limited the differential pressure across which the active valve could regulate flow. Although significant analysis work was performed on the experimental data containing this instability behavior and although a plausible explanation for the said behavior was put forth in the conclusions of this thesis, it is believed by the author that a vast number of fluid flow issues and questions must be further investigated and answered before the observed phenomena can be understood fully and before the impact on full MHT systems can be estimated. These issues focus on two major tasks: (1) the characterization

of the flow behavior through microvalve orifices and (2) the understanding of the interaction between this flow through microvalve orifices and any adjacent compliant structures. These tasks are detailed in the following sections.

### **Flow Characterization Through Microvalve Orifices**

The majority of experimental testing on valves for use within microsystems has been done on macroscale valves. The fluid models used throughout this thesis, in fact, were based on this method of testing, with the results being accepted at the microscale [2]. In order to fully understand the flow behavior as the Reynolds number passes from zero to in excess of 10,000 during valve opening and closing, and in particular, to understand the critical nature of the transition regime between laminar and turbulent flow, microscale valve experiments must be carried out. These experiments must utilize rigid valve cap structures that are in no way affected by the fluid flow, and conversely, that do not themselves influence the flow behavior. In this way, an understanding of vortex formation and flow instabilities can be obtained independent of adjacent compliant structures. Tests could be performed using many of the microfabricated layers used for the active valve in this thesis. However, one would need to incorporate a precisely controlled solenoid or long piezoelectric stack actuator bonded to a rigid valve cap (without an adjacent compliant membrane) which could be moved upward and downward against the fluid orifice. It is critical that no compliant structures exist in the region of the orifice flow so that the resulting flow behavior is solely a function of the orifice geometry and applied operating conditions. The following experimental tests could be carried out:

1. Slow static valve opening tests, identical to those performed in the instability section of Chapter 9, whereby the valve cap is lowered from its fully closed position against the valve orifice over a sufficiently long period of time ( $\sim 10$  minutes) to ensure flow behavior for a static valve opening. The valve cap deflection, flow rate, and dynamic pressure directly upstream and downstream of the valve cap should be measured and recorded real-time. Without a compliant structure (ie: the valve membrane) present during this test, an understanding of the relationships between differential pressure, flow rate, and dynamic pressure can be obtained and an estimation of the laminar, transition, and turbulent flow regimes could be carried out.
2. In conjunction with the test described above, flow velocimetry measurement techniques should be implemented to visualize the flow as it passes through the microvalve orifice. Vortex shedding and unsteady flow phenomena could be identified in an effort to evaluate the regions of laminar, transition, and turbulent flow as a function of Reynolds number. These velocimetry techniques are designed to illuminate and measure particle and surface motions using infrared wavelengths, taking advantage of the fact that silicon is largely

transmissive to light with wavelengths greater than  $1\mu m$ . Such a system could allow observation of particles within the flow stream inside of the silicon-based valve orifice microdevice [3]. By analyzing images using both time-of-flight and phase-locked techniques, quantitative measurements about the motion of the fluid could be taken.

3. Using both of the above testing methods, valve orifices with varying types of orifice “sharpness” could be evaluated. The creation of vortices in these microstructures is most likely enhanced by the sharp expansion that occurs as fluid flows radially outward across the membrane. Current MEMS fabrication processes limit the degree of “chamfering” that can be done on corners. It is possible, though, that future microfabrication processes will be developed to enable smoothing of these types of orifice structures.

With the experiments described above, a thorough characterization of the flow behavior through microvalve orifices could be obtained, independent from its interaction with adjacent compliant structures.

### **Flow-Induced Instabilities of Adjacent Valve Membrane Structure**

With a detailed understanding of the flow regimes through microvalve orifice geometries, experiments could be run to evaluate the impact of these flow regimes on the stability of adjacent compliant valve cap membrane structures. The structures tested could be similar to the full valves tested in this thesis. The following experimental tests could be carried out:

1. During the slow valve opening tests discussed previously, it would be very useful to capture instantaneous snapshots (with period  $\sim 10ms$ ) repeatedly during the full 10 minute long experimental test. This would require a more sophisticated A/D measurement system than was used in this thesis, in which low data sampling rates (ie: 10 data points per second) could be used for the extended period test and much higher sampling rates (ie: 1,000,000 data points per second) could be used for the snapshots. In this manner, during valve opening, as the valve cap transitions from stable to unstable oscillatory behavior, these snapshots could capture the nature of this transition behavior.
2. Additionally, during these tests, rather than measuring just the center point of the valve cap using the laser vibrometer system, it would be informative to scan over the entire surface of the valve cap. In this manner, tilting motion of the valve cap could be analyzed as a cause of any unstable flow behavior. Since the valve cap stiffness is minimal for tilting motions (no net volume change beneath the valve cap occurs), these motions could easily be caused by unstable flow regions around the valve cap or, conversely, unstable flow behavior (vortices) could be a result of valve cap tilting. Therefore, measurement of the valve cap tilting could be informative. The spot size of the laser vibrometer system

used in this thesis, however, is too large for such a spatial measurement procedure. Micro laser vibrometer systems could be attempted, however, these systems are typically housed within microscope stage set-ups, which would limit the ability to incorporate the active valve test-rig and jig under the lens. Further brainstorming ideas are needed for outfitting such a small spot size measurement technique.

3. In addition to measuring the whole valve cap motion during this testing, it would also be beneficial to spatially measure the deformation of the valve cap membrane. In this manner, the onset of structural oscillations could be matched with estimated flow regime phenomena. Unfortunately, in the current system, the valve membrane is not in the line of sight of the vibrometer laser beam, due to the presence of silicon layers above and below. Velocimetry (to measure the motion of a moving surface) could be a potential solution, as discussed earlier. Or other sensing methods could be used to measure the dynamic behavior of the membrane, such as incorporation of piezoresistive material in the membrane. This method, however, would require significant fabrication complexity and the need for electrical lead-ins and lead-outs to the membrane, which would only further increase the complexity of the device assembly and bonding procedures.
4. A further interesting experiment which could be performed on the existing active valve design would be to reverse the flow direction through the valve orifice and determine if the same flow-induced vibrations occur. Since in either flow direction the orifice is comprised of a contraction and an expansion of similar magnitude area ratio, the flow is expected to behave consistently. The one main difference, however, is that over the compliant membrane itself, the flow will be experiencing a contraction rather than an expansion, a difference which might result in less severe formation of vortices. The instability discussion in Chapter 9, however, did include schematics from the fluid mechanics literature that indicated similar vorticity fields for both expansion and contraction flow geometries.

A further recommended task would be to develop a theoretical model for the fluid-structural interaction between this flow behavior and the compliant valve structure, using FEM and CFD analyses. The major problem with this, however, is that these modeling procedures require user input for governing flow relations. Since transition regimes between laminar and turbulent flow are not understood theoretically, there would be no way to instruct these programs on how to behave. As a result, the models would be only as accurate as the user's understanding of the flow behavior, which unfortunately is severely limited.

### 10.2.3 Materials Characterization

In the development of this active valve device, single-crystal ferroelectric material was the desired material for use due to its enhanced strain capabilities in comparison to the polycrys-



talline PZT-5H material. The published [4] PZN-PT material properties ( $d_{33} = 2000pC/N$  and  $E_p = 9.01GPa$ ) used in the design and optimization chapters of this thesis were found to overpredict the actual capability of the material based on the experiments detailed in Chapters 7 and 9. As a result, overall valve deflection versus voltage was lower than designed for. More detailed characterization studies should be performed on this PZN-PT material to better understand its actuation capabilities under the high voltage and relatively high stress conditions experienced in these active valve devices. Additionally, further development efforts by the manufacturers of this material to improve its performance characteristics (and maintain consistency across different batches of material) would enable more reliable design iterations to take place. In general, this valve design desires a piezoelectric material with as large a  $d_{33}$  and as large a Youngs modulus  $E_p$  as possible.

Additionally from a materials standpoint, the reliability of the active valve device and its capabilities for operating against large pressures and with significant valve cap stroke are directly affected by the yield stress levels of the etched silicon membranes that form the valve and the drive piston tethers. Given a value for yield stress (ie: in the design and optimization section of this thesis a value of 1 GPa was used [5]), the systematic design procedure presented in Chapter 5 is able to generate an active valve geometry that guarantees a maximum stress during theoretical operation below this value of yield stress. This assumed limit, therefore, directly influences the resulting size and dimensions of the active valve device. Further work to better characterize this yield stress limit (based on defects in the etched structures) or further work to enhance the strength of these filleted features with possible post DRIE smoothing procedures would enable more compact valve designs that work at higher stress levels.

#### 10.2.4 Microfabrication Issues

From a fabrication and assembly standpoint, this active valve device is far from a cost-effective manufacturable entity, primarily due to the extremely intensive Silicon-on-Insulator wafer DRIE etching steps for Layers 4, 5, and 7. Currently these etch procedures require tight control of fillet radii dimensions at the base of  $300 - 400\mu m$  deep etches, a requirement which necessitates numerous human inspection and handling steps. If etch procedures could be developed that minimize the depth of this etch so as to improve fillet radius uniformity across a given valve membrane structure or piston tether, the processing time and human intervention requirements could be drastically reduced. Additionally, the reliabilities of wafer-level silicon-to-silicon fusion bonding and silicon-glass anodic bonding are far from optimal at present. Although improvements in yields on a given wafer have occurred over the course of this MHT program at MIT, further optimization and processing studies could only help to improve wafer yields.

Finally, this active valve device is a 9-layer silicon and glass structure with integrated piezoelectric material elements. A general philosophy is “the fewer number of layers, the better”, as

long as each of the reduced layers is not substantially increased in complexity. Efforts should be pursued to redesign this active valve structure to still maintain the required structural elements, yet do so in such a way that eliminates as many layers as possible. A further improvement to the device would be to find a way to create a micro-seal between the hydraulic amplification chamber and the piezoelectric material chamber without the need for solid annular tethered structures. Limitations exist now in the ability to create very deep, thin and smooth gap etches in silicon. If such a thin trench could be micromachined and if a relatively compliant polymer material of some sort could be made to fill that thin gap, then the drive element piston would be capable of moving up and down in response to the piezoelectric material voltage without the need for these micromachined annular tethers. Of course, new problems such as electrical contact to the top surface of the piezoelectric materials and the release of a free-standing piston structure present themselves. Fabrication brainstorming ideas such as these should be continued in an effort to progress to next-generation valve devices.

### 10.2.5 Future of MHTs

This chapter has reviewed the performance of the active valve and has outlined a series of future activities that could be pursued in an effort to improve its performance. In general, the piezoelectrically-driven hydraulic amplification microvalve documented in this thesis successfully outperforms all liquid-regulation active valves previously presented in the literature (see Chapter 1), in terms of simultaneously satisfying a set of high frequency ( $\sim 1kHz$ ), high pressure ( $\sim 300kPa$ ), and large stroke ( $\sim 40\mu m$ ) requirements. In this sense, the development of the device has been a success. However, the performance limitations observed through device experimentation indicate that, in order for this valve technology to be successful in the designed-for high specific power ( $\sim 1000\frac{W}{kg}$ ) micropumping applications (MHTs) introduced in Chapter 1, significant further research and redesign is required. Even with the current limited active valve capabilities observed in this thesis, however, full MHT micropumping systems incorporating these valves are estimated to operate with specific powers between  $25\text{--}30\frac{W}{kg}$ , at least an order of magnitude larger than the best micropumping systems ( $2.5\frac{W}{kg}$ ) presented in the literature and detailed in Chapter 1. With this future work, it may be possible to realize an active valve device capable of operating at the desired quasi-static operational frequency ( $> 10kHz$ ) and high differential pressure ( $> 1MPa$ ), enabling it to successfully regulate liquid flow within the higher specific power MHT systems.

As detailed in this chapter, a structural redesign effort should be pursued, incorporating updated finite-element models with inertia coupling and external fluid added mass effects, to achieve a valve design with quasi-static frequency in excess of  $10kHz$ . It is the belief of this author that, by simplifying the hydraulic amplification chamber geometry, increasing the valve membrane thickness, and increasing the piezoelectric material volume beneath the drive element

piston, this frequency enhancement could be readily achieved while maintaining similar stroke capability. However, this guarantees only that the structure can successfully operate as a high-frequency microactuator against a constant external loading. It is the differential pressure applied to the device, and the resulting fluid flow through the valve orifice structure that will most likely limit the flow regulation capability of the structure, as observed in this thesis. The future work to more comprehensively understand the fluid flow regimes through these small scale orifice structures and, more importantly, the interaction of this flow with the adjacent compliant valve membrane structure is, therefore, of vital importance to the success of higher-performing valve devices for use in MHT systems. It is quite possible that by increasing the valve membrane thickness, as discussed in this chapter, the valve flow-induced structural oscillations could be significantly reduced. However, this hypothesis can only be proven through the detailed fluid-structural coupling models and experimental procedures recommended in this chapter. It is, therefore, the belief of this author that this microvalve device can be successfully redesigned to meet the structural high frequency requirements for use in high specific power MHT systems. What is unknown in this stage of the research, however, is the expected nature of fluid-structural interaction and corresponding flow-induced vibrations of the valve cap and membrane at these higher drive frequency levels and higher differential pressures. Future research must address these issues.

# Bibliography

- [1] Y.H. Su, K.S. Chen, D.C. Roberts, and S.M. Spearing, “Large Deflection Analysis of a Pre-Stressed Annular Plate With a Rigid Boss Under Axisymmetric Loading,” *Journal of Micromech. Microeng.* 11 (2001) pp. 645-653.
- [2] J. Carretero and K.S. Breuer, “Measurement and Modeling of the Flow Characteristics of Micro Disk Valves,” Proceedings of the 1994 International Mechanical Engineering Conference and Exposition: Microfluidics Symposium, Orlando, FL, Nov. 2000.
- [3] K.S. Breuer, J.C. Bird, G. Han, and K.J.A. Westin, “Infrared Diagnostics for the measurement of fluid and solid motion in micromachined Devices,” Proceedings, ASME IMECE, New York, NY. November 2001.
- [4] S.E. Park and T.R. Shrout, “Characteristics of Relaxor-Based Piezoelectric Single Crystals for Ultrasonic Transducers,” IEEE Trans. Ultrasonics, Ferroelectrics, and Frequency Control, Vol.44, No.5, Sept. 1997, pp. 1140-1147.
- [5] K.T. Turner, An Evaluation of Critical Issues for Microhydraulic Transducers: Silicon Wafer Bonding, Strength of Silicon on Insulator Membranes and Gold-Tin Solder Bonding. MIT Master’s Thesis. June 2001.

## Appendix A

# Support Documentation for Active Valve Linear Model

## A.1 ChapterExample.mws

File: ChapterExample.mws

David C. Roberts

This file calculates the linear deflection and swept volume of an annular plate with outer radius a and inner radius b. There is an applied pressure P from inner radius b to outer radius a. The plate is guided at r=b and clamped at r=a. This problem is included in the modeling chapter as a demonstration example of how this linear theory is carried out. The pressure P serves to deflect the plate in the positive direction. These calculations include deflections due to bending and shearing effects, since the plate thickness is not necessarily << than the plate outer radius.

```
> restart;
> Digits:=40;
```

*Digits := 40*

### Calculate Deflection, Swept Volume Due to BENDING

#### Define Governing Plate Bending Equation and Shear Force

```
> eqn:='diff(1/r*diff(r*diff(w(r),r),r),r)=Q(r)/D';
```

$$eqn := \frac{\partial}{\partial r} \left( \frac{\partial}{\partial r} \left( \frac{r}{r} \frac{\partial}{\partial r} w(r) \right) \right) = \frac{Q(r)}{D}$$

Shear force in terms of P:

```
> Q(r):= P*Pi*(r^2-b^2)/(2*Pi*r);
```

$$Q(r) := \frac{1}{2} \frac{P(r^2 - b^2)}{r}$$

#### Integrate the Governing Plate Bending Equation

Calculate the deflection, w\_bending(r), due to bending:

```
> Q1(r):=(int(Q(r)/D,r)+C1)*r;
```

```
Q2(r):=(int(Q1(r),r)+C2)/r;
```

```
w_bending(r):=int(Q2(r),r)+C3;
```

$$Q1(r) := \left( \frac{1}{4} \frac{P r^2}{D} - \frac{1}{2} \frac{P b^2 \ln(r)}{D} + C1 \right) r$$

$$Q2(r) := \frac{\frac{1}{16} \frac{P r^4}{D} - \frac{1}{4} \frac{P b^2 r^2 \ln(r)}{D} + \frac{1}{8} \frac{P b^2 r^2}{D} + \frac{1}{2} C1 r^2 + C2}{r}$$

$$w\_bending(r) := \frac{1}{64} \frac{P r^4}{D} - \frac{1}{8} \frac{P b^2 r^2 \ln(r)}{D} + \frac{1}{8} \frac{P b^2 r^2}{D} + \frac{1}{4} C1 r^2 + C2 \ln(r) + C3$$

#### Apply BCs and Solve for W\_bending(r)

```
> BC1:=subs({r=a},w_bending(r))=0;
```

$$BC1 := \frac{1}{64} \frac{P a^4}{D} - \frac{1}{8} \frac{P b^2 a^2 \ln(a)}{D} + \frac{1}{8} \frac{P b^2 a^2}{D} + \frac{1}{4} C1 a^2 + C2 \ln(a) + C3 = 0$$

```
> BC2:=subs({r=a},diff(w_bending(r),r))=0;
```

$$BC2 := \frac{1}{16} \frac{P a^3}{D} - \frac{1}{4} \frac{P b^2 a \ln(a)}{D} + \frac{1}{8} \frac{P b^2 a}{D} + \frac{1}{2} C1 a + \frac{C2}{a} = 0$$

```
> BC3:=subs({r=b},diff(w_bending(r),r))=0;
```

$$BC3 := \frac{3}{16} \frac{P b^3}{D} - \frac{1}{4} \frac{P b^3 \ln(b)}{D} + \frac{1}{2} C1 b + \frac{C2}{b} = 0$$

```
> Set1:=solve({BC1,BC2,BC3},{C1,C2,C3});
```

Determine the general expression for plate deflection, W\_bending(r):

```
> W_bending(r):=collect(subs(Set1,w_bending(r)),{D,P});
```

Page 1

$$W\_bending(r) := \left( \left( \frac{1}{64} r^4 - \frac{1}{8} b^2 r^2 \ln(r) + \frac{1}{8} b^2 r^2 - \frac{1}{32} \frac{(-a^4 + 4 b^2 a^2 \ln(a) - 2 b^2 a^2 + 3 b^4 - 4 b^4 \ln(b)) r^2}{-a^2 + b^2} \right. \right. \\ \left. \left. - \frac{1}{16} \frac{b^2 a^2 \left( a^2 - b^2 + 4 b^2 \ln\left(\frac{b}{a}\right) \right) \ln(r)}{-a^2 + b^2} \right. \right. \\ \left. \left. - \frac{1}{64} \frac{a^2 (a^4 - 4 b^2 a^2 \ln(a) - 3 b^2 a^2 + 2 b^4 + 8 b^4 \ln(b) + 16 b^4 \ln(a)^2 - 4 b^4 \ln(a) - 16 b^4 \ln(a) \ln(b))}{-a^2 + b^2} \right) \right) / D$$

⌈ Determine the plate deflection at r=b. This is denoted Wb\_bending.

> **Wb\_bending:=collect(simplify(subs({r=b},W\_bending(r))),{D,P});**

$$Wb\_bending := -\frac{1}{64} \left( \left( 7 b^4 a^2 - 3 b^6 - 4 b^4 \ln(b) a^2 - 5 b^2 a^4 + 4 b^4 a^2 \ln(a) + 4 b^2 a^4 \ln(b) + 16 b^4 a^2 \ln\left(\frac{b}{a}\right) + a^6 \right. \right. \\ \left. \left. - 4 a^4 b^2 \ln(a) + 16 a^2 b^4 \ln(a)^2 - 16 a^2 b^4 \ln(a) \ln(b) \right) \right) / (D (-a^2 + b^2))$$

### [-] Calculate Swept Volume, dV\_bending, Due to Bending

⌈ This is the swept volume under only the plate. The swept volume from r=0 to r=b must also be considered.

> **dV\_bending:=collect(simplify(int(2\*Pi\*r\*W\_bending(r),r=b..a)),{Pi,D,P});**

$$dV\_bending := \frac{1}{192} P \pi \left( -a^8 + 10 a^6 b^2 - 24 a^4 b^4 - 48 a^4 b^4 \ln\left(\frac{b}{a}\right) \ln(a) + 24 a^4 b^4 \ln\left(\frac{b}{a}\right) - 48 a^4 b^4 \ln(a)^2 \right. \\ \left. + 48 a^4 b^4 \ln(a) \ln(b) + 22 b^6 a^2 - 7 b^8 + 48 b^6 a^2 \ln(b) \ln\left(\frac{b}{a}\right) - 24 b^6 a^2 \ln\left(\frac{b}{a}\right) + 48 b^6 a^2 \ln(a)^2 - 48 b^6 a^2 \ln(a) \ln(b) \right) \\ \left. \right) / (D (-a^2 + b^2))$$

### [-] Calculate Deflection, Swept Volume Due to SHEARING

#### [-] Define Governing Plate Shearing Equation and Integrate

> **eqn2:='diff(w(r),r)=-alpha\*Q(r)/G/h';**

$$eqn2 := \frac{\partial}{\partial r} w(r) = -\frac{\alpha Q(r)}{G h}$$

⌈ Calculate the deflection, W\_shearing, due to shear effects (shear coefficient, alpha=1.5):

> **w\_shearing(r):=int(-alpha\*Q(r)/G/h,r)+C4;**

$$w\_shearing(r) := -\frac{1}{4} \frac{\alpha P r^2}{G h} + \frac{1}{2} \frac{\alpha P b^2 \ln(r)}{G h} + C4$$

#### [-] Apply BC and Solve for W\_shearing(r)

> **BC4:=subs({r=a},w\_shearing(r))=0;**

$$BC4 := -\frac{1}{4} \frac{\alpha P a^2}{G h} + \frac{1}{2} \frac{\alpha P b^2 \ln(a)}{G h} + C4 = 0$$

> **Set2:=solve({BC4},{C4});**

> **W\_shearing(r):=subs(Set2,w\_shearing(r));**

$$W\_shearing(r) := -\frac{1}{4} \frac{\alpha P r^2}{G h} + \frac{1}{2} \frac{\alpha P b^2 \ln(r)}{G h} - \frac{1}{4} \frac{\alpha P (-a^2 + 2 b^2 \ln(a))}{G h}$$

⌈ Determine the plate deflection at r=b. This is denoted Wb\_shearing.

> **Wb\_shearing:=collect(simplify(subs({r=b},W\_shearing(r))),{P});**

$$Wb\_shearing := -\frac{1}{4} \frac{\alpha P (b^2 - 2 b^2 \ln(b) - a^2 + 2 b^2 \ln(a))}{G h}$$

### Calculate Swept Volume Due to Shearing, dV\_shearing

```
> dV_shearing:=collect(simplify(int(2*Pi*r*W_shearing(r),r=b..a)),{P});
```

$$dV_{shearing} := \frac{1}{8} \frac{\pi \alpha P (a^4 - 4 b^2 a^2 + 3 b^4 - 4 b^3 \ln(b) + 4 b^4 \ln(a))}{G h}$$

### Total Deflection and Swept Volume

Sum the deflections due to bending and shear into the total plate deflection at r=b, Wb:

```
> Wb:=collect(Wb_bending + Wb_shearing,{P});
```

$$Wb := \left( -\frac{1}{64} \left( 7 b^4 a^2 - 3 b^6 - 4 b^4 \ln(b) a^2 - 5 b^2 a^4 + 4 b^4 a^2 \ln(a) + 4 b^2 a^4 \ln(b) + 16 b^4 a^2 \ln(b) \ln\left(\frac{b}{a}\right) + a^6 - 4 a^4 b^2 \ln(a) + 16 a^2 b^4 \ln(a)^2 - 16 a^2 b^4 \ln(a) \ln(b) \right) \right) / (D (-a^2 + b^2)) - \frac{1}{4} \frac{\alpha (b^2 - 2 b^2 \ln(b) - a^2 + 2 b^2 \ln(a))}{G h} \Bigg) P$$

Sum the displaced volumes due to bending and shear into the total displaced volume, dV:

```
> dV:=collect(dV_bending+dV_shearing,{P});
```

$$dV := \left( \frac{1}{192} \pi \left( -a^8 + 10 a^6 b^2 - 24 a^4 b^4 - 48 a^4 b^4 \ln\left(\frac{b}{a}\right) \ln(a) + 24 a^4 b^4 \ln\left(\frac{b}{a}\right) - 48 a^4 b^4 \ln(a)^2 + 48 a^4 b^4 \ln(a) \ln(b) + 22 b^6 a^2 - 7 b^8 + 48 b^6 a^2 \ln(b) \ln\left(\frac{b}{a}\right) - 24 b^6 a^2 \ln\left(\frac{b}{a}\right) + 48 b^6 a^2 \ln(a)^2 - 48 b^6 a^2 \ln(a) \ln(b) \right) \right) / (D (-a^2 + b^2)) + \frac{1}{8} \frac{\pi \alpha (a^4 - 4 b^2 a^2 + 3 b^4 - 4 b^4 \ln(b) + 4 b^4 \ln(a))}{G h} \Bigg) P$$

### Substitution of Example Values

```
> Wb_EXAMPLE:=evalf(subs({alpha=1.5,a=3.15e-3,b=0.80e-3,E=165e9,nu=0.22,h=1000e-6},subs(P=1e6,D=E*h^3/(12*(1-nu^2)),G=E/2/(1+nu),Wb)));
```

$$Wb\_EXAMPLE := .986574732573098211629339004226204575890 \cdot 10^{-7}$$

```
> dV_EXAMPLE:=evalf(subs({alpha=1.5,a=3.15e-3,b=0.80e-3,E=165e9,nu=0.22,h=1000e-6},subs(P=1e6,D=E*h^3/(12*(1-nu^2)),G=E/2/(1+nu),dV)));
```

$$dV\_EXAMPLE := .1320442285992528857571432424955844654522 \cdot 10^{-11}$$

```
>
```



## A.2 FullActiveValve(LINEAR).mws [see Section 2.4]

```

File: FullActiveValve(LINEAR).mws
David C. Roberts
This file solves the linear valve analytical model described in Chapter 2 of thesis. The inputs are P1, P2, and Vp.
The valve behavior is calculated.
> restart;
> Digits:=40;

```

*Digits := 40*

**Step 1: Define Linear Quasi-Static Relations**

**Piezoelectric Material**

[ This relation assumes perfect d33 actuation (no effect of transverse clamping).  
> EQN1 := Z[p] = d[33]\*V[p] - (L[p]/E[p])\*T[p];

$$EQN1 := Z_p = d_{33} V_p - \frac{L_p T_p}{E_p}$$

[ This relation determines the piezo charge.  
> EQN2 := Q[p] = (eT[33]\*A[p]/L[p])\*V[p] + (d[33]\*A[p])\*T[p];

$$EQN2 := Q_p = \frac{eT_{33} A_p V_p}{L_p} + d_{33} A_p T_p$$

**Bottom Structural Compliance**

[ Circular plate with stress imposed over central region.  
> EQN3 := Z[bot] = (Xi[Zbot,T]) \* T[p];

$$EQN3 := Z_{bot} = \Xi_{Zbot, T} T_p$$

**Drive Element Tethers**

> EQN4 := Z[te] =  
(Xi[Ztetop,F]\*Xi[Ztebot,F]) / (Xi[Ztetop,F]+Xi[Ztebot,F]) \* (A[p]\*T[p]-A[piis]\*P[HAC]) -  
(Xi[Ztetop,P]\*Xi[Ztebot,P]) / (Xi[Ztetop,P]+Xi[Ztebot,P]) \* P[HAC];

$$EQN4 := Z_e = \frac{\Xi_{Ztetop, F} \Xi_{Ztebot, F} (A_p T_p - A_{pis} P_{HAC})}{\Xi_{Ztetop, F} + \Xi_{Ztebot, F}} - \frac{\Xi_{Ztetop, P} \Xi_{Ztebot, P} P_{HAC}}{\Xi_{Ztetop, P} + \Xi_{Ztebot, P}}$$

> EQN5 := dV[te] =  
(Xi[dVtetop,F]\*Xi[Ztebot,F]) / (Xi[Ztetop,F]+Xi[Ztebot,F]) \* (A[p]\*T[p]-A[piis]\*P[HAC]) -  
(Xi[dVtetop,P]\*Xi[Ztebot,P]) / (Xi[dVtetop,P]+Xi[Ztebot,P]) \* P[HAC] + A[piis]\*Z[te];

$$EQN5 := dV_e = \frac{\Xi_{dVtetop, F} \Xi_{Ztebot, F} (A_p T_p - A_{pis} P_{HAC})}{\Xi_{Ztetop, F} + \Xi_{Ztebot, F}} - \frac{\Xi_{dVtetop, P} \Xi_{Ztebot, P} P_{HAC}}{\Xi_{dVtetop, P} + \Xi_{Ztebot, P}} + A_{pis} Z_e$$

**Drive Element Piston**

> EQN6 := Z[piis] = Xi[Zpis,T]\*T[p] - Xi[Zpis,P]\*P[HAC];

$$EQN6 := Z_{pis} = \Xi_{Zpis, T} T_p - \Xi_{Zpis, P} P_{HAC}$$

> EQN7 := dV[piis] = Xi[dVpis,T]\*T[p] - Xi[dVpis,P]\*P[HAC];

$$EQN7 := dV_{pis} = \Xi_{dVpis, T} T_p - \Xi_{dVpis, P} P_{HAC}$$

**Fluid Compressibility**

> EQN8 := dV[fluid] = -(V[HAC]/K[f])\*(P[HAC]);

Page 1

$$EQN8 := dV_{fluid} = - \frac{V_{HAC} P_{HAC}}{K_f}$$

**Top Structural Compliance**

> EQN9 := Z[top] = Xi[Ztop,P]\*P[HAC] + Xi[Ztop,F]\*F[vm];

$$EQN9 := Z_{top} = \Xi_{Ztop,P} P_{HAC} + \Xi_{Ztop,F} F_{vm}$$

> EQN10 := dV[top] = Xi[dVtop,P]\*P[HAC] + Xi[dVtop,F]\*F[vm] + A[vm]\*Z[top];

$$EQN10 := dV_{top} = \Xi_{dVtop,P} P_{HAC} + \Xi_{dVtop,F} F_{vm} + A_{vm} Z_{top}$$

> EQN11 := F[vm] = (A[vm]-A[vc])\*(P[HAC]-P[2]) + A[vc]\*(P[HAC]-P[1]);

$$EQN11 := F_{vm} = (A_{vm} - A_{vc}) (P_{HAC} - P_2) + A_{vc} (P_{HAC} - P_1)$$

**Valve Cap/Membrane**

Note: I have included the contribution to valve cap deflection due to top chamber deflection.  
The corresponding volume contribution is already included in the Top Structural Compliance section.

> EQN12 := Z[vc] = Xi[Zvc,P]\*(P[HAC]-P[2]) + Xi[Zvc,F]\*F[vc] + Z[top];

$$EQN12 := Z_{vc} = \Xi_{Zvc,P} (P_{HAC} - P_2) + \Xi_{Zvc,F} F_{vc} + Z_{top}$$

> EQN13 := dV[vm] = Xi[dVvm,P]\*(P[HAC]-P[2]) + Xi[dVvm,F]\*F[vc] + A[vc]\*Z[vc];

$$EQN13 := dV_{vm} = \Xi_{dVvm,P} (P_{HAC} - P_2) + \Xi_{dVvm,F} F_{vc} + A_{vc} Z_{vc}$$

> EQN14 := F[vc] = (P[HAC]-P[1])\*A[vc];

$$EQN14 := F_{vc} = A_{vc} (P_{HAC} - P_1)$$

**Deflection, Swept Volume Conservation**

All structural deflections and swept volumes are defined to be positive in the upward direction.

> EQN15 := Z[p] + Z[bot] = Z[te] + Z[piis];

$$EQN15 := Z_p + Z_{bot} = Z_{te} + Z_{piis}$$

> EQN16 := 0 = dV[te] + dV[piis] + dV[fluid] - dV[top] - dV[vm];

$$EQN16 := 0 = dV_{te} + dV_{piis} + dV_{fluid} - dV_{top} - dV_{vm}$$

**Other Relations**

Variables as functions of other variables.

> EQN17 := Z[de] = Z[te] + Z[piis];

$$EQN17 := Z_{de} = Z_{te} + Z_{piis}$$

**Step 2: Define Geometric/Material Parameters**

Geometric Parameters:

> R[vc]:=0.31e-3: R[vm]:=0.80e-3: t[vm]:=10e-6: A[vc]:=Pi\*R[vc]^2: A[vm]:=Pi\*R[vm]^2:  
t[vc]:=400e-6:

> L[p]:=1e-3: R[p]:=1e-3: A[p]:=Pi\*R[p]^2:

> R[piis]:=3e-3: R[ch]:=3.225e-3: t[piis]:=800e-6: t[topte]:=10e-6: t[botte]:=10e-6:  
A[piis]:=Pi\*R[piis]^2:

> t[bot]:=1000e-6:

> H[HAC]:=400e-6: V[HAC]:=Pi\*R[ch]^2\*H[HAC] + Pi\*(R[vm]^2-R[vc]^2)\*t[vc]:

> t[top]:=1000e-6:

Material Parameters:

```
[ > d[33]:=2000e-12: sD[33]:=16.4e-12: sE[33]:=111e-12: E[p]:=1/sE[33]:
eT[33]:=d[33]^2/(sE[33]-sD[33]): E[sij]:=165e9: nu[sij]:=0.22: K[f]:=2e9: alpha[sij]:=1.25:
```

### Step 3: Calculate Linear Plate Coefficients

#### Bottom Stuctural Compliance

```
[ Circular plate clamped at outer radius (r=a) with stress imposed over central region (r=0 to r=b).
[ Positive deflection is upward, whereas positive stress acts downward. This relation includes
[ bending and shearing effects, see BottomChamberPlate(WORST).mws.
[ > eqn:='diff(1/r*diff(r*diff(Z(x),x),x),x)=Q(x)/D':
[ > Q_0b(x):=-Tp*Pi*x^2/(2*Pi*x):
[ > Q1(x):=(int(Q_0b(x)/D,x)+C1)*x:
[ > Q2(x):=(int(Q1(x),x))/x:
[ > Zbot_0b_bending(x):=int(Q2(x),x)+C3:
[ > BC1:=subs({r=b},Zbot_0b_bending(x))=Zb_bending:
[ > BC2:=subs({r=b},diff(Zbot_0b_bending(x),x))=dZb_bending:
[ > BC3:=subs({r=b},diff(diff(Zbot_0b_bending(x),x),x) +
[ > nu/r*diff(Zbot_0b_bending(x),x))=d2Zb_bending:
[ > eqn:='diff(1/r*diff(r*diff(Z(x),x),x),x)=Q(x)/D':
[ > Q_ba(x):=-Tp*Pi*b^2/(2*Pi*x):
[ > Q1(x):=(int(Q_ba(x)/D,x)+C4)*x:
[ > Q2(x):=(int(Q1(x),x)+C5)/x:
[ > Zbot_ba_bending(x):=int(Q2(x),x)+C6:
[ > BC4:=subs({r=a},Zbot_ba_bending(x))=0:
[ > BC5:=subs({r=a},diff(Zbot_ba_bending(x),x))=0:
[ > BC6:=subs({r=b},Zbot_ba_bending(x))=Zb_bending:
[ > BC7:=subs({r=b},diff(Zbot_ba_bending(x),x))=dZb_bending:
[ > BC8:=subs({r=b},diff(diff(Zbot_ba_bending(x),x),x) +
[ > nu/r*diff(Zbot_ba_bending(x),x))=d2Zb_bending:
[ > Set1:=solve({BC1,BC2,BC3,BC4,BC5,BC6,BC7,BC8},{C1,C3,C4,C5,C6,Zb_bending,dZb_bending,d
[ > 2Zb_bending}):
[ > Zbot_0b_BENDING(x):=collect(subs(Set1,Zbot_0b_bending(x)),{D,Tp}):
[ > Zbot_ba_BENDING(x):=collect(subs(Set1,Zbot_ba_bending(x)),{D,P}):
[ > dVbot_0b_BENDING:=collect(simplify(int(2*Pi*r*Zbot_0b_BENDING(x),r=0..b)),{Tp}):
[ > dVbot_ba_BENDING:=collect(simplify(int(2*Pi*r*Zbot_ba_BENDING(x),r=b..a)),{Tp}):
[ > eqn4:='diff(Z(x),x)=-alpha*Q_(x)/G/h':
[ > Zbot_0b_shearing(x):=int(-alpha*Q_0b(x)/G/h,x)+C7:
[ > BC9:=subs({r=b},Zbot_0b_shearing(x))=Zb_shearing:
[ > eqn4:='diff(Z(x),x)=-alpha*Q_(x)/G/h':
[ > Zbot_ba_shearing(x):=int(-alpha*Q_ba(x)/G/h,x)+C8:
[ > BC10:=subs({r=a},Zbot_ba_shearing(x))=0:
[ > BC11:=subs({r=b},Zbot_ba_shearing(x))=Zb_shearing:
[ > Set2:=solve({BC9,BC10,BC11},{C7,C8,Zb_shearing}):
[ > Zbot_0b_SHEARING(x):=collect(subs(Set2,Zbot_0b_shearing(x)),{D,Tp}):
[ > Zbot_ba_SHEARING(x):=collect(subs(Set2,Zbot_ba_shearing(x)),{D,Tp}):
```

```
[ > dVbot_0b_SHEARING:=collect(simplify(int(2*Pi*r*Zbot_0b_SHEARING(r),r=0..b)),{Tp}):
[ > dVbot_ba_SHEARING:=collect(simplify(int(2*Pi*r*Zbot_ba_SHEARING(r),r=b..a)),{Tp}):
[ > Zbot_0b(r):=collect(Zbot_0b_BENDING(r) + Zbot_0b_SHEARING(r),{Tp}):
[ > Zbot_ba(r):=collect(Zbot_ba_BENDING(r) + Zbot_ba_SHEARING(r),{Tp}):
[ > dVbot:=collect(dVbot_0b_BENDING + dVbot_ba_BENDING + dVbot_0b_SHEARING +
dVbot_ba_SHEARING,{Tp}):
[ > Xi[Zbot,T]:=subs({r=0,Tp=1},Zbot_0b(r));
Xi[Zbot,T]:=evalf(subs({a=R[ch],b=R[p],alpha=alpha[si],h=t[bot],D=E[si]*t[bot]^3/(12*(
1-nu[si]^2)),G=E[si]/(2*(1+nu[si]))},Xi[Zbot,T]));
```

$$\Xi_{Zbot,T} := -\frac{1}{64} \frac{b^2 \left( -3b^2 + 4a^2 + 4b^2 \ln\left(\frac{b}{a}\right) \right)}{D} - \frac{1}{4} \frac{\alpha b^2 (1 - 2 \ln(b) + 2 \ln(a))}{G h}$$

$$\Xi_{Zbot,T} := -.5212199372749083675326231687472284135238 \cdot 10^{-13}$$

#### Drive Element Tethers

```
TOP TETHER
Annular plate clamped at outer radius (r=a) and guided at inner radius (r=b) with pressure applied
downward over tether and concentrated force applied upward at inner radius (r=b). These relations
include bending effects only, see TetherTop2.mws.
[ > eqn:='diff(1/r*diff(r*diff(Z(r),r),r),r)=Q(r)/D':
[ > Q(r):=F[topte]/(2*Pi*r) - PHAC*Pi*(r^2-b^2)/(2*Pi*r):
[ > Q1(r):=(int(Q(r)/D,r)+C1)*r:
Q2(r):=(int(Q1(r),r)+C2)/r:
Ztether1_bending(r):=expand(int(Q2(r),r)+C3):
[ > BC1:=subs({r=a},Ztether1_bending(r))=0:
[ > BC2:=subs({r=a},diff(Ztether1_bending(r),r))=0:
[ > BC3:=subs({r=b},diff(Ztether1_bending(r),r))=0:
[ > Set1:=solve({BC1,BC2,BC3},{C1,C2,C3}):
[ > Ztether1_BENDING(r):=collect(subs(Set1,Ztether1_bending(r)),{F[topte],D,PHAC}):
[ > Ztether1:=collect(simplify(subs({r=b},Ztether1_BENDING(r))),{F[topte],D,PHAC}):
[ > dVtether1_BENDING:=collect(simplify(int(2*Pi*r*Ztether1_BENDING(r),r=b..a)),{Pi,F[topt
e],D,PHAC}):
[ > Xi[Ztetop,F] := subs({PHAC=0,F[topte]=1},Ztether1);
Xi[Ztetop,F]:=evalf(subs({a=R[ch],b=R[pi],h=t[topte],D=E[si]*t[topte]^3/(12*(1-nu[si]
^2))},Xi[Ztetop,F]));
```

$$\Xi_{Ztetop,F} := -\frac{1}{64} \frac{8b^2a^2 - 4b^4 + 16b^2a^2 \ln\left(\frac{b}{a}\right) \ln(b) - 4a^4 + 16a^2 \ln(a)^2 b^2 - 16a^2 \ln(a) b^2 \ln(b)}{\pi(a^2 - b^2)D}$$

$$\Xi_{Ztetop,F} := .3358560090822692575226480248142747504821 \cdot 10^{-5}$$

```
[ > Xi[Ztetop,P] := -subs({PHAC=1,F[topte]=0},Ztether1);
Xi[Ztetop,P]:=evalf(subs({a=R[ch],b=R[pi],h=t[topte],D=E[si]*t[topte]^3/(12*(1-nu[si]
^2))},Xi[Ztetop,P]));
```

$$\Xi_{Ztetop,P} := \frac{1}{64} \left( 7\pi b^4 a^2 - 3\pi b^6 - 5\pi a^4 b^2 + 4\pi b^4 a^2 \ln(a) - 4\pi b^4 \ln(b) a^2 + 4\pi b^2 a^4 \ln(b) + 16\pi b^4 a^2 \ln(b) \ln\left(\frac{b}{a}\right) \right)$$

```

+  $\pi a^6 - 4 \pi a^4 b^2 \ln(a) + 16 \pi a^2 \ln(a)^2 b^4 - 16 \pi a^2 \ln(a) b^4 \ln(b)$   $\Big) / (\pi (a^2 - b^2) D)$ 
 $\Xi_{Zetop, P} := .7246716855091782654098385470407258607940 \cdot 10^{-11}$ 
> Xi[dVtetop, F] := subs({PHAC=0, F[topte]=1}, dVtether1_BENDING);
Xi[dVtetop, F] := evalf(subs({a=R[ch], b=R[pi], h=t[topte], D=E[si]*t[topte]^3/(12*(1-nu[si]^2)), Xi[dVtetop, F]}));
 $\Xi_{dVtetop, F} := -\frac{1}{192} \left( -12 b^4 \ln(b) a^2 + 24 b^4 a^2 \ln\left(\frac{b}{a}\right) - 3 a^6 + 12 a^4 b^2 \ln(b) - 12 a^4 b^2 \ln(a) - 24 a^4 b^2 \ln\left(\frac{b}{a}\right) \right.$ 
 $\left. + 48 a^4 \ln(a)^2 b^2 + 48 a^4 b^2 \ln\left(\frac{b}{a}\right) \ln(a) - 48 a^4 \ln(a) b^2 \ln(b) + 15 a^4 b^2 + 48 a^2 \ln(a) b^4 \ln(b) - 48 b^4 a^2 \ln\left(\frac{b}{a}\right) \ln(b) \right.$ 
 $\left. - 48 a^2 \ln(a)^2 b^4 - 21 b^4 a^2 + 12 b^4 a^2 \ln(a) + 9 b^6 \right) / ((a^2 - b^2) D)$ 
 $\Xi_{dVtetop, P} := .7246716855091782654098385470406784 \cdot 10^{-11}$ 
> Xi[dVtetop, P] := -subs({PHAC=1, F[topte]=0}, dVtether1_BENDING);
Xi[dVtetop, P] := evalf(subs({a=R[ch], b=R[pi], h=t[topte], D=E[si]*t[topte]^3/(12*(1-nu[si]^2)), Xi[dVtetop, P]}));
 $\Xi_{dVtetop, P} := \frac{1}{192} \left( \left( 24 b^6 a^2 \ln\left(\frac{b}{a}\right) + a^8 - 48 a^4 \ln(a) b^4 \ln(b) + 48 a^4 b^4 \ln\left(\frac{b}{a}\right) \ln(a) + 48 a^4 \ln(a)^2 b^4 - 24 a^4 b^4 \ln\left(\frac{b}{a}\right) \right. \right.$ 
 $\left. + 24 a^4 b^4 - 10 a^6 b^2 - 48 b^6 a^2 \ln\left(\frac{b}{a}\right) \ln(b) - 48 a^2 \ln(a)^2 b^6 + 48 a^2 \ln(a) b^6 \ln(b) + 7 b^8 - 22 b^6 a^2 \right) \pi / ($ 
 $(a^2 - b^2) D)$ 
 $\Xi_{dVtetop, P} := .1672014327695025501669898411677512555127 \cdot 10^{-16}$ 
BOTTOM TETHER
Annular plate clamped at outer radius (r=a) and guided at inner radius (r=b) with concentrated
force applied upward at inner radius (r=b) and pressure over annulus. These relations include
bending effects only, see TetherBottom3.mws.
> eqn:='diff(1/r*diff(r*diff(Z(x), x), x), x)=Q(x)/D':
> Q(x):=F[botte]/(2*Pi*x) - PHAC*Pi*(x^2-b^2)/(2*Pi*x):
> Q1(x):=(int(Q(x)/D, x)+C1)*x:
> Q2(x):=(int(Q1(x), x)+C2)/x:
Ztether2_bending(x):=expand(int(Q2(x), x)+C3):
> BC1:=subs({x=a}, Ztether2_bending(x))=0:
> BC2:=subs({x=a}, diff(Ztether2_bending(x), x))=0:
> BC3:=subs({x=b}, diff(Ztether2_bending(x), x))=0:
> Set1:=solve({BC1, BC2, BC3}, {C1, C2, C3}):
> Ztether2_BENDING(x):=collect(subs(Set1, Ztether2_bending(x)), {F[botte], D, PHAC}):
> Ztether2:=collect(simplify(subs({x=b}, Ztether2_BENDING(x))), {F[botte], D, PHAC}):
> dVtether2_BENDING:=collect(simplify(int(2*Pi*x*Ztether2_BENDING(x), x=b..a)), {Pi, F[botte], D, PHAC}):
> Xi[Ztebot, F] := subs({PHAC=0, F[botte]=1}, Ztether2);
Xi[Ztebot, F] := evalf(subs({a=R[ch], b=R[pi], h=t[botte], D=E[si]*t[botte]^3/(12*(1-nu[si]^2)), Xi[Ztebot, F]}));

```

$$\Xi_{Zebot, F} := -\frac{1}{64} \frac{8b^2a^2 - 4b^4 + 16b^2a^2 \ln\left(\frac{b}{a}\right) \ln(b) - 4a^4 + 16a^2 \ln(a)^2 b^2 - 16a^2 \ln(a) b^2 \ln(b)}{\pi(a^2 - b^2) D}$$

$$\Xi_{Zebot, F} := .3358560090822692575226480248142747504821 \cdot 10^{-5}$$

```

> Xi[Ztebot, P] := -subs({PHAC=1, F[botte]=0}, Ztether2);
Xi[Ztebot, P] := evalf(subs({a=R[ch], b=R[pi], h=t[botte], D=E[si]*t[botte]^3/(12*(1-nu[si]^2)), Xi[Ztebot, P]}));
Xi[Ztebot, P] := 1/64 * (7*pi*b^4*a^2 - 3*pi*b^6 - 5*pi*a^4*b^2 + 4*pi*b^4*a^2*ln(a) - 4*pi*b^4*ln(b)*a^2 + 4*pi*b^2*a^4*ln(b) + 16*pi*b^4*a^2*ln(b)*ln(b/a) + pi*a^6 - 4*pi*a^4*b^2*ln(a) + 16*pi*a^2*ln(a)^2*b^4 - 16*pi*a^2*ln(a)*b^4*ln(b)) / (pi*(a^2 - b^2)*D)
Xi[Ztebot, P] := .7246716855091782654098385470407258607940 * 10^{-11}
> Xi[dVtebot, F] := subs({PHAC=1, F[botte]=1}, dVtether2_BENDING);
Xi[dVtebot, F] := evalf(subs({a=R[ch], b=R[pi], h=t[botte], D=E[si]*t[botte]^3/(12*(1-nu[si]^2)), Xi[dVtebot, F]}));
Xi[dVtebot, F] := -1/192 * (-12*b^4*ln(b)*a^2 + 24*b^4*a^2*ln(b/a) - 3*a^6 + 12*a^4*b^2*ln(b) - 12*a^4*b^2*ln(a) - 24*a^4*b^2*ln(b/a) + 48*a^4*ln(a)^2*b^2 + 48*a^4*b^2*ln(b/a)*ln(a) - 48*a^4*ln(a)*b^2*ln(b) + 15*a^4*b^2 + 48*a^2*ln(a)*b^4*ln(b) - 48*b^4*a^2*ln(b/a)*ln(b) - 48*a^2*ln(a)^2*b^4 - 21*b^4*a^2 + 12*b^4*a^2*ln(a) + 9*b^6) / ((a^2 - b^2)*D)
Xi[dVtebot, F] := .7246716855091782654098385470406784 * 10^{-11}
> Xi[dVtebot, P] := -subs({PHAC=1, F[botte]=0}, dVtether2_BENDING);
Xi[dVtebot, P] := evalf(subs({a=R[ch], b=R[pi], h=t[botte], D=E[si]*t[botte]^3/(12*(1-nu[si]^2)), Xi[dVtebot, P]}));
Xi[dVtebot, P] := 1/192 * ((24*b^6*a^2*ln(b/a) + a^8 - 48*a^4*ln(a)*b^4*ln(b) + 48*a^4*b^4*ln(b/a)*ln(a) + 48*a^4*ln(a)^2*b^4 - 24*a^4*b^4*ln(b/a) + 24*a^4*b^4 - 10*a^6*b^2 - 48*b^6*a^2*ln(b/a)*ln(b) - 48*a^2*ln(a)^2*b^6 + 48*a^2*ln(a)*b^6*ln(b) + 7*b^8 - 22*b^6*a^2)*pi) / ((a^2 - b^2)*D)
Xi[dVtebot, P] := .1672014327695025501669898411677512555127 * 10^{-16}

```

#### Drive Element Piston (More Compliant: Hinged Outer Circumference)

Circular plate hinged at outer radius (r=a) with pressure acting downward over entire plate (from r=0 to r=a) and stress acting upward in central region (from r=0 to r=b). Positive plate deflection is defined in the upward direction. These relations include bending and shearing effects, see Piston(WORST).mws.

```

> eqn:='diff(1/r*diff(x*diff(Z(x), x), x), x)=Q(x)/D':
> Q_0b(x):=(Tp-PHAC)*Pi*x^2/(2*Pi*x):
> Q1(x):=(int(Q_0b(x)/D, x)+C1)*x:
Q2(x):=(int(Q1(x), x))/x:
Zpis_0b_bending(x):=int(Q2(x), x)+C3:
> BC1:=subs({r=b}, Zpis_0b_bending(x))=Zb_bending:
> BC2:=subs({r=b}, diff(Zpis_0b_bending(x), x))=dZb_bending:
> BC3:=subs({r=b}, diff(diff(Zpis_0b_bending(x), x), x) +

```

```

[ nu/r*diff(Zpis_0b_bending(x),x)=d2Zb_bending:
[ > eqn:='diff(1/r*diff(r*diff(Z(x),x),x),x)=Q(x)/D':
[ > Q_ba(x):=Tp*Pi*b^2/(2*Pi*x) - PHAC*Pi*x^2/(2*Pi*x):
[ > Q1(x):=(int(Q_ba(x)/D,x)+C4)*x:
[ > Q2(x):=(int(Q1(x),x)+C5)/x:
[ > Zpis_ba_bending(x):=int(Q2(x),x)+C6:
[ > BC4:=subs({r=a},Zpis_ba_bending(x))=0:
[ > BC5:=subs({r=a},diff(diff(Zpis_ba_bending(x),x),x) +
[ nu/r*diff(Zpis_ba_bending(x),x))=0:
[ > BC6:=subs({r=b},Zpis_ba_bending(x))=Zb_bending:
[ > BC7:=subs({r=b},diff(Zpis_ba_bending(x),x))=dZb_bending:
[ > BC8:=subs({r=b},diff(diff(Zpis_ba_bending(x),x),x) +
[ nu/r*diff(Zpis_ba_bending(x),x))=d2Zb_bending:
[ > Set1:=solve({BC1,BC2,BC3,BC4,BC5,BC6,BC7,BC8},{C1,C3,C4,C5,C6,Zb_bending,dZb_bending,d
[ 2Zb_bending}):
[ > Zpis_0b_BENDING(x):=collect(subs(Set1,Zpis_0b_bending(x)),{D,Tp,PHAC}):
[ > Zpis_ba_BENDING(x):=collect(subs(Set1,Zpis_ba_bending(x)),{D,Tp,PHAC}):
[ > dVpis_0b_BENDING:=collect(simplify(int(2*Pi*r*Zpis_0b_BENDING(x),r=0..b)),{Tp,PHAC}):
[ > dVpis_ba_BENDING:=collect(simplify(int(2*Pi*r*Zpis_ba_BENDING(x),r=b..a)),{Tp,PHAC}):
[ > eqn4:='diff(Z(x),x)=-alpha*Q_(x)/G/h':
[ > Zpis_0b_shearing(x):=int(-alpha*Q_0b(x)/G/h,x)+C7:
[ > BC9:=subs({r=b},Zpis_0b_shearing(x))=Zb_shearing:
[ > eqn4:='diff(Z(x),x)=-alpha*Q_(x)/G/h':
[ > Zpis_ba_shearing(x):=int(-alpha*Q_ba(x)/G/h,x)+C8:
[ > BC10:=subs({r=a},Zpis_ba_shearing(x))=0:
[ > BC11:=subs({r=b},Zpis_ba_shearing(x))=Zb_shearing:
[ > Set2:=solve({BC9,BC10,BC11},{C7,C8,Zb_shearing}):
[ > Zpis_0b_SHEARING(x):=collect(subs(Set2,Zpis_0b_shearing(x)),{D,Tp,PHAC}):
[ > Zpis_ba_SHEARING(x):=collect(subs(Set2,Zpis_ba_shearing(x)),{D,Tp,PHAC}):
[ > dVpis_0b_SHEARING:=collect(simplify(int(2*Pi*r*Zpis_0b_SHEARING(x),r=0..b)),{Tp,PHAC}):
[ :
[ > dVpis_ba_SHEARING:=collect(simplify(int(2*Pi*r*Zpis_ba_SHEARING(x),r=b..a)),{Tp,PHAC}):
[ :
[ > Zpis_0b(x):=collect(Zpis_0b_BENDING(x) + Zpis_0b_SHEARING(x),{Tp,PHAC}):
[ > Zpis_ba(x):=collect(Zpis_ba_BENDING(x) + Zpis_ba_SHEARING(x),{Tp,PHAC}):
[ > Zpis_0:=subs({r=0},collect(Zpis_0b_BENDING(x) + Zpis_0b_SHEARING(x),{Tp,PHAC})):
[ > dVpist:=collect(simplify(dVpis_0b_BENDING + dVpis_ba_BENDING + dVpis_0b_SHEARING +
[ dVpis_ba_SHEARING),{Tp,PHAC}):
[ > Xil[Zpis,T] := subs({PHAC=0,Tp=1},Zpis_0);
[ Xil[Zpis,T]:=evalf(subs({a=R[pis],b=R[p],nu=nu[sis],alpha=alpha[sis],h=t[pis],D=E[sis]*t[
[ pis]^3/(12*(1-nu[sis]^2)),G=E[sis]/(2*(1+nu[sis]))},Xil[Zpis,T]));

```

$$\Xi l_{Zpis,T} := \frac{1}{64} \frac{-7b^4 + 12b^2a^2 + 4vb^2a^2 - 3vb^4 + 4\ln\left(\frac{b}{a}\right)b^4 + 4\ln\left(\frac{b}{a}\right)vb^4}{(1+v)D} - \frac{1}{4} \frac{\alpha(-b^2 + 2b^2\ln(b) - 2\ln(a)b^2)}{Gh}$$

 **Drive Element Piston (Less Compliant: Rigid Outer Circumference)**

```

> eqn:='diff(1/r*diff(r*diff(Z(x),x),x),x)=Q(x)/D':
> Q_0b(x):=(Tp-PHAC)*Pi*x^2/(2*Pi*x):
> Q1(x):=(int(Q_0b(x)/D,x)+C1)*x:
> Q2(x):=(int(Q1(x),x))/x:
> Zpis_0b_bending(x):=int(Q2(x),x)+C3:
> BC1:=subs({r=b},Zpis_0b_bending(x))=2b_bending:
> BC2:=subs({r=b},diff(Zpis_0b_bending(x),x))=d2b_bending:
> BC3:=subs({r=b},diff(diff(Zpis_0b_bending(x),x),x)+
nu/r*diff(Zpis_0b_bending(x),x))=d22b_bending:
> eqn:='diff(1/r*diff(r*diff(Z(x),x),x),x)=Q(x)/D':
> Q_ba(x):=(Pi*Pi*b^2/(2*Pi*x) - PHAC)*Pi*x^2/(2*Pi*x):
> Q1(x):=(int(Q_ba(x)/D,x)+C4)*x:
> Q2(x):=(int(Q1(x),x)+C5)/x:
> Zpis_ba_bending(x):=int(Q2(x),x)+C6:
> BC4:=subs({r=a},Zpis_ba_bending(x))=0:

```



```

[ > BC5:=subs({r=a},diff(Zpis_ba_bending(r),r))=0:
[ > BC6:=subs({r=b},Zpis_ba_bending(r))=Zb_bending:
[ > BC7:=subs({r=b},diff(Zpis_ba_bending(r),r))=dZb_bending:
[ > BC8:=subs({r=b},diff(diff(Zpis_ba_bending(r),r),r) +
[ nu/r*diff(Zpis_ba_bending(r),r))=d2Zb_bending:
[ > Set1:=solve({BC1,BC2,BC3,BC4,BC5,BC6,BC7,BC8},{C1,C3,C4,C5,C6,Zb_bending,dZb_bending,d
[ 2Zb_bending}):
[ > Zpis_0b_BENDING(r):=collect(subs(Set1,Zpis_0b_bending(r)),{D,Tp,PHAC}):
[ > Zpis_ba_BENDING(r):=collect(subs(Set1,Zpis_ba_bending(r)),{D,Tp,PHAC}):
[ > dVpis_0b_BENDING:=collect(simplify(int(2*Pi*r*Zpis_0b_BENDING(r),r=0..b)),{Tp,PHAC}):
[ > dVpis_ba_BENDING:=collect(simplify(int(2*Pi*r*Zpis_ba_BENDING(r),r=b..a)),{Tp,PHAC}):
[ > eqn4:='diff(Z(r),r)=-alpha*Q_(r)/G/h':
[ > Zpis_0b_shearing(r):=int(-alpha*Q_0b(r)/G/h,r)+C7:
[ > BC9:=subs({r=b},Zpis_0b_shearing(r))=Zb_shearing:
[ > eqn4:='diff(Z(r),r)=-alpha*Q_(r)/G/h':
[ > Zpis_ba_shearing(r):=int(-alpha*Q_ba(r)/G/h,r)+C8:
[ > BC10:=subs({r=a},Zpis_ba_shearing(r))=0:
[ > BC11:=subs({r=b},Zpis_ba_shearing(r))=Zb_shearing:
[ > Set2:=solve({BC9,BC10,BC11},{C7,C8,Zb_shearing}):
[ > Zpis_0b_SHEARING(r):=collect(subs(Set2,Zpis_0b_shearing(r)),{D,Tp,PHAC}):
[ > Zpis_ba_SHEARING(r):=collect(subs(Set2,Zpis_ba_shearing(r)),{D,Tp,PHAC}):
[ > dVpis_0b_SHEARING:=collect(simplify(int(2*Pi*r*Zpis_0b_SHEARING(r),r=0..b)),{Tp,PHAC}):
[ :
[ > dVpis_ba_SHEARING:=collect(simplify(int(2*Pi*r*Zpis_ba_SHEARING(r),r=b..a)),{Tp,PHAC}):
[ :
[ > Zpis_0b(r):=collect(Zpis_0b_BENDING(r) + Zpis_0b_SHEARING(r),{Tp,PHAC}):
[ > Zpis_ba(r):=collect(Zpis_ba_BENDING(r) + Zpis_ba_SHEARING(r),{Tp,PHAC}):
[ > Zpis_0:=subs({r=0},collect(Zpis_0b_BENDING(r) + Zpis_0b_SHEARING(r),{Tp,PHAC})):
[ > dVpist:=collect(simplify(dVpis_0b_BENDING + dVpis_ba_BENDING + dVpis_0b_SHEARING +
[ dVpis_ba_SHEARING),{Tp,PHAC}):
[ > Xi2[Zpis,T] := subs({PHAC=0,Tp=1},Zpis_0);
[ Xi2[Zpis,T]:=evalf(subs({a=R[pis],b=R[p],nu=nu[si],alpha=alpha[si],h=t[pis],D=E[si]*t[
[ pis]^3/(12*(1-nu[si]^2)),G=E[si]/(2*(1+nu[si]))},Xi2[Zpis,T]));
[
[ 
$$\Xi_{2_{Zpis,T}} := \frac{-\frac{3}{64}b^4 + \frac{1}{16}b^2a^2 + \frac{1}{16}\ln\left(\frac{b}{a}\right)b^4}{D} - \frac{1}{4} \frac{\alpha(-b^2 + 2b^2\ln(b) - 2\ln(a)b^2)}{Gh}$$

[ 
$$\Xi_{2_{Zpis,T}} := .7888483668699864076767250030356035147167 \cdot 10^{-13}$$

[ > Xi2[Zpis,P] := -subs({PHAC=1,Tp=0},Zpis_0);
[ Xi2[Zpis,P]:=evalf(subs({a=R[pis],b=R[p],nu=nu[si],alpha=alpha[si],h=t[pis],D=E[si]*t[
[ pis]^3/(12*(1-nu[si]^2)),G=E[si]/(2*(1+nu[si]))},Xi2[Zpis,P]));
[
[ 
$$\Xi_{2_{Zpis,P}} := \frac{1}{64} \frac{a^4}{D} + \frac{1}{4} \frac{\alpha a^2}{Gh}$$

[ 
$$\Xi_{2_{Zpis,P}} := .22306374289772727272727272727272727273 \cdot 10^{-12}$$

[ > Xi2[dVpis,T] := subs({PHAC=0,Tp=1},dVpist);

```

```

Xi2[dVpis,T]:=evalf(subs({a=R[pi],b=R[p],nu=nu[si],alpha=alpha[si],h=t[pi],D=E[si]*t
[pi]^3/(12*(1-nu[si]^2)),G=E[si]/(2*(1+nu[si]))},Xi2[dVpis,T]));


$$\Xi_{dVpis,T} := \frac{1}{192} \pi \left( 48 \alpha b^2 a^2 D - 24 \alpha b^4 D - 3 b^4 G h a^2 + 24 b^6 G h \ln\left(\frac{h}{a}\right) + 3 b^2 G h a^4 - 24 b^6 G h \ln(b) + 24 b^6 G h \ln(a) + b^6 G h \right) / (D G h)$$



$$\Xi_{dVpis,T} := .6341969310342016231443513844306627385162 \cdot 10^{-18}$$


> Xi2[dVpis,P] := -subs({PHAC=1,TP=0},dVpist);
Xi2[dVpis,P]:=evalf(subs({a=R[pi],b=R[p],nu=nu[si],alpha=alpha[si],h=t[pi],D=E[si]*t
[pi]^3/(12*(1-nu[si]^2)),G=E[si]/(2*(1+nu[si]))},Xi2[dVpis,P]));


$$\Xi_{dVpis,P} := -\frac{1}{192} \frac{\pi(-a^6 G h - 24 \alpha a^4 D)}{D G h}$$



$$\Xi_{dVpis,P} := .2347316925014454026966632223282621962794 \cdot 10^{-17}$$


```

#### Drive Element Piston (Averaged Compliance)

This section averages the compliances effects from the previous two sections on the piston.  
In reality, the tethers are compliant enough that they don't provide a rigid boundary condition at r=a, however they are not soft enough to provide a hinge there either. Therefore, the compliance is assumed as the average of the two. This effect has been shown with FEM.

```

> DERatio:=0.5;


$$DERatio := .5$$


> Xi[Zpis,T] := (1-DEratio)*Xi1[Zpis,T] + (DEratio)*Xi2[Zpis,T];


$$\Xi_{Zpis,T} := .1377449219142713680403997730308330787445 \cdot 10^{-12}$$


> Xi[Zpis,P] := (1-DEratio)*Xi1[Zpis,P] + (DEratio)*Xi2[Zpis,P];


$$\Xi_{Zpis,P} := .5035147372159090909090909090909090909092 \cdot 10^{-12}$$


> Xi[dVpis,T] := (1-DEratio)*Xi1[dVpis,T] + (DEratio)*Xi2[dVpis,T];


$$\Xi_{dVpis,T} := .1466311782062712642937790352294156777490 \cdot 10^{-17}$$


> Xi[dVpis,P] := (1-DEratio)*Xi1[dVpis,P] + (DEratio)*Xi2[dVpis,P];


$$\Xi_{dVpis,P} := .6312099450503241827158900246632211207317 \cdot 10^{-17}$$


```

#### Top Structural Compliance

Annular plate clamped at outer radius (r=a) and free at inner radius (r=b) with a pressure applied underneath plate from r=b to r=a and a concentrated force applied upward at r=b. Positive plate deflection is defined in the upward direction. These relations include bending and shearing effects, see TopChamberPlate.mws.

```

> eqn:='diff(1/x*diff(x*diff(Z(x),x),x),x)=Q(x)/D':
> Q(x):=Fvm/(2*Pi*x) + PHAC*Pi*(x^2-b^2)/(2*Pi*x):
> Q1(x):=(int(Q(x)/D,x)+C1)*x:

```

```

Q2(x):=(int(Q1(x),x)+C2)/x:
Ztop_bending(x):=int(Q2(x),x)+C3:
[ > BC1:=subs({r=a},Ztop_bending(x))=0:
[ > BC2:=subs({r=a},diff(Ztop_bending(x),x))=0:
[ > BC3:=subs({r=b},diff(diff(Ztop_bending(x),x),x) + nu/x*diff(Ztop_bending(x),x))=0:
[ > Set1:=solve({BC1,BC2,BC3},{C1,C2,C3}):
[ > Ztop_BENDING(x):=collect(subs(Set1,Ztop_bending(x)),{Fvm,D,PHAC}):
[ > Ztop_bend:=collect(simplify(subs({r=b},Ztop_BENDING(x))),{Fvm,D,PHAC}):
[ > dVtop_BENDING:=collect(simplify(int(2*Pi*r*Ztop_BENDING(x),r=b..a)),{Pi,Fvm,D,PHAC}):
[ > eqn2:='diff(Z(x),x)=-alpha*Q(x)/G/h':
[ > Ztop_shearing(x):=int(-alpha*Q(x)/G/h,x)+C4:
[ > BC4:=subs({r=a},Ztop_shearing(x))=0:
[ > Set2:=solve({BC4},{C4}):
[ > Ztop_SHEARING(x):=subs(Set2,Ztop_shearing(x)):
[ > Ztop_shear:=collect(simplify(subs({r=b},Ztop_SHEARING(x))),{Fvm,PHAC}):
[ > dVtop_SHEARING:=collect(simplify(int(2*Pi*r*Ztop_SHEARING(x),r=b..a)),{Fvm,PHAC}):
[ > Ztop1:=collect(Ztop_bend + Ztop_shear,{Fvm,PHAC}):
[ > dVtop1:=collect(dVtop_BENDING+dVtop_SHEARING,{Fvm,PHAC}):
[ > Xi[Ztop,P] := subs({PHAC=1,Fvm=0},Ztop1);
Xi[Ztop,P]:=evalf(subs({a=R[ch],b=R[vm],nu=nu[si],alpha=alpha[si],h=t[top],D=E[si]*t[top]^3/(12*(1-nu[si]^2)),G=E[si]/(2*(1+nu[si]))},Xi[Ztop,P]));

Xi[Ztop,P]:=-1/64*(3*pi*b^6*v-pi*b^4*a^2-16*pi*b^4*a^2*ln(b)*ln(b/a)*v-16*pi*b^4*a^2*ln(b)*ln(b/a)+4*pi*a^4*v*b^2*ln(a)
+16*pi*a^2*ln(a)*b^4*ln(b)-16*pi*a^2*ln(a)^2*b^4*v-4*pi*b^4*a^2*v*ln(a)+7*pi*b^6+4*pi*b^4*ln(b)*a^2*v-pi*a^6*v-4*pi*b^4*a^4*ln(b)*v
+16*pi*a^2*ln(a)*v*b^4*ln(b)+pi*a^6-7*pi*a^4*b^2-16*pi*a^2*ln(a)^2*b^4+4*pi*a^4*b^2*ln(a)-7*pi*b^4*a^2*v+5*pi*b^2*v*a^4
+20*pi*b^4*a^2*ln(a)-4*pi*b^2*a^4*ln(b)-20*pi*b^4*ln(b)*a^2)/(pi*(-a^2+a^2*v-b^2-v*b^2)*D)
+1/4*(alpha*(-b^2*pi+2*b^2*ln(b)*pi+a^2*pi-2*b^2*ln(a)*pi)/G*h*pi)
Xi[Ztop,P]:=.1442510763604847433456380046056248573029 10^-12

[ > Xi[Ztop,F] := subs({PHAC=0,Fvm=1},Ztop1);
Xi[Ztop,F]:=evalf(subs({a=R[ch],b=R[vm],nu=nu[si],alpha=alpha[si],h=t[top],D=E[si]*t[top]^3/(12*(1-nu[si]^2)),G=E[si]/(2*(1+nu[si]))},Xi[Ztop,F]));

Xi[Ztop,F]:=-1/64*(8*v*b^2*a^2+16*a^2*ln(a)^2*b^2+32*b^2*ln(b)*a^2-32*a^2*ln(a)*b^2-4*v*a^4-4*v*b^4+4*a^4
+16*b^2*a^2*ln(b)*ln(b/a)*v+16*b^2*a^2*ln(b/a)*ln(b)-16*a^2*ln(a)*v*b^2*ln(b)-16*a^2*ln(a)*b^2*ln(b)+16*a^2*ln(a)^2*v*b^2
+8*b^2*a^2-12*b^4)/(pi*(-a^2+a^2*v-b^2-v*b^2)*D)+1/4*(alpha*(-2*ln(b)+2*ln(a))/G*h*pi)
Xi[Ztop,F]:=.1775479105428133086725272014729944768799 10^-7

[ > Xi[dVtop,P] := subs({PHAC=1,Fvm=0},dVtop1);
Xi[dVtop,P]:=evalf(subs({a=R[ch],b=R[vm],nu=nu[si],alpha=alpha[si],h=t[top],D=E[si]*t[top]^3/(12*(1-nu[si]^2)),G=E[si]/(2*(1+nu[si]))},Xi[dVtop,P]));

```

$$\Xi_{dVtop,P} := -\frac{1}{192} \left( -2a^6b^2 - 13b^8 + a^8 + 12a^4b^4 + 2b^6a^2 - 48a^2\ln(a)v b^6\ln(b) + 22a^2vb^6 + 10a^6vb^2 \right. \\ \left. - 24a^4vb^4 - a^8v - 7vb^8 - 48a^4b^4\ln\left(\frac{b}{a}\right)v\ln(a) + 48a^2b^6\ln\left(\frac{b}{a}\right)v\ln(b) + 48a^4\ln(a)v b^4\ln(b) - 24b^6a^2\ln\left(\frac{b}{a}\right) \right. \\ \left. - 48a^4\ln(a)^2b^4 + 24a^4b^4\ln\left(\frac{b}{a}\right) + 48a^2\ln(a)^2b^6 + 48a^2\ln(a)^2b^6v + 48a^4\ln(a)b^4\ln(b) - 48a^4b^4\ln\left(\frac{b}{a}\right)\ln(a) \right. \\ \left. + 48b^6a^2\ln\left(\frac{b}{a}\right)\ln(b) - 48a^2\ln(a)b^6\ln(b) - 48a^4\ln(a)^2b^4v - 24a^2b^6\ln\left(\frac{b}{a}\right)v + 24a^4b^4\ln\left(\frac{b}{a}\right)v - 48b^6\ln(a)a^2 \right. \\ \left. + 48b^6\ln(b)a^2 \right) \pi \Bigg/ ((-a^2 + a^2v - b^2 - vb^2)D) - \frac{1}{8} \frac{\alpha(4b^2a^2\pi - a^4\pi - 3b^4\pi + 4b^4\ln(b)\pi - 4b^4\ln(a)\pi)}{Gh}$$

$$\Xi_{dVtop,P} := .1638097346275169420654979054561191650143 \cdot 10^{-17}$$

```
> Xi[dVtop,F] := subs({PHAC=0,Fvm=1},dVtop1);
Xi[dVtop,F]:=evalf(subs({a=R[ch],b=R[vn],nu=nu[si],alpha=alpha[si],h=t[top],D=E[si]*t[
top]^3/(12*(1-nu[si]^2)),G=E[si]/(2*(1+nu[si]))},Xi[dVtop,F]));
```

$$\Xi_{dVtop,F} := -\frac{1}{192} \left( -21a^4b^2 - 84b^4\ln(b)a^2 + 84b^4a^2\ln(a) - 3b^4a^2 + 3a^6 + 9vb^6 + 21b^6 - 48a^2\ln(a)^2vb^4 \right. \\ \left. - 24a^4b^2\ln\left(\frac{b}{a}\right)v + 48a^4\ln(a)^2vb^2 + 48a^4b^2\ln\left(\frac{b}{a}\right)v\ln(a) + 12a^2v\ln(a)b^4 - 12a^2vb^4\ln(b) \right. \\ \left. + 48a^2v\ln(a)b^4\ln(b) - 48b^4a^2\ln\left(\frac{b}{a}\right)v\ln(b) - 48a^4\ln(a)v b^2\ln(b) - 3a^6v + 24b^4a^2\ln\left(\frac{b}{a}\right)v + 15a^4vb^2 \right. \\ \left. - 12a^4\ln(a)v b^2 + 12a^4vb^2\ln(b) - 21a^2vb^4 + 48a^4b^2\ln\left(\frac{b}{a}\right)\ln(a) - 48a^4\ln(a)b^2\ln(b) + 48a^2\ln(a)b^4\ln(b) \right. \\ \left. - 48b^4a^2\ln\left(\frac{b}{a}\right)\ln(b) + 24b^4a^2\ln\left(\frac{b}{a}\right) + 12a^4b^2\ln(b) - 12a^4b^2\ln(a) - 24a^4b^2\ln\left(\frac{b}{a}\right) + 48a^4\ln(a)^2b^2 \right. \\ \left. - 48a^2\ln(a)^2b^4 \right) \Bigg/ ((-a^2 + a^2v - b^2 - vb^2)D) - \frac{1}{8} \frac{\alpha(-2a^2 + 2b^2 - 4b^2\ln(b) + 4\ln(a)b^2)}{Gh}$$

$$\Xi_{dVtop,F} := .1442510763604847433456380046056248573035 \cdot 10^{-12}$$


#### Valve Cap/Membrane

Annular plate clamped at outer radius (r=a) and guided at inner radius (r=b) with differentialia; pressure applied underneath plate from r=b to r=a and concentrated force applied upward at r=b. Positive plate deflection is defined in the upward direction. These relations only include bending effects, see ValveCapMembrane.mws.

```
> eqn:='diff(1/r*diff(r*diff(w(x),x),x),x)=Q(x)/D':
> Q(x):=Fvc/(2*Pi*x) + Fvm*Pi*(x^2-b^2)/(2*Pi*x):
> Q1(x):=(int(Q(x)/D,x)+C1)*x:
Q2(x):=(int(Q1(x),x)+C2)/x:
Zvm_bending(x):=expand(int(Q2(x),x)+C3):
> BC1:=subs({r=a},Zvm_bending(x))=0:
> BC2:=subs({r=a},diff(Zvm_bending(x),x))=0:
> BC3:=subs({r=b},diff(Zvm_bending(x),x))=0:
> Set1:=solve({BC1,BC2,BC3},{C1,C2,C3}):
> Zvm_BENDING(x):=collect(subs(Set1,Zvm_bending(x)),{Fvc,D,Fvm}):
> Zvc1:=collect(simplify(subs({r=b},Zvm_BENDING(x))),{Fvc,D,Fvm}):
> dVvm_BENDING:=collect(simplify(int(2*Pi*x*Zvm_BENDING(x),x=b..a)),{Pi,Fvc,D,Fvm}):
```

```

> Xi[Zvc,P] := subs({Fvc=0,Pvm=1},Zvc1);
Xi[Zvc,P]:=evalf(subs({a=R[vm],b=R[vc],h=t[vm],D=E[si]*t[vm]^3/(12*(1-nu[si]^2))},Xi[Zvc,P]));


$$\Xi_{Zvc,P} := \frac{1}{64} \left( 7\pi b^4 a^2 - 3\pi b^6 - 5\pi a^4 b^2 + 4\pi b^4 a^2 \ln(a) - 4\pi b^4 \ln(b) a^2 + 4\pi b^2 a^4 \ln(b) + 16\pi b^4 a^2 \ln(b) \ln\left(\frac{b}{a}\right) + \pi a^6 - 4\pi a^4 b^2 \ln(a) + 16\pi a^2 \ln(a)^2 b^4 - 16\pi a^2 \ln(a) b^4 \ln(b) \right) / (\pi(a^2 - b^2) D)$$



$$\Xi_{Zvc,P} := .1236306944873668358747037186342053319349 \cdot 10^{-9}$$


> Xi[Zvc,F] := subs({Fvc=1,Pvm=0},Zvc1);
Xi[Zvc,F]:=evalf(subs({a=R[vm],b=R[vc],h=t[vm],D=E[si]*t[vm]^3/(12*(1-nu[si]^2))},Xi[Zvc,F]));


$$\Xi_{Zvc,F} := \frac{1}{64} \frac{4a^4 - 16a^2 \ln(a)^2 b^2 + 4b^4 - 8b^2 a^2 - 16b^2 a^2 \ln\left(\frac{b}{a}\right) \ln(b) + 16a^2 \ln(a) b^2 \ln(b)}{\pi(a^2 - b^2) D}$$



$$\Xi_{Zvc,F} := .0001891300225883061570524241081849325118186$$


> Xi[dVvm,P] := subs({Fvc=0,Pvm=1},dVvm_BENDING);
Xi[dVvm,P]:=evalf(subs({a=R[vm],b=R[vc],h=t[vm],D=E[si]*t[vm]^3/(12*(1-nu[si]^2))},Xi[dVvm,P]));


$$\Xi_{dVvm,P} := \frac{1}{192} \left( \left( 24b^6 a^2 \ln\left(\frac{b}{a}\right) + a^8 - 48a^4 \ln(a) b^4 \ln(b) + 48a^4 b^4 \ln\left(\frac{b}{a}\right) \ln(a) + 48a^4 \ln(a)^2 b^4 - 24a^4 b^4 \ln\left(\frac{b}{a}\right) + 24a^4 b^4 - 10a^6 b^2 - 48b^6 a^2 \ln\left(\frac{b}{a}\right) \ln(b) - 48a^2 \ln(a)^2 b^6 + 48a^2 \ln(a) b^6 \ln(b) + 7b^8 - 22b^6 a^2 \right) \pi \right) / ((a^2 - b^2) D)$$



$$\Xi_{dVvm,P} := .9031509650514488184176314920963760635496 \cdot 10^{-16}$$


> Xi[dVvm,F] := subs({Fvc=1,Pvm=0},dVvm_BENDING);
Xi[dVvm,F]:=evalf(subs({a=R[vm],b=R[vc],h=t[vm],D=E[si]*t[vm]^3/(12*(1-nu[si]^2))},Xi[dVvm,F]));


$$\Xi_{dVvm,F} := \frac{1}{192} \left( -15a^4 b^2 - 9b^6 - 48a^2 \ln(a) b^4 \ln(b) + 48b^4 a^2 \ln\left(\frac{b}{a}\right) \ln(b) + 21b^4 a^2 + 48a^2 \ln(a)^2 b^4 + 12b^4 \ln(b) a^2 - 12b^4 a^2 \ln(a) - 24b^4 a^2 \ln\left(\frac{b}{a}\right) + 3a^6 - 48a^4 b^2 \ln\left(\frac{b}{a}\right) \ln(a) + 48a^4 \ln(a) b^2 \ln(b) - 48a^4 \ln(a)^2 b^2 - 12a^4 b^2 \ln(b) + 24a^4 b^2 \ln\left(\frac{b}{a}\right) + 12a^4 b^2 \ln(a) \right) / ((a^2 - b^2) D)$$



$$\Xi_{dVvm,F} := .123630694487366835874703718634205331944 \cdot 10^{-9}$$


```

#### Step 4: Solve Equations

```

> Solutions:=solve({EQN1,EQN2,EQN3,EQN4,EQN5,EQN6,EQN7,EQN8,EQN9,EQN10,EQN11,EQN12,EQN13,EQ
N14,EQN15,EQN16,EQN17},{Z[p],T[p],Z[bot],Z[te],P[HAC],dV[te],Z[piis],dV[piis],dV[fluid],Z[t
op],dV[top],F[vm],Z[vc],dV[vm],F[vc],Q[p],Z[de]}):
> SolutionsValues:=evalf(subs({P[1]=0.5e6,P[2]=0e6,V[p]=500},Solutions));

SolutionsValues := { T_p = .2231936350709793062278122870357821015647 10^7,
Z_bot = -.1163329724718546223813989792182145983230 10^6, Z_p = .7522550650712129700871283613902818672634 10^6,
dV_piis = .1872711788601659056212980592568417325255 10^-11, F_vm = .2949951827261501434908943661858065648750,

```

```

    }
    [ >
    Q_p = .8044211902127622847866619042834808352349 10^-7, dV_flnl = -.1525217750740688068517105409610629628775 10^-11,
    P_HAC = 221796.6922473865376986184401155057549960, dV_w = .1327480701927576751967670781787336404598 10^-10,
    Z_pis = .1957599951338435463759510228801996409326 10^-6, Z_vc = .00001157278902917103407170790367469559248067,
    dV_hyp = .4807373020567373342830674851203196699054 10^-12, F_vc = -.08399154105942311823880775989422955139809,
    Z_de = .6359220925993583477057293821720672689401 10^-6, Z_w = .4401620974655148013297783592918676280078 10^-6,
    dV_vm = .1314156375508000117308951551571083207255 10^-10, Z_hyp = .3723198942120302708075553839325050285056 10^-7
    }

```

## Appendix B

# Support Documentation for Non-Linear Valve Cap/Membrane

## B.1 NLValveCapMembrane-CaseA.m [see Section 3.5]

```
function [y,r,Vtotal,psi,W,theta,xi,thetaND,psiND,sigma_r_top,sigma_r_bot,yvc,maxstress] =
NLValveCapMembrane_CaseA(Pvm,Fvc,rb,ra,tvm,E,nu,flagNL,No)

%NLValveCapMembrane_CaseA.m

%David C. Roberts
%This Matlab code solves for the non-linear deflection behavior of the valve cap
%/membrane under loading Pvm and Fvc. The deflection, slope,
%curvature, swept volume, and membrane stress are calculated. Case A refers to the
%fact that we are applying both loading inputs Pvm and Fvc and determining the
%structural response. Prior to calling of this code, the user must define Pvm and
%Fvc as functions of P1, P2, and PHAC. The loadings are defined as follows:
% Pvm = pressure differential across valve membrane = PHAC-P2
% Fvc = force seen by valve cap = Avc*(PHAC-P1)
%The plate/membrane is characterized by inner radius rb, outer radius ra, thickness
%tvm, and material properties E and nu. If flagNL=0, only linear theory will be
%considered. If flagNL=1, non-linear theory will be considered. No is the value of
%the in-plane pretension. In this file yvc is the valve cap deflection (Zvc).

format long;

%%%%%%%%%%%%%%%%%%%%%%%%%%%%%%%%%%%%%%%%%%%%%%%%%%%%%%%%%%%%%%%%%%%%%%%%
%Convert Inputs to Dimensionless Qunatities
P = (Pvm*ra^4)/(E*tvm^4); %Dimensionless loading of pressure difference across
cap/membrane
F = (Fvc*ra^2)/(pi*E*tvm^4); %Dimensionless loading due to additional force on cap
%%%%%%%%%%%%%%%%%%%%%%%%%%%%%%%%%%%%%%%%%%%%%%%%%%%%%%%%%%%%%%%%%%%%%%%%

beta = sqrt((1-nu)/(1+nu))*(rb/ra);
k = (ra/tvm)*sqrt((12*(1-nu^2)*No)/(E*tvm*(1-beta^2)));
s = beta*k;

%%%%%%%%%%%%%%%%%%%%%%%%%%%%%%%%%%%%%%%%%%%%%%%%%%%%%%%%%%%%%%%%%%%%%%%%
%%Section 2: Define grid spacing and coordinate transformation parameters
%%for finite-difference method
%%%%%%%%%%%%%%%%%%%%%%%%%%%%%%%%%%%%%%%%%%%%%%%%%%%%%%%%%%%%%%%%%%%%%%%%
Npoints=200; %The total # of grid points to use (MUST KEEP IT EVEN)
alpha=1.01; %Grid density parameter
phi=(alpha+1)/(alpha-1); %Grid density ratio
hr = 1/(Npoints-1); %Size of grid spacing
eta = 0:hr:1; %Vector of evenly spaced points between 0 and 1

xi_b = rb/ra; %Non-dimensional position of inner radius
xi_c = (rb+ra)/(2*ra); %Non-dimensional position of midpoint along membrane
xi_a = ra/ra; %Non-dimensional position of outer radius

%For the grid points from xi_b to xi_c, define the derivatives of eta with respect to xi
for i=1:Npoints/2,
    xi(i) = xi_b + (alpha-1)*(xi_c-xi_b)*(phi-phi^(1-2*eta(i)))/(1+phi^(1-2*eta(i)));
    m = (alpha-1)*(xi_c-xi_b);
    m2 = m*phi - m + 2*xi_b;
    deta(i) = (0.5/log(phi))*(m*(1+phi))/((m*phi-(xi(i)-xi_b))*(m+(xi(i)-xi_b)));
    d2eta(i) = -(0.5/log(phi))*(m*(1+phi)*(m2-2*xi(i)))/((m*phi-(xi(i)-xi_b))*(m+(xi(i)-xi_b)))^2;
end

%For the grid points from xi_c to xi_a
for i=Npoints/2+1:Npoints,
    xi(i) = xi_b + (alpha-1)*(xi_c-xi_b)*(phi-phi^(1-2*eta(i)))/(1+phi^(1-2*eta(i)));
    m = (alpha-1)*(xi_c-xi_b);
    m2 = m*phi - m + 2*xi_b;
    deta(i) = (0.5/log(phi))*(m*(1+phi))/((m*phi-(xi(i)-xi_b))*(m+(xi(i)-xi_b)));
    d2eta(i) = -(0.5/log(phi))*(m*(1+phi)*(m2-2*xi(i)))/((m*phi-(xi(i)-xi_b))*(m+(xi(i)-xi_b)))^2;
end
```



```

%%%%%%%%%%%%%%%%%%%%%%%%%%%%%%%%%%%%%%%%%%%%%%%%%%%%%%%%%%%%%%%%%%%%%%%%%%%%%%
%%Section 3: Finite-Difference Implementation
%%%%%%%%%%%%%%%%%%%%%%%%%%%%%%%%%%%%%%%%%%%%%%%%%%%%%%%%%%%%%%%%%%%%%%%%%%%%%%

%Governing equations at internal points (from 2 to Npoints-1)
for i=2:Npoints-1,
    A(i,i-1) = (xi(i)^2*deta(i)^2)/(hr^2) - (xi(i)^2*d2deta(i) + xi(i)*deta(i))/(2*hr);
    A(i,i) = -( 2*xi(i)^2*deta(i)^2)/(hr^2) + (s^2+1) + xi(i)^2*k^2 );
    A(i,i+1) = (xi(i)^2*deta(i)^2)/(hr^2) + (xi(i)^2*d2deta(i) + xi(i)*deta(i))/(2*hr);

    B(i,i-1) = (xi(i)^2*deta(i)^2)/(hr^2) - (xi(i)^2*d2deta(i) + 3*xi(i)*deta(i))/(2*hr);
    B(i,i) = -(2*xi(i)^2*deta(i)^2)/(hr^2);
    B(i,i+1) = (xi(i)^2*deta(i)^2)/(hr^2) + (xi(i)^2*d2deta(i) + 3*xi(i)*deta(i))/(2*hr);

    C(i) = 6*(1-nu^2)*P*(xi(i)^3 - xi(i)*(rb/ra)^2) + 6*(1-nu^2)*F*xi(i);
end

%Boundary condition equations at xi_b (grid point #1)
A(1,1) = 1;
B(1,1) = -3*xi(1)*deta(1)/(2*hr) + (1-nu);
B(1,2) = 4*xi(1)*deta(1)/(2*hr);
B(1,3) = -xi(1)*deta(1)/(2*hr);
C(1) = 0;

%Boundary condition equations at xi_a (grid point #Npoints)
A(Npoints,Npoints) = 1;
B(Npoints,Npoints-2) = xi(Npoints)*deta(Npoints)/(2*hr);
B(Npoints,Npoints-1) = -4*xi(Npoints)*deta(Npoints)/(2*hr);
B(Npoints,Npoints) = 3*xi(Npoints)*deta(Npoints)/(2*hr) + (1-nu);
C(Npoints) = 0;

%%%%%%%%%%%%%%%%%%%%%%%%%%%%%%%%%%%%%%%%%%%%%%%%%%%%%%%%%%%%%%%%%%%%%%%%%%%%%%
%%Section 4: Provide an initial guess for the theta vector (plate slope), to be
%%used in the finite-difference iteration procedure.
%%%%%%%%%%%%%%%%%%%%%%%%%%%%%%%%%%%%%%%%%%%%%%%%%%%%%%%%%%%%%%%%%%%%%%%%%%%%%%

if k==0,
    %theta = (-0.75*(1-nu^2)*P*xi.*(1-xi.^2))'; %Linear result
    theta=xi';
else
    theta=xi';
end

%%%%%%%%%%%%%%%%%%%%%%%%%%%%%%%%%%%%%%%%%%%%%%%%%%%%%%%%%%%%%%%%%%%%%%%%%%%%%%
%%Section 5: Matrix Manipulation Procedure
%%%%%%%%%%%%%%%%%%%%%%%%%%%%%%%%%%%%%%%%%%%%%%%%%%%%%%%%%%%%%%%%%%%%%%%%%%%%%%

Niterations=500; %Perform up to 500 iterations
tolerance1=1e-8;
tolerance2=1e-8;
omega=0.45; %Under-relaxation parameter
if flagNL==1 %This variable is passed into file.
    NLoption=1; %0 = Linear solution; 1 = NonLinear solution
else
    NLoption=0;
end

for i=1:Niterations,
    i;
    for j=2:Npoints-1 %Define D vector for each iteration
        D(j) = -0.5*theta(j).^2;
    end
    D(1)=0;
    D(Npoints)=0;

    Sr = inv(B)*D'*NLoption; %Solve for Sr

```

```

v_Sr = 12*(1-nu^2)*xi'.^2.*Sr;          %Calculate non-linear correction term v_Sr
A2 = A - diag(v_Sr,0);                  %Subtract non-linear correction term from A
theta_new = inv(A2)*C';                  %Calculate new theta vector

inner_product = (theta_new'*theta)/sqrt(theta_new'*theta_new)/sqrt(theta'*theta);
length_ratio = sqrt(theta_new'*theta_new)/sqrt(theta'*theta);

if (1-inner_product) >= tolerance1 | (1-length_ratio) >= tolerance2
    theta = (1-omega)*theta + omega*theta_new;
else
    break;
end
end

%%%%%%%%%%%%%%%%%%%%%%%%%%%%%%%%%%%%%%%%%%%%%%%%%%%%%%%%%%%%%%%%%%%%%%%%%%%%%%
%%Section 6: Calculate Deflection, Curvature, Stress, and Swept Volume in this
%%post-processing section.
%%%%%%%%%%%%%%%%%%%%%%%%%%%%%%%%%%%%%%%%%%%%%%%%%%%%%%%%%%%%%%%%%%%%%%%%%%%%%%

%PLATE DEFLECTION: Calculate plate deflection vector from the final theta vector,
%using 2nd-order forward, backward, and central difference methods to express
%theta in terms of W. Then, using matrix inversion to obtain the vector W.
i=1;          %BC at rb
Wmatrix(i,i) = deta(i)*(-3/(2*hr));
Wmatrix(i,i+1) = deta(i)*(2/hr);
Wmatrix(i,i+2) = deta(i)*(-1/(2*hr));

for i=2:Npoints-1    %Inner grid points
    Wmatrix(i,i-1) = deta(i)*(-1/(2*hr));
    Wmatrix(i,i+1) = deta(i)*(1/(2*hr));
end

%BC at ra --> Do not do for the outer boundary condition. We already know that
%the deflection at ra is equal to zero.

W = inv(Wmatrix(1:Npoints-1,1:Npoints-1))*theta(1:Npoints-1);
W=[W;0];
%Done

%PLATE CURVATURE: Calculate plate curvature vector from the final theta vector,
%using 2nd-order forward, backward, and central difference methods.
i=1;          %BC at rb
psi(i) = deta(i)*(1/(2*hr))*(-3*theta(i) + 4*theta(i+1) - theta(i+2));

for i=2:Npoints-1    %Inner grid points
    psi(i) = deta(i)*(1/(2*hr))*(theta(i+1) - theta(i-1));
end

i=Npoints;    %BC at ra
psi(i) = deta(i)*(1/(2*hr))*(3*theta(i) - 4*theta(i-1) + theta(i-2));
%Done

%PLATE STRESS: Calculate the stress vectors in the plate.

for i=1:Npoints
    Sro(i) = (k^2/(12*(1-nu^2)))*(1 + beta^2/(xi(i)^2));
    sigma_r_top(i) = (E*tvrm^2/ra^2)*(Sro(i) + Sr(i) - (1/(2*(1-nu^2)))*(psi(i) +
(nu*theta(i))./xi(i)));
    sigma_r_bot(i) = (E*tvrm^2/ra^2)*(Sro(i) + Sr(i) + (1/(2*(1-nu^2)))*(psi(i) +
(nu*theta(i))./xi(i)));
end
if max(sigma_r_top) > max(sigma_r_bot)
    maxstress = abs(max(sigma_r_top));
else
    maxstress = abs(max(sigma_r_bot));
end

```

```

end
%Done

%CONVERSION TO NON_DIMENSIONAL PARAMETERS
r=xi*ra;
y=W*tvm;
thetaND=theta*tvm/ra;    %This non-dimensional theta is dw/dr
psiND=psi*tvm/(ra^2);    %This non-dimensional psi is d2w/dr2

%PLATE SWEPT VOLUME: Calculate total swept volume under cap and membrane.
V=0;
for i=1:Npoints-1
    dV(i) = pi*(r(i+1)^2-r(i)^2)*0.5*(y(i+1)+y(i));
    V = V + dV(i);
end
yvc = y(1);
Vcap = yvc*pi*rb^2;
Vtotal = Vcap + V;
%Done

```

## B.2 NLValveCapMembrane-CaseB.m [see Section 3.5]

```
function
[y,r,Vtotal,psi,W,theta,xi,thetaND,psiND,sigma_r_top,sigma_r_bot,yvc,Pvm,maxstress] =
NLValveCapMembrane_CaseB(Fvcstar,yvc_imposed,rb,ra,tv,E,nu,flagNL,No)

%NLValveCapMembrane_CaseB.m

%David C. Roberts
%This Matlab code solves for the non-linear deflection behavior of the valve cap/
%membrane under loading Fvcstar and a desired valve cap deflection at r=rb. The
%required Pvm to produce this deflection and the resulting deflection, slope,
%curvature, swept volume, and membrane stress are calculated. Case B refers to the
%fact that we are applying a known cap force (in addition to that due to Pvm) and
%imposing a cap deflection, and then solving for the required Pvm and the resulting
%structural response. Prior to calling of this code, the user must define Fvcstar
%as a function of P1 and P2. This Fvcstar loading is defined as follows:
% Fvcstar = Avc*(P2-P1)
%After running this code, the user can then back out PHAC using the following relation:
% PHAC = Pvm+P2
%The plate/membrane is characterized by inner radius rb, outer radius ra, thickness
%tvm, and material properties E and nu. If flagNL=0, only linear theory will be
%considered. If flagNL=1, non-linear theory will be considered. No is the value of
%the in-plane pretension. In this file, yvc is the valve cap deflection (Zvc).

format long;

%%%%%%%%%%%%%%%%%%%%%%%%%%%%%%%%%%%%%%%%%%%%%%%%%%%%%%%%%%%%%%%%%%%%%%%%
%Convert Inputs to Dimensionless Quantities
Wb=yvc_imposed/tvm;
F = (Fvcstar*ra^2)/(pi*E*tvm^4); %Dimensionless loading due to additional force on cap

%%%%%%%%%%%%%%%%%%%%%%%%%%%%%%%%%%%%%%%%%%%%%%%%%%%%%%%%%%%%%%%%%%%%%%%%

beta = sqrt((1-nu)/(1+nu))*(rb/ra);
k = (ra/tvm)*sqrt((12*(1-nu^2)*No)/(E*tvm*(1-beta^2)));
s = beta*k;

%%%%%%%%%%%%%%%%%%%%%%%%%%%%%%%%%%%%%%%%%%%%%%%%%%%%%%%%%%%%%%%%%%%%%%%%
%%Section 2: Define grid spacing and coordinate transformation parameters
%%for finite-difference method
%%%%%%%%%%%%%%%%%%%%%%%%%%%%%%%%%%%%%%%%%%%%%%%%%%%%%%%%%%%%%%%%%%%%%%%%
Npoints=200; %The total # of grid points to use (MUST KEEP IT EVEN)
alpha=1.01; %Grid density parameter
phi=(alpha+1)/(alpha-1); %Grid density ratio
hr = 1/(Npoints-1); %Size of grid spacing
eta = 0:hr:1; %Vector of evenly spaced points between 0 and 1

xi_b = rb/ra; %Non-dimensional position of inner radius
xi_c = (rb+ra)/(2*ra); %Non-dimensional position of midpoint along membrane
xi_a = ra/ra; %Non-dimensional position of outer radius

%For the grid points from xi_b to xi_c, define the derivatives of eta with respect to xi
for i=1:Npoints/2,
    xi(i) = xi_b + (alpha-1)*(xi_c-xi_b)*(phi-phi^(1-2*eta(i)))/(1+phi^(1-2*eta(i)));
    m = (alpha-1)*(xi_c-xi_b);
    m2 = m*phi - m + 2*xi_b;
    deta(i) = (0.5/log(phi))*(m*(1+phi))/((m*phi-(xi(i)-xi_b))*(m+(xi(i)-xi_b)));
    d2eta(i) = -(0.5/log(phi))*(m*(1+phi)*(m2-2*xi(i)))/((m*phi-(xi(i)-xi_b))*(m+(xi(i)-xi_b)))^2;
end

%For the grid points from xi_c to xi_a
for i=Npoints/2+1:Npoints,
    xi(i) = xi_b + (alpha-1)*(xi_c-xi_b)*(phi-phi^(1-2*eta(i)))/(1+phi^(1-2*eta(i)));
    m = (alpha-1)*(xi_c-xi_b);
    m2 = m*phi - m + 2*xi_b;
    deta(i) = (0.5/log(phi))*(m*(1+phi))/((m*phi-(xi(i)-xi_b))*(m+(xi(i)-xi_b)));
    d2eta(i) = -(0.5/log(phi))*(m*(1+phi)*(m2-2*xi(i)))/((m*phi-(xi(i)-xi_b))*(m+(xi(i)-xi_b)))^2;
end
```

```

end

%%%%%%%%%%%%%%%%%%%%%%%%%%%%%%%%%%%%%%%%%%%%%%%%%%%%%%%%%%%%%%%%%%%%%%%%%%%%%%
%%Section 3: Finite-Difference Implementation
%%%%%%%%%%%%%%%%%%%%%%%%%%%%%%%%%%%%%%%%%%%%%%%%%%%%%%%%%%%%%%%%%%%%%%%%%%%%%%

%Governing equations at internal points (from 2 to Npoints-1)
for i=2:Npoints-1,
    A(i,i-1) = (xi(i)^2*deta(i)^2)/(hr^2) - (xi(i)^2*d2deta(i) + xi(i)*deta(i))/(2*hr);
    A(i,i) = -( 2*xi(i)^2*deta(i)^2)/(hr^2) + (s^2+1) + xi(i)^2*k^2 );
    A(i,i+1) = (xi(i)^2*deta(i)^2)/(hr^2) + (xi(i)^2*d2deta(i) + xi(i)*deta(i))/(2*hr);

    B(i,i-1) = (xi(i)^2*deta(i)^2)/(hr^2) - (xi(i)^2*d2deta(i) + 3*xi(i)*deta(i))/(2*hr);
    B(i,i) = -(2*xi(i)^2*deta(i)^2)/(hr^2);
    B(i,i+1) = (xi(i)^2*deta(i)^2)/(hr^2) + (xi(i)^2*d2deta(i) + 3*xi(i)*deta(i))/(2*hr);

    C(i) = 6*(1-nu^2)*F*xi(i);
end

%Boundary condition equations at xi_b (grid point #1)
A(1,1) = 1;
B(1,1) = -3*xi(1)*deta(1)/(2*hr) + (1-nu);
B(1,2) = 4*xi(1)*deta(1)/(2*hr);
B(1,3) = -xi(1)*deta(1)/(2*hr);
C(1) = 0;

%Boundary condition equations at xi_a (grid point #Npoints)
A(Npoints,Npoints) = 1;
B(Npoints,Npoints-2) = xi(Npoints)*deta(Npoints)/(2*hr);
B(Npoints,Npoints-1) = -4*xi(Npoints)*deta(Npoints)/(2*hr);
B(Npoints,Npoints) = 3*xi(Npoints)*deta(Npoints)/(2*hr) + (1-nu);
C(Npoints) = 0;

%IMPORTANT: Since P is an unknown, an extra column and row are added to A to solve for P
%and therefore the added entry to C is the non-dimensional deflection Wb.

%Define entries in additional column of A
A(1,Npoints+1) = 0; %BC at r=rb
for i=2:Npoints-1 %central points
    A(i,Npoints+1) = -6*(1-nu^2)*(xi(i)^3);
end
A(Npoints,Npoints+1) = 0; %BC at r=ra
A(Npoints+1,Npoints+1) = 0; %This is a meaningless entry so it must be zero.

%Define entries in additional row of A
A(Npoints+1,1) = -(hr/2)/deta(1);
for i=2:Npoints-1
    A(Npoints+1,i) = -(hr)/deta(i);
end
A(Npoints+1,Npoints) = -(hr/2)/deta(Npoints);

%Define additional entry in C
C(Npoints+1) = Wb;

%%%%%%%%%%%%%%%%%%%%%%%%%%%%%%%%%%%%%%%%%%%%%%%%%%%%%%%%%%%%%%%%%%%%%%%%%%%%%%
%%Section 4: Provide an initial guess for the theta vector (plate slope), to be
%%used in the finite-difference iteration procedure.
%%%%%%%%%%%%%%%%%%%%%%%%%%%%%%%%%%%%%%%%%%%%%%%%%%%%%%%%%%%%%%%%%%%%%%%%%%%%%%

if k==0,
    %theta = (-0.75*(1-nu^2)*P*xi.*(1-xi.^2))'; %Linear result
    theta=xi';
else
    theta=whoops;
end

```

```

%%%%%%%%%%%%%%%%%%%%%%%%%%%%%%%%%%%%%%%%%%%%%%%%%%%%%%%%%%%%%%%%%%%%%%%%%%%%%%
%%Section 5: Matrix Manipulation Procedure
%%%%%%%%%%%%%%%%%%%%%%%%%%%%%%%%%%%%%%%%%%%%%%%%%%%%%%%%%%%%%%%%%%%%%%%%%%%%%%

Niterations=500;           %Perform up to 500 iterations
tolerance1=1e-8;
tolerance2=1e-8;
omega=0.45;               %Under-relaxation parameter
if flagNL==1               %This variable is passed into file.
    NLoption=1;            %0 = Linear solution; 1 = NonLinear solution
else
    NLoption=0;
end

for i=1:Niterations,
    1;
    for j=2:Npoints-1      %Define D vector for each iteration
        D(j) = -0.5*theta(j).^2;
    end
    D(1)=0;
    D(Npoints)=0;

    Sr = inv(B)*D'*NLoption; %Solve for Sr
    v_Sr = 12*(1-nu^2)*xi'.^2.*Sr; %Calculate non-linear correction term v_Sr
    v_Sr(Npoints+1) = 0; %Make v_Sr the proper length
    A2 = A - diag(v_Sr,0); %Subtract non-linear correction term from A
    theta_new = inv(A2)*C'; %Calculate new theta vector
    P_result = theta_new(Npoints+1); %Record the calculated value of P
    theta_new = theta_new(1:Npoints); %Remove the P entry from the theta vector

    inner_product = (theta_new'*theta)/sqrt(theta_new'*theta_new)/sqrt(theta'*theta);
    length_ratio = sqrt(theta_new'*theta_new)/sqrt(theta'*theta);

    if (1-inner_product) >= tolerance1 | (1-length_ratio) >= tolerance2
        theta = (1-omega)*theta + omega*theta_new;
    else
        break;
    end
end

%%%%%%%%%%%%%%%%%%%%%%%%%%%%%%%%%%%%%%%%%%%%%%%%%%%%%%%%%%%%%%%%%%%%%%%%%%%%%%
%%Section 6: Calculate Deflection, Curvature, Stress, and Swept Volume in this
%%post-processing section.
%%%%%%%%%%%%%%%%%%%%%%%%%%%%%%%%%%%%%%%%%%%%%%%%%%%%%%%%%%%%%%%%%%%%%%%%%%%%%%

%PRESSURE Pvm: Calculate the differential pressure across the membrane.
Pvm = P_result*E*tv_m^4/ra^4;
%Done

%PLATE DEFLECTION: Calculate plate deflection vector from the final theta vector,
%using 2nd-order forward, backward, and central difference methods to express
%theta in terms of W. Then, using matrix inversion to obtain the vector W.
i=1; %BC at rb
Wmatrix(i,i) = deta(i)*(-3/(2*hr));
Wmatrix(i,i+1) = deta(i)*(2/hr);
Wmatrix(i,i+2) = deta(i)*(-1/(2*hr));

for i=2:Npoints-1 %Inner grid points
    Wmatrix(i,i-1) = deta(i)*(-1/(2*hr));
    Wmatrix(i,i+1) = deta(i)*(1/(2*hr));
end

%BC at ra --> Do not do for the outer boundary condition. We already know that
%the deflection at ra is equal to zero.

W = inv(Wmatrix(1:Npoints-1,1:Npoints-1))*theta(1:Npoints-1);

```

```

W=[W;0];
%Done

%PLATE CURVATURE: Calculate plate curvature vector from the final theta vector,
%using 2nd-order forward, backward, and central difference methods.
i=1; %BC at rb
psi(i) = deta(i)*(1/(2*hr))*(-3*theta(i) + 4*theta(i+1) - theta(i+2));

for i=2:Npoints-1 %Inner grid points
    psi(i) = deta(i)*(1/(2*hr))*(theta(i+1) - theta(i-1));
end

i=Npoints; %BC at ra
psi(i) = deta(i)*(1/(2*hr))*(3*theta(i) - 4*theta(i-1) + theta(i-2));
%Done

%PLATE STRESS: Calculate the stress vectors in the plate.

for i=1:Npoints
    Sro(i) = (k^2/(12*(1-nu^2)))*(1 + beta^2/(xi(i)^2));
    sigma_r_top(i) = (E*tvm^2/ra^2)*(Sro(i) + Sr(i) - (1/(2*(1-nu^2)))*(psi(i) +
(nu*theta_bar(i))./xi(i)));
    sigma_r_bot(i) = (E*tvm^2/ra^2)*(Sro(i) + Sr(i) + (1/(2*(1-nu^2)))*(psi(i) +
(nu*theta_bar(i))./xi(i)));
end
if max(sigma_r_top) > max(sigma_r_bot)
    maxstress = abs(max(sigma_r_top));
else
    maxstress = abs(max(sigma_r_bot));
end
%Done

%CONVERSION TO NON_DIMENSIONAL PARAMETERS
r=xi*ra;
y=W*tvm;
thetaND=theta*tvm/ra; %This non-dimensional theta is dw/dr
psiND=psi*tvm/(ra^2); %This non-dimensional psi is d2w/dr2

%PLATE SWEPT VOLUME: Calculate total swept volume under cap and membrane.
V=0;
for i=1:Npoints-1
    dV(i) = pi*(r(i+1)^2-r(i)^2)*0.5*(y(i+1)+y(i));
    V = V + dV(i);
end
yvc = y(1);
Vcap = yvc*pi*rb^2;
Vtotal = Vcap + V;
%Done

```

## B.3 NLValveCapMembrane-CaseC.m [see Section 3.5]

```
function
[y,r,Vtotal,psi,W,theta,xi,thetaND,psiND,sigma_r_top,sigma_r_bot,yvc,Fvc,maxstress] =
NLValveCapMembrane_CaseC(Pvm,yvc_imposed,rb,ra,tvm,E,nu,flagNL,No)

%NLValveCapMembrane_CaseC.m

%David C. Roberts
%This Matlab code solves for the non-linear deflection behavior of the valve cap/
%membrane under loading Pvm and a desired valve cap deflection at r=rb. The required
%Fvc to produce this deflection and the resulting deflection, slope, curvature,
%swept volume, and membrane stress are calculated. Case C refers to the fact that
%we are applying Pvm and imposing a cap deflection, and then solving for the Fvc
%and the resulting structural response. Prior to calling this code, the user must
%define Pvm as a function of PHAC and P2. This Pvm loading is defined as follows:
% Pvm = PHAC-P2
%
%
%The plate/membrane is characterized by inner radius rb, outer radius ra, thickness
%tvm, and material properties E and nu. If flagNL=0, only linear theory will be
%considered. If flagNL=1, non-linear theory will be considered. No is the value of
%the in-plane pretension. In this file, yvc is the valve cap deflection (Zvc).

format long;

%%%%%%%%%%%%%%%%%%%%%%%%%%%%%%%%%%%%%%%%%%%%%%%%%%%%%%%%%%%%%%%%%%%%%%%%
%Convert Inputs to Dimensionless Qunatities
Wb=yvc_imposed/tvm;
P = (Pvm*ra^4)/(E*tvm^4); %Dimensionless loading of pressure across cap/membrane

%%%%%%%%%%%%%%%%%%%%%%%%%%%%%%%%%%%%%%%%%%%%%%%%%%%%%%%%%%%%%%%%%%%%%%%%

beta = sqrt((1-nu)/(1+nu))*(rb/ra);
k = (ra/tvm)*sqrt((12*(1-nu^2)*No)/(E*tvm*(1-beta^2)));
s = beta*k;

%%%%%%%%%%%%%%%%%%%%%%%%%%%%%%%%%%%%%%%%%%%%%%%%%%%%%%%%%%%%%%%%%%%%%%%%
%%Section 2: Define grid spacing and corrdinate transformation parameters
%%for finite-difference method
%%%%%%%%%%%%%%%%%%%%%%%%%%%%%%%%%%%%%%%%%%%%%%%%%%%%%%%%%%%%%%%%%%%%%%%%
Npoints=200; %The total # of grid points to use (MUST KEEP IT EVEN)
alpha=1.01; %Grid density parameter
phi=(alpha+1)/(alpha-1); %Grid density ratio
hr = 1/(Npoints-1); %Size of grid spacing
eta = 0:hr:1; %Vector of evenly spaced points between 0 and 1

xi_b = rb/ra; %Non-dimensional position of inner radius
xi_c = (rb+ra)/(2*ra); %Non-dimensional position of midpoint along membrane
xi_a = ra/ra; %Non-dimensional position of outer radius

%For the grid points from xi_b to xi_c, define the derivatives of eta with respect to xi
for i=1:Npoints/2,
    xi(i) = xi_b + (alpha-1)*(xi_c-xi_b)*(phi-phi^(1-2*eta(i)))/(1+phi^(1-2*eta(i)));
    m = (alpha-1)*(xi_c-xi_b);
    m2 = m*phi - m + 2*xi_b;
    deta(i) = (0.5/log(phi))*(m*(1+phi))/((m*phi-(xi(i)-xi_b))*(m+(xi(i)-xi_b)));
    d2eta(i) = -(0.5/log(phi))*(m*(1+phi)*(m2-2*xi(i)))/((m*phi-(xi(i)-xi_b))*(m+(xi(i)-xi_b)))^2;
end

%For the grid points from xi_c to xi_a
for i=Npoints/2+1:Npoints,
    xi(i) = xi_b + (alpha-1)*(xi_c-xi_b)*(phi-phi^(1-2*eta(i)))/(1+phi^(1-2*eta(i)));
    m = (alpha-1)*(xi_c-xi_b);
    m2 = m*phi - m + 2*xi_b;
    deta(i) = (0.5/log(phi))*(m*(1+phi))/((m*phi-(xi(i)-xi_b))*(m+(xi(i)-xi_b)));
    d2eta(i) = -(0.5/log(phi))*(m*(1+phi)*(m2-2*xi(i)))/((m*phi-(xi(i)-xi_b))*(m+(xi(i)-xi_b)))^2;
end
```



```

end

%%%%%%%%%%%%%%%%%%%%%%%%%%%%%%%%%%%%%%%%%%%%%%%%%%%%%%%%%%%%%%%%%%%%%%%%%%%%%%
%%Section 3: Finite-Difference Implementation
%%%%%%%%%%%%%%%%%%%%%%%%%%%%%%%%%%%%%%%%%%%%%%%%%%%%%%%%%%%%%%%%%%%%%%%%%%%%%%

%Governing equations at internal points (from 2 to Npoints-1)
for i=2:Npoints-1,
    A(i,i-1) = (xi(i)^2*deta(i)^2)/(hr^2) - (xi(i)^2*d2deta(i) + xi(i)*deta(i))/(2*hr);
    A(i,i) = -( 2*xi(i)^2*deta(i)^2)/(hr^2) + (s^2+1) + xi(i)^2*k^2 );
    A(i,i+1) = (xi(i)^2*deta(i)^2)/(hr^2) + (xi(i)^2*d2deta(i) + xi(i)*deta(i))/(2*hr);

    B(i,i-1) = (xi(i)^2*deta(i)^2)/(hr^2) - (xi(i)^2*d2deta(i) + 3*xi(i)*deta(i))/(2*hr);
    B(i,i) = -(2*xi(i)^2*deta(i)^2)/(hr^2);
    B(i,i+1) = (xi(i)^2*deta(i)^2)/(hr^2) + (xi(i)^2*d2deta(i) + 3*xi(i)*deta(i))/(2*hr);

    C(i) = 6*(1-nu^2)*P*(xi(i)^3 - xi(i)*(rb/ra)^2);
end

%Boundary condition equations at xi_b (grid point #1)
A(1,1) = 1;
B(1,1) = -3*xi(1)*deta(1)/(2*hr) + (1-nu);
B(1,2) = 4*xi(1)*deta(1)/(2*hr);
B(1,3) = -xi(1)*deta(1)/(2*hr);
C(1) = 0;

%Boundary condition equations at xi_a (grid point #Npoints)
A(Npoints,Npoints) = 1;
B(Npoints,Npoints-2) = xi(Npoints)*deta(Npoints)/(2*hr);
B(Npoints,Npoints-1) = -4*xi(Npoints)*deta(Npoints)/(2*hr);
B(Npoints,Npoints) = 3*xi(Npoints)*deta(Npoints)/(2*hr) + (1-nu);
C(Npoints) = 0;

%IMPORTANT: Since F is an unknown, an extra column and row are added to A to solve for F
%and therefore the added entry to C is the non-dimensional deflection Wb.

%Define entries in additional column of A
A(1,Npoints+1) = 0; %BC at r=rb
for i=2:Npoints-1 %central points
    A(i,Npoints+1) = -6*(1-nu^2)*xi(i);
end
A(Npoints,Npoints+1) = 0; %BC at r=ra
A(Npoints+1,Npoints+1) = 0; %This is a meaningless entry so it must be zero.

%Define entries in additional row of A
A(Npoints+1,1) = -(hr/2)/deta(1);
for i=2:Npoints-1
    A(Npoints+1,i) = -(hr)/deta(i);
end
A(Npoints+1,Npoints) = -(hr/2)/deta(Npoints);

%Define additional entry in C
C(Npoints+1) = Wb;

%%%%%%%%%%%%%%%%%%%%%%%%%%%%%%%%%%%%%%%%%%%%%%%%%%%%%%%%%%%%%%%%%%%%%%%%%%%%%%
%%Section 4: Provide an initial guess for the theta vector (plate slope), to be
%%used in the finite-difference iteration procedure.
%%%%%%%%%%%%%%%%%%%%%%%%%%%%%%%%%%%%%%%%%%%%%%%%%%%%%%%%%%%%%%%%%%%%%%%%%%%%%%

if k==0,
    %theta = (-0.75*(1-nu^2)*P*xi.*(1-xi.^2))'; %Linear result
    theta=xi';
else
    theta=xi';
end

```

```

%%%%%%%%%%%%%%%%%%%%%%%%%%%%%%%%%%%%%%%%%%%%%%%%%%%%%%%%%%%%%%%%%%%%%%%%
%%Section 5: Matrix Manipulation Procedure
%%%%%%%%%%%%%%%%%%%%%%%%%%%%%%%%%%%%%%%%%%%%%%%%%%%%%%%%%%%%%%%%%%%%%%%%

Niterations=500;           %Perform up to 500 iterations
tolerance1=1e-8;
tolerance2=1e-8;
omega=0.45;               %Under-relaxation parameter
if flagNL==1               %This variable is passed into file.
    NLoption=1;            %0 = Linear solution; 1 = NonLinear solution
else
    NLoption=0;
end

for i=1:Niterations,
    i;
    for j=2:Npoints-1      %Define D vector for each iteration
        D(j) = -0.5*theta(j).^2;
    end
    D(1)=0;
    D(Npoints)=0;

    Sr = inv(B)*D'*NLoption; %Solve for Sr
    v_Sr = 12*(1-nu^2)*xi'.^2.*Sr; %Calculate non-linear correction term v_Sr
    v_Sr(Npoints+1) = 0; %Make v_Sr the proper length
    A2 = A - diag(v_Sr,0); %Subtract non-linear correction term from A
    theta_new = inv(A2)*C'; %Calculate new theta vector
    F_result = theta_new(Npoints+1); %Record the calculated value of F
    theta_new = theta_new(1:Npoints); %Remove the F entry from the theta vector

    inner_product = (theta_new'*theta)/sqrt(theta_new'*theta_new)/sqrt(theta'*theta);
    length_ratio = sqrt(theta_new'*theta_new)/sqrt(theta'*theta);

    if (1-inner_product) >= tolerance1 | (1-length_ratio) >= tolerance2
        theta = (1-omega)*theta + omega*theta_new;
    else
        break;
    end
end

%%%%%%%%%%%%%%%%%%%%%%%%%%%%%%%%%%%%%%%%%%%%%%%%%%%%%%%%%%%%%%%%%%%%%%%%
%%Section 6: Calculate Deflection, Curvature, Stress, and Swept Volume in this
%%post-processing section.
%%%%%%%%%%%%%%%%%%%%%%%%%%%%%%%%%%%%%%%%%%%%%%%%%%%%%%%%%%%%%%%%%%%%%%%%

%CALCULATE Fvcstar
Fvc = F_result*(pi*E*tmv^4)/(ra^2); %Dimensionalize the additional cap force
%Done

%PLATE DEFLECTION: Calculate plate deflection vector from the final theta vector,
%using 2nd-order forward, backward, and central difference methods to express
%theta in terms of W. Then, using matrix inversion to obtain the vector W.
i=1; %BC at rb
Wmatrix(i,i) = deta(i)*(-3/(2*hr));
Wmatrix(i,i+1) = deta(i)*(2/hr);
Wmatrix(i,i+2) = deta(i)*(-1/(2*hr));

for i=2:Npoints-1 %Inner grid points
    Wmatrix(i,i-1) = deta(i)*(-1/(2*hr));
    Wmatrix(i,i+1) = deta(i)*(1/(2*hr));
end

%BC at ra --> Do not do for the outer boundary condition. We already know that
%the deflection at ra is equal to zero.

W = inv(Wmatrix(1:Npoints-1,1:Npoints-1))*theta(1:Npoints-1);
W=[W;0];

```

```

%Done

%PLATE CURVATURE: Calculate plate curvature vector from the final theta vector,
%using 2nd-order forward, backward, and central difference methods.
i=1; %BC at rb
psi(i) = deta(i)*(1/(2*hr))*(-3*theta(i) + 4*theta(i+1) - theta(i+2));

for i=2:Npoints-1 %Inner grid points
    psi(i) = deta(i)*(1/(2*hr))*(theta(i+1) - theta(i-1));
end

i=Npoints; %BC at ra
psi(i) = deta(i)*(1/(2*hr))*(3*theta(i) - 4*theta(i-1) + theta(i-2));
%Done

%PLATE STRESS: Calculate the stress vectors in the plate.

for i=1:Npoints
    Sro(i) = (k^2/(12*(1-nu^2)))*(1 + beta^2/(xi(i)^2));
    sigma_r_top(i) = (E*tvm^2/ra^2)*(Sro(i) + Sr(i) - (1/(2*(1-nu^2)))*(psi(i) +
(nu*theta(i))./xi(i)));
    sigma_r_bot(i) = (E*tvm^2/ra^2)*(Sro(i) + Sr(i) + (1/(2*(1-nu^2)))*(psi(i) +
(nu*theta(i))./xi(i)));
end
if max(sigma_r_top) > max(sigma_r_bot)
    maxstress = abs(max(sigma_r_top));
else
    maxstress = abs(max(sigma_r_bot));
end
%Done

%CONVERSION TO NON_DIMENSIONAL PARAMETERS
r=xi*ra;
y=W*tvm;
thetaND=theta*tvm/ra; %This non-dimensional theta is dw/dr
psiND=psi*tvm/(ra^2); %This non-dimensional psi is d2w/dr2

%PLATE SWEPT VOLUME: Calculate total swept volume under cap and membrane.
V=0;
for i=1:Npoints-1
    dV(i) = pi*(r(i+1)^2-r(i)^2)*0.5*(y(i+1)+y(i));
    V = V + dV(i);
end
yvc = y(1);
Vcap = yvc*pi*rb^2;
Vtotal = Vcap + V;
%Done

```



## Appendix C

# Support Documentation for Full Non-Linear Active Valve Model

## C.1 FullActiveValve(Non-Linear).mws [Section 4.1]

```
File: FullActiveValve(NON-LINEAR).mws
David C. Roberts
This file creates the active valve matrix used in the full non-linear active valve Matlab model developed by Dave Roberts.
This file defines all the active valve relations (except for the non-linear membrane relations which are solved for in the
Matlab code:NActiveValveMatlab.m) and solves for the coefficients of the valve matrix A.
> restart;
> Digits:=40;

Digits := 40
```

### Step 1: Define Linear Quasi-Static Relations

#### Piezoelectric Material

[ This relation assumes perfect d33 actuation (no effect of transverse clamping).

> EQN1 := Z[p] = d[33]\*V[p] - (L[p]/E[p])\*T[p];

$$EQN1 := Z_p = d_{33} V_p - \frac{L_p T_p}{E_p}$$

[ This relation determines the piezo charge.

> EQN2 := Q[p] = (eT[33]\*A[p]/L[p])\*V[p] + (d[33]\*A[p])\*T[p];

$$EQN2 := Q_p = \frac{eT_{33} A_p V_p}{L_p} + d_{33} A_p T_p$$

#### Bottom Structural Compliance

[ Circular plate with stress imposed over central region.

> EQN3 := Z[bot] = (Xi[Zbot,T]) \* T[p];

$$EQN3 := Z_{bot} = \Xi_{Zbot, T} T_p$$

#### Drive Element Tethers

> EQN4 := Z[te] =

(Xi[Ztetop,F]\*Xi[Ztebot,F]) / (Xi[Ztetop,F]+Xi[Ztebot,F]) \* (A[p]\*T[p]-A[pis]\*P[HAC]) -  
(Xi[Ztetop,P]\*Xi[Ztebot,P]) / (Xi[Ztetop,P]+Xi[Ztebot,P]) \* P[HAC];

$$EQN4 := Z_{te} = \frac{\Xi_{Ztetop, F} \Xi_{Ztebot, F} (A_p T_p - A_{pis} P_{HAC})}{\Xi_{Ztetop, F} + \Xi_{Ztebot, F}} - \frac{\Xi_{Ztetop, P} \Xi_{Ztebot, P} P_{HAC}}{\Xi_{Ztetop, P} + \Xi_{Ztebot, P}}$$

> EQN5 := dV[te] =

(Xi[dVtetop,F]\*Xi[Ztebot,F]) / (Xi[Ztetop,F]+Xi[Ztebot,F]) \* (A[p]\*T[p]-A[pis]\*P[HAC]) -  
(Xi[dVtetop,P]\*Xi[dVtebot,P]) / (Xi[dVtetop,P]+Xi[dVtebot,P]) \* P[HAC] + A[pis]\*Z[te];

$$EQN5 := dV_{te} = \frac{\Xi_{dVtetop, F} \Xi_{Ztebot, F} (A_p T_p - A_{pis} P_{HAC})}{\Xi_{Ztetop, F} + \Xi_{Ztebot, F}} - \frac{\Xi_{dVtetop, P} \Xi_{dVtebot, P} P_{HAC}}{\Xi_{dVtetop, P} + \Xi_{dVtebot, P}} + A_{pis} Z_{te}$$

#### Drive Element Piston

> EQN6 := Z[pis] = Xi[Zpis,T]\*T[p] - Xi[Zpis,P]\*P[HAC];

$$EQN6 := Z_{pis} = \Xi_{Zpis, T} T_p - \Xi_{Zpis, P} P_{HAC}$$

> EQN7 := dV[pis] = Xi[dVpis,T]\*T[p] - Xi[dVpis,P]\*P[HAC];

$$EQN7 := dV_{pis} = \Xi_{dVpis, T} T_p - \Xi_{dVpis, P} P_{HAC}$$

#### Fluid Compressibility

> EQN8 := dV[fluid] = -(V[HAC]/K[E])\*P[HAC];

$$EQN8 := dV_{fluid} = -\frac{V_{HAC} P_{HAC}}{K_f}$$

**Top Structural Compliance**

- >  $EQN9 := Z[top] = Xi[Ztop, P] * P[HAC] + Xi[Ztop, F] * F[vm];$   

$$EQN9 := Z_{top} = \Xi_{Ztop, P} P_{HAC} + \Xi_{Ztop, F} F_{vm}$$
- >  $EQN10 := dV[top] = Xi[dVtop, P] * P[HAC] + Xi[dVtop, F] * F[vm] + A[vm] * Z[top];$   

$$EQN10 := dV_{top} = \Xi_{dVtop, P} P_{HAC} + \Xi_{dVtop, F} F_{vm} + A_{vm} Z_{top}$$
- >  $EQN11 := F[vm] = (A[vm] - A[vc]) * (P[HAC] - P[2]) + A[vc] * (P[HAC] - P[1]);$   

$$EQN11 := F_{vm} = (A_{vm} - A_{vc}) (P_{HAC} - P_2) + A_{vc} (P_{HAC} - P_1)$$

**Valve Cap/Membrane**

- The only valve/cap membrane relation defined here is the sum of the forces on the valve cap.
- >  $EQN12 := F[vc] = (P[HAC] - P[1]) * A[vc];$   

$$EQN12 := F_{vc} = A_{vc} (P_{HAC} - P_1)$$

**Deflection, Swept Volume Conservation**

- All structural deflections and swept volumes are defined to be positive in the upward direction.
- >  $EQN13 := Z[p] + Z[bot] = Z[te] + Z[pis];$   

$$EQN13 := Z_p + Z_{bot} = Z_{te} + Z_{pis}$$

**Other Relations**

- Variables as functions of other variables.
- >  $EQN14 := Z[de] = Z[te] + Z[pis];$   

$$EQN14 := Z_{de} = Z_{te} + Z_{pis}$$


**Step 2: Define Geometric/Material Parameters**


- Geometric Parameters:
  - >  $R[vc] := 0.31e-3; R[vm] := 0.80e-3; t[vm] := 10e-6; A[vc] := Pi * R[vc]^2; A[vm] := Pi * R[vm]^2;$   
 $t[vc] := 400e-6;$
  - >  $L[p] := 1e-3; R[p] := 1e-3; A[p] := Pi * R[p]^2;$
  - >  $R[pis] := 3e-3; R[ch] := 3.225e-3; t[pis] := 800e-6; t[topte] := 10e-6; t[botte] := 10e-6;$   
 $A[pis] := Pi * R[pis]^2;$
  - >  $t[bot] := 1000e-6;$
  - >  $H[HAC] := 400e-6; V[HAC] := Pi * R[ch]^2 * H[HAC] + Pi * (R[vm]^2 - R[vc]^2) * t[vc];$
  - >  $t[top] := 1000e-6;$
- Material Parameters:
  - >  $d[33] := 2000e-12; sD[33] := 16.4e-12; sE[33] := 111e-12; E[p] := 1/sE[33];$   
 $eT[33] := d[33]^2 / (sE[33] - sD[33]); E[si] := 165e9; nu[si] := 0.22; K[f] := 2e9; alpha[si] := 1.25;$


**Step 3: Calculate Linear Plate Coefficients**

- Bottom Structural Compliance** [identical to FullActiveValve(LINEAR).mws]
- Drive Element Tethers** [identical to FullActiveValve(LINEAR).mws]
- Drive Element Piston (More Compliant: Hinged Outer Circumference)** [identical to

FullActiveValve(LINEAR).mws]

 Drive Element Piston (Less Compliant: Rigid Outer Circumference) [identical to FullActiveValve(LINEAR).mws]

 Drive Element Piston (Averaged Compliance) [identical to FullActiveValve(LINEAR).mws]

 Top Structural Compliance [identical to FullActiveValve(LINEAR).mws]

#### Step 4: Solve Equations

The variables [Zp, Tp, Qp, Zbot, Zte, dVte, Zpis, dVpis, dVfluid, Ztop, dVtop, Fvm, Fvc, and Zde] are solved for in terms of the other variables [Vp, P1, P2, and PHAC]. Once solved for, each of the coefficients is assigned to the proper location in matrix A, which are then passed to NLActiveValveMatlab.m.

```
> Solutions:=solve({EQN1,EQN2,EQN3,EQN4,EQN5,EQN6,EQN7,EQN8,EQN9,EQN10,EQN11,EQN12,EQN13,EQN14},{Z[p],T[p],Q[p],Z[bot],Z[te],dV[te],Z[dis],dV[dis],dV[fluid],Z[top],dV[top],F[vm],F[vc],Z[de]}):
```

```
[>
> A11:=evalf(subs({V[p]=1,P[1]=0,P[2]=0,P[HAC]=0},subs(Solutions,Z[p]))):
> A12:=evalf(subs({V[p]=0,P[1]=1,P[2]=0,P[HAC]=0},subs(Solutions,Z[p]))):
> A13:=evalf(subs({V[p]=0,P[1]=0,P[2]=1,P[HAC]=0},subs(Solutions,Z[p]))):
> A14:=evalf(subs({V[p]=0,P[1]=0,P[2]=0,P[HAC]=1},subs(Solutions,Z[p]))):
>
> A21:=evalf(subs({V[p]=1,P[1]=0,P[2]=0,P[HAC]=0},subs(Solutions,T[p]))):
> A22:=evalf(subs({V[p]=0,P[1]=1,P[2]=0,P[HAC]=0},subs(Solutions,T[p]))):
> A23:=evalf(subs({V[p]=0,P[1]=0,P[2]=1,P[HAC]=0},subs(Solutions,T[p]))):
> A24:=evalf(subs({V[p]=0,P[1]=0,P[2]=0,P[HAC]=1},subs(Solutions,T[p]))):
>
> A31:=evalf(subs({V[p]=1,P[1]=0,P[2]=0,P[HAC]=0},subs(Solutions,Q[p]))):
> A32:=evalf(subs({V[p]=0,P[1]=1,P[2]=0,P[HAC]=0},subs(Solutions,Q[p]))):
> A33:=evalf(subs({V[p]=0,P[1]=0,P[2]=1,P[HAC]=0},subs(Solutions,Q[p]))):
> A34:=evalf(subs({V[p]=0,P[1]=0,P[2]=0,P[HAC]=1},subs(Solutions,Q[p]))):
>
> A41:=evalf(subs({V[p]=1,P[1]=0,P[2]=0,P[HAC]=0},subs(Solutions,Z[bot]))):
> A42:=evalf(subs({V[p]=0,P[1]=1,P[2]=0,P[HAC]=0},subs(Solutions,Z[bot]))):
> A43:=evalf(subs({V[p]=0,P[1]=0,P[2]=1,P[HAC]=0},subs(Solutions,Z[bot]))):
> A44:=evalf(subs({V[p]=0,P[1]=0,P[2]=0,P[HAC]=1},subs(Solutions,Z[bot]))):
>
> A51:=evalf(subs({V[p]=1,P[1]=0,P[2]=0,P[HAC]=0},subs(Solutions,Z[te]))):
> A52:=evalf(subs({V[p]=0,P[1]=1,P[2]=0,P[HAC]=0},subs(Solutions,Z[te]))):
> A53:=evalf(subs({V[p]=0,P[1]=0,P[2]=1,P[HAC]=0},subs(Solutions,Z[te]))):
> A54:=evalf(subs({V[p]=0,P[1]=0,P[2]=0,P[HAC]=1},subs(Solutions,Z[te]))):
>
> A61:=evalf(subs({V[p]=1,P[1]=0,P[2]=0,P[HAC]=0},subs(Solutions,dV[te]))):
> A62:=evalf(subs({V[p]=0,P[1]=1,P[2]=0,P[HAC]=0},subs(Solutions,dV[te]))):
> A63:=evalf(subs({V[p]=0,P[1]=0,P[2]=1,P[HAC]=0},subs(Solutions,dV[te]))):
```



```

[ > A64:=evalf(subs({V[p]=0,P[1]=0,P[2]=0,P[HAC]=1},subs(Solutions,dV[te]))):
[ >
[ > A71:=evalf(subs({V[p]=1,P[1]=0,P[2]=0,P[HAC]=0},subs(Solutions,Z[pis]))):
[ > A72:=evalf(subs({V[p]=0,P[1]=1,P[2]=0,P[HAC]=0},subs(Solutions,Z[pis]))):
[ > A73:=evalf(subs({V[p]=0,P[1]=0,P[2]=1,P[HAC]=0},subs(Solutions,Z[pis]))):
[ > A74:=evalf(subs({V[p]=0,P[1]=0,P[2]=0,P[HAC]=1},subs(Solutions,Z[pis]))):
[ >
[ > A81:=evalf(subs({V[p]=1,P[1]=0,P[2]=0,P[HAC]=0},subs(Solutions,dV[pis]))):
[ > A82:=evalf(subs({V[p]=0,P[1]=1,P[2]=0,P[HAC]=0},subs(Solutions,dV[pis]))):
[ > A83:=evalf(subs({V[p]=0,P[1]=0,P[2]=1,P[HAC]=0},subs(Solutions,dV[pis]))):
[ > A84:=evalf(subs({V[p]=0,P[1]=0,P[2]=0,P[HAC]=1},subs(Solutions,dV[pis]))):
[ >
[ > A91:=evalf(subs({V[p]=1,P[1]=0,P[2]=0,P[HAC]=0},subs(Solutions,dV[fluid]))):
[ > A92:=evalf(subs({V[p]=0,P[1]=1,P[2]=0,P[HAC]=0},subs(Solutions,dV[fluid]))):
[ > A93:=evalf(subs({V[p]=0,P[1]=0,P[2]=1,P[HAC]=0},subs(Solutions,dV[fluid]))):
[ > A94:=evalf(subs({V[p]=0,P[1]=0,P[2]=0,P[HAC]=1},subs(Solutions,dV[fluid]))):
[ >
[ > A101:=evalf(subs({V[p]=1,P[1]=0,P[2]=0,P[HAC]=0},subs(Solutions,Z[top]))):
[ > A102:=evalf(subs({V[p]=0,P[1]=1,P[2]=0,P[HAC]=0},subs(Solutions,Z[top]))):
[ > A103:=evalf(subs({V[p]=0,P[1]=0,P[2]=1,P[HAC]=0},subs(Solutions,Z[top]))):
[ > A104:=evalf(subs({V[p]=0,P[1]=0,P[2]=0,P[HAC]=1},subs(Solutions,Z[top]))):
[ >
[ > A111:=evalf(subs({V[p]=1,P[1]=0,P[2]=0,P[HAC]=0},subs(Solutions,dV[top]))):
[ > A112:=evalf(subs({V[p]=0,P[1]=1,P[2]=0,P[HAC]=0},subs(Solutions,dV[top]))):
[ > A113:=evalf(subs({V[p]=0,P[1]=0,P[2]=1,P[HAC]=0},subs(Solutions,dV[top]))):
[ > A114:=evalf(subs({V[p]=0,P[1]=0,P[2]=0,P[HAC]=1},subs(Solutions,dV[top]))):
[ >
[ > A121:=evalf(subs({V[p]=1,P[1]=0,P[2]=0,P[HAC]=0},subs(Solutions,F[vm]))):
[ > A122:=evalf(subs({V[p]=0,P[1]=1,P[2]=0,P[HAC]=0},subs(Solutions,F[vm]))):
[ > A123:=evalf(subs({V[p]=0,P[1]=0,P[2]=1,P[HAC]=0},subs(Solutions,F[vm]))):
[ > A124:=evalf(subs({V[p]=0,P[1]=0,P[2]=0,P[HAC]=1},subs(Solutions,F[vm]))):
[ >
[ > A131:=evalf(subs({V[p]=1,P[1]=0,P[2]=0,P[HAC]=0},subs(Solutions,F[vc]))):
[ > A132:=evalf(subs({V[p]=0,P[1]=1,P[2]=0,P[HAC]=0},subs(Solutions,F[vc]))):
[ > A133:=evalf(subs({V[p]=0,P[1]=0,P[2]=1,P[HAC]=0},subs(Solutions,F[vc]))):
[ > A134:=evalf(subs({V[p]=0,P[1]=0,P[2]=0,P[HAC]=1},subs(Solutions,F[vc]))):
[ >
[ > A141:=evalf(subs({V[p]=1,P[1]=0,P[2]=0,P[HAC]=0},subs(Solutions,Z[de]))):
[ > A142:=evalf(subs({V[p]=0,P[1]=1,P[2]=0,P[HAC]=0},subs(Solutions,Z[de]))):
[ > A143:=evalf(subs({V[p]=0,P[1]=0,P[2]=1,P[HAC]=0},subs(Solutions,Z[de]))):
[ > A144:=evalf(subs({V[p]=0,P[1]=0,P[2]=0,P[HAC]=1},subs(Solutions,Z[de]))):
[ >

```

 **Step 5: Output Matrix to Matlab File**

Page 4

[ Now that all the matrix coefficients have been solved for, it is necessary to output these values to a file which Matlab can read.  
 Also,  
 output the important valve geometry parameters (rb, ra, tvn, E, nu) for use in the non-linear Matlab code.

```
[ > interface(echo=0);
> writeto('NLActiveValveMatrix.m');
> printf('A(1,1) = %+2.08e;',A11);
> printf('A(1,2) = %+2.08e;',A12);
> printf('A(1,3) = %+2.08e;',A13);
> printf('A(1,4) = %+2.08e;',A14);
> printf('A(2,1) = %+2.08e;',A21);
> printf('A(2,2) = %+2.08e;',A22);
> printf('A(2,3) = %+2.08e;',A23);
> printf('A(2,4) = %+2.08e;',A24);
> printf('A(3,1) = %+2.08e;',A31);
> printf('A(3,2) = %+2.08e;',A32);
> printf('A(3,3) = %+2.08e;',A33);
> printf('A(3,4) = %+2.08e;',A34);
> printf('A(4,1) = %+2.08e;',A41);
> printf('A(4,2) = %+2.08e;',A42);
> printf('A(4,3) = %+2.08e;',A43);
> printf('A(4,4) = %+2.08e;',A44);
> printf('A(5,1) = %+2.08e;',A51);
> printf('A(5,2) = %+2.08e;',A52);
> printf('A(5,3) = %+2.08e;',A53);
> printf('A(5,4) = %+2.08e;',A54);
> printf('A(6,1) = %+2.08e;',A61);
> printf('A(6,2) = %+2.08e;',A62);
> printf('A(6,3) = %+2.08e;',A63);
> printf('A(6,4) = %+2.08e;',A64);
> printf('A(7,1) = %+2.08e;',A71);
> printf('A(7,2) = %+2.08e;',A72);
> printf('A(7,3) = %+2.08e;',A73);
> printf('A(7,4) = %+2.08e;',A74);
> printf('A(8,1) = %+2.08e;',A81);
> printf('A(8,2) = %+2.08e;',A82);
> printf('A(8,3) = %+2.08e;',A83);
> printf('A(8,4) = %+2.08e;',A84);
> printf('A(9,1) = %+2.08e;',A91);
> printf('A(9,2) = %+2.08e;',A92);
> printf('A(9,3) = %+2.08e;',A93);
> printf('A(9,4) = %+2.08e;',A94);
> printf('A(10,1) = %+2.08e;',A101);
> printf('A(10,2) = %+2.08e;',A102);
> printf('A(10,3) = %+2.08e;',A103);
```

Page 5

```

[ > printf('A(10,4) = %+2.08e;',A104);
[ > printf('A(11,1) = %+2.08e;',A111);
[ > printf('A(11,2) = %+2.08e;',A112);
[ > printf('A(11,3) = %+2.08e;',A113);
[ > printf('A(11,4) = %+2.08e;',A114);
[ > printf('A(12,1) = %+2.08e;',A121);
[ > printf('A(12,2) = %+2.08e;',A122);
[ > printf('A(12,3) = %+2.08e;',A123);
[ > printf('A(12,4) = %+2.08e;',A124);
[ > printf('A(13,1) = %+2.08e;',A131);
[ > printf('A(13,2) = %+2.08e;',A132);
[ > printf('A(13,3) = %+2.08e;',A133);
[ > printf('A(13,4) = %+2.08e;',A134);
[ > printf('A(14,1) = %+2.08e;',A141);
[ > printf('A(14,2) = %+2.08e;',A142);
[ > printf('A(14,3) = %+2.08e;',A143);
[ > printf('A(14,4) = %+2.08e;',A144);
[ > printf('rvc = %+2.08e;',R[vc]);
[ > printf('rvm = %+2.08e;',R[vm]);
[ > printf('tvm = %+2.08e;',t[vm]);
[ > printf('Esi = %+2.08e;',E[si]);
[ > printf('nusi = %+2.08e;',nu[si]);
[ > writeto('terminal');
[ >

```

## C.2 NActiveValveMatlab.m [Section 4.1]

```
%[NActiveValveMatlab.m]      DAVID C. ROBERTS
%
% This file calculates the behavior of the active valve, with non-linear valve/cap
%membrane deformation included. First, the Maple file FullActiveValve(Non-Linear).mws
%is run in order to generate the matrix of linear valve relation coefficients. That matrix
%is then used in this file.

clear;
close all;
format long;
NActiveValveMatrix;          %Read in the linear matrix coefficients and the valve geometry
                              %from this file, which was generated by running
                              %NActiveValveMaple.mws. The matrix values go from A11,A12,A13,
                              %A14, A21, ..., A141,A142,A143,A144 and the valve geometry
                              %variables read in are rvc, rvm, tvn, Esi, nusi.

#####DEFINE INPUT PARAMETERS#####
Vp=500;          %Piezo Voltage
P1=0.5e6;        %Pressure on top of valve cap
P2=0e6;          %Pressure on top of valve membrane
flagNL=1;        %Include non-linearity if flagNL=1
No=0;            %Initial in-plane prestress

#####PROVIDE INITIAL GUESS FOR PHAC#####
PHACguess=0.0013e6;
PHAC1=PHACguess;
PHAC2=PHACguess;
check0=1;
check1=1;
i=0
j=0

%Determine Volume discrepancy for initial PHAC guess
U=[Vp P1 P2 PHAC1];          %Vector of input parameters to compliance matrix
S=A*U';                      %S is the vector of all linear responses
Fvc=S(13); Pvm=PHAC1-P2;     %Define these loadings for use in NActiveValve_MembraneCaseA.m
[y,r,Vtotal,psi,W,theta,xi,thetaND,psiND,sigma_r_top,sigma_r_bot,yvc,maxstress] =
NActiveValve_MembraneCaseA(Pvm,Fvc,rvc,rvm,tvm,Esi,nusi,flagNL,No);
dVvm=Vtotal; dVte=S(6); dVpis=S(8); dVfluid=S(9); dVtop=S(11);
check1 = (dVvm + dVtop - dVte - dVpis - dVfluid);
check0=check1;
%Done

%Determine range of PHAC (between PHAC0 and PHAC1) within which the real PHAC lies
while check0*check1/(abs(check0*check1))> 0
    i=0
    j=j+1

    PHAC0 = PHAC1;
    PHAC1 = PHAC2
    check0 = check1

    U=[Vp P1 P2 PHAC1];          %Vector of input parameters to compliance matrix
    S=A*U';                      %S is the vector of all linear responses
    Fvc=S(13); Pvm=PHAC1-P2;     %Define these loadings for use in
NActiveValve_MembraneCaseA.m
    [y,r,Vtotal,psi,W,theta,xi,thetaND,psiND,sigma_r_top,sigma_r_bot,yvc,maxstress] =
NActiveValve_MembraneCaseA(Pvm,Fvc,rvc,rvm,tvm,Esi,nusi,flagNL,No);
    dVvm=Vtotal; dVte=S(6); dVpis=S(8); dVfluid=S(9); dVtop=S(11);
    check1 = (dVvm + dVtop - dVte - dVpis - dVfluid);

    if check1 < 0
        PHAC2 = 10*PHAC1;
```

```

elseif check1 > 0
    PHAC2 = 0.1*PHAC1;
else
    break;
end
end

if PHAC1<PHAC0 %rearrange PHAC0 to be less than PHAC1
    PHACmax=PHAC0;
    PHACmin=PHAC1;
    PHAC1=PHACmax
    PHAC0=PHACmin
else
end
%DONE,it has been determined that PHAC lies between PHAC0 and PHAC1

j=0;

%Determine solution for Pvc
PHACm=0.5*(PHAC0+PHAC1);
firsthalf=0;

while abs((PHAC1-PHAC0)/PHAC0) > 0.0001

    i=1
    j=j+1

    if firsthalf==1

        U=[Vp P1 P2 PHACm]; %Vector of input parameters to compliance matrix
        S=A*U'; %S is the vector of all linear responses
        Fvc=S(13); Pvm=PHACm-P2; %Define these loadings for use in
        NActiveValve_MembraneCaseA.m
        [y,r,Vtotal,psi,W,theta,xi,thetaND,psiND,sigma_r_top,sigma_r_bot,yvc,maxstress] =
        NActiveValve_MembraneCaseA(Pvm,Fvc,rv,rv,rv,rv,tvm,Esi,nusi,flagNL,No);
        dVvm=Vtotal; dVte=S(6); dVpis=S(8); dVfluid=S(9); dVtop=S(11);
        checkm = (dVvm + dVtop - dVte - dVpis - dVfluid);

    else

        U=[Vp P1 P2 PHAC0]; %Vector of input parameters to compliance matrix
        S=A*U'; %S is the vector of all linear responses
        Fvc=S(13); Pvm=PHAC0-P2; %Define these loadings for use in
        NActiveValve_MembraneCaseA.m
        [y,r,Vtotal,psi,W,theta,xi,thetaND,psiND,sigma_r_top,sigma_r_bot,yvc,maxstress] =
        NActiveValve_MembraneCaseA(Pvm,Fvc,rv,rv,rv,rv,tvm,Esi,nusi,flagNL,No);
        dVvm=Vtotal; dVte=S(6); dVpis=S(8); dVfluid=S(9); dVtop=S(11);
        check0 = (dVvm + dVtop - dVte - dVpis - dVfluid);

        U=[Vp P1 P2 PHACm]; %Vector of input parameters to compliance matrix
        S=A*U'; %S is the vector of all linear responses
        Fvc=S(13); Pvm=PHACm-P2; %Define these loadings for use in
        NActiveValve_MembraneCaseA.m
        [y,r,Vtotal,psi,W,theta,xi,thetaND,psiND,sigma_r_top,sigma_r_bot,yvc,maxstress] =
        NActiveValve_MembraneCaseA(Pvm,Fvc,rv,rv,rv,rv,tvm,Esi,nusi,flagNL,No);
        dVvm=Vtotal; dVte=S(6); dVpis=S(8); dVfluid=S(9); dVtop=S(11);
        checkm = (dVvm + dVtop - dVte - dVpis - dVfluid);

    end

    if check0*checkm <= 0
        PHAC1=PHACm;
        firsthalf=1;
    else
        PHAC0=PHACm;
        firsthalf=0;
    end
end

```

```

        PHACm=0.5*(PHAC0+PHAC1)
end
PHAC=PHACm;
%DONE, PHAC solution has been determined

%Evaluate all parameters for last value of PHACm

U=[Vp P1 P2 PHACm];           %Vector of input parameters to compliance matrix
S=A*U';                       %S is the vector of all linear responses
Fvc=S(13); Pvm=PHACm-P2;      %Define these loadings for use in NLActiveValve_MembraneCaseA.m
[y,r,Vtotal,psi,W,theta,xi,thetaND,psiND,sigma_r_top,sigma_r_bot,yvc,maxstRes] =
NLActiveValve_MembraneCaseA(Pvm,Fvc,rvc,rvm,tvm,Esi,nusi,flagNL,No);

Zp=S(1)                        %Print to screen all results
Tp=S(2)
Qp=S(3)
Zbot=S(4)
Zte=S(5)
dVte=S(6)
Zpis=S(7)
dVpis=S(8)
dVfluid=S(9)
Ztop=S(10)
dVtop=S(11)
Fvm=S(12)
Fvc=S(13)
Zde=S(14)
Zvc=yvc+Ztop
dVvm=Vtotal
maxstress
%DONE

```

# Modeling, Simulation and Design of Piezoelectric Micro-Hydraulic Transducer Devices

O. Yaglioglu<sup>\*</sup>, Y.H. Su<sup>\*\*</sup>, D.C. Roberts<sup>\*</sup>, J. Carretero<sup>\*</sup> and N. W. Hagood<sup>\*</sup>

<sup>\*</sup>Active Material and Structures Laboratory, Massachusetts Institute of Technology, 77 Massachusetts Avenue, Rm. 37-315, Cambridge, MA 02139, onnik@mit.edu

<sup>\*\*</sup>State University of New York, Stony Brook, NY

## ABSTRACT

This paper reports on modeling, simulation and design considerations for piezoelectric Micro-Hydraulic Transducer (MHT) systems, focusing on power generation applications. Since these devices are complex fluid and structural systems, comprehensive simulation tools are needed for effective design. A system level simulation tool has been developed using Simulink<sup>TM</sup>, by integrating models for different energy domains, namely fluids, structures, piezoelectrics and circuitry. The simulation allows for the monitoring of important parameters such as chamber pressure, flowrate, and various structural component deflections and stresses. Using the simulation, the operation of the system is analyzed and important design considerations are evaluated. Results indicate that system efficiency is highly dependent on compliances within the device structure and the type of piezoelectric material used.

**Keywords:** microhydraulic, power generation, piezoelectric

## 1 CONFIGURATION AND OPERATION

Piezoelectric Micro-Hydraulic Transducers are compact high power density transducers, which can function bi-directionally as actuators/micropumps and/or power generators. These devices are comprised of a main pumping chamber, two actively controlled valves, a low-pressure reservoir and a high-pressure reservoir (Figure 1) [1].

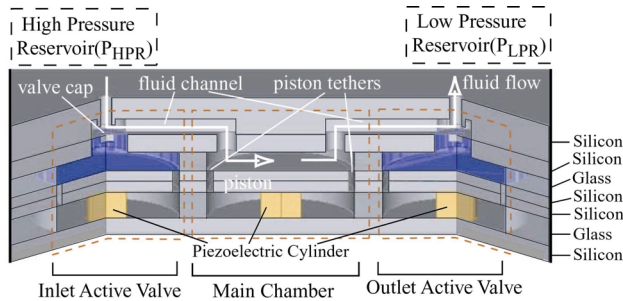


Figure 1: Device layout for power generator configuration. Top and bottom packaging pyrex layers not shown.

The active valves regulate fluid flow from the reservoirs into and out of the main chamber, which houses a piezoelectrically driven tethered piston. When operating as a pump, the electrical signal applied to the piezoelectric element results in pressure fluctuations inside the main chamber. When operating as a power generator, pressure fluctuations within the main chamber are converted to an electrical signal, which is rectified and stored in a battery. These devices are designed to generate 0.5-1W power at frequencies of ~15-20kHz, resulting in high power densities approaching 500-1000W/kg. This paper primarily focuses on modeling simulation and design considerations for MHT devices used as power generators.

A prototype MHT device consists of a 9-layer stack of pyrex and silicon micromachined layers (Figure 2). Sealing of the piston in the main chamber is provided by annular tethers which are created through Deep Reactive Ion Etching (DRIE) of a SOI wafer. The tether thickness (~10μm) is defined by the SOI device layer, and the buried oxide acts as an etch stop. All glass layers are patterned by conventional diamond core drilling. Piezoelectric cylinders are core drilled from piezoelectric substrate plates, onto which Ti-Pt-AuSn-Au multilayer film is sputter-deposited for eutectic bonding. The device assembly is accomplished through anodic bonding of the glass layers to the silicon layers at 300°C, a process which also enables the AuSn eutectic alloy to melt. Upon cooling, the alloy solidifies, bonding the piezoelectric cylinders to the silicon layers. [2].

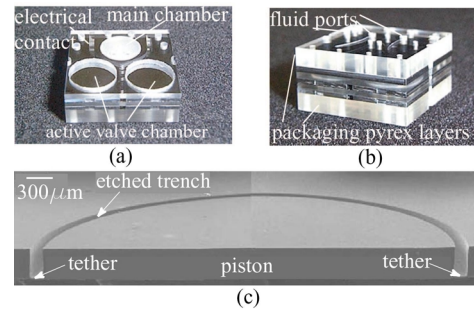


Figure 2: (a) 5-layer device for subcomponent testing (b) Complete 9-layer device (c) SEM of micromachined tethered piston structure.

## 2 MODELING

This section focuses on the development of a system level model to capture the behavior of the main chamber

portion of an MHT device under various operation conditions. The individual components considered for the main chamber are shown in Figure 3.

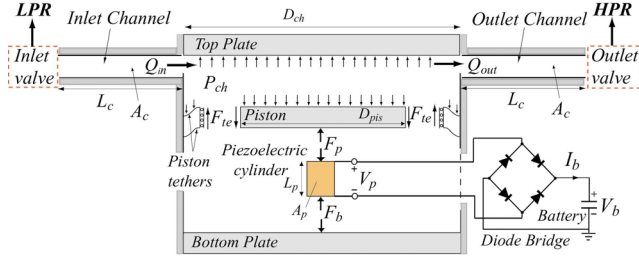


Figure 3: Modeling schematic of the main chamber and fluid channels. The active valves are not shown.

## 2.1 Piezoelectric Cylinder and Circuitry

Linear piezoelectric constitutive relationships are assumed. For a cross-sectional area  $A_p$  and length  $L_p$ , the net deflection of the piezoelectric element and the voltage across it can be expressed as:

$$x_p = \frac{L_p}{A_p} (s_{33}^D F_p + \frac{d_{33}}{\epsilon_{33}^T} Q_p) \quad (2a)$$

$$V_p = \frac{L_p}{A_p} (\frac{d_{33}}{\epsilon_{33}^T} F_p - \frac{1}{\epsilon_{33}^T} Q_p) \quad (2b)$$

where  $Q_p$  is the charge,  $F_p$  is the force on the piezoelectric cylinder,  $s_{33}^D$  is the open circuit compliance,  $d_{33}$  is the piezoelectric constant and  $\epsilon_{33}^T$  is the dielectric constant at constant stress for the case of compression parallel to polarization of the element. The governing equations for the diode bridge rectifier are derived using Kirchoffs laws and diode equations.

## 2.2 Chamber Continuity

The chamber converts hydraulic energy into mechanical energy via the piston, which then compresses the piezoelectric cylinder. Considering a control volume inside the chamber the continuity equation can be derived as:

$$\frac{dP_{ch}}{dt} = \frac{1}{C_{eff}} \left( Q_{in} - Q_{out} - \frac{dx_p}{dt} A_{pis} \right) \quad (3)$$

where  $P_{ch}$  is the chamber pressure,  $Q_{in}$  and  $Q_{out}$  are the flowrates into and out of the chamber respectively,  $x_p$  is the deflection of the piston,  $A_{pis}$  is the area of the piston and  $C_{eff}$  is the effective chamber compliance which is given by:

$$C_{eff} = \left( \frac{V_o}{\beta_f} + C_s \right) \quad (4)$$

where the first and second term correspond to the fluidic compliance ( $V_o$  is the initial volume of the chamber and  $\beta_f$  is the bulk modulus of the working fluid) and structural compliance, respectively. It is assumed that the volume displaced by the piston is much smaller than the initial volume of the chamber,  $V_o$ .

## 2.3 Structural Compliance

The structural compliance of the main chamber can be defined as:

$$C_s = \frac{\Delta V_s}{\Delta P_{ch}} \quad (5)$$

which represents the volume change of the chamber due to structural deformations in response to a change in chamber pressure. Individual structural compliances include the deformation of the top and bottom support structures, deformation of the piston and bending of the tethers. These deformations are calculated using linear plate theory [6]. Compliances of individual structural members act like parallel capacitors in an electric circuit analogy. Also, the stress distribution in the tether is calculated using linear plate theory. Finite-element models are then used to define appropriate stress concentration coefficients based on the fillet radius geometry [7]. In order to monitor important parameters in the simulation, such as chamber pressure, tether stress and volume changes due to individual members, the elastic equations of the respective components are simultaneously solved and the coefficients are fed to the Simulink<sup>TM</sup> simulation architecture (Figure 4). Additionally, within the simulation, look-up tables are incorporated which capture the non-linear large deflection behavior of the valve membrane structures [5]. A numerical code [4] is used to generate these look-up tables.

## 2.4 Valves and Channels

During system operation, the flow in the channels is inertia dominated due to the high Reynolds numbers. The valves are modeled using orifice flow relations. The form of the governing equations for the valves and the channels are as follows:

$$P_{HPR} - P_{ch} = R_i(Q_{in}, vo_{in})Q_{in}^2 + \left( \frac{\rho L_c}{A_c} \right) \frac{dQ_{in}}{dt} \quad (6a)$$

$$P_{ch} - P_{LPR} = R_o(Q_{out}, vo_{out})Q_{out}^2 + \left( \frac{\rho L_c}{A_c} \right) \frac{dQ_{out}}{dt} \quad (6b)$$

where  $P_{HPR}$  and  $P_{LPR}$  are the pressures of the high and low pressure reservoirs,  $L_c$  and  $A_c$  are the length and the cross sectional area of the fluid channels, and  $R_i$  and  $R_o$  are the flow resistances in the inlet and outlet valve, respectively, which are calculated based on the flowrate, the valve opening ( $vo_{in}$ ,  $vo_{out}$ ) and the valve geometry using look-up



tables where experimental discharge coefficients are incorporated into the simulation[3].

### 3 SIMULATION AND ANALYSIS

The equations and look up tables described in the previous section are incorporated into the Matlab<sup>TM</sup>/Simulink<sup>TM</sup> simulation software, as shown in Figure 4. The basic input/output relationships between the modules correspond to subcomponents of the device. Additional monitored parameters such as stresses and deflections are included in the simulation, although not shown in the figure.

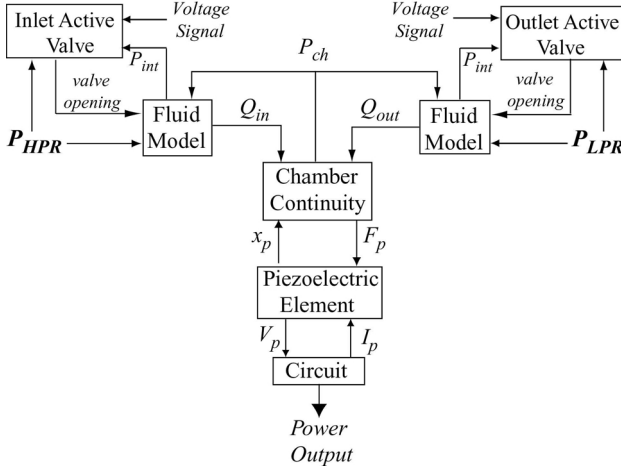


Figure 4: Modular Simulink<sup>TM</sup> simulation architecture for power generation configuration.

The device has been simulated for a sample geometry and operating conditions, where  $D_{pis} = 4.5mm$ ,  $P_{HPR} = 2MPa$ ,  $P_{LPR} = 0MPa$ ,  $f = 10kHz$  and  $V_b = 90V$ . The battery voltage is equal to one fourth of the open circuit voltage of the piezoelectric element for maximum power output. The valve size is determined such that the chamber pressure fluctuates between  $P_{HPR}$  and  $P_{LPR}$ . The time histories, which represent a typical duty cycle of the power generator, are shown in Figure 5. The corresponding force vs. deflection plot (i.e. the work cycle of the piezoelectric element) is shown in Figure 6).

The average flow rate can be found by integrating equation 3 to obtain:

$$Q_{ave} = A_{pis} \Delta x_p f + C_{eff} \Delta P_{ch} f \quad (7)$$

where  $\Delta x_p$  is the net piston deflection,  $\Delta P_{ch}$  is the maximum pressure difference in the chamber and  $f$  is the operation frequency. The electrical energy stored per cycle is equal to the area enclosed by the work cycle shown in Figure 6. The generated power can be obtained:

$$W = \frac{1}{4} (s_{33}^E - s_{33}^D) \sigma_d^2 A_p L_p f \quad (8)$$

where  $\sigma_d$  is the maximum stress on the piezoelectric element.

For negligible bottom plate deflection, the net piston deflection in a cycle is equal to the net compression of the piezoelectric cylinder, which can be expressed as:

$$\Delta x_p = \frac{1}{2} \sigma_d L_p (s_{33}^E + s_{33}^D) \quad (9)$$

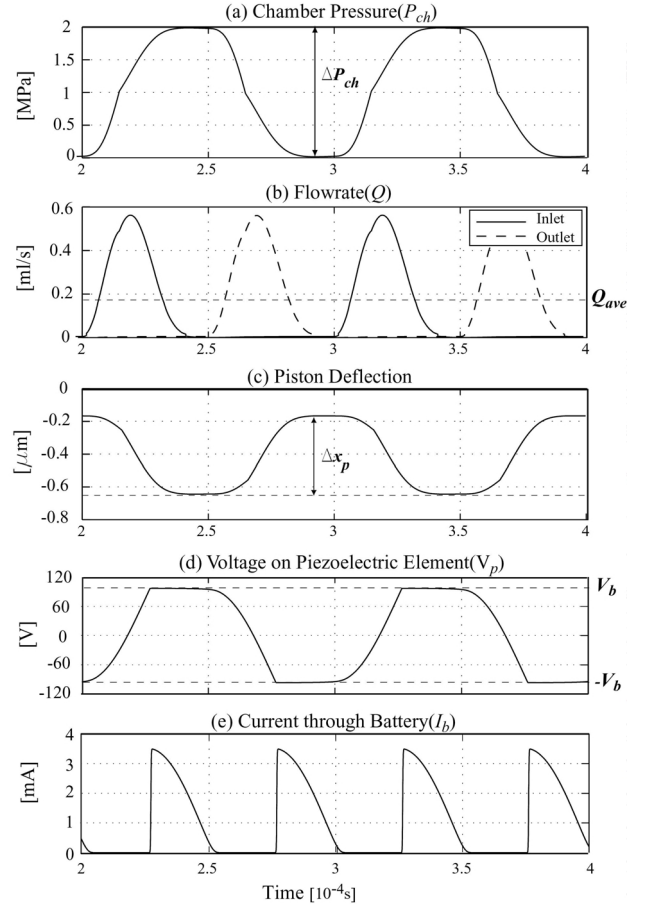


Figure 5: Typical duty cycle of the power generator. Generated power is equal to  $V_b I_b$ .

Using equations 7, 8 and 9 and assuming that the maximum pressure in the chamber is  $P_{HPR}$ , and the minimum pressure is zero, the average flow rate required for a given power requirement,  $W$ , can be calculated as:

$$Q_{ave} = \frac{2(s_{33}^E + s_{33}^D)W}{(s_{33}^E - s_{33}^D)P_{HPR}} + C_{eff} P_{HPR} f \quad (10)$$

The first term in equation 10 corresponds to the flowrate required to move the piston and the second term corresponds to the additional flowrate required due to the chamber compliance.

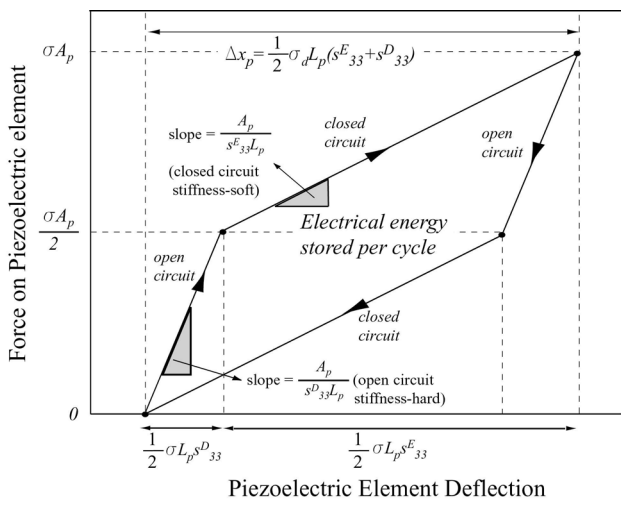


Figure 6: The work cycle of the piezoelectric element.

## 4 DESIGN CONSIDERATIONS

**Tether Optimization:** The tether structure has to be flexible enough to allow piston movement, yet stiff enough such that the additional compliance introduced by the tether is minimal. Also, the maximum stress shouldn't exceed 1GPa [7]. Tether thickness and width optimization studies have been performed, but are not covered in this paper.

**Fluidic Oscillations:** The fluid channels and the main chamber constitute a resonating system similar to a Helmholtz resonator. The  $L_c/A_c$  ratio of the fluid channels should be chosen such that it will satisfy the resonance conditions at the design frequency. The simulation tool is used for these studies.

**Piezoelectric Material and Efficiency:** The efficiency of the chamber, neglecting power consumption in the valves, can be calculated by dividing the electrical power output by the hydraulic power input. The maximum possible efficiency, which corresponds to the case where the effective chamber compliance  $C_{eff}$  is zero, can be obtained from equation 10:

$$\eta_{\max} = \frac{W}{Q_{\min} P_{HPR}} = \frac{k_{33}^2}{4 - 2k_{33}^2} \quad (11)$$

where  $Q_{\min}$  is the minimum required flowrate and  $k_{33}$  is the coupling coefficient of the piezoelectric element. Piezoelectric materials differ in their depolarization stress,  $\sigma_d$ , which determines the power density of the material, and coupling coefficient,  $k_{33}$  which determines the electromechanical energy conversion efficiency. Figure 7 shows a comparison of different piezoelectric materials in terms of system efficiency for the geometry discussed in the previous section and for a  $0.5W$  power requirement. It can be seen that the single crystal piezoelectric material PZN-PT is the most efficient material because of its very high coupling coefficient. However, due to its low depolarization

stress, it requires higher operational frequencies. The designed bandwidth of the active valves is  $\sim 20\text{kHz}$  and the operation frequency of the device should be below this value. Tradeoffs such as this need to be carefully considered in the design procedure.

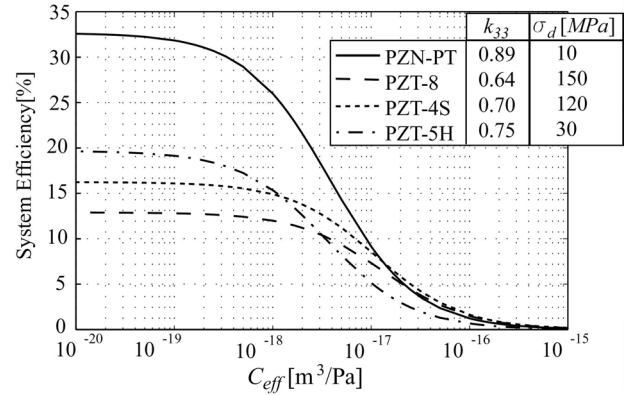


Figure 7: Comparison of different piezoelectric materials.

Using the simulation and the analysis discussed, design procedures have been carried on for building prototype MHT devices. Major design limitations are the depolarization stress of the piezoelectric material and maximum allowable stress in the tethers. Typical efficiencies are  $\sim 15\%$ . The main chamber design is complimented by the design of the active valves, detailed in [5].

## 5 CONCLUSIONS

A system level simulation tool has been developed which allows dynamic simulation of linear and nonlinear structural members, micro-fluid flow, piezoelectrics, circuitry and monitoring of important system parameters in different energy domains. The system is analyzed for power generator configuration and important design considerations are investigated. It is found that system efficiency highly depends on structural compliances and the type of piezoelectric material used.

## REFERENCES

- [1] N.W. Hagood *et al*, Proceedings of SPIE, Vol. 3985 (2000), pp. 680-688.
- [2] D.C. Roberts *et al*, Transducers 2001, Munich, Germany, June 2001.
- [3] J. Carretero *et al*, Proceedings of the ASME Microfluidics Symposium, Orlando, FL, Nov. 2000.
- [4] Y.H. Su, *et al*, Journal of Micromechanics and Microengineering, 11 (2001), pp.645-653.
- [5] D.C. Roberts *et al*, Proceedings of SPIE, Vol. 4327 (2001), pp.366-380.
- [6] S. Timoshenko, Theory of Plates and Shells, McGraw-Hill, New York, 1940.
- [7] K. Turner, S.M Thesis, MIT, 2001.

J.L. Steyn , H.Q. Li, D.C. Roberts, K.T. Turner, O. Yaglioglu, Y.-H. Su,  
M.A. Schmidt, S.M. Spearing, N.W. Hagood  
Massachusetts Institute of Technology  
Cambridge, MA 02139  
R. Mlcak  
Boston Microsystems, Inc.  
Woburn, MA 01801

## ABSTRACT

Hydraulic amplification devices for stroke amplification in MEMS devices have been designed, fabricated and evaluated experimentally. This work investigates the feasibility of using the concept of hydraulic amplification as a means of increasing the actuation stroke of a piezoelectric actuator in a microfabricated actuation system. The important aspects relating to the design of these devices are presented. This paper further provides a brief overview of the fabrication process used and then proceeds to address the topics related to the successful filling and sealing of small-scale hydraulic couplers. Both static and dynamic sealing techniques were used. Static tests were performed and stroke amplification ratios as high as 50:1 were obtained, with the peak-to-peak amplified stroke being approximately  $25\mu\text{m}$ . Results from a piezoelectrically driven hydraulic amplifier are also presented and show resonant behavior at approximately 5kHz, proving that high-frequency, high-force, large-stroke actuation can be performed on the microscale using piezoelectric hydraulic amplification.

## INTRODUCTION

Relying on Pascal's law, hydraulic amplification can be seen as a conceptually elegant means of increasing either the stroke or the force of an actuator. No mechanical linkages or mechanisms are used, and there are only two moving parts - the two pistons. The actuator can take any form, but in this work we are primarily concerned with a piezoelectric actuator requiring stroke amplification.

The work presented here forms part of a larger program at the Massachusetts Institute of Technology to develop piezoelectric MicroHydraulic Transducer (MHT) technologies. The goal of MHT technology is to use hydraulics in conjunction with piezoelectric materials to produce hydraulic pumps or generators for actuation and power generation applications. It is beneficial to operate the piezoelectric material at high frequencies for maximum power output [1]. High frequency operation requires mechanical systems with high natural frequencies if quasi-static operation is desired. The use of fabrication technologies associated with MicroElectroMechanical Systems (MEMS) presents the opportunity to build small hydraulic machines capable of operating quasi-statically at high frequencies. In addition, the small scale results in increased power densities.

A 3-dimensional section view of the full MHT device being developed is shown in Figure 1. This device has a piezoelectrically driven piston and two piezoelectrically driven active valves. The use of so-called "active" valves instead of the typical "passive"

check valves used in pumps allows for bi-directional operation, enabling this device to operate as both a pump and a generator. Both the main piston and the two valves employ a piezoelectric micro-actuator as described by Roberts *et al* [2].

The active valves (see [3]) require large stroke operation in the kHz range of frequencies. In addition, the device shown in Figure 1 is designed to operate at pressures as high as 2MPa, and therefore the valves should also be able to operate at these pressures. Piezoelectric materials have sufficient actuation force and bandwidth to drive these valves, but are lacking in stroke. For this device, hydraulic amplification was chosen as the most feasible means of increasing the uniaxial actuation of a piezoelectric element.

Macroscale examples of hydraulic amplifiers exist. (See, e.g. [4,5]). This work proceeds to present, for the first time, hydraulic amplification as a general means of stroke amplification for use in MEMS, with the use of the basic principle extending beyond that of piezoelectric valve operation. The relevant issues pertaining to the development of such devices are discussed, and experimental results are presented.

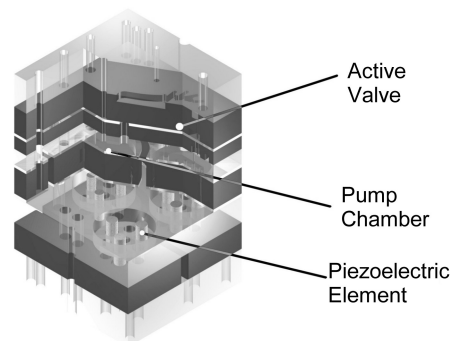


**Figure 1.** A 3D section view of the full MicroHydraulic Transducer device with two hydraulically amplified piezoelectrically driven active valves and a piezoelectrically driven main piston.

## DEVICE LAYOUT AND DESIGN CONSIDERATIONS

Figures 2 and 3 schematically show the layout of the devices that were evaluated. Figure 2 depicts a pressure operated hydraulic amplifier, and Figure 3 a piezoelectrically driven one.

L7 and L8, are silicon layers, and the other four, L1, L3, L6 and L9, are borosilicate glass. In both devices, a short stroke motion of the large piston in layers 4 and 5 is amplified to a large stroke motion of the small piston in layer 7. All pistons are formed using Silicon On Insulator (SOI) substrates, where the SOI device layer is used as an annular membrane tether to attach the piston to the device structure and to act as a flexural seal.

In the process of the designing these devices, the following aspects were considered: (a) The stiffness and strength of the membrane tethers. Within the constraints of available SOI thicknesses, device area available, manufacturing capabilities and the required deflections, the membranes were designed for maximum strength and minimum added compliance to the hydraulic amplification chamber (HAC). (b) The added compliance of the remaining device structure. By use of finite element analysis, suitable dimensions for the silicon and glass support structures were defined to enable a compact yet stiff device. (c) The height of the HAC. This chamber, formed in L6, was designed for minimum volume without introducing unnecessary squeeze film damping with a chamber height that is too low.

The results of both a pressure-operated, as well as a piezoelectrically driven hydraulic amplifier are presented here. Both devices had a large piston of diameter 6.8mm with a tether width of 225 $\mu$ m, and a small piston diameter of 0.51mm with corresponding tether width of 442 $\mu$ m. This gives a theoretical stroke amplification ratio of between 40:1 and 50:1, when taking into account all the relevant compliances in the system. Due to geometric nonlinearities in the small piston structure, the amplification ratio is not constant for the full range of travel of the two pistons.

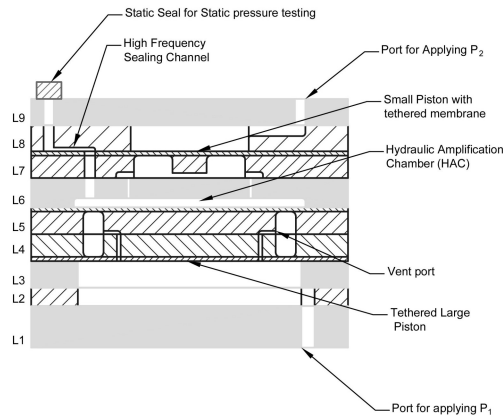


**Figure 2.** Static, pressure operated hydraulic amplifier.

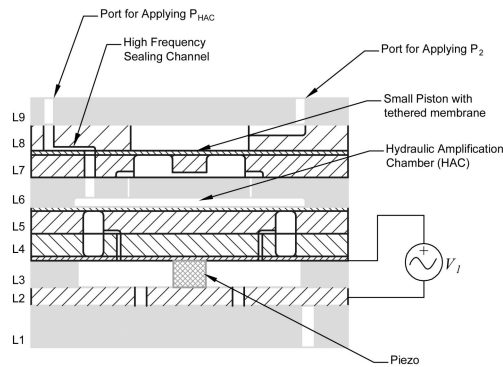


**Figure 3.** Dynamic, piezoelectrically driven hydraulic amplifier.

The silicon layers were bulk micromachined using Deep Reactive Ion Etching (DRIE). All glass layers (Pyrex<sup>TM</sup> 7740) were ultrasonically machined, on the wafer scale. In the case of Layer 6, a 200 $\mu$ m deep recess was made to form the HAC.

Wafer-level Si-Si fusion bonding was used to bond L4 to L5, as well as L7 to L8. Wafer-level anodic bonding was used to bond L6 to the L4-5 stack and also to bond L1 to L2. All other bonds were anodic bonds performed on the die level. For the piezoelectric device shown in Figure 3, a small bulk piezoelectric element was integrated in the final anodic bonding step, as described in [2].

Figure 4 shows the device subassemblies, with Figure 5 showing a completed device. The final device is a nine-layer Si-glass sandwich structure and has dimensions of 20x20x10mm.

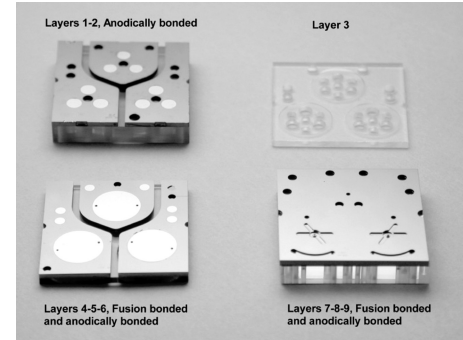


**Figure 4:** Subassemblies of the nine-layer hydraulic amplification device. Various unique fabrication techniques were used to produce these dies.

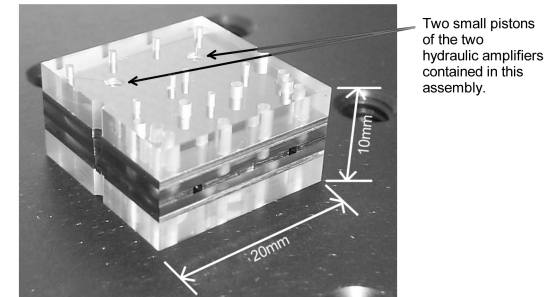


**Figure 5:** Assembled hydraulic amplification device. Each such stack contains two independent hydraulic amplifiers.

## FILLING TECHNIQUES

Effective hydraulic amplification relies on bubble-free filling of the HAC. To achieve this, a process was developed where the HAC is first evacuated and purged with the vapor of the hydraulic fluid. Afterwards, the chamber is filled with the fluid itself. This process ensured that any entrapped gases in the HAC would mostly consist of the vapor of the hydraulic fluid.

This method of vapor purging prior to filling required that the hydraulic fluid itself had a sufficiently high vapor pressure. The fluid of choice was hexamethyldisiloxane, with a viscosity at room temperature of ~0.65cst, and a vapor pressure of 6.7kPa. Using this silicone oil, bubble free filling of the HAC was attained through a 10 $\mu$ m x 10 $\mu$ m by 1000 $\mu$ m long filling channel.

Two methods were used for sealing the hydraulic amplifier. The first method, used for the pressure operated “static” devices, relied on a 125 $\mu\text{m}$  thick PTFE film backed by a brass plate and preloaded with an o-ring. This seal was placed over the filling hole in Layer 9. Minimal seal compression and creep was observed, and therefore the pressure inside the HAC remained unaffected.

For the piezoelectrically driven dynamic hydraulic amplifier, a “dynamic seal” was used. This seal consisted of a small (10 $\mu\text{m}$ x10 $\mu\text{m}$  cross section, 1000 $\mu\text{m}$  long) channel that acted as a fluid low pass filter. By using this sealing technique, it was possible to set the steady-state pressure inside of the HAC to a desired value using an outside pressure source, whilst maintaining high-frequency pressure fluctuations due to the piezoelectric actuation inside the HAC. Figure 6 illustrates the effectiveness of this channel. When driving the large piston, and observing the motion of the small piston, rolloff is detected at a frequency of 0.1Hz, well below the kHz operating frequencies of the device.

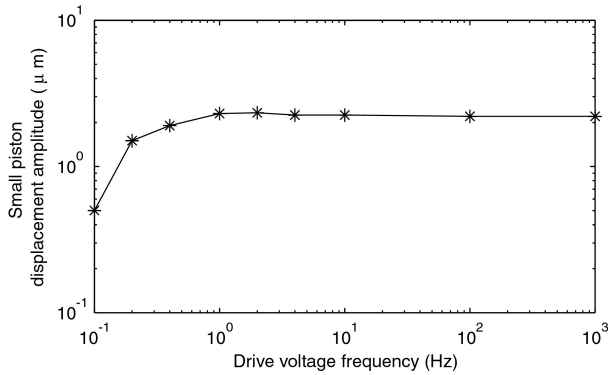


**Figure 6:** Frequency response of the dynamic seal. This seal acts as a low pass filter to the HAC.

## STATIC HYDRAULIC AMPLIFICATION

Static, pressure-operated hydraulic amplification tests were performed to evaluate the ability of the hydraulic amplification chamber to couple the motion of the two pistons. Pressures were applied to the large piston ( $P_1$ ) and the small piston ( $P_2$ ).  $P_1$  was varied from 0 to 200kPa for preset pressures of  $P_2 = 0, 53, 105, 153, 206$  and 253kPa. Loading the HAC in this manner made it possible to prove the stiffness of the coupler. Using a laser vibrometry system, the displacements of the small and large pistons were measured. The results of these tests are shown in Figures 7 and 8. From these results, one can calculate the amplification ratio (Figure 9), defined as the ratio of the difference in displacement of the small piston versus that of the large piston.

Figure 7 shows discrepancies between the predicted and actual motion. This is due to additional compliance in the HAC, which could be caused by a small bubble in the fluid in this particular case. The good agreement on the results in Figure 8, for the small piston, can be explained by the fact that the differential pressure across the large piston is not very large for the deflections seen. Therefore, the pressure on the large piston,  $P_1$ , is approximately equal to the pressure in the HAC,  $P_{HAC}$ . Therefore, Figure 8 is almost equivalent to a series of pressure-deflection tests on the small piston structure alone. Figure 9 shows similar

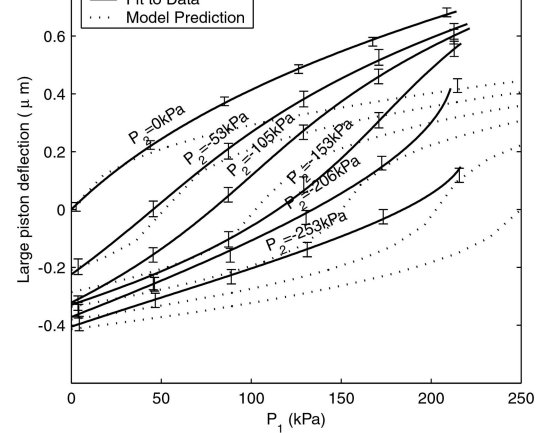


**Figure 7:** Motion of the large piston under applied pressure on both the large piston ( $P_1$ ), and the small piston ( $P_2$ ).

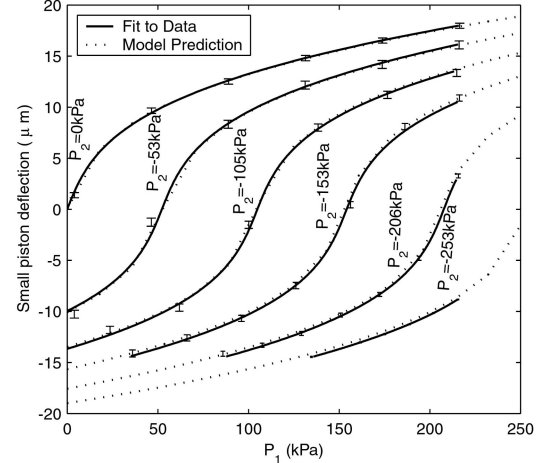


**Figure 8:** Motion of the small piston under applied pressure on both the large piston ( $P_1$ ), and the small piston ( $P_2$ ).

trends for both the predicted and measured amplification ratios, with the exception being the case where  $P_2=0\text{kPa}$ .

## VERIFICATION OF DYNAMIC OPERATION

To prove that the hydraulic amplifier can function as intended - that is, to amplify the stroke of a piezoelectric actuation element - tests were performed on a piezoelectrically driven hydraulic amplifier as was shown schematically in Figure 3. Figure 10 is an amplitude spectrum of the motion of the small piston, when excited using a sweep excitation on the piezoelectrically driven large piston. A first resonance of approximately 10kHz was observed when using gas to pressurize the small piston. When liquid was used on top of the small piston, this frequency reduced to approximately 5kHz due to the added mass effect of the fluid on the small piston.

Figure 11 shows the behavior of the small and large pistons for various excitation voltages at 1kHz sinusoidal excitation. In this case, the voltage replaces the applied large piston pressure used to create Figures 7 and 8. In the case of the dynamic hydraulic amplifier, much better correlation is seen between the predicted and measured results, most likely due to improved filling of the HAC. The same holds for the amplification ratio, depicted

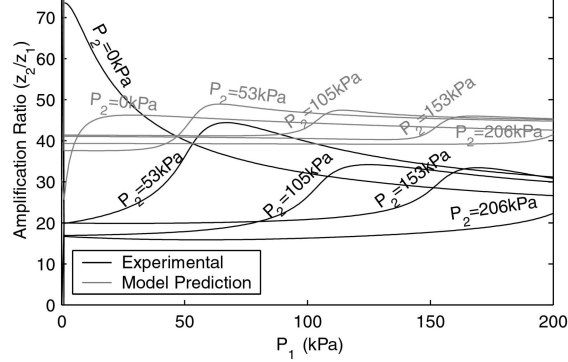


**Figure 9:** Amplification ratio for the static hydraulic amplifier.

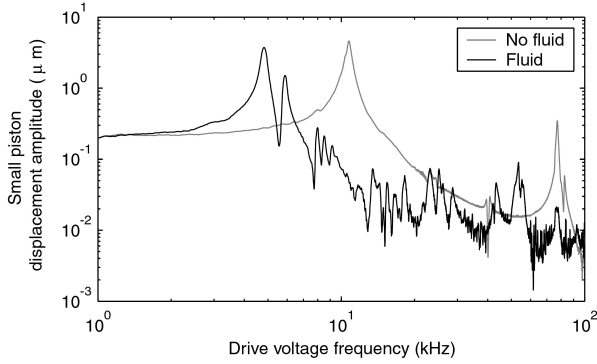


**Figure 10:** Displacement spectrum of the small piston. Excitation was 5Vp-p.

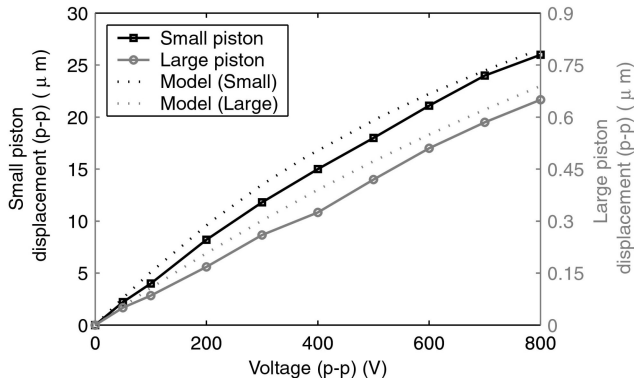


**Figure 11:** Displacement of the small and large pistons of the dynamic hydraulic amplifier for various excitation voltages. Sinusoidal excitation at 1kHz.

in Figure 12. Note that there is acceptable agreement between the amplification ratios observed during static and dynamic actuation.

## CONCLUSIONS

In this work we have developed and evaluated microfabricated hydraulic amplification devices. The important issues relating to the design of such devices on the microscale have been addressed. We have also demonstrated that filling and sealing of microfabricated dead volumes with hydraulic fluid is feasible, and stiff hydraulic couplers can be produced using the techniques described here. The experimental results show that microfabricated hydraulic amplification devices can have

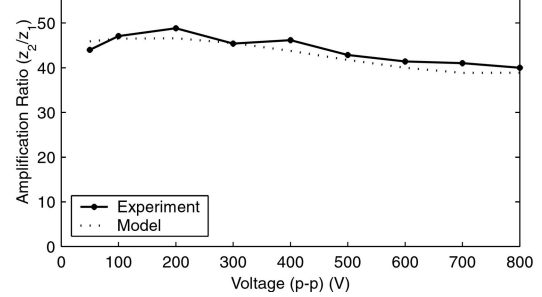


**Figure 12:** Amplification ratio results for the piezoelectric hydraulic amplifier.

sufficient stiffness and actuation authority for application in high-pressure microvalves and other types of micropositioning devices. It has also been shown that these devices can have sufficient bandwidth to allow for high frequency operation, with large amplification ratios.

## ACKNOWLEDGMENTS

All microfabrication was performed at the MIT Microsystems Technology Laboratories (MTL). The authors also wish to acknowledge the group of Prof. Liou at the University of Nebraska for all the Au-Sn sputter deposited films used to incorporate the piezoelectric elements. This work was performed under ONR grants N00014-01-1-0857 and N00014-97-1-0880 and DARPA grant DAAG55-98-1-0361.

## REFERENCES

1. N.W. Hagood IV, *et al.* "Micro-hydraulic Transducer Technology for Actuation and Power Generation", *SPIE 7<sup>th</sup> International Symposium on Smart Structures and Materials*, Newport Beach, CA, March 5-9, 2000.
2. D.C. Roberts *et al.*, "A High Frequency, High Stiffness Piezoelectric Micro-Actuator for Hydraulic Applications," *Proceedings of the 11th International Conference on Solid-State Sensors and Actuators*, Munich, Germany, June 10-14, 2001, pp. 686-689.
3. D.C. Roberts *et al.*, "Modeling, Design, and Simulation of a Piezoelectrically Driven Microvalve for High Pressure, High Frequency Applications," *Proceedings of the SPIE 8th International Symposium on Smart Structures and Materials*, Newport Beach, CA, March 5-8, 2001, Vol. 4327, pp. 366-380.
4. P. Tang, *et al.* "Combined Piezoelectric-Hydraulic Actuator Based Active Vibration Control for Rotordynamic System", *Trans. of the ASME - Journal of Vibration and Acoustics*, July 1995, Vol. 117, pp285-293
5. J. Garcia-Bonito, *et al.* "A novel high-displacement piezoelectric actuator for active vibration control", *Smart Materials and Structures*, Vol 7 1998, pp31-42, IOP
6. H.Q. Li, *et al.*, "A High Frequency, High Flow Rate Piezoelectrically Driven MEMS Micropump", *Technical Digest of the 2000 Solid-State Sensor and Actuator Workshop*, Hilton Head, SC, June 2000
7. J.L. Steyn, "Hydraulic Amplification for Actuation in MicroElectroMechanical Systems", Master's Thesis, MIT, 2002
8. D.C. Roberts, "Design, modeling, fabrication and testing of a piezoelectric microvalve for high pressure, high frequency hydraulic applications", PhD Thesis, MIT, 2002

# Hydraulic Amplification for Actuation in MicroElectroMechanical Systems

by

J. Lodewyk Steyn

B.Eng.(Mechanical), 1998  
University of Pretoria, South Africa

Submitted to the Department of Aeronautical and Astronautical Engineering  
in partial fulfillment of the requirements for the degree of

Master of Science

at the

MASSACHUSETTS INSTITUTE OF TECHNOLOGY

February 2002

© Massachusetts Institute of Technology, MMII. All rights reserved.

Author\_\_\_\_\_

Department of Aeronautical and Astronautical Engineering  
1 February 2002

Certified by\_\_\_\_\_

Nesbitt W. Hagood IV  
Associate Professor of Aeronautics and Astronautics  
Thesis Supervisor

Accepted by\_\_\_\_\_

Wallace E. VanderVelde  
Professor of Aeronautics and Astronautics  
Chairman, Committee on Graduate Students





# Hydraulic Amplification for Actuation in MicroElectroMechanical Systems

by  
J. Lodewyk Steyn

Submitted to the Department of Aeronautical and Astronautical Engineering  
on 1 February 2002, in partial fulfillment of the  
requirements for the degree of  
Master of Science

## Abstract

In this work the concept of hydraulic amplification as a means of stroke amplification is explored for applications in MicroElectroMechanical Systems (MEMS). Building on the batch fabrication technologies of the semiconductor industry, MEMS technology could enable the simultaneous fabrication of multiple microhydraulic systems of which hydraulic amplifiers would form part. Precision lithography would furthermore make dense arrays of microhydraulic systems possible, with the eventual goal being to create high power density microscale actuation and power generation systems.

This document provides an overview of the design considerations required for a successful microfabricated hydraulic amplifier, and proceeds to discuss the techniques developed to successfully fabricate, assemble and test such a device. Deep Reactive Ion Etching (DRIE) techniques were developed for creating strong tethered membrane structures using Silicon On Insulator (SOI) technology. Bonding techniques included silicon-silicon fusion bonding of fragile wafers and silicon-glass anodic bonding and alignment on the wafer and die level to produce multi-layered structures. Liquid filling of micromachined dead volumes through micron-size channels was performed. Static sealing techniques for leak-free sealing of micromachined, filled dead volumes with minimal seal compression and dynamic sealing techniques when quasi-static actuation is not a prerequisite were successfully developed.

Using these techniques, several hydraulic amplification devices have been produced. Testing of these devices revealed good correlation with theoretical predictions. Stroke amplification ratios as high as 48 : 1 have been observed. In addition, natural frequencies of up to  $10kHz$  were measured. In conclusion, this work verifies the viability of hydraulic amplification for applications in microscale actuation systems.

Thesis Supervisor: Nesbitt W. Hagood IV

Title: Associate Professor of Aeronautics and Astronautics



## Acknowledgments

This work was not an individual effort, and the author would like to thank the following persons for their contributions:

Professor Nesbitt Hagood, for his advice and guidance. Furthermore, Professors Kenny Breuer, Mark Spearing and Marty Schmidt for their advice.

Hanqing Li, for his constant advice and guidance and, most of all, for teaching me the art of microfabrication. It has been a truly eye-opening experience, which I will cherish for the rest of my career. The reader will also notice Hanqing's contributions throughout this work, with respect to mask design and process development.

Dave Roberts whose inputs in the whole development of this device were invaluable. In addition, for generating most of the model results for the hydraulic amplifier, for providing me with his code to use for the model-experiment correlation, and for his contributions to this document.

Developing MHT devices with Dave and Hanqing has been nothing but enjoyable, and it was a privilege to work with people of such caliber.

Jorge Carretero, for his words of wisdom and for his initial work on the fluid test bench.

Kevin Turner, for his feedback during our fillet radius process development.

Rick Mlcak, for his contributions in terms of fluid filling and the initial fabrication process development, on which these devices rely.

Onnik Yaglioglu, for the MHT device modeling.

Dave Robertson, AMSL lab manager, for his assistance and friendliness in the lab.

The following undergraduate students made significant contributions to this work under the MIT UROP program: Blair Connelly, for teaching us how to use the vibrometer, for making our chip trays, and other assistance in the lab. Geeta Gupta, for being my draftsman. Erik Stockham, for the LabView coding and his flowmeter, not mentioned in this document, but certainly very useful for the valves and the pumps and harvesters.

The author would further like to thank the MIT Microsystems Technology Laboratories for the use of their facilities. The following staff members were particularly helpful during the fabrication process: Bernard Alamariu, Kurt Broderick, Vicky Diadiuk, Paul McGrath and Paul Tierney.

The author expresses his gratitude to Professor Liou from the University of Nebraska for

the high-quality gold-tin thin film deposition performed on the piezoelectric materials used in the piezoelectrically driven hydraulic amplifiers.

In addition, I would like to thank my father, Professor Jasper Steyn, of the Department of Mechanical Engineering of the University of Pretoria, for his advice, guidance, and support and also for proofreading this document.

And then, in any such project, there are the people, family and friends, around oneself, not directly involved with the work, but still part of one's life, and thus indirectly involved and contributing and... always... supporting. To those people in my life I would like to extend this brief, personal, sincerest, "thank you".

This research was performed under ONR grants N00014-01-1-0857 and N00014-97-1-0880 and DARPA grant DAAG55-98-1-0361.

# Contents

---

<b>1</b>	<b>Introduction</b>	<b>19</b>
1.1	Objective . . . . .	19
1.2	Survey of previous work . . . . .	20
1.2.1	Macroscale hydraulic amplification . . . . .	20
1.2.2	Microscale stroke amplification . . . . .	22
1.2.3	Microfluidic and microhydraulic systems . . . . .	23
1.3	Motivation . . . . .	24
1.4	Method of investigation . . . . .	25
<b>2</b>	<b>Design considerations</b>	<b>29</b>
2.1	The ideal hydraulic amplifier . . . . .	29
2.2	The practical hydraulic amplifier . . . . .	30
2.3	The hydraulic amplifier evaluated in this work . . . . .	30
2.3.1	Design considerations . . . . .	32
2.3.2	Critical dimensions of the devices built . . . . .	33
2.4	Stiffness matrix . . . . .	33
2.4.1	A simple spring-based analogy . . . . .	35
2.4.2	An hydraulic amplifier with sliding seals . . . . .	36
2.4.3	An hydraulic amplifier with flexural seals . . . . .	38
2.5	The nonlinear case . . . . .	39
2.5.1	Nonlinear modeling and design of the hydraulic amplifier . . . . .	40
2.5.2	Nonlinear simulation results . . . . .	42
2.6	Summary . . . . .	42
<b>3</b>	<b>Fabrication and device assembly</b>	<b>49</b>

3.1	Fabrication overview . . . . .	49
3.2	Process flow for creating silicon membrane structures . . . . .	50
3.2.1	Membrane fillet radius control . . . . .	52
3.3	Silicon fusion bonding techniques . . . . .	54
3.4	Anodic bonding techniques and die-level assembly . . . . .	55
3.4.1	Wafer-scale anodic bonding . . . . .	55
3.4.2	Die-level assembly . . . . .	58
3.5	Summary . . . . .	61
<b>4</b>	<b>Filling and sealing techniques</b>	<b>63</b>
4.1	Filling techniques . . . . .	63
4.1.1	Fluid requirements . . . . .	63
4.1.2	Filling process . . . . .	64
4.1.3	Initial tests . . . . .	67
4.2	Sealing concepts . . . . .	68
4.2.1	Static sealing . . . . .	68
4.2.2	Dynamic sealing . . . . .	69
4.3	Summary . . . . .	72
<b>5</b>	<b>Experimental techniques</b>	<b>73</b>
5.1	Test rig requirements . . . . .	73
5.2	System overview . . . . .	73
5.3	Device test jigs . . . . .	74
5.4	The fluid test bench . . . . .	75
5.4.1	Gas pressure regulating module . . . . .	75
5.4.2	Gas-liquid pressurization module . . . . .	76
5.4.3	Pressure measurement and control module . . . . .	80
5.4.4	Vacuum module . . . . .	80
5.5	Displacement measurement . . . . .	83
5.6	Data acquisition . . . . .	83

5.7	Testing protocols . . . . .	83
5.7.1	Testing of static hydraulic amplifiers . . . . .	86
5.7.2	Testing of dynamic hydraulic amplifiers . . . . .	87
<b>6</b>	<b>Experimental results</b>	<b>89</b>
6.1	Overview . . . . .	89
6.2	Pressure Deflection results . . . . .	91
6.2.1	Pressure-deflection characteristics of the large piston . . . . .	91
6.2.2	Pressure-deflection characteristics of the small piston structures . . . . .	92
6.2.3	Summary: Pressure deflection results . . . . .	94
6.3	Static hydraulic amplification tests . . . . .	95
6.3.1	Testing: HAC Device 3 . . . . .	95
6.3.2	Amplification ratios: HAC Device 3 . . . . .	97
6.3.3	Stiffness matrix: HAC Device 3 . . . . .	99
6.3.4	Testing: HAC Device 4 . . . . .	105
6.3.5	Amplification ratios: HAC Device 3 . . . . .	105
6.3.6	Stiffness matrix: HAC Device 4 . . . . .	109
6.3.7	Static hydraulic amplification as a two-variable function . . . . .	112
6.4	Dynamic hydraulic amplification tests . . . . .	112
6.5	Summary of the test results . . . . .	116
<b>7</b>	<b>Conclusions and recommendations</b>	<b>117</b>
7.1	Conclusions . . . . .	117
7.2	Recommendations . . . . .	118
7.3	Final remarks . . . . .	119
<b>A</b>	<b>Material properties</b>	<b>125</b>
<b>B</b>	<b>Equipment list</b>	<b>127</b>
<b>C</b>	<b>Detail designs</b>	<b>131</b>

C.1	Die-level anodic bonding jig . . . . .	131
C.2	Test jig for the hydraulic amplifier . . . . .	145
<b>D</b>	<b>Computer code</b>	<b>157</b>
D.1	Matlab codes used for modeling of the HAC . . . . .	157
D.1.1	Bisection method iteration code for modeling of the HAC . . . . .	157
D.1.2	Nonlinear annular plate code . . . . .	161
D.2	Matlab code used for data analysis and computation . . . . .	166
<b>E</b>	<b>Masks</b>	<b>209</b>



# List of figures

---

1.1	MHT 3D section view . . . . .	20
1.2	MHT modes of operation: Pump vs. Generator . . . . .	21
1.3	MHT 3D layers . . . . .	25
1.4	MHT cross section . . . . .	26
1.5	The hydraulic amplifier . . . . .	27
1.6	Tethered piston . . . . .	27
2.1	The ideal hydraulic amplifier. . . . .	30
2.2	Hydraulic amplification device types . . . . .	31
2.3	Piston nomenclature . . . . .	33
2.4	A simple three-spring analogy . . . . .	36
2.5	An hydraulic amplifier with sliding seals . . . . .	36
2.6	HAC: Simplified schematic . . . . .	40
2.7	Large piston simulation results - 1 small piston . . . . .	43
2.8	Small piston simulation results - 1 small piston . . . . .	43
2.9	$P_{HAC}$ simulation results - 1 small piston . . . . .	44
2.10	Simulation results: Stress - 1 small piston . . . . .	45
2.11	Large piston simulation results - 10 small pistons . . . . .	45
2.12	Small piston simulation results - 10 small pistons . . . . .	46
2.13	$P_{HAC}$ simulation results - 10 small pistons . . . . .	47
2.14	Simulation results: Stress - 10 small pistons . . . . .	48
2.15	Simulation results in 3D . . . . .	48
3.1	Silicon membrane fabrication . . . . .	50
3.2	Large piston SEM . . . . .	51
3.3	SEM's of typical channel structures . . . . .	52

3.4	Fillet feature detail . . . . .	53
3.5	Fillet SEM's . . . . .	53
3.6	Layer 4 etch mask . . . . .	56
3.7	The basic principle of anodic bonding. . . . .	57
3.8	Anodic bonding jig. . . . .	58
3.9	Three-point alignment . . . . .	59
3.10	Anodic bonding jig with chip . . . . .	60
3.11	Assembled hydraulic amplifier photograph . . . . .	60
4.1	Bulk modulus vs. fluid pressure . . . . .	64
4.2	Vapor lines for a selection of linear siloxanes . . . . .	65
4.3	Filling system schematic . . . . .	65
4.4	Filling system photograph . . . . .	66
4.5	Filling test chip . . . . .	68
4.6	Static sealing concepts . . . . .	69
4.7	Schematic of the dynamic seal . . . . .	70
4.8	Model of the dynamic seal . . . . .	71
4.9	Dynamic seal results . . . . .	71
5.1	Test jig . . . . .	75
5.2	Top clamp . . . . .	76
5.3	Fluid system schematic . . . . .	77
5.4	The gas pressure regulating module. . . . .	78
5.5	The gas-liquid pressurization module. . . . .	79
5.6	Pressure measurement and control module. . . . .	81
5.7	Vacuum module. . . . .	82
5.8	Regulator bank . . . . .	84
5.9	The test rig . . . . .	85
5.10	The test rig - side view . . . . .	86
6.1	Static hydraulic amplifier . . . . .	91
6.2	Pressure deflection results . . . . .	93

6.3	Pressure deflection results . . . . .	93
6.4	Pressure deflection results . . . . .	94
6.5	Typical test run data . . . . .	96
6.6	HAC Large piston data . . . . .	97
6.7	HAC Small piston data . . . . .	98
6.8	HAC Large piston model correlation . . . . .	98
6.9	HAC Small piston model correlation . . . . .	99
6.10	Amplification ratio . . . . .	100
6.11	Amplification sensitivity . . . . .	100
6.12	Deflection results for Device 3 . . . . .	101
6.13	HAC Large piston model correlation . . . . .	103
6.14	HAC Small piston model correlation . . . . .	104
6.15	HAC Large piston data . . . . .	106
6.16	HAC Small piston data . . . . .	106
6.17	HAC Large piston model correlation . . . . .	107
6.18	HAC Small piston model correlation . . . . .	107
6.19	Amplification ratio . . . . .	108
6.20	Amplification sensitivity . . . . .	108
6.21	HAC Large piston model correlation . . . . .	110
6.22	HAC Small piston model correlation . . . . .	111
6.23	Results in 3D . . . . .	112
6.24	Dynamic hydraulic amplifier . . . . .	113
6.25	Frequency response . . . . .	114
6.26	Time history . . . . .	114
6.27	Deflection versus drive voltage . . . . .	115
6.28	Amplification ratio . . . . .	115
C.1	Assembly jig main part . . . . .	132
C.2	Assembly jig lower ceramic plate . . . . .	133
C.3	Assembly jig upper ceramic plate . . . . .	134
C.4	Assembly jig chip rest (ceramic) . . . . .	135

C.5	Assembly jig ceramic bushing . . . . .	136
C.6	Assembly jig stainless steel bushing . . . . .	137
C.7	Assembly jig ceramic alignment pin . . . . .	138
C.8	Assembly jig ceramic clamping pin . . . . .	139
C.9	Assembly jig wire clamp lower part . . . . .	140
C.10	Assembly jig wire clamp lower part . . . . .	141
C.11	Assembly jig leaf spring . . . . .	142
C.12	Assembly jig lower contact plate . . . . .	143
C.13	Assembly jig upper contact plate . . . . .	144
C.14	Test jig 3D view 1 . . . . .	146
C.15	Test jig 3D view 2 . . . . .	147
C.16	Test jig front view 1 . . . . .	148
C.17	Test jig front view 2 . . . . .	149
C.18	Test jig front section 1 . . . . .	150
C.19	Test jig front detail 1 . . . . .	151
C.20	Test jig front detail 2 . . . . .	152
C.21	Test jig front detail 3 . . . . .	153
C.22	Test jig side detail 1 . . . . .	154
C.23	Test jig rear view 1 . . . . .	155
C.24	Test jig mount . . . . .	156
E.1	Glass layers . . . . .	211
E.2	Layer 3 glass patterns . . . . .	212
E.3	Layer 4 masks . . . . .	213
E.4	Layer 5 masks . . . . .	214
E.5	Layer 7 masks . . . . .	215
E.6	Layer 8 masks . . . . .	216
E.7	Wafer scale masks of Layer 7 . . . . .	217
E.8	Plan view . . . . .	218

# List of tables

---

2.1	Large piston dimensions for all hydraulic amplifiers built . . . . .	34
2.2	Small piston dimensions for hydraulic amplifiers with a single small piston .	34
2.3	Small piston dimensions for hydraulic amplifiers with ten small pistons . . .	34
2.4	Other dimensions and values . . . . .	34
6.1	Outline of the hydraulic amplification devices assembled and tested . . . . .	90
6.2	Large piston inverse compressibility . . . . .	92
6.3	Small piston inverse compressibility for devices with a single small piston. .	94
6.4	Small piston inverse compressibility for devices with 10 small pistons. . . .	95
6.5	Inverse compressibilities for the pistons of HAC Device 3. . . . .	101
6.6	Inverse compressibilities for the pistons of HAC Device 4. . . . .	109



# Nomenclature

---

## Variables and constants

Name	Units	Description
$A$	$m^2$	Area
$AR$		Amplification ratio
$AS$		Amplification sensitivity
$C$	$m/Pa$	Compressibility matrix
$D$	$Pa/m$	Inverse compressibility matrix
$F$	$N$	Force
$h$	$m$	Height
$k$	$N/m$	Stiffness
$P$	$Pa$	Pressure
$r$	$m$	Radius
$t$	$m$	Thickness
$V$	$m^3$	Volume
$V$	$V$	Voltage
$w$	$m$	Width
$z$	$m$	Vertical displacement
$\beta$	$Pa$	Bulk modulus
$\gamma$	$m^{-1}$	Geometric ratio (Area/Volume)
$\psi$	$Pa/m$	Inverse compressibility

## Subscripts

$HAC$	Hydraulic Amplification Chamber property
$c$	Lumped chamber property
1	Large piston property
2	Small piston property
$f$	Chamber fluid property
$eff$	Effective
$m$	Membrane
$t$	Trench

<i>SOI</i>	Silicon On Insulator
<i>r</i>	Fillet radius feature
<i>w</i>	Wafer
<i>a</i>	Outer radius of tethered piston
<i>b</i>	Inner radius of tethered piston
<i>p – p</i>	Peak-to-peak

## Acronymns

AV	Active Valve
BOE	Buffered Oxide Etch
DRIE	Deep Reactive Ion Etching
HAC	Hydraulic Amplification Chamber
MEMS	MicroElectroMechanical Systems
MHT	MicroHydraulic Transducer
RIE	Reactive Ion Etching
SOI	Silicon On Insulator

## Hydraulic diagram naming conventions

APR	Absolute Pressure Regulator
BEV	BEllows Valve
BV	Ball Valve
CT	Cold Trap
FT	Filter
LN	Liquid Nitrogen
NV	Needle Valve
RV	Relief Valve
SPS	Static Pressure Sensor
SV	Solenoid Valve
TK	Tank
V	Valve
VG	Vacuum Gauge
VP	Vacuum Pump



# Introduction

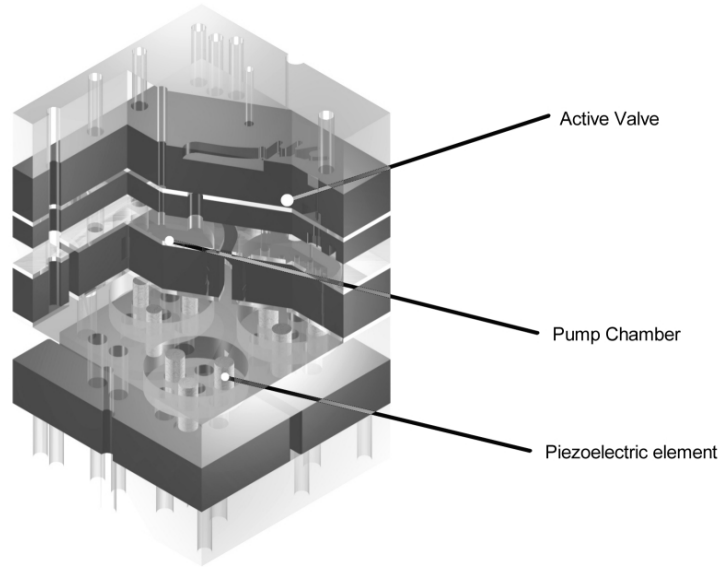
---

At a time when the mere existence of the air around us was a debatable topic, the French mathematician and scientist Blaise Pascal (1623-1662) presented a remarkable series of scientific studies on the behavior of fluids [1]. In 1653, his studies led to the formulation of what is now known as Pascal's law, which can be stated as: "Pressure applied to an enclosed fluid is transmitted undiminished to every portion of the fluid and the walls of the containing vessel" [2]. It is from this simple principle that the concept of hydraulic force amplification or stroke amplification can be derived. Hydraulic amplification is a conceptually elegant means of mechanical amplification, with few moving parts and no mechanisms.

## 1.1 Objective

The objective of the work presented here is to explore the feasibility of hydraulic coupling as a means of stroke amplification for actuation in a microscale hydraulic system. For the purposes of this discussion, the term "microscale" will refer to any device that is fabricated by means of microfabrication technology.

The microscale hydraulic system, in this case, is a piezoelectrically driven microfluidic prime mover with a piezoelectric piston and two piezoelectrically driven active valves. Thanks to its active valves, this device, also called a MicroHydraulic Transducer (MHT), pictured in Figure 1.1 can be operated as either a pump or a generator. The pump/generator modes of operation are shown in Figure 1.2. Due to the requirement of both large stroke and high frequency actuation of the active valves, direct actuation by piezoelectric elements is not feasible, and hydraulic amplification provides an attractive means for amplifying the stroke of the piezoelectric valve actuators. For background on this device, and the general concept of a MicroHydraulic Transducer, the reader is referred to [3],[4]. In this work, we will introduce the concept of hydraulic amplification for actuation in MicroElectroMechanical Systems (MEMS) by evaluating the performance of the hydraulic amplifiers of the



*3D Modeling by H.Q. Li. Rendering by J.L. Steyn*

Figure 1.1: 3D Section view of a MicroHydraulic Transducer Device.

MicroHydraulic Transducer shown in Figure 1.1.

## 1.2 Survey of previous work

Although hydraulic amplification has not been investigated for microfabricated devices, numerous macroscopic systems using hydraulic amplification have been reported. This section provides a brief overview of some previous work, and also some general work in microhydraulic and microfluidic systems.

### 1.2.1 Macroscale hydraulic amplification

Hydraulic *force* amplification forms an integral part of modern industry, where servo-hydraulic systems can be found in applications ranging from earthmoving equipment to aerospace applications. Hydraulic *stroke* amplification, however, is less common.

Tang presented an hydraulic stroke amplifier, employing very viscous, stiff fluids, so-called

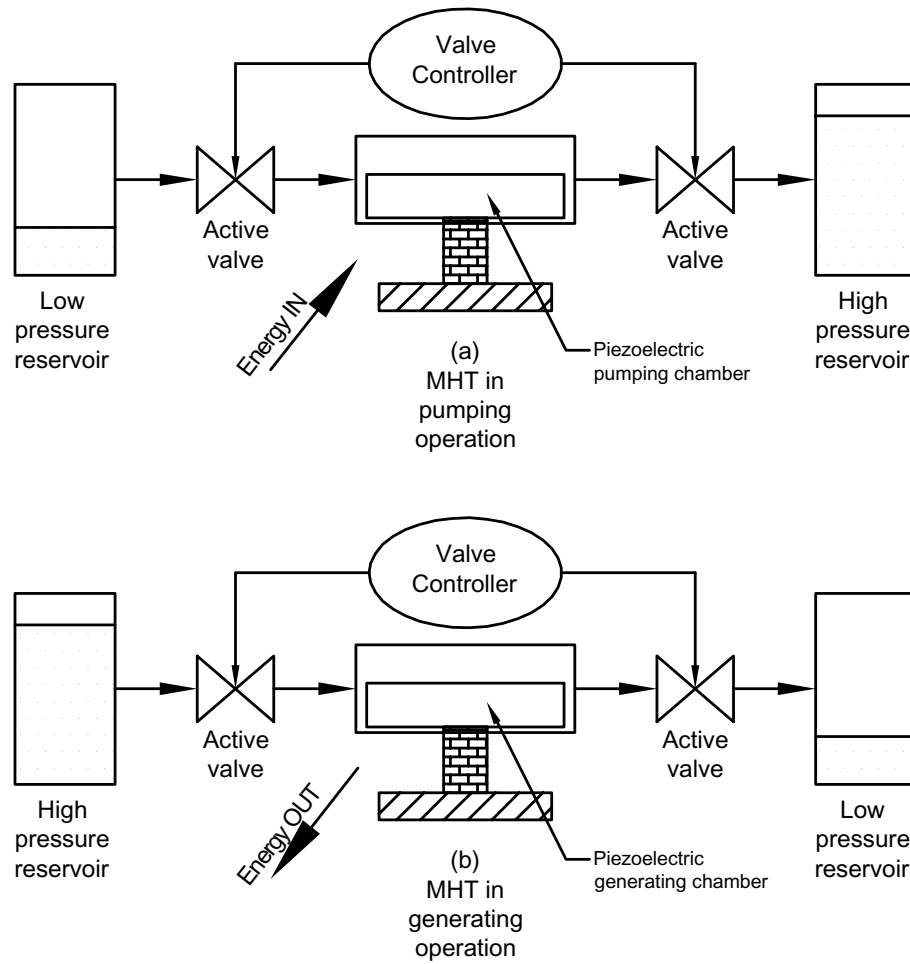


Figure 1.2: The two modes of operation for an active valve MHT device: (a) Pumping/Actuation and (b) Power generation.

liquid plastic PVC, for active vibration control of rotorblades. [5] Using ultrasonic techniques, bulk modulus measurements of the fluids are reported, and range from 1.9GPa to 2GPa, compared to a measured bulk modulus of 2.2GPa for water.

In [6] another application for active vibration control prompted the need for hydraulic amplification of piezoelectric actuation. Using ethylene glycol as the hydraulic fluid, a novel ring-type actuator was produced.

### 1.2.2 Microscale stroke amplification

Although hydraulic amplification of force and stroke has not been applied in the field of MEMS until now, other means of mechanical stroke amplification techniques have been explored. Where piezoelectric actuation is desired, bimorph beam structures have been fabricated to convert the in-plane strain of the piezoelectric element into an out-of-plane motion. The piezoelectric material takes the form of a thin film, either zinc oxide (*ZnO*) or ceramic lead zirconate titanate (*PZT*). These beam structures were claimed to have potential applications in, amongst others, mass sensing [7], sound generation [8] and thin film characterization [9].

In work by Rogers [10] a number of compliant flexure systems for stroke amplification is mentioned, with amplification ratios of 5 to 50 and efficiencies of greater than 80%, where the efficiency is defined, in this case, as<sup>1</sup>:

$$\eta_{mech} = \frac{(Force\ out) \times (Displacement\ out)}{(Force\ in) \times (Displacement\ in)} \quad (1.1)$$

These flexural linkage systems are visually quite impressive. A theoretical treatment on multi-stage cascaded flexural linkage systems is presented in [12]. Amplification ratios as high as 148:1 are reported. In general, the literature provides limited information on the actual stiffnesses of these mechanisms. However, it is apparent from the size of the devices discussed, as well as the method of fabrication - surface micromachining - that these flexural amplification devices are mostly suited for light-duty applications. In the work presented here we will strive to develop a stroke amplifier that will provide substantial (large force) actuation authority on the microscale.

---

<sup>1</sup>For a more comprehensive treatment on actuation efficiencies, based on macroscale stroke amplification devices, the attention of the reader is also drawn to the work of Precht and Hall [11].

### 1.2.3 Microfluidic and microhydraulic systems

Numerous microfluidic devices for various applications have been reported. Of these devices, micropumps and microvalves, in particular, could be used to construct microhydraulic systems. In any such system, the proposed microscale hydraulic amplification concept can be an enabling technology to accomplish such tasks as large stroke valve operation and general force or stroke amplified mechanical actuation. For completeness we present here an overview of some of the highlights in the development of micropumps and microvalves for potential use in small-scale hydraulic systems.

Often, hydraulic systems will require a prime mover that can take the form of a pump or a generator. In 1988 Van Lintel [13] reported a piezoelectrically driven micromachined silicon pump with a maximum flow rate of approximately  $0.6\mu l/min$  and a maximum pressure head of approximately  $2.5mH_2O$ . A year later Esashi [14] reported a piezoelectric micropump with a maximum flow and  $\Delta P$  of  $20\mu l/min$  and  $0.78mH_2O$  respectively. Recently, in the same project of which this study forms part, using features of the MHT technology described earlier [4], a seven layer silicon-glass piezoelectric micropump capable of delivering up to  $3000\mu l/min$ , or setting up differential pressures as high as  $450kPa$  was developed [15]. With functional dimensions of approximately  $8 \times 8 \times 10mm$ , this device demonstrated that small-scale high power density prime movers can become a reality. The performance of this pump is matched and, in some cases, even exceeded by elektrokinetic pumps as described, for example, in [16]. Electrokinetic pumps are mechanically very simple and robust, but suffer from a finite lifetime due to the electrochemical reaction that drives the flow.

A large number of microvalves for various applications have been developed and reported in the literature, and a detailed discussion of previous microvalves is not presented. Indeed, microvalves have seen development to the stage where they have already found commercial applications such as mass flow control and pilot valves. See, for example, [17]. It should be noted that valves developed specifically for liquid applications are less common than those for gas applications. This fact is also reflected in the review by Gravesen [18]. The reader is referred to this review for a more complete overview of the earlier microvalves. A newer, high-frequency, high-pressure, high-flowrate microvalve that was enabled by the hydraulic amplification technology discussed in this document is presented by Roberts [19], and the reader is encouraged to review his work in conjunction with the work presented here.

A brief remark has to be made on devices that are sometimes referred to as "fluidic amplifiers". Reported by Zdeblick [20] and later Vollmer [21] and also called "wall attachment

amplifiers”, these devices operate on flow streams to either amplify the flow rate or the pressure. These devices can also find useful applications in microhydraulic systems, but we want to emphasize that the device that we will refer to as an *hydraulic amplifier* in this work is completely different from devices previously developed and subsequently named *fluidic amplifiers*.

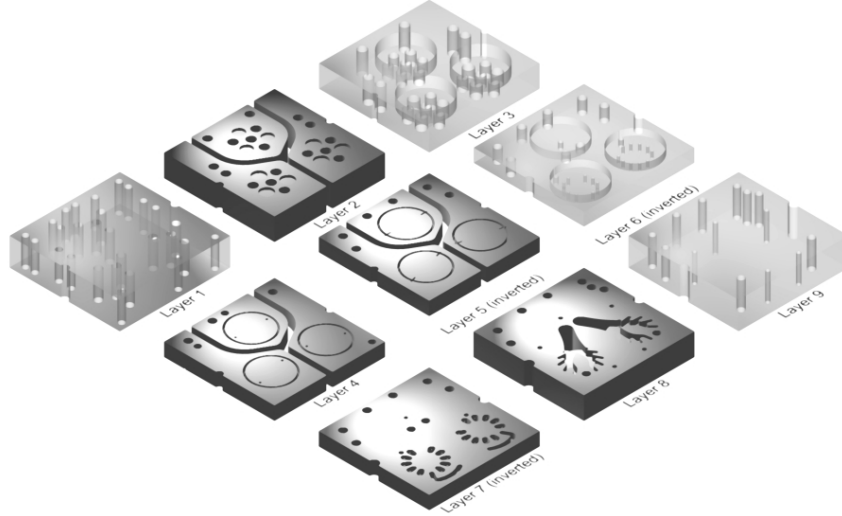
### 1.3 Motivation

Recent developments in MEMS have brought quite a number of devices that can be classified as “Power-MEMS” devices, with the purpose of performing meaningful mechanical work rather than simple sensing or chemical analysis. See for example, [22]. MHT technology, as discussed previously, also falls in this category by attempting to exploit the benefits of piezoelectric materials on the microscale.

As is shown in [3], piezoelectric materials can be made to operate efficiently as electromechanical transducers, even at high mechanical loads. Like most so-called “smart” materials, piezoelectric materials have the drawback of being able to provide only minimal actuation stroke. They can, however, operate at very high frequencies, usually with a minimal reduction in their actuation authority. Since the mechanical power output of a transducer will be proportional to  $Work/cycle \times frequency$ , it is clear that high frequency operation is desirable for high power output.

For high frequency operation of the piezoelectric material, the structure that is driven by this material should ideally have a high natural frequency. MEMS provides a means of producing small, stiff structures with high natural frequencies. MHT technology then uses hydraulic fluid as a rectifying medium. The energy is transferred from the piezoelectric element to the fluid, which can then be used to drive, say, an hydraulic actuator at a slightly lower frequency to provide actuation for “real-world” mechanical applications, where the desired frequency of operation might be in the  $1 - 100Hz$  range, compared to the  $10kHz$  operation desired for the piezoelectric actuation element.

Even on the microscale, however, the stroke provided by the piezoelectric material may not be sufficient to operate, for example, a microvalve in an MHT system. Therefore, for microscale applications of piezoelectric materials, there exists a definite need for stiff, compact stroke amplification mechanisms or devices.



3D Modeling by H.Q. Li. Rendering by J.L. Steyn

Figure 1.3: 3D View of the layers of the MHT Device.

The *primary motivation* for the development of a microscale hydraulic amplifier is this need for a "power-MEMS" type stroke amplifier for microscale piezoelectric applications, in contrast to previous stroke amplification devices, discussed in Section 1.2.2, and geared solely towards light-duty sensing and positioning applications. A *secondary motivation* for this research is the complete void in the field of MEMS in terms of either hydraulic force or stroke amplification, and the need to gain some insight into the requirements with respect to the design and operation of such devices.

## 1.4 Method of investigation

Using the MHT device mentioned previously as a test bed, this work demonstrates that hydraulic amplification is a viable and an elegant means for stroke amplification. Figures 1.3 and 1.4 show the major components of this device in more detail. As a full experimental microhydraulic transducer, this device has the following design features:

- Dimensions of  $20 \times 20 \times 10mm$
- Five silicon and four glass layers, making a nine layer device

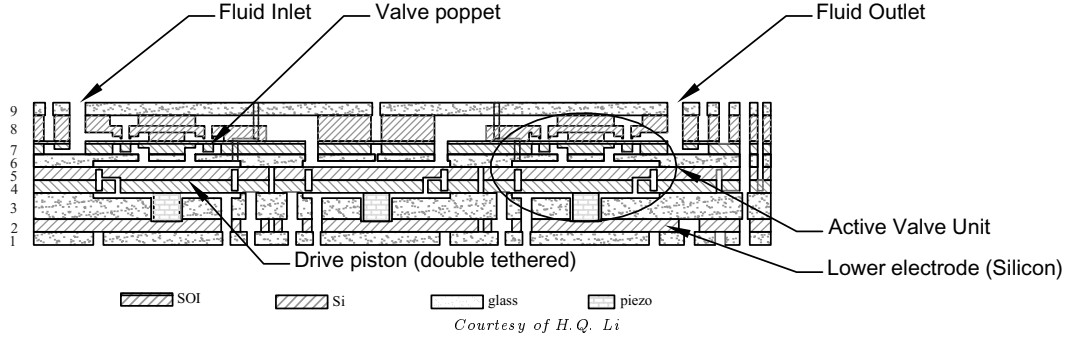


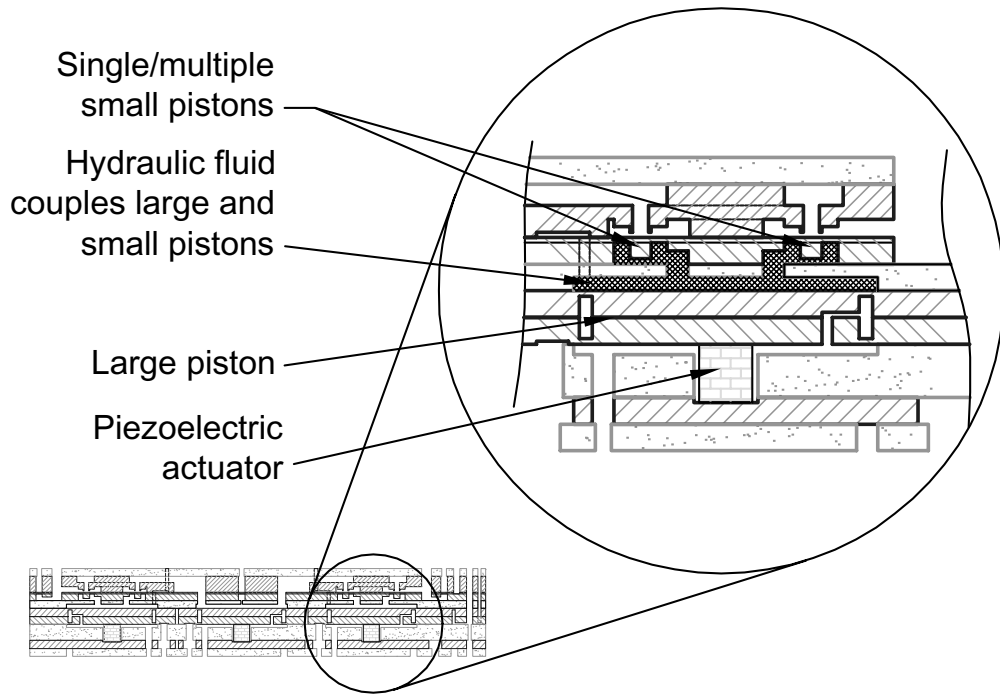
Figure 1.4: Expanded cross section view of the MHT Device.

- Three groups of three piezoelectric elements for three piezoelectrically driven microactuator structures
- Two hydraulically amplified active valves.
- One pumping (or energy generating) chamber

In this work, the hydraulic amplifier under consideration, as a subcomponent of the full MHT device, is shown in Figure 1.5. The MHT system, and therefore also the hydraulic amplifier as one of its subcomponents, rely heavily on the use of tethered piston structures to create moving pistons on the microscale. These tethered pistons with flexural seals and rigid center bosses are compatible with conventional micromachining techniques, as we will discuss in Chapter 3. The operation of a basic tethered piston is shown in Figure 1.6.

In the chapters that follow, the issues that had to be addressed with respect to the design, fabrication, fluid filling, sealing and eventual testing and evaluation of a successful MEMS hydraulic amplifier will be discussed. Finally experimental results with good agreement to theoretical predictions are presented.





*Courtesy of H. Q. Li*

Figure 1.5: The hydraulic amplifier as part of the MHT device.

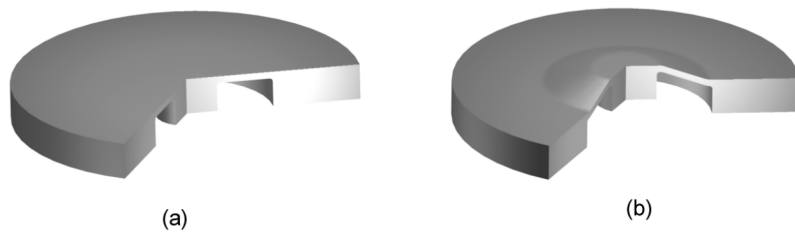


Figure 1.6: The operation of a tethered piston. All moving components rely on this mechanism. (a) Shows an undeflected tethered membrane, and (b) one that has been deflected, either by a load at the center (e.g. piezoelectric actuation) or by a pressure differential applied over the structure.



# Design considerations

---

In order to produce a successful hydraulic amplification device, whether be it on the microscale or the macroscale, certain aspects of its design require careful thought to ensure that the functional requirements established be met. This chapter provides a brief overview of the issues that were addressed in the design of the particular hydraulic amplification device mentioned in Chapter 1. For a more detailed treatment of some the material presented here, the reader is referred to [19].

## 2.1 The ideal hydraulic amplifier

When considering the design of a closed hydraulic system which, to first order, obeys Pascal's law, it is always beneficial to keep in mind the ideal hydraulic amplifier <sup>1</sup>. In the ideal hydraulic amplifier it is assumed that all structural components have infinite stiffness and that the coupling fluid is fully incompressible (i.e. infinite bulk modulus). Furthermore, it is assumed that the mass of all components are negligible, and that the device will have infinite bandwidth of operating frequency. It goes without saying that the device should be completely lossless. Figure 2.1 depicts a conceptually ideal hydraulic amplifier.

In this case, due to conservation of mass, the amplification is given by the area ratio:

$$\frac{z_1}{z_2} = \frac{A_2}{A_1} \quad (2.1)$$

---

<sup>1</sup>The electrical analogy to this would be the ideal transformer. See, for example [23]

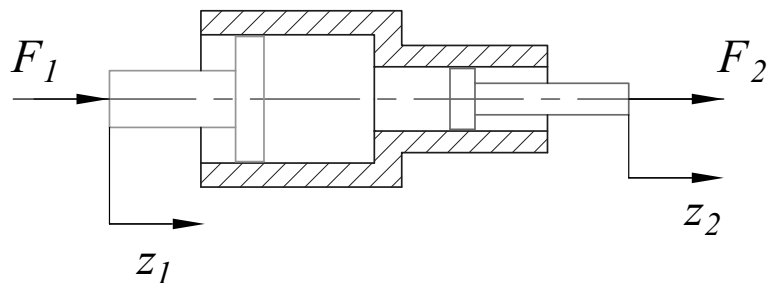


Figure 2.1: The ideal hydraulic amplifier.

## 2.2 The practical hydraulic amplifier

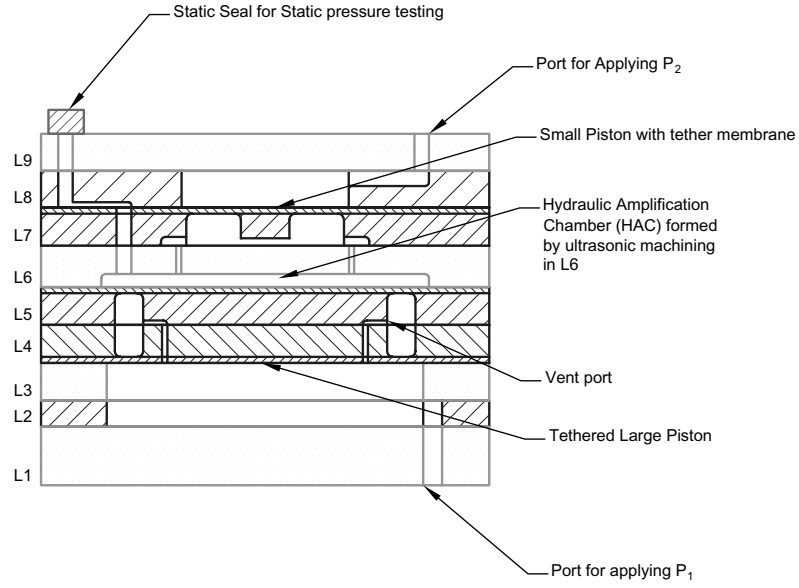
By changing the following assumptions, the ideal hydraulic amplifier is transformed into a practical hydraulic amplifier:

- The coupling fluid has a finite bulk modulus.
- The structural components have nonzero compliance.
- The structural components have mass.
- The fluid itself also has inertia.
- Provision should be made for losses. An example is viscous losses due to squeeze film damping, depending on the geometry of the device under consideration

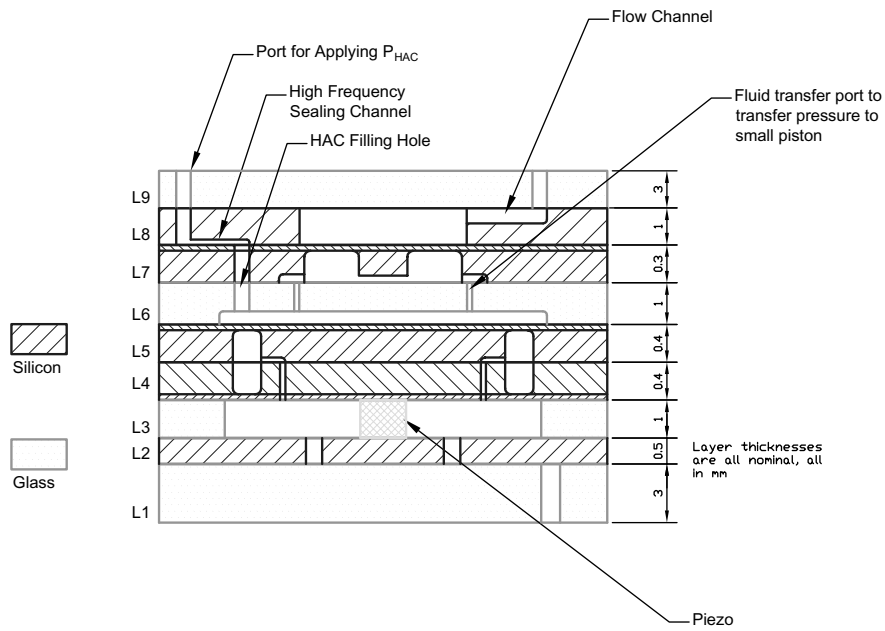
It will be obvious to the reader that, in particular, the added compliance (both fluidic and structural) of the practical hydraulic amplifier will be a dominant limiting factor in the static performance of such a device. In this work we will be concerned mostly with the static behavior of hydraulic amplifiers as actuation couplers.

## 2.3 The hydraulic amplifier evaluated in this work

The hydraulic amplification devices that were evaluated in this work are schematically shown in Figure 2.2. These devices are constructed using microfabrication techniques. They feature two tethered-membrane piston-type elements.



(a)



(b)

Figure 2.2: Hydraulic amplification devices evaluated in this work: a) Static pressure actuated and b) Dynamic piezoelectrically driven.

These devices have the following design features and associated aspects that need to be addressed in analysis, fabrication and testing:

- A nine layer device, with five silicon and four glass layers.
- A tethered large piston structure, with the annular tether thickness defined by the thickness of the Silicon-On-Insulator (SOI) layers of Layers 4 and 5 in Figure 2.2. All pressures and deflections relating to the large piston will have subscript 1. Note that this piston is a double-tethered piston, designed to increase the natural frequency of the structure [19].
- A tethered small piston structure with the annular tether thickness defined by the SOI layer of Layer 7 in Figure 2.2. All pressures and deflections relating to the small piston will have subscript 2. If needed, more than one small piston can be driven from a single large piston. This work investigates the behaviour of *two* small piston configurations, namely a device with a *single* small piston, and also one with an array of *ten* small pistons.
- An hydraulic amplification chamber formed by ultrasonic machining into glass Layer 6 in Figure 2.2.

In addition, the device can either be pressure actuated, as shown in Figure 2.2a, or it can be piezoelectrically driven, as shown in Figure 2.2b.

### 2.3.1 Design considerations

The design of the devices mentioned in Section 2.3 was accomplished through use of the following techniques <sup>2</sup>:

- Baseline design of the final MHT device as a starting point for the design process [4].
- System-level design of the final MHT device to determine the required pressures and deflections. These were used as the structural inputs for the design steps that followed [24], [19].

---

<sup>2</sup>The author gratefully acknowledges the work done by D.C. Roberts, O. Yaglioglu, Y.-H. Su and J.A. Carretero in terms of the structural and fluidic modeling of this device

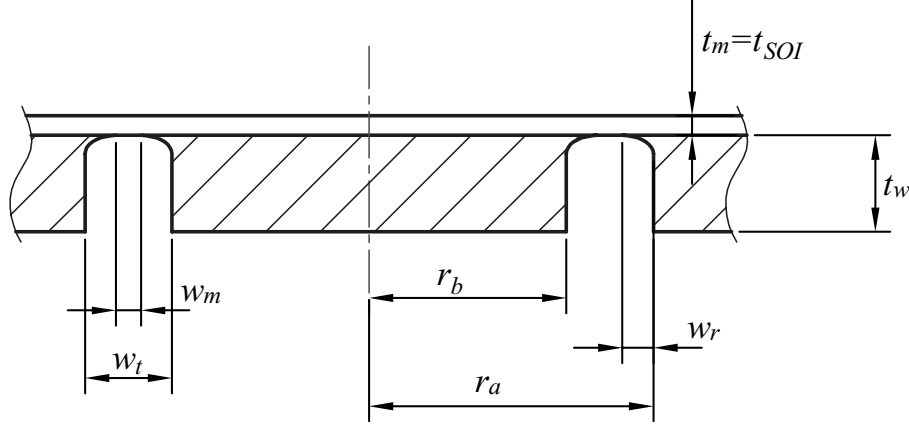


Figure 2.3: Nomenclature for a piston with microfabricated membrane tethers

- Preliminary design of the tethered membrane structures through use of a nonlinear annular plate code [25], [19]. This also included a coupled modeling of the HAC using a nonlinear plate code for the tether-membrane structures and a linear plate equation for the bending of the large piston to produce an iterative nonlinear model of the HAC.
- Verification of proper chamber height to minimize squeeze film damping effects [26].
- Verification of the initial design through finite element simulation [19].

### 2.3.2 Critical dimensions of the devices built

Figure 2.3 outlines the relevant dimensions that are important when designing a tethered piston structure. Tables 2.1, 2.2, 2.3 and 2.4 provide the dimensions obtained for two types of hydraulic amplifier, designed using the procedures described in 2.3.1. (See [19] and [24]) The associated material properties are given in Appendix A for reference.

## 2.4 The stiffness matrix of a flexural seal based hydraulic amplifier

To evaluate the stiffness of an hydraulic amplification device, it is sometimes useful to define a stiffness matrix to enable one to evaluate the performance of the device as a mechanical

$r_a$	$3613\mu m$	Outer radius
$r_b$	$3388\mu m$	Inner radius
$w_r$	$20\mu m$	Fillet width
$t_w$	$400\mu m$	Wafer thickness
$t_m = t_{SOI}$	$10\mu m$	SOI thickness

Table 2.1: Large piston dimensions for all hydraulic amplifiers built

$r_a$	$696\mu m$	Outer radius
$r_b$	$254\mu m$	Inner radius
$w_r$	$20\mu m$	Fillet width
$t_w$	$300\mu m$	Wafer thickness
$t_m = t_{SOI}$	$7\mu m$	SOI thickness

Table 2.2: Small piston dimensions for hydraulic amplifiers with a single small piston

$r_a$	$368\mu m$	Outer radius
$r_b$	$97\mu m$	Inner radius
$w_r$	$20\mu m$	Fillet width
$t_w$	$300\mu m$	Wafer thickness
$t_m = t_{SOI}$	$7\mu m$	SOI thickness

Table 2.3: Small piston dimensions for hydraulic amplifiers with ten small pistons

$V_c$	$8.3nl$	Chamber volume
$h_c$	$200\mu m$	Chamber height

Table 2.4: Other dimensions and values



transducer or coupler. This also aids in visualizing the effect of various compliances in the system, and assists in debugging, should fabricated devices not perform to expectations.

In such a device, various compliances of different orders of magnitude can be present. For example, the working fluid might be a very stiff part of the hydraulic amplifier, especially when dealing with flexure-sealed structures, as is the case for the devices considered in this work. In this scenario, the membranes themselves will typically be the most compliant elements and the effect of this compliance can readily be incorporated in the models used to design the hydraulic amplifiers [19]. However, the introduction of a bubble into the fluid might affect the effective bulk modulus of the chamber by orders of magnitude, hence making the fluid a compliance that needs to be considered as well.

We will introduce the concept of a stiffness matrix by considering a much simplified case, using, instead of fluid, pistons and pressures, a simple spring system. Thereafter, we will consider a fictitious hydraulic amplification device with perfect sliding seals, to introduce the concept of amplification into the stiffness matrix. Thereafter, we will consider the more complex case of a tethered structure where the fluid pressure is now acting not only on the pistons but on the membrane tethers themselves. In all the arguments presented, we will deal with a linear coupler. Introducing nonlinearity will invalidate the simple concept of a stiffness matrix and will require, rather, a *stiffness function* to be considered, as is mentioned in Section 2.5. In addition, we only consider a static, pressure actuated hydraulic amplification device in this argument.

### 2.4.1 A simple spring-based analogy

In this case, as shown in in Figure 2.4, we can write down the following stiffness matrix for the system:

$$\begin{Bmatrix} F_1 \\ F_2 \end{Bmatrix} = \begin{bmatrix} k_c + k_1 & -k_c \\ -k_c & k_c + k_2 \end{bmatrix} \begin{Bmatrix} z_1 \\ z_2 \end{Bmatrix} \quad (2.2)$$

The inverse of this matrix will be the *compliance matrix*. In Equation 2.2 the springs  $k_1$  and  $k_2$  are equivalent to the membrane tether stiffnesses in the hydraulic amplifier depicted in Figure 2.2, and the spring  $k_c$  is related to the *lumped* stiffness of the chamber itself, including the bulk modulus of the fluid as well as the compliance of the tether seals. Note that if

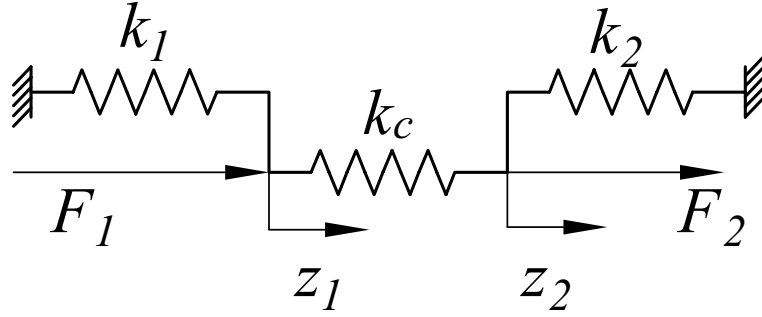


Figure 2.4: A simple three-spring coupler analogy

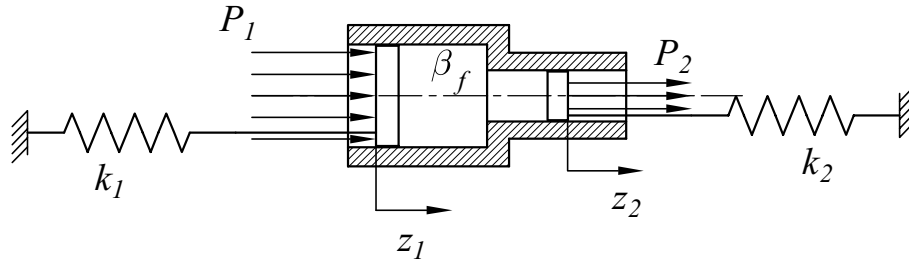


Figure 2.5: An hydraulic amplifier with sliding seals

$k_1 = k_2 = 0$ , the matrix will be singular. In general, soft springs are desirable for  $k_1$  and  $k_2$ , and a hard spring is desirable for  $k_c$ . This implies that, in general, the stiffness matrix will be *almost* singular. In the discussions that follow, both in this chapter, and also in Chapter 6, reference will be made to this fact. However simple it may be, this three-spring analogy proves to be the most useful in understanding and conveying the basic compliance effects that need to be considered when designing and testing an hydraulic amplifier. The paragraphs that follow will look at particular cases in more detail.

### 2.4.2 An hydraulic amplifier with sliding seals

Here an ideal hydraulic amplifier with return springs and a finite fluid bulk modulus is considered, as shown in Figure 2.5. In this case we can say the following about the pressure acting on the large piston:

$$\begin{aligned}
P_1 &= \frac{k_1}{A_1} z_1 + \frac{\beta_f \Delta V_1}{V_c} - \frac{\beta_f \Delta V_2}{V_c} \\
&= \frac{k_1}{A_1} z_1 + \frac{\beta_f A_1 z_1}{V_c} - \frac{\beta_f A_2 z_2}{V_c}
\end{aligned} \tag{2.3}$$

Note that, in this case, the chamber compliance only depends on  $\beta_f$ , the bulk modulus of the fluid. At this point it makes sense to introduce the concept of what can be defined as the *inverse compressibility matrix*, given in Equation 2.4, which gives as result a vector of pressures rather than a vector of forces when it operates on a displacement vector. It can therefore also be called a displacement-pressure operator. In the SI system it has units of  $Pa/m$ .

$$\begin{Bmatrix} P_1 \\ P_2 \end{Bmatrix} = \begin{bmatrix} \frac{\beta_f A_1}{V_c} + \frac{k_1}{A_1} & -\frac{\beta_f A_2}{V_c} \\ -\frac{\beta_f A_1}{V_c} & \frac{\beta_f A_2}{V_c} + \frac{k_2}{A_2} \end{bmatrix} \begin{Bmatrix} z_1 \\ z_2 \end{Bmatrix} \tag{2.4}$$

Note that the inverse compressibility matrix, as shown in Equation 2.4 is, in general, not symmetric. We can proceed to define the stiffness matrix as follows: In Equation 2.5, the effective force on the large piston can be defined.

$$F_{eff,1} = P_1 A_1 = k_1 z_1 + \frac{\beta_f A_1^2}{V_c} z_1 - \frac{\beta_f A_1 A_2}{V_c} z_2 \tag{2.5}$$

Similarly, we can also write the expression for the effective force on the small piston:

$$F_{eff,2} = P_2 A_2 = k_2 z_2 + \frac{\beta_f A_2^2}{V_c} z_2 - \frac{\beta_f A_1 A_2}{V_c} z_1 \tag{2.6}$$

This enables us to define the stiffness matrix for an hydraulic amplifier with sliding seals:

$$\begin{Bmatrix} F_1 \\ F_2 \end{Bmatrix} = \begin{bmatrix} \frac{\beta_f A_1^2}{V_c} + k_1 & -\frac{\beta_f A_2 A_1}{V_c} \\ -\frac{\beta_f A_1 A_2}{V_c} & \frac{\beta_f A_2^2}{V_c} + k_2 \end{bmatrix} \begin{Bmatrix} z_1 \\ z_2 \end{Bmatrix} \tag{2.7}$$

This stiffness matrix is symmetric. Furthermore, it is almost singular, just like the previous

matrices in Equations 2.2 and 2.4.

### 2.4.3 An hydraulic amplifier with flexural seals

We are now ready to consider an hydraulic amplifier of the type investigated in this work. A simplified schematic view is shown in Figure 2.6. In this case the flexural seals contribute to the compliance of the HAC, and it is necessary to revert to the *effective* chamber bulk modulus ( $\beta_c$ ) first introduced in Equation 2.2 to account for this additional compliance. In addition, the flexural seals, or tethers, also act as part of their respective pistons. It therefore becomes necessary to define an *effective* area for the pistons that includes a portion of the tether area. Introducing the changes into Equations 2.4 and 2.7, we obtain the following expressions:

$$\begin{Bmatrix} P_1 \\ P_2 \end{Bmatrix} = \begin{bmatrix} \frac{\beta_c A_{1,eff}}{V_c} + \frac{k_1}{A_{1,eff}} & -\frac{\beta_c A_{2,eff}}{V_c} \\ -\frac{\beta_c A_{1,eff}}{V_c} & \frac{\beta_c A_{2,eff}}{V_c} + \frac{k_2}{A_{2,eff}} \end{bmatrix} \begin{Bmatrix} z_1 \\ z_2 \end{Bmatrix} \quad (2.8)$$

$$\begin{Bmatrix} F_1 \\ F_2 \end{Bmatrix} = \begin{bmatrix} \frac{\beta_c A_{1,eff}^2}{V_c} + k_1 & -\frac{\beta_c A_{2,eff} A_{1,eff}}{V_c} \\ -\frac{\beta_c A_{1,eff} A_{2,eff}}{V_c} & \frac{\beta_c A_{2,eff}^2}{V_c} + k_2 \end{bmatrix} \begin{Bmatrix} z_1 \\ z_2 \end{Bmatrix} \quad (2.9)$$

The use of effective areas in the equations mentioned above brings with it the complication of correctly defining these areas. To correctly define the effective area, one needs to find the equivalent diameter of a rigid sliding piston, as discussed in Section 2.4.2 that will, for a given deflection,  $z$ , produce the same volume change,  $\Delta V$  as a piston with annular flexural seals. In the case where the deflections are small, this approximation is feasible. For large deformations, one will find that the effective area will change throughout the stroke of the piston.

Because all experimental work presented in Chapter 6 was done by means of applying pressure loadings and measuring resultant displacements, we will use the following version of Equation 2.8 from now on:

$$\begin{Bmatrix} P_1 \\ P_2 \end{Bmatrix} = \begin{bmatrix} \beta_c \gamma_1 + \psi_1 & -\beta_c \gamma_2 \\ -\beta_c \gamma_1 & \beta_c \gamma_2 + \psi_2 \end{bmatrix} \begin{Bmatrix} z_1 \\ z_2 \end{Bmatrix} \quad (2.10)$$

Or, in vector-matrix notation:

$$\mathbf{P} = \mathbf{D}\mathbf{z} \quad (2.11)$$

Where, in this inverse compressibility matrix, we note that, for small deflections of either the large piston or the small piston, when they are tested *individually*, and not as part of the coupler, we can write:

$$\begin{aligned} P_1 &= \psi_1 z_1 \\ P_2 &= \psi_2 z_2 \end{aligned} \quad (2.12)$$

And, furthermore:

$$\begin{aligned} \gamma_1 &= \frac{A_{1,eff}}{V_c} \\ \gamma_2 &= \frac{A_{2,eff}}{V_c} \end{aligned}$$

The inverse of this matrix, the compressibility matrix, will then have the form:

$$\begin{aligned} \begin{Bmatrix} z_1 \\ z_2 \end{Bmatrix} &= \frac{1}{\Delta} \begin{bmatrix} \beta_c \gamma_2 + \psi_2 & \beta_c \gamma_2 \\ \beta_c \gamma_1 & \beta_c \gamma_1 + \psi_1 \end{bmatrix} \begin{Bmatrix} P_1 \\ P_2 \end{Bmatrix} \\ \Delta &= \beta_c \gamma_1 \psi_2 + \beta_c \gamma_2 \psi_1 + \psi_1 \psi_2 \end{aligned} \quad (2.13)$$

Or:

$$\mathbf{z} = \mathbf{C}\mathbf{P} \quad (2.14)$$

## 2.5 The nonlinear case

When dealing with large displacements<sup>3</sup>, there no longer exists a stiffness matrix for the hydraulic coupler, but rather, a stiffness function. Or, in the case of pressures and displacements, an inverse compressibility function, as shown in 2.15 and a compressibility function

---

<sup>3</sup>In the case of plate structures, including the tethered piston shown in Figure 1.6, a "large displacement" is typically assumed to be approximately  $> 1/3$  of the plate thickness, in this case  $t_{SOI}$ .

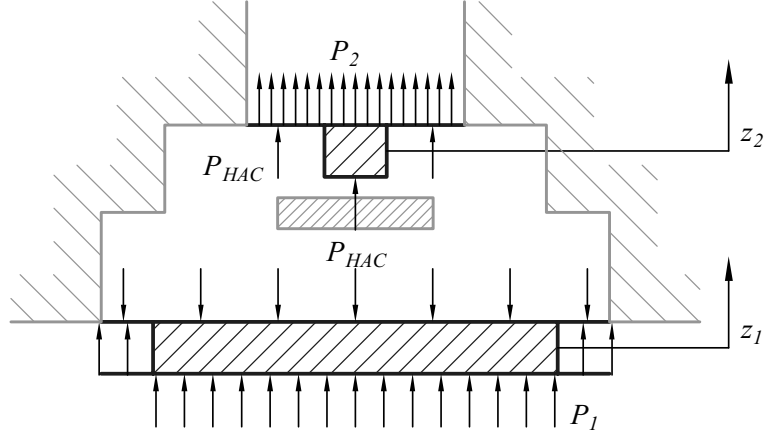


Figure 2.6: A simplified schematic of the static hydraulic amplifier

as in 2.16:

$$\begin{aligned} P_1 &= f(z_1, z_2) \\ P_2 &= g(z_1, z_2) \end{aligned} \quad (2.15)$$

$$\begin{aligned} z_1 &= \tilde{f}(P_1, P_2) \\ z_2 &= \tilde{g}(P_1, P_2) \end{aligned} \quad (2.16)$$

### 2.5.1 Nonlinear modeling and design of the hydraulic amplifier

Expressing the functions  $f, g, \tilde{f}$  and  $\tilde{g}$  shown in (2.15) and in (2.16) in analytical form is not trivial. Indeed, in this work, no closed-form expressions were ever derived for  $f, g, \tilde{f}$  or  $\tilde{g}$ . Using numerical modeling one can, however, evaluate these functions numerically.

Under numerical modeling, we also imply the numerical solution of the large deformation equations for an annular plate with a rigid center boss, as described in detail by Su and Roberts [25],[19]. With the theory described in these references, one can proceed to set up the nonlinear quasi-static model of the hydraulic amplifier in the following manner:

- Model the two tether structures, that is, the small piston tether and the large piston tether, using the nonlinear annular plate theory described in [25] and [19]. Note that the large piston deflections ( $z_1$ ) were small in this work, and a linear plate theory would also have sufficed for the large piston.
- Add additional compliance due to bending and shear of the large piston. Here, a linear thick plate theory, including shear deformation, can be used. The classical reference is Timoshenko [27]. The small piston center boss is assumed to be rigid. This assumption was valid for the geometry used.
- Model the fluid as a closed hydraulic volume with a constant bulk modulus.

We then have a coupled system. The inputs, or "loading" of the system are the two pressures,  $P_1$  and  $P_2$ . The unknown pressure is  $P_{HAC}$ . We know the following:

$$z_1 = f_1(P_1, P_{HAC}) \quad (2.17)$$

$$z_2 = f_2(P_2, P_{HAC}) \quad (2.18)$$

$$P_{HAC} = f_3(\Delta V_f) = \beta_f \frac{\Delta V_f}{V_c} \quad (2.19)$$

We further know that the volume change caused by the large piston, the volume change caused by the small piston and the volume change due to fluid compression must add up to zero<sup>4</sup>:

$$\Delta V_1 + \Delta V_2 = \Delta V_f \quad (2.20)$$

Furthermore, the volume changes can be described by :

$$\Delta V_1 = g_1(z_1) = g_1(f_1(P_1, P_{HAC})) \quad (2.21)$$

$$\Delta V_2 = g_2(z_2) = g_2(f_2(P_2, P_{HAC})) \quad (2.22)$$

$$\Delta V_f = \frac{V_c P_{HAC}}{\beta_f} \quad (2.23)$$

Where we note that  $\Delta V_1$  and  $\Delta V_2$  in (2.21) and (2.22) are now nonlinear functions of the inputs,  $P_1$  and  $P_2$ . The method for obtaining these functions is described in detail in the work by Roberts and Su.

The system in (2.21)-(2.23) can be solved iteratively in a cascaded iteration procedure. Iteration is performed to determine  $\Delta V_1$  and  $\Delta V_2$ , based on the nonlinear plate theory,

---

<sup>4</sup>Where everything that causes a volume reduction of the HAC is considered negative, and everything that causes an increase is positive in this relation.

using an assumed  $P_{HAC}$  as an initial guess. Then, by using Equation 2.20 with a suitable convergence criterium, the final coupled solution can be obtained. The functions for  $\Delta V_1$  and  $\Delta V_2$ , although nonlinear, are well-behaved, and most numerical techniques should work. In this work, a simple bisection method was used<sup>5</sup>. (See, for example [28].)

### 2.5.2 Nonlinear simulation results

Using the techniques described in Section 2.5.1, the two configurations (one or ten small pistons) of hydraulic amplifiers were modeled<sup>6</sup>. Figures 2.7 to 2.10 are the results of simulations on an hydraulic amplifier with one small piston, and Figures 2.11 to 2.14 show the expected behavior of a device with 10 small pistons. *Note:* The results shown here were computed for  $t_{SOI} = 8\mu m$  for the large piston and  $t_{SOI} = 6\mu m$  for the small piston. These values are closer to the measured and expected thicknesses of the actual devices that will be discussed in Chapter 6. It was therefore decided to show results that agree with the model predictions in Chapter 6, rather than results based on the design values mentioned in Section 2.3.2.

By performing suitable interpolation, the functions  $\tilde{f}$  and  $\tilde{g}$ , introduced in (2.16), can be plotted as 2-variable functions in three dimensions. The results are shown in Figure 2.15. These functions will receive some further attention in Chapter 6.

## 2.6 Summary

This chapter briefly addressed the relevant aspects that need to be considered in order to design a flexural seal based hydraulic amplifier. For a more detailed treatment of the design considerations the reader is referred to the works mentioned in Section 2.3.1. In addition, the concept of the hydraulic amplifier as a two-port coupler was introduced. In the linear case, a  $2 \times 2$  stiffness matrix can be defined for this coupler. In the nonlinear case, it becomes two coupled nonlinear functions. Designing a working hydraulic amplifier implies that careful consideration should also be given to the method by which it is going to be fabricated. The next chapter addresses the issues relating to the fabrication and assembly of the MEMS-based hydraulic amplifiers evaluated in this work.

---

<sup>5</sup>The relevant computer codes can be found in Appendix D

<sup>6</sup>D.C. Roberts kindly contributed the results presented in this section.



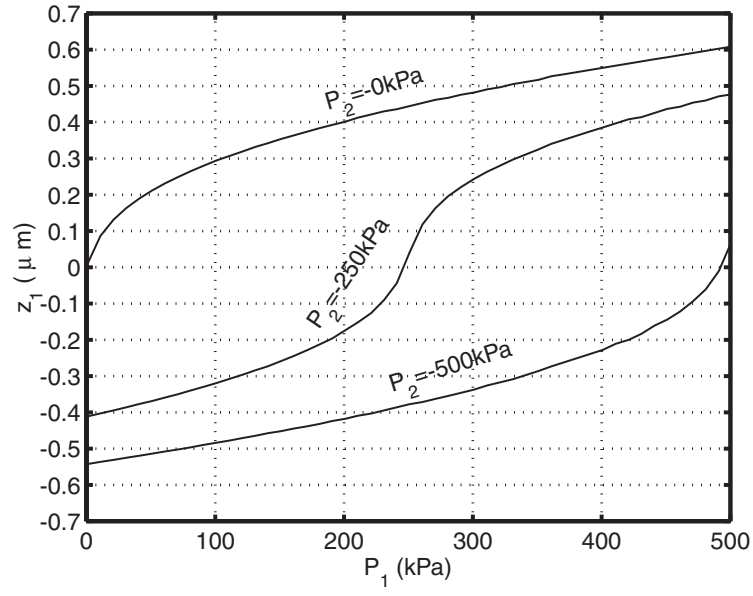


Figure 2.7: Large piston simulation results for an hydraulic amplifier with one small piston.  $t_{SOI,1} = 8\mu\text{m}$ ,  $t_{SOI,2} = 6\mu\text{m}$ .

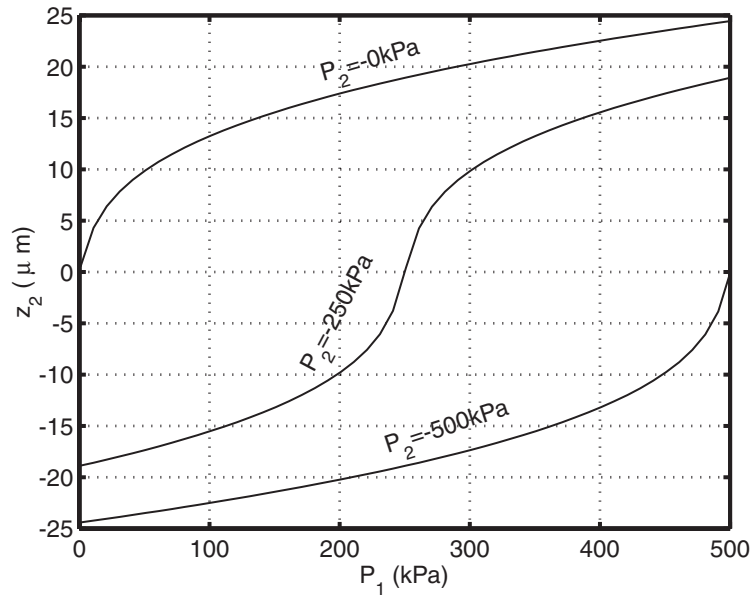


Figure 2.8: Small piston simulation results for an hydraulic amplifier with one small piston.  $t_{SOI,1} = 8\mu\text{m}$ ,  $t_{SOI,2} = 6\mu\text{m}$ .

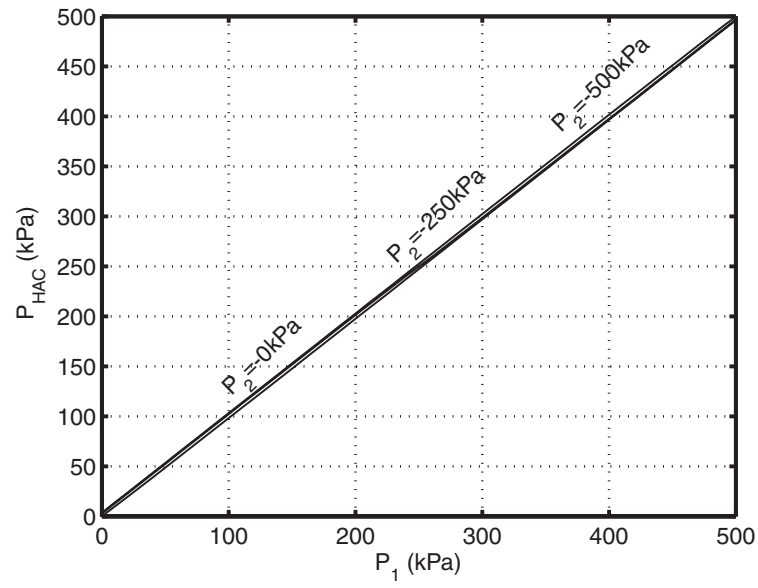


Figure 2.9:  $P_{HAC}$  as a function of  $P_1$  for an hydraulic amplifier with one small piston. Note that the slope of all three lines is approximately equal to 1, indicating that  $P_1 \approx P_{HAC}$ , which proves that the large piston essentially acts as a pressure transfer element for the geometries designed.  $t_{SOI,1} = 8\mu m$ ,  $t_{SOI,2} = 6\mu m$ .

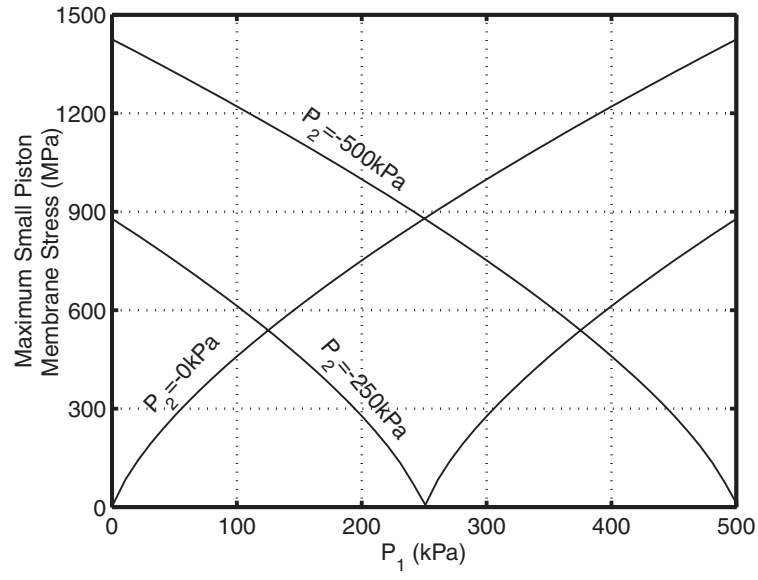


Figure 2.10: Maximum stress in the small piston membrane tether for an hydraulic amplifier with one small piston.  $t_{SOI,1} = 8\mu m$ ,  $t_{SOI,2} = 6\mu m$ .

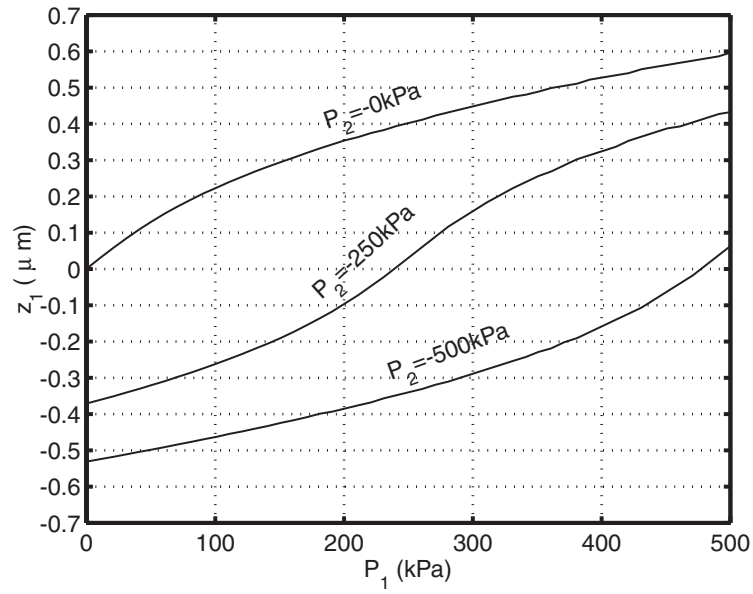


Figure 2.11: Large piston simulation results for an hydraulic amplifier with 10 small pistons.  $t_{SOI,1} = 8\mu m$ ,  $t_{SOI,2} = 6\mu m$ .

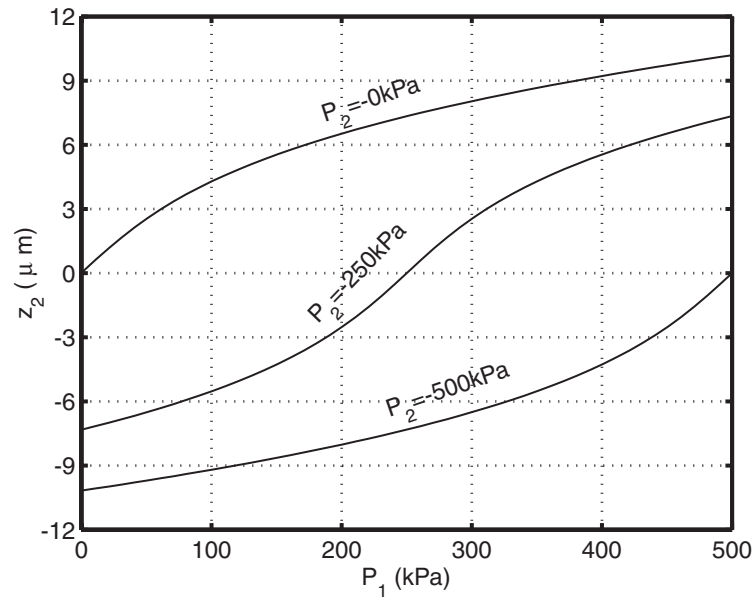


Figure 2.12: Small piston simulation results for an hydraulic amplifier with 10 small pistons.  
 $t_{SOI,1} = 8\mu\text{m}$ ,  $t_{SOI,2} = 6\mu\text{m}$ .

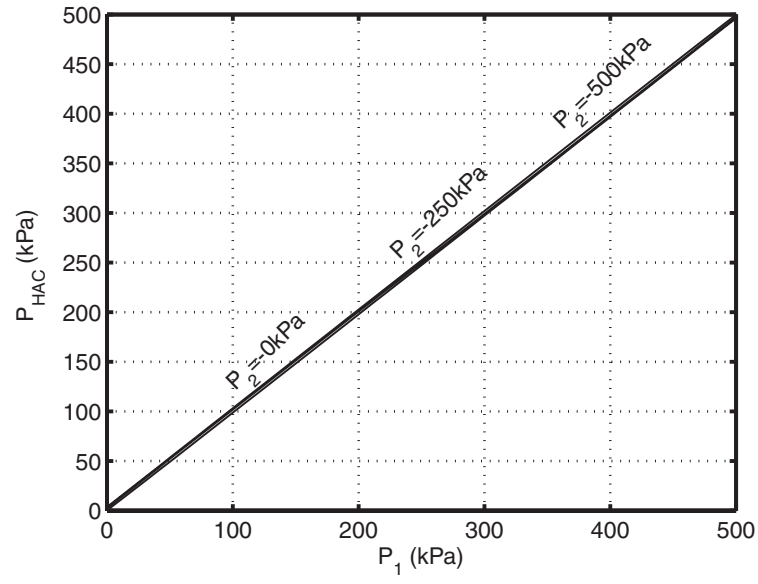


Figure 2.13:  $P_{HAC}$  as a function of  $P_1$  for an hydraulic amplifier with 10 small pistons. Note again that the slope of all three lines is approximately equal to 1, indicating that  $P_1 \approx P_{HAC}$ , which proves that the large piston essentially acts as a pressure transfer element for the geometries designed.  $t_{SOI,1} = 8\mu m$ ,  $t_{SOI,2} = 6\mu m$ .

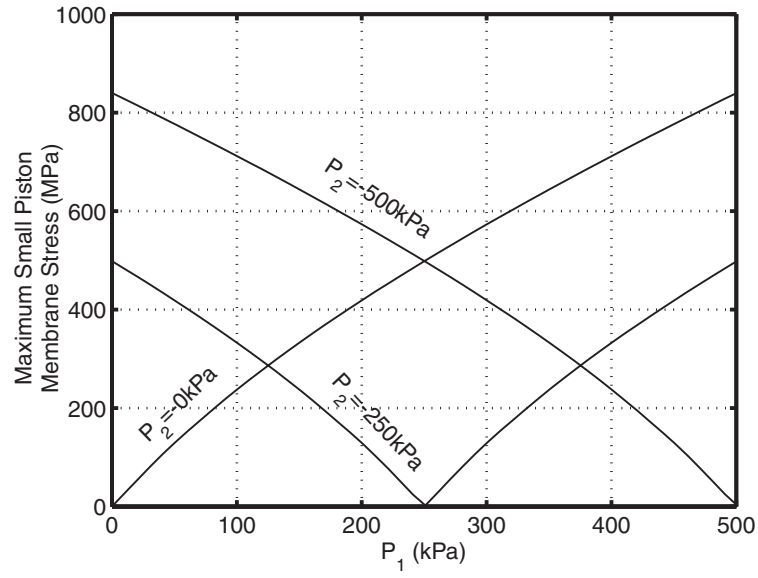


Figure 2.14: Maximum stress in the small piston membrane tether for an hydraulic amplifier with 10 small pistons.  $t_{SOI,1} = 8\mu m$ ,  $t_{SOI,2} = 6\mu m$ .

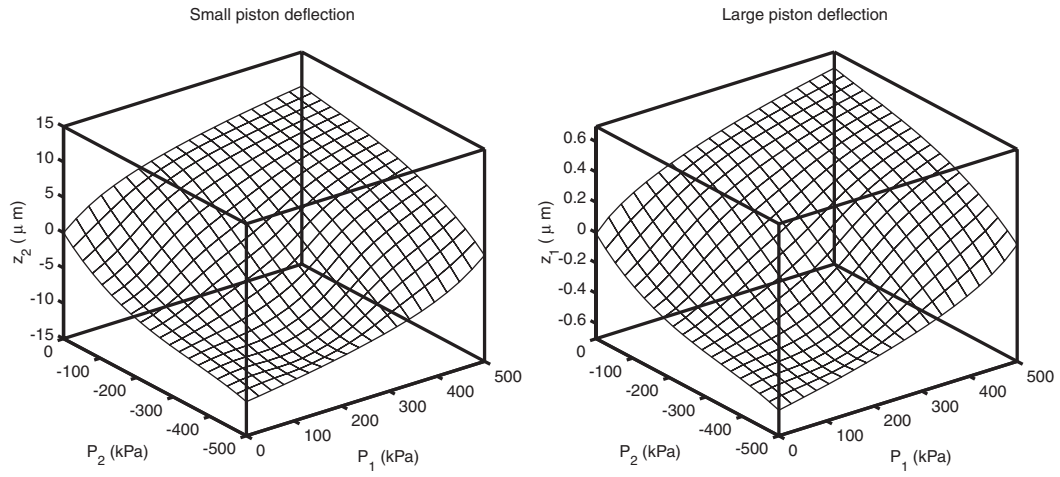


Figure 2.15: Small and large piston deflections as functions of both  $P_1$  and  $P_2$  for a device with 10 small pistons. These two graphs can be seen as numerical representations of  $\tilde{g}$  and  $\tilde{f}$  of Equation 2.16.

# Fabrication and device assembly

---

Effective fabrication of a fluidic-based power MEMS device is often a complex task. In many cases, where conventional micromachining technology is used, through-wafer etching is required. In addition, multiple layers are usually needed to create the desired three-dimensional structures that would make up a device consisting of moving parts, flow channels, inlet and outlet ports and electrical connections. In [22] an interesting example of such a multi-faceted process is presented. This chapter will address the fabrication techniques that were used to produce the hydraulic amplification devices evaluated in this work.

## 3.1 Fabrication overview

In Chapter 2 the two types of devices investigated in this document were introduced. For both devices shown in Figure 2.2, the fabrication process required to produce a device can be divided into the following major subtasks:

- Silicon tethered membrane fabrication, using Silicon-On-Insulator (SOI) wafers.
- Structural silicon layer fabrication. Double-side polished wafers are used for this purpose.
- Glass layer fabrication by ultrasonic machining. The glass used was *Pyrex*<sup>TM</sup> 7740 by Corning.
- Wafer scale fusion bonding of silicon-silicon wafer pairs and anodic bonding of silicon-glass wafer pairs.
- Die-level alignment and anodic bonding to complete the assembly.

In the case of the piezoelectrically driven device, a piezoelectric element has to be integrated during the final bond step. For more information, the reader is referred to [19] and to [29].

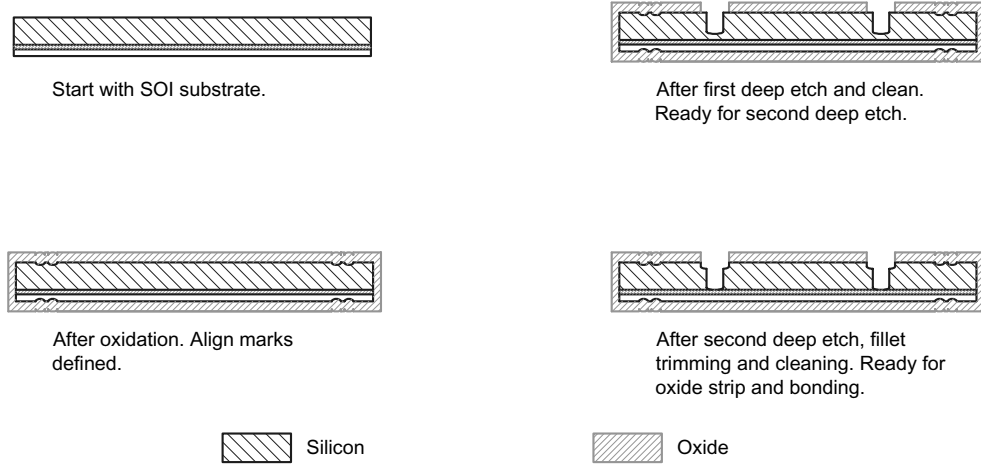


Figure 3.1: Selected steps of the process required to produce a tethered silicon membrane structure.

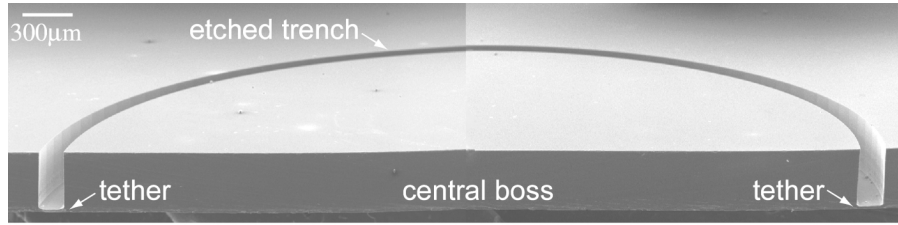
### 3.2 Process flow for creating silicon membrane structures

Figure 3.1 depicts the process used to produce the silicon membrane structures used in the devices characterized in this work<sup>1</sup>. A scanning electron micrograph of such a structure is shown in Figure 3.2. The process flow for creating a structure like this from an SOI substrate can be summarized in the following steps [30]:

1. Start with a Silicon on Insulator (SOI) wafer, double side polished. Device layer thicknesses of  $7\mu m$  to  $10\mu m$  were used. The wafer thicknesses ranged from 300 to  $400\mu m$ .
2. Grow first layer of protective thermal oxide at  $1100^\circ C$ ,  $0.6\mu m$  thick.
3. Pattern align marks on both sides, using OCG825 standard thin photoresist. Etch in 7:1 Buffered Oxide Etch (BOE).
4. Etch align marks in Silicon using reactive ion etching (RIE)..
5. Grow second layer of protective thermal oxide at  $1100^\circ C$ , to a total thickness of  $1.7\mu m$ .
6. Pattern oxide using BOE, to define the nested mask

<sup>1</sup>For corresponding mask sets, the reader is referred to Appendix E





*Courtesy of K.T. Turner. Created from two separate images.*

Figure 3.2: Scanning Electron Micrograph (SEM) of a prototype large piston. This piston was cut in half for illustrative purposes. Also note that this piston was fabricated using a single deep etch. No stepped features are visible on the sidewalls.

7. Recoat with photoresist, using Clariant AZ4620 thick photoresist. A thickness of approximately  $10\mu m$  after baking is desired. Define the first Deep Reactive Ion Etching (DRIE) etch mask. Mount the wafer on a handle substrate using AZ4620 photoresist.
8. Perform the first deep etch using an STS ICP DRIE tool <sup>2</sup> to approximately  $20\mu m$  away from the buried oxide. Dismount wafer in acetone and strip photoresist using a process consisting of burning the organic materials in an oxygen plasma ("ashing") and performing a chemical cleaning step, using a mixture of 3 parts  $H_2SO_4$  added to 1 part of  $H_2O_2$  ("Piranha cleaning").
9. Remount wafer on handle substrate and perform the final etch.
10. Dismount in acetone, and clean using again ashing and piranha. Just prior to fusion bonding, the oxide would be stripped with BOE and an RCA cleaning step would be performed.

The procedure described above will allow the fabrication of a basic tethered silicon membrane structure. It has been found that some amount of exposed silicon outside of the etched membrane features, as provided by the nested mask process, tends to simplify the fillet radius control procedure somewhat. This procedure is described in Section 3.2.1.

Additional features, e.g. flow channels, can be defined in the nested mask and the nested mask etch depth can be tailored (within the bounds of the wafer's structure) to suit the requirements of the features needed. Figure 3.3 shows two examples of what can be achieved

<sup>2</sup>Please refer to Appendix B for non-standard fabrication tools used.

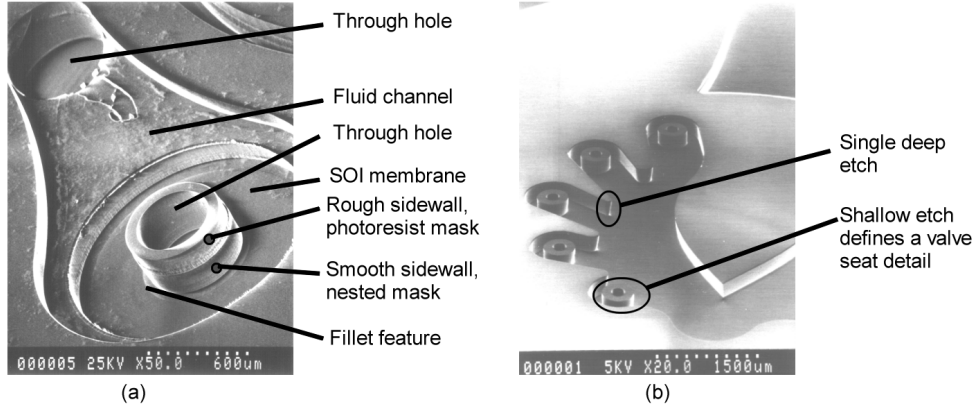


Figure 3.3: SEM images of typical channel structures that can be realized with a nested mask process. (a) depicts a checkvalve, as was used in the pump described in [15]. (b) shows a ten-valve manifold of the MHT device shown in Figure 1.1. This manifold has undergone its first deep etch, and is ready for the nested mask etch. Numerous shallow etches can be used, as is shown here, to define additional shallow features.

using the nested mask process. Note that in addition to the two deep etches allowed by the nested mask process, additional shallow features can be added. The depth of these shallow features is limited by the lithographic process. In this work it has been found that features deeper than approximately  $20\mu m$  (and of in-plane dimensions greater than  $\sim 500\mu m$ ) will not be well suited to an additional lithography step involving the spin-casting of photoresist and subsequent exposure. Another interesting observation is that the nested mask, a hard  $SiO_2$  mask, will generally provide a smoother sidewall than the initial photoresist mask. This can be attributed to a phenomenon sometimes referred to as "micromasking", where photoresist is removed from the top of the substrate by the DRIE process, and subsequently redeposited on the trench walls, leading to sidewall roughness.

### 3.2.1 Membrane fillet radius control

An aspect not addressed until now has been the nature of the fillet feature (See Figures 3.4 and 3.5) at the bottom of the etched trench after the final DRIE etch described above. It has been shown [29] that a proper fillet feature is critical when high strength membrane tethers are desired, as is the case for the MHT device. Attaining a good fillet feature can be a daunting task, primarily due to a combination of the following two effects:

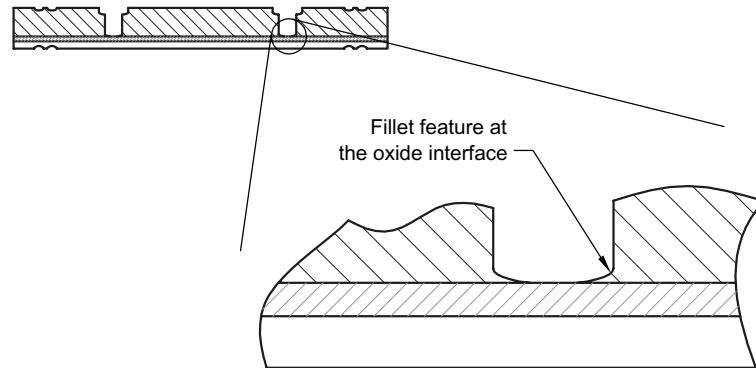
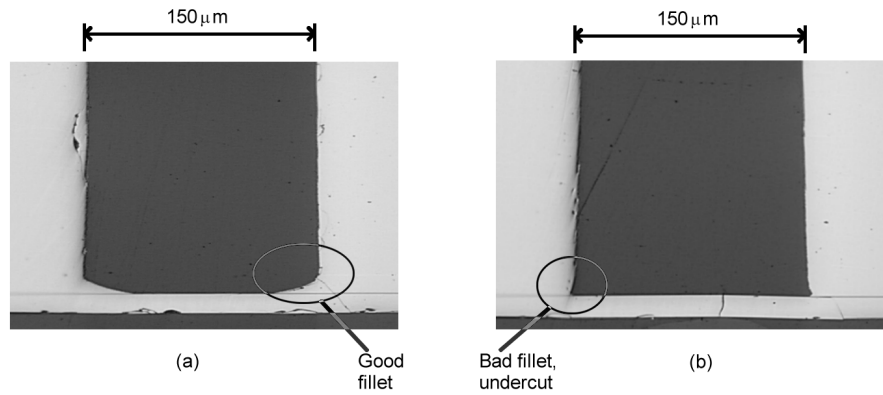


Figure 3.4: Idealized fillet feature at the bottom of the etched trench.



*Courtesy of K.T. Turner.*

Figure 3.5: Two possible outcomes after etching an SOI membrane using DRIE: (a) Good fillet feature obtained by proper timing of the deep etch and (b) an undercut fillet feature. Undercut will cause a stress concentration, significantly reducing the strength of the structure.

- Nonuniformity in the DRIE etching using current DRIE technologies.
- The natural tendency of the DRIE process to undercut and produce a "footing" feature, rather than the desired fillet feature, when the buried oxide etch stop is reached as is shown in Figure 3.5. (For an explanation of this phenomenon, see, for example, [31].)

In this work, the membranes were fabricated using an iterative process involving multiple etching and inspection steps for the width of these membranes. The membrane widths were estimated during processing using a microscope with a calibrated reticle. Membrane width was found to be the preferred parameter for fillet radius quality control, rather than the fillet width itself, due to difficulties associated with properly estimating the endpoint of the fillet.

Should, upon inspection, it be found that a particular membrane was properly etched, this membrane would then be covered with OCG825 photoresist using a bent wire to deposit a droplet of photoresist on the feature. The photoresist would then be baked for approximately 5 minutes, after which a second coating of photoresist would be applied, and another baking step for approximately 10 minutes would follow. Afterwards, the wafer would be returned to the DRIE tool for further etching.

This procedure would be repeated until all the membranes have been fully etched. After this step, the wafer would be prepared for fusion bonding.

It has also been shown that surface roughness can have a significant effect on the effective fracture strength of silicon, due to the fact that it is a brittle material with no plastic deformation at room temperature [32]. On the large piston tether membranes, the decision was made to switch to an isotropic etch recipe in the DRIE process in an attempt to further improve the surface finish of the fillet features. Tolerance constraints did not allow this procedure to be performed on the small piston membrane tethers.

### 3.3 Silicon fusion bonding techniques

Silicon fusion bonding is the process by which two silicon substrates having surfaces with roughness no greater than  $10\text{\AA}$  and minimal bow are brought into intimate contact. Van der Waals forces keep the wafers in contact. Subsequent annealing at temperatures above

1000°C will result in a bond strength approaching that of single crystal silicon [33]. For successful fusion bonding, substrate surface finish and cleanliness is of the utmost importance.

The devices evaluated in this work required two separate wafer-scale silicon-silicon fusion bonding steps to be performed:

- Bond Layers 4 and 5 to form a double-tethered piston structure. (For the layer numbers, see Figure 2.2)
- Bond Layer 7, the membrane layer, to Layer 8, the fluid channel layer that provides a pressurization path to the top of the membranes, and also forms a proper "clamped" boundary condition for the membrane tether.

The bond between Layers 4 and 5 proved to be challenging, due to the very compliant nature of the wafers being bonded. Figure 3.6 illustrates the large amount of material removed from these wafers during processing. To prevent these wafers from becoming stuck during alignment prior to bonding, it was necessary to increase the separation of the wafers from the 75 $\mu$ m normally used to approximately 150 $\mu$ m. All silicon fusion bonds were performed using an Electronic Visions EV450 aligner and AB1-PV bonder.

## 3.4 Anodic bonding techniques and die-level assembly

### 3.4.1 Wafer-scale anodic bonding

Due to electrical constraints in the full MHT device, it was required that the three large pistons of this device, as well as their lower electrodes, be fully electrically insulated from each other. The insulation was accomplished by etching a Y-shaped trench in each die. This enabled the three pistons to be insulated after die-sawing [30]. See Figure 3.6 and also Figure 1.3.

This feature required that Layers 4 and 5 in Figure 2.2 be anodically bonded to Layer 6 on the wafer scale prior to dicing. For the same reason, Layers 1 and 2 had to be bonded on the wafer scale for the piezoelectrically driven devices. In this particular case, it was crucial to ensure a proper surface finish on the glass after bonding to allow subsequent bonds to be performed in order to create a multi-layered sandwich structure.

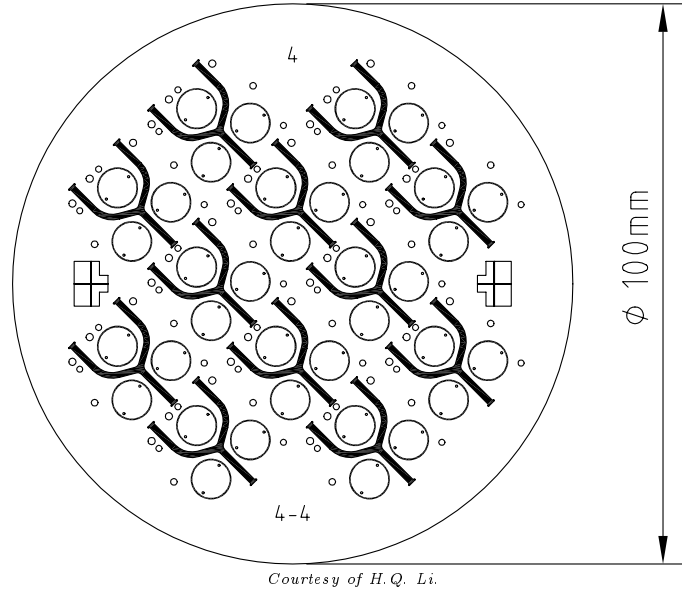


Figure 3.6: Deep etch mask for Layer 4. Note the Y-shaped trenches on each die. Removing large amounts of material may result in excessive wafer bow and problems with pre-alignment stiction.

Figure 3.7 illustrates the basic principle of anodic bonding. An anodic bond between silicon and a suitable glass (for example, *Pyrex*<sup>TM</sup> 7740) is formed by placing a smooth silicon surface in contact with a smooth glass surface. Thereafter, this silicon-glass stack is heated to mobilize the ions in the glass. An electric field is then applied across the glass by contacting the silicon and glass layers. This field acts to draw sodium ions away from the bond interface, leaving behind oxygen ions which then bond to the silicon, forming  $SiO_2$  [33]. The applied field also has the effect of causing an electrostatic attraction between the silicon and glass layers, ensuring intimate contact. Note that this field effectively acts only across the depletion zone shown in Figure 3.7, and the attraction is therefore quite strong.

From Figure 3.7 it should be clear to the reader that the sodium ions migrating away from the bond interface will eventually manifest themselves as a sodium compound ( $NaOH$ ) on the glass surface [34]. This accumulation of sodium is generally associated with surface damage. To minimize this damage, it was found to be necessary to create a uniform smooth and flat graphite electrode as a contact to the glass layer. It was found that any surface irregularities in the electrode would exacerbate the accumulation of sodium compounds in the regions of those irregularities.

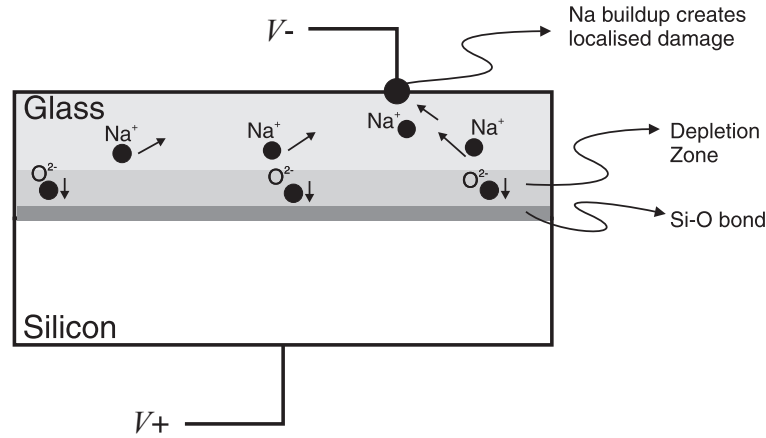


Figure 3.7: The basic principle of anodic bonding.

When assembling multi-layer Si-glass sandwich structures, it is also important to bear in mind that the bond time should be long enough to ensure a complete bond, but no longer. Any additional time after the bond is complete will once again only tend to exacerbate the accumulation of unwanted sodium on the electrode side of the glass. In addition, when performing the second anodic bond, it is possible to use the first bonded silicon layer as the glass contact for this bond. In this case, particular care should be taken not to overbond, as one will run the risk of forming precipitates in the glass, observed as brown speckles. A further discussion of this phenomenon is found in [35]. With all anodic bonding performed for the hydraulic amplification devices, it was found to be very useful to monitor the bond current during the bond. Usually, the bond was assumed to be complete when the current had fallen to approximately  $1/8$  of its initial value.

In all anodic bonding performed, both on the wafer level and the die level, a voltage of  $1000V$  was used, at a temperature of  $300^\circ C$ . The bond time depended on the thickness of the glass layer which ultimately determined both the field strength and the amount of sodium that had to be transported. In all cases, the  $1/8$  value criterium was used. All bonds were performed at atmospheric pressure, except for the final die-level bond on the piezoelectrically driven devices. This bond had to be performed in a reducing atmosphere [29].

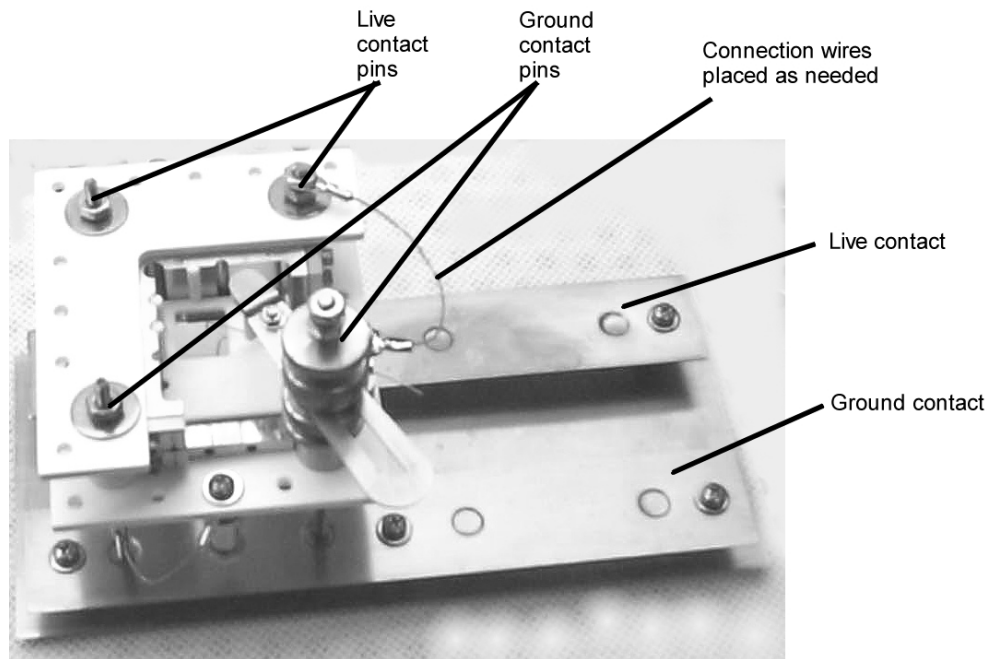


Figure 3.8: Anodic bonding jig.

### 3.4.2 Die-level assembly

To complete the assembly of an hydraulic amplification device, it was required to anodically bond, on the die level, the following sets of layers (See, again, Figure 2.2):

- Layers 1 and 2, wafer scale bonded anodically.
- Layer 3 - a seperate glass layer.
- Layers 4, 5 and 6, fusion bonded and anodically bonded on the wafer scale.
- Layers 7 and 8, fusion bonded on the wafer scale.
- Layer 9 - another seperate glass layer.

To facilitate alignment on the die-level, an alignment jig, shown in Figure 3.8 was built. (See Appendix C for the detail design of this jig.) This jig relies on 2D kinematic alignment of dies, and requires that all dies be the same size. This feat is accomplished by ensuring



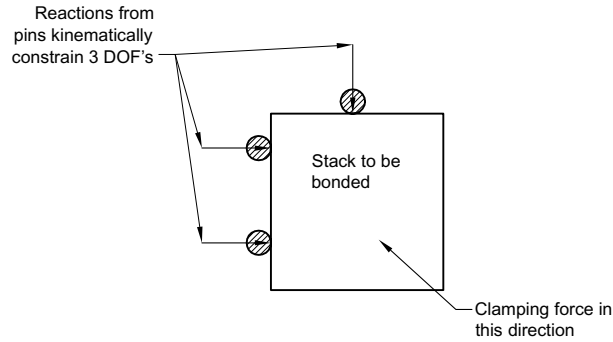


Figure 3.9: Three-point alignment as used in the anodic bonding jig. The three pins were made from glass-mica machineable ceramic.

that all dies are cut with the same blade during the dicing operation. The jig has three pins that allow the dies to be pushed into an alignment corner, as shown in Figure 3.9. This ensures that the three degrees of freedom are constrained. Figure 3.10 shows the jig with a device that is being bonded. The clamping, contacts and alignment pins are all visible.

The following bond sequence was used in the assembly:

1. Bond the Layer 1-2 pair to Layer 3.
2. Bond Layer 9 to the layer 7-8 pair.
3. Bond the stack of Layers 4-5-6 to Layers 7-8-9
4. Finally, bond the lower part of the device, Layers 1-2-3, to the upper part, Layers 4-5-6-7-8-9.

In the case of the piezoelectrically driven hydraulic amplifiers, the final anodic bond was performed together with a solder bond to attach the piezoelectric element to the large piston of the hydraulic amplifier. This procedure is described in detail in [19] and [29].

Figure 3.11 shows a fully assembled hydraulic amplifier.

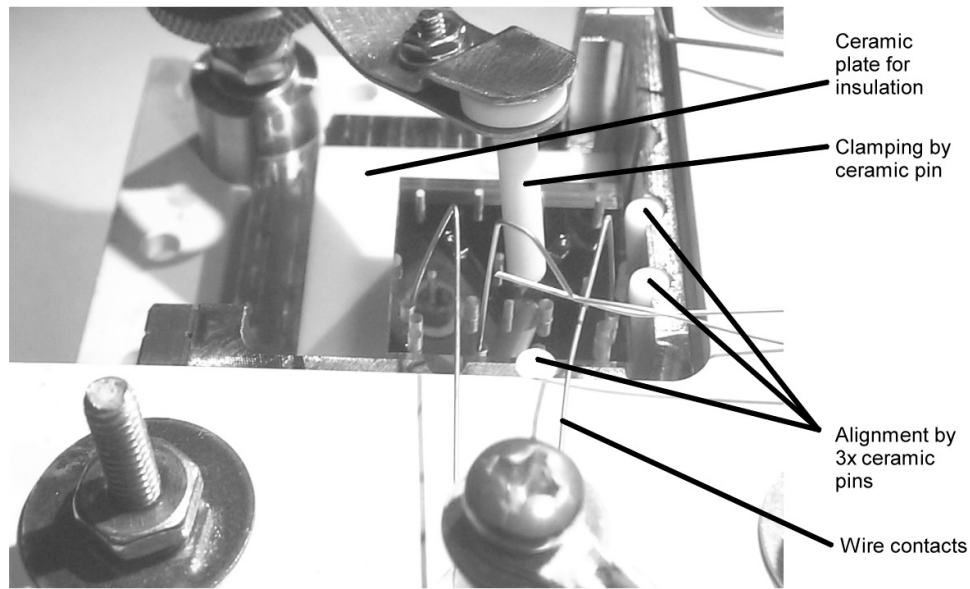


Figure 3.10: Close-up of the anodic bonding jig, with a device being bonded. Note the alignment by alignment pins, the wire contacts, the clamping method and the insulation.

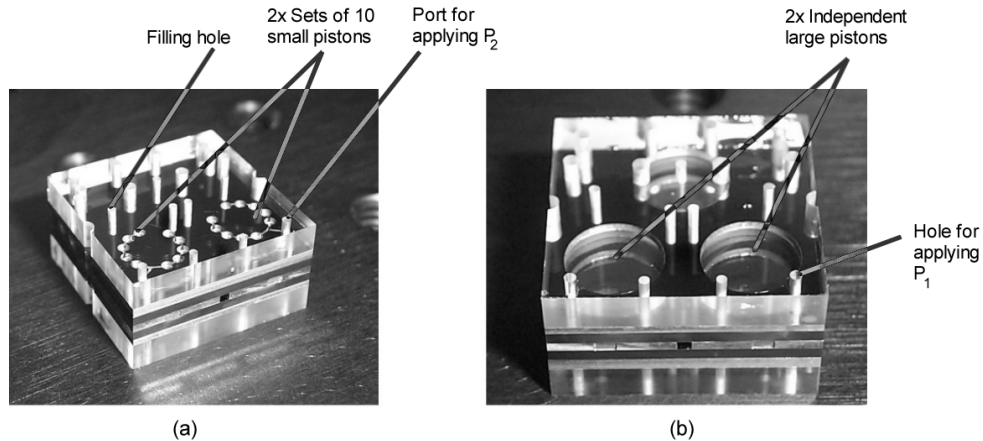


Figure 3.11: Assembled static hydraulic amplification device with ten small pistons and one large one. Each such stack contains two independent hydraulic amplification devices. (a) Shows a top view, with the two sets of ten small pistons, and (b) a bottom view, with the two large pistons. Note the third piston, which is not used for this device, but only for the full MHT device mentioned in Chapter 1.

## 3.5 Summary

In this chapter we looked at a typical process flow for producing a multi-layered silicon-glass bulk micromachined hydraulic amplification device. To build a device such as shown in Figure 3.11, it was necessary to develop, in addition to what can be considered a "conventional" DRIE-based process flow, techniques for:

- Controlling the fillet radii of deep etched trenches in SOI wafers and
- Wafer-level and die-level aligned anodic bonding to create silicon-glass sandwich structures.

After assembly, the hydraulic amplification device is still in a particulate-free condition. The next step, before operating the device, involves filling and sealing of hydraulic amplification chamber. These procedures are described in Chapter 4.



# Filling and sealing techniques

---

In Chapter 2 it was shown that, for effective hydraulic amplification, compliance of the system needs to be minimized. Hence, reliable filling and sealing techniques were required to ensure the stiffest hydraulic amplification chamber possible. This chapter describes filling techniques initially developed by Boston MicroSystems [36], and further refined for the particular devices tested here. It also addresses the sealing techniques that were developed to properly seal the hydraulic amplification chambers for either static or dynamic sealing purposes.

## 4.1 Filling techniques

### 4.1.1 Fluid requirements

For the full MHT device, the working fluid had to satisfy the following requirements [36]:

- Low viscosity, for minimal viscous losses.
- High bulk modulus, for minimal compliance.
- Should wet silicon surfaces well, to ease filling of small cavities.
- Should be dielectric, due to the high voltage operation of the device.

Based on these requirements a volatile silicone oil, Hexamethyldisiloxane (Produced by Dow Corning under the trade name DC200 0.65cst), was chosen as the system fluid. This was also the fluid used in all hydraulic amplifiers tested in this document. This is based on the assumption that the filling procedure used to fill the HAC's would also be used to fill the device itself at the same time, requiring that the fluid in the HAC be the same as the fluid

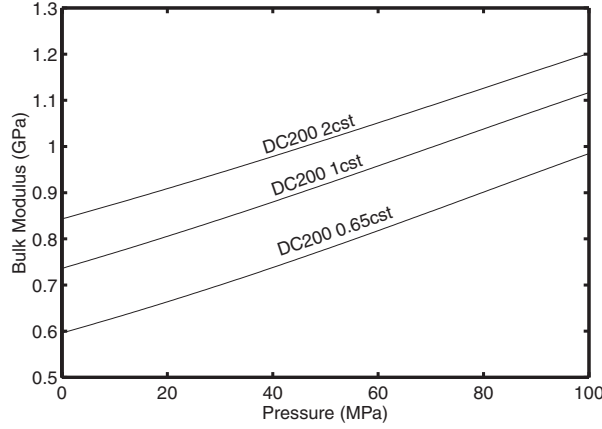


Figure 4.1: Bulk modulus vs. fluid pressure for a selection of volatile silicone oils, adapted from data as supplied by Dow Corning [37]. Note that the amount of outgassing performed on these fluids is unknown.

in the device. In other applications, or using different filling techniques, this requirement of using one type of oil for the whole MHT system could probably be relaxed.

The properties of various silicone oils indicate that there is a tradeoff between viscosity and bulk modulus. This is also shown in Figure 4.1. In the case where it is possible to use a different fluid in the HAC, it might pay off to investigate slightly more viscous fluids with higher bulk moduli. Note, however, that filling of the HAC, as described in the previous section, relies on the working fluid also possessing a high vapor pressure. This requirement eliminates most of the high viscosity oils. (See Figure 4.2)

#### 4.1.2 Filling process

To ensure bubble-free filling of the HAC, a filling system and associated filling process was developed. Figure 4.3 shows a schematic of the apparatus and Figure 4.4 is a photograph of the same apparatus.

To fill and seal an HAC, the following process was developed:

1. Set the initial condition of the system: All valves closed.
2. Open Tank B, and place the device test jig (Discussed in Chapter 5), as well as the

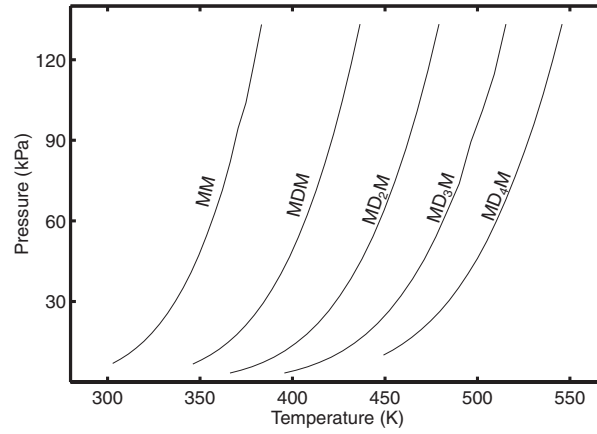


Figure 4.2: Vapor lines for a selection of linear siloxanes, adapted from [38]. The graphs show the vapor lines for Hexamethyldisiloxane ( $MM$ ), Octamethyltrisiloxane ( $MDM$ ), Decamethyltetrasiloxane ( $MD_2M$ ), Dodecamethylpentasiloxane ( $MD_3M$ ) and Tetradecamethylhexasiloxane ( $MD_4M$ ). Dow Corning DC200 0.65cst consists of  $MM$  and trace impurities. The other viscosities may contain blends of the compounds mentioned above.

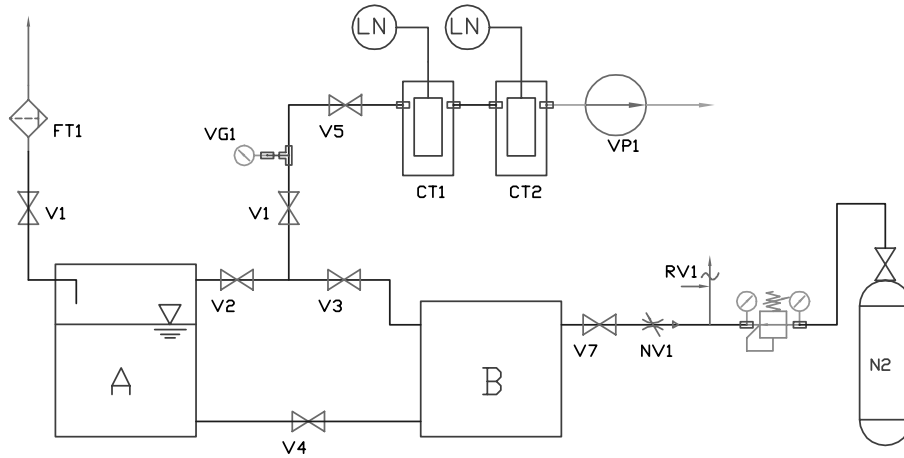


Figure 4.3: Schematic representation of the filling system



Figure 4.4: The fluid filling system. The cold traps are not shown in this photograph.

device, inside. Do not mount the device in the jig yet. This will be done after filling. Also do not install any o-rings in the jig. They are installed after filling. Close Tank B.

3. Start vacuum pump VP1.
4. When sufficient vacuum has been attained in the cold traps, CT1 and CT2, fill CT1 and CT2 with liquid nitrogen. Open ball valves V5 and V1.
5. *Substep if Tank A is not already filled with silicone oil:* Connect silicone oil reservoir (not shown) to Tank A via V6. FT1 will filter the inlet stream. Open V6 and V2. This will draw the silicone oil into Tank A, and simultaneously outgas the oil. Dissolved gases tend to reduce the effective bulk modulus of the oil, an undesired effect. After Tank A is filled, Close V6 and V2. Disconnect silicone oil reservoir and vent Tank A to atmosphere through V6.
6. Open V3. Evacuate Tank B to  $5\text{mmHg}$  or less.
7. *Vapor purging step:* Slowly open V4 and allow a small amount of silicone oil to flow into Tank B. In this case, a fluid level of approximately  $10\text{mm}$  was used in Tank B. Close V4.
8. Continue pumping on Tank B for approximately 90 minutes. All of the oil in Tank B



should have evaporated, and would have been caught in CT1. Ensure that Tank B is at a pressure of  $5\text{mmHg}$  or less.

9. *Filling:* Close V3. Slowly open V4 and allow the fluid to submerge the jig and the device. Close V4 when the contents of Tank B are submerged.
10. *Pressurising:* Open V7 and needle valve NV1. Adjust the regulator, APR1, to provide an absolute pressure of  $1.5\text{atm}$ . This will ensure that the pressure in the HAC asymptotes to a slightly higher pressure than atmosphere.
11. Reduce the pressure in Tank B to  $1\text{atm}$  absolute pressure, and open Tank B.
12. With the device and the jig still submerged, insert the o-ring seals into the jig, mount the device and clamp to seal.

#### 4.1.3 Initial tests

In this work it was necessary to fill a dead volume of approximately  $8.3\text{nl}$  through a channel of dimensions  $10\mu\text{m} \times 10\mu\text{m} \times 1\text{mm}$ . The motivation for this channel will be discussed in Section 4.2.2. The nature of the design of the hydraulic amplification devices prevented any visual inspection of the HAC for bubbles after filling. It was therefore essential to verify the filling procedure described in Section 4.1.2, and to ensure that it was very robust. To this end, a set of experimental devices was fabricated in such a manner that the filling procedure could be seen through a suitable glass window. A device consisting of a glass-silicon-glass sandwich structure was fabricated using DRIE and a simple two step lithography process. A completed filling test chip is shown in Figure 4.5. Assembly was performed on the die level, using simultaneous anodic bonding of the top and bottom glass layers. In this case, conventional machining, using diamond tools, was used to drill holes in the top glass layer.

Using the procedure as described above, and visually monitoring the filling of each chamber using a microscope, it was verified that bubble-free filling could be obtained. The filling time after initiating the pressurization step was found to be approximately 7 minutes. After this time, no visible bubbles were detected. Two of these devices were assembled, giving a total of four chambers to be filled. Both chips were filled successfully on the first attempts to fill them. These results provided the needed confidence to fill and test the full hydraulic amplification devices.

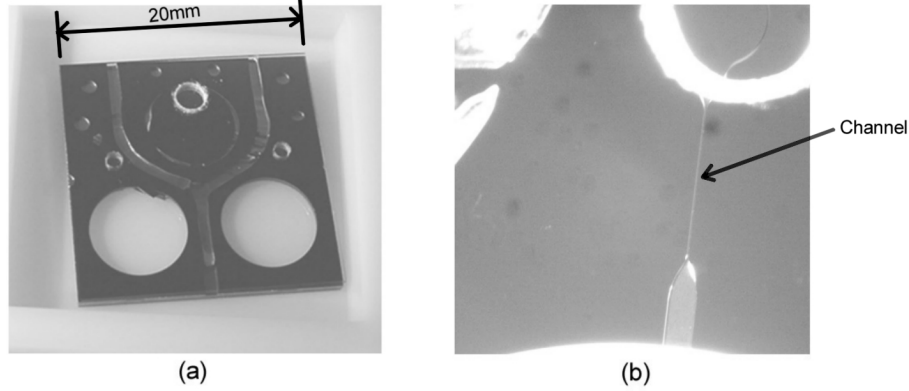


Figure 4.5: (a) Experimental filling test chip with two  $10\mu m \times 10\mu m \times 1mm$  channels and matching dead volumes. (b) Detail of the filling channel. The dead volume had to be evacuated through this channel prior to filling.

## 4.2 Sealing concepts

Sealing of an hydraulic amplifier can be challenging. As discussed in Chapter 2, one would like to maximize the stiffness of the hydraulic coupler. This also means that any imposed volume change, as might be introduced by a seal pressing against an opening and subsequently bulging could introduce a large pressure increase in the hydraulic amplification chamber. (See Figure 4.6a ). This led to the development of two sealing strategies for the two different types of tests performed on the hydraulic amplifiers evaluated in this work. The first type is a traditional static seal, as described above, and the second type, for high frequency hydraulic amplifiers, is a dynamic seal relying on a flow restriction.

### 4.2.1 Static sealing

For static sealing of the hydraulic amplifiers a seal consisting of a teflon sheet,  $125\mu m$  thick, backed by a brass plate and preloaded with an o-ring was used, as illustrated in Figure 4.6b. This method enabled reliable sealing of the hydraulic amplifiers while giving minimal seal compression and volume change in the HAC, even with a sealing hole diameter in the glass layer of  $800\mu m$ . Should seal compression be of greater concern, the sealing hole diameter can be further reduced by micromachining the inlet port to the HAC [30].

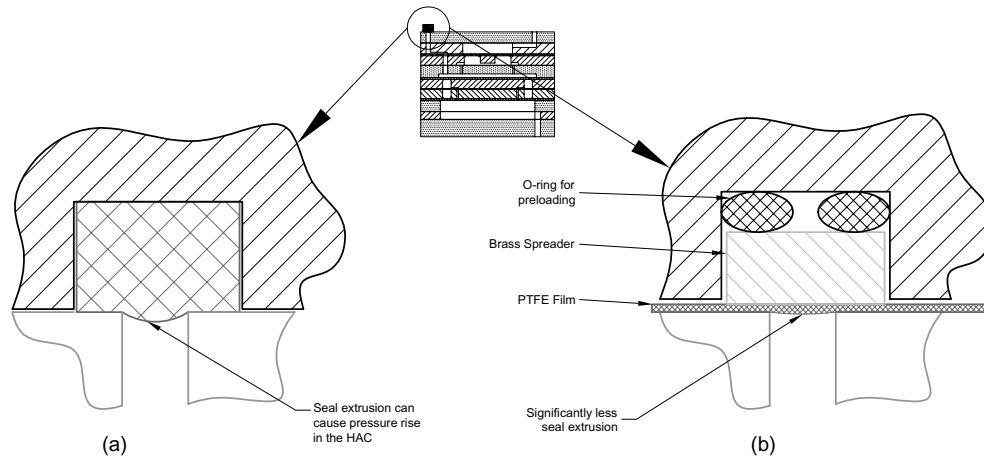
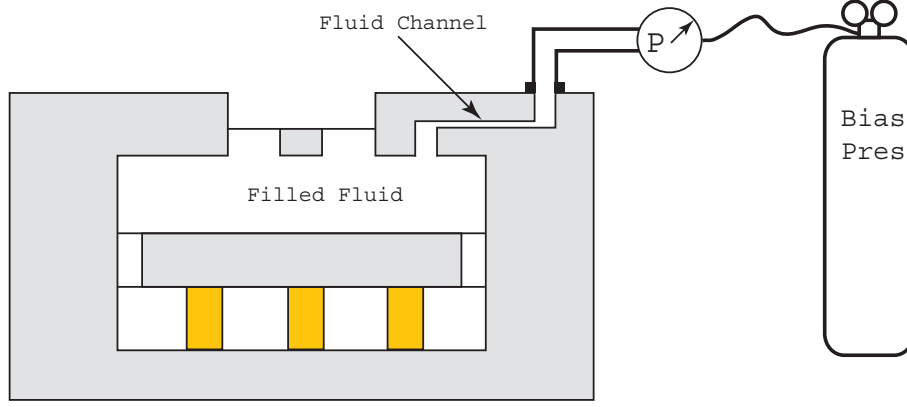


Figure 4.6: Static sealing of the hydraulic amplifier: a) The basic concept of an elastomeric or plastic seal. Seal compression could introduce large pressure changes in the HAC. b) Using a PTFE film for sealing, with a load spreader and a preloading element.

### 4.2.2 Dynamic sealing

If the hydraulic amplifier is to be operated only at high frequencies, another sealing technique can be used. By providing a suitable flow restriction on the inlet port to the HAC, it can be shown that high frequency pressure fluctuations generated by the large piston inside the HAC will not be transmitted to the outside. This restriction will have the effect of a low pass filter, allowing low frequency pressure variations to enter and leave the HAC. Using this sealing technique, the concerns related to seal compression are eliminated and it becomes easier to control the static pressure in the HAC. These benefits come at the cost of an external pressurization system that must be added to the device. For experimental purposes, this was not a concern. Figure 4.7 illustrates the basic principle. In addition, the external pressurization system provides the benefit of setting a constant pressure bias in the HAC. This in turn allows for balancing of the steady-state pressure on the small piston, and can also be used to control the static position of the small piston, should an offset be desired as, for example, in the case of a valve [19]. Furthermore, placing a bias pressure on the HAC reduces the likelihood of cavitation that could be induced by high frequency operation of the large piston.

A simple way to design this type of seal is to assume it to be a channel of suitable dimensions, containing a fluid slug. (See Figure 4.8.) By selecting the appropriate boundary conditions



*Courtesy of D.C. Roberts*

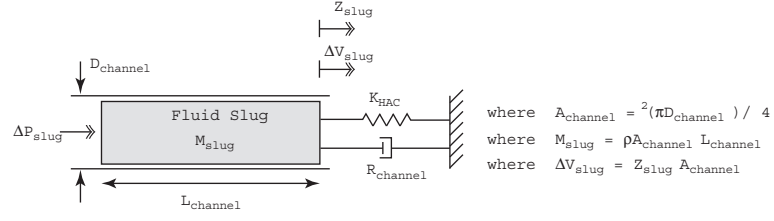
Figure 4.7: Schematic of the high resistance fluid channel between the HAC and an external bias pressure regulator. This channel was etched into the underside of Layer 7.

for the fluid slug in the channel, and by estimating the losses in the channel using Hagen-Poiseuille flow, one can predict the cutoff frequency of such a channel. As discussed in [19], such a channel was designed using the following equation of motion, as given by Roberts, as a starting point:

$$\left( \frac{M_{slug}}{A_{channel}^2} \right) \Delta \ddot{V}_{slug} + R_{channel} \Delta \dot{V}_{slug} + K_{HAC} \Delta V_{slug} = \Delta P_{slug} \quad (4.1)$$

A channel of dimensions  $10\mu m \times 10\mu m \times 1mm$  was designed. Letting  $L_{channel} = 1mm$ ,  $D_{channel} = 11.3\mu m$ ,  $K_{HAC} = 1.0e^{17} Pa/m^3$ ,  $\rho_{fluid} = 760kg/m^3$ , and  $\mu_{fluid} = 6.5e^{-4} kg/(ms)$  gives a frequency of  $48Hz$  for which  $\Delta V_{slug}$  is 1% of the large piston volume change. For a further treatment of this subject, the reader is referred to [19].

Test results, as shown in Figure 4.9 clearly indicate the effectiveness of this channel. A lower cutoff frequency of approximately  $0.1Hz$  was observed. This frequency is even less than the design cutoff frequency. It is also significantly less than the design frequency for the hydraulic amplifier, of between 1 and  $15kHz$ . This ensures that the full pressure swing created by the piezoelectric actuators acting on the large piston is transferred to the smaller piston. The results shown in Figure 4.9 were obtained with AV Device 1 that is discussed in Chapter 6. For information on the experimental equipment required to obtain the results in Figure 4.9, the reader is referred to Chapter 5.



Courtesy of D. C. Roberts.

Figure 4.8: Model of the high resistance fluid channel between the HAC and an external bias pressure regulator. A fluid slug within the channel is modeled. This slug is acted upon by an external stiffness associated with the HAC chamber stiffness. Additionally, the flow resistance of this slug through the channel is modeled using laminar Hagen-Poiseuille flow relations.

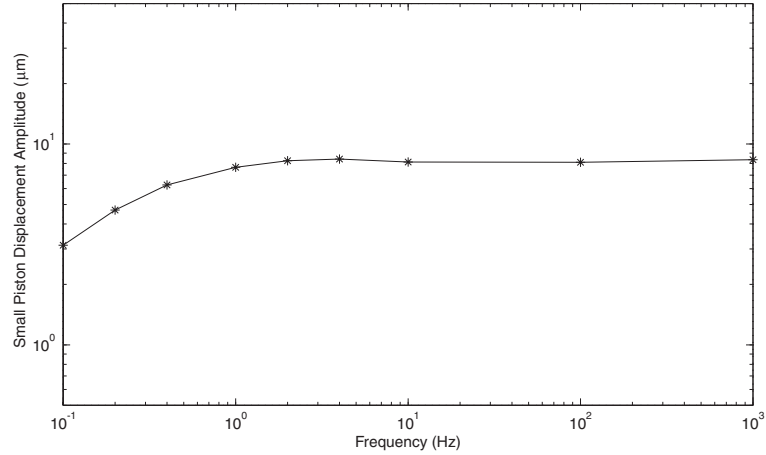


Figure 4.9: Experimental results of tests performed on a flow restriction-type dynamic seal. This test was performed by applying a sinusoidal excitation of  $200V_{p-p}$  to the piezoelectric element of the large piston, and measuring the displacement of the small piston for the frequencies shown. Note the good quasi-static performance down to 1Hz.

### 4.3 Summary

The bubble-free filling and successful sealing of the HAC can be seen as the two most critical steps in the process of producing an hydraulic amplifier. An improperly filled and sealed hydraulic amplifier cannot be expected to function as desired, regardless of its design or the fabrication techniques used. The procedures that were developed in this work have been proven to yield reliable filling and sealing results, as will be shown in Chapter 6. Before presenting the results, however, Chapter 5 will discuss the macroscale systems and test jigs required to enable the instrumentation and testing of the hydraulic amplifiers evaluated in this work.

# Experimental techniques

---

## 5.1 Requirements of the experimental setup

To enable experimental evaluation of the hydraulic amplification devices that had been built, an appropriate test bench had to be developed to enable the measuring of all important parameters. To evaluate the performance of an hydraulic amplification unit, such a test bench had to satisfy the following requirements:

- Enable fluid pressure to be applied to either one of both sides of the device. Also, to accurately measure the relevant pressures.
- Enable electrical connection to the device, in the case of a piezoelectrically driven device.
- Provide a means for measuring out of plane displacement of the tethered piston structures.
- Provide, in addition, a means for evacuating the device and refilling the device with fluid.<sup>1</sup>

## 5.2 System overview

To address all the requirements mentioned previously, a system containing the following five subsystems was built:

---

<sup>1</sup>This excludes the hydraulic amplification chamber itself. The filling and sealing of this chamber was dealt with in the previous chapter.

1. Device testing section, including the device test jig and the pressure measurement and control module, for measuring steady pressures.
2. Gas pressure regulating module.
3. Gas-liquid pressurization module, to enable pressurization of the working fluid.
4. Vacuum module, to enable evacuation and filling of the system.

It was found useful to construct the system in this modular fashion. The functioning of the various modules will be described in the sections that follow. For all equipment used, the reader is referred to Appendix B.

### **5.3 Device test jigs**

The purpose of a test jig is to provide an interface between the microfabricated device, in this case an hydraulic amplifier, and the macroscale environment with which it has to interact. Although the test jig could also be called the "packaging" for the device, as described at length in [39] and [31], a distinction is made here between a component to be used for testing the MEMS device, and a component used to package the device for use in commercial applications.

Figures 5.1 and 5.2 show the test jig designed for the static hydraulic amplifiers. The detail design of this jig is given in Appendix C. In the design of this test jig the following aspects were considered:

- Provide reliable sealing of all fluid connections to the device. Accomplished by o-rings.
- Provide sufficient, but not excessive, clamping force. Accomplished by using springs for preload.
- Expose as much of the device area as possible for ease of laser displacement measurement. This was done. In addition, the jig was manufactured from aluminum and anodized black, to minimize reflection.
- Ensure proper electrical insulation. The device was insulated from the jig with an acetal-type plastic insert.



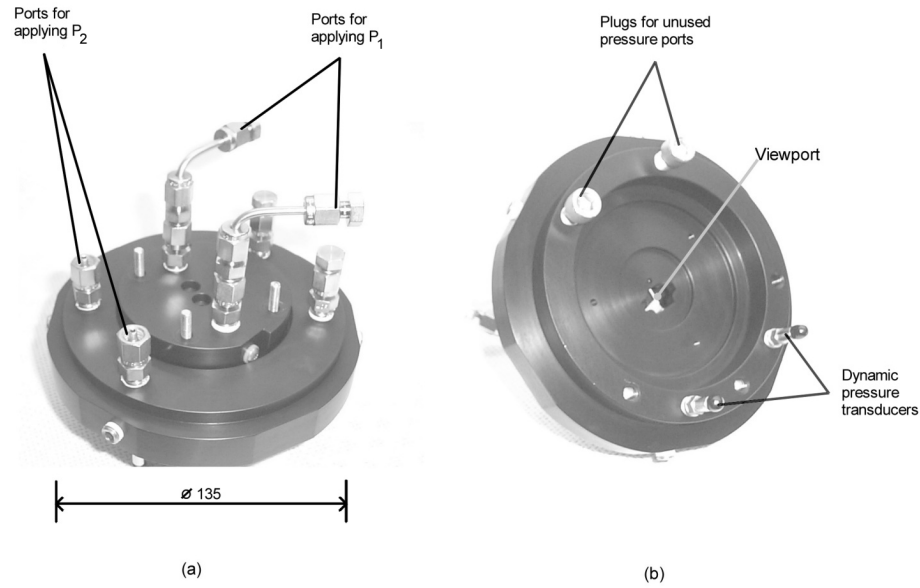


Figure 5.1: Two views of the test jig: Top view (a) and bottom view (b). Note the viewport for laser displacement measurement.

- Allow for measuring of dynamic pressure fluctuations near the device. Provision was made for the installation of PCB model 112A22 dynamic pressure transducers on the jig.
- Had to fit in the fluid filling system discussed in Chapter 4.

## 5.4 The fluid test bench

The remaining four modules mentioned in Section 5.2 will now be given attention. Figure 5.3 is a schematic drawing of all the modules, each of which will be discussed in detail.

### 5.4.1 Gas pressure regulating module

Figure 5.4 illustrates the layout of the pressure regulating module. This module supplies regulated pressure to the test bench, and relies on double regulation, using Concoa Series

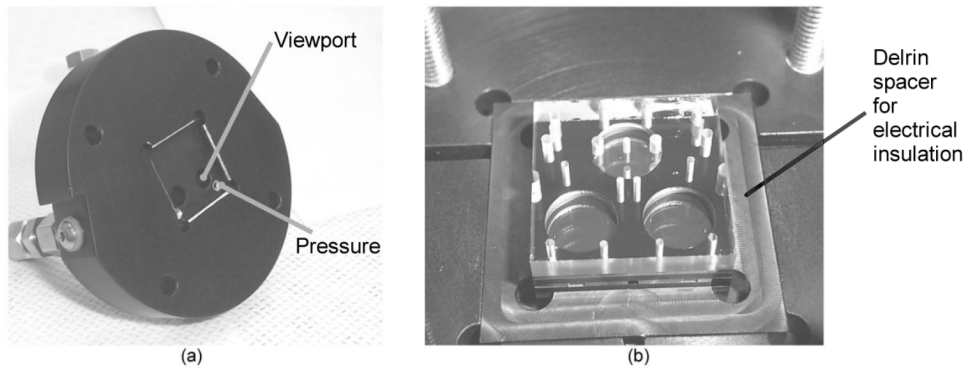


Figure 5.2: The top clamp (a) shows a recess for the device, two optical viewports and also two fluid pressurization ports. The device is inserted into the main jig (b) and then clamped with the top clamp.

402 regulators. Even with double regulation, a certain amount of leak-through and drift can still occur when using process-grade regulators. Therefore, a continuous bleed-off system, using two sets of two Swagelok SS-2SS needle valves, *NV1*, *NV2*, *NV4* and *NV5*, was utilized whenever exact pressure control was needed.

#### 5.4.2 Gas-liquid pressurization module

To provide the capability of pressurizing the hydraulic amplifier with a liquid instead of a gas, a gas-liquid pressurization module was added to the test bench. This is schematically shown in Figure 5.5. This module consists of a stainless steel tank, *TK2* - a Swagelok part number 304L - *HDF4* - 500 500cm<sup>3</sup> sample cylinder - pressurized from the top by nitrogen, and filled through a filling tube with DC200 0.65cst silicone oil. The oil is drawn into the vessel by vacuum, outgassing the liquid in the same process. A clear nylon tube, rated at 625psi working pressure, was added on the side of this vessel for level visualization. Stainless steel bellows valves (*BEV1*, *BEV3*), Swagelok part number SS-4H, were used for gas-liquid shutoff, and stainless steel ball valves (*BV1*, *BV3*, *BV5*) - Swagelok SS-42S4 - were used for all other shutoff purposes. For the most part, 1/4" seamless 304L stainless steel tubing was used in the construction of this module.

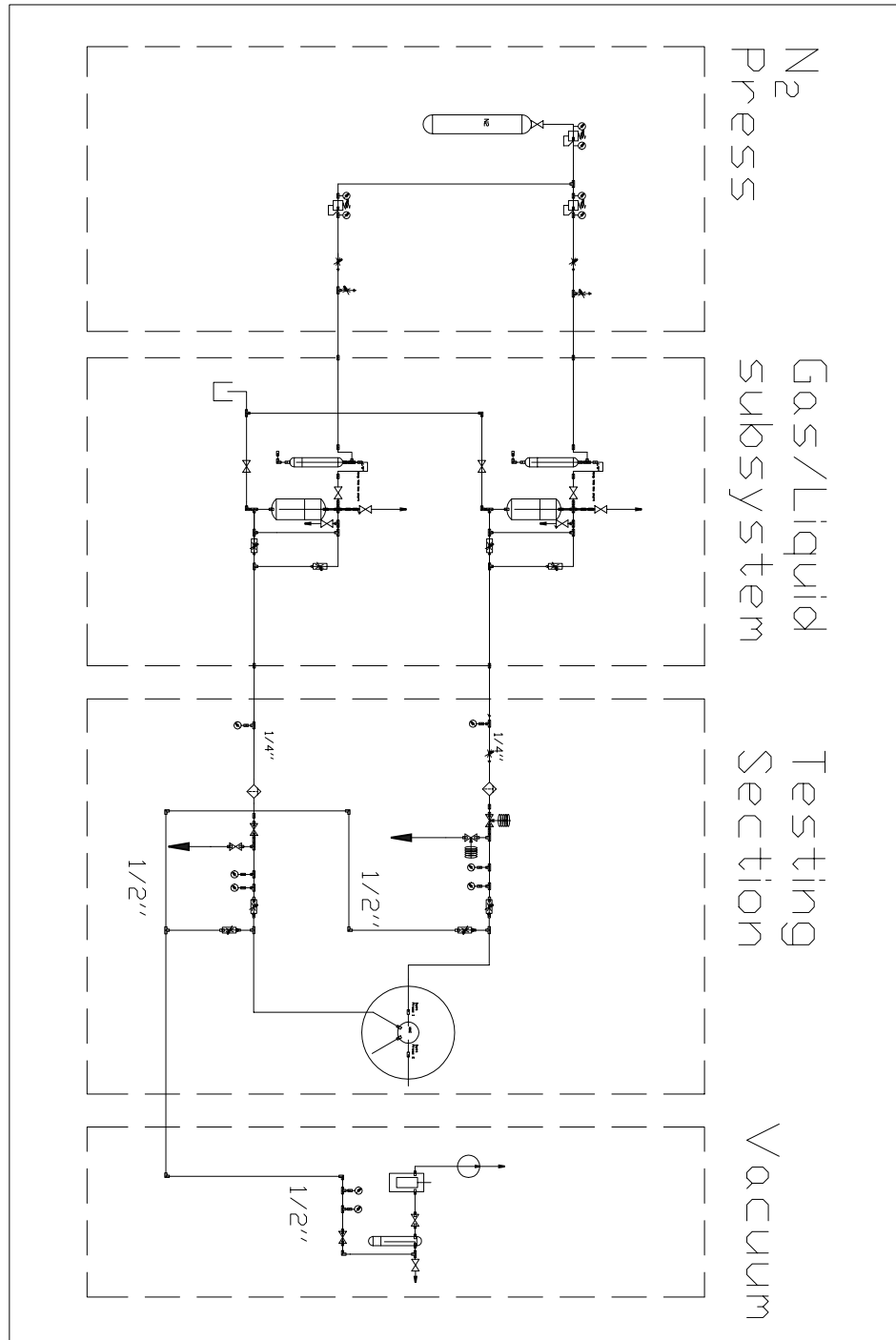


Figure 5.3: Schematic representation of the full fluidic testing system used for performing experiments on the Hydraulic Amplification Devices.

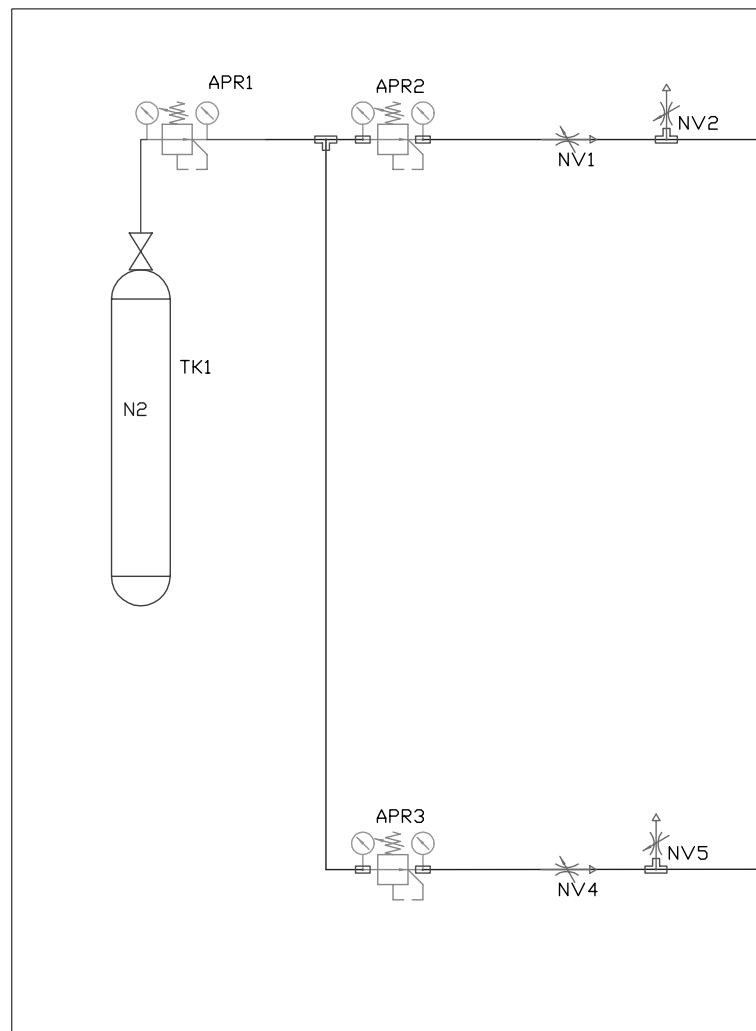


Figure 5.4: The gas pressure regulating module.

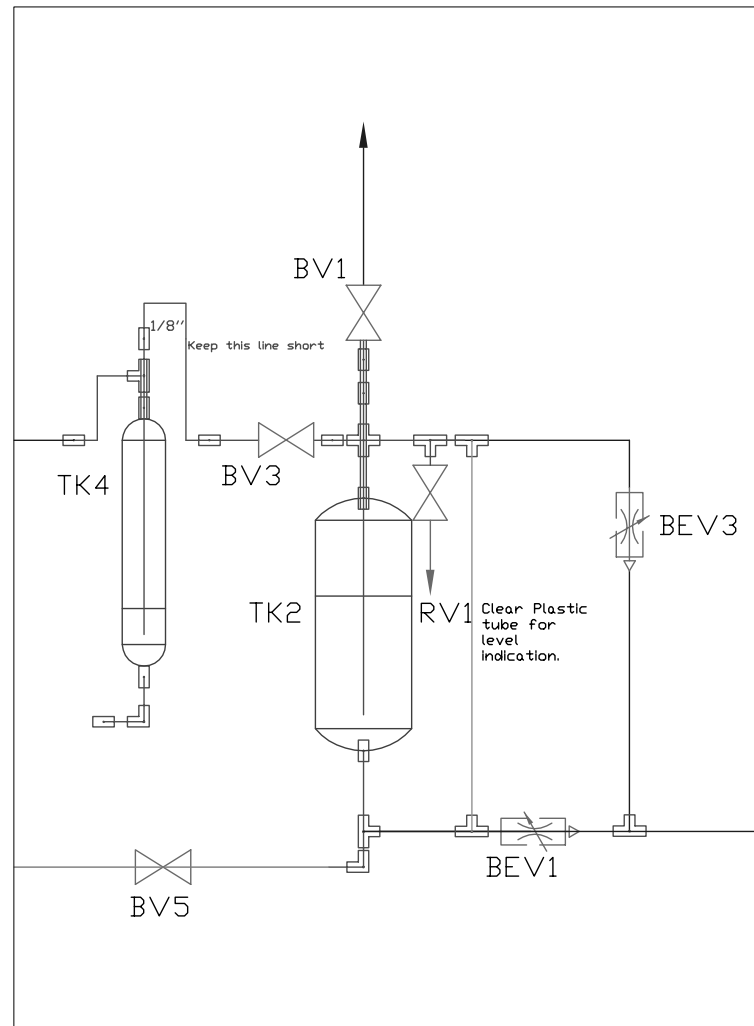


Figure 5.5: The gas-liquid pressurization module.

### 5.4.3 Pressure measurement and control module

The essence of the fluidic test bench for the hydraulic amplifier is contained within the pressure measurement and control module. In Figure 5.6 the following components are of importance:

- Two static gauge pressure transducers per pressurization line. Sensotec FP2000 type sensors ( $500\text{psig}, 0 - 5\text{VDC}, 0.1\%$  accuracy) (*SPS2, SPS4*) were used for high pressure measurements, and for low pressure measurements the same type of sensors, but with the following specifications: ( $100\text{psig}, 0 - 5\text{VDC}, 0.1\%$  accuracy) (*SPS7, SPS8*).
- Two Parker Series 9 fast acting high pressure solenoid valves (*SV1, SV2*) on one of the pressurization lines, to allow for rapid pressurization and venting of the device being tested. Controlled by a signal from the data acquisition system, these valves enabled, to a large extent, automation of the testing procedure. (See Figure 6.5)
- Two Swagelok SS-42S4 ball valves on the other pressurization line (*BV10, BV11*). These valves perform the same function as *SV1* and *SV2*, but in a manual fashion. Using solenoid valves worked so well that it is recommended that two sets of solenoid valves be used instead, should similar experiments ever be attempted.
- Swagelok SS-4TF-05  $0.5\mu\text{m}$  filters on both supply lines leading to the device.
- As in the case shown in Figure 5.5, stainless steel bellows valves (*BEV5 - BEV8*) were used for gas-liquid shutoff.

### 5.4.4 Vacuum module

The vacuum module, depicted schematically in Figure 5.7 encompasses the vacuum pump (*VP1*), cold trap (*CT1*) and a thermocouple vacuum gauge and meter (*SPS6*). All vacuum connections were made using  $1/2''$  tube, either in stainless steel or polypropylene. The vacuum module was used to evacuate flow systems prior to filling with silicone oil. A pressure of approximately  $5\text{mmHg}$  was found to be sufficient for bubble free filling of flow channels.

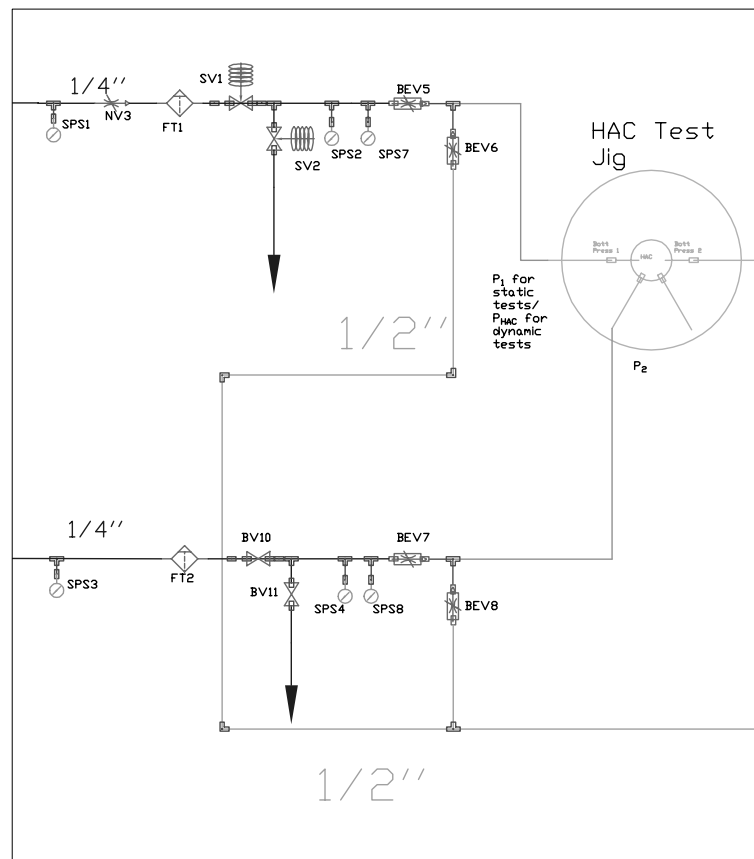


Figure 5.6: Pressure measurement and control module.

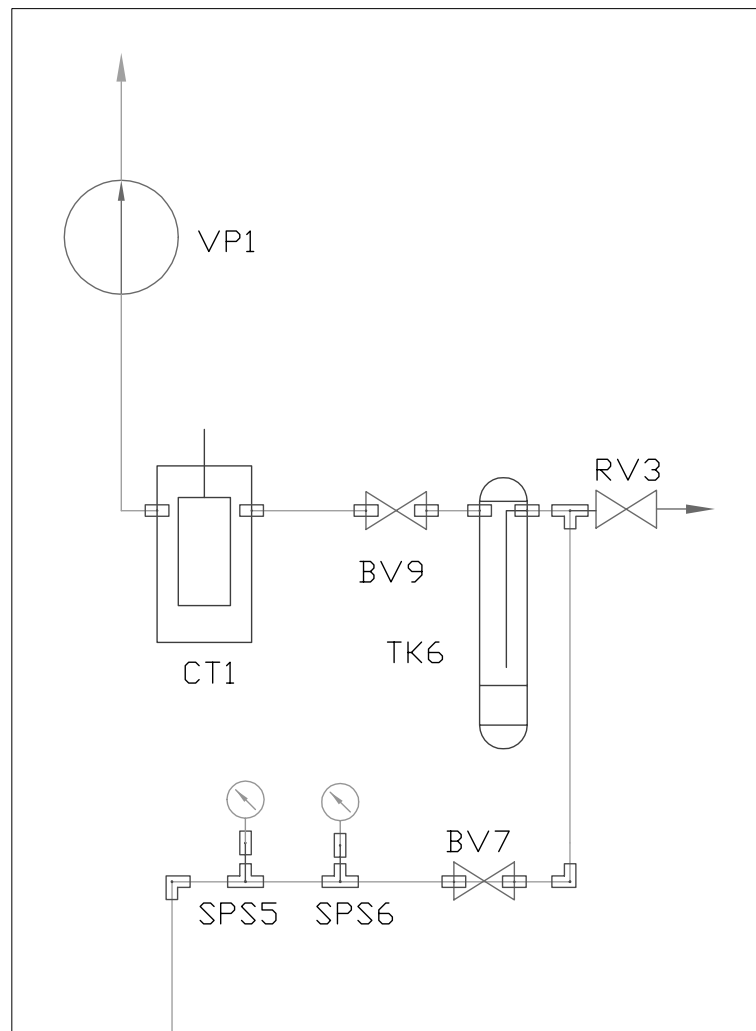


Figure 5.7: Vacuum module.



## 5.5 Displacement measurement

All displacement measurements were performed with a Polytec PI PSV-300 Scanning Laser Vibrometry system. Using doppler principles, this system measures the velocity of a moving target. By integration, displacement is obtained. The system was outfitted with a precision displacement measuring board with a rated resolution of  $2nm$ . Testing has shown that the actual resolution is dependent on the amount of ambient noise present, and also on the nature of the surface being measured. The best actual resolution obtained for near-zero frequency displacement measurements was found to be between 10 and  $50nm$ , depending on the noise present when the measurements were performed.

All of the instrumentation and hardware used to test the hydraulic amplification devices have now been discussed. Figures 5.8, 5.9 and 5.10 are photographs of the testing system that has, up until now, only been described schematically.

## 5.6 Data acquisition

All data acquisition was performed using two National Instruments PCI-6110 boards installed in a desktop computer with an Intel Pentium III  $700MHz$  processor and 128MB RAM. The data acquisition system allowed the simultaneous, synchronized, measurement of up to eight input channels, at sampling rates of up to  $4MHz$ . In addition, it also allowed for simultaneous synchronized generation of four arbitrary waveform outputs at frequencies up to  $25kHz$ , using data acquisition software as developed by [40] using the National Instruments LabView language.

## 5.7 Testing protocols

Prior to testing the device, either a static or dynamic hydraulic amplifier, it is filled using the procedures described in Chapter 4 and subsequently clamped in the test jig described in Section 5.3. For testing the devices, two different testing procedures were followed for the static and dynamic devices, and these will be discussed briefly.

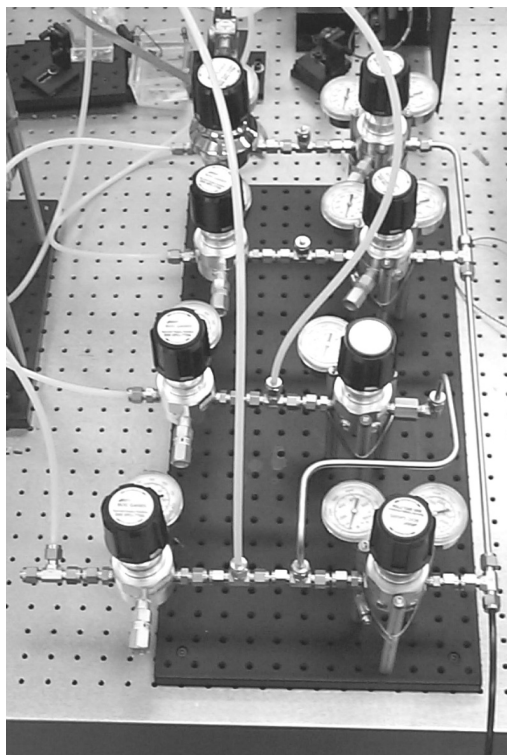


Figure 5.8: Regulator bank. Note that this is the regulator bank for the full MHT device. Only two sets of the four displayed are used. Note the double regulation from a regulated tank output.

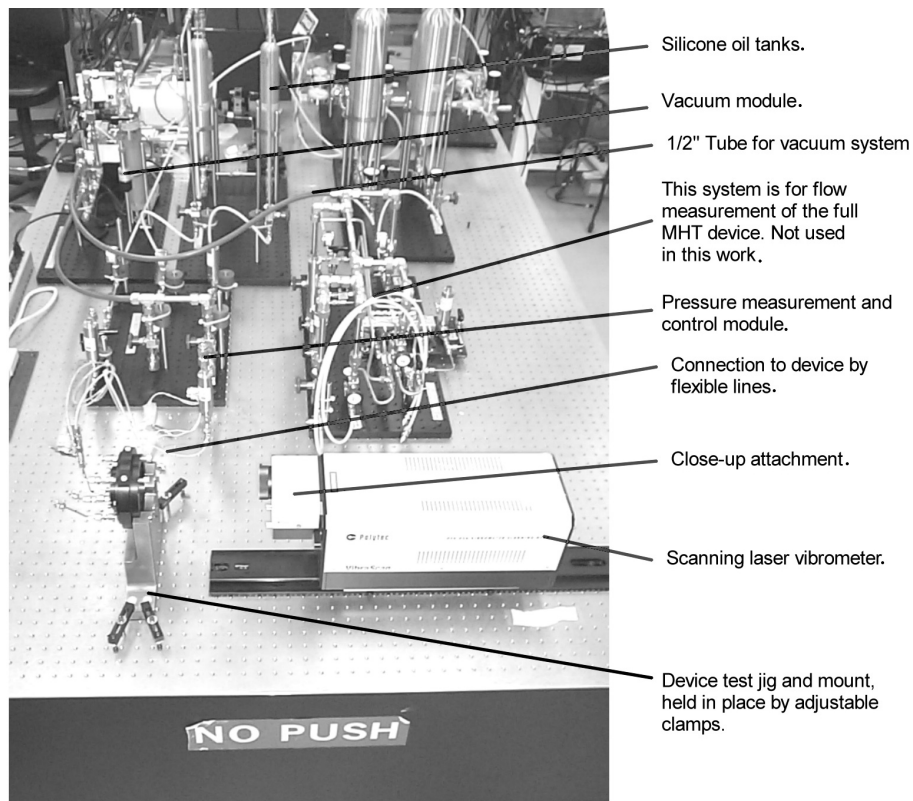


Figure 5.9: Photograph of the entire test rig. All tests were performed on an optical vibration isolation table.

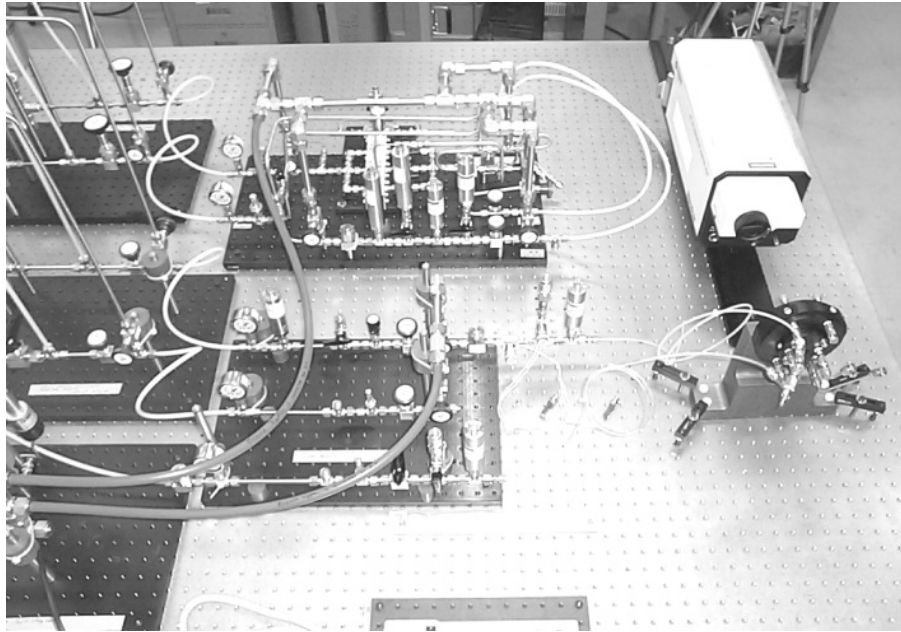


Figure 5.10: Side angle photograph of the test rig, with more detail on the pressure measurement and control module.

### 5.7.1 Testing of static hydraulic amplifiers

The following aspects, not necessarily in the order mentioned, should be considered during the testing of a static hydraulic amplifier:

- Decide whether the device is going to be tested in a full liquid system, a gas system, or a gas-liquid system. For static devices, for optical clarity, it was found desirable to test in a gas-liquid system.<sup>2</sup> In this configuration, *TK2* in Figure 5.5 is bypassed using *BEV3*.<sup>3</sup> Note that the device and the test jig were filled with liquid, but the pressurization lines were operated using nitrogen. Concerns about water hammer from operating *SV1*, *SV2* (Shown in Figure 5.6) were the motivation for not using a full liquid system in this case. The displacement measurement obtained from the

---

<sup>2</sup>Meaning measuring through silicone oil instead of gas. During the filling process, the device is filled with oil. If this oil is subsequently removed from the device, a residue often is left behind, which hinders measurements.

<sup>3</sup>The equivalents of *TK2* and *BEV3* are also used in this manner. These are not shown explicitly, but can be found in Figure 5.3

laser vibrometer had to be corrected for the different index of refraction of the fluid in all cases where the measurements were performed on an interface with silicone oil rather than air. It can be shown that dividing by the index of refraction gives the desired correction.

- Set the pressures  $P_1$  and  $P_2$  on *APR2* and *APR3*.
- Set the appropriate acquisition rate in the data acquisition system, and ready the system for testing.
- Start by switching *SV1* and *SV2* to provide a pulsing pressure for  $P_1$ . (See, again, Figure 6.5).
- Use *BV10* and *BV11* to vary  $P_2$ .
- In all these tests, *BEV5* and *BEV7* are fully open, and *BEV6* and *BEV8* are fully closed.

### 5.7.2 Testing of dynamic hydraulic amplifiers

- Once again, decide whether to use liquid, gas or gas-liquid. In this case, tests were generally performed using either a full gas system, or a full liquid system.
- In these tests,  $P_1$  and  $P_{HAC}$  are applied. They are not varied or pulsed as in the static case. Therefore, it is advisable to remove *SV1* and *SV2* from the system for these tests. *SV1* and *SV2* are normally closed valves, and although it is possible to apply a voltage to keep *SV1* open continuously, it is not desirable and may damage the valve coil.
- Set  $P_1$  and  $P_{HAC}$  on *APR2* and *APR3*. In all tests presented in this work  $P_1 = P_{HAC}$ . Therefore, in this case,  $P_1$  and  $P_{HAC}$  were controlled from the same regulator, using an appropriate tube to connect the two ports.
- Prepare the data acquisition system for testing.
- Apply the drive voltage to the piezoelectric element. This potential is named  $V_1$ , and is applied on Layers 2 and 4 of Figure 2.2. Tests were performed using either frequency sweeps or sinusoidal excitation.

With these testing protocols, it was possible to perform the experiments that will be described in Chapter 6.



# Experimental Evaluation of Hydraulic Amplification Devices

---

Having discussed all issues relevant to the successful design, fabrication and testing of an experimental hydraulic amplification device, this chapter deals with the subsequent tests performed on a selection of devices based on the MIT EH4 energy harvesting device discussed in the introduction.

## 6.1 Overview of the experimental work

In brief, the devices were characterized in the following manner:

- Pressure-deflection characteristics of the tethered piston structures.
- Static performance measurements on two hydraulic amplifiers: One with ten small pistons and one large one as well as a device with a single small piston. Gas pressurization techniques were used.
- Demonstration of dynamic performance of a device with one small piston and a piezo-electrically driven large piston.

In total, four hydraulic amplification devices were built and tested. Table 6.1 summarizes the devices built, and the tests performed on them.

Device number	Device type	Tests performed	Comments
HAC Device 1	Single small piston static hydraulic amplifier, no piezoelectric elements	Static Characterization of small and large pistons	Device cracked during initial testing due to excessive clamping force in test jig
HAC Device 2	Single small piston static hydraulic amplifier, no piezoelectric elements	Static Characterization of small and large pistons	Device cracked after filling due to excessive clamping force in test jig
HAC Device 3	Ten small piston static hydraulic amplifier, no piezoelectric elements	Static Characterization of small and large pistons, Characterization of hydraulic amplification capabilities	Device was subjected to full range of characterization tests without failure.
HAC Device 4	Single small piston static hydraulic amplifier, no piezoelectric elements	Characterization of hydraulic amplification capabilities	Device was subjected to full range of characterization tests without failure.
AV Device 1	Single small piston active valve device. Piezoelectrically driven	Dynamic testing of the hydraulic amplification concept, evaluation of the performance of the high-frequency sealing channel.	Device was subjected to full range of dynamic tests without failure.

Table 6.1: Outline of the hydraulic amplification devices assembled and tested



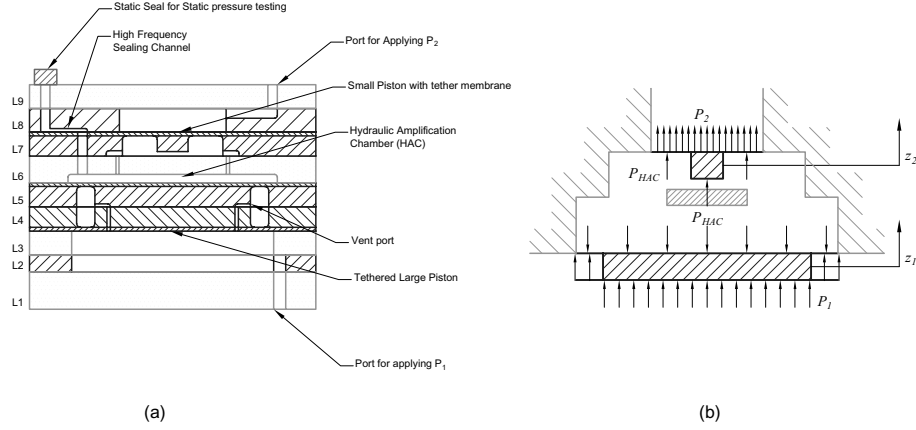


Figure 6.1: Two representations of the static hydraulic amplification device: (a) A detailed cross section schematic view, and (b) A simplified functional schematic, with nomenclature to be used.

## 6.2 Pressure Deflection results

The purpose of performing simple pressure deflection tests of the tethered structures is to determine the stiffnesses of the individual components of the hydraulic amplification device. These will later be used in correlating the experimental results of the full hydraulic amplification devices with the theoretical predictions. For each device, the pressure-deflection characteristics of both the large piston and the small piston were evaluated. Figure 6.1 illustrates the geometry under consideration and also the nomenclature that will be used. Note that, in this case,  $P_{HAC} = 0$ , and we only apply  $P_1$  for the large piston and  $P_2$  for the small piston. All results presented in this section reflect the aggregate of all tests performed on a given type of membrane structure, rather than discussing the testing of each individual membrane. This will maintain the focus of our discussion and will also give the reader a sense for the amount of variation from specimen to specimen that can be expected when using the fabrication techniques described in Chapter 3.

### 6.2.1 Pressure-deflection characteristics of the large piston

All of the devices listed in Table 6.1 had the exact same design geometry for the large pistons. However, due to variations in the fabrication process, all of the large pistons were slightly different. Figure 6.2 displays the pressure-deflection results obtained for a selection

$\psi_{1,exp}$	11.3
$\psi_{1,theo(8\mu m)}$	8.9
$\psi_{1,theo(9\mu m)}$	12.7
$\psi_{1,theo(10\mu m)}$	17.4

*Note: All units are in  $kPa/\mu m$ .*

Table 6.2: Large piston inverse compressibility

of these pistons, along with a prediction from the nonlinear model developed in [25].

We can further proceed, based on the information shown, to compute the linearized inverse compressibility coefficients for the experimental results and also for the theoretical predictions, as defined in Equation 2.13. The results are shown in Table 6.2. Referring back to Table 2.1 and also to Chapter 3, we recall that the design required a  $10\mu m$  thick SOI layer. The starting substrate for these pistons had a device layer thickness of, nominally,  $11\mu m$  with a variation of  $\pm 1\mu m$ . After the oxidation process, approximately  $0.7\mu m$  is removed, therefore reducing the SOI thickness to  $10.3 \pm 1\mu m$ . Measurements performed after processing on pieces from the wafer edge, using a KLA-Tencor P10 surface profilometer, indicate that the final thickness of the device layer at the edge location was  $8 \pm 0.5\mu m$  on various positions of the wafer edge. Therefore, for small deflections, the model agreement appears to be very good and within the bounds of measurement errors and fabrication tolerances.

### 6.2.2 Pressure-deflection characteristics of the small piston structures

As mentioned in Section 2.3, two types of small piston configurations were used. Figure 6.3 shows the pressure-deflection characteristics of a device with a single small piston, and Figure 6.4 shows the same for a device with ten smaller pistons.

For these two cases one can proceed and again compute the small-deflection inverse compressibility coefficients, as was done for the large pistons. Table 6.3 gives these coefficients for the devices having a single small piston, and Table 6.4 gives the coefficients for HAC Device 3. In both of these cases, the starting wafer had a device layer thickness of  $8 \pm 1\mu m$ . After processing, this thickness would be reduced to approximately  $7.3 \pm 1\mu m$ , based on the fabrication process. Post-fabrication measurements on the wafer edge gave a thickness of  $6 \pm 0.5\mu m$  on various positions of the wafer edge. Once again, the agreement with model predictions is good, and within the bounds of fabrication capabilities and measurement

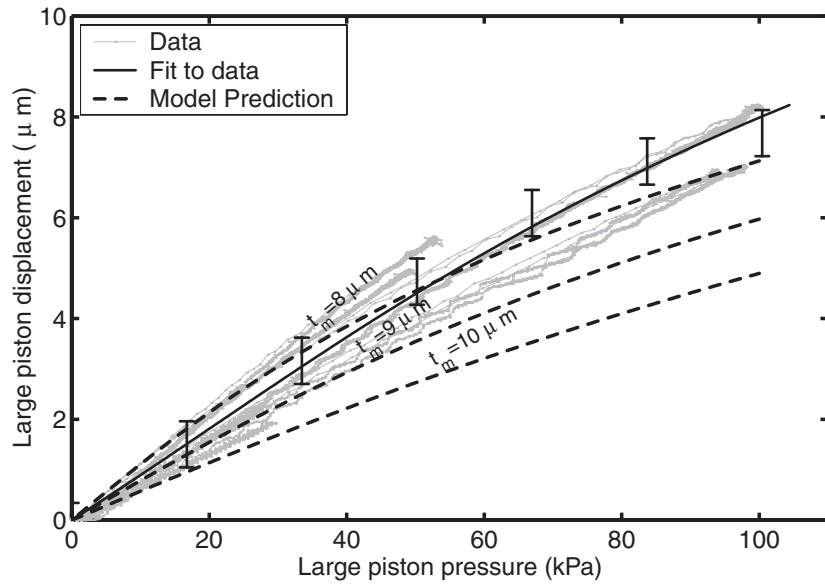


Figure 6.2: Results from pressure-deflection tests on the large pistons, obtained from HAC devices 1,2 and 3

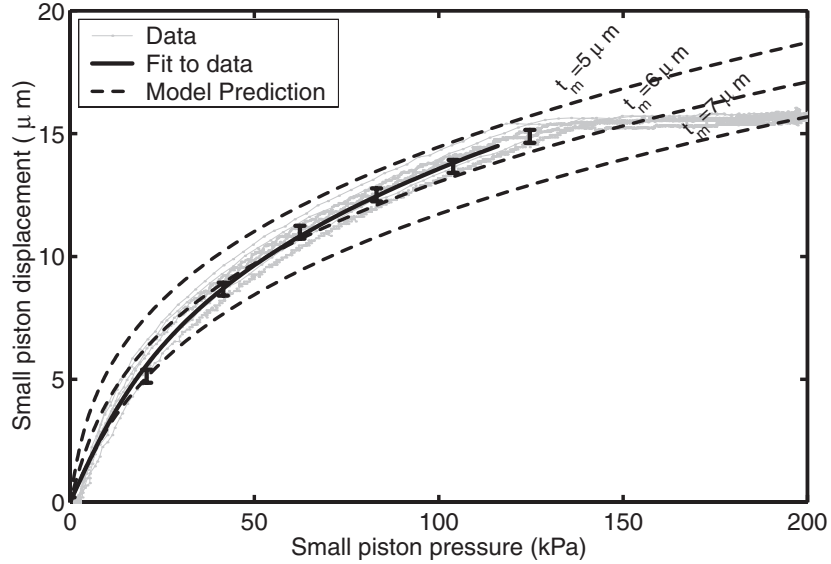


Figure 6.3: Results from pressure-deflection tests on a selection of small pistons from HAC Devices 1 and 2, both having one small piston per hydraulic amplifier.

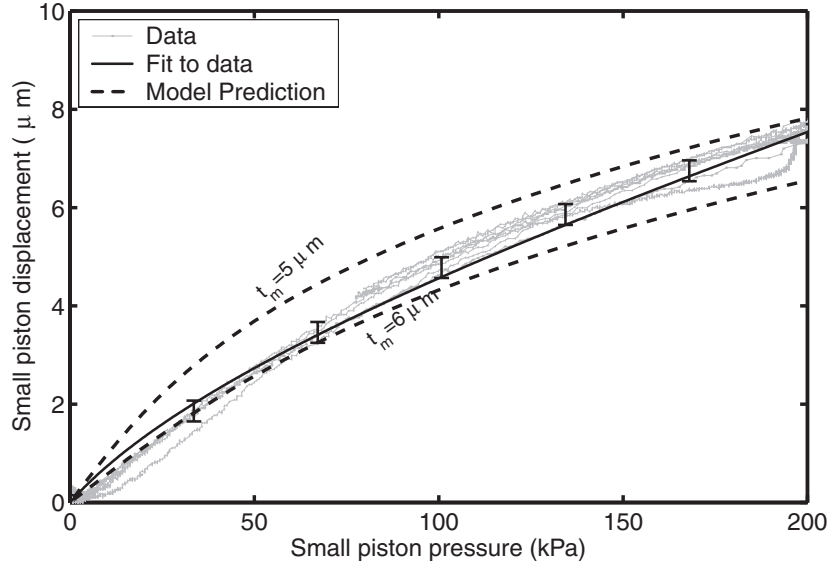


Figure 6.4: Results from pressure-deflection tests on a selection of small pistons from HAC Device 3, a device with ten small pistons per hydraulic amplifier.

$\psi_{2,exp}$	3.1
$\psi_{2,theo(5\mu m)}$	1.0
$\psi_{2,theo(6\mu m)}$	1.8
$\psi_{2,theo(7\mu m)}$	3.0

*Note: All units are in  $kPa/\mu m$ .*

Table 6.3: Small piston inverse compressibility for devices with a single small piston.

tolerances.

### 6.2.3 Summary: Pressure deflection results

This section presented pressure deflection data on the small and large piston geometries employed in the hydraulic amplifiers that were tested. In all results it appears that the pistons were slightly more compliant than predictions based on design values. After post-fabrication metrology and model corrections, it was shown that the values obtained were still within the bounds of tolerances quoted by the wafer suppliers, as well as tolerances in the subsequent fabrication processes. After performing these tests, the models were

$\psi_{2,exp}$	13.0
$\psi_{2,theo(5\mu m)}$	10.1
$\psi_{2,theo(6\mu m)}$	17.5

*Note: All units are in  $kPa/\mu m$ .*

Table 6.4: Small piston inverse compressibility for devices with 10 small pistons.

appropriately adjusted before continuing to the next section, which involves the testing of a filled hydraulic amplifier.

### 6.3 Static hydraulic amplification tests

Two devices mentioned in Table 6.1 underwent static hydraulic amplification tests: HAC Device 3 was a device with 10 small pistons and HAC Device 4 was a device with a single small piston. The static behavior of both devices was evaluated by pressurizing both the small piston(s) and the large piston, and measuring the displacement of both. Due to constraints in the measurement system, simultaneous measurements were not possible. However, by accurately controlling the respective pressures, reliable results were obtained. In all static tests performed,  $P_1$  was switched by the solenoid valves discussed in Section 5.4.3.  $P_2$  was switched manually using ball valves. Figure 6.5 shows representative time-histories obtained for a typical hydraulic amplification test run.

#### 6.3.1 Tests performed, and correlation with nonlinear models: HAC Device 3

Figures 6.6 and 6.7 show the deflections of the large piston and one of the small pistons for  $P_1$  varying from 0 to  $500kPa$  and for  $P_2$  having values 0, 92, 298 and  $500kPa$ . Keeping in mind the pressure-deflection results from Section 6.2.1 it should be clear to the reader that the large piston acts as a pressure transfer element with very little pressure differential across this piston for the deflections observed in Figure 6.6. The small piston in turn responds to the pressure transferred by the large piston. In both figures the data is displayed along with cubic fits to the data. In all subsequent analyses the *fitted* data will be used instead of the raw data. Note that the fits are cubic, and were performed on the *inverse* of the data shown. The reader should bear in mind that, to first order, the tethered membrane piston structure can be seen to be analogous to a Duffing-type spring, as described, for example,

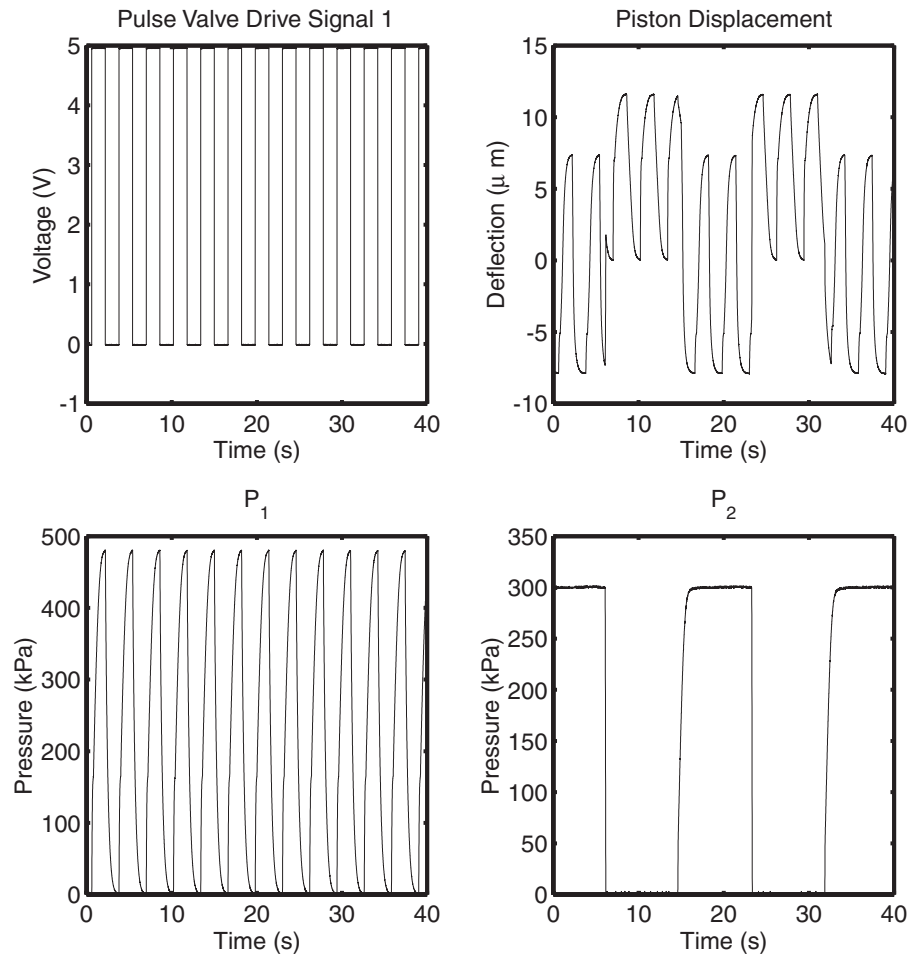


Figure 6.5: Typical data obtained from an hydraulic amplification test run. By accurately controlling  $P_2$  during each small piston - large piston measurement pair, it was possible to obtain good data without resorting to two-sided displacement measurement.

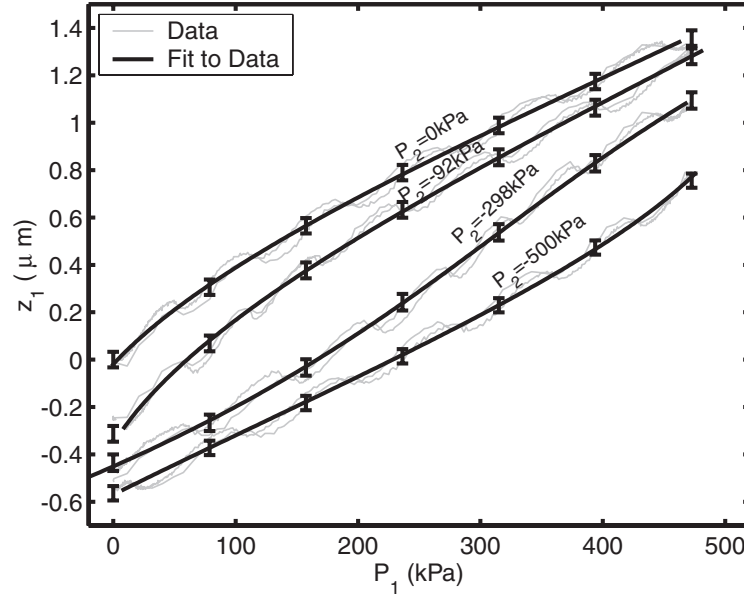


Figure 6.6: Hydraulic amplification data for the large piston of HAC Device 3. For all subsequent analysis, the fitted data will be used.

in [41]. In the case of a Duffing spring, the spring force is a cubic polynomial function of the deflection. The inverse - that the deflection is a cubic polynomial function of the spring force - does not hold. It is the same for the membrane structures, with the exception that a pressure takes the place of the force, as discussed in Chapter 2.

Figures 6.8 and 6.9 now show the model results plotted over the experimental results. Note that the large piston deflects significantly more than model predictions, indicating a reduced stiffness of the HAC.

### 6.3.2 Amplification ratio and amplification sensitivity: HAC Device 3

A suitable figure of merit in evaluating the performance of an hydraulic amplifier would be an amplification ratio or an amplification factor. This ratio can be computed using two different methods. The first method, which we will define as the amplification ratio, is defined as:

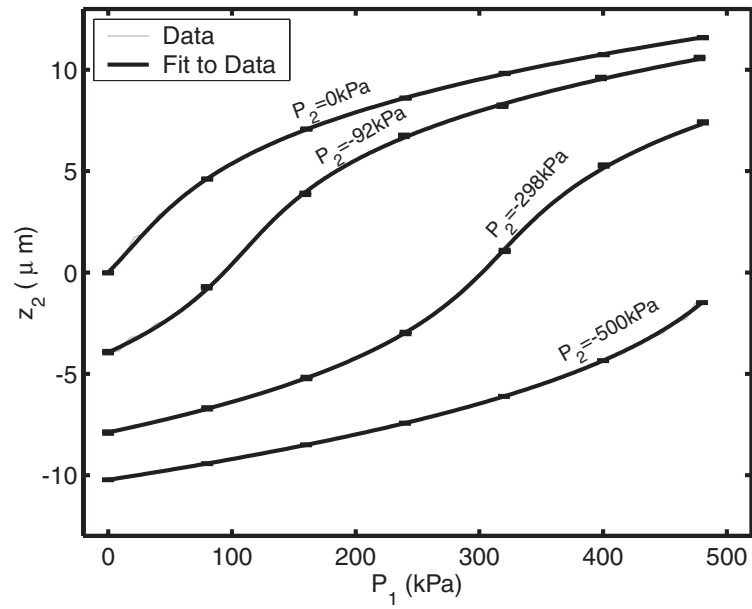


Figure 6.7: Hydraulic amplification data for the small piston of HAC Device 3. Note that the scatter in data for the small piston is very small, due to good measurement resolution and large amplitude motions.

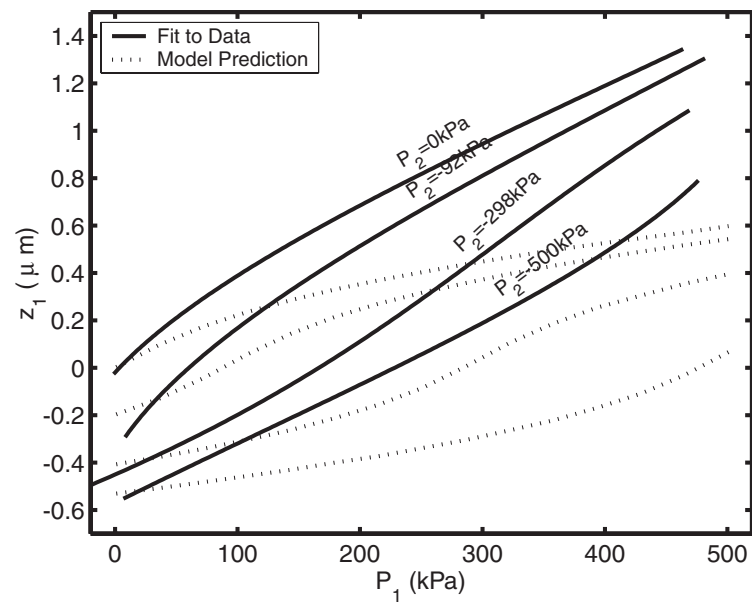


Figure 6.8: Adding model data to Figure 6.6. HAC Device 3.



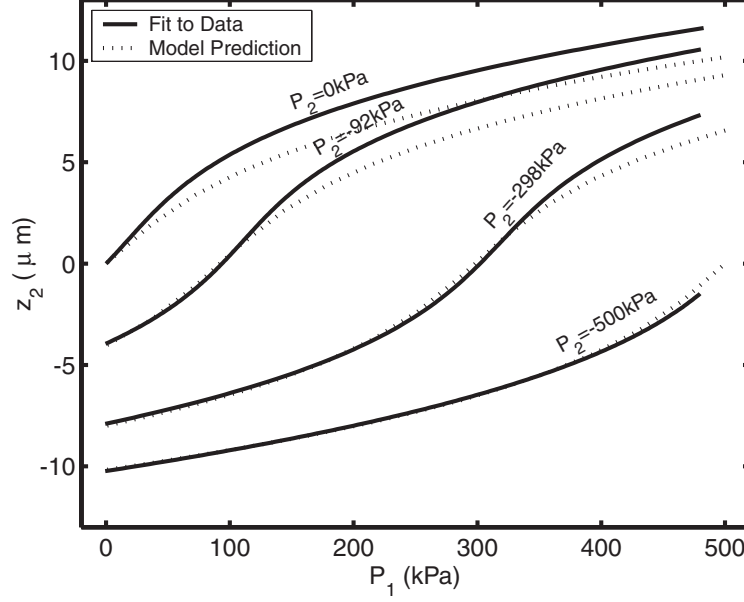


Figure 6.9: Adding model data to Figure 6.7. HAC Device 3.

$$AR = \left( \frac{z_2(P_1) - z_2(0)}{z_1(P_1) - z_1(0)} \right)_{P_2=const} \quad (6.1)$$

Figure 6.10 shows this amplification ratio. Note that the amplification ratio is always a maximum near the "linear region" of the operating regime. The second method, shown in Figure 6.11 uses the incremental displacement amplification which allows us to write an expression for the amplification sensitivity:

$$AS = \left( \frac{\partial z_2}{\partial z_1} \right)_{P_1, P_2=const} \quad (6.2)$$

### 6.3.3 Small deflection stiffness matrix comparisons: HAC Device 3

One can proceed and compute the small-deflection inverse compressibility matrix of the coupler, as described in Section 2.4. In Section 6.2 the results of the tests on all tethered piston structures are given. Figure 6.12 gives the results obtained for the large piston

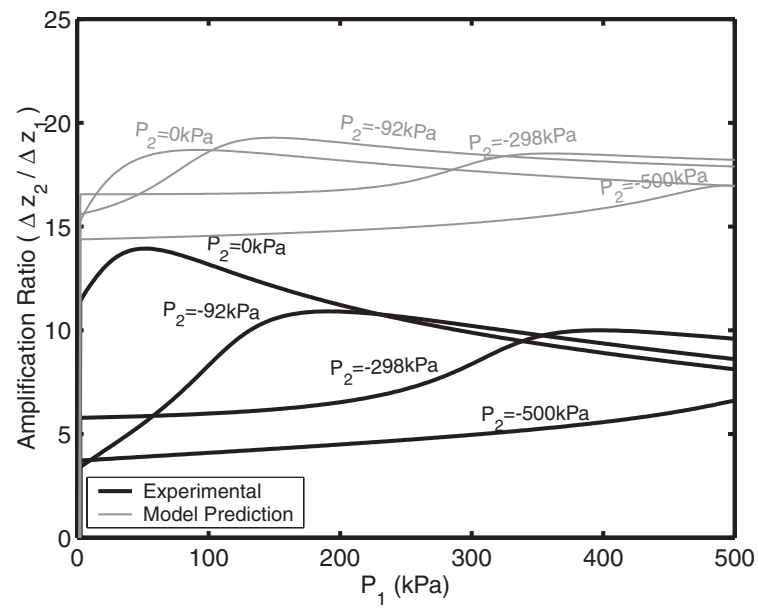


Figure 6.10: Amplification ratios for the tests performed. HAC Device 3.

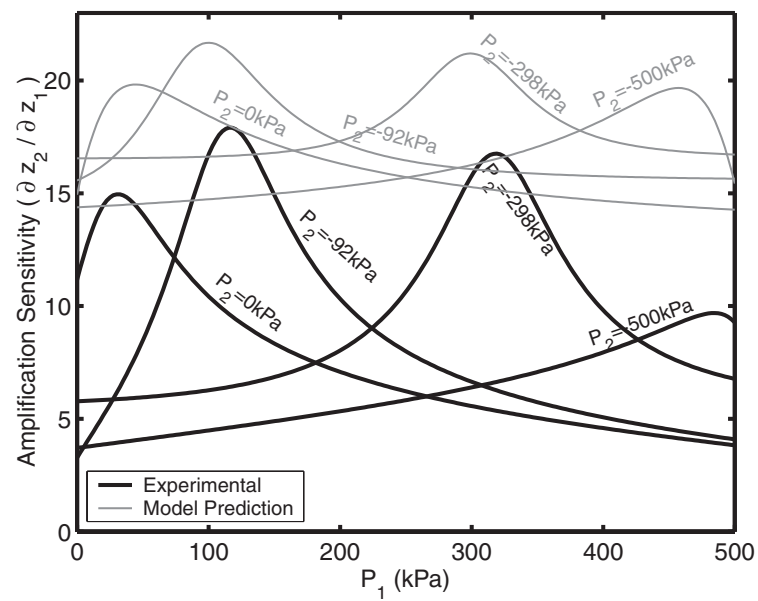


Figure 6.11: Amplification sensitivities for the tests performed. HAC Device 3.

$\psi_{1,exp}$	15.2
$\psi_{2,exp}$	15.4

*Note: All units are in kPa/ $\mu\text{m}$ .*

Table 6.5: Inverse compressibilities for the pistons of HAC Device 3.

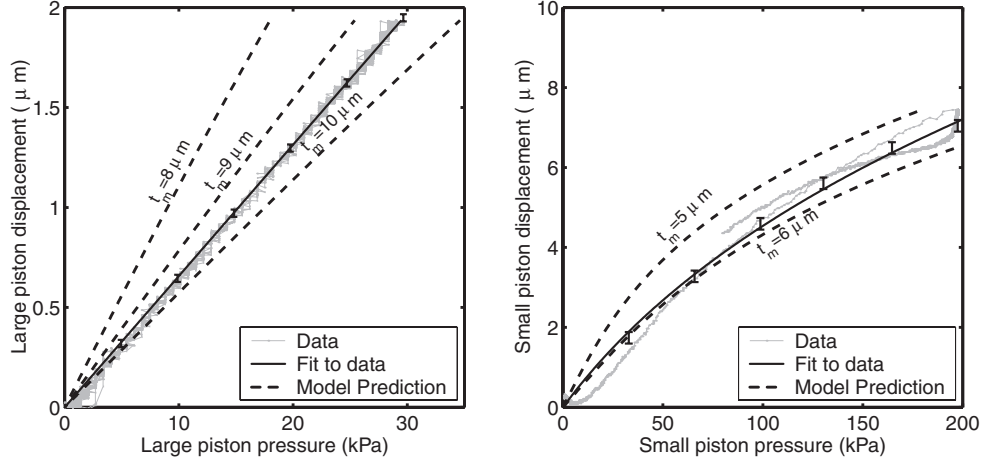


Figure 6.12: Pressure-deflection results for the large and small pistons of HAC Device 3.

and small piston tested in this section. For these individual tethered piston structures, the scatter in the data is significantly less, due to the elimination of variations in the fabrication process and variations in SOI device layer thickness as elements of uncertainty. For these particular structures, the inverse compressibilities,  $\psi_1$  and  $\psi_2$ , are given in Table 6.5.

We now proceed to compute the inverse compressibility matrix for this coupler. By taking two values of  $z_2$  at two values of  $P_2$  and a matching  $P_1$ , and then finding the corresponding values for  $z_1$  at those values of  $P_2$  and  $P_1$ , we can set up a system of linear equations, and solve for the four coefficients, as shown in Equation 6.3.

$$\begin{Bmatrix} P_{1a} \\ P_{2a} \\ P_{1b} \\ P_{2b} \end{Bmatrix} = \begin{bmatrix} z_{1a} & z_{2a} & 0 & 0 \\ 0 & 0 & z_{1a} & z_{2a} \\ z_{1b} & z_{2b} & 0 & 0 \\ 0 & 0 & z_{1b} & z_{2b} \end{bmatrix} \begin{Bmatrix} D_{11} \\ D_{12} \\ D_{21} \\ D_{22} \end{Bmatrix} \quad (6.3)$$

where:

$$\mathbf{D} = \begin{bmatrix} D_{11} & D_{12} \\ D_{21} & D_{22} \end{bmatrix} \quad (6.4)$$

and, recalling from Equation 2.11 that:

$$\mathbf{P} = \mathbf{D}\mathbf{z} \quad (6.5)$$

For  $z_{2a} = 1\mu m$ ,  $P_{2a} = -92kPa$  and  $z_{2b} = -1\mu m$ ,  $P_{2b} = -298kPa$ , and finding the matching values for  $P_1$  and  $z_1$  in both the experimental and theoretical cases, the following  $\mathbf{D}$ -matrices were computed:

$$\mathbf{D}_{theo} = \begin{bmatrix} 7.38 \times 10^3 & -3.49 \times 10^2 \\ -7.38 \times 10^3 & 3.67 \times 10^2 \end{bmatrix} kPa/\mu m \quad (6.6)$$

$$\mathbf{D}_{exp} = \begin{bmatrix} 6.34 \times 10^2 & -1.90 \times 10^1 \\ -6.32 \times 10^2 & 3.46 \times 10^1 \end{bmatrix} kPa/\mu m \quad (6.7)$$

Dividing (6.6) element-wise by (6.7), we find the following ratios:

$$\begin{bmatrix} 11.6 & 18.4 \\ 11.7 & 10.6 \end{bmatrix} \quad (6.8)$$

In a similar fashion, we can compute theoretical and experimental  $\mathbf{C}$ -matrices, as described in Equation 2.14, and we find, for the same values as used for the  $\mathbf{D}$ -matrices:

$$\mathbf{C}_{theo} = \begin{bmatrix} 2.75 \times 10^{-3} & 2.61 \times 10^{-3} \\ 5.53 \times 10^{-2} & 5.53 \times 10^{-2} \end{bmatrix} \mu m/kPa \quad (6.9)$$

$$\mathbf{C}_{exp} = \begin{bmatrix} 3.48 \times 10^{-3} & 1.91 \times 10^{-3} \\ 6.37 \times 10^{-2} & 6.39 \times 10^{-2} \end{bmatrix} \mu m/kPa \quad (6.10)$$

And, dividing (6.9) element-wise by (6.10):

$$\begin{bmatrix} 0.8 & 1.4 \\ 0.9 & 0.9 \end{bmatrix} \quad (6.11)$$

Note that, due to the almost-singular nature of the matrices, as discussed in Section 2.4, the apparent factor 10 discrepancy in (6.8) is not reflected as a factor 0.1 in (6.11). It should be pointed out that the tests performed were tests aimed at measuring *compressibility*, and not *inverse compressibility* - i.e. a load was applied, and a deflection was measured. For

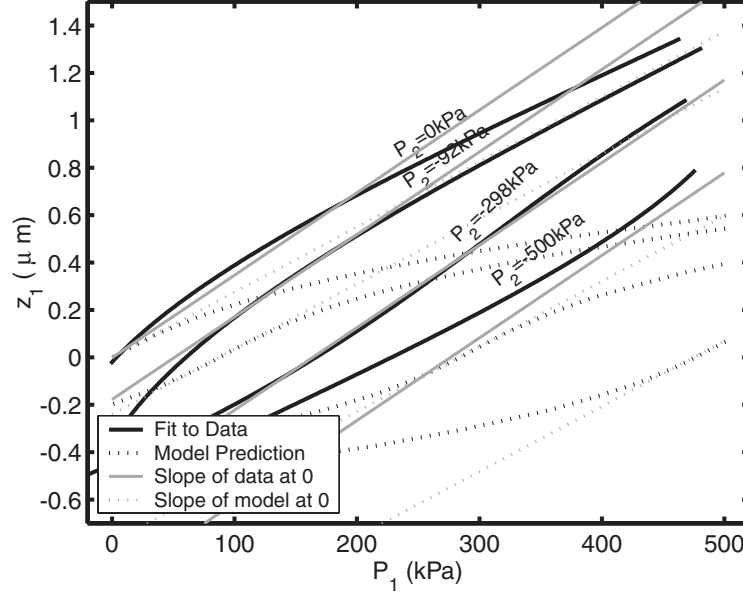


Figure 6.13: Large piston results with the linearization about 0 added. HAC Device 3.

measuring the inverse compressibility, or, in the case of a simple spring, the stiffness, we would have had to impose a displacement, and measure the resulting load.

Therefore, in Figures 6.8 and 6.9 we see no sign of a factor 10 discrepancy. Figures 6.13 and 6.14 are repeats of Figures 6.8 and 6.9, but with the linearizations given by (6.9) and (6.10) added to them.

A discrepancy that is apparent in both the theoretical and experimental data is that  $|D_{11}|$  is not significantly greater than  $|D_{21}|$  in (6.6) and (6.7). Recall from Equation 2.10 that:

$$D_{11} = \beta_c \gamma_1 + \psi_1$$

$$D_{21} = -\beta_c \gamma_1$$

The discrepancy in the *theoretical* case is readily explained by the fact that a chosen value of  $z_2 = \pm 1 \mu m$  already adds some nonlinearity to the system, combined with the fact that, in the theoretical case,  $D_{11} = O(10^3)$ , whereas  $\psi_1 = O(10)$ . The effect of  $\psi_1$  is almost negligible and easily masked by numerical artefacts. It has been verified that, for smaller values of  $z_2$ , the condition of  $|D_{11}| > |D_{21}|$  is obtained. In (6.7), we do have that  $|D_{11}| > |D_{21}|$ , but the difference, approximately  $2 kPa / \mu m$ , is less than the measured value of  $\psi_1 = 15.2 kPa / \mu m$ .

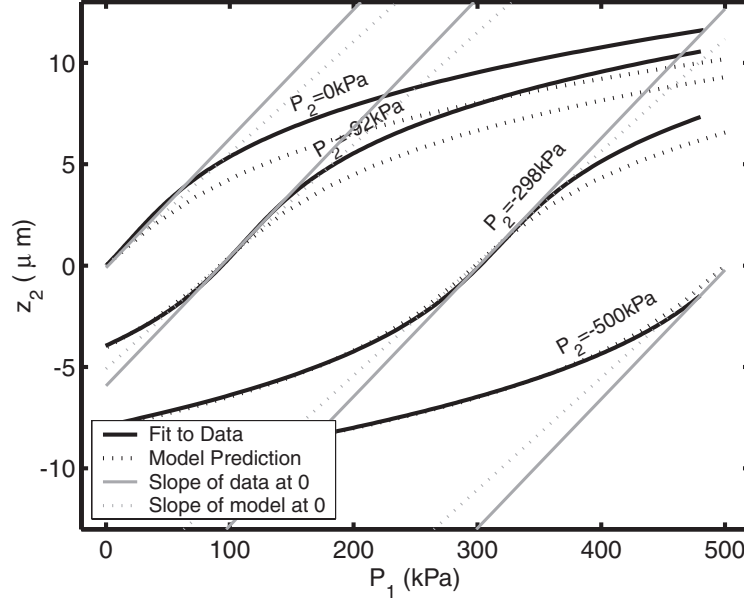


Figure 6.14: Small piston results with the linearization about 0 added. HAC Device 3.

This discrepancy can probably be attributed to an error in the measurements taken.

One more calculation remains to evaluate the quality of the data presented in this section. We can subtract the appropriate values for  $\psi_1$  and  $\psi_2$  from the theoretical and experimental  $\mathbf{D}$ -matrices, to get a matrix of the form:

$$\tilde{\mathbf{D}} = \begin{bmatrix} \beta_c \gamma_1 & -\beta_c \gamma_2 \\ -\beta_c \gamma_1 & \beta_c \gamma_2 \end{bmatrix} \quad (6.12)$$

In the theoretical and experimental cases we then obtain:

$$\tilde{\mathbf{D}}_{theo} = \begin{bmatrix} 7.37 \times 10^3 & -3.49 \times 10^2 \\ -7.38 \times 10^3 & 3.49 \times 10^2 \end{bmatrix} \quad (6.13)$$

$$\tilde{\mathbf{D}}_{exp} = \begin{bmatrix} 6.19 \times 10^2 & -1.90 \times 10^1 \\ -6.32 \times 10^2 & 1.92 \times 10^1 \end{bmatrix} \quad (6.14)$$

Element-wise division yields:

$$\begin{bmatrix} 11.9 & 18.4 \\ 11.7 & 18.2 \end{bmatrix} \quad (6.15)$$

We note that, in reality, (6.15) should have all entries be identical. We recall that in Equation 6.12:

$$\begin{aligned}\gamma_1 &= \frac{A_{1,eff}}{V_c} \\ \gamma_2 &= \frac{A_{2,eff}}{V_c}\end{aligned}$$

Therefore,  $\gamma_1$  and  $\gamma_2$  depend solely on geometry, which should be very similar from model to experiment. Therefore, one should expect to see all four entries in (6.15) reflect the ratio of:

$$\frac{\beta_{c,theo}}{\beta_{c,exp}}$$

The discrepancy in (6.15) is attributed to measurement errors. Any other variation would not violate the physics of the system.

#### 6.3.4 Tests performed, and correlation with nonlinear models: HAC Device 4

Both hydraulic amplifiers in HAC Device 4 were tested. The results of the two devices match closely, and only one set is discussed here. Figures 6.15 and 6.16 show the deflections of the large piston and the small piston for  $P_1$  varying from 0 to  $200kPa$  and for  $P_2$  having values 0, 53, 105, 153, 206 and  $253kPa$ . Again, the data is displayed along with cubic fits to the data.

Figures 6.17 and 6.18 now show the model results plotted over the experimental results. As was the case for HAC Device 3, the large piston deflects significantly more than model predictions, indicating a reduced stiffness of the HAC.

#### 6.3.5 Amplification ratio and amplification sensitivity: HAC Device 4

Using Equations 6.1 and 6.2, we proceed to compute the amplification ratio and amplification sensitivity for HAC Device 4. The results are shown in Figures 6.19 and 6.20. The amplification ratio is higher than predicted for  $P_2 = 0kPa$ . This could probably attributed to a measurement irregularity. Also, in this case, the amplification sensitivity is higher for the experimental case. This is due to a smaller incremental change in  $z_1$  for the measured values.

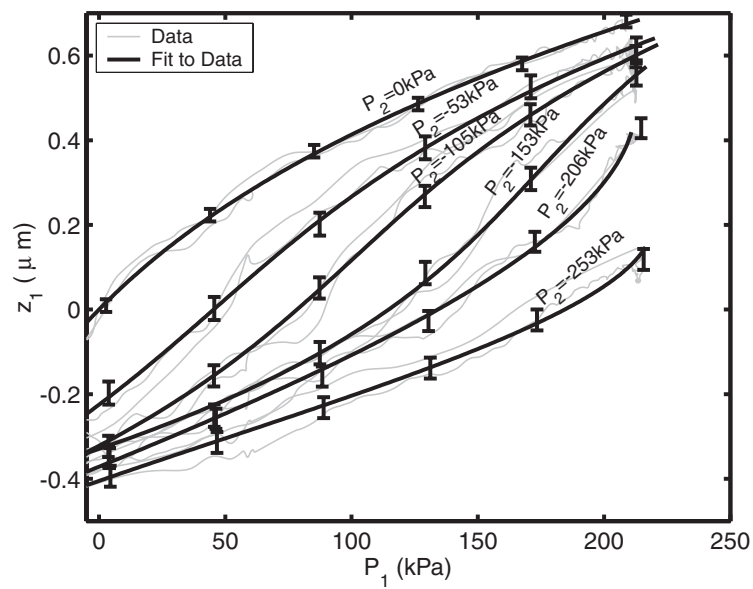


Figure 6.15: Hydraulic amplification data for the large piston of HAC Device 4.

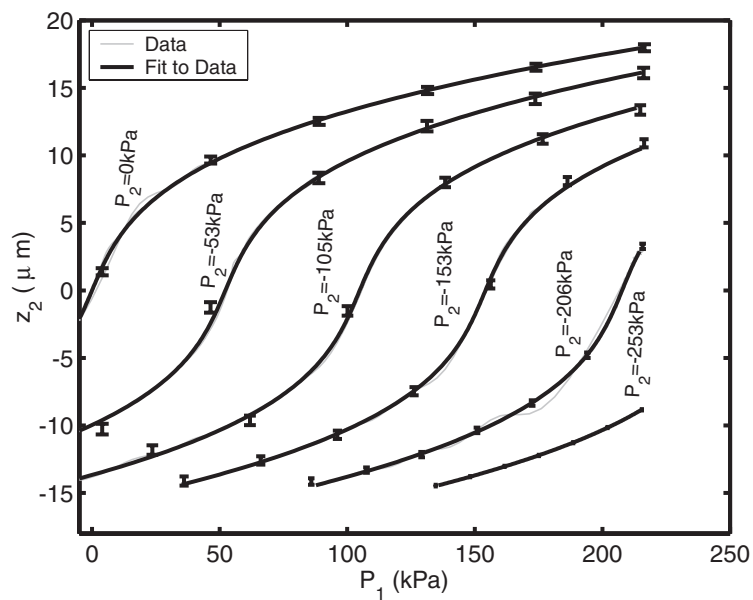


Figure 6.16: Hydraulic amplification data for the small piston of HAC Device 4.



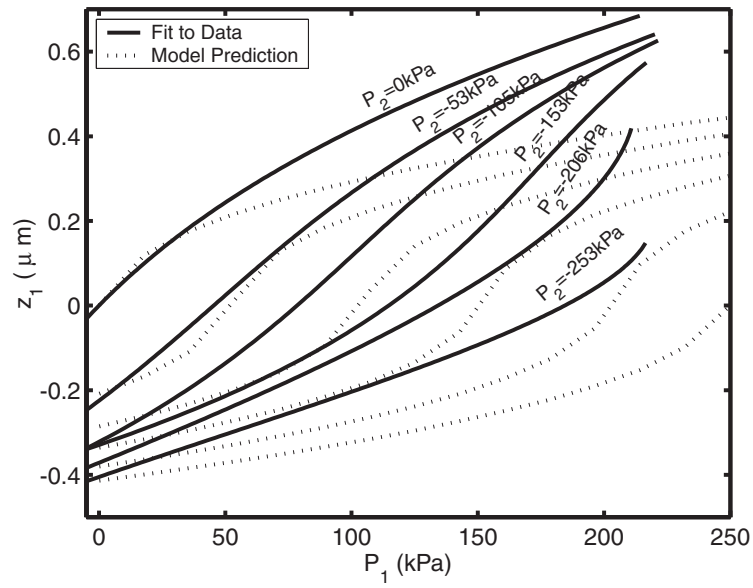


Figure 6.17: Adding model data to Figure 6.15. HAC Device 4.

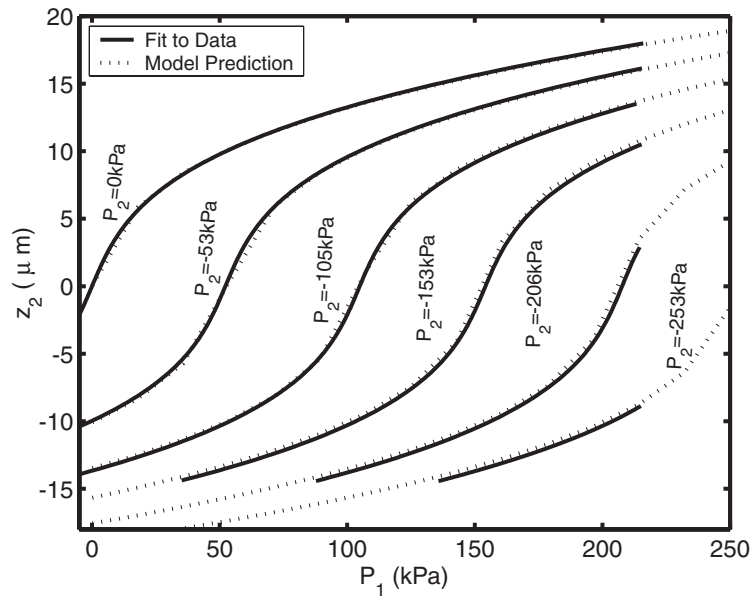


Figure 6.18: Adding model data to Figure 6.16. HAC Device 4. The good correlation is attributed to the fact that the large piston sees a very small  $\Delta P$ .

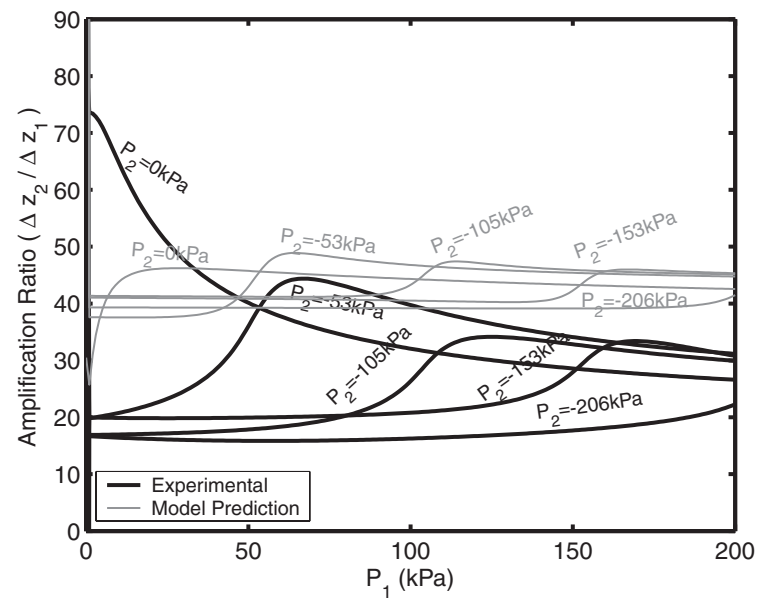


Figure 6.19: Amplification ratios for the tests performed. HAC Device 4.

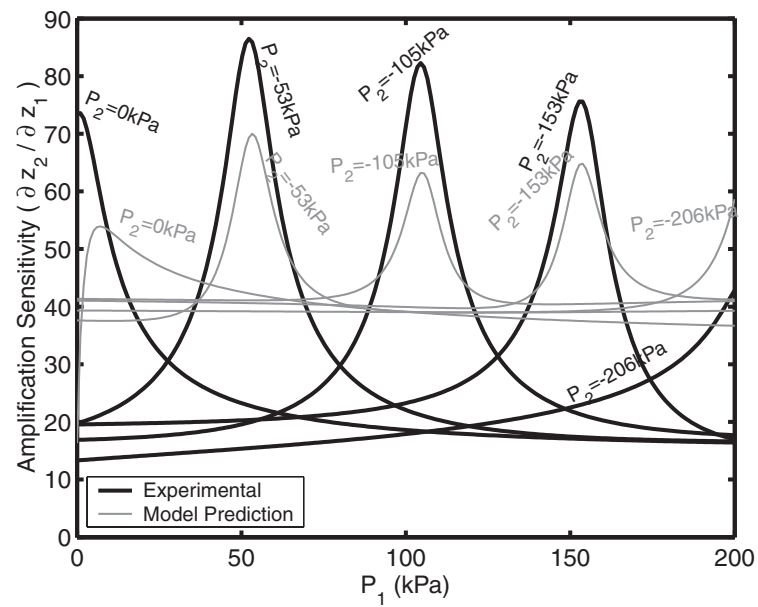


Figure 6.20: Amplification sensitivities for the tests performed. HAC Device 4.

$\psi_{1,exp}$	11.3
$\psi_{2,exp}$	3.1

*Note: All units are in  $kPa/\mu m$ .*

Table 6.6: Inverse compressibilities for the pistons of HAC Device 4.

### 6.3.6 Small deflection stiffness matrix comparisons: HAC Device 4

This section is a repeat of Section 6.3.3 for the hydraulic amplifier with a single small piston. No individual membrane characterizations were performed on this device. The results from HAC Devices 1 and 2 were used instead. The inverse compressibilities that were used,  $\psi_1$  and  $\psi_2$ , are given again in Table 6.6.

As was done in Section 6.3.3, we compute the inverse compressibility matrix. For  $z_{2a} = 1\mu m$ ,  $P_{2a} = 0kPa$  and  $z_{2b} = -1\mu m$ ,  $P_{2b} = -153kPa$ , and finding the matching values for  $P_1$  and  $z_1$  in both the experimental and theoretical cases, the following  $\mathbf{D}$ -matrices were computed:

$$\mathbf{D}_{theo} = \begin{bmatrix} 4.18 \times 10^3 & -1.12 \times 10^2 \\ -4.18 \times 10^3 & 1.14 \times 10^2 \end{bmatrix} kPa/\mu m \quad (6.16)$$

$$\mathbf{D}_{exp} = \begin{bmatrix} 7.67 \times 10^2 & -8.20 \\ -7.71 \times 10^2 & 9.40 \end{bmatrix} kPa/\mu m \quad (6.17)$$

Dividing (6.16) element-wise by (6.17), we find:

$$\begin{bmatrix} 5.4 & 13.6 \\ 5.4 & 12.1 \end{bmatrix} \quad (6.18)$$

We note that there seems to be slightly better correlation between the predicted and measured inverse compressibilities when (6.18) is compared to (6.8). This could be due to an HAC that was better filled. In a similar fashion, we compute theoretical and experimental  $\mathbf{C}$ -matrices:

$$\mathbf{C}_{theo} = \begin{bmatrix} 1.47 \times 10^{-2} & 1.45 \times 10^{-2} \\ 5.41 \times 10^{-1} & 5.41 \times 10^{-1} \end{bmatrix} \mu m/kPa \quad (6.19)$$

$$\mathbf{C}_{exp} = \begin{bmatrix} 1.06 \times 10^{-2} & 9.23 \times 10^{-3} \\ 8.68 \times 10^{-1} & 8.63 \times 10^{-1} \end{bmatrix} \mu m/kPa \quad (6.20)$$

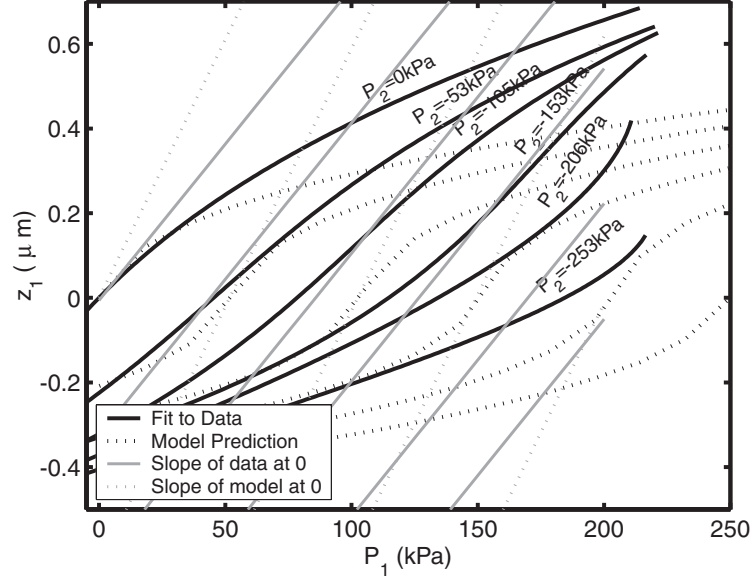


Figure 6.21: Large piston results with the linearization about 0 added. HAC Device 4.

And, dividing (6.19) element-wise by (6.20):

$$\begin{bmatrix} 1.4 & 1.6 \\ 0.6 & 0.6 \end{bmatrix} \quad (6.21)$$

Once again, the ratios seen in (6.21) are not the inverse of those seen in (6.18). Figures 6.21 and 6.22 are repeats of Figures 6.17 and 6.18 with the linearizations given by (6.19) and (6.20) added to them.

The discrepancy between  $|D_{11}|$  and  $|D_{21}|$  as discussed previously can once again be seen in (6.16) and (6.17). In (6.17), we now have that  $|D_{11}| < |D_{21}|$ . Measurement errors could cause such a discrepancy.

Subtracting the appropriate values for  $\psi_1$  and  $\psi_2$  from the theoretical and experimental **D**-matrices, we obtain:

$$\tilde{\mathbf{D}}_{theo} = \begin{bmatrix} 4.17 \times 10^3 & -1.12 \times 10^2 \\ -4.18 \times 10^3 & 1.12 \times 10^2 \end{bmatrix} \quad (6.22)$$

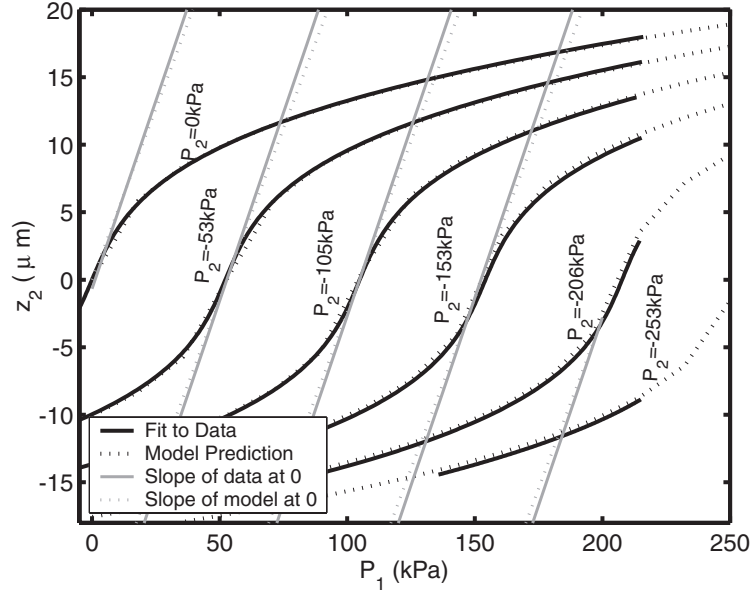


Figure 6.22: Small piston results with the linearization about 0 added. HAC Device 4.

$$\tilde{\mathbf{D}}_{exp} = \begin{bmatrix} 7.56 \times 10^2 & -8.20 \times 10^1 \\ -7.71 \times 10^2 & 6.30 \times 10^1 \end{bmatrix} \quad (6.23)$$

And element-wise division yields:

$$\begin{bmatrix} 5.5 & 13.6 \\ 5.4 & 17.8 \end{bmatrix} \quad (6.24)$$

Once again, as was the case in (6.15), the fact that all entries in (6.24) are not equal is attributed to measurement errors. Note that  $|D_{11,theo}| < |D_{21,theo}|$  because  $z_2$  was chosen to be relatively large. Choosing a smaller  $z_2$  will yield the correct result. For these experiments however, it was decided not to use a  $z_2$  that is too small, causing the analyses to be overly sensitive to possible measurement errors.

In summary, two static hydraulic amplifiers with different theoretical amplification ratios have been tested. The same trends have been seen in the tests of both HAC Device 3 and HAC Device 4, with the latter device, HAC Device 4, appearing to be the one that was better filled and sealed. Amplification ratios of up to 40:1 were observed, when ignoring the  $P_2 = 0 \text{ kPa}$  result for HAC Device 4. In addition, amplification sensitivities of approximately 80:1 were obtained.

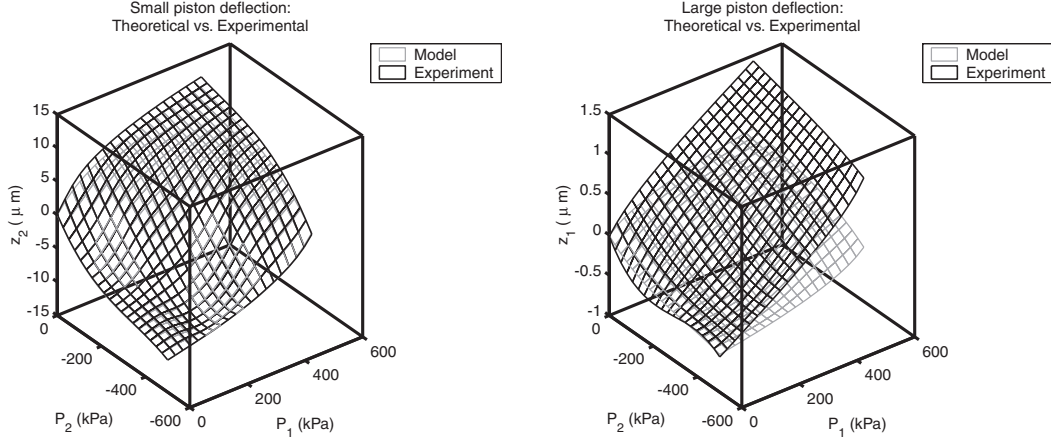


Figure 6.23: Small and large piston deflections as functions of both  $P_1$  and  $P_2$ . HAC Device 3.

### 6.3.7 Static hydraulic amplification as a two-variable function

For completeness, the attention of the reader is drawn to the fact that, as described in the section on the nonlinear case (Section 2.5), the deflections can be written as nonlinear functions of the two pressures, and vice-versa. Graphs from experimental and theoretical results can be constructed and, by using suitable interpolation, the theoretical and experimental responses can be visualized in a three-dimensional manner, as shown in Figure 6.23.

## 6.4 Dynamic hydraulic amplification tests

This section attempts to briefly demonstrate the dynamic capabilities of the hydraulic amplifiers developed in this work. The dynamic tests discussed here were performed on the HAC of a piezoelectrically driven active valve, as described in [19]<sup>1</sup>. In these tests the large piston was actuated by three radially equispaced PZN-PT single crystal piezoelectric elements, instead of the pressure that was previously used. Furthermore, the HAC was not statically sealed, but rather dynamically using the technique described in Section 4.2.2. The dynamic hydraulic amplifier is depicted schematically in Figure 6.24.

<sup>1</sup>In Table 6.1 this device is referred to as AV Device 1

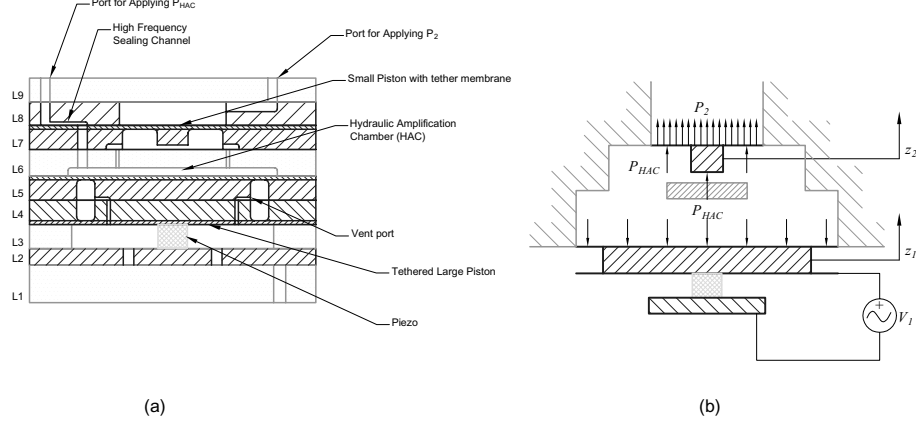


Figure 6.24: Two representations of the dynamic hydraulic amplification device: (a) A detailed cross section schematic view, and (b) A simplified functional schematic, with nomenclature to be used.

The device tested was one with a single small piston. The first test performed was a low amplitude frequency sweep to determine the bandwidth of the hydraulic amplifier. Figure 6.25 shows the results of this test. When no silicone oil is present on top of the small piston, the first resonance occurs at approximately  $10kHz$ . Adding oil introduces additional inertia, with a corresponding reduction in natural frequency to approximately  $5kHz$ . For a further discussion of this phenomenon, the reader is referred to [19].

In addition, quasi-static tests were performed at various voltage levels, at a frequency of  $1kHz$ . Figure 6.26 shows a typical time history of the small and large pistons for the case where  $V_1 = 400V \pm 400V$ ,  $P_{HAC} = P_2 = 500kPa$ . Figure 6.27 shows the deflection versus different values for  $V_1$ . The corresponding amplification ratio as a function of  $V_1$  is depicted in Figure 6.28. In this case, the amplification ratio is defined as:

$$AR = \frac{z_{2,p-p}}{z_{1,p-p}} \quad (6.25)$$

Note the equivalence of Figure 6.27 with Figures 6.6 and 6.7, where a voltage takes the place of pressure actuation for the dynamic tests. Varying  $P_2$  to obtain the same sets of curves as seen for the static case was not feasible, due to the fact that the dynamic seal used in the piezoelectric hydraulic amplifier would not allow for a quasi-steady pressure differential to be applied between  $P_{HAC}$  and  $P_2$  without changing the equilibrium position of the small piston. Changing  $P_2$  at sufficiently high frequency was not possible with the experimental equipment used.

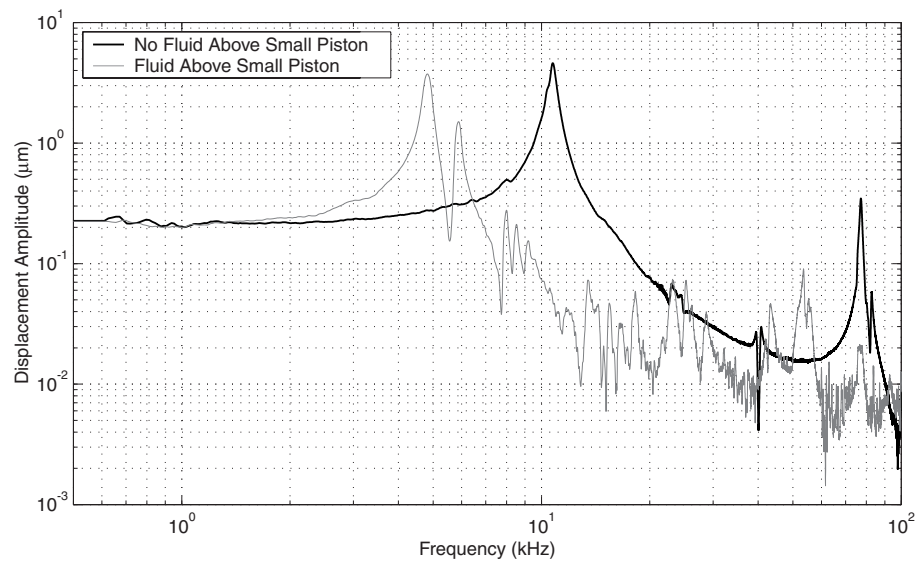


Figure 6.25: Frequency response of AV Device 1 with and without silicone oil on top of the small piston.  $V_1 = 0V \pm 5V$ ,  $P_{HAC} = P_2 = 500kPa$

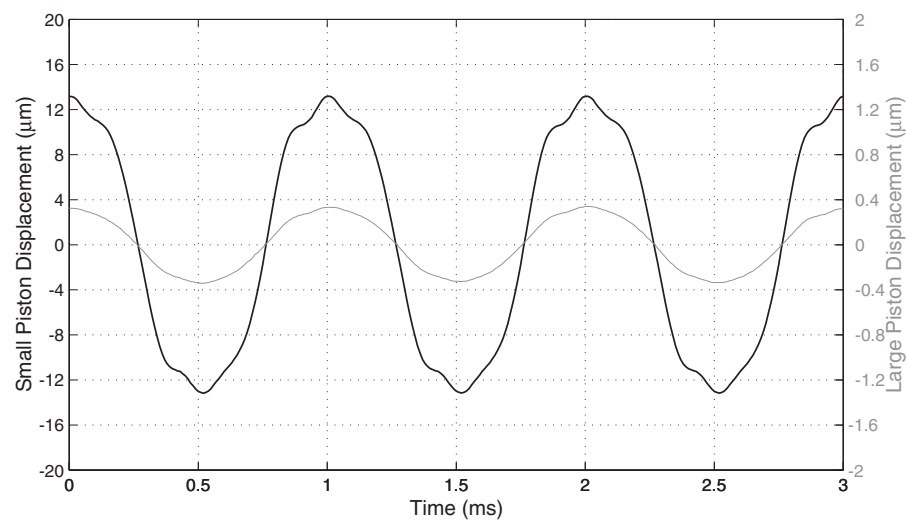


Figure 6.26: Time history of AV Device 1 with silicone oil on top of the small piston.



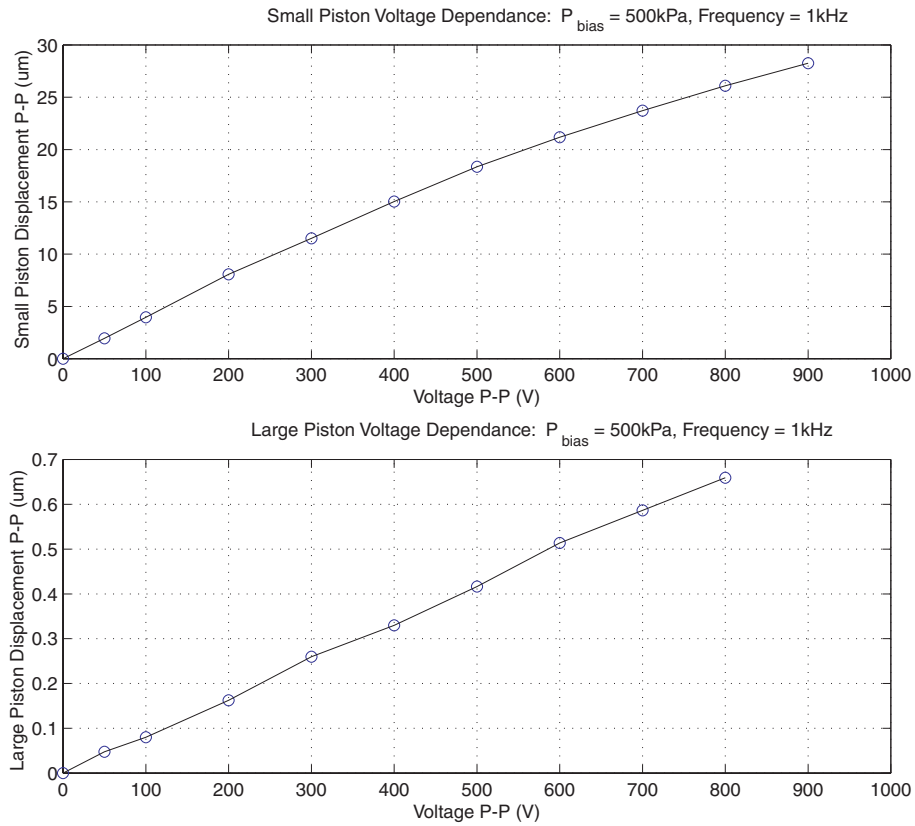


Figure 6.27: Deflection of the small and large pistons as a function of  $V_1$ .

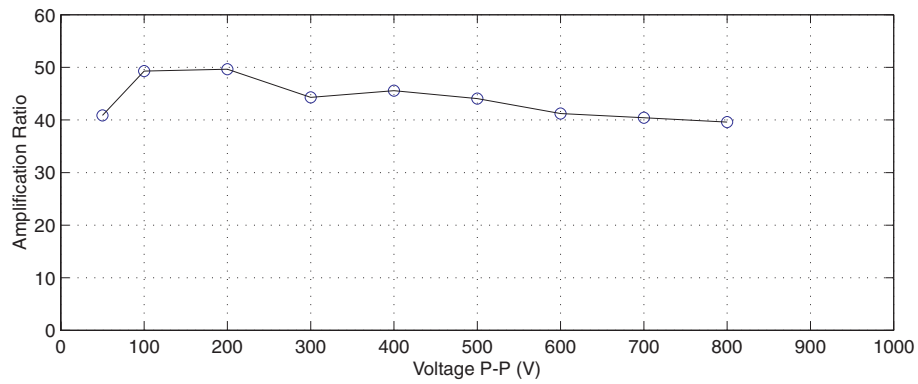


Figure 6.28: Amplification ratio as a function of  $V_1$ .

For a detailed discussion of these results, the reader is again referred to [19]. For the purposes of the argument presented in this document, it can be concluded that these dynamic tests indicate that the HAC has sufficient bandwidth for high frequency operation of microvalves and other micromanipulators. The added mass effect of the silicone oil on the natural frequency of the device shows that the effect of the system being driven by the hydraulic amplifier should be accounted for when designing a microscale hydraulic amplifier, as is the case for any actuator-load pair.

## 6.5 Summary of the test results

In this chapter we presented the following results:

- Pressure-deflection results for the three different types of tethered-membrane structures. It was shown that the measured results compared well with model predictions, when considering measurement errors and fabrication tolerances.
- Static hydraulic amplification results for two types of hydraulic amplifiers. The compressibility matrix coefficients, equivalent to a compliance matrix, were found to be close to those predicted by analytical models. See (6.11),(6.21). Further data analysis on the inverse compressibility matrices revealed possible measurement errors. Despite these errors, however, the data clearly indicates that a stiff hydraulic amplifier was produced.
- Dynamic hydraulic amplification results for a piezoelectrically driven hydraulic amplifier. These tests were performed to show that the hydraulic amplifier has sufficient bandwidth. A first natural frequency of approximately  $10kHz$  was achieved, reducing to  $5kHz$  when silicone oil was added on top of the small piston.

In conclusion these first test results on microfabricated hydraulic amplifiers prove that hydraulic amplification is a viable means of stroke enhancement for MEMS applications.

# Conclusions and recommendations

---

## 7.1 Conclusions

In this work, a number of significant accomplishments have been made, and these are summarized as follows:

- Fabrication techniques for fabricating high-quality tethered membrane structures have been developed [30].
- Reliable die-level alignment anodic bonding techniques have been developed and employed with success in the assembly of not only hydraulic amplification devices, but also complete MHT devices, significantly reducing the risks associated with full-wafer processing of fragile experimental wafers.
- Reliable filling procedures have been developed for the bubble-free filling of hydraulic dead volumes through channels of cross-section  $10\mu \times 10\mu m$  and  $1000\mu m$  in length.
- Static sealing techniques for experimental devices have been developed and proven to be reliable in sealing HAC's with minimal seal extrusion and HAC pressure rise.
- Dynamic sealing techniques, based on labyrinth seal technology, were conceived and proven to be a valid means of sealing an HAC that will operate at frequencies higher than the cutoff frequency of the dynamic seal.
- A fluid testing system was developed to enable the successful testing of HAC devices.
- A reliable test jig for the device was developed as a subsystem of the fluid testing system.
- Building on all items mentioned above, hydraulic amplification devices were successfully designed, fabricated and tested to prove the concept of hydraulic amplification for MEMS. The devices have been shown to have amplification ratios and stiffnesses that

agree well with theoretical predictions. In addition, it was shown that a microscale hydraulic amplifier, properly designed, will have sufficient bandwidth for high-frequency micromechanical actuation.

## 7.2 Recommendations

It is recommended that the following issues be addressed in further studies in hydraulic amplification devices.

- The fillet radius control techniques for fabricating the SOI membrane structures need substantial improvement. A process with minimal human intervention is required.
- This work dealt primarily with stroke amplification. The reverse application, namely force amplification, could be useful for increasing the force generated by, e.g. electrostatic actuation techniques. An investigation into this matter may prove fruitful.
- In addition to piezoelectric actuation, hydraulic amplifiers lend themselves to be driven by other types of actuation. The usefulness of hydraulic amplification in an electrostatic or electromagnetic system is worth investigating.
- The effect of various aspects of the device geometry on the natural frequency of the devices needs to be investigated in more detail. This study would also include the effect of geometry on the fluidic behavior of the device.
- The filling and sealing procedures, although robust, are tedious. Additional work to further improve and understand the filling process, as well as better sealing techniques for commercial applications, are recommended.
- It is probably wise to state that the per unit cost of devices, influenced by the aforementioned items in this list, as well as some others, needs to be reduced significantly to make hydraulic amplification commercially viable for MEMS. This is said with the understanding that the devices presented in this work were fabricated solely for research purposes, with cost not being a concern.

## 7.3 Final remarks

In conclusion it can be stated that hydraulic amplification for use in MEMS can now be considered feasible. Although this work has addressed the investigation from a mostly experimental point of view on a select few devices, it is safe to assume that the techniques developed and knowledge gained here, especially with reference to membrane fabrication and fluid filling and sealing, will enable future hydraulic amplification devices to rely on these building blocks for their success.



# References

---

- [1] B. Pascal. *Récit de Grande Expérience de l'Équilibre des Liquers*. A. Asher and Co., Berlin, 1893, reprinted from correspondence dated 1648.
- [2] H.D. Young. *University Physics - Extended Version with Modern Physics*. Addison Wesley Publishing Company, Reading, Massachusetts, USA, 8<sup>th</sup> edition, 1992.
- [3] N.W. Hagood *et al.* Development of micro-hydraulic transducer technology. *Proceedings ICAST '99*, October 11-13, 1999.
- [4] S. Pulitzer. Feasibility assessment and design of micro hydraulic solid-state transducers. Master's thesis, MIT, 1998.
- [5] P. Tang *et al.* Combined piezoelectric-hydraulic actuator based active vibration control for rotordynamic system. *Transactions of the ASME - Journal of Vibration and Acoustics*, 117:285–293, 1995.
- [6] J. Garcia-Bonito *et al.* A novel high-displacement piezoelectric actuator for active vibration control. *Smart Materials and Structures*, 7:31–42, 1998.
- [7] V. Ferrari *et al.* Development and application of mass sensors based on flexural resonances in alumina beams. *IEEE Trans. on Ultrasonics, Ferroelectrics and Frequency Control*, 43(4):601–608, 1996.
- [8] S.S. Lee and R. M. White. Self-excited piezoelectric cantilever oscillators. *Proc. of the 8th International Conference on Solid-State Sensors and Actuators, and Eurosensors IX, Stockholm, Sweden*, pages 417–420, 1995.
- [9] Luginbuhl *et al.* Piezoelectric cantilever beams actuated by pzt sol-gel thin film. *Proc. of the 8th International Conference on Solid-State Sensors and Actuators, and Eurosensors IX, Stockholm, Sweden*, pages 413–416, 1995.
- [10] M.S. Rogers *et al.* A new class of high-force, low voltage, compliant actuation systems. *Proceedings of the 2000 Solid State Sensor and Actuator Workshop, Hilton Head*, pages 210–213, 2000.
- [11] E.F. Prechtel and S.R. Hall. Design of a high efficiency, large stroke, electromechanical actuator. *Smart materials and structures*, 8(1):13–30, 1999.
- [12] X.-P.S. Su and H.S. Yang. Design of compliant microleverage mechanisms. *Sensors and Actuators A*, 87:146–156, 2001.

- [13] H.T.G. Van Lintel *et al.* A piezoelectric micropump based on micromachining of silicon. *Sensors and Actuators*, 15:153–167, 1988.
- [14] M. Esashi *et al.* Normally closed microvalve and micropump fabricated on a silicon wafer. *Sensors and Actuators*, 20:163–169, 1989.
- [15] H.Q. Li *et al.* A high frequency high flow rate piezoelectrically driven MEMS micropump. *Proceedings of the 2000 Solid State Sensor and Actuator Workshop, Hilton Head*, pages 69–72, 2000.
- [16] S. Zeng *et al.* Fabrication and characterization of electrokinetic micropumps. *Proceedings of the 2000 Inter Society Conference on Thermal Phenomena, IEEE*, pages 31–36, 2000.
- [17] J.S. Fitch *et al.* Pressure-based mass-flow control using thermopneumatically-actuated microvalves. *Proceedings of the 1998 Solid State Sensor and Actuator Workshop, Hilton Head*, pages 162–165, 1998.
- [18] P. Gravesen *et al.* Microfluidics - a review. *Journal of Micromechanics and Microengineering*, 3(4):168–182, 1993.
- [19] D.C. Roberts. *Design, modeling, fabrication and testing of a piezoelectric microvalve for high pressure, high frequency hydraulic applications*. PhD thesis, MIT, 2002.
- [20] M.J. Zdeblick *et al.* A microminiature fluidic amplifier. *Sensors and Actuators*, 15:427–433, 1988.
- [21] J. Vollmer *et al.* Bistable fluidic elements in LIGA technique for flow control in fluidic microactuators. *Sensors and Actuators A*, 43:330–334, 1994.
- [22] C.-C. Lin *et al.* Fabrication and characterization of a micro turbine/bearing rig. *Proceedings MEMS '99, IEEE*, pages 529–533, 1999.
- [23] P.C. Sen. *Principles of electric machines and power electronics*. John Wiley and Sons, New York, 2nd edition, 1997.
- [24] O. Yaglioglu. Modeling and design considerations for a microhydraulic piezoelectric power generator. Master's thesis, MIT, 2002.
- [25] Y.-H. Su *et al.* Large deflection analysis of a pre-stressed annular plate with a rigid boss under axisymmetric loading. *Journal of Micromechanics and Microengineering*, 11:645–653, 2001.
- [26] J.A. Carretero. Personal communication, 1999-2001.
- [27] S. Timoshenko and S. Woinowski-Krieger. *Theory of plates and shells*. McGraw-Hill, New York, 2nd edition, 1959.
- [28] R.L. Burden and J.D. Faires. *Numerical Analysis*. Brooks/Cole, Pacific Grove, California, USA, 6th edition, 1997.



- 
- [29] K.T. Turner. An evaluation of critical issues for microhydraulic transducers: Silicon wafer bonding, strength of silicon on insulator membranes and gold-tin solder bonding. Master's thesis, MIT, 2001.
  - [30] H.Q. Li. Personal communication, 1999-2001.
  - [31] N. Maluf. *An Introduction to Microelectromechanical Systems Engineering*. Artech House, Boston, 1st edition, 2000.
  - [32] K.-S. Chen, A.A. Ayon, and S.M. Spearing. Controlling and testing the fracture strength of silicon on the mesoscale. *J. Am. Ceram. Soc.*, 83(6):1476–84, 2000.
  - [33] M.A. Schmidt. Wafer-to-wafer bonding for microstructure formation. *Proc. of the IEEE*, 86(8):1575–1585, 1998.
  - [34] M. Despont *et al.* Fabrication of a silicon-pyrex-silicon stack by a.c. anodic bonding. *Sensors and Actuators A*, 55:219–224, 1996.
  - [35] M.M. Visser. Chemical analysis of bonded and debonded silicon-glass interfaces. *J. Micromech. Microeng.*, 11(5):N1–N6, 2001. Technical Note.
  - [36] R. Mlcak. Boston MicroSystems, Woburn, MA, Personal communication, 1999-2001.
  - [37] Dow Corning. *Compressibility at High Pressures of Various Dow Corning Silicone Fluids, as adapted from BridgeMan, P.W., Proc. Acad. Arts Sci., Vol. 77, No. 4, pp115-146, February 1949*. Midland, Michigan, U.S.A, March 1962.
  - [38] Dow Corning. *Data provided as published in Journal of Chemical and Engineering Data, Vol31, No.3 1986*. Midland, Michigan, U.S.A, 1986.
  - [39] S.D. Senturia. *Microsystem Design*. Kluwer Academic Publishers, Boston, 1st edition, 2001.
  - [40] E.S. Stockham. Personal communication, 2000-2001.
  - [41] A.H. Nayfeh and D.T. Mook. *Nonlinear Oscillations*. John Wiley and Sons, Inc., New York, USA, 1<sup>st</sup> edition, 1979.
  - [42] Swagelok. *General catalog*. Solon, Ohio, U.S.A, 2000.
  - [43] Concoa. *Regulators catalog*. Virginia Beach, Virginia, U.S.A, 2001.
  - [44] Parker Hannifin Corporation, General Valve Division. <http://www.pneutronics.com/gv/>. <http://www.parker.com/>.



## Material properties

---

The following material properties were used for performing calculations:

### Silicon, single crystal, (100)

Property name	Units	Quantity
Young's modulus (Effective)	$GPa$	165
Poisson's ratio (Effective)		0.22
Density	$kg/m^3$	2330
Tensile strength	$GPa$	1.0

### Glass (*Pyrex<sup>TM</sup>* 7740)

Property name	Units	Quantity
Young's modulus (Effective)	$GPa$	62.8
Poisson's ratio (Effective)		0.20
Density	$kg/m^3$	2230
Tensile strength	$MPa$	7

### Silicone oil - Hexamethyldisiloxane (*Dow Corning DC200 0.65cst*)

Property name	Units	Quantity
Bulk Modulus	$GPa$	0.6
Specific gravity		0.760
Viscosity	$cst$	0.65
Vapor pressure @ 25°C	$kPa$	6.7

Boiling point @ 1atm	<i>K</i>	373.15
----------------------	----------	--------

**Piezoelectric material - Single crystal PZT-PT (*TRS Ceramics*)**

<b>Property name</b>	<b>Units</b>	<b>Quantity</b>
Young's modulus (Effective)	<i>GPa</i>	6.76
Piezoelectric constant ( $d_{33}$ )	<i>pC/N</i>	1300
Density	<i>kg/m<sup>3</sup></i>	8315

# **Equipment list**

---

- (2×) Acopian Model 15EB100 15V AC-DC power supplies
- (1×) Bertan Associates Inc. Series 230 High Voltage Power Supply, 0-3kV, 0-5mA
- (1×) Branson Model 3510R-DTH ultrasonic cleaner
- (2×) Clear Air Products Model CAP412-5959A-1 Laminar flow workstations
- (3×) Concoa Model 4025301-580 regulators
- (2×) Concoa Model 4052001-000 regulators
- (1×) Dell XPS700r Desktop computer, Intel PentiumIII 700MHz Processor, 128MB RAM, SCSI HDD
- (1×) Dremel Model 395 Multipro tool
- (1×) Electronic Visions EV450 Aligner and AB1-Pv Bonder.
- (1×) GW Model GPS-3030D Lab Power Supply
- (1×) Hewlett Packard Model 33120A Function generator
- (2×) Industrial Test Equipment Model 112722-1 DC HV Power Supply
- (2×) Industrial Test Equipment Model 250A RF Amplifier
- (1×) MDC NW16 LN Foreline trap, KDFT-4075-2LN, P/N 434002
- (1×) MDC NW63 LN Foreline trap, LDFT-8250-2LN, P/N 434020
- (1×) Mitutoyo Digital Micrometer, Model 293-721-30, S/N 8084339
- (1×) MTI Model MTI-2000 Fotonic Sensor with fiber optic probes
- (2×) National Instruments BNC-2090 Connection units

- (2×) National Instruments PCI-6110 A/D in, D/A out Data acquisition boards
- (1×) Nikon Optiphot 88 microscope
- (1×) Olympus SZ60 Stereo microscope
- (1×) Omega Inc. Omegaette HH306 Thermometer
- (1×) Panasonic Model PV-7400 VCR unit
- (2×) Parker Hannifin Model 009-225-900 24VDC Fast acting solenoid valves
- (2×) PCB Piezotronics Model 112A22 dynamic pressure transducers
- (1×) PCB Piezotronics Series 481 signal conditioner
- (1×) Polytec PI OFV056 Scanning Head
- (1×) Polytec PI OFV056C Close-up attachment
- (1×) Polytec PI OFV3001 Vibrometer controller with 2nm resolution board
- (1×) Polytec PI OFV310 Focus controller
- (1×) Polytec PI PSV-Z-040-F Junction Box
- (7×) Red Bulls
- (1×) Sensotec FDD1BR.2D5A6A 0-5V 100psid pressure transducer, 0.1%
- (1×) Sensotec FDW1CJ.2D5A6A 0-5V 150psid pressure transducer, 0.1%
- (1×) Sensotec FPG1BR.2D5A6A 0-5V 100psig pressure transducer, 0.1%
- (2×) Sensotec FPG1CR.2D5A6A 0-5V 500psig pressure transducer, 0.1%
- (1×) Sony Model PVM-1350 Monitor
- (1×) Surface Technology Systems (STS) ICP Deep Reactive Ion Etch tool
- (15×) Swagelok SS-42S4 Ball valves
- (8×) Swagelok SS-4H Bellows valves
- (2×) Tektronix TDS210 Two-channel oscilloscopes
- (1×) T-M Vacuum Products Inc. Model SS806NS-14 Vacuum Oven

- (1×) Varian Convectorr vacuum gauge with Panelvac meter
- (1×) Welch vacuum pump Model 1392B-01 with Emerson Model S55NXMPF-6788 Electric motor





# Detail designs

---

### C.1 Die-level anodic bonding jig

The detail design for the die-level anodic bonding jig, as shown in Figure 3.8, is given here. All parts not shown are standard off-the-shelf components. Some of the standard knurled thumbwheels required minor modifications for this application. The four posts on the corners of the jig are standard 6-32 threaded rod. The bushings shown in Figures C.5 and C.6 require a piece of seamless 304L stainless steel tubing to be cut to protect the ceramic parts against abrasion from the threaded rods.

The complexity of this design comes from the requirements of being able to make contact to multiple layers in a silicon-glass sandwich structure, from both the top and bottom of the stack. In addition, this jig has to withstand temperatures as high as  $500^{\circ}C$ , eliminating most, if not all, polymers for use as insulators. In addition, care had to be taken to allow for thermal expansion. Therefore, the main stainless steel part is "floating", both mechanically and electrically, between the four posts, but the potential of this part is effectively set by the threaded rod contact that is connected to the post attached to Spacer2, shown in Figure C.6. This post was chosen to be at ground potential and the main part is pressed against it by springs acting on the opposite ceramic bushes. The use of a positive-negative switchable power supply made device stacking and pre-bonding assembly easy. After assembly, the power supply simply had to be set to ensure that the glass is at a negative potential with respect to the silicon.

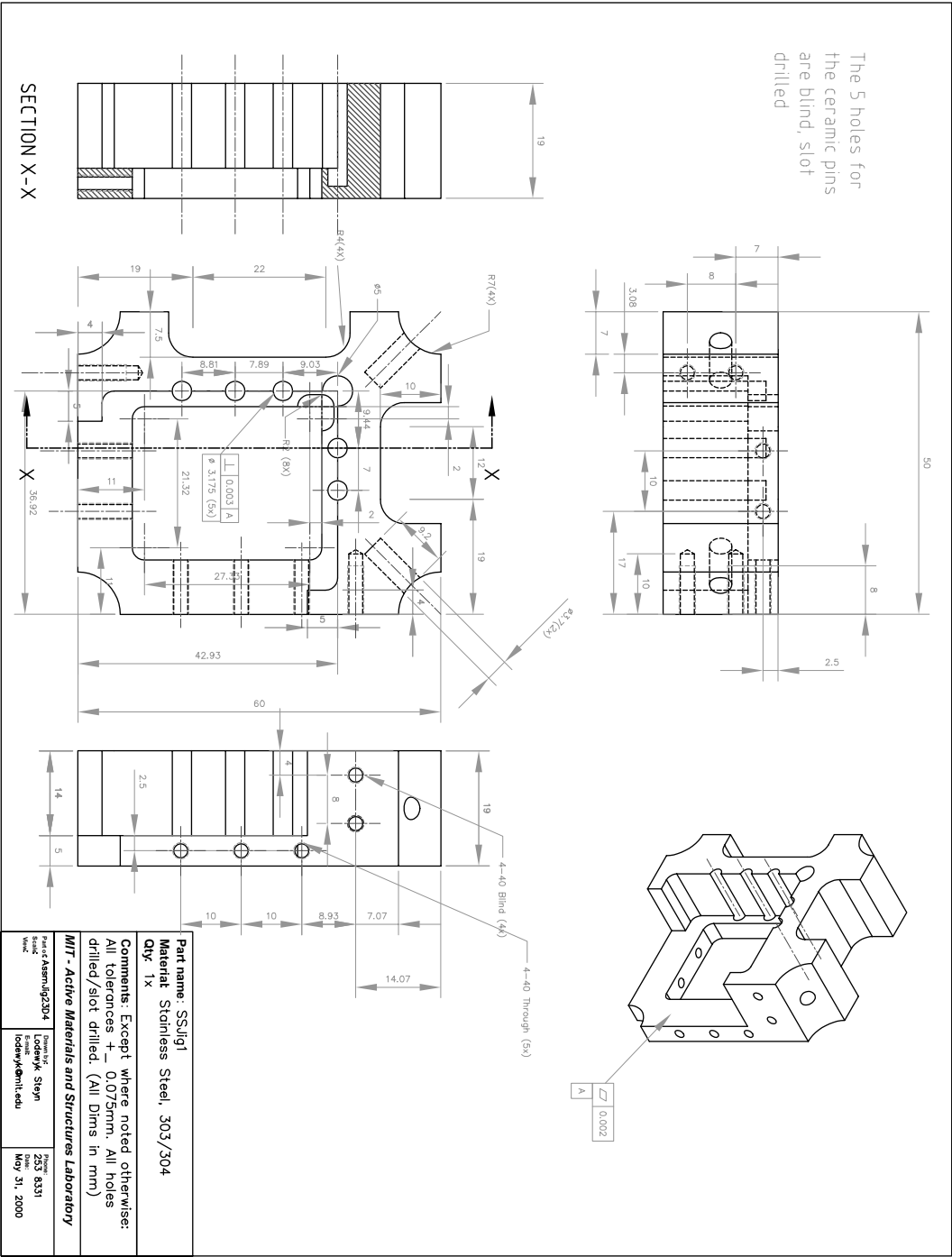


Figure C.1: Main stainless steel part

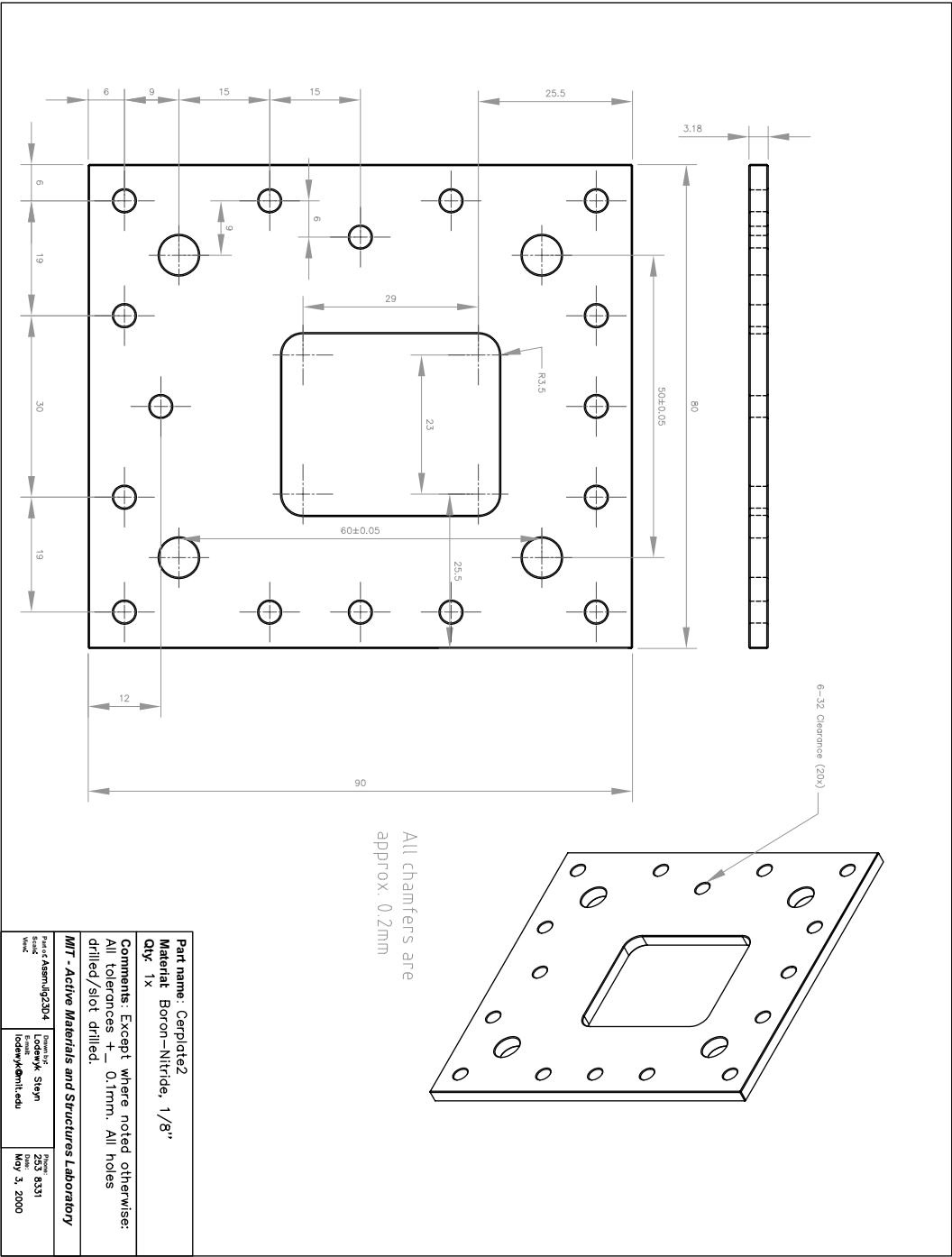


Figure C.2: Lower ceramic plate

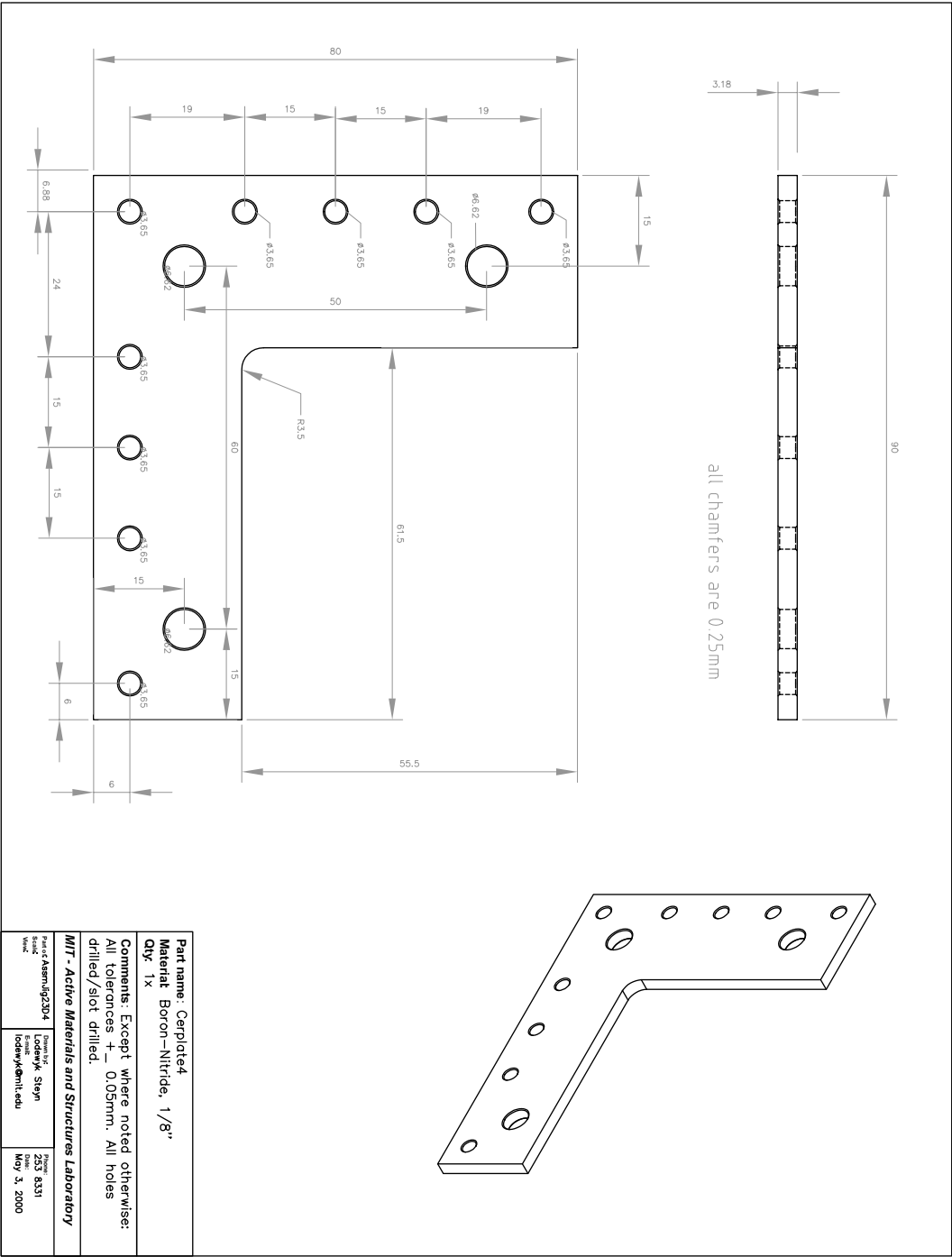


Figure C.3: Upper ceramic plate

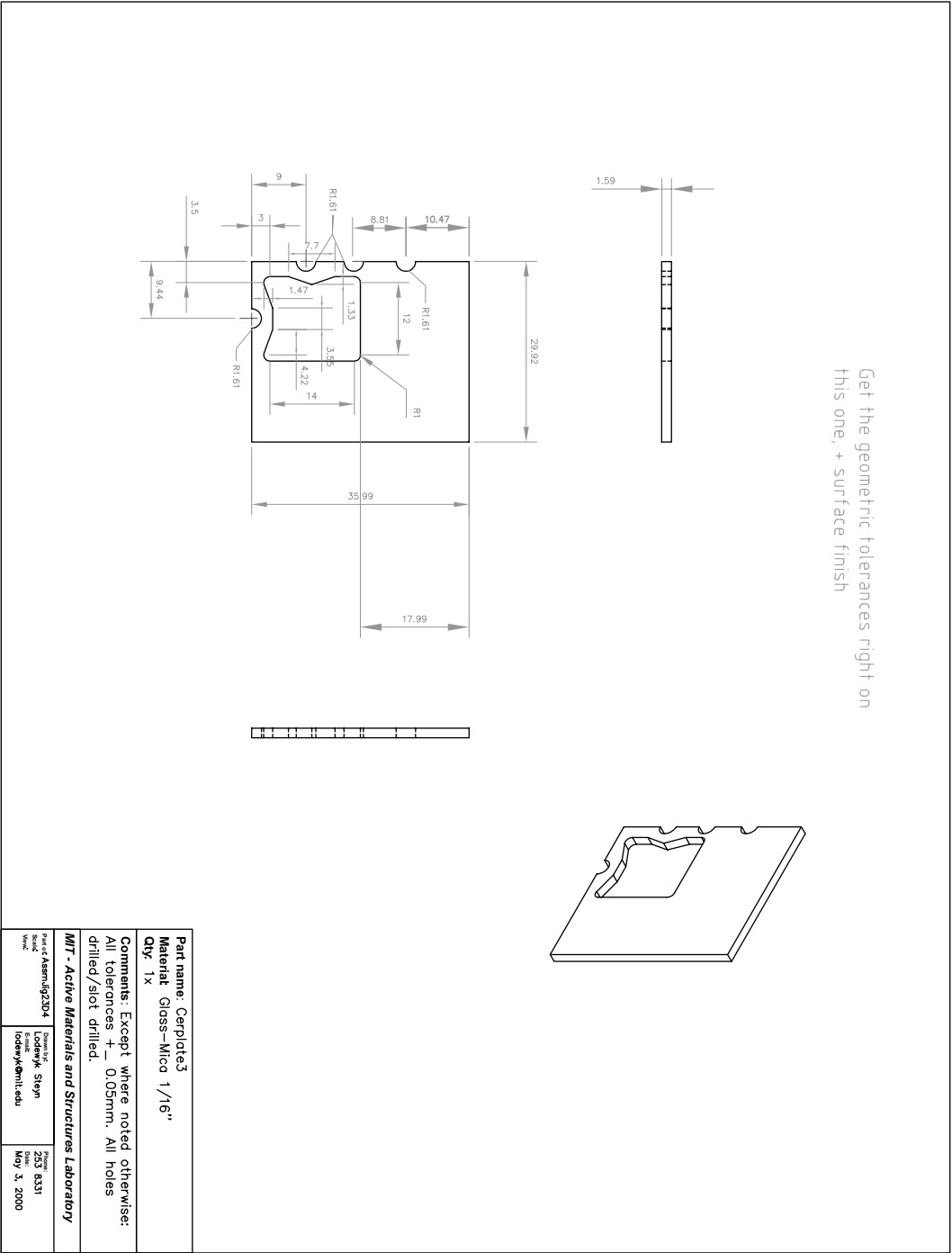


Figure C.4: Chip rest (ceramic)

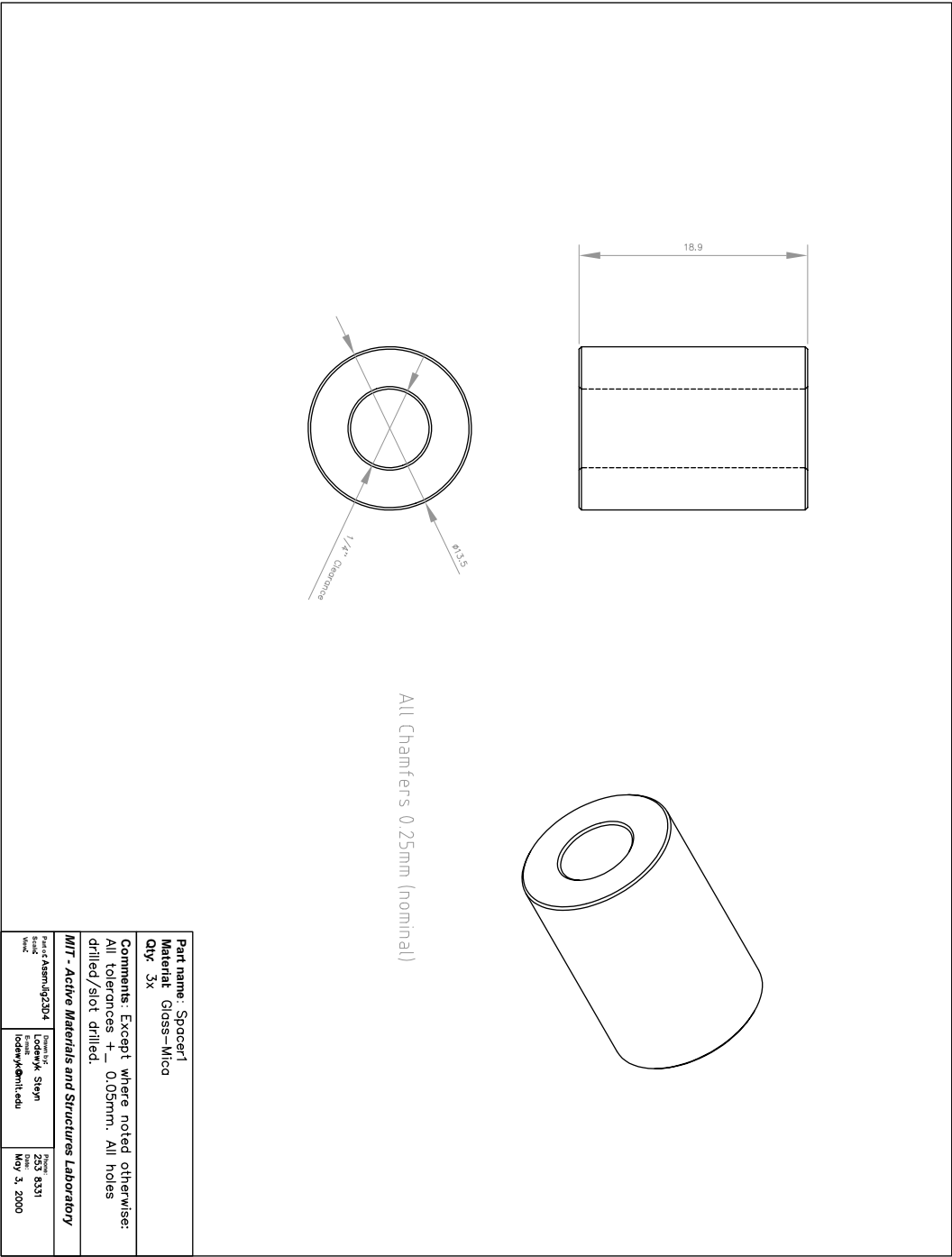


Figure C.5: Ceramic bushing

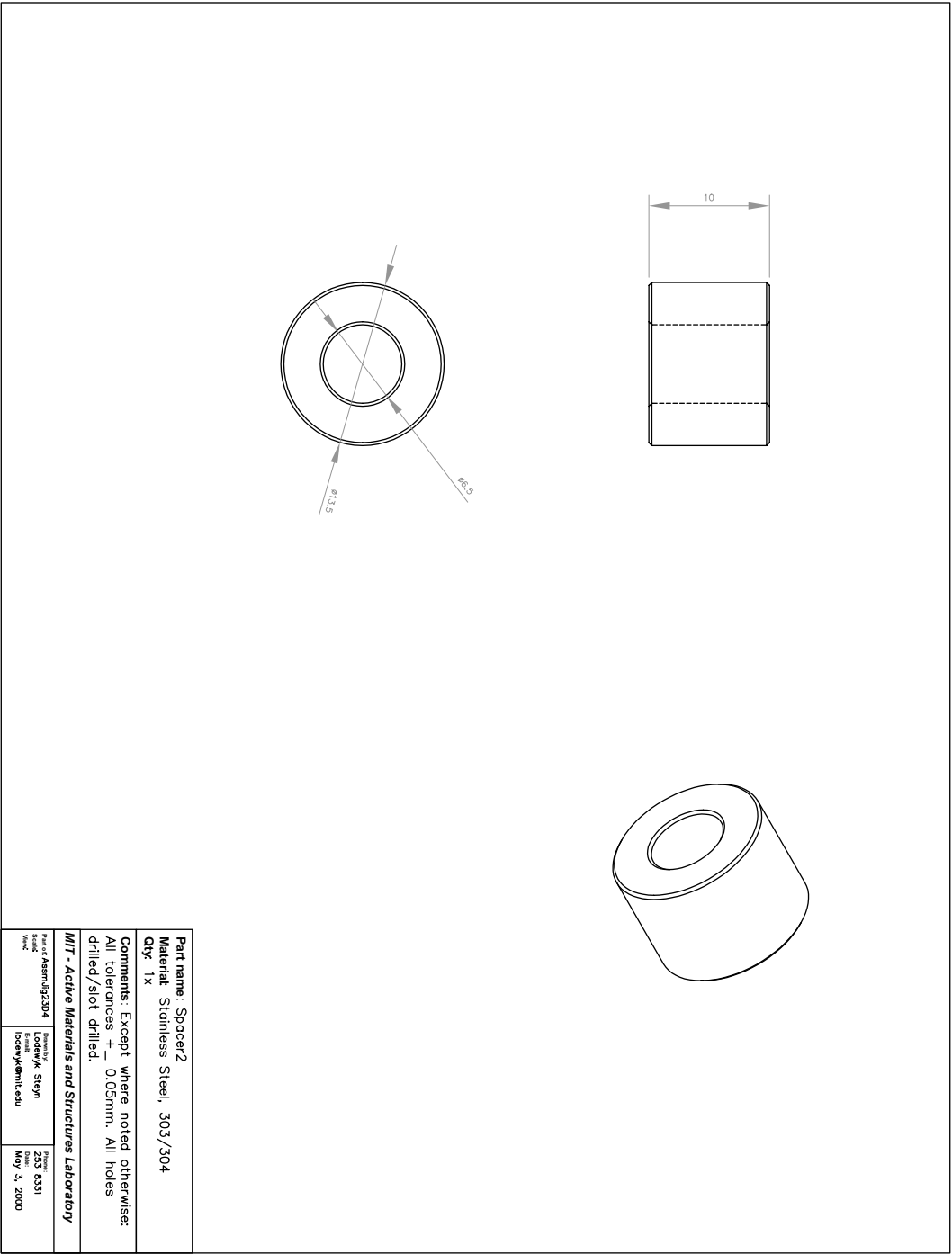


Figure C.6: Stainless steel bushing

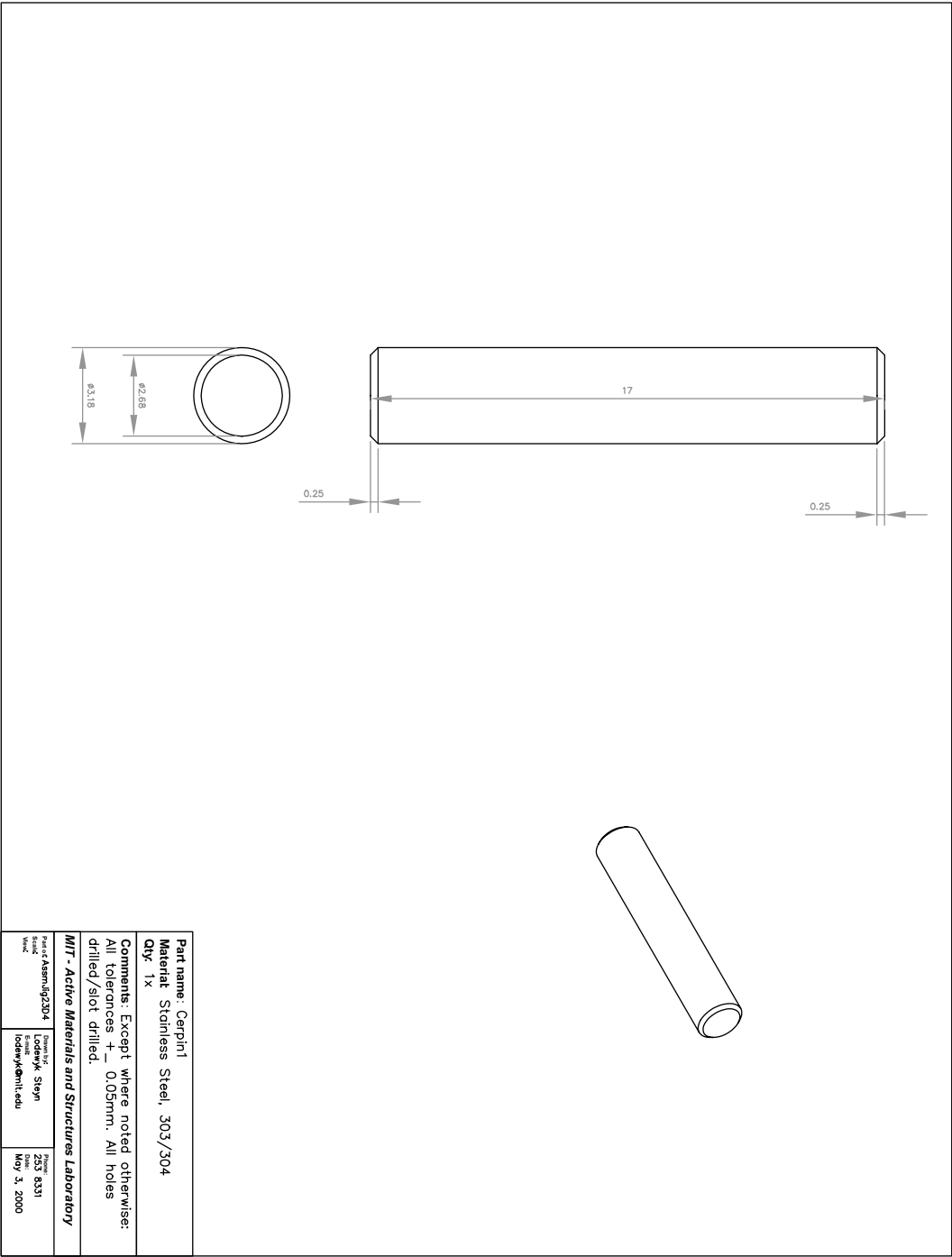


Figure C.7: Ceramic alignment pin



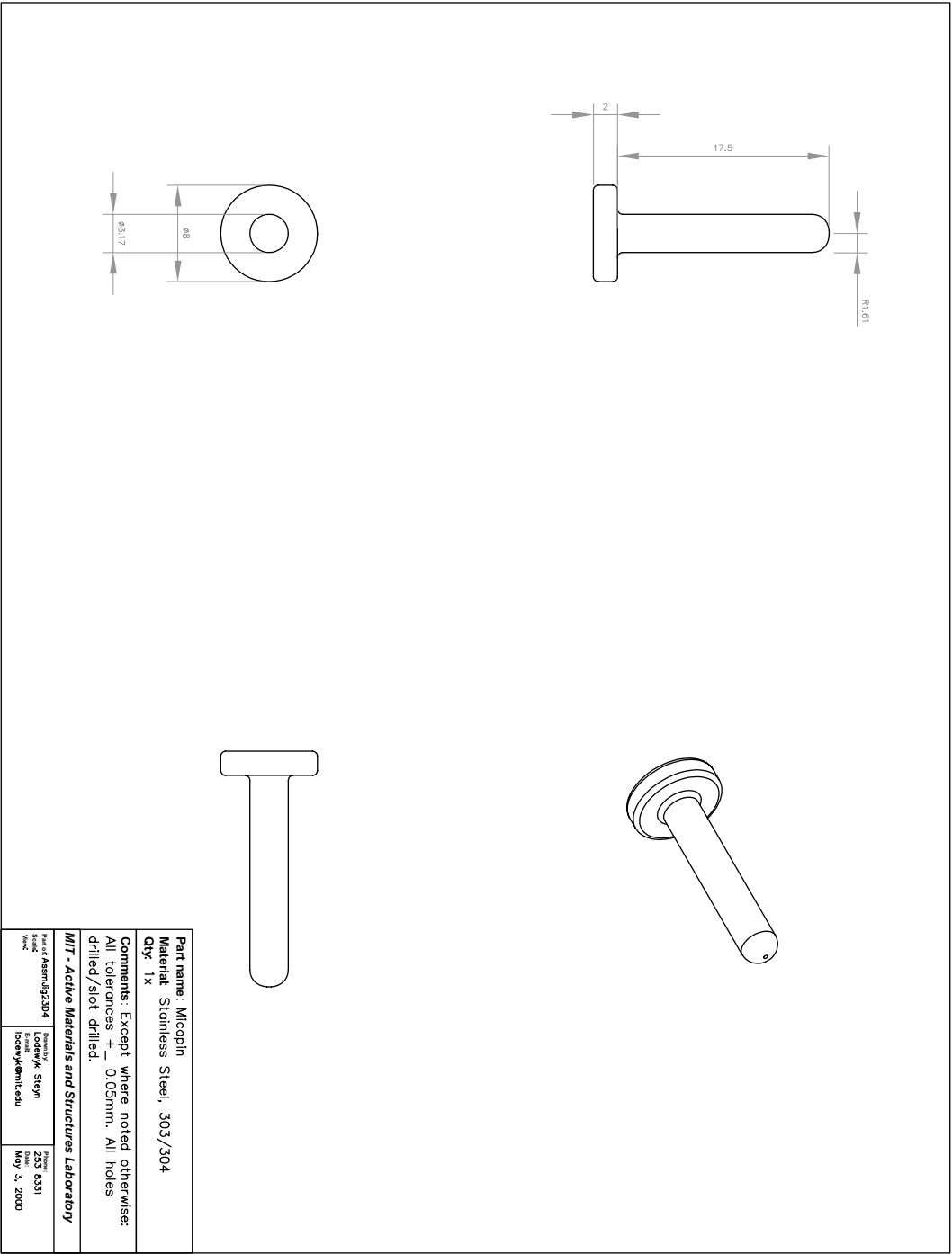


Figure C.8: Ceramic clamping pin

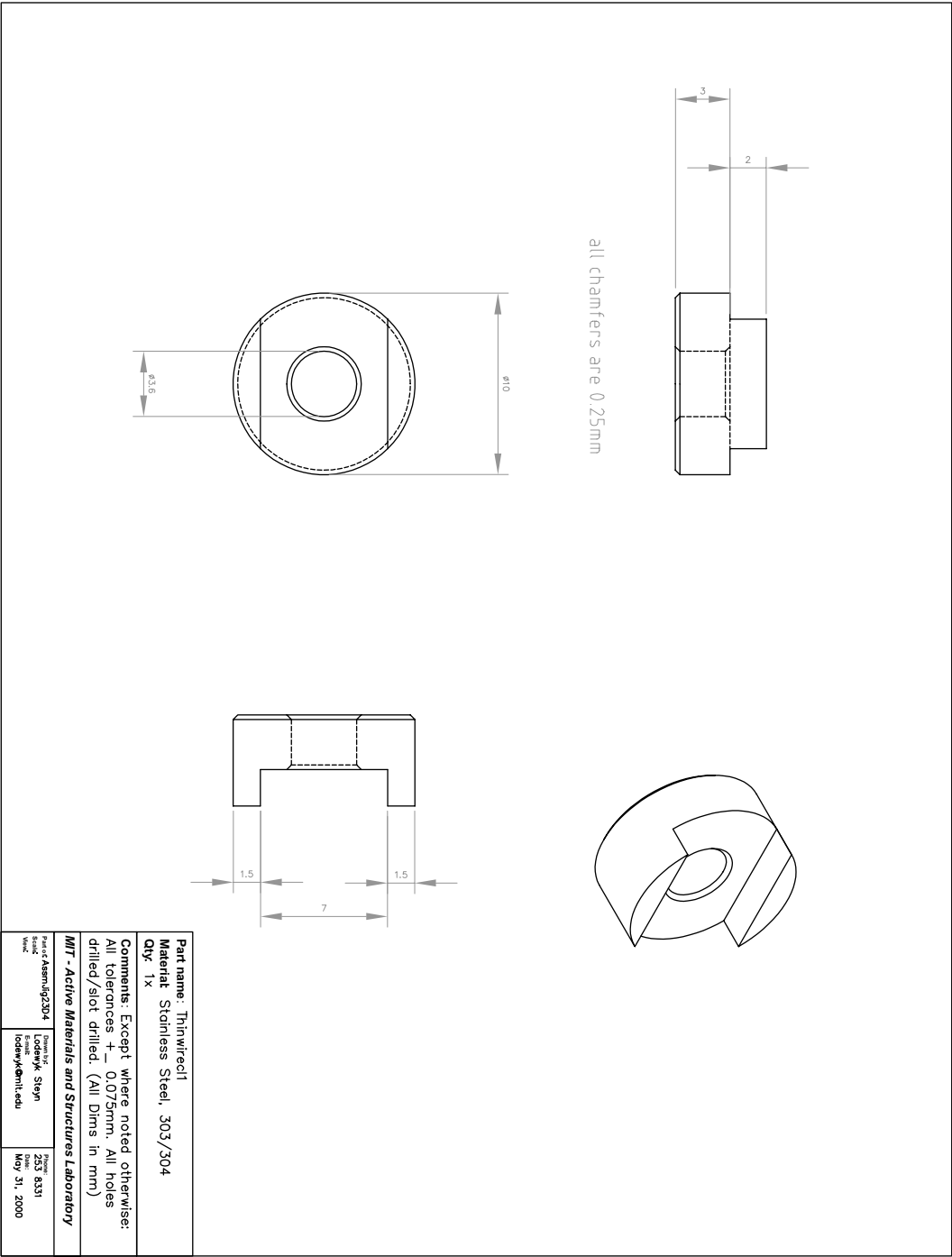


Figure C.9: Wire clamp lower part

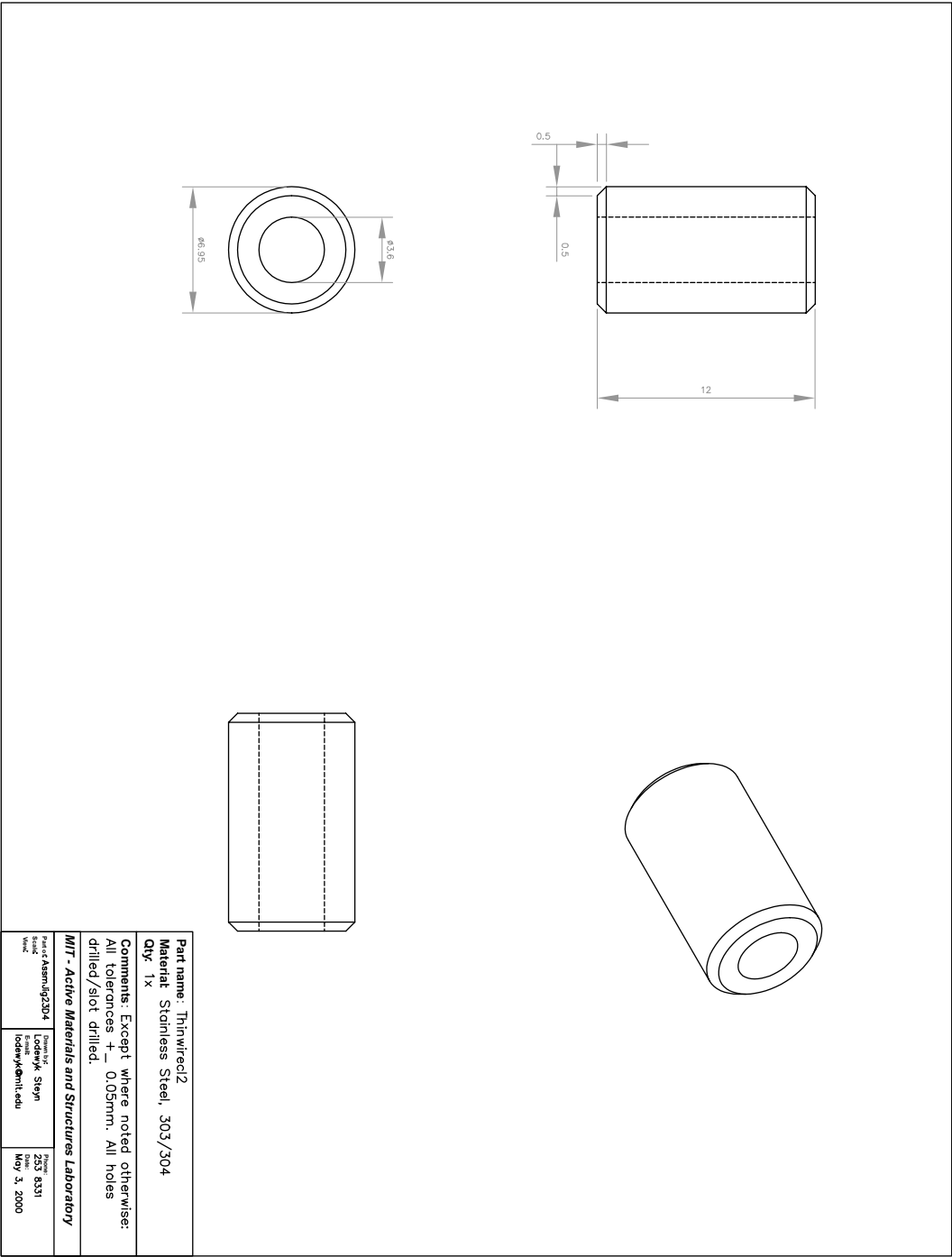


Figure C.10: Wire clamp upper part



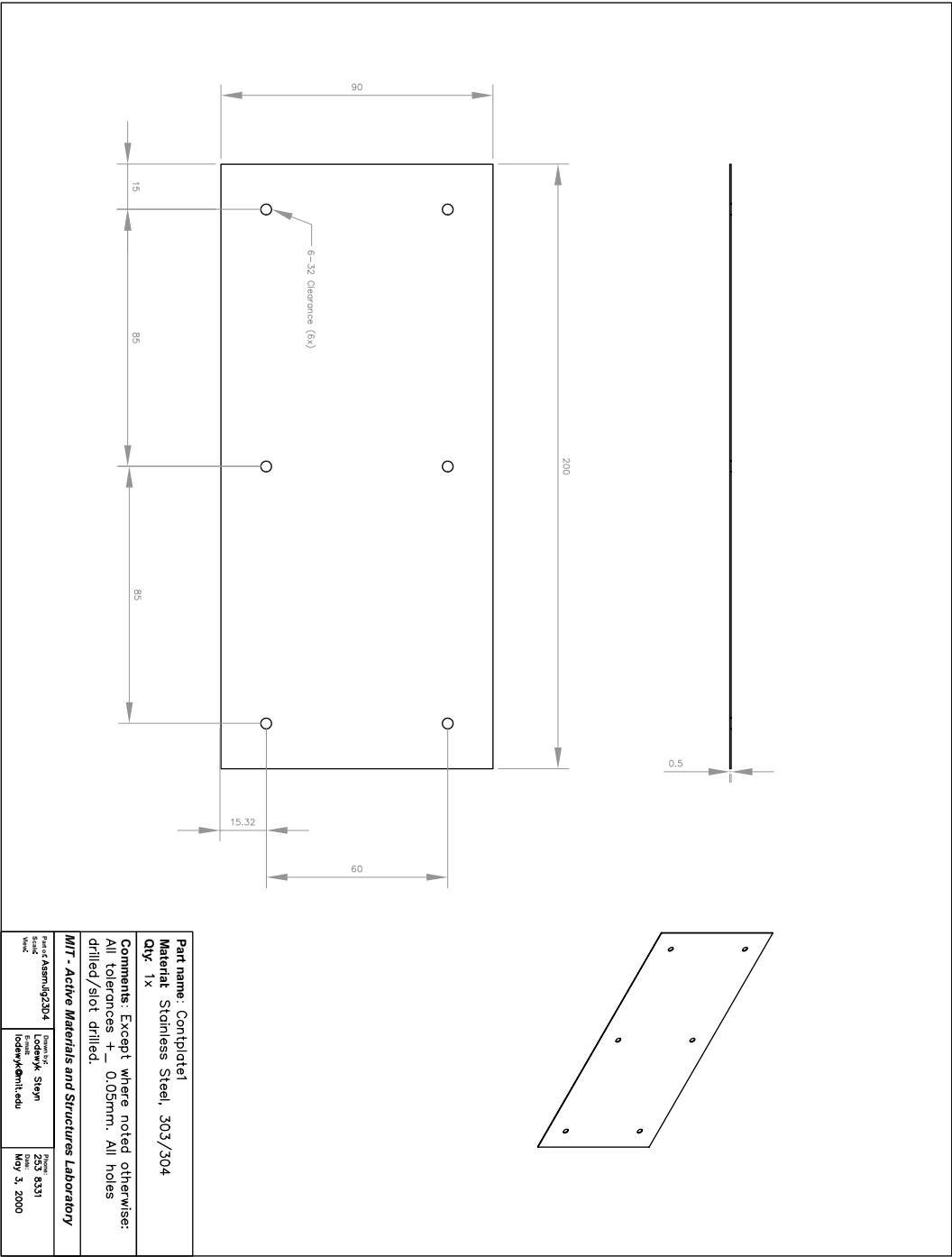


Figure C.12: Lower contact plate

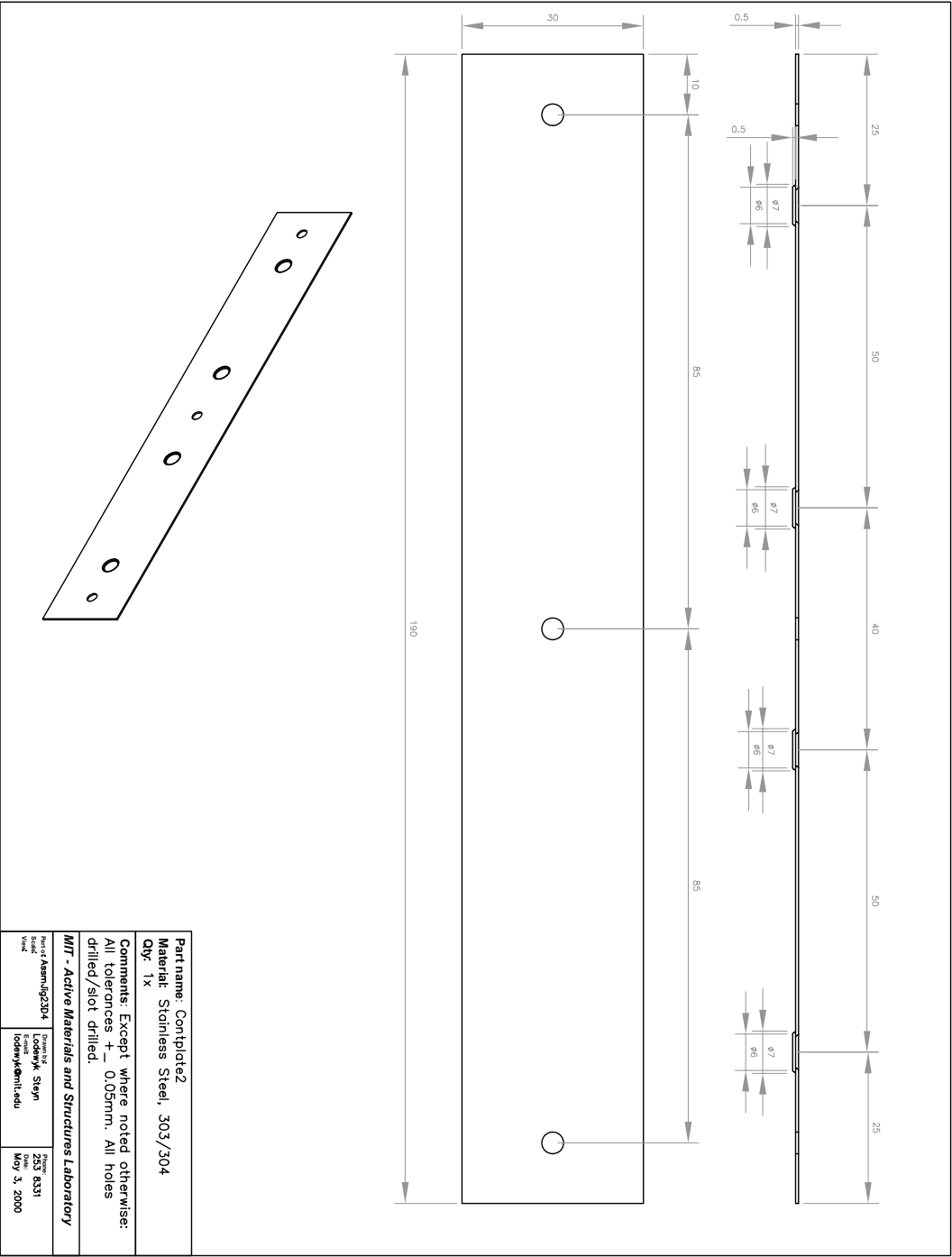


Figure C.13: Upper contact plate

## C.2 Test jig for the hydraulic amplifier

This section includes the detail drawings of the test jig that was used to test the hydraulic amplifier. The material used was 6061 – *T6* aluminum, and the jig was anodized black to prevent glare while performing optical measurements.









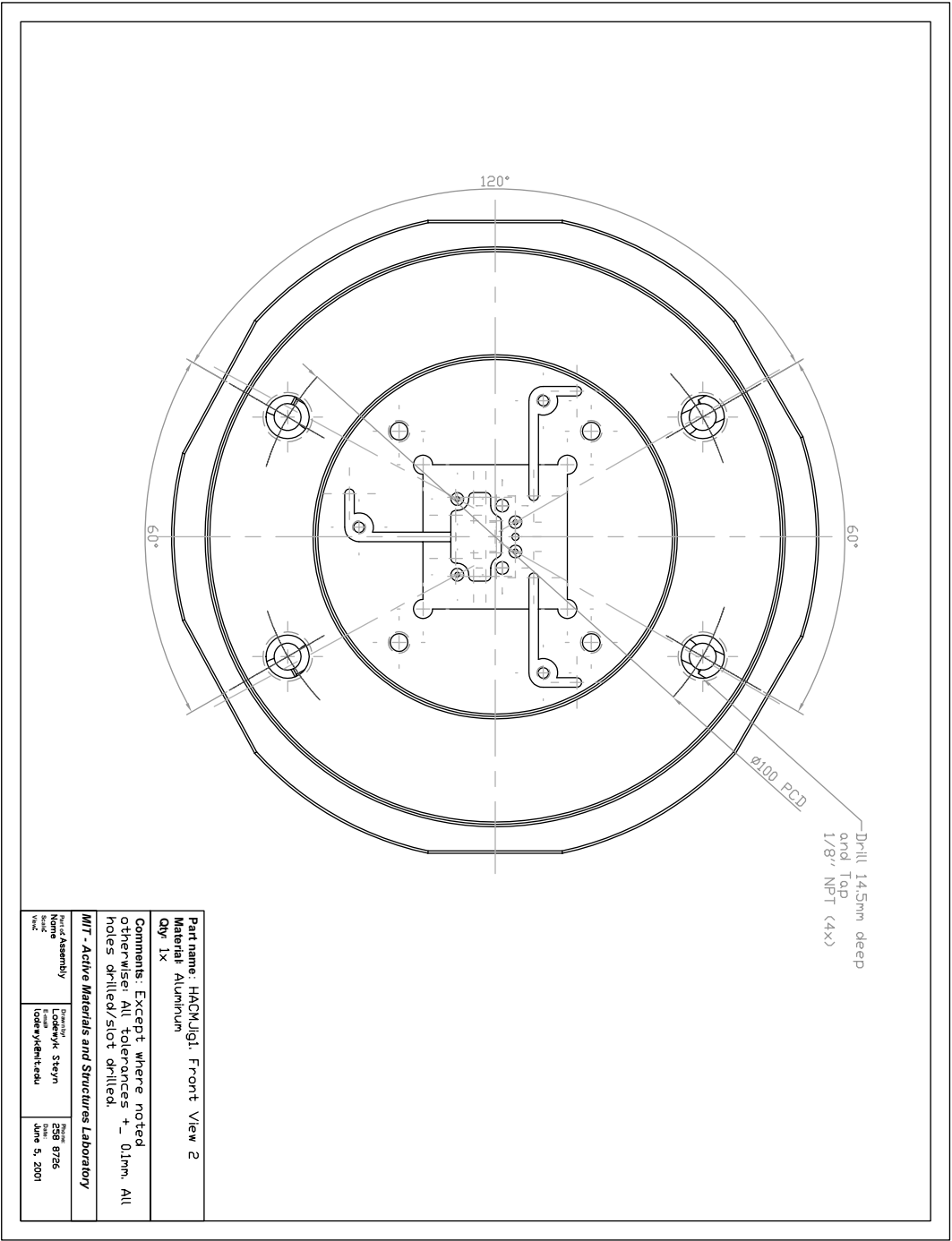


Figure C.17: Front view 2

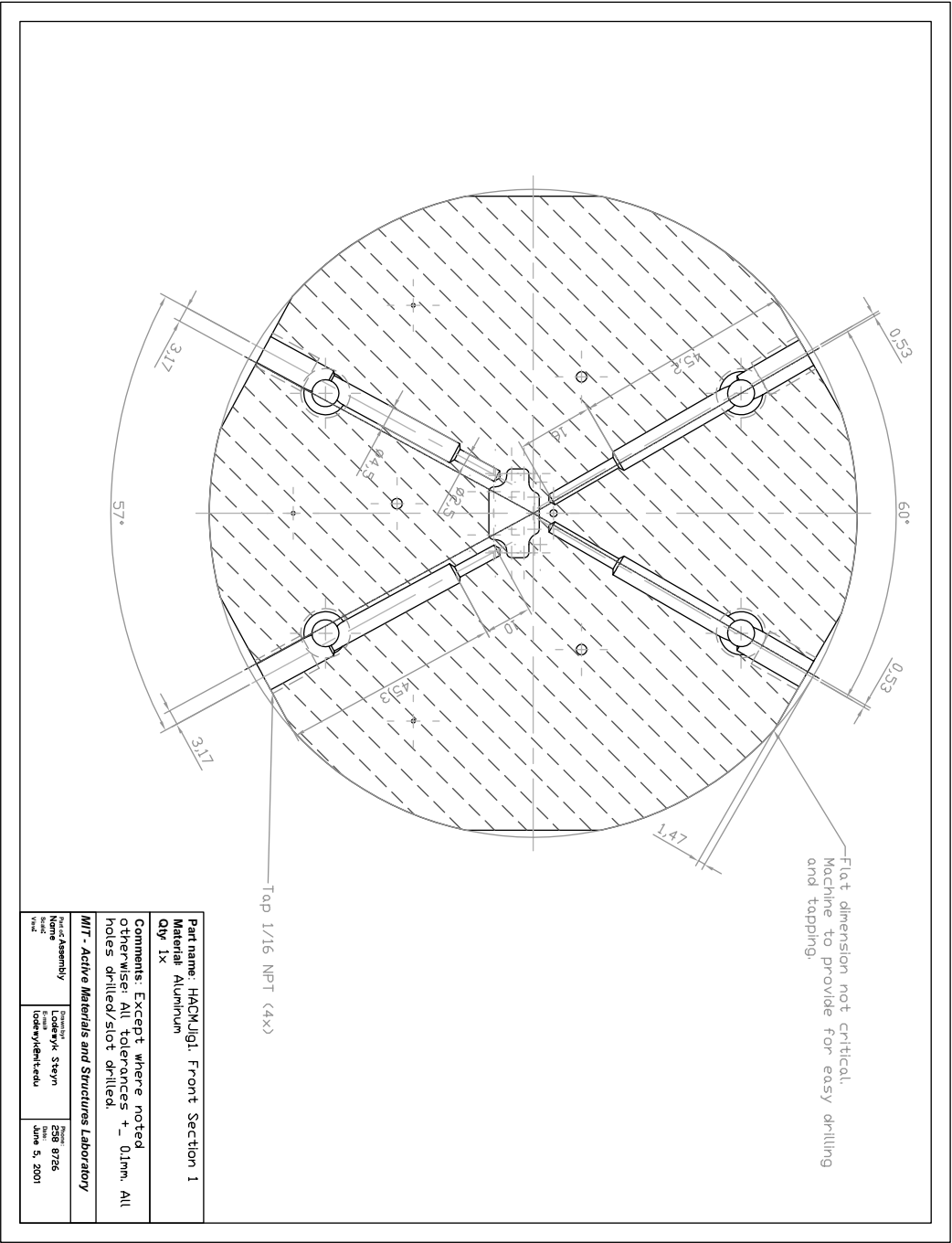


Figure C.18: Front section 1



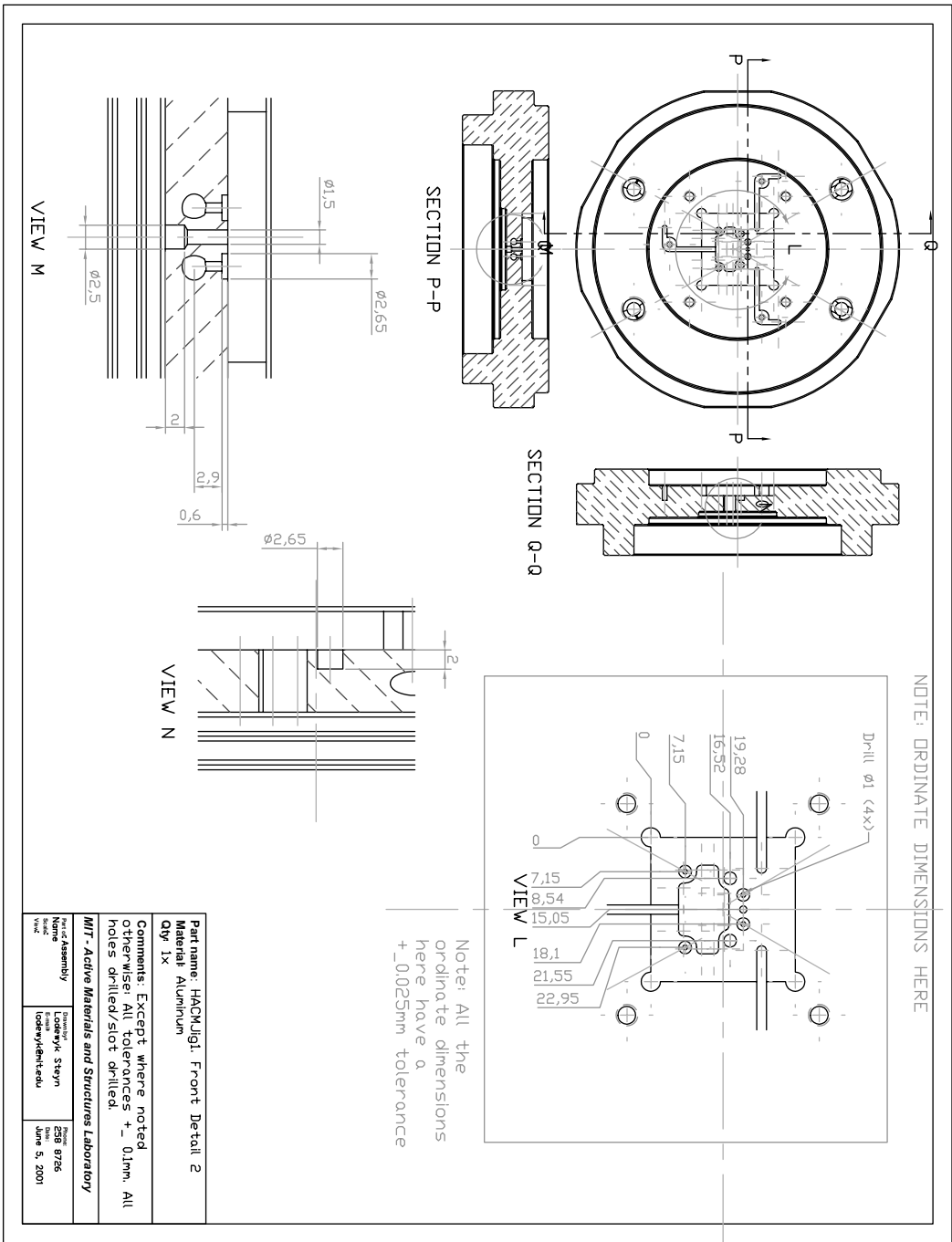


Figure C.20: Front detail 2

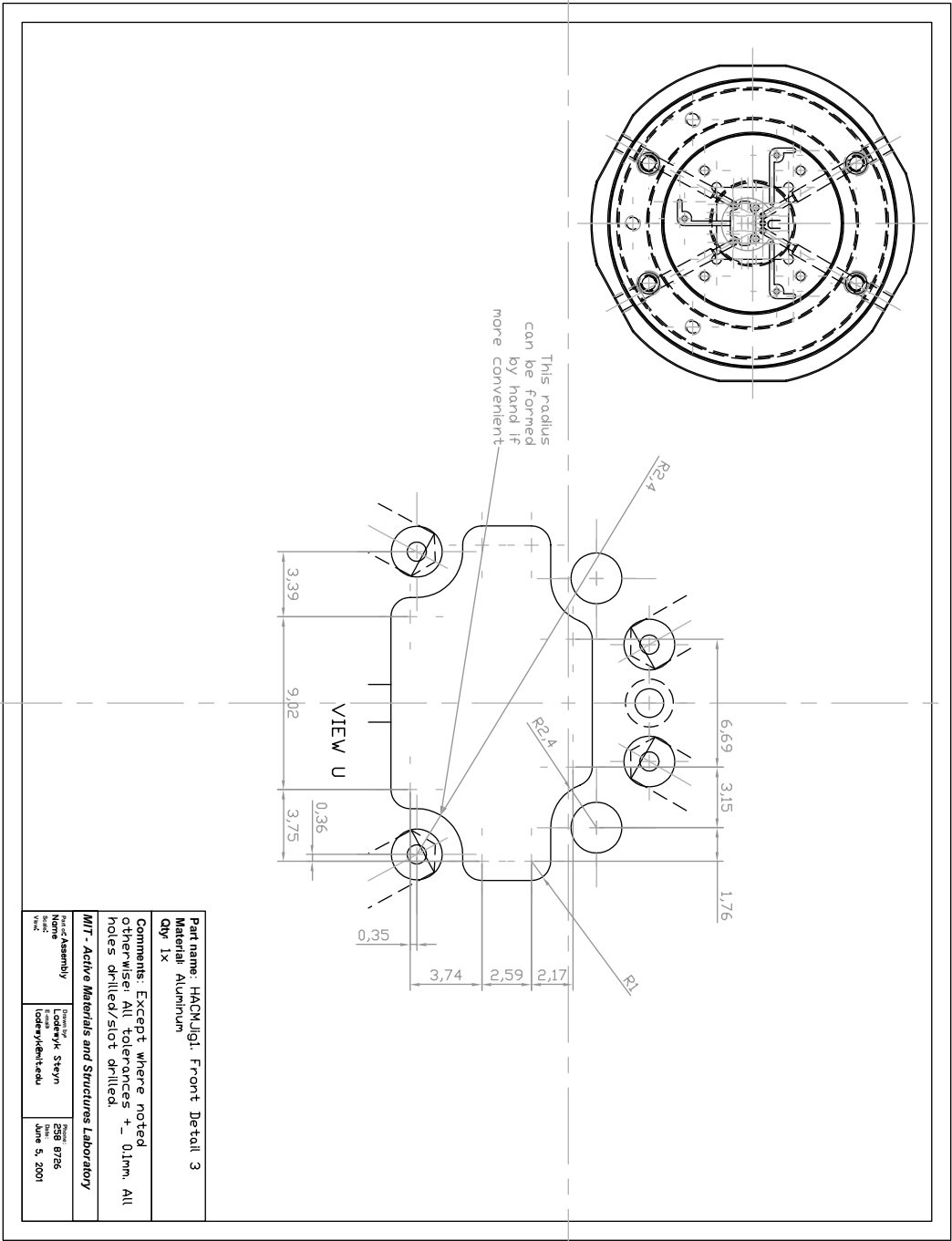


Figure C.21: Front detail 3

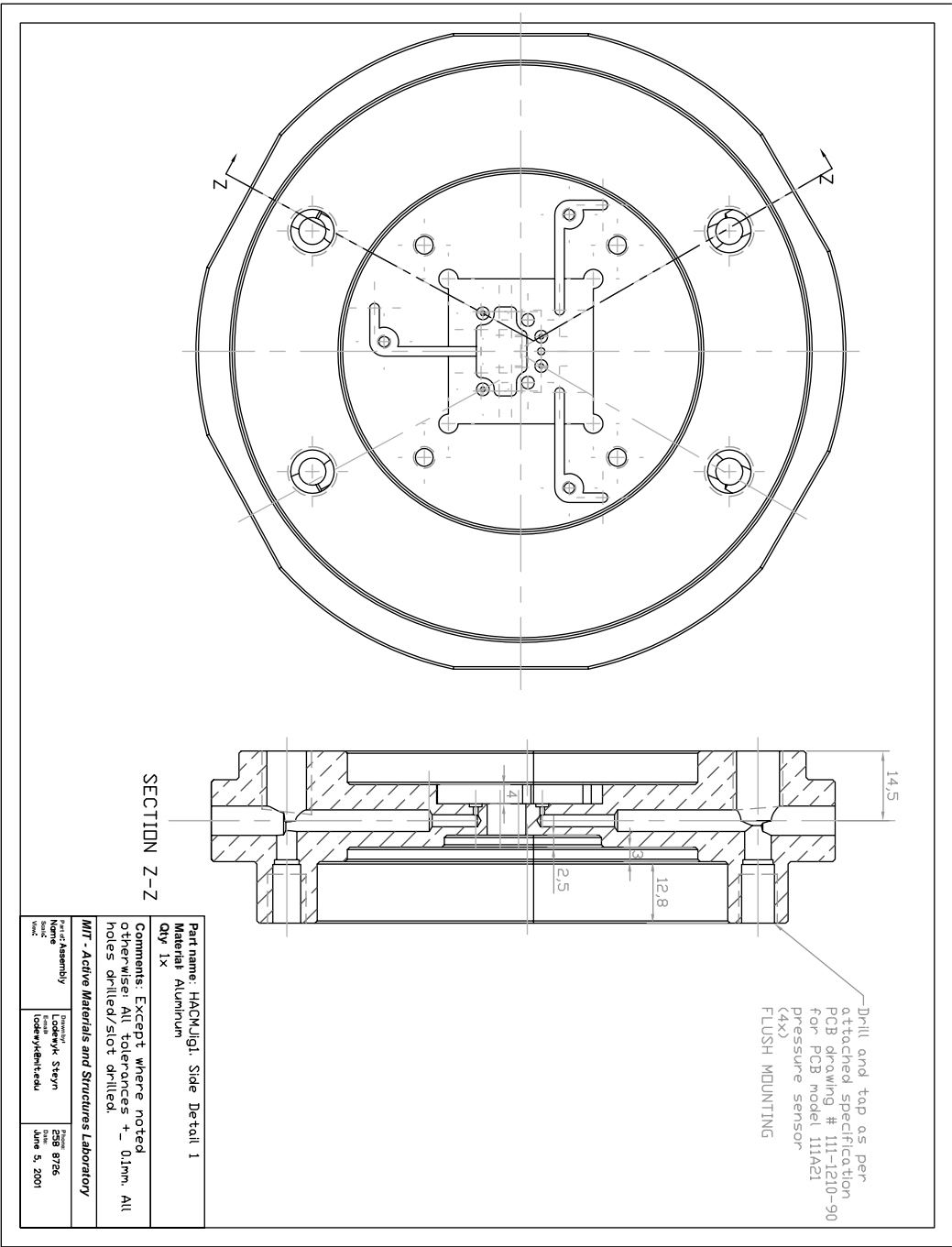


Figure C.22: Side detail 1



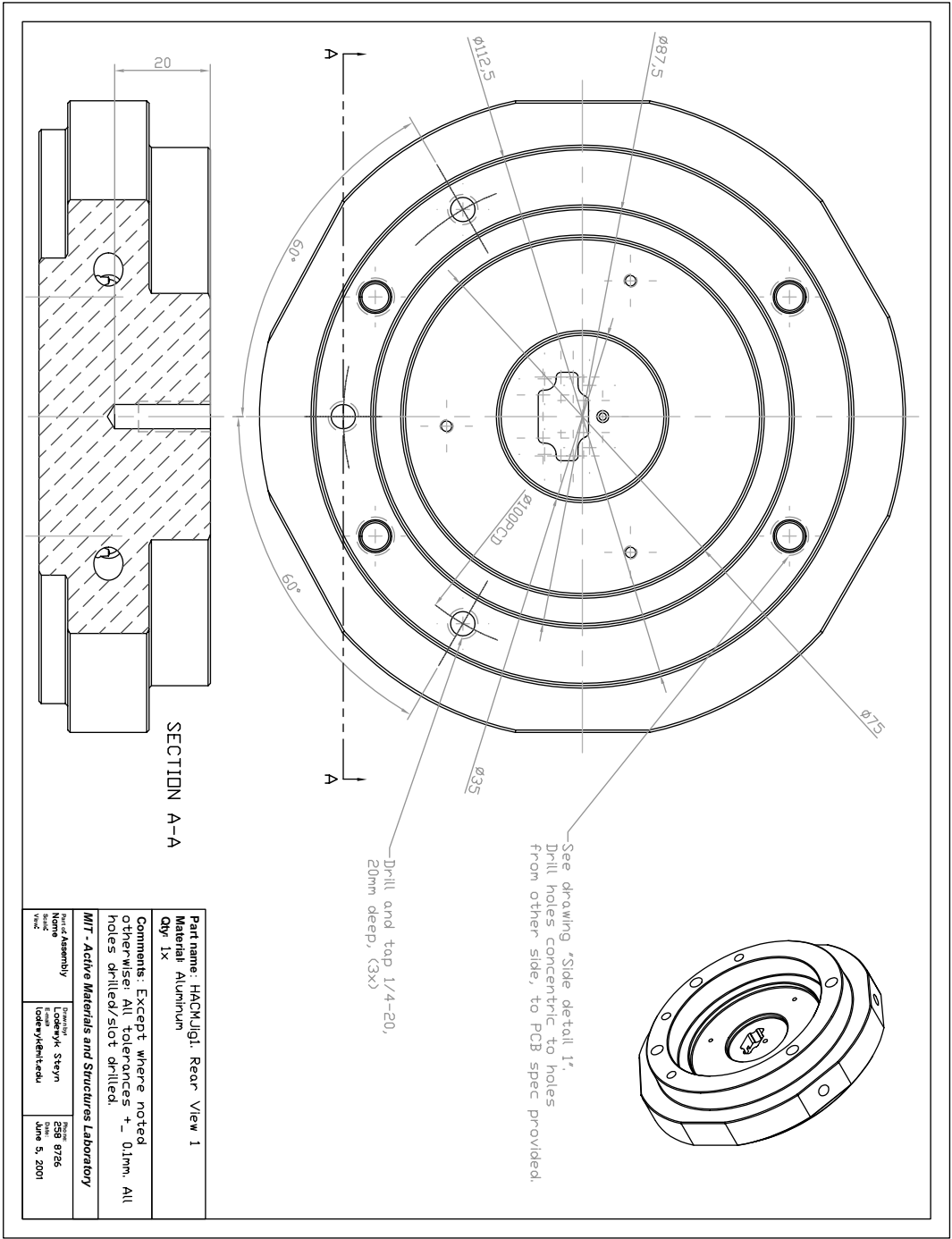


Figure C.23: Rear view 1



## Appendix D

# Computer code

---

### D.1 Matlab codes used for modeling of the HAC

*These codes were contributed by D.C. Roberts, and are included here for completeness.*

#### D.1.1 Bisection method iteration code for modeling of the HAC

This code calls the nonlinear plate code and uses bisection to solve for  $z_1$  and  $z_2$ , using the following equation as a convergence criterium (See (2.20)):

$$\Delta V_1 + \Delta V_2 = \Delta V_f \quad (\text{D.1})$$

```
function [Zte, dVte, dVfluid, Ztop, dVtop, Fvm, Zde, dVvm, Maxstress, Zvc, PHAC]...
    =HAC1ValveMatlabIterateSubCode(Ppis,PHPR)

%9-16-01 DAVID C. ROBERTS
%
% This file iterates in PHAC to determine the equilibrium solution
%for the HAC device behavior (1-Valve devices).

%Read in compliance coefficients from Maple generated .m file
HAC1ValveMatlabIterateMatrix; %Read in compliance coefficients

%%%%%%%%%%%%%%%%%%%%%%%%%%%%%%%%%%%%%%%%%%%%%%%%%%%%%%%%%%%%%%%%%%%%%%%%%%%%%%
flagNL=1; %Include non-linearity if flagNL=1
No=0; %Initial in-plane prestress

%%%%%%%%%%%%%%%%%%%%%%%%%%%%%%%%%%%%%%%%%%%%%%%%%%%%%%%%%%%%%%%%%%%%%%%%%%%%%%
%PROVIDE INITIAL GUESS FOR PHAC%%%%%%%%%%%%%%%%%%%%%%%%%%%%%%%%%%%%%%%%%%%%%%%%%%%%%%%%%%%%%%%%%%%%%%%%%%%%%%
PHACguess=0.0013e6;
PHAC1=PHACguess;
PHAC2=PHACguess;
check0=1;
check1=1;
```

```
i=0
j=0

%Determine Volume discrepancy for initial PHAC guess
U=[Ppis PHPR PHAC1]; %Vector of input parameters to compliance matrix
S=A*U'; %S is the vector of all linear responses
Fvc=Av*c*(PHAC1-PHPR); Pvm=PHAC1-PHPR; %Define these loadings for use in
%NLActiveValve_MembraneCaseA.m
[y,r,Vtotal,psi,W,theta,xi,thetaND,psiND,sigma_r_top,sigma_r_bot,yvc,maxstress]...
    = NLActiveValve_MembraneCaseA(Pvm,Fvc,rv,c,rv,m,tvm,Esi,nusi,flagNL,No);
dVvm=Vtotal; dVte=S(2); dVfluid=S(3); dVtop=S(5);
check1 = (dVvm + dVtop - dVte - dVfluid);
check0=check1;
%Done

%Determine range of PHAC (between PHAC0 and PHAC1) within which
%the real PHAC lies
while check0*check1/(abs(check0*check1))> 0
i=0
    j=j+1

    PHAC0 = PHAC1;
    PHAC1 = PHAC2
    check0 = check1

    U=[Ppis PHPR PHAC1]; %Vector of input parameters to
    %compliance matrix
    S=A*U'; %S is the vector of all
    %linear responses
    Fvc=Av*c*(PHAC1-PHPR); Pvm=PHAC1-PHPR; %Define these
    %loadings for use in NLActiveValve_MembraneCaseA.m
    [y,r,Vtotal,psi,W,theta,xi,thetaND,psiND,sigma_r_top,sigma_r_bot,yvc,...
        maxstress] = NLActiveValve_MembraneCaseA(Pvm,Fvc,rv,c,rv,m,tvm,Esi,nusi,flagNL,No);
    dVvm=Vtotal; dVte=S(2); dVfluid=S(3); dVtop=S(5);
    check1 = (dVvm + dVtop - dVte - dVfluid);

    if check1 < 0
        PHAC2 = 10*PHAC1;
    elseif check1 > 0
        PHAC2 = 0.1*PHAC1;
    else
        break;
    end
end

if PHAC1<PHAC0 %rearrange PHAC0 to be less than PHAC1
    PHACmax=PHAC0;
    PHACmin=PHAC1;
    PHAC1=PHACmax
    PHAC0=PHACmin
else
end
```

```

%DONE,it has been determined that PHAC lies between PHAC0 and PHAC1

j=0;

%Determine solution for PHAC
PHACm=0.5*(PHAC0+PHAC1);
firsthalf=0;

while abs((PHAC1-PHAC0)/PHAC0) > 0.0001

    i=1
    j=j+1

    if firsthalf==1

        U=[Ppis PHPR PHACm]; %Vector of input parameters to %
        %compliance matrix
        S=A*U'; %S is the vector of all
        %linear responses
        Fvc=Av*c*(PHACm-PHPR); Pvm=PHACm-PHPR; %Define these loadings
        %for use in NLAActiveValve_MembraneCaseA.m
        [y,r,Vtotal,psi,W,theta,xi,thetaND,psiND,...
            sigma_r_top,sigma_r_bot,yvc,maxstress] = ...
            NLAActiveValve_MembraneCaseA(Pvm,Fvc,rv,c,rv,m,tvm,Esi,nusi,flagNL,No);
        dVvm=Vtotal; dVte=S(2); dVfluid=S(3); dVtop=S(5);
        checkm = (dVvm + dVtop - dVte - dVfluid);

    else

        U=[Ppis PHPR PHAC0]; %Vector of input parameters to
        %compliance matrix
        S=A*U'; %S is the vector of all
        %linear responses
        Fvc=Av*c*(PHAC0-PHPR); Pvm=PHAC0-PHPR; %Define these loadings
        %for use in NLAActiveValve_MembraneCaseA.m
        [y,r,Vtotal,psi,W,theta,xi,thetaND,psiND,...
            sigma_r_top,sigma_r_bot,yvc,maxstress] = ...
            NLAActiveValve_MembraneCaseA(Pvm,Fvc,rv,c,rv,m,tvm,Esi,nusi,flagNL,No);
        dVvm=Vtotal; dVte=S(2); dVfluid=S(3); dVtop=S(5);
        check0 = (dVvm + dVtop - dVte - dVfluid);

        U=[Ppis PHPR PHACm]; %Vector of input parameters %
        %to compliance matrix
        S=A*U'; %S is the vector of all %
        %linear responses
        Fvc=Av*c*(PHACm-PHPR); Pvm=PHACm-PHPR; %Define these loadings for %
        %use in NLAActiveValve_MembraneCaseA.m
        [y,r,Vtotal,psi,W,theta,xi,thetaND,psiND,...
            sigma_r_top,sigma_r_bot,yvc,maxstress] = ...
            NLAActiveValve_MembraneCaseA(Pvm,Fvc,rv,c,rv,m,tvm,Esi,nusi,flagNL,No);
        dVvm=Vtotal; dVte=S(2); dVfluid=S(3); dVtop=S(5);

```

```
checkm = (dVvm + dVtop - dVte - dVfluid);

end

    if check0*checkm <= 0
        PHAC1=PHACm;
        firsthalf=1;
    else
        PHAC0=PHACm;
        firsthalf=0;
    end

    PHACm=0.5*(PHAC0+PHAC1)
end
PHAC=PHACm;
%DONE, PHAC solution has been determined

%Evaluate all parameters for last value of PHACm

U=[Ppis PHPR PHACm]; %Vector of input parameters
%to compliance matrix
S=A*U'; %S is the vector of all linear
%responses
Fvc=AvC*(PHACm-PHPR); Pvm=PHACm-PHPR; %Define these loadings for
%use in NActiveValve_MembraneCaseA.m
[y,r,Vtotal,psi,W,theta,xi,thetaND,psiND,...
    sigma_r_top,sigma_r_bot,yvc,maxstress] = ...
    NActiveValve_MembraneCaseA(Pvm,Fvc,rvC,rvm,tvm,Esi,nusi,flagNL,No);

Zte=S(1);
dVte=S(2);
dVfluid=S(3);
Ztop=S(4);
dVtop=S(5);
Fvm=S(6);
Zde=S(7);
dVvm=Vtotal;
Maxstress=maxstress;
Zvc=yvc+Ztop;
PHAC=PHACm;

%DONE
```

## D.1.2 Nonlinear annular plate code

```
function [y,r,Vtotal,psi,W,theta,xi,thetaND,psiND,sigma_r_top,sigma_r_bot,yvc,maxstress]...
    = NLActiveValve_MembraneCaseA(Pvm,Fvc,rb,ra,tvm,E,nu,flagNL,No)

%NLValveCapMembrane_CaseA.m

%David C. Roberts, 11-30-2000
%This Matlab code solves for the non-linear deflection behavior of the valve cap
%/membrane under loading Pvm and Fvc. The deflection, slope,
%curvature, swept volume, and membrane stress are calculated. Case A refers to the
%fact that we are applying both loading inputs Pvm and Fvc and determining the
%structural response. Prior to calling of this code, the user must define Pvm and
%Fvc as functions of P1, P2, and PHAC. The loadings are defined as follows:
% Pvm = pressure differential across valve membrane = PHAC-P2
% Fvcstar = force seen by valve cap = Avc*(PHAC-P1)
%The plate/membrane is characterized by inner radius rb, outer radius ra, thickness
%tvm, and material properties E and nu.

format long;

%%%%%%%%%%%%%%%%%%%%%%%%%%%%%%%%%%%%%%%%%%%%%%%%%%%%%%%%%%%%%%%%%%%%%%%%
%Convert Inputs to Dimensionless Qunatities
P = (Pvm*ra^4)/(E*tvm^4); %Dimensionless loading of pressure
%difference across cap/membrane
F = (Fvc*ra^2)/(pi*E*tvm^4); %Dimensionless loading due to additional
%force on cap

%%%%%%%%%%%%%%%%%%%%%%%%%%%%%%%%%%%%%%%%%%%%%%%%%%%%%%%%%%%%%%%%%%%%%%%%

beta = sqrt((1-nu)/(1+nu))*(rb/ra);
k = (ra/tvm)*sqrt((12*(1-nu^2)*No)/(E*tvm*(1-beta^2)));
s = beta*k;

%%%%%%%%%%%%%%%%%%%%%%%%%%%%%%%%%%%%%%%%%%%%%%%%%%%%%%%%%%%%%%%%%%%%%%%%
%%Section 2: Define grid spacing and corrdinate transformation parameters
%%for finite-difference method
%%%%%%%%%%%%%%%%%%%%%%%%%%%%%%%%%%%%%%%%%%%%%%%%%%%%%%%%%%%%%%%%%%%%%%%%
Npoints=200; %The total # of grid points to use (MUST KEEP IT EVEN)
alpha=1.01; %Grid density parameter
phi=(alpha+1)/(alpha-1); %Grid density ratio
hr = 1/(Npoints-1); %Size of grid spacing
eta = 0:hr:1; %Vector of evenly spaced points between 0 and 1

xi_b = rb/ra; %Non-dimensional position of inner radius
xi_c = (rb+ra)/(2*ra); %Non-dimensional position of midpoint along membrane
xi_a = ra/ra; %Non-dimensional position of outer radius

%For the grid points from xi_b to xi_c, define the derivatives of eta with respect to xi
for i=1:Npoints/2,
xi(i) = xi_b + (alpha-1)*(xi_c-xi_b)*(phi-phi^(1-2*eta(i)))/...
    (1+phi^(1-2*eta(i)));
```

```

m = (alpha-1)*(xi_c-xi_b);
m2 = m*phi - m + 2*xi_b;
deta(i) = (0.5/log(phi))*(m*(1+phi))/((m*phi-(xi(i)-xi_b))*...
    (m+(xi(i)-xi_b)));
d2eta(i) = -(0.5/log(phi))*(m*(1+phi)*(m2-2*xi(i)))/...
    ((m*phi-(xi(i)-xi_b))*(m+(xi(i)-xi_b)))^2;
end

%For the grid points from xi_c to xi_a
for i=Npoints/2+1:Npoints,
xi(i) = xi_b + (alpha-1)*(xi_c-xi_b)*(phi-phi^(1-2*eta(i)))/...
    (1+phi^(1-2*eta(i)));
m = (alpha-1)*(xi_c-xi_b);
m2 = m*phi - m + 2*xi_b;
deta(i) = (0.5/log(phi))*(m*(1+phi))/((m*phi-(xi(i)-xi_b))*...
    (m+(xi(i)-xi_b)));
d2eta(i) = -(0.5/log(phi))*(m*(1+phi)*(m2-2*xi(i)))/...
    ((m*phi-(xi(i)-xi_b))*(m+(xi(i)-xi_b)))^2;
end

%%%%%%%%%%%%%%%%%%%%%%%%%%%%%%%%%%%%%%%%%%%%%%%%%%%%%%%%%%%%%%%%%%%%%%%%
%%%%%%%%%%%%%%%%%%%%%%%%%%%%%%%%%%%%%%%%%%%%%%%%%%%%%%%%%%%%%%%%%%%%%%%%
%%Section 3: Finite-Difference Implementation
%(based on Equation ?? in Chapter 2, DCR Thesis)
%%%%%%%%%%%%%%%%%%%%%%%%%%%%%%%%%%%%%%%%%%%%%%%%%%%%%%%%%%%%%%%%%%%%%%%%
%%%%%%%%%%%%%%%%%%%%%%%%%%%%%%%%%%%%%%%%%%%%%%%%%%%%%%%%%%%%%%%%%%%%%%%%

%Governing equations at internal points (from 2 to Npoints-1)
for i=2:Npoints-1,
    A(i,i-1) = (xi(i)^2*deta(i)^2)/(hr^2) - (xi(i)^2*d2eta(i)...
        + xi(i)*deta(i))/(2*hr);
    A(i,i) = -(2*xi(i)^2*deta(i)^2)/(hr^2) + (s^2+1) + ...
        xi(i)^2*k^2);
    A(i,i+1) = (xi(i)^2*deta(i)^2)/(hr^2) + (xi(i)^2*d2eta(i) + ...
        xi(i)*deta(i))/(2*hr);

    B(i,i-1) = (xi(i)^2*deta(i)^2)/(hr^2) - (xi(i)^2*d2eta(i) + ...
        3*xi(i)*deta(i))/(2*hr);
    B(i,i) = -(2*xi(i)^2*deta(i)^2)/(hr^2);
    B(i,i+1) = (xi(i)^2*deta(i)^2)/(hr^2) + (xi(i)^2*d2eta(i) + ...
        3*xi(i)*deta(i))/(2*hr);

    C(i) = 6*(1-nu^2)*P*(xi(i)^3 - xi(i)*(rb/ra)^2) + 6*(1-nu^2)*F*xi(i);
end

%Boundary condition equations at xi_b (grid point #1)
A(1,1) = 1;
B(1,1) = -3*xi(1)*deta(1)/(2*hr) + (1-nu);
B(1,2) = 4*xi(1)*deta(1)/(2*hr);
B(1,3) = -xi(1)*deta(1)/(2*hr);
C(1) = 0;

```



```

%Boundary condition equations at xi_a (grid point #Npoints)
A(Npoints,Npoints) = 1;
B(Npoints,Npoints-2) = xi(Npoints)*deta(Npoints)/(2*hr);
B(Npoints,Npoints-1) = -4*xi(Npoints)*deta(Npoints)/(2*hr);
B(Npoints,Npoints) = 3*xi(Npoints)*deta(Npoints)/(2*hr) + (1-nu);
C(Npoints) = 0;

%%%%%%%%%%%%%%%%%%%%%%%%%%%%%%%%%%%%%%%%%%%%%%%%%%%%%%%%%%%%%%%%%%%%%%%%
%%%%%%%%%%%%%%%%%%%%%%%%%%%%%%%%%%%%%%%%%%%%%%%%%%%%%%%%%%%%%%%%%%%%%%%%
%%Section 4: Provide an initial guess for the theta vector
%(plate slope), to be
%%used in the finite-difference iteration procedure.
%%%%%%%%%%%%%%%%%%%%%%%%%%%%%%%%%%%%%%%%%%%%%%%%%%%%%%%%%%%%%%%%%%%%%%%%
%%%%%%%%%%%%%%%%%%%%%%%%%%%%%%%%%%%%%%%%%%%%%%%%%%%%%%%%%%%%%%%%%%%%%%%%

if k==0,
    %theta = (-0.75*(1-nu^2)*P*xi.*(1-xi.^2))'; %Linear result
    theta=xi';
else
    theta=xi';
end

%%%%%%%%%%%%%%%%%%%%%%%%%%%%%%%%%%%%%%%%%%%%%%%%%%%%%%%%%%%%%%%%%%%%%%%%
%%%%%%%%%%%%%%%%%%%%%%%%%%%%%%%%%%%%%%%%%%%%%%%%%%%%%%%%%%%%%%%%%%%%%%%%
%%Section 5: Matrix Manipulation Procedure
%%%%%%%%%%%%%%%%%%%%%%%%%%%%%%%%%%%%%%%%%%%%%%%%%%%%%%%%%%%%%%%%%%%%%%%%
%%%%%%%%%%%%%%%%%%%%%%%%%%%%%%%%%%%%%%%%%%%%%%%%%%%%%%%%%%%%%%%%%%%%%%%%

Niterations=500; %Perform up to 500 iterations
tolerance1=1e-8;
tolerance2=1e-8;
omega=0.45; %Under-relaxation parameter
if flagNL==1 %This variable is passed into file.
    NLoption=1; %0 = Linear solution; 1 = NonLinear solution
else
    NLoption=0;
end

for i=1:Niterations,
    i;
    for j=2:Npoints-1 %Define D vector for each iteration
        D(j) = -0.5*theta(j).^2;
    end
    D(1)=0;
    D(Npoints)=0;

    Sr = inv(B)*D'*NLoption; %Solve for Sr
    v_Sr = 12*(1-nu^2)*xi'.^2.*Sr; %Calculate non-linear correction term v_Sr
    A2 = A - diag(v_Sr,0); %Substract non-linear correction term from A

```

```
theta_new = inv(A2)*C'; %Calculate new theta vector

    inner_product = (theta_new'*theta)/sqrt(theta_new'*theta_new)/...
        sqrt(theta'*theta);
    length_ratio = sqrt(theta_new'*theta_new)/sqrt(theta'*theta);

    if (1-inner_product) >= tolerance1 | (1-length_ratio) >= tolerance2
        theta = (1-omega)*theta + omega*theta_new;
    else
        break;
    end
end

%%%%%%%%%%%%%%%%%%%%%%%%%%%%%%%%%%%%%%%%%%%%%%%%%%%%%%%%%%%%%%%%%%%%%%%%%%%%%%
%%%%%%%%%%%%%%%%%%%%%%%%%%%%%%%%%%%%%%%%%%%%%%%%%%%%%%%%%%%%%%%%%%%%%%%%%%%%%%
%%Section 6: Calculate Deflection, Curvature, Stress, and
%%Swept Volume in this
%%post-processing section.
%%%%%%%%%%%%%%%%%%%%%%%%%%%%%%%%%%%%%%%%%%%%%%%%%%%%%%%%%%%%%%%%%%%%%%%%%%%%%%
%%%%%%%%%%%%%%%%%%%%%%%%%%%%%%%%%%%%%%%%%%%%%%%%%%%%%%%%%%%%%%%%%%%%%%%%%%%%%%

%PLATE DEFLECTION: Calculate plate deflection vector from the final theta vector,
%using 2nd-order forward, backward, and central difference methods to express
%theta in terms of W. Then, using matrix inversion to obtain the vector W.
i=1; %BC at rb
Wmatrix(i,i) = deta(i)*(-3/(2*hr));
Wmatrix(i,i+1) = deta(i)*(2/hr);
Wmatrix(i,i+2) = deta(i)*(-1/(2*hr));

for i=2:Npoints-1 %Inner grid points
    Wmatrix(i,i-1) = deta(i)*(-1/(2*hr));
    Wmatrix(i,i+1) = deta(i)*(1/(2*hr));
end

%BC at ra --> Do not do for the outer boundary condition. We already know that
%the deflection at ra is equal to zero.

W = inv(Wmatrix(1:Npoints-1,1:Npoints-1))*theta(1:Npoints-1);
W=[W;0];
%Done

%PLATE CURVATURE: Calculate plate curvature vector from the final theta vector,
%using 2nd-order forward, backward, and central difference methods.
i=1; %BC at rb
psi(i) = deta(i)*(1/(2*hr))*(-3*theta(i) + 4*theta(i+1) - theta(i+2));

for i=2:Npoints-1 %Inner grid points
    psi(i) = deta(i)*(1/(2*hr))*(theta(i+1) - theta(i-1));
end
```

```

i=Npoints; %BC at ra
psi(i) = deta(i)*(1/(2*hr))*(3*theta(i) - 4*theta(i-1) + theta(i-2));
%Done

%PLATE STRESS: Calculate the stress vectors in the plate.

for i=1:Npoints
    Sro(i) = (k^2/(12*(1-nu^2)))*(1 + beta^2/(xi(i)^2));
    sigma_r_top(i) = (E*tvm^2/ra^2)*(Sro(i) + Sr(i) - ...
        (1/(2*(1-nu^2)))*(psi(i) + (nu*theta(i))./xi(i)));
    sigma_r_bot(i) = (E*tvm^2/ra^2)*(Sro(i) + Sr(i) + ...
        (1/(2*(1-nu^2)))*(psi(i) + (nu*theta(i))./xi(i)));
end
if max(sigma_r_top) > max(sigma_r_bot)
    maxstress = abs(max(sigma_r_top));
else
    maxstress = abs(max(sigma_r_bot));
end
%Done

%CONVERSION TO NON_DIMENSIONAL PARAMETERS
r=xi*ra;
y=W*tvm;
thetaND=theta*tvm/ra; %This non-dimensional theta is dw/dr
psiND=psi*tvm/(ra^2); %This non-dimensional psi is d2w/dr2

%PLATE SWEEP VOLUME: Calculate total swept volume under cap and membrane.
V=0;
for i=1:Npoints-1
    dV(i) = pi*(r(i+1)^2-r(i)^2)*0.5*(y(i+1)+y(i));
    V = V + dV(i);
end
yvc = y(1);
Vcap = yvc*pi*rb^2;
Vtotal = Vcap + V;
%Done

```

## D.2 Matlab code used for data analysis and computation

```
% Lodewyk Steyn
% Code to postprocess the HAC data taken in October 2001
% Computes the stiffness matrix
% Reads in theoretical data as generated by Dave's code
%

%%Polytec Calibration Factors:
%% for 50kPa tests --> 2um/V
%% for 100kPa tests --> 8um/V
%% for 150kPa tests --> 8um/V
%% for 200kPa tests --> 20um/V

clear all;
close all;

%*****
% USER INPUT

%The psi_1 psi_2 matrix, to be subtracted from the D matrices.
% the units are in kPa/um

psi1psi2E = [15.2 0
             0 15.4]

psi1psi2T = [8.9 0
             0 17.5]

% Plotstage % For the 2D plots
% Set to the following values:
% 1: Just experimental data and curve fits
% 2: Experimental curve fits, no error bars, and theoretical curves added
% 3: Experiment, model, and the linear lines

Plotstage = 3;

% number of plot points to plot for the model values on the curves
nmodcorrpts = 15;

% PHPR Question
% Make all PHPR's negative?

PHPRsgn = -1;

% Readflag
% Set = 1 if you want to read in a new datacell, or to 0 if you want to load the old one.
Readflag = 0
```

---

```

% Read model data
% Set = 1 if you want to read model data.
ModReadflag = 0

% Mplotflag
% Set to 1 if you want to plot all the time histories
Mplotflag = 0

% To do postprocessing or not
Postprocflag = 1;

% File to save datacell to
wfilename = 'PisBValB_workfile.mat'

wfilename_mod = 'PisBValB_workfile_mod.mat'

% Number of channels in each file
Nchannels = 4;

chan1str = 'Pulse Valve Drive Signal 1';
chan2str = 'Piston Displacement';
chan3str = 'P_1';
chan4str = 'P_2';

%Number of files to read:
nfiles1 = 6;

%Array of model file names to be read

modfilearray = {'HAC10ValveData_Phpr0kPa_8um_6um.mat'
                'HAC10ValveData_Phpr92kPa_8um_6um.mat'
                'HAC10ValveData_Phpr298kPa_8um_6um.mat'
                'HAC10ValveData_Phpr500kPa_8um_6um.mat'}

% Array of the corresponding PHPR's for the model files - NOTE - USE THE POSITIVE VALUES!!
modfileP_HPR_S = [0
                  92
                  298
                  500];

% Change the sign appropriately
modfileP_HPR_S = modfileP_HPR_S*PHPRsgn;

% Caption of the data to be stored in the model cell array
modfilecaption = 'PHAC PPisvary1 Zde1 Zvc1 maxstress1'

% Polytec Settings for each file % Also correct for index of refraction
PolytecFactors = [0.5/1.3745
                  0.5/1.3745
                  0.5/1.3745

```

```
8/1.3745
8/1.3745
8/1.3745];

% Values to shift the Polytec Channels by to get the correct zero values (in um)
% These are for each file, and are obtained after the first run of this code
% Subtract!! these values from the actual data...

PolytecYshifts = [-0.16
-0.25
-0.05
-0.05
-0.025
-0.05]

%%%%%%%%%%%%%%%%%%%%%%%%%%%%%%%%%%%%%%%%%%%%%%%%%%%%%%%%%%%%%%%%%%%%%%%%

% Create a matrix with all the drive element XY plots to be done.
% Columns are: Col1: File # Col2: Start time in Secs Col3: End time in Secs
DEplots = [3 24.4 26.9 % 0kPa PHPR
1 32.4 34.8 %100 kPa
2 16.5 19 % 300
3 16.4 19] % 500

DEsign = -1 % To make Data negative, make it -1, to Make it Pos, make it 1

VCplots = [5 8.5 11.7 % 0kPa
4 13.4 16.6 % 100
5 18.2 21.4 % 300
6 18.2 21.4] %500

VCsign = 1 % To make Data negative, make it -1, to Make it Pos, make it 1

%!!!! NOTE We compute P as a function of X, and not the other way around !!!!
% !!!! AND THEN WE PLOT THE INVERSE !!!!
% Why... Because if  $F = k_1*x + k_2*x^3$ , it
% DOES NOT MEAN THAT  $x = s_1*F + s_2*F^3$  !!!

% Define degree of polynomials to fit to the respective data

DEPolydeg = 3;

DEPolydeg_err = 3; % For error bars

VCPolydeg = 3;

VCPolydeg_err = 7; % For error bars

%*****
%*****
```

```

% 2D XY Plot axis limits
%*****
%*****

yde_lims = [-0.7 1.5]

yvc_lims = [-13 13]

xPde_lims = [-20 520]

%*****
% 2D and 3D plot Axis labels
%*****

xPde_labl = 'P_1 (kPa)';
xPde_labl3D = {'P_1 (kPa)'};
yPhpr_labl = 'P_2 (kPa)';
yPhpr_labl3D = {'P_2 (kPa)'};
zde_labl = 'z_1 ( \mu m)';
zvc_labl = 'z_2 ( \mu m)';

curvefract = 0.6 % for placing labels on the curves

%*****

%*****
% 2D Plot figure properties
%*****

% All units here in pixels

Plot1pos = [200 200 700 500]
Plot1axpos = [65 65 570 380]
Plot1units = 'pixels'
Plot1fontsize = 14
Plot1linewidth = 2

% Plot 2 will form part of a 2-plot set, for the drive element and the valve
Plot2pos = [250 250 500 500]
Plot2axpos = [65 65 370 370]
Plot2units = 'pixels'
Plot2fontsize = 14
Plot2linewidth = 2

% Plot r is for the raw data
Plotrpos = [150 100 700 700]
Plotrunits = 'pixels'
Plotrfontsize = 12
Plotrlinewidth = 2

```

```
% Font size for the curve legend:
curvelegfntsiz = 10

%*****
% Stiffness matrix parameters
%*****

% First Value of valve cap deflection to use in um
zVCsdef1 = 1;
% Second value of valve cap deflection
zVCsdef2 = -1

% Indices of the DEplots and VCplots to use for computing the stiffness matrix
% ONLY 2 allowed
Exp_Kidxs = [2
             3];

% Indices of the modfilearray to use for the stiffness matrix
% ONLY 2 Allowed
Theo_Kidxs = [2
             3];

%*****
% End Stiffness matrix parameters
%*****

%Number of points to plot for each curve fit
ncfitpts = 200;

FitLwidth = 1.5; % Linewidth of the fitted curves

% Number of points for error bars
nerrbpts = 7;

%%%%%%%%

% Static pressure sensor calibration factor
SensPressFact1 = 6.894*100/4.9939; %6.894 Pa/psi ; 4.9939 V/100psi (Sensotec FDDBR,2D5A6A, 769233)

%%%%%%%%
```



```

% Static Sensor 2 calibration factor
SensPressFact2 = 6.894*150/5.0111      % Sensotec FDW 150 psi differential sensor

% Define a color vector with the appropriate colors for the different lines
PColVect = ['r'
            'g'
            'b'
            'c'
            'm'
            'k'];

%*****
% 3D Plotting Parameters
%*****

% Number of points to use for the functions when doing the surface plots
nfcnpts = 200
% Number of points per axis for the surface plots
n3dpts = 20

% PPiston values for surface plots
Ppismin = 0
Ppismax = 500

% Note, Phprmin should obey the sign convention - IT WILL NOT BE AUTOMATICALLY CORRECTED
% Phpr values for surface plots
Phprmin = -500
Phprmax = 0

% END: USER INPUT
%*****
%*****
%*****

nmodfiles = size(modfilearray,1);

if Readflag == 1
    %*****
    % Section : Files read
    %*****

    % Open the files to generate the appropriate plots]

    fid_v = zeros(nfiles1,1)

```

```
% File 1:

fid_v(1,1) = fopen('HACDev3Fil3_PisB_PPis500kPa_PHPR100kPa_05umV_Run1.txt','r');
fid_v(2,1) = fopen('HACDev3Fil3_PisB_PPis500kPa_PHPR300kPa_05umV_Run1.txt','r');
fid_v(3,1) = fopen('HACDev3Fil3_PisB_PPis500kPa_PHPR500kPa_05umV_Run1.txt','r');
fid_v(4,1) = fopen('HACDev3Fil3_ValvB_PPis500kPa_PHPR100kPa_8umV_Mem7_Run1.txt','r');
fid_v(5,1) = fopen('HACDev3Fil3_ValvB_PPis500kPa_PHPR300kPa_8umV_Mem7_Run1.txt','r');
fid_v(6,1) = fopen('HACDev3Fil3_ValvB_PPis500kPa_PHPR500kPa_8umV_Mem7_Run1.txt','r');

% Read the sampling rates in Scans per second
% Create a cell array with the same amount of columns as the number of files

DataCell = cell(3,nfiles1);

for i1 = 1:nfiles1
    [DataCell{1,i1} count1]=fscanf(fid_v(i1,1),'%e',[1 1]); % Get the scanrate for each file
end

% Read the data into the cell array

for i1 = 1:nfiles1
    [A count1]=fscanf(fid_v(i1,1),'%e',[Nchannels inf]);
    fclose(fid_v(i1,1));

    DataCell{2,i1} = A'; % Assign the appropriate column in the dataset to the file
    %number read in above
end

%*****
% Files read Cell array assigned
%*****

save(wfilename,'DataCell');

else

    load(wfilename);

end

%*****
% Read Model Files
%*****

if ModReadflag == 1

%*****
%*****
```

```

% Import appropriate data from NL code
%*****
%*****

% Create a cell array that will store all the data of all of the
% model files in a single structure

ModelCell = cell(2,nmodfiles);

% Load the appropriate model files

%Your variables are:
%PHAC1      Pvary1      Zde1      Zvc1      maxstress1

for i1 = 1:nmodfiles
    load(modfilearray{i1,1}); % Load the model file\
    nptsmod = size(PHAC1,2); % Compute # of points in the file

    A = zeros(nptsmod,5);
    A(:,1) = PHAC1'/1000; % Get the p[ressure in kPa
    A(:,2) = Pvary1'/1000; % Get the pressure in kPa
    A(:,3) = Zde1'*1e6; % Get it in um
    A(:,4) = Zvc1'*1e6; % Get it in um
    A(:,5) = maxstress1'/1e6; % Get the stress in MPa

    ModelCell{1,i1} = modfilecaption;
    ModelCell{2,i1} = A;
end

%*****
% All Model Files Loaded
%*****

save(wfilename_mod,'ModelCell');

else

    load(wfilename_mod);
end

%*****
% Set the time Vectors
%*****

% Define the time interval

```

```
for i1 = 1:nfiles1
    dT1 = 1/DataCell{1,i1}; % Get the scanrate for the file under inspection

    npts = size(DataCell{2,i1},1);

    Time1 = zeros(npts,1);

    for i2=1:npts
        Time1(i2,1)=dT1*i2;
    end

    DataCell{3,i1} = Time1;

end

%*****
% Time Vectors Set
%*****

%*****
% Scale the data appropriately - convert the voltages into Data
%*****

for i1 = 1:nfiles1
    A = DataCell{2,i1};

    A(:,2) = A(:,2)*PolytecFactors(i1,1);
    A(:,3) = A(:,3)*SensPressFact1;
    A(:,4) = A(:,4)*SensPressFact2;

    DataCell{2,i1} = A;
end

%*****
% Data Scaled
%*****

%*****
% Adjust DC offsets on the Sensotec pressure transducers and also the Polytec
%*****

for i1 = 1:nfiles1
    A = DataCell{2,i1};
```

```

A(:,2) = A(:,2) - PolytecYshifts(i1,1);
A(:,3) = A(:,3) - min(A(:,3));
A(:,4) = A(:,4) - min(A(:,4));

DataCell{2,i1} = A;
end

%*****
% DC Offsets Adjusted
%*****

%*****
% Plot results for each file
%*****
if Mplotflag == 1

    % Set up the figure handles for these plots;

    hmplots = zeros(nfiles1,1);
    hmsubplots = zeros(nfiles1,4);
    hmsubhandls = zeros(nfiles1,4)
    xlabh = zeros(nfiles1,4);
    ylabh = zeros(nfiles1,4);
    tith = zeros(nfiles1,4);

    for i1 = 1:nfiles1

        A = DataCell{2,i1};
        Time1 = DataCell{3,i1};

        hmplots(i1,1) = figure('color','w','position',Plotrpos);

        hmsubplots(i1,1) = subplot(2,2,1);

        hmsubhandls(i1,1) = plot(Time1,A(:,1));
        %grid
        xlabh(i1,1) = xlabel('Time (s)')
        ylabh(i1,1) = ylabel('Voltage (V)')
        tith(i1,1) = title(chan1str)

        hmsubplots(i1,2) = subplot(2,2,2);
        hmsubhandls(i1,2) = plot(Time1,A(:,2));
        %grid
        xlabh(i1,2) = xlabel('Time (s)')
        ylabh(i1,2) = ylabel('Deflection (\mu m)')
        tith(i1,2) = title(chan2str)
    end
end

```

```
hmsubplots(i1,3) = subplot(2,2,3);
hmsubhandles(i1,3) = plot(Time1,A(:,3));
%grid
xlabelh(i1,3) = xlabel('Time (s)')
ylabelh(i1,3) = ylabel('Pressure (kPa)')
tith(i1,3) = title(chan3str)

hmsubplots(i1,4) = subplot(2,2,4);
hmsubhandles(i1,4) = plot(Time1,A(:,4));
%grid
xlabelh(i1,4) = xlabel('Time (s)')
ylabelh(i1,4) = ylabel('Pressure (kPa)')
tith(i1,4) = title(chan4str)
end

% Make the plots pretty:
set(hmsubplots,'fontsize',Plotrfontsize,'linewidth',Plotrlinewidth)
set(hmsubhandles,'color','k');

set(xlabelh,'fontsize',Plotrfontsize);
set(ylabelh,'fontsize',Plotrfontsize);
set(tith,'fontsize',Plotrfontsize);

end
%*****
% Plots Completed
%*****

if Postprocflag == 1

%*****
% Make the two X-Y plots
%*****

% Determine the length of the plot color vector

ncolors = size(PColVect,1);

%*****
% DE plots
%*****

% Create a cell array with all the XY data for the respective plots

nDEplt = size(DEplots,1);

DE_XYCell = cell(2,nDEplt);
```

---

```

h11 = figure('color','w');
h11a = axes('box','on');

DElinehandl = zeros(nDEplt,1);

for i1 = 1:nDEplt

    dat_idx = DEplots(i1,1);

    % Load the appropriate time data
    A = DataCell{2,dat_idx};
    Time1 = DataCell{3,dat_idx};

    npts = size(Time1,1);

    t1 = DEplots(i1,2);
    t2 = DEplots(i1,3);

    tmax = Time1(npts,1);

    % Approximate the data indices
    dat_idx_1 = floor(t1/tmax*npts);
    dat_idx_2 = floor(t2/tmax*npts);

    P_Save = A(dat_idx_1:dat_idx_2,3);
    Delta_Save = DESign*A(dat_idx_1:dat_idx_2,2);

    A_Save = [P_Save Delta_Save];

    PHPR_Save = mean(A(dat_idx_1:dat_idx_2,4)); % Define the average value of PHPR

    DE_XYCell{1,i1} = PHPR_Save*PHPRsgn; % Sign Change
    DE_XYCell{2,i1} = A_Save;

    % Get a color index for this plot
    col_idx = ceil(((i1/ncolors) - floor(i1/ncolors))*ncolors);

    axes(h11a);

    DElinehandl(i1,1) = line(P_Save,Delta_Save,'color',PColVect(col_idx,1))

end

xlabel('Pressure (kPa)');
ylabel('Deflection (um)');

```

```
%*****
% VC plots
%*****

% Create a cell array with all the XY data for the respective plots

nVCplt = size(VCplots,1);
VC_XYCell = cell(2,nVCplt);

h22 = figure('color','w');
h22a = axes('box','on');

VClinehandl = zeros(nVCplt,1);

for i1 = 1:nVCplt

    dat_idx = VCplots(i1,1);

    % Load the appropriate time data
    A = DataCell{2,dat_idx};
    Time1 = DataCell{3,dat_idx};

    npts = size(Time1,1);

    t1 = VCplots(i1,2);
    t2 = VCplots(i1,3);

    tmax = Time1(npts,1);

    % Approximate the data indices
    dat_idx_1 = floor(t1/tmax*npts);
    dat_idx_2 = floor(t2/tmax*npts);

    P_Save = A(dat_idx_1:dat_idx_2,3);
    Delta_Save = VCsign*A(dat_idx_1:dat_idx_2,2);

    A_Save = [P_Save Delta_Save];

    PHPR_Save = mean(A(dat_idx_1:dat_idx_2,4)); % Define the average value of PHPR

    VC_XYCell{1,i1} = PHPR_Save*PHPRsgn; % Sign change
    VC_XYCell{2,i1} = A_Save;

    % Get a color index for this plot
    col_idx = ceil(((i1/ncolors) - floor(i1/ncolors))*ncolors);

    axes(h22a);
```



---

```

VCl ine handl(i1,1) = line(P_Save,Delta_Save,'color',PColVect(col_idx,1))

end

xlabel('Pressure (kPa)');
ylabel('Deflection (um)');

%*****
% XY PLOTS COMPLETED
%*****

% Now we have the data for the XY plots

%*****
% Perform Curve fits on all the XY-plots
% We perform 2 types of curve fits
% One PROPER one, to be used for further computation
% And one inverse (incorrect) one, to be used for
% making errorbars
%*****

% Drive elements

% Create a cell array with two rows: One for the polynomial coefficients and one
% for the regression correlation structure
DE_PolyCell = cell(4,nDEplt);
DE_PolyCell_wrong = cell(2,nDEplt);

DEfithandl = zeros(nDEplt,1);
DEebarhandl = zeros(2,nDEplt); % Error bars have 2 handles, one for the bars, and one %
for the line

DElabhdl = zeros(nDEplt,1);

for i1 = 1:nDEplt

    % Load the XY data
    A = DE_XYCell{2,i1};

    % Fit a curve to it
    %!!!! NOTE We compute P as a function of X, and not the other way around !!!!!
    % !!!! AND THEN WE PLOT THE INVERSE !!!!!
    % Why... Because if  $F = k_1*x + k_2*x^3$ , it DOES NOT MEAN THAT  $x = s_1*F + s_2*F^3$  !!!
    [P,S] = polyfit(A(:,2),A(:,1),DEPolydeg); % Linear fit for this data

    %Store this data into the new cell array

    DE_PolyCell{1,i1} = P;

```

```
DE_PolyCell{2,i1} = S;

% Also fit the inverse curve, but this is not so nice.

[P,S] = polyfit(A(:,1),A(:,2),DEPolydeg_err);

%Store this data into the new cell array

DE_PolyCell_wrong{1,i1} = P;
DE_PolyCell_wrong{2,i1} = S;


% Determine the x-limits for this plot

xmin = min(A(:,2));
xmax = max(A(:,2));

% Create an x-vector with the appropriate number of points
Xvect = linspace(xmin,xmax,ncfitpts);

% Create y -vector with the correct curve fit
[Yvect,delta] = polyval(DE_PolyCell{1,i1},Xvect,DE_PolyCell{2,i1});

% Perform plot on the previous axes
col_idx = ceil(((i1/ncolors) - floor(i1/ncolors))*ncolors);

axes(h11a);
hold on;
% Plot the fit on the axes
DEfithandl(i1,1) = line(Yvect,Xvect,'color',PColVect(col_idx,1),'linewidth',FitLwidth)

%*****
% Store PHPR and the domain

P_hpr_x = DE_XYCell{1,i1}; % Also extract the corresponding PHPR

DE_PolyCell{3,i1} = P_hpr_x;
DE_PolyCell{4,i1} = [xmin xmax];
```

```

%*****
%*****

%*****
% Place text on the curves for each P2 (PHPR)

ctext1 = strcat('P_2=',strcat(num2str(modfileP_HPR_S(i1,1),'%4.0f'),'kPa'));

DElabhdl(i1,1) = curvelabel2(ctext1,h11a,xPde_lims,yde_lims,curvefract,Yvect,Xvect);

%*****

% Create the error bar plot
xemin = min(A(:,1));
xemax = max(A(:,1));

Xv_err = linspace(xemin,xemax,nerrbpts); % Use inverse data for error bars

[Yv_err,Edelta] = polyval(DE_PolyCell_wrong{1,i1},Xv_err,DE_PolyCell_wrong{2,i1});

DEebarhdl(:,i1) = errorbar(Xv_err,Yv_err,Edelta)

set(DEebarhdl(1,i1),'color',PColVect(col_idx,1),'linewidth',FitLwidth);

delete(DEebarhdl(2,i1)); % Delete the lines from the errobar plot

end

% Valve Caps

% Create a cell array with two rows: One for the polynomial coefficients and one
% for the regression correlation structure
VC_PolyCell = cell(4,nVCplt);
VC_PolyCell_wrong = cell(2,nVCplt);

VCfithandl = zeros(nVCplt,1);
VCebarhandl = zeros(2,nVCplt); % Error bars have 2 handles, one for the bars, and one for
%the line

VClabhdl = zeros(nVCplt,1);

for i1 = 1:nVCplt

    % Load the XY data
    A = VC_XYCell{2,i1};

```

```
% Fit a curve to it
%!!!! NOTE We compute P as a function of X, and not the other way around !!!!!
% !!!! AND THEN WE PLOT THE INVERSE !!!!!
% Why... Because if  $F = k_1*x + k_2*x^3$ , it DOES NOT MEAN THAT  $x = s_1*F + s_2*F^3$  !!!
[P,S] = polyfit(A(:,2),A(:,1),VCPolydeg); % Linear fit for this data

%Store this data into the new cell array

VC_PolyCell{1,i1} = P;
VC_PolyCell{2,i1} = S;

% Also fit the inverse curve, but this is not so nice.

[P,S] = polyfit(A(:,1),A(:,2),VCPolydeg_err);

%Store this data into the new cell array

VC_PolyCell_wrong{1,i1} = P;
VC_PolyCell_wrong{2,i1} = S;

% Determine the x-limits for this plot

xmin = min(A(:,2));
xmax = max(A(:,2));

% Create an x-vector with the appropriate number of points
Xvect = linspace(xmin,xmax,ncfitpts);

% Create y -vector with the correct curve fit
[Yvect,delta] = polyval(VC_PolyCell{1,i1},Xvect,VC_PolyCell{2,i1});

% Perform plot on the previous axes
col_idx = ceil(((i1/ncolors) - floor(i1/ncolors))*ncolors);

axes(h22a);
hold on;
% Plot the fit on the axes
VCfithandl(i1,1) = line(Yvect,Xvect,'color',PColVect(col_idx,1),'linewidth',FitLwidth)

%*****
% Store PHPR and the domain

P_hpr_x = VC_XYCell{1,i1}; % Also extract the corresponding PHPR
```

```

VC_PolyCell{3,i1} = P_hpr_x;
VC_PolyCell{4,i1} = [xmin xmax];

%*****
%*****

%*****
% Place text on the curves for each P2 (PHPR)

cext1 = strcat('P_2=',strcat(num2str(modfileP_HPR_S(i1,1),'%4.0f'),'kPa'));

VClabhdl(i1,1) = curvelabel2(cext1,h22a,xPde_lims,yvc_lims,curvefract,Yvect,Xvect);

%*****

% Create the error bar plot
xemin = min(A(:,1));
xemax = max(A(:,1));

Xv_err = linspace(xemin,xemax,nerrbpts); % Use inverse data for error bars

[Yv_err,Edelta] = polyval(VC_PolyCell_wrong{1,i1},Xv_err,VC_PolyCell_wrong{2,i1});

VCebarhdl(:,i1) = errorbar(Xv_err,Yv_err,Edelta)

set(VCebarhdl(1,i1),'color',PColVect(col_idx,1),'linewidth',FitLwidth);

delete(VCebarhdl(2,i1)); % Delete the lines from the errorbar plot

end

%*****
%*****
% Overplot the model over the measured data
%*****
%*****

DEmodhdl = zeros(nmodfiles,1);

```

```
VCmodhandl = zeros(nmodfiles,1);

for i1 = 1:nmodfiles

    % Retrieve Data from the cell array:

    A = ModelCell{2,i1};

    % Resample the model data to reduce the number of points, or otherwise
    % the plots will be garbage in B&W

    % get the x-vector;

    Xvecfop = A(:,2);
    Yvec1fop = A(:,3);
    Yvec2fop = A(:,4);

    xfopmin = min(Xvecfop);
    xfopmax = max(Xvecfop);
    Xfopred = (linspace(xfopmin,xfopmax,nmodcorrpts))';

    Yfop1red = interp1(Xvecfop,Yvec1fop,Xfopred,'spline');
    Yfop2red = interp1(Xvecfop,Yvec2fop,Xfopred,'spline');

    % Set the DE axes
    axes(h11a);

    DEmodhandl(i1,1) = line(Xfopred,Yfop1red,'color','k','linestyle','-', 'linewidth',0.8...
        , 'marker','p', 'markersize',5);

    axes(h22a);

    VCmodhandl(i1,1) = line(Xfopred,Yfop2red,'color','k','linestyle','-', 'linewidth',0.8...
        , 'marker','p', 'markersize',5);

end

%*****
% Next steps:

% 1. Do curve fits on the theoretical data, and get the appropriate polynomials

% 2. Compute the small deflection stiffness matrices - EASY!!!, because we already have
%     the curve fits, where  $P = f(z)$  - just keep  $z$  small!!

%*****
%*****
% Perform curve fits on the theoretical data from Dave's curves
```

```

%*****
%*****

% Create a cell array with two rows: One for the polynomial coefficients and one
% for the regression correlation structure
DE_PolyCell_mod = cell(4,nmodfiles);
%DE_PolyCell_wrong_mod = cell(2,nmodfiles);

VC_PolyCell_mod = cell(4,nmodfiles);
%VC_PolyCell_wrong_mod = cell(2,nmodfiles);

for i1 = 1:nmodfiles

    % Load the appropriate model data
    A = ModelCell{2,i1};

    %Remember: A has the following column structure:
    % PHAC Pvary1 zDE zVc stress

    % Fit a curve to the Drive element, and then the valve cap:
    %!!!! NOTE We compute P as a function of X, and not the other way around !!!!!
    % !!!! AND THEN WE PLOT THE INVERSE !!!!!
    % Why... Because if  $F = k_1x + k_2x^3$ , it DOES NOT MEAN THAT  $x = s_1F + s_2F^3$  !!!
    [P,S] = polyfit(A(:,3),A(:,2),DEPolydeg); %

    %Store this data into the new cell array

    DE_PolyCell_mod{1,i1} = P;
    DE_PolyCell_mod{2,i1} = S;

    % Now, we have to find the domain for this one

    xmin = min(A(:,3));
    xmax = max(A(:,3));

    %*****
    % Store PHPR and the domain

    P_hpr_x = modfileP_HPR_S(i1,1); % Also extract the corresponding PHPR

    DE_PolyCell_mod{3,i1} = P_hpr_x;
    DE_PolyCell_mod{4,i1} = [xmin xmax];

    %*****
    %*****

```

```
% Also fit the valve:
[P,S] = polyfit(A(:,4),A(:,2),VCPolydeg); % Linear fit for this data

%Store this data into the new cell array

VC_PolyCell_mod{1,i1} = P;
VC_PolyCell_mod{2,i1} = S;

% Now, we have to find the domain for this one

xmin = min(A(:,4));
xmax = max(A(:,4));

%*****
% Store PHPR and the domain

P_hpr_x = modfileP_HPR_S(i1,1); % Also extract the corresponding PHPR

VC_PolyCell_mod{3,i1} = P_hpr_x;
VC_PolyCell_mod{4,i1} = [xmin xmax];

%*****
%*****

end

%*****
%*****

% Now, we have all the fitted curves of  $P(z)$ .

%*****
%*****

% Note, we will now change the signs to keep everything consistent

%*****
%*****

% Let us compute the pressures corresponding to the valve cap deflection specified
% in the USER INPUT section

Pcoefs = VC_PolyCell{1,Exp_Kidxs(1,1)}
```



---

```

% Compute the first drive element pressure
PDE1 = polyval(Pcoefs,zVCsdef1)

% Now determine the PHPR, based on the average between the PHPR
% taken for the measurement on the valve, and
% that of the measurement taken on the drive element.

PHPR1 = (DE_XYCell{1,Exp_Kidxs(1,1)} + VC_XYCell{1,Exp_Kidxs(1,1)})/2

% also, determine the zDE corresponding to this zVC

Pcoefs = DE_PolyCell{1,Exp_Kidxs(1,1)}
% subtract PDE1 from the constant term, to find the root.

size_poly = size(Pcoefs,2);

Pcoefs(1,size_poly) = Pcoefs(1,size_poly) - PDE1

zDE_s = roots(Pcoefs)

% Now we have to pick the correct root.

zDEidx = input('Please type in the index of the correct zDE in the matrix above...')

% Now assign zDE
zDEsdef1 = zDE_s(zDEidx,1);

%*****
% Second Experimental pressure condition
%*****

Pcoefs = VC_PolyCell{1,Exp_Kidxs(2,1)}

% Compute the first drive element pressure
PDE2 = polyval(Pcoefs,zVCsdef2)

% Now determine the PHPR, based on the average between the PHPR
% taken for the measurement on the valve, and
% that of the measurement taken on the drive element.

PHPR2 = (DE_XYCell{1,Exp_Kidxs(2,1)} + VC_XYCell{1,Exp_Kidxs(2,1)})/2

% also, determine the zDE corresponding to this zVC

Pcoefs = DE_PolyCell{1,Exp_Kidxs(2,1)}
% subtract PDE1 from the constant term, to find the root.

size_poly = size(Pcoefs,2)

Pcoefs(1,size_poly) = Pcoefs(1,size_poly) - PDE2

```

```
zDE_s = roots(Pcoefs)

% Now we have to pick the correct root.

zDEidx = input('Please type in the index of the correct zDE in the matrix above...')

% Now assign zDE
zDEsdef2 = zDE_s(zDEidx,1);

%*****

%%%%%%%%%%%%%%%%%%%%%%%%%%%%%%%%%%%%%%%%%%%%%%%%%%%%%%%%%%%%%%%%%%%%%%%%%%%%%%
% Assign the matrices to solve for BOTH Stiffness AND COMPLIANCE
%%%%%%%%%%%%%%%%%%%%%%%%%%%%%%%%%%%%%%%%%%%%%%%%%%%%%%%%%%%%%%%%%%%%%%%%%%%%%%

Press_EXP = [PDE1
             PHPR1
             PDE2
             PHPR2];

Defls_EXP = [zDEsdef1 zVCsdef1 0 0
             0 0 zDEsdef1 zVCsdef1
             zDEsdef2 zVCsdef2 0 0
             0 0 zDEsdef2 zVCsdef2];

Dvect_EXP = [zDEsdef1
             zVCsdef1
             zDEsdef2
             zVCsdef2];

Pmatx_EXP = [PDE1 PHPR1 0 0
             0 0 PDE1 PHPR1
             PDE2 PHPR2 0 0
             0 0 PDE2 PHPR2];

%%%%%%%%%%%%%%%%%%%%%%%%%%%%%%%%%%%%%%%%%%%%%%%%%%%%%%%%%%%%%%%%%%%%%%%%%%%%%%

Betas_EXP = inv(Defls_EXP)*Press_EXP
Svect_EXP = inv(Pmatx_EXP)*Dvect_EXP

epsilon_EXP = (zDEsdef1-zDEsdef2)/(zDEsdef2)

delta_EXP = (zVCsdef1-zVCsdef2)/(zVCsdef2)

epsilon2_EXP = (PDE1-PDE2)/PDE1
delta2_EXP = (PHPR1-PHPR2)/PHPR1

%*****
%*****

% DO THE SAME FOR THE THEORETICAL DATA
```

```

%*****

Pcoefs = VC_PolyCell_mod{1,Theo_Kidxs(1,1)}

% Compute the first drive element pressure
PDE1 = polyval(Pcoefs,zVCsdef1)

% Now determine the PHPR, from user input

PHPR1 = modfileP_HPR_S(Theo_Kidxs(1,1),1)

% also, determine the zDE corresponding to this zVC

Pcoefs = DE_PolyCell_mod{1,Theo_Kidxs(1,1)};
% subtract PDE1 from the constant term, to find the root.

size_poly = size(Pcoefs,2);

Pcoefs(1,size_poly) = Pcoefs(1,size_poly) - PDE1;

zDE_s = roots(Pcoefs)

% Now we have to pick the correct root.

zDEidx = input('Please type in the index of the correct zDE in the matrix above...')

% Now assign zDE
zDEsdef1 = zDE_s(zDEidx,1);

%*****
% Second THEORETICAL pressure condition
%*****

Pcoefs = VC_PolyCell_mod{1,Theo_Kidxs(2,1)}

% Compute the first drive element pressure
PDE2 = polyval(Pcoefs,zVCsdef2)

PHPR2 = modfileP_HPR_S(Theo_Kidxs(2,1),1)

% also, determine the zDE corresponding to this zVC

Pcoefs = DE_PolyCell_mod{1,Theo_Kidxs(2,1)};
% subtract PDE1 from the constant term, to find the root.

size_poly = size(Pcoefs,2);

Pcoefs(1,size_poly) = Pcoefs(1,size_poly) - PDE2;

```

```
zDE_s = roots(Pcoefs)

% Now we have to pick the correct root.

zDEidx = input('Please type in the index of the correct zDE in the matrix above...')

% Now assign zDE
zDEsdef2 = zDE_s(zDEidx,1);

%*****

%%%%%%%%%%%%%%%%%%%%%%%%%%%%%%%%%%%%%%%%%%%%%%%%%%%%%%%%%%%%%%%%%%%%%%%%%%%%%%
% Assign the matrices to solve for BOTH Stiffness AND COMPLIANCE
%%%%%%%%%%%%%%%%%%%%%%%%%%%%%%%%%%%%%%%%%%%%%%%%%%%%%%%%%%%%%%%%%%%%%%%%%%%%%%

Press_THEO = [PDE1
              PHPR1
              PDE2
              PHPR2];

Defls_THEO = [zDEsdef1 zVCsdef1 0 0
              0 0 zDEsdef1 zVCsdef1
              zDEsdef2 zVCsdef2 0 0
              0 0 zDEsdef2 zVCsdef2];

Dvect_THEO = [zDEsdef1
              zVCsdef1
              zDEsdef2
              zVCsdef2];

Pmatx_THEO = [PDE1 PHPR1 0 0
              0 0 PDE1 PHPR1
              PDE2 PHPR2 0 0
              0 0 PDE2 PHPR2];

%%%%%%%%%%%%%%%%%%%%%%%%%%%%%%%%%%%%%%%%%%%%%%%%%%%%%%%%%%%%%%%%%%%%%%%%%%%%%%

format short e

Betas_THEO = inv(Defls_THEO)*Press_THEO
Svect_THEO = inv(Pmatx_THEO)*Dvect_THEO

% Output the "delta indicators" for the terms that are different
% in the matrices we are solving.
% If they are < 0.5, we are probably in trouble
epsilon_THEO = (zDEsdef1-zDEsdef2)/(zDEsdef1)
epsilon_EXP

delta_THEO = (zVCsdef1-zVCsdef2)/(zVCsdef1)

epsilon2_THEO = (PDE1-PDE2)/PDE1
delta2_THEO = (PHPR1-PHPR2)/PHPR1
```

```

delta_EXP

epsilon2_EXP
delta2_EXP

Betas_EXP
Svect_EXP

BetaME = [Betas_EXP(1,1) Betas_EXP(2,1)
          Betas_EXP(3,1) Betas_EXP(4,1)]

SmatxME = [Svect_EXP(1,1) Svect_EXP(2,1)
           Svect_EXP(3,1) Svect_EXP(4,1)]

BetaMT = [Betas_THEO(1,1) Betas_THEO(2,1)
          Betas_THEO(3,1) Betas_THEO(4,1)]

SmatxMT = [Svect_THEO(1,1) Svect_THEO(2,1)
           Svect_THEO(3,1) Svect_THEO(4,1)]

format short

%% NEXT STEP - plot the chosen points on the graphs!!!!

% Drive element piston
axes(h11a);

DEsEXPptshand = line([Press_EXP(1,1) Press_EXP(3,1)],...
                    [Defls_EXP(1,1) Defls_EXP(3,1)], 'color', 'r', 'linestyle', 'none', 'marker', '*', ...
                    'MarkerSize', 12);

DEsTHPptshand = line([Press_THEO(1,1) Press_THEO(3,1)],...
                    [Defls_THEO(1,1) Defls_THEO(3,1)], 'color', 'k', 'linestyle', 'none', 'marker', 'x', ...
                    'MarkerSize', 12);

%Valve Piston!!!!
axes(h22a);

VCsEXPptshand = line([Press_EXP(1,1) Press_EXP(3,1)],...
                    [Defls_EXP(1,2) Defls_EXP(3,2)], 'color', 'r', 'linestyle', 'none', 'marker', '*', ...
                    'MarkerSize', 12);

VCsTHPptshand = line([Press_THEO(1,1) Press_THEO(3,1)],...
                    [Defls_THEO(1,2) Defls_THEO(3,2)], 'color', 'k', 'linestyle', 'none', 'marker', 'x', ...
                    'MarkerSize', 12);

```

```
%*****
%*****
%*****
%*****

% Attempt at making 3d plots of the following:

% 1: Experimental data
% 2: Model data
% 3: Experimental stiffness plane
% 4: Theoretical stiffness plane

%*****
%*****
%*****
%*****
%*****

%*****
% Nonlinear plots first - they look cooler

% We will use the following variables:

% VC_PolyCell_mod
% VC_PolyCell
% DE_PolyCell_mod
% DE_PolyCell

% All of the above have the following structure:

% Row1: Polynomial Coefs for polyeval function
% Row2: An S-structure for error estimation
% Row3: The corresponding PHPR at which the fit was done
% Row4: The xmin and xmax values over which the curve fit
% is valid. THIS IS NB, because we hardcode invert the fcns!!!

%*****

[XMATX,YMATX,VCE_ZMATX] = hac3dinterp1(VC_PolyCell,nfcnpts,n3dpts,Ppismmin,Ppismmax,...
    Phprmin,Phprmax);
[XMATX,YMATX,VCT_ZMATX] = hac3dinterp1(VC_PolyCell_mod,nfcnpts,n3dpts,Ppismmin,...
    Ppismmax,Phprmin,Phprmax);
[XMATX,YMATX,DEE_ZMATX] = hac3dinterp1(DE_PolyCell,nfcnpts,n3dpts,Ppismmin,...
    Ppismmax,Phprmin,Phprmax);
[XMATX,YMATX,DET_ZMATX] = hac3dinterp1(DE_PolyCell_mod,nfcnpts,n3dpts,Ppismmin,...
    Ppismmax,Phprmin,Phprmax);
```

```

VCDE3Dihand1 = figure('color','w','position',[100 180 900 450]);

hold on;

VC3Daxes1 = subplot(1,2,1);
set(VC3Daxes1,'linewidth',2,'box','on');

VC3dmeshh1 = surface(XMATX,YMATX,VCT_ZMATX,'facecolor','none','edgecolor',...
    [0.6 0.6 0.6],'linewidth',0.8)
VC3dmeshh2 = surface(XMATX,YMATX,VCE_ZMATX,'facecolor','none','edgecolor',...
    [0 0 0],'linewidth',1)

% Set view before resize
view(-37.5,30);
% Set position after the plot is complete
set(VC3Daxes1,'units','pixels','position',[60 60 340 310]);

xlabel(xPde_labl3D);
ylabel(yPhpr_labl3D);
zlabel(zvc_labl);
title({'Small piston deflection:','Theoretical vs. Experimental'})
legend('Model','Experiment')


DE3Daxes1 = subplot(1,2,2);

set(DE3Daxes1,'linewidth',2,'box','on');

DE3dmeshh1 = surface(XMATX,YMATX,DET_ZMATX,'facecolor','none','edgecolor',...
    [0.6 0.6 0.6],'linewidth',0.8)
DE3dmeshh2 = surface(XMATX,YMATX,DEE_ZMATX,'facecolor','none','edgecolor',...
    [0 0 0],'linewidth',1)

% Set view before resize
view(-37.5,30);
% Set position after the plot is complete
set(DE3Daxes1,'units','pixels','position',[490 60 340 310]);

xlabel(xPde_labl3D);
ylabel(yPhpr_labl3D);
zlabel(zde_labl);
title({'Large piston deflection:','Theoretical vs. Experimental'})
legend('Model','Experiment')

%*****
%*****
%*****

```

```
% Now we compute xyz data for the linear functions, the stiffness estimates

% We have the following two matrices to use:

%SmatxME - experimental "compliance"

%SmatxMT - theoretical "compliance"

% [ zDE ] = [s11 s12] [PPIS]
% [ zVC ]   [s21 s22] [PHPR]

%*****
%*****
%*****

% This is very easy, because we have XMATX and YMATX:

DESE_ZMATX = zeros(n3dpts);
DEST_ZMATX = zeros(n3dpts);
VCSE_ZMATX = zeros(n3dpts);
VCST_ZMATX = zeros(n3dpts);

for i1 = 1:n3dpts %x-index, or the PDE index
    for i2 = 1:n3dpts % y-index or the PHPR index

        Pminivect = [XMATX(i1,i2)
                     YMATX(i1,i2)];

        DESE_ZMATX(i1,i2) = SmatxME(1,:)*Pminivect;

        DEST_ZMATX(i1,i2) = SmatxMT(1,:)*Pminivect;

        VCSE_ZMATX(i1,i2) = SmatxME(2,:)*Pminivect;

        VCST_ZMATX(i1,i2) = SmatxMT(2,:)*Pminivect;

    end
end

VCDE3D2hand1 = figure('color','w','position',[100 180 900 450]);

VC3Daxesh2 = subplot(1,2,1)
set(VC3Daxesh2,'linewidth',2,'box','on');

VC3dmeshh21 = surface(XMATX,YMATX,VCST_ZMATX,'facecolor','none','edgecolor','b')

VC3dmeshh22 = surface(XMATX,YMATX,VCSE_ZMATX,'facecolor','none','edgecolor','k')
```



---

```

% Set view before resize
view(-37.5,30);
% Set position after the plot is complete
set(VC3Daxesh2,'units','pixels','position',[60 60 340 310]);

xlabel(xPde_labl3D);
ylabel(yPhpr_labl3D);
zlabel(zvc_labl);
title({'Small piston linear stiffness:','Theoretical vs. Experimental'})
legend('Model','Experiment')

DE3Daxesh2 = subplot(1,2,2)
set(DE3Daxesh2,'linewidth',2,'box','on');

DE3dmeshh21 = surface(XMATX,YMATX,DEST_ZMATX,'facecolor','none','edgecolor','b')
DE3dmeshh22 = surface(XMATX,YMATX,DESE_ZMATX,'facecolor','none','edgecolor','k')

% Set view before resize
view(-37.5,30);
% Set position after the plot is complete
set(DE3Daxesh2,'units','pixels','position',[490 60 340 310]);

xlabel(xPde_labl3D);
ylabel(yPhpr_labl3D);
zlabel(zde_labl);
title({'Large piston linear stiffness:','Theoretical vs. Experimental'})
legend('Model','Experiment')

%*****
%*****
%*****

% Overplot the two experimental linear stiffness meshes with their corresponding
%nonlinear buddies.

VC3D3handl = figure('color','w','position',[100 180 900 450]);

VC3Daxesh3 = subplot(1,2,1)
set(VC3Daxesh3,'linewidth',2,'box','on');

```

```
VC3dmeshh31 = surface(XMATX,YMATX,VCE_ZMATX,'facecolor','none','edgecolor','b')

VC3dmeshh32 = surface(XMATX,YMATX,VCSE_ZMATX,'facecolor','none','edgecolor','r')

% Set view before resize
view(-37.5,30);
% Set position after the plot is complete
set(VC3Daxesh3,'units','pixels','position',[60 60 340 310]);

xlabel(xPde_lab13D);
ylabel(yPhpr_lab13D);
zlabel(zvc_lab1);
title({'Small piston Comparison:' ; 'Experimental Nonlinear vs. Linearised about  $z_{\{2\}} = 0\}$ })
legend('Experiment','Linearization')


DE3Daxesh3 = subplot(1,2,2)
set(DE3Daxesh3,'linewidth',2,'box','on');

DE3dmeshh31 = surface(XMATX,YMATX,DEE_ZMATX,'facecolor','none','edgecolor','b')

DE3dmeshh32 = surface(XMATX,YMATX,DESE_ZMATX,'facecolor','none','edgecolor','r')

% Set view before resize
view(-37.5,30);
% Set position after the plot is complete
set(DE3Daxesh3,'units','pixels','position',[490 60 340 310]);

xlabel(xPde_lab13D);
ylabel(yPhpr_lab13D);
zlabel(zde_lab1);
title({'Large piston Comparison:' ; 'Experimental Nonlinear vs. Linearised about  $z_{\{1\}} = 0\}$ })
legend('Experiment','Linearization')

%*****
%*****
%*****

%*****
%*****
%*****
% Create line plots to show the equivalence of the stiffness matrices
```

---

```

% Just overplot them over the original plots
% Both experimental and also theoretical

DEexpSMatH = zeros(nDEplt,1);
VCexpSMatH = zeros(nDEplt,1);

for i1 = 1:nDEplt

    % Displacement vector

    zde_vect_fop = zeros(n3dpts,1);

    % We will use XMATX again - why not?!

    PHPR1 = DE_PolyCell{3,i1};

    for i2 = 1:n3dpts
        Pminivect = [XMATX(i2,1)
                     PHPR1];
        zde_vect_fop(i2,1) = SmatxME(1,:)*Pminivect;
    end

    axes(h11a);
    DEexpSMatH(i1,1) = line(XMATX(:,1),zde_vect_fop);

    zde_vect_fop = zeros(n3dpts,1);

    % We will use XMATX again - why not?!

    PHPR1 = VC_PolyCell{3,i1};

    for i2 = 1:n3dpts
        Pminivect = [XMATX(i2,1)
                     PHPR1];
        zde_vect_fop(i2,1) = SmatxME(2,:)*Pminivect;
    end

    axes(h22a);
    VCexpSMatH(i1,1) = line(XMATX(:,1),zde_vect_fop);

end

% Now the theoretical overplots:

DEthSMatH = zeros(nDEplt,1);
VCthSMatH = zeros(nDEplt,1);

```



```

%*****
%*****

%*****
%*****

set(VCexpSMatH,'linestyle','-','color',[0.5 0.5 0.5],'marker','none','markersize',...
    4,'linewidth',0.5)
set(DEexpSMatH,'linestyle','-','color',[0.5 0.5 0.5],'marker','none','markersize',...
    4,'linewidth',0.5)

set(VCthSMatH,'linestyle','-','color',[0.5 0.5 0.5],'marker','p','markersize',4,...
    'linewidth',0.5)
set(DEthSMatH,'linestyle','-','color',[0.5 0.5 0.5],'marker','p','markersize',4,...
    'linewidth',0.5)

% Set the axes limits, labels and line thicknesses:

set(h11a,'xlim',xPde_lims,'ylim',yde_lims,'linewidth',2,'fontsize',12);
set(h22a,'xlim',xPde_lims,'ylim',yvc_lims,'linewidth',2,'fontsize',12);

axes(h11a)

xlabel(xPde_labl)
ylabel(zde_labl)
%title('Large piston motion vs. Applied pressure');

% Add a legend to the fits
%DElegendhandl = legend(DEfithandl,'P_2=0','P_2=92','P_2=298','P_2=500',2);

axes(h22a)
xlabel(xPde_labl)
ylabel(zvc_labl)
%VClegendhandl = legend(VCfithandl,'P_2=0','P_2=92','P_2=298','P_2=500',2);

set(DEfithandl,'color','k','linewidth',2);
set(VCfithandl,'color','k','linewidth',2);
set(DEebarhandl(1,:), 'color','k','linewidth',2);
set(VCebarhandl(1,:), 'color','k','linewidth',2);

set(DElabhdl,'fontsize',curvelegfntsiz);
set(VClabhdl,'fontsize',curvelegfntsiz);

set(DElinehandl,'linewidth',0.8,'color',[0.75 0.75 0.75])
set(VClinehandl,'linewidth',0.8,'color',[0.75 0.75 0.75])

```

```
% Get the graphs right for the stage of plotting we're in:

legends2d = cell(2,2);

switch Plotstage
case 1
    delete(DEmodhandl);
    delete(VCmodhandl);
    delete(DEexpSMatH);
    delete(VCexpSMatH);
    delete(DEthSMatH);
    delete(VCthSMatH);
    % Legend
    [legends2d{1,1},legends2d{1,2}] = legend(h11a,[DElinehandl(1,1) DEfithandl(1,1)]...
        , 'Data', 'Fit to Data', 2);
    [legends2d{2,1},legends2d{2,2}] = legend(h22a,[VClinehandl(1,1) VCfithandl(1,1)]...
        , 'Data', 'Fit to Data', 2);
case 2
    delete(DElinehandl);
    delete(VClinehandl);
    delete(DEebarhandl(1,:));
    delete(VCebarhandl(1,:));
    delete(DEexpSMatH);
    delete(VCexpSMatH);
    delete(DEthSMatH);
    delete(VCthSMatH);
    % Legend
    [legends2d{1,1},legends2d{1,2}] = legend(h11a,[DEfithandl(1,1) DEmodhandl(1,1)]...
        , 'Fit to Data', 'Model Prediction', 2);
    [legends2d{2,1},legends2d{2,2}] = legend(h22a,[VCfithandl(1,1) VCmodhandl(1,1)]...
        , 'Fit to Data', 'Model Prediction', 2);
case 3
    delete(DEebarhandl(1,:));
    delete(VCebarhandl(1,:));
    delete(DElinehandl);
    delete(VClinehandl);
    % Legend
    [legends2d{1,1},legends2d{1,2}] = legend(h11a,...
        [DEfithandl(1,1) DEmodhandl(1,1) DEexpSMatH(1,1) DEthSMatH(1,1)],...
        'Fit to Data', 'Model Prediction', 'Slope of data at 0', 'Slope of model at 0', 2);
    [legends2d{2,1},legends2d{2,2}] = legend(h22a,...
        [VCfithandl(1,1) VCmodhandl(1,1) VCexpSMatH(1,1) VCthSMatH(1,1)],...
        'Fit to Data', 'Model Prediction', 'Slope of data at 0', 'Slope of model at 0', 2);

end

set(legends2d{1,2}(1,1), 'fontsize', 10);
set(legends2d{2,2}(1,1), 'fontsize', 10);
```

```

%*****
%*****

%*****
%*****

%*****
%*****

%*****
%*****

%*****
%*****
%*****
%*****
%*****
%*****
%*****
%*****
%*****
%*****
%*****
%*****
%*****
%*****
%*****
%*****
%*****
%*****
%*****
%*****

% Plot out the stiffness matrices in a nice readable format:
disp(sprintf('*****'))
disp(sprintf('*****'))
disp(sprintf('***** Output of the stiffness matrix solutions *****'))
disp(sprintf('*****'))
disp(sprintf('*****'))
disp(sprintf('\n\nTheoretical inverse compressibility matrix, where:\n'))
disp(sprintf('{P1} = [b11  b12] {z1}'))
disp(sprintf('{P2} = [b21  b22] {z2}\n\n'))

disp(sprintf('Units are in kPa/um:'))

disp(sprintf('{P1} = [%11.3e  %11.3e] {z1}',BetaMT(1,1),BetaMT(1,2)))
disp(sprintf('{P2} = [%11.3e  %11.3e] {z2}',BetaMT(2,1),BetaMT(2,2)))

disp(sprintf('\n\nExperimental inverse compressibility matrix in kPa/um:\n'))

disp(sprintf('{P1} = [%11.3e  %11.3e] {z1}',BetaME(1,1),BetaME(1,2)))
disp(sprintf('{P2} = [%11.3e  %11.3e] {z2}',BetaME(2,1),BetaME(2,2)))

disp(sprintf('\n\nRatio of the elements of the matrices:\n'))

Betaratio = BetaMT./BetaME;

```

```
disp(sprintf('%6.1f %6.1f',Betaratio(1,1),Betaratio(1,2)))
disp(sprintf('%6.1f %6.1f',Betaratio(2,1),Betaratio(2,2)))

% Also substract the measured stiffnesses from the theo and exp data

BetaTildeTHEO = BetaMT - psi1psi2T;
BetaTildeEXP = BetaME - psi1psi2E;

disp(sprintf('\n\nD-Tilde, THEORETICAL in kPa/um:\n'))

disp(sprintf('%11.3e %11.3e',BetaTildeTHEO(1,1),BetaTildeTHEO(1,2)))
disp(sprintf('%11.3e %11.3e',BetaTildeTHEO(2,1),BetaTildeTHEO(2,2)))

disp(sprintf('\n\nD-Tilde, EXPERIMENTAL in kPa/um:\n'))

disp(sprintf('%11.3e %11.3e',BetaTildeEXP(1,1),BetaTildeEXP(1,2)))
disp(sprintf('%11.3e %11.3e',BetaTildeEXP(2,1),BetaTildeEXP(2,2)))

disp(sprintf('\n\nRatio of the elements of the D-Tilde matrices:\n'))

DTilderatio = BetaTildeTHEO./BetaTildeEXP;

disp(sprintf('%6.1f %6.1f',DTilderatio(1,1),DTilderatio(1,2)))
disp(sprintf('%6.1f %6.1f',DTilderatio(2,1),DTilderatio(2,2)))

disp(sprintf('*****'))
disp(sprintf('\n\nTheoretical compressibility matrix, where:\n'))
disp(sprintf('{z1} = [b11 b12] {P1}'))
disp(sprintf('{z2} = [b21 b22] {P2}\n\n'))

disp(sprintf('Units are in kPa/um:'))

disp(sprintf('{z1} = [%11.3e %11.3e] {P1}',SmatxMT(1,1),SmatxMT(1,2)))
disp(sprintf('{z2} = [%11.3e %11.3e] {P2}',SmatxMT(2,1),SmatxMT(2,2)))

disp(sprintf('\n\nExperimental Compressibility matrix in kPa/um:\n'))

disp(sprintf('{z1} = [%11.3e %11.3e] {P1}',SmatxME(1,1),SmatxME(1,2)))
disp(sprintf('{z2} = [%11.3e %11.3e] {P2}',SmatxME(2,1),SmatxME(2,2)))

disp(sprintf('\n\nRatio of the elements of the matrices:\n'))

Sratio = SmatxMT./SmatxME;

disp(sprintf('%6.1f %6.1f',Sratio(1,1),Sratio(1,2)))
disp(sprintf('%6.1f %6.1f',Sratio(2,1),Sratio(2,2)))

disp(sprintf('*****'))
disp(sprintf('*****'))
```



```

%*****
%*****
%*****
%*****
%*****
%*****
%***** COMPUTING AMPLIFICATION RATIOS *****
%*****
%*****
%*****
%*****
%*****
%*****
%*****
%*****
%*****

% This will make for a cool 3D plot sometime....

% This subprogram will compute the amplification ratios
% based on fitted theoretical and fitted experimental data
% by differentiating the polynomials and looking at the relative change in AR

hAR = figure('color','w');
hARa = axes('box','on');

ARexphndl = zeros(nDEplt,1);
ARmodhndl = zeros(nmodfiles,1);

ARexplabhdl = zeros(nDEplt,1);
ARmodlabhdl = zeros(nmodfiles,1);

curvefractAR = [0.2
    0.4
    0.6
    0.8];

% First, we look at the experimental data:

for i1 = 1:nDEplt

    A1 = DE_PolyCell{1,i1}; % Extract the Drive element polynomial
    A2 = VC_PolyCell{1,i1}; % Extract the Valve cap polynomial

    PHPRfop = modfileP_HPR_S(i1,1); % extract the estimated PHPR

    % compute the derivatives of the polynomials

```

```
dA1 = polyder(A1); % dP1/dz1
dA2 = polyder(A2); % dP2/dz2

% Find values for these
% at the appropriate values for z1,z2

z1lims = DE_PolyCell{4,i1};
z2lims = VC_PolyCell{4,i1};

z1vect = (linspace(z1lims(1,1),z1lims(1,2),ncfitpts))';
z2vect = (linspace(z2lims(1,1),z2lims(1,2),ncfitpts))';

% Also create a regularly spaced P1 vector, because we will interpolate
% So that we can eventually compare apples with apples

P1reg = (linspace(Ppismmin,Ppismmax,ncfitpts))';

% Now, we evaluate the derivative of the function at each value of z
% ALSO evaluate the function ITSELF at each value of z

P1_fz1_irreg = polyval(A1,z1vect);
P1_gz2_irreg = polyval(A2,z2vect);

%dP1dz1_dfz1 = polyval(dA1,z1vect);
%dP1dz2_dgz2 = polyval(dA2,z2vect);

% Interpolate to have irregular z vectors for each P1 vector

z1irregP1 = interp1(P1_fz1_irreg,z1vect,P1reg,'spline');
z2irregP1 = interp1(P1_gz2_irreg,z2vect,P1reg,'spline');

% Now, each of the irregular z's has a little friend in P1reg

% For each IRREGULAR z we can compute the corresponding dP/dz

dP1dz1_dfz1 = polyval(dA1,z1irregP1); % Now we have the derivatives
dP1dz2_dgz2 = polyval(dA2,z2irregP1);

% Each of the two functions above also has a matching value in P1reg

% The amplification ratio is dz2/dz1 ===== (dP1/dz1)/(dP1/dz2) - check it

AR_P1reg = dP1dz1_dfz1./dP1dz2_dgz2;

% Plot the amplification ratio on the graph

axes(hARa);

ARexphandl(i1,1) = line(P1reg,AR_P1reg);
```

```

%*****
% Place a legend for PHPR on the plot

ctext1 = strcat('P_2=',strcat(num2str(modfileP_HPR_S(i1,1),'%4.0f'),'kPa'));

ARexplabhdl(i1,1) = curvelabel2(ctext1,hARa,[0 500],[0 22],...
    curvefractAR(i1,1),P1reg,AR_P1reg);

%*****

%*****

end

%Now, the model:

for i1 = 1:nmodfiles

    A1 = DE_PolyCell_mod{1,i1}; % Extract the Drive element polynomial
    A2 = VC_PolyCell_mod{1,i1}; % Extract the Valve cap polynomial

    PHPRfop = modfileP_HPR_S(i1,1); % extract the estimated PHPR

    z1lims = DE_PolyCell_mod{4,i1};
    z2lims = VC_PolyCell_mod{4,i1};

    % compute the derivatives of the polynomials

    dA1 = polyder(A1); % dP1/dz1
    dA2 = polyder(A2); % dP2/dz2

    % Find values for these
    % at the appropriate values for z1,z2

    z1vect = (linspace(z1lims(1,1),z1lims(1,2),ncfitpts))';
    z2vect = (linspace(z2lims(1,1),z2lims(1,2),ncfitpts))';

    % Also create a regularly spaced P1 vector, because we will interpolate
    % So that we can eventually compare apples with apples

    P1reg = linspace(Ppismin,Ppismax,ncfitpts);

    % Now, we evaluate the derivative of the function at each value of z
    % ALSO evaluate the function ITSELF at each value of z

```

```
P1_fz1_irreg = polyval(A1,z1vect);
P1_gz2_irreg = polyval(A2,z2vect);

%dP1dz1_dfz1 = polyval(dA1,z1vect);
%dP1dz2_dfz2 = polyval(dA2,z2vect);

% Interpolate to have irregular z vectors for each P1 vector

z1irregP1 = interp1(P1_fz1_irreg,z1vect,P1reg,'spline');
z2irregP1 = interp1(P1_gz2_irreg,z2vect,P1reg,'spline');

% Now, each of the irregular z's has a little friend in P1reg

% For each IRREGULAR z we can compute the corresponding dP/dz

dP1dz1_dfz1 = polyval(dA1,z1irregP1); % Now we have the derivatives
dP1dz2_dgz2 = polyval(dA2,z2irregP1);

% Each of the two functions above also has a matching value in P1reg

% The amplification ratio is dz2/dz1 ===== (dP1/dz1)/(dP1/dz2) - check it

AR_P1reg = dP1dz1_dfz1./dP1dz2_dgz2;

% Plot the amplification ratio on the graph

axes(hARa);

ARmodhdl(i1,1) = line(P1reg,AR_P1reg,'color','k');
%*****
% Place a legend for PHPR on the plot
ctext1 = strcat('P_2=',strcat(num2str(modfileP_HPR_S(i1,1),'%4.0f'),'kPa'));

ARmodlabhdl(i1,1) = curvelabel2(ctext1,hARa,[0 500],[0 22],...
    curvefractAR(i1,1),P1reg,AR_P1reg);
%*****

end

% Make the plot pretty

set(hARa,'linewidth',2,'fontsize',12,'xlim',[Ppismmin Ppismax],'ylim',[0 23])
xlabel('P_1');
ylabel('Amplification Ratio (z_1/z_2)');

% Set the colors of the plots
set(ARexphhdl,'color','k','linewidth',2);
set(ARmodhdl,'color',[0.5 0.5 0.5],'linewidth',1);

set(ARmodlabhdl,'fontsize',10,'color',[0.5 0.5 0.5]);
```

[illegible]



## Appendix E

# Masks

---

This appendix contains a selection of masks from the set that was used to form the devices shown in Figure 2.2. It should give the reader an idea of what is involved in the creation of a multi-layered device with multiple silicon and glass layers. Figure E.1 shows the glass patterns of the full MHT device. All glass layers were ultrasonically machined. Prior to ultrasonic machining, wafer-scale align marks were patterned on the glass wafers using BOE. Care had to be taken during the exposure step, because the substrates were transparent. The ultrasonic machining was then done to the align marks provided. Figure E.2 shows different patterns for Layer 3, to be able to accommodate piezoelectric elements of various sizes. It also shows the pattern that was used for the static, pressure operated hydraulic amplifier (L3 Big Hole).

The masks for the large piston (Layers 4 and 5) are shown in Figures E.3 and E.4. Note the nearly identical process for the two layers. The main difference lies in the venting channels in Layer 5, and the venting holes in Layer 4.

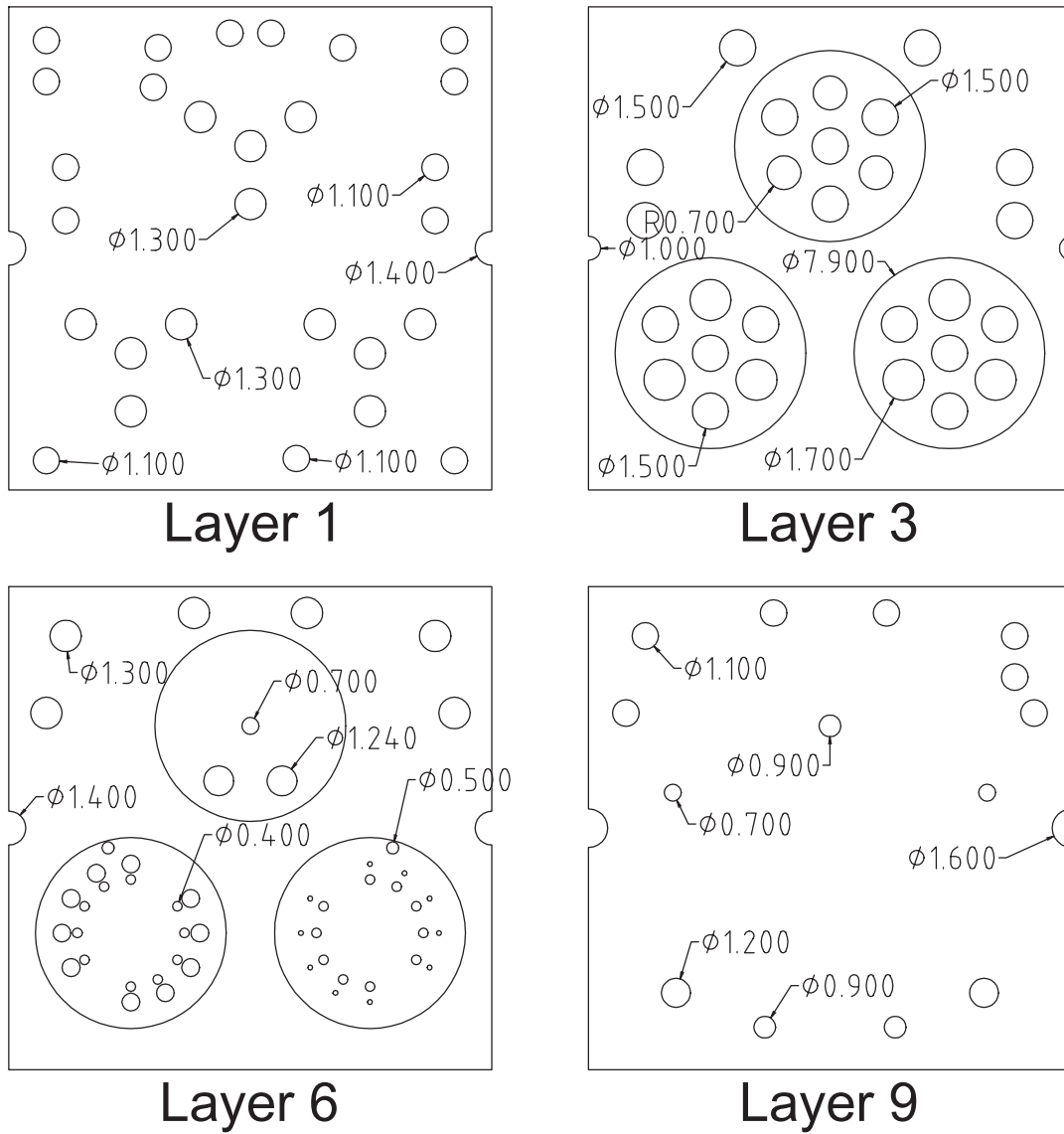
Figure E.5 shows the mask flow for Layer 7, the layer containing the small pistons. In this figure, a mask set for a device with a single small piston is shown. Ten small pistons were created using the same mask flow, but with different geometries.

In Figure E.6 the masks for Layer 8 are shown, along with a mask set for an hydraulic amplifier with two small pistons (which was not tested). Note, especially in this figure, the use of so-called "halo" masks to etch through-wafer features. Halo masks are often used for performing uniform DRIE etching when features of various sizes are present on the wafer. Keeping the trench width constant for all through-wafer features helps to maintain a constant etch rate.

Figure E.7 is the wafer scale process flow associated with Figure E.5. Note the steps for creating features such as align marks and cutting lines for the dicing operation.

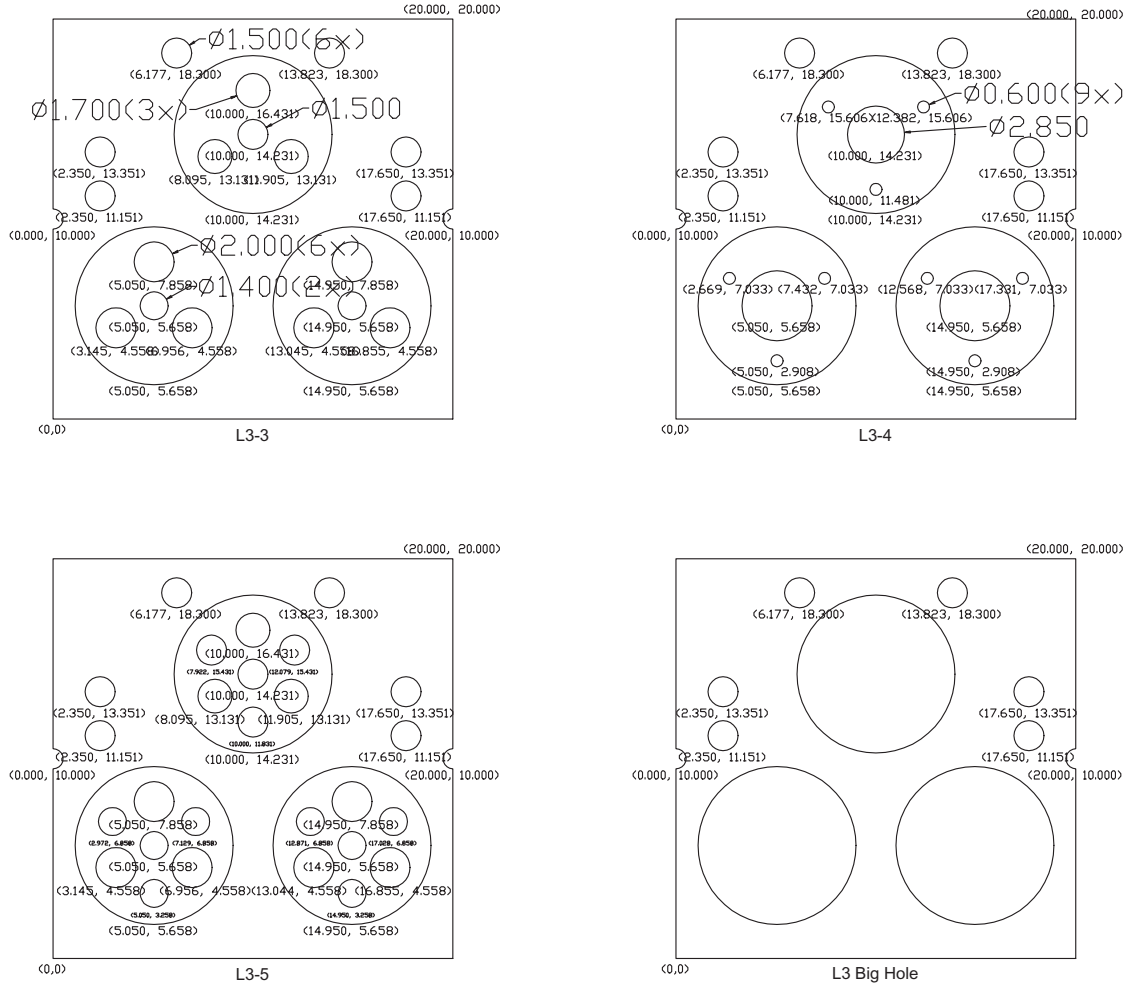
A plan view for all the layers of the full MHT device is shown in Figure E.8. This figure is an overlay of all the masks needed to fabricate the device.





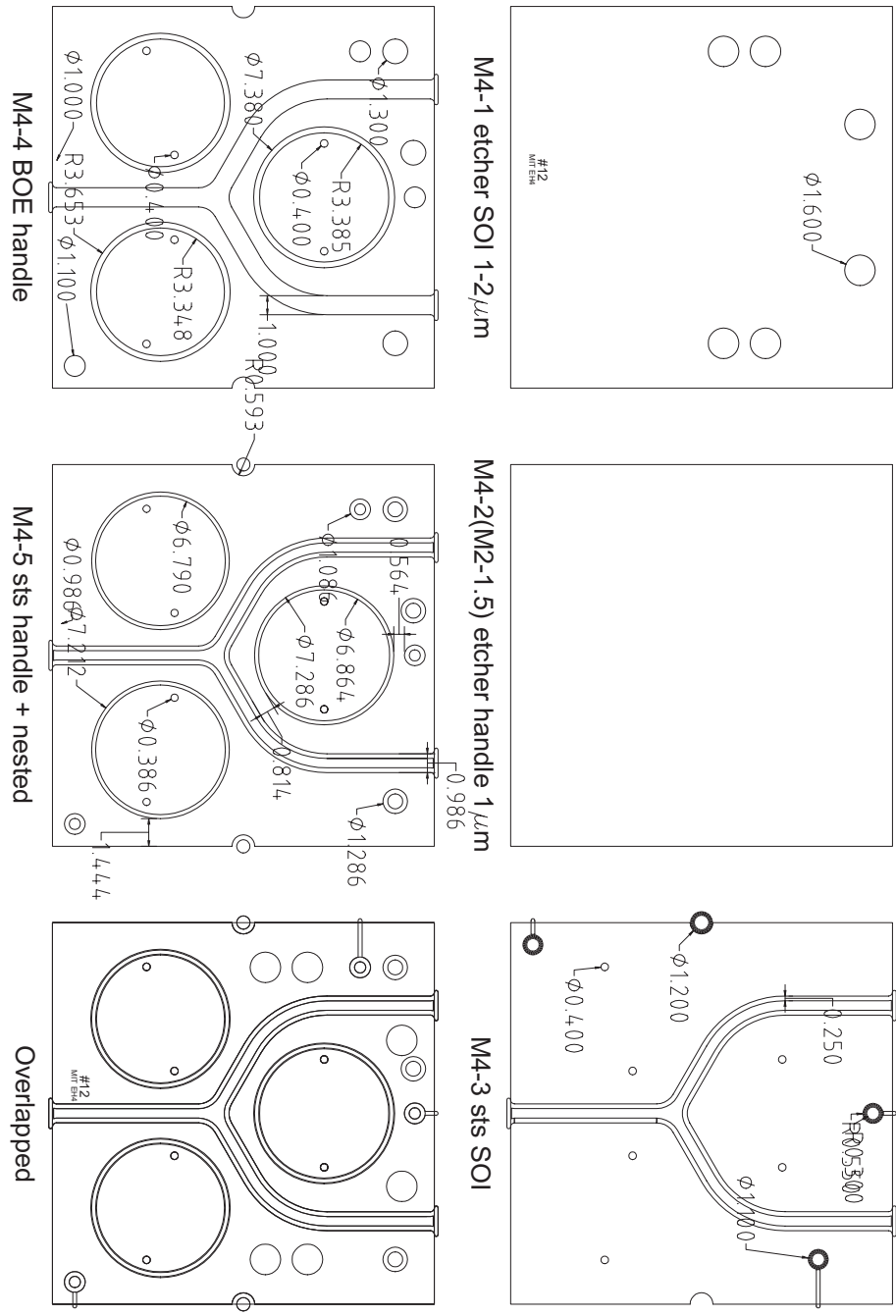
*Courtesy of H. Q. Li*

Figure E.1: The glass layers of the full ten valve MHT device.



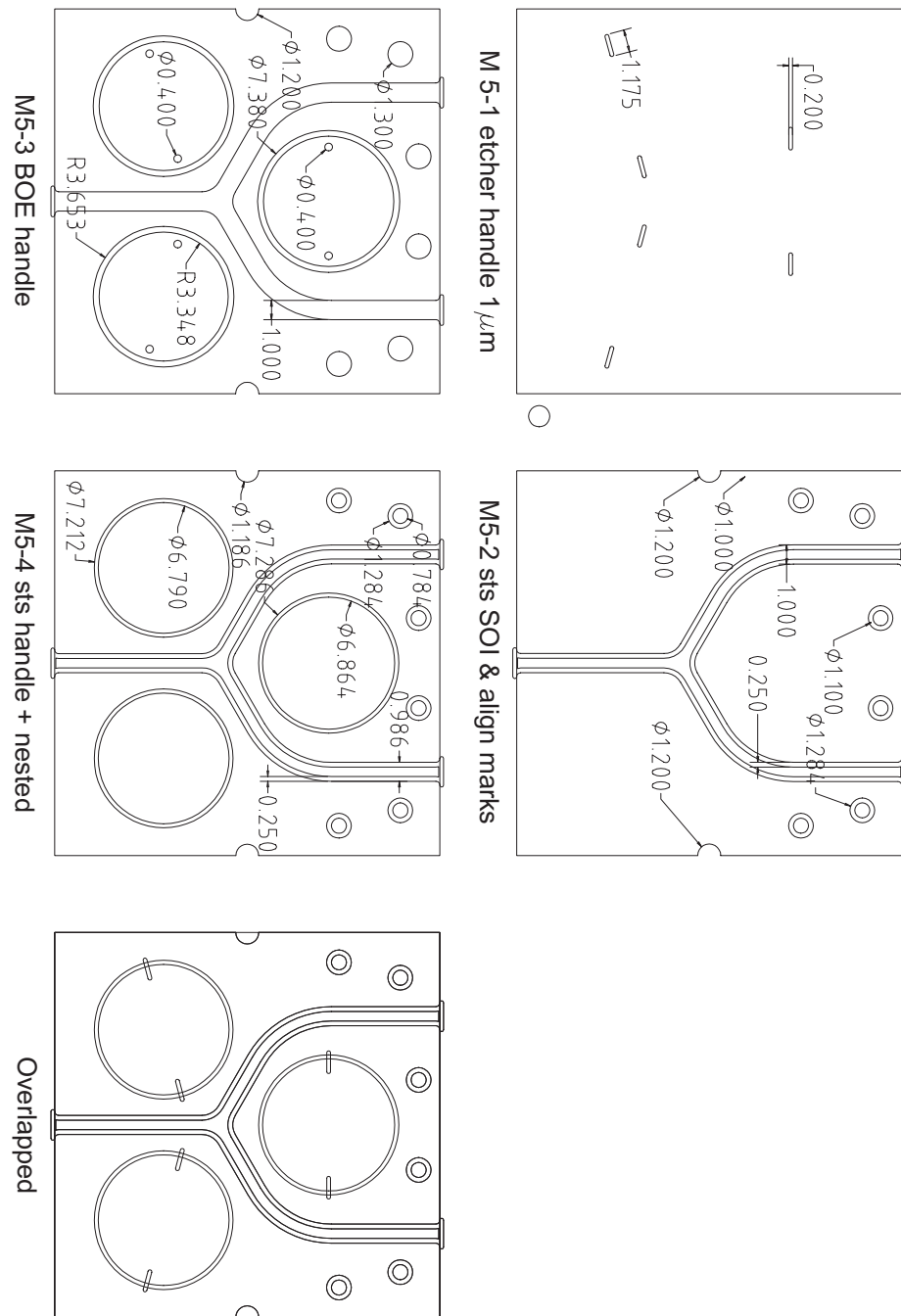
Courtesy of H. Q. Li

Figure E.2: Different configurations for Layer 3. L3-3 is the standard Layer 3, L3-4 is for accommodating a single large piezoelectric element, L3-5 has additional holes for optical displacement measurement and L3 Big Hole was used for the static hydraulic amplifiers.



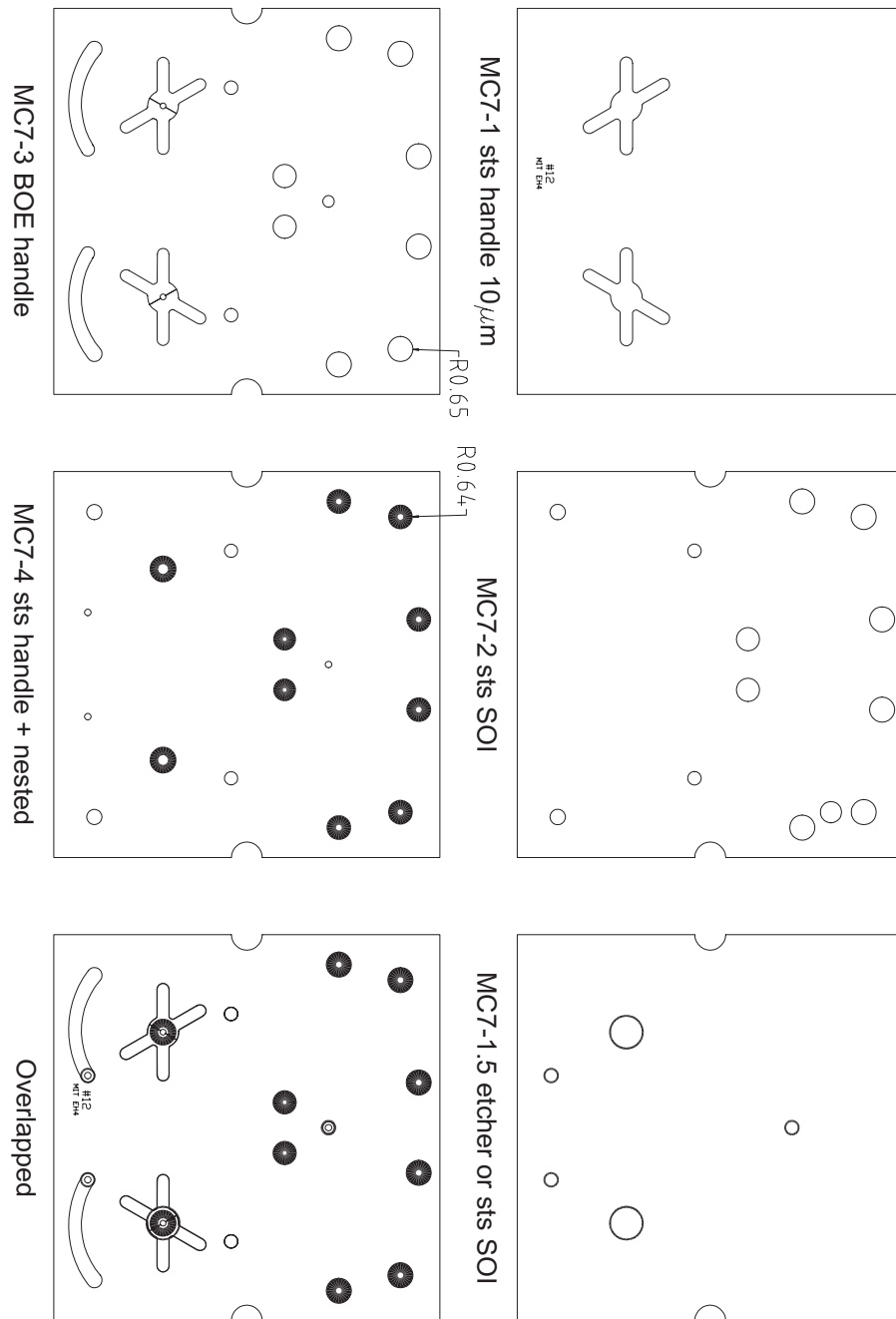
Courtesy of H.Q. Li

Figure E.3: Mask set for Layer 4.



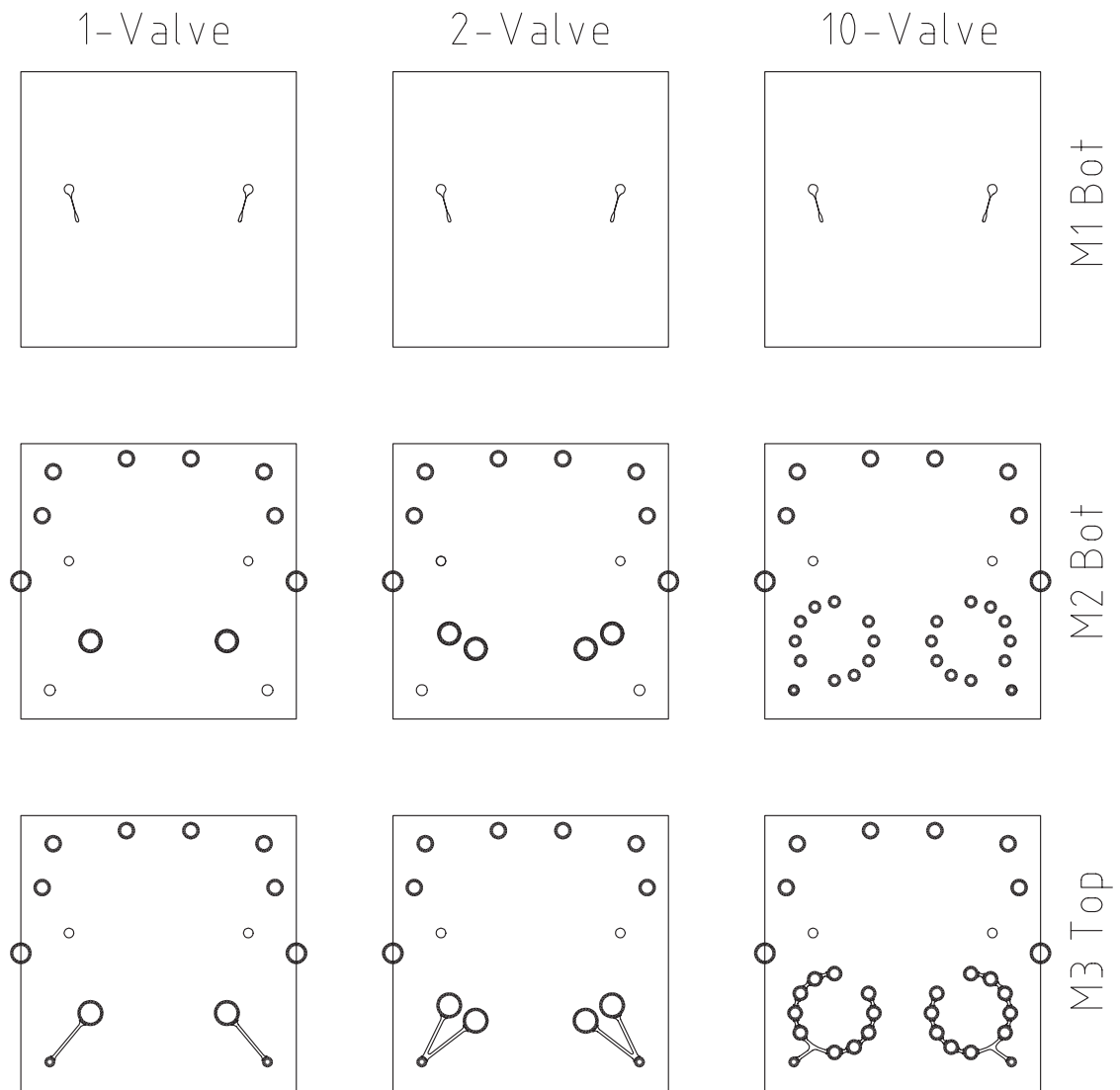
Courtesy of H.Q. Li

Figure E.4: Mask set for Layer 5.



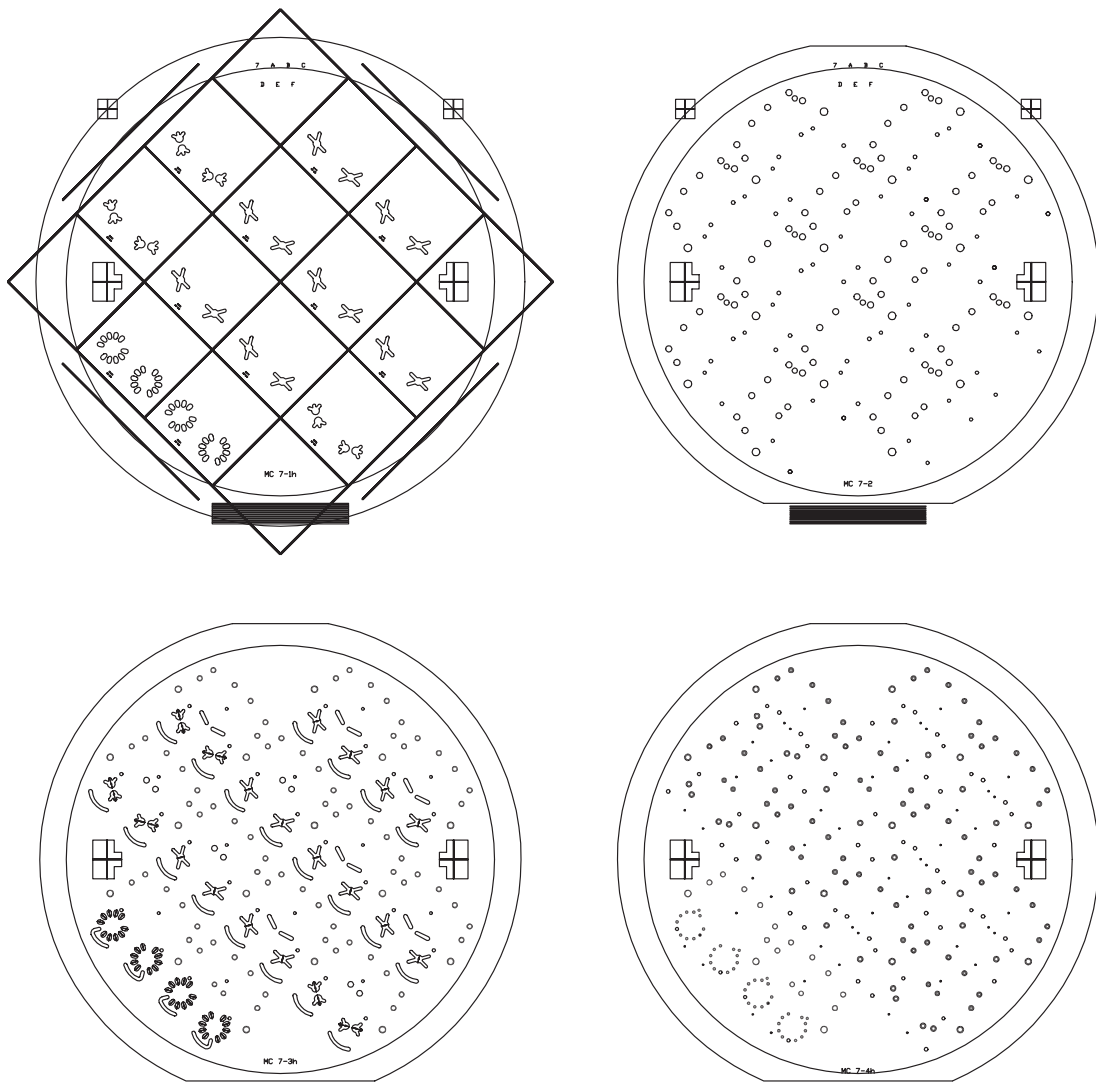
*Courtesy of H. Q. Li*

Figure E.5: Mask set for Layer 7. This is the mask set for the device with one small piston. The ones with ten small pistons have the same mask flow, but a different geometry.



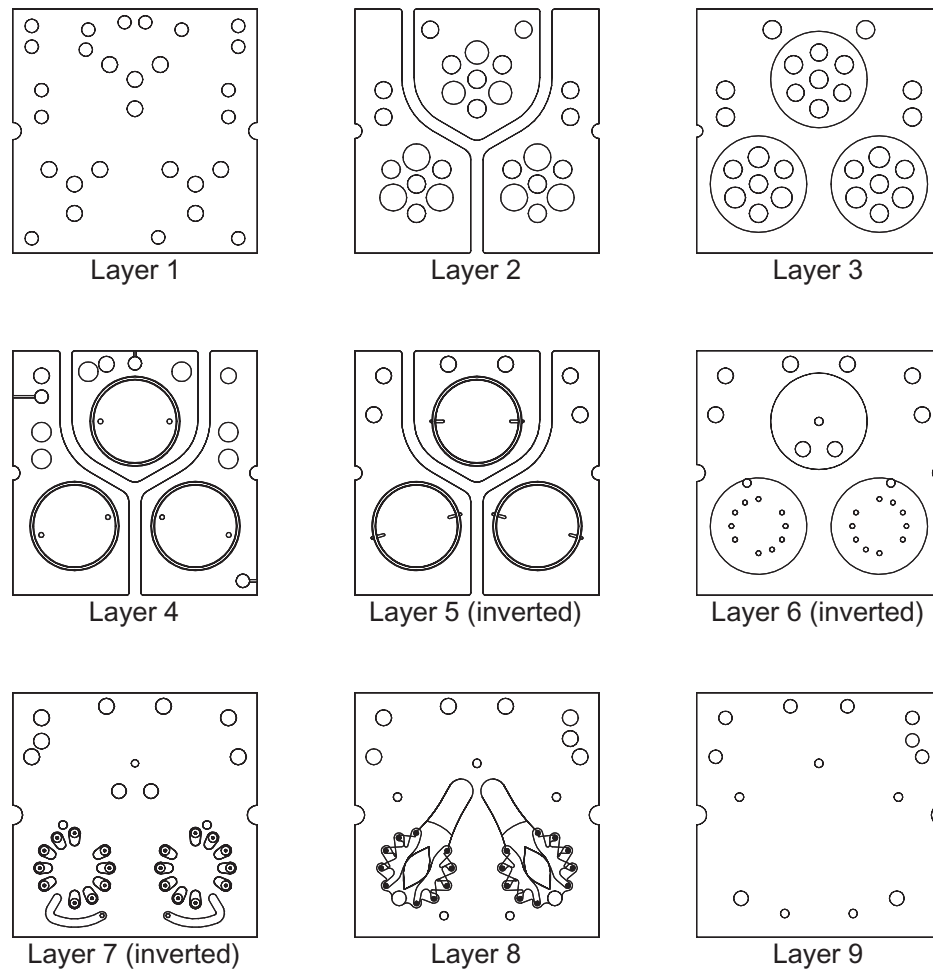
*Courtesy of H. Q. Li*

Figure E.6: Die-level mask set for Layer 8 of three types of hydraulic amplifiers: One, two and ten small pistons. Although dies with two small pistons were fabricated, as also shown in Figure E.7, none were tested in this work.



*Courtesy of H.Q. Li*

Figure E.7: Wafer scale masks of Layer 7. The first mask is also used to define align marks, globally aligned to the wafer, as well as cutting lines for the dicing operation.



*Courtesy of H. Q. Li*

Figure E.8: Plan view of all the layers of the full ten valve MHT device.



**Modeling and Design Considerations for a  
Micro-Hydraulic Piezoelectric  
Power Generator**

by:

Onnik Yaglioglu

Master's Thesis

Massachusetts Institute of Technology

February 2002

# Contents

<b>1</b>	<b>Introduction</b>	<b>21</b>
1.1	Microhydraulic Piezoelectric Transducers . . . . .	21
1.2	Configuration and Operation . . . . .	23
1.3	Preliminary Design Considerations . . . . .	26
1.4	Objective, Scope and Organization of the Thesis . . . . .	28
<b>2</b>	<b>Piezoelectric Power Generation and Circuitry</b>	<b>31</b>
2.1	Introduction . . . . .	31
2.2	Previous Work . . . . .	32
2.3	Theoretical Background . . . . .	36
2.4	Circuitry Considerations . . . . .	40
2.4.1	Modeling . . . . .	41
2.4.2	Simulation and Analysis . . . . .	44
2.5	Other Circuits . . . . .	59
2.6	Piezoelectric Material Comparison . . . . .	62
2.7	Conclusion . . . . .	66
<b>3</b>	<b>Energy Harvesting Chamber and Preliminary Design Considerations</b>	<b>67</b>
3.1	Configuration and Operation of the Energy Harvesting Chamber . . . . .	67
3.2	Modeling . . . . .	69
3.2.1	Piezoelectric Cylinder . . . . .	69
3.2.2	Chamber Continuity . . . . .	70
3.2.3	Fluid Model . . . . .	72

3.2.4	Circuitry . . . . .	77
3.3	Working Fluid . . . . .	77
3.4	Simulation and Analysis . . . . .	78
3.4.1	Energy Harvesting Chamber and Full Bridge Rectifier . . . . .	79
3.4.2	Energy Harvesting Chamber and Full Bridge Rectifier with Voltage De- tector Circuit . . . . .	83
3.5	Discussion . . . . .	91
3.6	Summary and Conclusion . . . . .	96
<b>4</b>	<b>Detailed Model of the Energy Harvesting Chamber</b>	<b>99</b>
4.1	Analysis of a Simplified Chamber Structure . . . . .	99
4.2	Detailed Analysis of Structural Components . . . . .	102
4.2.1	Top Support Structure . . . . .	102
4.2.2	Bottom Support Structure . . . . .	104
4.2.3	Piston . . . . .	106
4.2.4	Piston Tethers . . . . .	107
4.3	Simulation Architecture . . . . .	110
4.4	Conclusion . . . . .	114
<b>5</b>	<b>Further Design Considerations and Design Procedure</b>	<b>115</b>
5.1	Further Design Considerations . . . . .	115
5.1.1	Fluidic Oscillations . . . . .	115
5.1.2	Chamber filling and evacuation . . . . .	122
5.1.3	Tether Structure Optimization . . . . .	124
5.1.4	Operation Conditions and Trade-offs . . . . .	129
5.1.5	Bias Pressure . . . . .	135
5.1.6	Scaling Issues . . . . .	138
5.2	Design Procedure . . . . .	141
5.2.1	Preliminary design decisions . . . . .	141
5.2.2	Parameters imposed by active valve design . . . . .	142
5.2.3	Parameters imposed by fabrication process . . . . .	143

5.2.4	Design Procedure . . . . .	143
5.3	Design Examples . . . . .	147
5.3.1	Design Example 1 . . . . .	147
5.3.2	Design Example 2 . . . . .	148
5.4	Summary . . . . .	157
<b>6</b>	<b>Conclusions and Recommendations for Future Work</b>	<b>159</b>
6.1	Summary . . . . .	159
6.2	Recommendations for Future Work . . . . .	162
<b>A</b>	<b>Simulink Block Diagrams</b>	<b>171</b>
<b>B</b>	<b>Matlab Files</b>	<b>181</b>
<b>C</b>	<b>Maple Files</b>	<b>187</b>



# List of Figures

1-1	(a) Configuration of power generator (b) Configuration of actuator/ micropump. The actuator/micropump configuration can also be operated with check valves instead of active valves, which are necessary for power generator configuration. .	22
1-2	Device layout for power generator configuration. Top and bottom packaging pyrex layers not shown. . . . .	24
1-3	Generic operation duty cycle of the power generator. . . . .	25
1-4	(a) 5-layer device for subcomponent testing (b) Complete 9-layer device (c) SEM of micromachined tethered piston structure [7]. . . . .	27
1-5	Overall system architecture for the heel strike power generation configuration. . .	28
2-1	Graphic illustration of electromechanical energy conversion and definition of the piezoelectric coupling factor $k_{33}$ given in [18] (a) Conversion of energy from a mechanical source to electrical work (b) Conversion of energy from an electrical source to mechanical work. . . . .	38
2-2	Alternative idealized work cycles given in [8]. . . . .	39
2-3	Alternative circuits to rectify and store the electrical energy generated by the piezoelectric element. . . . .	41
2-4	Simulation architecture used to simulate the piezoelectric element connected to the full bridge rectifier. The force is imposed on the piezoelectric element. . . .	45
2-5	Time histories from the simulation of the piezoelectric element connected to the full bridge rectifier for the case of imposed force. The generated power is $I_b V_b$ . .	47
2-6	Force vs. deflection and voltage vs. charge plots of the piezoelectric element compressed under the applied force for the case of full bridge rectifier. . . . .	48

2-7	Effect of battery voltage on power. . . . .	49
2-8	Effect of bias force on the workcycle. . . . .	50
2-9	General presentation of the work cycle of the piezoelectric element in terms of stress, strain, electric field and charge density for the case of regular diode bridge.	52
2-10	Illustration of the effective coupling factor for the case of regular diode bridge. .	53
2-11	Time histories from the simulation of the piezoelectric element connected to the full bridge rectifier and voltage detector circuit. The time intervals between the dashed lines present the intervals where the switch(SCR) is in its "on" state. . . .	55
2-12	Force vs. deflection and voltage vs. charge plots of the piezoelectric element compressed under the applied force for the case of full bridge rectifier and voltage detector circuit. . . . .	56
2-13	General presentation of the work cycle of the piezoelectric element in terms of stress, strain, electric field and charge density for the case of the full bridge rectifier and voltage detector circuit. . . . .	57
2-14	Illustration of the effective coupling factor for the full bridge rectifier and voltage detection circuit. . . . .	58
2-15	Other alternative circuits for piezoelectric power generation. . . . .	59
2-16	Simulation results of the piezoelectric element shunted by a resistor for different resistance values. . . . .	60
2-17	Comparison of resistive shunting(at optimum resistance) with full bridge rectifier and full bridge rectifier with voltage detector. . . . .	61
2-18	Simulation results of the full bridge rectifier connected to a capacitor. . . . .	62
2-19	Force vs. deflection plot from the simulation of the full bridge rectifier with additional inductor. . . . .	63
2-20	Effective coupling factors of the diode bridge and the diode bridge with voltage detector as a function of the coupling coefficient. . . . .	64
2-21	Piezoelectric Material Comparison: (a) Effective coupling factor (b) Energy density.	65
3-1	Energy harvesting chamber configuration. . . . .	68
3-2	Duty cycles of generic operation of the energy harvesting chamber. The valve openings have the same duty cycle as the flowrates and are not shown here. . . .	68

3-3	Device schematics showing pressures at different locations. . . . .	73
3-4	Valve orifice representation:(a) Valve cap geometry and fluid flow areas, (b) Representation of flow through the valve as a flow contraction followed by a flow expansion. . . . .	74
3-5	Look-Up tables used for flow loss contraction and expansion coefficients. The loss coefficients are obtained from [51]. . . . .	75
3-6	Simulation architecture used in Simulink. . . . .	79
3-7	Simulation of the energy harvesting chamber attached to the full bridge rectifier circuit. . . . .	80
3-8	Force vs. displacement curve of the piezoelectric element from the simulation of the harvesting chamber attached to the full bridge rectifier. . . . .	82
3-9	Simulation of the energy harvesting chamber attached to the full bridge rectifier and voltage detector circuit. The time intervals between the dashed lines present the intervals where the switch(SCR) is in its "on" state. . . . .	84
3-10	Force vs. displacement curve of the piezoelectric element from the simulation of the energy harvesting chamber attached to the full bridge rectifier and voltage detector circuit. . . . .	85
3-11	Time histories of the force and deflection of the piezoelectric element. . . . .	85
3-12	Force vs. displacement curve of the piezoelectric element and slopes at different periods of operations. . . . .	87
3-13	The effect of effective chamber compliance on force vs. deflection curve and effective coupling factor. . . . .	90
3-14	Flowrate and frequency requirement for 0.5 W power requirement. . . . .	92
3-15	System efficiency as a function of the effective chamber compliance. . . . .	93
3-16	Required flowrates for 0.5 power generation. Comparison of different piezoelectric elements and different circuitry. . . . .	94
3-17	Required frequencies for the 0.5W power requirement. Comparison of different piezoelectric materials and circuitry. Note that the required frequency in the case of regular rectifier is independent of the chamber compliance. . . . .	95



3-18	Comparison of different piezoelectric materials and circuitry in terms of system efficiency. . . . .	96
3-19	Maximum system efficiency(which corresponds to the case where the effective compliance of the chamber is zero)as a function of the coupling coefficient. . . .	98
4-1	(a) Simplified chamber structure consisting of a fluid chamber with a compliant wall (b) Deformation of the top plate and swept volume. . . . .	100
4-2	Comparison of fluidic and structural compliances for a generic chamber structure at different chamber diameters for fixed chamber height and top plate thickness.	101
4-3	(a) Schematic illustrating the dimensional parameters of the chamber, (b) deformation of structural components and sign conventions, (c) free body diagrams and sign conventions. Deflections are exaggerated. . . . .	103
4-4	Model of the bottom support structure: circular plate with a circular hole at its center with guided boundary condition at inner radius b and clamped boundary condition at outer radius a. . . . .	105
4-5	Model of the piston: circular plate with a circular hole at its center with guided boundary condition at inner radius b and clamped boundary condition at outer radius a. . . . .	106
4-6	Model of the top tether: circular plate with a circular hole at its center with guided boundary condition at inner radius b and clamped boundary condition at outer radius a. . . . .	108
4-7	Simulation architecture used to integrate the elastic equations into system level simulation. . . . .	113
5-1	Helmholtz Resonator. . . . .	116
5-2	Simulation of the chamber with constant overall compliance for different channel geometries. . . . .	118
5-3	Comparison of flowrate time histories for different L/A ratios. . . . .	118
5-4	Simulation of the chamber attached to circuitry for different channel geometries.	119
5-5	Effect of L/A ratio on pressure band and generated power. . . . .	120
5-6	Effect of valve opening on the pressure band in the chamber. . . . .	123

5-7	Effect of operation frequency on the pressure band in the chamber. . . . .	123
5-8	(a) Schematic illustrating the hypotheticalal chamber (b) good tether design providing large piezoelectric element compression (c) poor tether design, either too thin or large width, resulting in low chamber pressure and small piezoelectric element compression (d) poor tether design, either very thick or small width, resulting in large pressures but small piezoelectric element compression. . . . .	125
5-9	(a) Piston deflection for different tether thicknesses and widths,(b) corresponding pressures in the chamber (c) compliance of the chamber. The dashed line corresponds to the hypotheticalal case where piston diameter is equal to chamber diameter and there is perfect sealing. . . . .	126
5-10	(a) Schetch illustrating tether deflection. (b),(c),and (d) show the stress components on the bottom surface and deflected shape of the tether for 3 different cases.(b) good tether design, (c) poor tether design where the tether is too compliant, and (d) poor tether design where the tether is too stiff. . . . .	127
5-11	(a) SEM picture of micromachined piston structure [7](b)detailed view of the tether and the fillet. . . . .	128
5-12	Comparison of different piezoelectric materials in terms of required operation frequency at different chamber diameters for a power requirement of 0.5W. . . .	131
5-13	Comparison of different piezoelectric materials in terms of required flowrate at different chamber diameters for a power requirement of 0.5W. . . . .	132
5-14	Comparison of different piezoelectric elements in terms of system efficiency for different reservoir pressures and chamber diameters. . . . .	134
5-15	Required operation frequency and flowrate for different power requirements at different chamber diameters ( $P_{HPR} = 2MPa$ , piezoelectric material: $PZN - PT$ ).135	
5-16	Schematic illustrating the effect of bias pressure.(a) not biased case (b) biased case136	
5-17	Effect of bias pressure on required frequency, flowrate and efficiency. . . . .	137
5-18	Design procedure. . . . .	144
5-19	(a) System layout (b) System level simulation architecture (c) The chamber and piezo block in the overall system architecture which was developed in Chapter 4. 146	
5-20	Tether structure design. Piston deflection shown for different tether widths. . .	148

5-21	Simulation time histories of the design example 1. . . . .	150
5-22	Simulation time histories of the design example 1. . . . .	151
5-23	Simulation time histories of the design example 1. . . . .	152
5-24	Simulation time histories of the design example 2. . . . .	154
5-25	Simulation time histories of the design example 2. . . . .	155
5-26	Simulation time histories of the design example 2. . . . .	156
A-1	Simulink model of the piezoelectric element. . . . .	172
A-2	Simulink model of the diode bridge. . . . .	173
A-3	Simulink model of the diode bridge attached to an inductor, voltage detector and SCR(Silicon Controlled Rectifier). . . . .	174
A-4	Implementation of the voltage detector circuit. . . . .	175
A-5	Simulink model of the full system including the chamber, piezoelectric element, fluid models and circuitry. . . . .	176
A-6	Simulink model of the main chamber and the piezoelectric element. . . . .	177
A-7	Simulink model of the inlet valve and fluid channel. . . . .	178
A-8	Simulink model of the outlet valve and fluid channel. . . . .	179
B-1	Matlab code used in Chapter 3 to calculate the required frequency, flowrate and efficiency for different circuitry. . . . .	182
B-2	Matlab code used in Chapter 5 to calculate the required frequency, flowrate and efficiency of the system attached to regular diode bridge for different reservoir pressures and chamber diameters. . . . .	183
B-3	Matlab code used for tether optimization. . . . .	184
B-4	Matlab code used for writing system parameters into the workplace to be read by the Simulink model for the system level simulation. . . . .	185

# List of Tables

2.1	Geometry and operation conditions used in simulation . . . . .	45
2.2	Comparison of circuitry in terms of energy density and effective coupling factor .	63
2.3	Properties of different piezoelectric materials . . . . .	66
3.1	Comparison of different working fluids . . . . .	78
3.2	The geometry and operation conditions used in the simulation . . . . .	78
3.3	Summary and comparison of circuitry in terms of performance indices . . . . .	97
5.1	Summary of preliminary design decisions applied to the design examples. . . . .	147
5.2	Summary of design and performance parameters of design example 1. . . . .	149
5.3	Summary of design and performance parameters of design example 2. . . . .	153



# Chapter 1

## Introduction

This chapter presents the configuration, operation and motivation of microhydraulic-piezoelectric power generators. Preliminary design considerations are discussed. The objective, scope and organization of the thesis are presented.

### 1.1 Microhydraulic Piezoelectric Transducers

Transducers are devices that convert physical energy from one form to another. Actuators and power generators are examples of transducer devices. The performance and usefulness of a transducer for most applications are highly dependent on two important characteristics: compactness and power density, that is, power output of the transducer per its unit volume. Conventional transducers, generally, not only tend to be heavy and bulky, but are also limited in terms of power transduction capabilities because of their low bandwidths. For instance, conventional hydraulic systems possess high single-stroke work, but their power densities are greatly reduced by their large mass. Recent advances in active materials technology have led to the development of many compact solid-state transducers. However, the power output from these solid-state transducers is fairly limited for most macro applications. Although the single-stroke work output of solid-state materials such as piezoelectric materials is relatively small, such materials possess very high bandwidths, and as such, are capable of high power output. However, since most applications do not require high frequency actuation, the high bandwidth potential of piezoelectric materials is not fully utilized. Since a transducer's power

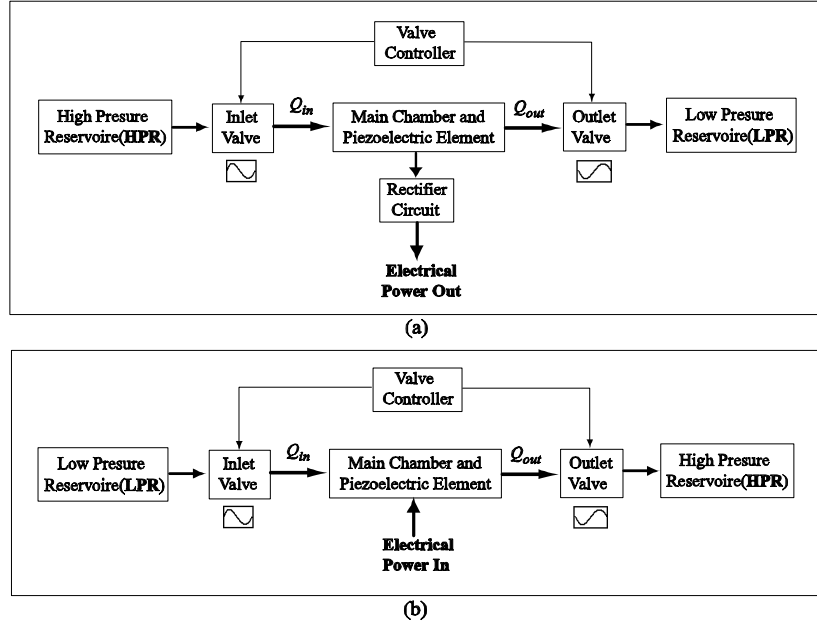


Figure 1-1: (a) Configuration of power generator (b) Configuration of actuator/ micopump. The actuator/micropump configuration can also be operated with check valves instead of active valves, which are necessary for power generator configuration.

output is the product of its single stroke energy and its bandwidth, it is feasible to create high performance transducers by combining high single-stroke force of a hydraulic system and high frequency displacements of a piezoelectric element in a synergistic manner[1]. This concept can be further exploited to create high performance transducers with very high power densities by miniaturizing the transducer systems. The state-of-the-art micromachining (or MEMS) technology has the potential to allow for the implementation of this concept at the micro scale.

Research and development of microfluidic devices has received a significant amount of interest in the past years. The feasibility of micromachining many of the key building blocks (flow channels, pumps, active/passive valves) of a micro-fluidic system including the integration of solid-state materials such as piezoelectric materials to actuate valves has already been demonstrated, and researchers are now striving to create complete microfluidic systems. However, the microfluidic devices developed thus far mostly feature small flow conductance, limited stroke, and low power density, and are mostly geared towards small flow/force applications such as microdosing of fluids. An extensive literature review on microfluidic devices can be found in

[2].

A unique feature of piezoelectric microhydraulic transducers is their ability to operate as both an actuator and a power generator, by merely reversing the direction of their operation. As actuators, these transducers transform electrical energy input into mechanical/hydraulic energy output, and as power generators, the transducers transform mechanical/hydraulic energy input into electrical energy that can be stored in a battery or a capacitor. These high performance transducers can significantly enhance the scope of micromachined transducers technology by enabling many novel applications. When utilized as actuators, they are capable of extending the usefulness of active material based structural actuation beyond small strain applications [1]. These actuators can also be useful in miniature robotics. As power generators, the transducers can extract electrical energy from wasted mechanical energy sources such as vibrations of operating machinery, heel strike of human gait, wind, sound and function as disposable batteries for numerous small electronic devices in both civilian and military applications. A literature survey about piezoelectric power generation will be presented in Chapter 2. Detailed information and comparisons of various transducers can be found in [2] where a feasibility analysis of Micro Hydraulic Transducers has been performed.

## 1.2 Configuration and Operation

The concept of piezoelectric micro-hydraulic transducer (MHT) is schematically illustrated in Figure 1-1 for actuator and power generator configurations. The transducers are comprised of the following generic components: the main chamber which houses a piezoelectrically driven tethered piston, two actively controlled valves, a low-pressure fluid reservoir (LPR), and a high-pressure fluid reservoir (HPR). The power generator configuration requires rectification circuitry to rectify and store the voltage generated by the piezoelectric element. The two active valves, one operating between the HPR and the main chamber and the other one operating between the main chamber and the LPR regulate the fluid flow into and out of the main chamber. The piezoelectric element within the pump chamber serves as the main energy transducing element. A detailed drawing of the device is shown in Figure 1-2.

When operating as an actuator/pump, the electrical signal applied to the piezoelectric



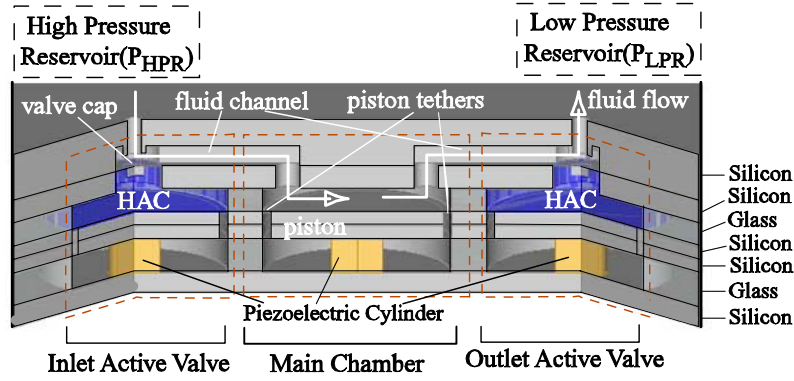


Figure 1-2: Device layout for power generator configuration. Top and bottom packaging pyrex layers not shown.

element results in pressure fluctuations inside the main chamber. When operating as a power generator, pressure fluctuations within the main chamber are converted to an electrical signal, which is rectified and stored in a battery or capacitor. In the actuator configuration, the voltage applied to the piezoelectric element induces a strain in the element resulting in a net volume change in the pump chamber. A controller synchronized with the pump signal cycles the active valves out of phase with each other in a specified duty cycle, transforming the volume oscillations of the chamber into a net fluid flow from the low pressure reservoir to the high pressure reservoir.

In the power generator configuration, the transducer operates in a manner that is reverse of the actuator. The controller toggles the valves with a phasing that allows fluid flow from the high pressure reservoir to the low pressure reservoir, thus transforming the static fluid pressure into high frequency pulses on the piezoelectric element via the piston. Valve actuation at high frequency creates a near sinusoidal cyclic stress on the piezoelectric element, thereby generating electrical charge across the element. Coupled circuitry rectifies this electrical energy and stores it in a battery or capacitor. It should be noted that, for the actuator/micropump configuration, check valves can also be used, instead of active valves, which is demonstrated in [3]. However, for the power generator configuration, active valves are necessary in order to convert the static pressure differential into pressure fluctuations on the piston. Generic operation duty cycle of the power generator configuration is shown in Figure 1-3.

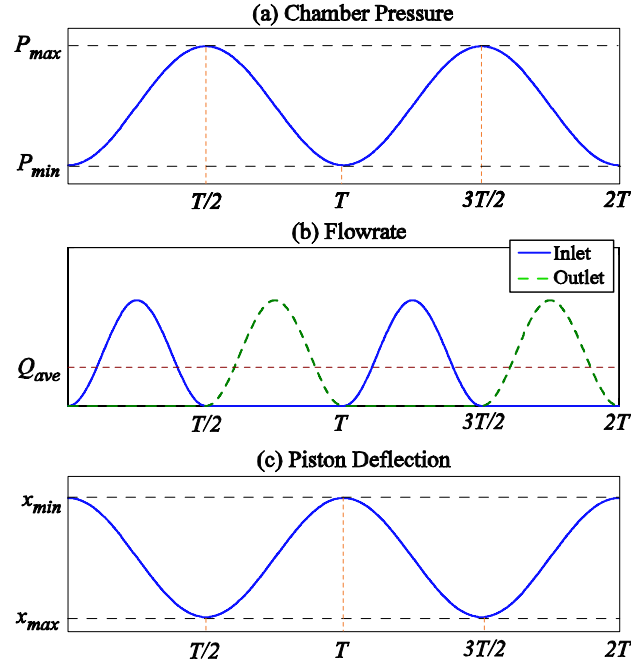


Figure 1-3: Generic operation duty cycle of the power generator.

Active valves are comprised of a similar chamber/piston structure, called hydraulic amplification chamber (HAC), which incorporates a fluid enclosed in the volume between the piston and the valve diaphragm, which effectively serves to amplify the small displacements of the piezoelectric material into significantly larger displacements of the valve cap and effectively transmits the high force actuation capability of the piezoelectric material. As the piston in the active valve is displaced by the piezoelectric element, the pressure of the compressed fluid acts to deform the smaller area valve membrane located at the top of the chamber. Deflection of the rigid cap at the center of the valve membrane blocks fluid flow through the corresponding fluid orifice. The utilization of the hydraulic amplification chamber also leads to minimization of the actuator material, and thus helps in achieving high power densities. The ability to micromachine the device provides the scope to further miniaturize the system to micro scales, leading to higher valve frequencies and therefore enhanced device power densities.

As shown in Figure 1-2, in each chamber, namely inlet HAC, main chamber (energy harvesting chamber) and outlet HAC, a piezoelectric element is sandwiched between the device

structure and a moveable piston plate. The piston plate is sufficiently thick for rigidity and is tethered to the chamber wall through thin flexible diaphragms that extend radially from the outer edges of the cylinder. The structure effectively constitutes a piston that can move vertically up and down when a net force is applied to it.

The prototype MHT device consists of a 9-layer stack of pyrex and silicon micromachined layers, as shown in Figure 1-2 and Figure 1-4. Sealing of the piston in the main chamber is provided by annular tethers which are created through Deep Reactive Ion Etching (DRIE) of a SOI wafer. The tether thickness ( $\sim 10\mu\text{m}$ ) is defined by the SOI device layer, and the buried oxide acts as an etch stop. All glass layers are patterned by conventional diamond core drilling. Piezoelectric cylinders are core drilled from piezoelectric substrate plates, onto which a Ti-Pt-AuSn-Au multilayer film is sputter-deposited for eutectic bonding. The device assembly is accomplished through anodic bonding of the glass layers to the silicon layers at  $300^{\circ}\text{C}$ , a process which also enables the AuSn eutectic alloy to melt. Upon cooling, the alloy solidifies, bonding the piezoelectric cylinders to the silicon layers. Detailed information about the fabrication techniques developed for piezoelectric micro-hydraulic transducers can be found in [3], [6], and [7].

### 1.3 Preliminary Design Considerations

The proposed MHT devices derive their enhanced performance from several inherent design features. For efficient device operation, the compliances within the system, which result from the deformations of the structural members like piston, tether and support structures, and compression of the working fluid within the chambers should be minimum. This implies that the chambers should have small volumes and the structural members should be as thick as possible. This introduces trade-offs between fabrication limitations and design requirements. The type of piezoelectric element also affects system efficiency since the coupling coefficient of the element determines the electromechanical energy conversion work-cycle. For the power generator configuration the rectifier circuit topology is another factor affecting system efficiency, since it determines the electromechanical energy conversion work-cycle along with the piezoelectric material.

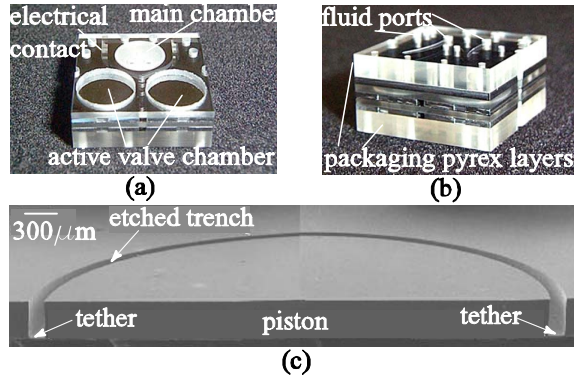


Figure 1-4: (a) 5-layer device for subcomponent testing (b) Complete 9-layer device (c) SEM of micromachined tethered piston structure [7].

Design of the piston tether structure is very crucial for system operation. The tethers should be flexible enough to allow sufficient motion of the piston, yet stiff enough to avoid introduction of excessive compliance into the system. Similar design consideration is also valid for the valve membrane. Achieving high power density critically depends on valves having high bandwidth (frequencies in the tens of kilohertz), sufficient actuation force to overcome large pressures ( $\sim 1\text{-}2$  MPa) and large stroke ( $\sim 20\text{-}30\mu m$ ). The valve membranes should be designed such that they are flexible enough to allow for large valve stroke and stiff enough to operate against high pressures and have high natural frequencies. Large stroke actuation of the valve cap generally results in nonlinear membrane behavior.

Possible fluidic and structural oscillations within the system should be considered. For example the fluid channels and the main chamber constitute a resonating system similar to a Helmholtz resonator. Similarly, piezoelectric element and piston dynamics, which affect the bandwidth of the device, should also be considered.

Important design limitations are maximum allowable stress in the membranes and the depolarization stress of the piezoelectric material. The stress in the tether structures shouldn't exceed 1GPa [7]. Piezoelectric materials also differ in their depolarization stress, which determines the energy density of the material. If during the operation, the stress on the piezoelectric element exceeds the depolarization stress, the element loses its functionality.

The choice of working fluid is also important since different fluids have different bulk moduli,

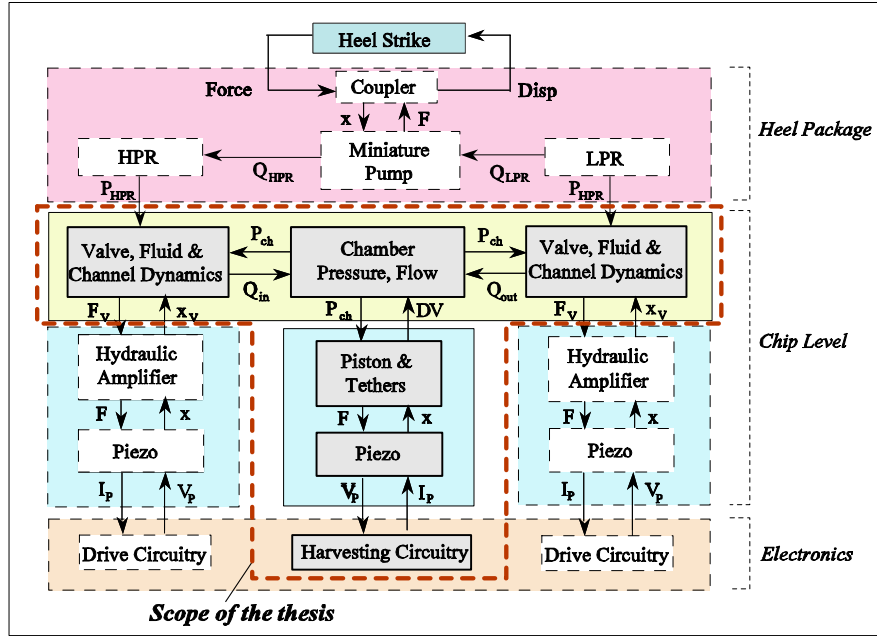


Figure 1-5: Overall system architecture for the heel strike power generation configuration.

densities and viscosities.

## 1.4 Objective, Scope and Organization of the Thesis

Since these devices are complex, comprehensive simulation tools are needed for effective design. Operation of each subcomponent of the device is highly coupled and every design decision should be made with remaining components in mind. The simulation tool should allow for the monitoring of important parameters such as chamber pressure, flowrate, and various structural component deflections and stresses. A system level simulation tool is needed which should be developed by integration of different energy domains, namely fluids, structures, piezoelectric material and circuitry. The challenges in modeling and simulation are: microscale fluid flow, incorporation of membrane behavior into dynamic simulation, prediction of structural compliances and incorporation of the elastic equations of the structural members into simulation.

The MHT group at MIT Active Material and Structures Laboratory(AMSL) has obtained good experimental correlation for subcomponent models from tests on piezoelectrically driven

piston/tether structure, hydraulic amplification chamber structure and valve membrane [6], flow tests through macro disc valves [4], and micropumps [3].

This thesis focuses on the modeling and design of piezoelectric microhydraulic transducers used as power generators. The system architecture for a possible application, namely heel strike power generation configuration is shown in Figure 1-5. The scope of the thesis is shown with the dashed line in the system architecture. The heel package design will not be discussed. Also design of the active valve structure will not be discussed, which is detailed in [5]. Orifice models developed in [4] are used for fluid flow through the valves.

The objectives of this thesis are:

- To develop a comprehensive system level model and simulation tool to analyze the main chamber and the associated fluid channels and valves,
- To gain insight into system operation and understand the factors affecting the system performance,
- Develop a design procedure, which should be complemented by the design of the active valves.

The organization of the thesis is as follows: Chapter 2 presents an analysis of piezoelectric power generation based on linear electromechanical energy conversion. Effect of circuitry and piezoelectric material on energy density and effective coupling factor is discussed. Chapter 3 presents a simple model of the energy harvesting chamber, simulations with the coupled circuitry and preliminary design considerations. The interaction of the main chamber and the circuitry is discussed. The circuits presented in Chapter 2 and different piezoelectric materials are compared in terms of flowrate and frequency requirements for a given pressure differential and power, and in terms of system efficiency. Chapter 4 presents the detailed modelling of the energy harvesting chamber and investigates the contribution of different structural components on the effective compliance of the chamber. It also presents the simulation architecture used for integrating elastic equations into system level simulation. Chapter 5 discusses further design considerations for choosing chamber geometry with regard to operation conditions like maximum pressure, operation frequency and flowrate. Parameter studies are performed and a design procedure is developed. Chapter 6 summarizes important results and conclusions presented in previous chapters and presents recommendations for future work.



## Chapter 2

# Piezoelectric Power Generation and Circuitry

This chapter presents an analysis of piezoelectric power generation based on linear electromechanical energy conversion. Effect of circuitry and piezoelectric material on electromechanical energy conversion and energy density is discussed.

### 2.1 Introduction

Piezoelectric materials are mostly used as sensors and actuators. Since they are capable of electromechanical energy conversion and some have high coupling coefficients, which is an indication of the efficiency of the electromechanical energy conversion, they can be also used as power generators from ambient vibration or impact energy, and as structural vibration dampers. The idea and the governing principles are the same for power generation and structural vibration damping, using piezoelectric elements and passive circuit elements. Damping of structural vibrations with passive electrical circuit elements is discussed in [15] and [14]. This method eliminates the need for viscoelastic materials or mechanical vibration absorbers attached to the structure, or complex amplifiers which are required by the piezoelectric materials for active structural control systems [15]. The coupling between mechanical and electrical domains provided by the piezoelectric effect allows the damping mechanism to be implemented as electrical circuit elements rather than physical masses, springs and dampers. Most of the discussions



which are valid for the structural damping applications with piezoelectric elements are valid for the power generation from ambient vibration or impact energy with piezoelectric elements. In both cases, the purpose is to transfer as much energy from the mechanical to the electrical domain. The transferred energy to the electrical domain can be either dissipated or stored. If a piezoelectric element is shunted with a resistor or with a resistor and inductor network, the converted electrical energy is basically dissipated. However, if the piezoelectric element is connected to a rectifier circuit, a diode bridge for example, with a capacitor or battery, the converted electrical energy can be stored.

## 2.2 Previous Work

Structural damping with piezoelectric elements shunted with a resistor and a resistor-inductor network is analyzed in [15]. In the resistive shunting the electromechanical energy conversion efficiency depends on the operation frequency, and the optimum frequency depends on the resistance value. In other words, optimum efficiency is obtained when the impedance of the piezoelectric element is equal to the impedance of the resistance. Shunting with a resistor and inductor introduces an electrical resonance, which can be optimally tuned to structural resonances for maximum vibration damping.

Linear shunting components such as resistive elements or resistive-inductive-capacitive circuits produce behavior analogous to that of viscoelastic damping materials and tuned proof-mass dampers. Nonlinear piezoelectric shunting for structural damping using a piezoelectric element attached to a diode bridge and a DC voltage is presented in [14]. The rectified DC shunt performs less well in terms of energy conversion efficiency compared with the resistive shunt at optimum frequency. However, unlike the resistive shunt, the rectified DC shunt is independent of frequency and the transferred energy can be recovered depending on the implementation of the DC voltage source.

Power generation characteristics of piezoelectric elements in response to impact loads are investigated in [9], [10] and [11]. In the first two, a ball is dropped from a certain height onto a piezoelectric plate vibrator. In the first one, the piezoelectric vibrator is shunted with a resistor and the efficiency of transformation from mechanical to electrical energy in terms of initial

height and shunted resistance value is investigated. The efficiency is defined as the ratio of the electrical energy dissipated in the resistor to the initial impact energy. The input mechanical impact energy effects the efficiency due to nonlinearity in the vibrator and as expected there is an optimum resistance value. They conclude that efficiency increases with decreasing input impact energy, increasing mechanical quality factor  $Q_m$ , increasing electromechanical coupling coefficient  $k_{33}^2$  and decreasing dielectric loss  $\tan \delta$ . They obtain a maximum efficiency of 52%.

The same authors of [9] investigate the power generation characteristics of the same system attached to a diode bridge and capacitor instead of a resistor in [10]. In this case the transformation efficiency is defined as the ratio of the impact energy to the energy stored in the capacitor. As the capacitance of the capacitor increases, the electric charge increases because the duration of the oscillation becomes longer and the output voltage decreases. They conclude that there exists an optimum capacitance value in terms of transformation efficiency. They obtain a maximum efficiency of 35%. It should be noted that, if a force were imposed on a piezoelectric element, the voltage on the capacitor would always increase until half of the open circuit voltage which corresponds to the maximum stress on the piezoelectric element, regardless of the capacitance of the capacitor. The value of the capacitance would change the duration in which the maximum voltage is reached and the stored energy in the capacitor would be proportional to its capacitance, since the maximum voltage is constant for a given maximum stress. In the paper discussed above, the force on the piezoelectric element is not imposed, it is determined depending on the impedances of the vibrator and the capacitor. In this case, the impedance matching principle cannot be applied since the system is nonlinear because of the diode bridge. No power density figures are reported in [9] and [10].

Piezoelectric power generation from thermal energy is presented in [20]. This paper discusses an energy conversion system in which thermal energy is converted to high frequency, high voltage electric a.c energy. The conversion system is composed of a thermal-acoustic natural heat engine and a piezoelectric transduction system to convert the acoustic energy to electric energy.

Another system to convert acoustic energy to electric energy is presented in [35]. The device is designed to convert waste acoustic energy, e.g. in automobile or airplane jet engines to electrical energy in a predetermined frequency range. The system consists of a piezoelectric bending element, means for mounting the piezoelectric bending element in an acoustic energy

path and a tuning means mounted on to the piezoelectric bending element to set the resonant frequency of oscillation of the piezoelectric bending element within the predetermined frequency range.

The idea of piezoelectric power generation from the ocean waves is patented in [27]-[32] by Ocean Power Technologies, Inc. The motivation in these studies is to utilize the enormous amount of mechanical energy present in the oceans. [27] relates to the generation of electrical power from waves on the surface of bodies of water, and particularly to the conversion of the mechanical energy of such waves to electrical energy by means of piezoelectric materials. The system consists of piezoelectric elements in the form of one or a laminate of sheets, each sheet having an electrode on opposite surfaces thereof, a support means for maintaining the structure in a preselected position within and below the surface of the water. In certain embodiments, the elements are designed to enter into mechanical resonance in response to the passage of waves thereover, increasing the mechanical coupling efficiency between the waves and the elements. Similar approaches are presented in [28] and [30]. In [28], a float on a body of water is mechanically coupled to a piezoelectric material member for causing alternate straining and de-straining of the member in response to the up and down movement of the member in response to passing waves, thereby causing the member to generate electric energy. The output impedance of the float is matched to the input impedance of the member for increasing the energy transfer from the float to the member. In [30], the system comprises a weighted member supported from a piezoelectric element for applying a preselected strain to the element. In one embodiment, the element is supported by a float floating on the surface of the water. In another embodiment, the element is supported above the surface of the water and the weighted member, of negative buoyancy, is immersed in the water. Means are provided for tuning the natural frequency of the system to cause it to enter into mechanical resonance in response to passing waves. Similar approaches are presented in [29], [31] and [32].

Some circuitry considerations for piezoelectric power generation are presented in [33] and [26]. [33] presents a DC bias scheme for improved efficiency for applications including electrostrictive materials, which have very weak piezoelectric characteristics. However, if a DC bias is applied, the piezoelectric characteristics can be significantly increased. [26] presents an alternative rectifier circuit, which includes an inductor, a SCR(silicon controlled rectifier) and

a voltage detection circuit in the conduction path between the piezoelectric element and the storage element, a capacitor for example. The object is to optimize the transfer of the energy produced by a piezoelectric transducer to a load. Another circuit designed for a wide variety of applications is presented in [36].

Piezoelectric power generation for electronic wristwatch applications is presented in [23]-[25]. [23] presents an electronic wristwatch having a piezoelectric generator in it. The generator converts energy from mechanical to electrical energy to drive the electronic wristwatch. The oscillation of a weight produces mechanical energy as it oscillates. A wheel train transmits the mechanical energy to the generator by applying a torque to the generator. The generated voltage is rectified with a diode bridge. Similar systems are presented in [24] and [25].

Piezoelectric power generation from wind energy is presented in [21] and [22]. The system presented in [22] consists of a piezoelectric transducer mounted on a resilient blade which in turn is mounted on an independently flexible support member. Fluid flow against the blade causes bending stresses in the piezoelectric polymer which produces electric power.

Other piezoelectric power generation systems are presented in [34], [39], [38] and [37]. [34] presents a piezoelectric fluidic-electric generator which consists of a piezoelectric bending element, means for driving the piezoelectric bending element to oscillate with the energy of the fluid stream, and electrodes connected to the piezoelectric element to conduct current generated by the oscillatory motion of the piezoelectric element. [39] presents a system which consists of a piezoelectric array which is mounted on one or more tires of a motor vehicle. As the vehicle drives on the road, the tire is flexed during each revolution to distort the piezoelectric elements and generate electricity.

Piezoelectric materials are also used in power electronics applications such as transformers. Piezoelectric transformers are composite resonators made of two bonded piezoelectric parts. The vibration of one part, excited by an input electric voltage, induces an output voltage across the other part [40]. In other words, a piezoelectric transformer works by using the direct and converse piezoelectric effects to acoustically transform power from one voltage and current level to another [44]. Detailed information about the operational characteristics of piezoelectric transformers can be found in [41] and [42].

Piezoelectric transformers have low-electric noise because they transmit power by mechan-

ical vibration. They can also operate efficiently at high frequencies, whereas conventional electromagnetic transformers are not efficient at high frequencies because of core loss and copper loss. Other advantages over the electromagnetic transformers can be stated as high voltage isolation between primary and secondary, high frequency operation leading to reduction in the filter capacitors and low weight and size [43]. Since piezoelectric transformers have much higher power densities than electromagnetic transducers, they are very promising as power electronic components for miniature and lightweight electrical equipment.

Fundamental limits on energy transfer of piezoelectric transformers are discussed in [44]. The discussion details similar considerations to those of the piezoelectric power generation concept. One has to consider the work cycle of electromechanical energy conversion and associated circuitry. Also the maximum electric field, the maximum surface charge density, the maximum stress and the maximum strain of the piezoelectric element are important criteria to consider when determining the limitations of power transfer in a piezoelectric transformer, as well as in a piezoelectric power generation system.

## 2.3 Theoretical Background

The linear electromechanical energy conversion process with piezoelectric ceramics is by far the easiest to handle, since the piezoelectric, dielectric and elastic constants can be applied directly [8]. In linear analysis, the coefficients mentioned above are assumed to be constant during the operation. The nonlinearity at high fields and hysteresis effects are ignored, i.e. the losses due to nonlinear effects are not considered. It is also assumed that the operation frequency is well below the lowest resonant frequency of the piezoelectric element, i.e. the operation can be considered as quasi-static. The linear constitutive relationships for a general piezoelectric element are:

$$\begin{bmatrix} D \\ S \end{bmatrix} = \begin{bmatrix} \epsilon^T & d \\ d_t & s^E \end{bmatrix} \begin{bmatrix} E \\ T \end{bmatrix} \quad (2.1)$$

where  $D$  is a vector of electric displacements or charge density(charge/area),  $S$  is the vector of material engineering strains,  $E$  is the vector of electrical field in the material(volts/meter),

$T$  is the vector of material stresses (force/area),  $\varepsilon$  is the matrix of dielectric constants,  $d$  is the matrix of piezoelectric constants and  $s$  is the matrix of compliance coefficients of the piezoelectric element. The superscripts  $()^T$  and  $()^E$  signify that the coefficients are measured at constant stress and constant electric field respectively and the subscript  $()_t$  denotes the matrix transpose. In this chapter, a specific case will be considered where the piezoelectric element is subjected to compression parallel to the polarization of the element. It is assumed that the lateral dimensions are small compared to the axial dimension, so that only the axial stress  $T_3$  needs to be considered ( $T_1 = T_2 \approx 0$ ). Or, it can be assumed that, the element is free to expand in lateral directions so that  $T_3$  is the only nonzero stress component. Under these conditions, equation 2.1 reduces to

$$\begin{bmatrix} D_3 \\ S_3 \end{bmatrix} = \begin{bmatrix} \varepsilon_{33}^T & d_{33} \\ d_{33} & s_{33}^E \end{bmatrix} \begin{bmatrix} E_3 \\ T_3 \end{bmatrix} \quad (2.2)$$

where the first and second subscripts of the piezoelectric, dielectric and elastic constants denote the orientation of the electric field and the stress respectively.

Quasi-static coupling factors, or coefficients, are very common and useful definitions for piezoelectric energy conversion. The coupling coefficients are dimensionless and thus they provide a useful comparison between different piezoelectric materials independent of the specific values of permittivity or compliance. The definition of the coupling coefficient described above is given in [18]. Figure 2-1 illustrates graphically the meaning of the coupling coefficient  $k_{33}$ . The cycle shown is as follows: first, the piezoelectric element is compressed under short circuit condition, then the compressive stress is removed under open circuit condition, and then the cycle is completed under constant stress condition by applying an ideal electric load. As work is done on the electric load, the strain returns to its initial state. For the idealized case illustrated in Figure 2-1(a), the coupling coefficient is defined as:

$$(k_{33})^2 = \frac{W_1}{W_1 + W_2} = \frac{s_{33}^E - s_{33}^D}{s_{33}^E} = \frac{d_{33}^2}{s_{33}^E \varepsilon_{33}^T} \quad (2.3)$$

where  $W_1$  is the work done on the electric load and  $W_2$  is the part of the energy unavailable to the electric load or the reversible stored elastic energy(strain energy).

Similarly, the coupling coefficient for energy conversion from electrical energy to mechanical

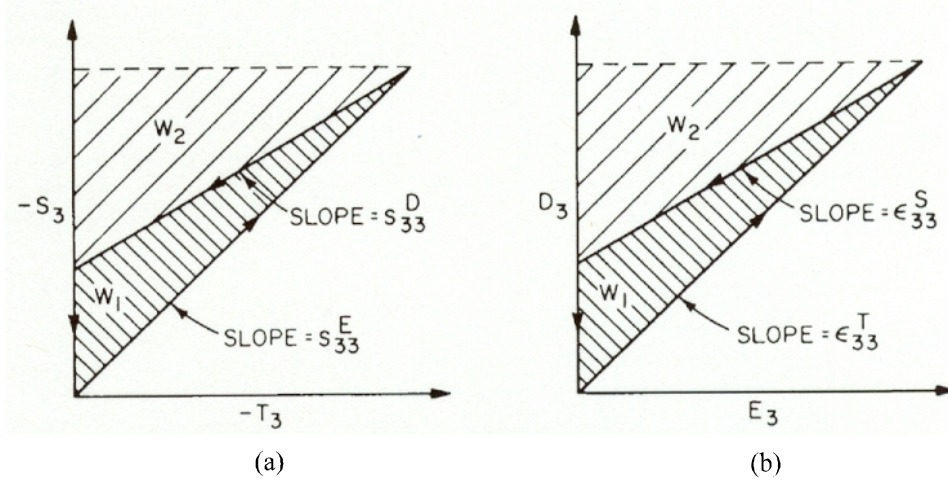


Figure 2-1: Graphic illustration of electromechanical energy conversion and definition of the piezoelectric coupling factor  $k_{33}$  given in [18] (a) Conversion of energy from a mechanical source to electrical work (b) Conversion of energy from an electrical source to mechanical work.

energy can be derived using the idealized cycle illustrated in Figure 2-1(b). First, the element is mechanically free when the electric source is connected. Then the element is blocked mechanically parallel to polarization before the electric source is disconnected. Then with  $E_3 = 0$  the mechanical block is removed and in its place a finite mechanical load is provided. For this idealized cycle of work illustrated in Figure 2-1(b), the coupling coefficient is defined as:

$$(k_{33})^2 = \frac{W_1}{W_1 + W_2} = \frac{e_{33}^T - e_{33}^{S_3=0}}{\epsilon_{33}^T} = \frac{d_{33}^2}{s_{33}^E \epsilon_{33}^T} \quad (2.4)$$

where  $W_1$  is the work done on the mechanical load and  $W_2$  is the part of the energy unavailable to the mechanical load.

The idealized work cycles illustrated in Figure 2-1 correspond to the standard definition of the piezoelectric coupling coefficient. Berlincourt proposes alternative work cycles of reversible electromechanical energy conversion in [8]. These cycles are shown in Figure 2-2. The first one, which is illustrated in Figure 2-2(a) corresponds to a case where the element is compressed with the electric load not connected, i.e. under open circuit conditions, then the electric load is connected with stress maintained, then the mechanical stress is reduced to zero with the electric load again disconnected and finally the electric load is connected and the element

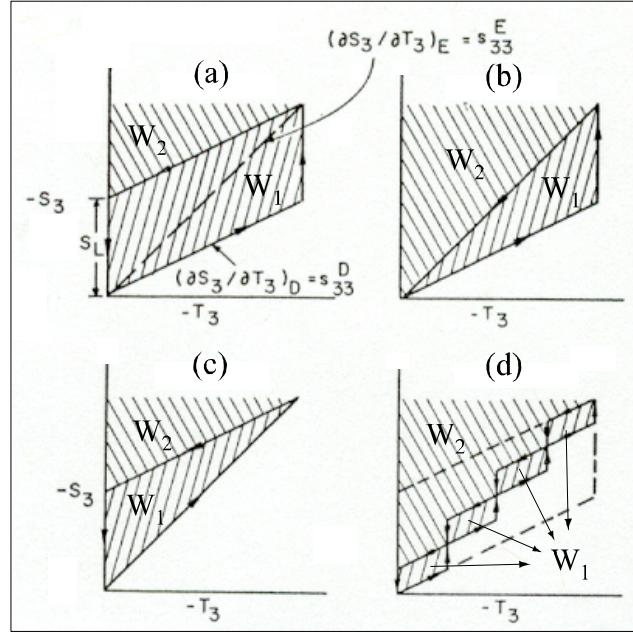


Figure 2-2: Alternative idealized work cycles given in [8].

returns to its initial state under constant stress. In the cycle illustrated in Figure 2-2(b), the element is compressed under open circuit condition, then the electric load is connected with stress maintained and finally the electric load is connected and the stress is reduced under closed circuit condition and the element returns to its initial state. The cycle in Figure 2-2(c) is identical to the cycle used for deriving the coupling coefficient in Figure 2-1. The cycle in Figure 2-2(d) corresponds to a case where the energy conversion occurs at several intermediate levels.

Berlincourt [8] defines an *effective coupling factor*, which is equal to

$$k_{eff}^2 = \frac{W_1}{W_1 + W_2} \quad (2.5)$$

He applies this definition to each of the different work cycles described above. Then he expresses the effective coupling factors for each of the different cycles in terms of the standard coupling coefficient given in Equation 2.3 as follows:



$$k_{eff(a)} = k_{33}\sqrt{2/(1 + k_{33}^2)} \quad (2.6)$$

$$k_{eff(b)} = k_{33}\sqrt{1 + k_{33}^2} \quad (2.7)$$

$$k_{eff(c)} = k_{33} \quad (2.8)$$

$$k_{eff(d)} = k_{33}\sqrt{2/(n + k_{33}^2)} \quad (2.9)$$

where  $k_{33}$  is the standard coupling coefficient and  $n$  is the number of intermediate levels in Figure 2-2(d). From equation 2.6 it is apparent that the coupling coefficient corresponding to the first case in Figure 2-2 is greater than the standard coupling coefficient defined previously.

It is important to note that, the cycles described so far are idealized or hypothetical cycles. The energy conversion process occurs with the mechanical and electrical energy sources connected and disconnected at will. However, no explanation has been given in terms of how these cycles can be achieved or approximated in a real application. In other words, the mechanical and electrical infrastructures which would allow these cycles to occur are not discussed. In this chapter, conversion from mechanical to electrical energy is considered, with emphasize on the circuitry used which basically determines the work-cycle. In other words, the rectifying circuitry is the electrical infrastructure in the power generation process. In the following sections two different circuit topologies will be analyzed in detail in terms of the effective coupling factor and energy density.

## 2.4 Circuitry Considerations

Although in the literature different mechanisms for piezoelectric power generation has been presented and some studies performed for piezoelectric material characterization for power generation, no detailed analysis has been presented in terms of effective coupling factor, energy density and piezoelectric material comparison with regard to circuitry. This section analyzes two different circuits for rectifying and storing the electrical energy generated by the piezoelectric element. These circuits constitute examples of nonlinear shunting of piezoelectric elements. The first one is a regular full bridge rectifier with a battery attached to it. The second circuitry is the same circuit proposed in [26] for piezoelectric power generation, which consists of a full bridge

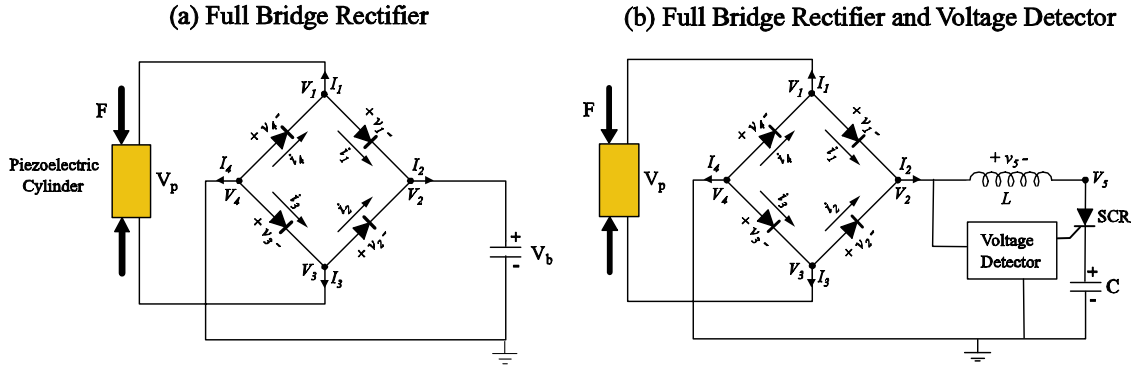


Figure 2-3: Alternative circuits to rectify and store the electrical energy generated by the piezoelectric element.

rectifier, an inductor, a silicon controlled rectifier (SCR), a voltage detector and a capacitor to store the electrical energy. The circuits are shown in Figure 2-3.

### 2.4.1 Modeling

This section presents the modeling of the piezoelectric element and the circuitry. The models are same for the two circuits under consideration except some small differences.

#### Piezoelectric Element

Linear piezoelectric constitutive relationships are assumed. The form of the constitutive equations used here is as follows:

$$\begin{bmatrix} S \\ E \end{bmatrix} = \begin{bmatrix} s_{33}^D & \frac{d_{33}}{\varepsilon_{33}^T} \\ \frac{d_{33}}{\varepsilon_{33}^T} & -\frac{1}{\varepsilon_{33}^T} \end{bmatrix} \begin{bmatrix} T \\ D \end{bmatrix} \quad (2.10)$$

where  $D$  is the charge field,  $S$  is the strain,  $E$  is the electric field, and  $T$  is the stress. For a cross-sectional area of  $A_p$  and length of  $L_p$ , the expressions for the deflection of the piezoelectric element and the voltage across it become:

$$x_p = \frac{L_p}{A_p} (s_{33}^D F_p + \frac{d_{33}}{\varepsilon_{33}^T} Q_p) \quad (2.11)$$

$$V_p = \frac{L_p}{A_p} \left( \frac{d_{33}}{\varepsilon_{33}^T} F_p - \frac{1}{\varepsilon_{33}^T} Q_p \right) \quad (2.12)$$

where  $x_p$  is the deflection,  $Q_p$  is the charge,  $F_p$  is the force applied on the piezoelectric cylinder, and  $V_p$  is the voltage across the piezoelectric cylinder. And the current through the piezoelectric element is given by:

$$I_p = \frac{dQ_p}{dt} \quad (2.13)$$

## Diode Bridge

The model of the diode bridge rectifier is based on [52]. The governing equations can be derived using Kirchoffs laws and diode equations. The notation in Figure 2-3 is used. Applying Kirchoffs Current Law (*KCL*) in the junctions 1,2,3,and 4, we get:

$$I_1 = i_4 - i_1 \quad (2.14)$$

$$I_2 = i_1 + i_2$$

$$I_3 = i_3 - i_2$$

$$I_4 = -i_3 - i_4$$

The voltages across the diodes are given by:

$$v_1 = V_1 - V_2 \quad (2.15)$$

$$v_2 = V_3 - V_2$$

$$v_3 = V_4 - V_3$$

$$v_4 = V_4 - V_1$$

Applying Kirchoffs Voltage Law (*KVL*) around the loops corresponding to the cases where  $V_p > 0$  and  $V_p < 0$  we get:

$$\begin{aligned}
-V_p + v_1 + V_b + v_3 &= 0 & \text{for } V_p > 0 \\
V_p + v_2 + V_b + v_4 &= 0 & \text{for } V_p < 0
\end{aligned} \tag{2.16}$$

For the case where  $V_p > 0$ , the currents flowing through diodes #1 and #3 are the same, and for the case where  $V_p < 0$ , the currents flowing through diodes #2 and #4 are the same. Since all the diodes have the same constitutive relationship, we can write:

$$\begin{aligned}
V_1 - V_2 &= V_4 - V_3 & \text{for } V_p > 0 \\
V_4 - V_1 &= V_3 - V_2 & \text{for } V_p < 0
\end{aligned} \tag{2.17}$$

Recognizing that  $V_p = V_1 - V_3$ ,  $V_2 = V_b$ ,  $V_4 = 0$ (ground) and using equation 2.17 we can write:

$$\begin{aligned}
V_1 &= \frac{V_b + V_p}{2} \\
V_3 &= \frac{V_b - V_p}{2}
\end{aligned} \tag{2.18}$$

The *voltage – current* relationships (constitutive law) of the diodes are:

$$\begin{aligned}
i_n &= I_o \left[ \exp \frac{qv_n}{\eta k T} - 1 \right], & v_n &\geq 0 \\
i_n &= 0 & v_n &< 0
\end{aligned} \tag{2.19}$$

where the subscript  $( )_n$  denotes the diode number,  $q = 1.60 \times 10^{-19}(C)$  is the electron charge,  $k = 1.38 \times 10^{-23}(J/K)$  is the Boltzman constant and  $T$  is the temperature( $T = 300K$ ).  $I_o$  and  $\eta$  are diode properties. For CS57-04 diode (Collmer Semiconductor, Inc.), whose values will be used throughout the thesis, they are measured to be:  $I_o = 10^{-6}$  and  $\eta = 17.25$  [19].

## Diode Bridge and Voltage Detection Circuit

For the diode bridge with the voltage detection circuit, the model is similar. The equations 2.14, 2.15, and 2.19 are valid. However because of the implementation of the voltage detection circuit and SCR, the simulation architecture is different [53], which is shown in Appendix A. The voltage detection circuit is not modeled. Only its function is implemented in Simulink. The Kirchoffs Voltage Law can be written for this case using the notation in Figure 2-3 as:

$$\begin{aligned} -V_p + v_1 + v_5 + V_{SCR} + V_c + v_3 &= 0 & \text{for } V_p > 0 \\ V_p + v_2 + v_5 + V_{SCR} + V_c + v_4 &= 0 & \text{for } V_p < 0 \end{aligned} \quad (2.20)$$

The voltage across the inductor is given by:

$$v_5 = L \frac{d(I_2)}{dt} \quad (2.21)$$

And we can also write

$$V_c = \frac{1}{C} \int I_2 \quad (2.22)$$

### 2.4.2 Simulation and Analysis

Simulations are performed using Matlab/Simulink. The Simulink blocks and additional details are given in the Appendix A. The Simulink architecture is shown in Figure 2-4. The piezoelectric element block includes the constitutive relationships and the circuit block includes the equations corresponding to the circuitry. The piezoelectric element is excited with an imposed force on it. The geometry and operation conditions chosen for the simulation are shown in Table 2.1.

The imposed force is sinusoidal with an offset, namely it fluctuates between zero and the force corresponding to the maximum applicable stress, which is the depolarization stress of the piezoelectric element. In the case of PZN-4.5%PT, the depolarization stress is measured to be around  $10MPa$  [19]. For the chosen piezoelectric cylinder diameter, the maximum force is  $31.4N$ . Detailed comparison of different piezoelectric materials will be presented in section 2.6.

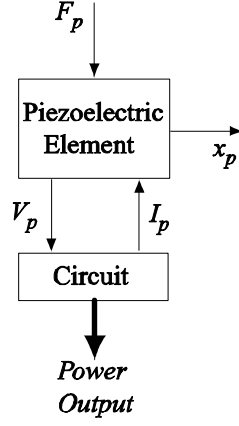


Figure 2-4: Simulation architecture used to simulate the piezoelectric element connected to the full bridge rectifier. The force is imposed on the piezoelectric element.

Length of the piezoelectric element, $L_p$	$1mm$
Diameter of the piezoelectric element, $D_p$	$2mm$
Operation frequency, $f$	$20kHz$
Maximum force, $F_p$	$31.4N$
Optimum battery voltage, $V_b$	$90V$
Piezoelectric material	$PZN - 4.5\%PT$

Table 2.1: Geometry and operation conditions used in simulation

## Full Bridge Rectifier

**Simulation** Simulation time histories are shown in Figure 2-5. The operation at steady state can be summarized as follows: During the compression of the piezoelectric element the voltage on it increases. If it reaches the battery voltage, current starts to flow through the battery and in fact the piezoelectric element voltage is a little bit higher than the battery voltage during this interval which causes the current to flow. The amount which the piezoelectric element voltage exceeds the battery voltage during this interval depends on the diode properties and other resistances in the system. When the force on the piezoelectric element begins decreasing, the voltage decreases too and when it becomes less than the battery voltage current stops flowing through the battery. As the force on the piezoelectric element keeps decreasing, the voltage on the piezoelectric elements keep decreasing until it reaches the negative value of the battery voltage. At this point, current begins to flow through the battery, now, however, from a different branch of the diode bridge, namely through different diodes. Again during this interval the voltage on the piezoelectric element exceeds the battery voltage a little bit (in this case it is lower than the negative value of the battery voltage). When the force begins increasing, the voltage begins increasing too and again no current flows through the battery. Throughout the operation, the voltage on the piezoelectric element fluctuates between the negative and positive values of the battery voltage.

In order to get insight into the energy conversion mechanism and to derive the governing equations in the next section, it is worthwhile to look at the force vs. deflection and voltage vs. charge plots of the piezoelectric element. These are plotted in Figure 2-6. The most important observation is that there are two major regimes during the operation: Operation under open circuit conditions, where the compliance of the piezoelectric element is small, i.e the piezoelectric element is hard; and operation under closed circuit conditions, where the compliance of the piezoelectric element is large, i.e the piezoelectric element is soft. The compliances in these regimes are  $s_{33}^D$  and  $s_{33}^E$  for open circuit and closed circuit conditions respectively. The shaded region in Figure 2-6 corresponds to the stored electrical energy in one cycle. The generated power is then simply this energy times the operation frequency.

The battery voltage has an important effect on the performance. The simulation results presented in Figure 2-5 and Figure 2-6 correspond to the optimum battery voltage (90V). The

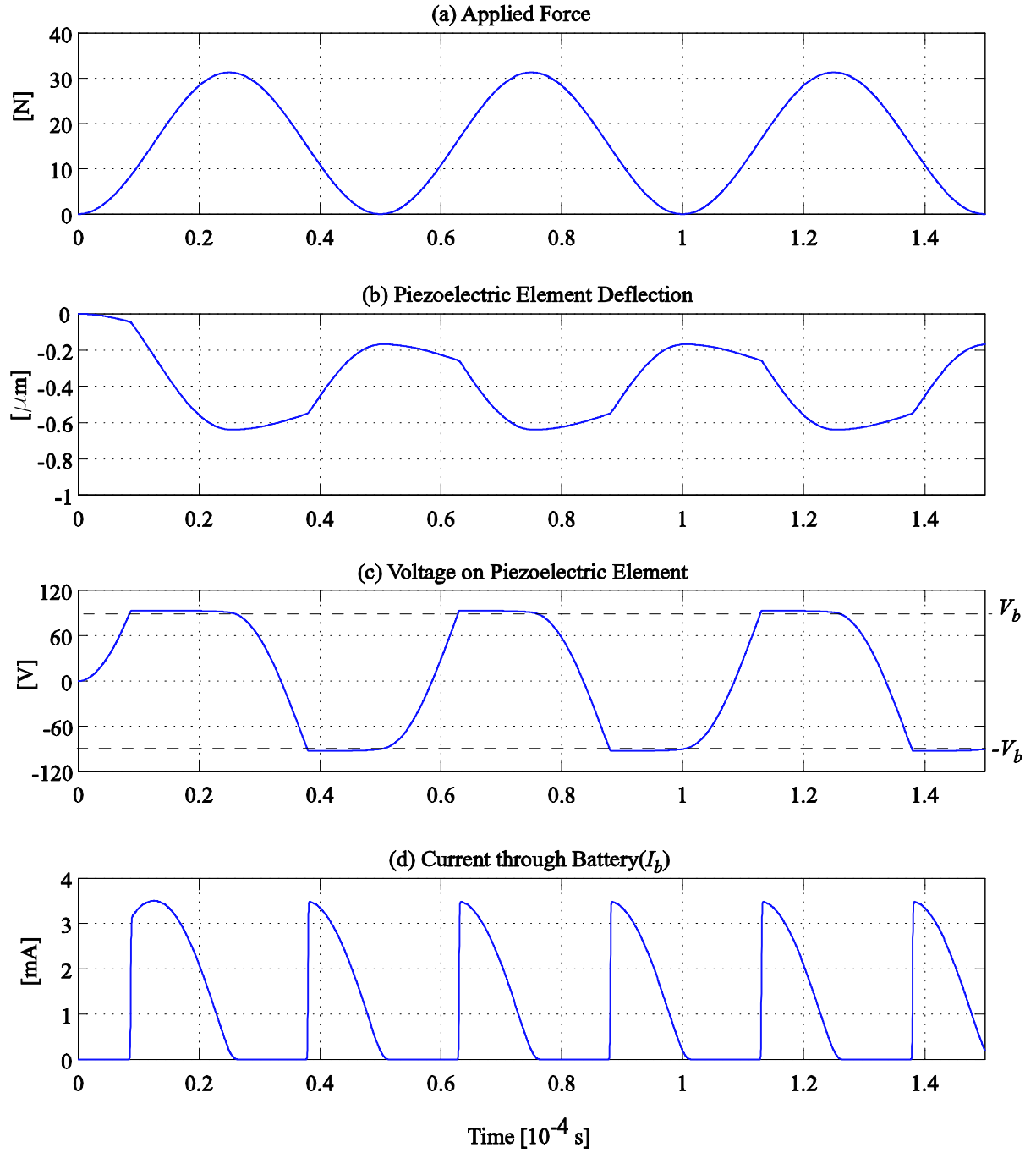


Figure 2-5: Time histories from the simulation of the piezoelectric element connected to the full bridge rectifier for the case of imposed force. The generated power is  $I_b V_b$ .



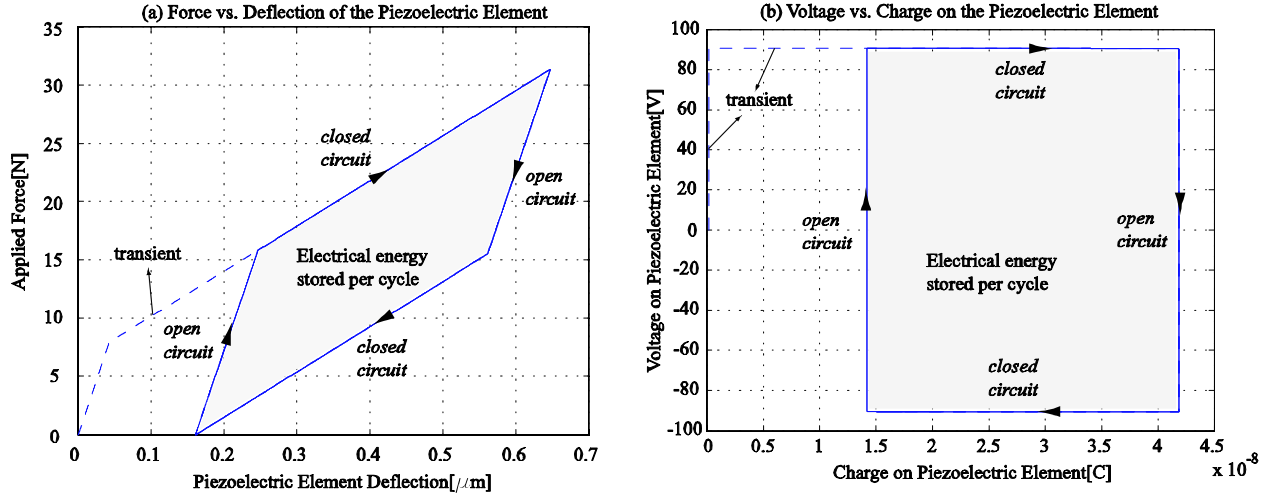


Figure 2-6: Force vs. deflection and voltage vs. charge plots of the piezoelectric element compressed under the applied force for the case of full bridge rectifier.

force vs. deflection of the piezoelectric element for different values of battery voltage is shown in Figure 2-7. It is found that, the maximum power is obtained with an optimum battery voltage of:

$$V_{b(opt)} = \frac{V_{oc}}{4} = \frac{1}{4} \frac{\sigma(s_{33}^E - s_{33}^D)L_p}{d_{33}} \quad (2.23)$$

where  $V_{oc}$  is the open circuit voltage of the piezoelectric element,  $s_{33}^E$  and  $s_{33}^D$  are the closed circuit and open circuit compliances of the piezoelectric element respectively,  $d_{33}$  is the piezoelectric coefficient,  $\sigma$  is the maximum stress on the piezoelectric element, and  $L_p$  is the length of the piezoelectric element. Open circuit voltage at a given stress is the voltage generated by the piezoelectric element when compressed under open circuit conditions. In fact the optimum battery is the voltage which optimizes the shape of the force vs. displacement curve for maximum enclosed area.

It should be noted that the above analysis is done for a case where the force on the piezoelectric element is varying between zero and a maximum value which corresponds to the depolarization stress of the piezoelectric element. In order to analyze the case where the force is biased, the system is simulated for nonzero positive or negative minimum forces. It has been discovered

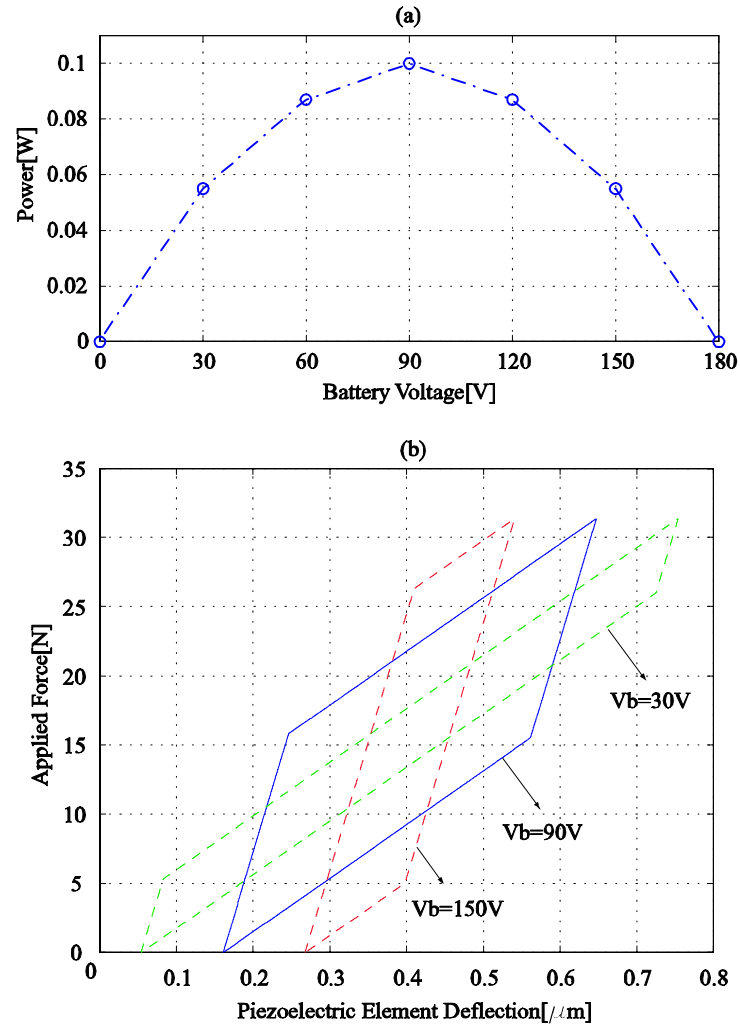


Figure 2-7: Effect of battery voltage on power.

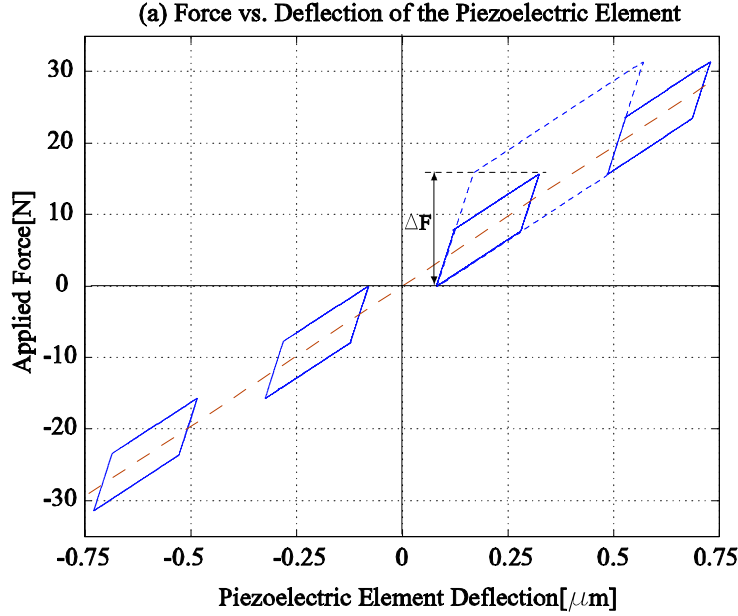


Figure 2-8: Effect of bias force on the workcycle.

that the optimum battery voltage depends only on the stress band on the piezoelectric element, namely on the difference of the maximum and minimum stresses on the piezoelectric element. Figure 2-8 shows the workcycles for different applied forces which have the same peak to peak values but different bias values. For each case the optimum battery voltage is the same since the stress band resulting from each case is the same. Equation 2.23 can be rewritten as:

$$V_{b(opt)} = \frac{1}{4} \frac{\Delta\sigma(s_{33}^E - s_{33}^D)L_p}{d_{33}} \quad (2.24)$$

where  $\Delta\sigma$  is the stress band on the piezoelectric element.

**Analysis** In order to investigate the work cycle of the piezoelectric element, we can analyze the stress vs. strain and electric field vs. charge density plots of the piezoelectric element in detail. Important features of the work cycle is shown in Figure 2-9 which corresponds to the optimum battery voltage case. It is important to not that, the dashed line, which corresponds to the case in which the piezoelectric element would be compressed in closed circuit conditions, passes through the middle of the stress vs. strain curve. We also know the slopes of the curve

in the two different regimes, namely open circuit and closed circuit regimes. Using simple geometry, we can derive the coordinates of the corner points. From the voltage vs. charge plot in Figure 2-6 we see that the voltage of the piezoelectric element fluctuates between the positive and negative values of the battery voltage. Using constitutive relationships to calculate the corresponding charge on the piezoelectric element at different states, we can get the electric field vs. the charge density plot. These are shown in Figure 2-9.

The electrical energy stored (per piezoelectric element volume) in the battery in one cycle for the case of optimum battery voltage, which is equal to the enclosed area by the stress vs. strain or electric field vs charge density curve can obtained using simple geometry from Figure 2-9 as:

$$E = \frac{1}{4}(s_{33}^E - s_{33}^D)\sigma^2 \quad (2.25)$$

where  $s_{33}^E$  and  $s_{33}^D$  are the closed circuit and open circuit compliances of the piezoelectric element respectively and  $\sigma$  is the maximum stress on the piezoelectric element.

Then, the generated power by the piezoelectric element can be expressed as:

$$W = \frac{1}{4}(s_{33}^E - s_{33}^D)\sigma^2 V_p f \quad (2.26)$$

where  $V_p$  is the volume of the piezoelectric element and  $f$  is the operation frequency. From the above equation it can be seen that the power depends heavily on the stress on the piezoelectric element. The most important limitation on piezoelectric power generation is the depolarization stress. For stresses larger than this, piezoelectric element coefficients degrade and performance decreases drastically. Each piezoelectric element has a different depolarization stress, which constitute an important factor when determining their feasibility as power generators. Detailed comparison of different piezoelectric elements will be presented in Section 2.6.

Effective coupling factor for an electromechanical energy conversion mechanism, in this case a system which converts mechanical energy into electrical energy is defined as the ratio of the mechanical work done on the system to the electrical energy stored in one cycle. This definition is the same as the one used to derive the coupling coefficient. This is illustrated in Figure 2-10. From the above definition we can write:

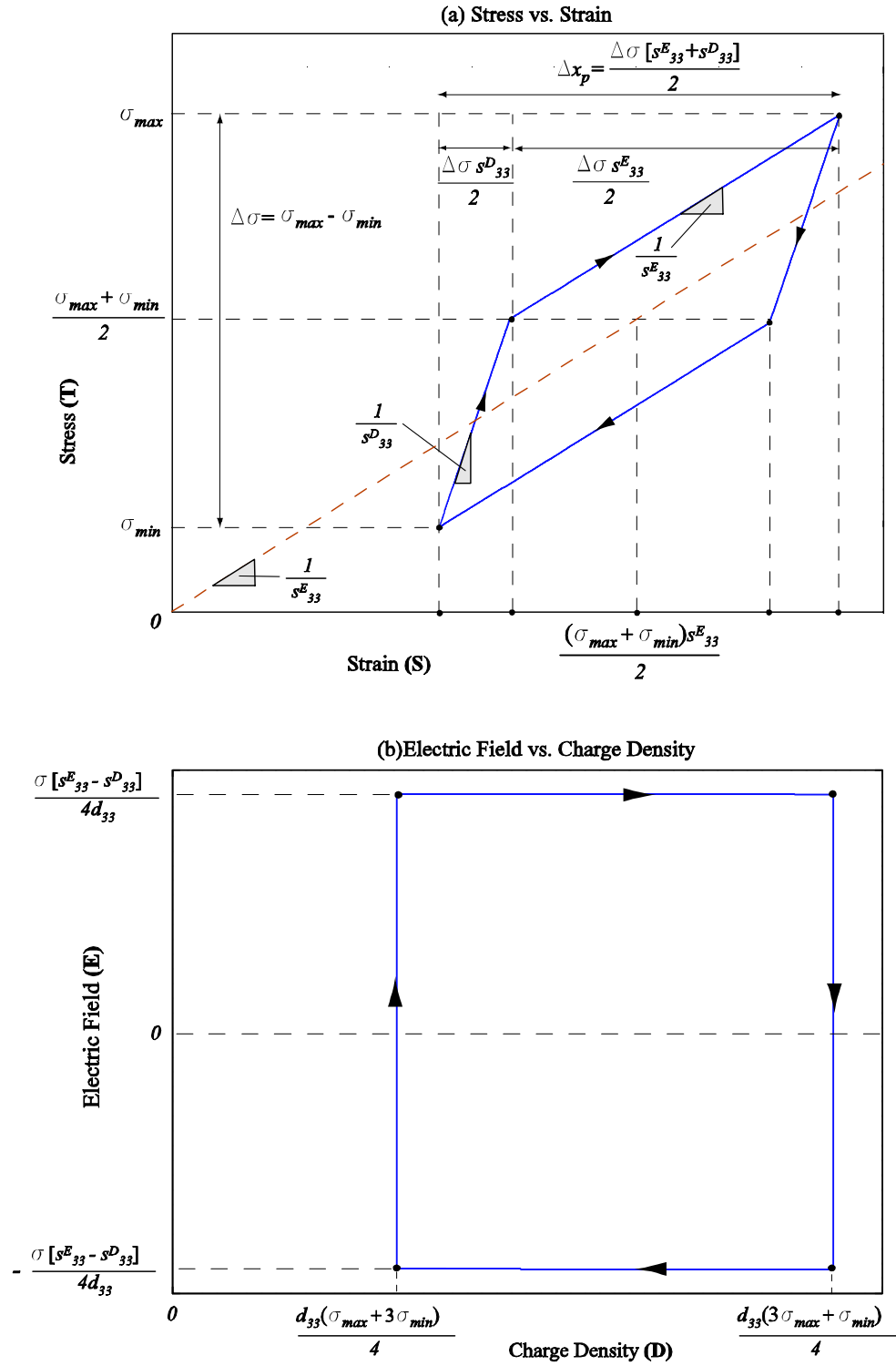


Figure 2-9: General presentation of the work cycle of the piezoelectric element in terms of stress, strain, electric field and charge density for the case of regular diode bridge.

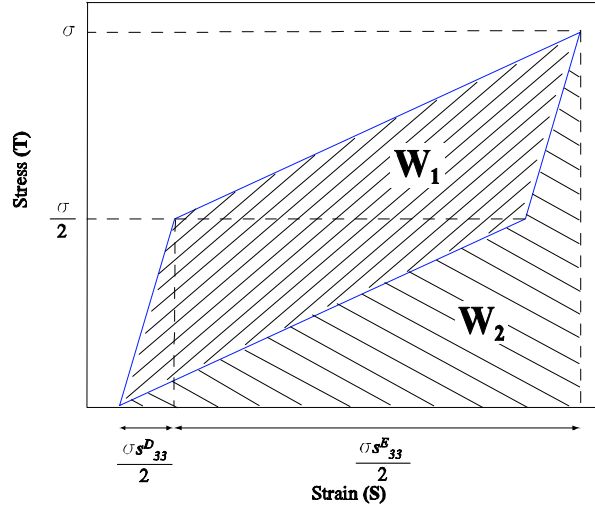


Figure 2-10: Illustration of the effective coupling factor for the case of regular diode bridge.

$$k_{eff}^2 = \frac{W_1}{W_1 + W_2} \quad (2.27)$$

Again using geometry, the effective coupling factor can be derived in terms of the piezoelectric material compliances as:

$$k_{eff}^2 = \frac{2(s_{33}^E - s_{33}^D)}{3s_{33}^E + s_{33}^D} \quad (2.28)$$

The definition of the coupling coefficient of a piezoelectric element was given in section 2.3. Using equations 2.3 and 2.28, the effective coupling factor for the full bridge rectifier case can be expressed in terms of the coupling coefficient as:

$$k_{eff}^2 = \frac{2k_{33}^2}{k_{33}^2 + 2} \quad (2.29)$$

### Full Bridge Rectifier and Voltage Detection Circuit

The operation of this circuit is as follows: The voltage detector circuit detects the voltage right after the diode bridge ( $V_2$ ). Initially, the SCR is in "off" state. If  $V_2$  reaches its maximum and begins decreasing, the voltage detector sends a current signal to SCR which turns it on. If the detected voltage reaches zero, the voltage detector sends another signal to SCR which turns it

off.

**Simulation** The simulation architecture is the same as in Figure 2-4. The implementation of the switching of the SCR and additional details of the Simulink model are presented in Appendix A. Again, the force is imposed on the piezoelectric element. The geometry, operation frequency and the piezoelectric material are the same as in the previous section. The time histories resulting from the simulation are shown in Figure 2-11.

Again, in order to get insight into the energy conversion mechanism and to derive the governing equations, it is worthwhile to look at the force vs. deflection and voltage vs. charge plots for the piezoelectric element. These are plotted in Figure 2-12. We can see that there are two basic operation regimes. The first one is operation under open circuit conditions, where the compliance of the piezoelectric element is low, i.e the piezoelectric element is hard. The second operation regime is defined with the *almost flat* lines in Figure 2-12. This regime corresponds to the time intervals, where the switch (SCR) is on. In this regime, the piezoelectric material behaves as a very soft material.

Since the SCR is initially closed, the piezoelectric element is first compressed under open circuit conditions, until the applied force reaches its maximum and begins to decrease (period 1-2). In this period, the voltage on the piezoelectric element reaches the open circuit voltage corresponding to the maximum stress applied on the element. Once the force begins to decrease, the detected voltage, which is the rectified piezoelectric element voltage, begins to decrease too, which causes the switch to turn on. After the switch turns on, the voltage decreases very fast and the piezoelectric element is compressed with a very small effective stiffness. The switch turns again off once the voltage reaches zero. During the period when the switch is on (2-3), the piezoelectric element is squeezed until the point, as if it was being squeezed under the same stress and closed circuit conditions. We can verify this by looking to the voltage vs. charge plot. In state 3, the voltage on the piezoelectric element is zero and the force on it is almost the maximum force. Of course, this rapid compression occurs in finite time and during this time interval, the force decreases a little bit, which results in the *almost flat* region in force vs. deflection plot. The shorter the "on" state, the flatter will be the line. It can be concluded that, the performance of the system with this cycle depends highly on the time history of the

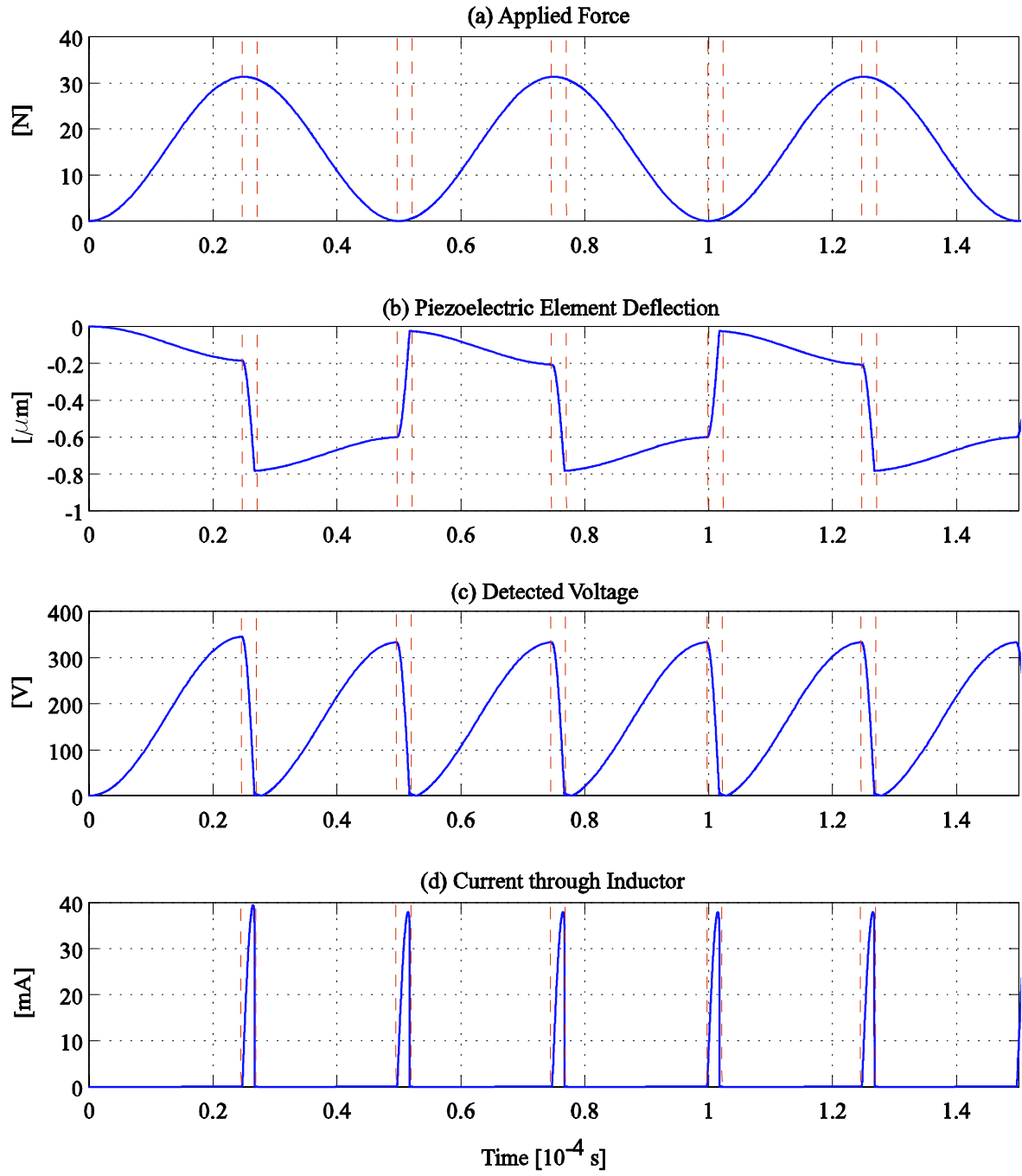


Figure 2-11: Time histories from the simulation of the piezoelectric element connected to the full bridge rectifier and voltage detector circuit. The time intervals between the dashed lines present the intervals where the switch(SCR) is in its "on" state.



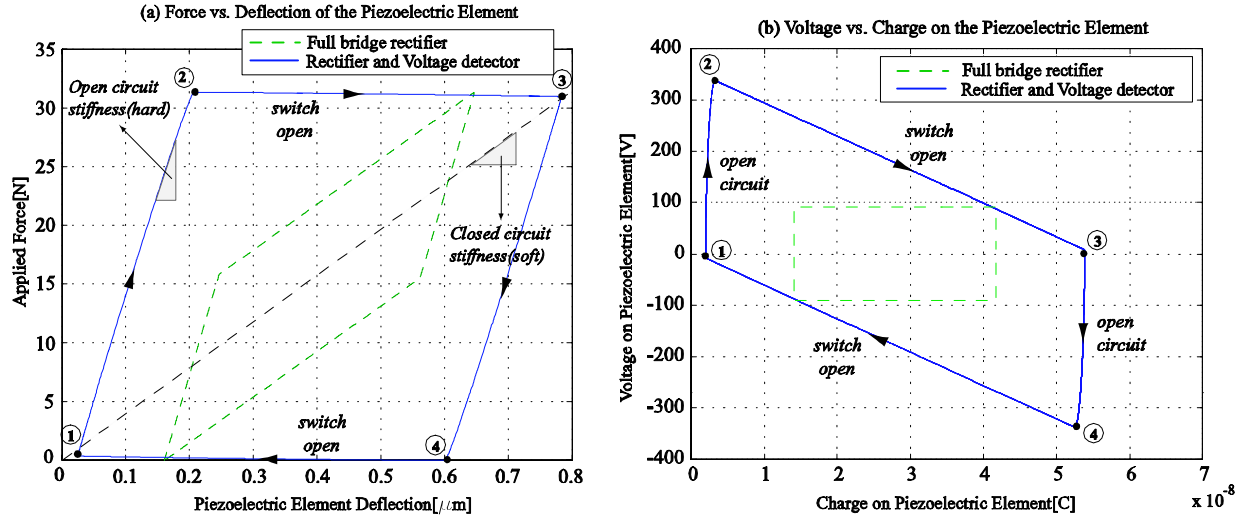


Figure 2-12: Force vs. deflection and voltage vs. charge plots of the piezoelectric element compressed under the applied force for the case of full bridge rectifier and voltage detector circuit.

applied force.

**Analysis** After the observations done in the previous section, we can derive the equations which determine the maximum strain and charge of the piezoelectric element, the energy stored per cycle and the effective coupling factor. To keep the analysis more general, we again analyze the work cycles in terms of stress vs. strain and electric field vs. charge density plots. Important features of the idealized work cycles are shown in Figure 2-13. As mentioned earlier, there is a finite time associated with the transition between states 2-3 and 4-1, where the force does not remain at its maximum value. This time interval depends highly on the value of the inductor used. In the simulation, an inductor of  $20\text{mH}$  is used. It should be also mentioned that, the capacitor has to be large enough to avoid saturation. The simulation results are very close to the idealized cycles, which can be seen comparing Figure 2-12 and Figure 2-13. It should be also mentioned that, the difference between these figures should be counted partly on a simulation artifact. The switch operation and open circuit and closed circuit conditions are simulated using very large and very small resistances respectively. It can be concluded that, the idealized curves in Figure 2-13 are very good approximations to the actual work cycles.

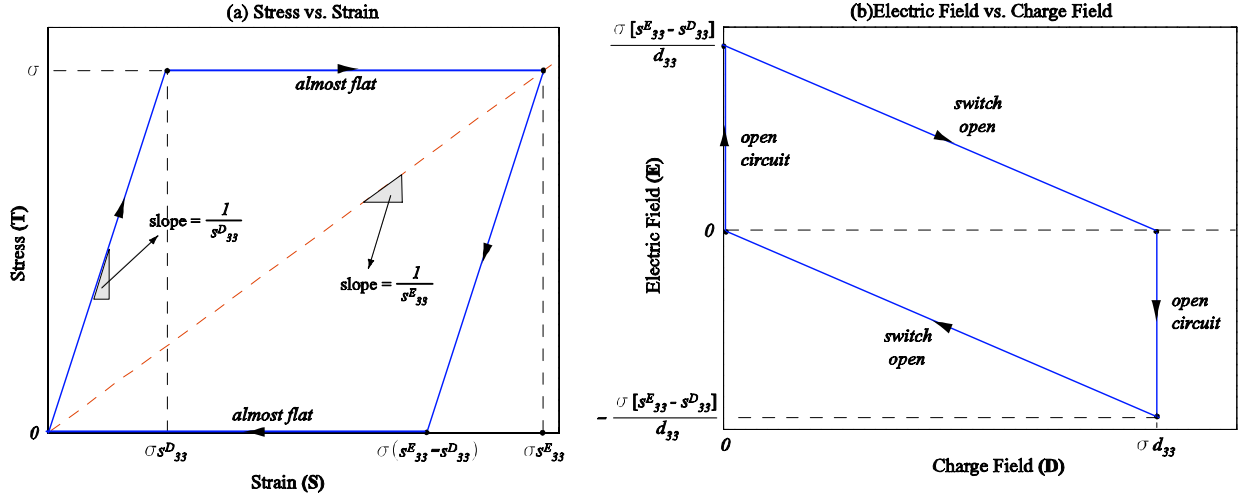


Figure 2-13: General presentation of the work cycle of the piezoelectric element in terms of stress, strain, electric field and charge density for the case of the full bridge rectifier and voltage detector circuit.

The derivation of the coordinates of the points in Figure 2-13 is straightforward. The strain values can be found by using the slopes of the stress vs. strain curve. The maximum charge can be calculated using the constitutive relationships for the condition of zero electric field and maximum stress. The electrical energy stored in the capacitor in one cycle, which is equal to the enclosed area by the stress vs. strain and electric field vs. charge density curve can be obtained easily as:

$$E = (s_{33}^E - s_{33}^D)\sigma^2 \quad (2.30)$$

where  $s_{33}^E$  and  $s_{33}^D$  are the closed circuit and open circuit compliances of the piezoelectric element respectively and  $\sigma$  is the maximum stress on the piezoelectric element.

Then, the generated power by the piezoelectric element can be expressed as:

$$W = (s_{33}^E - s_{33}^D)\sigma^2 V_p f \quad (2.31)$$

where  $V_p$  is the volume of the piezoelectric element and  $f$  is the operation frequency. From the above equation it can be seen that the power depends heavily on the stress on the piezo-

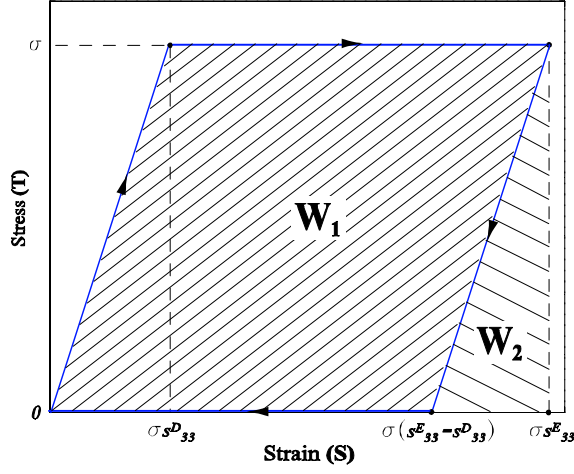


Figure 2-14: Illustration of the effective coupling factor for the full bridge rectifier and voltage detection circuit.

electric element. The power generated with this circuitry is four times bigger than the power generated using the full bridge rectifier under the same conditions, namely same applied force and frequency.

Using the definition in equation 2.27 and from Figure 2-14, the effective coupling factor can be obtained as:

$$k_{eff}^2 = \frac{W_1}{W_1 + W_2} = \frac{2(s_{33}^E - s_{33}^D)}{2s_{33}^E - s_{33}^D} \quad (2.32)$$

Using equations 2.3 and 2.32, we can express the effective coupling factor of the coupling coefficient as:

$$k_{eff}^2 = \frac{2k_{33}^2}{k_{33}^2 + 1} \quad (2.33)$$

It is very interesting to note that the diode bridge and the voltage detection circuit proposed by Smalser in [26] result in the hypothetical electromechanical energy conversion work-cycle proposed by Berlincourt [8]. This cycle is shown in Figure 2-2(a). The expression in equation 2.6 is identical to equation 2.33.

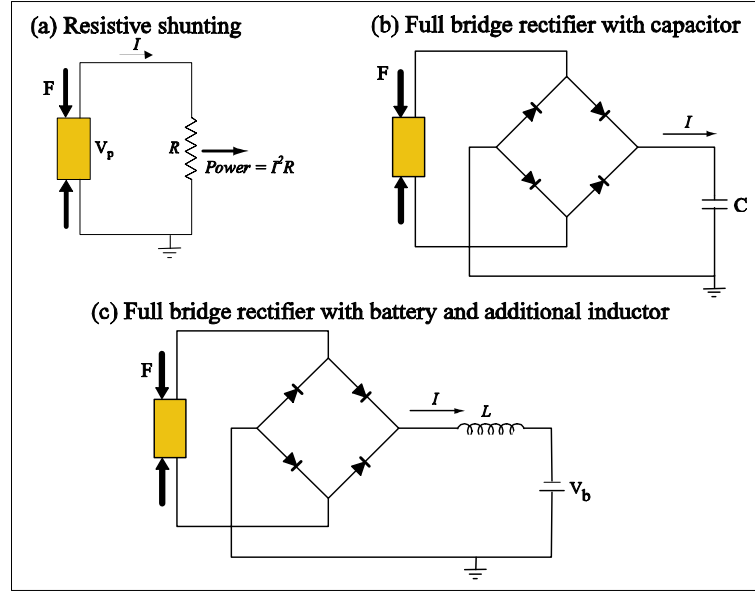


Figure 2-15: Other alternative circuits for piezoelectric power generation.

## 2.5 Other Circuits

This section discusses some other alternative circuits for piezoelectric power generation, shown in Figure 2-15. The geometry, operation frequency and the piezoelectric material used for the simulations are the same as in the previous section.

A much simpler circuit than the ones presented in previous sections is that involving just a resistor. Resistive shunting of piezoelectric elements for structural damping is discussed in [15]. The resistive shunting exhibits frequency dependent behavior and the converted electrical energy is dissipated, not stored. Figure 2-16 shows the force vs. deflection and voltage vs. charge plots from the simulation of the piezoelectric element shunted by a resistor. It can be seen that, for relatively small resistance values, the piezoelectric element behaves close to the closed circuit condition, whereas for large resistance values, it behaves close to the open circuit condition. It should be noted that the simulations presented in Figure 2-16 are performed at a certain frequency. If one were to keep the resistance constant and change the frequency, similar behavior would be observed. Namely, at very large frequencies the behavior would be close to open circuit behavior, whereas at very low frequencies, the behavior would be close to closed

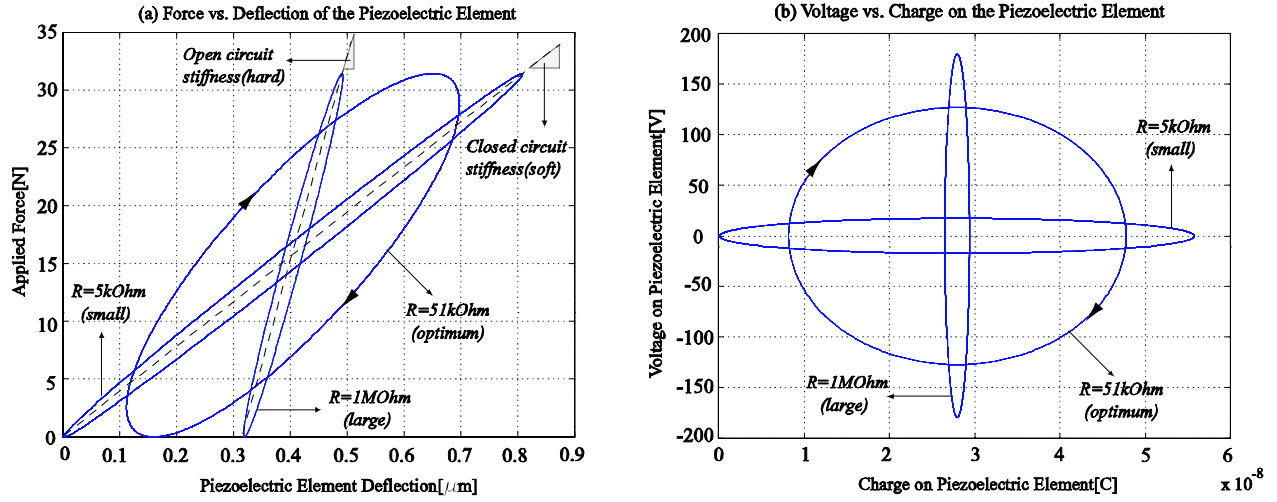


Figure 2-16: Simulation results of the piezoelectric element shunted by a resistor for different resistance values.

circuit behavior. Indeed, the maximum electromechanical energy conversion occurs when the impedance of the load, which is the resistor, is matched to the impedance of the piezoelectric element. In other words, for a given piezoelectric element and geometry, at any given resistance value there exists an optimum frequency, or at any given frequency there exists an optimum resistance value. The optimum resistance value is given as:

$$R_{opt} = \frac{1}{2\pi f C^T} \quad (2.34)$$

where  $f$  is the operation frequency and  $C^T$  is the capacitance of the piezoelectric element under constant stress, which can be expressed as:

$$C^T = \frac{e_{33}^T A_p}{L_p} \quad (2.35)$$

where  $e_{33}^T$  is the dielectric constant and  $A_p$  and  $L_p$  are the cross-sectional area and the length of the piezoelectric element respectively.

Figure 2-17 compares the resistive shunting (for optimum resistance value) with the circuits presented in previous sections. Resistive shunting performs better compared to the full bridge rectifier in terms of electromechanical energy conversion. However, as mentioned earlier, the

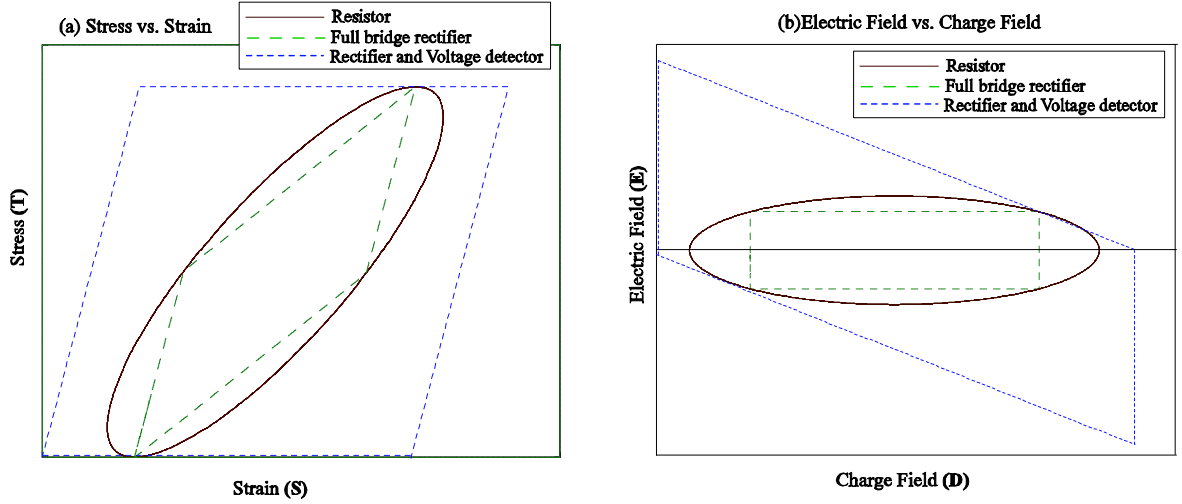


Figure 2-17: Comparison of resistive shunting(at optimum resistance) with full bridge rectifier and full bridge rectifier with voltage detector.

performance depends heavily on operation frequency and the electrical energy is not stored, which make resistive shunting not a suitable option for power generation.

An alternative circuit can be full bridge rectifier and a capacitor connected to it, instead of a battery or a DC voltage source as presented in section 2.4.2. This is actually the same circuit configuration as presented in [10]. The simulation results are shown in Figure 2-18. As can be seen from the plots, the behavior heavily depends on the value of the capacitor. Obviously, energy cannot be transferred to the capacitor after the voltage of the capacitor nearly reaches half of the open circuit voltage of the piezoelectric element, which corresponds to the maximum stress. As expected, the higher the capacitance, the larger is the stored energy, since the final voltage is the same regardless of the capacitance value. This statement contradicts with the conclusion made in [10] because in this simulation the force is imposed on the piezoelectric element. In [10], no force is imposed on the piezoelectric element. The dynamics of the system (falling ball, vibration of the plate etc.) is determined by the circuitry, i.e. the capacitor and there exists an optimum capacitance value for maximum energy transfer.

Another alternative would be to add an inductor to the full bridge rectifier in series with the battery. The simulation results corresponding to the optimum inductor value are shown in Figure 2-19. It can be seen that both the stored energy per cycle and the effective coupling

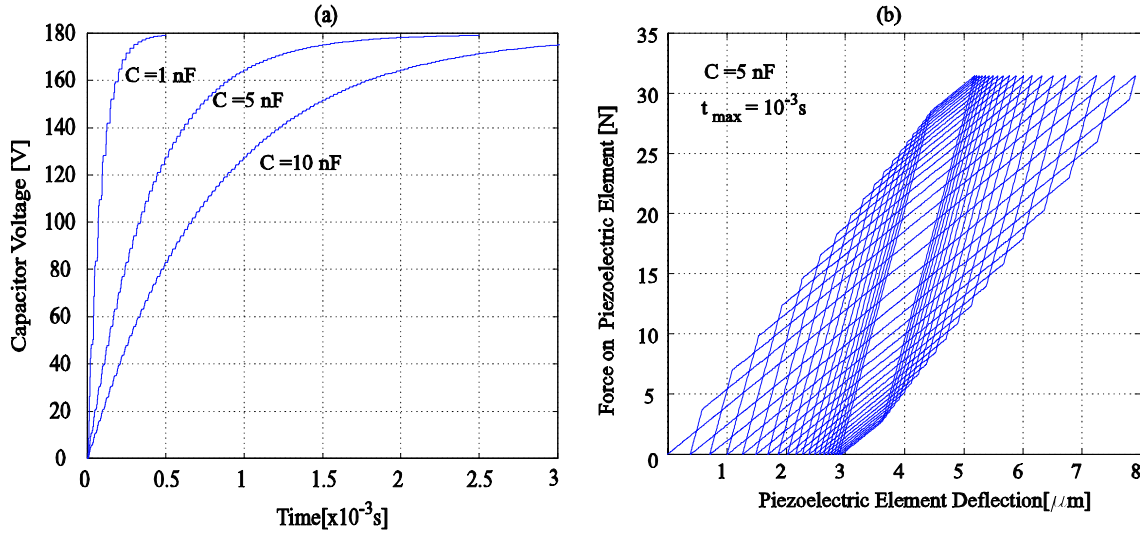


Figure 2-18: Simulation results of the full bridge rectifier connected to a capacitor.

factor increases with the addition of the inductor. However, in order to get this behavior, the value of the inductor should be tuned to the optimum value at a given frequency and for this particular example the required inductance is about 100mH, which is physically very large and not practical.

We can generally conclude that, the circuits discussed in the previous section are better suited for piezoelectric power generation since they can store the electrical energy and the behavior is not frequency dependent.

## 2.6 Piezoelectric Material Comparison

Section 2.4 presented an analysis of two different circuits and expressions derived for the effective coupling factor and generated power. This section presents a comparison of different piezoelectric materials in terms of energy density and effective coupling factor for different shunting conditions, i.e. with different circuits connected, using the expressions derived in Section 2.4. The important expressions for energy density and effective coupling factor are summarized in Table 2.2. The effective coupling factors for the two circuits presented in Table 2.2 are plotted as a function of the coupling coefficient in Figure 2-20. It can be seen that the effective coupling

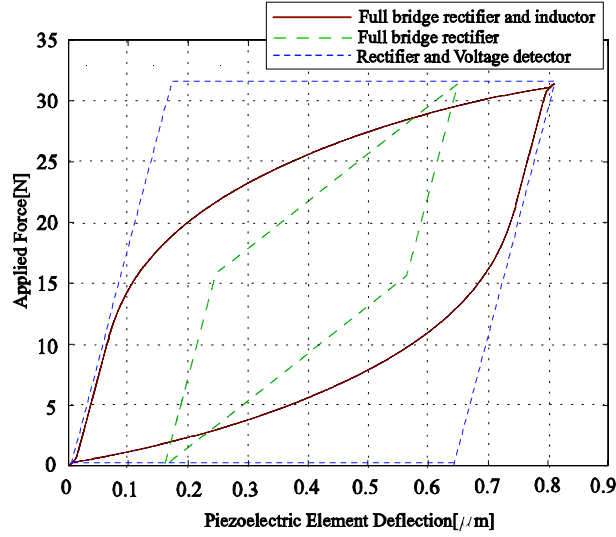


Figure 2-19: Force vs. deflection plot from the simulation of the full bridge rectifier with additional inductor.

	Rectifier	Rectifier+Voltage Detector
Energy Density	$ED = \frac{1}{4}(s_{33}^E - s_{33}^D)\sigma_d^2$	$ED = (s_{33}^E - s_{33}^D)\sigma_d^2$
Effective coupling factor	$k_{eff}^2 = \frac{2k_{33}^2}{k_{33}^2 + 2}$	$k_{eff}^2 = \frac{2k_{33}^2}{k_{33}^2 + 1}$

Table 2.2: Comparison of circuitry in terms of energy density and effective coupling factor

factor for the case of the diode bridge is always smaller than the coupling coefficient whereas the effective coupling factor for the case of the diode bridge with voltage detector is always larger than the coupling coefficient. This can be also presented with the following inequality:

$$\sqrt{\frac{2k_{33}^2}{k_{33}^2 + 2}} < k_{33} < \sqrt{\frac{2k_{33}^2}{k_{33}^2 + 1}} \quad (2.36)$$

which is valid since  $k_{33} < 1$ .

The energy density of a piezoelectric material, i.e. the maximum energy which can be extracted from a piezoelectric element in one cycle is mostly limited by the depolarization stress of the piezoelectric element, which means that if a stress higher than the depolarization stress



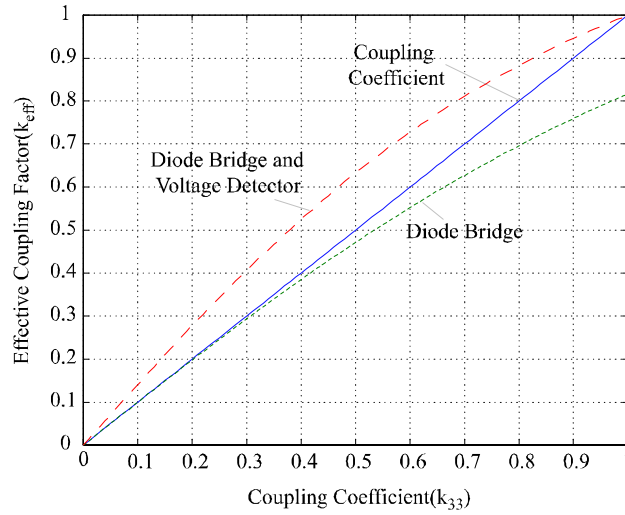


Figure 2-20: Effective coupling factors of the diode bridge and the diode bridge with voltage detector as a function of the coupling coefficient.

is applied, the material begins to dipole and the piezoelectric, dielectric and elastic coefficients begin to degrade. Behavior of different PZT ceramics and PZN-PT single crystal piezoelectric elements under high stress are investigated in [46] and [19] respectively. The assumption for the maximum stress limit, i.e. the assumed values for the depolarization stress are based on the above mentioned references. Other studies about piezoelectric elements under high fields are presented in [45]-[49]. Elastic and piezoelectric properties of different piezoelectric materials along with depolarization stress values are compiled in Table 3.3.

Different piezoelectric materials are compared in terms of their energy densities and effective coupling factors for different circuitry in Figure 2-10. It is interesting to note that, although the single crystal piezoelectric material(PZN-PT) has very high effective coupling factor, it has a very low energy density compared to PZT-8 or PZT-4S because of its small depolarization stress. We can generally say that, the effective coupling factor is a function of the coupling coefficient and the circuitry, whereas the energy density is a function of coupling coefficient, circuitry and the depolarization stress. As mentioned earlier, for a piezoelectric element, the energy density obtained with the diode bridge and voltage detector circuit is four times larger than the energy density obtained with just the diode bridge.

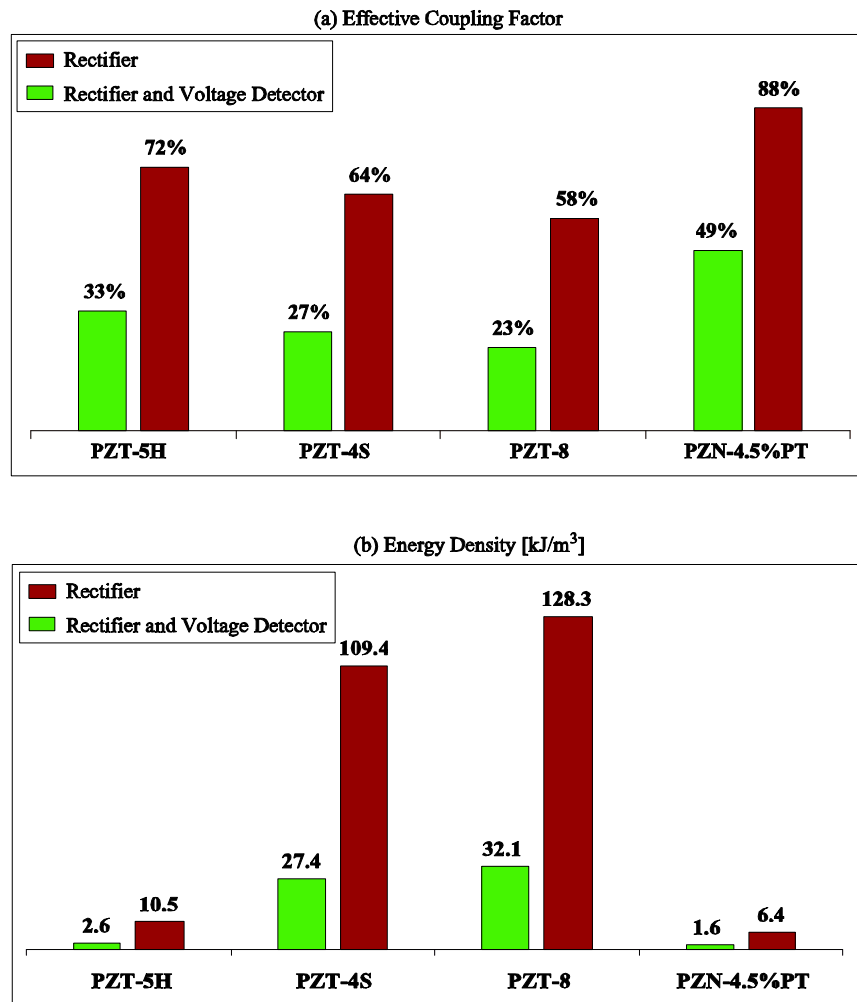


Figure 2-21: Piezoelectric Material Comparison: (a) Effective coupling factor (b) Energy density.

	PZT-4S	PZT-5H	PZT-8	PZN-4.5%PT
$s_{33}^E[10^{-12}m^2/N]$	15.5	20.7	13.9	81
$s_{33}^D[10^{-12}m^2/N]$	7.9	9.01	8.2	17
$k_{33}$	0.7	0.75	0.64	0.89
$d_{33}[10^{-12}m/V]$	350	593	250	1780
<i>Depolarization Stress</i> [MPa]	120	30	150	10

Table 2.3: Properties of different piezoelectric materials

## 2.7 Conclusion

This chapter presented an analysis of two different circuitries for piezoelectric power generation. Analytical expressions are derived for the generated power and effective coupling factor for a given piezoelectric material and circuitry. Different piezoelectric materials are compared in terms of their power generation characteristics. Among the materials analyzed, PZT-8 has the highest energy density. Despite its large coupling coefficient, the single crystal material PZN-PT has very low energy density, which is a consequence of its low depolarization stress. However, the coupling coefficient becomes an important criteria if the piezoelectric element is considered along with its surrounding system, for example the infrastructure which provides the force on the element, which is the energy harvesting chamber in the microhydraulic power generation device. It should be remembered that in the analysis presented in this chapter a prescribed force is imposed on the piezoelectric element. This issue will be addressed in the next chapter.

## Chapter 3

# Energy Harvesting Chamber and Preliminary Design Considerations

This chapter presents a simple model of the energy harvesting chamber, simulations with the coupled circuitry and preliminary design considerations. The interaction of the energy harvesting chamber and the circuitry is discussed. The two circuits presented in Chapter 2 and different piezoelectric materials are compared in terms of the flowrate and frequency requirements for a given pressure differential and power, and in terms of system efficiency.

### 3.1 Configuration and Operation of the Energy Harvesting Chamber

The Energy Harvesting Chamber consists of a fluid chamber, a piston and a piezoelectric cylinder. The configuration of the energy harvesting chamber and its basic components are shown in Figure 3-1.

The piston converts the pressure in the chamber to a force on the piezoelectric cylinder. The inlet and outlet valves operate  $180^\circ$  out of phase at high frequency and convert the static pressure differential ( $P_{HPR} - P_{LPR}$ ) into pressure fluctuations in the chamber. This results in cyclic compression of the piezoelectric cylinder, which is coupled to the circuitry. The generic operation and typical duty cycles are shown in Figure 3-2.

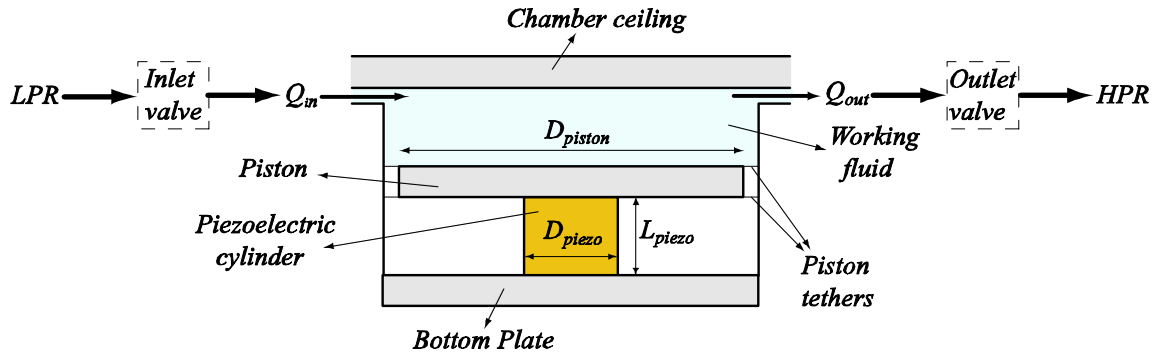


Figure 3-1: Energy harvesting chamber configuration.

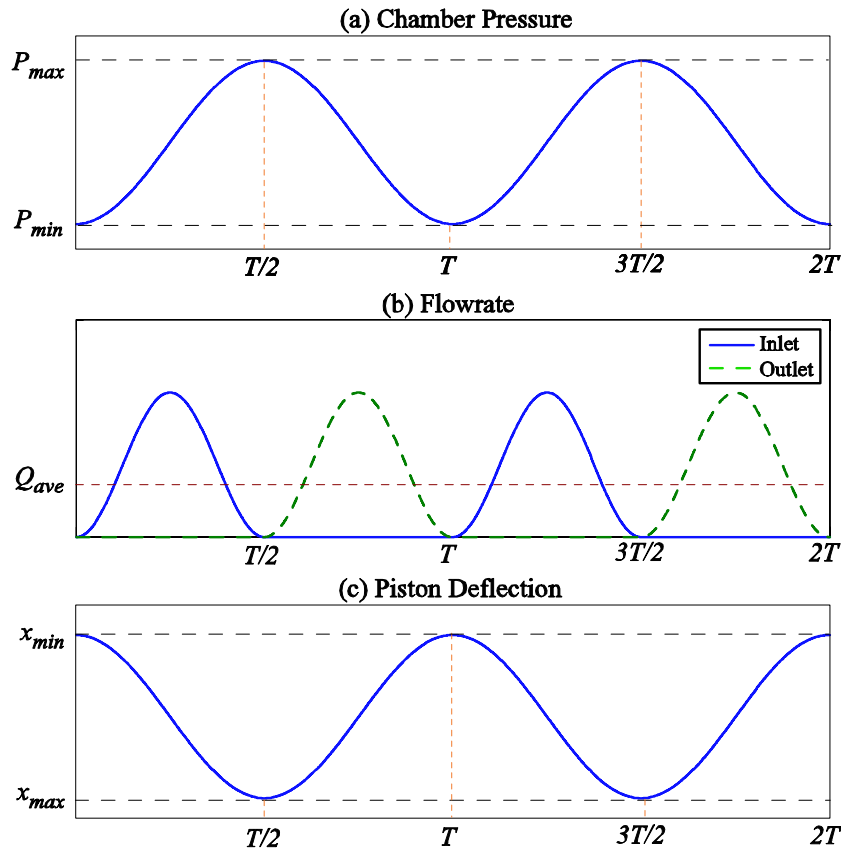


Figure 3-2: Duty cycles of generic operation of the energy harvesting chamber. The valve openings have the same duty cycle as the flowrates and are not shown here.

In the chamber, the hydraulic energy is converted into mechanical energy, which is converted into electrical energy in the piezoelectric element and then the electrical energy is stored in the coupled circuitry. There is a strong coupling between the hydraulic/mechanical system and the circuitry, in other words, the electrical circuit affects the behavior of the system dramatically, an issue which should be analyzed in detail.

## 3.2 Modeling

In order to understand the interaction between the hydraulic, mechanical and electrical system, a simple model of the energy harvesting chamber will be used to simulate a representative system. The basic assumptions are:

- The effect of piston tethers on the motion of the piston is neglected perfect sealing between the piston and the chamber walls is assumed
- An effective compliance,  $C_{eff}$ , is assigned for the chamber, which includes the combined effect of the bending of the piston, chamber ceiling (top plate), bottom plate and piston tethers as well as fluid compression inside the chamber.  $C_{eff}$  will be defined in section 3.2.2.
- Piston dynamics is neglected.

The detailed structural modeling and analysis of the compliance contributions of the structural members in the chamber will be presented in Chapter 4.

### 3.2.1 Piezoelectric Cylinder

The piezoelectric material is modeled using the same constitutive relationship given in Chapter 2, namely:

$$\begin{bmatrix} S \\ E \end{bmatrix} = \begin{bmatrix} s_{33}^D & \frac{d_{33}}{\epsilon_{33}^T} \\ \frac{d_{33}}{\epsilon_{33}^T} & -\frac{1}{\epsilon_{33}^T} \end{bmatrix} \begin{bmatrix} T \\ D \end{bmatrix} \quad (3.1)$$

where  $D$  is the charge field,  $S$  is the displacement field (strain),  $E$  is the electric field, and  $T$  is the stress. For a cross-sectional area of  $A_p$  and length of  $L_p$ , the expressions for the deflection

of the piezoelectric element and the voltage across it become:

$$x_p = \frac{L_p}{A_p} (s_{33}^D F_p + \frac{d_{33}}{\varepsilon_{33}^T} Q_p) \quad (3.2)$$

$$V_p = \frac{L_p}{A_p} (\frac{d_{33}}{\varepsilon_{33}^T} F_p - \frac{1}{\varepsilon_{33}^T} Q_p) \quad (3.3)$$

where  $x_p$  is the deflection,  $Q_p$  is the charge,  $F_p$  is the force applied on the piezoelectric cylinder, and  $V_p$  is the voltage across the piezoelectric cylinder. And the current through the piezoelectric element is given by:

$$I_p = \frac{dQ_p}{dt} \quad (3.4)$$

### 3.2.2 Chamber Continuity

The chamber converts the hydraulic energy into mechanical energy via the piston, which applies a force on the piezoelectric cylinder. In order to derive the expression for the chamber pressure, continuity equation inside the chamber should be considered. Consider an initial fluid volume inside the chamber. The time rate of the pressure change in the chamber is given by:

$$\frac{dP_{ch}}{dt} = \frac{\beta_f}{V_o} \frac{dV}{dt} \quad (3.5)$$

where  $\beta_f$  is the bulk modulus of the fluid,  $V_o$  is the initial volume of the fluid inside the chamber and  $\frac{dV}{dt}$  is the volume change of the fluid. Sources of the volume change are:

- Net flowrate into the chamber
- Piston Movement
- Additional volume created inside the chamber by the deformation of the structural members due to chamber pressure

Then, the time rate of the total volume change in the chamber can be expressed as:

$$\frac{dV}{dt} = Q_{in} - Q_{out} - \frac{dx_p}{dt} A_{pis} - \frac{dV_s}{dt} \quad (3.6)$$

where  $x_p$  is the displacement of the piston, which is equal to the deflection of the piezoelectric cylinder,  $A_{pis}$  is the cross-sectional area of the piston, and  $V_s$  is the total volume displaced by

the deformation of the structural members inside the chamber. The source of this additional volume might be the deformation of the top and bottom plate of the chamber, deformation of the piston tethers and deformation of the piston itself. The individual sources of the structural compliance of the chamber will be analyzed in detail in Chapter 4.

Combining equations 3.5 and 3.6, we get:

$$\frac{dP_{ch}}{dt} = \frac{\beta_f}{V_o} \left( Q_{in} - Q_{out} - \frac{dx_p}{dt} A_{pis} - \frac{dV_s}{dt} \right) \quad (3.7)$$

We can define the overall structural compliance as:

$$C_s = \frac{dV_s}{dP_{ch}} \quad (3.8)$$

From equations 3.7 and 3.8, we get the expression for the chamber pressure as:

$$\frac{dP_{ch}}{dt} = \left( \frac{V_o}{\beta_f} + C_s \right)^{-1} \left( Q_{in} - Q_{out} - \frac{dx_p}{dt} A_{pis} \right) \quad (3.9)$$

For simplicity, we can define an effective compliance for the chamber, which represents all the compliance sources as:

$$C_{eff} = \left( \frac{V_o}{\beta_f} + C_s \right) \quad (3.10)$$

where the first and the second terms correspond to the fluidic compliance and structural compliance respectively, which act like parallel capacitors in electrical circuit analogy.

We can rewrite 3.9 as follows:

$$\frac{dP_{ch}}{dt} = \frac{1}{C_{eff}} \left( Q_{in} - Q_{out} - \frac{dx_p}{dt} A_{pis} \right) \quad (3.11)$$

It is important to note that, in the above analysis the initial fluid volume inside the chamber,  $V_o$ , is assumed to be much larger than the volume displaced by the piston and the volume displaced due to the deformation of the structural members inside the chamber. If the deflection of the piston becomes comparable to the chamber height, the volume displaced by the piston becomes comparable with the initial volume of the chamber, and that effect should be taken into consideration, which will result in nonlinear behavior, i.e nonlinear compliance.



The generic duty cycle of the operation is shown in Figure 3-2. The average flowrate can be calculated using the following relationship:

$$Q_{ave} = \frac{\int_0^{T/2} Q_{in} dt}{T} = \frac{\int_{T/2}^T Q_{out} dt}{T} \quad (3.12)$$

It is also important to note that:

$$\int_{T/2}^T Q_{in} dt = \int_0^{T/2} Q_{out} dt = 0 \quad (3.13)$$

Integrating equation 3.11 from  $t = 0$  to  $t = \frac{T}{2}$ , using equation 3.12 and arranging terms, we get the expression for the average flowrate as:

$$Q_{ave} = A_{pis}(x_{\max} - x_{\min})f + C_{eff}(P_{\max} - P_{\min})f \quad (3.14)$$

where  $A_{pis}$  is the cross-sectional area of the piston and  $f$  is the operation frequency. The same expression can be obtained by integrating equation 3.11 from  $t = \frac{T}{2}$  to  $t = T$ . The first term in equation 3.14 corresponds to the flowrate required to move the piston and squeeze the piezoelectric element. The second term corresponds to the flowrate required due to the compliances in the chamber.

### 3.2.3 Fluid Model

The schematic of the device with pressures at different locations within the system is shown in Figure 3-3 where  $P_{int-in}$  is the intermediate pressure at the exit of the inlet channel, and  $P_{int-out}$  is the intermediate pressure at the entrance to the outlet valve. Inlet and outlet channels have the same geometry. Details of the Simulink architecture is given in the Appendix A.

### Valve Orifice Flow Relations

Work by previous researches has shown that for small openings, poppet valves, such as the valve cap in the active valves within the MHT systems, behave as long orifices in which the effects of flow separation and subsequent re-attachment dominate the valve flow dynamics[5].

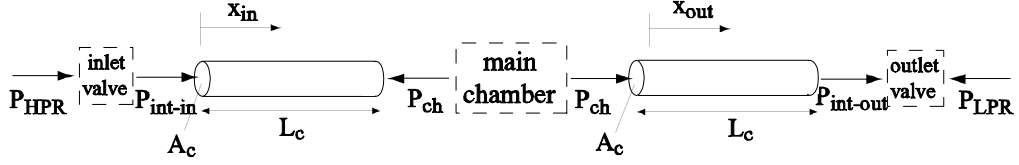


Figure 3-3: Device schematics showing pressures at different locations.

Qualitatively, the valve flow can be approximated by a simplified order-of-magnitude valve model. The valve orifice may be characterized as a flow contraction followed by a flow expansion as shown in Figure 3-4(a) and (b). An integral analysis gives a relationship for the combined effect of the flow expansion and contraction. The loss coefficient  $\zeta_{orifice}$  is defined as the total pressure drop  $\Delta P = P_{HPR} - P_{int}$  (for the inlet valve) over the dynamic pressure based on the orifice local mean velocity ( $\bar{u} = \frac{Q}{A_o}$ )

$$\zeta_{orifice} = \frac{\Delta P}{\frac{1}{2}\rho\bar{u}^2} = \left[ \frac{1}{2} \left( 1 - \frac{A_o}{A_1} \right)^{\frac{3}{4}} + \left( 1 - \frac{A_o}{A_2} \right)^2 \right] \quad (3.15)$$

where the upstream, throat and downstream flow areas can be approximated as:

$$A_2 = 2\pi R_{vc} H_c \quad (3.16)$$

$$A_o = 2\pi R_{vc} x_{vc} \quad (3.17)$$

$$A_1 = \pi R_{vc}^2 \quad (3.18)$$

respectively, where  $H_c$  is the height of the radial flow channel above the valve membrane,  $x_{vc}$  is the valve cap distance from the valve stop structure and  $R_{vc}$  is the radius of the valve cap.

This approximation, however, is independent of the Reynolds number and therefore holds only for  $Re \geq 10,000$ , where the flow is in fully turbulent regime. In the MHT power generator, Reynolds numbers are expected to fluctuate between approximately 10 and 20,000 as the valves

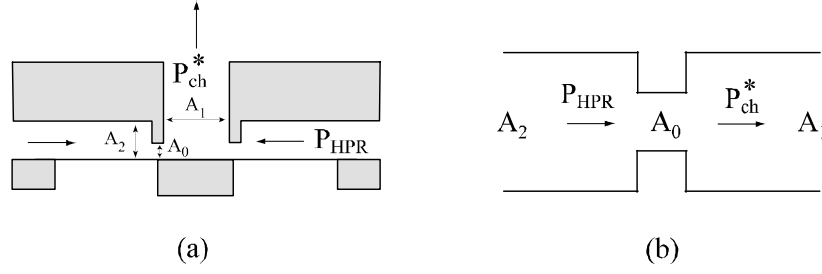


Figure 3-4: Valve orifice representation:(a) Valve cap geometry and fluid flow areas, (b) Representation of flow through the valve as a flow contraction followed by a flow expansion.

open and close. For this reason, correction factors obtained from experimental results need to be employed to obtain better estimates of the loss coefficients for these low turbulence and laminar flow regimes[4]. A loss coefficient for each of the contraction and expansion geometries,  $\zeta_{contraction}$  and  $\zeta_{expansion}$ , respectively, is used to approximate the total loss coefficient through the valve, as detailed in the following relation:

$$\zeta_{orifice}^* = \zeta_{contraction}\left(\text{Re}, \frac{A_o}{A_2}\right) + \zeta_{expansion}\left(\text{Re}, \frac{A_o}{A_1}\right) \quad (3.19)$$

where Reynolds number is defined as:

$$\text{Re} = \frac{1}{\pi} \frac{Q}{R_{vc} \nu} \quad (3.20)$$

Figure 3-5(a) plots  $\zeta_{contraction}$  as a function of Reynolds number and contraction area ratio  $\frac{A_o}{A_2}$ , and Figure 3-5(b) plots  $\zeta_{expansion}$  as a function of Reynolds number and the expansion area ratio  $\frac{A_o}{A_1}$ . As a result, the pressure-flow relation for the full valve orifice geometry can be written as:

$$\Delta P = \frac{1}{2} \rho \zeta_{orifice}^* \left( \frac{Q^2}{A_o^2} \right) \quad (3.21)$$

All subsequent fluid models discussed in this thesis incorporate these higher-order correction factors to obtain an accurate estimation of the flow behavior. These flow models are based on steady flow phenomenon and do not capture frequency dependent losses. For a specific value of valve cap opening at a given time during the cycle, a relationship therefore exists for the

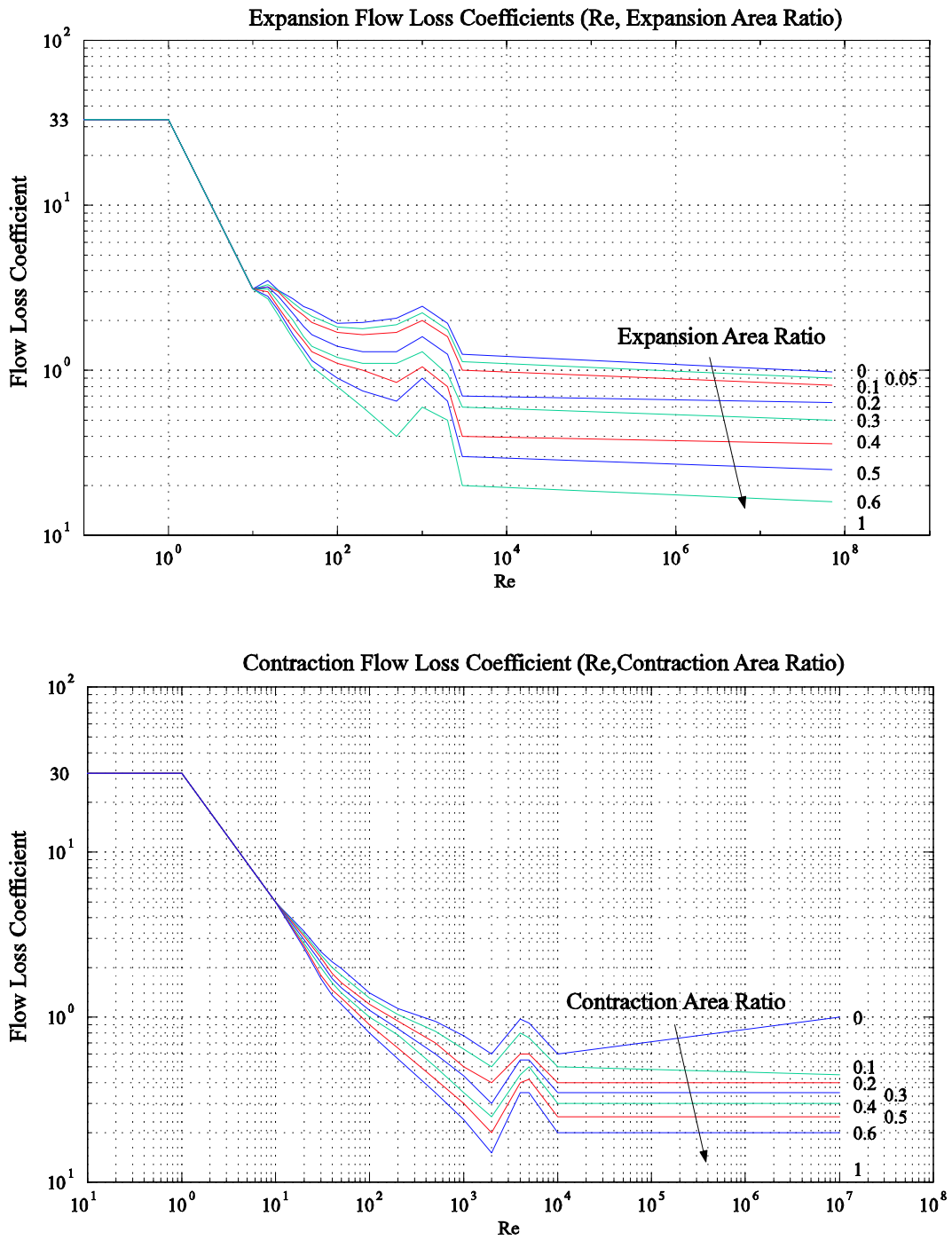


Figure 3-5: Look-Up tables used for flow loss contraction and expansion coefficients. The loss coefficients are obtained from [51].

instantaneous fluid flow through the valve as a function of the pressure drop across the valve.

Equation 3.21 can be rewritten for inlet and outlet valves using the notation in Figure 3-3 as:

$$P_{HPR} - P_{int-in}(t) = R_{in}(Q_{in}, v_{o_{in}})Q_{in}^2 \quad (3.22)$$

$$P_{int-out}(t) - P_{LPR} = R_{out}(Q_{out}, v_{o_{out}})Q_{out}^2 \quad (3.23)$$

where  $R_{in}$  and  $R_{out}$  represent the flow resistances of the inlet and outlet valves, respectively, which are functions of the flowrate and the corresponding valve opening at a given instant of time.

### Flow in the Channels

Due to the high Reynolds numbers, the flow in the channels is expected to be inertia dominated. Furthermore, the compliance in the fluid channels is usually negligible due to the fact that the channels are surrounded by rigid walls and their volume is much smaller than that of the chamber. Under this assumptions the flow inside the channels is modeled as one dimensional inviscid and incompressible flow. The pressure-flowrate relationship in this case is given as:

$$\Delta P = I \frac{dQ}{dt} = \left( \frac{\rho L_c}{A_c} \right) \frac{dQ}{dt} \quad (3.24)$$

where  $I$  is defined as the fluid inductance inside the channel,  $\rho$  is the fluid density and  $L_c$  and  $A_c$  are the length and cross-sectional area of the fluid channel respectively. For the case of inlet valve and outlet valve fluid channels, the pressure-flow relations can be written as:

$$P_{int-in}(t) - P_{ch}(t) = \left( \frac{\rho L_c}{A_c} \right) \frac{dQ_{in}}{dt} \quad (3.25)$$

$$P_{ch}(t) - P_{int-out}(t) = \left( \frac{\rho L_c}{A_c} \right) \frac{dQ_{out}}{dt} \quad (3.26)$$

For a long channel with small cross-sectional area, one can expect fluid inertial effects to

play a significant role as the pressure difference builds up to accelerate the fluid slug into the chamber. Conversely, for short channels with large cross-sectional areas, the inertial effects are negligible and the pressure  $P_{int-in}$  and  $P_{ch}$  or  $P_{ch}$  and  $P_{int-out}$  will not differ much. It is important to consider inertial effects when designing hydraulic systems containing small channels.

## Governing Equations

Combining equations 3.22, 3.23, 3.25, and 3.26 we can obtain the governing equations for the fluid flow in the system, which are integrated into the system level simulation, as:

$$P_{HPR} - P_{ch}(t) = R_{in}(Q_{in}, v_{o_{in}})Q_{in}^2 + \left(\frac{\rho L_c}{A_c}\right) \frac{dQ_{in}}{dt} \quad (3.27)$$

$$P_{ch}(t) - P_{LPR} = R_{out}(Q_{out}, v_{o_{out}})Q_{out}^2 + \left(\frac{\rho L_c}{A_c}\right) \frac{dQ_{out}}{dt} \quad (3.28)$$

Although not explicitly seen, the intermediate pressures can be easily calculated and monitored in the system level simulation, which are important in terms of stresses in the valve membranes and power consumption in the active valves since they are assumed to act on the valve cap, where the reservoir pressures are assumed to act on the membranes[6].

### 3.2.4 Circuitry

The same circuit models presented in Chapter 2 will be used.

## 3.3 Working Fluid

Fluid properties which are important in terms of system performance are listed in Table 3.3 for alternative working fluids. The density of a working fluid effects the dynamic behavior of the system because of the fluid inductance in the fluid channels. A low density fluid is desirable since it would increase the bandwidth of the system. The viscosity of a working fluid effects the energy dissipated in the valves. A more viscous fluid would provide the same amount of flowrate with larger valves or valve openings, causing an increase in power consumption in the

	Density[ $kg/m^3$ ]	Viscosity[ $Pa/s$ ]	Bulk Modulus[ $GPa$ ]
Water	1000	1.0e-3	2.24
Mercury	13,570	1.5e-3	25.0
Silicone Oil	760	4.9e-4	2.0(degassed)

Table 3.1: Comparison of different working fluids

<i>Length of the piezoelectric cylinder</i>	<i>1mm</i>
<i>Diameter of the piezoelectric cylinder</i>	<i>2mm</i>
<i>Diameter of the piston</i>	<i>4.5mm</i>
<i>Effective chamber compliance (<math>C_{eff}</math>)</i>	<i><math>2 \times 10^{-18}[m^3/Pa]</math></i>
<i><math>P_{HPR}</math></i>	<i>2MPa</i>
<i><math>P_{LPR}</math></i>	<i>0MPa</i>
<i>Operation Frequency</i>	<i>10kHz</i>
<i>Fluid channel length</i>	<i>1mm</i>
<i>Fluid channel cross-section</i>	<i>50<math>\mu m</math> x 100 <math>\mu m</math></i>
<i>Piezoelectric Material</i>	<i>PZN-4.5%PT</i>

Table 3.2: The geometry and operation conditions used in the simulation

valves. The bulk modulus effects the system compliance. Silicone oil is chosen as the working fluid because of its low density, low viscosity and a bulk modulus comparable to that of water.

### 3.4 Simulation and Analysis

The equations presented in the previous section will be simulated using Simulink. The coupled equations used to simulate the system are 3.2, 3.3, 3.4, 3.11, 3.27, 3.28 and equations for the circuitry, which were given in Chapter 2.

The simulation architecture is shown in Figure 3-6. For the analysis in this chapter, a representative system will be analyzed, for which the geometry and operation conditions are presented in Table 3.2.

In the following analysis, the valve openings are imposed and reservoir pressures are assumed to be constant. The valve size and opening are adjusted such that the pressure in the energy harvesting chamber attains the high pressure reservoir pressure ( $P_{HPR}$ ) and low pressure reservoir pressure ( $P_{LPR}$ ) as its maximum and minimum pressures respectively. In other words, the pressure inside the chamber fluctuates between  $P_{HPR}$  and  $P_{LPR}$ . The valves operate  $180^\circ$  out of phase.

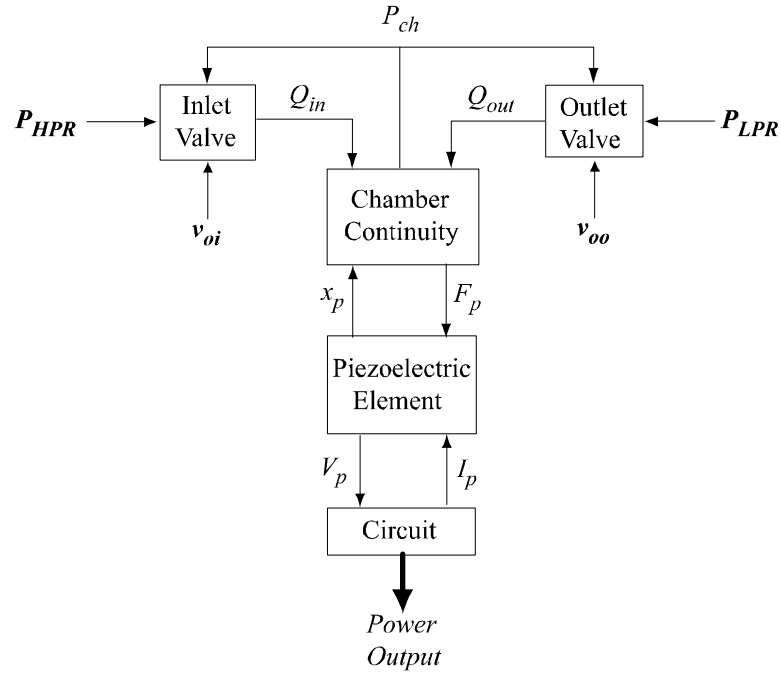


Figure 3-6: Simulation architecture used in Simulink.

### 3.4.1 Energy Harvesting Chamber and Full Bridge Rectifier

This section presents the simulation and analysis of the energy harvesting chamber attached to the full bridge rectifier using the model presented in the previous section. The time histories of the chamber pressure, flowrate and piston deflection, which is equal to the deflection of the piezoelectric element, are shown in Figure 3-7.

In order to understand the interaction between the hydraulic/mechanical system and the circuitry, and its implications on flowrate and frequency for a given power requirement, it is worthwhile to investigate the plot of force on the piezoelectric element vs displacement of the piezoelectric element. This is shown in Figure 3-8. It is interesting to note that the curve in Figure 3-8 has the exact same shape of the force vs. displacement curve presented in Chapter 2 for the case of the imposed force on a piezoelectric cylinder attached to a diode bridge. From this we can conclude that the force vs. displacement curve of a piezoelectric element attached to the full bridge rectifier does not depend on the time history of the applied force. So, the equations derived in Chapter 2 for the full bridge rectifier will be used here to derive



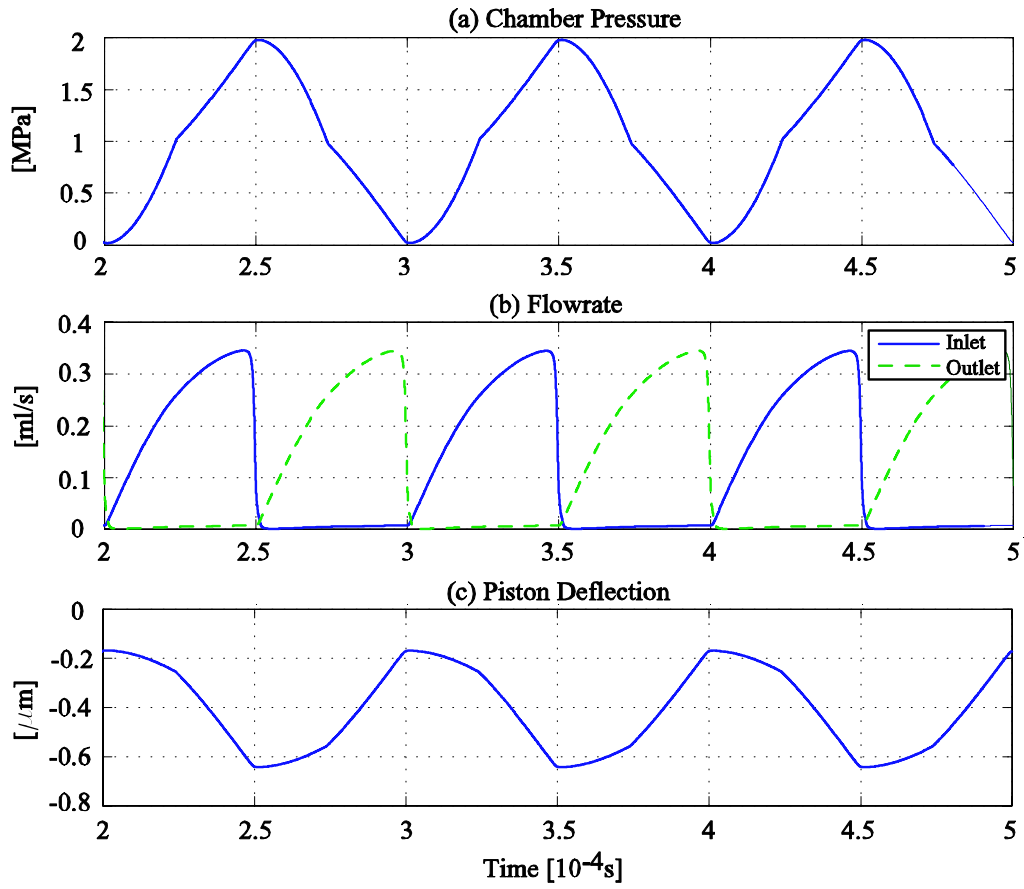


Figure 3-7: Simulation of the energy harvesting chamber attached to the full bridge rectifier circuit.

the governing equations for required frequency, flowrate and system efficiency.

For a given operation frequency and power requirement, the required cross-sectional area of the piezoelectric element can be obtained from equation 2.25 as:

$$A_p = \frac{4W}{(s_{33}^E - s_{33}^D)\sigma^2 L_p f} \quad (3.29)$$

where  $W$  is the generated power,  $L_p$  is the length of the piezoelectric cylinder and  $f$  is the operation frequency. Since the maximum pressure in the chamber is  $P_{HPR}$ , the cross-sectional area of the piston should be equal to:

$$A_{pis} = \frac{\sigma_d A_p}{P_{HPR}} \quad (3.30)$$

where  $\sigma_d$  is the depolarization stress of the piezoelectric element. From the results derived in Chapter 2, the total deflection of the piston/piezoelectric cylinder is given by:

$$\Delta x_p = \frac{1}{2} \sigma_d L_p (s_{33}^E + s_{33}^D) \quad (3.31)$$

Using equations 5.31, 3.29, 3.30, and 3.31, the required flowrate for a given power requirement and maximum chamber pressure can be derived as follows:

$$Q = \frac{2(s_{33}^E + s_{33}^D)W}{(s_{33}^E - s_{33}^D)P_{HPR}} + C_{eff} P_{HPR} f \quad (3.32)$$

The first term in equation 3.32 corresponds to the flowrate which is required just to move the piston. The second term corresponds to the additional flowrate required due to the chamber compliance. If we consider the ideal case, where the chamber is not compliant, i.e  $C_{eff} = 0$ , the minimum required flowrate is given by

$$Q_{\min} = \frac{2(s_{33}^E + s_{33}^D)W}{(s_{33}^E - s_{33}^D)P_{HPR}} \quad (3.33)$$

In order to evaluate the performance of the energy harvesting chamber, we can define the efficiency of the chamber as follows:

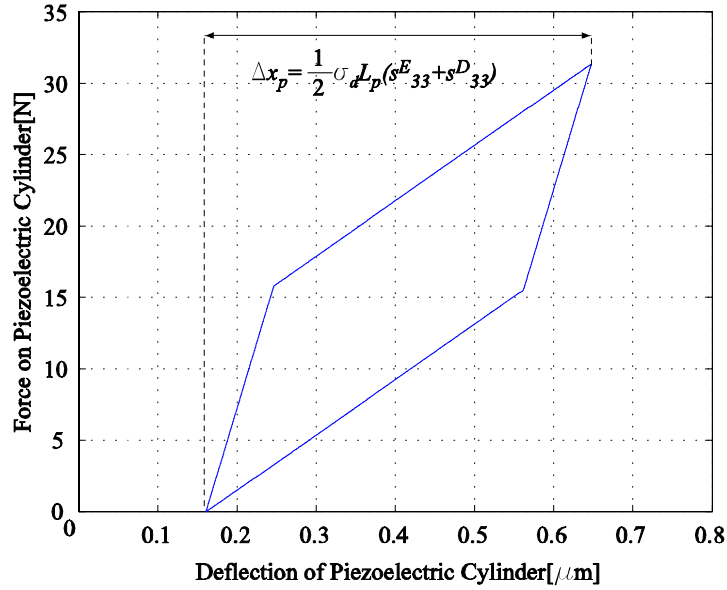


Figure 3-8: Force vs. displacement curve of the piezoelectric element from the simulation of the harvesting chamber attached to the full bridge rectifier.

$$\eta_{ch} = \frac{\text{Electrical Power Out}}{\text{Hydraulic Power In}} = \frac{W}{QP_{HPR}} \quad (3.34)$$

In the extreme case, where the effective chamber compliance is zero, the efficiency has its maximum value, which can be obtained from equations 3.32 and 3.34 as:

$$\eta_{ch \max} = \frac{(s_{33}^E - s_{33}^D)}{2(s_{33}^E + s_{33}^D)} = \frac{k_{33}^2}{4 - 2k_{33}^2} \quad (3.35)$$

It is interesting to note that the maximum efficiency of the chamber depends only on the coupling coefficient of the piezoelectric material. This suggests that, regardless of the geometry and operation conditions, the above expression puts an upper bound on the system efficiency, which is only a function of the piezoelectric element chosen. It is important to note that the above definition of the efficiency corresponds only to the energy harvesting chamber. If the overall system is considered, the electrical power consumption in the active valves should be taken into consideration.

### 3.4.2 Energy Harvesting Chamber and Full Bridge Rectifier with Voltage Detector Circuit

This section presents the simulation and analysis of the Energy Harvesting Chamber attached to the full bridge rectifier and voltage detector circuit. The geometry and the operation conditions are the same as in the previous section. The time histories of the chamber pressure, flowrate and piston deflection are shown in Figure 3-9.

It is interesting to note that there are sudden pressure drops inside the chamber and the time histories of the chamber pressure and the piston deflection are quite different from the time histories presented in the previous section. The most important observation is that during the periods when the switch is on, the pressure decreases/increases suddenly because the fluid cannot fill/evacuate the chamber immediately due to the fluid inertia of the fluid in the channels. In order to understand the interaction between the hydraulic/mechanical system and the circuit, and its implications on flowrate and frequency requirements for a given power, we can investigate the force vs. displacement plot of the piezoelectric element which is shown in Figure 3-10.

In Figure 3-10, the force vs. displacement curve of the piezoelectric element for this case is compared to the chamber attached to full bridge rectifier and to the case where the force is imposed on the piezoelectric element attached to the regular diode bridge and voltage detector. It is interesting to note that the new curve is much different than the imposed force case. In the latter case, which was discussed in Chapter 2, during the interval when the switch is on, the force is almost constant, and the portion of the curve corresponding to that period is almost flat. However, for the chamber, during the interval when the switch is on, the piezo becomes very soft, and the piston moves up or down very rapidly, which causes sudden pressure drops/rises inside the chamber, as can be seen in Figure 3-9. In order to analyze the behavior of the system, we can divide the time history into four periods, as shown in Figure 3-11.

In the periods 1-2 and 3-4 the piezoelectric element is open circuited, and the deflections at the states 1 and 3 correspond to the deflection as if the material was short circuited and the same force as in 1 and 3 was applied. In other words,  $F_1, F_3, x_1$ , and  $x_3$  should satisfy the following equations.

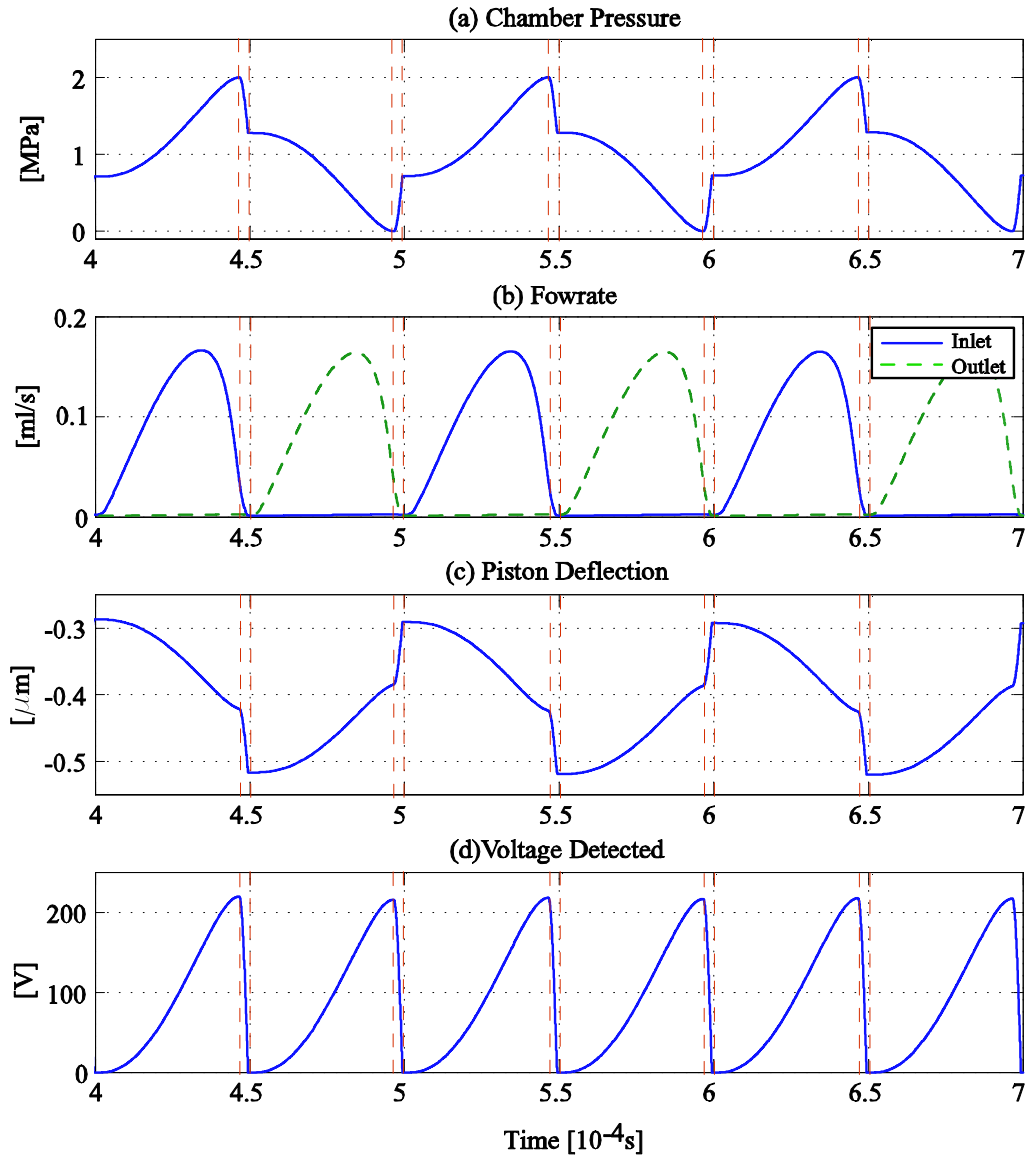


Figure 3-9: Simulation of the energy harvesting chamber attached to the full bridge rectifier and voltage detector circuit. The time intervals between the dashed lines present the intervals where the switch(SCR) is in its "on" state.

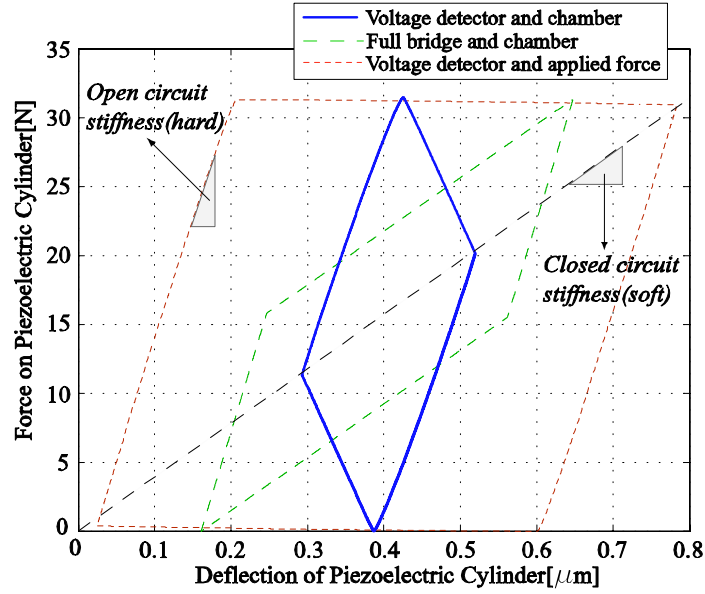


Figure 3-10: Force vs. displacement curve of the piezoelectric element from the simulation of the energy harvesting chamber attached to the full bridge rectifier and voltage detector circuit.

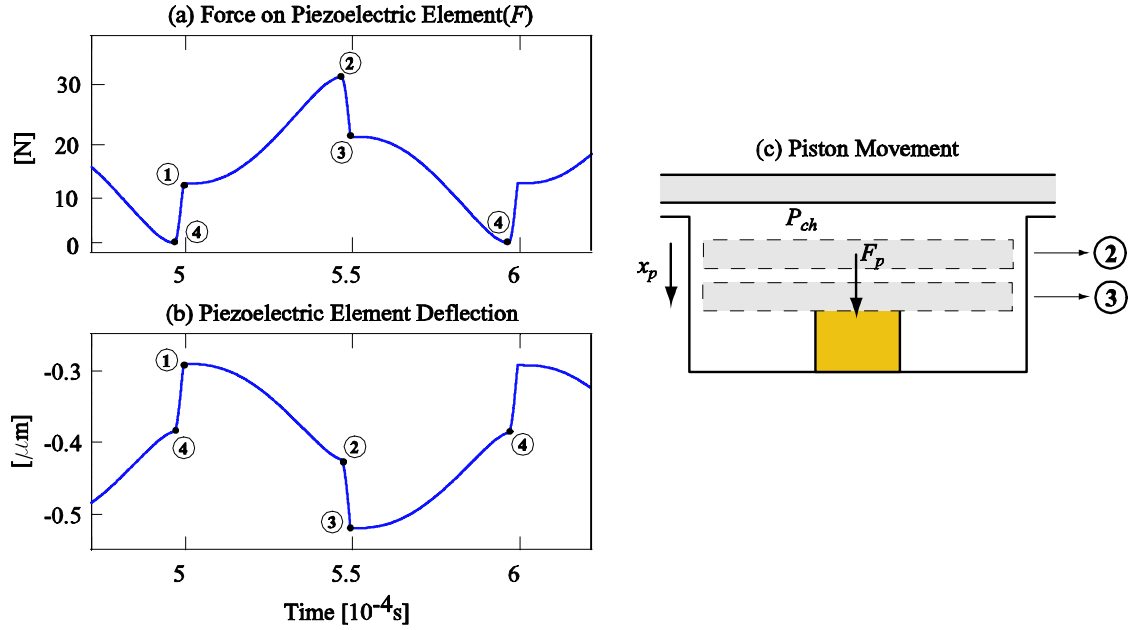


Figure 3-11: Time histories of the force and deflection of the piezoelectric element.

$$x_1 = F_1 \frac{s_{33}^E L_p}{A_p} \quad (3.36)$$

$$x_3 = F_3 \frac{s_{33}^E L_p}{A_p} \quad (3.37)$$

Since in the periods 1-2 and 3-4 the piezoelectric element is open circuited, the slope of the force vs deflection curve in these periods is simply the open circuit stiffness of the piezoelectric element and the following equations should be satisfied.

$$F_2 - F_1 = \frac{A_p}{s_{33}^D L_p} (x_2 - x_1) \quad (3.38)$$

$$F_3 - F_4 = \frac{A_p}{s_{33}^D L_p} (x_3 - x_4) \quad (3.39)$$

In order to understand the behavior in the periods 2-3 and 4-1, let us consider the period 2-3. At state 2, the pressure is maximum and at state 3, the voltage on the piezoelectric element is zero. In the period 2-3, there is almost no flowrate, which suggests that the pressure change in the chamber in this period, which is the sudden pressure drop, is only because of the volume change due to piston movement. In other words, the pressures at states 2 and 3 should satisfy the following equation.

$$P_2 - P_3 = (x_3 - x_2) \frac{A_{pis}}{C_{eff}} \quad (3.40)$$

where

$$P = \frac{F}{A_{pis}} \quad (3.41)$$

From equations 3.40 and 3.41, we can write:

$$F_2 - F_3 = (x_3 - x_2) \frac{(A_{pis})^2}{C_{eff}} \quad (3.42)$$

Similarly for the period 4-1, we can write:

$$F_1 - F_4 = (x_4 - x_1) \frac{(A_{pis})^2}{C_{eff}} \quad (3.43)$$

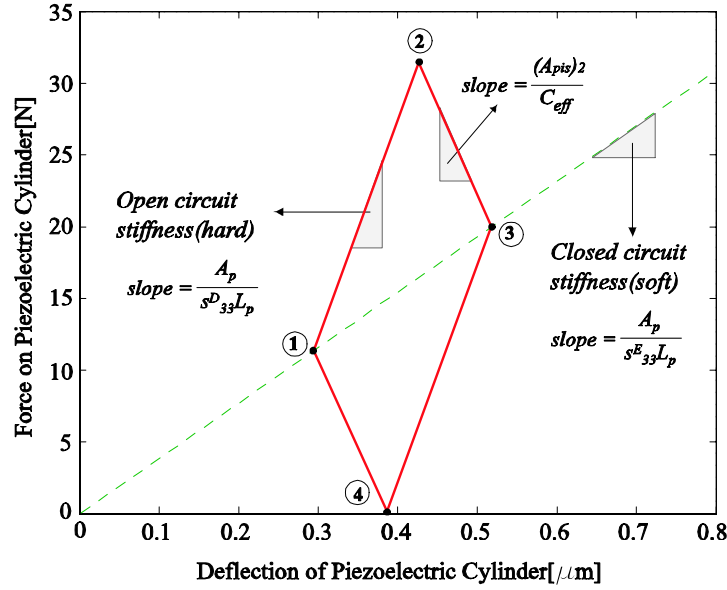


Figure 3-12: Force vs. displacement curve of the piezoelectric element and slopes at different periods of operations.

We also know that:

$$F_2 = \sigma_d A_p \quad \text{and} \quad F_4 = 0 \quad (3.44)$$

where  $\sigma_d$  is the depolarization stress of the piezoelectric element.

By solving equations 3.36, 3.37, 3.38, 3.39, 3.42, 3.43, and 3.44 we can determine the coordinates of the force vs. deflection curve of the piezoelectric element and we can also calculate the electrical energy stored per cycle, which is the area enclosed by the force vs. deflection curve, the effective coupling factor and system efficiency in terms of chamber geometry, piezoelectric cylinder geometry, chamber compliance and maximum pressure inside the chamber. The force vs. displacement curve of the piezoelectric element and the slopes of the curve at different periods are shown in Figure 3-12. It is interesting to note that in this case, the force vs. deflection curve depends on the chamber compliance, whereas in the case of the energy harvesting chamber attached to the full bridge rectifier, the slopes were determined only by the piezoelectric material geometry and properties.



The coordinates of the force vs displacement curve are as follows:

$$(x_1, F_1) = \left( \frac{\sigma_d A_{pis}^2 L_p^2 s_{33}^E (s_{33}^E - s_{33}^D)}{C_{eff} A_p + A_{pis}^2 L_p (2s_{33}^E - s_{33}^D)}, \frac{\sigma_d A_{pis}^2 L_p A_p (s_{33}^E - s_{33}^D)}{C_{eff} A_p + A_{pis}^2 L_p (2s_{33}^E - s_{33}^D)} \right) \quad (3.45)$$

$$(x_2, F_2) = \left( \frac{\sigma_d L_p^2 (s_{33}^E)^2 A_{pis}^2 + \sigma_d C_{eff} L_p A_p s_{33}^D}{C_{eff} A_p + A_{pis}^2 L_p (2s_{33}^E - s_{33}^D)}, \sigma_d A_p \right) \quad (3.46)$$

$$(x_3, F_3) = \left( \frac{\sigma_d L_p^2 (s_{33}^E)^2 A_{pis}^2 + \sigma_d C_{eff} L_p A_p s_{33}^E}{C_{eff} A_p + A_{pis}^2 L_p (2s_{33}^E - s_{33}^D)}, \frac{\sigma_d A_p L_p A_{pis}^2 s_{33}^E + \sigma_d C_{eff} A_p^2}{C_{eff} A_p + A_{pis}^2 L_p (2s_{33}^E - s_{33}^D)} \right) \quad (3.47)$$

$$(x_4, F_4) = \left( \frac{(\sigma_d s_{33}^E A_{pis}^2 L_p^2 + \sigma_d C_{eff} L_p A_p)(s_{33}^E - s_{33}^D)}{C_{eff} A_p + A_{pis}^2 L_p (2s_{33}^E - s_{33}^D)}, 0 \right) \quad (3.48)$$

Using the coordinates of the points given in the above equations, electrical energy stored per cycle can be calculated as:

$$E = \frac{\sigma_d^2 L_p A_p (s_{33}^E - s_{33}^D) (A_p C_{eff} + s_{33}^E A_{pis}^2 L_p) (A_p C_{eff} + s_{33}^D A_{pis}^2 L_p)}{[A_{pis}^2 L_p (2s_{33}^E - s_{33}^D) + C_{eff} A_p]^2} \quad (3.49)$$

From equation 5.31 we can write the expression for the flowrate as:

$$Q_{ave} = A_{pis} (x_3 - x_1) f + C_{eff} P_{HPR} f \quad (3.50)$$

For a given power requirement  $W$ , we can determine the required frequency using:

$$f = \frac{W}{E} \quad (3.51)$$

The required flowrate for a given power requirement can be derived from equations 3.45, 3.47, 3.49, 3.50, and 3.51 as:

$$Q_{ave} = \frac{W [s_{33}^E C_{eff} P_{HPR}^2 + \sigma_d^2 L_p A_p s_{33}^E (2s_{33}^E - s_{33}^D)]}{P_{HPR} (C_{eff} P_{HPR}^2 + \sigma_d^2 L_p A_p s_{33}^E) (s_{33}^E - s_{33}^D)} + \frac{W P_{HPR} C_{eff} [C_{eff} P_{HPR}^2 + \sigma_d^2 L_p A_p (2s_{33}^E - s_{33}^D)]^2}{\sigma_d^2 A_p L_p (s_{33}^E - s_{33}^D) (C_{eff} P_{HPR}^2 + \sigma_d^2 L_p A_p s_{33}^E) (C_{eff} P_{HPR}^2 + \sigma_d^2 L_p A_p s_{33}^D)} \quad (3.52)$$

In the extreme case where the effective chamber compliance is zero, namely  $C_{eff} = 0$ , the

expression for the required flowrate simply reduces to

$$Q_{\min} = \frac{(2s_{33}^E - s_{33}^D)W}{(s_{33}^E - s_{33}^D)P_{HPR}} \quad (3.53)$$

From the above expression we can get the maximum system efficiency using the definition given in equation 3.34 as

$$\eta_{ch \max} = \frac{(s_{33}^E - s_{33}^D)}{(2s_{33}^E - s_{33}^D)} = \frac{k_{33}^2}{1 + k_{33}^2} \quad (3.54)$$

where, as in the previous section, the maximum efficiency depends only on the coupling coefficient of the piezoelectric material.

Figure 3-13 shows the force vs. deflection curve of the piezoelectric element for different values of chamber compliance. It is interesting to note that, as the chamber compliance increases, the curve approaches the curve for the case where the force is imposed. One might think that having large compliance would have a positive effect on system performance, since the area inside the curve, which is the electrical energy stored per cycle, increases with increasing compliance. For a given power requirement lower frequencies and lower flowrates would be required. However, as the compliance increases, the required flowrate increases dramatically due to the second term in equation 3.50. This effect overwhelms the effect of decreased flowrate due to lower frequency requirement and the maximum system efficiency occurs again for the case where the chamber compliance is zero. The two extreme cases, namely  $C_{eff} = 0$  and  $C_{eff} = \infty$  are shown in Figure 3-13 (b).

The effective coupling factor from mechanical to electrical energy was defined in Chapter 2 and the expressions were derived for different circuits for the imposed force case. For the case of the energy harvesting chamber attached to the full bridge rectifier, the effective coupling factor is the same as the one for the imposed force case since for the full bridge rectifier, the force vs. displacement curve doesn't depend on the time history of the force on the piezoelectric element. However, it was found that, the force vs. displacement curve for full bridge rectifier and voltage detector depends on the time history of the force on the piezoelectric element, and in this case the curve depends on the chamber compliance. The effective coupling factor was defined in Chapter 2. From Figure 3-13 we can write:

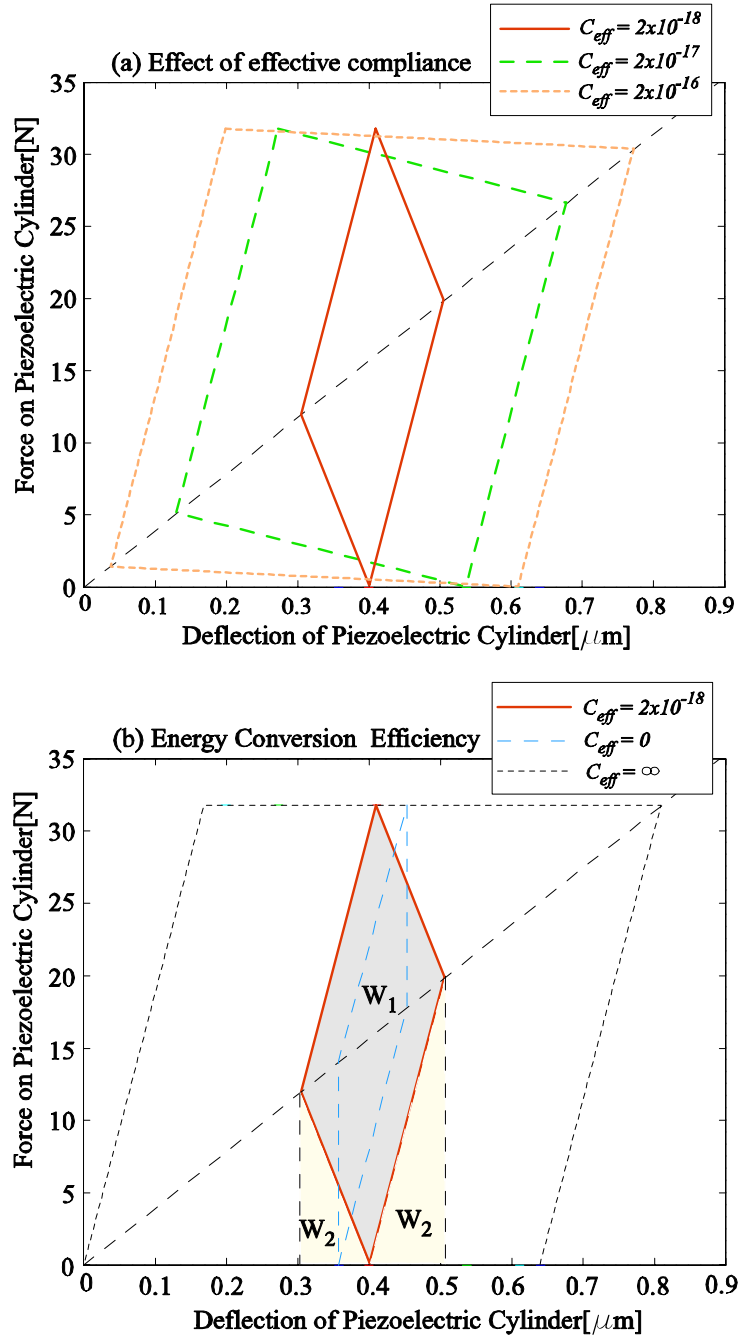


Figure 3-13: The effect of effective chamber compliance on force vs. deflection curve and effective coupling factor.

$$k_{eff}^2 = \frac{W_1}{W_1 + W_2} \quad (3.55)$$

The effective coupling factor can be calculated using the coordinates of the force vs. deflection curve. For the case where the effective chamber compliance is infinity, the effective coupling factor is:

$$C_{eff} = \infty \rightarrow k_{eff}^2 = \frac{2(s_{33}^E - s_{33}^D)}{2s_{33}^E - s_{33}^D} \quad (3.56)$$

for which case the electrical energy stored per cycle is:

$$E_{(C_{eff}=\infty)} = (s_{33}^E - s_{33}^D)\sigma_d^2 A_p L_p \quad (3.57)$$

which is the same amount of energy stored for the case of imposed force on piezoelectric element with the same circuitry.

For the case where the effective chamber compliance is zero, the effective coupling factor becomes:

$$C_{eff} = 0 \rightarrow k_{eff}^2 = \frac{2(s_{33}^E - s_{33}^D)}{3s_{33}^E - 2s_{33}^D} \quad (3.58)$$

for which case the electrical energy stored per cycle is:

$$E_{(C_{eff}=0)} = \frac{\sigma_d^2 A_p L_p (s_{33}^E - s_{33}^D) s_{33}^E s_{33}^D}{(2s_{33}^E - s_{33}^D)^2} \quad (3.59)$$

### 3.5 Discussion

This section presents a comparison of circuitry and piezoelectric materials in terms of their effect on important performance metrics such as flowrate, frequency and efficiency using the results obtained in previous sections of this chapter. Let us consider the system analyzed in Section 3.4, for which the geometric parameters were given in Table 3.2. Now, however, the effective chamber compliance will be varied and its effect on system performance will be investigated. This could be accomplished, for example, by changing the thicknesses of the structural members or by changing the chamber height. For a power requirement of  $0.5W$ , the required frequency

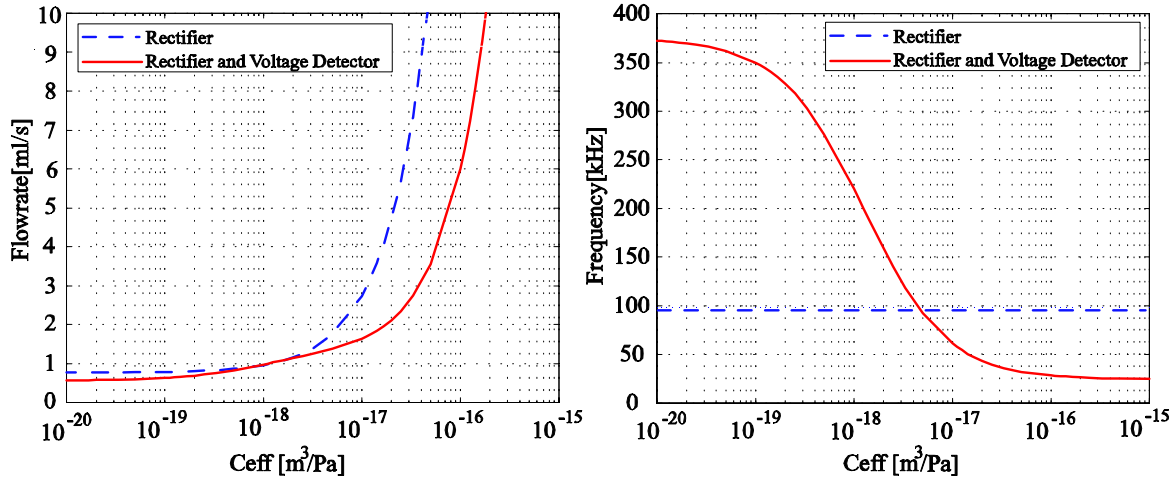


Figure 3-14: Flowrate and frequency requirement for 0.5 W power requirement.

and flowrate is plotted as a function of effective chamber compliance in Figure 3-14. It can be noted from Figure 3-14 that the frequency requirement for the full bridge rectifier case does not depend on effective chamber compliance since the force vs. displacement graph is the same for any chamber compliance and the energy stored per cycle depends only on the maximum stress on the piezoelectric element and piezoelectric material properties. However, since the force vs. displacement curve for the rectifier with voltage detector case depends heavily on the effective chamber compliance, the electrical energy stored per cycle depends on the compliance. So, for a given power requirement, the required frequency depends on the effective compliance as well. In terms of flowrate requirement, it can be easily seen that, as the system gets more compliant, the required flowrate increases dramatically. It should be pointed out that, for a microfluidic device, even flowrates on the order of  $1\text{ml/s}$  can be considered very high, and special high performance microvalves are needed. It is obvious that, prediction of the effective chamber compliance will constitute a crucial part of the modelling and design process. This will be addressed in Chapter 4.

The system efficiency, which was defined in equation 3.34 is plotted as a function of the effective chamber compliance in Figure 3-15. It can be noted that, as the effective chamber compliance gets smaller and smaller, in other words, as the chamber gets less and less compliant, the efficiency values approach their maximum values which were given in equations 3.35 and

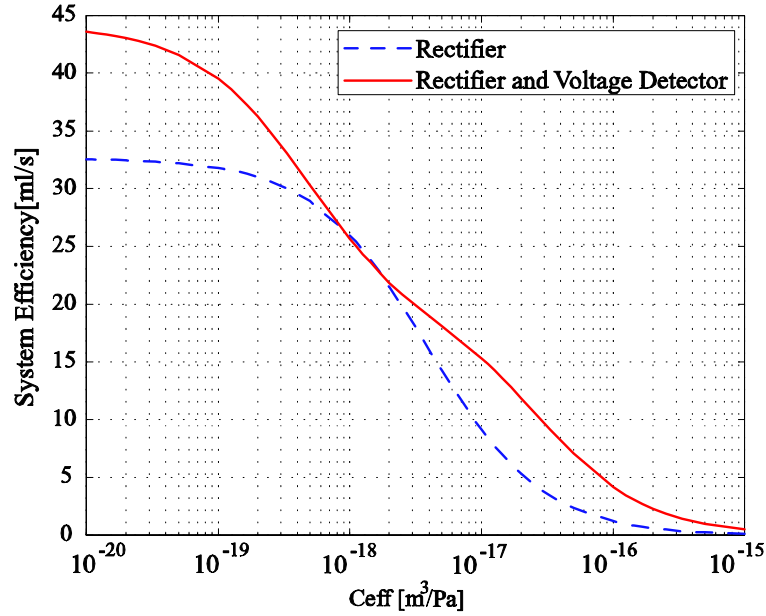


Figure 3-15: System efficiency as a function of the effective chamber compliance.

3.54 for the rectifier and rectifier and voltage detector circuit cases respectively. As mentioned earlier, these maximum efficiency values depend only on the piezoelectric material used.

Using the relations derived in previous sections, we can also compare different piezoelectric materials in terms of flowrate and frequency requirements and system efficiency. Again, let's consider the same system for the  $0.5W$  power requirement. Figure 3-16 shows the required flowrates for different piezoelectric materials and different circuitry as a function of effective chamber compliance. It should be noted that for each piezoelectric material, the piezo diameter,  $D_p$ , is adjusted such that at the maximum chamber pressure, the stress on the piezoelectric element is equal to its depolarization stress,  $\sigma_d$ . The required flowrates for the rectifier circuit with voltage detector are significantly less than the case with just the rectifier. It can be also observed that PZN-PT requires the least flowrate and PZT-8 requires the most flowrate at low compliance values.

The required frequencies for different piezoelectric materials are shown in Figure 3-17. As mentioned earlier the required operation frequency in the case of rectifier circuit is constant, regardless of the effective chamber compliance. Since the force vs. displacement curve in the

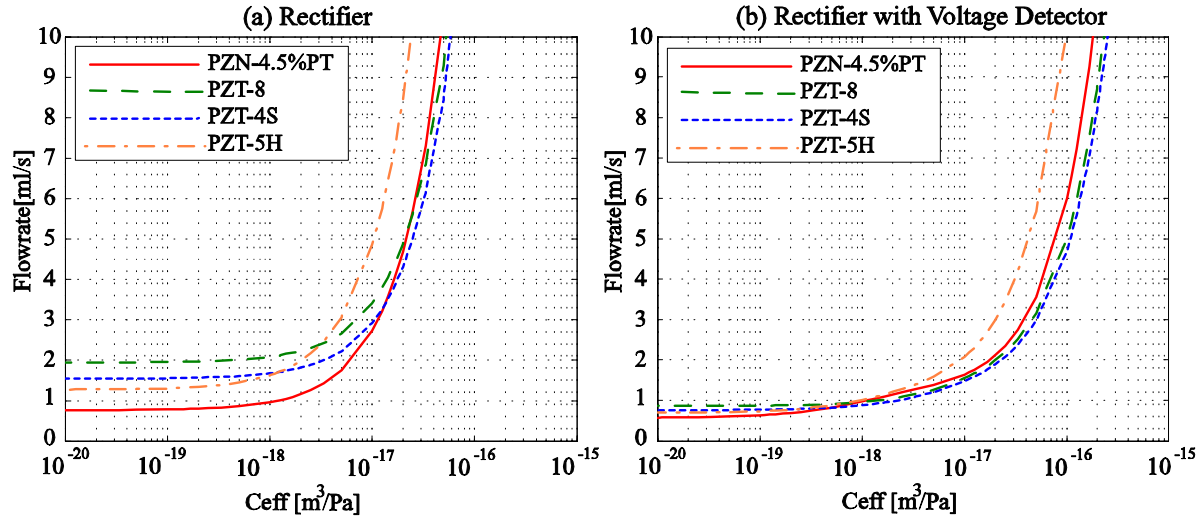


Figure 3-16: Required flowrates for 0.5 power generation. Comparison of different piezoelectric elements and different circuitry.

case of the rectifier and voltage detection circuit depends heavily on the effective chamber compliance, the required frequency for a certain power requirement depends on the effective chamber compliance. Since the materials PZT-8 and PZT-4S have very high depolarization stresses compared to PZT-5H and PZN-PT, the electrical energy stored per cycle for PZT-8 and PZT-4S is much larger, which means reduced frequency requirements for the same power requirement. For example, although PZN-PT has the highest coupling coefficient ( $k_{33} = 0.89$ ) among the piezoelectric materials discussed here, it requires higher operation frequencies due to its low depolarization stress.

Figure 3-18 shows the system efficiency for different piezoelectric materials and circuitry. It can be seen that, the chamber with the rectifier circuit and voltage detector is more efficient than the case with the rectifier. As the effective compliance gets smaller and smaller, the system efficiencies approach their maximum value, which are given by equations 3.35 and 3.54 for rectifier and rectifier with voltage detector cases respectively. As expected, PZN-PT is the most efficient material due to its high coupling coefficient ( $k_{33} = 0.89$ ) and PZT-8 is the least efficient material due to its low coupling coefficient ( $k_{33} = 0.64$ ). Although PZT-8 is the least efficient one, it might be a better suited material since the system with PZN-PT has very high

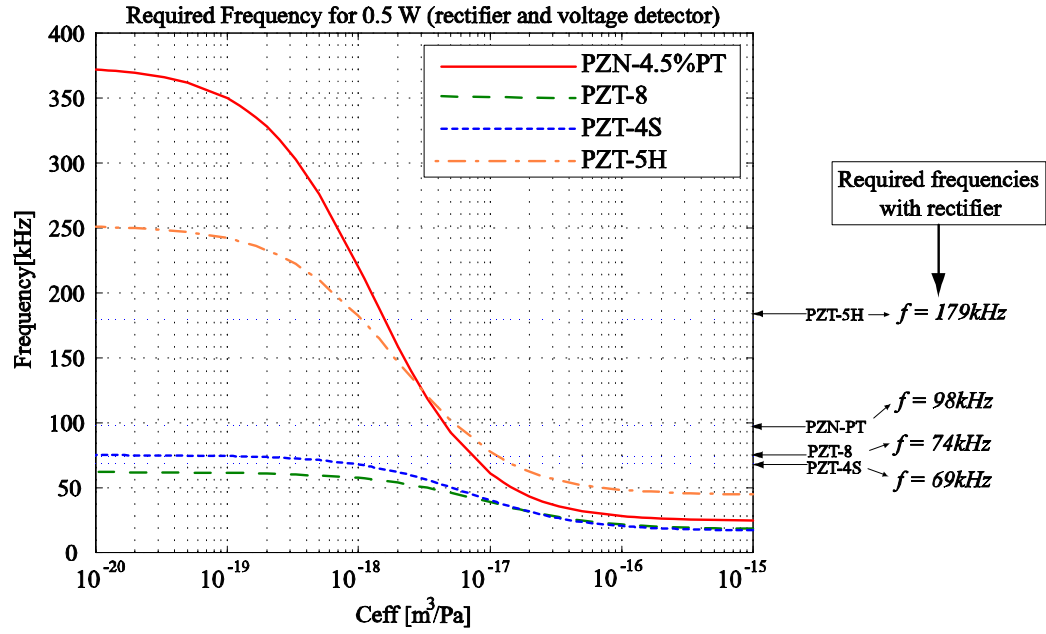


Figure 3-17: Required frequencies for the 0.5W power requirement. Comparison of different piezoelectric materials and circuitry. Note that the required frequency in the case of regular rectifier is independent of the chamber compliance.



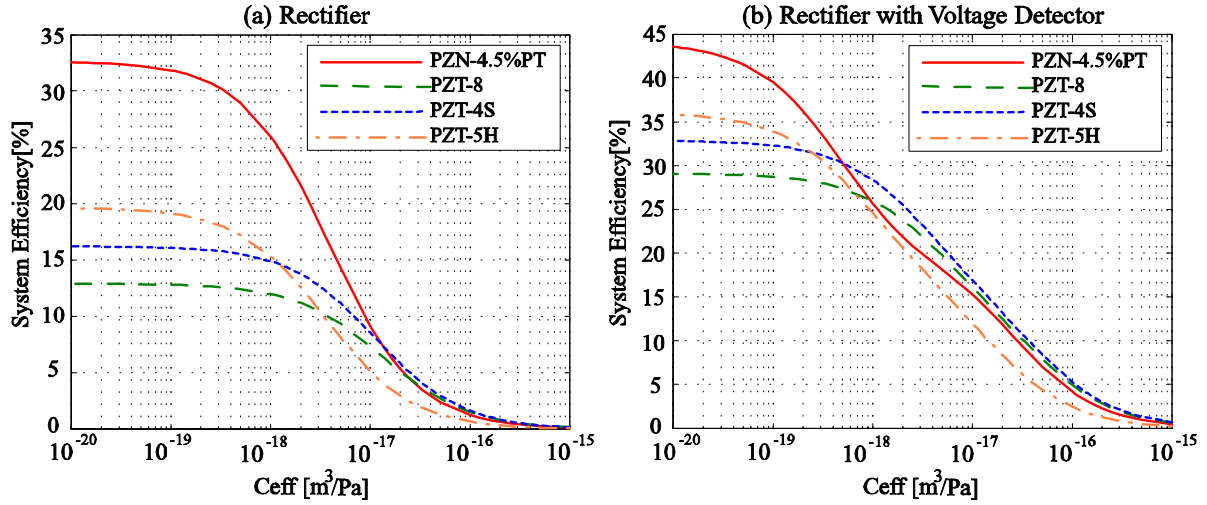


Figure 3-18: Comparison of different piezoelectric materials and circuitry in terms of system efficiency.

frequency requirements. The material selection process should address the design trade-offs and should take the remaining components of the system, for example the active valves, into consideration. One might choose to use PZN-PT which requires very high frequencies, but this frequency can exceed the bandwidth of the active valves. This issue will be addressed in Chapter 5.

One should remember that the analysis of the chamber attached to the rectifier and the voltage detector presented in this chapter assumed that the impedances(inductances) of the fluid channels are large enough such that there are sudden pressure drops inside the chamber and the governing equations are derived assuming that in the time interval where the SCR is in its "on" state, there is no net flowrate into the chamber.

### 3.6 Summary and Conclusion

This chapter presented a simple analysis of the energy harvesting chamber and a case study using a simulation for a predetermined chamber geometry and operating conditions. The interaction between the chamber and the circuitry has been investigated. Some of the important performance metrics derived in the previous sections are summarized in Table 3.3.

	Rectifier	Rectifier+Voltage Detector
Effective Coupling Factor	$k_{eff}^2 = \frac{2k_{33}^2}{k_{33}^2 + 2}$	$k_{eff(C_{eff}=0)}^2 = \frac{2k_{33}^2}{2k_{33}^2 + 1}$
Minimum Required Flowrate	$Q_{\min} = \frac{(4 - 2k_{33}^2)W}{k_{33}^2 P_{HPR}}$	$Q_{\min} = \frac{(1 + k_{33}^2)W}{k_{33}^2 P_{HPR}}$
Maximum System Efficiency	$\eta = \frac{k_{33}^2}{4 - 2k_{33}^2}$	$\eta = \frac{k_{33}^2}{1 + k_{33}^2}$

Table 3.3: Summary and comparison of circuitry in terms of performance indices

The first row summarizes the expressions obtained for the effective coupling factor for the two circuits analyzed in this chapter. The second expression in the first row represents the effective coupling factor for the rectifier with voltage detection circuit for the case where  $C_{eff} = 0$ , which corresponds to the most efficient operation condition for the energy harvesting chamber. However, maximum effective coupling factor for this circuit occurs when  $C_{eff} = \infty$ , which is the same as the effective coupling factor of the same circuit for the applied force case, which was presented in Chapter 2. The effective coupling factor for the full bridge rectifier case is the same regardless of the effective compliance of the energy harvesting chamber. The second row presents the minimum required flowrate for a given power requirement and maximum pressure in the chamber. The third row represent the maximum system efficiency. The second and third rows correspond to the case where  $C_{eff} = 0$ . As mentioned earlier, the maximum system efficiency of the energy harvesting chamber depends only on the piezoelectric material chosen, namely the coupling coefficient( $k_{33}$ ). The expressions are plotted as a function of the coupling coefficient in Figure 3-19. A comparison of different piezoelectric materials is also made on the same plot.

The expressions for the maximum system efficiency in Table 3.3 put an upper limit on the system efficiency. It is interesting to note that, at  $k_{33} = 1$  the two curves reach the same point, which is 50% efficiency. This means that, even with a perfect piezoelectric material( $k_{33} = 1$ ) and zero effective compliance, which are not possible, the system efficiency cannot exceed 50%.

The most important conclusion of this chapter is that the performance of the energy harvesting chamber depends on

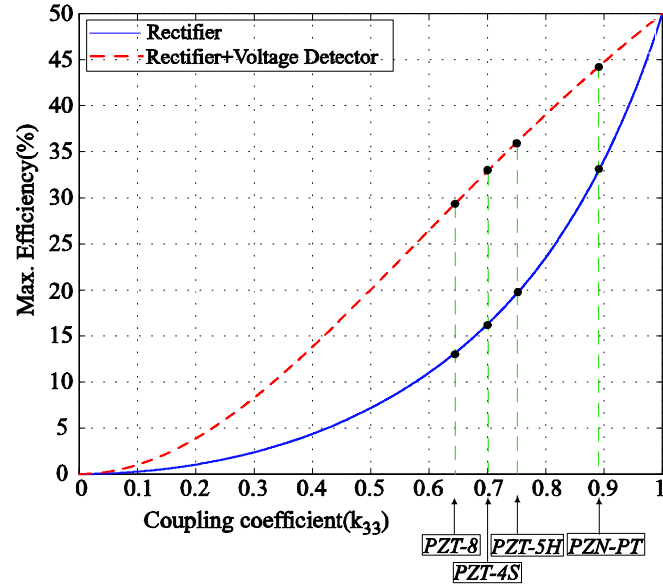


Figure 3-19: Maximum system efficiency(which corresponds to the case where the effective compliance of the chamber is zero)as a function of the coupling coefficient.

- Rectification circuit topology
- Piezoelectric material ( $k_{33}, \sigma_d$ )
- Chamber compliance( $C_{eff}$ )

Again it should be emphasized that the efficiency definition in this chapter corresponds only to the energy harvesting chamber. The electrical power consumption in the active valves is not considered.

## Chapter 4

# Detailed Model of the Energy Harvesting Chamber

This chapter presents the detailed modelling of the energy harvesting chamber. In Chapter 3, an effective chamber compliance ( $C_{eff}$ ) based on a typical MHT device was assumed to be used in the simulation and the effect of compliance on system performance was analyzed. This chapter investigates the contribution of different structural components on the effective compliance of the chamber. It also presents the simulation architecture used for integrating elastic equations into the system level simulation.

### 4.1 Analysis of a Simplified Chamber Structure

Consider a simple circular chamber structure consisting of a fluid chamber and rigid walls, except the top portion of the chamber, as shown in Figure 4-1. The compliant portion can be modeled as a clamped circular plate which deforms under the action of uniform pressure underneath. For small deflections, the deformation of the top plate can be assumed to be linear and can be analyzed using linear plate theory [50].

For a uniform pressure distribution  $P$  and a radius of  $a$ , the deflection of the top plate as a function of the radial distance is given as:

$$w(r) = \frac{P}{64D} (a^2 - r^2)^2 \quad (4.1)$$

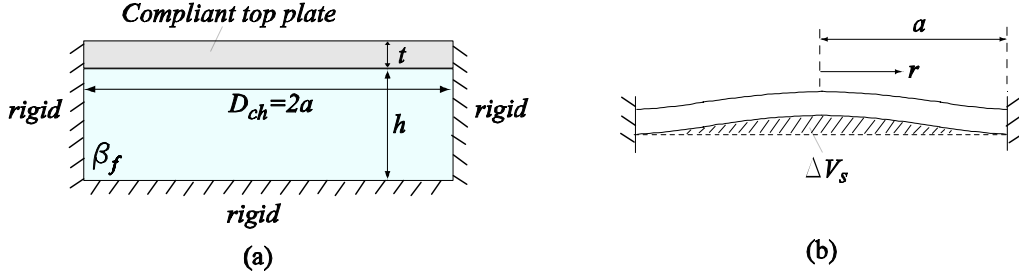


Figure 4-1: (a) Simplified chamber structure consisting of a fluid chamber with a compliant wall (b) Deformation of the top plate and swept volume.

where  $D$  is the flexural rigidity of the plate given by:

$$D = \frac{Et^3}{12(1 - \nu^2)} \quad (4.2)$$

where  $E$  and  $\nu$  is the Young Modulus and Poisson ratio of the material respectively, and  $t$  is the thickness of the plate. The additional volume created in the chamber due to the deformation of the plate can be calculated by integrating equation 4.1 over the plate:

$$\Delta V_s = \int_0^a w(r) 2\pi r dr = \frac{P\pi a^6(1 - \nu^2)}{16Et^3} \quad (4.3)$$

The structural compliance was defined in Chapter 3 as:

$$C_s = \frac{\Delta V_s}{\Delta P} \quad (4.4)$$

which represents the volume change of the chamber due to structural deformations in response to a change in chamber pressure. In this simple example, the top plate is the only compliant structural member. Using equations 4.4 and 4.3, the structural compliance can be calculated as:

$$C_s = \frac{\pi a^6(1 - \nu^2)}{16Et^3} \quad (4.5)$$

The effective chamber compliance can be obtained as:

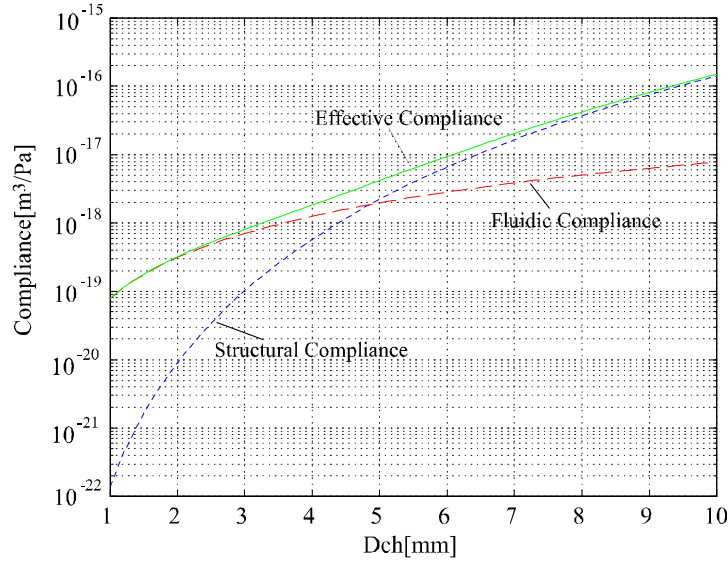


Figure 4-2: Comparison of fluidic and structural compliances for a generic chamber structure at different chamber diameters for fixed chamber height and top plate thickness.

$$C_{eff} = \left( \frac{V_o}{\beta_f} + C_s \right) = \left( \frac{\pi a^2 h}{\beta_f} + \frac{\pi a^6 (1 - \nu^2)}{16 E t^3} \right) \quad (4.6)$$

where  $V_o$  is the initial fluid volume inside the chamber,  $\beta_f$  is the bulk modulus of the fluid and  $h$  is the height of the chamber.

Consider a chamber with top plate thickness of  $500\mu m$  and chamber height of  $200\mu m$ . Figure 4-2 shows a comparison of fluidic and structural compliances for different chamber diameters. It can be seen that, for small chamber diameters, the compliance of the chamber is dominated by the fluidic compliance, whereas at large chamber diameters the structural compliance dominates. However, it should be noted that, if all the geometric parameters are scaled the same amount, the ratio of the fluidic and structural compliances will remain the same. This issue will be discussed further in Chapter 5.

## 4.2 Detailed Analysis of Structural Components

A simplified chamber structure consisting of a compliant top plate and a fluidic chamber has been analyzed in the previous section. This section will present detailed analysis of individual structural compliances of the energy harvesting chamber which will include the deformation of the top and bottom support structures, deformation of the piston and bending of the tethers. Figure 4-3 shows geometric parameters of the structural components, corresponding deformations and the free body diagrams which will be used in the formulations of the governing equations.

These deformations inside the energy harvesting chamber can be adequately represented by the linear plate theory [50]. Each component will be modeled as a plate with applied loading and boundary conditions to determine the deflections and swept volumes. In general, a symmetrically loaded circular plate will experience deflections due to bending as well as shearing. If the plate thickness is small compared to the plate outer radius, the deflection due to bending will be significantly larger than that due to shearing. Since the radii of the structural components analyzed are larger than the corresponding thicknesses, deformations only due to bending will be considered.

### 4.2.1 Top Support Structure

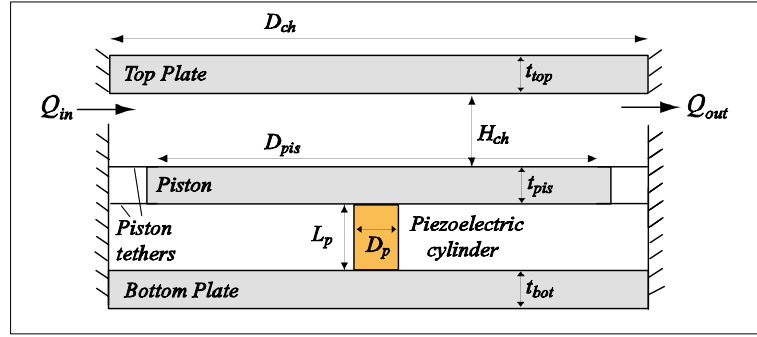
The top support structure is modeled as a clamped circular plate which deforms under the action of a uniform pressure distribution underneath. The governing differential equation for the symmetrical bending of a circular plate is given as:

$$\frac{d}{dr} \left[ \frac{1}{r} \frac{d}{dr} \left( r \frac{dw(r)}{dr} \right) \right] = \frac{Q(r)}{D} \quad (4.7)$$

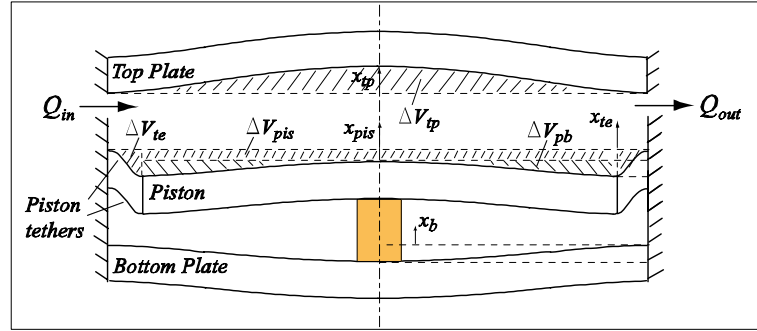
where  $D$  is the flexural rigidity given in equation 4.2,  $w(r)$  is the deflection of the plate, and  $Q(r)$  is the shear force per unit length. For a uniformly loaded circular plate the shear force per unit length is given as:

$$Q(r) = \frac{P_{ch}r}{2} \quad (4.8)$$

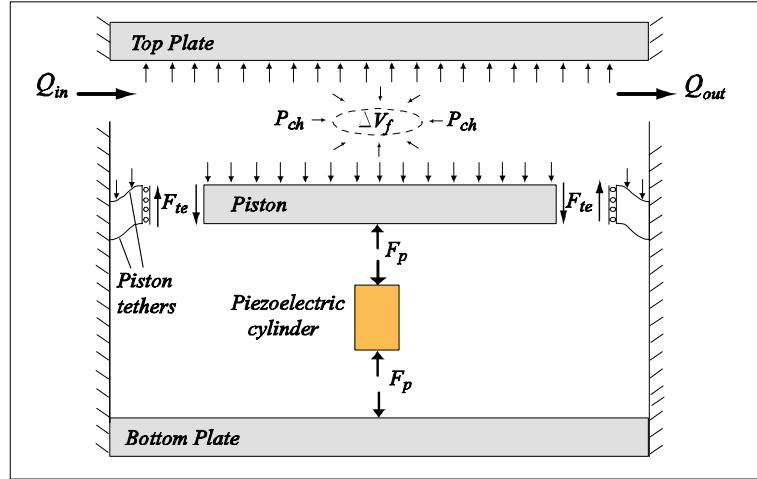
where  $P$  is the pressure. The boundary conditions are:



(a)



(b)



(c)

Figure 4-3: (a) Schematic illustrating the dimensional parameters of the chamber, (b) deformation of structural components and sign conventions, (c) free body diagrams and sign conventions. Deflections are exaggerated.



$$w(r = a) = 0 \quad (4.9)$$

$$\frac{dw}{dr}(r = a) = 0 \quad (4.10)$$

$$\frac{dw}{dr}(r = 0) = 0 \quad (4.11)$$

By integrating the governing differential equation and applying the boundary conditions, the deflection of the plate  $w(r)$  can be determined as:

$$w(r) = \frac{P_{ch}}{64D} (a^2 - r^2)^2 \quad (4.12)$$

The deflection of the midpoint of the top support structure can be obtained by calculating the deflection of the top plate at  $r = 0$  :

$$x_{tp} = \frac{3P_{ch}a^4(1 - \nu^2)}{16Et^3} = k_{dtp}P_{ch} \quad (4.13)$$

where  $k_{dtp}$  depends only on the chamber diameter and the top plate thickness.

The corresponding swept volume can be calculated by integrating equation 4.12 over the plate as:

$$\Delta V_{tp} = \int_0^a w(r)2\pi r dr = \frac{P_{ch}\pi a^6(1 - \nu^2)}{16Et^3} = k_{tp}P_{ch} \quad (4.14)$$

where  $k_{tp}$  depends only on the chamber diameter and the top plate thickness.

Equations 4.12 and 4.14 are the same equations used in the previous section.

### 4.2.2 Bottom Support Structure

A rigid bottom structure beneath the piezoelectric element would ensure that all of the deflection of the piston goes into the compression of the piezoelectric element. In reality, this structure is not rigid and as a result this bottom structure deformation results in less compression of the piezoelectric element at a given chamber pressure.

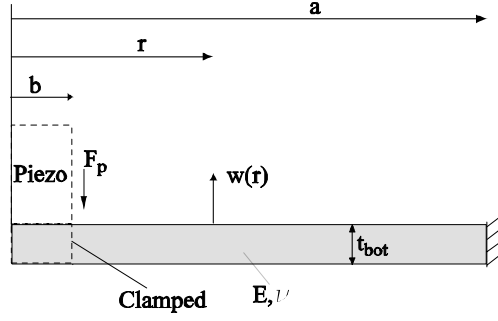


Figure 4-4: Model of the bottom support structure: circular plate with a circular hole at its center with guided boundary condition at inner radius  $b$  and clamped boundary condition at outer radius  $a$ .

The bottom support structure is modeled as a circular plate with a circular hole at the center which is clamped at its outer radius ( $r = a$ ) and guided at its inner radius ( $r = b$ ), shown in Figure 4-4. In this case the shear force per unit length is given as:

$$Q(r) = \frac{-F_p}{2\pi r} \quad (4.15)$$

where  $F_p$  is the force acting on the bottom support structure through the guided support in the inner radius ( $r = b$ ). The boundary conditions are:

$$w(r = a) = 0 \quad (4.16)$$

$$\frac{dw}{dr}(r = a) = 0 \quad (4.17)$$

$$\frac{dw}{dr}(r = b) = 0 \quad (4.18)$$

The deflection of the bottom plate,  $x_b$ , can be calculated by integrating equation 4.7 and applying the boundary conditions to obtain:

$$x_b = k_b F_p \quad (4.19)$$

where  $k_b$  is the stiffness of the bottom plate which depends on the thickness of the bottom plate,  $t_{bot}$ , inner radius ( $b = D_p/2$ ), and outer radius ( $a = D_{ch}/2$ ).

### 4.2.3 Piston

The piston is modeled as a circular plate with a circular hole at the center which is simply supported at its outer radius ( $r = a$ ) assuming that the tethers exert insignificant bending moments on the piston at its outer radius, and guided at its inner radius ( $r = b$ ), shown in Figure 4-5. In this case the shear force per unit length is given as:

$$Q(r) = \frac{F_p}{2\pi r} - \frac{P_{ch}r}{2} \quad (4.20)$$

where  $F_p$  is the force acting on the piston through the guided support in the inner radius ( $r = b$ ).

The boundary conditions are:

$$w(r = a) = 0 \quad (4.21)$$

$$M_r(r = a) = -D \left( \frac{d^2 w(r = a)}{dr^2} + \frac{\nu}{r} \frac{dw(r = a)}{dr} \right) = 0 \quad (4.22)$$

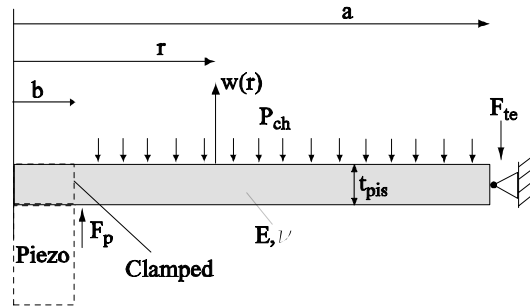


Figure 4-5: Model of the piston: circular plate with a circular hole at its center with guided boundary condition at inner radius b and clamped boundary condition at outer radius a.

$$\frac{dw}{dr}(r = b) = 0 \quad (4.23)$$

where  $M_r$  denotes the bending moment per unit length along circumferential sections of the plate. The deflection of the piston and the corresponding swept volume can be calculated by integrating equation 4.7 and applying the boundary conditions to obtain:

$$x_{pb} = x_{pis} - x_{te} = k_{p1}F_p + k_{p2}P_{ch} \quad (4.24)$$

$$\Delta V_{pb} = k_{p3}F_p + k_{p4}P_{ch} \quad (4.25)$$

where  $k_{p1}, k_{p2}, k_{p3}$ , and  $k_{p4}$  depend on the thickness of the piston,  $t_{pis}$ , inner radius ( $b = D_p/2$ ), and outer radius ( $a = D_{pis}/2$ ). The dynamics of the piston can be represented using the free body diagram in Figure 4-3 as:

$$M_{pis} \frac{d^2 x_{pis}}{dt^2} = -A_{pis}P_{ch} + F_p - F_{te} = F_{net} \quad (4.26)$$

#### 4.2.4 Piston Tethers

In this section, tethers corresponding to a double layer piston structure will be analyzed which consist of a top and bottom tether structure. In order to allow for flexibility in design, the top and bottom tethers are defined to have different thicknesses ( $t_{tetop}, t_{tobot}$ ). The top tether is modeled as a circular plate with a circular hole at the center which is clamped at its outer radius and guided at its inner radius, shown in Figure 4-6. It experiences a concentrated force,  $F_{tetop}$ , at its inner radius and a uniform pressure loading,  $P_{ch}$ . The shear force per unit length is given as:

$$Q(r) = \frac{F_{tetop}}{2\pi r} - \frac{P_{ch}(r^2 - b^2)}{2r} \quad (4.27)$$

The boundary conditions are:

$$w(r = a) = 0 \quad (4.28)$$

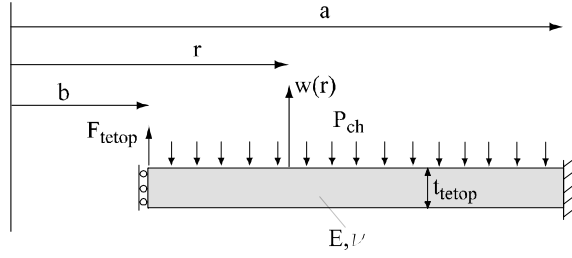


Figure 4-6: Model of the top tether: circular plate with a circular hole at its center with guided boundary condition at inner radius  $b$  and clamped boundary condition at outer radius  $a$ .

$$\frac{dw}{dr}(r = a) = 0 \quad (4.29)$$

$$\frac{dw}{dr}(r = b) = 0 \quad (4.30)$$

The deflection of the top tether and the corresponding swept volume can be calculated by integrating equation 4.7 and applying the boundary conditions to obtain:

$$x_{te} = k_{tt1}F_{tetop} + k_{tt2}P_{ch} \quad (4.31)$$

$$\Delta V_{te} = k_{tt3}F_{tetop} + k_{tt4}P_{ch} \quad (4.32)$$

where  $k_{tt1}$ ,  $k_{tt2}$ ,  $k_{tt3}$ , and,  $k_{tt4}$  depend on the thickness of the top tether,  $t_{tetop}$ , inner radius ( $b = D_{pis}/2$ ), and outer radius ( $a = D_{ch}/2$ ).

Since the tethers are much thinner than the support structures and the piston, it is important to consider the stress in the tethers and make sure that they don't exceed the critical value of  $1GPa$  [7]. For a circular plate subject to symmetrical bending, the two stress components can be calculated as:

$$\sigma_r = -\frac{6M_r}{h^2} \quad (4.33)$$

$$\sigma_t = -\frac{6M_t}{h^2} \quad (4.34)$$

where  $M_r$  and  $M_t$  are the bending moment per unit length along the circumferential sections of the plate and along the diametral section of the plate respectively, and  $h$  is the thickness of the plate. The bending moments are obtained as:

$$M_r = -D \left( \frac{d^2 w}{dr^2} + \frac{\nu}{r} \frac{dw}{dr} \right) \quad (4.35)$$

$$M_t = -D \left( \frac{1}{r} \frac{dw}{dr} + \nu \frac{d^2 w}{dr^2} \right) \quad (4.36)$$

where  $D$  is the flexural rigidity of the plate. Using the equations 4.33, 4.34, 4.35, 4.36, the stress components can be calculated after the governing plate equation 4.7 is integrated using appropriate boundary conditions and the deflection of the plate,  $w$ , is determined. As will be seen later in the next chapter,  $\sigma_r$  is generally bigger than  $\sigma_t$  and the maximum stress occurs at  $a = D_{ch}/2$ . Then we can write the maximum stress in the top tether as:

$$\sigma_{\max} = \sigma_{tt} = -\frac{6M_r(r = D_{ch}/2)}{t_{ttop}^2} \quad (4.37)$$

which can be alternatively expressed as:

$$\sigma_{tt} = s_{tt1}F_{ttop} + s_{tt2}P_{ch} \quad (4.38)$$

where  $s_{tt1}$  and  $s_{tt2}$  depend on the thickness of the top tether,  $t_{ttop}$ , inner radius ( $b = D_{pis}/2$ ), and outer radius ( $a = D_{ch}/2$ ).

The bottom tether is modeled in the same way as the top tether, except it experiences only a concentrated force,  $F_{tebot}$ , at its inner radius and no pressure loading. The shear force per unit length is:

$$Q(r) = \frac{F_{tebot}}{2\pi r} \quad (4.39)$$

The boundary conditions are the same as the boundary conditions for the top tether. The

deflection of the bottom tether, which is equal to the deflection of the top tether can be obtained by integrating equation 4.7 and applying the boundary conditions to obtain:

$$x_{te} = k_{tb}F_{tebot} \quad (4.40)$$

where  $k_{tb}$  depends on the thickness of the bottom tether,  $t_{tebot}$ , inner radius ( $b = D_{pis}/2$ ), and outer radius ( $a = D_{ch}/2$ ).

Similarly, the stress in the bottom tether can be calculated as:

$$\sigma_{tb} = s_{tb}F_{tebot} \quad (4.41)$$

where  $s_{tb}$  depends again on the thickness of the bottom tether,  $t_{tebot}$ , inner radius ( $b = D_{pis}/2$ ), and outer radius ( $a = D_{ch}/2$ )

We can also write:

$$F_{te} = F_{tetop} + F_{tebot} \quad (4.42)$$

which represents the force balance at the connection point of the tethers with the piston.

Detailed derivations of the elastic equations of the structural components are detailed in Appendix C.

### 4.3 Simulation Architecture

This section will present the simulation architecture used for integrating the elastic equations into the system level simulation.

#### Chamber Continuity

The continuity equation was derived in the previous chapter. In this section a more detailed equation will be derived considering the volume displaced in the chamber due to deformations of individual structural members. In the previous chapter, all the volume displaced by deformations was analyzed as a bulk value, namely  $\Delta V_s$ , and was used to define the structural compliance,  $C_s$ . Rewriting equation 3.5, we have:

$$\frac{dP_{ch}}{dt} = \frac{\beta_f}{V_o} \frac{dV}{dt} \quad (4.43)$$

where  $\beta_f$  is the bulk modulus of the fluid,  $V_o$  is the initial volume of the fluid inside the chamber and  $\frac{dV}{dt}$  is the rate of the volume change of the fluid. Sources of the volume change are net flowrate into the chamber, piston movement and additional volume created inside the chamber due to structural deformations. Considering these effects and integrating equation 4.43, we can write:

$$P_{ch} = \frac{\beta_f}{V_o} \left( \int_0^t (Q_{in} - Q_{out}) dt + \Delta V_{pis} + \Delta V_{pb} + \Delta V_{te} - \Delta V_{tp} \right) \quad (4.44)$$

where  $\Delta V_{pis}$ ,  $\Delta V_{pb}$ ,  $\Delta V_{te}$ ,  $\Delta V_{tp}$  represent the swept volume due to the motion of the piston, deformation of the piston, deformation of the top tether and deformation of the top support structure respectively. The swept volume due to the motion of the piston is simply equal to:

$$\Delta V_{pis} = x_{pis} A_{pis} \quad (4.45)$$

where  $A_{pis}$  is the area of the piston. By arranging equation 4.44 we can obtain:

$$P_{ch} = \left( \frac{V_o}{\beta_f} + C_{tp} \right)^{-1} \left( \int_0^t (Q_{in} - Q_{out}) dt + x_{pis} A_{pis} + \Delta V_{pb} + \Delta V_{te} \right) \quad (4.46)$$

where  $C_{tp}$  represents the structural compliance corresponding to the deformation of the top support structure, which is given by equation 4.5.

## Piezoelectric Cylinder

For a cross-sectional area of  $A_p$  and length  $L_p$ , the net deflection of the piezoelectric element and the voltage across it can be expressed using linear constitutive relationships as:

$$x_b - x_{pis} = \frac{L_p}{A_p} (s_{33}^D F_p + \frac{d_{33}}{\varepsilon_{33}^T} Q_p) \quad (4.47)$$

$$V_p = \frac{L_p}{A_p} \left( \frac{d_{33}}{\varepsilon_{33}^T} F_p - \frac{1}{\varepsilon_{33}^T} Q_p \right) \quad (4.48)$$



where  $Q_p$  is the charge on the piezoelectric element.

Equations 4.13, 4.14, 4.19, 4.24, 4.25, 4.26, 4.31, 4.32, 4.38, 4.40, 4.41, 4.42, 4.44, 4.47, and 4.48 (15eqns) can be solved for the 15 unknowns, namely  $V_p$ ,  $x_{tp}$ ,  $\Delta V_{tp}$ ,  $\Delta V_{te}$ ,  $\Delta V_{pb}$ ,  $x_b$ ,  $x_{te}$ ,  $F_{te}$ ,  $F_{te-top}$ ,  $F_{te-bot}$ ,  $\sigma_{tt}$ ,  $\sigma_{tb}$ ,  $F_p$ ,  $P_{ch}$ , and  $F_{net}$  in terms of  $Q_p$ ,  $x_{pis}$ , and  $Q_{net}$  where

$$Q_{net} = \int_0^t (Q_{in} - Q_{out}) dt \quad (4.49)$$

which represents the net fluid volume change inside the chamber due to the fluid flow into and out of the chamber [52]. The elastic equations along with the chamber continuity equation and piezoelectric element constitutive relationships are solved in Maple and the coefficients ( $A_{11}$ ,  $A_{12}$  ...) of the  $15 \times 3$  matrix required by the simulation architecture, shown in Figure 4-7, is calculated. The coefficients are then processed in a Matlab code to generate the  $15 \times 3$  matrix, which is fed to Simulink. The details are presented in Appendix B and Appendix C. The Simulink blocks of the system model are presented in Appendix A.

The matrix equation solved in Simulink is as follows:

$$\begin{bmatrix} V_p \\ x_{tp} \\ \Delta V_{tp} \\ \Delta V_{te} \\ \Delta V_{pb} \\ x_b \\ x_{te} \\ F_{te} \\ F_{te-top} \\ F_{te-bot} \\ \sigma_{tt} \\ \sigma_{tb} \\ F_p \\ P_{ch} \\ F_{net} \end{bmatrix} = \begin{bmatrix} A_{11} & A_{12} & A_{13} \\ A_{21} & A_{22} & A_{23} \\ A_{31} & A_{32} & A_{33} \\ A_{41} & A_{42} & A_{43} \\ A_{51} & A_{52} & A_{53} \\ A_{61} & A_{62} & A_{63} \\ A_{71} & A_{72} & A_{73} \\ A_{81} & A_{82} & A_{83} \\ A_{91} & A_{92} & A_{93} \\ A_{101} & A_{102} & A_{103} \\ A_{111} & A_{112} & A_{113} \\ A_{121} & A_{122} & A_{123} \\ A_{131} & A_{132} & A_{133} \\ A_{141} & A_{142} & A_{143} \\ A_{151} & A_{152} & A_{153} \end{bmatrix} \begin{bmatrix} Q_p \\ x_{pis} \\ Q_{net} \end{bmatrix} \quad (4.50)$$

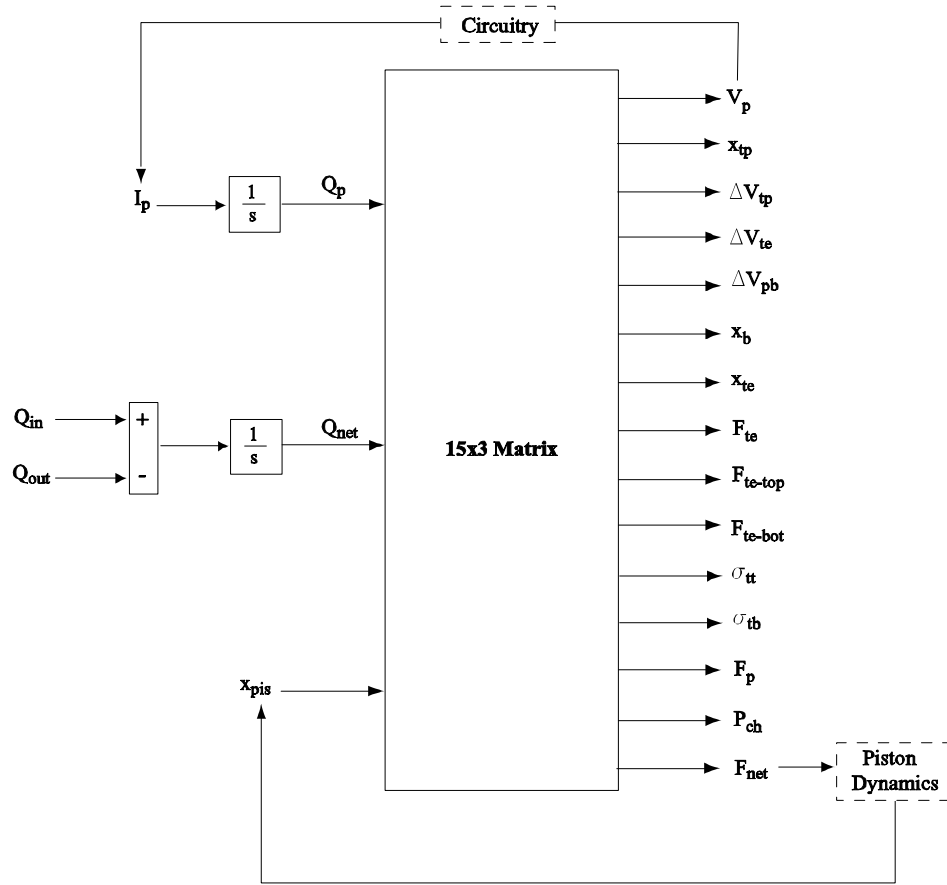


Figure 4-7: Simulation architecture used to integrate the elastic equations into system level simulation.

where the matrix coefficients are calculated using Maple.

The simulation architecture allows for integration of the elastic equations into the dynamic simulations as well as for monitoring important parameters like deflections and swept volumes of the individual structural components and stresses in the tethers.

## **4.4 Conclusion**

This chapter presented detailed analysis of the energy harvesting chamber in terms of the deformations of individual structural components. The deformations are analyzed using linear plate theory. It is assumed that the deflections due to bending are significantly larger than those due to shearing. A simulation architecture is presented to be included in the overall system level simulation, which allows for inclusion of the elastic equations into the dynamic simulation and allows for monitoring important parameters.

## Chapter 5

# Further Design Considerations and Design Procedure

This chapter presents further design considerations in addition to those issues discussed in Chapter 3. These are fluidic oscillations within the system, chamber filling and evacuation, tether structure optimization and the effect of operation conditions and geometry on system performance. At the end of the chapter, a design procedure along with two design examples and simulation results will be presented. The system is analyzed only for the case where the chamber is attached to the regular bridge.

### 5.1 Further Design Considerations

#### 5.1.1 Fluidic Oscillations

Inertial effects should be considered when designing hydraulic systems containing small channels. In fact, in the MHT devices, the fluid channels and the main chamber constitute a resonating system similar to a Helmholtz resonator, shown in Figure 5-1, which comprises a fluid channel and a chamber with an effective compliance  $C$ . The natural frequency of the Helmholtz resonator can be calculated by considering the free-body diagram of the fluid slug within the channel. The equation of motion of the fluid slug can be written as:

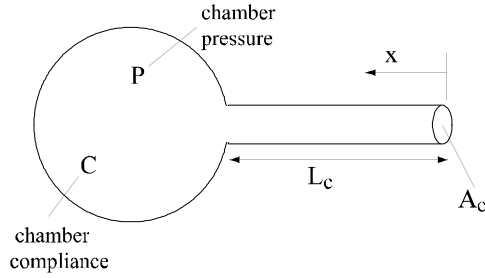


Figure 5-1: Helmholtz Resonator.

$$\rho A_c L_c \frac{d^2 x}{dt^2} + P A_c = 0 \quad (5.1)$$

where  $P$  is the pressure inside the chamber which builds up as a result of the additional fluid flow into the chamber, which can be expressed as:

$$P = \frac{A_c x}{C} \quad (5.2)$$

Combining equations 5.1 and 5.2 we can obtain the governing equation for the Helmholtz resonator as:

$$\ddot{x} + \left( \frac{A_c}{\rho C L_c} \right) x = 0 \quad (5.3)$$

The natural frequency of the resonator can be easily obtained from equation 5.3:

$$\omega_n = \sqrt{\frac{A_c}{\rho C L_c}} \quad (5.4)$$

We can conclude that the natural frequency of the oscillations similar to Helmholtz resonator within the system depends on the channel geometry ( $\frac{L_c}{A_c}$  ratio), the compliance of the chamber and the density of the working fluid. The chamber compliance here refers to the overall chamber, including the compression of the piezoelectric element. In Chapter 3, an effective chamber compliance,  $C_{eff}$ , was defined which took only the structural deformations and fluid compression into account, but not the compression of the piezoelectric element. In the context of this discussion, it is convenient to define an overall chamber compliance,  $C$ , which includes

the structural deformations, fluid compression, and the deformation of the piezoelectric element. The overall chamber compliance in this case can be defined as:

$$C = \frac{\Delta V_f}{\Delta P_{ch}} = \frac{\int (Q_{in} - Q_{out}) dt}{\Delta P_{ch}} \quad (5.5)$$

where  $\Delta V_f$  is the fluid volume change in the chamber due to the fluid flow. In fact, this compliance is not a constant value in the actual power generator since the stiffness of the piezoelectric element changes constantly (the stiffness flips between open-circuit and close-circuit stiffnesses of the piezoelectric element) during the operation, as discussed in Chapter 2 and Chapter 3. In the following two subsections, the fluidic oscillations will be analyzed for two cases. In the first case, a constant overall chamber compliance will be assumed for simplicity and in order to get insight, and in the second case the actual system, i.e. the chamber attached to the rectifier circuit will be analyzed in terms of fluidic oscillations.

### Analysis with Constant Overall Chamber Compliance

Consider a chamber with constant overall chamber compliance,  $C = 10^{-17} [m^3/Pa]$ , as defined in equation 5.5. Figure 5-2 shows the simulation of the system for different chamber geometries, i.e. for different  $L_c/A_c$  ratios. In the simulation, the operation conditions, valve size and openings are adjusted such that the chamber pressure fluctuates between  $P_{HPR}$  and  $P_{LPR}$  for the case where the inertial effects in the channels are negligible. These conditions are:  $P_{HPR} = 2MPa$ ,  $P_{LPR} = 0$ ,  $f = 10kHz$ ,  $R_{vc} = 200\mu m$ ,  $vo_{in} = vo_{out} = 20\mu m$ , and the working fluid is silicon-oil.

It can be seen that there exists an optimum  $L_c/A_c$  value for which the difference between the maximum and minimum pressures, i.e. the pressure band,  $\Delta P_{ch}$ , is maximum. This value is approximately  $25000(1/m)$ . The pressure band is not very sensitive to  $L_c/A_c$  around the optimum value, i.e.  $L_c/A_c = 24000$  or  $L_c/A_c = 26000$  results pretty much in the same pressure band. In fact, the optimum value of the  $L_c/A_c$  can be approximated using equation 5.4. Figure 5-3 shows the inlet flowrate time histories from the simulation. It can be seen that, the fluid inductance in the channel causes the flow to lag, i.e. the flowrate reaches its maximum at a later time compared to the case where the fluid inductance is negligible.

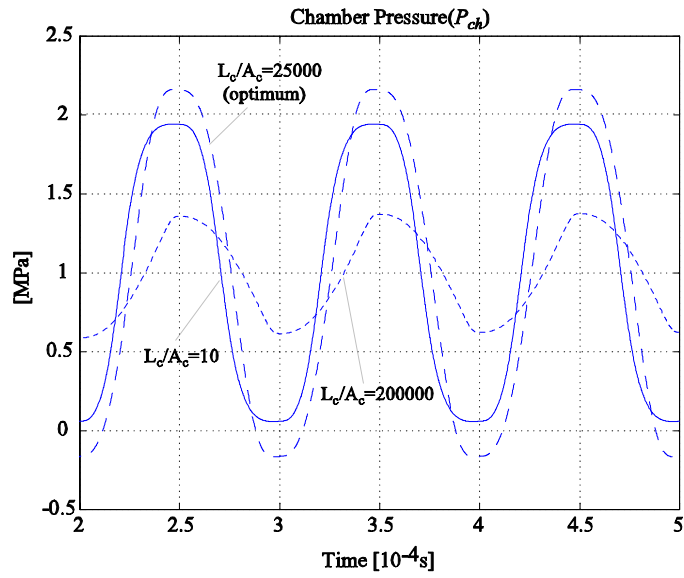


Figure 5-2: Simulation of the chamber with constant overall compliance for different channel geometries.

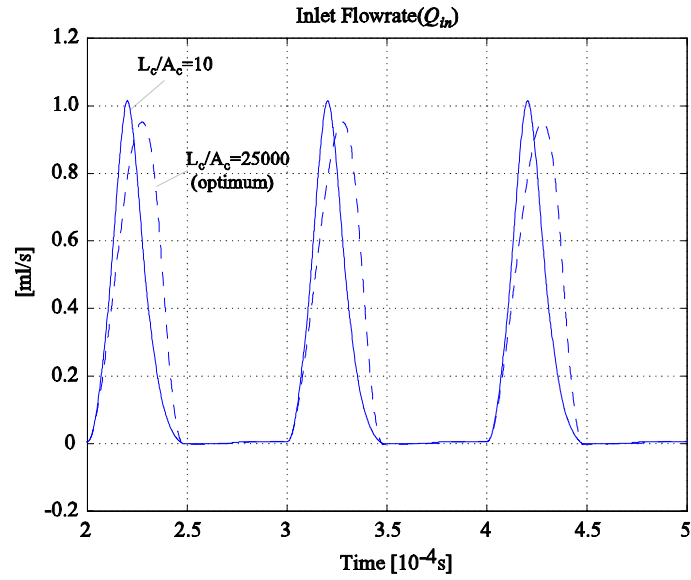


Figure 5-3: Comparison of flowrate time histories for different  $L/A$  ratios.

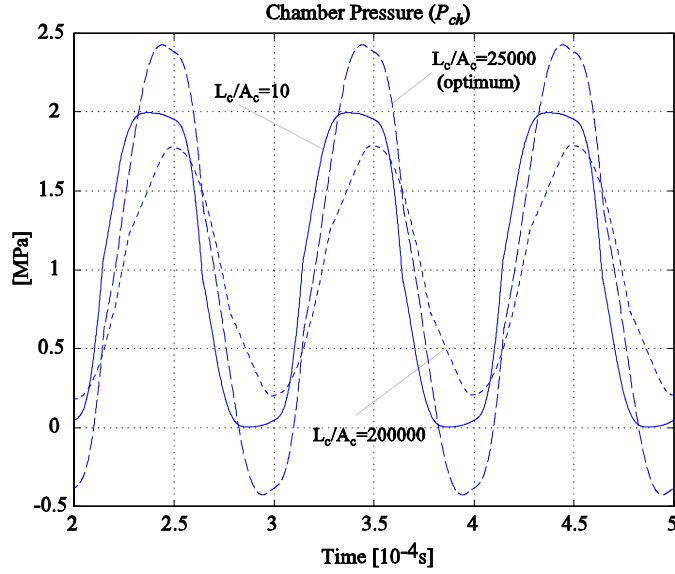


Figure 5-4: Simulation of the chamber attached to circuitry for different channel geometries.

### Analysis of the chamber attached to circuitry

Consider the chamber geometry, effective compliance and operation conditions presented in Table 3.2 of Chapter 3. Figure 5-4 shows the simulation of the same geometry for different  $L_c/A_c$  ratios. Again, the valve size and opening is adjusted such that the chamber pressure fluctuates between  $P_{HPR}$  and  $P_{LPR}$  for the case where the inertial effects in the channels are negligible. These conditions are:  $P_{HPR} = 2MPa$ ,  $P_{LPR} = 0$ ,  $f = 10kHz$ ,  $R_{vc} = 200\mu m$ ,  $vo_{in} = vo_{out} = 20\mu m$ , the working fluid is silicon-oil, and the battery voltage,  $V_b$ , is  $90V$ , which is optimized for a pressure band of  $2MPa$ . Similar to the case where a constant overall chamber compliance was assumed, there exists an optimum  $L_c/A_c$  value for which the difference between the maximum and minimum pressures, i.e. the pressure band,  $\Delta P_{ch}$ , is maximum.

Figure 5-5 shows the effect of  $L_c/A_c$  ratio on pressure band and generated power. Throughout the simulations the battery voltage was not changed. In fact, in a design, the battery voltage should be determined according to the expected pressure band, which determines the stress band on the piezoelectric element. For example, for the optimum  $L_c/A_c$  ratio, the pressure band is  $2.435MPa$ , which suggests a battery voltage of approximately  $125V$ . If the simulation is repeated with this value, the pressure band is now  $2.472MPa$ , which is slightly different than



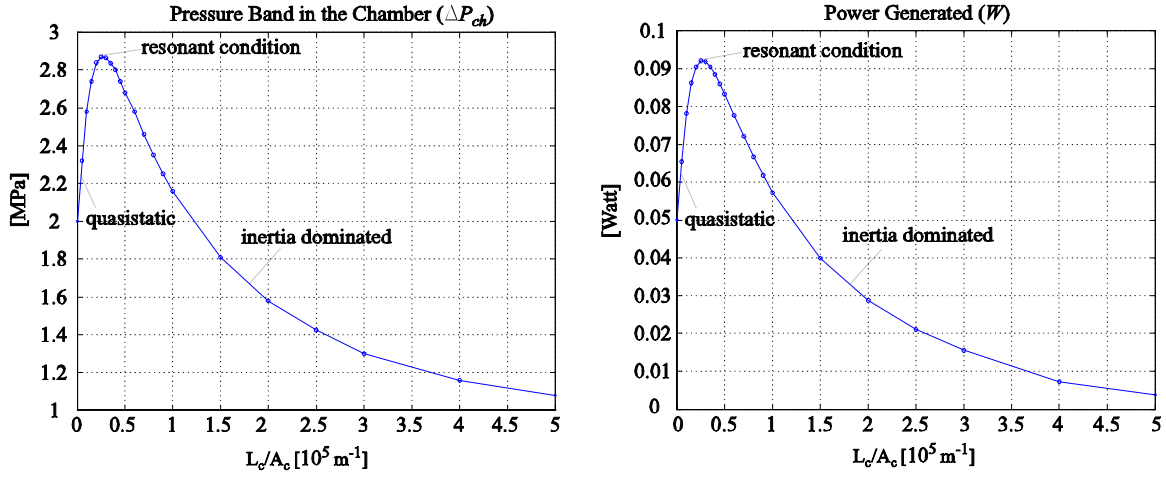


Figure 5-5: Effect of  $L/A$  ratio on pressure band and generated power.

the previous value, and the generated power is  $0.1068W$ . The slight change in the pressure band suggests that the change in the battery voltage caused a small change in the overall chamber compliance, because it basically determines the voltage level where the piezoelectric element will change its stiffness, and therefore effects the time intervals in which the piezoelectric element possesses the different stiffnesses. The expression for the optimum battery voltage was given in Chapter 2 as:

$$V_b = \frac{1}{4} \frac{\Delta\sigma(s_{33}^E - s_{33}^D)L_p}{d_{33}} \quad (5.6)$$

which can be written in terms of the pressure band in the chamber as:

$$V_b = \frac{1}{4} \frac{\Delta P_{ch} A_{pis}}{A_p} \frac{(s_{33}^E - s_{33}^D)L_p}{d_{33}} \quad (5.7)$$

where  $A_{pis}$  and  $A_p$  are the piston area and the cross-sectional area of the piezoelectric cylinder respectively, and  $\Delta\sigma$  is the stress band on the piezoelectric element. It should be noted that, when writing equation 5.7 the effect of tethers and piston dynamics is neglected. In other words, static force balance between the piston and piezoelectric element is assumed and the force applied by the tethers on the piston is neglected. This issue will be addressed later.

We can conclude that, for a given overall chamber compliance there exists an optimum  $L_c/A_c$  ratio at a certain operation frequency, or similarly, there exists an optimum operation

frequency for a certain overall compliance and  $L_c/A_c$  ratio. The fluidic oscillations should be considered in any design procedure and the channels should be designed accordingly. This will be addressed later in the discussion of the design procedure.

The overall chamber compliance was defined as the compliance of the chamber including the compliances due to structural deformations and fluidic compliance, which is represented by the effective compliance,  $C_{eff}$ , and the compliance due to the deflection of the piezoelectric element. The compliance due to the deflection of the piezoelectric element can be calculated considering the volume displaced by the piston due to the deflection of the element as a response to the pressure change in the chamber:

$$C_p = \frac{\Delta V_{pis}}{\Delta P_{ch}} = \frac{\Delta x_p A_{pis}}{\Delta P_{ch}} = \frac{\left( \frac{\Delta P_{ch} A_{pis}}{k_p} \right) A_{pis}}{\Delta P_{ch}} = \frac{A_{pis}^2}{k_p} \quad (5.8)$$

where  $k_p$  is the stiffness of the piezoelectric element, which can be expressed as:

$$k_p = \frac{A_p}{s_{33} L_p} \quad (5.9)$$

where  $A_p$  and  $L_p$  are the cross-sectional area and the length of the piezoelectric element respectively, and  $s_{33}$  is the compliance coefficient of the element. As mentioned earlier, the stiffness of the piezoelectric element changes constantly during the operation between the open circuit and closed circuit stiffnesses, which should be calculated using  $s_{33}^D$  and  $s_{33}^E$  respectively. Therefore the system is highly nonlinear and it is impossible to express the resonant frequency, or the optimum  $L_c/A_c$  ratio analytically. However we can get a first order estimation of the resonant frequency using one of the stiffnesses above. For example using the open circuit compliance coefficient,  $s_{33}^D$ , and from equations 5.4, 5.8, and 5.9 we obtain:

$$f_n = \frac{1}{2\pi} \sqrt{\frac{A_c}{L_c \rho (C_{eff} + C_p)}} = \frac{1}{2\pi} \sqrt{\frac{A_c}{L_c \rho \left( \frac{V_o}{\beta_f} + C_s + \frac{s_{33}^D L_p A_{pis}^2}{A_p} \right)}} \quad (5.10)$$

where  $C_{eff}$  is the effective chamber compliance.

It is very important to note that in the simulations presented in this and the previous

sections (Figures 5-2 and 5-4), the pressure in the chamber overshoot the reservoir pressures ( $P_{HPR}$  and  $P_{LPR}$ ) in the resonance conditions, which resulted in negative pressures, which should be avoided because of cavitation. In the design procedure, the operation conditions should be adjusted such that there won't be any cavitation. For example the system can be biased, i.e. the reservoir pressures can be increased keeping the difference the same. Or, the valve openings can be adjusted accordingly. The motivation for operating at resonance condition is that the same pressure band can be achieved with smaller valve cap sizes or valve openings compared to the case of negligible or very large fluid inductance in the channels, resulting in reduced power consumption in the active valves.

### 5.1.2 Chamber filling and evacuation

In order to attain the desired pressure bands inside the chamber, it is important to design the valve sizes, openings and the operation frequency accordingly. Consider the chamber attached to the circuitry discussed in the previous section. Figure 5-6 shows the effect of valve opening on pressure band in the chamber. A valve opening of  $20\mu m$  provides perfect filling and subsequent evacuation of the chamber in the required time interval and the chamber pressure fluctuates between the reservoir pressures. A small valve opening of  $5\mu m$  results in poor(slow) filling and evacuation, resulting in a reduced pressure band. A large valve opening of  $50\mu m$  provides very fast filling and evacuation, which causes the chamber pressure to retain its maximum and minimum values for long time intervals. The latter results in the same power generated, however it also results in more power consumption in the active valves due to the higher stroke. A similar result would be obtained by keeping the valve opening the same, but increasing the valve cap size. Again more power would be consumed in the active valves.

Figure 5-7 shows the effect of operation frequency on the pressure band in the chamber. It can be seen that, for a fixed valve opening, different operation frequencies result in system behaviors similar to the ones in Figure 5-6. At high frequency, there is not enough time for the valve to fill and evacuate the chamber in the required time interval. Similarly, at low frequency, there is more than enough time for the valves to fill and evacuate, which results in similar behavior to the case of large valve opening. This implies that, the valve opening can be reduced for reduced power consumption in the active valve and yet the same power can be

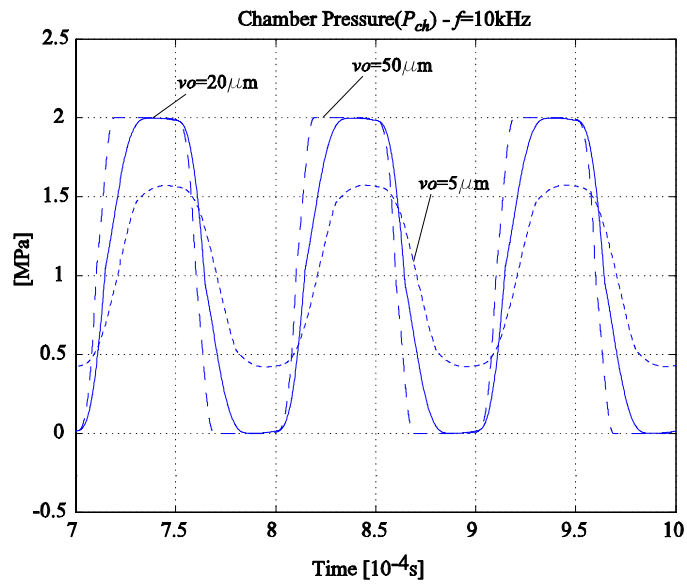


Figure 5-6: Effect of valve opening on the pressure band in the chamber.

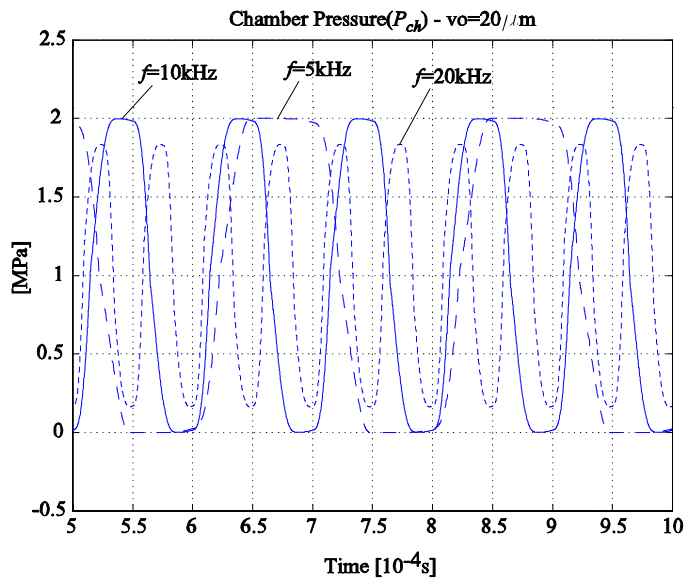


Figure 5-7: Effect of operation frequency on the pressure band in the chamber.

generated as long as the pressure band in the chamber is kept at the desired level.

In the two cases analyzed above, the valve cap size could be analyzed instead of valve opening, which would lead to the same conclusions. The combination of the valve size and the valve opening define the overall valve resistance. We can conclude that, for a designed operation frequency and pressure band, it is important to design the valve size and opening such that they will provide just enough filling and evacuation of the chamber in the required time interval, which is defined by the operation frequency, so that the chamber pressure fluctuates between the reservoir pressures in the most economical way. As will be addressed later, the pressure band is a very important design parameter, since the power generated is proportional to the square of the stress band on the piezoelectric element. Additional design considerations concerning the design of the valve size and opening is not within the scope of this thesis. The design optimization of the active valves is detailed in [5].

### 5.1.3 Tether Structure Optimization

Design of the piston tether structure is very crucial for system operation. The tethers should be flexible enough to allow sufficient motion of the piston, yet stiff enough to avoid introduction of excessive compliance into the system. The tethers have to be designed to allow maximum piezoelectric element compression for a given net fluid volume into the chamber, which occurs basically at every cycle during system operation. To analyze the tether structure, consider a simple hypothetical chamber which consists of a fluid chamber with rigid walls, a single layer piston attached to the wall with a single tether providing sealing, and a piezoelectric element. Figure 5-8 illustrates the hypothetical chamber and different tether designs. Figure 5-8(b) illustrates a good tether design where the tethers allow large piezoelectric element compression. Figure 5-8(c) illustrates a poor design where the tether is either too thin or the tether width,  $t_w$ , is very large ( $t_w = [D_{ch} - D_{pis}]/2$ ). This results in low pressure in the chamber and small compression of the piezoelectric element since the compliance introduced by the tether is very large. In other words, pressure doesn't built up inside the chamber because of the excessive bending of the tether. Figure 5-8(d) illustrates another poor design where the tether is either too thick or the tether width,  $t_w$ , is very small. In this case the pressure in the chamber is high but the compression of the piezoelectric element is still very small since the very stiff tethers

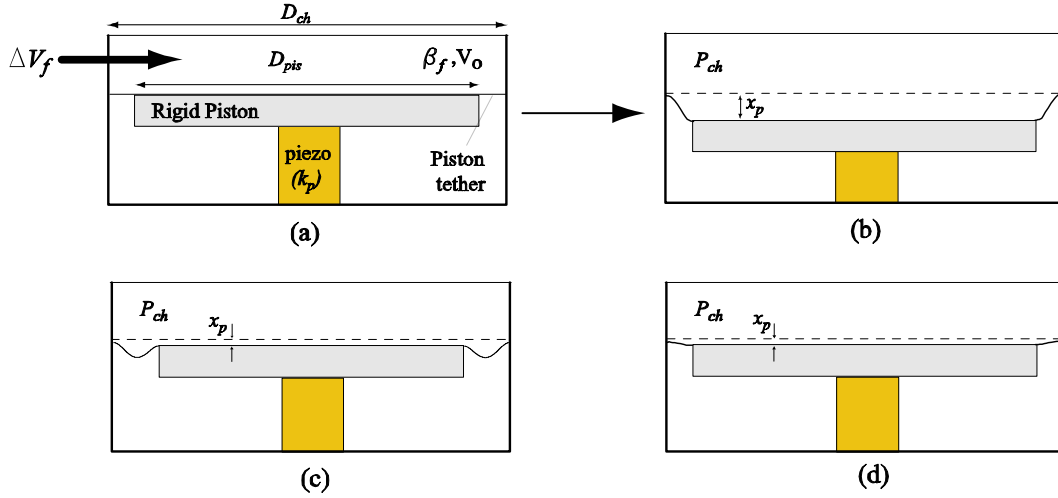


Figure 5-8: (a) Schematic illustrating the hypothetical chamber (b) good tether design providing large piezoelectric element compression (c) poor tether design, either too thin or large width, resulting in low chamber pressure and small piezoelectric element compression (d) poor tether design, either very thick or small width, resulting in large pressures but small piezoelectric element compression.

do not allow the piston to move although they introduce very small additional compliance into the system. This suggests that for a design where the chamber diameter(or piston diameter) is determined, the tether structure has to be optimized in conjunction with fabrication limitations, such as thickness of the tether, which is determined by the SOI wafer, or the maximum tether width which can be etched.

Consider a chamber of the following geometric parameters:  $D_{ch} = 5mm$ ,  $D_p = 1mm$ ,  $L_p = 1mm$ , and  $H_{ch} = 200\mu m$ . An additional fluid volume,  $\Delta V_f = 10^{-11}m^3$ , is introduced into the chamber. Figure 5-9 shows piston deflection/piezoelectric element deflection, pressure in the chamber and the compliance of the chamber for different tether thicknesses and widths. The tether width is varied by keeping the chamber diameter the same and changing the piston diameter. Since the tether width is very small compared to chamber or piston diameter, it doesn't matter which parameter is kept constant, i.e. the the piston diameter could be kept constant and the chamber diameter could be varied alternatively. Thus we can generalize this study for a nominal chamber diameter of  $5mm$ . It can be seen that for a tether thickness, there exists a range of values for tether widths where maximum deflection of the piston occurs. It

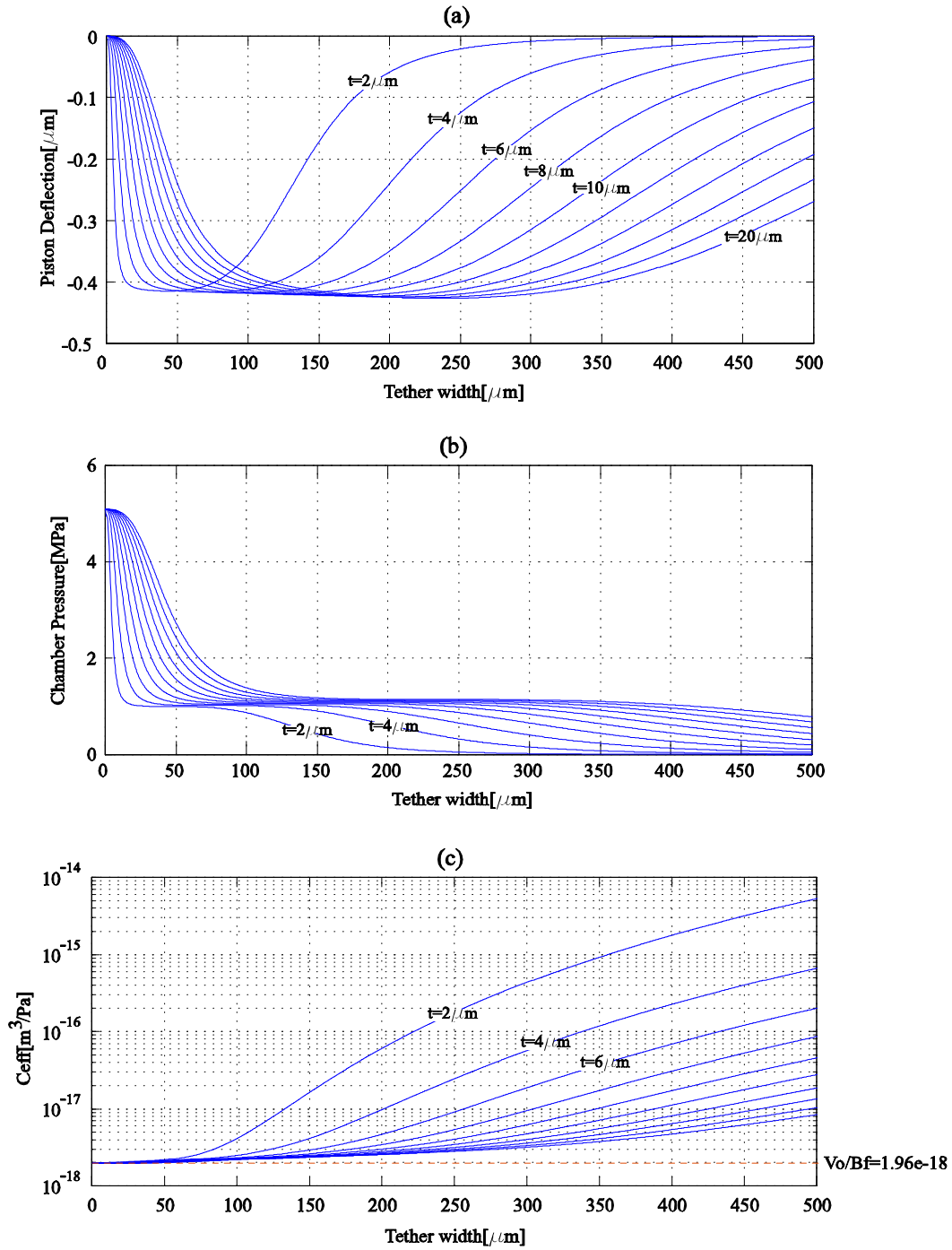


Figure 5-9: (a) Piston deflection for different tether thicknesses and widths, (b) corresponding pressures in the chamber (c) compliance of the chamber. The dashed line corresponds to the hypothetical case where piston diameter is equal to chamber diameter and there is perfect sealing.

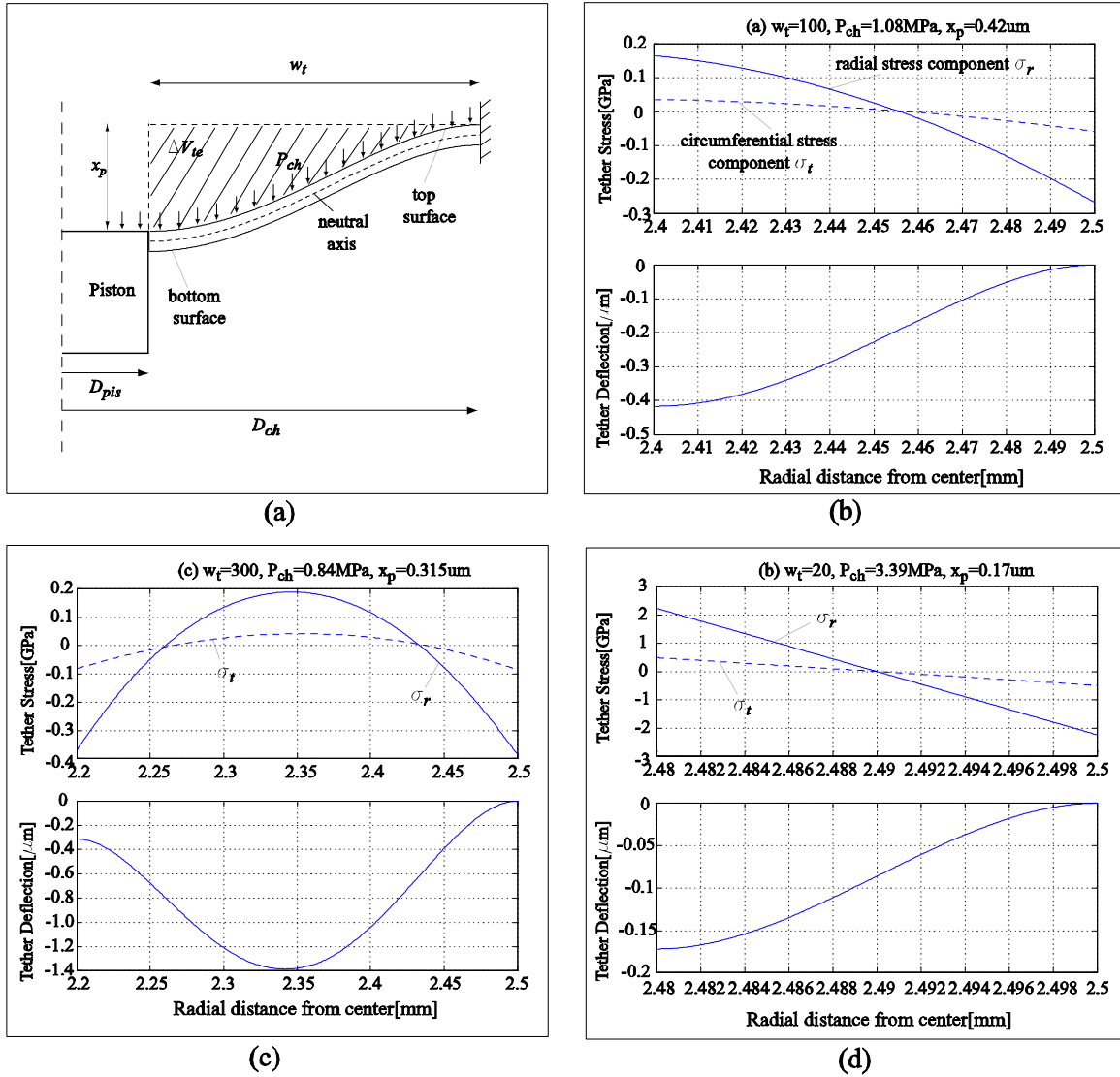


Figure 5-10: (a) Schetch illustrating tether deflection. (b),(c),and (d) show the stress components on the bottom surface and deflected shape of the tether for 3 different cases.(b) good tether design, (c) poor tether design where the tether is too compliant, and (d) poor tether design where the tether is too stiff.



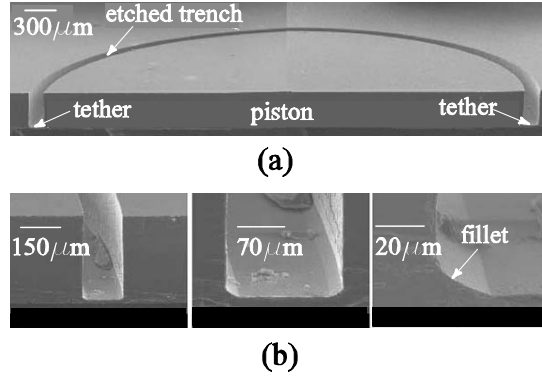


Figure 5-11: (a) SEM picture of micromachined piston structure [7](b)detailed view of the tether and the fillet.

can be also seen that for those values, the additional compliance introduced by the tethers is negligible.

Figure 5-10 illustrates the stresses and deflected shapes of the tether with a thickness of  $10\mu m$  for three different cases. Figure 5-10(b) illustrates a good design where the tether width is optimized. Figure 5-10(c) illustrates a poor design where the tether width is very large and therefore the pressure in the chamber and piston deflection are small. Figure 5-10(d) illustrates another poor design where the tether width is small and therefore the tether is very stiff, which results in small piston deflection even though the pressure built up in the chamber is high. It can be also seen that the stresses in this case are very large compared to the previous two cases.

It should be noted that linear plate theory is used for this analysis which means that the neutral axis coincides with the central axis of the tether. In general, in a well-designed tether structure, the bottom surface of the tether experiences compressive stress near the chamber wall and tensile stress near the piston, which is the case in Figure 5-10(b), and the maximum stress occurs at the point where the tether is attached to the wall. The top surface experiences stresses with opposite signs.

It is also very important to consider the effect of the fillet on the stress and to note that the stresses calculated from the linear plate theory should be corrected using the proper stress concentration factor. However the stresses calculated using linear theory give a reasonable estimate and provide first order prediction about stresses during the design procedure. A

detailed study of the fillet radius and stress concentration factors can be found in [7]. A fabricated piston structure and the fillets are shown in Figure 5-11.

#### 5.1.4 Operation Conditions and Trade-offs

In most of the analysis performed so far the basic parameters of the chamber, such as chamber diameter, and operation conditions such as reservoir pressures and operation frequency were fixed. This section will discuss how to choose chamber geometry and operation conditions for a given power requirement and will discuss trade-offs between operation conditions. The general design guidelines can be summarized as follows:

- The operation frequency should be kept as small as possible due to the bandwidth limitations imposed by the active valve structure,
- The flowrate should be kept as small as possible to minimize valve size and reduce power consumption in the valves,
- The maximum pressure in the chamber should be kept as small as possible in order to avoid high stresses in the tethers and active valve membranes.

For the analysis of this section, a relatively simple chamber structure will be assumed, namely the effect of the tethers, the deformation of the piston, and the deformation of the bottom plate will be ignored. This means that the effective compliance will be comprised of the fluidic compliance and structural compliance only due to the deflection of the top support structure. These assumptions are done for simplification of the analysis without loss of generality.

Fixed geometric parameters in this analysis are: chamber height,  $H_{ch} = 200\mu$ , length of piezoelectric element,  $L_p = 1mm$ , and top support structure thickness,  $t_{top} = 1mm$ . For each design point considered, piston area and cross-sectional area of the piezoelectric element satisfy the following relationship.

$$A_{pis} = \frac{\sigma_d A_p}{P_{HPR}} \quad (5.11)$$

which represents the static force balance between the piston and the piezoelectric element. The areas of the piston and the piezoelectric element are designed such that maximum stress on the piezoelectric element is equal to the depolarization stress,  $\sigma_d$ , for maximum power output.

It is assumed that the maximum and minimum pressures attained in the chamber are equal to the high and low pressure reservoirs respectively, where  $P_{LPR}$  is assumed to be zero for simplicity.

### Required operation frequency for a given power requirement

The required frequency in order to generate a certain amount of power,  $W$ , for the case of the chamber attached to regular diode bridge is given by:

$$f = \frac{4W}{(s_{33}^E - s_{33}^D)\sigma_d^2 A_p L_p} \quad (5.12)$$

where  $s_{33}^E$  and  $s_{33}^D$  are the closed circuit and open circuit compliances of the piezoelectric element respectively. Figure 5-12 compares different piezoelectric materials in terms of required frequency for a  $0.5W$  power requirement at different chamber diameters and reservoir pressures. It can be seen that,  $PZT - 4S$  and  $PZT - 8$  require lower frequencies because of their very high depolarization stress, even though they have smaller coupling coefficients compared to  $PZT - 5H$  and  $PZN - PT$ . It should be noted that, the required frequency does not depend on the chamber compliance, as can be seen from equation 5.12.

It is important to note that there is a trade-off between the maximum chamber pressure( $P_{HPR}$ ) and the operation frequency. For lower chamber pressures, higher operation frequencies are needed. In fact, for a given piston diameter the required frequency is inversely proportional to the reservoir pressure, as can be easily seen from equations 5.11 and 5.12. It can be also seen that, for larger chamber diameters, the required operation frequency is smaller since for larger chamber diameters, piezoelectric elements having larger diameter are used to satisfy equation 5.11, which results in lower frequency requirement due to the increased piezoelectric element volume.

### Required flowrate for a given power requirement

The required flowrate is given by the following equation, which was derived in Chapter 3:

$$Q = \frac{2(s_{33}^E + s_{33}^D)W}{(s_{33}^E - s_{33}^D)P_{HPR}} + C_{eff}P_{HPR}f \quad (5.13)$$

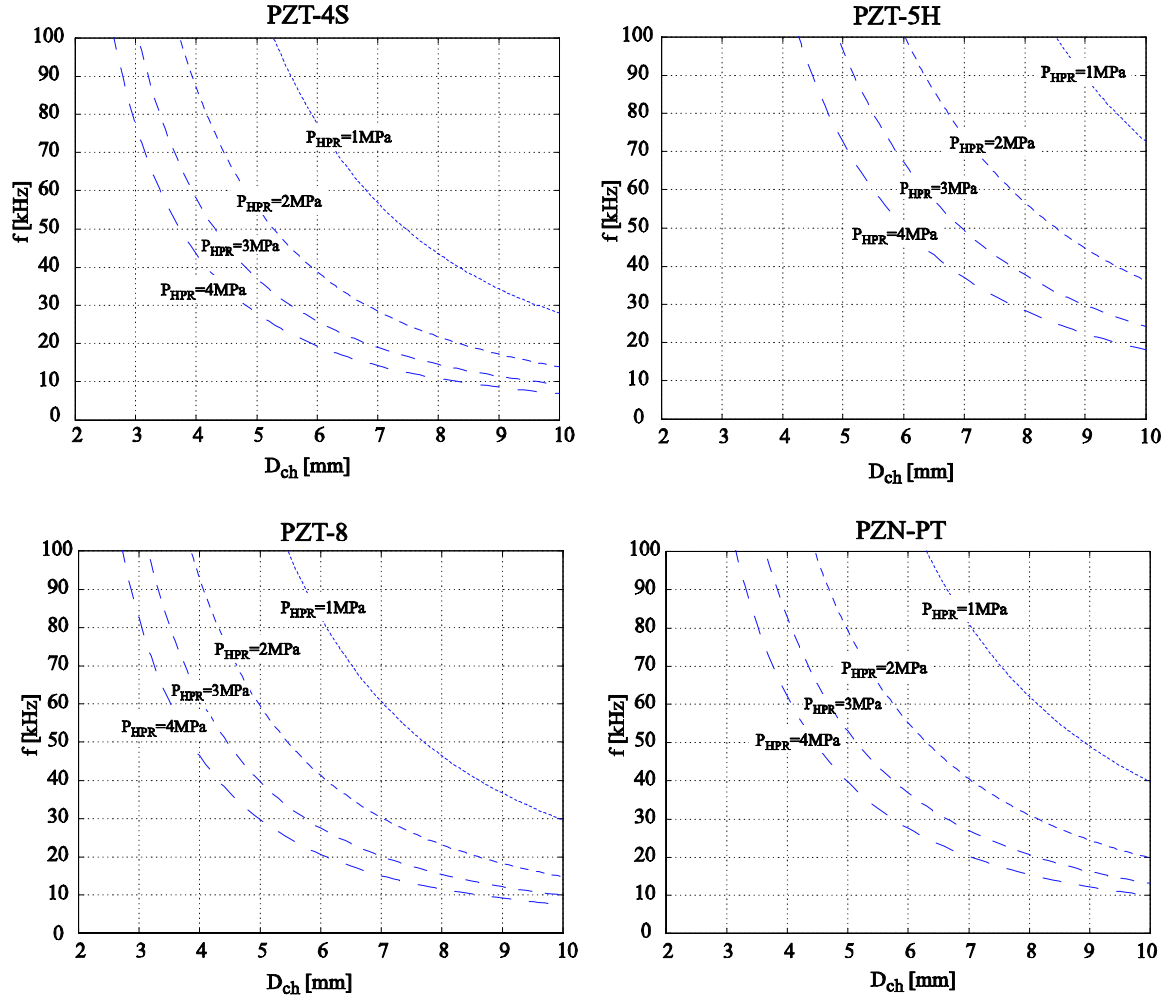


Figure 5-12: Comparison of different piezoelectric materials in terms of required operation frequency at different chamber diameters for a power requirement of 0.5W.

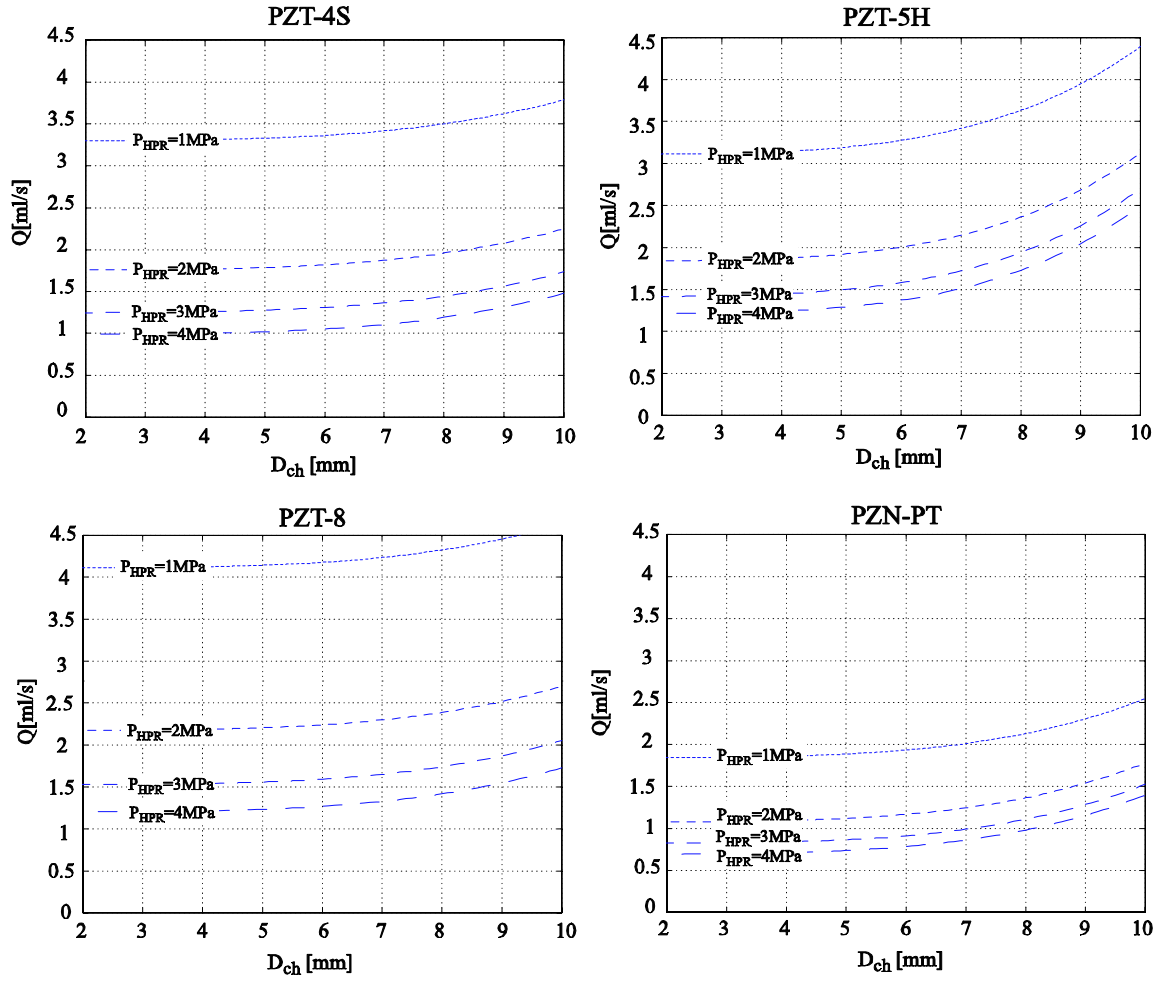


Figure 5-13: Comparison of different piezoelectric materials in terms of required flowrate at different chamber diameters for a power requirement of 0.5W.

where  $f$  is the required operation frequency corresponding to the power requirement at the particular chamber diameter and reservoir pressure, as discussed in the previous subsection. Figure 5-13 shows a comparison of different piezoelectric materials in terms of required flowrate at different reservoir pressures and chamber diameters.

It can be seen that  $PZN - PT$  requires the least flowrates due to its high coupling coefficient, which translates into higher system efficiencies as discussed in Chapter 3. It can be also noted that, for larger chamber diameters, higher flowrates are required. This can be explained by considering equation 5.13. There are in fact two competing effects. For larger chamber diameters, lower frequencies are needed, as shown in Figure 5-12, which suggest lower flowrates. However, larger chamber diameters result in increased chamber compliance, which is the dominating factor resulting in higher flowrates.

In this case, a trade-off exists between the required flowrate and maximum chamber pressure, namely for lower chamber pressures, higher flowrates are required.

## Efficiency

The efficiency of the system is given by:

$$\eta = \frac{W}{QP_{HPR}} \quad (5.14)$$

where the power consumption in the active valves is not considered. Figure 5-14 shows a comparison of different piezoelectric elements in terms of system efficiency for different reservoir pressures and chamber diameters. It can be seen that  $PZN - PT$  provides the most efficient power generation due to its high coupling coefficient. For larger chamber diameters, the efficiency is lower due to the fact that the flowrate is higher at larger chamber diameters, as shown in Figure 5-13. It is also important to note that the efficiency decreases as the reservoir pressure increases. This can be explained considering equations 5.11, 5.12 and 5.13. Combining these equations we get:

$$Q = \frac{2(s_{33}^E + s_{33}^D)W}{(s_{33}^E - s_{33}^D)P_{HPR}} + \frac{4C_{eff}W}{(s_{33}^E - s_{33}^D)\sigma_d A_{pis} L_p} \quad (5.15)$$

which is the explicit form of equation 5.13. Using equation 5.14 we get:

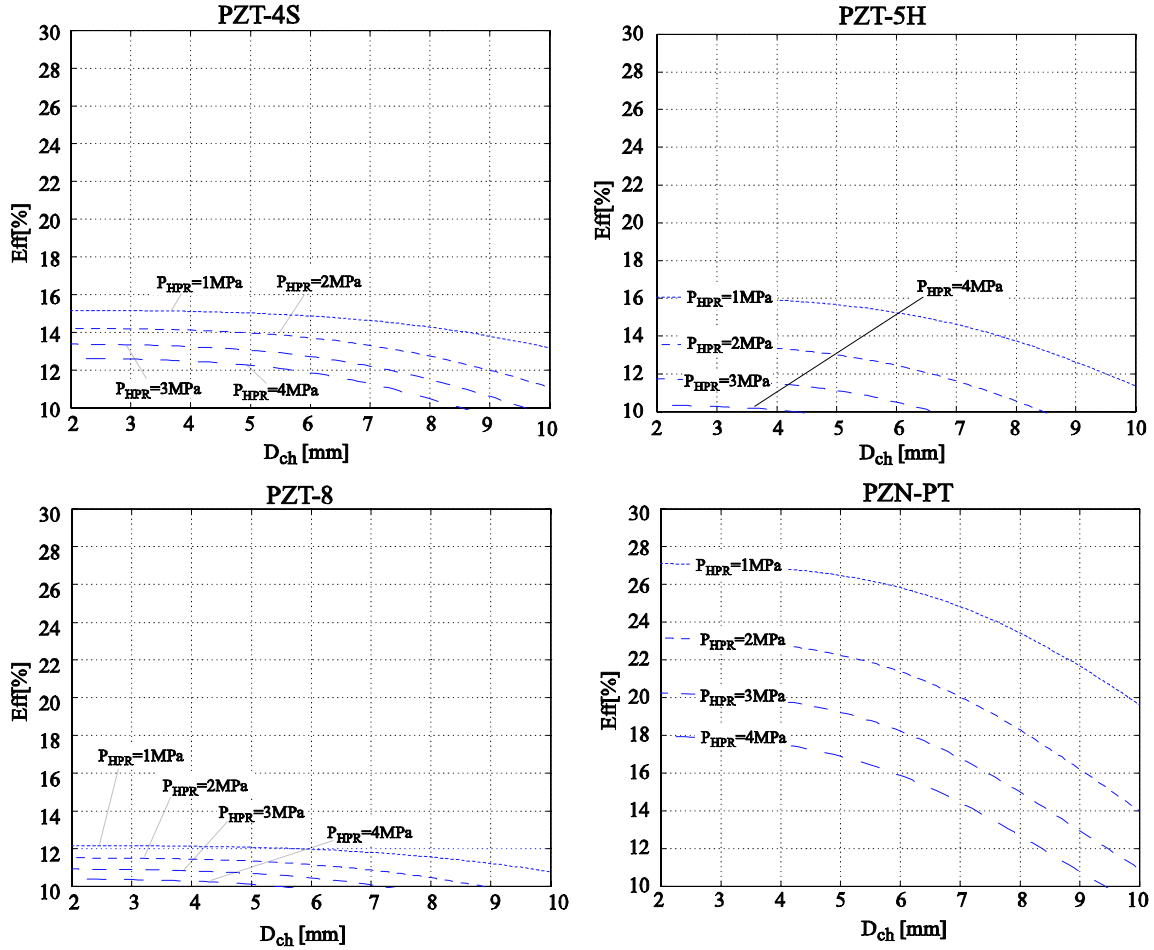


Figure 5-14: Comparison of different piezoelectric elements in terms of system efficiency for different reservoir pressures and chamber diameters.

$$\eta = \frac{W}{QP_{HPR}} = \left( \frac{2(s_{33}^E + s_{33}^D)}{(s_{33}^E - s_{33}^D)} + \frac{4C_{eff}P_{HPR}}{(s_{33}^E - s_{33}^D)\sigma_d A_{pis} L_p} \right)^{-1} \quad (5.16)$$

from which it can be easily seen that at a certain chamber diameter, the efficiency decreases with increasing reservoir pressure. It is also possible to observe that efficiency does not depend on the generated power.

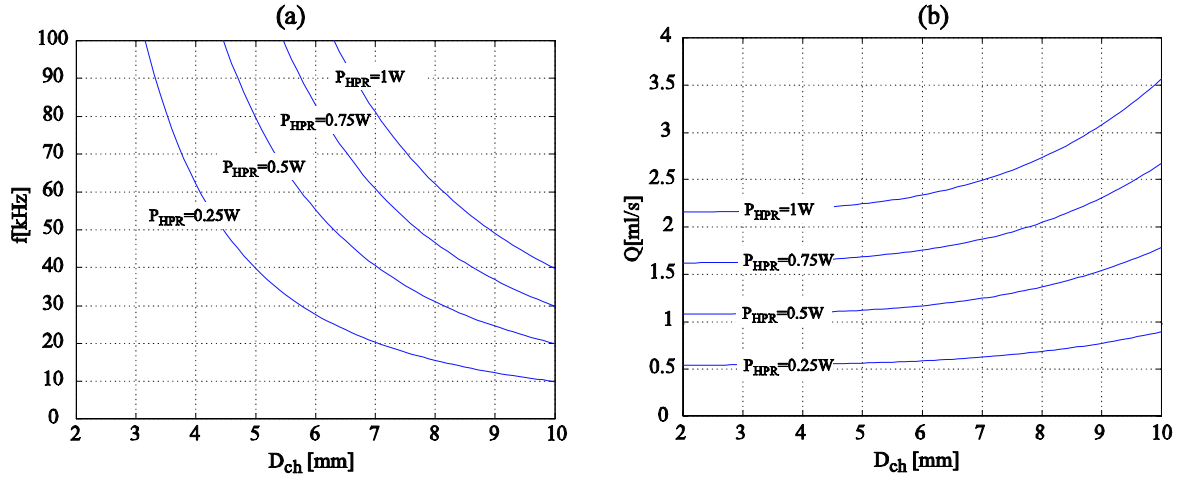


Figure 5-15: Required operation frequency and flowrate for different power requirements at different chamber diameters ( $P_{HPR} = 2MPa$ , piezoelectric material:  $PZN - PT$  ).

### Effect of power requirement

As can be seen from equations 5.12 and 5.16, the required operation frequency and flowrate are directly proportional to the generated power. Figure 5-15 illustrates the effect of power requirement on frequency and flowrate for the case where  $P_{HPR} = 2MPa$  and piezoelectric material:  $PZN - PT$ .

#### 5.1.5 Bias Pressure

As discussed in section 5.1.1, negative pressure in the chamber should be avoided due to cavitation. Even though the chamber is designed for positive pressure fluctuations, cavitation could occur due to unexpected fluidic resonances. Also the active valve design imposes minimum pressure requirements for the low pressure reservoir due to cavitation considerations inside the hydraulic amplification chamber. For a conservative design, the chamber pressure can be biased by a certain amount, by keeping the pressure differential  $P_{HPR} - P_{LPR}$  the same, aiming for the same power as would be generated with  $P_{LPR} = 0$ . However, since the depolarization stress of the piezoelectric element cannot be exceeded, the effective stress band reduces, even though the pressure band remains the same. For the case where  $P_{LPR} = 0$ , the stress band, i.e. the difference between the maximum and minimum stress on the piezoelectric element is equal to



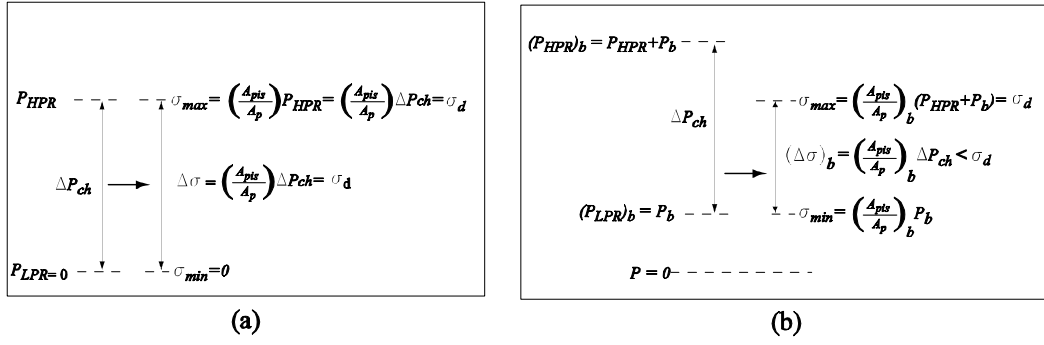


Figure 5-16: Schematic illustrating the effect of bias pressure.(a) not biased case (b) biased case

the depolarization stress, given by:

$$\Delta\sigma = \left(\frac{A_{pis}}{A_p}\right) \Delta P_{ch} = \sigma_d \quad (5.17)$$

However, for the biased case, where  $P_{LPR} \neq 0$ , the stress band is given by:

$$(\Delta\sigma)_b = \left(\frac{A_{pis}}{A_p}\right)_b \Delta P_{ch} < \sigma_d \quad (5.18)$$

which is smaller than the depolarization stress of the piezoelectric material. Figure 5-16 illustrates the effect of bias pressure. This means that for the same pressure differential, higher frequencies and flowrates are required, which can be seen from the following equations which are derived for the general case:

$$f_b = \frac{4W}{(s_{33}^E - s_{33}^D)(\Delta\sigma)_b^2 A_p L_p} \quad (5.19)$$

$$Q_b = \frac{2(s_{33}^E + s_{33}^D)W}{(s_{33}^E - s_{33}^D)\Delta P_{ch}} + C_{eff}\Delta P_{ch}f_b \quad (5.20)$$

or

$$Q_b = \frac{2(s_{33}^E + s_{33}^D)W}{(s_{33}^E - s_{33}^D)\Delta P_{ch}} + \frac{4C_{eff}W}{(s_{33}^E - s_{33}^D)(\Delta\sigma)_b A_{pis} L_p} \quad (5.21)$$

Figure 5-17 illustrates the effect of bias pressure on required frequency, flowrate and efficiency for the case of  $0.5W$  power requirement, where  $\Delta P_{ch} = P_{HPR} - P_{LPR} = 2MPa$ , and

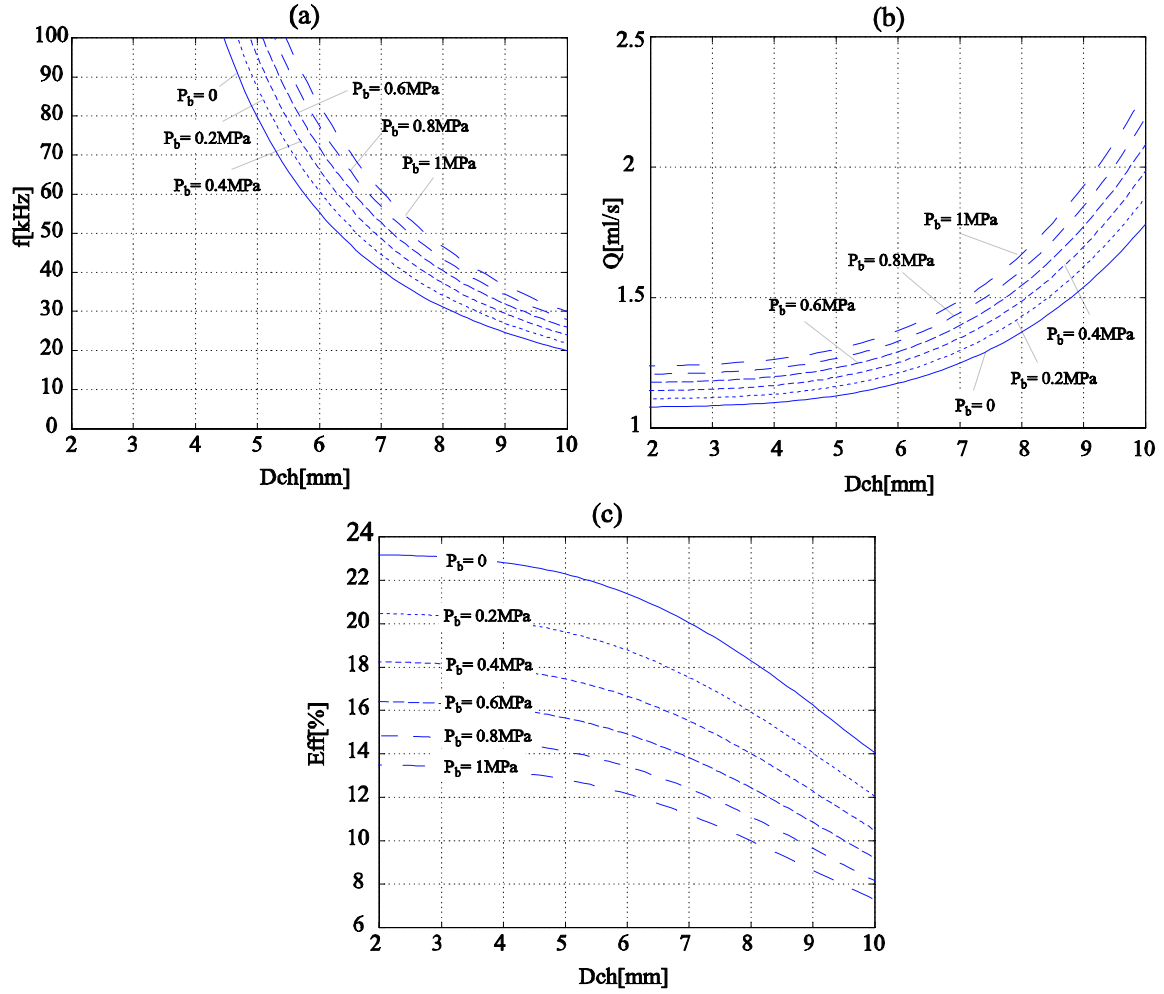


Figure 5-17: Effect of bias pressure on required frequency, flowrate and efficiency.

piezoelectric material is  $PZN - PT$ . It is important to note that the generated power is proportional to the square of stress band and therefore the bias pressure should be kept as small as possible. It can be easily shown that, for a given chamber diameter, the required frequency for the biased case and for the case where  $P_{LPR} = 0$  are related by:

$$\frac{f}{f_b} = \left( \frac{\Delta P_{ch}}{\Delta P_{ch} + P_b} \right)^2 \quad (5.22)$$

where  $P_b$  is the bias pressure. It is assumed that in both cases the pressure differential in the chamber is the same. Equation 5.22 implies that if the bias pressure is much smaller than the pressure band in the chamber, its effect is negligible. However for typical MHT devices this is not the case and the effect of bias pressure should be considered.

### 5.1.6 Scaling Issues

One of the many advantages of MEMS devices is their ability to operate at very high frequencies. In other words, they allow operation with much larger bandwidth due to their high natural frequencies. For linear systems, the scaling law for natural frequency can be obtained by considering a very simple system consisting a cantilever beam and a proof mass attached to the tip of the beam. The stiffness corresponding to the tip deflection of the beam in response to a force applied to the tip can be obtained from beam theory:

$$k = \frac{EWH^3}{4L^3} \quad (5.23)$$

where  $E$  is the Youngs modulus, and  $W$ ,  $H$ , and  $L$  are the width, the height and the length of the beam respectively. The natural frequency of this system can be calculated by:

$$\omega_n = \sqrt{\frac{k}{m}} \quad (5.24)$$

where  $m$  is the mass of the proof mass. If we define the scale factor,  $\lambda$ , as the ratio of the new scaled dimensions divided by the nominal, the dependence of the stiffness of the beam and the mass of the proof mass on the system scale are:

$$k \sim \lambda \quad \text{and} \quad m \sim \lambda^3 \quad (5.25)$$

where the scale dependence of the stiffness of the beam is obtained from equation 5.23.

The natural frequency of the system is then related to its size by:

$$f_n \sim \sqrt{\frac{\lambda}{\lambda^3}} = \frac{1}{\lambda} \quad (5.26)$$

which can be generalized to any linear structure.

Similarly we can obtain the scaling laws for the power generator considering the dependence of the natural frequency, required operation frequency and compliance of the system on system scale. Consider the simple chamber structure described in Section 4.1, which consists of a fluid chamber and a compliant top support structure. Here we assume that in the energy harvesting chamber the top support structure is the only compliant structure, and the piston is rigid and perfectly sealed to piston walls without tethers. The effective compliance for this case was derived in Section 4.1 as:

$$C_{eff} = \left( \frac{V_o}{\beta_f} + C_s \right) = \left( \frac{\pi D_{ch}^2 H_{ch}}{4\beta_f} + \frac{\pi D_{ch}^6 (1 - \nu^2)}{1024 E t_{top}^3} \right) \quad (5.27)$$

where  $D_{ch}$  is the chamber diameter,  $H_{ch}$  is the chamber height, and  $t_{top}$  is the thickness of the top support structure. The dependence of the effective chamber compliance on the system scale is then

$$C_{eff} \sim \lambda^3 \quad (5.28)$$

which suggests that as the system gets smaller, the compliance gets smaller. Lets consider a case where  $P_{LPR} = 0$  and the effective chamber compliance is given by equation 5.27. For a certain power requirement, the required operation frequency can be calculated as:

$$f_{req} = \frac{4W}{(s_{33}^E - s_{33}^D)\sigma^2 A_p L_p} \quad (5.29)$$

where  $\sigma$  is the stress band on the piezoelectric element, which is equal to the maximum stress since  $P_{LPR} = 0$ . As discussed earlier, in a design procedure, the chamber diameter and the piezo diameter are chosen such that the maximum stress on the piezoelectric element is equal to the depolarization stress of the piezoelectric element. If we assume that for any design scenario

this condition will be satisfied, then the dependence of the required frequency on system scale can be obtained as:

$$f_{req} \sim \frac{1}{\lambda^3} \quad (5.30)$$

which suggests that as the system gets smaller, larger frequencies are required due to the reduced piezoelectric element volume. The required flowrate is given by:

$$Q = \frac{2(s_{33}^E + s_{33}^D)W}{(s_{33}^E - s_{33}^D)P_{HPR}} + C_{eff}P_{HPR}f_{req} \quad (5.31)$$

From equations 5.28 and 5.30 we can obtain the dependence of the required flowrate on the system scale as:

$$Q \sim \lambda^0 \quad (5.32)$$

which suggests that the required flowrate does not depend on the system scale. In smaller scale, although the system compliance reduces, the required frequency increases in the same amount which results in the same required flowrate. Since this results were derived for constant  $P_{HPR}$  and required power,  $W$ , the system efficiency does not depend on the system scale either, which can be expressed as:

$$\eta = \frac{W}{P_{HPR}Q} \sim \lambda^0 \quad (5.33)$$

It should be noted that this analysis relies on the assumption that the active valves can operate at very high frequencies and the valves and channels can provide the required flowrates even when the system gets very small.

Consider a design case where the operation frequency is equal to the maximum bandwidth of the device. If we make the system 10 times smaller and keep the required power and  $P_{HPR}$  the same, we will need 1000 times the frequency to generate the same power from the smaller device. However we can increase the operation frequency only 10 times since the natural frequency is inversely proportional to the system scale, which is expressed in equation 5.26. This implies that we can extract only one percent of the required power from the small device. However

we can fit 1000 small devices inside the original volume, which means that we can generate 10 times the original power from the same volume. This suggests that the power density is inversely proportional to the system scale, which can be expressed as:

$$PD \sim \frac{1}{\lambda} \quad (5.34)$$

This suggests that, as the system gets smaller, the power density increases. Again, it should be mentioned that, this analysis assumed that, in the smaller scale the valves and channels can provide the required flowrate regardless of the system scale. However, it is expected that viscous losses in the valves will begin to dominate beyond a certain scale and scaling further down will not be more efficient. In order to perform this study, more detailed fluid models are needed. Nevertheless, the above analysis provides a general understanding about the scaling of the system.

## 5.2 Design Procedure

This section will present a design procedure for designing the microhydraulic piezoelectric power generator. First, the design decisions made considering the issues discussed in previous sections as well as those imposed by the active valve design and fabrication process will be presented. Then, the design procedure will be described and two design examples will be presented along with simulation results.

### 5.2.1 Preliminary design decisions

As discussed in Chapter 3, the working fluid is chosen to be silicone oil due to its low viscosity and low density. It also has a comparable bulk modulus to that of water. Choice of piezoelectric element is done considering the results in sections 5.1.4, 5.1.4, and 5.1.4. From Figure 5-12 it can be seen that the piezoelectric material  $PZT - 5H$  has very high frequency requirements,  $PZT - 4S$ ,  $PZT - 8$  have lower and very similar frequency requirements, and  $PZN - PT$  has comparable frequency requirements to those of  $PZT - 4S$  and  $PZT - 8$ . If we examine Figures 5-13 and 5-14, we can see that  $PZN - PT$  requires much lower flowrates and provides much efficient power generation compared to other piezoelectric materials. In Chapter 2 it was

concluded that  $PZN - PT$  has the smallest energy density among the piezoelectric elements considered, which is a result of its low depolarization stress. However due to its very high coupling coefficient it provides very efficient electromechanical energy conversion and requires the lowest flowrate for a given power requirement. It should be noted that, the implication of the low energy density of  $PZN - PT$  is that, larger piezoelectric material volume is needed compared to other piezoelectric materials for the same power output. However, the weight of the piezoelectric element constitutes only a small fraction of the overall system weight and the increased efficiency of  $PZN - PT$  due to its much higher coupling coefficient would still overwhelm the effect of increased weight in terms of the overall system power density. The chamber height is chosen to be  $200\mu m$ . A preliminary study has shown that chamber heights smaller than this could cause squeeze film damping effect inside the chamber and can result in undesired losses. And, larger chamber heights would increase the chamber compliance, which would decrease the efficiency of the system. The length of the piezoelectric element is chosen to be  $1mm$ . This parameter is basically determined considering the actuation in the active valves, since all the piezoelectric cylinders within the system, namely the ones in the active valves and the one in the energy harvesting chamber, have the same length because of the layered structure of the device, which was explained in Chapter 1. Larger lengths would decrease the stiffness of the piezoelectric elements inside the active valves, which reduces the actuation capability, and smaller lengths could cause dielectric breakdown.

### 5.2.2 Parameters imposed by active valve design

The basic limitation of the active valves is their bandwidth. Current active valve designs predict bandwidths in the order of  $10 - 20kHz$ . Typical trade-offs in the active valve design are stroke, bandwidth and force, which are detailed in [5]. Another important limitation is the pressures that the active valves can work against, which basically imposes the maximum high reservoir pressure possible. They can typically work against pressures of  $2 - 3MPa$ . Also the active valves impose a minimum pressure requirement due to cavitation considerations in the hydraulic amplification chamber(HAC) within the active valve structure. In the design example presented, the low pressure reservoir pressure,  $P_{HPR}$  is chosen as  $0.5MPa$ .

### 5.2.3 Parameters imposed by fabrication process

As briefly described in Chapter 1, the device consists of silicon and pyrex micromachined layers. The thickness of the layers basically dictate the thicknesses of individual components. For example, a double layer piston structure, which consist of two silicon layers bonded to each other, will have a thickness of  $t_{pis} = 800\mu m$ , which is the case in the design example. Since the tethers are created through deep reactive ion etching(DRIE) of a SOI wafer, the tether thickness is defined by the SOI layer. Also, the fillet radius control during the fabrication process imposes some limitations on the tether width. For example narrow tethers would be very stiff due to the relatively large fillet radius and the predictions of the linear theory used for the optimization would not valid beyond a certain tether width. The top tether thickness,  $t_{tetop}$ , is chosen to be  $10\mu m$ , whereas the bottom tether thickness is chosen to be thinner, namely,  $5\mu m$ , because the bottom tether does not have any functionality and therefore it should be kept as thin as possible so that it won't cause significant resistance to piston motion. The thicknesses of the top and bottom support structures are determined by the number of layers used, including the packaging layers on top and bottom portions of the device. As discussed in Chapter 3, the compliance of the system is very important in terms of system performance and they should be kept as small as possible. Therefore it is desirable to have very thick top and bottom support structures. The effective thickness would also depend on the structure of the auxiliary system in which the device is packaged. In the design examples, the top and bottom structures are assumed to have the same thicknesses, namely  $t_{top} = t_{bot} = 2.5mm$ , and they are assumed to comprise of all silicon layers.

### 5.2.4 Design Procedure

Figure 5-18 presents a design procedure, which will be followed after the initial design decisions are made using above considerations. The first part consists of analytical design calculations. The pressure band in the chamber is dictated by the bias pressure,  $P_b$ , and high pressure reservoir pressure,  $P_{HPR}$ . The piston diameter and piezo diameter are calculated using equations 5.11 and 5.19, and the battery voltage is calculated using equation 5.6.

These calculations are followed by the tether structure optimization, which determines the optimum tether width,  $w_t$ , for the given tether thicknesses and piston diameter. The designed



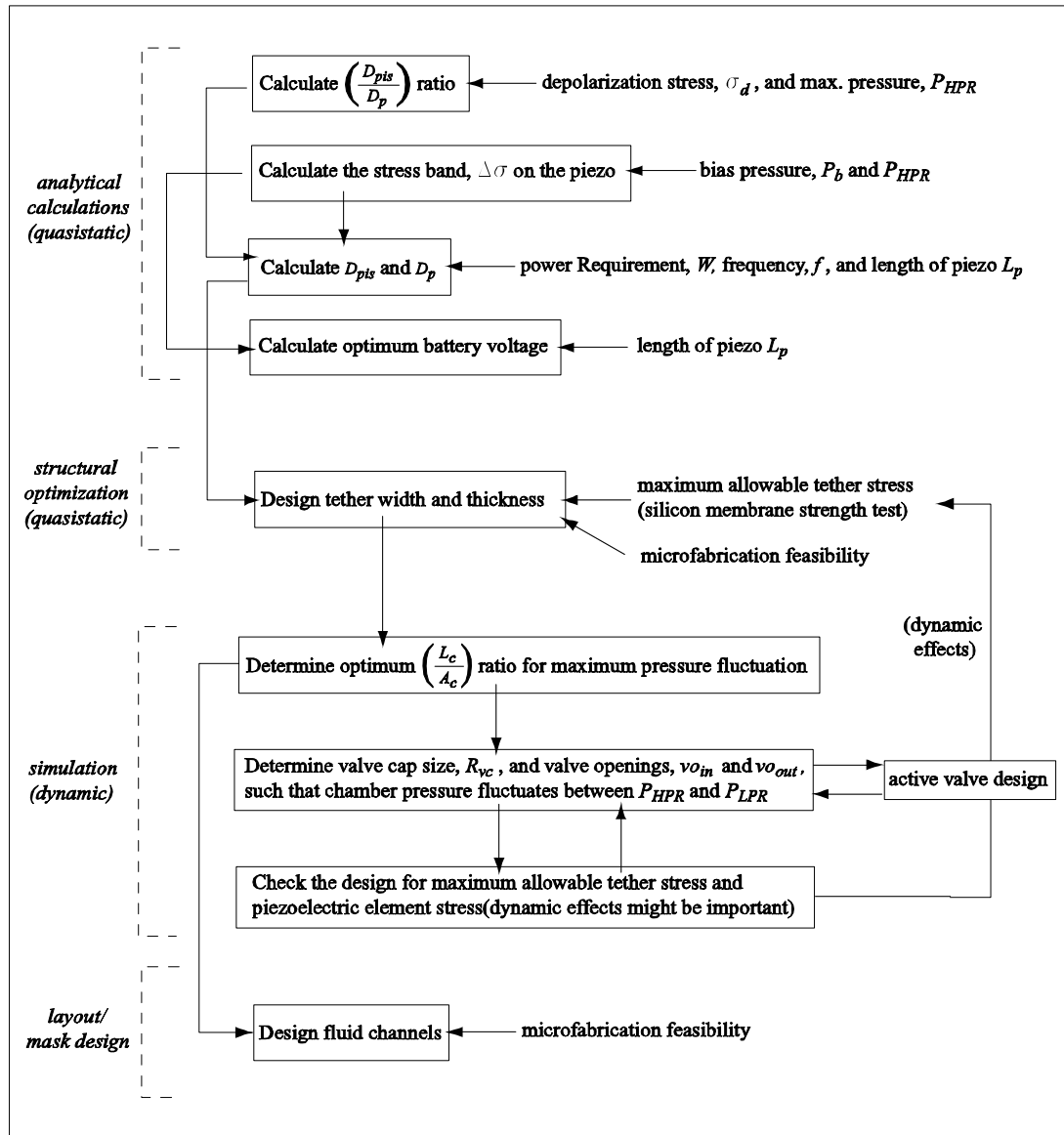


Figure 5-18: Design procedure.

tether width also determines the chamber diameter,  $D_{ch}$ . The geometric parameters along with the operation conditions are then fed to the system level simulation. The simulation architecture is shown 5-19 and the Simulink block diagrams are given in Appendix A.

First, simulations are performed to determine the optimum length to area ratio of the fluid channels, using arbitrary valve resistance, i.e. arbitrary valve cap size or valve openings. It is helpful to run these simulations with very small valve resistance, namely with very large valve opening or very large valve cap, since the fluidic oscillations are much more pronounced with lower valve resistances and it is easier to determine the optimum length to area ratio of the channels. Then, the valve cap size and valve opening are designed such that the chamber pressure fluctuates between reservoir pressures, namely between  $P_{HPR}$  and  $P_{LPR}$ . At this stage, it is important to consider structural limitations, which might be imposed by the active valves. For example, a large valve cap size requires a large membrane to allow sufficient valve motion, however this may cause excessive stresses in the membrane. Or, a very large valve opening can cause the same problem. Since the same effective valve resistance can be achieved with different combinations of valve opening and valve cap size, coupled iterations may be necessary with the active valve design procedure, which is not within the scope of this thesis. Detailed information about the active valve design procedure can be found in [5].

Finally, the system is simulated, stresses in the tethers and on the piezoelectric element are checked, and design iterations are performed if necessary. Although the valves are designed to achieve the desired pressure band in the chamber, the stress band may be a little bit different than expected. This can be explained by considering equation 5.11. This equation assumes static force balance between the piezoelectric cylinder and the piston. Also, the effect of the tether is neglected since the force exerted by the tethers on the piston is generally very small compared to the force exerted by the piezo and force due to chamber pressure. As will be seen in the design examples, the dynamics of the piston does not have a significant effect on system performance and it is reasonable to assume quasi-static force balance. However, if the operation frequency is much higher, the dynamics of the piston will be important and equation 5.11 will not be valid. The design procedure presented above is followed by the layout and mask design for the fabrication.

For the piston dynamics, a damping ratio of 5% is assumed, considering the piezoelectric

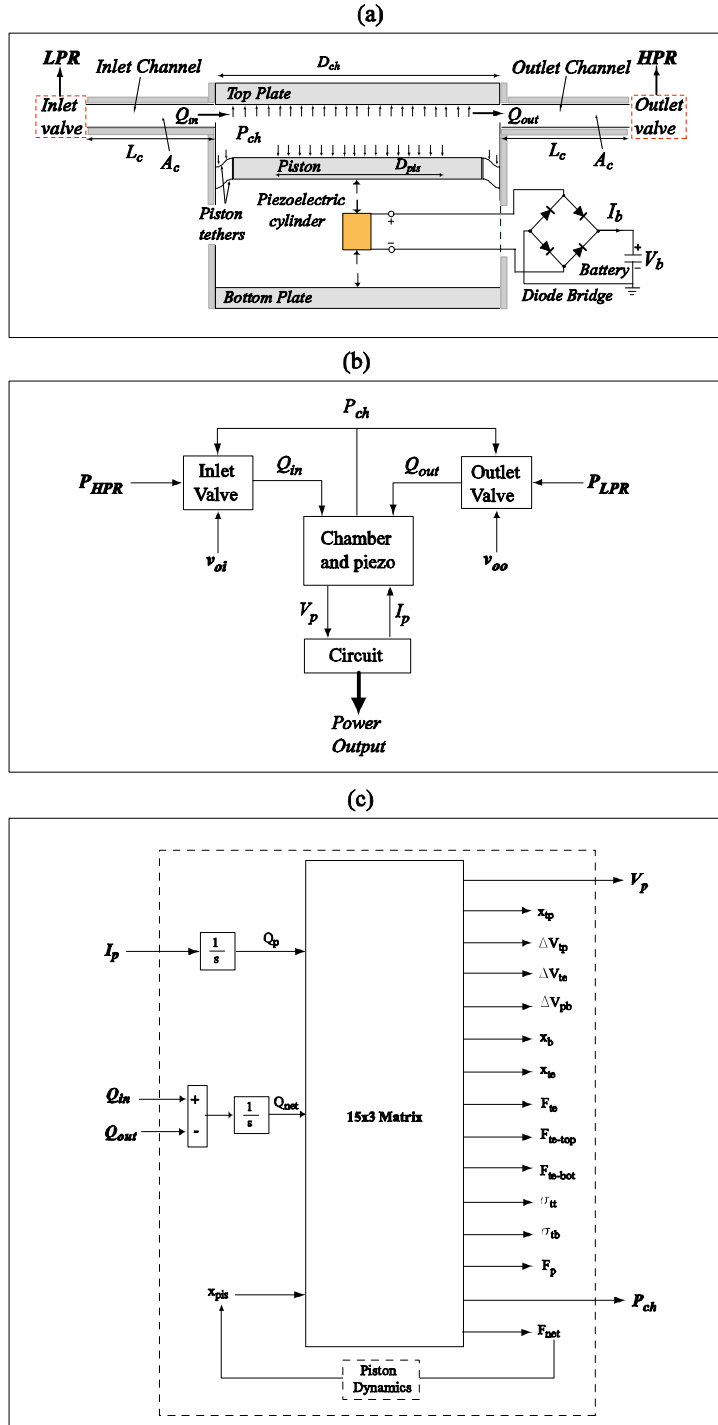


Figure 5-19: (a) System layout (b) System level simulation architecture (c) The chamber and piezo block in the overall system architecture which was developed in Chapter 4.

<b>Design Decisions</b>		
Piezoelectric material	PZN-PT	lowest flowrate requirement
Working fluid	silicone oil	low viscosity and density
Piezoelectric element length, $L_p$	1mm	active valve actuation
Chamber height, $H_{ch}$	200 $\mu m$	squeeze film damping
<b>Parameters imposed by fabrication process</b>		
Piston thickness, $t_{pis}$	800 $\mu m$	double layer piston
Top and bottom support structure thickness	2.5mm	packaging layers
Top tether thickness, $t_{tetop}$	10 $\mu m$	fabrication feasibility
Bottom tether thickness, $t_{tebot}$	5 $\mu m$	fabrication feasibility
<b>Material Limitations</b>		
Depolarization stress of piezoelectric element, $\sigma_d$	10MPa	shouldn't be exceeded
Maximum allowable stress in tethers	1GPa	shouldn't be exceeded
<b>Damping</b>		
Damping ratio of piston	5%	assumed

Table 5.1: Summary of preliminary design decisions applied to the design examples.

element as the effective spring. Namely the damping coefficient is calculated as:

$$c = 2\zeta\sqrt{m_{pis}k_p} = 2\zeta\sqrt{m_{pis}\frac{A_p}{s_{33}^D L_p}} \quad (5.35)$$

where  $\zeta$  is the damping ratio and  $s_{33}^D$  is the open circuit compliance of the piezoelectric element.

## 5.3 Design Examples

This section will present two design examples who have different operational requirements due to the limitations imposed by the active valves. The preliminary design decisions, parameters imposed by fabrication process and material limitations, which are valid for both examples are summarized in Table 5.1.

### 5.3.1 Design Example 1

The parameters imposed by the active valves, the design parameters obtained by applying the design procedure discussed in the previous section, and performance parameters are summarized in Table 5.2. Simulation results are shown in Figure 5-21, Figure 5-22 and Figure 5-23. The

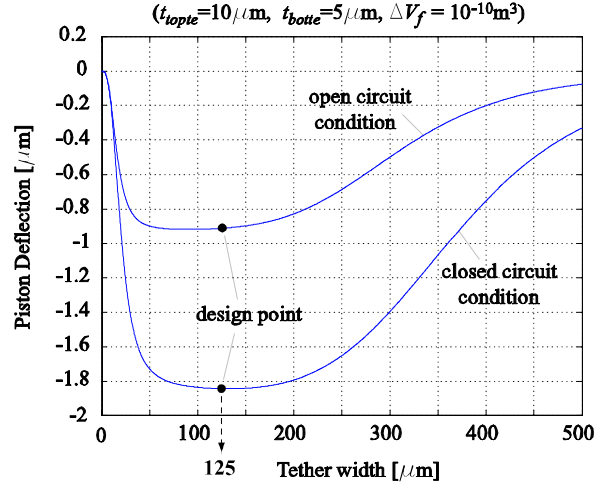


Figure 5-20: Tether structure design. Piston deflection shown for different tether widths.

tether structure optimization is shown in Figure 5-20 where the piston deflection is plotted as a function of the tether width for an added fluid volume of  $\Delta V_f = 10^{-10} m^3$ .

Figure 5-22 shows simulation results for the deflections and swept volumes of individual structural components. It can be seen that, as expected, the deflection of the bottom support structure is much smaller than the piston deflection, which is desirable for maximum piezoelectric element compression. Also, it can be seen that the volume swept due to tether bending, piston deformation and top support structure deformation is much smaller than the volume swept by the piston motion, which is again desirable for maximum piezoelectric element compression.

### 5.3.2 Design Example 2

The parameters imposed by the active valves, design parameters and performance parameters are summarized in Table 5.3. In this example, the performance of the active valves are very limited, which results in very small power output compared to the first example. Simulation results are shown in Figure 5-24, Figure 5-25 and Figure 5-26. The observations done for the deflections and swept volumes of the individual structural members in the first design example are also valid for this example. Namely, the deflection of the bottom support structure is

Power Requirement	0.25W	Electrical power output
<b>Parameters imposed by active valve design</b>		
Operation frequency, $f$	20kHz	bandwidth of active valves
Bias Pressure, $P_b$	0.5MPa	cavitation in HAC chamber
High Pressure Reservoir Pressure, $P_{HPR}$	3MPa	membrane stress limitation
<b>Important parameters resulting from operation conditions</b>		
Pressure band in the chamber, $\Delta P_{ch}$	2.5MPa	-
Stress band on piezoelectric element, $\Delta\sigma$	8.33MPa	-
<b>Designed parameters</b>		
Piston Diameter, $D_{pis}$	6.95mm	-
Piezoelectric cylinder diameter, $D_p$	3.8mm	-
Battery voltage, $V_b$	74.9V	-
Tether width, $w_t$	125 $\mu$ m	optimization
Chamber diameter, $D_{ch}$	7.2mm	-
Fluid channel length to area ratio, $\frac{L_c}{A_c}$	5000m <sup>-1</sup>	same for inlet and outlet
Valve cap radius, $R_{vc}$	400 $\mu$ m	same for inlet and outlet
Valve opening, $vo_{in}, vo_{out}$	24 $\mu$ m	same for inlet and outlet
<b>Performance parameters</b>		
Net flowrate, $Q_{net}$	0.52ml/s	-
Hydraulic power input	1.3W	$(P_{HPR} - P_{LPR})Q_{net}$
Efficiency, $\eta$	19.2%	$\frac{\text{Electrical power output}}{\text{Hydraulic power input}}$

Table 5.2: Summary of design and performance parameters of design example 1.

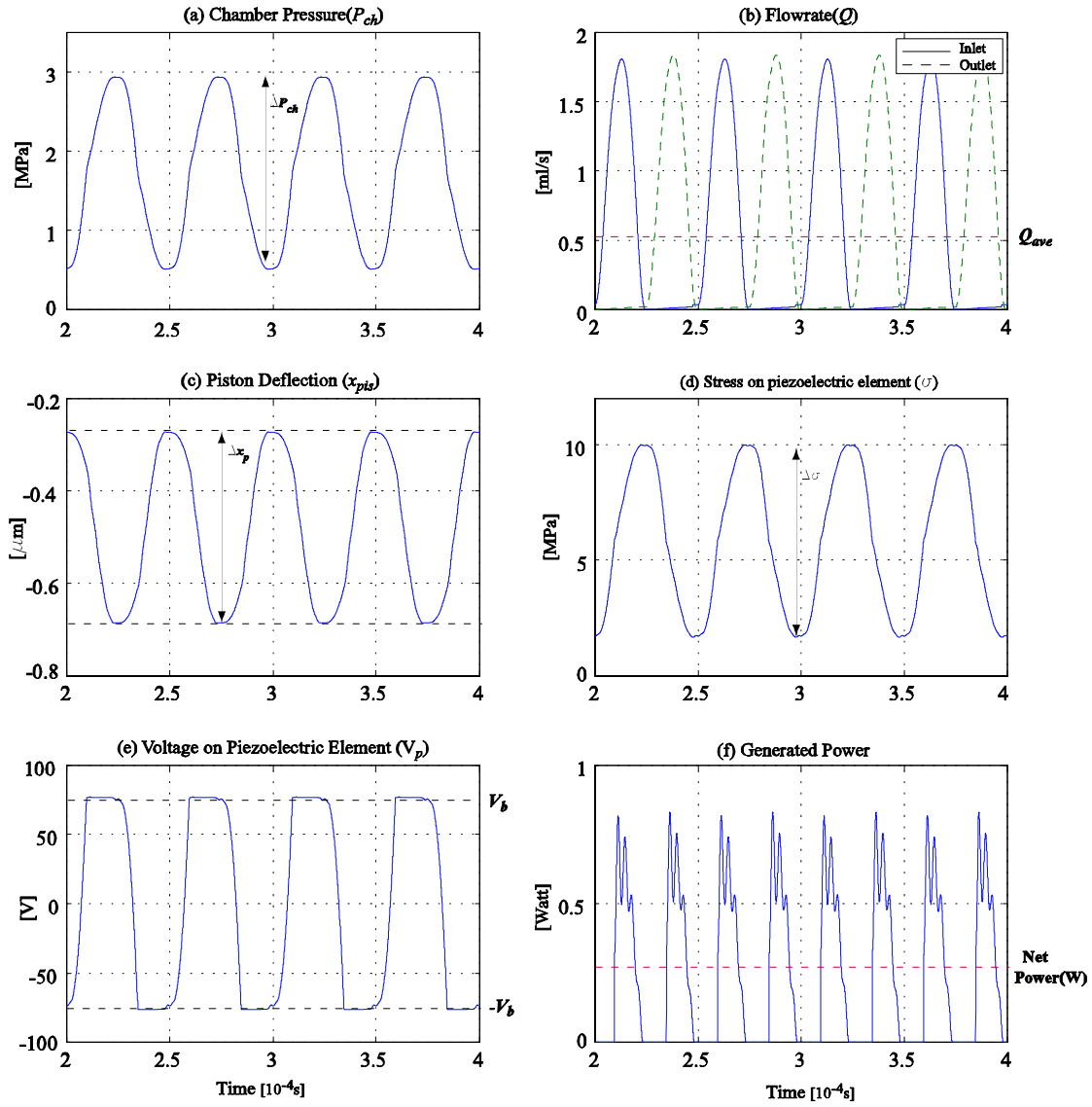


Figure 5-21: Simulation time histories of the design example 1.

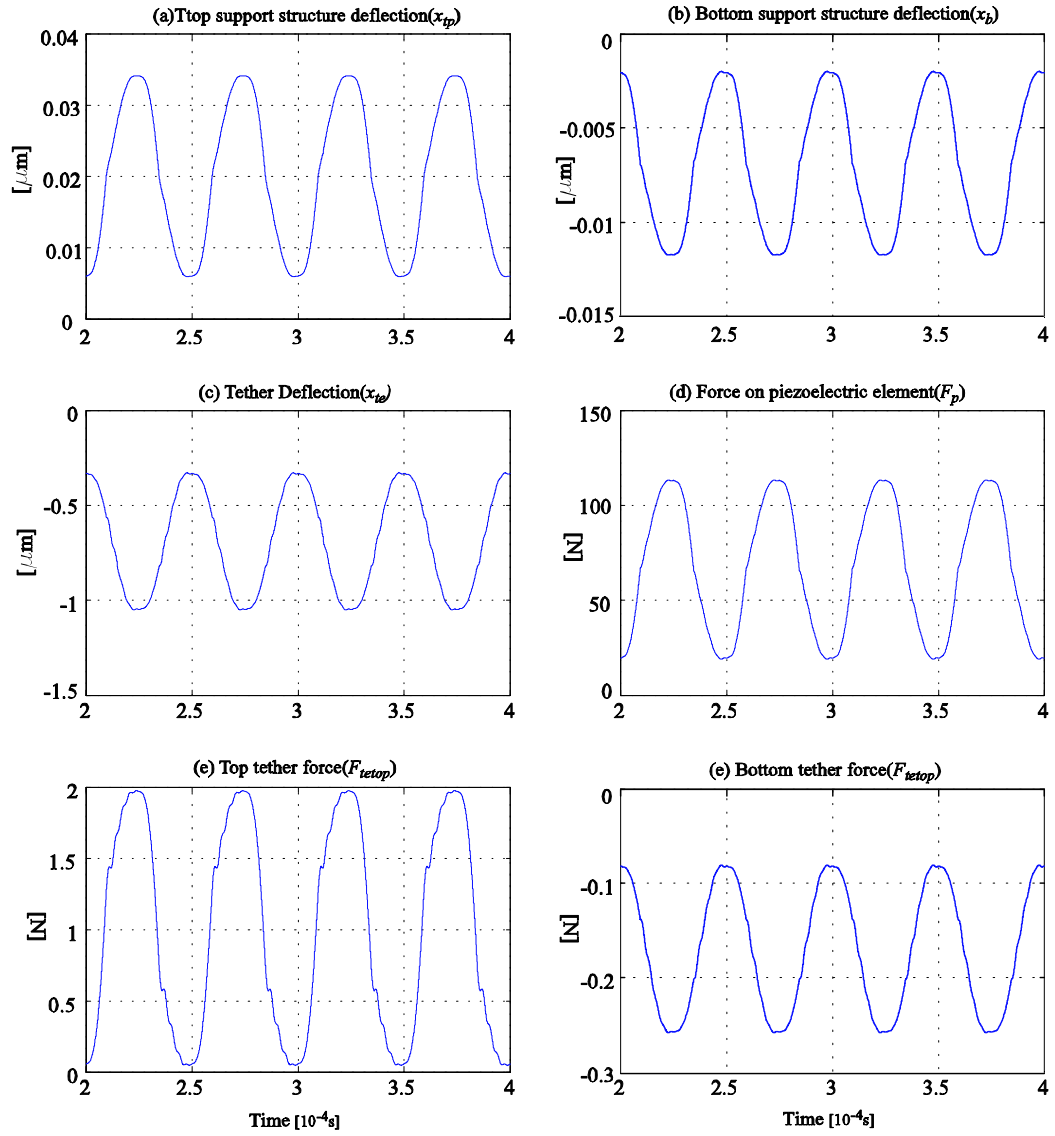


Figure 5-22: Simulation time histories of the design example 1.



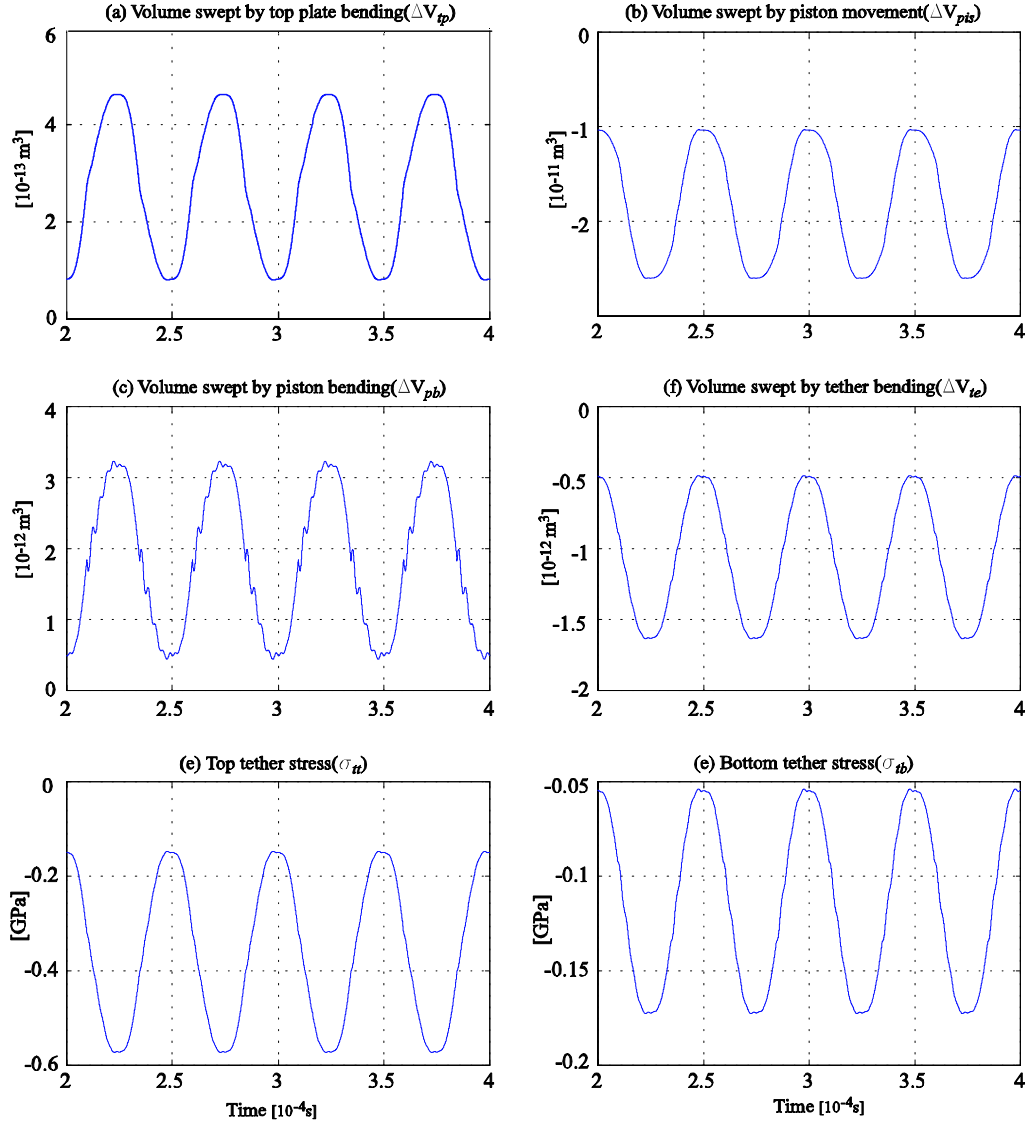


Figure 5-23: Simulation time histories of the design example 1.

Power Requirement	0.01W	Electrical power output
<b>Parameters imposed by active valve design</b>		
Operation frequency, $f$	5kHz	bandwidth of active valves
Bias Pressure, $P_b$	0.5MPa	cavitation in HAC chamber
High Pressure Reservoir Pressure, $P_{HPR}$	1.5MPa	membrane stress limitation
<b>Important parameters resulting from operation conditions</b>		
Pressure band in the chamber, $\Delta P_{ch}$	1MPa	-
Stress band on piezoelectric element, $\Delta\sigma$	6.67MPa	-
<b>Designed parameters</b>		
Piston Diameter, $D_{pis}$	4.89mm	-
Piezoelectric cylinder diameter, $D_p$	1.89mm	-
Battery voltage, $V_b$	59.9V	-
Tether width, $w_t$	125 $\mu$ m	optimization
Chamber diameter, $D_{ch}$	5.19mm	-
Fluid channel length to area ratio, $\frac{L_c}{A_c}$	110000m <sup>-1</sup>	same for inlet and outlet
Valve cap radius, $R_{vc}$	150 $\mu$ m	same for inlet and outlet
Valve opening, $vo_{in}, vo_{out}$	9.3 $\mu$ m	same for inlet and outlet
<b>Performance parameters</b>		
Net flowrate, $Q_{net}$	0.042ml/s	-
Hydraulic power input	0.042W	$(P_{HPR} - P_{LPR})Q_{net}$
Efficiency, $\eta$	23.8%	$\frac{\text{Electrical power output}}{\text{Hydraulic power input}}$

Table 5.3: Summary of design and performance parameters of design example 2.

much smaller than the piston deflection, which is desirable for maximum piezoelectric element compression and the volume swept due to tether bending, piston deformation and top support structure deformation is much smaller than the volume swept by the piston motion, which is again desirable for maximum piezoelectric element compression.

As discussed in the previous chapters, the generated power is a strong function of the stress band on the piezoelectric element and the operation frequency. As the maximum operating frequency reduces due to active valve design limitations, much larger piezoelectric elements and chamber structures are needed to generate the same amount of power. In the second design example, in order to generate the same power as in design example 1, huge chamber diameters, larger than 20mm, is needed, which is not feasible due to the increased compliance and size constraints. As discussed earlier in Section 5.1.6, it is feasible to make smaller and multiple devices which would fit in the original volume. In section 5.1.6 it was concluded that the efficiency does not depend on system scale. As can be seen from Tables 5.2 and 5.3 the

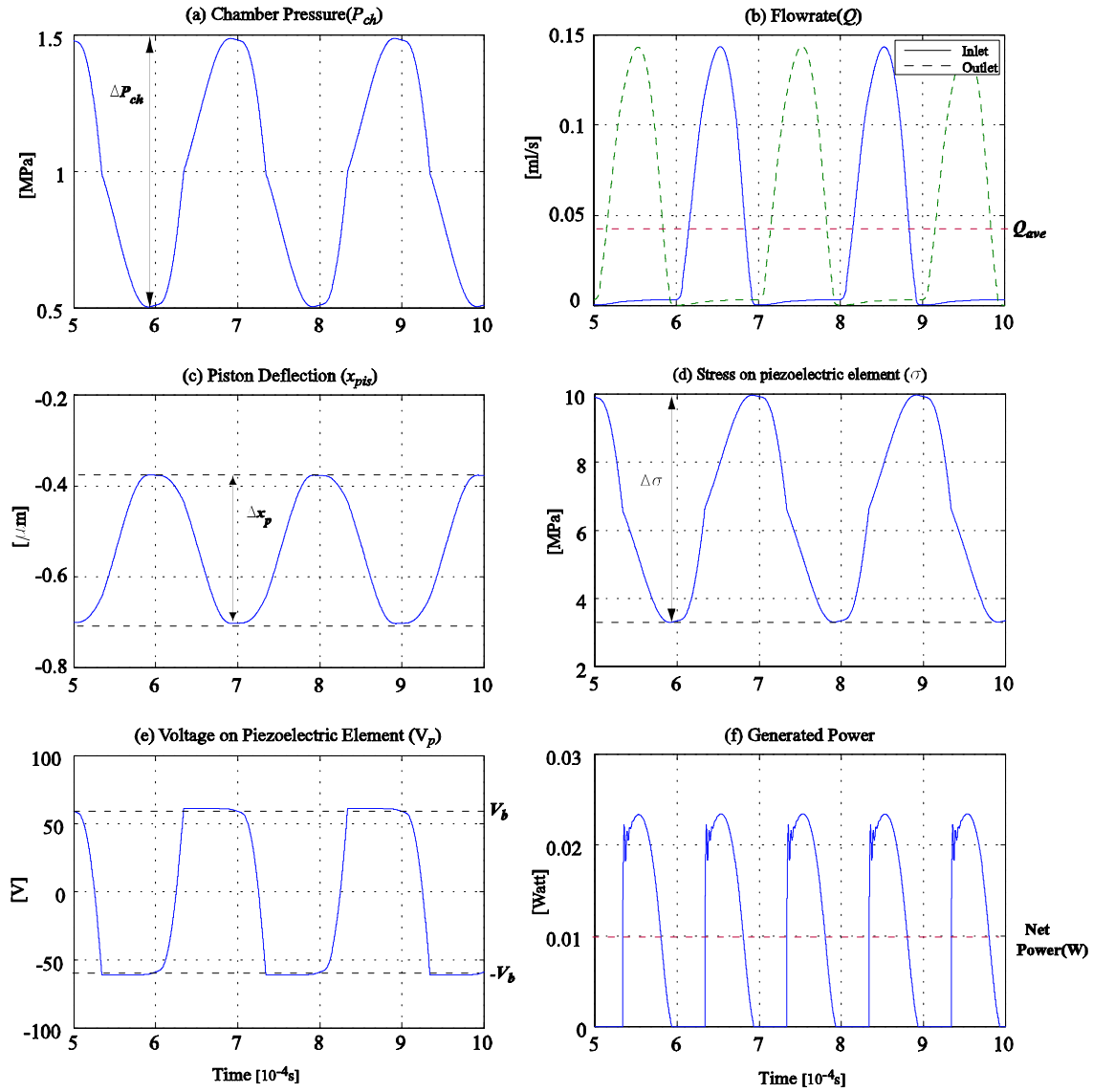


Figure 5-24: Simulation time histories of the design example 2.

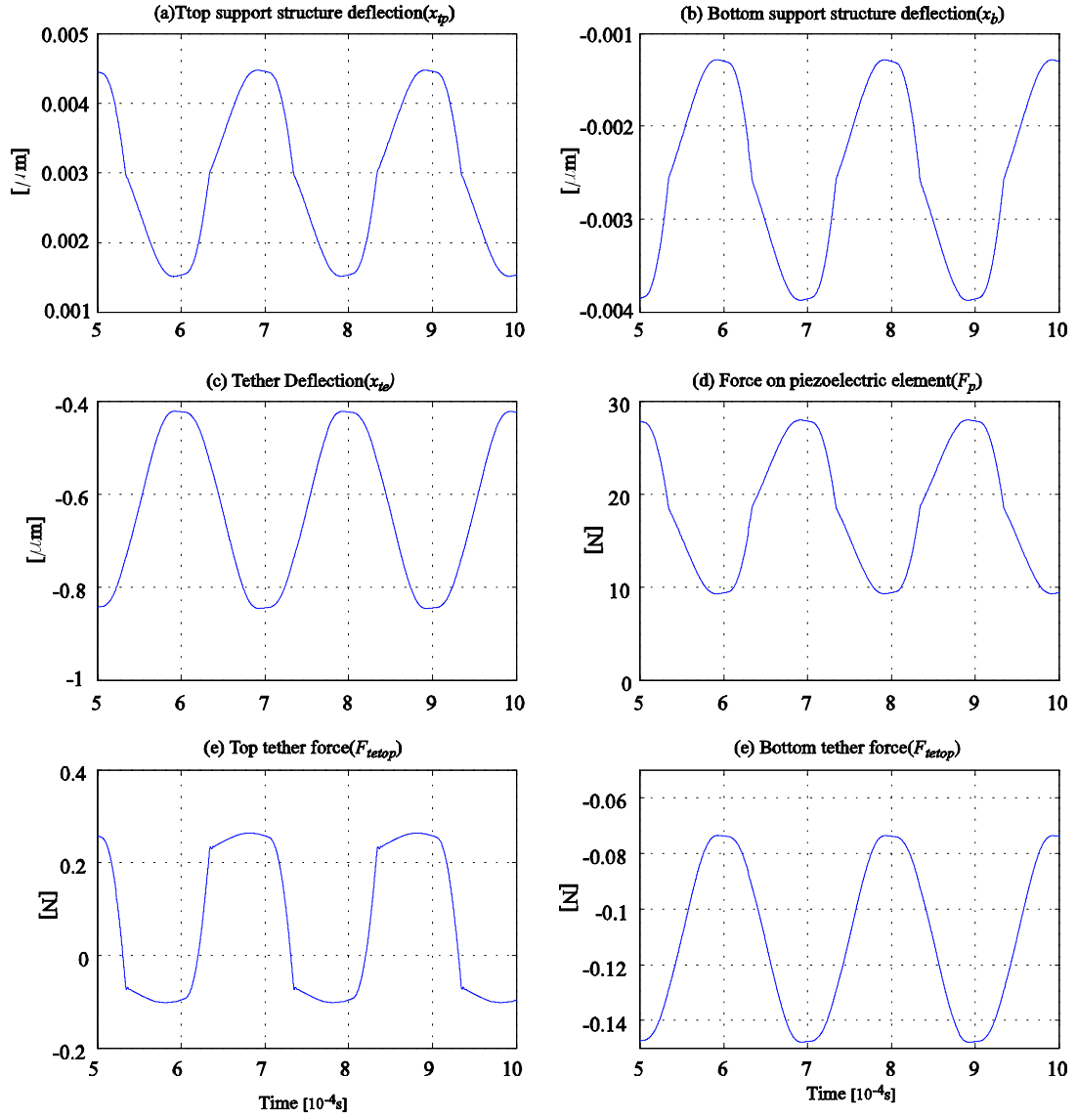


Figure 5-25: Simulation time histories of the design example 2.

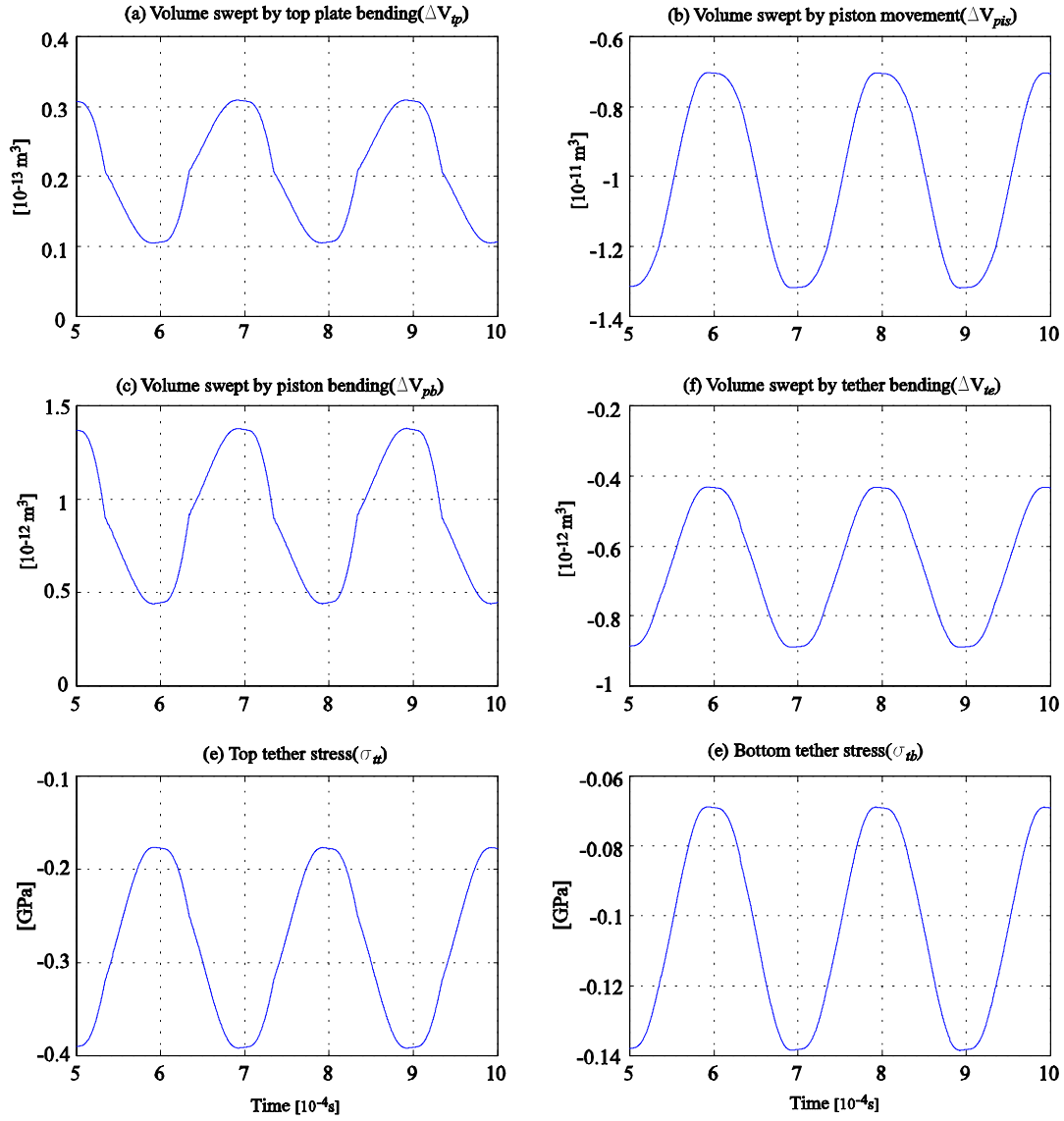


Figure 5-26: Simulation time histories of the design example 2.

second device, which is smaller than the first one, has higher efficiency. This is due to the fact that in the example, only the chamber diameter and piezo diameter are smaller. The length of the piezoelectric element, chamber height and structural thicknesses are kept constant. This resulted in a stiffer chamber compared to the case where all the dimensions were reduced. The explicit relationships and effect of geometric parameters on system scale can be seen in equation 5.27, which represents a simpler case than the actual chamber.

## 5.4 Summary

This chapter presented further design considerations and a design procedure along with two design examples. Fluidic oscillations within the system and conditions for sufficient chamber filling and evacuation is analyzed. An optimization procedure for the tether structure is presented. Trade-offs between operation conditions and their effect on the performance is discussed. Effect of system scale on the performance is discussed. Effect of the fabrication process and the active valves on the design is discussed.



## Chapter 6

# Conclusions and Recommendations for Future Work

### 6.1 Summary

The objectives of this thesis were:

- To develop a comprehensive system level model and simulation tool to analyze the main chamber and the associated fluid channels and valves of piezoelectric microhydraulic power generation devices
- To gain insight into system operation and understand the factors affecting the system performance
- Develop a design procedure, which should be complemented by the design of the active valves.

Chapter 1 presented the configuration, operation and motivation of microhydraulic-piezoelectric power generators. Primary challenges and preliminary design considerations is discussed.

Chapter 2 presented an analysis of piezoelectric power generation based on linear electromechanical energy conversion. Effect of circuitry and piezoelectric material on energy density and effective coupling factor is discussed. Models for two different circuit topologies are developed, simulations are performed and analytical expressions are derived for the generated power and effective coupling factor. Different piezoelectric materials are compared in terms of their energy densities and energy conversion efficiencies for different circuitry. It has been concluded



that, although the single crystal piezoelectric material (PZN-PT) has very high effective coupling factor, it has a very low energy density compared to PZT-8 or PZT-4S because of its small depolarization stress. Another important conclusion of this chapter is that, for a piezoelectric element, the energy density obtained with the diode bridge and voltage detector circuit is four times bigger than the energy density obtained with only the diode bridge. The effective coupling factor is a function of the coupling coefficient and the circuitry, whereas the energy density is a function of coupling coefficient, circuitry and the depolarization stress. Indeed, the effective coupling factor becomes an important criteria if the piezoelectric element is considered along with its surrounding system, for example the infrastructure which provides the force on the element, which is the energy harvesting chamber in the microhydraulic power generation device. It should be remembered that in the analysis presented in this chapter a prescribed force is imposed on the piezoelectric element. This issue is addressed in Chapter 3.

Chapter 3 presented a simple model of the energy harvesting chamber, simulations with the coupled circuitry and preliminary design considerations. The interaction of the energy harvesting chamber and the circuitry is discussed. The two circuits presented in Chapter 2 and different piezoelectric materials are compared in terms of the flowrate and frequency requirements for a given pressure differential and power requirement, and in terms of system efficiency. Analytical expressions are derived for the generated power, required flowrate, effective coupling factor and system efficiency. The most important conclusion of this chapter is that the performance of the energy harvesting chamber depends on

- Circuit topology
- Piezoelectric material( $k_{33}, \sigma_d$ )
- Chamber compliance( $C_{eff}$ ).

It is also concluded that, as  $k_{33}$  approaches 1 and  $C_{eff}$  approaches 0, the system efficiency for the two circuits analyzed approaches 50%. This means that, even with a perfect piezoelectric material( $k_{33} = 1$ ) and zero effective chamber compliance, which are not possible, the system efficiency cannot exceed 50%. It should be emphasized that the efficiency definition throughout the thesis corresponds only to the energy harvesting chamber. The electrical power consumption in the active valves is not considered.

Chapter 4 presented detailed modelling of the energy harvesting chamber. In Chapter 3,

an effective chamber compliance ( $C_{eff}$ ) was assumed to be used in the simulation and in the following analysis. This chapter investigated the contribution of different structural components on the effective compliance of the chamber. Deformations of individual structural members are calculated using linear plate theory. It is assumed that the deflections due to bending are significantly larger than that due to shearing. A simulation architecture is presented to be included in overall system level simulation, which allows for inclusion of the elastic equations into dynamic simulation as well as monitoring important parameters.

Chapter 5 presented further design considerations in addition to the design issues discussed in Chapter 3. These were fluidic oscillations within the system, chamber filling and evacuation, tether structure optimization, effect of operation conditions on system performance and trade-offs, and scaling issues. The system is analyzed only for the case where the chamber is attached to the regular bridge. A design procedure along with two design examples is presented. The design decisions made considering the issues discussed in previous chapters as well as those imposed by the active valve design and fabrication process is discussed. Simulation results are shown. In Chapter 2 it was concluded that  $PZN - PT$  has the smallest energy density among the piezoelectric elements considered, which is a result of its low depolarization stress. However due to its very high coupling coefficient it provides very efficient electromechanical energy conversion and requires lowest flowrate for a given power requirement. It should be noted that, the implication of the low energy density of  $PZN - PT$  is that, larger piezoelectric material volume is needed compared to other piezoelectric materials for the same power output. However, the weight of the piezoelectric element constitutes only a small fraction of the overall system weight and the increased efficiency of  $PZN - PT$  due to its much higher coupling coefficient would still overwhelm the effect of increased weight in terms of the overall system power density.

This thesis developed a framework to analyze piezoelectric microhydraulic power generators. Insight into system operation is gained and important factors affecting system performance are analyzed.

## 6.2 Recommendations for Future Work

Recommendations for future work in terms of modeling and design can be summarized in the following subgroups:

### Piezoelectric Element

The analysis presented in this thesis is based on linear electromechanical energy conversion. More detailed analysis including nonlinear effects is required to obtain better predictions for system performance. Also, piezoelectric element coefficients only in 3-3 direction is used since the piezoelectric element is subjected to compression parallel to the polarization of the element and assuming that the element is free to expand in lateral directions, so that  $T_3$  is the only nonzero stress component. However, this is not the case since the piezoelectric cylinder is bonded to the piston and bottom support structure. Finite element analysis is required to calculate the effective coefficients in 3-3 direction, namely effective  $d_{33}$ ,  $s_{33}^E$  and  $s_{33}^D$ .

### Fluid Structure Interaction

The system is analyzed for relatively low frequencies where the fluid channels were the only components whose dynamic behavior was important for system performance. At higher frequencies, the modal behavior of the piezoelectric element and the piston structure along with the fluid contained in the chamber might be important (added mass effect of the fluid). Detailed finite element models are needed to investigate the fluid structure interaction within the chamber.

### Fluid model

In this thesis, a simple fluid model based on discharge coefficients taken from published data is used. These models do not provide accurate estimation of the power consumption in the valves since it is not possible to predict the force exerted on the valve cap and valve membrane by the flow. Detailed CFD analysis can provide more insight into the fluid flow in the valve. This is very important because of the complicated geometry of the valves.

## **Squeeze film damping**

Squeeze film damping is a common problem in MEMS devices. Although not presented in this thesis, a preliminary analysis has shown that, for the chamber height used in the design, squeeze film effects are not important. However, for smaller devices, squeeze film damping can effect system performance significantly. Detailed analytical models and/or finite element studies are required to investigate this effect.

## **Scaling Study**

As the system size gets smaller, the power density increases, however, only until a certain scale. Beyond that scale, it is expected that viscous losses in the valves will begin to dominate and scaling further down will not be more efficient. In order to perform this study, more detailed fluid models are needed as mentioned earlier.

## **System level analysis**

This thesis concentrated on the main chamber, also called the energy harvesting chamber, of the piezoelectric microhydraulic power generators. System level simulations, including full active valve structure, should be performed to obtained better predictions about system performance and efficiency. However, it should be emphasized that, these simulations would provide realistic predictions provided that good fluid models exist, as discussed above.



# Bibliography

- [1] N.W Hagood, D.C. Roberts, L. Saggere, K.S. Breuer, K.S.Chen, J.A. Carretero, H. Li, R. Mlcak, S. Pulitzer, M. A. Schmidt, S. M. Spearing, Y.H.Su. "Micro Hydraulic Transducer Technology for Actuation and Power Generation". *Proceedings of the SPIE Annual International Symposium on Smart Structures and Materials*, 7:680-688, 2000.
- [2] Seward Webb Pulitzer III, "Feasibility Assesment and Design of Micro Hydraulic Solid-State Transducers". *SM Thesis, Masssachusetts Institute of Technology*, 2001.
- [3] H.Q. Li, D.C. Roberts, J.L. Steyn, K.T. Turner, J. A. Carretero, O. Yaglioglu, Y.H. SU, L. Saggere, N.W. Hagood, S.M. Spearing, M.A. Schmidt, R. Mlcak, K.S. Breuer. "A High Frequency High Flow Rate Piezoelectrically Driven MEMS Micropump". *Solid-State Sensor and Actuator Workshop*, pp. 69-72, 2000.
- [4] J. A. Carretero. "Measurement and Modeling of the Flow Characteristics of Micro Disc Valves". *SM Thesis, Masssachusetts Institute of Technology*, 2001.
- [5] D. C Roberts, O. Yaglioglu, J. Carretero, Y.H Su, L. Saggere, N.W. Hagood. " Modeling, Design, and Simulation of a Piezoelectrically Driven Microvalve for High Pressure, High Frequency Applications, SPIE Proceedings, 4327:366-380, 2001
- [6] D. C. Roberts. "Design, Modeling, Fabrication, and Testing of a Piezoelectric Microvalve for High Pressure, High Frequency Hydraulic Applications". *PhD Thesis, Masssachusetts Institute of Technology*, 2002.

- [7] K. Turner, " An Evaluation of Critical Issues for Microhydraulic Transducers: Silicon Wafer Bonding, Strength of Silicon on Insulator Membranes and Gold-Tin Solder Bonding" , *SM Thesis, Massachusetts Institute of Technology*, 2001.
- [8] D.A. Berlincourt. "Piezoelectric and Ferroelectric Energy Conversion".*IEEE Transactions on Sonics and Ultrasonics*, S-15(2):89-97,1968.
- [9] M. Umeda, K.Nakamura, S. Ueha. " Analysis of the Transformation of Mechanical Impact Energy to Electric Energy Using Piezoelectric Vibrator".*Jpn. Journal of Applied Physics*, 35:3267-3273, 1996.
- [10] M. Umeda, K.Nakamura, S. Ueha. "Energy Storage Characteristics of a Piezo-Generator using Impact Induced Vibration ".*Jpn. Journal of Applied Physics*, 36:3146-3151, 1997.
- [11] C. N. Xu, M. Akiyama, K. Nonaka, T. Watanabe. " Electrical Power Generation Characteristics of PZT Piezoelectric Ceramics". *IEEE Transactions on Ultrasonics, Ferroelectrics, and Frequency Control*, 45(4):1065-1070, 1998.
- [12] M. Goldfarb, L. D. Jones."On the Efficiency of Electric Power Generation With Piezoelectric Ceramic". *Journal of Dynamic Systems, Measurement, and Control*, Transactions of ASME, 121:566-571, 1999
- [13] P. G. Jones, S. P. Beeby, E. P. James, N. M. White."The Modelling of a Piezoelectric Vibration Powered Generator for Microsystems. In *Transducers '01*, 2001
- [14] D. J. Warkentin, N. W. Hagood. "Nonlinear Piezoelectric Shunting for Structural Damping". *Proceedings of SPIE*, 3041:747-757, 1997.
- [15] N. W. Hagood, A. von Flotow. " Damping of Structural Vibrations with Piezoelectric Materials and Passive Electrical Networks". *Journal of Sound and Vibration*, 146(2):243-268, 1991.
- [16] N. W. Hagood, W. H. Chung, A. von Flotow. " Modelling of Piezoelectric Actuator Dynamics for Active Structural Control". *Journal of Intelligent Material Systems and Structures*, 1(3):327-354, 1990.

- [17] W. P. Mason. "An Electromechanical Representation of a Piezoelectric Crystal Used as a Transducer". *Proceedings of the Institute of Radio Engineers*, 23(10):1252-1263, 1935.
- [18] IEEE Std 176-1987 IEEE Standard on Piezoelectricity, The Institute of Electrical and Electronics Engineers. 1987
- [19] Ching-Yu Lin. "Material Characterization and Modeling for Piezoelectric Actuation and Power Generation under High Electromechanical Loading". *PhD Thesis, Massachusetts Institute of Technology*, 2002
- [20] J. M. Hall, W. E. Dillon, W. C. Nunnally. "Thermo-Acoustic-Piezoelectric Power Generation". Proceedings of the 26th Intersociety Energy Conversion Engineering Conference-IECEC'91, 2001.
- [21] V. H. Schmidt. "Piezoelectric Energy Conversion in Windmills". Proceedings of IEEE: Ultrasonic Symposium, 2:897-904, 1992.
- [22] V. H. Schmidt. "Piezoelectric Wind Generator". *United States Patent #4,536,674*. August 20, 1985.
- [23] S. Nagao. "Electronic Wristwatch With Generator". *United States Patent #5,939,707*. Assignee: Seiko Epson Corporation, July 3, 1990.
- [24] O. Takahashi, Y. Hashimoto, E. Nagasaka, H. Miyazaki, T. Funasaka. "Piezoelectric Power Generator For a Portable Power Supply Unit and Portable Electronic Device Equipped With Same ". *United States Patent #5,751,091*. Assignee: Seiko Epson Corporation, May 12, 1998.
- [25] Y. Hashimoto, O. Takahashi, H. Miyazaki, T. Funasaka, M. Furahata. "Power Generation Method and Power Generator Using a Piezoelectric Element and Electronic Device Using The Power ". *United States Patent #5,835,996*. Assignee: Seiko Epson Corporation, November 10, 1998.
- [26] P. Smalser. "Power Transfer of Piezoelectric Generated Energy". *United States Patent #5,703,474*. Assignee: Ocean Power Technologies Inc., December 30, 1997.



- [27] G. W. Taylor, J. R. Burns. "Power Generation From Waves Near the Surface of Bodies of Water". *United States Patent* #4,404,490. September 13, 1983.
- [28] J. R. Burns. "Ocean Wave Energy Conversion Using Piezoelectric Material Members". *United States Patent* #4,685,296. August 11, 1987.
- [29] M. Y. Epstein, C. B. Carroll. "Piezoelectric Electric Energy Generator". *United States Patent* #5,512,795. Assignee: Ocean Power Technologies, Inc., April 30, 1996.
- [30] M. Y. Epstein. "Piezoelectric Generation of Electrical Power From Surface Waves on Bodies of Water Using Suspended Weighted Members". *United States Patent* #5,578,889. Assignee: Ocean Power Technologies, Inc., November 26, 1996.
- [31] M. Y. Epstein, G. W. Taylor. "Water Craft Using Piezoelectric Materials". *United States Patent* #5,621,264. Assignee: Ocean Power Technologies, Inc., April 15, 1997.
- [32] C. B. Carroll. "Frequency Multiplying Piezoelectric Generators". *United States Patent* #5,814,921. Assignee: Ocean Power Technologies, Inc., September 29, 1998.
- [33] J. R. Burns. "DC Bias Scheme For Field Induced Piezoelectric Power Generators". *United States Patent* #6,201,336. Assignee: Ocean Power Technologies, Inc., March 13, 2001.
- [34] E. A. Kolm, H. H. Kolm. "Piezoelectric Fluid-Electric Generator". *United States Patent* #4,387,318. Assignee: Piezo Electric Products, Inc., June 7, 1983.
- [35] H. H. Kolm, E. A. Kolm. "Piezoelectric Acousto-Electric Generator". *United States Patent* #4,467,236. Assignee: Piezo Electric Products, Inc., August 21, 1984.
- [36] P. A. Todd, B. R. Walker. "Piezoelectric Circuit". *United States Patent* #5,065,067. November 12, 1991.
- [37] M. Kimura. "Piezo-Electricity Generation Device". *United States Patent* #5,801,475. Assignee: Seiki Company, Ltd., September 1, 1998.
- [38] S. Yamashita. "Portable Piezoelectric Electric Generation Device". *United States Patent* #4,091,302. May 23, 1978.

- [39] C. G. Triplett. "Vehicular Mounted Piezoelectric Generator". *United States Patent* #4,504,761. March 12, 1985.
- [40] E. Dieulesaint, D. Royer, D. Mazerolle, P. Nowak. "Piezoelectric Transformers". *Electronic Letters*, 24(7):444-445, 1998.
- [41] G. Ivensky, I. Zafrany, S. B. Yaakov. "Generic Operational Characteristics of Piezoelectric Transformers". *Proceedings of IEEE: Power Electronics Specialists Conference*, 3:1657-1662, 2000.
- [42] S. H. Lee, J. Hong, J.H. Yoo, G. S. Gong. "Characteristics of Piezoelectric Transformer for Power Supply". *Proceedings of IEEE: Ultrasonics Symposium*, 1:971-975, 1998.
- [43] J. Navas, T. Bove, J.A. Cobos, F. Nuno, K. Brebol. "Miniaturised Battery Charger Using Piezoelectric Transformers". *Proceedings of IEEE: Applied Power Electronics Conference and Exposition*, 1:492-496, 2001.
- [44] A. M. Flynn, S. R. Senders. "Fundamental Limits on Energy Transfer and Circuit Considerations for Piezoelectric Transformers". *Proceedings of Power Electronic Specialists Conference, IEEE Transactions*, 2:1463-1471, 1998.
- [45] S. E. Park, V. Vedula, M. J. Pan, W. S. Hackenbauer, P. Pertsch, T. Shrout. "Relaxor Based Ferroelectric Single Crystals For Electromechanical Actuators". *Proceedings of the SPIE*, 3324:136-144, 1998.
- [46] Q. M. Zhang, J. Zhao, K. Uchino, J. Zheng. "Change of the Weak-Field Properties of  $\text{PB}(\text{ZrTi})\text{O}_3$  Piezoceramics With Compressive Uniaxial Stresses and Its Links to the Effect of Dopants on the Stability of the Polarizations in the Materials". *J. Mater. Res.*, 12(1):226-234, 1997.
- [47] V. D Kugel, Q. M. Zhang, B. Xu, Q. M. Wang, S. Chandran, L.E. Cross. "Behavior of Piezoelectric Actuators under High Electric Field". *Proceedings of the Tenth IEEE International Symposium on Applications of Ferroelectrics*, 2:655-658, 1996.

- [48] J. Zhao, Q. M. Zhang. "Effect of Mechanical Stress on the Electromechanical Performance of PZT and PMN-PT Ceramics". *Proceedings of the Tenth IEEE International Symposium on Applications of Ferroelectrics*, 2:971-974, 1996.
- [49] G. Yang, W. Ren, S.F. Liu, A. J. Masys, B. K. Mukherjee. "Effects of Uniaxial Stress and DC Bias Field on the Piezoelectric, Dielectric, and Elastic Properties of Piezoelectric Ceramics". *Proceedings of IEEE: Ultrasonics Symposium*, 2:1005-1008 , 2000.
- [50] S. Timoshenko. "Theory of Plates and Shells". McGraw-Hill, NewYork, NY, 1940.
- [51] I.E. Idelchik. "Handbook of Hydraulic Resistance", FL, 1994
- [52] Y.H. Su. Personal communication. *Massachusetts Institute of Technology*, 2000
- [53] V. Caliskan. Personal communication. *Massachusetts Institute of Technology*, 2001

# Appendix A

## Simulink Block Diagrams

This section presents the simulink models used in this thesis. Figure A-1 shows the model of the piezoelectric element model used in Chapter 2 in order to simulate the case of applied force. Later in the thesis, namely in Chapter 4 and Chapter 5, the piezoelectric element constitutive equations are solved along with the elastic equations of the structural members of the main chamber and incorporated into the simulation architecture with a 15x3 matrix, as described in Chapter 4. Figures A-2 and A-3 present the simulink models of the regular diode bridge and the diode bridge attached to the voltage detector, respectively, used throughout the thesis. Figure A-4 presents the simulink blocks used to implement the function of the voltage detection circuit. Figure A-5 shows the simulink architecture of the full system including the main chamber, fluid models and circuitry, used in Chapter 5. Simulations in Chapter 3 are performed with a similar model. Figures A-6, A-7 and A-8 present the simulink models for the main chamber presented in Chapter 4 and the fluid models presented in Chapter 3. The circuit model used for the simulations in Chapter 5, where the system is simulated only with regular diode bridge, is the same as in Figure A-2.

**Implementation of the voltage detector circuit and silicon controlled rectifier** The operation of the voltage detection circuit was described in Chapter 2. The function of the voltage detector is implemented as follows: The voltage detector block in the Simulink model sends a signal to the switch/resistor block which is either 1 or zero depending on the detected voltage,  $V_2$ . The logic is as follows:

$$\begin{aligned}
&\text{If } \frac{dV_2}{dt} < 0 \quad \text{and} \quad V_2 > 0 \quad \text{signal}=1 \text{ (switch on)} \\
&\text{If } \frac{dV_2}{dt} > 0 \quad \text{and} \quad V_2 > 0 \quad \text{signal}=0 \text{ (switch off)} \\
&\text{If } \frac{dV_2}{dt} < 0 \quad \text{and} \quad V_2 < 0 \quad \text{signal}=0 \text{ (switch off)} \\
&\text{If } \frac{dV_2}{dt} > 0 \quad \text{and} \quad V_2 < 0 \quad \text{signal}=0 \text{ (switch off)}
\end{aligned}$$

The switch function is implemented with a resistor in the place of the SCR, whose value depends on the signal. If the signal value is 1, the value of the resistor is very small and the switch is in "on" state. If the signal value is 0, the value of the resistor is very large and the switch is in "off" state. The following parameter values are used:

Large resistance:  $10^6 \text{ Ohm}$ , small resistance:  $10^{-6} \text{ Ohm}$ , capacitance value:  $10^{-7} \text{ F}$ , inductor value:  $20 \text{ mH}$ ,  $m = 5$ ,  $K = 10^7$ ,  $\omega = 5 \times 10^{12}$ .

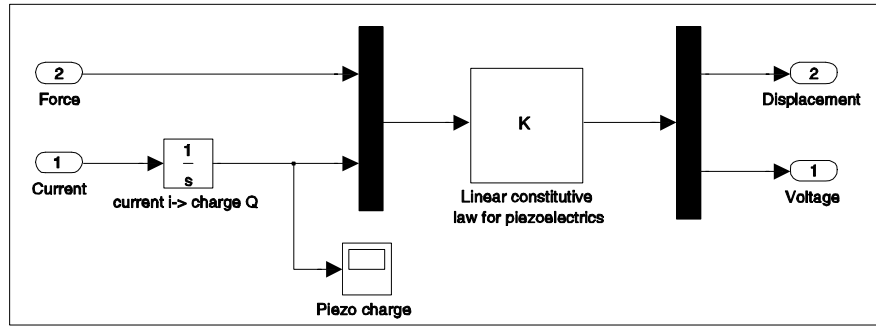


Figure A-1: Simulink model of the piezoelectric element.

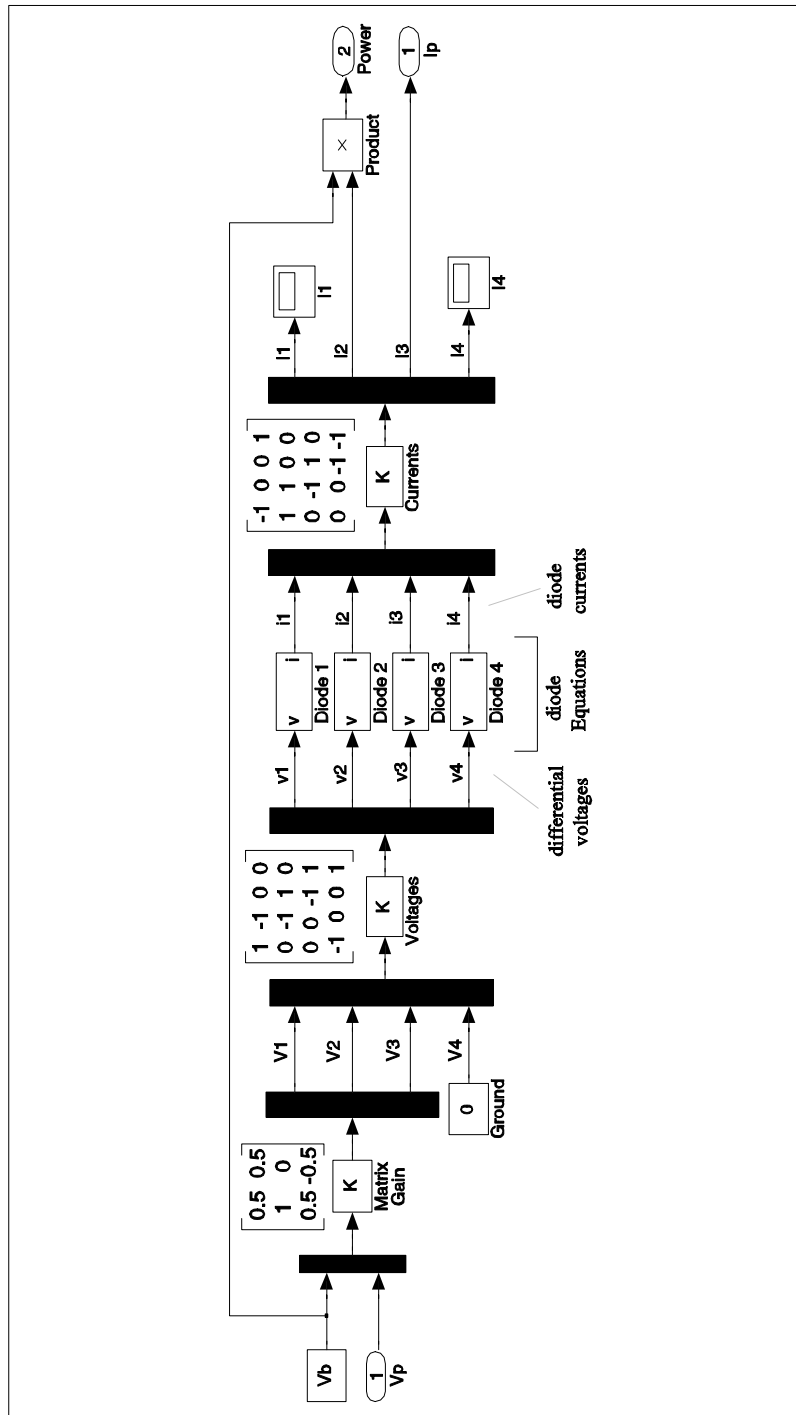


Figure A-2: Simulink model of the diode bridge.

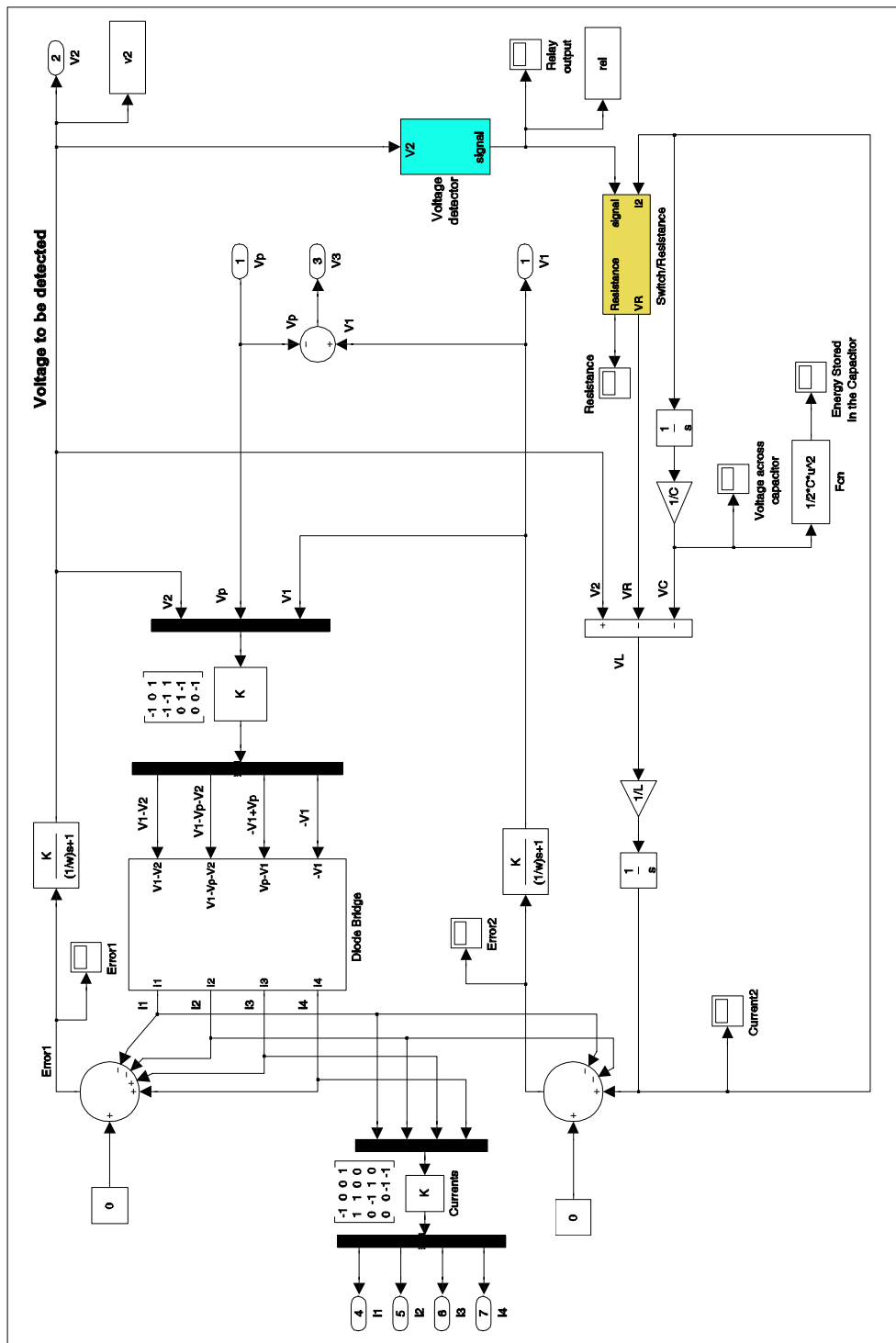


Figure A-3: Simulink model of the diode bridge attached to an inductor, voltage detector and SCR(Silicon Controlled Rectifier).

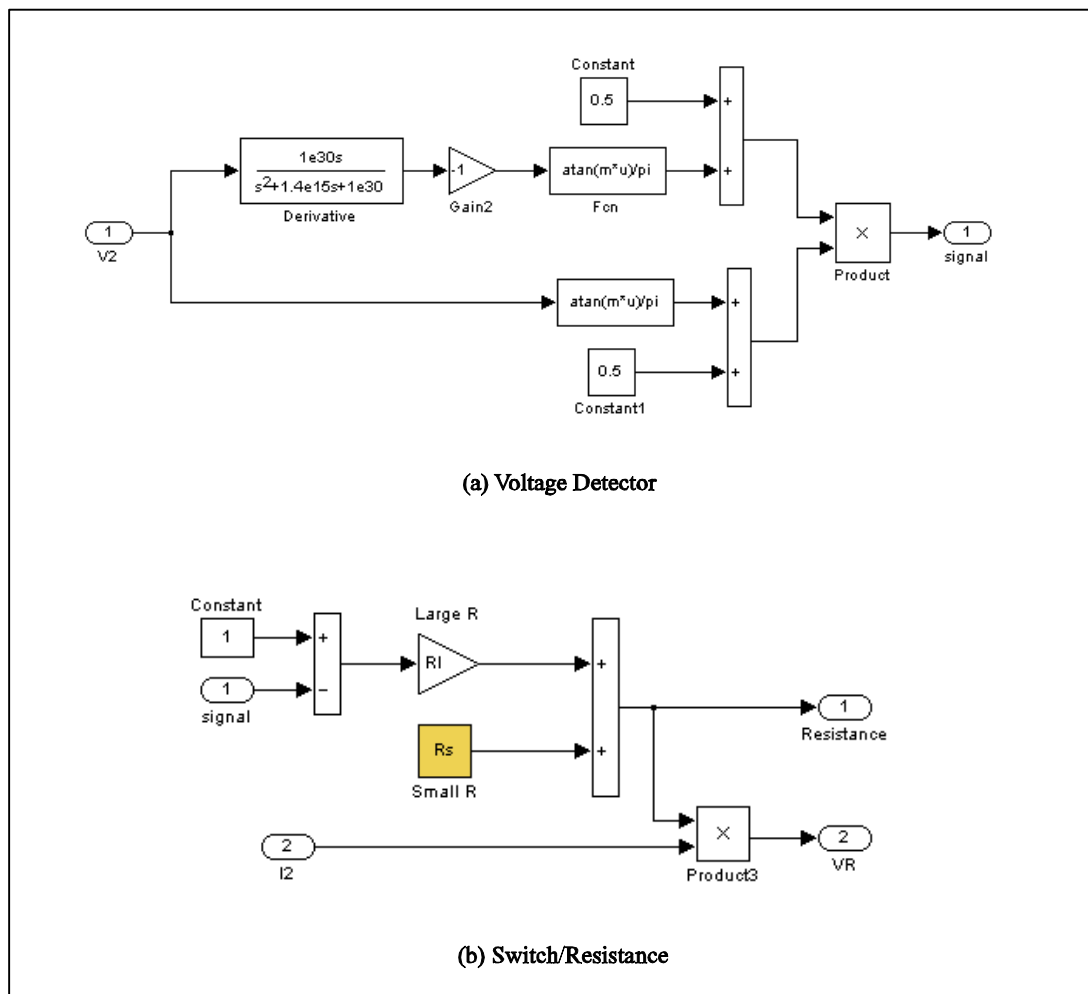


Figure A-4: Implementation of the voltage detector circuit.





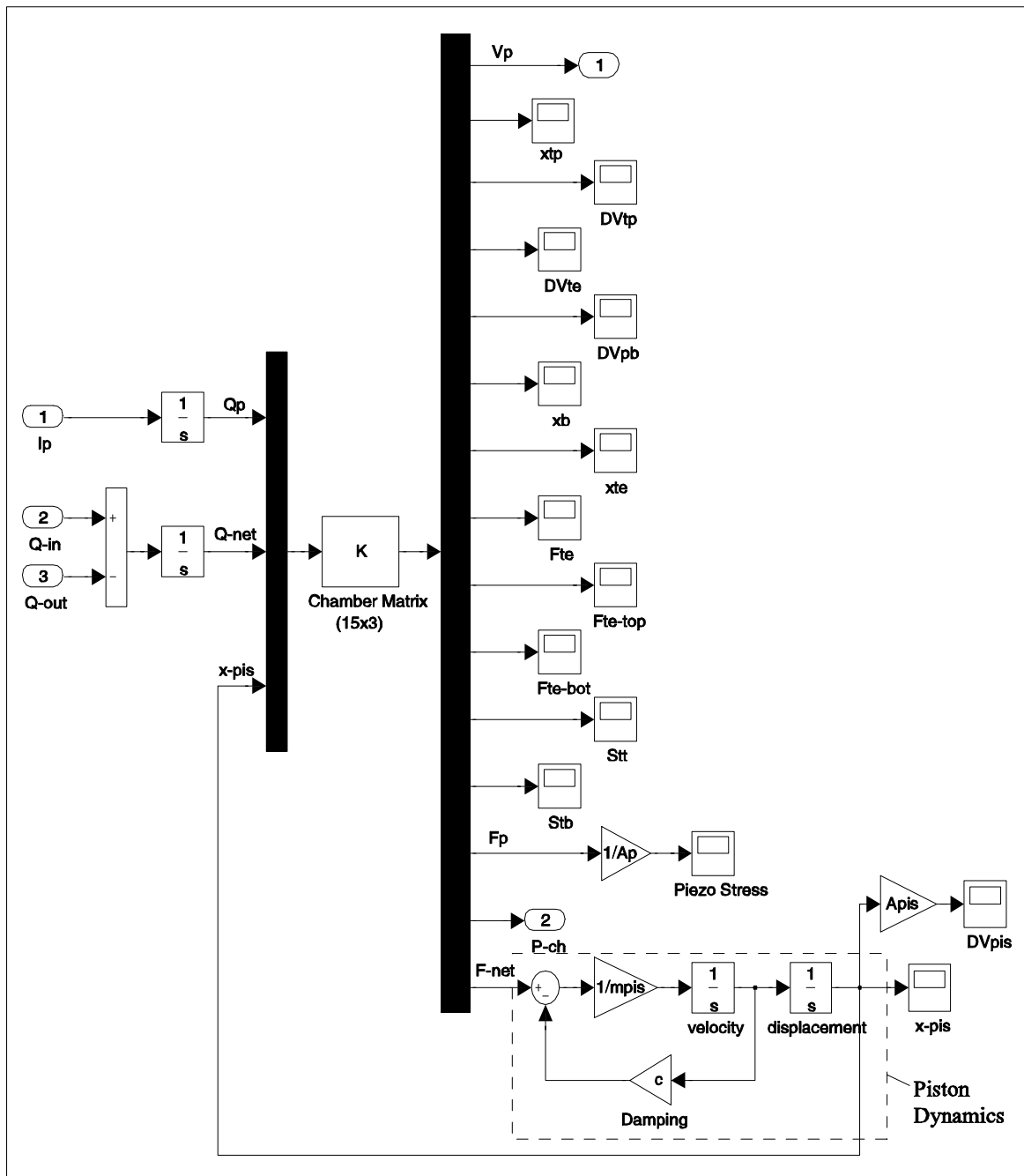


Figure A-6: Simulink model of the main chamber and the piezoelectric element.

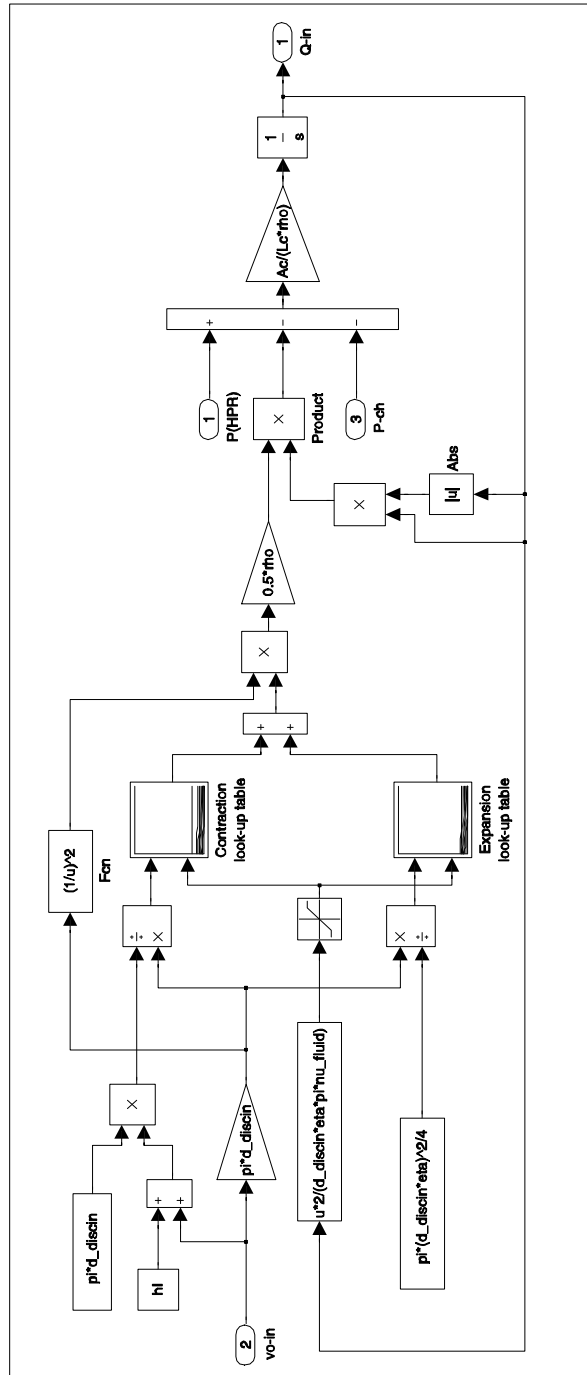
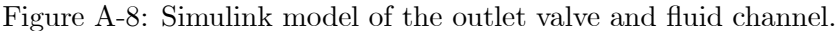


Figure A-7: Simulink model of the inlet valve and fluid channel.





# Appendix B

## Matlab Files

This section presents important Matlab codes used in the thesis.

Figure B-1 presents the code used in Chapter 3 to calculate the required frequency, flowrate and efficiency for different circuitry.

Figure B-2 presents the code used to calculate the required frequency, flowrate and efficiency of the system attached to regular diode bridge for different reservoir pressures and chamber diameters in Chapter 5.

Figure B-3 presents the Matlab code used in Chapter 5 for tether optimization. The elastic equations and equations governing the chamber behavior are solved in Maple, which is presented in Appendix C.

Figure B-4 presents the Matlab code used in Chapter 5 which writes the operational and some of the geometric parameters into the Matlab workspace, which can be read by the Simulink model for the system level simulation. Also, the 15x3 matrix required by the Simulink model (Appendix A) is generated, whose coefficients are calculated by Maple, which is presented in Appendix C.

```

% This code calculates the required frequency, flowrate and efficiency for two different circuitries.
% Effect of tethers is neglected and perfect sealing between the piston and the chamber walls is assumed.

clear all;

% Piezo properties (PZN-4.5kPT)

s33E = 81e-12 ; % Closed circuit compliance
s33D = 17e-12 ; % Open circuit compliance
Sd = 10e6; % Depolarization stress
PHPR = 2e6 ; % High pressure reservoir
W = 0.5 ; % Power requirement

% Dimensions

Dpis = (4.5e-3); % Piston diameter (=chamber diameter since the effect of tethers is neglected)
Aps = (Dpis^2)*pi/4; % Piston area
Ap = Aps*PHPR/Sd; % Piezo area
Dp = sqrt(4*Ap/pi); % Piezo diameter
Lp = (1e-3) ; % Piezo length
Vp = Ap*Lp ; % Piezo volume

% Chamber stiffness

Keff = [1e15, 2e15, 3e15, 4e15, 5e15, 6e15, 7e15, 8e15, 9e15, 1e16, 2e16, 3e16, 4e16, 5e16, ...
        6e16, 7e16, 8e16, 9e16, 1e17, 2e17, 3e17, 4e17, 5e17, 6e17, 7e17, 8e17, 9e17, 1e18, 2e18, ...
        3e18, 4e18, 5e18, 6e18, 7e18, 8e18, 9e18, 1e19, 2e19, 3e19, 4e19, 5e19, 6e19, 7e19, 8e19, 9e19, 1e20];

% RECTIFIER

% Energy stored per cycle
Er = ((s33E-s33D).*(Sd).^2.*Vp)/4;

% Required frequency [kHz]
fr = W./Er./1000;

% Required flowrate [ml/s]
Qr = (2.*(s33E+s33D).*W./((s33E-s33D).*(PHPR)+(PHPR.*1000./Keff)).*1e6 ;

% Efficiency
Eayr = (W./((Qr.*1e-6).*(PHPR)).*100;

% RECTIFIER+VOLTAGE DETECTOR

% Energy stored per cycle
Es = -(s33D-s33E).*(Sd.^2.*Lp.*Ap.*(s33E.*Lp.*Keff.*Aps.^2+Ap).*(s33D.*Lp.*Keff.*Aps.^2+Ap)/...
      ((Ap+2.*s33E.*Lp.*Keff.*Aps.^2-s33D.*Lp.*Keff.*Aps.^2).^2);

% Required frequency [kHz]
fs = W./Es./1000 ;

% Required flowrate [ml/s]
Qs = (W.*(PHPR.^2+2.*s33E.*Lp.*Keff.*Sd.^2.*Ap-s33D.*Lp.*Keff.*Sd.^2.*Ap).*(...
      (3.*s33E.*Lp.*Keff.*Sd.^2.*Ap.*PHPR.^2+s33E.*Lp.^2.*Keff.^2.*Sd.^4.*Ap.^2.*s33D+PHPR.^4-PHPR.^2.*s33D.*Lp.*Keff.*Sd.^2.*Ap)/...
      (PHPR.*(s33E.*Lp.*Keff.*Sd.^2.*Ap+PHPR.^2).*(-s33D+s33E).*(Ap.*Sd.^2.*Lp.*(PHPR.^2+s33D.*Lp.*Keff.*Sd.^2.*Ap).*(Keff)).*1e6;

% Efficiency
Eays = ((s33E.*Lp.*Keff.*Sd.^2.*Ap+PHPR.^2).*(-s33D+s33E).*(Ap.*Sd.^2.*Lp.*(PHPR.^2+s33D.*Lp.*Keff.*Sd.^2.*Ap).*(Keff./...
      ((PHPR.^2+2.*s33E.*Lp.*Keff.*Sd.^2.*Ap-s33D.*Lp.*Keff.*Sd.^2.*Ap).*(...
      (3.*s33E.*Lp.*Keff.*Sd.^2.*Ap.*PHPR.^2+s33E.*Lp.^2.*Keff.^2.*Sd.^4.*Ap.^2.*s33D+PHPR.^4-PHPR.^2.*s33D.*Lp.*Keff.*Sd.^2.*Ap))*100;

Ceff=1./Keff; % Effective compliance

figure(1)
h=semilogx(Ceff,Qr,'b--',Ceff,Qs,'r-');
set(h,'LineWidth',2)
title('Study3')
xlabel('Ceff [m^3/Pa]')
ylabel('Flowrate [ml/s]')
legend('Rectifier','Rectifier+Voltage Detector')
grid on
axis([1e-20 1e-15 0 10])

figure(2)
h=semilogx(Ceff,fr,'b--',Ceff,fs,'r-');
set(h,'LineWidth',2)
xlabel('Ceff [m^3/Pa]')
ylabel('Frequency [kHz]')
grid on

figure(3)
h=semilogx(Ceff,Eayr,'b--',Ceff,Eays,'r-');
set(h,'LineWidth',2)
xlabel('Ceff [m^3/Pa]')
ylabel('System Efficiency [ml/s]')
legend('Rectifier','Rectifier+Voltage Detector')
grid on

```

Figure B-1: Matlab code used in Chapter 3 to calculate the required frequency, flowrate and efficiency for different circuitry.

```

% This code calculates the required frequency, flowrate and efficiency of
% the system for different reservoir pressures and chamber diameters

clear all;

% Power requirement
W = 0.5 ; % Power requirement

% Piezo properties (PZN-PT)
s33E = 81e-12 ; % Closed circuit compliance
s33D = 17e-12 ; % Open circuit compliance
Sd = 10e6; % Depolarization stress

% Silicon material properties
v = 0.22; % Poissons ratio
E = 165e9 ; % Youngs modulus

% Silicon oil bulk modulus
Bf = 2e9 ; % Fluid bulk modulus

% Operation condition: varying PHPR
for PHPR = 1e6:1e6:4e6;

% Geometric dimensions
n = 1:0.1:10;

Dch = 1e-3*n ; % Chamber diameter

Hch = 200e-6 ; % Chamber height
Ach = (Dch.^2)*pi/4; % Chamber area
Ap = Ach.*PHPR./Sd; % Piezo area
Lp = 1e-3 ; % Piezo lenght
htp = 1e-3 ; % Top plate thickness

% Calculation of compliances
Cs = (16.*E.*htp.^3./(pi.*(1-v.^2).*(Dch./2).^6)).^-1; % Top plate compliance
Cf = (Bf./(Ach.*Hch)).^-1 ; % Fluidic compliance
Ceff= Cs+Cf; % Effective compliance

% Calculation of required frequency, flowrate and efficiency
f = 4.*W./((s33E-s33D).*Sd.^2.*Lp.*Ap); % Required frequency
Q = 2.*(s33E+s33D).*W./((s33E-s33D).*PHPR)+Ceff.*PHPR.*f; % Required flowrate
Eff = W./(Q.*PHPR); % Efficiency

% Plotting results
figure(1)
grid
plot(Dch/1e-3,f/1e3)
title('Required frequency vs. piston diameter')
xlabel('Dpis[mm]')
ylabel('f[kHz]')
hold on

figure(2)
grid
plot(Dch/1e-3,Q/1e-6)
title('Required flowrate vs. piston diameter')
xlabel('Dpis[mm]')
ylabel('Q[ml/s]')
hold on

figure(3)
grid
plot(Dch/1e-3,Eff*100)
title('Efficiency vs. piston diameter')
xlabel('Dpis[mm]')
ylabel('Eff[%]')
hold on

end

```

Figure B-2: Matlab code used in Chapter 5 to calculate the required frequency, flowrate and efficiency of the system attached to regular diode bridge for different reservoir pressures and chamber diameters.



```

% Matlab code used in tether structure optimization.(Double layer piston)
% The expressions for kxf, kxp, kvf, kvp, xpt, P, Ppt and Ceff are obtained using Maple.

clear all;

dVf = 1e-10; % Input flow volume into the chamber

Dch = 7.2e-3; % Chamber diameter
Dp = 3.8e-3; % Piezo diameter
Lp = 1e-3; % Piezo length
Ap = Dp^2*pi/4; % Piezo area
Hch = 200e-6; % Chamber height

E = 165e9; % Youngs modulus
v = 0.22; % Poisson ratio
Bf = 2e9; % Bulk modulus
s33D = 81e-12; % Open circuit compliance

a = Dch/2; % Piezo stiffness
kp = Ap/s33D/Lp; % Initial volume of chamber
Vo = Hch*Dch^2*pi/4;

ttopte = 10e-6;
tbotte = 5e-6;

d = E*ttopte^3/(12*(1-v^2));
ds = E*tbotte^3/(12*(1-v^2));

for k= 1:1:2e3;

Dpis = (Dch)-k*0.0005e-3;

b = Dpis/2;
Apis = Dpis^2*pi/4;

% Top tether

kxf = -1/16*(b^4-2*b^2*a^2+4*b^2*a^2*log(a/b)*log(b)+a^4-4*a^2*log(a)^2*b^2+4*a^2*log(a)*b^2*log(b))/(d*pi*(b^2-a^2));
kxp = -1/64*(3*b^6-7*b^4*a^2+4*b^4*log(b)*a^2+5*b^2*a^4-4*b^4*a^2*log(a)-4*b^2*log(b)*a^4+16*b^4*log(b)*a^2*log(a/b)...
-a^6+4*a^4*b^2*log(a)-16*a^2*log(a)^2*b^4+16*a^2*log(a)*b^4*log(b))/(d*(b^2-a^2));
kvf = 1/64*pi*(16*b^4*log(b)*a^2*log(a/b)+16*a^2*log(a)*b^4*log(b)+5*b^2*a^4-4*b^4*log(b)*a^2+4*b^4*a^2*log(a)+4*b^2*...
log(b)*a^4-4*a^4*b^2*log(a)-16*a^2*log(a)^2*b^4-a^6-7*b^4*a^2+3*b^6-16*a^4*log(a)*b^2*log(b)-8*b^4*a^2*log(a/b)...
+16*a^4*log(a)^2*b^2+8*a^4*b^2*log(a/b)-16*a^4*b^2*log(a/b)*log(a))/(d*pi*(b^2-a^2));
kvp = 1/192*pi*(24*a^4*b^4*log(a/b)+24*a^4*b^4-22*b^6*a^2+8*b^8-48*a^4*b^4*log(a/b)*log(a)-48*a^4*log(a)*b^4*log(b)...
+48*a^4*log(a)^2*b^4+48*b^6*a^2*log(a/b)*log(b)+48*b^6*a^2*log(a)*log(b)-48*b^6*a^2*log(a)^2-24*b^6*a^2*log(a/b)-...
10*a^6*b^2)/(d*(b^2-a^2));

% Bottom tether

kxfb = 1/8*b^2*log(b)/(pi*ds)-1/8*b^2/(pi*ds)+1/16*(-2*a^2*log(a)+a^2+2*b^2*log(b)-b^2)*b^2/(pi*ds*(a^2-b^2))+1/4*b^2*...
a^2*log(a/b)*log(b)/(pi*ds*(a^2-b^2))+1/16*a^2*(a^2-2*b^2*log(b)-b^2-4*b^2*log(a)^2+2*b^2*log(a)+4*b^2*log(a)*...
log(b))/(pi*ds*(a^2-b^2));

% Overall equations

xpis = -kxfb*(kxf*Apis-kxp)*dVf/Bf/(kxfb*Vo+kxfb*Bf*kvf*Apis-kxfb*Bf*kvp+kxf*Vo-kxf*Bf*kvp+kxf*kp*kxfb*Vo-kxf*kp*kxfb*...
Bf*kvp+kxf*Apis^2*Bf*kxfb+kxp*Bf*kvf+kxp*Bf*kvf*kp*kxfb-kxp*Bf*kxfb*Apis);
P = Bf*dVf*(kxfb+kxf+kxf*kp*kxfb)/(kxfb*Vo+kxfb*Bf*kvf*Apis-kxfb*Bf*kvp+kxf*Vo-kxf*Bf*kvp+kxf*kp*kxfb*Vo-kxf*kp*kxfb*Bf*...
*kvp+kxf*Apis^2*Bf*kxfb+kxp*Bf*kvf+kxp*Bf*kvf*kp*kxfb-kxp*Bf*kxfb*Apis);
Ceff = Vo/Bf+(kxfb*kvf*Apis+kxp*kvf+kxp*kvf*kp*kxfb-kxfb*kvp-kxf*kvp-kxf*kp*kxfb*kvp)/(kxfb+kxf+kxf*kp*kxfb);

xp(k) = xpis;
Pch(k) = P;
Comp(k) = Ceff;
Dpisan(k) = Dpis;

end

figure(2)
subplot(3,1,1)
plot((Dch-Dpisan)*1e6/2,xp/1e-6)
hold on
title('Dch fixed,Dpis varied')
ylabel('Piston Deflection[um]')
grid
subplot(3,1,2)
plot((Dch-Dpisan)*1e6/2,Pch/1e6)
hold on
ylabel('Chamber Pressure[NPa]')
grid
subplot(3,1,3)
semilogy((Dch-Dpisan)*1e6/2,Comp)
hold on
ylabel('Ceff[m^3/Pa]')
xlabel('tether width')
grid

```

Figure B-3: Matlab code used for tether optimization.

```

% This code writes the system parameters to the Matlab workspace to be read by Simulink.
% It also generates the 15x3 matrix used in Simulink, whose coefficients are calculated using Maple.

clear all;

% Fluid Properties
rho      = 760 ; % fluid density [kg/m^3];
nu_fluid = 0.65e-6; % viscosity [m^2/sec];
mu_fluid = rho*nu_fluid; % viscosity [Pa/sec];

% Valve geometry
d_discin = 2*400e-6 ; % inlet valve cap diameter[m];
d_discout = d_discin ; % outlet valve cap diameter[m];

hI = 100e-6;
eta = 0.965 ;

% Valve Channel Geometry
lk = 5e-7 ; % Leakage[m]
Lc = 5000; % Channel length
Ac = 1; % Channel area

% Note: Since only L/A ratio is important in this study,
% no exact channel geometry is defined, only the ratio is determined.

% Diode Properties for the rectifier circuit
T = 300;
k = 1.38e-23;
eta = 17.25/5;
q = 1.6e-19;
Io = 1e-6;

% Operation Conditions
voi = 24e-6 ; % Inlet valve opening[m]
voo = 24e-6 ; % Outlet valve opening[m]
wn = 20000 ; % Operation frequency[Hz]
Vb = 74.9; % Battery Voltage[V]
PHPR = 3e6; % High Pressure Reservoir Pressure
PLPR = 0.5e6; % Low Pressure Reservoir Pressure

% Expansion look-up table
Re = [0, 0.05,0.1,0.2,0.3,0.4,0.5,0.6,0.9] ;
Ce = [1,10,15,20,30,40,50,100,2e2,5e2,1e3,2e3,3e3,1e15] ;
Te = [33,3,1,3,5,3,04,2,7,2,42,2,32,1,92,1,94,2,07,2,45,1,92,1,25,0,98;
33,3,1,3,3,3,02,2,56,2,29,2,13,1,83,1,79,1,89,2,23,1,76,1,13,0,9;
33,3,1,3,2,3,2,4,2,15,1,95,1,7,1,65,1,7,2,1,6,1,0,81;
33,3,1,3,2,2,8,2,2,1,85,1,65,1,4,1,3,1,3,1,6,1,25,0,7,0,64;
33,3,1,3,1,2,6,2,1,6,1,4,1,2,1,1,1,1,3,0,95,0,6,0,5;
33,3,1,3,0,2,4,1,8,1,5,1,3,1,1,1,1,0,85,1,05,0,8,0,4,0,36;
33,3,1,2,8,2,3,1,65,1,35,1,15,0,9,0,75,0,65,0,9,0,65,0,3,0,25;
33,3,1,2,7,2,15,1,55,1,25,1,05,0,8,0,6,0,4,0,6,0,5,0,2,0,16;
33,3,1,2,6,2,1,4,1,1,0,9,0,4,0,3,0,1,8e-2,5e-2,2e-2,1,8e-2] ;

% Contraction look-up table
Rc = [0,0.1,0.2,0.3,0.4,0.5,0.6,1] ;
Cc = [1,10,20,30,40,50,1e2,2e2,5e2,1e3,2e3,4e3,5e3,1e4,1e15] ;
Tc = [30,5,3,3,2,5,2,16,1,98,1,4,1,13,0,94,0,77,0,6,0,97,0,92,0,6,1;
30,5,3,2,2,4,2,1,8,1,3,1,04,0,82,0,64,0,5,0,8,0,75,0,50,0,45;
30,5,3,1,2,3,1,84,1,62,1,2,0,95,0,7,0,5,0,4,0,6,0,6,0,4,0,4;
30,5,2,95,2,15,1,7,1,5,1,1,0,85,0,6,0,44,0,30,0,55,0,55,0,35,0,35;
30,5,2,8,2,0,1,6,1,4,1,0,78,0,5,0,35,0,25,0,45,0,5,0,3,0,3;
30,5,2,7,1,8,1,46,1,3,0,9,0,65,0,42,0,3,0,2,0,4,0,42,0,25,0,25;
30,5,2,6,1,7,1,35,1,2,0,8,0,56,0,35,0,24,0,15,0,35,0,35,0,20,0,20;
30,5,2,6,1,7,1,20,0,8,0,6,0,40,0,15,0,01,0,05,0,15,0,15,0,10,0,10] ;

% Preparation of the matrix to be fed into Simulink
ThesisSimMatrix; % Read in matrix values from ThesisSimMatrix.m

for i=1:15
    for j=1:3
        eval(['Amatrix(i,j)=A' num2str(i) num2str(j) ','']);
    end
end

```

Figure B-4: Matlab code used for writing system parameters into the workplace to be read by the Simulink model for the system level simulation.



## Appendix C

# Maple Files

This section presents important Maple files used in the Thesis.

The first two codes are the Maple files used for tether optimization in Chapter 5. The first one solves the elastic equations of the tether structures. The second one solves the governing equation for the chamber behavior. The coefficients calculated are then fed to the Matlab code used for tether optimization presented in Appendix B.

The third code solves the elastic equations of all the structural components within the system along with the equations governing the chamber continuity and piezoelectric element behavior. The equations are solved and the coefficients for the 15x3 matrix required by the Simulink model architecture, which is described in Chapter 4, are calculated. These coefficients are written in a Matlab m.file which are then read by another Matlab code (Appendix B) to generate the 15x3 matrix. The assumptions and derivation of these equations are presented in Chapter 4.

```

[ This file solves the elastic equations corresponding to the tether structure.
  Double layer piston is considered.
  It is assumed that everything except the tethers are rigid.
[ > restart;
[ > Digits:=40:

- Top tether

- Define governing DE for bending of circular plate and shear force
[ Governing DE
[ > eqn:='diff(1/r*diff(r*diff(w(r),r),r),r)=Q(r)/d':
[ Shear force in terms of Pch(chamber pressure) and Fpt (force applied by the piston on the top tether)
[ > Q(r):=Fpt/(2*P1*r) - (1/2)*P*(r^2-b^2)/r:

- Integrate the DE
[ > Q1(r):=(int(Q(r)/d,r)+C1)*r:
[ > Q2(r):=(int(Q1(r),r)+C2)/r:
[ > w(r):=int(Q2(r),r)+C3:

- Apply BC's
[ > BC1:=subs({r=a},w(r))=0:
[ > BC2:=subs({r=a},diff(w(r),r))=0:
[ > BC3:=subs({r=b},diff(w(r),r))=0:
[ > Set:=solve({BC1,BC2,BC3},{C1,C2,C3}):
[ > W(r):=subs(Set,w(r)):

- Calculation of linear coefficients for deflection and swept volume
[ > kxf:=subs({P=0,Fpt=1},subs({r=b},W(r))):
[ > kxp:=subs({P=1,Fpt=0},subs({r=b},W(r))):
[ > kvf:=subs({P=0,Fpt=1},collect(simplify(int(2*pi*r*W(r),r=b..a)),{d,P})):
[ > kvp:=subs({P=1,Fpt=0},collect(simplify(int(2*pi*r*W(r),r=b..a)),{d,P})):

- Bottom tether

- Define governing DE for bending of circular plate and shear force
[ Governing DE
[ > eqn:='diff(1/r*diff(r*diff(w(r),r),r),r)=Q(r)/ds':
[ Shear force in terms of Fpb (force applied by the piston on the bottom tether)
[ > Q(r):=Fpb/(2*P1*r):

- Integrate the DE
[ > Q1(r):=(int(Q(r)/ds,r)+C1)*r:
[ > Q2(r):=(int(Q1(r),r)+C2)/r:
[ >
[ > w(r):=int(Q2(r),r)+C3:

- Apply BC's
[ > BC1:=subs({r=a},w(r))=0:
[ > BC2:=subs({r=a},diff(w(r),r))=0:
[ > BC3:=subs({r=b},diff(w(r),r))=0:
[ > Set:=solve({BC1,BC2,BC3},{C1,C2,C3}):
[ > W(r):=subs(Set,w(r)):

- Calculation of linear coefficient for deflection
[ > kxfb:=subs({P=0,Fpb=1},subs({r=b},W(r))):

```

File: Compl.mws

This file solves the overall equations governing the chamber behavior including piston deflection, swept volume, chamber pressure, force on piezo and force on tethers.

Also the effective compliance of the system is calculated. The elastic equations governing the tether behavior are calculated using another maple file.

The results of both maple files are then fed to Matlab for tether structure optimization.

```
> restart;
```

```
> Digits:=40:
```

#### Equations Governing top tether deflection

```
> eqn1:=xpis=kxf*Fpt+kxp*P:
```

```
> eqn2:=dVt=kvf*Fpt+kvp*P:
```

#### Equation Governing bottom tether deflection

```
> eqn3:=xpis=kxfb*Fpb:
```

#### Force Balance at piston-tether connection

```
> eqn4:=Fp=Fpt+Fpb:
```

#### Fluid Compliance

```
> eqn5:=P=((dVf+dVt+xpis*Apis)/(Vo))*Bf:
```

#### Piston and Piezo

```
> eqn6:=P*Apis+Fp+kp*xpis=0:
```

#### Solve equations for input dVf

```
> sys:=solve({eqn1,eqn2,eqn3,eqn4,eqn5,eqn6},{xpis,Fp,dVt,P,Fpt,Fpb}):
```

```
> assign(sys);
```

```
> Ceff:=collect(simplify((dVf+xpis*Apis)/P),{Vo,Bf}):
```

*File: ThesisSimComp.mws*

Within the simulink model, an 15 x 3 matrix is needed, which takes as inputs ( Qp, Qnet, xpis) and solves for the outputs (Vp, xtp, DVtp, DVte, DVpb, xb, xte, Fte, Fte-top, Fte-bot, Stt, Stb, Fp, Pch, Fnet).

This code calculates the coefficients of this matrix.

```
[ > restart;
[ > Digits:=40:
```

## **Governing Equations**

### **Top support structure**

```
[ > EQN1 := x[tp]=k[dtpl]*P[ch] :
[ > EQN2 := DV[tp]=k[tp]*P[ch] :
```

### **Bottom Support Structure**

```
[ > EQN3 := x[b] = k[b]*F[p] :
```

### **Piston**

```
[ > EQN4 := x[pis]-x[te]=k[p1]*F[p]+k[p2]*P[ch] :
[ > EQN5 := DV[pb]=k[p3]*F[p]+k[p4]*P[ch] :
[ > EQN6 := F[net]=-A[pis]*P[ch]+F[p]-F[te] :
```

### **Piston Tethers**

```
[ > EQN7 := x[te]=k[tt1]*F[tetop]+k[tt2]*P[ch] :
[ > EQN8 := DV[te]=k[tt3]*F[tetop]+k[tt4]*P[ch] :
[ > EQN9 := Str[tt]=s[tt1]*F[tetop]+s[tt2]*P[ch] :
[ > EQN10 := x[te]=k[tb]*F[tebot] :
[ > EQN11 := Str[tb]=s[tb]*F[tebot] :
[ > EQN12 := F[te]=F[tetop]+F[tebot] :
```

### **Chamber continuity**

```
[ > EQN13 := P[ch]=B[f]/V[o]*(Q[net]+x[pis]*A[pis]+DV[pb]+DV[te]-DV[tp]) :
```

### **Piezoelectric Material**

```
[ Linear constitutive relations.
[ > EQN14 := x[b]-x[pis] = L[p]/A[p]*(sD[33]*F[p]+d[33]/eT[33]*Q[p]) :
[ > EQN15 := V[p] = L[p]/A[p]*(d[33]/eT[33]*F[p]-1/eT[33]*Q[p]) :
```

## **Geometric and Material Parameters**

Geometric Parameters:

```
[ > L[p]:=1e-3: d[p]:=3.8e-3: A[p]:=(Pi*d[p]^2)/4:
[ > d[pis]:=6.95e-3: w[t]:=125e-6: d[ch]:=d[pis]+2*w[t]: t[pis]:=800e-6:
[ A[pis]:=(Pi*d[pis]^2)/4:
[ > t[tetop]:=10e-6: t[tebot]:=5e-6:
[ > t[bot]:=2500e-6: t[top]:=2500e-6:
[ > H[ch]:=200e-6: V[o]:=Pi*(d[ch]^2/4)*H[ch] :
[ Material Parameters:
[ > d[33]:=1780e-12: sD[33]:=17e-12: sE[33]:=81e-12: eT[33]:=d[33]^2/(sE[33]-sD[33]):
[ > E[si]:=165e9: nu[si]:=0.22: B[f]:=2e9: rho[si]:=2230: M[pis]:=-rho[si]*A[pis]*t[pis] :
```

## **Calculate Linear Plate Coefficients**

### **Top Support Structure**

```
[ Circular plate clamped at its outer radius(r=a).
[ Positive deflection is upward.
[ > eqn:='diff(1/r*diff(r*diff(z(x),x),x),r)=Q(x)/Ds':
[ > Q(x):=P[ch]*r/2:
```

```
[ > Q1(r):=(int(Q(r)/Ds,r)+C1)*r:
[ > Q2(r):=(int(Q1(r),r)+C2)/r:
[ > wtp(r):=subs({C2=0},int(Q2(r),r)+C3):
[ > BC1:=subs({r=a},wtp(r))=0:
[ > BC2:=subs({r=a},diff(wtp(r),r))=0:
[ > Set:=solve({BC1,BC2},{C1,C3}):
[ > Wtp:=simplify(subs(Set,wtp(r))):
[ > DVtp:=int(2*Pi*r*Wtp,r=0..a):
[ > Wtpo:=subs({r=0},Wtp):
[ > k[dtpl]:=subs({P[ch]=1},Wtpo):
[ > k[dtpl]:=evalf(subs({a=d[ch]/2, Ds=E[s1]*t[top]^3/(12*(1-nu[s1]^2))},k[dtpl])):
[ > k[tp]:=subs({P[ch]=1},DVtp):
[ > k[tp]:=evalf(subs({a=d[ch]/2, Ds=E[s1]*t[top]^3/(12*(1-nu[s1]^2))},k[tp])):
```

#### **Bottom Support Structure**

```
[ Circular plate with a circular hole at the center which is clamped at its outer radius(r=a) and guided at its inner radius(r=b).
[ Positive deflection is upward.
[ > eqn:='diff(1/r*diff(r*diff(Z(r),r),r),r)=Q(r)/Ds':
[ > Q(r):=-F[p]/2/Pi/r:
[ > Q1(r):=(int(Q(r)/Ds,r)+C1)*r:
[ > Q2(r):=(int(Q1(r),r)+C2)/r:
[ > wb(r):=int(Q2(r),r)+C3:
[ > BC1:=subs({r=a},wb(r))=0:
[ > BC2:=subs({r=a},diff(wb(r),r))=0:
[ > BC3:=subs({r=b},diff(wb(r),r))=0:
[ > Set:=solve({BC1,BC2,BC3},{C1,C2,C3}):
[ > Wb:=simplify(subs(Set,wb(r))):
[ > k[b]:=simplify(subs({F[p]=1},subs({r=b},Wb))):
[ > k[b]:=evalf(subs({a=d[ch]/2, b=d[p]/2, Ds=E[s1]*t[bot]^3/(12*(1-nu[s1]^2))},k[b])):
```

#### **Piston**

```
[ Circular plate with a circular hole at the center which is simply supported at its outer radius(r=a) and guided at its inner
[ radius(r=b).
[ Positive deflection is upward.
[ > eqn:='diff(1/r*diff(r*diff(Z(r),r),r),r)=Q(r)/Ds':
[ > Q(r):=F[p]/2/Pi/r-P[ch]*r/2:
[ > Q1(r):=(int(Q(r)/Ds,r)+C1)*r:
[ > Q2(r):=(int(Q1(r),r)+C2)/r:
[ > wp(r):=int(Q2(r),r)+C3:
[ > BC1:=subs({r=a},wp(r))=0:
[ > BC2:=subs({r=a},diff(wp(r),r^2)+nu/r*diff(wp(r),r))=0:
[ > BC3:=subs({r=b},diff(wp(r),r))=0:
[ > Set:=solve({BC1,BC2,BC3},{C1,C2,C3}):
[ > Wp:=simplify(subs(Set,wp(r))):
[ > DVpb:=simplify(int(2*Pi*r*Wp,r=0..a)):
[ > k[p1]:=simplify(subs({P[ch]=0,F[p]=1},subs({r=b},Wp))):
[ > k[p1]:=evalf(subs({a=d[pis]/2, b=d[p]/2, Ds=E[s1]*t[pis]^3/(12*(1-nu[s1]^2)),
[ nu=nu[s1]},k[p1])):
[ > k[p2]:=simplify(subs({P[ch]=1,F[p]=0},subs({r=b},Wp))):
[ > k[p2]:=evalf(subs({a=d[pis]/2, b=d[p]/2, Ds=E[s1]*t[pis]^3/(12*(1-nu[s1]^2)),
[ nu=nu[s1]},k[p2])):
[ > k[p3]:=simplify(subs({P[ch]=0,F[p]=1},DVpb)):
[ > k[p3]:=evalf(subs({a=d[pis]/2, b=d[p]/2, Ds=E[s1]*t[pis]^3/(12*(1-nu[s1]^2)),
[ nu=nu[s1]},k[p3])):
[ > k[p4]:=simplify(subs({P[ch]=1,F[p]=0},DVpb)):
[ > k[p4]:=evalf(subs({a=d[pis]/2, b=d[p]/2, Ds=E[s1]*t[pis]^3/(12*(1-nu[s1]^2)),
[ nu=nu[s1]},k[p4])):
```



## [-] Drive Element Tethers

### Top Tether

Annular plate clamped at outer radius ( $r=a$ ) and guided at inner radius ( $r=b$ ) with pressure applied downward over tether and concentrated force applied upward at inner radius ( $r=b$ ).

```
[ > eqn:='diff(1/r*diff(r*diff(Z(x),x),x),x)=Q(x)/Ds':
[ > Q(x):=F[tetop]/(2*Pi*r)-P[ch]*(x^2-b^2)/(2*x):
[ > Q1(x):=(int(Q(x)/Ds,x)+C1)*x:
[ > Q2(x):=(int(Q1(x),x)+C2)/x:
[ > wtt(x):=int(Q2(x),x)+C3:
[ > BC1:=subs({x=a},wtt(x))=0:
[ > BC2:=subs({x=a},diff(wtt(x),x))=0:
[ > BC3:=subs({x=b},diff(wtt(x),x))=0:
[ > Set:=solve({BC1,BC2,BC3},{C1,C2,C3}):
[ > Wtt:=simplify(subs(Set,wtt(x))):
[ > DVtt:=simplify(int(2*Pi*r*Wtt,r=b..a)):
[ > k[tt1]:=simplify(subs({P[ch]=0,F[tetop]=1},subs({x=b},Wtt))):
[ > k[tt1]:=evalf(subs({a=d[ch]/2, b=d[pl]/2,
[ > Ds=E[s1]*t[tetop]^3/(12*(1-nu[s1]^2)),k[tt1]}):
[ > k[tt2]:=simplify(subs({P[ch]=1,F[tetop]=0},subs({x=b},Wtt))):
[ > k[tt2]:=evalf(subs({a=d[ch]/2, b=d[pl]/2,
[ > Ds=E[s1]*t[tetop]^3/(12*(1-nu[s1]^2)),k[tt2]}):
[ > k[tt3]:=simplify(subs({P[ch]=0,F[tetop]=1},DVtt)):
[ > k[tt3]:=evalf(subs({a=d[ch]/2, b=d[pl]/2,
[ > Ds=E[s1]*t[tetop]^3/(12*(1-nu[s1]^2)),k[tt3]}):
[ > k[tt4]:=simplify(subs({P[ch]=1,F[tetop]=0},DVtt)):
[ > k[tt4]:=evalf(subs({a=d[ch]/2, b=d[pl]/2,
[ > Ds=E[s1]*t[tetop]^3/(12*(1-nu[s1]^2)),k[tt4]}):
[ > Stt:=simplify(6*(Ds*(diff(Wtt,r^2)+nu/r*diff(Wtt,x)))/(h^2)):
[ > s[tt1]:=simplify(subs({P[ch]=0,F[tetop]=1},subs({x=a},Stt))):
[ > s[tt1]:=evalf(subs({a=d[ch]/2, b=d[pl]/2, Ds=E[s1]*t[tetop]^3/(12*(1-nu[s1]^2)),
[ > nu=nu[s1], h=t[tetop]},s[tt1]}):
[ > s[tt2]:=simplify(subs({P[ch]=1,F[tetop]=0},subs({x=a},Stt))):
[ > s[tt2]:=evalf(subs({a=d[ch]/2, b=d[pl]/2, Ds=E[s1]*t[tetop]^3/(12*(1-nu[s1]^2)),
[ > nu=nu[s1], h=t[tetop]},s[tt2]}):
```

### Bottom Tether

Annular plate clamped at outer radius ( $r=a$ ) and guided at inner radius ( $r=b$ ) with concentrated force applied upward at inner radius ( $r=b$ ).

```
[ > eqn:='diff(1/r*diff(r*diff(Z(x),x),x),x)=Q(x)/Ds':
[ > Q(x):=F[tebot]/(2*Pi*r):
[ > Q1(x):=(int(Q(x)/Ds,x)+C1)*x:
[ > Q2(x):=(int(Q1(x),x)+C2)/x:
[ > wtb(x):=int(Q2(x),x)+C3:
[ > BC1:=subs({x=a},wtb(x))=0:
[ > BC2:=subs({x=a},diff(wtb(x),x))=0:
[ > BC3:=subs({x=b},diff(wtb(x),x))=0:
[ > Set:=solve({BC1,BC2,BC3},{C1,C2,C3}):
[ > Wtb:=simplify(subs(Set,wtb(x))):
[ > k[tb]:=simplify(subs({F[tebot]=1},subs({x=b},Wtb))):
[ > k[tb]:=evalf(subs({a=d[ch]/2, b=d[pl]/2, Ds=E[s1]*t[tebot]^3/(12*(1-nu[s1]^2)),
[ > nu=nu[s1]},k[tb]}):
[ > Stb:=simplify(6*(Ds*(diff(Wtb,r^2)+nu/r*diff(Wtb,x)))/(h^2)):
[ > s[tb]:=simplify(subs({F[tebot]=1},subs({x=a},Stb))):
[ > s[tb]:=evalf(subs({a=d[ch]/2, b=d[pl]/2, Ds=E[s1]*t[tebot]^3/(12*(1-nu[s1]^2)),
[ > nu=nu[s1], h=t[tebot]},s[tb]}):
```

## [-] Solve Equations

In the Simulink model, the inputs to the matrix block are Qn, Onet and xpis. It is desired to solve for each of the output variables in

terms of these inputs. The output variables are Vp, xtp, DVtp, DVte, DVpb, xb, xte, Fte, Fte-top, Fte-bot, Stt, Stb, Fp, Pch, Fnet. Once solved, each of the coefficients is assigned to the proper location in the matrix.

All the matrix coefficients are then fed to matlab matrix file, which is then called by a matlab preparation file to run the Simulink model.

```
> Solutions:=solve({EQN1,EQN2,EQN3,EQN4,EQN5,EQN6,EQN7,EQN8,EQN9,EQN10,EQN11,EQN12,EQN13,
,EQN14,EQN15},{V[p],x[tp],DV[tp],DV[te],DV[pb],x[b],x[te],F[te],F[tetop],F[tebot],Str[
tt],Str[tb],F[p],P[ch],F[net]}):
> A11:=evalf(subs({Q[p]=1,Q[net]=0,x[pis]=0},subs(Solutions,V[p]))):
> A12:=evalf(subs({Q[p]=0,Q[net]=1,x[pis]=0},subs(Solutions,V[p]))):
> A13:=evalf(subs({Q[p]=0,Q[net]=0,x[pis]=1},subs(Solutions,V[p]))):
> A21:=evalf(subs({Q[p]=1,Q[net]=0,x[pis]=0},subs(Solutions,x[tp]))):
> A22:=evalf(subs({Q[p]=0,Q[net]=1,x[pis]=0},subs(Solutions,x[tp]))):
> A23:=evalf(subs({Q[p]=0,Q[net]=0,x[pis]=1},subs(Solutions,x[tp]))):
> A31:=evalf(subs({Q[p]=1,Q[net]=0,x[pis]=0},subs(Solutions,DV[tp]))):
> A32:=evalf(subs({Q[p]=0,Q[net]=1,x[pis]=0},subs(Solutions,DV[tp]))):
> A33:=evalf(subs({Q[p]=0,Q[net]=0,x[pis]=1},subs(Solutions,DV[tp]))):
> A41:=evalf(subs({Q[p]=1,Q[net]=0,x[pis]=0},subs(Solutions,DV[te]))):
> A42:=evalf(subs({Q[p]=0,Q[net]=1,x[pis]=0},subs(Solutions,DV[te]))):
> A43:=evalf(subs({Q[p]=0,Q[net]=0,x[pis]=1},subs(Solutions,DV[te]))):
> A51:=evalf(subs({Q[p]=1,Q[net]=0,x[pis]=0},subs(Solutions,DV[pb]))):
> A52:=evalf(subs({Q[p]=0,Q[net]=1,x[pis]=0},subs(Solutions,DV[pb]))):
> A53:=evalf(subs({Q[p]=0,Q[net]=0,x[pis]=1},subs(Solutions,DV[pb]))):
> A61:=evalf(subs({Q[p]=1,Q[net]=0,x[pis]=0},subs(Solutions,x[b]))):
> A62:=evalf(subs({Q[p]=0,Q[net]=1,x[pis]=0},subs(Solutions,x[b]))):
> A63:=evalf(subs({Q[p]=0,Q[net]=0,x[pis]=1},subs(Solutions,x[b]))):
> A71:=evalf(subs({Q[p]=1,Q[net]=0,x[pis]=0},subs(Solutions,x[te]))):
> A72:=evalf(subs({Q[p]=0,Q[net]=1,x[pis]=0},subs(Solutions,x[te]))):
> A73:=evalf(subs({Q[p]=0,Q[net]=0,x[pis]=1},subs(Solutions,x[te]))):
> A81:=evalf(subs({Q[p]=1,Q[net]=0,x[pis]=0},subs(Solutions,F[te]))):
> A82:=evalf(subs({Q[p]=0,Q[net]=1,x[pis]=0},subs(Solutions,F[te]))):
> A83:=evalf(subs({Q[p]=0,Q[net]=0,x[pis]=1},subs(Solutions,F[te]))):
> A91:=evalf(subs({Q[p]=1,Q[net]=0,x[pis]=0},subs(Solutions,F[tetop]))):
> A92:=evalf(subs({Q[p]=0,Q[net]=1,x[pis]=0},subs(Solutions,F[tetop]))):
> A93:=evalf(subs({Q[p]=0,Q[net]=0,x[pis]=1},subs(Solutions,F[tetop]))):
> A101:=evalf(subs({Q[p]=1,Q[net]=0,x[pis]=0},subs(Solutions,F[tebot]))):
> A102:=evalf(subs({Q[p]=0,Q[net]=1,x[pis]=0},subs(Solutions,F[tebot]))):
> A103:=evalf(subs({Q[p]=0,Q[net]=0,x[pis]=1},subs(Solutions,F[tebot]))):
> A111:=evalf(subs({Q[p]=1,Q[net]=0,x[pis]=0},subs(Solutions,Str[tt]))):
> A112:=evalf(subs({Q[p]=0,Q[net]=1,x[pis]=0},subs(Solutions,Str[tt]))):
> A113:=evalf(subs({Q[p]=0,Q[net]=0,x[pis]=1},subs(Solutions,Str[tt]))):
> A121:=evalf(subs({Q[p]=1,Q[net]=0,x[pis]=0},subs(Solutions,Str[tb]))):
> A122:=evalf(subs({Q[p]=0,Q[net]=1,x[pis]=0},subs(Solutions,Str[tb]))):
> A123:=evalf(subs({Q[p]=0,Q[net]=0,x[pis]=1},subs(Solutions,Str[tb]))):
> A131:=evalf(subs({Q[p]=1,Q[net]=0,x[pis]=0},subs(Solutions,F[p]))):
> A132:=evalf(subs({Q[p]=0,Q[net]=1,x[pis]=0},subs(Solutions,F[p]))):
> A133:=evalf(subs({Q[p]=0,Q[net]=0,x[pis]=1},subs(Solutions,F[p]))):
> A141:=evalf(subs({Q[p]=1,Q[net]=0,x[pis]=0},subs(Solutions,P[ch]))):
> A142:=evalf(subs({Q[p]=0,Q[net]=1,x[pis]=0},subs(Solutions,P[ch]))):
> A143:=evalf(subs({Q[p]=0,Q[net]=0,x[pis]=1},subs(Solutions,P[ch]))):
> A151:=evalf(subs({Q[p]=1,Q[net]=0,x[pis]=0},subs(Solutions,F[net]))):
> A152:=evalf(subs({Q[p]=0,Q[net]=1,x[pis]=0},subs(Solutions,F[net]))):
> A153:=evalf(subs({Q[p]=0,Q[net]=0,x[pis]=1},subs(Solutions,F[net]))):
```

## Generation of output matrix to Matlab file

Output matrix coefficient values to a file which Matlab/Simulink can read.

```
> interface(echo=0);
> writeto('ThesisSimMatrix.m');
```

```

[ > printf(`A11 = %+2.08e;`,A11);
[ > printf(`A12 = %+2.08e;`,A12);
[ > printf(`A13 = %+2.08e;`,A13);
[ > printf(`A21 = %+2.08e;`,A21);
[ > printf(`A22 = %+2.08e;`,A22);
[ > printf(`A23 = %+2.08e;`,A23);
[ > printf(`A31 = %+2.08e;`,A31);
[ > printf(`A32 = %+2.08e;`,A32);
[ > printf(`A33 = %+2.08e;`,A33);
[ > printf(`A41 = %+2.08e;`,A41);
[ > printf(`A42 = %+2.08e;`,A42);
[ > printf(`A43 = %+2.08e;`,A43);
[ > printf(`A51 = %+2.08e;`,A51);
[ > printf(`A52 = %+2.08e;`,A52);
[ > printf(`A53 = %+2.08e;`,A53);
[ > printf(`A61 = %+2.08e;`,A61);
[ > printf(`A62 = %+2.08e;`,A62);
[ > printf(`A63 = %+2.08e;`,A63);
[ > printf(`A71 = %+2.08e;`,A71);
[ > printf(`A72 = %+2.08e;`,A72);
[ > printf(`A73 = %+2.08e;`,A73);
[ > printf(`A81 = %+2.08e;`,A81);
[ > printf(`A82 = %+2.08e;`,A82);
[ > printf(`A83 = %+2.08e;`,A83);
[ > printf(`A91 = %+2.08e;`,A91);
[ > printf(`A92 = %+2.08e;`,A92);
[ > printf(`A93 = %+2.08e;`,A93);
[ > printf(`A101 = %+2.08e;`,A101);
[ > printf(`A102 = %+2.08e;`,A102);
[ > printf(`A103 = %+2.08e;`,A103);
[ > printf(`A111 = %+2.08e;`,A111);
[ > printf(`A112 = %+2.08e;`,A112);
[ > printf(`A113 = %+2.08e;`,A113);
[ > printf(`A121 = %+2.08e;`,A121);
[ > printf(`A122 = %+2.08e;`,A122);
[ > printf(`A123 = %+2.08e;`,A123);
[ > printf(`A131 = %+2.08e;`,A131);
[ > printf(`A132 = %+2.08e;`,A132);
[ > printf(`A133 = %+2.08e;`,A133);
[ > printf(`A141 = %+2.08e;`,A141);
[ > printf(`A142 = %+2.08e;`,A142);
[ > printf(`A143 = %+2.08e;`,A143);
[ > printf(`A151 = %+2.08e;`,A151);
[ > printf(`A152 = %+2.08e;`,A152);
[ > printf(`A153 = %+2.08e;`,A153);
[ > printf(`Ap = %+2.08e;`,evalf(A[p]));
[ > printf(`Apis= %+2.08e;`,evalf(A[pl]));
[ > printf(`Mpis= %+2.08e;`,evalf(M[pl]));
[ > writeto(terminal);

```

**Material Characterization and Modeling for Piezoelectric  
Actuation and Power Generation under High  
Electromechanical Driving Levels**

by

Ching-Yu Lin

Submitted to the Department of Aeronautics and Astronautics  
in partial fulfillment of the requirements for the degree of  
Doctor of Philosophy in Aeronautics and Astronautics

at the

MASSACHUSETTS INSTITUTE OF TECHNOLOGY

June 2002

© Massachusetts Institute of Technology 2002. All rights reserved.

Author .....  
Department of Aeronautics and Astronautics  
May 3, 2002

Certified by .....  
Nesbitt W. Hagood  
Principal Research Scientist  
Department of Aeronautics and Astronautics  
Thesis Supervisor

Certified by .....  
S. Mark Spearing  
Associate Professor  
Department of Aeronautics and Astronautics  
Thesis Supervisor

Certified by .....  
Yet-Ming Chiang  
Professor  
Department of Material Science and Engineering  
Thesis Supervisor

Accepted by .....  
Wallace E. Vander Velde  
Professor  
Department of Aeronautics and Astronautics  
Chair, Committee on Graduate Students



# Material Characterization and Modeling for Piezoelectric Actuation and Power Generation under High Electromechanical Driving Levels

by

Ching-Yu Lin

Submitted to the Department of Aeronautics and Astronautics  
on May 3, 2002, in partial fulfillment of the  
requirements for the degree of  
Doctor of Philosophy in Aeronautics and Astronautics

## Abstract

High electromechanical loads parallel to piezoelectric polarization might result in depolarization of the material, depending on the material property itself and the external excitations such as electrical field, electrical driving frequency, stress and stress duration. In this work, material properties under these effects were first characterized experimentally. The experiments included monitoring general piezoelectric responses of PZT-5H and PZT-5A subjected to large electric excitations (butterfly curves) under various static compressions and measuring generalized piezoelectric constants under short and open circuit conditions for actuation of PZT-5A and power generation of PZT-5H, single crystals PZN-PT, and single crystals PMN-PT.

To model these observed material behaviors, one- and three-dimensional rate dependent nonlinear constitutive models based on thermodynamic potentials for PZT-5H and PZT-5A piezoelectric materials were then developed. An internal variable, net remnant polarization  $D^*$ , was used to simulate the hysteric behaviors of piezoelectric materials. An evolution law of  $D^*$  was derived to specify the rate dependent responses of the materials. The parameters of the material models were determined by minimizing the error between the data and the models. The material models were capable of describing the responses subjected to large electric excitations under static compression, but incapable of predicting accurate piezoelectric constants under dynamic compression. This flaw was believed due to the absence of stress rate dependency in the models. It was also found that the PZT-5A model performed worse than the PZT-5H model because of its highly hysteretic strain-polarization relation. This hysteresis could be explained by the slow switching rate of 90-degree domain movement.

Finally, to simulate devices under non-uniform field or with irregular geometries using these material models, differential algebraic equations for mixed finite element analysis of 3-D nonlinear rate dependent piezoelectric materials were formulated and solved numerically by DASP solver. Using 4-node tetrahedral elements, this formulation was demonstrated by examples with uniform and skewed electric excitations. The combination of the nonlinear mixed FEM model and the material model provided a useful tool for modeling the response of active devices with complicated geometries and irregular boundary conditions.

Thesis Supervisor: Nesbitt W. Hagood  
Title: Principal Research Scientist  
Department of Aeronautics and Astronautics

Thesis Supervisor: S. Mark Spearing  
Title: Associate Professor  
Department of Aeronautics and Astronautics

Thesis Supervisor: Yet-Ming Chiang  
Title: Professor  
Department of Material Science and Engineering

## Acknowledgments

First, I would like to thank my advisor, Professor Nesbitt Hagood, for his encouraging advice. The additional assistance from Professors Yet-Ming Chiang, Mark Spearing, John Dugundji and Marthinus van Schoor is also acknowledged. Other assistance from people in AMSL, Dave Robertson, Mauro Atalla, Mai Nguyen, Mary Jones, Kamyar Ghandi, Aaron Bent, Chris Dunn, Timothy Glenn, Benon Janos, Dave Roberts, Lodewyk Steyn, Onnik Yaglioglu, Malinda Lutz, Yong Shi, and Michael Fripp, is thanked, too.

I would also like to thank my family for their support. My parents educated me well so that I could come to MIT. My brother and sister set good examples for me. My beloved wife Chun-Ling (Lindsey), who helps me focus on this doctoral thesis, is mostly appreciated.

Funding for this research was provided by U.S. Army Research Office (ARO) under contract DAAH04-95-1-0104 monitored by Dr. Gary Anderson and by DARPA under contract of Active Fiber Composite Consortium (AFCC, 49620-97-0527) monitored by Dr. William Coblenz and Dr. Spencer Wu. Support also came from Office of Naval Research (ONR) under contract N00014-01-1-0857 monitored by Dr. Smith Wallace and from DARPA under contract DAAG55-98-1-036 monitored by Dr. Robert Nowak and Dr. Richard Paur.





# Contents

<b>1</b>	<b>Introduction</b>	<b>27</b>
1.1	Piezoelectricity . . . . .	27
1.1.1	What is a piezoelectric material? . . . . .	27
1.1.2	How does it work? . . . . .	28
1.2	Application . . . . .	33
1.2.1	Actuator . . . . .	33
1.2.2	Sensor . . . . .	36
1.2.3	High Voltage Source and Energy Harvester . . . . .	37
1.3	Thesis Motivation and Objectives . . . . .	38
1.4	Thesis Outline . . . . .	41
<b>2</b>	<b>Material Characterization</b>	<b>43</b>
2.1	Experimental Setup . . . . .	44
2.1.1	Mechanical Loading and Measurement . . . . .	44
2.1.2	Electrical Loading and Measurement . . . . .	49
2.2	Characterization for Actuation Application . . . . .	58
2.2.1	Actuation under Load . . . . .	58
2.2.2	Residual Actuation and Compression Duration . . . . .	66
2.2.3	Summary of Actuation Characterization . . . . .	71
2.3	Characterization for Energy Harvesting Application . . . . .	74
2.3.1	Resistive Load vs. Rectifying Circuitry . . . . .	74
2.3.2	Characterization of Generalized Material Constants . . . . .	77
2.3.3	Diode Selection and Characterization . . . . .	81

2.3.4	Characterization of Material Energy Density . . . . .	83
2.3.5	Single Crystal vs. Polycrystalline Ceramics . . . . .	86
2.3.6	Summary of Piezoelectric Energy Harvesting . . . . .	87
2.4	Characterization for Material Modeling . . . . .	88
2.5	Summary of Important Material Characteristics . . . . .	104
<b>3</b>	<b>Development of Material Model</b>	<b>105</b>
3.1	Literature Review of Material Models . . . . .	105
3.1.1	Model by Soukhojak and Chiang . . . . .	106
3.1.2	Introduction to Thermodynamic Potential . . . . .	109
3.1.3	Thermodynamically Consistent Model . . . . .	111
3.2	Development of a 1-D Rate and Stress Dependent Piezoelectric Model . . .	114
3.2.1	Assumption of Electric Conduction Effect . . . . .	115
3.2.2	Probabilistic Effect . . . . .	117
3.2.3	Rate and Stress Effects of Polarization . . . . .	119
3.2.4	Parametric Study . . . . .	121
3.3	1-D Material Parameters . . . . .	123
3.3.1	Construction of $D^*$ . . . . .	126
3.3.2	Selection of Polynomials . . . . .	128
3.3.3	Optimization of Polynomial Coefficients . . . . .	129
3.3.4	Optimization of $\tau$ , $\Delta D_c$ , and $\alpha$ . . . . .	130
3.3.5	Optimized 1-D Model Parameters for PZT-5H . . . . .	134
3.3.6	Optimized 1-D Model Parameters for PZT-5A . . . . .	139
3.3.7	Discrepancy of Domain Switching Process between PZT-5A and PZT-5H . . . . .	152
3.4	Development of a 3-D Rate and Stress Dependent Piezoelectric Model . . .	156
3.4.1	Introduction to Ghandi's Tensor Invariants . . . . .	156
3.4.2	3-D Rate Rules . . . . .	160
3.5	Finding 3-D Material Parameters . . . . .	160
3.5.1	Optimized 3-D PZT-5H Model Parameters . . . . .	162
3.5.2	Optimized 3-D PZT-5A Model Parameters . . . . .	167

3.6	Summary of Model Development . . . . .	173
<b>4</b>	<b>Model Validation for Application at Stage 3</b>	<b>175</b>
4.1	PZT-5H Minor Loop Validation . . . . .	175
4.2	Model Validation for PZT-5H Power Generation . . . . .	179
4.2.1	Validation of Generalized Piezoelectric Constants under Short Circuit	179
4.2.2	Validation of Generalized Piezoelectric Constants under Open Circuit	180
4.2.3	Validation of Diode Circuit Response . . . . .	181
4.2.4	Explanation of Poor Correlation: Stress Rate Dependency . . . . .	185
4.3	Model Validation for PZT-5A Actuation . . . . .	186
4.3.1	Validation of Single Loop Test . . . . .	186
4.3.2	Validation of Multiple Loop Test . . . . .	188
4.4	Summary of Model Validation at Stage 3 . . . . .	191
<b>5</b>	<b>3-D Analysis Using Finite Element Method</b>	<b>193</b>
5.1	Mixed Formulation . . . . .	194
5.1.1	Problem Statement of an Electroelastic Continuum . . . . .	194
5.1.2	Equations of Equilibrium . . . . .	195
5.2	Implementation of Material Model . . . . .	197
5.3	Implementation of Spatial Discretization . . . . .	198
5.3.1	4-node Tetrahedra . . . . .	198
5.4	Solution Techniques . . . . .	201
5.4.1	Differential Algebraic Formulation . . . . .	201
5.4.2	Time-stepping Numerical Algorithm . . . . .	204
5.4.3	Software Implementation . . . . .	206
5.5	Case Study . . . . .	207
5.5.1	Element Tests . . . . .	207
5.5.2	Piezoelectric Response under Uniform Loading . . . . .	211
5.5.3	Piezoelectric Response under Skewed Loading . . . . .	214
5.5.4	Limitation of Large Scale Problem . . . . .	220
5.6	Summary of 3-D Nonlinear Rate Dependent Finite Element Analysis . . . .	221

<b>6</b>	<b>Conclusions</b>	<b>223</b>
6.1	Summary and Future Work . . . . .	223
6.2	Contributions . . . . .	227
<b>A</b>	<b>Simulink Graphical Model</b>	<b>233</b>
A.1	Linear Piezoelectricity with Resistive Load . . . . .	234
A.2	Linear Piezoelectricity with Diode Bridge . . . . .	235
A.3	1-D Nonlinear Short Circuit Piezoelectricity . . . . .	238
A.4	3-D Nonlinear Short Circuit Piezoelectricity . . . . .	240
A.5	1-D Nonlinear Open Circuit Piezoelectricity . . . . .	242
A.6	1-D Nonlinear Open Circuit Piezoelectricity with Conduction . . . . .	243
A.7	3-D Nonlinear Open Circuit Piezoelectricity . . . . .	244
A.8	3-D Nonlinear Open Circuit Piezoelectricity with Conduction . . . . .	246
A.9	1-D Nonlinear Piezoelectricity with Diode Circuit . . . . .	247
A.10	3-D Nonlinear Piezoelectricity with Diode Circuit . . . . .	248
<b>B</b>	<b>S-Function</b>	<b>249</b>
B.1	Dsraterule.m . . . . .	249
B.2	sfuncES.m . . . . .	251
B.3	Dsraterule3D.m . . . . .	253
B.4	sfuncES3D.m . . . . .	255

# List of Figures

1-1	Schematic structure of a fictitious ferroelectric crystal. . . . .	28
1-2	Schematic potential wells. . . . .	29
1-3	Schematic P-E and S-E loops. . . . .	30
1-4	S-E (solid line) and $\alpha P $ -E (dashed line) loops, where $\alpha$ is a scale factor. . . .	31
1-5	Schematic P-E and S-E loops under compression. . . . .	31
1-6	Piezo stacks . . . . .	34
1-7	Piezoelectric wafer with Interdigitated Electrodes (IDE). . . . .	34
1-8	Active Fiber Composites . . . . .	35
1-9	Active Fiber Composites for integral actuation of helicopter blades . . . . .	35
1-10	Piezo-based load cell vs. strain-based load cell . . . . .	36
1-11	Schematics of accelerameter . . . . .	36
1-12	Diode bridge circuitry . . . . .	38
1-13	Preliminary data implies rate dependent piezoelectricity . . . . .	39
1-14	Three major axes of dependencies: electric field, compression, and driving frequency	40
2-1	Axial test configurations: (a) longitudinal test and (b) transverse test. . . . .	44
2-2	Axial test configurations: (a) longitudinal test and (b) transverse test. . . . .	45
2-3	Experimental setup: Test fixture consisted of a spherical joint and alumina disks.	46
2-4	Instron Test Machine . . . . .	47
2-5	Component Testing Machine . . . . .	47
2-6	Component Testing Machine . . . . .	48
2-7	Simple equivalent circuit of piezoelectric material . . . . .	50
2-8	High potential voltmeter . . . . .	50
2-9	High potential voltmeter, considering dynamics of the resistor . . . . .	51

2-10 Pole-zero mapping of high potential voltmeter, considering dynamics of the resistor	52
2-11 Schematics of active filter . . . . .	52
2-12 High potential voltmeter using high voltage power amplifier feedback to compensate the dynamics of the resistor . . . . .	53
2-13 The final configuration of open circuit voltage meter used in this thesis work: (a) $10\text{G}\Omega$ with filtered output, (b) $100\text{M}\Omega$ . . . . .	53
2-14 High potential voltmeter, considering capacitance of cable . . . . .	53
2-15 Transfer function of high potential voltmeter, considering dynamics of the resistor	54
2-16 Transfer function of compensated high potential voltmeter using active filter . .	55
2-17 Transfer function of high potential voltmeter: one with $10\text{G}\Omega$ resistor operates from 1 to 100Hz, one with $100\text{M}\Omega$ resistor operates from 100Hz to 4kHz. . .	56
2-18 Charge amplifier. . . . .	57
2-19 Current amplifier. . . . .	57
2-20 The compression profile of the single loading cycle test. . . . .	60
2-21 Test results of single loading cycle subjected to different electric fields. . . . .	60
2-22 The compression profile of the test using multiple loading cycles . . . . .	62
2-23 Multiple loading cycles with $\pm 16\% E_c$ (upper) and $\pm 40\% E_c$ (lower): (1A) cycle 1, loading, (1B) cycle 1, unloading, (2A) cycle 2, loading, (2B) cycle 2, unloading, (3A) cycle 3, loading, (3B) cycle 3, unloading, (4A) cycle 4, loading, (4B) cycle 4, unloading, (5A) cycle 5, loading, (5B) cycle 5, unloading, (6A) single loading cycle, and (6B) single unloading cycle. . . . .	63
2-24 Multiple loading cycles with $\pm 70\% E_c$ (upper) and $\pm 90\% E_c$ (lower): (1A) cycle 1, loading, (1B) cycle 1, unloading, (2A) cycle 2, loading, (2B) cycle 2, unloading, (3A) cycle 3, loading, (3B) cycle 3, unloading, (4A) cycle 4, loading, (4B) cycle 4, unloading, (5A) cycle 5, loading, (5B) cycle 5, unloading, (6A) single loading cycle, and (6B) single unloading cycle. . . . .	64
2-25 Reversibility: (A) Recovery percentage of residual actuation vs. electric field and maximum exposure stress. (B) Residual actuation vs. electric field and maximum exposure stress. . . . .	65
2-26 The load profile of testing the residual actuation at zero stress after exposure to compressions for a duration of $\Delta t$ . . . . .	67

2-27 The residual actuation after exposure to compressions for 30 seconds is normalized by the initial actuation at zero stress. . . . .	67
2-28 Type A was driving electric actuation at zero stress only, while Type B was driving at both zero and nonzero stress. . . . .	68
2-29 Normalized residual actuations for different compression duration and different electric fields: (A) Results using Type A actuation (B) Results using Type B actuation (C) Results using low Type B actuation, $\pm 9\% E_c$ (D) Results using high Type B actuation, $\pm 70\% E_c$ . . . . .	70
2-30 Illustration of the dipoles restituted by the internal electric fields induced by the unequilibrium free charges: (A) the original equilibrium state before compression, (B) the unequilibrium state after compression, (C) the equilibrium after compression. . . . .	71
2-31 Effect of the limited current source on a $RC$ circuit. . . . .	75
2-32 Simulation of force-displacement relation of piezoelectric specimen with resistive load. . . . .	75
2-33 Diode bridge circuitry . . . . .	76
2-34 Simulation of force-displacement relation of piezoelectric specimen with a resistor or a rectifying diode bridge. . . . .	77
2-35 Generalized material constants $d_{33}$ and $s_{33}^E$ as functions of stress at 10Hz and 400Hz for PZT-5H, PZN-PT and PMN-PT. . . . .	79
2-36 Generalized material constants $g_{33}$ and $s_{33}^D$ as functions of stress at 10Hz and 400Hz for PZT-5H, PZN-PT and PMN-PT. . . . .	80
2-37 $k_{33}^2$ . . . . .	81
2-38 Diode forward test circuitry . . . . .	82
2-39 Diode characteristics . . . . .	82
2-40 Diode reverse test circuitry . . . . .	83



2-41	Data and simulation of low and high stress response: (a) the force-displacement relation at low stress, 400Hz, $V_{DC} = 300\text{V}$ ; (b) the simulated and measured current at low stress 400Hz, $V_{DC} = 300\text{V}$ ; (c) driving force history of low stress condition; (d) the force-displacement relation at high stress, 400Hz, $V_{DC} = 400\text{V}$ ; (e) the simulated and measured current at high stress 400Hz, $V_{DC} = 400\text{V}$ ; (f) driving force history of high stress condition. . . . .	84
2-42	Power vs. $V_{DC}$ . . . . .	85
2-43	Maximum energy density using rectifying circuitry. The curves labeled as "Fitted" are obtained from Eq. 2.22 using generalized material constants described in Eq. 2.5, 2.6, 2.7, 2.11, 2.12, and 2.13. The curve labeled as "Linear" are obtained from Eq. 2.22 assuming constant material coefficients $d_{33}$ and $g_{33}$ at zero stress . . . . .	86
2-44	The test planes of stress and electric fields versus frequency and electric field .	88
2-45	Rate dependency of PZT-5H: P-E loops(left) and S-E loops(right) . . . . .	89
2-46	Rate dependency of PZT-5A: P-E loops(left) and S-E loops(right) . . . . .	89
2-47	The data of repolarizing PZT-5A (Batch A) material behavior under longitudinal compression test. . . . .	91
2-48	The data of repolarizing PZT-5A (Batch A) material behavior under longitudinal compression test. . . . .	92
2-49	The data of repolarizing PZT-5A (Batch A) material behavior under longitudinal compression test. . . . .	93
2-50	The data of repolarizing PZT-5A (Batch B) material behavior under transverse compression test. . . . .	94
2-51	The data of repolarizing PZT-5A (Batch B) material behavior under transverse compression test. . . . .	95
2-52	The data of repolarizing PZT-5A (Batch B) material behavior under transverse compression test. . . . .	96
2-53	The data of repolarizing PZT-5A (Batch B) material behavior under transverse compression test. . . . .	97
2-54	The data of repolarizing PZT-5A (Batch B) material behavior under longitudinal compression test (up to 56MPa). . . . .	98

2-55	The data of repolarizing PZT-5A (Batch B) material behavior under longitudinal compression test (up to 56MPa). . . . .	99
2-56	The data of repolarizing PZT-5A (Batch B) material behavior under longitudinal compression test (up to 56MPa). . . . .	100
2-57	The data of repolarizing PZT-5A (Batch B) material behavior under longitudinal test with higher compression (up to 112MPa). . . . .	101
2-58	The data of repolarizing PZT-5A (Batch B) material behavior under longitudinal test with higher compression (up to 112MPa). . . . .	102
2-59	The data of repolarizing PZT-5A (Batch B) material behavior under longitudinal test with higher compression (up to 112MPa). . . . .	103
3-1	The dielectric polarization as a function of sinusoidal electric field $E$ at different frequencies, assuming $\tau_d = 5\text{ms}$ in Soukhojak's model. . . . .	107
3-2	The net fraction of polarization as a function of sinusoidal electric field $E$ at different frequencies, assuming $\tau_{sw} = 5\text{ms}$ in Soukhojak's model. . . . .	108
3-3	The total polarization as a function of sinusoidal electric field $E$ at different frequencies, assuming $\tau_{sw} = 0.5\text{ms}$ and $\tau_d = 1\text{ms}$ in Soukhojak's model. . . . .	108
3-4	Potentials of a ferroelectric material proposed by Devonshire. . . . .	112
3-5	Electric constitutive relations. Dotted line indicates the portions of the curve which are thermodynamically unstable. . . . .	112
3-6	Stress dependence of material response using Devonshire model. Dotted line indicates the portions of the curve which are thermodynamically unstable. . . . .	113
3-7	The simulated polarization using Ghandi's model . . . . .	115
3-8	Equivalent circuitry of piezoelectric ceramics under voltage source control (left) and charge source control (right). . . . .	116
3-9	Non-contact electrode of AFC makes its piezoelectric fiber under charge source control. . . . .	117
3-10	Probability density function (left) and cumulative probability density function (right). . . . .	118
3-11	Weibull probability density function (left) and its cumulative probability density function (right). . . . .	118

3-12 Effect of $D^*$ on $E$ - $D$ and $E$ - $S$ relations, assuming $T = 0$ and $f = 1$ Hz. For non zero $D^*$ case, $\Delta D_c = 0.5$ , $\tau = 0.001$ , and $\alpha = 1$ are used in Eq. 3.34. . .	122
3-13 Effect of $\alpha$ on $E$ - $D$ and $E$ - $S$ relations, assuming $f = 1\text{Hz}$ , $\Delta D_c = 0.6$ , $T = 0$ , $\tau = 0.001$ , and varying $\alpha = \{1, 2, \text{ or } 3\}$ . . . . .	123
3-14 Effect of $\Delta D_c$ on $E$ - $D$ and $E$ - $S$ relations, assuming $f = 1\text{Hz}$ , $T = 0$ , $\alpha = 1$ , $\tau = 0.001$ , and varying $\Delta D_c = \{0.2, 0.5, \text{ or } 0.8\}$ . . . . .	124
3-15 Effect of $\tau$ on $E$ - $D$ and $E$ - $S$ relations, assuming $f = 1\text{Hz}$ , $T = 0$ , $\Delta D_c = 0.5$ , $\alpha = 1$ , and varying $\tau = \{0.0005, 0.001, \text{ or } 0.0015\}$ . . . . .	124
3-16 Effect of driving frequency on $E$ - $D$ and $E$ - $S$ relations, assuming $T = 0$ , $\Delta D_c = 0.05$ , $\alpha = 3$ , $\tau = 0.0005$ , and varying $f = \{0.1, 1, \text{ or } 10\}\text{Hz}$ . . . . .	125
3-17 Effect of stress on $E$ - $D$ and $E$ - $S$ relations, assuming $f = 1\text{Hz}$ , $\Delta D_c = 0.05$ , $\alpha = 1$ , $\tau = 0.001$ , and varying $T = \{-1, 0, \text{ or } 1\}$ . . . . .	125
3-18 Finding $D^*$ for virgin specimen. . . . .	127
3-19 Finding $D_0^*$ for poled specimen: (left) time history of measured $D$ , simulated $D^{**}$ with initial guessed $D_0^{**}$ , and simulated $D^*$ with converged $D_0^*$ ; (right) zoomed time history. . . . .	127
3-20 Finding $D_0^*$ for poled specimen. (left) initial guessed $D_0^{**}$ , (right) converged $D_0^*$	128
3-21 Unreasonable strain and polarization response at various stresses using inappropriate parameter optimization. Data was obtained by Ghandi[35]. . . . .	133
3-22 Unreasonable strain and polarization response at various frequencies using inappropriate parameter optimization. . . . .	134
3-23 Simulated rate dependent behaviors of PZT-5H using 1-D model. . . . .	135
3-24 Data and simulated stress dependent behaviors of PZT-5H using 1-D model. .	136
3-25 Data and simulated stress dependent behaviors of PZT-5H using 1-D model (Cont).	137
3-26 Overall data and simulated stress dependent behaviors of PZT-5H using 1-D model. . . . .	138
3-27 Data and simulated stress dependent behaviors of PZT-5A, Batch A, using 1-D model. . . . .	140
3-28 Data and simulated stress dependent behaviors of PZT-5A, Batch A, using 1-D model(Cont). . . . .	141

3-29 Overall data and simulated stress dependent behaviors of PZT-5A, Batch A, using 1-D model. . . . .	142
3-30 Simulated rate dependent behaviors of PZT-5A, Batch A, using 1-D model. . .	143
3-31 Simulated rate dependent behaviors of PZT-5A, Batch B, 0–50MPa, using 1-D model. . . . .	144
3-32 Data and simulated stress dependent behaviors of PZT-5A, Batch B, 0–50MPa, using 1-D model. . . . .	145
3-33 Data and simulated stress dependent behaviors of PZT-5A, Batch B, 0–50MPa, using 1-D model (Cont). . . . .	146
3-34 Overall data and simulated stress dependent behaviors of PZT-5A, Batch B, 0–50MPa, using 1-D model. . . . .	147
3-35 Simulated rate dependent behaviors of PZT-5A, Batch B, 0–100MPa, using 1-D model. . . . .	148
3-36 Data and simulated stress dependent behaviors of PZT-5A, Batch B, 0–100MPa, using 1-D model. . . . .	149
3-37 Data and simulated stress dependent behaviors of PZT-5A, Batch B, 0–100MPa, using 1-D model (Cont). . . . .	150
3-38 Overall data and simulated stress dependent behaviors of PZT-5A, Batch B, 0–100MPa, using 1-D model. . . . .	151
3-39 Comparison between S-D curves of PZT-5H and PZT-5A. Right lower plot shows all data. . . . .	153
3-40 Discrepancy of domain switching between PZT-5A((a),(b),(c)) and PZT-5H((d),(e),(f)).	154
3-41 Correlation between 3-D model and data of PZT-5H transverse tests. . . . .	163
3-42 Correlation between 3-D model and data of PZT-5H transverse tests (Cont.) .	164
3-43 Correlation between 3-D model and data of PZT-5H longitudinal tests. . . . .	165
3-44 Correlation between 3-D model and data of PZT-5H longitudinal tests (Cont.)	166
3-45 Simulated rate dependency of PZT-5H using 3-D model . . . . .	167
3-46 Correlation between 3-D model and data of PZT-5A transverse tests. . . . .	169
3-47 Correlation between 3-D model and data of PZT-5A transverse tests (Cont.) .	170
3-48 Correlation between 3-D model and data of PZT-5A longitudinal tests. . . . .	171
3-49 Correlation between 3-D model and data of PZT-5A longitudinal tests (Cont.)	172

3-50	Simulated rate dependency of PZT-5A using 3-D model . . . . .	173
4-1	Electric driving command for minor loop test. . . . .	176
4-2	Time history correlation between modeled and measured electric displacement of minor loop test for PZT-5H. . . . .	177
4-3	Time history correlation between modeled and measured strain of minor loop test for PZT-5H. . . . .	177
4-4	Correlation between modeled and measured electric displacement of minor loop test for PZT-5H. Left: 1-D model; right: 3-D model. . . . .	178
4-5	Correlation between modeled and measured strain of minor loop test for PZT-5H. Left: 1-D model; right: 3-D model. . . . .	178
4-6	Comparison between the predicted and measured generalized $d_{33}$ (left) and $s_{33}^E$ (right). . . . .	179
4-7	Comparison between the predicted and measured generalized $g_{33}$ (left) and $s_{33}^D$ (right). . . . .	181
4-8	The current output of the diode circuit. The piezoelectric specimen is under 105N compression. Upper plot shows the time history of current. Lower plot shows the time history of input force. . . . .	182
4-9	The current output of the diode circuit. The piezoelectric specimen is under 677N compression. Upper plot shows the time history of current. Lower plot shows the time history of input force. . . . .	183
4-10	The current output of the diode circuit. The piezoelectric specimen is under 1573N compression. Upper plot shows the time history of current. Lower plot shows the time history of input force. . . . .	184
4-11	Comparison between the predicted and measured generalized $s_{33}^E$ of PZT-5H. .	185
4-12	Load rate of butterfly curve test at various stresses. . . . .	186
4-13	Simulation of single loop test with $\pm 0.09E_c$ (upper), $\pm 0.16E_c$ (middle), and $\pm 0.40E_c$ (lower) driving electric field. . . . .	187
4-14	Simulation of single loop test with $\pm 0.09E_c$ (upper), $\pm 0.16E_c$ (middle), and $\pm 0.40E_c$ (lower) driving electric field. Maximum compression of first loop is 30MPa. . . . .	189

4-15 Simulation of single loop test with $\pm 0.09E_c$ (upper), $\pm 0.16E_c$ (middle), and $\pm 0.40E_c$ (lower) driving electric field. Maximum compression of first loop is 20MPa. . . . .	190
5-1 4-node (left) and 10-node (right) tetrahedral elements. . . . .	199
5-2 Test 1. Results: deformed body. Displacement is not in scale. . . . .	208
5-3 Test 1. Results: polarization (left) and displacement (right) vs. driving voltage. . . . .	208
5-4 Test 2. Results . . . . .	209
5-5 Test 2 result: comparison between nodal voltage and driving voltage. . . . .	210
5-6 Test 2. results: polarization (left) and displacement (right) vs. driving voltage. . . . .	210
5-7 Representative volume of specimen under uniform electric field. . . . .	212
5-8 Mesh of representative volume for the case under uniform electric field. . . . .	212
5-9 Solved voltage on the nodes. . . . .	213
5-10 Solution of displacement on the nodes (left) and electric displacement on the elements (right). . . . .	213
5-11 Representative volume of specimen under skewed electric field. . . . .	215
5-12 Mesh of representative volume for the case under skewed electric field. . . . .	215
5-13 Solved voltage on the nodes. . . . .	216
5-14 Solved voltage on the nodes. . . . .	216
5-15 Electric displacement vs. driving voltage under skewed electric field on various elements. . . . .	217
5-16 Displacement vs. driving voltage under skewed electric field on various nodes. . . . .	218
5-17 Deformed body under skewed electric field at various time steps. . . . .	219
A-1 Linear piezoelectricity with resistive load . . . . .	234
A-2 The block "Piezo" shown in Figure A-1. . . . .	234
A-3 Linear piezoelectric device with diode bridge. . . . .	236
A-4 Labels of voltages and currents in rectifying diode circuit. . . . .	236
A-5 The details of the block "Rectifying Diode Bridge" in Figure A-3. . . . .	237
A-6 Implementation of constitutive law of each " Diode element" in Figure A-5 . . . . .	237
A-7 1-D nonlinear short circuit simulation. . . . .	238
A-8 Details of block "Piezo" in Figure A-7. . . . .	239

A-9 3-D nonlinear short circuit simulation. . . . .	240
A-10 Details of block “Piezo” in Figure A-9. . . . .	241
A-11 1-D nonlinear open circuit simulation. . . . .	242
A-12 Details of block “Piezo” in Figure A-11. . . . .	242
A-13 1-D nonlinear open circuit simulation with conduction. . . . .	243
A-14 3-D nonlinear open circuit simulation. . . . .	244
A-15 Details of block “Piezo” in Figure A-14. . . . .	245
A-16 3-D nonlinear open circuit simulation with conduction. . . . .	246
A-17 1-D nonlinear “Piezo” block for diode circuit simulation used in Figure A-3. .	247
A-18 3-D nonlinear “Piezo” block for diode circuit simulation used in Figure A-3. .	248

# List of Tables

1.1	Task and targeted precision of the model . . . . .	40
2.1	Selection of piezoelectric materials for testing . . . . .	43
2.2	Summary of PZT-5A Compressive Depolarization. (● indicates the test condition.)	73
3.1	Thermodynamic potentials . . . . .	109
3.2	Polynomial terms of thermodynamic potentials . . . . .	128
3.3	Coefficients of PZT-5H thermodynamic potential expanded by polynomial terms. This will result in poor rate behavior, despite the good stress dependent response	132
3.4	Coefficients of PZT-5H thermodynamic potential expanded in polynomial terms.	135
3.5	Coefficients of thermodynamic potential expanded by polynomial terms PZT-5A, Batch A. . . . .	139
3.6	Coefficients of thermodynamic potential expanded in polynomial terms for PZT- 5A, Batch B, 0–50MPa . . . . .	144
3.7	Coefficients of thermodynamic potential expanded in polynomial terms for PZT- 5A, Batch B, 0–100MPa . . . . .	148
3.8	Derivatives of various invariants of symmetric tensor $T_{ij}$ and vectors $D_i$ and $a_i$ , where $\mathbf{e} = [1 \ 1 \ 1 \ 0 \ 0 \ 0]^\top$ and $\mathbf{R} = \text{diag}([1 \ 1 \ 1 \ 2 \ 2 \ 2])$ . . . . .	159
3.9	Energy expansions for PZT-5H in 3-D and their optimal coefficients. . . . .	162
3.10	Energy expansions for PZT-5A in 3-D and their optimal coefficients. . . . .	168
6.1	Model comparison with literatures . . . . .	230





# Nomenclature

$\alpha$	Parameter of Weibull function.
$\beta$	Ferroelectric domain switching function in Soukhojak's model.
$\Delta D_c$	Critical value to determine the initialization of the repolarization.
$\Delta E$	Energy barrier.
$\eta$	Diode property.
$\dot{\hat{\mathbf{D}}}^*$	Derivative of $\hat{\mathbf{D}}^*$ with respect to time $t$ .
$\hat{\mathbf{D}}$	Electric displacement degree of freedom in finite element analysis.
$\hat{\mathbf{D}}^*$	Fictitious electric displacement degree of freedom in finite element analysis.
$\hat{\mathbf{U}}_{\mathbf{a}}$	Unknown displacement degree of freedom in finite element analysis.
$\hat{\mathbf{U}}_{\mathbf{b}}$	Prescribed displacement degree of freedom in finite element analysis.
$\hat{\mathbf{U}}$	Displacement degree of freedom in finite element analysis.
$\hat{\mathbf{V}}_{\mathbf{a}}$	Unknown voltage degree of freedom in finite element analysis.
$\hat{\mathbf{V}}_{\mathbf{b}}$	Prescribed voltage degree of freedom in finite element analysis.
$\hat{\mathbf{V}}$	Voltage degree of freedom in finite element analysis.
$\mathbf{a}, a_i$	Reference vector of tensor invariants.
$\mathbf{D}^*, D_i^*$	Fictitious internal variable for hysteretic electric displacement in matrix and tensor forms.

$\mathbf{D}, D_i$	Electric displacement in matrix and tensor forms.
$\mathbf{E}, E_i$	Electric field in matrix and tensor forms.
$\mathbf{S}, S_{ij}$	Strain in matrix and tensor forms.
$\mathbf{T}, T_{ij}$	Stress in matrix and tensor forms.
$\mathcal{P}$	Power.
$\Omega$	Energy Density.
$\sigma$	Entropy.
$\tau$	Time constant.
$\tau_d$	Dielectric time constant in Soukhojak's model.
$\tau_{sw}$	Time constant of domain switching in Soukhojak's model.
$\theta$	Temperature.
$A$	Helmholtz free energy.
$D, D_3$	Electric displacement in 3 direction. To be rigorous, the transformation between the polarization( $P$ ) and electric displacement( $D$ ) is $D = P + \epsilon_0 E$ . The difference is negligible, since $\epsilon_0$ is comparatively small.
$D^*, D_3^*$	Fictitious electric displacement.
$d_{ij}$	Piezoelectric constant.
$E, E_3$	Electric field in 3 direction.
$E_0$	Normalization field in Soukhojak's model.
$E_c$	Coercive field.
$f$	Frequency in Hz.
$G$	Gibbs free energy.
$G_1$	Elastic Gibbs energy.

$G_2$	Electric Gibbs energy.
$g_{ij}$	Piezoelectric constant.
$H$	Enthalpy.
$H_1$	Elastic enthalpy.
$H_2$	Electric enthalpy.
$I_0$	Diode property.
$k$	Boltzmann constant
$k_{ij}$	Coupling coefficient.
$n$	Net fraction of dipoles pointing up, as defined in Soukhojak's model.
$P, P_3$	Polarization in 3 direction.
$P_d$	Dielectric polarization in Soukhojak's model.
$P_F$	Ferroelectric polarization in Soukhojak's model.
$P_r$	Remnant polarization.
$P_s$	Spontaneous polarization.
$P_{sat}$	Saturation of polarization in Soukhojak's model.
$S, S_{33}, S_3$	Strain in 3 direction.
$s_{ij}^D$	Elastic constant at open circuit condition.
$s_{ij}^E$	Elastic constant at short circuit condition.
$T, T_{33}, T_3$	Stress in 3 direction.
$U$	Internal energy.
$V_{DC}$	Battery voltage.
$w_E$	Weights of least squares regression for electric field.
$w_S$	Weights of least squares regression for strain.



# Chapter 1

## Introduction

### 1.1 Piezoelectricity

#### 1.1.1 What is a piezoelectric material?

Piezoelectric materials are those certain crystalline materials which have the ability to develop an electric charge proportional to an applied mechanical stress. It was first discovered by J. and P. Curie in 1880. Soon it was realized that materials showing this phenomenon must also have the converse behavior, a geometric strain (deformation) proportional to an applied voltage[47]. Since then, piezoelectric materials have become the common electromechanical transducers which can transfer energy between electrical and mechanical forms. Compared to electro-magnetic transducers, a piezoelectric has the advantages of its high stiffness and broad bandwidth.

Various types of ceramics with different material composition have been discovered and improved since 1940s. The early commercial piezoelectric barium titanate products were phonograph pickup devices marketed by Sonotone Corporation. Composition modification was found desirable to improve the temperature stability and to gain moderate improvement in voltage output. An advance of great practical importance was the discovery of very strong and stable piezoelectric effects in lead zirconate titanate (PZT) solid solutions. Lead zirconate titanate with various additives has since become the dominant piezoelectric ceramic. The most common piezoelectric material used today includes the PZT family commercialized by Morgan Matroc. Recently, single crystal piezoelectric materials such as lead

zinc niobate-lead titanate (PZN-PT) and lead magnesium niobate-lead titanate (PMN-PT) have gained the attention of engineers who need high coupling coefficients, i.e. efficient power transformation.

### 1.1.2 How does it work?

To describe the essential features of the ferroelectric phenomenon, Jona and Shirane[48] used a hypothetical ferroelectric crystal. The model is simplified such that only a two dimensional crystal is considered having the chemical formula  $AB$  and a fictitious structure illustrated in Figure 1-1(a).

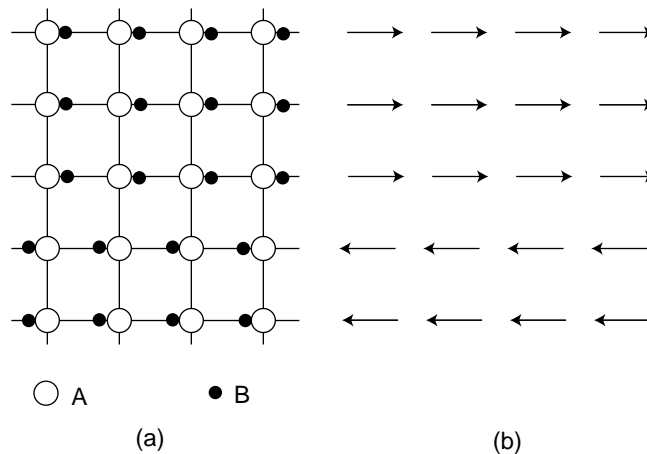


Figure 1-1: Schematic structure of a fictitious ferroelectric crystal.

The  $A$  ions, assumed to carry a negative charge, are located on the lattice points of a simple square net. Beside the  $A$  ions on the horizontal lines are the positively charged  $B$  ions. The equilibrium positions of the  $B$  ions are such that they always bond closer to one of the two adjacent  $A$  ions than to the other. This is a possible situation if the potential between two adjacent  $A$  ions is one of the types sketched in Figure 1-2(a). For a  $B$  ion on the line between two  $A$  ions, two equilibrium points correspond to the same minimum value of the energy. The  $B$  ions can shift from one equilibrium to the other. To do so, they must be supplied with sufficient energy to overcome the energy barrier  $\Delta E$ .

At a given temperature  $T$ , all  $A$  ions are closer to their  $B$  partners on the right. Each pair  $AB$  can be seen as an electric dipole and the structure can then be schematically represented

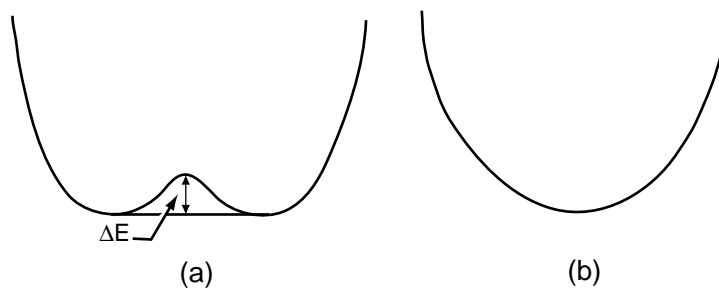


Figure 1-2: Schematic potential wells.

by an array of dipoles aiming all in the same direction, as illustrated in the three upper rows of Figure 1-1(b). This kind of crystal is considered spontaneously polarized. Alignment of the electric dipoles may extend only over a region of the crystal, while in another region the direction of the spontaneous polarization may be reversed, as shown in the lower part of Figure 1-1(b). Such regions of uniform polarization are called domains.

Suppose now that an electric d.c. field in the horizontal direction of Figure 1-1 is applied. The dipoles which are already oriented in the direction of the field will remain so aligned, but those which are oriented in the direction opposite to the field will show a tendency to reverse their orientation. If the applied field is sufficiently large, the  $B$  ions of this model will be able to overcome the barrier  $\Delta E$ , and in so doing will cause the corresponding dipoles to flip over into the direction of the field. This phenomenon of polarization reversal takes place by way of a nucleation process and domain-wall motion. If this  $AB$  crystal is initially composed of an equal number of positive and negative domains, the overall polarization of the crystal is zero. If a small electric field in the positive direction is applied, the material will follow a linear  $P$ - $E$  relation as shown by the OA portion in the plot of  $P$  vs.  $E$  in Figure 1-3.

### Nonlinearity and Hysteresis

If the electric field strength is increased, the linearity will no longer hold. A number of the negative domains will switch over in the positive direction and the polarization will increase rapidly (portion AB), until the material reaches a state in which all the domains are aligned in the positive direction: this is a state of saturation (portion BC) and the crystal consists



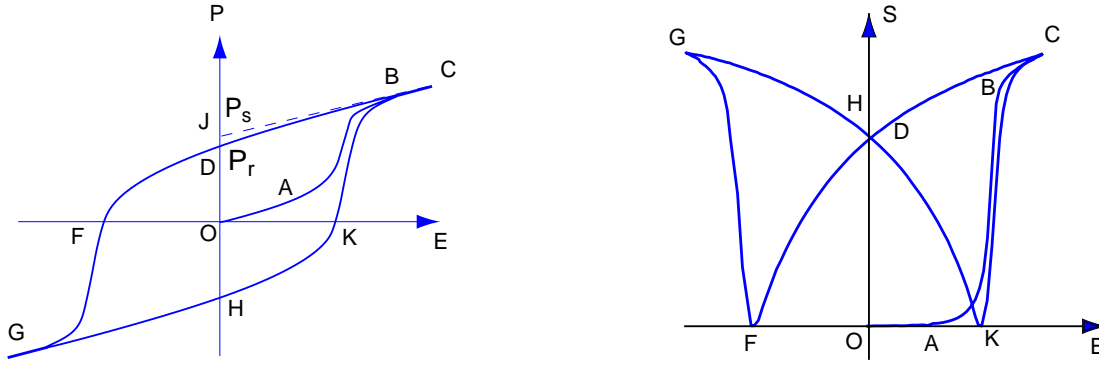


Figure 1-3: Schematic P-E and S-E loops.

now of a single domain. If the field strength is decreased, the polarization will generally not return to zero but rather follow the path CD of Figure 1-3. When the field is reduced to zero, some of the domains will remain aligned in the positive direction and the crystal will exhibit a remnant polarization  $P_r$  (OD).

It is possible to reduce polarization by applying an electric field in the opposite direction. The value of this field is called the coercive field  $E_c$ . Further increase of the field in the negative direction will cause complete alignment of the dipoles in this direction (FG) and the cycle can be completed by reversing the field direction once again (GHC). The relation between P and E is thus represented by a hysteresis loop (CDGHC), which is the most important characteristic of a ferroelectric crystal. The essential feature of a ferroelectric is thus not the fact that it has a spontaneously polarized domain, but rather the fact that this spontaneously polarized domain can be reversed by means of applying an electric field.

The strain of the material induced by the applied field is also illustrated in Figure 1-3. The strain response is approximately linear to the magnitude of the material polarization as illustrated in Figure 1-4. This shows that the material deformation is due to the growth of dipole and domain movement. Although the dipole may either orient to the left or right in Figure 1-1(b), the deformation only depends on the projected magnitude of the dipole. This explains how electric field induces the deformation of the materials.

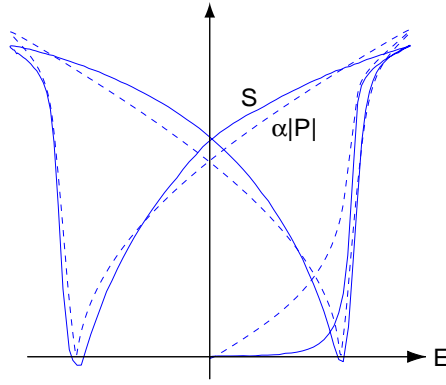


Figure 1-4: S-E (solid line) and  $\alpha|P|$ -E (dashed line) loops, where  $\alpha$  is a scale factor.

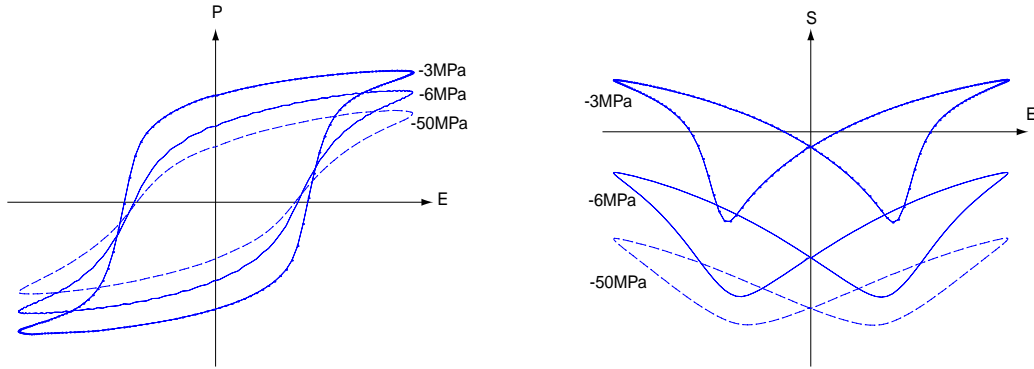


Figure 1-5: Schematic P-E and S-E loops under compression.

## Stress Dependency

If a compressive stress parallel to the polarization is applied to the material, obviously more energy needs to be overcome for ion B to change the equilibrium position. If the same electric field is applied, as in Figure 1-5, the polarization of material under compression may not increase to the same value as the stress-free material. For the same reason, the deformation of the material is suppressed by the compression. The material can also be subjected to tensile stress. The effect of tension is converse for the compression; however, it is not practical to apply tension on piezoelectric ceramics because of their fragility.

## Linearization

In general, piezoelectric response (outputs) such as electric displacement<sup>1</sup> and mechanical strain can be described as functions of applied electric field and stress (inputs), for example:

$$\begin{aligned}\mathbf{D} &= \mathbf{D}(\mathbf{E}, \mathbf{T}) \\ \mathbf{S} &= \mathbf{S}(\mathbf{E}, \mathbf{T})\end{aligned}\tag{1.1}$$

As can be seen in Figure 1-5, these two functions involve a high order of nonlinearity. The nonlinearity, hysteresis, and stress dependency make it difficult to model and design a piezoelectric device for advanced application. In the next section, a discussion of these issues will be presented. Before that, it is useful to linearize the material response using material constants. For example, assuming that the piezoelectric material is polarized in the 3 direction, the response in Eq. 1.1 can be linearized as:

$$\left\{ \begin{array}{c} D_1 \\ D_2 \\ D_3 \\ S_{11} \\ S_{22} \\ S_{33} \\ 2S_{23} \\ 2S_{13} \\ 2S_{12} \end{array} \right\} = \left[ \begin{array}{cccccccccc} \epsilon_{11}^T & 0 & 0 & 0 & 0 & 0 & 0 & d_{15} & 0 \\ 0 & \epsilon_{22}^T & 0 & 0 & 0 & 0 & d_{15} & 0 & 0 \\ 0 & 0 & \epsilon_{33}^T & d_{31} & d_{31} & d_{33} & 0 & 0 & 0 \\ 0 & 0 & d_{31} & s_{11}^E & s_{12}^E & s_{13}^E & 0 & 0 & 0 \\ 0 & 0 & d_{31} & s_{12}^E & s_{11}^E & s_{13}^E & 0 & 0 & 0 \\ 0 & 0 & d_{33} & s_{13}^E & s_{13}^E & s_{33}^E & 0 & 0 & 0 \\ 0 & d_{15} & 0 & 0 & 0 & 0 & s_{44}^E & 0 & 0 \\ d_{15} & 0 & 0 & 0 & 0 & 0 & 0 & s_{44}^E & 0 \\ 0 & 0 & 0 & 0 & 0 & 0 & 0 & 0 & s_{66}^E \end{array} \right] \left\{ \begin{array}{c} E_1 \\ E_2 \\ E_3 \\ T_{11} \\ T_{22} \\ T_{33} \\ T_{23} \\ T_{13} \\ T_{12} \end{array} \right\} \tag{1.2}$$

This form is useful to calculate the linear response of materials under the short circuit condition. For materials under the open circuit condition, it is convenient to use another

---

<sup>1</sup>To be rigorous, the transformation between the polarization ( $P$ ) and electric displacement ( $D$ ) is  $D = P + \epsilon_0 E$ . The difference is negligible, since  $\epsilon_0$  is comparatively small.

form:

$$\left\{ \begin{matrix} E_1 \\ E_2 \\ E_3 \\ S_{11} \\ S_{22} \\ S_{33} \\ 2S_{23} \\ 2S_{13} \\ 2S_{12} \end{matrix} \right\} = \begin{bmatrix} \beta_{11}^T & 0 & 0 & 0 & 0 & 0 & 0 & -g_{15} & 0 \\ 0 & \beta_{22}^T & 0 & 0 & 0 & 0 & -g_{15} & 0 & 0 \\ 0 & 0 & \beta_{33}^T & -g_{31} & -g_{31} & -g_{33} & 0 & 0 & 0 \\ 0 & 0 & g_{31} & s_{11}^D & s_{12}^D & s_{13}^D & 0 & 0 & 0 \\ 0 & 0 & g_{31} & s_{12}^D & s_{11}^D & s_{13}^D & 0 & 0 & 0 \\ 0 & 0 & g_{33} & s_{13}^D & s_{13}^D & s_{33}^D & 0 & 0 & 0 \\ 0 & g_{15} & 0 & 0 & 0 & 0 & s_{44}^D & 0 & 0 \\ g_{15} & 0 & 0 & 0 & 0 & 0 & 0 & s_{44}^D & 0 \\ 0 & 0 & 0 & 0 & 0 & 0 & 0 & 0 & s_{66}^D \end{bmatrix} \left\{ \begin{matrix} D_1 \\ D_2 \\ D_3 \\ T_{11} \\ T_{22} \\ T_{33} \\ T_{23} \\ T_{13} \\ T_{12} \end{matrix} \right\} \quad (1.3)$$

## 1.2 Application

As mentioned earlier, the first piezoelectric device was a phonograph pickup marketed by Sonotone Corporation. Since then, underwater sonar has been the major application. After the concept of smart structures proposed by Crawley and Deluis[50], piezoelectric materials are primarily used as sensors and actuators. Other applications include electrical transformers and electrical power harvesters. In this section, several common sensors, actuators and energy harvesters are introduced.

### 1.2.1 Actuator

An early application of piezoelectric materials was an underwater sound transducer used by the navy for submarine detection. This application needs broad bandwidth but only small deformation. However, to achieve successful smart structures, such as space structures and aircraft wings, engineers have made an effort to maximize the strain of the piezoelectric materials with minimum driving voltage.

To achieve this goal, one method is to drive the piezoceramics with large amplitude electric field. However, due to their natural characteristics, the piezoceramics behave non-linearly at high electric fields, as shown in Figure 1-3. It is essential to have a good model to predict these behaviors in order to design the devices and take advantage of this large deformation. Another way to achieve large deformation is to configure the device as a stack, as illustrated in Figure 1-6(a). Using this technique, one can reduce the driving voltage but

increase the actuation stroke. However, the arrangement of connecting leads may not be easy. An alternative configuration in Figure 1-6(b) used by Morgan Matroc<sup>2</sup> improves this problem. However, the drawbacks of this design include a costly manufacturing process and stress concentration at the ends of electrodes. This nonuniform stress may degenerate the performance of the material. As shown in Figure 1-7, the same problem also exists in a piezoelectric wafer with Interdigitated Electrodes (IDE), proposed by Hagood *et al.*[49]. To realize this stress concentration, sophisticated nonlinear models and finite element tools are essential.

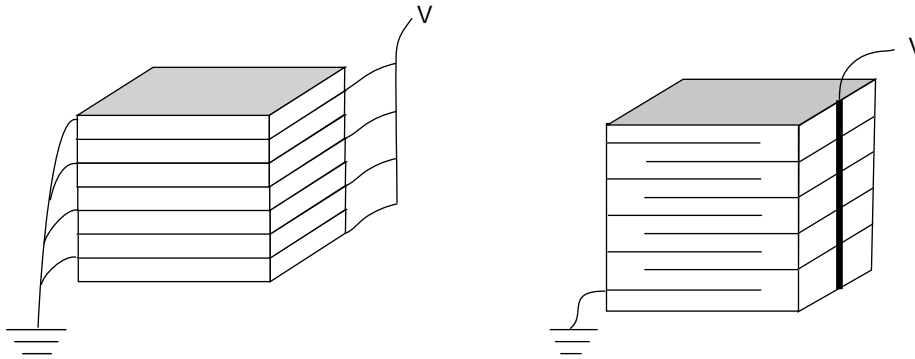


Figure 1-6: Piezo stacks

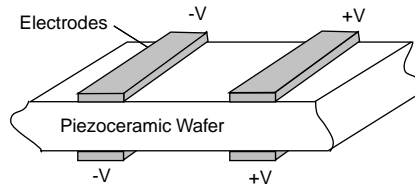


Figure 1-7: Piezoelectric wafer with Interdigitated Electrodes (IDE).

Another problem of common piezo-actuators is their fragility. It is also difficult to re-shape the materials. A novel actuator, Active Fiber Composites(AFCs), was invented by MIT researchers to solve this problem[27]. The application of AFCs includes integral actuation of helicopter blades[51], as shown in Figure 1-9. As shown in Figure 1-8, piezoelectric

---

<sup>2</sup>Morgan Matroc, Inc. Bedford, Ohio 44146

materials made in fiber forms are sandwiched by two layers of interdigitated electrodes. Between the layers is epoxy material cured to protect the piezoelectric fibers and to increase the overall strength of the composites. The voltage is applied such that major electric fields go through the fiber direction. This results in direct actuation of the piezoelectric in 33-mode, which means the deformation is along the applied field.

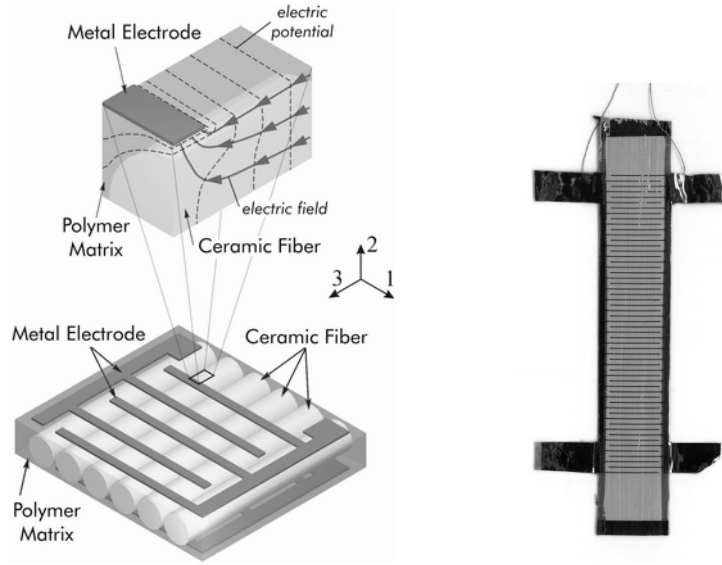


Figure 1-8: Active Fiber Composites

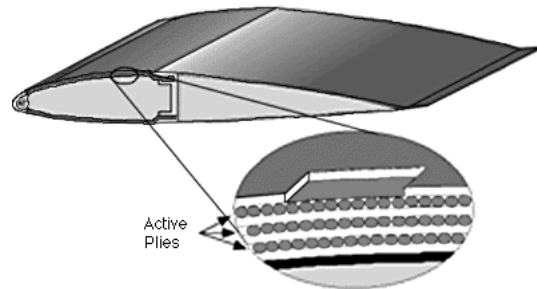


Figure 1-9: Active Fiber Composites for integral actuation of helicopter blades

Some applications may need the materials to deform in large strain instead of high force output. For instance, precision optical devices may need large actuating deformation but low force, while some applications need material to generate large actuating forces.

To achieve large actuating force, hard materials such as PZT-5A or PZT-8<sup>3</sup> are usually desired, despite their small deformations. In contrast, to achieve large actuating strain, soft materials such as PZT-5H<sup>4</sup> or single crystal material PZN-PT, in spite of their small forces, are usually selected.

### 1.2.2 Sensor

Typical sensors made of piezoelectric materials include load cells, accelerometers, and microphones. Figures 1-10 and 1-11 are the schematics to show how they work. The load cells utilize the fact that the induced charge is proportional to the applied force. The same concept was used for accelerometers since the force applied on the piezoelectric materials is proportional to the product of mass and acceleration, according to Newton's law.

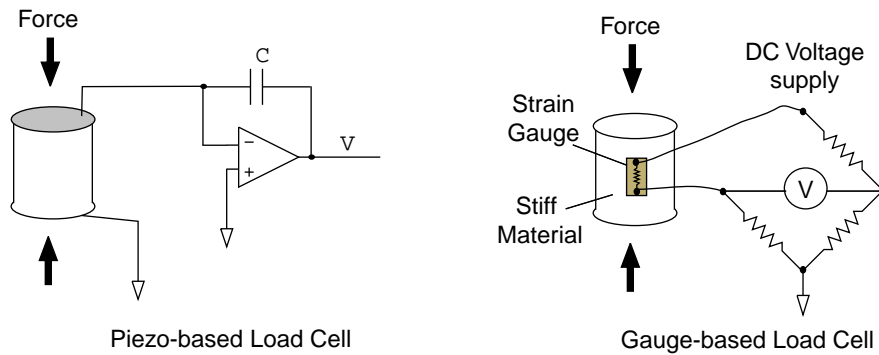


Figure 1-10: Piezo-based load cell vs. strain-based load cell

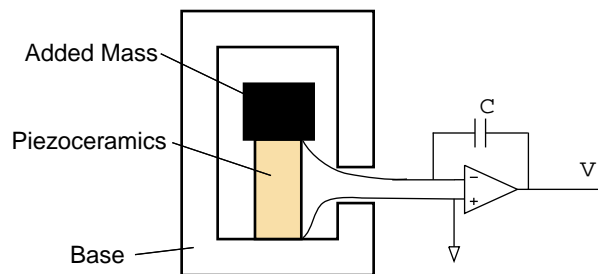


Figure 1-11: Schematics of accelerometer

<sup>3</sup>Trademark of Morgan Matroc

<sup>4</sup>Trademark of Morgan Matroc

Using piezoelectric materials as sensors can benefit from their broad bandwidth and high frequency response. Compared to strain-based load cells which rely on resistive strain gages to obtain force, piezo-based load cells can measure response that ranges from several Hz to kHz or MHz, while strain-based load cells can only measure response from DC to several 100Hz. One of the drawbacks of piezo-based sensor, however, is its poor performance at very low frequency, say 1/10 Hz. This is due to the capacitive impedance of the piezoelectric material.

In addition to bandwidth, a good sensor also needs precise calibration and is preferred to operate linearly. For application with large range response, in order to operate linearly, the stiffness is usually increased by reducing thickness and expanding cross section. However, some applications in micro-electromechanical systems (MEMS) may not allow this design approach. In this case, a precisely calibrated and accurate nonlinear piezoelectric material model is essential to make a sensor function properly.

### **1.2.3 High Voltage Source and Energy Harvester**

By analogy to load cell operation, if the charge generated by squeezing piezoelectric materials can be collected and stored, this harvested electric energy can be used to do work. Practical levels of compression, say up to 20 MPa, will generate open circuit fields in the range of 5-15 kV/cm. Devices using this feature can provide the spark for gasoline motor ignition[47].

Other applications, such as the micro hydraulic energy harvester, are under development by a group of MIT researchers[52]. The electric power transformed from mechanical energy can be harvested through circuitry. For instance, as demonstrated in Figure 2-33, the current can be rectified by diode bridges to recharge a battery. The greater and faster the compressive action is, the more energy per second (i.e. power) is collected in the battery. The reason to make the device in micro scale is to increase the natural frequency so that the piezoceramics can be driven much faster.

One of the major obstacles in developing this micro hydraulic energy harvesting technique is the compressive depolarization of the piezoelectric material. As can be imagined, the high compression can depolarize the poled piezoceramics and therefore degenerate the expected performance. Due to the nonlinearity of piezoelectric material, it is also diffi-



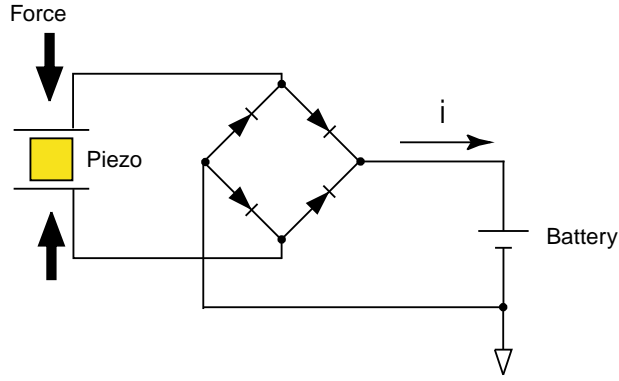


Figure 1-12: Diode bridge circuitry

cult to predict the behavior of this compressive depolarization without accurate material characterization or a material model.

### 1.3 Thesis Motivation and Objectives

#### Motivation

As mentioned earlier, nonlinearity and hysteresis make it difficult to analyze and design a piezoelectric device for smart structure application, such as actuating and sensing components as well as energy harvesters. As a result, this thesis is initially motivated to characterize the hysteretic behavior and to develop an analytical model and the tools to predict this behavior.

In addition to hysteresis, compressive depolarization is also a major concern in terms of performance. Most actuators, sensors, and even energy harvesters operate at high compression. This compression, which usually is parallel to the poling direction, will depolarize the material and degenerate the performance. One of the goals is to characterize this phenomenon and embed it in the material model.

The preliminary experiments, as illustrated schematically in Figure 1-13, showed that the response is dependent upon not only the applied fields (electric and mechanical) but also the driving frequency. It is also the objective to observe this behavior and include it into the material model.

It is also of interest to investigate the difference between hard and soft materials such

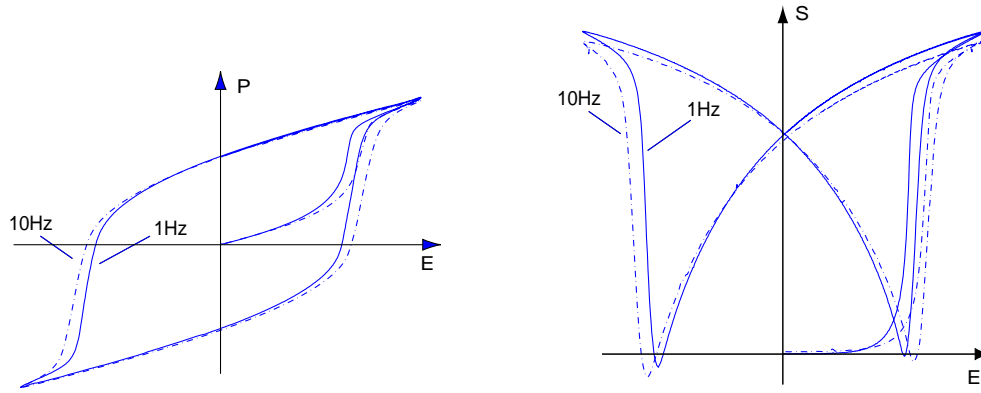


Figure 1-13: Preliminary data implies rate dependent piezoelectricity

as PZT-5A/5H versus single crystal PZN-PT and PMN-PT. For most actuation applications, PZT-5A is the most common selection because of its moderate piezoelectric constant, stiffness, and cost. For power generation, PZT-5H, PZN-PT, and PMN-PT are the best candidates. These materials have different characteristics subjected to applied compression. It is also the goal to establish a library of these material properties.

One of the obstacles to make AFCs function properly is to predict the actual electric field along the fibers. This prediction can help determine the poling voltage and design the gap between the electrodes. However, to do so, a three dimensional analysis tool such as the finite element method is desired because of the complicated boundary conditions of AFCs,.

## Objectives

Motivated by the discussion above, this thesis is aimed at characterizing the material under different loading conditions. As shown in Figure 1-14, the test matrix consists of three axes of dependencies: electric field, compression, and driving frequency. The phenomena of interest include

1. nonlinearity and hysteresis
2. electric field dependency
3. compressive stress dependency
4. rate dependency

5. difference between hard and soft material
6. three dimensional material properties for finite element analysis

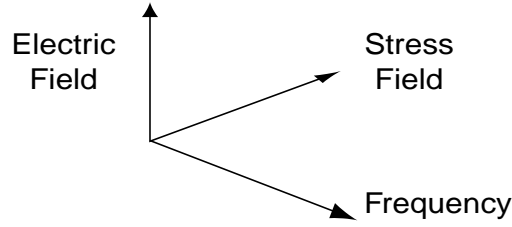


Figure 1-14: Three major axes of dependencies: electric field, compression, and driving frequency

It is also the goal to build a reliable model to simulate these behaviors. The approach is to establish a physical framework within which empirical descriptions of the behavior of some of the variables are embedded. The development of the model has three stages, as listed in Table 1.1. The description of these stages follows the guideline set forth by Ashby[70]. Each stage has its targeted task and corresponding precision. To improve the accuracy of the model, it is necessary to proceed to the next developing stage to increase the complexity of the model.

Table 1.1: Task and targeted precision of the model

Stage	Precision	Task	Required Mechanisms
1st	Factor 10	To gain understanding and insight	1-D, electric rate, static stress
2nd	Factor 2	FEM, stress analysis	3-D tensor invariants
3rd	Factor 1.1	data condensation, design guide	(stress-rate, S-D hysteresis)

The first stage is to understand the electric rate and static stress dependent effects. For such purpose, accuracy of factor 10 is the precision target. At this stage, an evolution law of internal state variables  $D^*$  was proposed; only electric rate dependence was included; a parametric study was performed; only 1-D model was considered.

The second stage is to make the model more useful and to capture these major effects into equations and code for the use of the finite element method. To do this, 3-D tensor invariants were included in addition to Level 1. The finite element analysis is often used to predict the stress of active devices. For such purpose, the factor of 2 accuracy is targeted at this stage.

The third stage is to condense the data into material constants so that a material library or a design guide for material selection can be built. For this purpose, a 1.1 precision factor is desired in order to differentiate the characteristics of various materials and compositions. If this can be done, one can perform the butterfly curve test and find the parameters of the model for each material. The piezoelectric constants for power generation and actuation applications can then be extracted from this model. No additional tests are required to obtain these constants.

The model should also be based on consistent thermodynamic potentials so that the model can be implemented into fully three dimensional finite element analysis. Without the consistent thermodynamic potentials, the electric energy and mechanical energy may not be interchangeable. Namely, it will fail to couple the electromechanical degrees of freedom in the finite element formulation. In addition to developing a material model, a finite element analysis tool is to be built in this thesis in order to simulate the response of devices with irregular loading conditions.

## 1.4 Thesis Outline

Chapter 2 will first document the approach and the result of material characterization. Two types of material characterization, minor and major loops, were conducted. The minor loop test with moderate amplitudes of field applied is primarily for specific applications, such as actuation and power generation. In contrast, the major loop test with large amplitudes of field applied (butterfly curves) is intended to find the general material parameters for model development.

Although a number of material models have been proposed since decades ago, none of them are capable of fulfilling the needs of the desired model. Fortunately, some of them provide good insights and physical explanation of the material behaviors. Chapter 3 will start with the review of these existing models, followed by the development of a rate dependent material model. To simplify the derivation and to emphasize the essence of the material model, a 1-D model will be first introduced. A parametric study will be performed to show the effects of material parameters. After understanding the 1-D material model, a 3-D model using tensor invariants will then be developed. In this chapter, the parameters

of both the 1-D and 3-D material models for PZT-5A and PZT-5H will be also optimized by minimizing the error between the model and the data acquired in Chapter 2. Chapter 4 will validate the material models with the minor loop data for energy harvesting and actuation applications.

To analyze piezoelectric devices with complicated geometry or non-uniform loading, a differential algebraic formulation of mixed finite element analysis will be developed in Chapter 5. Solution techniques to this differential algebraic equation system will be discussed in detail. Several cases will be studied to demonstrate this finite element approach. In Chapter 6, the test results will be summarized, and the developed model will be evaluated. Future work will be recommended, and the contributions of this thesis will be detailed.

## Chapter 2

# Material Characterization

Before building the material model, it is important to first observe the detailed material behaviors under different driving conditions. Three categories of experiments were conducted to investigate the material behaviors regarding actuation application, energy harvesting application, and material model development. In addition to electric field dependency, stress dependency and rate dependency are also of interest in these tests.

There are numerous types of piezoelectric materials. It is impossible to test all of them. However, the testing task can be minimized by selecting important materials for special applications. Table 2.1 shows the linear material constants of common materials. This table will help to decide the material selection. For actuation application, PZT-5A was examined in this work because it has moderate piezoelectric constants and stiffness. It is therefore suitable for actuation application. In addition, it was selected as fibers in AFCs[27]. To understand and correlate the behavior of AFCs, it is essential to test the PZT-5A bulk material. For energy harvesting application, PZT-5H was tested because of its availability and low cost. It is also because PZT-5H has higher  $d_{33}$  than PZT-5A. PZN-PT and PMN-

Table 2.1: Selection of piezoelectric materials for testing

	$d_{33}$ (pC/N)	$s_{33}^E$ (pm <sup>2</sup> /N)	$k_{33} = (d_{33}g_{33}/s_{33}^E)^{1/2}$
PZT-5H [53]	593	20.7	0.752
PZT-5A[53]	374	18.8	0.705
PZN-PT[54]	2000	111	0.93
PMN-PT[55]	2000	133	0.92

PT single crystal materials were also tested because of their extremely high  $d_{33}$  constants. For model development, the goal is to establish a material library for engineers. PZT-5A and PZT-5H were targeted because they are the most commonly used piezoelectric material. Due to the limited availability of PZN-PT and PMN-PT single crystal materials, they were not intensively tested for model development.

In this chapter, the electrical and mechanical experiment setups will be first introduced. It will be followed by the approach and results of three types of material characterizations.

## 2.1 Experimental Setup

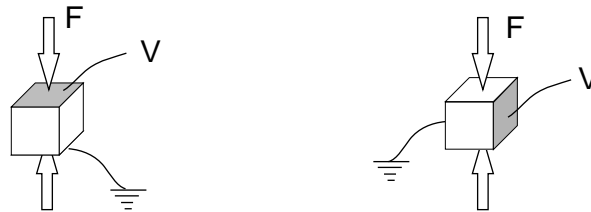


Figure 2-1: Axial test configurations: (a) longitudinal test and (b) transverse test.

Two types of tests under load can be performed: longitudinal and transverse tests, as illustrated in Figure 2-1. In the longitudinal test, the mechanical load is parallel to the electric field, while in the transverse test, the mechanical load is perpendicular to the electric field. This section will discuss how the specimen is prepared and how the electromechanical loadings are applied.

### 2.1.1 Mechanical Loading and Measurement

#### Specimen Preparation

To investigate the stress dependency, it is desired to measure the response only under uniform fields. In order to guarantee a uniform stress field on the specimen, the aspect ratios of the specimen should be increased. Ghandi[35] determined that at least a 3-to-1 ratio is required to eliminate the clamping effect and to provide the uniform field in the center of the specimen.

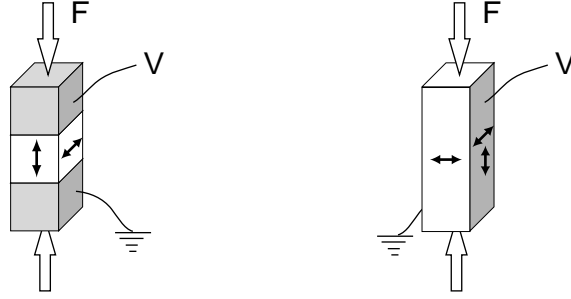


Figure 2-2: Axial test configurations: (a) longitudinal test and (b) transverse test.

In order to increase the aspect ratio of the longitudinal test specimen, the specimen shown in Figure 2-2(a) was sandwiched by two end pieces of the same unpoled material. These end pieces were coated with nickel electrodes on six faces by the vendor. By fully plating the end pieces, the electric fields in the end pieces and the net charges on their surfaces were constrained to zero, and the voltages were applied via two end pieces using alligator clips. The strains on the longitudinal specimen along its longitudinal and transverse directions were measured by attaching opposing strain gage pairs<sup>1</sup> to the four side faces of the specimen. The solid arrows shown in Figure 2-2(a) indicate the measured strain directions. These gage pairs were also used to ensure no bending moment on the specimen.

The aspect ratio of specimens in the transverse test was also increased to 3 to 1. However, instead of three stacks, one slender piece as shown in Figure 2-2(b) was used because of the way electric field was applied. The strain gauges were attached in pairs such that the bending moment could be monitored.

After the gauges were attached, the specimen was finally coated with polyurethane and submerged in silicone oil to avoid dielectric breakdown during the test. To avoid electrical damage to the computer system, a customized isolated strain gauge conditioning electronic device[35] was used to isolate the high voltage drive level from the strain gauge signal level.

The specimen size was determined by several factors: (1) the saturation field  $E_s$  of the material, (2) the maximum load capability of the testing machine, (3) the strain gauge size, (4) the electric power amplifier, and (5) the maximum isolation voltage of the strain gauge conditioner. Different tests use different sizes of specimens. The specific sizes of specimens

---

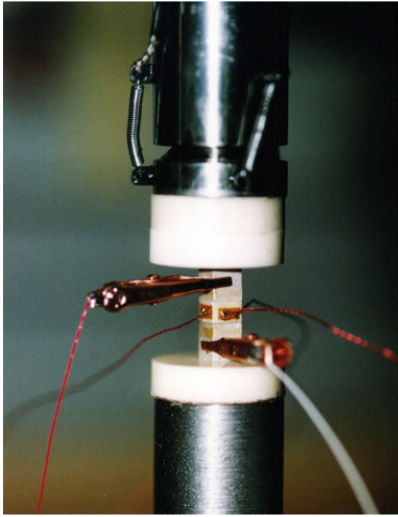
<sup>1</sup>EA-06-031EC-350 and EA-06-031DE-350 from Measurements Group Inc.



will be described in detail later when the different test sets are discussed.

### **Bending Reliever**

As shown in Figure 2-3, a test fixture incorporating a spherical joint was customized to help align the testing specimen. This fixture not only interfaced the loading between the specimen and testing machine, but also relieved the bending moment on the specimen due to any misalignment.



(A)

Figure 2-3: Experimental setup: Test fixture consisted of a spherical joint and alumina disks.

### **Low Frequency Test**

Low frequency up to 100Hz and high mechanical load up to 10kN was performed using an Instron hydraulic testing machine shown in Figure 2-4. The load was monitored using either an Instron load cell (Model 2518-603) or a piezo-based Kistler load cell (Model 9342) connected in series. The Instron load cell was required for load feedback control, while the piezo-based load cell was optional for high frequency load monitoring.

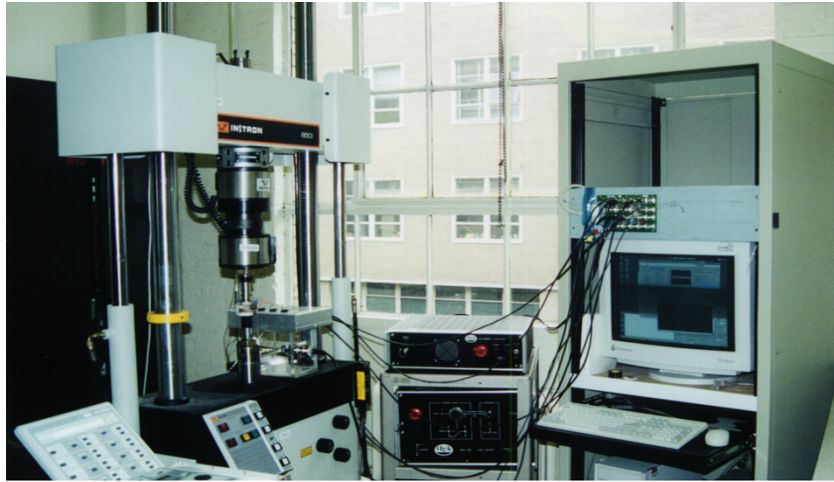


Figure 2-4: Instron Test Machine

### High Frequency Test

High frequency up to 1kHz and low mechanical load up to 400N was performed on a piezo-based component tester developed at MIT[39], as shown in Figure 2-5. The tester used three actuators<sup>2</sup> in parallel to move against the specimen fixed on the blocking plate and therefore generated mechanical compression. In addition, a membrane was used to support the specimen in order to prevent the buckling of a slender specimen. The details of the original design can be found in Lutz's work[39].

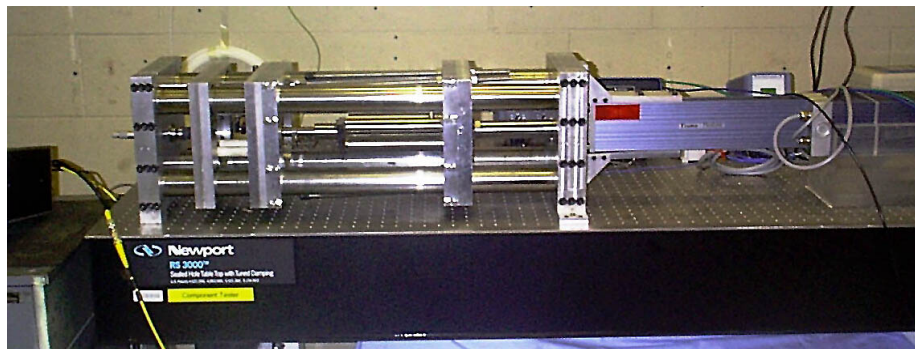


Figure 2-5: Component Testing Machine

Several modifications were made in order to maximize the load output of this tester.

---

<sup>2</sup>Kinetic Ceramics, Inc.

The original design using three actuators in parallel works well if the specimen has higher stiffness than the actuators. However, as illustrated in Figure 2-6, if the specimen is less stiff than the actuator, placing the actuators in series instead of in parallel may be beneficial. As a result, two actuators were connected in series to drive the specimen. The number of actuators in series is limited by the space between the two blocking plates. It is also essential

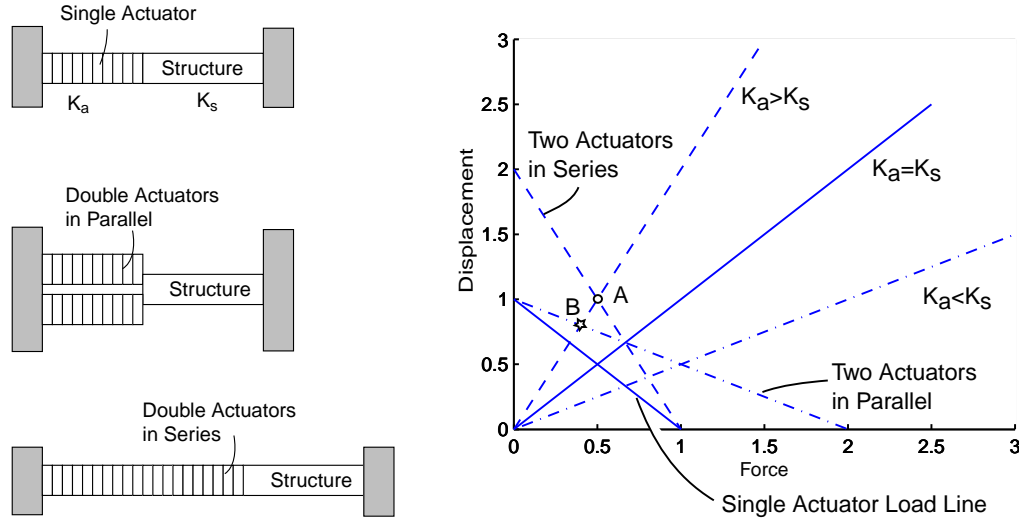


Figure 2-6: Component Testing Machine

to find the weakest link of the structure in series. This structure includes all components such as the load cell and connectors but not the actuators. If one of the components is very soft, the whole structure will be compliant. Unfortunately, the piezoelectric load cell used by the original design was found very compliant compared to the other components. To solve this problem, a piezo-based load washer by Kistler (Model 9212) was used together with a strain gauge-based load cell by Entran (Model ELH-TC790-3000) to monitor the load. The piezo-based load washer can provide high frequency load reading, while the strain gauge-based load cell is primarily used to measured DC load offset.

Another major contributor resulting in incorrect force measurement is the supporting membrane because it carries load against the actuators. To remedy this problem, the membrane was replaced by a linear bearing. The final problem of this tester is that its performance is limited by the budget and the current limit of the power amplifier that drives the piezoelectric actuators. The current limit of the amplifier is 3A, the maximum

voltage is 800V, and the actuator capacitor is  $1.5\mu\text{C}$ . From the relation

$$\left|\frac{V}{I}\right| = \left|\frac{1}{2\pi fC}\right| \quad (2.1)$$

the maximum frequency of the tester at maximum voltage is about 400Hz.

In summary, the exact maximum load generated by this component tester depends on the stiffness of the specimen and the interlinked devices such as the load cells. The stiffer the specimen or the interlinked structure is, the more blocking force can be generated by the driving piezoelectric actuators. The maximum driving frequency is restricted by the current limit of the power amplifier that is used to drive piezoelectric stacks.

## 2.1.2 Electrical Loading and Measurement

### Electrical Driving Instruments

Electric field was generated using a 20kV power amplifier, Model 20/20B by Trek Inc. A 10kV and a 4kV power amplifiers were also available. These amplifiers were used for different purposes. The 20kV and 10kV amplifiers were primarily used for poling process and large electric field characterization. For thicker specimen, 20kV could provide more electric field, however, less current. 4kV was preferred to drive minor loop with smaller electric field because its current monitor had higher signal to noise ratio.

### Measurement of Electrical Properties at Open Circuit

In order to characterize the electrical properties of the piezoelectric at constant electric displacement, i.e. open circuit, a high potential voltmeter with high impedance was developed. An equivalent circuit of a piezoelectric material shown in Figure 2-7 can be helpful in designing a high potential voltmeter.

The high potential voltmeter shown in Figure 2-8 consists of a feedback resistor  $R_f$ , a high impedance resistor  $R$ , and an inverting operational amplifier. Using this configuration, one can measure the open circuit voltage with frequency higher than

$$f_{low} = \frac{1}{2\pi RC}$$

where  $C$  is the capacitance of the piezoelectric test specimen, and the gain of measurement

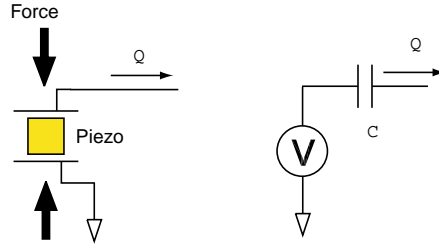


Figure 2-7: Simple equivalent circuit of piezoelectric material

is

$$\frac{V_{piezo.}}{V_{out}} = -\frac{R}{R_f}$$

By measuring the open circuit voltage while subject to compression, one can calculate the  $g_{33}$  constant.

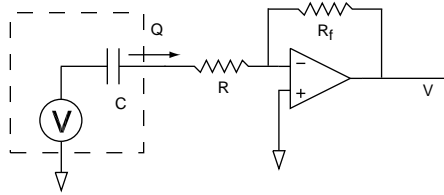


Figure 2-8: High potential voltmeter

The frequency dependence characterized in this thesis work ranges from 1Hz to 1kHz. The capacitance of the specimen ranges from 100pF to 200pF. As a result, the resistor  $R$  must be at least  $10G\Omega$  in order to satisfy the lower bound of frequency range. Unfortunately, the impedance of the resistor is not just ideally pure resistance but also contains capacitance and inductance. The virtual capacitance and inductance of the high impedance resistor, as illustrated in Figure 2-9, result in frequency dependency of the voltage meter. In order to avoid unstable dynamics at high frequency, a capacitor  $C_f$  was added in parallel with the feedback resistor  $R_f$ . With  $R = 10G\Omega$ ,  $R_f = 10M\Omega$ ,  $L = 3.6MH$ ,  $C_f = 15pF$ , and  $C = 0.07pF$ , the simulated transfer function of  $V$  to  $V_p$

$$\frac{V_{out}}{V_p} = -\frac{R_f}{R} \frac{LCs^2 + sRC + 1}{(1 + sR_fC_f)(R + sL)} \quad (2.2)$$

is compared to the measured one, as shown in Figure 2-15. The pole-zero mapping of

this dynamic system is also shown in Figure 2-10. To make a precise open circuit voltage meter, an additional filter circuit must be designed to compensate this dynamic effect. An active filter [40] using three operation amplifiers shown in Figure 2-11 has been successfully implemented to ensure  $\pm 1\%$  error within 125 Hz, as demonstrated in Figure 2-16. For frequencies higher than 125Hz, it is necessary to develop a new technique. One possible compensation can be made by using high voltage power amplifier feedback to compensate the dynamics of the resistors, as shown in Figure 2-12. However, it is easier to use another resistor with a smaller value for high frequency, since a resistor with a smaller value has less capacitive and inductive effects. Instead of the  $10\text{G}\Omega$  resistor, a  $100\text{M}\Omega$  resistor for  $R$  was used to obtain a voltage meter with bandwidth from 100Hz to 4kHz and gain error within  $\pm 2\%$ .

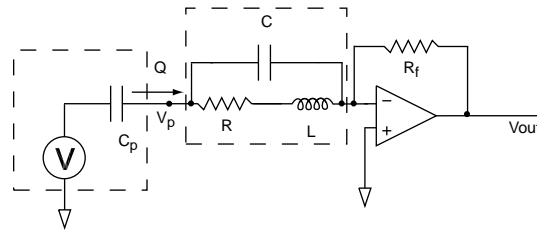


Figure 2-9: High potential voltmeter, considering dynamics of the resistor

In summary, two open circuit voltage meters were developed for this thesis work. One is for test frequencies less than 100Hz, and the other is for frequencies higher than 100Hz up to 4kHz. Figures 2-13 and 2-17 summarize their final configurations and transfer functions. These two meters were calibrated using the Trek amplifier at different voltage levels ranging from  $\pm 200\text{V}$  to  $\pm 2000\text{V}$ . The transfer functions demonstrate that these voltage meters operate linearly in the specified bandwidth.

A final note on using the open circuit voltmeters is that a precaution must be taken to minimize the cable capacitance. This is due to the limited charge source of the piezoelectric material. If the piezoelectric output port somehow forms a capacitive path to the ground, as illustrated in Figure 2-14, part of the limited charge source will be drained to the ground. This leakage charge will result in measurement error of the open circuit voltage. As a result, the length of wire between the piezoelectric output and volt meter input must be designed

as short as possible to minimize the error due to wire capacitance.

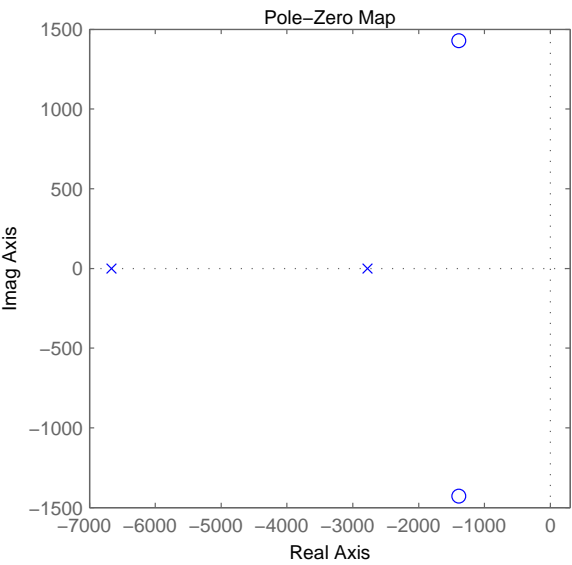


Figure 2-10: Pole-zero mapping of high potential voltmeter, considering dynamics of the resistor

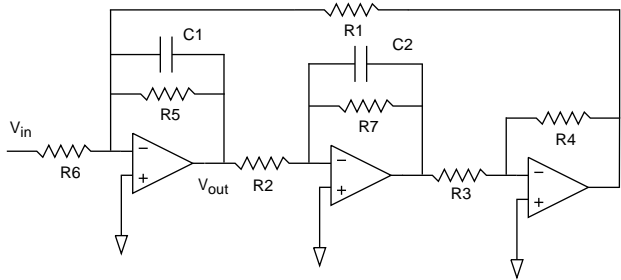


Figure 2-11: Schematics of active filter

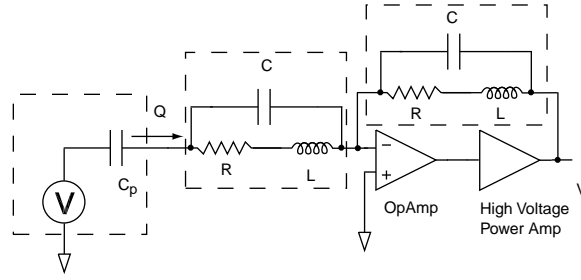
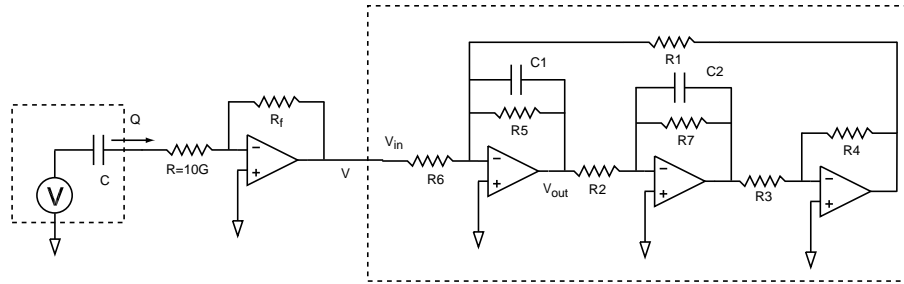
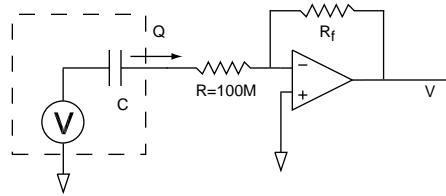


Figure 2-12: High potential voltmeter using high voltage power amplifier feedback to compensate the dynamics of the resistor



(a)



(b)

Figure 2-13: The final configuration of open circuit voltage meter used in this thesis work: (a)  $10\text{G}\Omega$  with filtered output, (b)  $100\text{M}\Omega$

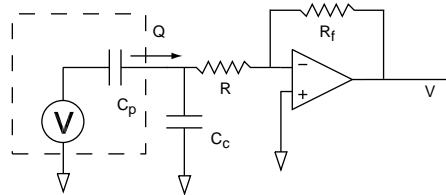


Figure 2-14: High potential voltmeter, considering capacitance of cable



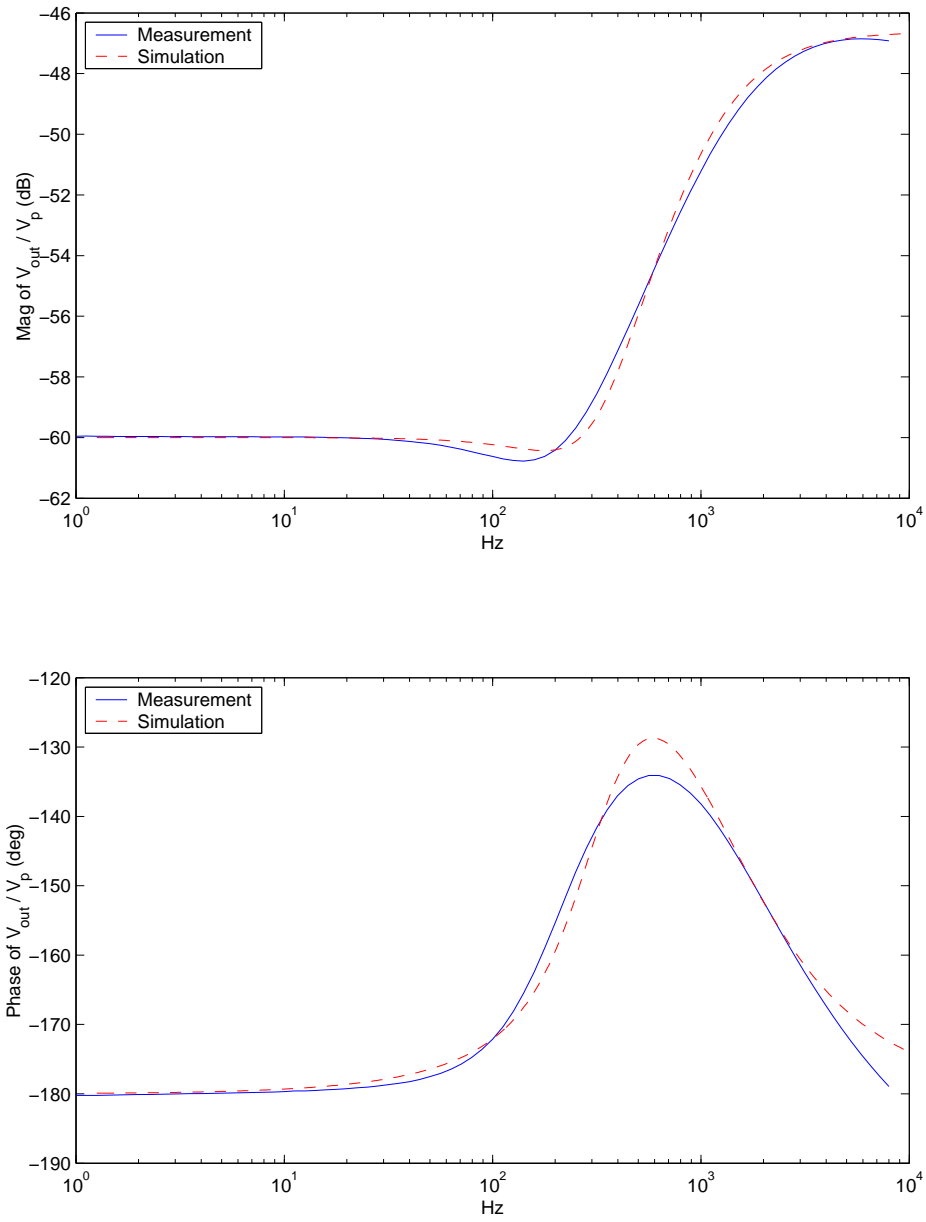


Figure 2-15: Transfer function of high potential voltmeter, considering dynamics of the resistor

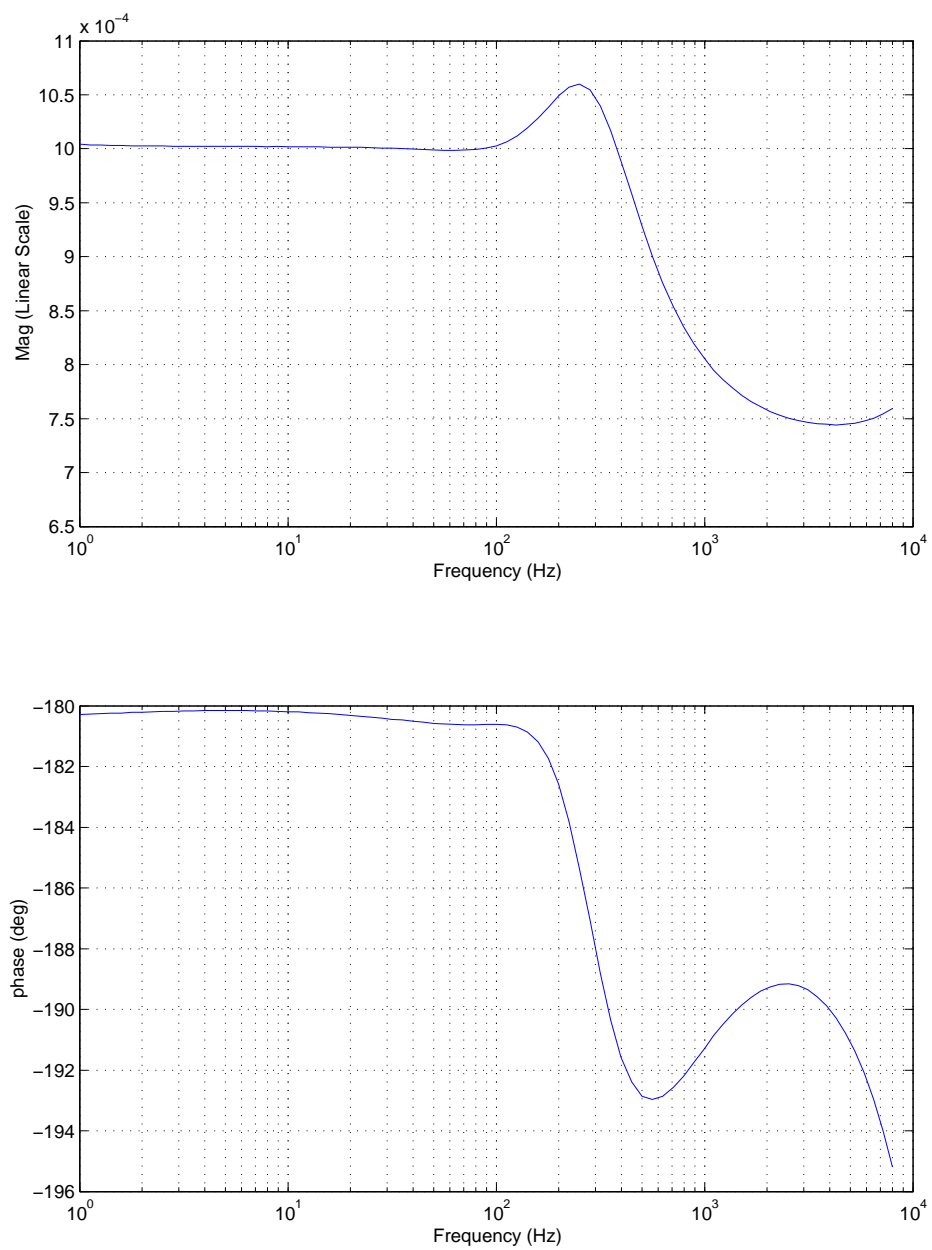


Figure 2-16: Transfer function of compensated high potential voltmeter using active filter

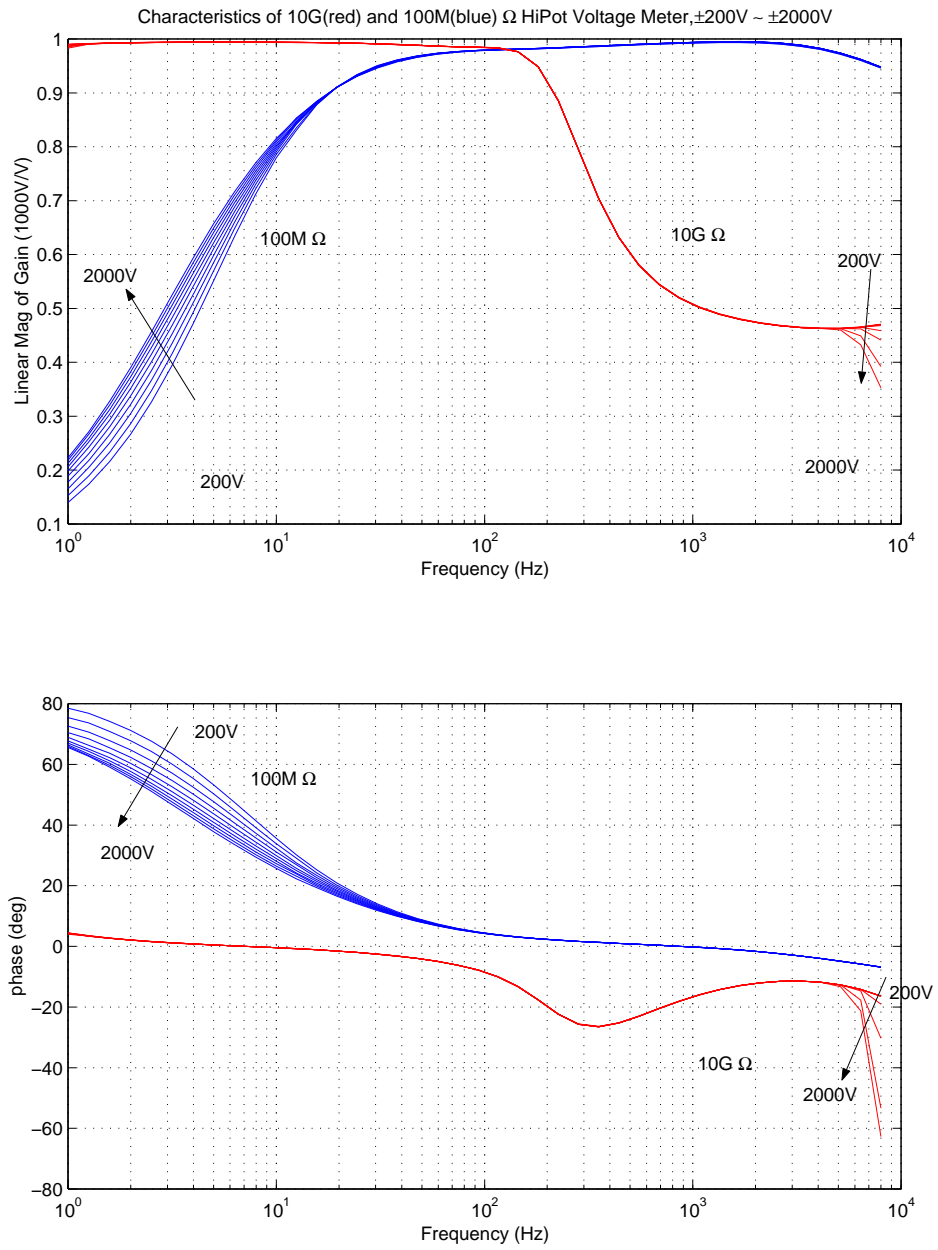


Figure 2-17: Transfer function of high potential voltmeter: one with 10G $\Omega$  resistor operates from 1 to 100Hz, one with 100M $\Omega$  resistor operates from 100Hz to 4kHz.

## Measurement of Electrical Properties at Short Circuit

In order to measure short circuit properties, one must use a charge/current amplifier which consists of an inverting operational amplifier and a feedback capacitor or resistor as shown in Figures 2-18 and 2-19. With the feedback capacitor or resistor, the operational amplifier amplifies charge or current, respectively. The gain for the charge amplifier [42] is

$$Q(j\omega) = -\frac{V(j\omega)}{j\omega C}$$

and for the current amplifier [43] is

$$I(j\omega) = -\frac{V(j\omega)}{R}.$$

Operational amplifier OPA111<sup>3</sup> was selected because of its high impedance.

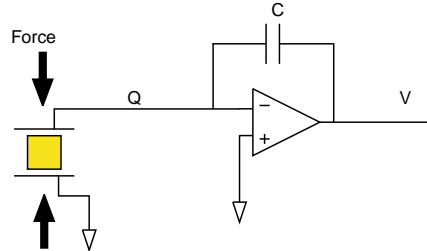


Figure 2-18: Charge amplifier.

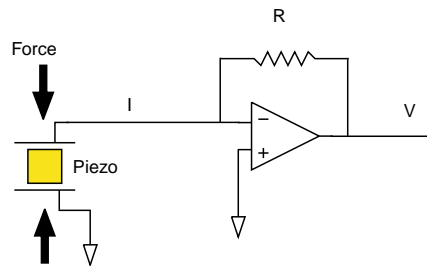


Figure 2-19: Current amplifier.

---

<sup>3</sup>Burr-Brown Corporation, Tucson, AZ 85706

## 2.2 Characterization for Actuation Application

This work is motivated by the depolarization of PZT-5A piezoelectric fibers in AFCs, because the fibers may be exposed to high stress field after manufacturing. For example, during the curing process, the difference between the coefficients of thermal expansion of the epoxy matrix and the piezoelectric fibers may result in compression of the fibers. In addition, during the fiber poling process, the fibers may extend against the epoxy that surrounds them. In such situation, the fibers may experience additional compression. Exposure to these high electromechanical loads parallel to the material poling direction may result in the depolarization of the material, depending on the material composition and on environmental variables such as temperature, electric field, and stress. In addition, the stress duration effect may influence the depolarization.

Early studies on the effects of static stress on piezoelectric materials have been conducted by Krueger [28] and Zhang [29]. These studies only investigated the low electric field material properties affected by static compressive stresses while many applications operate the material at relatively high electric fields. There may be a possibility that high electric excitation can resist depolarization to some extent. Hence, this section will examine the compressive depolarization of commercial lead zirconate titanate PZT-5A piezoelectric ceramics by evaluating the electric actuation strain at different electric fields, compressive stresses, and compression durations. Varying the combinations of these parameters allows further understanding of the coupling effects among them.

In this section, the detailed data and test procedure of PZT-5A will be presented. The difference between single and multiple loop loading cycles used to investigate the actuation under load will be exhibited. The effect of the compression duration on the residual actuation will be reported.

### 2.2.1 Actuation under Load

#### Single Loading Cycle

The objectives of this test were to identify the limit of compression without permanently depolarizing the material and to investigate the possibility that high electric field could avert compressive depolarization of the material. In this test, the compressive load was

monotonically increased up to 150 MPa in 10 MPa increments and then released to 0 MPa also in 10 MPa decrements, as shown in Figure 2-20. The actuation strain was measured five minutes after each change in load. In order to compare the effects of low and high electric fields, the test procedure used by Zhang [29] was modified, and the specimen was excited by 1Hz sinusoidal waves with amplitudes of 9%, 16%, 40%, 70%, 90% and 110% of the coercive field ( $E_c$ ), which is 1.12 kV/mm for PZT-5A. To evaluate the actuation at high electric field, a generalized piezoelectric constant  $d_{33}^*$  was defined as the ratio of peak-to-peak actuation strain to peak-to-peak electric field [44]. To measure the constant  $d_{33}^*$  in the low field region and to increase the signal-to-noise ratio of actuation strain measurement, the sinusoidal wave with 9%  $E_c$  amplitude was used to represent the low field behavior. 9%  $E_c$  was validated to be low enough to represent the low field properties by comparing the measured data with published low field data [29]. The difference between the two sets of data was within  $\pm 5\%$  error. A freshly poled specimen that had not been exposed to any compression was tested for each selected electric field. What follows is the detailed test procedure:

1. Measure and record the actuation strain resulting from the selected electric field at zero stress.
2. Compress the sample by 10MPa increments and hold for 5 minutes. The sample electrodes were short-circuited during compression so that the charge generated by the compression could be discharged and balanced. By doing so, it is believed that the material will be more easily depolarized.
3. Measure and record the actuation strain resulting from the selected electric field. The compressive load remained on the sample during the electric actuation.
4. Repeat Steps 2 and 3 until the compressive load is 150MPa.
5. Reduce the compressive load by 10MPa and hold for 5 minutes. Short-circuit the electrodes of the specimen during compression.
6. Measure and record the actuation strain resulting from the selected electric field. The compressive load remained on the sample during the electric actuation.

7. Repeat Steps 5 and 6 until the compressive load was 0MPa.

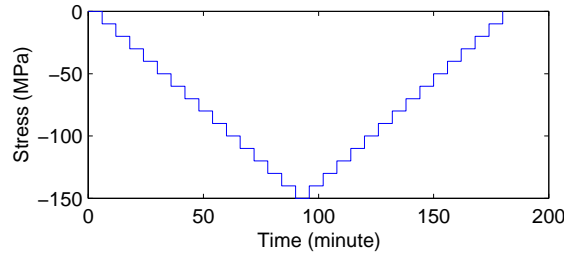


Figure 2-20: The compression profile of the single loading cycle test.

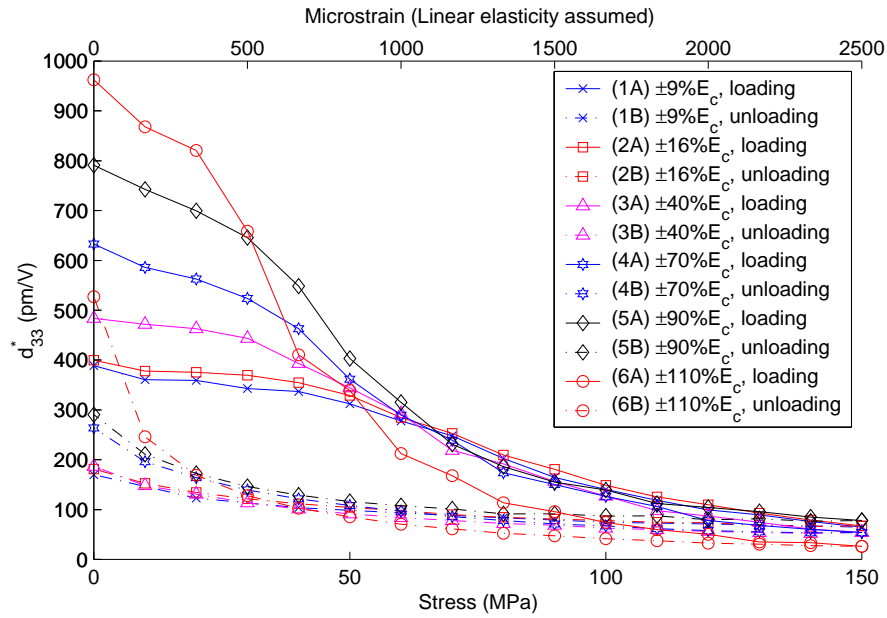


Figure 2-21: Test results of single loading cycle subjected to different electric fields.

Figure 2-21 shows the actuation under load while subject to different electric fields. The low field result at 9%  $E_c$  was similar to the one reported by Zhang [29]. Before any compressive load was applied, higher electric field yielded higher actuation. However, higher electric field did not prevent the reduction of actuation when the compressive load was increased. Furthermore, electric fields higher than the coercive field tended to decrease the

actuation more quickly because the negative component of the electric field expedited the depolarization of the material. It was also found that most of the electric actuation did not recover even when the compressive load was totally released except for the slight recovery of the sample using  $110\%E_c$ . This was because the electric field was higher than the coercive field and would have repolarized the piezoelectric material. In summary, this test result showed that even high electric AC fields had little success in preventing depolarization due to high compressive stresses, although positive DC bias might help achieve this goal.

### Multiple Loading Cycles

In the single loading cycle test, the material properties during the unloading cycle were governed by the maximum exposure stress, which was 150MPa. It is also of interest to investigate the unloading material properties determined by different levels of maximum exposure stress less than 150MPa. For this purpose, a new test using multiple loading cycles was designed. In the new test, the total range of 150MPa compression was partitioned into five equal subranges, namely, 30, 60, 90, 120 and 150MPa. Starting from the lowest loading range followed by the higher ones, five loading cycles corresponding to these five subranges were conducted in the test. At each loading cycle, the compression on the specimen was loaded up to the peak of the corresponding loading range in 10MPa increments and then unloaded to zero stress also in 10MPa decrements, as shown in Figure 2-22. Sinusoidal waves with amplitudes of 16%, 40%, 70% and 90%  $E_c$  at 1Hz were driven to actuate the specimen 5 minutes after the load was changed. A freshly poled specimen was tested for each selected electric field. The detailed test procedures is:

1. Measure and record the actuation strain resulting from the selected electric field at zero stress.
2. Compress the sample by 10MPa increments and hold for 5 minutes. Short-circuit the electrodes of the specimen during compression.
3. Measure and record the actuation strain resulting from the selected electric field. The compressive load remained on the sample during the electric actuation.
4. Repeat Steps 2 and 3 until the compressive load reached the peak of the loading range corresponding to the current loading cycle.



5. Reduce the compressive load by 10MPa and hold for 5 minutes. Short-circuit the electrodes of the specimen during compression.
6. Measure and record the actuation strain resulting from the selected electric field. The compressive load remained on the sample during the electric actuation.
7. Repeat Steps 5 and 6 until the compressive load was zero.
8. Repeat Steps 2 to 7 for the next loading range which had not yet been applied.

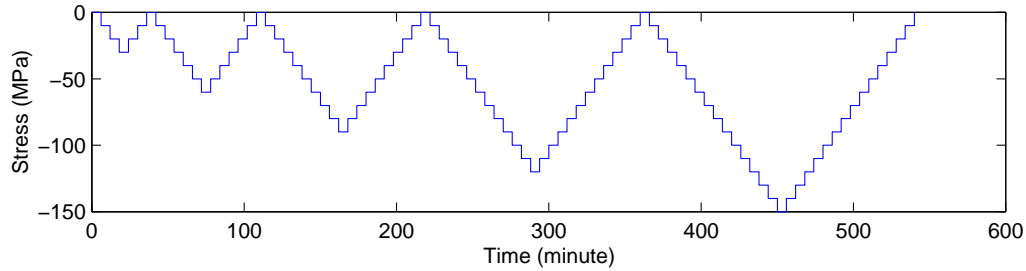


Figure 2-22: The compression profile of the test using multiple loading cycles

Figures 2-23 and 2-24 show the actuation during multiple compressive loading cycles using  $\pm 16\%$ ,  $\pm 40\%$ ,  $\pm 70\%$  and  $\pm 90\%$   $E_c$  electric fields, respectively. In loading cycle 1, under maximum compression of 30MPa, actuation under load shows complete reversibility after reduction of compression. In loading cycle 2, under maximum compression of 60MPa, actuation under load shows slight reversibility after reduction of compression. For the loading cycles 3, 4, and 5, the irreversible behavior shows the obvious depolarization of the material. Figure 2-25 illustrates the reversibility as a function of the electric field and the maximum exposure stress. As shown in Figure 2-25(A), compared to the maximum exposure stress, the applied electric fields are found to be relatively less relevant to the reversibility, although high electric field results in high electric actuation, as shown in Figure 2-25(B). The reversibility clearly indicates the confident operating range of the compression without depolarizing the material. It is also found that the actuation during the multiple loading cycles is clearly enveloped by the actuation under the single loading cycle, as shown in each figure.

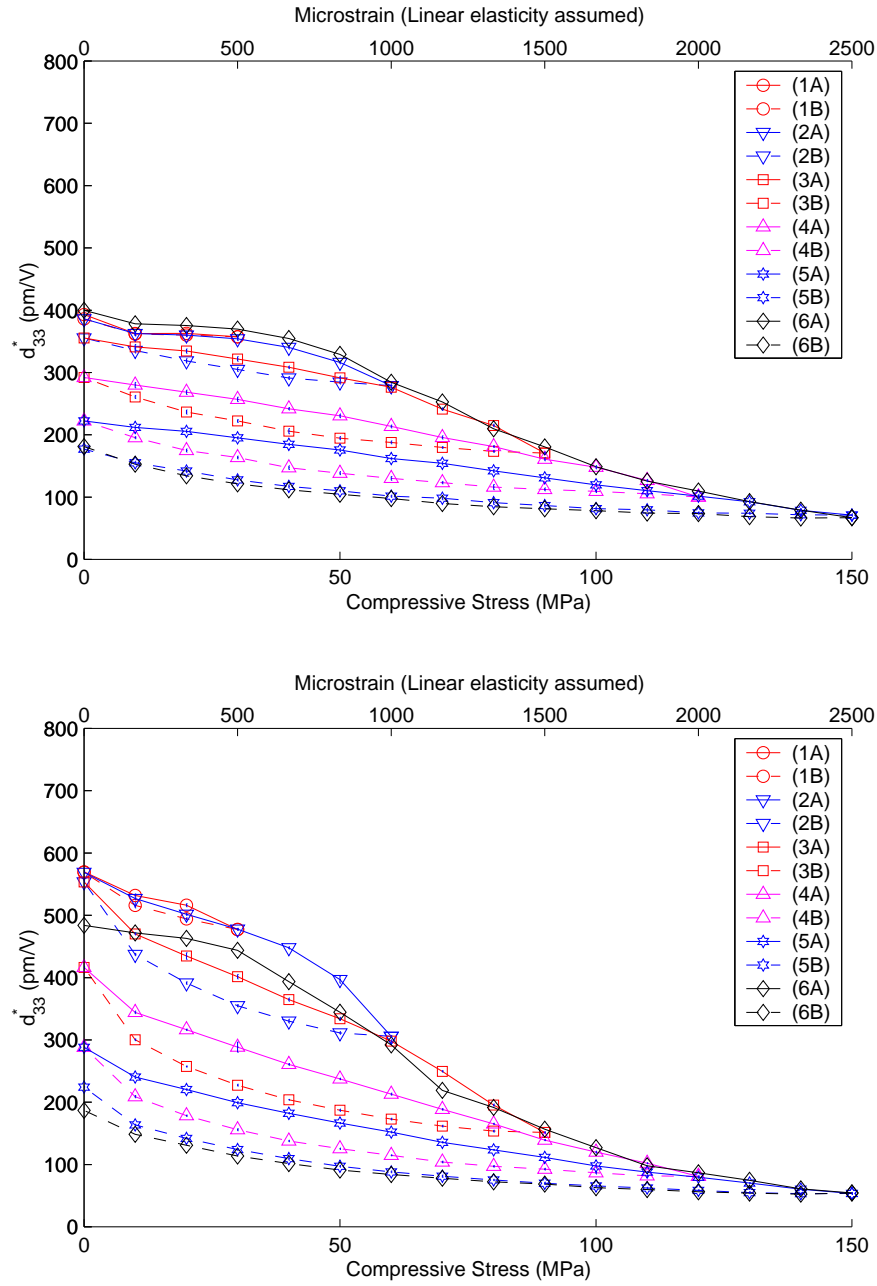


Figure 2-23: Multiple loading cycles with  $\pm 16\%$   $E_c$  (upper) and  $\pm 40\%$   $E_c$  (lower): (1A) cycle 1, loading, (1B) cycle 1, unloading, (2A) cycle 2, loading, (2B) cycle 2, unloading, (3A) cycle 3, loading, (3B) cycle 3, unloading, (4A) cycle 4, loading, (4B) cycle 4, unloading, (5A) cycle 5, loading, (5B) cycle 5, unloading, (6A) single loading cycle, and (6B) single unloading cycle.

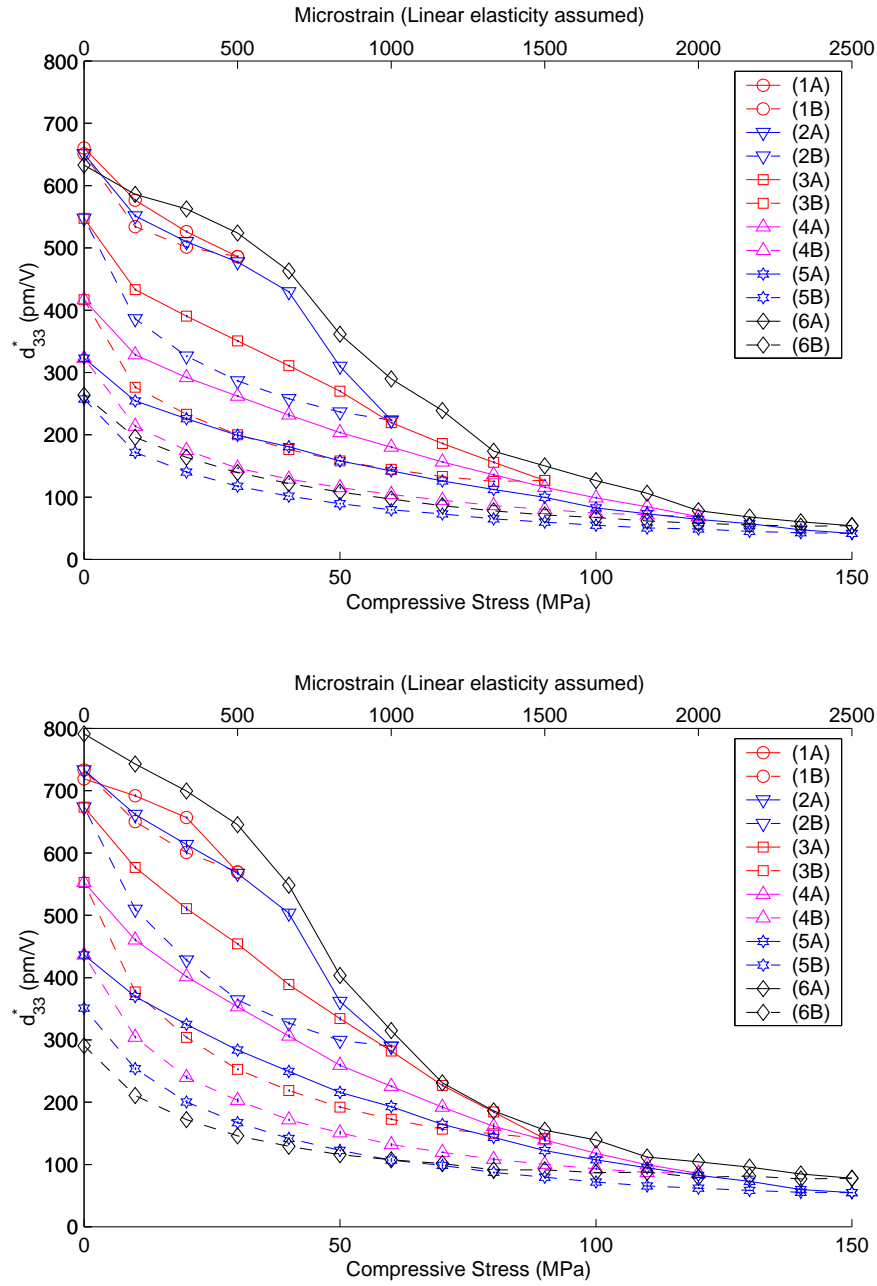


Figure 2-24: Multiple loading cycles with  $\pm 70\% E_c$  (upper) and  $\pm 90\% E_c$  (lower): (1A) cycle 1, loading, (1B) cycle 1, unloading, (2A) cycle 2, loading, (2B) cycle 2, unloading, (3A) cycle 3, loading, (3B) cycle 3, unloading, (4A) cycle 4, loading, (4B) cycle 4, unloading, (5A) cycle 5, loading, (5B) cycle 5, unloading, (6A) single loading cycle, and (6B) single unloading cycle.

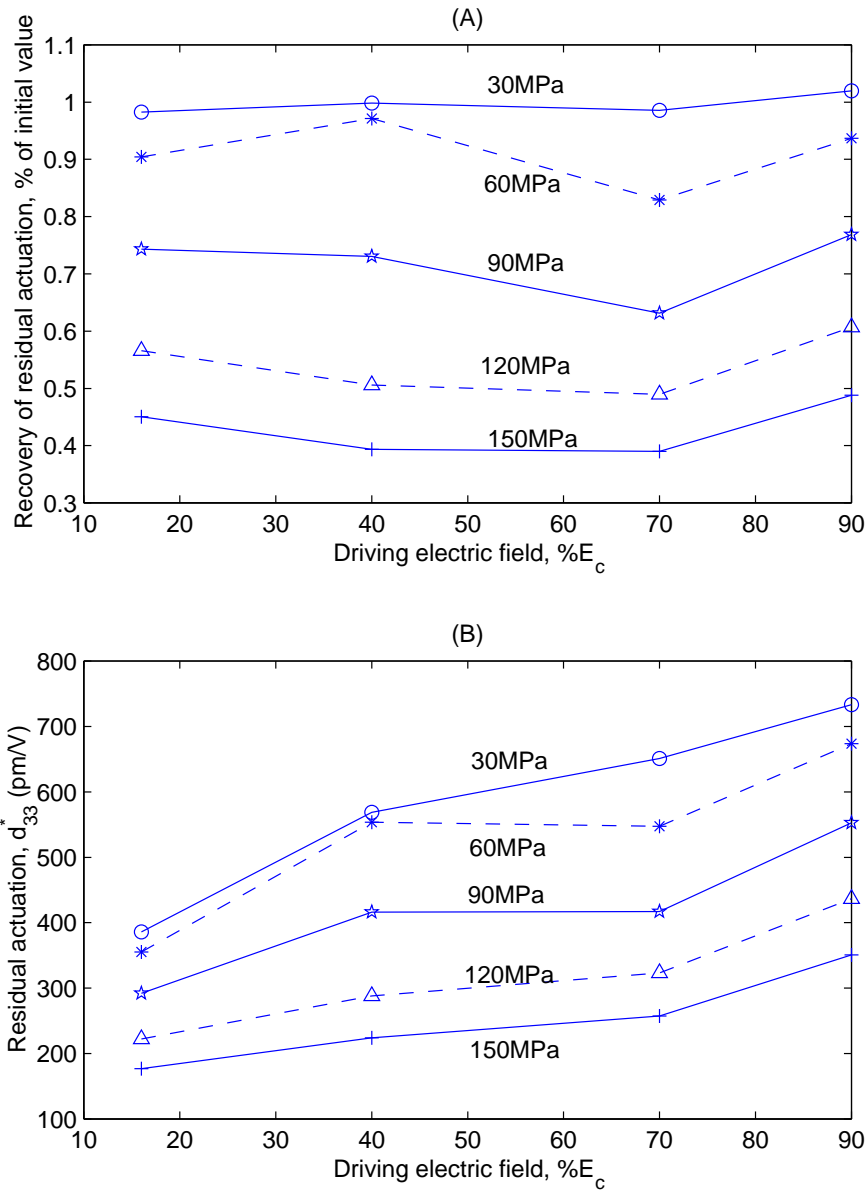


Figure 2-25: Reversibility: (A) Recovery percentage of residual actuation vs. electric field and maximum exposure stress. (B) Residual actuation vs. electric field and maximum exposure stress.

## 2.2.2 Residual Actuation and Compression Duration

### Residual Actuation

In order to characterize the residual actuation at zero stress after a small period of exposure to the compressive load, a test similar to the one conducted on AFCs by Morris *et al.* [56] was performed. It was reported that the AFCs retained their initial actuation at zero stress even after exposure to 150MPa compression stress for 30 seconds. In order to mirror the test performed on AFCs, 30 second compression exposure time was used in this experiment, as shown in Figure 2-26. Sinusoidal waves with the amplitudes of 9%, 17%, 34%, 51% and 68%  $E_c$  at 1Hz were selected to actuate the specimen in this experiment. A freshly poled sample was tested for each selected electric field. The detailed procedure is:

1. Measure and record the actuation strain resulting from the selected electric field at zero stress.
2. Compress the sample by 10MPa and hold for 30 seconds. Short-circuit the sample electrodes during compression.
3. Release the load and wait for 30 seconds.
4. Measure and record the residual actuation strain resulting from the selected electric field at zero stress.
5. Repeat steps 2 to 4 with 10MPa load increments until the compressive load was 150MPa.

As shown in Figure 2-27, the residual actuation after exposure to the compression for 30 seconds is normalized by the initial actuation at zero stress. Using lower electric fields ( $< 50\% E_c$ ), the residual actuation reduced as the compressive load was increased. In contrast, using higher electric fields ( $> 50\% E_c$ ), the residual actuation slightly increased even as the compression load was increased. This result correlated with the similar phenomenon observed on AFCs by Morris *et al.* [56] It is of interest to explore this phenomenon further.

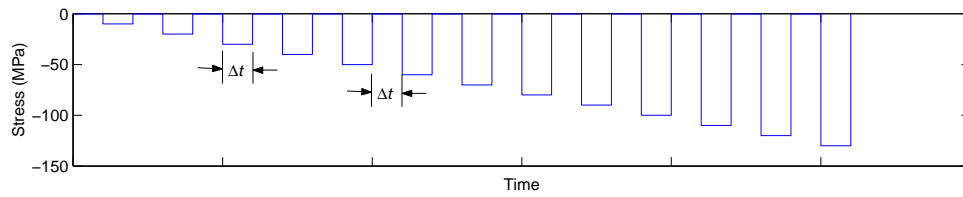


Figure 2-26: The load profile of testing the residual actuation at zero stress after exposure to compressions for a duration of  $\Delta t$ .

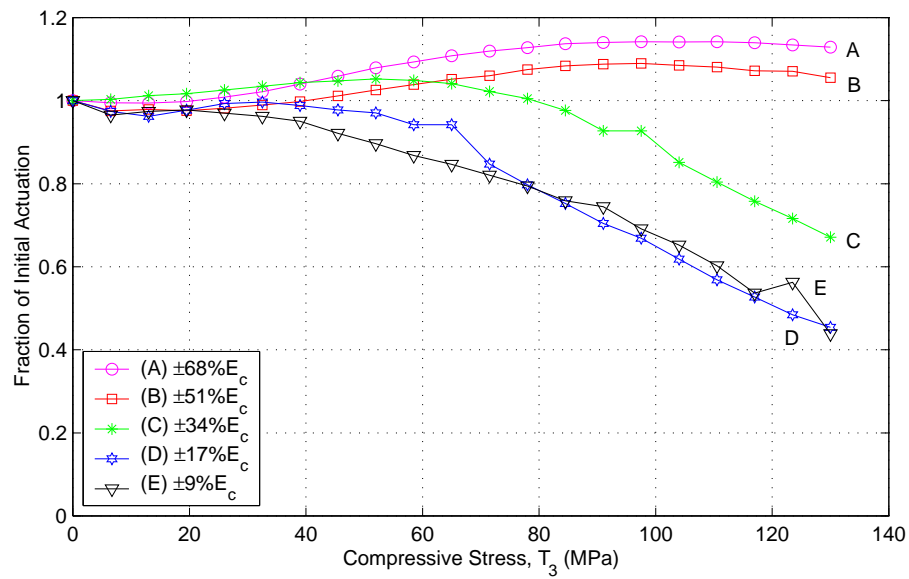


Figure 2-27: The residual actuation after exposure to compressions for 30 seconds is normalized by the initial actuation at zero stress.

## Compression Duration Issue

The data of  $\pm 70\%$   $E_c$  residual actuation shown in Figure 2-27 slightly increased even as the load increased. However, Figure 2-24 shows the reduction of  $\pm 70\%$   $E_c$  residual actuation at zero stress after each of the multiple loading cycles. The only difference between these two data is the compression duration. The data shown in Figure 2-24 used 5 minute duration for each step, and the specimen totally experienced 25 minutes of nonzero compression for the first loading cycle, while the data shown in Figure 2-27 used 30 second duration. Comparison implied the dependency of stress duration. The same phenomenon that actuation is dependent upon compression duration has also been reported by Zhang[29]. In order to study this phenomenon, more tests were conducted by using 5 minute and 30 minute compression durations instead of 30 seconds in the residual actuation test, as shown in Figure 2-26. In addition, in order to exclude the high electric field effect under high compression, two electric excitations distinguished as Types A and B were designed as shown in Figure 2-28. Type A was driving electric actuation at zero stress only, while Type B was driving at both zero and nonzero stress.

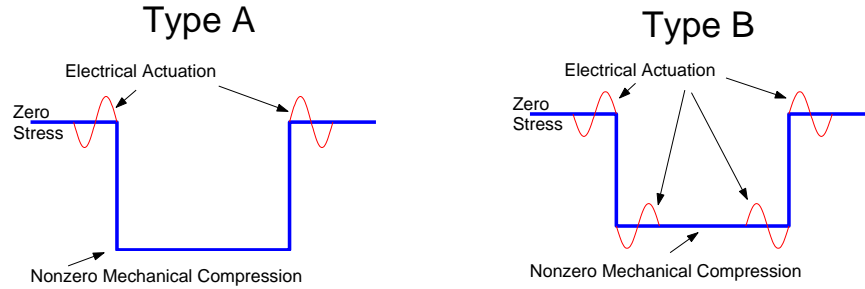


Figure 2-28: Type A was driving electric actuation at zero stress only, while Type B was driving at both zero and nonzero stress.

Figure 2-29(A) shows the test result using Type A actuation and Figures 2-29(B), (C), and (D) show the test result using Type B actuation. Some observations are concluded as the following:

- For Type A actuation using short compression duration, high electric drive can maintain the initial residual actuation even after exposure to high compressive stress, as

illustrated in Lines A1 and A2 in Figure 2-29(A).

- For Type A actuation using high electric drive level, longer compression duration results in reduced residual actuation, as shown in Lines A2 and A3 in Figure 2-29(A).
- Comparing Figures 2-29(A) and (B) shows the difference between Types A and B that the first two statements do not hold for Type B actuation.
- By comparing different durations, Lines C1–C3 in Figure 2-29(C) or Lines D1–D3 in Figure 2-29(D), one can conclude that Type B actuation has little compression duration effect.
- By comparing Line  $C_i$  to Line  $D_i$ , where  $i=1...3$ , for different electric driving fields in Figures 2-29(C) and (D), one can observe that Type B actuation has no ability to resist compressive depolarization, although high electric fields in Figure 2-29(D) result in 10% more actuation than low electric drive in Figure 2-29(C) after exposure to 150MPa.

The mechanism of duration effect on the residual actuation can be explained by the hypothesis that the depoled dipoles can be restituted by the internal electric field induced by unbalanced free charges due to compression until these free charges reach equilibrium. The compression duration matters because it takes time for free charges to reach such equilibrium. Figure 2-30 illustrates how this mechanism works. Before any compression, as shown in Figure 2-30(A), the dipoles in the material align along the poling direction, and the free charges and dipoles stay in equilibrium such that no internal electric field exists. After the compression is applied, the dipoles are flipped, as shown in Figure 2-30(B). At this moment, the unbalanced free charges and the flipped dipoles form internal electric fields which can reorient the dipoles back to the original alignment. This is true until these free charges migrate and compensate with the dipoles such that no more induced internal electric field exists, i.e. reaching equilibrium, as shown in Figure 2-30(C). As a consequence, if the stress is removed before equilibrium, the dipoles will be turned back by the induced internal electric field. This restitution depends on the extent of being in equilibrium that has been achieved by the migrating free charges and the restoring dipoles. In addition, any high electric field applied at this unbalanced state will help reconstitute the dipoles. This explains



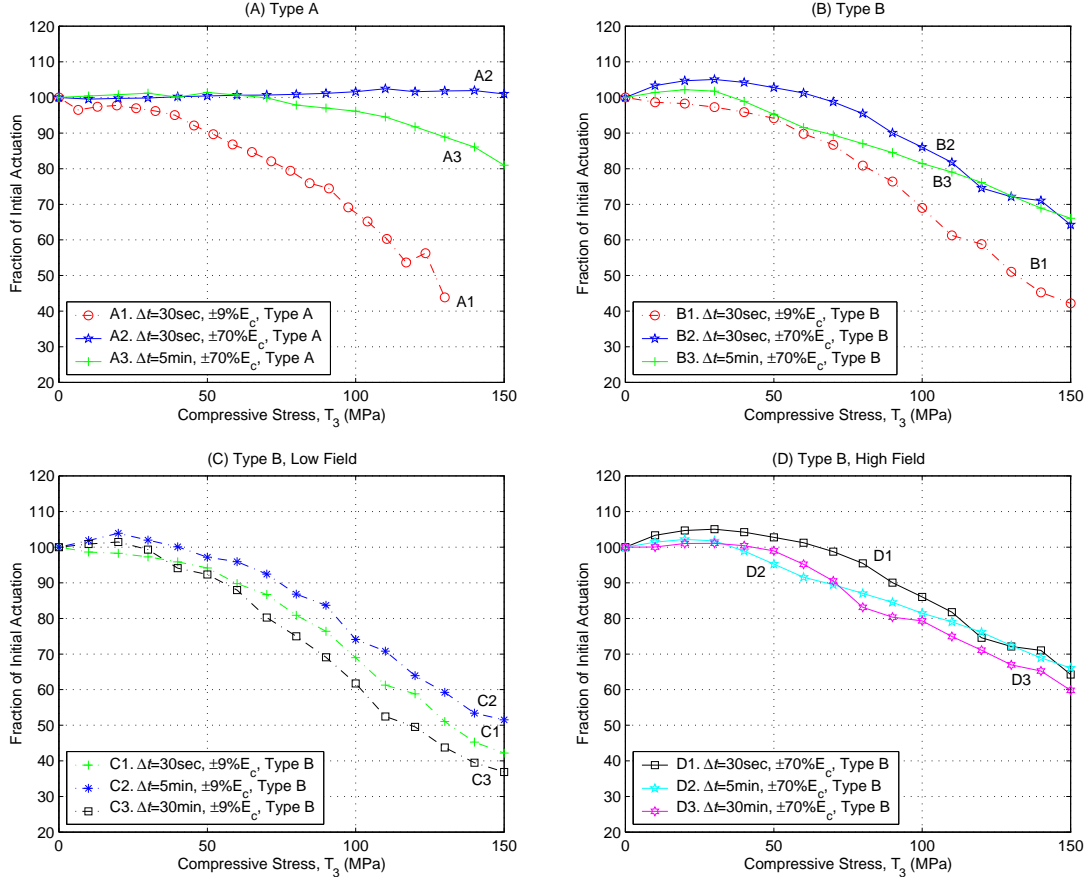


Figure 2-29: Normalized residual actuations for different compression duration and different electric fields: (A) Results using Type A actuation (B) Results using Type B actuation (C) Results using low Type B actuation,  $\pm 9\% E_c$  (D) Results using high Type B actuation,  $\pm 70\% E_c$ .

why using Type A actuation for short duration and high electric actuation can maintain the original actuation. However, this does not hold for Type B actuation because, in addition to compressive stress, the negative component of the electric field at nonzero compressive stress has further depolarized the material and therefore impedes the restitution of dipoles.

The surprising result that high electric actuation under short duration retains initial actuation provides promising driving conditions for controlled structures. Engineers may take the advantage of this result if short duration of a high compression environment is unavoidable. An example of such a situation is helicopter rotor blades subjected to a sudden gust. High electric actuation with  $\pm 70\% E_c$  at zero stress can prevent high compression

depolarization for such short duration. If the high electric actuation under short duration of high compression is necessary, biased electric actuation without negative field is strongly recommended to prevent further depolarization of the material.

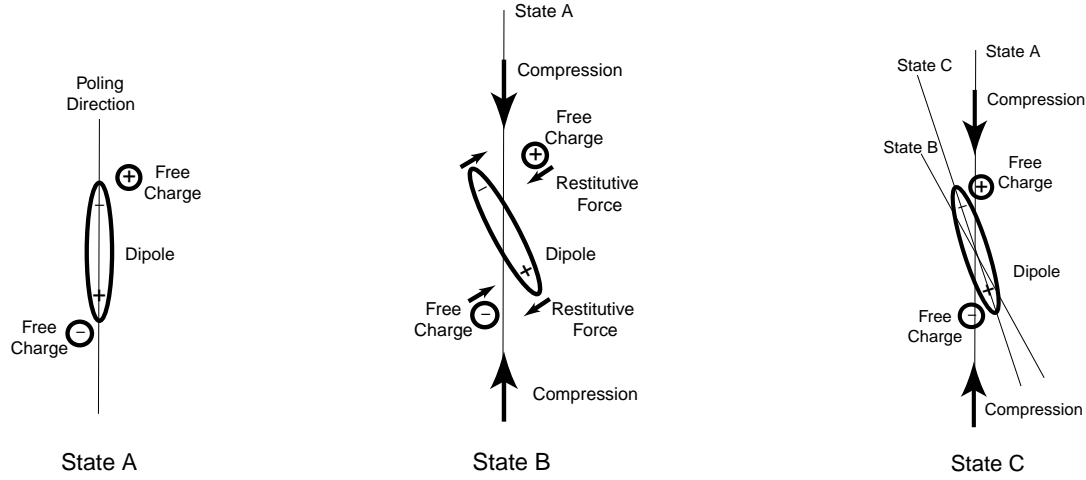


Figure 2-30: Illustration of the dipoles restituted by the internal electric fields induced by the unequilibrium free charges: (A) the original equilibrium state before compression, (B) the unequilibrium state after compression, (C) the equilibrium after compression.

### 2.2.3 Summary of Actuation Characterization

The compression limit of PZT-5A without depolarizing the material has been investigated in this section by testing the material at different levels and combinations of electric fields, compressive stresses and stress durations. The test results of actuation under load for a single loading cycle showed that the material was depolarized at high compressive stress even for high applied electric field. Once the material was depolarized by 150MPa compressive load, the polarization did not recover even after the complete removal of the load. The reversibility of actuation under load was observed only in the case subjected to the compressive load less than 30 MPa, as indicated by the test results of actuation under load using multiple loading cycles. Slight recovery of electric actuation was observed for the loading case below 60 MPa. The data of actuation under loads higher than 60 MPa indicated that the material suffered severe compressive depolarization and lost most actuation performance even for high electric field.

The properties of the residual actuation at zero stress after removal of the compressive load varied with applied electric field, compression duration, and whether the negative electric field was applied along with the compression. Without negative electric field driven with compressive load, the residual actuation at zero stress by high enough electric field (70%  $E_c$ ) will remain constant even after exposure to short duration of high compression (less than 30 seconds). However, this is not true for those situations consisting of any combination of low electric field, long duration of compression, and occurrence of high negative electric field along with high compression.

Table 2.2 summarizes a matrix of possible situations leading to material depolarization. This table provides engineers a design guide for active devices under high compression environment. In particular, engineers may take reasonable advantage of certain results observed in this work that indicate that the active devices subjected to short duration of high compression (less than 30 seconds) will retain major actuation performance if high enough electric field (70%  $E_c$ ) is applied and no compression is applied along with this electric excitation.

Table 2.2: Summary of PZT-5A Compressive Depolarization. (● indicates the test condition.)

	E-Field $\pm 9\%E_c$	E-Field $\pm 70\%E_c$	Compression $\leq 30MPa$	Compression $\geq 30MPa$	Duration $\leq 30sec.$	Duration $t \geq 5min.$	Loss of Actuation	Reversible
Actuation Under Load	●		●			●	little	Yes
	●			●		●	Yes	No
		●	●			●	25% loss	Yes
		●		●		●	Yes	No
Residual Actuation	●		●		●		little	
	●			●	●		Yes	
		●	●		●		No	
		● <sup>4</sup>		●	●		No	
		● <sup>5</sup>		●	●		Yes	
		●	●			●	No	
		●		●		●	Yes	
		●		●		●	Yes	

<sup>4</sup>No negative electric field was applied along with compression

<sup>5</sup>Negative electric field was applied along with compression

## 2.3 Characterization for Energy Harvesting Application

The most exciting feature of a piezoelectric material is that one can generate electric power by squeezing it very hard and fast. However, it is a major concern that the high compression parallel to the piezoelectric polarization direction may depolarize the materials[47]. Therefore, engineers desire to know the limit of compressive load without degenerating the material. Another concern is the frequency dependency. A previous study by Goldfarb[57] showed that piezoelectric generation using resistive load had low efficiency at high frequency. However, the new study in this work shows that the frequency dependency depends on the use of circuitry. A new test in this work using a rectifying diode circuit demonstrates that the energy can be harvested in a battery and that the efficiency is independent of frequency below the specimen natural frequency.

Hence, this section will fully investigate the frequency and stress effects of the piezoelectric energy harvesting application. Piezoceramics connected with a resistor and diode circuit will be first realized. The material characterization of generalized piezoelectric constants under short and open circuits will then be conducted. Diodes used for power measurement will be selected and characterized. Finally, the power harvested by diode circuitry will be reported. The common commercial piezoceramics PZT-5H<sup>6</sup> was selected for testing because its moderate piezoelectric and elastic constants, availability, and low cost. Other modern engineered materials such as single crystal PZN-PT<sup>7</sup> and PMN-PT<sup>8</sup> were also chosen because of their high piezoelectric constants, as shown in Table 2.1.

### 2.3.1 Resistive Load vs. Rectifying Circuitry

In order to study the difference between resistive load and rectifying circuitry, a linear electromechanically coupled model was built using SIMULINK<sup>TM</sup> by Mathworks Inc. In this model, the material constants are assumed independent of stress and frequency. This model can be used to simulate response of the piezoelectric specimen subjected to a mechanical load and connected to circuitry such as resistors and rectifying diodes. More details of the model can be found in Appendix A.

---

<sup>6</sup>6.35mm cube supplied by Staveley Sensors Inc, E. Hartford, CT.

<sup>7</sup>PZN-4.5%PT, 5.5mm cube, supplied by TRS Ceramics, Inc., State College, PA.

<sup>8</sup>6mm × 6mm × 4mm supplied by Crystal Associates Inc., East Hanover, NJ.

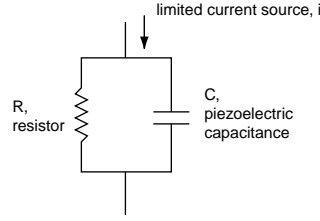


Figure 2-31: Effect of the limited current source on a  $RC$  circuit.

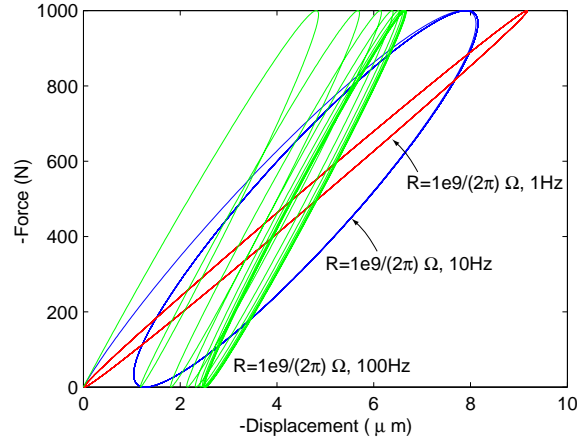


Figure 2-32: Simulation of force-displacement relation of piezoelectric specimen with resistive load.

Before simulating the resistive circuitry, an understanding must be emphasized that only a limited current can be generated by compressing a piezoelectric material. Due to this limited current source and the capacitive impedance of the piezoelectric material itself, the current flowing through the resistor is frequency dependent. As shown in Figure 2-31, in order to maximize the current flowing through the resistor, the value of the resistor ( $R$ ) must match the impedance of the specimen ( $C$ ):

$$|R| = \left| \frac{1}{j2\pi fC} \right| \quad (2.3)$$

or

$$R = \frac{1}{2\pi fC} \quad (2.4)$$

where  $j$  equals  $\sqrt{-1}$  and  $f$  is the driving frequency of the mechanical load. Figure 2-32 shows the simulated force-displacement relation of the specimen in the resistor circuit.

The enclosed area by this force-displacement relation represents the mechanical energy transformed into electrical energy. As a result, for a given amplitude of the input force, the larger the enclosed area is, the higher the efficiency is. As shown in the Figure 2-32, for a 100pF specimen with a  $1/(2\pi) \times 10^9 \Omega$  resistor, the maximum efficiency occurs at 10Hz. This correlates the test result by Goldfarb. However, the same efficiency at different frequency can be obtained by matching the impedance, for instance, using a resistors of  $1/(2\pi) \times 10^{10} \Omega$  at 1Hz or a resistor of  $1/(2\pi) \times 10^8 \Omega$  at 100Hz. This analysis demonstrates that the frequency dependency comes from the mismatch between the resistor and the impedance of the specimen. Unfortunately, the factor of impedance mismatch is not considered by Goldfarb.

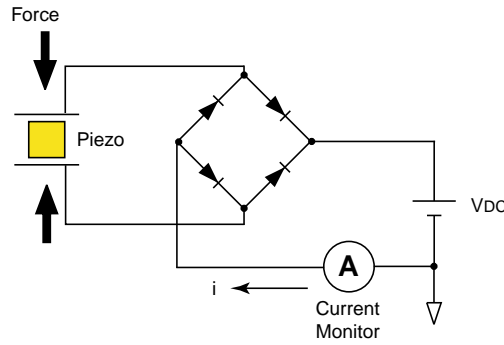


Figure 2-33: Diode bridge circuitry

In contrast to the resistive load, the rectifying circuit shown in Figure 2-33 will result in efficiency that is independent of frequency. Figure 2-34 shows a comparison of the simulated force-displacement relationships for the resistive load and rectifying circuit. Although the maximum efficiency of the rectifying circuit is slightly smaller than that of the resistive circuit, the benefit using the rectifying circuit includes frequency independence and the fact that electric power can be harvested in a battery. As a result, the diode circuit will be used later in this section to characterize the stress effects on the power density generated by piezoelectric materials.

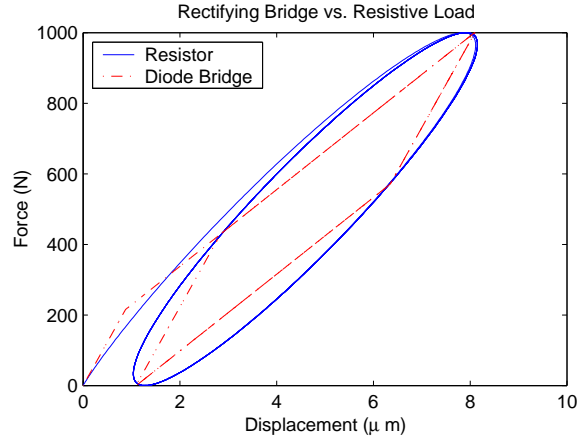


Figure 2-34: Simulation of force-displacement relation of piezoelectric specimen with a resistor or a rectifying diode bridge.

### 2.3.2 Characterization of Generalized Material Constants

The simulation used in the previous discussion is based on the assumption that the material properties are independent of stress and frequency. This linearity may not be true in practice. As a result, it is of interest to obtain experimental data of material constants as a function of stress and frequency. To do so, a generalized material constant is first defined as the linear slope of material response with respect to the stress at different amplitudes and frequencies of the input stress. These generalized material constants include piezoelectric coupling constants  $d_{33}$  and  $g_{33}$  and compliances  $s_{33}^E$  and  $s_{33}^D$ , each a required input of the simulation model. The  $d_{33}$  constant determines how much current can be drawn from the specimen at short circuit condition. The  $g_{33}$  constant determines how much potential can be generated on the specimen at open circuit condition. The stiffness determines how much displacement the specimen deforms and how much power is delivered into the specimen for a given input force.

The test was performed using the high frequency tester shown in Figure 2-5. Under short circuit condition, strain and charge were measured by the strain gauges and charge amplifier shown in Figure 2-18. Under open circuit condition, strain and voltage were measured by the strain gauges and voltmeter shown in Figure 2-13. Figures 2-35 and 2-36 show the data of  $s_{33}^E$ ,  $s_{33}^D$ ,  $d_{33}$ , and  $g_{33}$  as functions of stress at 10Hz and 400Hz for PZT-5H,



PZN-PT and PMN-PT. As can be seen, the material properties are significant functions of the driving stress but not obvious functions of the driving frequency. The variance of single crystal data at different frequency might be due to the variance of different samples. A slight misalignment of cutting of a single crystal specimen may result in huge variance of material properties, while the cutting has no major effect of a polycrystalline PZT-5H specimen. Each data set can be fitted using a polynomial function of compressive stress  $T$  (in MPa):

$$d_{33}^{PZT-5H} = 679.18 + 11.035T - 0.28434T^2 \quad (2.5)$$

$$d_{33}^{PMN-PT} = 958.75 + 17.235T - 0.72036T^2 \quad (2.6)$$

$$d_{33}^{PZN-PT} = 1576.8 + 47.839T - 1.8197T^2 \quad (2.7)$$

$$s_{33}^{EPZT-5H} = 23.753 + 0.11773T - 0.0052678T^2 \quad (2.8)$$

$$s_{33}^{EPMN-PT} = 39.285 + 0.70661T - 0.0080949T^2 \quad (2.9)$$

$$s_{33}^{EPZN-PT} = 78.076 + 0.71686T + 0.0066186T^2 \quad (2.10)$$

$$g_{33}^{PZT-5H} = 0.020196 + 0.00012746T - 0.000041935T^2 + \\ 0.0000023240T^3 - 0.000000057743T^4 \quad (2.11)$$

$$g_{33}^{PMN-PT} = 0.027015 + 0.00051050T - 0.000107110T^2 + \\ 0.0000031697T^3 - 0.000000028433T^4 \quad (2.12)$$

$$g_{33}^{PZN-PT} = 0.036175 + 0.00071800T - 0.00019501T^2 + \\ 0.0000067482T^3 - 0.000000071305T^4 \quad (2.13)$$

$$s_{33}^{DPZT-5H} = 10.2763 - 0.035048T + 0.0012802T^2 \quad (2.14)$$

$$s_{33}^{DPMN-PT} = 15.525 + 0.59993T + 0.014338T^2 \quad (2.15)$$

$$s_{33}^{DPZN-PT} = 15.792 + 0.10766T - 0.15070T^2 + \\ 0.040328T^3 - 0.0017931T^4 + 0.000023619T^5 \quad (2.16)$$

where the units of  $d_{33}$  and  $g_{33}$  are pC/N and Vm/N, respectively, and  $s_{33}^E$  and  $s_{33}^D$  are in pm<sup>2</sup>/N. Among the four constants,  $g_{33}$  decreases most rapidly as the compression is increased. This also results in the sharp degeneration of the coupling coefficients  $k_{33}$  shown in Figure 2-37 and defined as:

$$k_{33}^2 = \frac{d_{33}g_{33}}{s_{33}^E} \quad (2.17)$$

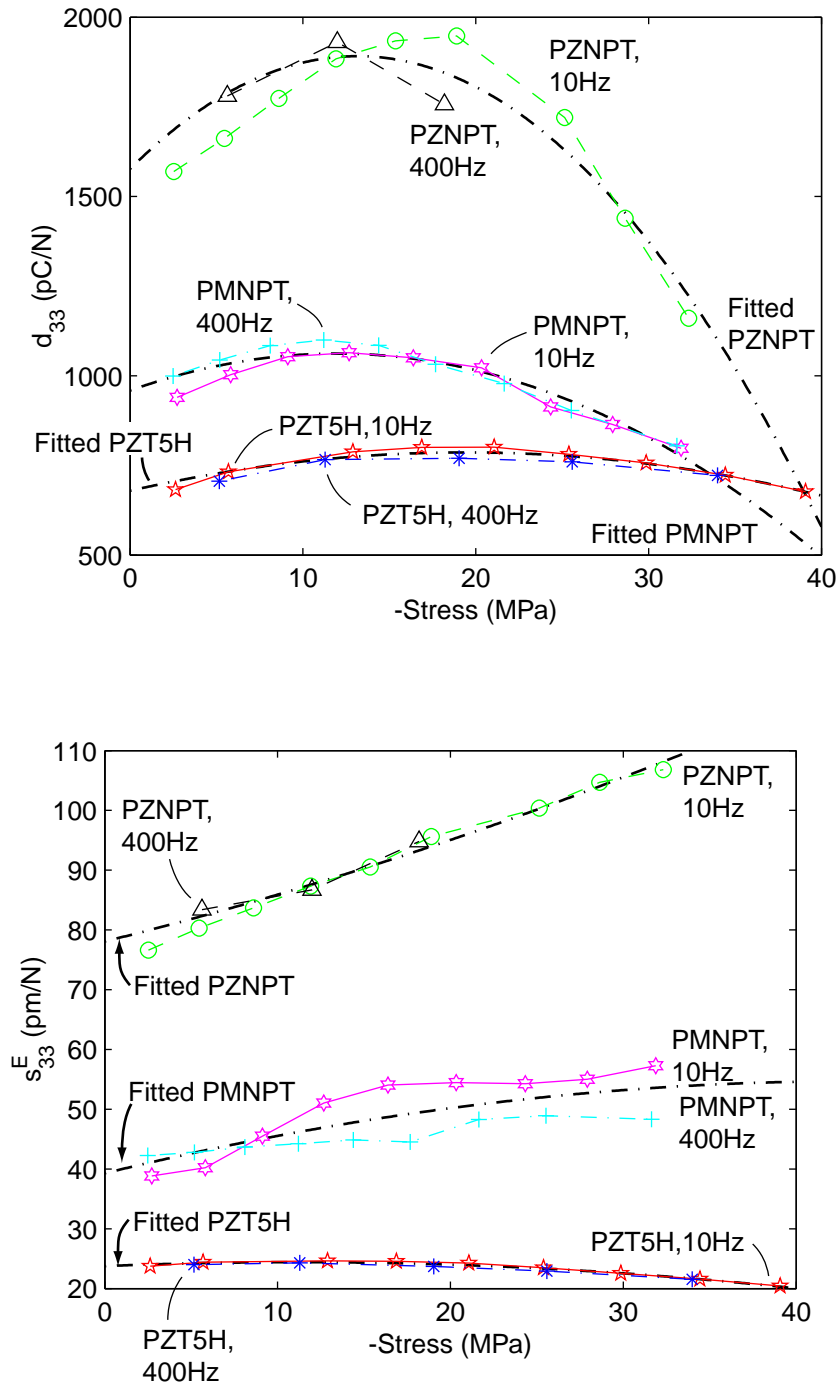


Figure 2-35: Generalized material constants  $d_{33}$  and  $s_{33}^E$  as functions of stress at 10Hz and 400Hz for PZT-5H, PZN-PT and PMN-PT.

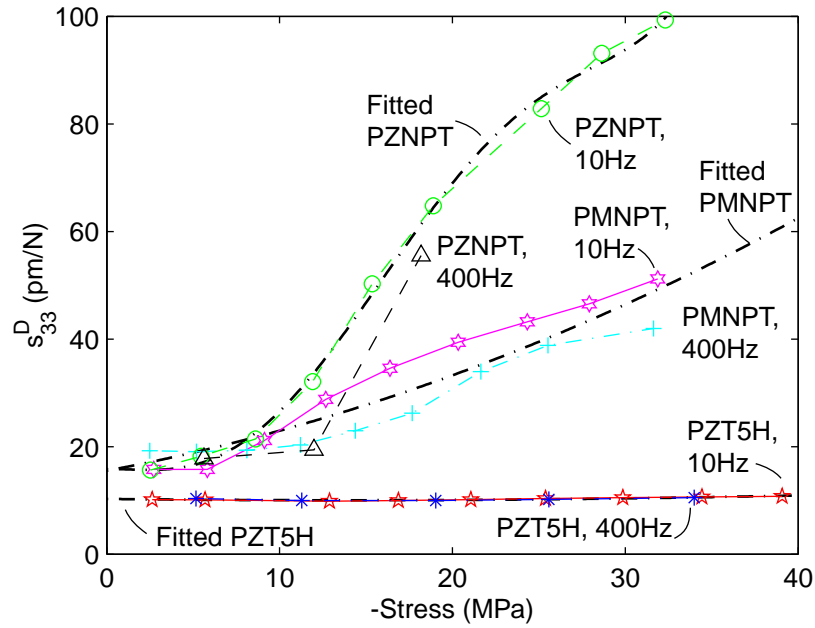
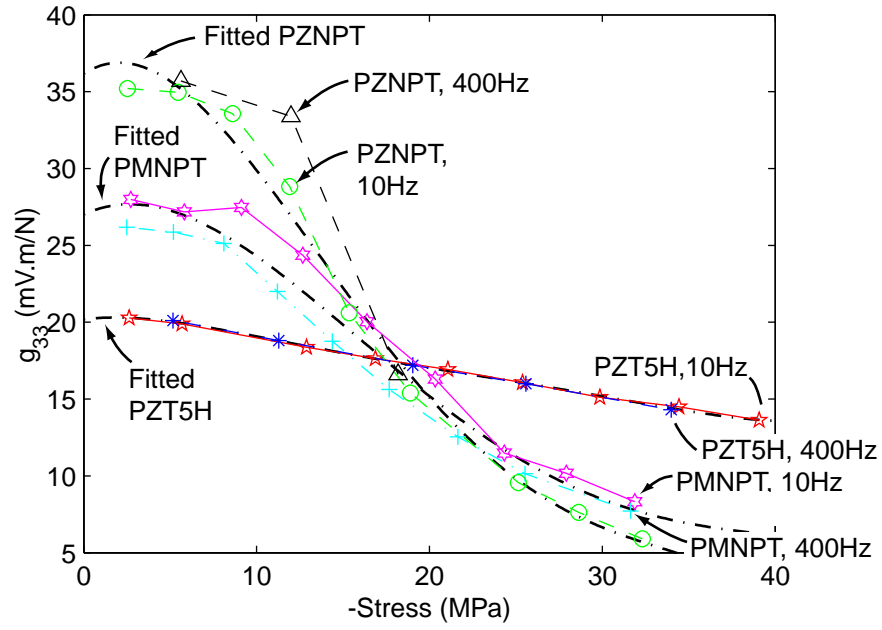


Figure 2-36: Generalized material constants  $g_{33}$  and  $s_{33}^D$  as functions of stress at 10Hz and 400Hz for PZT-5H, PZN-PT and PMN-PT.

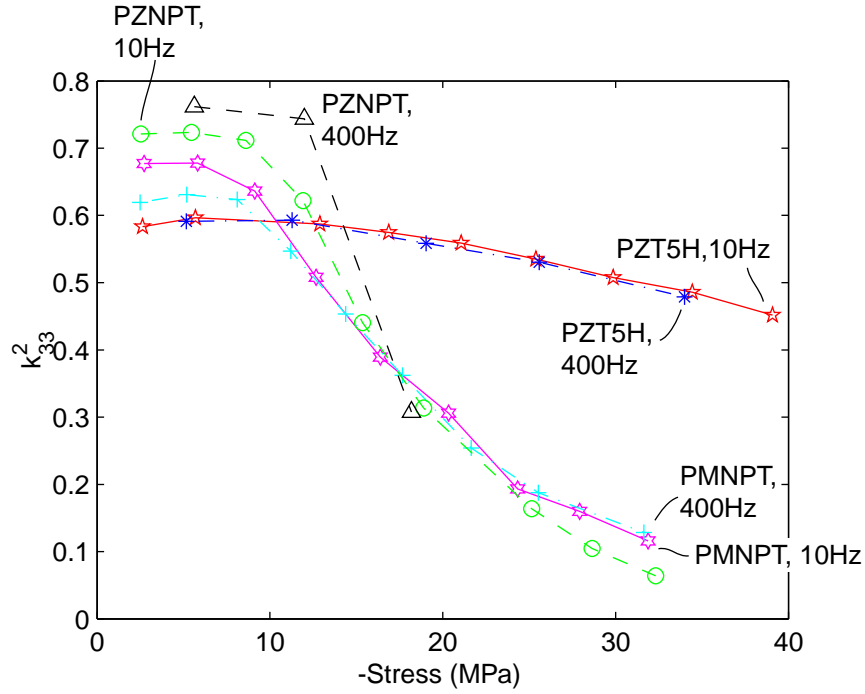


Figure 2-37:  $k_{33}^2$

### 2.3.3 Diode Selection and Characterization

As mentioned earlier, compressive stress, say up to 20MPa, can easily generate up to 5-15kV/cm open circuit electric field, which corresponds to 3-9kV on a 0.6cm thick specimen. The reverse breakdown voltage of the diode must be higher than the voltage level generated by the piezoelectric materials. The diode CS57-04<sup>9</sup> was therefore chosen to construct a rectifying bridge. A common model can be used to describe the characteristics of the diodes:

$$i = \begin{cases} I_0 \left[ \exp\left(\frac{qv}{\eta k \theta}\right) - 1 \right], & v \geq 0. \\ 0 & v < 0. \end{cases} \quad (2.18)$$

where  $q = 1.60 \times 10^{-19}$ (C) is the electron charge,  $k = 1.38 \times 10^{-23}$ (J/K) is the Boltzmann constant, and  $\theta$  is the temperature.  $I_0$  and  $\eta$  are material properties to be determined from experiment using the circuit shown in Figure 2-38. For CS57-04 diode, parameters were

<sup>9</sup>Collmer Semiconductor, Inc.

found by fitting the model to the data shown in Figure 2-39:

$$I_0 = 1.35 \times 10^{-11}, \quad \text{and} \quad \eta = 5.6.$$

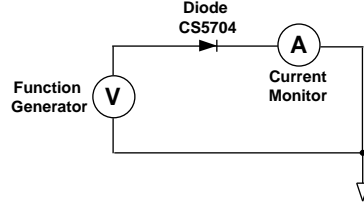


Figure 2-38: Diode forward test circuitry

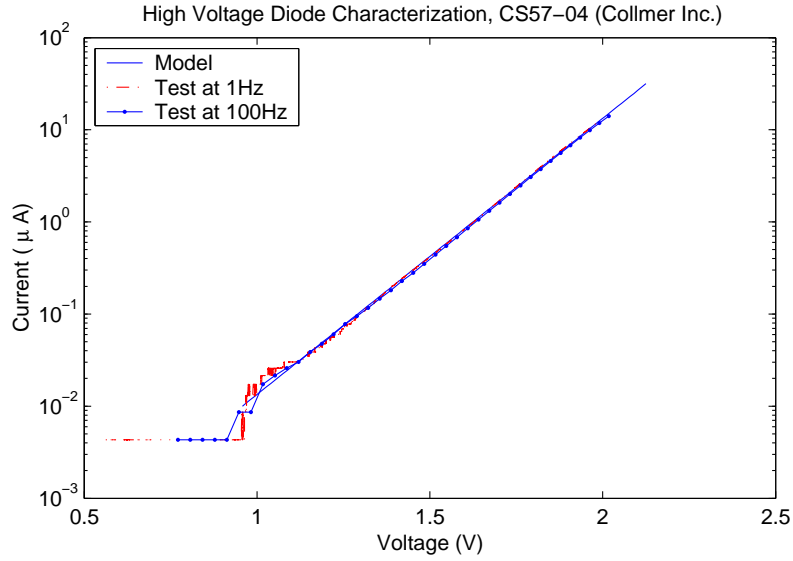


Figure 2-39: Diode characteristics

It is also essential to verify that the reverse current is low enough so that the loss is minimized. This can be done using the test configuration described in Figure 2-40, with current amplifier gain  $10^6 \text{V/A}$  and reverse voltage up to 4kV. The current in reverse diode mode was found to be less than  $0.02 \mu\text{A}$ , which is much less than the forward current range 1 to  $100 \mu\text{A}$  in this thesis work. For convenience, the reverse diode current is therefore assumed zero as in Eq. 2.18.

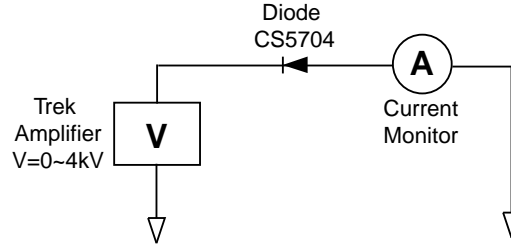


Figure 2-40: Diode reverse test circuitry

### 2.3.4 Characterization of Material Energy Density

Using the rectifying circuit shown in Figure 2-33, one can obtain the power output by

$$\mathcal{P} = i \times V_{DC} \quad (2.19)$$

where  $V_{DC}$  is the DC voltage of the battery, and  $i$  is the current flowing into the battery. The specimens of different materials were tested under different frequencies, forces, and battery voltages. Using the generalized material properties measured earlier, one can simulate the response using the Simulink model developed earlier.

Figures 2-41(a), (b), and (c) show good correlation between the measured and simulated response of PZN-PT under low stress at which the material behaves linearly. Unfortunately, the material does not behave linearly under high stress condition. The nonlinear material is the reason why the simulation does not correlate with the measured data very well, as shown in Figures 2-41(c), (d), and (e). Figure 2-42 shows the measured and simulated power as a function of the battery voltage at both low stress and high stress conditions. As can be seen again, the linear simulation predicts the power output much better at low stress than at high stress. In addition, maximum power output occurs approximately when the battery voltage equals one half of the specimen's open circuit voltage.

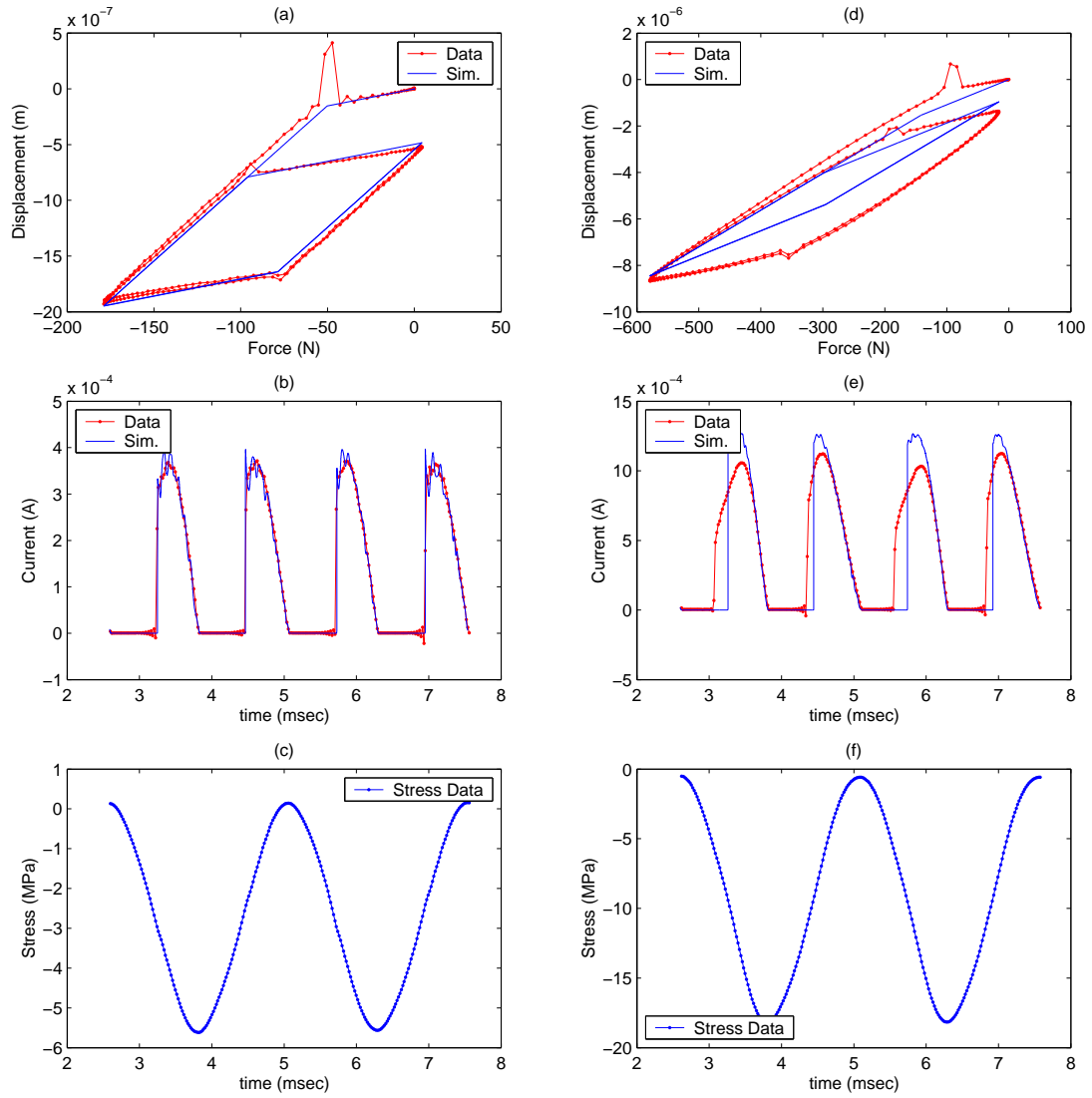


Figure 2-41: Data and simulation of low and high stress response: (a) the force-displacement relation at low stress, 400Hz,  $V_{DC} = 300V$ ; (b) the simulated and measured current at low stress 400Hz,  $V_{DC} = 300V$ ; (c) driving force history of low stress condition; (d) the force-displacement relation at high stress, 400Hz,  $V_{DC} = 400V$ ; (e) the simulated and measured current at high stress 400Hz,  $V_{DC} = 400V$ ; (f) driving force history of high stress condition.

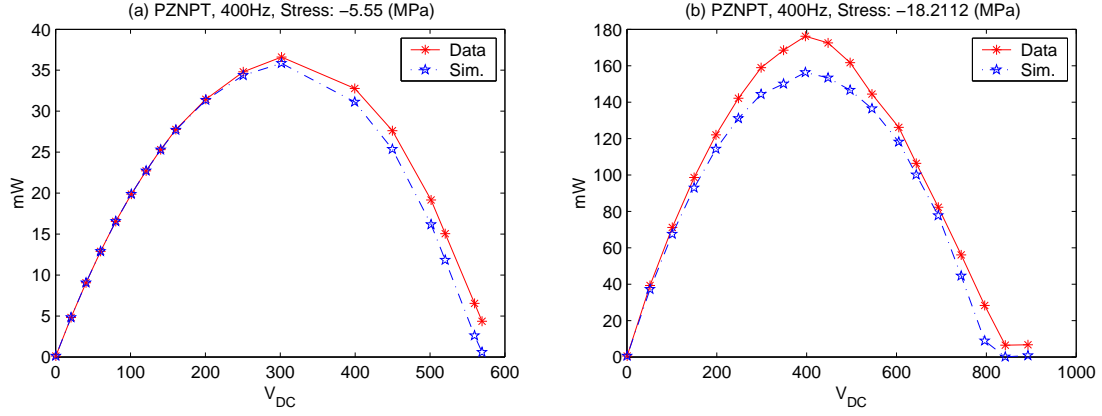


Figure 2-42: Power vs.  $V_{DC}$

In order to compare the harvested electric energy for different sizes of specimens and different driving frequencies, it is convenient to normalize the power  $\mathcal{P}$  by the frequency  $f$  and specimen volume  $V$  and to define an energy density:

$$\Omega = \frac{\mathcal{P}}{fV} \quad (2.20)$$

If the material properties are linear, the maximum energy density obtained using rectifying circuitry is proportional to the square of the stress and is given by[58]

$$\Omega_{max} = \frac{1}{4}k_{33}^2T_{33}^2s_{33}^E \quad (2.21)$$

or

$$\Omega_{max} = \frac{1}{4}g_{33}d_{33}T_{33}^2 \quad (2.22)$$

where  $T_{33}$  is the compressive stress. Figure 2-43 shows the maximum energy density of different materials as a function of compressive stress using rectifying circuitry. The dashed lines are obtained assuming the materials are linear; however, the experiment shows that the materials degenerate at higher stress. The generalized material constants obtained earlier are also useful to predict this result. Substituting Eq. 2.5, 2.6, 2.7, 2.11, 2.12, and 2.13 into Eq. 2.22 yields a good approximation of maximum energy density, as shown in Figure 2-43.



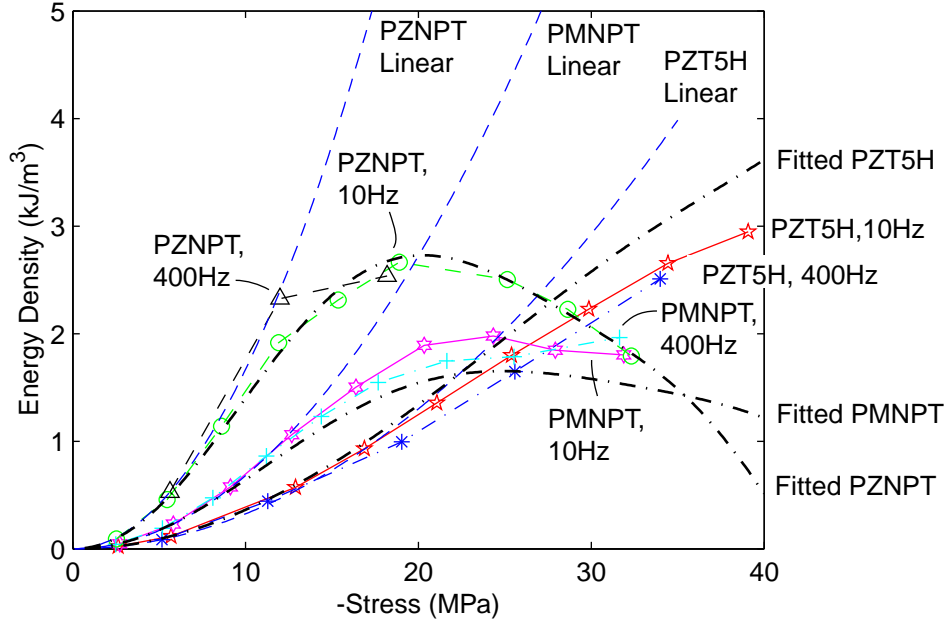


Figure 2-43: Maximum energy density using rectifying circuitry. The curves labeled as "Fitted" are obtained from Eq. 2.22 using generalized material constants described in Eq. 2.5, 2.6, 2.7, 2.11, 2.12, and 2.13. The curve labeled as "Linear" are obtained from Eq. 2.22 assuming constant material coefficients  $d_{33}$  and  $g_{33}$  at zero stress

### 2.3.5 Single Crystal vs. Polycrystalline Ceramics

From the data of  $s_{33}^E$  as a function of compression, the single crystal PZN-PT and PMN-PT show *softening* phenomenon, while polycrystalline material PZT-5H shows *hardening* behavior. This softening result implies (but not necessarily means) that the material structure of the single crystals might have been damaged by high compression.<sup>10</sup> This damage might be able to explain why the  $g_{33}$  constants of the single crystal materials drop more rapidly. For the sake of discussion, it is assumed the undamaged single crystal specimen is perfectly dielectric. When the structure of the single crystal specimen is damaged, the free charge or vacancy might build up, which is the major source of channelling or conductivity. Although the damaged specimen is conductive now, it still has finite resistance. Because of this resistance, the open circuit voltage will decrease and so will the  $g_{33}$  constants. In contrast, this resistance has little influence on  $d_{33}$  because it is measured under the short circuit con-

<sup>10</sup>Similar damage has also been reported by Lynch[67] that single crystal PZN tends to develop cracks when driving the material with high electric fields.

dition. On the other hand, for the polycrystalline PZT material, the hardening behavior suggests that only domain movement or switching (but little damage) happens while under high compression. This hypothesis qualitatively explains the discrepancies between polycrystalline PZT-5H and single crystal PZNPT and PMN-PT, whereas an additional study using microscopic observation is needed to fully understand this discrepancy.

### 2.3.6 Summary of Piezoelectric Energy Harvesting

In this work, the material properties for an energy harvesting application were tested and show a significant dependence on applied stress but not a significant dependence on frequency. These material properties can be represented by generalized material constants as functions of stress, as shown in Figures 2-36 and 2-35. For PZT-5H, the material starts to depole when the compression is higher than 22MPa, while the material starts to degenerate at stresses higher than 11MPa for PZN-PT and 15MPa for PMN-PT. Among others, PZN-PT at low stress has the largest energy density which is beneficial. However, this is not necessarily true at higher stress. It might be beneficial if PZT-5H is used at stress higher than 30MPa, according to the result shown in Figure 2-43.

In addition, it is also discovered in this work that both  $d_{33}$  and  $g_{33}$  are essential to predict the capability of piezoelectric power generation at high compression, according to Eq. 2.22. The literature[54] that only published  $d_{33}$  as a function of stress is not sufficient for the purpose of designing a successful energy harvester.

## 2.4 Characterization for Material Modeling

Although it is possible to characterize each material at each design loading point, the cost is too high. As a result, the ultimate aim of this thesis is to build a full model which can capture the characteristics observed in Sections 2.2 and 2.3. If this can be done, a lot of testing work can be saved. To reach this goal, it is essential to characterize the material under the largest amplitude of practical driving conditions. The approach follows Ghandi's work in which PZT-5H was characterized. In this thesis work, PZT-5A was also tested because it is primarily used in the commercial AFCs. In addition to the study of stress dependency, the study of frequency dependence is also of interest. However, to minimize the number of tests, the effects of frequency and stress are assumed decoupled. By this assumption, only two planes of a three dimensional testing domain needs to be conducted. As shown in Figure 2-44, one is electric field and stress; the other is electric field and frequency.

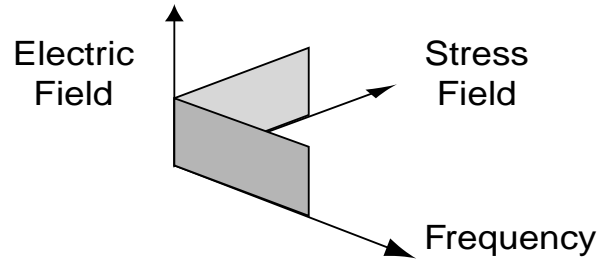


Figure 2-44: The test planes of stress and electric fields versus frequency and electric field

### Rate Dependency

Before characterizing the material behavior under compression, one can first examine the rate dependency of the piezoelectric material. To complete the full test matrix, PZT-5H was first driven by electric fields at different frequencies: 0.1Hz, 1Hz and 10Hz. Figures 2-45 shows the result that higher frequency tends to expand the butterfly curves and P-E loops. Figure 2-46 shows the same trends for PZT-5A. Similar phenomena of this expansion have also been found in Magnetic Particle Active Fiber Composites(mpAFC)[73]. These frequency dependent P-E and S-E data will be the basis of the rate dependent model in

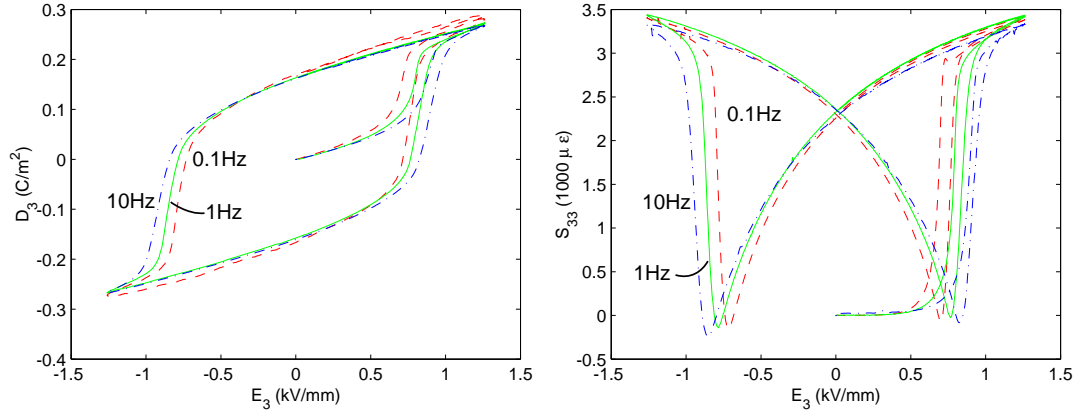


Figure 2-45: Rate dependency of PZT-5H: P-E loops(left) and S-E loops(right)

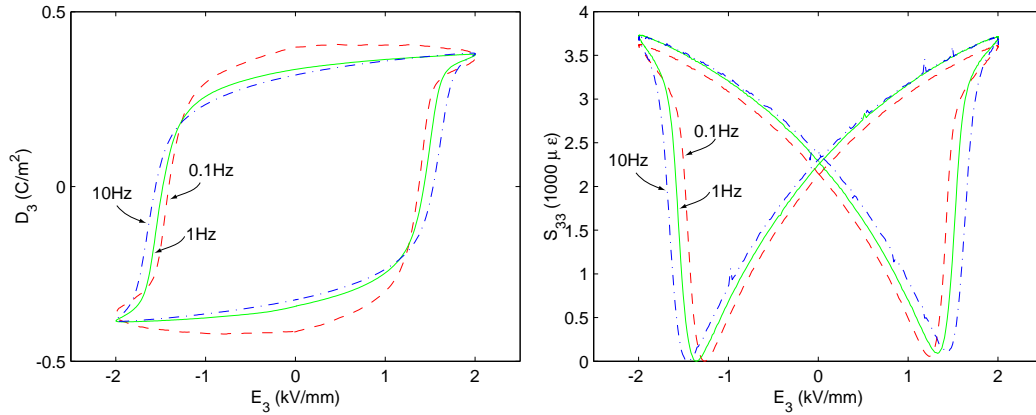


Figure 2-46: Rate dependency of PZT-5A: P-E loops(left) and S-E loops(right)

### Stress Dependency

After the test of rate dependence, stress dependence was also of interest in this thesis work. The same test for PZT-5H has been done by Ghandi[35]. Therefore, only PZT-5A will be tested in this thesis. Two configurations, the transverse and the longitudinal tests, shown in Figure 2-2, were used. In the longitudinal test of PZT-5A, the specimen was 6mm by 6mm by 4mm. The buffer blocks were sized 6mm by 6mm by 7mm. By applying  $T_{33}$  and  $E_3$ , one

can measure the response of  $S_{11}(= S_{22})$ ,  $S_{33}$ , and  $D_3$ . In the transverse test of PZT-5A, the specimen is 4mm by 4mm by 12mm. By applying  $T_{11}$  and  $E_3$ , one can measure the response of  $S_{11}$ ,  $S_{22}$ , and  $S_{33}$ .

Figures 2-47, 2-48, and 2-49 showed the result of the longitudinal test of PZT-5A (Batch A). Figures 2-50, 2-51, 2-52, and 2-53 showed the result of the transverse test of PZT-5A (Batch B). Unfortunately, these two tests were conducted using two different batches of specimens. Comparing the coercive fields shown in Figure 2-47 and 2-50, the variance of these two batches were very significant. This may cause difficulty in developing the material model later. As a result, an additional longitudinal test using Batch B was repeated, as shown in Figures 2-54, 2-55, and 2-56. The new longitudinal test data of PZT-5A (Batch B) showed a better correlated coercive field.

The tests mentioned above were under compression up to 50MPa. Since the actuation tests in Section 2.2 are under compression up to 150MPa, it was also of interest to perform similar tests under higher compression. However, to avoid the failure of the specimen under high compression and high electric field simultaneously, only the longitudinal tests under compression up to 100MPa were repeated, as shown in Figures 2-57, 2-58, and 2-59. As can be seen, the material was significantly depolarized by higher compression.

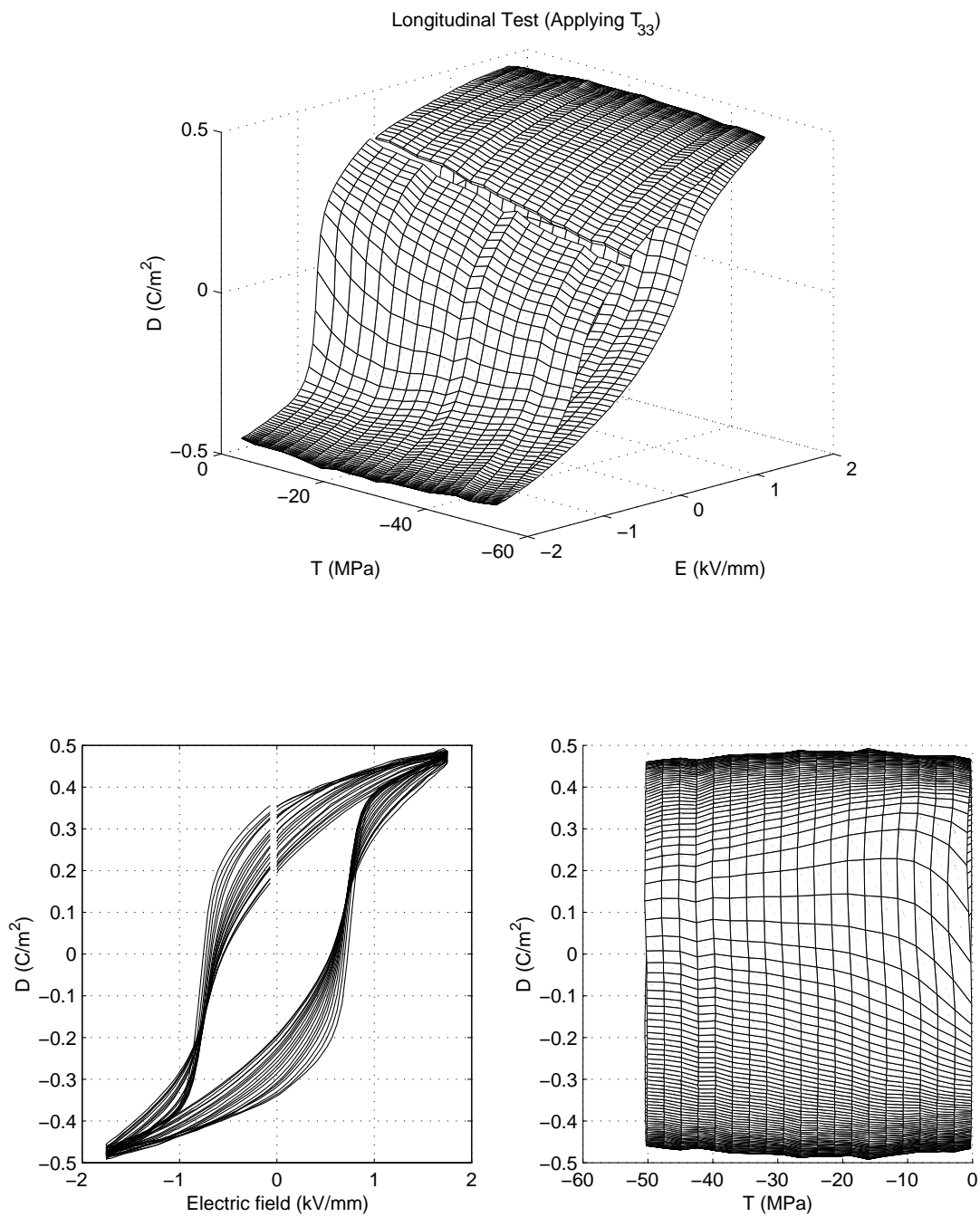


Figure 2-47: The data of repolarizing PZT-5A (Batch A) material behavior under longitudinal compression test.

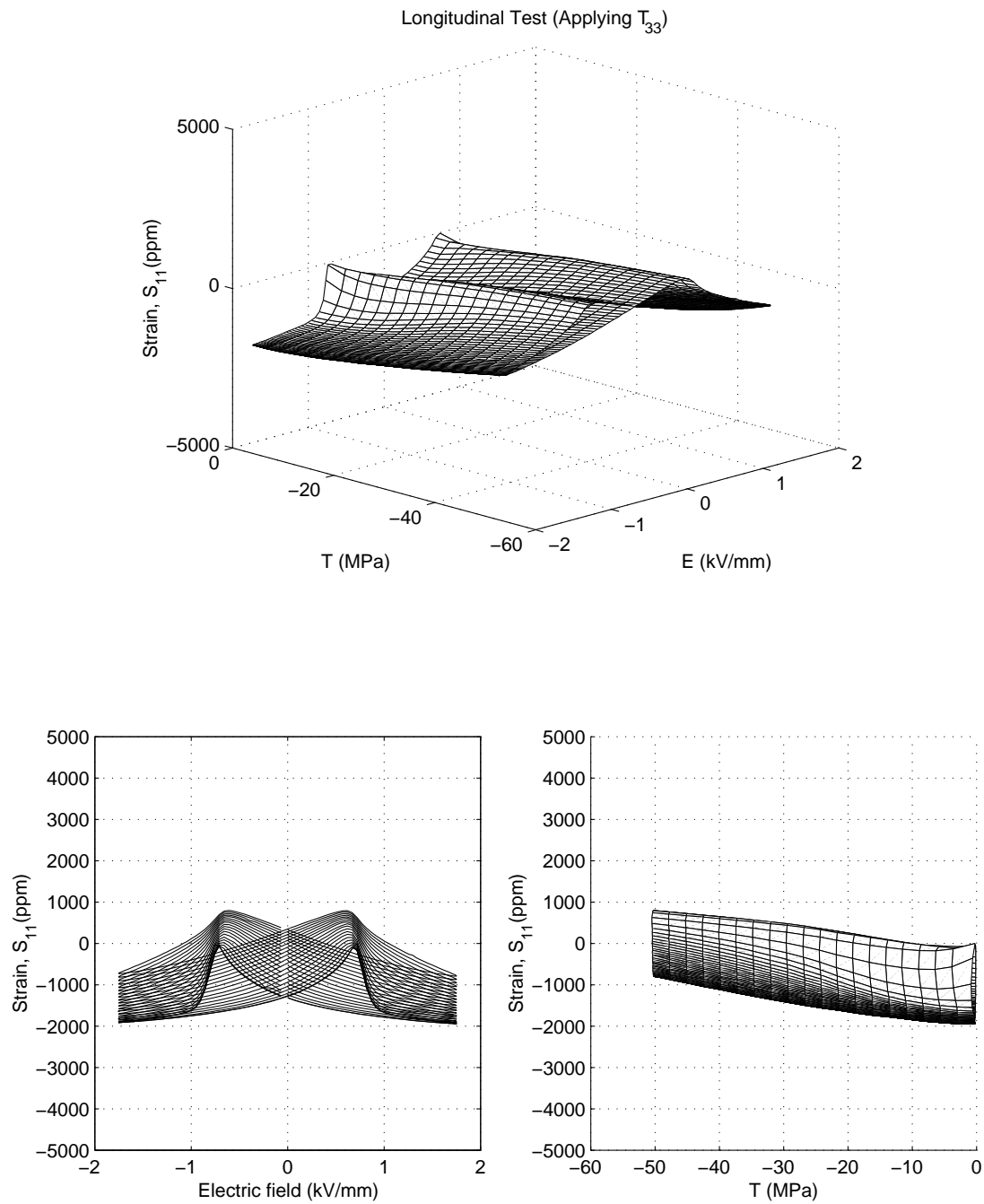


Figure 2-48: The data of repolarizing PZT-5A (Batch A) material behavior under longitudinal compression test.

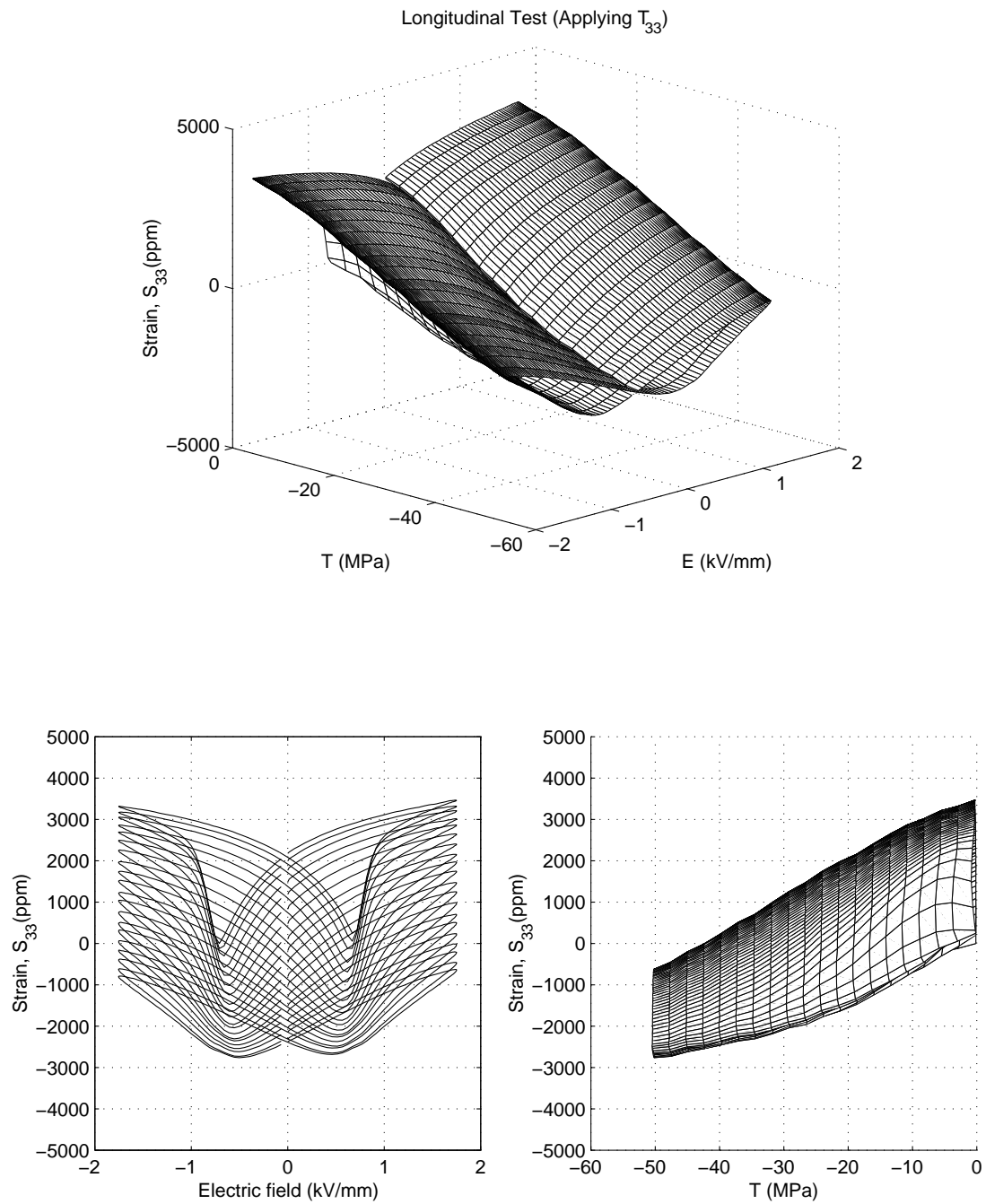


Figure 2-49: The data of repolarizing PZT-5A (Batch A) material behavior under longitudinal compression test.



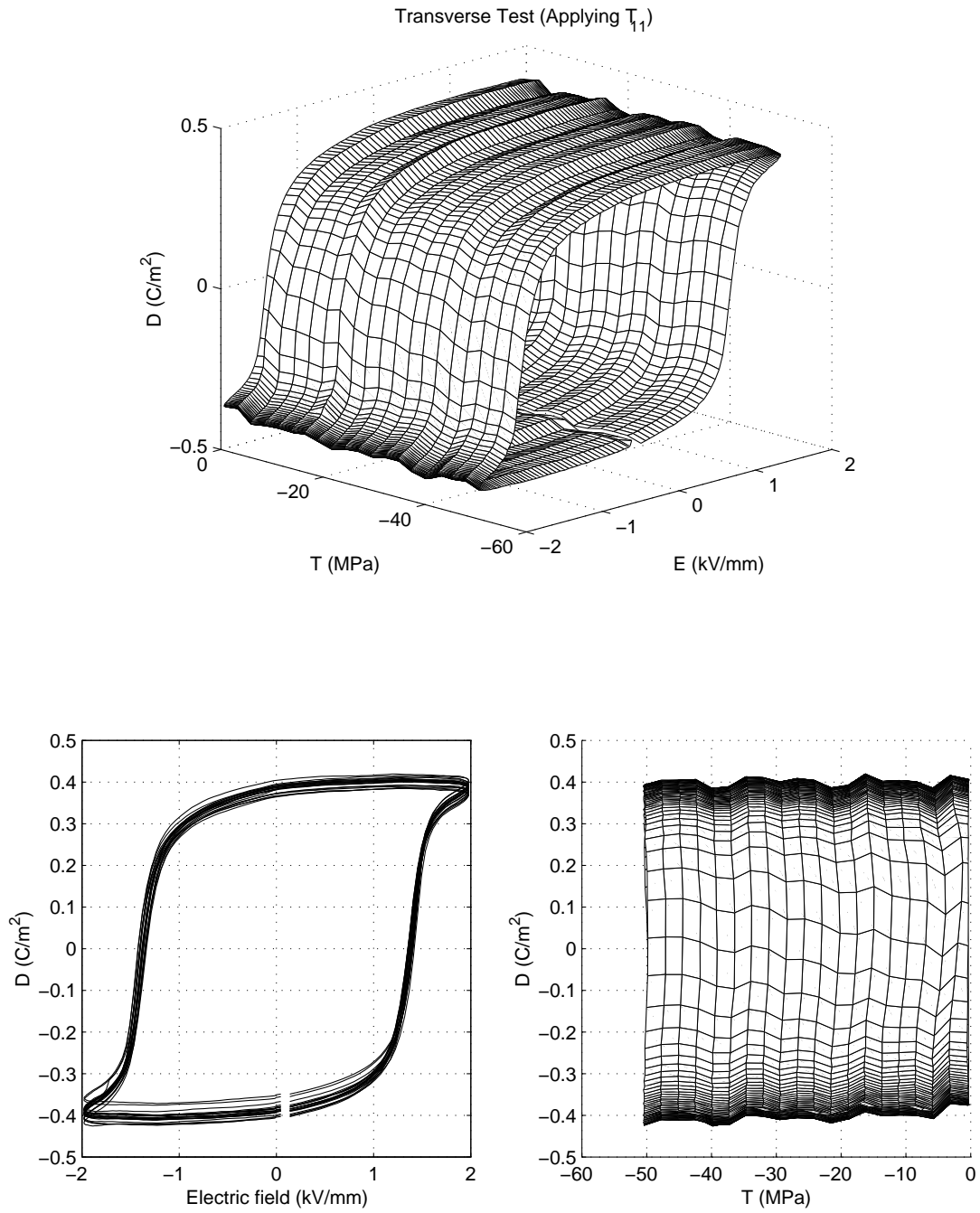


Figure 2-50: The data of repolarizing PZT-5A (Batch B) material behavior under transverse compression test.

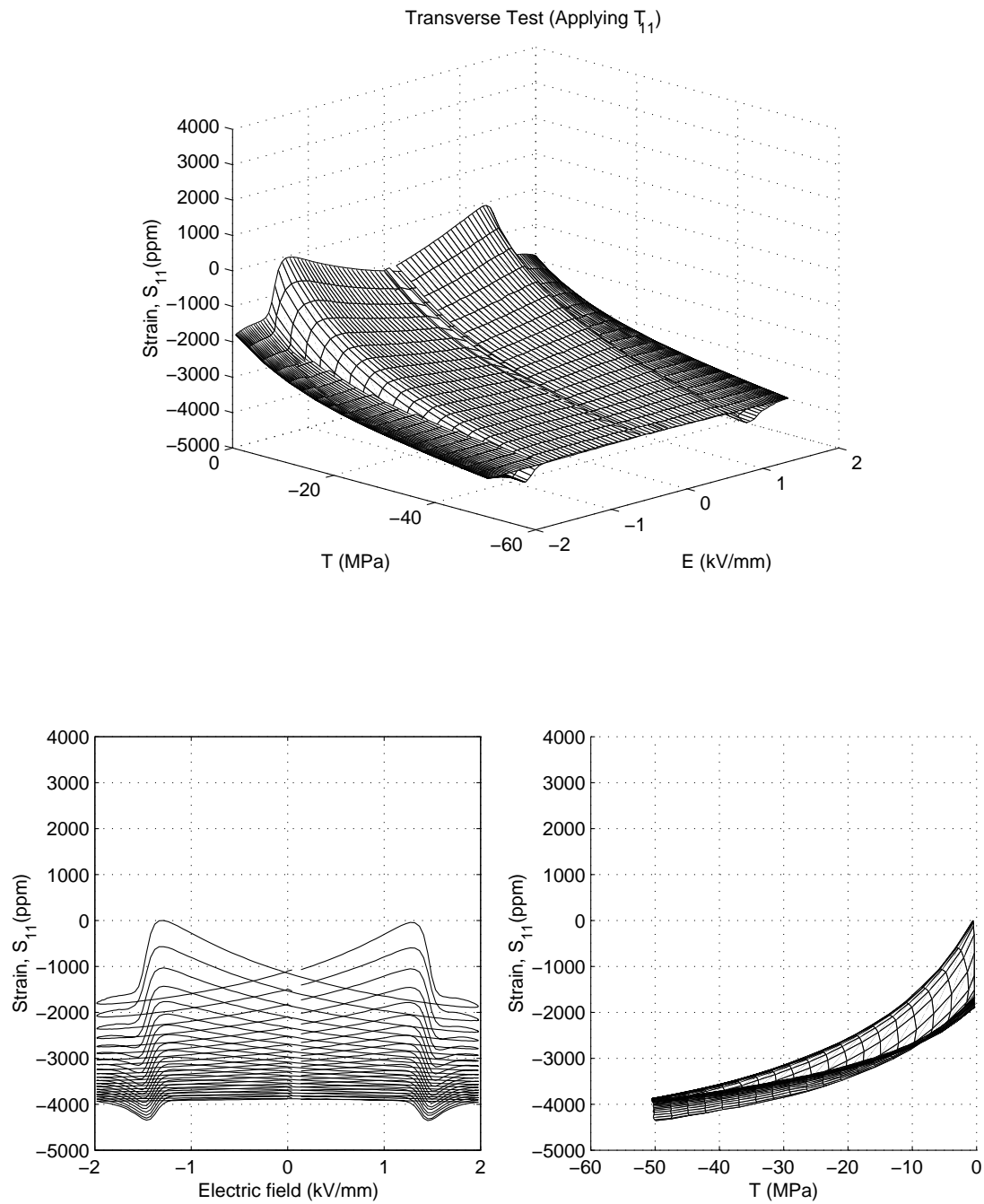


Figure 2-51: The data of repolarizing PZT-5A (Batch B) material behavior under transverse compression test.

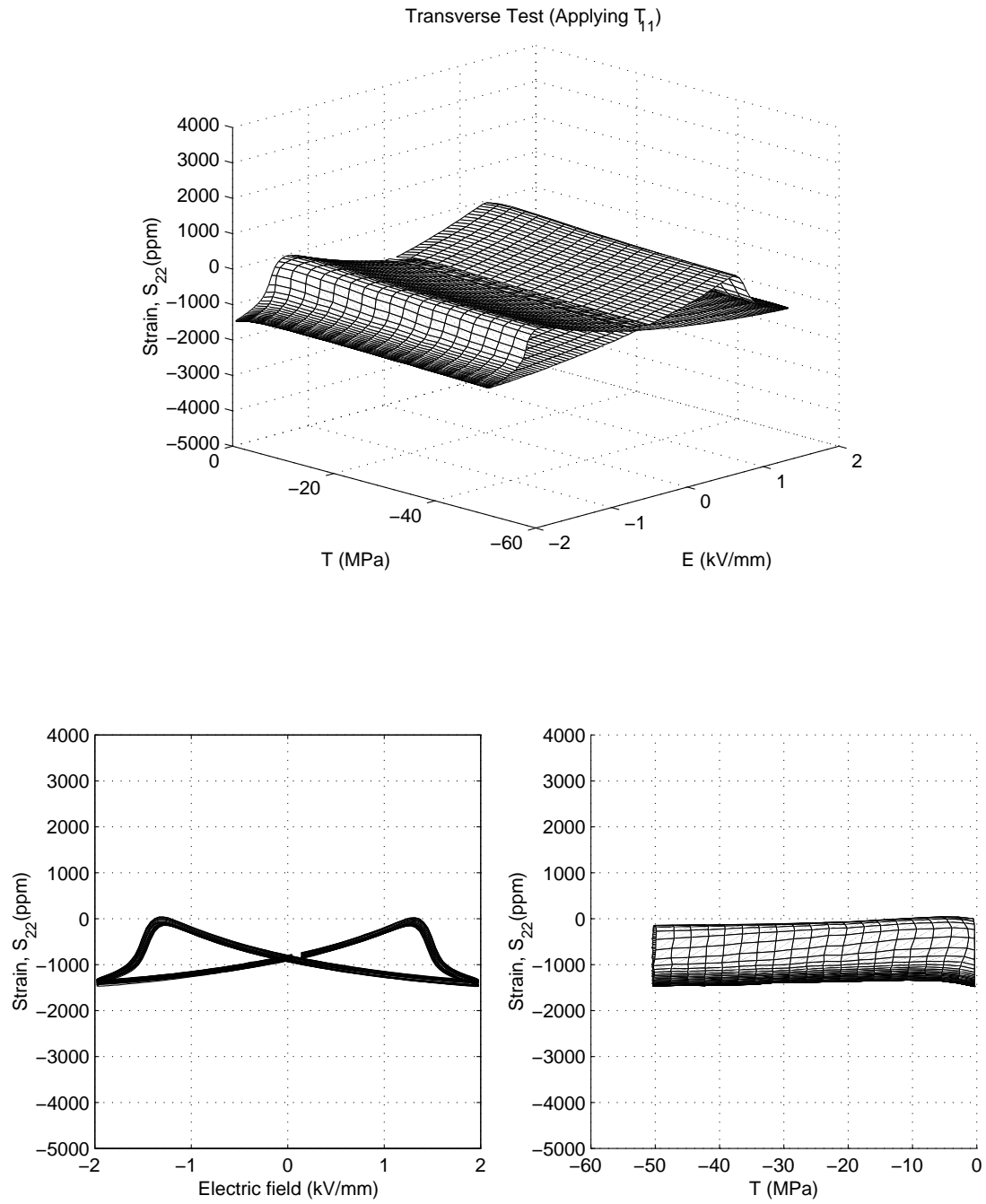


Figure 2-52: The data of repolarizing PZT-5A (Batch B) material behavior under transverse compression test.

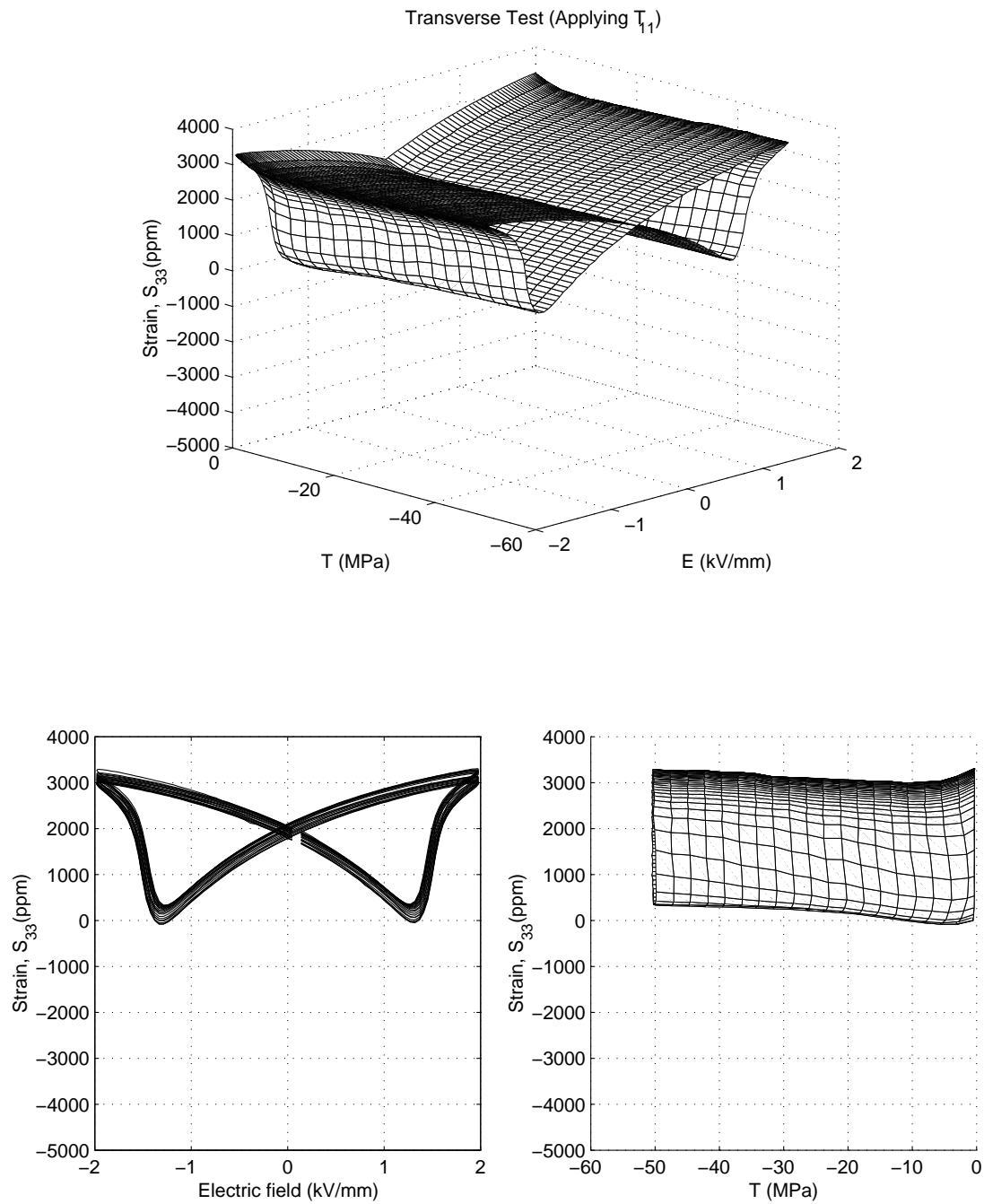


Figure 2-53: The data of repolarizing PZT-5A (Batch B) material behavior under transverse compression test.

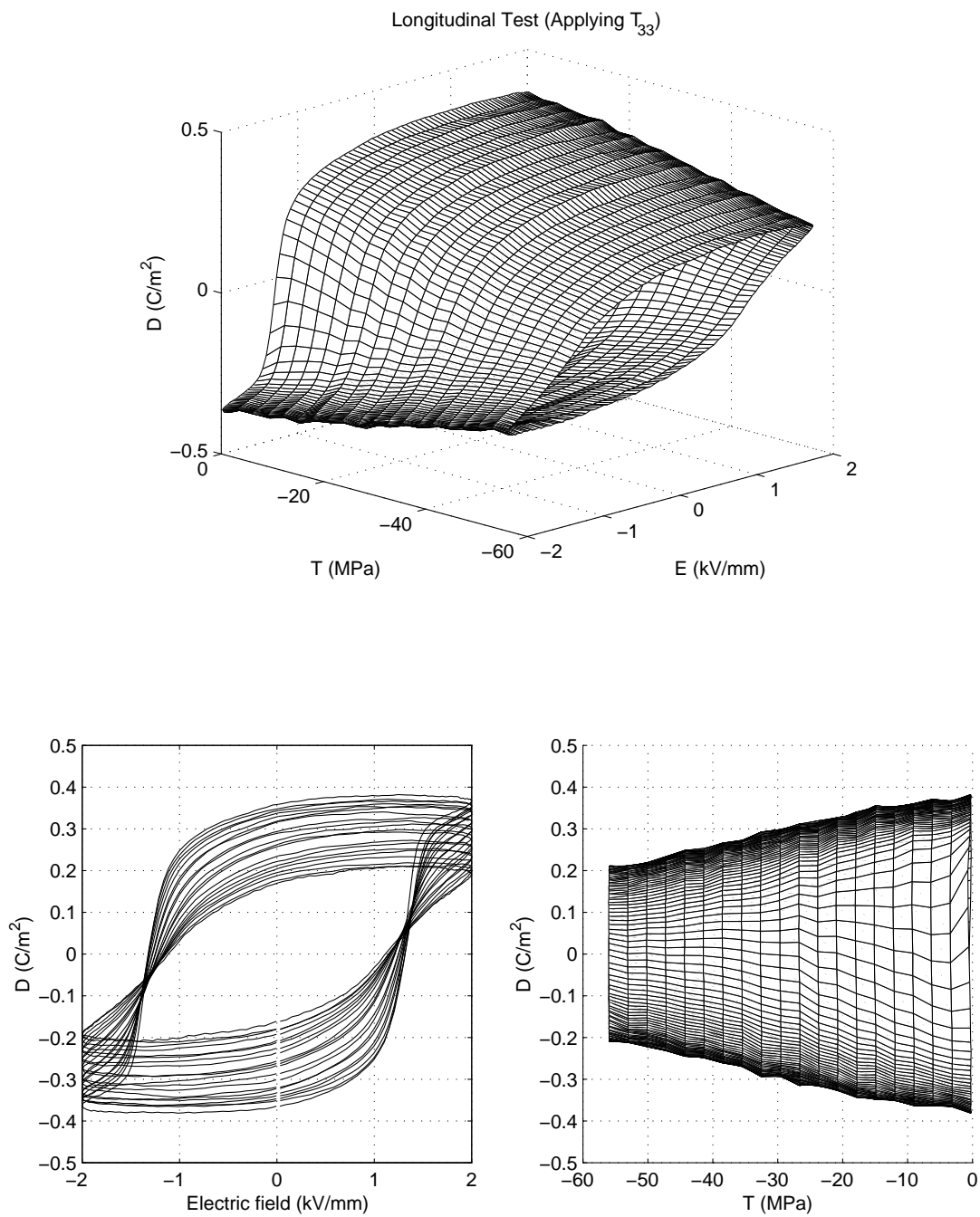


Figure 2-54: The data of repolarizing PZT-5A (Batch B) material behavior under longitudinal compression test (up to 56MPa).

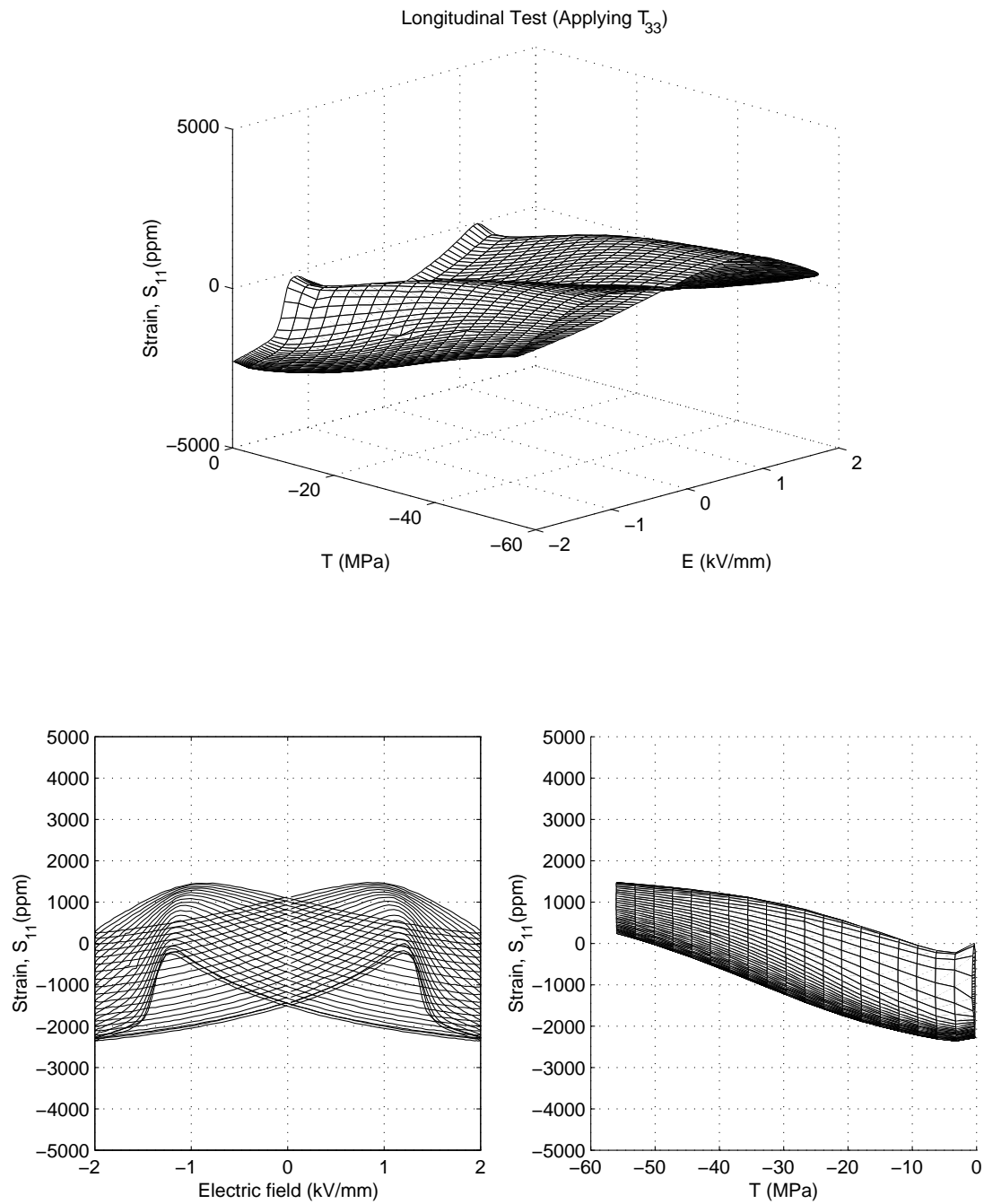


Figure 2-55: The data of repolarizing PZT-5A (Batch B) material behavior under longitudinal compression test (up to 56MPa).

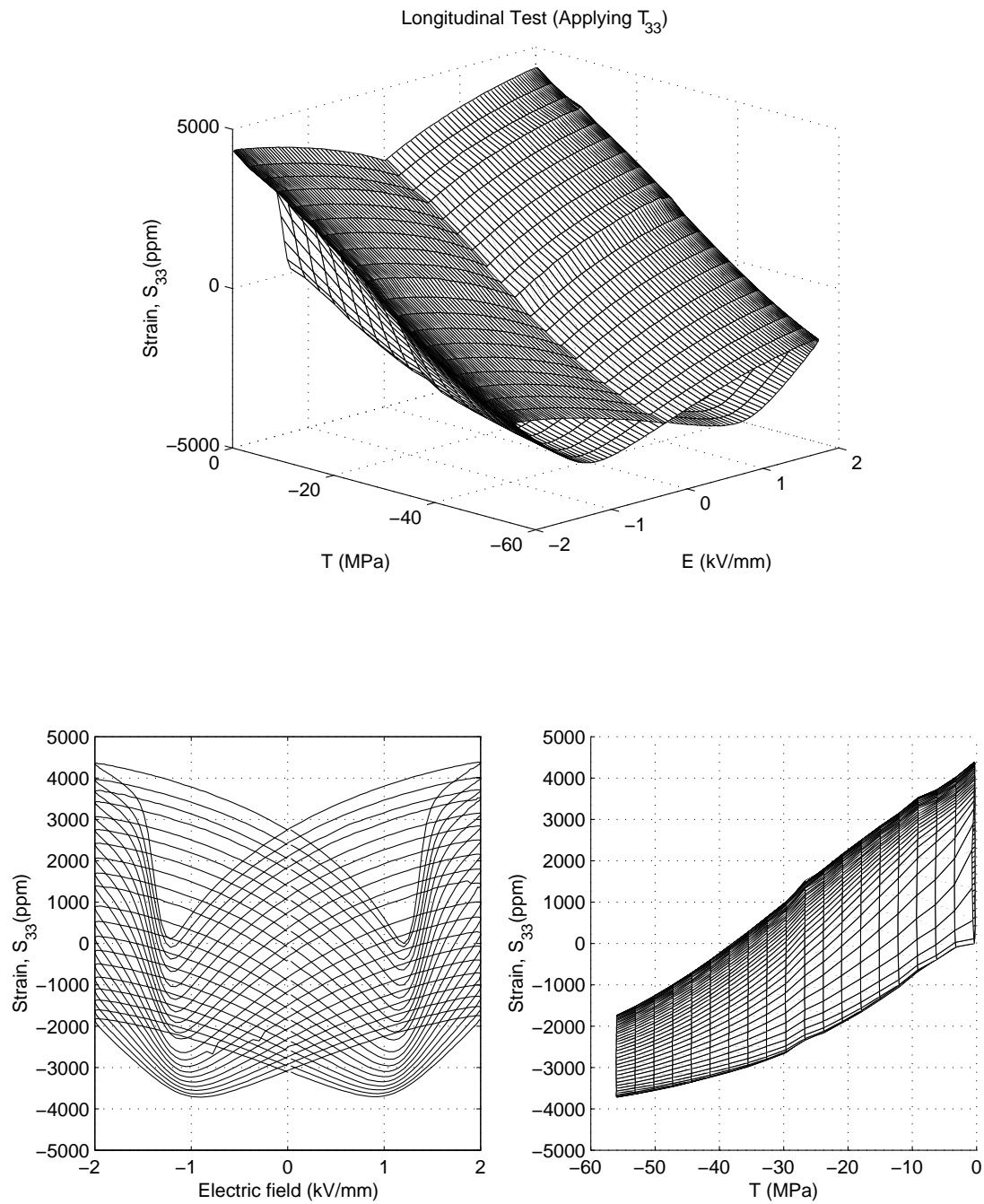


Figure 2-56: The data of repolarizing PZT-5A (Batch B) material behavior under longitudinal compression test (up to 56MPa).

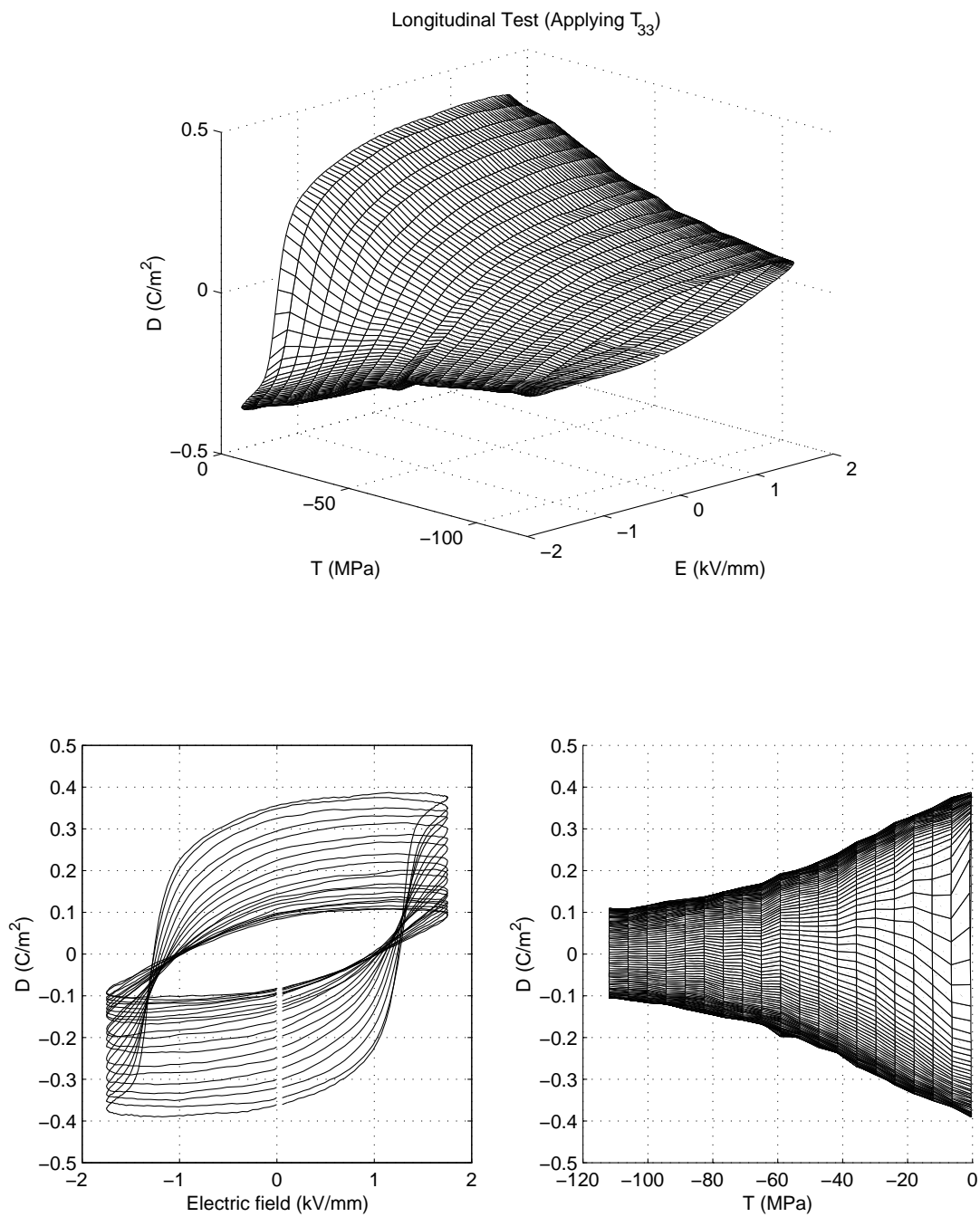


Figure 2-57: The data of repolarizing PZT-5A (Batch B) material behavior under longitudinal test with higher compression (up to 112MPa).



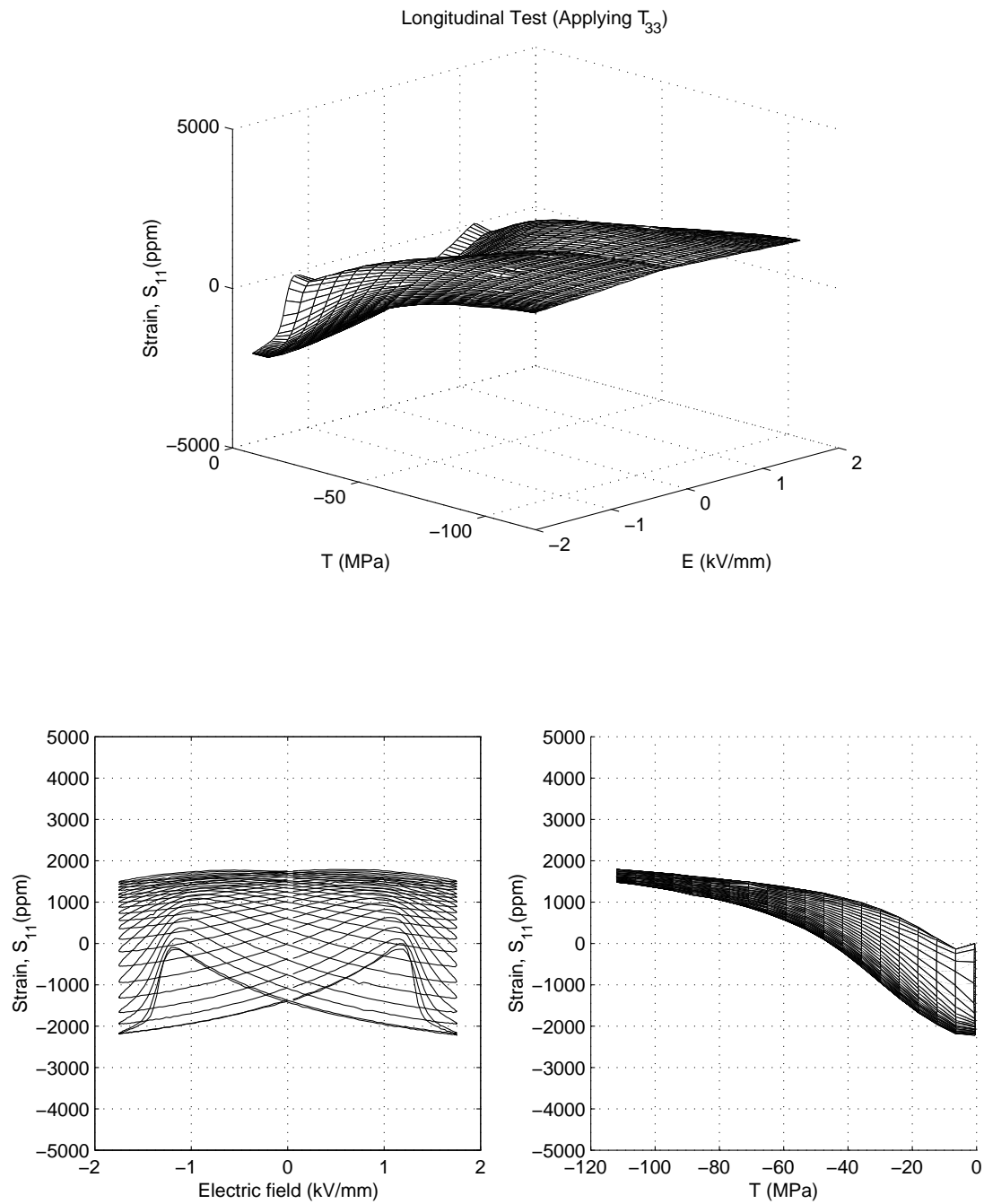


Figure 2-58: The data of repolarizing PZT-5A (Batch B) material behavior under longitudinal test with higher compression (up to 112MPa).

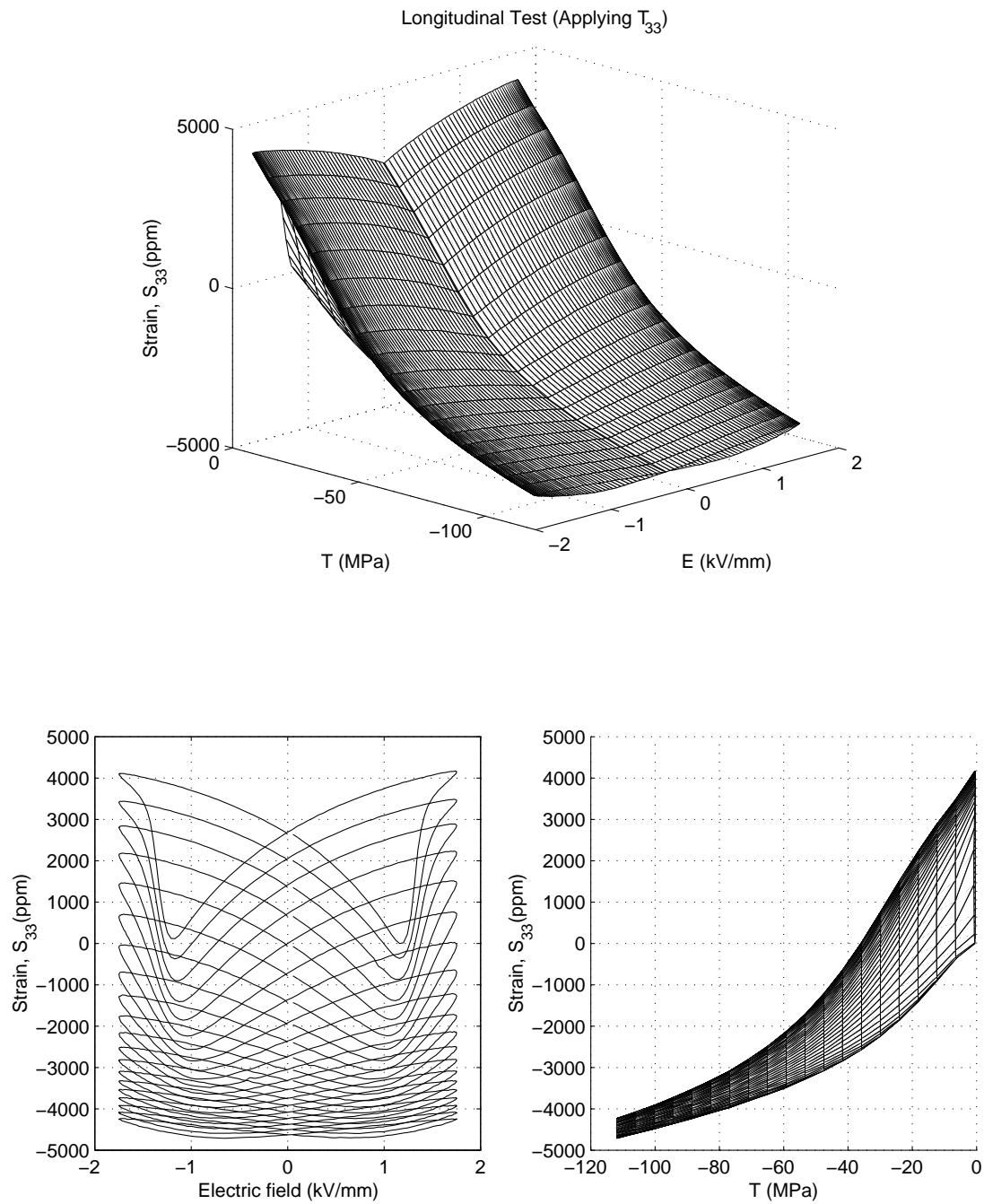


Figure 2-59: The data of repolarizing PZT-5A (Batch B) material behavior under longitudinal test with higher compression (up to 112MPa).

## 2.5 Summary of Important Material Characteristics

Four major phenomena, electric field dependency, rate dependency, stress dependency, and material composition dependency, have been observed in this chapter. What follows is a summary of these important material characteristics.

### Electric Field Dependency

The actuation strongly depends nonlinearly upon the driving level of electric field. In addition, the polarization and strain response show serious hysteresis under high amplitude electric excitation.

### Rate Dependency

The rate dependency of piezoelectric materials was found in two conditions. One is the residual actuation caused by varying compression duration (i.e. stress rate); the other is the expansion of butterfly curves and P-E loops caused by higher driving electric field (i.e. electric rate). However, the generalized piezoelectric constants for energy harvesting do not show significant frequency dependency.

### Stress Dependency

Compression parallel to the poling direction suppresses the growth of dipoles at high electric field. This makes the butterfly curves or P-E loops look flat at high compression. In addition to electric field, stress field is also a major factor of material nonlinear behavior.

### Hard vs. Soft Materials

The difference between hard and soft materials includes: (a) hard material has smaller piezoelectric constant  $d_{33}$ , and (b) hard materials tend to have higher coercive field.

It is the goal of this thesis to model these phenomena as accurately as possible. In the next chapter, currently available material models in the literature will be reviewed to examine whether these material models can well predict the material behaviors observed in this chapter. A new model will be developed to improve the accuracy of these models.

## Chapter 3

# Development of Material Model

The primary objective of this thesis work is to obtain the state equations for the material (constitutive relations) that relate the variables strain ( $\mathbf{S}$ ), stress ( $\mathbf{T}$ ), electric field ( $\mathbf{E}$ ), and electric displacement ( $\mathbf{D}$ ). For instance, the constitutive equations can be written as:

$$\mathbf{D} = \mathbf{D}(\mathbf{E}, \mathbf{T}), \quad (3.1)$$

$$\mathbf{S} = \mathbf{S}(\mathbf{E}, \mathbf{T}). \quad (3.2)$$

In addition to electric and stress fields, the desired model has to be able to simulate the rate dependent material response, as discussed in the previous chapter. To reach this goal, the most advanced material models in the literature will be first examined in this chapter to see whether they meet the requirement of the desired models. After finding the shortcomings of these models, a new model will also be developed in this chapter by improving upon these models.

### 3.1 Literature Review of Material Models

Two major categories of piezoelectric material models have been proposed since two decades ago. One was based on thermodynamic potentials; the other was based on the phenomenological observation of material response. In this section, a phenomenological model by Soukhovjak and Chiang[2] will first be discussed and followed by an introduction to the theory of thermodynamics. At the end, two thermodynamically consistent models by Devonshire[59] and Ghandi[35] will be examined.

### 3.1.1 Model by Soukhojak and Chiang

Soukhojak and Chiang expanded Chen and Montgomery's model for anti-ferroelectrics and elasto-ferroelectrics. It is assumed that the total polarization  $P$  can be categorized into  $P_d$ , the dielectric polarization, and  $P_F$ , the polarization due to ferroelectric domain switching:

$$P = P_d + P_F. \quad (3.3)$$

The dielectric polarization accounts for the dynamic hysteresis, while polarization due to ferroelectric domain switching accounts for the static hysteresis. Equilibrium dielectric polarization is given by an odd function of the electric field

$$P_{d,e} = P_{sat} \tanh\left(\frac{E}{E_0}\right), \quad (3.4)$$

where  $P_{sat}$  is the saturation of polarization, and  $E_0$  is the normalization field. The change rate of dielectric polarization is given by

$$\frac{dP_d}{dt} = \frac{1}{\tau_d}(P_{d,e} - P_d), \quad (3.5)$$

where  $\tau_d$  is the dielectric time constant. Equations 3.4 and 3.5 solve for  $P_d$  as a function of  $E$ . Figure 3-1 shows the dielectric polarization as a function of sinusoidal electric field  $E$  driving at different frequencies, assuming  $\tau_d=5\text{ms}$ .

Polarization due to ferroelectric switching is given by

$$P_F = nP_s, \quad (3.6)$$

where  $P_s$  is the spontaneous polarization, and  $n$  is the net fraction of dipoles pointing "up":  $-1 \leq n \leq 1$ . This parameter exhibits a static hysteresis. The rate equation for  $n$  is given by

$$\frac{dn}{dt} = \frac{\beta - n|\beta|}{\tau_{sw}}, \quad (3.7)$$

where  $\beta$  is the ferroelectric domain switching function.  $\beta$  can be expressed analytically as

$$\beta = \tanh^3\left(\frac{E}{E_c}\right)^{2m-1}, \quad (3.8)$$

where  $E_c$  is the coercive field and  $m$  is a positive integer that characterizes the abruptness of the switching function  $\beta$  in the vicinity of  $E_c$ . Equations 3.7 and 3.8 solve for the dynamics

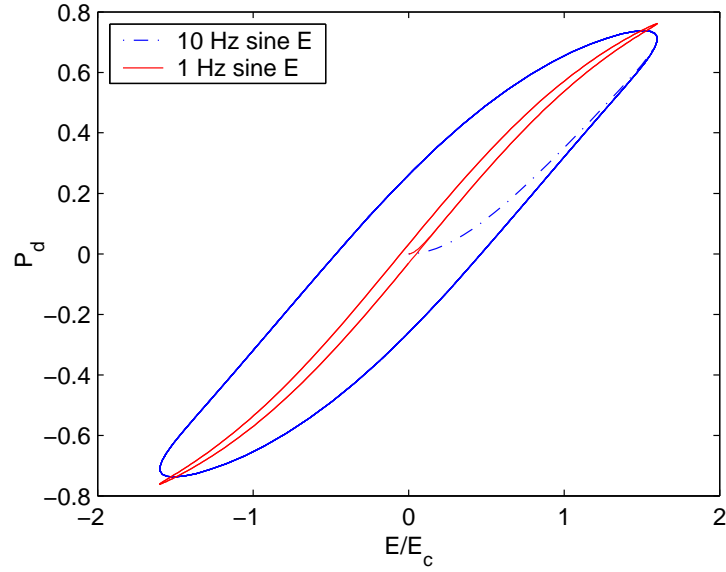


Figure 3-1: The dielectric polarization as a function of sinusoidal electric field  $E$  at different frequencies, assuming  $\tau_d=5\text{ms}$  in Soukhojak's model.

of  $n$  as a function of  $E$ . Figure 3-2 shows the net fraction of polarization as a function of the sinusoidal electric field  $E$  at different frequencies, assuming  $\tau_{sw}=5\text{ms}$ .

Figure 3-3 shows the total polarization as a function of sinusoidal electric field  $E$  at different frequencies, assuming  $\tau_{sw}=0.5\text{ms}$  and  $\tau_d=1\text{ms}$ . As can be seen, the model is able to capture the hysteresis of polarization. It can also capture the expansion of polarization at high frequency. However, it is difficult to apply a three dimensional model using this frame work.

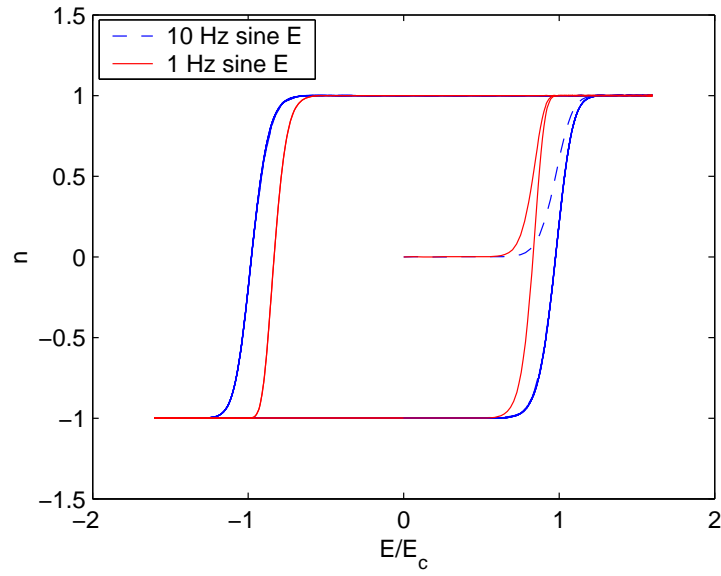


Figure 3-2: The net fraction of polarization as a function of sinusoidal electric field  $E$  at different frequencies, assuming  $\tau_{sw} = 5\text{ms}$  in Soukhojak's model.

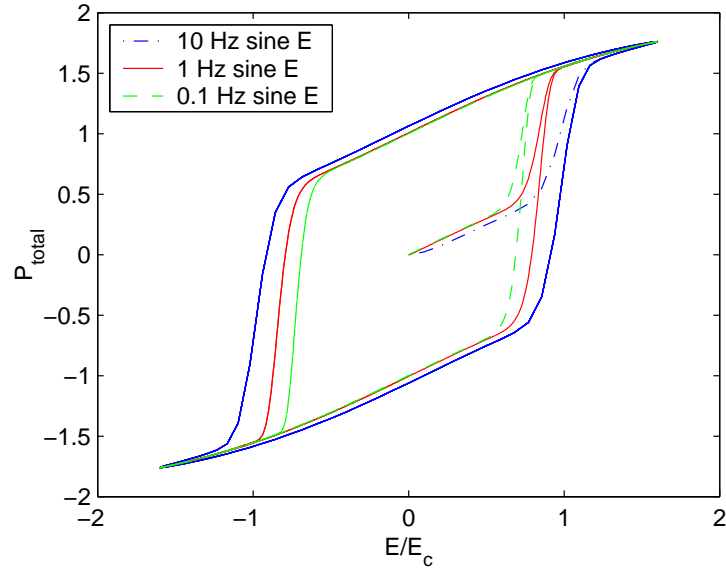


Figure 3-3: The total polarization as a function of sinusoidal electric field  $E$  at different frequencies, assuming  $\tau_{sw} = 0.5\text{ms}$  and  $\tau_d = 1\text{ms}$  in Soukhojak's model.

### 3.1.2 Introduction to Thermodynamic Potential

One can express thermodynamic potentials for the material in terms of any 3 independent variables selected from the conjugate pairs  $(\mathbf{S}, \mathbf{T})$ ,  $(\mathbf{D}, \mathbf{E})$ , and  $(\sigma, \theta)$ . Eight possible representations of thermodynamic potentials are listed in Table 3.1. The variables temperature  $(\theta)$  and entropy  $(\sigma)$  have been included in the list for completeness. They are relevant when the material response is a function of temperature. Selection of the thermal properties  $(\sigma, \theta)$  depends on whether an isothermal or adiabatic condition is considered. In this thesis work, all the tests and models are based on the isothermal condition (i.e. constant  $\theta$ ). To simplify the remaining discussion, the terms associating  $\theta$  and  $\sigma$  are dropped from the energy expression.

Table 3.1: Thermodynamic potentials

Internal Energy	$dU = \theta d\sigma + \mathbf{T}d\mathbf{S} + \mathbf{E}d\mathbf{D}$
Enthalpy	$dH = \theta d\sigma - \mathbf{S}d\mathbf{T} - \mathbf{D}d\mathbf{E}$
Elastic enthalpy	$dH1 = \theta d\sigma - \mathbf{S}d\mathbf{T} + \mathbf{E}d\mathbf{D}$
Electric enthalpy	$dH2 = \theta d\sigma + \mathbf{T}d\mathbf{S} - \mathbf{D}d\mathbf{E}$
Helmholtz free energy	$dA = -\sigma d\theta + \mathbf{T}d\mathbf{S} + \mathbf{E}d\mathbf{D}$
Gibbs free energy	$dG = -\sigma d\theta + \mathbf{S}d\mathbf{T} - \mathbf{D}d\mathbf{E}$
Elastic Gibbs energy	$dG1 = -\sigma d\theta + \mathbf{S}d\mathbf{T} + \mathbf{E}d\mathbf{D}$
Electric Gibbs energy	$dG2 = -\sigma d\theta + \mathbf{T}d\mathbf{S} - \mathbf{D}d\mathbf{E}$

From each energy function listed in Table 3.1, a set of constitutive relations can be obtained. For instance, given  $H$  as a function of the state variables  $(\mathbf{T}, \mathbf{E})$ , one can obtain the constitutive relations:

$$\mathbf{S} = \frac{\partial H}{\partial \mathbf{T}}, \quad \mathbf{D} = \frac{\partial H}{\partial \mathbf{E}}. \quad (3.9)$$

These constitutive relations obtained from thermodynamic potentials satisfy the Maxwell relation:

$$\frac{\partial \mathbf{S}}{\partial \mathbf{E}} = \frac{\partial \mathbf{D}}{\partial \mathbf{T}}. \quad (3.10)$$

Formulating a nonlinear model using arbitrary expressions for  $\mathbf{T}(\mathbf{S}, \mathbf{D})$  and  $\mathbf{E}(\mathbf{S}, \mathbf{D})$  may lead to a system which violates the Maxwell relations and hence the first law of thermodynamics.

The selection of different thermodynamic potentials listed in Table 3.1 depends on the choice of independent variables. Since only isothermal conditions are of interest in this



thesis work, only 4 thermodynamic potentials are possible. Ghani[35] summarized how these various forms of thermodynamic potentials can be used.

If the strain  $\mathbf{S}$  and electric field  $\mathbf{E}$  are chosen as independent state variables, electric Gibbs energy  $G_2$  is the appropriate form of thermodynamic potential and results in the constitutive relations:

$$\mathbf{T} = \frac{\partial G_2}{\partial \mathbf{S}}, \quad \mathbf{D} = -\frac{\partial G_2}{\partial \mathbf{E}}. \quad (3.11)$$

This form is useful for a conventional finite element model that utilizes nodal displacement and voltage degrees of freedom. In such an approach, the strain and electric field are computed from the nodal degrees of freedom. The material model is then used to compute the stress and electric displacement in the material.

If the strain  $\mathbf{S}$  and electric displacement  $\mathbf{D}$  are chosen as independent state variables, the Helmholtz free energy  $A$  is the appropriate form of thermodynamic potential and results in the constitutive relations:

$$\mathbf{T} = \frac{\partial A}{\partial \mathbf{S}}, \quad \mathbf{E} = \frac{\partial A}{\partial \mathbf{D}}. \quad (3.12)$$

This form is useful for material modeling since electric displacement is the state variable linked directly to the polarization in the material.

If the stress  $\mathbf{T}$  and electric field  $\mathbf{E}$  are chosen as independent state variables, the Gibbs energy  $G$  is the appropriate form of thermodynamic potential and results in the constitutive relations:

$$\mathbf{S} = -\frac{\partial G}{\partial \mathbf{T}}, \quad \mathbf{D} = -\frac{\partial G}{\partial \mathbf{E}}. \quad (3.13)$$

This form is useful for material testing since it is in general easier to apply a uniaxial stress than a uniaxially constrained strain on a specimen. In addition, using this form, one can test the specimen under voltage control.

If the stress  $\mathbf{T}$  and electric displacement  $\mathbf{D}$  are chosen as independent state variables, elastic Gibbs energy  $G_1$  is the appropriate form of thermodynamic potential and results in the constitutive relations:

$$\mathbf{S} = -\frac{\partial G_1}{\partial \mathbf{T}}, \quad \mathbf{E} = \frac{\partial G_1}{\partial \mathbf{D}}. \quad (3.14)$$

This form is useful for material testing if the specimen is tested under current control instead of voltage control.

### 3.1.3 Thermodynamically Consistent Model

#### Devonshire Single Crystal Model

From Section 3.1.2, it is known that constitutive equations can be derived from thermodynamic potentials. The question is how to obtain these energy expansions such that the material behavior can be well-presented by these constitutive relations.

Devonshire presented the first 1-D energy based model for repolarization in single domain crystal ferroelectrics[59]. The free energy is expanded in terms of polynomials of the electric displacement:

$$A = -\frac{1}{2}\alpha D^2 + \frac{1}{4}\beta D^4, \quad (3.15)$$

where  $\alpha$  and  $\beta$  are material constants. Two local minima can be found in this potential as a function of electric displacement. These correspond to two possible states of spontaneous polarization. Under an applied electric field, equilibrium is achieved when

$$dA - dW = 0, \quad dW = EdD. \quad (3.16)$$

This is the first law of thermodynamics, where  $EdD$  represents the work done by an applied electric field in causing a change in electric displacement. Equivalently, it can be stated that the system is at equilibrium whenever the energy  $A - ED$  is at a local minimum.

Figure 3-4 shows plots of  $A - ED$  at different electric fields. As the electric field  $E$  is increased, the location of the local minima changes corresponding to a change in the electric displacement of the system. As  $E$  is increased beyond a critical level, the system undergoes a phase transition. In other words, the spontaneous polarization of the material changes. If these local minima are plotted as a function of the applied electric field  $E$ , as shown in Figure 3-5, one can obtain the electric constitutive relation. This electric constitutive relation can be also obtained by differentiating Eq. 3.15 according to 3.12:

$$E = -\alpha D + \beta D^3. \quad (3.17)$$

To study the mechanical response, one can include the elastic energy in terms of strain  $S$  into the free energy expansion:

$$A = \frac{1}{2}cS^2 - hSD^2 - \frac{1}{2}\alpha D^2 + \frac{1}{4}\beta D^4, \quad (3.18)$$

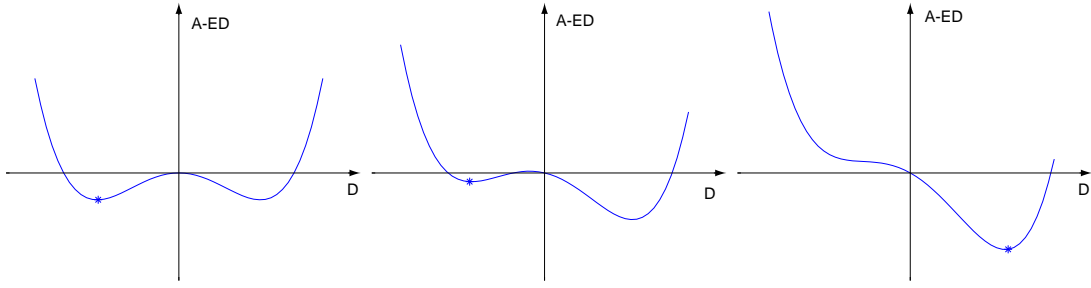


Figure 3-4: Potentials of a ferroelectric material proposed by Devonshire.

[h]

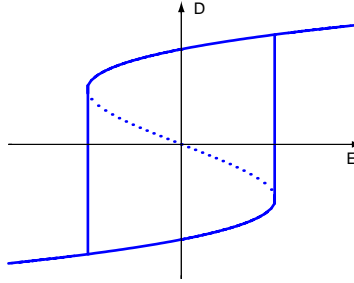


Figure 3-5: Electric constitutive relations. Dotted line indicates the portions of the curve which are thermodynamically unstable.

where the first term represents the elastic energy, and the second term considers the electromechanical coupling. Using this energy expansion, one can obtain the mechanical constitutive relation by differentiating Eq. 3.18 according to Eq. 3.12:

$$T = cS - hD^2. \quad (3.19)$$

Rewriting this equation as

$$S = (T + hD^2)/c, \quad (3.20)$$

and combining with Eq. 3.17 yields

$$E = -(2T/c + \alpha)D + (\beta - 2h/c)D^3. \quad (3.21)$$

Using Eq. 3.20 and 3.21, one can visualize the stress dependence in Figure 3-6. As expected, the applied stress produces a change in the coercive field and the magnitude of the polarization. The applied stress also changes the strain level due to the elasticity of the material.

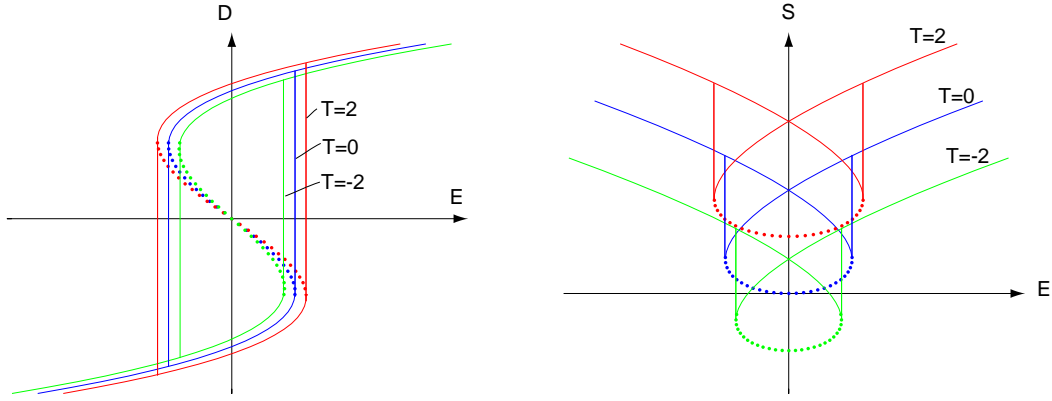


Figure 3-6: Stress dependence of material response using Devonshire model. Dotted line indicates the portions of the curve which are thermodynamically unstable.

### Ghandi and Hagood

In general, a polycrystalline piezoelectric can be considered as an assembly of an infinite number of small single domains with randomly oriented polarization. Using this assumption, Chan[60] developed a multiple family model based on Devonshire's single crystal model. One can imagine that quite a few families are required to produce a smooth response in the three-dimensional case. Performing this kind of computation for multiple families for each individual domain is very expensive.

To reduce the computational load, an approximation by Ghandi[35] is used to represent the response of a polycrystalline model. A thermodynamic potential of Helmholtz free energy is first assumed to have the form

$$G_1 = 5D^4 + 10(\Delta D)^2, \quad (3.22)$$

where

$$\Delta D = D - D^*,$$

$D$  is the electric displacement, and  $D^*$  is an internal variable representing the net remnant polarization. According to Eq. 3.14, the electric field can then be presented

$$E = \frac{\partial G_1}{\partial D}, \quad (3.23)$$

or

$$E = 20D^3 + 20\Delta D. \quad (3.24)$$

To determine the polarization state, the repolarization rule has to be used:

$$\begin{aligned}
& \text{if } |\Delta D| < \Delta D_c, \\
& \quad {}^{t+\Delta t}D^* = {}^tD^*, \\
& \text{if } |\Delta D| > \Delta D_c, \\
& \quad {}^{t+\Delta t}D^* = {}^tD^* + \Delta D \left(1 - \frac{\Delta D_c}{|\Delta D|}\right),
\end{aligned} \tag{3.25}$$

where

$$\Delta D = {}^{t+\Delta t}D - {}^tD^*,$$

$\Delta D_c$  is the magnitude of the critical difference between the electric displacement and the net remnant polarization. This critical value  $\Delta D_c$  governs the hysteretic behavior of the system. The response of the system is assumed to be reversible if

$$|\Delta D| < \Delta D_c. \tag{3.26}$$

That is, no repolarization occurs under these conditions. In contrast the system is assumed to undergo repolarization when

$$|\Delta D| = \Delta D_c. \tag{3.27}$$

$|\Delta D| > \Delta D_c$  is considered to be inadmissible.  $\Delta D_c$  is assumed to be constant. The nonlinear repolarizing system described by Eq. 3.22 and 3.25 can be solved using Newton-Raphson iteration. Figure 3-7 shows the electric displacement and net spontaneous polarization for different  $\Delta D_c$ . As expected, higher  $\Delta D_c$  results in expansion of polarization and higher coercive fields.

Although this model captures most of the important phenomena of piezoelectric ceramics, the evolution rule using discrete time step makes it difficult to implement the rate dependence in the model. In addition, due to the discrete time model, it is also difficult to obtain smooth response at the repolarizing region.

## 3.2 Development of a 1-D Rate and Stress Dependent Piezoelectric Model

The primary goal of this thesis is to develop a rate dependent nonlinear material model based on consistent thermodynamic potentials. The frame work of this material model evolves

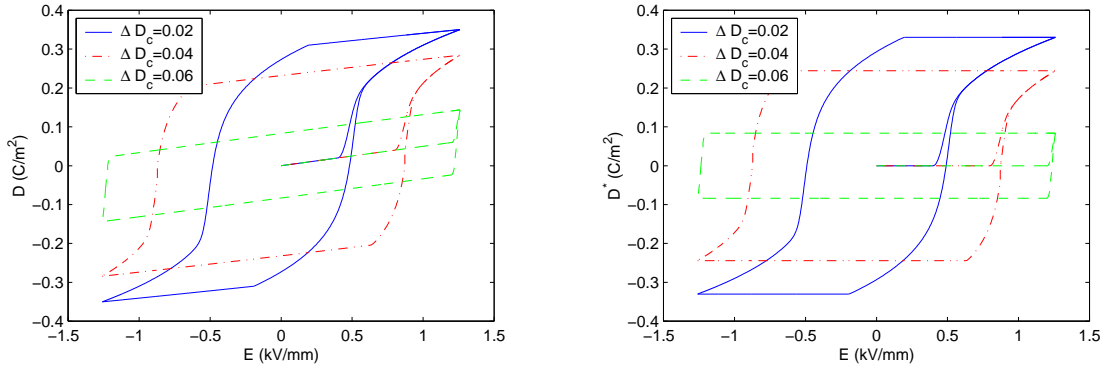


Figure 3-7: The simulated polarization using Ghandi's model

from Ghandi's model and the Weibull probabilistic function. This section will first discuss the assumption of electric conduction effect and then present the derivation of the model in 1-D example. A rate rule mechanism will be introduced to describe the hysteretic behavior of the material. The whole model can also be simplified as a system of differential-algebraic equations (DAE).

### 3.2.1 Assumption of Electric Conduction Effect

It is important to clarify the conduction effect before developing the material model. A piezoelectric material is not a perfect dielectric material. In other words, the material may be conductive. As shown in Figure 3-8, a piezoelectric material can be simulated by a nonlinear capacitor  $C_p$  and a nonlinear resistor  $R$  connected in parallel. The conduction through the resistor  $R$  may influence the material behavior depending on whether the driving condition is voltage source or charge source control.

#### Voltage Control vs. Charge Control

An example of voltage control includes the tests for actuation and model development conducted in Section 2.4. In these tests, the specimen is excited by the controlled voltage source from power amplifier. The power amplifier will supply enough current or charge to maintain the voltage commanded by users. Under this voltage source control, the voltage across the specimen is independent of  $I_r$ , the current in resistor  $R$ . In addition, it is

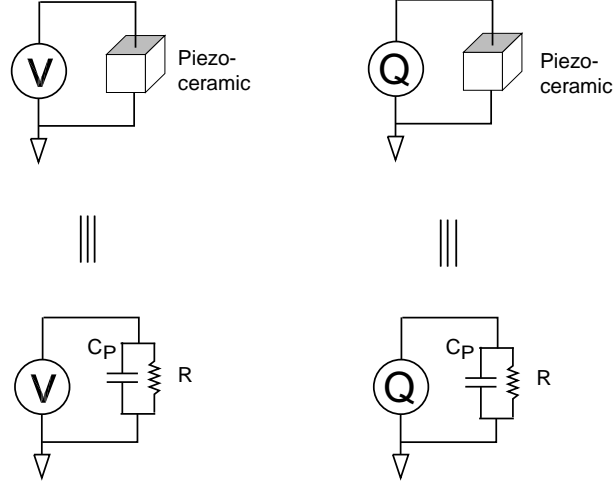
**Voltage Source Control****Charge Source Control**

Figure 3-8: Equivalent circuitry of piezoelectric ceramics under voltage source control (left) and charge source control (right).

reported [53] that the volume resistivity is larger than  $10^{11}\Omega\text{M}$  and the time constant is about 2000 seconds assuming the relative dielectric constant ( $\epsilon_{33}^T/\epsilon_0$ ) is 3400. This implies that the impedance of  $R$  is relatively large compared to dielectrics at frequencies above 0.1Hz at which the rate dependent tests were performed in Section 2.4. Consequently, the conduction effect can be neglected in this thesis work as the specimen is under voltage source control.

In contrast, the voltage across the specimen varies with  $R$  if the material is under limited charge source control. Some of the charge will be dissipated in resistor  $R$ . This dissipation will cause the voltage to drop. The energy harvester is a good example of charge source control. The finite charge source generated by external compression in the specimen may be dissipated via the conduction. Another example is the active fiber composite shown in Figure 3-9. The piezoelectric fibers are essentially under control of a limited charge source dielectrically generated on the epoxy-fiber interface. In such case, the conduction of the piezoelectric material is important to the overall response of the AFC. This effect has been studied by Harper[36].

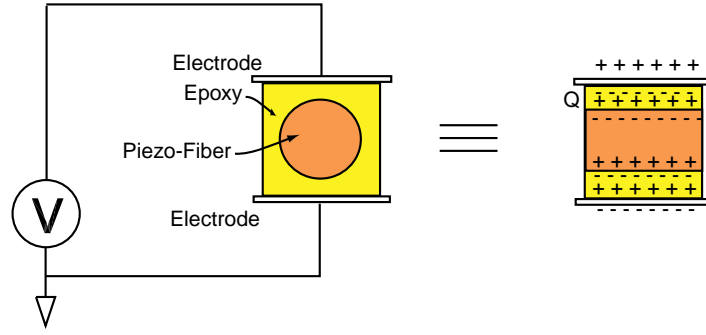


Figure 3-9: Non-contact electrode of AFC makes its piezoelectric fiber under charge source control.

## Conclusion

Based on the above arguments, the conduction effect can be neglected in the following discussion of the material model because the model will be developed from the observation of material response under voltage source control. In the case when the driving condition is under charge control, a linear conduction model can be used to supplement the non-conduction material model.

### 3.2.2 Probabilistic Effect

In Ghandi's model, Equation 3.25 implies that all the dipoles in polycrystalline ceramics repolarize at the same time when  $|\Delta D| \geq \Delta D_c$ . This simultaneous response can be described using the probability density function and the cumulative probability density function shown in Figure 3-10. With help of this interpretation, one can easily imagine that in practice not all the dipoles in a polycrystalline piezoelectric ceramics will respond to the applied electric field at the same time. Based on this assumption, one can further assume that the reaction of dipoles has a Weibull distribution[61] with respect to  $\Delta D$ :<sup>1</sup>

$$f(\Delta D) = \frac{\alpha}{\Delta D_c} \left( \frac{\Delta D}{\Delta D_c} \right)^{\alpha-1} \exp \left[ - \left( \frac{\Delta D}{\Delta D_c} \right)^{\alpha} \right], \text{ for } \Delta D \geq 0, \quad (3.28)$$

<sup>1</sup>Although the Weibull function represents an unsymmetric distribution, it is easier to use the Weibull distribution instead of the normal distribution because of the existence of a closed form of the cumulative Weibull distribution.



where  $\alpha$  is a distribution shape parameter. As  $\alpha \rightarrow \infty$ , the distribution becomes a impulse function, and the cumulative function of the Weibull distribution

$$F(\Delta D) = 1 - \exp \left[ - \left( \frac{\Delta D}{\Delta D_c} \right)^\alpha \right], \text{ for } \Delta D \geq 0 \quad (3.29)$$

becomes a step function. Figure 3-11 shows the Weibull probability density function and the Weibull cumulative probability density function as a function of  $\Delta D$  for various  $\alpha$ .

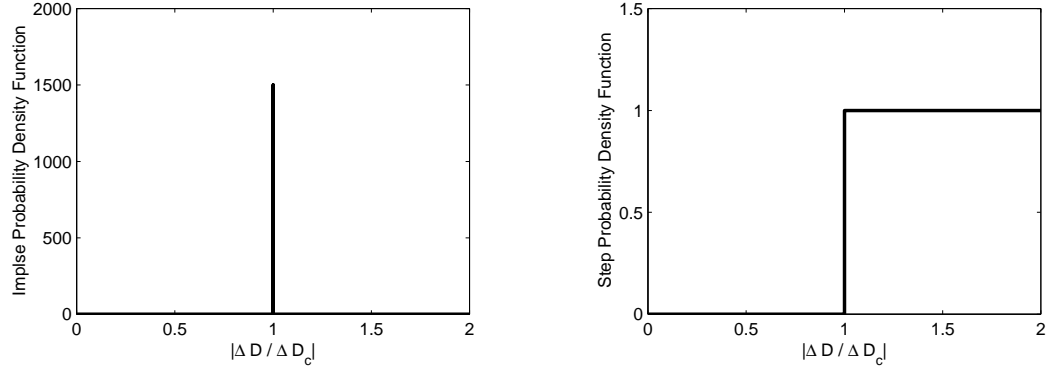


Figure 3-10: Probability density function (left) and cumulative probability density function (right).

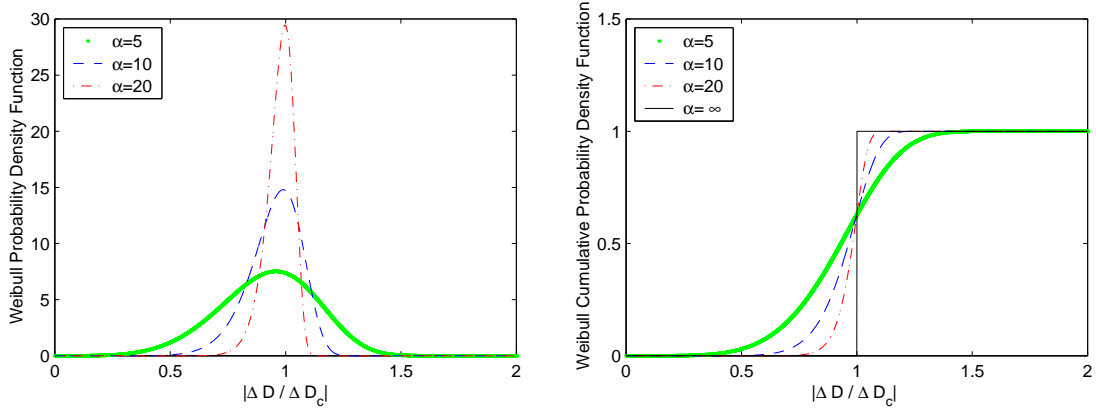


Figure 3-11: Weibull probability density function (left) and its cumulative probability density function (right).

As a consequence, the repolarizing rule, Equation 3.25, can be modified as

$${}^{t+\Delta t}D^* = {}^tD^* + \Delta D \left(1 - \frac{\Delta D_c}{|\Delta D|}\right) \left\{1 - \exp \left[- \left(\frac{|\Delta D|}{\Delta D_c}\right)^\alpha\right]\right\}. \quad (3.30)$$

To eliminate the singularity at  $\Delta D = 0$  and for convenience, it is desirable to rewrite Equation 3.30 as

$$\Delta D^* = {}^{t+\Delta t}D^* - {}^tD^* = [\Delta D - \text{sign}(\Delta D)\Delta D_c] \left\{1 - \exp \left[- \left(\frac{|\Delta D|}{\Delta D_c}\right)^\alpha\right]\right\}. \quad (3.31)$$

However, this equation is still not valid because the term  $[\Delta D - \text{sign}(\Delta D)\Delta D_c]$  has the opposite sign to  $\Delta D$  when  $\Delta D < \Delta D_c$ . This was not a problem for Ghandi's original model because  $\Delta D$  is 0 when  $\Delta D < \Delta D_c$ . In order to fix this problem, the simplest way is to modify Equation 3.31 as

$$\Delta D^* = {}^{t+\Delta t}D^* - {}^tD^* = \Delta D \left\{1 - \exp \left[- \left(\frac{|\Delta D|}{\Delta D_c}\right)^\alpha\right]\right\}. \quad (3.32)$$

Note that the term  $\Delta D \left(1 - \frac{\Delta D_c}{|\Delta D|}\right)$  in Equation 3.30 has been simply replaced by  $\Delta D$ . This simplification may, to some extent, change the characteristics of the original evolution rule (Eq. 3.25), but the difference between Eq.3.25 and 3.32 can be corrected by the parameters in the Weibull function. These parameters can be obtained by comparing the model and experimental data, as will be discussed later.

### 3.2.3 Rate and Stress Effects of Polarization

#### Rate Dependency

To account for the rate effect, Equation 3.32 can be modified as

$$\frac{dD^*}{dt} = \frac{\Delta D}{\tau} \left\{1 - \exp \left[- \left(\frac{|\Delta D|}{\Delta D_c}\right)^\alpha\right]\right\}, \quad (3.33)$$

where  $\tau$  is a time constant characterizing the change rate of the net remnant polarization  $D^*$ . This equation may not be perfect for differentiation because the derivative of the absolute function is not continuous. The purpose of this absolute function is to guarantee a behavior of an even function. As a result, Eq. 3.33 can be further modified by replacing the absolute function with an even function such as

$$\frac{dD^*}{dt} = \frac{\Delta D}{\tau} \left\{1 - \exp \left[- \left(\frac{\Delta D}{\Delta D_c}\right)^{2\alpha}\right]\right\}, \quad (3.34)$$

where  $\alpha$  now is a positive integer. Again, this modification will not affect the overall development of the model because all the parameters have not been determined yet.

Eq. 3.34 is the final version of the rate rule of the net remnant polarization  $D^*$ . This rate rule not only describes the material behavior in continuous time, but also considers the probabilistic response of the domains in polycrystalline ceramics. Using this rate rule and the constitutive relation (Eq. 3.24) derived from thermodynamic potential described in Eq. 3.22, one can well define the polarization response of piezoelectric materials. This system is a set of differential algebraic equations of index-1:

$$\begin{cases} \dot{D}^* = f(D, D^*), \\ 0 = g(D, D^*) - E, \end{cases} \quad (3.35)$$

which can be solved by a number of numerical software package, such as DASPK[46].

### Stress Dependency

To model the stress effect of polarization, it is more appropriate to use the elastic Gibbs Energy, as discussed in Section 3.1.2. Adding elastic energy in Eq. 3.22, for instance, one can expand the energy function using Taylor's series in terms of  $D$ ,  $D^*$ , and  $T$ :

$$\begin{aligned} G_1 = & (a_1 D + a_2 D^2 + a_3 D^3 + a_4 D^4 + a_5 D D^* + \dots) \\ & -(b_0 + b_1 D + b_2 D^2 + b_3 D^3 + b_4 D^4 + b_5 D D^* + \dots) T \\ & -(c_0 + c_1 D + c_2 D^2 + c_3 D^3 + c_4 D^4 + c_5 D D^* + \dots) T^2 \\ & + \text{H.O.T.} \end{aligned} \quad (3.36)$$

where the coefficients of this expansion can be obtained by curve fitting to the data obtained in Section 2.4. The detailed procedure will be discussed in the next section. Consequently, the system can be described using the rate rule (Eq.3.34), the corresponding electric constitutive relation, and the elastic constitutive relations

$$\begin{aligned} E = \frac{\partial G_1}{\partial D} = & (a_1 + 2a_2 D + 3a_3 D^2 + 4a_4 D^3 + a_5 D^* + \dots) \\ & -(b_1 + 2b_2 D + 3b_3 D^2 + 4b_4 D^3 + b_5 D^* + \dots) T \\ & -(c_1 + 2c_2 D + 3c_3 D^2 + 4c_4 D^3 + c_5 D^* + \dots) T^2 \\ & + \text{H.O.T.} \end{aligned} \quad (3.37)$$

$$\begin{aligned}
S = -\frac{\partial G_1}{\partial T} &= (b_0 + b_1 D + b_2 D^2 + b_3 D^3 + b_4 D^4 + b_5 D D^* + \dots) \\
&\quad 2(c_0 + c_1 D + c_2 D^2 + c_3 D^3 + c_4 D^4 + c_5 D D^* + \dots)T \\
&\quad + \text{H.O.T.}
\end{aligned} \tag{3.38}$$

### 3.2.4 Parametric Study

Before finding the coefficients in Eq. 3.36, it is essential to investigate how the parameters in the rate rule (Eq. 3.34) influence the model. In addition, it is of interest to understand how the rate and stress affect the materials using this model. To do this in the simplest manner, the following coefficients are first assumed in Eq. 3.36:

$$a_2 = 1, \quad a_4 = 1, \quad a_5 = -2, \quad b_2 = 0.5, \quad c_0 = 0.1, \quad c_1 = 0.001, \tag{3.39}$$

and the others are assumed zero.

#### Effect of $D^*$

First it is of interest to see the effect of  $D^*$ , which is the major factor of piezoelectric hysteresis. If the rate change of  $D^*$  is zero, i.e.

$$\frac{dD^*}{dt} = 0, \tag{3.40}$$

the response shown in Figure 3-12 is non-hysteric as expected. This result can be compared to the hysteretic case where  $\frac{dD^*}{dt}$  is not zero as described by Eq. 3.34.

#### Effect of $\alpha$

Figure 3-13 shows the effect of  $\alpha$ , assuming  $f = 1\text{Hz}$ ,  $T = 0$ ,  $\Delta D_c = 0.6$ ,  $\tau = 0.001$ , and varying  $\alpha = \{1, 2, \text{ or } 3\}$ . As expected from the characteristics of the Weibull function shown in Figure 3-11, the polarization in the beginning starts to increase earlier for smaller  $\alpha$  because of the wider distribution for smaller  $\alpha$  in Figure 3-11.

#### Effect of $\Delta D_c$

Figure 3-14 shows the effect of  $\Delta D_c$ , assuming  $f = 1\text{Hz}$ ,  $T = 0$ ,  $\alpha = 1$ ,  $\tau = 0.001$ , and varying  $\Delta D_c = \{0.2, 0.5, \text{ or } 0.8\}$ . As expected, the polarization in the beginning starts to increase earlier for smaller  $\Delta D_c$ .

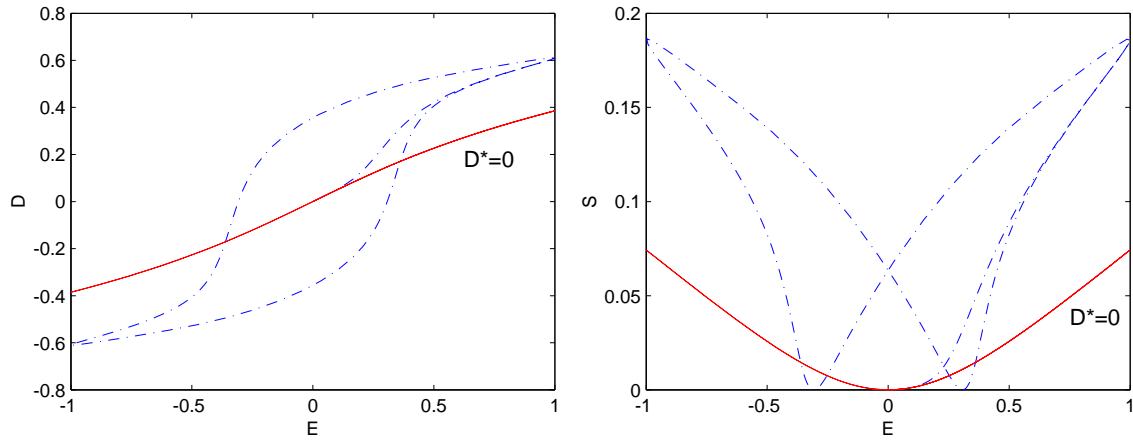


Figure 3-12: Effect of  $D^*$  on  $E$ - $D$  and  $E$ - $S$  relations, assuming  $T = 0$  and  $f = 1$  Hz. For non zero  $D^*$  case,  $\Delta D_c = 0.5$ ,  $\tau = 0.001$ , and  $\alpha = 1$  are used in Eq. 3.34.

### Effect of $\tau$

Figure 3-15 shows the effect of  $\tau$ , assuming  $f = 1$ Hz,  $T = 0$ ,  $\Delta D_c = 0.5$ ,  $\alpha = 1$ , and varying  $\tau = \{0.0005, 0.001, \text{ or } 0.0015\}$ . As can be seen, a larger time constant  $\tau$  results in expansion of the polarization and strain response.

### Effect of Frequency

Figure 3-16 shows the effect of frequency  $f$ , assuming  $T = 0$ ,  $\Delta D_c = 0.05$ ,  $\alpha = 3$ ,  $\tau = 0.0005$ , and varying  $f = \{0.1, 1, \text{ or } 10\}$ Hz. As can be seen, higher frequency  $f$  also results in expansion of the polarization and strain response. This correlates with the observation in Section 2.4.

### Effect of Stress

Figure 3-17 shows the effect of  $T$ , assuming  $f = 1$ Hz,  $\Delta D_c = 0.05$ ,  $\alpha = 1$ ,  $\tau = 0.001$ , and varying  $T = \{-1, 0, \text{ or } 1\}$ . As expected, the compressive stress results in flat polarization and strain response, which correlates with the behavior observed in Section 2.4. Although no experimental data of material in tension is available, the simulated response of material in tension shows reasonable stretch in polarization and strain.

Compared to the data observed in Section 2.4, the parametric study discussed above

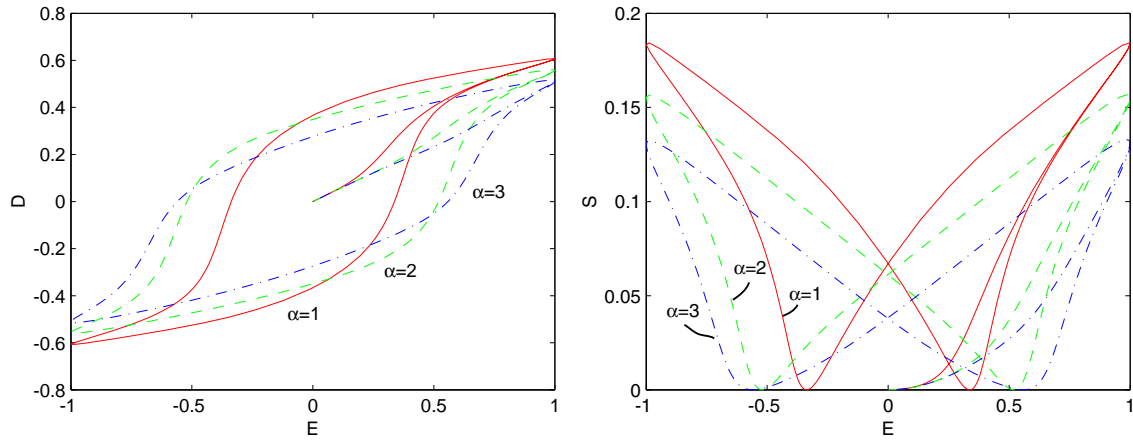


Figure 3-13: Effect of  $\alpha$  on  $E$ - $D$  and  $E$ - $S$  relations, assuming  $f = 1\text{Hz}$ ,  $\Delta D_c = 0.6$ ,  $T = 0$ ,  $\tau = 0.001$ , and varying  $\alpha = \{1, 2, \text{ or } 3\}$ .

shows that the parameters  $\Delta D_c$ ,  $\alpha$ , and  $\tau$  in the rate rule (Eq.3.34) and the energy expansion (Eq.3.36) are sufficient to describe the rate and stress dependency as well as the major hysteretic behaviors of piezoelectric materials. The next step is to calibrate those coefficients in the energy expansion shown in Eq. 3.36 using a curve fitting technique such that the error between the model and data is minimized.

### 3.3 1-D Material Parameters

This section will demonstrate how to calibrate the parameters of the material model by fitting the model to the test data obtained in Section 2.4. The optimal parameters for PZT-5A and PZT-5H will be presented with the correlation of data and the model. For the purpose of understanding the mechanisms, the targeted precision is set within an order of magnitude, as discussed in Section 1.3

The parameters of the material model needing to be found include the rate parameters in Eq. 3.34 and the polynomial coefficients in the energy expansion. The polynomial coefficients can be found using standard least squares regression. Unfortunately, the rate parameters appear in the the system in a nonlinear fashion. No efficient algorithm is currently available to optimize these nonlinear parameters. As a result, an intensive simulation for different combinations of rate parameters has to be conducted, and the optimal rate pa-

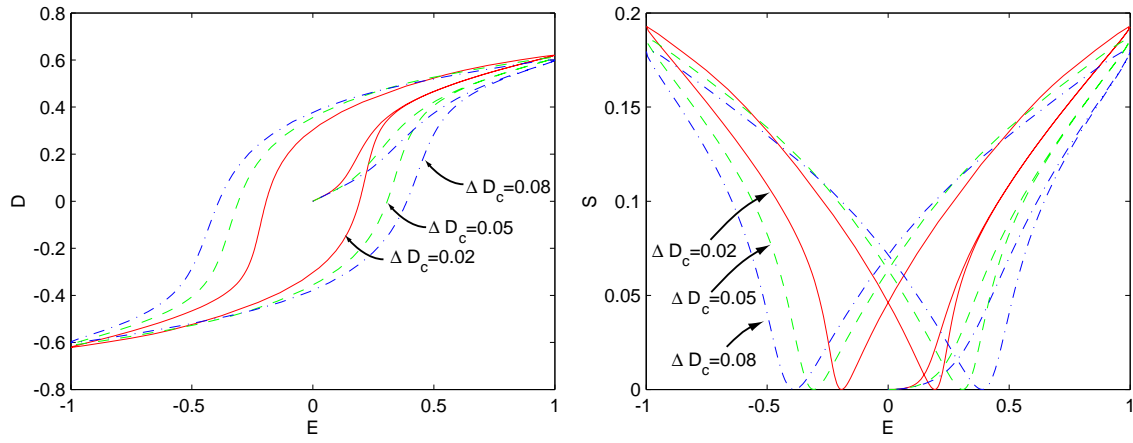


Figure 3-14: Effect of  $\Delta D_c$  on  $E$ - $D$  and  $E$ - $S$  relations, assuming  $f = 1\text{Hz}$ ,  $T = 0$ ,  $\alpha = 1$ ,  $\tau = 0.001$ , and varying  $\Delta D_c = \{0.2, 0.5, \text{ or } 0.8\}$ .

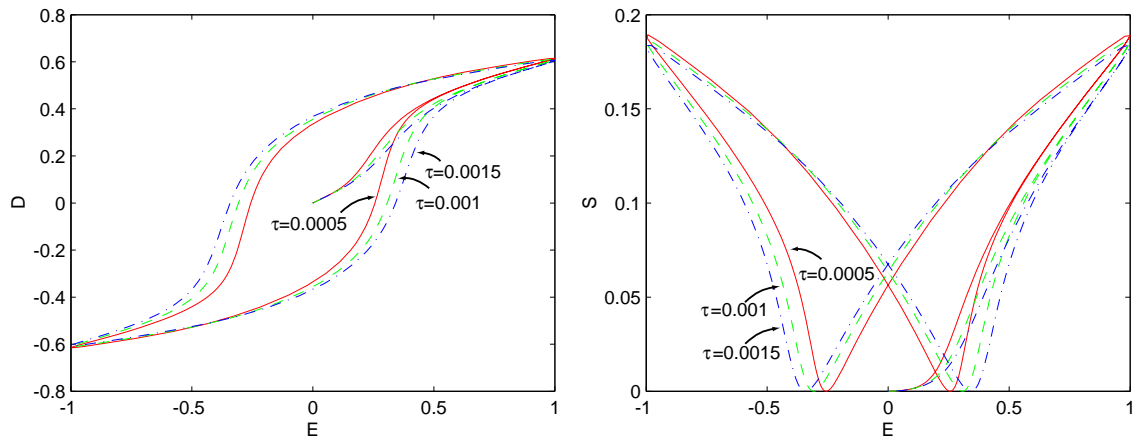


Figure 3-15: Effect of  $\tau$  on  $E$ - $D$  and  $E$ - $S$  relations, assuming  $f = 1\text{Hz}$ ,  $T = 0$ ,  $\Delta D_c = 0.5$ ,  $\alpha = 1$ , and varying  $\tau = \{0.0005, 0.001, \text{ or } 0.0015\}$ .

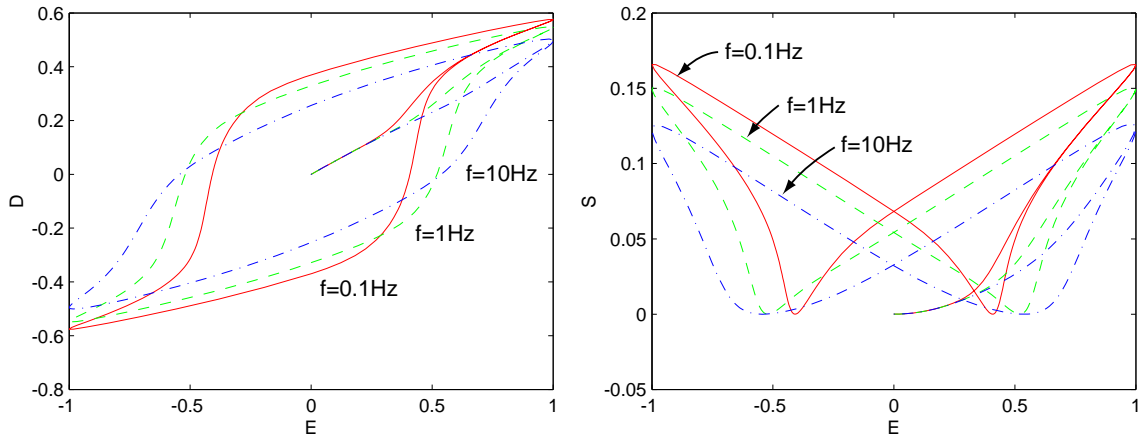


Figure 3-16: Effect of driving frequency on  $E$ - $D$  and  $E$ - $S$  relations, assuming  $T = 0$ ,  $\Delta D_c = 0.05$ ,  $\alpha = 3$ ,  $\tau = 0.0005$ , and varying  $f = \{0.1, 1, \text{ or } 10\}\text{Hz}$ .

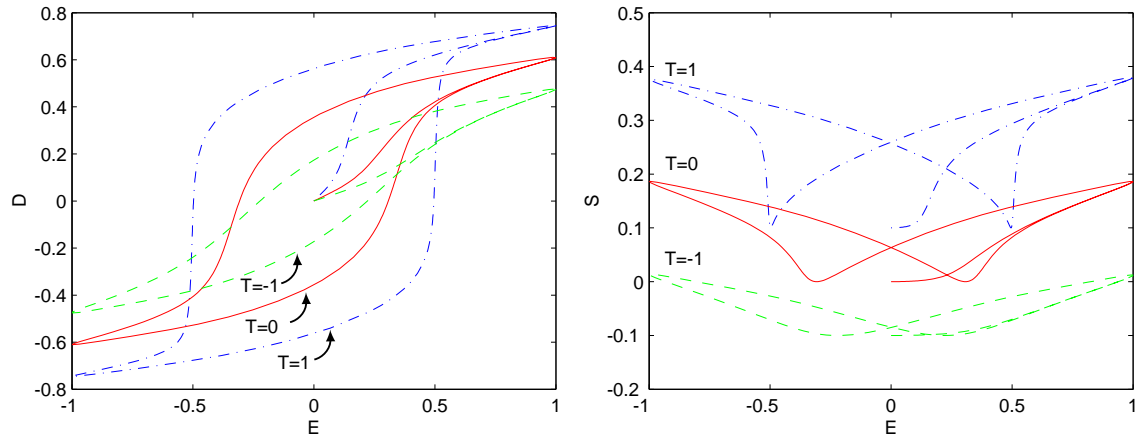


Figure 3-17: Effect of stress on  $E$ - $D$  and  $E$ - $S$  relations, assuming  $f = 1\text{Hz}$ ,  $\Delta D_c = 0.05$ ,  $\alpha = 1$ ,  $\tau = 0.001$ , and varying  $T = \{-1, 0, \text{ or } 1\}$ .



rameters with minimal error will be found. Below is a summary of the general procedure which is followed by a detailed description.

1. Construct  $D^*$  from data of  $D$  using Eq. 3.34 with assumed  $\tau$ ,  $\Delta D_c$ , and  $\alpha$ .
2. Assume polynomial terms of energy expansion  $G_1$  as a function of  $D$ ,  $D^*$ , and  $T$ .
3. Perform linear least squares regression and calculate the error for optimal coefficients of the assumed polynomial terms and rate rule parameters  $\tau$ ,  $\Delta D_c$ , and  $\alpha$ .
4. Repeat Steps 1 to 3 for different combinations of rate rule parameters  $\tau$ ,  $\Delta D_c$ , and  $\alpha$ . Then compare all the results and find the minimum error for the optimal  $\tau$ ,  $\Delta D_c$ , and  $\alpha$ .

### 3.3.1 Construction of $D^*$

As discussed earlier,  $D^*$  is a fictitious variables which cannot be measured by any instruments that are currently available. To find the coefficients of the polynomial terms that are functions of  $D$  and  $D^*$ ,  $D^*$  must be simulated from measured  $D$ .

In this step, a set of rate parameters  $\tau$ ,  $\Delta D_c$ , and  $\alpha$  should be assumed first. The typical range of  $\tau$  is from 0.1 to 10 millisecond;  $\Delta D_c$  is from 0.01 to 0.1 C/m<sup>2</sup>, and  $\alpha$  is from 3 to 10. These values are the conclusion of the parametric study in the previous section. Using these assumed  $\tau$ ,  $\Delta D_c$ , and  $\alpha$  and measured  $D$ , one can then find the simulated  $D^*$  by solving the differential equation (Eq. 3.34). Two sets of initial conditions of this differential equation are possible: one is zero, and the other is nonzero.

If the material data of polarization  $D$  is recorded from the freshly unpoled state, the initial condition of  $D$  and  $D^*$  are therefore zero. With these initial conditions, the simulated  $D^*$  can be solved numerically from Eq. 3.34. Figure 3-18 shows the simulated result and the relation between  $D$  and  $D^*$ .

Unfortunately, most data for stress dependency study obtained in Section 2.4 did not start from the virgin state of the material, i.e. remanent polarization exists in the material. In other words, the initial values of  $D$  and  $D^*$  for each cycle are not zero. As a result, iteration for  $D_0^*$ , the initial condition of  $D^*$ , must be conducted by first assuming  $D_0^* = D_0/0.8$  and then solving for  $D^*$  for a cycle. The value of  $D^*$  at the end of this cycle can

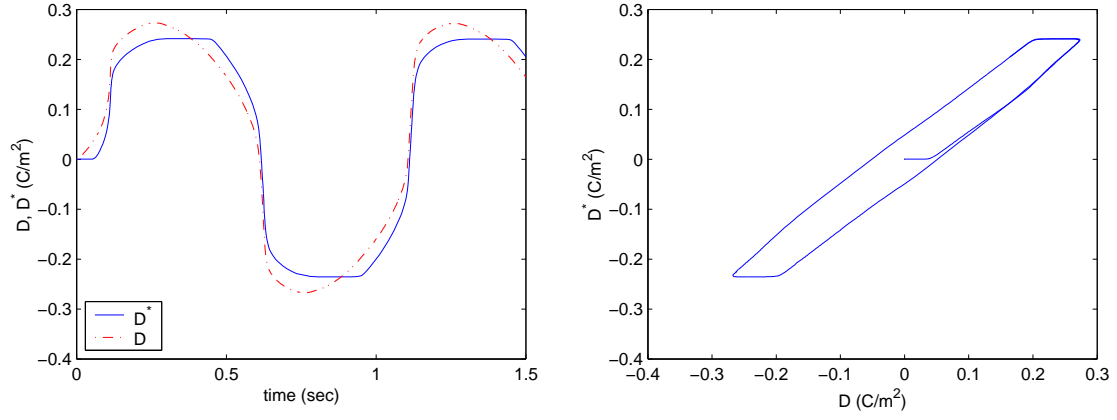


Figure 3-18: Finding  $D^*$  for virgin specimen.

be used as the new initial guess of  $D_0^*$  for the next integration cycle. This integration process must be continued until the value of  $D_0^*$  converges. In general, only two cycles of integration are needed to obtain a converged  $D_0^*$  for each stress value. Figure 3-19 shows the time history of measured  $D$ , simulated  $D^{**}$  with initial guessed  $D_0^{**}$ , and simulated  $D^*$  with converged  $D_0^*$ . The right plot of 3-19 shows the zoomed data that  $D^{**}$  converges rapidly to  $D^*$ . Figure 3-20 shows the relation between  $D$  and  $D^*$ . The left plot shows how  $D^{**}$  with initial guessed  $D_0^{**}$  converges to  $D^*$ . The right plot shows the relation between measured  $D$  and converged  $D^*$ .

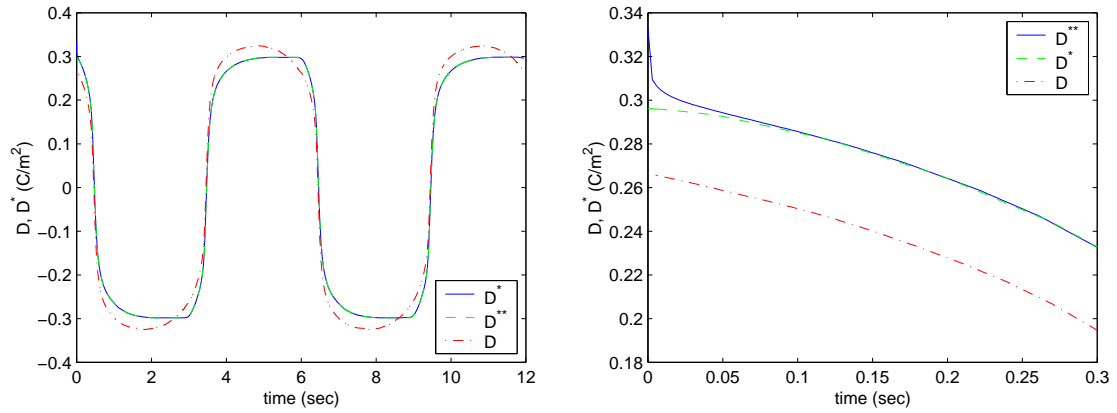


Figure 3-19: Finding  $D_0^*$  for poled specimen: (left) time history of measured  $D$ , simulated  $D^{**}$  with initial guessed  $D_0^{**}$ , and simulated  $D^*$  with converged  $D_0^*$ ; (right) zoomed time history.

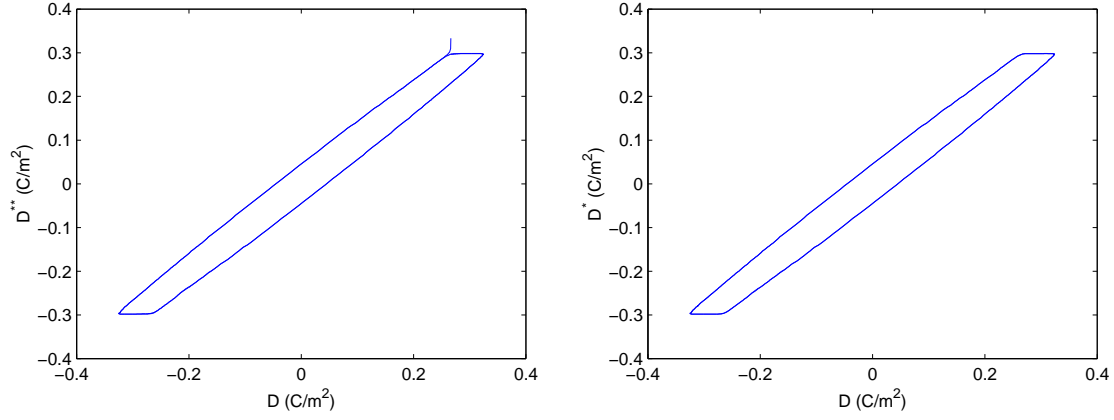


Figure 3-20: Finding  $D_0^*$  for poled specimen. (left) initial guessed  $D_0^{**}$ , (right) converged  $D_0^*$

### 3.3.2 Selection of Polynomials

Table 3.2: Polynomial terms of thermodynamic potentials

$\sigma_1 D$	$\sigma_6 D^*$	$\sigma_{11} D D^*$
$\sigma_2 D^2$	$\sigma_7 D^{*2}$	$\sigma_{12} D D^{*2}$
$\sigma_3 D^3$	$\sigma_8 D^{*3}$	$\sigma_{13} D^2 D^{*2}$
$\sigma_4 D^4$	$\sigma_9 D^{*4}$	$\sigma_{14} D^2 D^*$
$\sigma_5 D^5$	$\sigma_{10} D^{*5}$	$\sigma_{15} D^3 D^*$
		$\sigma_{16} D^3 D^{*2}$
		$\sigma_{17} D^3 D^{*3}$
		$\sigma_{18} D^2 D^{*3}$
		$\sigma_{19} D D^{*3}$

First,  $G_1$  is assumed to have a form of

$$G_1 = f_a(D, D^*) - f_b(D, D^*)T - f_c(D, D^*)T^2 - f_d(D, D^*)T^4, \quad (3.41)$$

where the terms related to  $T^3$  are neglected by observing strain ( $S$ ) is an odd function of stress ( $T$ ). The corresponding strain and electric field are then

$$S = f_b(D, D^*) + 2f_c(D, D^*)T + 4f'_d(D, D^*)T^3, \quad (3.42)$$

$$E = f'_a(D, D^*) - f'_b(D, D^*)T - f'_c(D, D^*)T^2 - f'_d(D, D^*)T^4, \quad (3.43)$$

where  $f'$  denotes the partial derivative of  $f$  with respect to  $D$ . Table 3.2 shows the polynomial terms used in this work for  $f_a(D, D^*)$ ,  $f_b(D, D^*)$ ,  $f_c(D, D^*)$ , and  $f_d(D, D^*)$ . The coefficient corresponding to each term is denoted by  $\sigma_i$ , where  $\sigma$  represents the subscript of  $f_a$ ,  $f_b$ ,  $f_c$ , and  $f_d$  in general. Namely, for instance,  $f_a$  is given by

$$f_a(D, D^*) = a_1 D + a_2 D^2 + \cdots a_{18} D D^{*3}.$$

Higher order terms can be included in this expansion of the energy function to improve the performance of the model. However, the terms selected in Table 3.2 are found to be sufficient to simulate the observed data. After selection of these polynomial terms, the next step is to obtain the corresponding coefficients using least squares regression such that the error between model and data can be minimized.

### 3.3.3 Optimization of Polynomial Coefficients

Since the rate parameters are assumed,  $D^*$  is simulated from the measured and  $D$ , and the polynomial terms of the elastic Gibbs energy are selected, this step is to optimize the coefficients of the energy expansion subjected to the assumed rate parameters. For convenience of discussion, rewriting the elastic Gibbs free energy as

$$G_1 = \sum_k x_k G_1^{(k)}(T, D, D^*) \quad (3.44)$$

yields expressions of  $E$  and  $S$  as

$$E = \sum_k x_k E^{(k)}(T, D, D^*), \quad (3.45)$$

$$S = \sum_k x_k S^{(k)}(T, D, D^*), \quad (3.46)$$

where  $x_k$  includes all the coefficients of  $a_i$ ,  $b_i$ ,  $c_i$ , and  $d_i$ .

With the expression of  $S$  and  $E$  in Eq. 3.46 and 3.45 and the measured data  $\hat{S}$  and  $\hat{E}$  from Section 2.4, the weighted cost function for optimization can be defined by summing all the weighted errors for  $n$  data points:

$$\mathbf{e} = \sum_{z=1}^n w_{E_z} (E_z(\hat{D}_z, \hat{D}_z^*, \hat{T}_z) - \hat{E}_z)^2 + \sum_{z=1}^n w_{S_z} (S_z(\hat{D}_z, \hat{D}_z^*, \hat{T}_z) - \hat{S}_z)^2 \quad (3.47)$$

where  $n$  is the number of data points,  $w_E$  and  $w_S$  are weighting functions, and  $\hat{D}$ ,  $\hat{D}^*$ , and  $\hat{T}$  are the measured values from Section 2.4. This cost function can be also defined from a

weighted linear system

$$\mathbf{W}\mathbf{A}\mathbf{x} = \mathbf{W}\mathbf{b} \quad (3.48)$$

where  $\mathbf{x}$  is the vector of  $x_k$ ,  $\mathbf{W}$  is given by a diagonal matrix of the vector  $[\mathbf{w}_E \ \mathbf{w}_S]^T$ , and  $\mathbf{b}$  is an appended vector of measured  $\hat{E}_z$  and  $\hat{S}_z$ :

$$\mathbf{b} = \begin{bmatrix} \hat{\mathbf{E}} \\ \hat{\mathbf{S}} \end{bmatrix}. \quad (3.49)$$

The corresponding  $\mathbf{A}$  can be partitioned as

$$\mathbf{A} = \begin{bmatrix} \mathbf{A}^E \\ \mathbf{A}^S \end{bmatrix}, \quad (3.50)$$

where the respective components of  $\mathbf{A}^E$  and  $\mathbf{A}^S$  are

$$A_{zk}^E = E^{(k)}(\hat{D}_z, \hat{D}_z^*, \hat{T}_z), \quad (3.51)$$

$$A_{zk}^S = S^{(k)}(\hat{D}_z, \hat{D}_z^*, \hat{T}_z). \quad (3.52)$$

The vector  $\mathbf{x}$  that minimizes the weighted cost function  $\mathbf{e}$  or  $\mathbf{W}\|\mathbf{A}\mathbf{x} - \mathbf{b}\|$  is the solution to the weighted normal equations[62]:

$$\mathbf{A}^T \mathbf{W} \mathbf{A} \mathbf{x} = \mathbf{A}^T \mathbf{W} \mathbf{b} \quad (3.53)$$

i.e.  $\mathbf{x} = (\mathbf{A}^T \mathbf{W} \mathbf{A})^{-1} \mathbf{A}^T \mathbf{W} \mathbf{b}$ .

### 3.3.4 Optimization of $\tau$ , $\Delta D_c$ , and $\alpha$

In the previous discussion, the coefficients of the energy expansion are optimized for certain assumed rate parameters  $\alpha$ ,  $\tau$  and  $\Delta D_c$ . However, these rate parameters are not optimized yet. Unlike the polynomial coefficients, these rate parameters influence the system in a nonlinear manner, and therefore it is difficult to optimize them using least squares regression. The only possible approach is to intensively repeat the same procedure described in Sections 3.3.1, 3.3.2, and 3.3.3 for different combinations of rate parameters. The optimized rate parameters can be therefore obtained by identifying the minimum value of the cost function. The data of the stress effect as well as the rate effect must be included in this evaluation of the cost function; otherwise, the model may result in unreasonable behavior. For instance,

using the parameters  $\alpha = 3$ ,  $\Delta D_c = 0.15C/m^2$ , and  $\tau = 1ms$  and the energy expansion with the coefficients listed in Table 3.3:

$$\begin{aligned}
G_1 = & a_2 D^2 + a_4 D^4 + a_{11} D D^* + a_{12} D D^{*2} + a_{13} D^2 D^{*2} \\
& + a_{14} D^2 D^{*2} + a_{15} D^3 D^* + a_{16} D^3 D^{*2} + a_{17} D^3 D^{*3} + a_{18} D^2 D^{*3} \\
& + a_{19} D D^{*3} + a_{20} D^6 + a_{21} D^4 D^* + a_{22} D^4 D^{*2} + a_{23} D^4 D^{*3} \\
& + (b_2 D^2 + b_4 D^4 + b_7 D^{*2} + b_9 D^{*4} + b_{11} D D^* + b_{12} D D^{*2} \\
& + b_{13} D^2 D^{*2} + b_{14} D^2 D^* + b_{15} D^3 D^* + b_{16} D^3 D^{*2} + b_{17} D^3 D^{*3} + b_{18} D^2 D^{*3} \\
& + b_{19} D D^{*3} + b_{20} D^6 + b_{21} D^4 D^* + b_{22} D^4 D^{*2} + b_{23} D^4 D^{*3}) T \\
& + (c_0 + c_2 D^2 + c_4 D^4 + c_7 D^{*2} + c_9 D^{*4} + c_{11} D D^* + c_{12} D D^{*2} \\
& + c_{13} D^2 D^{*2} + c_{14} D^2 D^* + c_{15} D^3 D^* + c_{16} D^3 D^{*2} + c_{17} D^3 D^{*3} + c_{18} D^2 D^{*3} \\
& + c_{19} D D^{*3} + c_{20} D^6 + c_{21} D^4 D^* + c_{22} D^4 D^{*2} + c_{23} D^4 D^{*3}) T^2 \\
& + (d_0 + d_2 D^2 + d_4 D^4 + d_7 D^{*2} + d_9 D^{*4} + d_{11} D D^* + d_{12} D D^{*2} \\
& + d_{13} D^2 D^{*2} + d_{14} D^2 D^* + d_{15} D^3 D^* + d_{16} D^3 D^{*2} + d_{17} D^3 D^{*3} + d_{18} D^2 D^{*3} \\
& + d_{19} D D^{*3} + d_{20} D^6 + d_{21} D^4 D^* + d_{22} D^4 D^{*2} + d_{23} D^4 D^{*3}) T^4, \tag{3.54}
\end{aligned}$$

one can correlate the model well with stress dependent data as shown in Figure 3-21. However, this combination of parameter shows a very poor result with respect to rate dependency, as shown in Figure 3-22. As a result, this set of parameters is not valid.

Table 3.3: Coefficients of PZT-5H thermodynamic potential expanded by polynomial terms. This will result in poor rate behavior, despite the good stress dependent response

					( $\times 10^4$ )		( $\times 10^5$ )
				$c_0$	0.0035	$d_0$	-0.0269
$a_2$	0.1127	$b_2$	217.1444	$c_2$	0.3758	$d_2$	-1.6482
$a_4$	297.9421	$b_4$	-13885.0000	$c_4$	-26.8084	$d_4$	-207.0929
		$b_7$	118.4422	$c_7$	0.3037	$d_7$	-1.2494
		$b_9$	-11910.0000	$c_9$	-25.8064	$d_9$	-100.2973
$a_{11}$	-3.6804	$b_{11}$	-326.2087	$c_{11}$	-0.7135	$d_{11}$	3.9120
$a_{12}$	0.6607	$b_{12}$	-28.7464	$c_{12}$	-0.0443	$d_{12}$	-0.0989
$a_{13}$	1252.0000	$b_{13}$	-75620.0000	$c_{13}$	-157.2291	$d_{13}$	-723.4826
$a_{14}$	-0.5245	$b_{14}$	28.0433	$c_{14}$	0.0490	$d_{14}$	-0.3229
$a_{15}$	-983.0483	$b_{15}$	52618.0000	$c_{15}$	105.4464	$d_{15}$	616.6637
$a_{16}$	59.0330	$b_{16}$	-277.7209	$c_{16}$	0.0469	$d_{16}$	-22.9987
$a_{17}$	140.9955	$b_{17}$	-2712.1000	$c_{17}$	0.1323	$d_{17}$	202.0744
$a_{18}$	-45.1711	$b_{18}$	264.5240	$c_{18}$	-0.2842	$d_{18}$	36.2788
$a_{19}$	-697.9519	$b_{19}$	49214.0000	$c_{19}$	104.7170	$d_{19}$	394.5847
$a_{20}$	48.8821						
$a_{21}$	-17.3723						
$a_{22}$	-171.4751						
$a_{23}$	-35.5942						

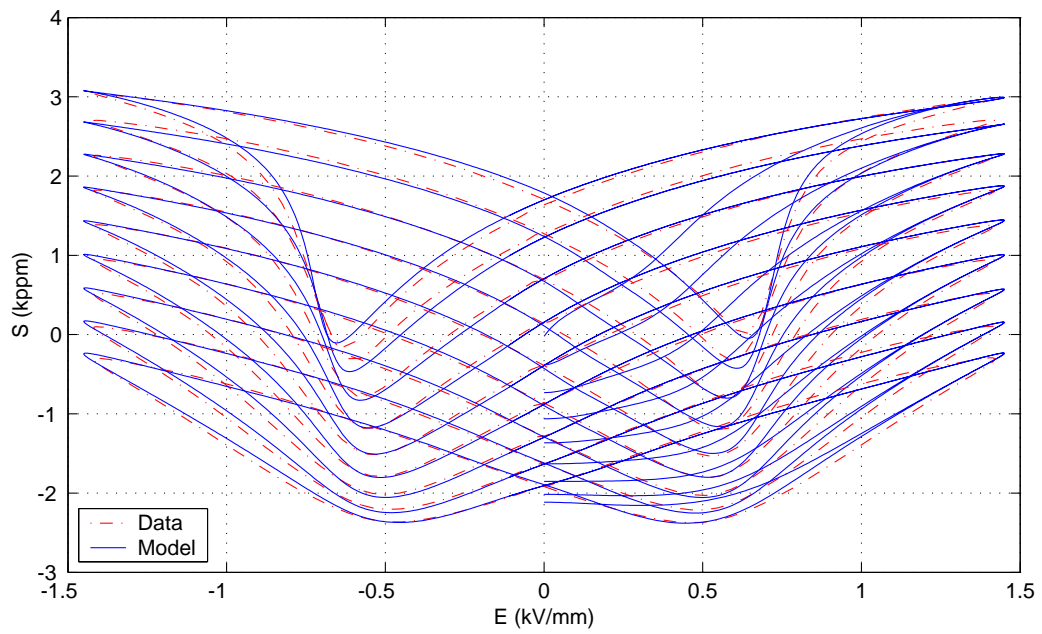
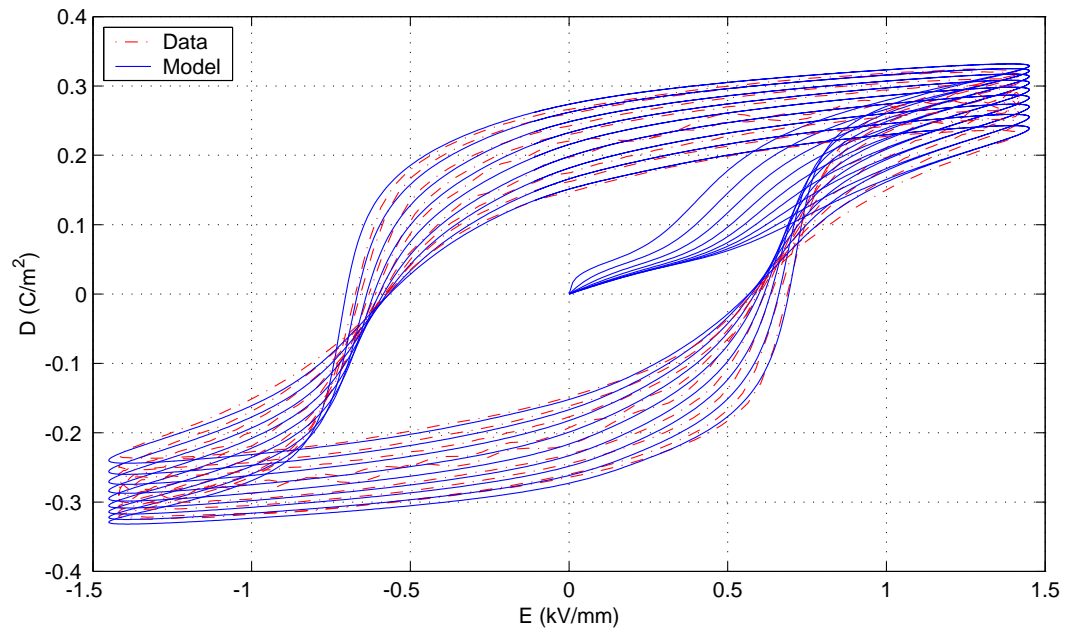


Figure 3-21: Unreasonable strain and polarization response at various stresses using inappropriate parameter optimization. Data was obtained by Gandhi[35].



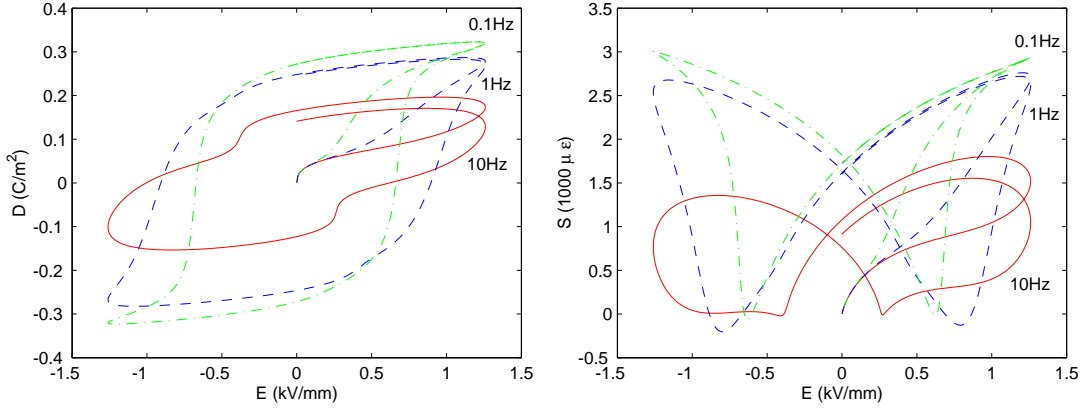


Figure 3-22: Unreasonable strain and polarization response at various frequencies using inappropriate parameter optimization.

### 3.3.5 Optimized 1-D Model Parameters for PZT-5H

Following the procedures described in Sections 3.3.1–3.3.4 with weight  $w_i = 1$ , one can find the optimized 1-D rate parameters for PZT-5H:  $\tau=0.1$  (ms),  $\Delta D_c=0.03$  (C/m<sup>2</sup>),  $\alpha=7$ . To simplify the model and to avoid the fact that higher order terms may cause unstable solution of the differential algebraic equations at high frequency, only the following terms shall be included in the expansion of the elastic Gibbs free energy  $G_1$ :

$$\begin{aligned}
 G_1 = & a_2 D^2 + a_4 D^4 + a_{11} D D^* + a_{12} D D^{*2} + a_{13} D^2 D^{*2} + a_{14} D^2 D^* \\
 & + (b_2 D^2 + b_4 D^4) T \\
 & + (c_0 + c_2 D^2 + c_4 D^4) T^2 \\
 & + (d_0 + c_2 D^2 + c_4 D^4) T^4
 \end{aligned} \tag{3.55}$$

Since  $E$  is an odd function of  $D$ , terms such as  $D$  and  $D^3$  are excluded from  $G_1$ . In addition, since  $S$  is also an odd function of  $T$ , terms related with  $T^3$  are excluded from  $G_1$ . To increase the performance, cross terms between  $D$  and  $D^*$  up to second order are included. To scale the system so that the ill-conditioned matrix  $\mathbf{A}^T \mathbf{W} \mathbf{A}$  in Eq. 3.53 can be avoided while performing least square regression, the units of  $T$  and  $D$  in GPa and C/m<sup>2</sup> are used, respectively. The units of the resulting  $E = \partial G_1 / \partial D$  and  $S = -\partial G_1 / \partial T$  are therefore in kV/mm and kppm, respectively.

The corresponding coefficients of the energy expansion are summarized in Table 3.4. Figure 3-23 shows the rate response of the model, which captures the expansion behavior of the rate data shown in Figure 2-45. Figures 3-24, 3-25, and 3-26 show the correlation between the measured data and the simulated material response under different compression levels. As can be seen, the model well-predicts the shrinking effect of compression on the strain and polarization response. In addition, this 1-D PZT-5H model not only achieves the targeted accuracy at Stage 1 but also at Stage 2, as defined in Table 1.1.

Table 3.4: Coefficients of PZT-5H thermodynamic potential expanded in polynomial terms.

$a_2$	14.4665	$b_2$	27.4074	$c_0$	38.1430	$d_0$	$-2.8570 \times 10^3$
$a_4$	-1.5161	$b_4$	11.6303	$c_2$	-88.2369	$d_2$	$24.8750 \times 10^3$
$a_{11}$	-29.2314			$c_4$	-537.7735	$d_4$	$-351.4483 \times 10^3$
$a_{12}$	0.3759						
$a_{13}$	18.1391						
$a_{14}$	-0.1526						

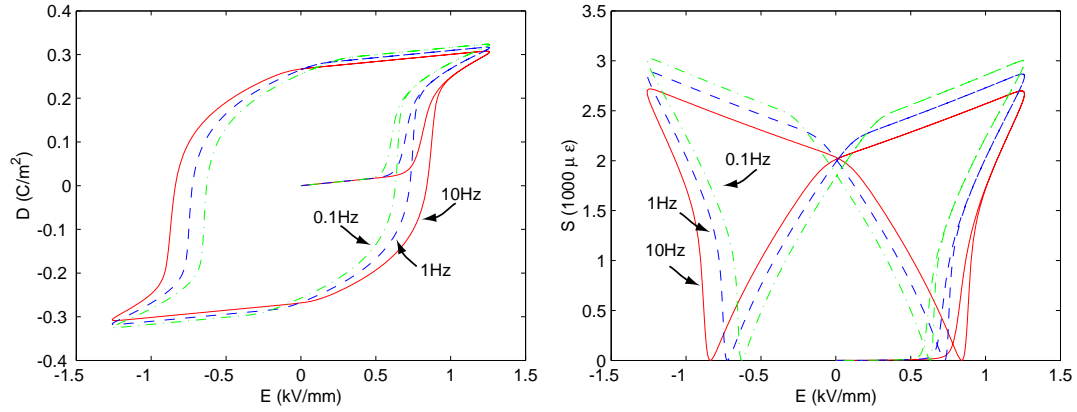


Figure 3-23: Simulated rate dependent behaviors of PZT-5H using 1-D model.

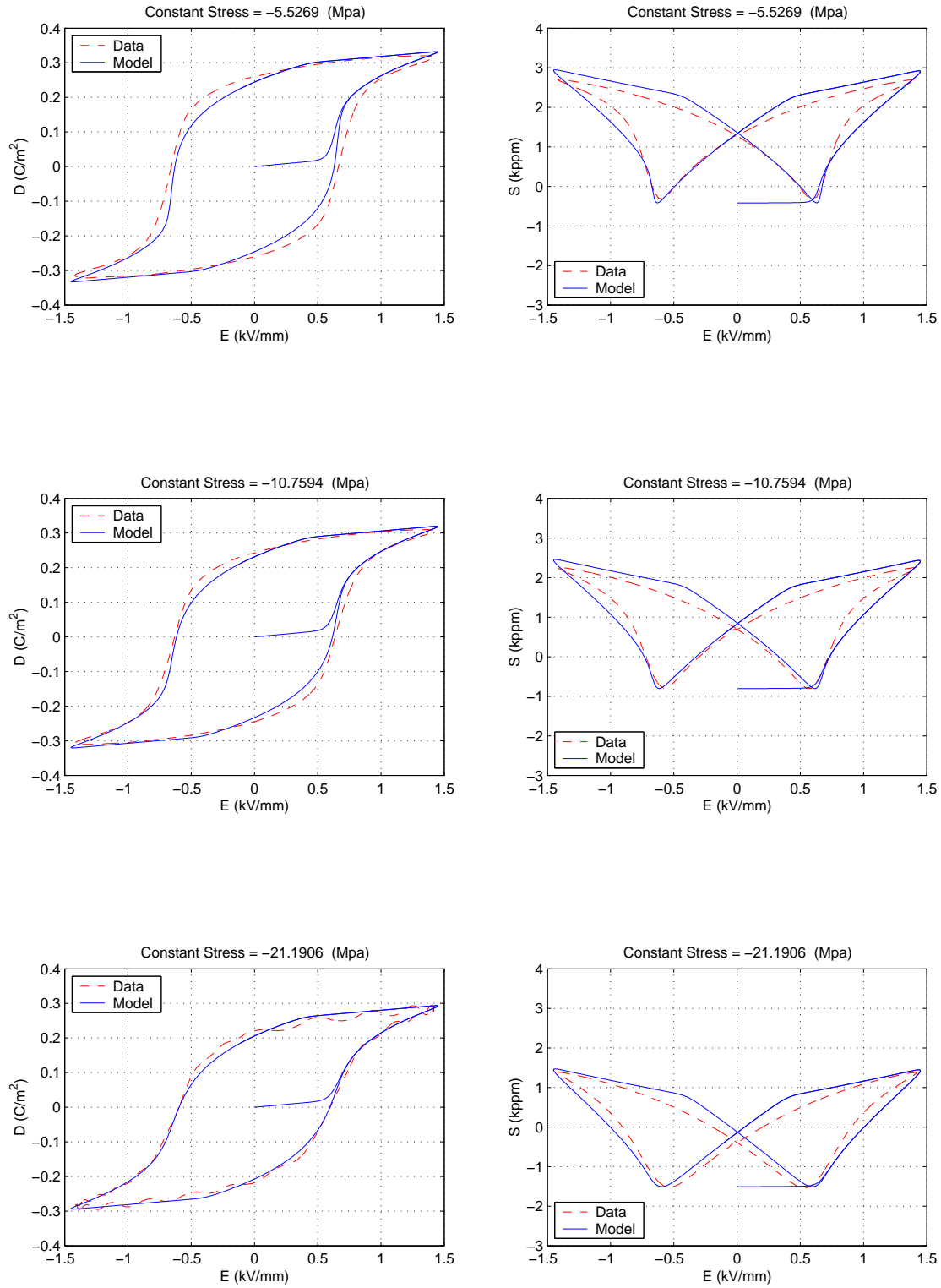


Figure 3-24: Data and simulated stress dependent behaviors of PZT-5H using 1-D model.

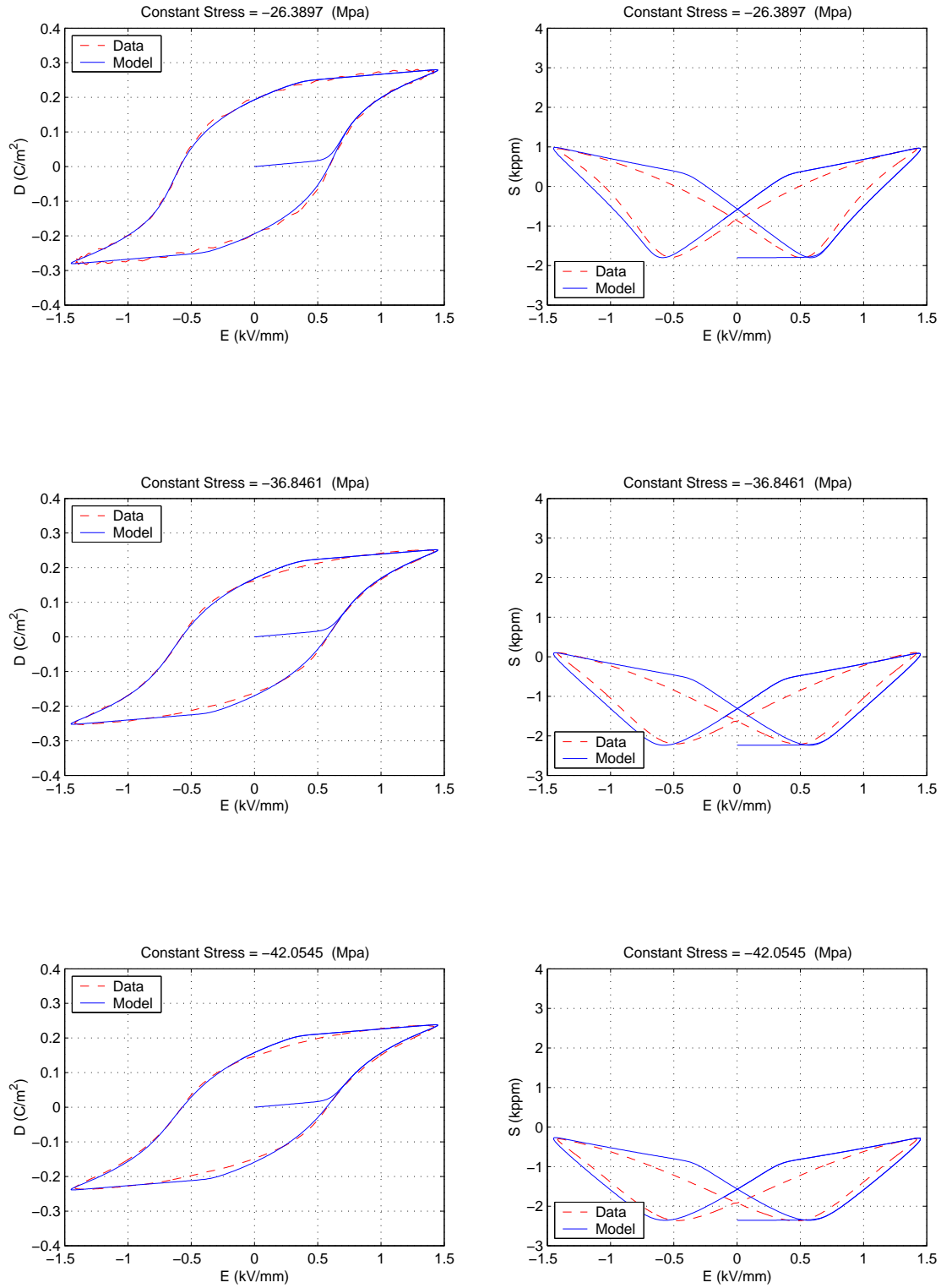


Figure 3-25: Data and simulated stress dependent behaviors of PZT-5H using 1-D model (Cont).

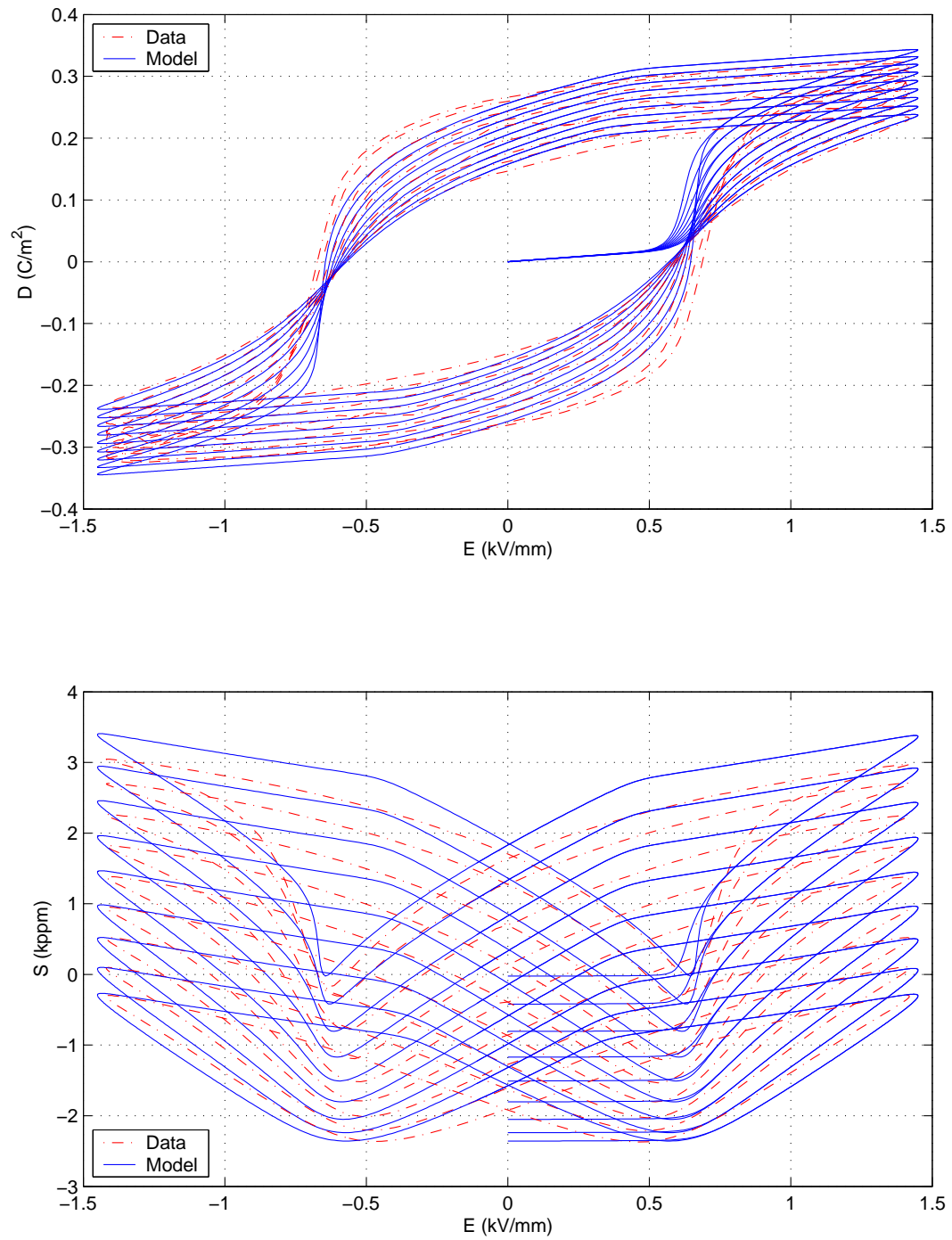


Figure 3-26: Overall data and simulated stress dependent behaviors of PZT-5H using 1-D model.

### 3.3.6 Optimized 1-D Model Parameters for PZT-5A

As described in Chapter 2, three sets of data under longitudinal test were acquired: (1) Batch A, 0–50MPa; (2) Batch B, 0–50MPa; (3) Batch B, 0–100MPa. Batch A exhibits an abnormal coercive field and therefore is not considered a good batch. In spite of this, it is of interest to see how well the modeling framework developed here can predict a wide range of material behaviors. Based on this motivation, the optimal material parameters defining all sets of data will be obtained using the same procedure and energy expansion for PZT-5H.

#### PZT-5A (Batch A, 0–50MPa)

As summarized in Table 3.5, the optimized coefficients for this data set can be found using  $w_i=1$  and the optimal rate parameters  $\tau=0.1$  (ms),  $\Delta D_c=0.03$  (C/m<sup>2</sup>), and  $\alpha=7$ . Figures 3-27, 3-28, and 3-29 show the correlation between the measured data and the simulated material response under different compression levels. Figure 3-30 shows the rate response of the model, which captures the expansion behavior of the rate data shown in 2-46. In addition, this 1-D PZT-5A model not only achieves the targeted accuracy at Stage 1 but also at Stage 2, as defined in Table 1.1.

Table 3.5: Coefficients of thermodynamic potential expanded by polynomial terms PZT-5A, Batch A.

$a_2$	8.5107	$b_2$	20.8161	$c_0$	44.7726	$d_0$	$-3.7552 \times 10^3$
$a_4$	-2.5740	$b_4$	-26.2853	$c_2$	7.5421	$d_2$	$32.0817 \times 10^3$
$a_{11}$	-17.3906			$c_4$	-74.7835	$d_4$	$-74.0138 \times 10^3$
$a_{12}$	-1.9810						
$a_{13}$	12.1964						
$a_{14}$	0.9194						

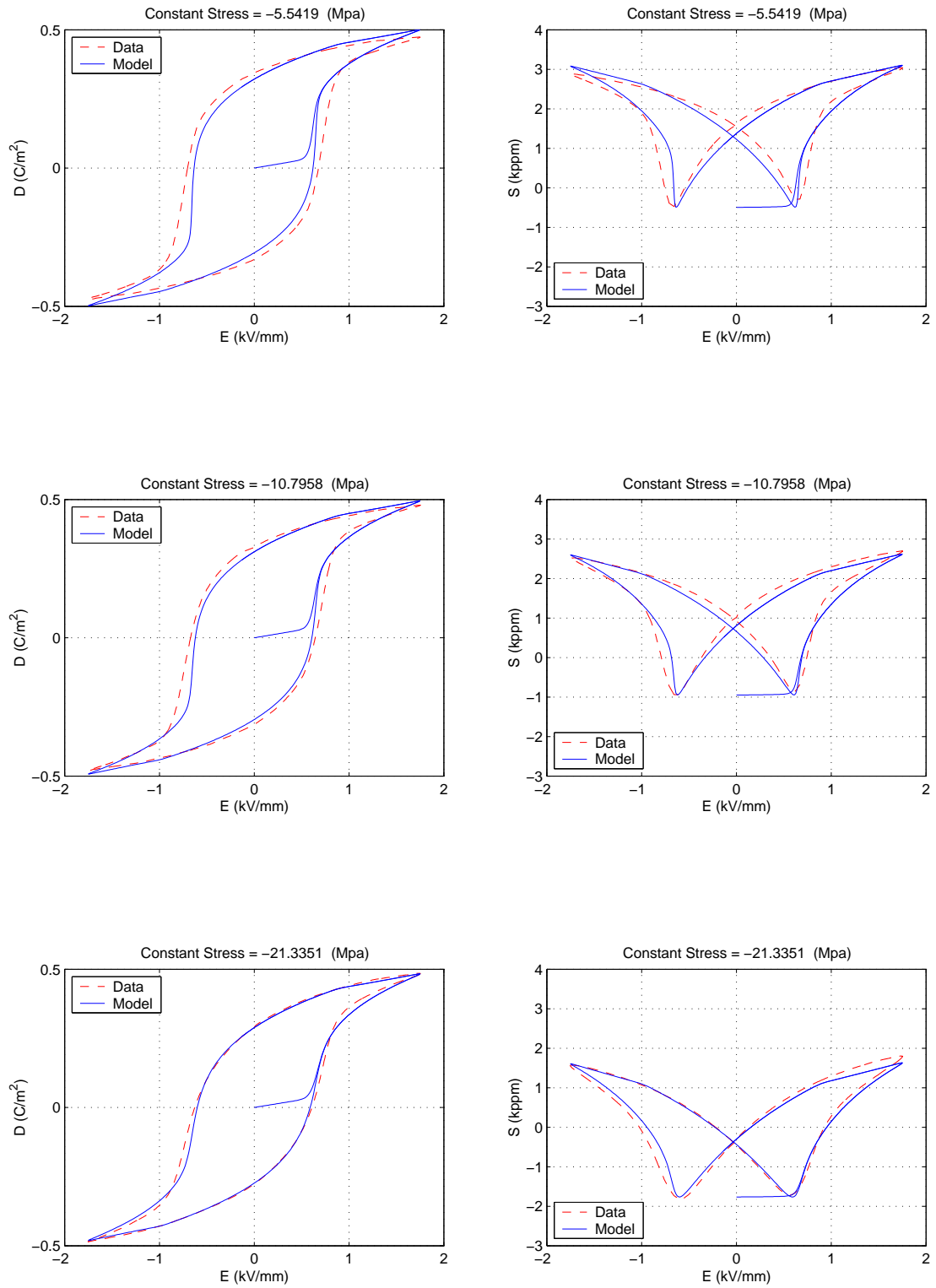


Figure 3-27: Data and simulated stress dependent behaviors of PZT-5A, Batch A, using 1-D model.

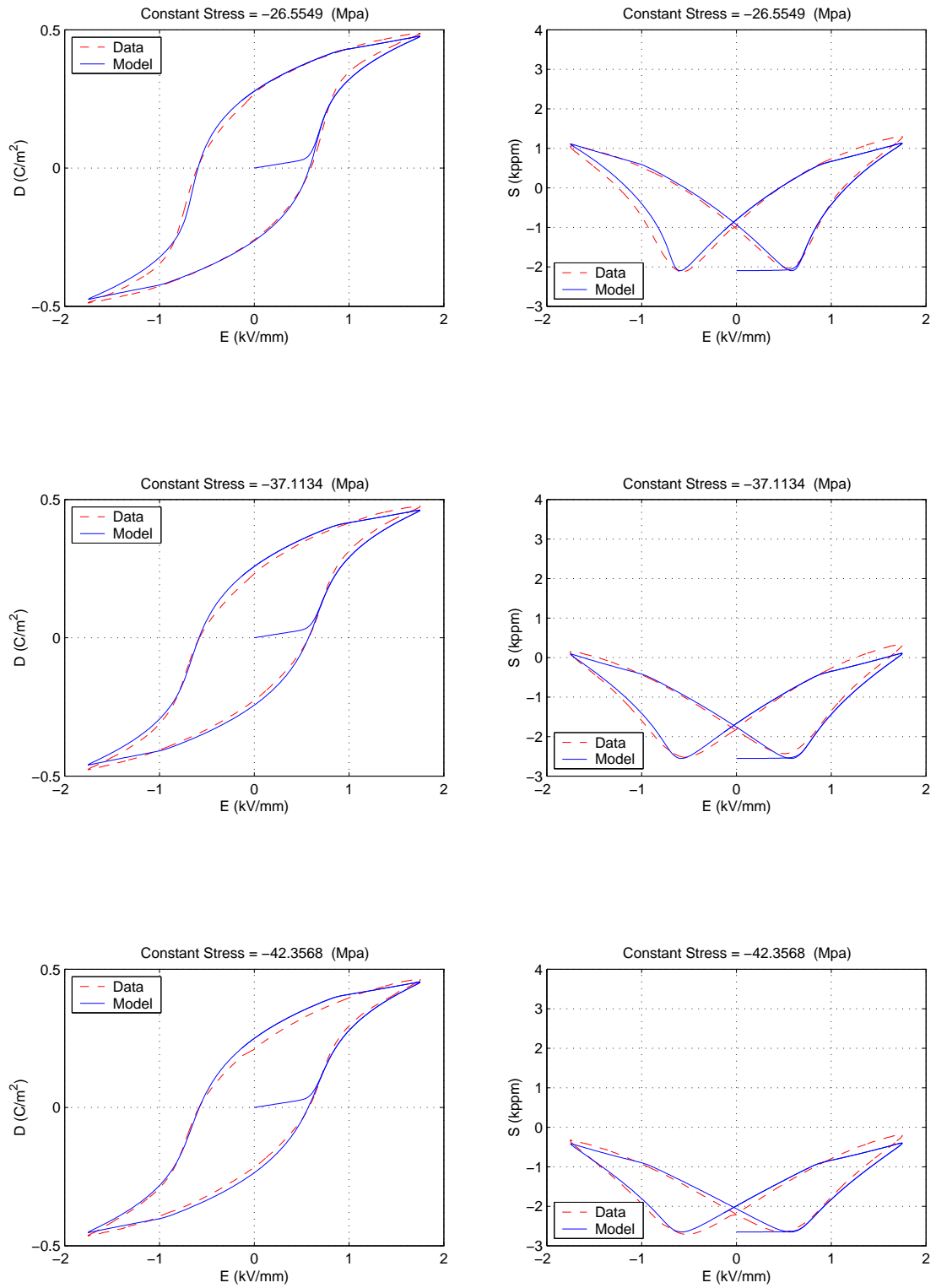


Figure 3-28: Data and simulated stress dependent behaviors of PZT-5A, Batch A, using 1-D model(Cont).



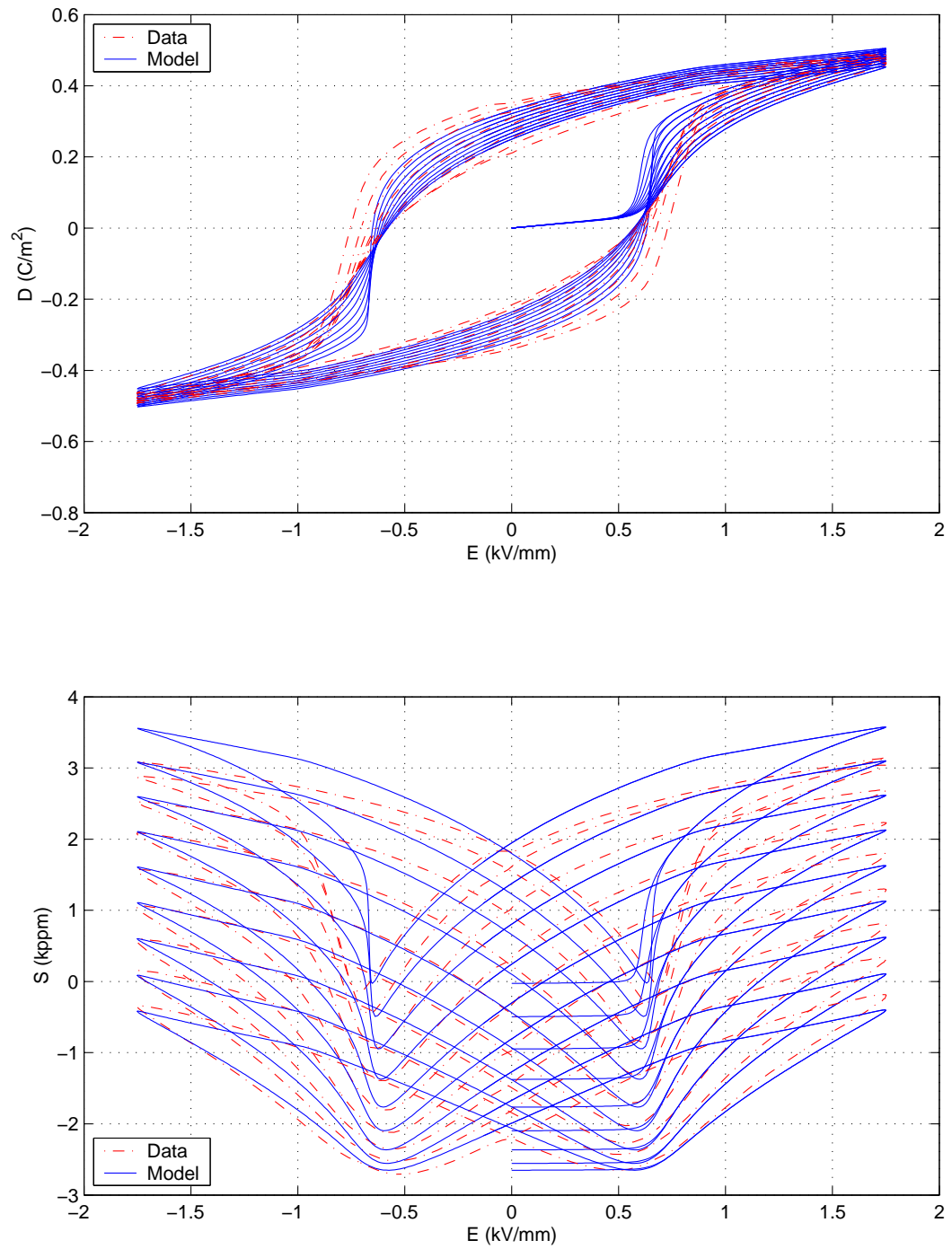


Figure 3-29: Overall data and simulated stress dependent behaviors of PZT-5A, Batch A, using 1-D model.

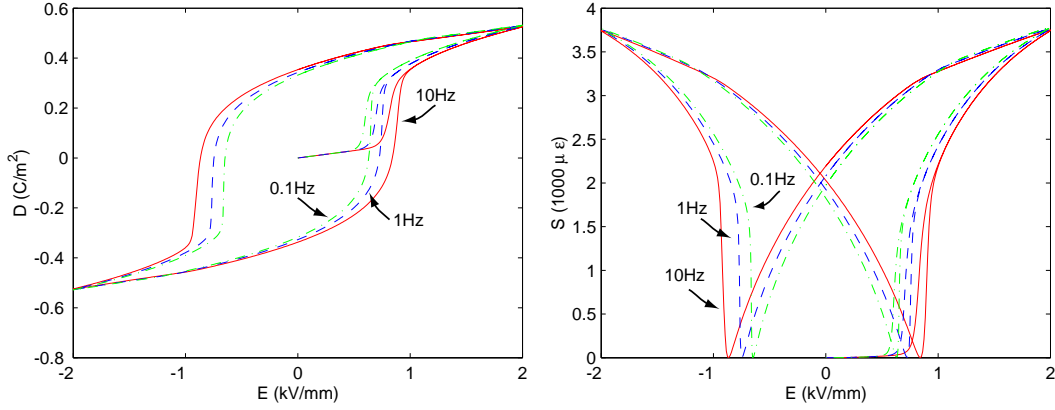


Figure 3-30: Simulated rate dependent behaviors of PZT-5A, Batch A, using 1-D model.

#### PZT-5A (Batch B, 0–50MPa)

Similarly, using  $w_i=1$  and the optimal rate parameters  $\tau=0.1$  (ms),  $\Delta D_c=0.01$  (C/m<sup>2</sup>), and  $\alpha=7$ , the optimized coefficients for this data set can be found as summarized in Table 3.6. Figure 3-31 shows the rate response of the model, which captures the expansion behavior of the rate data shown in 2-46. Figures 3-32, 3-33, and 3-34 show the correlation between the measured data and the simulated material response under different compression levels. In addition, this 1-D PZT-5A model not only achieves the targeted accuracy at Stage 1 but also at Stage 2, as defined in Table 1.1.

Table 3.6: Coefficients of thermodynamic potential expanded in polynomial terms for PZT-5A, Batch B, 0–50MPa

$a_2$	86.0048	$b_2$	33.7068	$c_0$	33.5042	$d_0$	57.0187
$a_4$	-29.4160	$b_4$	-33.2464	$c_2$	52.9584	$d_2$	$-2.1257 \times 10^4$
$a_{11}$	-171.7265			$c_4$	$-1.2124 \times 10^3$	$d_4$	$-2.9374 \times 10^4$
$a_{12}$	9.9571						
$a_{13}$	66.3547						
$a_{14}$	-4.8116						

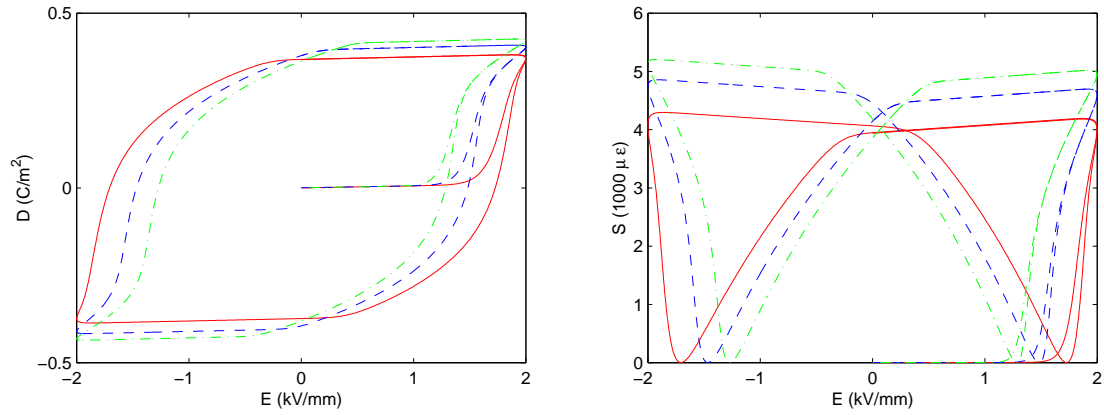


Figure 3-31: Simulated rate dependent behaviors of PZT-5A, Batch B, 0–50MPa, using 1-D model.

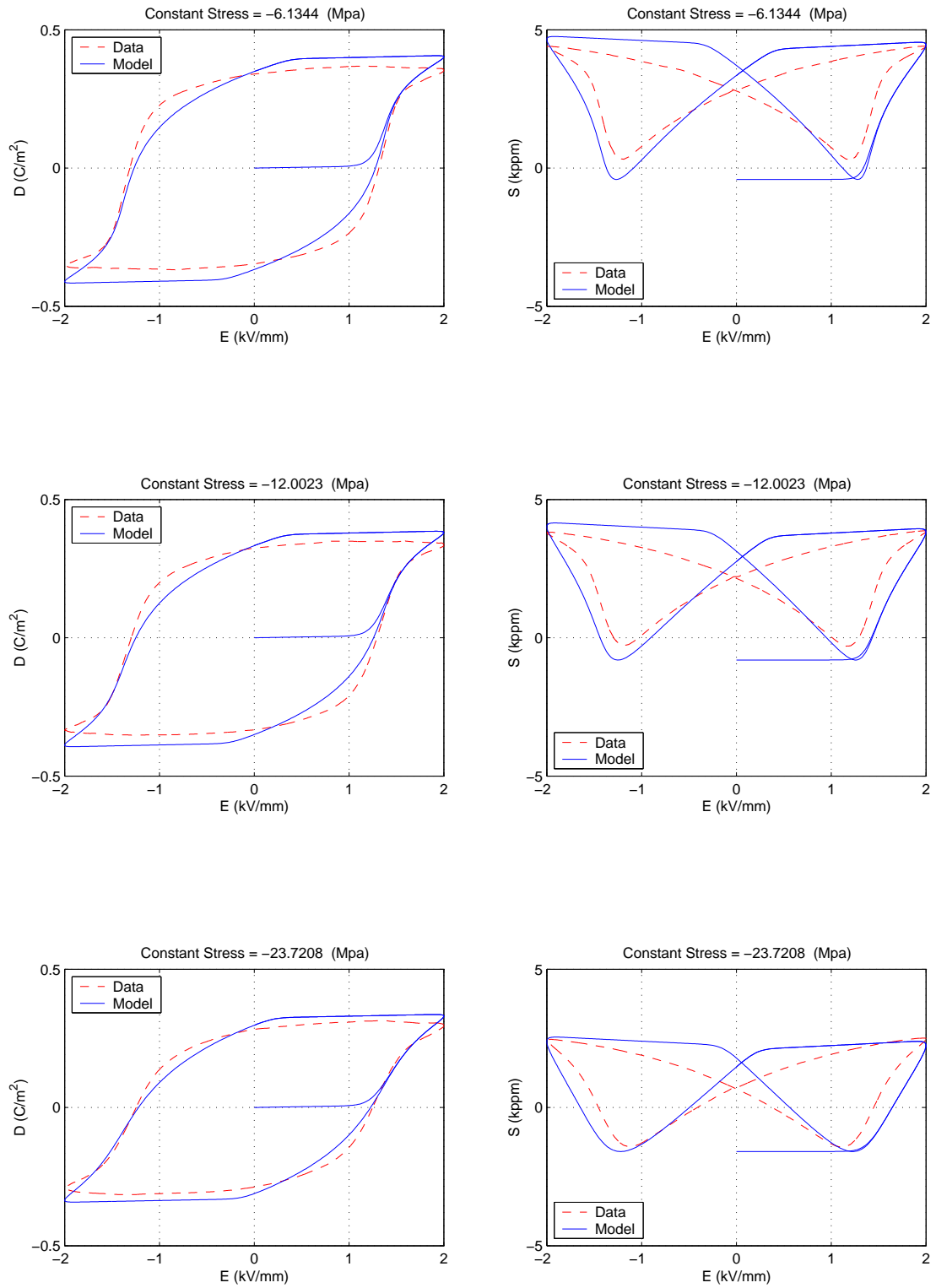


Figure 3-32: Data and simulated stress dependent behaviors of PZT-5A, Batch B, 0–50MPa, using 1-D model.

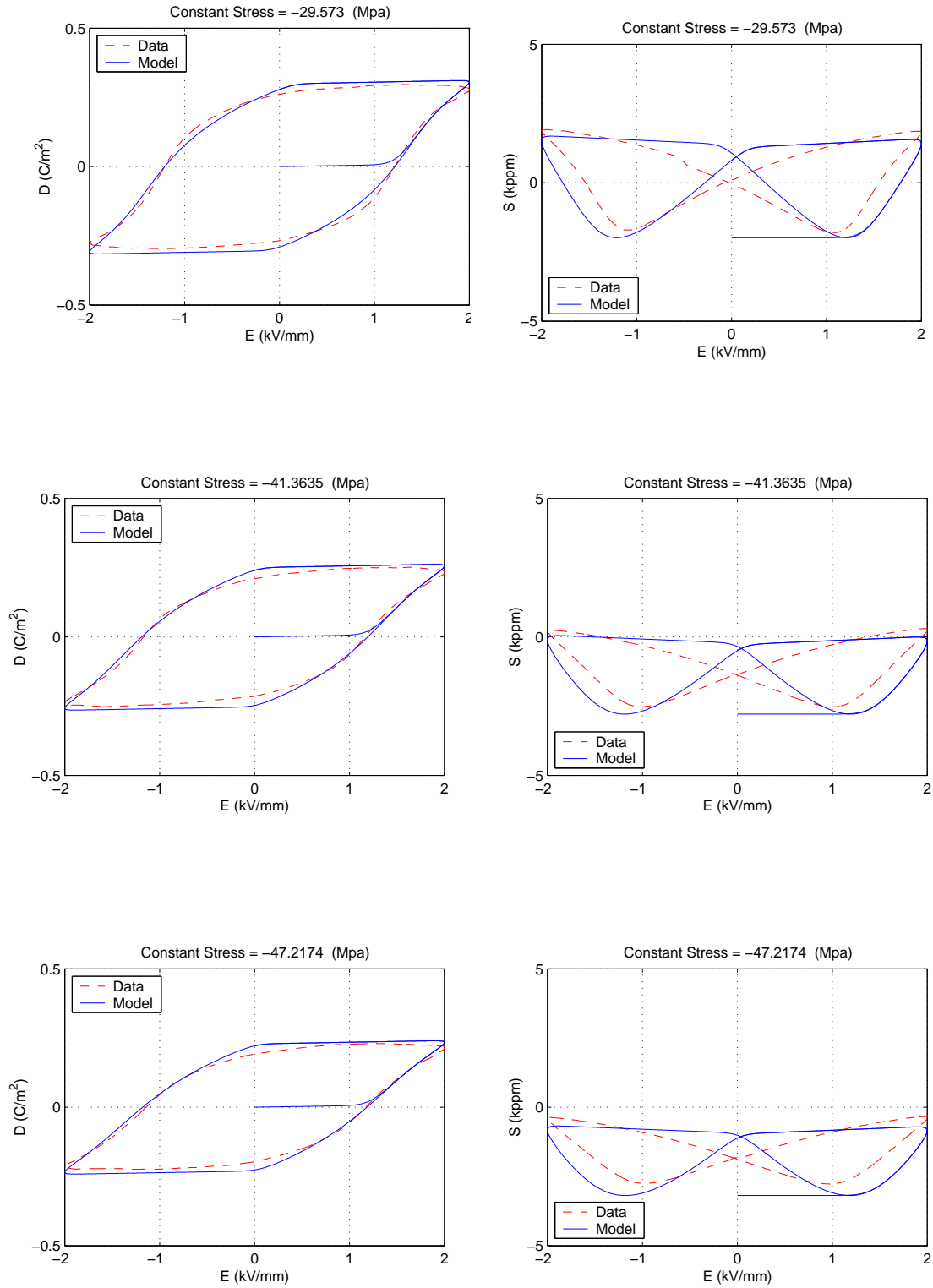


Figure 3-33: Data and simulated stress dependent behaviors of PZT-5A, Batch B, 0–50MPa, using 1-D model (Cont).

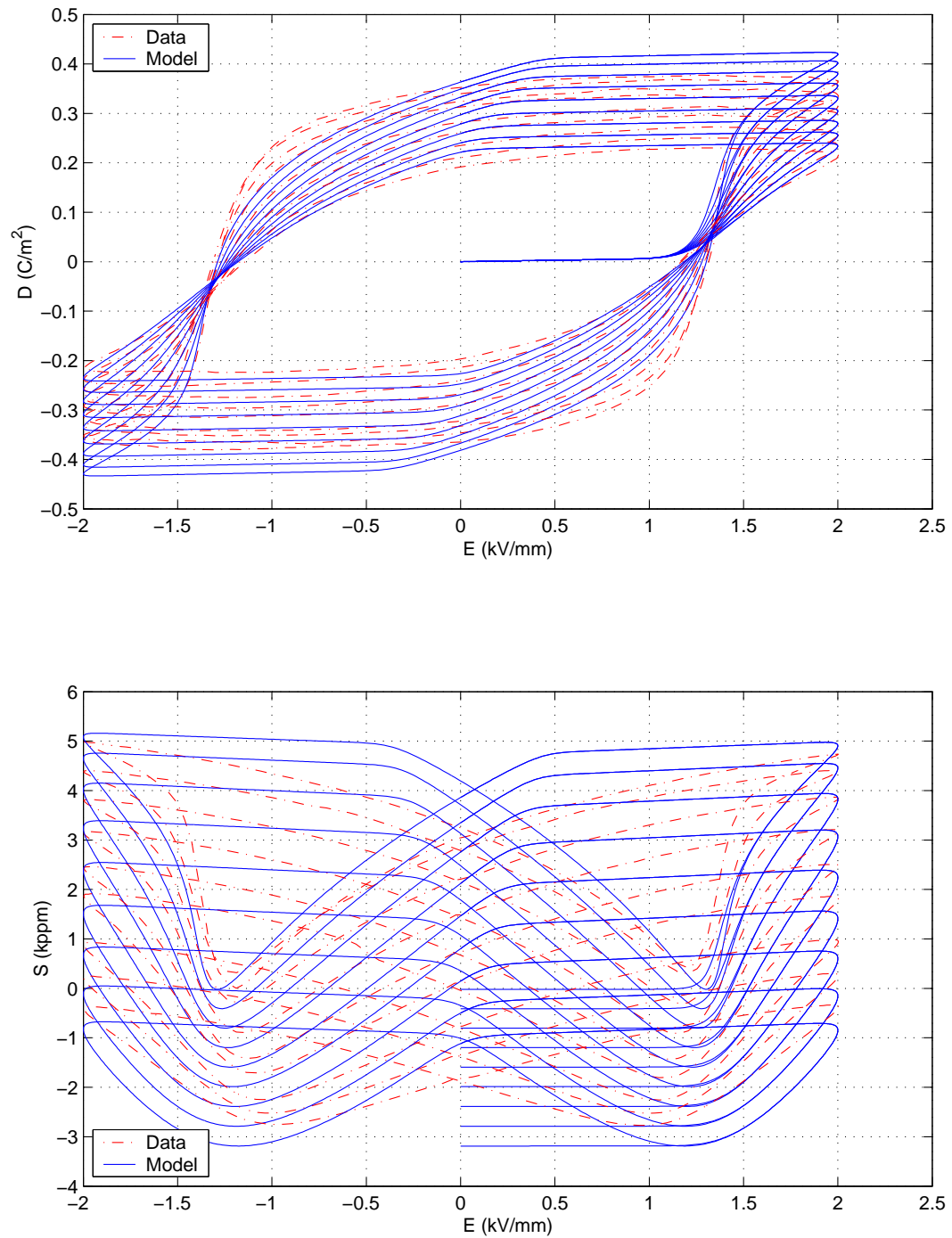


Figure 3-34: Overall data and simulated stress dependent behaviors of PZT-5A, Batch B, 0–50MPa, using 1-D model.

### PZT-5A (Batch B, 0–100MPa)

Similarly, using  $w_i=1$  and the optimal rate parameters  $\tau=0.1$  (ms),  $\Delta D_c=0.01$  (C/m<sup>2</sup>), and  $\alpha=7$ , the optimized coefficients for this data set can be found as summarized in Table 3.7. Figure 3-35 shows the rate response of the model, which captures the expansion behavior of the rate data shown in 2-46. Figures 3-36, 3-37, and 3-38 show the correlation between the measured data and the simulated material response under different compression levels. In addition, this 1-D PZT-5A model not only achieves the targeted accuracy at Stage 1 but also at Stage 2, as defined in Table 1.1.

Table 3.7: Coefficients of thermodynamic potential expanded in polynomial terms for PZT-5A, Batch B, 0–100MPa

$a_2$	72.2932	$b_2$	16.4705	$c_0$	37.9313	$d_0$	-764.8502
$a_4$	-26.6186	$b_4$	56.4527	$c_2$	-169.0589	$d_2$	$1.7444 \times 10^3$
$a_{11}$	-143.1599			$c_4$	377.5831	$d_4$	$-4.2211 \times 10^4$
$a_{12}$	-7.4087						
$a_{13}$	55.6369						
$a_{14}$	3.6222						

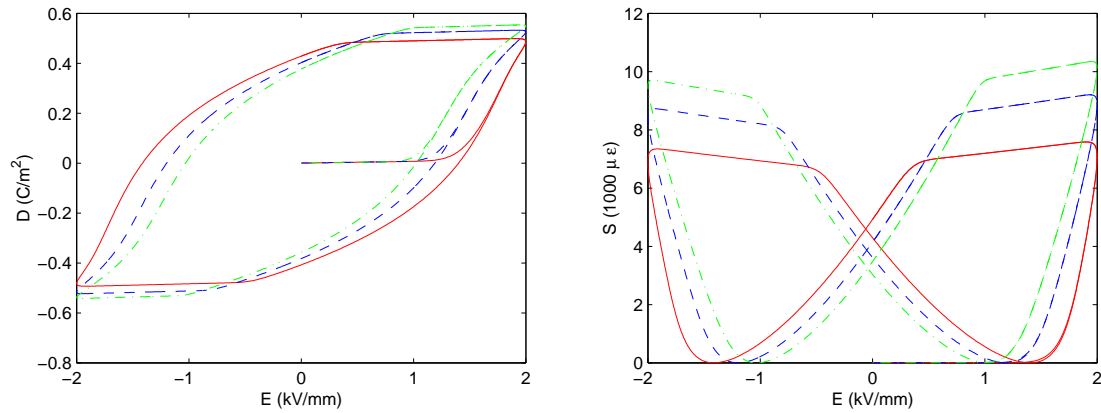


Figure 3-35: Simulated rate dependent behaviors of PZT-5A, Batch B, 0–100MPa, using 1-D model.

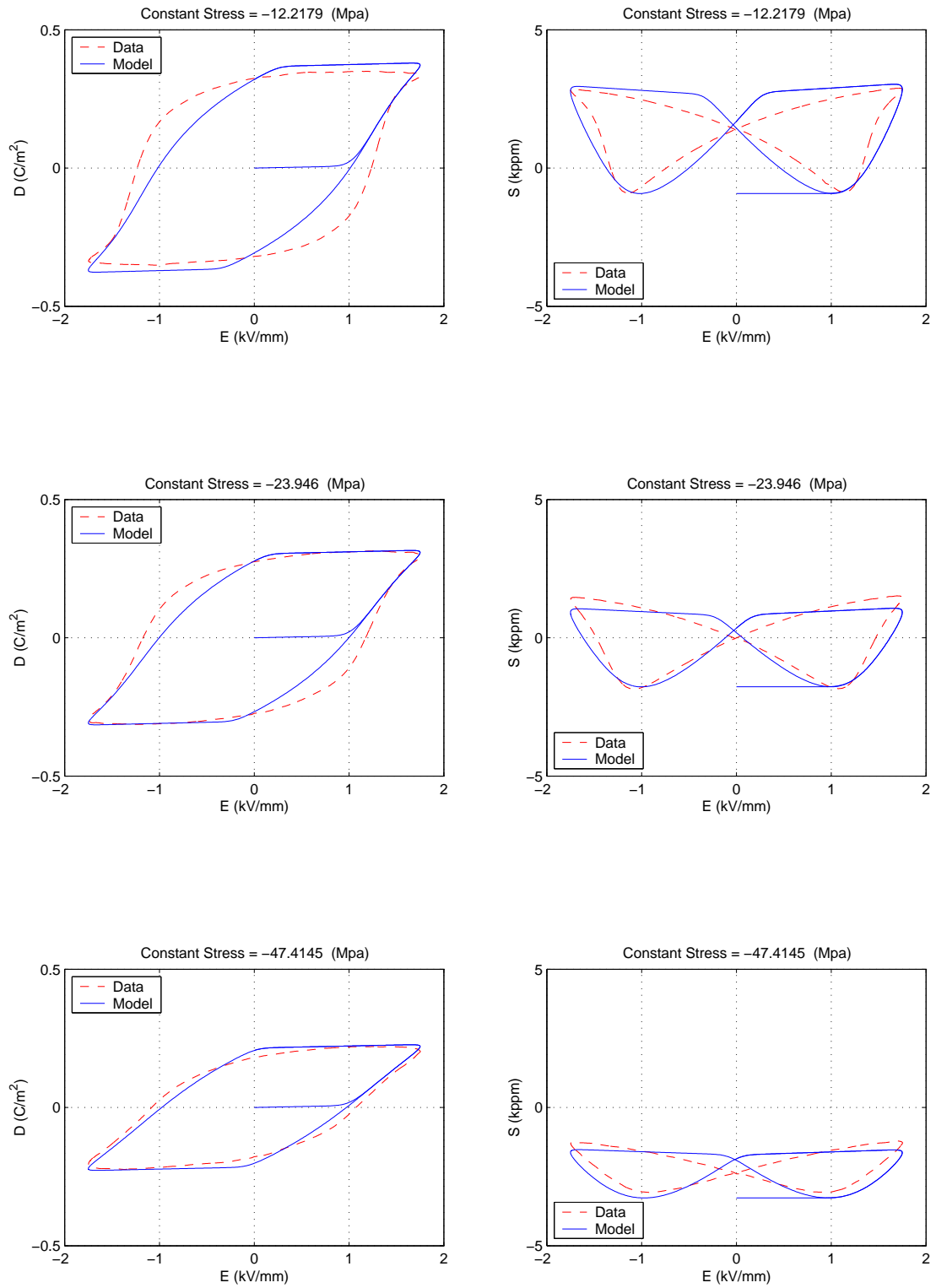


Figure 3-36: Data and simulated stress dependent behaviors of PZT-5A, Batch B, 0–100MPa, using 1-D model.



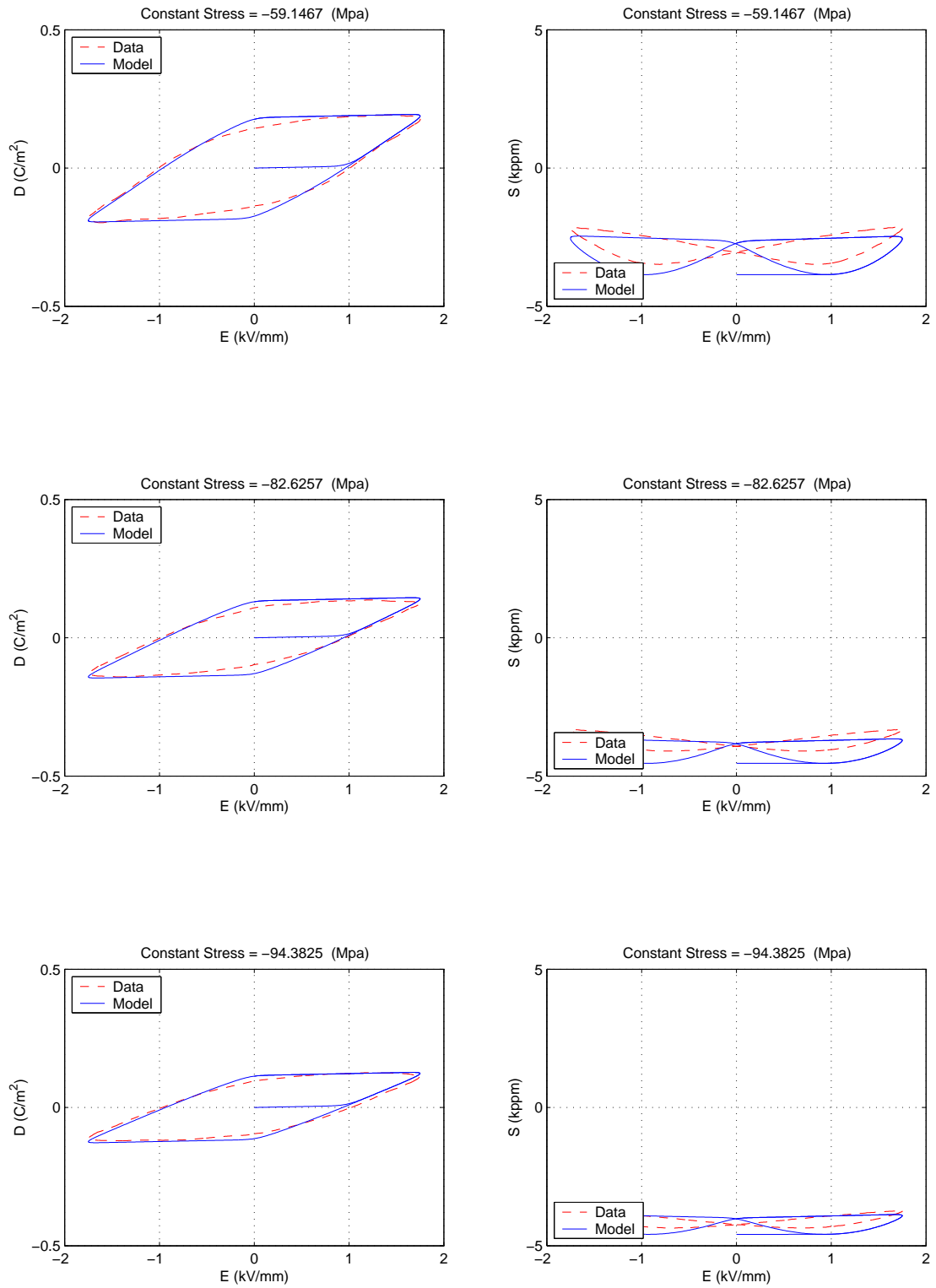


Figure 3-37: Data and simulated stress dependent behaviors of PZT-5A, Batch B, 0–100MPa, using 1-D model (Cont).

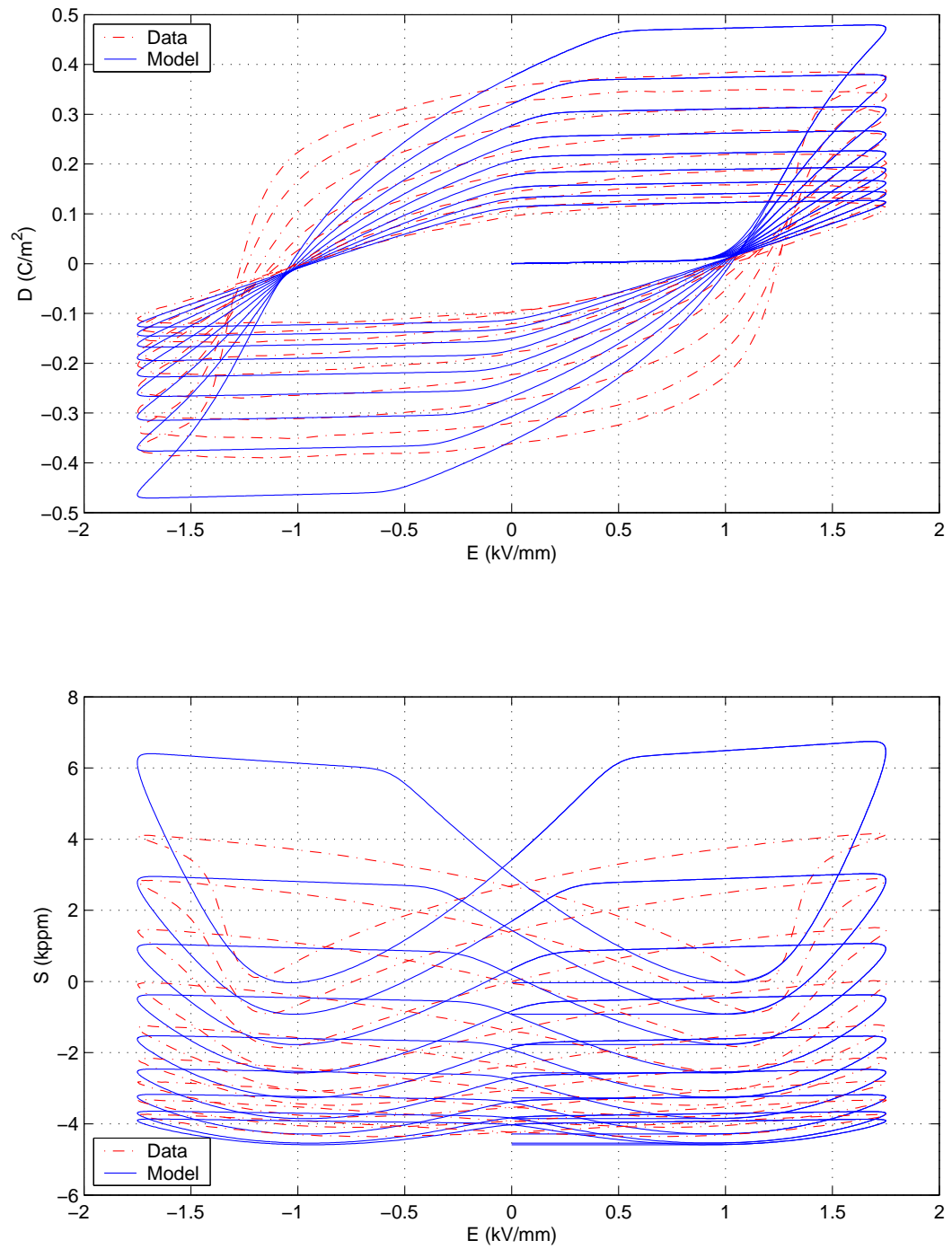


Figure 3-38: Overall data and simulated stress dependent behaviors of PZT-5A, Batch B, 0–100MPa, using 1-D model.

### 3.3.7 Discrepancy of Domain Switching Process between PZT-5A and PZT-5H

Compared to the models of PZT-5H and Batch A of PZT-5A, the model for Batch B of PZT-5A shows worse correlation with the data. This can be explained by the special relationship between strain (S) and electric displacement (D) of PZT-5A<sup>2</sup>. If S is plotted versus D, an important discrepancy between PZT-5H and PZT-5A can be found, as shown in Figure 3-39. The S-D relationship of PZT-5A shows more hysteretic behavior than that of PZT-5H, while a simple non-hysteretic parabolic function can be used to approximate the S-D curve of PZT-5H. Similar phenomena have also been reported by Zhou *et al.* [65], except that the discrepancy was found for a single material at different frequencies. He also proposed a 90°/180° domain switching hypothesis to explain this phenomenon. The hysteresis of the S-D curve is due to two successive 90° domain switching processes, instead of an instantaneous 180° process.

It is well known that PZT ceramics in the tetragonal phase state have two kinds of domain structures: 180° domains and 90° domains. Strong electric fields (higher than  $E_c$ ) induce switching of the 180° domains and the reorientation of 90° domains (ferroelectric switching).<sup>3</sup> 180° domain reversal does not contribute to the induced strain, only 90° rotation does, whereas the 180° domain reversal contributes mainly to the polarization[66][65].

The domain switching process of PZT-5A is illustrated in Figure 3-40(c). Most of the domains undergo a 90° switching from points A and a to B for the first time due to the increasing electric field (still less than  $E_c$ ), but there are still some domains remaining at the previous poling direction. Hence, the polarization is still negative and the strain reaches its minimum value at point B, but it may not be zero. From point B to b, part of the domains experiences a second 90° reorientation. Domains with an opposite poling direction make the net polarization zero, but the strain has already started to increase. At point b, most of the domains undergo a 90° switch for the second time. From points b to C and c, both 90° and 180° switching processes may happen, since the electric field is larger than  $E_c$ . At points C and c, nearly all the domains have been aligned to the direction of a positive electric field. Hence, both polarization and strain are saturated. The domain switching

---

<sup>2</sup>For convenience, Batch B of PZT-5A will represent PZT-5A in the rest of the discussion, unless it is specified.

<sup>3</sup>90° domain reorientation can also be induced by stress (ferroelastic switching).

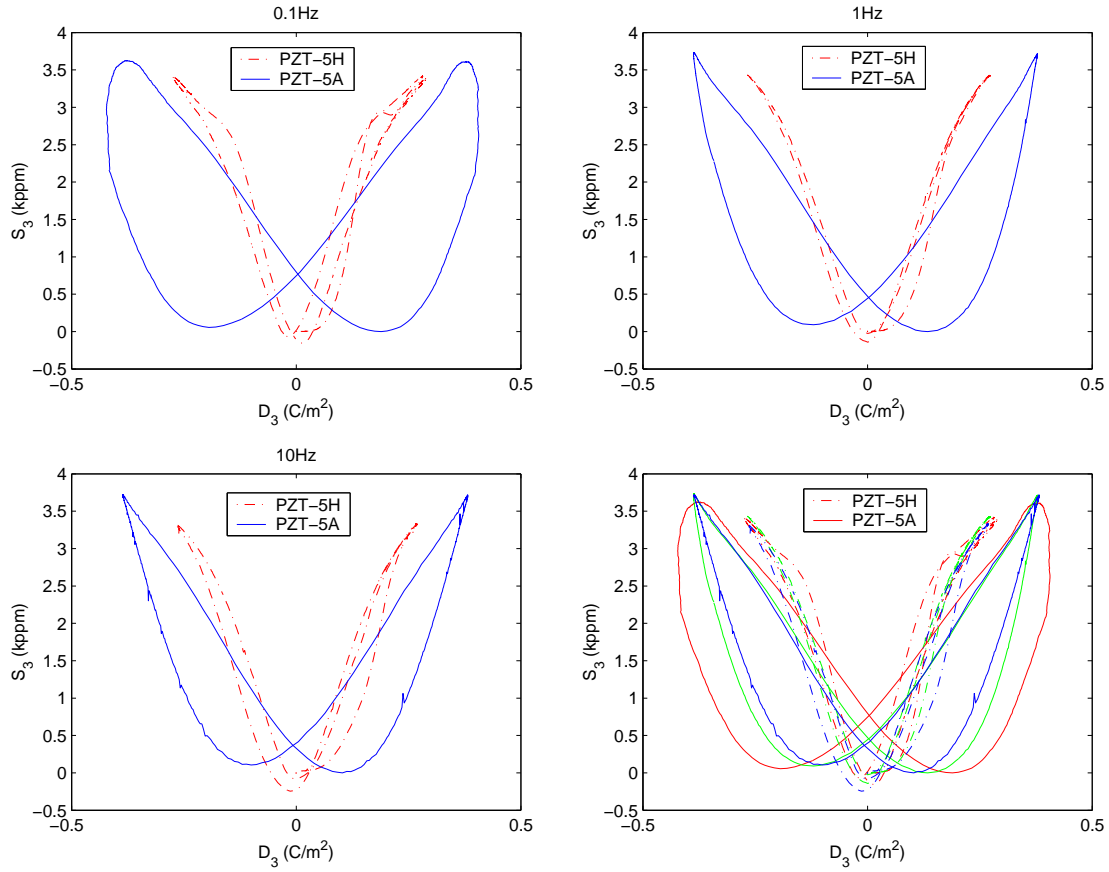


Figure 3-39: Comparison between S-D curves of PZT-5H and PZT-5A. Right lower plot shows all data.

process of the following sequence of D, d-E-e-F, f-G, g is nearly the same, just that the direction is opposite.

The domain switching process of PZT-5H is illustrated in Figure 3-40(f). Some domains still keep their negative polarization direction from points A and a to points B and b. In the meantime, unlike PZT-5A, a small number of PZT-5H domains have completed their  $180^\circ$  reversals and changed their polarization to the positive direction. This is because PZT-5H is considered “softer” than PZT-5A and therefore both  $90^\circ$  and  $180^\circ$  switching processes may occur even though the electric field is smaller than  $E_c$ . Since the number of domains with opposite polarization is the same, the net polarization of the specimen is zero. From points b to C and c, PZT-5H domains undergo the same switching process as PZT-5A domains do.

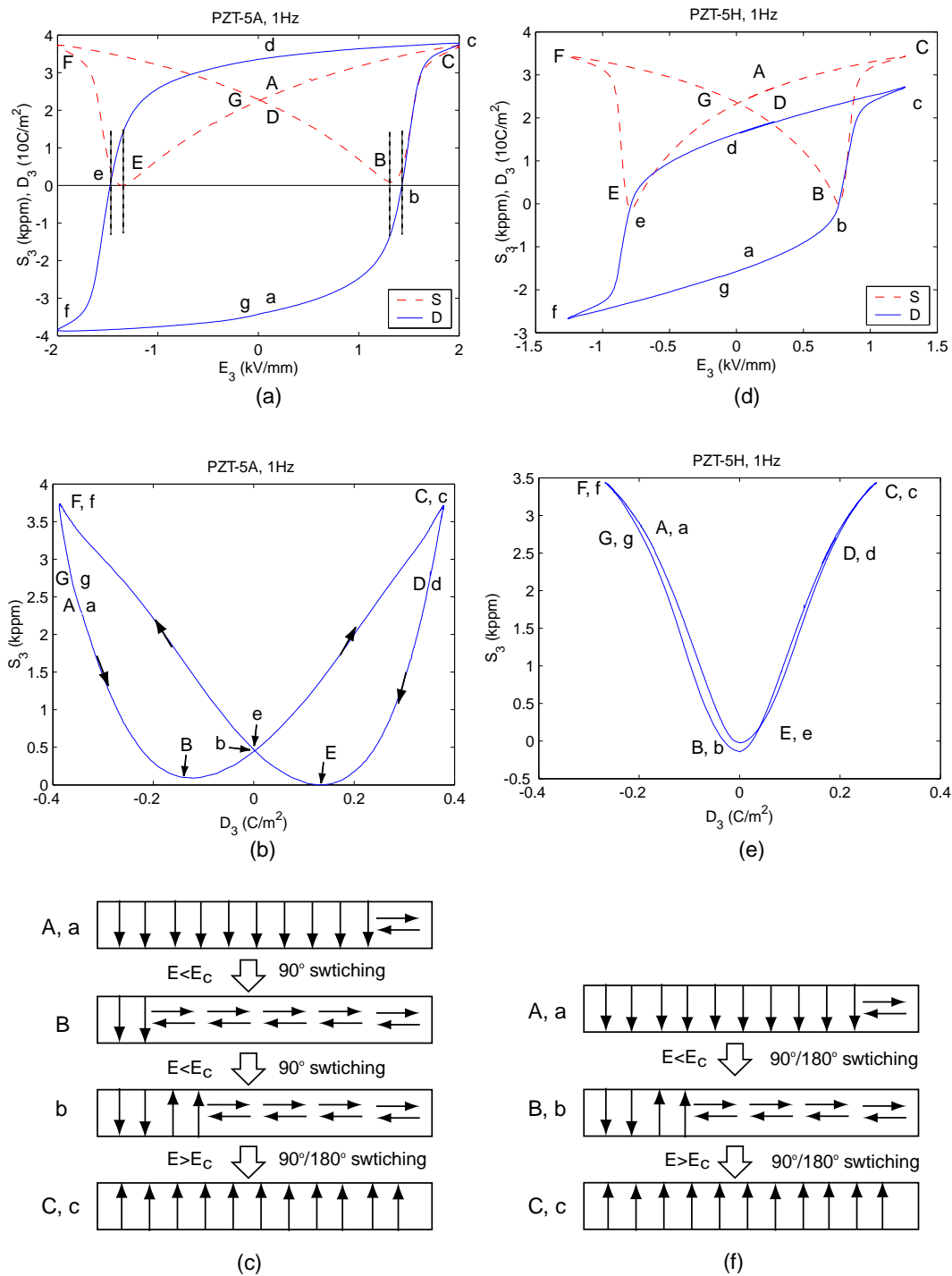


Figure 3-40: Discrepancy of domain switching between PZT-5A((a),(b),(c)) and PZT-5H((d),(e),(f)).

The key discrepancy between PZT-5A and PZT-5H is that PZT-5A requires two successive  $90^\circ$  reorientations to fulfill a domain reversal, which can be accomplished by an instantaneous  $180^\circ$  reversal for a softer material, such as PZT-5H. For hard material(PZT-5A), this is because only  $90^\circ$  reorientation is allowed when electric field is smaller than  $E_c$ . In contrast, both  $90^\circ$  and  $180^\circ$  switching processes may occur for soft material (PZT-5H) even though electric field is smaller than  $E_c$ . In addition, experimental results reported by Tsurumi *et al.*[68] also indicated that the velocity of the  $90^\circ$  domain wall motion was relatively low. As a result, the hysteresis of PZT-5A S-D curve is due to this slower  $90^\circ$  domain wall motion.

According to the findings by Zhou *et al.*[65], significant hysteresis was observed in the S-D curves at low frequencies, while simple parabolic S-D curves were observed at high frequencies. This is because there is enough time for the two-step  $90^\circ$  domain switching to take place at low frequencies. Although this phenomenon is not detected in each data of PZT-5A and PZT-5H in this work, as shown in Figure 3-39, similar observation can be found in the rate data of PZT-5A: the S-D curves at low frequency (0.1Hz or 1Hz) show more hysteretic behavior than that at high frequency (10Hz).

In summary, in order to improve the material model for PZT-5A, the hysteresis observed in the S-D curve must be included in the model. Although it may not be difficult to describe this hysteresis by a differential equation or a new internal variable, making the model thermodynamically consistent is the key obstacle. As a result, this modification will be left as a recommendation for future work.

## 3.4 Development of a 3-D Rate and Stress Dependent Piezoelectric Model

In the previous section, a rate dependent model of a piezoelectric material in one dimension has been developed. Although the 1-D models achieve second level accuracy, a fully 3-D model is still absent. In order to reach the second level goal, as defined in Table 1.1, the approach of the 1-D model is extended to three dimensions in this section.

### 3.4.1 Introduction to Ghandi's Tensor Invariants

It is natural to expand the energy function in three dimensions in terms of classic tensors proposed by Lines and Glass[63]:

$$A = \frac{1}{2}c_{ijkl}^D S_{ij} S_{kl} - \frac{1}{2}h_{ijkl} S_{ij} D_k D_l + \frac{1}{2}\beta_{ij}^S + \frac{1}{4}\xi_{ijkl}^S D_j D_j D_k D_l. \quad (3.56)$$

This expression depends on the choice of coordinates and is only useful for single crystal materials because this expression is dependent on the choice of the coordinate system. However, piezoelectric ceramics have no preferred orientation because they are composed of various domains with arbitrary orientations. Consequently, the internal energy expression for ceramics shall be invariant with respect to rotations. To do so, Ghandi proposed an expression of free energy in terms of invariant inner products of the internal variables in the expansion. For example, consider the term  $c_{ijkl}^D S_{ij} S_{kl}$  in Eq. 3.56. The tensor contains 81 elements which may be reduced to two independent quantities for an isotropic material. This term can be replaced by two terms with scalar coefficients:

$$c_{ijkl} S_{ij} S_{kl} \Rightarrow a S_{ii} S_{jj} + b S_{ij} S_{ji}. \quad (3.57)$$

Thus, the invariant form of Eq. 3.56 may be written as

$$U = a S_{ii} S_{jj} + b S_{ij} S_{ji} + c S_{ii} D_j D_j + d S_{ij} D_i D_j + e D_i D_i + f D_i D_i D_j D_j. \quad (3.58)$$

### Transversely Isotropic Tensor Invariants

Since a poled piezoelectric material is transversely isotropic, a unit vector along the direction of polarization of the material  $a_i$  is used in addition to the strain  $S_{ij}$  and the electric displacement  $D_i$  in the expansion of the energy function. It is essential to specify an

expression for the energy in terms of  $S_{ij}$  and  $D_i$  which satisfies rotational symmetry about the polarization axis  $a_i$ . From an integrity basis for the isotropic functions by Zhang[64] and using the fact that any complete representation for isotropic functions of  $S_{ij}$ ,  $D_i$ , and  $a_i$  may be regarded as a complete representation for a function of  $S_{ij}$  and  $D_i$  under the symmetry group characterized by rotation about  $a_i$ , Ghandi summarized a complete set of the corresponding tensor invariants :

$$\begin{aligned}
& S_{ii}, & S_{ij}S_{ji}, & S_{ij}S_{jk}S_{ki}, \\
& D_iD_i, & S_{ij}D_iD_j, & S_{ij}S_{jk}D_iD_k, \\
& a_ia_i, & D_{ij}a_ia_j, & S_{ij}S_{jk}a_ia_k, \\
& a_iD_i, & (S_{ij} + S_{ji})a_iD_j, & (S_{ij}S_{jk} + S_{kj}S_{ji})a_iD_k.
\end{aligned} \tag{3.59}$$

Ghandi also presented these invariants in terms of  $T_{ij}$  and  $D_i$ :

$$\begin{aligned}
& I_1 = a_ia_i, & I_2 = a_iD_i, & I_3 = D_iD_i, \\
J_0 = T_{ii}, & J_1 = T_{ij}a_ia_j, & J_2 = T_{ij}(a_iD_j + a_jD_i), & J_3 = T_{ij}D_iD_j, \\
K_0 = T_{ij}T_{ji}, & K_1 = T_{ik}T_{kj}a_ia_j, & K_2 = T_{ik}T_{kj}(a_iD_j + a_jD_i), & K_3 = T_{ik}T_{kj}D_iD_j, \\
L_1 = T_{ij}T_{jk}T_{ki}.
\end{aligned} \tag{3.60}$$

Using these tensor invariants, Ghandi suggested that a Taylor series expansion of the energy may be presented as:

$$\begin{aligned}
G_1 &= f + f_0J_0 + f_1J_1 + f_3J_3 + f_{00}J_0J_0 + f_{01}J_0J_1 + f_{02}J_0J_2 + f_{03}J_0J_3 \\
&+ f_{11}J_1J_1 + f_{12}J_1J_2 + f_{13}J_1J_3 + f_{22}J_2J_2 + f_{23}J_2J_3 + f_{33}J_3J_3 \\
&+ g_0K_0 + g_1K_1 + g_2K_2 + g_3K_3 + \dots,
\end{aligned} \tag{3.61}$$

where each  $f$  and  $g$  is a function of the electric invariants ( $I_1, I_2, I_3$ ) to an arbitrary order. Selection of the terms to be included is determined by the availability of experimental data when conducting the least squares regression for model optimization.

### Matrix Implementation of Tensor Invariants and their Derivatives

To implement the model in the finite element code, Ghandi also expressed these tensor invariants and their derivatives in matrix notation as summarized in Table 3.8 where  $T$



denotes stress in Voigt notation and  $\hat{\mathbf{T}}$  denotes stress as a  $3 \times 3$  matrix. That is:

$$\hat{\mathbf{T}} = \begin{bmatrix} T_{11} & T_{12} & T_{13} \\ T_{12} & T_{22} & T_{23} \\ T_{13} & T_{23} & T_{33} \end{bmatrix}, \quad T = \begin{bmatrix} T_{11} & T_{22} & T_{33} & T_{23} & T_{13} & T_{12} \end{bmatrix}^T. \quad (3.62)$$

An additional operator  $(\ )^\times$  was introduced by Ghani to map a  $3 \times 1$  vector into a  $3 \times 6$  matrix as follows:

$$\mathbf{v}^\times = \begin{bmatrix} v_1 & 0 & 0 & 0 & v_3 & v_2 \\ 0 & v_2 & 0 & v_3 & 0 & v_1 \\ 0 & 0 & v_3 & v_2 & v_1 & 0 \end{bmatrix}. \quad (3.63)$$

Using this operator, one can express the tensor inner product of a symmetric tensor and a vector  $(T_{ij}D_j)$  in two various notations:

$$T_{ij}D_j \quad \Leftrightarrow \quad \hat{\mathbf{T}}\mathbf{D} = \mathbf{D}^\times\mathbf{T}. \quad (3.64)$$

The first notation is useful for differentiating the invariant with respect to  $\mathbf{D}$ , while the second notation is appropriate for the derivatives with respect to  $\mathbf{T}$ .

### Relationship between $a_i$ and $D_i^*$

The invariant tensors listed in Eq. 3.60 show a complete representation for a function of  $S_{ij}$  and  $D_i$  under the symmetry group characterized by rotation about  $a_i$ . The vector  $a_i$  used to specify the direction of transverse isotropy in the energy expansion is exactly the same vector as the net remnant polarization of the ceramics,  $D_i^*$ . Hence, all occurrences of  $a_i$  in the three dimensional model shall be substituted by  $D_i^*$ .

Table 3.8: Derivatives of various invariants of symmetric tensor  $T_{ij}$  and vectors  $D_i$  and  $a_i$ , where  $\mathbf{e} = [1 \ 1 \ 1 \ 0 \ 0 \ 0]^\top$  and  $\mathbf{R} = \text{diag}([1 \ 1 \ 1 \ 2 \ 2 \ 2])$ .

	$G_1$	$G_1$	$\partial G_1 / \partial \mathbf{T}$	$\partial^2 G_1 / \partial \mathbf{T}^2$	$\partial G_1 / \partial \mathbf{D}$	$\partial^2 G_1 / \partial \mathbf{D}^2$	$\partial^2 G_1 / (\partial \mathbf{T} \partial \mathbf{D})$
$I_1$	$a_i a_i$	$\mathbf{a}^\top \mathbf{a}$	$\mathbf{0}$	$\mathbf{0}$	$\mathbf{0}$	$\mathbf{0}$	$\mathbf{0}$
$I_2$	$D_i a_i$	$\mathbf{D}^\top \mathbf{a}$	$\mathbf{0}$	$\mathbf{0}$	$\mathbf{a}$	$\mathbf{0}$	$\mathbf{0}$
$I_3$	$D_i D_i$	$\mathbf{D}^\top \mathbf{D}$	$\mathbf{0}$	$\mathbf{0}$	$2\mathbf{D}$	$2\mathbf{I}$	$\mathbf{0}$
$J_0$	$T_{ii}$	$\mathbf{T}^\top \mathbf{e}$	$\mathbf{e}$	$\mathbf{0}$	$\mathbf{0}$	$\mathbf{0}$	$\mathbf{0}$
$K_0$	$T_{ij} T_{ji}$	$\mathbf{T}^\top \mathbf{R} \mathbf{T}$	$2\mathbf{R} \mathbf{T}$	$2\mathbf{R}$	$\mathbf{0}$	$\mathbf{0}$	$\mathbf{0}$
$J_1$	$T_{ij} a_i a_j$	$\mathbf{a}^\top \hat{\mathbf{T}} \mathbf{a}$	$\mathbf{a}^{\times \top} \mathbf{a}$	$\mathbf{0}$	$\mathbf{0}$	$\mathbf{0}$	$\mathbf{0}$
$J_2$	$T_{ij}(D_i a_j + a_i D_j)$	$\mathbf{a}^\top \hat{\mathbf{T}} \mathbf{D} + \mathbf{a}^\top \hat{\mathbf{T}} \mathbf{a}$	$\mathbf{a}^{\times \top} \mathbf{D} + \mathbf{D}^{\times \top} \mathbf{a}$	$\mathbf{0}$	$2\hat{\mathbf{T}} \mathbf{a}$	$\mathbf{0}$	$2\mathbf{a}^{\times}$
$J_3$	$T_{ij} D_i D_j$	$\mathbf{D}^\top \hat{\mathbf{T}} \mathbf{D}$	$\mathbf{D}^{\times \top} \mathbf{D}$	$\mathbf{0}$	$2\hat{\mathbf{T}} \mathbf{D}$	$2\hat{\mathbf{T}}$	$2\mathbf{a}^{\times}$
$K_1$	$T_{ik} T_{kj} a_i a_j$	$\mathbf{a}^\top \hat{\mathbf{T}}^2 \mathbf{a}$	$2\mathbf{a}^{\times \top} \mathbf{a}^{\times \top} \mathbf{T}$	$2\mathbf{a}^{\times \top} \mathbf{a}^{\times}$	$\mathbf{0}$	$\mathbf{0}$	$\mathbf{0}$
$K_2$	$T_{ik} T_{kj}(D_i a_j + a_i D_j)$	$\mathbf{a}^\top \hat{\mathbf{T}}^2 \mathbf{D} + \mathbf{D}^\top \hat{\mathbf{T}}^2 \mathbf{a}$	$2\mathbf{a}^{\times \top} \mathbf{D}^{\times \top} \mathbf{T} + 2\mathbf{D}^{\times \top} \mathbf{a}^{\times \top} \mathbf{T}$	$\mathbf{a}^{\times \top} \mathbf{D}^{\times} + \mathbf{D}^{\times \top} \mathbf{a}^{\times}$	$2\hat{\mathbf{T}}^2 \mathbf{a}$	$\mathbf{0}$	$2(\hat{\mathbf{T}} \mathbf{a}^{\times} + (\hat{\mathbf{T}} \mathbf{a})^{\times})$
$K_3$	$T_{ik} T_{kj} D_i D_j$	$\mathbf{D}^\top \hat{\mathbf{T}}^2 \mathbf{D}$	$2\mathbf{D}^{\times \top} \mathbf{D}^{\times \top} \mathbf{T}$	$2\mathbf{D}^{\times \top} \mathbf{D}^{\times} \mathbf{T}$	$2\hat{\mathbf{T}}^2 \mathbf{D}$	$2\hat{\mathbf{T}}^2$	$2(\hat{\mathbf{T}} \mathbf{D}^{\times} + (\hat{\mathbf{T}} \mathbf{D})^{\times})$

### 3.4.2 3-D Rate Rules

After expanding the energy in terms of tensor invariants, the next step is to specify the evolution rule of  $\mathbf{D}^*$  for three dimensional problems. This can be done by modifying the rate rule in Eq. 3.34 as

$$\frac{d\mathbf{D}^*}{dt} = \frac{\mathbf{D} - \mathbf{D}^*}{\tau} \left\{ 1 - \exp \left[ - \left( \frac{\|\mathbf{D} - \mathbf{D}^*\|}{\Delta D_c} \right)^{2\alpha} \right] \right\}, \quad (3.65)$$

where  $\mathbf{D}$  and  $\mathbf{D}^*$  are vectors in three dimensions, i.e.

$$\mathbf{D} = [D_1, D_2, D_3]^\top, \quad \mathbf{D}^* = [D_1^*, D_2^*, D_3^*]^\top,$$

and  $\|\mathbf{D} - \mathbf{D}^*\|$  is the  $\ell_2$  norm of the vector  $(\mathbf{D} - \mathbf{D}^*)$ .

## 3.5 Finding 3-D Material Parameters

The procedure for finding optimized 1-D material parameters can be modified to find 3-D material parameters. To do so, the elastic Gibbs free energy shall be first expanded in terms of tensor invariants:

$$G_1 = \sum_k x_k G_1^{(k)}(\mathbf{T}, \mathbf{D}, \mathbf{D}^*), \quad (3.66)$$

where  $x_k$  is the coefficient of the selected energy function. This expression yields the electric field and strain as

$$\mathbf{E} = \sum_k x_k \mathbf{E}^{(k)}(\mathbf{T}, \mathbf{D}, \mathbf{D}^*), \quad (3.67)$$

$$\mathbf{S} = \sum_k x_k \mathbf{S}^{(k)}(\mathbf{T}, \mathbf{D}, \mathbf{D}^*), \quad (3.68)$$

where  $\mathbf{E}$  is a  $3 \times 1$  vector and  $\mathbf{S}$  is a  $6 \times 1$  vector. Next, the strain and polarization response subjected to both longitudinal and transverse tests shall be included in the cost function such that Eq. 3.47 becomes:

$$\mathbf{e} = \sum_{z=1}^n w_{E_z} (E_{3z}(\hat{\mathbf{D}}_z, \hat{\mathbf{D}}_z^*, \hat{\mathbf{T}}_z) - \hat{E}_{3z})^2 + \sum_{z=1}^n \sum_{i=1}^3 w_{S_z} (S_{iz}(\hat{\mathbf{D}}_z, \hat{\mathbf{D}}_z^*, \hat{\mathbf{T}}_z) - \hat{S}_{iz})^2, \quad (3.69)$$

where  $(\hat{\cdot})$  denotes the measured data.  $E_{3z}$  and  $S_{iz}$  are the corresponding components in Eq. 3.67 and 3.68. Since only  $E_3$ ,  $S_1$ ,  $S_2$ , and  $S_3$  are measured in Chapter 2, only these components in Eq. 3.67 and 3.68 are included in the cost function, Eq. 3.69.

After defining this cost function, one can then obtain the optimized material model in three dimensions by minimizing the cost function subjected to various rate parameters of the 3-D rate rule in Eq. 3.65. The detailed procedure has been described in Section 3.3.1–3.3.4 except that the cost function (Eq. 3.69), the rate rule (Eq. 3.65), and the energy expansion (Eq. 3.66) shall be used instead.

### 3.5.1 Optimized 3-D PZT-5H Model Parameters

Using this modification for the 3-D model and following the procedure described in Section 3.3.1 –3.3.4, one can obtain the optimized material parameters for PZT-5H as characterized in Chapter 2. To fit the data, weights  $w_E=50$  and  $w_S=1$  were used, and the Gibbs energy function was expanded in 27 terms as suggested by Ghandi. Table 3.9 lists these terms and their optimal coefficients. The optimized rate parameters are found to be  $\tau=0.1(\text{ms})$ ,  $\Delta D_c=0.03 \text{ (C/m}^2\text{)}$ , and  $\alpha=7$ .

Table 3.9: Energy expansions for PZT-5H in 3-D and their optimal coefficients.

$G_1^{(k)}$	$x_k$	$G_1^{(k)}$	$x_k$	$G_1^{(k)}$	$x_k$
$I_2$	-29.0122	$J_3$	-73.7834	$K_0$	-34.7323
$I_3$	14.4313	$J_3I_2$	$-2.8420 \times 10^3$	$K_0I_1$	$-1.7861 \times 10^3$
$I_3I_3$	7.1147	$J_3I_3$	$1.8671 \times 10^3$	$K_0I_2$	$2.8609 \times 10^3$
$J_0I_1$	9.3314	$J_0J_0$	9.6466	$K_0I_3$	-810.6531
$J_0I_2$	3.5402	$J_0J_0I_1$	$1.6667 \times 10^3$	$K_1$	$4.7744 \times 10^3$
$J_0I_3$	3.2426	$J_0J_0I_2$	$-2.3131 \times 10^3$	$K_2$	$-4.0868 \times 10^3$
$J_0I_3I_3$	-9.9131	$J_0J_0I_3$	606.0236	$K_3$	$3.3175 \times 10^3$
$J_1$	-55.1078	$J_0J_1$	$-5.1591 \times 10^3$		
$J_1I_2$	$1.0125 \times 10^3$	$J_0J_2$	$4.1821 \times 10^3$		
$J_2$	40.8231	$J_0J_3$	$-3.3173 \times 10^3$		

Figures 3-41–3-44 show the correlation between the data and the model for PZT-5H. As can be seen, the material model effectively captures the significant trends of the piezoelectric behaviors under various mechanical loading conditions. In addition, compared to the data shown in Figure 2-45, this 3-D model is able to simulate the rate dependency of PZT-5H as shown in Figure 3-45. Finally, this 3-D PZT-5H model also achieves the targeted precision of Stage 2, as defined in Table 1.1.

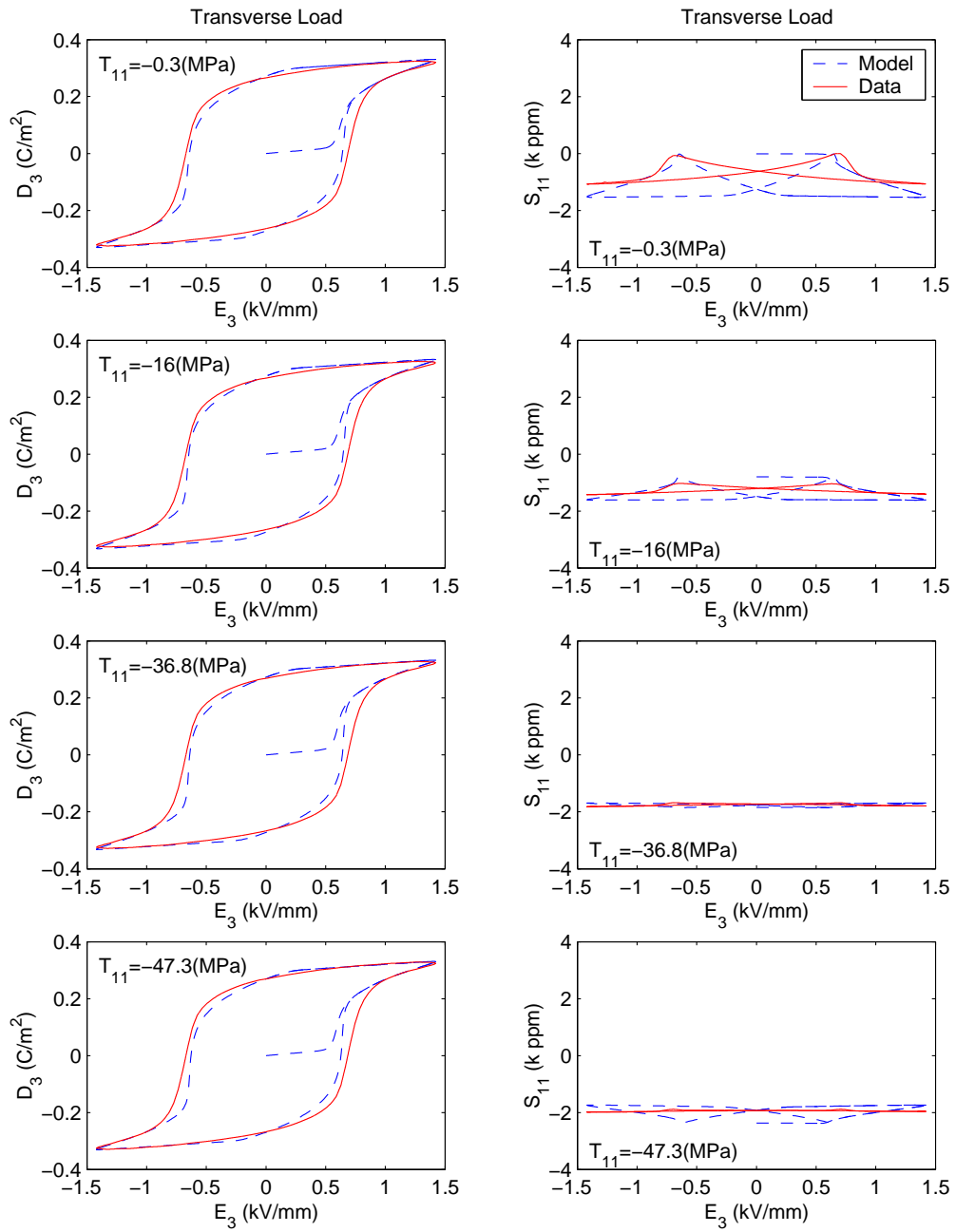


Figure 3-41: Correlation between 3-D model and data of PZT-5H transverse tests.

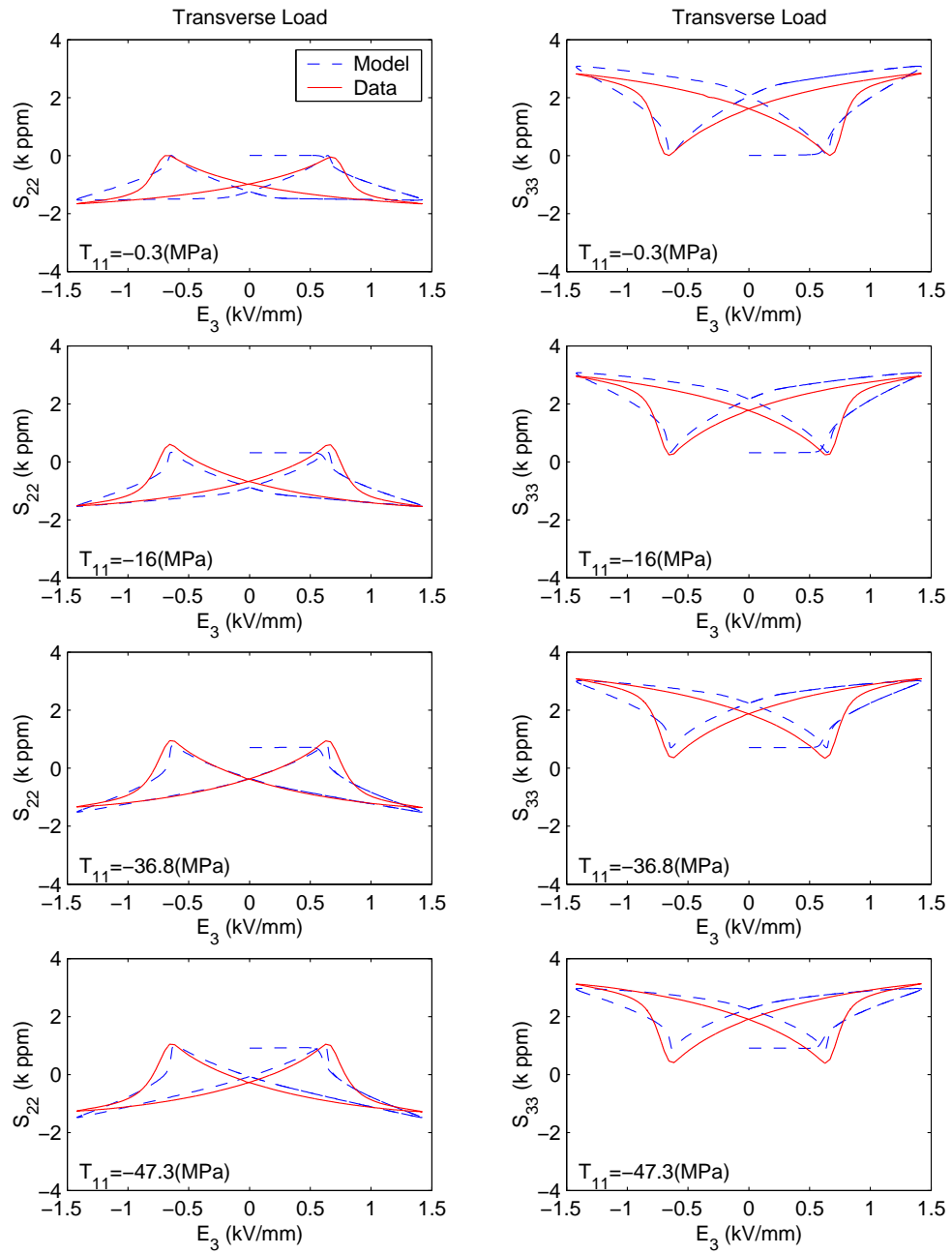


Figure 3-42: Correlation between 3-D model and data of PZT-5H transverse tests (Cont.)

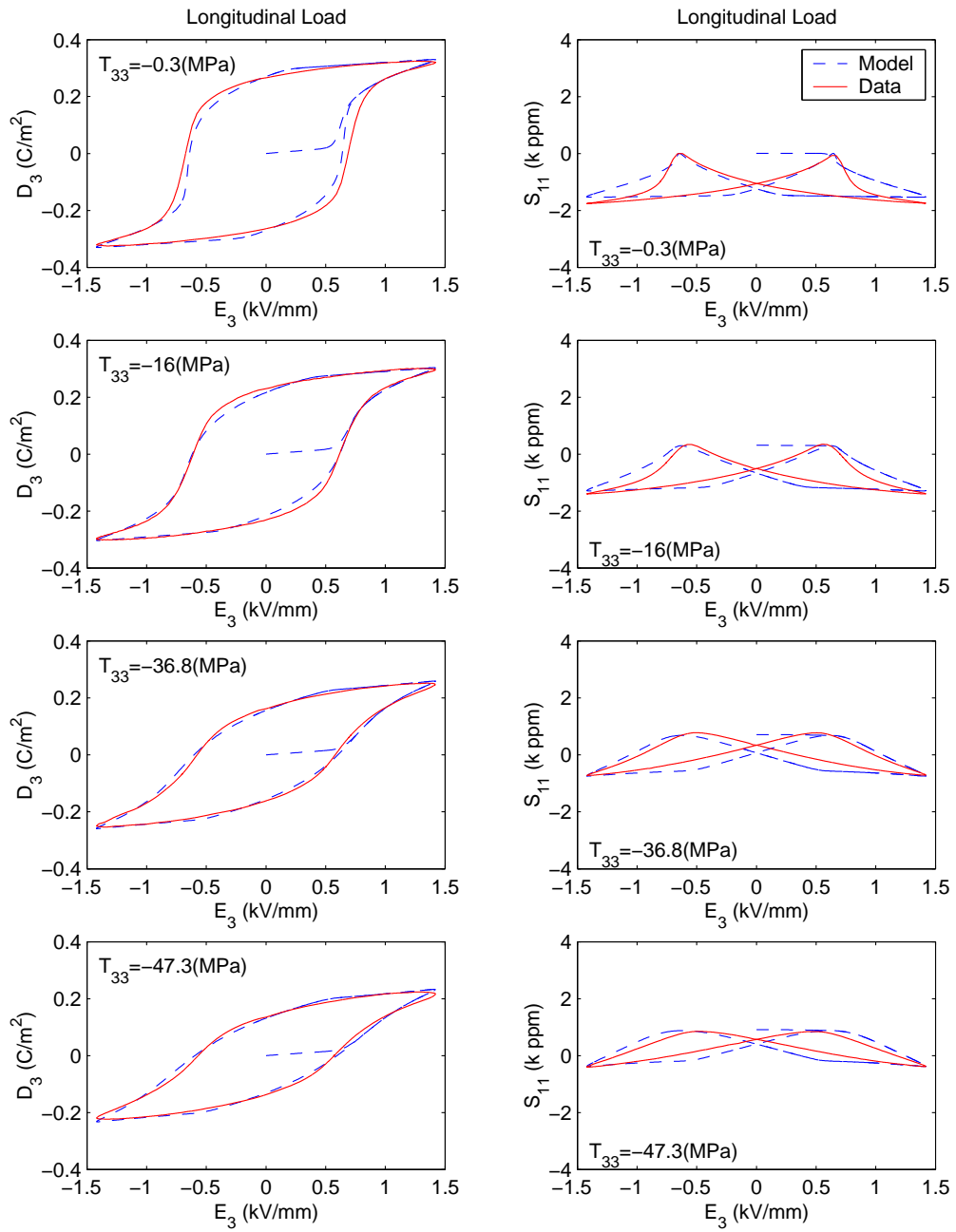


Figure 3-43: Correlation between 3-D model and data of PZT-5H longitudinal tests.



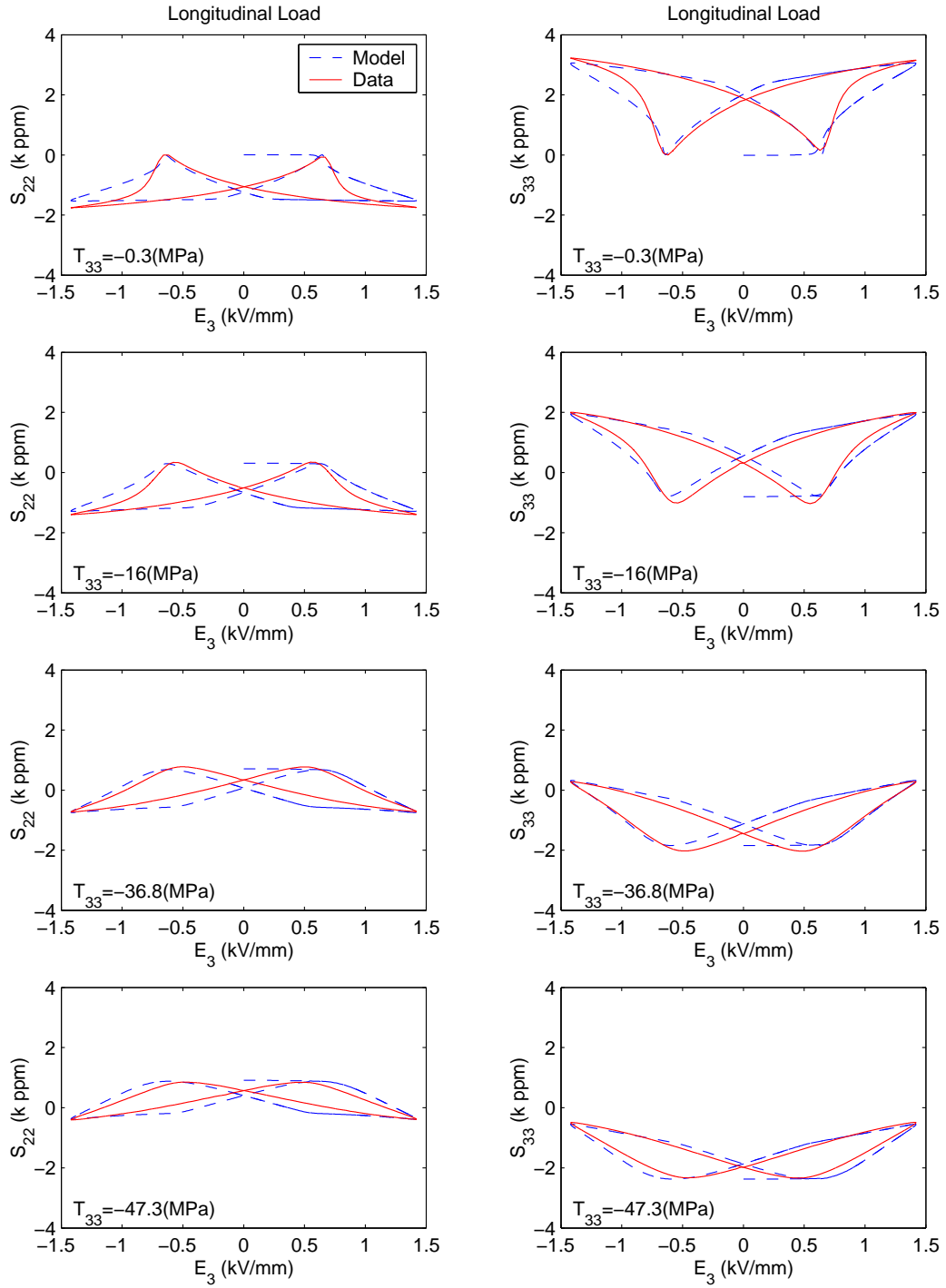


Figure 3-44: Correlation between 3-D model and data of PZT-5H longitudinal tests (Cont.)

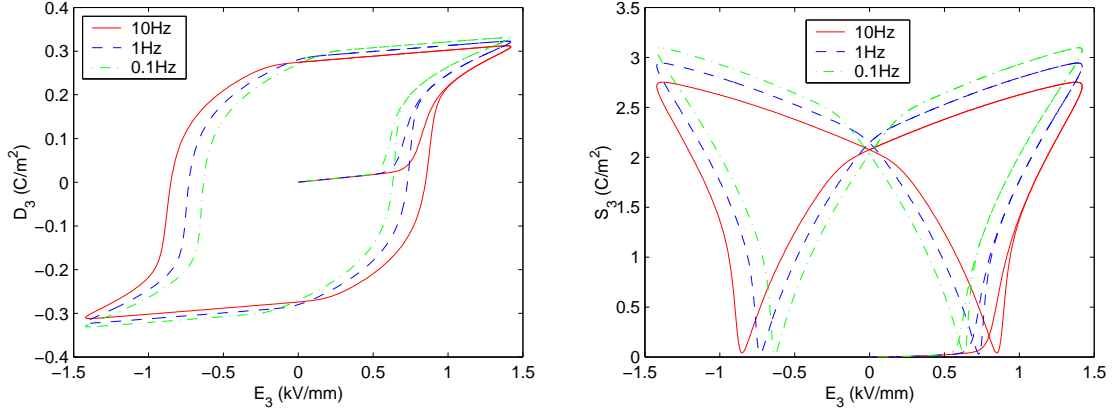


Figure 3-45: Simulated rate dependency of PZT-5H using 3-D model

### 3.5.2 Optimized 3-D PZT-5A Model Parameters

As presented in Chapter 2, Batch A and Batch B of PZT-5A specimens show inconsistent coercive fields. This inconsistency may cause difficulty in optimizing the material properties. To avoid this problem, the data of both transverse and longitudinal tests for the least squares regression shall be chosen from the same specimen batch. As a result, Batch-B data under compression up to 50MPa, shown in Figures 2-50–2-56, were used to obtain the optimized parameters. With the weights  $w_E=50$  and  $w_S=1$  and the same energy expansion for PZT-5H, one can find the optimized coefficients of energy functions as listed in Table 3.10. These results are based on the following optimized rate parameters:  $\tau=0.1(\text{ms})$ ,  $\Delta D_c=0.01(\text{C/m}^2)$ , and  $\alpha=7$ .

Figures 3-46–3-49 show the correlation between the data and the model for PZT-5A. As can be seen, the material model effectively captures the significant trends of piezoelectric behaviors under various mechanical loading conditions. In addition, compared to the data shown in Figure 2-46, this 3-D model is able to simulate the rate dependency of PZT-5A as shown in Figure 3-50. However, this 3-D PZT-5A model barely accomplishes the targeted accuracy and does not perform as well as the 3-D PZT-5H model. This can be explained by the same reason as discussed in Section 3.3.7, specifically that PZT-5A exhibits a special hysteretic relation between strain and electric displacement that simple Taylor expansion

cannot simulate well. To improve the model, a new internal variable must be defined, and its rate rule must be also derived to specify the S-D hysteresis of PZT-5A.

Table 3.10: Energy expansions for PZT-5A in 3-D and their optimal coefficients.

$G_1^{(k)}$	$s_k$	$G_1^{(k)}$	$s_k$	$G_1^{(k)}$	$s_k$
$I_2$	-169.2308	$J_3$	-565.8915	$K_0$	-43.7857
$I_3$	85.0693	$J_3 I_2$	-12967	$K_0 I_1$	152930
$I_3 I_3$	2.4812	$J_3 I_3$	8627.7	$K_0 I_2$	-308880
$J_0 I_1$	-81.0137	$J_0 J_0$	11.5568	$K_0 I_3$	156050
$J_0 I_2$	178.1540	$J_0 J_0 I_1$	-155280	$K_1$	-237990
$J_0 I_3$	-77.2817	$J_0 J_0 I_2$	313630	$K_2$	242210
$J_0 I_3 I_3$	-28.2338	$J_0 J_0 I_3$	-158360	$K_3$	-246150
$J_1$	-572.5728	$J_0 J_1$	228990		
$J_1 I_2$	4378.9	$J_0 J_2$	-233590		
$J_2$	543.0814	$J_0 J_3$	238000		

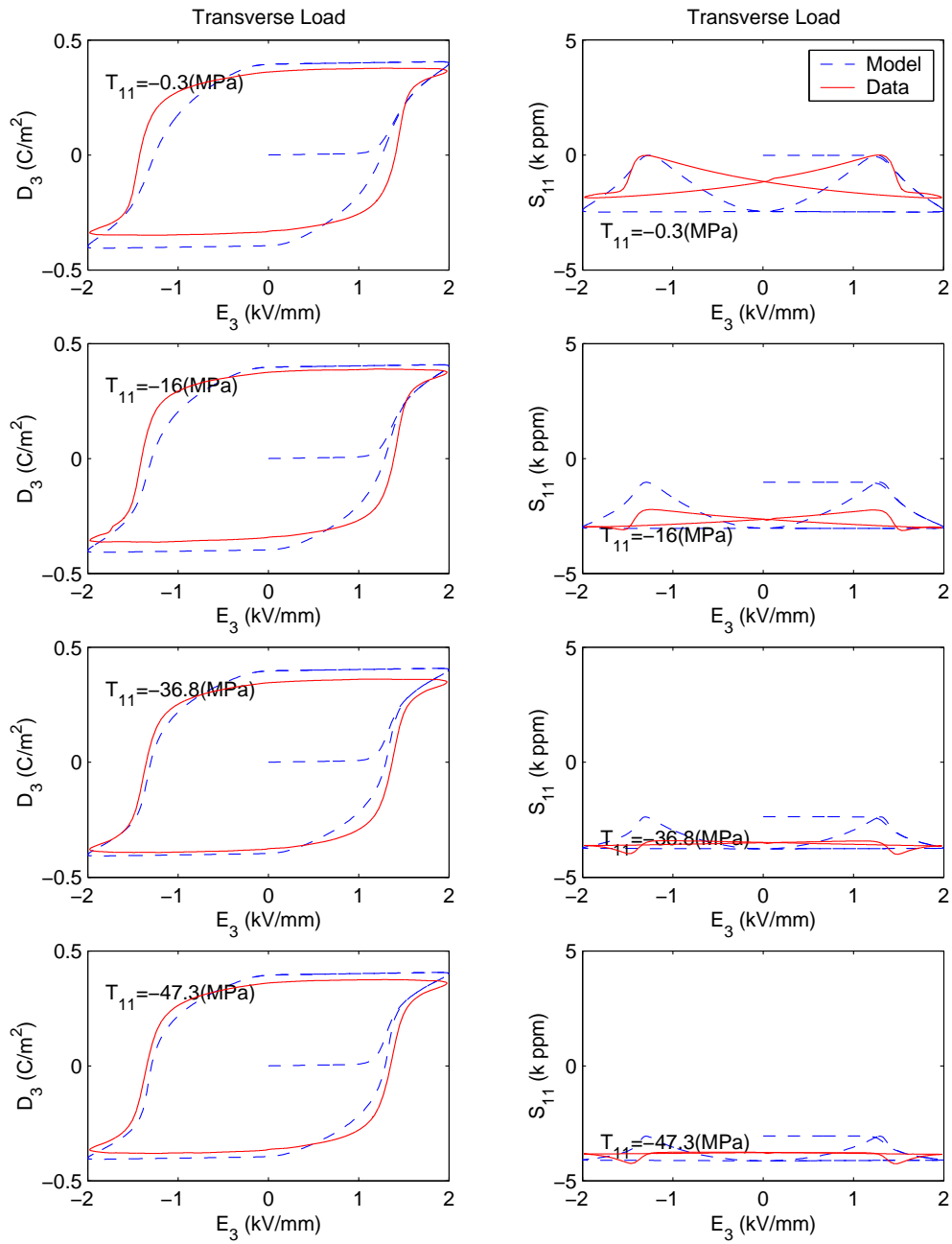


Figure 3-46: Correlation between 3-D model and data of PZT-5A transverse tests.

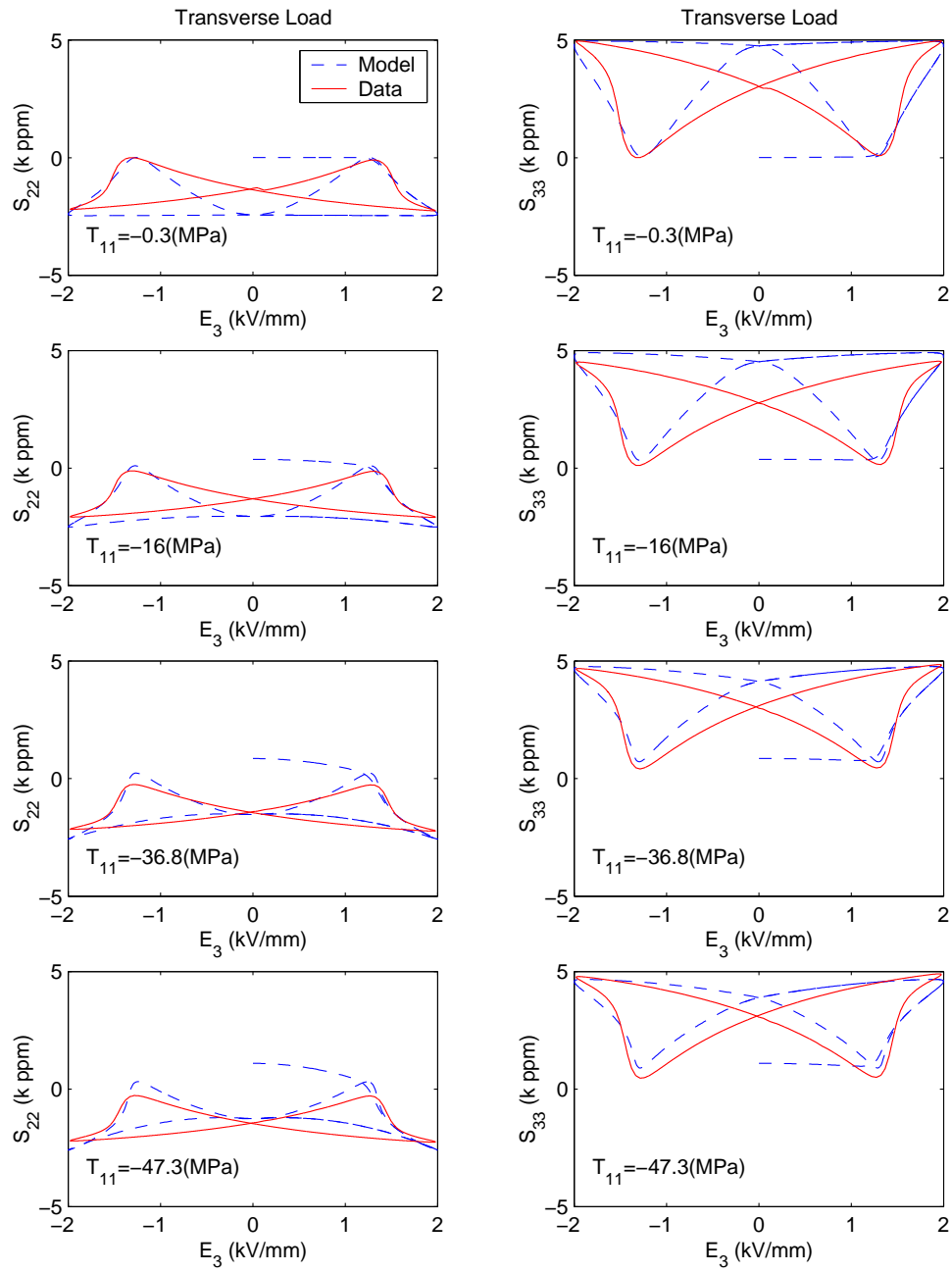


Figure 3-47: Correlation between 3-D model and data of PZT-5A transverse tests (Cont.)

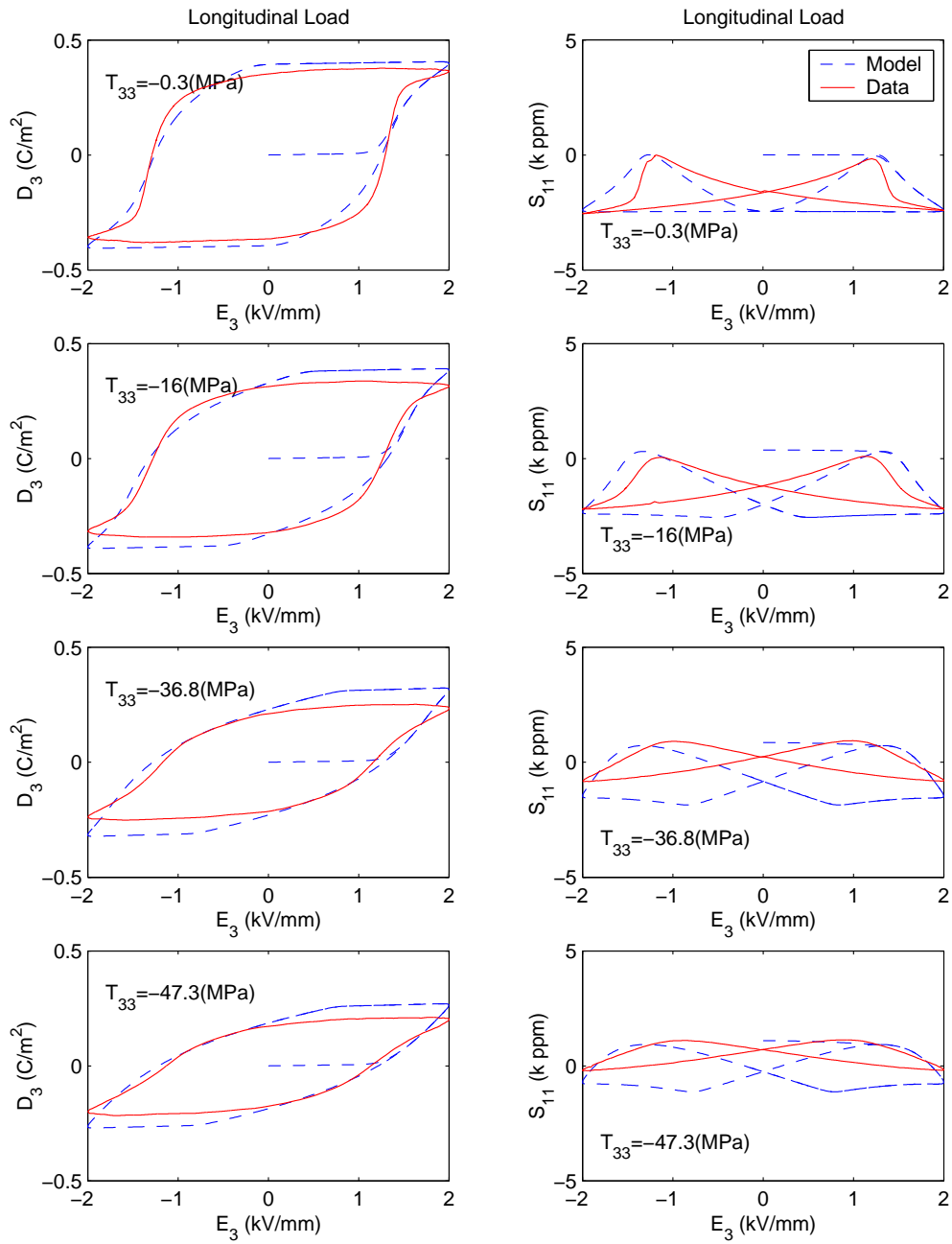


Figure 3-48: Correlation between 3-D model and data of PZT-5A longitudinal tests.

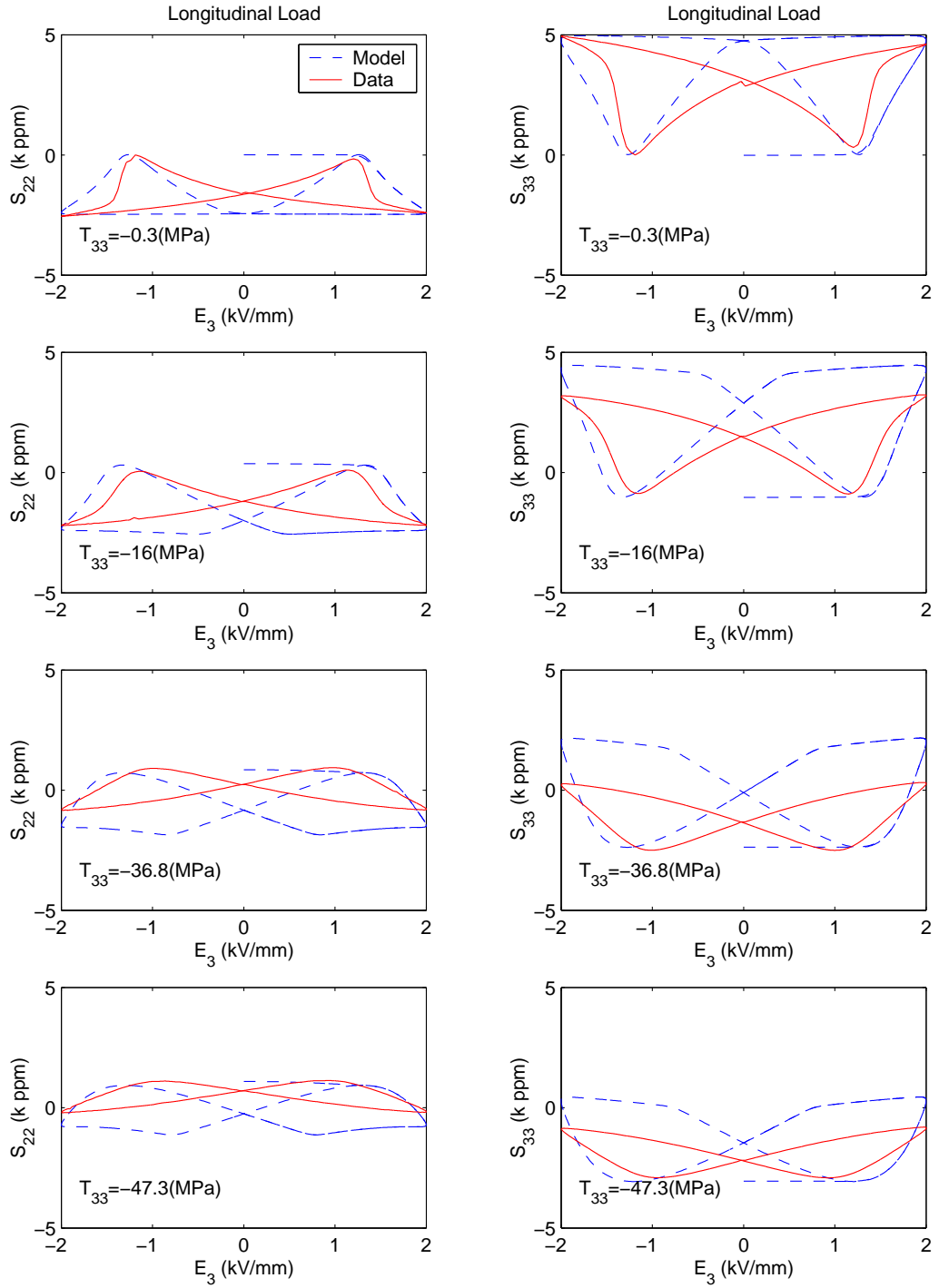


Figure 3-49: Correlation between 3-D model and data of PZT-5A longitudinal tests (Cont.)

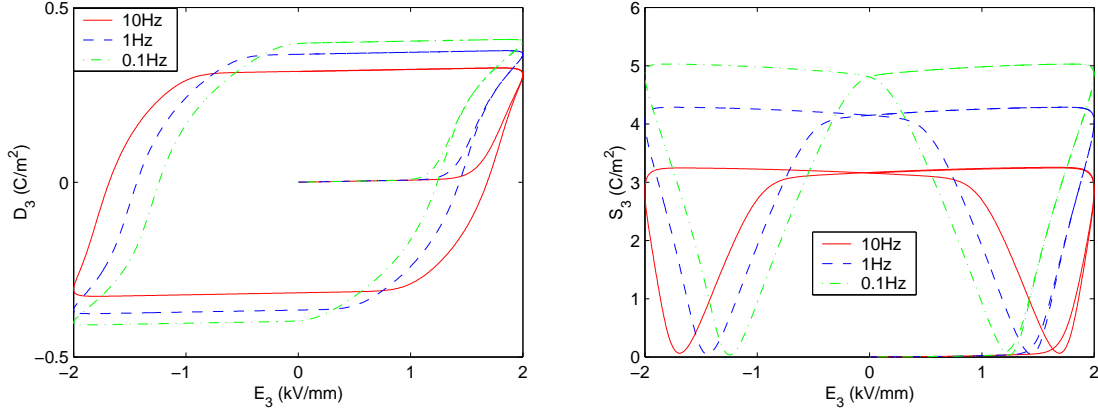


Figure 3-50: Simulated rate dependency of PZT-5A using 3-D model

### 3.6 Summary of Model Development

In this chapter, models for one and three dimensional piezoelectric response under various loading conditions have been developed using a thermodynamic framework and an evolution rule of the internal variable  $D^*$ . The model parameters for PZT-5A and PZT-5H have been optimized by minimizing the error between model fits and measured data. In general, the models are capable of predicting major trends of the material response, such as stress dependency and rate dependency, within the targeted accuracy of Stages 1 and 2, as defined in Table 1.1. However, it is found that the PZT-5H model performs much better than the PZT-5A model. This is because of the special hysteric relationship between strain and polarization of PZT-5A, which can be explained by the variance between  $90^\circ$  and  $180^\circ$  domain switching processes. In order to improve the material model for PZT-5A, a new rate rule is required that incorporates a new internal variable to describe this S-D hysteresis. Although it may not be difficult to do so, making the model thermodynamically consistent is the key obstacle. As a result, this modification will be left as a future work for the successors. Despite this, it is also of interest to test the models developed in this chapter against the criteria of Stage 3. This examination will be discussed in the next chapter.





## Chapter 4

# Model Validation for Application at Stage 3

In the previous chapter, the model correlated well with the data within the targeted precision of Stages 1 and 2. It is also of interest to test the models against the criteria of Stage 3. The task of Stage 3 is to condense the data into a material library or a design guide for material selection. This includes the information for actuation and energy harvesting applications. Since this information is obtained from the minor loop test, this chapter will first examine the minor loop performance. This will be followed by the model validation for PZT-5H power generation. The PZT-5A actuation predicted by the model will then be evaluated. Finally, the model performance against Stage 3 criteria will be summarized.

### 4.1 PZT-5H Minor Loop Validation

The purpose of the minor loop test is to examine the response while subject to moderate electric fields, usually below the coercive field so that the material will not be re-polarized by high electric fields. To validate the minor loop behavior, a test in addition to those in Chapter 2 was also conducted. Figure 4-1 shows the driving command of the electric field  $E_3$  of this test. During the test, behaviors of strain  $S_3$  and electric displacement  $D_3$  were recorded and have been compared to the simulated response by the 1-D and 3-D models developed in the previous section. In order to facilitate the simulation for different loading conditions, graphical simulation block diagrams using SIMULINK were built and documented

in detail in Appendix A. Since the test was performed by exciting an electric field, the short circuit simulations in Appendices A.3 and A.4 shall be used for 1-D and 3-D, respectively.

Figures 4-2 and 4-3 show the time history correlation between data and simulation. Figures 4-4 and 4-5 also present the modeled and measured relations between electric field and electric displacement and electric field and strain. As can be seen, both 1-D and 3-D models are capable of simulating the minor loop response including the small hysteretic loops shown in the data. However, the values predicted by the models are not accurate. This is not surprising because the models are not perfectly flawless as discussed in the previous chapter. In addition, the PZT-5H specimen of this minor loop test is not from the same batch as those test specimens used by Ghandi [35]. Compared to the test data shown by Ghandi [35], the peak strain and electric displacement of this minor loop test specimen are higher. Nevertheless, the models are able to predict the minor loop behaviors within the factor of 2.

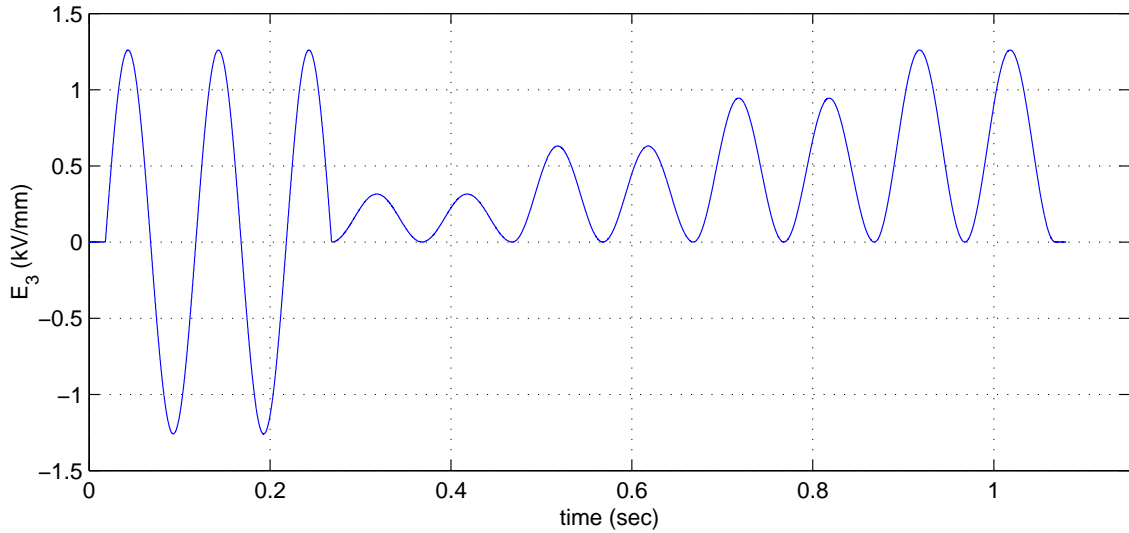


Figure 4-1: Electric driving command for minor loop test.

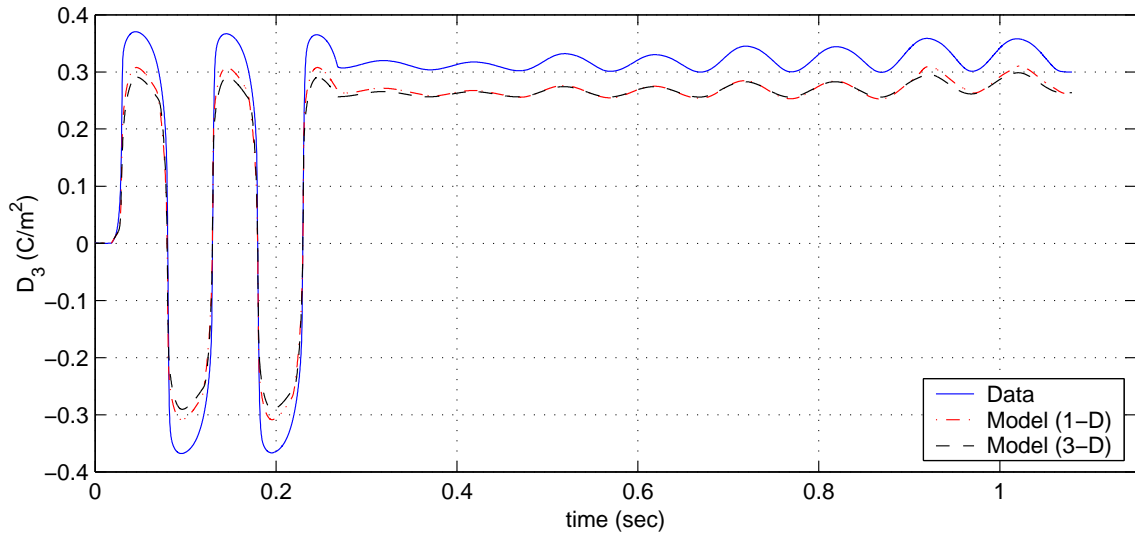


Figure 4-2: Time history correlation between modeled and measured electric displacement of minor loop test for PZT-5H.

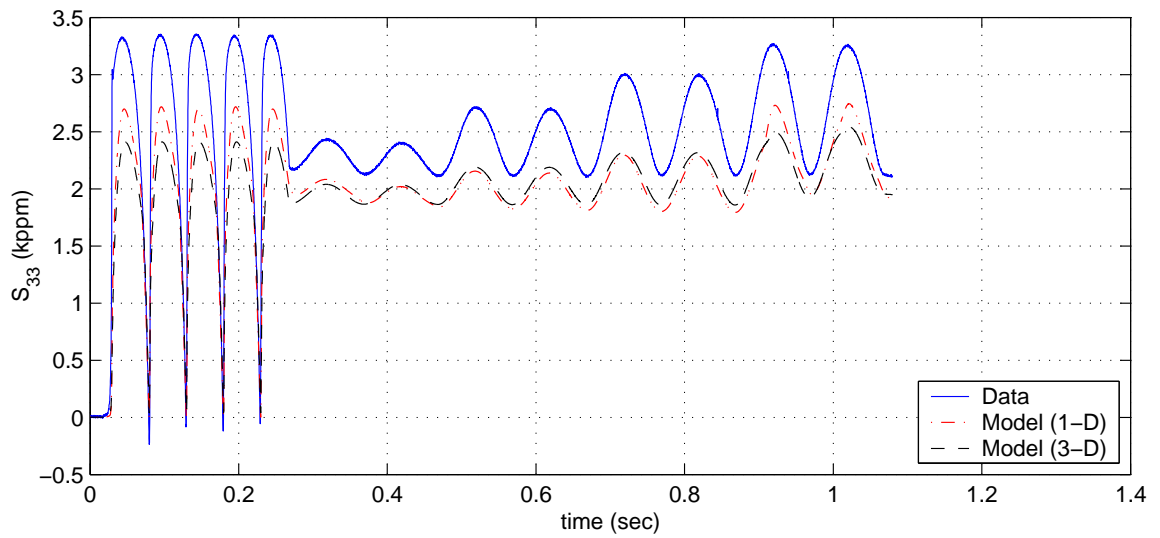


Figure 4-3: Time history correlation between modeled and measured strain of minor loop test for PZT-5H.

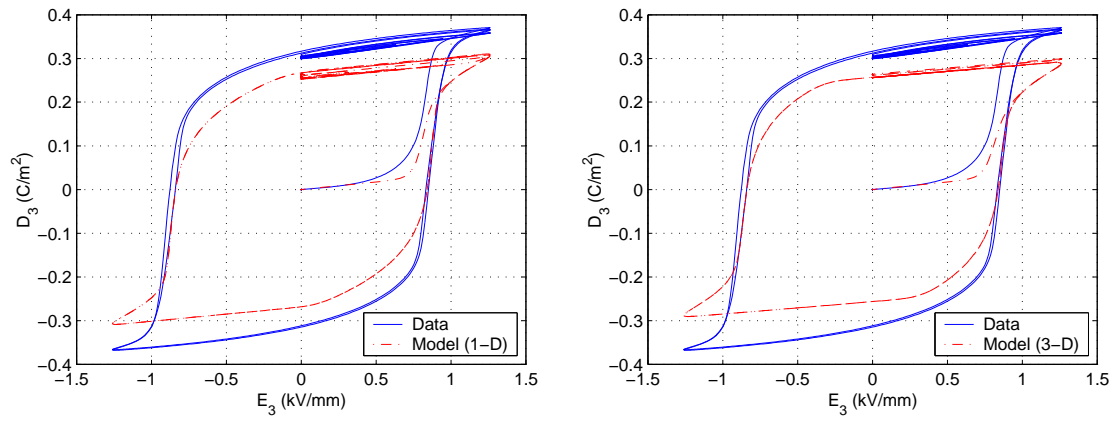


Figure 4-4: Correlation between modeled and measured electric displacement of minor loop test for PZT-5H. Left: 1-D model; right: 3-D model.

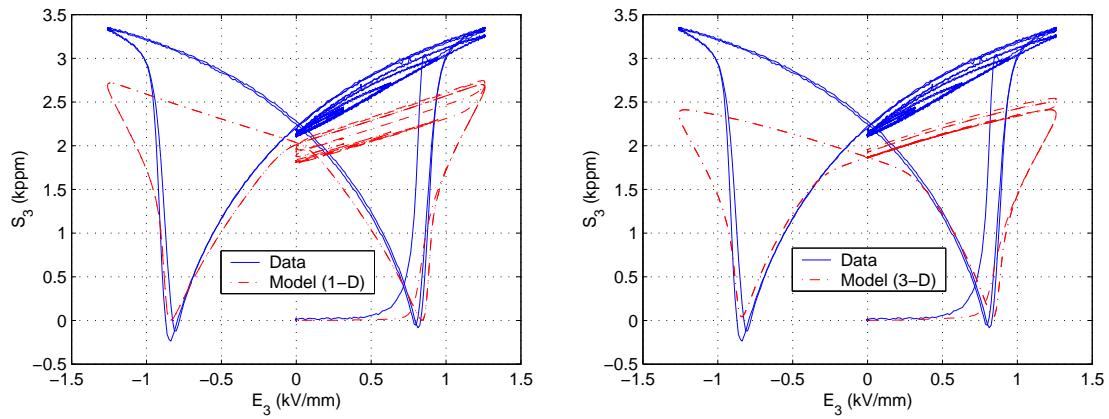


Figure 4-5: Correlation between modeled and measured strain of minor loop test for PZT-5H. Left: 1-D model; right: 3-D model.

## 4.2 Model Validation for PZT-5H Power Generation

It is also of interest to investigate if both 1-D and 3-D models are capable of predicting the material properties of PZT-5H for piezoelectric energy harvesting application. To do so, generalized piezoelectric constants including those under short circuit and open circuit tests shall be examined first. In addition, the response of piezoelectric specimens subjected to compression and shunted by the diode circuit shall be analyzed.

### 4.2.1 Validation of Generalized Piezoelectric Constants under Short Circuit

In order to simulate the generalized piezoelectric constant under short circuit, the same SIMULINK block diagram for the minor loop test discussed in the previous section can be used without change. To produce a poled piezoelectric specimen in the model, half a cycle of a 0.1Hz sinusoidal wave can be used as the polarizing signal. The final values of simulated  $D$  and  $D^*$  during this excitation represent the states of the poled material.

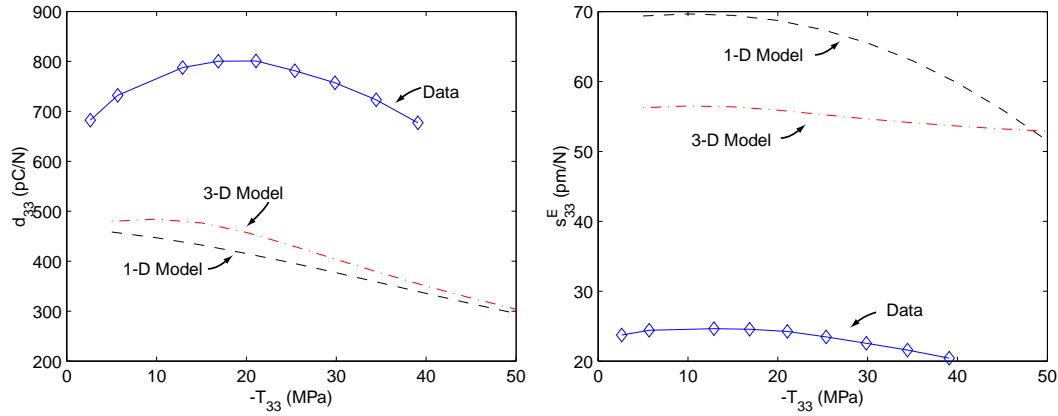


Figure 4-6: Comparison between the predicted and measured generalized  $d_{33}$  (left) and  $s_{33}^E$  (right).

To predict the generalized  $d_{33}$  and  $s_{33}^E$  constants, a 10Hz sinusoidal compression wave was used as a driving signal under the condition that electric field is constrained to be zero. The generalized constants were extracted using the same definition in Chapter 2. Figure 4-6 presents the comparison between the predicted and measured generalized  $d_{33}$  and  $s_{33}^E$ .

constants. Unfortunately, the models fail to predict accurate values of the generalized constants under the short circuit condition. The explanation of this bad correlation will be discussed at the end of this section. However, the models do show the trend that the generalized constants decrease as compression increases. In addition, as can be seen, the 3-D model performs better than the 1-D model.

#### 4.2.2 Validation of Generalized Piezoelectric Constants under Open Circuit

In order to simulate the generalized piezoelectric constant under open circuit, new SIMULINK models were built and are shown in detail in Appendices A.5 and A.7. Values of  $D$  and  $D^*$  which represent the poled states of the materials are also required as the initial conditions of the models. To predict the generalized  $g_{33}$  and  $s_{33}^D$  constants, a 10Hz sinusoidal compression wave was used as a driving signal under the condition that electric displacement is constrained to be constant. The generalized constants were extracted using the same definition in Chapter 2. Figure 4-7 presents the comparison between the predicted and measured generalized  $g_{33}$  and  $s_{33}^D$  constants, respectively.

Unfortunately, both the 1-D and 3-D models fail to predict accurate values of the generalized constants under open circuit condition. The explanation of this bad correlation will be discussed at the end of this section. In addition, the models do not capture the decreasing trend of  $g_{33}$  as compression increases. This is because no conduction effect is considered in the models. Recall the discussion in Section 3.2.1 that the electric conduction plays a significant role in the material behavior if it is under charge source control. This is the same situation with the measurement of  $g_{33}$ . During the test, two paths of conduction are possible: one is the internal resistance of the material itself, and the other is the finite impedance of the voltage meter. The former has been measured by Harper [36], and its corresponding resistance is converted to be  $1.87\text{G}\Omega$ . The latter is exactly known as  $10\text{G}\Omega$  for the 10Hz test. To account for the loss due to this electric conduction, the SIMULINK models were modified by including a resistor  $R$ , as shown in Appendices A.6 and A.8. Although this modification does not improve the capability of predicting an accurate  $g_{33}$  constant, both the 1-D and 3-D models have been improved to capture the phenomenon shown in Figure 4-7 that the  $g_{33}$  constant decreases as the compression increases.

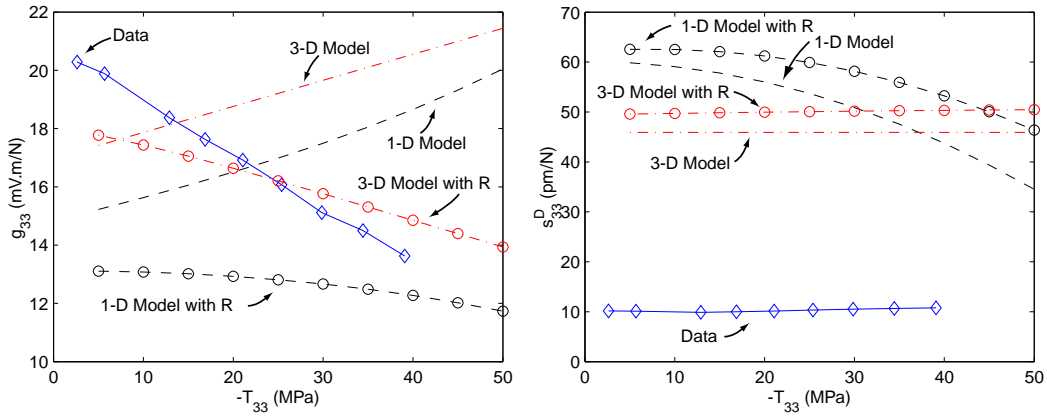


Figure 4-7: Comparison between the predicted and measured generalized  $g_{33}$  (left) and  $s_{33}^D$  (right).

#### 4.2.3 Validation of Diode Circuit Response

To simulate the nonlinear response of a piezoelectric specimen subjected to compression and connected to the diode circuit, appropriate SIMULINK models were built and are shown in detail in Appendices A.9 and A.10. Figures 4-8, 4-9, and 4-10 show the comparison of the simulated response and data of the current flowing through the battery in the diode circuit shown in Figure 2-33 for 2.62MPa, 16.8MPa, and 39MPa compressions, respectively. As can be seen, neither the 1-D nor the 3-D model can predict the response well because both models have difficulty simulating accurately the generalized piezoelectric constants. Ironically, the linear piezoelectric model using measured generalized piezoelectric constants outperforms the nonlinear models.



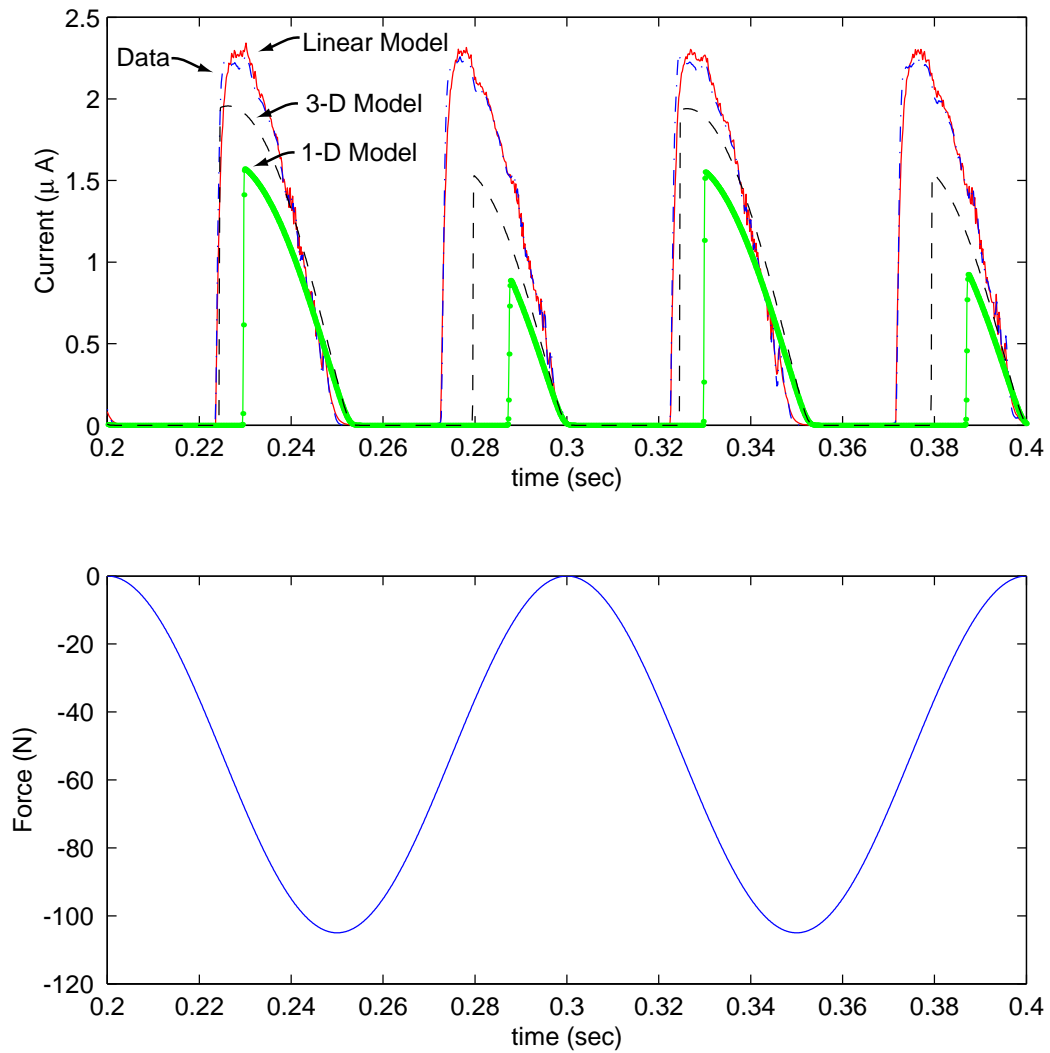


Figure 4-8: The current output of the diode circuit. The piezoelectric specimen is under 105N compression. Upper plot shows the time history of current. Lower plot shows the time history of input force.

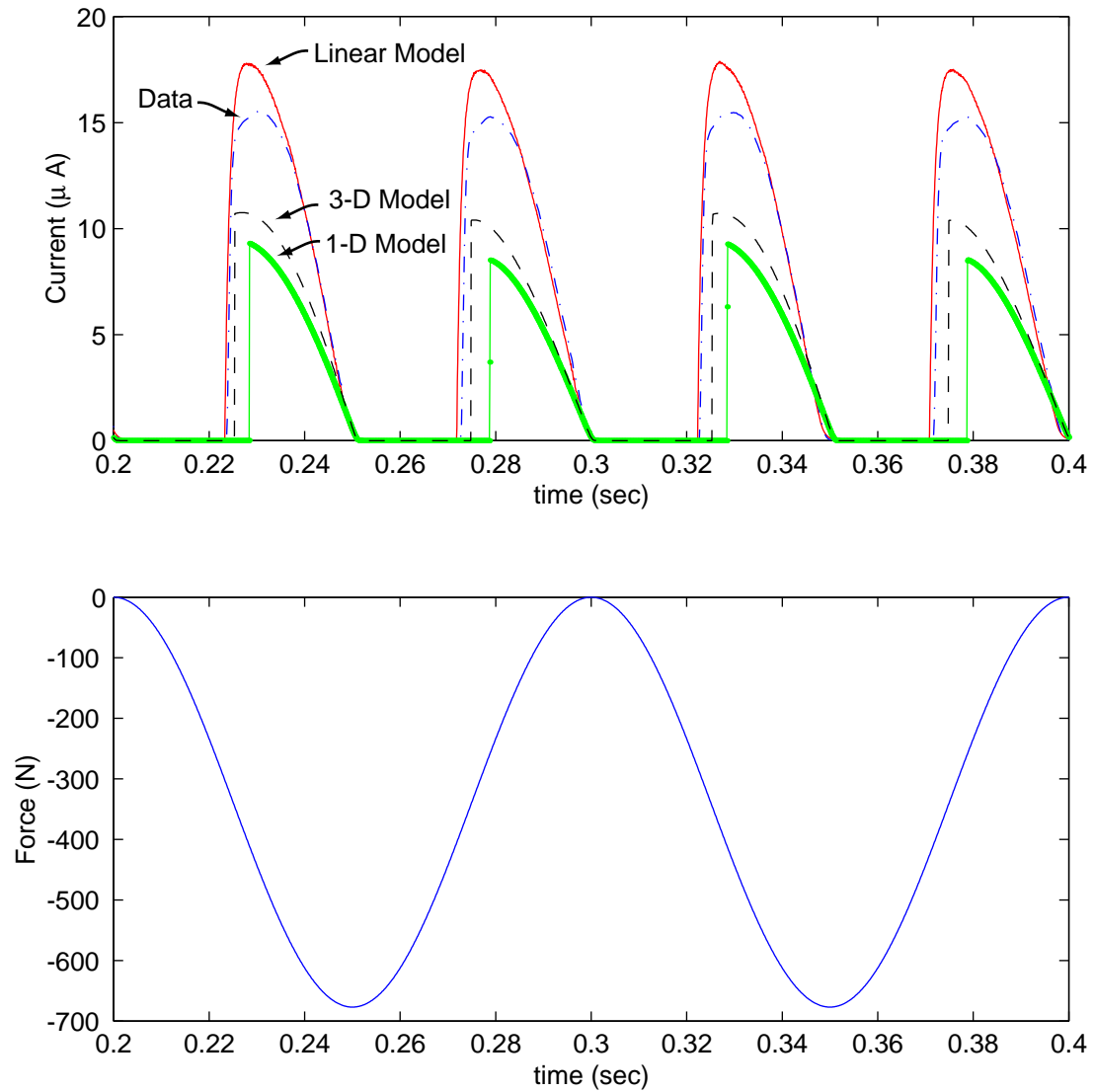


Figure 4-9: The current output of the diode circuit. The piezoelectric specimen is under 677N compression. Upper plot shows the time history of current. Lower plot shows the time history of input force.

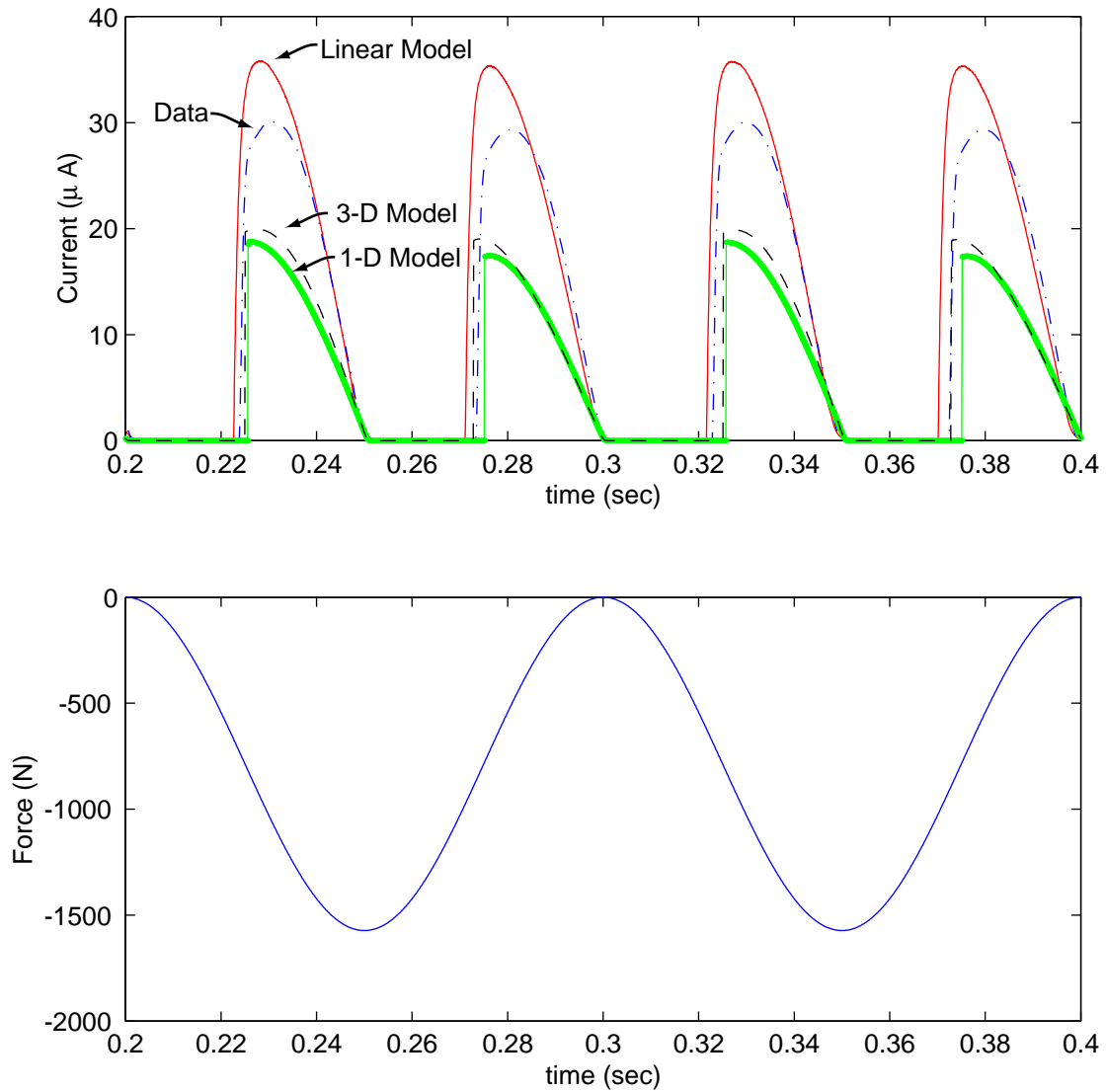


Figure 4-10: The current output of the diode circuit. The piezoelectric specimen is under 1573N compression. Upper plot shows the time history of current. Lower plot shows the time history of input force.

#### 4.2.4 Explanation of Poor Correlation: Stress Rate Dependency

As discussed above, the nonlinear models developed in the previous chapter fail to predict the response accurately within the targeted precision. This might be due to the neglect of the stress rate dependency in the material model. To explain this, the remnant strain of a PZT-5H specimen at zero electric field in Figures 3-24 and 3-25 are first plotted as a function of stress as shown in Figure 4-11 (right). Using this plot,  $s_{33}^E$  can be approximated as 88pm/N. Note that the stress rate of this data is very low as shown in Figure 4-12.

The stress rate dependence can be found by comparing two data sets of  $s_{33}^E$ : one is for PZT-5H power generation as shown in Figure 4-11 (left) and the other is extracted from PZT-5H butterfly curve under various stresses shown in Figure 4-11 (right). The former  $s_{33}^E$  is approximately 25pm/N and is obtained by exciting 10Hz compression at zero electric field (i.e. short circuit condition) while the latter is approximately 88pm/N and is obtained at very low stress rate as shown in Figure 4-12. In addition, the latter  $s_{33}^E$  is closer to the model prediction because the model is built by the data set of the same stress rate.

As a result, it is obvious that stress rate dependence can be inferred from Figure 4-11. This stress rate dependence therefore contributed to the bad correlation of  $s_{33}^E$  shown in Figure 4-11 (left) as well as the other piezoelectric and elastic constants for power generation ( $d_{33}$ ,  $g_{33}$ , and  $s_{33}^D$ ).

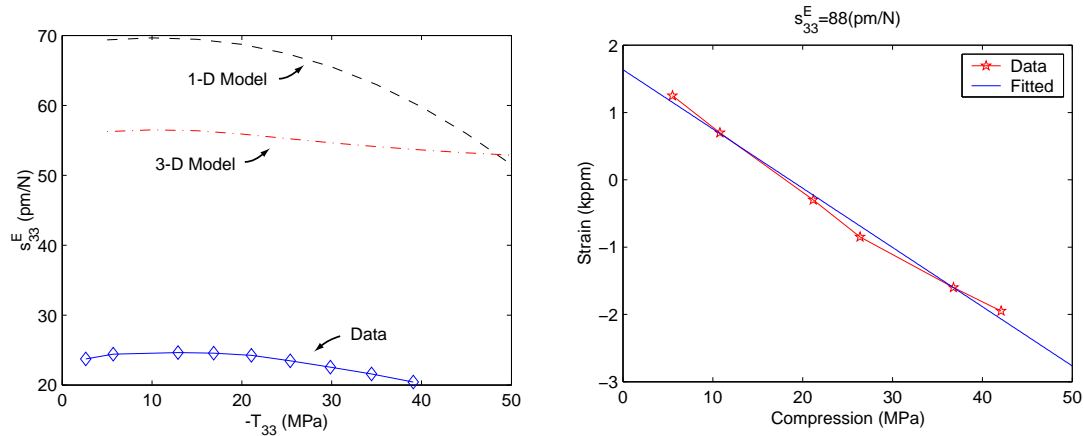


Figure 4-11: Comparison between the predicted and measured generalized  $s_{33}^E$  of PZT-5H.

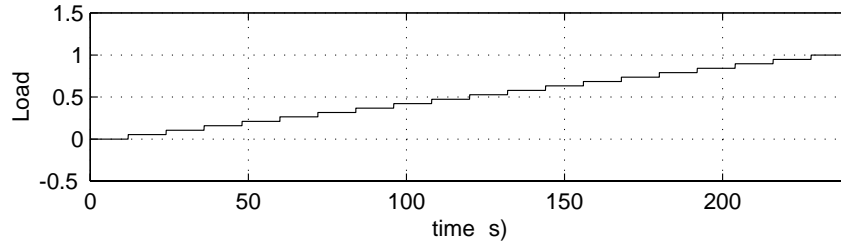


Figure 4-12: Load rate of butterfly curve test at various stresses.

### 4.3 Model Validation for PZT-5A Actuation

It is also of interest to investigate if the nonlinear model is capable of predicting the material properties of PZT-5A for piezoelectric actuation. This includes the behaviors of the single loop and multiple loop tests presented in Section 2.2. The compression of these data ranges from 0 to 150MPa, while none of the nonlinear model developed in the previous chapter is valid up to 150MPa compression.

Although the 1-D model for PZT-5A (Batch B) is valid up to 112MPa, the bad correlation might not be good enough to simulate the test result of actuation. Among the three 1-D models of PZT-5A developed in Chapter3, the model for PZT-5A (Batch A) shows better correlation and therefore will be chosen to simulate the piezoelectric actuation test in the following. For comparison, the driving electric field is normalized by the coercive field which is 0.75kV/mm for PZT-5A (Batch A). The same simulink simulation block diagram used for the minor loop test in Section 4.1 can be used for this type of simulation, except that the material parameters must be replaced by the coefficients listed in Table 3.5.

#### 4.3.1 Validation of Single Loop Test

Figure 4-13 shows the converse generalized  $d_{33}^*$  subjected to electric fields of  $\pm 9\% E_c$ ,  $\pm 16\% E_c$  and  $\pm 40\% E_c$ , respectively. As can be seen, the model fails to predict correct values of the converse generalized  $d_{33}^*$  because of the difficulty in finding the exact parameters for the model, as discussed in the previous chapter. In spite of this flaw, the model well describes the decreasing  $d_{33}^*$  of the material under high compression.

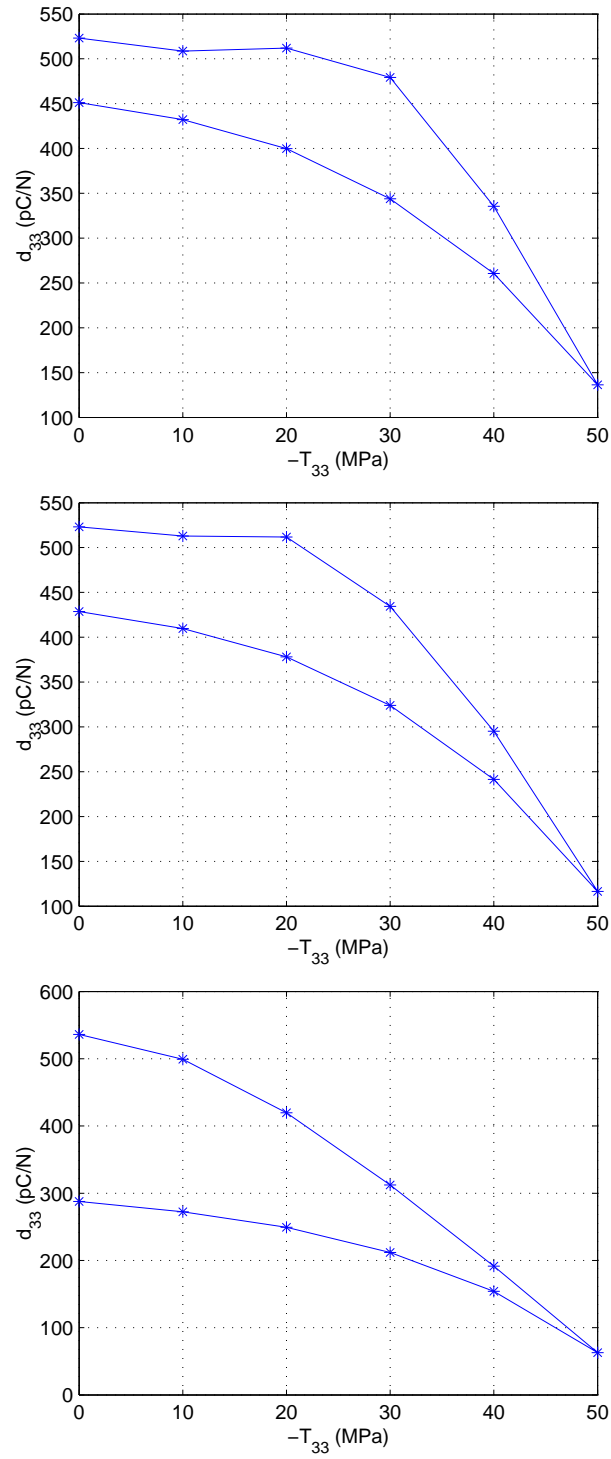


Figure 4-13: Simulation of single loop test with  $\pm 0.09E_c$  (upper),  $\pm 0.16E_c$  (middle), and  $\pm 0.40E_c$  (lower) driving electric field.

### 4.3.2 Validation of Multiple Loop Test

Because the material model is only valid up to 50MPa, the simulated multiple loop test uses the peak load first up to 30MPa and then to 50MPa. As shown in Figure 4-14, the actuation slightly recovers from the first peak load but not as completely as the data shown in Section 2.2. In addition, the material begins to exhibit compressive depolarization after the compression up to 50MPa, which correlates with the data shown in Section 2.2.

To see if the material actuating properties can recover after slight compression, an additional set of tests is done by using the first peak load only up to 20MPa and then to 50MPa for the second one. As shown in Figure 4-15, the actuation completely recovers from the first peak load if the negative driving electric field is low enough (less than  $\pm 16\% E_c$ ). In contrast, high enough negative driving electric field may result in incomplete recovery of actuation after experiencing the first peak load. This is because the high electric field in negative polarization also tends to depolarize the material. These simulated results show qualitatively that the model is capable of describing the phenomenon observed in Section 2.2, although the value is not accurate.

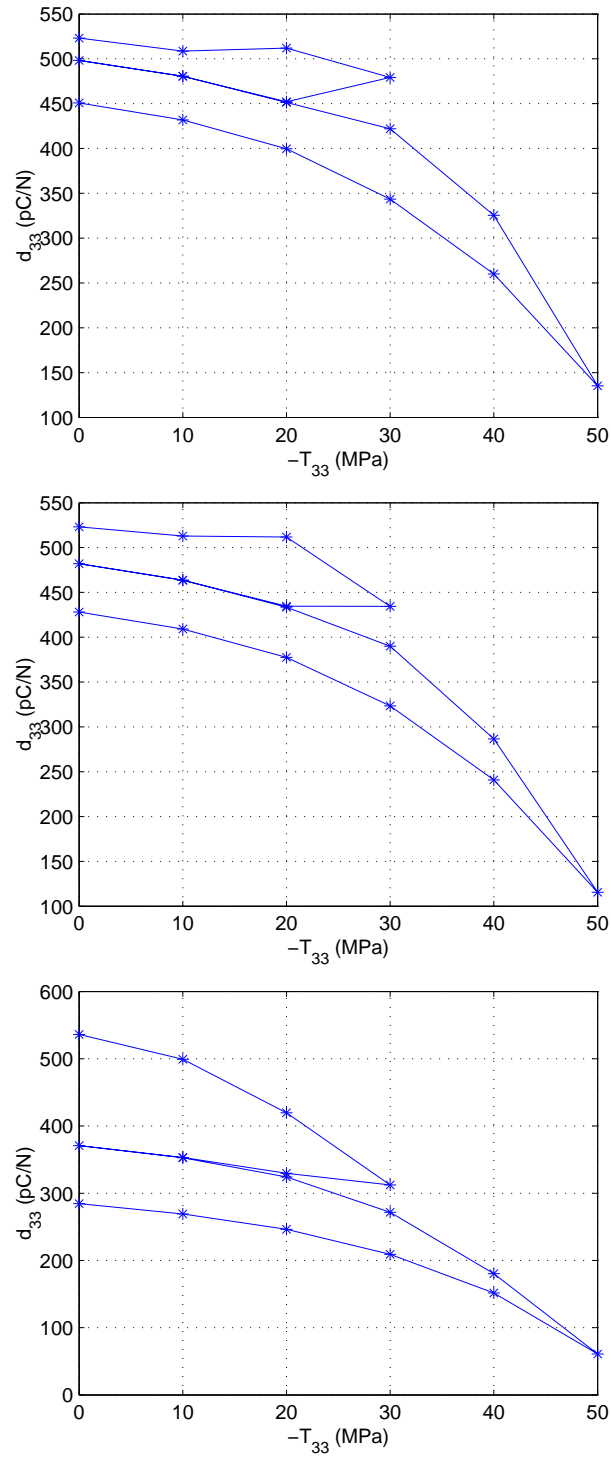


Figure 4-14: Simulation of single loop test with  $\pm 0.09E_c$  (upper),  $\pm 0.16E_c$  (middle), and  $\pm 0.40E_c$  (lower) driving electric field. Maximum compression of first loop is 30MPa.



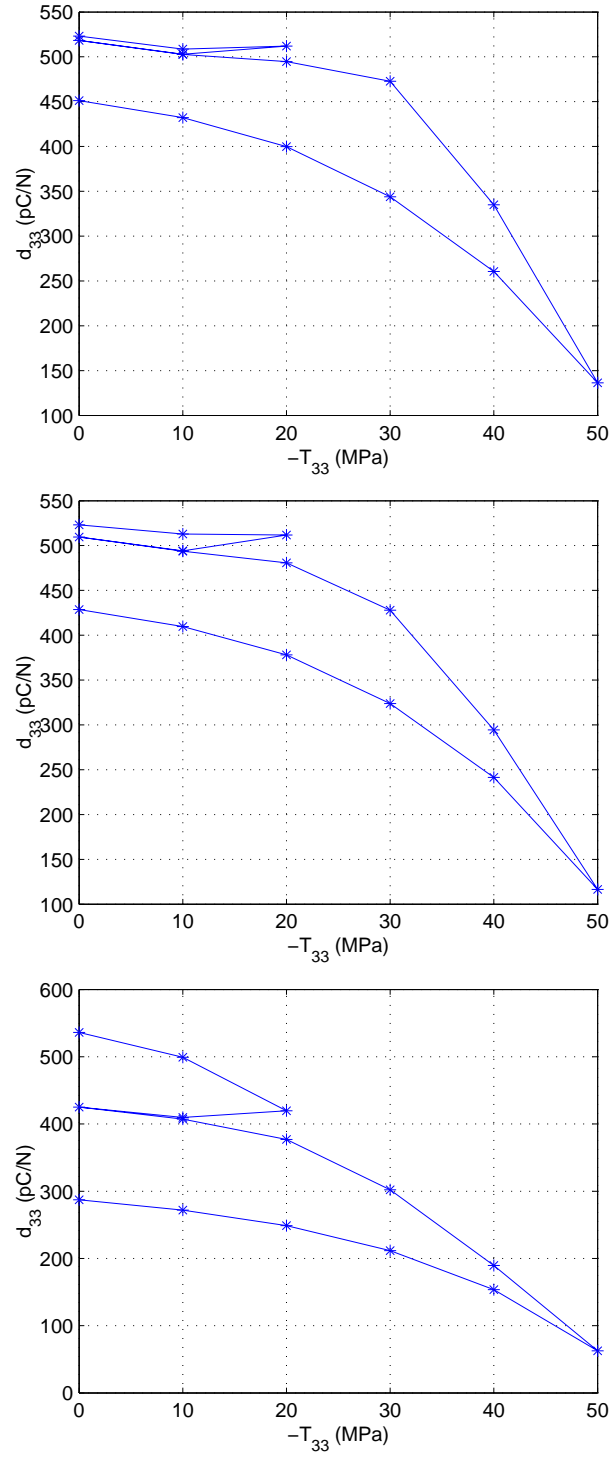


Figure 4-15: Simulation of single loop test with  $\pm 0.09E_c$  (upper),  $\pm 0.16E_c$  (middle), and  $\pm 0.40E_c$  (lower) driving electric field. Maximum compression of first loop is 20MPa.

## 4.4 Summary of Model Validation at Stage 3

This chapter examined the capability of the material models in predicting the minor loop behaviors and the material constants. Although the material models are able to capture major trends of material behaviors under various stresses and driving frequencies, they fail to forecast accurate piezoelectric constants for actuation and energy harvesting applications, which is the required task at Level 3. Several reasons contribute to this deficiency:

1. There was significant variance among the material batches.
2. S-D hysteresis was not modeled.
3. Stress rate effect was neglected in the material model.
4. The material parameters were obtained by fitting the model with the wide range data.

However, this methodology may not be efficient in predicting local derivatives of the response.

To improve the model, it is recommended to include two new internal variables: one is to describe the S-D hysteresis of PZT-5A; the other is to specify the stress rate dependency. In addition, higher order terms in the energy expansion may help improve the local derivative of the material response.



## Chapter 5

# 3-D Analysis Using Finite Element Method

It is the goal of this thesis to develop a method to analyze electromechanically coupled devices with irregular geometries or boundary conditions. Finite element method has been used to solve this type of problem for a long time. The first linear piezoelectric finite element method was formulated by Allik and Hughes [8]. This linear formulation was later commercialized in the finite element software package ANSYS. Unfortunately, none of the currently available software packages are capable of analyzing or implementing the nonlinearity and hysteresis of piezoelectric materials.

The most advanced work in finite element analysis of nonlinear piezoelectric materials was done by Ghandi [35]. Unlike the conventional formulation used by Allik [8], Ghandi developed a mixed formulation using electric displacement  $D$  as an additional degree of freedom, in addition to the potential  $V$  and displacement  $u$ . However, the solution technique described in [35] is only appropriate for the rate independent nonlinear piezoelectric material model, i.e. discrete time model. Since a new rate dependent material model has been developed in this thesis work, the mixed finite element formulation by Ghandi as well as its solution technique shall be modified to implement the system in the continuous time domain. It is therefore the objective of this chapter to demonstrate the feasibility of a rate dependent mixed finite element analysis of nonlinear piezoelectric materials.

This chapter will start with a complete summary of the rate dependent mixed formula-

tion, followed by the implementation of the material model and the spatial discretization. The techniques of the numerical solution will then be addressed. In the end, element tests and case studies will be shown to demonstrate the solution technique.

## 5.1 Mixed Formulation

### 5.1.1 Problem Statement of an Electroelastic Continuum

The goal of this thesis is to calculate the response of an electroelastic continuum subjected to different boundary conditions and loading. To do so, the problem shall be specified first as the following. A material volume  $V$  bounded by surface  $S = S_f + S_u$  is subject to mechanical surface traction  $f_i^{S_f}$  on  $S_f$  and mechanical displacement constraints  $u_i^{S_u}$  on  $S_u$ . These are the essential and natural mechanical boundary conditions, respectively:

$$u_i = u_i^{S_u} \text{ on } S_u, \quad (5.1)$$

$$T_{ij}n_j = f_i^{S_f} \text{ on } S_f. \quad (5.2)$$

Within the body of this continuum, applied body forces must balance the internal stresses:

$$T_{ij,j} + f_i^B = 0. \quad (5.3)$$

Portions of the surface may be covered by electrical conductors. On such portions,  $S_\phi$ , the electric potential is specified. The remainder of the surface,  $S_q$ , is insulated, and a surface charge is specified. These are the essential and natural electrical boundary conditions, respectively:

$$\phi = \phi^{S_\phi} \text{ on } S_\phi, \quad (5.4)$$

$$D_i n_i = -q^{S_q} \text{ on } S_q. \quad (5.5)$$

Gauss's equation for charge equilibrium can be written as

$$D_{i,i} - q^B = 0. \quad (5.6)$$

In addition, strain-displacement and electric field-potential relations can be written as

$$S_{ij} = \frac{1}{2}(u_{i,j} + u_{j,i}), \quad (5.7)$$

$$E_i = -\phi_{,i}. \quad (5.8)$$

Finally, the stress and electric field are related to strain and electric displacement by the material constitutive equation developed in Chapter 3:

$$T_{ij}(S_{kl}, D_m), \quad (5.9)$$

$$E_n(S_{kl}, D_m). \quad (5.10)$$

### 5.1.2 Equations of Equilibrium

The first step in solving the problem stated above using the finite element method is to discretize the body into numerous elements and to describe the degrees of freedom on each element in terms of shape functions:

$$\begin{aligned} \mathbf{u} &= \mathbf{H}_u \hat{\mathbf{U}}, \\ \phi &= \mathbf{H}_v \hat{\mathbf{V}}, \\ \mathbf{D} &= \mathbf{H}_D \hat{\mathbf{D}}, \end{aligned} \quad (5.11)$$

where  $\hat{\mathbf{U}}$  is the vector of nodal displacement degrees of freedom for the element,  $\hat{\mathbf{V}}$  is the vector of nodal voltage degrees of freedom, and  $\hat{\mathbf{D}}$  is the vector of electric displacement. The matrices  $\mathbf{H}_u$ ,  $\mathbf{H}_v$ , and  $\mathbf{H}_D$  contain the shape functions for displacement, potential, and electric displacement, respectively. In addition, the strain  $\mathbf{S}$  and electric potential gradient  $\nabla\phi$  can also be described in terms of derivatives of the shape functions:

$$\begin{aligned} \mathbf{S} &= \mathbf{B}_u \hat{\mathbf{U}}, \\ \nabla\phi &= \mathbf{B}_v \hat{\mathbf{V}}, \end{aligned} \quad (5.12)$$

where the matrices  $\mathbf{B}_u$  and  $\mathbf{B}_v$  contain the shape functions of strain and gradient of potential. These shape functions are determined by the spatial discretization of the problem which will be discussed later. The mixed formulation of equations of equilibrium for finite element analysis using this approximation has been derived by Ghandi [35]:

$$\int_V \mathbf{B}_u^T \mathbf{T}(\mathbf{S}, \mathbf{D}, \mathbf{D}^*) dV - \int_V \mathbf{H}_u^T \mathbf{f}^B dV - \int_{S_f} \mathbf{H}_u^T \mathbf{f}^{S_f} dS = 0, \quad (5.13)$$

$$\int_V \mathbf{B}_v^T \mathbf{D} dV + \int_V \mathbf{H}_v^T q^B dV + \int_{S_q} \mathbf{H}_v^T q^{S_q} dS = 0, \quad (5.14)$$

$$\int_V \mathbf{H}_D^T (\mathbf{E}(\mathbf{S}, \mathbf{D}, \mathbf{D}^*) + \nabla\phi) dV = 0. \quad (5.15)$$

The first equation is the equilibrium of mechanical force, and the second equation is an expression of Gauss's equation. The third equation describes the constraint between electric displacement  $\mathbf{D}$  and the gradients of potential  $\phi$ . The detailed derivation of these equations can be found in Ghandi's work [35].

### Generalized Degrees of Freedom

To simplify the discussion of the solution algorithm, Ghandi has defined generalized degree of freedom  $\hat{\mathbf{X}}$ , generalized internal loads  $\mathbf{F}_I$ , and generalized external loads  $\mathbf{F}_E$  as

$$\hat{\mathbf{X}} = \begin{bmatrix} \hat{\mathbf{U}} \\ \hat{\mathbf{D}} \\ \hat{\mathbf{V}} \end{bmatrix}, \quad \mathbf{F}_I(\hat{\mathbf{X}}) = \begin{bmatrix} \mathbf{R}_I(\hat{\mathbf{X}}) \\ \mathbf{L}(\hat{\mathbf{X}}) \\ -\mathbf{Q}_I(\hat{\mathbf{X}}) \end{bmatrix}, \quad \mathbf{F}_E = \begin{bmatrix} \mathbf{R}_E \\ \mathbf{0} \\ -\mathbf{Q}_E \end{bmatrix}, \quad (5.16)$$

where equivalent nodal forces due to internal stress ( $\mathbf{R}_I$ ), equivalent nodal forces due to external loads ( $\mathbf{R}_E$ ), equivalent nodal charges corresponding to the internal electric field ( $\mathbf{Q}_I$ ), equivalent nodal charges due to distributed body and surface charges ( $\mathbf{Q}_E$ ), and the constraint equation ( $\mathbf{L}$ ) are

$$\mathbf{R}_I(\hat{\mathbf{X}}) = \int_V \mathbf{B}_u^T \mathbf{T}(\mathbf{S}, \mathbf{D}, \mathbf{D}^*) dV, \quad (5.17)$$

$$\mathbf{Q}_I(\hat{\mathbf{X}}) = - \int_V \mathbf{B}_v^T \mathbf{D} dV, \quad (5.18)$$

$$\mathbf{L}(\hat{\mathbf{X}}) = \int_V \mathbf{H}_D^T \mathbf{E}(\mathbf{S}, \mathbf{D}, \mathbf{D}^*) dV + \int_V \mathbf{H}_D^T \nabla \phi dV, \quad (5.19)$$

$$\mathbf{R}_E = \int_V \mathbf{H}_u^T \mathbf{f}^B dV + \int_{S_f} \mathbf{H}_u^T \mathbf{f}^{S_f} dS, \quad (5.20)$$

$$\mathbf{Q}_E = \int_V \mathbf{H}_v^T q^B dV + \int_{S_q} \mathbf{H}_v^T q^{S_q} dS. \quad (5.21)$$

Thus the finite element equilibrium equations (Eq. 5.13, 5.14, and 5.15) may be written as:

$$\mathbf{F}(\hat{\mathbf{X}}) = \mathbf{F}_I(\hat{\mathbf{X}}) - \mathbf{F}_E \quad (5.22)$$

However, this is not considered a complete representation of the system yet. There are four variables ( $\mathbf{D}$ ,  $\mathbf{D}^*$ ,  $\mathbf{U}$ , and  $\mathbf{V}$ ) but only three equations in the defined system. The equation for the internal variables  $\mathbf{D}^*$  has not been specified. For the discrete time material model, the evolution of  $\mathbf{D}^*$  is implicitly specified in the 3-D version of Eq. 3.25 in Ghandi's

work [35], while for the continuous time material model developed in this thesis work,  $\mathbf{D}^*$  is explicitly described in Eq. 3.65 or can be simplified as:

$$\dot{\hat{\mathbf{D}}}^* = \mathbf{f}(\hat{\mathbf{D}}, \hat{\mathbf{D}}^*) \quad (5.23)$$

where  $(\dot{\phantom{x}})$  is the derivative with respect to time  $t$ .

In summary, the complete set of system equations includes Eq. 5.22 and 5.23, and the nonlinearity of the material response enters through the functions  $\mathbf{T}(\mathbf{S}, \mathbf{D}, \mathbf{D}^*)$  and  $\mathbf{E}(\mathbf{S}, \mathbf{D}, \mathbf{D}^*)$ . This system is essentially a set of differential-algebraic equations (DAE). Unlike the discrete system by Ghandi, which is just a set of nonlinear equations, the differential-algebraic formulation of the continuous system has a special feature that the initial conditions must be consistent. As a result, the objective of the FEM code is to compute nodal displacement/potentials and elemental electric displacement such that Eq. 5.22 and Eq. 5.23 are satisfied at all time.

## 5.2 Implementation of Material Model

In the material model, the strain and electric fields are functions of the electric displacement and stress

$$\begin{aligned} \mathbf{S} &= \mathbf{S}(\mathbf{D}, \mathbf{D}^*, \mathbf{T}), \\ \mathbf{E} &= \mathbf{E}(\mathbf{D}, \mathbf{D}^*, \mathbf{T}). \end{aligned} \quad (5.24)$$

However, to implement the finite element method, the constitutive law must be in the form of

$$\begin{aligned} \mathbf{T} &= \mathbf{T}(\mathbf{D}, \mathbf{D}^*, \mathbf{S}), \\ \mathbf{E} &= \mathbf{E}(\mathbf{D}, \mathbf{D}^*, \mathbf{S}). \end{aligned} \quad (5.25)$$

Since the strain is restricted as a first order function of stress when the tensor invariants were chosen, one can rewrite the equations as

$$\mathbf{S} = \mathbf{s}^{\mathbf{D}} \mathbf{T} + \mathbf{S}^0, \quad (5.26)$$

where

$$\mathbf{s}^{\mathbf{D}} = \frac{\partial \mathbf{S}}{\partial \mathbf{T}}, \quad (5.27)$$

and

$$\mathbf{S}^0 = \mathbf{S}(\mathbf{T} = \mathbf{0}, \mathbf{D}, \mathbf{D}^*).$$



Note that  $\mathbf{s}^{\mathbf{D}}$  and  $\mathbf{S}^0$  now are functions of  $\mathbf{D}$  and  $\mathbf{D}^*$  only and are independent of  $\mathbf{T}$ . The stress can be represented as a function of  $\mathbf{S}$ ,  $\mathbf{D}$ , and  $\mathbf{D}^*$ :

$$\mathbf{T} = (\mathbf{s}^{\mathbf{D}})^{-1}(\mathbf{S} - \mathbf{S}^0) \quad (5.28)$$

Substituting Eq. 5.28 into Eq. 5.24, one can represent electric field as a function of  $\mathbf{D}$ ,  $\mathbf{D}^*$ , and  $\mathbf{S}$ . Hence, by transforming the material model from the form of Eq. 5.24 into the form of Eq. 5.25, one can implement the material model in the finite element analysis.

### 5.3 Implementation of Spatial Discretization

Detailed convergence tests of various element types have been discussed by Ghandi [35]. Among those convergeable element types, tetrahedral elements are most attractive because they can easily mesh complex geometry. Both the 4-node and 10-node tetrahedral elements shown in Figure 5-1 have been considered in this thesis work to demonstrate the finite element analysis. The 4-node element represents uniform fields for each element, while the 10-node element represents linearly distributed fields for each element. Apparently, higher order elements such as 10-node show faster converging rates than lower order elements. However, due to the nonlinear material model implemented in the finite element formulation, the integration in Eq. 5.13 and 5.14 might be a problem. These integrations are usually carried out by summing up the functionals at the Gaussian points. According to Gellert [45], 20 numerical integration points are required to meet the degree of precision of 5. This means 20 times the computational effort compared to that of the 4-node element. In addition, the way that the material model is formulated needs a degree of precision of at least 6. More derivation is needed to obtain the formula for degree higher than 5. Based on the purpose of demonstration only, the derivation of a new formula is out of the scope of this thesis work. As a result, only 4-node elements are used in the rest of the discussion.

#### 5.3.1 4-node Tetrahedra

Although the shape functions of the 4-node tetrahedon can be easily found in any text of finite element analysis, they are summarized here for completeness. First, the isoparametric

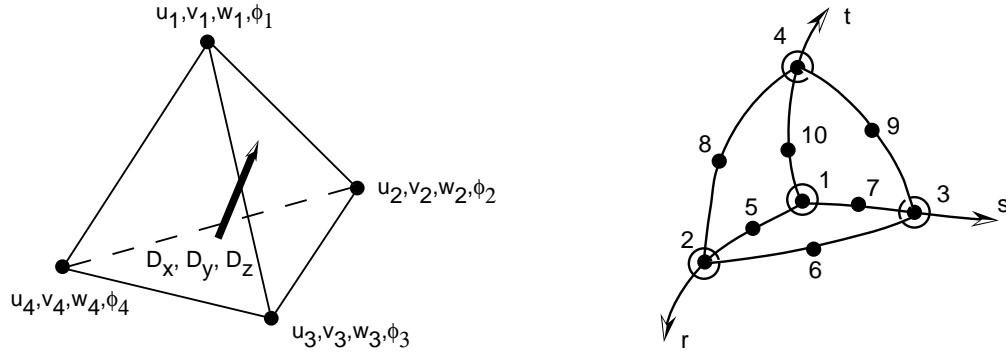


Figure 5-1: 4-node (left) and 10-node (right) tetrahedral elements.

shape functions are defined as:

$$\begin{aligned}
 h_1 &= 1 - r - s - t, \\
 h_2 &= r, \\
 h_3 &= s, \\
 h_4 &= t.
 \end{aligned} \tag{5.29}$$

Hence, the shape function for the displacement degrees of freedom on each element is

$$\mathbf{H}_{\mathbf{u}}^{(e)} = \begin{bmatrix} h_1 & 0 & 0 & h_2 & 0 & 0 & \cdots & h_4 & 0 & 0 \\ 0 & h_1 & 0 & 0 & h_2 & 0 & \ddots & 0 & h_4 & 0 \\ 0 & 0 & h_1 & 0 & 0 & h_3 & \cdots & 0 & 0 & h_4 \end{bmatrix}, \tag{5.30}$$

the shape function for the potential degrees of freedom on each element is

$$\mathbf{H}_{\mathbf{v}}^{(e)} = \begin{bmatrix} h_1 & h_2 & h_3 & h_4 \end{bmatrix}, \tag{5.31}$$

and the shape function for the electric displacement degrees of freedom on each element is

$$\mathbf{H}_{\mathbf{D}}^{(e)} = \begin{bmatrix} 1 & 0 & 0 \\ 0 & 1 & 0 \\ 0 & 0 & 1 \end{bmatrix}. \tag{5.32}$$

Since the strain is the spatial derivative of the displacement

$$\mathbf{S} = \begin{bmatrix} u_{,x} & v_{,y} & w_{,z} & v_{,z} + w_{,y} & u_{,z} + w_{,x} & u_{,y} + v_{,x} \end{bmatrix}^T, \tag{5.33}$$

the shape function of strain on each element is

$$\mathbf{B}_{\mathbf{u}}^{(e)} = \begin{bmatrix} h_{1,x} & 0 & 0 & h_{2,x} & 0 & 0 & \cdots & h_{4,x} & 0 & 0 \\ 0 & h_{1,y} & 0 & 0 & h_{2,y} & 0 & \ddots & 0 & h_{4,y} & 0 \\ 0 & 0 & h_{1,z} & 0 & 0 & h_{2,z} & \ddots & 0 & 0 & h_{4,z} \\ 0 & h_{1,z} & h_{1,y} & 0 & h_{2,z} & h_{2,y} & \ddots & 0 & h_{4,z} & h_{4,y} \\ h_{1,z} & 0 & h_{1,x} & h_{2,z} & 0 & h_{2,x} & \ddots & h_{4,z} & 0 & h_{4,x} \\ h_{1,y} & h_{1,x} & 0 & h_{2,y} & h_{2,x} & 0 & \cdots & h_{4,y} & h_{4,x} & 0 \end{bmatrix}, \quad (5.34)$$

and the shape function of electric field on each element is

$$\mathbf{B}_{\mathbf{v}}^{(e)} = \begin{bmatrix} h_{1,x} & h_{2,x} & h_{3,x} & h_{4,x} \\ h_{1,y} & h_{2,y} & h_{3,y} & h_{4,y} \\ h_{1,z} & h_{2,z} & h_{3,z} & h_{4,z} \end{bmatrix}. \quad (5.35)$$

Note that

$$\mathbf{J} = \begin{bmatrix} \frac{\partial x}{\partial r} & \frac{\partial y}{\partial r} & \frac{\partial z}{\partial r} \\ \frac{\partial y}{\partial s} & \frac{\partial y}{\partial s} & \frac{\partial z}{\partial s} \\ \frac{\partial z}{\partial t} & \frac{\partial y}{\partial s} & \frac{\partial z}{\partial t} \end{bmatrix}, \quad (5.36)$$

and therefore

$$\begin{bmatrix} \frac{\partial}{\partial x} \\ \frac{\partial}{\partial y} \\ \frac{\partial}{\partial z} \end{bmatrix} = \mathbf{J}^{-1} \begin{bmatrix} \frac{\partial}{\partial r} \\ \frac{\partial}{\partial s} \\ \frac{\partial}{\partial t} \end{bmatrix}, \quad (5.37)$$

and the matrix  $\mathbf{B}_{\mathbf{v}}$  is

$$\mathbf{B}_{\mathbf{v}}^{(e)} = \mathbf{J}^{-1} \begin{bmatrix} h_{1,r} & h_{2,r} & h_{3,r} & h_{4,r} \\ h_{1,s} & h_{2,s} & h_{3,s} & h_{4,s} \\ h_{1,t} & h_{2,t} & h_{3,t} & h_{4,t} \end{bmatrix}. \quad (5.38)$$

In addition, the element in matrix  $\mathbf{B}_{\mathbf{u}}^{(e)}$  can be extracted from matrix  $\mathbf{B}_{\mathbf{v}}^{(e)}$  in Eq. 5.38.

Since the shape function for the 4-node tetrahedron is a first-order function, the Jacobian matrix is just a function of nodal coordinates but not a function of isoparametric natural coordinates:

$$\mathbf{J} = \begin{bmatrix} x_2 - x_1 & y_2 - y_1 & z_2 - x_1 \\ x_3 - x_1 & y_3 - y_1 & z_3 - z_1 \\ x_4 - x_1 & y_4 - y_1 & z_4 - z_1 \end{bmatrix}. \quad (5.39)$$

## Numerical Integration

Since all the functions are constant along each element, the integration on the volume of each element can be carried out easily.

### Assembly

To assemble all the elements into the global finite element system, a connectivity matrix  $\mathbf{N}$  which attributes the element nodal index to global nodal index is needed. The connectivity matrix  $\mathbf{N}$  has size of  $m \times n$ , where  $m$  is the number of total elements, and  $n$  is the number of nodes per element. In addition, two index vectors  $\mathbf{I}_v$  and  $\mathbf{I}_u$  are needed to indicate the prescribed potential and displacement degrees of freedom, respectively.

## 5.4 Solution Techniques

### 5.4.1 Differential Algebraic Formulation

The variables that need to be solved include  $\hat{\mathbf{U}}$ ,  $\hat{\mathbf{V}}$ ,  $\hat{\mathbf{D}}$ , and  $\hat{\mathbf{D}}^*$ , which are defined by Eq. 5.22 and 5.23. Using the numerical integration or so called Gaussian-Quadrature which transforms the spatial integration into summation  $\sum$ , one can rewrite the system as

$$\dot{\hat{\mathbf{D}}}^* - \mathbf{f}(\hat{\mathbf{D}}, \hat{\mathbf{D}}^*) = 0, \quad (5.40)$$

$$\sum \mathbf{J} \mathbf{B}_u^T \mathbf{T}(\mathbf{B}_u \hat{\mathbf{U}}, \mathbf{H}_D \hat{\mathbf{D}}, \hat{\mathbf{D}}^*) - \mathbf{R}_E = 0, \quad (5.41)$$

$$\sum \mathbf{J} \mathbf{H}_D^T \mathbf{E}(\mathbf{B}_u \hat{\mathbf{U}}, \mathbf{H}_D \hat{\mathbf{D}}, \hat{\mathbf{D}}^*) + \sum \mathbf{J} \mathbf{H}_D^T \mathbf{B}_v \hat{\mathbf{V}} = 0, \quad (5.42)$$

$$\sum \mathbf{J} \mathbf{B}_v^T \mathbf{H}_D \hat{\mathbf{D}} - \mathbf{Q}_E = 0. \quad (5.43)$$

Eq. 5.40, 5.41, 5.42, and 5.43 can be further renamed and simplified, respectively, as

$$\dot{\hat{\mathbf{D}}}^* - \mathbf{F}_1(\hat{\mathbf{D}}, \hat{\mathbf{D}}^*) = 0, \quad (5.44)$$

$$\mathbf{F}_U(\hat{\mathbf{U}}, \hat{\mathbf{D}}, \hat{\mathbf{D}}^*) - \mathbf{R}_E = 0, \quad (5.45)$$

$$\mathbf{F}_D(\hat{\mathbf{U}}, \hat{\mathbf{D}}, \hat{\mathbf{D}}^*, \hat{\mathbf{V}}) = 0, \quad (5.46)$$

$$\mathbf{F}_V(\hat{\mathbf{D}}) - \mathbf{Q}_E = 0. \quad (5.47)$$

With this representation, one can easily trace the dependent variables in the equations. If some of the displacement and potential degrees of freedom are prescribed, one can partition

them as

$$\hat{\mathbf{U}} = \begin{bmatrix} \hat{\mathbf{U}}_{\mathbf{a}} \\ \hat{\mathbf{U}}_{\mathbf{b}} \end{bmatrix}, \quad \hat{\mathbf{V}} = \begin{bmatrix} \hat{\mathbf{V}}_{\mathbf{a}} \\ \hat{\mathbf{V}}_{\mathbf{b}} \end{bmatrix}, \quad (5.48)$$

where  $\hat{\mathbf{U}}_{\mathbf{a}}$  and  $\hat{\mathbf{V}}_{\mathbf{a}}$  are the unknown displacement and potential degrees of freedom, and  $\hat{\mathbf{U}}_{\mathbf{b}}$  and  $\hat{\mathbf{V}}_{\mathbf{b}}$  are the prescribed displacement and potential degrees of freedom, respectively.

Similarly,  $\mathbf{R}_{\mathbf{E}}$  and  $\mathbf{Q}_{\mathbf{E}}$  can be partitioned into

$$\mathbf{R}_{\mathbf{E}} = \begin{bmatrix} \mathbf{R}_{\mathbf{E}_{\mathbf{a}}} \\ \mathbf{R}_{\mathbf{E}_{\mathbf{b}}} \end{bmatrix}, \quad \mathbf{Q}_{\mathbf{E}} = \begin{bmatrix} \mathbf{Q}_{\mathbf{E}_{\mathbf{a}}} \\ \mathbf{Q}_{\mathbf{E}_{\mathbf{b}}} \end{bmatrix}, \quad (5.49)$$

where  $\mathbf{R}_{\mathbf{E}_{\mathbf{a}}}$  is the prescribed force on the unknown displacement  $\hat{\mathbf{U}}_{\mathbf{a}}$ , and  $\mathbf{R}_{\mathbf{E}_{\mathbf{b}}}$  is the reaction force on the prescribed displacement  $\hat{\mathbf{U}}_{\mathbf{b}}$ . Similarly,  $\mathbf{Q}_{\mathbf{E}_{\mathbf{a}}}$  is the prescribed charge on the unknown voltage degree of freedom  $\hat{\mathbf{V}}_{\mathbf{a}}$ , and  $\mathbf{Q}_{\mathbf{E}_{\mathbf{b}}}$  is the reaction charge on the prescribed voltage degree of freedom  $\hat{\mathbf{V}}_{\mathbf{b}}$ . These partitions can be conducted in the computer program using the vectors  $\mathbf{I}_{\mathbf{u}}$  and  $\mathbf{I}_{\mathbf{v}}$ . Although  $\hat{\mathbf{D}}$  and  $\hat{\mathbf{D}}^*$  are degrees of freedom, in general they are difficult to be prescribed.

With these partitions, Eq. 5.45 can be rearranged into

$$\mathbf{F}_2(\hat{\mathbf{U}}_{\mathbf{a}}, \hat{\mathbf{U}}_{\mathbf{b}}, \hat{\mathbf{D}}, \hat{\mathbf{D}}^*) - \mathbf{R}_{\mathbf{E}_{\mathbf{a}}} = 0, \quad (5.50)$$

$$\mathbf{F}_3(\hat{\mathbf{U}}_{\mathbf{a}}, \hat{\mathbf{U}}_{\mathbf{b}}, \hat{\mathbf{D}}, \hat{\mathbf{D}}^*) - \mathbf{R}_{\mathbf{E}_{\mathbf{b}}} = 0, \quad (5.51)$$

and Eq. 5.46 can be rewritten as

$$\mathbf{F}_4(\hat{\mathbf{U}}_{\mathbf{a}}, \hat{\mathbf{U}}_{\mathbf{b}}, \hat{\mathbf{D}}, \hat{\mathbf{D}}^*, \hat{\mathbf{V}}_{\mathbf{a}}, \hat{\mathbf{V}}_{\mathbf{b}}) = 0. \quad (5.52)$$

In addition, Eq. 5.47 can be partitioned into

$$\mathbf{F}_5(\hat{\mathbf{D}}) - \mathbf{Q}_{\mathbf{E}_{\mathbf{a}}} = 0, \quad (5.53)$$

$$\mathbf{F}_6(\hat{\mathbf{D}}) - \mathbf{Q}_{\mathbf{E}_{\mathbf{b}}} = 0. \quad (5.54)$$

To make it clear, the equations to be solved are recollected again from Eq. 5.40, 5.50,

5.51, 5.52, 5.53, and 5.54:

$$\dot{\hat{\mathbf{D}}}^* - \mathbf{F}_1(\hat{\mathbf{D}}, \hat{\mathbf{D}}^*) = 0, \quad (5.55)$$

$$\mathbf{F}_2(\hat{\mathbf{U}}_a, \hat{\mathbf{U}}_b, \hat{\mathbf{D}}, \hat{\mathbf{D}}^*) - \mathbf{R}_{\mathbf{E}_a} = 0, \quad (5.56)$$

$$\mathbf{F}_3(\hat{\mathbf{U}}_a, \hat{\mathbf{U}}_b, \hat{\mathbf{D}}, \hat{\mathbf{D}}^*) - \mathbf{R}_{\mathbf{E}_b} = 0, \quad (5.57)$$

$$\mathbf{F}_4(\hat{\mathbf{U}}_a, \hat{\mathbf{U}}_b, \hat{\mathbf{D}}, \hat{\mathbf{D}}^*, \hat{\mathbf{V}}_a, \hat{\mathbf{V}}_b) = 0, \quad (5.58)$$

$$\mathbf{F}_5(\hat{\mathbf{D}}) - \mathbf{Q}_{\mathbf{E}_a} = 0, \quad (5.59)$$

$$\mathbf{F}_6(\hat{\mathbf{D}}) - \mathbf{Q}_{\mathbf{E}_b} = 0. \quad (5.60)$$

The input of these equations are  $\hat{\mathbf{U}}_b$ ,  $\hat{\mathbf{V}}_b$ ,  $\mathbf{R}_{\mathbf{E}_a}$ , and  $\mathbf{Q}_{\mathbf{E}_a}$ . The unknown variables to be solved are  $\hat{\mathbf{V}}_a$ ,  $\hat{\mathbf{U}}_a$ ,  $\hat{\mathbf{D}}$ ,  $\hat{\mathbf{D}}^*$ ,  $\mathbf{R}_{\mathbf{E}_b}$ , and  $\mathbf{Q}_{\mathbf{E}_b}$ . Since  $\mathbf{R}_{\mathbf{E}_b}$  and  $\mathbf{Q}_{\mathbf{E}_b}$  are the reaction force and charge, to solve this system, it is convenient to solve for  $\hat{\mathbf{V}}_a$ ,  $\hat{\mathbf{U}}_a$ ,  $\hat{\mathbf{D}}$ , and  $\hat{\mathbf{D}}^*$  first from Eq. 5.55, 5.56, 5.58, and 5.59. Once  $\hat{\mathbf{V}}_a$ ,  $\hat{\mathbf{U}}_a$ ,  $\hat{\mathbf{D}}$ , and  $\hat{\mathbf{D}}^*$  are solved, the reaction force ( $\mathbf{R}_{\mathbf{E}_b}$ ) and charge ( $\mathbf{Q}_{\mathbf{E}_b}$ ) can be obtained easily from Eq. 5.57 and 5.60. As a result, the final set of equations to be solved includes Eq. 5.55, 5.56, 5.58, and 5.59, which shall be recollected here again for convenience:

$$\dot{\hat{\mathbf{D}}}^* - \mathbf{F}_1(\hat{\mathbf{D}}, \hat{\mathbf{D}}^*) = 0, \quad (5.61)$$

$$\mathbf{F}_2(\hat{\mathbf{U}}_a, \hat{\mathbf{U}}_b, \hat{\mathbf{D}}, \hat{\mathbf{D}}^*) - \mathbf{R}_{\mathbf{E}_a} = 0, \quad (5.62)$$

$$\mathbf{F}_4(\hat{\mathbf{U}}_a, \hat{\mathbf{U}}_b, \hat{\mathbf{D}}, \hat{\mathbf{D}}^*, \hat{\mathbf{V}}_a, \hat{\mathbf{V}}_b) = 0, \quad (5.63)$$

$$\mathbf{F}_5(\hat{\mathbf{D}}) - \mathbf{Q}_{\mathbf{E}_a} = 0. \quad (5.64)$$

This is essentially a set of differential algebraic equations (DAE) again, which can be rewritten in the general form

$$F(t, \mathbf{z}, \dot{\mathbf{z}}) = 0. \quad (5.65)$$

where  $\mathbf{z}$  is a vector of state variables to be solved:

$$\mathbf{z} = \begin{bmatrix} \hat{\mathbf{D}}^* \\ \hat{\mathbf{U}}_a \\ \hat{\mathbf{D}} \\ \hat{\mathbf{V}}_a \end{bmatrix}. \quad (5.66)$$

### 5.4.2 Time-stepping Numerical Algorithm

The basic idea for solving a DAE system is to replace the solution and its derivative in Eq. 5.65 by a finite difference approximation and to solve the resultant equations for the solution at the current time  $t_n$  using Newton's method. For example, replacing the derivative by the backward difference in Eq. 5.65 gives the first order formula

$$F(t_n, \mathbf{z}_n, \frac{\mathbf{z}_n - \mathbf{z}_{n-1}}{h_n}) = 0, \quad (5.67)$$

where  $h_n = t_n - t_{n-1}$ . This equation can be solved at each time step using a modified Newton method:

$$\mathbf{z}_n^{(m+1)} = \mathbf{z}_n^{(m)} - \left( \frac{1}{h_n} \frac{\partial F}{\partial \dot{\mathbf{z}}} + \frac{\partial F}{\partial \mathbf{z}} \right)^{-1} F \left( t, \mathbf{z}_n^{(m)}, \frac{\mathbf{z}_n^{(m)} - \mathbf{z}_{n-1}}{h_n} \right), \quad (5.68)$$

where  $m$  is the iteration index. Solving this requires solution of the linear system

$$\mathbf{A} \mathbf{x} = \mathbf{b}, \quad (5.69)$$

where

$$\mathbf{A} = \left( \frac{1}{h_n} \frac{\partial F}{\partial \dot{\mathbf{z}}} + \frac{\partial F}{\partial \mathbf{z}} \right) \quad (5.70)$$

is an  $N \times N$  iteration matrix,  $\mathbf{x} = \mathbf{z}_n^{(m+1)} - \mathbf{z}_n^{(m)}$  is an  $N$ -vector, and

$$\mathbf{b} = -F \left( t, \mathbf{z}_n^{(m)}, \frac{\mathbf{z}_n^{(m)} - \mathbf{z}_{n-1}}{h_n} \right)$$

is an  $N$ -vector.  $N$  is the total number of the degrees of freedom to be solved.

#### Calculation of Iteration Matrix $\mathbf{A}$

The iteration matrix (Eq. 5.70) can be calculated numerically using a finite difference scheme. However, to improve the convergence, it is recommended to calculate the iteration matrix analytically if possible. From Eq. 5.55, the term  $\frac{\partial F}{\partial \dot{\mathbf{z}}}$  can be written as

$$\frac{\partial F}{\partial \dot{\mathbf{z}}} = \begin{bmatrix} \mathbf{I} & 0 \\ 0 & 0 \end{bmatrix}, \quad (5.71)$$

where  $\mathbf{I}$  is a  $q \times q$  identity matrix.  $q$  is the size of the vector  $\hat{\mathbf{D}}^*$ . From Eq. 5.61, 5.62, 5.63 and 5.64, the term  $\frac{\partial F}{\partial \mathbf{z}}$  can be written as

$$\frac{\partial F}{\partial \mathbf{z}} = \begin{bmatrix} \mathbf{K}_{ss} & 0 & \mathbf{K}_{sd} & 0 \\ \mathbf{K}_{us} & \mathbf{K}_{uu} & \mathbf{K}_{ud} & 0 \\ \mathbf{K}_{ds} & \mathbf{K}_{du} & \mathbf{K}_{dd} & \mathbf{K}_{dv} \\ 0 & 0 & \mathbf{K}_{vd} & 0 \end{bmatrix}, \quad (5.72)$$

where

$$\mathbf{K}_{ss} = \frac{\partial \mathbf{F}_1}{\partial \hat{\mathbf{D}}^*},$$

$$\mathbf{K}_{sd} = \frac{\partial \mathbf{F}_1}{\partial \hat{\mathbf{D}}},$$

$$\mathbf{K}_{us} = \frac{\partial \mathbf{F}_2}{\partial \hat{\mathbf{D}}^*} = \int_V \mathbf{B}_u^T \frac{\partial \mathbf{T}}{\partial \mathbf{D}^*} \mathbf{H}_D dV,$$

$$\mathbf{K}_{uu} = \frac{\partial \mathbf{F}_2}{\partial \hat{\mathbf{U}}} = \int_V \mathbf{B}_u^T \frac{\partial \mathbf{T}}{\partial \mathbf{S}} \mathbf{B}_u dV,$$

$$\mathbf{K}_{ud} = \frac{\partial \mathbf{F}_2}{\partial \hat{\mathbf{D}}} = \int_V \mathbf{B}_u^T \frac{\partial \mathbf{T}}{\partial \mathbf{D}} \mathbf{H}_D dV,$$

$$\mathbf{K}_{ds} = \frac{\partial \mathbf{F}_3}{\partial \hat{\mathbf{D}}^*} = \int_V \mathbf{H}_D^T \frac{\partial \mathbf{E}}{\partial \mathbf{D}^*} \mathbf{H}_D dV,$$

$$\mathbf{K}_{du} = \frac{\partial \mathbf{F}_3}{\partial \hat{\mathbf{U}}} = \int_V \mathbf{H}_D^T \frac{\partial \mathbf{E}}{\partial \mathbf{S}} \mathbf{B}_u dV,$$

$$\mathbf{K}_{dd} = \frac{\partial \mathbf{F}_3}{\partial \hat{\mathbf{D}}} = \int_V \mathbf{H}_D^T \frac{\partial \mathbf{E}}{\partial \mathbf{D}} \mathbf{H}_D dV,$$

$$\mathbf{K}_{dv} = \frac{\partial \mathbf{F}_3}{\partial \hat{\mathbf{V}}} = \int_V \mathbf{H}_D^T \mathbf{B}_v dV,$$

$$\mathbf{K}_{vd} = \frac{\partial \mathbf{F}_4}{\partial \hat{\mathbf{D}}} = \int_V \mathbf{B}_v^T \mathbf{H}_D dV.$$



As can be seen, the matrices  $\mathbf{K}_{us}$ ,  $\mathbf{K}_{uu}$ ,  $\mathbf{K}_{ud}$ ,  $\mathbf{K}_{ds}$ , and  $\mathbf{K}_{du}$  are dependent upon the material properties. To calculate these matrices, one must first change the variables as the following:

$$\frac{\partial \mathbf{T}}{\partial \mathbf{D}^*} = \frac{\partial \mathbf{T}}{\partial \mathbf{S}} \frac{\partial \mathbf{S}}{\partial \mathbf{D}^*}, \quad (5.73)$$

$$\frac{\partial \mathbf{T}}{\partial \mathbf{D}} = \frac{\partial \mathbf{T}}{\partial \mathbf{S}} \frac{\partial \mathbf{S}}{\partial \mathbf{D}}, \quad (5.74)$$

$$\frac{\partial \mathbf{E}}{\partial \mathbf{S}} = \frac{\partial \mathbf{E}}{\partial \mathbf{T}} \frac{\partial \mathbf{T}}{\partial \mathbf{S}}, \quad (5.75)$$

where  $\frac{\partial \mathbf{S}}{\partial \mathbf{D}^*}$ ,  $\frac{\partial \mathbf{S}}{\partial \mathbf{D}}$ ,  $\frac{\partial \mathbf{E}}{\partial \mathbf{D}^*}$ , and  $\frac{\partial \mathbf{E}}{\partial \mathbf{T}}$  can be obtained symbolically from the material model (Eq. 5.24), and  $\frac{\partial \mathbf{T}}{\partial \mathbf{S}}$  can be obtained by inverting Eq. 5.27.

In summary, Eq. 5.71 and 5.72 give the iteration matrix  $\mathbf{A}$ . With this iteration matrix, Eq. 5.65 can be solved numerically.

### 5.4.3 Software Implementation

Solving a large scale system of DAEs such as the one in Eq. 5.65 is not a trivial problem. A well-known DAE solver, DASSL, has been developed by Pezold[46]. A sophisticated version of DASSL called DASPK scales and preconditions the iteration matrix ( $\mathbf{A}$ ) so that the system  $\mathbf{Ax} = \mathbf{b}$  is solved with  $\mathbf{A}$  virtually close to an identity matrix. For this reason, this thesis work implemented the DASPK solver to solve the system defined in Eq. 5.65.

## 5.5 Case Study

This section will demonstrate the capability of the nonlinear finite element code developed above. It is important to study how these elements perform before emulating real problems. Hence, this section will first examine a simple element under various loading conditions to assure the result. After the element tests, large scale problems, such as a chunk of material under uniform and skewed loading, will be simulated to demonstrate the contribution of this nonlinear finite element code.

### 5.5.1 Element Tests

#### Test 1. Single element with complete prescribed voltage

It is the intention to see how the polarization in the element responds to the applied electric fields. The first test case, as shown in Figure 5-2, examines the response of an element with four nodes subjected to prescribed voltage. Node 1, 2, and 3 are ground, while Node 4 is driven with a 1.4kV cyclic voltage at 0.1Hz. In addition, the following displacements are constrained to be zero:  $u_x^{(1)}$ ,  $u_y^{(1)}$ ,  $u_z^{(1)}$ ,  $u_x^{(2)}$ ,  $u_y^{(3)}$ ,  $u_x^{(4)}$ , and  $u_y^{(4)}$ , where the number in ( ) denotes the nodal number. In this case, all the voltage degrees of freedom are prescribed; that is,  $\mathbf{V} = \mathbf{V}_b$ . This means that  $\mathbf{V}_a$  and  $\mathbf{Q}_{E_a}$  are actually null vectors in the system. As a result, the system of Eq. 5.61, 5.62, 5.63, and 5.64 becomes

$$\dot{\hat{\mathbf{D}}}^* - \mathbf{F}_1(\hat{\mathbf{D}}, \hat{\mathbf{D}}^*) = 0, \quad (5.76)$$

$$\mathbf{F}_2(\hat{\mathbf{U}}_a, \hat{\mathbf{U}}_b, \hat{\mathbf{D}}, \hat{\mathbf{D}}^*) - \mathbf{R}_{E_a} = 0, \quad (5.77)$$

$$\mathbf{F}_4(\hat{\mathbf{U}}_a, \hat{\mathbf{U}}_b, \hat{\mathbf{D}}, \hat{\mathbf{D}}^*, \hat{\mathbf{V}}_b) = 0. \quad (5.78)$$

Therefore, only  $\hat{\mathbf{D}}$ ,  $\hat{\mathbf{U}}_a$ , and  $\hat{\mathbf{D}}^*$  need to be solved. Figure 5-3 shows the polarization and displacement response of different nodes versus applied cyclic voltage signal. The polarization direction and deformed body can be visualized in Figure 5-2.

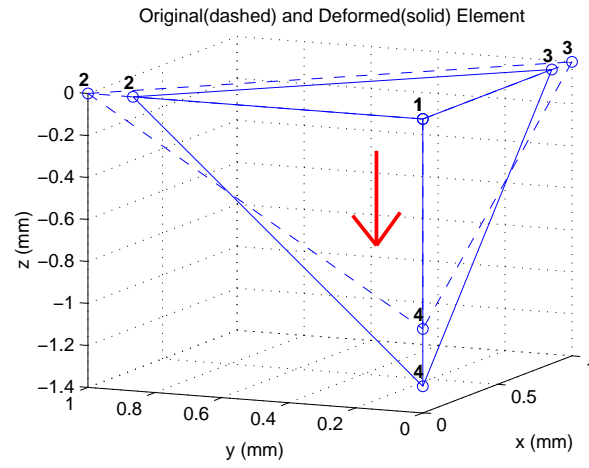


Figure 5-2: Test 1. Results: deformed body. Displacement is not in scale.

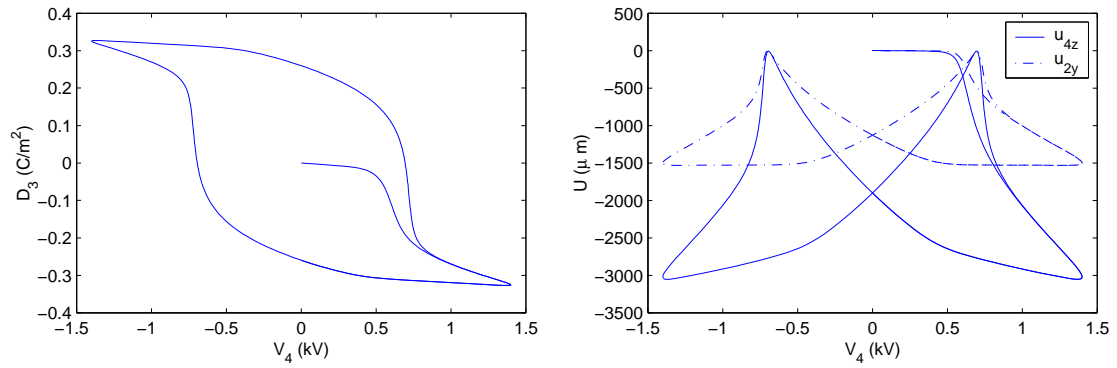


Figure 5-3: Test 1. Results: polarization (left) and displacement (right) vs. driving voltage.

## Test 2. Single element with incomplete prescribed voltage

It is also important to investigate if the FEM code can solve for unprescribed nodal voltages on the element. As illustrated in Figure 5-4, Node 4 is prescribed with a 0.1Hz and 1.4kV cyclic voltage, and Node 1 is ground, while voltage on Nodes 2 and 3 are left undetermined. In addition, the following displacements are constrained to be zero:  $u_x^{(1)}$ ,  $u_y^{(1)}$ ,  $u_z^{(1)}$ ,  $u_x^{(2)}$ ,  $u_y^{(3)}$ ,  $u_x^{(4)}$ , and  $u_y^{(4)}$ . Compared to the applied voltage, Figure 5-5 shows the voltage solved by the FEM code. Due to the boundary condition prescribed on the nodal displacement, the element may undergo stress as the electric field increases. This induced stress will cause the nodal potential to decrease as shown in Figure 5-5. Figure 5-6 shows the polarization and displacement response of different nodes versus applied voltage. The polarization direction and deformed body can be visualized in Figure 5-4.

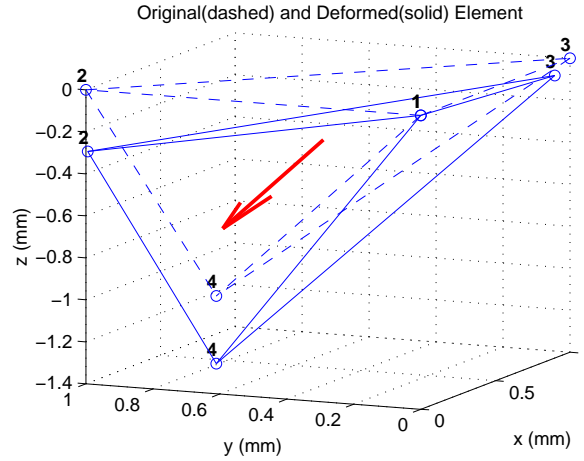


Figure 5-4: Test 2. Results

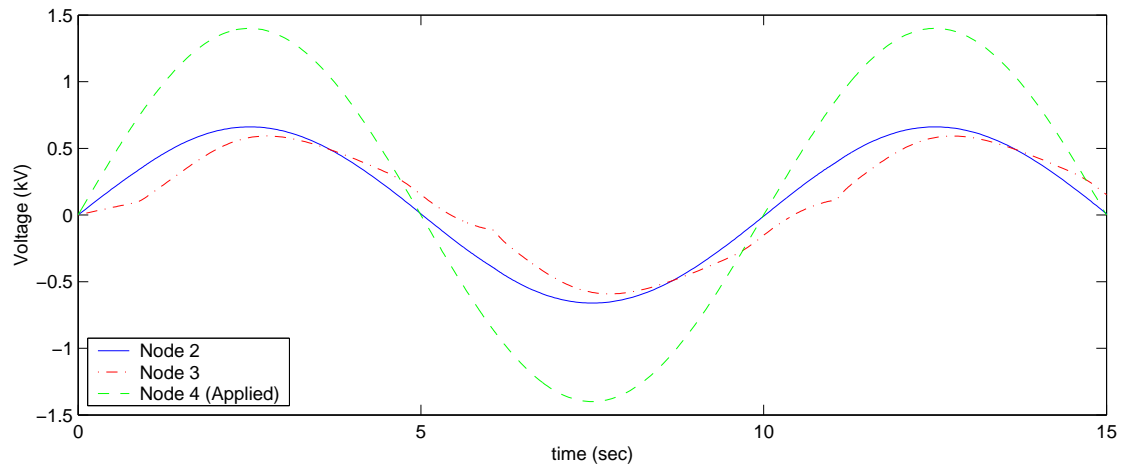


Figure 5-5: Test 2 result: comparison between nodal voltage and driving voltage.

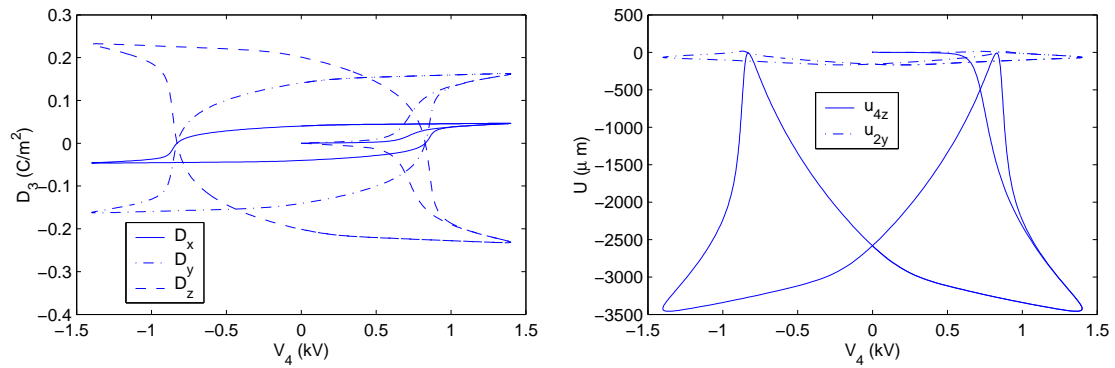


Figure 5-6: Test 2. results: polarization (left) and displacement (right) vs. driving voltage.

### 5.5.2 Piezoelectric Response under Uniform Loading

Before solving the problem with irregular boundary conditions or geometries, it is also essential to examine the case under uniform electric field, as shown in Figure 5-7. By symmetry, one can re-define the case with the representative volume shown in Figure 5-7 under the following boundary conditions:

$$\phi = V \sin(\omega t), \quad \text{at } z = H,$$

$$\phi = 0, \quad \text{at } z = 0,$$

$$u_x = 0, \quad \text{at } x = 0,$$

$$u_y = 0, \quad \text{at } y = 0,$$

$$u_z = 0, \quad \text{at } z = 0.$$

For demonstration purposes, the dimensions of the representative volume are  $a=1\text{mm}$ ,  $b=1\text{mm}$ , and  $H=3\text{mm}$ , and its driving voltage is a 1Hz cyclic wave with an amplitude of 4.35kV. The representative volume is meshed into 36 elements by 19 nodes, shown in Figure 5-8 (left).

Figure 5-8 (right) shows the simulated results of the deformed body and the polarization direction on each element at time = 1.5s. As can be seen, the representative volume extends along the polarization direction while it shrinks in the transverse directions. Figure 5-9 shows the time history of the nodal voltages solved by the code. As can be seen, the potentials on the nodes are proportional to their z-coordinates because the volume is under uniform electric field along the z-direction. For the same reason, the whole volume exhibits a uniform polarization as shown in Figure 5-10 (right), and the displacements are also proportional to their z-coordinates as shown in Figure 5-10 (left).

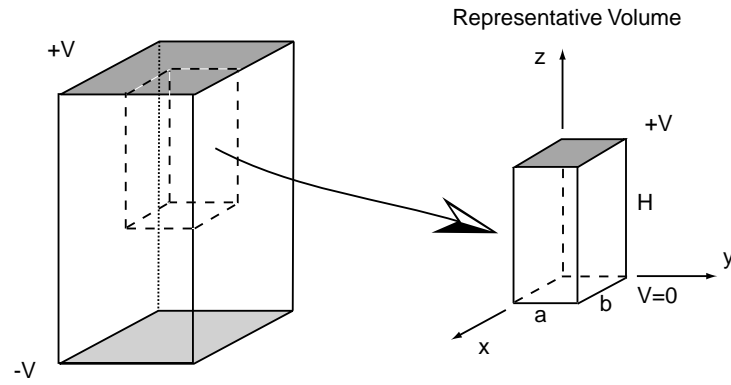


Figure 5-7: Representative volume of specimen under uniform electric field.

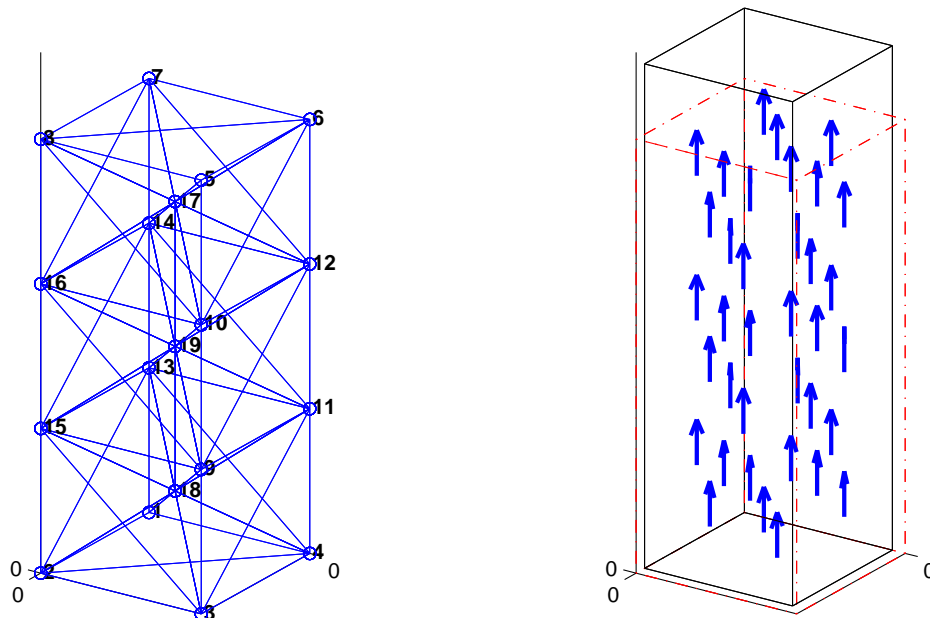


Figure 5-8: Mesh of representative volume for the case under uniform electric field.

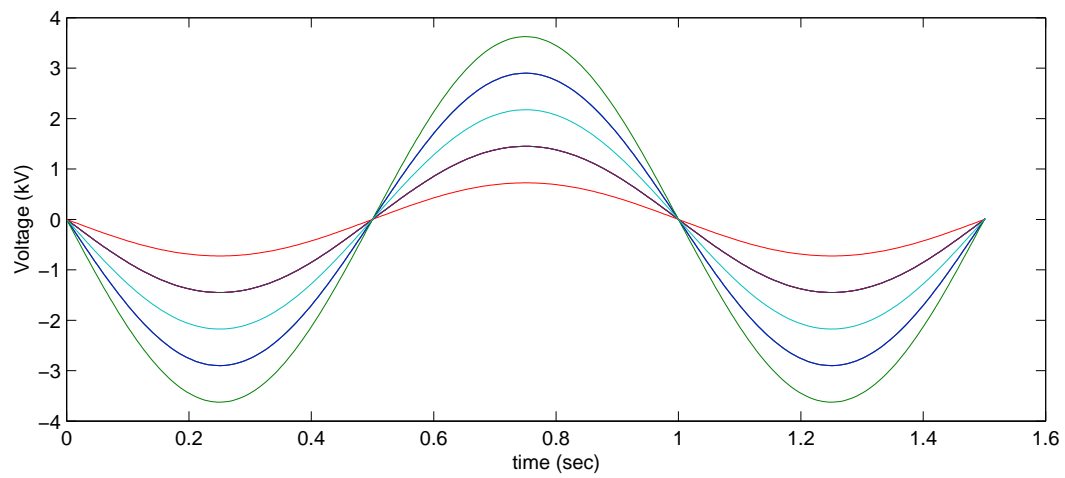


Figure 5-9: Solved voltage on the nodes.

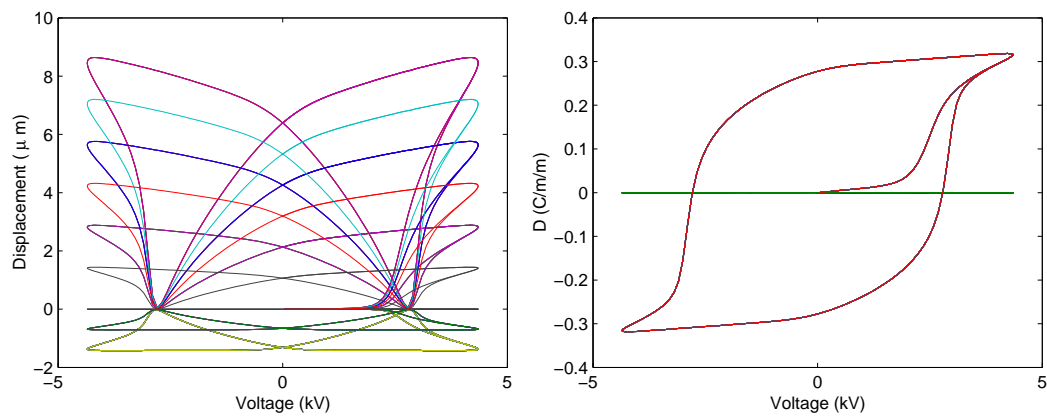


Figure 5-10: Solution of displacement on the nodes (left) and electric displacement on the elements (right).



### 5.5.3 Piezoelectric Response under Skewed Loading

It is the ultimate goal of this thesis to simulate the material response for irregular geometry or non-uniform boundary conditions. To demonstrate this capability of this code, a chunk of material with four electrodes on its edges is used, as illustrated in Figure 5-11. By symmetry, one can re-define the case with the representative volume shown in Figure 5-11 under the following boundary conditions:

$$\begin{aligned}\phi &= V \sin(\omega t), & \text{at } z = b, \quad d < x < c + d, \\ \phi &= 0, & \text{at } x = 0, \\ u_x &= 0, & \text{at } x = 0, \\ u_y &= 0, & \text{at } y = 0, \\ u_z &= 0, & \text{at } z = 0.\end{aligned}$$

For demonstration purposes, the dimensions of the representative volume are a=1mm, b=1mm, c=1mm, and d=2mm, and its driving voltage is a 0.126Hz cyclic wave with an amplitude of 2.8kV. The representative volume is also meshed into 36 elements by 19 nodes, shown in Figure 5-12.

Figures 5-13 and 5-14 first show the results of the simulated potentials on the nodes compared to the cyclic driving voltage. As can be seen, some of the nodal potentials are not exactly proportional to the the driving voltage. This is because some of the element is experiencing stress while other elements are polarized. This phenomenon is very severe for the coarsely meshed volume especially when meshed by the 4-node tetrahedral element like the one used in this case, because this type of element exhibits very stiff characteristics<sup>1</sup>. For the same reason, the polarizations and displacements of some of the elements exhibit strange behavior, as shown in Figures 5-15 and 5-16. The polarization direction of each element and the deformed body compared to the original volume at various time steps are shown in Figure 5-17. As can be seen, the representative volume exhibits slight shear deformation due to the skewed electric field. Despite this, the deformation of the body shows significant elongation along the x-direction after 1.5 cycles of driving voltage. This is exactly the case for the actuator with interdigitated electrodes introduced in Chapter 1.

---

<sup>1</sup>The strain field and electric displacement are assumed uniform on the element. As a result, it shows little flexibility of its response

Unfortunately, the results discussed above are not converged to the real problem yet because of the coarse mesh used in this problem. In order to increase the accuracy, a much finer mesh must be used to relieve the stiff characteristics of the 4-node tetrahedral element.

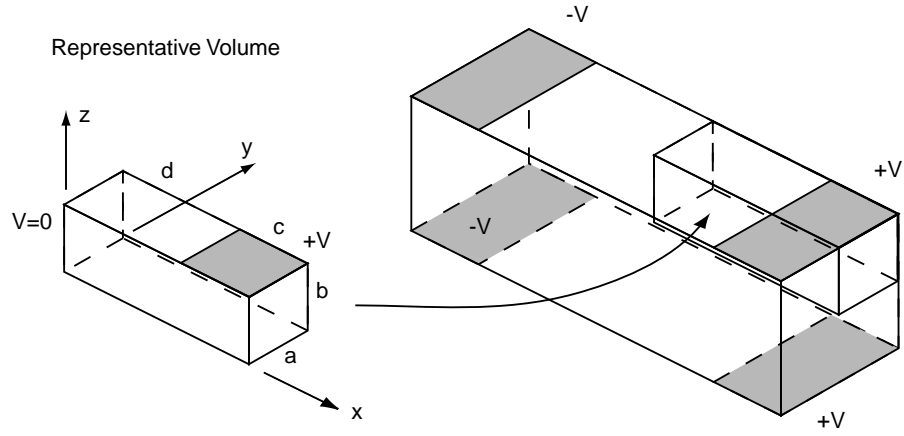


Figure 5-11: Representative volume of specimen under skewed electric field.

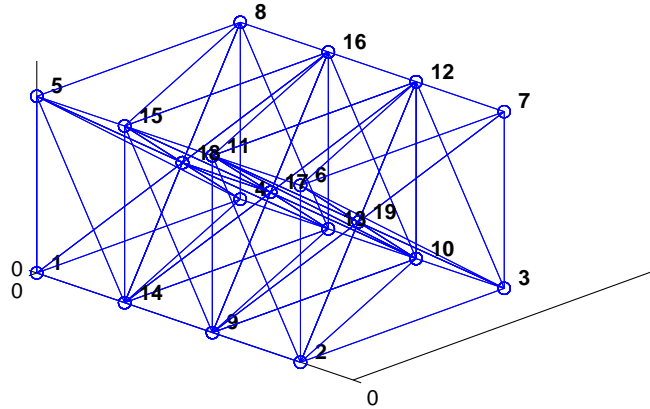


Figure 5-12: Mesh of representative volume for the case under skewed electric field.

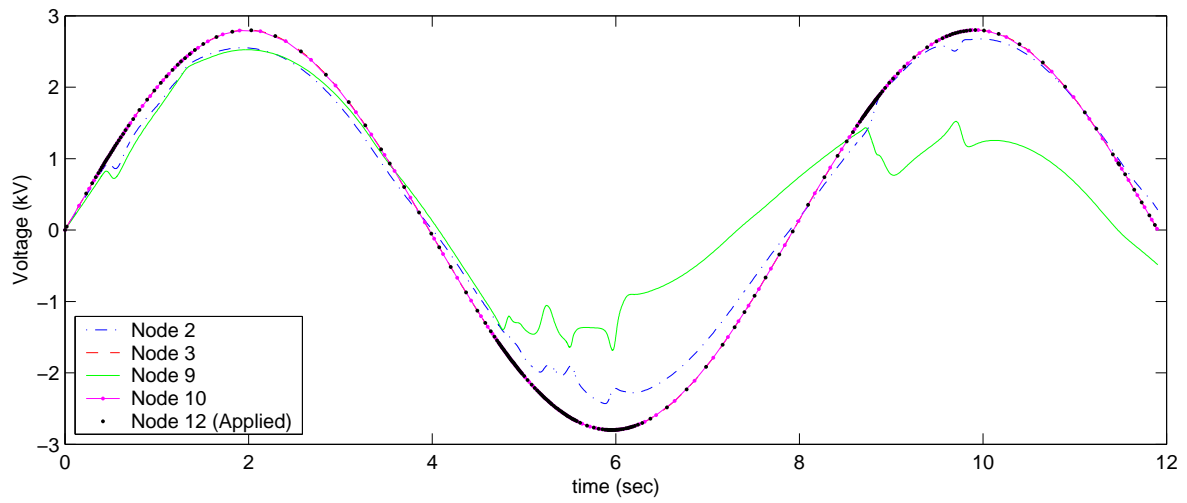


Figure 5-13: Solved voltage on the nodes.

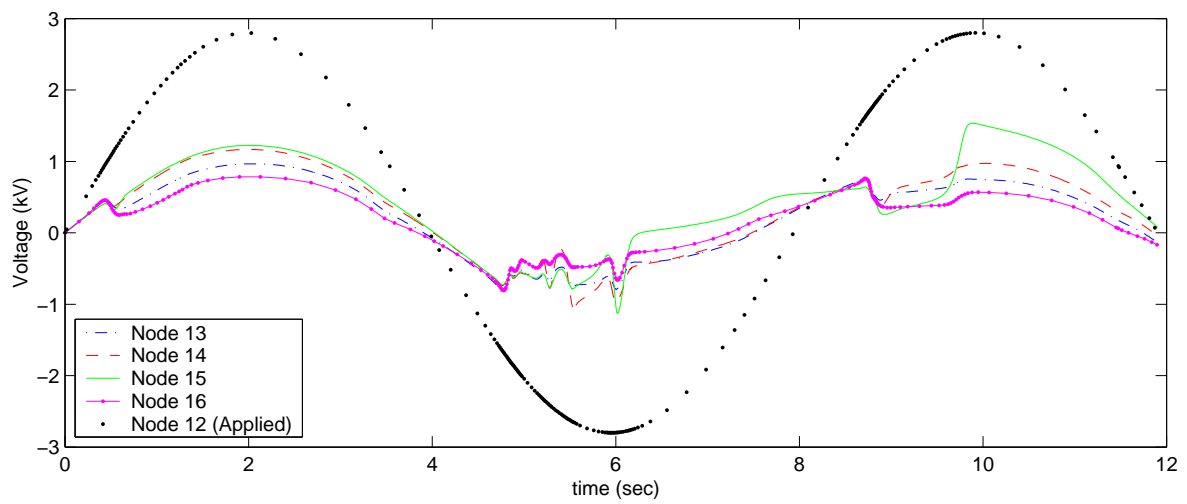


Figure 5-14: Solved voltage on the nodes.

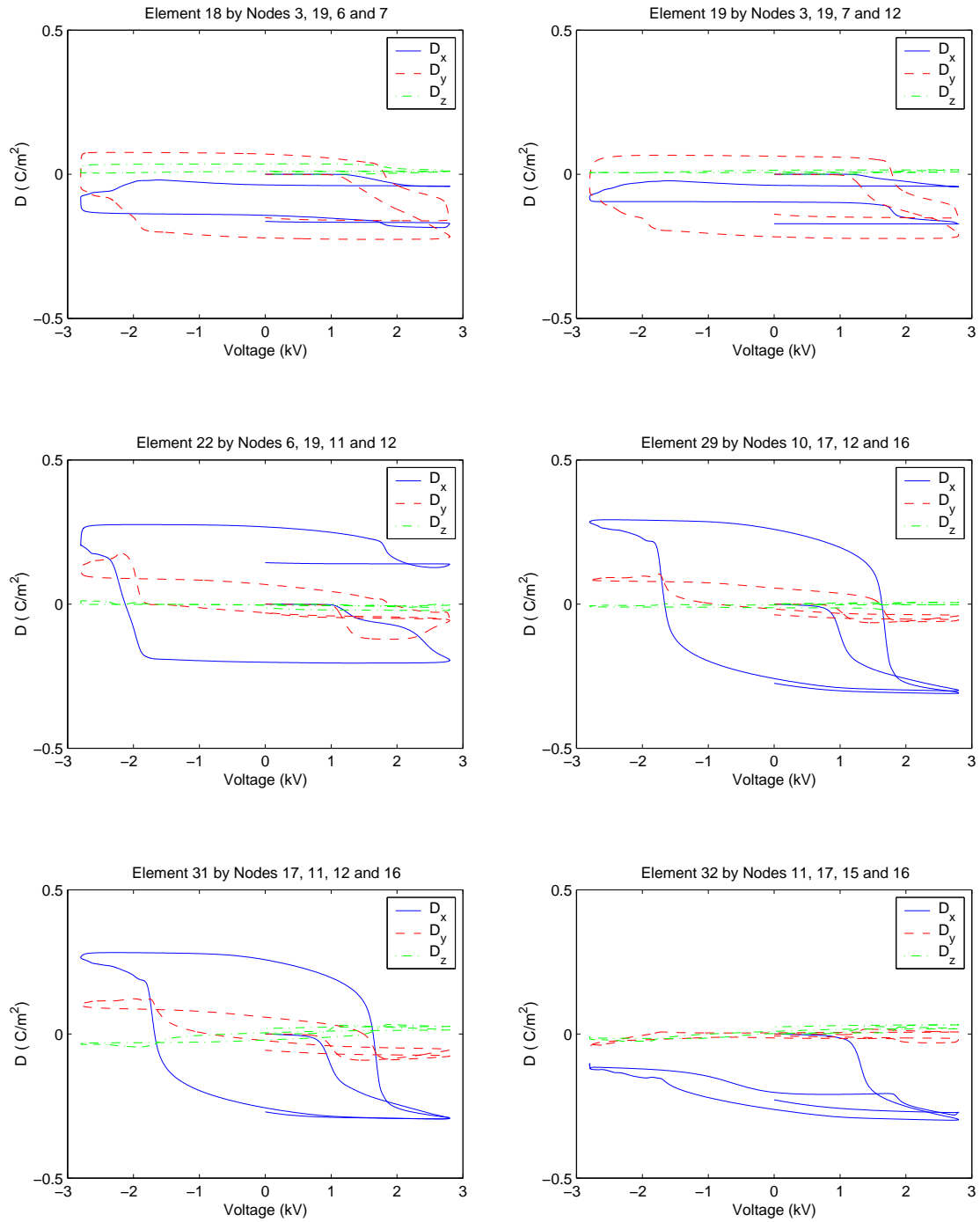


Figure 5-15: Electric displacement vs. driving voltage under skewed electric field on various elements.

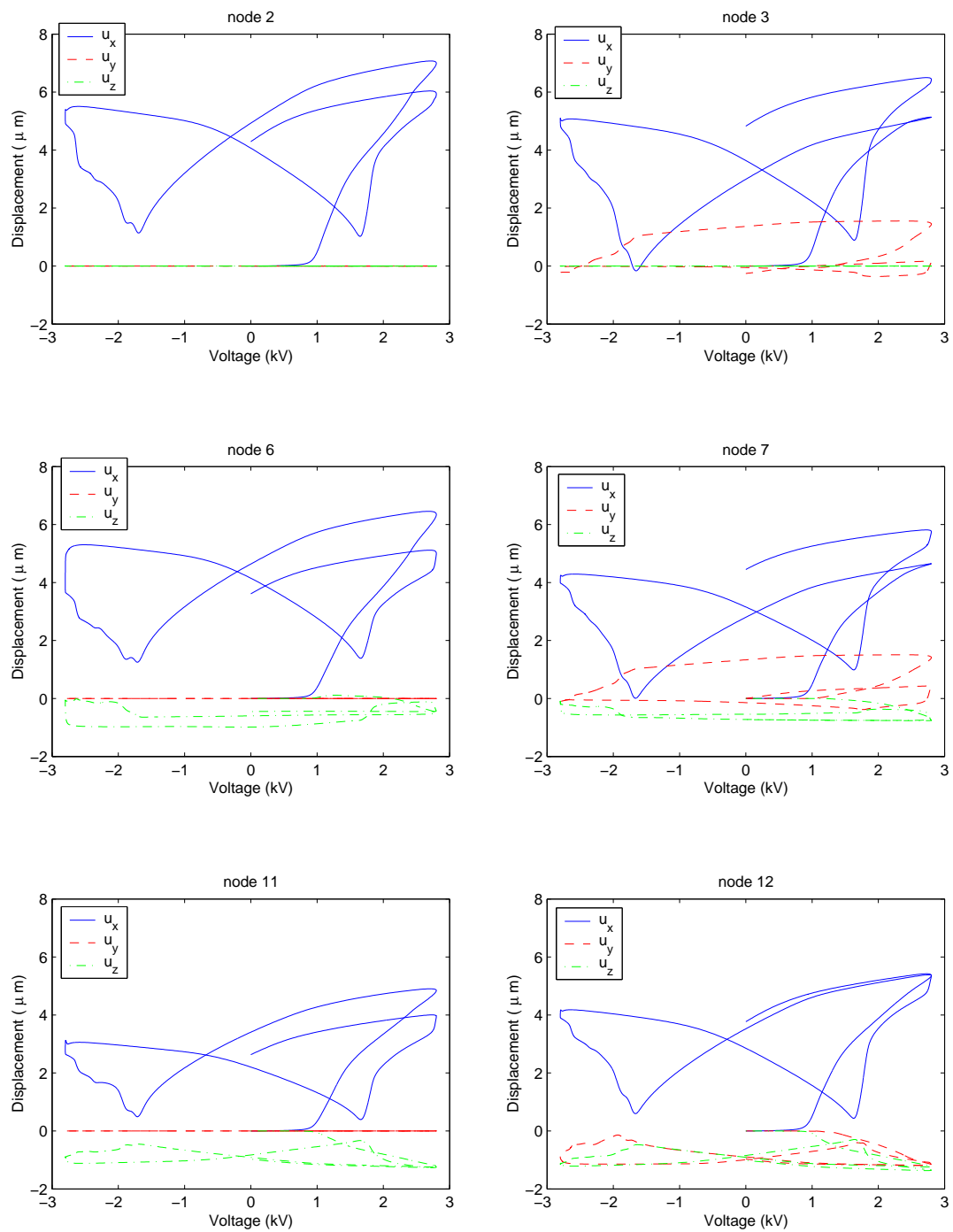


Figure 5-16: Displacement vs. driving voltage under skewed electric field on various nodes.

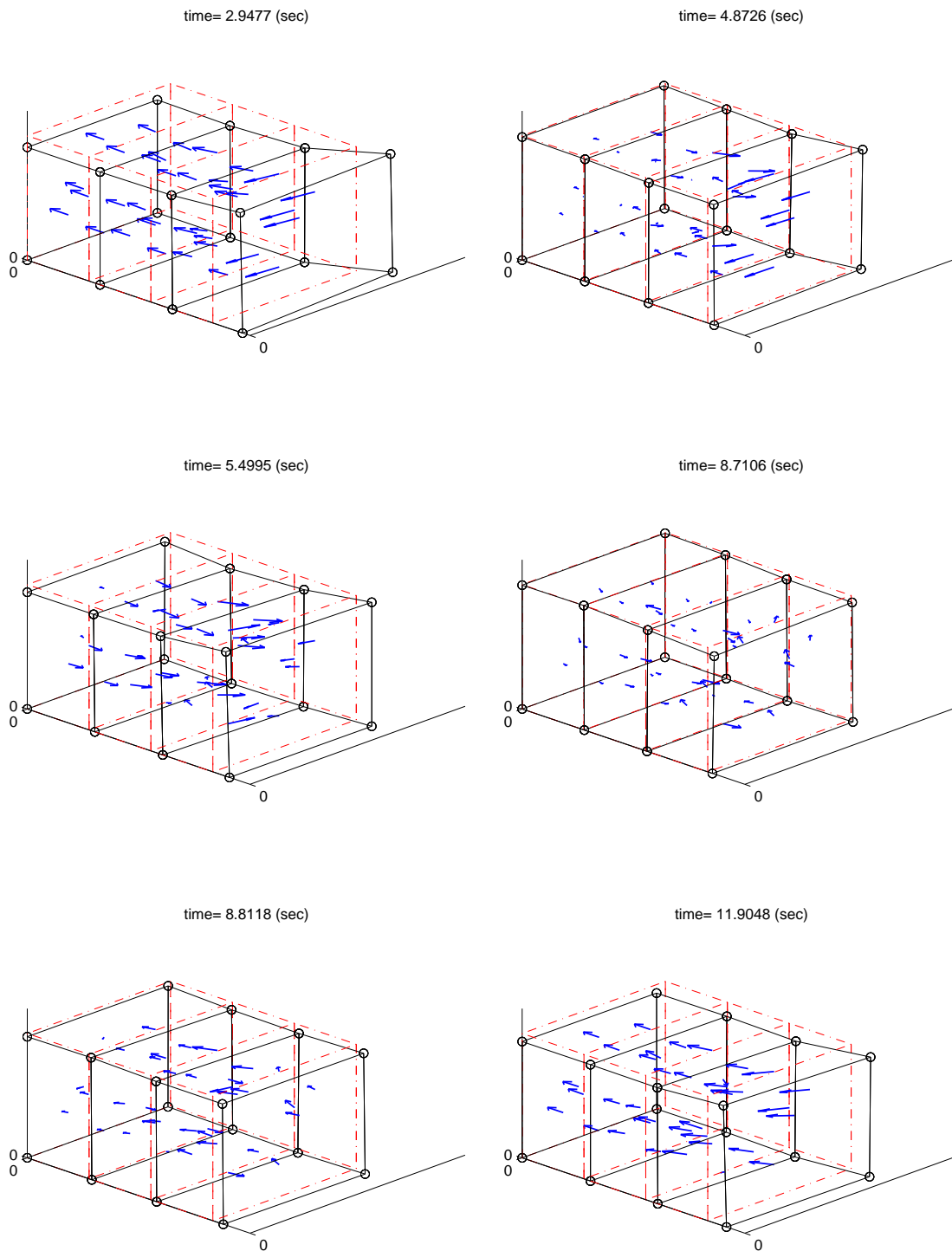


Figure 5-17: Deformed body under skewed electric field at various time steps.

### 5.5.4 Limitation of Large Scale Problem

As mentioned earlier, in order to increase the accuracy of the simulation, a much finer mesh must be used to eliminate the stiff characteristics of the 4-node tetrahedral element. This refined mesh will result in rapid growth of the degrees of freedom. As the scale of the problem grows, the tolerance control of iteration becomes very important for the DAE code to reach the converged solution.

An attempt has been made to simulate the previous case under skewed loading with a finer mesh. Unfortunately, the finite element code using the DASPK solver fails to converge the solution under the specified tolerance. This failure is believed to be caused by the inefficient tolerance control used by the DASPK solver. In DASPK, the tolerance is controlled by the root-mean-square norm of the residues of the algebraic-differential equations:[46]

$$\|\mathbf{x}\|_{RMS} = \left[ N^{-1} \sum_i^N (x_i)^2 \right]^{1/2} \quad (5.79)$$

where  $N$  is the degree of freedom. This algorithm shows no difficulty in solving small scale problems. However, as the degree of freedom increases, the error seen by the solver decreases because the error has been divided by  $N$ . To remedy this problem, it is recommended that the tolerance should be controlled by the  $\ell_2$  norm

$$\|\mathbf{x}\|_2 = \left[ \sum_i^N (x_i)^2 \right]^{1/2} \quad (5.80)$$

or by the  $\ell_\infty$  norm

$$\|\mathbf{x}\|_\infty = \max(x_i) \quad (5.81)$$

instead of root-mean-square norm.

Unfortunately, it is impossible to modify the DASPK solver without violating its copyright, and developing a new solver is beyond the scope of this thesis work. The only thing that can be done is to tighten the tolerance manually according to the size of the problem,  $N$ . However, by doing so, more computational efforts are required to solve the problem. Due to the limitation of the current computing capability, a large scale problem cannot be solved within the schedule of this thesis. As a result, solving for a large scale problem shall be left as future work. Nevertheless, the study in the previous case that is under skewed loading has successfully demonstrated the formulation and the solution technique of the 3-D rate dependent piezoelectric finite element analysis.

## 5.6 Summary of 3-D Nonlinear Rate Dependent Finite Element Analysis

To provide a compatible analysis tool for problems with irregular geometries using the material model developed in this thesis, based on the mixed FEM formulation by Ghandi[35], a differential algebraic formulation of finite element method was derived, coded, and solved using the DASPK DAE solver in this chapter. The computer code successfully demonstrated simple examples with uniform and skewed loadings. However, the size of solvable problem was limited by the tolerance control algorithm and speed of computing machines.





# Chapter 6

## Conclusions

This chapter summarizes the critical data of the piezoelectric material properties and the development of the material models. The limitations of the model and finite element analysis are revealed. Possible future work is also recommended. Finally, the essential contributions advanced by this thesis are detailed.

### 6.1 Summary and Future Work

Nonlinearity and hysteresis make it difficult to analyze and design a piezoelectric device for smart structures applications, such as actuating and sensing components as well as energy harvesters. In addition, compressive depolarization is a major concern in terms of performance. Most actuators, sensors, and even energy harvesters operate at high compression. This compression, which is usually parallel to the poling direction, will depolarize the material and degenerate the performance. Moreover, frequency dependence is a well-known characteristic of piezoelectric materials. As a result, this thesis is motivated by these obstacles to characterize in details the nonlinear and hysteric behaviors while subject to various loading conditions. It is also the goal to develop an analytical model and a finite element analysis tool to predict these behaviors.

Since PZT-5A has been used as fibers in commercial active fiber composites, and it has moderate piezoelectric constant and stiffness, PZT-5A was selected for the actuation tests in this work. Single crystal PZN-PT and PMN-PT were chosen for the power generation tests because of their high piezoelectric constants. PZT-5H was also tested for energy harvesting

because of its low cost and moderate piezoelectric constants. In addition to these tests, repolarizing material behaviors of both PZT-5A and PZT-5H subjected to high electric excitations and under static compression were also characterized to obtain a full range of information for material modeling.

To study the actuation performance of PZT-5A, several tests were designed: a single loop test was aimed at depicting the envelope of actuation during compressive loading and unloading situations, a multiple loop test was aimed at identifying the reversibility of the actuation after various intermediate levels of compressive, and a residual test with various compression duration was aimed at revealing the stress rate effects. The tests unveiled the following facts:

1. Compression starts to depolarize the PZT-5A material at 30 MPa.
2. PZT-5A actuation capability can fully recover after 30MPa compression and slightly rebound after 60MPa. However, after 90MPa, PZT-5A loses approximately 70% of its actuation, depending on the level of electric excitation.
3. High electric field cannot prevent the depolarization.
4. Short compression duration with positive high electric excitation can result in actuation recovery.

To measure the energy harvesting capability of PZT-5H and single crystal PZN-PT and PMN-PT, an open circuit voltage divider and a short circuit charge amplifier were designed, built and calibrated. To apply high frequency force, the piezo-actuating component testers developed by Lutz and Shi were modified to obtain accurate and sufficient compression. The piezoelectric and elastic constants,  $g_{33}$ ,  $d_{33}$ ,  $s_{33}^E$ , and  $s_{33}^D$  while subject to various amplitudes of compression were first measured and curve-fitted as polynomial functions of the compression. The electrical power generated by various amplitudes of compression was then obtained using a rectifying diode circuit and correlated with the estimated power output using the fitted piezoelectric constants.

An essential trend was found for single crystal PZN-PT and PMN-PT that  $g_{33}$  decreased drastically as the compression was increased. This significantly degenerated the electric power output at high compression. In addition, unlike PZT-5H, single crystal showed softening tendency as the compression was enhanced. This implied that the single crystal structure might be damaged by the high compression. Lessons learned from this test include:

both  $g_{33}$  and  $d_{33}$  are the critical material properties with regard to the energy harvesting capability; PZT-5H starts to deteriorate at 22MPa, while single crystal materials start to degenerate at 11MPa for PZN-PT and 15MPa for PMN-PT; using PZN-PT at low compression for energy harvesters is beneficial, while using PZT-5H is more profitable at compression higher than 30MPa.

To develop a material model, which was targeted to capture full-range nonlinear and hysteretic behaviors as well as material constants, repolarizing responses of PZT-5A were also characterized using longitudinal and transverse tests. These tests were originally developed for PZT-5H by Ghandi but were modified in this work specially for PZT-5A. In addition, rate dependent repolarizing data of both PZT-5A and PZT-5H under stress free conditions were acquired.

Another goal of this thesis is to develop a material model by establishing a physical framework within which empirical descriptions of the behavior of some of the variables are embedded. The development of the model consists of three stages: to gain understanding and insight of material behaviors; to capture major effects into equations and computer codes for the use of finite element method; to condense material data as constants to establish a material library or design guide for material selection. The description of these stages follows the guideline by Ashby[70]. Each stage has its objective task and corresponding precision. Additional mechanisms shall be taken into consideration to proceed to the more accurate level.

The goal of the first stage was to understand the electric rate and static stress dependent effects. At this stage, only the 1-D model was considered and the precision was targeted within an order of magnitude. The model was formulated using the thermodynamically consistent framework developed by Ghandi who introduced an internal variable  $D^*$ , a net remnant polarization, to govern the material hysteresis. An additional evolution law of  $D^*$  was proposed using the Weibull function to describe the electric rate dependence in this work. A parametric study was performed to evaluate the influence of the rate rule constants:  $\Delta D_c$  controls the initiation of repolarization,  $\alpha$  governs abruptness of repolarizing transition, and both  $\alpha$  and  $\tau$  determine the rate dependence of coercive field. The material models for PZT-5H and PZT-5A were determined by optimizing the coefficients of energy expansion and by tuning the rate rule constants. At this first stage, this 1-D model successfully

offered significant insights into rate dependence and stress dependence of the materials and achieved the targeted precision.

In order to formulate the model for the use of the full 3-D finite element analysis at the second stage with the targeted precision factor of 2, 3-D tensor invariants originally proposed by Ghandi were included in the 1-D model developed in the first level. The 1-D evolution law of  $D^*$  was modified into three dimensions. 3-D models for PZT-5H and PZT-5A were also obtained by optimizing the coefficients of energy expansion and by tuning the rate rule constants. This 3-D model also achieves the targeted precision of Stage 2 .

The model developed at Stage 2 was tested directly against the criteria of the third stage without adding new mechanisms. Unfortunately, the model failed to achieve the targeted precision of 1.1 due to the following factors:

1. Stress rate dependence is absent.
2. Unlike PZT-5H, a special rate rule describing the hysteresis between  $S$  and  $D$  is required to improve the PZT-5A model.
3. Least squares fit using large amplitude data makes it difficult to predict the small signal response accurately, unless the data is perfectly fit by the model.

These factors are recommended as future work for a better material model. Although it may not be difficult to derive a new rate rule managing the hysteresis between  $S$  and  $D$ , the major obstacle is to guarantee the model to be thermodynamically consistent.

To provide a compatible analysis tool for problems with irregular geometries using this material model, based on the mixed FEM formulation by Ghandi[35], a differential algebraic formulation of the finite element method was derived, coded, and solved using the DASPK DAE solver. The computer code successfully demonstrated simple examples with uniform and skewed loadings. However, the size of the solvable problem was limited by the tolerance control algorithm and the speed of the available computing machines. To improve the stability of convergence, a new tolerance control algorithm using  $\ell_\infty$  norm of the residues of the algebraic-differential equations was proposed for future work,

$$\|\mathbf{x}\|_\infty = \max(x_i), \quad (6.1)$$

instead of original root-mean-square norm used by DASPK:

$$\|x\|_{RMS} = \left[ N^{-1} \sum_i^N (x_i)^2 \right]^{1/2}, \quad (6.2)$$

where  $N$  is the number of the degrees of freedom, and  $\mathbf{x}$  is the residue vector of the differential algebraic equations. To facilitate the computation, parallel computing is feasible and recommended.

The combination of the nonlinear mixed FEM model and the material model provides a useful tool for modeling the response of active devices with complicated geometries and irregular boundary conditions. This tool permits investigation of the nonuniform polarization in such devices and its effect of the phenomenological response of the system. This tool also permits analysis of internal stress originated by nonuniform spontaneous strain in the material which can cause actuator failure.

## 6.2 Contributions

### Piezoelectric Actuation Constants

Piezoelectric actuation constants  $d_{33}$  under various stresses have been reported by Zhang [29] and Krueger [28]. However, these data were obtained using small electric excitation.

In this work, piezoelectric actuation constants  $d_{33}$  under various static stresses were measured using various levels of electric signals. In addition, new methodologies such as the multiple loop test and the residual actuation test were conducted to identify how the material recovers from the degeneration of compressive depolarization. Moreover, the compression duration issues were discovered and tested.

### Piezoelectric Power Generation Constants

Both  $g_{33}$  and  $d_{33}$  are essential to determine the electric energy output of piezoelectric materials. In addition,  $s_{33}^E$  and  $s_{33}^D$  are essential to determine the required mechanical input energy and coupling coefficients.

Although these data of PZT-5H have been measured and published by the vendor[53], the test conditions were limited to low stress.  $d_{33}$  constants of PZN-PT at high stress have also been published by the vendor[54], but the data was obtained from the actuation test

and therefore is not valid for an energy harvesting application. In addition, no complete sets of single crystal PZN-PT and PMN-PT data are available in the literature.

In this work, systematic material characterization for power generation was performed under various amplitudes and frequencies of compression.  $d_{33}$ ,  $g_{33}$ ,  $s_{33}^D$ , and  $s_{33}^E$  constants are extracted from the experiments and fitted as functions of compression. These results successfully correlate with the measured power data using the rectifying circuit. Comparison between polycrystalline PZT-5H and single crystal PZN-PT and PMN-PT were performed.

This work also found that  $g_{33}$  plays an important role in determining the maximum electric power output under high stress because  $g_{33}$  decreases drastically as compression is increased. Moreover, from the data of  $s_{33}^E$  as a function of compression, the single crystal PZN-PT and PMN-PT show *softening* phenomenon, while polycrystalline material PZT-5H shows *hardening* behavior. This result implies that the material structure of the single crystal specimens might have been damaged by high compression. This might explain why  $g_{33}$  of the single crystals drops more rapidly. Additional study is needed to fully understand this discrepancy.

## Demonstration of Piezoelectric Power Generation at High Frequency

It is a goal of this thesis to demonstrate that piezoelectric power generation can still work at high frequency. Although the piezoelectric power generation was first demonstrated by Umeda [32][33] using a diode circuit and a ball drop as the mechanical input, it is difficult to examine the result as a function of stress and frequency. The recent study by Goldfarb [57] reported that the efficiency of piezoelectric power generation is frequency dependent and that the efficiency is very low at high frequency.

However, a further study in this work shows that the frequency dependency depends upon the impedance of the circuit that is used to characterized the power. In Goldfarb's result, the test was implemented using a resistor whose impedance will cause problems, especially at high frequency. Unlike Goldfarb's approach but similar to Umeda's, this work systematically designed a test procedure using the high frequency tester and demonstrated frequency independency which disproved Goldfarb's statement. In addition, this work also identified the limitation caused by high compression.

### **3-D Repolarizing Material Behavior of PZT-5A**

The 3-D repolarizing material behavior of PZT-5H under various stresses has been reported by Ghandi[35]. However, data of PZT-5A, which is used in the commercial AFCs, would be essential to improve the performance of AFCs but is absent in the literature. As a result, one of the goals in this work is to obtain sufficient material data of PZT-5A for analyzing AFCs.

The challenge of testing PZT-5A is the preparation of the specimen. The higher coercive field of PZT-5A makes it difficult to obtain fully repolarizing behavior with saturation. Due to the 8kV isolation limitation of the strain gauge conditioner, the specimen has to be small enough to obtain high enough electric driving field. On the other hand, the specimen has to be large enough to accommodate the strain gauges and to prevent electric arcing. This work has overcome these obstacles and has successfully obtained the 3-D repolarizing data of PZT-5A. In addition, rate dependent data of both PZT-5A and PZT-5H were acquired.

### **3-D Rate Dependent Model**

Table 6.2 shows a comparison of various models found in the literature. None of the models in the literature are capable of simulating 3-D nonlinear repolarizing material behavior under various stresses and frequencies. For instance, Ghandi[35] developed a 3-D thermodynamically consistent model. Ghandi's model only considers stress dependency but not frequency dependency. Another example is the model by Soukhojak and Chiang[2] who has modeled 1-D behavior of materials under various stresses and frequencies. But it is difficult to expand this framework into a 3-D model.

Based on the 3-D model developed by Ghandi, a new 3-D rate dependent model was developed in this work. To do so, a novel evolution law was derived to describe the rate dependency of the materials. In addition, a material model library of PZT-5A and PZT-5H was established.

### **Discrepancy of Domain Switching Process between PZT-5A and PZT-5H**

A major discrepancy between hard and soft materials was found by comparing the S-D curves of PZT-5A and PZT-5H. The hysteresis of the PZT-5A S-D curve was the reason why the PZT-5A model did not perform as well as PZT-5H's. In addition, this hysteresis



Table 6.1: Model comparison with literatures							
	1-D	3-D	Rate dependent	Stress dependent	Strain response	Polarization response	Comment
Tikare et. al.[1]	•		•			•	Monte Carlo
Fan et. al.[6]	•			•	•		Nonlinear spring
Chen and Lynch[24]	•			•	•	•	
Hwang et. al.[22]	•			•	•	•	
Smith and Ounaies[7]	•		•			•	ODE
Bassinouny et.al.[11]	•		•	•		•	
Chen and Montgomery[13]	•		•		•	•	
Chen and Tucker[15]	•					•	
Soukhojak and Chiang[2]	•		•	•	•	•	ODE
Ghandi and Hagood[35]	•	•		•	•	•	
This work	•	•	•	•	•	•	Tensor invariants DAE

was explained by a  $90^\circ/180^\circ$  domain switching hypothesis modified from Zhou's theory[65]. Although Zhou has reported similar hysteretic behavior in an S-D curve, his results were limited to a single material at various frequencies. In contrast, the result shown in this work covers two distinguishable materials at various frequencies.

This finding also shows the significance of the PZT-5A characterization accomplished in this work. Without this, the flaw in Ghandi's framework[35] and in this material model would not have been revealed.

### **Differential Algebraic Formulation of Finite Element Analysis**

Because the 3-D rate dependent material model was newly developed, none of commercial finite element software packages could support this model. To provide a compatible analysis tool, based on the mixed FEM formulation by Ghandi[35], a differential algebraic formulation of the finite element method was derived, coded, and demonstrated successfully by simple examples. Although the performance of this code was limited by the current computing facility, this code is expected to contribute to solving real problems when advanced computing machines are made available.



# Appendix A

## Simulink Graphical Model

This appendix documents the simulation of the Simulink models used in this thesis. These models include:

1. Linear piezoelectricity with resistive load<sup>1</sup>.
2. Linear piezoelectricity with diode bridge<sup>2</sup>.
3. 1-D nonlinear short circuit piezoelectricity.
4. 3-D nonlinear short circuit piezoelectricity.
5. 1-D nonlinear open circuit piezoelectricity.
6. 1-D nonlinear open circuit piezoelectricity with conduction.
7. 3-D nonlinear open circuit piezoelectricity.
8. 3-D nonlinear open circuit piezoelectricity with conduction.
9. 1-D nonlinear piezoelectricity with diode circuit.
10. 3-D nonlinear piezoelectricity with diode circuit.

The reader is encouraged to consult the manual of Simulink[71]. Some graphical simulation blocks make use of S-functions[72], which will be listed in Appendix B.

---

<sup>1</sup>Linear piezoelectric block was constructed with help from K. Ghandi.

<sup>2</sup>Diode bridge block was constructed with help from Y.-H. Su.

## A.1 Linear Piezoelectricity with Resistive Load

Figure A-1 shows the graphical simulation of linear piezoelectricity with resistor R. The block "Piezo" in Figure A-1 is detailed in Figure A-2. The matrix gain "K" in Figure A-2 describes the constitutive relation between the inputs (force and charge) and outputs (voltage and displacement):

$$\frac{L}{A} \begin{bmatrix} \beta_{33}^T & -g_{33} \\ g_{33} & s_{33}^D \end{bmatrix}, \quad (\text{A.1})$$

where  $L$  is the thickness of the specimen, and  $A$  is the area of the cross section.

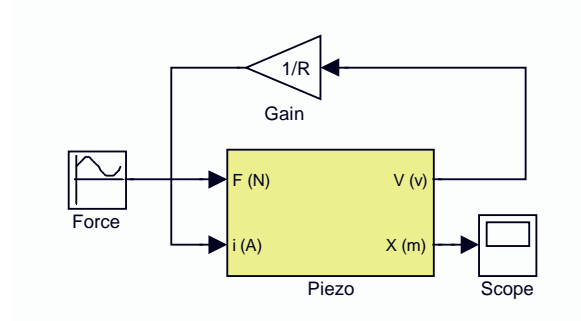


Figure A-1: Linear piezoelectricity with resistive load

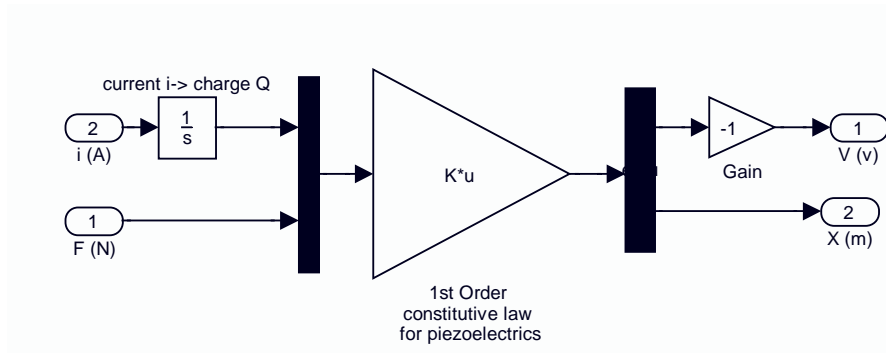


Figure A-2: The block "Piezo" shown in Figure A-1.

## A.2 Linear Piezoelectricity with Diode Bridge

Figure A-3 shows the graphical simulation of linear piezoelectricity with a rectifying diode bridge whose voltage and current are labeled in Figure A-4: the voltages and currents at four junctions are  $V_k$  and  $I_k$ ,  $k = 1 \cdots 4$ , respectively; the voltages across the diodes and the currents through the diodes are  $v_k$  and  $i_k$ ,  $k = 1 \cdots 4$ , respectively.

The block “Piezo” in Figure A-3 is the same as the one specified in Figure A-2. The gain matrix in Figure A-3 relates the voltage differences between the piezoceramics and the battery:

$$\begin{bmatrix} 0.5 & 0.5 \\ 1.0 & 0.0 \\ 0.5 & -0.5 \end{bmatrix}. \quad (\text{A.2})$$

The block “Rectifying Diode Bridge” in Figure A-3 is detailed in Figure A-5. The first gain matrix in Figure A-5, labeled as “Voltages(Junction->Diode)”, links the global nodal voltage to the local diode voltages:

$$\begin{Bmatrix} v_1 \\ v_2 \\ v_3 \\ v_4 \end{Bmatrix} = \begin{bmatrix} 1 & -1 & 0 & 0 \\ 0 & -1 & 1 & 0 \\ 0 & 0 & -1 & 1 \\ -1 & 0 & 0 & 1 \end{bmatrix} \begin{Bmatrix} V_1 \\ V_2 \\ V_3 \\ V_4 \end{Bmatrix}. \quad (\text{A.3})$$

From Kirchhoff’s law, the second gain matrix in Figure A-5, labeled as “Currents(Diode->Junction)”, relates the local diode currents to the global junction currents:

$$\begin{Bmatrix} I_1 \\ I_2 \\ I_3 \\ I_4 \end{Bmatrix} = \begin{bmatrix} -1 & 0 & 0 & 1 \\ 1 & 1 & 0 & 0 \\ 0 & -1 & 1 & 0 \\ 0 & 0 & -1 & -1 \end{bmatrix} \begin{Bmatrix} i_1 \\ i_2 \\ i_3 \\ i_4 \end{Bmatrix}. \quad (\text{A.4})$$

Each block, labeled “Diode element” in Figure A-5, defines the constitutive law for each diode (Eq. 2.18) and is implemented in Figure A-6.

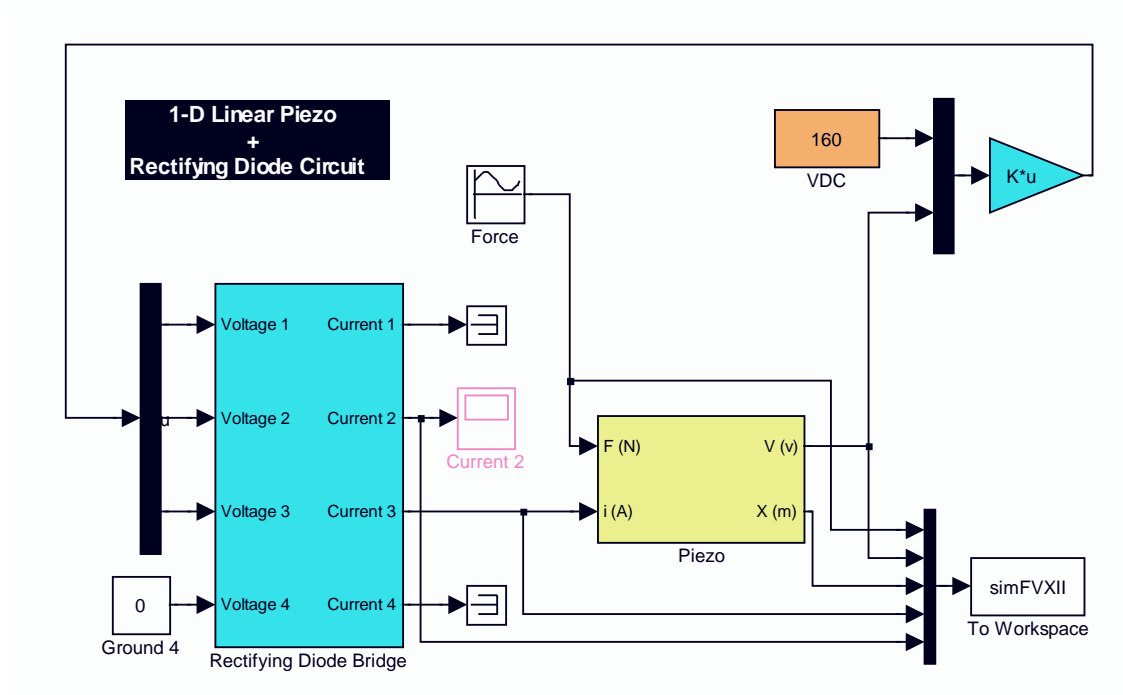


Figure A-3: Linear piezoelectric device with diode bridge.

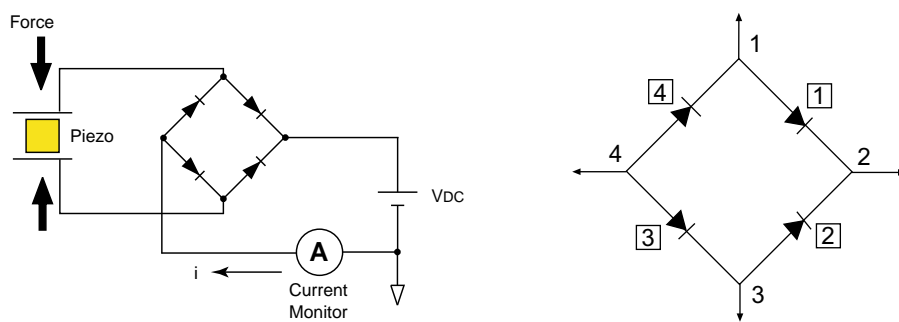


Figure A-4: Labels of voltages and currents in rectifying diode circuit.

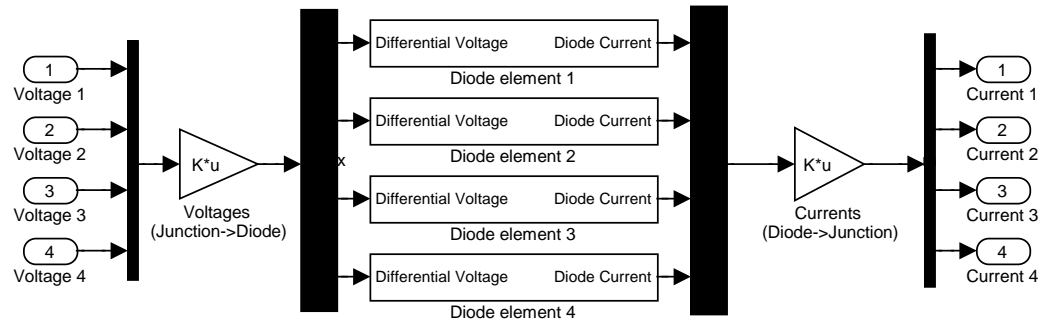


Figure A-5: The details of the block “Rectifying Diode Bridge” in Figure A-3.

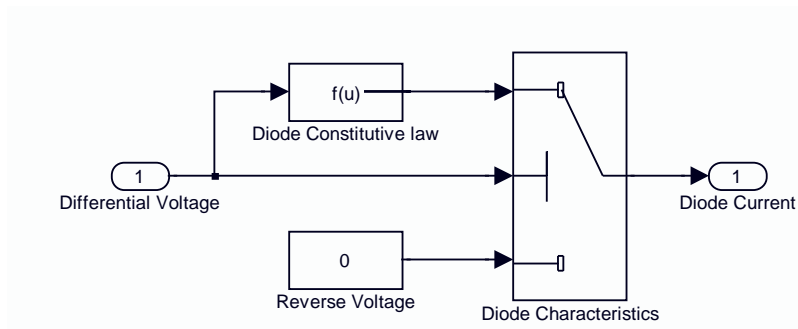


Figure A-6: Implementation of constitutive law of each “Diode element” in Figure A-5 .



### A.3 1-D Nonlinear Short Circuit Piezoelectricity

Figure A-7 shows the graphical simulation of the 1-D nonlinear piezoelectric response under short circuit condition using the 1-D model developed in this thesis. The block labeled “Piezo” is detailed in Figure A-8. The s-functions “Dsraterule” and “sfuncES”, which code the rate rule (Eq. 3.34) and the constitutive relations

$$E = E(D, D^*, T), \quad (\text{A.5})$$

$$S = S(D, D^*, T) \quad (\text{A.6})$$

are listed in Appendices B.1 and B.2, respectively.

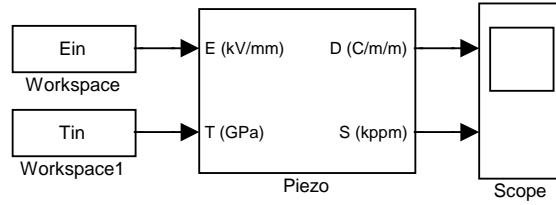


Figure A-7: 1-D nonlinear short circuit simulation.

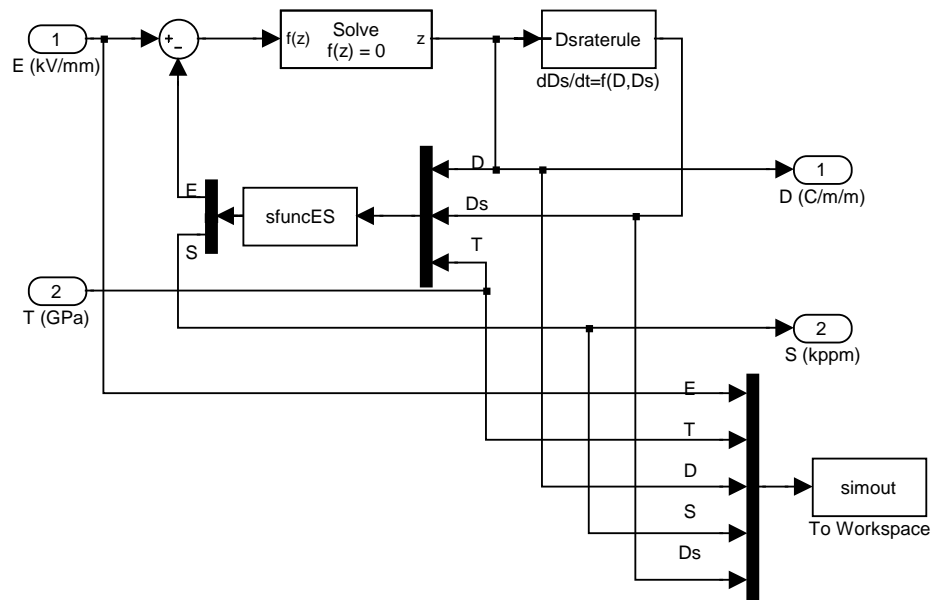


Figure A-8: Details of block “Piezo” in Figure A-7.

## A.4 3-D Nonlinear Short Circuit Piezoelectricity

Figure A-9 shows the graphical simulation of the 3-D nonlinear piezoelectric response under short circuit condition using the 3-D model developed in this thesis. The block labeled “Piezo” is detailed in Figure A-10. The s-functions “Dsraterule3D” and “sfuncES3D”, which code the rate rule (Eq. 3.65) and the 3-D constitutive relations

$$\mathbf{E} = \mathbf{E}(\mathbf{D}, \mathbf{D}^*, \mathbf{T}), \quad (\text{A.7})$$

$$\mathbf{S} = \mathbf{S}(\mathbf{D}, \mathbf{D}^*, \mathbf{T}) \quad (\text{A.8})$$

are listed in Appendices B.3 and B.4, respectively.

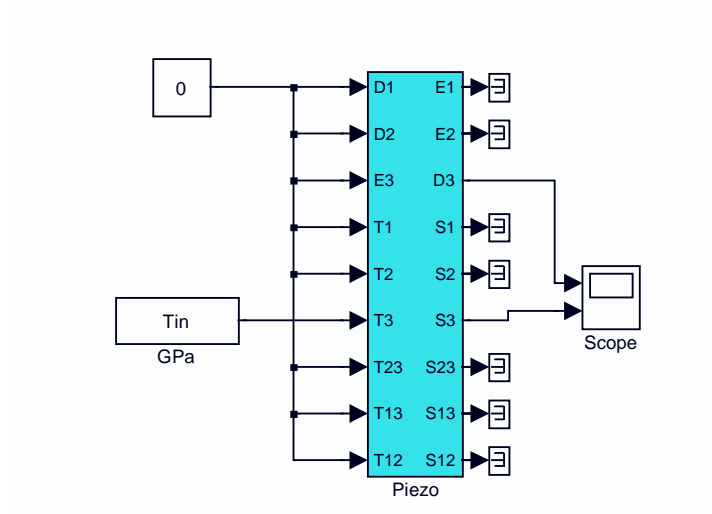


Figure A-9: 3-D nonlinear short circuit simulation.

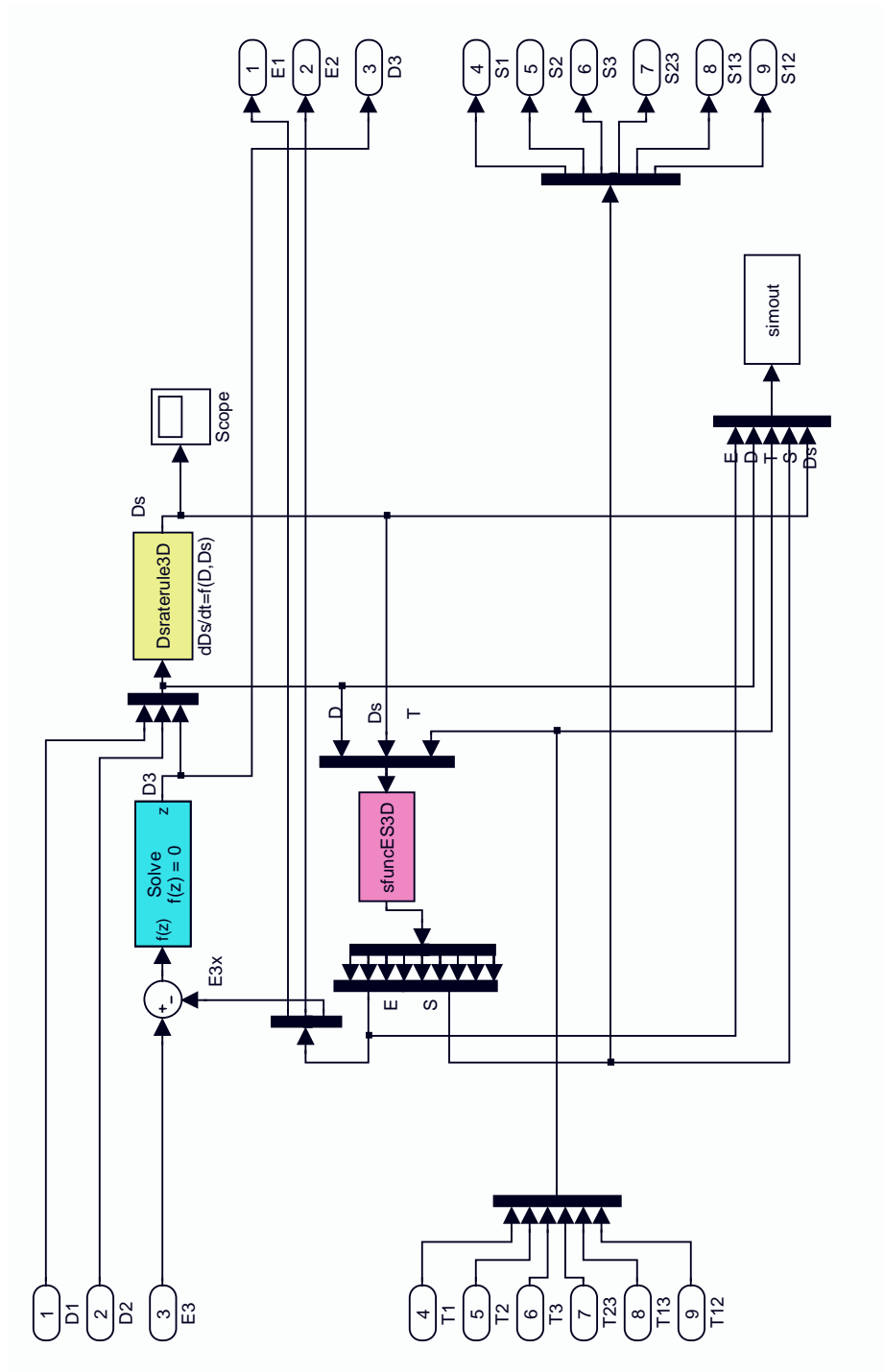


Figure A-10: Details of block “Piezo” in Figure A-9.

## A.5 1-D Nonlinear Open Circuit Piezoelectricity

Figure A-11 shows the graphical simulation of the 1-D nonlinear piezoelectric response under open circuit condition using the 1-D model developed in this thesis. The block labeled “Piezo” is detailed in Figure A-12. The s-functions “Dsraterule” and “sfuncES” are listed in Appendices B.1 and B.2, respectively. The initial conditions of  $D$  and  $D^*$  are specified at the block named “D0” and the s-function “Dsraterule”, respectively. The initial conditions of  $D$  and  $D^*$  are specified at the block named “D0” and the s-function “Dsraterule”, respectively.

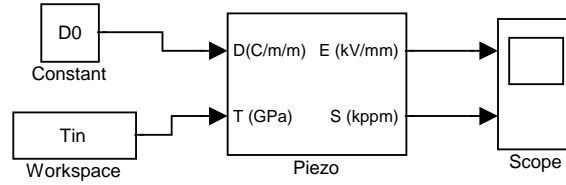


Figure A-11: 1-D nonlinear open circuit simulation.

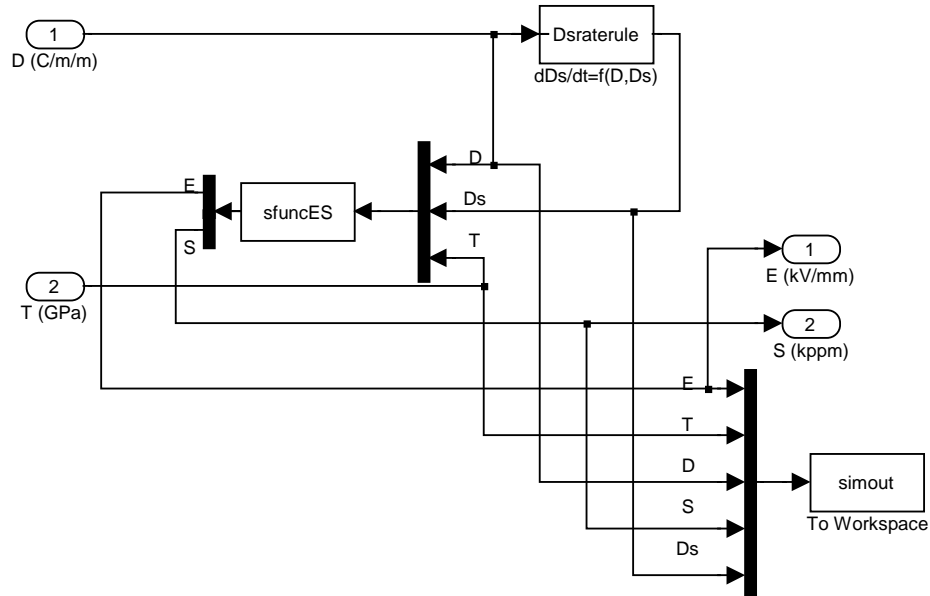


Figure A-12: Details of block “Piezo” in Figure A-11.

## A.6 1-D Nonlinear Open Circuit Piezoelectricity with Conduction

To account for the internal conduction of the piezoelectric specimen under open circuit condition, the 1-D model shown in Figure A-11 has been modified by including a linear resistor  $R$  as illustrated in Figure A-13. The block labeled “E2V” converts electric field to voltage via the specimen thickness. The block labeled “Q2D” converts charge to electric displacement via the area of the specimen cross section. The block labeled “Piezo” is detailed in Figure A-12. The initial conditions of  $D$  and  $D^*$  are specified at the block named “D0” and the s-function “Dsraterule”, respectively.

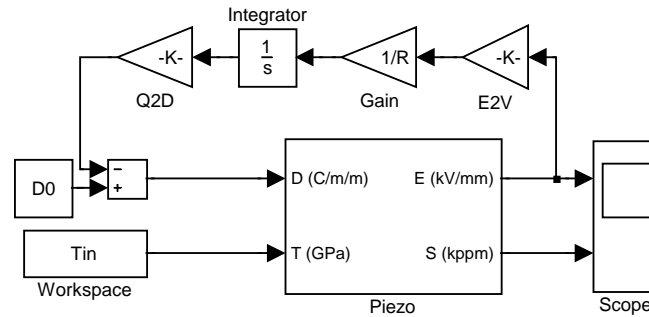


Figure A-13: 1-D nonlinear open circuit simulation with conduction.

## A.7 3-D Nonlinear Open Circuit Piezoelectricity

Figure A-14 shows the graphical simulation of the 3-D nonlinear piezoelectric response under open circuit condition using the 3-D model developed in this thesis. The block labeled “Piezo” is detailed in Figure A-15. The s-functions “Dsraterule3D” and “sfuncES3D” are listed in Appendices B.3 and B.3, respectively. The initial conditions of  $D$  and  $D^*$  are specified at the block named “D0” and the s-function “Dsraterule3D”, respectively.

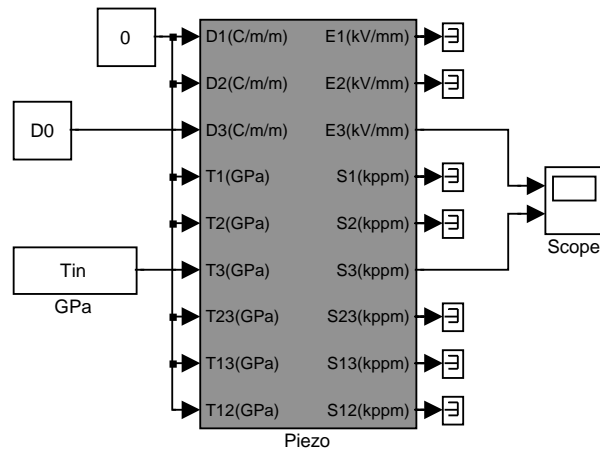


Figure A-14: 3-D nonlinear open circuit simulation.





## A.8 3-D Nonlinear Open Circuit Piezoelectricity with Conduction

To account for the internal conduction of the piezoelectric specimen under open circuit condition, the 3-D model shown in Figure A-14 has been modified by including a linear resistor  $R$  as shown in Figure A-16. The block labeled “E2V” converts electric field to voltage via the specimen thickness. The block labeled “Q2D” converts charge to electric displacement via the area of the specimen cross section. The block labeled “Piezo” is detailed in Figure A-15. The initial condition of  $D$  and  $D^*$  are specified at the block named “D0” and the s-function “Dsraterule3D”, respectively.

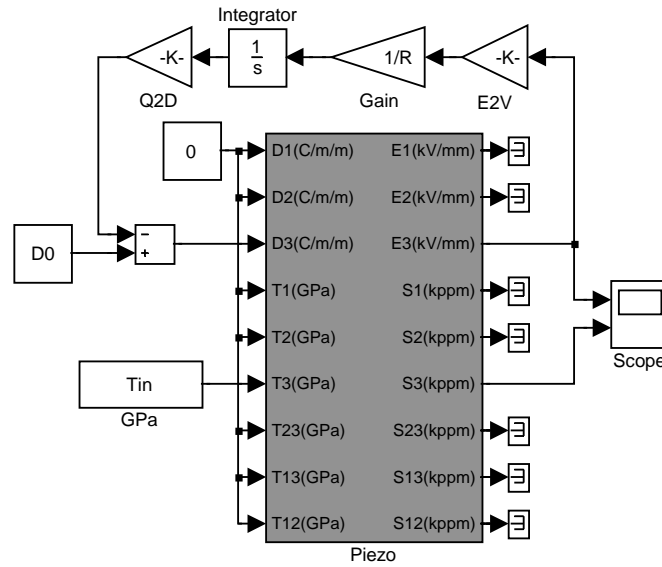


Figure A-16: 3-D nonlinear open circuit simulation with conduction.

## A.9 1-D Nonlinear Piezoelectricity with Diode Circuit

To simulate 1-D nonlinear piezoceramics with the diode circuit, the simulation shown in Figure A-3 has been modified by replacing the block labeled “piezo” with the one detailed in Figure A-17. The block labeled “E2V” converts electric field to voltage via the specimen thickness. The block labeled “Q2D” converts charge to electric displacement via the area of the specimen cross section. The block labeled “F2T” converts force to stress via the area of the specimen cross section. The block labeled “S2x” converts strain to displacement via the specimen thickness. The initial conditions of  $D$  and  $D^*$  are specified at the block named “D0” and the s-function “Dsraterule”, respectively.

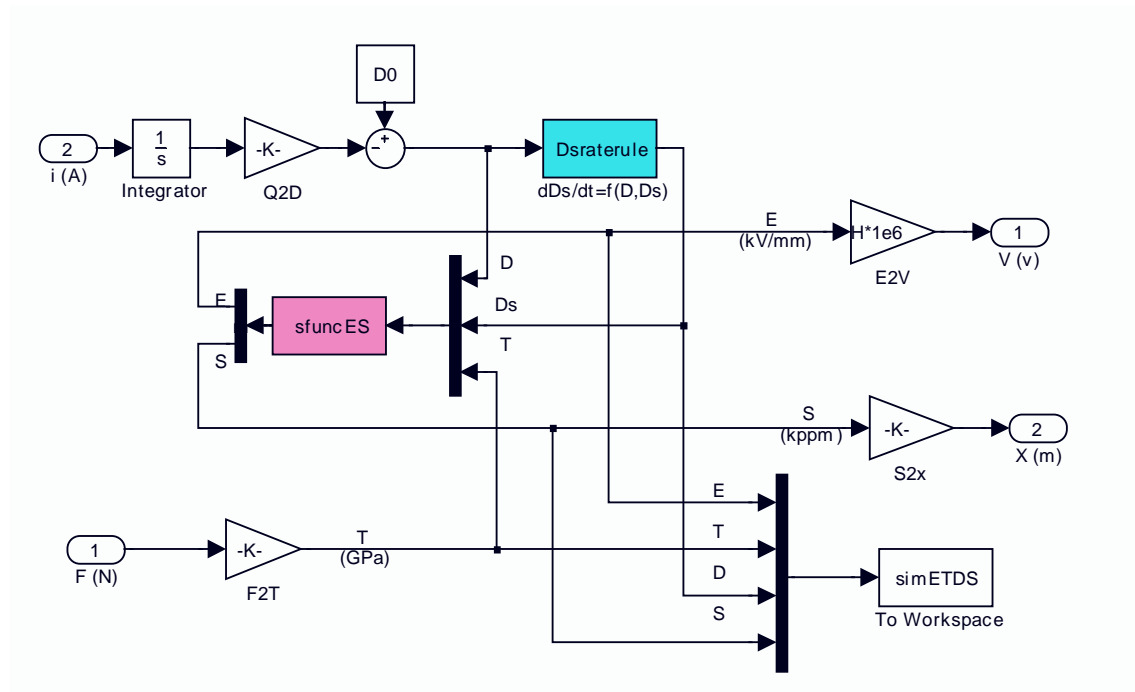


Figure A-17: 1-D nonlinear “Piezo” block for diode circuit simulation used in Figure A-3.

## A.10 3-D Nonlinear Piezoelectricity with Diode Circuit

To simulate 3-D nonlinear piezoceramics with the diode circuit, the simulation shown in Figure A-3 has been modified by replacing the block labeled “piezo” with the one detailed in Figure A-18. The block labeled “E2V” converts electric field to voltage via the specimen thickness. The block labeled “Q2D” converts charge to electric displacement via the area of the specimen cross section. The block labeled “F2T” converts force to stress via the area of the specimen cross section. The block labeled “S2x” converts strain to displacement via the specimen thickness. The block labeled “Piezo” in Figure A-18 is detailed in Figure A-15. The initial conditions of  $D$  and  $D^*$  are specified at the block named “D0” and the s-function “Dsraterule3D”, respectively.

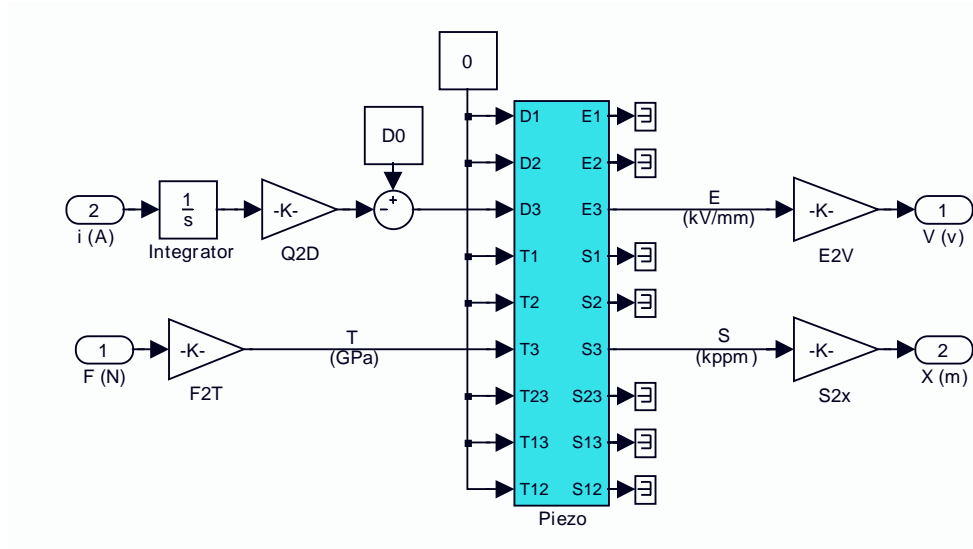


Figure A-18: 3-D nonlinear “Piezo” block for diode circuit simulation used in Figure A-3.

## Appendix B

# S-Function

### B.1 Dsraterule.m

```
function [sys,x0,str,ts] = Dsraterule(t,x,u,flag,tau,dDc,a,Ds0)
switch flag,
%%%%%%%%%%%%%%
% Initialization %
%%%%%%%%%%%%%%
case 0,
[sys,x0,str,ts]=mdlInitializeSizes(t,x,u,tau,dDc,a,Ds0);
%%%%%%%%%%%%%%
% Derivatives %
%%%%%%%%%%%%%%
case 1,
sys=mdlDerivatives(t,x,u,tau,dDc,a);
%%%%%%%%%%%%%%
% Outputs %
%%%%%%%%%%%%%%
case 3,
sys=mdlOutputs(t,x,u,tau,dDc,a);
%%%%%%%%%%%%%%
% Unhandled flags %
%%%%%%%%%%%%%%
case { 2, 4, 9 },
sys = [ ];
%%%%%%%%%%%%%%
% Unexpected flags %
%%%%%%%%%%%%%%
otherwise
error(['Unhandled flag = ',num2str(flag)]);
```

```

end
% end csfunc
%
%=====
% mdlInitializeSizes
% Return the sizes, initial conditions,
% and sample times for the S-function.
%=====
%
function [sys,x0,str,ts]=mdlInitializeSizes(t,x,u,tau,dDc,a,Ds0)
sizes = simsizes;
sizes.NumContStates = 1;
sizes.NumDiscStates = 0;
sizes.NumOutputs = 1;
sizes.NumInputs = 1;
sizes.DirFeedthrough = 1;
sizes.NumSampleTimes = 1;
sys = simsizes(sizes);
x0 = Ds0;
str = [ ];
ts = [0 0];
% end mdlInitializeSizes
%
%=====
% mdlDerivatives
% Return the derivatives for the continuous states.
%=====
%
function sys=mdlDerivatives(t,x,u,tau,dDc,a)
D=u;
Ds=x;
sys=(D-Ds)/tau*(1-exp(-((D-Ds)/dDc)^(2*a)));
% end mdlDerivatives
%
%=====
% mdlOutputs
% Return the block outputs.
%=====
%
function sys=mdlOutputs(t,x,u,tau,dDc,a) D=u; Ds=x;
sys=x;
% end mdlOutputs

```

## B.2 sfuncES.m

```
function [sys,x0,str,ts] = sfuncES(t,x,u,flag)
switch flag,
    %%%%%%%%%%%
    % Initialization %
    %%%%%%%%%%%
    % Initialize the states, sample times, and state ordering strings.
    case 0
        [sys,x0,str,ts]=mdlInitializeSizes;
        %%%%%%%%%%%
        % Outputs %
        %%%%%%%%%%%
        % Return the outputs of the S-function block.
    case 3
        sys=mdlOutputs(t,x,u);
        %%%%%%%%%%%
        % Unhandled flags %
        %%%%%%%%%%%
        % There are no termination tasks (flag=9) to be handled.
        % Also, there are no continuous or discrete states,
        % so flags 1,2, and 4 are not used, so return an emptyu
        % matrix
    case { 1, 2, 4, 9 }
        sys=[];
        %%%%%%%%%%%
        % Unexpected flags (error handling)%
        %%%%%%%%%%%
        % Return an error message for unhandled flag values.
    otherwise
        error(['Unhandled flag = ',num2str(flag)]);
end
%
%=====
% mdlInitializeSizes
% Return the sizes, initial conditions, and sample times for the S-function.
%=====
%
function [sys,x0,str,ts] = mdlInitializeSizes()
sizes = simsizes;
sizes.NumContStates = 0;
sizes.NumDiscStates = 0;
sizes.NumOutputs = 2;
sizes.NumInputs = 3;
sizes.DirFeedthrough = 1; % has direct feedthrough
```

```

sizes.NumSampleTimes = 1;
sys = simsizes(sizes);
str = [];
x0 = [];
ts = [-1 0]; % inherited sample time
% end mdlInitializeSizes
%
%=====
% mdlOutputs
% Return the output vector for the S-function
%=====
%
function sys = mdlOutputs(t,x,u)
D=u(1);
Ds=u(2);
T=u(3);
sys(1)= % E(D,Ds,T)
sys(2)= % S(D,Ds,T)

```

## B.3 Dsraterule3D.m

```

function [sys,x0,str,ts] = Draterule(t,x,u,flag,tau,dDc,a,Ds0)
switch flag,
    %%%%%%%%%%%%%%%
    % Initialization %
    %%%%%%%%%%%%%%%
    case 0,
        [sys,x0,str,ts]=mdlInitializeSizes(Ds0);
        %%%%%%%%%%%%%%%
        % Derivatives %
        %%%%%%%%%%%%%%%
    case 1,
        sys=mdlDerivatives(t,x,u,tau,dDc,a);
        %%%%%%%%%%%%%%%
        % Outputs %
        %%%%%%%%%%%%%%%
    case 3,
        sys=mdlOutputs(t,x,u,tau,dDc,a);
        %%%%%%%%%%%%%%%
        % Unhandled flags %
        %%%%%%%%%%%%%%%
    case { 2, 4, 9 },
        sys = [];
        %%%%%%%%%%%%%%%
        % Unexpected flags %
        %%%%%%%%%%%%%%%
    otherwise
        error(['Unhandled flag = ',num2str(flag)]);
end
% end csfunc
%
%=====
% mdlInitializeSizes
% Return the sizes, initial conditions, and sample times for the S-function.
%=====
%
function [sys,x0,str,ts]=mdlInitializeSizes(Ds0)
sizes = simsizes;
sizes.NumContStates = 3;
sizes.NumDiscStates = 0;
sizes.NumOutputs = 3;
sizes.NumInputs = 3;
sizes.DirFeedthrough = 0;
sizes.NumSampleTimes = 1;

```



```

sys = simsizes(sizes);
x0 = [Ds0]; % a vector of 3 element
str = [];
ts = [0 0];
% end mdlInitializeSizes
%
%=====
% mdlDerivatives
% Return the derivatives for the continuous states.
%=====
%
function sys=mdlDerivatives(t,x,u,tau,dDc,a)
D=u;
Ds=x;
% concise form
sys=(D-Ds)/tau*(1-exp(-(norm(D-Ds)/dDc)^(2*a)));
% end mdlDerivatives
%
%=====
% mdlOutputs
% Return the block outputs.
%=====
%
function sys=mdlOutputs(t,x,u,tau,dDc,a)
sys=x;
%end mdlOutputs

```

## B.4 sfuncES3D.m

```
function [sys,x0,str,ts] = sfuncES(t,x,u,flag) switch flag,
%%%%%%%%%%%%%%%%%%%%%%%%%%%%%%%%%%%%%%%%%%%%%%%%%%%%%%%%%%%%%%%%%%%%%%%%
% Initialization %
%%%%%%%%%%%%%%%%%%%%%%%%%%%%%%%%%%%%%%%%%%%%%%%%%%%%%%%%%%%%%%%%%%%%%%%%
% Initialize the states, sample times, and state ordering strings.
case 0
[sys,x0,str,ts]=mdlInitializeSizes;
%%%%%%%%%%%%%%%%%%%%%%%%%%%%%%%%%%%%%%%%%%%%%%%%%%%%%%%%%%%%%%%%%%%%%%%%
% Outputs %
%%%%%%%%%%%%%%%%%%%%%%%%%%%%%%%%%%%%%%%%%%%%%%%%%%%%%%%%%%%%%%%%%%%%%%%%
% Return the outputs of the S-function block.
case 3
sys=mdlOutputs(t,x,u);
%%%%%%%%%%%%%%%%%%%%%%%%%%%%%%%%%%%%%%%%%%%%%%%%%%%%%%%%%%%%%%%%%%%%%%%%
% Unhandled flags %
%%%%%%%%%%%%%%%%%%%%%%%%%%%%%%%%%%%%%%%%%%%%%%%%%%%%%%%%%%%%%%%%%%%%%%%%
% There are no termination tasks (flag=9) to be handled.
% Also, there are no continuous or discrete states,
% so flags 1,2, and 4 are not used, so return an emptyu
% matrix
case { 1, 2, 4, 9 }
sys=[];
%%%%%%%%%%%%%%%%%%%%%%%%%%%%%%%%%%%%%%%%%%%%%%%%%%%%%%%%%%%%%%%%%%%%%%%%
% Unexpected flags (error handling)%
%%%%%%%%%%%%%%%%%%%%%%%%%%%%%%%%%%%%%%%%%%%%%%%%%%%%%%%%%%%%%%%%%%%%%%%%
% Return an error message for unhandled flag values.
otherwise
error(['Unhandled flag = ',num2str(flag)]);
end
%
%=====
% mdlInitializeSizes
% Return the sizes, initial conditions, and sample times for the S-function.
%=====
%
function [sys,x0,str,ts] = mdlInitializeSizes()
sizes = simsizes;
sizes.NumContStates = 0;
sizes.NumDiscStates = 0;
sizes.NumOutputs = 9;
sizes.NumInputs = 12;
sizes.DirFeedthrough = 1; % has direct feedthrough
sizes.NumSampleTimes = 1;
```

```

sys = simsizes(sizes);
str = [];
x0 = [];
ts = [-1 0]; % inherited sample time
% end mdlInitializeSizes
%
%=====
% mdlOutputs
% Return the output vector for the S-function
%=====
%
function sys = mdlOutputs(t,x,u)

D1=u(1);
D2=u(2);
D3=u(3);
Ds1=u(4);
Ds2=u(5);
Ds3=u(6);
T1=u(7);
T2=u(8);
T3=u(9);
T23=u(10);
T13=u(11);
T12=u(12);
sys(1)= % E1(D1,D2,D3,Ds1,Ds2,Ds3,T1,T2,T3,T23,T13,T12)
sys(2)= % E2(D1,D2,D3,Ds1,Ds2,Ds3,T1,T2,T3,T23,T13,T12)
sys(3)= % E3(D1,D2,D3,Ds1,Ds2,Ds3,T1,T2,T3,T23,T13,T12)
sys(4)= % S1(D1,D2,D3,Ds1,Ds2,Ds3,T1,T2,T3,T23,T13,T12)
sys(5)= % S2(D1,D2,D3,Ds1,Ds2,Ds3,T1,T2,T3,T23,T13,T12)
sys(6)= % S3(D1,D2,D3,Ds1,Ds2,Ds3,T1,T2,T3,T23,T13,T12)
sys(7)= % S4(D1,D2,D3,Ds1,Ds2,Ds3,T1,T2,T3,T23,T13,T12)
sys(8)= % S5(D1,D2,D3,Ds1,Ds2,Ds3,T1,T2,T3,T23,T13,T12)
sys(9)= % S6(D1,D2,D3,Ds1,Ds2,Ds3,T1,T2,T3,T23,T13,T12)

```

# Bibliography

- [1] V. Tikare B. G. Potter, Jr. and B. A. Tuttle. "Monte Carlo Simulation of Ferroelectric Domains Structure and Applied Field Response in Two Dimensions," *Journal of Applied Physics*, Vol. 87, No. 9, pp. 4415-4424, 2000.
- [2] Andrey N. Soukhojak and Yet-Ming Chiang. "Generalized Rheology of Active Materials," *Journal of Applied Physics*, Vol. 88, No. 11, pp. 6902-6909, 2000.
- [3] Alberto Garcia and David Vanderbilt, "Electromechanical Behavior of BaTiO<sub>3</sub> from First Principles," *Applied Physics Letters*, Vol. 72, No. 23, pp. 2981-2983, 1998.
- [4] *IEEE Standard on Piezoelectricity*, ANSI/IEEE Std 176-1987.
- [5] Sang-Joo Kim and Sunggi Kim, "On the Effects of the Heat Generated during an Electric Field-induced Ferroelectric Domain Switching," *International Journal of Solids and Structure*, Vol. 38, pp. 1311-1325, 2001.
- [6] J. Fan, W. A. Stoll, and C. S. Lynch, "Nonlinear Constitutive Behavior of Soft and Hard PZT: Experiments and Modeling," *Acta Materialia*, Vol. 47, No. 17, pp. 4415-4425, 1999.
- [7] Ralph C. Smith and Zoubeida Ounaies, "A Domain Wall Model for Hysteresis in Piezoelectric Materials," *ICASE Report*, No. 99-52, 1999.
- [8] Henno Allik and Thomas J. R. Hughes "Finite Element Method for Piezoelectric Vibration," *International Journal for Numerical Methods in Engineering*, Vol. 2, pp. 151-157, 1970
- [9] E. Bassiouny, A. F. Ghaleb and G. A. Maugin "Thermodynamical Formulation for Coupled Electromechanical Hysteresis Effects - I. Basic Equations," *International Journal of Engineering Science*, Vol. 26, No. 12, pp. 1279-1295, 1988
- [10] E. Bassiouny, A. F. Ghaleb and G. A. Maugin "Thermodynamical Formulation for Coupled Electromechanical Hysteresis Effects - II. Poling of Ceramics," *International Journal of Engineering Science*, Vol. 26, No. 12, pp. 1297-1306, 1988
- [11] E. Bassiouny and G. A. Maugin "Thermodynamical Formulation for Coupled Electromechanical Hysteresis Effects - III. Basic Equations," *International Journal of Engineering Science*, Vol. 27, No. 8, pp. 975-987, 1989

- [12] E. Bassiouny and G. A. Maugin “Thermodynamical Formulation for Coupled Electromechanical Hysteresis Effects - IV. Combined Electromechanical Loading,” *International Journal of Engineering Science*, Vol. 27, No. 8, pp. 989-1000, 1989
- [13] Peter J. Chen and Stephen T. Montgomery “A Macroscopic Theory for the Existence of the Hysteresis and Butterfly Loops in Ferroelectricity,” *Ferroelectrics*, Vol. 23, pp. 199-208, 1980
- [14] Peter J. Chen and P. S. Peerey “One Dimensional Dynamic Electromechanical Constitutive Relations of Ferroelectric Materials,” *Acta Mechanica*, Vol. 31, pp. 231-241, 1979
- [15] Peter J. Chen and T. J. Tucker “Determination of the Polar Equilibrium Properties,” *Acta Mechanica*, Vol. 38, pp. 209-218, 1981
- [16] Peter J. Chen, C. E. Land, and Marcella M. Madsen “A Theory of the Influences of Space-Charge Field on Domain Switching in PLZT 7/65/35 Ceramic,” *Acta Mechanica*, Vol. 43, pp. 61-72, 1982
- [17] Peter J. Chen, “Characterization of the Three Dimensional Properties of Poled PZT 65/35 in the Absence of Losses,” *Acta Mechanica*, Vol. 47, pp. 95-106, 1983
- [18] Peter J. Chen, C. E. Land, and Marcella M. Madsen “Three Dimensional Constitutive Relations for Ferroelectric Materials in the Presence of Quasi-Static Domain Switching,” *Acta Mechanica*, Vol. 48, pp. 31-42, 1983
- [19] J. S. Cory and J. L. McNichols, Jr., “Nonequilibrium Thermostatistics” *Journal of Applied Physics*, Vol. 58. No. 9, pp. 3283-3294, 1985
- [20] Craig L. Hom and Natarajan Shankar, “A Fully Coupled Constitutive Model for Electrostrictive Ceramic Materials” *Journal of Intelligent Material Systems and Structures*, Vol. 5, pp. 795-801, 1994
- [21] M. Kamlah, U. Bhle, D. Munz, and Ch. Tsakmakis, “Macroscopic Description of the Nonlinear Electromechanical Coupling in Ferroelectrics” *Smart Structures and Materials 1997: Smart Structures and Integrated Systems, San Diego, CA, USA, Proceedings of SPIE - The International Society for Optical Engineering*, Vol. 3039, pp. 144-155, 1997.
- [22] S. C. Hwang, C. S. Lynch and R. M. McMeeking, “Ferroelectric/Ferroelastic Interactions and a Polarization Switching Model” *Acta Metallurgica et Materialia*, Vol. 43, No. 5, pp. 2073-2084, 1995
- [23] C. S. Lynch “Effect of Uniaxial Stress on the Electro-mechanical Response of 8/65/35 PLZT” *Acta Materialia*, Vol. 44, No. 10, pp. 4137-4148, 1996
- [24] W. Chen and C. S. Lynch “A Micro-electro-mechanical Model for Polarization Switching of Ferroelectric Materials” *Acta Materialia*, Vol. 46, No. 15, pp. 5303-5311, 1998
- [25] G. A. Maugin and J. Pouget, “Electroacoustic Equations for One-domain Ferroelectric Bodies,” *Journal of the Acoustical Society of America*, Vol. 68, No. 2, pp. 575-587, 1980

- [26] E. F. Prechtel and S. R. Hall, "Design of a High Efficiency, Large Stroke, Electromechanical Actuator," *Smart Materials and Structures*, Vol. 8, No. 1, pp. 13, Feb. 1999.
- [27] N. W. Hagood and A. A. Bent, "Development of Piezoelectric Fiber Composites for Structural Actuation," *34th AIAA/ASME/ASCE/AHS/ASC Structures, Structural Dynamics, and Materials Conference*, LaJolla, CA, pp. 3625-3638, 1993.
- [28] H. H. A. Krueger and D. Berlincourt, "Effects of High Static Stress on the Piezoelectric Properties of Transducer Materials," *Journal of the Acoustical Society of America*, Vol. 33, pp. 1339-44, 1961.
- [29] Q. M. Zhang, J. Zhao, K. Uchino, and J. Zheng, "Change of the Weak-field Properties of Pb(ZrTi)O<sub>3</sub> Piezoceramics with Compressive Uniaxial Stresses and its Links to the Effect of Dopants on the Stability of the Polarizations in the Materials," *Journal of Materials Research*, Vol. 12, pp. 226-234, 1997.
- [30] B. Jaffe, W. R. Cook, and H. Jaffe, *Piezoelectric Ceramics*. London, New York,: Academic Press, 1971.
- [31] D. J. Warkentin and N. W. Hagood, "Nonlinear Piezoelectric Shunting for Structural Damping," *Smart Structures and Materials 1997: Smart Structures and Integrated Systems, San Diego, CA, USA*, pp. 747-757: *Proceedings of SPIE - The International Society for Optical Engineering*. v 3041 1997. Society of Photo-Optical Instrumentation Engineers, Bellingham, WA, USA.
- [32] M. Umeda, K. Nakamura, and S. Ueha, "Analysis of the Transformation of Mechanical Impact Energy to Electric Energy Using Piezoelectric Vibrator," *Japanese Journal of Applied Physics, Part 1-Regular Papers Short Notes and Review Papers*, Vol. 35, pp. 3267-3273, 1996.
- [33] M. Umeda, K. Nakamura, and S. Ueha, "Energy Storage Characteristics of a Piezo-generator Using Impact Induced Vibration," *Japanese Journal of Applied Physics Part 1-Regular Papers Short Notes and Review Papers*, Vol. 36, pp. 3146-3151, 1997.
- [34] T. Michelitsch and W. S. Kreher, "Simple Model for the Nonlinear Material Behavior of Ferroelectrics," *Acta Materialia*, Vol. 46, pp. 5085-5094, 1998.
- [35] K. Ghandi, "Nonlinear Modeling and Characterization Techniques for Phase Transitions in Electromechanically Coupled Devices," Ph.D. Thesis, Massachusetts Institute of Technology, 1998
- [36] J. E. Harper, "Analysis of Nonlinear Electroelastic Continua with Electric Conduction," S.M. Thesis, Massachusetts Institute of Technology, 1999
- [37] W. Chen and C. S. Lynch, "Micro-electro-mechanical Model for Polarization Switching of Ferroelectric Materials," *Acta Materialia*, Vol. 46, pp. 5303-5311, 1998.
- [38] C. Kim, A. E. Glazounov, F. D. Flippen, A. Pattnaik, Q. M. Zhang, and D. Lewis, III, "Piezoelectric Ceramic Assembly Tubes for Torsional Actuators," *Proceedings of Spie - the International Society for Optical Engineering*. Vol. 3675, 1999, pp. 53-62.

- [39] M. Lutz and N. W. Hagood, "Actuation Efficiency in Piezoelectrically Driven Linear and Non-linear Systems," *Proceedings of Spie - the International Society for Optical Engineering*. Vol. 3668, pp. 780-796, 1999
- [40] L. P. Huelsman, *Active and Passive Analog Filter Design* McGraw-Hill, Inc., 1993.
- [41] D. G. Morris, N. W. Hagood and A. Pizzochero, "Experimental Investigation on the Effect of Environmental Stress on Active Fiber Composite Actuators," *Proceedings of Spie - the International Society for Optical Engineering*. Vol. 3674, pp. 296-305, 1999
- [42] T. G. Beckwith, R. D. Marangoni and J. H. Lienhard V, *Mechanical Measurements*. Addison-Wesley Publishing Company, 1993.
- [43] A. J. Peyton and V. Walsh, *Analog Electronics with Op Amps, A source Book of Practical Circuits*. Cambridge University Press, 1993.
- [44] E. H. Anderson, "Piezoceramic Induced Strain Actuation of One - and Two-dimensional Structures," M.S. Thesis, Massachusetts Institute of Technology, 1989.
- [45] M. Gellert and R. Harbord, "Moderate Degree Cubature Formulas for 3-D Tetrahedral Finite-Element Approximations," *Communications in Applied Numerical Methods*, Vol. 7, pp. 487-495, 1991.
- [46] K. E. Brenan, S. L. Campbell and L. R. Petzold, *Numerical Solution of Initial-Value Problems in Differential-Algebraic Equations*, Society for Industrial and Applied Mathematics, 1996.
- [47] B. Jaffe, W. Cook, and H. Jaffe, *Piezoelectric Ceramics*, Academic Press Limited, 1971.
- [48] F. Jona and G. Shirane, *Ferroelectric Crystals*, Dover Publications, Inc. 1993.
- [49] N. Hagood, R. Kindel, K. Ghandi, and P. Gaudenzi, "Improving Transverse Actuation of Piezoceramics using Interdigitated Surface Electrodes," Paper No. 1917-25, *Proc. of SPIE's Symposium on Smart Structures and Intelligent Systems*, Albuquerque, NM, 1993.
- [50] E. F. Crawley, J. Deluis, "Use of Piezoelectric Actuators as Elements of Intelligent Structures," *AIAA Journal*, Vol. 25. No. 10, 1987, pp. 1373-1385.
- [51] J. Rodgers, "Development of An Integral Twist-Actuated Rotor Blade for Individual Blade Control," Ph.D. Thesis, Massachusetts Institute of Technology, 1998
- [52] N.W. Hagood, D.C. Roberts, L. Saggere, K.S. Breuer, K.-S. Chen, J.A. Carretero, H.Q. Li, R. Mlcak, S. Pulitzer, M.A. Schmidt, S.M. Spearing, and Y.-H. Su, "Micro Hydraulic Trans-ducer Technology for Actuation and Power Generation," *Proceedings of the SPIE 7th Annual International Symposium on Smart Structures and Materials*, Vol. 3985, pp. 680-688, Newport Beach, CA, March 5-9, 2000.
- [53] D. Berlincourt and H. H. A. Krueger, "Important Properties of Morgan Matroc Piezoelectric Ceramics", TP-226, Morgan Matroc, Inc. Bedford, OH 44146.

- [54] Seung-Eek Park, Venkata Vedula, Ming-Jen Pan, Wesley S. Hackenberger, Patrick Pertsch and Thomas R. Shrout, “Relaxor Based Ferroelectric Single Crystals for Electromechanical Actuators”, TRS Ceramics, Inc. PA
- [55] Crystal Associates, Inc. East Hanover, NJ 07936
- [56] D. G. Morris, N. W. Hagood and A. Pizzochero, “ Experimental Investigation on the Effect of Environmental Stress on Active Fiber Composite Actuators,” *Proceedings of Spie - the International Society for Optical Engineering.* vol. 3674, pp. 296-305, 1999
- [57] M. Goldfarb and L. D. Jones, “On the Efficiency of Electric Power Generation with Piezoelectric Ceramic,” *Journal of Dynamic System, Measurement, and Control. Transaction of ASME*, vol. 121, September 1999, pp. 566 - 571
- [58] O. Yaglioglu, “Modeling and Design Considerations for a Micro-Hydraulic Piezoelectric Power Generator”, S.M. Thesis, Massachusetts Institute of Technology, Cambridge, MA, June 2002.
- [59] A. F. Devonshire, “Theory of Ferroelectrics”, *Philosophical Magazine*, Vol. 3, No. 10, April 1954, pp. 85-130.
- [60] K. H. Chan, “ Nonlinear Modeling of High Field Ferroelectric Ceramics for Structural Actuation”, S.M. Thesis, Massachusetts Institute of Technology, Cambridge, MA, 1994.
- [61] A. W. Drake, *Fundamentals of Applied Probability Theory*, McGraw-Hill, Inc.
- [62] *Optimization Tool Box*, Mathworks, Natick, MA 01760
- [63] M. E. Lines and A. M. Glass, *Principles and Applications of Ferroelectrics and related Materials*, Clarendon Press, Oxford, 1977.
- [64] Q. S. Zheng, “ On Transversely Isotropic, Orthotropic and Relative Isotropic Functions of Symmetric Tensors, Skew-Symmetric Tensors and Vectors, Part I: Two Dimensional Orthotropic and Relative Isotropic Functions and Three Dimensional Relative Isotropic Functions”, *International Journal of Engineering and Science*, Vol. 31, No. 10, 1993, pp. 1399-1409.
- [65] D. Zhou, M. Kamlah and D. Munz, “Rate Dependence of Soft PZT Ceramics under Electric Dield Loading,” *SPIE Proceddings, Smart Structures and Materials, 2001*, Vol. 4333, pp. 64-70.
- [66] Kenji Uchino, *Ferroelectric devices*, New York, 2000
- [67] S. Wan and C.S. Lynch, “ Characterization of PZN Single Crystals”, 12th IEEE International Symposium on the Application of Ferroelectrics, Honolulu, Hawaii, 2000.
- [68] T. Tsurumi, Y. Kumano, N. Ohashi, T. Takenaka and O. Fukunaga, “ 90 ° domain reorientation and electric-field-induced strain of tetragonal Lead Zirconate Titanate ceramics”, *Japan Journal of Applied Physics*, Vol. 36, pp. 5970-5975, 1997.



- [69] B.K. Mukherjee, W. Ren, S.-F. Liu, A.J. Masys, and G. Yang, “Non-linear properties of piezoelectric ceramics” *Proceedings of the Conference on Smart Structures and Materials 2001, Newport Beach, CA, Mar. 5-8, 2001*, SPIE Proceedings. Vol. 4333, 2001, p. 41-54
- [70] M.F. Ashby, “Physical Modelling of Materials Problems”, *The Institute of Materials*, 1992
- [71] *Using Simulink*, Mathworks, Natick, MA 01760
- [72] *Writing S-Functions*, Mathworks, Natick, MA 01760
- [73] B. Janos, “Design, Development, and Characterization of Magnetic Particle Active Fiber Composites,” Ph.D. Thesis, Massachusetts Institute of Technology, 2001

# FABRICATION OF A MICROVALVE WITH PIEZOELECTRIC ACTUATION

H.Q. Li, D.C. Roberts, J.L. Steyn, K.T. Turner, O. Yaglioglu,  
N.W. Hagood, S.M. Spearing, and M.A. Schmidt  
Massachusetts Institute of Technology  
Cambridge, MA 02139, USA

## ABSTRACT

The fabrication of an active MEMS micro valve driven by integrated bulk single crystal piezoelectric actuators is reported. The valve has a nine-layer structure of glass, Si, and silicon on insulator (SOI) assembled by wafer level fusion bonding and anodic bonding, as well as die level anodic bonding and eutectic bonding. Valve head strokes as large as  $20\mu\text{m}$  were realized through hydraulic amplification of small stroke the piezoelectric actuator. Flow rate of  $0.21\text{ml/s}$  was obtained at  $1\text{kHz}$ . The fabrication, bonding and assembly process, as well as some test results will be described.

## INTRODUCTION

In a micro hydraulic transducer (MHT) system for high energy density actuation and power generation applications [1], a key component is actively controlled micro valves that regulate high liquid flow under high pressure and at high frequencies, have small volume, and consume minimum power. There have been many studies on various types of MEMS micro valves [2-5], but operation of the MHT devices demands a new approach in the valve design and fabrication. The fabrication processes of the valve have to be compatible to those of the core units of the MHT devices to simplify the fabrication and device integration of the whole system. Since single crystal piezoelectric material is used in MHT devices for actuation, it was preferred that the valve uses the same to reduce redundant actuator integration and process development. The use of piezoelectric material brought about the challenges of electric contacts, insulation, integration of small piezoelectric material pieces in a MEMS device. Another challenge is the conversion of the intrinsically high frequency, small strokes of the piezoelectric material into large strokes of the valve motion at the same frequency for high flow rate under high pressure. Our solution to this challenge is hydraulic amplification in the valve. The design and testing of this valve will be published elsewhere [6]. This paper will present the structure of the device, fabrication and assembly procedures, as well as some test results.

## VALVE STRUCTURE

Figure 1 shows the schematic cross-section of the device. It includes four Pyrex glass layers, L1, L3, L6, and L9, two Si layers, L2 and L8, and three SOI layers, L4, L5, and L7. One or three actuators of single crystal piezoelectric material (PZN-PT) (14) are nested in L3 holes. Fig. 1 only shows one actuator for simplicity. The electrical contacts to the piezoelectric actuators are on L2 and the device layer of L4.

Recessed seats are etched into L2 for actuator height compensation. In L4 and L5 there is a bonded circular double layer piston (10),  $6.8\text{mm}$  in diameter and  $2 \times 450\mu\text{m}$  thick, attached to annular SOI membranes (12),  $10\mu\text{m}$  thick and  $225\mu\text{m}$  wide, that allow the piston's vertical motion at the actuation of the piezoelectric material. The valve head, composed of a circular piston (5),  $0.5\text{mm}$  in diameter and  $310\mu\text{m}$  thick, and an attached annular SOI membrane,  $7\mu\text{m}$  thick and  $450\mu\text{m}$  wide, is in L7. The valve orifice (4)  $470\mu\text{m}$  in diameter, and flow inlet (2) and outlet (6) are in L8. The pistons and membranes in L4 and L5 are identical except for the venting channel (9) that is composed of a shallow lateral channel in L5 and a through hole in L4. Connecting the valve head and the drive piston is a hydraulic amplification

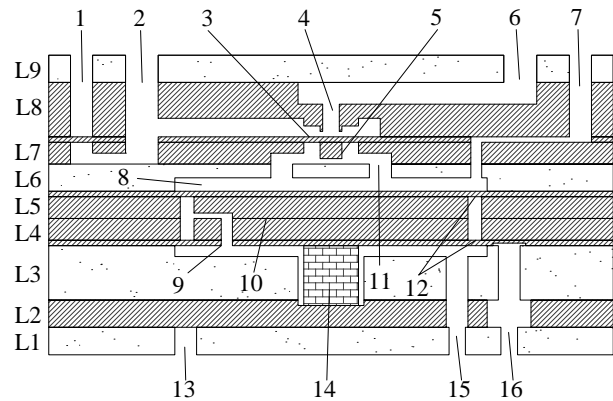


Figure 1. Schematic cross-section view of the microvalve, Layers L1, L3, L6 and L9 are glass. Layers L2 and L8 are Si. Layers L4, L5, and L7 are SOI.

chamber (HAC) in L6. It consists of a recessed volume (8) and through holes (11). The recessed volume (8) has a larger diameter than the drive membrane in L5 to allow the drive piston move up. Similar recessed volume is also formed in L3 for the downward motion of the drive piston. Glass is used for L6 to insulate the actuator electrode from the Si layer above it and for convenience of device assembly. The HAC is filled with high bulk modulus silicone oil and hermetically sealed through a filling hole (7). When the piezoelectric actuator pushes the drive piston up, the silicone oil in the HAC in turn pushes the valve head up a much larger distance due to the area difference. Bubble-free filling is critical to high frequency response of the valve to the piezoelectric actuation. Sealing without significant HAC volume change is important for membrane performance. A systematic study of HAC was previously reported [7]. L9 covers the outlet channel and accommodates all the fluid ports, as well as a port for inlet pressure sensor (1) build in L7 in the form of a SOI membrane. Observation windows

(15) for drive piston deflection measurements are through L1 to L3. All the electric connections, (13) to L2 and (16) to L4 are arranged at the bottom of the device and all the fluid connections are arranged on the top of the device as seen in Fig. 1. The separation of the fluidic ports and electric ports helps to make the testing of the micro valve convenient.

## PROCESSES

All the glass layers were patterned using ultrasonic trilling. The tolerance of this process is about  $25\mu\text{m}$ , much larger than that of contact photolithography used for Si and SOI wafer. Because of this, large tolerance was designed into critical features such as the recesses for drive piston in L3 and L6. Global align marks were patterned by photo lithography and etched by BOE for bonding alignment to Si and SOI layers. All Si and SOI wafers were thermally oxidized at the beginning of the fabrication and the oxide were to be removed only right before fusion bonding, a commonly used technique to protect the bonding surfaces. 22 photo masks were used to pattern the Si and SOI wafers. Surface oxide and buried oxide in SOI wafers were etched using buffered oxide etcher (BOE). Deep Si features were etched by deep reactive ion etch process. Oxide nested mask technique was used to form 2 deep steps on one side of the wafers. As an example, Figure 2 shows the process flow for L4 that includes the drive piston and its membrane, a key feature of the device. It starts, in step 1, with a SOI wafer that has a  $10\mu\text{m}$  thick device layer,  $2\mu\text{m}$  thick buried oxide

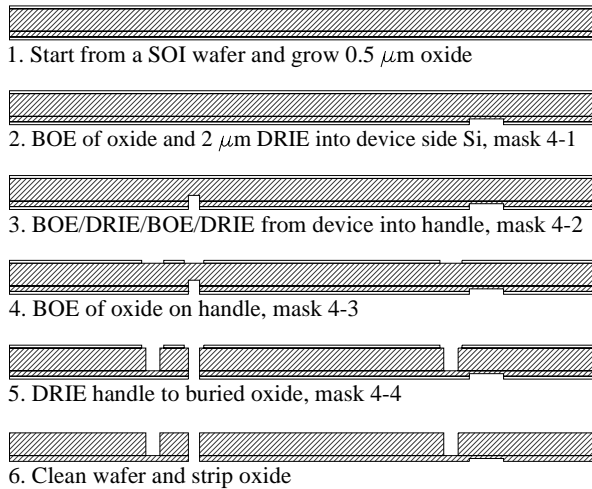


Figure 2. The process flow of L4, a SOI layer with the drive piston and membrane. L5 and L7 use similar processes.

layer and  $440\mu\text{m}$  thick handle layer.  $0.5\mu\text{m}$  oxide was thermally grown on both sides of the wafer by thermal oxidation and then (not shown) bonding alignment marks were etched on both sides first through the oxide by BOE and then  $0.2\text{-}0.3\mu\text{m}$  into Si by DRIE. In step 2,  $2\text{-}3\mu\text{m}$  deep electrode recesses were etched into Si by BOE and DRIE using mask 4-1. In step 3, mask 4-2 for the fusion bonding venting hole was used to have the device layer etched

through by DRIE, the buried oxide layer removed by BOE, and the handle side etched by DRIE for 30 to  $40\mu\text{m}$ . Etching a distance into handle from the device side is a unique feature of L4 process. The purpose is to compensate the RIE lag of the small venting holes relative to larger piston membranes when etching from the handle side, so that the buried oxide starts to expose some time after the small venting holes are etched through. Therefore the piston membrane fillet control is not affected by the finish time of the venting holes. In step 4, donut shape oxide patterns offsetting the drive piston membranes by  $6\mu\text{m}$  were etched by BOE using mask 4-3. DRIE etch of drive piston membranes were done with mask 4-4 as shown in step 5. The oxide offsetting from the membranes allows the membranes to be defined by thick resist patterns that are usually smoother. It is important to keep the whole circle of the membrane as smooth as possible to avoid stress concentration. The membrane DRIE stopped at the buried oxide layer. Careful control was taken to make sure the each membrane in a wafer has a  $15\text{-}20\mu\text{m}$  fillet at the bottom. Any sharp corner and footing would greatly lower the strength of the membranes. Because of the non-uniformity of the DRIE process, dies around the edge of wafers were finished earlier than the center dies, sometimes more than 10 minute earlier. If the center dies are to be finished with good fillets, the edge dies would have sharp corners or footings in the membranes. One solution was constantly stopping the etching, inspecting the wafers under microscope, covering the finished edge dies with resist, and etching the remaining dies.

The processes of the L5 and L7 are designed to be similar to L4 process for fabrication simplicity. Si layers L2 and L8 use nested oxide masks that are patterned by a BOE etch prior to one DRIE step and used as the mask for another DRIE step.

## ASSEMBLY SEQUENCES

The assembly of the device involves wafer level fusion bonding and anodic bonding, die level anodic bonding, and eutectic bonding performed at the same time as the final anodic bonding. For the assembly of a multiplayer structure, it is preferred to include die level bonding steps for better yield. Since die level multiplayer fusion bonding technology is not yet mature, and this micro valve device requires insulation in L1, L3 and L6, die level anodic bonding of glass to Si was selected for device assembly.

Figures 3a, 3b, 3c, and 3d show the assembly sequence of the micro-valve. First the glass wafers are ultrasonically drilled and the Si and SOI wafers were etched. Fusion bonding on wafer level was done to bond L4 to L5 and L7 to L8, as seen in Fig. 3a. The conditions for fusion bonding are  $1100^\circ\text{C}$  anneal for 1 hour after alignment and pressing using an EVG Group aligner and bonder. Then wafer level anodic bonding was done to bond L1 to L2, and L6 to the stack of L4 and 5, as shown in Fig. 3b, using the same align

tool as fusion bonding. The anodic bonding was done at 300°C and at a voltage of 800V. Wafer level bonding is necessary to these wafers because there are 2 valves in each die and they are laterally insulated in L2 and in L4/L5 stack by through etches across the die. The bonding of L4/L5 stack to L6, and the bonding of L2 to L1 on wafer level help to hold the two devices together after dicing.

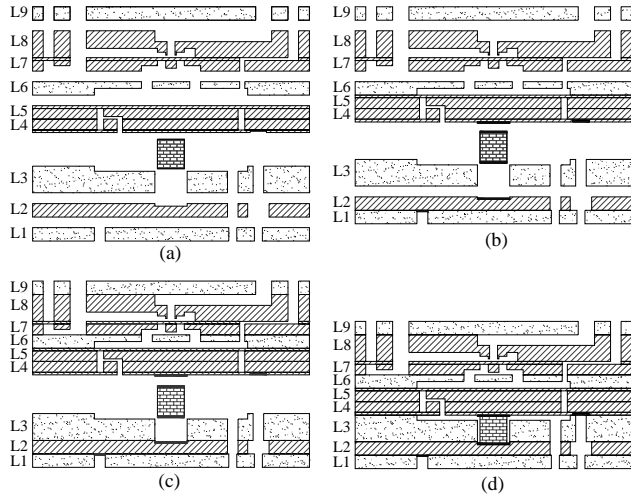


Figure 3. The assembly sequence of the microvalve, (a) wafer level fusion bonding of L4 to L5 and L7 to L8, (b) wafer level anodic bonding of L6 to L4/L5 stack, flowed by dicing, cleaning, and electrode depositions, (c) die-level anodic bonding of layers L4 to L9 and L1-L3, and (4) final anodic bonding of L3 to L4 and the eutectic bonding of piezoelectric actuators to the L2 and L4.

All the wafers or wafer stacks were diced into 20 mm by 20mm dies thereafter, with special care taken to avoid any die-saw slurry or other debris entering the devices. Next, 500nm of gold film were deposited on L4 device side and top of L2 using different shadow masks by e-beam deposition. The top and bottom surfaces of the piezoelectric material piece were coated with 2  $\mu\text{m}$  of 80%-20% Au-Tin alloys and 50 nm of gold film by sputtering. A thin Ti layer was put down first in each deposition for surface wetting enhancement. One thing to point out is that the cleaning after dicing is very important for high quality film deposition and anodic bonding. The device wafers were sealed using a glass wafer by crystal bond during dicing. After a thorough rinse with DI water, the crystal bond was dissolved in acetone to release the glass pieces. Cleaning of the dies as done by repeated acetone, methanol, and isopropanol soaking and rinsing. A photograph of the dies before die level bonding is show in Figure 4. Next, L1-L3 and L4-L9 are anodically bonded respectively as shown in Fig. 3c. The actuators were dropped in L3 holes that are just slightly bigger than the largest dimensions of the actuators so no extra alignments were needed. Finally, as seen in Fig. 3d, the anodic bonding of L3 and L4 and the eutectic bonding of the piezoelectric actuators to L4 and L2 were done at the same time to finish the die assembly. A completed die with two single valve head device is show in the photograph in Figure 5. At the top and bottom are 3mm

thick glass layers L9 and L1 respectively. Two curved bright features in the middle of the die are two HACs in L6.

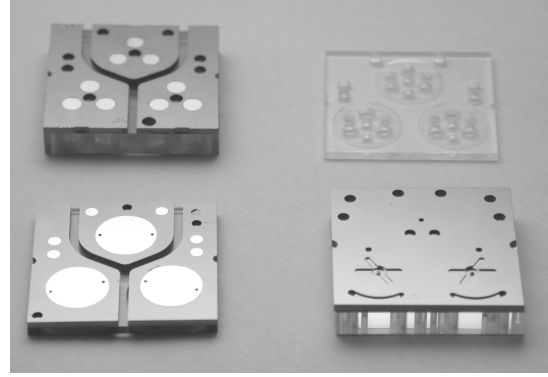


Figure 4. Photograph of dies before assembly on die level. Clockwise from top left are bonded layer 1 and 2 with layer 2 on top, layer 3, bonded layer 4, 5 and 6 with layer 4 on top, and bonded layer 7, 8 and 9 with layer 7 on top. Gold films were deposited with shadow masks on layer 2 and layer 5 for electric contacts to the piezoelectric actuators. In each die there are 2 microvalves units that share layer 1-6 with the final MHT device.

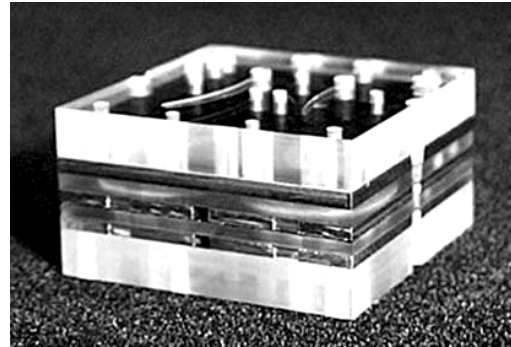


Figure 5. Photograph of an assembled chip of about 20x20x10mm. 3 mm thick glass wafers were used in layer 1 and 9 to give the device a strong structural support.

The approach of die level bonding and assembling described above has several advantages for this type of prove of concept device development. First it provides the flexibility of choosing best dies in wafers of every layer to construct high quality devices, therefore increasing the yield. Secondly, it reduces the risk of loosing all dies as in the event of wafer level bonding and assembling failure. Thirdly, different components of a device can be constructed using dies in common layers and minimum new wafer fabrication. A component of the active valve, the HAC component device [7], shares L1 to L6 with the valve. In fact the valve itself also only differs from the MHT devices in layers L7 to L9.

## TEST RESULTS

After being mounted in a test jig, filled with silicone oil and sealed, the micro valve was tested for membrane deflection, flow rate, pressure, voltage, frequency and power. From simultaneous deflection measurement of the valve membranes and the drive membranes using a laser

vibrometer, an HAC amplification ratio of about 40 was obtained, consistent with calculation based on the device geometry. Two real time valve head motion curves under a differential pressure of 35kPa are shown in Figure 6. The frequency of the voltage applied on the piezoelectric actuators is 1kHz. As the drive voltage increases the valve opening increases until the valve head reaches the orifice. The flat tops of the curve at higher voltage indicate that the valve was in close position. The dependence of flow rate on differential pressure is plotted in Figure 7. The duty cycle of 0% means that the valve is fully closed and the duty cycle of 100% means that it is fully open. This figure proves that flow regulation was achieved at high frequency. The highest flow rate achieved in this device is 0.21ml/s under the conditions of a differential pressure of 260kPa, a 1kHz peak to peak sinusoidal drive voltage of 500V, and a peak valve opening of 17 $\mu$ m.

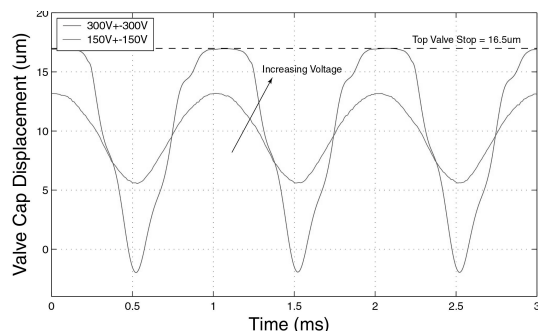


Figure 6. Valve head motion curves at different actuation voltages at 1 kHz. The pressure differential across the valve membrane is 50 kPa. The flat tops of the curves at high voltages indicate that the valve head is in the closed position.

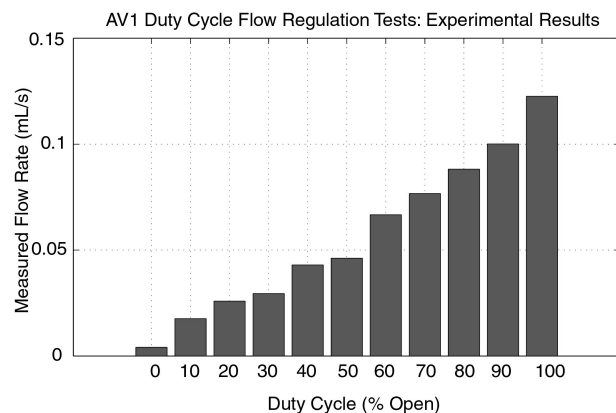


Figure 7. Flow rate vs. duty cycle of a microvalve. The actuation frequency is 1kHz, and the pressure differential is 35kPa.

## SUMMARY

In conclusion, we developed a reliable and flexible fabrication and assembly process and successfully fabricated a multilayer MEMS micro valve with piezoelectric actuation that was amplified at the valve head by a sealed hydraulic chamber. Combinations of wafer level fusion bonding, wafer level anodic bonding, and die-level anodic bonding contributes greatly in the success of the assembly of this multilayer structure. Large valve opening and large flow rate at high pressure and high frequency were achieved. The study of this micro valve paves the way for the MHT devices.

## REFERENCES

- [1] N.W. Hagood, D.C. Roberts, L. Saggere, K.S. Breuer, K.-S. Chen, J.A. Carretero, H.Q. Li, R. Mlcak, S. Pulitzer, M.A. Schmidt, S.M. Spearing, and Y.-H.Su, "Micro hydraulic transducer technology for actuation and power generation" Proceedings of the SPIE 7<sup>th</sup> Annual International Symposium on Smart Structures and Materials, New Port Beach, CA, March 5-9, 2000, Vol, 3985, pp.680-688, 2000.
- [2] S. Shoji and M. Esashi, "Microflow devices and systems" Journal of Micromechanics and Microengineering, 4, pp 157-171, 1994.
- [3] H. van Lintel, F. van de Pol, and A. Bouwstra, "piezoelectric micropump based on micromachining of silicon" Sensors and Actuators" 15, pp 153-167, 1988.
- [4] V. Gasss, B. van der Schoot, S. Jeanneret and N. de Rooij, "Integrated flow-regulated siliconmicropump" Sensors and Actuators A 43, pp. 335-338, 1994
- [5] M. Koch, A.G.R. Evans, and A. Brunnschweiler, "The dynamic micropump driven with a screen printed PZT actuator" Journal of Micromechanics and Microengineering, 8, p. 119, 1998.
- [6] D.C. Roberts, H.Q. Li, J.L. Styen, O. Yaglioglu, S.M. Spearing, M.A. Schmidt, and N.W. Hagood, "A piezoelectric microvalve for compact high-frequency, high differential pressure micropumping systems" to be published in Journal of Microelctromechemical Systems.
- [7] J.L. Styen, H.Q. Li, D.C. Roberts, R. Mlcak, K.T. Turner, O. Yaglioglu, Y.-S. Su, M.A. Schmidt, S.M. Spearing, and N.W. Hagood, Proceedings of the IEEE Solid-State Sensor and Actuator Workshop, Hilton Head, SC, June 4-7, 2002, pp. 50-54. 2002.

# A Piezoelectric Microvalve for Compact High-Frequency, High-Differential Pressure Hydraulic Micropumping Systems

David C. Roberts, Hanqing Li, J. Lodewyk Steyn, Onnik Yaglioglu, S. Mark Spearing, *Member, ASME*, Martin A. Schmidt, *Senior Member, IEEE*, and Nesbitt W. Hagood

**Abstract**—A piezoelectrically driven hydraulic amplification microvalve for use in compact high-performance hydraulic pumping systems was designed, fabricated, and experimentally characterized. High-frequency, high-force actuation capabilities were enabled through the incorporation of bulk piezoelectric material elements beneath a micromachined annular tethered-piston structure. Large valve stroke at the microscale was achieved with an hydraulic amplification mechanism that amplified ( $40 \times -50 \times$ ) the limited stroke of the piezoelectric material into a significantly larger motion of a micromachined valve membrane with attached valve cap. These design features enabled the valve to meet simultaneously a set of high frequency ( $\geq 1$  kHz), high pressure ( $\geq 300$  kPa), and large stroke ( $20\text{--}30\text{ }\mu\text{m}$ ) requirements not previously satisfied by other hydraulic flow regulation microvalves. This paper details the design, modeling, fabrication, assembly, and experimental characterization of this valve device. Fabrication challenges, such as deep-reactive ion etching of the piston and valve membrane structures, wafer-level silicon-to-silicon fusion bonding, wafer-level and die-level silicon-to-glass anodic bonding, preparation and integration of piezoelectric material elements within the micromachined tethered piston structure, and filling of degassed fluid within the hydraulic amplification chamber are detailed. [829]

**Index Terms**—Hydraulic amplification, MEMS, micropump, microvalve, piezoelectric.

## I. INTRODUCTION

THE development of a fluidic microvalve, capable of high-frequency control of high-differential pressure liquid fluid flows, is a key task in the realization of compact high performance micropumping technology. Currently, many research efforts around the world are underway to develop compact liquid micropumping systems, the term “micro” referring to devices which are created with fabrication procedures capable of  $\mu\text{m}$ -size tolerances and which produce overall micropump dimensions on the order of a few millimeters to a few centimeters. However, the vast majority of these systems are designed for low pressure and low flow rate applications (i.e., drug dispensing and microdosing) [1]–[8]. The higher performing

of these systems are capable of pumping liquids with flow rates on the order of  $1000\text{--}3000\text{ }\mu\text{L}/\text{min}$  ( $0.017\text{--}0.050\text{ mL/s}$ ) against differential pressures of no more than  $10\text{--}50$  kPa.

In an effort to develop higher differential pressure and higher flow rate micropumping systems for both actuation and power generation applications, a novel class of micro-hydraulic transducer (MHT) devices has been introduced [9]–[13]. These devices, which integrate bulk piezoelectric materials within stiff micromachined structures to form a fluid pumping chamber and two active valves, are designed to enable high frequency pumping of fluid ( $1\text{--}10$  kHz) against pressure differentials on the order of  $\sim 0.4\text{--}1$  MPa, creating flow rates near or in excess of  $0.5\text{ mL/s}$ . The performance of these MHT systems is directly governed by the pressurization, stroke, and frequency capabilities of the active valves employed. The development of a microvalve for use within these MHT systems is the subject of this paper.

Although a significant amount of literature is available describing the development of active valve devices and technology, few if any have been designed for high frequency control of high differential pressure liquid fluid flows. Microvalve designs using thermopneumatic actuation [14], [15], thermal bimetallic actuation [16], SMA actuation [17], electrostatic actuation [18], [19], electromagnetic actuation [20], [21], piezoelectric bender-type actuation (both thin-film and thick film) [22], [23], and piezoelectric stack-type actuation [24]–[26] have been presented. All of these microvalves share a common operational geometry in that a valve cap is affixed to a diaphragm or membrane structure which carries the cap through a predetermined stroke. Based on the reported capabilities, none of these valves is capable of simultaneously satisfying the set of high frequency, high differential pressure, and large stroke requirements needed within full MHT liquid micropumping systems.

The thermal actuation designs (based on thermopneumatic, thermal bimetallic, and shape memory alloy principles) potentially can achieve large stroke and reasonable actuation force. However, these devices exhibit excessive power consumption and poor response times on the order of seconds. High-frequency actuation in the kHz range is unachievable. The electrostatic devices are limited in their deflection and pressure generation capabilities, since the electrostatic force generated between two parallel plates scales inversely with their spacing and since electrical breakdown across the gap must be avoided. The electromagnetic concepts are impeded by the overall size of external solenoid and housing structures

Manuscript received March 18, 2002; revised July 12, 2002. This research was assisted by the staff at the Microsystems Technology Laboratory at MIT and supported by DARPA under Grant #DAAG55-98-1-0361 and by ONR under Grant #N00014-97-1-0880. Subject Editor H. Fujita.

D. C. Roberts and N. W. Hagood are with the Continuum Photonics, Inc., Billerica, MA 01821 USA (e-mail: droberts@continuumphotonics.com).

H. Li, J. L. Steyn, O. Yaglioglu, S. M. Spearing, and M. A. Schmidt are with the Massachusetts Institute of Technology (MIT), Cambridge, MA 02139 USA.

Digital Object Identifier 10.1109/JMEMS.2002.807471

needed to actuate the valve structure. Piezoelectric thin-film and thick-film bender-type designs are limited in their ability to generate both high force and large deflection output. The work in [24]–[26] aimed at solving this limited valve stroke problem through the use of a stack-type piezoelectric actuator material attached directly to the valve membrane. In order to achieve a reasonable stroke of  $8\text{ }\mu\text{m}$ , however, the piezoelectric stack material was required to be quite long ( $\sim 9\text{ mm}$ ), and the valve membrane structure was designed to be relatively compliant to compensate for the tolerance mismatch between the stack and the surrounding structure. These characteristics resulted in limited differential pressure ( $< 50\text{ kPa}$ ) and limited frequency ( $< 50\text{ Hz}$ ) capabilities for the valve device.

A promising concept for achieving high frequency operation ( $\geq 1\text{ kHz}$ ) in conjunction with large differential pressure ( $\geq 300\text{ kPa}$ ) and large valve stroke ( $20\text{--}30\text{ }\mu\text{m}$ ) capabilities involves the use of miniature-sized bulk piezoelectric elements (for example  $1\text{ mm}$  in thickness—almost an order of magnitude smaller in length than those in [24]–[26]), actuating a stiff micromachined piston-type structure, with an integrated area-ratio hydraulic amplification mechanism for amplifying the limited deflection of the piezoelectric material into a significantly larger valve cap stroke. This concept for microscale systems has been introduced in [12] and [13]. Numerous macroscale piezoelectric hydraulic amplification mechanisms have been presented in the literature. In an application for active vibration control, a piezoelectric actuator uses the volume change of a piezoelectric ring to create a large deflection of a smaller area contact surface [27]. In an application for vibration control of a rotary dynamic system, the deflection of a stack-type piezoelectric actuator is coupled through an hydraulic line to a smaller size piston, which helps to control the motion of a rotating shaft [28]. These and other [29] piezoelectric hydraulic amplification mechanisms are novel in design, yet do not face the difficult fabrication, assembly, and tolerancing challenges inherent in the development of microscale systems.

This paper details the development of a compact piezoelectric hydraulic amplification microvalve to enable the realization of high frequency, high differential pressure micropumping systems. The paper is organized as follows. Section II describes the microvalve geometry and its principle of operation. Section III presents modeling tools and dynamic simulations that were developed to design the valve structure. Section IV outlines the fabrication and assembly procedures developed to create the active valve device. Section V details the results of two sub-component studies carried out to validate the concept of the active valve. Section VI outlines the final active valve design geometry. Section VII presents an overview of the measurement set-up and experimental test plan to evaluate the valve performance. Section VIII discusses the experimental results and provides model-experiment correlation for the quasistatic and dynamic performance of the active valve device. Last, Section IX presents conclusions for this research work.

## II. PRINCIPLE OF OPERATION

The microvalve geometry is shown in Fig. 1. The active valve consists of three primary components: a piezoelectric drive ele-

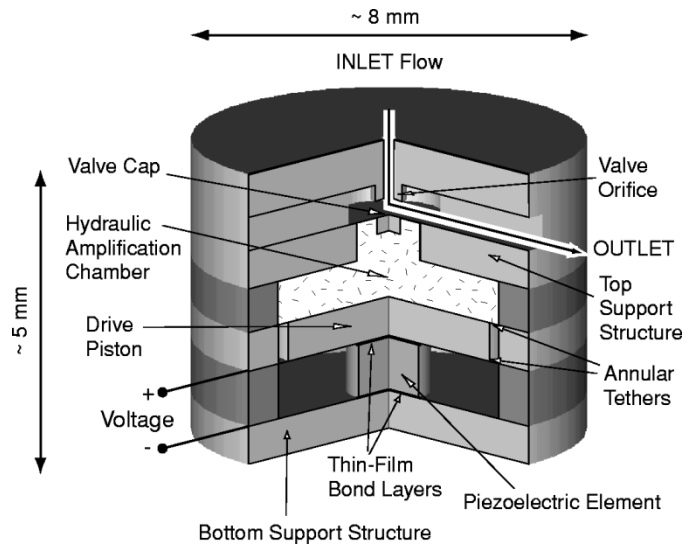


Fig. 1. A schematic of the piezoelectrically driven hydraulic amplification microvalve. The primary structural components are designated with arrows. External hydraulic system pressure loading is applied on the top surface of the valve cap and membrane.

ment, an enclosed hydraulic amplification chamber (HAC), and a membrane with attached valve cap. The drive element incorporates a circular piston structure supported from beneath by one or more small bulk piezoelectric cylinders and is suspended circumferentially from a surrounding support structure by thin annular micromachined tethers. This novel compact “piston-type” design enables high frequency actuation against a large external pressurization due to the high stiffness of the piston structure and integration of miniature bulk piezoelectric elements beneath the piston using a thin-film bond layer.

The lateral dimensions of the tethers are designed to make the tethers compliant enough to allow for rigid piston motion up and down, yet stiff enough to resist bowing under pressurization caused by the hydraulic fluid above the tether during actuation. The tethers provide a seal between the hydraulic fluid above the piston and the piezoelectric chamber below the piston, and also provide a path for electrical contact to the top surface of the piezoelectric cylinders. The fluid chamber resides between the top surface of the drive element piston and the bottom surface of a thin, smaller diameter silicon micromachined valve cap membrane. In response to applied piezoelectric voltage, the piezoelectric material strains. The resulting deflection of the drive element piston generates a pressure within the hydraulic amplification chamber which in turn deflects the valve cap and membrane against a fluid orifice, thereby regulating fluid flow through the external hydraulic system. The pressure loadings on the valve cap and membrane during device operation depend on the external microfluidic system application. The piezoelectric material capabilities, the ratio of the piston diameter to the valve membrane diameter, the compliances of the fluid and structural elements in the chamber, the severity to which the valve cap membrane experiences nonlinear behavior, and the nature of the external loading all contribute to the performance of this microvalve device.



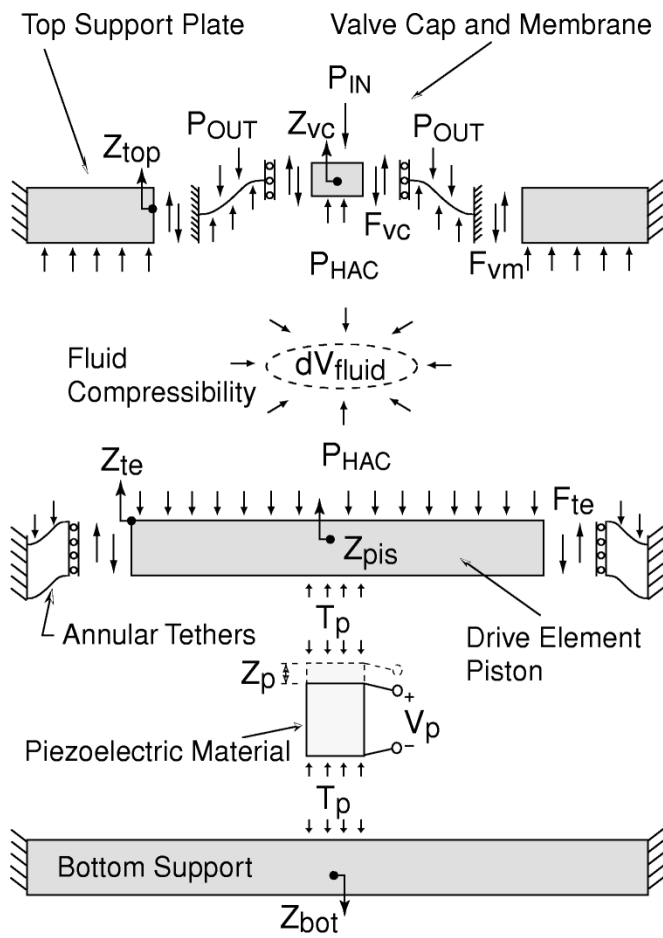


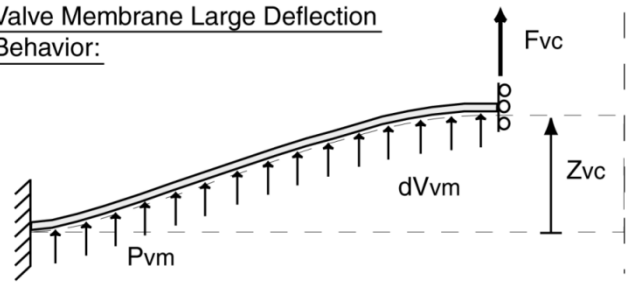
Fig. 2. Structural components included within active valve analytical model. All structures were modeled using linear theory, except for the valve cap and membrane structure, which required the development of nonlinear numerical modeling tools.

### III. MODELING AND SIMULATION

Comprehensive quasistatic and dynamic analytical modeling tools were developed in an effort to design the valve structure based on operational requirements and subsequently to predict the valve behavior in response to applied piezoelectric material voltage and external pressure loading. As shown in Fig. 2, the piezoelectric material behavior, the bending of the drive element piston and deformation of the annular tethers, the hydraulic amplification chamber fluid compressibility, the structural compliance of the top support plate, the structural deformation of the bottom support plate, and the deformation of the valve cap and membrane structure were captured by these modeling tools (see Fig. 3).

The deformations of the plate structures were modeled using bending and shearing relations to determine the structural deflections and fluid swept volumes. Detailed discussions of these active valve modeling procedures are found in previous publications [12], [13]. Although the majority of structural deformations within the valve could be evaluated using linear plate theory, the modeling of the valve cap and membrane structure had to include in-plane tensile relations to properly capture the nonlinear large deflection behavior associated with valve cap deflections in excess of the membrane thickness. Associated

#### Valve Membrane Large Deflection Behavior:



#### Look-Up Tables:

Table $F_{vc}$	→	Given: $Z_{vc}$ , $P_{vm}$	Interpolate: $F_{vc}$
Table $dV_{vm}$	→	Given: $Z_{vc}$ , $P_{vm}$	Interpolate: $dV_{vm}$
Table $\sigma_{max}$	→	Given: $Z_{vc}$ , $P_{vm}$	Interpolate: $\sigma_{max}$

Fig. 3. Numerical modeling tools were used to generate look-up tables for the nonlinear large deflection behavior of the valve cap and membrane. Given a prescribed valve cap displacement  $Z_{vc}$  and pressure loading across the membrane  $P_{vm}$ , a look-up table for each of  $F_{vc}$ ,  $dV_{vm}$ , and  $\sigma_{vm}$  was generated.

numerical modeling tools, detailed in [30], were incorporated into the overall active valve structural model for this purpose.

To capture the nonlinear effects of the valve membrane deformation at high frequency, and to include important dynamic effects, such as the drive element piston inertia and the valve cap inertia and damping, a Simulink simulation architecture was developed. The structural compliances within the active valve simulation were based upon the linear and nonlinear modeling tools discussed above. Look-up tables were implemented within the simulation to enable efficient calculation of the valve membrane deflections and stresses at every time step. Taking as inputs the valve cap displacement  $Z_{vc}$  and the net pressure across the valve membrane  $P_{vm} = P_{HAC} - P_{OUT}$ , a lookup table was employed for each of the following output variables: the valve cap force on the membrane  $F_{vc}$ , the swept volume beneath the valve cap and membrane  $dV_{vm}$ , and the maximum radial stress in the membrane  $\sigma_{vm}$ .

Dynamic relations for the valve cap and drive element piston, schematically shown in Fig. 4, were also implemented to incorporate structural mass and damping. The dynamic behavior of the drive piston structure and the valve cap structure can be described by the following relations, respectively,

$$M_{pis}\ddot{Z}_{te} + C_{pis}\dot{Z}_{te} = A_p T_p - A_{pis} P_{HAC} + F_{te} \quad (1)$$

$$M_{vc}\ddot{Z}_{vc} + C_{vc}\dot{Z}_{vc} = A_{vc}(P_{HAC} - P_{IN}) + F_{vc} \quad (2)$$

where  $A_{pis}$  is the piston area,  $M_{pis}$  is the piston mass,  $A_p$  is the piezoelectric material area,  $A_{vc}$  is the valve cap area, and  $M_{vc}$  is the valve cap mass. The damping coefficient  $C_{pis}$  is a lumped parameter that includes the effects of structural damping in the tethers and damping due to fluid-structural interaction within the hydraulic amplification chamber. The damping coefficient  $C_{vc}$  is a lumped parameter that includes the effects of structural damping in the valve membrane and potential squeeze film



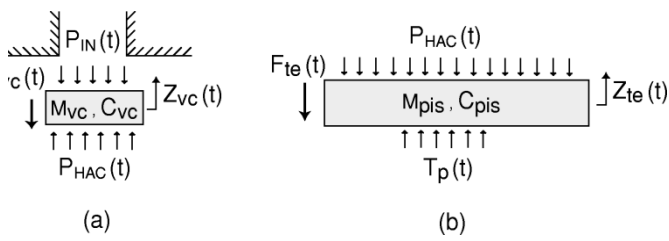


Fig. 4. Dynamic modeling of the valve cap and drive element piston structures: (a) valve cap mass,  $M_{vc}$ , and damping,  $C_{vc}$ ; (b) piston mass,  $M_{pis}$ , and damping,  $C_{pis}$ . Values for the damping coefficients were estimated, then verified through experimentation.

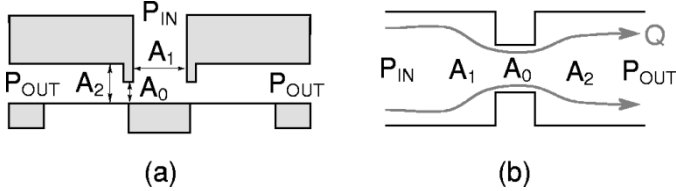


Fig. 5. Valve orifice representation: (a) valve cap geometry and fluid flow areas and (b) representation of flow through valve as a flow contraction followed by a flow expansion.

damping due to the valve cap motion as it closes against the fluid orifice.

Pressure-flow relations through the valve orifice were included in the overall valve simulation, with the orifice structure being represented by a flow contraction followed by a flow expansion. An integral analysis gives a relationship for the combined effect of this flow expansion and contraction. The loss coefficient  $\zeta_{orifice}$  is defined as the total pressure drop  $\Delta P = P_{IN} - P_{OUT}$  over the dynamic pressure based on the orifice local mean velocity ( $\bar{u} = Q/A_0$ ),

$$\zeta_{orifice} = \frac{\Delta P}{\frac{1}{2}\rho\bar{u}^2} = \left[ \frac{1}{2} \left( 1 - \frac{A_0}{A_1} \right)^{\frac{3}{4}} + \left( 1 - \frac{A_0}{A_2} \right)^2 \right] \quad (3)$$

where the upstream flow area is defined as  $A_1$ , the throat area is defined as  $A_0$ , and the downstream flow area is defined as  $A_2$  (see Fig. 5).

This approximation holds only for Reynolds numbers in excess of 10 000 (i.e., fully turbulent flow). In high-performance micropumping systems, Reynolds numbers fluctuating between 10 and 20 000 are expected as the valve cap opens and closes [31]. For this reason, empirical correction factors were employed to obtain better estimates for the loss coefficients of the laminar and turbulent flow regimes within this range [31]. These higher order loss effects were represented with a Reynolds number dependent coefficient  $C(Re)$  as a multiplier of  $\zeta_{orifice}$ , thereby altering the pressure-flow relation for the orifice,

$$\Delta P = P_{IN} - P_{OUT} = \frac{1}{2}\rho C(Re)\zeta_{orifice} \left( \frac{Q^2}{A_0^2} \right). \quad (4)$$

The structural and fluidic modeling tools presented in this section were combined to form a system-level Simulink simulation that was then used to design the active valve geometry

to satisfy performance requirements and to provide model correlation for subsequent experimental results. The simulation architecture for the structural components of the active valve consisted of four major subsystems, as shown in Fig. 6: a matrix of linear coefficients describing the active valve structural behavior, including that of the piezoelectric material, a collection of nonlinear look-up tables that captures the large-deflection valve membrane deformation and stress behavior, a valve cap dynamics block, and a drive piston dynamics block.

#### IV. FABRICATION AND ASSEMBLY

The fabrication process flow for the microvalve involved the micromachining and assembly of three silicon-on-insulator layers, two silicon layers, and four glass layers. A cross-section schematic of the microvalve device is shown in Fig. 7. The drive element tethered-piston structure was created through deep-reactive ion etching of Layers 4 and 5 separately, followed by wafer-level fusion bonding of the two wafers together to form a double-layer piston structure. During etching of the annular tethers in each of Layers 4 and 5, control of the fillet radii at the oxide etch-stop was critical, in order to minimize stress concentrations [32], [33]. Fig. 8 presents scanning-electron micrograph (SEM) images of a Layer 4 piston structure with well-controlled fillet radii, prior to bonding with Layer 5. The valve cap and membrane structure was also created using deep-reactive ion etching, with a similar requirement for good dimensional control of the fillet radii.

The middle glass layer (Layer 3) forms the drive element support structure and the top (Layer 9) and bottom (Layer 1) glass layers provide structural support. The bottom silicon layer (Layer 2) and drive piston silicon layers (Layers 4,5) provide a path for electrical contact to the piezoelectric cylinders. The top four silicon layers (Layers 4,5,7,8) and glass layer (Layer 6) house the hydraulic amplification chamber, valve cap and membrane structure, and fluid inlet and outlet channels. In order to provide a bottom structural stop for the valve cap as it moves away from the orifice, the Layer 6 glass layer was designed with a series of small through holes to connect the bottom portion of the hydraulic amplification chamber above the drive element piston to the top portion of the chamber directly beneath the valve cap and membrane. Although not shown in Fig. 7, a small fluid channel connecting the valve HAC chamber to an external pressure regulator was micromachined in Layer 7. This channel enabled control of a bias pressure  $P_{bias}$  within the chamber during device testing, however, due to its flow impedance characteristics, effectively allowed high frequency  $P_{HAC}$  pressure oscillations about the bias pressure during active valve operation. All glass wafers were machined ultrasonically. All silicon-silicon wafer interfaces were bonded with a wafer-level high-temperature ( $\sim 1300^\circ\text{C}$ ) fusion bonding procedure, and all silicon-glass layer interfaces were bonded using a low temperature ( $\sim 300^\circ\text{C}$ ) anodic bonding process (either at the wafer-level or die-level depending on the process step) with an applied voltage of 1000 V. Thin venting channels were etched in Layers 4 and 5 to prevent pressurization and potential plastic deformation or fracture of the piston tethers during the high temperature fusion bonding procedure. Attachment of the



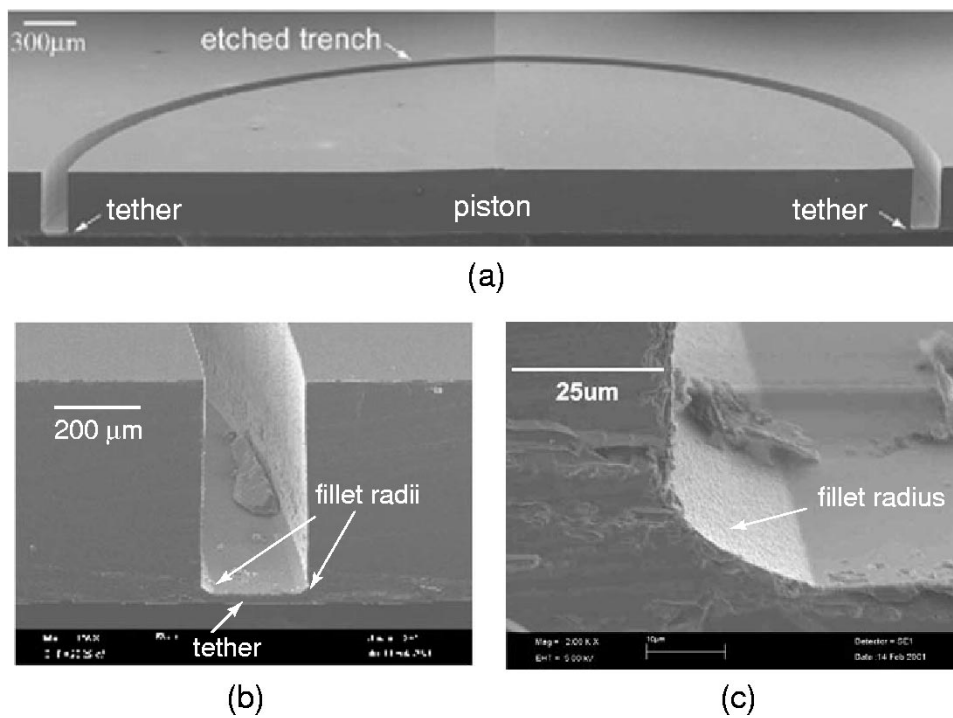


Fig. 8. SEM images of a Layer 4 etched drive element piston: (a) a cross section of the SOI piston structure, (b) a close-up of the etched trench, and (c) a further close-up of the fillet radius. In this structure, a 20–25  $\mu\text{m}$  fillet radius was achieved. Debris in background was generated during die-saw procedures.

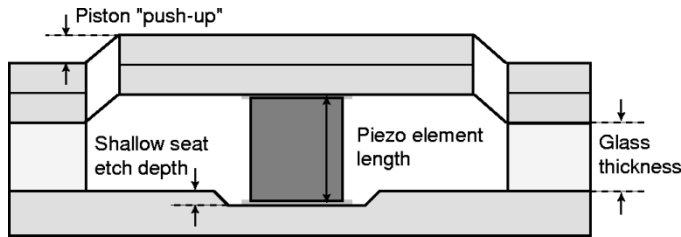


Fig. 9. Tolerancing of the piezoelectric element within the drive element structure was accomplished by etching shallow seats in the top surface of Layer 2. Precise control of the etch depth was necessary to achieve a controlled “push-up” of the drive element piston during bonding operations.

## V. VALVE SUBCOMPONENT VALIDATIONS

The development program for this active valve device involved the validation of two primary subcomponent device platforms prior to assembly and characterization of the complete active valve device. These two subcomponent platforms were 1) the piezoelectric drive element structure, encompassing the challenge of integrating the miniature piezoelectric element(s) beneath the micromachined tethered piston structure and 2) the hydraulic amplification unit, as a means to prove the capability to fill the HAC chamber with degassed fluid and to achieve amplification of the piston motion into a significantly larger valve cap deflection.

### A. Drive Element Subcomponent Validation

The purpose of this effort was to evaluate the fabrication and assembly process flow for integrating piezoelectric material elements within the micromachined drive element structure and to obtain quasistatic and high-frequency experimental data on the

completed actuator structures. The previously published work [11] provides a comprehensive overview of this subcomponent study. In general, this study, through the assembly and testing of a series of drive element devices, proved the ability to integrate both single and multiple (three) piezoelectric material elements beneath double-layer micromachined tethered-piston structures, as shown in Fig. 11. The presence of three elements spread out beneath the piston enabled higher stiffness actuation capabilities by eliminating tilting and bending behavior of the piston structure. Additionally, this study verified that high-strain capability single-crystal (PZN-PT) piezoelectric material [36], in addition to standard polycrystalline PZT-5H material, could be successfully incorporated. Three-cylinder PZN-PT devices were experimentally characterized up to a frequency of 200 kHz for drive voltages between 50 V and 1000 V. Results showed that these microactuator structures exhibited negligible bending and tilting for quasistatic operation up to 15 kHz and that first modal behavior did not occur until frequencies in excess of 80 kHz [11].

### B. Hydraulic Amplification Validation

The purpose of this effort was to validate the concept of hydraulic amplification between the piston and valve cap structures. HAC devices, consisting of Layers 4 through 9, were constructed to validate fluid filling and device operation without the effects of piezoelectric material integration beneath the piston structure. The previously presented work [35] provides a comprehensive overview of this subcomponent study. The assembled devices were successfully filled with degassed silicone oil (hexamethyldisiloxane, produced by Dow Corning under the trade name DC200 0.65 centistoke) and device amplification ratios up to 40 $\times$  were measured.

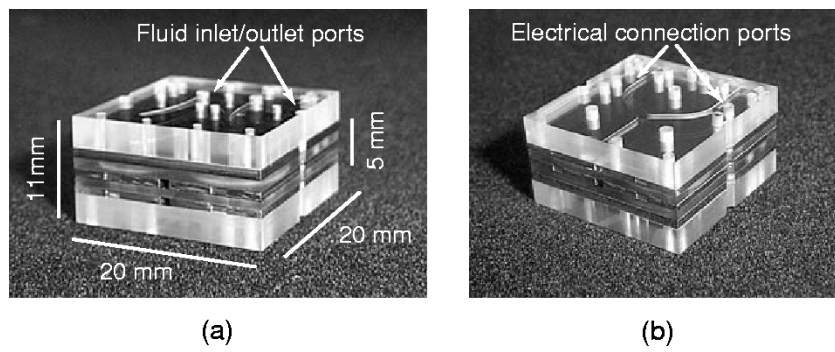


Fig. 10. Photograph of a nine-layer silicon and glass piezoelectrically driven hydraulic amplification microvalve, as part of a full MHT system. Dimensions of the valve structure within the full MHT chip are 8 mm×8 mm×5 mm.

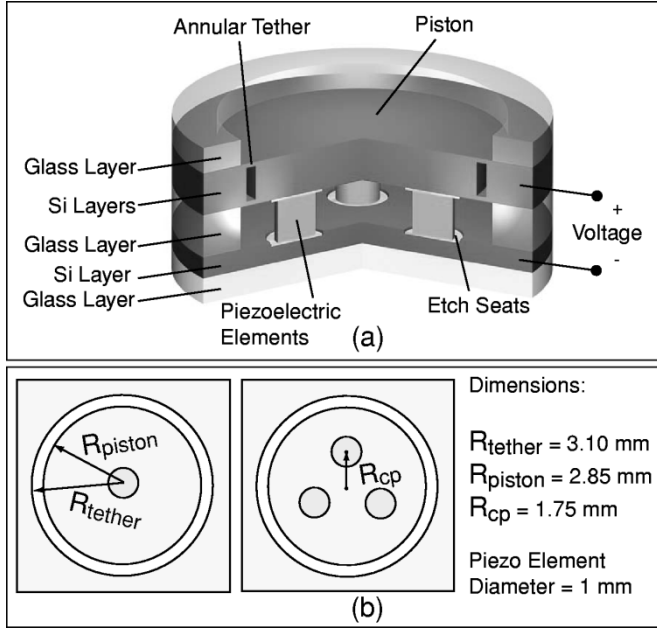


Fig. 11. Three-dimensional schematic of a piezoelectric drive element device. Three piezoelectric cylinders are sandwiched between a lower support silicon layer and an upper double silicon layer tethered-piston structure. Voltage is carried along the upper and lower silicon layers.

## VI. FINAL ACTIVE VALVE DIMENSIONS

The dimensions of the fabricated final active valve device are illustrated in Fig. 12. The device incorporated three PZN-PT piezoelectric square elements (each with cross-sectional area 1.06 mm×1.06 mm) beneath a double-layer tethered piston structure. The top and bottom tethers of the piston were each 250  $\mu\text{m}$  in width and each had a thickness of 8  $\mu\text{m}$ . A valve cap and membrane structure was positioned above the hydraulic amplification chamber, with a structural stop (formed by the glass Layer 6 within the HAC chamber)  $\sim 16.5 \mu\text{m}$  below the equilibrium position of the valve cap. Glass Layer 6 contained a series of “HAC through-holes” to carry the fluid from the lower to upper portion of the HAC chamber. The valve cap had a diameter of 500  $\mu\text{m}$  and the valve membrane had an outer diameter of 1400  $\mu\text{m}$  and thickness of 6  $\mu\text{m}$ . A valve orifice was located  $\sim 16.5 \mu\text{m}$  above the valve cap equilibrium position. The orifice had an inner diameter of 450  $\mu\text{m}$ .

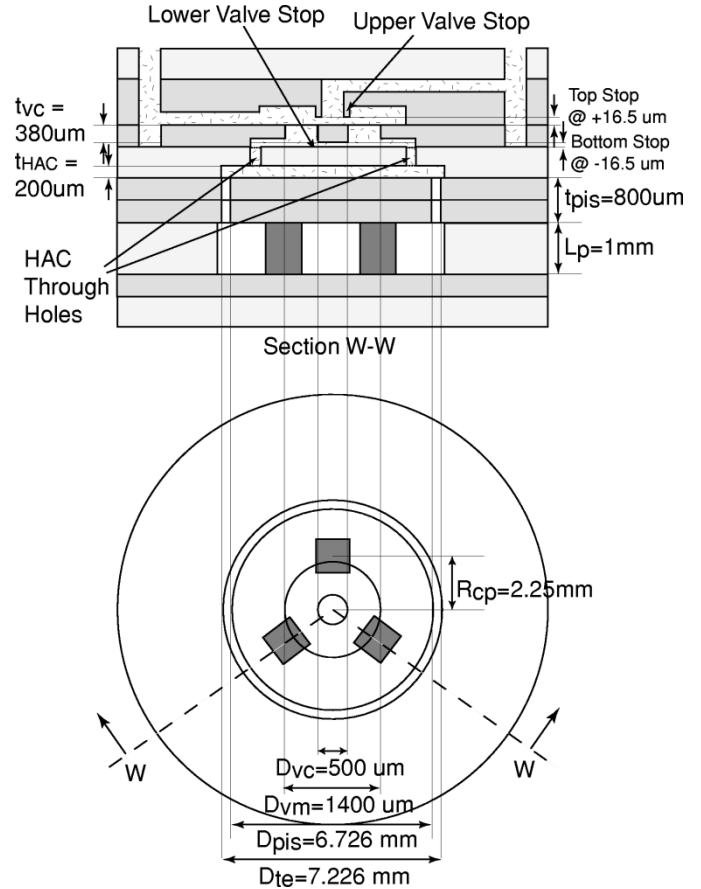


Fig. 12. Dimensions of the fabricated active valve devices. Three square PZN-PT elements were incorporated beneath a double-layer tethered piston. A valve cap and membrane structure interacts with the fluid orifice structure at  $Z_{vc} = +16.5 \mu\text{m}$  and with the glass Layer 6 structure within the HAC chamber at  $Z_{vc} = -16.5 \mu\text{m}$ .

## VII. EXPERIMENTAL TEST PLAN

Testing of the active valve device was divided into two primary efforts. The first effort focused on characterizing the actuation capabilities of the valve structure without the effects of differential pressure and flowing fluid above the structure. In this effort, the dynamic behavior of the active valve device was evaluated and the range of driving frequency for which the valve behaved in a quasistatic manner was determined. Additionally, at the determined maximum quasistatic operational frequency,

the structural amplification ratio of the valve device was characterized as a function of applied voltage to the piezoelectric drive element. Once the device was proven to be a successful actuator, the second effort focused on evaluating its flow regulation capabilities and limitations. In this effort, the flow regulation capability of the valve device at the maximum quasistatic operational frequency of the structure was evaluated as a function of increasing differential pressure across the valve orifice. In this manner, the valve performance limitations could be determined as the differential pressure was increased.

The aforementioned tests required the development of testing rigs and experimental procedures to measure accurately the drive element piston and valve cap structural vibrations within the multilayered device. A laser vibrometer system, with a micro-lens attachment, was used for these vibration measurements [37]. The active valve chip-level device was mounted in a test-jig which included fluid inlet and outlet ports to the chip, as well as through-holes for alignment of the vibrometer laser beam on the key structural components within the device. The accompanying fluids testing rig was comprised of fluid reservoirs, absolute and differential pressure sensors for measuring the inlet and outlet pressures into the device, and a calibrated real-time flow sensor for measuring flow rates through the valve. Additionally, a data-acquisition system was implemented to enable real-time drive signals to the device and measurements from the device and testing rig.

## VIII. RESULTS AND DISCUSSION

### A. Device Actuation Capabilities

To characterize the frequency-dependent behavior of the active valve device, a low-voltage ( $0\text{ V} \pm 5\text{ V}$ ) sweep signal from 500 Hz to 100 kHz was applied to the piezoelectric drive element structure. The valve cap and piston velocities were measured using the laser vibrometer system. The corresponding displacements were obtained through post-process integration of the velocity signals. Fig. 13 overlays the frequency response of the drive element piston with that of the valve cap, for the case in which oil is present above the valve structure but for which no differential pressure or flowing fluid occurred across the valve orifice. These tests were performed with  $P_{\text{bias}} = 500\text{ kPa}$  to eliminate the possibility of cavitation within the HAC chamber. Additionally, the pressures above the valve cap and membrane were maintained at  $P_{\text{IN}} = P_{\text{OUT}} = 500\text{ kPa}$ .

The piston and valve responses both followed the same patterns across the frequency range. The valve first modal frequency was observed to occur at  $\sim 5\text{ kHz}$ . The additional peaks in the response were most likely a result of fluid-structure interactions between the oil and the experimental test-jig flow tubes external to the device or between the oil and the flow channels internal to the device. The increase in piston displacement amplitudes at frequencies below 1 kHz was due to measurement limitations in the vibrometer system. Below 1 kHz, the measured velocities were of the same order as the noise floor, whereas at higher drive frequencies, the measured velocities were sufficiently above the noise floor to provide accurate measurements. The results indicate that the amplification ratio of the valve device was steady (between  $40 \times$  to  $50 \times$ ) over the range of frequencies below resonance.

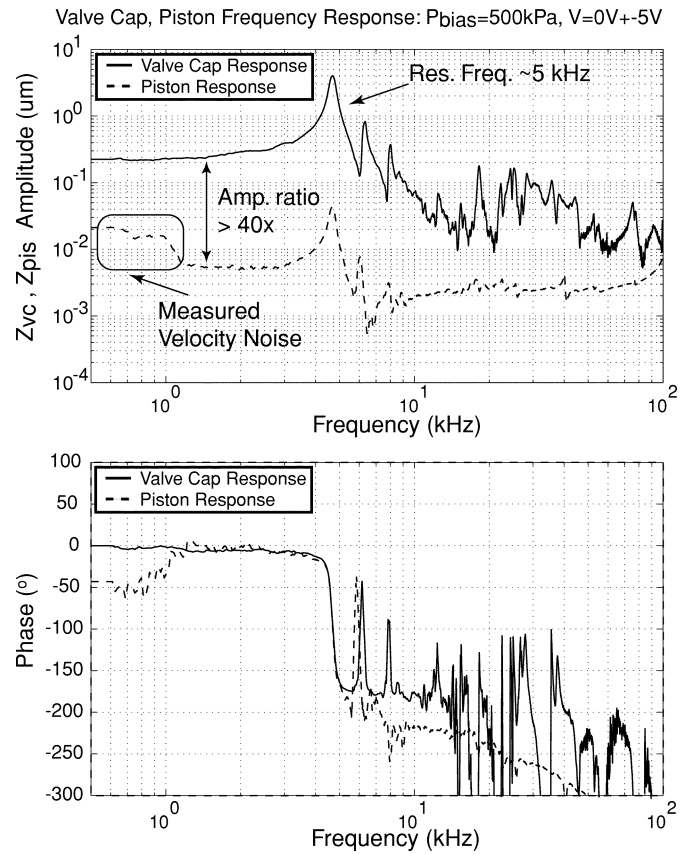


Fig. 13. Low-voltage ( $0\text{ V} \pm 5\text{ V}$ ) piston and valve cap frequency responses from 500 Hz to 100 kHz, with oil present above the valve structure. The top figure plots the valve cap and piston amplitudes, while the bottom figure plots the corresponding phase. The bias pressure in these tests was maintained at  $P_{\text{bias}} = 500\text{ kPa}$ . An amplification ratio between  $40 \times$  to  $50 \times$  is observed for frequencies below 5 kHz.

The previous frequency sweep experimental tests found the 1st modal frequency of the device to be  $\sim 5\text{ kHz}$ . In order to evaluate the quasistatic performance of the structure under the larger drive voltage levels at which the valve was designed to operate, a frequency of operation of 1 kHz was chosen. Fig. 14 plots the valve cap and piston displacement time histories, respectively, at this drive frequency over a range of applied voltages from 50 Vpp to 800 Vpp. In Fig. 14(a), the dotted lines at  $\pm 16.5\text{ }\mu\text{m}$  indicate the position of the upper and lower valve stops, respectively. For an applied voltage of 50 Vpp, the response of the valve cap was purely sinusoidal.

As the voltage was increased to 800 Vpp, the resulting valve cap displacement time history contained small amplitude higher frequency ( $\sim 5\text{ kHz}$ ) oscillations due to the nonlinear nature of the valve membrane structure. These oscillations became more pronounced as the voltage was increased. In Fig. 14(b), the drive element deflection time histories were somewhat rough in nature due to the noise level of the measurement system. As the deflections increased in amplitude, the effect of this noise floor diminished. It is important to note that for a voltage of 800 V, the valve was not deflected sufficiently to close against the valve orifice. This was due to the fact that the actual piezoelectric material coefficient was only  $\sim 75\%$  of the expected value used for the original valve design (see further discussion in subsequent paragraphs).

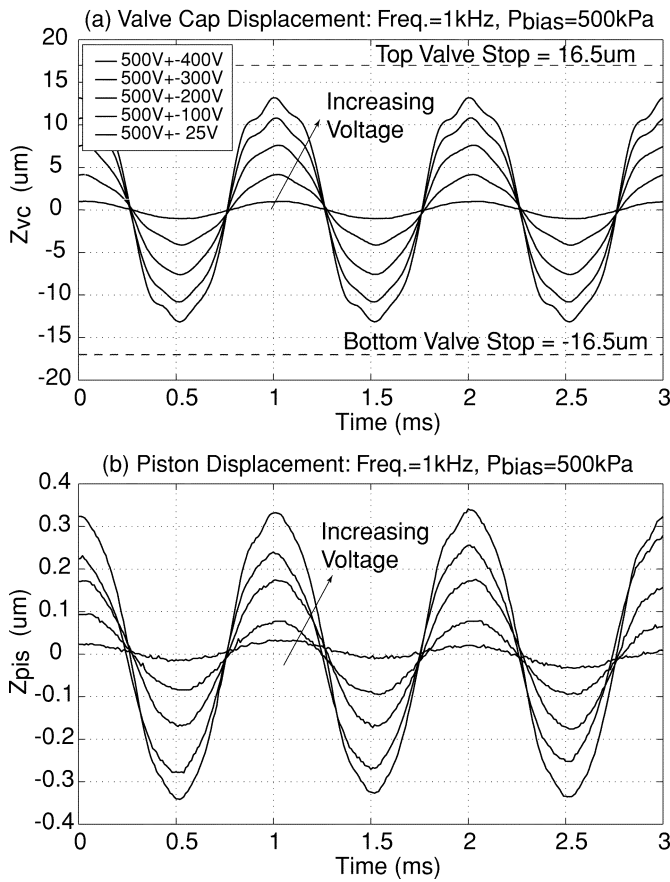


Fig. 14. Experimental valve cap and piston deflection time histories for a series of 1 kHz sinusoidal drive voltage levels. As the voltage was increased, small amplitude 5 kHz oscillations appeared in the deflection responses. Note that a voltage of 800 Vpp was not sufficient to close valve cap against the valve orifice.

Fig. 15 takes these deflection time histories and plots the valve cap peak–peak displacement, piston peak–peak displacement, and corresponding device amplification ratio as a function of applied voltage to the piezoelectric drive element. The amplification ratio was observed to decrease from 50 to 40 as the voltage was increased, as illustrated in Fig. 15(c).

If the structural system was composed of elements operating only in their linear deformation regimes, this amplification ratio would remain constant over the voltage range. Due to the nonlinear stiffness of the valve membrane, however, constant incremental changes in voltage result in increased incremental changes in the chamber pressure and reduced incremental changes in valve cap deflection, as shown in Fig. 15(a). A similar result for the piston deflection is shown in Fig. 15(b). This curve, however, exhibits slightly more linearity than the valve cap deflection curve, due to the increased incremental changes in compressed fluid volume change and structural chamber deformation as the voltage is increased. In essence, as the voltage is increased, a smaller percentage of the piston swept volume is transformed into valve membrane swept volume, thereby resulting in a decreasing amplification ratio.

Fig. 15 also includes model predictions for this behavior. Shown on this plot are three curves generated from the active valve simulation tools discussed previously. The first curve is the predicted response based on the assumed piezo-

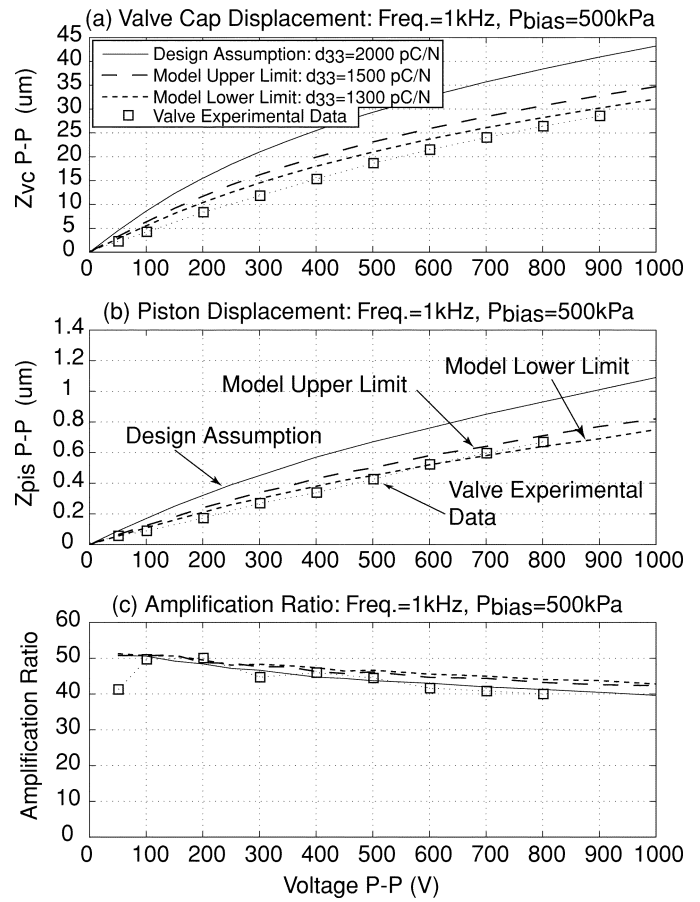


Fig. 15. Active valve quasistatic 1 kHz model correlation for increasing applied voltage: (a) the valve cap deflection curve was 5–10% below the limiting bounds for  $d_{33} = 1300 - 1500 \text{ pC/N}$ , (b) the piston deflection curve fell within the limiting bounds for large voltage, and (c) the device amplification ratio (between  $40\times$  and  $50\times$ ) agreed very closely with the predicted limiting bounds.

electric material coefficient value of  $d_{33} = 2000 \text{ pC/N}$  used in the original design of the active valve device. The second two model curves are based on limiting values of  $d_{33} = 1300 - 1500 \text{ pC/N}$  determined by measuring a large number of individual piezoelectric elements and observing the range of piezoelectric coefficients. Active valve performance was therefore compared to these limiting model cases rather than the ideal case since the piezoelectric elements were determined to be inferior to original design assumptions. The model correlation indicates that the experimental valve cap deflection curve falls slightly short (at 800 Vpp for example, the cap deflection was  $26 \text{ μmP-P}$  versus the predicted  $31 \text{ μmP-P}$ ) of the prediction limits for  $d_{33} = 1300 - 1500 \text{ pC/N}$ , while the experimental piston deflection curve falls within these limits for large enough applied voltage. Based on these results, it can be concluded that an additional compliance mechanism must exist within the HAC chamber, most likely due to a smaller than expected value of fluid bulk modulus. A fluid bulk modulus of  $K_f = 2 \text{ GPa}$  was assumed in the active valve models and simulations [37]. The corresponding device amplification ratio, as shown in Fig. 15(c) decreased slightly from  $\sim 50\times$  for a low voltage of 100 Vpp to  $\sim 40\times$  for a high voltage of 800 Vpp, consistently within 5–10% of the limiting model predictions.

TABLE I  
ACTIVE VALVE ACTUATION CAPABILITIES

Performance Characteristics	Experimental Results	Model Predictions
1st Modal Frequency	5 kHz	14 kHz
Piston Deflection (@1kHz, 800Vpp)	0.65 $\mu\text{m}$ pp	0.72 $\mu\text{m}$ pp
Valve Cap Deflection (@1kHz, 800Vpp)	26 $\mu\text{m}$ pp	31 $\mu\text{m}$ pp
Amplification Ratio (@1kHz, 800Vpp)	40x	43x

Table I summarizes the critical actuation capabilities of the active valve device in comparison to model predictions. As discussed previously, the valve 1st modal frequency occurred at  $\sim 5$  kHz. Finite-element models of this valve structure had predicted a 1st modal frequency of 14 kHz, however, these models did not include the presence of oil above the valve cap and membrane structure. It was this added mass of the oil that reduced the 1st modal frequency of the valve structure. Future modeling of the valve should more carefully include this added mass effect when predicting modal behavior. As for quasistatic operation at 1 kHz, as already discussed, the measured device valve cap deflection fell slightly short of predictions. However, the amplification ratio was in excellent agreement with model predictions. Overall, this encouraging device performance enabled further investigations into the valve's flow regulation capabilities.

### B. Device Flow Regulation Capabilities

To evaluate the capability of the active valve device to regulate flow at 1 kHz, a series of tests was carried out for increasing imposed differential pressure across the valve orifice. Flow regulation tests were performed for differential pressures  $P_{\text{IN}} - P_{\text{OUT}} = 24$  kPa, 95 kPa, 145 kPa, 200 kPa, 260 kPa, and 340 kPa. A volatile silicone oil (hexamethyldisiloxane, produced by Dow Corning under the trade name DC200 0.65 centistoke) was used as the flow regulation fluid. By controlling  $P_{\text{HAC}}$  with respect to the magnitude of  $P_{\text{IN}}$  and  $P_{\text{OUT}}$  (using the high-frequency channel and corresponding bias pressure regulator set-up discussed previously), the valve cap was displaced statically upward to a deflection of  $Z_{vc} = 11 \mu\text{m}$ . A sinusoidal voltage of 500 Vpp was then applied to the piezoelectric drive element at 1 kHz to actuate the valve cap upward against the valve orifice and downward toward the original equilibrium position of the valve cap. In all test runs, it was desired to just barely close the valve cap against the orifice at its maximum displacement, and to maintain  $Z_{vc} = 0$  at its minimum displacement. In others words, it was desired to always ensure a valve opening stroke of 16.5  $\mu\text{m}$ .

Fig. 16 plots the experimentally measured flow rates for each of the differential pressure test cases. An applied voltage of 500 Vpp was held constant for all of the test cases, and the corresponding measured stroke of the valve cap during actuation is printed inside of each data bar. Fig. 16 also plots the experimental results versus the model expectations obtained using the active valve simulation tools detailed previously. Model predictions for chosen limiting valve strokes of  $Z_{vc,PP} = 13 \mu\text{m}$  and  $Z_{vc,PP} = 17 \mu\text{m}$  are shown. The model correlation indicates that the active valve regulates flow in excellent correlation

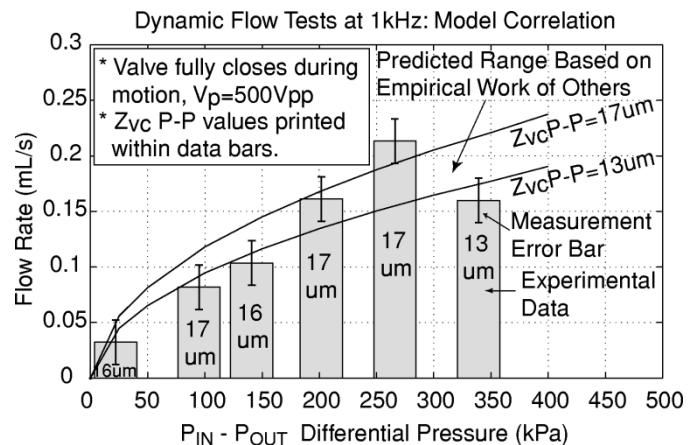


Fig. 16. Dynamic flow regulation model correlation at 1 kHz for varying differential pressures. Correlation is good over range of differential pressures. Error bars on the data indicate the measurement error, which was estimated based on the flow sensor calibration error and the accuracy of the applied differential pressure.

with the model predictions. Since the flow loss coefficients used within the models discussed previously were based on a compilation of empirical Re data from other researchers, the line of predicted behavior in Fig. 16 is understood to be of only "limited accuracy," in other words, it is not based on exact theory.

Subsequent test runs at differential pressures in excess of  $P_{\text{IN}} - P_{\text{OUT}} = 340$  kPa resulted in unstable oscillatory motion of the valve cap structure, and eventually fracture of the valve membrane. The nature of the flow behavior (based on Reynolds number) was investigated for a variety of valve opening situations in subsequent studies. The results indicated that these self-excited valve cap oscillations were most probably a result of transitional flow (between laminar and turbulence) through the valve orifice structure, a regime which limited the valve operation to relatively low differential pressures of no more than 340 kPa. A comprehensive overview of these unstable oscillatory valve cap experiments is detailed in [37]. Future research work should focus on a better understanding of the flow regimes through these microscale orifice structures, especially as a function of different viscosity fluids, and on a redesign effort to develop a valve geometry which is less sensitive to the flow behavior passing through the orifice. Additionally, this redesign should include an effort to increase the 1st modal frequency of the device, to potentially enable operation at or above a frequency of 10 kHz. With these redesign efforts, a higher frequency, higher flow rate microvalve could be achieved.

## IX. CONCLUSION

A compact piezoelectrically-driven hydraulic amplification microvalve was successfully fabricated and tested for the first time. This concept of hydraulically amplifying the limited stroke of a miniature bulk piezoelectric material into a significantly larger motion of a valve cap structure enables the valve to simultaneously meet a set of high frequency ( $\geq 1$  kHz), high pressure ( $\geq 300$  kPa), and large stroke (20–30  $\mu\text{m}$ ) requirements not previously satisfied by other hydraulic flow regulation microvalves. The active valve structural behavior and flow regulation capabilities were evaluated over a range

of applied piezoelectric voltages, actuation frequencies, and differential pressures across the valve. For applied piezoelectric voltages up to 500 Vpp at 1 kHz, the valve devices demonstrated amplification ratios of drive element deflection to valve cap deflection of  $40 \times -50\times$ . These amplification ratios correlated within 5–10% of the model expectations. Flow regulation experiments proved that a maximum average flow rate through the device of 0.21 mL/s for a 1 kHz sinusoidal drive voltage of 500 Vpp, with valve opening of 17  $\mu\text{m}$ , against a differential pressure of 260 kPa could be obtained. Tests revealed that fluid-structural interactions between the valve cap and membrane components and flow instabilities (due to transition between the laminar and turbulent flow regimes through the valve orifice) limited the valve performance capabilities. This work has proven this valve technology as a viable component within compact high performance hydraulic micropumping systems.

#### ACKNOWLEDGMENT

The authors are grateful to the following individuals who have supported this research work: K. Turner, for issues related to fillet radius control and eutectic bonding; J. Carretero and Dr. K. Breuer, for fluid flow modeling at the microscale; Dr. R. Mlcak, for fluid filling and sealing procedural development; Dr. Y.-H. Su, for nonlinear structural modeling contributions; and Dr. K.-S. Chen and Dr. L. Saggere, for additional structural modeling work. Additionally, the authors wish to acknowledge Dr. S.-H. Liou at the University of Nebraska for his generous support in the deposition of AuSn eutectic alloys and associated films on the piezoelectric materials used in this work.

#### REFERENCES

- [1] H. Van Lintel, F. van de Pol, and A. Bouwstra, "Piezoelectric micropump based on micromachining of silicon," *Sens. Actuators*, vol. 15, pp. 153–167, 1988.
- [2] M. Stehr, S. Messner, H. Sandmaier, and R. Zengerle, "The VAMP—a new device for handling liquids or gases," *Sens. Actuators, Phys. A*, vol. 57, pp. 153–157, 1996.
- [3] V. Gass, B. van der Schoot, S. Jeanneret, and N. de Rooij, "Integrated flow-regulated silicon micropump," *Sensors and Actuators A*, vol. 43, pp. 335–338, 1994.
- [4] S. Shoji and M. Esashi, "Microflow devices and systems," *J. Micromech. Microeng.*, vol. 4, pp. 157–171, 1994.
- [5] K. Ikuta, T. Hasewaga, and T. Adachi, "The optimized SMA micro pump chip applicable to liquids and gases," in *Proceedings of the 2001 International Conference on Solid-State Sensors and Actuators (Transducers '01)*, 2001.
- [6] M. Koch, N. Harris, R. Maas, A. Evans, N. White, and A. Brunnenschweiler, "Novel micropump design with thick-film piezoelectric actuation," *Measure. Sci. Technol.*, vol. 8, no. 1, pp. 49–57, Jan. 1997.
- [7] P. Watler and M. Sefton, "A piezoelectric driven controlled release micropump for insulin delivery," *Trans. Amer. Soc. Artif. Intern. Organs*, vol. XXXVI, pp. 70–77, 1990.
- [8] B. Wagner, H. Quenzer, S. Hoerschelmann, T. Lisec, and M. Juerss, "Micromachined bistable valves for implantable drug delivery systems," in *Proc. 18th Annu. Int. Conf. IEEE Engineering in Medicine and Biology Society*, 1997, pp. 254–255.
- [9] N. W. Hagood, D. C. Roberts, L. Saggere, K. S. Breuer, K.-S. Chen, J. A. Carretero, H. Q. Li, R. Mlcak, S. Pulitzer, M. A. Schmidt, S. M. Spearing, and Y.-H. Su, "Micro hydraulic transducer technology for actuation and power generation," in *Proc. SPIE 7th Annu. Int. Symp. Smart Structures and Materials*, vol. 3985, Newport Beach, CA, Mar. 5–9, 2000, pp. 680–688.
- [10] H. Q. Li, D. C. Roberts, J. L. Steyn, K. T. Turner, J. A. Carretero, O. Yaglioglu, Y.-H. Su, L. Saggere, N. W. Hagood, S. M. Spearing, M. A. Schmidt, R. Mlcak, and K. S. Breuer, "A high frequency high flow rate piezoelectrically driven MEMS micropump," in *Proc. IEEE Solid-State Sensor and Actuator Workshop*, Hilton Head, SC, June 4–8, 2000, pp. 69–72.
- [11] D. C. Roberts, J. L. Steyn, H. Q. Li, K. T. Turner, R. Mlcak, L. Saggere, S. M. Spearing, M. A. Schmidt, and N. W. Hagood, "A high-frequency, high-stiffness piezoelectric micro-actuator for hydraulic applications," in *Proc. 11th Int. Conf. Solid-State Sensors and Actuators (Transducers '01)*, Munich, Germany, June 10–14, 2001, pp. 686–689.
- [12] D. C. Roberts, N. W. Hagood, Y.-H. Su, H. Q. Li, and J. A. Carretero, "Design of a piezoelectrically-driven hydraulic amplification microvalve for high pressure, high frequency applications," in *Proc. SPIE 7th Annu. Int. Symp. Smart Structures and Materials*, vol. 3985, Newport Beach, CA, Mar. 5–9, 2000, pp. 616–628.
- [13] D. C. Roberts, O. Yaglioglu, J. Carretero, Y.-H. Su, L. Saggere, and N. W. Hagood, "Modeling, design, and simulation of a piezoelectric microvalve for high pressure, high frequency applications," in *Proc. SPIE 8th Annu. Int. Symp. Smart Structures and Materials*, vol. 4327, Newport Beach, CA, Mar. 4–8, 2001, pp. 366–380.
- [14] K. Henning, "Liquid and gas-liquid phase behavior in thermopneumatically actuated microvalves," *Proc. SPIE—The Int. Soc. Optic. Eng.*, vol. 3515, pp. 53–63, 1998.
- [15] C. Rich and K. Wise, "A thermopneumatically-actuated microvalve with improved thermal efficiency and integrated state sensing," in *Proc. IEEE Solid-State Sensor and Actuator Workshop*, Hilton Head, SC, 2000, pp. 234–237.
- [16] H. Jerman, "Electrically-activated, micromachined diaphragm valves," in *Proc. 1991 Int. Conf. Solid-State Sensors and Actuators (Transducers '91)*, 1991, pp. 1045–1048.
- [17] M. A. Huff and W. L. Benard, "Thin film titanium-nickel shape memory alloy microfluidic devices," in *Proc. Third Int. Symp. Microstructures and Microfabricated Systems*, 1997, pp. 26–38.
- [18] M. A. Huff, "Silicon Micromachined Wafer-Bonded Valves," Ph.D. dissertation, Massachusetts Institute of Technology, Cambridge, 1993.
- [19] M. Shikida, K. Sato, S. Tanaka, Y. Kawamura, and Y. Fujisaki, "Electrostatically driven gas valve with high conductance," *J. Microelectromech. Syst.*, vol. 3, no. 2, pp. 76–80, June 1994.
- [20] F. Pourahmadi, L. Christel, K. Petersen, J. Mallon, and J. Bryzek, "Variable-flow micro-valve structure fabricated with silicon fusion bonding," in *Proc. IEEE Solid-State Sensor and Actuator Workshop*, Hilton Head, SC, 1990, pp. 78–81.
- [21] A. Meckes, J. Behrens, and W. Benecke, "Electromagnetically driven microvalve fabricated in silicon," in *Proc. 1997 Int. Conf. on Solid-State Sensors and Actuators (Transducers '97)*, 1997, pp. 821–824.
- [22] J. G. Smits, "Piezoelectric micropump with microvalves," in *Proc. Eighth Bienn Univ Gov Ind Microelectron Symp. (IEEE n 89CH2769-8)*, Piscataway, NJ, pp. 92–94.
- [23] S. Kluge, G. Neumayer, U. Schaber, and M. Wackerle, "Pneumatic silicon microvalves with piezoelectric actuation," in *Proc. 2001 Int. Conf. on Solid-State Sensors and Actuators (Transducers '01)*, 2001.
- [24] M. Esashi, S. Shoji, and A. Nakano, "Normally closed microvalve and micropump fabricated on a silicon wafer," *Sens. Actuators*, vol. 20, pp. 163–169, 1989.
- [25] M. Esashi, "Integrated micro flow control systems," *Sens. Actuators*, vol. A21–A23, pp. 161–167, 1990.
- [26] S. Shoji, B. Van der Schoot, N. de Rooij, and M. Esashi, "Smallest dead volume microvalves for integrated chemical analyzing systems," in *Proc. 1991 Int. Conf. Solid-State Sensors and Actuators (Transducers '91)*, 1991, pp. 1052–1055.
- [27] J. Garcia-Bonito, M. J. Brennan, S. J. Elliot, A. David, and R. J. Pinnington, "A novel high-displacement piezoelectric actuator for active vibration control," *Smart Mater. Struct.*, vol. 7, pp. 31–42, 1998.
- [28] P. Tang, A. Palazzolo, A. Kascak, G. Montague, and W. Li, "Combined piezoelectric-hydraulic actuator based active vibration control for rotor-dynamic system," *J. Vibration Acoust.*, vol. 117, pp. 285–293, 1995.
- [29] W. Tsukamoto, "Piezo-actuator's displacement magnifying mechanism," U.S. Pat. 5 233 834, 1993.
- [30] Y. H. Su, K. S. Chen, D. C. Roberts, and S. M. Spearing, "Large deflection analysis of a pre-stressed annular plate with a rigid boss under axisymmetric loading," *J. Micromech. Microeng.*, vol. 11, pp. 645–653, 2001.
- [31] J. A. Carretero and K. S. Breuer, "Measurement and modeling of the flow characteristics of micro disk valves," in *Proc. 1994 Int. Mechanical Engineering Congress and Exposition: Microfluidics Symposium*, Orlando, FL, Nov. 2000.



- [32] K. S. Chen, A. A. Ayon, and S. M. Sparing, "Controlling and testing the fracture strength of silicon on the Mesoscale," *J. Amer. Ceramic Soc.*, vol. 83, no. 6, pp. 1476–1484, 2000.
- [33] K. T. Turner, "An evaluation of critical issues for microhydraulic transducers: silicon wafer bonding, strength of silicon on insulator membranes and gold-tin solder bonding," S. M. thesis, Massachusetts Institute of Technology, Cambridge, June 2001.
- [34] K. T. Turner, R. Mlcak, D. C. Roberts, and S. M. Sparing, "Bonding of bulk piezoelectric material to silicon using a gold-tin eutectic bond," in *2001 MRS Fall Meeting*, Boston, MA.
- [35] J. L. Steyn, H. Q. Li, D. C. Roberts, R. Mlcak, K. T. Turner, O. Yagliglu, Y.-H. Su, M. A. Schmidt, S. M. Sparing, and N. W. Hagood, "Hydraulic amplification devices for microscale actuation," in *Solid-State Sensor, Actuator and Microsystems Workshop*, Hilton Head Island, SC, June 2–6, 2002.
- [36] S. E. Park and T. R. Shrout, "Characteristics of relaxor-based piezoelectric single crystals for ultrasonic transducers," *IEEE Trans. Ultrason., Ferroelect., Freq. Contr.*, vol. 44, pp. 1140–1147, Sept. 1997.
- [37] D. C. Roberts, "Design, modeling, fabrication, and testing of a piezoelectric microvalve for high pressure, high frequency hydraulic applications," Ph.D. dissertation, Massachusetts Institute of Technology, Cambridge, Feb. 2002.
- [38] O. Yagliglu, Y. H. Su, D. C. Roberts, J. Carretero, and N. W. Hagood, "Modeling, simulation and design of piezoelectric micro-hydraulic transducer devices," in *Proc. Fifth Int. Conf. on Modeling and Simulation of Microsystems*, San Juan, Puerto Rico, Apr. 21–25, 2002.



**David C. Roberts** received the S.B., S.M., and Ph.D. degrees in mechanical engineering from the Massachusetts Institute of Technology (MIT), Cambridge, in 1995, 1998, and 2002, respectively. His doctoral research in the Active Materials and Structures Laboratory at MIT was focused on the development of high-performance piezoelectrically driven microvalve and microactuator devices for hydraulic applications.

His research areas of interest include mechanical design and structural dynamics, as they relate to the development of microfabricated actuators and systems. He is employed as a mechanical engineer at Continuum Photonics, Inc., in Billerica, MA.



**Hanqing Li** received the B.S. degree in physics from Peking University, Beijing, China, in 1982 and the M.S. degree in material science at the General Research Institute for Non-ferrous Metals, Beijing, China, in 1985. He received the Ph.D. degree from the University of Nebraska-Lincoln, in 1998.

He was a Guest Scientist at NIST-Boulder, CO, from 1995 to 1998, a Postdoc at MIT between 1998–1999, and is currently a Research Scientist at Massachusetts Institute of Technology (MIT), Cambridge. His primary research interests are in

MEMS fabrication and testing and superconducting devices.



**Lodewyk Steyn** received the B.Eng. degree in mechanical engineering from the Department of Mechanical and Aeronautical Engineering, University of Pretoria, in 1998. He is currently pursuing a Doctoral degree in the Department of Aeronautics and Astronautics at the Massachusetts Institute of Technology (MIT), Cambridge. His research interests include the fabrication, packaging, instrumentation, and testing of piezoelectrically driven microfluidic devices for actuation and power generation applications.



**Onnik Yagliglu** received the S.B. degree in mechanical engineering from Bogazici University, Istanbul, in 1999 and the S.M. degree in mechanical engineering from the Massachusetts Institute of Technology (MIT), Cambridge, in 2002. His Master's research in the Active Materials and Structures Laboratory at MIT was focused on the modeling, simulation and design of piezoelectric microhydraulic transducer devices. He is currently working towards the Ph.D. degree in the Mechanical Engineering Department at MIT.

His research areas of interest include power MEMS, RF MEMS, power generation from ambient vibration, and microfluidics.



**S. Mark Sparing** received the Ph.D. degree from the Engineering Department at Cambridge University, U.K., in 1990.

From 1990 to 1992, he worked as a research engineer at University of California, Santa Barbara, where he produced analytical models for the failure of high-temperature ceramic materials and for Carborundum Microelectronics, where he was a member of the electronic packaging technology development team from 1992 to 1994. He is an Associate Professor of Aeronautics and Astronautics

at the Massachusetts Institute of Technology (MIT), Cambridge, where he has been since 1994. His technical interests include materials and structural analysis and design of MEMS, development of wafer bonding technologies, electronic packaging and advanced composites. Since 1995, he has been responsible for materials, structural design, and packaging tasks of the MIT MicroEngine, MicroRocket, Micro-chemical power, and MicroHydraulic transducer projects as well as conducting cross-cutting underpinning technology development.

Dr. Sparing is a Member of the ASME.



**Martin A. Schmidt** (S'88–M'88–SM'00) received the B.S.E.E. degree in electrical and computer engineering from Rensselaer Polytechnic Institute, Troy, NY, in 1981. He received the S.M. and Ph.D. degrees in electrical engineering and computer science from Massachusetts Institute of Technology (MIT), Cambridge, in 1983 and 1988, respectively.

In addition to his professorship in the Department of Electrical Engineering, he is the Director of the Microsystems Technology Laboratories at MIT. He investigates microfabrication technologies for integrated

circuits, sensors, and actuators; design of micromechanical sensor and actuator systems; mechanical properties of microelectronic materials, with emphasis on silicon wafer bonding technology; integrated microsensors; and microfluidic devices. His current research projects involve novel applications of MEMS technologies to a variety of fields, including miniature gas turbines, miniature chemical reactors, microswitches, biological applications and sensors monolithically integrated with electronics.



**Nesbitt W. Hagood** received the S.B., S.M., and Ph.D. degrees from the Department of Aeronautics and Astronautics from Massachusetts Institute of Technology (MIT), Cambridge, in 1985, 1988, and 1991, respectively.

He is co-founder and currently Chief Technology Officer of Continuum Photonics, Inc. He was formerly a tenured Associate Professor of Aeronautics and Astronautics at MIT and Director of the Active Materials and Structures Laboratory. He specializes in the analysis, design and development of solid

state actuation devices, microfabricated systems, and applications.

Dr. Hagood is an ONR Young Investigator and has received the Presidential Early Career Award in Science and Technology.

<b>REPORT DOCUMENTATION PAGE</b>			<b>Form Approved OMB NO. 0704-0188</b>	
Public Reporting burden for this collection of information is estimated to average 1 hour per response, including the time for reviewing instructions, searching existing data sources, gathering and maintaining the data needed, and completing and reviewing the collection of information. Send comment regarding this burden estimates or any other aspect of this collection of information, including suggestions for reducing this burden, to Washington Headquarters Services, Directorate for information Operations and Reports, 1215 Jefferson Davis Highway, Suite 1204, Arlington, VA 22202-4302, and to the Office of Management and Budget, Paperwork Reduction Project (0704-0188,) Washington, DC 20503.				
1. AGENCY USE ONLY ( Leave Blank)		2. REPORT DATE 10/15/2003		3. REPORT TYPE AND DATES COVERED Final Technical Report: June 1, 2001 to May 31, 2002
4. TITLE AND SUBTITLE Relaxor Ferroelectric Single Crystal Based Hybrid Actuator for Underwater Acoustic Noise Generation			5. FUNDING NUMBERS N00014-01-1-0857	
6. AUTHOR(S) J. Lodewyk Steyn and Nesbitt W. Hagood IV				
7. PERFORMING ORGANIZATION NAME(S) AND ADDRESS(ES) Massachusetts Institute Of Technology 77 Massachusetts Ave. Cambridge, MA 02139			8. PERFORMING ORGANIZATION REPORT NUMBER	
9. SPONSORING / MONITORING AGENCY NAME(S) AND ADDRESS(ES) Office of Naval Research Ballston Centre Tower One 800 North Quincy St. Arlington, VA 22217-5660			10. SPONSORING / MONITORING AGENCY REPORT NUMBER	
11. SUPPLEMENTARY NOTES The views, opinions and/or findings contained in this report are those of the author(s) and should not be construed as an official Office of Naval Research position, policy or decision, unless so designated by other documentation.				
12 a. DISTRIBUTION / AVAILABILITY STATEMENT Approved for public release; distribution unlimited.			12 b. DISTRIBUTION CODE	
13. ABSTRACT (Maximum 200 words)  This report details the development of a microfabricated pump for underwater acoustic noise generation. The goal of MicroHydraulic Transducer (MHT) technology is to provide high power density servohydraulic actuation systems that can be used in a variety of applications. Hydroacoustic actuation is a good application for such technology. The goal here is to develop an acoustic noise source capable of radiating approximately 0.25-0.5W of acoustic power under water at frequencies ranging from 100-1000Hz. This translates to pressure and flow rate requirements of 15-30kPa and 300-500ml/s respectively. The MHT relies on the incorporation of discrete piezoelectric elements into a microfabricated device to produce compact, high stiffness actuation at high frequencies. These piezoelectric elements, used in conjunction with a piezoelectric piston, enable the design of a stiff, efficient electric to fluidic energy conversion mechanism with a high power density. The device relies on the DRIE fabrication of high-strength silicon membranes to form pistons with membrane tethers. A final device was built and tested, and a maximum flow rate and pressure differential of 4ml/min and 350kPa were obtained. It is shown that suitable modifications will enable a future MHT device to match the pressure and flow rate requirements for underwater acoustic noise generation.				
14. SUBJECT TERMS  Piezoelectric, Microvalve, Hydraulic amplification, Silicon Membrane, SOI, Die-level bonding, Power MEMS, Active valve, Fluid filling, Microhydraulic Transducer, MHT, Hydroacoustic, Micropump, Bi-directional.			15. NUMBER OF PAGES 1460	
			16. PRICE CODE	
17. SECURITY CLASSIFICATION OR REPORT UNCLASSIFIED	18. SECURITY CLASSIFICATION ON THIS PAGE UNCLASSIFIED	19. SECURITY CLASSIFICATION OF ABSTRACT UNCLASSIFIED	20. LIMITATION OF ABSTRACT UL	